

29TH EUROPEAN SYMPOSIUM ON COMPUTER AIDED CHEMICAL ENGINEERING

PART A

Edited by

ANTON A. KISS, EDWIN ZONDERVAN
RICHARD LAKERVELD AND LEYLA ÖZKAN



COMPUTER-AIDED CHEMICAL ENGINEERING, 46

29TH EUROPEAN SYMPOSIUM ON
COMPUTER AIDED PROCESS
ENGINEERING

PART A

This page intentionally left blank

29TH EUROPEAN SYMPOSIUM ON COMPUTER AIDED PROCESS ENGINEERING

PART A

Edited by

Anton A. Kiss

*The University of Manchester, United Kingdom
Manchester, M13 9PL*

Edwin Zondervan

*University of Bremen, Germany
D. Bremen, 28359*

Richard Lakerveld

*The Hong Kong University of Science and Technology
Clear Water Bay, Kowloon, Hong Kong*

Leyla Özkan

*Eindhoven University of Technology, The Netherlands
Postbus 513, 5600 MB*



ELSEVIER

Amsterdam – Boston – Heidelberg – London – New York – Oxford
Paris – San Diego – San Francisco – Singapore – Sydney – Tokyo

Elsevier
Radarweg 29, PO Box 211, 1000 AE Amsterdam, Netherlands
The Boulevard, Langford Lane, Kidlington, Oxford OX5 1GB, UK
50 Hampshire Street, 5th Floor, Cambridge, MA 02139, USA

Copyright © 2019 Elsevier B.V. All rights reserved.

No part of this publication may be reproduced or transmitted in any form or by any means, electronic or mechanical, including photocopying, recording, or any information storage and retrieval system, without permission in writing from the publisher. Details on how to seek permission, further information about the Publisher's permissions policies and our arrangements with organizations such as the Copyright Clearance Center and the Copyright Licensing Agency, can be found at our website: www.elsevier.com/permissions.

This book and the individual contributions contained in it are protected under copyright by the Publisher (other than as may be noted herein).

Notices

Knowledge and best practice in this field are constantly changing. As new research and experience broaden our understanding, changes in research methods, professional practices, or medical treatment may become necessary.

Practitioners and researchers must always rely on their own experience and knowledge in evaluating and using any information, methods, compounds, or experiments described herein. In using such information or methods they should be mindful of their own safety and the safety of others, including parties for whom they have a professional responsibility.

To the fullest extent of the law, neither the Publisher nor the authors, contributors, or editors, assume any liability for any injury and/or damage to persons or property as a matter of products liability, negligence or otherwise, or from any use or operation of any methods, products, instructions, or ideas contained in the material herein.

British Library Cataloguing in Publication Data

A catalogue record for this book is available from the British Library

Library of Congress Cataloging-in-Publication Data

A catalog record for this book is available from the Library of Congress

ISBN (Part A): 978-0-128-19939-8

ISBN (Set) : 978-0-128-18634-3

ISSN: 1570-7946

For information on all Elsevier publications visit our website at <https://www.elsevier.com/>



Working together
to grow libraries in
developing countries

www.elsevier.com • www.bookaid.org

Publisher: Joe Hayton

Acquisition Editor: Kostas Marinakis

Editorial Project Manager: Kelsey Connors

Production Project Manager: Paul Prasad Chandramohan

Designer: Greg Harris

Typeset by SPi Global, India

Contents

Preface	xxiii
1. On the implementation of generalized polynomial chaos in dynamic optimization under stochastic uncertainty: a user perspective <i>Satyajeet Bhonsale, Philippe Nimmegeers, Dries Telen, Joel A. Paulson, Ali Mesbah and Jan Van Impe</i>	1
2. On the role of H ₂ storage and conversion for wind power production in the Netherlands <i>Lukas Weimann, Paolo Gabrielli, Annika Boldrini, Gert Jan Kramer and Matteo Gazzani</i>	7
3. Fuzzy Control Applied to Combustion in Sugarcane Bagasse Boilers <i>Fernando M. de Mello, Antonio J. G. da Cruz, Ruy de Sousa Jr.</i>	13
4. Dynamics and Control of a Fully Heat-Integrated Complex Distillation Column <i>Manuel Rodríguez, Ignacio P. Fernández Arranz</i>	19
5. Optimal dose administration of renally excreted drugs <i>Giuseppe Pesenti, Adriana Savoca, Davide Manca</i>	25
6. Automating HAZOP studies using D-higraphs <i>Borja Martínez, Manuel Rodríguez, Ismael Díaz</i>	31
7. A Novel Optimizable Inherent Safety Index Based on Fuzzy Logic <i>Daniel Vázquez, Rubén Ruiz-Femenia, José A. Caballero</i>	37
8. Optimization under uncertainty of melatonin dosing for critically ill patients <i>Adriana Savoca, Giuseppe Pesenti, Davide Manca</i>	43
9. Simultaneous design and controllability optimization for the reaction zone for furfural bioproduction <i>A.G. Romero-García, O.A. Prado-Rúbio, G. Contreras-Zarazúa, C. Ramírez-Márquez, J.G. Segovia-Hernández</i>	49
10. Design and Optimization of Azeotropic and Extractive Distillation to Purify Furfural Considering Safety, Environmental and Economic Issues <i>G. Contreras-Zarazúa, M.E. Jasso-Villegas, E. Sanchez-Ramirez, J.A. Vazquez-Castillo, J.G. Segovia-Hernandez</i>	55

11. Revisiting Classic Acetic Acid Synthesis: Optimal Hydrogen Consumption and Carbon Dioxide Utilization
Juan D. Medrano-García, Rubén Ruiz-Femenia, Jose A. Caballero 61
12. Innovative application of statistical analysis for the optimization of CO₂ absorption from flue gas with ionic liquid
Grazia Leonzio, Edwin Zondervan 67
13. Optimization of a shell-and-tube heat exchanger using the grey wolf algorithm
Oscar D. Lara-Montaña and Fernando I. Gómez-Castro 73
14. Optimization Under Uncertainty Based on a Datadriven Model for a Chloralkali Electrolyzer Cell
Erik Esche, Joris Weigert, Thomas Budiarto, Christian Hoffmann and Jens-Uwe Repke 79
15. Parameter Estimation for Thermodynamic Models Using an Identifiability Analysis and Subset Selection
Christian Hoffmann, Joris Weigert, Erik Esche and Jens-Uwe Repke 85
16. Evaluation of Discretization Methods for Modeling the Chloralkali Membrane Process
Thomas Budiarto, Joris Weigert, Christian Hoffmann, Erik Eschea and Jens-Uwe Repke 91
17. Synthesis, Design and Optimization of Schemes to Produce 2, 3-Butanediol Considering Economic, Environmental and Safety issues
Eduardo Sánchez-Ramírez, Juan José Quiroz-Ramírez, Juan Gabriel Segovia-Hernandez 97
18. ORC on tour: Integrated design of dynamic ORC processes and working fluids for waste-heat recovery from heavy-duty vehicles
Dominik Tillmanns, Jonas Petzschmann, Johannes Schilling, Christoph Gertig and André Bardow 103
19. The impact of sustainable supply chain on waste-to-energy operations
Maryam Mohammadi, Iiro Harjunkoski 109
20. Automating a shuttle-conveyor for multi-stockpile level control
Jeffrey D. Kelly, Brenno C. Menezes 115

21. High-quality blend scheduling solution for sizing, selecting, sequencing, slotting and spotting in the processing industries
Brenno C. Menezes, Jeffrey D. Kelly 121
22. A simple modeling approach to control emulsion layers in gravity separators
Christoph Josef Backi, Samuel Emebu, Sigurd Skogestad and Brian Arthur Grimes 127
23. Improving Waste Water Treatment Plant Operation by Ammonia Based Aeration and Return Activated Sludge Control
Melinda Várhelyi, Vasile Mircea Cristea, Marius Brehar 133
24. Combining the Advantages of Discrete- and Continuoustime MIP Scheduling Models
Hojae Lee and Christos T. Maravelias 139
25. A steady-state and dynamic simulation tool for solid oxide fuel cell operation applications
Amirpiran Amiri, Khaliq Ahmed, Moses O. Tadó 145
26. Thermal conductivity prediction of molten salt-based nanofluids for energy storage applications
B.H. Mahmoud, L.F. Mortimer, M. Fairweather, H.P. Rice, J. Peakall, D. Harbottle 151
27. Nanoparticle behaviour in multiphase turbulent channel flow
B.H. Mahmoud, L.F. Mortimer, M. Fairweather, H.P. Rice, J. Peakall, D. Harbottle 157
28. Multi-objective optimisation of chemical processes via improved genetic algorithms: A novel trade-off and termination criterion
Viviane De Buck, Carlos André Muñoz López, Philippe Nimmegeers, Ihab Hashem and Jan Van Impe 163
29. Economic Nonlinear Model Predictive Control of Multi-Product Air Separation Processes
A. Caspari, Y. Martin Pérez, Chr. Offermanns, P. Schäfer, A.-M. Ecker, A. Peschel, F. Schliebitz, G. Zapp, A. Mhamdi, and A. Mitsos 169
30. DyOS - A Framework for Optimization of Large-Scale Differential Algebraic Equation Systems
A. Caspari, A. M. Bremen, J. M. M. Faust, F. Jung, C. D. Kappatou, S. Sass, Y. Vaupel, R. Hannemann-Tamás, A. Mhamdi and A. Mitsos 175

31. Optimisation of multi effect distillation based desalination system for minimum production cost for freshwater
O.M.A.Al-hotmani, M. A. Al-Obaidi, G. Filippini, F. Manenti, R.Patel, and I. M. Mujtaba 181
32. Rate-based modelling and simulation of pilot scale distillation column
Mayra M. May-Vázquez, Fernando I. Gómez-Castro, Mario A. Rodríguez-Ángeles 187
33. An MPEC model for Strategic Offers in a Jointly Cleared Energy and Reserve Market under Stochastic Production
Evangelos G. Tsimopoulos, Michael C. Georgiadis 193
34. Decision-making of online rescheduling procedures using neuroevolution of augmenting topologies
Teemu J. Ikonen and Iiro Harjunkoski 199
35. Model-Based Bidding Strategies for Simultaneous Optimal Participation in Different Balancing Markets
Pascal Schäfer, Nils Hansmann, Svetlina Ilieva and Alexander Mitsos 205
36. Optimal CSP-waste based polygeneration coupling for constant power production
Ester de la Fuente, Mariano Martín 211
37. A model-based approach for optimizing petroleum refinery configuration for heavy oil processing
Cheng Seong Khor, Tareq A. Albahri, Ali Elkamel 217
38. Optimal short-term Scheduling of Industrial Packing Facilities
Apostolos P. Elekidis, Francesc Corominas, Michael C. Georgiadis 223
39. Computer-Assisted Experiments for the Identification of the Two-Phase Viscosity of Fluids
Xenia Gabrisch, Jens-Uwe Repke 229
40. From Single Process Simulation and Optimization to Decision Making Based on a Multitude of Solutions
Norbert Asprion, Roger Böttcher, Johannes Höller, Patrick Schwartz, Jan Schwientek, Michael Bortz 235
41. A Neural Network-Based Framework to Predict Process-Specific Environmental Impacts
Johanna Kleinekorte, Leif Kröger, Kai Leonhard and André Bardow 241

42. Performance Evaluation of Reverse Osmosis Brackish Water Desalination Plant with Different Recycled Ratios of Retentate
A. A. Alsarayreh, M. A. Al-Obaidi, A. M. Al-Hroub, R. Patel, and I. M. Mujtaba 247
43. Deciphering Latent Uncertainty Sources with Principal Component Analysis for Adaptive Robust Optimization
Chao Ning, Fengqi You 253
44. Increasing the Reliability of Parameter Estimates by Iterative Model-based Design of Experiments Using a Flowsheet-Simulator
Maria Yliruka, Norbert Asprion, Roger Böttcher, Johannes Höller, Patrick Schwartz, Jan Schwientek, Michael Bortz 259
45. Globally Optimal Design of Double Pipe Heat Exchangers using Local Properties and Discretized Models
Alice Peccini, André Costa, Miguel Bagajewicz 265
46. Incipient Fault Detection, Diagnosis, and Prognosis using Canonical Variate Dissimilarity Analysis
Karl Ezra S. Pilario, Yi Caoc and Mahmood Shafiee 271
47. One-point temperature control of reactive distillation: A thermodynamics-based assessment
Mihai Daniel Moraru, Costin Sorin Bildea 277
48. Optimization of Biogas to Syngas via Combined Super-Dry and Tri-Reforming. Analysis of Fischer-Tropsch Fuels Production
Borja Hernández, Mariano Martín 283
49. Multi-objective spatio-temporal optimisation for simultaneous planning, design and operation of sustainable and efficient value chains for rice crop
Stephen S. Doliente, Sheila Samsatli 289
50. Estimating mixture properties from batch distillation using semi-rigorous and rigorous models
Michael Bortz, Raoul Heese, Alexander Scherrer, Thomas Gerlach, Thomas Runowski 295
51. The Effect of Indirect GHG Emissions Costs on the Optimal Water and Energy Supply Systems
Negar Vakilifard, Parisa A. Bahri, Martin Anda, Goen Ho 301
52. An MILP Approach for Short-term Scheduling of Batch Operations
Hossein Mostafaei, Iiro Harjunkoski 307

53.	Synthesis and optimization of refinery hydrogen network using surrogate models <i>Shihui Wang, Li Zhou, Xu Ji and Yagu Dang</i>	313
54.	Optimising European supply chains for carbon capture, transport and sequestration, including uncertainty on geological storage availability <i>Federico d'Amore, Nixon Sunny, Diana Iruretagoyena, Fabrizio Bezzo, Nilay Shah</i>	319
55.	Real-time design space description in pharmaceutical manufacturing <i>Gabriele Bano, Pierantonio Facco, Marianthi Ierapetritou, Fabrizio Bezzo, Massimiliano Barolo</i>	325
56.	Short-term Scheduling of a Multipurpose Batch Plant Considering Degradation Effects <i>Ouyang Wu, Giancarlo Dalle Ave, Iiro Harjunkoski, Lars Imsland, Stefan Marco Schneider, Ala E.F. Bouaswaig and Matthias Roth</i>	331
57.	Real-time determination of optimal switching times for a H ₂ production process with CO ₂ capture using Gaussian Process Regression models <i>Luca Zanella, Marcella Porru, Giulio Bottegal, Fausto Gallucci, Martin van Sint Annaland and Leyla Özkan</i>	337
58.	Applying a Sustainability Metric in Energy, Water and Food Nexus Applications; A Biomass Utilization Case Study to Improve Investment Decisions <i>Ahmed AlNouss, Sarah Namany, Gordon McKay, Tareq Al-Ansari</i>	343
59.	A Framework for the Integration of Holistic Sustainability Assessment in Computer-Aided Molecular Design <i>Athanasios I. Papadopoulos, Gulnara Shavaliyeva, Stavros Papadokonstantakis, Panos Seferlis</i>	349
60.	Flexibility Assessment of a Distillation Train: Nominal vs Perturbated Conditions Optimal Design <i>Alessandro Di Pretoro, Ludovic Montastruc, Flavio Manenti, Xavier Joulia</i>	355
61.	Dynamic Optimisation and Visualisation of Industrial Beer Fermentation with Explicit Heat Transfer Dynamics <i>Alistair D. Rodman, Megan Weaser, Lee Griffiths, Dimitrios I. Gerogiorgis</i>	361
62.	Statistical Modelling for Optimisation of Mash Separation Efficiency in Industrial Beer Production <i>Qifan (Frank) Shen, Megan Weaser, Lee Griffiths, Dimitrios I. Gerogiorgis</i>	367

63. Technoeconomic MINLP Optimisation of Liquid-Liquid Extraction (LLE) Cascades for Continuous Pharmaceutical Manufacturing (CPM) of Atropine
Samir Diab, Nikolaos Mytis, Andreas G. Boudouvis, Dimitrios I. Gerogiorgis 373
64. Dynamic Modelling and Simulation of Chinese Hamster Ovary (CHO) Cell Fermentation for Advanced Biopharmaceutical Manufacturing
Haruku Shirahata, Samir Diab, Hirokazu Sugiyama, Dimitrios I. Gerogiorgis 379
65. A Multiperiod Optimisation Approach to Enhance Oil Field Productivity during Secondary Petroleum Production
Emmanuel I. Epelle, Dimitrios I. Gerogiorgis 385
66. Statistical diagnosis of process-model mismatch by means of the Lagrange multiplier test
Marco Quaglio, Eric S. Fraga and Federico Galvanin 391
67. Fast Fourier Transforms for Microgrid Climate Computing
Paolo Fracas, Edwin Zondervan 397
68. End-of-Pipe Zero Liquid Discharge Networks for different brine water qualities
Fatima Mansour, Sabla Y. Alnouri 403
69. An Advanced Data-Centric Multi-Granularity Platform for Industrial Data Analysis
Marco S Reis, Tiago J. Rato 409
70. Optimal Operation and Control of Fluidized Bed Membrane Reactors for Steam Methane Reforming
Alejandro Marquez-Ruiz, Jiaen Wu, Leyla Özkan, Fausto Gallucci, Martin Van Sint Annaland 415
71. Optimal design of experiments for the identification of kinetic models of 5-hydroxymethylfurfural hydrogenation
Andrea Bortoli, Fabrizio Bezzo and Federico Galvanin 421
72. Iterative Medium-Term Production Scheduling of an Industrial Formulation Plant
Vassilios Yfantis, Thomas Siwczyk, Matthias Lampe, Nicolai Kloye, Manuel Remelhe and Sebastian Engell 427
73. On the Solution of the Smoluchowski Coagulation Equation Using a Conservative Discretization Approach (CDA)
Menwer Attarakih and Hans-Jörg Bart 433

74.	Multi-product reactive distillation process for higher acrylates production <i>Mihai Daniel Moraru, Anton Alexandru Kiss, Costin Sorin Bildea</i>	439
75.	Stochastic nonlinear model predictive control of a batch fermentation process <i>Eric Bradford and Lars Imsland</i>	445
76.	Control structure design for a CO ₂ - refrigeration system with heat recovery <i>Adriana Reyes-Lúa, Glenn Andreassen, Lars F. S. Larsen, Jakob Stoustrup and Sigurd Skogestad</i>	451
77.	A PLSR Model for Consumer Preference Prediction of Yoghurt from Sensory Attributes Profiles <i>Kexin Bi, Dong Zhang, Zifeng Song, Tong Qiu, Yizhen Huang</i>	457
78.	Coordination of multiple production and utility systems in a multi-leader multi-follower Stackelberg game <i>Ludger Leenders, Kirstin Ganz, Björn Bahl, Maike Hennena and André Bardow</i>	463
79.	A point estimate method-based back-off approach to robust optimization: application to pharmaceutical processes <i>Victor N. Emenike, Xiangzhong Xie, Ulrike Krewera, b and René Schenkendorf</i>	469
80.	From peak power prices to seasonal storage: Long-term operational optimization of energy systems by time-series decomposition <i>Nils Baumgärtner, David Shu, Björn Bahl, Maike Hennen and André Bardow</i>	475
81.	Real-Time Optimisation of Closed-Loop Processes Using Transient Measurements <i>Jack Speakman_ and Grégory François</i>	481
82.	A Financial Accounting based Model of Carbon Footprinting: Built Environment Example <i>Alex Veys, Virginia Acha, Sandro Macchietto</i>	487
83.	Fouling and Cleaning of Plate Heat Exchangers for Milk Pasteurisation: A Moving Boundary Model <i>Abhishek Sharma and Sandro Macchietto</i>	493
84.	Scale-up Modeling of a Pharmaceutical Antisolvent Crystallization via a Hybrid Method of Computational Fluid Dynamics and Compartmental Modeling <i>Merve Öner, Stuart M. Stocks, Jens Abildskov, Gürkan Sin</i>	499

85. Design and Operation Optimization for Water and Power Cogeneration System by Reverse Osmosis and Renewable Energy Technologies
Yousef Saif, Muhammad Rizwan, Ali Almansoori, Ali Elkamel 505
86. Modelling of bubble column hydrodynamics using CFD and SQMOM as a population balance solver
Jan Schäfer, Mark W. Hlawitschka, Menwer Attarakih and Hans-Jörg Bart 511
87. Single-shooting optimization of an industrial process through co-simulation of a modularized Aspen Plus Dynamics model
Mikael Yamanee-Nolin, Anton Löfgren, Niklas Andersson, Bernt Nilsson, Mark Max-Hansen and Oleg Pajalic 517
88. Process Dynamic Analysis and Control Strategy for COGEN option Used for Flare Utilization
Monzure-Khoda Kazi, Fadwa Eljack, Saad Ali Al-Sobhi, Nikolaos Kazantzis, Vasiliki Kazantzi 523
89. Satellite based Vegetation Indices variables for Crop Water Footprint Assessment
Haile Woldesellasse, Rajesh Govindan, Tareq Al-Ansari 529
90. Modelling of extractive heterogeneous-azeotropic distillation in dividing wall column
Andras Jozsef Toth, Daniel Fozer, Tibor Nagy, Eniko Haaz, Judit Nagy, Peter Mizsey 535
91. A Discrete-time MILP Formulation for the Optimal Scheduling of Maintenance Tasks on Oil and Gas Wells and Surface Facilities
Victoria G. Achkar, Vanina G. Cafaro, Carlos A. Méndez, Diego C. Cafaro 541
92. Optimization of an Integrated First- and Second- Generation Ethanol Production Plant with Focus on Hydrolysis Parameters
Roymel R. Carpio, Roberto C. Giordano, Argimiro R. Secchi 547
93. Optimization of seaweed-based biorefinery with zero carbon emissions potential
Rofice Dickson, Jay Liu 553
94. Optimal design for integrated macroalgae-based biorefinery via mixed alcohol synthesis
Rofice Dickson, Peyman Fasahati, Jay Liu 559
95. Global Optimization of Counter Current Gasketed Plate Heat Exchanger
Natália Martins, Peam Cheali, André Costa, and Miguel Bagajewicz 565

96. Efficient robust nonlinear model predictive control via approximate multi-stage programming: A neural networks based approach
Wachira Daosud, Paisan Kittisupakorn, Miroslav Fikar, Sergio Lucia and Radoslav Paulen 571
97. Optimal design of multi-stage depressurization systems using dynamic modelling
Juan Quattordio, Sander Groenendijk, Robert Kedzierski, Hans Göebel 577
98. Innovative mapping method for screening reactive distillation designs
Rahma Muthia, Megan Jobson, Anton A. Kiss 583
99. Filter-based Constraints to Easier Plant Feasibility in Modifier Adaptation Schemes
A. Papasavvas and G. Francois 589
100. An optimization model for a biorefinery system based on process design and logistics
Christos Galanopoulos, Aristide Giuliano, Diego Barletta, Edwin Zondervan 595
101. Design of smart liquid-liquid extraction columns for downstream separations of biopharmaceuticals using deep Q-learning algorithm
Soonho Hwangbo, Merve Öner, Gürkan Sin 601
102. Process design and techno-economic analysis of a pineapple wine production plant under the context of the Choco-Colombia region
Juan Fernando Murcia Palacios, Rolando Barrera, Edwin Zondervan 607
103. A dynamic model for automated control of directed self-assembly of colloidal particles at low densities
Baggie W. Nyande, Yu Gao & Richard Lakerveld 613
104. Towards Model-Based Optimization for Quality by Design in Biotherapeutics Production
Alireza Ehsani, Chrysoula Dimitra Kappatou, Adel Mhamdi, Alexander Mitsos, Andreas Schuppert, Sebastian Niedenfuehr 619
105. Population Balance Equation Applied to Microalgae Filtration
Pui Ying Lee, Keat Ping Yeoh, Chi Wai Hui 625
106. Optimisation of Aqueous Two-Phase Systems
Emma Chandler, Robert Falconer and Solomon Brown 631
107. Integrated Process and Controller Design Software Tool – ProCACD
Jialiang Wang, Peng Ji, Xi Chen, Anjan Tula, Rafiqul Gani 637

108. Computational Fluid Dynamics of Rectangular Monolith Reactor vs. Packed-Bed Column for Sorption-Enhanced Water-Gas Shift
Vlad C. Sandu, Ionela Dumbrava, Ana-Maria Cormos, Arpad Imre-Lucaci, Calin C. Cormos, Paul D. Cobden, Robert de Boer 643
109. Review of override control methods
Jan Schuurmans 649
110. Development of a biorefinery scheme to produce biofuels from waste cooking oil
Araceli Guadalupe Romero-Izquierdo, Fernando Israel Gómez-Castro, Claudia Gutiérrez-Antonio, Rogelio Cruz Barajas, Salvador Hernández 655
111. A novel process monitoring approach based on Feature Points Distance Dynamic Autoencoder
Feifan Cheng and Jinsong Zhao 661
112. A comparison of the performance of multi-objective optimization methodologies for solvent design
Ye Seol Lee, Edward Graham, George Jackson, Amparo Galindo and Claire S. Adjiman 667
113. Real-time feasible model-based crystal size and shape control of crystallization processes
Botond Szilagyí, Zoltan K. Nagy 673
114. Automated open-loop control of directed self-assembly with multiple electrokinetic actuators in microfluidic devices
Yu Gao, Richard Lakerveld 679
115. A network model-based optimisation analysis for the utilisation of CO₂ in Qatar's chemical industries
Ali Attiq Al-Yaeshi, Tareq Al-Ansari, Rajesh Govindan 685
116. A Framework for Multi-level Life Cycle Analysis of the Energy System
Emre Gençer, Francis M. O'Sullivan 691
117. Contract Settlements for Exchanging Utilities through Automated Negotiations between Prosumers in Eco-Industrial Parks using Reinforcement Learning
Dan E. Kröhling, Ernesto C. Martínez 697
118. Integration of Max-Plus-Linear Scheduling and Control
Risvan Dirza, Alejandro Marquez-Ruiz, Leyla Özkan and Carlos S. Mendez-Blanco 703

119. Nonlinear dynamic analysis of chemical engineering processes described by differential-algebraic equations systems <i>Ataíde S. Andrade Neto, Argimiro R. Secchia and Príamo A. Melo</i>	709
120. Life Cycle Assessment of Petroleum Coke Gasification to Fischer-Tropsch Diesel <i>Ikenna J. Okeke, Thomas A. Adams II</i>	715
121. Superstructure Optimization for the Production of Fuels, Fertilizers and Power using Biomass Gasification <i>Ahmed AlNouss, Gordon McKay, Tareq Al-Ansari</i>	721
122. Parameter Estimation for Thermal Runaway of Li-ion cells: a Gaussian Process approach <i>Robert Milton, Peter Bugryniec and Solomon Brown</i>	727
123. Techno-Economic-Environmental Study for Recovery of Novel Water Source within a Power Plant - Desalination Complex <i>Ahmed AlNouss, Fadwa Eljack</i>	733
124. Molecular tracking: A novel approach for multicomponent distillation column design <i>Nima Nazemzadeh, Isuru A. Udugama, Michael A. Taube, Jens Abildskov, Seyed Soheil Mansouri</i>	739
125. Improved Design of Experiments for Identification of MIMO Systems <i>Kurt E. Häggblom</i>	745
126. Nonlinear Model Predictive Control of Haemodialysis <i>Tianhao Yu, Vivek Dua</i>	751
127. Machine Learning of Molecular Classification and Quantum Mechanical Calculations <i>Jie-Jiun Chang, Jia-Lin Kang, David Shan-Hill Wong, Cheng-Hung Chou, Hsuan-Hao Hsu³, Chen-Hsuan Huang³ and Shang-Tai Lin</i>	757
128. Comparative CFD analysis of thermal energy storage materials in photovoltaic/thermal panels <i>Aya Al-Hmoud, Daniel Sebastia-Saez, Harvey Arellano-Garcia</i>	763
129. Development of a Model-Based Quality-by-Control Framework for Crystallization Design <i>Ayşe Eren, Botond Szilágyi, Justin Quon, Masashi Furuta, Charles Papageorgiou, Zoltán K. Nagy</i>	769
130. DEM Study of a Mixer for Core Manufacturing System <i>Jiwon. Roh, Junghwan. Kim, Man Sig. Lee, Il. Moon</i>	775

131. Automatic synthesis of distillation processes for the separation of azeotropic multi-component systems
Thulasi Sasi, Jonas Wesselmann, Hanns Kuhlmann and Mirko Skiborowski 781
132. Development of Guidelines for Optimal Operation of a Cogeneration System
Jia-Lin Kang, Hsu-Hung Chang, Shyan-Shu Shieh, Shi-Shang Jang, Jing-wei Ko, Hsiang-Yao Sun 787
133. On the Optimization of Production Scheduling in Industrial Food Processing Facilities
Georgios P. Georgiadis, Chrysovalantou Ziogou, Georgios Kopanos, Borja Mariño Pampín, Daniel Cabo, Miguel Lopez, Michael C. Georgiadis 793
134. A Systematic Parameter Study on Film Freeze Concentration
Jan-Eise Vuist, Maarten Schutyser and Remko Boom 799
135. A Stacked Auto-Encoder Based Fault Diagnosis Model for Chemical Process
Yi Qiu, Yiyang Dai 805
136. Simulation-based reinforcement learning for delivery fleet optimisation in CO₂ fertilisation networks to enhance food production systems
Rajesh Govindan, Tareq Al-Ansari 811
137. Exergoeconomic Analysis for a Flexible Dry Reforming Power Plant with Carbon Capture for Improved Energy Efficiency
Szabolcs Szima, Calin-Cristian Cormos 817
138. Structured millichannel multiphase reactors
J. Ruud van Ommen, John Nijenhuis, Johan T. Padding 823
139. Systematic decision-support methodology for identifying promising platform technologies towards circular economy
Dominic Silk, Beatrice Mazzali, Isuru A. Udugama, Krist V. Gernaey, Manuel Pinelo, John Woodley, and Seyed Soheil Mansouri 829
140. Variations of the shrinking core model for effective kinetics modeling of the gas hydrate-based CO₂ capture process
Hossein Dashti, Daniel Thomas, Amirpiran Amiri, Xia Lou 835
141. Multi-objective optimization approach to design and planning hydrogen supply chain under uncertainty: A Portugal study case
Diego Câmara, Tânia Pinto-Varela, Ana Paula Barbósa-Povoa 841
142. Global Uncertainty and Sensitivity Analysis for Robust Design of a Rotary Kiln Process
Thomas B. Iversen, Gürkan Sin 847

143. A novel scenario aggregation framework based on network community detection methods
Sergio Medina-González, Ioannis Gkioulekas, Vivek Dua, Lazaros G. Papageorgiou 853
144. Towards development of a decision support tool for conceptual design of wastewater treatment plants using stochastic simulation optimization
Resul Al, Chitta Ranjan Behera, Krist V. Gernaey, Gürkan Sin 859
145. Optimization of semi-permeable membrane systems for biogas upgrading
Diego Filipetto, Federico Capra, Francesco Magli, Manuele Gatti, Emanuele Martelli 865
146. A Fuzzy Analytic Hierarchy Process (FAHP) Approach to Multi-Objective Optimisation of Oil Palm Value Chains
John Frederick Tapia, Sheila Samsatli 871
147. Numerical Simulation of Forced Convection in a Microchannel with Realistic Roughness of 3D Printed Surface
Seyed Alborz Manavi, Eugeny Y. Kenig 877
148. Morris screening for FMECA of valve failure modes on offshore gas reinjection
Emil Krabbe Nielsen, Jérôme Frutiger and Gükan Sin 883
149. Optimization of a large-scale biorefinery problem by decomposition
Varun Punnathanam and Yogendra Shastri 889
150. Planning of Supply Chains Threatened by Extreme Events: Novel Heuristic and Application to Industry Case Studies
Michael Ehrenstein, Chi-Hsiang Wang and Gonzalo Guillén-Gosálbez 895
151. Optimal Maintenance Scheduling for Washing of Compressors to Increase Operational Efficiency
Frederik Schulze Spüntrup, Giancarlo Dalle Ave, Lars Imsland and Iiro Harjunkoski 901
152. Turbulent flow modeling in continuous oscillatory flow baffled reactor using STAR CCM+
Nikola Kljajić, Branislav Todić, Danijela Slavnić, Nikola Nikačević 907
153. Overpotentials in Water Electrolysis: In-Silico Comparison of PEM-cell and GAP-cell performance
Luisa C. Brée, Tobias Schiekkel and Alexander Mitsos 913
154. Study on the formation of chemical wave patterns for the Belousov–Zhabotinsky reaction system
Jiali Ai, Wei Sun, Chi Zhai 919

155. Efficient design of intensified extractive distillation processes based on a hybrid optimization approach
Kai Fabian Kruber, Tamara Grueters, Mirko Skiborowski 925
156. Flux Balance Analysis Incorporating a Coarse-grained Proteome Constraint for Predicting Overflow Metabolism in *Escherichia Coli*
Hong Zeng, Aidong Yang 931
157. A Quality-by-Control Approach in Pharmaceutical Continuous Manufacturing of Oral Solid Dosage via Direct Compaction
Qinglin Su, Sudarshan Ganesh, Dan Bao Le Vo, Anushaa Nukala, Yasasvi Bommireddy, Marcial Gonzalez, Gintaras V. Reklaitis, Zoltan K. Nagy 937
158. Targeting of sustainable chemical processes using data envelopment analysis: application to liquid fuels for transportation
Daniel F. Rodríguez-Vallejo, Ángel Galán-Martín, Gonzalo Guillén-Gosálbez Benoit Chachuat 943
159. Design and Planning of Agri-Food Supply Chains
Lourenço Cruz, João Pires-Ribeiro and Ana Barbosa-Póvoa 949
160. Production scheduling of semi-continuous milk processing facility
Utkarsh Konge and Sivakumar Subramanian 955
161. Fast Bypass Selection Method during the Heat Exchanger Network Synthesis
Rupu YANG, Cong Toan Tran, Assaad Zoughaib 961
162. Integrating Oil Refineries and Bio-refineries: Upgrading Acetone, Butanol and Ethanol to High-Value Products
Elham Ketabchi, Laura Pastor-Perez, Tomas Ramirez Reina, Harvey Arellano-Garcia 967
163. Dynamic transitions in a reactive distillation column for the production of silicon precursors
Salvador Tututi-Avila, Nancy Medina-Herrera, Luis Ricardez-Sandoval and Arturo Jiménez-Gutiérrez 973
164. Adjoint system method in shape optimization of some typical fluid flow patterns|
Alexis Courtais, François Lesage, Yannick Privat, Pascal Frey and Abderrazak Latifi 979
165. Dynamics and control of a heat pump assisted azeotropic dividing-wall column (HP-A-DWC) for biobutanol purification
Iulian Patraşcu, Costin Sorin Bîldea, Anton A. Kiss 985

166. Integrated white-box models for designing freezing processes of human induced pluripotent stem cells considering diversity within a container
Yusuke Hayashi, Ikki Horiguchi, Masahiro Kino-oka, Masahiko Hirao, Hirokazu Sugiyama 991
167. Heat-Integrated Reactive distillation processes to produce Ethyl Levulinate: Design and Optimization including Environmental, Safety and Economics Aspects
J.A. Vazquez-Castillo, G.Contreras-Zarazúa J.G. Segovia-Hernandez 997
168. An Explicit Online Resource-Task Network Scheduling Formulation to Avoid Scheduling Nervousness
Giancarlo Dalle Ave, Mert Alici, Iiro Harjunkoski, and Sebastian Engell 1003
169. A systemic approach for agile biorefineries
Michelle Houngré, Anne-Marie Barthe-Delanoë, Stéphane Négny 1009
170. Closed-loop dynamic real-time optimization of a batch graft polymerization reactor
Ryad Bousbia-Salah, François Lesage, Miroslav Fikar, Abderrazak Latifi 1015
171. Optimizing Return on Investment in Biomass Conversion Networks under Uncertainty Using Data-Driven Adaptive Robust Optimization
Jack Nicoletti, Chao Ning, Fengqi You 1021
172. Improving the prediction of multi-component tablet properties from pure component parameters
Hikaru G. Jolliffe, Foteini Papathanasiou, Elke Prasad, Gavin Halbert, John Robertson, Cameron J. Brown, Alastair J. Florence 1027
173. Targeting material exchanges in industrial symbiosis networks
Ana Somoza-Tornos, Valeria Giraldo-Carvajal, Antonio Espuña, Moisés Graells 1033
174. Total Organic Carbon Prediction with Artificial Intelligence Techniques
Eda Goz, Mehmet Yuceer, Erdal Karadurmus 1039
175. On the Design and Implementation of a Process Modelling Language for Uncertainty
Pedro I. O. Filho and Eric S. Fraga 1045
176. Simulation of Food Waste Pyrolysis for the Production of Biochar: A Qatar Case Study
Samar Elkhalfifa, Ahmed AlNouss, Tareq Al-Ansari, Hamish R Mackey, Prakash Parthasarathy, Gordon Mckay 1051

177. The robust pooling problem <i>Johannes Wiebe, Inês Cecílio and Ruth Misener</i>	1057
178. A model identification approach for the evaluation of plant efficiency <i>Keivan Rahimi-Adli, Patrick D. Schiermoch, Benedikt Beisheim, Simon Wenzel and Sebastian Engell</i>	1063
179. Risk-conscious approach to optimizing bioenergy investments in the Brazilian sugarcane industry <i>Victoria M. Mutrana,b, Celma O. Ribeiroa, Claudio O. A. Nascimentoa and Benoît Chachuat</i>	1069
180. Modeling and Multi-Objective Optimization of Syngas Fermentation in a Bubble Column Reactor <i>Elisa M. de Medeiros, John A. Posada, Henk Noorman, Rubens Maciel Filho</i>	1075
181. Production of chemicals from syngas: an enviroeconomic model-based investigation <i>Andrea Bernardi, Jose E. A. Graciano and Benoît Chachuat</i>	1081
182. Application of cyclic operation to acetic / water separation <i>Catalin Patrut, Elena Catalina Udrea, Costin Sorin Bildea</i>	1087
183. Control analysis of batch reactive distillation column with intermittent fed <i>C F. Rodriguez-Robles, S. Hernandez-Castro, H. Hernandez-Escoto, J. Cabrera-Ruiz, F. O. Barroso-Muñoz, J. E. Terrazas-Rodriguez</i>	1093
184. New Methodology for Bias Identification and Estimation – Application to Nuclear Fuel Recycling Process <i>Amandine Duterme, Marc Montuir, Binh Dinh, Julia Bisson, Nicolas Vigier, Pascal Floquet, Xavier Joulia</i>	1099
185. Reinforcement Learning for Batch-to-Batch Bioprocess Optimisation <i>P. Petsagkourakis, I. Orson Sandoval, E. Bradford, D. Zhang and E.A. del Rio-Chanona</i>	1105
186. A new index for chemical process design considering risk analysis and controllability <i>Nancy Medina-Herrera, Salvador Tututi-Avila, Arturo Jiménez-Gutierrez</i>	1111
187. A primal bounding approach for multistage stochastic programs of resource-constrained planning and scheduling with stochastic task success <i>Zuo Zeng, Selen Cremaschi</i>	1117
188. Rigorous Bayesian Inference VS New Approximate Strategies for Estimation of the Probability Distribution of the Parameters of DAE Models <i>Francesco Rossi, Linas Mockus, Gintaras Reklaitis</i>	1123

This page intentionally left blank

Preface

This volume of the Computer-Aided Chemical Engineering series puts together a selection of the contributions presented at the 29th European Symposium on Computer-Aided Process Engineering (ESCAPE), held in Eindhoven, The Netherlands, from June 16th to 19th, 2019.

This 29th event of the ESCAPE series is a continuation of the conferences under the auspices of the CAPE Working Party of the European Federation of Chemical Engineering (EFCE), Nederland Procestechologie (NPT), and Process Systems Engineering NL (PSE-NL).

The conference has been organised since 1992, starting with two meetings in 1992 in Denmark and France, and since then having one event annually. Hosting countries to the conference have been Austria (1993, 2018), Ireland (1994), Slovenia (1995, 2016), Greece (1996, 2011), Norway (1997), Belgium (1998), Hungary (1999, 2014), Italy (2000, 2010), Denmark (1992, 2001, 2015), The Netherlands (2002), Finland (2003, 2013), Portugal (2004), Spain (2005, 2017), Germany (2006), Romania (2007), France (1992, 2008), Poland (2009), and the United Kingdom (2012). Having organised the event in 2002, The Netherlands takes on the torch of research and knowledge exchange with organising ESCAPE-29.

ESCAPE-29 is jointly organized by a team of skilled professionals from Eindhoven University of Technology, Delft University of Technology, University of Twente, and Upfield (The Netherlands), University of Bremen (Germany), The University of Manchester (UK), and The Hong Kong University of Science and Technology (Hong Kong). The main vision was to collaborate in organizing the event and coordinating the scientific program, such that besides traditional themes it offers a platform for additional topics covering a wide range of topics: *from molecule to enterprise*.

The themes of ESCAPE-29 have been selected after a comprehensive discussion with the CAPE Working Party members and the scientific community. The particular topics within these overarching themes have been formulated to allow researchers from CAPE-related sciences to present their results and exchange valuable knowledge and experience. The themes and topics include:

1. **Process-product synthesis, design and integration:** structured products, process integration, single- and multi-objective synthesis and design of processes, modular plants, integration of intensified process units, product-process design: property-prediction- based synthesis and design, synthesis of different supply-chains.
2. **Methods, models and computational tools for PSE:** generation and development of concepts for CAPE/PSE, advances in multi-scale modelling, modelling in different CAPE/PSE applications, numerical methods and tools, numerical analysis, process simulation, large-scale and multi-level optimization, process plant data analysis, agent based modelling.
3. **Process control and operations:** scheduling, operability, flexibility and optimization under uncertainty, supply-chains optimization and logistics,

cyber-physical structures, interaction and information infrastructure, off-line and on-line control, smart sensors, analysis of dynamic plant data, plant-wide control, remote plant control, operational excellence, real-time optimization, operator training.

4. **CAPE/PSE in sustainable development and food industry:** food & water issues, biorefineries, solar refineries, life cycle analysis, industrial infrastructures, infrastructures for sustainable production, sustainability indicators and footprints, risk assessment, safety, waste reduction and management, waste valorisation, waste-water treatment, conversions of fossil-free energy and materials.
5. **CAPE/PSE in energy transition:** heat and power integration, waste-to-energy applications, renewable resources in total-site integration, novel approaches to address the complex system integration challenges, electrification of chemical industry, integration of energy sources and sinks, reliable dynamic supply and demand.
6. **CAPE/PSE in hi-tech micro/nano-devices and processes:** frontiers at tiny scales: micro-, nano scale products & systems, micro- and nano-scale engineering, semi-conductors, solid state, advanced materials, self-assembly, energy storage.
7. **Education in CAPE/PSE & knowledge transfer:** best practices in academia, continued training in a changing professional practice, effective selling of top quality PSE solutions to industry, knowledge transfer hurdles and lessons, effective exploitation of CAPE/PSE tools.

ESCAPE-29 attracted over 300 contributions from five continents (Europe, Americas, Africa, Asia and Australia), and the International Scientific Committee (ISC) selected 120 oral presentations out of these contributions, the rest of them being presented as posters. The scientific program is rounded up by five plenary lectures given by renowned experts from academia and industry, as well as 20 keynotes given by academic and industrial leaders in their field. Putting together all this would have been impossible without the help of 8 topic coordinators, as well as the 86 members of the ISC. We are deeply thankful for timely and careful reviews by these committees, as well as their invaluable help in suggesting plenary and keynote speakers.

As editors of this special volume, we hope that the contributions in this edition of Computer Aided Process Engineering are excellent illustrations of the current state of the art in their respective field.

Anton A. Kiss
The University of Manchester | University of Twente

Edwin Zondervan
University of Bremen

Leyla Özkan
Eindhoven University of Technology

Richard Lakerveld
The Hong Kong University of Science and Technology

On the implementation of generalized polynomial chaos in dynamic optimization under stochastic uncertainty: a user perspective

Satyajeet Bhonsale^a, Philippe Nimmegeers^a, Dries Telen^a, Joel A. Paulson^b, Ali Mesbah^b and Jan Van Impe^{a,*}

^a*KU Leuven, Department of Chemical Engineering, BioTeC+ & OPTEC, Ghent, Belgium*

^b*Department of Chemical and Biomolecular Engineering, University of California, Berkeley, USA*

**jan.vanimpe@kuleuven.be*

Abstract

Throughout the past century, numerous frameworks have been presented to address different types of uncertainty in model-based (dynamic) optimization. One of the most successful and promising frameworks to address uncertainty in dynamic optimization is generalized polynomial chaos (gPC). This framework is applicable to uncertainties modeled as random variables with generic (e.g., correlated and bimodal) probability distributions. An accurate and efficient approximation of the mean and variances of the model responses can then be readily computed from the coefficients of the gPC expansion. Two types of formulations exist to compute the gPC coefficients: intrusive and non-intrusive. In this paper, a tutorial and critical comparison are presented on the implementation of gPC. More specifically, an intrusive Galerkin approach and two non-intrusive approaches (probabilistic collocation and least-squares regression) have been implemented on a continuously stirred tank reactor case study.

Keywords: probabilistic uncertainty, generalized polynomial chaos, dynamic optimization

1. Introduction

Mathematical models are indispensable tools for the analysis, control and optimization of a wide range of complex technical systems. As models are only an approximate representation of reality, uncertainty is inherently present. This uncertainty can be structural, parametric or initial condition uncertainty as well as the impact of external disturbances and process variability which are typically present in the control and optimization of dynamic processes. In order to account for these sources of uncertainty systematically, two approaches can be followed, i.e., *stochastic* and *robust* optimization. In the former approach, the uncertainty is considered to be of a stochastic nature for which the probability distribution information is available. The latter assumes that the uncertainty is known to be fully contained within a given set and usually leads to the formulation where all constraints must be satisfied in the *worst case* scenario (Diehl et al., 2008). In this paper, stochastic uncertainty is considered in the model parameters and/or initial conditions. A key requirement to account for uncertainty in nonlinear optimization is accurate uncer-

tainty propagation while maintaining a computationally tractable formulation.

This paper focuses on generalized polynomial chaos (Wiener, 1938) which exploits information on the distribution to approximate both mean and variance. To this extent a polynomial expansion is derived for which the coefficients need to be determined. A recent historical perspective on the use of polynomial chaos for optimization of dynamic systems has been presented by Kim et al. (2013) and a recent summary of the known theoretical results is provided in Paulson and Mesbah (2017). Two different approaches exist to determine the PCE coefficients: intrusive and non-intrusive formulations. The main contributions of this article, are a tutorial and critical comparison on the implementation of gPC formulations. In addition, an intrusive Galerkin formulation and two non-intrusive formulations (probabilistic collocation and least-squares regression) have been implemented on a continuously stirred tank reactor case study.

2. Dynamic optimization under stochastic uncertainty with gPC

2.1. Dynamic optimization under stochastic uncertainty

Consider the dynamic optimization problem under stochastic uncertainty in the interval $t \in [0, t_f]$:

$$\begin{aligned} \min_{u(\cdot)} \quad & \mathbb{E}\{J(x, u, \theta)\} + \alpha_0 \text{Var}\{J(x, u, \theta)\}, \\ \text{subject to:} \quad & \dot{x} = f(x, u, \theta), \\ & x(0) = x_0(\theta), \\ & \mathbb{E}\{g_i(x, u, \theta)\} + \alpha_i \text{Var}\{g_i(x, u, \theta)\} \leq 0, \quad i = 1, \dots, n_c, \\ & \theta \sim p_\theta, \end{aligned} \tag{1}$$

with $x \in \mathbb{R}^{n_x}$ the state vector, $u \in \mathbb{R}^{n_u}$ the control vector, $\theta \in \mathbb{R}^n$ the uncertain parameters, $x_0(\theta)$ is the initial condition, f the model equations, p_θ the parameter probability density function and $J(x, u, \theta)$ and $\{g_i(x, u, \theta)\}_{i=1}^{n_c}$ the optimization objective and constraints, respectively. The parameters $\boldsymbol{\alpha} = (\alpha_0, \alpha_1, \dots, \alpha_{n_c})$ directly control the tradeoff between the mean and variance.

The main difficulty in solving (1), lies in the evaluation of the multidimensional integrals related to the expectation and variance operators $\mathbb{E}\{\cdot\}$ and $\text{Var}\{\cdot\}$ in the above formulation, since $\mathbb{E}\{R_k(\theta)\} = \int_{\theta \in \Theta} R_k(\theta) p_\theta(\theta) d\theta$ and $\text{Var}\{R_k(\theta)\} = \mathbb{E}\{(R_k(\theta) - \mathbb{E}\{R_k(\theta)\})^2\}$ are generally defined in terms of a multidimensional integral for any function $R_k(\theta)$. Unless these integrals can be evaluated analytically as a function of the decision variables, these need to be approximated using a sampling-based method that can either be *deterministic* (e.g., Gauss quadrature) or *random* (e.g., Monte Carlo sampling) (Debusschere et al., 2004). Deterministic sampling methods result in $N = 100^n$, in case 100 points are spaced equally throughout the n uncertainty dimensions. Random sampling methods require less samples, but can still require a very large N to practically converge as e.g. in Monte Carlo where the convergence rate is quite low $O(1/\sqrt{N})$.

2.2. Generalized polynomial chaos (gPC)

The gPC method approximates a model response y as a sum of orthogonal polynomials which are a function of the uncertain parameters for which stochastic information is avail-

able. The d -th order polynomial chaos expansion (PCE) of a model response y is defined as follows:

$$y_{\text{PCE}}(\boldsymbol{\theta}) = \sum_{j=0}^L \hat{y}_j \Phi_j(\boldsymbol{\theta}), \quad (2)$$

with \hat{y}_j the unknown PCE coefficients and $\Phi_j(\boldsymbol{\theta})$ the multivariate orthogonal polynomials and j a term based index ($j = 0, \dots, L$) and $L + 1 = (n_\theta + d)! / (n_\theta! d!)$.

These multivariate orthogonal polynomials can be written as a function of univariate orthogonal polynomials as it is typically assumed in polynomial chaos that the uncertain parameters are independent. In gPC, the uncertain parameters are written as a function of a standard distributed uncertain variable ξ . The Wiener-Askey can then be used to define generalized orthogonal polynomials as a function of ξ (Wiener, 1938; Xiu and Karniadakis, 2002). Recently, Paulson et al. (2017) proposed a further generalization, termed arbitrary polynomial chaos (aPC), to define the basis directly in terms of the *moments* of the uncertain variables.

The expected value and variance of R_y can be approximated with PCE as:

$$\mathbb{E}[y] \approx \hat{y}_0 \quad (3)$$

$$\text{Var}[y] \approx \sum_{j=1}^L (\hat{y}_j)^2 \mathbb{E}[\Phi_j^2(\boldsymbol{\theta})]. \quad (4)$$

Note that $\mathbb{E}[\Phi_j^2(\boldsymbol{\theta})]$ can be computed upfront and equals 1 for standard normalized polynomials.

3. Computing the PCE coefficients

Remark that up till now, it is not yet mentioned how the unknown PCE coefficients \hat{y}_j can be computed. Two classes of methods exist to compute these unknown coefficients: *intrusive* and *non-intrusive* methods. The dynamic optimization problem formulations are presented in Table 1. In *intrusive methods* a deterministic set of equations is developed for the coefficients \hat{y} based on a Galerkin projection of the approximation error between the model response function and its polynomial chaos expansion. For *intrusive* methods the model response needs to be explicitly known and preferably the explicit model response function is a polynomial function. More details on intrusive methods can be found in e.g., Ghanem and Spanos (1991), Debusschere et al. (2004). In *non-intrusive methods* the model is considered as a black box and exact expressions for the model response are not required. All *non-intrusive* methods can be considered as a weighted sum of model response evaluations in n_s sampling points. The non-intrusive Galerkin, probabilistic collocation and least squares regression differ in the number of sampling points n_s that are selected and the weighting matrices as indicated in Table 1.

Note that the intrusive gPC problem formulation no longer has any random variables appearing so that it can be solved using standard dynamic optimization methods. However, the complexity of evaluating the right-hand side inner products of the equations above

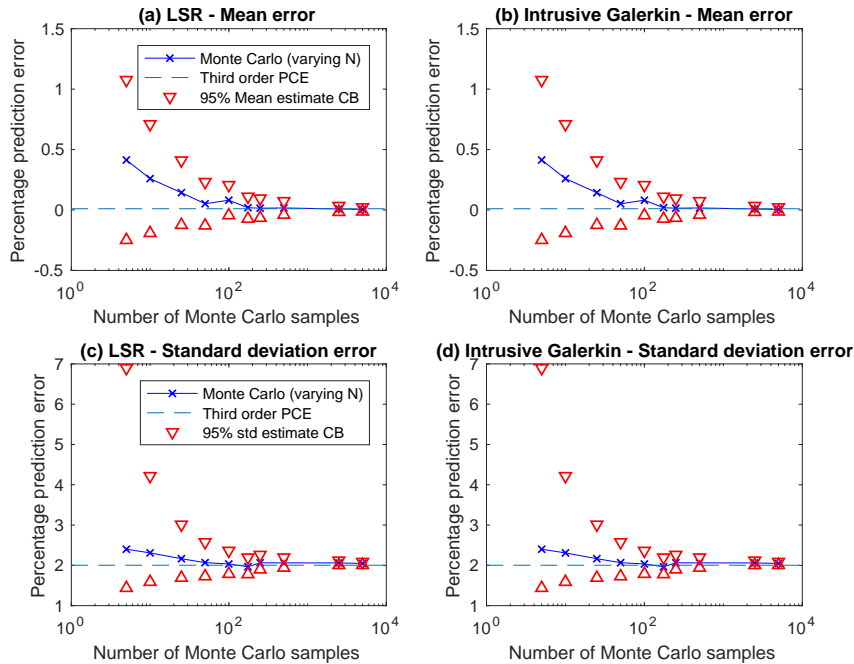


Figure 1: Prediction errors for mean and standard deviation for LSR (a,c) and intrusive Galerkin (b,d).

(which may not even have closed-form expressions) and the fact that there is no clear exploitable structure due to the strong correlation between all the variables. The fact that the number of terms in the right-hand side grows exponentially with order of the polynomial also implies gradient calculations will be very expensive, which is a key bottleneck in many optimization algorithms including interior point and active set methods.

4. Results for a CSTR case study

4.1. Case study

The continuously stirred tank reactor (CSTR) case study from Lucia et al. (2017) has been implemented to compare three different gPC implementations: intrusive Galerkin with non-intrusive probabilistic collocation (PCM) and least squares regression (LSR). In this CSTR the reactants A and B react to form a product C. The objective of the problem is to maximize the amount of C. The model consists of 7 differential equations, describing the change of the reactor volume with respect to time, the concentration mass balances of A, B and C, the dynamics of the reactor temperature and jacket temperature and the dynamics of the inlet jacket temperature. The controls are the reactor inflow and the set-point of the thermostat. Two uncertain parameters have been considered to be uniformly distributed within the interval $[0.7\theta_{\text{nom}}, 1.3\theta_{\text{nom}}]$: the molar reaction enthalpy ΔH_R and the reaction constant k . The dynamic optimization problems have been discretized using an orthogonal collocation scheme.

4.2. Prediction error as function of order and method

As a measure the final temperature has been chosen and 10000 Monte Carlo (MC) samples have been taken as a benchmark for comparison with the prediction of mean and variance. Figure 1 indicates a minor effect on mean approximation while variance approximation improves with increasing order. The prediction error between MC and PCE has been plotted as a function of the number of parameter samples for both LSR as intrusive Galerkin.

Table 1: Dynamic optimization problem formulations for intrusive and non-intrusive gPC.

Intrusive Galerkin formulation		
$\min_{u(\cdot)} J_0 + \alpha_0 \sum_{i=1}^L J_i^2 \langle \Phi_i^2 \rangle$ $\text{subject to: } \hat{g}_{i,0} + \alpha_i \sum_{j=1}^L \hat{g}_{i,j}^2 \langle \Phi_j^2 \rangle \leq 0$		
$\frac{d\hat{x}_k(t)}{dt}$	$=$	$\frac{1}{\langle \Phi_k^2 \rangle} \langle f(\sum_{i=0}^L \hat{x}_i \Phi_i(\xi), u(t), \sum_{i=0}^L \hat{\theta}_i \Phi_i(\xi)), \Phi_k \rangle,$
$\hat{x}_k(0)$	$=$	$\frac{\langle x_0 \Phi_k \rangle}{\langle \Phi_k^2 \rangle},$
\hat{f}_k	$=$	$\frac{1}{\langle \Phi_k^2 \rangle} \langle J(\sum_{i=0}^L \hat{x}_i \Phi_i(\xi), u(t), \sum_{i=0}^L \hat{\theta}_i \Phi_i(\xi)), \Phi_k \rangle,$
$\hat{g}_{i,k}$	$=$	$\frac{1}{\langle \Phi_k^2 \rangle} \langle g(\sum_{i=0}^L \hat{x}_i \Phi_i(\xi), u(t), \sum_{i=0}^L \hat{\theta}_i \Phi_i(\xi)), \Phi_k \rangle,$
$\forall k$	$=$	$0, \dots, L, \forall i = 1, \dots, n_c.$
Non-intrusive formulations		
$\min_{u(\cdot)} J_0 + \alpha_0 \sum_{i=1}^L J_i^2 \langle \Phi_i^2 \rangle$ $\text{subject to: } \dot{x}^j = f(x^j, u, \theta^j), j = 1, \dots, N,$		
$x^j(0)$	$=$	$x_0(\theta^j), j = 1, \dots, N,$
\hat{f}_k	$=$	$\sum_{j=1}^N w_{k,j} J(x^j, u, \theta^j), k = 0, \dots, L,$
$\hat{g}_{i,k}$	$=$	$\sum_{j=1}^N w_{k,j} g_i(x^j, u, \theta^j), i = 1, \dots, n_c, k = 0, \dots, L,$
0	\geq	$\hat{g}_{i,0} + \alpha_i \sum_{j=1}^L \hat{g}_{i,j}^2 \langle \Phi_j^2 \rangle, i = 1, \dots, n_c,$
		$\hat{\mathbf{y}} = \mathbf{W}\mathbf{y}$ with $\mathbf{y} = [y(\theta^1), \dots, y(\theta^N)]$
Non-intrusive Galerkin	Probabilistic collocation	Least squares regression
$\begin{bmatrix} \frac{q^1 \Phi_0(\theta^0)}{\langle \Phi_0^2 \rangle} & \dots & \frac{q^N \Phi_0(\theta^{n_s-1})}{\langle \Phi_0^2 \rangle} \\ \vdots & \vdots & \vdots \\ \frac{q^1 \Phi_L(\theta^0)}{\langle \Phi_L^2 \rangle} & \dots & \frac{q^N \Phi_L(\theta^{n_s-1})}{\langle \Phi_L^2 \rangle} \end{bmatrix}$	$\left((\mathbf{\Lambda}^{(d)})^T \right)^{-1}$	$\left(\mathbf{\Lambda}^{(d)} \left(\mathbf{\Lambda}^{(d)} \right)^T \right)^{-1} \mathbf{\Lambda}^{(d)}.$
with weights q^i from the quadrature rule	with $\mathbf{\Lambda}^{(d)} =$	with $\mathbf{\Lambda}^{(d)} =$
	$\begin{bmatrix} \Phi_0(\theta^0) & \dots & \Phi_0(\theta^{n_s-1}) \\ \vdots & \ddots & \vdots \\ \Phi_L(\theta^0) & \dots & \Phi_L(\theta^{n_s-1}) \end{bmatrix}$	$\begin{bmatrix} \Phi_0(\theta^0) & \dots & \Phi_0(\theta^{n_s-1}) \\ \vdots & \ddots & \vdots \\ \Phi_L(\theta^0) & \dots & \Phi_L(\theta^{n_s-1}) \end{bmatrix}$

For the mean MC never seems to outperform the PCE accuracy. More than 1000 MC samples are required to outperform PCE.

4.3. CPU time

The IPOPT main loop times for the three different methods are displayed in Table 2 for different PCE orders. All states are initialized at a fixed value, not exploiting the advantage of non-intrusive approaches which can use the nominal state profiles as initialization. PCM outperforms LSR and intrusive Galerkin in all cases except for the first order PCE, where performance is similar. LSR and intrusive Galerkin have a similar performance, although intrusive Galerkin requires $\frac{(n+d)!}{n!d!} n_x$ states and LSR $n^{d+1} n_x$ states.

Table 2: CPU times in seconds for different orders obtained with LSR, PCM and intrusive Galerkin.

First order			Second order			Third order		
LSR	PCM	Galerkin	LSR	PCM	Galerkin	LSR	PCM	Galerkin
0.936	0.713	1.058	3.696	2.317	9.805	17.711	1.817	12.426

5. Conclusions

In this article a comparison between the different gPC formulations has been presented and an intrusive Galerkin, PCM and LSR have been implemented on a CSTR case study. Results indicate that non-intrusive formulations are preferred over intrusive due to the generally lower CPU time and potential further decrease in CPU time due to the parallelizable sampling-based structure of the dynamic optimization problem (Jiang et al., 2017).

Acknowledgements

The research is supported by: FWO-G.0863.18 and SB holds a Baekeland PhD grant from the Agency for Innovation through Science and Technology in Flanders.

References

- B. Debusschere, H. Najm, P. Pébay, O. Knio, R. Ghanem, O. L. Maitre, 2004. Numerical challenges in the use of polynomial chaos representations for stochastic processes. *SIAM Journal on Scientific Computing* 26, 698–719.
- M. Diehl, J. Gerhard, W. Marquardt, M. Mönnigmann, 2008. Numerical solution approaches for robust nonlinear optimal control problems. *Computers and Chemical Engineering* 32, 1287–1300.
- R. Ghanem, P. Spanos, 1991. *Stochastic Finite Elements A Spectral Approach*. SpringerVerlag.
- Y. Jiang, P. Nimmegeers, D. Telen, J. Van Impe, B. Houska, 2017. A distributed optimization algorithm for sampling-based stochastic optimal control. In: *Proceedings of the 20th IFAC World Congress*. pp. 11755–11760.
- K.-K. Kim, D. Shen, Z. Nagy, R. Braatz, 2013. Wiener’s polynomial chaos for the analysis and control of nonlinear dynamical systems with probabilistic uncertainties [historical perspectives]. *IEEE Control Systems* 33 (5), 58–67.
- S. Lucia, A. Tătulea-Codrean, C. Schoppmeyer, S. Engell, 2017. Rapid development of modular and sustainable nonlinear model predictive control solutions. *Control Engineering Practice* 60, 51 – 62.
- J. Paulson, E. Buehler, A. Mesbah, 2017. Arbitrary polynomial chaos for uncertainty propagation of correlated random variables in dynamic systems. *Proceedings of the IFAC World Congress*, 3607 – 3612.
- J. A. Paulson, A. Mesbah, 2017. An efficient method for stochastic optimal control with joint chance constraints for nonlinear systems. *International Journal of Robust and Nonlinear Control* 21 (1).
- N. Wiener, 1938. The homogeneous chaos. *American Journal of Mathematics* 60 (4), 897 – 936.
- D. Xiu, E. Karniadakis, 2002. The Wiener-Askey polynomial chaos for stochastic differential equations. *SIAM Journal of Scientific Computation* 24, 619 – 644.

On the role of H₂ storage and conversion for wind power production in the Netherlands

Lukas Weimann^a, Paolo Gabrielli^b, Annika Boldrini^a, Gert Jan Kramer^a and Matteo Gazzani^{a*}

^a*Utrecht University, Princetonlaan 8a, 3584 CB Utrecht, The Netherlands*

^b*ETH Zurich, Sonneggstrasse 3, 8092 Zurich, Switzerland*
m.gazzani@uu.nl

Abstract

Mixed integer linear programming (MILP) is the state-of-the-art mathematical framework for optimization of energy systems. The capability of solving rather large problems that include time and space discretization is particularly relevant for planning the transition to a system where non-dispatchable energy sources are key. Here, one of the main challenges is to realistically describe the technologies and the system boundaries: on the one hand the linear modeling, and on the other the number of variables that can be handled by the system call for a trade-off between level of details and computational time. With this work, we investigate how modeling wind turbines, H₂ generation via electrolysis, and storage in salt cavern affect the system description and findings. We do this by implementing methodological developments to an existing MILP tool, and by testing them in an exemplary case study, i.e. decarbonization of the Dutch energy system. It is found that modeling of wind turbines curtailment and of existing turbines are key. The deployment of H₂ generation and storage is driven by the interplay between area availability, system costs, and desired level of autarky.

Keywords: MILP, wind turbines, energy storage, technology modeling, energy transition

1. Introduction

A high penetration of non dispatchable renewable energy sources (NDRES) comes with the necessity for energy storage capacity. While batteries show a very high round-trip efficiency and suitability for intra-day storage, they are not suited for long-term storage, especially seasonal, due to their energy losses over time. (Gabrielli et al. (2018a)) The production of hydrogen via power-to-gas (PtG) is a more promising candidate for such long-term storage. Nevertheless, the large volumes required on a national or even international scale require alternatives to conventional gas tanks. Hydrogen storage in salt caverns is a proven technology (Lord et al. (2014)) that features large point storage capacity, especially in the Netherlands and in Germany. Previous studies focusing on Germany (Welder et al. (2018)) have already shown the potential of the described system. Understanding the trade-offs between offshore vs. onshore wind farms, and planning the replacement of old wind installations is a challenging task that benefits from the adaptation of rigorous MILP frameworks. Therefore, this work aims at grasping the aforementioned trade-offs by analyzing a hypothetical Dutch energy system consisting of onshore and offshore wind turbines, and PtG systems with hydrogen storage in salt caverns. Furthermore,

the extent of autarky achievable with such a system will be quantified.

2. Methodology

The model discussed in this work builds upon the MILP modeling framework reported by Gabrielli et al. (2018b). Following, we focus on new developments within this framework.

2.1. Wind turbine modeling

Various approaches to model wind turbines showing different levels of detail can be found in literature, ranging from detailed wind power plant modeling as reported by Gebraad et al. (2017) to simplified models for the use in MILP energy system optimization (Weber and Shah (2011)). In this work, we model the wind turbines using power curves as a function of cut-in, rated, and cut-out windspeed (v_{in} , v_r and v_{out} , respectively) as described by Jerez et al. (2015).

Implementation into the MILP framework: Using wind profiles for the full analyzed time horizon allows to tackle the non linearity arising from the power curve in a pre-processing step. The maximum power output P_{max} for a wind turbine is calculated for every hour of the year and passed on to the optimization as a constant vector. Note that P_{max} , being the uncurtailed output for a given windspeed, is different from P_r , the rated power correlating to v_r . The actual output P_{out} is then calculated as

$$\begin{aligned} P_{out,i,t} &\leq P_{max,i,t} \cdot S_i \\ 0 &\leq S_i \text{ for all } i \in \{1, I\} \text{ and } t \in \{1, T\} \end{aligned} \quad (1)$$

where the integer decision variable S is the number of turbines, I the number of types of turbines and T the length of the time horizon. The optimization can choose to build new turbines from a discrete set (offshore: 3.5 MW and 6 MW, onshore: 0.9 MW, 2.5 MW and 4.5 MW). The treatment of existing turbines is more complicated owing to the limited amount of information open databases provide.

Existing turbines: Detailed modeling of existing turbines is required to decide upon replacement and continuous operation. While it is easy to model a certain turbine in detail, the vast variety of existing turbines calls for a more generalized approach, which is described in this section. A data set consisting of 43 turbines, accounting for about 78 % of Dutch turbines, was used. The only clear correlation was found between the P_r and the total integral of the power curve. Based on this observation and the aforementioned set of turbines, an algorithm to calculate estimates of v_{in} , v_r and v_{out} for arbitrary turbines was developed. The algorithm takes P_r and the manufacturer of the wind turbine to be analyzed as an input as well as the 43 turbines data set. Knowing that the maximum hourly windspeeds are usually around 10-20 ms^{-1} , v_{out} usually ranging from 20-25 ms^{-1} is of minor importance and hence neglected here. If a match for the manufacturer is found, the set is reduced to that manufacturer. Otherwise, the full set is used. The resulting data set is compared for P_r . Depending on how many matches are found, 3 cases are distinguished.

- *Case 1: 1 match for P_r found:* The algorithm uses the match from the dataset to simulate the turbine of interest.

- *Case 2: >1 match for P_r found:* A target power curve integral I_t is determined as

$$I_t = \frac{\sum_{i=1}^{N_m} \int_0^{v_{r,max}} P_i(v_{in}, v_r, v) dv}{N_m} \quad (2)$$

where $v_{r,max}$ is the maximum rated windspeed found in the data set and N_m is the total number of P_r -matches found. v_{in} and v_r are then calculated solving eq. (3)

$$\begin{aligned} \min_{v_{in}, v_r} g &= \left| \int_0^{v_{r,max}} P(v_{in}, v_r, v) dv - I_t \right| \\ \text{s.t. } v_{in,min} &\leq v_{in} \leq v_{in,max} \\ v_{r,min} &\leq v_r \leq v_{r,max} \end{aligned} \quad (3)$$

v_{out} is returned as the average of the values in the considered data subset.

- *Case 3: No turbines found* In this particular case, the turbines with the next higher and next lower P_r are chosen. If more than one turbine each is found, their integrals are averaged as seen in eq. (2) to end up with one upper and one lower value. I_t is then obtained by interpolation. If P_r of the turbine of interest is higher or lower than all turbines in the considered subset, the whole subset forms the basis for a linear fit that allows to calculate I_t by means of extrapolation. Once I_t is obtained, the remaining procedure is identical to Case 2, i.e. solving eq. (3) for v_{in} and v_r and averaging v_{out} .

Curtailment: While the inequality in eq. (1) already allows for curtailment, this formulation is imprecise from a physical point of view since wind turbines are curtailed in a discrete manner. They are either curtailed, i.e. turned off, or operated following their power curves. To account for this effect, the curtailment C was introduced as an additional integer decision variable, describing how many turbines are turned off. The power output can then be formulated as

$$\begin{aligned} P_{out,i,t} &= P_{max,i,t} \cdot (S_i - C_{i,t}) \\ 0 &\leq C_{i,t} \leq S_i \\ 0 &\leq S_i \\ r^2 \pi \cdot \sum_i S_i &\leq A_{max} \end{aligned} \quad (4)$$

Note that the strict equality in eq. (4), as compared to eq. (1), is reducing the flexibility of the system. This formulation allows for a physical-based description of curtailment, but it also increases significantly the complexity of the problem as discussed in the results. The total number of turbines is constraint by the maximum available land A_{max} . It is assumed that the distance between two wind turbines has to be at least 500 m, giving each turbine a radius r of 0.25 km.

2.2. Power-to-gas and hydrogen storage

The power-to-gas system consists of a polymer electrolyte membrane (PEM) electrolyzer and fuel cell, operating with water and air, respectively. Their modeling is reported in detail by Gabrielli et al. (2018b). Hydrogen is considered to be stored in cylindrical salt caverns as described in Gabrielli et al. (2018c).

3. Results

The problem was formulated in MATLAB R2018b using YALMIP (Löfberg (2004)) and solved with Gurobi v8.1 on an Intel Xeon E5-1620 3.60 GHz machine with 16 GB RAM.

Case study 1: To quantify the effect of discrete compared to continuous curtailment, a hypothetical offshore-island - aimed at providing the whole Dutch electricity demand - was analyzed. The set of technologies encompasses a 3.5 MW wind turbine ($v_{in} = 3 \text{ ms}^{-1}$, $v_r = 14 \text{ ms}^{-1}$), a 6 MW wind turbine ($v_{in} = 4 \text{ ms}^{-1}$, $v_r = 13 \text{ ms}^{-1}$) and a PtG system. Due to the absence of salt caverns off-shore, traditional tank storage was assumed. In addition, the currently existing Dutch offshore turbines are considered but can be replaced through new turbines. The analysis was conducted with and without PtG system, both with discrete and continuous curtailment, ultimately resulting in 4 scenarios whose results are summarized in Table 1. As opposed to case study 2, no spatial constraints are assumed. As expected, dissipation of electricity occurs with discrete curtailment only and results from the fact that the costs for dissipation and import are equal at 10^5 euro per kWh. Hence, building an additional turbine and dissipating energy can be more favorable than importing. The application of PtG systems reduces the dissipation by an order of magnitude and the import by a quarter. Surprisingly, the PtG system is not utilized with continuous curtailment. Given the assumptions used, it is most likely that this is a result of the missing cost benefit of avoiding dissipation by using storage. Using discrete curtailment, the computational time is increased by about 80 % without PtG and by 1000 % with PtG. This indicates that the computational effects of discrete curtailment scale with the complexity of the system as a whole. This can easily lead to unsolvable systems due to a lack of memory, as experienced in case study 2. The preference of the 3.5 MW turbines over the 6.0 MW turbines can be explained by comparing their v_{in} with the wind profile, showing that the 3.5 MW turbine operates for 6366 hours per year while the 6.0 MW turbine only operates for 4674 hours per year. This significant downtime for both also explains the high amount of imported electricity despite the high amount of installed turbines. Furthermore, this also shows the need of large scale energy storage; the storage installed in scenario 4 is at its maximum of $4.9290 \cdot 10^7$ kWh.

Case study 2: The system under investigation consists of 3 nodes, hereafter called onshore-node (ONN), offshore-node (OFFN), and cavern-node (CN). All data refers to the Netherlands and is hourly resolved for 2017. Wind turbines can be installed in ONN and OFF, and PtG systems with storage in CN and without storage in ONN. The country's electricity demand is an input profile for ONN and wind profiles are considered as input for ONN and OFFN. Full connectivity between the nodes is assumed for the electricity network while the hydrogen network needs to be built if required, i.e. investment costs occur. The optimization decides upon selection, sizing, and scheduling of the technologies as well as the flows between the nodes with the levelized costs of the total system as objective. While there is no export of electricity allowed, electricity can be imported at a

Table 1: Effect of discrete curtailment on technology selection. Scenarios: (1) no PtG, continuous curtailment (2) PtG, continuous curtailment (3) no PtG, discrete curtailment (4) PtG, discrete curtailment. For simplicity, only the storage of the PtG system is shown. Import, Dissipation and Storage are given in kWh.

Scenario	WTex	WT-3.5	WT-6.0	Import	Dissipation	Storage
1	79	13356752	0	1.08 E10	0	-
2	79	13356753	0	1.08 E10	0	0
3	79	13356753	0	1.08 E10	1.07 E06	-
4	79	13356752	0	8.27 E09	1.04 E05	4.93 E07

Table 2: Sensitivity of technology implementation towards level of autarky. The sizes for electrolyzer (PEMEC) and fuel cell (PEMFC) are in kW capacity, and for the wind-turbines (WT) in built units. The number next to *WT* refers to its maximum capacity in MW

Autarky	PEMEC	PEMFC	WT-0.9	WT-2.5	WT-4.5	WT-3.5	WT-6.0
0.625	42586	423.8	0	26944	4792	1077	24
0.475	0	0	0	15223	0	0	0
0.325	0	0	0	7520	0	0	0
0.175	0	0	0	3687	0	0	0
0.025	0	0	0	531	0	0	0
0	0	0	0	0	0	0	0

price of 0.032 euro per kWh and an emission factor of 0.676 kg_{CO_2} per kWh. A CO_2 -tax of 20 euro per tonne was applied, corresponding to the current ETS prices. The available land for ONN was assumed to be 15 % of the total land (WorldBank (2018), McKenna et al. (2015)). For OFFN, a total available area of 2900 km^2 (Dutch Government (2014)) was assumed. Although being spatially reduced to only 3 nodes, the study is based on realistic assumptions and constraints in terms of electricity demand, wind speed, available area and existing turbines. Putting the focus on achievable autarky using PtG, and considering the issues found in case study 1, continuous curtailment is used and existing turbines are neglected. Since imported electricity is the only source of emissions, the maximum achievable autarky was determined by applying a CO_2 -tax of 10^6 euro per tonne giving an autarky of 62.5 % (defined as the fraction of the produced electricity over the total demand). Following, the autarky was implemented as a constraint and the sensitivity of the technology selection towards this constraint was investigated using the real CO_2 -tax (see Table 2). It can be observed that in order to achieve the upper limit of autarky, oversizing of production technologies and installation of PtG is necessary. As soon as the constraint on autarky is relaxed, undersizing of production technologies and compensation with import is the preferred combination. Note that this result is also sensitive to the import price, the CO_2 -tax, and the emission factor of imported electricity. The difference in size between PEMEC and PEMFC indicates that the amplitudes in overproduction are greater than in overdemand. Nevertheless, it does not necessarily follow that the total production for a year is higher than the demand.

4. Conclusions

In this work, the implementation of wind turbines with its various aspects into an MILP framework, and in particular the consideration of existing turbines, was discussed. A first analysis of the Dutch case study shows how the level of targeted autarky affects the selection of technologies. For the considered assumptions and constraints in this study, an upper limit to autarky is given by the available land, and PtG is required to approach this limit. From a computational point of view, the description of the wind turbine curtailment strongly affects the problem complexity and can cause an up to 10-fold increase of computation time for discrete curtailment. The exact impact depends on the overall system complexity. This becomes especially crucial when existing turbines are considered, because each type of turbine is treated as separate technology. Hence, existing turbines intrinsically lead to a vast increase in system complexity.

5. Acknowledgement

ACT ELEGANCY, Project No 271498, has received funding from DETEC (CH), BMWi (DE), RVO (NL), Gassnova (NO), BEIS (UK), Gassco, Equinor and Total, and is co-funded by the European Commission under the Horizon 2020 programme, ACT Grant Agreement No 691712.

References

- P. Gabrielli, M. Gazzani, E. Martelli, M. Mazzotti, 2018a. Optimal design of multi-energy systems with seasonal storage. *Applied Energy* 219, 408–424.
- P. Gabrielli, M. Gazzani, M. Mazzotti, 2018b. Electrochemical conversion technologies for optimal design of decentralized multi-energy systems: Modeling framework and technology assessment. *Applied Energy* 221, 557–575.
- P. Gabrielli, A. Poluzzi, C. Spiers, M. Mazzotti, M. Gazzani, 2018c. Seasonal energy storage through hydrogen salt caverns: Technology modeling for system optimization and assessment of emissions reduction potential. in preparation.
- P. Gebraad, J. Thomas, A. Ning, P. Fleming, K. Dykes, 2017. Maximization of the annual energy production of wind power plants by optimization of layout and yaw-based wake control. *Wind Energy* 20, 97–107.
- S. Jerez, F. Thairs, I. Tobin, M. Wild, A. Colette, P. Yiu, R. Vautard, 2015. The CLIMIX model: A tool to create and evaluate spatially-resolved scenarios of photovoltaic and wind power development. *Renewable and Sustainable Energy Reviews* 42, 1–15.
- J. Löfberg, 2004. Yalmip : A toolbox for modeling and optimization in matlab. In: *Proceedings of the CACSD Conference*. Taipei, Taiwan.
- A. Lord, P. Kobos, D. Borns, 2014. Geologic storage of hydrogen: Scaling up to meet city transportation demands. *International Journal of Hydrogen Energy* 39, 15570–15582.
- R. McKenna, S. Hollnaicher, P. O. v. d. Leye, W. Fichtner, 2015. Cost-potentials for large onshore wind turbines in europe. *Energy* 83, 217–229.
- Dutch Government, 2014. White paper on offshore wind energy. <https://www.government.nl/documents/reports/2015/01/26/white-paper-on-offshore-wind-energy>, (accessed 14 November 2018).
- C. Weber, N. Shah, 2011. Optimisation based design of a district energy system for an eco-town in the United Kingdom. *Energy* 36, 1292–1308.
- L. Welder, D. Yberg, L. Kotzur, T. Grube, M. Robinius, d. Stolten, 2018. Spatio-temporal optimization of a future energy system for power-to-hydrogen applications in Germany. *Energy* 158, 1130–1149.
- WorldBank, 2018. Arable land. <https://data.worldbank.org/indicator/AG.LND.ARBL.ZS?view=chart>, (accessed 14 November 2018).

Fuzzy Control Applied to Combustion in Sugarcane Bagasse Boilers

Fernando M. de Mello^{a,b}, Antonio J. G. da Cruz^{b,c}, Ruy de Sousa Jr.^{b,c,*}

^a*Tereos, Rod. Assis Chateaubriand km 155, Olimpia 15400-000, Brazil*

^b*Graduate Program in Chemical Engineering, Rod. Washington Luís km 235, São Carlos 13565-905, Brazil*

^c*Department of Chemical Engineering, Federal University of São Carlos, Rod. Washington Luís km 235, São Carlos 13565-905, Brazil*

ruy@ufscar.br

Abstract

In the sugarcane industry, boilers are widely used for cogeneration. This industry uses mainly sugarcane bagasse as the primary fuel source, followed by other types of biomass. Fuel price has a major impact on the industry results, due to the scenario of the energy market. Therefore, optimizing the combustion is an important lever to reduce this cost. Real-time measurement of oxygen content in the boilers flue gas is one of the requirements for this optimization. Due to the capital cost and the requirements for personnel qualification for maintenance and calibration, sugarcane mills rarely apply such analyzers in closed loop. In this work, a fuzzy control was implemented in the combustion air flowrate of a large boiler in the Tereos group, to maintain the oxygen content in the combustion products within the optimum range. A tool was used to identify the process dynamics and to tune the control loop in real time. After downloading the new strategy in the factory control system and tuning the controller, the oxygen control loop started operation in automatic mode. After twenty-four hours of continuous operation, regulatory and servo controls were able to keep the desired setpoint with low variability ($\pm 1.2\%$ variation in excess air coefficient) and respond to setpoint changes with good response speed (1.5-20 minutes) and overshoot (8-56%). No previous references were found in the literature on the use of fuzzy logic for the combustion control of sugarcane bagasse-fired boilers, especially high pressure and high steam throughput boilers. Results reached so far demonstrate the applicability of fuzzy control for combustion in boilers on sugarcane bagasse, with 40% less variability than a PID controller, and 69% less variability compared to operation in manual mode.

Keywords: sugarcane bagasse boiler, oxygen control, fuzzy logic.

1. Introduction

In the sugarcane industry, boilers are widely used for cogeneration (i.e., simultaneous generation of thermal and electrical energy from the same fuel source). The main fuel used is sugarcane bagasse, followed by other types of biomass, such as cane straw, woodchips and corn stover. According to the Brazilian Sugarcane Industry Union (UNICA), and the National Electric Energy Agency (ANEEL), the granted capacity of electricity supply from biomass represents 9% of the Brazilian energy matrix. The cane harvest period, which occurs between the months of April and November in the southeast of Brazil, is an advantage for electricity generation from bagasse, since it

matches the drier seasons of the year. During this period, the generation demand from thermoelectric power plants is increased. In this scenario, the price of sugarcane biomass (bagasse and straw) has a significant impact on the financial results of sugarcane mills. Since the process of manufacturing sugar and ethanol consumes large amounts of steam, the production of electricity from the very steam consumed at the mills is an inexpensive way of generating electricity. Therefore, it is essential that plants with a focus on bioelectricity generation invest in energy efficiency, to maximize the biomass surplus and its conversion into electricity, which reduces the risk exposure to the biomass market. Excess air is an impact factor on combustion efficiency: boilers use an air/fuel curve to maintain excess air as predicted by the manufacturer. However, variations in fuel quality, mainly humidity, require corrections on this curve. The main mechanism to correct the air/fuel curve is the oxygen control in the outlet duct of the effluent gases. This type of control is still little used in sugarcane bagasse boilers. Advanced control may have advantages over PID in this type of application. Thus, this work presents a fuzzy logic approach for the combustion control.

2. Literature Review

Fuel composition defines the combustion's stoichiometry, which in turn defines the theoretical air for the fuel's complete combustion. However, due to furnace mixing deficiencies, an excess amount of air is required to maintain a sufficient amount of oxygen until the end of the burning. One way of expressing the air/fuel ratio is the excess air coefficient, which is the ratio of the total amount of air used in the combustion to the amount of stoichiometric air. The excess air controls the volume and the enthalpy of the flue gases, which are determinant for the boiler's efficiency. A large excess of air is undesirable because it lowers the flame temperature and increases heat losses by enthalpy of the dry gas. On the other hand, a low excess of air can result in incomplete combustion and the formation of CO, soot and smoke, in addition to an accumulation of unburnt fuel, causing risk of explosion. Therefore, an optimum excess air coefficient is required to minimize both losses. In a boiler's design, manufacturers define a curve known as the air/fuel curve. This curve relates the air inlet as a function of the fuel throughput, and aims to maintain the excess air coefficient within the targeted range for each type of boiler. However, variations in fuel composition cause deviations from this curve, and the boiler no longer operates with the best combustion efficiency. Humidity is the main factor of variation in fuel composition throughout the crop. This is mainly due to limitations in the control of imbibition water in the sugar extraction process, cane throughput variability, wear of the drying/dewatering mills. An oxygen level control in the flue gas can correct the air/fuel curve in real time.

Zadeh (1965) introduced the concept of fuzzy sets, which, as the name suggests, is a theory of sets (or classes) whose boundaries are indefinite. He established that a fuzzy set would be a class with varying membership degrees. That is, each element would be allowed a certain degree of membership to the set. Fuzzy logic provides a means of quantifying states and overlapping between them (eg, High and Low), assigning degrees of membership (truth) to each of them (Akisue et al., 2018). Bhandari et al. (2016) simulated the combustion control of a low pressure (20 kgf/cm²) and low capacity (30 t/h) coal boiler using fuzzy logic, and applied this strategy to the equipment's PLC for testing during load variations. In another work, Li and Chang (1999) combined fuzzy logic control with neural networks in the combustion in coal-fired boilers. This approach aimed to adapt a base of membership functions and rules through a neural

network, from previous system responses, until the desired control performance was achieved. As mentioned, the works referenced in this document are based on the operation of coal boilers. No references were found in the literature on the use of fuzzy logic for the combustion control of sugarcane bagasse-fired boilers, especially high pressure (above 65 bar) and high steam throughput (from 200 t/h) boilers. The present work aims to fill this gap, with the implementation of a fuzzy logic controller in the combustion control loop of a bagasse-fired boiler with 67 bar pressure and 200 t/h of steam throughput.

3. Methodology

The implementation of the closed loop oxygen control, controller tuning and data collection was performed in a high-pressure boiler with an oxygen analyzer at the flue gas outlet. The boiler used in this work, model ZS-2T-200/67-525, is a ZANINI-SERMATEC steam generator with a pin hole grate. It has water wall panels, single pass convection beam, two drums supported by the top of the metal structure, with natural circulation and a bagasse burning system in suspension.

Among the boiler's main control loops is the combustion control: variable frequency drives on primary and secondary air fans adjust the airflow based on the air/bagasse curve, in order to guarantee the required excess air under different operating regimes. The air/bagasse curve operates according to a curve determined by the manufacturer. This curve is corrected by an oxygen control loop by fuzzy logic, which was implanted as object of the present work.

The gas analyzer installed in the boiler is the EL3040 model, manufactured by ABB. It consists of two probes, one infrared probe Uras26 for CO analysis, and the other an electrochemical probe Endura AZ20 for O₂ analysis. The O₂ sensor, object of this work, is based on a zirconium oxide cell. This cell is mounted on the tip of the probe that is inserted into the gas duct. The oxygen concentration in the effluent gases is measured using an in situ wet analysis method. The output signal generated by the zirconium cell is processed in the transmitter, providing a local O₂ reading and a 4-20 mA retransmission signal covering the 0-100% O₂ range.

The plant's main control system is Emerson's DeltaV[®]. It has development tools that allowed the addition of fuzzy logic blocks to the oxygen control loop, and a tuning application (DeltaV Insight[®]) adjust the scaling factors. All data was stored using OSIsoft's PI System[®].

The controller uses, as input signals, the error and change in error of the O₂ concentration, and the change of the control action for correcting the air/bagasse curve as the output signal (input and output linguistic variables). The relationships between these three variables represent a nonlinear controller. The two linguistic values for error and change in error are Negative and Positive. For the output change, a third linguistic value, Zero, is added. The values of error and change in error, along with the membership scaling, respectively, S_e and $S_{\Delta e}$, determine the degree of membership (memberships to Negative linguistic values are maximum for $-S_e$ and $-S_{\Delta e}$; memberships to Positive linguistic values are maximum for $+S_e$ and $+S_{\Delta e}$). The membership functions of the output change are singletons. A singleton represents a fuzzy set whose support is a single point with a membership function equal to 1. Singletons are usually employed in the industry for output changer in order to simplify the computational demand for defuzzification, since they eliminate the need for numerical integration. The membership scaling ($S_{\Delta u}$) determines the magnitude of the output change, positive or negative, for a given error and change in error. There are four

fuzzy logic rules that the controller uses for a reverse control action. These rules are described in Table 1, with N, P and ZO being Negative, Positive and Zero, respectively.

Table 1. Fuzzy logic rules in DeltaV.

Rule 1	If error is N and change in error is N, make change in output P.
Rule 2	If error is N and change in error is P, make change in output ZO.
Rule 3	If error is P and change in error is N, make change in output ZO.
Rule 4	If error is P and change in error is P, make change in output N.

Tuning can be used to establish the scaling factors (Se , $S\Delta e$ and $S\Delta u$). For small control errors and setpoint changes smaller than a nominal value (ΔY_{sp}), the scaling factors of the fuzzy controller are related to the proportional gain (K_p) and the integral time (T_i) that would be used in a PI block being executed with a scan time (Δt) of 1 second to control the same process. Those relationships are expressed in Eq. (1), (2) and (3).

$$S\Delta e = \beta \Delta Y_{SP} \quad (1)$$

$$S\Delta u = 2S\Delta e K_p \quad (2)$$

$$Se = Se_0 = T_i S\Delta e \quad (3)$$

Where:

$S\Delta e$	=	change in error scaling factor
Se	=	error scaling factor
$S\Delta u$	=	change in output scaling factor
Se_0	=	error scaling factor for a 1 second scan time

Beta is a function of the process dead time and time constant, and ranges between 0.2 and 0.5. The nominal setpoint change value for ΔY_{sp} is 1%. When the change in setpoint is higher than the nominal setpoint change value (ΔY_{sp}), scaling factors are internally augmented by the FLC block.

Once a control loop is set up to govern a process, it needs to be tuned. The tuning application used in this work applies an on-demand process test to provide tuning recommendations automatically. This on-demand tuning is based on Aström-Hägglund's patented algorithm to calculate the tuning parameters of a closed loop (Aström and Hägglund, 1988). Emerson enhanced this algorithm with the incorporation of a patented technique to identify the process' dead time. During tuning, the output of the controller is determined by a known function that acts as a relay with hysteresis. This relay provides a two-state control and causes a process oscillation with a small, controlled amplitude. From the amplitude and frequency of this oscillation, the tuning software calculates the process' critical gain and critical time. The controller parameters are then computed based on the classical Ziegler-Nichols' rules.

To follow the process variable, manipulated variable and setpoint of the boiler's combustion control loop, OSIsoft's PI System[®] was used. It is a Plant Information Management System (PIMS), used for plant information management, which collects process data residing in distinct sources and stores it in a single database.

4. Results

After the construction of the oxygen control loop with the FLC block (fuzzy logic controller) and the implementation in the DCS (distributed control system), the combustion control loop was switched to automatic. After starting the operation with this new strategy, the tuner was used to obtain the controller's scaling factors. This step resulted in the following recommendation of scaling factors of the membership functions for the linguistic variables error, change in error and change in output:

- Se (error) = 28.74%; $S\Delta e$ (change in error) = 0.4%; $S\Delta u$ (change in output) = 0.68

The controller's parameters recommended by the tuning were updated in the DCS, and the controller returned its operating mode to automatic. A specialized company carried out a combustion regulation of the ZS-2T-200 boiler, measuring gas concentration (O_2 , CO and CO_2) at various points in the circuit with portable analyzers, as well as an evaluation of the inlet and exhaust fans. A 2.5% setpoint for the O_2 concentration in the boiler effluent was recommended due to an offset of 2 percentage points caused by the probe's position. This corresponds to a 4.5% O_2 content in the center of the gas duct.

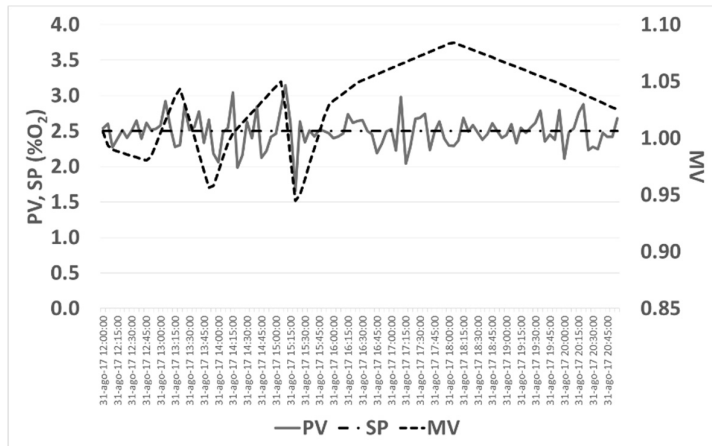


Figure 1. History data from eight operating hours with flue gas' oxygen control loop in automatic mode with the fuzzy controller. PV, SP data on left axis, and MV on the right axis. Source: PI System.

Figure 1 shows the historical data of setpoint (SP), process variable (PV) and manipulated variable (MV) during eight hours of operation of the boiler with the control loop in automatic. During this period, the setpoint was set at 2.5% and the variability of the PV (regulatory control) was evaluated. The mean value of PV in this period was 2.49%, with a standard deviation of 0.22. This deviation represents a variation of $\pm 1.2\%$ in the excess air coefficient. One can also observe, in Figure 1, that the MV acted without saturation during the entire period.

After eight hours of automatic operation with fixed setpoint, tests were performed to evaluate the controller's performance to setpoint changes (servo control), and to maintain the new setpoint values. Figure 2 shows the total interval of 24 hours of testing between servo and regulatory controls. After twenty-four hours of continuous operation, regulatory and servo controls were able to keep the desired setpoint with low variability ($\pm 1.2\%$ variation in excess air coefficient) and respond to setpoint changes with good response speed (1.5-20 minutes) and overshoot (8-56%).

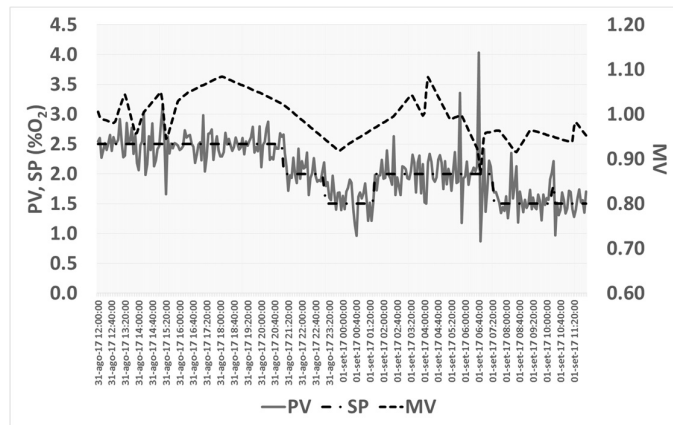


Figure 2. Controller's performance test in servo and regulatory modes over 24 hours. PV, SP data on left axis, and MV on the right axis. Source: PI System.

Compared to previous PID and manual control results (de Mello, 2018) from Tereos, it was observed 40% less variability than the PID controller, and 69% less variability than operation in manual mode.

5. Conclusions

The implementation of a closed loop oxygen control, controller tuning and data collection was performed in a high-pressure boiler with an oxygen analyzer at the flue gas outlet. Results presented here demonstrate the applicability of fuzzy control for combustion in boilers on sugarcane bagasse.

References

- R. A. Akisue, A. C. L. Horta and R. Sousa Jr., 2018, Development of a fuzzy system for dissolved oxygen control in a recombinant *Escherichia coli* cultivation for heterologous protein expression, *Computer Aided Chemical Engineering*, v. 43, p. 1129-1134.
- K. J. Aström and T. Hägglund, 1988, *Automatic Tuning of PID Controllers*, ISA, RTP.
- S. S. Bhandari, P. Makwana and D. K. Maghade, 2016, Solid fuel fired boiler combustion control using fuzzy logic algorithm, *ICACDOT*, Pune, India, p. 473-476.
- W. Li and X. Chang, 1999, A neuro-fuzzy controller for a stoker-fired boiler, based on behavior modeling, *Control Engineering Practice*, v. 7, p. 469-481.
- F. M. de Mello, 2018. Controle nebuloso (“fuzzy”) aplicado à combustão em caldeiras a bagaço de cana. Master's Thesis. Federal University of São Carlos - Brazil.
- L. A. Zadeh, 1965, Fuzzy Sets, *Information and Control*, v. 8, n. 3, p. 338–353.

Acknowledgements

To Tereos and São Paulo Research Foundation, FAPESP (grant number 2011/51902-9).

Dynamics and Control of a Fully Heat-Integrated Complex Distillation Column

Manuel Rodríguez ^{a*}, Ignacio P. Fernández Arranz ^a

^a *Universidad Politécnica de Madrid, José Gutiérrez Abascal 2, 28006 Madrid, Spain*

Abstract

Distillation is the most widely used in the separation section of a process. It consumes an important amount of energy (close to 40 % of the energy of chemical process). Many different configurations to increase its thermodynamic efficiency have been proposed. In this paper a new distillation column configuration developed by Toyo Engineering Corporation called SuperHIDiC is analysed. This new column is simulated and compared with a conventional distillation column. Its dynamic performance and control structure performance are also analysed. Results show that SuperHIDiC achieves an important reduction in energy consumption and that a conventional control configuration can be used in order to have a stable operation.

Keywords: Heat integration, complex distillation, process control

1. Introduction

Energy consumption is one of the problems that our world faces in this century. In 2017 energy consumption increased 2.3 % versus 1.1 % increase in 2016 according to the Global Energy Statistical Yearbook 2018, and it is expected to expand by 30 % between today and 2040 as indicated by the International Energy Agency. United States energy consumption by use is depicted in Fig 1. industrial consumption amounts to more than 30 % of the total being almost half of it consumed in separation process being distillation the consumer of half of the energy of the separation processes (i.e. around 8 % of the total energy consumption in the U.S.).

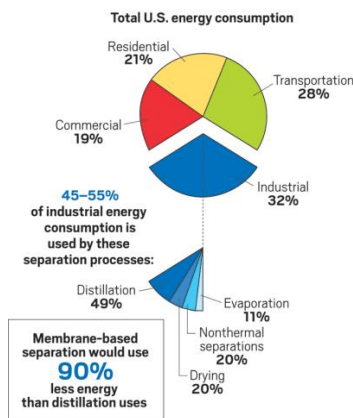


Figure 1. United States energy consumption (Ritter, 2017)

Conventional distillation is a very inefficient process in terms of energy, being its efficiency below 10 %. The idea of more efficient distillation columns is not new, in 1977 (Mah et al. 1977) proposed the first method to save energy through heat integration. In the following years based on Mah's idea, different researchers proposed and patented heat integrated distillation configurations like Seader (1980), Aso (1996), Nakaiwa (2000), etc. These types of columns called HIDiC (*Heat Integrated Distillation Column*) have been studied and its feasibility and profitability demonstrated for low relative volatility separations and tight product specifications (Leon Pulido et al., 2010). Although HIDiCs can achieve (theoretically) almost 60 % energy reduction, their use in industry is far from being high, mainly due to complex (and costly) construction and high maintenance costs. In this paper we explore a new HIDiC developed by Toyo Corp. denominated SuperHIDiC. Next section this new type of column is described, then a simulation of its performance and energy savings is presented, section four shows a dynamic model and a valid control structure and finally in the last section comments on the obtained conclusions.

2. SuperHIDiC column concept

SUPERHIDiC[®] is HIDiC configuration developed by Toyo Inc. In this setup the stripping and rectifying columns switch positions, being the stripping section at the top and the rectifying section at the bottom, side heat exchange is accomplished by thermo-siphon and/or gravity without pumping. The operating pressure in rectifying section is higher, this makes a transfer of the excess heat duty in the rectifying section to the stripping one possible. Fig 2. shows the configuration of the SuperHIDiC column.

Feed goes into the stripping section. This section operates only with the reboiler, and it has (at least) one side heat exchanger to take advantage of heat integration. The stream at the top of the column goes to a compressor and then exchanges heat before going to the rectifying column. This, high pressure, column operates only with the condenser and it has (at least) one side heat exchanger. The number of side heat exchangers, which can be up to five, depends on the type of separation and operating conditions. Reboiler and condenser duty are significantly reduced due to the heat integration achieved with the side heat exchangers. There is no need of special equipment, so maintenance can be conducted

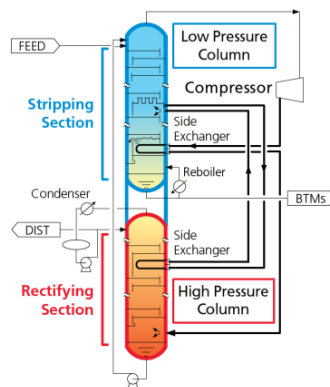


Figure 2. SuperHIDiC distillation column concept (Toyo Engineering, 2017)

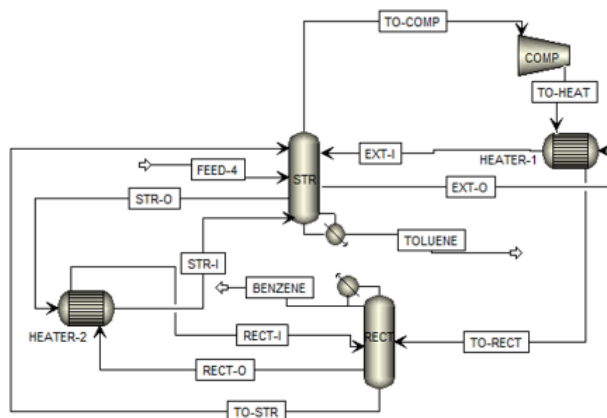


Figure 3. SuperHIDiC simulation configuration using Aspen Plus

by conventional means. Toyo engineers (Toyo Engineering Corporation, 2018) claim to achieve up to a 50 % energy reduction. Main applications are in installations where:

- Temperature difference between the overhead and the bottom is lower than 80 °C.
- Utilities are expensive.
- Condenser and/or reboiler duties are large.

3. SuperHIDiC Simulation

The system to separate using this technology is a stream composed of benzene and toluene. Feed composition is equimolar and its temperature and pressure are 94 °C and 100 kPa respectively. Total flow is 100 kmol/h. Molar purity of both products is 99.5 % molar. The fully heat integrated distillation column has been simulated using Aspen Plus as shown in Fig 3. and the physical properties packages used is RK-SOAVE. The configuration is equivalent to the SuperHIDiC column, it has two columns (stripping and rectifying) with side extractions to the heat exchangers.

The stripping column has 15 stages with side extractions in stages 4 and 13. The rectifying column has also 15 stages with a side stream in stage 4, it operates with a reflux ratio of 2.2. The compressor discharge pressure is 350 kPa.

Table 1. Energy consumption comparison between conventional distillation and SuperHIDiC

	CONVENTIONAL	SUPERHIDIC	REDUCTION (%)
CONDENSER	1.395 MW	0.951 MW	31.87
REBOILER	1.240 MW	0.619 MW	50.10
COMPRESSOR	-	0.275 MW	-
TOTAL	2.635 MW	1.844 MW	30.01

The separation has also been implemented using a conventional distillation column. The conventional column has 30 stages and it operates at a reflux ratio of 2. The obtained results show a significant reduction in energy consumption, see Table 1.

Around 32 % reduction in the condenser and a 50 % reduction in the reboiler. Adding the power needed for the compressor the overall reduction is 30 %, it appears that even considering the extra capital expenses of this new type of column, it can be a better option than the conventional approach. Besides other aspects should be considered as the environmental impact which is much lesser.

The energy savings are 0.791 MW, taking 8760 h/y the resulting annual energy savings are 6929.2 MWh. Considering an emission factor of 0.39 kg CO₂/kWh (Ministry of agriculture, 2018) the greenhouse gas emission reduction is 2702.4 t CO₂/y. The OPEX savings obtained considering an energy price of 52.24 €/MWh (OMIE, 2018) are 3.6M €/y.

4. SuperHIDiC Control

According to Toyo Inc. a conventional control structure allows for a stable operation of the distillation column. Pressure control in the stripping column is obtained manipulating compressor speed, and composition control is achieved through inference with temperature. In the rectifying column pressure is control with the condenser duty and distillate flow is also controlled. Inventories in both columns are controlled. This conventional control scheme shown in Fig 4.

It has been implemented in a dynamic simulation in order to check its validity. The simulation has been done with Aspen Dynamics (Fig 5.) using the steady state model developed previously and adding the dynamic information needed. Feed composition and feed flow disturbances have been applied to the process.

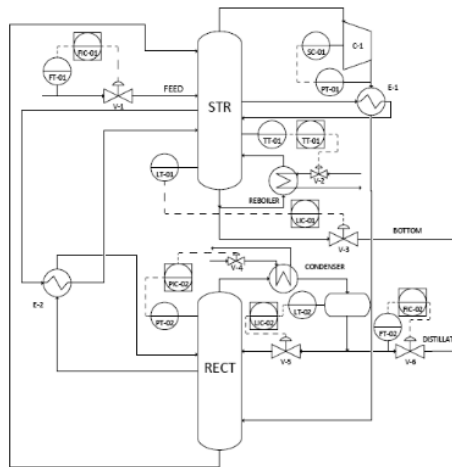


Figure 4. Control scheme to operate the heat integrated column

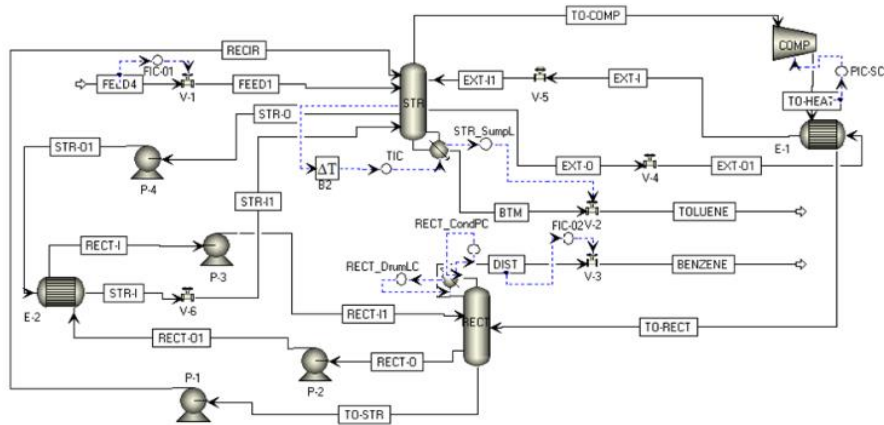


Figure 5. Dynamic simulation of the SuperHIDiC and its control structure

Fig 6. and 7 show the behaviour of the control system flow disturbance (changed from 100 kmol/h to 150 kmol/h which is higher than expected in a real plant as these columns are design for a turndown between 70-100%) and composition disturbance (change of 10% in benzene composition). Both are rejected and the control system exhibits good performance.

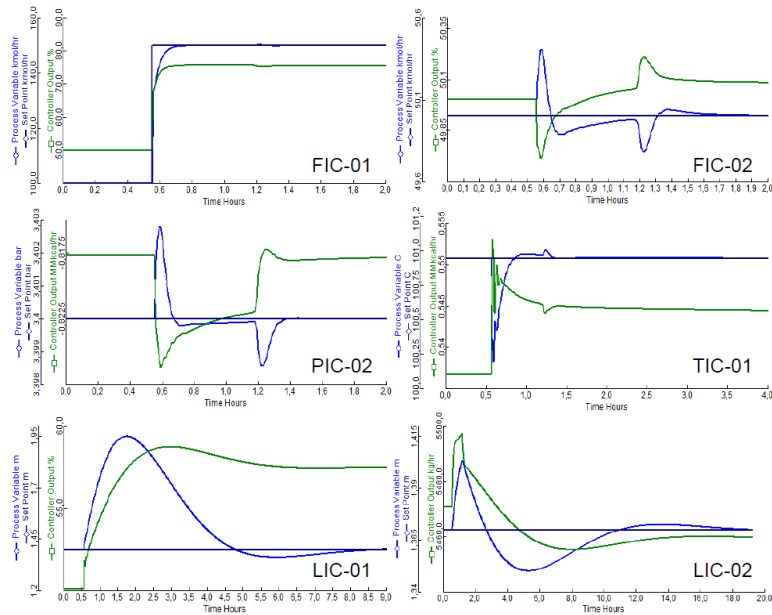


Figure 6. SuperHIDiC control performance under feed flow disturbance

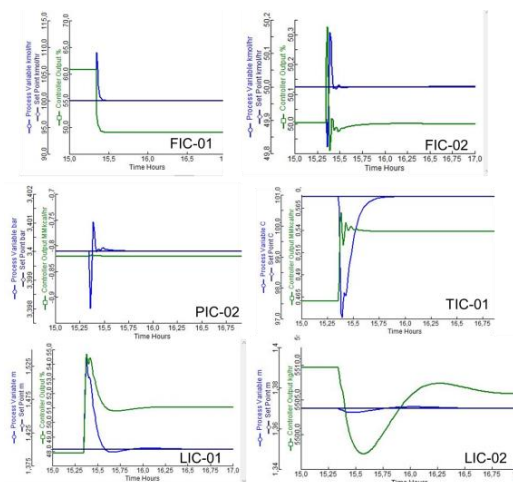


Figure 7. SuperHIDiC control performance under composition disturbance

5. Conclusions and further work

In this work a new distillation configuration to save energy consumption called SuperHIDiC has been tested. A comparison with a conventional distillation column results in significant energy savings (although not so high as claimed by the designers Toyo Inc.) and an important reduction in greenhouse gas emission. A dynamic simulation has also been implemented with its associated control structure. The conclusion is that a conventional control configuration allows good operation of the column. Further work will compare the capital expenses of this configuration with the conventional approach to have a complete economic comparison and will implement advanced control to the column to compare it with the conventional control scheme applied in this work.

References

- K. Aso, H. Matuso, T. Noda, N. Takada, N. Kobayashi, 1996. U.S. Patent n° 5.788.047.
- J. L. Pulido, M. W. Maciel, R. M. Filho, 2010. Nuevas perspectivas en procesos de separación: Simulación Columna de Destilación con Integración Interna de Calor. Revista ION, 7-12.
- R. Mah, J. Nicholas, R. Wodnik, 1977. Distillation with Secondary Reflux and Vaporization, a Comparative Evaluation. AIChE J, 651-658.
- Ministry of Agriculture, Fisheries and Food of Spain, 2018. Factores de Emisión: Registro de Huella de Carbono, Compensación y Proyectos de Absorción de Dióxido de Carbono.
- M. Nakaiwa, K. Huang, K. Naito, A. Endo, M. Owa, T. Akiya, T. Takamatsu, 2000. A New Configuration of Ideal Heat Integrated Distillation Columns. Computers and Chemical Engineering, 239 - 245.
- OMIE, 2017. Informe de Precios (Electricity price report, Spain).
- S.K. Ritter, 2017, Putting distillation out of business in the chemical industry, Chemical and Engineering News, vol. 95, 25, 18-21
- J. Seader, 1978, U.S. Patent n° 4.284.891.
- Toyo Engineering, 2017, Toyo Communications. TOYO TIMES, 10.
- Toyo Engineering Corporation, 2018, <http://www.toyoeng.com/jp/en/products/environment/superhidic/>

Optimal dose administration of renally excreted drugs

Giuseppe Pesenti, Adriana Savoca, Davide Manca*

*PSE-Lab, Dipartimento di Chimica, Materiali e Ingegneria Chimica "Giulio Natta"
Politecnico di Milano, Piazza Leonardo da Vinci 32, Milano 20133, Italy*

davide.manca@polimi.it

Abstract

The paper presents and discusses a basic pharmacokinetic model for vancomycin, an antibiotic that is principally excreted by kidneys. The model accounts for the degree of renal function by employing the CKD-EPI equation. Only one parameter of the model is identified by a nonlinear regression of experimental data, while the other parameters are evaluated *a priori* via correlations from the scientific literature.

We simulate the pharmacokinetic time-curves of vancomycin by accounting for different values of the glomerular filtration rate and show the strong influence of the degree of renal function on the drug pharmacokinetics. In addition, the model can be used to determine the optimal dose for patients featuring varying degrees of renal function. Results underline the importance of individualized treatment.

Keywords: pharmacokinetics, optimal dose, renal function, GFR, vancomycin.

1. Introduction

The assessment of the optimal dose for drug administration is a critical choice for clinical doctors and calls for considering the individual characteristics of patients. Since drugs are typically tested on healthy subjects, dosage guidelines and PK studies are often available for average healthy individuals. Conversely, in clinical practice, drugs are administered to ill and/or elderly patients, who often suffer from varying degrees of renal impairment. About 31% of administered drugs are mainly cleared by the kidneys (Varma et al., 2009). For these drugs, the patient's degree of renal function strongly affects the concentration profile of the drug and the administered dose is critical. The glomerular filtration rate (GFR) represents the volumetric flow of plasma that is filtered by the kidneys and is a useful measure to estimate the degree of renal function.

Renal function declines with age and may be further affected by renal diseases. Renal impairment is extremely common, even though a large fraction of people who suffer from it are unaware of their status (Girndt et al., 2016). Chronic kidney disease (CKD) at stages 3-5 is defined as a condition when $GFR < 60 \text{ mL/min/1.73 m}^2$ for 3 months. This corresponds to the loss of more than half of the normal kidney function. According to Hill et al. (2016), 10.6% of the general world population suffers from CKD at stages 3-5. For patients with renal impairment, drug dosage is often suboptimal and drug dosing errors are common (Kim et al., 2016), which trigger adverse effects and reduce life quality and life expectancy.

We developed a pharmacokinetic (PK) model that can be applied as a tool to determine the optimal dose of a drug that is mainly cleared via renal filtration. The optimal dose is personalized according to the individual characteristics of the patients, *i.e.* age, sex, height, weight, and serum creatinine levels. These parameters, in particular, allow

estimating GFR, and therefore the renal function, according to the CKD-EPI equation (Levey et al., 2009).

The PK model is applied to vancomycin, an antibiotic that is almost completely cleared by renal filtration and whose metabolism is negligible. Vancomycin is routinely administered in clinical settings especially to critically ill patients, who typically display heterogeneous characteristics and, in particular, an extremely wide range of degrees of renal function.

2. Methods

A rather simple PK model comprising only three compartments was developed to explicitly focus on renal function. The compartments (Figure 1) are (i) the global circulatory system, (ii) the renal circulatory system, and (iii) the other tissues.

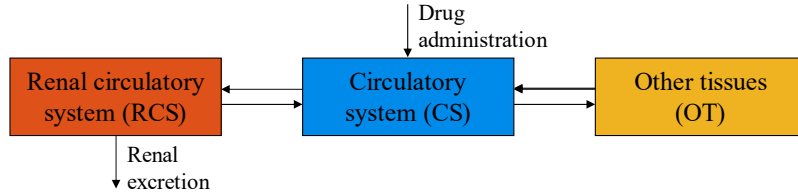


Figure 1 – Compartments of the PK model.

The global circulatory system (CS) involves the plasma contained in the whole circulatory system but the fraction that passes through the kidneys, which is described by the renal circulatory system (RCS) compartment. The third compartment lumps the other tissues and organs (OT) where the drug diffuses through the exchange between plasma and interstitial fluid at the capillaries.

The model consists of three ordinary differential equations (Eqs. 1-3) that quantify the material balances of vancomycin in each of the three compartments, including the exchange between them and the excretion due to renal filtration.

$$\begin{aligned} \frac{dm_{CS}}{dt} = & \dot{m}_W - \frac{Q_{CS \leftrightarrow RCS}}{V_{CS}} m_{CS} + \frac{Q_{CS \leftrightarrow RCS}}{V_{RCS}} m_{RCS} + \\ & - \frac{K_{CS \leftrightarrow OT}}{V_{CS}} m_{CS} (1-R) + \frac{K_{CS \leftrightarrow OT}}{V_{OT}} m_{OT} \end{aligned} \quad (1)$$

$$\frac{dm_{RCS}}{dt} = \frac{Q_{CS \leftrightarrow RCS}}{V_{CS}} m_{CS} - \frac{Q_{CS \leftrightarrow RCS}}{V_{RCS}} m_{RCS} - \frac{Q_{GFR}}{V_{RCS}} m_{RCS} (1-R) \quad (2)$$

$$\frac{dm_{OT}}{dt} = \frac{K_{CS \leftrightarrow OT}}{V_{CS}} m_{CS} (1-R) - \frac{K_{CS \leftrightarrow OT}}{V_{OT}} m_{OT} \quad (3)$$

m_{CS} , m_{RCS} and m_{OT} are the mass of drug (in mg) in the CS, RCS and OT compartments. \dot{m}_W is the intravenous (IV) infusion rate of vancomycin (in mg/h) administered to the patient, R is the fraction of vancomycin bound to blood proteins, $Q_{CS \leftrightarrow RCS}$ is the volumetric flow (mL/h) of plasma that reaches the kidneys, and $K_{CS \leftrightarrow OT}$ is a mass transfer

coefficient (mL/h) related to capillary exchange. Finally, V_{CS} , V_{RCS} , and V_{OT} are the volumes (mL) of plasma or interstitial fluid in the corresponding compartments.

Q_{GFR} is the volumetric GFR and is estimated via the CKD-EPI equation (Levey et al., 2009) as a function of sex, age, serum creatinine, and body surface area (BSA), which in turn depends on the height and weight of the patient. The plasma flow to the kidneys $Q_{CS \leftrightarrow RCS}$ is calculated as 19% of the overall cardiac output, which is estimated as $3.5 BSA$ (Cowles et al., 1971) multiplied by the average volumetric fraction of plasma in the blood, *i.e.* 0.53 for men and 0.58 for women.

The plasma volumes of CS and RCS are evaluated from the total mass of blood as a function of weight (Brown et al., 1997), its density (Vitello et al., 2014), and the fraction of blood that is contained in the RCS (Leggett et al., 1995). According to Butterfield et al. (2011), the average factor for vancomycin protein binding R is 0.415.

Since vancomycin poorly diffuses into bones, CNS, and lungs (Giuliano et al., 2010), these elements were excluded from the OT compartment. Following the approach of Abbiati et al. (2016), both mass and density of the overall OT compartment were estimated from Brown et al. (1997) as 70.3% of the total mass and 1.005 g/mL respectively. The OT compartment volume is estimated as their ratio.

The total flow exchanged at the capillaries is proportional to the global capillary exchange area and therefore to the number of capillaries in the body. Therefore, $K_{CS \leftrightarrow OT}$ is assumed to be proportional to the estimated OT compartment mass (Eq. 4).

$$K_{CS \leftrightarrow OT} = m_{OT} \cdot k_{CS \leftrightarrow OT}^m \quad (4)$$

For the sake of simplicity, we assume that $k_{CS \leftrightarrow OT}^m$ is constant for all the individuals and its value is identified via a nonlinear regression of clinical data. To minimize the distance between the simulated PK profiles and the measured values of vancomycin plasma concentration, the weighted sum of squared errors (SSE) between each experimental and simulated value j (over the N_i^{exp} values), for each patient i (over the N_p patients), is minimized (Eq. 5).

$$\min_{k_{CS \leftrightarrow OT}^m} SSE = \frac{1}{N_p} \min_{k_{CS \leftrightarrow OT}^m} \sum_{i=1}^{N_p} \left(\frac{1}{N_i^{exp}} \sum_{j=1}^{N_i^{exp}} \left(\frac{c_{CS,ij}^{sim} - c_{CS,ij}^{exp}}{c_{CS,ij}^{exp}} \right)^2 \right) \quad (5)$$

The proposed model is not a physiologically-based pharmacokinetic (PBPK) model, as it features a basic 3-compartment structure and lumps all the organs and tissues of the human body other than the kidneys in just one compartment. However, its description is consistent with the physiological processes in the human body and this allows determining quantitatively the whole set of model parameters but one, *i.e.* $k_{CS \leftrightarrow OT}^m$.

The experimental data were extracted from Turner et al. (2018), who published rich pharmacokinetic data of experimental vancomycin profiles for a heterogeneous population of critically ill patients in an intensive care unit (ICU). Vancomycin was administered with periodic infusions at a maximum rate of 1000 mg/h. Each patient received a different dose intravenously (in the range 500-1750 mg) over 0.7-2 h intervals. After a specific period (8, 12 or 24 h), a new cycle was repeated. The desired therapeutic target was to maintain vancomycin concentration above the 15-20 mg/L threshold for the whole time interval. This target, called trough concentration, can be achieved with periodic infusions (*e.g.*, 0.7-2 h) over long time intervals (*e.g.*, 8-24 h) as the elimination

half-life of vancomycin is about 6-12 h (Rybak, 2006).

The initial values of CS concentration were linearly extrapolated from the two initial experimental points in Turner et al. (2018), and the initial RCS concentration was approximated with the CS one (due to the lack of further details in the experimental data). As far as the initial OT concentration values are concerned, the experimental points were collected from patients that had already received at least three successive vancomycin doses. To estimate the accumulation of vancomycin in the OT compartment, three consecutive cycles were simulated, each time using the final OT concentration as the next OT initial condition for the following simulation to achieve a plausible initial value.

3. Results

The regression was performed using the data of five patients from Turner et al. (2018) and yielded a value of 843.68 mL/h/kg for $k_{CS \leftrightarrow OT}^m$. For the sake of space, Figures 2 (a-c) show the simulated concentration profiles in CS, RCS, and OT and the experimental CS measures of three of the patients. As SSE (the average squared relative error for each experimental point, see also Eq. 5) is pretty low (0.1440), the regression is considered successful. Accordingly, Figures 2 (a-c) show a good fit of the experimental data. Figure 2 (d) shows the simulated time-profiles of drug mass over the three compartments for just one patient.

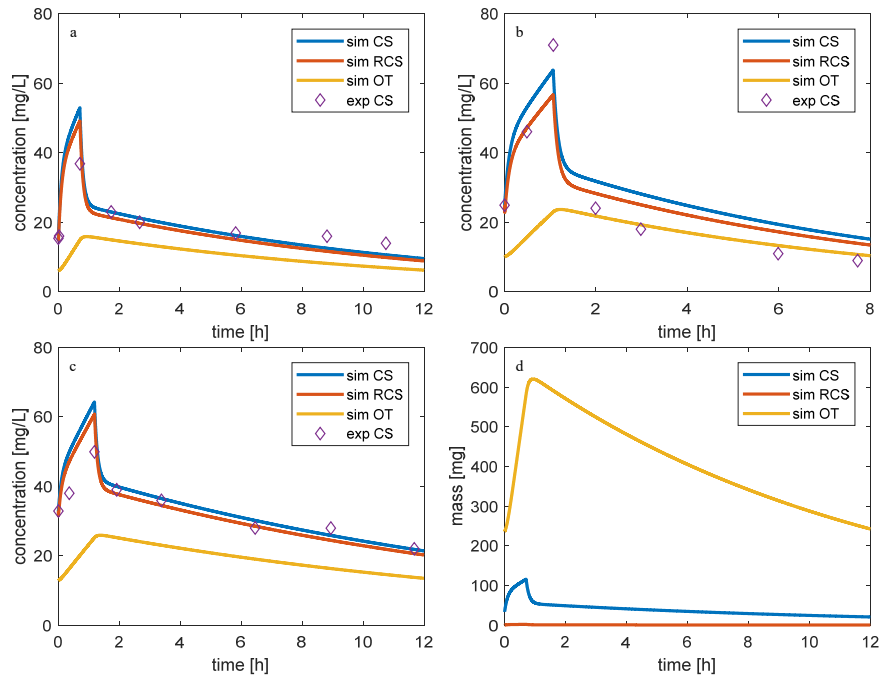


Figure 2 – (a-c) Simulated and experimental vancomycin concentration for patients #1-3. (d) Simulated mass profiles in the three compartments of the PK model for patient #1.

Once successfully identified, the model was employed to investigate the effect of the degree of renal function. Thus, we simulated the CS concentration dynamics of a specific

virtual patient for a fixed vancomycin dose at different GFR degrees. The simulated individual was determined from the average characteristics of the abovementioned 5 patients: male, 57.8 years old, 85 kg, and 174 cm. This virtual patient received an infusion of 1000 mg over 1 h. The initial values of CS and RCS were assumed equal to 20 mg/L, whereas the initial OT concentration was estimated by simulating three previous cycles. The simulated GFR range (29-199 mL/min) is the same of patients from Turner et al. (2018), estimated according to the CKD-EPI equation. The results highlight simulated curves which vary widely for different values of GFR, as shown in Figure 3. In case of the highest GFR considered, for example, the peak and trough concentrations are 46.72 and 10.40 mg/L respectively, whereas in case of the lowest GFR they are 88.58 and 55.98 mg/L. It is worth observing that the simulated dose does not allow respecting the target trough concentration in case of the two highest GFR values, whereas it would lead to excessive vancomycin levels for the two patients with the lowest GFR. Horey et al. (2012) report a significant occurrence of nephrotoxicity (81.8%) when trough levels are higher than 35 mg/L.

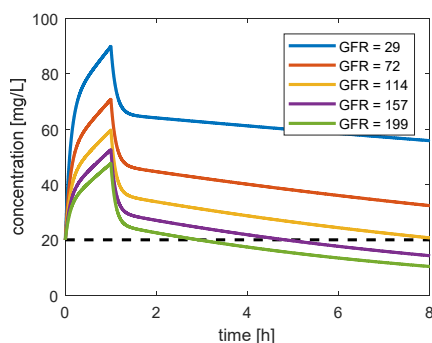


Figure 3 – Simulated plasma concentration of vancomycin for a virtual averaged patient as a function of their GFR (mL/min). The horizontal dashed line is the target trough concentration.

Finally, the PK model is used to find the optimal dose for the averaged individual, as a function of their GFR. A fixed infusion rate of 1000 mg/h is administered *in silico* for a varying time interval, with a period of 8 h between consecutive infusions. As in previous cases, we assume that the patient has already undergone three cycles and starts with an initial CS concentration of 20 mg/L. The dose is optimized individually so that the CS concentration at the end of the simulated interval is equal to 20 mg/L, which guarantees the target trough concentration. Table 1 reports the optimal doses, which display a marked difference (a ratio higher than 6) between the highest and lowest quantities of vancomycin to be administered. Over 24 h, the simulated doses cover the 924-5667 mg range, which is comparable with the 1000-5250 mg range reported in Turner et al. (2018).

Table 1 – Optimal vancomycin doses for a virtual averaged patient as a function of their renal function (estimated via GFR).

GFR [mL/min]	29	72	114	157	199
Optimal dose [mg]	308.0	593.9	964.6	1403.8	1889.0

4. Conclusions

Whenever renally-excreted drugs are concerned, the degree of renal function must be taken into account to determine the optimal dose for individual administration. In fact, as

shown in Figure 3, the degree of renal function dramatically influences the drug concentration profile. The administered drug dosages can be optimized for each patient according to their bodily characteristics (*i.e.* sex, age, weight, and height) and serum creatinine, by employing suitable PK models, which can lead to improved compliance with therapeutic targets and reduced side effects by avoiding excessive drug concentrations. The proposed PK model allows medical doctors improving the design of personalized clinical treatments.

References

- Abbiati, R.A., Lamberti, G., Grassi, M., Trotta, F., Manca, D. (2016). Definition and validation of a patient-individualized physiologically-based pharmacokinetic model. *Comput. Chem. Eng.* 1/4;84:394-408.
- Brown, R.P., Delp, M.D., Lindstedt, S.L., Rhomberg, L.R., Beliles, R.P. (1997) Physiological parameter values for physiologically based pharmacokinetic models. *Toxicol. Ind. Health* 13(4):407-84.
- Butterfield, J.M., Patel, N., Pai, M.P., Rosano, T.G., Drusano, G.L., Lodise, T.P. (2011). Refining Vancomycin Protein Binding Estimates: Identification of Clinical Factors That Influence Protein Binding. *Antimicrob Agents Chemother. Sep*; 55(9): 4277–4282.
- Cowles, A.L., Borgstedt, H.H., Gillies, A.J. (1971). Tissue Weights and Rates of Blood Flow in Man for the Prediction of Anesthetic Uptake and Distribution. *Anesthesiology*. November 1;35(5):523-6.
- Girndt, M., Trocchi, P., Scheidt-Nave, C., Markau, S., Stang, A. (2016). The Prevalence of Renal Failure. Results from the German Health Interview and Examination Survey for Adults, 2008-2011 (DEGS1). *Dtsch Arztebl Int.* Feb 12;113(6):85-91.
- Giuliano, C., Haase, K.K., Hall, R. (2010). Use of vancomycin pharmacokinetic-pharmacodynamic properties in the treatment of MRSA infections. *Expert Rev Anti Infect Ther.* Jan;8(1):95-106.
- Hill, N.R., Fatoba, S.T., Oke, J.L., Hirst, J.A., O'Callaghan, C.A., Lasserson, D.S., Lasserson, D.S. (2016). Global Prevalence of Chronic Kidney Disease – A Systematic Review and Meta-Analysis. *PLoS ONE* 11(7): e0158765.
- Horey, A., Mergenhagen, K.A., Mattappallil, A. (2012). The Relationship of nephrotoxicity to vancomycin trough serum concentrations in a veteran's population: a retrospective analysis. *Ann Pharmacother.* Nov;46(11):1477-83.
- Kim, G.J., Je, N.K., Kim, D.S., Lee, S. (2016). Adherence with renal dosing recommendations in outpatients undergoing haemodialysis. *Journal of Clinical Pharmacy and Therapeutics*, 41, 26–33.
- Leggett, R., Williams, L., Eckerman, K. (1995). A Proposed Blood Circulation Model for Reference Man. *Health Physics* 69(2):187-201.
- Levey, A.S., Stevens, L.A., Schmid, C.H., Zhang, Y.L., Castro, A.F., Feldman, H.I., Kusek, J.W., Eggers, P., Van Lente, F., Greene, T., Coresh, C. (2009). A New Equation to Estimate Glomerular Filtration Rate. *Ann Intern Med.* May 5; 150(9): 604–612.
- Rybak, M.J. (2006). The Pharmacokinetic and Pharmacodynamic Properties of Vancomycin. *Clinical Infectious Diseases*; 42:S35–9.
- Turner, R.B., Kojiro, K., Won, R., Chang, E., Chan, D., Elbarbry, F. (2018). Prospective evaluation of vancomycin pharmacokinetics in a heterogeneous critically ill population, *Diagn. Microbiol. Infect. Dis.*, <https://doi.org/10.1016/j.diagmicrobio.2018.06.022>
- Varma, M.V.S., Feng, B., Obach, R.S., Troutman, M.D., Chupka, J., Miller, H.R., El-Kattan, A. (2009). Physicochemical Determinants of Human Renal Clearance. *J. Med. Chem.* 52, 4844–4852.
- Vitello, D.J., Ripper, R.M., Fettiplace, M.R., Weinberg, G.L., Vitello, J.M. (2014). Blood Density Is Nearly Equal to Water Density: A Validation Study of the Gravimetric Method of Measuring Intraoperative Blood Loss. *Journal of veterinary medicine* 12/01;2015:152730.

Automating HAZOP studies using D-higraphs

Borja Martínez,^a Manuel Rodríguez,^{a*} Ismael Díaz,^a

^a *Universidad Politécnica de Madrid, José Gutiérrez Abascal 2, 28006 Madrid, Spain*

Abstract

In this paper we present a methodology to perform guided HAZOP studies using a functional modelling framework: D-higraphs. It is a formalism that gathers in a single model the functional as well as the structural information about the process considered of any given system. This tool uses an expert system to predict the behaviour of the modelled process in order to achieve a semi-automatic and systematic HAZOP analysis. In this paper it is applied to an industrial case showing the easy understanding of the proposed methodology and comparing the obtained results to those obtained conducting the HAZOP study in the conventional way.

Keywords: Functional modelling; HAZOP; Risk assessment.

1. Introduction

Throughout the history of the process industry there have been a lot of important aspects to be considered in the consequences of accidents: environmental impact, pollution, operators' occupational health and economy. This situation can involve lots of losses associated to shutdowns, reparations, compensations or fines, so avoiding accidents is not only a direct way to save money on losses, but also the incomes are increased because productivity does (De la Mata and Rodríguez, 2010).

According to the design stage of the process plant, Process Hazard Analyses (PHA) are carried out to identify the potential safety problems in order to provide possible solutions that enhance the safety of the plant, such as process changes, new control strategies or the use of safety instrumentation. There are a broad variety of methods but the most widely used is the Hazard and Operability Study (HAZOP) (Zhao et al., 2005). However, this technique consumes a lot of time an effort, so in the last decades a lot of work and resources have been put to develop tools and methodologies that automate this process.

Some of these tools are HAZOPEXpert (Venkatasubramanian et al., 2000), PHASuite (Zhao et al., 2005), Functional HAZOP assistant (Rossing et al., 2010a, 2010b), Layered Digraph Model (Cui et al., 2008) and PetroHAZOP (Zhao et al., 2009).

In order to do this automation, expert systems (or production rule systems) are used to perform calculations functions of the causes and consequences due to a possible deviation that happened in the process, with a view to understand the severity of the situation.

In this work a new HAZOP assistant is developed based on a modelling technique called D-higraphs, which considers structural and functional information of the system under analysis. This methodology has been implemented using a production rule system called CLIPS (CLIPS, 2018). It has been applied to a standard scenario and its results are compared to those obtained doing the HAZOP study as usual.

2. D-higraphs: merging function and structure

2.1. Dualization: from Higraphs to D-higraphs

Higraphs are a general kind of diagramming objects well suited to specify the behavior of complex concurrent systems but not process system (Harel, 1987).

On the other hand, D-higraphs are an adaptation of Higraphs that consist of blobs, representing transitions, and edges, representing states. This adaptation of Higraphs was first presented in Rodríguez and Sanz (2009) as a modeling technique that merges functional and structural information of the system modeled.

It has to be noted that a D-higraphs is not a dual higraphs, obtained from changing blobs by edges and edges by blobs. The duality lies in their interpretation and properties.

2.2. Elements of a D-higraphs: Blobs and Edges

The two main elements of a D-higraphs are depicted in Figure 1, where the basic blob is represented in the left-hand-side, and the different types of edges are shown in the center. Blobs represent functions that are performed by an ACTOR producing state 2 if state 1 is enabled. Edges represent flows of mass, energy, or information, which are responsible of the interactions in a process system (Lind, 1994). The main properties of blobs and edges are described in De la Mata and Rodríguez (2010).

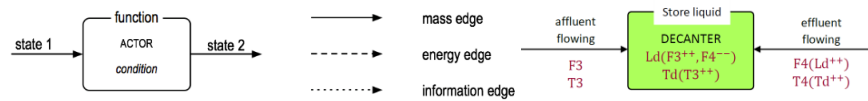


Figure 1. Basic blob and different types of edges.

2.3. Causal and qualitative reasoning

D-higraphs integrate a series of causation rules relating two events that allow us to track the evolution of failures across the system. These rules combined with sensor data of the plant enables the performance of Fault Detection and Isolation analysis using D-higraphs. However, certain analyses require the use of deviations and not only failures, like HAZOP studies. In a certain way, we need to simulate qualitatively the system in order to propagate these deviations. The description of a system is made in three different layers (Kuipers, 1984):

1. *Structural description*: described by variables, such as flow (F), pressure (P), temperature (T), composition (x), energy (E), information (I), level (L), valve opening (A), etc.
2. *Behavioral description*: potential behavior of the system as a network. The M^+ and M^- constraints (Kuipers, 1986) provide this information, but in some behaviors they need to be modified according to: M^{++} , M^{0+} , M^{+-} , M^{-0} , M^{00} , M^{-0} , M^{+0} , M^{0-} y M^{-} . The first sign shows the monotonicity for values under the expected one, and the other sign does for values above it. In Figure 2 some examples are shown.
3. *Functional description*: describes the purpose of a structural component and its connections provided by the D-higraphs layout.

The three layers of this representation are shown in the right-hand-side of Figure 1, where there is a physical device (DECANTER) whose main purpose is to *store liquid*. The decanter has two characteristic variables: level (Ld) and temperature (Td). Ld is affected by the inflow F3 with variations of the same sign (an increment of F3 increases Ld) and by the outflow F4 in the opposite way. In the same way, the flow F4 is affected by the level of the decanter in the same direction.

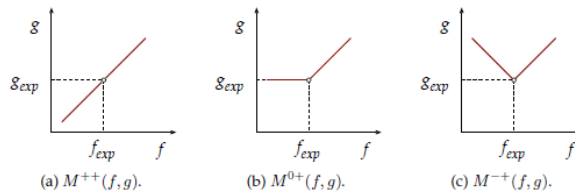


Figure 2. Some examples of the M constraints (De la Mata and Rodríguez, 2010).

3. D-higraphs and the CLIPS environment

The D-higraphs models are implemented using a graphic tool that has as input the P&ID of the process and it uses a D-higraphs built using a template (Álvarez, 2010). Once the model has been developed, it is loaded into the expert system that obtains the report of the deviation thanks to the rule database. The HAZOP study is performed feeding the deviations to the reasoning engine. The result of the analysis is provided to the user and it can be fed back in order to make changes into the process or D-higraphs.

CLIPS is the expert system that performs the analysis by entering the command “Assert” followed by the desired deviation, which is formed with a HAZOP guide word, and the process variable.

4. Case study

In this section, we present the oil vaporizer unit, which is designed to achieve superheated oil vapor from oil liquid, due to a furnace containing a heating coil and burners, where the natural gas combines with air to burn (BS IEC 61882:2001). To that end, this process uses two control loops: the first one has the goal to regulate the incoming oil flow, besides a low flow alarm of liquid oil, and the second one deals with the temperature of the outgoing vaporized oil flow manipulating the flow of natural gas to the burners. In addition to these control loops, there is an auto regulated valve that controls the pressure of the natural gas flow. A simplified P&ID of the unit is shown in Figure 3.

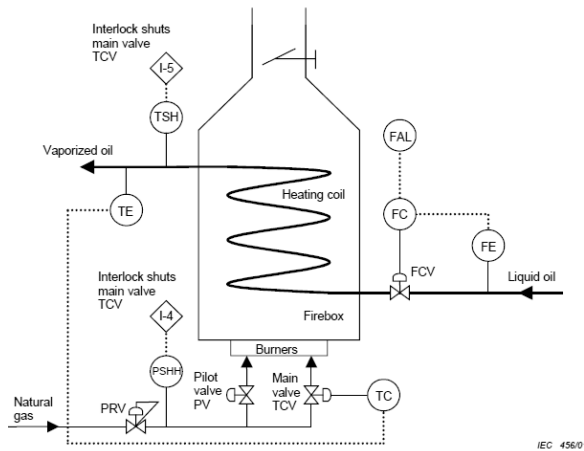


Figure 3. Oil vaporizer unit (BS IEC 61882:2001).

4.1. Functional decomposition

The main goal of the overall unit is to obtain oil vapor from the combustion between natural gas and external air, as said in the process description. To that end, the system can be decomposed into two subsystems that perform the necessary subgoals, in the following way: (1) Oil flow section: provide a constant feed of liquid oil and emerges vapor flow under operation conditions; (2) Burners section: provide through combustion the needed heat to vaporize the oil. This functional decomposition can be continued until the desired level of detail is obtained. Thanks to that and the P&ID, the D-higraphs can be developed. It is shown in Figure 4.

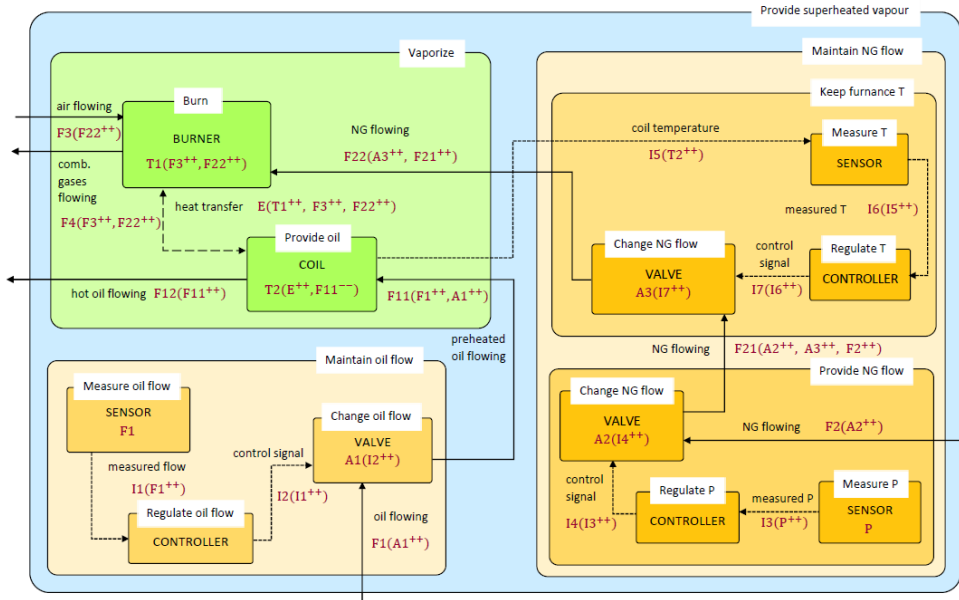


Figure 4. D-higraphs.

5. Hazop and D-higraphs results

In this section the results obtained for “No oil flow” deviation are shown. This deviation consists of the variable “oil flow” that passes through the heating coil and the HAZOP guide word “no”. It should be noted that due to space constraints, only this deviation is shown, but the complete study has been conducted, applying all the HAZOP deviations.

5.1. HAZOP analysis

A modified table of the HAZOP report obtained for the case study is featured below in Table 1. It shows relevant details, such as the HAZOP team, the considered part of the process, the design intent and the deviation, which is where we focus on this paper. The HAZOP team points out that the main reasons for the lack of flow are due to a failure of the supply line, the flow control valve FCV or a failure of the vaporizer.

At the same time, the possible consequences of this deviation are reflected, where the overheating of the vaporizer is highlighted, as well as the safeguards and the actions required as preventive measures.

Table 1. Example HAZOP worksheet. No oil flow deviation (BS IEC 61882:2001).

STUDY TITLE: OIL VAPORIZER									
Drawing No. :					REVISION No.:			DATE:	
TEAM COMPOSITION: MG, NE, DH, EK, LB					MEETING DATE:				
PART CONSIDERED: Vaporizer coil from oil inlet (before flow measurement), to vapour exit to process (after temperature control)					DESIGN INTENT: Inputs: Oil flow from the feed line, heat from the furnace Activities: Vaporize, superheat and transfer oil vapour to the process				
No.	Guide word	Element	Deviation	Possible causes	Consequences	Safeguards	Comments	Actions required	Action by
1	No	Oil flow	No oil flow	- Supply failure - Flow control valve PCV closed	Vaporizer coil overheats and may fail	Low flow alarm FAL High temperature trip TSH	Safeguard depends on quick operator response	Consider low flow element FE to close main burner valve TCV	LB
				- Plugging of coil - Blockage downstream of vaporizer	Oil in vaporizer will boil: Possible overheating and coking of heating coil	Low flow alarm FAL High temperature trip TSH		Check whether these safeguards are adequate and the ease with which the coil could be cleaned	NE

5.2. D-higraphs - CLIPS analysis

As it has been said before, once the topology and the rules of causes or consequences have been loaded, the analysis begins. For this, the “Assert” command is used, followed by the guide Word “No” (“Fail”, in CLIPS) and the parameter “oil flow” (“hot_oil_flow”). It is necessary to specify whether this variable belongs to an edge or blob. The CLIPS report is featured below.

CAUSES

```
CLIPS> (assert (Report))
<Fact-1>
CLIPS> (assert (Fail edge
[hot_oil_flow]))
<Fact-2>
CLIPS> (run)
```

The causative Edges are:

```
[preheated_oil_flow]
[heat_transfer]
[air_flow]
[NG_flow]
[measured_T]
[NG_flow]
[control_signal]
[NG_flow]
[measured_P]
[control_signal]
[coil_temperature]
[control_signal]
[oil_flow]
[measured_flow]
```

The causative Blobs are:

```
[PROVIDE_OIL]
[BURN]
[CHANGE_NG_FLOW]
[CHANGE_NG_FLOW]
[REGULATE_P]
[MEASURE_P]
[REGULATE_T]
[MEASURE_T]
[PROVIDE_OIL]
[CHANGE_OIL_FLOW]
[REGULATE_OIL_FLOW]
[MEASURE_OIL_FLOW]
```

CONSEQUENCES

```
CLIPS> (assert (Report))
<Fact-1>
CLIPS> (assert (Fail edge
[hot_oil_flow]))
<Fact-2>
CLIPS> (run)
```

The affected Edges are:

```
[hot_oil_flow]
[coil_temperature]
[measured_T]
[control_signal]
[NG_flow]
[comb_gases_flow]
[heat_transfer]
```

The affected Blobs are:

```
[PROVIDE_OIL]
[VAPORIZE]
[MEASURE_T]
[REGULATE_T]
[KEEP_FURNACE_T]
[CHANGE_NG_FLOW]
[BURN]
```

There have been double fail in:

```
[PROVIDE_OIL]
```

There have been triple fail in:

```
[hot_oil_flow]
[coil_temperature]
[MEASURE_T]
[PROVIDE_OIL]
```

There have been quadruple fail in:

```
[measured_T]
[hot_oil_flow]
[coil_temperature]
```

The Hazard Level of this fail is: 14

5.3. Comparing the results

According to the results, CLIPS is useful to show all those edges and blobs that are involved in the contingency created and it also lists a series of devices that are not present in the HAZOP report. However, CLIPS does not go into much detail of the type of failure. That is why this methodology is only helpful to find possible sources, such as [BURN], where it warns that the cause can be due to a failure in the device that provides the energy to oil. In the same way it happens with the consequences, where it also highlights multiple failures in edges and blobs, implying that those devices have a high importance. This guided HAZOP can save a lot of time to the HAZOP team and avoid missing some causes or consequences as it follows every possible path in the process.

6. Conclusions and further work

In this paper we have presented a methodology to perform systematic guided HAZOP studies based on D-higraphs. It has been applied to an industrial process in order to show its applicability and compare a traditional HAZOP study with CLIPS. The results are easy to understand and helpful in order to broaden the field of analysis of the process, to make it more complete and deeper, increasing thus the security of the analysis. On the other hand, future work will be devoted to the implementation of a “translator”, which will transform P&IDs models to D-higraphs, avoiding the text template that can be a human error source, hindering its quick implementation. In addition, the rules of causes and consequences should be analysed to give more depth in the analysis of each HAZOP guide word and to increase the level of detail in the CLIPS report.

References

- Álvarez, M. E. 2010. Diagnosis de fallos en procesos químicos mediante modelos D-higraph. Final Project. Department of Chemical Engineering, Technical University of Madrid.
- British Standard IEC 61882:2001. Hazard and operability studies (HAZOP studies) – Application guide, 52.
- CLIPS. 2018. CLIPS, A Tool for Building Expert Systems. <http://clipsrules.sourceforge.net>
- Cui, L., Zhao, J., Qiu, T., & Chen, B. 2008. Layered digraph model for HAZOP analysis of chemical processes. *Process Safety Progress*, 27(4), 293–305.
- De la Mata, J. L., Rodríguez, M. 2010. Abnormal situation diagnosis using D-higraphs. *Proc. of the 20th European Symposium on Computer Aided Process Engineering*, pp. 1477-1482.
- Harel, D. 1987. Statecharts: A visual formalism for complex systems. *Sci. Comput. Program.*, 8.
- Kuipers, B. 1984. Commonsense reasoning about causality. *Artificial Intelligence*, 24.
- Kuipers, B. 1986. Qualitative simulation. *Artificial Intelligence*, 29.
- Lind, M. 1994. Modeling goals and functions of complex Industrial plant. *Applied Artificial Intelligence*, 8 (2).
- Rodríguez, M., Sanz, R. 2009. Development of integrated functional-structural models. *Computer Aided Process Engineering*, 27.
- Rossing, N. L., Lind, M., Jensen, N., Jørgensen, S. B. 2010a. A functional HAZOP methodology. *Computers and Chemical Engineering*, 34 (2).
- Rossing, N. L., Lind, M., Jensen, N., & Jørgensen, S. B. 2010b. A goal based methodology for HAZOP analysis. *Nuclear Safety and Simulation*, 1(2).
- Venkatasubramanian, V., Zhao, C., Viswanathan, S. 2000. Intelligent systems for HAZOP analysis of complex process plants. *Computers and Chemical Engineering*, 24 (9-10).
- Zhao, C., Bhushan, M., & Venkatasubramanian, V. 2005. PHASuite: An Automated HAZOP Analysis Tool for Chemical Processes. *Process Safety and Environment Protection*, 83 (6).
- Zhao, J., Cui, L., Zhao, L., Qiu, T., & Chen, B. 2009. Learning HAZOP expert system by case-based reasoning and ontology. *Computers & Chemical Engineering*, 33(1).

A Novel Optimizable Inherent Safety Index Based on Fuzzy Logic

Daniel Vázquez^{a*}, Rubén Ruiz-Femenia^a, José A. Caballero^a

^a*Institute of Chemical Process Engineering, University of Alicante, PO 99, E-3080 Alicante, Spain*

vazquez.vazquez@ua.es

Abstract

In our days, the concept of inherent safety is gaining popularity thanks to its ability to assess the safety level of a plant at an early design stage. Hence, safety can be considered one of the core design principles, instead of a post-design add-on. In this work, we propose a novel index to assess the inherent safety level of a design. This index is based on the principles of fuzzy logic, which allow the user to shift the importance in the safety criteria easily, and its main objective is to provide an optimizable framework. In order to achieve an optimizable fuzzy index, some concessions must be made in its methodology. As such, the presented index is not as quantitative as other safety indexes. However, this shortcoming is compensated with the comparative ability and modifiability that this index provides the decision maker with. As a conclusion, we showcase the ability of this novel index in assessing the inherent safety level of an example case.

Keywords: Inherent Safety, Fuzzy Logic, Optimization.

1. Introduction

In order to consider the design of a chemical process from a holistic point of view, it is necessary to have a method able to assess the safety level of a plant at an early design stage. The concept of inherent safety, coined by Kletz (Kletz & Amyotte, 2010), presents itself useful for this objective. The four main principles of inherent safety are: intensification, substitution, attenuation and limitation. The consideration of these principles allows the designer to give safety aspects the same importance as economic and environmental issues. Therefore, safety is considered a key design variable, instead of an afterthought once the main variables are fixed.

Safety analysis tend to be performed with the aid of safety indexes, such as Dow's (AIChE, 1994) and Safety Weighted Hazard Index (Khan et al., 2001). Some techniques, like the Hazard and Operability (HAZOP) method, consist in a committee of experts discussing the weak and hazardous points of a design. They use keywords, such as "high" and "low", which cannot be immediately quantified. This methodology resembles spoken language, and the use of fuzzy logic allows the designer to assemble spoken language with mathematical quantifiable rules (Zadeh, 1999). In this work, we use Mamdani's method (Mamdani & Assilian, 1975) in order to extract mathematical information from keywords. Mamdani's method comprises four steps: fuzzification of the inputs, establishment of the relationships among the inputs and outputs, aggregation of the conclusions and defuzzification of the output.

A problem that many safety indexes exhibit is that the mathematical expressions to compute them are nonconvex. Since they work with multiple variables at the same level,

such as flows, temperatures, enthalpies and pressures, they must use nonlinear operators. More complex indexes that use dispersion models are highly nonlinear and nonconvex. Since this work has the objective of providing an optimizable index, the calculations must be maintained the most linear possible. The defuzzification step includes a nonlinear equation which is unavoidable, but the fuzzification and the relationships among fuzzy sets can be made completely linear with the inclusion of Generalized Disjunctive Programming (GDP).

Therefore, this work presents a novel optimizable (in the sense that it can be systematically optimized) inherent safety (in that it is calculated according to the principles of inherent safety) index based on fuzzy logic (which allows the user to connect keywords and establish relationships input-output maintaining a mostly linear model). The index is divided into sub-indices that account for each inherent safety principle. In this paper we present the sub-indices for intensification and attenuation. These are then part of a multi-objective optimization (MOO) problem.

2. Intensification sub-index

The intensification principle, also named minimization principle, is based on the core idea of diminishing the inventory inside a process unit. The inventory refers to both the amount of chemical in the unit (or exiting the unit in a period of time) and the amount of energy that these chemicals carry. The index is obtained as shown in Eq. (1).

$$II = (II_{energy} \wedge II_{inventory}) \quad (1)$$

Where II stands for Intensification Index, II_{energy} stands for the part of the sub-index that takes into account the energy in the unit, and $II_{inventory}$ stands for the part of the sub-index that takes into account the amount of mass in the unit, as well as the streams that go out of the unit.

Each of these parts is calculated by an equation, shown in Eq. (2).

$$II_{energy} = \sum_{i=1}^C \Delta Hc_i x_i + \Delta Hr \quad (2)$$

$$II_{inventory} = FEV \cdot \rho + \dot{m}_{t=10min}$$

Where:

- ΔHc_i stands for the combustion enthalpy of the chemical i of C components in the unit, in kJ/kg.
- ΔHr stands for the reaction enthalpy in the unit, if a reaction is happening, in kJ/kg
- x_i stands for the mass fraction of the chemical $i \in C$ inside the process unit.
- FE, V, ρ stand for the equipment factor, volume and density respectively. The equipment factor is a parameter that relates the volume of the unit with the amount of chemical inside. An example is 0.8 for reactors and tanks. If you are

using the volume of chemical directly, its value is 1. The units of the volume and density are m^3 and kg/m^3 respectively.

- $\dot{m}_{t=10min}$ stands for the mass of chemical that leaves the process unit in a time interval of ten minutes, in kg.

In order to continue Mamdani’s method, we have to fuzzify the input values for both parts of the index. As such, an interval must be fixed by the designer. Then, a fuzzification function is used to assign a membership value to each crisp input. It is recommended to use linear functions, such as the triangular or trapezoid functions. An example of fuzzification for both parts of the sub-index is shown in Table 1.

Table 1. Fuzzification of the input. Intensification index.

Semantic pointer	Range	Fuzzification function
Low (L)	0 – 60 % of the interval	Gaussian
Medium (M)	5 – 95 % of the interval	Triangular
High (H)	40 – 100 % of the interval	Gaussian

While the Gaussian function is nonlinear, it is chosen in this work as an example of how, the index is still able to provide a satisfactory result even when dealing with more nonlinearities than the one strictly needed. These intervals are examples. The safety experts of the plant must decide how many intervals are necessary and how wide they are in order to correctly classify the safety level of the design.

The experts must define as well the relationships between the two parts of the sub-index (Eq. (1)). Some decision making techniques, such as Analytical Hierarchy Process, can be useful to ensure that the relationships remain coherent. Each relationship has to be assigned to an output fuzzy set. For example, in order to illustrate this, in this work the relationships are shown in Table 2.

Table 2. Relationships among inputs

Output fuzzy set / Risk level	Implications ($I_{energy} \wedge I_{inventory}$)
Minimal	$(L \wedge L)$
Low	$(L \wedge M) \vee (M \wedge L)$
Medium	$(M \wedge M) \vee (L \wedge H) \vee (H \wedge L)$
Moderate	$(H \wedge M) \vee (M \wedge H)$
High	$(H \wedge H)$

In order to defuzzify the output, we need to know how these output fuzzy sets are created. The chosen outputs of the intensification index are fuzzified as shown in Table 3.

Table 3. Fuzzification of the output

Semantic Pointer	Value of the index	Fuzzification function
Minimal Risk	0 – ~10	Gaussian
Low Risk	4 – 15	Triangular
Medium Risk	15-35	Triangular
Moderate Risk	35-45	Triangular
High Risk	~40-50	Gaussian

After the step of aggregation, we obtain an aggregated output that can be defuzzified using a centroid.

3. Attenuation sub-index

The attenuation principle is based on the idea of diminishing the hazardous conditions during operation. As such, the main variables considered for its calculation are the operating temperature and the operating pressure, although these are not the only parameters that the index takes into account.

The methodology is analogous to the intensification sub-index one. As such, we present only the equations and example fuzzification intervals and relationships.

The equations are as shown in Eq. (3) and Eq. (4)

$$AI = (AI_T \wedge AI_P) \quad (3)$$

Where AI_T stands for the part of the index that depends on the temperature parameters and AI_P stands for the part of the index that depends on the pressure parameters.

$$\begin{aligned} AI_T &= T_{op} + Pen_T \cdot \max(0, T_{op} - T_b) - R w_T \cdot \max(0, T_b - T_{op}) \\ AI_P &= P_{op} + Pen_P \cdot \max(0, P_{vap} - P_{op}) \end{aligned} \quad (4)$$

Where T_{op}, T_b stand for the operating temperature and the boiling temperature in °C and P_{op}, P_{vap} stand for the operating pressure and vapour pressure in bar. Pen_T , $R w_T$ and Pen_P are penalization and reward parameters that reward the unit when working with subcooled liquids and penalize it when it works with overheated vapours. In this work, their values are set to 0.5, 0.1 and 0.5 respectively.

A possible fuzzification is shown in Table 4.

Table 4. Fuzzification of the input. Attenuation index.

Semantic Pointer	Range in temperature (°C)	Range in pressure (bar)	Fuzzification function
Atmospheric (A)	~30	~1.5	Gaussian
Low (L)	10 – 50	1 – 6	Triangular
Medium (M)	40 – 80	4 – 10	Triangular
High (H)	70 - > 100	8 - > 12	Gaussian

A possible set of relationships is shown in Table 5.

Table 5. Relationships among inputs. Attenuation index

Output fuzzy set/ Risk level	Implications ($AI_T \wedge AI_P$)
Minimal	$(A \wedge A) \vee (A \wedge L)$
Low	$(L \wedge L) \vee (L \wedge A) \vee (A \wedge M) \vee (L \wedge M)$
Medium	$(M \wedge M) \vee (A \wedge H) \vee (M \wedge L) \vee (L \wedge H) \vee (M \wedge A)$
Moderate	$(H \wedge A) \vee (H \wedge L) \vee (M \wedge H)$
High	$(H \wedge H) \vee (H \wedge M)$

The fuzzification of the output is analogous to the one shown in Table 3.

4. Example and Results

We consider a number of units that work with certain operating conditions. No reaction is occurring inside these units. The properties of the chemicals inside the units are shown in Table 6.

Table 6. Data of the example case

Properties	Unit #01	Unit #02	Unit #03	Unit #04	Unit #05	Units
$\sum_{i=1}^C \Delta H c_i x_i$	14.25	17.20	10.43	8.29	5.34	MJ/kg
$FEV \cdot \rho$	20000	15000	34000	10000	5000	kg
$\dot{m}_{t=10min}$	3000	2000	2000	1000	3000	kg
T_{op}, T_b	50, 50	30, 60	50, 30	40, 70	80, 40	°C
P_{op}, P_{vap}	1, 1	3, 2	4, 6	8, 7	8, 12	bar
Inventory range			0 – 40			t
Energy range			0 – 20			MJ/kg
Temperature range			0 – 100			°C
Pressure range			0 – 12			Bar

We consider the global index as the aggregation of both the intensification and attenuation sub-indices. The resultant optimization model, based on Generalized Disjunctive Programming (GDP), is a Mixed Integer Non-Linear Programming (MINLP) problem. The nonlinearities are found in the defuzzification of the output step, which is performed using the centroid, and in the Gaussian fuzzification functions of the inputs. The rest of the calculations are linear. The results are shown in Table 7.

Table 7. Results of the optimization

Order from best to worst	Global Index	II	AI
Unit #02	39.86	29.98	9.88
Unit #04	43.40	20.22	23.18
Unit #03	52.74	32.74	20.00
Unit #01	53.10	28.11	24.99
Unit #05	66.26	16.27	49.99

It can be observed that the index is able to rank the different process units regarding its inherent safety level. In this example, an aggregation of both the intensification sub-index and the attenuation sub-index is performed. This is not the only option, since there are multiple possibilities to treat MOO problems. Another alternative is a weighted sum, giving more importance to one sub-index over the other. It is the duty of the decision maker to assign the correct importance to each sub-index.

An important remark is the case of Unit #05. Its attenuation sub-index has a value of practically 50, which is the highest value that the index achieves. If we look at the definition of the fuzzy sets for the input, Table 4, we can see that the high semantic pointer (H) starts at around 70 °C and 8 bar. If we apply Eq. (4), we obtain the values of $AI_T = 100$ °C and $AI_P = 10$ bar. While the temperature part of the attenuation index is indeed at its maximum allowed by the chosen range, the pressure part stills has room for an increment. However, any higher pressure, e.g., 11, 12 bar, will still result in an index of 50. This nuance shows that the decision maker must choose carefully the range of the intervals and the fuzzification functions of the inputs, as well as its ranges.

5. Conclusions

In this work we present the initial step in creating a novel inherent safety index based on fuzzy logic. The index is divided in sub-indices that refer to each main principle of inherent safety. The use of fuzzy logic allows the user to maintain a mostly linear model, which can be made strictly linear except for the objective function. It also allows the user to easily and quickly change parameters in order to fit the index to different problems. This is both an advantage and a disadvantage. While the modifiability of the index increases its versatility, it also forces the user to know the system of possibilities beforehand. Ranges must be chosen regarding the corresponding problem at hand, and so must be the relationships. The user has to know where to put more emphasis in the safety analysis. In some units, it may be better to give more importance to the pressure than to the temperature, and this must be reflected in the chosen relationships among input fuzzy sets.

The index proves its efficiency as an optimizable inherent safety index able to rank alternatives depending on their safety level. While its main use is comparative, due to the fact that each sub-index depends on a series of user-chosen parameters and ranges, with the appropriate considerations, i.e., relationships and ranges, it could be used as a global index for a process, with the advantage of being systematically optimizable and modifiable. For future works, it is intended to implement an analogous methodology to obtain an index for the substitution index, using the NFPA(2012) standard as the main variable.

Acknowledgments

The authors acknowledge financial support from the Spanish “Ministerio de Economía, Industria y Competitividad” (CTQ2016-77968-C3-02-P, FEDER, UE).

References

- AICHE. (1994). Dow's Fire & Explosion Index Hazard Classification Guide. In.
- Khan, F. I., Husain, T., & Abbasi, S. A. (2001). Safety Weighted Hazard Index (SWeHI). *Process Safety and Environmental Protection*, 79, 65-80.
- Kletz, T., & Amyotte, P. (2010). *A Handbook for Inherently Safer Design (Second Edition ed.)*.
- Mamdani, E. H., & Assilian, S. (1975). An experiment in linguistic synthesis with a fuzzy logic controller. *International Journal of Man-Machine Studies*, 7, 1-13.
- NFPA. (2012). NFPA 704: Standard System for the Identification of the Hazards of Materials for Emergency Response. In.
- Zadeh, L. A. (1999). Fuzzy Sets as a Basis for a Theory of Possibility. *Fuzzy Sets and Systems*, 100.

Optimization under uncertainty of melatonin dosing for critically ill patients

Adriana Savoca, Giuseppe Pesenti, Davide Manca*

*PSE-Lab, Dipartimento di Chimica, Materiali e Ingegneria Chimica "Giulio Natta"
Politecnico di Milano, Piazza Leonardo da Vinci 32, Milano 20133, Italy*

davide.manca@polimi.it

Abstract

Computer-aided modelling and simulation are effective tools to provide guidance in the design of clinical experiments and treatments. Simulations with physiologically-based pharmacokinetic (PBPK) models combine the drug material balances within the body to its real physiological and anatomical features and can be used to optimize drugs dosing and administration timing. We focus on melatonin administration to critically ill patients, a challenging population because of their high inter-individual variability in the pharmacokinetics (due to their heterogeneous and severe conditions). We show how the optimization problem can be suitably formulated to tackle this uncertainty, and compare the results obtained for critically ill patients and healthy individuals. The approach can be easily transferred to any other drug routinely administered in intensive care units whenever a desired pharmacokinetic profile is available.

Keywords: optimization, modelling, simulation, uncertainty, pharmacokinetics.

1. Introduction

Recent years have seen an increasing interest in melatonin. Although it is particularly well-known as a cure for sleep disturbances and restoration of circadian rhythms, researchers are investigating additional physiological and pathophysiological functions. Indeed, there is evidence of anti-cancer, anti-oxidative, anti-inflammatory, and analgesic properties (Brzezinski, 1997). Healthy individuals produce melatonin endogenously by means of the pineal gland according to the day-night rhythm. Melatonin production onsets with darkness (around 9-10 PM) and peaks at 2-4 AM. Healthy plasma peak levels are in between 60-100 pg/mL. After the peak, melatonin levels settle to the low daily baseline (5-10 pg/mL). Collaboration with Intensive Care Unit (ICU) of Ospedale San Paolo di Milano (Italy) allowed focusing on critically ill patients. Such patients exhibit disorders in melatonin secretion rhythm and/or lower levels compared to healthy individuals. This phenomenon is correlated to the lack of sleep, which likely increases both patients' morbidity and probability of mortality. There is evidence that exogenous melatonin has beneficial effects on these patients, mainly for treatment of sleep disorder, delirium, and oxidative stress (Bourne and Mills, 2006; Mistraletti et al., 2010). Several studies investigated the optimal dose with the purpose of reproducing the desired physiological levels of melatonin and proposed different doses (regimens) to restore the healthy endogenous rhythm. While physiological levels are desirable to restore circadian rhythms, pharmacological levels (*i.e.* supraphysiological levels, for instance about 3 orders of magnitude higher) are more suitable for anti-oxidant or anti-cancer purposes (Reiter et al., 2014). We show that computer simulation is an efficient tool to design and/or integrate such pharmacokinetic (PK) studies, with the advantage of reducing times

and costs of the experiments. In addition, simulations using physiologically-based pharmacokinetic (PBPK) models allow comparing and evaluating the pharmacokinetics from not only different doses but also routes of administration. In fact, our first goal is to select the administration route that best mimics human physiological levels. Subsequently, we focus on that route and optimize dosing, also by comparing results for healthy individuals (by neglecting the endogenous contribution for the sake of clarity) and critically ill patients. The main issue with critically ill patients is that they are intrinsically rather heterogeneous, because of their different conditions (*e.g.*, age, dysfunctions, organs failure) (Mistraletti et al., 2010). This feature enhances inter-individual variability of melatonin pharmacokinetics. To deal with this problem, we propose a prospective approach to drug dosing optimization.

2. Methods

Figure 1 shows the structure of a multi-route compartmental PBPK model. The reference model for this work is Abbiati et al. (2016), where organs and tissues of the human body are represented by homogenous compartments. We complemented those compartments number and model structure to melatonin features and administration routes, by adding (i) the pineal gland, which is the source of endogenous melatonin, and (ii) the salivary glands (Savoca et al., 2018). A further equation accounts for the dynamics of main melatonin metabolite: 6-sulfatoxymelatonin (aMT6s) both in plasma and in urine. In case of oral administration (PO, *per os*, see also Figure 1), the model consists of material balances on either single or lumped homogenous compartments.

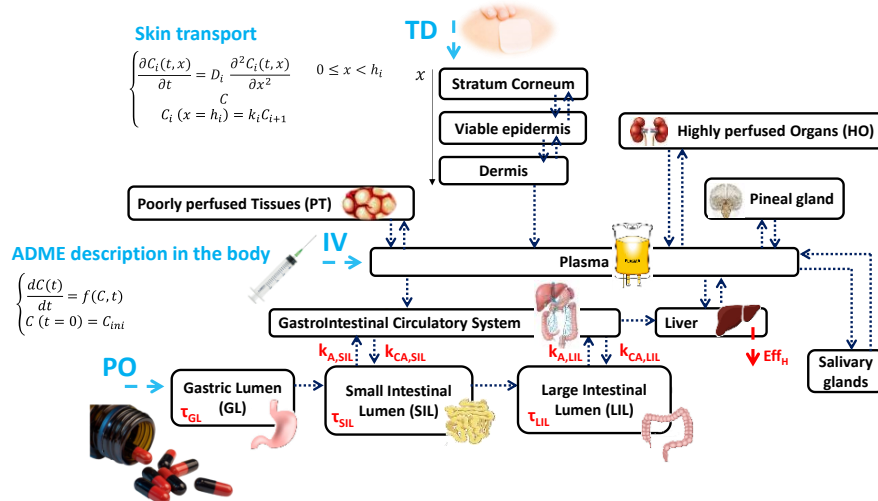


Figure 1 - Scheme of the PBPK model for description of melatonin ADME processes. Parameters in red are associated to the main processes responsible for inter-patient variability. While skin transport is described via PDEs discretized with respect to skin depth x , the other body compartments feature melatonin material balances in the form of ODEs.

These are the gastric lumen (GL), the small and large intestinal lumina (SIL and LIL), the gastrointestinal circulatory system (GICS), the plasma, the liver, the poorly perfused tissues (PT, lumping adipose tissue, skin, and muscles), and the highly perfused organs

(HO, lumping brain, lungs, and spleen). In case of intravenous (IV) route, the gastrointestinal compartments are neglected. Finally, in case of transdermal (TD) administration, skin is assumed as a separate compartment from PT and described by a set of partial differential equations (PDEs) with proper boundary conditions for skin TD absorption. The model features three skin layers: (i) stratum corneum, (ii) viable epidermis (also a metabolism site), and (iii) dermis, from which the drug is supposed to reach the systemic circulation. These PDEs are discretized with respect to the spatial coordinate (*i.e.* skin depth) and converted to ODEs and merged to those of the other compartments (Savoca et al., 2018). Model parameters include (i) individualized and assigned parameters that are either calculated as a function of patient's characteristics or found in the literature, and (ii) adaptive parameters (*e.g.*, diffusivities, transfer coefficients, metabolic constants) that are obtained via a non-linear regression of experimental data from the literature. Firstly, we use the multi-route PBPK simulations to compare levels resulting from PO, IV, and TD administration routes. Secondly, we perform an optimization based only on PO controlled release (CR), as it resulted the most suitable to mimic endogenous pharmacokinetics. Based on experimental release curves from the scientific literature, the optimal melatonin amount and time of administration are identified for three *in silico* individuals, (i) a healthy male, (ii) a healthy female, and (iii) an ICU patient. The PBPK model parameters for healthy individuals are identified with melatonin PK experimental data of healthy volunteers. Equally, the parameters that describe the PK of ICU patients are identified via regression with experimental data of the critically ill.

To account for considerable inter-individual variability, the optimization problem considers the uncertainty related to the (patho)physiological differences of such patients. The processes that most likely produce inter-subject variability are (i) absorption from the intestinal walls into gastrointestinal circulation (characterized by absorption constants $k_{A,SIL}$, $k_{A,LIL}$, $k_{CA,SIL}$, and $k_{CA,LIL}$ and residence times in gastrointestinal region τ_{GL} , τ_{SIL} , and τ_{LIL}) and (ii) hepatic metabolism (described by hepatic efficiency Eff_H). These model parameters are randomized within a proper range, which is chosen referring to physiology for the transit times, and model uncertainty for the others, to produce different PK profiles for the ICU virtual patient, VP. These additional NS "scenarios" embody the structure of the optimization problem in Eq. (1), where NM is the number of experimental data C_i^{ideal} that describe the healthy endogenous plasma concentration profile (Voultsios et al., 1997). The degrees of freedom are: *dose* and t_{adm} (*i.e.* timing of administration).

$$\min_{dose, t_{adm}} \sum_{k=1}^{NS} \left(\frac{\sum_{i=1}^{NM} (C_i^{ideal} - C_i^{VP,k})^2}{NM} \right) \quad (1)$$

3. Results

3.1. Comparison of administration routes

The physiochemical properties of melatonin (*e.g.*, lipophilicity and low molecular weight) make it suitable for at least three administration routes, *i.e.* PO, IV, and TD. As far as the PO route is concerned, we consider both immediate and controlled release (CR) formulations. Figure 2 allows comparing the pharmacokinetics of these different routes under the same melatonin dose (1.5 mg in the left panel, 12 mg in the right panel). The characteristic slowness of TD absorption is particularly appropriate to mimic the sustained endogenous levels produced by the pineal gland. Equally, the PO (CR)

formulation provides continued levels (T_{max} about 4 h), coupled with a steeper absorption.

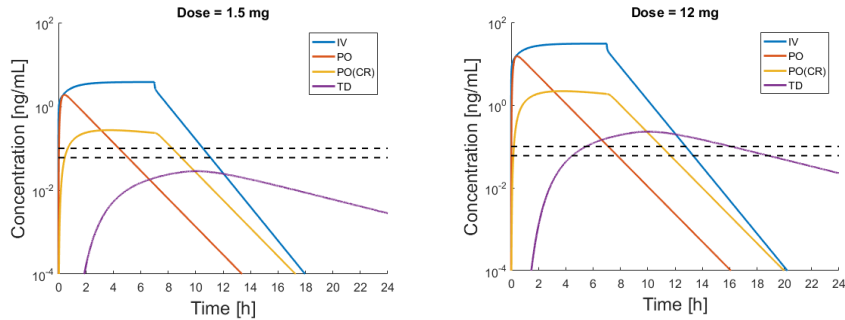


Figure 2 – PK simulations of a healthy individual with IV, PO (immediate release and controlled release (CR) formulations), and TD administrations of melatonin. Black dashed horizontal lines show the range of concentration peak after healthy endogenous production (60-100 pg/mL).

The difference in the velocity of early absorption affects the selection of the optimal administration timing as it affects the onset time of the pharmacological and physiological effects. Predictably, even low doses of continuous IV infusion produce the highest levels, thus it is probably the most appropriate to achieve prompt pharmacological (*i.e.* supraphysiological) levels. On the contrary, TD administration should be excluded for that purpose, even in case of higher doses. In case of PO immediate-release formulation, the melatonin concentration decreases rapidly after administration. However, even for low doses, this administration formulation allows reaching pharmacological levels, alternatively to IV infusion. This conclusion is in line with experimental studies where oral doses higher than 0.3 mg produce supra-physiological levels.

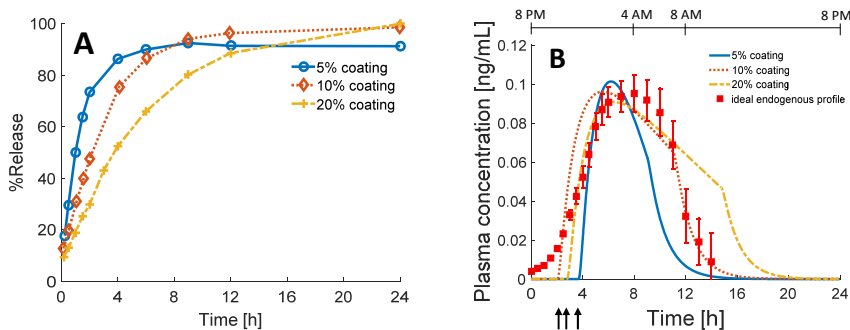


Figure 3 – (A) Experimental release curves for different formulations, as in Lee et al. (1995). (B) Optimized PK levels (continuous, dashed, and dotted lines) in ICU and ideal (experimental) healthy endogenous data (red squares). Black arrows indicate optimal timing of administration.

3.2. Optimization for PO CR route

Panel A of Figure 3 compares three PO (CR) formulations with different percentages of polymer coating (5-10-20%) that generate three different release curves as in Lee et al. (1995). Panel B of Figure 3 shows experimental data of the endogenous profile of a healthy individual (red squares, from Voultsios et al. (1997)), while continuous, dotted, and dashed lines are the optimized pharmacokinetics of an ICU patient who receives tablets featuring the three different release curves. The most suitable release curve

corresponds to the 10%-coating tablet that best approaches the PK endogenous profile.

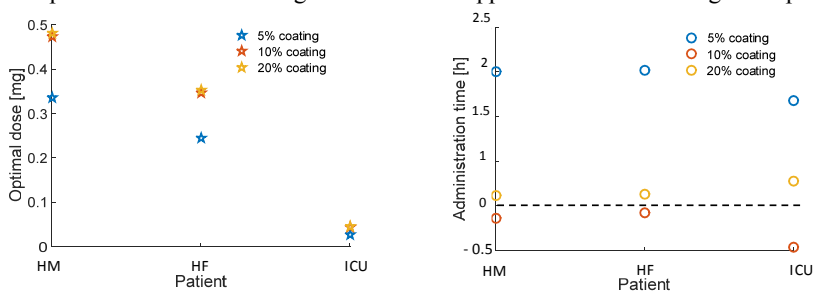


Figure 4 – Optimal melatonin dose (left panel) and timing of administration (right panel) for HM and HF (healthy male and female individuals) and ICU (critically ill patient). Dashed horizontal line (right panel) indicates the desired time of onset of melatonin effects.

Figure 4 shows the melatonin optimal doses and timing of administration. On the x-axis, HM and HF stand for the male and female healthy individuals, while ICU stands for the critically ill patient. It is worth noticing that the lowest dose is associated to the ICU patient. Indeed, for the same dose, PK studies show higher melatonin concentrations in critically ill patients, compared to healthy individuals. Probably, the continuous enteral nutrition of ICU patients facilitates melatonin absorption. Notably, PBPK model simulations are consistent with this behavior.

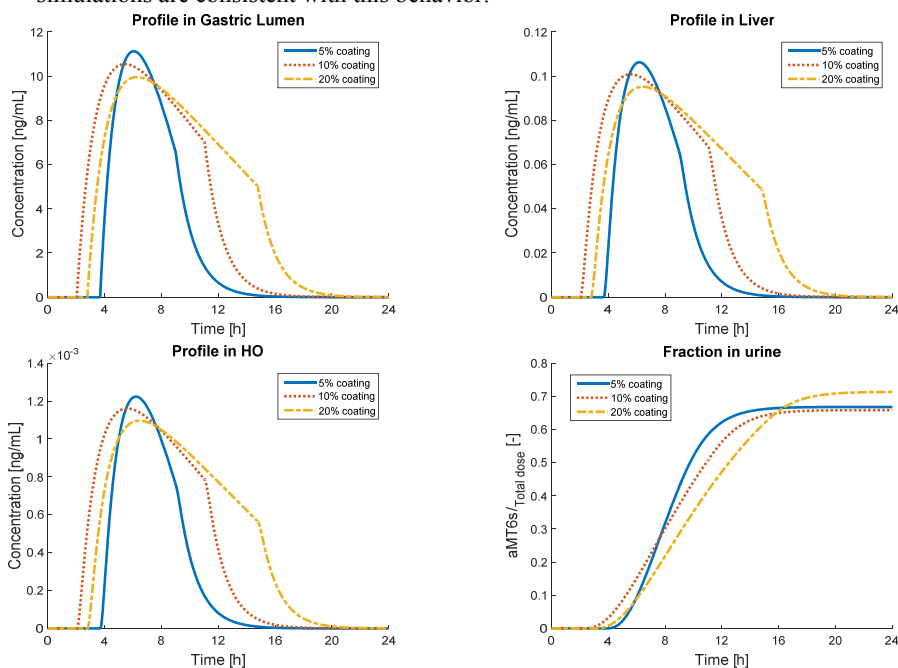


Figure 5 - PBPK model simulations for the critically ill patient in Gastric Lumen, Liver, HO (Highly perfused Organs), and aMT6s fraction in urine.

In addition, optimal dose values for the healthy individuals are in line with the results of experimental studies (as already mentioned, oral doses higher than 0.3 mg produce

supraphysiological levels). Our results are not so far from this approximate value. Figure 4 (right panel) shows the optimal timing of administration in relation to the desired onset time for melatonin effects (see the horizontal dashed line at 0). In case of 10%-coating, the optimal administration timing for the ICU patient is about 30 min before the desired onset, while it is shorter for healthy individuals. This is consistent with the fact that critically ill patients exhibit higher levels of melatonin after exogenous administration. In all the other cases, to mimic the endogenous profile optimally, the administration timing should occur *after* the desired onset time, which evidently makes no sense. This confirms that the 10%-coating formulation is the most optimal to deliver physiological levels of melatonin. Finally, Figure 5 shows melatonin PK simulations in different compartments (*i.e.* Gastric Lumen, Liver, and HO, Highly perfused Organs) and the eliminated amount of melatonin metabolite, aMT6s, after the optimal administration of PO (CR) formulation to the ICU patient. Low levels in HO are consistent with the typical tissue hypoperfusion of critically ill patients. Experimentally, the eliminated melatonin is usually higher than 85%, while this threshold is not reached in our simulations. This may be related to two different reasons: (i) from the modeling point of view, our model underestimates aMT6s metabolic production as we consider (for simplicity) the liver contribution only, (ii) from the physical point of view, ICU patients may exhibit lower metabolism compared to healthy patients.

4. Conclusions

PBPK model simulations are an effective tool in melatonin optimal pharmacotherapy. We optimized melatonin dosing by comparing healthy individuals and critically ill patients. As the latter ones represent an extremely heterogeneous population, we proposed an approach that allows accounting for inter-subject variability generated by the gastrointestinal absorption and metabolic processes. Results are in line with conclusions from past experimental PK studies and can provide aid in future study for the challenging identification of melatonin optimal dose regimens in critically ill patients.

References

- Abbiati, R.A., Depetri, V., Scotti, F., Manca, D. (2016). A new approach for pharmacokinetic model application towards personalized medicine, *CACE*, 38, 1611-1616.
- Bourne, R.S., Mills, G.H. (2006). Melatonin: possible implications for the postoperative and critically ill patient. *Intensive Care Med*, 32, 371-379.
- Brzezinski, A. (1997). Melatonin in humans. *N Engl J Med*, 336, 186-195.
- Lee, B.J., Parrott, K.A., Ayres, J.W., Sack, R.L. (1995). Design and evaluation of an oral controlled release delivery system for melatonin in human subjects. *Int J Pharm*, 124, 119-127.
- Mistraletti, G., Sabbatini, et al. (2010). Pharmacokinetics of orally administered melatonin in critically ill patients. *J Pineal Res*, 48, 142-147.
- Reiter, R.J., Tan, D.X., Galano, A. (2014). Melatonin: exceeding expectations. *Physiology (Bethesda)*, 29, 325-333.
- Savoca, A., Mistraletti, G., Manca, D. (2018). A physiologically-based diffusion-compartment model for transdermal administration – The melatonin case study. *Computers & Chemical Engineering*, 113, 115-124.
- Voultzios, A., Kennaway, D.J., Dawson, D. (1997). Salivary melatonin as a circadian phase marker: validation and comparison to plasma melatonin. *J Biol Rhythms*, 12, 457-466.

Simultaneous design and controllability optimization for the reaction zone for furfural bioproduction

A.G. Romero-García,^a O.A. Prado-Rúbio,^b G. Contreras-Zarazúa,^a C. Ramírez-Márquez,^a J.G. Segovia-Hernández,^a

^a *Universidad de Guanajuato, Campus Guanajuato, División de Ciencias Naturales y Exactas, Departamento de Ingeniería Química, Noria Alta S/N, Guanajuato, Gto., 36050, México*

^b *Departamento de Ingeniería Química, Universidad Nacional de Colombia, Km 9 vía al Aeropuerto La Nubia, Campus La Nubia, Bloque L, Manizales, Caldas, Colombia.*
Corresponding author. Email: gsegovia@ugto.mx

Abstract

In this work is presented the simultaneous optimization of design parameters and control properties, using a stochastic method named Differential Evolution with Tabu List Algorithm, as study case the reaction zone in the production process of furfural from biomass. In the objective function, the Total Annual Cost, eco-indicator 99 and condition number are combined as economic, environmental and control criteria respectively. From the multi-objective optimization, results show the direct influence that design parameters have over the control properties having an antagonist behaviour. As consequence, it is possible to see that to have the best control properties there is an increase in TAC and eco-indicator. Based on results, operating conditions founded allows having an acceptable furfural production of 2014.4 kg/h by reducing costs in a 39% and environmental impact in a 42% in a system with good control properties in dynamic state.

Keywords: Furfural, Optimization, Total Annual Cost, Eco-Indicator99, Control Properties.

1. Introduction

Furfural is a chemical compound produced by biomass rich in pentoses content in the hemicellulose as raw material, in a reaction catalysed in presence of strong acids. Is used as a potential platform to produce biofuels. In recent years, furfural has received special attention as a potential platform to produce biofuels and biochemicals. In a study conducted by the Department of Renewable Energy of the United States, furfural was selected as one of the 30 main chemicals that can be manufactured from biomass (Cai et al., 2014). Industrially, it is a very versatile chemical because of its multiple applications: utilized as a raw material to produce phenol-furfural-resins (Brown, 1959), or can be converted furfuryl alcohol, tetrahydrofurfuryl alcohol, furan, tetrahydrofuran and diols (Bhogeswararao, 2015). The Quaker Oats process is the oldest commercial form of producing furfural industrially. This process was created by the Quaker Oat company using oat cereal waste as raw material, which is mixed with sulfuric acid. The process consists in two steps, first the reaction zone in which the biomass reacted with a solution of sulfuric acid to convert the xylan fraction into furfural, then high vapour

stream is introducing to the reactor to remove the furfural as fast as possible in order to avoid furfural polymerization (Marcotullio, 2011). The vapor stream from the reactor is condensed to feed the azeotropic distillation sequences in order to remove the excess of water and some by-products such as methanol and acetic acid (Marcotullio, 2011).

Under the economy circle concept, the study of the reaction zone in the production of furfural is important because it allows to reduce the excessive use of water, high energy consumption and the formation of decomposition products by reducing the separation costs. In this work aims to present a novel proposal for the simultaneous optimization having as objective function TAC as economic criteria, Condition Number as a control indicator and EI99 as environmental conditions in order to improve reactor productivity in the reaction zone in the furfural production process. So far, there are no publications reported in the literature where the multi-objective optimization methodology for the furfural reaction zone is solved.

2. Methodology

In this work it is consider as raw material, stem of date-palm tree with a composition of: cellulose (glucan) 66.6 wt%, hemicellulose (xylan)14.52 wt%, lignin 13.72 wt% lignin. Experimental data are taken from Bamufleh et.al (2013) to propose a kinetic model and parameters. The model proposed, is analogous to the proposed by Saeman, (1945) on the hydrolysis of cellulose catalyzed by dilute sulfuric acid. In the proposed reaction, furfural is obtained from xylan and the furfural reacts to form the corresponding decomposition products such as methanol and acetic acid (Marcotullio, 2011). For simplicity, decomposition products are condensed in a unique expression as is shown in Eq. (1).



The r_i value it is expressed as Eq. (2). Kinetic parameters k_o , b and E were estimated with experimental data reported by Bamufleh using the Curve fitting tool from the software Matlab. From Eq. (1), it is reported two reaction rates, which kinetic parameters estimated are: $k_{o1}=6.24 \times 10^8 \pm 2.28 \times 10^9$ (min^{-1}), $b_1=1.20 \pm 0.21$, $E_1=93.44 \pm 11.16$ (kJ/mol), $k_{o2}=1.74 \pm 7.33$ (min^{-1}), $b_2=2.06 \pm 0.56$ and $E_2=33.63 \pm 11.72$ (kJ/mol). The adjustment has a correlation coefficient of 0.96447, indicating a good parameter fitting.

$$r = k_o C h^b \exp\left(\frac{-E}{RT}\right) \quad (2)$$

To produce furfural, a continuous CSTR reactor with continuous agitation is proposed. From a generalized balance the equations that describe the dynamic of the system are shown in Eq. (3), Eq. (4) and Eq. (5).

$$\frac{dC_{xylan}}{dt} = \frac{F_{in}}{V} (C_{in-xylan} - C_{xylan}) + r_{xylan} \quad (3)$$

$$\frac{dC_{Furfural}}{dt} = r_{Furfural} - C_{Furfural} \frac{F_{in}}{V} \quad (4)$$

$$\frac{dC_{D,P}}{dt} = r_{D,P} - C_{D,P} \frac{F_{in}}{V} \quad (5)$$

From Eq. (3), Eq. (4) and Eq. (5): the feed flow is represented by F_{in} [kg / h], the fraction of xylan at the entrance of the reactor $C_{in-xylan}$ [kg/L]. For this system, two other variables to consider are: temperature T [°K] and the concentration of the sulfuric acid Ch [% w], it is reported that the manipulation of acidic conditions and temperature play an important role in the reaction kinetics to produce furfural (Marcotullio, 2011). Within the reactor, it is of interest to study the behaviour that will have during the reaction time: first the degradation of the raw material C_{xylan} [kg/L], as well, the formation of furfural $C_{Furfural}$ [kg/L] and Decomposition Products $C_{D,P}$ [kg/L].

The reaction system presented, has significant number of variables to be optimized order to have an optimal design and operation conditions, by aiming a maximum production of furfural, the best control criteria, lowest environmental impact and lowest cost possible. In this context, the reaction system described as case study is a good model to be optimized simultaneous control and design parameters. Additional factors: the model proposed shows the dynamic behaviour of the system and there is no work in literature where the optimization of design parameters and simultaneous control for furfural reactor are reported. The design variables for the study case are shown in Table 1.

Table 1. Design variables for the multi-objective optimization

Variables	Type Variable	Symbol	Range	Units
Relation of solid (raw material) and water	Continue	LSR	1-15	ml/gr
Feed Flow	Continue	F_{in}	$1 \times 10^3 - 6 \times 10^6$	kg/h
Temperature	Continue	T	373 - 413	K
Acid Concentration	Continue	Ch	5 - 15	% w
Volume	Continue	V_o	300 – 520000	L

A multi-objective optimization technique referred to as Differential Evolution with Tabu List (DETL) proposed by Srinivas and Rangaiah (2007) is employed. This technique works as a combined system between the biological evolution from Differential Evolution technique and the random search method from the Tabu search technique. The objective function involves three important axes to analyse: Total Annual Cost (TAC) as an indicator of the economy of the process by calculating the annualized cost of the process equipment and the operating cost, Condition Number (γ^*) as an indicator of the dynamic behaviour of the process considering low condition number for systems with good controllability and Eco-indicator 99 (EI99) to quantify the environmental impact. Similar works have been reported by Sánchez-Ramírez et. al. (2017) applying this index for distillation columns. The objective function is expressed as Eq. (6).

$$\min[TAC, \gamma^*, EI99] = f(LSR, F_{in}, T, Ch, V_o) \quad (6)$$

$$\text{Subject to: } \begin{aligned} y_{i,F} &\geq x_{i,F} \\ w_{i,F} &\geq u_{i,F} \end{aligned} \quad (7)$$

The objective functions are restricted to satisfy the mass flowrate ($u_{i,PC}$) specifications of furfural. The minimum mass flowrate for furfural were fixed to 2000kg/ hr. The values of parameters required by DETL method are: Population size: 120 individuals, Generation number: 710, Tabu list size: 60, Tabu radius: 0.01, Crossover fractions: 0.8, Mutation fractions: 0.3.

3. Results

To represent the main results of the simultaneous optimization of the reactor for furfural bioproduction, Pareto charts are used to identify the best option to produce furfural satisfying in the multi-objective function. Pareto fronts of reactor for furfural bioproduction are presented: a) Condition Number vs Total Annual Cost, b) Total Annual Cost vs Eco-indicator 99 and c) Condition Number vs Eco-indicator 99, all of them comparing with the respective furfural yield %. (See Figure 1).

In Figure 1, each point represents a different design. The best design selected is marked as red square. It was selected according to utopian point methodology where two objectives cannot improve more, both are in equilibrium (Wang and Rangaiah, 2017). The red square corresponds to solutions closer to utopic point. Figure 1.a, shows antagonist behaviour between condition number and total annual cost. To explain this trend variable such as temperature and volume, are related both to the costs and to the control properties. When temperature increase, energy consumption will increase having a direct increase in TAC. Referring to the volume, a bigger volume will require more building material and increment the feed flow having an increment in TAC, moreover, for control properties, having an increase in volume the disturbances have less influence on the system thus improving control properties.

Figure 1.b shows a relation between total annual cost vs eco-indicator 99, in this case both objectives presents the same behaviour strongly influenced by energy supply and cost of energy. To have a reactor of this magnitude it is necessary to increase the heat supply (this represent a direct increase in TAC) and to increase the steel used for the equipment, it is demonstrated that steel has a strong influence in EI99 (Sanchez-Ramirez et al., 2016). In this case is shown a unique minimum but it is not possible to choose it as the optimum because that minimum is an extreme when is evaluated in other index. Figure 1.c shows also an antagonist behaviour between control properties and eco-indicator 99, such as the presented in Figure 1.a, when volume is increased eco-points will increase because of the increment of steel used for equipment as well; and simultaneously when volume is increased perturbations has less influence in the system improving controllability. For all the designs the yield % is around 15-30% for an industrial production similar to the reported experimentally by Bamufleh, et al. (2013). The optimal design parameters are presented in Table 2.

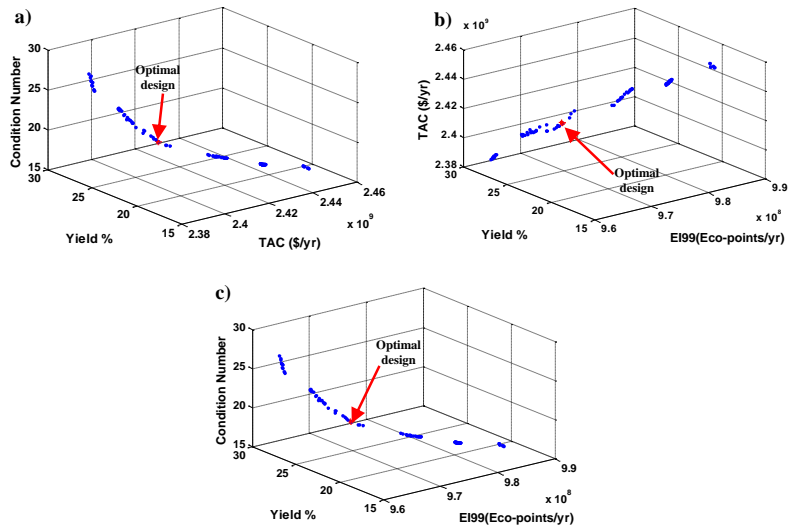


Figure 1. Pareto fronts from the reactor of furfural bioproduction.

Table 2. Optimal design parameters for the reactor.

Design Variables	Symbol	Value	Units
Reactor Volume	V_o	518880.77	L
Diameter	D	7.61	M
Height	H	11.41	M
Temperature	T	411.26	$^{\circ}\text{K}$
Acid concentration	Ch	12.31	% w
Feed flow	F_{in}	728422.31	kg/h
Solid and water relation	LSR	10.497	ml/gr
Total energy Consumed (kJ/hr)	Q	5608969.50	kW
Furfural	Furf	2014.4	kg/h
Decomposition Product	D.P	1731.6	kg/h
Furfural yield	---	25.43	%
Utilities cost	---	2411.46	(million\$/yr)
Equipment cost	---	0.322	(million\$/yr)
TAC	TAC	2411.786	(million\$/yr)
EI99	EI99	970.162	(millionEco-points/yr)
Condition Number	γ^*	18.55	-----

4. Conclusions

In this work the reactor zone to produce furfural from palm-date has been optimized. Based on results, is possible to find many possible designs in which furfural yield is

maximized as well cost and eco-points are minimizing in a controllable system. Optimal operation conditions found for the system, like temperature 411.26 °K and acid concentration 12.31%w have strong influence in reaction rate, this conditions allows to maximize furfural yield to 25.43% with a production of 2014.4 kg/h, this represents an improvement compering with the reported by Bamufleh et. al. (2013), with a furfural yield between 11-22% in non-optimal conditions of cost, environmental effects and control properties. As well, dimensions found for the reactor (volume of 518880.77 L) allows to minimize the TAC, eco-points and this size of reactor allows the system to have good control properties.

5. References

- Bamufleh, H. S., Alhamed, Y. A., & Daous, M. A. (2013). Furfural from midribs of date-palm trees by sulfuric acid hydrolysis. *Industrial Crops and Products*, 42(1), 421–428.
- Brown L. H., Watson D. D. (1959) ; Phenol-furfural resins. *Industrial and Engineering Chemistry*, 51(5), 683-684
- Bhogeswararao S., Srinivas D. (2015); Catalytic conversion of furfural to industrial chemicals over supported Pt and Pd catalysts. *Journal of Catalysis*, 327, 65-77.
- Cai, C. M., Zhang, T., Kumar, R., & Wyman, C. E. (2014). Integrated furfural production as a renewable fuel and chemical platform from lignocellulosic biomass. *Journal of Chemical Technology and Biotechnology*, 89(1), 2-10.
- Long, N. V. D., Kim, S., & Lee, M. (2016). Design and optimization of intensified biorefinery process for furfural production through a systematic procedure. *Biochemical Engineering Journal*.
- Lu, Y., & Mosier, N. S. (2008). Kinetic modeling analysis of maleic acid-catalyzed hemicellulose hydrolysis in corn stover. *Biotechnology and Bioengineering*, 101(6), 1170–1181.
- Marcotullio, G. (2011). The chemistry and technology of furfural production in modern lignocellulose feedstock biorefineries. TU Delft, Delft University of Technology.
- Rijnsdorp JE, Bekkers P. (1992). Early integration of process and control design. IFAC Workshop on Interactions between Process Design and Process Control; London, UK; 17–22.
- Saeman, J. F. (1945). “Kinetics of wood saccharification-hydrolysis of cellulose and decomposition of sugars in dilute acid at high temperature,” *Industrial & Engineering Chemistry Research* 37(1), 43-52.
- Sánchez-Ramírez, E., Quiroz-Ramírez, J. J., Segovia-Hernández, J. G., Hernández, S., Ponce-Ortega, J. M. (2016). Economic and environmental optimization of the biobutanol purification process. *Clean Technologies and Environmental Policy*, 18(2), 395-411.
- Sánchez-ramírez, E., Quiroz-ramírez, J. J., Hernández, S., Segovia-hernández, J. G., & Kiss, A. A. (2017). Optimal hybrid separations for intensified downstream processing of biobutanol, 185, 149–159.
- Srinivas M., Rangaiah G. P. (2007). Differential evolution with TL for solving nonlinear and mixed-integer nonlinear programming problems, *Industrial & Engineering Chemistry Research*, 46, 7126-7135.
- Wang, Z., & Rangaiah, G. P. (2017) Application and analysis of methods for selecting an optimal solution from the Pareto-optimal front obtained by multiobjective optimization. *Industrial & Engineering Chemistry Research*, 56(2), 560-574.

Design and Optimization of Azeotropic and Extractive Distillation to Purify Furfural Considering Safety, Environmental and Economic Issues.

G. Contreras-Zarazúa,^a M.E. Jasso-Villegas,^a E. Sanchez-Ramirez,^a J.A. Vazquez-Castillo,^a J.G. Segovia-Hernandez^{a,*}

^a *Department of Chemical Engineering University of Guanajuato, Noria Alta S/N, Guanajuato, Gto., 36000, Mexico.*

^b *Faculty of Chemical Sciences Autonomous University of Chihuahua, Circuito Universitario 8, Campus II, Chihuahua, Chih. 31125,*

g_segovia@hotmail.com

Abstract

In this work have been designed and optimized simultaneously three different process separations for purify furfural, using Differential Evolution with Tabu List Algorithm. The study cases are a conventional Quaker Oats process, a thermally coupled process and liquid-liquid extraction process. The objective of this work is select the best alternative to purify furfural taken into consideration economic, environmental and safety issues. The results show which the thermally coupled process has several improvements and reductions on the risk, similar cost and environmental impact compared with Quaker Oats process. While the liquid-liquid extraction process does not have any improvement in the objective function, these results are associated with the use of entrainer in this sequence with respect to Quaker Oats Process. Therefore, due to the important improvements in safety issues the TCP process is choosing as the best alternative.

Keywords: Furfural, Process Bio-Refinery, Safety, Optimization Processes.

1. Introduction

In the last years the furfural has aroused a special interest due to it is a chemical produced from biomass, which can compete with the petrochemicals. The US National Renewable Energy Laboratory (NREL) has listed the furfural as one of the 30 most important chemicals produced from biomass, due to their wide applications such as precursor in the production furfural-acetone polymers, extract agents, lubricant oils, nematocide and in the production of furfuryl alcohol which is used in the production of thermoset polymers (Niehn et al. 2016).

The furfural is produced from five carbon sugars as xylose and arabinose which are contained in the hemicellulose fraction of biomass. In an industrial scale the furfural is produced through Quaker Oats process, which is used since 1922. This process is based in two zones: a reaction and separation zones. In the reaction zone, the biomass is treated with sulphuric acid in order to release xylose and convert it into furfural, then a high pressure vapour stream is introduced to reactor in order to remove the furfural and avoid their resinification. During the purification stage, the vapour from the reactor which is

rich in water, methanol, acetic acid and furfural is condensed and then it is feeding to a distillation sequence where the furfural is purified. This process has several disadvantages, one of the most important is the high separation cost due to large amount of water contained in the stream that is introduced to the purification zone. The presences of water imply the formation of azeotropes and therefore, is necessary the use of complex and expensive separation alternatives. However, despite the high separation costs of the Quaker Oats process has been used until now, because their easy implementation and lower cost compared with other alternatives (Zeitsch; 2000). Therefore, in this work are studied three different process separation alternatives for purify furfural. The total annual cost (TAC), eco-indicator (EI99) and the individual risk (IR) as economic, environmental and safety indexes respectively are used to evaluate. The novelty of this work since the point of view of circular economy is that, the optimization and identification of best process parameters allow for get a sustainable and profitable process for purify furfural with the less emissions and residues (Geissdoerfer et al. 2017). In the same time, the determination of best optimal parameters allows for the identification of safest process and operating conditions. In other hand the optimization of these 3 objective functions provide the generation of green and friendly process with the environment according with the reported by Jiménez-González and Constable, (2011).

2. Methodology

In this work three different processes distillation to purify furfural have been studied; the Quaker Oats process (QO), a thermally coupled process (TCP) and extractive distillation process (ED). The QO process consist in three distillation columns, the first equipment is an azeotropic distillation column (C1), wherein the mixture is concentrated until the heterogeneous azeotrope concentration. In the column C2 the methanol is recovered by the top if this equipment, and the column C3 where the furfural is purified in the bottoms column and the bottoms and the top products of columns C2 and C3 are sent to decanter. A side stream is withdrawn between the top and bottom of C1, this stream contains a mixture rich in water and furfural, which is sent to a decanter where the organic phase rich in furfural is purified in a third column (C3) (Zeitsch; 2000). In the case of TCP process is generated from the Quaker Oats process by the replacement of condenser associated to the first column, which was substituted by vapour and liquid streams that are linked in the last and penultimate stages of the rectification zone. The last scheme is the liquid-liquid extraction coupled with a distillation process (ED), which consist a liquid-liquid extractive column (E1) where the butyl-chloride is used as entrainer for separate the furfural from the water mixture according to reported by Nhien et al. 2016. Stream rich in solvent and furfural is obtained by the top of extractive column and subsequently the butyl-chloride and furfural are separated in a conventional distillation column (C1) whereas the C2 is used as a prefractionator and C3 is used for purify the methanol. This scheme was studied previously by Nhien et al. 2016. The Figure 1 shows the schemes of the study cases.

In order to perform this study, the most general and extendible possible to the majority of furfural plants, the average composition reported by Zeitsch has been considered. This composition consists in water 90 %wt, furfural 6 %wt, methanol 2 %wt, and acetic acid 2 %wt. The mass flow rate considered in this work is 105,000 kg/hr that corresponds to the estimated global furfural demand reported by Nhien et al 2016. The thermodynamic property model used to simulate the liquid-liquid-vapour equilibrium is Non-random Two-Liquids with Hayden-O'Connell equation of state (NRTL-HOC), which takes into

account the two liquid phases and the dimerization and solvation characteristics of mixtures with carboxylic acids. All processes separations were simulated rigorously using the software Aspen Plus. The Total Annual Cost (TAC), Eco-Indicator 99 (EI99) and the individual risk (IR) as objective functions to be minimized.

The total annual cost has been computed using the Guthrie methodology, wherein the cost is calculated as the sum annualized of capital cost (cost of all equipments process) and the operating cost, which are associated with the use of steam, cooling water and electricity. All parameters used for calculated the TAC were taken from Turton et al. 2008. Ten years were assumed as payback period, whereas carbon steel is considered as construction material for the process equipments. The operating costs included cooling utilities, heating utilities and 8500 hours per year of operation for each alternative have been considered. Mathematically, the TAC can be defined according with Eq. (1).

$$TAC = \frac{\text{Capital cost}}{\text{Payback period}} + \text{Operating cost} \quad (1)$$

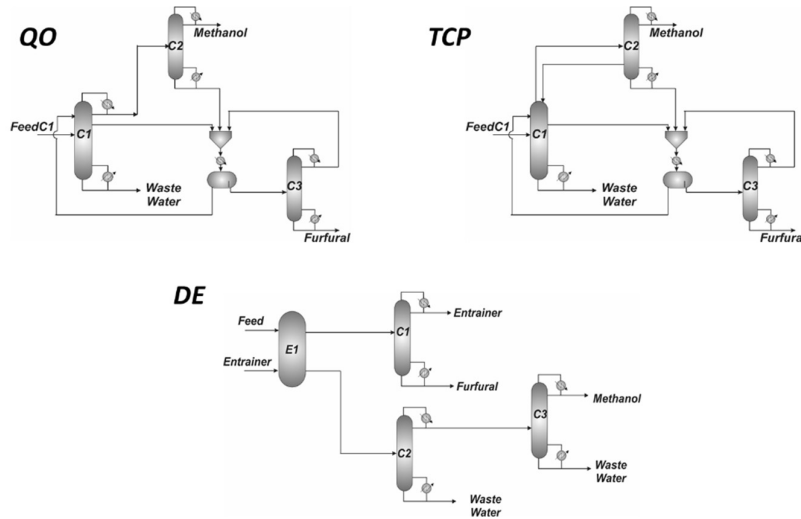


Figure 1. Processes separation schemes.

The EI99 is used to calculate the environmental impact that provokes of each case of study. This approach is based in the evaluation of three impact categories: human health, ecosystem quality, and resources depletion. This method has been successfully implemented in some previous works as the showed by Quiroz-Ramirez et al 2017. According to importance of three major impact categories the weighting for eco-indicator 99 was considered as follows: damages to human health and damage to ecosystem quality are of equal importance, thus these were equally weighted while the damage to the resources was considered to be half of importance weight. The EI99 can be expressed mathematically as:

$$EI99 = \sum_b \sum_d \sum_{k \in K} \delta_d \omega_d \beta_b \alpha_{b,k} \quad (2)$$

where β_b represents the total amount of chemical b released per unit of reference flow due to direct emissions, $\alpha_{b,k}$ is the damage caused in category k per unit of chemical b released to the environment, ω_d is a weighting factor for damage in category d , and δ_d is a normalization factor for damage of category d , respectively. the weights and the values for the impact categories were taken from Quiroz-Ramirez et al 2017.

Finally, the individual risk is an index used to quantify the security of a process, it is calculated through a quantitative risk analysis wherein the damage caused by accident is identified and quantified. For all the cases of study have been identified seven possible accidents divided in two categories. Instantaneous incidents: Boiling liquid expanding vapour explosion (BLEVE), unconfined vapour cloud explosion (UVCE), flash fire and toxic release, and whereas the continuous release incidents are: jet fire, flash fire and toxic release. For Calculate the individual risk a reference distance of 50m were chosen. The complete set equations for calculate the IR is showed by Medina-Herrera et al. 2014. The mathematical equation that describes the individual risk is the following:

$$IR = \sum f_i P_{x,y} \quad (3)$$

where f_i is the occurrence frequency of incident i , whereas $P_{x,y}$ is the probability of injury or decrease caused by the incident i .

The multi-objective optimization problem was solved using the mathematic technique called differential evolution with tabu list (DETL.). The values of parameters required by DETL method are: Population size: 120 individuals, Generations Number: 710, Tabu List size: 60 individuals, Tabu Radius: 0.01, Crossover fractions: 0.8, Mutation fractions: 0.3. The DETL method and the objective functions were implemented in a hybrid platform, which link Aspen PlusTM and Microsoft ExcelTM through Visual Basic. The design variables for the different study cases are showed in the Table 1.

Finally, the overall optimization problem can be mathematically expressed as in Eq. (4) and Eq. (5):

$$\min Z = \{TAC; Eco99; IR\} = \left\{ \frac{\text{Capital cost}}{\text{Payback period}} + \text{Operating cost}; \sum_b \sum_d \sum_{k \in K} \delta_d \omega_d \beta_b \alpha_{b,k}; \sum f_i P_{x,y} \right\} \quad (4)$$

$$\text{Subject to: } \begin{aligned} y_{i,F} &\geq x_{i,F} \\ w_{i,F} &\geq u_{i,F} \end{aligned} \quad (5)$$

The objective functions are restricted to satisfy the purity ($x_{i,PC}$) and mass flowrate ($u_{i,PC}$) specifications of furfural. The minimum purity of mass flowrate for furfural were fixed to 99.2%tw and 6200kg/ hr respectively.

3. Results

In this section is showed the results obtained during the simultaneous design and optimization for the three alternatives. In order to simplify the results analysis, the Pareto graphs are studied. The Figure 2 shows a representative Pareto front for TCP scheme,

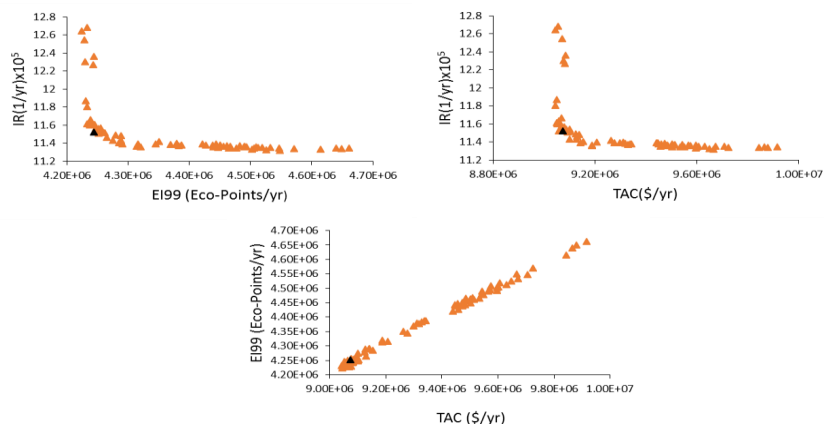
wherein the QO and DE processes shows exactly the same behaviour. In the Figure 2, can be observed that Pareto front of total annual cost versus eco-indicator 99 have a linear dependency with an only one minimum to both objectives, while the other two charts show an opposite behaviour where the minimum TAC and EI corresponds to a design with highest risk and vice versa. The points selected as the best designs corresponds to black point, these were chosen, because are the points that provides an equilibrium between the three objectives. In the same way the designs for QO were chosen. The Table 1 shows the optimal design specifications for all separation schemes.

Table 1. Values of design variables for all process.

Design specifications	QO	TCP	DWC
Stages, C1	55	91	53
Stages, C2	12	40	50
Stages, C3	6	8	50
Stages E1	-----	-----	17
Feed stage recycle of C1	22	15	-----
Feed stage, C1	27	55	35
Stage of side stream C1	16	39	-----
Feed stage C2	8	16	27
Feed stage C3	3	2	9
Diameter of C1, m	.44	1.1	1
Diameter of C2, m	.42	.9	3.0
Diameter of C3, m	1.63	1.67	1.2
Diameter of E1, m	-----	-----	.58
Entrainer flowrate kg/hr			38945.2
Reflux ratio of C1	18.5	-----	0.2
Reflux ratio of C2	0.21	25.45	18.5
Reflux ratio of C3	0.208	.353	5.1
Heat duty of C1, kW	19096.8	19357	5490.51
Heat duty of C2, kW	770.17	115.702	21912
Heat duty of C3, kW	456	1007.4	3030.4
Interlinking flow, kg h ⁻¹	-----	3649.2	-----
Values of objective functions			
TAC (\$/yr)x10 ⁶	9.334	9.301	13.91
Eco99 (Eco-points) x10 ⁶	4.335	4.3623	6.534
IR (1/yr) x10 ⁵	18.674	13.548	36.00

Due to the large amount of water in the feed stream, the column C1 in the process QO and TCP has the greater contribution for energy, thus is the biggest equipment and it has more impact in the economic and environmental indexes. In the case of DE process, it does not have important reductions in the TAC and EI99 because the large amount of water is removed in the liquid-liquid extraction column, which need be purify in order to purify the methanol. In other hand, the DE process has not any saving or improves on TAC, EI99 and IR, which makes it the worst option. The results obtained in the DE process can be explained due to the addition of the solvent. The entrainer need be recovered in a distillation column, increasing the separation cost and the environmental impact caused by the use of energy. In the case of IR, an increment in the risk is observed because the C1 column contains mainly large amounts of solvent increasing the likelihood of releases and fires, and damage caused by a probable accident. TCP process is choosing as the best option of the three alternatives studied. The TCP process has similar EI99 and

TAC respect to Quaker Oats process, however the replacing of condenser in C1 column results in a shorter resident times and lower inventory inside of C1 reducing the risk.



4. Conclusions

In this work three different process separation of furfural have been designed and optimized simultaneously, considering economic, environmental and safety issues, in order to find the most sustainable and safest process. The results indicate that ED process has not improvements with respect to any objective due to the addition of important amounts of solvent which need be separate. The entrainer used in ED process is an organic component, which is flammable and toxic and therefore its use affects the safety index. In other hand, the TCP do not have important savings in TAC and EI99 with respect to Quaker Oats process, but the interconnection flows between the top of C1 and the C2 promotes that the concentration of water inside of C2 be greater which causes a dilution of methanol and reduce the risk. The TCP process is chosen as the best alternative due to it has important improvements in security aspects.

References

- Geissdoerfer, M., Savaget, P., Bocken, N. M., & Hultink, E. J. (2017). The Circular Economy—A new sustainability paradigm?. *Journal of cleaner production*, 143, 757-768.
- Jiménez-González, C., & Constable, D. J. (2011). *Green chemistry and engineering: a practical design approach*. John Wiley & Sons.
- Medina-Herrera, N., Jiménez-Gutiérrez, A., & Mannan, M. S.; Development of inherently safer distillation systems. *Journal of Loss Prevention in the Process Industries*, 2014, 29, 225-23
- Nhien L. C., Van Duc Long N., Lee M.; (2017) Process design of hybrid extraction and distillation processes through a systematic solvent selection for furfural production. *Energy Procedia*, 105, 1084-1089
- Quiroz-Ramírez, J. J., Sánchez-Ramírez, E., Hernández-Castro, S., Segovia-Hernández, J. G., Ponce-Ortega, J. M.; (2017). Optimal planning of feedstock for butanol production considering economic and environmental aspects, *ACS Sustainable Chemistry & Engineering*, 5(5), 4018-4030.
- Turton, R., Bailie, R. C., Whiting, W. B., & Shaeiwitz, J. A. (2008). *Analysis, synthesis and design of chemical processes*. Pearson Education
- Zeitsch, K. J. (2000). *The chemistry and technology of furfural and its many by-products* (Vol. 13). Elsevier.

Revisiting Classic Acetic Acid Synthesis: Optimal Hydrogen Consumption and Carbon Dioxide Utilization

Juan D. Medrano-García,* Rubén Ruiz-Femenia, Jose A. Caballero

*Institute of Chemical Process Engineering, University of Alicante, PO 99E-03080
Alicante, Spain*

jd.medrano@ua.es

Abstract

Acetic acid is a bulk chemical with many applications in the manufacture of several important products. The carbon footprint of its classic synthesis process (methanol carbonylation) is around 1.3921 - 1.8746 kg CO₂-eq/kg, which adds up as the commodity is used in further syntheses. Hence, a reduction in the acetic acid synthesis Global Warming Potential (GWP) would impact in many end products GWP. We propose an acetic acid synthesis superstructure, including different syngas synthesis processes, gas separation technologies and methanol synthesis, which is aimed at reducing both the cost and GWP of the process. Results show that, integrating the methanol synthesis process provides the best results in both objectives. When minimizing the cost (classic synthesis) is best to use an Auto-thermal Reforming (ATR) and CO absorption configuration (0.388 \$/kg, 1.832 kgCO₂-eq/kg). Adding a fuel cell and a Reverse Water Gas Shift (RWGS) reactor overall reduces both cost and emission (0.280 \$/kg, 1.590 kgCO₂-eq/kg) of the synthesis and changes the configuration to Partial Oxidation (POX) and cryogenic distillation. Minimum emission (0.102 kgCO₂-eq/kg) can also be achieved with the fuel cell plus RWGS combo, POX and Pressure Swing Adsorption (PSA), although the cost is almost tripled (0.978 \$/kg).

Keywords: CO₂ utilization, methane reforming, carbon monoxide separation, reverse water gas shift, acetic acid synthesis

1. Introduction

Acetic acid, with a high and ever-increasing annual production of more than 14 Mt (2017), is an important chemical used to synthesize vinyl acetate (vinyl acetate monomer, VAM), terephthalic acid (polyethylene terephthalate, PET) and acetate anhydride (cellulose flake) among others (“IHS Markit: Acetic Acid,” 2018). However, the most extended process for acetic acid production, methanol carbonylation, whose two main raw materials are carbon monoxide and methanol, provokes an appreciable carbon footprint of 1.3921 - 1.8746 kg CO₂-eq/kg (“Ecoinvent Database 3.4,” 2017). On the other hand, it is well-known that in methanol synthesis it is possible to consume CO₂. Furthermore, the main source of CO is syngas separation, hence CO₂ can also be used in syngas synthesis (Medrano-Garcia et al., 2017) allowing for further consumption of the gas. Therefore, consuming CO₂ and decreasing the overall Global Warming Potential (GWP) in acetic acid synthesis would accomplish a significant reduction in global CO₂ emissions due to the relevance and high production of this commodity.

We propose a process superstructure in which carbon monoxide and methanol synthesis are integrated with the production of acetic acid. Seven different syngas synthesis processes, both classic and CO₂-consuming (Table 1) along with several gas separation technologies (adsorption, absorption and cryogenic distillation) for each gas component are considered. In addition, the hydrogen byproduct in the CO separation step can be used as fuel elsewhere in the process, as a methanol raw material or as reactant in the reverse water gas shift reactor (RWGS) to increase CO production while consuming additional CO₂. Additionally, heat integration is included across the whole model. We address the existence or non-existence of the units using the Generalized Disjunctive Programming (GDP) and then transforming the disjunctions into algebraic equations using the Hull reformulation (Lee and Grossmann, 2000). We perform multi-objective optimizations of the resulting MINLP model using the epsilon constraint method, minimizing the cost (\$/kg) (1) as our economic indicator and the Global Warming Potential (GWP) (kg CO₂-eq/kg) (2) as our environmental indicator:

$$cost = \frac{\text{Annualized Capital Cost} + \text{Raw material Cost} + \text{Utility Cost}}{\text{Acetic acid production}} \quad (1)$$

$$emission = \frac{\text{Raw material GWP} + \text{Utility GWP} + \text{Outlet CO}_2 - \text{Inlet CO}_2}{\text{Acetic acid production}} \quad (2)$$

Results show that the RWGS reactor acts as an important sink of CO₂ while reducing the raw materials needed in the syngas synthesis step, and therefore reducing the overall cost and emission of the process. Emissions can be reduced, approximately, 1 kg CO₂-eq per kg of acetic acid.

Table 1. Reforming agents used in methane reforming technologies.

	SMR	POX	ATR	CR	DMR	BR	TR
Steam	X		X	X		X	X
O₂		X	X	X			X
CO₂					X	X	X

SMR: Steam Methane Reforming; POX: Partial Oxidation; ATR: Auto-thermal Reforming; CR: Combined Reforming; DMR: Dry Methane Reforming; BR: Bi-Reforming; TR: Tri-Reforming.

2. Methodology

2.1. Superstructure overview

The aim of this work is the reduction of the GWP in the production of acetic acid using the methanol carbonylation classic process. This technology requires both a methanol and carbon monoxide feed. In the proposed superstructure, carbon monoxide is produced by separation of syngas. On the other hand, methanol is manufactured using a mixture of this syngas, H₂ separated as the result of purifying the CO, and a fraction of the CO itself, in addition to possibly being bought from an external source. Furthermore, removed H₂ can be used as fuel or as feedstock in a Reverse Water Gas Shift (RWGS) reactor that, while consuming CO₂, produces additional CO. In addition, depending on its purity, it can be used in a fuel cell that supplies the system electricity. The off-gas produced by the gas separation can also burn as fuel or be partially recycled in order to further remove valuable gases from it. The proposed superstructure is shown in Figure 1.

First, the raw materials, which include methane and a reforming agent (steam, oxygen, carbon dioxide or a combination), enter the syngas synthesis section of the superstructure. Here, the feedstock is compressed and heated up to the reaction pressure and temperature. Then, the mixture enters the reformer reactor where syngas is the product. Each syngas process operates at different feed ratios, pressures and temperatures, in addition to producing syngas with different compositions. These process variables are fixed to the most common values found in the bibliography for industrial operation. These values and employed models for the syngas synthesis section can be found in Medrano-Garcia et al. (2017). The syngas stream is then headed to the gas separation section, where it first encounters a phase separator (40 °C) that removes all the water contained in the gas. The option of capturing CO₂ is given next in a diglycolamine (DGA) absorber. This CO₂ can be used as feedstock in the syngas synthesis step and RWGS reactor, or just be assigned for storage. The RWGS reactor works using an H₂/CO₂ inlet ratio fixed at seven, operating temperature of 300, 350, 400 or 450 °C and according CO₂ conversion of 11.6, 45.0, 77.6 or 85.9 % (Wolf et al., 2016). Next, a Pressure Swing Adsorption (PSA) unit targeting H₂ can be used to remove this gas from the syngas. This H₂, due to the purity a PSA separation can achieve, is a valid option for fuelling the fuel cell, in addition to be used as fuel or as feedstock in the methanol synthesis loop and/or RWGS reactor. After the H₂ removal option, a fraction of the syngas can be diverted in order to feed the methanol synthesis loop. The remaining syngas then arrives to the CO separation section of the superstructure, where cryogenic distillation, chemical absorption or a CO-targeting PSA can be chosen for the task. These technologies provide an off-gas in addition to the CO-rich product stream and, in the case of cryogenic distillation, also an H₂-rich stream. The off-gas can burn as fuel or be partially recycled back just before the H₂ PSA in order to further remove valuable gases from it. The H₂-rich stream can also be used as fuel or as a raw material for the RWGS reactor or the methanol synthesis loop. Note that the H₂-rich steam purity is insufficient for its use in the fuel cell, and hence this option is not considered. Finally, the CO-rich stream is given the possibility of removing any remaining CO₂ contained in it with a second ammine absorber. After this step, it can be split so that it can feed both the acetic acid synthesis process and the methanol synthesis loop if needed.

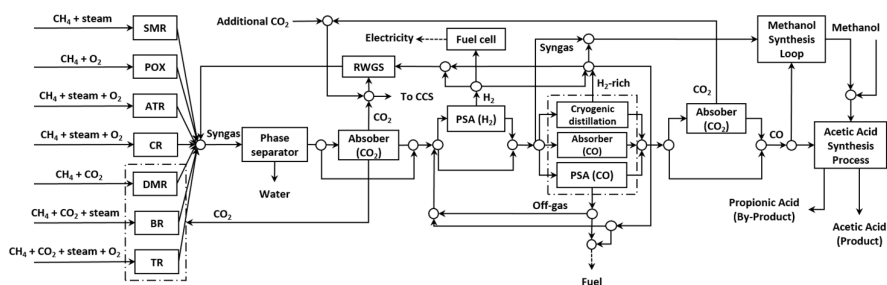


Figure 1. Proposed process superstructure for the integration, synthesis and separation of syngas, methanol and acetic acid.

2.2. Methanol synthesis loop

The methanol synthesis loop can be seen in Figure 2. The loop is modelled using linear equations derived from simulations studies in Aspen HYSYS v9.0 with the aim of achieving minimum cost and emission in the synthesis (Medrano et al., 2017). Syngas at 40 °C and 30 bar, with an $(\text{H}_2\text{-CO}_2)/(\text{CO}+\text{CO}_2)$ ratio of 2.00 (2.04 in the reactor inlet) and

5 % CO₂ content enters the loop and is compressed to 76.5 bar and heated up to 284.2 °C. The reaction takes place in a plug flow reactor modelled after (Bussche and Froment, 1996) kinetics. The resulting stream then gets depressurized and cooled down to 10 bar and 40 °C. In a phase separator, crude methanol (96.4 % wt. methanol content) is obtained and sent to the acetic acid synthesis process. The unreacted syngas stream is partially purged (5 %, to burn as fuel), recompressed and recycled back to the heating stage.

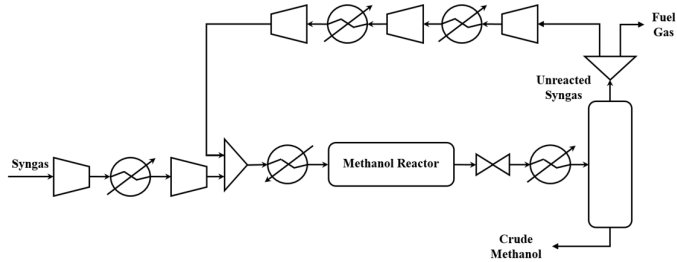


Figure 2. Proposed methanol synthesis loop embedded in the superstructure.

2.3. Acetic acid synthesis

The acetic acid synthesis process is shown in Figure 3 (Cheung et al., 2000):

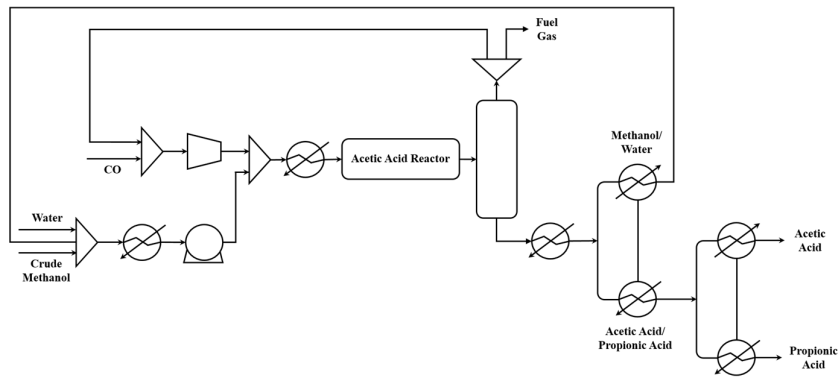
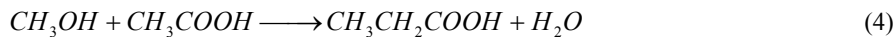


Figure 3. Proposed acetic acid synthesis process embedded in the superstructure.

Methanol, CO (40 °C, 1 and 30 bar respectively, 1:1 molar ratio) and water (40 °C, 1 bar), enter the process and are compressed and heated up to 30 bar and 175 °C. The catalyst needs water (4.0 - 4.5 % wt.) in order to activate the carbonylation reaction, which allows the use of crude methanol as a feedstock for the process, hence resulting in the omission of the methanol purification column. Inside the reactor, the following reactions take place:



For the main reaction, the synthesis of acetic acid (3), a CO conversion of 60 % is considered. The parallel reaction of the formation of propionic acid (4) as a byproduct transforms 1 % of the produced acetic acid in reaction (3). Lastly, the Water Gas Shift

(WGS) equilibrium reaction (5), is assumed to have a CO conversion of 10 %. After the reaction, the gaseous phase is recycled (50 % purged, to fuel gas) and the liquid phase is separated (86.25 °C, 1 bar, 62 stages) into a methanol-water stream, which is recycled, and an acetic acid-propionic acid stream which is further separated (116.97 °C, 1 bar, 62 stages) into the product (99.87 % wt. acetic acid) and byproduct (99.13 % wt. propionic acid).

3. Results and discussion

The resulting MINLP model consists of 2,029 equations and 1,587 variables, 25 of which are binary variables. The solving time was 1,667 s per case in an Intel Core 2 Quad with an 8GB RAM. The multi-objective optimization is performed applying the epsilon constraint method and using the solver ANTIGONE (Misener and Floudas, 2014) within GAMS (GAMS, 2018). The main results are shown in Figure 4. The use of specific syngas synthesis processes is separated into areas by dashed lines, while dotted lines split RWGS operating conditions and CO separation units. In addition, all solutions include the integrated methanol synthesis process.

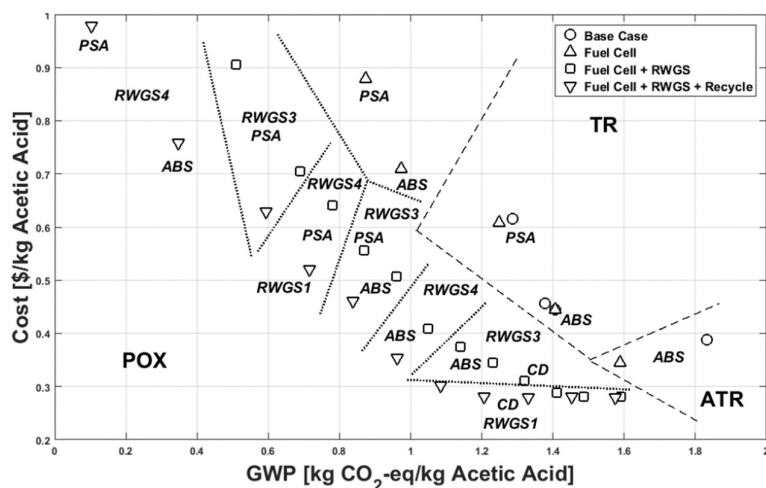


Figure 4. Results of the multi-objective optimization for the synthesis of acetic acid.

Results show that, minimizing the cost in classic (base case) acetic acid synthesis (0.388 \$/kg, 1.832 kgCO₂-eq/kg) requires ATR as the syngas synthesis process and absorption of CO (ABS) as the CO separation technology. Including a fuel cell reduces overall cost and emission (0.345 \$/kg, 1.587 kgCO₂-eq/kg) without changing the main configuration units. Adding the RWGS reactor provides a significant decrease in cost (0.280 \$/kg, 1.590 kgCO₂-eq/kg) and changes the configuration into using POX and cryogenic distillation (CD). Allowing the partial recycle of off-gas streams (0.280 \$/kg, 1.575 kgCO₂-eq/kg) barely reduces the emission maintaining cost invariable. On the other hand, when minimizing the emission, the addition of the fuel cell (0.873 \$/kg, 0.879 kgCO₂-eq/kg) more than doubles the synthesis cost of the base case while reducing GWP value almost by 1 kgCO₂-eq/kg. The RWGS reactor inclusion (0.906 \$/kg, 0.510 kgCO₂-eq/kg) further reduces emission and increases the cost. Finally, when off-gas streams are free to recycle (0.978 \$/kg, 0.102 kgCO₂-eq/kg) the cost of the synthesis peaks, almost tripling the base case, while the emission reaches its minimum, reducing the base case emission by more than 1.7 kgCO₂-eq/kg; almost achieving carbon neutrality.

4. Conclusions

In this work, we propose an acetic acid synthesis superstructure in order to minimize both the cost and the emission of the production of this commodity. Integrating several methane reforming processes, gas separation technologies and methanol synthesis, we perform multi-objective optimizations of the resulting MINLP model in order to achieve the optimal configurations. Results show that for all cases, methanol should be produced simultaneously with acetic acid to minimize both cost and emissions.

Comparison with the minimum cost configuration (0.388 \$/kg, 1.832 kgCO₂-eq/kg) states that the cost of the synthesis can be further reduced using a fuel cell and a RWGS reactor with POX and cryogenic distillation (0.280 \$/kg, 1.590 kgCO₂-eq/kg), while recycling the process off-gases barely has an effect. On the other hand, emissions can be significantly decreased with the same configuration but using a PSA instead (0.906 \$/kg, 0.510 kgCO₂-eq/kg), however, off-gas recycling does have an effect in further reducing the emission (0.978 \$/kg, 0.102 kgCO₂-eq/kg), where the decrease surpasses 1.7 kgCO₂-eq/kg.

Acknowledgements

The authors gratefully acknowledge financial support to the Spanish «Ministerio de Economía, Industria y Competitividad» under project CTQ2016-77968-C3-2-P (AEI/FEDER, UE) and «Generalitat Valenciana: Conselleria de Educació, Investigació, Cultura y Deporte» for the Ph.D. grant (ACIF/2016/062).

References

- Bussche, K.M.V., Froment, G.F., 1996. A Steady-State Kinetic Model for Methanol Synthesis and the Water Gas Shift Reaction on a Commercial Cu/ZnO/Al₂O₃Catalyst. *J. Catal.* 161, 1–10.
- Cheung, H., Tanke, R.S., Torrence, G.P., 2000. Acetic Acid, in: *Ullmann's Encyclopedia of Industrial Chemistry*. Wiley-VCH Verlag GmbH & Co. KGaA, Weinheim, Germany.
- Ecoinvent Database 3.4 [WWW Document], 2017. URL <https://www.ecoinvent.org/> (accessed 7.15.18).
- GAMS Development Corporation. General Algebraic System (GAMS) Release 25.0.3. Washington, DC, USA, 2018, n.d.
- IHS Markit: Acetic Acid [WWW Document], 2018. URL <https://ihsmarkit.com/products/acetic-acid-chemical-economics-handbook.html> (accessed 2.1.18).
- Lee, S., Grossmann, I.E., 2000. New algorithms for nonlinear generalized disjunctive programming. *Comput. Chem. Eng.* 24, 2125–2141.
- Medrano-García, J.D., Ruiz-Femenia, R., Caballero, J.A., 2017. Multi-objective optimization of combined synthesis gas reforming technologies. *J. CO₂ Util.* 22, 355–373.
- Medrano, J.D., Ruiz-Femenia, R., Caballero, J.A., 2017. Multi-objective Optimization of a Methanol Synthesis Process Superstructure with Two-step Carbon Dioxide Consumption. *Comput. Aided Chem. Eng.* 40, 721–726.
- Misener, R., Floudas, C.A., 2014. ANTIGONE: Algorithms for coNTinuous / Integer Global Optimization of Nonlinear Equations. *J. Glob. Optim.* 59, 503–526.
- Wolf, A., Jess, A., Kern, C., 2016. Syngas Production via Reverse Water-Gas Shift Reaction over a Ni-Al₂O₃ Catalyst: Catalyst Stability, Reaction Kinetics, and Modeling. *Chem. Eng. Technol.* 39, 1040–1048.

Innovative application of statistical analysis for the optimization of CO₂ absorption from flue gas with ionic liquid

Grazia Leonzio,^{a,*} Edwin Zondervan,^b

^a*Department of Industrial and Information Engineering and Economics, University of L'Aquila, Via Giovanni Gronchi 18, 67100 L'Aquila, Italy*

^b*Laboratory of Process Systems Engineering, Department of Production Engineering, Universität Bremen, Leobener Str. 6, 28359 Bremen, Germany*

grazia.leonzio@graduate.univaq.it

Abstract

In this research, a model for the physical absorption of CO₂ from flue gas with [hmim][Tf₂N] ionic liquid, an innovative solvent used in the last CO₂ absorption processes, is developed in Aspen Plus and optimized through a central composite design by using Minitab. Then a unique combination of simulation and statistical analysis is carried out for the process. The aim is to find the optimal operating conditions that can maximize the amount of captured CO₂ while minimizing the total costs. The study shows the percentage of CO₂ removal is 93.7%, operating costs are 0.279 trillion euro/a and capital costs are 21.9 million euro/year. The obtained results are in agreement with other works reported in literature, considering the high cost for ionic liquid.

Keywords: CO₂ capture, ionic liquid, process simulation, statistical analysis, optimization.

1. Introduction

From the combustion of natural gas, oil, fuels-coal, globally 30 gigatons (Gt) per year of carbon dioxide are emitted impacting the environment dramatically (Wilcox et al., 2014; Tlili et al., 2014). Reducing emissions is critical, but at this time it is also important to capture carbon dioxide efficiently from emission sources. Chemical absorption by with amines is a common technology to capture carbon dioxide from flue gases (Nittaya et al., 2014; Lin et al., 2011). High reactivity, low cost, good absorption capacity, high affinity to carbon dioxide are some positive aspects of this technology. However, there are also serious disadvantages such as tendency for corrosion, high energy demand for regeneration and loss of solvent. Ionic liquids (ILs) are a promising and green alternative due to their low volatility, good dissolution, high decomposition temperature and stability, excellent chemical tunabilities, that allow to reduce the losses of solvent and energy for regeneration (Luo and Wang, 2017; Ma et al., 2018). Using ionic liquids as a solvent for CO₂ absorption is still a rather new carbon capture process. As an example: Valencia-Marquez et al. (2017) developed a mixed-integer nonlinear programming (MINLP) problem for absorption process to design the best ionic liquid that can ensure a recovery of CO₂ higher than 90% with a simultaneous optimal product and process design. Currently no study that employs ANOVA analysis, response surface methodology (RSM) by using central composite design has been used for optimizing the absorption

process of CO₂ by using ionic liquid. In particular, a process for the physical absorption of carbon dioxide from flue gas (coming from power plant) with 1-n-hexyl-3-methylimidazolium bis(trifluoromethylsulfonyl)amide ([hmim][Tf2N]) ionic liquid is developed in Aspen Plus. A similar work is not present in literature. The model is used to carry out a face centered central composite design (FCCCD) according to the response surface methodology (RSM) by using Minitab software with the aim to find the optimal operating conditions. In this way the factors (geometric and operating) and combination of factors that are significant can be identified. The aim is to improve the efficiency of the process reducing the costs. The inlet temperature of flue gas, absorption column pressure, the carbon dioxide composition of flue gas, the height of absorption column are the considered factors, while the percentage of carbon dioxide removal, operating costs (OPEX) and capital costs (CAPEX) are the analyzed responses.

2. Materials and methods

2.1 Description of the absorption process

A process for the absorption of CO₂ by flue gas of power plant is developed in Aspen Plus as in figure 1. In this process flue gas is composed by Ar, CH₄, H₂, N₂, CO, CO₂, H₂O, NH₃, H₂S. Absorber (RADFRAC model) is a packed bed with plastic pall rings of 0.025 m and packing surface area of 205 m²/m³. The height of each stage is 3 m. Compressed flue gas is fed at the bottom of the absorber, where IL contacts the flue gas, remove CO₂ and discharges the clean gas to the air. The stream existing at the bottom of absorber is rich in IL so it is sent to a flash to recover it and to recirculate to the absorber. The stream gas existing at the top of flash is mainly composed by CO₂ and water. Then it is cooled to 288 K in order to separate any water present, so that captured CO₂ can be compressed up to 150 bar in the following refrigerated compressors.

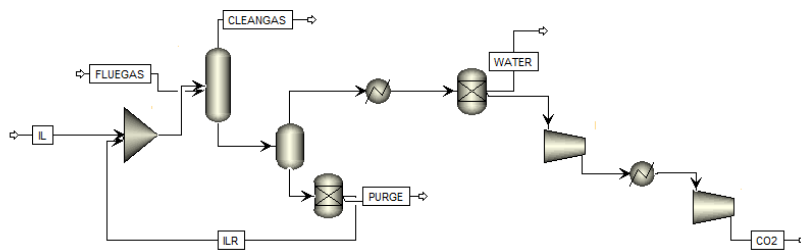


Figure 1 Process scheme of CO₂ absorption process from flue gas with IL in Aspen Plus environmental

The IL [hmim][Tf₂N] is characterized in Aspen Plus as new component by defining density, viscosity, surface tension, vapor pressure, heat capacity and critical properties as reported in Basha et al. (2013). The Peng Robinson Equation of State is chosen as thermodynamic model, by setting binary interaction parameter between each component

via regression analysis (Basha et al., 2013). The amount of flue gas entering the column is 25.63 kg/s, while the amount of fed IL is 280 kg/s.

2.2 Response surface methodology

A face centered central composite design is setup for the absorption process using the response surface methodology principle (Montgomery, 2005). From this design, the surface plots of considered responses with respective second order polynomial models can be obtained. The flue gas inlet temperature, column pressure, CO₂ composition in flue gas and the height of absorber are the selected factors. It is evident as operating and design factors are selected for the optimization of the process. The percent of CO₂ removal from flue gas, operating (costs of raw material and utilities) and capital costs are the analyzed responses. These costs are evaluated by using Aspen Process Economic Analyzer (APEA), considering a price for IL of 20 €/kg over a period of 20 year (Ramdin et al., 2012). Table 1 shows the values set for each level of factor. As shown, three levels are considered for each factor. For the statistical analysis, 31 simulation tests are carried out including 16 cube points, 7 axial points, 7 central points and 1 replication. Star points are set on the centers of each factorial face: the value of α is 1. The significance of each term in the obtained model is validated by analysis of variance.

Table 1 Values of level for each factor in FCCCD analysis

Code	Factor	Level		
		(-1)	0	(+1)
A	Flue gas inlet temperature (K)	323	411.5	500
B	Column pressure (bar)	15	22.5	30
C	CO ₂ composition in flue gas (mol%)	3	13.5	24
D	Height of absorber (m)	2	26	50

3. Results and discussions

The process scheme developed in Aspen Plus is used to carry out different simulations according to the face centered central composite design. From the parameters obtained from the simulation, a mathematical model is obtained for each analyzed response, as the capital costs, the operating costs, the percent of CO₂ removal from flue gas, respectively, as the following equations (Eqs 1-3):

$$CAPEX \text{ (euro)} = 22370478 - 427029 \cdot A + 1076170 \cdot B + 1288803 \cdot D \quad (1)$$

$$OPEX \left(\frac{\text{euro}}{\text{year}} \right) = 2.85 \cdot 10^{11} + 3.76 \cdot 10^9 \cdot DD \quad (2)$$

$$\begin{aligned} CO_2 \text{ removal (\%)} \\ = 72.42 + 23.59 \cdot B + 1.13 \cdot BC + 1.02 \cdot BD + 1.02 \cdot CD - 0.91 \\ \cdot D - 3.36 \cdot BB \end{aligned} \quad (3)$$

where factor A is the flue gas inlet temperature, factor B is the column absorber pressure, factor C is the CO₂ composition in flue gas and factor D is the height of column absorber. Results show that factor B, interaction BC, BD, CD have a positive effect on the percentage of carbon dioxide removal, while factor D and interaction BB have a negative effect on this response. For the operating costs the interaction DD has a positive effect. In addition, for the capital costs factor D and B have a positive effect, while factor A has a negative effect. It is evident that factors B, C and D have an overall stronger influence on the process while factor A only influences the capital costs. Figures 2, 3, and 4 show the surface plots for CAPEX, OPEX and CO₂ removal respectively obtained by Minitlab as function of two factors, while the others are set to a value of 0 level. It is possible to see especially for the surface plots of CAPEX and OPEX, that even if interactions between factors are not significant, they are present.

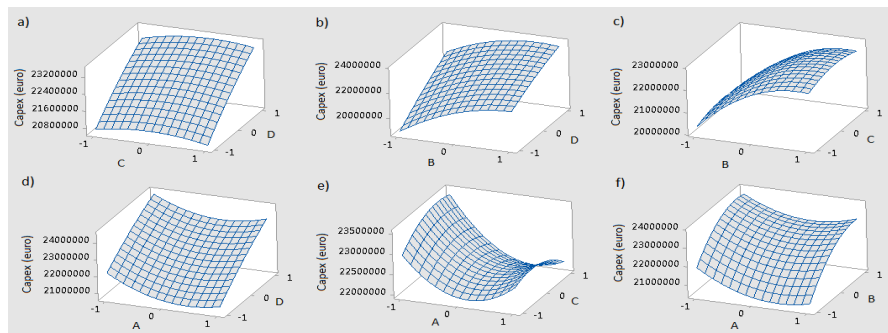


Figure 2 Response surface plots for CAPEX (euro): a) CAPEX (euro) as function of factor C and D; b) CAPEX (euro) as function of B and D; c) CAPEX (euro) as function of B and C; d) CAPEX (euro) as function of factor A and D; e) CAPEX (euro) as function of factor A and C; f) CAPEX (euro) as function of factor A and B. (Hold values: A=B=C=D=0).

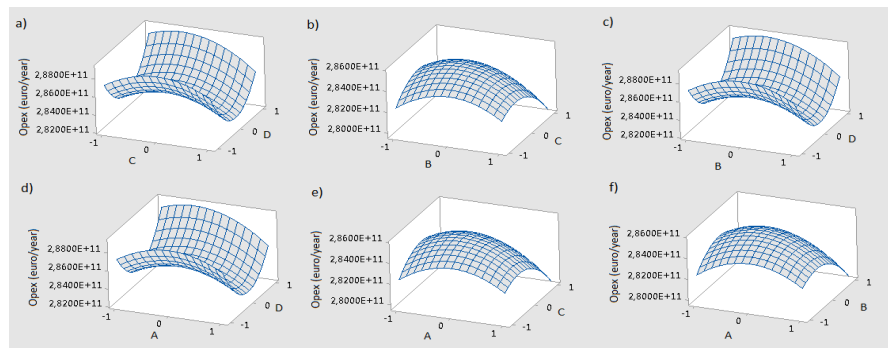


Figure 3 Response surface plots for OPEX (euro/year): a) OPEX (euro/year) as function of factor C and D; b) OPEX (euro/year) as function of factor B and C; c) OPEX (euro/year) as function of factor B and D; d) OPEX (euro/year) as function of factor A and D; e) OPEX (euro/year) as function of factor A and C; f) OPEX (euro/year) and function of factor A and B. (Hold values: A=B=C=D=0).

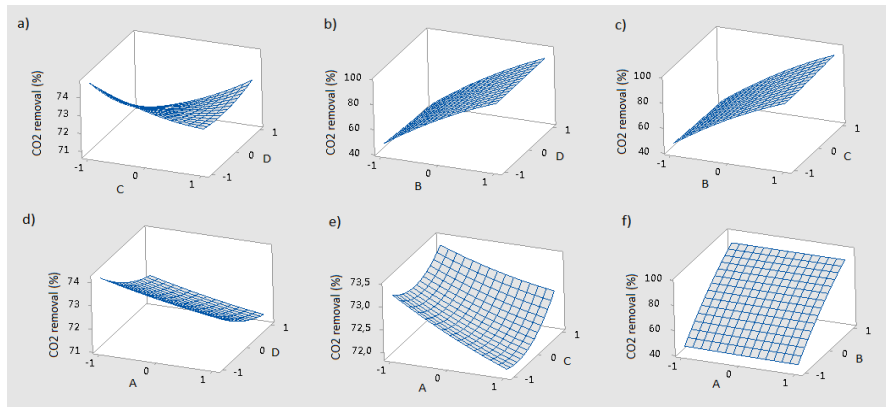


Figure 4 Response surface plots for CO₂ removal (%): a) CO₂ removal as function of factor C and D; b) CO₂ removal as function of factor B and D; c) CO₂ removal as function of factor C and B; d) CO₂ removal as function of factor A and D; e) CO₂ removal as function of factor A and C; f) CO₂ removal as function of factor A and B. (Hold values: A=B=C=D=0).

The operating conditions that maximize the capture of carbon dioxide and minimize the costs using a desirability function are found: factor A, B, C and D should be respectively equal to 500 K, 30 bar, 24 mol% and 1.36 m. The percentage of carbon dioxide removal is equal to 93.7%, the operating costs are 0.279 trillion euro/year and the capital costs are 21.9 million euro. The obtained values are supported by other studies. Significant reductions are made as compared to for example (Nguyen and Zondervan, 2018; de Riva et al., 2017). Capital and operating costs have not been reported for [himm][Tf2N] and comparison is not that easy. For other ionic liquids such as [Bmim][Ac], [bmim][BF₄] and [bmim][PF₆] economic data has been reported (Ma et al., 2017; Shiflett et al., 2010) but a straight comparison cannot be made. In the current study, the relation suggested by Nguyen and Zondervan (2018) for calculation of operating and capital costs in the case of [bmim][Ac] ionic liquid as function of flue gas flow rate and carbon dioxide composition is used. Results show that capital costs are in the same order, while a higher value for operating cost is obtained may be due to the high flow rate required and the cost of used IL.

4. Conclusions

In this research, an innovative optimization of physical absorption process to capture CO₂ from flue gas through ionic liquid ([himm][Tf₂N]) is developed and a similar work can not be found in literature. A new solution, as ionic liquid is considered due to its better properties compared to traditional ones. However, the high cost of this ionic liquid suggested to find the optimal operating conditions in order to maximize the amount of captured CO₂ and to reduce costs. A face centered central composite design is developed considering as factors flue gas inlet temperature, column absorber pressure, CO₂ composition in flue gas and the height of column absorber. Operating and capital costs and the amount of reduced CO₂ are considered as responses. Results show that to have an optimized process, flue gas inlet temperature, column absorber pressure, CO₂ composition in flue gas and the height of column absorber should be respectively equal

to 500 K, 30 bar, 24 mol% and 1.36 m. In this way, operating costs, capital costs and the percent of CO₂ removal are respectively 0.279 trillion euro/year, 21.9 million euro and 93.7%.

References

- Basha, O.M., Keller, M.J., Luebke, D.R., Resnik, K.P., Morsi, B.I., 2013. Development of a Conceptual Process for Selective CO₂ Capture from Fuel Gas Streams Using [hmim][Tf₂N] Ionic Liquid as a Physical Solvent, *Energy Fuels*, 2013, 27 (7) 3905–3917.
- de Rivaa, J., Suarez-Reyesa, J., Morenoa, D., Díaz, I., Ferro, V., Palomara, J., 2017. Ionic liquids for post-combustion CO₂ capture by physical absorption: Thermodynamic, kinetic and process analysis. *International Journal of Greenhouse Gas Control* 61, 61–70.
- Lin, Y.J., Pan, T.H., Wong, S.H., Jang, S.S., Chi, Y.W., Yeh, C.H., 2011. Plantwide control of CO₂ capture by absorption and stripping using monoethanolamine solution. *Am. Control Conf.* 50 (3), 1338–1345.
- Luo, X., Wang C., 2017. The development of carbon capture by functionalized ionic liquids, *Current Opinion in Green and Sustainable Chemistry* 3, 33-38.
- Ma, Y., Gao, J., Wang, Y., Hu, J., Cui, P., 2018. Ionic liquid-based CO₂ capture in power plants for low carbon emissions. *International Journal of Greenhouse Gas Control* 75, 134–139.
- Ma, T., Wang, J., Du, Z., Abdeltawab, A., Al-Enizi, A.M., Chen, X., Yu, G., 2017. Process simulation study of CO₂ capture by ionic liquids. *International Journal of Greenhouse Gas Control*, 58, 223-231.
- Montgomery, D.C. 2005. *Design and Analysis of Experiments*; John Wiley & Sons: New York, NY, USA.
- Nittaya, T., Douglas, P.L., Croise, E., Ricardez-Sandoval, L.A., 2014. Dynamic modelling and control of MEA absorption processes for CO₂ capture from power plants. *Fuel* 116, 672–691.
- Ramdin, M., de Loos, T.W., Vlugt, T.J.H., 2012. State-of-the-Art of CO₂ Capture with Ionic Liquids. *Ind. Eng. Chem. Res.* 2012, 51, 8149–8177
- Wilcox, J., Haghpanah, R., Rupp, E.C., He, J.J., Lee, K., 2014. Advancing Adsorption Membrane Separation Processes for the gigaton carbon capture challenge, *Annu. Rev. Chem. Biomol. Eng.* 5, 479-480.
- Shiflett, M.B., Drew, D.W., Cantini, R.A., Yokozeki, A., 2010. Carbon Dioxide Capture Using Ionic Liquid 1-Butyl-3-Methylimidazolium Acetate. *Energy Fuels*, 24 (10) 5781-5789.
- Tlili, A., Frogneux, X., Blondiaux, E., Cantat, T., 2014. Creating added value with a waste: methylation of amines with CO₂ and H₂, *Angew. Chem. Int. Ed.* 53, 2543-2545.
- Valencia-Marquez, D., Flores-Tlacuahuac, A., Vasquez-Medrano, R., 2017. An optimization approach for CO₂ capture using ionic liquids. *Journal of Cleaner Production* 168, 1652-1667

Optimization of a shell-and-tube heat exchanger using the grey wolf algorithm

Oscar D. Lara-Montaña^a and Fernando I. Gómez-Castro^a

^a*Departamento de Ingeniería Química, División de Ciencias Naturales y Exactas, Campus Guanajuato, Universidad de Guanajuato, Noria Alta S/N, Guanajuato, Guanajuato 36050, Mexico*
fgomez@ugto.mx

Abstract

Most chemical processes require heat exchangers to modify the temperatures of the streams involved in the production steps. Due to their many applications, the rigorous design of such exchangers is of interest, aiming to determine the physical characteristics required to obtain the desired variation in temperature. The mathematical models representing such devices have several degrees of freedom and non-linear equations, thus robust optimization algorithms are required to obtain the optimal solution in a short time. In this work, the use of the grey wolf algorithm is proposed for the optimization of a shell-and-tube heat exchanger, modeled by the Bell-Delaware equations. With the proposed method, a minimum total annual cost of 3,978.2 USD was obtained, in a mean time of 0.7976 seconds.

Keywords: meta-heuristic optimization, shell-and-tube heat exchanger, grey wolf algorithm.

1. Introduction

Heat exchangers are among the most used auxiliary equipment in chemical industry, since cooling and heating are common operations which allow modifying the temperature, or even the phase, of process streams, according to the operational requirements. This implies that heat exchangers are necessary for almost any chemical process. Shell-and-tube exchangers are widely used in industry to obtain wide ranges of temperature variations for streams from low to high flow rates, with high heat transfer efficiency due to the turbulence occurring on the shell. The design of a shell-and-tube heat exchanger involves several variables, which are usually related through energy balances and empirical correlations. One of the most common strategies to design heat exchangers in the industry is the Bell-Delaware method, which considers the variations of the convective heat transfer coefficient with the baffle configuration and phenomena occurring in the baffles, as leakage, pass partition bypass, among others. Nevertheless, the equations which model the heat exchanger are highly non-linear and non-convex, mainly due to the presence of fractional and logarithmic terms in the mathematical model. Moreover, some of the variables are integer, as the number of tubes, and other variables can be taken as continuous, but in practice they take discrete values, as the internal and external diameter of the tubes, which are constrained by the standard dimensions for commercial tubes. Thus, a robust method is necessary to obtain proper solutions to the optimal design problem of the heat exchanger. The use of meta-heuristic optimization strategies offers a viable alternative to the solution of such problem. In this work, a recently reported stochastic optimization method, namely, the grey wolf optimization algorithm, is proposed to solve the optimization problem for a shell-and-tube heat exchanger, represented by the Bell-Delaware model, aiming to the minimization of the total annual cost. The grey wolf optimization algorithm emulates the hunting mechanisms of grey wolves, and it has been reported that it possesses a superior

exploitation capacity than other meta-heuristic algorithms, together with a high capacity to avoid local optima (Mirjalili et al., 2014)

2. Grey Wolf Optimizer

Grey Wolf Optimizer (GWO) emulates the hunting technic of wolves. It was modeled by Mirjalili et al. (2014). This optimization algorithm considers the wolves hierarchy; alpha (α), is not necessarily the strongest but is the one who makes important decisions that affect the whole group; beta (β) wolves help the alpha in decision making activity, these wolves respect the alpha but command the other lower level wolves; omega (ω) are the lowest ranked wolves in the hierarchy, although they are the least important, they help to maintain the structure of the pack; delta (δ) wolves are those that are not in any of the previous categories, they have a lower hierarchy than alpha and betas but higher than the omega.

The GWO algorithm takes into account different actions within the hunting process:

- Tracking, chasing, and approaching the prey.
- Pursuing, encircling, and harassing the prey until it stops moving.
- Attack towards the prey.

2.1. Mathematical model

The GWO algorithm defines the fitness solution as alpha α , the second and third best solutions are beta β and gamma γ , respectively. Other solutions are named omega ω . The optimization process is guided by α, β and γ . As mentioned before, wolves tend to encircle its prey. This behaviour is modeled with the equations 1 and 2.

$$\vec{D} = |\vec{C} \cdot \vec{X}_p(t) - \vec{X}(t)| \quad (1)$$

$$\vec{X}(t+1) = \vec{X}_p(t) - \vec{A} \cdot \vec{D} \quad (2)$$

\vec{X}_p is the position vector of the prey, \vec{X} is the position vector of a grey wolf, \vec{A} and \vec{C} are coefficient vectors, and t is the current iteration. The vectors \vec{A} and \vec{C} are calculated according to the equations 3 and 4

$$\vec{A} = 2\vec{a} \cdot \vec{r}_1 - \vec{a} \quad (3)$$

$$\vec{C} = 2 \cdot \vec{r}_2 \quad (4)$$

where components of the vector \vec{a} are linearly decreased from 2 to 0 as the iterations pass, r_1 and r_2 are random vector with elements between 0 and 1.

In nature, grey wolves know where the prey is, however, in the mathematical framework we don't know where the optimum is (prey). To overcome this problem, it's supposed that the alpha, beta and delta wolves have a better idea about the position of the prey. Assumed this, the best three results are saved and oblige the other search agents to update their position. To simulate this, the equations 5-7 are used.

$$\vec{D}_\alpha = |\vec{C}_1 \cdot \vec{X}_\alpha - \vec{X}|, \vec{D}_\beta = |\vec{C}_2 \cdot \vec{X}_\beta - \vec{X}|, \vec{D}_\delta = |\vec{C}_3 \cdot \vec{X}_\delta - \vec{X}| \quad (5)$$

$$\vec{X}_1 = \vec{X}_\alpha - \vec{A}_1 \cdot (\vec{D}_\alpha), \vec{X}_2 = \vec{X}_\beta - \vec{A}_2 \cdot (\vec{D}_\beta), \vec{X}_3 = \vec{X}_\delta - \vec{A}_3 \cdot (\vec{D}_\delta) \quad (6)$$

$$\vec{X}(t+1) = \frac{\vec{X}_1 + \vec{X}_2 + \vec{X}_3}{3} \quad (7)$$

In summary, the population of wolves begins randomly within the search space. Each position of the wolves is a possible solution. The parameter \bar{a} decreases in each iteration from 2 to 0, this parameter indicates the exploration and exploitation capacity of the GWO. If the value of $|A \geq 1|$, the wolf diverges from the prey, if $|A \leq 1|$ the wolf converges towards the prey.

3. Heat Exchanger Mathematical Model

3.1. Heat transfer of shell side

The Bell-Delaware mathematical model is used to predict the shell-side convective heat transfer coefficient h_s . This model considers different parameters and geometrical variables (Shah and Sekulic, 2003). An ideal convective heat transfer coefficient h_i is calculated and corrected using five parameters j according to the equation 8.

$$h_s = h_i j_c j_l j_b j_s j_t \quad (8)$$

h_i is evaluated as

$$h_i = j \frac{C_{ps} Pr_s^{-2/3}}{A_{o,cr}} \quad (9)$$

where C_{ps} is the fluid heat capacity, Pr_s is the Prandtl number, and j_c, j_l, j_b, j_s, j_t are correction factors for baffle configuration, shell to baffle and tube to baffle leakage effects, bundle pass and partition bypass, baffle spacing, and temperature gradient, respectively. $A_{o,cr}$ is the flow area near the shell center-line for one cross-flow section and j is the Colburn factor, it is calculated with the equation 10 (Wildi-Tremblay and Gosselin, 2007). The variable a is determined with 11. The parameters a_1, a_2, a_3 and a_4 are reported in Wildi-Tremblay and Gosselin (2007).

$$j = a_1 \left(\frac{1.33}{Pt/d_o} \right)^a (Re_s)^{a_2} \quad (10)$$

$$a = \frac{a_3}{1 + 0.14 Re_s^{a_4}} \quad (11)$$

$$(12)$$

The Reynolds number Re_s is evaluated with equation 13, μ_s is fluid viscosity, m_s is the mass flow rate in shell-side and d_o is the tube external diameter.

$$Re_s = \frac{m_s d_o}{\mu_s A_{o,cr}} \quad (13)$$

The area of the heat exchanger area is calculated with the Equation 14.

$$A = \frac{Q}{U \Delta T_{ml} F_t} \quad (14)$$

where Q is the heat transfer rate, U is the global heat transfer coefficient, T_{LMDT} is the logarithmic mean temperature difference and F_t is a correction factor. The U coefficient depends of the convective heat transfer of shell and tube side as well as fouling resistance of both sides, it is calculated with the Equation 15

$$U = \frac{1}{\frac{1}{h_s} + R_{fs} + \frac{d_o \ln\left(\frac{d_o}{d_i}\right)}{2k_w} + R_{ft} \frac{d_o}{d_i} + \frac{1}{h_t} \frac{d_o}{d_i}} \quad (15)$$

h_t is convective heat transfer coefficients for tube side, k_w is the material thermal conductivity, R_{fs} and R_{ft} are the fouling factors for shell and tubes. The tube internal diameter, d_i , is calculates as $d_i = 0.8d_o$.

3.2. Heat transfer in tube side

To calculate h_t , the equation 16 is used, this equation only works when the fluid in tubes is water (Sinnott and Towler, 2009). T_{C_m} is the medium fluid temperature and v_t is the fluid velocity in tubes that is calculated with the equation 17. Where ρ_t fluid density, m_t is the mass flow rate and N_t is the total number of tubes, is calculated according the equation

$$h_t = \frac{4200(1.35 + 0.02T_{C_m})v_t^{0.8}}{d_i^{0.8}} \quad (16)$$

$$v_t = \frac{s}{N_t} \frac{m_t}{\pi \frac{d_i^2}{4} \rho_t} \quad (17)$$

3.3. Pressure drop calculations

The pressure drop in the tubes side is calculated with the equation 18, the friction factor, f , is evaluated as $f = 0.046Re_t^{-0.2}$, s is the the pass number and L the length of tubes that is calculated using 19.

$$\Delta P_t = s \left(\frac{4fL}{d_i} + 2.5 \right) \frac{\rho_t v_t}{2} \quad (18)$$

$$L = \frac{A}{\pi d_o N_t} \quad (19)$$

The expression 20 is used to calculate the pressure drop in shell-side

$$\Delta P_s = [(N_b - 1)\Delta P_{b,id}\zeta_b + N_b\Delta P_{w,id}] \zeta_l + 2\Delta P_{b,id} \left(1 + \frac{N_{r,cw}}{N_{r,cc}} \right) \zeta_b \zeta_s \quad (20)$$

where N_b is the number of baffles, $\Delta P_{b,id}$ is the ideal pressure drop in the central section, $N_{r,cw}$ is the effective tubes en the cross flow, $N_{r,cc}$ is the effective number of tubes rows crossed, ζ is a correction factor.

3.4. Cost estimation

In this study, the total annual cost (TAC) is used, this is the sum of fixed, C_f and operation cost C_{op} . To calculate the fixed cost the equation 22 is used (Smith, 2005). The purchase price C_p is corrected using the factors f_m , f_p and f_c for construction material, operating pressure and operation temperature, respectively. While the C_{op} is evaluated with equation 23.

$$C_p = 32800 \left(\frac{A}{80} \right)^{0.68} \quad (21)$$

$$C_f = C_p f_m f_p f_c \quad (22)$$

$$C_{op} = \frac{(E_s + E_t) Ec Hr}{1000} \quad (23)$$

$$TAC = C_f \frac{r(1+r)^n}{(1+r)^n - 1} + C_{op} \quad (24)$$

where E_s and E_t is the pump power (Watts) used in shell and tube side, respectively. Ec is the energy cost (\$/kWh), Hr is the operational hours per year, n is the projected life time and r the interest rate per year. The optimization is performed using eleven parameters that can have a value between a given range, those are:

- Diameter of shell (D_s): 300mm -1000mm.

- Outer diameter of tube (d_o): 15.87mm 63.5mm.
- Tube pitch P_t : $[1.25d_o, 1.5d_o]$.
- Tube layout angle (TL): $[30^\circ, 45^\circ, 90^\circ]$
- Baffle spacing at center (L_{bc}): $0.2D_s - 0.55D_s$
- Baffle spacing at the inlet and outlet ($L_{bo} = L_{bi}$): $L_{bc} - 1.6L_{bc}$
- Baffle cut (B_c): $[25\%, 30\%, 40\%, 45\%]$
- Number of tube passes (s): $[1, 2, 4]$
- Tube-to-baffle diametrical clearance (δ_{tb}): $0.01d_o - 0.1d_o$
- Diametrical clearance of shell-to-baffle (δ_{sb}): $0.01D_s - 0.1D_s$
- Outer diameter of tube bundle (D_{otl}): $0.8(D_s - d_{sb}) - 0.95(D_s - d_{sb})$

The optimization process is subject to constrains for maximum allowed pressure drop in tube-side and shell-side, fluid velocity, and length to shell-diameter ratio, as follows:

$$\Delta P_s, \Delta P_t \leq \Delta P_a \quad (25)$$

$$1\text{m/s} \leq v_t \leq 3\text{m/s} \quad (26)$$

$$L/D_s < 15 \quad (27)$$

The equation 28 is the fitness function. The constants r_1 , r_2 , r_3 and r_4 are penalty values, if a constrain is violated a penalty value is activated.

$$FF = TAC + r_1 \max[(\Delta P_s - \Delta P_a), 0] + r_2 \max[(\Delta P_t - \Delta P_a), 0] + r_3 [\max\{(1 - v_t)\} + \max\{(3 - v_t)\}, 0] + r_4 \max[(L/D_s - 15), 0] \quad (28)$$

4. Case study

The case study is taken from Wildi-Tremblay and Gosselin (2007). It is required to design a heat exchanger with a flow rate of 18.8 kg/s of cooling water, the inlet temperature is 33 °C and the outlet temperature is 37.2 °C. The hot fluid is nafta, the inlet temperature is 114 °C and the outlet temperature is 40 °C. Water is placed in tube-side and nafta in shell-side. The construction material for tube and shell side is stainless steel and carbon steel, respectively.

Calculations are performed using a 5 % interest rate, 20 years life time period, 5000 operation hours per year, a pump efficiency of 0.85 and an electricity cost of 0.1 \$/kWh. The maximum allowed pressure drop is 70,000 Pa. The factors to modify the purchase cost are $f_m = 1.7$, $f_i = 1.0$ and $f_p = 1.0$.

5. Results

MATLAB was used as codification environment for the heat exchanger mathematical model and GWO model. A population of 50 individuals was used with 50 iterations. To generate statistical information 30 runs were made. An average cost of 4,095.36 USD was found with a standard deviation of 103.57 USD. The minimum value was 3,977.76 USD. Particle swarm optimization (PSO) algorithm was also used to solve the problem as a comparison. With PSO an average cost of 4,197.56 USD with a standard deviation of 220.07 USD, the minimum value was 3,976.38 USD. The Table 1 shows the parameters value for both optimization methods. It can be seen that both method reached a similar solution. The computing time was 1.0161s for GWO and 2.1881s for PSO.

Table 1: Parameters for optimal heat exchanger configuration.

Parameter	D_s	d_o	N_t	A	L	P_t	TL	s	L_{bc}	L_{bo}	B_c
Unit	mm	mm		m^2	m	mm	°		mm	mm	%
GWO	302.36	15.87	144	32.35	4.50	19.83	90	1	60.47	60.47	25
PSO	301.90	15.87	143	32.30	4.53	19.83	90	1	60.38	60.38	25
Parameter	δ_{fb}	δ_{sb}	D_{out}	N_b	v_t	L/D_s	ΔP_t	ΔP_c	C_{op}	C_f	TAC
Unit	mm	mm	mm		m/s		Pa	Pa	\$/year	\$/year	\$/year
GWO	0.15	3.02	284.37	74	1.64	14.90	8938.76	12843.52	189.20	3789.08	3978.29
PSO	0.15	3.02	283.93	74	1.66	15.00	9028.80	12889.25	190.91	3784.94	3975.85

6. Conclusion

The Grey Wolf Optimizer has been proposed as a technique to solve the design and optimization of a shell-and-tube heat exchanger, modeled through the Bell-Delaware method. The optimization model is a MINLP, which is codified and solved in a MATLAB routine. The method has been proved to be efficient, reaching the optimal solution in a relatively low computing time. Moreover, the standard deviation between the obtained solutions in different tests is low, implying that the method tends to reach very similar optimal points for a number of runs.

References

- S. Mirjalili, S. M. Mirjalili, A. Lewis, 2014. Grey wolf optimizer. *Advances in engineering software* 69, 46–61.
- R. K. Shah, D. P. Sekulic, 2003. *Fundamentals of heat exchanger design*. John Wiley & Sons.
- R. K. Sinnott, G. Towler, 2009. *Chemical engineering design: SI Edition*. Elsevier.
- R. Smith, 2005. *Chemical process: design and integration*. John Wiley & Sons.
- P. Wildi-Tremblay, L. Gosselin, 2007. Minimizing shell-and-tube heat exchanger cost with genetic algorithms and considering maintenance. *International Journal of Energy Research* 31 (9), 867–885.

Optimization Under Uncertainty Based on a Data-driven Model for a Chloralkali Electrolyzer Cell

Erik Esche^{a,*}, Joris Weigert^a, Thomas Budiarto^a, Christian Hoffmann^a and Jens-Uwe Repke^a

^a*Technische Universitaet Berlin, Process Dynamics and Operations Group, Sekr. KWT 9, Str. des 17. Juni 135, D-10623, Berlin, Germany*
erik.esche@tu-berlin.de

Abstract

Data-driven models are increasingly used to model chemical processes with the long-term goal of using them for real-time optimization. At the moment, the uncertainty contained in these models is scarcely modeled or mostly assumed to adhere to a multivariate normal distribution. In this contribution, we model both the input-output relation of a rigorous model as well as the uncertainty. During the training process of surrogate models, both accuracy as well as smoothness of the resulting models are ensured. For the case study of a Chloralkali electrolyzer cell, snapshots are generated based on a rigorous model. Surrogate models for input-output relationships and uncertainty are trained and compared regarding their fit, smoothness, and their applicability in chance-constrained optimization. Based on this methodology, a Gaussian process was developed for the input-output modeling and a functional covariance matrix with separate models for the entries using both artificial neural networks and linear regression for separate entries. The models were tested in a chance-constrained optimization framework showing excellent performance regarding speed of the computation and validity of the results.

Keywords: Data-driven modeling, surrogate, models, optimization under uncertainty

1. Introduction and Motivation

Data-driven models are increasingly used in chemical engineering applications for the support of optimal process operation. Examples of data-driven models recently used are linear regressions, artificial neural networks, support vector regression, gaussian process regression (also known as kriging), etc. Data to train and validate these models can stem from different sources, either experimental data or simulation snapshots from existing first principle models.

These sets of training data, of course, contain uncertainty: on the one hand through experimental measurement error or on the other hand through known uncertain parameters of an original model. This uncertainty information should be considered in the actual description of the data-driven model's output uncertainty.

Given the way how data-driven models are derived, it is well understood that their applicability is limited to the domain of the original data they are trained and validated upon. Beyond that, extrapolation and sometimes even interpolation between sparsely scattered data points becomes highly unreliable. There are a couple of techniques available to make sure that optimization solvers operating on data-driven models stay within the area of applicability, e.g. the implementation of inequality constraints regarding the domain of the model or the introduction of uncertainty maps as model elements.

In this contribution, we investigate possibilities to extend typical data-driven surrogate models by uncertainty models for the description of the uncertainty of each output variable, while standard data-driven techniques only provide static descriptions of the model’s uncertainty. Furthermore, we evaluate these models regarding their performance in a framework for optimization under uncertainty.

2. Modeling of Input-Output Relationships and Uncertainty

To derive models for both input-output relationships as well as the uncertainty, we pursue a two-stage procedure. In the first stage, the input-output relationship is modeled, in the second stage the uncertainty of the outputs is then described. This is in contrast to most modeling strategies typically followed in machine-learning, wherein the assumptions for the input-output model often also contain the description of the uncertainty. However, this is then mostly limited to multivariate normal distributions or discontinuous probability density models and only describes the uncertainty of the data-driven model.

For all further discussions here, a set of input and output data points is already given, which could stem from either experiments or sampling on a simulation model. Henceforth, a rigorous model will be taken as the basis.

2.1. Modeling of Input-Output Relationships

For modeling the input-output relationships, we assume that the input and output data have already been clustered, i.e. points in input space close to one another have been aggregated. Hence, clustering techniques will not be discussed here. Building upon existing implementations of various data-driven models in scikit-learn (Pedregosa et al., 2011), our python framework generates linear regression (LR), Gaussian process regression (GPR), and artificial neural networks (ANN) based on a wide selection of options for kernels, model parameters, optimization settings, and of course the ratio between the number of training data and test data.

After training the various models, they are evaluated with different statistical metrics describing their deviation to the testing data and the smoothness of the resulting surface functions for outputs plotted over inputs. The finally selected model is henceforth denoted as g with input variables u and output variables y , see Eq. (3).

2.2. Modeling of Uncertainty

Based on the chosen model for the input-output relationships, the deviations of all data points compared to that model are then computed and taken as the basis for modeling the uncertainty. For this purpose, we take two different approaches, which are sketched in Fig. 1. In the first approach, modeling the uncertainty is solely based on the deviations of the outputs and is independent of any input values. In the second approach, the input values are also considered, so that influences of the inputs on the uncertainty of the outputs may be incorporated.

As ansatz models for the uncertainty, multivariate normal distribution, Dirichlet distribution (multivariate beta distribution), and kernel density estimation are considered. Yet again, these models are trained/fitted to the present data and compared regarding their capabilities to describe the uncertainty. As above, the eventually selected uncertainty model is denoted as \tilde{g} , which describes the uncertain outputs \tilde{y} depending on the outputs y generated by model g , some model parameters \hat{p} , and optionally the inputs u , see Eq. (4).

For the model generation, relevant uncertainty data for the respective ansatz is created at every input point. For a multivariate normal distribution, this would be the covariance of the outputs and for the Dirichlet distribution the model parameters α . Based on this data, the uncertainty model is trained and tested using the same python framework as for the input-output model generation.

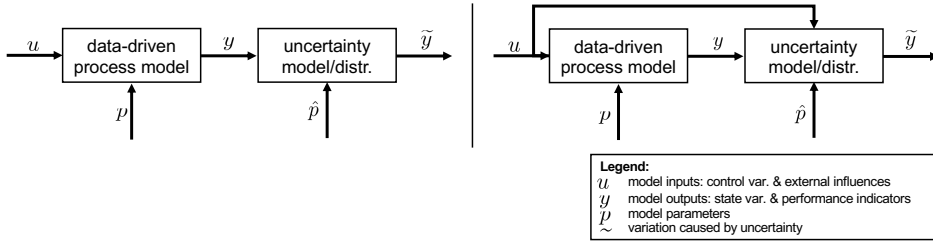


Figure 1: Two different modeling strategies pursued herein to accurately model the uncertainty contained in original data and induced by input-output model.

3. Framework for Optimization Under Uncertainty

The framework for optimization under uncertainty is fully implemented in python and builds upon the department's existing framework for chance-constrained optimization - the DoCCE (dynamically optimized chance constraint evaluator (Werk et al., 2012)). The extended framework developed for this contribution now supports systems as characterized by the following nonlinear programming problem (NLP) with objective function f , data-driven model g , uncertainty model \tilde{g} , and the desired probability level α :

$$\min_x f(x) \quad (1)$$

$$\text{s.t. } \Pr\{h(x) \geq 0\} \geq \alpha \quad (2)$$

$$y = g(u) \quad (3)$$

$$y, u \subset x \quad \wedge \quad y \cap u = \emptyset$$

$$\tilde{y} = \tilde{g}(y, p) \quad \forall \quad \tilde{y} = \tilde{g}(y, u, \hat{p}) \quad (4)$$

$$\tilde{y} \subseteq y$$

For additional information on DoCCE's capabilities for mixed-integer nonlinear programming problems refer to (Esche et al., 2016).

4. Case Study - Chloralkali Electrolyzer Cell

To test the performance of input-output and uncertainty models inside the framework for optimization under uncertainty, a rigorous, steady-state model of the anolyte half cell of a Chloralkali electrolyzer cell (CEC) is used as a small-scale example.

The anolyte cell is modeled as a CSTR for a five component mixture (Na^+ , Cl^- , OH^- , H_3O^+ , H_2O). The model consists of 32 equations including descriptions for the chlorine production by the anode reaction, the autoprotolysis of water, the migration based sodium ion flux, and descriptions for water leaving by electroosmosis and with the chlorine gas stream.

4.1. Generation of Snapshots

The rigorous model is implemented in MOSAICmodeling (Esche et al., 2017) and from there exported to AMPL (Fourer et al., 2003) and solved as a simulation problem with IPOPT (Wächter and Biegler, 2005). For the case study, the input variables (feed volume flow and current density of CEC) are varied between a given set of bounds and the model parameters (feed temperature and electroosmosis factor) are assumed to follow a multivariate normal distribution. Samples for

the output variables (outgoing liquid volume flow, mass fractions of all components) are generated by sampling 1 000 times from the input variables with a Latin Hypercube sampling and 20 times from the parameters following the normal distribution. Hence, 20 000 output samples are present, which can easily be clustered along the input samples. The output samples obtained from AMPL are then filtered to eliminate randomly appearing, non-converged solutions and the remainder is stored for subsequent training and testing.

4.2. Input-output Model

Based on the aforementioned number of samples, Gaussian process regression shows the best performance regarding match and smoothness of the resulting surface functions compared to the other tested model types. Randomly, 70 % of the generated snapshots are taken for training the Gaussian process with a squared exponential covariance function as kernel. The remaining data is used for testing and shows a mean squared error of 10^{-5} , an R^2 value of around 0.96, and a mean percentual deviation of around 2.7 %. The input-output model describes two inputs (feed volume flow, current density of CEC) and six outputs (outgoing liquid volume flow, mass fractions of all components). For the first two outputs (outgoing liquid volume flow, mass fraction of Na^+), the resulting surface functions are shown in Fig. 2 (plots (a) and (b)).

4.3. Uncertainty Model

For modeling the difference between data-driven model and original snapshot data, a number of different probability density functions were tested. The best fit was achieved with a functional covariance matrix describing all outputs of the data-driven model as follows:

$$\tilde{y} = \tilde{g}(y, Cov(u)) = y + \mathcal{N}(0, Cov(u)) \quad (5)$$

Every entry of the covariance matrix Cov is a function of the input variables u , which corresponds to the second approach sketched in Fig. 1. Depending on the form of variance and covariance of the respective output variables, either linear regression or gaussian process regression are used to describe the functional relationship between input and output uncertainty distribution. For the application here, all six output variables are taken as uncertain, resulting in a six-by-six covariance matrix. The surface function describing the relationship between the two inputs and the variance of output no. 2 and the covariance between outputs 1 and 2 are plotted in Fig. 2 (plots (c) and (d)). Of the 36 entries of the covariance matrix, eight entries are described with linear regression models, the remaining ones are described by individual ANNs.

To ensure that the reliability of the input-output model tends to zero outside of its training region, the models for the variance/diagonal entries in Cov are there set to the magnitude of the respective output y . This allows for an indirect hull formulation, which does not need to be added as an additional constraint and is adaptive to further training with new data.

4.4. Chance-constrained Optimization

To test the usability of the derived input-output and uncertainty models, a simple chance-constrained optimization problem is formulated based on the CEC example. As objective function, the outlet flow of sodium ions is minimized while a chance constraint is implemented to enforce an upper bound on the pH value of 2.88 (mass fraction of H_3O^+ equal to $2.5 \cdot 10^{-5}$) inside the cell. Always starting from the same initial point, the enforced probability level α of the chance constraint is steadily increased. The resulting increase in the objective function value is plotted over the probability level in Fig. 3. The objective function value shows the expected increase with the steadily increased constraint probability. The CPU seconds necessary for the computation appear independent of the enforced probability and are in a very reasonable range at below 25 seconds.

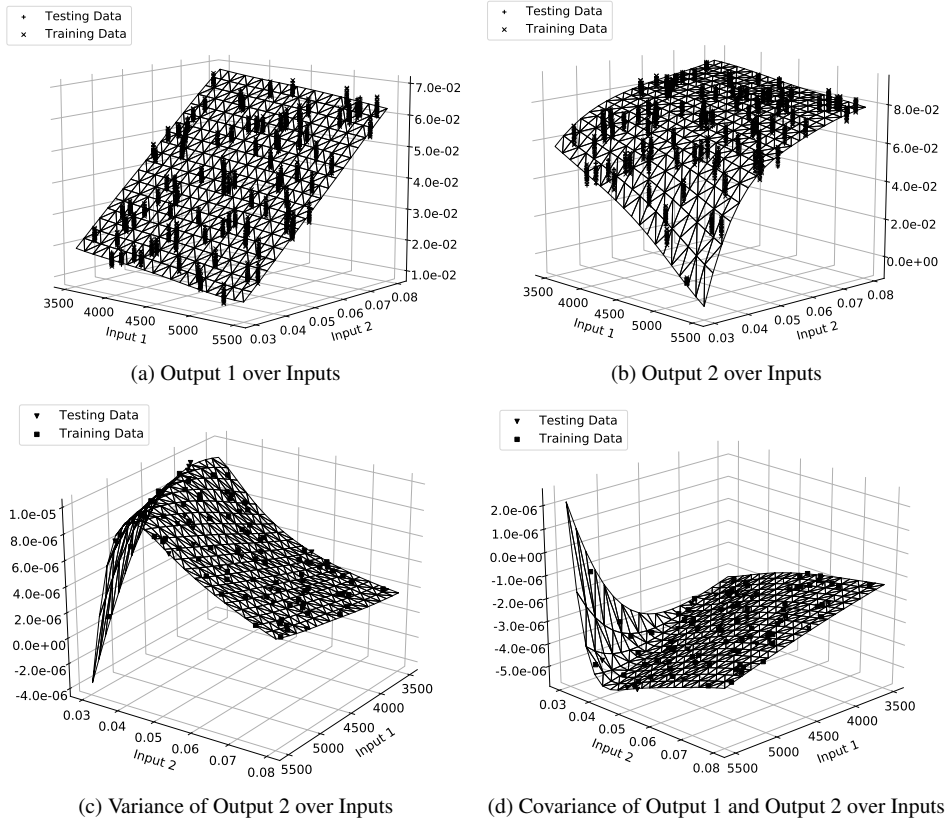


Figure 2: Figures (a) and (b) showing outputs 1 and 2 plotted over the two input variables. Figures (c) and (d) showing variance of output 2 and covariance between output 1 and output 2 plotted over both inputs. x/square: training data, +/triangle: testing data; surface functions: predicted data and uncertainty models respectively.

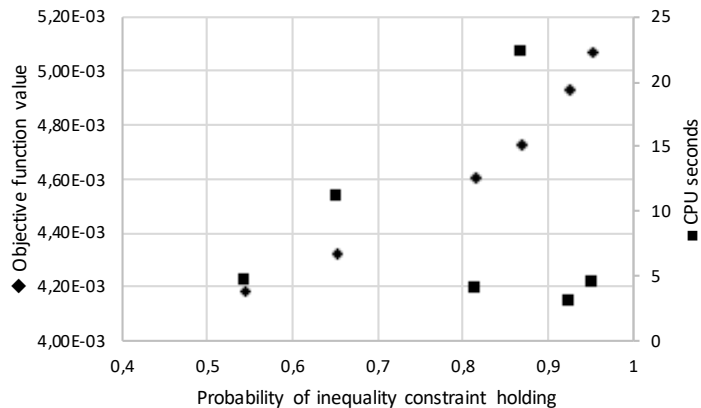


Figure 3: Objective function plotted over the enforced probability level. CPU seconds given on the secondary axis.

For the computation of the chance constraint's probability a five-dimensional sparse grid is used (first five outputs). For every single grid point the position is computed, at which the sixth output variable ensures the equality of the inner constraint ($h(x) = 0$; mass fraction of H_3O^+ equal to $2.5 \cdot 10^{-5}$). Given the variation of the covariance matrix over the input space, the sparse grid is adapted to the covariance matrix at every single iteration, i.e. at a probability computation.

The computation of the inner constraint is done by the secant method. The DoCCE framework by default uses Newton's or Haley's method in case first or even second derivatives are available. However, on using the data-driven input-output models, the framework falls back to the derivative-free approach. This is naturally highly inefficient, but given the speed of the input-output models the many function calls necessary for the secant method can be easily handled.

5. Conclusions & Outlook

Up to now, offline or even online application of optimization under uncertainty is still a major challenge with the time required for computing uncertain scenarios or integrating over the uncertainty space being the main hurdles. Using surrogate models to describe both input-output relations and uncertainty of an existing rigorous model or of plant data can be a building block to allow for the wide-spread fast application of optimization under uncertainty.

By initially comparing several different types of surrogate models for the input-output relationship, both a good match and sufficient smoothness can be ensured. Based on the hence obtained model, the uncertainty is then described with an additional model. Here, good results were obtained using a functional description of a covariance matrix of all the outputs of the input-output surrogate model. Using these two models together for optimization under uncertainty ensures both speed and reliability of the optimization results given their high accuracy in modeling the original data and their explicit model structures.

In future work, the derivatives will be added to both input-output as well as uncertainty models to further speed up the optimization run. In addition, the continuous retraining of both models will be exercised in online applications to continuously reduce the model uncertainty and extend the range of validity of these models while optimally running a plant. Furthermore, the minimally required training effort based on rigorous simulation snapshots will need to be discussed and hence also the design of computer experiments to limit the number of potentially expensive simulation runs.

6. Acknowledgements

The research project ChemEFlex (funding code 0350013A) is supported by the German Federal Ministry for Economic Affairs and Energy.

References

- E. Esche, C. Hoffmann, M. Illner, D. Müller, S. Fillinger, G. Tolksdorf, H. Bonart, G. Wozny, J.-U. Repke, 2017. Mosaic - enabling large-scale equation-based flow sheet optimization. *Chem. Ing. Tech.* 89 (5), 620–635.
- E. Esche, D. Müller, S. Werk, I. E. Grossmann, G. Wozny, 2016. Solution of chance-constrained mixed-integer nonlinear programming problems. In: Z. Kravanja, M. Bogataj (Eds.), *Proceedings of the 26th European Symposium on Computer Aided Process Engineering - ESCAPE 26*. No. 38. Elsevier, pp. 91–94.
- R. Fourer, D. M. Gay, B. W. Kernighan, 2003. *AMPL – A Modeling Language for Mathematical Programming*, 2nd Edition. Brooks/Cole – Thomson Learning.
- F. Pedregosa, G. Varoquaux, A. Gramfort, V. Michel, B. Thirion, O. Grisel, M. Blondel, P. Prettenhofer, R. Weiss, V. Dubourg, J. Vanderplas, A. Passos, D. Cournapeau, M. Brucher, M. Perrot, E. Duchesnay, 2011. Scikit-learn: Machine learning in Python. *Journal of Machine Learning Research* 12, 2825–2830.
- A. Wächter, L. Biegler, 2005. On the implementation of an interior-point filter line-search algorithm for large-scale nonlinear programming. *Math. Program. Ser. A*.
- S. Werk, T. Barz, H. Arellano-Garcia, G. Wozny, 2012. Performance analysis of shooting algorithms in chance-constrained optimization. In: I. A. Karimi, R. Srinivasan (Eds.), *11th International Symposium on Process Systems Engineering*. Vol. 31 of *Computer Aided Chemical Engineering*. Elsevier, pp. 1512 – 1516.

Parameter Estimation for Thermodynamic Models Using an Identifiability Analysis and Subset Selection

Christian Hoffmann^{a,*}, Joris Weigert^a, Erik Esche^a and Jens-Uwe Repke^a

^a*Technische Universität Berlin, Process Dynamics and Operations Group, Sekr. KWT 9, Straße des 17. Juni 135, Berlin 10623, Germany*

**c.hoffmann@tu-berlin.de*

Abstract

Parameter estimation problems are solved on a regular basis to fit thermodynamic models to experiments. However, conducting these experiments with a high accuracy is time-consuming. Hence, methods to identify parameters as fast as possible have to be used. In this contribution, subset selection is applied to parameter estimation problems with different datasets, such as VLE and excess enthalpy data. It is demonstrated that performing a subset selection with sensitivity analysis leads to an efficiently reduced set of estimated parameters. The results of the subset selection could additionally be used for an optimal design of experiments as the information gain of the different experimental datasets (VLE data, excess enthalpy) is different.

Keywords: Parameter estimation, Subset selection, Thermodynamic models

1. Introduction

Thermodynamics are a fundamental aspect of process design, modeling, simulation, and optimal operation in process engineering as evidenced by many publications on this subject in the past decades, e.g. (Hendriks et al., 2010). Many models have been suggested to describe the various phase equilibria appearing in multicomponent mixtures, such as activity models, (semi-)empirical cubic equations of state, and advanced equations of state (SAFT family, CPA, etc.).

Most thermodynamic models are highly nonlinear and hold several parameters, which are fitted to experimental data. At the same time, there is often little measurement data available and obtaining additional high-quality experimental data is time-consuming. By consequence, a number of issues can arise when performing parameter estimation on complex thermodynamic models: Noisy measurement data can be overfitted, identifiability of parameters cannot be ensured, and this in turn may lead to ill-conditioned parameter estimation problems, which show poor convergence and yield large variances of the estimated parameters. In addition, little can be found regarding parameter identifiability or their sensitivity with respect to the objective for thermodynamic applications, although there have been studies on parameter identifiability in general in the past few years, e.g. (Nogueira and Pontes, 2017).

Due to these shortcomings, this contribution investigates the identifiability of parameters in thermodynamic models in further detail. For this purpose, two parameter estimation problems were selected: the binary VLE of methanol and water and the dilution of sodium chloride in water. Both are described with appropriate activity models, which are briefly outlined in the next section. Activity models were selected because of their wide use in practical applications in the process industry. On top of that, they are preferred for low pressure applications for which the fugacity coefficient can usually be neglected. However, the approach is not limited to them and will certainly be extended to other property models in the future, especially equations of state.

2. Theoretical Fundamentals

In this section, the theoretical fundamentals of thermodynamic phase equilibria, the applied activity models and the parameter estimation framework are briefly discussed.

2.1. Thermodynamics

Thermodynamic equilibria can be described using the γ - ϕ -approach for the isofugacity criterion. Under low pressure assumptions, this yields Raoult's Law, extended by the activity coefficient in the liquid phase:

$$x_i \gamma_i P_{0,i}^{VL} = y_i P, \quad (1)$$

where x_i and y_i are the liquid and vapor mole fraction of component i , γ_i is the activity coefficient, $P_{0,i}^{VL}$ is the vapor pressure of the pure component and P is the pressure of the mixture. The activity coefficient is computed with the Wilson and the NRTL equation (Wilson, 1964; Renon and Prausnitz, 1968) for the methanol/water system and eNRTL (Chen and Evans, 1986) for the NaCl/water system.

Wilson: The expression for the activity coefficient is

$$\ln \gamma_i = 1 - \ln \left(\sum_{j=1} A_{ij} x_j \right) - \sum_{j=1} \frac{A_{ji} x_j}{\sum_k A_{jk} x_k}; \quad A_{ij} = \frac{v_j}{v_i} \exp(-\lambda_{ij}), \quad A_{ii} = 1, \quad (2)$$

where v_i is the molar volume of component i . The binary interaction parameters λ_{ij} are the two parameters to be estimated. However, λ is often assumed to be temperature-dependent. This leads to a parameter estimation problem of up to ten parameters:

$$\lambda_{ij} = a_{ij} + \frac{b_{ij}}{T} + c_{ij} \ln T + d_{ij} T + e_{ij} T^2. \quad (3)$$

NRTL and eNRTL: The activity coefficient of the solvent is given by the product of the long-range contribution (LR) from the Debye-Hückel equation and the short-range contribution (SR) from the eNRTL equations. The equations for the LR term are not shown here because they do not hold any parameters for this estimation. The reader is referred to the literature (Chen and Evans, 1986). The equation for the SR term is (Chen and Evans, 1986):

$$\begin{aligned} \ln \gamma_{i=m}^{eNRTL} &= \frac{\sum_j X_j G_{jm} \tau_{jm}}{\sum_k X_k G_{km}} + \sum_{m'} \frac{X_{m'} G_{mm'}}{\sum_k X_k G_{km'}} \left(\tau_{mm'} - \frac{\sum_k X_k G_{km'} \tau_{km'}}{\sum_k X_k G_{km'}} \right) \\ &+ \sum_c \sum_{a'} \frac{X_{a'}}{\sum_{a''} X_{a''}} \frac{X_c G_{mc,a'c}}{\sum_{k \neq c} X_k G_{kc,a'c}} \left(\tau_{mc,a'c} - \frac{\sum_{k \neq c} X_k G_{kc,a'c} \tau_{kc,a'c}}{\sum_{k \neq c} X_k G_{kc,a'c}} \right) \\ &+ \sum_a \sum_{c'} \frac{X_{c'}}{\sum_{c''} X_{c''}} \frac{X_a G_{ma,c'a}}{\sum_{k \neq a} X_k G_{ka,c'a}} \left(\tau_{ma,c'a} - \frac{\sum_{k \neq a} X_k G_{ka,c'a} \tau_{ka,c'a}}{\sum_{k \neq a} X_k G_{ka,c'a}} \right), \end{aligned} \quad (4)$$

where m , c , and a stand for molecule, cation, and anion. The equations for the cations and anions are not shown here due to space limitations. In addition, $G_{ji,ki}$ is given by:

$$G_{ji,ki} = \exp(-\alpha_{ji,ki} \tau_{ji,ki}). \quad (5)$$

The binary interaction parameters $\tau_{ji,ki}$ and the non-randomness parameter $\alpha_{ji,ki}$ are the three parameters subject to the estimation. Again, τ and also α are however often assumed to be temperature-dependent. Here, we limit ourselves to the temperature dependence of τ . This leads to a parameter estimation problem of up to seven (eNRTL) or eleven (NRTL) parameters:

$$\tau_{ji,ki}^{eNRTL} = a_{ji,ki} + \frac{b_{ji,ki}}{T} + c_{ji,ki} \left[\frac{T^{ref} - T}{T} + \ln \left(\frac{T}{T^{ref}} \right) \right]; \quad \tau_{ji}^{NRTL} = a_{ji} + \frac{b_{ji}}{T} + c_{ji} \ln(T) + d_{ji} T^{e_{ji}}. \quad (6)$$

2.2. Parameter Estimation Framework with Subset Selection

The parameter estimation and identifiability analysis is carried out using the algorithm presented in (Müller et al., 2014). Its two main features are the regularization of the estimation problem via subset selection and an estimate of the covariance matrix of the parameters. First of all, data must be sampled, i.e. thermodynamic equilibrium data must be collected. Secondly, lower and upper bounds as well as initial guesses must be supplied. More details on this step are given below. Afterwards, a first parameter estimation is performed using the complete parameter set. Based on the results, the Fisher Information matrix (FIM) is approximated by

$$FIM \approx S^T \Sigma^{-1} S, \quad (7)$$

where S is the sensitivity matrix containing all derivatives of the model responses (temperatures, pressures, and vapor mole fractions) with respect to the parameters, and Σ is a matrix holding all variances of the measurements on its diagonal. In the following, the parameters are ranked according to their identifiability based on a singular value decomposition of the FIM. Parameters that cannot be identified are fixed to their current values and the parameter estimation is repeated until no changes in the active set take place. The lower bound of the standard deviation of the estimated parameters is estimated with the Cramér-Rao inequality. Hence, the standard deviations are the roots of the diagonal elements of the inverted FIM (Müller et al., 2014). The objective function f of the parameter estimation problem is

$$\min_p f = \sum_{DP} \sum_{DType} \left(\frac{DType^{exp}_{DP} - DType^{calc}_{DP}}{\sigma_{DType,DP}} \right)^2 \quad (8)$$

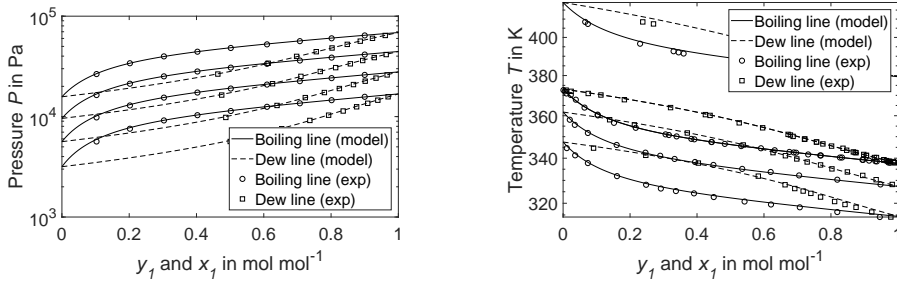
where the first sum ranges over all experimental isothermal and isobaric data points DP , the inner sum iterates all data types $DType$ (e.g. temperature, pressure, or mole fraction), and σ is the standard deviation of the measurement error. However, these are not always stated in the original datasets. In these cases, σ_p , σ_T , and σ_{y_i} were assumed to be 100 Pa, 0.1 K, and 0.01, respectively, which are typical values in the literature.

Table 1: Results of parameter estimation for methanol/water in step 1 (Wilson), experimental data at 328 K, taken from (Fu et al., 1989). Full-scale problem did not converge for 8 and 10 parameters.

Estimated parameters	Identifiable parameters	$\frac{\sigma_{a_{12}}^{PE,Full}}{ a_{12} }$	$\frac{\sigma_{a_{21}}^{PE,Full}}{ a_{21} }$	$\frac{\sigma_{b_{12}}^{PE,Full}}{ b_{12} }$	$\frac{\sigma_{b_{21}}^{PE,Full}}{ b_{21} }$	$\frac{\sigma_{c_{12}}^{PE,Full}}{ c_{12} }$	$\frac{\sigma_{c_{21}}^{PE,Full}}{ c_{21} }$
2	2	4.7E-7	1.5E-8	-	-	-	-
4	2	4.4E-1	1.1E-1	3.8E-1	9.9E-2	-	-
6	2	1.7E+0	1.1E+1	4.8E+2	8.4E+2	2.91E-1	1.78E+0

3. Results and Discussion

To analyze the behavior of the subset selection, the results are presented in three parts: In the first step, the parameter estimation is performed on equilibrium data only at a single constant temperature. In a second step, the number of different experimental temperatures is increased and typical temperature-dependent expressions for the parameters are introduced. Finally, additional data, such as excess enthalpies, are added to the parameter estimation problem. For all cases, the number of identifiable parameters and their variances are analyzed to demonstrate the merit of applying subset selection. Initial guesses for the parameters are always set to the arbitrary vectors $p_{init}^{NRTL} = [\alpha, a_{12}, a_{21}]^T = [0.2, 1, 2]^T$, $p_{init}^{Wilson} = [a_{12}, a_{21}]^T = [1, 2]^T$, and $p_{init}^{eNRTL} = [\alpha, a_{12}, a_{21}]^T = [0.2, 4, -8]^T$. Other parameters are initially set to zero. The algorithm has been implemented in Matlab 2017a using lsqnonlin.



(a) Experimental data taken from (Fu et al., 1989) at 298, 308, 318, and 328 K.

(b) Experimental data taken from (Swami et al., 1956; Álvarez et al., 2011; Yang et al., 2011, 2012) at 0.4, 0.67, 1, and 4.3 bar.

Figure 1: P-x-y (a) and T-x-y (b) diagram for methanol (1) and water, calculated with the NRTL equation; $a_{12} = -0.01$, $a_{21} = 0.79$, and $\alpha = 0.5$.

3.1. Step 1: One dataset

In this first section, only one dataset at constant temperature is used. The results are shown in Tab. 1 for the methanol/water system and the Wilson equation. The algorithm determines that only two of up to ten parameters are identifiable. This is no surprise as the λ values are constants for a given temperature. These results can hence be seen as a plausibility check. Moreover, Tab. 1 shows the estimated standard deviation of the estimation divided by their expected value for the full-scale set (all parameters are active, first iteration of the algorithm) for 2, 4, and 6 estimated parameters. These values increase, the more parameters are added to the problem, until the standard deviation becomes larger than the expected value itself (last line in Tab. 1). Hence, the estimated parameters become more and more uncertain.

3.2. Step 2: Several datasets

In the next step, more experimental data are added to identify additional parameters in the temperature dependence of the interaction energies. The results of the parameter estimation are shown in Fig. 1 for the NRTL equation. The results for the Wilson equation are not shown here. Both activity models can accurately describe the VLE of methanol and water. However, only up to 4 parameters are identifiable for both models. The results for the parameter estimation of the full set (all parameters active, no subset selection) are given in Tab. 2 for NRTL. They show that adding additional data does not necessarily reduce the uncertainty of the parameters. For NRTL, the non-randomness factor α remains unidentifiable for all datasets. Secondly, it is observed that the number of identifiable parameters can decrease when more parameters are added to the problem. In addition to the larger dimensionality of the problem, this further complicates the parameter estimation as it leads to small gradients of the objective function hyperplane. Typically, the standard deviation of the parameter subset SsS0 is at least two orders of magnitude smaller than for the full set (see first line in Tab. 1 and 2). Thirdly, it must be noted that the excess enthalpy is poorly described if it is not considered in the parameter estimation problem (not shown here).

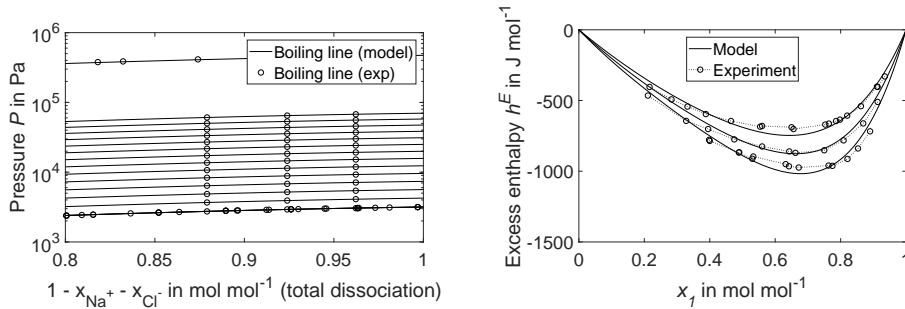
A second parameter estimation was performed for the water/NaCl system, for which total dissociation was assumed. The results are shown in Fig. 2a. Although the parameters are estimated over a temperature range from 298 to 423 K, only three parameters of seven (1 in 3) can be identified. All those three parameters describe the temperature dependence of the same binary interaction energy, meaning that the system can well be described by estimating only one binary interaction and set the other to an arbitrary value.

Table 2: Results of parameter estimation for methanol/water in step 2 (NRTL), experimental data as stated in Fig. 1.

Estimated parameters	Identifiable parameters	$\frac{\sigma_{a_{12}}^{PE,Full}}{ a_{12} }$	$\frac{\sigma_{a_{21}}^{PE,Full}}{ a_{21} }$	$\frac{\sigma_{b_{12}}^{PE,Full}}{ b_{12} }$	$\frac{\sigma_{b_{21}}^{PE,Full}}{ b_{21} }$	$\frac{\sigma_{c_{12}}^{PE,Full}}{ c_{12} }$	$\frac{\sigma_{c_{21}}^{PE,Full}}{ c_{21} }$
3	2	5.0E-6	9.5E-8	-	-	-	-
5	4	2.8E-6	2.7E-6	2.7E-6	5.8E-6	-	-
7	4	6.5E-6	8.4E-6	6.3E-6	9.0E-6	6.5E-6	8.7E-6
11	2	2.3E-2	2.8E-4	2.8E-2	6.0E-4	2.3E-2	2.0E-4
		$\frac{\sigma_{d_{12}}^{PE,Full}}{ d_{12} }$	$\frac{\sigma_{d_{21}}^{PE,Full}}{ d_{21} }$	$\frac{\sigma_{e_{12}}^{PE,Full}}{ e_{12} }$	$\frac{\sigma_{e_{21}}^{PE,Full}}{ e_{21} }$	$\frac{\sigma_{\alpha}^{PE,Full}}{ \alpha }$	
3	2	-	-	-	-	3.8E-4	
5	2	-	-	-	-	4.0E-4	
7	2	-	-	-	-	4.0E-4	
11	2	8.4E-2	4.1E-6	3.8E-2	7.4E-6	1.6E-3	

3.3. Step 3: Additional information

In this last step, additional information for the parameter estimation is given by including data of the excess enthalpy, which is correlated to the activity model by the Gibbs-Helmholtz equation. The results for the calculation of the excess enthalpy are displayed in Fig. 2b. Contrary to previous estimations, the excess enthalpy can now be well described without losing accuracy in the phase equilibria. Adding excess enthalpy data has a decisive effect on the parameter estimation problem as just one set of excess enthalpy data makes four of five parameters identifiable for the NRTL equation. This was not possible by using four different isothermal sets of VLE data in the parameter estimation and leads to an important message with respect to experimental investigations: If one excess enthalpy dataset yields more information gain than three additional VLE sets, significant costs and time can be saved by performing a subset selection with sensitivity analysis on a regular basis to plan the next experiments. As the measurement of thermodynamic equilibria is



(a) calculated with the eNRTL equation, $a_{12} = 955.61$, $a_{21} = -1.12$, and $\alpha = 0.5$, experimental data at temperatures between 298 and 423 K from (Pepela and Dunlop, 1972; Mashovets et al., 1973; Berling et al., 1999; Nasirzadeh et al., 2004).

(b) calculated with the NRTL equation, $a_{12} = 0.98$, $a_{21} = 0.43$, $b_{12} = -321.95$ K, $b_{21} = 95.12$ K, and $\alpha = 0.5$, experimental data at 278.15, 298.15, and 323.15 K from (Tomaszkiewicz et al., 1986).

Figure 2: P-x-y diagram for water and dissociated NaCl (a) and h^E -x diagram for methanol and water (b). Only one parameter remains identifiable for the NaCl/water system.

quite time-consuming if done correctly, subset selection will be a valuable asset for optimal design of experiments in thermodynamic application.

4. Conclusion and Outlook

This contribution demonstrated the application of parameter estimation with subset selection for methanol/water and NaCl/water using different activity models. It was shown that thermodynamic models can contain unidentifiable parameters, e.g. the non-randomness parameter α in the NRTL model. This justifies the conventional suggestion to fix α in parameter estimations. The second major result concerns complex parameter estimation problem, for example in electrolyte chemistry. For these applications, the number of parameters could be drastically reduced by using a subset selection to simplify the parameter estimation problem. This may lead to more reliable thermodynamic models for gas treatment or electrolysis. The third important aspect is the improved parameter identifiability of activity models by using excess enthalpy data instead of additional VLE data. This could be related to the additional derivative information on the activity model that is introduced when using excess enthalpy data. In future work, the algorithm will be used for more complex phenomena, such as Vapor-Liquid-Liquid Equilibria, and more complex models, such as equations of state, to investigate its performance.

References

- V. Álvarez, S. Mattedi, M. Iglesias, R. Gonzalez-Olmos, J. Resa, 2011. Phase equilibria of binary mixtures containing methyl acetate, water, methanol or ethanol at 101.3 kPa. *Physics and Chemistry of Liquids* 49 (1), 52–71.
- D. Berling, B. Jönsson, G. Olofsson, 1999. The use of isothermal heat-conduction calorimetry in direct measurements of solvent vapor pressure. *Journal of Solution Chemistry* 28, 693–710.
- C.-C. Chen, L. B. Evans, 1986. A local composition model for the excess gibbs energy of aqueous electrolyte systems. *AIChE Journal* 32 (3), 444–454.
- J. Fu, K. Wang, Y. Hu, 1989. Studies on vapor-liquid and liquid-liquid vapor equilibria for the ternary system methanol-methyl methacrylate-water (I) three binary systems. *Chinese Journal of Chemical Engineering*.
- E. Hendriks, G. M. Kontogeorgis, R. Dohrn, J.-C. de Hemptinne, I. G. Economou, L. F. Žilnik, V. Vesovic, 2010. Industrial requirements for thermodynamics and transport properties. *Industrial & Engineering Chemistry Research* 49 (22), 11131–11141.
- V. Mashovets, V. Zarebo, M. Fedorov, 1973. Vapor pressure of aqueous NaCl, NaBr, and NaI at temperatures from 150–350 C. *Zh. Prikl. Khim* 46, 650–652.
- D. Müller, E. Esche, D. C. López, G. Wozny, 2014. An algorithm for the identification and estimation of relevant parameters for optimization under uncertainty. *Computers & Chemical Engineering* 71, 94–103.
- K. Nasirzadeh, D. Zimin, R. Neueder, W. Kunz, 2004. Vapor-pressure measurements of liquid solutions at different temperatures: apparatus for use over an extended temperature range and some new data. *Journal of Chemical & Engineering Data* 49 (3), 607–612.
- I. B. Nogueira, K. V. Pontes, 2017. Parameter estimation with estimability analysis applied to an industrial scale polymerization process. *Computers & Chemical Engineering* 96, 75–86.
- C. N. Pepela, P. J. Dunlop, 1972. A re-examination of the vapour pressures of aqueous sodium chloride solutions at 25 C. *The Journal of Chemical Thermodynamics* 4 (2), 255–258.
- H. Renon, J. M. Prausnitz, 1968. Local compositions in thermodynamic excess functions for liquid mixtures. *AIChE Journal* 14 (1), 135–144.
- D. Swami, V. K. Rao, N. N. Rao, 1956. Vapour-liquid equilibrium still for miscible liquids at atmospheric and subatmospheric pressures. *Trans. Indian Inst. Chem. Eng* 9, 32–46.
- I. Tomaszewicz, S. Randzio, P. Gierycz, 1986. Excess enthalpy in the methanol-water system at 278.15, 298.15 and 323.15 K under pressures of 0.1, 20 and 39 MPa. II. experimental results and their analytical presentation. *Thermochimica Acta* 103 (2), 281–289.
- G. M. Wilson, 1964. Vapor-liquid equilibrium. XI. a new expression for the excess free energy of mixing. *Journal of the American Chemical Society* 86 (2), 127–130.
- C. Yang, S. Ma, X. Yin, 2011. Organic salt effect of tetramethylammonium bicarbonate on the vapor-liquid equilibrium of the methanol-water system. *Journal of Chemical & Engineering Data* 56 (10), 3747–3751.
- C. Yang, F. Sun, S. Ma, X. Yin, H. Zeng, 2012. Organic salt effect on vapor-liquid equilibrium of the methanol + water system at subatmospheric pressure. *Journal of Chemical & Engineering Data* 57 (10), 2696–2701.

Evaluation of Discretization Methods for Modeling the Chloralkali Membrane Process

Thomas Budiarto^a, Joris Weigert^a, Christian Hoffmann^a, Erik Esche^a and Jens-Uwe Repke^{a,*}

^a*Technische Universität Berlin, Process Dynamics and Operation Group, Sekr. KWT 9, Str. des 17. Juni 135, Berlin 10623, Germany*
t.budiarto@campus.tu-berlin.de

Abstract

A chloralkali membrane cell process is modeled based on a macro-homogeneous approach. The Poisson-Nernst-Planck (PNP) equation is applied to model the multi-ion transport in the system. A steep gradient problem arises at the membrane's interfaces. The finite differences method, Hermite collocation on finite elements, and the Galerkin finite elements method are compared to determine the most efficient method to tackle the problem. A logarithmic reformulation is also investigated to evaluate its compatibility to solve the problem. The finite differences method and the Hermite collocation method turn out the best results, respectively in terms of the computational time and accuracy. Afterwards, the finite differences method is applied to model a solution-membrane system based on the 1D PNP equation, whose results are discussed further regarding their subsequent applicability for extensive simulation studies.

Keywords: Hermite Collocation, Galerkin Finite Elements, The Poisson Nernst Planck equation, Chloralkali electrolysis

1. Introduction

The chloralkali membrane process is a potential energy buffer for demand-side management in the electricity market. Although this is an economically promising solution, the resulting dynamic operation is highly challenging. The chloralkali membrane electrolyzer is one among many critical apparatuses, which are fragile to dynamic load changes and also devalue considerably during dynamic operation. The total reaction in the electrolyzer is formulated as:



A model of a chloralkali membrane process is developed to enable further investigation of the dynamic characteristics of this equipment during flexible operation. The macro-homogeneous modeling approach introduced by Verbrugge and Hill (1990) and also validated by Verbrugge and Hill (1992) is considered to model the chloralkali process. It is already widely used to model electrochemical systems due to its reasonable accuracy and low computational cost, while it is adequately able to predict necessary phenomena for practical applications. This approach assumes that the modeled components are continuously distributed over the modeled spatial domain and can be represented by macroscopic variables, such as concentrations. Some authors (Moshtarikhah et al. (2017), Fíla and Bouzek (2003), Kodým et al. (2016)) have modeled the chloralkali membrane cell using this approach for a high current density regime. A numerical challenge in modeling such a system usually comes from the steep gradient at phase boundaries. Zheng and Wei (2011) successfully reduced the boundary layer complexity by incorporating the Boltzmann equation into

the PNP system despite of the narrowed model validity under the overlimiting current regime. Various discretization methods have been applied in modeling the problem. However, the most suitable one remains a question. In the present contribution, a logarithmic reformulation and three well-known discretization methods: the finite differences method, the finite elements method with Hermite collocation, and the Galerkin finite elements method are benchmarked to justify the suitability in solving such problems.

2. Model Description

The modeled system depicted in Fig. 1 considers three main components in the chloralkali membrane cell, i.e. Na^+ ($i = 1$), Cl^- ($i = 2$) and OH^- ($i = 3$), which are assumed to have a continuous distributions in space. The domain is divided into three different parts: an anolyte diffusion layer (ADL), the cation exchange membrane (CM), and a catholyte diffusion layer (CDL).

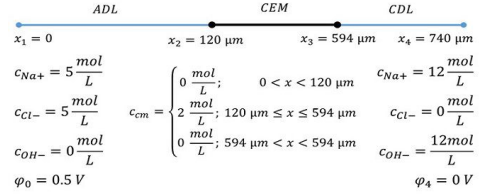


Figure 1: Schematic of the solution-membrane system

2.1. The Poisson Nernst Planck equation

The Poisson Nernst Planck (PNP) model considers the concentration of the three ionic components c_i and the electric potential φ in the modeled spatial domain. The 1D steady-state Poisson-Nernst-Planck system consists of:

$$D_i \left(\frac{d^2 c_i}{dx^2} + \frac{z_i F}{RT} \left(\frac{dc_i}{dx} \frac{d\varphi}{dx} + c_i \frac{d^2 \varphi}{dx^2} \right) \right) = 0 \quad (1)$$

$$\frac{d^2 \varphi}{dx^2} = -\frac{F}{\epsilon} \left(z_m c_m + \sum_i^{N_i} z_i c_i \right) \quad (2)$$

D_i is the diffusion coefficient of component i . z_i , R , and T in Eq. (1) are the charge number of component i , the ideal gas constant ($8.314 \text{ JK}^{-1} \text{ mol}^{-1}$), and the temperature (K) of the modeled system, respectively. ϵ and F are the permittivity of the medium (assumed $\epsilon \approx 3.9825 \times 10^{-10} \text{ F m}^{-1}$) and the Faraday constant (96485 C mol^{-1}). z_m and c_m denote the charge number of the fixed charges in the ion exchange membrane and their concentration.

2.2. The 1D linear model

To be able to benchmark the discretization methods, an analytical solution of a 1D linear model is derived and considered as a reference function. The linear differential system models an ionic liquid system in 1D space between two Dirichlet boundary conditions: $c_i(x = 0) = C_0$ and $c_i(x = L) = C_L$, wherein L is the length of the 1D space. The linear model assumes a linear electric potential distribution over the spatial domain. This assumption reduces the PNP equation into a second order homogeneous linear differential equation:

$$D_i \left(\frac{d^2 c_i}{dx^2} + \frac{z_i F}{RT} \beta \frac{dc_i}{dx} \right) = 0, \quad (3)$$

wherein β is the constant value of the electric potential gradient $\frac{d\varphi}{dx}$. An analytical solution has been derived for the linear model and leads to the following general solution: $c_i(x) = A_1 + A_2 e^{-k_i \beta x}$ with $k_i = \frac{z_i F}{RT}$. The coefficients A_1 and A_2 are determined by the spatial boundary conditions C_0 and C_L . These boundary conditions lead to a particular solution of the linear model:

$$c_i(x) = c_0 + \frac{C_0 - C_L}{1 - e^{-k_i \beta L}} (e^{-k_i \beta x} - 1) \quad (4)$$

3. The Discretization Methods

We benchmarked the linear model using the three mentioned discretization techniques in comparison to the analytic solution. Space is discretized into $Nn - 1$ equidistant partitions, $0 = x_{n=1} < x_{n=2} < \dots < x_{n=Nn} = L$. In the subsequent sections, the evaluated methods will only be briefly reviewed. Further details and fundamental background on these methods can be found in literature (Finlayson (1980)).

3.1. The finite differences method

For the first method, central finite differences are applied. The 1D space is divided into $Nn - 1$ partitions with an equal length of Δx . Eq. (5) shows the discretized form of Eq. (3). The equation system of the finite differences method holds $Nn - 2$ balance equations (Eq. (5)) and two boundary conditions C_0 and C_L .

$$D_i \left(\frac{c_{i,n+1} - 2c_{i,n} + c_{i,n-1}}{\Delta X^2} + \frac{z_i F}{RT} \beta \frac{c_{i,n+1} - c_{i,n-1}}{\Delta X} \right) = 0 \quad (5)$$

3.2. The finite elements method

In this contribution, Hermite collocation and Galerkin are applied on finite elements to approximate the solution. The approximation is carried out on $Nn - 1$ elements by a linear combination of basis functions. To simplify the discretization, the global variable x is transformed into local variable u by $u = \frac{x-x_n}{h_n}$. h_n is the length of the n -th element, given by $h_n = x_{n+1} - x_n$. Within each element, the solution is approximated by a linear combination of some basis function $N_j(u)$ shown in Eq. (6). The coefficients $a_{i,j,n}$ are then solved numerically to provide the approximated solution.

$$c_{i,n}(u) = \sum_{j=1}^{Nj} a_{i,j,n} N_{j,n}(u) \quad (6)$$

For Hermite collocation, four cubic Hermite polynomials are used as basis functions, which are $N_{j=1,n}(u) = (1-u)^2(1+2u)$, $N_{j=2,n}(u) = u(1-u)^2 h_n$, $N_{j=3,n}(u) = (u)^2(3-2u)$, and $N_{j=4,n}(u) = u^2(u-1)h_n$. As shown by Finlayson (1980) and Arora et al. (2006), it is convenient to choose the roots of shifted orthogonal Legendre polynomial ($P_2^{0,0}(u)$) as collocation points: $u_1 = 0$, $u_2 = \frac{1}{2}(1 + \frac{1}{\sqrt{3}})$, $u_3 = \frac{1}{2}(1 - \frac{1}{\sqrt{3}})$, $u_4 = 1$.

Eq. (6) is substituted into Eq. (3) resulting in the discretized form in Eq. (7). Eq. (7) is then evaluated at the inner collocation points, u_2 and u_3 . The Hermite polynomials guarantee C^1 continuity at the element boundaries. Hence, only the two global boundary conditions $a_{i,n=1,j=1} = C_0$ at $x = 0$ and $a_{i,n=Nn-1,j=3} = C_L$ at $x = L$ need to be described. The equation system to be solved consists of $2(Nn - 1)$ balance equations (Eq. (7)) and the two overall boundary conditions.

$$D_{i,n} \left(\frac{1}{h_n^2} \sum_{j=1}^{Nj=4} a_{i,n,j} \frac{d^2 N_{j,n}(u)}{du^2} + \frac{z_i F}{RT} \frac{\beta}{h_n} \sum_{j=1}^{Nj=4} a_{i,n,j} \frac{d N_{j,n}(u)}{du} \right) = 0 \quad (7)$$

For the Galerkin method, three second order Lagrange polynomials are applied as basis functions ($N_j(u)$) of Eq. (6). Those polynomials are $N_{j=1} = 2(u-1)(u-1/2)$, $N_{j=2} = 4u(1-u)$, and $N_{j=3} = 2u(u-1/2)$. By substituting Eq. (6) into Eq. (3) and applying Galerkin'S method, the linear model turns into Eq. (8). Two additional boundary conditions in every element, $\frac{dc_{i,n}}{du} - \frac{dc_{i,n-1}}{du} = 0$ and $c_{i,n} - c_{i,n-1} = 0$ are added to the equation system to guarantee C^1 continuity at the element boundaries. C_0 and C_L are also added to the equation system as the outer boundary conditions of the spatial domain.

$$\int_0^L D_i \left(\frac{1}{h_n} \sum_{j=1}^{Nj=3} a_{i,n,j} \frac{d^2 N_{j,n}(u)}{du^2} + \frac{z_i F}{RT} \beta \sum_{j=1}^{Nj=3} a_{i,n,j} \frac{d N_{j,n}(u)}{du} \right) N_{j=2,n}(u) du = 0 \quad (8)$$

3.3. Logarithmic reformulation

In addition to the discretization, a logarithmic reformulation is applied to influence the scaling of the model. For this purpose, all concentrations are replaced by $c_i(x) = e^{\ln(c_i(x))} = e^{\tilde{c}_i(x)}$ and the model is then solved in terms of \tilde{c}_i . The assumption is that this scales better and also guarantees positivity of all concentration values. The reformulated model shown in Eq. (9) is then discretized with the central finite differences method to solve it numerically.

$$D_i e^{\tilde{c}_i(x)} \left(\frac{d^2 \tilde{c}_i(x)}{dx^2} + \left(\frac{d\tilde{c}_i(x)}{dx} \right)^2 + \frac{z_i F}{RT} \beta \frac{d\tilde{c}_i(x)}{dx} \right) = 0 \quad (9)$$

4. Comparison of the Methods

To benchmark the methods introduced in Section 3, a simulation study on the linear model is set up to determine concentrations of anions ($z_{i=1} = -1$) and cations ($z_{i=2} = +1$) in a solution system. The spatial domain L has a length of $10^{-3}m$ bounded by two Dirichlet boundary conditions for both ions, namely $C_0 = 12$ and $C_L = 10^{-7} \text{ mol m}^{-3}$, which represent the maximum concentration difference in the simulation of the electrolyzer model. The diffusion coefficients are $D_{i=1} = 10^{-11}$ and $D_{i=9} = 10^{-9} \text{ m}^2 \text{ s}^{-1}$, which represent the maximum and minimum values of diffusion coefficients in the electrolyzer model. The temperature is set to be 363 K, which is the typical operation temperature of the process. And the β is -500 V m^{-1} , determined by the electric potential difference of 0.5 V divided by L . The condition number of the Jacobian matrix, the computation time and the maximum absolute error or deviation from the analytic solution are also presented in Table 1. The termination tolerance of 10^{-14} is set to end the computation. All equation systems are solved using fsolve of MATLAB with the Trust-Region-Dogleg algorithm.

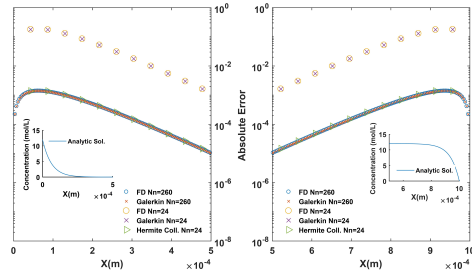


Figure 2: The comparison of the absolute error resulted by three discretization methods. The left side and the right side graphs show respectively the error profile of the negative component ($z_{i=1} = -1$) and the positive component ($z_{i=2} = +1$). The small graphs show the analytic solution of the corresponding model.

4.1. The finite differences and the finite elements methods

As initial guesses, the concentrations of all components are set to 1 mol/L. The equation systems are discretized using the finite differences (FD) and both finite elements methods (FE). All simulation problems successfully converged with the absolute value of the function residuals smaller than the required termination tolerance. The simulation results plotted in Figure 2 show that the accuracies of the evaluated methods differ in regions of higher gradient values. The Hermite collocation method overall shows a higher accuracy compared to the other two. Tab. 1 shows that

Table 1: Numerical performance: Hermite collocation, finite differences, and Galerkin method

Parameters	Hermite Coll.(HC)		Finite Differences (FD)		Galerkin Method (GM)	
	24	24	24	260	24	260
Condition number	$8.59 \cdot 10^7$	$7.38 \cdot 10^3$	$9.31 \cdot 10^5$	$4.68 \cdot 10^{13}$	$5.55 \cdot 10^{15}$	
Computation time (s)	0.9958	0.2218	0.9974	0.4347	10.2488	
Max.absolute error	0.0014	0.1781	0.0014	0.1781	0.0014	

by increasing the number of discrete points/elements (Nn) to 260, the finite difference and the Galerkin method can achieve a similar accuracy resulted by the Hermite collocation method with 24 discrete elements. To achieve this accuracy, the finite differences method needs approximately similar computation time to that of the Hermite collocation.

4.2. The logarithmic reformulation

The logarithmically reformulated model is evaluated by comparing its performance to the non-reformulated model. The central finite differences is applied to discretize both models. Nn is set to 36, which is reasonably accurate for the finite differences method based on the previous results. The analytic solution is used as an initial guess. To investigate the convergence range of the reformulation method, four variations of boundary conditions (C_0 and C_L in molL^{-1}) are simulated: 24 and 2×10^{-1} , 12 and 2 , 12×10^4 and 2 , 12×10^{-4} and 2×10^{-9} . The other model parameters remain unchanged. The variation of the boundary conditions yields four different condition numbers for the reformulated model, which are 9.49×10^5 , 9.06×10^3 , 2.20×10^9 and 4.12×10^{12} , respectively. While the condition number of the non-reformulated model remains constant at 1.70×10^4 in all variations of the boundary conditions. Only for the second case of the logarithmic problem, the reformulated model successfully converged. The convergence of the reformulated method starts to breakdown as the solution value approaches one, because of the singularity of the log function as its value approaches zero. The reformulated model obtains higher accuracy only in the region with a concave upward profile as shown in Fig. 3. Since the aim of the current investigation is a selection of the discretization method, necessary further investigations to improve the reformulation method is not done here.

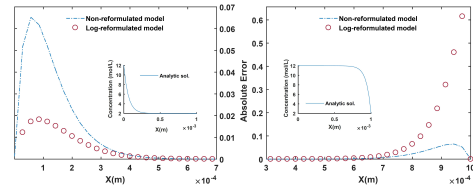


Figure 3: The comparison of the absolute error resulted by the log-reformulated model and the non-reformulated model. The left side and the right side graphs show respectively the error profile of the negative component ($z_{i=1} = -1$) and the positive component ($z_{i=2} = +1$). The small graphs show the analytic solution of the non-reformulated model for both components.

5. Modeling the Solution-Membrane System of the Chloralkali Electrolyzer

In this section, the application of the Poisson-Nernst-Planck equation to model a system of three ions in a membrane and two diffusion layers (shown by Figure 1) is presented. The model is an approximation of a chloralkali process in a segment of the membrane reactor. D_i and the size of the spatial domain are adopted from Kodým et al. (2016) and Fíla and Bouzek (2003). Continuity of the dependent variables and ion fluxes are applied at both solution-membrane interfaces (x_2 and x_3). Eq. (1) and Eq. (2) are discretized using the central finite differences method due to

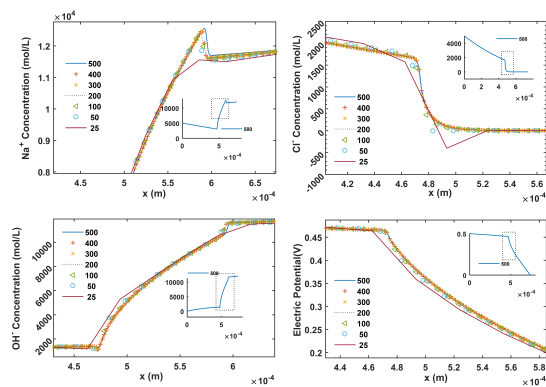


Figure 4: Profiles of the ions concentration and the electric potential in the 1D PNP system (Fig. 1) resulted from simulations with various numbers of discrete points.

its relative simple initialization and low computational cost while preserving reasonable accuracy. The number of the discrete elements (Nn) was varied from 25 to 500 elements to justify the minimum number of elements necessary to obtain adequate accuracy. The simulations were converged with a tolerance of 10^{-14} . Fig. 4 shows the obtained profiles of the ion concentration and the electric-potential. Almost all of the discretization variants provide a similar overall profile. They only differ at the solution-membrane interface ($x = 474\mu m$ and $x = 594\mu m$), where the steepest gradient appears. Increasing the number of elements to more than 300 does not improve the accuracy significantly.

6. Conclusions and Outlook

Three discretization methods: the central finite differences, Hermite collocation on finite elements, and the Galerkin finite elements method have been evaluated using a 1D linear differential model. In comparison with its analytic solution, the Hermite collocation on finite elements method shows the highest accuracy, particularly in regions of steep gradients. However, with extra number of the discrete points the central finite differences method can also achieve the similar accuracy in an approximately similar computation time. A logarithmic reformulation was evaluated while using the central finite differences as the discretization method. The results show that this method makes the condition number of the Jacobian matrix more dependent on the actual solution range. Further investigation and modification of this method for tackling the dependency are necessary to make this method more applicable. The 1D Poisson-Nernst-Planck model has been adopted to model a solution-membrane system, approximating a chloralkali membrane process. The presented results show that the method is capable of being implemented in such a case by considering an appropriate number of elements to achieve a desired accuracy.

In future work, we will investigate non-equidistant discretizations. In regions of smaller gradient values, lower numbers of discrete points or finite elements could be applied and consequently the computational cost of the discretization techniques can be further reduced.

7. Acknowledgment

The LPDP (Indonesian Endowment Fund for Education) is gratefully acknowledged for supporting this research through the Ph.D. funding for the author. The German Federal Ministry for Economic Affairs and Energy is also gratefully acknowledged for supporting the research project ChemEflex (funding code 0350013A).

References

- Arora, S., Dhaliwal, S., Kukreja, V., 2006. Simulation of washing of packed bed of porous particles by orthogonal collocation on finite elements. *Computers and Chemical Engineering* 30, 1054–1060.
- Fíla, V., Bouzek, K., 2003. A mathematical model of multiple ion transport across an ion-selective membrane under current load conditions. *Journal of Applied Electrochemistry* 33, 675–684.
- Finlayson, B. A., 1980. *Nonlinear Analysis in Chemical Engineering*. McGraw-Hill.
- Kodým, R., Fíla, V., Šnita, D., Bouzek, K., 2016. Poisson-Nernst-Planck model of multiple ion transport across an ion-selective membrane under conditions close to chlor-alkali electrolysis. *Journal of Applied Electrochemistry* 46, 679–694.
- MoshtariKhah, S., Oppers, N., Groot, M., Keurentjes, J., Schouten, J., Schaaf, J. v. d., 2017. Nernst–Planck modeling of multicomponent ion transport in a Nafion membrane at high current density. *Journal of Applied Electrochemistry* 47, 51–62.
- Verbrugge, M. W., Hill, R. F., 1990. Ion and Solvent Transport in Ion-Exchange Membranes: I. A Macrohomogeneous Mathematical Model. *Journal of The Electrochemical Society* 137, 886–893.
- Verbrugge, M. W., Hill, R. F., 1992. Measurement of ionic concentration profiles in membranes during transport. *Electrochimica Acta* 37, 221–229.
- Zheng, Q. and Wei, G.-W., 2011. Poisson–Boltzmann–Nernst–Planck Model. *Journal of Chemical Physics* 134, 194101.1–17.

Synthesis, Design and Optimization of Schemes to Produce 2, 3-Butanediol Considering Economic, Environmental and Safety issues

Eduardo Sánchez-Ramírez,^{a*} Juan José Quiroz-Ramírez,^b Juan Gabriel Segovia-Hernández^a

^a*Universidad de Guanajuato, Noria Alta S/N, Guanajuato 36050, México*

^b*CONACyT – CIATEC A.C. Centro de Innovación Aplicada en Tecnologías Competitivas, Omega 201 Col. Industrial Delta, León 37545, México*

eduardo.sanchez@ugto.mx

Abstract

2, 3-Butanediol is a very promising chemical due to its several applications and may be produced by microbial production. The recovery of 2, 3-Butanediol from the fermentation broth is yet a challenge due to its low concentration. Moreover, a broader point of view is also necessary since current needs require a process with low environmental impact and high inherent safety. In this work, the inherent risk will be approached at early-stages at the same time that economic and environmental issues. The aim of this paper is to synthesis, design and optimize some alternatives to purify 2,3-Butanediol based on distillation, those alternatives are synthesized in such way that is obtained as results thermally coupled, thermodynamically equivalent and intensified sequences. The alternatives were designed and optimized considering three objective functions: the total annual cost as an economic index, the eco-indicator 99 as an environmental index, and the inherent risk of the process (analyzed as individual risk). In general terms, the intensified alternative presented 15 % reduction of the TAC and 14% of the environmental impact. Moreover, the same alternative presented the lowest inherent risk with a reduction of about 50% in comparison with the reference alternative.

Keywords: 2,3-Butanediol, Multi-Objective Optimization, Downstream Process, Individual Risk.

1. Introduction

2,3-Butanediol (2,3-BD) is a renewable chemical if its production is based on biomass. Several reports pointed out 2,3-BD as a quite interesting bio-based compound since its application covers several industrial sectors. Currently, 2, 3-BD has shown its potential for being used in the manufacturing of printing inks, perfumes, explosives, etc. Moreover, an interesting consideration of this bio-based chemical is its use as potential liquid fuel with a heating value of 27.19 kJ/g; additionally, 2,3-BD is an intermediate to produce methyl-ethyl-ketone (MEK) a quite promising biofuel, using a dehydrogenation process. 2,3-Butanediol coming from fermentation comes with a high content of water, making its purification a challenge (Koutinas et al. 2016).

On the other hand, since the boiling point of 2,3-BD is about 180°C at atmospheric pressure and it does not form an azeotrope with water, the use of conventional

distillation seems a natural alternative. While this unit operation has many advantages, one drawback is its significant energy requirement. Therefore, energy consumption plays a major role in the operational costs of a process. Despite at first sight the use of distillation it might be not profitable, it is possible to implement several synthesis alternatives to reduce both capital and energy cost. Regarding the synthesis and design of separation process Errico et al. (2016) have presented an ordered and sequential methodology to generate subspaces of separation alternatives. This kind of methodologies jointly with optimization strategies have shown important improvements. Despite the usefulness of many synthesis and optimization approaches, they have focused mostly on the economic issue which is indeed a critical point. On the other hand, an important issue like inherent safety has been disregarded or considered as an afterthought following the design. So, do not include the risk involved in the downstream process can lead to misleading risk assessment. An effective alternative would be, to include inherent safety, economic and environmental issues on early design stages, guaranteeing in this way a process with low economic and environmental impact and also accounts the risk assessment on each alternative. In this manner, with all background mentioned, this work aims to synthesize, design and optimize some new alternatives to separate and purify an effluent of 2,3-Butanediol coming from fermentation. This approach proposes to produce purification alternatives which consider the balance among several targets, in other words, the optimization procedure will find separation alternatives which considers economic, environmental, and safety issues in order to accomplish the current industrial necessities.

2. Problem statement and methodology

Although 2,3-butanediol is a very useful chemical bio bulk, its microbial production involves a dilute broth which requires further purification. However, according to the state of the art of 2,3- butanediol, this downstream process is not well explored so far. Recently, Penner et al. (2017) proposed a conventional alternative for this task (see Figure 1a). However, it is clear the necessity for new alternatives which improve performance indexes. With this in mind, the schemes in Figure 1a)-b) will be considered as the references cases for further synthesis and design methodology. The complete methodology is described below.

Step 1: Identification of conventional distillation column: The schemes presented in Figure 1a)-b) were considered as reference cases. Initially, (Penner et al. 2017) proposed the direct sequence presented in Figure 1a), the natural complement for Figure 1a is the indirect sequence in Figure 1b).

Step 2: Generation of thermally coupled alternatives: having both cases of Figure 1 as a reference, it is possible to generate the subspace of the modified thermally coupled sequences by the substitution of heat exchangers (reboiler and condenser as appropriate) associated to no-product stream with a liquid/vapor interconnection (See Figure 2). In other words, where the streams of no-product are located, it is possible to set a thermally coupling if either a reboiler or condenser is eliminated, and a stream of steam and liquid is considered instead.

Step 3: Generation of thermodynamically equivalent alternatives. Now, with the thermal couplings already introduced, there are column sections where the condenser/reboiler provides a common reflux ratio/vapor boil-up between two consecutive columns. With

this in mind, it is possible to move this section to generate thermodynamically equivalent alternatives in Figure 3. i. e. Figure 3a) is obtained if section 4 of Figure 2a) is moved below section 2 in Figure 3a).

Step 4 Generation of intensified alternatives: the following methodology is simple and consists of the elimination of the side columns which have only one column section (See Figure 4). i.e. Figure 4a) is obtained if section 3 in Figure 3a) is eliminated.

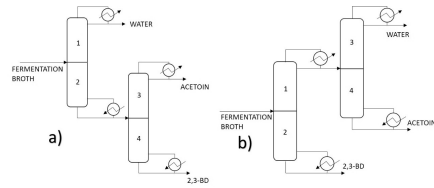


Fig. 1 Pure distillation schemes

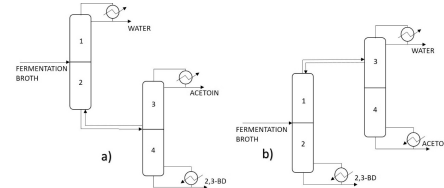


Fig. 2 Thermally Coupled schemes

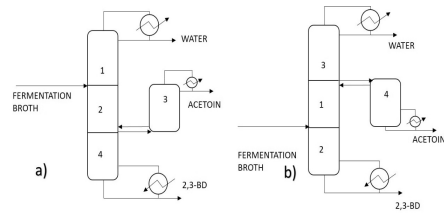


Fig. 3 Thermodynamic Equivalent schemes

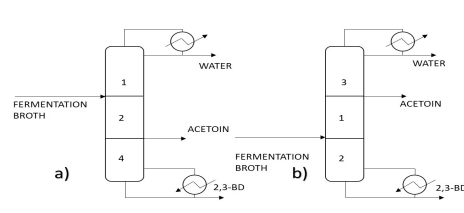


Fig. 4 Intensified schemes

According to their result in fermentation, the Diol concentration is 150 g/L and 10 g/L of 2,3-Butanediol and Acetoin, respectively. In this work, we considered the same mass fractions and a mass flow of 73,170 kg h⁻¹. All alternatives were modeled using Aspen Plus modeler using the NRTL thermodynamic model, which according to Penner et al. (2017), it describes better the interactions among all components. The minimum purities were fixed on a mass base as 99.5% for 2,3-BD and water, and 99.0% for acetoin. The objective function and the optimization method are described below.

2.1 Multi-objective Optimization and Objective Functions

The objective function included the simultaneous minimization of the total annual cost (TAC), the eco-indicator 99 (EI99) and the Inherent Risk (IR) measured as individual risk. The minimization of these objectives was subject to the required recoveries and purities in each product stream (see Eq. 1).

$$\text{Min}(TAC, EI99, IR) = f(N_m, N_{fn}, R_m, F_m, F_{rn}, F_{vn}, D_{cn}, P_{cn}, FC_{cn}) \quad (1)$$

Where N_m are total number of column stages, N_{fn} is the feed stage in column, R_m is the reflux ratio, F_m is the distillate/bottoms flux, F_{rn} and F_{vn} are the interconnection liquid/vapor flow, D_{cn} is the column diameter, P_{cn} and F_{cn} are physicochemical properties for IR calculation such as molecular weight, heat of combustion, LC50 and so on. This multi-objective minimization considered 25 continuous and discrete variables. TAC was calculated through the Guthrie method according to the equation $TAC = (\text{Capital Costs}/\text{Payback Period}) + \text{Operating Costs}$, all the parameters for the equipment were taken from (Turton R. 2001). The Eco-Indicator 99 (EI99) was used to

evaluate the sustainability of the processes by means of the equation $EI_{99} = \sum \sum \sum$ (Amount of chemical x damage caused x weighting factor x normalization factor), this methodology is based on lifecycle analysis of different categories where individual scores are assigned depending on the category, three impact categories (steel, electricity, and vapor) were considered according to work presented by Errico et al. (2016) where this indicator has been utilized to quantify the environmental impact in some chemical processes. In the case of the safety, the individual risk was calculated through quantitative risk analysis technique, which is a methodology of inherent safety where the main objective is to evaluate the frequency and probability of decease or injury due to accidents like explosions or toxic release. The inherent risk is evaluated by the equation $IR = \sum f * P$, being f the frequency of accident and P the probability of affection. This methodology has been successfully used to evaluate the risk on the chemical process (Medina-Herrera, et al. 2014), the equations and procedure were realized to a distance of 50m from the equipment according to reported by American Institute of Chemical Engineers, 2000.

To optimize the process route for biobutanol production, a stochastic optimization method, Differential Evolution with Tabu List (DETL) was used, which have shown being robust to optimize intensified separation systems. Srinivas & Rangaiah, (2007) showed that the use of some concepts of the metaheuristic tabu could improve the performance of DE algorithm. The implementation of this optimization approach was made using a hybrid platform where the DETL method was coded using Microsoft Excel (ME). Initially, the method proposes a vector which is sent to Aspen Plus by means of dynamic data exchange (DDE). In there the separation process was rigorously simulated. For the optimization of process routes analyzed in this study, the following parameters for DETL method were used: 200 individuals, 500 generations, a tabu list of 50% of total individuals, a tabu radius of 0.0000025, 0.80 and 0.6 for crossover and mutation fractions, respectively.

3. Results

Although the three objective functions are evaluated, the obtained results are shown in Table 1. All Pareto fronts were obtained after 100,000 evaluations, as afterward, the vector of decision variables did not produce any meaningful improvement. Initially, note the pure distillation schemes present a difference of 32%. The high difference in TAC is high enough to select as the best option the direct sequence between both conventional alternatives. For such reason, since the direct alternative has been identified, only the schemes derived for that configuration are considered for optimization procedure. After the optimization process, some trends among objective function were observed. Note, in Figure 5, when the TAC is evaluated jointly IR, it is clear the competitive connection between both targets, as long as the TAC increase, the individual risk decreases and vice versa. Figure 5 also shows the antagonist behavior between the environmental impact and the individual risk associated with the conventional downstream process. It is possible to obtain process with low environmental impact, however, the probability of individual accident increase and vice versa.

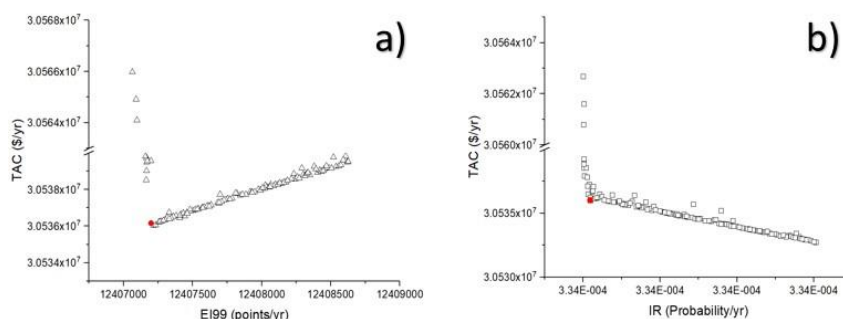


Fig. 5 Pareto fronts between EI99/TAC and TAC/IR for the intensified scheme

Table 1. Objective function values

Objective Function	TAC [$\$ y^{-1}$]	EI99 [points y^{-1}]	IR [P Y^{-1}]
Direct	35,032,419	14,328,558	0.0006686
Indirect	51,155,609	22,627,903	0.0006663
T Coupled	31,360,313	12,559,191	0.0006795
T Equivalent	31,055,124	12,557,857	0.0006684
Intensified	30,536,031	12,407,199	0.0003341

Table 2. Intensified scheme 4a) parameters

	C1
Number of stages	87
Reflux ratio	0.333
Feed-stage	42
Column diameter (m)	0.675
Distillate ($kg h^{-1}$)	3,416.07
Side stage	49
Side flow ($kmol h^{-1}$)	8.155
Condenser duty (kW)	51,507
Reboiler duty (kW)	61,457

Regarding the evaluation of TAC and IR, it is pretty interesting the reason for such reduction on this incident probability. Since IR calculation considers continuous and instantaneous chemical releases, it is clear that as long as internal flows increase, IR will increase because of the quantity of inventory inside the column increase, which it will provoke that if an accident happens the affectation and duration of the events or probability of death will be greater due to there is more mass that is source to fires, explosion, and toxic releases. This is the general tendency, however, note that for IR calculations several physicochemical properties are involved, such as heat of combustion, flammability limits and so on. With this in mind, note that the feed stream to be separated is mainly composed of water, which obviously for its physicochemical properties generates a contrary behavior. In other words, the IR increases with high internal flows (caused by high reflux or high diameters), however in this case of study for almost all sequences, the first columns separate mainly water, consequently, the internal flows are enriched with water. This amount of water solubilizes the other component to separates and its flammability and toxicity decrease.

Furthermore, at second column acetoin and 2,3-BD are separated, but at this instance, the internal flows follow the common IR behavior, because the quantity of water is fewer in comparison with the first column. In this manner, the IR calculation does not generate a proportional behavior with TAC because of this associated conflict. Finally, when is observed the tendency of EI99 evaluated jointly IR in Pareto front of Figure 5, similar behavior is observed. The internal flows play an interesting role already mentioned. However, those flows must be heated. So, in almost all alternatives, the first column separates the water and implies a significant amount of steam, impacting directly on EI99 value. However, the concentration of flammable compounds decreases. On the other hand, the last column to reduce both IR and TAC values is composed mainly by small columns, which indeed needs fewer services than the first column. Table 2 shows the main parameters of the intensified scheme.

4. Conclusions

This approach has been performed using a multi-objective optimization problem, finding through Pareto fronts the most balanced solution among all objective function, in other words, it was possible to find a solution where all objective functions reach its minimum values. Once the optimization test was applied to the proposed alternatives by a synthesis procedure, the initial results showed that between the two conventional alternatives the direct sequence is better than the indirect scheme. Derived from the direct sequence, the intensified alternatives, which separate and purify the feed stream in a single column, showed the best performance index (economic, environmental and safety) in comparison with all alternatives. It was possible to reach economic savings of about 15% in comparison with the direct sequences, a reduction of about 14% on the environmental impact and a reduction of about 50% regarding the IR. Regarding IR evaluation, it was clear the high dependence of this index with the size of the equipment, the amount of internal flows and the kind of chemical to be separated.

References

- Koutinas, A. A., Yopez, B., Kopsahelis, N., Freire, D. M., de Castro, A. M., Papanikolaou, S., & Kookos, I. K. 2016. Techno-economic evaluation of a complete bioprocess for 2, 3-butanediol production from renewable resources. *Bioresource technology*, 204, 55-64.
- Errico, M., Sanchez-Ramirez, E., Quiroz-Ramirez, J. J., Segovia-Hernandez, J. G., & Rong, B. G. 2016. Synthesis and design of new hybrid configurations for biobutanol purification. *Computers & Chemical Engineering*, 84, 482-492.
- Penner, D., Redepenning, C., Mitsos, A., & Viell, J. 2017. Conceptual Design of Methyl Ethyl Ketone Production via 2, 3-Butanediol for Fuels and Chemicals. *Industrial & Engineering Chemistry Research*, 56(14), 3947-3957.
- Turton, R., Bailie, R. C., Whiting, W. B., & Shaeiwitz, J. A. 2008. Analysis, synthesis, and design of chemical processes. Pearson Education.
- Medina-Herrera, N., Jiménez-Gutiérrez, A., & Mannan, M. S. 2014. Development of inherently safer distillation systems. *Journal of Loss Prevention in the Process Industries*, 29, 225-239.
- Srinivas, M., & Rangaiah, G. P. 2007. Differential evolution with tabu list for solving nonlinear and mixed-integer nonlinear programming problems. *Industrial & Engineering Chemistry Research*, 46(22), 7126-7135.

ORC on tour: Integrated design of dynamic ORC processes and working fluids for waste-heat recovery from heavy-duty vehicles

Dominik Tillmanns^a, Jonas Petzschmann^a, Johannes Schilling^a,
Christoph Gertig^a and André Bardow^{a,b*}

^a*Institute of Technical Thermodynamics, Schinkelstraße 8, 52062 Aachen, Germany*

^b*Institute of Energy and Climate Research – Energy Systems Engineering (IEK-10),
Wilhelm-Johnen-Straße, 52425 Jülich, Germany*

andre.bardow@itt.rwth-aachen.de

Abstract

Organic Rankine Cycles (ORC) convert low temperature heat into power. To maximize conversion efficiency, both ORC process and working fluid have to be tailored to the specific application. Common solution approaches for the resulting integrated design of ORC process and working fluid are limited to steady-state applications. However, for applications in dynamic settings, steady-state design approaches can lead to suboptimal solutions due to the neglect of the dynamic behavior. In this work, we present an approach for the integrated design of ORC process and working fluid considering the dynamics. The approach is based on the Continuous-Molecular Targeting–Computer-aided Molecular Design (CoMT-CAMD) framework. Herein, the physically based Perturbed-Chain Statistical Associating Fluid Theory (PC-SAFT) is used as thermodynamic model. To capture the ORC behavior under dynamic conditions, dynamic models for the ORC equipment are integrated into the process model. The result is an optimal control problem (OCP) yielding an optimal working fluid and the corresponding optimal process control for a given dynamic input. This so-called dynamic CoMT-CAMD approach is applied to an ORC for waste-heat recovery on a heavy-duty vehicle. Whereas steady-state design approaches fail, the presented approach identifies the optimal working fluid and the corresponding optimal control of the ORC process.

Keywords: CoMT-CAMD, integrated design, dynamic, PC-SAFT, Modelica

1. Introduction

Nearly 30 % of the on-road CO₂ emissions in 2014 were emitted by heavy-duty vehicles (HDV) in the European Union (Muncrief and Sharpe, 2015). CO₂ emissions of HDVs can be decreased by reducing their fuel consumption. To reduce the fuel consumption of HDVs, the exhaust gas waste heat of the engine can be transformed into mechanical power by an Organic Rankine Cycle (ORC). An ORC improves the compliance with future CO₂-regulations and the total cost of ownership (TCO) (Eichler et al., 2015). However, ORCs on HDVs have high investment costs and low power output due to low conversion efficiencies. To maximize conversion efficiency and thus render ORCs profitable, a tailor-made ORC is needed. To tailor an ORC, working fluid design has to be integrated into process optimization (Gani, 2004). To solve the resulting large-

scale mixed-integer nonlinear program (MINLP), many solution approaches have been developed as recently reviewed by Papadopoulos et al. (2018). In our previous work, we developed the Continuous-Molecular Targeting – Computer-Aided Molecular Design (CoMT-CAMD) approach for the integrated design of processes and molecules (Bardow et al., 2010; Lampe et al., 2015). In CoMT-CAMD, the physically-based Perturbed-Chain Statistical Associating Fluid Theory (PC-SAFT) is used as thermodynamic model (Gross and Sadowski, 2001). In the first stage of CoMT-CAMD (CoMT stage), the discrete pure component parameters representing a working fluid in PC-SAFT are relaxed to identify a hypothetical optimal working fluid, the so-called target. In the second stage (Structure-Mapping stage), a second-order Taylor approximation around the target and a CAMD formulation are used to identify real working fluids in a mixed-integer quadratic program (MIQP).

So far, CoMT-CAMD and other integrated design approaches are limited to steady-state input. However, for ORCs on HDVs, the exhaust gas waste heat shows dynamic behavior resulting in transient temperature and mass flow rates of the ORC heat source. The design of ORC processes with dynamic heat sources leads to large-scale dynamic optimization problems (Huster et al., 2018). However, the optimal working fluid also depends on temperature and mass flow of the heat source (Colonna et al., 2015) as well as the control strategy for the ORC (Zarogiannis et al., 2017). Thus, a steady-state design point is not sufficient for working fluid design, and the process dynamics has to be considered within the integrated design to capture all process-related trade-offs.

In this work, we present the dynamic CoMT-CAMD approach for the integrated design of dynamic processes and fluids. For this purpose, dynamic models for the equipment are integrated into the process model of CoMT-CAMD leading to an optimal control problem (OCP). The solution of dynamic CoMT-CAMD is an optimal working fluid and the corresponding optimal process for a given dynamic input.

2. Dynamic CoMT-CAMD

The CoMT-CAMD approach was developed for the integrated design of steady-state applications (Bardow et al., 2010; Lampe et al., 2015). In this work, we extend the CoMT-CAMD approach to applications with dynamic inputs. For this purpose, dynamic models for the equipment are integrated into the process model to capture the dynamic behavior. Thereby, the original MINLP of the integrated design is transformed into a large-scale mixed-integer optimal control programming (MIOCP) problem. To efficiently solve this problem, we split the MIOCP into an optimal control problem (OCP) (CoMT stage, see section 2.1) and an MIQP (Structure-Mapping stage, see section 2.2) according to the idea of the original CoMT-CAMD approach (Figure 1). Finally, the identified working fluids are assessed by individual dynamic process optimizations (see section 2.3).

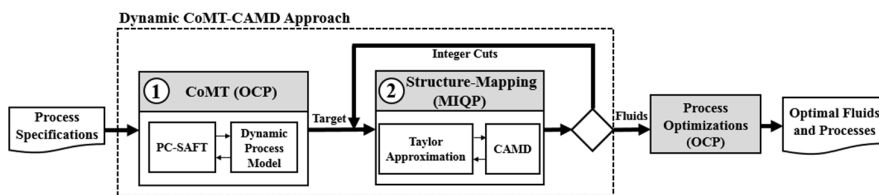


Figure 1: Workflow of the dynamic CoMT-CAMD approach

2.1. Continuous-molecular targeting (CoMT)

A working fluid is described by a set of pure component parameters in PC-SAFT. In the first stage, the CoMT stage, these discrete pure component parameters representing the working fluid are relaxed to transform the MIOCP into an OCP given by:

$$\begin{aligned}
 & \max_{x(t), u(t), p_{pr}, p_{wf}} \tilde{f} = \int_{t_0}^{t_1} f(x(t), u(t), p_{pr}, \theta(t)) dt && \text{objective} \\
 & s.t. \quad \left. \begin{aligned}
 \dot{x}(t) &= k(x(t), u(t), p_{pr}, \theta(t)) \\
 g_1(x(t), u(t), p_{pr}, \theta(t)) &= 0 \\
 g_2(x(t), u(t), p_{pr}, \theta(t)) &\leq 0 \\
 \theta(t) &= h(x(t), u(t), p_{pr}, p_{wf}) \\
 x_{\min} &\leq x(t) \leq x_{\max} \\
 u_{\min} &\leq u(t) \leq u_{\max} \\
 p_{pr, \min} &\leq p_{pr}(t) \leq p_{pr, \max} \\
 p_{wf, \min} &\leq p_{wf}(t) \leq p_{wf, \max}
 \end{aligned} \right\} \begin{array}{l}
 \text{DAE process model} \\
 \text{PC-SAFT} \\
 \text{dynamic states} \\
 \text{input signals} \\
 \text{process parameters} \\
 \text{working fluid}
 \end{array} \quad (1)
 \end{aligned}$$

Herein, the objective function \tilde{f} (e.g., the mean net power output) depends on dynamic states $x(t)$ (e.g., time-dependent temperatures), input signals $u(t)$ (e.g., time-dependent control of the pump), process parameters p_{pr} (e.g., nominal pressure levels) and equilibrium properties of the working fluid $\theta(t)$ (e.g., enthalpies). The process model consists of a system of differential equations for the dynamic states $\dot{x}(t)$ (e.g. energy balances), equality constraints g_1 (e.g. isentropic efficiencies) and inequality constraints g_2 (e.g., pressure limits). The equilibrium properties of the working fluid $\theta(t)$ are calculated using the PC-SAFT equation of state h .

The result of the CoMT stage in problem 1 is a hypothetical optimal working fluid, the so-called target, and the corresponding optimal control of the process. The target is characterized by its optimal pure component parameters p_{wf}^* , the optimal objective function value \tilde{f}^* and the derivatives of \tilde{f} at the target.

To reduce the programming effort for the development of new processes, the process model is implemented in Modelica enabling easy drag-and-drop flowsheeting and the use of existing model libraries. The OCP in problem 1 is typically solved within hours using the multiple shooting algorithm MUSCOD-II (Leineweber et al., 2003).

2.2. Structure-Mapping using Computer-aided molecular design (CAMD)

In the second stage, the Structure-Mapping stage, a second-order Taylor-approximation around the target \tilde{f} is used to estimate the objective function value \tilde{f} of real working fluids. To design molecular structures with a performance closest to the target in the resulting MIQP, a computer-aided molecular design (CAMD) formulation is used:

$$\begin{aligned}
 & \max_n \hat{f}(p_{wf}) = \tilde{f}(p_{wf}^*) + \frac{\partial \tilde{f}}{\partial p_{wf}} \Big|_{p_{wf}=p_{wf}^*} (p_{wf} - p_{wf}^*) + \frac{1}{2} (p_{wf} - p_{wf}^*)^T \frac{\partial^2 \tilde{f}}{\partial p_{wf}^2} \Big|_{p_{wf}=p_{wf}^*} (p_{wf} - p_{wf}^*) \\
 & s.t. \quad k(n) = p_{wf} && \text{group contribution method} \\
 & \quad n \in \mathbb{Z} && \text{molecular structure}
 \end{aligned} \quad (2)$$

Herein, the objective function \hat{f} is the second-order Taylor approximation around the target $\tilde{f}^* = \tilde{f}(p_{wf}^*)$. The homosegmented group-contribution (GC) method for PC-SAFT (Sauer et al., 2014) is used to predict the pure component parameters of PC-SAFT p_{wf} from the molecular structure of the working fluid n . Here, the vector n contains the number of functional groups constituting the molecular structure of the working fluid. In this work, we consider the following non-polar, non-associating functional groups: $-\text{CH}_3$, $-\text{CH}_2-$, $>\text{CH}-$, $>\text{C}<$ for alkanes, $=\text{CH}_2$, $=\text{CH}-$, $>\text{C}=\text{}$ for alkenes, $-\text{C}\equiv\text{CH}$ for 1-alkynes,

$-\text{CH}^{\text{Arom}=\text{}}$, $>\text{C}^{\text{Arom}=\text{}}$ for aromatic compounds, $-\text{CH}_2^{\text{Hex}-}$, $>\text{CH}^{\text{Hex}-}$ for branched cyclohexanes and $-\text{CH}_2^{\text{Pent}-}$, $>\text{CH}^{\text{Pent}-}$ for branched cyclopentanes.

To overcome shortcomings of the Taylor approximation, a ranking of working fluids is calculated. For this purpose, the MIQP in problem 2 is solved repeatedly using integer cuts (Grossmann and Kravanja, 1995) to exclude previous solutions from the design space. The result of the Structure-Mapping stage is a ranking of optimal working fluids based on the Taylor approximation. The MIQP in problem 2 is typically solved within a few seconds using the software GAMS.

2.3. Final process optimization

Finally, to overcome shortcomings of the Taylor approximation, the working fluids identified in the Structure-Mapping stage are individually optimized using the dynamic process model of the CoMT stage. Thereby, we obtain a more accurate objective function value \tilde{f} for the promising working fluids and the corresponding optimal control of the ORC process. The final optimal control problems are also solved with MUSCOD-II as for the CoMT stage.

3. Case study

3.1. Specifications

The presented dynamic CoMT-CAMD approach is applied to the integrated design of an ORC for waste heat recovery from heavy-duty vehicles based on Eichler et al. (2015) (see figure 2). The dynamic heat input of the ORC is characterized by time series for the temperature and mass flow of the exhaust gas after the exhaust gas after-treatment. We approximate these time series by sine waves with mean values and amplitudes based on time series from Dünnebeil et al. (2015). We assume cyclic steady-state constraints and thus only one sine wave of the slowest oscillating profile is needed to represent the full time series.

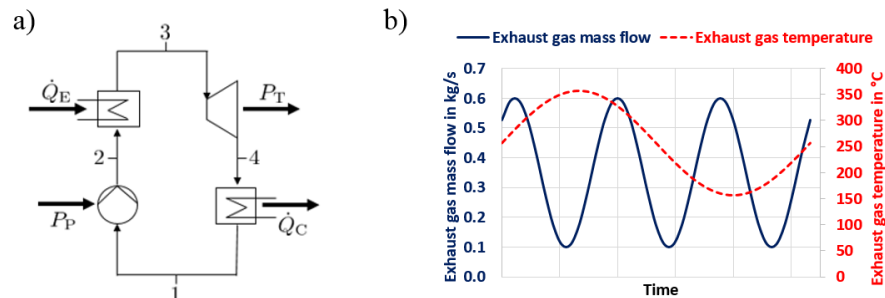


Figure 2: ORC process in (a) flowsheet and (b) temperature and mass flow of the exhaust gas after exhaust gas after-treatment.

The mean net power output of the ORC \bar{P} is considered as objective $\tilde{f} = \bar{P} = \frac{1}{t_f - t_0} \int_{t_0}^{t_f} P(x(t), u(t), p_{pr}, \theta(t)) dt$ in problem 1.

To react to the dynamic input of the ORC, the pump can be used to control the ORC process. For this purpose, the pump is modelled using affinity laws (Calise et al., 2015). The inertia of the pump is captured by a first-order lag element with a time constant $\tau_p = 1$ s (Esposito et al., 2015; Quoilin, 2011). An isentropic pump efficiency of $\eta_{p,s} = 0.5$ is

assumed. For the evaporator, we use a 0-D model based on Peralez et al. (2015) that assumes a homogeneous temperature of the heat exchanger wall T_W . The mass of the heat exchanger wall mass is $m_W = 13$ kg. The expander is modelled by assuming a constant isentropic efficiency of $\eta_{E,s} = 0.7$. In the condenser, we assume a minimal approach temperature of $\Delta T_{\min} = 20$ K and for the cooling water, an inlet temperature of $T_{CW,in} = 75$ °C and an outlet temperature of $T_{CW,out} = 80$ °C. For this case study, the dynamic states $x(t) = (T_W, n_{rel})^T$ are the temperature of the evaporator heat exchanger wall T_W and the relative rotational speed of the pump n_{rel} calculated as the ratio of the rotational speed n and the nominal rotational speed n_N . The input signal $u(t)$ is the control variable of the nominal speed of the pump. The process parameters $p_{pr} = (p_{l,N}^{red}, p_{u,N}^{red}, \dot{m}_N)^T$ are the nominal mass flow rate of the working fluid \dot{m}_N , the nominal lower reduced pressure level $p_{l,N}^{red}$ and the nominal upper reduced pressure level $p_{u,N}^{red}$. Additionally, limits on the absolute pressure levels $p_{\min} = 1$ bar and $p_{\max} = 35$ bar are assumed. Furthermore, a maximal number of functional groups per working fluid of $n_{\max} = 25$ is considered in the CAMD problem.

3.2. Results

Dynamic CoMT-CAMD is applied to the integrated design of the described ORC. In this case study, the target has a mean net power output $\bar{P} = 3.20$ kW (see table 1).

All working fluids of the top 5 working fluids identified in the Structure-Mapping stage are short-chained alkanes, alkenes or alkynes. The best 2 working fluids consist of 5 carbon atoms and have an unstable triple bond. Thus, these working fluids would probably not be used in ORC applications. The following 3 working fluids consist of 4 carbon atoms and have just single or double bonds, which are more stable than triple

Table 1: The mean net power output of the target and top 5 identified working fluids.

Rank	Name	\bar{P} / kW
Target	-	3.20
1	3-Methyl-1-butyne	2.79
2	1-Pentyne	2.66
3	Isobutane	1.77
4	1-Butene	1.66
5	Isobutene	1.54

bonds. The best identified working fluid without triple bond is isobutane with $\bar{P} = 1.77$ kW, which is 45 % lower than the mean net power output of the target and 37 % lower than the best working fluid with triple bond, 3-methyl-1-butyne. For isobutane, the net power varies between $P_{\min} = 0.44$ kW and $P_{\max} = 3.49$ kW during one cycle.

The results are compared to the integrated design based on a steady-state input calculated as the mean value of the temperature and mass flow of the dynamic heat source (cf. figure 2b). The steady-state design overestimates the mean net power output of isobutane by 20 %. For 1-butene and isobutene the net power output is overestimated by 23 % and 30 %, respectively. Thus, a steady-state design point is not sufficient for the selection of the optimal working fluid for dynamic ORC applications. Instead, the integrated design based on a dynamic process model is required, which is enabled by the presented dynamic CoMT-CAMD approach.

4. Conclusions

The dynamic CoMT-CAMD approach is presented for the integrated design of molecules and processes with dynamic input such as ORCs for waste heat recovery on HDVs. The underlying CoMT-CAMD approach was limited to steady-state applications. This limitation is overcome in the presented dynamic CoMT-CAMD approach by using

dynamic models for the ORC equipment in Modelica. MUSCOD-II is used in the CoMT stage to identify a hypothetical optimal working fluid in the resulting optimal control problem. Subsequently, a CAMD algorithm is used to identify real working fluids with a performance closest to the hypothetical optimum.

The resulting dynamic CoMT-CAMD approach is successfully applied to the design of an ORC for waste heat recovery on an HDV. Here, isobutane is identified as optimal stable working fluid for the dynamic application. In comparison, the integrated design based on a steady-state input calculated as the mean value of the temperature and mass flow of the dynamic heat source overestimates the mean net power output of the top 5 identified working fluids by up to 30 %. Therefore, the integrated design based on a dynamic process model is required, which is enabled by the presented dynamic CoMT-CAMD approach.

Acknowledgements

We thank the Deutsche Forschungsgemeinschaft (DFG) for funding this work (BA2884/4-2).

References

- Bardow A, Steur K, Gross J. Continuous-Molecular Targeting for Integrated Solvent and Process Design. *Ind. Eng. Chem. Res.* 2010;49(6):2834–40.
- Calise F, d'Accadia MD, Vicidomini M, Scarpellino M. Design and simulation of a small-scale solar CHP system based on evacuated flat-plate solar collectors and Organic Rankine Cycle. *Energy Conversion and Management* 2015;90:347–63.
- Colonna P, Casati E, Trapp C, Mathijssen T, Larjola J, Turunen-Saaresti T, et al. Organic Rankine Cycle Power Systems: From the Concept to Current Technology, Applications, and an Outlook to the Future. *J. Eng. Gas Turbines Power* 2015;137(10):100801.
- Dünnebeil F, Reinhard C, Lambrecht U, Kies A, Hausberger S, Rexeis M. Future measures for fuel savings and GHG reduction of heavy-duty vehicles. Federal Environment Agency (Germany), Nr. 32; 2015.
- Eichler K, Jekhouni Y, Ritterskamp C. Fuel Economy Benefits for Commercial Diesel Engines with Waste Heat Recovery. *SAE Int. J. Commer. Veh.* 2015;8(2):491–505.
- Esposito MC, Pompini N, Gambarotta A, Chandrasekaran V, Zhou J, Canova M. Nonlinear Model Predictive Control of an Organic Rankine Cycle for Exhaust Waste Heat Recovery in Automotive Engines. *IFAC-PapersOnLine* 2015;48(15):411–8.
- Gani R. Chemical product design: Challenges and opportunities. *Comput. Chem. Eng.* 2004;28(12):2441–57.
- Gross J, Sadowski G. Perturbed-Chain SAFT: An Equation of State Based on a Perturbation Theory for Chain Molecules. *Ind. Eng. Chem. Res.* 2001;40(4):1244–60.
- Huster WR, Vaupel Y, Mhamdi A, Mitsos A. Validated dynamic model of an organic Rankine cycle (ORC) for waste heat recovery in a diesel truck. *Energy* 2018;151:647–61.
- Lampe M, Stavrou M, Schilling J, Sauer E, Gross J, Bardow A. Computer-aided molecular design in the continuous-molecular targeting framework using group-contribution PC-SAFT. *Comput. Chem. Eng.* 2015;81:278–87.
- Leineweber DB, Schäfer A, Bock HG, Schlöder JP. An efficient multiple shooting based reduced SQP strategy for large-scale dynamic process optimization. *Computers & Chemical Engineering* 2003;27(2):167–74.
- Muncrief R, Sharpe B. Overview of the heavy-duty vehicle market and CO₂ emissions in the European Union. Washington, DC: The International Council on Clean Transportation 2015.
- Papadopoulos AI, Tsivintzelis I, Linke P, Seferlis P. Computer-Aided Molecular Design: Fundamentals, Methods, and Applications. In: Reedijk J, editor. Reference module in chemistry, molecular sciences and chemical engineering: Elsevier; 2018.
- Peralez J, Tona P, Nadri M, Dufour P, Sciarretta A. Optimal control for an organic rankine cycle on board a diesel-electric railcar. *Journal of Process Control* 2015;33:1–13.
- Sauer E, Stavrou M, Gross J. Comparison between a Homo- and a Heterosegmented Group Contribution Approach Based on the Perturbed-Chain Polar Statistical Associating Fluid Theory Equation of State. *Ind. Eng. Chem. Res.* 2014;53(38):14854–64.
- Zarogiannis T, Papadopoulos A, Seferlis P, Linke P. The Impact of Novel and Conventional Working Fluids on the Control Performance in Organic Rankine Cycles. *Comput. Aided Chem. Eng.* 2017;40:2443–48.

The impact of sustainable supply chain on waste-to-energy operations

Maryam Mohammadi,^a Iiro Harjunoski^{a,b,*}

^a*Department of Chemical and Metallurgical Engineering, School of Chemical Engineering, Aalto University, FI-00076 Espoo, Finland*

^b*ABB Corporate Research Center Germany, Wallstadter Str. 59, 68526 Ladenburg, Germany*

iiro.harjunoski@aalto.fi; iiro.harjunoski@de.abb.com

Abstract

This paper addresses the optimal planning of an integrated supply chain (SC) network for waste-to-energy (WtE) systems. A mixed integer linear programming (MILP) model is presented, which simultaneously considers the tactical and operational decisions related to transportation, inventory, production, and distribution. The objective of the proposed model is to find a balance between SC costs, waste reduction, and using the generated waste efficiently. It also ensures environmental sustainability in the operations of WtE systems and continuous feedstock supply. The considered waste type is combustible non-biodegradable municipal solid waste (MSW) with low moisture content, and the employed technologies are pyrolysis, gasification, and combined heat and power (CHP) to produce electricity and heat. The proposed MILP model is formulated and solved using GAMS/CPLEX.

Keywords: municipal solid waste, waste-to-energy, supply chain, sustainability, mixed integer linear programming.

1. Introduction

WtE is an energy recovery process that utilizes waste conversion technologies to generate heat and electricity from non-reusable and non-recyclable waste materials. WtE excels the other waste management (WM) strategies (e.g., reusing and recycling) as it can be used to meet the increasing energy demands and to reduce the dependency on energy imports and natural resources, in addition to reducing the waste amount for disposal. WtE also provides superior economic and environmental benefits because of the produced products through the WtE processes (e.g., transportation fuels, synthetic natural gas, chemicals, ferrous and non-ferrous metals, energy), emitting less carbon dioxide (CO₂) compared to power plants using non-renewable resources, and producing less greenhouse gas emissions (such as methane) compared to landfilling. It can also supply base-load power throughout the year to the community. Hence, WtE has become a promising alternative for many countries as an effective WM solution in a sustainable way and as the superior method of waste disposal. The three main thermochemical technologies for extracting energy from waste include conventional incineration, pyrolysis, and gasification. Moreover, CHP, used for simultaneous electricity and heat generation, can significantly increase operational efficiency of the plant, more than the facilities only generating electricity, and thereby decrease the energy costs.

WM can be considered as an SC problem since it involves determining the number, location, and size of production facilities, stocking and sourcing points, capacity allocation, inventory control, distribution and transportation planning, and order fulfilment. Therefore, to optimize the waste flows and decrease the negative impacts of involved processes, as well as ensuring the sustainability of the system, it is crucial to integrate the SC strategies into energy system planning and management. The literature study shows that many models exist, where the production and logistics problems in WtE practices are separately considered (Ahn et al., 2015; Balaman et al., 2018; Mohammadi et al., 2018; Quddus et al., 2018), but not the integrated WtE SC problem for sustainable heat and electricity production. A well-designed WtE SC results in a smooth flow of waste to treatment plants, balancing the waste supply lots and vehicle loads, reducing inventory levels and the stock-out risks, and better re-use of waste for cost-effective renewable energy production. It also contributes to a significant reduction in the total cost of the SC network and environmental emissions. Accordingly, this paper presents an integrated SC model that aims to maximize the total system profit by producing sustainable energy from waste materials while satisfying existing capacity and environmental constraints.

2. Mathematical Model Formulation

The proposed model covers waste collection at cities, separation and pre-treatment of waste in separation centers, processing for energy recovery in WtE plants, and selling the energy products to the markets, as shown in Figure 1.

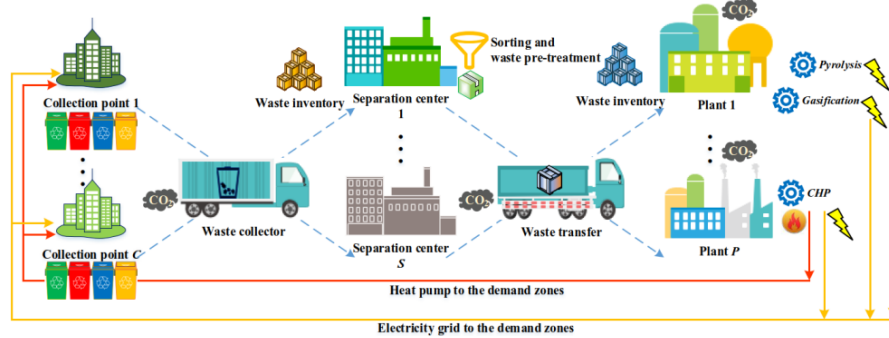


Figure 1. The addressed WtE SC network

The integrated WtE SC problem is formulated as an MILP model. The indices used in the formulation are: w (waste), \tilde{w} (treated waste), c (city), s (separation center), p (plant), j^s, j^{int}, j^e (technologies for waste pre-treatment, intermediate production, and energy production), n^{int} (intermediate product), n^{el} (electricity), n^h (heat), and t (time period). Equation (1) shows the objective function of the proposed model, where the revenue from the selling of heat and electricity is maximized, from which the total cost of the entire SC network is deducted. The selling price of electricity and heat is shown by P_{nct} . The total cost includes waste collection (C_{ct}^{col}), waste separation (C_{wst}^{sep}), waste pre-treatment (C_{wst}^{treat}), waste storage in separation centers ($C_{wst}^{stor}, C_{wst}^{stor}$), waste storage in

plants ($C_{\tilde{w}pt}^{stor}$), waste processing for intermediates production in plants ($C_{\tilde{w}pj}^{oper}$), intermediates processing for energy production in plants ($C_{n^{int}pj}^{oper}$), fixed and variable transportation (C^{fix}, C^{var}), and heat and electricity distribution costs (C_{npct}^{dist}).

$$\begin{aligned}
Max f = & \sum_{n \in \{n^{el} \cup n^h\}} \sum_c \sum_t P_{nct} \cdot q_{nct} - \left(\sum_w \sum_c \sum_t C_{ct}^{col} \cdot A_{wct} + \sum_w \sum_c \sum_s \sum_t C_{wst}^{sep} \cdot q_{wst} \right. \\
& + \sum_w \sum_s \sum_t C_{wst}^{treat} \cdot q_{wst}^{sep} + \sum_w \sum_s \sum_t C_{wst}^{stor} \cdot i_{wst} + \sum_{\tilde{w}} \sum_s \sum_t C_{\tilde{w}st}^{stor} \cdot i_{\tilde{w}st} + \sum_{\tilde{w}} \sum_p \sum_t C_{\tilde{w}pt}^{stor} \cdot i_{\tilde{w}pt} \\
& + \sum_{\tilde{w}} \sum_p \sum_{j^{int}} \sum_t C_{\tilde{w}pj}^{oper} \cdot q_{\tilde{w}pj}^{int} + \sum_{n^{int}} \sum_p \sum_{j^e} \sum_t C_{n^{int}pj}^{oper} \cdot q_{n^{int}pj}^{e_t} + \sum_c \sum_s \sum_t (C^{fix} + C^{var} \cdot d_{cs}) \cdot v_{cst} \\
& \left. + \sum_s \sum_p \sum_t (C^{fix} + C^{var} \cdot d_{sp}) \cdot v_{spt} + \sum_{n \in \{n^{el} \cup n^h\}} \sum_p \sum_c \sum_t C_{npct}^{dist} \cdot q_{npct} \right) \quad (1)
\end{aligned}$$

The produced MSW in a city (A_{wct}) is distributed to different separation centers (q_{wct}) as given in Eq. (2). Equation (3) shows that the total amount of waste inlet to a separation center should not exceed its maximum input capacity (SC_{wst}^{max}). Equation (4) shows the amount of separated waste (q_{wst}^{sep}) using a separation rate for each waste type (R_{ws}^{sep}). Equation (6) shows the amount of waste shipped to the pre-treatment technologies in separation center ($q_{wsj^s t}^{sep}$), which is limited by the technology capacity ($SC_{wsj^s}^{low}, SC_{wsj^s}^{up}$) as given in Eq. (7). The binary variable $z_{wsj^s t}^{treat}$ indicates whether the waste is sent for pre-treatment to a technology or not. Equation (8) shows the amount of treated waste (q_{wst}^{treat}) using a pre-treatment rate for each waste type ($R_{\tilde{w}wsj^s}^{treat}$). Equations (5) and (9) define the inventory levels of initial waste and treated waste in a separation center ($i_{wst}, i_{\tilde{w}st}$), which cannot exceed its storage capacity ($S_{ws}, S_{\tilde{w}s}$).

$$A_{wct} = \sum_s q_{wct} \quad \forall w \in W, c \in C, t \in T \quad (2)$$

$$\sum_c q_{wct} \leq SC_{wst}^{max} \quad \forall w \in W, s \in S, t \in T \quad (3)$$

$$q_{wst}^{sep} = \sum_c q_{wct} \cdot R_{ws}^{sep} \quad \forall w \in W, s \in S, t \in T \quad (4)$$

$$i_{wst} = i_{ws(t-1)} + q_{wst}^{sep} - \sum_{j^s} q_{wsj^s t}^{sep} \quad \text{and} \quad i_{wst} \leq S_{ws} \quad \forall w \in W, s \in S, t \in T \quad (5)$$

$$\sum_{j^s} q_{wsj^s t}^{sep} \leq i_{ws(t-1)} + q_{wst}^{sep} \quad \forall w \in W, s \in S, t \in T \quad (6)$$

$$SC_{wsj^s}^{low} \cdot z_{wsj^s t}^{treat} \leq q_{wsj^s t}^{sep} \leq SC_{wsj^s}^{up} \cdot z_{wsj^s t}^{treat} \quad \forall w \in W, s \in S, j^s \in J^s, t \in T \quad (7)$$

$$q_{wst}^{treat} = \sum_w \sum_{j^s} q_{wsj^s t}^{sep} \cdot R_{\tilde{w}wsj^s}^{treat} \quad \forall \tilde{w} \in \tilde{W}, s \in S, t \in T \quad (8)$$

$$i_{\tilde{w}st} = i_{\tilde{w}s(t-1)} + q_{wst}^{treat} - \sum_p q_{\tilde{w}spt} \quad \text{and} \quad i_{\tilde{w}st} \leq S_{\tilde{w}s} \quad \forall \tilde{w} \in \tilde{W}, s \in S, t \in T \quad (9)$$

Equation (10) shows the amount of treated waste that can be shipped from separation centers to plants ($q_{\tilde{w}spt}$). Equation (11) calculates the number of vehicles used for the

transportation of waste from cities to separation centers (v_{cst}) and from separation centers to plants (v_{spt}) considering the vehicle capacity respecting the waste volume ($VC_w, VC_{\tilde{w}}$). Equation (12) limits the CO₂ emissions emitted from transportation by $TE_{st}^{CO_2}$ considering the distance (D_{cs}, D_{sp}), fuel consumption (F), and emission emitted from per liter of fuel (E^{CO_2}). Equation (13) shows that the total waste inlet to a plant is limited by the input capacity of the plant ($PC_{\tilde{w}pt}^{max}$). Equation (14) presents the waste inventory level in a plant ($i_{\tilde{w}pt}$), which cannot exceed the storage capacity ($S_{\tilde{w}p}$) of the plant. Equation (15) limits the amount of waste that can be transferred to processing technologies ($q_{\tilde{w}pj^{int}_t}$), which cannot exceed the capacity limits of the technology ($PC_{\tilde{w}pj^{int}_t}^{low}, PC_{\tilde{w}pj^{int}_t}^{up}$) as shown in Eq. (16). $z_{\tilde{w}pj^{int}_t}^{conv}$ is a binary variable that equals 1 if the waste is sent to conversion technologies for the production of intermediate products.

$$\sum_p q_{\tilde{w}spt} \leq i_{\tilde{w}s(t-1)} + q_{\tilde{w}st}^{reat} \quad \forall \tilde{w} \in \tilde{W}, s \in S, t \in T \quad (10)$$

$$v_{cst} - 1 \leq \sum_w \frac{q_{wcst}}{VC_w} \leq v_{cst} \text{ and } v_{spt} - 1 \leq \sum_{\tilde{w}} \frac{q_{\tilde{w}spt}}{VC_{\tilde{w}}} \leq v_{spt} \quad \forall c \in C, s \in S, p \in P, t \in T \quad (11)$$

$$\left(\sum_c D_{cs} \cdot v_{cst} + \sum_p D_{sp} \cdot v_{spt} \right) \cdot F \cdot E^{CO_2} \leq TE_{st}^{CO_2} \quad \forall s \in S, t \in T \quad (12)$$

$$\sum_s q_{\tilde{w}spt} \leq PC_{\tilde{w}pt}^{max} \quad \forall \tilde{w} \in \tilde{W}, p \in P, t \in T \quad (13)$$

$$i_{\tilde{w}pt} = i_{\tilde{w}p(t-1)} + \sum_s q_{\tilde{w}spt} - \sum_{j^{int}} q_{\tilde{w}pj^{int}_t} \text{ and } i_{\tilde{w}pt} \leq S_{\tilde{w}p} \quad \forall \tilde{w} \in \tilde{W}, p \in P, t \in T \quad (14)$$

$$\sum_{j^{int}} q_{\tilde{w}pj^{int}_t} \leq i_{\tilde{w}p(t-1)} + \sum_s q_{\tilde{w}spt} \quad \forall \tilde{w} \in \tilde{W}, p \in P, t \in T \quad (15)$$

$$PC_{\tilde{w}pj^{int}_t}^{low} \cdot z_{\tilde{w}pj^{int}_t}^{conv} \leq q_{\tilde{w}pj^{int}_t} \leq PC_{\tilde{w}pj^{int}_t}^{up} \cdot z_{\tilde{w}pj^{int}_t}^{conv} \quad \forall \tilde{w} \in \tilde{W}, p \in P, j^{int} \in J^{int}, t \in T \quad (16)$$

Equation (17) calculates the amount of produced intermediates ($q_{n^{int}_{pj^e}}$) using the

conversion rate of $R_{\tilde{w}n^{int}_{pj^{int}}}^{conv}$. Equation (18) shows that the total amount of intermediate

product is transferred to energy conversion technologies ($q_{n^{int}_{pj^e}}$), which is restricted to

the capacity limits of the technology ($PC_{n^{int}_{pj^e}}^{low}, PC_{n^{int}_{pj^e}}^{up}$) as shown in Eq. (19). The

binary variable $z_{n^{int}_{pj^e}}^{energy}$ indicates whether the intermediate product is sent to energy

production technologies or not.

$$q_{n^{int}_{pj^e}} = \sum_{\tilde{w}} \sum_{j^{int}} q_{\tilde{w}pj^{int}_t} \cdot R_{\tilde{w}n^{int}_{pj^{int}}}^{conv} \quad \forall n^{int} \in N^{int}, p \in P, t \in T \quad (17)$$

$$\sum_{j^e} q_{n^{int}_{pj^e}} = q_{n^{int}_{pj^e}} \quad \forall n^{int} \in N^{int}, p \in P, t \in T \quad (18)$$

$$PC_{n^{int}_{pj^e}}^{low} \cdot z_{n^{int}_{pj^e}}^{energy} \leq q_{n^{int}_{pj^e}} \leq PC_{n^{int}_{pj^e}}^{up} \cdot z_{n^{int}_{pj^e}}^{energy} \quad \forall n^{int} \in N^{int}, p \in P, j^e \in J^e, t \in T \quad (19)$$

Equation (20) shows the conversion of intermediate products to electricity ($q_{n^{el}pt}$) considering the conversion rate of $\tau_{n^{int}n^{el}pj^e}$ and efficiency of $\varphi_{n^{int}n^{el}pj^e}$. Since an intermediate can be converted to both heat and electricity, the coefficient $\lambda_{n^{int}pt}^{el}$ is used, which is the percentage of intermediate product conversion to electricity, and the rest can be converted to heat. Equation (21) shows the heat production considering the conversion rate of $\tau_{n^{int}n^h pj^e}$ and efficiency of $\varphi_{n^{int}n^h pj^e}$. Equation (22) indicates the amount of CO₂ emissions from operating waste ($E_{\tilde{w}pj^{int}}^{CO_2}$) and intermediates ($E_{n^{int}pj^e}^{CO_2}$), which is limited to the pre-determined emission level ($OE_{pt}^{CO_2}$). Equation (23) limits the electricity and heat generation to the production capacity of plant (PC_{npt}^{max}), and the binary variable z_{npt}^{prod} is to check if energy products are produced by the plant or not. Equation (24) shows the total energy transmitted from a plant to cities (q_{npt}), and Eq. (25) shows the energy products received by cities (q_{nct}), which cannot exceed the product demand (D_{nct}).

$$q_{n^{el}pt} = \sum_{n^{int}} \sum_{j^e} \lambda_{n^{int}pt}^{el} \cdot q_{n^{int}pj^e} \cdot \tau_{n^{int}n^{el}pj^e} \cdot \varphi_{n^{int}n^{el}pj^e} \quad \forall n^{el}, p \in P, t \in T \quad (20)$$

$$q_{n^hpt} = \sum_{n^{int}} \sum_{j^e} (1 - \lambda_{n^{int}pt}^{el}) \cdot q_{n^{int}pj^e} \cdot \tau_{n^{int}n^h pj^e} \cdot \varphi_{n^{int}n^h pj^e} \quad \forall n^h, p \in P, t \in T \quad (21)$$

$$\sum_{\tilde{w}} \sum_{j^{int}} q_{\tilde{w}pj^{int}} \cdot E_{\tilde{w}pj^{int}}^{CO_2} + \sum_{n^{int}} \sum_{j^e} q_{n^{int}pj^e} \cdot E_{n^{int}pj^e}^{CO_2} \leq OE_{pt}^{CO_2} \quad \forall p \in P, t \in T \quad (22)$$

$$q_{npt} \leq PC_{npt}^{max} \cdot z_{npt}^{prod} \quad \forall n \in \{n^{el} \cup n^h\}, p \in P, t \in T \quad (23)$$

$$q_{npt} = \sum_c q_{nptc} \quad \forall n \in \{n^{el} \cup n^h\}, p \in P, t \in T \quad (24)$$

$$q_{nct} = \sum_p q_{nptc} \quad \text{and} \quad q_{nct} \leq D_{nct} \quad \forall n \in \{n^{el} \cup n^h\}, c \in C, t \in T \quad (25)$$

3. Results and Discussions

The considered multi-echelon SC problem consists of two cities as waste sources and consumer locations, two separation centers for waste separation and pre-treatment operations with two pre-treatment technologies, and three WtE plants to generate electricity and heat. The total MSW generation is 1,164 kt during a year. The presented MILP model is solved efficiently in a reasonable computational time (0.22 CPU-s) using GAMS/CPLEX. Considering the pyrolysis and gasification with the energy potential of 660 kWh/ton waste and the CHP plant with the capacity of 585 kWh/ton waste, 383 GWh of electricity and 171 GWh of heat are produced in a year. Figure 2 (a) presents the generated electricity and heat by the considered WtE plants. As demonstrated, pyrolysis produced the smallest amount of electricity, meeting 21 % of electricity demand, and the gasification plant met 49 % of electricity demand. Operation of CHP plant depends on the heat demand, and afterward, the range of electricity generation is determined; i.e., the more heat is produced the less energy is available for electricity production. The CHP generated 113.85 GWh of electricity during a year and satisfied 100 % of the heat demand. Therefore, CHP is a more profitable conversion technology than the other two WtE alternatives. However, it is most cost-effective when

there is a constant heat demand, e.g., from adjacent industrial plants or district heating systems. The feedstock in pyrolysis was mostly plastic waste with lower calorific value compared to the considered mixed waste, which justifies the lower electricity generation by pyrolysis compared to the other two technologies. As shown in Figure 2 (b), the SC performance is greatly affected by the changes in electricity demand. Regarding the environmental aspects, pyrolysis and gasification are promising technologies in terms of clean energy production and having lower negative environmental impacts, whereas CHP led to the production of higher CO₂ emissions.

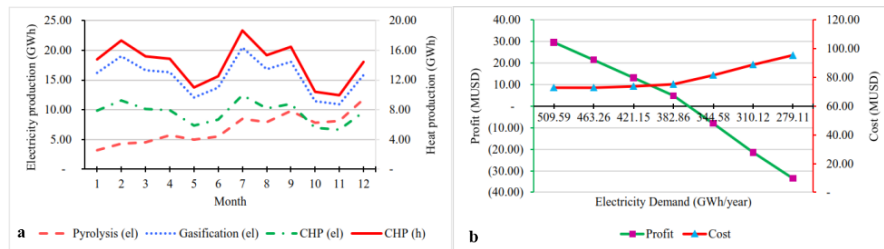


Figure 2 (a): Energy generation by WtE plants; 2 (b): Effect of fluctuations in electricity demand on the SC performance

4. Conclusions

The purpose of this study is to measure the environmental impacts and economic costs of the WtE SC network in order to check the economic and ecological feasibility of the entire system. In such systems, the production process, waste availability, energy demand, plant capacity, and level of energy efficiency affect the performance of WtE plants. Moreover, the coordination between SC entities has a substantial impact on the system performance by minimizing the overall costs, satisfying capacity restrictions at each level of the SC network, and fulfilling the demand requirements. The proposed model provides quantifiable information to make effective and optimum decisions regarding the treatment of waste while ensuring the most feasible (sustainable and cost-efficient) operations.

References

- Y.C. Ahn, I.B. Lee, K.H. Lee, J.H. Han, 2015, Strategic Planning Design of Microalgae Biomass-To-Biodiesel Supply Chain Network: Multi-period Deterministic Model, *Applied Energy*, 154, 528-542.
- Ş.Y. Balaman, D.G. Wright, J. Scott, A. Matopoulos, 2018, Network Design and Technology Management for Waste to Energy Production: An Integrated Optimization Framework under the Principles of Circular Economy, *Energy*, 143, 911-933.
- M. Mohammadi, I. Harjunkoski, S. Mikkola, S-L, Jämsä-Jounela, 2018, Optimal Planning of a Waste Management Supply Chain, 13th International Symposium on Process Systems Engineering - PSE 2018, San Diego, California, USA, 1609-1614.
- M.A. Quddus, S. Chowdhury, M. Marufuzzaman, F. Yu, L. Bian, 2018, A Two-stage Chance-constrained Stochastic Programming Model for a Bio-fuel Supply Chain Network, *International Journal of Production Economics*, 195, 27-44.

Automating a shuttle-conveyor for multi-stockpile level control

Jeffrey D. Kelly,^{a,*} Brenno C. Menezes^b

^a*Industrial Algorithms Ltd., 15 St. Andrews Road, Toronto M1P 4C3, Canada*

^b*Center for Information, Automation and Mobility, Technological Research Institute, Av. Prof. Almeida Prado 532, São Paulo 05508-901, Brazil*

jdkelly@industrialalgorithms.ca

Abstract

We describe the application of an online dynamic and discrete scheduling optimization, also known as real-time hybrid model predictive control, applied to a shuttle-conveyor / tripper car intermittently delivering crushed-ore containing copper, iron, etc., to several stockpiles. Each stockpile continuously feeds an apron feeder located in a tunnel underneath the stockpile where multiple of these are combined to a belt feeder to charge a grinding mill which ultimately produces concentrates of minerals. Crushed-ore from a mine several kilometres upstream is transported by both conveyor belt and automatic trains. The shuttle-conveyor is the discrete actuation or manipulated variable depositing the solids onto each stockpile where we vary the time over each stockpile to automatically control to a setpoint or target their levels sensed by industrial radar. In the field, the motion of the shuttle-conveyor is known as sweeping as it moves from one stockpile (or tunnel) to the next in a fixed sequence. The purpose of our application is to improve the stockpile level control performance by automatically adjusting the up-time, fill-time or run-length of the shuttle-conveyor tripper car over each stockpile based on real-time level measurement feedback and the application which is referred to as *smart sweeping*.

Keywords: Mixed-integer linear programming (MILP), Hybrid dynamic control, Stockpile live inventory, Smart sweeping.

1. Introduction

Advances in manufacturing toward the Industry 4.0 (I4) age push the re-examination of industrial systems to identify opportunities to (re) execute them into an improved production state. For such, the information and communication technologies (ICT), high-performance computing (HPC) and mechatronics (MEC) are evolving together with the advances in modelling and solving algorithms (MSA). Considering this I4 era in manufacturing, we explore the MSA aspects in an application found in the mining field (see the Future of Mining in the 21st Century in Lottermoser, 2017). In the system, shuttle-conveyors are modeled in terms of their sequencing and timing as they travel from one position or location to the next on the shuttle-carriage, whereby stockpile levels are used as setpoints to influence the movements of the shuttle-conveyors. Automated belt conveyor systems integrated with intelligent decision-making core is a successful application of I4 in the mining value chain (Braun et al., 2017).

In the proposed work, the design basis of the advanced control system for managing simultaneously multiple stockpile levels for each feeder in the ore land field, warehouse,

bunker or barn uses the mixed-integer linear programming (MILP) optimization for the positioning, placement, movement or manipulation of the shuttle-conveyors / tripper cars, the discrete (integer), whereas the stockpile levels are continuous. In addition, the supply (filling) and demand (drawing) of crushed-ore in the ore barn is semi-continuous or intermittent especially considering the nature of how crushed-ore travels from the mine to the barn and how crushed-ore is feed to autogenous mills via the feeders.

The proposed problem is known in the control literature as hybrid model predictive control (HMPC) as there is a mix of discrete and continuous variables with a receding or moving prediction time-horizon. The MILP solution defines the shuttle positions which will collectively manage the stockpile levels over each feeder given the supply and demand of crushed-ore. MILP is a search-based algorithm known as branch-and-bound (B&B) which will evaluate quickly many possible scenarios, samples or situations to find the best solution that optimizes the objective function also taking into consideration both the continuous and discrete nature of the controlled and manipulated variables subject to hard constraints (i.e., lower and upper bounds) and soft constraints (target).

Supported by the I4 fundamentals, a high-end radar sensing system (for virtual reality) measures the mineral stockpile level (opening inventory) in real-time for the determination of discrete positions and time-slots of the reversing shuttle-conveyor that creates the stockpiles (ST1 to ST8) for feeding multiple fixed discharge points. A reversing shuttle-conveyor in Figure 1 is a belt conveyor sweeping onto a rail system in both directions which manipulates, belt direction and shuttle movement, and can be automated or controlled manually by an operator.

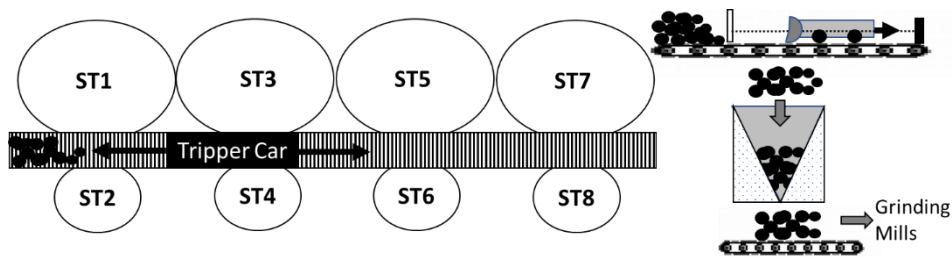


Figure 1. Tripper car shuttle-conveyor schematics.

2. Problem statement

The objective function will minimize the absolute deviations (1-norm performance) of the stockpile estimated *live* inventories (controlled variables) as well as minimizing the absolute excursions or penalties from its lower and upper holdup bounds should any infeasibilities be detected both in the present and in the future. The decision or manipulated variables are the shuttle-conveyor positions (in time-steps) subject to their sequence and timing constraints. In the problem, the shuttle-conveyor (SC) supplies crushed-ore to the ore barn which contains the wet-mills Mill1 and Mill2 as seen in Figure 2. To these mills are fed crushed-ore by eight (8) feeders with corresponding stockpiles (ST1, ST2, ..., ST8) connected to them by tunnels or zones below the stockpiles where apron-feeders gravity load crushed-ore onto belt-conveyors on an incline to be sent to the wet-mills for grinding.

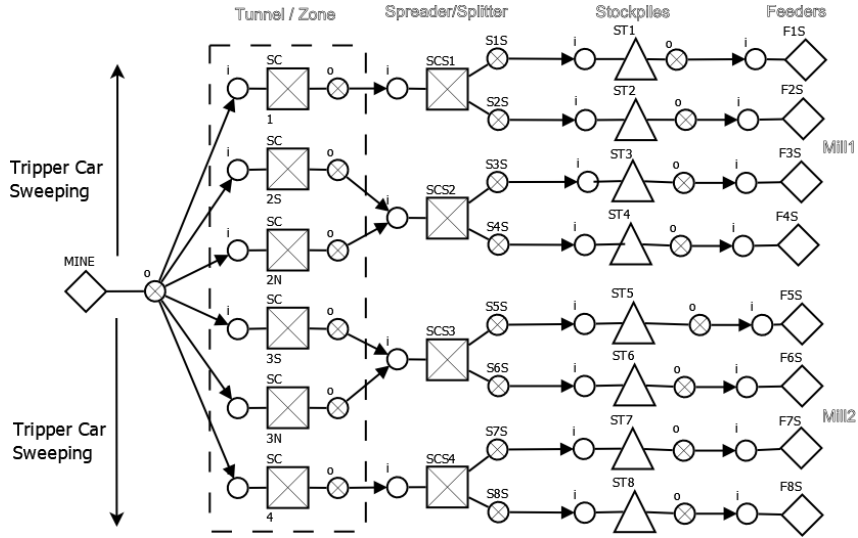


Figure 2. Stockpile control system.

The shuttle-conveyor position sequencing policies are based on the notion of whether the placement sequence from one tunnel to the next and the amount of time the shuttle-conveyor spends over each tunnel are fixed or variable. Sweeping is the name given to a fixed-sequence / variable-time policy with SC traveling forward and backward between tunnels 1 to 4. Figure 2 above depicts a flowsheet for how crushed-ore material from the mine can be moved from SC (tunnels) to the stockpiles (ST1, ..., ST8) and ultimately to the wet-mill feeders via the spreader / splitter objects shown. These separation structures or shapes are required to model the non-ideal flow of how crushed-ore flow distributes or spreads over to both stockpiles at each tunnel. It should be emphasized that since SC is a unary or single-use resource only one of the six operations configured (1, 2S, 2N, 4, 3S, 3N) can be setup, active, on, open, etc., within any given time-period. Sweeping is similar to the notion of *phasing* found in project scheduling (Menezes et al., 2015) as there is a fixed-sequence of how each shuttle-conveyor traverses its area of the ore warehouse or barn, i.e., from one phase, task or operation to the next and so on.

3. Mathematical formulation

The network in Figure 2 uses the unit-operation-port-state superstructure (UOPSS) formulation (Kelly, 2005). The objects are: a) unit-operations m for sources and sinks (\diamond), stockpiles (\triangle) and continuous-processes (\boxtimes) and b) the connectivity involving arrows (\rightarrow), in-port-states i (\circ) and out-port-states j (\otimes). Unit-operations and arrows have binary and continuous variables (y and x , respectively). In the mixed-integer linear (MILP) problem (P), the objective function (1) minimizes the absolute deviation of the stockpile inventories, levels or holdups $xh_{m,t}$. The performance constraint (2) defines the lower and upper deviation variables ($xh_{m,t}^{LD}$ and $xh_{m,t}^{UD}$, respectively) around the stockpile holdup target ($\bar{x}h_{m,t}$) with w^D as weight. The semi-continuous constraint (3) limits the stockpile holdup by its lower and upper bounds ($\bar{x}h_{m,t}^L$ and $\bar{x}h_{m,t}^U$), whereby the excursion variables or penalties $xh_{m,t}^{LE}$ and $xh_{m,t}^{UE}$ are included to avoid infeasibilities (with w^E as weight). Similarly, there are semi-continuous constraints for flows of process-units $x_{m,t}$ and arrows $x_{j,i,t}$, although without excursion variables as for the stockpile holdups. Unit-

operations m for the mine, shuttle-conveyor, spreader, stockpile, and feeder belong, respectively, to the sets M_{MN} , M_{SC} , M_{SD} , M_{ST} , and M_{FD} . For $x \in \mathbb{R}^+$, $y, yg \in \{0,1\}$ and $zsu_{m,t}, zsd_{m,t}, zsw_{m,t} \in [0,1]$:

$$(P) \text{ Max } Z = \sum_t \sum_{m \in M_{ST}} [w^D(xh_{m,t}^{LD} + xh_{m,t}^{UD}) + w^E(xh_{m,t}^{LE} + xh_{m,t}^{UE})] \quad \text{s.t.} \quad (1)$$

$$xh_{m,t} - \bar{x}h_{m,t} + xh_{m,t}^{LD} - xh_{m,t}^{UD} = 0 \quad \forall m \in M_{ST}, t \quad (2)$$

$$\bar{x}h_{m,t}^L y_{m,t} - xh_{m,t}^{LE} \leq xh_{m,t} \leq \bar{x}h_{m,t}^U y_{m,t} + xh_{m,t}^{UE} \quad \forall m \in M_{ST}, t \quad (3)$$

$$\frac{1}{\bar{x}_{m,t}^U} \sum_{j \in M_{MN}} x_{j,i,t} \leq y_{m,t} \leq \frac{1}{\bar{x}_{m,t}^L} \sum_{j \in M_{MN}} x_{j,i,t} \quad \forall (i, m) \in M_{SC}, t \quad (4)$$

$$\frac{1}{\bar{x}_{m,t}^U} \sum_i x_{j,i,t} \leq y_{m,t} \leq \frac{1}{\bar{x}_{m,t}^L} \sum_i x_{j,i,t} \quad \forall (m, j) \in (M_{MN}, M_{SC}, M_{SD}), t \quad (5)$$

$$\frac{1}{r_{i,t}^U} \sum_j x_{j,i,t} \leq x_{m,t} \leq \frac{1}{r_{i,t}^L} \sum_j x_{j,i,t} \quad \forall (i, m) \in (M_{SC}, M_{SD}), t \quad (6)$$

$$\frac{1}{r_{j,t}^U} \sum_i x_{j,i,t} \leq x_{m,t} \leq \frac{1}{r_{j,t}^L} \sum_i x_{j,i,t} \quad \forall (m, j) \in (M_{SC}, M_{SD}), t \quad (7)$$

$$xh_{m,t} = xh_{m,t-1} + \sum_{j_{up}} x_{j_{up},i,t} - \sum_{i_{do}} x_{j_{i_{do}},t} \quad \forall (i, m, j) \in M_{ST}, t \quad (8)$$

$$\sum_{m \in M_{SC}} y_{m,t} \leq 1 \quad \forall t \quad (9)$$

$$\sum_{m \in M_{SC}} y_{m,t} \geq 1 \quad \forall t \quad (10)$$

$$y_{m_{up},t} + y_{m,t} \geq 2y_{j_{up},i,t} \quad \forall (m_{up}, j_{up}, i, m), t \quad (11)$$

$$y_{m,t} - y_{m,t-1} - zsu_{m,t} + zsd_{m,t} = 0 \quad \forall m \in M_{SC}, t \quad (12)$$

$$y_{m,t} + y_{m,t-1} - zsu_{m,t} - zsd_{m,t} - 2zsw_{m,t} = 0 \quad \forall m \in M_{SC}, t \quad (13)$$

$$zsu_{m,t} + zsd_{m,t} + zsw_{m,t} \leq 1 \quad \forall m \in M_{SC}, t \quad (14)$$

$$\sum_{g \in G_{SC}} yg_{u,g,t} = 1 \quad \forall u \in U_{SC}, t \quad (15)$$

$$\sum_{(m \in M_{SC}) \subset G_{SC}} y_{m,t} \leq yg_{u,g,t} \quad \forall u \in U_{SC}, g \in G_{SC}, t \quad (16)$$

$$yg_{u,g,t} - yg_{u,g,t-1} \leq zsu_{m \subset g,t} \quad \forall u \in U_{SC}, g \in G_{SC}, t \quad (17)$$

$$yg_{u,g,t-1} - yg_{u,g,t} \leq zsu_{m \subset g',t} \quad \forall u \in U_{SC}, g \in G_{SC}, g' \in G_{SC}, t \quad (18)$$

Equations (4) and (5) represent, respectively, the sum of the arrows arriving in the in-port-states i (or mixers) or leaving from the out-port-states j (or splitters) and their summation must be between the bounds of the unit-operation m connected to them. Equations (6) and (7) consider bounds on yields, both inverse ($r_{i,t}^L$ and $r_{i,t}^U$) and direct ($r_{j,t}^L$ and $r_{j,t}^U$), since the unit-operations m can have more than one stream arriving in or leaving from their connected ports. The quantity balance of inventory or holdup for unit-operations of tanks ($m \in M_{ST}$) in Eq. (8) considering initial inventories $xh_{m,t-1}$ and inlet and outlet streams of the tanks, whereby the port-states j_{up} and i_{do} represent upstream and downstream ports connected, respectively, to the in-port-states i and out-port-states j of the stockpile unit-operations m as represented in Figure 2. In Eq. (9), for all physical units, at most one unit-operation m (as $y_{m,t}$ for procedures, modes or tasks) is permitted in U_{SC} at a time t . Equation (10) is the zero-downtime constraint to activate SC in all time t . Equation (11) is the structural transition logic valid cut of 4 objects (m', j, i, m) to reduce the tree search in branch-and-bound methods.

The sequencing operation of the multiple SC is controlled by the temporal transition constraints (12) to (14) from Kelly and Zyngier (2007). The setup or binary variable $y_{m,t}$ manages the dependent start-up, switch-over-to-itself and shut-down variables ($zsu_{m,t}$, $zsw_{m,t}$ and $zsd_{m,t}$, respectively) are relaxed in the interval $[0,1]$ instead of considering them as logic variables. Equation 12 is necessary to guarantee the integrality of the relaxed variables. By fixing the sequence (neighbor to neighbor) of the SC modes of operation (time-slots of the positions), the grouping constraints (15) to (18) coordinate the grouping setup variable $yg_{u,g,t}$ to update the shuttle-conveyor operation-group to operation-group sequence-dependent *phasing* (or fixed transition between neighbor modes of the SC, e.g., $1 \rightarrow 2S \rightarrow 3S \rightarrow 4 \rightarrow 3N \rightarrow 2N \rightarrow 1$). Other constraints related to uptime of the SC and the shutting-when-full relationship are found in Zyngier and Kelly (2009).

4. Example

The example in Figure 2 uses the structural-based UOPSS framework found in the semantic-oriented modelling and solving platform IMPL (Industrial Modeling & Programming Language) from Industrial Algorithms Limited using Intel Core i7 machine at 3.4 GHz (in 8 threads) with 64 GB of RAM. The optimization for the proposed MILP for a 2 hours time-horizon with 2 minute time-steps (30 time-periods) is solved in 4.07 seconds (with GUROBI 8.1.0). There are 5,472 constraints (1,593 equality) for 2,823 continuous variables and 900 binary variables with 2,130 degrees-of-freedom. Figure 3 shows the Gantt chart for the shuttle-conveyor and spreader time-slot positions (in min).

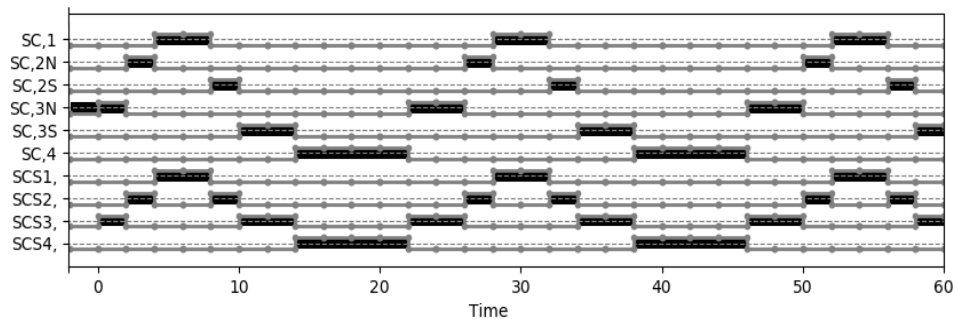


Figure 3. Gantt chart for shuttle-conveyor (SC) and spreader (SCS) time-slot positions.

5. Conclusions

By automating a shuttle-conveyor position in variable time-slots of minutes, a hybrid dynamic control problem coordinates the stockpile *live* inventory of crushed-ore of minerals in the mining field. With advanced automation of mining sub-systems, it may be possible to replace human operators in the field in certain areas and functions. One place to start can be the integration of the synchronization of the sensing, calculating and actuating cycle (within minutes) as in the mining system proposed in this paper. The position of the tripper car reached the level of sensing and calculating technologies to be integrated to automatically program the time-slot of positions of the shuttle conveyor system.

Integrated to the decision-making core proposed in this paper (the hybrid dynamic control), for the advances in the infrastructure of cyber-physical systems (CPS) for a digital twin of the reality in the mining system there are needs of other three smart manufacturing foundations. They are: a) information and communication technologies (ICT), with the ecosystem match of the internet of the things and computing edges as the cloud and fog (Bittencourt, 2018), to capture the *live* inventory using the radar apparatus; b) the high-performance computing (HPC), to solve extremely fast the discrete and continuous problems in distributed machine cores; and c) the mechatronics (MEC) to actuate automatically considering an integrated envelop of the main I4 attributes around the sensing, calculation and actuation cycle of an I4-age manufacturing system.

Acknowledgements

The first author acknowledges the financial support from the São Paulo Research Foundation (FAPESP) under grant #2018/26252-0 for the project over the application of the Industry 4.0 concepts in the mining field.

References

- L. Bittencourt, R. Immich, R. Sakellariou, N. Fonseca, E. Madeira, M. Curado, L. Villas, L. Da Silva, C. Lee, O. Rana, 2018, The Internet Of Things, Fog and Cloud Continuum: Integration And Challenges. *Internet of Things*, 3-4, 134-155.
- T. Braun, A. Henning, B.G. Lottermoser, 2017, The Need for Sustainable Technology Diffusion in Mining: Achieving the Use of Belt Conveyor Systems in the German Hard-Rock Quarrying Industry, *Journal of Sustainable Mining*, 16, 24-30.
- J.D. Kelly, 2005, The Unit-Operation-Stock Superstructure (UOSS) and the Quantity-Logic-Quality Paradigm (QLQP) for Production Scheduling in The Process Industries, In *Multidisciplinary International Scheduling Conference Proceedings*: New York, United States, 327-333.
- J.D. Kelly, D. Zyngier, 2007, An Improved MILP Modeling of Sequence-Dependent Switchovers for Discrete-Time Scheduling Problems, *Industrial Engineering Chemistry Research*, 46, 4964.
- B.G. Lottermoser, 2017, The Future of Mining in the 21st Century. *Georesources Journal*, 2, 5-6.
- B.C. Menezes, J.D. Kelly, I. E. Grossmann, A. Vazacopoulos, 2015, Generalized Capital Investment Planning of Oil-Refineries using MILP and Sequence-Dependent Setups, *Computer and Chemical Engineering*, 80, 140-154.
- D. Zyngier, J.D. Kelly, 2009, Multi-product Inventory Logistics Modeling in The Process Industries. In: Wanpracha Chaovalitwongse, Kevin C. Furman, Panos M. Pardalos (Eds.) *Optimization and Logistics Challenges in the Enterprise*. Springer optimization and its Applications, 30, Part 1, 61.

High-quality blend scheduling solution for sizing, selecting, sequencing, slotting and spotting in the processing industries

Brenno C. Menezes,^a Jeffrey D. Kelly^{b,*}

^a*Center for Information, Automation and Mobility, Technological Research Institute, Av. Prof. Almeida Prado 532, São Paulo 05508-901, Brazil*

^b*Industrial Algorithms Ltd., 15 Saint Andrews Road, Toronto M1P 4C3, Canada*

jdkelly@industrialalgorithms.ca

Abstract

High-quality process system engineering (PSE) solutions for production scheduling evolve to a wider scope and scale when moving from simulation- to optimization-based approaches, generally by using mixed-integer programming (MIP) in discrete-time formulations. To reach as we state in this paper as the spotting level of service, into the scheduling operational details and time-step within a time-horizon of planning, the novel aspect of these types of PSE solutions is to integrate automated logistics or blend logistics decisions regarding: (1) sizing the future blend volumes for blending (or throughputs of unit-operations for processing); (2) selecting a product tank for the blends (or modes of operation for the process units); (3) sequencing the blended product grades (i.e., regular before premium, etc.) in multi-product blender (or the sequence of modes of operation for units/tanks); (4) slotting the start-times of the blends (or processing-time of units) into time-periods; and (5) spotting the future product shipments to steward to the plan. Examples of scheduling optimization effectively implemented are: (1) the production of lubes and asphalts with sequence-dependent switchovers between modes of operation; and (2) the gasoline blend scheduling operations using decomposition strategies and cuts based on nominal qualities. Faster results are obtained by tailored solutions of decomposing these industrial problems.

Keywords: Effective knowledge transfer, Industrial PSE applications, Spot markets.

1. Introduction

Integration of planning and scheduling in the processing industries can be achieved by solving a scheduling problem (in terms of time-step, level of details, etc.) within a planning time-horizon (in general for a month or longer). In such a way, the proposed planning-scheduling solution can be considered (in a product point of view) what we name in the paper as spotting, since there are potentials to increase the profit by exploring the higher gains from spot market opportunities when compared with its concurrent and complementary contract market dividends. In this case, for the producer, there is a reasonable degree of confidence in the day-by-day (optimized or prescribed) production by extending a schedule from a week to a month time-horizon. By addressing such high-quality PSE solutions into the spotting state, sellers are still in time to negotiate products in the spot market, which requires by half to one month in advance for the time-restricted contract to be made.

However, major considerations to reach the spotting stage (in a process point of view) must consider the following challenges for such integrated decision-making systems. What is the necessary time-grid of the scheduling solutions for a specific process, varying from online solutions (≤ 1 -hour) to 1-day discrete time-step? What planning and scheduling integration strategies exist? What degree of process details is demanded in the modelling? Which advanced manufacturing attribute can be explored and integrated in the optimization core, such as information and communication technologies (ICT) and auxiliary mechatronics (MEC) to automatically sample, analyse and communicate?

Franzoi et al. (2018a) proposed a refinery-wide scheduling approach to investigate the limits or capabilities of an enterprise-wide optimization (EWO) by solving simultaneously the supply, production, and demand chains using MILP. This solution fixes time-varying setups of unit-operations and connections that construct the flowsheet operations for further NLPs (Kelly et al., 2017a). Such EWO scope and scale may use additional detailed calculations within other edges such as in the depooling of aggregated tanks by considering their actual topology and operations (Menezes et al., 2018). Furthermore, Kelly et al. (2018a) introduce the concept of planuling that is a portmanteau of planning and scheduling where we schedule slow processes and plan fast processes together inside the slower process time-horizon, which demands an extra calculation for the fast processes, but henceforth as a scheduling problem.

To achieve the spotting solution in the matters of operational and economical standpoints may be accomplished by reducing the problem complexity when we exclude, relax and fixate part of it. These procedures must be coupled with high-performance computing (HPC) for faster calculations in parallel cores. Additionally, model and plant differences can be reduced by using closed-loop parameter feedback (Franzoi et al., 2018b) with the support of ICT and MEC capabilities. For the integrated planning and scheduling approach toward the spotting service level, we present solutions with 1-week to 2-months as time-horizon varying from 2-hours to 1-day as time-step. The effective implementation of the industrial examples uses the best technologies of modelling and solving algorithms (MSA) to optimize the problem.

2. From planning and scheduling to spotting

Benefit areas from this moving to optimization-based decisions using MILP as a prescriptive analytics application for sizing, selecting, sequencing, slotting and spotting (blend volumes and throughputs) in the processing industries are as follows:

- a) optimized (vs. simulated) schedules which maximize profit and performance given pricing and discretizing on a sub-day or sub-hour basis;
- b) better coordination with sales and marketing by providing optimized and achievable blend production schedules for all future product (and saleable component) shipments;
- c) improved stewardship to the monthly feedstock selection and operations plan which coordinates the supply and demand of all the refinery site production;
- d) increased ability to capture spot market opportunities after contract sales have been fulfilled respecting bottlenecks, in-progress blends, planned recipes, etc.;
- e) blend schedules matching product quality specifications to reduce key property giveaway and to decrease the chances of off-specification blends to product tanks.

3. Effective knowledge transfer: high-quality PSE solution for spotting

Recently, state-of-the-art technology on modelling and solving algorithms (MSA), one of the ground bases of the *Industry 4.0* mandate, was implemented in an oil and gas company in Southern Asia. The company’s call of technology winner has beaten the dominant petroleum scheduling technology sellers since they still deliver simulation-based scheduling solutions with limited optimization capabilities. The potentials of the cutting-edge MSA technologies are used in the examples.

Similar scope and scale to those implemented in crude-oil refineries, the examples are configured in the modelling platform named Industrial Modeling & Programming Language (IMPL) seamlessly coupled with GUROBI’s superior simplex and barrier LP algorithms as one of today’s most efficient solvers. These technologies optimize the production considering time-horizons for (a) 1-month with 1 day as time-step and (b) 7-days to 30-days with 2h as time-step. They are robustly and reliably solved within minutes combined for both the logistics and the quality sub-problems or any sort of decomposition. The object constructs of the examples (Figures 1 and 2) consider the unit-operation-port-state superstructure (UOPSS) formulation (Kelly, 2005) built-in with IMPL (see IMPL manual in Kelly, 2018). The unit-operation and arrow objects have binary and continuous variables (y and x , respectively) such as: a) unit-operations m for sources and sinks (\diamond), tanks (Δ) and continuous-processes (\boxtimes) and b) the connectivity involving arrows (\rightarrow), in-port-states i (\circ) and out-port-states j (\otimes).

4. Examples

4.1. Scheduling for production of lubes and asphalts

Reduced crude-oil distilled streams or atmospheric residue from crude-oil distillation units are fed to vacuum distillation units to produce fractions of lubes and asphalts (Kyungseok et al., 2017). To schedule the blocks, campaigns or conjugated modes of operation (or grades of lube base oils) in further steps of processing in solvent extraction (EU), dewaxing (DU) and hydrotreating units as in Figure 1, the MILP optimization uses the sequence-dependent switchovers introduced by Kelly and Zyngier (2007).

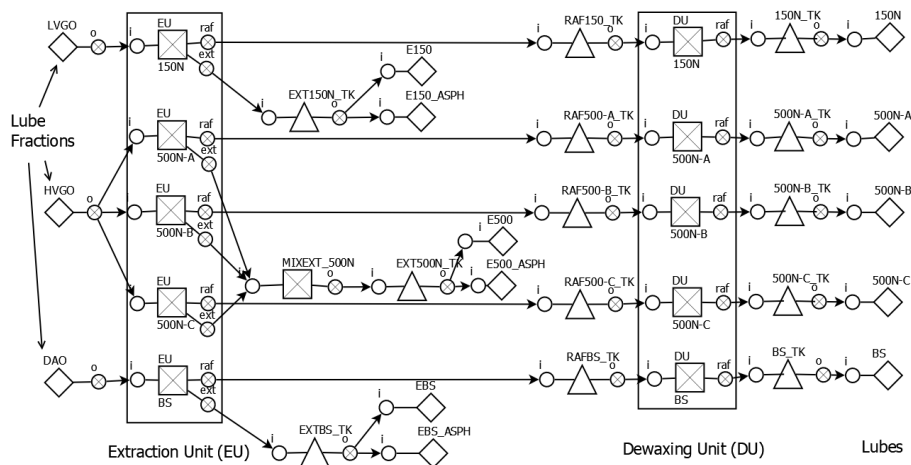


Figure 1. Production flowsheet for Lubes.

The proposed solution of the flowsheet in Figure 1 solves a 60-day horizon with 1-day time-steps, allowing opportunities of exploring the dynamics of the contract and spot markets. The MILP for a 60-day time-horizon with 1-day time-steps (60 time-periods) is solved in 30.7 seconds (with GUROBI 8.1.0) and 40.9 seconds (with CPLEX 12.8.0) at 0.0% of MILP relaxation gap using an Intel Core i7 machine at 3.4 GHz (in 8 threads) with 64 GB of RAM. There are 10,247 constraints (2,942 equality) for 5,102 continuous variables and 3,120 binary variables with 5,280 degrees-of-freedom. Figure 2 shows the Gantt chart for the dewaxing (DU) operations in time-slot positions.

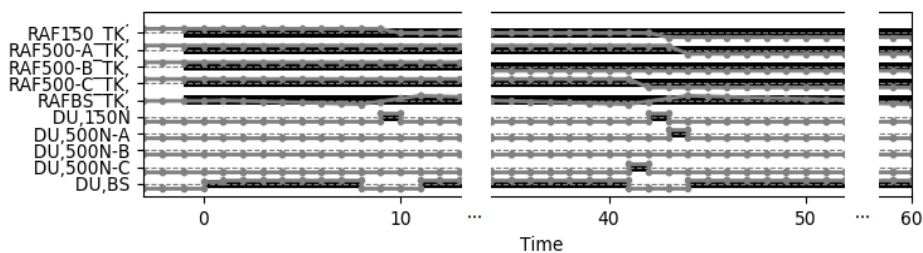


Figure 2. Dewaxing (DU) modes of operation and the holdup in their feed tanks (TK).

4.2. Gasoline blend scheduling

The gasoline blend scheduling is solved for the logistics (MILP) problem including nominal quality balances (Kelly et al., 2018b) in the MILP solution instead of neglecting the quality relationships completely. In the problem, without preferred recipes initialization as in Mendez et al. (2006), slack or surplus variables are calculated to balance the amounts of quality around the blender unit-operations and a successive MILP can be iterated to meet the quality specifications by using the slack or surplus variables and their distances from their lower and upper respective specifications. In such a way, cuts based on nominal qualities may avoid impending quality NLP infeasibilities if the NLP is needed after the MILP setup variables fixation. In this case, successive linear programming (SLP) technology can be used for these industrially-sized nonlinear dynamic optimizations since any infeasibilities or inconsistencies due to poor opening quantities and qualities, as example, are quickly detected and identified by the user in terms of the offending variable and/or constraint.

The proposed solution solves a 7- to 30-day horizon (time-step of 2 hours) for the problem in Figure 3. Table 1 shows the MILP solution (using nominal quality cuts) at 2% of MILP relaxation gap in an Intel Core i7 machine at 3.4 GHz (in 8 threads) with 64 GB of RAM. Although all cases converged, to reduce the CPU time in the full space MILP when > 60 minutes, we use a temporal decomposition heuristic known as rolling-horizon with crossover (RHC) in the time windows of the neighbouring time-horizon splits (Kelly, 2002) as shown in the additional CPU (in minutes).

Table 1. Statistics for 7, 14, 21 and 30 days (2 h time-step).

CPU (min)				CPU (min)				Equations (for 14d)	Continuous/ Binary Variables (for 14d)
GUROBI (8.1.0)				CPLEX (12.8.0)					
7d	14d	21d	30d	7d	14d	21d	30d		
2.4	6.1	> 60	> 60	25.9	> 60	> 60	> 60	99,300	47,091/ 13,992
RHC		+ 11.1	+8.5	RHC + 37.3		> 60	> 60		

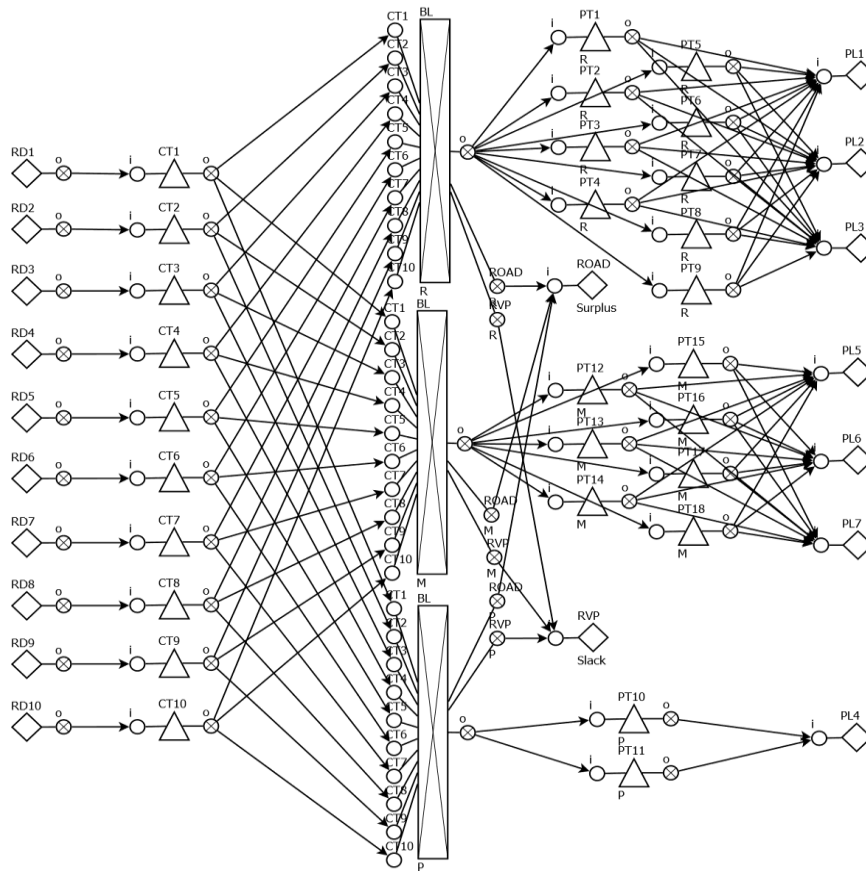


Figure 3. Gasoline blend scheduling with regular, medium and premium grade modes.

As an example of a result in the gasoline blend scheduling problem, Figure 4 shows the Gantt chart of the blender unit-operations (R, M and P) for 14 days as time-horizon solved using MILP with cuts on nominal qualities or factors for qualities (Kelly et al., 2018) in octane number (Road) and Reid vapor pressure (RVP) as shown in the flowsheet in Figure 3. The sequence of modes of operation (R, M and P in the blender BL unit) attend the supply of detailed and specific demands of the different grades of gasoline. The gasoline premium grade (P) has a reduced demand and production with punctual deliveries as seen in the holdups of the PT10 and PT11 tanks of the P grade.

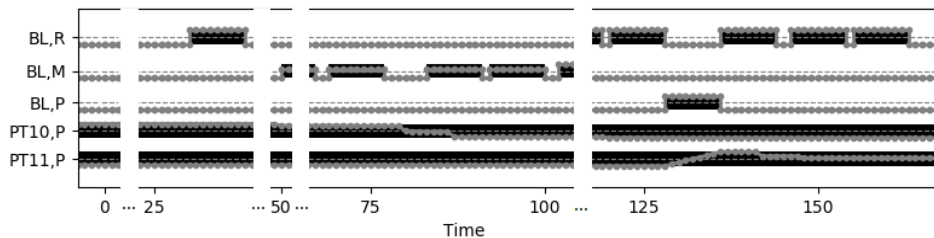


Figure 4. Blender (BL) modes of operation and tanks (PT10 and PT11) holdups (14 d).

5. Conclusions

We have exposed the knowledge around PSE solutions transferred to the processing industries. They are configured into a process industry specific domain programming language (IMPL) and solved using one of the best commercial solvers GUROBI. By solving the problems in a planning horizon with a scheduling level of detail (i.e., in time-step and operational relationships), any company's profit and performance may be improved by exploring their spot markets in a timely fashion. It may reduce management gaps between production and market segments inside the plant and teams in headquarters. The dynamics of both contracted and spot market require decisions within quarters and months in advance. For that, in the examples of PSE solutions in this paper, the planning and scheduling merge in the necessary spotting level of service.

Acknowledgements

The first author gratefully acknowledges the financial support from the São Paulo Research Foundation (FAPESP) under grant #2018/26252-0.

References

- R.E. Franzoi, B.C. Menezes, J.D. Kelly, J.W. Gut, 2018a, Refinery-Wide Scheduling for Optimization of Multiple Unit-Operations in the Supply, Production, and Demand Chains in Fuels, Lubes, Asphalts and Petrochemicals Industries. In: AICHE Annual Meeting, Pittsburgh, United States.
- R.E. Franzoi, B.C. Menezes, J.D. Kelly, J.W. Gut, 2018b, Effective Scheduling of Complex Process-Shops Using Online Parameter Feedback in Crude-Oil Refineries. *Computer Aided Chemical Engineering*, 44, 1279-1284.
- J.D. Kelly, 2018, IMPL Manual, www.industrialalgorithms.ca.
- J.D. Kelly, 2002, Chronological Decomposition Heuristic for Scheduling: Divide and Conquer Method. *AICHE Journal*, 48, 2995-2999.
- J.D. Kelly, 2005, The Unit-Operation-Stock Superstructure (UOSS) and the Quantity-Logic-Quality Paradigm (QLQP) for Production Scheduling in The Process Industries. In *Multidisciplinary International Scheduling Conference Proceedings: New York, United States*, 327-333.
- J.D. Kelly, B.C. Menezes, F. Engineer, I.E. Grossmann, 2017, Crude-Oil Blend Scheduling Optimization of an Industrial-Sized Refinery: a Discrete-Time Benchmark. In: *Foundations of Computer Aided Process Operations*, Tucson, United States.
- J.D. Kelly, R.E. Franzoi, B.C. Menezes, J.W. Gut, 2018a, Planuling: A Hybrid Planning and Scheduling Optimization to Schedule Slow and Plan Fast Processes. In: AICHE Annual Meeting, Pittsburgh, United States.
- J.D. Kelly, B.C. Menezes, I.E. Grossmann, 2018b, Successive LP Approximation for Nonconvex Blending in MILP Scheduling Optimization Using Factors for Qualities in the Process Industry. *Industrial and Engineering Chemistry Research*, 57, 11076-11093.
- N. Kyungseok, S. Joohyun, J.H. Lee, 2017, An Optimization Based Strategy for Crude Selection in a Refinery with Lube Hydro-Processing. *Computer and Chemical Engineering*, 116, 91-111.
- C.A. Mendez, I.E. Grossmann, I. Harjunkoski, P.A. Kabore, 2006, A Simultaneous Optimization Approach for Off-Line Blending and Scheduling of Oil-Refinery Operations. *Computer and Chemical Engineering*, 30, 614-634.
- B.C. Menezes, J.D. Kelly, I.E. Grossmann, 2018, Logistics Optimization for Dispositions and Depooling of Distillates in Oil-Refineries: Closing the Production Scheduling and Distribution Gap. *Computer Aided Chemical Engineering*, 40, 1135-1140.

A simple modeling approach to control emulsion layers in gravity separators

Christoph Josef Backi^{a,b,*}, Samuel Emebu^b, Sigurd Skogestad^b and Brian Arthur Grimes^b

^a*BASF SE, 63056 Ludwigshafen am Rhein, Germany*

^b*Department of Chemical Engineering, Norwegian University of Science and Technology (NTNU), 7491 Trondheim, Norway*
christoph.backi@ntnu.no

Abstract

This paper presents an extension to a gravity separator model that has been previously introduced by some of the authors. It expands the existing model by adding differential states for emulsion layer thickness between the oil- and the water-continuous phases in addition to the gas pressure, the overall liquid level and the water-continuous layers. These differential states can ultimately be used for controller design in order to regulate the layer thickness by adding demulsifiers to the inflow. Due to the fact that demulsifiers are a primary factor to promote coalescence of complex petroemulsions, the demulsifier inflow is a critical variable to incorporate into a control model for gravity separation of petroemulsions.

Keywords: Gravity separator, oil and gas, emulsion layer, modeling, control

1. Introduction

The inflows of dispersed droplets into the new emulsion layers are obtained from a simplified interfacial coalescence relationship presented by Grimes (2012). In this formulation, the product Γ of the interfacial tension σ and retarded Hamaker constant Ha are directly related to the influence of the demulsifier. Realistic combinations of the interfacial tension and Hamaker constant that provide increasing and decreasing emulsion layer thicknesses were determined and a feedback control model was formulated to adjust the demulsifier inflow based on measurement of the thickness of the emulsion layers through the parameter σ . The controllers of simple PI-type were tuned according to the SIMC rule, see e.g. Skogestad (2003), and the theoretical developments of this work are demonstrated in a simulation case study.

2. Mathematical model

The basic principles for the gravity separator model without emulsion layers have been introduced in Backi and Skogestad (2017) and Backi et al. (2018). Three dynamic state variables were defined, where the first describes the dynamics of the overall liquid level (oil plus water), h_L ,

$$\frac{dh_L}{dt} = \frac{dV_L}{dt} \frac{1}{2L\sqrt{h_L(2r-h_L)}} \quad (1)$$

where r is the separator's radius and L is the length of the active separation zone. Furthermore, $\frac{dV_L}{dt} = q_{L,in} - q_{L,out}$ is the volumetric change in overall liquid, where $q_{L,out} = q_{W,out} + q_{O,out}$. The manipulated variables are the outflows of water $q_{W,out}$ and oil $q_{O,out}$, respectively.

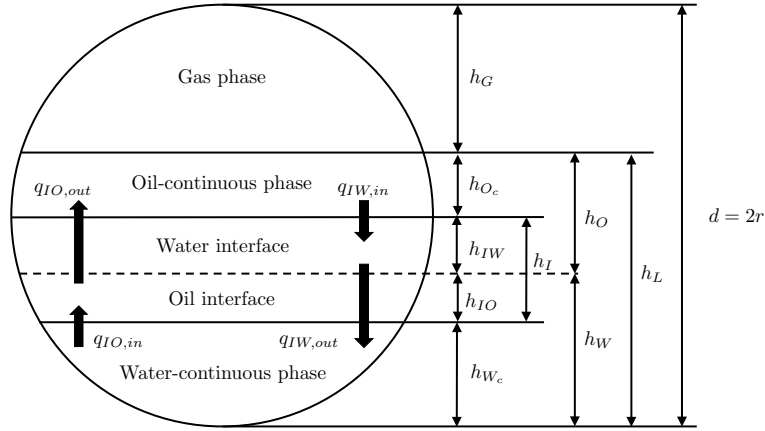


Figure 1: Schematic over the different variables in a cross-sectional view of the gravity separator

The second variable introduces the change in the water-continuous level, h_W ,

$$\frac{dh_W}{dt} = \frac{dV_W}{dt} \frac{1}{2L\sqrt{h_W(2r-h_W)}} \quad (2)$$

with $\frac{dV_W}{dt} = q_{W,in} - q_{W,out}$, where $q_{W,in} = \gamma q_{L,in}$ is a fraction γ of the total liquid inflow $q_{L,in}$ entering the water-continuous phase. Thereby, $\gamma = \alpha \phi_{ww} + (1 - \alpha)(1 - \phi_{oo})$, where α is the water cut of the inflow, ϕ_{ww} describes the fraction of inflowing water entering the water-continuous phase, and ϕ_{oo} is the fraction of inflowing oil entering the oil-continuous phase.

The third variable describes the pressure dynamics derived from the ideal gas law with temperature T constant

$$\frac{dp}{dt} = \frac{RT \frac{\rho_G}{M_G} (q_{G,in} - q_{G,out}) + p(q_{L,in} - q_{L,out})}{V_{Sep} - A_L L}, \quad (3)$$

where R denotes the universal gas constant, M_G is the molar mass of the gas, ρ_G describes the gas density, and $q_{G,in}$ and $q_{G,out}$ give the in- and outflows of gas, where latter is a manipulated variable.

In addition to the dynamic part of the original model, an algebraic part is introduced. In short, the algebraic part compares horizontal to vertical residence times of different droplet size classes. Based on this calculation, a droplet size class is either separated, not separated, or partially separated. Thereby, several assumptions hold, for example that Stokes' law is the main driving force for separation and that no coalescence or breakage are considered. For further details, the authors refer to Backi and Skogestad (2017) and Backi et al. (2018).

As an extension to the model, two new state variables are introduced in order to represent the emulsion layer between the oil- and the water-continuous layers in a gravity separator. In Figure 1, a schematic of the cross-sectional areas and the variables in such a separator are given.

2.1. Oil interface layer h_{IO}

We derive a differential equation for the oil interface layer, which builds up on top of the water-continuous layer. We write the cross-sectional area of the oil interface layer (index IO) as

$$A_{IO} = A_W - A_{W-IO}, \quad (4)$$

with the two cross-sectional areas A_W (index W for water layer) and A_{W-IO} (index $W-IO$ for water-continuous layer minus oil interface layer) defined as

$$A_W = \frac{r^2}{2} \left(2 \arccos \left(\frac{r-h_W}{r} \right) - \sin \left(2 \arccos \left(\frac{r-h_W}{r} \right) \right) \right), \quad (5)$$

$$A_{W-IO} = \frac{r^2}{2} \left(2 \arccos \left(\frac{r-(h_W-h_{IO})}{r} \right) - \sin \left(2 \arccos \left(\frac{r-(h_W-h_{IO})}{r} \right) \right) \right). \quad (6)$$

After differentiating (4)–(6), we receive the expression

$$\begin{aligned} \frac{dA_{IO}}{dt} &= \frac{dh_{IO}}{dt} \left[2\sqrt{(h_W-h_{IO})(2r-(h_W-h_{IO}))} \right] \\ &+ \frac{dh_W}{dt} \left[2 \left(\sqrt{h_W(2r-h_W)} - \sqrt{(h_W-h_{IO})(2r-(h_W-h_{IO}))} \right) \right], \end{aligned} \quad (7)$$

where $\frac{dh_W}{dt}$ is introduced in (2) leading to

$$\begin{aligned} \frac{dA_{IO}}{dt} &= \frac{dh_{IO}}{dt} \left[2\sqrt{(h_{IO}+h_W)(2r-(h_{IO}+h_W))} \right] \\ &+ \frac{dV_W}{dt} \frac{1}{L} \left(1 - \sqrt{\frac{(h_{IO}+h_W)(2r-(h_{IO}+h_W))}{h_W(2r-h_W)}} \right). \end{aligned} \quad (8)$$

Ultimately, we receive the differential equation for the oil interface layer

$$\begin{aligned} \frac{dh_{IO}}{dt} &= \frac{dV_{IO}}{dt} \frac{1}{2L} \frac{1}{\sqrt{(h_W-h_{IO})(2r-(h_W-h_{IO}))}} \\ &- \frac{dV_W}{dt} \frac{1}{2L} \left(\frac{1}{\sqrt{(h_W-h_{IO})(2r-(h_W-h_{IO}))}} - \frac{1}{\sqrt{h_W(2r-h_W)}} \right), \end{aligned} \quad (9)$$

with $\frac{dV_W}{dt} = q_{W,in} - q_{W,out}$ and $\frac{dV_{IO}}{dt} = q_{IO,in} - q_{IO,out}$; latter is calculated using the algebraic part of the model.

2.2. Water interface layer h_{IW}

For the water interface layer (index IW) forming on the bottom of the oil-continuous layer, it holds

$$A_{IW} = A_{O+G} - A_{O+G-IW} \quad (10)$$

with the two cross-sectional areas A_{O+G} (index $O+G$ for the sum of the oil-continuous layer plus the gas phase) and A_{O+G-IW} (index $O+G-IW$ for oil-continuous layer plus gas phase minus water interface layer) defined as

$$A_{O+G} = \frac{r^2}{2} \left(2 \arccos \left(\frac{r-h_{O+G}}{r} \right) - \sin \left(2 \arccos \left(\frac{r-h_{O+G}}{r} \right) \right) \right), \quad (11)$$

$$A_{O+G-IW} = \frac{r^2}{2} \left(2 \arccos \left(\frac{r-(h_{O+G}-h_{IW})}{r} \right) - \sin \left(2 \arccos \left(\frac{r-(h_{O+G}-h_{IW})}{r} \right) \right) \right). \quad (12)$$

Differentiating (10), (11), and (12) and defining $h_{O+G} = 2r - h_W$, we obtain

$$\begin{aligned} \frac{dA_{IW}}{dt} &= \frac{dh_{IW}}{dt} \left[2\sqrt{(h_{IW}+h_W)(2r-(h_{IW}+h_W))} \right] \\ &+ \frac{dh_W}{dt} \left[2 \left(\sqrt{(h_{IW}+h_W)(2r-(h_{IW}+h_W))} - \sqrt{h_W(2r-h_W)} \right) \right] \end{aligned} \quad (13)$$

where, again, $\frac{dh_W}{dt}$ is presented in (2) and hence

$$\begin{aligned} \frac{dA_{IW}}{dt} = & \frac{dh_{IW}}{dt} \left[2\sqrt{(h_{IW} + h_W)(2r - (h_{IW} + h_W))} \right] \\ & + \frac{dV_W}{dt} \frac{1}{L} \left(\sqrt{\frac{(h_{IW} + h_W)(2r - (h_{IW} + h_W))}{h_W(2r - h_W)}} - 1 \right). \end{aligned} \quad (14)$$

Finally, we receive the differential equation for the water interface layer

$$\begin{aligned} \frac{dh_{IW}}{dt} = & \frac{dV_{IW}}{dt} \frac{1}{2L} \frac{1}{\sqrt{(h_{IW} + h_W)(2r - (h_{IW} + h_W))}} \\ & - \frac{dV_W}{dt} \frac{1}{2L} \left(\frac{1}{\sqrt{h_W(2r - h_W)}} - \frac{1}{\sqrt{(h_{IW} + h_W)(2r - (h_{IW} + h_W))}} \right) \end{aligned} \quad (15)$$

with $\frac{dV_W}{dt} = q_{W,in} - q_{W,out}$ and $\frac{dV_{IW}}{dt} = q_{IW,in} - q_{IW,out}$. It must be pointed out that here $\frac{dV_W}{dt} = q_{W,in} - q_{W,out}$ excludes the oil leaving the water into the interface. Furthermore, $\frac{dV_{IW}}{dt} = q_{IW,in} - q_{IW,out}$ is calculated using the algebraic part of the model.

3. Controller Design

The controllers of PI type in the shape $K(s) = K_P + T_I \frac{1}{s}$ have the aim to regulate the gas pressure and the levels of overall liquid and water as well as the oil and the water interface layer levels. The first three controllers have already been introduced and developed in Backi and Skogestad (2017) and Backi et al. (2018), where the manipulated variables (MVs) are the outflows of water $q_{W,out}$, oil $q_{O,out}$ and gas $q_{G,out}$. Hence, in this work the focus lies on the design of the controllers for the oil and water interface layers.

3.1. Theoretical developments

In order to control the layer thickness of emulsions in gravity separators, the addition of demulsifiers to the inlet stream is necessary. Depending on the type of oil and the thickness of the emulsion, more or less demulsifier has to be added. We derive a relationship between the outflow of oil and water from the respective interface layers into their bulk phases and the coalescence time t_c for droplets with the volumetric outflow given by

$$q_{I,out} = A_I \int_0^\infty \frac{r_d}{3t_c} f(r_d) dr_d \cong \frac{A_I r_1}{3t_c}, \quad (16)$$

where $A_I = 2L\sqrt{h_W(r - h_W)}$ is the interfacial area, r_d are droplet radii, r_1 is a lumped, unified, theoretic droplet radius and t_c is the coalescence time

$$t_c = 1.046 \frac{\mu_c (\rho_d - \rho_c) g_z r_1^{9/2}}{\sigma^{3/2} Ha^{1/2}}, \quad (17)$$

where μ_c is the dynamic viscosity of the continuous phase, ρ_d and ρ_c are the densities of the dispersed and continuous phases, respectively, g_z is the gravitational acceleration, and finally Ha describes the retarded Hamaker constant and σ is the interfacial tension. Latter is the manipulated variable for the controller, hence by changing σ we can affect the volumetric outflow (16). In a first step, we aim to find a relation between the retarded Hamaker constant and the interfacial tension in order to affect the coalescence time, which affects the outflow of oil or water from the respective interfaces. Since the retarded Hamaker constant and the interfacial tension are related by the function

$$\Gamma = \sigma^{3/2} Ha^{1/2} \quad (18)$$

we first investigate pairings of these values that give reasonable values for Γ and then ultimately find the theoretic, lumped droplet radii r_1 for water and oil droplets in the respective interfaces. Furthermore, we can reduce the parameter space by one if we find an expression that links the retarded Hamaker constant Ha with the interfacial tension σ , namely $Ha = f(\sigma)$, and hence $\Gamma = \sigma^{3/2} [f(\sigma)]^{1/2}$. A function that satisfies the property that the retarded Hamaker constant is decreasing as the interfacial tension is rising is

$$f(\sigma) = \sigma \left[1.7564 \cdot 10^{-\left(20 + \frac{\sigma}{\sigma_{min}}\right)} \right] \ln \left(1 + \frac{0.0001}{\sigma} \right), \quad (19)$$

where $\sigma_{min} = 0.005 \text{ N m}^{-1}$.

Expressions for the outflows can be obtained by combining (16), (17) and (18)

$$\begin{aligned} q_{IO,out} &= \frac{A_I r_{IO,1}}{3t_{IO,c}} = \frac{2L\sqrt{h_W(r-h_W)}}{3.138 \mu_{IO,c}(\rho_d - \rho_c) g_z r_{IO,1}^{7/2}} \frac{\Gamma_{IO}}{r_{IO,1}^{7/2}}, \\ q_{IW,out} &= \frac{A_I r_{IW,1}}{3t_{IW,c}} = \frac{2L\sqrt{h_W(r-h_W)}}{3.138 \mu_{IW,c}(\rho_d - \rho_c) g_z r_{IW,1}^{7/2}} \frac{\Gamma_{IW}}{r_{IW,1}^{7/2}}, \end{aligned} \quad (20)$$

and it becomes apparent that the only tuning variables affecting the outflow are the water level h_W and furthermore the combined parameters Γ_{IO} and Γ_{IW} as well as the theoretic, lumped droplet radii $r_{IO,1}$ and $r_{IW,1}$.

As can be seen from (19) and ultimately (20), the interfacial tensions σ_{IW} and σ_{IO} , which are the MVs for the two controllers, can never be zero or negative. From these equations it can be inferred that large σ give small outflows and vice versa.

4. Results

Figure 2 shows simulation results incorporating the model and the controllers presented in sections 2 and 3, respectively. The subplots $S_{i,i}$ are thereby numerated according to entries in a matrix, hence $S_{1,1}$ is the top left plot, etc.

$S_{1,1}$ and $S_{2,1}$ show the liquid level h_L and the water level h_W in solid lines with their respective reference values in dashed lines. The water level is increased at time $t = 200$ s from initially 1.2 m to 1.4 m while the liquid level is held constant at 2.5 m. This is done to demonstrate that all controllers can handle this occurrence. $S_{1,2}$ and $S_{2,2}$ depict the outflows from the oil- and water-continuous phases, $q_{W,out}$ and $q_{O,out}$, respectively.

$S_{3,1}$ presents the oil interface level with its outflow $q_{IO,out}$ in $S_{3,2}$. One can see that $q_{IO,out}$ is initially held constant at a very low flow rate resulting in the oil interface level to increase. The controller and hence the addition of demulsifier is activated at $t = 100$ s causing the oil interface level to be brought back to zero. Accordingly, the water interface level is depicted in $S_{4,1}$ with its outflow $q_{IW,out}$ in $S_{4,2}$. Like for the oil interface level described above, initially $q_{IW,out}$ is constant and the water interface level increases. Again, the controller is turned on at $t = 100$ s, which leads to a decrease in the water interface level.

For completeness, the interfacial tensions for the two interface layers over time are presented in $S_{3,3}$ and $S_{4,3}$, respectively. Furthermore, the oil-continuous level is shown in $S_{1,3}$ and $S_{2,3}$ depicts the water-continuous level.

Due to space limitations we refer to Backi et al. (2018), where the majority of simulation parameters are presented. The only simulation parameters specific for this work are $r_{IO,1} = 90 \text{ }\mu\text{m}$ and $r_{IW,1} = 110 \text{ }\mu\text{m}$ as well as the tuning parameters for the interface layer controllers, $K_{P,IW} = 1.84$, $T_{I,IW} = 0.092$, $K_{P,IO} = 2.19$ and $T_{I,IO} = 0.11$.

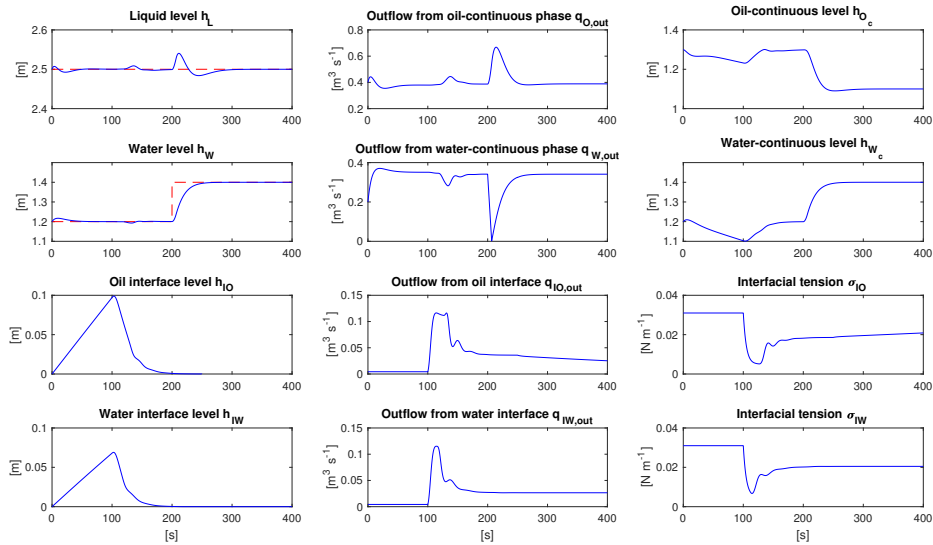


Figure 2: The different state variables with the manipulated variables

5. Conclusion

We presented a simple modeling approach in order to regulate the thickness of emulsion layers in gravity separators. The simplicity of the model makes it usable for easy controller design, as is demonstrated in the Results section. Although the approach describing two interface layers on top of each other does not strictly fulfill physical principles, the model showed itself useful. However, it must be noted that from a strict physical viewpoint, the water interface forming on top of the oil interface will not happen in reality. It rather is a way to describe the emulsion interface between the water- and oil-continuous phases in a systematic manner. We refer to Hartland and Jeelani (1987), who describe sedimentation and dense-packed zones, which inspired our approach.

6. Acknowledgement

The authors gratefully acknowledge the financial support provided by the Norwegian Research Council in the project SUBPRO (Subsea production and processing).

References

- C. J. Backi, B. A. Grimes, S. Skogestad, 2018. A Control- and Estimation-Oriented Gravity Separator Model for Oil and Gas Applications Based upon First-Principles. *Ind. Eng. Chem. Res.* 57 (21), 7201–7217.
- C. J. Backi, S. Skogestad, May 24–26 2017. A simple dynamic gravity separator model for separation efficiency evaluation incorporating level and pressure control. In: *Proceedings of the American Control Conference*. Seattle, USA, pp. 2823–2828.
- B. A. Grimes, 2012. Population Balance Model for Batch Gravity Separation of Crude Oil and Water Emulsions. Part I: Model Formulation. *J. Dispersion Sci. Technol.* 33 (4), 578–590.
- S. Hartland, S. A. K. Jeelani, 1987. Choice of model for predicting the dispersion height in liquid/liquid gravity settlers from batch settling data. *Chem. Eng. Sci.* 42 (8), 1927–1938.
- S. Skogestad, 2003. Simple analytic rules for model reduction and PID controller tuning. *J. Process Control* 13, 291–309.

Improving Waste Water Treatment Plant Operation by Ammonia Based Aeration and Return Activated Sludge Control

Melinda Várhelyi, Vasile Mircea Cristea*, Marius Brehar

Babeş-Bolyai University, Faculty of Chemistry and Chemical Engineering, 11 Arany Janos Street, Cluj-Napoca 400028, Romania

mcristea@chem.ubbcluj.ro

Abstract

Wastewater Treatment Plant (WWTP) is a very important part of every urban infrastructure, which has to achieve the desired effluent quality with cost-effective operation. Modelling and simulation help to find better operation scenarios and design alternatives, but also to investigate different control strategies. A dynamic WWTP simulator implemented in Matlab and Simulink was first calibrated with the configuration and process measured data from the local municipal WWTP. Then, the calibrated model was used for the investigation of different control strategies. This paper presents the investigation of five different ammonia based aeration control (ABAC) structures applying feedback and feedforward control. The latter is based on the ammonia influent disturbance. Five different return activated sludge (RAS) ratio control structures, coupled to the influent flow rate of wastewater, are also investigated in association to the nitrate recirculation (NR) control. According to the performed simulations, when applying ABAC with a feedforward component added to the setpoint of the dissolved oxygen (DO) controller, the air flow rate and the aeration energy can be reduced up to 45% and the effluent quality can be improved. Following the investigation of the RAS ratio-control, it was shown that flow rate of RAS and the pumping energy can be reduced up to 37% while the effluent quality remains high. This research demonstrated the benefits of applying ABAC and RAS control.

Keywords: wastewater treatment, modelling, simulation, ammonia based aeration control, return activated sludge control.

1. Introduction

Control of the Wastewater Treatment Plants (WWTPs) is a complex task due to the disturbances consisting in the wastewater influent concentrations and flow rates, the complicated behaviour of the microorganisms and the prescribed effluent quality requirements. WWTPs confront with the problem of high operational costs represented by the aeration and pumping energy, asking for control strategies to reduce them. Control strategies may be investigated by modelling and simulation, before their implementation in the WWTPs (Ostace et al., 2012).

Ammonia based aeration control (ABAC) is a cascade control in which the dissolved oxygen (DO) controller is combined with an ammonia controller (Rieger et al., 2014). The reason to apply ABAC is to reduce the aeration costs due to the implied aeration

energy and to react efficiently to the ammonia disturbances appearing in the influent wastewater and at the end of the aerobic zone (Ozturk et al., 2016; Zhu et al., 2017).

Return activated sludge (RAS) flow rate is essential for the biological wastewater treatment because RAS has the role to return the activated sludge from the secondary settlers to the input of the biodegradation basins ensuring the necessary concentration of the biomass in the anaerobic and aerobic tanks (Olsson, 2012).

This paper focuses on two main control strategies: ammonia based aeration control in which the flow rate of air entering the aerated bioreactors is computed by ammonia controller in cascade with three dissolved oxygen controllers and the RAS control which is based on the flow rate of the wastewater entering the WWTP.

2. Development of the Dynamic WWTP Simulator

The WWTP model used in this study is an extension of Benchmark Simulation Model No. 1 (BSM1) (Copp, 2002) with a nonreactive primary clarifier based on Otterpohl model. The model was calibrated with the reactors and flows configuration of the investigated municipal WWTP and the measured data collected during May 2016 from this plant. The municipal WWTP under study has an anaerobic-anoxic-aerobic (A2O) configuration, according to which the nitrate (internal) recirculation from the end of the aerobic zone is entering between the anaerobic and anoxic zones of the basin. The dynamic WWTP Simulator was implemented in Matlab and Simulink. The equations of the primary clarifier, the bioreactors according to the Activated Sludge Model No. 1 (ASM1) and the nonreactive secondary settler based on Takács clarifier model were written in C programming language and introduced in the Simulink environment by S-function blocks. The model was calibrated in steady state using different optimisation methods and then tested by dynamic simulations. This calibrated model was used in the further presented studies.

3. Implemented Control Strategies

In the study of the ammonia based aeration control, the calibrated model was complemented with 3 Proportional-Integral (PI) feedback dissolved oxygen (DO) controllers in cascade configuration, as slave controllers, associated to an ammonia master controller. This control structure was augmented with the ratio based feedforward control of both the RAS and the NR, based on the WWTP leading influent flow rate. The configuration of this control strategy is presented in Figure 1. Ammonia concentration is measured at the aerated zone outlet and is used by the ammonia controller to keep the $1 \text{ g NH}_3\text{-N/m}^3$ setpoint value. The ammonia master controller computes the reference value for the first DO controller, which can be supplemented by an extra value based on the ammonia disturbances in the influent. This added value can be a constant, proportional or in linear relationship with the influent ammonia concentration. In this research 5 cases were tested as presented in Table 1: switching the added DO setpoint value from 0 to $0.5 \text{ g O}_2\text{/m}^3$ when the ammonia concentration in the influent exceeds $30 \text{ g NH}_3\text{-N/m}^3$ (case A), respectively $20 \text{ g NH}_3\text{-N/m}^3$ (case E). Based on the $30 \text{ g NH}_3\text{-N/m}^3$ ammonia concentration limit, it was studied a proportional (case B) and a linear (case C) dependency of the supplement. It was also defined a linear function for the DO setpoint supplement, depending on the influent ammonia

concentration, the coefficients of the linear equation being determined by optimisation. This latter approach was taking into consideration the quality of the effluent and the necessary air flow rate entering the aerobic zone (case D). The third DO controller computes the flow rate of the air entering equally into the 3 aerated reactors. The flow rate of the RAS is considered to be equal with the influent flow rate; the NR is controlled by a nitrate controller combined with a 0.7 factor of the wastewater flow rate. The simulations were performed for 66 days (three times the collected measured data of 22 days).

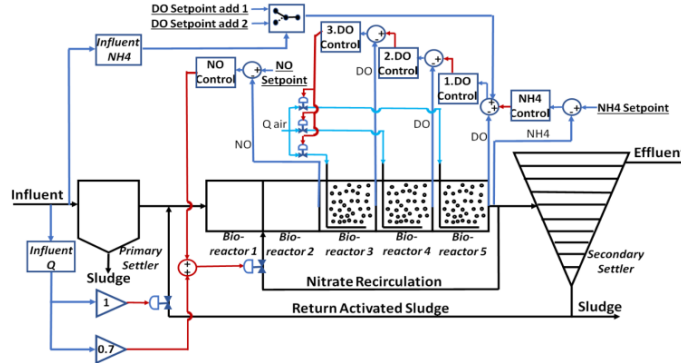


Figure 1. ABAC with supplementing the dissolved oxygen setpoint computed by the ammonium controller, control of RAS and control of NR based on the wastewater influents

Table 1. Investigated cases of ammonia based aeration control

CASE	DESCRIPTION
ABAC Case A	$\text{If } C_{NH_inf} \geq 30 \text{gN} / \text{m}^3 \text{ then } y_{ref_DO_R5} = y_{c_NHcontroller} + 0.5 \quad (1)$ $\text{else } y_{ref_DO_R5} = y_{c_NHcontroller}$
ABAC Case B	$\text{If } C_{NH_inf} \geq 30 \text{gN} / \text{m}^3 \text{ then } y_{ref_DO_R5} = y_{c_NHcontroller} + 0.03 \cdot C_{NH_inf} \quad (2)$ $\text{else } y_{ref_DO_R5} = y_{c_NHcontroller}$
ABAC Case C	$\text{If } C_{NH_inf} \geq 30 \text{gN} / \text{m}^3 \text{ then } y_{ref_DO_R5} = y_{c_NHcontroller} + (0.074 \cdot C_{NH_inf} - 2.217) \quad (3)$ $\text{else } y_{ref_DO_R5} = y_{c_NHcontroller}$
ABAC Case D	$y_{ref_DO_R5} = y_{c_NHcontroller} + (0.0307 \cdot C_{NH_inf} + 0.0101) \quad (4)$
ABAC Case E	$\text{If } C_{NH_inf} \geq 20 \text{gN} / \text{m}^3 \text{ then } y_{ref_DO_R5} = y_{c_NHcontroller} + 0.5 \quad (5)$ $\text{else } y_{ref_DO_R5} = y_{c_NHcontroller}$

In the second part of this research, the DO setpoint supplement based on the ammonia influent concentration in the ABAC structure was eliminated; the configuration of the calibrated model with the investigated control structures is presented in Figure 2. Considering the RAS (Q_{RAS}) and NR (Q_{NR}) control, a study was carried out to find the optimal values of the factors k_{RAS} and k_{NR} for the associated flow rates, as described by Eq. (6) and (7). The investigated cases are presented in Table 2. The optimized values were found and simulations were performed for 22 days period.

$$Q_{RAS} = k_{RAS} \cdot Q_{Influent} \quad (6)$$

$$Q_{NR} = k_{NR} \cdot Q_{Influent} + y_{c_NOcontroller} \quad (7)$$

Table 2. The investigated cases with RAS control and basic ABAC structure

CASE	DESCRIPTION
RAS Case A	$k_{RAS}=0.8323$, $k_{NR}=0.5509$ optimized values for the whole period of time
RAS Case B	k_{RAS} and k_{NR} changing optimized values from day to day – I.
RAS Case C	k_{RAS} and k_{NR} changing optimized values from day to day – II.
RAS Case D	k_{RAS} changing optimized values from day to day, $k_{NR}=0.7$
RAS Case E	$k_{RAS}=0.7761$ optimized value for the whole period, $k_{NR}=0.7$

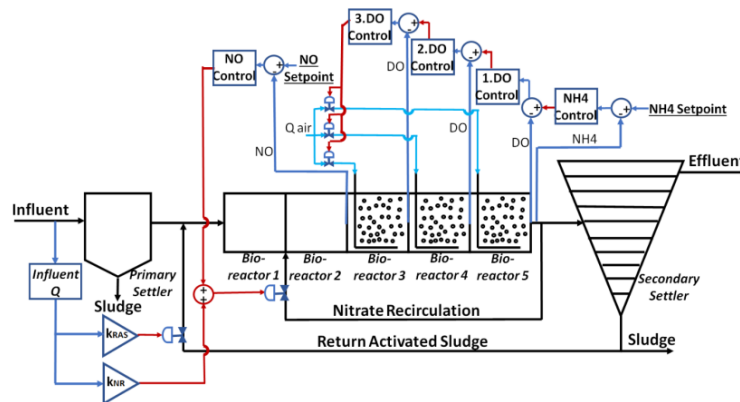


Figure 2. Return activated sludge and nitrate recirculation control associated to ABAC

4. Results and discussions

4.1. Ammonia Based Aeration Control with variable supplement of the DO setpoint

This control system design proposes the reduction of aeration energy, and consequently the operational costs at the aerated basins and the improvement of effluent quality by applying ABAC. To the ABAC structure found in literature (Rieger et al., 2014), i.e. to the control signal of the ammonia controller, it was added a supplement based on the average values obtained from simulations of the effluent concentrations and the RAS, NR and air flow rates, when the supplemented DO setpoint value was designed based on different principles. In all investigated cases it may be observed the reduction of nitrates and total nitrogen effluent concentration and the reduction of the air flow rate comparatively to the municipal WWTP.

Considering the average effluent concentrations and flow rate values, it can be stated that the most efficient case is ABAC – Case D. In Figure 3 and Figure 4 it is represented the comparison between the municipal WWTP and the simulated WWTP with ABAC – Case D.

Table 3. Comparison between the municipal WWTP measured data and the results of the simulated ABAC cases with supplemented DO setpoint

	Municipal WWTP	ABAC Case A	ABAC Case B	ABAC Case C	ABAC Case D	ABAC Case E
COD Effluent [g/m ³]	19.36	22.18	22.14	22.18	22.05	22.17
NH Effluent [g N/m ³]	0.17	1.00	1.00	1.00	0.99	1.00
NO Effluent [g N/m ³]	3.76	0.60	0.60	0.59	0.57	0.61
N total Effluent [g N/m ³]	5.70	3.60	3.61	3.60	3.57	3.62
Air flow rate [m ³ /day]	127,770	70,791	71,133	70,738	70,575	71,115
RAS flow rate [m ³ /day]	112,530	119,220	119,220	119,220	119,220	119,220
NR flow rate [m ³ /day]	138,350	136,390	133,260	136,380	139,340	134,180

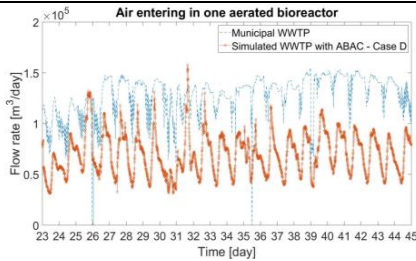


Figure 3. Comparison between the flow rate of air entering one bioreactor measured at the municipal WWTP and the simulated WWTP with ABAC – Case D

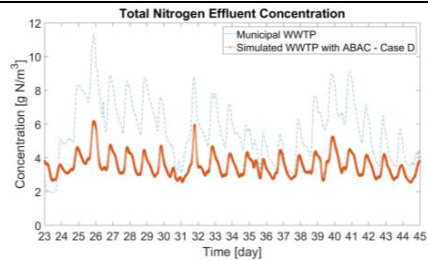


Figure 4. Comparison between the concentration of total nitrogen in effluent measured at the municipal WWTP and the simulated WWTP with ABAC – Case D

4.2. Return Activated Sludge Control

The flow rate of the RAS is dependent on the influent flow rate. An investigation, for the different RAS designs of Table 2, was performed in order to find the best factor value for RAS and, in some cases, for NR too. Table 4 presents the obtained results.

Table 4. Comparison between the municipal WWTP measured data and the results of the simulated WWTP with the different RAS cases

	Municipal WWTP	RAS Case A	RAS Case B	RAS Case C	RAS Case D	RAS Case E
COD Effluent [g/m ³]	19.36	20.66	21.17	20.07	19.02	20.39
NH Effluent [g N/m ³]	0.17	0.99	0.99	0.99	0.99	0.99
NO Effluent [g N/m ³]	3.76	0.79	0.69	0.90	1.08	0.83
N total Effluent [g N/m ³]	5.70	3.71	3.62	3.80	3.92	3.73
Air flow rate [m ³ /day]	127,770	71,178	71,417	70,739	70,317	71,114
RAS flow rate [m ³ /day]	112,530	99,231	118,860	86,601	71,336	92,534
NR flow rate [m ³ /day]	138,350	114,140	127,930	99,606	113,230	123,330

Considering the cases of the RAS flow rate designs, the case of changing the factor value for RAS every day and setting 0.7 for the k_{NR} (RAS – Case D) led to the flow rate of RAS reduced by 36.6%, associated to pumping energy and cost reduction. RAS – Case D also presents a reduction of the NR flow rate by 18.2%. Figure 5 and Figure 6 show the benefits of applying RAS – Case D. Figure 7 shows reduction of air flow rate entering one bioreactor and Figure 8 presents the effluent total nitrogen concentration.

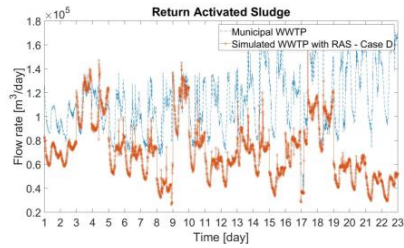


Figure 5. Comparison between RAS flow rate of measured at the municipal WWTP and simulated WWTP with RAS – Case D

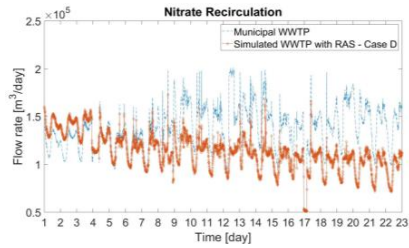


Figure 6. Comparison between the NR flow rate measured at the municipal WWTP and simulated WWTP with RAS – Case D

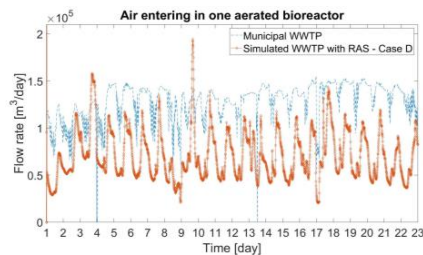


Figure 7. Comparison between the air entering one aerobic bioreactor measured at the municipal WWTP and simulated WWTP with RAS – Case D

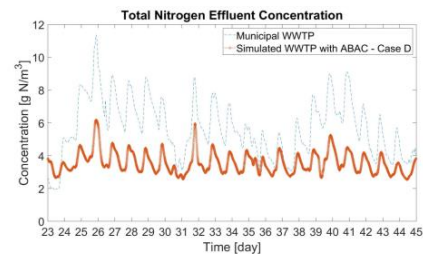


Figure 8. Comparison between total nitrogen effluent concentration measured at the municipal WWTP and simulated WWTP with RAS – Case D

5. Conclusions

New ammonia based aeration control designs associated to the return activated sludge control were investigated by simulation for WWTP control. In the ABAC structure based on the ammonia inlet concentration disturbance, the DO setpoint value handled by the ammonia controller was supplemented with a component calculated based on different principles. The RAS ratio control was coupled with the inlet wastewater flow rate and the implied factor values were computed by optimization. The investigated control strategies demonstrated benefits for WWTPs, reducing the aeration and pumping energies and improving the effluent quality.

References

- J. B. Copp, 2002, The COST Simulation Benchmark: Description and Simulator Manual
- G. Olsson, 2012, ICA and me – A Subjective Review, *Water Research*, 46, 6, 1585-1624
- G. S. Ostace, V. M. Cristea, P. S. Agachi, 2012, Evaluation of different control strategies of the waste water treatment plant based on a modified activated sludge model no. 3, *Environmental Engineering and Management Journal*, 11, 1, 147-164
- M. C. Ozturk, F. M. Serrat, F. Teymour, 2016, Optimization of aeration profiles in the activated sludge process, *Chemical Engineering Science*, 139, 1-14
- L. Rieger, R. M. Jones, P. L. Dold, C. B. Bott, 2014, Ammonia-based feedforward and feedback aeration control in activated sludge process, *Water Environment Research*, 86, 1, 63-73
- Z. Zhu, R. Wang, Y. Li, 2017, Evaluation of the control strategy for aeration energy reduction in a nutrient removing wastewater treatment plant based on the coupling of ASM1 to an aeration model, *Biochemical Engineering Journal*, 124, 44-53

Combining the Advantages of Discrete- and Continuous-time MIP Scheduling Models

Hojae Lee^a and Christos T. Maravelias^a

^a*Department of Chemical and Biological Engineering, University of Wisconsin-Madison, 1415 Engineering Dr., Madison, WI 53706, USA
christos.maravelias@wisc.edu*

Abstract

A solution algorithm that harnesses the strengths of discrete- and continuous-time scheduling models is proposed. It is a three stage algorithm consisting of (i) a discrete-time MIP scheduling model, (ii) a mapping algorithm, and (iii) a continuous-time LP model. It enables fast and accurate solution of scheduling problems, by quickly obtaining approximate solutions and improving their accuracy, while maintaining feasibility. Through a computational study, it is shown that the proposed method is capable of finding high quality solutions up to 4 orders of magnitude faster, compared to stand-alone discrete- and continuous-time models.

Keywords: chemical production scheduling, solution algorithm, continuous-time model, discrete-time model

1. Introduction

All existing grid-based mixed-integer programming (MIP) scheduling models can be classified into two categories based on the type of grids they employ: discrete- and continuous-time models. While continuous-time models provide more accurate solutions, discrete-time models are, in general, faster in large-scale instances and can accommodate various process features without additional computational cost (Floudas and Lin, 2004; Sundaramoorthy and Maravelias, 2011). In this work, we propose a solution algorithm, namely the Discrete-Continuous Algorithm, that combines the advantages of both discrete- and continuous-time scheduling models, while overcoming their limitations.

We consider a short-term chemical production scheduling problem in network environments. Given the facility data, resource availability and demand information, the objective is to find a schedule that satisfies the customer demand, while minimizing makespan. We use the state-task network (STN) representation throughout the paper (Kondili et al., 1993). We use set $\mathbf{I} \ni i$ to denote tasks, $\mathbf{J} \ni j$ to denote units, and $\mathbf{K} \ni k$ to denote materials. We also define the following subsets: \mathbf{I}_j to denote tasks that can be executed in unit j , $\mathbf{I}_k^+/\mathbf{I}_k^-$ to denote tasks that produce/consume material k , and \mathbf{J}_i to denote units that can process task i .

2. Discrete-continuous algorithm

The Discrete-Continuous Algorithm (DCA) consists of three components: (i) a discrete-time MIP scheduling model, (ii) a mapping algorithm, and (iii) a continuous-time LP

model. In the first stage, an approximate solution is obtained with a relatively large discretization step length (δ), which gets mapped on to two new types of continuous-time grids in the second stage. Finally, in the third stage, some components of the first stage solution (e.g. timing of events, batch sizes, etc.) are recomputed to obtain a more accurate, and potentially better, solution. More details can be found in Lee and Maravelias (2018). Although not the scope of this work, we note that extending the algorithm to an iterative procedure may provide guaranteed bounds on the solution quality.

2.1. Stage 1: Discrete-time MIP scheduling model

While the algorithm can employ any discrete-time scheduling model, the STN model proposed by Shah et al. (1993) is used in this study. We divide the horizon into intervals of equal length, δ . The resulting time points are represented by $n \in \mathbf{N}$. We round-up the processing times (i.e. $\bar{\tau}_{ij} = \lceil (\tau_{ij}^F + \tau_{ij}^V \beta_j^{max}) / \delta \rceil$), and round-down the horizon (i.e. $\bar{H} = \lfloor H / \delta \rfloor$) to ensure feasibility, where $\tau_{ij}^F / \tau_{ij}^V$ are the fixed/variable processing time of task i performed on unit j , and H is the horizon. The key decision variable for the first stage model is the *start of task* binary, X_{ijn} , which is equal to 1 if task i starts in unit j at time point n . The readers are encouraged to refer to Shah et al. (1993) for the full model. In the first stage, the model is solved with a chosen δ to obtain an approximate solution fast.

2.2. Stage 2: Mapping algorithm

In the second stage, we map the first stage solution onto two continuous-time grids that we introduce: (i) material-, and (ii) unit-specific grids. The batches in the first stage solution that produce/consume each material are mapped onto the corresponding material-specific grid, collecting the information regarding the sequencing of these batches. The batches that are executed in each unit are mapped onto the corresponding unit-specific grid, collecting information regarding the batch-unit assignment and the batch sequencing within each unit. By denoting the set of grid points as $\mathbf{M} \ni m$, each grid point on a given grid can be represented using an index pair (e.g. 2nd grid point on unit U1 grid is represented as (U1,m2)).

We introduce the following binary algorithmic parameters to store the information collected: $f_{ikm}^1 = 1$ if task i is mapped to grid point (k,m) ; $f_{jkm}^2 = 1$ if a task mapped to grid point (k,m) is performed in unit j ; $f_{kmm'}^3 = 1$ if grid point where material k is produced (i.e. (k,m)) is before where it is consumed (i.e. (k,m')); $f_{ijkmm'}^4 = 1$ if task i is mapped to grid points (j,m) and (k,m') . The mapping algorithm is given in Table 1.

2.3. Stage 3: Continuous-time LP model

Based on the algorithmic parameters obtained in the previous stage, the timing of events, batch sizes and inventory levels are recomputed to obtain a more accurate solution. We define the following nonnegative continuous variables: batch size of the task mapped to grid point (k,m) , B_{km}^C ; inventory level of material k at grid point (k,m) , S_{km}^C ; time of grid point (j,m) , T_{jm}^U ; time of grid point (k,m) , T_{km}^M .

Table 1: Mapping algorithm

```

0: Initialize:  $M_j^U = 0 \quad \forall j, M_k^M = 0 \quad \forall k, f^{1\sim 4} = 0, \mathbf{M}_k^P = \mathbf{M}_k^C = \emptyset \quad \forall k$ 
1: Loop  $n \in \mathbf{N}$ 
2:   Loop  $k \in \mathbf{K}$ 
3:     Loop  $i \in \mathbf{I}_k^+$ 
4:       Loop  $j \in \mathbf{J}_i$ 
5:         If  $X_{ij(n-\bar{\tau}_{ij})} = 1$ 
6:            $M_k^M \leftarrow M_k^M + 1; M_j^U \leftarrow \sum_{n' < n} \sum_{i' \in \mathbf{I}_j} X_{i'jn'}$ 
7:            $\mathbf{M}_k^P \leftarrow \mathbf{M}_k^P \cup \{M_k^M\}$ 
8:            $f_{ik,m(=M_k^M)}^1 \leftarrow 1; f_{jk,m(=M_k^M)}^2 \leftarrow 1; f_{ijk,m(=M_j^U),m'(=M_k^M)}^4 \leftarrow 1$ 
9:         EndIf
10:      EndLoop x2
11:     Loop  $i \in \mathbf{I}_k^-$ 
12:       Loop  $j \in \mathbf{J}_i$ 
13:         If  $X_{ijn} = 1$ 
14:            $M_k^M \leftarrow M_k^M + 1; M_j^U \leftarrow \sum_{n' \leq n} \sum_{i' \in \mathbf{I}_j} X_{i'jn'}$ 
15:            $\mathbf{M}_k^C \leftarrow \mathbf{M}_k^C \cup \{M_k^M\}$ 
16:            $f_{ik,m(=M_k^M)}^1 \leftarrow 1; f_{jk,m(=M_k^M)}^2 \leftarrow 1; f_{ijk,m(=M_j^U),m'(=M_k^M)}^4 \leftarrow 1$ 
17:            $f_{kmm'}^3 \leftarrow 1 \quad \forall m < M_k^M, m \in \mathbf{M}_k^P, m' = M_k^M$ 
18:         EndIf
19:      EndLoop x4
20:   EndLoop x4
    
```

We ensure the sequencing of batches on material- and unit-specific grids.

$$T_{km}^M \leq T_{km'}^M \quad \forall k, m, m' : f_{kmm'}^3 = 1 \quad (1)$$

$$T_{jm}^U + (\tau_{ij}^F + \tau_{ij}^V B_{km'}^C) \leq T_{j(m+1)}^U \quad \forall i, j, k, m, m' : f_{ijkmm'}^4 = 1 \quad (2)$$

Time matching constraints are enforced to ensure that the timing of grid points that originate from the same batch are the same.

$$T_{jm}^U = T_{km'}^M \quad \forall i, j, k, m, m' \in \mathbf{M}_k^C : f_{ijkmm'}^4 = 1 \quad (3)$$

$$T_{jm}^U = T_{km'}^M - (\tau_{ij}^F + \tau_{ij}^V B_{km'}^C) \quad \forall i, j, k, m, m' \in \mathbf{M}_k^P : f_{ijkmm'}^4 = 1 \quad (4)$$

We enforce unit capacity constraints, as well as batch size matching constraints to ensure that the batch sizes that correspond to the same batch are identical.

$$\beta_j^{\min} \leq B_{km}^C \leq \beta_j^{\max} \quad \forall j, k, m : f_{jkm}^2 = 1 \quad (5)$$

$$B_{km'}^C = B_{k'm''}^C \quad \forall i, j, k, k', m, m', m'' : f_{ijkmm'}^4 = f_{ijk'mm''}^4 = 1, k < k' \quad (6)$$

The inventory level of material k at grid point m is equal to the sum of initial inventory, γ_k , and the amount produced/consumed up to that point. We make sure the demand for material k , ξ_k is satisfied.

$$S_{km}^C = \gamma_k + \sum_{m > m' \in \mathbf{M}_k^P} \sum_{i \in \mathbf{I}_k^+ : f_{ikm'}^1 = 1} \rho_{ik} B_{km'}^C + \sum_{m \geq m' \in \mathbf{M}_k^C} \sum_{i \in \mathbf{I}_k^- : f_{ikm'}^1 = 1} \rho_{ik} B_{km'}^C \quad \forall k, m \in \mathbf{M}_k^C \quad (7)$$

$$S_{k, M_k^M}^C \geq \xi_k \quad \forall k \quad (8)$$

We minimize makespan, MS :

$$\min MS : MS \geq T_{km}^M \quad \forall k, m \in \mathbf{M}_k^P \quad (9)$$

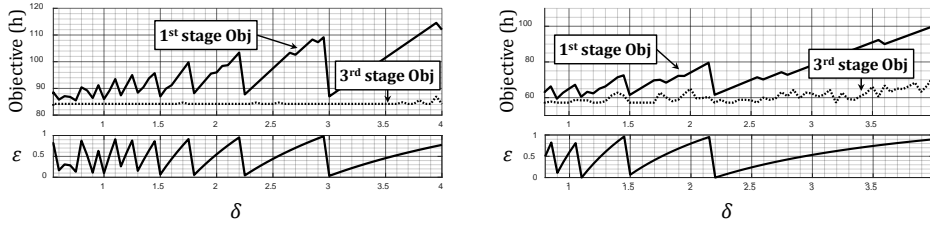


Figure 1: Using the error evaluation function, $\varepsilon(\delta)$, as a metric to determine δ 's, illustrated for (a) instance 1, and (b) instance 2

3. Determining the key model parameter, δ

As mentioned earlier, DCA requires the user to select the discretization step length, δ , in the first stage model. If chosen carefully, the speed and accuracy of DCA can be improved significantly. However, selecting δ 's that bring such results is non trivial.

In order to find the best performing δ , we introduce an error evaluation function denoted as $\varepsilon(\delta)$. For a given instance, $\varepsilon(\delta)$ measures the amount of discretization error introduced by the chosen δ , considering how much the shortage of each unit is constraining the objective value.

$$\varepsilon(\delta) = \frac{1}{\delta} \sum_i \sum_{j \in \mathbf{J}_i} \omega_{ij} |\tau_{ij} - \delta \bar{\tau}_{ij}|, \quad \omega_{ij} = \left(\frac{N_{ij}}{\sum_i N_{ij}} \right) \left(\frac{D_j}{\sum_j D_j} \right) \quad (10)$$

$$D_j = \sum_n \lambda_{jn}^* \quad \forall j \quad (11)$$

$$N_{ij} = \sum_n X_{ijn}^* \quad \forall i, j \in \mathbf{J}_i \quad (12)$$

where, X_{ijn}^* is the solution of the LP relaxed model of the first stage, and λ_{jn}^* is the dual variable associated with the allocation constraints (Eq. 9 in Shah et al. (1993)) in the LP relaxed model.

As shown in Figure 1, $\varepsilon(\delta)$ is an accurate metric to quantify the amount of discretization error introduced. Specifically, DCA obtains high quality first and third stage solutions, whenever δ 's that lead to low values of $\varepsilon(\delta)$ are used. Although only shown for two instances, we observed similar results for all other instances tested.

4. Generating multiple solutions

In industrial applications, it is desired to obtain multiple solutions rather than just one. By having multiple options, the operators can choose a schedule that minimizes the potential risks that may arise from the discrepancy between the problem data and the actual plant operation conditions.

DCA offers a systematic way of obtaining multiple solutions with varying degrees of accuracy in problem data approximation. This can be achieved by running DCA with different δ 's that are identified by our method (see Figure 1). More importantly, depending on the δ chosen, the users have the flexibility to decide which problem data (e.g. processing time of a specific task) to approximate more accurately.

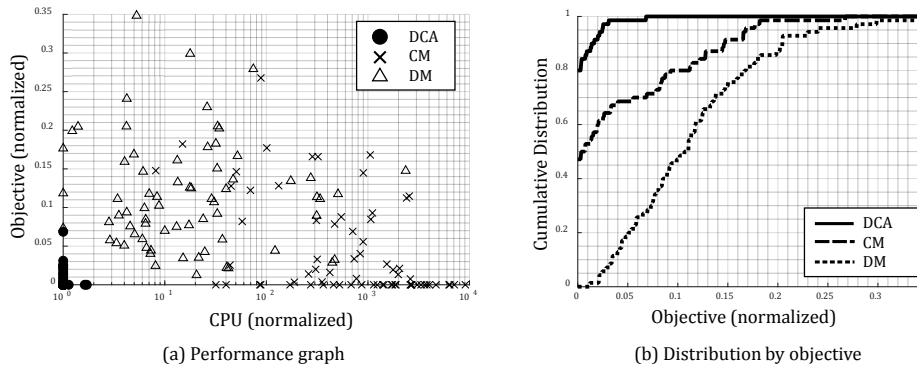


Figure 2: Performance comparison between the three approaches, DCA, DM and CM: (a) performance graph, and (b) distribution by objective value

5. Computational study

5.1. Performance test

We compare the performance of DCA with systematically determined δ against a discrete-time model (Shah et al., 1993) and one of the best performing continuous-time model (Sundaramoorthy and Karimi, 2005), denoted as DM and CM, respectively. We consider 7 networks from the literature with 10 variations each (total of 70 instances).

Figure 2a shows the performance of the three approaches. The abscissa of the graph represents the CPU time normalized with respect to the fastest approach, while the ordinate represents the objective value normalized with respect to the best. In terms of computational speed, DCA outperforms the other two approaches by up to 4 orders of magnitude. Figure 2b shows the cumulative distribution of instances as a function of normalized objective value. DCA finds the best solutions in 80% of the instances, and high quality solutions (i.e. 0~3% inferior than best found) in 98% of the instances. In general, DCA yields substantially better and often rather different schedules compared to the other approaches.

5.2. Case study

A network from (Papageorgiou and Pantelides, 1996) that consists of 19 tasks performed on 8 units producing 4 products is considered (Figure 3a). The objective is to minimize makespan while satisfying a given demand until the end of 120 h horizon. The example is solved using three different approaches, and the results are given in Table 2. DCA with $\delta = 1.85$ h finds the best solution of 56.4 h in less than 4 seconds, being the fastest approach (see Figure 3b).

Table 2: Computational results

	DM	CM	DCA
δ or #Slots	1.00	25	1.85
Constraints	8,550	5,732	4,598
Disc. Var.	2,156	742	1,166
Cont. Var.	4,782	4,829	2,577
LP Relax.	5.9	43.2	10.3
Obj (h)			59.2
(Refined)	62	57	56.4
CPU (s)	35.1	18,000.1	3.8
Nodes	1,872	$>10^5$	2,291
Gap (%)	-	13.5	-

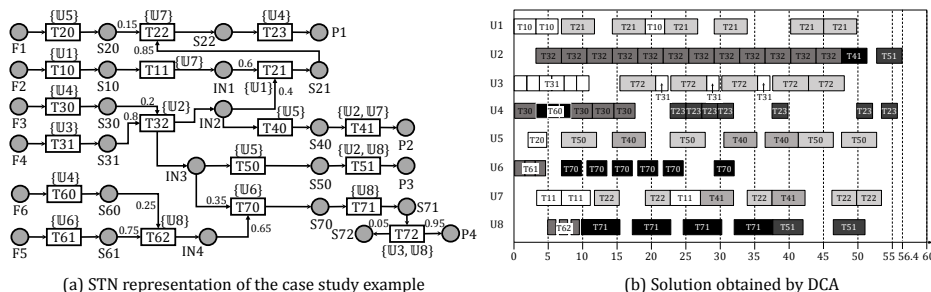


Figure 3: Case study: (a) STN representation, and (b) solution obtained by DCA

6. Conclusion

The two types of grids adopted in grid-based mathematical programming models for chemical production scheduling exhibit distinctive advantages. Discrete-time models are generally faster and have higher modeling flexibility, while continuous-time models provide more accurate solutions.

In this work, we proposed a new solution algorithm, namely the Discrete-Continuous Algorithm, that enable us to exploit the advantages of both time grids. DCA is capable of obtaining accurate solutions fast, while also allowing us to model different process characteristics, such as intermediate shipments and deliveries, limited shared utilities, etc. In addition, we proposed a systematic method to choose the discretization step length, δ , used in the first stage model, which has a significant impact on the performance of DCA. Furthermore, DCA offers a systematic way to generate multiple alternative solutions with varying degrees of accuracy in problem data approximation.

Through computational study, it was shown that DCA is capable of finding high quality solutions much faster than stand-alone discrete- and continuous-time models. Specifically, we showed that it finds the best solution in 80% of test instances while being up to 4 orders of magnitude faster.

References

- C. A. Floudas, X. X. Lin, 2004. Continuous-time versus discrete-time approaches for scheduling of chemical processes: a review. *Computers & Chemical Engineering* 28 (11), 2109–2129.
- E. Kondili, C. C. Pantelides, R. W. H. Sargent, 1993. A general algorithm for short-term scheduling of batch-operations – I. MILP formulation. *Computers & Chemical Engineering* 17 (2), 211–227.
- H. Lee, C. T. Maravelias, 2018. Combining the advantages of discrete- and continuous-time scheduling models: Part 1. framework and mathematical formulations. *Computers & Chemical Engineering* 116, 176–190.
- L. G. Papageorgiou, C. C. Pantelides, 1996. Optimal campaign planning scheduling of multipurpose batch semicontinuous plants .2. A mathematical decomposition approach. *Industrial & Engineering Chemistry Research* 35 (2), 510–529.
- N. Shah, C. C. Pantelides, R. W. H. Sargent, 1993. A general algorithm for short-term scheduling of batch-operations – II. computational issues. *Computers & Chemical Engineering* 17 (2), 229–244.
- A. Sundaramoorthy, I. A. Karimi, 2005. A simpler better slot-based continuous-time formulation for short-term scheduling in multipurpose batch plants. *Chemical Engineering Science* 60 (10), 2679–2702.
- A. Sundaramoorthy, C. T. Maravelias, 2011. Computational study of network-based mixed-integer programming approaches for chemical production scheduling. *Industrial & Engineering Chemistry Research* 50 (9), 5023–5040.

A steady-state and dynamic simulation tool for solid oxide fuel cell operation applications

Amirpiran Amiri,^{a,*} Khaliq Ahmed,^b Moses O. Tadé^b

^a*European Bioenergy Research Institute (EBRI), School of Engineering and Applied Science, Aston University, Birmingham, B4 7ET, United Kingdom*

^b*Centre for Process Systems Computations, Department of Chemical Engineering, Curtin University, Kent Street, Bentley, WA 6102, Australia*

a.p.amiri@aston.ac.uk

Abstract

A modular simulator of dynamic behaviour of the Solid Oxide Fuel Cell (SOFC) system, suitable for use as a training tool is presented in this article, as an alternative to expensive practical tests. This simulator, developed in Aspen Custom Modeller (ACM), captures all of the processes in an SOFC module: mass, energy, and charge balances, overpotentials, ohmic losses and electrochemical reaction kinetics. The challenges relevant to programming and mathematical skills needed for models deployment are minimised. Application of the simulator is demonstrated through i) a basic steady-state simulation and 1D optimisation followed by estimation of the stack's distributed variables and ii) illustration of the transient behaviour of the SOFC unit. Interpretation of SOFC operation dynamics, in particular, is emphasised to show the effectiveness of the simulator for training purposes and for laboratory demonstrations. The results show the key features of the SOFC module simulator for practical applications and for virtual laboratories. It also opens up opportunities for developing an in-built SOFC simulator module in a flowsheet simulation software such as Aspen Plus and Aspen HYSYS.

Keywords: SOFC, Simulator, Dynamic, Laboratory, ACM,

1. Introduction

Fuel cell, an emerging technology for future green energy production, is an active area of interest as a teaching unit and for research at chemical engineering departments at universities and industrial research and development (R&D) laboratories worldwide (Baker and Açar, 2011). The expensive fuel cell test rigs have been used for cutting-edge research and occasionally for training purposes. However, lower cost, simplicity, safety, and speed are some of the advantages of numerical simulators compared to the experimental set-up. Moreover, convenient access to a computational tool, in contrast to the real-life experimental set-up, resolves the space and time limitations that are usually a hindrance to laboratory-based work (Aguiar et al., 2005, Lai et al., 2011). Since fuel cell is at its infancy stage, there is a shortage in existence of efficient and user-friendly simulators for it. Aspen Custom modeller (ACM) is used in this paper to develop a user-friendly SOFC simulator as depicted in Figure 1. The mathematical model that predicts the cell performance and behaviour has been demonstrated in our previous work (Amiri et al., 2015). The model provides user with the flexibility needed for an insightful simulation of an SOFC module, as dominant process variables and simulation parameters

are conveniently accessible. The user first sets the main model parameters such as the SOFC configuration parameters. This involves the SOFC physical dimensions and the thermal and electrical properties of its material. Operating conditions such as the cell operating voltage, air and fuel flows and the temperatures at the cell inlet, are also among the user-specified information. The thermal and electrical metrics are the main output of the simulator. The module is modifiable, as its programming interface is readily accessible. In order to estimate the species and mixtures properties, *Aspen Properties* and *ACM* are integrated. Such a modelling framework—founded on the application of ACM for SOFC and other types of fuel cells – contributes to this new technology process taking advantage of the established in-built unit operations and the thermodynamical property estimation packages.

2. Demonstration of the capabilities of the Simulator

The simulator developed in this work is demonstrated by carrying out a number of case studies, which are presented below.

2.1. Case study I: Lumped parameter simulation of SOFC

Extraction of essential characteristic information including V-I data is always the preliminary step for the evaluation of fuel cell performance and for an assessment of the model's accuracy. In practice, it can be accomplished through ramping the operating voltage and recording the corresponding current. Normalisation of the estimated current, i.e., current/area, allows comparing cells/stacks with different sizes. Interpretation of the V-I characteristic curve and its connection to the underlying fundamental processes is critical in training and research applications. The V-I simulation results using the simulator developed in this work (Figure 1) is compared against experimental data as shown in Figure 2(a). The simulator is capable of generating V-I curves under various operating conditions as shown in Figure 2(b). Supporting data including detailed information for streams and cell internal variables allow further evaluation of the cell's performance. Figure 2(c) shows the variation of fuel utilisation, caused by a change in the operating current at constant voltage, when the inlet temperature is varying.

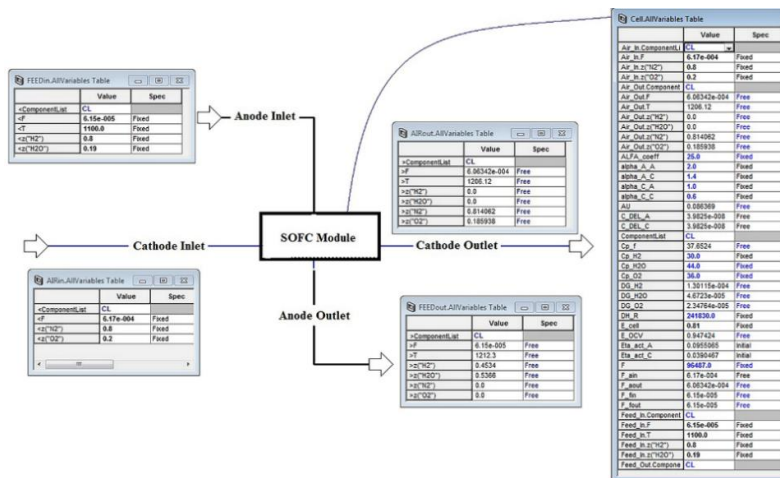


Figure 1: User-friendly SOFC simulator interface developed in ACM.

Since a lumped parameter analysis is presented in this section of the paper, the fuel-air flow configuration does not play a role in this case study. However, the flow pattern is important in the distributed parameter simulations that are presented in the following sections. In all of the cases presented in this work, the cell is assumed to operate adiabatically. Moreover, cell-to-cell and cell-to-surroundings heat transfer are ignored in this model, assuming a well-insulated stack.

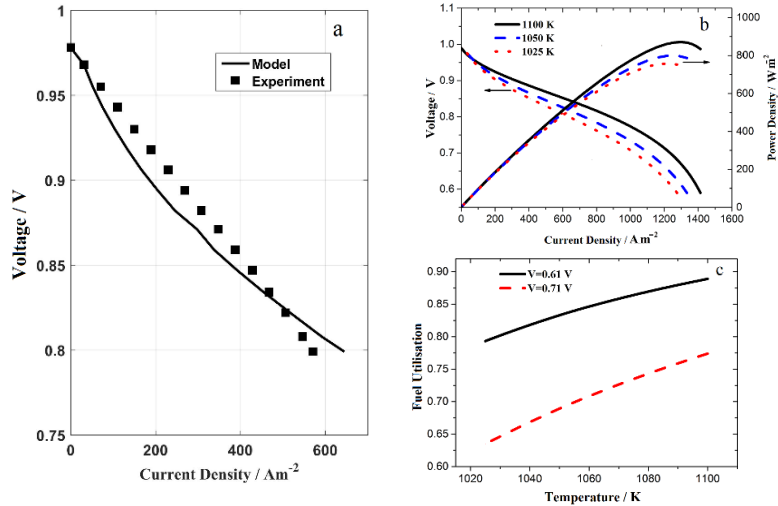


Figure 2: (a) Model validation using data from Tang et al. (2016); (b) Illustrative generation of V-I characteristics profile for different fuel temperatures

by using modular simulator capable of describing voltage losses regions; (c) cell's fuel utilisation for a range of fuel temperatures and under two operating voltages.

2.2. Case Study II: Distributed parameter simulation of SOFC

Visualisation of the distributed variables along the stack dimensions provides an illustrative tool to present the impact of system's variables on cell/stack performance homogeneity. This feature is of practical importance for process analysis of the entire system along with the stack's distributed variables. For 2D and 3D simulation, researchers have used CFD (Ni, 2013), COMSOL modelling facilities (Lai et al., 2011), finite volume model (Ma et al., 2015), and specifically developed tools (Khaleel, 2012). This type of analysis, however, still faces geometry complexity and calculation load challenges making their applications limited to the specific expertise and computational powers. This paper proposes an approach for capturing the stack's distributed variables in *Aspen Plus*, with drastically reduced computational time, approximately of the same order of magnitude of time needed for the simulation of other BoP components. Networking of 0D compartments allows simulating the SOFC as a more realistic reactor as internal spatial distributions of the state variables always exist. This is a straightforward task after exporting the developed module (Figure 1) from the *ACM* environment to the *Aspen Plus* environment. The number of compartments in series, however, must be estimated based on experimental Residence Time Distribution data (Amiri et al., 2015). The distributed parameter model is used to optimise the air (coolant) supply to each part of a cross flow SOFC to achieve a lower temperature variation across the cell. Optimum design and operation of SOFC needs to be examined against the performance characteristics

measures including, durability, reliability and efficiency (Secanell et al., 2011). Some of these targets are to some extent mutually exclusive. For example, high efficiency necessitates operation at high fuel utilisation but may detrimentally impact on the SOFC lifetime, potentially due to the high rates of degradation at the higher levels of utilisation. Durability also depends on the reduction of thermal stresses. This can be achieved by using surplus coolant gas but the system efficiency will reduce as a consequence of the parasitic loss (Tang et al., 2016). From this viewpoint, the optimisation task for either the stack or the system as a whole is a multi-objective optimisation problem with some compromise in operational measures. The optimisation task in this article is an user-defined single objective function (Eq. (1)),

$$\min f = \frac{1}{\bar{T}} \sqrt{\sum_{i=1}^n (T_i - \bar{T})^2}, \quad \bar{T} = \frac{1}{n} \sum_{i=1}^n T_i \quad (1)$$

with the constraint: each compartment must receive at least 5% of total air preventing oxygen starvation, where T_i and \bar{T} stand for local and average temperature of the compartment, respectively. Figure 4 depicts the PEN (Positive electrode-Electrolyte-Negative electrode) temperature profile along the cell's length under different total excess air and with normal and optimised air flow distributions. As can be seen, this strategy is more influential at the lower range of the excess air flows. The wavy temperature profile in Figure 3(a) might be attributed to the discretisation method which is a limitation for developing the distributed models inside the flowsheeting platform. Either increasing the number of intervals or interpolating the values inside the intervals resolves such a flaw as can be seen in Figure 3(b). However, it must be noted that the profiles' trends suffice for schematically presenting the overall performance of the objective function and optimisation effort in a training task.

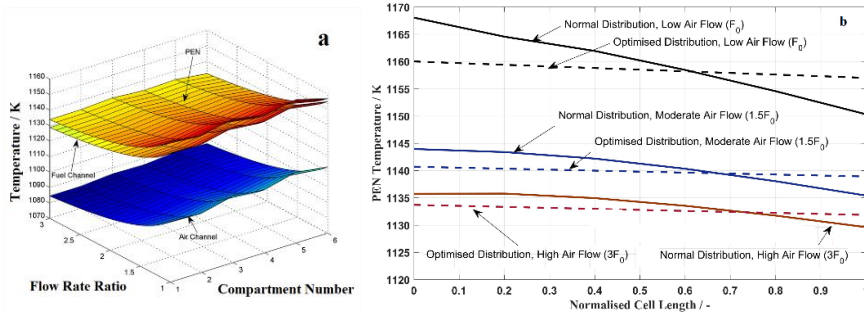


Figure 3. 3D and 2D presentations of the temperature gradient minimisation along the fuel flow path by coolant (air) distribution strategy and for different coolant's flow ratio (ratio of flow to basis-flow).

2.3. Case Study III: Transient simulation of SOFC

The open loop responses of current density, solid temperature, hydrogen concentration, voltage losses, and air/fuel utilisations, upon the inlet gas temperature changes in a stepwise pattern, are shown in Figure 4. Variation of ± 20 K in the inlet gas temperature significantly impacts the cell's dynamics and also the final steady values of the state variables. The significant increase in the PEN temperature has its roots in two causes,

namely the decline in cooling rate due to use of the hotter air, +20 K, and the extra heat released from the promoted exothermic electrochemical reaction. The rate of reaction increases as a result of the increase in the PEN temperature. A feature of the transient temperature behaviour is the equality of absolute value of the final temperature change ($\approx 36\text{K}$) and also the settling time ($\approx 200\text{s}$), for both, negative and positive inlet changes. From this viewpoint it might be concluded that the solid's temperature responses are almost linear. However, the average current shows under- and over-shoots which are not equal in absolute values. This is the case for the hydrogen concentration and OCV histories too. The trainee could explore and interpret the connection between these observations to understand how a non-linear system may behave in unstable circumstances. For instance, the presented scenario indicates the impact of the initial temperature in estimation of the current value at the moment of change implementation. In other words, the higher the difference between initial and final values of the temperature, the more significant is the under/over-shoots in current and other temperature-dependent profiles. Explanation of the dynamic observations based on the utilised empirical and physical correlations allows for the demonstration of the application of these predictive equations. As an example, one may focus on the OCV profile aiming to explain the connection between this voltage and the state variables' profiles based on the Nernst equation. OCV profile, Figure 4, is a strong function of temperature and the species concentration changes. Explanation of reaction rates by using the current profile along with the temperature and concentration histories is another learning practice. Analysis of the dynamic voltage losses will lead to a detailed understanding of the share of each term in the total voltage losses and thus the operating voltage dynamics. A stable operation requires the voltage fluctuations to be minimised. Since oscillations in the operating voltage are caused by instability in OCV and overpotentials, an insight of the time-dependent weight of each term of voltage equation (i.e., OCV, anode and cathode activation loss, concentration loss, ohmic loss) can help to understand the voltage element(s) that dominate(s) the operating voltage dynamics and to propose control strategies for steady operation of the SOFC.

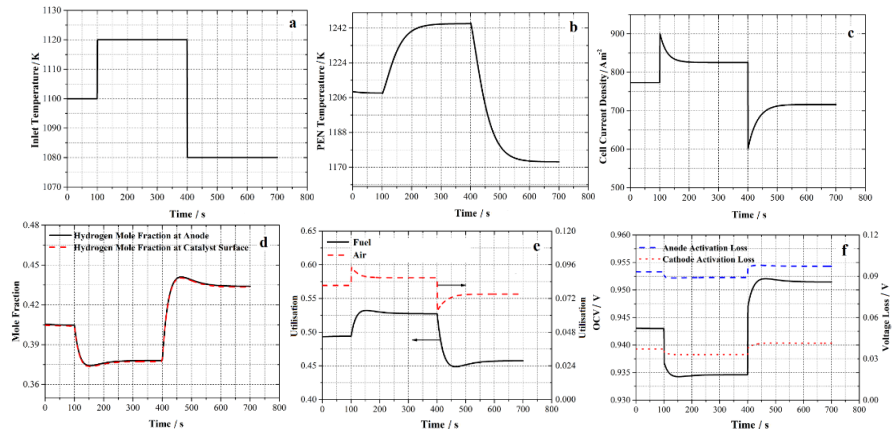


Figure 4. Dynamics of the SOFC state variables in response to a stepwise change in the inlet gases temperature.

3. Conclusions

This article provides an effective modelling simplification without compromising the dominant SOFC process phenomena. Complicated mathematics and the necessity of professional numerical skills make the application of academic models difficult particularly for non-academic users. This is an important motivation to develop simulators that reduces the demand of such skills for applied purposes. Compared to the literature, for instance the authors' previous publications (Amiri et al., 2015, 2016), the simulation approach presented in this work offers a considerable simplicity without sacrificing the model details. While the formers are beneficial for technical research purposes, the later, this work, is beneficial for both training and research. ACM further offers advanced applications including, but not limited to, model predictive control, process optimisation, knowledge based decision-making, model-based fault diagnosis, and process flowsheet simulation which makes it a very effective and convenient tool for intelligent automation of fuel cell process operations. The dynamic analysis presented in this article was to demonstrate this.

References

- P. Aguiar, C.S. Adjiman, , N.P. Brandon, , 2005, Anode-supported intermediate-temperature direct internal reforming solid oxide fuel cell: II. Model-based dynamic performance and control, *J. Power Sources*, 147, 136-147.
- A. Amiri, P. Vijay, M.O. Tadé, K. Ahmed, G.D. Ingram, V. Pareek, R. Utikar, 2015, Solid oxide fuel cell reactor analysis and optimisation through a novel multi-scale modelling strategy, *Comput. Chem. Eng.*, 78, 10-23.
- A. Amiri, P. Vijay, M.O. Tadé, K.Ahmed, , G.D. Ingram, V. Pareek, R. Utikar, 2016, Planar SOFC system modelling and simulation including a 3D stack module, *Int. J. Hydrogen Energy*, 41, 2919-2930.
- D.K. Baker, E. Ađar, 2011, International Summer Engineering Program on fuel cells for undergraduate engineering students, *Int. J. Hydrogen Energy*, 36, 3712-3725.
- M. Khaleel, 2012, Overview of SOFC Modeling and Simulation: Recent Progress, 13th Annual SECA Workshop, National Energy Technology Laboratory, Pittsburgh, PA.
- K. Lai, B.J. Koepfel, K.S. Choi, K.P. Recknagle, X. Sun, L.A. Chick, V. Korolev, M. Khaleel, 2011, A quasi-two-dimensional electrochemistry modeling tool for planar solid oxide fuel cell stacks, *J. Power Sources*, 196, 3204-3222.
- T. Ma, M. Yan, M. Zeng, J.-l. Yuan, Q.-y. Chen, B. Sundén, Q.-w. Wang, 2015, Parameter study of transient carbon deposition effect on the performance of a planar solid oxide fuel cell, *Appl. Energy*, 152, 217-228.
- M.Ni, 2013, Modeling and parametric simulations of solid oxide fuel cells with methane carbon dioxide reforming, *Energy Convers. Manage.*, 70, 116-129.
- M. Secanell, J. Wishart, P. Dobson, 2011, Computational design and optimization of fuel cells and fuel cell systems: A review, *J. Power Sources*, 196, 3690-3704.
- S. Tang, A. Amiri, P. Vijay, M.O. Tadé, 2016, Development and validation of a computationally efficient pseudo 3D model for planar SOFC integrated with a heating furnace, *Chem. Eng. J.*, 290, 252-262.

Thermal conductivity prediction of molten salt-based nanofluids for energy storage applications

B.H. Mahmoud^{a*}, L.F. Mortimer^a, M. Fairweather^a, H.P. Rice^a, J. Peakall^b,
D. Harbottle^a

^a*School of Chemical and Process Engineering, and* ^b*School of Earth and Environment, University of Leeds, Leeds LS2 9JT, UK*

**bgv9bm@leeds.ac.uk*

Abstract

Molten salt-based nanofluids (nano-salts) form an important class of thermal fluids that can act as both heat transfer and thermal energy storage media for high temperature applications, including solar thermal systems. Among these, the class of binary nitrate salts (60:40 wt. % NaNO₃:KNO₃) and their mixtures with metal oxide nanoparticles are the most prominent. This study evaluates the stability of nano-salts using a computational technique based on Lagrangian particle tracking, with the model considering the motion of solid nanoparticles suspended in a molten fluid. The technique enables various multiscale forces, with different characteristics, to be established. The system considered consists of 25-71 nm Al₂O₃ ceramic nanoparticles at volume fractions ranging from 1.0 to 5.0% suspended in fluids of different density ratios, with homogeneous temperature distributions from 250-600 °C. The simulation results demonstrate the effectiveness of the technique, with predictions elucidating the role of oscillatory structural, Brownian motion and particle collision forces, and their influence on the enhancement of thermal conductivity. The liquid structuring of salt melts around the embedded nanoparticles is found to play a key role in the nano-salts' thermal behaviour, with predictions in agreement with previous theoretical and experimental studies. The outcome of this research forms the basis for the potential use of nano-salts in solar thermal systems.

Keywords: Nanofluids, oscillatory structural force, thermal conductivity, energy storage.

1. Introduction

Binary mixtures of NaNO₃:KNO₃, like many other salts, contain ionic compounds such as sodium (Na⁺), potassium (K⁺) and nitrate (NO₃⁻) ions and are, therefore, classified as alkali metal nitrates. When two nanoparticles (with smooth surfaces) are immersed in an ionic liquid such as molten nitrate salt, an oscillatory force exists between the particles due to the ordering of the confined liquid molecules in the thin film between the two surfaces. Theoretical predictions demonstrate that the ordering of liquid molecules reaches an energetic minimum at separations which correspond roughly to the diameter of a liquid molecule, as illustrated in Fig 1. At present, little is known about the thermal properties of this interfacial layer, however, theoretical analyses and numerical simulations predict that it acts as a thermal bridge, particularly in high temperature ionic fluids like molten salts. It is believed that these layered fluid molecules are in an intermediate physical state between that of the bulk fluid and the solid surfaces, thus

forming a solid-like nanolayer of liquid molecules which leads to higher thermal conductivity than that of the bulk fluid (Choi, 2003).

In this study, a novel method is used to describe the oscillating layered structure of molten salt fluids (represented by the matrix of liquid molecules around the nanoparticles), and the influence of the interfacial layer thickness on the system conductivity. An explanation of this phenomenon was first given by Israelachvili (2011) who noted that the structural force arises once there is a change in the liquid density at the surface of nanoparticles, as they approach one other. This force may be thought of as the van der Waals force at small separations, with the molecular properties and density variations of the medium taken into account. This force is consequently dependent on the size, type and surface properties of the particles as well as the ionic concentration and density of the continuum.

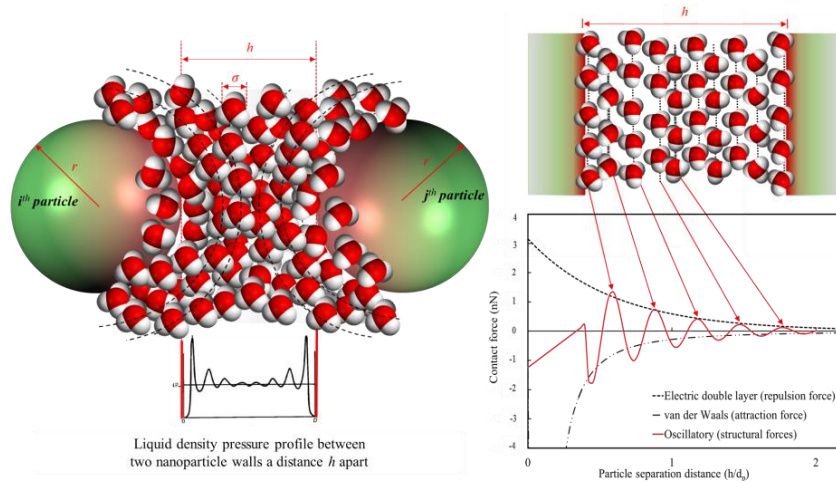


Figure 1. Schematic of structuring of molten nitrate molecules between two smooth spherical particles submerged in an ionic continuum (left); and period of force, i.e. diameter of small liquid molecules, causing oscillatory structural forces with monotonically decaying amplitude (right).

2. Computational Setup and Model Description

This work extends previous simulations (Mahmoud et al, 2018) performed using an in-house code embodying the multiscale numerical model. The model applies a Lagrangian particle tracking approach to investigate the dynamics of, and heat transfer mechanisms in, high temperature salt-based nanofluids. The three-dimensional computational region examined consists of a $1 \mu\text{m}$ cube filled with stagnant molten nitrate salt. This volume element is composed of a collection of 25-71 nm Al_2O_3 ceramic nanoparticles (50-1500 in number) that are injected uniformly across the domain. The motion of the embedded nanoparticles in the fluid is treated using an Eulerian-Lagrangian approach with fixed time stepping. The dynamic properties of both phases are coupled to the ambient temperature of the fluid suspension, that being molten nitrate salt at $250\text{-}600^\circ\text{C}$.

The model describes the dynamic interactions between the i -th and j -th spherical nanoparticles in the normal unit direction, \mathbf{n}_{ij} , according to the approach of Fujita and Yamaguchi (2007). Particle collisions are resolved using a soft sphere approach as

described by the Hertzian normal contact theory (Timoshenko and Goodier, 1970). The oscillatory structural force is considered by adding an extra term, Π^{os} , to the classical DLVO expression for the disjoining pressure (Denkov and Kralchevsky, 1995):

$$\Pi(h) = \Pi^{vW}(h) + \Pi^{el}(h) + \Pi^{os}(h) \quad (1)$$

where Π^{vW} is the van der Waals attractive force:

$$\Pi^{vW} = -\frac{A_H}{6\pi h_{ij}^3} \quad (2)$$

and h is the film thickness, A_H the Hamaker constant, and Π^{el} is the electric double layer repulsive force:

$$\Pi^{el} = \frac{64\pi r n k_b T \theta^2 e^{-\kappa h_{ij}}}{\kappa} \quad (3)$$

Here, r is the sphere radius, n the number density of electrolyte ions, k_b the Boltzmann constant, T the temperature of the suspension, θ the polarisability factor, and κ the inverse of the Debye length.

The dependence of the oscillatory structural component of disjoining pressure on the film thickness can be specified using the formula of Denkov and Kralchevsky (1995):

$$\begin{aligned} \Pi^{os}(h) &= P_0 \cos\left(\frac{2\pi h}{d_1}\right) \exp\left(\frac{d^3}{d_1^2 d_2} - \frac{h}{d_2}\right), \text{ for } h > d \\ \Pi^{os}(h) &= -P_0, \text{ for } 0 < h < d \end{aligned} \quad (4)$$

where σ is the diameter of the smaller fluid hard spheres (≈ 0.45 nm for molten salt molecules), d_1 the oscillatory period and d_2 the characteristic decay length, which are related to the particle volume fraction, φ , as follows:

$$\frac{d_1}{d} = \sqrt{\frac{2}{3} + a_1 \Delta\varphi + a_2 (\Delta\varphi)^2}; \quad \frac{d_2}{\sigma} = \frac{b_1}{\Delta\varphi} - b_2 \quad (5)$$

Here, $\Delta\varphi = \varphi_{max} - \varphi$, with $\varphi_{max} = \pi/3\sqrt{2}$ the value of φ at close packing, and a_1 , a_2 , b_1 and b_2 are correlation coefficients determined theoretically with respect to φ . The particle osmotic pressure, P_0 , is taken from the formula of Carnahan and Starling (1969):

$$P_0 = \rho_s k_b T \frac{1 + \varphi + \varphi^2 - \varphi^3}{(1 - \varphi)^3} \quad (6)$$

in which ρ_s is the particle number density of the small fluid spheres given by $\rho_s = 6\varphi/\pi\sigma^3$. For $h > \sigma$ the structural disjoining pressure oscillates around P_0 as defined in Eq. (6). However, for $h < \sigma$ the small particles are expelled from the gap into the neighbouring bulk suspension by the depletion attraction, described by Eq. (4). When $h = \sigma$ there is a finite discontinuity as the interaction switches from an oscillatory to a depletion regime. The contribution of the interaction free energy per unit area of the film can be obtained by integrating the oscillatory structural forces:

$$f_{os}(h) = \int_h^\infty \Pi^{os}(h') dh' \quad (7)$$

and from Eq. (4) and (7) one obtains:

$$\begin{aligned} f_{os}(h) &= \mathbf{F}(h), \text{ for } h \geq \sigma \\ f_{os}(h) &= \mathbf{F}(\sigma) - P_0(\sigma - h), \text{ for } 0 \leq h \leq \sigma \end{aligned} \quad (8)$$

where

$$\mathbf{F}(h) = \frac{P_0 d_1 \exp(d^3/d_1^2 d_2 - h/d_2)}{4\pi^2 + (d_1/d_2)^2} \left[\frac{d_1}{d_2} \cos\left(\frac{2\pi h}{d_1}\right) - 2\pi \sin\left(\frac{2\pi h}{d_1}\right) \right] \quad (9)$$

It should be noted that although soft sphere particle collisions are assumed, Eqs. (4) and (9) are applicable for hard sphere fluid molecules of diameter σ . However, the interparticle potential may still be ‘soft’ due to the actions of some long range forces.

3. Results and Discussion

Simulations were performed using the model, with results analysed to consider the forces and mechanisms responsible for nanoparticle dynamics, structural and surface property effects, and thermal conductivity enhancement. First, the spontaneous ordering process of nanoparticles in a suspension was examined, followed by the formation of a structured nanolayer (of liquid molecules around the seeded nanoparticles) and of percolation networks of nanostructures using a system under forced aggregation conditions.

A schematic diagram of the structural forces is given in Fig. 1 illustrating the dynamic properties of liquid films confined between two smooth particle surfaces. This shows the concentration dependence of the structural force in the oscillatory regime and how it is dominated by the decay length d_2 , in line with Eqs. (4) and (9). The period of the force is equivalent to the diameter of the small liquid molecules σ , and shows an oscillatory nature close to the particle surface with an amplitude that decays monotonically with h (e.g. for a given h , the disjoining pressure increases almost five times for a 10% increase in the volume fraction ϕ of the liquid molecules). Furthermore, the model predicts the effect of temperature and nanoparticle size on the overall thermal conductivity of the system, with Fig. 2 giving model predictions (coloured) for pure molten salt which are in good agreement with experimental data (Ma and Banerjee, 2017). The figure also gives predictions of thermal conductivities of nanofluids for a fixed concentration of 1 vol. % and temperatures over the range shown. The results are compared with the theoretical work of Maxwell (1892), the data of Ma and Banerjee (2017) and other model predictions (Xuan and Li, 2000; Pang et al., 2016; Prasher et al., 2005), with good agreement found. It should be noted that the existing model showed more sensitivity to particle size in predicting conductivity than the other theoretical models illustrated in Fig. 2

Regarding size dependence, the model predicts that the conductivity of nanofluids containing 20nm Al_2O_3 particles is significantly greater than those containing 25nm and 71nm particles, by nearly 11% and 22%, respectively, although no systematic experimental investigation of size-dependant conductivities has been performed. Fig. 3 shows the thermal conductivity of the nanofluids, normalised by the conductivity of the base fluid, plotted as a function of the solid volume fraction, Φ , for the 71nm Al_2O_3 particles. The results show the contribution of the nanolayer and aggregation, and the nanolayer only, to the thermal conductivity, and how this increases with particle volume fraction. With regards to the effect of the nanolayer, at concentrations < 3 vol. % the majority of nanoparticles collide, although the formation of aggregates remains low. Hence, the thermal conductivity enhancement is dominated by the formation of

nanolayers between particles. At $\Phi \geq 3$ vol. %, however, the combined effect curves show that the conductivity is enhanced by a factor of two to three, and at such concentrations aggregates (nanoclusters) form in addition to the nanolayers between them, although the interparticle distance is very small (0.5-1 nm). This leads to the conclusion that at high concentrations the effect of Brownian motion is dramatically reduced and instead percolation effects dominate due to reduced interparticle distances and increased particle nanolayering and aggregation.

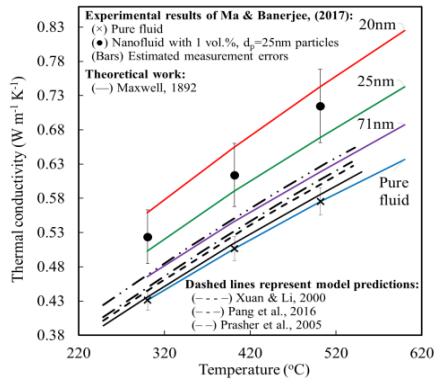


Figure 2. Comparison of model predictions of thermal conductivity with experimental measurements and analytical models for molten salt (Al_2O_3) nanofluids.

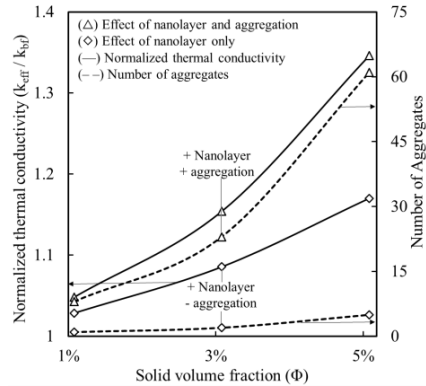


Figure 3. Nanoparticle concentration dependent thermal conductivities of nanofluids and effect of nanolayer and number of aggregates formed at 350 °C.

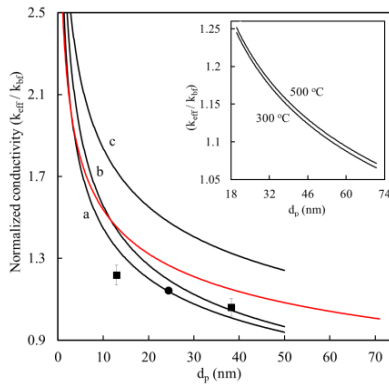


Figure 4. Effect of particle diameter d_p on thermal conductivity ratio. Insert shows conductivity ratio of nanolayer plotted as function of temperature.

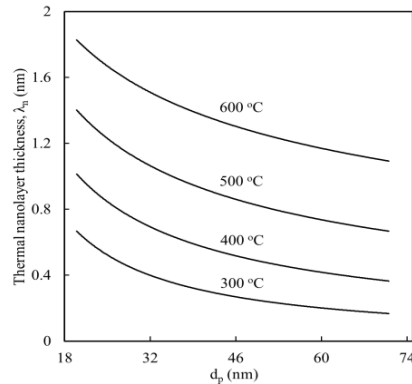


Figure 5. Thermal conductivity ratio of nanolayer as function of particle diameter at fixed concentration of 1 vol. %.

Fig. 4 shows the effect of particle diameter on the thermal conductivity for $\Phi = 1$ vol. %. The predictions indicate that as the particle size is decreased, the interparticle distance decreases and, consequently, conduction-like effects become dominant, increasing the conductivity. The smaller the nanoparticles, therefore, the more the enhancement in the conductivity of nano-salts. Corresponding results for the effect of particle diameter on the nanolayer thickness are given in Fig. 5, with predicted values at different temperatures.

This demonstrates that the thickness of the nanolayer increases with reducing particle diameter, and with temperature due to Brownian motion effects. Hence both particle size and system temperature can be used to enhance the thermal conductivity of nanofluids.

4. Conclusions

Key variables related to the oscillatory structural force acting between two spherical nanoparticles, and the thermal conductivity of salt-based ionic nanofluids, have been examined using multiscale simulation. The thermal properties of nanofluids were found to be enhanced compared to those of the pure molten salt bulk fluid. The model has been found to perform well in comparison with similar studies, and provides confirmation of the effect of interparticle distance, particle concentration, temperature, and the formation of nanolayer and percolation networks, on the thermal conductivity of nano-salts. Future work will extend the current model's application to include the dynamic forces considered to be important in three-dimensional flows, as found in solar thermal heat storage systems, by coupling the tracking approach with direct numerical simulations.

Acknowledgements

BHM is grateful for the financial support of the Kuwait Institute for Scientific Research.

References

- N.F. Carnahan, K.E. Starling, 1969, Equation of State for Nonattracting Rigid Spheres, *J. Chem. Phys.*, 51, 635-637.
- S.U.S. Choi, 2003, Thermal Conductivity of Nanofluids: Vision and Key Features, *Thermal Conductivity 27/Thermal Expansion 15*, 143-152.
- N.D. Denkov, P.A. Kralchevsky, 1995, Colloid Structural Surface Forces in Thin Liquid Films, *Prog. Colloid Polymer Sci.*, 98, 18-22.
- M. Fujita, Y. Yamaguchi, 2007, Multiscale Simulation Method for Self-Organization of Nanoparticles in Dense Suspension, *J. Comput. Phys.*, 223, 108-119.
- J.N. Israelachvili, 1992, *Intermolecular and Surface Forces*, 2nd Edition, Academic Press, London.
- B. Ma, D. Banerjee, 2017, Experimental Measurements of Thermal Conductivity of Alumina Nanofluid Synthesized in Salt Melt, *AIP Advances* 7, 115124.
- B.H. Mahmoud, M. Fairweather, L.F. Mortimer, J. Peakall, H.P. Rice, D. Harbottle, 2018, Prediction of Stability and Thermal Conductivity of Nanofluids for Thermal Energy Storage Applications, *Computer-Aided Chemical Engineering*, 43, 61-66.
- J.C. Maxwell, 1873, *A Treatise on Electricity and Magnetism*, Clarendon Press, Oxford.
- C. Pang, J.W. Lee, Y.T. Kang, 2016, Enhanced Thermal Conductivity of Nanofluids by Nanoconvection and Percolation Network, *Heat Mass Transfer* 52, 511-520.
- R. Prasher, P. Bhattacharya, P.E. Phelan, 2005, Thermal Conductivity of Nanoscale Colloidal Solutions (Nanofluids), *Phys. Rev. Lett.*, 94, 025901.
- S.P. Timoshenko, J.N. Goodier, 1970, *Theory of Elasticity*, McGraw-Hill, New York.
- Y. Xuan, Q. Li, 2003, Investigation on Convective Heat Transfer and Flow Features of Nanofluids, *J. Heat Transfer* 125(1), 151-155.

Nanoparticle behaviour in multiphase turbulent channel flow

B.H. Mahmoud^{a*}, L.F. Mortimer^a, M. Fairweather^a, H.P. Rice^a, J. Peakall^b,
D. Harbottle^a

^a*School of Chemical and Process Engineering, and* ^b*School of Earth and Environment, University of Leeds, Leeds LS2 9JT, UK*

**bgv9bm@leeds.ac.uk*

Abstract

The behaviour of dispersed nanoparticles within a turbulent wall-bounded flow is investigated, with the fluid phase properties chosen to represent a thermofluid flow typical of those present in solar thermal power plants. The continuous phase is modelled using direct numerical simulation with the open source spectral element-based solver, Nek5000, with predictions of a statistically steady turbulent channel flow at shear Reynolds number $Re_\tau = 180$ first obtained and validated. A Lagrangian particle tracking routine is subsequently implemented to simulate the dispersed phase, and is capable of accommodating one-, two- and four-way coupling between the fluid and discrete phases. In order to investigate the effect that the turbulence field has on the dispersion properties of the solid nano-particulate phase, mean fluid and particle velocities, and turbulence statistics, are obtained and presented. Particle mean velocities are observed to lag behind the fluid flow in the outer layer for all coupling methods. Particle streamwise velocity fluctuations are lower than those of the fluid in the bulk region of the flow, but are greater than the latter in the buffer layer, with the addition of particle agglomeration augmenting this effect. Particle concentrations in the near-wall region are observed to increase over time due to turbophoresis.

Keywords: Direct numerical simulation, Lagrangian particle tracking, nanofluids, agglomeration, turbophoresis

1. Introduction

Particle-laden fluids have gained a lot of attention in recent years because of their existing and potential industrial applications. Of particular interest are nanofluids, which are dilute fluid suspensions of nanoparticles (1-100 nm) at relatively low concentrations (0.05-2.0% volume fraction) (Choi, 1995). They are prepared by dispersing nanoparticles with significantly higher thermal conductivity values (i.e. 10-430 $Wm^{-1}K^{-1}$ for pure elements) in conventional thermofluids with modest thermal conductivity (i.e. 0.1-0.6 $Wm^{-1}K^{-1}$ at 25°C) such as water, oil, molten salt or ethylene glycol. Unlike conventional fluids, the significant enhancement of thermal properties when solid nanoparticles are added presents new application opportunities, particularly in the energy sector. In this sector, the efficiency of heat removal and thermal management systems presents the greatest technological challenge. Hence, the heat transfer potential of nanofluids is now gaining interest by researchers and developers in the academic and industrial communities due to their advantageous thermal properties.

On the other hand, understanding transport phenomena such as the dispersion behaviour of particles in nanofluid flows is challenging, particularly in experimental studies where obvious difficulties occur. Hence, apart from constraints due to the size of nanoparticles and potentially difficult conditions (e.g. high temperatures), many other complications arise from the various forces acting on the particles at various magnitudes and time scales. In addition, there is currently a lack of a reliable theory capable of making accurate predictions of the flow and heat transfer behaviour of nanofluids (with relatively low solid volume fractions). A numerical approach is therefore proposed to investigate dispersion behaviour. More specifically, the work described develops a multi-scale computational model using Lagrangian particle tracking coupled with direct numerical simulation (DNS) to investigate the influence of dispersed nanoparticles on the surrounding carrier fluid, and the effect of the turbulence field on the dispersion and aggregation properties of the solid nano-particulate phase. The advantage of the model developed is its ability to study in detail phenomena such as interparticle collisions, turbophoresis and thermophoresis, with the approach also of value in investigations of the long-term stability of nanoparticle dispersions which as yet has not been considered in detail. It is also possible that the agglomeration of nanoparticles to form larger particles could lead to their deposition, surface impact and erosion, although evidence of this in the literature is contradictory (Buongiorno, 2009), with very few existing quantitative studies.

2. Computational Setup and Model Description

The simulations were performed using a numerical multi-scale model with the continuous phase predicted using the open source spectral element-based DNS code, Nek5000 (Fischer et al, 2008). This code was chosen based on its extensive testing, efficient parallelization capabilities and validation history. Within the code, the incompressible Navier-Stokes equations (mass and momentum conservation) are solved to high accuracy, with the code applied to a Cartesian grid consisting of $27 \times 18 \times 23$ 8th order elements (i.e. 5.7 M nodes) used to represent a turbulent channel flow at shear Reynolds number $Re_\tau = 180$. The elements were scaled such that those closest to the wall were distributed more densely. The geometry of the channel was $14\delta \times 2\delta \times 6\delta$, with $\delta = 0.1$ mm. For the purpose of this study, the computational coordinates (x, y, z) were used to represent the three-dimensional geometry of the channel, with x being the streamwise direction, y the wall-normal direction, and z the spanwise direction. Periodic boundary conditions were enforced in the streamwise and spanwise directions, while the wall-normal axis used no-slip conditions at $y = \pm\delta$. The flow was driven and maintained by a constant pressure gradient.

The dispersed phase was represented by 500k 100 nm diameter Al_2O_3 particles which were tracked through the fluid field. These were simulated using a Lagrangian particle tracking routine, which was developed for this work and implemented to interface concurrently with Nek5000. The motion of each nanoparticle is described using the Langevin equation (Sloan et al, 2012), where the translational velocity of the i -th particle is obtained from the principle of conservation of linear momentum. At each timestep, the force on each particle was calculated accounting for the particle contact force, the electric double layer repulsive force, the van der Waals attractive force, the fluid force and the random Brownian motion force. Other body forces such as gravity and buoyancy were found to be negligible for all length and time scales since their magnitudes are much

smaller than the aforementioned surface forces. Further details can be found elsewhere (Mahmoud et al, 2018).

The model described was used to simulate the dynamics and mechanisms responsible for nanoparticle dispersion and aggregation using different levels of coupling. Consideration of solely fluid forces acting upon the particulate phase is known as one-way coupling. Two-way coupling was achieved by implementing the point-source-in-cell method whereby particle forces are fed back to the local fluid cells. Particle collisions (four-way coupling) were resolved using the soft sphere approach, as described by Hertzian normal contact theory (Timoshenko and Goodier, 1970). Finally, four-way coupled predictions were extended to include DLVO interparticle van der Waals attractive and electric double layer repulsive forces to allow the prediction of particle-particle agglomeration events (see Mahmoud et al, 2018). Chemical and mechanical properties were chosen to match Al_2O_3 in water, with the parameters used in the simulations provided in Table 1.

Table 1. Parameters used in the simulations.

Parameter	Carrier phase (water)	Particle phase (Al_2O_3)
Shear Reynolds number, Re_τ	180	-
Bulk Reynolds number, Re_B	2800	-
Particle diameter, d_p / nm	-	100
Number of particles, N_p	-	500,000
Volume, V / m^3	1.58×10^{-10}	4.07×10^{-13}
Volume fraction, Φ / vol %	-	0.26
Temperature, T / $^\circ\text{C}$	25	25
Bulk velocity, U_B / m s^{-1}	25.67	25.68
Density, ρ / kg m^{-3}	997.1	3850
Viscosity, η_F / $\text{m}^2 \text{s}^{-1}$	0.917×10^{-6}	-

The simulations were first run as an unladen single-phase flow using a standard initial turbulence profile with added chaotic terms in the wall-normal and spanwise directions. Once turbulence was established, fluid statistics were monitored every 1.95 ns until the mean and fluctuating velocities reached a statistically steady state. Particles were then injected uniformly throughout the channel and given an initial velocity equal to that of the local fluid. Particle statistics in the wall-normal direction were obtained by splitting the domain into 120 equal volume cuboidal regions, and by averaging over all particles within each region. The statistics presented below represent those at a state where the near-wall particle concentration was approximately stationary with respect to time. From this steady state condition, two-way coupled runs were started, reducing the fluid and particle time step initially to avoid divergences in the flow field due to the impact of particle forces. Fluid and particle statistics were then recorded to determine when the system had finished responding to the addition of momentum-coupling. Once satisfied, statistics were determined as noted. This approach was repeated to obtain four-way coupled simulations, and results for four-way coupling plus particle agglomeration.

3. Results and Discussion

The results of each simulation were analysed to elucidate the behaviour of the fluid and the nanoparticles within the channel flow. The predictions demonstrated how particle concentrations increased with time in the near-wall regions due to turbophoresis, as illustrated in Fig 1. Preferential concentration of particles within low-speed streaks close to the walls was also noted.

Figures 2 and 3 compare the fluid streamwise mean velocity profile, and normal and shear stress profiles, for the single phase flow with those obtained by Moser et al. (1999) who also used DNS, with excellent agreement obtained.

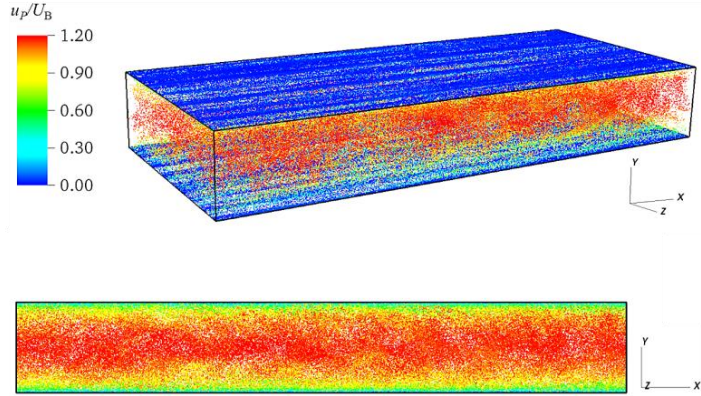


Figure 1. Particle distribution within $Re_t = 180$ channel flow, colours indicate particle to bulk velocity ratio, u_p/U_B (top); and snapshot of streamwise particle velocity on vertical plane (bottom).

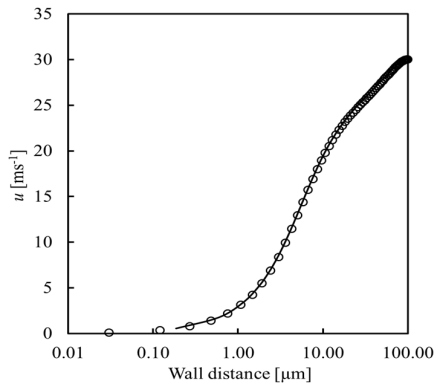


Figure 2. Comparison of fluid streamwise mean velocity profiles (— present, \circ Moser et al, 1999).

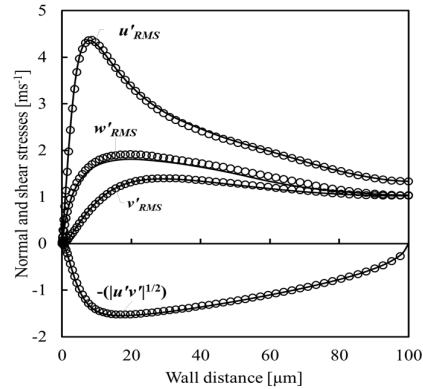


Figure 3. Comparison of fluid normal and shear stress profiles (— present, \circ Moser et al, 1999).

Figure 4 compares the particulate phase streamwise mean velocity against that of the unladen flow for each coupling mechanism considered. It is observed that for all the coupled cases, the particles lag slightly behind the unladen fluid flow between the turbulent region and the channel centre. This indicates that the coupling and interaction mechanisms all have a slight effect on the mean streamwise motion of the particles, albeit of the same order. However, Fig. 5 shows the root-mean-square of the velocity fluctuations, a measure of turbulence intensity, in each coordinate direction. In this case it is clear that for two-way and four-way coupling, the particulate phase exhibits similar velocity fluctuations in all three directions. More specifically, reduced turbulence fluctuations are observed compared to the single phase in the spanwise and wall normal directions, whilst the streamwise normal stress is greater in the turbulent region of the flow, but lower close to the channel centre. On introduction of the DLVO attractive and

repulsive forces, a further slight increase in the streamwise normal stress is observed which is most significant in the turbulent region. This is likely due to the aggregation of particles in this region which leads to increased particle inertia due to their larger size, with such particles exhibiting greater decoupling from the local fluid velocities.

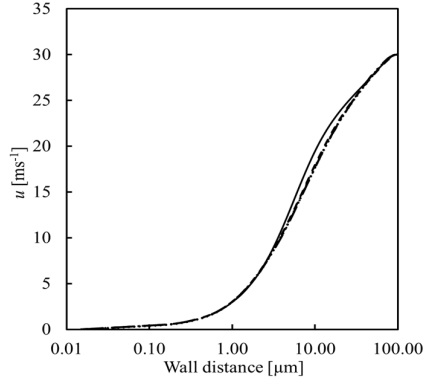


Figure 4. Comparison of streamwise mean velocity profiles (— unladen flow, - - - particles (two-way), ··· particles (four-way), - · - particles (four-way + agglomeration).

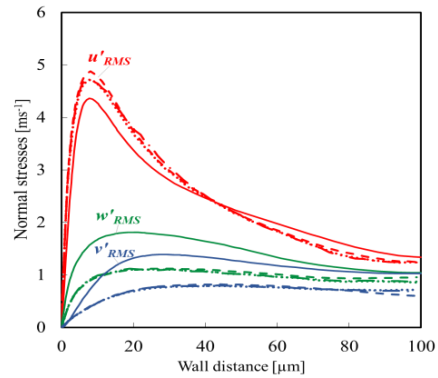


Figure 5. Comparison of normal stresses (— unladen flow, - - - particles (two-way), ··· particles (four-way), - · - particles (four-way + agglomeration).

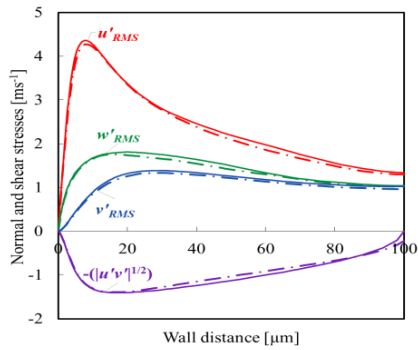


Figure 6. Fluid normal and shear stress profiles (— unladen flow, - · - two-way).

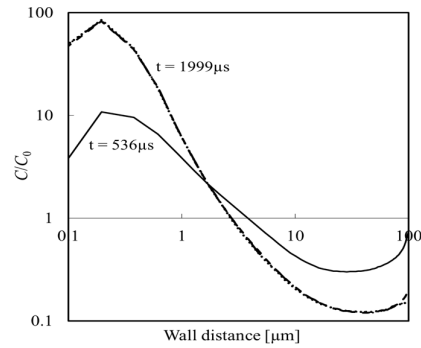


Figure 7. Particle concentration at 536 μ s (— four-way + agglomeration), and 1999 μ s (- · - two-way, ··· four-way, - - four-way + agglomeration).

Figure 6 considers the effect of two-way coupling on the fluid normal and shear stresses in order to determine how the particles modify the turbulence properties of the flow. The results demonstrate that two-way coupling has only a small influence on these statistics. Specifically, all three components of the normal stress and the Reynolds shear stress are attenuated, indicating that the presence of nanoparticles at the concentration considered reduces slightly the magnitude of turbulence in the flow. Since the effect is strongest in those regions which show greatest deviation between particle stresses and those of the unladen flow, this is likely due to greater slip velocities in those regions, meaning that the particles work to dampen the energy in the local turbulent eddies.

Finally, Fig. 7 compares the particle concentration distribution relative to the initial concentration, C_0 , for each simulation. It is clear from the results that over the course of the simulations turbophoresis takes place, with a similar final behaviour observed for all

cases considered. Over time this leads to a build-up of nano-particulate concentrations close to the walls. This has consequences for the agglomeration rate since the local concentration in these regions is nearly 100 times greater than the initial concentration once the system has reached a steady state. This also implies that, with time, particle deposition rates will likely increase due to the migration towards the walls. Interestingly, and despite the slight differences in particle velocity fluctuations for the different coupling mechanisms, there is very little difference in the eventual concentration distributions. This implies that the agglomerate structures do not, over the time studied, show preferential concentration in different regions of the channel when compared to the other particle flows considered.

4. Conclusions

The dispersion properties of a nanoparticle-laden channel flow have been studied using various coupling mechanisms between the particles and the fluid flow. The particles are found to be slightly decoupled from the fluid flow in that they lag behind the mean flow beyond the turbulent region for all coupling regimes. Velocity fluctuations indicate that the particles exhibit increased normal stresses in the streamwise direction in the turbulent region, but reduced values in the other coordinate directions. Interestingly, the inclusion of particle agglomeration increases the magnitude of this effect in the streamwise direction. Two-way coupling is shown to lead to a slight dampening effect on the flow turbulence. Concentration plots also indicate a time varying particle distribution, with a noticeable increase in particle concentration in the near-wall regions over the run times considered that is insensitive to the mode of coupling. Future work will further consider relating the effects observed to the rate of particle collision and agglomeration within the channel in order to better understand the dynamics which lead to the particle behaviour observed, and to allow conclusions to be reached regarding the implications for thermal energy storage systems using nanofluids.

Acknowledgements

BHM is grateful for the financial support of the Kuwait Institute for Scientific Research.

References

- J. Buongiorno, L. Hu, 2009, Nanofluid Heat Transfer Enhancement for Nuclear Reactor Applications, Proc. ASME. 43918; Second International Conference on Micro/Nanoscale Heat and Mass Transfer, 3, 517-522.
- S.U.S. Choi, 1995, Enhancing Thermal Conductivity of Fluids with Nanoparticles, in Developments and Applications of Non-Newtonian Flows, D.A. Siginer, H.P. Wang (Eds.), FED-V.231/MD-V.66, 99-105, ASME, New York.
- P.F Fischer, J.W. Lottes, S.G. Kerkemeier, 2008, Nek5000 web page <http://nek5000.mcs.anl.gov>.
- B.H. Mahmoud, M. Fairweather, L.F. Mortimer, J. Peakall, H.P. Rice, D. Harbottle, 2018, Prediction of Stability and Thermal Conductivity of Nanofluids for Thermal Energy Storage Applications, Computer-Aided Chemical Engineering, 43, 61-66.
- R.D. Moser, J. Kim, N.N. Mansour, 1999, Direct Numerical Simulation of Turbulent Channel Flow up to $Re_\tau = 590$, Phys. Fluids, 11, 943-945.
- G. Sloan, Z.-G. Feng, K. Bhaganagar, D. Banerjee, 2012, Coupled Direct Numerical Simulation and Experimental Approach to Develop Framework for Nano Fluids, ASME International Mechanical Engineering Congress and Exposition, 7, 2877-2882.
- S.P. Timoshenko, J.N. Goodier, 1970, Theory of Elasticity, McGraw-Hill, New York.

Multi-objective optimisation of chemical processes via improved genetic algorithms: A novel trade-off and termination criterion

Viviane De Buck^a, Carlos André Muñoz López^a, Philippe Nimmegeers^a, Ihab Hashem^a and Jan Van Impe^{a,*}

^a*KU Leuven, Department of Chemical Engineering, BioTeC+ & OPTEC, Ghent, Belgium*

**jan.vanimpe@kuleuven.be*

Abstract

A sustainable chemical process operation often requires optimality with respect to multiple conflicting objectives as economic, societal and environmental aspects need to be addressed. Multi-objective optimisation aims at solving such problems. A single optimal solution for all objectives does not exist as one cannot improve with respect to one objective without worsening with respect to one of the other objectives. The result of a multi-objective optimisation algorithm is hence a Pareto set comprising equally optimal trade-off solutions. In this contribution an improved version of NSGA-II, one of the current state-of-the-art algorithms in evolutionary multi-objective optimisation, is presented and applied to the optimisation of an industrially relevant case. The proposed novel algorithm overcomes, amongst others, one of the major shortcomings of the currently used evolutionary multi-objective optimisation algorithms: the inability to distinguish between solutions based on their trade-off and distribution. This results in a Pareto front cluttered with irrelevant solutions. The performance of the improved algorithm has been evaluated for the multi-objective optimisation of a methane tri-reforming process for methanol production. Three objectives have been studied: (i) minimisation of the total energy demand, (ii) maximisation of the carbon efficiency and (iii) an economic profit function. For this INPROP, the recently developed interface between Matlab and Aspen Plus for multi-objective optimisation of chemical processes, is extended to perform multi-objective optimisation using the proposed method. Up till now, INPROP only exploited scalarisation-based multi-objective optimisation methods. Scalarisation methods convert the multi-objective optimisation problem (MOOP) in a sequence of single objective optimisation problems, which are solved separately using deterministic gradient-based methods. Evolutionary algorithms, like NSGA-II, are vector-based and tackle the MOOP in its entirety. The results obtained with the improved evolutionary algorithm are compared with earlier presented scalarisation-based multi-objective process optimisation results.

Keywords: Multi-objective optimisation, NSGA-II, Evolutionary algorithms, Trade-off, PIT-region, t-domination

1. Introduction

To maintain a competitive position in the current worldwide market, companies need to operate their processes as optimally as possible with respect to different, often conflicting,

objectives (e.g. societal, environmental, and economical aspects). In such case, no one optimal solution exists, and decision makers need to resort to Pareto-optimal solutions. These optimisation problems are called multi-objective optimisation problems (MOOPs) and the solutions of such problems are a Pareto front, comprising all equally optimal trade-off solutions. The decision maker (DM) will choose one optimal solution from the Pareto front as the operating point. Computing (an approximation of) this Pareto front is the main goal when solving a MOOP. It is desirable to produce a diverse Pareto set in a minimal computing time. MOOPs are mathematically challenging problems and are generally solved via the use of dedicated algorithms. The two major algorithm categories are scalarisation methods and vectorisation methods. Since this contribution focuses on vectorisation methods, scalarisation methods will not be further discussed. The interested reader is referred to Das and Dennis (1997, 1998); Messac et al. (2003); Logist et al. (2010) for more information on this type of optimisation methods.

Vectorisation methods use stochastic algorithms to solve a MOOP and tackle the optimisation problem in its entirety (Deb et al., 2002). A sub-field of the stochastic algorithms are the evolutionary algorithms (EA), which are based on Darwin's evolution theory. EAs can generate multiple Pareto-optimal solutions in a single run, making them an excellent choice to solve MOOPs, especially if the decision maker is interested in a diverse set of solutions. Additionally, EAs have no need for derivative information which makes them suitable for black box optimisation. The considered evolutionary algorithm in this article is Non-dominated Sorting Genetic Algorithm-II (NSGA-II) (Deb et al., 2002). NSGA-II is an elitist evolutionary algorithm, equipped with a fast non-dominated sorting algorithm and a crowding distance parameter to obtain a diverse solution set.

The overall goal of this contribution is (i) to present a novel EA that overcomes the shortcomings of the NSGA-II algorithm, (ii) demonstrate its performance in the `INPROP` interface between `Matlab` and `Aspen Plus` and (iii) apply for the tri-objective optimisation of a methane tri-reforming process.

2. Multi-objective optimisation problems

2.1. Mathematical description of a MOOP

The following MOOP formulation is used throughout this article (Das and Dennis, 1997):

$$\min_{\mathbf{u} \in C} \mathbf{F}(\mathbf{x}, \mathbf{u}) = \{J_1(\mathbf{x}, \mathbf{u}) \dots J_M(\mathbf{x}, \mathbf{u})\} \quad (1)$$

with $\mathbf{u} \in \mathbb{R}^{n_u}$ the controls of the considered process, $\mathbf{x} \in \mathbb{R}^{n_x}$ the variables, $J_i(\mathbf{x}, \mathbf{u})$ the i -th objective function ($i \in \{1 \dots M\}$), and with C the constraint solution space:

$$C = \{(\mathbf{x}, \mathbf{u}) : \mathbf{h}(\mathbf{x}, \mathbf{u}) = 0; \mathbf{g}(\mathbf{x}, \mathbf{u}) \leq 0; \mathbf{a} \leq \mathbf{u} \leq \mathbf{b}\} \quad (2)$$

$$\mathbf{y} = [\mathbf{u}^T, \mathbf{x}^T]^T \quad (3)$$

With $\mathbf{h}(\mathbf{x}, \mathbf{u}) : \mathbb{R}^{n_u+n_x} \mapsto \mathbb{R}^{n_e}$ the n_e equality constraints, $\mathbf{g}(\mathbf{x}, \mathbf{u}) : \mathbb{R}^{n_u+n_x} \mapsto \mathbb{R}^{n_i}$ the n_i inequality constraints and $\mathbf{a} \in \mathbb{R}^{n_u}$ and $\mathbf{b} \in \mathbb{R}^{n_u}$ the respectively lower and upper boundaries for the controls. A solution \mathbf{y}^* of the MOOP is Pareto-optimal or non-dominated if there exists no other solution \mathbf{y} for which $\mathbf{F}(\mathbf{y}) \leq \mathbf{F}(\mathbf{y}^*)$ and $\exists k : J_k(\mathbf{y}) < J_k(\mathbf{y}^*)$ with $k \in \{1 \dots M\}$ (Das and Dennis, 1997; Munoz Lopez et al., 2018).

2.2. Non-dominated sorting genetic algorithm II (NSGA-II)

NSGA-II is an evolutionary algorithm developed as an answer to the shortcomings of early evolutionary algorithms, which lacked elitism and used a sharing parameter in order to sustain a diverse Pareto set. NSGA-II uses a fast non-dominated sorting algorithm, sharing, elitism, and crowded comparison. Elitism implies that the best solutions of the previous iteration are kept unchanged in the current one. This significantly increases the convergence speed of the algorithm. Additionally, its use of a fast non-dominated sorting algorithm contributes to a significant reduction of its computational complexity. For more details, the interested reader is referred to Deb et al. (2002).

3. The tDOM-algorithm

Despite its significant improvement in comparison to its evolutionary predecessors, NSGA-II has two major shortcomings: (i) its inability to distinguish between solutions based on their trade-off, and (ii) its use of an arbitrary and problem-irrelevant stopping criterion. The presented novel tDOM-algorithm is based on the general framework of NSGA-II and is developed to remedy these shortcomings. To achieve this, the tDOM-algorithm employs t-domination instead of non-domination, via the introduction of a trade-off function and PIT-regions. This enables the tDOM-algorithm to distinguish between solutions based on their trade-off. Additionally, this allowed for the introduction of a non-arbitrary stopping criterion.

3.1. Preliminaries

PIT-region: Regions of practical insignificant trade-off (PIT-regions) are spatial structures which are constructed around the solutions in the objective space. The dimensions of the PIT-region are defined by a minimal trade-off Δt and distribution Δr . If two solutions are located in each others' PIT-region, both solutions are considered insignificantly different from one another by the DM and therefore one of these solutions can be filtered out of the population set (Mattson et al., 2004).

t-Domination: A solution \mathbf{p} t-dominates solution \mathbf{q} if $\mathbf{F}(\mathbf{p}) \leq \mathbf{F}(\mathbf{q})$, $\exists k : J_k(\mathbf{p}) < J_k(\mathbf{q})$, and $\mathbf{p} \notin PIT(\mathbf{q})$.

Trade-off function: The trade-off function determines the crowdedness of the PIT-regions of the obtained solutions. During the selection step, solutions are additionally sorted in ascending order according to crowdedness of their PIT-region, thus more emphasis is set on high trade-off solutions. Concurrently, the trade-off function establishes whether all the solutions of two subsequent generations are located within each others' PIT-regions. If this is the case, the `stop` Boolean is set to `true`, and the algorithm stops.

3.2. Algorithm description

The tDOM-algorithm uses the NSGA-II framework, but it is equipped with the multi-functional trade-off function that determines the trade-off between solutions and the algorithm's stopping criterion. Hashem et al. (2017) presented the idea of using the trade-off of solutions as a stopping criterion. In their divide and conquer scheme for deterministic algorithms, the exploration of a certain area of the Pareto front is ceased if the generated solutions no longer display the required trade-off or distribution. This idea is adapted for evolutionary algorithms via the PIT-regions in the tDOM-algorithm.

During the first iteration, N initial random solutions are generated in the parent set P_0 , which is used to generate a first offspring set Q_1 ($|Q_1| = N$). Offspring solutions are obtained via crossovers and mutations of the parent solutions. At the t -th generation of the tDOM-algorithm, after offspring solutions are generated, the parent set P_{t-1} and offspring set Q_t are merged into a combined solution set R_t ($|R_t| = 2N$), enabling elitism. Subsequently, the solutions of R_t are sorted into their non-dominated front, and their crowding distance and trade-off are determined. Additionally, the stopping parameter `stop` is determined via the trade-off function. Based on the rank of their non-dominated front, their crowding distance, and their trade-off, only the best N solutions of R_t are retained. These solutions form the parent set P_t of the $(t + 1)$ -th iteration. The tDOM-algorithm is interrupted when the stopping parameter `stop` is set to `true` during the trade-off function.

4. Results and discussion

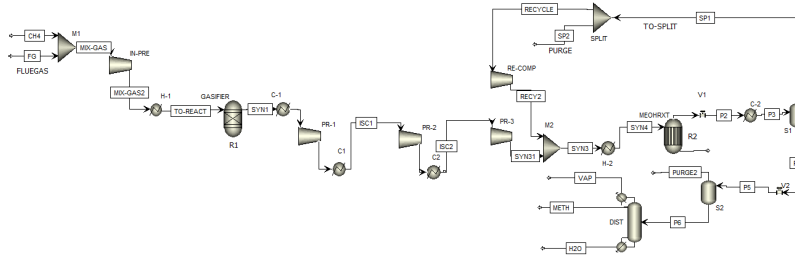


Figure 1: Methanol production via methane tri-reforming (Munoz Lopez et al., 2018).

A methane tri-reforming process converts flue gasses and a methane stream into methanol and water. This process was modelled by Munoz Lopez et al. (2018) in Aspen Plus (see Figure 1). To optimise this process the tDOM-algorithm is implemented in Matlab 2018a. The interface between the process simulator Aspen Plus and Matlab is referred to as INterface for PProcess Optimisation (INPROP) (Munoz Lopez et al., 2018). During the optimisation, the controls \mathbf{u} and variables \mathbf{x} are transferred from Aspen Plus to Matlab. The controls \mathbf{u} are subsequently optimised using the tDOM-algorithm and are send back to Aspen Plus, where the corresponding variables \mathbf{x} are determined and send back to Matlab, continuing the optimisation procedure. This process repeats itself until the stopping criterion is satisfied. Three objectives were optimised, subject to a minimal required methanol purity of 98 % and a maximum methanol fraction of 85 % in the water stream (Munoz Lopez et al., 2018):

$$J_1(\mathbf{x}, \mathbf{u}) = -\frac{[MEOH]_{METH}}{([CH_4] + [CO_2]_{FG})} [-] \quad (4) \quad J_2(\mathbf{x}, \mathbf{u}) = \frac{(|\dot{W}| + |\dot{Q}|)}{([MEOH]_{METH}/3600)} \left[\frac{MJ}{kmol} \right] \quad (5)$$

$$J_3(\mathbf{x}, \mathbf{u}) = -\left(a_1 [MEOH]_{METH} - (a_2 [CH_4] + 3600 \times a_3 (|\dot{Q}| + |\dot{W}|)) - \frac{ann.cc}{8000} \right) [€/h] \quad (6)$$

subject to

$$0 < p_{S1} - p_{S2} \leq 70 \quad (7) \quad 0 < p_{S2} - p_{DIST} \leq 25 \quad (8)$$

$$p_{PR-3} - p_{R2} = 0 \quad (9) \quad 0.98 - [MEOH]_{METH} \leq 0 \quad (10)$$

$$[MEOH]_{H2O} - 0.85 \leq 0 \quad (11)$$

Objective J_1 is the carbon efficiency of the process, with $[MEOH]_{METH}$ the methanol stream [kmol/h], $[CH_4]$ the methane stream [kmol/h], and $[CO_2]_{FG}$ the carbon dioxide in the flue gas stream [kmol/h]. Objective J_2 is the total energy demand required for the production of 1 kmol $MEOH$, with $|\dot{W}|$ the total amount of work [MW], and $|\dot{Q}|$ the total

amount of thermal energy [MW]. Objective J_3 is the profit-cost balance with a_1 the unit price of $MEOH$, a_2 the unit price of CH_4 , and a_3 the unit price of electricity. The obtained results and Pareto fronts are represented in Table 1 and Figure 2 respectively. For more information on the controls, the interested reader is referred to Munoz Lopez et al. (2018).

Table 1: Lower (a) and upper (b) boundaries of the controls \mathbf{u} , anchor points of the Pareto front, and the original problem (adapted from Munoz Lopez et al. (2018)).

Results		a	b	Carbon effic. maximised	Total energy demand minimised	Profit maximised	Original process	Units
Controls	$[CH_4]$	200.00	800.00	345.93	378.80	366.23	400.00	kmol/h
	PR_1	1.05	5.00	1.00	3.74	2.44	1.00	MPa
	TR_1	400	980	980	943	974	850	K
	PR_2	50	300	300	174	52	50	MPa
	TR_2	200	300	200	200	204	220	K
	PS_1	25.00	40.00	40.00	31.80	39.40	24.00	MPa
	TS_1	25.00	50.00	25.00	31.62	26.00	25.00	K
	$[SP2]/[SP1]$	0.05	0.30	0.05	0.30	0.06	0.05	-
	PS_2	20.00	30.00	9.12	9.00	13.00	10	MPa
	$PDIST$	9.00	20.00	9.00	9.00	13.00	10.00	MPa
	$RRDIST$	1.5	3.0	3	1.5	1.5	1.5	-
	$D/FDIST$	0.950	0.988	0.988	0.988	0.980	0.988	-
Objective	J_1	-	-	-0.9546	-0.8432	-0.8442	-0.7584	-
	J_2	-	-	1567.0	994.9	1189.5	1538.8	MJ/kmol
	J_3	-	-	-1078.0	-4244.0	-4407.5	-2537.2	€/h

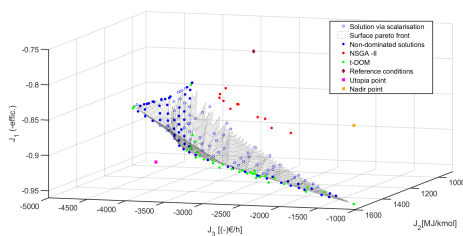


Figure 2: Pareto fronts generated via tDOM-algorithm, NSGA-II, and scalarisation method.

For all the objectives, Δt was defined as 10% and Δr as 15%. Note that in practical applications Δt and Δr can have different values for each objective. The values of Δt_i and Δr_i quantify the importance attached to the i -th objective. Visual analysis of the results displayed in Figure 2 raises two main observations. First, the results obtained via the scalarisation method (blue dots) and the surface interpolated from them seem to offer a well-defined approximation of the Pareto front for this MOOP. However, numerous solutions generated via the scalarisation method are non-Pareto-optimal, and therefore could be misleading for the DM. Logist et al. (2010) confirms this observation by stating that scalarisation methods can be prone to generate non-Pareto-optimal solutions, in contrast to EAs and the proposed tDOM-algorithm. Secondly, if the results generated by the tDOM-algorithm are compared with the results generated with the original NSGA-II algorithm, the tDOM-algorithm outperforms the NSGA-II algorithm. When the same conditions in terms of population size and number of generations were kept for both algorithms, the proposed algorithm converges to the actual Pareto front while the solutions from NSGA-II remain far from it. The normalised average distance to the Utopia point (i.e., all the individual objective minimisers) of the tDOM-solutions is 0.6914, while that of the NSGA-II solutions amounts to 1.0447, placing it significantly closer to the Nadir point (i.e., all the individual objective maximisers). This proves that the proposed tDOM-algorithm overcomes the limitations of the NSGA-II algorithm and produces a more informative Pareto front that is not affected with the presence of non-optimal solutions.

Finally, regarding the numerical results as presented in Table 1, the original process is non-optimal. All the generated solutions result in lower integral costs than those of the reference conditions. For instance, the most carbon efficient solution results in a gain of 20.55%. Strikingly, the energy consumption of this solution is only 1.80% higher than the original process. Despite this, a 57.51% loss in profit is displayed, compared to the original process, making the process economically infeasible. Again, note that the density of tDOM-solutions in this Pareto front area is sparser than in the more economically interesting knee of the Pareto front.

5. Conclusions

A sustainable process requires optimality with respect to multiple, often conflicting, objectives. In such cases, no single optimal solution exists, but instead multiple trade-off solutions. Determining the most optimal solutions is achieved via a multi-objective optimisation problem (MOOP). NSGA-II is a widely applied optimisation algorithm, used to solve MOOPs. However, it is unable to distinguish between solutions based on their trade-off, and it uses an arbitrary stopping criterion. To overcome these shortcomings, the tDOM-algorithm is presented. Via the introduction of regions of practically insignificant trade-off (PIT), solutions with a high trade-off are emphasised. Additionally, by applying the concept of t-domination, the tDOM-algorithm is equipped with a problem-relevant stopping criterion. The advantages of the tDOM-algorithm were demonstrated for the MOO of the methane tri-reforming process. Using the `INPROP` interface it was found that tDOM-algorithm is able of producing a diverse set of relevant Pareto-optimal solutions. This in strong contrast to solutions produced by NSGA-II, which do not converge to the Pareto front, and the solution set generated via a scalarisation method, which is populated with non-Pareto-optimal solutions.

Acknowledgements

This work was supported by KU Leuven Research Fund [PFV/10/002] Center-of-Excellence Optimization in Engineering (OPTEC). CAM holds a VLAIO-Baekeland [HBC.2017.0239] grant. IH is supported by FWO-SB grant 1S54217N.

References

- Das, I., Dennis, J., 1997. A closer look at drawbacks of minimizing weighted sums of objectives for pareto set generation in multi-criteria optimization problems. *Structural Optimization* 14.
- Das, I., Dennis, J., 1998. Normal-boundary intersection: A new method for generating the pareto surface in nonlinear multicriteria optimization problems. *SIAM Journal on Optimization* 8.
- Deb, K., Pratap, A., Agarwal, S., Meyarivan, T., 2002. A fast and elitist multiobjective genetic algorithm: NSGA-II. *Evolutionary Computation, IEEE Transactions on* 6(2), 182–197.
- Hashem, I., Telen, D., Nimmegeers, P., Logist, F., Van Impe, J., 2017. A novel algorithm for fast representation of a pareto front with adaptive resolution: Application to multi-objective optimisation of a chemical reactor. *Computers and Chemical Engineering* 106.
- Logist, F., Houska, B., Diehl, M., Van Impe, J., 2010. Fast pareto set generation for nonlinear optimal control problems with multiple objectives. *Structural and Multidisciplinary Optimization* 42, 591–603.
- Mattson, C., Mullur, A., Messac, A., 2004. Smart pareto filter: obtaining a minimal representation of multiobjective design space. *Engineering Optimization* 36(6), 721–740.
- Messac, A., Ismail-Yahaya, A., Mattson, C., 2003. The normalized normal constraint method for generating the pareto frontier. *Structural and Multidisciplinary Optimization* 25.
- Munoz Lopez, C., Telen, D., Nimmegeers, P., Cabianca, L., Logist, F., Van Impe, J., 2018. A process simulator interface for multiobjective optimization of chemical processes. *Computers and Chemical Engineering* 109, 119–137.

Economic Nonlinear Model Predictive Control of Multi-Product Air Separation Processes

A. Caspari^a, Y. Martin Pérez^a, Chr. Offermanns^a, P. Schäfer^a, A.-M. Ecker^b,
A. Peschel^b, F. Schliebitz^b, G. Zapp^b, A. Mhamdi^a, and A. Mitsos^{a,*}

^a*AVT Process Systems Engineering, RWTH Aachen University, 52056 Aachen, Germany*

^b*Linde plc, Engineering Division, 82049 Pullach, Germany*

amitsos@alum.mit.edu

Abstract

Multi-product air separation units produce important gases such as nitrogen and oxygen from ambient air. Their high electricity demand suggests an economic advantage of flexible operation depending on fluctuating electricity prices. Flexible operation can be achieved using economic model predictive control by solving an economic dynamic optimization directly on the process controller level. The goal of the controller is to operate economically optimal with respect to operational cost while satisfying product purities and other operational constraints in the presence of disturbances, such as varying feed air temperatures. We solve the resulting large-scale dynamic online optimization problem using a suboptimal method based on direct single-shooting. The results show that economic model predictive control is viable for the optimal operation of air separation units in real-time. We demonstrate that it improves the process economics by around 4% compared to the stationary benchmark operation while satisfying all operational constraints. The control strategy is implemented in Python using a Modelica model and our dynamic optimization framework DyOS.

Keywords: economic model predictive control, demand side management, air separation process

1. Introduction

The integration of renewable energy sources into the electricity grid leads to fluctuating energy prices and promises an economic advantage of flexible process operation and demand side management (e.g., Daryanian et al. (1989); Ghoheity and Mitsos (2010)). This advantage is significant in the case of energy-intensive processes, like cryogenic air separation units (ASUs). Since the dominant time constants of the ASU are in the same range as the electricity price fluctuations, the process dynamics have to be taken into account by the process operation strategy.

Economic nonlinear model predictive control (eNMPC) (e.g., Engell (2007); Amrit et al. (2013)) can be used for flexible and economically optimal process operation. To reduce the solution times of the dynamic optimizations required for eNMPC, fast-update methods (cf. Wolf and Marquardt (2016)) have been proposed, which approximate the optimal solution. In the considered suboptimal fast-update methods the iteration number of sequential quadratic programming (SQP) algorithms used for dynamic optimization are restricted (e.g., Diehl et al. (2005)).

The application of eNMPC to an ASU has been in the focus of research recently. Huang and Biegler (2012) used an advanced-step model predictive controller for the rectification column section of a multi-product ASU. However, the heat exchanger and compressor

were not considered, although they are main parts of an ASU. Pattison et al. (2016) applied a combined dynamic scheduling and tracking controller approach to a liquid nitrogen ASU. Caspari et al. (2018) applied a suboptimal method to an ASU for liquid nitrogen production based on direct single-shooting.

The application of eNMPC to a complete multi-product ASU comprising a heat exchanger, two columns, a feed air compressor, and additional utilities has not yet been focused on. We show that eNMPC can be applied to realize demand side management without using a scheduling layer for a large-scale process in real-time.

The article is structured as follows: Section 2 describes the process, and process model and the eNMPC framework. Section 3 discusses the closed-loop case-study results before the work is finally concluded in Section 4.

2. Air Separation Process and Economic Model Predictive Control Method

We consider a multi-product ASU producing both liquid and gaseous oxygen and gaseous nitrogen. The flowsheet of the process, shown in Fig. 1, is similar to the one presented by Miller et al. (2008). However, the argon part of the ASU and the nitrogen product liquefier are not considered here. We add an oxygen storage tank to buffer the product to improve the process flexibility. Ambient air enters the process and is compressed at the beginning to 58 bar before one part of the stream is expanded to 5.5 bar and enters the high pressure column (HPC). The other part is cooled down further in the heat exchanger and is fed to the HPC and to the low pressure column (LPC) at a pressure of 1.424 bar.

The two columns are interconnected by the heat integrated condenser and reboiler. Gaseous and liquid oxygen product (GOX and LOX, respectively) is withdrawn from the reboiler. The gaseous nitrogen product (GNP) is taken from the LPC top. One part of the oxygen product stream is stored in the buffer tank, the other part is compressed to 5.5 bar and vaporized in the heat exchanger to cool down the feed air stream and exits the process as GOX. We developed a first-principle model of the ASU. The models used are similar to the models used by Huang and Biegler (2012) and Pattison et al. (2016). The main model assumptions are summarized in the following.

Thermodynamics: The vapor-liquid equilibrium is calculated using the isofugacity condition. The vapor pressure of the pure components are computed using the extended Antoine equation. The ideal gas law is used for the vapor phase. The liquid phase activity coefficient is calculated using the NRTL model. All parameter values for the thermody-

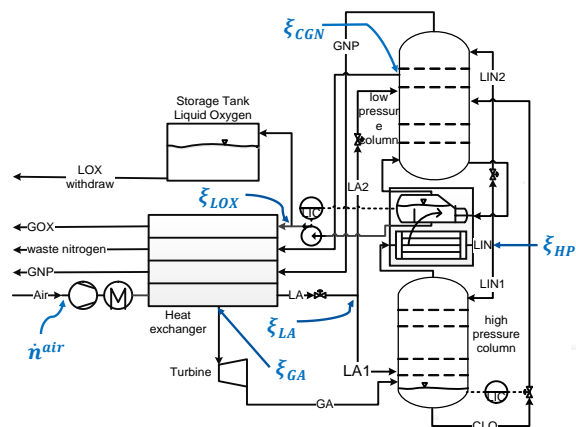


Figure 1: Process flowsheet of the multi-product ASU. The control variables for the eNMPC are illustrated in blue letters. \dot{n}_{air} is the feed air stream entering the process, ξ_i are split factors for the respective streams.

dynamic models are retrieved from Aspen Plus version 8.8 (Aspen Technology, 2018).

LPC/HPC: The rectification columns are described by a stage-by-stage model. The column stages are modeled with dynamic MESH-equations using the following assumptions: (i) negligible vapor hold up, (ii) quasi-stationary energy balance, (iii) a constant pressure difference between neighboring stages and (iv) a linear relation for stage hydraulics. We modeled the LPC with 60 stages and the HPC with 30 stages.

Heat exchanger: The heat exchanger is described by a spatially-distributed model discretized using steady-state energy and mass balance equations for the fluid streams and dynamic energy balances for the heat exchanger wall elements. A discretization of 10 segments is used for each stream and the wall. The temperature profile has been regressed as function of enthalpy, pressure, and composition, allowing to handle phase transitions in the heat exchanger easily.

Compressors/Turbine: The compressors and the turbine are modeled using isentropic efficiencies of maximum 80% at steady-state operating point and quadratically decreasing in off-design operation.

The entire model results in a nonlinear index-1 differential-algebraic equation system (DAE) comprising of 300 differential and about 22500 algebraic equations.

2.1. eNMPC framework

In eNMPC, a dynamic optimization problem is solved repeatedly online during process operation on a moving horizon. An economic objective function is minimized subject to a DAE system defined by the model equations and further operational constraints, such as the product quality. As we use a large-scale nonlinear model, the high computational effort for solving the dynamic optimization problem impede real-time tractability and thus the application in process control. To overcome this issue, we use a suboptimal fast-update method (Diehl et al., 2005) to approximate the optimal solution of the dynamic optimization problem. We restrict iterations of the optimization algorithm, such that the optimization stops before the optimality conditions are satisfied. The optimization problems are solved using direct single-shooting (Brusch and Schapelle, 1973; Sargent and Sullivan, 1978), where a DAE integrator is used inside the optimization algorithm to solve the DAE. This guarantees the model equations to be solved exactly within the integrator tolerances at each iteration of the optimization algorithm and the NLP solver does not influence the physical reliability of the solution. In that sense, single-shooting is particularly suited for suboptimal fast-update methods. Moreover, delay compensation by prediction (Wolf and Marquardt, 2016) is used to improve the eNMPC performance; we use the control variable values from the last controller iteration to predict the system state over a time horizon that is defined by the computational time required to solve the eNMPC problem. This leads to a more aggressive controller reaction since the controller has less time to react to potential disturbance. The time delay is estimated a priori. All disturbances that may occur during operation are assumed to be time invariant over the complete control horizon.

2.2. Implementation

We implement the mechanistic model in Modelica (Modelica, 2018). We export it as functional mock-up unit (FMU) (FMI 2 standard, 2014) and use it in the dynamic optimization framework DyOS (DyOS, 2018). We apply the integrator NIXE (Hannemann et al., 2010) and the SQP optimization algorithm SNOPT (Gill et al., 2005). Integrator and optimizer are implemented in C++ and Fortran. Thus, the numerics are performed in those languages. We implement the overall eNMPC framework in Python (Python,

2018). We use a Windows 7 desktop computer equipped with an Intel Core(TM) i3-6100 processor running at 3.7 GHz and 8 GB RAM.

3. Closed-Loop Case-Study

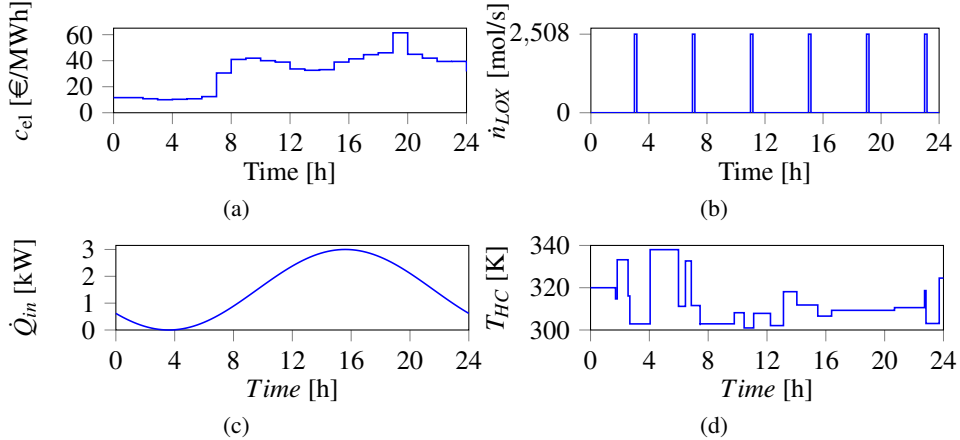


Figure 2: Input and disturbance profiles for the closed-loop case-study. (a) Electricity price of the day ahead auction for the 12th February, 2018 (Epexspot, 2018). (b) Liquid oxygen product rate withdrawn from the storage tank. (c) Heat transfer rate to each tray due to solar radiation. (d) Feed air temperature entering the heat exchanger.

3.1. Operational Scenario and eNMPC formulation

The goal of the eNMPC is to control the process economically optimal with respect to the electricity cost, satisfy the product demand, and reject disturbances. We compare the eNMPC performance to a constant production rate as benchmark, i.e., time-invariant process input variables. The values of the input variables are the same as the initial input variable values of the eNMPC. We assume full state feedback and the electricity prices profile shown in Fig. 2a. Using the eNMPC problem formulation, we ensure that both the closed-loop process and the benchmark produce the same amount of product. We use an operation scenario where liquid oxygen product is withdrawn from the tank six times every day (cf. Fig. 2b) in an amount that corresponds to the oxygen produced by the benchmark production. This may correspond to product withdrawal and distribution by tank wagons. The eNMPC has to control the process such that the initial storage tank content is achieved again by the end of each control horizon. Additionally, the eNMPC has to guarantee the gaseous oxygen product amount to be the same as in the benchmark by using an endpoint constraint. We constrain product purities by path-constraints in order to guarantee the required product quality during the complete time horizon. We bound column stage temperatures to additionally support the product purities. We assume two disturbances during operation: (i) the feed air temperature profile corresponding to temperature fluctuations and (ii) heat streams entering the columns (Fig. 2c and 2d). In the eNMPC, we minimize the economic objective function $\phi = \int_{t_0}^{t_0+\Delta t_c} c_{el}(t)(P_{com}(t) - P_{tur}(t))dt$, where t_0 is the initial time of the eNMPC controller, i.e., the current time on the moving horizon, Δt_c is the control horizon, i.e., the horizon over which the optimization problem is solved in the eNMPC controller, c_{el} is the fluctuating electricity price. P_{com} and P_{tur} are the compressor and turbine electricity demand, respectively. We bound control variables (cf. Fig. 1) by: $\dot{n}_{air} \in [1500, 2800]$ mol/s, $\xi_{GA} \in [0.31, 0.41]$, $\xi_{LA} \in [0.83, 0.9]$, $\xi_{LOX} \in [0.65, 0.84]$,

$\xi_{HP} \in [0.536, 0.579]$, and $\xi_{CGN} \in [0.56, 0.64]$. In order to compare the two operational modes we use the economic improvement measure $\eta = 1 - \frac{\Phi_{eNMPC}^*/n_{eNMPC}^*}{\Phi_{benchmark}^*/n_{benchmark}^*}$, where Φ_{eNMPC}^* and n_{eNMPC}^* is the objective function value and the total product amount resulting from the eNMPC controlled closed-loop simulation, respectively, and $\Phi_{benchmark}^*$ and $n_{benchmark}^*$ are the respective values corresponding to the constant benchmark operation. An eNMPC sampling time of 7.5 min and a control horizon of 8 h are used. We restrict the SQP algorithm to a single iteration. We assume full state feedback and no plant-model mismatch. Partial state feedback or plant-model mismatch would require the use of state estimation techniques. A PI controller is used for the HPC liquid tank holdup. We use absolute and relative integrator tolerances, and the optimality and feasibility tolerances of SNOPT of 10^{-3} . We select 0.1 as maximum major step length in SNOPT.

3.2. Results and Discussion:

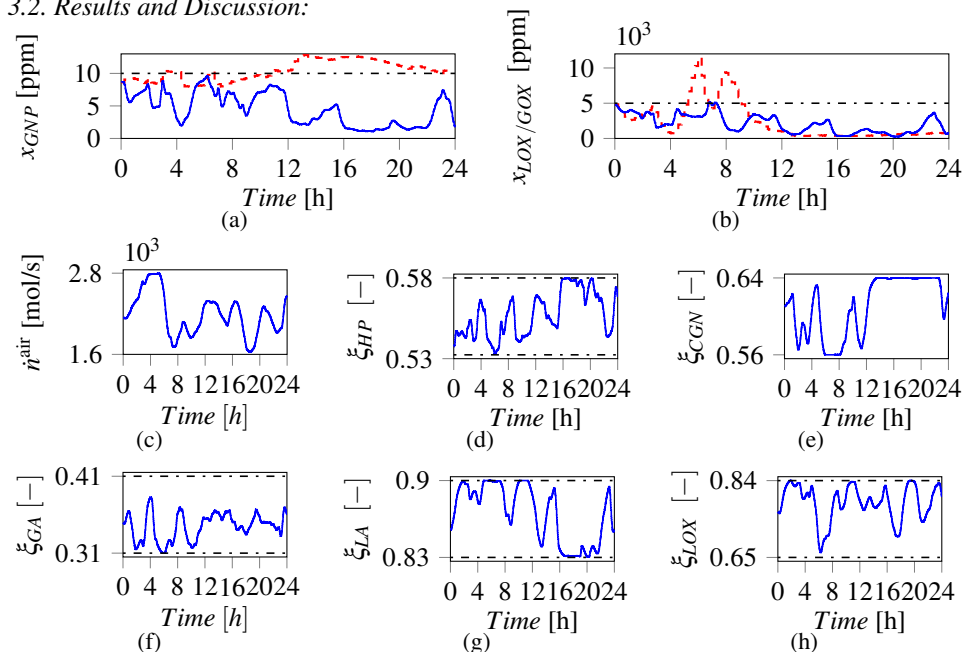


Figure 3: Top: Selected state profiles of benchmark operation (dashed red lines) and closed-loop (solid blue lines) simulation; dash-dotted lines the upper bounds. Rows 2 - 3: selected control profiles of the closed-loop simulation. (a) Impurities of the GNP product stream. (b) Impurities of the LOX and GOX product streams. (c) Feed air stream. (d)-(h) Split factors.

The eNMPC achieves an economic improvement of 3.7 % compared to the benchmark operation. The cost effectiveness can be expected to be further improved by using additional SQP iterations (Caspari et al., 2018). For comparison, we simulated the process benchmark operation, i.e., open-loop without eNMPC, using the same disturbance and electricity price profiles. From Fig. 3a and 3b, we see that the product quality constraints are violated in the benchmark operation due to the presence of the disturbances, as expected. The nitrogen product quality is violated especially in times of high heat streams after 16 h. The oxygen product impurity exceeds its upper bound in those times when the feed air temperature is higher. With eNMPC, the constraints are satisfied, as shown in Fig. 3a and 3b. The corresponding control variable profiles are depicted in Fig. 3c -

3h. We see, that the eNMPC varies the control variables in the whole range within the allowed bounds. The air feed stream (Fig. 3c) is low in times of low electricity prices (Fig. 2a). This is intuitive, since this stream directly corresponds to the electricity consumption of the main compressor. The split factor shown in Fig. 3d corresponds to the reflux ratio of the HP. A high split factor leads to a high reflux ratio and, thus, to higher purities. Increased reflux ratios are, hence, reasonable in times of high heat streams into the column in order to achieve the product purities. The average computational time for the suboptimal fast-update is about 50 s, i.e., about 18% of the control horizon.

4. Conclusion

We present a case study of eNMPC applied to a multi-product ASU based on direct single-shooting. We limit the number of SQP iterations of the NLP solver to reduce computational time. We use a large-scale first principle model as controller model and considered disturbances in the closed-loop simulation. Using the eNMPC we improved the process operational cost by almost 4 % compared to stationary operation. The constraints that are violated in the benchmark operation are satisfied using the eNMPC operation. The computational times indicate that the method presented is applicable in real time. Further computational time reduction could be achieved using model reduction techniques or further algorithmic improvements, such as neighboring extremal updates (cf. Wolf and Marquardt (2016)), which however require the efficient computation of the second order sensitivities. SNOPT uses a BFGS approximation to calculate these starting with the unity matrix.. The use of exact second order sensitivities can improve both computational times and process economics (Würth et al., 2009).

Acknowledgments: The authors gratefully acknowledge the financial support of the Kopernikus project SynErgie by the Federal Ministry of Education and Research (BMBF) and the project supervision by the project management organization Projektträger Jülich (PtJ). The authors thank J. Faust and F. Jung from AVT for fruitful discussions.

References

- R. Amrit, J. B. Rawlings, L. T. Biegler, 2013. *Comput. Chem. Eng.* 58, 334–343.
- I. Aspen Technology, 2018. <https://www.aspentech.com/>.
- R. G. Brusch, R. H. Schapelle, 1973. *AIAA Journal* 11 (2), 135–136.
- A. Caspari, J. M. M. Faust, P. Schäfer, A. Mhamdi, A. Mitsos, 2018. *IFAC-PapersOnLine*.
- B. Daryanian, R. E. Bohn, R. D. Tabors, 1989. *IEEE Power Engineering Review* 4, 36–36.
- M. Diehl, H. G. Bock, J. P. Schlöder, 2005. *SIAM Journal on Control and Optimization* 43, 1714–1736.
- DyOS, 2018. <http://permalink.avt.rwth-aachen.de/?id=295232>.
- S. Engell, 2007. *J. Process Control* 17, 203–219.
- Epexspot, 2018. <https://www.epexspot.com/de/marktdaten/dayaheadauktion>.
- FMI 2 standard, 2014. <http://fmi-standard.org>.
- A. Ghousey, A. Mitsos, 2010. *Desalination* 263, 76–88.
- P. E. Gill, W. Murray, M. A. Saunders, 2005. *SIAM Review* 47, 99–131.
- R. Hannemann, W. Marquardt, U. Naumann, B. Gendler, 2010. *Procedia Comput. Sci.* 1, 297–305.
- R. Huang, L. T. Biegler, 2012. *Comput. Aided Chem. Eng.* 31, 1612–1616.
- J. Miller, W. L. Luyben, P. Belanger, S. Blouin, L. Megan, 2008. *Ind. Eng. Chem. Res.* 47, 394–404.
- Modelica, 2018. <https://www.modelica.org/>.
- R. Pattison, C. R. Touretzky, T. Johansson, M. Baldea, I. Harjunkoski, 2016. *IFAC-PapersOnLine* 49, 681–686.
- Python, 2018. <https://www.python.org/>.
- R. W. H. Sargent, G. R. Sullivan, 1978. In: *Optimization Techniques*. Springer-Verlag, pp. 158–168.
- I. J. Wolf, W. Marquardt, 2016. *J. Process Control* 44, 162–183.
- L. Würth, R. Hannemann, W. Marquardt, 2009. *J. Process Control* 19, 1277–1288.

DyOS - A Framework for Optimization of Large-Scale Differential Algebraic Equation Systems

A. Caspari^a, A. M. Bremen^a, J. M. M. Faust^a, F. Jung^a, C. D. Kappatou^a, S. Sass^a,
Y. Vaupel^a, R. Hannemann-Tamás^a, A. Mhamdi^a and A. Mitsos^{a, b, c, *}

^a*AVT Process Systems Engineering, RWTH Aachen University, 52056 Aachen, Germany*

^b*JARA-CSD, RWTH Aachen University, 52056 Aachen, Germany*

^c*IEK-10, Forschungszentrum Jülich, 52425 Jülich, Germany*

amitsos@alum.mit.edu

Abstract

Dynamic optimization problems arise in many fields of engineering. Typically, they are subject to models of differential-algebraic equations and further process constraints. To promote and investigate the application of methods based on dynamic optimization, an efficient and modular implementation of numerical algorithms for their solution is essential. We present the current status of the open-source software DyOS for the solution of large-scale dynamic optimization problems. DyOS has been applied to optimal operation, model-predictive control and process design problems in various case studies. DyOS is based on direct adaptive shooting algorithms and it allows for multi-stage problem formulations including binary decision making. Models can either be imported as standardized functional mock-up units, flat Modelica models, or C++ models. The modular implementation of DyOS enables the use of various open-source and commercial integrators and nonlinear programming solvers based on various numerical methods. DyOS can be accessed via Matlab or Python interfaces. As an illustrative large-scale application, we present the results of optimal operation of an air separation process under fluctuating electricity prices. An open-source version of DyOS including several parts of the framework presented is available at <http://permalink.avt.rwth-aachen.de/?id=295232>.

Keywords: dynamic optimization, direct adaptive shooting, open-source framework

1. Introduction

The solution of optimization problems constrained by differential algebraic equation systems (DAEs) is a common challenge in many fields. Among others, dynamic optimization of DAEs is used in process control, operation, and design. The direct optimization methods full discretization (Cuthrell and Biegler, 1987), single shooting (Brusch and Schapelle, 1973; Sargent and Sullivan, 1978; Kraft, 1985), and multiple shooting (Bock and Plitt, 1984) make use of discretization to treat the DAEs. There are already several software frameworks, which implement these methods. A list can be found in Nicholson et al. (2017). Open source implementations include `pyomo:dae` (Nicholson et al., 2017), `ACADO` (Houska et al., 2010), `Optimica` and `JModelica` (Åkesson et al., 2010), and `TACO` (Kirches and Leyffer, 2013). We present the current status of the open-source framework DyOS (Dynamic Optimization Software) for dynamic optimization based on direct adaptive shooting methods, which is tailored to large-scale DAEs. DyOS integrates several software packages including different integration and optimization methods, dif-

ferent nonlinear and linear equation solvers, and a graph coloring algorithm into a large framework for the efficient solution of dynamic optimization problems. Using the standardized modeling language Modelica and the standard Functional Mockup Unit (FMU), it allows straightforward model provision and optimization problem set-up. The remainder of the manuscript is structured as follows. The methods used, the implementation and the problems solved in the past are summarized in Section 2. A large-scale case study is shown in Section 3, before the work is concluded in Section 4.

2. Methods and Implementation

The optimization framework DyOS solves a multi-stage mixed-integer dynamic optimization problem of the form

$$\min_{\mathbf{u}, \mathbf{z}, \mathbf{p}} \sum_i^N \Phi(\mathbf{x}(t_i^-)) \quad (1a)$$

$$\text{s.t. } \mathbf{M}\dot{\mathbf{x}}(t) = \mathbf{f}_i(\mathbf{x}(t), \mathbf{y}(t), \mathbf{u}(t), \mathbf{p}, \mathbf{z}), \quad \forall t \in \mathcal{T}_i, 0 \leq i < N \quad (1b)$$

$$\mathbf{0} = \mathbf{g}_i(\mathbf{x}(t), \mathbf{y}(t), \mathbf{u}(t), \mathbf{p}, \mathbf{z}), \quad \forall t \in \mathcal{T}_i, 0 \leq i < N \quad (1c)$$

$$\mathbf{0} = \mathbf{h}_i(\mathbf{x}(t_i^+), \mathbf{x}(t_i^-), \mathbf{y}(t_i^-), \mathbf{p}, \mathbf{z}), \quad 1 \leq i < N \quad (1d)$$

$$\mathbf{0} \geq \mathbf{c}_i(\mathbf{x}(t), \mathbf{y}(t), \mathbf{u}(t), \mathbf{p}, \mathbf{z}), \quad \forall t \in \mathcal{T}_i, 0 \leq i < N \quad (1e)$$

on a finite time horizon $\mathcal{T} = \bigcup_{i=1}^N \mathcal{T}_i$, where N is the number of stages and $\mathcal{T}_i = [t_i, t_{i+1}]$ are the time horizons of the stage i , $\mathbf{f}_i : \mathbb{X} \rightarrow \mathbb{R}^{n_x}$ and $\mathbf{g}_i : \mathbb{X} \rightarrow \mathbb{R}^{n_y}$ define the semi-explicit differential-algebraic system of index 1 with the invertible matrix $\mathbf{M} \in \mathbb{R}^{n_x \times n_x}$, while $\mathbf{h}_i : \mathbb{R}^{n_x} \times \mathbb{R}^{n_x} \times \mathbb{R}^{n_y} \times \mathbb{R}^{n_p} \times \mathbb{R}^{n_z} \rightarrow \mathbb{R}^{n_x}$ indicates the initial conditions and $\mathbf{c}_i : \mathbb{X} \rightarrow \mathbb{R}^{n_c}$ the constraints, with $\mathbb{X} := \mathbb{R}^{n_x} \times \mathbb{R}^{n_y} \times \mathbb{R}^{n_u} \times \mathbb{R}^{n_p} \times \mathbb{R}^{n_z}$. Problem (1) aims at finding optimal control trajectories $\mathbf{u} : \mathcal{T} \rightarrow \mathbb{R}^{n_u}$, differential and algebraic state trajectories $\mathbf{x} : \mathcal{T} \rightarrow \mathbb{R}^{n_x}$ and $\mathbf{y} : \mathcal{T} \rightarrow \mathbb{R}^{n_y}$, respectively, for parameter values $\mathbf{p} \in \mathbb{R}^{n_p}$ and integer variables $\mathbf{z} \in \mathbb{N}^{n_z}$, that minimize an objective in Mayer form $\Phi : \mathbb{R}^{n_x} \rightarrow \mathbb{R}$. The superscripts $+$ and $-$ denote the upper and lower one-sided limits of t_i . The algorithms in DyOS are based on adaptive direct single- and multiple-

shooting (Schlegel et al., 2004; Assassa and Marquardt, 2014), where the control variable profile discretization is automatically adapted. Two types of grid adaptation methods can be selected: one based on the objective function improvement using wavelet analysis (Schlegel et al., 2004) and the other based on the necessary optimality conditions (Assassa and Marquardt, 2016). Grid adaptation allows the user to start the optimization using a coarse discretization grid and get a fine grid at the end of the optimization. Thus, grid adaptation can reduce the overall

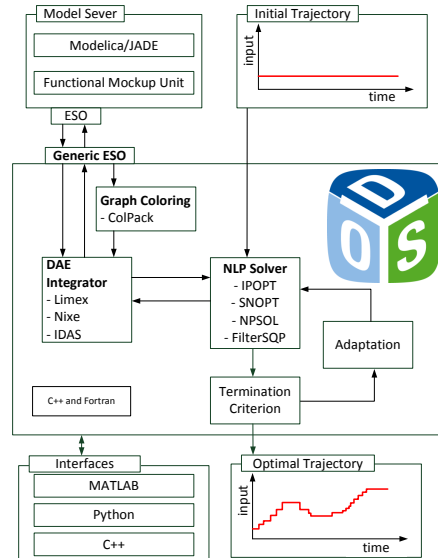


Figure 1: DyOS implementation structure.

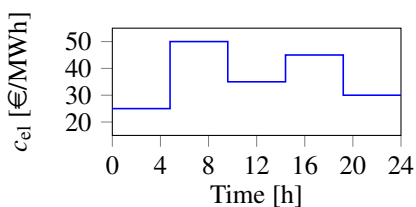
CPU time by avoiding an abundant parameterization. This can be used to avoid over-parameterized solution, and the use of control structure detection can significantly reduce the granularity of the discretization without losing information (Assassa and Marquardt, 2015). Using a branch-and-bound algorithm, DyOS can solve mixed-integer optimization problems (Oldenburg et al., 2003; Frankl et al., 2012). Moreover, a unique feature of DyOS are the special approaches to provide the Jacobian and the Hessian of the Lagrangian. The first- and second-order sensitivities can be provided by forward sensitivity integration and first-order adjoint equations. The Hessian can be provided using composite adjoints of the Lagrangian (Hannemann and Marquardt, 2007; Jorgensen, 2007). The modified discrete adjoint solver NIXE (Hannemann et al., 2010) serves as an integrator for the composite adjoint sensitivity system. The Jacobian of the models can be calculated in both forward and reverse mode, and the Hessian matrix can be calculated in reverse mode. A generic integrator interface implementation facilitates coupling of existing DAE integrator codes to DyOS. Wrappers for three different integrators are currently implemented: the semi-implicit extrapolation methods NIXE (Hannemann et al., 2010) and sLIMEX (Schlegel et al., 2004), as well as the backward differentiation formula IDAS (Serban et al., 2018). The architecture of DyOS is shown in Fig. 1. A generic optimizer interface enables coupling nonlinear programming codes to DyOS. Four different NLP solvers are currently available: SNOPT (Gill et al., 2005), NPSOL (Gill et al., 1986), IPOPT (Wächter and Biegler, 2005), and FilterSQP (Fletcher and Leyffer, 2002). A generic model interface is implemented, which allows to couple different models to DyOS. The model interface currently supports the functional mockup interface standard (FMI, 2014) and parsed Modelica models. In the latter case C++ code of the model residuals is generated and processed by the algorithmic differentiation tool dcc (Naumann, 2012) to generate first- and second-order derivatives. DyOS focuses on the solution of large-scale optimization problems by making use of adaptation strategies and the integration of efficient numerical software packages. Thus, several packages are used to support this purpose: the graph coloring package ColPack (Gebremedhin et al., 2013) for efficient Jacobian and Hessian calculation, nonlinear solver CMINPACK, as well as linear solvers KLU, SuperLu, and CSparse. Three front ends are implemented to access DyOS from C++, Matlab and Python. A minor limitation is the restriction to a constant matrix \mathbf{M} and a system with a differential index of 1. However, every non-index-1 system can be reformulated to an index-1 system with constant matrix \mathbf{M} , and, thus, this limitation is not severe. In the past, DyOS has been used for solving many challenging chemical engineering problems either as standalone solver, e.g., for dynamic optimization of batch recipes or as a subsolver embedded in an algorithm, e.g., in nonlinear model predictive control (NMPC) applications. Table 1 presents a non-exhaustive, yet exemplary, list of problems solved with DyOS which shows its wide range of applicability and its capability to handle large-scale DAE systems.

3. Dynamic Optimization of an Air Separation Process

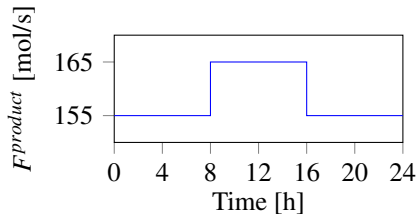
Since air separation units (ASU) are electricity intensive processes, their flexible operation for demand-side management is economically promising due to the penetration of fluctuating renewable energy. In this section, an offline dynamic optimization of an ASU using DyOS is presented based on the work of Caspari et al. (2018). The flowsheet of the process is depicted in Fig. 4. Air is compressed from its ambient state at 1 bar to 10 bar and cooled down by a heat-exchanger and expansion in a turbine. It is separated into its components in a rectification column at a pressure of 6.6 bar comprising of an integrated

Table 1: Published contributions which make use of DyOS.

Reference	Problem Type	Problem Size
Caspari et al. (2018)	eNMPC	127 differential equations 2940 algebraic equations
Frankl et al. (2012)	Integrated Scheduling and Control	1500 equations 9 binary variables
Hartwich and Marquardt (2010)	DO	1752 differential equations 10779 algebraic equations
Kadam et al. (2007)	DO	200 differential equations 2500 algebraic equations
Oldenburg et al. (2003)	MIDO	330 DAEs 32 binary variables
Pontes et al. (2015)	DRTO	148 differential equations 2435 algebraic equations



(a) Electricity price of the day ahead auction (Fraunhofer ISE, 2018).



(b) Assumed product demand rate.

Figure 2: Input parameters for the dynamic optimization.

reboiler and condenser. Nitrogen is withdrawn either from the storage tank or directly from the heat exchanger. The main energy consumers of the process are the feed air compressor and the nitrogen product liquefier. A nonlinear first-principle process model is used comprising of 127 differential and 2940 algebraic states and 5 input variables. The model is implemented in Modelica and connected via the Functional Mock-Up Interface. The economic objective function $L(t) = \int_{t_0}^{t_{\text{end}}} c_{el}(t)(P_{comp}(t) + P_{liq}(t) - P_{tur}(t))dt$ is minimized, where $P_{comp/liq/tur}$ is the power demand/supply of the compressor, liquefier, and turbine, respectively, and c_{el} is the fluctuating electricity price. t_0 and t_{end} are the initial and final time of the control horizon. The operational cost is compared to a constant operation benchmark. The electricity price profile used is shown in Fig. 2a. The profile of the product flowrate from the process is shown in Fig. 2b. The product purity is path-constrained to guarantee a predefined product quality. The storage tank holdup is endpoint-constrained to guarantee a minimum amount of product produced during the optimization horizon. The process operation is optimized over a time horizon of one day. We use wavelet-based grid adaptation with an adaptation of maximum five adaptation steps and an initial equidistant grid with eight piecewise constant control elements. SNOPT is used as NLP solver and sLIMEX as integrator with the tolerances set to 10^{-6} . The results of the dynamic optimization and of the benchmark operation strategy are shown in Fig. 3. We see that the tank is loaded when the electricity price is low and unloaded when it is

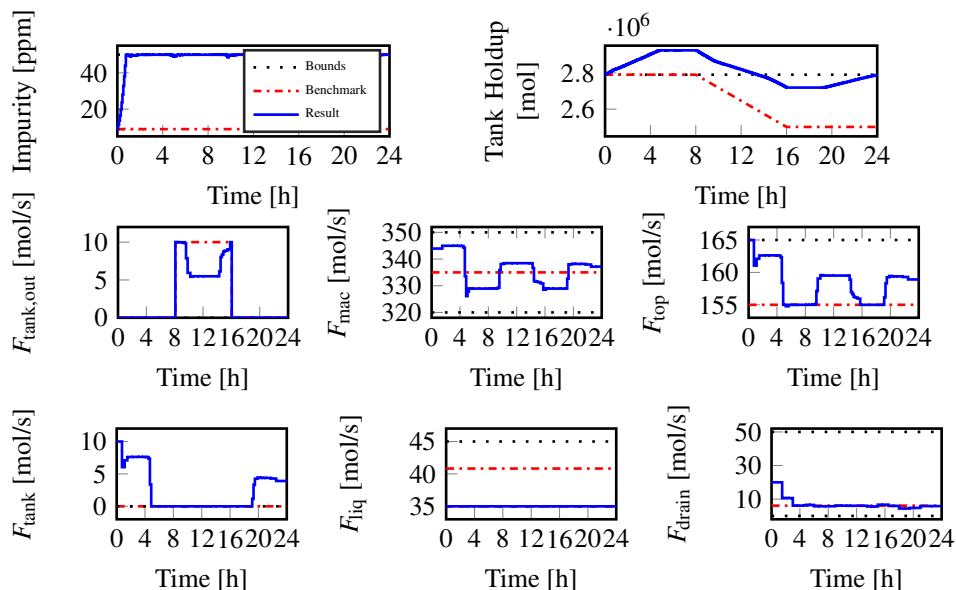


Figure 3: State and input trajectories of ASU case-study. The optimal operation (solid blue) is compared to a benchmark (dash-dotted red) corresponding to constant production rate. Top: Trajectories of selected constrained states. Rows 2 - 3: Trajectories of input variables.

high, as expected. The highest tank level is kept constant when the electricity price is at its maximum value, which is less intuitive. However, it can be explained by the increased product stream from 8 h on. In the benchmark operation the tank is unloaded due to the higher product demand. This difference is accounted for by the economic evaluation. Moreover, the product impurity are at their bounds throughout the considered time horizon. The control variable profiles are shown in Fig. 3, where successful grid adaptation is demonstrated. They have a fine discretization where needed, e.g., for F_{mac} , and a coarse if not, e.g., for F_{liq} . The total runtime including the five grid adaptation steps took about 8 hours of CPU time. A Windows 7 computer is used with an Intel Core i3-6100 processor having 3.7 GHz and 8 GB RAM. The optimization results in a cost reduction of about 2 % with respect to the benchmark operation.

4. Conclusion

We present the dynamic optimization framework DyOS that is tailored to large-scale DAE systems. We review existing work which used DyOS for large-scale optimization problems. Finally, we demonstrate the application of the wavelet-based adaptation to an optimization of an air separation process.

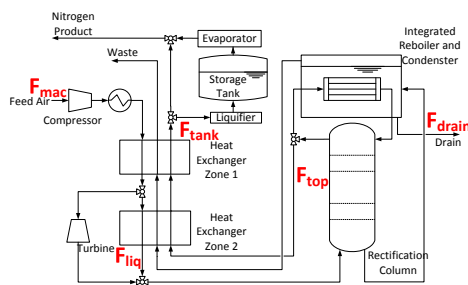


Figure 4: Air separation process flowsheet with control variables (bold red letters).

Acknowledgement: The implementation of DyOS presented here is based on earlier versions that have been developed over many years by several researchers and programmers in the group of Wolfgang Marquardt. We thank him and them. We thank Uwe Naumann for allowing us to ship their algorithmic differentiation software `dcc` free of charge. We gratefully acknowledge the financial support of the Kopernikus project SynErgie by the Federal Ministry of Education and Research (BMBF) and the project supervision by the project management organization Projektträger Jülich (PTJ), the Deutsche Forschungsgemeinschaft (DFG) in the Collaborative Research Center SFB 985 Functional Microgels and Microgel Systems within Project B4, the Federal Ministry of Education and Research (BMBF) for funding of the project CO2Min (FKZ: 033RC014), the European Union Horizon 2020 research and innovation programme under the Marie Skłodowska-Curie Grant Agreement No. 675251, and the Helmholtz Association under the Joint Initiative Energy System 2050 - A Contribution of the Research Field Energy".

References

- J. Åkesson, K.-E. Årzén, M. Gäfvert, T. Bergdahl, H. Tummescheit, 2010. *Comput. Chem. Eng.* 34 (11), 1737–1749.
- F. Assassa, W. Marquardt, 2014. *Comput. Chem. Eng.* 60, 242–259.
- F. Assassa, W. Marquardt, 2015. *Comput. Chem. Eng.* 73, 82–101.
- F. Assassa, W. Marquardt, 2016. *problems. Comput. Chem. Eng.* 92, 189–203.
- H. Bock, K. Plitt, 1984. *IFAC Proceedings Volumes* 17 (2), 1603–1608.
- R. G. Brusch, R. H. Schapelle, feb 1973. *AIAA Journal* 11 (2), 135–136.
- A. Caspari, J. M. Faust, P. Schäfer, A. Mhamdi, A. Mitsos, 2018. *IFAC-PapersOnLine* 51 (20), 295 – 300.
- J. E. Cuthrell, L. T. Biegler, 1987. *AIChE J.* 33 (8), 1257–1270.
- R. Fletcher, S. Leyffer, 2002. *Math. Program.* 91 (2), 239–269.
- FMI, 2014. <http://fmi-standard.org>.
- K. Frankl, J. Brenner, W. Marquardt, 2012. ESCAPE-22 conference.
- Fraunhofer ISE, 2018. <https://www.energy-charts.de>.
- A. H. Gebremedhin, D. Nguyen, M. M. A. Patwary, A. Pothén, 2013. *ACM Transactions on Mathematical Software* 40 (1), 1–31.
- P. E. Gill, W. Murray, M. A. Saunders, 2005. *SIAM Review* 47 (1), 99–131.
- P. E. Gill, W. Murray, M. A. Saunders, M. H. Wright, 1986. *NPSOL 5.0 User's Guide*. Stanford University. Dept of Management Science and Engineering.
- R. Hannemann, W. Marquardt, 2007. *IFAC Proceedings Volumes* 40 (5), 105–110.
- R. Hannemann, W. Marquardt, U. Naumann, B. Gendler, 2010. *Procedia Comput. Sci.* 1 (1), 297–305.
- A. Hartwich, W. Marquardt, 2010. *Comput. Chem. Eng.* 34 (11), 1873–1889.
- B. Houska, H. J. Ferreau, M. Diehl, 2010. *Optimal Control Applications and Methods* 32 (3), 298–312.
- J. B. Jorgensen, 2007. In: *European Control Conference (ECC)*. IEEE, pp. 3649–3656.
- J. V. Kadam, W. Marquardt, B. Srinivasan, D. Bonvin, 2007. *AIChE J.* 53 (3), 627–639.
- C. Kirches, S. Leyffer, apr 2013. *Mathematical Programming Computation* 5 (3), 227–265.
- D. Kraft, 1985. On converting optimal control problems into nonlinear programming problems. In: *Computational Mathematical Programming*. Springer Berlin Heidelberg, pp. 261–280.
- U. Naumann, 2012. *The Art of Differentiating Computer Programs. An Introduction to Algorithmic Differentiation*. No. 24 in *Software, Environments, and Tools*. SIAM.
- B. Nicholson, J. D. Siirola, J.-P. Watson, V. M. Zavala, L. T. Biegler, 2017. *Mathematical Programming Computation* 10 (2), 187–223.
- J. Oldenburg, W. Marquardt, D. Heinz, D. B. Leineweber, 2003. *AIChE J.* 49 (11), 2900–2917.
- K. V. Pontes, I. J. Wolf, M. Embiruçu, W. Marquardt, 2015. *Ind. Eng. Chem. Res.* 54 (47), 11881–11893.
- R. W. H. Sargent, G. R. Sullivan, 1978. In: *Optimization Techniques*. Springer-Verlag, pp. 158–168.
- M. Schlegel, W. Marquardt, R. Ehrig, U. Nowak, 2004. *Appl. Numer. Math.* 48 (1), 83–102.
- M. Schlegel, K. Stockmann, T. Binder, W. Marquardt, 2005. *Comput. Chem. Eng.* 29 (8), 1731–1751.
- R. Serban, C. Petra, A. C. Hindmarsh, 2018. *User Documentation for IDAS v2.2.1*. Center for Applied Scientific Computing, Lawrence Livermore National Laboratory.
- A. Wächter, L. T. Biegler, 2005. *Math. Program.* 106 (1), 25–57.

Optimisation of multi effect distillation based desalination system for minimum production cost for freshwater

O.M.A.Al-hotmani^a, M. A. Al-Obaidi^{a, b}, G. Filippini^c, F. Manenti^c, R.Patel^a,
and I. M. Mujtaba^{a,*}

^a *Department of Chemical Engineering, Faculty of Engineering and Informatics,
University of Bradford. Bradford, West Yorkshire BD7 1DP, UK*

^b *Middle Technical University, Technical Institute of Baquba, Dayala – Iraq*

^c *Chemical Engineering Department, Politecnico di Milano, Milan, Italy*

I.M.Mujtaba@bradford.ac.uk

Abstract

The multi effect distillation (MED) process has been extensively used for seawater desalination as a prominent process to produce high quality freshwater. However, the impact of number of effects in the MED process-based seawater desalination on the fresh water production cost has not been critically evaluated in the literature. Therefore, the aim of this study is to resolve this particular challenge via the simulation for a given seawater concentration and temperature conditions. The simulation is carried out using a comprehensive MED process model coupled with appropriate cost functions within gPROMS model builder software. The simulation results show that selecting the optimal number of the MED effects as 17 is important to achieve the lowest fresh water production cost for a given seawater operating conditions.

Keywords: Seawater desalination, MED process, Simulation, Fresh water production cost.

1. Introduction

The Multi Effect Distillation (MED) process is the oldest technique for seawater desalination and was first reported back in the middle of the 19th century. Essentially, the thermal and membrane processes are considered as the main adopted technologies used for seawater desalination. These technologies are employed to overcome the scarcity of fresh water due to restricted available resources (Sadri et al., 2017). Specifically, the thermal process characterises by using heat to evaporate and distil the seawater. However, massive research efforts need to be paid to improve the system's efficiency and decrease the fresh water production cost. In this respect, the main concern of thermal process is to improve the steam economy and specifically the Gained Output Ratio GOR (defined as the ratio of the produced distilled water in kilograms to steam consumed in kilograms) (Darwish and AL-Juwayhel, 2006). Recently, MED process gained more attention than other thermal processes (such as Multi Stage Flash, MSF) due to its high effectiveness, straightforward operation and maintenance and feasible economic characteristics. Ettouney and El-Dessouky (1999) stated that the thermal desalination processes, in particular MED process is the more

significant method for desalting seawater to obtain conductivity in very low level, which has a strong impact in power plant. More specifically, the MED process becomes a superior desalination processes due to its low specific energy consumption (Darwish and Abdulrahim, 2008) and low top brine temperature which ranges between 60 – 70 °C (Al-Sahali and Ettouney, 2007). Therefore, it is not surprised to notice that about 65% of the total capacity of production in the desalination industry is attributed to the thermal desalination including the MED process. Up to the authors' knowledge, the research on MED process is still required to alleviate the fresh water production cost by enhancing the performance efficiency besides keeping high-quality water. Specifically, the optimal number of effects in the MED process-based seawater desalination that attains the lowest fresh water production cost via model-based simulation has not been yet explored. Therefore, this research focuses on the implementation of an earlier model developed by the authors for MED process and an economic model gathered from the literature to investigate the optimal number of effects which can attain the lowest fresh water production cost for specified sweater operating conditions.

2. MED process model

Figure 1 shows the MED process that involves of a number of effects. External heat is used to rise the brine temperature within the first stage in order to evaporate the brine. The vapour from each stage supplies energies to the brine in subsequent stages. MED process is typically designed at different capacity that vary from 600 to 30,000 m³/day, and the design is made according to two main arrangements: (a) the seawater boils in a vertical tube in a thin film flowing within the tube and vapour condensate on the heat-transfer tubes (b) the horizontal tube where the seawater feed is sprayed onto the outside surface of the tubes and vapour flows inside the horizontal tubes, which is condensed to produce the water. Table 1 shows the process model taken from our earlier work (Filippini et al., 2018)

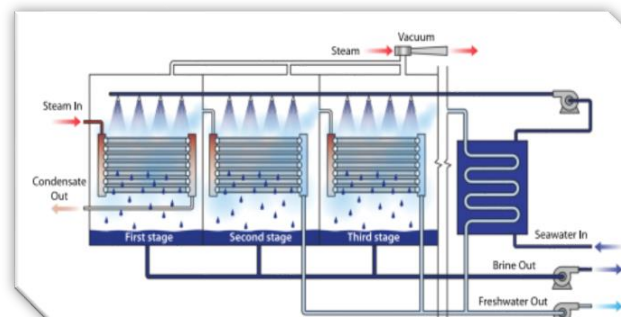


Figure 1. Schematic diagram of MED process (Adapted from Alkaraghoul, 2013)

3. Economic model of MED process

The economic model developed by Druetta et al. (2014) and given in Table 2 was used to calculate the total production cost for MED process. In this respect, Table 3 presents the parameters used in the economic model of MED process. In this respect, the fresh

water production cost is the division of total annual production cost and the total annual productivity of MED process. Specifically, for any seawater thermal desalination process, the total annual cost (*TAC*) is the sum of the total capital cost (*TCC*) and annual operational cost (*AOC*). Principally, the total capital cost comprises the installation, equipment, and indirect costs. However, some other related costs such as the steam cost, chemicals cost, labour, etc. are listed in the operational and maintenance cost.

Table 1. The model equations of MED process (Filippini et al. 2018)

No.	Title	Unit	Equation
1	Temperature drop among effects first attempt	(°C)	$\Delta T = \frac{T_1 - T_b}{n-1}$ or $\Delta T = \frac{T_s - T_b}{n}$
2	Temperature drop among pre-heaters first attempt	(°C)	$\Delta T = \Delta t$
3	Mean temperature in the plant	(°C)	$T_{mean} = \frac{T_1 + T_b}{2}$
4	Mean salinity	(ppm)	$x_{mean} = \frac{xf + xb}{2}$
5	Fraction of flashed distillate	(-)	$\alpha = \frac{cp(T_{mean}, x_{mean})\Delta T}{\lambda(T_{mean})}$
6	Fraction of total distillate boiled in each evaporator	(-)	$\beta = \frac{\alpha[xb(1-\alpha)^n - xf]}{(xb - xf)[1 - (1-\alpha)^n]}$
7	Heat load in i-th effect	(kJ/s)	$Q_i = D_{boiled,i-1}\lambda(Tv_{i-1})$
8	Sensible heat used in first effect	(kJ/kg)	$Q_{sensible} = Mf \int_{t_1}^{T_1} cp(T_1, x_1)dT$
9	Feed flowrate	(kJ/s)	$Mf = \frac{Ms \lambda(T_s)}{Q_{sensible} + Q_{latent}}$
10	Latent heat in first effect	(kJ/s)	$Q_{latent} = D_1\lambda(Tv_1)$
11	Rejected brine flowrate	(kg/s)	$Mb = Mf - Md$
12	Feed flow rate	(kg/s)	$Mf = Md \frac{xb - xf}{xb}$
13	Distillate produced by boiling in i-th evaporator	(kg/s)	$D_{boiled,i} = \beta Md$
14	Total distillate produced in i-th effect	(kg/s)	$D_i = D_{boiled,i} + D_{flash,i}$
15	Brine rejected in the i-th effect	(kg/s)	$B_i = B_{i-1} - D_i$
16	Mean salinity in the plant	(ppm or w/w%)	$x_i = \frac{x_{i-1}B_{i-1}}{B_i}$
17	Feed temperature in first effect	(°C)	$t_1 = tn + (n-1)\Delta t$
18	Temperature of the vapour phase in i-th effect	(°C)	$Tv = T - BPE(T, x)$
19	Driving force for heat exchange in i-th pre-heater	(°C)	$\Delta t_{log,i} = \frac{\Delta t}{\log(\frac{Tv_i - t_{i+1}}{Tv_i - t_i})}$
20	Gained Output Ratio	(-)	$GOR = \frac{Md}{Ms}$
21	Performance Ratio	(-)	$PR = GOR \frac{2330 \text{ kJ/kg}}{\lambda(T_s)}$
22	Specific total area	(m ² s/kg)	$Atot_s = \frac{Atot}{Ms}$
23	Specific seawater intake	(-)	$Mw_s = \frac{Md}{Mw}$
24	Area of i-th effect	(m ²)	$A_{ev,mean} = \frac{Q_i}{U_{ev,i} \Delta T_{ex,i}}$

Table 2. The economic model of Druetta et al. (2014)

No.	Title	Unit	Equation
1	Total Capital cost	(\$)	$TCC = CAPEX_{dir} + CAPEX_{indir}$
2	Indirect CAPEX	(\$)	$CAPEX_{indir} = 0.25CAPEX_{dir}$
3	Civil work cost	(\$)	$CAPEX_{civil_work} = 0.15CAPEX_{equipment}$
4	MED process cost	(\$)	$C_{med} = K_{MED} C_{mat_MED} A_{MED}^{0.64}$
5	Fresh water production cost	(\$/m ³)	$FWC_{MED} = \frac{TAC}{M_{fresh,MED} THY (3600)}$
6	Annual operating cost	(\$/yr)	$AOC = AOC_{chem} + AOC_{lab} AOC_{pow} + AOC_{man} + AOC_{steam}$
7	Seawater intake and pre-treatment cost	(\$)	$C_{intake} = \frac{K_{intake} 243600 M_{seawater_MED}}{2a}$
8	Capital recovery factor	(1/yr)	$CAF = \frac{lr(1 + lr)^{lft}}{(1 + lr)^{lft} - 1}$
9	Cost of human labor	(\$/yr)	$AOC_{lab} = \frac{C_{lab} THY 3600 M_{fresh,MED}}{\rho}$
10	Cost of manutention	(\$/yr)	$AOC_{man} = 0.002TCC$
11	Cost of external steam	(\$/yr)	$AOC_{steam} = \frac{C_{steam} THY (Ts-40) M_{steam}}{80} + 0.005 TCC$
12	Total Annual Cost	(\$/yr)	$TAC = AOC + CRF \times TCC$
13	Equipment cost	(\$)	$CAPEX_{equipment} = C_{intake} + C_{MED} + C_{cond}$
14	Direct CAPEX	(\$)	$CAPEX_{dir} = CAPEX_{equipment} + CAPEX_{civil_work}$
15	Cost of power for pumps	\$/yr	$AOC_{POW} = \frac{C_{pow} THY 100 M_{fresh,MED}}{\rho \mu} f(\Delta P)$
16	Final condenser cost	(\$)	$C_{cond} = K_{cond} C_{cond} C_{mat_cond} A_{cond}^{0.8}$
17	Cost of chemical treatment	(\$/yr)	$AOC_{chem} = \frac{C_{chem} THY 3600 M_{seawater_MED}}{\rho}$

Table 3. Parameters used in the economic model of MED process (Al-Obaidi et al., 2019)

Parameter	Description	Value	Unit	Parameter	Description	Value	Unit
$C_{mat-MED}$	Material of MED process	3644	(\$/m ²)	K_{MED}	Coeff. for MED process	1.4	-
Ir	Interest rate	0.07	(-)	C_{Lab}	Labour	0.05	(\$/m ³)
$C_{mat-cond}$	Material of condenser	500	(\$/m ²)	THY	Total hour per year	8760	(hr/yr)
f(ΔP)	Pressure losses	3571	(-)	C_{chem}	Chemical treatment	0.024	(\$/m ³)
μ	Efficiency of power generation	0.75	(-)	C_{pow}	Power	0.09	(\$/kWh)
life	Life of the plant	25	(year)	K_{intake}	Seawater intake	50	\$ day/m ³
C_{steam}	External steam	0.004	(\$/kg)	K_{cond}	Coeff. for condenser	2.8	-

4. Simulation of the MED Process

The simulation of the MED process is carried out at specified seawater conditions of feed concentration and temperature of 39000 ppm and 25 °C, respectively. Moreover, Steam flow rate M_s and steam temperature T_s are assumed to be known as 8 (kg/s) and 70 (°C), respectively. The case study analysed in this paper corresponds the desalination plants installed in Gulf regions with somehow high seawater salinity. Figure 2 (a) shows the fresh water production cost ($\$/m^3$) against the number of effects in MED process. This in turn showed that the optimum number of effects of 17 has entailed the lowest fresh water production cost for seawater desalination at the selected seawater operating conditions. Specifically, the lowest fresh water production cost is around 0.615 $\$/m^3$. Interestingly, the fresh water production cost exponentially decreases with number of effects below 17. However, a slow progress in the fresh water production cost is observed as a result to increasing number of effects up to 17. Also, the simulation results of the Figure 2 (b) shows that the total annual cost is increased with increasing the number of effects. Basically, this is attributed to increasing both capital costs (from 5118362.5 \$ to 19055098 \$) and operating costs (from 862693.1 $\$/yr$ to 1190574 $\$/yr$) as a result to increasing the number of effects from 8 to 20 in the MED process. Therefore, the minimum fresh water production cost observed in Figure 2 (a) can be ascribed to the progress of distillate flow rate that rapidly increased as a result to increasing number of effects. This in turn causes a rapid decrease in fresh water production cost despite the increase of total annual cost (Eq. (5) presented in Table 2). However, the increase of distillate flow rate beyond 17 effects was insignificant compared to a continuous increase in the total annual cost, which in turn results in a slow increase in the fresh water production cost (Figure 2 (a)). Figure 2 (c) shows the improvement in Gained Output Ratio (GOR) due to increasing number of effects. GOR value raised to its optimum of 17.06 as the number of effects hits 20. However, GOR alone cannot be the unique tool to measure the performance of thermal process as it does not account the impact of capital and other operating costs (such as pumping etc.). More important, the minimum fresh water production cost corresponds to an optimum GOR of 14.5 at 17 effects.

5. Conclusions

In this paper, an earlier model developed by the authors for multi effects desalination MED process was coupled with cost model to estimate the fresh water production cost under different number of effects and fixed seawater operating conditions. The cost model accounts for both capital and operating costs (such as steam, pumping, etc). The optimum number of effects was investigated via repetitive simulation, which illustrates the lowest fresh water production cost for seawater desalination. In this research, the optimum number of effects was obtained to be 17 with the corresponding minimum cost of 0.614 $\$/m^3$. In this respect, the optimum GOR has been discovered for the optimum design. This current research can be used as a powerful tool to design the MED process and specially to address the optimum number of effects for any specified seawater operating conditions. It is fair to realise the insignificant implementation of the current methodology for an already instilled MED plant. Therefore, a comprehensive simulation-based optimisation methodology needs to be explored to investigate the optimal seawater operating conditions and steam flow rate that minimises the fresh water production cost for a fixed number of effects. This would be an interesting scope of the future research.

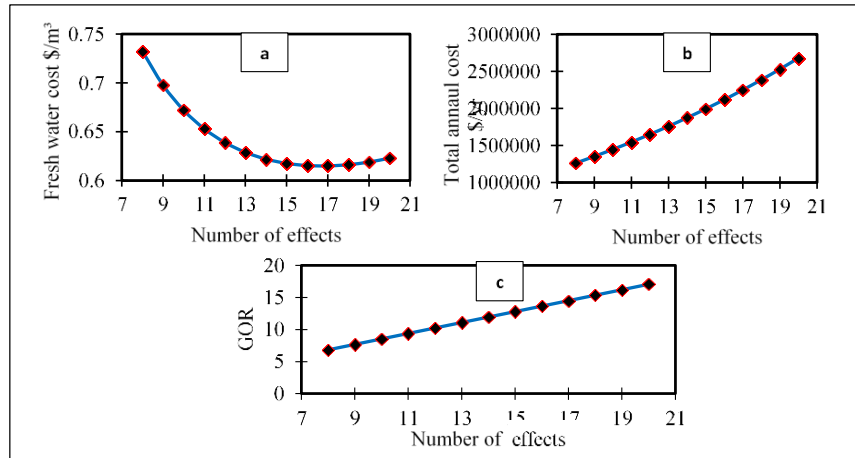


Figure 2. (a) Fresh water cost against number of effects (b) Total annual cost against number of effects (c) Gained output ratio against number of effects

References

- Al-Sahali M., Ettouney H., 2007. Developments in thermal desalination processes: Design, energy, and costing aspects. *Desalination*, 214, 227–240.
- Al-Obaidi M.A., Filippini G., Manenti F., Mujtaba I. M., 2019. Cost evaluation and optimisation of hybrid multi effect distillation and reverse osmosis system for seawater desalination. *Desalination*, 456, 136–149.
- Al-Karaghoul, A. and Kazmerski, L.L., 2013. Energy consumption and water production cost of conventional and renewable-energy-powered desalination processes. *Renewable and Sustainable Energy Reviews*, 24, pp.343-356.
- Darwish M.A., Al-Juwayhel F., Abdulraheim H.K., 2006. Multi-effect boiling systems from an energy viewpoint. *Desalination*, 194, 22–39
- Darwish M.A., Abdulrahim H.K. 2008. Feed water arrangements in a multi-effect desalting system. *Desalination*, 228, 30–54.
- Druetta P., Aguirre P., Mussati S., 2014. Minimizing the total cost of multi effect evaporation systems for seawater desalination. *Desalination*, 344, 431–445.
- Ettouney H.M., El-Dessouky H., 1999. A simulator for thermal desalination process. *Desalination*, 125, 277–291.
- Filipini G., Al-Obaidi M.A., Manenti F., Mujtaba I.M., 2018. Performance analysis of hybrid system of multi effect distillation and reverse osmosis for seawater desalination via modeling and simulation. *Desalination*, 448, 21–35.

Rate-based modelling and simulation of pilot scale distillation column

Mayra M. May-Vázquez, ^a Fernando I. Gómez-Castro, ^{a,*} Mario A. Rodríguez-Ángeles ^b

^a*Departamento de Ingeniería Química, División de Ciencias Naturales y Exactas, Campus Guanajuato, Universidad de Guanajuato, Noria Alta S/N Noria Alta, Guanajuato, Guanajuato 36050, Mexico*

^b*Departamento de Ingeniería en Plásticos, Universidad Politécnica de Juventino Rosas, Calle Hidalgo 102, Comunidad de Valencia, Santa Cruz de Juventino Rosas, Guanajuato 38253, Mexico*

fgomez@ugto.mx

Abstract

Batch distillation is perhaps the oldest operation used for separation of liquid mixtures. It is commonly used to produce fine chemicals and specialised products as alcoholic beverages, essential oils, perfume, pharmaceutical and petroleum products. Rigorous modelling of batch distillation can be developed by assuming phase equilibrium, or by rate-based approaches. The last approach represents in a more realistic way the phenomena occurring in the column, since it considers the heat and mass transfer rates for vapor and liquid phases. Due to the nature of their operation, batch distillation columns are modelled by a set of differential and algebraic equations (DAE). The present work concerns the simulation of a batch distillation column using the rate-based model, using a simplified approach for the calculation of the mass transfer rates. The pilot scale column modelled in this work has four trays, a total condenser and a pot. This column was used for separating a mixture of 75% mol methanol and 25% mol ethanol. As a first approach, mass transfer rates are obtained through rate-based simulations in Aspen Plus V8.8 for a pseudo-batch distillation column, using the Ideal thermodynamic model. The set of equations representing the rate-based batch column was solved using a specialized software (Polymath 6.0), taking the mass transfer rates as constant and equal to those obtained in the Aspen Plus simulation. The operating time of the batch column was 80 minutes, the thermal duty was kept as 500 W for the whole operation time, and the final composition in the pot was 72% mol methanol. The proposed strategy allows obtaining the composition and temperature profiles for the column, although it is still necessary to develop a proper mass transfer model to be included in the set of equations.

Keywords: batch distillation, rate-based modelling, mass transfer rates.

1. Introduction

Batch distillation is commonly used in the chemical, petroleum, polymers and pharmaceutical industries, and in the production of other fine chemicals. It is preferred over continuous distillation when the production is relatively small, when high added-value products are obtained, or it is required to produce different products in a single column.

For years the modelling and simulation of distillation columns has been the subject of several research. Several works have been presented for the modelling of the batch columns starting with the most elementary, as the one presented by Rayleigh, to the most robust formulation presented by Mujtaba (2004).

Two different approaches are available for the rigorous modelling of the interactions between phases in batch distillation columns, namely, equilibrium model and rate-based (nonequilibrium) model. The first one assumes vapor and liquid to be in thermodynamic equilibrium, using the efficiency of Murphree to describe the deviation from equilibrium. Thus, the accuracy of the predictions depends on the values assumed for this efficiency. The rate-based model doesn't require assuming the efficiency of Murphree, however, it requires good predictions of mass transfer coefficients, interfacial areas and diffusion coefficients (Sorensen, 2014).

In a trayed distillation column, the vapor from a lower stage is brought into contact with the liquid from an upper stage, allowing the two phases to exchange mass and energy across their common interface. Krishnamurthy and Taylor (1985) developed a nonequilibrium model based on general multicomponent mass and energy transport and using different correlations for the calculation of the binary mass transfer coefficient. A nonequilibrium or rate-based model employs the film model and equations based on transport phenomena to predict the mass transfer rates. This model is based on the MERSHQ equations, which consist of total and component material balances, energy balances, mass and energy rates of transfer across the interface, summation of mole fractions, hydraulic equation for pressure drop and equilibrium equations at vapor-liquid interface. The rate-based model is accurate (Taylor et al. 2000), but much more complicated than equilibrium model, therefore a more robust computing equipment is required to solve the system of equations. Ramesh et al. (2007) comments that an accurate mathematical model is necessary for the study of the dynamic characteristics and control of a distillation column, which is particularly important for batch distillation. López-Saucedo et al. (2016) presented the rigorous modelling for the simulation and optimization of a reactive batch distillation column. In the present work, a model for the representation of a pilot-scale batch distillation column is developed, taking as bases the model developed by López-Saucedo et al. (2016) but avoiding the reactive terms, and adding the mass and heat transfer contribution. As a first approach, mass transfer rates are assumed as constants, and a strategy to determine preliminary values for such rates is presented. The accuracy of such assumption is validated by comparison with experimental data.

2. Case of study

The present work concerns the modelling and simulation of a batch distillation column using the rate-based model. The work is divided in four stages: experimental, modelling of the pilot scale column, simulation in Aspen Plus V8.8 and solution of the obtained system of equations (DAE), using a specialized software (Polymath 6.0).

The experimental work was performed in a batch distillation column consisting of four sieve trays, a pot and a total condenser (Figure 1). This column was used to separate a mixture of alcohols with initial composition of 75% mol of methanol and 75% mol of ethanol, with initial charge of 0.196 kmol of the mixture. The characteristics of the column are shown in Table 1. The operating time of the batch column was 80 minutes, the thermal duty was kept as 500 W for the whole operation time. Samples were taken in each stage and then analysed in a gas chromatographer.



Figure 1.-Pilot scale column

Table 1.-Physical parameters of the batch column

Parameter	Value
Pot diameter	0.3 m
Pot height	0.27 m
Tray diameter	0.06 m
Tray Spacing	0.09 m

The rate-based mathematical model was developed for the column under study, with the following assumptions: the vapor-liquid interface reaches thermodynamic equilibrium, the trays are in mechanical equilibrium, the condenser operates at total condensation, the pot and the condenser are equilibrium stages, and the pressure along the column is constant. This last assumption is valid due to the small size of the column.

To obtain a preliminary estimate of the mass and heat transfer rates, a simulation of the pilot scale column was performed in Aspen Plus V8.8, representing the system a pseudo-batch column, by simulating a continuous column with feed on the bottoms and a reflux ratio of 1 and heat duty of 500 W. The column is represented with the RadFrac module, using the rate-based option. Thermodynamic equilibrium is modelled through the *Ideal* thermodynamic model.

The solution of the model for the batch column requires initial values for all the time-dependent variables. Such values are estimated by using the Aspen Batch Modeler V8.8, which assumes equilibrium for all the stages. The main specifications for this simulation are shown in Figure 2. Using the initial values obtained in this simulation for an initial condition of total reflux, the rate-based model is codified and solved in Polymath 6.0, aiming to obtain the liquid composition profile.

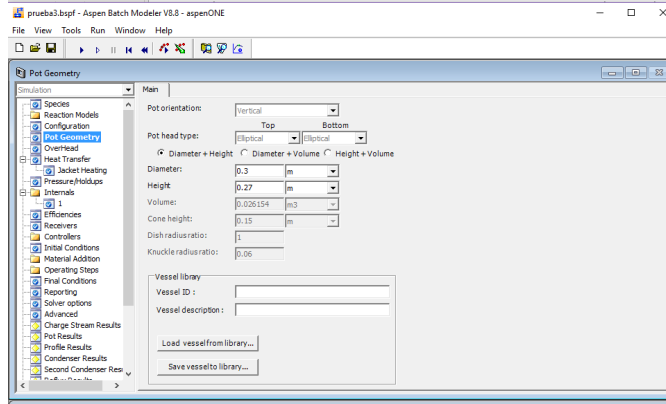


Figure 2.-Data for Aspen Batch Modeler

3. Results

The equations used to model the behaviour of the trays on the column are presented in this section. The total material balances for the vapor and liquid phases are:

$$\frac{dM_j^V}{dt} = V_{j-i} - V_j - N_{T,j} \quad (1)$$

$$\frac{dM_j^L}{dt} = V_{j+i} - V_j + N_{T,j} \quad (2)$$

The component material balances for component i in vapor and liquid phases on stage j are:

$$\frac{dy_{i,j}}{dt} = \frac{V_{j-1}}{M_j^V} y_{i,j-1} - \frac{V_j}{M_j^V} y_{i,j} - \frac{N_{i,j}^V}{M_j^V} \quad (3)$$

$$\frac{dx_{i,j}}{dt} = \frac{L_{j+1}}{M_j^L} x_{i,j+1} - \frac{L_j}{M_j^L} x_{i,j} + \frac{N_{i,j}^L}{M_j^L} \quad (4)$$

The energy balances of vapor and liquid phases on stage j are:

$$\frac{dH_i}{dt} = \frac{V_{j-1}}{M_j^V} H_{j-1} - \frac{V_j}{M_j^V} H_j - \frac{e_j^V}{M_j^V} \quad (5)$$

$$\frac{dh_i}{dt} = \frac{L_{j+1}}{M_j^L} h_{j+1} - \frac{L_j}{M_j^L} h_j + \frac{e_j^L}{M_j^L} \quad (6)$$

Rate of mass and energy transfer across interface is given by:

$$N_{i,j}^V = N_{i,j}^L \quad (7)$$

$$e_j^V = e_j^L \quad (8)$$

The mass and heat transfer rates in each stage are shown in Table 2. The stage 1 corresponds to the tray over the pot and the stage 4 corresponds to the tray below the condenser.

Table 2.-Mass and heat transfer rates (kmol/s)

Stage	Mass transfer rates (kmol/s)		Heat transfer rates (kJ/s)
	Methanol	Ethanol	Liquid
4	-3.30E-07	2.93E-07	-0.00211
3	-2.75E-07	2.44E-07	-0.00181
2	-2.23E-07	1.99E-07	-0.00151
1	-1.78E-07	1.59E-07	-0.00123

The trend of the composition in the pot is to increase because the amount of methanol in the reboiler decreases, while the distillate contains mostly methanol. As expected, the mol fractions of methanol tend to decrease from the upper to the lower stages for both, experimental and simulated results (Figure 3).

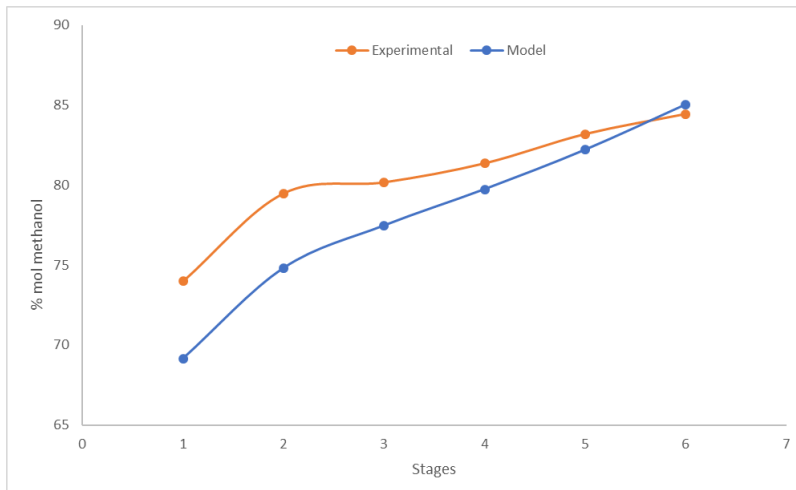


Figure 3.- Comparison of simulated and experimental profiles for liquid composition of methanol.

For the studied mixture, the composition of the pot changed from 75 mol% to a final composition of 74 mol% of methanol in the experimental system, while the model

predicts a variation from 75 mol% to 69.13 mol% of methanol. This represents a difference of approximately 5.87 mol% between the experimental and the numerical results. This gap is reduced as the profile reaches the top of the column. The difference between experimental and numerical data is attributed to the assumption of constant mass transfer rates. Thus, as a part of our future work, a mass transfer model applicable to the studied system will be developed and validated.

4. Conclusions

A rate-based model has been developed to represent the separation of an alcohol mixture in a pilot scale batch column, assuming constant mass and heat transfer rates.

The mol compositions are similar between the experimental and simulation of the case of study. The experimental time was 80 minutes, while the simulation time was 53 minutes; in both case the same amount of distillate was obtained. The error between the experimental and simulated composition of methanol was 6% maximum and 1% minimum. The rate-based model developed provides a good approximation with the experimental results, although a reliable mass transfer model is still required.

Acknowledgements

The authors acknowledge the financial support provided by Universidad de Guanajuato and CONACYT, through the scholarship granted to M.M. May-Vázquez.

References

- R. Krishnamurthy, R. Taylor, 1985, A Nonequilibrium Stage Model of Multicomponent Separation Processes. Part II: Comparison with Experiment, *AIChE J.*, 31, 3, 456-465.
- R. Taylor, R. Krishna, H. Kooijman, 2003, Real-World Modeling of Distillation, *Chem. Eng. Prog.*, July, 28-39.
- K. Ramesh, N. Aziz, S.R. Adb Shukor, M. Ramasamy, 2007, Dynamic Rate-Based and Equilibrium Model Approaches for Continuous Tray Distillation Column, *J. Appl. Sci. Res.*, 3, 12, 2030-2041.
- E. Sorensen, 2014, Design and Operation of Batch Distillation, in: *Distillation Fundamentals and Principles*, A. Górak and E. Sorensen (Eds.), Elsevier, UK, p. 187-224.
- I. M. Mujtaba, 2004, *Batch Distillation Design and Operation*, Imperial College Press, UK, p. 56-115.
- E. S. Lopez-Saucedo, I. E. Grossman, J. G. Segovia-Hernandez, S. Hernández, 2016, Rigorous modeling, simulation and optimization of a conventional batch reactive distillation column: A comparative study of dynamic optimization approaches, *Chem. Eng. Res. Des.*, 111, July, 83-99.

An MPEC model for Strategic Offers in a Jointly Cleared Energy and Reserve Market under Stochastic Production

Evangelos G. Tsimopoulos, Michael C. Georgiadis*

Aristotle University of Thessaloniki, Department of Chemical Engineering, 54124 Thessaloniki, Greece

mgeorg@auth.gr

Abstract

This work, based on Stackelberg hypothesis, considers a conventional power producer exercising their dominant position in an electricity pool with high penetration of wind power production. A bi-level optimization model is used to provide optimal offer strategies for the aforementioned producer in a jointly cleared energy and reserve pool settled through an hourly auction process. The upper-level problem illustrates the expected profit optimization of the strategic producer while the lower-level problem represents the energy-only market clearing process through a two-stage stochastic program. The first stage clears the day ahead market, and the second stage presents the system operation in balancing time through a set of plausible wind power production realizations. The bi-level problem is recast into mathematical programming with equilibrium constraints (MPEC) which is then reformulated into an MILP. These transformations occur using the Karush-Kuhn-Tucker optimality conditions and the strong duality theory. The suggested model provides optimal strategic offers and local marginal prices under different levels of wind penetration and network line transmission capacities.

Keywords: MPEC, energy-only markets, LMPs, strategic offers, wind uncertainty

1. Introduction

In recent years the electricity generation industry has experienced a remarkable penetration of renewable energy resources. However, the inherently uncontrollable fluctuations of renewable generation have resulted in the change of operational framework, the development of new tools to handle the stochastic nature of non-dispatchable production, and the redesign of market clearing algorithms (Conejo et al. 2011). Concerning the strong penetration of renewable sources supported by a generous mechanism of subsidized production and priority dispatch, the role of conventional energy production is diminishing. Although the market recognises the critical role of the thermal plants as capacity providers, the latter are faced with unequal treatment and have to adopt specific strategic behaviour to ensure competitiveness. Within the above context, and considering the conventional energy production, this work investigates the reaction of an incumbent firm and examines its incentives to exert market power and ensure its dominant position to avoid energy profit losses.

2. Problem Statement

This work analyses the optimal offering strategies of a conventional (thermal) power producer which participates with other conventional as well as wind power producers in a jointly cleared energy and balancing auction under network constraints. A bi-level programming model is developed based on Stackelberg leader-follower hypothesis. The upper-level problem determines expected profit maximization of the considered strategic producer which depend on clearing local marginal prices (LMPs) of day ahead (DA) and real time (RT) $\lambda_{n\omega}^{RT}$ market obtained at the lower level problem. On the other hand, the lower-level problem represents the clearing price process ensuing the least cost of energy dispatch conducted by the system operator (SO). Thus, the lower-level problem is formulated in a linearized DC network as two-stage stochastic programming. The first stage facilitates the DA market and results in the optimal anticipated dispatch (DA scheduled energy production), and the LMPs received as dual variables. The second stage represents the balancing market under the realization of all the plausible wind production scenarios and derives real time dispatch (reserve deployments) and RT prices (Morales et al. 2012). For the following formulation the indices i , o and j indicate the strategic conventional units, the nonstrategic conventional units and the wind farms respectively while the index d indicates the demands of the system. Additionally, the indices b and f refer to power blocks offered by the conventional units i , o and the wind farms j , the index k refers to power blocks consumed by load d and the index ω refers to wind power production scenarios. The sets Ψ_n^i , Ψ_n^o , Ψ_n^j and Ψ_n^d map the generation units and loads on to the system and the set Θ_n defines the connection of the bus n with the other buses of the network. The parameters c_{ib} , c_{ob} , c_{jf}^{DA} and u_{dk} represent the marginal cost of offered power blocks of generation units and the marginal utility of load blocks. In addition, the parameters c_i^{up} , c_o^{up} , c_i^{down} , c_o^{down} and $c_{j\omega}^{RT}$ indicate the cost of offered regulations and wind power realization at balancing stage. In addition, the parameter B_{nm} denotes the susceptance of the line n - m . The *here* and *now* decision variables P_{ib}^{DA} , P_{ob}^{DA} and W_{jf}^{DA} represent the scheduled production of conventional units and wind farms respectively and the δ_n^o represents the voltage angle at DA stage. The *wait* and *see* variables $r_{i\omega}^{up}$, $r_{o\omega}^{up}$, $r_{i\omega}^{down}$ and $r_{o\omega}^{down}$ refer to upward and downward reserves offered by units i and o , the $W_{j\omega}^{sp}$ indicates the wind power production spillage of wind farm j under scenario ω , the $L_{d\omega}^{sh}$ indicates the load shedding of demand d under scenario ω and the $\delta_{n\omega}$ indicates the voltage angle at RT stage. Finally, O_{ib}^{DA} defines the price offer of generation block b of strategic unit i in DA market while O_i^{up} and O_i^{down} define the price offer of upward and downward reserves of strategic unit i in RT market respectively.

2.1 Bi-level Formulation

The bi-level stochastic optimization model is formulated to derive its optimal offers as follows:

Upper level problem

$$\begin{aligned}
 \text{maximize} \quad & \sum_{(i \in \Psi_n^i) b} \lambda_n^{DA} P_{ib}^{DA} - \sum_{ib} c_{ib} P_{ib}^{DA} + \sum_{(i \in \Psi_n^i) \omega} \lambda_{n\omega}^{RT} \\
 & - \sum_{i\omega} \pi_\omega c_i^{up} r_{i\omega}^{up} - \sum_{(i \in \Psi_n^i) \omega} \lambda_{n\omega}^{RT} r_{i\omega}^{down} + \sum_{i\omega} \pi_\omega c_i^{down} r_{i\omega}^{down}
 \end{aligned} \tag{1}$$

Lower level problem

$$\begin{aligned}
 \text{minimize} \quad & \sum_{ib} O_{ib}^{DA} P_{ib}^{DA} + \sum_{i\omega} \pi_{\omega} O_i^{up} r_{i\omega}^{up} - \sum_{i\omega} \pi_{\omega} O_i^{down} r_{i\omega}^{down} \\
 & + \sum_{ob} c_{ob} P_{ob}^{DA} + \sum_{o\omega} \pi_{\omega} c_o^{up} r_{o\omega}^{up} - \sum_{o\omega} \pi_{\omega} c_o^{down} r_{o\omega}^{down} \\
 & + \sum_{jf} c_{jf}^{DA} W_{jf}^{DA} + \sum_{j\omega} \pi_{\omega} c_{j\omega}^{RT} \left(W_{j\omega}^{RT} - \sum_f W_{jf}^{DA} - W_{j\omega}^{sp} \right) \\
 & - \sum_{dk} u_{dk} L_{dk}^{DA} + \sum_{d\omega} \pi_{\omega} v L O L_d L_{d\omega}^{sh} \tag{2}
 \end{aligned}$$

$$\begin{aligned}
 \text{s.t.} \quad & - \sum_{(i \in \Psi_n^i) b} P_{ib}^{DA} - \sum_{(o \in \Psi_n^o) b} P_{ob}^{DA} - \sum_{(j \in \Psi_n^j) f} W_{jf}^{DA} \\
 & + \sum_{(d \in \Psi_n^d) k} L_{dk}^{DA} + \sum_{m \in \Theta_n} B_{nm} (\delta_n^o - \delta_m^o) = 0 \quad : (\lambda_n^{DA}) \quad \forall n \tag{3}
 \end{aligned}$$

$$\begin{aligned}
 & - \sum_{i \in \Psi_n^i} r_{i\omega}^{up} + \sum_{i \in \Psi_n^i} r_{i\omega}^{down} - \sum_{o \in \Psi_n^o} r_{o\omega}^{up} + \sum_{o \in \Psi_n^o} r_{o\omega}^{down} - \sum_{d \in \Psi_n^d} L_{d\omega}^{sh} \\
 & - \sum_{j \in \Psi_n^j} W_{j\omega}^{RT} + \sum_{(j \in \Psi_n^j) f} W_{jf}^{DA} + \sum_{j \in \Psi_n^j} W_{j\omega}^{sp} \\
 & + \sum_{m \in \Theta_n} B_{nm} (\delta_{n\omega} - \delta_n^o + \delta_m^o - \delta_{m\omega}) = 0 \quad : (\lambda_{n\omega}^{RT}) \quad \forall n, \forall \omega \tag{4}
 \end{aligned}$$

$$\sum_b P_{ib}^{DA} + r_{i\omega}^{up} \leq \sum_b P_{ib}^{MAX} \quad : (\mu_{i\omega}^{max}) \quad \forall i, \forall \omega \tag{5}$$

$$\sum_b P_{ob}^{DA} + r_{i\omega}^{up} \leq \sum_b P_{ob}^{MAX} \quad : (\mu_{o\omega}^{max}) \quad \forall o, \forall \omega \tag{6}$$

$$r_{i\omega}^{down} - \sum_b P_{ib}^{DA} \leq 0 \quad : (\mu_{i\omega}^{min}) \quad \forall i, \forall \omega \tag{7}$$

$$r_{o\omega}^{down} - \sum_b P_{ob}^{DA} \leq 0 \quad : (\mu_{o\omega}^{min}) \quad \forall o, \forall \omega \tag{8}$$

$$0 \leq W_{j\omega}^{sp} \leq W_{j\omega}^{RT} \quad : (\kappa_{j\omega}^{min}, \kappa_{j\omega}^{max}) \quad \forall j, \forall \omega \tag{9}$$

$$0 \leq L_{d\omega}^{sh} \leq \sum_k L_{dk}^{DA} \quad : (v_{d\omega}^{min}, v_{d\omega}^{max}) \quad \forall d, \forall \omega \tag{10}$$

The objective function (1) optimizes the expected profit of the strategic producer, and it is defined by the revenues from the day DA and RT market minus the actual incurred cost. The objective function (2) optimizes the expected cost of the power system operation conducted by SO. It consists of the scheduled production cost and the scenario dependent reserve deployment, spilling wind power and shedding load cost in real time operation. Constraint (3) enforces the energy balance at each node and the transmission capacity limits between them at DA. Thus, the total power flowing into bus n , which is the algebraic sum of generation and load at the bus, should be equal to the power flowing away from the bus. Constraint (4) counterbalances the imbalance occurred in RT due to the uncertain wind production arranging the reserve deployment

and the load curtailments. Constraints (5), (6), (7) and (8) ensure that unit generation is above zero and below maximum capacity P_{ib}^{MAX} and P_{ob}^{MAX} of units i and o capturing the coupling between anticipated dispatch and deployed reserve. Constraints (9) and (10) indicate that the wind energy spillage cannot exceed the scenario dependent actual wind energy production $W_{j\omega}^{RT}$ and the involuntary load curtailment cannot exceed the actual load consumption. Moreover, other constraints enforce transmission capacity limits between two buses, upper and lower bounds of voltage angle at each bus. Finally, the bus $n1$ is defined as slack bus thus δ_{n1}^o and $\delta_{(n1)\omega}^o$ equal to zero.

2.2 MPEC formulation and linearization

Considering the continuity and the convexity of the lower problem, the bi-level problem is reduced to an MPEC through first-order KKT optimality conditions. In this case, the Lagrange multipliers have the same meaning with the dual variables in linear programming. Using disjunctive constraints to linearize the KKT complementarity constraints (Fortuny-Amat and McCarl, 1981) as well as the strong duality theorem in combination with some of the KKT equality constraints to eliminate the non-linear terms within objective function (1) (Ruiz and Conejo, 2009), the MPEC is reformulated in an MILP solvable by commercial solvers such as GAMS/CPLEX.

3. Illustrative example

The proposed clearing market formulation is applied in a six-node system sketched in Fig. 1. The conventional generating units $i1$, $i2$, $i3$ and $i4$ belong to the strategic producer and the $o1$, $o2$, $o3$ and $o4$ belong to non-strategic producers. The technical data of the units is taken from Ruiz and Conejo (2009). Two wind farms $j1$ and $j2$, located at bus $n2$ and $n5$, have installed capacity of 100 MW and 70 MW, and their scheduled power production is offered in one block with zero marginal cost. Wind farms' uncertain power production is realized through three scenarios, $\omega1$ (high production) with 100 MWh and 70 MWh, $\omega2$ (medium production) with 50 MWh and 35 MWh, and $\omega3$ (low production) with 20 MWh and 15 MWh while occurrence probability of each scenario is 0.2, 0.5 and 0.3 respectively. A total demand of 1 GWh is allocated according to Figure 1. Load $d1$ accounts for 19 % and loads $d2$, $d3$ and $d4$ account for 27 % of the total demand each. Additionally, data about demand bids (energy and utility marginal cost) for each period of time comes from Ruiz and Conejo (2009). Finally, the value of the involuntary load reduction is 200 euro/MWh for all demands and all the connecting lines have a transmission capacity of 500 MW with susceptance equal to 9412 per unit.

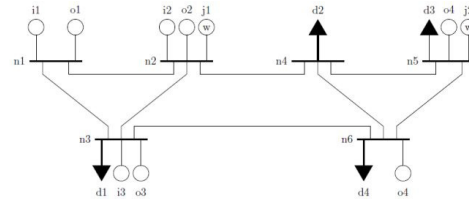


Figure 1. six-bus system

4. Results

4.1. Uncongested network solution

Based on the above information the proposed MILP model is applied to the system and solved using GAMS/CPLEX. When the strategic producer offers at marginal cost, the DA clearing price is constant throughout the 24-period time at a level of 11.260 /MWh. However, when the strategic producer exerts their market power the DA

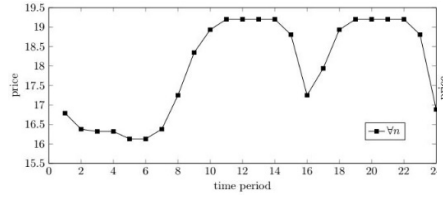


Figure 2. DA clearing prices [€/MWh]

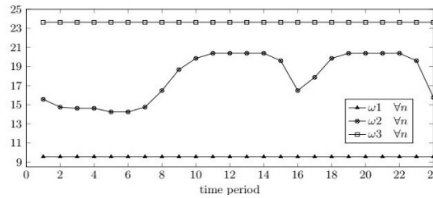


Figure 3. RT clearing prices [€/MWh]

clearing price is raised, while fluctuating between 16.130 and 19.200 €/MWh as shown in Figure 2. Similarly, the RT clearing prices are raised too. More specifically, in high wind scenario

ω_1 realization the RT price increases from 9.280 to 9.570 €/MWh, in medium wind scenario ω_2 the RT clearing price leaves the level of 11.470 €/MWh and moves in a range between 14.254 and 20.394 €/MWh, and in low wind scenario ω_3 the price rockets from 12.230 to 23.630 €/MWh as presented in Figure 3. In both cases, the prices are the same in all buses at each time period as line capacities are enough to facilitate the energy transaction. The proposed model results in an increase in the total expected profit of the strategic producer from 9,326 € to 67,556 € even though the producer's scheduled power production as well as its deployed reserve decreases in all wind scenarios.

4.2. Congested network solution

In the previous case the maximum power flow through line 3-6 is 227 MW. If the line capacity is reduced at the level of 240 MW, slightly above the maximum flow, the results

remain the same when the strategic producer acts as price taker. However, the proposed MILP formulation shows that the strategic producer can make offers in such a way that the system becomes congested resulting in different LMPs of DA and RT clearing prices at specific time periods as illustrated in Figures 4 and 5 respectively. It can be seen that bus n6 exhibits the highest price giving the strategic producer the opportunity

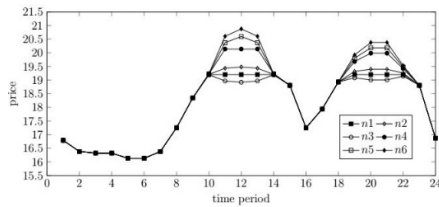


Figure 2. DA clearing prices [/MWh]

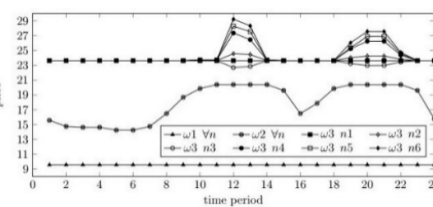


Figure 3. RT clearing prices [/MWh]

to increase the profit of unit i4. In that way the total expected profit of the strategic producer is slightly higher compared to that of uncongested network. Additionally, in the uncongested case the maximum power flow through line 4-6 is 24 MW. If the capacity of the line is reduced to 20 MW, slightly below the maximum flow, the network becomes congested under cost offer optimization, resulting in different LMPs and profit losses for the strategic producer. However, applying the proposed MILP formulation, the strategic producer changes the mixture of units' production keeping the line uncongested and the profit high.

4.3. Wind power production increment

In this case, the level of wind power penetration increases from 10 % to 14.16 % of the total installed capacity. More specifically, the power production of the wind farms j1 and j2 is 150 MW and 100 MW respectively in high wind scenario ω_1 , 75 MW and 50 MW in medium wind scenario ω_2 , and 30 MW and 20 MW in low wind scenario ω_3 . It can be seen in Fig.6 that the expected profits of units i1 and i2 are reduced in all wind scenarios. Considering unit i4 the expected profits decrease in high wind scenario ω_1 ; however, the expected profits increase in medium and low wind scenarios as the unit becomes more involved in reserve supply. Nevertheless, even if the total expected profits of unit i4 rise, the total expected profits of strategic producer decrease from 67,556 euro to 59,589 euro, indicating that wind power production can be used as a tool for market power mitigation.

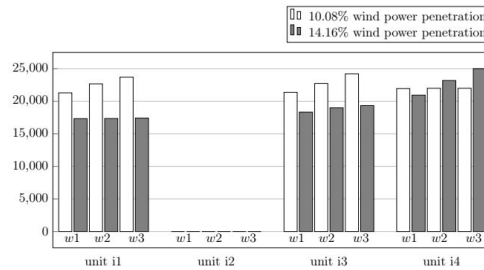


Figure 4. Profit of strategic units under different level of wind power penetration

5. Conclusions

In this work based on Stackelberg hypothesis, an MILP is developed to derive optimal offer strategies for a conventional power producer participating in a jointly cleared energy and reserve market under high penetration of wind power production. The model concerns energy-only markets. Co-optimizing scheduled energy and reserve deployment through two-stage stochastic programming, it gives insight information on LMPs and the way they are configured when the strategic producer exercises its dominant position in the market. Furthermore, the model provides information about how line capacities and network congestions can be used for the benefit of the strategic producer and indicates that wind power production can be used as an instrument of market power mitigation. Future work should involve a larger number of wind production scenarios and scenario reduction techniques. The model should also incorporate intertemporal constraints such as units' ramp-up and ramp-down limitations as well as non-convexities, e.g., unit minimum power production and unit start-up and shut-down

References

- A. J. Conejo, J. M. Morales and J. A. Martinez, (2011). Tools for the analysis and design of distributed resources Part III: Market studies. *IEEE Transactions on Power Delivery*, 26(3), 1663-1670.
- J. Fortuny-Amat and B. McCarl, (1981). A representation and economic interpretation of a two-level programming problem. *Journal of the operational Research Society*, 32(9), 783-792.
- J. M. Morales, A. J. Conejo, K. Liu and J. Zhong, (2012), Pricing electricity in pools with wind producers. *IEEE Transactions on Power Systems*, 27(3), 1366-1376.
- C. Ruiz and A. J. Conejo, (2009), Pool strategy of a producer with endogenous formation of locational marginal prices, *IEEE Transactions on Power Systems*, 24(4), 1855-1866.

Decision-making of online rescheduling procedures using neuroevolution of augmenting topologies

Teemu J. Ikonen^a and Iiro Harjunoski^{a,b,*}

^a*Aalto University, School of Chemical Engineering, Kemistintie 1, 02150 Espoo, Finland*

^b*ABB Corporate Research, Wallstadter Str. 59, 68526 Ladenburg, Germany*

**iiro.harjunoski@aalto.fi*

Abstract

Online scheduling requires appropriate timing of rescheduling procedures, as well as the determination of relevant horizon length. Optimal choices of these quantities are highly dependent on the uncertainty of the scheduling environment and may vary over time. We propose an approach where a neural network is trained to make online decisions on these quantities, as well as on the choice of the rescheduling method (mathematical programming or metaheuristics). In our approach, the neural network is trained using neuroevolution of augmenting topologies (NEAT) in a simulated environment. In this paper, we also optimize the rescheduling interval and horizon length of a conventional periodically occurring rescheduling on a dynamic routing problem. The resulting approach is the baseline for the development of the proposed neural network approach.

Keywords: online scheduling, horizon length, scheduling interval, neural network, NEAT

1. Introduction

Online scheduling of industrial processes is a demanding task, mainly due to a large number of solution candidates and uncertainty in scheduling parameters. Considering batch processes, the most common optimization approach in offline scheduling is mixed-integer programming (MIP), using modeling formalisms, e.g. resource-task network (Pantelides, 1994), state-task network (Kondili et al., 1993) or generalized disjunctive programming (Raman and Grossmann, 1994). Given a reasonably large amount of computational time, these approaches can often find the optimal solution. However, in online scheduling, the duration of the optimization process is constrained due to the moving time horizon, which significantly compromises the optimality of the solution. Another aspect to consider is that the later the optimization process is initiated, the more accurate are its scheduling parameters. This raises questions, such as what is the optimal rescheduling interval and what is a relevant length for the scheduling horizon. For a recent review of online scheduling, the reader may wish to consult the paper by Gupta et al. (2016).

We propose an approach where an artificial neural network trained to decide when to initiate a rescheduling process, what length to define for the time horizon and which optimization strategy (mathematical programming or metaheuristics) to use. In many previous studies, neural networks have been used to learn dispatching rules from the historical data of scheduling decisions (Priore et al., 2014). However, this approach can typically only mimic the historical decisions, and therefore the optimality of the scheduling solu-

tions is highly dependent on the quality of the given historical data. Our neural network approach operates at a higher level; it exploits the strength of MIP at finding the optimal, or near-optimal solution, and focuses on the allocation of the computational resources in the changing scheduling environment.

More specifically, we propose to use neuroevolution of augmenting topologies (NEAT), introduced by Stanley and Miikkulainen (2002), to train the neural network. NEAT is a genetic algorithm that simultaneously evolves the topology and weighting parameters of the neural network. Such et al. (2017) report the performance of the evolutionary neuroevolution algorithms to compare well against the gradient-based backpropagation algorithms. A key feature of NEAT is that the evolution process is initiated from very simple neural networks, the topology of which is then incrementally increased complexity during the evolution. The feature reduces unnecessary complexity of the final neural network, and is not possible using gradient-based algorithms. Recently, Hausknecht et al. (2014) applied NEAT to train a neural network to play 61 different Atari 2600 games, where the controls for the player are to move a joystick and press a button. The controls for our neural network are also of a similar low level of complexity (see the second paragraph), but the critical aspect is their timely execution.

In this paper, we first define a rescheduling problem (Section 2), suitable to be used as a test case for our neural network-based rescheduling approach. For the sake of simplicity, we define the underlying optimization problem to be a routing problem. However, our approach is also applicable to rescheduling of other industrial processes, e.g. batch processes. In Section 3, we tune the horizon length and rescheduling interval of the conventional periodically occurring rescheduling approach. This approach is a benchmark for our neural network-based approach. Finally, in Section 4, we describe the intended input and output signals for the neural network.

2. Dynamic routing problem

Let us consider a square region, having dimensions 1000×1000 m, and a vehicle traveling in the region at a constant speed of $v = 10$ m/s. The purpose of the vehicle is to visit n sites in the region before site-specific due dates. Each site has an order date, at which the vehicle receives the location and due date of the site. The objective of the optimization problem is to minimize the delay sum of visiting the n sites. Since scheduling decision must be made with limited information, finding the optimal solution to the problem requires rescheduling.

As an optimizer, we here use ant colony optimization (ACO) (Dorigo and Gambardella, 1997), which is a probabilistic metaheuristic search method of finding good paths in a graph. In the method, ants communicate by laying pheromone on paths between nodes. The laid pheromone concentration of an ant is proportional to the objective function value of the route the ant traveled. When a new ant is at node i , it chooses the path to node j with probability

$$p_{ij} = \frac{\phi_{ij}^\alpha d_{ij}^\beta}{\sum_{i,j=1}^n \phi_{ij}^\alpha d_{ij}^\beta}, \quad (1)$$

where ϕ_{ij} and d_{ij} are the pheromone level and desirability¹ of the path (i, j) . where α and β are influence parameters². We use a population size of 200. We have implement ACO using the Python module ACOPy (Grant, 2018).

In this and the next section, we study periodic rescheduling with fixed interval and horizon length. At $t = 0$, the vehicle starts to follow an initial path, determined by a greedy algorithm (which is defined to always choose the node lying closest to the current node). The path is then updated when the first rescheduling procedure is finished. The computational budget of all the rescheduling procedures during the time span is restricted to 50 CPU seconds. The computational budget is distributed evenly between the rescheduling processes. Therefore, a frequent rescheduling will have a small computation budget per rescheduling process, and vice versa. Each rescheduling procedure is associated with times t_{info} and t_{exe} , the difference of which is the duration of the procedure. The rescheduling is conducted using the information available at t_{info} , whereas t_{exe} is the planned start time of the new schedule.

2.1. A simple numerical example

Let us next present a solution to a simple routing problem of nine sites. The sites are randomly distributed inside the region (Figure 1(a)), and their due dates are randomly selected from the time interval of $[0, 500\text{s}]$ (Table 1). Further, the order dates of sites 1 to 7 are set to 0 s, while the order dates of sites 8 and 9 are randomly selected from the time interval of $[0, t_{\text{due}}]$, where t_{due} is the due date of the site (Table 1).

Table 1: Order and due dates for the sites in the simple numerical example.

site [-]	order date [s]	due date [s]	site [-]	order date [s]	due date [s]
1	0	46	6	0	400
2	0	198	7	0	346
3	0	343	8	4	43
4	0	14	9	185	439
5	0	279			

In this numerical example, we choose to use a scheduling interval of 50 s and horizon length of 500 s (i.e. the entire time span of the problem). Figure 1(a) shows the initial route (determined by a greedy search) for the vehicle. Further, Figures 1(b)-1(d) visualize intermediate states of the process. At $t_{\text{exe}} = 5$ s, the optimizer schedules the visit to the most critical site 1 before visiting sites 6 and 2. At $t_{\text{exe}} = 55$ s and $t_{\text{exe}} = 205$ s, the optimizer includes visits to sites 8 and 9, respectively, in the schedule. The locations and due dates of these sites were not known at the start of the time span. Figure 1(e) shows the final (realized) route of the vehicle. The delay sum of the final route is 235.30 s, which is caused by the vehicle failing to meet the due dates at sites 1, 4 and 8 (see Figure 1(f)).

3. Tuning of the rescheduling interval and horizon length

The purpose of the numerical example in the previous section was to provide an introduction to the dynamic routing problem, which we intend to study with the neural network

¹In this work, we use the distance of a path as its desirability measure.

²In this work, we use values $\alpha = 1$ and $\beta = 3$.

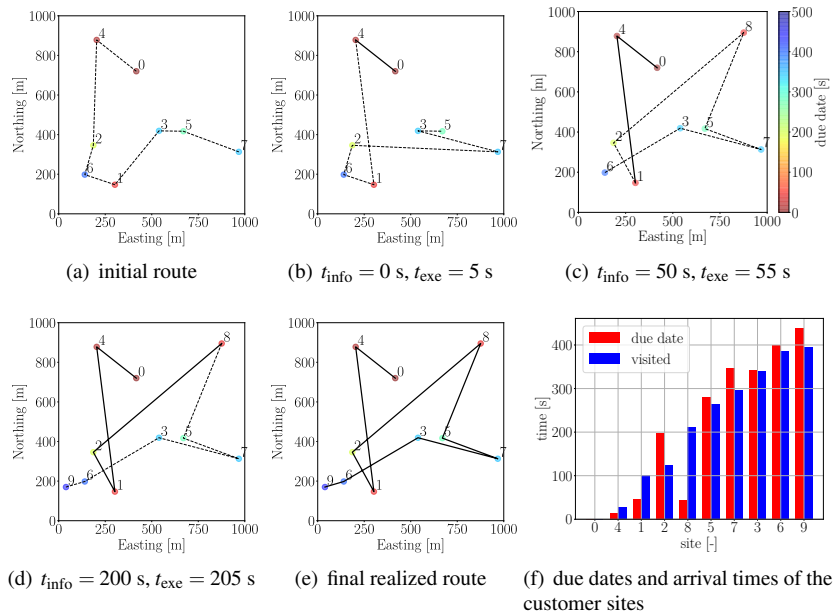


Figure 1: Representative states and the final results of the rescheduling procedure with nine sites to be visited. The locations and due dates of sites 8 and 9 are received at $t = 4$ s and 185 s, respectively, whereas the other orders are already known at $t = 0$. Continuous path represents realized route of the vehicle, and dashed line the scheduled route.

based approach. In this section, we examine a similar, but larger, routing problem with a total of 50 sites, and a time span of 1000 s. The locations and due dates of 40 sites are known at $t = 0$, whereas for the remaining 10 sites the information is obtained again at a random time point in the interval of $[0, t_{\text{due}}]$, where t_{due} is the due date of the site.

When using the periodically occurring rescheduling procedures, the optimal values for the rescheduling interval and horizon length are problem-dependent. Thus, in this section, we also use a grid search to systematically seek an optimized combination of the two parameters. The results of the grid search are shown in Figure 3. Out of the tested parameter combinations, the best final objective value (i.e. the delay sum) is obtained by the scheduling interval of 120 s and the horizon length of 500 s. We omit those parameter combinations, in which the scheduling interval is larger than the scheduling horizon (see the bottom right corner of Figure 3), as the vehicle would need to wait at certain sites for the schedule to be updated. Based on the results, the performance of the rescheduling procedure is poor for combinations lying close to this constraint, but also for combinations with very frequent rescheduling and long horizon length. In the former, the algorithm does not exploit enough information it has about the future, whereas in the latter the algorithm does not have enough computational time to find good solutions (to relatively large scheduling problems).

Finally, let us examine the rescheduling procedure with the optimized rescheduling interval and horizon length. Figures 2 and 4 visualize the initial route, the intermediate state at

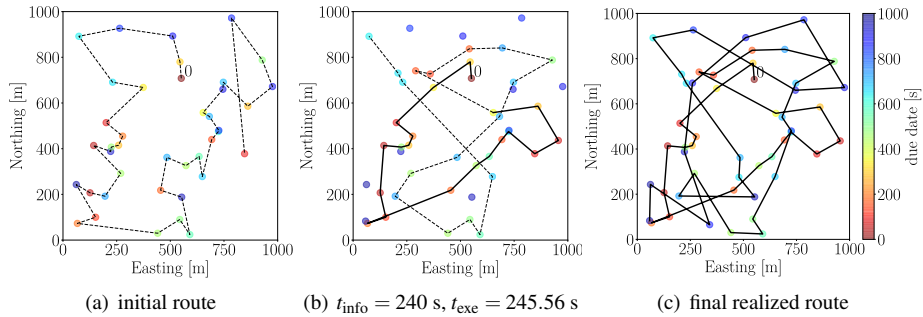


Figure 2: Representative states and the final results of the rescheduling procedure with 50 sites.

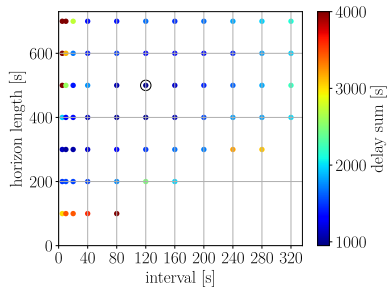


Figure 3: A grid search of best-performing rescheduling interval and horizon length. The best parameter combination is highlighted by a circle. Darkest red points exceed the scale.

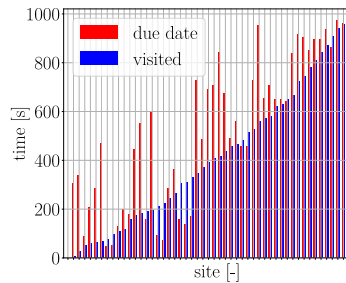


Figure 4: Due dates and arrival times of the final route (Figure 2(c)).

$t_{\text{exe}} = 245.56$ s and the final realized route of the rescheduling procedure. The delay sum of the final route is 992.89 s. Despite being a solution to a larger scale problem, the same features are also present here as in the simple example (Section 2.1): sites with urgent due dates are prioritized and, as the time proceeds, new orders are included in the schedule.

4. Proposed input and output signals

The periodically occurring rescheduling with tuned interval and horizon length seems to work reasonably well for these relatively small-scale scheduling problems. Another possible approach would be to trigger the rescheduling always when new information is obtained. However, the rescheduling decisions made by these approaches may be compromised, especially in larger problems, or if new information is obtained more frequently.

Thus, we propose the scheduling decisions to be made using a neural network that is trained by the NEAT algorithm. Figure 5 shows the input nodes we propose for the neural network. The input signals represent changes in the scheduling environment, the status of the ongoing rescheduling procedure, and the remaining computational resources.

At each evaluation, the neural network decides to either run a rescheduling procedure, using metaheuristics or mathematical programming, or to do nothing (depending which of the three top output nodes receives the highest signal). In addition, the neural network includes signals for the horizon length and allocated computational time for the possible rescheduling procedure.

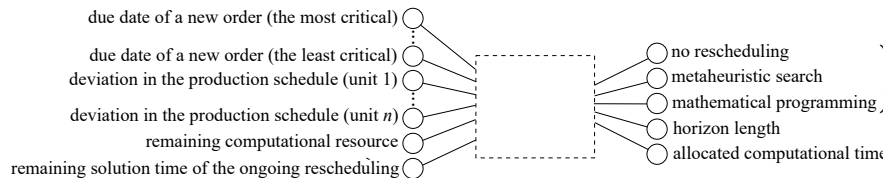


Figure 5: Proposed input and output signals for the neural network. Here, the neural network is depicted as a box as in NEAT its topology is decided during the training procedure.

5. Conclusions

We propose the rescheduling decision in online scheduling to be made by a neural network, trained using the NEAT algorithm. As a first step, this paper presents a dynamic routing problem suitable to be used as a demonstration and benchmarking problem for our approach. We optimized the rescheduling interval and horizon length of the conventional periodically occurring rescheduling procedure, in order to obtain a relevant baseline approach. The future work involves training and evaluation of the NEAT algorithm for the presented routing problem.

Acknowledgment: Financial support is gratefully acknowledged from the Academy of Finland project "SINGPRO", Decision No. 313466.

References

- M. Dorigo, L. M. Gambardella, 1997. Ant colony system: a cooperative learning approach to the traveling salesman problem. *IEEE Transactions on evolutionary computation* 1 (1), 53–66.
- R. Grant, 2018. Acopy [accessed on the 15th of october, 2018]. <https://github.com/rhgrant10/acopy>.
- D. Gupta, C. T. Maravelias, J. M. Wassick, 2016. From rescheduling to online scheduling. *Chemical Engineering Research and Design* 116, 83–97.
- M. Hausknecht, J. Lehman, R. Miikkulainen, P. Stone, 2014. A neuroevolution approach to general atari game playing. *IEEE Transactions on Computational Intelligence and AI in Games* 6 (4), 355–366.
- E. Kondili, C. C. Pantelides, R. W. H. Sargent, 1993. A general algorithm for short-term scheduling of batch operations—I. MILP formulation. *Computers & Chemical Engineering* 17 (2), 211–227.
- C. C. Pantelides, 1994. Unified frameworks for optimal process planning and scheduling. In: *Proceedings on the second conference on foundations of computer aided operations*. Cache Publications New York, pp. 253–274.
- P. Priore, A. Gómez, R. Pino, R. Rosillo, 2014. Dynamic scheduling of manufacturing systems using machine learning: An updated review. *AI EDAM* 28 (1), 83–97.
- R. Raman, I. E. Grossmann, 1994. Modelling and computational techniques for logic based integer programming. *Computers & Chemical Engineering* 18 (7), 563–578.
- K. O. Stanley, R. Miikkulainen, 2002. Evolving neural networks through augmenting topologies. *Evolutionary computation* 10 (2), 99–127.
- F. P. Such, V. Madhavan, E. Conti, J. Lehman, K. O. Stanley, J. Clune, 2017. Deep neuroevolution: genetic algorithms are a competitive alternative for training deep neural networks for reinforcement learning. *arXiv preprint arXiv:1712.06567*.

Model-Based Bidding Strategies for Simultaneous Optimal Participation in Different Balancing Markets

Pascal Schäfer^a, Nils Hansmann^a, Svetlina Ilieva^b and Alexander Mitsos^{a,*}

^a*Aachener Verfahrenstechnik – Process Systems Engineering, RWTH Aachen University, Aachen, Germany*

^b*TRIMET Aluminium SE, Essen, Germany*
amitsos@alum.mit.edu

Abstract

Due to the increasing share of intermittent renewable energy sources, energy-intensive enterprises are nowadays motivated to actively participate in electricity markets. They can do so by marketing their operational flexibility either at spot markets or by offering ancillary services on demand, such as balancing power. We propose an optimization-based methodology to select which capacity to offer at which market. We extend our framework for optimizing the bidding strategy at the primary balancing market (Schäfer et al. (2019)) to a simultaneous participation in both the primary and the secondary balancing market. We solve the resulting optimization problem using a hybrid stochastic-deterministic approach. The framework applies a genetic algorithm with a subordinated mixed-integer linear solver that allows for marketing the remaining flexibility at spot markets through solving a scheduling problem. For an industrial aluminum electrolysis, we demonstrate the efficacy of the approach to identify profitable bidding strategies. We show for an exemplary week with price data from 2018 that by optimal participation in balancing markets, savings of more than 10 % in weekly costs are enabled compared to a non-flexible operation.

Keywords: Demand side management, Aluminum electrolysis, Ancillary service markets, Mixed-integer nonlinear programming, Model-based bidding strategies

1. Introduction

The increasing share of electricity generation from intermittent renewable sources and the involved increasing volatility at electricity markets represent a severe challenge for the energy-intensive industry (Mitsos et al. (2018)). However, at the same time, flexible consumers can also benefit from these circumstances by adapting their consumption to fluctuating market signals (e.g., Ghoheity and Mitsos (2010); Mitra et al. (2012)). In addition to that, consumers also have the opportunity to offer parts of their flexibility range at ancillary service markets, which opens further promising revenue potentials (Paulus and Borggrefe (2011); Dowling et al. (2017)). It is thus crucial to have systematic approaches for selecting which capacity to offer at which market (e.g., Zhang et al. (2015); Otashu and Baldea (2018)), as usually a reserve capacity is not allowed to be marketed at the same time at multiple markets. Furthermore, in some important market environments like the European balancing market, the prices that market participants ask for the provision of the ancillary services are of high relevance as they not only determine the probability of acceptance of an offer but also define the potential revenues. In order to balance these trade-offs, we recently proposed to formulate the optimal bids at the market for primary balancing power (PRL) as a two-stage stochastic optimization problem where remaining capacities after acceptance or rejection of the individual bids can be used for optimization at spot electricity markets (Schäfer et al. (2019)).

In this work, we extend the formulation to cope with more than one balancing market simultaneously. More precisely, we also consider the market for secondary balancing power (SRL) that opens further revenue potentials, but also poses different rules for bidding than the PRL market. In order to cope with the increased complexity of the resulting optimization problem, we use a hybrid stochastic-deterministic solution approach. We apply the approach to an industrial aluminum electrolysis to calculate the optimal bidding strategy for one exemplary week from 2018. Finally, we discuss revenue potentials that are enabled via the optimal strategy in comparison to a pure marketing at the spot market and a single bidding at the PRL market only.

2. Primary and secondary balancing market

Both the German PRL and SRL market are auction markets where all participants are allowed to submit their individual bids. In case of PRL, one bid consists of a capacity [MW] reserved for balancing power for the entire horizon (one week) and a capacity price [EUR/MW] that the bidder is willing to accept as compensation. Once the auction is closed, those bids with the lowest capacity prices are accepted, until the total demand of PRL is satisfied. Note that if the bid is accepted, the capacity price is paid irrespectively of whether the held capacity is actually retrieved. The smallest capacity that can be offered at the PRL market is 1 MW. The increment is 1 MW. At the SRL market, there are three important differences: (i) the horizon is subdivided into periods that take into account the varying demand for balancing power in the course of the horizon, (ii) capacities for a load reduction and a load increase can be offered separately, and (iii) participants need to further submit an asked energy price [EUR/MWh] that is only paid for the actual retrieval of the balancing power. These energy prices determine how often the capacities are retrieved, i.e., capacities with low energy prices are retrieved more often. The smallest capacity that can be offered at the SRL market is 5 MW. The increment is again 1 MW.

3. Model-based bidding

3.1. Definitions and preliminary assumptions

For marketing the remaining flexibility, we herein only consider the day-ahead market. We assume that day-ahead prices for the entire week are known when the bidding takes place. Price data is retrieved from EPEX SPOT (www.epexspot.com). All data concerning balancing power is retrieved from the central auction platform REGELLEISTUNG.NET (www.regelleistung.net).

For each balancing power product j , we consider only one submitted bid. Placing more than one bid has been shown in our previous work to have only minor influences on potential revenues (Schäfer et al. (2019)). A bidding strategy thus comprises 14 variables: a capacity P_j and a capacity price CP_j for PRL as well as for each of the four considered SRL products (two load directions *POS* and *NEG* with each two periods denoted by *HT* and *NT*) plus an energy price EP_j for each of the SRL products. The decision variables are summarized in the vector \mathbf{x} . We assume that the individual bids are accepted once the submitted asked capacity prices are lower than the upcoming maximum accepted ask prices for the respective products. For methods to estimate the marginal price, we refer to the relevant literature (e.g., Box and Jenkins (1994)). To simplify the presentation and discussion, we herein assume that the maximum accepted ask price of product j is normally distributed around its real value μ_j with a standard deviation of $\sigma_j = 0.05\mu_j$. Thus, the probability of acceptance p_j for the offered capacity for product j reads

$$p_j = \frac{1}{2} \left(1 - \operatorname{erf} \left(\frac{CP_j - \mu_j}{\sqrt{2}\sigma_j} \right) \right), \quad j \in \{PRL, POSHT, NEGHT, POSNT, NEGNT\}. \quad (1)$$

Other probability distributions can be used as well, as long as the respective cumulative distribution functions can be computed. Note that when using the hybrid stochastic-deterministic solution approach presented, no further assumptions on the probability distribution are required, e.g., concerning availability of gradients or relaxations.

The compensation payments, i.e., the revenues from a balancing power product R_j , can be calculated using the following equations. In case of PRL, capacity and capacity price are just multiplied (Eq. (2)). In case of the SRL products, a second term is added for the compensation of the actual retrieved energy E_j over the entire horizon (Eq. (3)). We express the relation between E_j and OP_j via an exponential function. Parameters of the functions are fitted to historic retrieval data.

$$R_j = CP_j \cdot P_j, \quad j \in \{PRL\} \quad (2)$$

$$R_j = CP_j \cdot P_j + OP_j \cdot E_j, \quad j \in \{POSHT, NEGHT, POSNT, NEGNT\} \quad (3)$$

$$E_j = P_j \cdot \exp(a_j + b_j \cdot OP_j), \quad j \in \{POSHT, NEGHT, POSNT, NEGNT\} \quad (4)$$

3.2. Formulation of the optimization problem

We minimize the expected weekly costs ϕ , wherein the compensation payments from the balancing markets are considered as negative costs. ϕ itself can be written as a probability-weighted sum over mutually exclusive scenarios (Eq. (5)). The scenarios arise from the combination possibilities of acceptance and rejection of the individual bids. Considering one bid for each of the five balancing power products, there are $N = 2^5 = 32$ possible scenarios. Scenario i can be characterized by the set of accepted bids j_i^* . The probability for one scenario p_i as well as the revenues R_i can be calculated by summation or multiplication of the individual p_j 's (Eq. (6)) and R_j 's (Eq. (7)) respectively. Furthermore, in each of the scenarios, the remaining flexibility range, i.e., the part of the original flexibility range which has not been reserved for provision of balancing power, can be marketed at the day-ahead market in order to lower the weekly costs without the revenues (C_i 's). This is done by solving an integrated scheduling model which is denoted as the function $C^*(\cdot)$ in the following.

$$\min_{\mathbf{x}} \phi = \sum_{i=1}^N p_i (C_i - R_i) \quad (5)$$

$$\text{s.t. } p_i = \left(\prod_{j \in j_i^*} p_j \right) \cdot \left(\prod_{j \notin j_i^*} (1 - p_j) \right), \quad i = 1 \dots N \quad (6)$$

$$R_i = \sum_{j \in j_i^*} R_j, \quad i = 1 \dots N \quad (7)$$

$$\text{Eq. (1)-(4)} \quad (8)$$

$$C_i = C^* \left(P_{j \in j_i^*}, E_{j \in j_i^*} \right), \quad i = 1 \dots N \quad (9)$$

$$P_j \in \{1, \dots, P_{j,max}\} \quad (10)$$

For setting up the function $C^*(\cdot)$ for the process considered in the case study - an industrial aluminum process - we refer to Schäfer et al. (2019). Therein, we describe a mixed-inter linear programming (MILP) scheduling formulation for optimizing the electricity consumption of the process considering operating limits, off-design efficiency losses and opportunity costs due to the provision of balancing power. In this work, we only slightly adjust the model by accounting for surpluses or deficits in the energy balance of the cell due to the retrieval of SRL. The maximum capacity that can be offered in product j are set to 10 MW for PRL and 22 MW for SRL.

3.3. Hybrid stochastic-deterministic solution algorithm

As discussed in Schäfer et al. (2019), the mixed-inter nonlinear optimization program (MINLP) given in Eq. (5)-(9) shows a similarity with two-stage stochastic programs. That is, selecting a bidding strategy \mathbf{x} represents the first stage, the subordinated MILP scheduling problems (Eq. (9)) represent the second stage. A direct solution of (5)-(9) using state-of-the-art deterministic MINLP solvers is considered prohibitive. One possible approach to a deterministic solution would be the use of tailored decomposition algorithms exploiting the structure.

As an alternative, the use of a hybrid stochastic-deterministic method appears promising here. More precisely, the stochastic solver that varies the first-stage variables \mathbf{x} invokes an external MILP solver in a black-box manner. The single MILP problems for each scenario can be solved efficiently within short time using state-of-the-art MILP solvers. Furthermore, parallelization of the optimizations for single scenarios is easily possible. We herein use a genetic algorithm (GA) as stochastic solver. The framework (see, Figure 1) uses the GA supplied in MATLAB R2018a's Global Optimization Toolbox (Mathworks, Inc). The subordinated scheduling problems are implemented in GAMS v.25.1 (GAMS Development Corp.) and are solved using CPLEX v.12.8 (IBM Corp.).

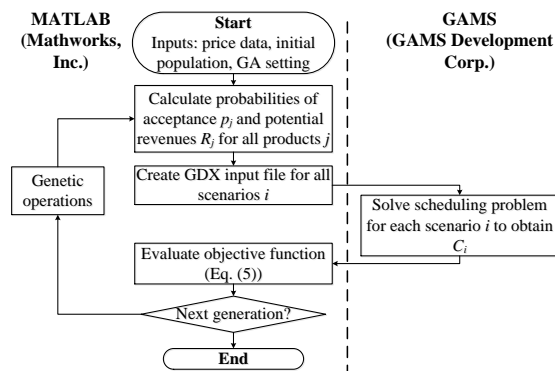


Figure 1: Flow diagram of the hybrid stochastic-deterministic solution algorithm.

4. Case study

As a case study, we calculate the optimal bidding strategy for the second calendar week of 2018. We conduct all calculations on a server with two Intel[®] Xeon[®] CPUs X5690 with 3.47 GHz and 96 GB RAM. For solution of the subordinated MILPs in parallel, the GAMS Grid Facility is used. The GA is stopped after evaluation of 300 generations with a population size of 70. The respective convergence plots of the GA are given in Figure 2 (a). Six cases are considered: no balancing market participation, a pure bidding at the PRL market, and a simultaneous bidding at the PRL and the SRL market, each of them once with the possibility to optimally market the remaining flexibility at the spot market (day-ahead) and once without this possibility. The longest run (bidding at PRL and SRL market with optimization at the spot market) took approximately 72 h, all others finished in substantially less time. Note however that all runs converged to the final value within a relative tolerance of 10^{-3} in less than 100 generations. This runtime is not prohibitive considering a horizon of the bids of one week. Calculations have been repeated with

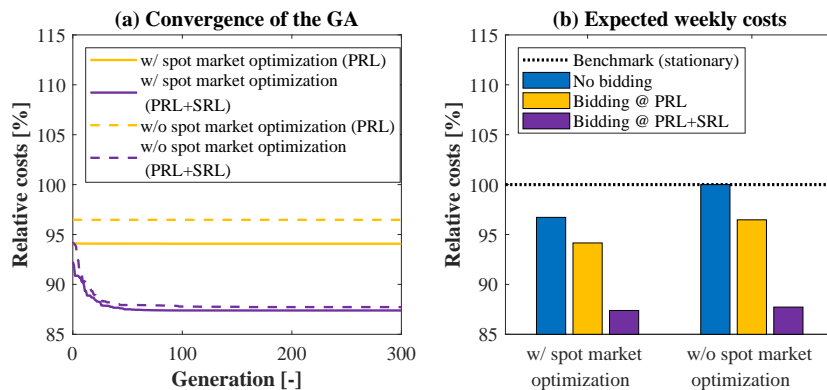


Figure 2: (a) Convergence plot of the GA. Lines indicate strongest individual of each generation. Solid lines: with optimal scheduling at spot market, dashed lines: without. Colors like in (b). (b) Economic evaluation of the optimal bidding strategy once with optimization at spot market and once without. The dotted black line is the benchmark case with constant production and spot prices. Blue bars: no balancing market participation, orange bars: bidding only at PRL market, purple bars: bidding at both PRL and SRL market.

different GA settings, however no significant differences neither in optimal variable values nor in the objective values have been found.

Figure 2 (b) further compares the expected costs following the optimal bidding strategy on both the SRL and the PRL market to a pure optimization at the spot market. We consider a stationary operation under day-ahead prices as a benchmark scenario. One sees strong economic benefits in actively marketing the operational flexibility in the considered week, which allows for overall savings of $> 10\%$ compared to a non-flexible operation. Figure 3 gives additional information about the selected bidding strategies. Note that in both cases (with and without optimization at the spot market) the most probable scenario by far is that all bids are accepted and that therefore all capacities depicted likely have to be reserved for balancing power. One sees only a minor influence of the spot market optimization in the sense that slightly more conservative prices are asked (decreased probability of the scenario) and that only a little larger part of the entire flexibility remains that is not offered as balancing reserves. Together with Figure 2 (b), this indicates a strong advantage of the balancing over the spot markets for that week. That is, the optimal bidding strategy aims - when possible - at offering almost the entire flexibility range at balancing markets and ensures that all offered capacities are likely accepted by asking conservative prices. The ability to market remaining flexibility at the spot market does not significantly change this strategy and consequently, does not enable additional savings.

5. Conclusion

We present a framework for model-based bidding at the market for primary and secondary balancing power simultaneously. We solve the resulting optimization problem using a tailored hybrid stochastic-deterministic solution approach. Considering an exemplary week from 2018, we calculate the optimal bidding strategy for an industrial aluminum electrolysis. We demonstrate that the approach effectively identifies bidding strategies which allow for substantial savings. Furthermore, we show that a balancing market participation can show substantially greater economic potentials than a pure trading at spot markets. Future work should aim at the rigorous deterministic solution of the bidding problem, e.g., through application or tailoring of decomposition techniques

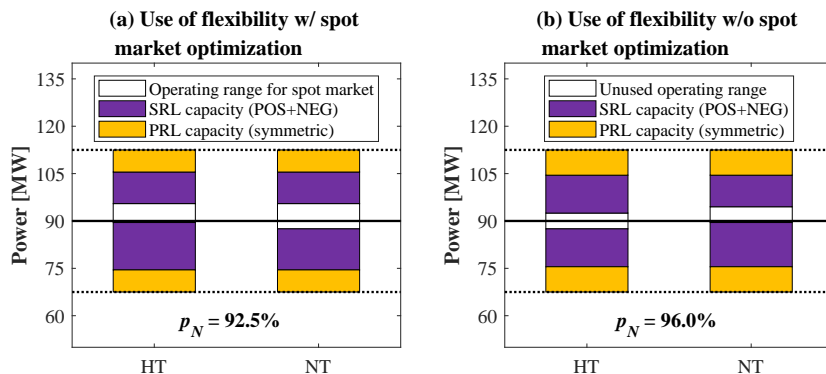


Figure 3: Capacity that is offered as balancing power (orange: PRL, purple: SRL) for the two time periods. (a) is with optimization at spot market and (b) without. Solid black line represents the nominal operating point, dotted black lines correspond to bounds of the operating range. p_N denotes the probability that all bids are accepted. Note that in (a), the remaining white part corresponds to the capacity available for spot market trading.

for MINLPs that would allow for a separation into nonlinear bidding and MILP scheduling sub-problems. Here, the reader is referred to, e.g., Li et al. (2012) for nonconvex generalized Benders decomposition or Mouret et al. (2011) for sophisticated Lagrangian methods.

6. Acknowledgment

The authors gratefully acknowledge the financial support of the Kopernikus project SynErgie by the Federal Ministry of Education and Research (BMBF) and the project supervision by the project management organization Projektträger Jülich. The authors further thank H. Hauck from TRIMET SE for valuable discussions.

References

- G. E. P. Box, G. M. Jenkins, 1994. Time Series Analysis: Forecasting and Control, 3rd Edition. Prentice Hall PTR.
- A. W. Dowling, R. Kumar, V. M. Zavala, 2017. A multi-scale optimization framework for electricity market participation. Applied Energy 190, 147–164.
- A. Ghoheity, A. Mitsos, 2010. Optimal time-dependent operation of seawater reverse osmosis. Desalination 263 (1), 76–88.
- X. Li, Y. Chen, P. I. Barton, 2012. Nonconvex generalized Benders decomposition with piecewise convex relaxations for global optimization of integrated process design and operation problems. Industrial & Engineering Chemistry Research 51 (21), 7287–7299.
- S. Mitra, I. E. Grossmann, J. M. Pinto, N. Arora, 2012. Optimal production planning under time-sensitive electricity prices for continuous power-intensive processes. Computers & Chemical Engineering 38, 171–184.
- A. Mitsos, N. Aspiron, C. A. Floudas, M. Bortz, M. Baldea, D. Bonvin, A. Caspari, P. Schäfer, 2018. Challenges in process optimization for new feedstocks and energy sources. Computers & Chemical Engineering 113, 209–221.
- S. Mouret, I. E. Grossmann, P. Pestiaux, 2011. A new Lagrangian decomposition approach applied to the integration of refinery planning and crude-oil scheduling. Computers & Chemical Engineering 35 (12), 2750–2766.
- J. I. Otashu, M. Baldea, 2018. Grid-level “battery” operation of chemical processes and demand-side participation in short-term electricity markets. Applied Energy 220, 562–575.
- M. Paulus, F. Borggrefe, 2011. The potential of demand-side management in energy-intensive industries for electricity markets in Germany. Applied Energy 88 (2), 432–441.
- P. Schäfer, H. Westerholt, A. M. Schweidtmann, S. Ilieva, A. Mitsos, 2019. Model-based bidding strategies on the primary balancing market for energy-intensive processes. Computers & Chemical Engineering 120, 4–14.
- Q. Zhang, I. E. Grossmann, C. F. Heuberger, A. Sundaramoorthy, J. M. Pinto, 2015. Air separation with cryogenic energy storage: Optimal scheduling considering electric energy and reserve markets. AIChE Journal 61 (5), 1547–1558.

Optimal CSP-waste based polygeneration coupling for constant power production

Ester de la Fuente, Mariano Martín*

*Departamento de Ingeniería química- Universidad de Salamanca. Plz. Caidos 1-5,
37008, Salamanca, Spain*

mariano.m3@usal.es

Abstract

This work addresses the integration of a biogas-based Brayton Cycle with a concentrated solar power facility. A heat exchanger network generates steam out of flue gas or molten salts to be used in a regenerative Rankine cycle to produce power. A multiperiod scheme is formulated for the design of the hybrid facility determining the waste required as back up to mitigate seasonal solar availability. The steam turbine is responsible for power production while the gas turbine works mainly as a combustion chamber. In the South of Spain, a 50% excess of biogas is produced during summer yielding a production cost of electricity of 0.17 €/kWh with an investment of 380 M€ for a production facility of 25MW. A scale-up study is also carried out.

Keywords: Circular economy, biogas turbine, CSP, renewable power, mathematical optimization

1. Introduction

The transition from fossil-based power to a renewable based economy faces an important challenge, the variability of the largest energy resource on Earth. Solar availability is highly volatile, it is subjected to seasonality in the longer term, but weather also results in hourly or subhourly fluctuations. Meeting power demand over time requires the use of integrated systems to help mitigate the variation in power production (Yaun and Chen, 2012). Hybrid concentrated solar power (CSP) facilities use a second energy source to mitigate the lack of Sun (Peterseim, et al 2013). Apart from the use of fossil resources, renewables have already been considered. Vidal and Martín (2015) optimized the operation of a facility that used lignocellulosic biomass gasification, providing hot streams to heat up the molten salts, and a gas turbine as buffer technology to operate a CSP facility. This integration suggested the use of a syngas powered gas turbine and the possibility of storing power in the form of hydrogen as energy vector if solar availability was enough to meet the power demand. The molten salts were not heated up using thermal energy from the hot gases nor a syngas furnace was used. However, the diversification of the use of lignocellulosic raw materials for the production of chemicals and the large and distributed availability of waste in isolated areas (Taifouris and Martín, 2018) suggest its use as back-up to mitigate the solar variability. In this work a mathematical optimization framework is developed to evaluate the integration of waste and CSP within a renewable-based power plant. The system considers waste anaerobic digestion and a gas turbine to produce power from

residues. The hot flue gas and/or the heat transfer fluid, molten salts, can be used for the production of the steam required by the steam turbine of a regenerative Rankine cycle

2. Process description

The process consists of five major sections: Biogas production and purification, gas turbine, solar collection technologies, heat exchanger network and a regenerative Rankine cycle.

Waste and water are fed to a digester. The mixture is anaerobically digested for 25 days to produce biogas and a digestate. The biogas is sent to purification to remove CO_2 and traces of NH_3 , using a Pressure Swing Adsorption (PSA) system, and to eliminate the H_2S in a fixed-bed reactor. Once biomethane is obtained, a Brayton cycle is used to produce power. The flue gas produced is sent to a heat exchanger network (HEN) to produce steam.

The CSP facility consists of the heliostat field including the receiver and the molten salts storage tanks and a HEN. The salts are used to generate superheated steam to be used in a steam turbine following a regenerative Rankine cycle.

The Rankine cycle is common for both energy resources. In order for the molten salts and the flue gas to be used, a system of heat exchangers in parallel is considered. For heating up and evaporating water, the entire flow of the molten salts is used while only a fraction was used for reheating and overheating the steam. However, the higher temperature of the flue gas suggests a different lay out. The entire flow is used for overheating the steam before feeding the high-pressure turbine whereas it is split to reheat the steam before feeding it into the medium pressure turbine and to heat-up and evaporate the water coming from the deaerator. In the second stage of the turbine, a fraction of the steam is extracted at a medium pressure and it is used to heat up the condensate. The rest of the steam is finally expanded to an exhaust pressure, condensed and recycled. A cooling tower is used to cool down the cooling water, see Figure 1.

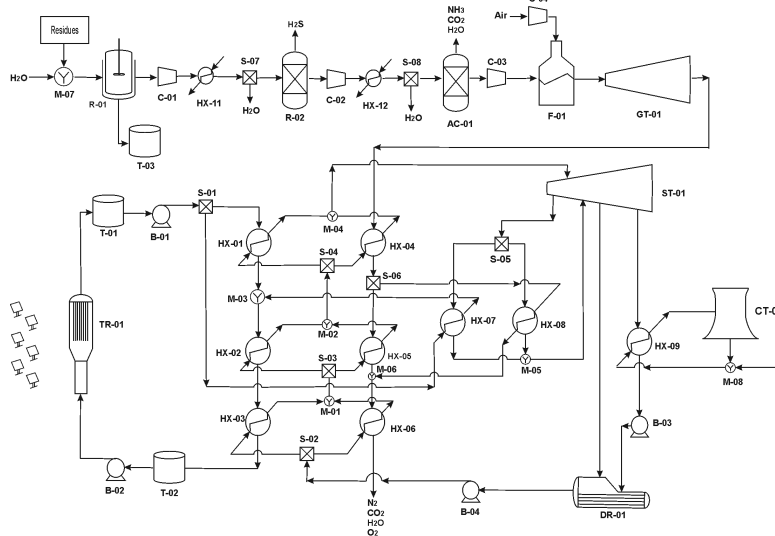


Figure 1. Integrated power facility

3. Problem formulation

The different technologies described in the flowsheet of Figure 1 are modelled using mass and energy balances, for the digester, the heat exchangers, mixers and splitters, thermodynamics for the gas compression and expansion, the steam turbine is modelled based on enthalpy and entropy balances where surrogate models are developed for the enthalpy and entropy of the steam as a function of the temperature and pressure (León and Martín, 2016), rules of thumb are used to estimate the compressor and turbine efficiencies (Walas, 1990), design equations are used to model the solar Receiver, and reduced order models are developed for the adsorption beds. The model is written in terms of the total mass flows, component mass flows, component mass fractions, and temperatures of the streams in the network. These are the main variables whose values have to be determined from the optimization. The components in the system correspond to the ones in the set $J = \{ \text{Wa, CO}_2, \text{O}_2, \text{N}_2, \text{H}_2\text{S, NH}_3, \text{CH}_4 \}$

The problem is a multiperiod NLP of 9600 vars and 4800 eqs. written in GAMS, that is solved maximizing eq. (1) on a monthly basis for the selection of the best use of waste to mitigate the lack of sun, either the production of power in a biogas fuelled gas turbine and/or the use of the flue gas to produce steam together with the molten salts. The objective function includes the net power production and the annualized cost ($K=1/3$) of the mirrors, the digesters, each of 6000m^3 at 365 €/m^3 , and the linearized cost for the turbines as a function of the power

$$Z = C_{\text{Electricity}} \cdot (W_{(\text{Turbgas})} + W_{\text{Total}} - W_{(\text{Comp1})} - W_{(\text{Comp2})} - W_{(\text{Comp3})} - W_{(\text{Comp4})}) - (120 \cdot \text{AreaTotal} + C_{\text{Digester}} \cdot N_{\text{digester}} + (335.27 \cdot (W_{(\text{Turbgas})}) + 36.211) - (270.5 \cdot W_{\text{Total}} + 2 \cdot 10^6)) \cdot (K) \quad (1)$$

A case study is presented for a region in Spain, Badajoz, where hybrid plants are already installed but using fossil backup energy (<http://es.csptoday.com>). The large availability of poultry and solar incidence makes its integration an interesting alternative to the use of fossil resources. A net production of 25 MW is considered. The framework is flexible to study the use of other residues and evaluate the operation in other regions.

4. Results

4.1. Plant operation

The plant allocation in the northern hemisphere dictates its operation. Summer operation is based on the use of solar energy, reducing the use of waste and the usage of the digestors, see Figure 2. This is an important feature since the use of the digestors at full capacity can allow the production of chemicals such as methanol or methane (Hernández and Martín, 2016) for energy storage purposes. It turns out that, in summer, additional 12 MW of power are available. Furthermore, an interesting feature unveiled from the optimization is the fact that the gas turbine actually operates as a furnace providing little power but generating a high temperature stream to be used in the heat exchanger network. As a result, the two heat exchanger networks, the one that uses the molten salts and the one that uses the hot flue gas, operate the entire year. Figure 3 summarizes the operation of both turbines and shows the contribution of the solar energy and the poultry manure. In winter up to 40% of the energy is provided by the manure while in summer, the solar energy is enough to reach the desired power production of 25 MW.

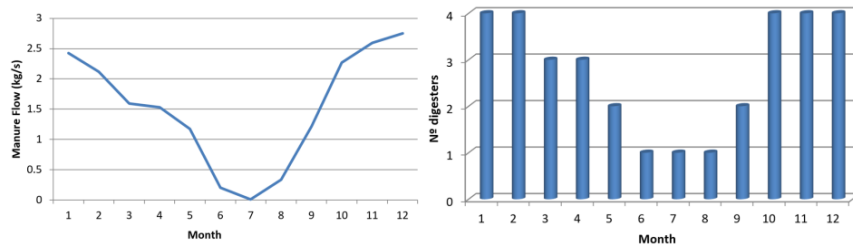


Figure 2. Waste consumption and digestors usage.

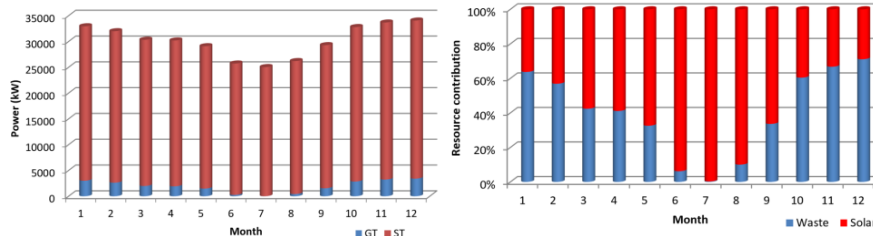


Figure 3. Contribution of the two sections of the process to power production

4.2. Economic evaluation

The production cost and investment costs of the integrated facility are estimated and compared to the stand alone CSP plant and other integrated facilities.

The investment cost is estimated using the factorial method (Sinnot 1999). It relies on the equipment cost, updated from Matche (Matche 2014). We consider the units described in the flowsheet given by Figure 1. Digesters cost is assumed to be 365 €/m³ (Taifouris and Martín, 2018) and the heliostat costs are 120 €/m². We assume that each heliostat has an area of 120 m². The installed equipment is assumed to represent 1.5 times the equipment cost. Piping, isolation, instrumentation and utilities represent 20 %, 15 %, 20 % and 10 % of the equipment cost respectively. Land and buildings cost are assumed to be 8 M€, and the load of molten salts is priced at 0.665 €/kg. These items add up to the fix cost (319 M€). The fees represent 3 % of the fix cost, other administrative expenses and overheads and the plant layout represent 10 % of the direct costs (fees plus fix capital) and 5 % of the fix cost respectively. The plant start-up cost represents 15 % of the investment. The investment adds up to 380 M€. Figure 4 shows the contribution to the cost of the different sections of the facility, the solar field is the larger contribution, over a third of the total, followed by the turbine and the heat exchanger network. The digestors, a total of 4 in the facility, represent 7.5% of the units. An interesting comparison between this plant and the stand-alone plant presented in (Martín and Martín, 2013) reveals that the investment cost is around 50% larger, but the production capacity was variable over time. Thus, the investment to secure constant production capacity was of around 130 M€.

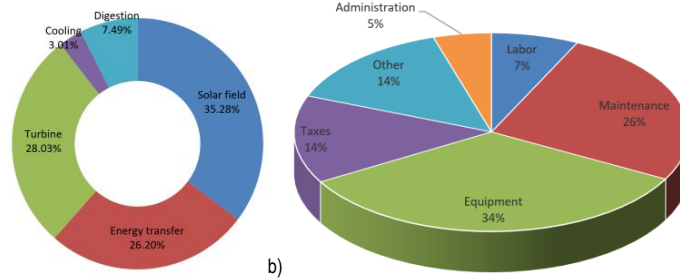


Figure 4.- a) Contribution of the facility sections to the final cost b) Distribution of the production costs

The production costs of the electricity generated, without considering the possibility of producing additional power, chemicals or credit from the digestate, can be seen in Figure 4b. The labour costs are assumed to be 0.5% of the investment, equipment maintenance around 2.5 % of fix costs, the amortization linear with time in 20 years, the taxes and the overheads 1 % of the investment each, and the administration around 5 % of labour, equipment maintenance, amortization, taxes and overheads. The production costs add up to 0.17 €/kWh, slightly higher than the values reported for the CSP facility of similar sized operating alone (Martín and Martín, 2013) that shows a production costs of around 0.15 €/kWh but that secures constant production using renewable resources. That additional 10% in the electricity cost is to secure the continuous production of power over time.

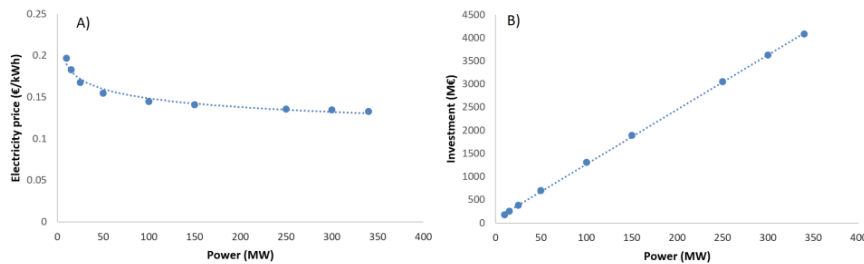


Figure 5.-Scale up/down of the integrated waste-CSP facility. A) Production cost; B) Investment

An additional comparison can be made with the integration of lignocellulosic biomass and CSP by Vidal and Martin (2015). Note that the collection of miscanthus is easier due to its higher density and easier transportation which allowed considering a larger facility of 340 MW benefiting from economies of scale. Furthermore, in that case, the integration considered the use of hot streams to heat up the molten salts, not to produce steam directly. The optimal integrated process consisted of the use of a syngas fueled gas turbine that produced power in parallel to the one obtained from the steam turbine from the CSP section. Finally, when solar power was enough to meet the power demand, the syngas was used to produce hydrogen using a WGSR, providing additional income. The larger scale allowed electricity production costs of 0.073 €/kWh with an investment cost of 3225 M€. In this work the integration is different since the hot streams were not intended to be used in heating up the molten salts but to directly produce steam. The gas turbine is merely used as a furnace and the excess of biogas can be stored or further processed to methane or methanol. Reaching that production capacity requires more than 50 digesters and processing around a peak of 40 kg/s of

manure which is far larger facility than any available. For the proper comparison, a scale up study is required. Figure 5 shows the results of the scale up/down of the economics of the integrated facility analyzed in this work. For a 340 MW integrated facility, an investment of 4080M€ is required for an electricity production cost of 0.133 €/kWh. Note that no credit is assumed from the digestate or the additional biogas production capacity

5. Conclusions

A superstructure for the integration of waste-to-power and a concentrated solar facility has been proposed embedding anaerobic digestion, a Brayton Cycle, solar field, molten salts system and a regenerative Rankine cycle. The solution of the multiperiod optimization problem decides on the use of each energy source.

The low yield to power of the poultry manure and the allocation of the plant results in an excess of capacity during summer of about 50%, so that the demand of 25MW is met in winter. The steam turbine is the one responsible for producing the power, while the gas turbine operates mostly as a combustion chamber. The production cost to secure power production are 5% larger than the ones of the stand-alone plant, 0.17 €/kWh, but the investment cost increases by 50% up to 380 M€. However, the excess of capacity can be used to produce chemicals that will be an asset to the process in terms of additional income or providing flexibility to its operation. The digestate can also be further used as a fertilizer. The large number of units involved makes difficult that the future lower costs of heliostats result in large investment savings per kW installed. Integration of waste is suggested at smaller scales compared to lignocellulosic biomass. The formulation is useful to evaluate trade-offs related to the location of the plant as function of the availability of the raw materials, solar energy and waste.

Acknowledgments

The authors acknowledge PSEM3 group and JCYL under grant SA026G18

References

- B. Hearnandez, M. Martín, 2016 Optimal Process operation for biogas reforming to methanol: effects of dry reforming and biogas composition IECR. 55 (23), 6677–6685,
- L. Martín, M. Martín 2013. Optimal year-round operation of a Concentrated Solar Energy Plant in the South of Europe *App. Thermal Eng.* 59:627-633.
- Matche (2014) <http://www.matche.com/prod03.htm>. (last accessed March 2018)
- J.H. Peterseim, S. White, A Tadros, W Hellwig, 2013. Concentrated solar power hybrid plants, which technologies are best suited for hybridisation. *Renew. Energ.* 57, 520-532
- R.K. Sinnott Coulson and Richardson, *Chemical Engineering*. 3rdEd. Butterworth Heinemann, Singapore. 1999.
- M.R. Taifouris, M. Martín, 2018. Multiscale scheme for the optimal use of residues for the production of biogas across Castile and Leon, *J. Clean. Prod.*, 185, 239-251
- M. Vidal, M. Martín 2015. Optimal coupling of biomass and solar energy for the production of electricity and chemicals. *Comp. Chem. Eng.* 72, 273-283
- S.M. Walas, 1990, *Chemical Process Equipment. Selection and Design* Butherworth Heinemann. Elsevier. Oxford UK.
- Z. Yuan, B Chen, 2012, *Process Synthesis for Addressing the Sustainable Energy Systems and Environmental Issues. AIChE J.* ,58 (11), 3370-3389
- <http://es.csptoday.com/mercados/arranca-el-proyecto-de-la-planta-termsolar-astexol-2>

A model-based approach for optimizing petroleum refinery configuration for heavy oil processing

Cheng Seong Khor,^{a*}Tareq A. Albahri,^bAli Elkamel^{c,d}

^a*Chemical Engineering Department, Universiti Teknologi PETRONAS, 32610 Seri Iskandar, Perak Darul Ridzuan, Malaysia*

^b*Chemical Engineering Department, Kuwait University, P.O. Box 5969, Safat 13060, Kuwait*

^c*Department of Chemical Engineering, University of Waterloo, Waterloo, ON N2L 3G1, Canada*

^d*Department of Chemical Engineering, Khalifa University, The Petroleum Institute, Abu Dhabi United Arab Emirates*

**chengseong.khor@utp.edu.my, khorchengseong@gmail.com*

Abstract

This work presents a model-based optimization approach to determine the configuration of a petroleum refinery for a new (grassroots) or an existing site for heavy oil processing of atmospheric distillation unit residue. We develop a high-level superstructure representation for the refinery configuration that encompass many possible alternatives comprising the technologies and their interconnections. The superstructure is postulated by decomposing it to include representative heavy oil processing scheme alternatives that center on the technologies for atmospheric residual hydrodesulfurization (ARDS), vacuum residual hydrodesulfurization (VRDS), and residual fluid catalytic cracking (RFCC). We formulate a mixed-integer nonlinear optimization model (MINLP) appended with logic propositions devised from experience and heuristics to aid solution convergence. Implementation on a case study of Kuwaiti refineries demonstrate the applicability and practicality of the proposed approach when validated against existing real-world refinery configurations.

Keywords: petroleum refinery configuration, heavy oil, mixed-integer linear programming, superstructure; logic propositions

1. Introduction

An important aspect of process synthesis and design is to identify the best flowsheet structure that performs a specific task while achieving a set of objectives, which mainly involve maximizing profit or minimizing cost and/or environmental emissions. Within this scope, the task complexity entailed in determining an optimal refinery configuration requires developing systematic approaches that can rigorously consider the interactions among numerous process variables and tradeoffs involving multiple possibly conflicting design objectives. In the literature, three available approaches for process synthesis are heuristic methods, pinch analysis, and optimization for which optimization allows developing decision making tools that can handle the complexities mentioned (Khor and Elkamel, 2010).

In the last decade, the superstructure-based mixed-integer nonlinear programming (MINLP) optimization approach has been proposed for synthesizing biorefinery or biomass-based processes. Zondervan et al. (2011) presents an MINLP based on the transshipment model to determine optimal processing routes to produce fossil fuel substitute chemicals for gasoline blending. The model considers individual objectives for yield maximization and waste minimization besides conventional economic cost functions. Quaglia et al. (2015) extends the superstructure-based MINLP methodology with systematic data management. A simultaneous economic and environmental-based multiobjective MINLP model derived from a large scale superstructure is proposed by del Rio-Chanona et al. (2017). A recent review of this area is offered by Cremaschi (2015).

The present work attempts to contribute by demonstrating the applicability of a MINLP model for large scale grassroots refinery configuration synthesis using a common business tool (Excel). The formulation considers rigorous process models with nonlinearities representative of major commercial refining technologies in terms of material balances, product yields and qualities, and costs. The model is implemented on an industrial case study of Kuwaiti refineries with the results validated against existing real-world refinery configurations to elucidate the practicality of the approach.

2. Problem statement

We consider the structural optimization problem to devise a petroleum refinery configuration. Given the following data is available: amount, properties, and cost of a mixture of crude oils (petroleum) as raw materials; a set of refining process units with known processing or throughput capacities and capital and operating costs; and amount and properties or qualities of a set of refining products. Our goal is to determine an optimal configuration by computing the continuous variables on material stream component flowrates (denoted by F_i for each component i) and the binary variables on selecting and sequencing the process units that satisfy an objective to minimize the total refinery cost (denoted by U_k for each unit k).

3. Superstructure representation

In the superstructure representation in Figure 1, crude oil is separated by a crude oil distillation unit (CDU) into gases, naphtha, kerosene, diesel, and atmospheric residue. CDU products are usually high in sulfur (also called sour products) and require treatment. The sour gas is typically treated for sulfur removal using a gas treating unit (GAS) and amine treating unit (AMN). The recovered hydrogen sulfide gas is converted to sulfur in the sulfur recovery unit (SULF). Straight run naphtha, kerosene, and diesel are hydrotreated in separate catalytic hydrotreaters (NHT, DHT, and KHT, respectively) to lower the amount of sulfur and other objectionable materials to meet environmental regulations for sale. Hydrotreated naphtha is typically separated into light and heavy naphtha using naphtha splitter (NAPS). Heavy naphtha is upgraded in a catalytic reformer (REF) while that of light naphtha in a catalytic isomerizer (ISO) to produce high octane gasoline blending stock. Alkylation (ALK1–2) and polymerization (POLY) units produce alkylate and polymerate blending stocks to supplement gasoline production. The olefin gas feed to the alkylation and polymerization units are supplied by fluid catalytic cracker (FCC), residue fluid catalytic cracker (RFCC), and delayed

coker (DCOK). Three main alternative processing schemes for heavy oil processing are incorporated in the superstructure. In the first alternative for atmospheric residual treating, high sulfur atmospheric residue is first processed in an atmospheric residue desulfurizer (ARDS) to produce low sulfur atmospheric residue that can be sold, or physically separated in a vacuum rerun unit (VRU) to produce low sulfur vacuum gas oil and low sulfur vacuum residue, or catalytically cracked in a residue fluid catalytic cracker (RFCC) to produce gasoline and other fuel types. In the second alternative of vacuum residual treating, the high sulfur atmospheric residue is physically separated in VRU into high sulfur vacuum gas oil and high sulfur vacuum residue. The latter (high sulfur vacuum residue) can be converted to low sulfur vacuum residue in vacuum residue desulfurizer (VRDS) to reduce the sulfur content and produce more valuable products such as transportation fuels. High sulfur vacuum gas oil is either sold after conversion to low sulfur vacuum gas oil in gas oil hydrotreater (GOHT) or converted to lighter products in hydrocracker (HCR) or fluid catalytic cracker (FCC1). We can sell low sulfur vacuum residue as fuel oil or further process it in DCOK or RFCC to produce lighter materials with or without prior visbreaking (VIS). In the third processing alternative called atmospheric residual cracking, the high sulfur atmospheric residue is first desulfurized in ARDS to produce low sulfur atmospheric residue that is either cracked in to produce lighter materials with or without a prior VIS. Typically, there is no vacuum pressure-operated unit in this configuration although some studies have shown the potential to process a feed from such units (Reynolds et al., 1992; Ancheyta, 2011).

4. Model formulation

The MINLP formulation for refinery configuration design is as follows:

$$F_i + \sum_k Q_{ik} X_k = P_i, \quad \forall i \in I \quad (1)$$

$$F_i \leq S_i, \quad \forall i \quad (2)$$

$$X_k \leq L_k B_k, \quad \forall k \quad (3)$$

$$FP_{i,k,p} = f(VS_{i,k}, VP_{i,k}), \quad \forall i, k, p \quad (4)$$

$$PP_{i,k,p} = f(FP_{i,k,p}, XU_k), \quad \forall i, k, p \quad (5)$$

$$F_k \leq M_k U_k, \quad \forall k \quad (6)$$

Eq. (1) describes the material balances where F_i = feed amount of component i , Q_{ik} = yield coefficient of component i in process unit k , X_k = capacity of unit k , and P_i = total amount of component i . Eq. (2) imposes maximum feed supply S_i for each component i . Eq. (3) allows designing additional trains of the same unit as given by a multiple number L_k of the capacity B_k of a single unit k . Eq. (4) and (5) governs feed and product properties of the process units, respectively. The objective function as given by Eq. (7) maximizes product sales minus the associated costs of raw materials (cf), capital (CC), and operation (CR) including utilities, maintenance (CM), and payroll (CP).

$$\text{maximize } \sum_i sp_i P_i - \sum_j cf_j F_j - \sum_k (CC_k + CR_k) - CM - CP \quad (7)$$

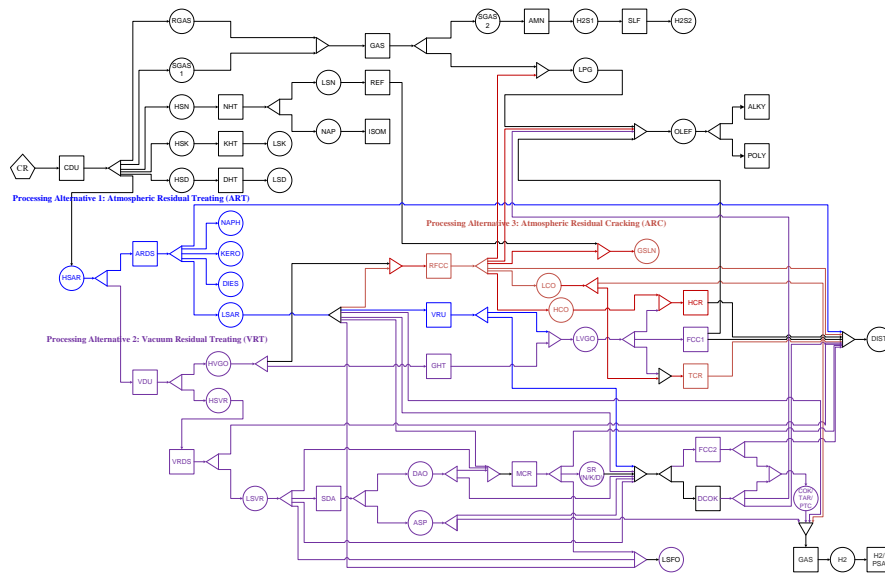


Figure 1. Superstructure representation of petroleum refinery configurations

5. Solution strategy

We develop a computational procedure that first generates and assigns a set of binary values (0–1) to the structural variables in generating a new refinery configuration at each iteration as based on the superstructure (Step 1). Then the procedure invokes a nonlinear optimizer to compute the unit conversions and product cuts in a corresponding configuration to maximize total profit-based objective function (Step 2). Figure 2 presents the described procedure flow.

The master module alternates the structural variable binary values U_k between 1 and 0 to indicate the selection or rejection, respectively of a process unit in an overall refinery scheme. Thus the algorithm can consider all possible alternatives within the superstructure that give rise to refinery configurations, which are given as inputs into the optimization submodule. The Excel submodule contains information on the superstructure element interconnections as well as their rigorous correlations for the material balances, product yields and qualities, utility requirements, feed and product prices, and associated running costs for all the units. The model accounts for all interconnections between the units and gathering pools for the intermediates and final products, and they involve both linear and nonlinear relations.

The submodule optimizes the unit conversions and product cuts in each configuration developed by the master module to determine the unit capacities and flow rates of intermediate and final product streams. By computing the capital and running costs, the submodule maximizes the objective function of total profit using the generalized reduced gradient-based method called GRG2 available in Excel Solver (Frontline

Systems, 2018). The master module then reads the new configuration profit from the submodule results and compares it with the current value to decide in storing the binary variable and objective variable values associated with that of higher profit; otherwise, we retain that of the previous scheme.

This algorithm terminates when all possible configurations are considered to determine an optimal configuration. Thus, our algorithm is one of complete enumeration as different from a partial enumeration approach such as branch-and-bound. Expectedly, our method entails more iterations to converge to optimality, hence motivating us to incorporate use of 0–1-based logic propositions on design and structural specifications to reduce the computational time but without compromising the solution quality.

6. Results and discussion

The model solution indicates that a configuration resembling the residual fluid catalytic cracking (RFCC) route is more economical than to use a combined vacuum unit and delayed coker with or without visbreaker, which is consistent with the literature on refinery configurations (Khor et al., 2011; Meyers, 2016; Albahri et al., 2018). Using RFCC to process atmospheric residue is favored to physical separation combined with thermal cracking mainly because we can improve the selectivity and yield of the desired product flows. RFCC-based configuration also entails less process units than that of ARDS and VRDS, hence promotes lower capital and running costs.

Although a low sulfur vacuum residue can be produced from the vacuum unit which can then be processed in the RFCC unit, that route is not an optimal choice because it is less economical. Moreover, unless preceded by ARDS, RFCC removes only 30 to 50% of sulfur in the feed, and its products therefore require hydrotreating. The selected optimal technologies show that hydrotreating straight-run products is favored cost-wise and essential too. Hydrotreating straight-run distillates from crude distillation unit is more economic than selling them due to the lower price of high sulfur products. In our model runs over different price sets and scenarios, the solutions preferentially choose naphtha, kerosene, and diesel hydrotreaters as part of the configurations, hence we decide to include these units as fixed structures (i.e., they are not evaluated by means of the binary variables) to enhance convergence and reduce computational time.

The total capital investment estimated is US\$2.1 billion, which is consistent with reported values for a refinery of this size (Maiti et al., 2001). Our optimal result run shows that a configuration that employs RFCC is the most profitable with a net profit of 8.40 US\$/barrel (20 cent/gallon). While the computed values may differ for a specific case's cost values (e.g. for erection and running expenses) and sale prices, the relative trend and conclusion remain valid for a similar comparison made.

7. Conclusions

This work presents an approach to synthesize an optimal petroleum refinery configuration during the preliminary screening of design alternatives. The configuration determined shows good agreement with refinery configurations in practice. We obtain an optimal processing scheme for a specific crude oil mixture to be that of residual fluid catalytic cracking (RFCC) of desulfurized atmospheric residue, without a need for a vacuum distiller or vacuum residue desulfurizer (VRDS). The latter structure conventionally forms part of the former (as incorporated in our superstructure), but the MINLP approach applied finds such a configuration to be actually suboptimal.

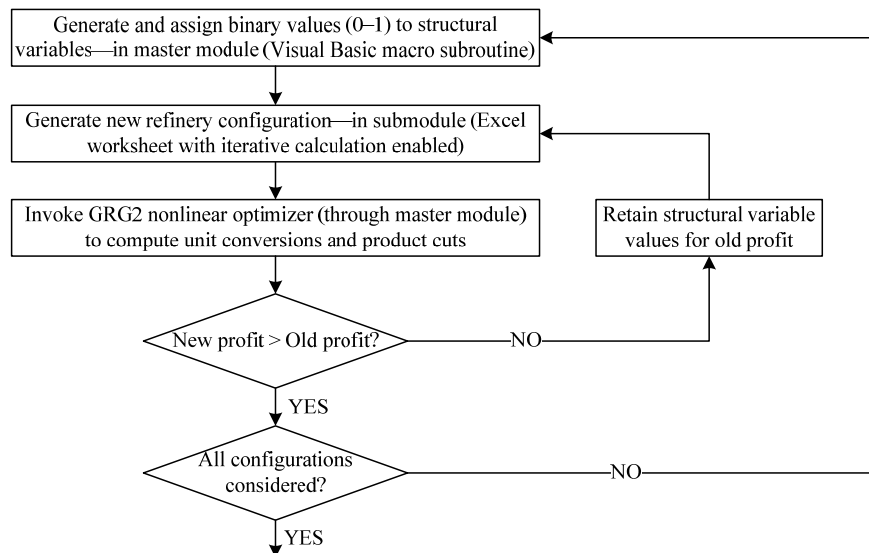


Figure 2. Flowchart on solution strategy used

References

- T. A. Albahri, C. S. Khor, M. Elsholkami, and A. Elkamel, 2018, Optimal Design of Petroleum Refinery Configuration Using a Model-Based Mixed-Integer Programming Approach with Practical Approximation, *Ind Eng Chem Res*, 57, 7555-7565.
- J. Ancheyta, 2011, Modeling and Simulation of Catalytic Reactors for Petroleum Refining, Wiley, p. 35.
- S. Cremaschi, 2015, A Perspective on Process Synthesis: Challenges and Prospects, *Comp Chem Eng*, 81, 130-137.
- E.A. del Rio-Chanona, D. Zhang, and N. Shah, 2018, Sustainable Biopolymer Synthesis via Superstructure and Multiobjective Optimization, *AIChE J*, 64, 91-103.
- Frontline Systems, 2018, FrontlineSolvers, USA.
- C. S. Khor and A. Elkamel, 2010, Superstructure Optimization for Oil Refinery Design, *Petroleum Science & Technology*, 28, 1457-1465.
- C. S. Khor, X. Q. Yeoh, and N. Shah, 2011, Optimal Design of Petroleum Refinery Topology Using a Discrete Optimization Approach with Logical Constraints, *J App Sci*, 11, 3571-3578.
- R. A. Meyers, 2016, Handbook of Petroleum Refining Processes, 4th ed., McGraw Hill.
- A. Quaglia, C. L. Gargalo, S. Chairakwongsa, G. Sin, and R. Gani, 2015, Systematic Network Synthesis and Design: Problem Formulation, Superstructure Generation, Data Management and Solution, *Comp Chem Eng*, 72, 68-86.
- B. E. Reynolds, E. C. Brown, and M. A. Silverman, 1992, Clean Gasoline via VRDS/RFCC, *Hydrocarbon Processing*, pp. 43-51.
- E. Zondervan, M. Nawaz, A. B. de Haan, J. M. Woodley, and R. Gani, 2011, Optimal Design of a Multi-Product Biorefinery System, *Comp Chem Eng*, 35, 1752-1766.

Optimal short-term Scheduling of Industrial Packing Facilities

Apostolos P. Elekidis ^{a,b}, Francesc Corominas ^c, Michael C. Georgiadis ^{a,b,*}

^a *Department of Chemical Engineering, Aristotle University of Thessaloniki, University Campus, Thessaloniki, 54124, Greece*

^b *Chemical Process and Energy Resource Institute (CPERI), Centre for Research and Technology Hellas (CERTH), PO Box 60361, 57001, Thessaloniki, Greece*

^c *Procter & Gamble, Temselaan 100, 1853 Strombeek-Bever, Belgium*

mgeorg@auth.gr.

Abstract

The simultaneous lot-sizing and production scheduling problem of a real-life large-scale industrial facility of packaged consumer goods is considered in this work. The problem under consideration is mainly focused on the packing stage which constitutes the major production bottleneck. Several packing lines, illustrating different design and operational characteristics, operate continuously in parallel. An efficient solution strategy is implemented to reduce the high computational cost. A Mixed-Integer Linear Programming model (MILP) is used in parallel with a decomposition-based algorithm. Appropriate constraints, referring to the production/formulation stage of the plant, are also imposed in order to ensure the generation of feasible production schedules. The model relies on tight timing and sequencing and products allocation constraints. The main objective is the minimization of the makespan. A number of different case studies have been considered and detailed optimal production schedules have been generated for over 130 products scheduled weekly. The obtained results lead to nearly-optimal scheduling solutions in reasonable computation times. The proposed model can assist decision makers towards rigorous scheduling plans in a dynamic production environment under realistic uncertainty.

Keywords: production scheduling, consumer goods industry, mixed integer linear programming, decomposition technique

1. Introduction

Modern multi-product, multipurpose plants play a key role within the overall current climate of business globalization, aiming to produce highly diversified products that can address the needs and demands of customers spread over wide geographical areas. The inherent size and diversity of these processes gives rise to the need for planning and scheduling problem, of large-scale industrial production operations. Over the past 20 years the literature illustrates a large-number of scheduling models, which have been mostly applied on generic but relatively small problem instances (Méndez et al., 2006). However, current real-world industrial applications include hundreds of different final products, produced in flexible multi-purposes facilities, under several tight design and operating constraints (Harjunkski et al., 2014). A few approaches have been used to solve large-scale industrial scheduling problems, utilizing advances in Mixed-Integer

optimisation (Kopanos, Puigjaner and Georgiadis, 2011). Furthermore, hybrid methods for large scale industrial problems have been proposed. Kopanos et al. (2010), proposed a decomposition strategy for large-scale scheduling problems in multiproduct multistage pharmaceutical batch plants. Baumann and Trautmann (2014) proposed a hybrid method for large-scale short-term scheduling of make-and-pack production processes. In this work an MILP-based decomposition algorithm is proposed for large scale scheduling problems in a multiproduct continuous plant. The model focuses on the packing stage, taking also into account constraints referring to the production formulation stage in order to ensure the generation of feasible production schedules.

2. Problem Statement

This work considers the scheduling of packaged consumer goods in a real-life industry. More than 300 products can be produced continuously in parallel packing lines. The production process consists of the formulation/production and the packing stage. In the formulation stage a number of intermediate products are produced. In most cases, more than one final product can be produced from the same intermediate product in the packing stage. Each packing line is connected to its own production/formulation unit. Sequence dependent changeovers take place in both stages. The changeover times differ among the various sequences, depending on the package size, the package color, the intermediate product etc. All changeovers, in the two stages, take place simultaneously and therefore the most time-consuming changeover determines the total changeover time for a product sequence. In addition, in the formulation stage, due to technical plant restrictions, the total number of intermediate products' changeovers should not exceed an upper limit. The short-term scheduling horizon of interest is one week, and both the packing and the formulation units are available 24 hours per day. Products' due dates are taken into account along with the necessary planned maintenance activities. The main objective is the minimization of the makespan and the minimization of products' changeover times.

3. MILP-based Decomposition Algorithm

For the aforementioned problem, an MILP-based decomposition algorithm has been developed. The original large-scale problem is decomposed into smaller scheduling sub-problems in an iterative mode. At each iteration, a subset of the involved product orders is scheduled. The main model decisions are a) the allocation of products to the packing lines, taking into account underlying equipment technical constraints, b) the relative sequence of products in the packing lines and c) the starting and completion time of product orders in the packing stage. The proposed MILP-based decomposition algorithm consists of: a) the insertion policy, b) the MILP model and c) a decomposition technique. If maintenance periods are to be taken into account, extra "maintenance-product" orders are scheduled, with processing time equal to the maintenance time. The ending times of these product orders are fixed to the ending times of the associated maintenance activities.

3.1. Insertion policy

In order to solve the original problem iteratively, the number and sequencing of the inserted products should be decided. Two insertion criteria are used in order to avoid the generation of infeasible schedules. The products with the earliest due dates are inserted first. Furthermore, according to the plant's technical restrictions, the products with the

same recipe (intermediate product) are inserted first, in order to minimize the total number of intermediate products' changeovers. Several real test cases have illustrated, that a 5-by-5 product insertion policy is the optimal one, as by increasing the number of products the solution is not improved while the computational cost is increased. In case that maintenance periods have to be taken into account these "maintenance-product" orders are inserted first.

3.2. MILP model

The MILP model applied in this case study is an extension of a general-immediate precedence framework as developed by Kopanos, Mendez and Puigjaner (2010). A brief description of the model is presented below:

$$\sum_{j \in i_j} Y_{i,j} = 1 \quad \forall i \quad (1)$$

$$X_{i',i,j} + X_{i,i',j} + 1 \geq Y_{i',j} + Y_{i,j} \quad \forall i, i' > i, j \in (i_j \cap i'_{j'}) \quad (2)$$

$$C_{i'} \geq C_i + T_{i'} + XX_{i,i',j} \text{changeover}_{i,i'} - M(1 - X_{i,i',j}) \quad (3)$$

$$\forall i, i' \neq i, j \in (i_j \cap i'_{j'})$$

$$2(X_{i',i,j} + X_{i,i',j}) \leq Y_{i',j} + Y_{i,j} \quad \forall i, i' > i, j \in (i_j \cap i'_{j'}) \quad (4)$$

$$Z_{i,i',j} + XX_{i,i',j} \geq X_{i,i',j} \quad \forall i, i', j \in (i_j \cap i'_{j'}) \quad (5)$$

$$Z_{i,i',j} = \sum_{i'' \neq i, i', j \in (i_j \cap i'_{j'})} (X_{i,i'',j} + X_{i'',i',j}) + M(1 - XX_{i,i',j}) \quad (6)$$

$$\forall i, i', j \in (i_j \cap i'_{j'})$$

$$\sum_i \sum_{\substack{i' \neq i \\ \text{formula}_{i'} \neq \text{formula}_i}} (XX_{i',i,j}) \leq \text{Limit}_j \quad \forall j \quad (7)$$

$$\min C_{\max} \geq C_i \quad \forall i, j \quad (8)$$

Constraint (1) forces that every product order i goes through one packing line j via the allocation binary variable $Y_{i,j}$. Constraint (2), (3) and (4) give the relative sequencing of product orders. The big-M constraint (3) determines the completion time $C_{i'}$ of a product order i' to be greater than the completion time and the processing time $T_{i'}$ of whichever product i is produced beforehand at the same unit, and greater than the changeover time, $\text{changeover}_{i,i'}$, only if the binary variable $X_{i,i',j}$ is active. The binary variable $X_{i,i',j}$ is active only if product i' is produced after product i . The constraints (2) and (4) state that when two products are produced at the same unit, only one global sequencing binary

variable has to be active and when one of the binary variable $X_{i',i,j,s}$ and $X_{i',i,j}$ is active at least one of the $Y_{i,j}$ and $Y_{i',j}$ has to be active as well. The variable $Z_{i,i',j}$ signifies the position difference among two products produced in the same packing line. When $Z_{i,i',j}$ is equal to 0, the product i is produced exactly before the i' . The variable $Z_{i,i',j}$ is calculated in equation (6). As a result, from equation (5) the immediate precedence binary variable $XX_{i,i',j}$ takes the value 1 only when the variable $Z_{i,i',j}$ is equal to 0. The binary variable $XX_{i,i',j}$ takes the value 1 when the product i' is produced exactly after the product i . The constraint (7) ensures that the number of sequences between products with different recipe ($formula_i$) does not exceed an upper limit ($Limit_j$) which is determined by the plants' technical restrictions. In order this constraint to be included in the model both the immediate and the general precedence binary variables are used. Finally, the objective function of the model is expressed by constraints (8), which is the minimization of the total production makespan, C_{max} , hence it also considers the minimization of changeovers and unnecessary idle times.

3.3. Decomposition Algorithm

The large-scale industrial scheduling problem is decomposed into smaller problems in an iterative fashion. In each iteration a subset of the product orders is scheduled. In this way the MILP subproblems are solved much easier while the computational time is significantly decreased. A number of inserted products are scheduled in each iteration until all product orders are scheduled. After the resolution of the MILP model at each iteration, the global sequencing variables, as well as the allocation variables of the inserted products are fixed. However, the timing variables (ending time) and the immediate precedence binary variables remain free. When all products are inserted, the final schedule is constructed. Each iteration, aims to find a solution with a 0% integrality gap. However, industrial requirements impose an upper bound on the total computational time. Therefore, a time limit of 10 minutes, has been set for the solution of each subproblem. Figure 1 illustrates the proposed decomposition technique.

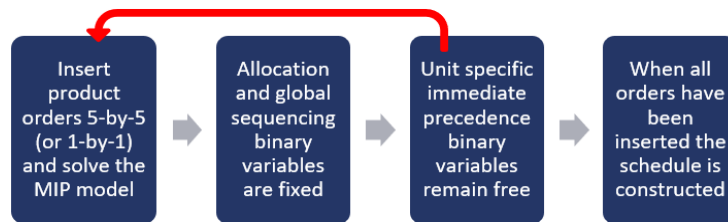


Figure 1: Decomposition-based solution algorithm

4. Results

A representative industrial case study of 178 final products and 6 packing lines is used to illustrate the applicability and efficiency of the proposed solution strategy. All data have been provided from a real-life, large-scale consumer goods industry. Technical packing lines restrictions do not allow full flexibility of the products' allocation. The first 80 products can be solely allocated to the first 3 packing lines, as the remaining 98 products can be processed only in the next 3 packing lines. Utilizing the aforementioned decomposition algorithm 5 products are scheduled at each iteration, except for the last

one, where the remaining 3 products are scheduled. The decomposition technique, was implemented in GAMS and solved using the CPLEX 12.0 solver. Figure 2. illustrates the final schedule, of the study under consideration. Maintenance activities have also been taken into account.

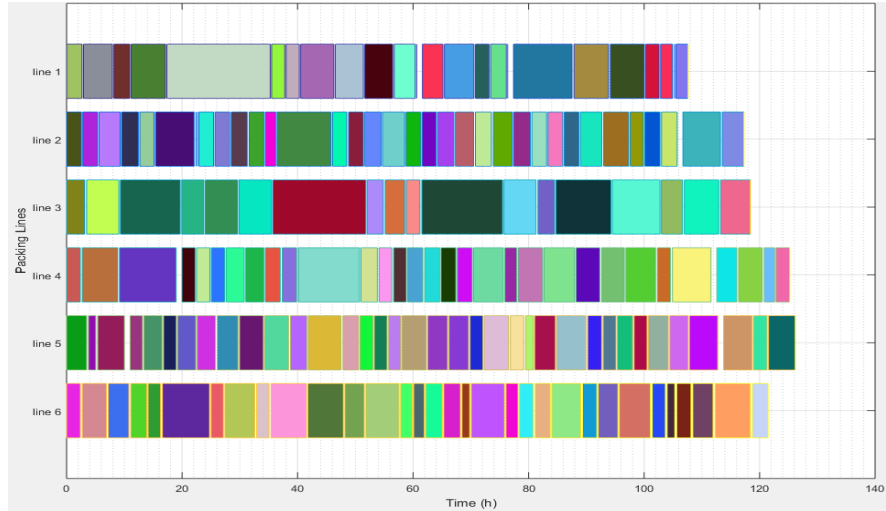


Figure 2: Gantt chart of the packing lines referring to the examined case study

Table 1: Comparison between the exact MILP model and the decomposition approach applying different insertion policies

	Exact MILP Approach	Decomposition Approach		
		Insertion policy 1-by-1	Insertion policy 5-by-5	Insertion policy 10-by-10
Makespan (hrs)	118.9	122.6	120.2	120.8
Computational CPU Time (minutes)	15	1.6	2.46	31.4

Another medium-scale problem instance including 80 products and 3 packing lines, has been also studied, in order to assess the solutions of the proposed decomposition technique. The study is solved using both the decomposition algorithm and the exact MILP model, described above. The results are illustrated in the Table 1. It is observed that the decomposition algorithm leads to nearly optimal solutions. In addition, the computation time is significantly decreased using the decomposition algorithm, when the products are inserted 1-by-1, or 5-by-5. The application of the 10-by-10 insertion policy, increases the complexity of the subproblems and the zero integrality gap cannot be achieved in several of the iterations without exceeding the underlying solution time limit.

As a result, the computational time is increased and higher makespan values are obtained. The aforementioned exact MILP model can only be applied to medium problem instances. For larger problem instances the computational cost becomes prohibitively high and even a feasible solution cannot be guaranteed.

5. Conclusions

The main contribution of this work is the application of an MILP-based decomposition technique, in large scale, industrial packing facilities. A continuous, real-life, industrial facility is considered. More specifically, the packing stage of a consumer goods facility is scheduled, taking also into account constraints related to the formulation/production stage. The proposed decomposition-based approach leads to nearly optimal solutions for large-scale problem instances. On the other hand, the exact MILP model can only be applied to medium-sized problem instances. The solution strategy can assist decision makers to take rigorous scheduling plans in a dynamic production environment under realistic uncertainty. Current work considers an additional improvement algorithm step to further improve the efficiency of the proposed scheduling technique.

Acknowledgements

The work leading to this publication has received funding from the European Union's Horizon 2020 research and innovation programme under grant agreement No 723575 (Project CoPro) in the framework of the SPIRE PPP.

References

- G.M. Kopanos, L. Puigjaner, M.C. Georgiadis, 2010, Production scheduling and lot-Sizing in dairy plants: The yoghurt production line, *Industrial & Engineering Chemical Research*, 49, 2, 701-718
- C.A. Méndez, J. Cerdá, I.E. Grossmann, I. Harjunoski, M. Fahl, 2006, State-of-the-art review of optimization methods for short-term scheduling of batch processes, *Computer & Chemical Engineering*, 30, 6-7, 913-94.
- I. Harjunoski, C.T. Maravelias, P. Bongers, P. M. Castro, S. Engell, I. E. Grossmann, J. Hooker, C.Méndez, G. Sand, J. Wassick, 2014, Scope for industrial applications of production scheduling models and solution methods, *Computers & Chemical Engineering*, 62, 161-193
- P. Baumann, N. Trautmann, 2014, A hybrid method for large-scale short-term scheduling of make-and-pack production processes, *European Journal of Operational Research*, 236, 2, 718-735
- G.M. Kopanos, C.A. Méndez, L. Puigjaner, 2010, MIP-based decomposition strategies for large-scale scheduling problems in multiproduct multistage batch plants: A benchmark scheduling problem of the pharmaceutical industry, *European Journal of Operational Research*, 207, 2, 718-735

Computer-Assisted Experiments for the Identification of the Two-Phase Viscosity of Fluids

Xenia Gabrisch^{a,*}, Jens-Uwe Repke^a

^aChair of Process Dynamics and Operation, Technical University of Berlin, Straße des 17. Juni 135, 10623 Berlin, Germany

xenia.gabrisch@tu-berlin.de

Abstract

The description of several transport phenomena requires the information about the viscosity of fluids. One application is a capillary tube that is operated as throttle device in the context of a heat pump. The two-phase pressure drop in the capillary tube can commonly be described using the homogenous flow model, which requires a valid correlation of the two-phase viscosity. Yet, no reliable correlation is available in literature, such that it is predictive for an extensive operation area. A lack of consistent and detailed experimental data as well as the lack of precise capillary specification complicates the matching of experimental and numerical results of the two-phase viscosity. For this reason, this work presents a systematic and comprehensive procedure in order to be able to identify a reliable two-phase viscosity. The procedure is a symbiosis of systematical numerical and experimental analysis of a two-phase refrigerant flow through a capillary tube. The numerical pre-analysis serves to identify sensitive parameters, which are experimentally refined afterwards. Comprehensive experimental investigations of the two-phase flow through the capillary provide understanding of different flow phenomena, which are inadequately described up to now. Numerical pre-analysis and extensive experimental investigations are the precondition for a computer-aided identification of the two-phase viscosity based on the experimental database.

Keywords: Computer-Assisted Experiments, Two-Phase Viscosity, Two-Phase Pressure Drop, Metastability, Hysteresis Effect

1. Introduction

Correlations of the two-phase viscosity of fluids are needed in order to describe various transport phenomena of fluids in process engineering. One application is the two-phase flow of a refrigerant through a capillary tube as a part of a heat pump system. The capillary serves as throttle device in rather smaller heat pump applications where it substantially determines the operation point. A predictive overall model of the heat pump is highly worth aspiring for, since it makes affordable a vast investigation of part components and their sensitivity towards the whole system. A precondition for this is a valid dynamic and predictive capillary model, i.e., the description of the two-phase flow through the capillary. The homogenous flow approach is a common assumption for the flow through a capillary tube. It requires the description of the two-phase viscosity of the considered refrigerant that is still an unsatisfactorily explored subject. Little data exists on natural and/or green refrigerants as statistics show (Dubba and Kumar, 2017). However, the latter are of growing importance in the context of the F-Gas Regulation. Sempértegui-Tapia and Ribatski (2017) stressed that a lot of the existing database on two-phase flow through

capillaries goes along with imprecise data on the inner diameter and the absolute roughness of the inner surface of the capillary. Nevertheless, these parameters have a strong influence on the two-phase pressure drop in the capillary as numerical sensitivity investigations show. Imprecise parametrization of the according flow model leads to difficulties in validation and identification of an appropriate two-phase viscosity. The numerical results can hardly match the experimental data provided when only the viscosity correlation serves as adjusting screw.

Furthermore, experimental databases seldom provide information on metastability as well as the hysteresis effect on vaporization of the flow in a capillary tube. In fact, experimental investigations show that the impact of these effects on e.g. the measured pressure drop in a capillary tube are significant, hence, they need to be considered. Meyer and Dunn (1998) discussed the presence of a hysteresis curve that correlates with the metastability of the refrigerant flow. They proposed a coherent collection of experimental data since the experimental results depend on the history of previous measurements and conditions, respectively. Yet, little researchers followed the proposed experimental technique. Consequently, most experimental data is inconsistent in terms of the mentioned flow phenomena. Meyer and Dunn also advised to implement a memory function into the numerical capillary model that is able to capture the hysteresis effect. Especially, within the context of an overall heat pump model, the effect needs to be considered, as the hysteresis of the capillary is passed through within the operation of the heat pump. However, existing experimental data are insufficient to develop and implement a memory function that predicts a broad operation range, yet.

This work presents a computer-aided approach for a systematic gathering of experimental data that enables the identification of an appropriate correlation of the two-phase viscosity of fluids.

2. Homogenous Flow Model

The homogenous flow model is a common way to describe the pressure drop in a capillary tube. The total pressure drop Δp is simplified to the sum of the pressure drop of the liquid refrigerant Δp_{liq} and the two-phase pressure drop Δp_{tp} , see Eq. 1-3.

$$\Delta p = \Delta p_{liq} + \Delta p_{tp} \quad (1)$$

$$\Delta p_{liq} = \left(L_{liq} \cdot \frac{f}{2 \cdot d} + \xi \right) \cdot \frac{G^2}{\rho} \quad (2)$$

$$\Delta p_{tp} = \Delta \left\{ \frac{G^2 \cdot x^2}{\alpha \rho_v} + \frac{G^2 \cdot (1-x)^2}{(1-\alpha) \cdot \rho_v} \right\} + f \cdot \frac{G^2}{2 \cdot d \cdot \rho} \cdot L_{tp} \quad (3)$$

In Eq. 1-3 d is the inner diameter of the capillary tube. L_{liq} and L_{tp} mark the lengths inside the capillary that are occupied by liquid flow and two-phase flow, respectively. Further, ρ represents the density of the refrigerant and ξ the entrance pressure drop coefficient due to sudden contraction of the flow channel. The indices v and l denote the vapour and liquid density, respectively. G indicates the mass flux, α the void fraction and

x the vapour quality. The friction factor follows the correlation of Colebrook (1939), see Eq. 4.

$$\frac{1}{\sqrt{f}} = 1.14 - 2 \cdot \log\left(\frac{e}{d}\right) + \frac{9.3}{Re \cdot \sqrt{f}} \quad (4)$$

The calculation of the friction factor (Eq. 4) requires the inner diameter d , the absolute roughness of the inner surface of the capillary e , as well as the Reynolds-Number Re of the flow. However, the calculation of the Reynolds-Number depends on the dynamic viscosity μ alongside the inner diameter, the flow velocity v and the density of the refrigerant – see Eq. 5.

$$Re = \frac{v \cdot d \cdot \rho}{\mu} \quad (5)$$

Whereas the dynamic viscosity for the liquid phase of refrigerants is well determined, there is disagreement on the appropriate two-phase viscosity. As stated by Sempértegui-Tapia and Ribatski (2017), imprecise capillary parametrization in terms of diameter and roughness can shadow the actual influence of the viscosity correlation.

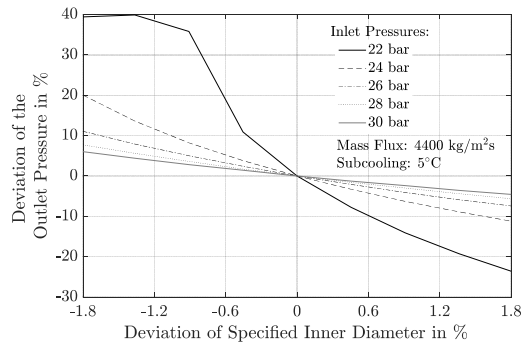


Figure 1: Impact of inner diameter uncertainty on the calculated outlet pressure

A sensitivity analysis (see Fig. 1) conducted with the given equation set (Eq. 1-5) shows how sensitive the calculated outlet pressure is towards a small degree of uncertainty of the inner diameter. The deviation of $\pm 1.8\%$ corresponds to the manufacturer's specification of the tolerance of the inner diameter. It further becomes visible that the sensitivity increases for lower inlet pressures. An uncertainty of the inner diameter of only 1.2% affects an uncertainty in the calculated outlet pressure of almost 40% . Comprehensive studies show that the sensitivity increases for smaller degrees of subcooling and higher mass fluxes. It is only reasonable to identify any appropriate viscosity correlation if the uncertainty of the inner diameter is narrowed. The same applies for the absolute roughness. Within this work, the capillary diameter is determined by the means of a light microscope and the roughness by the means of a white light

interferometry. Pre-investigations show that it is possible to narrow the tolerance of the inner diameter for capillaries of one production charge to at least $\pm 0.9\%$.

3. Experimental Investigations of the Two-Phase Pressure Drop

The experimental test rig presented in Fig. 1 serves for a comprehensive collection of two-phase pressure drop of propane for various conditions at the capillary inlet. The inlet condition of propane comprises the inlet pressure (PR-1), the inlet temperature (TR-1) and the mass flux (FIRC-1) of propane. The design of the experimental apparatus enables a wide operation range (PR-1: 10-30 bar, TR-1: 393-453 K, FIRC-1: 2-20 kg/h). The temperature is measured by thermocouples of type T providing a measuring error of ± 0.5 K. The measuring error of the piezo-resistive pressure sensors is specified to $\pm 0.7\%$; the error of the Coriolis mass flow meter to $\pm 0.3\%$.

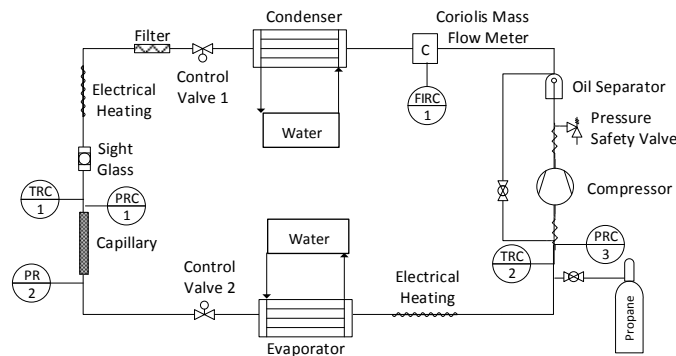


Figure 2: Experimental Apparatus

The capillary inside a heat pump is operated at flexible conditions depending on the application and outer circumstances of the operation. For a predictive and reliable capillary model, it is indispensable to validate the viscosity correlation against a wide range of operation conditions. However, the occurrence of hysteresis requires a coherent experimental data acquisition that drastically expands the original design of experiments. Hence, a systematic sensitivity analysis is conducted in order to understand whether the hysteresis effect is negligible for certain operation conditions. More precisely, the differences in pressure drop within hysteresis curves are examined for different inlet pressures, inlet temperatures and mass fluxes. Fig. 3 shows one exemplary hysteresis curve that depends on the increasing and decreasing of the subcooling. It makes clear that the different degrees of subcooling cannot be measured independently but depend on the previously performed subcooling. Furthermore, a discontinuity in the recorded pressure drops occurs at a subcooling of $7\text{ }^{\circ}\text{C}$ and $5\text{ }^{\circ}\text{C}$. Although the operation conditions remained constant at this point, a sudden increase in pressure drop was recorded. Meyer and Dunn (1998) interpreted this phenomenon as the collapse of a metastable region.

Yet, understanding of how the metastable regions develop and what causes the collapse is still not well investigated and modelled (García-Valladares, 2007) (Dubba and Kumar,

2017). Little attention has been paid to explain the phenomenon of the hysteresis on vaporization as it appears in Fig. 3 since Meyer and Dunn presented their findings in 1998. However, knowledge and understanding of the hysteresis is crucial when modelling a capillary in the context of a heat pump.

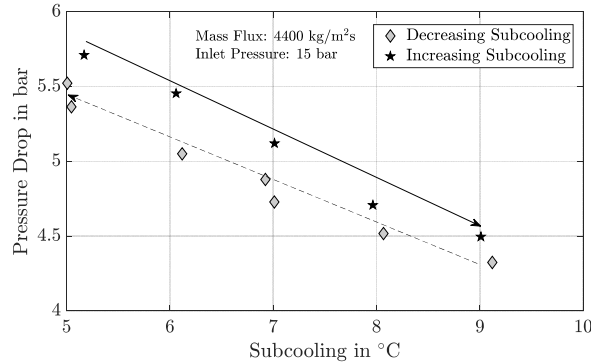


Figure 3: Hysteresis on vaporization depending on increasing and decreasing subcooling

4. Conclusions

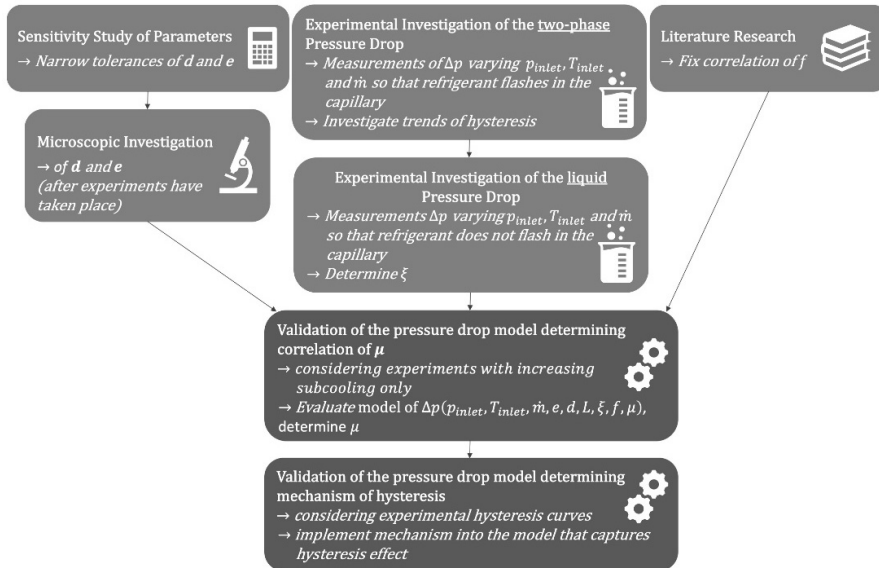


Figure 4: Systematic computer-aided approach for the validation of the pressure drop model

One reason for the fact that until today no satisfactory predictive two-phase correlation has been identified, is that the experimental database is not consistent and detailed enough. Because of that, this work aims for a systematic procedure to provide reliable data for the identification of the two-phase viscosity. For the systematic approach to

obtain a predictive two-phase viscosity correlation, the presented experimental apparatus in Fig. 2 serves for extensive data gathering. A wide range of operation conditions is performed whereby hysteresis curves are recorded so that the influence of the inlet pressure, inlet temperature and mass flux through the capillary on the hysteresis becomes clear. Comprehensive data on hysteresis curves also serves to identify and mathematically describe the occurrence and possible correlation between hysteresis and metastability of the flow. This means, that the equation set of Eq. 1-5 needs to be complemented by the gathered understanding of both phenomena, e.g. by implementing a memory function that takes into account the history of simulated capillary inlet conditions. Liquid pressure drop experiments provide a base of validation data against which the entrance pressure drop coefficient is determined. Following the systematic concept for the model validation of the pressure drop in the capillary in Fig 4. and Eq. (2), only ξ is unknown at this point. Once, extensive data collection at the experimental apparatus is completed, the inner diameter and the absolute roughness of the considered capillary are investigated by the designated optical measurement techniques in order to provide a more precise parametrization of the capillary model. The numerical sensitivity analysis indicates that e.g. the diameter should at least be refined to an uncertainty of $\pm 0.5\%$ in order to have less than 10% uncertainty in the calculated outlet pressure. The symbiosis of profound numerical and experimental analysis, thus, is necessary to reduce the overall degree of uncertainties of the capillary model in order to identify a predictive two-phase viscosity correlation of fluids. However, uncertainties still need to be considered when evaluating the viscosity correlation from the gathered experimental data, since any impacts cannot be captured by viscosity correlations. All in all, this work provides a systematic technique that, if followed by more researchers, delivers a reliable and precise data base in order to validate the two-phase pressure drop model of refrigerants.

References

- Z.H. Chen, R.Y. Li, S. Lin, Z.Y. Chen, 1990, A Correlation for Metastable Flow of Refrigerant 12 Through Capillary Tubes, ASHRAE Transactions, Vol. 96, No. 1, pp. 550-554
- C. F. Colebrook, 1939, Turbulent Flow in Pipes, with Particular Reference to the Transition Region between Smooth and Rough Pipe Laws, Journal of the Institution of Civil Engineers, Vol. 11, No. 4, pp. 133-156
- S. K. Dubba and R. Kumar, 2017, Flow of Refrigerants Through Capillary Tubes: A State-of-the-Art, Experimental Thermal and Fluid Science, Vol. 81, pp. 370-381
- O. García-Valladares, 2007, Numerical Simulation of Non-Adiabatic Capillary Tubes Considering Metastable Region. Part I: Mathematical Formulation and Numerical Model, International Journal of Refrigeration, Vol. 30, pp. 642-653
- J. J. Meyer and W. E. Dunn, 1998, New Insights into the Behavior of the Metastable Region of an Operating Capillary Tube, HVAC & Research, Vol. 4, No. 1, pp. 105-115
- D. F. Sempértegui-Tapia and G. Ribatski, 2017, Two-Phase Frictional Pressure Drop in Horizontal Micro-Scale Channels: Experimental Data Analysis and Prediction Method Development, International Journal of Refrigeration, Vol. 79, pp. 143-163

From Single Process Simulation and Optimization to Decision Making Based on a Multitude of Solutions

Norbert Asprion,^{a,*} Roger Böttcher,^a Johannes Höller,^b Patrick Schwartz,^b Jan Schwientek,^b Michael Bortz^b

^a *BASF SE, Chemical Process Modeling, Carl-Bosch-Str. 38, 67056 Ludwigshafen , Germany*

^b *Fraunhofer Institute for Industrial Mathematics ITWM, Fraunhofer Platz 1, 67663 Kaiserslautern, Germany*

norbert.asprion@basf.com

Abstract

Quite often process simulation is only used as a representation of experimentally developed processes. With today's availability of computation power and advanced simulation and optimization methods much more than providing a closed heat and mass balance and some data for process unit design is possible. There is a need for a shift in paradigm to a model-centric process development. Supporting decision making to find out which design variables or model parameters are significant, which experiments should be done, how optimality could be reached, should be addressed in an iterative workflow and a supporting framework. This is discussed in the present contribution.

Keywords: process simulation, multi-criteria optimization, sensitivity analysis, surrogate modeling.

1. Introduction

Most common process simulation tools are focussing on generating and managing only a single process simulation. However, in process development, for rational decisions in general a broader and more transparent view on achievable simulation and optimization results is desirable. Parallelization reduces computation time to explore the solution space. Therefore, tools for a holistic view on several simulation and optimization runs and for decision support enabling efficient and fast access to large data bases including many simulations are needed. Furthermore, a workflow for an iterative modelling, simulation and optimization should be supported to improve models and results continuously with increasing information and knowledge. The paper is organized as follows: After a brief description of the workflow, examples of applications and visualizations using a multitude of solutions for different tasks within process development will be discussed before a conclusion is given.

2. Process Simulation and Optimization for Decision Making

In the present contribution a concept for an iterative use of process simulation and optimization (cf. Fig. 1) during different stages of process development will be discussed, which relies on comparisons and visualizations of a multitude of process simulations and optimization to support decision making. A more detailed discussion can be found in

Asprion and Bortz (2018). The novelty is the holistic approach to support the various workflow aspects of process development in one simulation environment.

In an early phase of process development, process simulation and optimization might help to identify and compare most promising process concepts. The comparison of Pareto sets (set of best compromises between competing objectives) in a decision support system helps to find sound decisions and allows to investigate trade-offs between the competing objectives. Furthermore, an investigation of the impact of uncertainties (sensitivity analysis) on simulation and optimization results helps to identify model parameters which have to be determined with decreased uncertainty or to minimize risk by a robust or stochastic optimization. This might be useful for the design of mini-plants since in this phase many relationships are rather unclear like for example the impact of impurities on catalyst behavior and expected yield. In a laboratory setup or in a mini-, pilot or production plant, model-based design of experiments enables an efficient (faster, less costly) and effective (doing the right experiments) investigation, which might be used for model discrimination, model parameter estimation or verification of optimization results. Independent of the type of process development – either for a new or an existing plant – in a certain stage there will be plant data available – either from a mini- or pilot plant or from the existing production plant. These data can and should be used for the validation and adjustment of the process model before an extensive simulation or optimization study starts. In case of missing models for specific units greybox modeling can be used to setup a model combining scientific models with data-driven parts (cf. Asprion et al., 2019). Finally, a multi-criteria optimization of the process model will identify Pareto sets for the design of a new plant or design modifications for existing plants. Here again a combination with sensitivity analysis helps to evaluate and/or minimize risks evoked by uncertainties. A framework supporting the workflow of Fig. 1 requires data management and visualization to support decision making and documentation (incl. versioning). Of course, in most cases there will be iteration loops. One such loop might, for example, include design of experiment, experiments in a plant for parameter estimation or for verifying optimization results and subsequent model adjustment until an acceptable parameter estimation or optimization result is obtained. A process simulator should support the different tasks shown in Fig. 1 for an efficient and effective decision making in process development.

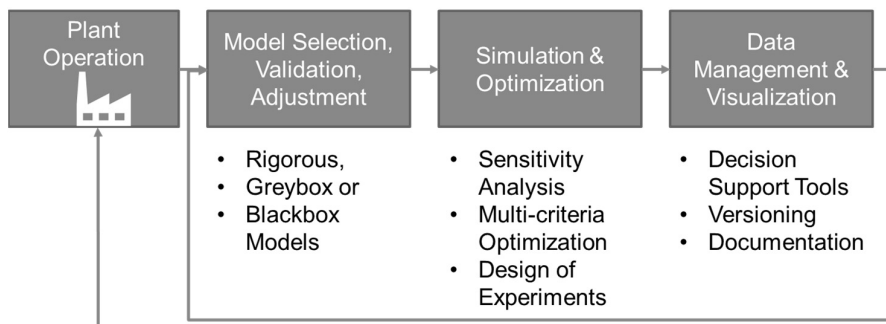


Figure 1: Workflow for an iterative use of process simulation and optimization to support decision making in process development

3. Examples

In the following examples for comparisons of a multitude of solutions including visualization for decision support in different phases of process development are presented.

3.1. Decision support for process concepts

In this example, four different concepts for the separation of three different mixtures of hexane, heptane and octane by distillation are compared based on Pareto sets (cf. Fig. 2). The optimization variables are summarized in Tab. 1. As objectives of the multi-criteria optimization the heptane product purity and the molar flow of heptane are maximized, whereas the total costs are minimized. As constraints the hexane and octane product streams should have a purity ≥ 99 mol%.

Table 1: Range of the optimization variables (N-number of stages, f-feed, sd-side draw, RR-reflux ratio, pf-pre-fractionator, ldw, hdw- lower and higher end of dividing wall, s-split) for the design of the column configurations for the separation of hexane, heptane, octane mixtures (600 kmol/h).

	N ₁	N _{f,1}	RR ₁	N ₂	N _{f,2}	RR ₂	n / kmol/h			n / kmol/h	
Indirect sequence	20-50	5-45	1-5	20-50	5-45	1-5	Hex:320-480; 160-260;60-140			Hep:60-140; 160-260;60-140	
Direct sequence	20-50	5-45	1-5	20-50	5-45	1-5	Oct:60-140; 160-260;320-480			Hep:60-140; 160-260;60-140	
	N ₁	N _{f,1}	RR ₁	N _{sd}	n / kmol/h			n / kmol/h		Constraint	
Side-draw	20-50	5-45	1-20	10-40	Oct:60-140; 160-260;320-480			Hep:60-140; 160-260;60-140		N _{sd} > N _{f,1}	
	N _{pf}	N _{f,1}	RR ₁	N ₁	N _{sd}	N _{ldw}	N _{hdw}	S _{ldw}	S _{hdw}	n / kmol/h	
Dividing wall col.	5-41	5-45	1-20	20-50	10-40	1-40	10-50	0,2-0,9	0,1-0,9	Oct:60-140; 160-260;320-480 Hep:60-140; 160-260;60-140	

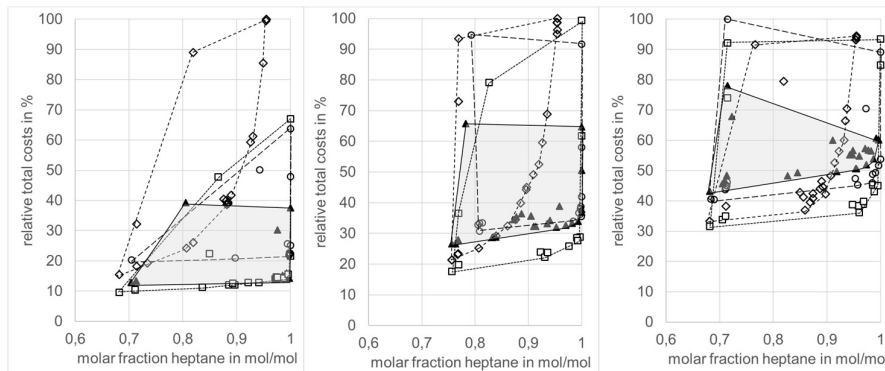


Fig. 2: Comparison of Pareto sets (lines representing convex hulls covering the full range of solutions also for the third objective, i.e. molar flow of heptane, gray area is only for better distinction) of 4 different concepts to separate mixtures of hexane, heptane and octane. \blacktriangle direct sequence of 2 columns, \circ indirect sequence of 2 columns, \diamond side-draw column, \square dividing wall column. Left: light feed (molar fractions: 2/3 hex., 1/6 hep. and 1/6 oct.), middle: equimolar feed, right: heavy feed (molar fractions: 1/6 hex., 1/6 hep. and 2/3 oct.)

As can be seen for all three mixtures, the dividing wall column is the cheapest concept. The side-stream column is only feasible for heptane purities < 95 mol%. In terms of total

costs at the same heptane purity, for the mixture with high light boiler (hexane) content, as expected, the direct sequence is more favorable as the indirect sequence, whereas for an equimolar feed both concepts are close to each other and for the mixture with large high boiler (octane) content the indirect sequence is more favorable than the direct one. Methods and further examples how to estimate Pareto sets and how a decision support system can be used to explore trade-offs are described in Bortz et al. (2014), Burger et al. (2014) and Hashem et al. (2017).

3.2. Sensitivity Analysis for Process Design

In this case the impact of uncertainties of an activity coefficient model on the design of a distillation column to separate a methanol-water mixture is considered (similar to Asprion et al. (2015), section 6.2 NQ Curve). In Fig. 3 on the left-hand side the impact of the uncertainties on the McCabe-Thiele can be seen, which look rather small, but since the purity specification of the product methanol is very high, there is a huge impact on the design. For the worst case this results in much higher number of stages required for a constant reboiler duty or significant higher reboiler duties at constant number of stages compared to the nominal model.

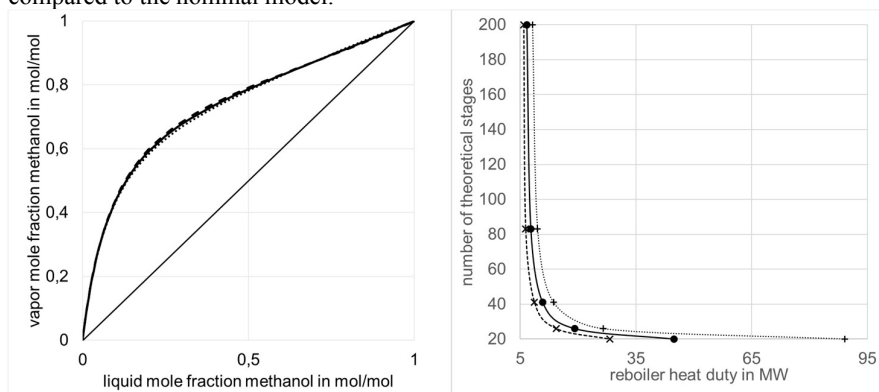


Fig. 3: Impact of uncertainties of a NRTL activity coefficient model for methanol-water on the design of distillation column with high purity of methanol. Left: McCabe-Thiele diagram at 1 bar and right part: N-Q curve for 3 different models: ●, — : Nominal model, ×, ---: model with 10% higher limiting activity coefficient of water in methanol, +, ···: model with 10% lower limiting activity coefficient. Uncertainties effect the necessary number of stages and/or reboiler heat duty.

Further examples can be found in Chinen et al. (2018), Bortz et al. (2017), von Harbou et al. (2017) and Asprion et al. (2017), which partly also include examples for robust/stochastic optimization to minimize the impact of uncertainties.

3.3. Surrogate Modeling for Process Optimization

The next example demonstrates that tools originally developed for a different application as described in chapter 2 can be used in different contexts.

In this example for a process model of a cumene plant (for details see Asprion et al., 2017), the whole model is replaced by a surrogate model to be used for a multi-criteria optimization. These results will be compared with the results of the optimization (variables see Table 2) of the original, rigorous process model (cf. Asprion et al., 2017, Fig.7, VLE2; k1; k2) to demonstrate the feasibility of that approach.

In a first step, a sensitivity analysis of the rigorous process model is performed using a Quasi-Monte-Carlo sampling based on Sobol sequences. To start with, this was done in

the range given in Table 2, leading however to a very high number (>70%) of infeasible, divergent simulation runs. Therefore, in a second step the range was reduced as given in Table 3. The number of samples (scenarios considered in the sensitivity analysis) was set to 10 per optimization variable yielding in this case 70 samples. From these a subset of 60 could be used to train surrogate models. The setup of the models was done using a functionality originally developed for greybox modeling (cf. Asprion et al., 2019).

Table 2: Range of the optimization variables for optimization of the rigorous process model: inlet temp. of the reactor T_{in} , propen to benzene ratio (p to b), reflux ratio (RR) and logarithmic cumene split ratio ($\ln(CR)$) of column 1 and 2 (cf. Asprion et al., 2017 for details).

	$T_{in}/^{\circ}C$	p to b	RR ₁	$\ln(CR_1)$	RR ₂	$\ln(CR_2)$	load
min	340	0.2	0.1	-12	0.1	-12	0.6
max	400	0.9	1	-1	1	-1	1.2

Table 3: Range of the variables for sampling of the rigorous model based on Sobol sequences (taken from Asprion et al., 2019, supplement, Table A1).

	$T_{in}/^{\circ}C$	p to b	RR ₁	$\ln(CR_1)$	RR ₂	$\ln(CR_2)$	load
min	340	0.5	0.1188	-3.1	0.3	-10.5	0.6
max	345	0.6	0.4188	-2.5	0.4	-9	1.2

The objective *capacity* is proportional to the *load*, which was used directly in the surrogate model. For the objectives *OpEx* (operational expenditure discounted for 10 years per ton of cumene) and *GWP* (global warming potential) artificial neural networks with one hidden and one output layer with 7 neurons each (according to the 7 variables used as input, see Table 3) were trained (regression coefficients $R^2=0.99$ and 0.92). To account for the 21 constraints used in the original optimization problem, these corresponding functions have also been modeled using neural nets. 15 functions could be modeled without a hidden layer ($R^2=0,87-1$) and 6 have been modeled ($R^2=0,98-1$) with a net with the same structure as the net for the objectives *OpEx* and *GWP*. All nets use a α -sigmoid function with $\alpha=2$. These models have been used in a multi-criteria optimization: minimizing *OpEx*, *GWP*, *load* and maximizing *capacity* as can be seen in Fig. 4.

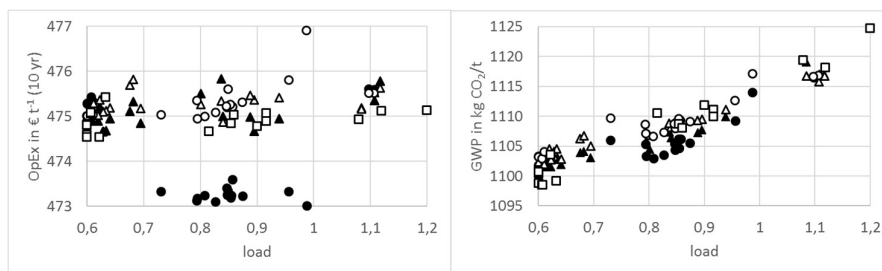


Fig. 4: Comparison of the results of a rigorous process model ($\square, \circ, \triangle$) of a cumene plant with the results of different versions of a surrogate model (\bullet, \blacktriangle). First a surrogate model has been created using a quasi-Monte-Carlo sampling (Sobol sequences) of the rigorous model. This model has been used for multi-criteria optimization (\bullet) and is compared with the optimization results of the original model (\square). Verification with the rigorous model using the optimization variables of the surrogate (\circ) shows larger deviation. Therefore, this data has been added and used to retrain the surrogate. $\blacktriangle, \triangle$ are representing the results of the optimization of the improved surrogate and the corresponding verification with the rigorous model.

The surrogate model (●) in general predicts too low values for the objectives and when using the estimated optimization variables as inputs of the rigorous model (○), the objectives are higher than the optimal values of the rigorous model (□). Therefore, in a second iteration the 22 verification runs together with the original samplings have been used to retrain the surrogate model. The optimization with this second surrogate model (▲) shows a good agreement with the objectives obtained from optimizing the rigorous model (□) and also the verification with the optimization variables (△) has only small deviations (mean absolute deviation OpEx < 0,067%; GWP < 0,13%). During the optimization the validity range of the models has been accounted for by using convex hulls, which were used to setup a constraint allowing for an extrapolation of 10% outside the validity range. This is the reason why the load range is not fully covered. One possibility would be to proceed with iterative retraining of the model and optimization until the full range is exploited. The agreement between the objectives of the surrogate and the verification can be used as a stopping criterion for an iterative optimization and retraining of surrogate models.

Further examples for surrogate modeling can be found in McBride and Sundmacher (2019).

4. Conclusions and Outlook

In process development many decisions have to be made concerning process concepts, experiments, models and model parameters, risk quantification and mitigation measures, which can be supported by process modeling, simulation and optimization. As was shown in the examples, it is essential that a process simulator supports methods like for example multi-criteria optimization, sensitivity analysis and surrogate modeling. Here an efficient data management for a multitude of solutions and helpful visualizations are required to enable comparisons, exploring the solution space and thus offering support to arrive at sound, documented decisions.

References

- N. Asprion, M. Bortz, 2018, *Chem. Ing. Tech.*, 90, No. 11, 1727–1738.
- N. Asprion, R. Benfer, S. Blagov, R. Böttcher, M. Bortz, M. Berezhnyi, J. Burger, E. von Harbou, K.-H. Küfer, H. Hasse, 2015, *Chem. Ing. Tech.*, 87 (12) 1810-1825.
- N. Asprion, S. Blagov, R. Böttcher, J. Schwientek, J. Burger, E. von Harbou, M. Bortz, 2017, *Chem. Ing. Tech.*, 89 (5) 665-674, DOI: 10.1002/cite.201600098
- N. Asprion, R. Böttcher, R. Pack, M.-E. Stavrou, J. Höller, J. Schwientek, M. Bortz, 2019, *Chem. Ing. Tech.*, 91 (3), DOI: 10.1002/cite.201800086
- M. Bortz, J. Burger, N. Asprion, S. Blagov, R. Böttcher, U. Nowak, A. Scheithauer, R. Welke, K.-H. Küfer, and H. Hasse, 2014, *Comp. Chem. Eng.*, 60, 354–363.
- M. Bortz, J. Burger, E. von Harbou, M. Klein, J. Schwientek, N. Asprion, R. Böttcher, K.-H. Küfer, H. Hasse, *Ind. Eng. Chem. Res.* 2017, 56 (44), 12672 – 12681.
- J. Burger, N. Asprion, S. Blagov, R. Böttcher, U. Nowak, M. Bortz, R. Welke, K.-H. Küfer, H. Hasse, *Chem. Ing. Tech.* 2014, 86 (7), 1065-1072.
- A.S. Chinen, J.C. Morgan, B. Omell, D. Bhattacharyya, C. Tong, D.C. Miller, 2018, *Ind. Eng. Chem. Res.*, 57 (31)10448-10463
- E. von Harbou, O. Ryll, M. Schrabback, M. Bortz and H. Hasse, *Chem. Ing. Tech.* 2017, 89, No. 10, 1315-1324.
- I. Hashem, D. Telen, P. Nimmegeers, F. Logist, J. Van Impe, 2017, *Comp. Chem. Eng.*, 106, 544–558.
- K. McBride, K. Sundmacher, 2019, *Chem. Ing. Tech.*, 91, No. 3, DOI: 10.1002/cite.201800091

A Neural Network-Based Framework to Predict Process-Specific Environmental Impacts

Johanna Kleinekorte^a, Leif Kröger^a, Kai Leonhard^a and André Bardow^{a,b,*}

^a*Institute for Technical Thermodynamics, RWTH Aachen University, Schinkelstraße 8, 52062 Aachen, Germany*

^b*Institute of Energy and Climate Research (IEK-10), Forschungszentrum Jülich, Wilhelm-Johnen-Straße, 52425 Jülich, Germany*
andre.bardow@itt.rwth-aachen.de

Abstract

Growing environmental concern and strict regulations led to an increasing effort of the chemical industry to develop greener production pathways. To ensure that this development indeed improves environmental aspects requires an early-stage estimation of the environmental impact in early process design. An accepted method to evaluate the environmental impact is Life Cycle Assessment (LCA). However, LCA requires detailed data on mass and energy balances, which is usually limited in early process design. Therefore, predictive LCA approaches are required. Current predictive LCA approaches estimate the environmental impacts of chemicals only based on molecular descriptors. Thus, the predicted impacts are independent from the chosen production process. A potentially greener process cannot be distinguished from the conventional route. In this work, we propose a fully predictive, neural network-based framework, which utilizes both molecular and process descriptors to distinguish between production pathways. The framework is fully automatized and includes feature selection, setup of the network architecture, and predicts 17 environmental impact categories. The pathway-specific prediction is illustrated for two examples, comparing the CO₂-based production of methanol and formic acid to their respective fossil production pathway. The presented framework is competitive to LCA predictions from literature but can now also distinguish between process alternatives. Thus, our framework can serve as initial screening tool to identify environmentally beneficial process alternatives.

Keywords: predictive life cycle assessment, artificial neural network, early process development stage, comparison of pathway alternatives

1. Introduction

Today, the chemical industry is mainly based on fossil fuels leading to greenhouse gas (GHG) emissions. To reduce these GHG emissions and the dependency on fossil resources, process alternatives are developed using renewable resources such as CO₂ as feedstock. To quantify environmental reduction potentials resulting from technological change and to support the investment decision process, these process alternatives have to be assessed environmentally in an early design stage. An accepted method for environmental assessment is Life Cycle Assessment (LCA). Life Cycle Assessment is a holistic approach, which avoids emission shifting between life cycle phases or types of environmental impacts. However, LCA requires detailed data, which is limited in early process design stages. Therefore, so-called streamlined LCA approaches are required.

Streamlined LCA approaches reduce the scope of the assessment or simplify the required data

(Hunt et al., 1998; Casamayor and Su, 2012). One possibility of streamlining is the use of machine learning. Current machine learning approaches for predictive LCA of chemicals are based on artificial neural networks (ANN). To transform the characteristics of a molecule into an input vector for the ANN, these models use molecular descriptors, e.g., molecular weight or functional groups (Song et al., 2017; Calvo-Serrano et al., 2017; Wernet et al., 2009). The main drawback of molecular descriptors is that the ANN cannot distinguish between production pathways leading to the same chemical. Therefore, molecular descriptors cannot resolve environmental reduction potentials due to process alternatives.

In this work, we propose an ANN-based framework that considers both, molecular and process descriptors. Thereby, the model can obtain process-dependent impacts and capture trade-offs of different production pathways.

2. Fully Automated Algorithm for Environmental Impact Prediction

Artificial neural networks are non-linear function approximators (Hornik et al., 1989), which usually have a greater generalization ability than linear regression models. The network consists of input, output and hidden layers, whereby each layer consists of neurons (see Figure 1, upper part). The neurons of each layer are connected by edges to the following layer. In a neuron, the inputs x_j are weighted according to their edge weight $w_{k,j}$, summed and the result is projected into a non-linear space by the activation function φ (see Figure 1, lower part). The edge weights are determined during the training process.

In this work, we propose a fully automated framework including the selection of a suitable subsets of descriptors, also called feature selection, and optimization of the network architecture (see Figure 2): In a first step, suitable descriptors are selected using stepwise regression. Afterwards, a genetic algorithm (GA) determines the optimal network architecture to predict a given environmental impact. The prediction quality of the resulting network is quantified and compared to the prediction error of a former loop. If the tolerance ε is reached, the GA stops and the optimal architecture is stored. In the last step, the generated ANN is used to predict the environmental impact for a given chemical.

To distinguish between several production pathways leading to the same chemical, we use a combination of molecular descriptors and process descriptors. The process descriptors are based on the environmental indicators proposed by Patel et al. (2012).

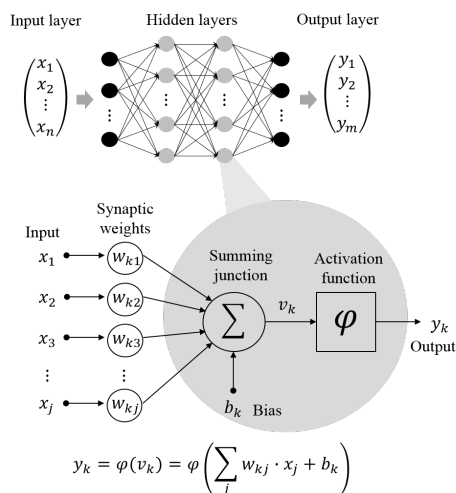


Figure 1: General structure of an ANN, including a zoom of a single neuron. The input values x_j of a general neuron k are weighted by $w_{k,j}$ and summed subsequently. The bias b_k allows for shifting the output by constant value. The resulting output v_k is passed to an activation function φ , which is usually a sigmoid function. As a result of the sigmoid function, the output y_k lies in a range of $[-1; 1]$. The output is then passed to the neurons of the subsequent layer.

2.1. Feature Selection

Feature selection reduce the input dimension by selecting a subset of suitable descriptors from all available descriptors to . We use stepwise regression as feature selection algorithm under the assumption that a sufficient linear correlation indicats also a non-linear correlation. Due to limited LCA data available for the training and to avoid overfitting, the final number of descriptors used in the ANN is limited to 10 % of the number of training samples.

We consider 185 possible descriptors in total, consisting of 178 molecular descriptors and 7 process descriptors. Molecular descriptors describe the main product of a process based on physical and chemical properties as well as classical functional groups. Process descriptors are based on the impact indicators proposed by Patel et al. (2012). E.g., the concentration of each component at the reactor outlet is calculated assuming ideal phase and chemical equilibrium. This process descriptor is assumed to correlate to the required separation effort. The temperature-dependent enthalpies and entropies are obtained from quantum mechanics calculations for each component. An additional process descriptor is given by the environmental impact EI of the reactants. The environmental impacts are summed according to the stoichiometric reaction equation $EI_{\text{stoichio}} = \sum_i \frac{v_i M_i}{v_{\text{mp}} M_{\text{mp}}} \cdot EI_i, i \in [1, \dots, n]$, wherein v_i is the stoichiometric coefficient of reactant i out of n reactants, M_i is the molar weight of reactant i , v_{mp} is the stoichiometric coefficient and M_{mp} the molar weight of the main product. Considering the sum of environmental impacts of the reactants transforms the reaction equation into a scalar input for the ANN and thus delivers a lower bound of the expected environmental impact of the product. If co-products occur in the reaction, mass allocation is applied to divide the impact of the upstream on all products. After feature selection, the descriptors are normalized to the range of $[-1; 1]$.

2.2. Network Setup

Our framework generates automatically a feedforward neural network for a given training set. The set up procedure of the neural networks requires the definition of so-called hyperparameters. These hyperparameters include the number of hidden layers, the number of neurons in each hidden layer, the regularization parameter, the number of maximum epochs and the kind of training algorithm. Typically, hyperparameters are chosen based on expert knowledge or using genetic algorithms. In this work, we use the GA of the MATLAB toolbox (The MathWorks, Release 2016a). The objective of the GA is to minimize the ratio between the root mean squared error (RMSE) and the coefficient of determination (R_p^2). The coefficient of determination is given as

$$R_p^2 = \left(\frac{\sum_i (t_i - \bar{t})(y_i - \bar{y})}{\sqrt{\sum_i (t_i - \bar{t})^2 \sum_i (y_i - \bar{y})^2}} \right)^2, \text{ wherein } t_i \text{ is the target value of sample } i, \bar{t} \text{ the mean of all target values, } y_i \text{ the estimation of sample } i \text{ and } \bar{y} \text{ the mean of all estimations. A value of 1 repre-}$$

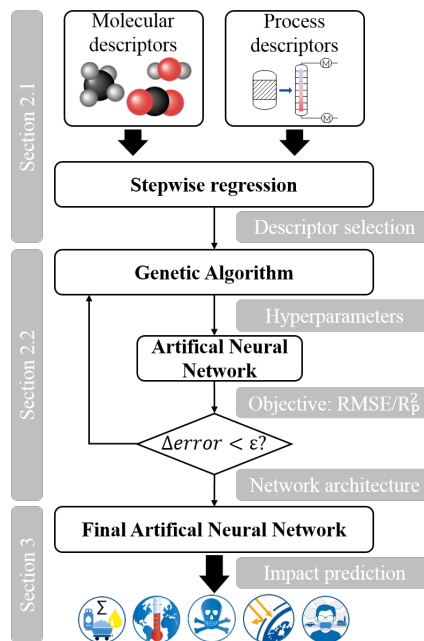


Figure 2: Algorithm to set up a neural network to predict environmental impacts. $\Delta error$ is the difference between the objective value of the former loop and the objective value of the current loop for a given architecture. ϵ is the chosen tolerance for convergence.

sents perfect correlation, while a value of 0 corresponds to no prediction ability of the ANN. The objective is defined as ratio of two error measures to minimize the absolute error (RMSE) as well as possible trends (R_p^2). Minimizing only the RMSE tends to lead to constant predictions of the average impact value, while minimizing only the coefficient of determination improves predictions of trends but increases absolute prediction errors.

Initially, the available training data is divided into 3 sets: (1) a training set (containing 85% of the overall data), which is used to train the ANN in each loop of the GA, (2) a validation set (10%), which is used to qualify the generalization ability of the regarded network architecture in each GA loop, (3) and a final test set (5%), which is used to qualify the results generated by the GA. The validation set is used to calculate the objective value of the GA in each loop. The test set is used to calculate the final objective value and to validate the final optimized network architecture.

The GA suggests possible hyperparameters in each loop. Using the suggested hyperparameters, an ANN is trained on the training set. Afterwards, the generalization ability is tested on the validation set. This loop is iterated until the GA has found a local optimum. Due to the local nature of the GA, we use a multistart approach, running several GA instances parallel. The optimal architecture is used afterwards for estimating the regarded environmental impact category.

3. Case study: Component vs. Process-Specific Networks

The proposed framework is employed to generate 17 neural networks, each predicting one of 17 Recipe v1.08 (H) Midpoint categories (Goedkoop et al., 2009). Here, we exemplified the framework for predicting the impact on Climate Change of methanol and formic acid. For training, we use LCA data of 63 organic chemicals obtained from the Gabi Database (PE International, 2012). The training data includes two alternative pathways for methanol and formic acid, respectively. Since the number of data samples is limited, the number of descriptors selected during feature selection is set to 6. For the validation set, 6 samples are chosen randomly in the beginning of each GA run, corresponding to 10 % of the available training data. The samples are kept constant during the optimization of one GA run to guarantee convergence of the GA. For the test set, the two process alternatives for methanol and formic acid, respectively, are chosen manually to test the assessment of competing process alternatives. This procedure allows for validating the process-specific prediction ability.

3.1. Prediction Performance

To validate the prediction performance of the process-specific network, we compare the process-specific ANN to an ANN solely based on molecular descriptors, called component-specific ANN in the following (Figure 3). The ANN are compared based on the coefficient of determination R_p^2 . The coefficient of determination is calculated for the training set of each network using leave-one-out cross validation. Each sample in the training set is left out once, the ANN is trained based on the remaining training set and the left out sample is predicted. Thus, the coefficient of determination is calculated using the prediction of each sample.

The process-specific ANN increase the prediction performance for 10 of 17 Recipe v1.08 (H) Midpoint indicators (Figure 3). The maximum improvement in terms of the coefficient of determination is achieved for Marine Ecotoxicity (MET) with an increase of 0.64 using the process-specific network in contrast to the component-specific network. The maximum decline is obtained for Photochemical Oxidant Formation (POF) with a reduction of 0.29. Although the absolute coefficients of determinations are still small with values lower than 0.4 for 16 of 17 impact categories, the use of process-descriptors has improved clearly prediction performance.

To compare our results to literature, we apply an literature-based ANN on our training data using the architecture and hyperparameters proposed by Wernet et al. (2008, 2009). The literature ANN achieves worse coefficients of determination for 14 of 17 impact categories compared to the process-specific ANN (Figure 3). Since Wernet et al. (2009) obtained coefficients of determina-

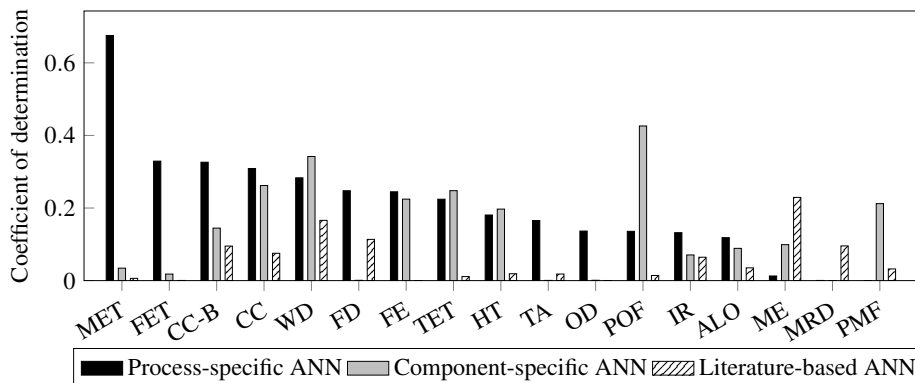


Figure 3: Comparison of the coefficient of determination for the process-specific ANN (black) and the component-specific network (grey), respectively, given for 17 Recipe 1.06 Midpoint categories: Marine Ecotoxicity (MET), Freshwater Ecotoxicity (FET), Climate Change exclusive biogenic carbon (CC-B), Climate Change (CC), Water Depletion (WD), Fossil Resource Depletion (FD), Freshwater Eutrophication (FE), Terrestrial Ecotoxicity (TET), Human Toxicity (HT), Terrestrial Acidification (TA), Ozone Depletion (OD), Photochemical Oxidant Formation (POF), Ionising Radiation (IR), Agricultural Land Occupation (ALO), Marine Eutrophication (ME), Mineral Resource Depletion (MRD), and Particulate Matter Formation (PMF). The shaded bars are the results from an ANN based on the descriptors and architecture given in Wernet et al. (2008, 2009).

tion of 0.41 up to 0.69 using similar hyperparameters, but other training data, the lower coefficient of determination shown in Figure 3 results from small training data set and its poor data quality. The coefficient of determination obtained for Climate Change by leave-one-out on our training set is comparable to the $R_p^2 = 0.31$ presented in Song et al. (2017).

3.2. Process-Specific Prediction

The proposed process-specific network is able to distinguish between alternative production pathways. To show this potential, the impact on Climate Change is predicted for two production alternatives for both methanol and formic acid (Figure 4). For this purpose, a network is trained without data for the production pathways of methanol and formic acid. Two pathway alternatives are then predicted: a fossil-based pathway, utilizing synthesis gas from steam methane reforming as carbon source, and a CO₂-based pathway utilizing CO₂ from an ammonia plant as carbon source. For both pathways, hydrogen is supplied by steam methane reforming and electricity is assumed as the current European grid mix. The impacts on Climate Change of both pathways are predicted using both the component-specific and the process-specific network. The predictions are compared to literature LCA values from Gabi (PE International, 2012) for the fossil-based pathways and from Artz et al. (2018) for the CO₂-based pathways.

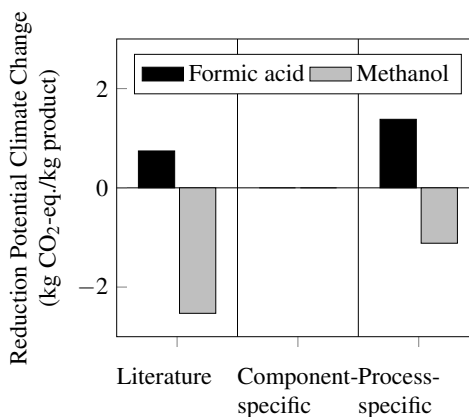


Figure 4: Comparison of the reduction potential in Climate Change for methanol and formic acid, calculated as the difference between fossil-based pathway and CO₂-based pathway alternative.

In literature, the CO₂-based production of formic acid causes a smaller impact on Climate Change than the fossil-based production pathway, resulting in a positive reduction potential (Figure 4). In contrast, the CO₂-based production of methanol is less environmentally friendly than the fossil-based pathway, resulting in a negative reduction potential. The component-specific ANN is not able to distinguish between different production pathways. Therefore, no reduction potential can be identified using the component-specific ANN. In comparison, the pathway-specific ANN can distinguish between process alternatives, resulting in a positive predicted reduction potential of the CO₂-based pathway for formic acid and a negative predicted reduction potential of the CO₂-based pathway for methanol. Although the potentials are overestimated by the process-specific ANN, the trends in reduction potentials are predicted correctly. Thus, the process-specific neural network can be used for comparison of pathway alternatives in early design stages.

4. Conclusion

In this work, we present a neural network-based framework to predict process-specific environmental impacts. The framework is fully automated including feature selection and architecture optimization of the ANN. In addition to molecular descriptors, process descriptors are used to enable process-specific predictions. The process descriptors increase the coefficient of determination up to 0.64. Importantly, process descriptors enable the network to distinguish between production pathways. The process-specific prediction ability is exemplified for methanol and formic acid: for each chemical, two production scenarios are predicted, one fossil-based and one CO₂-based. The trends in the environmental impact are predicted correctly, showing that our framework can serve as initial screening tool for identifying environmentally beneficial process alternatives. More training data would be desirable to increase the quantitative accuracy.

5. Acknowledgement

The authors thank the German Federal Ministry of Education and Research (BMBF) for funding within the project consortium “Carbon2Chem” under Contract 03EK3042C.

References

- J. Artz, T. E. Muller, K. Thenert, J. Kleinekorte, R. Meys, A. Sternberg, A. Bardow, W. Leitner, 2018. Sustainable conversion of carbon dioxide: an integrated review of catalysis and life cycle assessment. *Chemical reviews* 118 (2), 434–504.
- R. Calvo-Serrano, M. González-Miquel, S. Papadokostantakis, G. Guillén-Gosálbez, 2017. Predicting the cradle-to-gate environmental impact of chemicals from molecular descriptors and thermodynamic properties via mixed-integer programming. *Computers & Chemical Engineering* 108, 179–193.
- J. L. Casamayor, D. Su, 2012. Integration of detailed/screening lca software-based tools into design processes. In: *Design for Innovative Value Towards a Sustainable Society*. Springer, pp. 609–614.
- M. Goedkoop, R. Heijungs, M. Huijbregts, A. de Schryver, J. Struijs, R. van Zelm, 2009. Recipe 2008 - a life cycle impact assessment method which comprises harmonised category indicators at the midpoint and the endpoint level.
- K. Hornik, M. Stinchcombe, H. White, 1989. Multilayer feedforward networks are universal approximators. *Neural Network* 2 (5), 359–366.
- R. G. Hunt, T. K. Boguski, K. Weitz, A. Sharma, 1998. Case studies examining lca streamlining techniques. *The International Journal of Life Cycle Assessment* 3 (1), 36.
- A. D. Patel, K. Meesters, H. den Uil, E. de Jong, K. Blok, M. K. Patel, 2012. Sustainability assessment of novel chemical processes at early stage: Application to biobased processes. *Energy & Environmental Science* 5 (9), 8430–8444.
- PE International, 2012. Gabi lca software and lca database.
URL <http://www.gabi-software.com/databases/gabi-databases/>
- R. Song, A. A. Keller, S. Suh, 2017. Rapid life-cycle impact screening using artificial neural networks. *Environmental science & technology* 51 (18), 10777–10785.
- I. The MathWorks, Release 2016a. Matlab neural network toolbox.
- G. Wernet, S. Hellweg, U. Fischer, S. Papadokostantakis, K. Hungerbühler, 2008. Molecular-structure-based models of chemical inventories using neural networks. *Environmental science & technology* 42 (17), 6717–6722.
- G. Wernet, S. Papadokostantakis, S. Hellweg, K. Hungerbühler, 2009. Bridging data gaps in environmental assessments: Modeling impacts of fine and basic chemical production. *Green Chemistry* 11 (11), 1826–1831.

Performance Evaluation of Reverse Osmosis Brackish Water Desalination Plant with Different Recycled Ratios of Retentate

A. A. Alsarayreh ^a, M. A. Al-Obaidi ^{a,b}, A. M. Al-Hroub ^c, R. Patel ^a, and I. M. Mujtaba ^{a, *}

^a *School of Engineering, Faculty of Engineering and Informatics. University of Bradford. Bradford, West Yorkshire BD7 1DP, UK*

^b *Middle Technical University, Iraq – Baghdad*

^c *Senior Chemical Engineer, Energy and Water Directorate, Arab Potash Company, Jordan*

I.M.Mujtaba@bradford.ac.uk

Abstract

Reverse Osmosis (RO) process can be considered as one of the most widely utilised technologies for brackish water desalination due to its capabilities of retaining salts and producing high-quality water. This paper focuses on the retentate recycle design of an industrial medium-sized spiral wound brackish water RO desalination plant (1200 m³/day) of Arab Potash Company (APC) located in Jordan. The plant is essentially designed as a multistage and multi pass RO system including a low salinity retentate recycle stream from the 2nd pass and a high salinity retentate disposal from the 1st pass. However, in this work, we have considered recycle of high salinity retentate stream from the 1st pass and explored the impact of different recycled ratio on the process performance indicators such as the fresh water salinity, overall recovery rate, and specific energy consumption. The simulation is carried out using the model developed earlier by us for the specified RO plant using gPROMS software. The results indicate the possibility of increasing the product capacity by around 3% with 100% retentate recycle ratio.

Keywords: Reverse Osmosis; Brackish Water Desalination, Simulation, Retentate Recycle, Energy Consumption.

1. Introduction

Broadly speaking, water scarcity is a major environmental challenge facing Jordan since the early 1960s until these days. Jordan occupies the 10th rank in the world in terms of the shortage and insufficient of water resources (Hadadin et al., 2010). Therefore, it is important to exploit the brackish water using desalination to be used as a main source of drinking water and industrial requirements. In this respect, the Arab Potash Company (APC) implemented a power plant including brackish water RO desalination plant capacity of 1200 m³/day to produce low-salinity water (i.e. conductivity of less than 0.641 ppm) to be used in the ion exchangers (Al-Obaidi et al., 2018).

The RO process has affirmed its robustness as a superior technology for brackish water desalination due to its high performance of salt rejection and water permeation

(Ghaffour et al., 2015). Moreover, the application of RO process is interestingly increased due to its low cost and energy consumption compared to other conventional thermal technologies (Al-Karaghouli and Kazmerski, 2013). The multistage RO process is originally designed in several configurations to satisfy the specifications of the produced water. Specifically, the permeate and retentate recycling designs were employed by several researchers and their impacts on the process performance were investigated. For instance, Al-Bastaki and Abbas (1999) used a small-scale spiral wound RO water desalination plant of water solution (with concentration of 10,000 mg NaCl/l) in a cyclic mode to study the performance of permeate flow rate and salt rejection. They confirmed a reduction in the concentration polarisation that increased the permeate flux as a result of applying the cyclic mode of operation. Al-Bastaki and Abbas (2003) studied the impact of permeate recycled design on the performance of a small-scale spiral wound RO desalination plant. The simulation results of permeate recycle ratios between 0% to 25% confirmed a reduction in the concentration polarisation which entirely improved the product quality despite a reduced production rate. Specifically, the product concentration is reduced by 15% at 25% of recycling ratio compared to the case of no recycle mode. Whereas, the production rate is reduced by 22% compared to the case of no recycle mode.

Al-Obaidi et al. (2018) have demonstrated an extensive study to evaluate the performance of brackish water desalination plant of APC located in Jordan and based on multistage RO process via modelling and simulation. The model developed is validated with an actual data collected from APC and then used to carry out a sensitivity analysis to predict the plant performance against the variation of operating conditions. However, up to the authors' knowledge, the influence of different ratios of retentate stream recycle (that combined with raw water stream) on the process performance indicators has not yet been explored. In this respect, the performance of RO process with 10% to 100% high salinity retentate stream of the 1st pass will be investigated. Then, the process performance would be compared against the original experimental data of no recycle mode that carried out at specified operating conditions.

2. Description of BWRO desalination plant of APC

Fig.1 depicts the configuration of BWRO plant which contains 120 membranes, 20 pressure vessels (6 membranes in each) and includes two passes with retentate reprocessing design. The 1st pass comprises 2 stages arranged in parallel of 6 pressure vessels with configuration (4:2) and the 2nd pass comprises 3 stages of 4 pressure vessels with configuration (2:1:1).

The low-pressure permeates of 1st pass (position 1) are combined and pumped to the 2nd pass. Therefore, two forwarding high pumps are used to drive the water through the membranes in the 2nd pass. However, the high salinity retentate from the 1st pass is discharged into drain system (position 4). The permeate streams of 2nd pass are gathered to form the plant product stream, which is collected in product tank with salinity around 2 ppm (position 3). However, the low salinity retentate stream from the 2nd pass (position 2) is recycled back to be coupled with the main stream of raw water (with salinity 1098.62 ppm).

Table.1 shows the transport parameters and membranes specification. Also, the operating parameters of BWRO plant of APC are listed in Al-Obaidi et al. (2018).

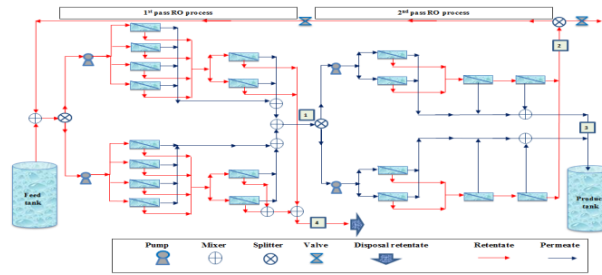


Figure 1. Schematic diagram of BWRO desalination plant of APC (Adapted from Al-Obaidi et al., 2018).

Table 1. Specifications of the spiral wound membrane element (Adapted from Al-Obaidi et al., 2018).

Parameter	Feed water salinity [ppm]	Feed water flow rate [m ³ /h]	Feed temperature [°C]	Daily production capacity [m ³ /day]	Average product salinity [ppm]	Total system rejection [%]
Value	(1098.62)	(74)	(25)	(1200)	(1.96)	(99.80)

3. RO process modelling

The steady state model for an individual spiral wound RO process is developed by Al-Obaidi et al. (2018) and successfully used to characterise the complete mathematical model of multistage brackish water RO plant of Arab Potash Company (APC). The complete mathematical model has been coded and solved within the gPROMS software suite. The model developed is validated with the actual data collected from APC and showed a good agreement.

4. Impact of recycling the retentate of 1st pass on process performance

The performance of the BWRO process of APC plant is investigated in this section by varying the 1st pass retentate stream recycle ratio from 10% to 100% in a step change of 10%. It is noteworthy to confirm that the RO plant is currently working at no recycle mode of 0% retentate recycle ratio. More importantly, this study is based on investigating the process performance against a step change of a spontaneous retentate recycle. The process performance indicators include the total plant recovery (Rec), total plant rejection (Rej), product flow rate and concentration (Q_p, C_p), retentate flow rate and concentration (Q_r, C_r), and energy consumption. Also, the current simulation is carried out at fixed values of 1098.62 ppm, 74 m³/h, 9.22 atm, and 25°C, of raw water concentration, feed flow rate, operating pressure, and temperature, respectively.

Fig. 2. shows insignificant variation of total plant rejection in an exponential relationship and a continuous drop in total plant recovery in a linear relationship against the increased retentate recycle ratio of 1st pass. In this respect, it can be said that 40% of recycled ratio has attained the optimal value of rejection. More importantly, the reduction of water recovery ratio can be attributed to an increase in the plant feed flow rate due to an increase in the retentate recycle ratio of 1st pass coupled with retentate

stream from the 2nd pass and with the raw water stream. This in turn causes an increase in the bulk velocity of all the membrane stages that accompanied with a reduction in the residence time of solution inside the feed channel. Moreover, the continuous increase of feed concentration has passively impacted the concentration polarisation that entirely reduces the permeated water through the membranes. Therefore, the total permeate flow rate of 1st pass is decreased as a response to increasing retentate ratio. This in consequence had reduced the total water recovery as noticed in Fig. 2. Subsequently, it is fair to expect an increase of the energy consumption due to increasing the recycle ratio. It is worth noting that a decrease in total recovery means that the requirements for energy consumption will be higher. This is already highlighted in Table.3.

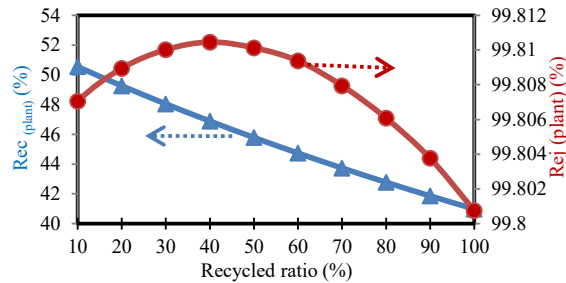


Figure 2. Impact of ratio variation on total plant recovery and rejection.

The influence of increasing the 1st pass recycle ratio of retentate on the product and retentate plant flow rates is shown in Fig. 3. It is clear that the product flow rate and retentate flow rate are significantly increased and decreased, respectively. The increasing of product flow rate is belonging to a lower velocity inside the module caused by decreasing the inlet feed flow rate of 2nd pass with increasing recycled ratio of retentate. It is important to realise that the total permeate of 1st pass is used as feed stream of 2nd pass. Up to this point, this would be associated with a lower residence time that reduced the retentate flow rate and increased water recovery of 2nd pass. However, the total water plant recovery keeps down due to a high progress of feed flow rate compared to a lower progress in product flow rate.

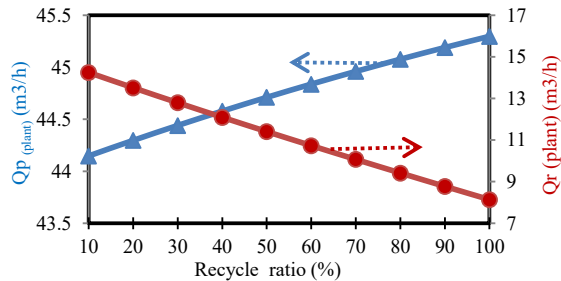


Figure 3. Impact of ratio variation on product and retentate plant flowrate.

The simulation results of Fig. 4 confirm that increasing of recycled retentate ratio causes a considerable increase in both product and retentate concentrations. This is ascribed to increasing the plant feed water concentration due to increasing the recycle ratio of high-

salinity stream. Furthermore, these results support the findings of Fig. 2 that associated with a continuous reduction of total water recovery.

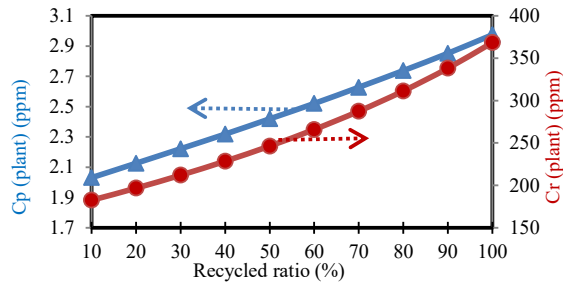


Figure 4. Impact of ratio variation on product and retentate plant concentration.

Table 3 presents the simulation results of energy consumption with the tested recycle ratios of the 1st pass retentate at fixed operating pressure and raw water concentration. Basically, the energy consumption is significantly increased by around (15%) as a response to this variation. This is might attributed to the progress of plant feed flow rate that dominated the energy consumption despite the noticeable improvement of product flow rate with increasing recycle ratio.

Table 3. The energy consumption simulation results with variation of recycled retentate.

Recycle ratio	10%	20%	30%	40%	50%
Power consumption [kWh/m ³]	0.860	0.873	0.887	0.900	0.914
Recycle ratio	60%	70%	80%	90%	100%
Power consumption [kWh/m ³]	0.929	0.944	0.959	0.975	0.992

To understand the performance of multistage RO process with no recycle mode (0% retentate ratio), Table. 4 presents the simulation results of several performance indicators with 40% and without recycle mode for comparison purposes. Specifically, it is noticed that no recycle mode can keep the process at the lowest product concentration and highest water recovery that commensurate with the lowest energy consumption.

However, the highest total product flow rate is achieved at 100% retentate recycle of the 1st pass which involved a slight increase of product concentration from 1.937 to 2.974 ppm at the same operating conditions. Therefore, this would enhance the productivity of fresh water which might be a possible negotiable point despite the necessity of increasing the requirements of energy consumption by around 17% within almost fixed solute rejection.

5. Conclusions

The performance of multistage and multi pass RO brackish water desalination plant of Arab Potash Company (APC) with different recycled ratios of 1st pass retentate is investigated via simulation. This is occurred in terms of several performance indicators. The simulation is carried out at fixed raw water flow rate, concentration, pressure, and temperature. This in turn explored that 100% retentate recycle can perform the highest production capacity with increased energy consumption.

This is originally compared to no recycle mode that currently used in the RO process of APC plant, and showed the lowest product concentration at the minimum product capacity.

Table 4. The simulation results of process performance indicators with 100%, 40%, and without recycle mode.

Indicators of process performance at recycle ratio from 1 st pass = 0 % [APC plant]		Indicators of process performance at recycle ratio from 1 st pass = 40 %		Indicators of process performance at recycle ratio from 1 st pass = 100 %	
Rej_plant [%]	99.804	Rej_plant [%]	99.811	Rej_plant [%]	99.801
Rec_plant [%]	51.898	Rec_plant [%]	46.889	Rec_plant [%]	40.981
Qp_plant [m ³ /h]	43.991	Qp_plant [m ³ /h]	44.578	Qp_plant [m ³ /h]	45.297
Qr_recycle from 2 nd pass [m ³ /h]	15.005	Qr_recycle from 2 nd pass [m ³ /h]	12.095	Qr_recycle from 2 nd pass [m ³ /h]	8.139
Cp_plant [ppm]	1.937	Cp_plant [ppm]	2.319	Cp_plant [ppm]	2.975
Cr_recycle [ppm]	169.159	Cr_recycle [ppm]	228.545	Cr_recycle [ppm]	368.465
power consumption pump [kWh/m ³]	0.848	power consumption pump [kWh/m ³]	0.900	power consumption pump [kWh/m ³]	0.991

References

- AL-Bastaki, N. & Abbas, A. 1999. Improving the permeate flux by unsteady operation of a RO desalination unit. *Desalination*, 123, 173-176.
- AL-Bastaki, N. & Abbas, A. 2003. Permeate recycle to improve the performance of a spiral-wound RO plant. *Desalination*, 158, 119-126.
- AL-Obaidi, M. A., Alsarayreh, A. A., AL-Hroub, A. M., Alsadaie, S. & Mujtaba, I. M. 2018. Performance analysis of a medium-sized industrial reverse osmosis brackish water desalination plant. *Desalination*, 443, 272-284.
- Hadadin, N., Qaqish, M., Akawwi, E. & Bdour, A. 2010. Water shortage in Jordan Sustainable solutions. *Desalination*, 250, 197-202.
- Sharma, A., Jelemensky, M., Paulen, R. & Fikar, M. 2017. Modeling and optimal operation of batch closed-loop diafiltration processes. *Chemical Engineering Research and Design*, 122, 198-210.
- Toray membrane USA INC., M. T. S. O., Maintenance and handling manual, 2015. Available: <http://www.toraywater.com/> [Accessed 10/3/2018].

Deciphering Latent Uncertainty Sources with Principal Component Analysis for Adaptive Robust Optimization

Chao Ning, Fengqi You *

Cornell University, Ithaca, New York, 14853, USA

fengqi.you@cornell.edu

Abstract

This paper proposes a novel data-driven robust optimization framework that leverages the power of machine learning for decision-making under uncertainty. By performing principal component analysis on uncertainty data, the correlations among uncertain parameters are effectively captured, and latent uncertainty sources are identified. Uncertainty data are then projected onto each principal component to facilitate extracting distributional information of latent uncertainties with kernel density estimation technique. To explicitly account for asymmetric uncertainties, we introduce forward and backward deviation vectors in an uncertainty set. The resulting data-driven uncertainty set is general enough to be employed in adaptive robust optimization model. The proposed framework not only significantly ameliorates the conservatism of robust optimization but also enjoys computational efficiency and wide applicability. An application of optimization under uncertainty on batch process scheduling is presented to demonstrate the effectiveness of the proposed general framework. We also investigate a data-driven uncertainty set in a low-dimensional subspace and derive a theoretical bound on the performance gap between ARO solutions due to the dimension reduction of uncertainties.

Keywords: big data, optimization under uncertainty, principal component analysis

1. Introduction

As a promising alternative paradigm, robust optimization characterizes uncertain parameters using an uncertainty set (Mulvey et al. 1995; Ben-Tal et al., 2009;). Uncertainty set-induced robust optimization can be divided broadly into two categories, namely static robust optimization and adaptive robust optimization (ARO). In static robust optimization, all the decisions are made “here-and-now” before uncertainty realizations. By introducing “wait-and-see” decisions, ARO approach well models the sequential nature of decision-making processes, and ameliorates the conservatism issue (Ben-Tal and Nemirovski, 2002). In recent years, robust optimization methodology has found a fruitful of applications, such as biomass processing network (Gong et al., 2016), production scheduling (Shi et al., 2016), supply chain (Yue et al., 2016), energy systems (Gong et al., 2017), and model-based control (Shang et al., 2019).

Despite the burgeoning popularity of robust optimization, conventional robust optimization methods have some potential limitations (Ning and You, 2017a). First, they do not take advantage of the power of machine learning and big data analytics to leverage uncertainty data for decision-making under uncertainty (Shang and You,

2017). Moreover, their adopted uncertainty sets fail to account for the correlations or asymmetry among uncertainties. Neglecting relevant information embedded in uncertainty data, such as correlations and asymmetry, could render the induced robust optimization solution conservative. With the explosion in uncertainty data and great advances in machine learning techniques, data-driven optimization paves a new way to decision-making under uncertainty (Ning and You, 2017b). Based on all the concerns above, the research objective of our work is to develop a general data-driven robust optimization framework that exploits uncertainty data for decision-making under uncertainty. In this paper, we propose a general data-driven decision-making framework that bridges machine learning with robust optimization methodology directly. A theoretical analysis on the impact of uncertainty dimension reduction on the quality of ARO solutions is also performed within the proposed framework.

2. Data-Driven Uncertainty Set Construction

Consider an uncertainty data matrix $\mathbf{X} = [\mathbf{u}^{(1)}, \dots, \mathbf{u}^{(N)}]^T \in R^{N \times m}$, in which each row represents an uncertainty data point in m -dimensional space. There are a total number of N uncertainty data points. We first scale matrix X to zero-mean in (4) for principal component analysis (PCA) modelling (Murphy, 2012; Friedman et al. 2001), as shown in Eq. (1).

$$\mathbf{X}_0 = \mathbf{X} - \mathbf{e}\boldsymbol{\mu}_0^T \quad (1)$$

where \mathbf{X}_0 is an uncertainty data matrix after scaling, \mathbf{e} denotes a column vector of all ones, and $\boldsymbol{\mu}_0$ represents the mean vector of uncertainty data.

The covariance matrix of uncertain parameters can be approximated with the sample covariance matrix \mathbf{S} , as shown in $\mathbf{S} = 1/(N-1)\mathbf{X}_0^T\mathbf{X}_0$. Through the eigenvalue decomposition, we can obtain $\mathbf{S} = \mathbf{P}\boldsymbol{\Lambda}\mathbf{P}^T$. The square matrix $\mathbf{P} = [\mathbf{p}_1, \dots, \mathbf{p}_m] \in R^{m \times m}$ consists of all the m eigenvectors (corresponding to the principal components), and $\boldsymbol{\Lambda} = \text{diag}\{\lambda_1, \dots, \lambda_m\}$ is a diagonal matrix consisting of all the eigenvalues.

Consider the projection of an uncertainty data point $\mathbf{u}^{(i)}$ onto the k -th principal component, shown as follows,

$$\mathbf{t}_k^{(i)} = \mathbf{p}_k^T [\mathbf{u}^{(i)} - \boldsymbol{\mu}_0] \quad (2)$$

Let ξ_k be a latent uncertainty along the k -th principal component, $\hat{f}_{KDE}^{(k)}(\xi_k)$ denotes the estimated probability density function of ξ_k by using the kernel density estimation approach, and $\hat{F}_{KDE}^{(k)}(\xi_k)$ be the corresponding cumulative density function. The corresponding quantile function can be expressed as follows:

$$\hat{F}_{KDE}^{(i)-1}(\alpha) = \min \left\{ \xi_k \in R \mid \hat{F}_{KDE}^{(k)}(\xi_k) \geq \alpha \right\} \quad (3)$$

which provides the minimum value of ξ_k based on a specific parameter α .

We propose the data-driven uncertainty set with uncertainty budget, as shown below.

$$U = \left\{ \mathbf{u} \left| \begin{array}{l} \mathbf{u} = \boldsymbol{\mu}_0 + \mathbf{P}\boldsymbol{\xi}, \boldsymbol{\xi} = \underline{\boldsymbol{\xi}}\mathbf{oz}^- + \bar{\boldsymbol{\xi}}\mathbf{oz}^+, \\ \mathbf{0} \leq \mathbf{z}^-, \mathbf{z}^+ \leq \mathbf{e}, \mathbf{z}^- + \mathbf{z}^+ \leq \mathbf{e}, \mathbf{e}^T(\mathbf{z}^- + \mathbf{z}^+) \leq \Phi \end{array} \right. \right\} \quad (4)$$

where \mathbf{z}^- is a backward deviation vector, \mathbf{z}^+ is a forward deviation vector, \mathbf{e} is a column vector of all ones, and Φ is an uncertainty budget. $\boldsymbol{\xi}$ is the latent uncertainty vector, its lower bound vector $\underline{\boldsymbol{\xi}}$ is defined in Eq. (5), and the upper bound vector $\bar{\boldsymbol{\xi}}$ is defined in Eq. (6).

$$\underline{\boldsymbol{\xi}} = \left[\hat{F}_{KDE}^{(1)-1}(\alpha), \dots, \hat{F}_{KDE}^{(m)-1}(\alpha) \right]^T \quad (5)$$

$$\bar{\boldsymbol{\xi}} = \left[\hat{F}_{KDE}^{(1)-1}(1-\alpha), \dots, \hat{F}_{KDE}^{(m)-1}(1-\alpha) \right]^T \quad (6)$$

A novel feature of the data-driven uncertainty set in Eq. (4) is that PCA and kernel density estimation are utilized to accurately capture the principal components and distributions embedded within the uncertainty data. Additionally, the proposed uncertainty set U does not necessarily be symmetric by introducing the positive and negative deviations separately.

3. Data-Driven Adaptive Robust Optimization Framework

In this subsection, we propose a data-driven two-stage ARO model to organically integrate uncertainty data with adaptive optimization model, as shown in Eq. (7).

$$\begin{aligned} & \min_{\mathbf{x}} \mathbf{c}^T \mathbf{x} + \max_{\mathbf{u} \in U} \min_{\mathbf{y} \in \Omega(\mathbf{x}, \mathbf{u})} \mathbf{b}^T \mathbf{y} \\ & \text{s.t. } \mathbf{Ax} \geq \mathbf{d}, \quad \mathbf{x} \in R_+^{n_1} \times Z^{n_2} \\ & \quad \Omega(\mathbf{x}, \mathbf{u}) = \{ \mathbf{y} \in R_+^{n_3} : \mathbf{Wy} \geq \mathbf{h} - \mathbf{T}\mathbf{x} - \mathbf{Mu} \} \end{aligned} \quad (7)$$

where \mathbf{x} is the first-stage decision made “here-and-now” before the uncertainty \mathbf{u} is realized, while the second-stage decision or recourse decision \mathbf{y} is postponed in a “wait-and-see” mode after the uncertainties reveal themselves. \mathbf{x} includes both continuous and integer variables, while \mathbf{y} only includes continuous variables. \mathbf{c} and \mathbf{b} are the vectors of the cost coefficients. U is the data-driven uncertainty set in Eq. (4).

This data-driven adaptive robust optimization model is a tri-level optimization problem, which cannot be solved directly by any off-the-shelf optimization solvers. The key idea is to decompose the multi-level MILP shown in (7) into a master problem and a sub-problem. The master problem (8) contains only a part of extreme points, so it provides a relaxation of the original problem.

$$\begin{aligned} & \min_{\mathbf{x}, \eta, \mathbf{y}^k} \mathbf{c}^T \mathbf{x} + \eta \\ & \text{s.t. } \mathbf{Ax} \geq \mathbf{d} \\ & \quad \eta \geq \mathbf{b}^T \mathbf{y}^k, \quad k = 1, \dots, r \\ & \quad \mathbf{T}\mathbf{x} + \mathbf{W}\mathbf{y}^k \geq \mathbf{h} - \mathbf{M}\mathbf{u}^k, \quad k = 1, \dots, r \\ & \quad \mathbf{x} \in R_+^{n_1} \times Z^{n_2}, \quad \mathbf{y}^k \in R_+^{n_3}, \quad k = 1, \dots, r \end{aligned} \quad (8)$$

where \mathbf{u}^k is the enumerated uncertainty realization at the k th iteration, \mathbf{y}^k is its corresponding recourse variable, and r represents the current number of iterations.

4. Application on Batch Process Scheduling

Planning and scheduling are typical operations in process systems engineering. Batch process scheduling plays a critical role in manufacturing industries (Chu et al., 2015). In this section, an industrial multipurpose batch process is presented to demonstrate the advantages of the proposed data-driven ARO approach. Figure 1 depicts the state-task network of this batch process (Chu et al., 2013). In this application, the product demands are uncertain.

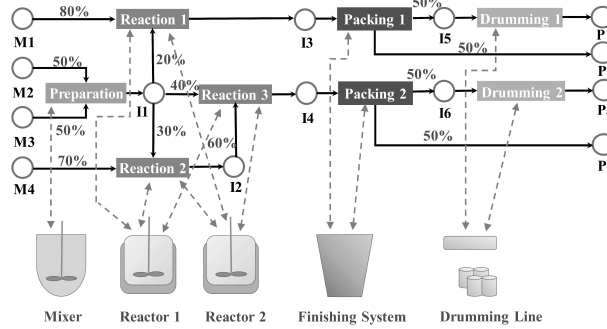


Figure 1. State task network of a multipurpose batch process.

The conventional method only utilizes the bounds of demand data, whereas the proposed approach leverages machine learning to dig out the correlation information among different product demands for scheduling decisions. As a result, the proposed approach is less conservative, and returns \$299 more profits than the conventional ARO method, and the Gantt chart of the proposed approach is displayed in Figure 2.

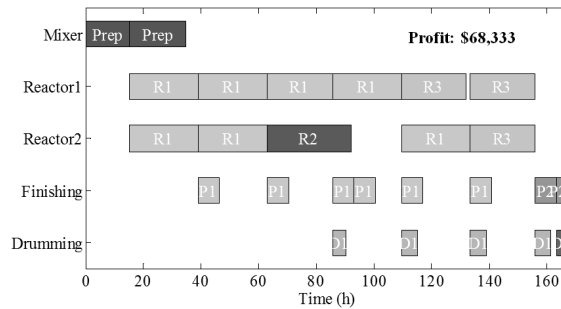


Figure 2. Optimal schedule decisions determined by the proposed data-driven approach.

5. Theoretical Analysis

High-dimensional uncertainty data often lies close to a low-dimensional subspace (Ferreira et al., 2012). Therefore, an extension of the proposed approach is to decipher the low-dimensional structure to perform “uncertainty dimension reduction” for ARO. Moreover, the discovered low-dimensional structure holds the potential to provide insights into the management of uncertainty. Only a small number of principal

components can be used to retain much uncertainty information (Xu et al., 2016). The ARO problem without performing uncertainty data compression is shown as (ARO-H).

$$(ARO-H) \quad \min_{\mathbf{x} \in X} \left\{ \mathbf{c}^T \mathbf{x} + \max_{\mathbf{u} \in U} Q(\mathbf{x}, \mathbf{u}) \right\}$$

where $Q(\mathbf{x}, \mathbf{u})$ is the recourse function. We define problem (ARO-L) as follows:

$$(ARO-L) \quad \min_{\mathbf{x} \in X} \left\{ \mathbf{c}^T \mathbf{x} + \max_{\mathbf{u} \in \hat{U}} Q(\mathbf{x}, \mathbf{u}) \right\}$$

where the uncertainty set $\hat{U} = \{\hat{\mathbf{u}} \mid \exists \mathbf{u} \in U \quad \hat{\mathbf{u}} = \Pi(\mathbf{u})\}$.

Note that $\Pi(\mathbf{g})$ is an operator of projecting uncertainty onto a low-dimensional subspace. The projected vector has the same dimension as the original vector. Suppose that \mathbf{x}^* and $\hat{\mathbf{x}}$ are the optimal solutions of problems (ARO-H) and (ARO-L), respectively. We are concerned with the difference in their worst-case performance in an uncertain environment where the real uncertainty realization is still in a high-dimensional space. The following theorem provides a theoretical bound on the solution quality due to the uncertainty data compression for the ARO problem.

Theorem. Given that \mathbf{x}^* and $\hat{\mathbf{x}}$ are the optimal solutions of problems (ARO-H) and (ARO-L), respectively. We have

$$0 \leq \left[\mathbf{c}^T \hat{\mathbf{x}} + \max_{\mathbf{u} \in \hat{U}} Q(\hat{\mathbf{x}}, \mathbf{u}) \right] - \left[\mathbf{c}^T \mathbf{x}^* + \max_{\mathbf{u} \in U} Q(\mathbf{x}^*, \mathbf{u}) \right] \leq \alpha \cdot \beta \quad (9)$$

where parameter $\alpha = \max_{\mathbf{u} \in U} \|\mathbf{u} - \Pi(\mathbf{u})\|_2$, parameter $\beta = \max_{\boldsymbol{\varphi} \in \Phi} \|\mathbf{M}^T \boldsymbol{\varphi}\|_2$ and set

$$\Phi = \{\boldsymbol{\varphi} \mid \mathbf{W}^T \boldsymbol{\varphi} \leq \mathbf{b}, \boldsymbol{\varphi} \geq \mathbf{0}\}.$$

Proof of Theorem. Since \mathbf{x}^* is an optimal solution of problem (ARO-H), and $\hat{\mathbf{x}}$ is a feasible solution of problem (ARO-H), we can arrive at the following inequality:

$$0 \leq \left[\mathbf{c}^T \hat{\mathbf{x}} + \max_{\mathbf{u} \in \hat{U}} Q(\hat{\mathbf{x}}, \mathbf{u}) \right] - \left[\mathbf{c}^T \mathbf{x}^* + \max_{\mathbf{u} \in U} Q(\mathbf{x}^*, \mathbf{u}) \right].$$

Similarly, because $\hat{\mathbf{x}}$ is an optimal solution of problem (ARO-L), and \mathbf{x}^* is a feasible solution of problem (ARO-H), we can arrive at the following inequality: $\mathbf{c}^T \hat{\mathbf{x}} + \max_{\mathbf{u} \in \hat{U}} Q(\hat{\mathbf{x}}, \mathbf{u}) \leq \mathbf{c}^T \mathbf{x}^* + \max_{\mathbf{u} \in U} Q(\mathbf{x}^*, \mathbf{u})$.

Based on strong duality, we can have $Q(\mathbf{x}, \mathbf{u}) = \max_{\boldsymbol{\varphi} \in \Phi} [\mathbf{h} - \mathbf{T}\mathbf{x} - \mathbf{M}(\bar{\mathbf{u}} + \mathbf{u})]^T \boldsymbol{\varphi}$, where dual

feasible region is $\Phi = \{\boldsymbol{\varphi} \mid \mathbf{W}^T \boldsymbol{\varphi} \leq \mathbf{b}, \boldsymbol{\varphi} \geq \mathbf{0}\}$. Based on $\hat{U} \subseteq U$, we have

$$\mathbf{c}^T \mathbf{x}^* + \max_{\mathbf{u} \in \hat{U}} Q(\mathbf{x}^*, \mathbf{u}) \leq \mathbf{c}^T \mathbf{x}^* + \max_{\mathbf{u} \in U} Q(\mathbf{x}^*, \mathbf{u}).$$

$$\begin{aligned} & \mathbf{c}^T \hat{\mathbf{x}} + \max_{\mathbf{u} \in \hat{U}} Q(\hat{\mathbf{x}}, \mathbf{u}) \\ &= \mathbf{c}^T \hat{\mathbf{x}} + \max_{\mathbf{u} \in \hat{U}} \max_{\boldsymbol{\varphi} \in \Phi} [\mathbf{h} - \mathbf{T}\hat{\mathbf{x}} - \mathbf{M}(\bar{\mathbf{u}} + \Pi(\mathbf{u}))]^T \boldsymbol{\varphi} \\ &\geq \mathbf{c}^T \hat{\mathbf{x}} + \max_{\substack{\mathbf{u} \in \hat{U} \\ \boldsymbol{\varphi} \in \Phi}} [\mathbf{h} - \mathbf{T}\hat{\mathbf{x}} - \mathbf{M}(\bar{\mathbf{u}} + \mathbf{u})]^T \boldsymbol{\varphi} + \min_{\substack{\mathbf{u} \in U \\ \boldsymbol{\varphi} \in \Phi}} [\mathbf{M}(\mathbf{u} - \Pi(\mathbf{u}))]^T \boldsymbol{\varphi} \\ &= \mathbf{c}^T \hat{\mathbf{x}} + \max_{\mathbf{u} \in \hat{U}} Q(\hat{\mathbf{x}}, \mathbf{u}) - \max_{\substack{\mathbf{u} \in U \\ \boldsymbol{\varphi} \in \Phi}} [(-1) \cdot \mathbf{M}(\mathbf{u} - \Pi(\mathbf{u}))]^T \boldsymbol{\varphi} \\ &\geq \mathbf{c}^T \hat{\mathbf{x}} + \max_{\mathbf{u} \in \hat{U}} Q(\hat{\mathbf{x}}, \mathbf{u}) - \max_{\substack{\mathbf{u} \in U \\ \boldsymbol{\varphi} \in \Phi}} \|\mathbf{u} - \Pi(\mathbf{u})\|_2 \cdot \|\mathbf{M}^T \boldsymbol{\varphi}\|_2 \end{aligned} \quad (10)$$

which concludes the proof. \square

6. Conclusions

In this paper, we proposed a novel data-driven ARO framework based on PCA. By employing PCA on uncertainty data matrix, latent uncertainty sources were identified. The forward and backward deviation vectors were introduced into the data-driven uncertainty set. An application on batch scheduling was presented. The results showed that the proposed data-driven ARO approach enjoyed a less conservative solution compared with other methods. Additionally, a theoretical bound was also derived.

References

- A. Ben-Tal, L. El Ghaoui, A. Nemirovski, 2009, Robust optimization: Princeton University Press.
- A. Ben-Tal, A. Nemirovski, 2002, Robust optimization - methodology and applications. *Mathematical Programming*, 92, 453-480.
- A. Ben-Tal, D. den Hertog, J.-P. Vial, 2015, Deriving robust counterparts of nonlinear uncertain inequalities. *Mathematical Programming*, 149, 265-299.
- D. Bertsimas, V. Gupta, N. Kallus, 2017, Data-driven robust optimization. *Mathematical Programming*, 1-58.
- Y. Chu, J.M. Wassick, F. You, 2013, Efficient scheduling method of complex batch processes with general network structure via agent-based modeling, *AIChE Journal*, 59, 2884-2906.
- Y. Chu, F. You, 2015, Model-based integration of control and operations: Overview, challenges, advances, and opportunities, *Computers & Chemical Engineering*, 83, 2-20.
- R.S. Ferreira, L.A. Barroso, M.M. Carvalho, 2012, Demand response models with correlated price data: A robust optimization approach, *Applied Energy*, 96, 133-149.
- J. Friedman, T. Hastie, R. Tibshirani, 2001, *The elements of statistical learning*, Springer, Berlin.
- J. Gong, D.J. Garcia, F. You, 2016, Unraveling optimal biomass processing routes from bioconversion product and process networks under uncertainty: an adaptive robust optimization approach, *ACS Sustainable Chemistry & Engineering*, 4, 3160-3173.
- J. Gong, F. You, 2018, Resilient design and operations of process systems: Nonlinear adaptive robust optimization model and algorithm for resilience analysis and enhancement. *Computers & Chemical Engineering*, 116, 231-252.
- J. M. Mulvey, R. J. Vanderbei, S. A. Zenios, 1995, Robust Optimization of Large-Scale Systems. *Operations Research*, 43, 264-281.
- K. P. Murphy, *Machine learning: A probabilistic perspective*: MIT press, 2012.
- C. Ning, F. You, 2017a, A data-driven multistage adaptive robust optimization framework for planning and scheduling under uncertainty. *AIChE Journal*, 63, 4343-4369.
- C. Ning, F. You, 2017b, Data-driven adaptive nested robust optimization: General modeling framework and efficient computational algorithm for decision making under uncertainty. *AIChE Journal*, 63, 3790-3817.
- C. Ning, F. You, 2018, Data-driven stochastic robust optimization: General computational framework and algorithm leveraging machine learning for optimization under uncertainty in the big data era. *Computers & Chemical Engineering*, 111, 115-133.
- C. Shang, X. Huang, F. You, 2017, Data-driven robust optimization based on kernel learning. *Computers & Chemical Engineering*, 106, 464-479.
- C. Shang, F. You, 2019, A data-driven robust optimization approach to scenario-based stochastic model predictive control. *Journal of Process Control*, 75, 24-39.
- H. Shi, F. You, 2016, A computational framework and solution algorithms for two-stage adaptive robust scheduling of batch manufacturing processes under uncertainty, *AIChE Journal*, 62, 687-703.
- H. Xu, C. Caramanis, and S. Mannor, 2016, Statistical optimization in high dimensions, *Operations Research*, 64, 958-979.
- D. Yue, F. You, 2016, Optimal supply chain design and operations under multi-scale uncertainties: Nested stochastic robust optimization modeling framework and solution algorithm, *AIChE Journal*, 62, 3041-3055.

Increasing the Reliability of Parameter Estimates by Iterative Model-based Design of Experiments Using a Flowsheet-Simulator

Maria Yliruka,^a Norbert Asprion,^a Roger Böttcher,^a Johannes Höller,^b Patrick Schwartz,^b Jan Schwientek,^b Michael Bortz^{b,*}

^a *BASF SE, Chemical Process Modeling, Carl-Bosch-Str. 38, 67056 Ludwigshafen, Germany*

^b *Fraunhofer Institute for Industrial Mathematics ITWM, Fraunhofer Platz 1, 67663 Kaiserslautern, Germany*

michael.bortz@itwm.fraunhofer.de

Abstract

The reliability of flowsheet simulation results depends heavily on the knowledge of model parameters, among which are, for example, kinetic parameters of chemical reactions or substance property data describing thermodynamic behavior. These parameters are usually estimated by nonlinear regression with respect to data from a laboratory setup, mini-plant or operating data from a production process. Applying model-based design of experiments (DoE), operating conditions can be identified which maximize the information content of the resulting data for the regression problem. In this contribution, we present gradient-plots in order to make DoE-plans more transparent to the engineer. In a second step, we report on the implementation of an iterative DoE-scheme in a flowsheet-simulator. Thus, the interplay between estimating model parameters, planning experiments, adding resulting experimental data and re-adjusting the parameters is supported.

Keywords: process simulation, design of experiments, nonlinear regression, parameter estimation.

1. Introduction

To maximize the accuracy of least-square estimates of model parameters, model-based design-of-experiment-strategies have been established. Assuming a reasonable initial guess of the model parameters, these strategies yield a set of operating conditions by finding the optimal value of a scalar measure of the Fisher information matrix. After implementing the optimal set of operating conditions at the real plant, the model is adjusted to the measured responses in order to obtain more accurate model parameter estimations. The application of this approach to flowsheet simulations has previously been reported by Asprion et al. (2018).

In industrial applications, when implementing the optimal experimental plan, deviations from the proposed operating conditions might occur. A poor initial guess of the model parameters model-based design of experiments can lead to a poor experimental plan. Furthermore, in real experiments, generally deviations occur when applying the optimized experimental plan, i.e. realizing the different operating conditions.

To cope with these issues, we propose two extensions: In a first step, gradient plots are exploited to make the DoE-result more transparent to the planner. Together with the DoE-

results for different criteria, these gradient plots, give an insight into how much the quality of an experimental plan depends on each of the experimental inputs.

In a second step, the following iterative approach is described in this contribution: Again, an initial estimate of the model parameters is assumed. A reduced experimental plan is then obtained from a Fisher information matrix that is calculated from derivatives. After the realization of the resulting reduced experimental plan at the plant, a new estimate of all model parameters is obtained. One then modifies the Fisher matrix of the previous step by including the already realized experiments and allowing a small number of additional experiments as new degrees of freedom. A new experimental plan is obtained and realized at the plant. This procedure can be repeated until some termination criterion is reached.

This article is organized as follows: In the next section, the formalism of iterative DoE is presented. Section three contains the concept of gradient plots, illustrated for the estimation of binary NRTL-parameters of different binary mixtures. Section four illustrates the iterative workflow. The article ends with a conclusion. Throughout, to generate the simulation results, the BASF inhouse flowsheet simulator Chemasim was used.

2. Iterative DoE approach

First, the notation required to formalize the iterative DoE-workflow is introduced.

In order to obtain a new estimate p_0^* of the model parameter vector p of length N_p , a weighted sum of squared residuals is minimized. Hereby, the deviation between the model predictions and the measured data is reduced.

$$p_0^* = \arg \min_p \sum_{i=1}^{N_e^0} \sum_{j=1}^{N_m} r_j(p, x_i)^2 \quad \text{with } r_j(p, x_i) = \sqrt{w_{i,j}} \left(\frac{\hat{y}_{i,j} - y_j(p, x_i)}{\sigma_{\hat{y}_{i,j}}} \right) \quad (1)$$

The j -th measured property in the i -th experiment is denoted by $\hat{y}_{i,j}$. The corresponding model prediction $y_j(p, x_i)$ depends on the model parameter vector p and the design variable vector x_i of the i -th experiment. Additionally, weighting factors $w_{i,j}$ and standard deviations $\sigma_{\hat{y}_{i,j}}$ of $\hat{y}_{i,j}$ are included. N_e^0 corresponds to the number of experiments and the number of measured outputs is denoted by N_m .

The uncertainty of p_0^* stems from two sources (cf. Bates, Watts, 1990), namely the accuracy of the measurements (described by $\sigma_{\hat{y}_{i,j}}$) and the correlation within x_i . This correlation is measured with respect to x_i 's impact on the gradients of y_j with respect to p . On a more formal level, the Fisher information matrix (FIM) F (dimension $N_p \times N_p$) has to be calculated (cf. e.g. Schittkowski, 2007a) in order to estimate the covariance matrix of the p_0^*

$$F^0 = \sum_{i=1}^{N_e^0} \sum_{j=1}^{N_m} J_j(p_0^*, x_i)^T J_j(p_0^*, x_i) \quad (2)$$

with the Jacobians J_j (dimension $N_e^0 \times N_p$) consisting of column vectors

$$J_j(p_0^*, x_i) = \left(\left(\frac{\partial r_j}{\partial p_1} (p_0^*, x_i) \right)^T ; \dots ; \left(\frac{\partial r_j}{\partial p_{N_p}} (p_0^*, x_i) \right)^T \right) \quad (3)$$

The covariance matrix C^0 corresponds to the inverse of the FIM F^0 .

Let us now extend F^0 as follows: Apart from the x_i that defined the conditions of the already realized measurements $\hat{y}_{i,j}$, additional $x_{i=N_e^0+1, \dots, N_e^0+N_e^1}$ are included. These additional x_i describe experiments still to be realized, on the basis of the estimates p_0^* . This extended Fisher matrix is called F^1 . Well-known scalar DoE-criteria ϕ are considered as a function of $x_{i=N_e^0+1, \dots, N_e^0+N_e^1}$ and used to formulate an optimization problem to determine a new experimental plan:

$$\min \phi(x_{i=N_e^0+1, \dots, N_e^0+N_e^1}) \quad (4)$$

Possible DoE-criteria ϕ are , for example, for the A-criterion, $\phi = \text{trace} ([F^1]^{-1}) = \sum_{i=1}^{N_p} \frac{1}{\lambda_i}$, or the D-criterion, $\phi = \det ([F^1]^{-1}) = \prod_{i=1}^{N_p} \frac{1}{\lambda_i}$, where λ_i are the eigenvalues of F^1 . The resulting x_i constitute the new experimental plan.

After the experiment, new parameter estimates p_1^* are found by minimizing a sum of squared residuals as in Eq. (1), now augmented by the additional experiments. Their covariance matrix can be estimated from the Fisher matrix F^1 . New experiments follow from extending this matrix to a new F^2 by including $x_{i=N_e^0+N_e^1+1, \dots, N_e^0+N_e^1+N_e^2}$ as optimization variables, determined by solving a DoE task analogous to Eq. (4). This procedure is repeated until some termination criterion is fulfilled. A certain limit on the number of experiments or a threshold value for the accuracy of the estimates present suitable termination criteria.

In the following, a concrete example, namely a binary vapor-liquid flash, is used in order to illustrate the procedure described above. In a given experimental set up, the pressure P and the concentration of substance 1 in the liquid phase x_1 can be adjusted. The temperature T and the concentration of substance 1 in the vapor phase y_1 are measured as experimental outputs. The NRTL-parameters $A_{12}, A_{21}, B_{12}, B_{21}$ are to be estimated. Applying the procedure, P and x_1 should be chosen such that the reliability of the parameter estimates are maximized.

3. Gradient plots

First, $N_e^0 = 0$ is set and an experimental plan is to be designed from scratch. To gain some intuitive insight, the gradients $\partial(w_{y_1}y_1)/\partial p'$ and $\partial(w_T T)/\partial p'$ with $p' = 5 \frac{p-p_{min}}{p_{max}-p_{min}} + 5$, $p \in \{A_{12}, A_{21}, B_{12}, B_{21}\}$, $w_{y_1} = 100$, $w_T = 10$, are calculated for all x_1 at fixed P and for all P at fixed x_1 . Using p' turned out to show favorable numerical results. For a mixture of methanol and water, these gradients are visualized in Figs. 1 and 2.

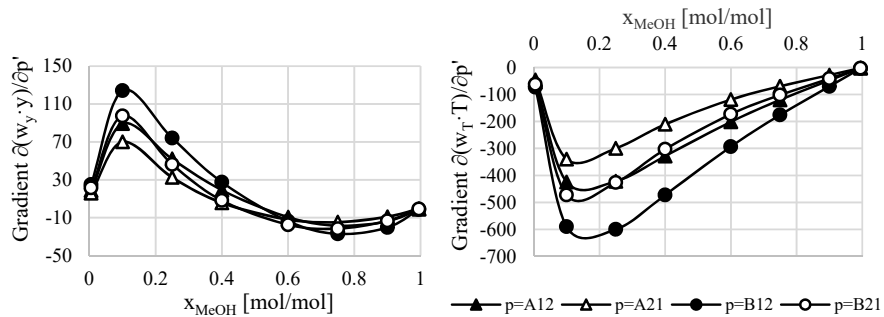


Figure 1: Gradient plots for experimental output functions y_1 (left) and T (right) for a mixture of water and methanol for constant $P = 1$ bar .

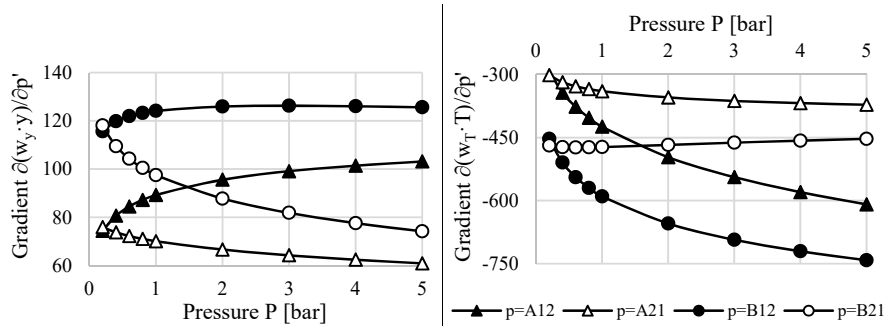


Figure 2: Gradient plots for experimental output functions y_1 (left) and T (right) for a mixture of water and methanol for constant $x_1 = 0.1$ mol/mol.

From Fig. 1 it follows that the highest dependence on the NRTL-parameters is observed for concentrations $x_1 < 0.4$. The monotonic dependence of the gradients on the pressure at $x_1 = 0.1$ mol/mol is shown in Fig. 2. Hence, designs at the upper and lower boundary for the allowed pressure values are favored. Furthermore, the relative variation of the gradients with respect to the pressure at constant x_1 is much smaller than its variation with respect to x_1 at constant P (Fig. 1). Thus, we expect the optimal design points in the $x_1 - P$ -plane to be located at P -values close to the bounds imposed by the experimental set up ($P = 0.1$ bar and $P = 5$ bar), and at x_1 -values between 0 mol/mol and 0.4 mol/mol. Furthermore, it is to be expected that the parameter estimates will be highly correlated as the gradient plots show correlated behavior of the gradients over the entire P and x_1 ranges. These findings will be confirmed in section 4.

For a comparison, a binary azeotropic mixture of methanol and acetone is considered in an equivalent setup. The corresponding gradient plots are presented in Figure 3 and 4.

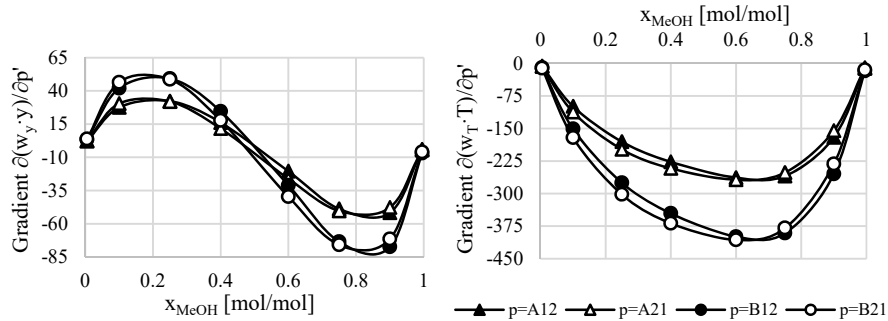


Figure 3: Gradient plots for experimental output functions y_1 (left) and T (right) for a mixture of methanol (1) and acetone (2) for constant $P = 1$ bar.

In contrast to the binary system of methanol-water, significant contributions to $\partial(w_{y_1}y_1)/\partial p$ now occur in two regions, namely for $0.1 < y_1 < 0.5$ and $0.5 < y_1 < 0.9$. But for the pressure, again a monotonic dependence is observed.

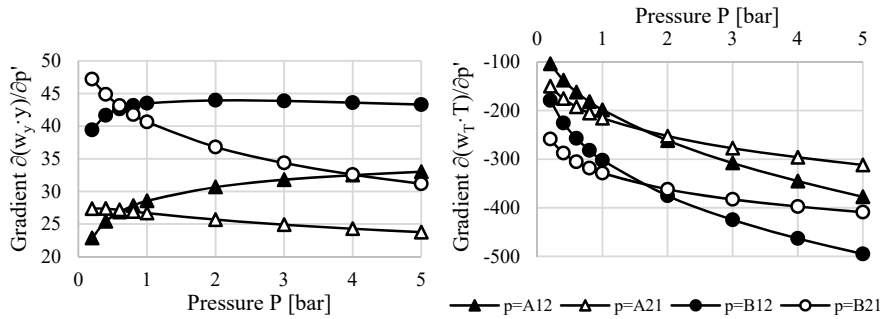


Figure 4: Gradient plots for experimental output functions y_1 (left) and T (right) for a mixture of methanol (1) and acetone (2) for constant $x_1 = 0.3$ mol/mol.

4. Illustration of iterative workflow

The gradient plots in the section 3 give some useful insights to how the optimal experimental plans will look like. In this section, the DoE-task in Eq. (4) is solved as a non-linear optimization problem for four experimental points from scratch, i.e. $N_e^0 = 0$, starting from different initial configurations. The results are presented in Fig. 5 which are in agreement with the gradient plots in section 3.

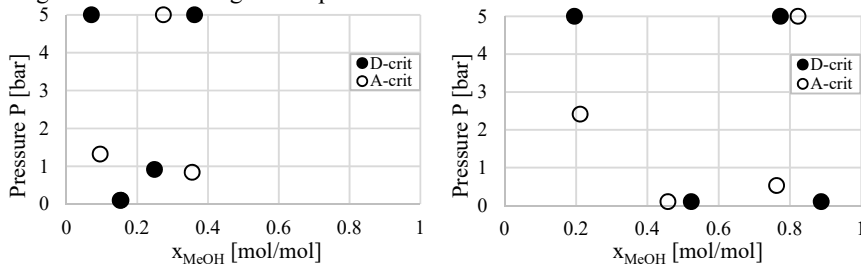


Figure 5: A- and D-optimal designs for mixtures of methanol-water (left) and methanol-acetone (right). These designs meet the expectations based on the gradient plots in section 3.

In the following, the discussion focuses on the binary mixture of methanol and water. In total, eight additional experiments should be realized after having performed the first experiments as shown in Fig. 5. Three different implementations of the additional experiments are considered:

- I. $N_e^0 = 4$, $N_e^{1,2,3,4}=1$, that is, four additional iterations with one experiment in each iteration.
- II. $N_e^0 = 4$, $N_e^1=4$, i.e., one additional iteration with four experiments
- III. Four experiments at $P = 1$ bar and four experiments at $P = 5$ bar, each with $x_1 = 0.05, 0.35, 0.75, 0.95$ mol/mol.

The first $N_e^0 = 4$ experiments of alternatives I and II are shown in Fig. 5. Pseudo-measurements are generated by adding a random Gaussian error to the predictions of the true model in each iteration. The corresponding experimental plans are shown in Fig. 6. One observes that if model-based DoE-strategies are applied, the designs cluster in the regions where the gradients are highest, in agreement with the gradient plots shown in the previous section. In order to avoid the clustering, one could also imagine a hybrid DoE

strategy, where the model-based approach is combined with a space-filling strategy, if a sufficient number of experiments are available. This is the subject of current research. To assess the quality of the plans, residual plots are shown in Fig. 7 for the differences between the measured and predicted values for T and y_1 . From the values of these residuals, all of the three alternatives I-III seem to lead to comparable results.

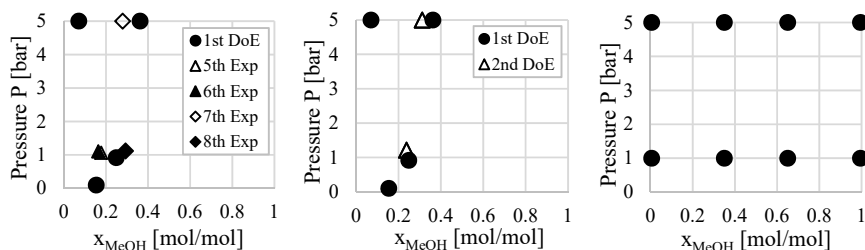


Figure 6: Experimental plans obtained for the three alternatives I-III (from left to right) described in the main text.

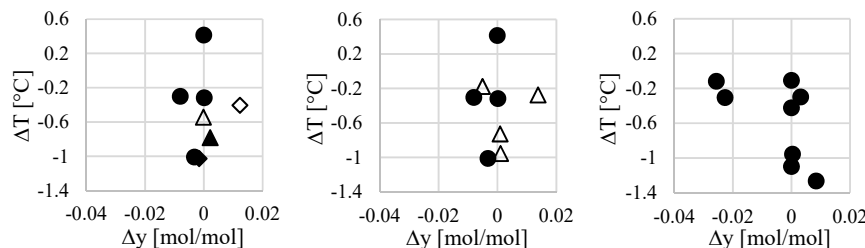


Figure 7: Residual plots for the three alternatives I-III, where the symbols in the plots have the same meaning as in Fig. 6. The axes show the residuals between measured and adjusted data for temperature (ΔT) and methanol concentration in the vapor phase (Δy).

5. Conclusion and outlook

Two extensions of the common DoE approach have been developed and implemented in BASF's inhouse flowsheet simulator Chemasim: The first extension consists in gradient plots which help to gain an intuitive insight into the correlations between parameter estimates and into promising regions for optimal experimental plans. The second extension supports an iterative workflow, where additional experiments are planned by fixing the ones already realized. The results suggest the development of a hybrid strategy, where a model-based DoE is combined with a space-filling strategy.

References

- N. Asprión, J. Ritter, R. Böttcher, M. Bortz, 2018, Proceedings of the 28th European Symposium on Computer Aided Process Engineering, pp43-48
- Bates, Watts, 1990, Nonlinear Regression Analysis and its Applications, John Wiley
- K. Schittkowski, 2007a, Ind. Eng. Chem. Res., 46, 9137-9147.

Globally Optimal Design of Double Pipe Heat Exchangers using Local Properties and Discretized Models

Alice Peccini^a, André Costa^b, Miguel Bagajewicz^{c,*}

^a*Federal University of Rio de Janeiro (UFRJ), Escola de Química CT, Bloco E, Ilha do Fundão, CEP 21949-900, Rio de Janeiro, RJ, Brazil*

^b*Rio de Janeiro State University (UERJ), Rua São Francisco Xavier, 524, Maracanã, CEP 20550-900, Rio de Janeiro, RJ, Brazil*

^c*School of Chemical, Biological and Materials Engineering, University of Oklahoma, Norman, Oklahoma, USA 73019*

bagajewicz@ou.edu

Abstract

The design of heat exchangers in general, including double pipe, is typically performed using methods based on simplifying assumptions (e.g. uniform overall heat transfer coefficient based on averaged physical properties, mostly). However, these assumptions may sometimes result in considerable under or oversizing, especially when ample variations of the physical properties with temperature take place. Aiming at circumventing this limitation, we present a novel MILP (globally optimal) formulation of the optimization of hairpin double-pipe heat exchangers using rigorous models and discretization. Numerical results illustrate the importance of the utilization of the proposed approach in relation to the traditional analytical models, showing to what extent one can undersize or oversize severely the heat exchanger.

Keywords: optimization, mathematical programming, linear programming, double pipe heat exchanger.

1. Introduction

Due to the importance of heat exchangers in chemical process plants, a large number of papers has focused on optimal design optimization procedures. Gonçalves et al. (2017) contains a brief overview of the main solution approaches. Independently of the approach, all of these papers rely on calculating the heat transfer coefficients using constant values of the physical properties.

This paper presents a novel mathematical programming formulation that is able to consider the variation of the overall heat transfer coefficient along the heat transfer surface. The resultant formulation, applied for hairpin double-pipe exchangers, is a mixed-integer linear programming problem (MILP), thus rendering globally optimum solutions.

2. Proposed Approach

The optimization problem corresponds to the minimization of a structure composed of a set of hairpin heat exchangers connected in series, as it is illustrated in Figure 1. One

wants to find the inner tube diameter, the outer tube diameter, the length of each hairpin and the number of hairpins that minimize the heat transfer area. The model encompasses energy balances, heat transfer coefficient equations and flow velocity bounds. The flow is assumed to be turbulent, without phase change.

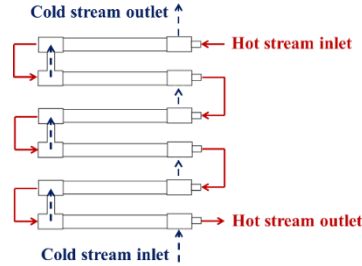


Figure 1: A set of three double pipe hairpins arranged in series.

Instead of modelling the heat exchanger using overall analytical descriptions, like the LMTD approach (i.e. $Q = U \cdot A \cdot \Delta T_{LM}$), which may involve large prediction errors, we propose to explore the original differential equations in the modelling:

$$\frac{dQ}{dz} = U \cdot (T_h - T_c) \cdot \pi \cdot dt_e \quad (1)$$

When applying a discretization procedure, the value of the overall heat transfer coefficient at each point along the mesh depends on the stream temperatures. As a consequence, the resultant model would be nonlinear and therefore would present the usual numerical problems (need of good initial estimate and possible existence of multiple local optima).

Our proposal to circumvent this problem is to apply the discretization procedure to one of the streams temperature range (in this case the hot stream, as shown in Figure 2) rather than to the length of the equipment. This approach is used so that the temperatures in the discretization points become known parameters, while the distance between mesh points becomes the variable. In this way, the physical properties also become parameters, eliminating all nonlinearities in the model equations.

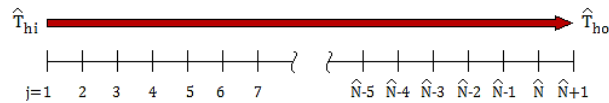


Figure 2: Hot stream discretization mesh.

For each adjacent pair of discrete temperature points, there is a corresponding length between them required for heat transfer. Thus, we rewrite Eq. (2), as follows:

$$\frac{dz}{dT_h} = \frac{\dot{m}_h \cdot C_{p_h}}{U \cdot (T_h - T_c) \cdot \pi \cdot dt_e} \quad (2)$$

For the corresponding cold stream temperatures between both intervals, we have (the mark (^) above symbols represents known parameters):

$$\frac{dT_c}{dT_h} = \frac{\hat{m}_h \cdot Cp_h}{\hat{m}_c \cdot Cp_c} \quad (3)$$

We highlight that the uniform mesh in the hot stream temperature does not correspond to a uniform mesh in the length of the equipment. Figure 3 illustrates it by showing, in a generic temperature curve, the relation between both meshes:

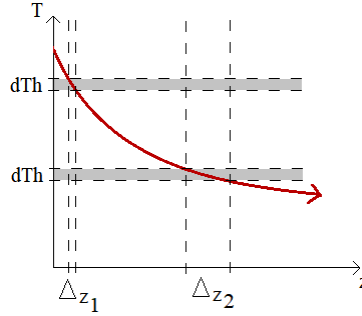


Figure 3: Discretization applied to the hot stream temperature curve.

For the discretization shown in Eq. (2), a second order central finite difference approximation for the intermediary points and a second-degree polynomial approximation for the last point, as well as a boundary condition for the first point are used, yielding, where $\Delta\hat{T}$ is the increment associated to the temperature mesh:

$$z_j = 0 \quad \text{for } j = 1 \quad (4)$$

$$\frac{z_{j+1} - z_{j-1}}{2 \cdot \Delta\hat{T}} = \frac{-\hat{m}_h \cdot \hat{C}p_{h,j}}{U_j \cdot (\hat{T}_{h,j} - \hat{T}_{h,j}) \cdot \pi \cdot dte} \quad \text{for } j = 2, \dots, N \quad (5)$$

$$\frac{z_{j-2} - 4z_{j-1} + z_j}{2 \cdot \Delta\hat{T}} = \frac{-\hat{m}_h \cdot \hat{C}p_{h,j}}{U_j \cdot (\hat{T}_{h,j} - \hat{T}_{h,j}) \cdot \pi \cdot dte} \quad \text{for } j = N + 1 \quad (6)$$

Knowing that tubes come in discrete options, we use discrete representations of the design variables. One of these, the one for inner tube diameter is shown in Eq. (7):

$$dte = \sum_{sd=1}^{sdmax} \hat{p}dte_{sd} \cdot yd_{sd} \quad (7)$$

$$\sum_{sd=1}^{sdmax} yd_{sd} = 1 \quad (8)$$

Similar equations are written for the other design variables. We now replace the design variables by the corresponding binaries and reformulate to obtain an equivalent linear

formulation (no loss of rigor). Gonçalves et al., (2017) show specific details of this procedure. After such manipulations, Eq. (5) becomes:

$$\frac{z_{j+1} - z_{j-1}}{2 \cdot \Delta \hat{T}} = \frac{-\hat{m}_h \cdot \hat{C}p_{h,j}}{(\hat{T}_{h,j} - \hat{T}_{h,j}) \cdot \pi} \sum_{sd=1}^{sd \max} \sum_{sD=1}^{sD \max} \hat{X}_{j,sd,sD} \cdot wdD_{sd,sD} \quad (9)$$

where $\hat{X}_{j,sd,sD}$ is now a parameter representing the value of $[U_j dte]^{-1}$ written for each instance of yd_{sd} and yD_{sD} .

$$\begin{aligned} \hat{X}_{j,sd,sD} = & \frac{\hat{p}dti_{sd}^{0.8}}{\hat{k}_{c,j} \cdot 0.023 \cdot \hat{P}r_{c,j}^{0.4} \cdot \left(\frac{4\hat{m}_c}{\pi \hat{\mu}_{c,j}} \right)^{0.8}} + \frac{\hat{R}f_c}{\hat{p}dti_{sd}} + \frac{\ln(\hat{p}dte_{sd} \cdot [\hat{p}dti_{sd}]^{-1})}{2 \cdot \hat{k}_{tube}} + \\ & + \frac{\hat{R}f_h}{\hat{p}dte_{sd}} + \frac{\hat{p}As_{sd,sD}^{0.8} \cdot \hat{p}dh_{sd,sD}^{0.2}}{\hat{k}_{h,j} \cdot 0.023 \cdot \hat{P}r_{h,j}^{0.3} \cdot \left(\frac{\hat{m}_h}{\hat{\mu}_{h,j}} \right)^{0.8}} \cdot \hat{p}dte_{sd} \end{aligned} \quad (10)$$

$$wdD_{sd,sD} \leq yd_{sd} \quad (11)$$

$$wdD_{sd,sD} \leq yD_{sD} \quad (12)$$

$$wdD_{sd,sD} \geq yd_{sd} + yD_{sD} - 1 \quad (13)$$

3. Results

The formulation proposed was applied to obtain the optimal design for the service described in Table 1. Polynomial fittings were applied to experimental data from Incropera et al (2011) to obtain the functions that describe the variation of the physical properties with the temperature. The sets of discrete options available for the optimization are depicted in Table 2.

Table 1: Stream data for the optimization problem.

Stream		Flow mass (kg/s)	Inlet Temperature (K)	Outlet Temperature (K)
Hot stream	Engine Oil	1.3	310	295
Cold stream	Cooling water	1.3	280	286

Table 2: Structural discrete options (pipe schedule 40).

Parameter	Discrete Options								
Number of hairpins	1	to	20						
Tube length (m)	3.048	6.096	9.144	12.192	15.240				
Inner tube OD (m)	0.021	0.027	0.033	0.042	0.048	0.060	0.073	0.089	0.102
Outer tube OD (m)	0.042	0.048	0.060	0.073	0.089	0.102	0.144	0.127	0.168

In order to illustrate the importance of accounting for the property’s variations, four scenarios were considered. Scenario 1 shows the results using the proposed approach, taking into account the temperature influence on the physical properties. The other three scenarios explored consider the physical properties constant, which incidentally generates the same results as the usual analytical approaches. Scenario 2: properties calculated using a mean temperature for each stream; Scenario 3: properties calculated using the lowest temperature for each stream, a more conservative approach; and Scenario 4: the overall heat transfer coefficient is set to be the mean between its values calculated in the inlet and outlet temperatures. The results obtained are shown in Table 3.

Table 3: Optimal solutions obtained for the three different scenarios.

Scenario	Inner tube OD (m)	Outer tube OD (m)	Tube length (m)	Number of hairpins	Total heat exchanger area (m ²)
1	0.042	0.060	15.24	15	30.28
2	0.042	0.060	15.24	14	28.26
3	0.042	0.060	15.24	20	40.37
4	0.042	0.060	9.144	20	24.22

For constant physical properties (Scenario 2) and using an average value of the overall heat transfer coefficient (Scenario 4), we obtain severe underestimation of the area. The conservative approach (Scenario 3) renders an area that is 32% higher.

These results point out the risk that a designer takes by using the simplified approach of adopting average or conservative temperatures, achieving a design that cannot fulfil the heat transfer task, or one that exceeds it, rendering a larger cost.

These disparities can be explained due to the nature of the hot stream. The example studied involves an engine oil stream with a large variation of the viscosity with the temperature. Such a large variation in viscosity affects the heat transfer coefficient on the oil side (from 144.7 W/(m²K) in the inlet to 57.7 W/(m²K) in the outlet).

4. Conclusions

We showed that modeling a double-pipe exchanger using the LMTD analytical method with uniform overall heat transfer coefficient can involve significant deviations from a more accurate solution obtained through discretization. When applied to a problem where physical properties vary substantially with temperature (the viscosity in our case), there is a significant risk of either obtaining an infeasible solution for the heat transfer task, or a significantly oversized exchanger. The implications for other cases (i.e. shell and tube exchangers) and other thermal tasks (i.e. condensers or vaporizers) is obvious. In addition, we also show that the spatial discretization, which leads to a nonlinear model, can be replaced by a temperature discretization, which generates a linear MILP, thus allowing globally optimal solutions.

5. Appendix

The symbols applied in this paper are shown in Table 4

Table 4: Stream data for the optimization problem.

Symbol	Description	Symbol	Description
ΔT	Temperature increment (K)	Pr	Prandtl number
Cp	Heat capacity (J/(kg.K))	Q	Heat load (W)
dte	Internal tube OD (m)	T	Stream temperature (K)
k	Thermal conductivity (W/(m.K))	U	Global heat transfer coefficient (W/(m ² .K))
m	Stream flow mass (kg/s)	wdPd	Substitution for binary product yd.yD.yP
pAs	Annular flow areas (m ²)	yd	Binary for internal tube diameter selection
pdh	Hydraulic diameters (m)	yD	Binary for external tube diameter selection
pdte	Internal tube ODs (m)	z	Position (m)
pdti	Internal tube ID (m)		

Acknowledgments

Alice Peccini thanks the Coordination of Superior Level Staff Improvement (CAPES) for her scholarship. André L. H. Costa thanks the National Council for Scientific and Technological Development (CNPq) for the research productivity fellowship (Process 311225/2016-0) and the Rio de Janeiro State University through the Prociência Program.

References

- C.O. Gonçalves, A.L.H. Costa, M.J. Bagajewicz, 2017, Shell and Tube Heat Exchanger Design Using Mixed-Integer Linear Programming, *AIChE Journal*, 63, 6, 1907-1922.
- F.P. Incropera, D.P. Dewitt, T.L. Bergman, A.S. Lavine, 2011, Appendix A, Fundamentals of Heat and Mass Transfer, Seventh Edition, John Wiley & Sons, Hoboken, NJ.

Incipient Fault Detection, Diagnosis, and Prognosis using Canonical Variate Dissimilarity Analysis

Karl Ezra S. Pilario^{a,b,*}, Yi Cao^c and Mahmood Shafiee^a

^a*Department of Energy and Power, Cranfield University, College Road, Bedfordshire, MK43 0AL, United Kingdom*

^b*Department of Chemical Engineering, University of the Philippines, Diliman, Quezon City 1101, Philippines*

^c*College of Chemical and Biological Engineering, Zhejiang University, Hangzhou, China*
k.pilario@cranfield.ac.uk

Abstract

Industrial process monitoring deals with three main activities, namely, fault detection, fault diagnosis, and fault prognosis. Respectively, these activities seek to answer three questions: ‘Has a fault occurred?’, ‘Where did it occur and how large?’, and ‘How will it progress in the future?’ As opposed to abrupt faults, incipient faults are those that slowly develop in time, leading ultimately to process failure or an emergency situation. A recently developed multivariate statistical tool for early detection of incipient faults under varying operating conditions is the Canonical Variate Dissimilarity Analysis (CVDA). In CVDA, a dissimilarity-based statistical index was derived to improve the detection sensitivity upon the traditional canonical variate analysis (CVA) indices. This study aims to extend the CVDA detection framework towards diagnosis and prognosis of process conditions. For diagnosis, contribution maps are used to convey the magnitude and location of the incipient fault effects, as well as their evolution in time. For prognosis, CVA state-space prediction and Kalman filtering during faulty conditions are proposed in this work. By covering the three main process monitoring activities in one framework, our work can serve as a baseline strategy for future application to large process industries.

Keywords: canonical variate analysis (CVA), incipient fault, Kalman filter (KF), dynamic process monitoring

1. Introduction

Data-driven methods for industrial process monitoring, known in general as multivariate statistical process monitoring (MSPM) techniques, have attained significant development in the last few decades (Reis and Gins, 2017). By addressing challenges such as high-dimensionality, temporal correlation, nonlinearity, non-Gaussianity, etc. in the plant data, MSPM tools have become more reliable for the automated detection of various faults in the plant (Ge et al., 2013).

However, in the larger perspective, fault detection must be followed by fault diagnosis and prognosis (Chiang et al., 2005). Fault diagnosis aims to determine the location and magnitude of a detected fault, while fault prognosis aims to predict its evolution in time. Indeed, Reis and Gins (2017) noted an increasing trend of research focus in the area of fault diagnosis and prognosis in the process industries. By developing more reliable diagnostic and prognostic tools, well-informed decisions can be made during production and maintenance operations planning, even when the fault continues to degrade the process performance. In addition, the ability to address

the aforementioned challenges in handling plant data must be present in all three process monitoring activities. Hence, it is beneficial to establish them under an integrated framework.

Among the various types of faults, the incipient fault is deemed as that which requires prognosis (Li et al., 2010). As opposed to abrupt faults, incipient faults are those that start at small magnitudes, but slowly worsen in time (Isermann, 2005). If an incipient fault is left to degrade the process, it may ultimately lead to process failure or an emergency situation (Pilario and Cao, 2017). Hence, incipient fault monitoring is an important issue that needs to be addressed by more advanced diagnostic and prognostic tools.

For the sensitive detection of incipient faults under dynamically varying conditions, the Canonical Variate Dissimilarity Analysis (CVDA) method was recently developed (Pilario and Cao, 2018). This method is based on the well-known Canonical Variate Analysis (CVA) (Odiwei and Cao, 2010) but uses a dissimilarity-based statistical index for enhanced sensitivity by measuring the predictability of the hidden states of the process. In this work, the CVDA fault detection methodology is extended to fault diagnosis and prognosis. Specifically, we aim to: (i) formulate a contributions-based approach for diagnosis using the canonical variate dissimilarity index; and, (ii) propose a prognostic tool using CVA state-space modelling and Kalman filtering under faulty conditions.

This paper is structured as follows. The CVDA methodology is revisited in Section 2. The proposed diagnosis and prognosis procedures are given in Section 3. Section 4 demonstrates the monitoring performance in a simulated CSTR case study. Lastly, concluding remarks are given.

2. CVDA for Fault Detection

The CVDA detection method proceeds by performing CVA to calculate the state and residual variables from the input-output process data, and then computing the statistical indices T^2 , Q , and D , which serve as health indicators of the process.

Given N samples of input and output data at normal conditions, denoted as $\mathbf{u}_k \in \mathbb{R}^{m_u}$ and $\mathbf{y}_k \in \mathbb{R}^{m_y}$ at the k th sampling instant, respectively, the past and future column vectors are formed as:

$$\mathbf{p}_k = [\mathbf{u}_{k-1}^T \quad \mathbf{u}_{k-2}^T \quad \cdots \quad \mathbf{u}_{k-p}^T \quad \mathbf{y}_{k-1}^T \quad \mathbf{y}_{k-2}^T \quad \cdots \quad \mathbf{y}_{k-p}^T]^T \in \mathbb{R}^{mp} \quad (1)$$

$$\mathbf{f}_k = [\mathbf{y}_k^T \quad \mathbf{y}_{k+1}^T \quad \mathbf{y}_{k+2}^T \quad \cdots \quad \mathbf{y}_{k+f-1}^T]^T \in \mathbb{R}^{m_y f} \quad (2)$$

where p and f are the number of lags in the past and future windows of data, respectively, and $m = m_u + m_y$. The number of lags are chosen large enough to capture autocorrelation in the output data (Odiwei and Cao, 2010).

The sample covariance matrices are then obtained using $\Sigma_{pp} = \frac{1}{M-1} \mathbf{Y}_p \mathbf{Y}_p^T$, $\Sigma_{ff} = \frac{1}{M-1} \mathbf{Y}_f \mathbf{Y}_f^T$, and $\Sigma_{fp} = \frac{1}{M-1} \mathbf{Y}_f \mathbf{Y}_p^T$, where $\mathbf{Y}_p = [\mathbf{p}_{p+1} \quad \mathbf{p}_{p+2} \quad \cdots \quad \mathbf{p}_{p+M}]$ and $\mathbf{Y}_f = [\mathbf{f}_{p+1} \quad \mathbf{f}_{p+2} \quad \cdots \quad \mathbf{f}_{p+M}]$ are the past and future Hankel matrices, respectively, and $M = N - p - f + 1$.

CVA aims to find vectors $\mathbf{a} \in \mathbb{R}^{m_y f}$ and $\mathbf{b} \in \mathbb{R}^{mp}$ so that the correlation between the linear combinations $\mathbf{a}^T \mathbf{f}_k$ and $\mathbf{b}^T \mathbf{p}_k$ are maximized (Odiwei and Cao, 2010). The algebraic solution is given by the singular value decomposition (SVD) of the scaled Hankel matrix:

$$\mathbf{H} = \Sigma_{ff}^{-1/2} \Sigma_{fp} \Sigma_{pp}^{-1/2} = \mathbf{U} \Sigma \mathbf{V}^T \quad (3)$$

where $\mathbf{U} = [\mathbf{u}_1, \mathbf{u}_2, \dots, \mathbf{u}_r]$ and $\mathbf{V} = [\mathbf{v}_1, \mathbf{v}_2, \dots, \mathbf{v}_r]$ are the left and right singular matrices, $\Sigma = \text{diag}(\sigma_1, \sigma_2, \dots, \sigma_r)$ is the diagonal matrix of descending non-zero singular values, and r is the rank of \mathbf{H} . The singular values, σ_i , are the maximum solutions of Eq. (3), which are also the canonical correlations between projected past and future data. Taking only the first n projections, corresponding to the n largest canonical correlations, the states, residuals, and dissimilarity

features at the k th sampling instant are computed as:

$$\mathbf{z}_k = \mathbf{J}_n \mathbf{p}_k \in \mathbb{R}^n \quad (4)$$

$$\mathbf{e}_k = \mathbf{F}_n \mathbf{p}_k \in \mathbb{R}^{mp} \quad (5)$$

$$\mathbf{d}_k = \mathbf{L}_n \mathbf{f}_{k-f+1} - \boldsymbol{\Sigma}_n \mathbf{J}_n \mathbf{p}_{k-f+1} \in \mathbb{R}^n \quad (6)$$

where $\mathbf{J}_n = \mathbf{V}_n^T \boldsymbol{\Sigma}_{pp}^{-1/2} \in \mathbb{R}^{n \times mp}$, $\mathbf{F} = (\mathbf{I} - \mathbf{V}_n \mathbf{V}_n^T) \boldsymbol{\Sigma}_{pp}^{-1/2} \in \mathbb{R}^{mp \times mp}$, $\mathbf{L}_n = \mathbf{U}_n^T \boldsymbol{\Sigma}_{ff}^{-1/2} \in \mathbb{R}^{n \times m_y f}$, \mathbf{V}_n and \mathbf{U}_n are the first n columns of \mathbf{V} and \mathbf{U} , respectively, and $\boldsymbol{\Sigma}_n$ is a diagonal matrix of the n largest singular values in Eq. (3). Finally, the statistical indices at the k th sampling instant are given by:

$$T_k^2 = \mathbf{z}_k^T \mathbf{z}_k \quad (7)$$

$$Q_k = \mathbf{e}_k^T \mathbf{e}_k \quad (8)$$

$$D_k = \mathbf{d}_k^T (\mathbf{I} - \boldsymbol{\Sigma}_n^2)^{-1} \mathbf{d}_k \quad (9)$$

which measure departures from the usual state subspace, residual subspace, and predictability of future states from the past states, respectively.

In the CVDA training phase, the distributions of T^2 , Q , and D , are estimated using kernel density estimation (KDE) without any assumption of Gaussianity in the data. Upper control limits (UCLs) are computed as the values of T_{UCL}^2 , Q_{UCL} , and D_{UCL} at which $P(T^2 < T_{\text{UCL}}^2) = \alpha$, $P(Q < Q_{\text{UCL}}) = \alpha$, and $P(D < D_{\text{UCL}}) = \alpha$, respectively. Throughout this paper, a significance limit of $\alpha = 99\%$ is adopted. During online monitoring, the process condition is deemed faulty when either of the indices exceeded their respective UCLs.

3. CVDA for Fault Diagnosis and Prognosis

3.1. Fault Diagnosis

To achieve fault diagnosis, the value of a statistical index at time point k can be decomposed into parts contributed by each measured variable. Hence, the measured variable/s with the largest contributions can be identified as most associated with the fault that occurred. Incipient fault diagnosis results must be reported using contribution maps instead of the traditional contribution bar plots, so that the fault evolution and propagation across time can be visually illustrated.

Contributions from the traditional CVA indices were already given by Jiang et al. (2015). In this paper, we derive the contributions for the dissimilarity index, D , as well. Altogether, the contributions of the i th measured variable ($i = 1, \dots, m$) to statistical index J at time point k , denoted by $C_{i,k}^J$ with $J \in \{T^2, Q, D\}$, are given by:

$$C_{i,k}^{T^2} = \sum_{j=0}^{p-1} \left| \mathbf{z}_k^T \left(\mathbf{J}_n^{(i+mj)} \mathbf{p}_k^{(i+mj)} \right) \right| \quad (10)$$

$$C_{i,k}^Q = \sum_{j=0}^{p-1} \left| \mathbf{e}_k^T \left(\mathbf{F}_n^{(i+mj)} \mathbf{p}_k^{(i+mj)} \right) \right| \quad (11)$$

$$C_{i,k}^D = \begin{cases} \sum_{j=0}^{p-1} \left| \mathbf{d}_k^T (\mathbf{I} - \boldsymbol{\Sigma}^2)^{-1} \left(\mathbf{L}_n^{(i-m_u+m_y j)} \mathbf{f}_{k-f+1}^{(i-m_u+m_y j)} - \boldsymbol{\Sigma}_n \mathbf{J}_n^{(i+mj)} \mathbf{p}_{k-f+1}^{(i+mj)} \right) \right| & i > m_u \\ \sum_{j=0}^{p-1} \left| \mathbf{d}_k^T (\mathbf{I} - \boldsymbol{\Sigma}^2)^{-1} \left(-\boldsymbol{\Sigma}_n \mathbf{J}_n^{(i+mj)} \mathbf{p}_{k-f+1}^{(i+mj)} \right) \right| & i \leq m_u \end{cases} \quad (12)$$

where $\mathbf{J}_n^{(l)}$, $\mathbf{F}_n^{(l)}$, $\mathbf{L}_n^{(l)}$ denote the l th columns in matrices \mathbf{J}_n , \mathbf{F}_n , \mathbf{L}_n , respectively, and $\mathbf{p}_k^{(l)}$, $\mathbf{f}_k^{(l)}$ denote the l th element in column vectors \mathbf{p}_k , \mathbf{f}_k , respectively. For Eq. (12) to apply, we assume that $p = f$ and that measured variables are sorted as all inputs followed by all outputs.

Using Eqs. (10)-(12), contributions from a fault-free training data set are first taken. For online use, relative contributions are computed by removing the mean normal contribution from $C_{i,k}^J$, and scaling by the standard deviation of the normal contributions (Deng and Tian, 2011):

$$C_{i,k}^{J,rel} = \frac{C_{i,k}^J - \text{mean}(C_{i,k}^J | \text{normal})}{\text{std}(C_{i,k}^J | \text{normal})}. \quad (13)$$

3.2. Fault Prognosis

CVA is distinguished from other process monitoring methods in that it is also a system identification method (Larimore, 1990). This benefit is useful for prognosis under the CVDA framework. In CVA, the system is assumed to be represented by the following state-space model:

$$\mathbf{x}_{k+1} = \mathbf{A}\mathbf{x}_k + \mathbf{B}\mathbf{u}_k + \mathbf{w}_k \quad (14)$$

$$\mathbf{y}_k = \mathbf{C}\mathbf{x}_k + \mathbf{D}\mathbf{u}_k + \mathbf{v}_k \quad (15)$$

where $\mathbf{A}, \mathbf{B}, \mathbf{C}, \mathbf{D}$ are the state-space matrices, \mathbf{w}, \mathbf{v} are the process and measurement noise, respectively, and $\mathbf{x}, \mathbf{y}, \mathbf{u}$ are the states, outputs, and inputs, respectively. After Eq. (4), CVA identification is achieved by letting $\mathbf{x}_k := \mathbf{z}_k$ and performing multivariate regression to estimate $\hat{\mathbf{A}}, \hat{\mathbf{B}}, \hat{\mathbf{C}}, \hat{\mathbf{D}}$ as follows (Larimore, 1990):

$$\begin{bmatrix} \hat{\mathbf{A}} & \hat{\mathbf{B}} \\ \hat{\mathbf{C}} & \hat{\mathbf{D}} \end{bmatrix} = \Sigma \left[\begin{pmatrix} \mathbf{x}_{k+1} \\ \mathbf{y}_k \end{pmatrix}, \begin{pmatrix} \mathbf{x}_k \\ \mathbf{u}_k \end{pmatrix} \right] \cdot \Sigma^{-1} \left[\begin{pmatrix} \mathbf{x}_k \\ \mathbf{u}_k \end{pmatrix}, \begin{pmatrix} \mathbf{x}_k \\ \mathbf{u}_k \end{pmatrix} \right] \quad (16)$$

where $\Sigma[\cdot, \cdot]$ denotes the sample covariance operation. Moreover, since the noise can be recovered as $\hat{\mathbf{w}}_k = \mathbf{x}_{k+1} - \hat{\mathbf{A}}\mathbf{x}_k - \hat{\mathbf{B}}\mathbf{u}_k$ and $\hat{\mathbf{v}}_k = \mathbf{y}_k - \hat{\mathbf{C}}\mathbf{x}_k - \hat{\mathbf{D}}\mathbf{u}_k$, then the noise covariances can be computed as $\hat{\mathbf{Q}} = \Sigma[\hat{\mathbf{w}}_k, \hat{\mathbf{w}}_k]$ and $\hat{\mathbf{R}} = \Sigma[\hat{\mathbf{v}}_k, \hat{\mathbf{v}}_k]$. Meanwhile, $\hat{\mathbf{P}}_0 = \Sigma[\hat{\mathbf{x}}_k, \hat{\mathbf{x}}_k]$ is the initial state covariance.

Given a future input sequence, the estimated state-space model can be used for predicting the output variables during normal operation. When a fault occurs, the state-space model must be re-trained by applying Eq. (16) to the samples obtained during the early stages of degradation (Ruiz-Cárcel et al., 2016). However, an incipient fault can bring changes in both the state-space model parameters and the states \mathbf{x}_k themselves. Re-training only corrects the model parameters. Hence, in this paper, we propose the use of Kalman filtering (KF) to correct changes in the states in conjunction with model re-training. In KF, the pertinent equations are:

$$\mathbf{x}_{k|k-1} = \hat{\mathbf{A}}\mathbf{x}_{k-1|k-1} + \hat{\mathbf{B}}\mathbf{u}_k \quad (17)$$

$$\hat{\mathbf{P}}_{k|k-1} = \hat{\mathbf{A}}\hat{\mathbf{P}}_{k-1|k-1}\hat{\mathbf{A}}^T + \hat{\mathbf{Q}} \quad (18)$$

$$\mathbf{x}_{k|k} = \mathbf{x}_{k|k-1} + \mathbf{K}_k(\mathbf{y}_k - \hat{\mathbf{C}}\mathbf{x}_{k|k-1}) \quad (19)$$

$$\hat{\mathbf{P}}_{k|k} = (\mathbf{I} - \mathbf{K}_k\hat{\mathbf{C}})\hat{\mathbf{P}}_{k|k-1} \quad (20)$$

where $\mathbf{K}_k = \hat{\mathbf{P}}_{k|k-1}\hat{\mathbf{C}}^T(\hat{\mathbf{C}}\hat{\mathbf{P}}_{k|k-1}\hat{\mathbf{C}}^T + \hat{\mathbf{R}})^{-1}$ is the Kalman gain.

To apply Eq. (17)-(20), the initial states are first estimated using Eq. (4) on the first p samples. Assuming that $\mathbf{x}_k, \hat{\mathbf{w}}_k$ and $\hat{\mathbf{v}}_k$ are Gaussian-distributed, KF is used to update \mathbf{x}_k at every time step. Note that changes due to other incipient faults, such as drifts in the noise statistics, may be difficult to track upon using the Kalman filter. This is a topic for future work.

4. Case Study

To evaluate the performance of CVDA for fault diagnosis and prognosis, a closed-loop CSTR case study is used, which is available in (Pilario, 2017). Data are simulated from a system of 4 state

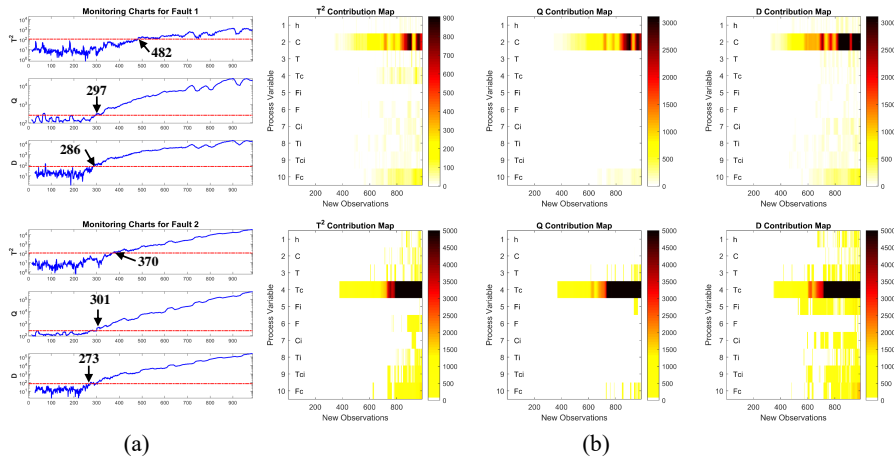


Figure 1: Monitoring results for: (a) fault detection (Arrows - detection time, mins; Red dash - UCLs; Blue solid - detection index); and (b) fault diagnosis. Top: Catalyst decay, Bottom: Fouling. For (b), the contributions maps are for T^2 , Q , and D from left to right.

equations, with 2 cascade control loops to maintain liquid level, h , and reactor temperature, T . The measured variables are $\mathbf{u} = [F_i, C_i, T_i, T_{ci}]^T$ and $\mathbf{y} = [h, C, T, T_c, F, F_c]^T$. The input variables are being perturbed every 30 sampling times to simulate disturbance changes.

Using a data set of 1000 samples at normal operation, CVDA was trained so as to generate the projection matrices, the UCLs, and the state-space model. The number of lags and number of states are selected as 14 and 8, respectively. These are chosen using autocorrelation analysis and the dominant singular values method (Odiowei and Cao, 2010). Two incipient faults are studied in the CSTR, namely, catalyst decay (Fault 1) and heat transfer fouling (Fault 2). In the faulty data sets, both faults are slow drifts introduced after an initial 200 min of normal operation.

Fig. 1(a) shows detection results for the faulty data sets. As shown, the D index incurs the earliest detection time for both faults. To locate and track the magnitude of the detected fault, contribution maps are generated using Eqs. (10)-(13), and are shown in Fig. 1(b). The most associated variables to catalyst decay and fouling faults are shown to be the outlet concentration, C , and outlet temperature of the coolant, T_c . These are, indeed, the expected results for fault diagnosis. Moreover, the maps were able to illustrate how the fault effects propagate to other variables further in time. Notably, the D contribution maps revealed not only the fault-affected variables, but also the input variables that contributed to the dissimilarity between past and future states. Hence, we suggest to use all three contribution maps in conjunction to better capture incipient fault signatures.

The 1-step ahead prediction of the top 2 faulty variables in each fault case is given in Fig. 2. The estimated data are Kalman-filter predictions from a state-space model re-trained every 20 sampling times using the latest 400 samples while under faulty conditions. Table 1 gives the R^2 measure of fit of the predictions, showing that without KF, the faulty variables cannot be tracked accurately. Hence, KF improves CVDA fault prognosis in this case study.

5. Conclusion

In this paper, an incipient fault detection, diagnosis, and prognosis methodology is presented under an integrated framework, namely, Canonical Variate Dissimilarity Analysis (CVDA). Using a CSTR case study involving 2 parametric incipient fault scenarios, the method was shown to

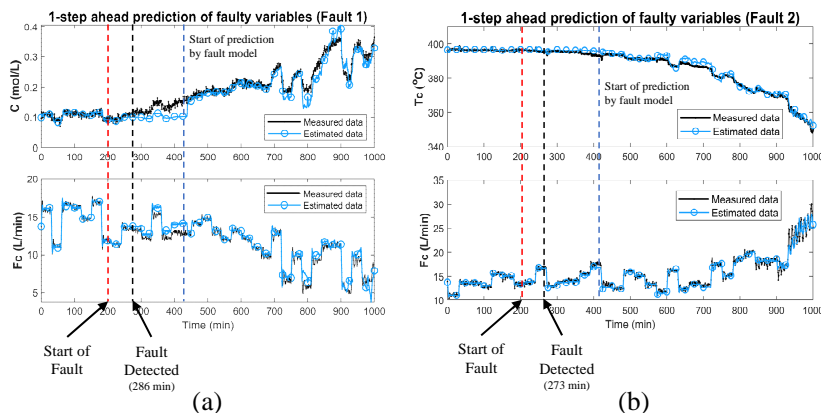


Figure 2: Fault prognosis results for the top 2 faulty variables in: (a) Catalyst decay fault; (b) Fouling fault. See Table 1 for R^2 fitness on all the charts.

Table 1: R^2 fitness values of the predictions of the faulty variables

Fault 1	with KF	without KF	Fault 2	with KF	without KF
C	90.57 %	-135.0 %	T_c	98.32 %	-35.3 %
F_c	94.41 %	27.30 %	F_c	96.52 %	12.93 %

provide early detection, reliable diagnosis, and accurate tracking of faulty variables. Hence, the framework constitutes a baseline strategy for industrial process monitoring.

References

- L. H. Chiang, E. L. Russell, R. D. Braatz, 2005. Fault Detection and Diagnosis in Industrial Systems. Springer-Verlag, London.
- X. Deng, X. Tian, 2011. A new fault isolation method based on unified contribution plots. Proceedings of the 30th Chinese Control Conference, CCC 2011 (10), 4280–4285.
- Z. Ge, Z. Song, F. Gao, 2013. Review of recent research on data-based process monitoring. Industrial and Engineering Chemistry Research 52, 3543–3562.
- R. Isermann, 2005. Model-based fault-detection and diagnosis - status and applications. Annual Reviews in Control 29 (1), 71–85.
- B. Jiang, D. Huang, X. Zhu, F. Yang, R. D. Braatz, 2015. Canonical variate analysis-based contributions for fault identification. Journal of Process Control 26 (2015), 17–25.
- W. E. Larimore, 1990. Canonical variate analysis in identification, filtering, and adaptive control. Proceedings of the IEEE Conference on Decision and Control 2, 596–604.
- G. Li, S. J. Qin, Y. Ji, D. Zhou, 2010. Reconstruction based fault prognosis for continuous processes. Control Engineering Practice 18 (10), 1211–1219.
- P.-E. Odiwei, Y. Cao, 2010. Nonlinear dynamic process monitoring using canonical variate analysis and kernel density estimations. IEEE Transactions on Industrial Informatics 6 (1), 36–45.
- K. E. Pilario, 2017. Cascade-controlled CSTR for Fault Simulation.
URL <https://www.mathworks.com/matlabcentral/fileexchange/65091-cascade-controlled-cstr-for-fault-simulation>
- K. E. Pilario, Y. Cao, sep 2017. Process incipient fault detection using canonical variate analysis. In: 2017 23rd International Conference on Automation and Computing (ICAC). IEEE, pp. 1–6.
- K. E. S. Pilario, Y. Cao, 2018. Canonical variate dissimilarity analysis for process incipient fault detection. IEEE Transactions on Industrial Informatics.
- M. Reis, G. Gins, 2017. Industrial Process Monitoring in the Big Data/Industry 4.0 Era: from Detection, to Diagnosis, to Prognosis. Processes 5 (3), 35.
- C. Ruiz-Cárcel, L. Lao, Y. Cao, D. Mba, 2016. Canonical variate analysis for performance degradation under faulty conditions. Control Engineering Practice 54, 70–80.

One-point temperature control of reactive distillation: A thermodynamics-based assessment

Mihai Daniel Moraru,^{a,b,*} Costin Sorin Bildea^b

^a*Department of Process Technology and Development, Hexion, Seattleweg 17, 3195 ND Pernis, The Netherlands*

^b*Department of Chemical and Biochemical Engineering, University Politehnica of Bucharest, Str. Gh. Polizu 1-7, 011061 Bucharest, Romania*

mihai.moraru@hexion.com

Abstract

A recent study introduced a new class of control structures using one-point temperature control applicable to heterogeneous reactive distillation. The feed rate of one reactant sets the plant capacity. The inventory of the other reactant is inferred from measuring the reflux rate or reflux ratio and is managed by adjusting the second feed flow. This idea can be implemented in different ways. Here, the applicability of these structures to various esterification systems of industrial importance is assessed. The analysis is based on key thermodynamic data: boiling points, azeotropy and liquid-liquid equilibria. As a rule-of-thumb, if water is the lightest and the ester the heaviest boiler in the system, and if at least the alcohol forms a minimum boiling heterogeneous azeotrope with water, then the new class of control structures may be applicable.

Keywords: acetates, acrylates, esterification, propionates, process control

1. Introduction

Reactive distillation (RD) offers significant advantages such as reduced investment and operating costs. However, the controllability of the process is as important as the economics, in order to meet important objectives such as process stability, production rate and product purity. Recently, we proposed a new class of control structures using one-point temperature control that are applicable to heterogeneous reactive distillation (Moraru et al., 2018). The *heterogeneous* attribute refers to systems that present minimum boiling heterogeneous azeotropy making possible a liquid-liquid split after vapor condensation. Hence, these control structures are appropriate for industrially important chemical systems which share this particular thermodynamic property.

Many acetates, acrylates and propionates are esters of industrial importance which have in common the minimum boiling heterogeneous azeotropy. They are produced in large quantities and used in a variety of applications. These esters are usually obtained in the reaction between an alcohol and the respective acid, which is typically performed in liquid phase and in the presence of a homogeneous catalyst. Whenever feasible, the RD technology using solid catalysts is preferred as alternative to the conventional processes (i.e., reactors followed by distillation systems).

In the perspective of showing the broad applicability of these new control structures using one-point temperature control, we study the basic thermodynamic properties of six important esterification systems: two acetates, two acrylates and two propionates;

the two acrylates were already used to test the concept of the new control structures and serve here as comparison for the other esterification systems. In the first part, the basic control idea applicable to the heterogeneous reactive distillation is presented; dynamic simulation results proving the control performance are also briefly presented. In the second part of the study, the common key properties that suggest the applicability of the new control structures are described. The azeotropy and liquid-liquid equilibria of each system are compared and discussed in detail. Aspen is used as computer-aided process engineering tool to make the analysis.

2. Basic control idea

The basic idea behind the new one-point temperature control structures addresses three basic control objectives: setting plant capacity, achieving the required product purity, and maintaining the component inventory. The latter is the key element of the concept.

To better describe the concept, we start by describing the RD process. A general esterification system which can be efficiently performed by RD comprises two reactants (A, B) and two products (C, D). Often, one product is the high-boiling species and is obtained as bottom stream, while the other is involved in a low-boiling azeotrope and is obtained as distillate. This azeotrope has the beneficial effect of displacing the chemical equilibrium, but also the disadvantage of an impure distillate. However, when the heterogeneity of the azeotrope makes possible a liquid-liquid split of the condensed distillate, the reactant-rich phase can be returned to the column as reflux, while the product-rich phase has the composition on the side of the distillation boundary which allows obtaining the top-product with a relatively high-purity. Figure 1 (left) shows a typical example. The heavy reactant B (acid or alcohol) is fed as liquid at the top of the reactive zone of the RD column. The light reactant A (acid or alcohol) is fed as vapor at the bottom of the reactive zone. The reactants flow in counter-current and reaction takes place in the liquid phase. The heavy product C (ester) is recovered in the stripping zone of the column, being obtained as high purity bottom stream. The light product D (water) forms several binary and ternary low-boiling heterogeneous azeotropes. Thus, water is removed from the liquid mixture with the result of increased reaction rate due to equilibrium displacement. The distillate is condensed, cooled, and sent to liquid-liquid separation. The organic phase is refluxed. The aqueous phase is the top product. If required, a flash can remove the small amounts of organics that are still dissolved.

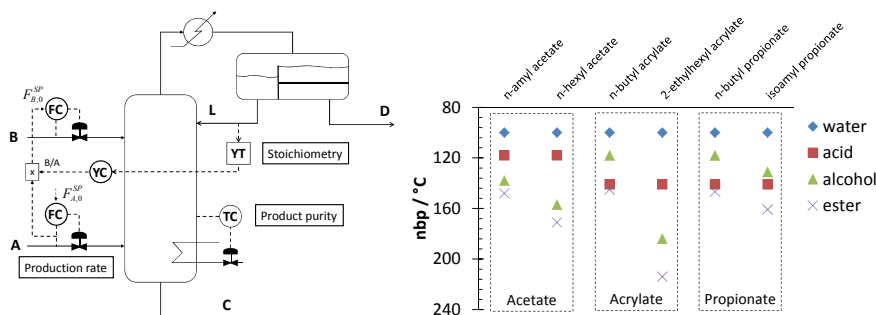


Figure 1. Basic control idea for RD process (left); different types of esterification systems (right)

During operation, the feed flow rate of one reactant sets the plant capacity. The requirement to feed the reactants in the stoichiometric ratio is addressed by feedback control. The inventory of the other reactant is inferred from the reflux rate or reflux ratio, which both can be easily measured. When this reactant is not fed in the correct stoichiometric ratio, it will either accumulate in the system or get depleted, which will be reflected by a change of the reflux rate. Thus, corrective action (change of the fresh feed rate) can be taken. This simple solution does not require concentration measurements and does not use any temperature control loop. Consequently, the reboiler duty becomes available to be used as manipulated variable in a quality-control loop. Several control strategies are possible based on this idea.

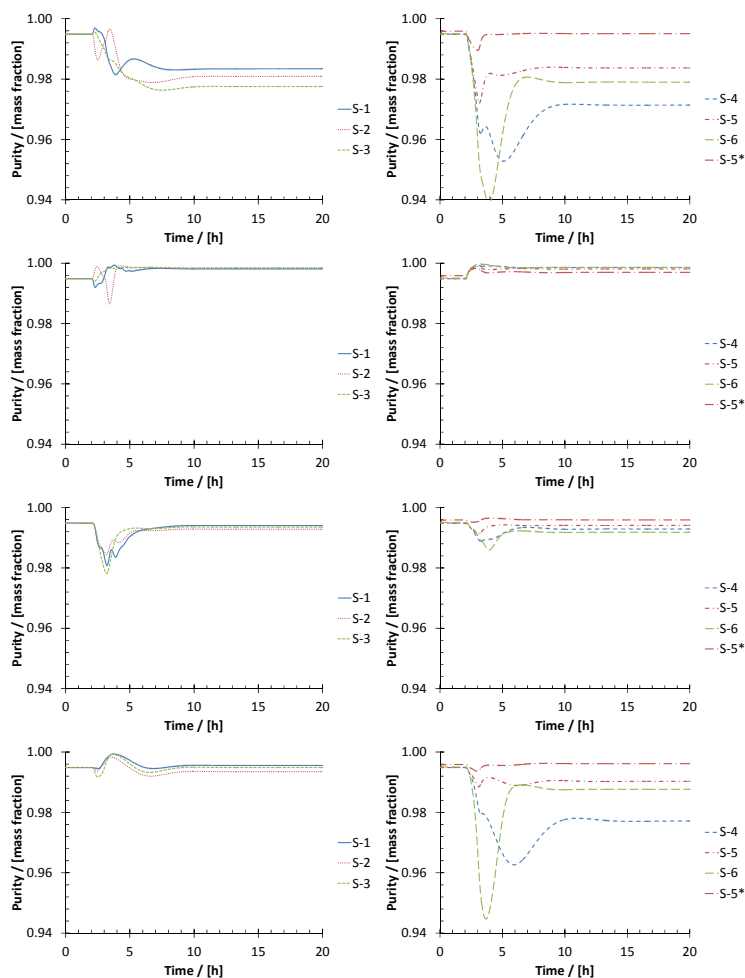


Figure 2. Process dynamics associated with each control structure (left column: literature structures S-1, S-2, S-3; right column: novel structures S-4, S-5, S-6 (S-5* uses pressure-compensated control and can be implemented to any of these six structures)) at various perturbations: top diagrams: +25% production; middle-top diagrams: -25% production; middle-bottom diagrams: 5 %mass water in fresh acid; bottom diagrams: 5 %mass water in fresh alcohol.

Figure 2 compares the performance of several control structures from the literature (S-1, S-2, (Luyben and Yu, 2008) and S-3 (Zeng et al, 2004)) with control structures based on the idea presented above (S-4, S-5, S-6). S-1 sets the production rate by the reboiler duty and uses two temperature measurements for inferential control of reactants inventory: the top feed controls a temperature in the stripping section while the bottom feed controls a temperature on the top of the reactive zone. S-2 sets the production rate directly, by changing the feed rate of the light reactant. The second reactant and the reboiler duty are used to control two temperatures in the stripping and reactive sections, respectively. S-3 uses only one temperature control loop, fixing the ratio between the reboiler duty and the flow rates of fresh reactants. In S-4 and S-5, the accumulation / depletion of one reactant is inferred from the reflux ratio and the reflux rate, respectively. S-6 takes a different approach: the reflux ratio is fixed and the alcohol is fed at two different locations: at the top of the reactive section, and directly in the decanter. This second feed provides an additional degree of freedom which is used to control the level of the organic phase, maintaining in this way the component balance. Among the new control structures, S-5 is the best, showing comparable performance with S-1 in terms of speed of disturbance rejection and offset in product purity.

3. Common key properties

The applicability of the new control concept to reactive distillation processes of industrial importance can be assessed based on key physical properties. This perspective is discussed in the remaining of this chapter.

3.1. Thermodynamic model

The model parameters for calculating the physical properties of pure components and mixtures are available in the Aspen database. The azeotropes and phase equilibria are calculated using the UNIQUAC or NRTL liquid activity coefficient models. The HOC equation of state is also considered to account for the dimerization of acids in the vapor phase. The binary interaction parameters are taken from published literature or retrieved from the Aspen databanks, including the parameters for the HOC equation.

3.2. Boiling points of pure components

The order of boiling points of the pure components in the system determines the structure of the RD column: addition of feeds and withdrawal of products. Figure 1 (right) orders by their normal boiling points the components (alcohol, acid, water and ester) of each of the esterification system considered in this work. In all systems, the ester is the highest boiler, and is obtained as bottoms; the heterogeneous azeotropes are the lightest, making possible to obtain the water as distillate (after decantation); the reactants are intermediates (acids lighter or heavier than alcohols), and are fed to the column at the bottom and top of the catalytic section. In addition, these six systems present various characteristics which shows that the proposed control structures are applicable to a wide range of esterification processes: (i) combination between 3 acids and 5 alcohols, (ii) wide boiling range for acids (118-141 °C), alcohols (118-184 °C) and esters (145-214 °C).

Note that other esterification systems (not presented in this study) such as *n*-butyl acetate, *n*-decyl acrylate and cyclohexyl acrylate, can be included in this list of industrially important esters.

3.3. Azeotropy and liquid-liquid equilibria

The formation of heterogeneous azeotropes and formation of two liquid phases after condensation are the key elements on the control concept. This allows to control the inventory of one component by monitoring the refluxed organic phase and adjusting one of the fresh feeds. Table 1 shows the azeotropes calculated at 1.013 bar for all esterification systems. Each system presents at least two binary heterogeneous azeotropes: water/alcohol and water/ester. With the exception of the 2-ethylhexyl acrylate, all the other systems also present a ternary heterogeneous azeotrope: water/alcohol/ester. All these azeotropes have a boiling point very close to that of water and will be found in the vapor distillate. Excepting the *n*-hexyl acetate system, the acid is involved in homogeneous azeotropy either with water (*n*-butyl propionate) or with the alcohol or ester. These azeotropes have a high boiling point, close to that of the ester in some cases. They are important since they may contaminate the ester product.

Figure 3 shows that all systems have large immiscibility areas, meaning that the water product is obtained with a relatively high purity; when this is not the case (*n*-butyl acrylate), an additional flash can recover the alcohol and obtain high-purity water. This is possible due to the minimum boiling heterogeneous azeotrope water / alcohol.

Table 1. Azeotropy^a (mass based) at 1.013 bar of the six esterification systems

#	type ^b	T_B / [°C]	water	acid	alcohol	ester
<i>n</i> -amyl acetate						
1	het.	94.7	0.411		0.107	0.481
2	het.	94.9	0.404			0.596
3	het.	95.9	0.541		0.459	
4	hom.	140.0		0.154	0.572	0.284
5	hom.	140.3		0.193	0.807	
<i>n</i> -hexyl acetate						
1	het.	97.4	0.586		0.139	0.276
2	het.	97.6	0.579			0.421
3	het.	98.0	0.690		0.310	
<i>n</i> -butyl acrylate						
1	het.	92.3	0.397		0.498	0.106
2	het.	92.4	0.417		0.583	
3	het.	95.4	0.435			0.868
4	hom.	139.8		0.868	0.132	
5	hom.	148.5		0.047		0.953
2-ethylhexyl acrylate						
1	het.	99.1	0.809		0.191	
2	het.	99.6	0.855			0.145
<i>n</i> -butyl propionate						
1	het.	92.9	0.411		0.436	0.153
2	het.	93.0	0.422		0.558	
3	het.	94.5	0.388			0.612
4	hom.	99.9	0.834	0.166		
isoamyl propionate						
1	het.	95.3	0.472		0.286	0.242
2	het.	95.7	0.541		0.459	
3	het.	96.2	0.466			0.534
7	hom.	142.1		0.754	0.246	

^athe calculations are performed using the *Distillation Synthesis* tool in Aspen Properties

^bazeotrope type: heterogeneous (het.) or homogeneous (hom.)

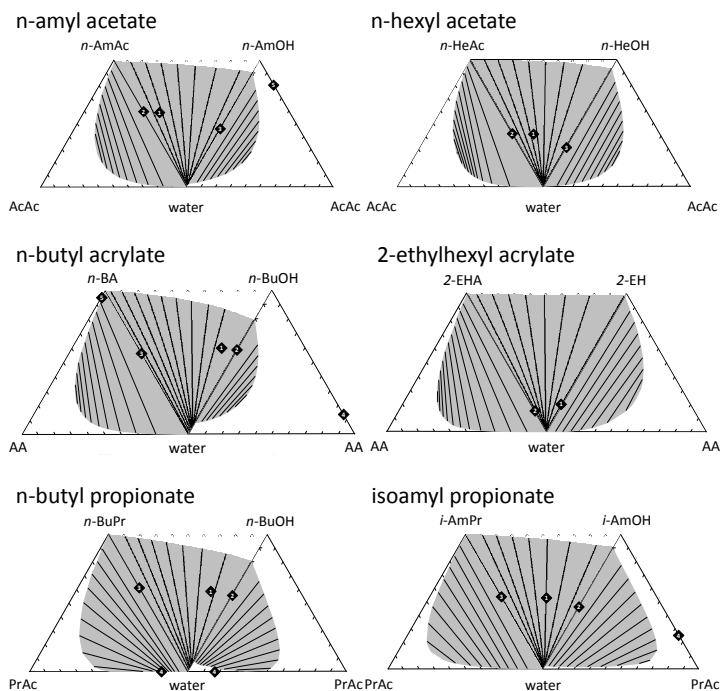


Figure 3. Liquid-liquid equilibria (mass based) at 1.013 bar and 35 C of the six esterification systems; numbering of the azeotropes as in Table 1

4. Conclusions

The applicability to a given esterification system of the basic control concept can be assessed based on key physical property data. As a rule-of-thumb, if the pure components have the right nbp order, and if at least the alcohol forms a minimum boiling heterogeneous azeotrope with water, then the new class of control structures may be applicable.

References

- M.D. Moraru, E. Zaharia, C.S. Bildea, 2018, Novel Control Structures for Heterogeneous Reactive Distillation, *Chem. Eng. Trans.* 69, 535-540.
- M.D. Moraru, C.S. Bildea, 2017, Process for n-butyl acrylate production using reactive distillation: Design, control and economic evaluation. *Chem. Eng. Res. Des.* 125, 130-145.
- M.D. Moraru, C.S. Bildea, 2018, Process for 2-Ethylhexyl Acrylate Production Using Reactive Distillation: Design, Control and Economic Evaluation, *Ind. Eng. Chem. Res.* 57, 15773–15784.
- W.L. Luyben, C.C. Yu, 2008, *Reactive Distillation Design and Control*, Wiley-AIChE.
- K.L. Zeng, C.L. Kuo, I.L. Chien, 2006, Design and control of butylacrylate reactive distillation column system, *Chem. Eng. Sci.* 61, 4417–4431.

Optimization of Biogas to Syngas via Combined Super-Dry and Tri-Reforming. Analysis of Fischer-Tropsch Fuels Production

Borja Hernández,^{a*} Mariano Martín,^a

^a*Departamento de Ingeniería Química. Universidad de Salamanca. Pza. Caidos 1-5, 37008 Salamanca, Spain.*

borjahb@usal.es

Abstract

This work presents an optimization approach to compare tri-reforming and super dry reforming for the production of syngas. Next, this section is integrated with the synthesis of Fischer-Tropsch liquids at low and high temperatures. The optimization of the tri-reforming technology is carried out introducing a parametric approach to evaluate different O₂:Biogas ratios. Tri-reforming is always selected to produce syngas. The biogas composition depends on the purpose of the syngas including ethanol, FT or methanol production. The large amount of hydrogen required in the last option is achieved introducing more steam in the WGS reactor in the tune-up section. In the second part of the work, the integration of previous reforming types with FT processes suggests that the operation in the LT mode is more profitable (\$3.3/gal of diesel) than the HT (\$5.4/gal). However, both are far from other production costs reported in literature that reach up to \$0.34/gal.

Keywords: Biogas, CO₂, circular economy, reforming, optimization.

1. Introduction

Current developed societies generate large volumes of wastes. Waste needs to be treated before disposing them. Anaerobic digestion represents a technology that allows not only processing and stabilizing the waste, but that also generates additional value in the form of biogas and digestate. For decades, biogas was only used for the production of power and as a source of methane for natural gas networks (Wellinger et al., 2013). However, biogas is an interesting source of carbon not only because of the methane, but also due to its CO₂ content since it can be used for the production of chemicals via dry reforming (DR) (Hernández et al., 2017). The DR technology has been evaluated by integrating it with other reforming technologies such as in combined steam and dry reforming (Hernández and Martín, 2016) or in tri-reforming (TR) (Chein et al. 2017, Vita et al. 2018). Apart from its combination, another relevant technology has been recently developed by intensifying the process (Buelens et al., 2016). Super-dry reforming (SDR) has been created by intensifying DR with the objective of maximizing the conversion of CO₂. It is based on eliminating the reverse WGS reaction, obtaining the global reaction presented in Eq. (1).



The optimization and comparison of TR with other reforming technologies was only recently addressed by Balasubramanian et al. (2018). They performed an MINLP

optimization selecting the optimal reforming type for different $H_2:CO$ syngas ratios and using natural gas as raw material. However, SDR was not taken into account. Thus, this work presents a comparison including the SDR technology within the superstructure and using biogas as raw material. Furthermore, the work is extended integrating the previous reformers with the production of Fischer-Tropsch (FT) fuels via low and high temperatures.

2. Modelling Issues.

The problem presented in this work is divided in two parts. First, in section 2.1 the superstructure for the production of syngas with different $H_2:CO$ ratios using biogas as raw material and with parallel TR and SDR is presented. Next, the integration of TR and SDR for the optimal production of FT fuels is presented in section 2.2.

2.1 Tri-Reforming versus Super-Dry Reforming for Syngas Production.

The problem addressed in this section is presented in the superstructure given by Figure 1, where only the main operations of the process are defined. The modelling of these units is briefly defined in the following paragraphs. Other units such as heat exchangers and compressors are not included in Figure 1 but they are also modelled based on thermodynamics, mass and energy balances.

The biogas fed in the system is a mixture of gases whose optimal composition is also desired to be obtained. It is fed in the system, and split into three streams: one for processing and the other two ones used as fuel for heating up the reforming reactors. The biogas fed to the process section is initially sent to a bed for removing the ammonia and H_2S that would reduce the catalyst efficiency of the reformer in later stages.

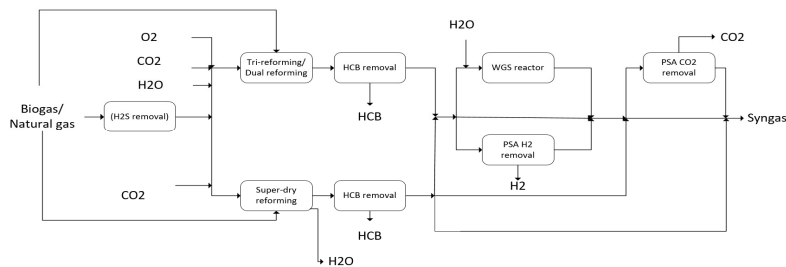


Figure 1. Superstructure of the Reforming Selection Problem for Syngas Production.

After cleaning the biogas, it is split in two streams. The first is sent to the TR reactor and the other one is sent to the SDR reactor. The TR is modelled dividing the reactor in two stages as presented by Hernández and Martín (2018). In the first stage, partial oxidation occurs and in the second stage the concentration of the components is computed based on chemical equilibrium. The oxygen required in this TR reactor is evaluated using different ratios by mean of a parametric optimization. The SDR reactor is modelled using a reduced order model, Eq. (2), that it is based on the thermodynamic results presented by Buelens et al. (2016). Two streams leave this SDR reactor: one for the water captured by the absorbent during regeneration and another one for the CO and unreacted gases produced.

$$X_{CH_4} = 8.13 + 0.76 \ln\left(\frac{\text{molCO}_2}{\text{molCH}_4}\right) - \frac{4746.4}{T(K)} - 2.6 \cdot 10^{-3} \text{gT}(K) - 6.3 \cdot 10^{-4} \text{gT}(K) \ln\left(\frac{\text{molCO}_2}{\text{molCH}_4}\right) \quad (2)$$

The syngas coming out from both reactors needs to be treated and its composition adjusted to ensure the H₂:CO ratio desired in the syngas. First, the traces of methane are removed in order to avoid carbon deposition on the catalyst of future synthesis or WGS reactors. The removal efficiency of the beds is assumed to be 100%. Then, the H₂:CO ratio is adjusted by considering three technologies: a WGS reactor to increase the concentration of H₂ (modeled as an equilibrium), a by-pass to keep constant the ratio and a hybrid membrane-PSA system to remove the H₂. The last stage assumed in the modelling of the tune-up section is the CO₂ removal since large concentrations of CO₂ promote the carbon deposition on the catalyst of synthesis reactors.

2.2 Super-dry and Tri-reforming for Fischer-Tropsch liquids production.

The previous syngas production can be integrated with the production of different chemicals and, among them, FT fuels. The superstructure for FT fuels production is presented in Figure 2. It considers two modes of operation depending on the reactor operating conditions: at high (HT), 590K-630K, and low temperatures (LT), 440K-530K. In both cases, the mass product distribution, w_i , follows the Anderson-Schulz-Flory distribution that depends on the number of carbons of the component, n_c , and the chain growth, α , as presented in Eq. (3). α is also dependent on the reactor temperature and molar fractions (Hernández and Martín, 2018).

$$w_i = \alpha^{n_c-1} (1-\alpha) \cdot n_c \quad (3)$$

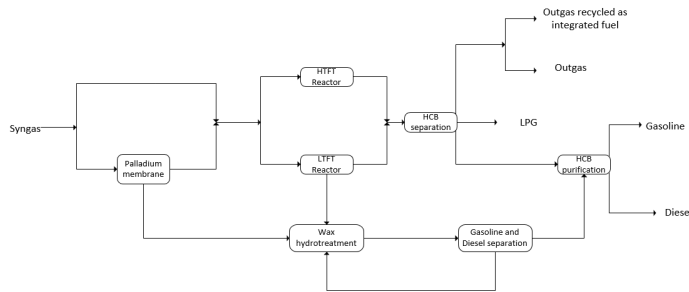


Figure 2. Superstructure for the Integration of FT-Fuels.

When the FT reactor operates at HT, light products are dominant and waxes only appear as traces. Thus, the product obtained from the reactor is sent to a separation stage composed by a flash separator to remove the unreacted gases of the syngas and fractions lighter than C₃. The products heavier than C₃ are expanded and separated in a tri-separator that has three outlets: a gas stream in the top that contains the LPG, a bottom stream with the water fraction and an intermediate stream with the organics with a chain larger than C₄. These organics are later separated in a distillation column in two fractions: gasoline and diesel.

The FT reactor operating at LT produces fuels with larger chain lengths, including waxes. In order to provide an added value to these waxes, an integrated recovering procedure based on hydrogenation is proposed. The hydrogenation reactor is modelled following a reduced model (Hernández and Martín, 2018). It requires H₂, which is

separated from the syngas before the FT reactor, see Figure 2. After separating the H₂, the syngas is sent to the LT-FT reactor, whose products are separated as follows. First, the waxes are separated at the exit of the reactor as liquids. The rest of components are gases that are cooled down and sent to a flash separator. Second, the flash separator removes the unreacted syngas and hydrocarbons (HCB) with a chain length shorter than C₃. The hydrocarbons with a chain larger than C₃ and water are sent to a tri-separator that separates the fractions as in the previous HTFT process. Finally, the hydrocarbons with a chain larger than C₄ (gasoline and diesel) are separated in a distillation column together with the fractions recovered from the waxes hydrogenation.

3. Solution procedure.

3.1 Tri-Reforming versus Super-Dry Reforming for Syngas Production.

The first part of this work focuses on the optimization of the syngas production using two type of reformers: super-dry and tri-reforming. This problem is solved maximizing the profit obtained from the process. It is computed following Eq. (4) as function of the product costs (\$), the fluxes (F_i), power (W_i) and heat (Q_i) consumptions. This objective function completes the definition of the NLP optimization problem that is composed by 1,200 equations and 1,400 variables that are written in GAMS and solved using a multi-start approach with CONOPT 3.0.

$$\begin{aligned} \text{profit} = & \$_{H_2} F_{H_2} - \$_{elec} \sum_{i \in \text{Compressors}} W_i - \$_{CH_4} \sum_{i \in CH_4 \text{ inlets}} F_{CH_4} - \$_{CO_2} \sum_{i \in CO_2 \text{ inlets}} F_{CO_2} - \$_{O_2} \sum_{i \in O_2 \text{ inlets}} F_{O_2} \\ & - \$_{H_2O} \sum_{i \in H_2O \text{ inlets}} F_{H_2O} - \$_{steam} \sum_{j \in Q_{heat}} Q_j + \$_{H_2Oref.} \sum_{k \in Q_{ref}} Q_k - \$_{H_2S} \sum_{i \in H_2S_{recovered}} F_{H_2S} \end{aligned} \quad (4)$$

3.2 Integrated Super-dry and Tri-reforming with Fischer-Tropsch processes.

The second part of this work focuses on the optimization of the integrated process that combines the reforming technology with the production of FT fuels. In this case, the integrated MINLP problem defined in the super-structures of Figure 1 and 2 is divided in two NLP sub-problems that are independently written in GAMS for the maximization of their profit. The problem involving the HT-FT reactor mode is composed over 2,100 equations and 2,500 variables, meanwhile the problem involving the LT-FT reactor model consists of 2,600 equations and 3,100 variables. Both cases are solved in GAMS using a multi-start approach with CONOPT 3.0.

4. Results

4.1 Syngas production from Tri-Reforming and Super-dry Reforming.

The optimization of the syngas production provides the optimal biogas composition for different products, the technologies selected and the operating conditions. The optimal composition of the biogas fed to the process is presented in Table 1. It can be seen that for ethanol production, the biogas composition required is approximately 48% of CO₂ and 52% of CH₄, while for FT and methanol production the methane content is to be at the upper bound. The large amount of hydrogen required to produce methanol is obtained by increasing the steam added in the WGS reactor of the tune-up stage.

After specifying the feed composition, the reforming technology selected is always the TR. Thus, oxygen is also needed in the process requiring 0.275 molO₂:mol Biogas for syngas used for methanol and FT, and 0.035 molO₂:mol Biogas ethanol. The

temperature in this reactor is suggested to be 1273 K for methanol and FT production and 1231 K for ethanol production.

In the tune-up section, the production of a syngas with a H₂:CO ratio of 1:1 only requires to remove the unreacted HCB. The production of a syngas with a H₂:CO ratio of 1.7 requires the removal of HCB, the use of a WGS reactor and the addition of 0.06 mol of steam per mol of biogas fed in the process. Finally, the production of a syngas with a H₂:CO ratio of 2.5 requires all the units defined in the tune-up section: a silica bed to remove the unreacted HCB, a WGS reactor that needs 0.21 mol of steam per mol of biogas fed in the process and a PSA system that removes the excess of CO₂ and receives the 66% of the syngas produced.

Table 1- Optimal Compositions of Biogas an Boundaries (% vol.).

Comp.	Methanol (H ₂ :CO=2.5)	FT (H ₂ :CO=1.7)	Ethanol, DME (H ₂ :CO=1)	Minimum	Maximum
CO ₂	0.25	0.25	0.479	0.37	0.75
CH ₄	0.75	0.75	0.521	0.25	0.50
H ₂ O	1·10 ⁻¹⁰	1·10 ⁻¹⁰	1·10 ⁻¹⁰	1·10 ⁻¹⁰	0.17
N ₂	1·10 ⁻⁴	1·10 ⁻⁴	1·10 ⁻⁴	1·10 ⁻⁴	2·10 ⁻³
H ₂ S	2·10 ⁻⁵	2·10 ⁻⁵	2·10 ⁻⁵	2·10 ⁻⁵	0.031
NH ₃	1·10 ⁻⁶	1·10 ⁻⁶	1·10 ⁻⁶	1·10 ⁻⁶	3.5·10 ⁻⁶

4.2 Integrated Super-dry and Tri-reforming with Fischer-Tropsch processes.

The second part of the problem focuses on integrating the selection of the two previous technologies with the production of FT fuels from syngas. The problem has been divided in two parts according to the operating mode in the reactor.

On the one hand, if the FT reactor operates at HT, the process shows a profit of $7 \cdot 10^{-4}$ per mol of biogas fed in the process. This process produces a large amount of HCB with short chain length that are less valuable than other fractions. However, the reduced income is balanced with a lower consumption of utilities. According to the process operation, the suggested biogas composition is 62% of CH₄ and 38% of CO₂. This biogas is processed selecting a TR reactor and the PSA system for removing the CO₂ in the tune-up section. As a result, the syngas obtained to be fed in the FT reactor has a ratio of 1.2. On the other hand, when the FT reactor operates at LT the profitability of the process is improved up to $2.2 \cdot 10^{-2}$ per mol of biogas fed in the process. The products obtained from this process are mainly gasoline, diesel and LPG. Thus, in spite of the higher consumption of utilities, the income is larger than in the previous mode and the process profitability is improved. Apart from the utilities, another characteristic variable is the biogas composition in the feed, similar to the previous one, 69% CH₄ and 31% CO₂. In this case, the TR reactor and PSA system for the removal of CO₂ are also selected, obtaining a syngas with a H₂:CO ratio of 1.

The optimization of the process is completed with an economic evaluation. For a plant fed with 12Mm³/y of biogas, the CAPEX is estimated to be \$8 M for the HT-FT process and \$19M for the LT-FT process. The production cost of the HT-FT process is estimated to be \$610/ton for LPG, \$2.57/gal for gasoline and \$3.02/gal for diesel. For the LT-FT process this production cost is estimated to be \$520/ton for LPG, \$1.25/gal for gasoline and \$1.67/gal for diesel. The production cost of the FT processes developed

can be scaled-up to a facility that processes 3100 kt/y of manure and compared with a previous renewable process as it is presented in Table 2. As a result from this comparison, it can be seen that the HT-FT and LT-FT are less competitive than the previous work (Hernández and Martín, 2017).

Table 2- Production costs of different processes for the production of fuels.

Process	Production cost.
HT-FT	\$5.4/gal
LT-FT	\$3.3/gal
Hernández and Martín (2017)	\$0.34/gal

5. Conclusions

This manuscript presents an optimization of biogas to syngas processes comparing super-dry and tri-reforming technologies. To optimize the TR process a parametric approach has been introduced since different O₂:biogas ratios are required. The results show that TR is always selected as the most profitable technology. However, SDR consumes more CO₂ in the reaction, being necessary further works to analyse its environmental impact. The different H₂:CO ratios are achieved by modifying the biogas compositions operating conditions and technologies in the tune-up section.

The work is completed integrating the syngas production section with two FT processes, at low and high temperature. The LT-FT shows to be more profitable than the HTFT process but none of the processes is not competitive with other renewable processes developed before.

References

- P. Balasubramanian, I. Bajaj, M.M.F. Hasan, 2018, Simulation and optimization of reforming reactors for carbon dioxide utilization using both rigorous and reduced models. *Journal of CO2 Utilization*, 23, 80-104.
- L.C. Buelens, V.V. Galvita, H. Poelman, C. Detavernier, G.B. Marin, 2016, Super-dry reforming of methane intensifies CO₂ utilization via Le Chatelier's principle. *Science*, 354, 449-452.
- R.Y. Chein, C.Y. Wang, C. Yu, 2017, Parametric study on catalytic tri-reforming of methane for syngas production. *Energy*, 118, 1-17.
- B. Hernández, E. León, M. Martín, 2017, Bio-waste selection and blending for the optimal production of power and fuels via anaerobic digestion. *Chemical Engineering Research and Design*. 121, May 2017, 163-172.
- B. Hernández, M. Martín, 2016, Optimal process operation for biogas reforming to methanol: effects of dry reforming and biogas composition. *Industrial and Engineering Chemistry Research*, 55, 23, 6677-6685.
- B. Hernández, M. Martín, 2017, Optimal Integrated Plant for Production of Biodiesel from Waste. *ACS Sustainable Chemistry & Engineering*, 5, 8, 6756-6567.
- B. Hernández, M. Martín, 2018, Optimization for biogas to chemicals via tri-reforming. Analysis of Fischer-Tropsch fuels from biogas. *Energy Conversion and Management*, 174, 998-1013.
- A. Vita, C. Italiano, D. Previtali, C. Fabiano, A. Palella, F. Freni, G. Bozzano, L. Pino, F. Manenti, 2018, Methanol synthesis from biogas: A thermodynamic analysis. *Renewable Energy*, 118, 673-684.
- A. Wellinger, J. Murphy, D. Baxter, 2013, *The biogas handbook: Science, production and applications*. Woodhead, Publishing.

Multi-objective spatio-temporal optimisation for simultaneous planning, design and operation of sustainable and efficient value chains for rice crop

Stephen S. Doliente,^{a,b} Sheila Samsatli^{a,*}

^a *Department of Chemical Engineering, University of Bath, Claverton Down, Bath BA2 7AY, United Kingdom*

^b *Department of Chemical Engineering, College of Engineering and Agro-Industrial Technology, University of the Philippines Los Baños, Batong Malake, Los Baños, Laguna 4031, Philippines*

**S.M.C.Samsatli@bath.ac.uk*

Abstract

The rice value chain, especially in the Philippines, can potentially progress in terms of efficiency and sustainability, as well as create more value by effectively utilising the crop residues of rice production. However, generating multiple products will lead to a complex decision-making process in supply chains, especially in the case of rice crop, which is vital for the Philippines' food security. Thus, systematic planning techniques are needed to address important decisions along the stages in rice value chains. This study presents a mixed integer linear programming (MILP) model developed for the planning, design and operation of multi-product rice value chains. In order to capture the spatial-dependencies of the problem, such as the candidate locations for rice farms and processing facilities, and location of demands, 81 cells represented the Philippines. The temporal aspect of the model considers a long planning horizon, out to 2050, and the time varying demands for white rice and the crop residues of farming and milling. The model determines design and operating decisions such as where to locate the farms and processing facilities, what products to produce, how to transport resources, among others. Different objectives are considered such as maximisation of the net present value and minimisation of CO₂ emissions. The Pareto set generated represents the optimal solutions representing the different trade-offs between economic gain and environmental protection.

Keywords: rice value chain optimisation, multi-product value chain, multi-objective optimisation, spatio-temporal modelling, mixed-integer linear programming

1. Introduction

Rice consumption in many developing countries of the tropics is rapidly growing due to rising population and increasing urbanisation. Compelled to secure sufficient rice supply, these nations had been enhancing farm productivity and expanding agricultural land. Despite resource scarcity, rice production in these nations has remained a highly land-use-, energy-, and water-intensive activity (Sims et al., 2015). Recently, extreme-weather events related to climate change have caused damage and losses to these nations' agricultural sectors such as rice. All of these drivers instil more pressure and inevitably disrupt the food-energy-water nexus that support rice value chains in the tropics (Keairns et al., 2016). Therefore, understanding and formulating better strategies in managing and

operating rice value chains are crucial. In the case of the Philippines, rice sufficiency improvements have yet to result in economic benefits due to mismatched policies and lack of infrastructure (Briones, 2014). Harvest losses and inefficient logistics interrupt the country's rice supply chain (Mopera, 2016). Rice cultivation is a major greenhouse gas emitter in the Philippines because the majority of the carbon-rich crop residues, rice straw and rice husk, are burnt and untapped. If these wasted resources are managed and valorised, the rice value chain can contribute to the country's economic and environmental sustainability. Motivated by the desire for rice value chains to be more secure, efficient, profitable and sustainable, the aim of this work is to develop a mixed integer linear programming (MILP) model for planning, design and operation of multi-product rice value chains. The multi-objective optimisation model is used to perform a number of case studies to determine the Pareto set of solutions that represent a compromise between economic and environmental criteria.

2. Problem statement

The problem involves simultaneous determination of design and operating decisions, such as: where to farm rice crop; how much farm land to allocate; what and how much resources to utilise and what products to generate (e.g. food, energy, fuels and chemicals); what conversion technologies to invest in and where to locate them; whether or not to densify/pre-process crop residues before conversion and/or transportation; and how to transport raw materials and distribute products to customers; all of these in order to maximise of the net present value of the value chain while at the same time minimising CO₂ emissions.

3. Mathematical model

The mathematical model was based on the Value Web Model (Samsatli & Samsatli, 2018; Samsatli et al., 2015), a spatio-temporal MILP model configured for the United Kingdoms' energy value chains for natural gas and wind power. For the first time, this model was applied to rice value chains with a vastly different configuration for the Philippines. A planning horizon of 32 years, from 2018 to 2050, was considered. The model comprised multiple time scales: planning periods $y \in \mathbb{Y}$, seasonal time steps $t \in \mathbb{T}$, day type of the week $d \in \mathbb{D}$ and hourly intervals $h \in \mathbb{H}$. For the spatial representation, Philippines was divided into 81 cells corresponding to its provinces (Fig. 1). Each cell, $z \in \mathbb{Z}$, has information on the available farm land, the paddy rice yield, the cost of paddy rice production, existing technologies, if any, and existing transport infrastructures, if any. In addition, each cell has coordinates (x_z, y_z) calculated from the population density, in order to represent the demand centres and to calculate the transport distance $d_{zz'}$ (km) from cell z to cell z' .

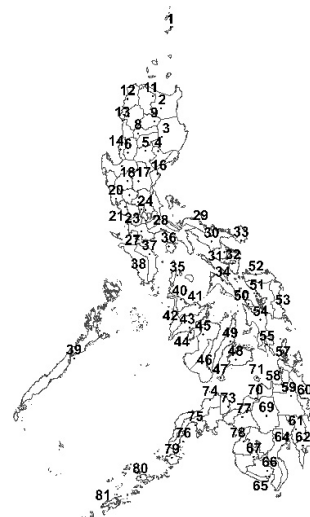


Figure 1. Spatial representation of the Philippines in the model

3.1. Objective function

Eq. (1) shows the objective function to be minimised:

$$Z = \sum_{my} w_m (J_{my}^P + J_{my}^Q + J_{my}^{fp} + J_{my}^{fq} + J_{my}^{vp} + J_{my}^{vq} + J_{my}^i + J_{my}^e + J_{my}^u - J_{my}^{Rev}) \quad (1)$$

Each term inside the parenthesis represents an impact in year y on performance metrics m . These include the following: the total net present capital impact of technologies for conversion J_{my}^P and transport J_{my}^Q ; the total net present fixed operating impact of technologies for conversion J_{my}^{fp} and transport J_{my}^{fq} ; the total net present variable operating impact of technologies for conversion, J_{my}^{vp} and transport J_{my}^{vq} ; the total net present impact of importing resources J_{my}^i ; the total net present impact of exporting resources J_{my}^e ; the total net present impact of utilising resources J_{my}^u ; and the total net present revenue from the sale of resources (e.g. white rice, bio-electricity, biofuels, etc.) J_{my}^{Rev} .

3.2. Constraints

Eq. (2) expresses the resource balance that considers various input and output terms for every resource $r \in \mathbb{R}$ in cell z during hour h of day type d in season t of planning period y . Eq. (3) states that the rate of utilisation, U_{rzhdt} , cannot exceed the maximum availability u_{rzhdt}^{max} (t/h or MW). Eq. (4) states that the total amount of biomass, represented by index c , utilised in each season cannot exceed the seasonal availability. Eqs. (5) and (6) are the local and national land footprint constraints, which respectively ensure that the allocated area A_{czt}^{Bio} (ha) for biomass c in cell z during planting period y , cannot be more than the maximum portion of suitable area in each cell z ; and total allocated area for biomass cannot be more than the maximum portion of the total suitable area at the national level. The net rate of resource production (or consumption) P_{rzhdt} (t/h or MW) is expressed by Eq. (7); where α_{rpy} is the conversion factor of a resource r in technology $p \in \mathbb{P}$ in planning period y . The rate of operation of a single conversion technology \mathcal{P}_{pzhdt} is limited by its minimum and maximum capacities, p_p^{\min} and p_p^{\max} , respectively, as given by Eq. (8). Furthermore, Eq. (9) states that the number of commercial conversion technologies invested N_{pzy}^{PC} cannot exceed the maximum number BR_{py} that can be built in planning period y . The net rate of transport Q_{rzhdt} (t/h or MW) of resource r between cells z and z' is given by Eq. (10) where $\bar{\tau}_{lr, dst, y}$ and $\bar{\tau}_{lr, dst, y}$ are the conversion factors for distance-dependent and distance-independent transport technology $l \in \mathbb{L}$ of resource r during planning period y , respectively. Eqs. (11) and (12) limit the operation of a transport technology $q_{lzz'ndty}$ up to its maximum capacity and the total operation rate of all transport technology up to the capacity of infrastructure $b \in \mathbb{B}$, respectively. The model categorises between two demands: those that must always be complied D_{rzhdt}^{comp} (t/h or MW) and those that may be optionally complied D_{rzhdt}^{opt} . Since the optimisation determines what and how much product to generate from a resource and what demands to satisfy, Eq. (13) determines the optional demand satisfied D_{rzhdt}^{sat} . Lastly, the rate of import I_{rzhdt} in Eqs. (14) and rate of export E_{rzhdt} in Eq. (15) cannot exceed the maximum import and export capacities I_{rzhdt}^{max} and E_{rzhdt}^{max} , respectively (all in t/h or MW).

$$U_{rzhdt} + I_{rzhdt} + P_{rzhdt} + Q_{rzhdt} \geq D_{rzhdt}^{comp} + D_{rzhdt}^{sat} + E_{rzhdt} \quad (2)$$

$$\forall r \in \mathbb{R}, z \in \mathbb{Z}, h \in \mathbb{H}, d \in \mathbb{D}, t \in \mathbb{T}, y \in \mathbb{Y} \quad (3)$$

$$U_{rzhdt} \leq u_{rzhdt}^{max} \quad \forall r \in \mathbb{R} - \mathbb{C}, z \in \mathbb{Z}, h \in \mathbb{H}, d \in \mathbb{D}, t \in \mathbb{T}, y \in \mathbb{Y} \quad (4)$$

$$\sum_{hd} U_{czt} n_h^{hd} n_d^{dw} n_t^{wt} \leq A_{czt}^{Bio} A_{czt}^{Bio} \quad \forall c \in \mathbb{C}, z \in \mathbb{Z}, t \in \mathbb{T}, y \in \mathbb{Y} \quad (5)$$

$$\sum_{hd} A_{czt}^{Bio} \leq f_{zy}^{loc} A_{zy}^{Bio, max} \quad \forall z \in \mathbb{Z}, y \in \mathbb{Y} \quad (6)$$

$$\sum_{cz} A_{czt}^{Bio} \leq f_y^{nat} \sum_z A_{zy}^{Bio, max} \quad \forall y \in \mathbb{Y} \quad (7)$$

$$P_{rzhdy} = \sum_p \mathcal{P}_{pzhdy} \alpha_{rpy} \quad \forall r \in \mathbb{R} - \mathbb{C}, z \in \mathbb{Z}, h \in \mathbb{H}, d \in \mathbb{D}, t \in \mathbb{T}, y \in \mathbb{Y} \quad (7)$$

$$N_{pzy}^{PC} p_p^{\min} \leq \mathcal{P}_{pzhdy} \leq N_{pzy}^{PC} p_p^{\max} \quad \forall p \in \mathbb{P}^C, z \in \mathbb{Z}, h \in \mathbb{H}, d \in \mathbb{D}, t \in \mathbb{T}, y \in \mathbb{Y} \quad (8)$$

$$\sum_c N_{pzy}^{PC} \leq BR_{py} \quad \forall p \in \mathbb{P}^C, y \in \mathbb{Y} \quad (9)$$

$$Q_{rzhdy} = \sum_{z' | \forall z' = 1} \sum_{l \in \mathbb{L}} [(\bar{\tau}_{lr, dst, y} + \bar{\tau}_{lr, dst, y} d_{zz'}) q_{lzz'zhdy}] + \sum_{z' | \forall z' = 1} \sum_{l \in \mathbb{L}} [(\bar{\tau}_{lr, dst, y} + \bar{\tau}_{lr, dst, y} d_{zz'}) q_{lzz'hdy}] \quad (10)$$

$$\forall r \in \mathbb{R}, z \in \mathbb{Z}, h \in \mathbb{H}, d \in \mathbb{D}, t \in \mathbb{T}, y \in \mathbb{Y}$$

$$q_{lzz'hdy} \leq \sum_{b \in \mathbb{B}} q_l^{\max} N_{bzz'y}^B |LB_{lb} = 1 \wedge v_{zz'} = 1 \quad \forall l \in \mathbb{L}; z, z' \in \mathbb{Z}; h \in \mathbb{H}, d \in \mathbb{D}, t \in \mathbb{T}, y \in \mathbb{Y} \quad (11)$$

$$\sum_{l \in \mathbb{L}} q_{lzz'hdy} LB_{lb} \leq b_b^{\max} N_{bzz'y}^B \quad \forall b \in \mathbb{B}; z, z' \in \mathbb{Z}; h \in \mathbb{H}, d \in \mathbb{D}, t \in \mathbb{T}, y \in \mathbb{Y} \quad (12)$$

$$D_{rzhdy}^{\text{sat}} \leq D_{rzhdy}^{\text{opt}} \quad \forall r \in \mathbb{R}, z \in \mathbb{Z}, h \in \mathbb{H}, d \in \mathbb{D}, t \in \mathbb{T}, y \in \mathbb{Y} \quad (13)$$

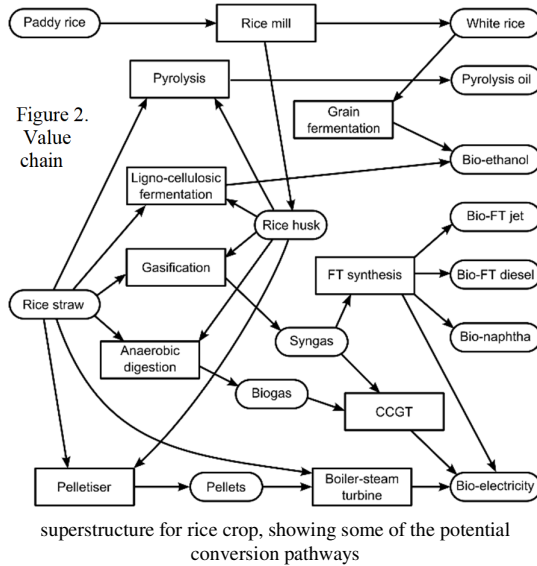
$$I_{rzhdy} \leq I_{rzhdy}^{\max} \quad \forall r \in \mathbb{R}, z \in \mathbb{Z}, h \in \mathbb{H}, d \in \mathbb{D}, t \in \mathbb{T}, y \in \mathbb{Y} \quad (14)$$

$$E_{rzhdy} \leq E_{rzhdy}^{\max} \quad \forall r \in \mathbb{R}, z \in \mathbb{Z}, h \in \mathbb{H}, d \in \mathbb{D}, t \in \mathbb{T}, y \in \mathbb{Y} \quad (15)$$

3.3. Network superstructure

Whereas food only (i.e. white rice) is produced in conventional rice value chains, many non-food products can also be generated as supplementary sources of income. The value chain superstructure in Fig. 2 shows potential pathways for multi-product generation from rice crop and its residues, e.g. the rice straw from farming and the rice husk from milling. The residues can be processed via thermo- and bio-chemical conversion technologies such as boiler-steam turbine, anaerobic digestion and combine cycle gas turbine (CCGT) for energy (i.e. bio-electricity); lignocellulosic (LC) fermentation and pyrolysis for fuels (i.e. bio-ethanol, pyrolysis oil); and gasification and Fischer Tropsch (FT) synthesis for chemicals (i.e. bio-naphtha).

The value chain (Fig. 2) also includes a pelletiser for the densification of the residues. The inputs to the optimisation model include the spatial and temporal availability of paddy rice and product demands (white rice, bio-electricity, bio-ethanol and bio-naphtha). The model also requires the characteristics of each conversion and transport technologies (capital expenditure, operation and maintenance costs, conversion factors etc). The key constraints are given in Section 3.2. For a given objective (maximise NPV or minimise CO₂ emissions), the model determines the optimal location for rice crop farming and the sites of the conversion technologies. The demands for food has to be satisfied all the time but the model can choose whether to produce non-food products from rice straw and/or rice husk, up to a specified maximum demand for a non-food product. Furthermore, the model also decides between barge and/or truck transport of white rice and/or paddy rice and the operation of these transport networks.



3.4. Multi-objective optimisation

The model was formulated as a multi-objective optimisation problem to allow the evaluation of trade-offs between conflicting objectives (Samsatli & Samsatli, 2018). The weighting method was used to transform the multi-objective optimisation problem into a single objective optimisation problem using different combinations of the weighting factors for the economic and environmental impacts. The weighting method can be expressed as $\min Z = \sum_{m=1}^N w_m Z_m$, where Z_m represents the individual impacts; w_m are the weighting factors, which can assume values between 0 and 1, with $\sum_{m=1}^N w_m = 1$. The optimal solutions obtained at different combinations of the weighting factors form a Pareto set, which represents the compromise between the different objectives (Ang et al., 2010). In this study, the performance metrics are $m \equiv \{Cost, CO_2\}$. Therefore, when $w_m \equiv \{1, 0\}$, the problem is the maximisation of net present value; and when $w_m \equiv \{0, 1\}$ the problem is the minimisation of CO₂ emissions.

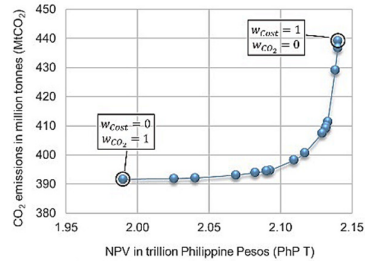


Figure 3. Pareto set for the multi-objective rice value chain optimisation problem

4. Case studies

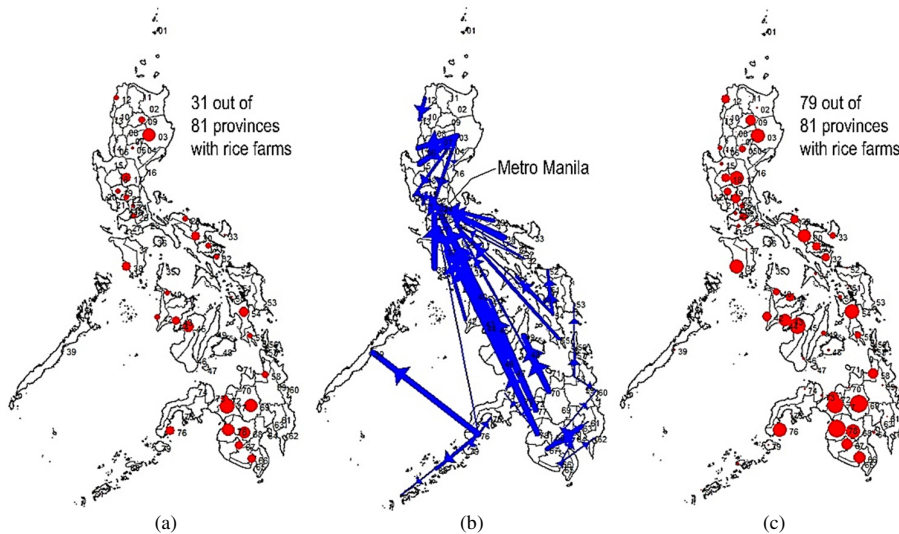


Figure 4. Optimisation results: (a) allocated farm lands in case 1; (b) transport of white rice by barges in case 1; and (c) allocated farm lands in case 2.

Two cases have been considered for this paper. Case 1 examines the optimal solution for maximising NPV and minimising CO₂ emissions for the Philippine rice value chains considering food production only. The Pareto set generated in Fig. 3 shows the compromise between these two objectives for a planning horizon of 32 years with white rice demand of 11 Mt/yr. The highest point on the right represents the optimal solution for maximising NPV. For this solution, the NPV is PhP 2.14 T (USD 40.26 bn) and the CO₂ emissions are 439 MtCO₂. The lowest point in the left represents the optimal solution for minimising CO₂ emissions, with NPV of PhP 1.99 T (USD 37.43 bn) and CO₂

emissions of 392 MtCO₂. Moving from the bottom-left of the curve to the top-right represents solutions with increasing profit at the expense of higher CO₂ emissions. Depending on the policies, this Pareto set presents an opportunity for the Philippines to decarbonise its current rice value chain. The model has also determined barges as the main mode of transport mode in delivering white rice to provinces with the highest demand (for example Metro Manila the capital city in cell 23), as shown in Fig. 4(b). Compared to transport by truck, the cost and CO₂ emissions of transport by barge is significantly lower, which is more beneficial for an archipelagic country like the Philippines. Furthermore, compared to the existing trend of farming rice, despite suitability, in all provinces of the country (e.g. using >50% of the total farm land area), the model recommends rice crop farming in selected provinces of the country with high paddy rice yield and low farming cost as shown in Fig. 4(a). The Case 2 study determined the profitability of a multi-product rice value chain wherein demand for white rice at 11 Mt/yr was always satisfied while annual demands for bio-electricity, bio-ethanol and bio-naphtha were *optionally* satisfied at up to 908 GWh/yr, 2.1 TWh/yr, and 17 GWh/yr, respectively. The model revealed that this multi-product rice value chain is profitable at NPV of PhP 2.41 T (or USD 45 bn) with 1.3 GtCO₂ emissions. In contrast to Case 1, the model suggested rice crop farming throughout the country (rice farms are now present in 79 out of 81 provinces – see Fig. 4(c)). When transformed into a multi-product rice value chain, the currently food-only rice value chain in the Philippines can become more profitable at PhP 0.6 m/ha (USD 11 k/ha), a 12% increase in NPV, since the non-food products can become additional revenue sources. Furthermore, the model recommended an optimal integrated rice value chain with *full* utilisation of rice husk and rice straw processed by LC fermentation, gasification, FT synthesis, boiler-steam turbine and CCGT. The model sited these technologies locally where the resources are available. Finally, the model also recommended transport by barge for both white rice and paddy rice. Paddy rice transport facilitated movement of rice husk to comply with demands of non-food products.

5. Conclusions

A multi-objective, spatio-temporal MILP model was developed for the simultaneous planning, design and operation of multi-product rice value chains. For the food-only scenario in the Philippines, the model generated a Pareto set representing the trade-offs between economic gain and environmental protection. The model recommended rice crop farming in provinces with high yields and low farming cost. To meet the demand for white rice, model showed that it is more cost-effective and environmentally sound to use barge over truck. For the multi-product rice value chain for the Philippines, the model was able to demonstrate that it was more profitable over a food-only rice value chain. Furthermore, advanced biomass conversion technologies to process rice straw and rice husk are going to be important for the feasibility of a multiproduct rice value chain.

References

- Ang, S. M. C., Brett, D. J. L., & Fraga, E. S., 2010, *Journal of Power Sources*, 195, 2754-2763.
- Briones, R. M., 2014, Philippine Institute for Development Studies. Discussion Paper Series No. 2015-04.
- Keairns, D. L., Darton, R. C., & Irabien, A., 2016, *Annual Review of Chemical and Biomolecular Engineering*, 7, 239-262.
- Mopera, L. E., 2016, *Journal of Developments in Sustainable Agriculture*, 11, 8-16.
- Samsatli, S., & Samsatli, N. J., 2018, *Applied Energy*, 220, 893-920.
- Samsatli, S., Samsatli, N.J., & Shah, N., 2015, *Applied Energy*, 147, 131-160.
- Sims, R., Flammini, A., Puri, S., & Bracco, S., 2015, In: *Food and Agriculture Organization United States Agency for International Development*. ISBN 978-92-5-108959-0.

Estimating mixture properties from batch distillation using semi-rigorous and rigorous models

Michael Bortz,^{a,*} Raoul Heese,^a Alexander Scherrer,^a Thomas Gerlach,^b Thomas Runowski^b

^a*Fraunhofer Institute for Industrial Mathematics, Fraunhofer Platz 1, 67663 Kaiserslautern, Germany*

^b*Bayer AG, Engineering & Technology, 51368 Leverkusen, Germany*

**michael.bortz@itwm.fraunhofer.de*

Abstract

Batch distillation experiments on laboratory scale are conducted in order to estimate NRTL parameters describing thermodynamic mixture properties. For this purpose, distillate composition and column temperatures are measured as functions of the batch hold-up and then used to fit model parameters with a non-linear regression approach. Two different models are presented, a semi-rigorous model relying on the assumption of constant molar overflow and a rigorous model from the commercial flowsheet simulator Aspen Custom Modeler. For both models, the NRTL parameters are estimated with good agreement to the experimental data. However, the semi-rigorous model is much simpler and therefore requires far less computational effort.

Keywords: batch distillation, constant molar overflow, non-linear regression, NRTL parameter estimation

1. Introduction

The knowledge of thermodynamic mixture properties is most relevant for reliable distillation process simulations. For many industrial applications, lab scale batch distillation experiments can be used to gain information about the separation behavior of complex multi-component mixtures. In this contribution, we address the question to which extent it is possible to estimate NRTL parameters reliably from this data. The estimation of such parameters from mixture properties is a numerically challenging problem as discussed by Gau et al (2000).

A detailed simulation of a distillation process based on a rigorous model requires expert knowledge for the fine-tuning of the model and is often computationally demanding. In order to reduce the complexity of the problem, a semi-rigorous model is set up based on the equilibrium stage model assuming constant molar overflows within the column and empty column hold-ups. This leads to decoupled mass and energy balances and therefore to considerable simplifications of the MESH equations, and allows for a product stream composition parametrized by the batch hold-up. Such a simplification has already been discussed by Doherty and Perkins (1978) in detail and has been applied to batch distillation column models by Dongen and Doherty (1985), however, with an additional simplification of the column profile.

Both semi-rigorous and rigorous model are used to estimate NRTL parameters from minimizing the sum of squared residuals between calculated and experimentally measured compositions and temperatures. For this purpose, the semi-rigorous model makes use of Matlab's native Levenberg-Marquardt optimizer. The rigorous model is realized in a prototypic software framework, which combines numerical simulation with Aspen Custom Modeler based on an implementation in its specific modeling language with a gradient-based optimization routine, see Schittkowski (2009). This software feeds NRTL parameters into a simulation instance and obtains simulation results from there, computes function values and numerical gradients for the optimization routine and obtains updated NRTL parameters from there, see Figure 1.

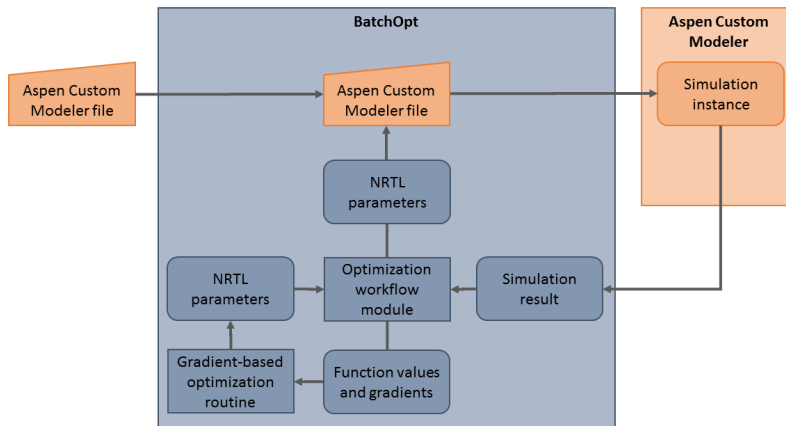


Figure 1: Software framework BatchOpt with its interfaces to Aspen Custom Modeler and gradient-based optimization routine.

This paper is organized as follows: Section 2 presents the semi-rigorous model and derives the equations used for the numerical simulation. Section 3 contains a short account on the experimental setup in the laboratory and compares measured data with simulated data from the two models using NRTL parameters from literature. Section 4 contains the results obtained from solving the corresponding regression problem. The paper ends with a conclusion.

2. Semi-rigorous model

The rigorous model used to model a batch distillation is based on coupled theoretical equilibrium stages within the MESH equation framework, see Stichlmair and Fair (1998). This means that each equilibrium stage i is described by variables H_i (liquid hold-up in kmol), V_i (vapour stream leaving stage i , in kmol/h), L_i (liquid stream leaving stage i , in kmol/h), x_i (composition of L_i in mol/mol), y_i (composition of V_i in mol/mol), temperature T_i (in K) and pressure p_i (in bar). The stages are numbered such that $i = 0$ corresponds to the batch, and $i = N$ corresponds to the topmost stage. Above the topmost stage a total condenser ($i = N + 1$) is fed with the vapor stream V_N and a liquid distillate stream D with composition $x_{N+1} = x_D$ is withdrawn in addition to the liquid backflow L_{N+1} to the topmost stage. The reflux ratio $R = L_{N+1}/D$ describes the relation of these streams. To model the hold-up in each equilibrium stage as a function of time, the

MESH-equations must be combined with a suitable hydrodynamic model. For a detailed discussion of the rigorous model, we refer to the aforementioned literature.

For the semi-rigorous model the stage hold-ups in the packed column are neglected based on the assumption of a comparatively small packing hold-up in comparison to the pot. Therefore, the $H_{i>0}$ are dropped such that no further model of the column hydraulics is required. Component Mole balances then read

$$\begin{aligned} \frac{d}{dt}(\mathbf{x}_0 H_0) &= -D\mathbf{x}_D \\ V_i \mathbf{y}(\mathbf{x}_i) &= L_{i+1} \mathbf{x}_{i+1} + D\mathbf{y}(\mathbf{x}_N), i = 0, \dots, N-1 \\ D\mathbf{x}_D &= V_N \mathbf{y}(\mathbf{x}_N) - L_{N+1} \mathbf{x}_D \end{aligned}$$

The first equation contains the total balance, the second the balances for the intermediate stages and the last for the top stage. Here the VLE relation $\mathbf{y} = \mathbf{y}(\mathbf{x})$ has been used. Dependence on the constant pressure $p_i = p$ and stage temperatures T_i have not been included in order to keep the notation simple. The total condenser enforces $\mathbf{y}(\mathbf{x}_N) = \mathbf{x}_{N+1} = \mathbf{x}_D$. In the next step, the approximation of constant molar overflows is made, which eliminates the stage dependence of internal streams, resulting in constant streams $V_i \equiv V$ and $L_i \equiv L$. Furthermore, a new pseudo-time variable $\tau = \ln \frac{H_0(t=0)}{H_0(t)}$ is introduced in order to parametrize the complete solution in terms of the relative batch hold-up. Time dependence is therefore completely eliminated, which means that energy balance is decoupled from mass balances.

These steps yield

$$\begin{aligned} (R+1)\mathbf{y}(\mathbf{x}_i) - R\mathbf{x}_{i+1} &= \mathbf{x}_0 - \frac{d}{d\tau} \mathbf{x}_0, i = 0, \dots, N-1 \\ \mathbf{y}(\mathbf{x}_N) &= \mathbf{x}_0 - \frac{d}{d\tau} \mathbf{x}_0 \end{aligned}$$

This differential-algebraic system of equations constitutes the semi-rigorous model. It is completely determined once R and $\mathbf{x}_0(t=0)$ are given.

3. Experimental setup

The experimental data is obtained from a real experiment in an industrial lab. The batch distillation column that was used for the experiment is a DN 50 column with 1.3 m of random packing (glass rings, 4 mm diameter, 4 mm length). Approximately 2 kg of the initial solvent mixture was prepared for the experiment. The mixture consisted of 30 wt% acetone, 30 wt% methanol, and 40 wt% butanone. The distillation was performed at 1 bar. During the start-up at the beginning of the experiment and after an intermediate shut-down the column was initialized at infinite reflux ratio R , otherwise a constant reflux ratio of 5 was applied. The medium temperature of the sump heat bath was continuously adjusted to ensure a constant pressure drop within the expected limits of the packing. The head temperature as well as the pot vapor and liquid temperatures were continuously logged. The distillate was fractionated into approximately 40 separate samples, which were further analyzed using GC analyses with an FID-detector. Additional analyses were performed of the pot content before and after the distillation to ensure agreement with the

mass balance. Feeding the semi-rigorous and the rigorous model with NRTL parameters from the Aspen data base yields good accordance with the measured data, see Figure 2.

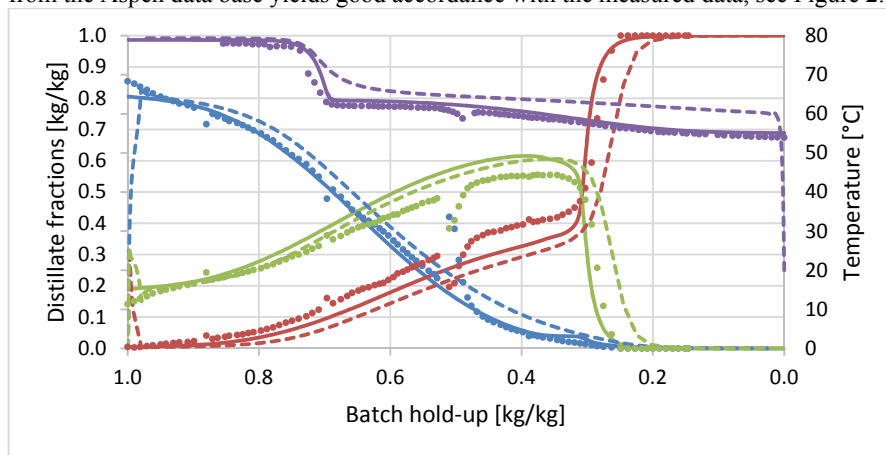


Figure 2: Distillate concentrations and head temperatures (violet) for initial NRTL parameters from experiment (dots), semi-rigorous model (solid lines) and rigorous model (dashed lines) for Acetone (blue), Methanol (green) and MEK (red).

The semi-rigorous model clearly achieves a better prediction of the experimental data than the rigorous model. The reason for this surprising behaviour is unknown to the authors, but might be an interesting starting point for further studies. Nevertheless, both models appear suitable for a fitting of NRTL parameters. This presumption will be confirmed in the next section.

4. Fitting of NRTL parameters

We exemplarily fit the two NRTL parameters B_{12} and B_{21} describing the mutual interactions between Acetone and Methanol and use fixed literature values for all other NRTL parameters. Thus, the joint fitting parameter $\theta = (B_{12}, B_{21})$ is two-dimensional and the regression problem can be formulated as

$$\hat{\theta} = \operatorname{argmin}_{\theta} \sum_n w_n |d_n - m_n(\theta)|^2$$

Here $\hat{\theta}$ denotes the optimal NRTL parameters, d_n describes the measured data point n and $m_n(\theta)$ the corresponding calculated data point obtained from the chosen model (semi-rigorous or rigorous) for a specific choice of θ . The sum index n over all measured mixture concentrations in distillate x_D and measured head temperatures T_N . The non-negative weights w_n allow for a tuning of the influence of different measurement points on the fitting result.

An appropriate pre-processing of the measurement data has been performed in such a way that outliers are omitted and all data points operate on the same scale. The weights w_n have been defined proportional to the inverse density of the neighboring data points. This choice compensates the varying density of the data with respect to the batch hold-up and therefore avoids an overfitting of densely measured regions. As an initial guess for the fitting parameters we choose deliberately displaced values $\theta_{\text{guess}} = (-50, -500)$ in

relation to the Aspen values $\Theta_{\text{Aspen}} = (102, 114)$. In case of the rigorous model fit we have neglected the initial data points d_n in the sum of squared residuals so that the transient behavior of the simulation has no effect on the fitting. Moreover, we also reduced the total number of data points in order to reduce the influence of numerical noise on numerical gradient computation and thereby improve the convergence of the optimization process. Such a data-dependent noise arises because the Aspen simulation has a relatively low numerical accuracy which can accumulate with an increasing number of sampling points in the regression problem. To suppress this effect we have excluded all temperature data and used only about one sixth of the measured concentrations suitably distributed over the hold-up. A major benefit of our semi-rigorous model becomes apparent: Although the rigorous model might in principle lead to simulations which are closer to the physical reality, its numerical evaluation can still be less precise for practical purposes than a simplified model.

The fitting results are shown in Figures 3 and 4. We find that both the semi-rigorous and the rigorous model lead to a reasonably good fit.

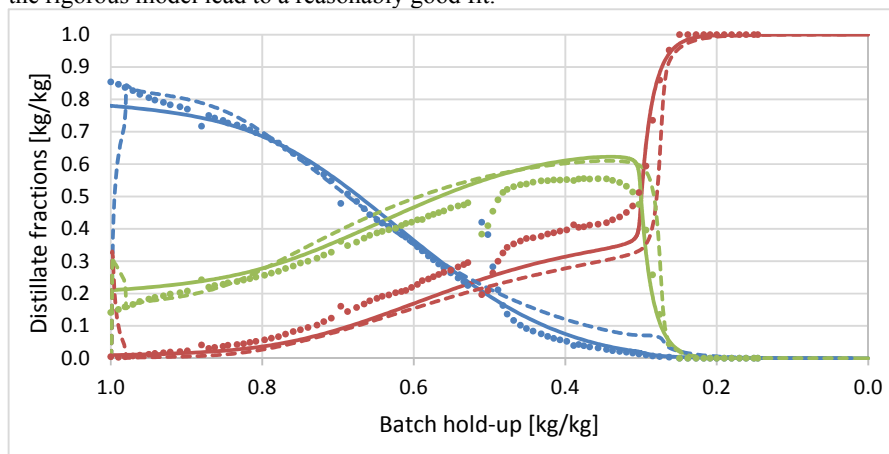


Figure 3: Distillate concentrations for fitted NRTL parameters from experiment (dots), semi-rigorous model (solid lines) and rigorous model (dashed lines) for Acetone (blue), Methanol (green) and MEK (red).

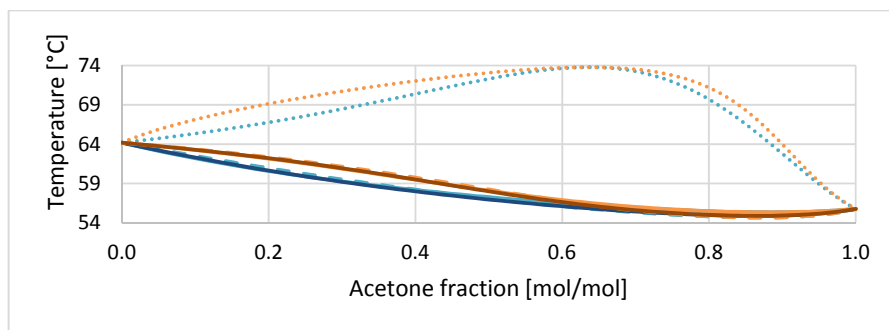


Figure 4: Phase diagram with liquid (blue) and vapour (orange) Acetone fractions for initial (dotted lines) and literature (solid lines in dark color) NRTL parameters and NRTL parameters fitted with semi-rigorous (solid lines) and rigorous model (dashed lines).

Summarized, starting from the initially chosen parameters $\Theta_{\text{guess}} = (-50, -500)$ we have recovered two different sets of optimal parameters $\hat{\Theta}_{\text{semi-rigorous}} = (-57, 284)$ and $\hat{\Theta}_{\text{rigorous}} = (272, -36)$, respectively, from the two different models by numerically solving a regression problem with data from a real experiment. Despite the quality of the fits, it is interesting to mention that the two resulting sets of parameters are different and do both not correspond to the original values from the Aspen data base $\Theta_{\text{Aspen}} = (102, 114)$. This ambiguity of the NRTL parameters is well-known and poses a major challenge for their estimation, see Gau et al. (2000). Further research would be required to analyze in detail to which extend the resulting parameters depend on the chosen models or the formulation of the regression problem.

5. Conclusions

Using the approximation of constant molar overflow we have derived a semi-rigorous batch distillation model for which energy balances are decoupled from mass balances. This approach yields a simplified system of differential-algebraic equations, where distillation time is replaced by the relative batch hold-up. We have shown that although evaluations of this semi-rigorous model require far less computational effort than evaluations of a rigorous model from a commercial flowsheet simulator, it is still able to predict the experimental data from an industrial lab with equally good precision. Furthermore, we have used both semi-rigorous and rigorous model to successfully fit NRTL parameters to the experimental data by means of a non-linear regression approach as a proof of concept. Our results highlight the ambiguity of the NRTL parameters and show that our semi-rigorous model can in practice be superior to the rigorous model despite its simplifications.

In conclusion, the semi-rigorous model approach presented herein allows for estimation of thermodynamic mixture properties based on experimental data from batch distillations using a packed column with multiple stages.

References

- M. F. Doherty, J. D. Perkins, 1978, On the Dynamics of Distillation Processes – I, Chem. Eng. Science, 33, 281-301
- D. Van Dongen, M.F. Doherty, (1985), Design and synthesis of homogeneous azeotropic distillations. 1. Problem formulation for a single column. Industrial & Eng. Chem. Fund. 24
- C.-Y. Gau, J.F. Brennecke, M. A. Stadtherr, 2000, Reliable nonlinear parameter estimation in VLE modeling, Fluid Phase Equilibria 168, 1-18
- H.Z. Kister, 1992: Distillation Design, McGraw-Hill Education, 510-512
- K. Schittkowski, 2009, NLPQLP: A Fortran implementation of a sequential quadratic programming algorithm with distributed and non-monotone line Search - User's guide, Version 3.1, Technical report, Dep. of Comp. Science, University of Bayreuth
- J. G. Stichlmair and J. R. Fair, 1998, Multistage Batch Distillation in Distillation – Principles and Practices, 284-327
- E. F. Wijn, 1999, Weir flow and liquid height on sieve and valve trays, Chem. Eng. Journal 73, 191-204

The Effect of Indirect GHG Emissions Costs on the Optimal Water and Energy Supply Systems

Negar Vakilifard, Parisa A. Bahri*, Martin Anda, Goen Ho

School of Engineering and Information Technology, Murdoch University, 90 South Street, Murdoch, Perth, Western Australia 6150, Australia

P.Bahri@murdoch.edu.au

Abstract

This study investigates the effect of indirect greenhouse gas (GHG) emissions on the optimal long-term planning and short-term operational scheduling of a desalination-based water supply system. The system was driven by grid-electricity and surplus output from residential rooftop photovoltaics to deliver water and energy to urban areas. The interactive two-level mixed integer linear programming model took into account demands, system configurations, resources capacities and electricity tariffs as well as GHG emission factor associated with the source of grid electricity. Both system and carbon abatement costs were considered in the formulation of the objective function. The optimal decisions for Perth (Australia) resulted in \$47,449,276 higher discounted total cost but 51,301.3 tCO₂eq less GHG emissions over 15 years planning horizon compared to when only system costs were minimised. Finally, the predominant effect of the indirect GHG emissions costs over system costs on the optimal solutions indicated their high sensitivity towards the source of purchased grid electricity.

Keywords: Grid electricity, Photovoltaics, GHG emissions, Desalination, Optimisation.

1. Introduction

Climate change and increasing water demand in urban areas have made it inevitable to incorporate drought-proof technologies such as desalination in water supply systems. However, meeting their intensive energy demand from fossil-fuel sources leads to higher indirect greenhouse gas (GHG) emissions, which adversely affects the existing water resources and therefore adds further complexities to sustainable supply. Considering renewable energy sources in the energy mix of this water supply option, therefore, could be a potential solution to decrease this effect.

In (Vakilifard et al., 2017), we proposed the idea of employing surplus residential grid-connected photovoltaics (PVs) output in conjunction with grid electricity to drive urban desalination-based water supply system. Using this source of energy not only assists in sustainably meeting the water-related energy demand but also mitigates the barrier of increasing the PVs installation to the existing electrical grid. In (Vakilifard et al., 2018), we developed a mixed integer linear programming (MILP) model to provide optimal strategic decisions of such water supply system incorporating short-term operational scheduling considering PV installation density as a parameter for any given year. In this paper, we extended the model to also investigate the effect of indirect GHG emissions costs associated with purchasing grid electricity on the optimal solutions and to determine to what extent they vary by the source of this energy. Additionally, the interactive effect of added water-related energy demand and installation density (as variable) was addressed through the two-run solving strategy. The results for an urban area located in the north-western corridor of Perth (Australia) were then discussed.

2. Problem statement

The problem was defined in three time frames (yearly, seasonal and hourly) for the planning horizon of 15 years (beginning from 2017). Water and energy needs were determined in 4 distinct zones in the studied area based on the demands per capita, annual population growth and service area of zone substations using ArcGIS 10 integrated with Excel analysis. It was assumed that a decentralised water supply system consisting of desalination plants, storage tanks, and a pipeline network delivers water to the zones. Plants were presumed to be operated in flexible (hourly) mode. The extra water could be desalted when renewable energy was available and could be stored for later use. Plant capacities were selected from 6 discrete values (20,000-120,000 m³/day) considering the plant factor of 0.85. For storage tanks, the capacities were chosen from 10,000 and 20,000 m³. Two pipeline capacities associated with the diameters of 30 and 54 in were also taken into account. The potential locations of water supply components in each zone, energy consumption per unit of water produced, stored and distributed as well as the capital and operational and maintenance (O&M) costs were according to (Vakilifard et al., 2018). Grid electricity and PV output supplied residential and water-related electricity demands. The maximum grid electricity that could be delivered to each zone was ascertained based on the associated substations capacities. The maximum capacity of available renewable energy was achieved based on the performance analysis of a 4 kW PV system output conducted in system advisor model (Vakilifard et al., 2017) and the installation density. The latter is the number of households equipped with PV systems in each zone divided by the total number of households and was determined by the model considering the economic-subjectivity index.

This index, in fact, is the product of economic and subjectivity indexes accounting for the economic preference of PV uptake and households' free will, respectively. To determine the economic index, Excel analysis was done based on the methodology described in (Miranda et al., 2015). This binary index is considered to be 1 if it is beneficial to install a PV system. The subjectivity index could be determined by the decision maker and could get any value between 0 and 1. It is the ratio of the households who decide to uptake PV systems (in case it is economically beneficial) to the total households. In this study, it was assumed the economic-subjectivity index is 1 meaning that in case it is economical to install a PV system, all households would decide to be equipped with one. Grid electricity price tariffs as well as the net feed-in tariff were taken from Synergy, the electricity retailer of Perth. The real discount rates for residential and business sectors were adopted from (AEC, 2017; ERA, 2017). The GHG emission factor of 0.7 for purchasing grid electricity from the south west interconnected system (SWIS), the electricity network in Perth, was adopted from (DEE, 2017). It is to be noted that this emission factor is only associated with the environmental impact of the fuels combustion in stationary sources (operational stage). The cost of carbon abatement was considered \$ 40/tCO₂eq, taken from (WSAA, 2012). All cost data was converted to 2017 real Australian dollar using appropriate exchange rates from (RBA, 2017).

3. Optimisation strategy

The model was formulated as a two-level MILP model. In the first level of optimisation, the objective function maximised the economic benefits for the households equipped with PV systems (z_1). This included savings from avoiding purchasing grid electricity as well as revenues from feeding surplus PV output back into the grid. The outcome of this level of optimisation, namely PV installation density, share of grid electricity in

supplying residential energy demand and surplus PV output, were introduced to the level-two optimisation where the optimal decisions for the water supply system were achieved. The objective function at this stage concerned minimisation of the discounted total cost of the water supply system including indirect GHG emissions costs associated with purchasing grid electricity for water supply (z_2). The model constraints of the level-one optimisation are presented in Eqs. (1)-(10). The constraints of level-two optimisation were based on our previous study (Vakilifard et al., 2017, 2018).

$$z_1 : Max \sum_t DF_t^r \cdot \sum_s nd_s \cdot \left[\sum_i \sum_b Ce_{t,s,b}^r \cdot RE_{t,i,s,b}^r + Cr_t \cdot Surp_{t,i,s,b} \right]$$

$$z_2 : Min \sum_t DF_t^{bi} \cdot \sum_s nd_s \cdot \left[Cfe_{t,i}^{bi} + \sum_i \sum_b Cr_t^{bi} \cdot RE_{t,i,s,b}^w + Ce_{t,s,b}^{bi} \cdot P_{t,i,s,b}^w + COM_{t,i,s,b} \cdot Q_{t,i,s,b} + Cs_t \cdot V_{t,i,s,b} \right]$$

$$+ \sum_t DF_t^{bi} \cdot \sum_c \left[Cap_{t,i,c}^{DP} \cdot XW_{t,i,c} + \sum_m Cap_{t,m}^{STT} \cdot X_{t,i,m} \right]$$

$$+ \sum_t DF_t^{bi} \cdot \left[\sum_{(i,j) \in \{AL_{i,j} | i=j\}} Cap_{t,i,j}^{PI} \cdot np_{t,i,j} \cdot L_{i,j} \cdot convf_2 + \sum_{(i,j) \in \{AL_{i,j} | i \neq j\}} Cap_{t,i,j}^{PI} \cdot np_{t,i,j} \cdot L_{i,j} \cdot convf_2 \right]$$

$$+ \sum_t DF_t^{bi} \cdot CTax \cdot f^{GHG} \cdot \sum_i \sum_s nd_s \cdot \sum_b P_{t,i,s,b}^w$$

Residential energy balance (with PVs): $P_{t,i,s,b}^r + RE_{t,i,s,b}^r = k_{t,i} \cdot D_{t,i,s,b}$ (1)

Added share of each energy source: $P_{t,i,s,b}^r = P_{t-1,i,s,b}^r + addP_{t,i,s,b}^r$ (2)

$$RE_{t,i,s,b}^r = RE_{t-1,i,s,b}^r + addRE_{t,i,s,b}^r$$
 (3)

Residential energy balance (without PVs): $P_{t,i,s,b}^m + RE_{t,i,s,b}^m = (1 - k_{t,i}) \cdot D_{t,i,s,b}$ (4)

Max. potential PV output: $MaxR_{t,i,s,b} = k_{t,i} \cdot dur_b \cdot PV_{s,b} \cdot exisR_{t,i}$ (5)

$$MaxR_{t,i,s,b} = MaxR_{t-1,i,s,b} + addk_{t,i} \cdot kp_t \cdot dur_b \cdot PV_{s,b} \cdot (exisR_{t,i} - exisR_{t-1,i})$$
 (6)

Surplus PV output: $Surp_{t,i,s,b} = MaxR_{t,i,s,b} - RE_{t,i,s,b}^r$ (7)

PV share constraints: $RE_{t,i,s,b}^r \leq MaxR_{t,i,s,b}$ (8)

Grid share constraint: $P_{t,i,s,b}^r + P_{t,i,s,b}^m + P_{t,i,s,b}^w \leq dur_b \cdot MaxPS_{t,i}$ (9)

Unused surplus energy: $Surp_{t,i,s,b} - RE_{t,i,s,b}^m - RE_{t,i,s,b}^w \cong 0$ (10)

The optimal solution was achieved in two runs using an interactive approach. In the first run, the initial estimation of the optimal water supply system was obtained regardless of remaining unused surplus PV output (relaxation of Eq. (10)). This led to the maximum PV installation density in the area and the initial estimation of the optimal decisions for water supply system while there was the highest access to the renewable energy. Considering this constraint (Eq. (10)), the initial estimation was then applied in the second run to adjust the installation density and achieve the final optimal solution. Each run included both levels of optimisation.

4. Optimal strategic and operational decisions

The model was coded into GAMS 24.3.1 software and solved by CPLEX 12.6. Two scenarios were considered. In the “minimum system and GHG costs” scenario, the objective function minimised the discounted cost of the system including capital and O&M costs as well as the carbon abatement cost over the planning horizon. This scenario was then compared with “minimum system costs” scenario, which only concerned the minimisation of discounted capital and O&M costs of the system. The

optimal results for the minimum system and GHG costs scenario led to \$ 2,291,309,369 discounted total cost, around \$ 47,449,276 higher than minimum system costs scenario. It also resulted in 51,301.3 tCO₂eq less GHG emissions over 15 years of system operation. The optimal results are presented in Figures 1 and 2.

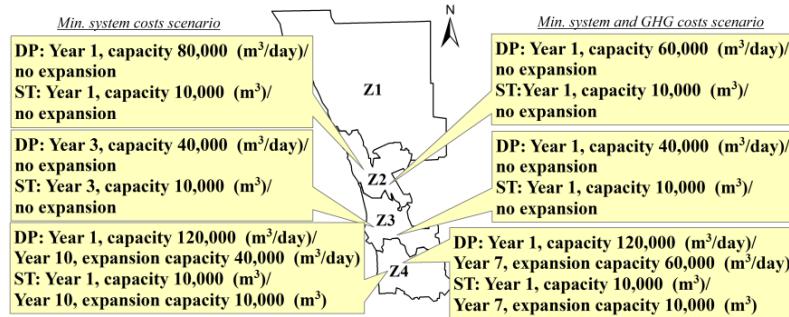


Figure 1: Optimal desalination plants (DP) and storage tanks (ST) capacities located in 4 discrete zones (z) in Min. system costs and Min. system and GHG costs scenarios

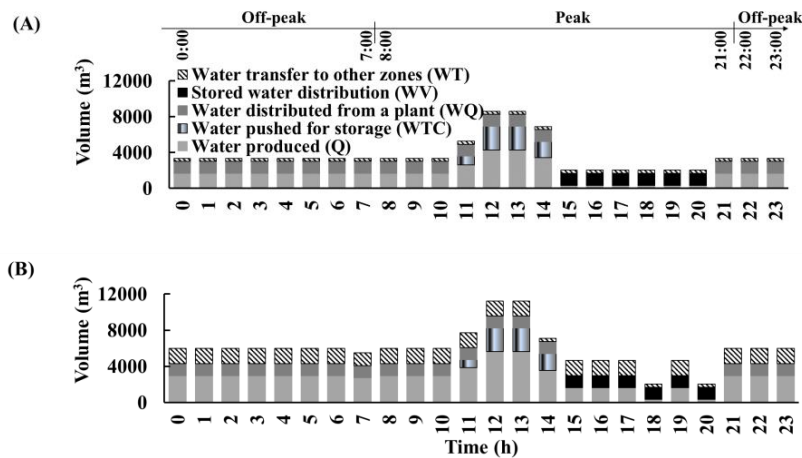


Figure 2: Operational scheduling of the water supply system in the representative zone 2 and year 2018 in: (A) Min. system costs and (B) Min. system and GHG costs scenarios

In both scenarios, three zones of 2, 3 and 4 were equipped with desalination plants (Figure 1); however, in terms of capacities and the timing of construction/expansion of the water supply components, they were different. In minimum system and GHG costs scenario, the model equipped both zones of 2 and 3 with desalination plants and associated storage tanks from the beginning of the planning horizon. Thus, despite the lack of economies of scale of the smaller desalination plants, it located a desalination plant with the capacity of 60,000 m³/day in zone 2 as opposed to the capacity of 80,000 m³/day in minimum system costs scenario. Instead, it placed a desalination plant with the capacity of 40,000 m³/day in zone 3 in year 1 versus year 3 in minimum system costs scenario. The reason is to reduce the energy consumption of water transfer among allowable zones (around 3,640 MWh over 2 years) and decrease indirect GHG

emissions costs. It is worth mentioning that although the expansion capacity of the desalination plant in zone 4 in the minimum system and GHG costs scenario was larger than minimum system cost scenario, the earlier time of the expansion neutralised the economic benefits of the larger scale expansion capacity.

Figures 2(A) and 2(B) show the optimal operational scheduling of the water supply system in both scenarios for a representative zone 2 and year 2018. Given flexible mode of operation for water supply system, the paradigm of the daily operational scheduling was achieved relatively the same for both scenarios. Accordingly, the highest water production and storage occurred when renewable energy was available, although it was concurrent with the peak electricity pricing hours. The stored water was then used for providing the water demand in the same zone when it was still during the peak electricity hours but no surplus PV output was available that could be assigned to the water-related electricity demand. The level of water production in zone 2 during peak electricity hours when there was no access to the renewable energy was limited to the demand of its adjacent zones (1 and/or 3). In off-peak electricity hours, the water demand was supplied directly from the desalination plant located in this zone.

5. Sensitivity analysis

Figure 3 depicts the sensitivity of the optimal solution towards purchasing grid electricity from 6 different sources in the minimum system and GHG costs scenario. The associated data was achieved from (Gifford, 2011). The results indicate a relatively high sensitivity towards emission factors higher than 0.148 (municipal waste). In fact, in higher emission factors, the effect of environmental impact was more significant and thus the optimal solution was mainly driven by indirect GHG emissions costs, which led to higher discounted total cost. By decreasing the emission factor, the effect of indirect GHG emissions costs reduced and from a certain point, it did not change the optimal decisions. Thus, the system cost turned to the predominant factor affecting the optimal results. This also explains the relatively same discounted total costs of the system with the minimum system costs scenario in lower emission factors.

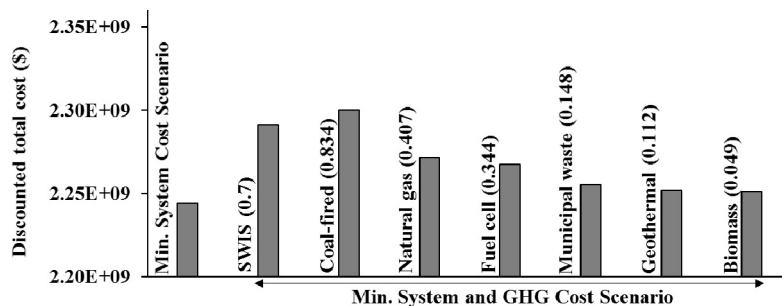


Figure 3: Sensitivity analysis towards purchasing electricity generated from different sources

6. Conclusions

In this study, we proposed an interactive optimisation model for the strategic and operational decisions of an urban water supply system driven by surplus PV output and grid electricity considering both system and carbon abatement costs in the formulation of the objective function. The optimal solutions for an urban area located in the north-western corridor of Perth (Australia) led to less GHG emissions but higher discounted total cost compared to the case where the system costs were the only components of the objective function. Finally, the results of the sensitivity analysis towards purchasing

grid electricity from different sources showed the predominant effect of indirect GHG emissions costs over system costs on the optimal solutions in higher emission factors.

Nomenclatures

Sets:

AL = allowable zones for water transfer

c = discrete points of plant capacities

i, j = zone

m = discrete points of storage tank capacities

t, s, b = planning horizon, season and time

block, respectively

Continuous variables:

$addP$ = added share of grid electricity (kWh)

$addRE$ = added share of PV output

$addk$ = added PV installation density (%)

k = PV installation density (%)

$MaxR$ = Max. PV output (kWh)

P = share of grid electricity (kWh)

Q = desalinated water produced (m³)

RE = share of renewable energy (kWh)

V = existing water storage (m³)

Parameters:

Cap = capital cost for plant (\$) and for pipeline (\$/km)

Ce = variable grid electricity cost (\$/kWh)

Cfe = fixed grid electricity cost (\$/day)

COM = plants O&M cost (\$/m³)

$conv2$ = conversion factor (km/m)

Cr = renewable electricity cost (\$/kWh)

Cs = O&M cost of water storage (\$/m³)

D = residential energy demand (kWh)

$CTax$ = Carbon abatement cost (\$/kgCO₂)

$exisR$ = number of existing residential rooftops

f^{GHG} = GHG emission factor (kgCO₂/kWh)

DF = discount factor

dur = duration of the time block (h)

kp = economic-subjectivity index

L = distance (m)

$MaxPS$ = Max. substation capacity (kW)

nd = number of days (day)

PV = PV system output (kW)

$Surp$ = surplus PV output (kWh)

Binary variables:

np, npI, J = decisions for construction/ expansion capacity of the pipeline

X, XW = decisions for storage tank size and plant capacity, respectively

Superscripts associated with:

bi = business sector; w = water

DP = plant; PI = pipeline; STT = storage tank

r, rm = households with and without PVs, respectively

References

- AEC, 2017, Australian Energy Council, Solar report, <https://www.energycouncil.com.au>, [accessed 11.01.18].
- DEE, 2017, Department of the Environment and Energy, National greenhouse accounts factors, <https://www.environment.gov.au>, [accessed 02.02.18].
- ERA, 2017, Economic Regulation Authority, The efficient costs and tariffs of the Water Corporation, Aqwest and Busselton Water, <https://www.erawa.com.au>, [accessed 17.02.18].
- J. Gifford, 2011, Survey and sustainability of energy technologies [M.Sc. Thesis], Iowa State University.
- R. F. C. Miranda, A. Szklo, R. Schaeffer, 2015, Technical-economic potential of PV systems on Brazilian rooftops, *Renewable Energy*, 75, 694-713.
- RBA, 2017, Reserve Bank of Australia Exchange rate data, mountly data, <http://www.rba.gov.au/statistics/historical-data.html#exchange-rates>, [accessed 02.01.17].
- N. Vakilifard, P. A. Bahri, M. Anda, G. Ho, 2017, Water security and clean energy, co-benefits of an integrated water and energy management, In: *Computer aided process engineering*, Elsevier, 40, 1363-1368.
- N. Vakilifard, P. A. Bahri, M. Anda, G. Ho, 2018, Integrating real-time operational constraints in planning of water and energy supply, In: *Computer aided process engineering*, Elsevier, 43, 313-318.
- WSAA, 2012, Water Services Association of Australia Ltd. , Occasional paper 28: Cost of carbon abatement in the urban water industry, <https://www.wsaa.asn.au/publications?page=13>, [accessed 18.01.18].

An MILP Approach for Short-term Scheduling of Batch Operations

Hossein Mostafaei^a, Iiro Harjunoski^{a,b,*}

^a*Process Control and Automation, School of Chemical Engineering, Aalto University, Espoo 02150, Finland*

^b*ABB AG, Corporate Research Center, Ladenburg, Germany*

iiro.harjunoski@de.abb.com

Abstract

In this paper, we address the short-term scheduling of multipurpose batch plants, a challenging problem that has received growing attention in the past few years. We present a new mixed integer linear programming (MILP) framework based on the state-task network (STN), which employs a multi-grid continuous-time approach. Compared to other formulations in the literature, the proposed model leads to smaller and simpler mathematical models with strong LP-relaxations, which is reflected in the ability to find the optimal solutions in shorter CPU times. We demonstrate the performance of our model with a complex and comprehensive case study from the literature.

Keywords: Batch plant, Scheduling, MILP, Mathematical modeling.

1. Introduction

Short-term scheduling of batch processes has received growing attention over the past two decades. It consists of allocating limited resources to activities over time to optimize the plant operation in terms of some specific performance criteria such as maximum profit or minimum makespan. Earlier work in this area can be found in Vaselenak et al. (1987). Research on the short-term scheduling of multipurpose batch plants has used mixed integer linear programming (MILP) considering the time representation within the planning horizon as either discrete or continuous. Discrete-time representations divide the time horizon into slots of equal and fixed duration, whereas continuous-time representations relax such assumption. Extensive reviews can be found in Floudas and Lin (2004) and Harjunoski et al. (2014). Continuous-time models can be further classified into two: single-grid (Castro et al., 2004; Maravelias and Grossmann, 2003; Sundaramoorthy and Karimi, 2005) and multi-grid (Ierapetritou and Floudas, 1998, Shaik and co-workers 2009; 2012). In the former, time slots are common for all units, while the latter provides each unit to have its own set of time intervals, which is not shared with other units.

Kondili et al. (1993) were the first to develop a discrete-time MILP based on the state-task network (STN) representation. In this model, the length of the time slots are determined from the greatest common factor among the processing times involved in the problem. For the same problem, Ierapetritou and Floudas (1998) developed an efficient multi-grid continuous-time MILP formulation that defines the duration of tasks by the optimization. The model needs less number of events (or time slots) compared to the single-grid models (Castro et al., 2004; Maravelias and Grossmann, 2003; Sundaramoorthy and Karimi, 2005). Based on the model by Ierapetritou and Floudas (1998), Shaik and Floudas (2009) presented an MILP formulation that can be utilized in

both batch and continuous plants. In this paper, we propose a new multi-grid continuous-time MILP scheduling model for multipurpose batch plants, based on the STN representation. Compared to other models in the literature, the proposed model is very tight and does not use any tightening constraint to generate a small integrality gap. We define a new set of sequencing constraints, which result in fewer continuous variables and constraints compared to previous multi-grid approaches. Furthermore, compared to literature, the proposed model leads to the same number of binary variables without decoupling tasks from units.

2. Problem statement

We focus on short-term scheduling of multipurpose batch plants, where a set of products are manufactured using a number of shared production units. Given the processing time data and the state-task network (STN) representation for the plant, we aim to optimally define the sequencing and timing of tasks in each units in order to maximize the total profit during a specific time horizon or minimize the total time required to meet demands. To sequence tasks in units, we use the concept of run $r \in R$; run r should start after the completion of $r-1$ in unit j . If run r is executed in unit j , one of tasks $i \in I_j$ (set of tasks that can be processed in unit j) is being processed in this unit.

3. Scheduling model

3.1. Task allocation, batch size and processing time

If binary variable $X_{i,j,r} = 1$, a certain volume of task i is being processed in unit j during run r ($V_{i,j,r}$). The processing time of task i in unit j at run r is assumed to be given by a constant plus a term proportional to the related batch size, where $cp_{i,j}$ and $vp_{i,j}$ are the constant and variable processing times of task i in unit j , respectively. In turn, $X_{j,r}^{\text{no task}} = \text{true}$ means that task i is not allocated to unit j and so the continuous variables $LR_{i,j,r}$ and $V_{i,j,r}$ are set to zero. We have thus the following disjunction (Mostafaei and Castro 2017; Castro and Mostafaei 2017; Castro et al. 2018):

$$\bigvee_{i \in I_j} \left[\begin{array}{c} X_{i,j,r} \\ v_{i,j}^{\min} \leq V_{i,j,r} \leq v_{i,j}^{\max} \\ LR_{i,j,r} = cp_{i,j} + vp_{i,j} V_{i,j,r} \end{array} \right] \vee \left[\begin{array}{c} X_{j,r}^{\text{no task}} \\ V_{i,j,r} = 0 \quad \forall i \in I_j \\ LR_{i,j,r} = 0 \quad \forall i \in I_j \end{array} \right] \quad \forall j, r \quad (1)$$

The MILP format of the above disjunction is described through eqs. (2)-(4).

$$\sum_{i \in I_j} X_{i,j,r} \leq 1 \quad \forall j, r \quad (2)$$

$$v_{i,j}^{\min} X_{i,j,r} \leq V_{i,j,r} \leq v_{i,j}^{\max} X_{i,j,r} \quad \forall i \in I_j, j, r \quad (3)$$

$$LR_{i,j,r} = cp_{i,j} X_{i,j,r} + vp_{i,j} V_{i,j,r} \quad \forall i \in I_j, j, r \quad (4)$$

3.2. Material balance

The excess amount of state s at the start of run r ($F_{s,r}$) is computed through eq. (5), where f_s^{initial} is the initial inventory of state s . In eq. (5), $\rho_{i,s}^p$ and $\rho_{i,s}^c$ are the proportion of state s produced or consumed from task i , respectively.

$$F_{s,r} = f_s^{\text{initial}} + \sum_{r' < r} \sum_{i \in (I_i^p \cap I_j)} \rho_{i,s}^p \sum_j V_{i,j,r'} - \sum_{r' \leq r} \sum_{i \in (I_i^c \cap I_j)} \rho_{i,s}^c \sum_j V_{i,j,r'} \quad \forall s, r \quad (5)$$

3.3. Sequencing process runs

Process run r in unit j should not start before the end of run $r-1$ in the same unit. Besides, the start of run r in unit j consuming state s should be after the end of process run $r-1$ in unit j' feeding the same state. The sets J_s^p and J_s^c in (7) include units that feed and consume state s , respectively.

$$SR_{j,r} \geq SR_{j,r-1} + \sum_{i \in I_j} LR_{i,j,r-1} \quad \forall j, r \geq 2 \quad (6)$$

$$SR_{j,r} \geq SR_{j',r-1} + \sum_{i \in I_j} LR_{i,j',r-1} \quad \forall j \in J_s^c, j' \in J_s^p (j \neq j'), s \in S, r \geq 2 \quad (7)$$

The completion time of the last process run in each unit should not surpass the horizon length, h_{\max} .

$$SR_{j,r} + \sum_{i \in I_j} LR_{i,j,r} \leq h_{\max} \quad \forall j, r \geq |R| \quad (8)$$

3.4. Sequence-dependent changeovers

If tasks i' and i are processed in unit j during runs $r-1$ and r respectively, there will be a constant changeover time of $\tau_{i',i,j}$ associated to the start of run r in unit j .

$$X_{i,j,r} \wedge X_{i',j,r'} \wedge \neg \left(\bigcup_{r''=r'+1}^{r-1} \bigcup_{i'' \in I_j} X_{i'',j,r''} \right) \Rightarrow X_{i,i',j,r',r}^{\text{changeover}} \quad \forall i, i' \in I_j (i \neq i'), j \in J, r \geq r' \quad (9)$$

$$\bigvee_{i \in I_j} \bigvee_{i' \in I_j} \left[X_{i,i',j,r',r}^{\text{changeover}} \right. \\ \left. SR_{j,r} - (SR_{j,r-1} + LR_{i',j,r-1}) \geq \tau_{i',i,j} \right] \quad \forall j, r > r' \quad (10)$$

We can now eliminate variable $X_{i,i',j,r',r}^{\text{changeover}}$ from the formulation by combining the constraints derived from form Eqs. (9-10), giving rise to the following equation:

$$SR_{j,r} - (SR_{j,r-1} + LR_{i',j,r-1}) \geq \tau_{i',i,j} (X_{i',j,r} + X_{i',j,r'} - \sum_{r''=r'+1}^{r-1} \sum_{i'' \in I_j} X_{i'',j,r''} - 1) \quad (11)$$

$$\forall i, i' \in I_j (i \neq i'), j \in J, r \geq r'$$

3.5. Meeting demand

Demands at states $s \in SM \subset S$ storing final products are enforced as a hard constraint in eq (14).

$$\sum_r \sum_{i \in I_i^p} \rho_{i,s}^p \sum_{j \in J_i} V_{i,j,r} \geq d_s \quad \forall s \in SM \quad (12)$$

3.6. Objective function

Two alternative objectives are considered. They are:

- (1) The maximization of profit given in eq (13), where the parameter vs_s is the value of state s :

$$\max z = \sum_s vs_s \sum_r \sum_{i \in I_r^p} \rho_{i,s}^p \sum_{j \in J_i} V_{i,j,r} \quad (13)$$

The model for profit maximization consists of eqs. (2)-(8),(11) and (13).

- (2) The minimum makespan given in (14):

$$\min z = H \quad (14)$$

where the continuous variable H is an upper bound on the completion time of last run in each unit:

$$SR_{j,r} + \sum_{i \in I_j} LR_{i,j,r} \leq H \quad \forall j, r \geq |R| \quad (15)$$

The model for makespan minimization consists of eqs. (2)- (7), (11)-(12), (14) and (15).

Remarks: Eq (16) below, the so-called *tightening* constraint, is a common constraint used e.g. in Shaik and co-workers (2009, 2012) and Marvelias and Grossmann (2003) and leads to strong LP-relaxations. It helps speed up the branch and bound solution search, and consequently decrease the solution CPU times. When minimizing the makespan the time horizon parameter in (16) needs to be replaced by the continuous variable H . We will show that our proposed model does not need the tightening constraint.

$$\sum_r \sum_{i \in I_j} LR_{i,j,r} \leq h_{\max} \quad \forall j \quad (16)$$

4. Case Study: A complex and comprehensive problem in the literature

The performance of our model is compared to a similar previous work by Shaik and Floudas (2006), hereafter referred to as SF. We consider a complex and comprehensive case study (Example 3) in Sundaramoorthy and Karimi (2005). Since our model does not allow tasks to span over multiple events and for the sake of a fair comparison, we only consider $\Delta n = 0$ in SF model and remove the big-M term in constraint (16), which makes it exactly equivalent to the model by Vooradi and Shaik (2012). Both the proposed model and SF model were implemented in GAMS/ CPLEX 12.7.1 (using 4 threads in parallel) on an Intel Core i5-7300U (3.33 GHz and 8 GB of RAM).

The model statistics and computational results when maximizing the total profit for two different time horizons are given in Table 1. From this table, both approaches need the same number of runs (events) to confirm the optimum and perform equally well. However, our model has fewer continuous variables and constraints and exhibits strong LP-relaxations with 6 runs for the first scenario and with 8 runs for the second scenario. Table 1 also summarizes the results for both models without the tightening constraint (16). As can be observed, the LP-relaxations (RMILP) do not change without the tightening constraint for the purposed model, which is not the case for the SF model.

Table 1: Results for the case study when maximizing total profit

	R	CPU (s)	Nodes	Binary variables	Total variables	Eqs	MILP (\$)	RMILP ^a (\$)
				$(h_{\max} = 8 \text{ h})$				
SF	5	0.43	304	55	286	457	1583.4	2100.0

	5*	0.34	340	55	286	451	1583.4	2100.0
	6	0.87	5744	66	343	551	1583.4	2750.9
	6*	0.82	4878	66	343	545	1583.4	2826.7
Our	5	0.34	428	55	261	365	1583.4	2100.0
	5*	0.28	309	55	261	359	1583.4	2100.0
	6	0.53	2827	66	313	440	1583.4	2563.2
	6*	0.71	3276	66	313	434	1583.4	2563.2
$(h_{\max} = 12 \text{ h})$								
SF	7	0.50	619	77	400	645	3041.2	3465.6
	7*	0.35	299	77	400	639	3041.2	3465.6
	8	1.29	2017	88	457	739	3041.2	3988.4
	8*	0.67	1066	88	457	733	3041.2	4059.3
Our	7	0.43	492	77	365	515	3041.2	3463.9
	7*	0.31	192	77	365	509	3041.2	3463.9
	8	0.59	1245	88	417	590	3041.2	3846.0
	8*	0.73	1088	88	417	584	3041.2	3846.0

*Results without the tightening constraint (16), ^aRelaxed Solution of MILP

Table 2 shows the results for the case study when minimizing the makespan for two different demand scenarios. In the first scenario i.e., $d_{s_{12}} = d_{s_{13}} = 250$ mass unit (mu), both models work equally well, but our model again leads to smaller and tighter mathematical models. For the second scenario and with the tightening constraint, our proposed model finds the optimum in just 2.95s and confirms it in 44.54 s. This represents a one-order-of-magnitude time saving compared to the SF's model, which takes 1567.2 s to confirm the optimality of solution confronted with 26 events. Without the tightening constraint, the proposed model again exhibits the same LP-relaxation and can confirm the optimality just in few seconds (12.92s). This is not the case for the SF model, which exhibits week LP-relaxations and takes minutes to prove the optimality.

Table 2: Results for the case study when minimizing the makespan

	R	CPU (s)	Nodes	Binary variables	Total variables	Eqs	MILP (h)	RMILP (h)
$(d_{s_{12}} = d_{s_{13}} = 250 \text{ mu})$								
SF	10	0.39	167	110	572	918	17.02	14.27
	10*	0.58	187	110	572	912	17.02	12.76
	11	0.87	824	121	629	1012	17.02	14.27
	11*	1.04	755	121	629	1006	17.02	12.62
Our	10	0.32	0	110	522	742	17.02	14.53
	10*	0.31	181	110	522	736	17.02	14.53
	11	0.92	967	121	574	817	17.02	14.39
	11*	0.76	746	121	574	811	17.02	14.39
$(d_{s_{12}} = d_{s_{13}} = 750 \text{ mu})$								
SF	26	144.9	158743	286	1484	2422	47.01	44.48
	26*	139.1	86100	286	1484	2416	47.01	37.86
	27	1567.2	1701164	297	1541	2516	47.01	44.48
	27*	1368.5	880148	297	1541	2510	47.01	37.66

Our	26	2.95	2468	286	1354	1942	47.01	44.84
	26*	3.75	3591	286	1354	1936	47.01	44.84
	27	44.54	67710	297	1406	2017	47.01	44.64
	27*	12.92	12883	297	1406	2011	47.01	44.64

*Results without the tightening constraint (18)

5. Conclusions

A multi-grid continuous-time MILP formulation for the short term scheduling of multipurpose batch plants has been developed. We relied on the STN representation to derive the problem constraints. It has been shown that the proposed model exhibits the same LP-relaxation with and without the tightening constraint frequently used in the literature. We validated the proposed model using a complex and comprehensive case study from the literature. The results demonstrated that the proposed model is smaller and significantly faster than previous similar work.

Acknowledgements

Financial support is gratefully acknowledged from the Academy of Finland project "SINGPRO", Decision No. 313466.

References

- J.A. Vaselenak, I.E. Grossmann, A.W. Westerberg, 1987, An embedding formulation for the optimal scheduling and design of multipurpose batch plants, *End. Eng. Chem. Res.*, 26, 139-148.
- C.A. Floudas, X. Lin, 2004, Continuous-time versus discrete-time approaches for scheduling of chemical processes: A review, *Comput. Chem. Eng.*, 28: 2109-2129.
- I. Harjunoski et al., 2014, Scope for industrial applications of production scheduling models and solution methods *Comput. Chem. Eng.*, 62, 161-193.
- E. Kondili, C.C. Pantelides, R. Sargent, 1993, A general algorithm for short-term scheduling of batch operations-I. MILP formulation *Comput. Chem. Eng.*, 17, 211-227.
- M.G. Ierapetritou, C.A. Floudas, 1998, Effective continuous-time formulation for short-term scheduling. 1. multipurpose batch processes, *Ind. Eng. Chem. Res.*, 37, 4341-4359.
- P. M. Castro, A.P. Barbosa-Povoa, H. Matos, A. Novais, 2004, Simple continuous-time formulation for short-term scheduling of batch and continuous processes, *Ind. Eng. Chem. Res.*, 43, 105-118.
- C.T. Maravelias, I.E. Grossmann, 2003, New general continuous-time state-task network formulation for short-term scheduling of multipurpose batch plants *Ind. Eng. Chem. Res.*, 42, 3056-3074.
- A. Sundaramoorthy, I.A. Karimi, 2005, A simpler better slot-based continuous time formulation for short-term scheduling in multipurpose batch plants *Chem. Eng. Sci.*, 60, 2679-2702.
- M.A. Shaik, C.A. Floudas, 2009, Novel unified modeling approach for short-term scheduling *Ind. Eng. Chem. Res.*, 48 6, 2947-2964.
- R. Vooradi, M. Shaik, 2012, Improved three-index unit-specific event-based model for short-term scheduling of batch plants, *Comput. Chem. Eng.*, 43, 148-172.
- H. Mostafaei, P.M. Castro, 2017, Continuous- time scheduling formulation for straight pipelines *AIChE*, 63, 1923-1936.
- P.M. Castro, H. Mostafaei, 2017, Product-centric continuous-time formulation for pipeline scheduling. *Computers and Chemical Engineering*, 104, 283-295.
- P.M. Castro, I.E. Grossmann, Q. Zhang, 2018, Expanding scope and computational challenges in process scheduling *Comput. Chem. Eng.*, 114, 14-42.

Synthesis and optimization of refinery hydrogen network using surrogate models

Shihui Wang^a, Li Zhou^{a,*}, Xu Ji^a and Yagu Dang^a

^a*School of Chemical Engineering, Sichuan University, No.24 South Section 1, Yihuan Road, Chengdu, 610065, P. R. China*
chezli@scu.edu.cn

Abstract

Previous works have developed methodologies for hydrogen network optimization, with a simplistic assumption of constant equilibrium distribution coefficient (K-value) for separation process, which leads to an inaccuracy of the solution. To address this problem, a surrogate-assisted modeling and optimization method for the design of refinery hydrogen network has been developed. The established models fully considered the changing characteristics of K-value in flash units, as well as the chemical processes happened in hydrotreaters, such as property of the processed crude oil (mainly the sulfide and 3+ring core aromatic content), formation of H₂S and light hydrocarbons (C1-C5). These process characteristics were reflected through the employment of surrogate modelling technique, which can be employed to compensate the computationally time-consuming nature of the corresponding first-principles-based models, due to its versatility. Polynomial surrogate model can be easily built using the least square method, and low order models are sufficient to approximate equipment models. A case study involving four hydrogen consumers is solved to indicate the efficacy of the proposed approach, and an NLP model is formulated. Compared to the result obtained by method proposed by the literature, the proposed method suggests more of gas flow to fuel system, since the calculated H₂S content in the product flow is comparatively high. Therefore, it can be concluded that the proposed method can deliver a more realistic result.

Keywords: Hydrogen network, Surrogate model, Design, Optimization

1. Introduction

The methodologies for the synthesis and optimization of refinery hydrogen networks can be divided into two categories: pinch analysis and mathematical programming. The latter shows more advantages because it takes into account some underlying constraints. It was originally developed by Hallale and Liu (2001). The research was continued by Kumar et al. (2010), considering several practical constraints (such as pressure constraints and hydrogen purity constraints) to obtain realistic solutions. Jia and Zhang (2011) proposed an improved modeling approach which defined the K-values in the flash separation units and incorporated the flash units into hydrogen consumer models. Umana et al. (2014) introduced an empirical model to predict the hydrogen consumption and the formulation of light hydrocarbons, and modeled the new hydrogen networks synthesis problem as an NLP (nonlinear programming).

Simplified equipment models were employed in the superstructure of optimization mod-

els in the previous works. In order to capture a more realistic behavior of the system, more accurate models should be used to represent equipments. However, the use of realistic models would be difficult due to high computational time in solution of the hydrogen network synthesis problem in an optimization algorithm.

This work proposes the use of surrogate modelling technique for hydrogen networks synthesis problems. It can capture the complicated chemical and physical processes involved in the hydrotreating and flash process, in the meanwhile, it requires less computation effort. Hence, more realistic solutions can be obtained in a reasonable time by applying the proposed methodology. This paper is structured as follows. Section 2 describes the methodology of building surrogate models. Section 3 provides a case study and shows a methodology to solve the hydrogen network synthesis problem by using surrogate models to represent equipment models, while Section 4 presents some conclusions.

2. Surrogate modeling and optimization: steps and strategies

The use of surrogate models in synthesis and optimization problems has been reported in many cases, e.g. Graciano and Le Roux (2013) and Sikorski et al. (2016). A surrogate model can be used to approximate the behaviors of a complicated system by only taking into account nature of the input-output relationship. Due to the simplicity of forms, a surrogate model can usually be solved with much lower computational efforts, compared to the original model. The steps of surrogate-assisted modeling and optimization used in this study are summarized below:

1. Selecting a set of input-output variables that are independent, as the characteristic indicators for the concerned processes.
2. Generating a set of sampling data for the selected input variables within the respective operational ranges (as described in Section 2.2).
3. Producing output values for each sampling point, by employing first principle models or commercial software packages.
4. Training the selected surrogate models with a portion (80% in this case) of the generated input-output data sets. The selection of a preferable surrogate model will be described later in Section 2.1.
5. Validating the obtained surrogate model with the remaining portion (20% in this case) of the generated input-output data sets.
6. Integrating the established surrogate models into the hydrogen network optimization problem.

2.1. Selection of surrogate models

There are several types of surrogate models such as polynomial, kriging, support vectors machine and artificial neural network. Polynomial can be built easily by using least square method and are sufficient to fit most models or data. In this work, polynomial surrogate model was employed to approximate hydrotreaters and flash unit models, due to its simplicity of forms and accuracy. For more detailed information about the selected surrogate models, the readers are referred to Forrester et al. (2008).

2.2. Sampling and validating plans

The sample sets were generated using Sobol sequences, developed by Sobol (1967), a type of quasi-random and low-discrepancy sequences which can achieve faster space-filling over other sequences. A number of accuracy measures were used including R^2 , root-mean-square-error (RMSE) and residual plot.

3. Case Study

The case study was taken from Umana et al. (2014), it consists of two possible hydrogen producers and four consumers, which again contains one hydrotreater and one flash unit.

3.1. Surrogate model fitting for flash units and hydrotreaters

3.1.1. Flash units

In order to overcome the drawback of constant K-value assumption in the previous works, Aspen Plus was used to model the flash separation units based on the operation conditions given in Jia and Zhang (2011). The model then served as a data generator for surrogate model fitting. In this case, ten indicators for the reaction effluent were chosen as the input variables, and eight were chosen for the gaseous stream, which is given in 1.

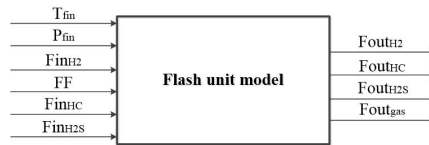


Figure 1: Flash unit model indicating input variables and output variables.

where T_{fin} is temperature, P_{fin} is pressure, Fin_{H_2} is inlet hydrogen flow rate, Fin_{HC} is inlet light hydrocarbons flow rate, Fin_{H_2S} is inlet H_2S flow rate, $Fout_{H_2}$ is outlet hydrogen flow rate, $Fout_{H_2S}$ is outlet H_2S flow rate, $Fout_{Ci}$ is outlet light hydrocarbons flow rate and $Fout_{gas}$ is outlet gas flow rate of the flash unit.

The results are represented in Table 1 and residual plots are illustrated in Fig 2. The R^2 is close to 1 and RMSE are relatively minor, indicating a good correlation by the surrogate models. Meanwhile, residual plots show that residuals are in random distribution.

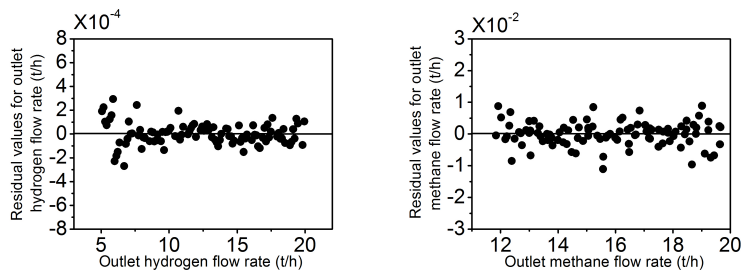


Figure 2: Plot of residuals for polynomial fit.

Table 1: Indicators for the flash unit model fitting results.

Output variables (t/h)	Polynomial RMSE	Polynomial R ²
Fout _{H2}	9.18×10 ⁻⁵	0.999997
Fout _{C1}	3.78×10 ⁻³	
Fout _{C2}	3.20×10 ⁻³	
Fout _{C3}	5.24×10 ⁻³	
Fout _{C4}	1.12×10 ⁻³	
Fout _{C5}	4.85×10 ⁻⁴	
Fout _{H2S}	1.40×10 ⁻²	
Fout _{gas}	1.25×10 ⁻²	

3.1.2. Hydrotreaters

The empirical model for the hydrotreaters provided by Umana et al. (2014) was reformulated into a much simpler form. For the hydrotreater, six input variables and eight output variables were chosen which is illustrated in Fig 3.

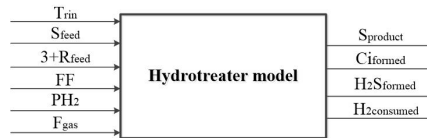


Figure 3: Hydrotreater model with input variables and output variables.

where T_{rin} is temperature, S_{feed} is sulphur content in the feed flow, $3+R_{feed}$ is 3+ring core aromatic content in the feed flow, FF is inlet oil flow rate, P_{H_2} is hydrogen partial pressure, F_{gas} is inlet gas flow rate, $S_{product}$ is sulphur content in the product, C_{formed} is amount of light hydrocarbons formed, $C_i=C1-C5$, H_2S_{formed} is amount of H_2S formed, and $H_{2consumed}$ is hydrogen consumption of the hydrotreater.

Table 2: Indicators for the hydrotreater model fitting results.

Output variables	Polynomial RMSE	Polynomial R ²
$S_{product}$ (ppwm)	9.88×10 ⁻²	0.999986
$C1_{formed}$ (t/h)	2.09×10 ⁻⁶	
$C2_{formed}$ (t/h)	3.90×10 ⁻⁶	
$C3_{formed}$ (t/h)	1.27×10 ⁻⁵	
$C4_{formed}$ (t/h)	1.40×10 ⁻⁵	
$C5_{formed}$ (t/h)	4.86×10 ⁻⁶	
H_2S_{formed} (t/h)	8.53×10 ⁻⁴	
$H_{2consumed}$ (t/h)	7.17×10 ⁻⁵	

Table 2 and Fig. 4 give the results for the hydrotreater surrogate model fitting. The indicators and residual plots all suggest good fitting.

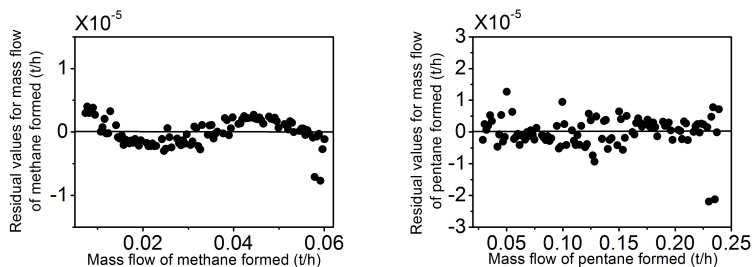


Figure 4: Plot of residuals for polynomial fit.

3.2. Synthesis and optimization of the hydrogen network

As noticed, the use of first-principles-based models in an optimization platform would be unfeasible due to high computational time and technical difficulties. Surrogate models developed in Section 3.1 can be employed in the solution of the synthesis problem, due to their great versatility. The objective function is to minimize the operating cost that accounts for the hydrogen production cost and fuel gas value. Operation conditions (T and P) for the flash units were set as fixed, constraint for sulphur content in oil product were imposed and the required hydrogen consumption for each hydrotreater were optimization variables for this problem. It was solved in GAMS which takes 0.172 s to give a result. The result is shown in Figure 5. For the flash unit, the established surrogate models fully consider the changing characteristics of K-value along with the conditions of feed flow. The details of inlet conditions were provided by Umana et al. (2014). When compared with the previous work (Table 3), it indicates a comparatively higher production rate of H₂S in the outlet of the flash unit which may cause more H₂S in the recycle stream sent to the reactor. As a result, more of the purge gas from DHT unit was suggested to be sent to the fuel system. In other words, the necessary constraint for H₂S accumulation in the system prevented further reuse of the DHT purge gas. Thus, it can be concluded that a more accurate model for the flash process is necessary in obtaining a more accurate simulation result for the hydrotreating process.

Table 3: Results comparison between the proposed method and the literature.

		Outlet of DHT flash units	
		This study	Previous study
Flowrate (t/h)		42.905	46.811
	H ₂	0.1404	0.3939
Compositions(mass fraction)	C ₁	0.3842	0.5895
	C ₂	0.0048	0.0053
	C ₃	0.0082	0.0034
	C ₄	0.0037	0.0017
	C ₅	0.0005	0.0007
	H ₂ S	0.4582	0.0055

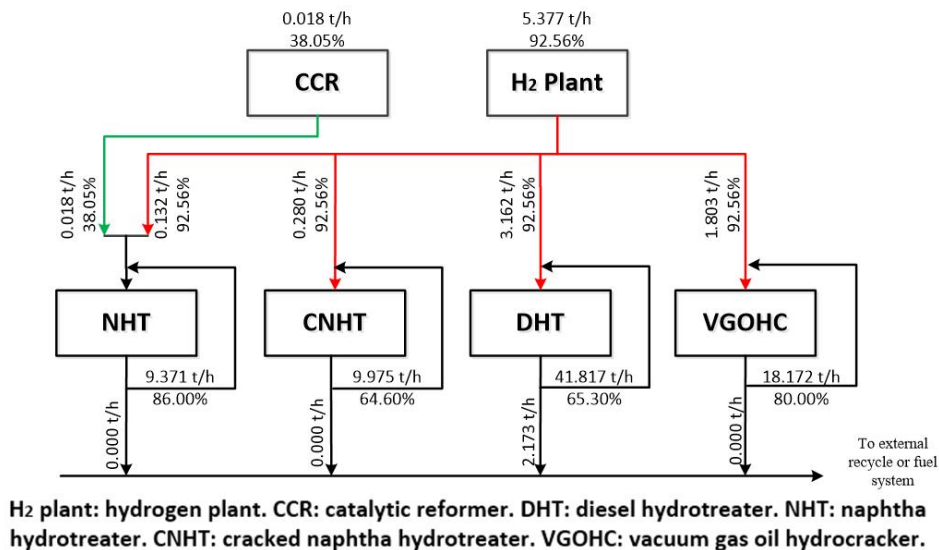


Figure 5: Integrated hydrogen network under varying hydrogen consumption

4. Conclusion

This paper introduces a methodology to optimize the design of refinery hydrogen network by using surrogate models to reflect the chemical and physical process in the hydrotreaters and flash units. When applied in a case study, the established surrogate models achieved reasonable fit, and the synthesis problem can be solved efficiently. Compared with results provided in the previous work, it was noticed that necessary constraints of inlet H₂S flow rate should be considered, causing by a large amount of outlet H₂S flow of the DHT flash unit. This difference can be attributed to the consideration of the changing separation efficiency of flash units along with the feed flow conditions. As a result, more realistic results can be obtained by using the proposed models.

References

- A. I. J. Forrester, A. Sobester, A. J. Keane, 2008. *Engineering Design via Surrogate Modelling: A Practical Guide*. Wiley , .
- J. E. A. Graciano, G. A. C. Le Roux, 2013. Improvements in surrogate models for process synthesis. Application to water network system design. *Computers and Chemical Engineering* 59, 197–210.
- N. Hallale, F. Liu, 2001. Refinery hydrogen management for clean fuels production. *Advances in Environmental Research* 6, 81–98.
- N. Jia, N. Zhang, 2011. Multi-component optimization for refinery hydrogen networks. *Energy* 36, 4663–4670.
- A. Kumar, G. Gautami, S. Khanam, 2010. Hydrogen distribution in the refinery using mathematical modelling. *Energy* 35, 3763–3772.
- J. Sikorski, G. Brownbridge, S. Mosbach, M. Kraft, 2016. Parameterisation of a biodiesel plant process flow sheet model. *Computers and Chemical Engineering* 95, 108–122.
- I. M. Sobol, 1967. Distribution of points in a cube and approximate evaluation of integrals. *Ussr Computational Mathematics and Mathematical Physics* 7, 86–112.
- B. Umana, A. Shoaib, N. Zhang, R. Smith, 2014. Integrating hydroprocessors in refinery hydrogen network optimization. *Applied Energy* 133, 169–182.

Optimising European supply chains for carbon capture, transport and sequestration, including uncertainty on geological storage availability

Federico d'Amore^a, Nixon Sunny^b, Diana Iruretagoyena^b, Fabrizio Bezzo^{a,*},
Nilay Shah^b

^aCAPE-Lab - Computer-Aided Process Engineering Laboratory, Department of Industrial Engineering, University of Padova, via Marzolo 9, Padova PD 35131, Italy

^bCPSE - Centre for Process Systems Engineering, Chemical Engineering Department, Imperial College London; South Kensington Campus, London SW7 2AZ, United Kingdom

fabrizio.bezzo@unipd.it

Abstract

Carbon capture and storage is considered a key option for decarbonising the energy sector. However, both the necessity of deploying large-scale infrastructures between the nodes of production and sequestration of CO₂, and the uncertainty related to the effective storage availability of sequestration basins still represent major challenges. Here, a mixed integer linear programming approach is proposed for the optimisation of a European supply chain model for carbon capture, transport, and storage. A quantitative assessment of storage uncertainty is incorporated to represent the volumetric capacity of basins to date considered capable of efficiently trapping the anthropogenic CO₂ emissions (i.e., deep saline aquifers, hydrocarbon fields and coal fields). The objective is to minimise the total expected cost required to install and operate, over a 10 years' time horizon, the overall network for carbon capture, transport and storage, while also taking into account the financial risk that is generated by uncertainty in geological capacity. The model defines economically optimal European supply chains, whilst simultaneously minimising the financial risk generated by uncertainty in local sequestration availability to ensure a robust design.

Keywords: Carbon capture transport and storage, European supply chain optimisation, Mixed integer linear programming, Uncertainty in storage capacity and risk.

1. Introduction

Addressing global warming through the reduction of CO₂ emissions is a crucial international goal. To constrain the mean global temperature rise below 2 °C by 2100, the planet must collectively keep the level of CO₂ equivalent below 550 ppm (Luderer et al., 2013). The power and industry sectors combined dominate current global CO₂ emissions, accounting for about 60 % of the total anthropogenic CO₂ generation, which must be drastically reduced by 2050 to meet COP21 targets (IPCC, 2018). Accordingly, carbon capture, transport, and storage (CCS) technologies have been highlighted as potential key players, considering their efficacy in delivering low carbon heat and dispatchable power, decarbonising industry, and facilitating the net removal of CO₂ from the atmosphere. The

feasibility of implementing a European CCS infrastructure has been investigated through a number of studies and demonstration plants in different countries, and this resulted in the development of a variety of technological and infrastructural options, whilst providing no clear consensus on which to deploy in any given context. To tackle this complexity, it is fundamental to establish engineering and cost analyses related to the whole CCS supply chain (SC), and in this sense, mathematical programming and optimisation techniques constitute the ideal methodological approach, in order to assess high-level, highly-combinatorial decisional problems, such as CCS. In particular, mixed integer linear programming (MILP) is frequently used in the modelling of large-scale energy systems, occasionally of continent-level CCS networks (Han and Lee, 2013; d'Amore and Bezzo, 2017; d'Amore et al., 2018). When designing CCS SCs, comparatively little attention has been paid to storage-related uncertainties such as geological volumes and long-term storage capacity, which are not usually known to a sufficient degree of accuracy before operation. As geological uncertainties may have a significant impact on overall sequestration costs, a more flexible pipeline network may be necessary rather than that designed using deterministic storage capacity data alone. Accordingly, the necessity of dealing with geological uncertainties in the planning and design of the infrastructure in terms of capacity must be highlighted as a primary action to improve the economic feasibility and manage the risks of large-scale CCS infrastructure. Amongst recent advances in the optimisation of process systems under uncertainty (Grossmann et al., 2016; Yue and You, 2016), several MILP models have been proposed for the optimisation of CCS networks under uncertainty, typically through either stochastic/probabilistic or robust techniques (e.g., Jin et al., 2017). Despite underlying the broad variety of investigated parameters (e.g., economics, storage injectivity, leakage, policy) and the abundance of employed methodologies (e.g., multiple scenario realisation, inexact optimisation), none of the previous studies focused on the quantification of risk that may emerge as a consequence of uncertainty in the actual geological volume that is available for CO₂ sequestration. This paper proposes a novel adaptive methodology for the calculation of risk based on uncertainties in local storage capacities in the European context. A MILP methodology that optimises the SC in terms of resiliency on risk was developed and applied. The model defines economically optimal designs of European SCs, whilst simultaneously minimising the economic risk generated by uncertainties in local sequestration availability to ensure a robust design. Risk is quantified as additional infrastructure costs that may emerge from the rerouting of CO₂ flowrates, upon realisation of geological uncertainty. Therefore, monetary consequences can be interpreted as additional investment costs that may need to be incurred to improve the flexibility of a European CCS infrastructure.

2. Material and methods

This contribution proposes a MILP optimisation under uncertainty based on the deterministic CCS SC model described in d'Amore and Bezzo (2017). Here, we address uncertainty related to the effective volumetric efficacy of those European basins that are nowadays considered capable of efficiently trapping the anthropogenic CO₂ emissions for long-term storage. The objective is to minimise the total costs required to install and operate, along a 10 years' time horizon, the overall network for CCS, considering the financial risks that are generated by uncertainties in both onshore and offshore European sequestration basins. The 10 years' time horizon is discretised according to a set $t = \{1, \dots, 10\}$. European large-stationary sources are described according to data retrieved from

d'Amore and Bezzo (2017). The capture stage and associated constraints are implemented through a set of technological options $k = \{\text{post-combustion from coal power plant, post-combustion from gas power plant, pre-comb from gas power plant, oxy-fuel combustion}\}$. The transport set includes different options $l = \{\text{onshore pipeline, offshore pipeline, ship}\}$, each discretised through a set of possible flowrate capacities $p = \{1, \dots, 7\}$ that ranges from a minimum of 1 Mt of CO₂/year to a maximum of 30 Mt of CO₂/year. The entire European area is discretised based on a grid of regions $g = \{1, \dots, 134\}$. A terrain factor is implemented to consider local geomorphology. The sequestration basins are distinguished into different categories according to a set $s = \{\text{deep saline aquifers, hydrocarbon fields, coal fields}\}$ (EU GeoCapacity Project, 2009). Overall, the main inputs are: the spatial distribution of European upstream sources of CO₂; the techno-economic parameters of capture options k ; the European carbon reduction target α to be pursued along the time horizon t ; the techno-economic parameters of transport means l ; the spatial distribution of deterministic minimum and maximum upper bounds of local geological potential of sequestration basins s ; the random matrix (generated through Mersenne Twister algorithm) of uncertain minimum upper bounds of local geological potential of sequestration basins. The key variables to be optimised are: location, scale and cost of the capture system, of the transport infrastructure, and of the deterministic-driven sequestration system; the adaptive, uncertainty-dependent upper bound of local geological potential for storage; location, scale and consequent risk of the uncertainty-driven sequestration system; the differential flowrates that may be generated (i.e., surplus and deficit) between the deterministic and the uncertainty-driven sequestration stage; the total risk generated by uncertainty according to the planning features and the location of the sequestration infrastructure.

3. Mathematical formulation

The model addresses uncertainty through a unique objective function that aims to minimise the total cost TC [€] of CCS, including cost for capture TCC [€], transport TTC [€], sequestration TSC [€], and total financial $risk$ [€] generated by the sequestration stage:

$$\forall it, loop [objective = \min(TC); TC = TCC + TTC + TSC + risk(it)] \quad (1)$$

Quantities TCC , TTC , and TSC of Eq.(1) are evaluated as in d'Amore and Bezzo (2017). Uncertainty is here introduced through a novel approach that aims at evaluating adaptive regional sequestration potential and, therefore, minimising its associated $risk$ through Eq.(1). The latter is given by the contribution on risk of both inter-connection between regions g and g' ($risk_{it,g,t}^I$ [€]), and intra-connection within region g ($risk_{it,g,t}^{II}$ [€]):

$$risk = \sum_{it,g,t} (risk_{it,g,t}^I + risk_{it,g,t}^{II}) / N_{it} \quad (2)$$

Indeed, either inter-connection or intra-connection related risks can be defined, at each sample it in region g at time period t , as the additional costs (i.e., with respect to TTC) to install and operate further transport links between different regions or basins:

$$risk_{it,g,t}^I = \sum_{g'} \Delta Q_{it,g,g',t} \cdot c^l \cdot LD_{g,g'} \cdot \tau_g \quad \forall it, g, t \quad (3)$$

$$risk_{it,g,t}^{II} = \sum_s S_{it,s,g,t}^{deficit} \cdot c^{II} \cdot LD_g \cdot \tau_g \quad \forall it, g, t \quad (4)$$

In particular, c^I [€/t/km] and c^{II} [€/t/km] (i.e., the average inter- or intra-connection unitary costs, respectively), $LD_{g,g'}$ [km] and LD_g [km] (i.e., the linear distances between region g and g' and the size of region g , respectively) and the tortuosity factor τ_g , are retrieved from d'Amore and Bezzo (2017). Variable $\Delta Q_{it,g,g',t}$ [t/year] represents the flowrates of CO₂ that must be transported at sample it between regions g and g' at time period t according to sequestration discrepancies between the deterministic and the uncertain models, whereas $S_{it,s,g,t}^{deficit}$ (t/year), together with its specular $S_{it,s,g,t}^{surplus}$ (t/year), are variables that define the differences between the uncertain and the deterministic amounts of CO₂ that are stored on basin s in region g at time period t . Overall, the yearly deterministic $S_{s,g,t}^D$ (t/year) and uncertain $S_{it,s,g,t}^U$ (t/year) stored amounts, are compared with surpluses ($S_{it,s,g,t}^{surplus}$) and deficits ($S_{it,s,g,t}^{deficit}$) in local sequestration capacities and with potential additional flowrates ($\Delta Q_{it,g,g',t}$) through the following mass balances:

$$S_{it,s,g,t}^U = S_{s,g,t}^D - S_{it,s,g,t}^{deficit} + S_{it,s,g,t}^{surplus} \quad \forall it, s, g, t \quad (5)$$

$$\sum_s S_{it,s,g,t}^{deficit} + \sum_{g'} \Delta Q_{it,g',g',t} = \sum_{g'} \Delta Q_{it,g,g',t} + \sum_s S_{it,s,g,t}^{surplus} \quad \forall it, g, t \quad (6)$$

According to Eq.(5) for each sample it , if a basin s in region g presents at time period t a value of $S_{it,s,g,t}^U \geq S_{s,g,t}^D$, this implies that $S_{it,s,g,t}^{surplus} \geq 0$ is generated in g (which is capable at receiving a deficit from g'). Conversely, when $S_{it,s,g,t}^U \leq S_{s,g,t}^D$, then $S_{it,s,g,t}^{deficit} \geq 0$, implying that a deficit occurs in region g and must be transported either to a different basin s , or region g' according to Eq.(6). The overall uncertain stored amount $S_{it,s,g,t}^U$ is then constrained to be lower than the local adaptive sequestration capacity:

$$\sum_t S_{it,s,g,t}^U \leq \sum_t \left[S_{it,s,g,t}^{U,min} \cdot Y_{it,s,g,t}^{start} + 0.1 \cdot (S_{s,g,t}^{D,max} - S_{it,s,g,t}^{U,min}) \cdot Y_{it,s,g,t}^{keep} \right] \quad \forall it, s, g \quad (7)$$

In particular, $S_{it,s,g}^{U,min}$ [t] is the matrix of uncertain minimum upper bounds of local sequestration capacity, constituted by random values comprised within the deterministic range $[S_{s,g}^{D,min}, S_{s,g}^{D,max}]$ (EU GeoCapacity Project, 2009). Furthermore, $Y_{it,s,g,t}^{start}$ and $Y_{it,s,g,t}^{keep}$ are binary variables that define, respectively, when the injection starts and/or continues being performed at it on basin s in region g at time period t . Overall, Eq.(7) defines the uncertainty in sequestration according to two contributions: a precautionary base storage potential preventively defined at the beginning of the operations, and the possibility of a yearly rate of increase (fixed to 0.1 year⁻¹ to exploit 10 years' simulation).

4. Results and discussion

Scenario A will be considered, in which the aim is to achieve a yearly European carbon reduction target $\alpha=50$ % of CO₂ emissions from large stationary sources. Results are compared with those from Scenario 0 (a risk-neutral network in which risk is not included within the objective function). The model was implemented in GAMS and optimised using the CPLEX solver on a 24-Core cluster (96 GB RAM). The uncertainty in sequestration capacity is approximated by $10 \leq N_{it} \leq 400$ random samples in order to test the efficacy of the proposed methodology, and show that the model achieves reliable results

for $it=100$ (Figure 1a). The design resulting from this sampling should constitute the initial design for future CCS optimisations.

Scenario A entails (Figure 1b) a TC for installing and operating the CCS system (including the contribution of financial risk) of 232.1 G€ (i.e., 38.302 €/t of sequestered CO_2), of which the major contribution is represented by TCC of 216.0 G€ (i.e., 35.637 €/t of sequestered CO_2). Interestingly, TTC (with 14.4 G€, i.e. 2.377 €/t of sequestered CO_2) and TSC (with 1.8 G€, i.e. 0.287 €/t of sequestered CO_2) constitute altogether only the 7 % of TC . With respect to $risk$, its final value is negligible, thus demonstrating the robustness of this solution on storage uncertainty. However, comparing the results with those from Scenario 0, despite having almost identical TC (+0.1 % with respect that of Scenario 0), the drawback of managing to keep such low values of risk is constituted by higher TTC (+11.2 % with respect to that of Scenario 0) and TSC (+5.5 % with respect to that of Scenario 0) costs. These additional infrastructural costs are a direct consequence of the choice of improving flexibility to nullify the contribution of risk to overall costs. In fact, regarding the SC configuration, under Scenario A (Figure 2a), the number of basins in which a deficit may occur is minimised and in general it is strategically chosen to exploit the sequestration potential of a larger number of regions (and basins) compared to Scenario 0 (Figure 2b), with the drawback of increasing transport costs. Accordingly, to distribute the investment for storage across different European regions, is an effective hedging strategy. In fact, the regions near the Baltics and Northern Poland are the only areas in which storage risk necessitates the balancing of deficits and surpluses, but these result in a range of $33 \leq \Delta Q_{g,g',t} \leq 720$ kt of CO_2 /year, therefore minimal with respect to the CO_2 shipped between regions (up to 30 Mt/year). When some risk is unavoidable, slightly risky basins are chosen in areas in which nearby regions are likely to receive a surplus of CO_2 , in order to minimise additional transport costs. In fact other deficits are scattered in Slovenia and near the Black Sea, but the CO_2 is diverted towards different basins within the same region and constitutes only a minor contribution to total economic risk, overall still negligible with respect to the total cost to install and operate the CCS network.

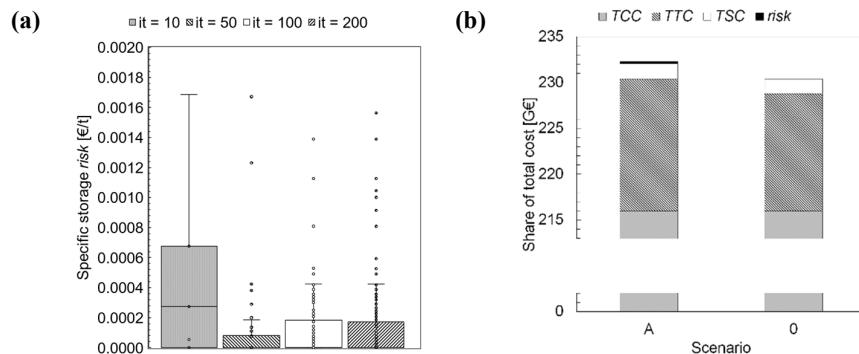


Figure 1. Scenario A, (a) dependency of $risk$ [€/t] from it , and (b) share of costs [G€].

5. Conclusions

This contribution proposed a MILP modelling framework for the economic optimisation of a European CCS SC, with uncertainty in effective volume capacity of sequestration basins. The effects of uncertainty were quantified in terms of risk related to the necessity of installing further transport links with respect to the risk-neutral solution of the model, with the aim of improving the intrinsic flexibility of European CO_2 infrastructures in

opposition to geological uncertainties. The proposed tool provides economically optimal network configurations resilient on risk and allows a decision-maker to understand the financial penalties associated with designing infrastructure in the absence of uncertainty. It was shown that only minor modifications and investments should be taken into account with respect to a European deterministic CO₂ network, in order to increase the level of flexibility of the transport infrastructure long enough to guarantee that uncertainty in storage capacity does not affect the final deployment of the overall system.

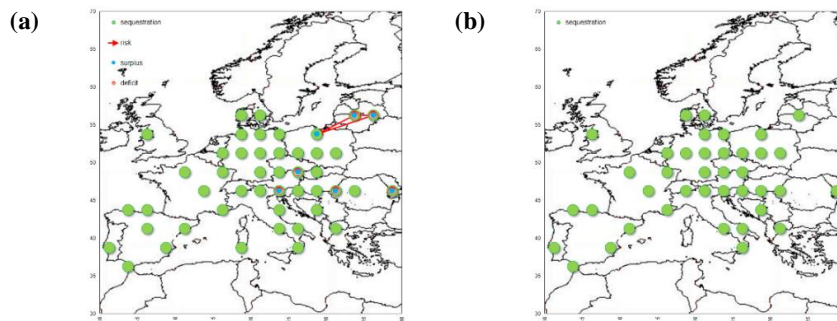


Figure 2. SC configuration for (a) Scenario A; and (b) Scenario 0.

References

- F. d'Amore, F. Bezzo, 2017, Economic optimisation of European supply chains for CO₂ capture, transport and sequestration, *Int. J. Greenh. Gas Control*, 65, 99-116.
- F. d'Amore, P. Mocellin, C. Vianello, G. Maschio, F. Bezzo, 2018, Economic optimisation of European supply chains for CO₂ capture, transport and sequestration, including societal risk analysis and risk mitigation measures, *Appl. Energy*, 223, 401-415.
- EU GeoCapacity Project, 2009, Assessing European Capacity for Geological Storage of Carbon Dioxide.
- I. E. Grossmann, et al., 2016, Recent advances in mathematical programming techniques for the optimization of process systems under uncertainty, *Comput. Chem. Eng.*, 91, 3-14.
- J. H. Han, I. B. Lee, 2013, A comprehensive infrastructure assessment model for carbon capture and storage responding to climate change under uncertainty, *Ind. Eng. Chem. Res.*, 52, 3805-3815.
- IPCC, 2018, Global warming of 1.5 °C. An IPCC special report on the impacts of global warming of 1.5 °C above pre-industrial levels and related global greenhouse gas emission pathways, in the context of strengthening the global response to the threat of climate change.
- S. W. Jin, Y. P. Li, S. Nie, J. Sun, 2017, The potential role of carbon capture and storage technology in sustainable electric-power systems under multiple uncertainties, *Renew. Sustain. Energy Rev.*, 80, 467-480.
- G. Luderer, et al., 2013, Economic mitigation challenges: How further delay closes the door for achieving climate targets, *Environ. Res. Lett.*, 8, 1-8.
- D. Yue, F. You, 2016, Optimal Supply Chain Design and Operations Under Multi-Scale Uncertainties: Nested Stochastic Robust Optimization Modeling Framework and Solution Algorithm, *AIChE J.*, 62, 3041-3055.

Real-time design space description in pharmaceutical manufacturing

Gabriele Bano,^a Pierantonio Facco,^a Marianthi Ierapetritou,^b Fabrizio Bezzo,^a Massimiliano Barolo^{a*}

^a*CAPE-Lab, Department of Industrial Engineering, University of Padova, Italy*

^b*Rutgers University, 98 Brett Road, Piscataway, NJ, 08854, USA*

max.barolo@unipd.it

Abstract

In this paper, we present a methodology to assist the offline description and online maintenance of the design space of a pharmaceutical product. The methodology is intended as a proactive risk-management tool to be included in a design space submission. First, classical feasibility analysis is exploited to obtain an offline model-based description of the design space (e.g., at the process development stage). Then, a dynamic state estimator is used to continuously adapt the model during plant operation, using measurements available from plant sensors. Surrogate-based feasibility analysis is used to continuously update the model-based description of the design space based on the up-to-date model returned by the state estimator. The tracking effectiveness of the methodology is shown for a co-milling process of a pharmaceutical production.

Keywords: quality by design, design space, state estimation, pharmaceutical manufacturing, model maintenance

1. Introduction

Following the recent FDA ICH Q12 draft guideline (ICH, 2018), the design space (DS) of a pharmaceutical product represents a set of established conditions (raw material properties and critical process parameters, CPPs) that guarantee to fulfill predefined specifications on the product critical quality attributes (CQAs).

The DS is typically obtained at the product/process development stage by exploiting a process model (either mechanistic or data-driven) and targeted laboratory experimentation. In principle, if all disturbances and sources of uncertainty that may affect the model predictions were accounted for at this stage, working within the resulting model-based representation of the DS would guarantee the desired product quality. In practice, however, there is no guarantee that the prediction fidelity of the model will remain unchanged as process operation progresses (Pantelides and Renfro, 2013). Process-model mismatch may in fact arise from parameter drifts (e.g., a heat exchange coefficient may change due to fouling), or insufficient/inappropriate description of the underlying physical phenomena driving the process (e.g., unmodeled physical phenomena that could not be observed at the laboratory scale, such as the effect of downstream/upstream units or of environmental factors). The fact that, along a plant lifecycle, the model may not be able to accurately reproduce the actual plant behavior, questions the appropriateness of the operating conditions selected by using the DS description obtained at the development stage. In this regard, the recent ICH Q12 draft

guideline (ICH, 2018) acknowledges that “(...) it may be necessary to change approved established conditions as a result of knowledge gained during product lifecycle...” and aims at providing a comprehensive regulatory framework on how to perform this in practice.

In this study, we propose a methodology to perform two sequential tasks: *i*) obtain an offline model-based description of the design space at the development stage; *ii*) obtain an up-to-date description of the design space as process operation progresses, by continuously reconciling the model predictions with the observed plant behavior. We intend the two activities (offline DS description and online DS maintenance) as complementary, making them appealing for a joint inclusion in a design space submission (i.e., for regulatory approval), in such a way as to reduce the burden of post-approval revision processes. We discuss the ability of the methodology to track the DS of a simulated de-lumping process of a pharmaceutical production using a conical miller.

2. Proposed methodology

Let us consider a dynamic system for the production of a pharmaceutical drug. The state-space representation of a pharmaceutical unit (or process) is typically given by a system of nonlinear differential-algebraic equations (DAEs) of the form:

$$\begin{bmatrix} \dot{\mathbf{x}}_1(t) \\ \mathbf{0} \end{bmatrix} = \begin{bmatrix} \mathbf{f}_1(\mathbf{x}_1(t), \mathbf{x}_2(t), \mathbf{q}(t), t) \\ \mathbf{f}_2(\mathbf{x}_1(t), \mathbf{x}_2(t), \mathbf{q}(t), t) \end{bmatrix} + \begin{bmatrix} \mathbf{w}_1(t) \\ \mathbf{w}_2(t) \end{bmatrix} \quad (1)$$

subject to initial conditions:

$$\mathbf{x}_1(0) = \mathbf{x}_{1,0} + \mathbf{w}_1(0) \quad (2)$$

where $\mathbf{x}_1(t)[N_1 \times 1]$ is the differential state vector, $\mathbf{x}_2(t)[N_2 \times 1]$ is the algebraic state vector, $\mathbf{w}_1(t)[N_1 \times 1]$ and $\mathbf{w}_2(t)[N_2 \times 1]$ are zero-mean random processes with unknown statistics representing the model error related to the differential and algebraic states respectively, and $\mathbf{q}(t)[M \times 1]$ is the vector collecting the raw material properties and CPPs (i.e., process parameters that have a strong effect on the product critical quality attributes). Formulation (1) assumes that there are no control variables (i.e., an open-loop scenario is considered). The model equations can also be concisely expressed in the implicit form:

$$\mathbf{F}(\dot{\mathbf{x}}_1(t), \dot{\mathbf{x}}_2(t), \mathbf{x}_1(t), \mathbf{x}_2(t), \mathbf{q}(t), t) = \mathbf{0} \quad (3)$$

We assume the availability of measurements from plant sensors at each time step t_k . The L -dimensional measurement vector at time t_k is denoted as $\mathbf{y}(t_k)$, and its relation $\mathbf{h}(\cdot)$ with the state vector is given by:

$$\mathbf{y}(t_k) = \mathbf{h}(\mathbf{x}_1(t_k), \mathbf{x}_2(t_k), t_k) + \mathbf{v}(t_k); \quad k = 1, 2, \dots, K \quad (4)$$

where $\mathbf{v}(t_k)[L \times 1]$ is the measurement noise.

The proposed methodology can be summarized in four steps.

Step #1: offline DS description. This activity is typically performed at the development stage. Given the process model (3), we define the feasibility function $\Psi(\mathbf{q}(t), \mathbf{x}_1(t), \mathbf{x}_2(t), t)$ as the maximum value of the I quality constraints imposed on the product CQAs:

$$\Psi(\mathbf{q}(t), \mathbf{x}_1(t), \mathbf{x}_2(t), t) = \max_{i \in I} g_i(\mathbf{q}(t), \mathbf{x}_1(t), \mathbf{x}_2(t), t), \quad i = 1, \dots, I \quad (5)$$

where $g_i(\mathbf{q}(t), \mathbf{x}_1(t), \mathbf{x}_2(t), t), i = 1, \dots, I$ is the set of quality constraints.. Based on this definition, the model-based description \overline{DS} of the design space (i.e. the set of CPPs and raw material properties that allow satisfying all quality constraints) is obtained by exploiting classical feasibility analysis (Halemane and Grossmann, 1983) according to:

$$\overline{DS} = \{\mathbf{q}(t) | \Psi(\mathbf{q}(t), \mathbf{x}_1(t), \mathbf{x}_2(t), t) \leq 0\}. \quad (6)$$

The description of the DS as expressed by Eq. (6) requires the solution of the following bilevel optimization problem (also called flexibility test problem (Halemane and Grossmann, 1983)):

$$\chi = \max_{\mathbf{q}(t) \in \mathbf{Q}(t)} \Psi(\mathbf{q}(t), \mathbf{x}_1(t), \mathbf{x}_2(t), t) \quad \text{subject to} \quad (7)$$

$$\mathbf{F}(\dot{\mathbf{x}}_1(t), \mathbf{x}_1(t), \mathbf{x}_2(t), \mathbf{q}(t), t) = \mathbf{0}; \quad \mathbf{x}_1(0) = \mathbf{x}_{1,0} \quad (8)$$

$$\mathbf{Q}(t) = \{\mathbf{q}(t) | \mathbf{q}^{lo}(t) \leq \mathbf{q}(t) \leq \mathbf{q}^{up}(t)\} .$$

The DS description obtained according to Eq. (6) through the solution of (7)-(8) represents the best representation of the DS that can be obtained with the available process model and with the best estimate of the model parameters obtained at the laboratory scale.

Step #2: uncertain model parameters determination. The underlying assumptions that we make is that process-model mismatch can be compensated for by continuously updating the system state and recalibrating some of the original model parameters. The parameters that should be recalibrated online can be chosen according to two criteria:

- a) if prior knowledge on the uncertainty or disturbances that may affect plant operation is available, the parameters are determined by preliminary qualitative diagnosis of the model structure;
- b) if condition a) does not hold true, sensitivity analysis can be used to determine the parameters that most affect the product CQAs. Only these parameters will be continuously adjusted during plant operation, as they are strongly related with the accuracy of the model-based description of the DS.

The set of parameters that are recalibrated online is denoted as $\mathbf{p}(t)[V \times 1]$, with $V \leq L$.

Step #3: state estimation and online parameter recalibration. The state estimator proposed by Cheng *et al.* (1997) is exploited to obtain the current system state and to perform the parameter recalibration at each time step t_k . The peculiarity of this state estimator is that, despite the traditional extended Kalman filter (EKF), its derivation is directly obtained from the DAE formulation (1) and does not require any assumptions on the form of the distributions of the state vector and measurement vector (which are assumed as normally distributed in the standard EKF formulation). The ability of this state estimator to handle large nonlinear DAE systems (involving more than 200 differential equations and 14,000 algebraic equations) has been discussed recently (Pantelides *et al.*, 2016). The mathematical formulation of this estimator can be found in the cited reference.

The online parameter recalibration is obtained through a state augmentation procedure (Ricker and Lee, 1995), by augmenting the differential state vector $\mathbf{x}_1(t)$ with the set of

uncertain parameters $\mathbf{p}(t)$. At each time step t_k , the state estimator returns the up-to-date values of $\mathbf{x}_1(t_k)$, $\mathbf{x}_2(t_k)$ and $\mathbf{p}(t_k)$.

Step #4: online DS maintenance. The up-to-date system state and parameter values returned by the state estimator are used to update the model-based description of the DS. The DS can be updated with the same measurement interval Δt_k at which measurements are collected from the plant or with a user-defined time interval Δt_m , provided that $\Delta t_m \geq \Delta t_k$. At each time t_m , the up-to-date DS representation is obtained according to:

$$\widehat{DS}_m = \{\mathbf{q}(t_m) | \Psi_m(\mathbf{q}(t_m), \mathbf{x}_1(t_m), \mathbf{x}_2(t_m), \mathbf{p}(t_m), t_m) \leq 0\} \quad (9)$$

by solving the flexibility test problem. The computational time required for the solution of the flexibility test problem must be smaller than the DS update interval Δt_m . If this condition does not hold true, surrogate-based feasibility analysis using a kriging or radial-basis function (RBF) surrogate can be used to make the online implementation viable. Mathematical details on this approach are discussed in Wang et al. (2017). For multidimensional design spaces (i.e., when the number of CPPs and raw material properties is greater than two), the joint projection to latent structures/RBF feasibility analysis approach proposed by Bano et al. (2018) can be exploited to reduce the problem dimensionality.

3. Test example

The application of the proposed methodology is illustrated for a simulated de-lumping operation of a pharmaceutical powder using a conical miller. The model proposed by Wang et al. (2017) is used to simulate the system behaviour. The model equations are given by Eq. (10)-(13) with the initial conditions and nominal values of the parameters reported in Table 1. The three state variables to be collected in vector $\mathbf{x}_1(t)$ are the mass holdup $M(t)$ in the co-mill, the outlet mass fraction $w_{API}(t)$ of the active pharmaceutical ingredient (API), and the outlet mass fraction $w_{ex}(t)$ of the excipient. The only algebraic state variable is the 90% D-value of the particle size distribution of the bulk material at the outlet $d_{90}^b(t)$, i.e. the diameter at which 90% of the bulk mass is comprised of smaller particles. Following the regulatory parlance, d_{90}^b is the product CQA, the impeller blade speed ω is a CPP, and the 90% D-value of the API at the inlet $d_{90,API}^in$ is a raw material property affecting the product CQA. Both ω and $d_{90,API}^in$ are considered as time-invariant.

4. Simulation set-up and results

It is desired to obtain a bulk material that satisfies the condition $222.5 \leq d_{90}^b \leq 224$ [μm] within 100s of co-milling operation. The design space for this process is defined as the set of combinations of $(\omega, d_{90,API}^in)$ that guarantee to obtain the desired specifications for $d_{90}^b(t)$ within the desired time frame.

Table 1. Initial conditions for the differential state variables and nominal values of the parameters of model (10)-(13).

Variable/ parameter	Units	Value
M_0	[kg]	0.19
$w_{API,0}$	[-]	0
$w_{ex,0}$	[-]	1
τ_{max}	[s]	40
ω_{min}	[rad/s]	104.62
a	[rad/s]	10.47
b	[m ³ /s]	1

$$\bar{\tau} \frac{dM(t)}{dt} + M(t) = \bar{\tau} F^{in}; \quad (10)$$

$$\frac{d(w_i^{out}M(t))}{dt} = w_i^{in}F^{in} - \frac{w_i^{out}M(t)}{\bar{\tau}} \quad i=API,ex; \quad (11)$$

$$\bar{\tau} = \tau_{max} \left[1 - \exp\left(-\frac{a}{\omega-\omega_{min}} - \frac{b}{F^{in}}\right) \right]; \quad (12)$$

$$d_{90}^b(t) = w_{API}(t)d_{90,API}^{in} + w_{ex}(t)d_{90,API}^{in} \quad (13)$$

The empirical relation (12) for the mean residence time is obtained from residence time distribution (RTD) experiments performed at the laboratory scale, and the regression parameters (τ_{max}, a, b) are therefore subject to a high degree of uncertainty when used to simulate a full-scale operation. Moreover, obtaining accurate initial values for the mass holdup and mass fractions (which both depend on upstream units) can be cumbersome.

In order to test the DS tracking performance of the proposed methodology, a situation was investigated where the model structure was correct, but erroneous values of the model parameters were used as well as an incorrect initial estimate of the system state. Specifically, a +10% deviation on the initial state estimate M_0 and a +35% deviation on the nominal value of parameter τ_{max} were enforced. The choice of enforcing a parametric mismatch on τ_{max} was dictated by the fact that its effect on the product CQA is considerably stronger than the other two regression parameters (a, b). Synthetic measurements of mass holdup to be fed to the estimator were generated at a frequency of 1 Hz; noise was simulated by adding the random error $v(t_k) \sim N(0,0.01^2)$ to the simulation results. The covariance for the model error $\mathbf{w}_1 \sim (0, \mathbf{Q})$ state estimator was set by trial and error to the value $\mathbf{Q} = \text{diag}(0.05^2; 0.001^2; 0.001^2)$ for each time step t_k .

The DS that can be obtained from model (10)-(13) with the correct initial state and nominal values of τ_{max} of Table 1 is denoted as the actual DS of the process. On the other hand, the DS as predicted by the estimator is denoted as the estimated DS. The actual DS is shown in the contour plot of Fig. 1a (i.e., the portion of the input domain within which the feasibility function is smaller than 0). Fig. 1b shows the discrepancy between the actual DS and the estimated DS that would be obtained at the development stage with a wrong estimate of the initial state of the system and of the parameter τ_{max} . Fig. 1c-1f show the tracking ability of the proposed methodology after 5,10,15 and 20 s of process operation (i.e., $\Delta t_m = 5s$). A RBF surrogate was exploited to reconstruct the boundary of the DS given the up-to-date model returned by the state estimator. The actual DS is recovered after ~ 20 s of operation, i.e., in less than 1/5 of the total co-milling operation.

5. Conclusions

The aim of this study was to propose a systematic methodology to assist the offline description and online maintenance of the design space of a pharmaceutical product. First,

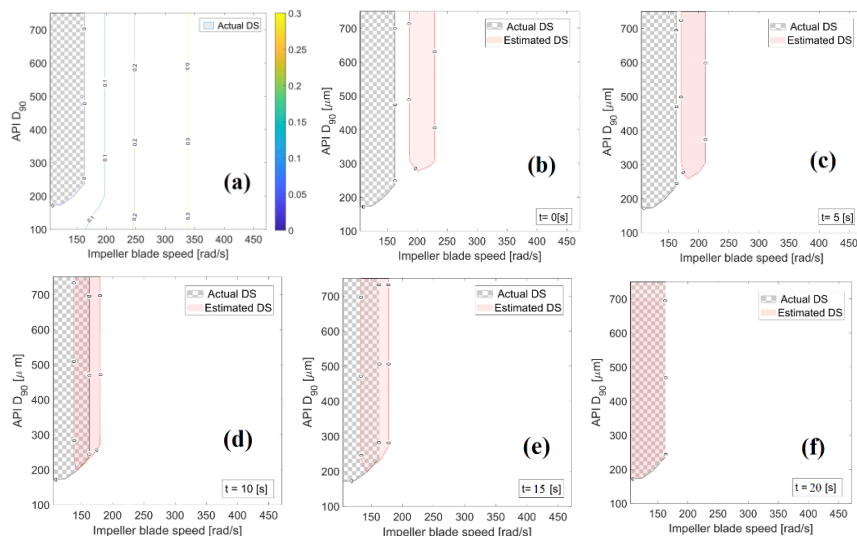


Figure 1. (a) Actual design space, (b) Estimated DS and actual DS at the development stage; estimated DS and actual DS after (c) 5s, (d) 10s, (e) 15s and (f) 20s of plant operation.

surrogate-based feasibility analysis was exploited to obtain an initial offline description of the design space using the available process model. Then, given few online measurements made available by plant sensors, an automatic strategy was proposed to continuously update the design space as plant operation progresses. The ability of the proposed approach to track a 35% parametric mismatch and a 10% error on the initial state estimate for a co-mill process of a pharmaceutical powder was shown. Applications of the proposed DS maintenance tool include open-loop decision support, real-time optimization, definition of optimal set-points or set-point trajectories within the boundary of the up-to-date design space.

References

- Bano, G., Wang Z., Facco, P., Bezzo, F., Barolo, M., Ierapetritou M. (2018) A novel and systematic approach to identify the design space of pharmaceutical processes. *Comput. Chem. Eng.* **115**, 309-322.
- Cheng, Y.S., Mongkhonsi, T., Kershenbaum, L.S (1997) Sequential estimation for nonlinear differential and algebraic systems- theoretical development and application. *Comput. Chem. Eng.* **21**,1051-1067.
- Halemane, K. P., Grossmann, I. E. (1983) Optimal process design under uncertainty. *AIChE J.*, **29**: 425-433.
- ICH (2018) Q12 - Technical and regulatory considerations for pharmaceutical product lifecycle management. Core guideline for industry.
- Pantelides, C. C., Renfro, J. G. (2013) The online use of first-principles models in process operations: Review, current status and future needs. *Comput. Chem. Eng.* **51**, 136-148
- Pantelides, C.C., Bano, G., Cheng Y.S., Spatenka S., Matzopoulos M., *Model-based real time monitoring of ethylene cracking furnaces*, 2016 AIChE Spring Meeting & 12th Global congress on process safety: Houston, TX; paper 444934
- Ricker, N. L., and Lee, J. H. (1995). Nonlinear modeling and state estimation for the Tennessee Eastman challenge process. *Comput. Chem. Eng.* **19**, 983-1005
- Wang, Z., Escotet-Espinoza, M. S., & Ierapetritou, M. (2017). Process analysis and optimization of continuous pharmaceutical manufacturing using flowsheet models. *Comput. Chem. Eng.*, **107**, 77-91.

Short-term Scheduling of a Multipurpose Batch Plant Considering Degradation Effects

Ouyang Wu^{a,b}, Giancarlo Dalle Ave^{c,d}, Iiro Harjunoski^c, Lars Imsland^b, Stefan Marco Schneider^a, Ala E.F. Bouaswaig^a and Matthias Roth^a

^a*Automation Technology, BASF SE, 67056 Ludwigshafen, Germany*

^b*Department of Engineering Cybernetics, NTNU, 7491 Trondheim, Norway*

^c*ABB Corporate Research Germany, 68526 Ladenburg, Germany*

^d*Dept. of Biochemical & Chemical Engineering, TU Dortmund, 44221 Dortmund, Germany*
ouyang.wu@ntnu.no

Abstract

Fouling is a typical type of degradation in the process industries, which results in significant negative effects on the efficiency of plants. This paper considers a case study, where production tasks with different recipes contribute to the batch-to-batch fouling evolution depending on their sequence. The scheduling of the production tasks is improved by explicit consideration of the degradation effects, resulting in an optimized production sequence. A set of continuous-time MILP-based scheduling models integrated with degradation models are employed to formulate this batch scheduling problem. The proposed formulations are tested for different problem sizes of the case study illustrating the effectiveness of each of the proposed approaches.

Keywords: multipurpose batch scheduling, sequence-dependent degradation, continuous-time MILP formulation, disjunctive model, precedence model

1. Introduction

Multipurpose chemical batch plants are often a challenge to schedule. These processes typically produce a large number of products requiring several processing steps. When scheduling such processes several factors must be taken into account including, but not limited to, process throughput, storage constraints, equipment condition, and maintenance concerns. When creating scheduling models, one of the major decisions is the time representation chosen for the problem. The time representation can either be continuous or discrete. Continuous time problems in general result in far fewer variables than their discrete counterparts and provide an explicit representation of timing decisions. Continuous time scheduling formulations are broadly classified into precedence, single, or multiple time grid based models (Méndez et al., 2006). Continuous time models have been applied to many different scenarios. Castro and Grossmann (2012) used generalized disjunctive programming to derive generic continuous-time scheduling models.

One aspect of scheduling that has been gaining attention in literature lately is that of integrating equipment condition into production scheduling. Vieira et al. (2017) studied the optimal planning of a continuous biopharmaceutical process with decaying yield. They formulated the problem as a continuous single-time grid formulation making both production scheduling and maintenance scheduling decisions. Other applications of combined maintenance and production scheduling can be found in Biondi et al. (2017) and Dalle Ave et al. (2019) who studied the joint production and maintenance problem of steel plant scheduling under different conditions.

The goal of this work is to investigate the production scheduling of a chemical batch plant with unit degradation. A batch reactor case study considering fouling is presented in which the fouling

prolongs the time needed to complete a batch and is highly influenced by the sequence of products produced in the reactor. The problem is formulated using a set of continuous-time MILP-based scheduling models which will be described and compared in the remainder of this work.

2. Problem description

This case study focuses on a batch polymerization process. Firstly, the product monomers are mixed in a single tank before being homogenized and dispatched to the reactors. Once the monomers have reacted they are dispatched via a shared piping system to storage. The major cause of degradation in this process is fouling in the reactors; polymer residues are accumulated on the inner surfaces of the reactors, heat exchangers, and pipes. This causes reduced heat transfer from the product to the coolant thereby decreasing cooling efficiency and prolonging batch duration. Moreover, the flow resistance due to fouling leads to an increased pressure drop over the heat exchanger. A pressure-based key performance indicator (KPI) was developed to indicate the degree of fouling for each batch run using a state estimation approach, and in this approach many interfering factors due to batch production are excluded from the fouling KPI (Wu et al., 2019). The batch-to-batch behaviors of the fouling evolution discussed in Wu et al. (2018, 2019) indicate that different batch recipes contribute to the fouling evolution differently. Hence, a linear model based the fouling KPI is developed to describe the effects of batch sequences on the batch-to-batch fouling growth, given as:

$$f_{k,j} = A_{R_{k-1,j}} \cdot f_{k-1,j} + B_{R_{k-1,j}} \quad (1)$$

where, $R_{k,j} = r$ indicates Recipe r at the k th batch of Unit j ; $f_{k,j}$ is the fouling KPI for the k th batch of Unit j , which is assumed to follow recipe-based unit-specific linear dynamics $\{(A_{rj}, B_{rj}) \mid r = 1, 2, \dots, |R|, j = 1, 2, \dots, |J|\}$.

The recipe determines the total processing time at each unit, and the reaction duration, which is also affected by the coolant temperature and the fouling. The degree of fouling is approximated using eq. (1), and the coolant temperature is considered as an external disturbance due to uncertainties among the cooling capacities and the demands. Moreover, the reactors and other units are not identical, which also leads to differences in the processing time. A linear model structure is applied to fit the processing time as a function of the fouling KPI and the coolant temperature given the recipe $R_{k,j}$ in Unit j , the coolant temperature is assumed to be fixed for the scheduling scenario. Therefore, the processing time is calculated using only the fouling KPI as eq. (2) shows:

$$Du_{k,j} = AD_{R_{k,j}} \cdot f_{k,j} + BD_{R_{k,j}} \quad (2)$$

where, $Du_{k,j}$ is the reaction processing time at the k th batch of Unit j ; $\{AD_{rj}, BD_{rj}\}$ are the model parameters for Recipe r at Unit j . The degradation impairs the batch production capacity and therefore needs to be explicitly considered in production scheduling. Provided the quantitative models in eqs. (1) and (2), a new scheduling problem considering degradation effects is formulated by integrating the degradation models into existing scheduling optimization approaches. In the next section, continuous-time MILP approaches using precedence concepts are presented for the aforementioned batch scheduling problem.

3. Methodology

In this section, four continuous-time MILP scheduling formulations are presented which integrate the sequence-dependent degradation model using precedence-based constraints. Furthermore, no changeover time and no intermediate storage are considered for the process specifications. Note that while this work focuses on a particular case study, the methodology presented here is generic and could be adapted to other scenarios.

3.1. Nomenclature

I, J, L, R	Sets of batch orders ($i = 1, 2, \dots, I $), units ($j = 1, 2, \dots, J $), stages ($l = 1, 2, \dots, L $) and batch recipes ($r = 1, 2, \dots, R $),
J_l, J_{de}, L_{de}	Sets of units belonging to Stage l , units suffered from degradation and stages containing units suffered from degradation,
Ts_{il}, Te_{il}	Start time and end time of Order i in Stage l ,
Tp_{ij}, Tr_l	Processing time of Order i at Unit j , transfer time in Stage l ,
Ta_{ij}	Additional processing time of Order i at Unit j due to degradation,
f_{ij}, FI_j, R_{ri}	Degradation (fouling) KPI for Order i at Unit j , initial fouling KPI at Unit j , recipe binary indicator for Order i using Recipe r ,
A_{rj}, B_{rj}	Degradation model parameters for Recipe r at Unit j , see eq. (1),
AD_{rj}, BD_{rj}	Duration model parameters for Recipe r at Unit j , see eq. (2),
$X_{i'i'j}^{ui}, W_{ij}$	Sequencing binary variables for a unit-specific immediate precedence model,
$X_{i'l}^{im}, Y_{ij}, W_{ij}$	Sequencing binary variables for an immediate precedence model,
$X_{i'l}^g, Y_{ij}$	Sequencing binary variables for a general precedence model,
S_{ij}	Absolute position of Order i in the sequence of Unit j ,

3.2. Sequence-dependent degradation

The continuous-time immediate precedence fits the form of the sequence-dependent degradation model as shown in eq. (1). Using a unit-specific immediate precedence model, the degradation initialization and propagation are presented in the form of disjunctive constraints as eqs. (3) and (4) show: if Order i is immediately processed after Order i' at Unit j ($X_{i'i'j}^{ui} = 1$), then the batch degradation KPI (f_{ij}) is calculated from its previous value ($f_{i'j}$) using eq. (1); if Order i is processed first in the sequence of unit j ($W_{ij} = 1$), then f_{ij} equals an initial value of the fouling KPI. To avoid nonlinear constraints, the processing time of Order i at Unit j is further divided into a varying duration due to fouling (Ta_{ij}) and a constant duration (Tp_{ij}) according to eq. (2), where the calculations of Ta_{ij} and Tp_{ij} are presented in eq. (4).

$$\bigvee_{i, i' \in I: i \neq i', j \in J_{de}} \begin{bmatrix} X_{i'i'j}^{ui} \\ f_{ij} \geq AS_{ij} \cdot f_{i'j} + BS_{ij} \\ f_{ij} \leq AS_{ij} \cdot f_{i'j} + BS_{ij} \end{bmatrix}, \quad \bigvee_{i \in I, j \in J_{de}} \begin{bmatrix} W_{ij} \\ f_{ij} \geq FI_j \\ f_{ij} \leq FI_j \end{bmatrix} \quad (3)$$

$$Ta_{ij} = \sum_{r \in R} R_{ri} \cdot AD_{rj} \cdot f_{ij}, \quad Tp_{ij} = \sum_{r \in R} R_{ri} \cdot BD_{rj}, \quad \forall i \in I, j \in J_{de} \quad (4)$$

where, $AS_{ij} = \sum_{r \in R} R_{ri} A_{rj}$, and $BS_{ij} = \sum_{r \in R} R_{ri} B_{rj}$.

3.3. Unit-specific immediate precedence model [M1]

A single-stage unit-specific immediate precedence model is proposed in Cerdá et al. (1997), and an adapted version for multistage problems considering unit degradation is presented as follows: given the sequence binaries ($X_{i'i'j}^{ui} = 1$, if Order i is processed immediate after Order i' at Unit j , $W_{ij} = 1$ if Order i is processed in the first place of the sequence at Unit j), the unit-specific immediate precedence constraints are presented in eqs. (5) and (6); the order timing constraints for a single order are presented in eq. (7); the order sequencing and timing constraints for two orders in a single unit are presented using disjunctive constraints as shown in eq. (8). The order sequencing and timing constraints for two orders in neighboring stages considering no immediate storage are presented in eq. (9) (the transfer procedure occupies both units in the two stages); the degradation and duration model constraints are presented in eqs. (3) and (4).

$$\sum_{i \in I} W_{ij} = 1, \quad \forall j \in J \quad (5)$$

$$\sum_{j' \in J_l} W_{ij'} + \sum_{i' \in I: i' \neq i, j' \in J_l} X_{i'i'j'}^{ui} = 1, \quad \sum_{i' \in I: i' \neq i, j' \in J_l} X_{i'i'j'}^{ui} \leq 1, \quad \forall i \in I, l \in L \quad (6)$$

$$Te_{il} = Ts_{il} + \sum_{j \in J_l} [Tp_{ij}(W_{ij} + \sum_{i' \in I: i' \neq i} X_{i'i'j}^{ui}) + Ta_{ij}], \quad Ts_{i(l+1)} \geq Te_{il} + Tr_l, \quad \forall i \in I, l \in L \quad (7)$$

$$\bigvee_{i,i' \in I: i \neq i', l \in L} \left[\begin{array}{c} \sum_{j \in J_l} X_{i'ij}^{ui} \\ Te_{i'l} + Tr_l \leq Ts_{il} - Tr_{(l-1)} \end{array} \right] \quad (8) \quad \bigvee_{i,i' \in I: i \neq i', l \in L: l < |l|} \left[\begin{array}{c} \sum_{j \in J_l} X_{i'ij}^{ui} \\ Ts_{il} \geq Ts_{i'(l+1)} + Tr_l \end{array} \right] \quad (9)$$

3.4. Immediate precedence model [M2]

In contrast to M1, the immediate precedence model (Gupta and Karimi, 2003) uses two types of binary variables $\{X_{i'il}^{im}, Y_{ij}\}$ ($X_{i'il}^{im} = 1$ indicates Order i is immediately processed after Order i' in some units of Stage l ; $Y_{ij} = 1$ indicates Order i is assigned to Unit j), which fits into the sequence-dependent degradation in eq. (3) by replacing $X_{i'ij}^{ui}$ with $X_{i'il}^{im} \wedge Y_{ij} \wedge Y_{i'j}$. The order assignment and immediate precedence constraints are presented in eqs. (5), (10) and (11), and the order timing constraints for a single order are presented in eq. (12). Lastly, the order sequencing and timing constraints for two orders in a single unit and neighboring stages are presented in eq. (13).

$$\sum_{j \in J_l} Y_{ij} = 1, \sum_{j \in J_l} W_{ij} + \sum_{i' \in I: i' \neq i} X_{i'il}^{im} = 1, \sum_{i' \in I: i' \neq i, l \in L} X_{i'il}^{im} \leq 1, \forall i \in I, l \in L \quad (10)$$

$$Y_{ij} \leq Y_{i'j} + 1 - X_{i'il}^{im} - X_{i'j}^{im}, \forall i, i' \in I: i \neq i', j \in J_l, l \in L \quad (11)$$

$$Te_{il} = Ts_{il} + \sum_{j \in J_l} (Tp_{ij} Y_{ij} + Ta_{ij}), Ts_{i(l+1)} \geq Te_{il} + Tr_l, \forall i \in I, l \in L \quad (12)$$

$$\bigvee_{i,i' \in I: i \neq i', l \in L} \left[\begin{array}{c} X_{i'il}^{im} \\ Te_{i'l} + Tr_l \leq Ts_{il} - Tr_{(l-1)} \end{array} \right], \quad \bigvee_{i,i' \in I: i \neq i', l \in L: l < |l|} \left[\begin{array}{c} X_{i'il}^{im} \\ Ts_{il} \geq Ts_{i'(l+1)} + Tr_l \end{array} \right] \quad (13)$$

3.5. Hybrid precedence model [M3]

When comparing to M1 and M2, general precedence models proposed by Méndez and Cerdá (2003) generally prevail with less computation cost. These models use binary variables $X_{i'il}^g = 1, Y_{ij} = 1, Y_{i'j} = 1$ to represent that Order i is processed after i' at Unit j in Stage l . But unlike M1 and M2, it does not provide immediate precedence relations. Given that the sequence-dependent degradation only occurs in certain stages, a hybrid precedence model is developed by replacing M2 with general precedence constraints in the stages requiring no immediate precedence information ($l \in L_n = L \wedge \neg L_{de}$). The precedence constraints are presented in eq. (14), and the order timing constraints for a single order are the same as M2 as eq. (12) shows. The order sequencing and timing constraints for two orders in the same stage or neighboring stages are presented in eq. (15).

$$\sum_{j \in J_l} Y_{ij} = 1, X_{i'il}^g + X_{i'j}^g = 1, \forall i, i' \in I: i \neq i', l \in L - L_{de} \quad (14)$$

$$\bigvee_{\substack{i,i' \in I: i' \neq i, \\ j \in J_l, l \in L_n}} \left[\begin{array}{c} X_{i'il}^g \wedge Y_{ij} \wedge Y_{i'j} \\ Te_{i'l} + Tr_l \leq Ts_{il} - Tr_{(l-1)} \\ Ts_{il} \geq Ts_{i'(l+1)} + Tr_l \end{array} \right], \quad \bigvee_{i,i' \in I: i' \neq i, l \in L_n} \left[\begin{array}{c} X_{i'il}^g \\ Ts_{i'l} + Tr_l \leq Ts_{il} \end{array} \right] \quad (15)$$

3.6. General precedence based model [M4]

A general precedence based model for sequence-dependent changeovers is proposed in Aguirre et al. (2012, 2017), which also can be adapted to the scheduling problem considering sequence-dependent degradation. The general precedence model presented in M3 is extended to all stages, and the immediate precedence binary variables $X_{i'il}^{im}, W_{ij}$ are introduced for the stages and units having sequence-dependent behaviors ($j \in J_{de}, l \in L_{de}$). By introducing a continuous variable S_{ij} , defined as the absolute position of batch i in the sequence of Unit j , the immediate precedence variables are connected to the general precedence model using eq. (16).

$$\bigvee_{i,i' \in I: i \neq i', j \in J_l, l \in L_{de}} \left[\begin{array}{c} X_{i'il}^g \wedge Y_{ij} \wedge Y_{i'j} \\ S_{ij} \geq S_{i'j} + 1 \\ X_{i'il}^{im} + S_{ij} - 1 \geq S_{i'j} + 1 \end{array} \right], \quad Y_{ij} \leq S_{ij} \leq \sum_{i \in I} Y_{ij}, \forall i \in I, j \in J_{de} \quad (16)$$

3.7. Big-M reformulation and objective function

The disjunctive programming constraints in the precedence models are reformulated into the MILP frameworks using the big-M approach. More details can be found in Castro and Grossmann (2012). This objective function considered in this work is the minimization of makespan considering fouling-influenced batch time.

4. Case study: computational results

Size	M1	M2	M3	M4
12(6,6)	3495.02 (53%)	3495.02(74sec)	3495.02(37%)	3495.02(37%)
15(7,8)	4315.79 (70%)	4266.73(979sec)	4282.61(42%)	4266.73(42%)
18(7,8,3)	5164.13 (79%)	5589.43(84%)	5116.97(46%)	5164.13(47%)
25(6,5,4,5,5)	7237.93 (91%)	13339.37(94%)	7034.91(51%)	7375.89(53%)

Table 1: Computational results of different formulations: objective function and optimality gap

Referring to the aforementioned case studies, the monomer make-up section and the reaction section are taken as the two production stages with one monomer vessel (U1) in Stage L1 and two non-identical reactors (U2 and U3) in Stage L2. The process topology can be viewed in Figure 1. Due to the lack of intermediate storage, the homogenization section (L1-Tr) is modeled as a transfer procedure between the stages. This transfer occupies both the discharging mixer as well as the reactor that is being charged, which is modeled using eq. (9) for model M1. Additionally, the only pipeline (L2-Tr) transfers product from either U2 or U3 into storage. To prevent multiple orders overlapping in L2-Tr, the ordering and timing constraints are used in a similar way as shown in eq. (8) by introducing an artificial precedence binary for this unit. In this case study, when minimizing makespan, it is not possible for jobs to overtake one another in L2 and therefore the precedence binary variable for L2-Tr same one for L1. In addition, an operational threshold is added on the degradation indicator.

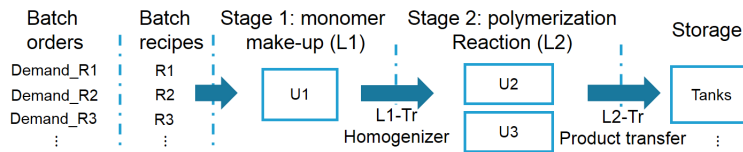


Figure 1: The topology of the batch process

Each of the four models defined earlier were tested for varying problem sizes. Take 15(7,8) for example, 15 refers to the total amount of product demand, and the values inside the parentheses (7,8) refer to the demands for different recipes. The parameters of the scheduling problem are obtained from the case study and the historical data. The models are implemented in GAMS 25.1 and solved using CPLEX 12.8, and the time limit is set to 1200 CPU seconds. The Gantt chart and fouling curves for the 25-order case using M3 are illustrated in fig. 2; the normalized fouling KPI data are presented for two units (U2 and U3) with different symbols denoting the recipes from R1 to R5, and the threshold for the normalized fouling KPI is one. Furthermore, the computational results are presented in table 1 with objective values and relative optimality gaps. Results show that the small-size problems using M2 are solved to zero gap before 20 minutes but the computation cost increases dramatically with larger problem size; M3 has better computational performance (smaller value of objective function and smaller relative optimality gap) for the problem sizes 18(7,8,3) and 25(6,5,4,5,5).

5. Conclusions

A short-term batch scheduling problem considering sequence-dependent degradation was formulated using different continuous-time MILP methods. Taking an industrial case study as example,

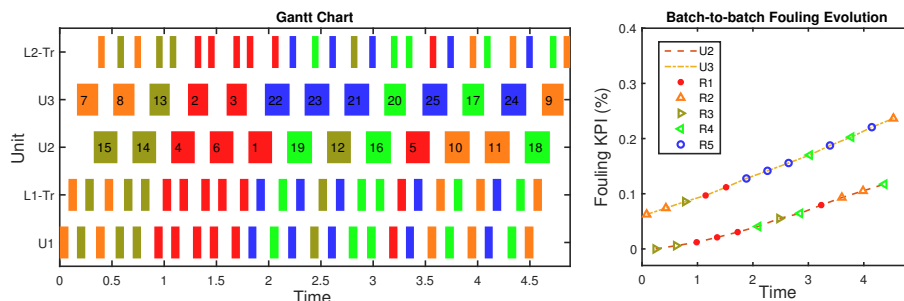


Figure 2: Result of the 25-order problem using M3

the recipe-based degradation models are integrated with the precedence models to improve the scheduling of batch production. Four integrated MILP formulations are compared by running the scheduling models with different problem sizes, and the hybrid precedence model is shown to have the best computation performance for relatively large-size problems. However, the investigated formulations do not find a provably optimal solution within 20 minutes; future work involves improving the computational performance of such models.

Acknowledgments: Financial support is gratefully acknowledged from the Marie Skłodowska Curie Horizon 2020 EID-ITN project “PRONTO”, Grant agreement No 675215.

References

- A. M. Aguirre, S. Liu, L. G. Papageorgiou, 2017. Mixed integer linear programming based approaches for medium-term planning and scheduling in multiproduct multistage continuous plants. *Industrial & Engineering Chemistry Research* 56 (19), 5636–5651.
- A. M. Aguirre, C. A. Méndez, P. M. Castro, C. De Prada, 2012. Milp-based approach for the scheduling of automated manufacturing system with sequence-dependent transferring times. In: *Computer Aided Chemical Engineering*. Vol. 30. Elsevier, pp. 477–481.
- M. Biondi, G. Sand, I. Harjunkoski, 2017. Optimization of multipurpose process plant operations: A multi-time-scale maintenance and production scheduling approach. *Computers & Chemical Engineering* 99, 325 – 339.
- P. M. Castro, I. E. Grossmann, 2012. Generalized disjunctive programming as a systematic modeling framework to derive scheduling formulations. *Industrial & Engineering Chemistry Research* 51 (16), 5781–5792.
- J. Cerdá, G. P. Henning, I. E. Grossmann, 1997. A mixed-integer linear programming model for short-term scheduling of single-stage multiproduct batch plants with parallel lines. *Industrial & Engineering Chemistry Research* 36 (5), 1695–1707.
- G. Dalle Ave, J. Hernandez, I. Harjunkoski, L. Onofri, S. Engell, 2019. Demand side management scheduling formulation for a steel plant considering electrode degradation. In: *IFAC International Symposium on Dynamics and Control of Process Systems (DYCOPS)*.
- S. Gupta, I. Karimi, 2003. An improved milp formulation for scheduling multiproduct, multistage batch plants. *Industrial & engineering chemistry research* 42 (11), 2365–2380.
- C. A. Méndez, J. Cerdá, 2003. An milp continuous-time framework for short-term scheduling of multipurpose batch processes under different operation strategies. *Optimization and Engineering* 4 (1-2), 7–22.
- C. A. Méndez, J. Cerdá, I. E. Grossmann, I. Harjunkoski, M. Fahl, 2006. State-of-the-art review of optimization methods for short-term scheduling of batch processes. *Computers & Chemical Engineering* 30 (6-7), 913–946.
- M. Vieira, T. Pinto-Varela, A. P. Barbosa-Pvoa, 2017. Production and maintenance planning optimisation in biopharmaceutical processes under performance decay using a continuous-time formulation: A multi-objective approach. *Computers & Chemical Engineering* 107, 111 – 139.
- O. Wu, A. E. F. Bouaswaig, S. M. Schneider, F. Moreno Leira, L. Imsland, M. Roth, 2018. Data-driven degradation model for batch processes: a case study on heat exchanger fouling. In: *Computer Aided Chemical Engineering*. Vol. 43. Elsevier, pp. 139–144.
- O. Wu, L. Imsland, E. Brekke, S. M. Schneider, A. E. F. Bouaswaig, M. Roth, 2019. Robust state estimation for fouling evolution in batch processes using the em algorithm. In: *IFAC International Symposium on Dynamics and Control of Process Systems (DYCOPS)*.

Real-time determination of optimal switching times for a H₂ production process with CO₂ capture using Gaussian Process Regression models

Luca Zanella^a, Marcella Porru^{b,*}, Giulio Bottegal^b, Fausto Gallucci^b, Martin van Sint Annaland^b and Leyla Özkan^b

^a*University of Padova, Via Marzolo 9, Padova, 35131, Italy*

^b*Eindhoven University of Technology, Eindhoven, 5600 MB, The Netherlands*

* *m.porru@tue.nl*

Abstract

This work presents a systematic methodology to determine in real-time the optimal durations of the three stages of a new Ca-Cu looping process for H₂ production with integrated CO₂ capture. Economic and quality criteria are proposed to determine the appropriate time to switch between the stages. These criteria rely on the time-profiles of some key variables, such as product concentrations. Given the delayed nature of hardware sensor measurements, the real-time determination of such variables is based on soft-sensors. For this purpose, Gaussian Process Regression models are employed. The predictive capabilities of these models are tested on several datasets, yielding reliable predictions in most of the cases. The values of the optimal switching times computed with the proposed method differ from the actual values by 4 %, at most.

Keywords: machine learning, gaussian process regression models, CO₂ capture, process intensification, process monitoring.

1. Introduction

The calcium-copper (Ca-Cu) looping technology is a cyclic, three-stages process for H₂ production with integrated CO₂ capture conducted in dynamically operated packed bed reactors (Abanades et al., 2010). While a satisfactory understanding of the underlying phenomena is available, investigations in the field of process automation are needed to efficiently upscale the process. Since the behaviour of each stage is inherently dynamic, one issue is the assessment of the optimal duration. The main aim of this work is to develop a methodology to identify the appropriate time instant to switch between stages. This is crucial to match satisfactory operating targets, including economic profitability and product quality specifications. Once suitable switching criteria have been defined, the optimal duration of the stages can be either scheduled or computed in real-time. The second approach is preferable, because it allows more flexibility in dealing with disturbances and process uncertainties. In practice, not all the variables needed for the evaluation of the switching criteria can be sensed in real-time. This is the case of composition measurements obtained via hardware analysers, which are often affected by substantial time-delays. Instead, soft-sensors can be employed as virtual analysers. Soft-sensors are models that allow the estimation of hard-to-measure, primary variables, making use of

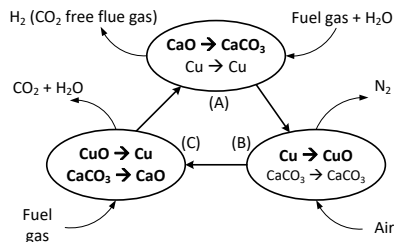


Figure 1: The three stages Ca-Cu chemical looping process for H₂ production.

secondary variables, that are easily sensed online. Several soft-sensing techniques have been reported in literature. A common classification is based on the type of models employed, either first principle or data-driven. First principle models usually allow reliable extrapolation (Porru et al., 2013), but lack of knowledge in some aspects of the underlying physics might result in poor performance (Porru and Özkan, 2017). Moreover, model complexity might make their solution too computationally demanding for real-time applications (Shokry et al., 2017). Conversely, data-driven models may suffer from limited extrapolation capabilities, since they only encode information available in the training data (Bonvin et al., 2016). Hence, the amount of data required for their training is usually large. A major advantage compared to first-principle models is that a deep knowledge of the process is not necessary. Hence, data-driven soft-sensors are particularly suitable to monitor complex and recursive processes, such as the Ca-Cu looping for H₂ production. Among a plethora of data-driven models, Gaussian Process Regression (GPR) is a method for supervised learning (Rasmussen and Williams, 2006). It allows performing regression without giving explicit parametrization to the underlying function, instead determining a distribution over the possible functions that are consistent with the observed data. The application of GPR has several advantages over popular machine learning methods used in process engineering, such as artificial neural networks. These include limited number of parameters to be estimated, the capability of automatically providing confidence intervals for the predictions and that of dealing with noisy measurements, by acting as *smoothing devices*. Although GPR has received great interest in recent years, its use for soft-sensing is still rather limited (Mei et al., 2016). Here, GPR models are proposed as soft-sensors to evaluate the conditions that trigger the switch from one stage to the next.

2. The Ca-Cu looping process

The Ca-Cu looping process is a novel concept for high purity H₂ production from CH₄ with integrated CO₂ capture. The process has been gaining increasing attention as a low-CO₂ emission solution for both power generation and H₂ production (Martini et al., 2016, 2017). The process consists of three stages, conducted cyclically in packed bed reactors. Switching between stages is performed by alternating the gaseous reactants fed to the reactor and changing the operating conditions in the fixed bed, mainly temperature and pressure. Figure 1 schematically shows the inlet and outlet flows of the stages and the main reactions involved in the solid phase. Data sets employed in the present work are collected via an experimental campaign. The solid bed contains three different solids: a Ni-based catalyst, to catalyse the reforming reactions, CaO, employed as CO₂-sorbent

material and Cu which is involved in the regeneration of CaO. The available set up allows the measurement of the following variables: temperature of the solid bed along the axial profile, $T_s(z)$, inlet and outlet gas temperatures, T_G^0 and T_G^{out} , inlet and outlet gas pressure, P_G^0 and P_G^{out} , outlet (dry) volume fractions, x_i^{out} and outlet (dry) volume flow rate, \dot{V}_{tot}^{out} .

In Stage A, sorption enhanced reforming takes place. The reactor is fed with a mixture of CH_4 and steam with a given steam-to-carbon ratio (S/C). The three main reactions are steam-methane reforming (SMR), water-gas shift (WGS) and carbonation of CaO. The last reaction allows the removal of the CO_2 formed, increases H_2 purity, CH_4 and CO conversions by shifting the SMR and WGS equilibria toward the products. In addition, the combination of these reactions makes the overall stage exothermic, so that the only energy duty is the one needed to compensate for the heat losses. This stage is considered terminated when the CaO is fully converted to $CaCO_3$, indicating that no more CO_2 can be captured by the fixed bed. To allow continuous operation, the $CaCO_3$ formed in this stages is regenerated to CaO by the Cu/CuO chemical loop carried out in stages B and C. In stage B, Cu is oxidized to CuO by feeding pressurized diluted air to the reactor. This stage is considered concluded when most of the Cu has been oxidised. The high pressure and low O_2 content prevent the calcination of $CaCO_3$.

Switching to stage C is performed by changing the feed to H_2 or other reducing species at lower pressure, such as syngas or CH_4 . The reduction of CuO to Cu provides the energy required for the calcination of $CaCO_3$ that regenerates the CO_2 sorbent. When most of the CuO has been reduced, switching to stage A is performed again.

3. Switching criteria

Economic and quality criteria are proposed to determine the appropriate time to switch (t_s) to the next stage. In the previous section the definition of end times was based on the state assumed by the solid bed. However, measurements of the solid bed composition are not available, nor easy to perform in-situ at industrial scale. Therefore, the course of each stage should be monitored employing other variables, such as temperature or gas composition. In this work, t_s is determined via an optimization-based approach. Table 1 reports the objective functions to be maximized and constraints. P (€/time) is a profit

Table 1: Switching criteria employed for stages A, B and C.

Stage	Objective Function	Constraint
A	$\int_0^t P(\tau) d\tau$	$x_{H_2}^{out}(t) \geq 0.85$
B	$T_s^{out}(t)$	$\dot{M}_{O_2}^{out}(t)/\dot{M}_{O_2}^0(t) \leq 0.35$
C	$T_s^{out}(t)$	$\dot{M}_{H_2}^{out}(t)/\dot{M}_{H_2}^0(t) \leq 0.35$

function, depending on several variables, including \dot{V}_{tot}^{out} , x_i^{out} , prices of chemicals, carbon tax on CO_2 emissions etc. \dot{M}_i is the mass flow rate of species i , computed with the ideal gas law. T_s^{out} is the outlet bed temperature. Although quite simple, the selected criteria aim to fulfil multiple requirements. For stage A, operation should last until it is economically profitable while the required H_2 purity constraint is not violated. For stages B and C, the proposed criteria aim to maximize the amount of Cu oxidation and reduction, respectively.

The constraint is motivated by the fact that a release of considerable amounts of O_2 and H_2 is an indication of the two stages coming to an end. The behaviour of the objective functions has been studied offline (i.e. after completion of the batches, and collection of the data), finding that they admit a unique maximum. These criteria are applied to all the datasets collected, considering the stages separately, resulting in a wide dispersion of the optimal durations, even at fixed operating conditions. Such differences are mainly linked to run-to-run variations of hardly controllable variables, such as the solid bed state. This makes it necessary to implement the criteria in real-time (i.e. during the batch run, as soon as a new data point is collected), to enable timely switching. The application of these criteria lies on the availability of the time-profiles of concentrations of several components with delayed measurements. Therefore, an inferential model is needed to allow their estimation in real-time. This is achieved by employing GPR.

4. Method: Gaussian Process Regression models

Let $\mathcal{D} = \{(\mathbf{x}_i, y_i) \mid i = 1, \dots, n\}$ be a training set of input-output pairs, where n is the number of measurement points, \mathbf{x}_i is a vector collecting the inputs (often collected in a matrix X) and y_i is the measured output at point i (often collected in a vector \mathbf{y}). The goal of GPR is to perform nonlinear regression without giving explicit parametrization of the underlying function. A prior probability is assigned to any possible function, such that higher probabilities are given to those functions which are considered more likely to describe the input-output observations (Mackay, 1998). The functions providing the best representation of the data are found by performing Bayesian inference collectively at the training points. Training of GPR models consists of two main steps:

- a. Model selection. It consists of the choice of a kernel, k , which is a function of two arguments that set qualitative properties of the unknown function, such as smoothness or periodicity. The kernel measures the similarity between two training points x_i and x_j .
- b. Model training. This step involves the tuning of a few hyperparameters, denoted by $\boldsymbol{\theta}$, through which k is parametrized in order to give flexibility to the selected model. In this work, the estimation of $\boldsymbol{\theta}$ is achieved by maximization of marginal likelihood (we refer to Rasmussen and Williams (2006), Ch. 5, for details on marginal likelihood estimation).

Once the model is trained, the prediction of the output y_* at any point x_* that does not belong to the training set is computed assuming that its conditional probability given the training data follows a Gaussian distribution, namely $y_* | \mathbf{y} \sim \mathcal{N}(K_*(K + \gamma I)^{-1} \mathbf{y}, K_{**} - K_*(K + \gamma I)^{-1} K_*^\top)$, where K is a covariance matrix containing kernel evaluation of each pair of points that belong to the training set, γ is a hyperparameter tuning the smoothness of the function, K_* is the vector containing the kernel evaluations between all training points and the test point and K_{**} is the variance on the test point. The predicted value y_* is computed as the mean of the previous distribution: $y_* = \bar{y}_* = K_*(K + \gamma I)^{-1} \mathbf{y}$. The method automatically provides the confidence interval of the predicted value of the function as the posterior variance of the Gaussian distribution through the simple expression: $var(y_*) = K_{**} - K_*(K + \gamma I)^{-1} K_*^\top$.

5. Online determination of the switching time

The use of criteria in Table 1 makes it necessary to predict in real-time the following primary variables, \mathbf{y} : \dot{V}_{tot}^{out} , $x_{H_2}^{out}$, $x_{CO_2}^{out}$ during stage A, \dot{V}_{tot}^{out} , $x_{O_2}^{out}$ during stage B and \dot{V}_{tot}^{out} , $x_{H_2}^{out}$

during C. Separate GPR models have been trained for each of them, because the method holds for scalar outputs. Both training and test sets are a subset of the data sets employed in the previous section. As the computational time needed to train a model is $\mathcal{O}(n^3)$, model training is performed offline. The MATLAB[®] routine `fitrgp` is employed for this purpose. Among all the variables sensed in the set up, the predictors are selected as the ones satisfying two requirements: (i) being influential on the outputs, since employing non-influential variables is observed to cause overfitting and large prediction variances; (ii) being available in real-time. Based on these considerations, t , P_G^0 and inlet compositions, specifically S/C , $x_{O_2}^0$ and $x_{H_2}^0$ in stages A, B and C, respectively, are employed as predictors to target all the outputs. Other variables are expected to be influential on the outputs. However, their variability in the available datasets is rather limited, hence including them would be of little use. The predictor matrices, X_A , X_B and X_C for the three stages are constructed as $X_A = [\mathbf{t} \ \mathbf{P}_G^0 \ S/C]$, $X_B = [\mathbf{t} \ \mathbf{P}_G^0 \ x_{O_2}^0]$ and $X_C = [\mathbf{t} \ \mathbf{P}_G^0 \ x_{H_2}^0]$, respectively. Bold symbols identify vectors, whose entries are the values of the variable along the time series, \mathbf{t} . Due to the computational demand of GPR, the number of training data is set equal to a few thousand, building matrices of dimensions $\dim X_A = 1464 \times 3$, $\dim X_B = 3927 \times 3$ and $\dim X_C = 1791 \times 3$, respectively. The observations included in X_A belong to 24 datasets, 4 for each set of nominal operating conditions ($S/C = 3, 4, 5$ and $P_G^0 = 2$ and 7 bar), those in X_B belong to 49 datasets, 7 for each set of operating conditions ($x_{O_2}^0 = 3\%, 5\%, 10\%$ and P_G^0 variable in the interval 3-8 bar) and the ones in X_C belong to 36 datasets, 12 for each value of $x_{O_2}^0$ (equal to 20%, 39% and 58%). Predictors are standardised to reduce complexity during calculation and to avoid those having greater order of magnitude dominating those of a smaller one. The squared exponential (k_{se}) and rational quadratic (k_{rq}) kernels are employed to model \hat{V}_{tot}^{out} and x_i^{out} , respectively.

The predictive capabilities of the models are tested on 38, 97 and 221 datasets of the three stages. Figure 2 shows the predicted profiles of two key variables employed in stage A. These plots are representative of most of the results. GPR provides very reliable predictions, the underlying functions are quite smooth and the confidence intervals are sufficiently tight.

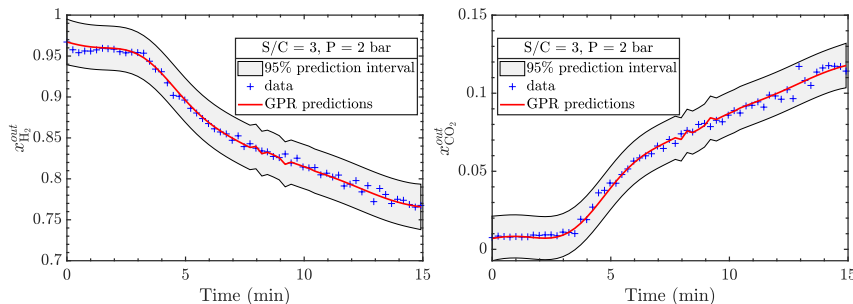


Figure 2: Time-profiles of: (a) $x_{H_2}^{out}$ and (b) $x_{CO_2}^{out}$ for stage A.

The real-time determination of t_s is simulated for several runs of each stage, by employing the GPR-based soft-sensors. At each sampling time (1 s), GPR soft-sensors use the measured values of the secondary variables to infer the values of the primary variables.

This way, the value of the objective function and constraints in Table 1 are computed. When the value of the objective function at the current time is smaller than the previously calculated one or the constraint is being hit, then switching is triggered (assuming that the constraint has a unique maximum). The use of GPR-based soft sensors, even in critical experimental runs, results in satisfactory performance. As an example, the actual value of t_s computed for one experimental run of stage A at $S/C = 5$, $P_G^0 = 5$ bar, results in 9.43 min. Conversely, scheduling the duration of t_s as the average of the values computed offline for all the data sets at the same operating conditions would result in $t_s = 11.59$ min, corresponding to an error of 23 %. In addition, such a time duration would not have allowed satisfying the constraint. The use of the GPR-based soft-sensors allows a real-time estimation of $t_s = 9.80$ min, which corresponds to a reduction in the error to only 3.89 %, which is a satisfactory performance for this application.

6. Conclusions

This work deals with the real-time determination of the switching instants of a cyclic process for H_2 production with integrated CO_2 capture. The proposed methodology is based on online evaluation of switching criteria, aiming to maximize economic and quality indicators. GPR-based soft sensors have been developed to make online predictions of these criteria. The use of GPR-based soft-sensors allows a real-time estimation of the optimal times to switch with a maximum error of only 4 % in the investigated runs. Future work should be devoted to identify reliable principles for a quantitative assessment of model performance and to improve model update techniques. This fact is crucial to abate process-model mismatches.

References

- J. Abanades, R. Murillo, J. Fernandez, G. Grasa, I. Martínez, 2010. New CO_2 capture process for hydrogen production combining Ca and Cu chemical loops. *Environ. Sci. Technol.* 44, 6901–6904.
- D. Bonvin, C. Georgakis, C. C. Pantelides, M. Barolo, M. A. Grover, D. Rodrigues, R. Schneider, D. Dochain, 2016. Linking models and experiments. *Ind. Eng. Chem. Res.* 55, 6891–6903.
- D. J. C. Mackay, 1998. Introduction to gaussian processes. NATO ASI Series F Computer and Systems Sciences 168, 133–166.
- M. Martini, I. Martínez, M. Romano, P. Chiesa, F. Gallucci, M. van Sint Annaland, 2017. Increasing the carbon capture efficiency of the Ca-Cu looping process for power production with advanced process schemes. *Chem. Eng. J.* 328, 304 – 319.
- M. Martini, A. van den Berg, F. Gallucci, M. van Sint Annaland, 2016. Investigation of the process operability windows for Ca-Cu looping for hydrogen production with CO_2 capture. *Chem. Eng. J.* 303, 73 – 88.
- C. Mei, M. Yang, D. Shu, H. Jiang, G. Liu, Z. Liao, 2016. Soft sensor based on gaussian process regression and its application in erythromycin fermentation process. *Chem. Ind. Chem. Eng. Q.* 22, 127–135.
- M. Porru, J. Alvarez, R. Baratti, 2013. A distillate composition estimator for an industrial multicomponent ic4-nc4 splitter with experimental temperature measurements. *IFAC Proceedings volumes 46 (32)*, 391–396.
- M. Porru, L. Özkan, 2017. Monitoring of batch industrial crystallization with growth, nucleation, and agglomeration. part 1: Modeling with method of characteristics. *Ind. Eng. Chem. Res.* 56 (20), 5980–5992.
- C. Rasmussen, C. Williams, 2006. *Gaussian Processes for Machine Learning*. MIT Press, Cambridge, Massachusetts.
- A. Shokry, M. Pérez-Moya, M. Graells, A. E. na, 2017. Data-driven dynamic modeling of batch processes having different initial conditions and missing measurements. *Comput. Aided Chem. Eng.* 40, 433–438.

Applying a Sustainability Metric in Energy, Water and Food Nexus Applications; A Biomass Utilization Case Study to Improve Investment Decisions

Ahmed AlNouss,^{a,b} Sarah Namany,^b Gordon McKay,^b Tareq Al-Ansari^{b,*}

^aDepartment of Chemical Engineering, College of Engineering, Qatar University,

Doha, Qatar

^bDivision of Sustainable Development, College of Science and Engineering, Hamad Bin

Khalifa University, Qatar Foundation, Doha, Qatar

talansari@hbku.edu.qa

Abstract

The demand for energy, water and food (EWF) resources will continue to increase, especially as the population is expected to reach 9 billion by 2050. The consequences of this include resource exhaustion and environmental degradation. Global pressures, such as climate change and resources depletion have encouraged the deployment of alternative energy systems and integration of carbon capture and sequestration processes. Currently, most chemicals and energy carriers are derived from finite fossil fuels which are susceptible to price fluctuation. Biomass, a renewable carbon-based fuel can be considered a promising substitute that can reduce environmental footprints in various applications. Gasification is a preferred route for handling biomass, in which the gas mixture (syngas) product is utilised to drive gas turbines and produce clean energy. Moreover, it can also be used to substitute natural gas in the petrochemical plants for methanol and ammonia production. Analysing the utilisation strategy of diverse biomass feedstocks represents a fertile research problem that can be addressed from a EWF Nexus perspective, which enables the quantification of impacts of biomass utilization strategies on the EWF systems. In this study, the utilisation strategy of biomass gasification feedstock for the poly-generation of different products is evaluated from an economic perspective. The Aspen Plus simulation models an oxygen-steam gasification technology to generate the optimal characteristics for each utilisation technique. Moreover, a sustainability metric was utilised to quantify the effect of each technique on EWF resources and to extend the investment decision making. Preliminary results generated from the simulation are integrated into a linear programming optimisation model that identifies the optimum biomass utilisation techniques that consider environmental and economic performances. The framework developed enables the selection of the optimal mix of biomass techniques that maximises sustainability indices for EWF resource systems, whilst ensuring a positive generation of the three corresponding resources. The results demonstrate that urea production and power generation are the most viable biomass utilisation techniques.

Keywords: Biomass Gasification, EWF Nexus, Sustainability, Optimisation, Decision Making

1. Introduction

The notion of producing renewable chemicals and fuels is driving sustainable development in the modern society towards a decreasing dependency on fossil fuels. The annual global production of petrochemicals is very large and implies a need to identify alternative routes to replace the fossil-based feedstocks to reduce GHG emissions as part of the global sustainable development agenda (Andersson, 2013). One of the main solutions considered for achieving large reductions in GHG emissions, is the increased production and usage of bioenergy. Considering the current total energy supply of 475 EJ, the International Panel on Climate Change (IPCC) expects that 120 to 155 EJ of the annually supplied primary energy can be extracted from biomass by 2050 (IPCC, 2011). Gasification is considered as the most flexible biomass feedstock route for the generation of various advanced biofuels, such as Fischer-Tropsch diesel or methanol. Bio-methanol produced via gasification of biomass has the potential to replace petrol in conventional combustion engines which can secure the transportation sector with renewable energy. Biomass gasification is also useful for green chemical production where green ammonia can be produced, thereby reducing the dependency on fossil fuels and reducing the emissions of greenhouse gases from the fertiliser industry (Andersson, 2013).

Numerous studies have been conducted to highlight the potential for producing value added products from biomass recycling. Arora et al. investigated the production of a small-scale ammonia plant from biomass to ensure sustainable and profitable production. The study emphasised the techno-economic benefits resulting from ammonia biomass-based production. Calculations produced using Aspen Plus simulation illustrated a 54-68% reduction in CO₂ emissions in comparison to the fossil-based conventional ammonia plants. Moreover, a wider spectrum of studies have been conducted to review the current status of the biomass technology and its utilisation in the production of value added products (Arora et al., 2016). Pike et al. discussed the wide range of opportunities to produce value added products generation from biomass. The study adopted the chemical complex analysis system to evaluate the introduction of plants producing multiple biomass-based chemicals. The developed superstructure of biomass-based chemical production system determined the optimal configuration of plants, considering economic, environmental and sustainable perspectives (Pike et al., 2008).

EFW Nexus systems have been widely used in recent years to address complex resource management challenges, and assess the significance and magnitude of the environmentally possible impacts when supplying a service or product. Integrated analysis considering an EFW Nexus approach enables the identification of key synergies and trade-offs that may exist in the design and operation of EFW sub-systems. Moreover, renewable energy technologies when integrated into EFW Nexus system analysis can address some of the trade-offs between EFW resources (Ferroukhi et al., 2015). Al-Ansari et al. developed an EFW Nexus tool based on a life cycle assessment (LCA) where EFW Nexus sub-systems are transformed from a linear system to highly efficient closed loop systems. The Nexus tool integrates biomass gasification combined cycle (IBGCC) and CO₂ capture to assess the environmental impact of a hypothetical food security scenario in Qatar. The results illustrated near relative carbon neutrality can be achieved through the integration of photovoltaic (PV), biomass gasification coupled with carbon capture for the system considered (Al-Ansari et al., 2016, 2017).

In this study, the utilisation strategy of biomass gasification feedstock for the poly-generation of different products is evaluated from an economic perspective. An Aspen

Plus model simulating gasification technology is utilised to generate the optimal characteristics for each utilisation technique. Moreover, a sustainability metric is integrated into the model in order to quantify the effect of each utilisation technique on EWF resources and to improve the investment decision.

2. Model development

Advanced system models are necessary in order to undertake reliable process economic and energy efficiency analyses of integrated biomass gasification routes. As such, a flowsheet of the biomass gasification system is simulated using Aspen Plus software evaluating Qatar’s biomass characteristics. This study is an expansion of previous work (AlNouss et al., 2018) and is novel as it optimises a unique set of biomass feedstock which includes date pits, food waste, manure and bio-sludge. The simulation takes advantage of oxygen and steam in the gasification of different feedstocks to generate H₂-rich syngas, utilized in the production of value-added products i.e. methanol, urea, power through IBGCC and Fischer-Tropsch liquids (FTL). Table 1 summarizes the elemental analyses of the biomass feedstocks considered in the study based on Qatar’s characteristics.

Table 1: Proximate and ultimate analyses of biomass feedstock

	Manure	Dried Sewage Sludge	Date Pit waste	Food Waste
Mass Flow (tons/y)	5.27x10 ⁵	3.65x10 ⁴	7.60x10 ³	7.0x10 ³
Proximate analyses (wt %)				
Volatile matter	65.0	8.8	81.8	86.1
Fixed carbon	13.5	19.4	17.2	7.7
Ash	21.6	71.8	1.0	6.2
Moisture	27.4	8.3	5.0	75.1
Ultimate analyses (wt %)				
C	37.1	19.1	49.8	46.4
H	5.1	2.3	6.8	6.9
O	31.4	5.7	37.9	37.4
N	3.7	1.1	4.5	3.1
S	0.5	0.1	0.0	0.0
Cl	1.0	0.0	0.0	0.0
Ash	21.4	71.8	1.0	6.2
LHV (dry basis) (MJ/kg)	19.09	16.40	25.30	19.84

The generated H₂-rich syngas is utilized in the production of value-added products: methanol, urea, power through IBGCC and Fischer-Tropsch liquids (FTL). Both urea and methanol production are described as petrochemical processes that utilise the produced syngas in a series of sections to produce the aforementioned value-added products. The main uses of methanol are as fuel, solvent and anti-freeze, whereas urea is mainly used as fertilizer. The liquid fuels and power production are described as emerging processes that utilise the produced syngas in a series of sections to produce the value-added products. Liquid fuels are used in many sectors such as aviation, transportation, heating and lightning, whereas power is mainly used to drive turbines. After the simulation of the four processes, an economic evaluation was conducted to quantify revenue, capital and operating costs. In addition, the EWF Nexus system considered is quantified based on the footprint of each of the three resources for every utilisation technique. Preliminary results from the simulation are integrated into a linear program to identify the optimal biomass utilisation strategies that enhance both economic and environmental performances, through minimising sustainability indexes for EWF systems while ensuring a positive generation of the three corresponding resources.

3. Results and discussion

The results from EWF footprints for each utilisation technique are quantified by comparing the consumption and generation of each resource. Table 2 summarises the main results from the economic evaluation and the EWF Nexus system. Subsequently, a sustainability metric introduced recently by (El-Halwagi, 2017), is used to quantify the effect of the footprints compared to the economic benefit for each process. To do this, the return on investment (ROI) is first calculated using equation 1, and then compared to the EWF footprints using the sustainability weighted return on investment metric (SWROIM) calculated using equation 2.

Table 2: EWF net values for the four utilization techniques

	Ammonia/ Urea	Methanol	Liquid Fuels	IBGCC
Total Capital Cost [\$]	1.4E+08	1.2E+08	1.3E+08	1.4E+08
Revenue [\$y]	4.2E+07	3.1E+07	3.0E+06	1.1E+07
Water Consumption [kg/h]	4.4E+04	9.2E+04	2.0E+04	1.7E+05
Water Generation [kg/h]	5.0E+04	9.2E+04	3.6E+04	2.1E+05
Net [ton/h]	5.8E+00	-8.2E-02	1.6E+01	3.5E+01
Food Waste Consumption [kg/h]	8.0E+02	8.0E+02	8.0E+02	8.0E+02
Food/Fertilizer* [kg/kg] (MDPS), 2018; WorldBank, 2018)	2.6E+03			
Food Generation [tons/h]	3.1E+04			
Net Food [tons/h]	3.1E+04	8.0E-01	8.0E-01	8.0E-01
Energy Consumption [kW]	4.2E+04	4.0E+04	4.2E+04	3.9E+04
Energy Generation [kW]				8.1E+04
Net Energy (MW)	-4.2E+01	-4.0E+01	-4.2E+01	4.2E+01

$$ROI_p = \frac{AEP_p}{TCI_p} \quad \text{eq.(1)}$$

Where the term AEP abbreviates the net annual economic profit, and the term TCI abbreviates the total capital investment.

$$SWROIM_p = \frac{AEP_p \left[1 + \sum_{i=1}^{N_{indicators}} w_i \left(\frac{Indicator_{p,i}}{Indicator_{i}^{Target}} \right) \right]}{TCI_p} \quad \text{eq. (2)}$$

Where the index i is for the considered sustainability indicators apart from the net annual economic profit with $i=1, 2, \dots, N_{indicators}$. w_i is the weighing factor indicating the relative importance ratio of the i^{th} sustainability indicator compared to the net annual economic profit. The associated ratios with EWF footprints are all assumed to be 0.25. They are manipulated to determine the effect of each footprint on the overall sustainability metric. $Indicator_{p,i}$ term corresponds to the value of the i^{th} sustainability indicator linked with the p^{th} alternative. The term $Indicator_i^{Target}$ represents the benchmark value of the i^{th} sustainability indicator. The comparison between results generated from sustainability metric (SWROIM) computations for each EWF Nexus system and the corresponding return on investment (ROI) demonstrated that urea production and power generation are the only techniques selected. Methanol and liquid fuels production are excluded due to their low SWROIM value which illustrates their negative impact on sustainability. Figure 1 illustrates the results of the ROI and SWROIM for each utilisation technique.

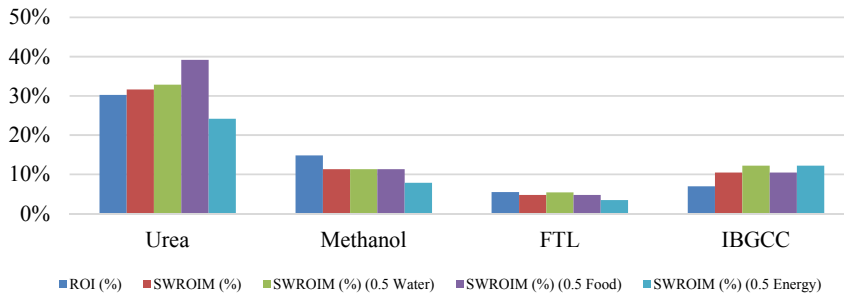


Figure 1: ROI and SWROIM results for different utilization techniques

In order to further refine the results and identify the best performing biomass utilisation techniques that considers both environmental and economic performances; a linear programming optimisation model is developed allowing the selection of optimal mix of biomass techniques that maximizes sustainability indices for EWF systems. The model, presented in Table 3 also takes into consideration the flow of resources into each application through imposing a positive net generation of EWF.

Table 3. Model formulation

Objective function	Water	$\max \sum_{i=1}^4 w_i \times x_i^w$
	Energy	$\max \sum_{i=1}^4 e_i \times x_i^e$
	Food	$\max \sum_{i=1}^4 f_i \times x_i^f$
Constraints	$\sum_{i=1}^4 nw_i \times x_i^w \geq 0$	$\sum_{i=1}^4 x_i^w = 1$
	$\sum_{i=1}^4 ne_i \times x_i^e \geq 0$	$\sum_{i=1}^4 x_i^e = 1$
	$\sum_{i=1}^4 nf_i \times x_i^f \geq 0$	$\sum_{i=1}^4 x_i^f = 1$

Where x_i^w, x_i^e and x_i^f are decision variables representing the percentage of contribution of each technology in each sector. w_i, e_i and f_i are the SWROIM for water, energy and food, respectively, for each technique. The first three equations ensure a positive net amount of EWF such that nw_i, ne_i and nf_i are the net values defined by the difference between generation and consumption amounts of a source. The final three equations impose the sum of percentages of each type of decision variable to be 100%. The results generated support findings from the first part as urea is selected again as a sustainable biomass utilisation technique as it demonstrates the largest SWROIM for both water and food. As for energy, utilising a combination of urea generation and power production results in a high SWROIM and a positive net energy generation. The results from the two methods are illustrated in Table 4.

Table 4: Optimal sustainability indexes results

Technique	Urea	Methanol	Liquid Fuels	IBGCC
ROI (%)	32%	11%	5%	10%
SWROIM (%) (0.25 each)	33%	11%	5%	12%
SWROIM (%) (0.5 Water, 0.25 others)	39%	11%	5%	10%
SWROIM (%) (0.5 Food, 0.25 others)	24%	8%	3%	12%
SWROIM (%) (0.5 Energy, 0.25 others)	32%	11%	5%	10%
Decision variable (Water)	1	0	0	0
Decision variable (Food)	1	0	0	0
Decision variable (Energy)	0.504	0	0	0.496

4. Conclusion

There has been significant global progress worldwide to diversify resource utilization options in order to limit GHG emissions and to prolong natural resources. This study is novel as it considers an EWF Nexus framework with an emphasis on biomass utilisation to design a system that will utilize the waste biomass from built environment in Qatar to produce a high-energy combustible gas. A utilisation strategy of biomass gasification feedstocks is evaluated from an economical perspective considering oxygen-steam gasification technology. Quantification of the effect for each utilisation technique on the EWF resources is conducted in which a EWF sustainability metric is utilised to inform and enhance investment decisions. Finally, urea production demonstrated that it is the most attractive amongst the utilisation techniques considered.

5. Acknowledgment

The authors acknowledge the support of Qatar National Research Fund (QNRF) (a member of Qatar Foundation) by GSRA grant No GSRA4-1-0518-17082.

References

- M.o.D.P.a.S. (MDPS), 2018, Agricultural Statistics.
- T. Al-Ansari, A. Korre, Z. Nie, and N. Shah, 2016, Integration of Biomass Gasification and CO₂ Capture in the LCA Model for the Energy, Water and Food Nexus, *Computer Aided Chemical Engineering*, 38, 2085-90.
- T. Al-Ansari, A. Korre, Z. Nie, and N. Shah, 2017, Integration of greenhouse gas control technologies within the energy, water and food nexus to enhance the environmental performance of food production systems, *Journal of Cleaner Production*, 162, 1592-606.
- A. AlNouss, G. McKay, and T. Al-Ansari, 2018, Optimum Utilization of Biomass for the Production of Power and Fuels using Gasification, *Computer Aided Chemical Engineering*, 43, 1481-86.
- J. Andersson, 2013, Techno-economic analysis of integrated biomass gasification for green chemical production, Luleå tekniska universitet.
- P. Arora, A.F.A. Hoadley, S.M. Mahajani, and A. Ganesh, 2016, Small-Scale Ammonia Production from Biomass: A Techno-Enviro-Economic Perspective, *Industrial & Engineering Chemistry Research*, 55, 22, 6422-34.
- M.M. El-Halwagi, 2017, A return on investment metric for incorporating sustainability in process integration and improvement projects, *Clean Technologies and Environmental Policy*, 19, 2, 611-17.
- R. Ferroukhi, D. Nagpal, A. Lopez-Peña, T. Hodges, R. Mohtar, B. Daher, and M. Keulertz, 2015, Renewable energy in the water, energy & food nexus, The International Renewable Energy Agency (IRENA).
- IPCC, 2011, IPCC special report on renewable energy sources and climate change mitigation.
- P. Pike, D. Sengupta, and T. Hertwig, 2008, Integrating biomass feedstocks into chemical production complexes using new and existing processes, Minerals Processing Research Institute, Louisiana State University, Baton Rouge, LA.
- WorldBank, 2018, Fertilizer consumption (kilograms per hectare of arable land), <https://data.worldbank.org/indicator/AG.CON.FERT.ZS>

A Framework for the Integration of Holistic Sustainability Assessment in Computer-Aided Molecular Design

Athanasios I. Papadopoulos^{a*}, Gulnara Shavaliyeva^b, Stavros Papadokonstantakis^b, Panos Seferlis^{a,c}

^a*Chemical Process and Energy Resources Institute, Centre for Research and Technology-Hellas, 57001 Themi, Greece*

^b*Chalmers University of Technology, Department of Space, Earth and Environment, Division of Energy Technology, SE-412 96 Gothenburg, Sweden*

^c*Department of Mechanical Engineering, Aristotle University of Thessaloniki, PO Box 454, Thessaloniki, Greece*
spapadopoulos@cperi.certh.gr

Abstract

We propose the integration of a holistic sustainability assessment framework in computer-aided molecular design (CAMD). The framework enables the assessment of life cycle (LCA) and safety, hazard and environmental (SHE) impacts from cradle-to-gate of chemicals designed through CAMD. It enables the calculation of an overall of 14 sustainability-related indices, with some of them aggregating several impact categories. Lack of models and data gaps in property prediction are addressed systematically through a data mining approach which exploits on-line similarity assessment with existing molecules for which data exist or can be predicted. The framework is implemented both simultaneously with CAMD or after CAMD to assess the designed solvents. A case study is presented on the design of phase-change solvents for chemisorption-based post-combustion CO₂ capture. Results indicate that the proposed approach enables the identification of verifiably useful phase-change solvents which exhibit favourable performance trade-offs compared to a reference CO₂ capture solvent.

Keywords: CAMD, Sustainability, LCA, SHE, Post-combustion CO₂ capture

1. Introduction

CAMD has been used widely in applications to design molecules of improved performance (Papadopoulos et al., 2018). The most common performance criteria include molecular or process properties pertaining to the thermodynamic and/or process performance of the evaluated molecular structures. While these are very important, the sustainability behavior of the evaluated molecules is also worth investigating; many chemicals exhibit significant environmental, health and safety impacts, rendering them undesired despite their otherwise favorable performance. Previous efforts incorporate sustainability-related considerations into CAMD, such as the work of Ten et. al (2016) where inherent safety and occupational health indices are considered and the work of Khor et. al (2017) which includes safety and health indices to select sustainable solvents for palm oil extraction. While these are among the few works which attempt to consider aspects of sustainability, in most publications the potential impact to the environment is either not assessed or considered to a limited extent through indices such as toxicity,

flammability, emissions etc. Systematic sustainability assessment requires a holistic view of the chemical life-cycle, at least considering all the upstream processes employed for the chemical production together with the potential hazards associated with its use. Such an approach, and its incorporation in CAMD, calls for the use of much more comprehensive indices including resource depletion and requirements, energy demands, emissions etc., to achieve a reliable differentiation over a certain, typically large, number of molecules. However, due to data gaps, several of the necessary properties cannot be predicted using group contribution (GC) methods which are predominantly used in existing CAMD implementations. Data mining methods (Lu et al., 2014) can be used to analyse, interpret and exploit molecular similarities to supplement GC models to predict dangerous properties, to potentially improve their predictive capabilities and to expand the range of sustainability indicators that can be predicted. However, such approaches have not yet been investigated as part of sustainability-based CAMD implementations.

2. Proposed approach

2.1 Framework overview

Papadopoulos et al. (2016) proposed the integration of CAMD with sustainability assessment in an approach where the latter was considered as an afterthought to solvent design. We hereby propose for the first time an approach for simultaneous CAMD and sustainability assessment. Compared to Papadopoulos et al. (2016) we employ the same sustainability indicators, but here data gaps in sustainability property prediction are addressed through data mining, while the method may account for solvents exhibiting either vapour-liquid or vapour-liquid-liquid phase-changes.

The framework supports evaluation of two main categories: (1) the holistic environmental benefit at the cradle-to-process gate level and (2) the substance hazard identification for evaluation of the harm potential in accidental scenarios (Table 1). Category (1) is approached through a Life Cycle Assessment (LCA) methodology used to calculate indices such as cumulative energy demand, global warming potential and EI99, with the latter comprising impacts over 11 categories, defining human health, eco-system quality and resource depletion damages. The LCA metrics are predicted by “black box” type models in the form of neural networks based on the molecular structure of the studied compound (for details see Wernet et al., 2009). Category (2) includes safety, health and environmental hazard (SHE) assessment Predictions for the necessary properties are performed using GC models when available. Lack of models and data gaps are addressed systematically through a data mining approach which exploits on-line similarity assessment with existing molecules for which data exist or can be predicted. In SHE assessment, single *S*, *H* and *E* scores are calculated based on various dangerous property values, shown in Table 1. Dangerous property parameters are obtained from a database (if available), calculated by the GC+ method (Hukkerikar et al., 2012a) or estimated by a similarity approach based on the local lazy learning method (LLL). For a given compound with a missing experimental or GC+ method parameter, the LLL method identifies its nearest neighbours (the most structurally similar molecules) in a given dataset and then uses these molecules to predict the compound property as follows:

$$y_{pre} = \sum_{i=1}^n \frac{S_i}{\sum_{j=1}^n S_j} * y_{i,db} \quad (1)$$

where y_{pre} is the predicted value of the query compound, $y_{i,db}$ is the property value of the i -th nearest neighbour from the dataset, S_i is the Tanimoto coefficient indicating the similarity value between the compound and the i -th neighbour, and n is the optimized

number of employed nearest neighbours. Details are reported in Shavaliieva et al. (2018).

Table 1: Dangerous properties and estimation methods used for SHE assessment.

Dangerous Property	Parameter	Estimation method
Safety (S)		
Mobility	Difference between boiling point of the pure substance and highest process temperature	GC (Hukkerikar et al., 2012b)
Fire/ Explosion	Difference between flashpoint of the pure substance and highest process temperature	GC (Hukkerikar et al., 2012b)
Acute toxicity	LD50 _{oral} (rat) – the amount of orally ingested chemical that causes death to 50% of rats (mg/kg body weight)	GC+ (Hukkerikar et al., 2012a)
Health (H)		
Chronic toxicity	Permissible exposure level (PEL) – a US legal exposure limit (mg/m ³) of an employee to a chemical, given as the average exposure concentration over 8 hours	GC+ (Hukkerikar et al., 2012a)
Environment (E)		
Water-mediated effects	Toxicity (LC50/EC50 _{aquatic}) - concentration (mg/l) of a chemical in water causing death to 50% of most sensitive aquatic species	Similarity (Lu et al., 2014; Shavaliieva et al., 2018)
Degradation in the environment	Persistence (days) - half-life of a chemical in the environment (water)	Similarity (Lu et al., 2014; Shavaliieva et al., 2018)
Air-mediated effects	Chronic toxicity index	GC+ (Hukkerikar et al., 2012a)
Accumulation	Bioconcentration factor (BCF) assesses chemical accumulation in a living organism.	Similarity (Lu et al., 2014; Shavaliieva et al., 2018)

2.2 Incorporation into CAMD

The framework obtains molecular structure information from CAMD and returns the values of the desired sustainability indices. It can be used either simultaneously with CAMD or after the molecules are obtained from CAMD, using criteria to evaluate their sustainability performance. The molecular structures in CAMD are represented by first order functional groups, hence they are compositions of the contained groups and their appearance frequency. For each structure the proposed implementation enables the generation of all potential isomers through RDKit (Landrum, 2016) in the form of SMILES (Simplified Molecular Input Line Entry System). For each isomer, the corresponding SMILE is further used for the calculation of SHE and LCA scores. LCA values are computed and incorporated to FineChem models (Wernet et al., 2009). Dangerous properties required to compute *S* and *H* scores are generated by the GC+ method (Hukkerikar et al., 2012a). The dangerous property values required for *E* are computed by the similarity and GC+ methods. When the similarity approach is used, the numbers are calculated for each isomer and then averaged to give a single index to be used for *E* score calculation. The outcome of the calculation for *CED*, *GWP*, *EI99*, *S*, *H* and *E* values is returned back to CAMD to be used in the molecule selection process.

3. Case study details and mathematical problem formulation

The aim is to design solvents for chemisorption-based, post-combustion CO₂ capture. In this work we focus for the first time on phase-change solvents, exhibiting vapour-liquid-liquid phase changes, which hold great promise to reduce the regeneration energy

requirements of CO₂ capture processes by over 50% (Zhang et al., 2012). Such solvents exhibit a liquid-liquid phase change upon reaction with CO₂ and increase of temperature. This enables mechanical solvent separation prior to introducing a reduced amount of CO₂-solvent product into the thermal regeneration step, which occurs at lower temperature than in conventional solvents, hence reducing regeneration energy. Results from the following cases are discussed:

- 1) Case A, where we use the proposed sustainability model simultaneously with CAMD.
- 2) Case B, where solvents are first designed using CAMD and their sustainability characteristics are calculated at a post-design step.

The implementation follows the multi-objective CAMD formulation of Papadopoulos et al. (2016), as shown in Table 2 for cases A (Eq. (2) and (4)) and B (Eq. (3) and (4)). In case B the sustainability properties are evaluated only for the solvents of the Pareto front obtained from CAMD.

Table 2: Mathematical formulation of Cases A and B

Case A		Case B	
$\max_G \rho$		$\max_G \rho$	
$\min_G P_{vp}, C_p, n, RED,$	(2)	$\min_G P_{vp}, C_p, n, RED$	(3)
$GWP, CED, EI99, S, H, E$			
s.t. $T_m < T_{Abs}, T_{bp} > T_{Des}, \left \delta^s - \delta^{CO_2} \right _{T_{Abs}} < \varepsilon, \left \delta^s - \delta^{H_2O} \right _{T_{Des}} > \varepsilon$		(4)	

Based on Papadopoulos et al. (2016) density (ρ) should be maximized, whereas vapour pressure (P_{vp}), heat capacity (C_p), viscosity (n) and relative energy difference (RED) should be minimized. RED is a scaled measure of CO₂ solubility in the solvent. Melting point temperature (T_m) should be less than absorption temperature (T_{Abs}) and boiling point temperature (T_{bp}) should be higher than desorption temperature (T_{Des}). The solubility parameter difference between solvent (δ^s) and CO₂ (δ^{CO_2}) should be lower than a value ε to ensure solvent-CO₂ miscibility and the same difference between δ^s and δ^{H_2O} should be higher than ε at T_{Des} to support liquid-liquid phase separation. We consider the following groups: CH₃-, -CH₂-, >CH-, >C<, -OH, -CH₂-NH₂, -CH₂-NH-, -CH₂-N<, >CH-NH₂, >CH-NH-, CH₃-NH-, CH₃-N<. The total number of groups allowed in each molecule range from 6 to 16, with up to 1 amine group. The latter allows for generation of simpler molecules, with fewer isomers, hence facilitating the use of the similarity approach in Case A. T_{Abs} is set to 40°C and T_{Des} to 90°C. The ε value is set to 7 (MPa)^{0.5} (Papadopoulos et al., 2016). The sustainability indices are calculated as averages over all generated isomers for each molecule. Properties P_{vp} , ρ , δ^s and RED are calculated from Hukkerikar et al. (2012b), n from Conte et al. (2008) and C_p from Kolska et al. (2008).

Comparison between cases is facilitated by an aggregate index J_i to generate Pareto fronts between the index and each property. The latter indicates how the overall performance of each solvent (i.e. in all properties considered simultaneously) is affected by changes in each property separately (Papadopoulos et al., 2016). The resulting multi-criteria selection problem includes the identification of the Pareto structures by generation of a Pareto front per property $j \in Pr$, with $Pr = \{\rho, P_{vp}, C_p, n, RED, GWP, CED, EI99, S, H, E\}$, considering the index J for every molecule i against each one of the properties.

4. Results and discussion

Indicative results are shown in Figure 1 (left) as a Pareto front of RED vs. J , for Cases A and B. The ID numbers correspond to solvents numbered within an original, larger set obtained from CAMD. The Pareto front shows that the two cases include few similar and

few different solvents. In the latter case their RED and J values are close. Due to space limitations the Pareto fronts of all properties against J are omitted. Observation of all other diagrams shows similar results to Figure 1 (left), except for properties P_{vp} , S , H and E . Consideration of the latter, results in molecules exhibiting better performance in Case A, compared to Case B. A similar trend also appears in Figure 1 (right). It shows the optimum value obtained for each property in Cases A and B (the values may correspond to a different solvent). Values for the 4 aforementioned properties are clearly different, whereas values for C_p , n , RED , V_m , GWP , CED and $EI99$ are either the same or similar. A very intense difference appears in P_{vp} . This means that when sustainability is considered during CAMD the designed molecular structures exhibit lower P_{vp} . This indicates a reasonable correlation between high sustainability performance and P_{vp} . Solvents with lower P_{vp} exhibit lower emissions hence enhancing some sustainability indicators. Figure 1 (right) also compares the performance of the obtained molecules with MEA (monoethanolamine), which is the reference solvent in CO_2 capture. In several performance indicators the performance of the obtained molecules is better than MEA.

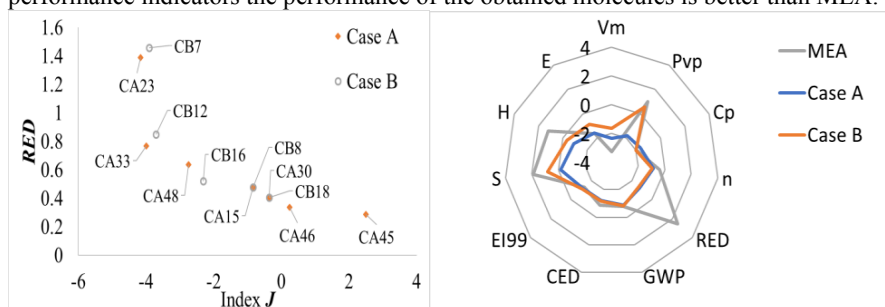


Figure 1: Pareto fronts between RED (sovent- CO_2 solubility) vs. index J (left), Optimum property values obtained by solvents in Cases A and B compared to MEA (right).

Table 3: Composition of selected, highly performing solvents from Cases A and B

ID	Groups	Frequency of appearance
CA23	[-CH ₃ ,>CH ₂ ,-OH,-CH ₂ -N<]	2,3,1,1
CA26	[-CH ₃ ,>CH ₂ ,-OH,>CH-NH-]	2,3,1,1
CA55	[-CH ₃ ,>CH ₂ ,-CH ₂ -NH-] (DBA)	2,5,1
CB7	[-CH ₃ ,>CH ₂ ,-OH,-CH ₂ -N<]	2,2,1,1
CB12	[-CH ₃ ,>CH ₂ ,-CH ₂ -NH ₂] (HEXA)	1,4,1
CB16	[-CH ₃ ,>CH ₂ ,-CH ₂ -NH-] (DPA)	2,3,1

Table 3 shows molecular structures selected through observation of Pareto fronts for all properties vs. index J . It includes solvents such as Dibutylamine (DBA), Hexylamine (HEXA) and Dipropylamine (DPA) which are known phase-change solvents (Zhang et al., 2012). This indicates that CAMD identifies such solvents in both Cases A and B. Notice that some structures contain a OH group. In Case A they are 75% of all the designed solvents, whereas in Case B they are only 21% of the entire set. This is a clear indication that when sustainability is considered during CAMD it drives the search toward OH-containing structures. Such structures may not favor phase-change behavior because OH enhances solvent-water miscibility, whereas solvent-water immiscibility is desired. Figure 2 shows the performance of the structures in all properties, compared to MEA. The overall performance, expressed by J , is better than MEA for all solvents. In 7 of the 11 properties the performance is better or similar to MEA.

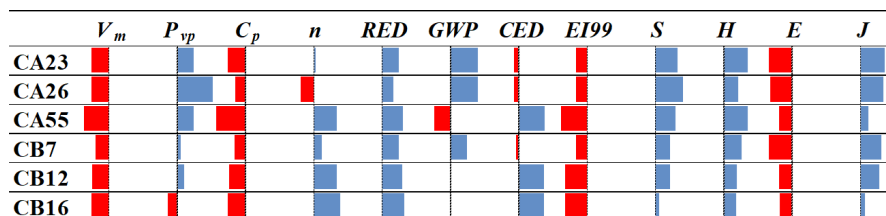


Figure 2: Performance of selected solvents compared to MEA, blue bars pointing right indicate better performance, red bars pointing left indicate worse performance

5. Conclusions

This work presents the integration into CAMD of a holistic sustainability assessment framework. The framework can be used simultaneously with CAMD or after CAMD (sequentially) for the assessment of the designed molecular structures. Implementation shows that both the simultaneous and sequential approaches enable the identification of solvents which are verifiably good candidates for phase-change, CO₂ capture operations. The solvents obtained from the simultaneous approach exhibit a preference toward hydroxyl containing groups which may hinder the appearance of phase-change phenomena in this particular application. The overall performance of the proposed solvents, obtained with both approaches, is better than MEA.

Acknowledgements

This project has received funding from the EU's Horizon 2020 program under agreement 727503 - ROLINCAP – H2020-LCE-2016-2017/H2020-LCE-2016-RES-CCS-RIA.

References

- Papadopoulos, A.I., Tsivintzelis, I., Linke, P., Seferlis, P., 2018, In: Reedijk, J. (Ed.) Reference Module in Chemistry, Molecular Sciences and Chemical Engineering. Waltham, MA: Elsevier. DOI:10.1016/B978-0-12-409547-2.14342-2
- Ten, J. Y., Hassim, M. H., Chemmangattuvalappil, N., Ng, D. K. S., 2016, *J. Loss Prev. Process Ind.*, 40, 67-80.
- Khor, S. Y., Liam, K. Y., Loh, W. X., Tan, C. Y., Ng, L. Y., Hassim, M. H., Ng, D. K. S., Chemmangattuvalappil, N. G., 2017, *Process Saf. Environ. Prot.*, 106, 211-23.
- Lu, J., Peng, J., Wang, J., Shen, Q., Bi, Y., Gong, L., Zheng, M., Luo, X., Zhu, W., Jiang, H., Chen, K., 2014, *J. Cheminf.*, 6(1), 26.
- Wernet, G., Papadokostantakis, S., Hellweg, S., Hungerbühler, K., 2009, *Green Chemistry*, 11(11), 1826-31.
- Hukkerikar, A. S., Kalakul, S., Sarup, B., Young, D.M., Sin, G., Gani, R., 2012a, *J. Chem. Inf. Model.*, 52 (11), 2823-39.
- Hukkerikar, A.S., Sarup, B., Ten Kate A., Abildskov, J., Sin, G., Gani, R., 2012b, *Fluid Phase Equilibria*, 321, 25-43.
- Shavaliyeva, G., Papadopoulos, A.I., Badr, S., Seferlis, P., Papadokostantakis, S., 2018, *Comput. Aided Chem. Eng.*, 44, 823-28.
- Landrum, G., 2016. An overview of the RDKit — The RDKit 2018.03.1 documentation. Available at: <http://www.rdkit.org/docs/Overview.html> [Accessed 5 Nov. 2018].
- Papadopoulos, A.I., Badr, S., Chremos, A., Forte, E., Zarogiannis, T., Seferlis, P., Papadokostantakis, S., Galindo, A., Jackson, G., Adjiman, C.S., 2016, *Mol. Syst. Des. Eng.*, 1 (3), 313-34
- Zhang, J., Qiao, Y., Agar, D.W., 2012, *Energy Procedia*, 23, 92-101.
- Conte E., Martinho A., Matos H.A., Gani R., 2008, *Ind. Eng. Chem. Res.*, 47, 7940-54.
- Kolská, Z., Kukul, J., Zábanský, M., Růžička, V., 2008, *Ind. Eng. Chem. Res.*, 47, 2075-85.

Flexibility Assessment of a Distillation Train: Nominal vs Perturbated Conditions Optimal Design

Alessandro Di Pretoro^{a,b}, Ludovic Montastruc^{a*}, Flavio Manenti^b, Xavier Joulia^a

^aLaboratoire de Génie Chimique, Université de Toulouse, CNRS/INP/UPS, Toulouse, France

^bPolitecnico di Milano, Dipartimento di Chimica, Materiali e Ingegneria Chimica "Giulio Natta", Piazza Leonardo da Vinci 32, 20133 Milano, Italia

ludovic.montastruc@ensiacet.fr

Abstract

Multicomponent mixtures can be separated into their single components by mean of different distillation train configurations. The standard design procedure consists of the assessment of the optimal columns configuration according to the economic and operational aspects. Anyway this optimal design is strictly related to the operating conditions, i.e. perturbations, when present, can seriously turn the tables. In these cases a flexibility analysis could be of critical importance to assess the operating conditions range of better performance for a system configuration with respect to another one.

This is the typical case of biorefineries (and bio-processes in general) where the composition perturbations downstream the fermenter across the year's seasons are completely normal due to the floating nature of the feedstock. Since no similar studies have been found in literature, a brand new ABE/W (acetone, n-butanol, ethanol, water) mixture separation case study has been set up; this mixture derives from an upstream microbial conversion process and the successful recovery of at least biobutanol and acetone is crucial for the profitability of the operation.

Therefore the purpose of this paper is the comparison between the possible distillation train configurations from a flexibility point of view. We are interested in particular in highlighting the differences, if present, between the economic optimal solution and flexibility optimal configuration that sometimes could not be the same, causing this way a very profitable design to be much less performant under perturbated conditions.

The flexibility assessment has been performed with an established procedure introduced in previous papers; all the flexibility indexes proposed in literature have been used both of simple and most complex usage in order to refine the analysis and a flexibility economic assessment has been carried out as well. Finally the two different configurations as well as the two different procedures (operating conditions based vs perturbated conditions based) have been compared both from a design and an economic point of view; then analogies and differences as well as their consequences from a decision making point of view have been highlighted and discussed.

Keywords: flexibility analysis, design optimization, distillation, column trains

1. Introduction

In refinery operations distillation has always been the leading separation process. In designing a distillation column, given the inlet streams (T, P, partial flowrates), column

top pressure, type of condenser (total or partial) and two design (separation) specifications, one degree of freedom stays unfilled. Either reflux ratio R (or ratio R/R_{\min}) or number of stages N should be fixed in order to univocally determine the unit design, anyway no physical constraints can help us to make a choice.

The standard decision making process to select the number of stages is indeed an economic-based optimization. Capital and operating costs for given specifications are calculated at different number of stages N (i.e. reflux ratios); due to the increasing CAPEX and the decreasing OPEX trends with respect to N , the total cost function shows a minimum for the R and N values corresponding to the most profitable column design. However it is worth selecting less profitable solutions whether the optimum point is located close to R_{\min} or N_{\min} conditions.

When multicomponent mixtures have to be treated, distillation trains need to be designed. Several distillation train configurations are possible according to the amount of components present in the feed and how many of them are worth to be recovered. For instance the simplest configurations for a multicomponent mixture with two components recovery required are shown in Figure 1. They're namely defined as:

- A) indirect configuration (sequential recovery from the heaviest to the lightest component);
- B) direct configuration (sequential recovery from the lightest to the heaviest component);
- C) midsplit configuration (a preliminary split between heaviest and lightest components is performed, then the separation is refined to achieve specification).

Each single column (and related equipment) is then designed on the basis of the lowest total cost and the cheapest train configuration is selected.

This procedure is well established and it has always worked well so far, anyway it has a main limitation: the economic assessment and equipment design are strictly related to the nominal operating conditions, i.e. they don't take into account feedstock or operating conditions perturbations that could occur. This means that, whether a feed composition perturbation occurs, the system could not be able to achieve the separation specifications or at least a relevant increase of operating costs can be detected causing the most profitable design not to be as profitable as expected.

In refinery's operation these problem are less appreciable since long-term contracts for crude oil supplying and blending processes ensure an almost constant and stable feedstock quality. However, during last 15 years there has been an increasing interest for the production of chemicals and fuels from renewable resources because of growing concerns about global warming and climatic change, increasing crude oil price and existing legislations restricting the use of non-renewable energy sources. The direct consequence of this trend results in an even more increasing demand for bio-based fuels and raw materials, i.e. bio-refinery processes. Anyway bio-processes are highly subjected to composition perturbations downstream the fermenter across the year's seasons due to the floating nature of the feedstock.

Being fermentation usually carried out as a batch process, in order to ensure the desired daily productivity, several fermenters working at the same time are required. On the other hand, even when continuous fermenters are used, their scale up and then the feed flowrate that can be processed have a limit. These conditions cause the fermentation process section to be very expensive, therefore a constantly good performance of the products recovery section is of critical importance for the profitability of the plant.

In the light of the above an a priori flexibility analysis of the different distillation train configurations is non-optional for this kind of separation in order to allow the decision maker to make a multi-criteria-based choice about the optimal design to be selected.

2. Objectives and methodology

The purpose of the paper is the economic and flexibility based comparison between different distillation train configurations aimed to the same separation specifications.

As already mentioned, the economic optimal design provided was determined by mean of the usual procedure; capital and operating costs have been estimated using Guthrie (1969) – Ulrich (1984) - Navarrete (2001) correlations.

Flexibility analysis has been performed both from a deterministic (Swaney & Grossmann, 1985; Saboo and Morari, 1985) and a stochastic (Pistikopoulos & Mazzuchi, 1990) point of view and coupled with economics according to the procedure shown by Di Pretoro et al. (2019).

ProSim Plus® process simulator has been used to assess the feasibility of the separation as well as to estimate all process parameters.

Since no former application of flexibility analysis to distillation trains has been found in literature, a new case study referring to the separation of an ABE/W mixture, coming from a fermentation process and a preliminary dewatering operation, has been proposed. The feed composition is listed in Table 1.

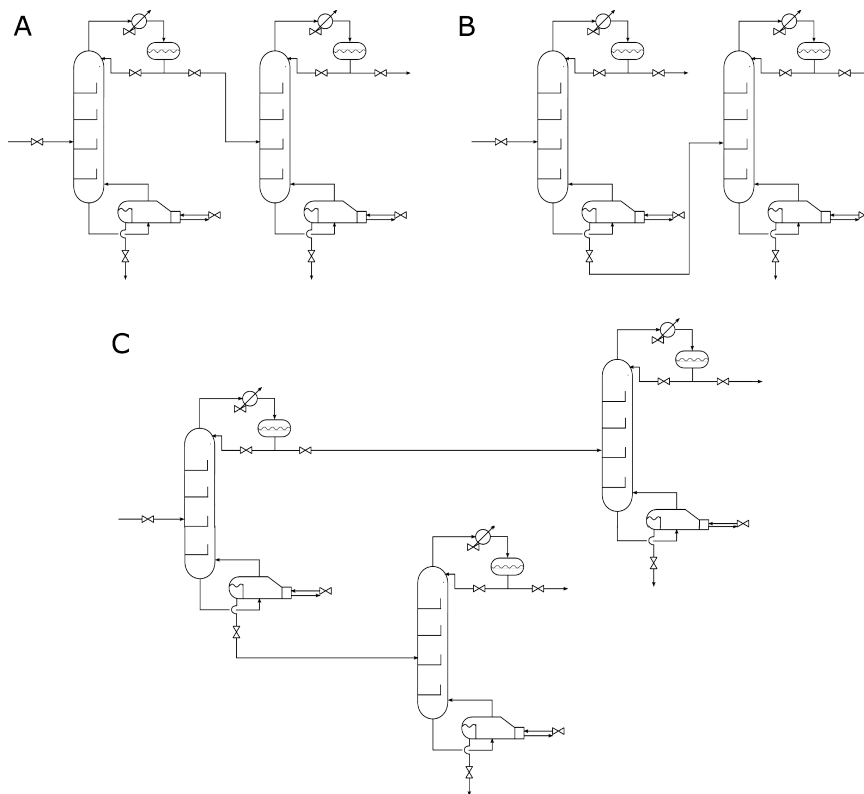


Figure 1 - Distillation train configurations for two components recovery

Table 1 - Feed components partial flowrates

Component	Partial flowrate (mol/s)
Acetone	12.030
Ethanol	3.839
n-Butanol	61.328
Water	12.428

The successful recovery of at least biobutanol and acetone is considered crucial for the profitability of the operation. In order to do this, a minimum of two distillation columns are required and three configurations are possible as previously shown in Figure 1. Midsplit configuration specifications are as follows:

1. Split column:
 - 1.1. Acetone recovery ratio in the distillate: 0.995;
 - 1.2. n-Butanol recovery ratio in the bottom: 0.98;
2. Acetone recovery column (top column):
 - 2.1. Acetone recovery ratio in the distillate: 0.995;
 - 2.2. Distillate acetone mass fraction: 0.995;
3. n-Butanol recovery column (bottom column):
 - 3.1. n-Butanol recovery ratio in the bottom: 0.98;
 - 3.2. Bottom n-butanol mass fraction: 0.99.

Specifications for direct and indirect configuration can be easily deduced from the midsplit ones. The direct configuration has resulted to be highly unfeasible since we should recover in the first column a highly acetone concentrated stream from a feed with a very low acetone molar fraction. Therefore only indirect and midsplit configurations will be compared.

3. Optimal design and flexibility assessment

As already mentioned, the standard design procedure has been conducted as usual; optimal number of stages and relative annual total cost for each column are listed in Table 2. With an overall annual cost of 933,509 \$/y vs 1,084,082 the indirect configuration results to be the most convenient with respect to the midsplit one.

The addition of a preliminary column indeed does not substantially affect the acetone column utilities consumption.

Table 2 - Distillation train optimal design

	1 st column		2 nd column		3 rd column	
	N (feed)	Cost (\$/y)	N (feed)	Cost (\$/y)	N (feed)	Cost (\$/y)
Indirect	16 (10)	580,016	50 (46)	353,493	/	/
Midsplit	35 (9)	455,493	50 (47)	352,224	16 (8)	276,365

First of all a flexibility analysis based only on the actual feasibility of the separation (i.e. without taking into account equipment sizing) has been performed. The most critical parameters, as well as the most likely to change, are water and butanol fractions; therefore water and butanol partial flowrates were then considered the uncertain parameters for the analysis.

Despite what usually happens in these situations and what we expected, the midsplit configuration, i.e. the one with one column more, doesn't result to be more flexible than the indirect one as shown in Figure 2. On the contrary it is slightly less performant. For a water vs. n-butanol ratio higher than 0.23 (0.22 for the midsplit) indeed the separation is not feasible at all.

According to the Swaney & Grossmann index (F_{SG}), that assesses the highest simultaneous perturbation of all uncertain parameters that the system is able to withstand, the indirect configuration flexibility is about 5% (midsplit about 4%). According to Saboo & Morari the Resilience Index (RI), that defines the largest total disturbance load a system is able to withstand independently of the direction of the disturbance, stays around 8% (midsplit about 7%). Finally, according to the Pistikopoulos & Mazzuchi stochastic flexibility index, evaluating the probability that the system could absorb the disturbance, we find $SF=77.86\%$ (75.85% for the midsplit) in case of a normal probability perturbation distribution with a 10% variance. These values don't take into account the equipment sizing but thermodynamics only; it means no matter how much we pay for a bigger reboiler or a larger column, no higher flexibility value can be achieved. The same feasibility region has been obtained by changing the columns number of stages between approximately 0.75 and 1.5 times N_{opt} . Flexibility analysis and economic assessment have then been coupled as shown in Di Pretoro et al. (2019). Total annual costs vs. partial flowrates perturbations have been plotted for the indirect configuration in Figure 3.a. An analogous trend has been obtained for the midsplit configuration.

However, the three columns configuration keeps being more expensive than the two column one, i.e. even under perturbed condition the external duties overconsumption is not compensated by the additional equipment despite what usually happens in standard distillation cases.

Costs result to be higher whether a bigger oversizing is necessary, i.e. positive deviation for both water and butanol flowrates, and along the operating conditions close to the feasibility boundary.

Moreover, the additional cost vs. flexibility plot for the deterministic indexes is reported in Figure 3.b as well; since F_{SG} represents the flexibility related to the simultaneous deviation of all uncertain variables, it implies a higher cost compared to the same RI value.

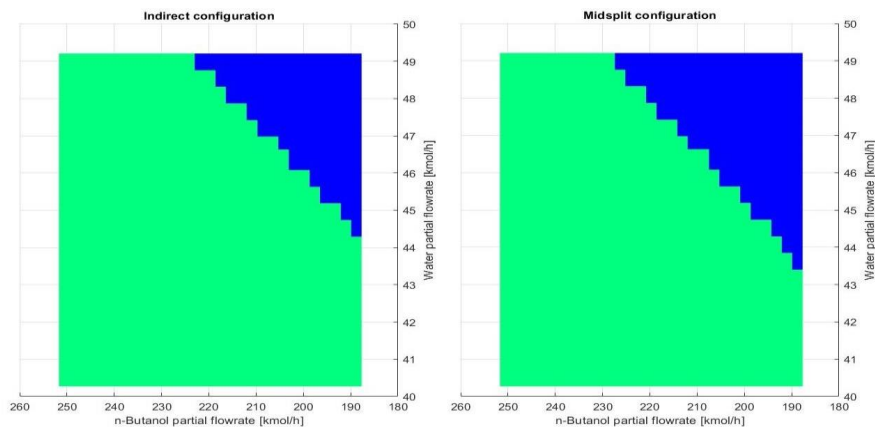


Figure 2 - Feasibility diagrams (Green = Feasible, Blue = Unfeasible)

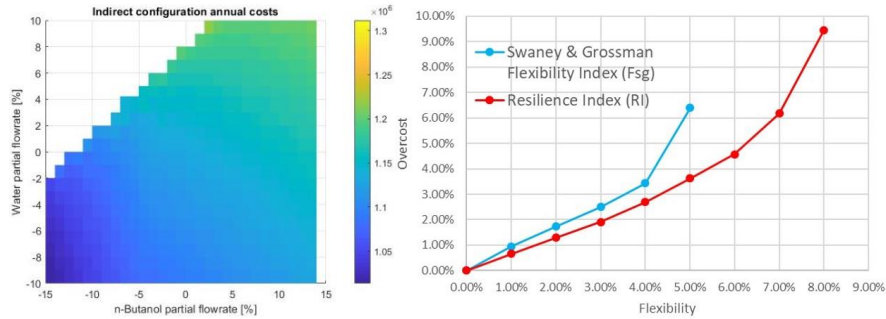


Figure 3 - Economic assessment (Indirect configuration): a. Costs vs. partial flowrates; b. Costs vs. flexibility

4. Conclusions

This paper introduces the comparison of distillation trains configurations both on a flexibility and economical basis. Flexibility assessment of distillation trains (involving both series and parallel columns) have been successfully performed with deterministic as well as stochastic indexes. Results have then been coupled with an economic assessment in order to obtain the overcost vs. flexibility analysis plot providing a critical tool to the decision maker.

The indirect configuration, that was the cheapest one, resulted to be also a little bit more flexible than the midsplit configuration, despite the expectation. The economic gap due to the additional column is conserved also under uncertain conditions as well as non-optimal column design. Moreover we can state that beyond a $F_{SG}=4\%$ or $RI=7\%$ it is less worth investing since the additional costs line becomes steeper.

However, beside the numerical results that are case-specific, the outcome of general validity is that, in thermodynamically constrained system, the feasibility and flexibility boundaries cannot go over a certain value by adding separation stages to the distillation column or, in general, investing more. An a priori flexibility analysis and economic assessment could then be crucial for making the best design choice and to know the limitation of our system if perturbations are likely to occur.

References

- [1] K. M. Guthrie, 1969, 'Capital Cost Estimating', *Chemical Engineering*, 76.3, 114-142.
- [2] G. D. Ulrich, 1984, 'A Guide to Chemical Engineering Process Design and Economics', Wiley.
- [3] P. F. Navarrete and W. C. Cole, 2001, 'Planning, Estimating, and Control of Chemical Construction Projects', 2nd Edition, CRC Press.
- [4] R.E. Swaney and I.E. Grossmann, 1985, 'An Index for Operational Flexibility in Chemical Process Design. Part I: Formulation and Theory', *AIChE Journal*, 31, 621-630.
- [5] Ak Saboo, M. Morari, and De Woodcock, 1985, 'Design of Resilient Processing Plants .8. a Resilience Index for Heat-Exchanger Networks', *Chemical Engineering Science*, 40.8, 1553-1565.
- [6] E. N. Pistikopoulos and T. A. Mazzuchi, 1990, 'A Novel Flexibility Analysis Approach for Processes with Stochastic Parameters', *Computers & Chemical Engineering*, 14.9, 991-1000.
- [7] A. Di Pretoro, L. Montastruc, F. Manenti, X. Joulia, 2019, 'Flexibility analysis of a distillation column: indexes comparison and economic assessment', Accepted by *Computers and Chemical Engineering* the 2nd February 2019.

Dynamic Optimisation and Visualisation of Industrial Beer Fermentation with Explicit Heat Transfer Dynamics

Alistair D. Rodman,^a Megan Weaser,^b Lee Griffiths,^b Dimitrios I. Gerogiorgis^{a*}

^a *School of Engineering (IMP), University of Edinburgh, Edinburgh, EH9 3FB, UK*

^b *Carling House, Molson Coors Brewing Co, Burton-On-Trent DE14 1JZ, UK*

D.Gerogiorgis@ed.ac.uk

Abstract

Demand for beer products fluctuates throughout the year, with a substantial increase occurring for the duration of global sporting events. Beer fermentation is frequently the production bottleneck due to its significant duration (often exceeding 1 week). Therein lies a strong incentive for fermentation optimisation and batch duration reduction such that maximum production capacity can be elevated during peak demand periods. Beer fermentation optimisation has received considerable attention, however a limitation of prior work is the universal assumption of direct and instantaneous control of fermentor temperature. With the addition of only two more ODEs to the system model, heat transfer dynamics is approximated in this work. A novel, comprehensive visualisation of the attainable performance maps for key process variables is presented, obtained via a large-scale dynamic simulation campaign of viable cooling policies. These attainable performance maps are compared to equivalent results produced previously, to elucidate how fermentor performance varies once production scale increases beyond the point of the previous simplifying assumption. Utilising orthogonal polynomials on finite elements allows a finite dimensional optimisation NLP problem to be formulated for ethanol yield maximisation, which has been solved with IPOPT. Optimal operation involves a novel cooling policy to effectively manage the active yeast population in the fermentor for improved performance versus previous approaches for beer fermentation.

Keywords: Dynamic optimisation, Dynamic simulation, Beer fermentation

1. Introduction

Fermentation is a key step in the production of consumer alcohol products, frequently presenting a production bottleneck due to its significant duration (often >1 week). Demand for beer products fluctuates throughout the year, with a substantial increase occurring for the duration of global sporting events (e.g., the World Cup). Therein lies a strong incentive for process optimisation and batch duration reduction such that maximum production capacity can be elevated during peak demand periods without the need to increase plant equipment sizes, which would incur significant capital investment for vessels which would be underutilised for much of the year. Beer fermentation is an extremely complex biochemical process (Vanderhaegen et al., 2006), whose mathematical representation and parameter estimation are possible only via reduced-order models (Dochain, 2003) considering only the most essential subset of reactions via selective aggregation. The system's complexity (>600 species) renders comprehensive parameter estimation infeasible and dynamic optimisation cumbersome.

A number of studies towards improved beer fermentation via temperature profile optimisation have been performed on the basis of simplified models, exploring the inherent trade-off between attainable ethanol concentration and required batch time. These have addressed both the single objective case for batch time minimisation or

ethanol yield maximisation (de Andrés-Toro et al., 1998; Carrillo-Ureta et al., 2001) or both (Rodman and Gerogiorgis, 2016). A rigorous dynamic optimisation has been performed via a NLP formulation employing orthogonal collocation on finite elements, computing the optimal temperature trajectory for the process duration (Rodman and Gerogiorgis, 2017). It is highly uncommon for brewers to monitor batch progression online during the fermentation process. Rather a prescribed temperature manipulation is followed, after which select terminal state concentrations may be sampled to confirm an adequate product quality. Herein, the design of a model predictive controller would be of little value to industry, who seek off-line computation of optimal dynamic manipulations to be implemented with a generic temperature feedback control loop.

A limitation of prior work (in the interest of simplification towards computational manageability) is the assumption of direct and instantaneous control of fermentor temperature. This is less realistic as the scale increases; industrial fermentation tanks can exceed 4,000 hectolitres, so the characteristic lag time for heat transfer from the reaction broth through the fermentor cooling jacket cannot be reliably considered as negligible. To this end, we build upon our published contributions by explicit modelling of the fermentor cooling jacket heat transfer dynamics. This requires only two addition model ODEs, where the rate of change of the reactor contents' temperature becomes a function of the jacket power supply and thermophysical properties of the system.

2. Beer Fermentation Modelling

The de Andrés-Toro (1998) fermentation model describes five components in the wort: ethanol (C_E), sugar (C_S) biomass (X_i) and two flavour-tarnishing compounds, diacetyl (C_{DY}) and ethyl acetate (C_{EA}). The single sugar species represents the sum of all sugars in the wort. Biomass is distinguished into three forms: active (X_A), latent (X_L) and dead (X_D) cells. Active cells can promote fermentation and duplicate and grow over time; however, a portion will die and no longer contribute to fermentation, settling at the bottom of the vessel. Latent (lag) cells are unable to promote fermentation, but over time they develop into active cells, responsible for consumption of the fermentable material in the wort. A diagram of the model scheme, and the corresponding kinetic rate equations are in Fig. 1. Arrhenius growth rates (μ_i) describe species progression with a stoichiometric yield factor (Y) and an inhibition factor, f , on ethanol production. A fundamental simplifying assumption of the fermentation model is that spatial variation of concentrations and temperature may be neglected. While some degree of variation is inevitable in practice, CO_2 generation from the primary reaction pathway and the cylindroconical vessel leads to considerable mixing. The lumped parameter model has been extensively validated as suitable for representing the process on an industrial scale.

The model is extended to consider heat transfer between the exothermic fermentor contents and the surrounding cooling jacket. Eq. 13 defines the bulk temperature inside the vessel, where energy generated by sugar fermentation at a rate of (ΔH) heats the wort according to its mean physio-thermal properties (ρ_R, C_{PR}).

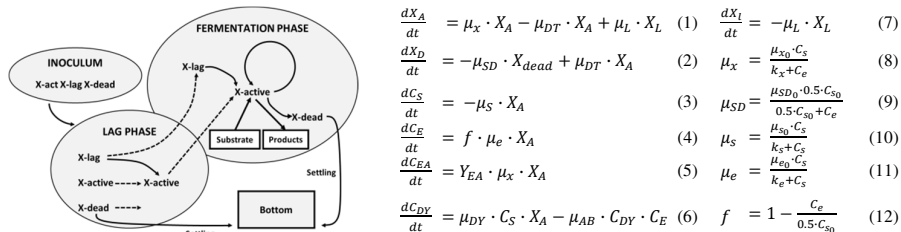


Figure 1: Model for dynamic simulation of beer fermentation (de Andrés-Toro, 1998).

Table 1: Heat transfer model parameters.

Symbol	Definition	Units	Value
T	Reaction Temperature	°C	–
T_C	Jacket Temperature	°C	–
T_{C0}	Coolant Feed Temperature	°C	4
F	Coolant Feed Rate	m ³ hr ⁻¹	–
ΔH	Enthalpy of Reaction	kJ kg ⁻¹	587
ρ_R	Mean Density of Wort	kg m ⁻³	1,030
ρ_C	Density of Coolant	kg m ⁻³	1,042
C_{PR}	Wort Heat Capacity	J kg ⁻¹ K ⁻¹	4,065
C_{PC}	Coolant Heat Capacity	J kg ⁻¹ K ⁻¹	3,914
A_h	Heat Transfer Area	m ²	221.4
U	Overall Heat Transfer Coefficient	W m ⁻² K ⁻¹	200
V_R	Wort Volume	m ³	400
V_C	Jacket Volume	m ³	3.8

The cooling rate is a function of the jacket temperature (T_C), the jacket/fermentor heat transfer area A_h , overall heat transfer coefficient (OHTC, U) and wort volume (V_h). The temperature of the jacket (volume = V_C) is described by Eq. 14, cooled with fresh coolant at ($T = T_{C0}$) at a volumetric rate (F). Heat losses to the surroundings are negated as the vessel jacket is close to ambient conditions. A typical large capacity industrial specification vessel is modelled. The 400,000 L vessel has a 3,800 L jacket, cooled by a propylene glycol:water mixture. A 4 °C coolant temperature is first assumed, with $U = 200 \text{ W m}^{-2} \text{ K}^{-1}$. Table 1 details the additional parameter values used in Eq. 13–14.

$$\frac{dT}{dt} = \frac{dC_s}{dt} \frac{\Delta H}{\rho_R C_{PR}} + \frac{A_h U}{V_R \rho_R C_{PR}} (T - T_C) \quad (13)$$

$$\frac{dT_C}{dt} = \frac{F}{V_C} (T_{C0} - T_C) + \frac{A_h U}{V_C \rho_C C_{PC}} (T_C - T) \quad (14)$$

3. Dynamic Simulation of Attainable Performance

Prior work investigating the potential for process improvement versus current plant fermentation operation involved an algorithm that rapidly generated and simulated plausible temperature manipulations adhering to realistic operability heuristics, while relying on the simplifying assumption that vessel temperature may be directly manipulated (Rodman and Gerogiorgis, 2016). Attainable performance maps were generated, allowing rapid visualisation of the viable output space permitted by operational modifications. To elucidate how fermentor performance varies once production scale increases, we perform a similar simulation campaign using the extended model. To exhaustively enumerate comparable performance maps for the most simple cooling policies five discrete coolant rates ($F = [0:5:20]$) are permitted, which may be only be switched at the end of a 20 hr interval across the 160 hr span considered. Thus $5^9 = 1,953,125$ cooling policies are considered for implementation.

Fig. 2 depicts the performance maps from the new cooling policy campaign (grey markers) alongside those from Rodman and Gerogiorgis (2016) which assumed direct temperature control (black markers). An immediate observation across all metrics is that the addition of the temperature model considerably reduces the broad range of viable terminal product concentrations, particularly for both by-product species. This is despite the solution set for coolant control being significantly larger ($\sim 1.9 \times 10^6$ policies) than that for direct temperature control ($\sim 1.75 \times 10^5$). The observation can be attributed to the fact that in the absence of any external heat source the vessel temperature can only rise

from its initial temperature at a rate governed by the exothermic fermentation reaction: there is considerably less scope to vary the vessel temperature during primary fermentation, where the temperature is capped by how quickly it can rise from the reaction enthalpy. This contrasts with prior work where the vessel temperature could instantaneously rise as high as 16 °C, which is not feasible in practice, leading to a subset of simulations corresponding to very short batch times and high by-product concentrations, highlighted by the black markers lying to the upper left in Fig. 2a.

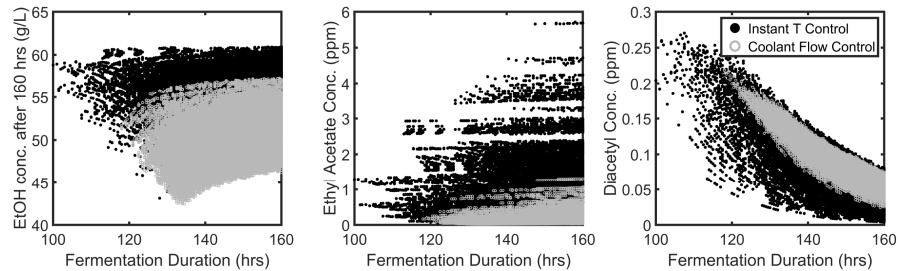


Figure 2: Comparison between attainable envelopes: direct $T(t)$ control vs. $F(t)$ control.

Of all cooling policies considered, the most favorable for alcohol (EtOH) maximisation is presented in Fig. 3 with the corresponding state trajectories. Here, the preferable approach is to begin cooling the jacket once the temperature exceeds 15 °C after 60 hr, increasing the cooling duty at 80 hr and reducing at 100 hr before turning the coolant flow off at 120 hr to allow the temperature to rise. This manages the active yeast population, preventing substantial cell death if the temperature were to rise further.

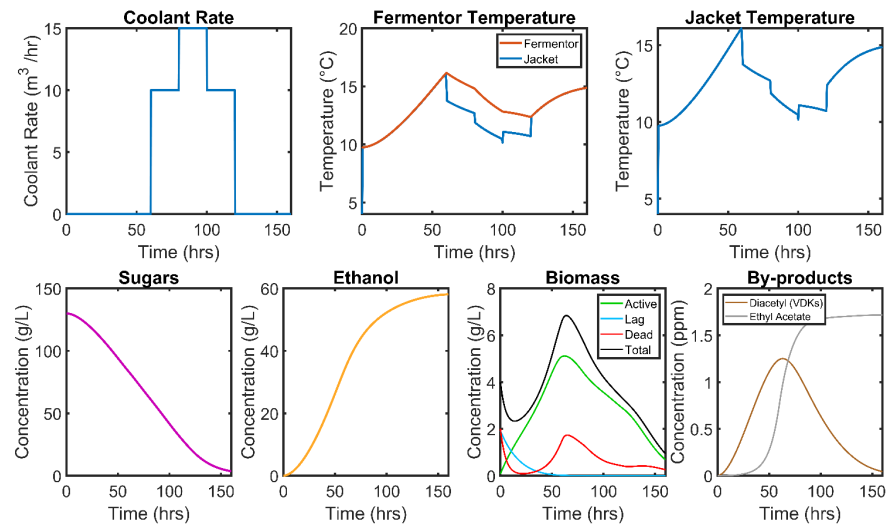


Figure 3: Best solution from exhaustive cooling policy campaign.

4. Dynamic Optimisation

Here, we describe the formulation of the nonlinear dynamic optimisation problem to maximise EtOH concentration. To formulate a finite dimensional optimisation problem, orthogonal polynomials on finite elements are used to approximate the control (coolant flowrate) and state (system species concentrations) trajectories to produce a large scale nonlinear programme (NLP). The differential algebraic equation (DAE) system is converted to a system of algebraic equations (AEs), where decision variables of the derived NLP problem include the coefficients of the linear combinations of these AEs.

The optimisation is performed using the DynOpt package in MATLAB (Cizniar et al., 2006). Fixing 16 elements across the time horizon, with 3 collocation points per element for the nine state ODEs and one collocation point (piecewise constant) per element for the control (F) leads to a $16 \times (3+1) \times 9 + 16 \times 1 \times 1 = 592$ variable NLP, able to accurately approximate the continuous dynamics of the system. For a single objective ethanol maximisation problem the NLP is solved using IPOPT (Wächter and Biegler, 2006). A multi-start initialisation procedure is used to best approximate global optimality.

The optimal control profile is presented in Fig. 4 with the corresponding jacket and vessel temperature trajectories. Similarities are observed between Figs. 3 and 4, with intermediate cooling to manage the active cell population evident as being the optimal policy to maximise the ethanol yield. The optimal policy computed here is to rapidly begin cooling after a favorable temperature is reached ($\sim 15^\circ\text{C}$) and to slowly lower the coolant rate over the following 70 hr to facilitate gradual, sustained cooling of the wort.

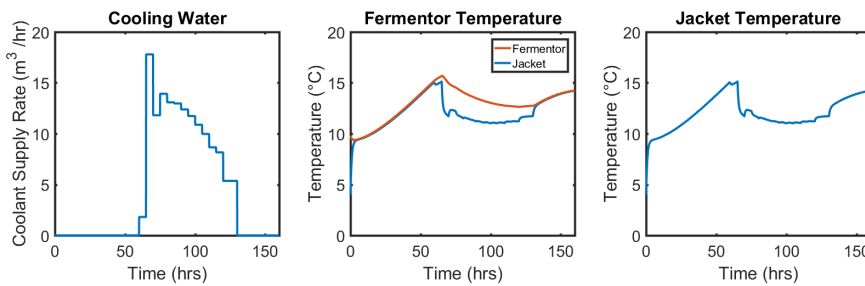


Figure 4: Optimal solution for maximum EtOH in 160 hrs.

5. Optimal Solution Sensitivity with respect to Jacket Design Variables

We investigate the impact of coolant temperature and U on the optimal cooling policy. The same dynamic optimisation problem is solved for a range of values for these process parameters. Fig. 5 shows the solutions for a range of values of U , while Fig. 6 shows the same for coolant temperatures. It is shown in Fig. 5 that with decreasing U , the same cooling policy profile form is utilised with increasing required coolant rate. Beyond a critical point ($U < 100 \text{ W m}^{-2} \text{ K}^{-1}$) the solution is at the maximum coolant rate. The third panel highlights how the jacket temperature differs in these cases with the increasing coolant rate, which lead to near identical temperature trajectories in the fermentor (centre panel), with the exception of the dark blue case ($U = 50 \text{ W m}^{-2} \text{ K}^{-1}$), which takes a less favourable path due to being limited by the maximum coolant rate. A wide range of values of U have been considered here; clarification of practiced values will further elucidate promising dynamic coolant rate trajectories for implementation.

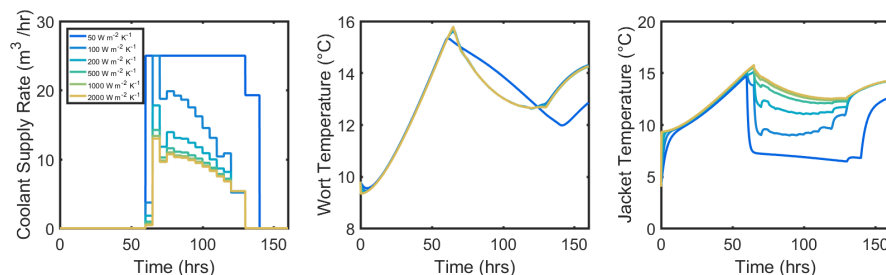


Figure 5: Overall Heat Transfer Coefficient (U) effect on optimal coolant supply rate.

In Fig. 6, it is similarly demonstrated how the same cooling policy form is computed regardless of the coolant temperature. Across all cases considered, it is possible to maintain essentially the same jacket-side temperature by adjusting the coolant rate such that the wort temperature and corresponding fermentation progression are unchanged. This highlights that in the common scenario where coolant feed temperature varies over time (ambient condition variability), adjustments can be made by varying the volumetric supply rate to adhere to the same temperature progression within the batch itself.

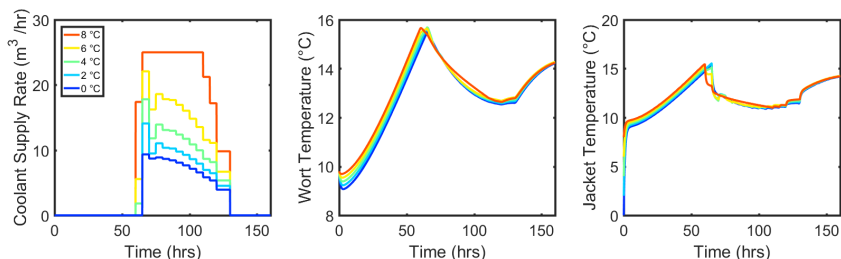


Figure 6: Coolant temperature effect on optimal coolant supply rate.

8. Conclusions

Consideration of explicit fermentor jacket heat transfer marks a significant improvement over the fidelity of prior work, which assumed that temperature may freely manipulated. Visualisation of attainable performance reveals that a vast portion of operation cases considered previously are unobtainable on an industrial scale, highlighting the importance of the improved approach. Utilising orthogonal polynomials on finite elements allows a finite dimensional NLP optimisation problem to be formulated for ethanol yield maximisation, which has been solved with the IPOPT solver. Optimal operation involves a novel cooling policy to effectively manage the active yeast population in the reactor, capable of improved performance versus established approaches. Sensitivity analysis of the solution dependence on heat transfer process and design parameters shows how adjustments in the coolant rate can be made to maintain the preferred optimal temperature trajectory of the fermenting wort in the vessel.

References

- B. de Andrés-Toro, J.M. Giron-Sierra, J.A. Lopez-Orozco, C. Fernandez-Conde, J.M. Peinado and F. Garcia-Ochoa., 1998, A kinetic model for beer production under industrial operational conditions, *Math. Comput. Simulat.*, 48, 1, 65–74.
- C. Boulton and D. Quain. 2008, *Brewing yeast and fermentation*, Wiley.
- G. Carrillo-Ureta, P. Roberts and V. Becerra, 2001, Genetic algorithms for optimal control of beer fermentation, *Proc. IEEE Int. Symp. Intell. Control*, 391–396.
- M. Cizniar, M. Fikar and M.A. Lati, 2006, MATLAB dynamic optimisation code DYNOPT, User's guide, Bratislava, Slovak Republic.
- D. Dochain, 2003, State and parameter estimation in chemical and biochemical processes: a tutorial, *J. Proc. Control*, 13, 8, 801–818.
- A. Rodman and D.I. Gerogiorgis, 2016, Multi-objective process optimisation of beer fermentation via dynamic simulation, *Food Bioprod. Proc.*, 100, A, 255–274.
- A. Rodman and D.I. Gerogiorgis, 2017, Dynamic optimization of beer fermentation: sensitivity analysis of attainable performance vs. product flavor constraints, *Comput. Chem. Eng.*, 106, C, 582–595.
- B. Vanderhaegen, H. Neven, H. Verachtert, and G. Derdelinckx, 2006, The chemistry of beer aging – a critical review, *Food Chem.*, 95, 3, 357–381.
- A. Wächter and L.T. Biegler, 2006, On the implementation of an interior-point filter line-search algorithm for large-scale nonlinear programming, *Math. Programming*, 106, 1, 25–57.

Statistical Modelling for Optimisation of Mash Separation Efficiency in Industrial Beer Production

Qifan (Frank) Shen,^a Megan Weaser,^b Lee Griffiths,^b Dimitrios I. Gerogiorgis^{a*}

^a *School of Engineering (IMP), University of Edinburgh, Edinburgh, EH9 3FB, UK*

^b *Carling House, Molson Coors Brewing Co, Burton-On-Trent DE14 1JZ, UK*

D.Gerogiorgis@ed.ac.uk

Abstract

Mash separation is a critical pre-processing step in beer production, ensuring that a high-quality stream of solubilised grain carbohydrates and nutrients (wort) is fed to the fermentors, in which sugars are then biochemically converted to ethanol. This essential pre-fermentation step is performed via either of two key units (lauter tuns or mash filters); the output quality of the clarified liquid stream (wort) depends on numerous critical variables (grain composition and size distribution, mash mixture physicochem. properties, brewing recipe, separation conditions). While first-principles mathematical descriptions may remain elusive, a multitude of available (input-output) industrial data can be used to improve understanding. This paper explores causality via statistical (Partial Least Squares) models for two types of beer, and performs a sensitivity analysis using the proposed input-output correlations towards mash separation improvements. Strong wort volume and incoming feed quality to the mash filter emerge as having the strongest effect on filtration time, a key industrial performance metric for optimisation.

Keywords: Statistical modelling, mashing, separation, beer, Partial Least Squares (PLS)

1. Introduction

Mashing is an enzymatic conversion and extraction process, during which the insoluble high molecular-weight (HMW) substances in the malt are converted into soluble sugars by physical and enzymatic action (Bamforth, 2006), to ensure that a purified stream of dissolved grain carbohydrates is reliably fed to the fermentor (Meussdoerffer, 2009). The ground malt is mixed with hot water in the mash vessel to enhance extraction rates. This process involves the participation of several enzymes, notably α - and β -amylases, whose activity is crucial for high efficiency. Thus, mashing temperature greatly affects the efficiency of mashing. In practice, temperatures close to the upper limit of enzyme activity are used, as they increase the filtration run-off rate. Wort concentration, pH and mashing time are key parameters for high mashing efficiency. Three common variants employed are infusion, decoction, and temperature-controlled mashing (Bühler, 1996).

Mash separation is a solid-liquid separation process, during which malt compounds dissolved during mashing are separated from grain components, thus increasing extract yield and removing substances adversely affecting beer flavour (Bühler, 1996). Modern breweries typically produce 10-12 batches per day, including maintenance downtime. Mash separation is a rate-limiting process, therefore the strategic goal of increasing its efficiency can boost productivity and reduce total production cost (Bamforth, 2006).

The two leading technologies for mash separation employ either a mash filter or a lauter tun, exploiting wort permeability through beds in very different ways (Bamforth, 2006). A *mash filter* is operated under external pressure, which drives a filtrate flow through the bed. The filtrate remaining in the filter cake is extracted by squeezing the latter (spent grains) using flexible membranes incorporated into the unit. A *lauter tun* maintains permeability through large mean particle size and employ mechanical force to loosen the bed (the filtrate is obtained by gravity). Although mash unit design varies, wort separation equipment normally use solid substances in mash as filter medium, and therefore the properties of solid particles play an important role in mash separation. Mash filtering achieves higher filtration performance in terms of wort clarity and filtration efficiency, at a higher capital investment and maintenance cost (Bühler, 1996).

Mash filters are made of rectangular polypropylene plates, which are pressed together by a hydraulic ram to create a water-tight pocket between them. Alternates are equipped with elastic membranes which can be inflated with compressed air to squeeze the mash against permeable polypropylene cloth. The space between uninflated cloths is 40 mm and is reduced significantly to about 25-30 mm when compressed (Bamforth, 2006).

Figure 1 illustrates mash filter operation. Mash is pumped into it via the bottom inlets and chambers are vented until the filter is filled; then point vents are closed and wort outlets are opened (*filling*). Withdrawing strong wort, the mash is continuously pumped into the mash filter, and solid particles deposited in the chambers accumulate, forming a filter cake (*filtration*). When mash transfer is complete, inlets are closed and elastic membranes are inflated by compressed air to squeeze the filter (*pre-compression*). Once membranes are inflated, sparge water is fed to the chamber (*sparging*), and the membrane is inflated again to recover filtrate remaining in the filter (*final compression*). The cycle is repeated until wort concentration is acceptably low: then, plate separation cause spent grain cake drop (*discharge*) to a hopper/screw conveyor (O'Rourke, 2003).

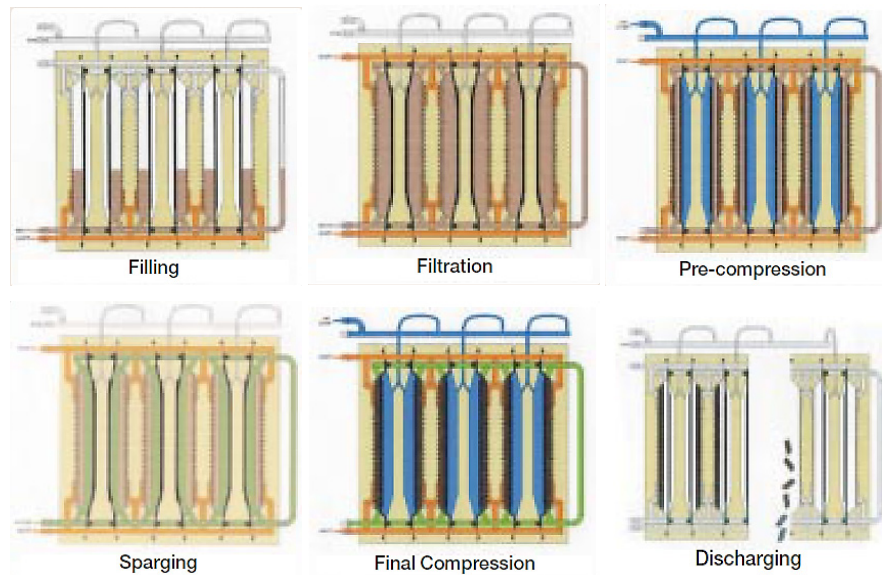


Figure 1. Mash filter operation stages (O'Rourke, 2003).

2. Methodology

The importance of process modelling, simulation and optimisation for the beer industry is well documented (Muster-Slawitch et al., 2014), although biochemical complexity of unit operations, mashing, fermenting and aging is immense (Vanderhaegen et al., 2006). The optimisation of mash separation is crucial, due to the substantial time requirement, and its influence on final product quality (Schneider et al., 2005; Kühbeck et al., 2006). First-principles models of filtration operations are useful (Wakeman & Tarleton, 1999), but their parameterisation may be laborious and elusive. Conversely, a multitude of statistical (data-driven) techniques can be used to improve our understanding of this industrial unit operation, on condition of production data availability and reliability.

This statistical modelling paper aims to explore causality in mash separation variability, develop input-output correlations for beer brands (here, type A) and propose viable improvements to the process by means of the Partial Least Squares (PLS) method, which is an established approach (MacGregor et al., 1994; Esposito Vinzi et al., 2010). A literature survey reveals that statistical (esp. PLS) models have been employed to improve product quality in the food (Poveda et al., 2004) and drink (Aznar et al., 2003) industry, and more specifically in regard to bottled lager beer aging (Liu et al., 2008). Nevertheless, to the best of our knowledge, such a statistical (esp. a PLS) approach has hitherto not been pursued to improve mash separation efficiency, despite its industrial importance (Schneider et al., 2005; Montanari et al., 2005; Kühbeck et al., 2006).

The parameters related to mash separation are not only numerous but also highly correlated, inducing significant modelling challenges. Conventional modelling methods, e.g. multiple linear regression (MLR) and ordinary least squares (OLS) cannot meet the set goals. Therefore, PLS regression is employed to capture mash separation variability. The algorithm is presented in Fig. 2 (Esposito Vinzi et al., 2010; Mehmood et al., 2012).

Step 1. Transform X and Y to normalized matrices F_0 , E_0 (m : indep., n : dep. variables)

Step 2. Extract the first component t_1 as the eigenvector corresponding to the largest eigenvalue of matrix $E_0^T F_0 F_0^T E_0$ (score vectors: $\hat{t}_1 = E_0 t_1$).

Step 3. Calculate the residual matrix E_0 as: $E_0 = t_1 p_1' + E_1$, where: $p_1 = \frac{E_0^T t_1}{\|t_1\|^2}$

Step 4. Replace E_0 with the residual matrix E_1 ; extract the second component, t_2 .

Repeat above steps to get all components.

Step 5. Determine the number of components k by cross-validation.

Step 6. Perform ordinary least squares on F_0 using extracted components (t_1, \dots, t_k) .

$$F_0 = \hat{t}_1 \beta_1^T + \dots + \hat{t}_k \beta_k^T + F_k$$

$$t_i = u_{i1}^* x_1 + \dots + u_{im}^* x_m (i=1, \dots, k)$$

$$Y = t_1 \beta_1 + \dots + t_k \beta_k$$

Step 7. Perform regression modelling to obtain the input (x)-output (y) correlation as:

$$y_j = a_{j1} x_1 + \dots + a_{jm} x_m (j = 1, \dots, n)$$

Figure 2: Partial Least Squares (PLS) algorithm used for input (X) and output (Y) data.

3. Results and Discussion

A statistical (PLS) model is derived for the mash separation of a beer brand (type A) this PLS regression model can accurately predict the filtration time of the mash separation process, as per Table 1 (for $r=4$ PLS variables selected). The 14 variables (x_i) in order, are: QM1, QM2, QM3: incoming feed quality parameters; MT: mashing time; CTT: compression total time; WTV: wort to copper volume; PVV: presparging volume; SWV: strong wort volume; CT1: compression1 time; SF3: sparge3 flowrate; PCV: pre-compress volume; SF1: sparge1 flowrate; SF2: sparge2 flowrate; SV3: sparge3 volume.

Table 1: Correlation coefficients of the 14 key variables considered (4 PLS variables).

	QM1	QM2	QM3	MT	CTT	WTV	PVV	SWV	C1T	SF3	PCV	SF1	SF2	SV3
QM1	1.00													
QM2	0.82	1.00												
QM3	0.90	0.86	1.00											
MT	0.44	0.47	0.47	1.00										
CTT	-0.50	-0.61	-0.51	-0.47	1.00									
WTV	0.83	0.59	0.71	0.37	-0.32	1.00								
PVV	0.04	0.13	0.13	0.26	-0.33	-0.16	1.00							
SWV	0.06	-0.07	0.13	0.19	0.10	0.09	-0.12	1.00						
C1T	-0.40	-0.58	-0.42	-0.46	0.94	-0.20	-0.32	0.09	1.00					
SF3	0.29	0.43	0.42	0.54	-0.64	0.09	0.27	0.15	-0.59	1.00				
PCV	-0.80	-0.71	-0.77	-0.52	0.47	-0.65	-0.07	-0.25	0.36	-0.55	1.00			
SF1	0.51	0.51	0.58	0.55	-0.51	0.31	0.19	0.25	-0.40	0.86	-0.72	1.00		
SF2	0.47	0.53	0.57	0.56	-0.57	0.25	0.25	0.16	-0.47	0.92	-0.70	0.97	1.00	
SV3	0.98	0.82	0.90	0.45	-0.50	0.86	-0.04	0.07	-0.38	0.36	-0.85	0.57	0.53	1.00

The variable importance projection (VIP) value is used to determine whether a variable should be retained in the PLS model: it is a weighted sum of squares of PLS weights, calculated from the amount of dependent variable variance of each PLS component, and it is an indicator showing the contribution of each independent variable to the model:

$$VIP = \sqrt{\frac{p}{Rd(Y; t_1, \dots, t_m)} \sum_{h=1}^m Rd(Y; t_h) w_{hj}^2} \quad (1)$$

Here, w_{hj} is the weight of the j th predictor variable; $Rd(Y; t_h)$ is the Y-variance fraction explained by component t_h ; $Rd(Y; t_1, \dots, t_m)$ is the cumulative fraction of Y-variance explained by components t_1, \dots, t_m , and p are the components retained (this work: $p = 4$). The VIP values that have been computed for the 14 independent variables of our PLS model are presented in Table 2 (all others with $VIP < 0.8$ scores have been discarded).

Table 2: VIP values of 14 retained independent variables (retention criterion: $VIP > 0.8$)

	QM1	QM2	QM3	MT	CTT	WTV	PVV	SWV	C1T	SF3	PCV	SF1	SF2	SV3
VIP	0.83	0.83	0.84	0.81	1.23	0.81	1.03	1.11	1.10	1.52	0.88	1.32	1.46	0.84

3.1. PLS model from odd-numbered batches validated vs. even-numbered batches

The input-output correlation obtained for filtration time (the critical output of industrial significance) vs. 14 independent variables from odd-batch data (in the order defined):

$$\text{Filtration time (s)} = y = 626.9886 + 0.2404x_1 + 0.9265x_2 + 0.5015x_3 + 32.2516x_4 + 48.5300x_5 - 0.3995x_6 - 62.6566x_7 + 11.1106x_8 + 23.0814x_9 - 2.2046x_{10} - 2.0042x_{11} - 2.9928x_{12} - 3.3516x_{13} + 2.0214x_{14} \quad (2)$$

The agreement of PLS model with plant data is great (error ca. 4% in outlier batch 24).

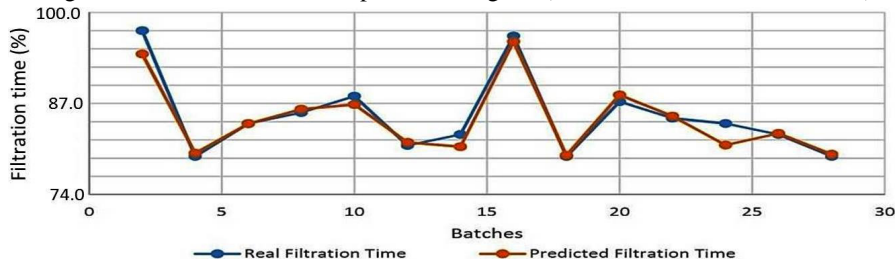


Figure 3. Filtration time prediction of odd (model) vs. even (data) separation batches.

3.2. PLS model from even-numbered batches validated vs. odd-numbered batches

Similarly, the input-output correlation obtained for filtration time (the critical output) vs. the same 14 independent variables from even-batch data (in the order defined):

$$\text{Filtration time (s)} = y = 1879.0100 + 0.2234x_1 - 0.3054x_2 + 0.2676x_3 + 18.119x_4 + 26.3076x_5 + 3.8418x_6 - 60.2435x_7 + 12.3015x_8 - 3.8380x_9 - 2.3208x_{10} - 0.8541x_{11} - 3.9576x_{12} - 3.0716x_{13} + 2.8110x_{14} \quad (3)$$

Great agreement of PLS model with plant data, again (error 3%, 4% in batches 1, 19).

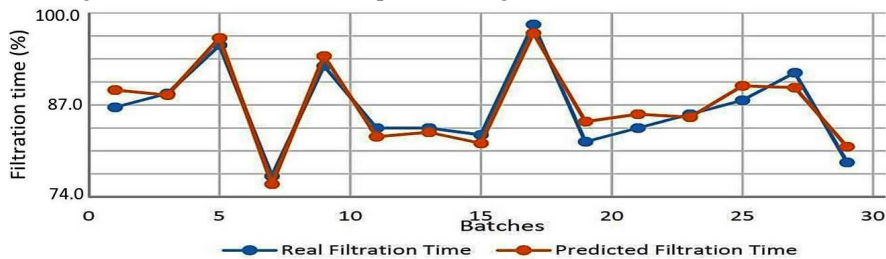


Figure 4. Filtration time prediction of even (model) vs. odd (data) separation batches.

3.3. Sensitivity analysis

Clearly, SWV, QM1, QM3, SF1, SF2 (in decr. order) are the strongest filtration drivers.

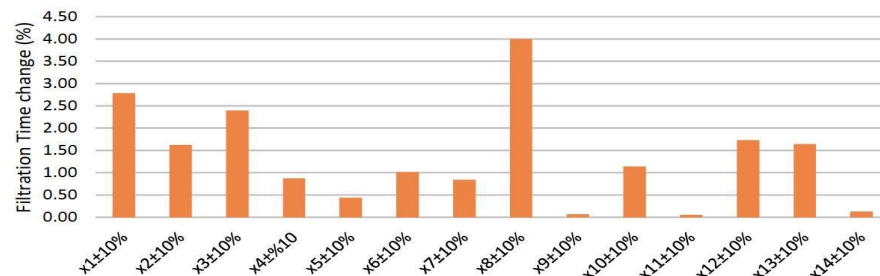


Figure 5: Sensitivity analysis of relative influence of input variables on filtration time.

4. Conclusions

This paper develops and discusses statistical (Partial Least Squares/PLS) models of mash separation for two beer types, and presents a sensitivity analysis in order to better understand which operational modifications are feasible and most promising in order to improve mash separation efficiency and benefit beer production and its supply chain. The agreement obtained between predicted and real filtration time is very good, and the analysis is repeated for different (odd/even) data subsets, to explore trends and outliers. A sensitivity plot shows that strong wort volume (SWV) and feed quality (QM1, QM3) have the strongest effect on filtration time (y), the key industrial performance metric. This concurs with industrial experience, but none of these are convenient manipulation variables: however, sparging flowrates (SF1, SF2) are, and thus can be effectively used. Mashing time (MT), pre-sparging and (pre-)compression metrics are not key factors. PLS models may require (re-)calibration to avoid drift, but clearly have business value.

Acknowledgements

The authors acknowledge instrumental help and helpful discussions with Molson Coors staff engineers and technicians, and EPSRC/IAA and MSc in Adv. Chem. Eng. project funding (School of Engineering, University of Edinburgh). Dr. Dimitrios I. Gerogiorgis also acknowledges a Royal Academy of Engineering (RAEng) Industrial Fellowship.

References

- M. Aznar et al., 2003, Prediction of aged red wine aroma properties from aroma chemical composition: Partial least squares regression models, *J. Agr. Food. Chem.* 51, 2700–2707.
- C. Bamforth, 2006, *Brewing: New Technologies*, Woodhead Publishing, Cambridge, UK.
- T. Bühler, 1996, *Effects Of Physical Parameters in Mashing on Lautering Performance*, Doctoral Thesis, Loughborough University, UK.
- V. Esposito Vinzi et al. (eds.), 2010, *Handbook of Partial Least Squares: Concepts, Methods and Applications*, Springer, Heidelberg.
- F. Kühbeck et al., 2006, Influence of lauter turbidity on wort composition, fermentation performance and beer quality in large-scale trials, *J. Inst. Brewing* 112, 222–231.
- J. Liu et al., 2008, Multivariate modeling of aging in bottled lager beer by principal component analysis and multiple regression methods, *J. Agr. Food Chem.* 56, 7106–7112.
- J.F. MacGregor et al., 1994, Process monitoring and diagnosis by multiblock PLS methods, *AIChE J.* 40, 826–838.
- T. Mehmood et al., 2012, A review of variable selection methods in Partial Least Squares regression, *Chemometr. Intell. Lab.* 118, 62–69.
- F.G. Meussdoerffer, 2009, A comprehensive history of beer brewing, in *Handbook of Brewing: Processes, Technology, Markets*, Wiley-VCH, Weinheim, Germany.
- L. Montanari et al., 2005, Effect of mashing procedures on brewing, *Eur. Food Res. Tech.*, 221, 175–179.
- B. Muster-Slawitsch et al., 2014, Process modelling and technology evaluation in brewing, *Chem. Eng. Process.* 84, 98–108.
- J.M. Poveda et al., 2004, Application of partial least squares (PLS) regression to predict the ripening time of Manchego cheese, *Food Chem.* 84, 29–33.
- J. Schneider et al., 2005, Study on the membrane filtration of mash with particular respect to the quality of wort and beer, *J. Inst. Brewing* 111, 380–387.
- R. Wakeman, S. Tarleton, 1999, *Filtration: Equipment Selection, Modelling, Process Simulation*, Elsevier, Amsterdam.

Technoeconomic MINLP Optimisation of Liquid-Liquid Extraction (LLE) Cascades for Continuous Pharmaceutical Manufacturing (CPM) of Atropine

Samir Diab,^a Nikolaos Mytis,^b Andreas G. Boudouvis,^b Dimitrios I. Gerogiorgis^{a*}

^a *School of Engineering (IMP), University of Edinburgh, Edinburgh, EH9 3FB, UK*

^b *School of Chemical Engineering, National Technical University of Athens, Athens 15780, Greece*

D.Gerogiorgis@ed.ac.uk

Abstract

Continuous pharmaceutical manufacturing (CPM) has the potential to revolutionise the production of active pharmaceutical ingredients (APIs), offering operational and economic benefits over the currently dominant batch methods implemented by industry. Atropine is a nerve agent API, whose demonstrated continuous flow synthesis facilitates process modelling and optimisation. This work implements MINLP optimisation for total cost minimisation of the upstream CPM of atropine for rapid process synthesis. The process model considers reactor design from regressed reaction kinetic parameters, solute partitioning between LLE phases for different solvent systems, UNIFAC-modelled ternary liquid-liquid equilibria and mass transfer correlations for continuous LLE design. Optimisation results indicate toluene as the best (cost optimal) LLE solvent choice. This work demonstrates the utility of the described methodology for rapid process synthesis and comparative technoeconomic evaluation in early CPM process development stages.

Keywords: Continuous pharmaceutical manufacturing (CPM); Atropine; MINLP; Superstructure; Economic analysis.

1. Introduction

Continuous pharmaceutical manufacturing (CPM) is an emerging research field with the potential for significant technical, operational and economic benefits over currently prevalent batch methods (Koenig and Dillon, 2017). Despite demonstrations of active pharmaceutical ingredient (API) continuous synthesis, a lack of integrated continuous separation methods is an important obstacle (Baxendale et al., 2015); elucidation of optimal process designs is imperative for successful implementation (Teoh et al., 2015).

Atropine is a World Health Organisation (WHO) API for the treatment of nerve agents (Marrs and Rice, 2016), whose continuous flow synthesis features two plug flow reactor (PFRs) followed by liquid-liquid extraction (LLE) (Bédard et al., 2016). Systematic comparative evaluation of LLE design configurations can be implemented via MINLP optimisation. This work implements steady-state modelling and MINLP optimisation for atropine CPM, including upstream continuous flow synthesis and continuous LLE. Reactor design using kinetic parameters regressed from published data, thermodynamic models and mass transfer correlations for LLE design and an established costing methodology for pharmaceutical manufacturing are implemented. Optimisation results corresponding to cost optimal LLE design configurations and minimum total costs are then presented for different designs with an outlook on this vibrant research field.

2. Process Modelling and MINLP Optimisation

2.1. Continuous Flow Synthesis

The flowsheet for the CPM of atropine is shown in Fig. 1. The API continuous flow synthesis is demonstrated by Bédard et al. (2016), featuring three reactions in two PFRs. The first (PFR-1) features the esterification of tropine **2** (in DMF) and neat phenylacetyl chloride **3** at 100 °C to form tropine ester HCl **4** (reaction 1), the free form of which (**5**) is formed by the addition of NaOH (aq). It is assumed that PFR-1 attains the same conversion of 99% of **2** to **4** at 100 °C as reported in the literature. The second reactor (PFR-2) features the addition of formaldehyde (CH₂O) to **5** (reaction 2a) under basic conditions to produce API. An undesired elimination of API to apotatropine **6** (reaction 2b) is also reported. Interrogation of the published kinetic data for reaction 2a shows a second-order (first-order in both **5** and CH₂O) to be the most plausible rate law with an estimated second-order rate constant of $k_2 = 1.68 \text{ L mol}^{-1} \text{ h}^{-1}$; this allows explicit modelling of reactor performance for PFR volume calculation in the process model.

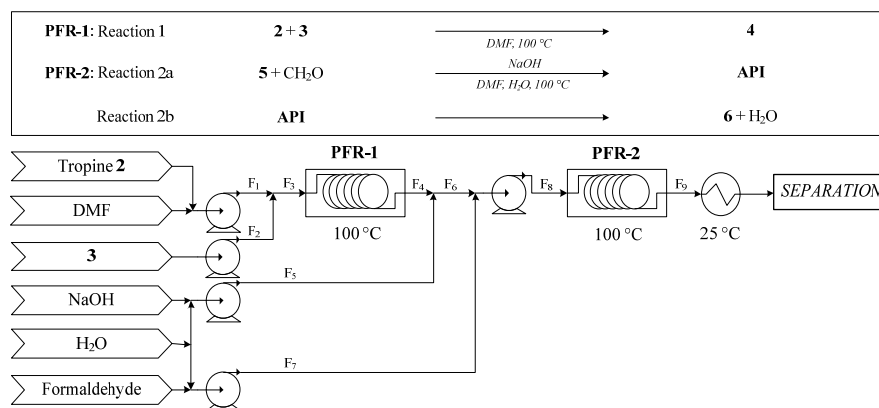


Figure 1: Flowsheet for the CPM of atropine: continuous synthesis and LLE.

2.2. Continuous Liquid-Liquid Extraction (LLE): Thermodynamics

This work considers a continuous purification via LLE following the API continuous flow synthesis. The continuous LLE is operated at $T_{\text{LLE}} = 25 \text{ }^\circ\text{C}$ for partitioning of structurally similar impurities (**2**, **5**, **6**) into the extract (aqueous phase) while retaining API in the raffinate (organic phase). Candidate LLE solvents for investigation must induce rapid phase splitting with the feed solvent mixture of DMF + H₂O from the continuous API synthesis; thus, modelling of candidate CPM-LLE designs requires liquid-liquid equilibria data for the ternary solvent system DMF + H₂O + LLE solvent. Ternary systems containing candidate LLE solvents were screened for their propensity to form an immiscible mixture via UNIFAC modelling. According to these criteria, the LLE solvents considered in this work are diethyl ether (Et₂O), butyl acetate (BuOAc) and toluene (PhMe), whose ternary diagrams are shown in Fig. 2. Partition coefficients of API and impurity solutes between organic and aqueous phases for different considered solvent systems at $T_{\text{LLE}} = 25 \text{ }^\circ\text{C}$ are available in the literature (Bédard et al., 2016) and are used here for solute distribution estimation and LLE modelling. Partition coefficients describe the distribution of solute components under equilibrium, i.e. non-steady-state conditions.

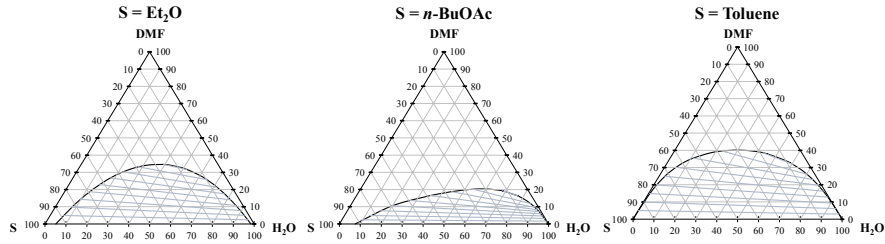


Figure 2: Ternary diagrams for the LLE systems DMF + H₂O + {Et₂O, BuOAc, PhMe}.

2.3. Continuous Liquid-Liquid Extraction (LLE): Mass Transfer Correlations

Calculation of inefficiencies associated with continuous (i.e., steady-state) operation compared to equilibrium conditions must be considered in the process model. The continuous LLE efficiency (E_{LLE}) is a function of the overall mass transfer coefficient (K), interfacial area (a) and tank residence time (τ_{LLE}). Here, k_i, Sh_i = phase mass transfer coefficients and Sherwood numbers, respectively, d_{32} = Sauter mean droplet diameter, D_{API} = API diffusivity, ϕ = dispersed phase volume fraction, Sc = Schmidt number, Fr = Froude number, Eu = Eotvos number, Re_i = impeller Reynolds' number, d_i, d_t = impeller and tank diameters, respectively, We = Weber number, N_i = impeller rotation speed, ρ_c = continuous phase density and σ = surface tension. The calculation of all terms uses the Skelland and Moetti (1990) correlation for continuous LLE modelling as mixer-settlers.

$$E_{LLE} = ((Ka\tau_{LLE})^{-1} + 1)^{-1} \quad (1)$$

$$K = (k_c^{-1} + k_d^{-1})^{-1} \quad (2)$$

$$a = \frac{6\phi}{d_{32}} \quad (3)$$

$$Sh_d = \frac{k_d d_{32}}{D_{API,d}} \approx 6.6 \quad (4)$$

$$Sh_c = \frac{k_c d_{32}}{D_{API,c}} = 1.25 \times 10^{-5} Sc_c^{1/3} Fr_c^{5/12} Eu^{5/4} \phi^{-1/2} Re^{2/3} \left(\frac{d_i}{d_{32}}\right)^2 \left(\frac{d_{32}}{d_t}\right)^{1/2} \quad (5)$$

$$d_{32} = \begin{cases} 0.052 d_i We^{-0.6} \exp 4\phi & , We < 10^3 \\ 0.390 d_i We^{-0.6} & , We > 10^3 \end{cases} \quad (6)$$

$$We = \frac{d_i^3 N_i^2 \rho_c}{\sigma} \quad (7)$$

2.4. MINLP Optimisation Problem Formulation

The MINLP LLE superstructure is illustrated in Fig. 3; the location and number of LLE solvent feed points and tanks affects the LLE performance and total costs and is varied in the considered superstructure. The objective of the MINLP optimisation problem is to minimise the total plant cost ($Cost$, Eq. 8). Integer decision variables are the number of LLE tanks, N_{LLE} , allowed a maximum number of 3 (Eq. 9), binary integer variable, y_i , which determines the number and location of fresh LLE solvent feed points (Eqs. 10–11). When the sum of $y_i = 0$, a purely countercurrent LLE configuration is implemented, i.e., no fresh LLE solvent is added; when $y_i > 0$, fresh LLE solvent is fed to tank i in addition to the countercurrent extract entering tank N_{LLE} and flowing through remaining tanks.

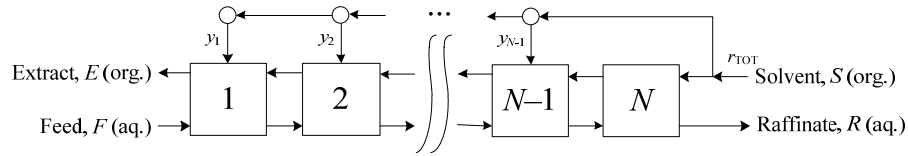


Figure 3: MINLP superstructure for the continuous liquid-liquid extraction (LLE), with continuous (tank volume, V_i , solvent feed rate, r_{TOT}) and integer variables (no. tanks, N_{LLE} and allocation of fresh solvent feed, y_i , and solvent choice).

Continuous decision variables are the total solvent-to-feed ratio (r_{TOT}), for which fresh solvent is divided equally between tanks to which a crossflow LLE solvent feed is specified (i.e., where $y_i = 1$) and constrained within values to ensure that the LLE process mixture is always fully immiscible (Eq. 13) for total LLE solvent addition, S_i (Eq. 11) and LLE tank volumes (V_i), each allowed to have a minimum volume of 1 L (Eq. 14). The problem is solved for separate instances of LLE solvent. For N_{LLE} implemented tanks, there are $N_{LLE} + 1$ continuous decision variables (V_i and r_{TOT}) and $N_{LLE} - 1$ integer decision variables (y_i), i.e. a total of $2N_{LLE}$ decision variables per instance. A multistart routine using multiple initial guesses of each decision variable is implemented in order to find as near to a global minima as possible. The considered plant capacity in all cases is $Q_{API} = 10^3$ kg API yr^{-1} . The current MINLP formulation has a small number of discrete variables, which could be solved as separate NLP instances; however, the current framework can be easily adapted to consider greater numbers of possible LLE tanks (N_{LLE}), which rapidly increases the number of discrete variables, for which applying MINLP is more suitable.

$$\min Cost = CapEx + \sum_{j=1}^t \frac{OpEx}{(1+k)^j} \quad (8)$$

s.t.

$$N_{LLE} \in \{1, 2, 3\} \quad (9)$$

$$y_i \in \{0, 1\}, i = 1 \dots N_{LLE} - 1 \quad (10)$$

$$S_i = \frac{y_i r_{TOT} F}{\sum y_{j+1}} \text{ for } i = 1 \dots N_{LLE}, j = 1 \dots N_{LLE} \quad (11)$$

$$\sum_{i=1}^{N_{LLE}-1} y_i \leq N_{LLE} - 1 \quad (12)$$

$$0.25 \leq r_{TOT} \leq 5 \quad (13)$$

$$1 \leq V_i \quad (14)$$

Total costs ($Cost$) are calculated as the sum of capital expenditure ($CapEx$), assumed spent at year zero, and the sum of time-discounted operating expenditure ($OpEx$) over the considered plant lifetime, $t = 20$ yr. The discount rate ($k = 5\%$) accounts for inflation over the plant lifetime. Annual operation of 8,000 hr is considered. Capital expenditure includes battery limits installed costs, construction and working capital; operating expenditure is the sum of material costs, utilities and waste handling costs. The implemented costing methodology in this work is applicable to both continuous and batch API pharmaceutical manufacturing processes (Jolliffe and Gerogiorgis, 2016).

3. Results and Discussion

Fig. 4 shows the optimal design configuration for each LLE solvent choice. All solvent choices result in the same flowsheet configuration, $N_{LLE} = 3$ tanks, with an extra fresh solvent feed to the first tank, but varying optimal tank volumes and LLE solvent-to-feed ratios. Tank volumes vary, with the largest being the first tank in all design cases, with the largest tanks required for BuOAc implementation. Consideration of longer cascades (i.e., more tanks), may lead to lower unit volumes and will affect the resulting efficiency and minimum total costs. The total LLE-solvent-to-feed ratio (r_{TOT}) varies between solvents, but all are typically mid-range with respect to the constraints applied to ensure process mixtures remain fully immiscible. The LLE MINLP superstructure considered in this work (Fig. 3) can be expanded further to consider splitting the fresh feed stream as well as splitting product from intermittent stages and the as possible implementation of solvent recycling. Consideration of subsequent crystallisation process requirements on LLE product streams should also be integrated with solvent harmonisation during the early stages of design to aid CPM development and mitigate plantwide operational issues.

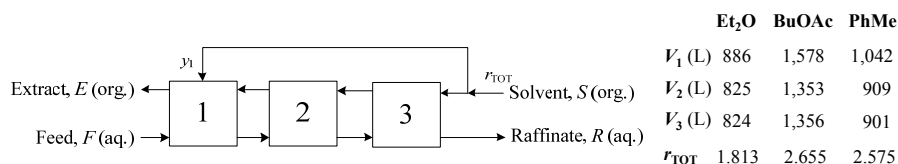


Figure 4: Optimal LLE MINLP superstructure and design and operating parameters corresponding to minimum plant total costs for different design assumptions.

Fig. 5 shows minimum total cost components corresponding to optimal LLE configurations presented in Fig. 4. *CapEx* is dominated by *BLIC* in all cases while material costs dominate *OpEx* due to expensive reagents. Despite high *CapEx* associated with large tank volumes, the benefits associated with increased LLE efficiency on reducing material requirements and waste is required due to the high contribution of *OpEx* components to total costs. Optimisation results show that toluene (PhMe) is the best LLE solvent choice, attaining the lowest total costs. Toluene exhibits the widest envelope of immiscibility of the LLE solvents considered; rapid and wide phase splitting allows for enhanced LLE performance. Further corroboration of optimisation results with experimental validation as well as solvent harmonisation with crystallisation processes is essential. Although toluene is more economically favourable, it has less favourable EHS criteria compared to BuOAc. Explicit consideration of solvent selection heuristics based upon EHS criteria has been useful in previous CPM efforts (Diab and Gerogiorgis, 2017).

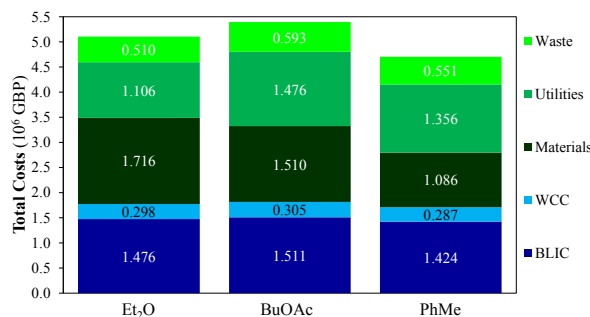


Figure 5: Minimum total cost components for different LLE solvent choices.

4. Conclusions

This work has formulated and solved a MINLP optimisation problem for the total cost minimisation of the plantwide CPM of atropine, a societally-important API with a variety of applications. Optimisation of a conceptual continuous LLE following the continuous flow synthesis for different LLE solvent choices was used to elucidate promising designs. Ternary phase equilibria were estimated via UNIFAC modelling and solute distribution between LLE phases used published partition coefficient data. The optimal LLE configuration for all cases implements three LLE tanks in series in a countercurrent arrangement with additional fresh LLE solvent fed to the first tank in the cascade. Investigation of more complex LLE superstructures accounting for greater numbers of tanks and recycle options will further elucidate optimal process design. Toluene emerges as the most economically favourable LLE solvent choice, offering significant total cost savings over other LLE designs with acceptable material efficiencies for pharmaceutical manufacturing applications. Consideration of downstream unit operation requirements for LLE solvent selection and harmonisation following the upstream CPM plant considered here will provide further insight into optimal process configuration and designs. This work demonstrates the value of conducting technoeconomic optimisation studies during the early stages of design towards economically viable end-to-end CPM.

Acknowledgements

Mr. Samir Diab gratefully acknowledges the financial support of the Engineering and Physical Sciences Research Council (EPSRC) via a Doctoral Training Partnership (DTP) PhD Fellowship (Grant # EP/N509644/1). Mr. Nikolaos Mytis acknowledges the support of an Erasmus+ Teaching Exchange Travel Scholarship. Dr. Dimitrios I. Gerogiorgis acknowledges a Royal Academy of Engineering (RAEng) Industrial Fellowship. The authors acknowledge the support of the Nagai and Great Britain Sasakawa Foundations.

References

- A.C. Bédard, A.R. Longstreet, J. Britton, Y. Wang, H. Moriguchi, R.W. Hicklin, W.H. Green and T.F. Jamison, 2016, Minimizing E-factor in the continuous-flow synthesis of diazepam and atropine, *Bioorg. Med. Chem.*, 25, 23, 6233–6241.
- I.R. Baxendale, R.D. Braatz, B.K. Hodnett, K.F. Jensen, M.D. Johnson, P. Sharratt, J.-P. Sherlock, A.J. Florence, Achieving continuous manufacturing: technologies and approaches for synthesis, workup, and isolation of drug substance, *J. Pharm. Sci.*, 104, 3, 781–791.
- S. Diab and D.I. Gerogiorgis, 2017, Process modeling and technoeconomic evaluation for continuous manufacturing of diphenhydramine, *Org. Process Res. Dev.*, 21, 7, 924–946.
- H.G. Jolliffe and D.I. Gerogiorgis, 2016, Plantwide design and economic evaluation of two continuous pharmaceutical manufacturing cases, *Comput. Chem. Eng.*, 91, 269–288.
- S. Koenig and B. Dillon, 2017, Driving toward greener chemistry in the pharmaceutical industry, *Curr. Opin. Green Sust. Chem.*, 7, 56–59.
- T. Marrs and P. Rice, Chemical terrorism and nerve agents, 2016, *Medicine*, 44, 2, 106–108.
- A.H.P. Skelland and L.T. Moetti, 1990, Mechanism of continuous-phase mass transfer in agitated liquid-liquid systems, *Ind. Eng. Chem. Res.*, 29, 11, 2258–2267.
- S.K. Teoh, C. Rathi and P. Sharratt, 2015, Practical assessment methodology for converting fine chemicals processes from batch to continuous, *Org. Process Res. Dev.*, 20, 2, 414–431.

Dynamic Modelling and Simulation of Chinese Hamster Ovary (CHO) Cell Fermentation for Advanced Biopharmaceutical Manufacturing

Haruku Shirahata,^a Samir Diab,^b Hirokazu Sugiyama,^a Dimitrios I. Gerogiorgis^{b*}

^a *Department of Chemical System Engineering, University of Tokyo, 113-8656, Japan*

^b *School of Engineering (IMP), University of Edinburgh, Edinburgh, EH9 3FB, UK*

D.Gerogiorgis@ed.ac.uk

Abstract

Chinese hamster ovary (CHO) cells are widely used in fermentation processes towards biopharmaceutical manufacturing of monoclonal antibodies (mAbs). This work presents dynamic models of two different fermentation modes: batch mode to produce interferon (IFN)- γ and perfusion mode to produce mAbs. The models predict concentration profiles of cells, substrate, by-product and product, which are validated versus experimental results from the literature. Sensitivity analyses were conducted to establish important parameters for dynamic states that can be investigated in process design. Time and operating costs were evaluated using dynamic models for batch and perfusion modes. Varying initial cell concentration shows a trade-off between production time and cost towards modelling and optimisation of advanced biopharmaceutical manufacturing.

Keywords: Chinese hamster ovary (CHO) cells; Fermentation; Process design.

1. Introduction

The biopharmaceuticals market is growing rapidly compared to that of conventional pharmaceuticals (Otto, Santagostino and Schrader, 2014). Typical manufacturing processes comprise of drug substance manufacturing, including fermentation and purification to produce active pharmaceutical ingredients (APIs), and drug product manufacturing for formulation (Fig. 1). Fermentation of mammalian cells is widely implemented in different operation modes for biopharmaceuticals; batch and fed-batch modes are commonly implemented, and perfusion operations are developed towards continuous manufacturing (Bielser et al., 2018). Dynamic modelling of fermentation processes can be implemented for quantitative comparative evaluation of different designs prior to expensive and laborious experimental campaigns and pilot plant studies.

Chinese hamster ovary (CHO) cell fermentation is often implemented for the production of monoclonal antibodies (mAbs), a class of biopharmaceuticals produced in high sales volumes (Ecker, Jones and Levine, 2015). Different fermentation modes are implemented in the literature for the production of various mAbs (Kelley, 2009). This work implements dynamic modelling incorporating CHO cell fermentation kinetics for two different culture modes (batch and perfusion) for advanced biopharmaceutical manufacturing process design. Model validation versus experimental results is implemented to establish which biological phenomena are well represented by the models. Parametric sensitivity analyses are then implemented to elucidate critical kinetic and design parameters in the models. Process design and economic evaluation under varying assumptions are then presented.

2. Dynamic Process Modelling of Fermentation Processes

Biopharmaceutical products from fermentation are synthesised as metabolites of biological cells following substrate consumption and accompanied by cell growth and waste generation. Fermentation processes are typically operated in either batch, fed-batch or perfusion modes prior to purification and formulation of the final drug product, as shown in Fig. 1. Batch operation begins with all cells and culture media in the bioreactor, and solution containing products is removed at the end of the run. Fed-batch mode feeds substrate intermittently to control nutrient concentrations throughout the batch cycle. Perfusion mode fermentation constantly feeds and harvests the bioreactor, with bleeding to control cell concentrations, in an effort towards attaining the operational benefits of continuous manufacturing, which is being adopted for certain APIs in conventional pharmaceutical manufacturing. This work considers batch fermentation for interferon (IFN)- γ production and perfusion fermentation to produce fully-humanised mAb.

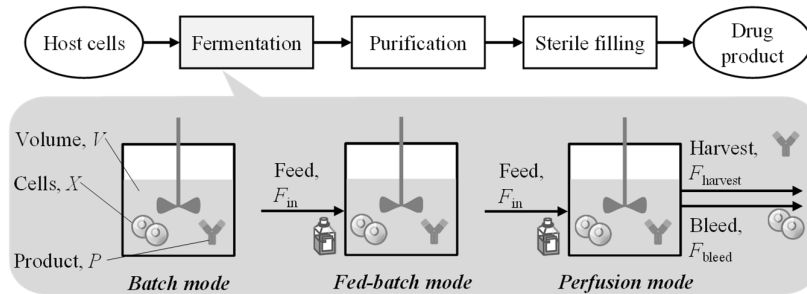


Figure 1: Typical biopharmaceutical manufacturing process and different culture modes.

2.1. Batch Mode Fermentation

Fox et al. (2004) developed a dynamic model for the batch CHO cell fermentation to produce IFN- γ , described by Eqs. 1–5. The model describes concentration profiles of cells (X), substrate (glucose, S), and product (IFN- γ , P) as a function of time (t). The specific cell growth (μ) and substrate consumption (q_s) are explicitly considered via Monod kinetics; the specific product formation rate (q_p), maximum specific growth rate (μ_{\max}), maximum specific substrate consumption rate (q_{\max}), Monod constant (K) and substrate consumption rate (K_s) are defined in the literature. The value of μ depends on S with respect to the threshold substrate concentration (S_t) (Fox et al., 2004).

$$\frac{dX}{dt} = \mu X \quad (1)$$

$$\frac{dS}{dt} = -q_s X \quad (2)$$

$$\frac{dP}{dt} = q_p X \quad (3)$$

$$q_s = \frac{q_{\max} S}{K_s + S} \quad (4)$$

$$\mu = \frac{\mu_{\max} S}{K + S} \quad (S \geq S_t); \mu = 0 \quad (S < S_t) \quad (5)$$

2.2. Perfusion Mode Fermentation

Karst et al. (2017) developed a dynamic model for the perfusion mode fermentation of CHO cells to produce fully-humanised mAb, described by Eqs. 6–10. In addition to concentration profiles of cells (X), substrate (S) and product (mAb, P), the perfusion model also describes concentration profile of waste product ammonia (A), which requires a value for the specific ammonia production rate (q_{amm}), defined in the literature (Karst et al., 2017), as well as the working volume variation (V). Steady-state operation and constant working volume are assumed by controlling the feed (F_{in}) and product (F_{out}) stream flowrates of the perfusion reactor; thus the time differential of the working volume (Eq. 9) is equal to zero. The outlet flowrate is controlled via the harvest (F_{harvest}) and bleed (F_{bleed}) rates, which depends on the working volume and the specific growth rate (μ). Bleed and harvest rates are calculated via Eq. 9. Monod kinetics describe μ , μ_{max} and the ammonia growth inhibition constant ($K_{\mu,\text{amm}}$) available in the literature (Karst et al., 2017).

$$\frac{d(VX)}{dt} = \mu VX - F_{\text{bleed}}X \quad (6)$$

$$\frac{d(VP)}{dt} = q_p VX - F_{\text{harvest}}P \quad (7)$$

$$\frac{d(VA)}{dt} = q_{\text{amm}} VX - F_{\text{out}}A \quad (8)$$

$$\frac{dV}{dt} = F_{\text{in}} - F_{\text{out}} = 0; F_{\text{out}} = F_{\text{harvest}} + F_{\text{bleed}}; F_{\text{bleed}} = \mu V \quad (9)$$

$$\mu = \frac{\mu_{\text{max}} K_{\mu,\text{amm}}}{K_{\mu,\text{amm}} + A} \quad (10)$$

The implemented models for batch (Fox et al., 2004) and perfusion (Karst et al., 2017) mode fermentations do not account for cell death or the production or consumption of other compounds, e.g. lactate produced during the reaction due to the lack of parameters available for such phenomena. Development of these models to account for concentration profiles of additional species should be implemented given sufficient experimental data.

3. Results and Discussion

3.1. Dynamic Model Sensitivity Analysis

Sensitivity analyses were conducted for dynamic states for different fermentation modes to establish design and operating parameters for investigation during process design. Model parameters are perturbed individually by $\pm 20\%$ from their base values. The sensitivity of dynamic states on various design and operating parameters is measured by:

$$R = \frac{i_{0,\text{perturbed}} - i_{\text{end,perturbed}}}{i_{0,\text{basecase}} - i_{\text{end,basecase}}} - 1 \quad (11)$$

Here, R is the sensitivity ratio, $i_{0,\text{perturbed}}$ and $i_{0,\text{basecase}}$ are initial dynamic states with and without perturbations, respectively, while $i_{\text{end,perturbed}}$ and $i_{\text{end,basecase}}$ are the equivalent final dynamic states. The sensitivity of product concentration, P , to various kinetic and operating parameters is considered for both batch and perfusion fermentation processes.

Fig. 2 shows the sensitivity of product concentration (R_p) to various kinetic and operational parametric perturbations. For the batch fermentation, kinetic parameters K , K_S , q_{max} , q_P and μ_{max} have the greatest effect on product concentration, while S_i has a lesser effect. The batch fermentation initial cell and substrate concentrations (X_0 and S_0 , respectively) affect product concentration more than initial product concentration (P_0). For the perfusion mode fermentation, product concentration is very sensitive to the value of q_P compared to other model kinetic parameters. The perfusion mode values for $F_{harvest}$, X_0 and V_0 have the most significant effect on product concentration compared to A_0 and P_0 . Sensitivity analyses on dynamic models are important to elucidate key kinetic parameters that must be fit to a high degree of accuracy during parameter regression from experimental data as well as operating parameters that can be tuned during process design.

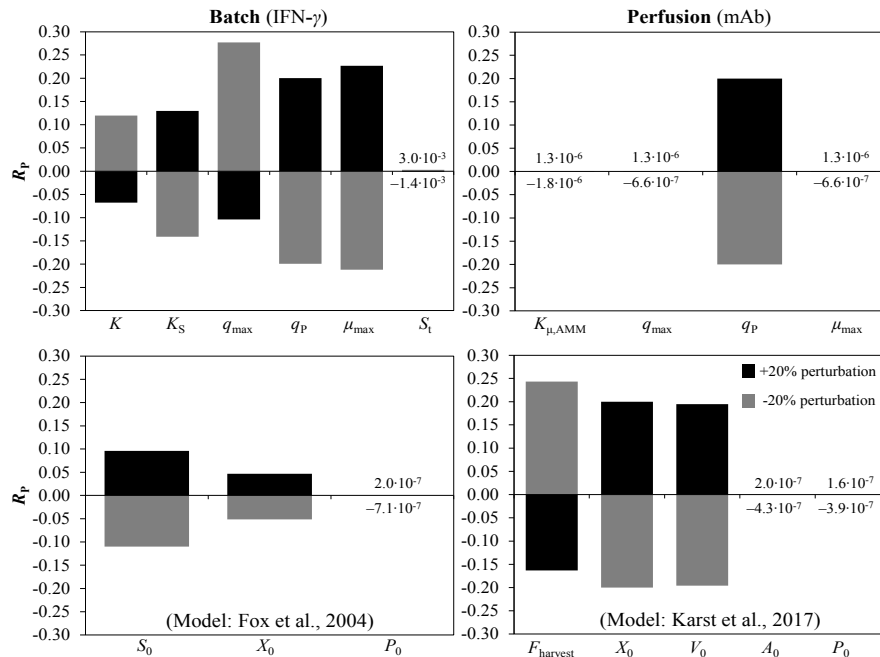


Figure 2: Product concentration sensitivity to different kinetic and operating parameters.

3.2. Dynamic Model Validation

The implemented dynamic models for batch and perfusion fermentation modes were compared versus published experimental data for model validation purposes. Fig. 3 shows profiles of X , S , A , P , and V for the batch and perfusion fermentation modes. The models were validated by t -testing, which showed good reproducibility with a significance level of 0.05 for both modes. The batch model reproduces the data well until $t = 98$ hr, after which cell concentration profiles significantly deviate due to the lack of cell death expressions in the model. For process design purposes, the maximum batch run time is assumed to equal 98 hr to ensure the model is viable. The perfusion model generally reproduces the experimental data well, with a slight over-prediction of P . Consideration of cell death in the model as well as concentration profiles of other significant biological compounds will enhance our understanding of the kinetic behaviour of this process.

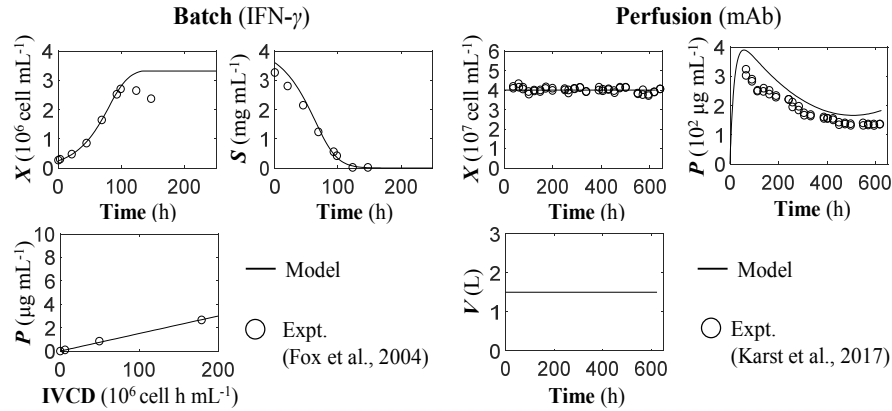


Figure 3: Model validation vs. experimental data (IVCD = integral of viable cell density).

3.3. Process Design Space Investigation and Economic Analysis

Economic evaluation of different process designs is imperative to elucidate promising cost-effective configurations. The current analysis investigates the effect of varying initial cell concentration on required production time and the corresponding normalised operating costs with respect to mass of product and bioreactor working volume. Operating costs (C_{OpEx}) are composed of cell (C_{cells}), media (C_{media}) and agitation ($C_{agitation}$) costs.

$$C_{OpEx} = C_{cells} + C_{media} + C_{agitation} \quad (12)$$

Fig. 4 shows production time and operating costs per unit product mass per unit bioreactor working volume for both batch and perfusion fermentation processes. In both cases, there is a trade-off between the processing time and the operating cost with varying initial cell concentration; as cell concentration increases, production time decreases, but a corresponding increase in cost is observed associated with increased cell quantities present in the fermentation broth. Cost calculations do not account for optimal batch numbers, sizes and scheduling, which will allow for improved costs and provide further insight into optimal design of the considered batch fermentation. Provision of production requirements, product sales prices and additional economic data for these particular processes will elucidate absolute cost components for clarification of economic viability.

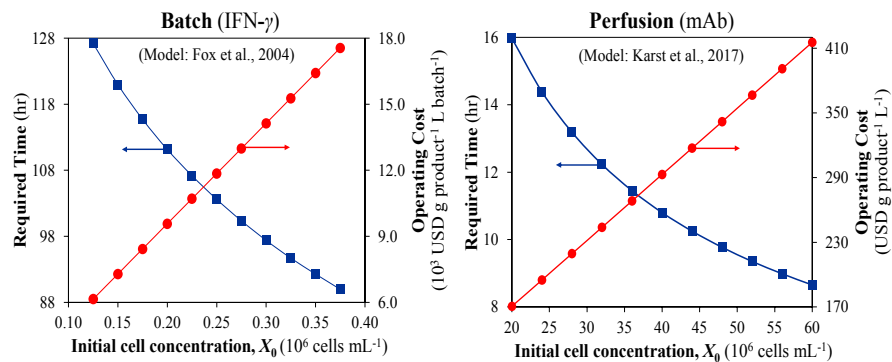


Figure 4: Production time and operating costs for batch and perfusion operations.

Consideration of perfusion downtimes and numbering-out/up of unit operations is another important consideration. Incorporation of detailed capital expenditure calculations into the total costs requires reliable cost-capacity correlations for specific biopharmaceutical manufacturing unit operations in order to gain insight into forecasted total costs. Provided accurate economic parameters, unit cost correlations and reduced model discrepancies with respect to experimental data, a dynamic optimisation problem formulation incorporating the kinetic models described in this work can allow elucidation of optimal control strategies of different dynamic parameters to meet specific economic objectives.

4. Conclusions

Dynamic models of different modes of fermentation of CHO cells were developed for manufacturing of different biopharmaceutical products: batch mode to produce IFN- γ and perfusion mode to produce fully-humanised mAb. The models were validated with experimental values from the literature, with the models for batch and perfusion modes showing good reproducibility. Sensitivity analyses of different operating parameters' effects on product concentrations established initial cell and substrate concentrations as important design variables for batch and perfusion modes. A trade-off between the production time and costs is observed for both fermentation modes. This work is the first to implement the described dynamic models for batch (Fox et al., 2004) and perfusion (Karst et al., 2017) CHO cell fermentation for process design and economic analysis of different biopharmaceutical manufacturing routes. Future work will implement the models into a dynamic optimisation problem formulation to establish optimal operating and design parameters for advanced biopharmaceutical manufacturing from CHO cells.

5. Acknowledgements

Ms. Haruku Shirahata acknowledges the support of the Global Leader Program for Social Design and Management and a Grant-in-Aid for JSPS Research Fellowship. Mr. Samir Diab acknowledges the support of the Engineering and Physical Sciences Research Council (EPSRC) via a Doctoral Training Partnership PhD Fellowship. Dr. Hirokazu Sugiyama acknowledges a Grant-in-Aid for Young Scientists Fellowship. All authors acknowledge the financial support of the Nagai and Great Britain Sasakawa Foundations.

References

- J.M. Bielser, M. Wolf, J. Souquet, H. Broly and M. Morbidelli, 2018, Perfusion mammalian cell culture for recombinant protein manufacturing – a critical review, *Biotechnol. Adv.*, 36, 1328–1340.
- D.M. Ecker, S.D. Jones and H.L. Levine, 2015, The therapeutic mAb market, *mAbs*, 7, 1, 9–14.
- S.R. Fox, U.A. Patel, M.G.S. Yap and D.I.C. Wang, 2004, Maximizing IFN- γ production by chinese hamster ovary cells through temperature shift optimization, *Biotechnol. Bioeng.*, 85, 2, 177–184.
- D.J. Karst, E. Scibona, E. Serra, J.M. Bielser, J. Souquet, M. Stettler, H. Broly, M. Soos, M. Morbidelli and T.K. Villiger, 2017, Modulation and modeling of monoclonal antibody N-linked glycosylation in mammalian cell perfusion reactor, *Biotechnol. Bioeng.*, 114, 9, 1978–1990.
- B. Kelley, 2009, Industrialization of mAb production technology: the bioprocessing industry at a crossroads, *mAbs*, 1, 5, 443–452.
- R. Otto, A. Santagostino and U. Schrader, 2014, The beauty and the beast: a perspective on biopharmaceuticals, *McKinsey&Company*, 9–18.

A Multiperiod Optimisation Approach to Enhance Oil Field Productivity during Secondary Petroleum Production

Emmanuel I. Epelle, Dimitrios I. Gerogiorgis*

School of Engineering (IMP), University of Edinburgh, Edinburgh, EH9 3FB, UK

D.Gerogiorgis@ed.ac.uk

Abstract

Water injection rate allocation across different injection wells in an oil and gas field undergoing secondary production is one of the most economical ways to increase hydrocarbon production. Exploiting a process systems engineering description of a rate allocation problem via mathematical optimisation can improve operational planning. We simultaneously address a production and injection optimisation problem with an economic objective function, the net present value (NPV), subject to practical constraints ensuring operational feasibility. A case study with a constant water injection rate is compared to another in which optimal dynamic injection rates and water sharing ratio among the respective injection wells are determined. With the formulated optimisation (NLP) problem, an optimal water injection strategy that reduces field water consumption and increases profitability is obtained. MATLAB's `fmincon` and IPOPT optimisation solvers are employed for solution, observing superiority of IPOPT compared to `fmincon`.

Keywords: Net present value (NPV), Optimal injection strategy, Production optimisation

1. Introduction

Secondary production via water flooding is one of the most implemented enhanced oil recovery methods in the oil and gas industry, involving the injection of water to increase the reservoir's pressure and sweep residual oil in order to consequently increase oil production. Cost reductions and improved productivity during secondary production are dependent on the dynamic rate allocation to different injection wells, the underlying reservoir permeability distribution and other rock and fluid properties. Applying reservoir and multiphase flow simulation (wellbore and pipeline hydraulics) in an integrated manner can aid practical operational decisions during early design stages (Kosmidis et al., 2004, Gerogiorgis et al., 2006; Van Essen et al., 2011). Current oil and gas production optimisation studies in the literature address problems such as well placement, production and drill rig scheduling, pipeline and surface facility routing, infrastructure installation and geological and economic uncertainty (Scheidt et al., 2010; Gupta and Grossmann, 2012; Gunnerud et al., 2013; Tavallali et al., 2013; Epelle and Gerogiorgis, 2017).

A common limitation of these studies that motivates our work is the lack of a detailed water flooding model that incorporates the intricacies of the reservoir behaviour and its dynamic fluid and well properties (gas oil ratio, water cut, productivity indices and well allocation factors). Here, we demonstrate that streamline simulation is a powerful tool that facilitates accurate and optimal determination of the injection rates to different wells. Compared to previous studies, in which the adopted wellbore geometries are vertical, the multiphase flow complexities in deviated well geometries are also incorporated in our approach. Furthermore, the inherent property of the petroleum production system that allows its components to be treated independently is significantly exploited. This is achieved by optimising an economic objective function that captures the overall system behaviour. The coupling of reservoir and pressure drop simulation via proxy-modelling enhances the adaptability of the implemented framework to real field operations via speedy computation.

2. Simulation Methodology and Optimisation Formulation

The model is first built in a numerical reservoir simulator using permeability, porosity and saturation data of a sandstone reservoir. The field contains four production wells and four injection wells (Fig. 1). Two of each class are horizontal wells and the others are vertical. In running the reservoir model, ECLIPSE 100 (Schlumberger, 2017), it is assumed that water injection commences in the third year. A production forecast for a 6-year duration is done to obtain the field pressure, productivity indices, water cut and gas oil ratios of the wells at each time step ($\Delta t = 1$ yr). These data are fed into a multiphase flow simulator, PIPESIM 2017 (Schlumberger, 2017), in which the wellbore and pipeline models are built.

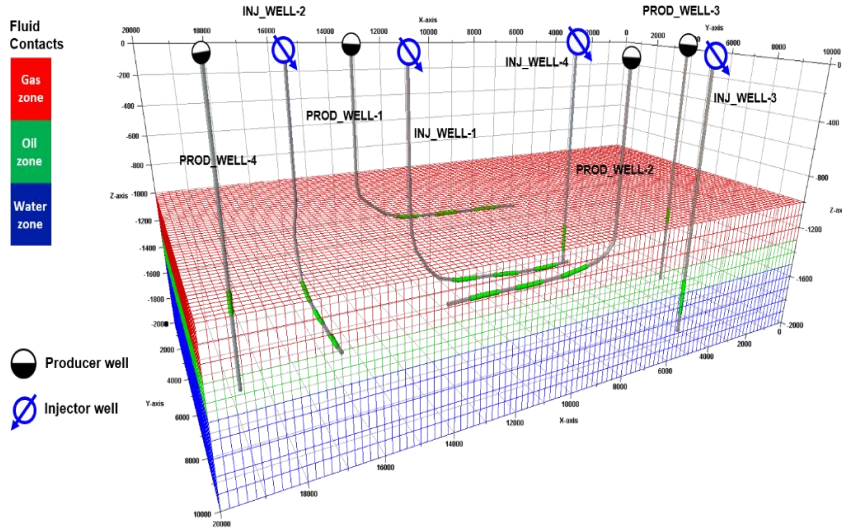


Figure 1: Reservoir structure with drilled wells. The surface network built in PIPESIM additionally consists of 2 main pipelines, 2 manifolds, 8 valves and 2 separators.

The objective function and operational constraints of the proposed formulation are outlined in Table 1. Compared to previous studies which maximise production (Kosmidis et al., 2004; Gunnerud et al., 2013), we maximise the net present value (NPV) by maximising oil and gas production (Eqs. 2–3) and limiting water production rates (Eq. 4) and injection costs (Eq. 5) (Guo and Reynolds, 2018). Here, TOP and TGP are the revenues from total oil and gas produced, respectively, TWP and TWI represent the cost incurred for water production and injection, respectively, r_{OP} and r_{GP} are oil and gas prices, respectively, r_{WP} and r_{WI} are the water production and injection unit costs, respectively, N_{prod} and N_{inj} are the number of producers and injectors, respectively, Δt is the timestep, b is the discount rate for reference time, t_{ref} ; q_{OP} , q_{GP} , q_{WP} and q_{WI} are the flow rates of produced oil, produced gas, produced water and injected water at time t , respectively. Subscripts i , j and l represent the injection wells, production wells, and pipelines, respectively. The capacity constraint of the field is represented by Eq. 6, where $C_{p,sep}$ is the separator capacity.

The pressure-rate relationship of the production and injection wells and pipelines are described via proxy-modelling. Deciding which form of surrogate modelling technique to be used considered various factors, such as the feasibility of implementation for our particular case studies, the ability to capture the system's dynamic nonlinearities and accuracy, the solution time and the modelling effort and ease of automation. Of all candidate forms considered, an algebraic/polynomial proxy model was best suited for application, yielding an error of $<2\%$ with respect to the simulation data obtained for

wells and pipelines (Gunnerud and Foss, 2010). These proxy models developed for each time period in the entire time horizon constitute the constraints fed to the optimisation routine. The proxy models for description of component flowrates and pressure drops in pipelines are shown in Eqs. 7–9. Here, subscript l indicates the pipeline, superscript m the manifold and s the separator, so P_l , P_m and P_s represent the pipeline, manifold and separator pressures, respectively, while the subscript t denotes their values at the particular time interval. Variables q_{io} , q_{lw} and q_{lg} are flowrates of oil, water and gas in pipeline l , respectively. Sensitivity analyses are performed over wells and pipelines at each Δt to obtain the proxy model coefficients a_n , b_n and c_n for $n = 1, 2, 3, 4$. Other constraints include the separator capacity and formation fracture pressure limitations. Forward flow of fluids towards the separator is described via Eqs. 10–11. Formation fracture due to high injection pressures (reducing the sweep efficiency) is avoided via Eq. 12, material balance constraints between wells and pipelines are denoted by Eq. 13 and the maximum allowable injection rate for the respective injection wells is limited by the available field water via Eq. 14. Here, P_l , P_m , P_s and P_j^w are the pipeline, manifold, separator and wellhead pressures, respectively, P_{inj} and P_{frac} are the water injection and formation fracture pressures and $Q_{inj,tot}$ is the total daily volumetric flowrate of water available for injection.

The number of variables, model nonlinearities and non-convexities and the adopted local optimisation solvers (fmincon and IPOPT) imply that solutions will be sensitive to the initial guess supplied. To address this challenge, streamline simulation is adopted for the determination of the dynamic well allocation factors (WAFs), which are used in the calculation of the dynamic injector efficiencies (Theile and Batycky, 2006; Azamipour et al., 2018). With these calculated efficiencies, the best performing injection well can be identified and consequently allocated the highest injection rate as an initial guess. Using these practical initial guesses obtained by applying streamline simulation, we enforce bounds on the decision variables, assuming a uniform distribution between the upper and lower bounds of the respective variables and perturb the initial guess 1,000 times between the bounds, thus facilitating convergence to a global solution. The final optimisation formulation consists of 198 variables and 252 constraints (nonlinear, linear, equality and inequality). These constraints and the objective function are written in MATLAB and solved using the fmincon and IPOPT solvers via the object-based OPTI toolbox platform.

Table 1: Objective function and constraints of the optimisation framework.

Objective Function	$q_{p,j,t} = a_1 + a_2 P_{j,t}^{w} + a_3 (P_{j,t}^{w})^2$	(7)
$\max NPV = \sum_{t=1}^{N_t} \frac{TOP^t + TGP^t - (TWP^t + TWI^t)}{(1+b)^{t_{ref}}}$	(1) $q_{p,i,t} = b_1 + b_2 P_{i,t}^{w} + b_3 (P_{i,t}^{w})^2$	(8)
$TOP^t = r_{OP} \sum_{j=1}^{N_{prod}} q_{OP,j,t}$	(2) $\Delta P_{l,t} = c_1 + c_2 q_{lg,t} + c_3 q_{lo,t} + c_4 q_{lw,t} + c_5 (q_{lg,t})^2 + c_6 (q_{lo,t})^2 + c_7 (q_{lw,t})^2 + c_8 q_{lg,t} q_{lw,t} + c_9 q_{lg,t} q_{lo,t} + c_{10} q_{lo,t} q_{lw,t}$	(9)
$TGP^t = r_{GP} \sum_{j=1}^{N_{prod}} q_{GP,j,t}$	(3) $P^s = P^m - P_{l,t}$	(10)
$TWP^t = r_{WP} \sum_{j=1}^{N_{prod}} q_{WP,j,t}$	(4) $P^m < P_j^w$	(11)
$TWI^t = r_{WI} \sum_{j=1}^{N_{prod}} q_{WI,j,t}$	(5) $P_{inj} < P_{frac}$	(12)
Constraints	$\sum_{j=1}^{N_{prod}} q_{p,j,t} = q_{p,l,t}$	(13)
$\sum_{j=1}^{N_{prod}} q_p \leq C_{p,sep}$	(6) $\sum_{j=1}^{N_{prod}} q_{w,inj} = Q_{inj,tot}$	(14)

3. Simulation and Optimisation Results

Two optimisation case scenarios are presented. In Scenario-1, the injection rates and production rates are optimised and in Scenario-2, the injection rates are maintained at the maximum allowable rate (constant) for each injection well and only the production rates optimised. Before discussing the optimisation results, the results of the simulation procedure are analysed. These results (Fig. 2) are the production and injection performances, based on a 6-year simulation forecast. It is observed that PROD_WELL-1 slightly outperforms PROD_WELL-2 (Fig. 2a); their respective equidistant locations from the INJ_WELL-1 (in the reservoir model – Fig. 1) and the similarity of the underlying local permeability distribution implies they experience similar levels of pressure support from the injection well. Also observed is the reduced productivity of the vertical wells (PROD_WELL-3 and 4) compared to the horizontal wells (PROD_WELL-1 and 2). This is inevitably due to the higher drainage area that the horizontal wells are exposed to in the reservoir. The large disparity observed in the well productivity profiles is not present in the streamline-derived injection efficiencies (Fig. 2b). Despite the favourable well geometry of INJ_WELL-2 (horizontal) compared to INJ_WELL-4 (vertical), they both exhibit similar efficiencies. The interaction of INJ_WELL-1 with the horizontal producers is the main factor contributing to its high efficiencies as determined from the WAFs obtained from streamline simulation. With the available daily field water injection rate and injection efficiencies, it was possible to propose initial injection rates for the optimisation algorithm.

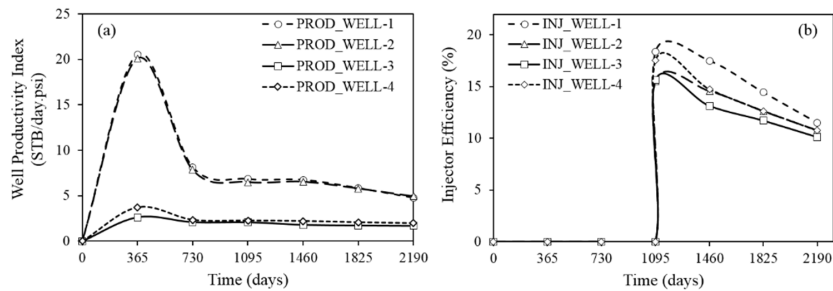


Figure 2: Production and injection well performances.

The production rate profiles for the oil, gas and water phases of the respective production wells for the two optimisation scenarios considered are compared in Fig. 3. The optimisation algorithm captures the increment in oil production at the start of injection (at 1,095 days) and the reduced decline rate after injection commences (Fig. 3a). Similar to the oil production rate profile, the gas production rates (Fig. 3b) of the respective wells also show an increment in production due to water injection and is more significant for the horizontal wells. The commencement of water injection is accompanied by a rapid increase in the water production rates, particularly for PROD_WELL-3 and 4. The horizontal wells (PROD_WELL-1 and 2) display a rather gradual increase in the water production rate compared to the vertical ones. It is also observed that the superior performance of the horizontal wells has been exploited by the optimisation algorithm for the improvement of the total oil production (Fig. 3a). This improvement mostly occurs in the plateau region (i.e. when constant oil production is observed). Compared to the oil production rates, the water and gas production rates of the horizontal wells only increase marginally; this happens towards the end of the production horizon (Fig. 3b–c). As for the other vertical producers, there is no difference between the observed production rates for the optimal and constant injection scenarios; this difference can be increased by incorporating well placement optimisation for the exploration of highly productive sites (with good permeability) in the reservoir. This would require the application of stochastic optimisation techniques and integer variables representing a grid block allocation method, introducing further complexity to the considered problem, which is beyond the scope of this paper.

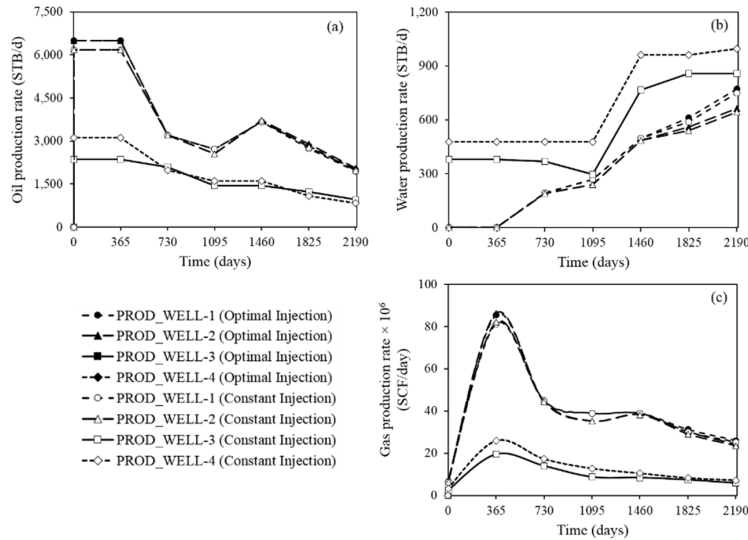


Figure 3: Optimal flow rates of oil gas and water from the production wells.

The optimal injection strategy and the corresponding cumulative injection rate for each well are shown in Figs. 4a–b. It is shown that a stepwise increase in the injection rate for INJ_WELL-1 and a constant injection for the rest of the wells is guaranteed to increase the NPV of the field by 6% (Fig. 4d) and reduce total water consumption by 11%. Furthermore, it is shown in Fig. 4c that the water production rates of PROD_WELL-3 and 4 (vertical wells) are higher than those of the horizontal wells, further demonstrating the desirable performance of the horizontal wells. Additionally, PROD_WELL-3 experiences a significantly lower water production compared to PROD_WELL-4 but with a similar oil production. Hence, PROD_WELL-3 can be considered the best performing vertical well.

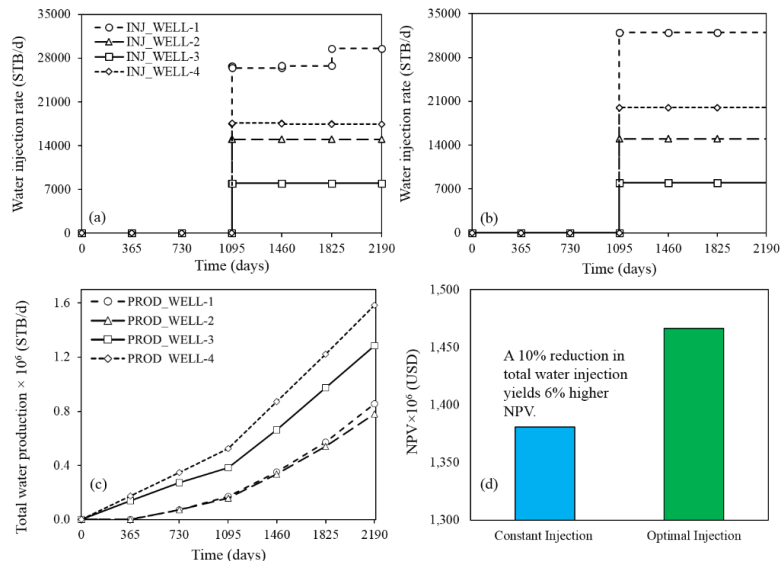


Figure 4: Water injection rates for (a) the optimal scenario and (b) the constant injection scenario; (c) cumulative water production rates of the optimal scenario and (d) the economic analysis of both scenarios.

A comparison of the solver performances showed that the MATLAB's `fmincon` was unable to yield satisfactory results that met convergence criteria. The IPOPT solver implementing an interior point line-search filter method was able to converge successfully.

4. Conclusion

A production and injection optimisation problem with an economic objective function subject to practical constraints that ensure operational feasibility has been thoroughly addressed. The application of streamline-based well allocation factors and injector efficiencies served as a reliable method of obtaining good initial guesses for the time-dependent injection rates, enabling faster performance of the optimisation algorithm. The implementation of algebraic proxy models was sufficient for accurate representation of the simulator output with a maximum error of <2 %. The optimisation framework has shown that a systematic variation of the injection rates, well head pressures and production rates yields increased field profitability. In the considered scenario, a 6% improvement in the NPV and a corresponding 11% decrease in the total field water consumption is attained.

5. References

- V. Azamipour, M. Assareh, M.R. Dehghani and G.M. Mittermeir, 2017, An efficient workflow for production allocation during water flooding, *J. Energy Resour. Technol.*, 139, 3, 1–10.
- E.I. Epelle and D.I. Gerogiorgis, 2017, A multiparametric CFD analysis of multiphase annular flows for oil and gas drilling applications, *Comput. Chem. Eng.*, 106, 645–661.
- D.I. Gerogiorgis, M. Georgiadis, G. Bowen, C.C. Pantelides and E.N. Pistikopoulos, 2006, Dynamic oil and gas production optimization via explicit reservoir simulation, *Comput. Chem. Eng.*, 21, 179–184.
- V. Gunnerud and B. Foss, 2010, Oil production optimization—A piecewise linear model solved with two decomposition strategies, *Comput. Chem. Eng.*, 34, 1803–1812.
- Z. Guo and A.C. Reynolds, 2018, Robust life-cycle production optimization with a support-vector-regression proxy, *SPE Journal*, 23, 6, 2409–2427.
- V. Gupta and I.E. Grossmann, 2012, An efficient multiperiod MINLP model for optimal planning of offshore oil and gas field infrastructure, *Ind. Eng. Chem. Res.*, 51, 19, 6823–6840.
- V.D. Kosmidis, J.D. Perkins and E.N. Pistikopoulos, 2004, Optimization of well oil rate allocations in petroleum fields, *Ind. Eng. Chem. Res.*, 43, 14, 3513–3527.
- Schlumberger, Eclipse User Manual, 2017, Technical Description, *Schlumberger Ltd.*
- Schlumberger, Pipesim User Manual, 2017, *Schlumberger Ltd.*
- C. Scheidt, J. Caers, Y. Chen and L. Durlowski, 2010, Rapid construction of ensembles of high-resolution reservoir models constrained to production data. In *ECMOR XII-12th European Conference on the Mathematics of Oil Recovery*, Oxford, UK.
- M.S. Tavallali, I.A. Karimi, K.M. Teo, D. Baxendale and S. Ayatollahi, 2013, Optimal producer well placement and production planning in an oil reservoir, *Comput. Chem. Eng.*, 55, 109–125.
- M.R. Thiele and R.P. Batycky, 2006, Using streamline-derived injection efficiencies for improved waterflood management, *SPE Reservoir Eval. Eng.*, 9, 2, 187–196.
- G. Van Essen, P. Van den Hof and J.D. Jansen, 2011, Hierarchical long-term and short-term production optimization, *SPE Journal*, 16, 1, 191–199.

Statistical diagnosis of process-model mismatch by means of the Lagrange multiplier test

Marco Quaglio^a, Eric S. Fraga^a and Federico Galvanin^{a,*}

^a*Department of Chemical Engineering, University College London (UCL),
Torrington Place, WC1E 7JE London, United Kingdom*

**f.galvanin@ucl.ac.uk*

Abstract

Modelling chemical processes frequently requires the construction of complex systems of differential and algebraic equations involving a high number of state variables and parameters. Whenever a model structure is proposed, its adequacy is checked with a goodness-of-fit test. The goodness-of-fit test is capable of detecting the presence of over-fitting or under-fitting. However, when some modelling error is detected, the test does not provide guidance on how to modify the model equations to match the behaviour of the physical system under analysis. In this work, a test statistic is derived from a tailored Lagrange multiplier test with the aim of diagnosing potential sources of process-model mismatch and to provide guidance on how to evolve approximated model structures towards a higher level of complexity. The proposed test is applied on a simulated case study of a yeast growth model in a fed-batch bioreactor.

Keywords: model misspecification, model building, Lagrange multiplier, maximum likelihood, Fisher information

1. Introduction

The construction of a parametric model from observations of process behaviour generally requires significant effort both for i) building an opportune functional form for the model equations and ii) for precisely estimating its parameters. The former aspect frequently leads to the formulation of approximate model structures. A classical approach for assessing the adequacy of a process model is the goodness-of-fit test, which compares the model residuals against their expected distribution under the null hypothesis that the model structure is exact (Silvey, 1975). Two types of modelling errors can be detected with a two-tailed goodness-of-fit test:

- Over-fitting. The model involves an excessive number of free parameters, i.e. a simpler model structure shall be preferred to describe the process behaviour.
- Under-fitting. The model is neglecting relevant parameters and/or variables, i.e. the model structure is not sufficiently complex to capture the process behaviour. When the model is under-fitting there is a significant discrepancy between process observations and model predictions, i.e. a process-model (PM) mismatch.

Systematic approaches are available to amend the structure of an over-fitting model. One may perform further tests, e.g. the Wald test (Wald, 1943) or the univariate *t*-test for

parameter significance (Asprey and Naka, 1999), with the aim of testing the hypothesis that some model parameters satisfy certain constraints. As an example, one may test the null hypothesis that some parameters equal zero. If there is not enough evidence to disprove this hypothesis, one shall favour the constrained model and fix those parameters to zero. This is frequently equivalent to excluding parameters (and the variables whose presence is controlled by those parameters) from the model structure. In the under-fitting case, the amendment of the model structure generally poses substantial challenges to the modeller. In fact, there may be significant uncertainty on which model components are correlated to the PM mismatch and on how to evolve the model structure for reducing and eventually eliminating the mismatch.

The importance of diagnosing the sources of PM mismatch is recognised in the literature on process monitoring (Wang et al., 2012; Badwe et al., 2009), but the problem is considered only in the context of linear, black-box models for control applications. An approach for diagnosing PM mismatch in first principle models was proposed by Meneghetti et al. (2014), where a latent variable model is used to highlight differences between process and model in the distribution of some auxiliary variables. These auxiliary variables represent user-defined combinations of variables and parameters appearing in the model. However, defining opportune auxiliary variables may not be obvious and the diagnosis is sensitive to their definition. A superstructure-based approach was suggested by Engle (1982), where the under-fitting model is regarded as a constrained instance of one or multiple alternative superstructures. A Lagrange multiplier test (Silvey, 1959) is then employed to challenge the model against the more complex alternatives. A limitation of this approach is that the definition of the superstructures relies entirely on the intuition of the modeller.

In this work, a model building approach is proposed where a Lagrange multiplier test is used to diagnose PM mismatch. The test does not require the definition of alternative model structures or the use of superstructures. Instead, the test aims at falsifying the hypothesis that a given model parameter is a state-independent constant. The test involves the computation of a score statistic which is proportional to the marginal fitting cost associated to the aforementioned hypothesis. It is shown that the score provides a useful index for guiding the evolution of the model towards a higher level of complexity. A high score associated to a parameter indicates strong evidence for justifying the evolution of the parameter into a state-dependent function.

2. Methodology

A model structure is proposed in Eq. (1) to describe a physical process of interest. In Eq. (1), \mathbf{f} is a $N_f \times 1$ array of model functions, \mathbf{x} is a $N_x \times 1$ array of state variables, $\dot{\mathbf{x}}$ is a $N_x \times 1$ array of time derivatives for the state variables, \mathbf{u} is a $N_u \times 1$ array of manipulable system inputs, t is time and $\boldsymbol{\theta} \in \Theta$ is a $N_\theta \times 1$ array of model parameters $\theta_1, \dots, \theta_{N_\theta}$. In Eq. (1), $\hat{\mathbf{y}}$ is a $N_y \times 1$ array of model predictions for N_y measurable system states \mathbf{y} . Model predictions are expressed as a $N_y \times 1$ array of functions \mathbf{h} .

$$\mathbf{f}(\dot{\mathbf{x}}, \mathbf{x}, \mathbf{u}, t, \boldsymbol{\theta}) = \mathbf{0}; \quad \hat{\mathbf{y}} = \mathbf{h}(\mathbf{x}, \mathbf{u}, t, \boldsymbol{\theta}) \quad (1)$$

A dataset Y is available to estimate the parameters $\boldsymbol{\theta}$. The dataset Y consists of N samples of \mathbf{y} where the i -th sample \mathbf{y}_i is collected setting the system inputs to \mathbf{u}_i and sampling at time t_i , i.e. $Y = \{(\mathbf{u}_i, t_i, \mathbf{y}_i)$ with $i = 1, \dots, N\}$. Measurements for \mathbf{y} are affected by Gaussian

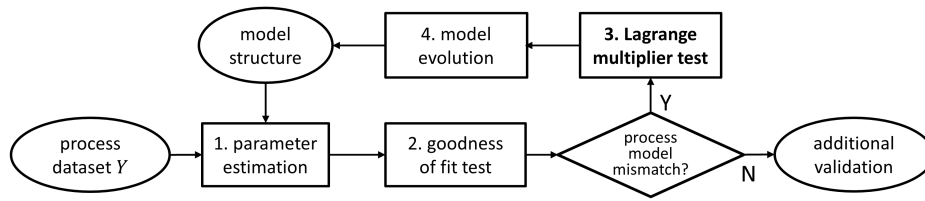


Figure 1: Simplified diagram showing the proposed model building approach.

noise with covariance matrix Σ . A model building framework implementing a step of PM mismatch diagnosis is introduced in Figure 1. The procedure involves the following steps:

1. A parameter estimation step. At this stage the model parameters θ are fitted to the available dataset Y employing a maximum likelihood approach.
2. A goodness-of-fit test. A test on the goodness-of-fit is performed to detect the presence of PM mismatch.
3. A Lagrange multiplier test. If PM mismatch is detected, a Lagrange multiplier test is performed to test the hypotheses that model parameters are state-independent constants by computing a likelihood-based score statistic.
4. A model evolution step. Parameters with the highest score statistic are evolved into state-dependent functions and the procedure is repeated from Step 1.

The iterative process interrupts when no PM mismatch is detected. One shall then proceed with additional model validation procedures, e.g. improving the precision of parameter estimates. Steps 1-3 in the procedure are further detailed in the following subsections. It is recognised that the convergence of the proposed approach relies on the selection of appropriate functional forms to evolve model parameters in the model evolution step. This aspect is going to be the focus in future research activities.

2.1. Parameter estimation

Let $\Phi(\theta|Y)$ be the log-likelihood function (Bard, 1974). The maximum likelihood estimate $\hat{\theta}$ is obtained solving the N_θ unconstrained likelihood equations Eq. (2).

$$\nabla\Phi(\hat{\theta}|Y) = \mathbf{0} \tag{2}$$

2.2. Goodness-of-fit test

The goodness-of-fit is evaluated with a 95% χ^2 test. The critical value χ_{ref}^2 is computed from the χ^2 distribution with degree of freedom $N \cdot N_y - N_\theta$. If the test fails, PM mismatch is diagnosed by means of the Lagrange multiplier test illustrated in the following section.

2.3. Lagrange multiplier test

It is assumed that the elimination of the mismatch requires the replacement of a certain parameter with an opportune state-dependent function. A statistical test for diagnosing PM mismatch is now introduced with the aim of testing the hypothesis that a certain parameter θ_i is a state-independent constant. The competing hypotheses under test are:

- Null hypothesis: θ_i and θ_j , with $j \neq i$, are all state-independent constants.
- Alternative hypothesis: θ_i is a state-dependent quantity and θ_j , with $j \neq i$, are state-independent constants.

Without loss of generality, it is assumed that the parameter under analysis is $\theta_i = \theta_1$. The log-likelihood function is written assuming that θ_1 is a state-dependent quantity, i.e. $\theta_1 = g(\mathbf{x}, \mathbf{u}, t)$ (knowledge of the functional form of g is not required in the test). The parameter set θ is extended to the $(N + N_\theta - 1) \times 1$ array of parameters $\theta_E = [\theta_{11}, \theta_{12}, \dots, \theta_{1N}, \theta_2, \theta_3, \dots, \theta_{N_\theta}]$. In θ_E , parameter $\theta_{1i} = g(\mathbf{x}, \mathbf{u}_i, t_i)$ represents the value of function g at experimental conditions \mathbf{u}_i and sampling time t_i . Let $\Phi_E(\theta_E|Y)$ be the log-likelihood function written for dataset Y under parametrisation θ_E .

$$\begin{aligned} \Phi_E(\theta_E|Y) = & -\frac{N}{2} [N_y \ln(2\pi) + \ln(\det(\Sigma))] \\ & - \frac{1}{2} \sum_{i=1}^N [\mathbf{y}_i - \hat{\mathbf{y}}(\mathbf{u}_i, t_i, \theta_{1i}, \theta_2, \dots, \theta_{N_\theta})]^T \Sigma^{-1} [\mathbf{y}_i - \hat{\mathbf{y}}(\mathbf{u}_i, t_i, \theta_{1i}, \theta_2, \dots, \theta_{N_\theta})] \end{aligned} \quad (3)$$

Under parametrisation θ_E , the i -th element in the sum in Eq. (3) is a function of parameters $\theta_{1i}, \theta_2, \dots, \theta_{N_\theta}$. The set of $N - 1$ constraints $\mathbf{s} = (\theta_{11} - \theta_{12}, \dots, \theta_{1N-1} - \theta_{1N}) = \mathbf{0}$ is defined. The imposition of constraints $\mathbf{s} = \mathbf{0}$ is equivalent to assuming that g is a parameter, i.e. the functional form g is constant and independent from the states. The constrained maximum likelihood estimate $\hat{\theta}_E$ is obtained solving the constrained likelihood equations.

$$\begin{aligned} \nabla \Phi_E(\hat{\theta}_E|Y) + \nabla \mathbf{s} \hat{\boldsymbol{\alpha}} &= \mathbf{0} \\ \mathbf{s} &= \mathbf{0} \end{aligned} \quad (4)$$

In Eq. (4), $\hat{\boldsymbol{\alpha}}$ is the estimate for the $N - 1 \times 1$ array of Lagrange multipliers. Notice that $\hat{\theta}_{1i} = \hat{\theta}_1 \forall i = 1, \dots, N$ because of the constraints $\mathbf{s} = \mathbf{0}$. As shown by Silvey (1959); Engle (1982), if the null hypothesis is true, the score statistic ξ_1 in Eq. (5) (subscript 1 refers to the parameter θ_1 under diagnosis) is distributed as a χ^2 distribution with degree of freedom equal to the number of imposed constraints, i.e. $N - 1$.

$$\xi_1 = \hat{\boldsymbol{\alpha}}^T \nabla \mathbf{s}^T \mathbf{H}^{-1} \nabla \mathbf{s} \hat{\boldsymbol{\alpha}} \sim \chi^2 \quad (5)$$

In Eq. (5), \mathbf{H} is the $(N + N_\theta - 1) \times (N + N_\theta - 1)$ Fisher information matrix associated to the estimates $\hat{\theta}_E$ (Bard, 1974). The critical value for the test ξ_{ref} is calculated from a χ^2 distribution with $N - 1$ degrees of freedom and 95% of significance. A $\xi_1 > \xi_{ref}$ shall be interpreted as evidence of θ_1 being a state-dependent quantity given that $\theta_2, \dots, \theta_{N_\theta}$ are state-independent parameters. The score ξ_i may be computed for the generic i -th parameter following the above procedure. If $\xi_i > \xi_{ref}$ and $\xi_j > \xi_{ref}$, the fitting quality is expected to increase by relaxing the constraints either on θ_i or on θ_j . However, a $\xi_i > \xi_j > \xi_{ref}$ suggests that the evidence for justifying the evolution of parameters into state-dependent functions is stronger for parameter θ_i than for parameter θ_j .

3. Case study and results

The illustrated Lagrange multiplier test is demonstrated with a case study on a fed-batch bio-reactor system simulated in silico (Asprey and Macchietto, 2000). The process be-

haviour is described by the set of equations Eq. (6) with a Cantois-type kinetic Eq. (7).

$$\frac{dx_1}{dt} = (r - u_1 - \theta_4)x_1; \quad \frac{dx_2}{dt} = -\frac{rx_1}{\theta_3} + u_1(u_2 - x_2); \quad \frac{dx_3}{dt} = \theta_5 u_2 \quad (6)$$

$$\text{"true" process rate: Cantois} \rightarrow r = \frac{\theta_1 x_2}{\theta_2 x_1 + x_2} \quad (7)$$

In Eq. (6) and Eq. (7), $x_1(t)$ is the biomass concentration [g/L], $x_2(t)$ is the substrate concentration [g/L], $u_1(t)$ is the dilution factor [h^{-1}], $u_2(t)$ is the substrate concentration in the feed [g/L] and x_3 is a dummy process variable with no physical meaning. The set of equations involves a set of five parameters $\theta = [\theta_1, \theta_2, \theta_3, \theta_4, \theta_5]$. The candidate model structure involves the set of equations Eq. (6) with a Monod-type kinetic Eq. (8).

$$\text{assumed rate: Monod} \rightarrow r = \frac{\theta_1 x_2}{\theta_2 + x_2} \quad (8)$$

Experimental data are generated in-silico by integrating the model equations with the "true" Cantois-type rate law. The parameter set assumed to simulate the experiments is $\theta^* = [0.310, 0.180, 0.550, 0.050, 0.200]$. The dataset Y consists of $N = 28$ samples of $\mathbf{y} = [x_1, x_2, x_3]$ collected in four dynamic experiments performed at different combinations of dilution factor and substrate concentration in the feed considering two levels for each variable $u_1 = \{0.050, 0.20\}$ and $u_2 = \{5.0, 35.0\}$. In each experiment, seven samples are collected at intervals of 3.0 hours. Initial conditions are fixed at $x_1(0) = 1.0$, $x_2(0) = 0.01$ and $x_3(0) = 0.1$. Measurements are affected by uncorrelated Gaussian noise with standard deviation $5 \cdot 10^{-2}$ [various units].

The estimate $\hat{\theta} = [0.305, 0.288, 0.524, 0.047, 0.199]$ for the candidate model parameters is obtained fitting the dataset Y . Subsequently, a 95% goodness-of-fit test is performed. A sum of squared residuals of 2301.6, larger than $\chi_{ref}^2 = 100.7$, highlights the presence of PM mismatch.

The mismatch is diagnosed using the proposed Lagrange multiplier test. The critical value used in the test is $\xi_{ref} = 40.1$. Score statistics are reported in the radar chart in Figure 2a. As one can see from Figure 2a, the smallest score is associated to θ_5 , i.e. $\xi_5 = 21$. The score suggests that parameter θ_5 is the least correlated to the root of the PM mismatch. Since $\xi_5 < \xi_{ref}$, the replacement of θ_5 with a function of the states is not expected to significantly improve the fitting quality. The scores associated to parameters $\theta_1 - \theta_4$ are higher than the reference value, i.e. $\xi_i > \xi_{ref} \forall i = 1, \dots, 4$. The highest scores are $\xi_2 = 2245$ and $\xi_1 = 2218$, suggesting that parameters θ_2 and θ_1 , which appear in the misspecified Eq. (8), are the most correlated to the source of PM mismatch. Also the scores associated to θ_3 and θ_4 , i.e. $\xi_3 = 684$ and $\xi_4 = 1829$, are significantly higher than $\xi_{ref} = 40.1$. However, since $\xi_2 > \xi_1 > \xi_4 > \xi_3$, the evidence for justifying the replacement of a parameter with a state-dependent function is stronger for θ_2 and θ_1 when compared to the evidence associated to parameters θ_4 and θ_3 . The scores can be interpreted as indexes for driving parameter evolution into functions, as represented in Figure 2b.

The modelling activity may proceed by evolving the parameters with the highest score into state-dependent functions. The PM mismatch can be eliminated by evolving θ_2 into the function $\theta_2 x_1$, but also by evolving θ_1 into $\theta_1(\theta_2 + x_2)/(\theta_2 x_1 + x_2)$. In future research activities, further tests will be formulated for evolving parameters into functions by supporting the construction of appropriate functional forms of the process variables.

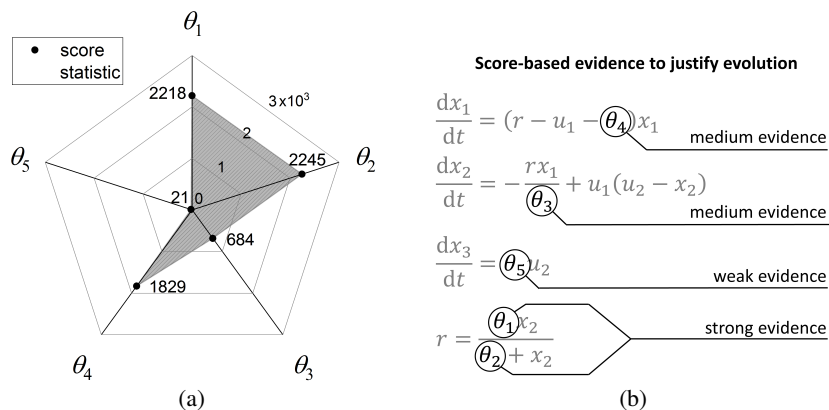


Figure 2: (a) Score statistics for parameters in the candidate model. (b) Score-based evidence for justifying the evolution of parameters into state-dependent functions.

4. Conclusions

When under-fitting is detected by challenging a parametric model against process data, model complexity shall be increased. The lack of systematic approaches to increase model complexity frequently leads to the full rejection of the model and the formulation of alternative model structures from scratch. A statistical test is proposed in this work to diagnose process-model mismatch which could inform the evolution of the model. The proposed score statistic is proportional to the marginal fitting cost associated to the assumption that a given parameter is a state-independent constant. A high score indicates strong evidence for expecting an improvement on the fitting quality if the parameter were evolved into a state-dependent function. Future work will focus on developing tests for unravelling functional relationships between state variables and the parameters selected for evolution.

References

- Asprey, S. P., Macchietto, S., 2000. Statistical tools for optimal dynamic model building. *Computers & Chemical Engineering* 24 (2), 1261–1267.
- Asprey, S. P., Naka, Y., 1999. Mathematical Problems in Fitting Kinetic Models - Some New Perspectives. *Journal of Chemical Engineering of Japan* 32 (3), 328–337.
- Badwe, A. S., Gudi, R. D., Patwardhan, R. S., Shah, S. L., Patwardhan, S. C., 2009. Detection of model-plant mismatch in MPC applications. *Journal of Process Control* 19 (8), 1305–1313.
- Bard, Y., 1974. *Nonlinear Parameter Estimation*. Academic Press.
- Engle, R. F., 1982. A general approach to lagrange multiplier model diagnostics. *Journal of Econometrics* 20 (1), 83–104.
- Meneghetti, N., Facco, P., Bezzo, F., Barolo, M., 2014. A Methodology to Diagnose Process/Model Mismatch in First-Principles Models. *Industrial & Engineering Chemistry Research* 53 (36), 14002–14013.
- Silvey, S. D., 1959. The Lagrangian Multiplier Test. *The Annals of Mathematical Statistics* 30 (2), 389–407.
- Silvey, S. D., 1975. *Statistical Inference*. CRC Press.
- Wald, A., 1943. Tests of statistical hypotheses concerning several parameters when the number of observations is large. *Transactions of the American Mathematical Society* 54 (3), 426–482.
- Wang, H., Xie, L., Song, Z., 2012. A Review for Model Plant Mismatch Measures in Process Monitoring. *Chinese Journal of Chemical Engineering* 20 (6), 1039–1046.

Fast Fourier Transforms for Microgrid Climate Computing

Paolo Fracas^a, Edwin Zondervan^{a,b,*}

^a *Genport srl – Spinoff del Politecnico di Milano, Via Lecco 61, Vimercate, 20871, Italy*

^b *University of Bremen, Leobener Str. 6, Bremen, 28359, Germany*

paolo.fracas@genport.it

Abstract

Solar panels and wind turbines are key technologies for a sustainable low-carbon energy transition. The large diffusion of weather-dependent renewable energy generators face the challenge to fit the demand of uncertain loads with the most appropriate mix of distributed energy resources. The availability of accurate climate variables projections is essential to identify the best combination among distributed generators, energy storages and power loads in each geographical location. From the European Centre for Medium-Range Weather Forecasts (ECMWF) datasets of several climate variables are available for renewable energy resources yield forecasting. This paper presents different approaches to manipulate ECMWF datasets by combining Fast Fourier Transform with polynomial and forest tree regression models to predict climate variables over a one-year period, typical for microgrid simulations. An example of climate datasets forecasts related to the city of Bremen is presented with the evaluation of performances during test and training scenarios phases.

Keywords: FFT, IFFT, ECMW, Renewable Energy Systems, Climate Monthly Datasets.

1. Introduction

1.1. Scope of this work

The European Centre for Medium-Range Weather Forecasts (ECMWF) provides a large number of climate datasets for public use updated until three months of real time; these datasets are available in ERA5, the fifth generation ECMWF atmospheric reanalysis of climate variables, built by combining models from across the world into a globally consistent database. Our work has been focus on developing an approach to extrapolate multiple ERA5 datasets by manipulating just a single dataset. In order to reach this result, Fast Fourier Transform (FFT) has been combined with Inverse Fast Fourier Transform (IFFT) and polynomial regression. The novelty of work mainly consists in the application of this method to the most updated ERA5 gridded datasets. The result is a viable route for improving the accuracy in wind and solar energy simulations, by avoiding the errors introduced with real weather data (D. Quiggin et al. - 2012) and old average climate datasets (NASA/SSE - 2008).

1.2. State of Art

The spectral transform method has been successfully applied in climate datasets for more than thirty years. The Fourier Transform method was introduced to numerical weather prediction starting from the work of Eliassen et al. (1970) and Orszag (1970).

Later works show an extensive use of monthly climate data: Joly and Voldoire, (2009) have developed a method to manipulate gridded datasets with Fast Fourier Transform (FFT) to better understand the coupled ocean–atmosphere processes. Kentat et al. (2013) analysed climate measurements, satellite retrievals of monthly mean marine Wind Speed to validate the accuracy required in calculation of air–sea heat fluxes. Wang and Zeng (2015) have elaborated climate data to quantify the land surface air Temperature. Amendola et al. (2017) used Fourier Transform to recombine Gaussian distributions obtained via Neural Network for seasonal weather forecasts. Wang et al. (2018) using monthly mean, have constructed indices of boreal sea surface Temperature in equatorial Pacific. Andres and Agostaa (2014), elaborated the correlations among atmospheric, oceanic gridded data with lunar nodal by using filtered climate data and Fast Fourier Transform.

2. Methods to manage the climate datasets and detect the errors

Fourier analysis is a method for expressing a complex function as a sum of periodic components, and for recovering the function from those components. Cooley and Tukey (1965) and later Press et al. (2007) provided a computing approach to Fourier analysis for discretized counterparts: the Fast Fourier Transform (FFT).

2.1. Fast Fourier Transforms for monthly climate predictions

Manipulation of datasets arrays, computing optimizations, FFT algorithms and regression analysis has been conducted with Python programming language. The following ECMWF monthly means of daily means has been elaborated: solar net surface Radiation [kWh/m²], 10 meter Wind Speed [m/s] Temperature at 2 meters from soil [K], Cloud Cover [%]. Two predicting curves of n-dimension respectively: n=72 and n=12 inherent the four climate datasets are generated. The first set of curves (n=72) was utilized to train the IFFT model; the second set (n=12), to test the model over one-year timeframe (June 2017 to June 2018). The developed FFT models (1) returned a transformed complex array ($y_d[k]$) and the corresponding frequency spectrum. A first complex array in the frequency domain (CAY) of k_1 -dimension was generated with original n=72 datasets. A second complex array (CAA) of k_2 -dimension, with n=12 array was created with the averages of monthly datasets.

$$y_d[k] = \sum_{n=0}^{N-1} e^{-2\pi j \frac{kn}{N}} x_d[n] \quad (1)$$

The two complex arrays have been used as input to return into the time domain the training and test predicting curves by using the inverse discrete transform (IFFT) as defined as:

$$x_f[n] = \frac{1}{M} \sum_{k=0}^{M-1} e^{2\pi j \frac{kn}{N}} y_f[k] \quad (2)$$

For testing purposes a typical test period of a simulation (n=12) was selected, suitable for conversion in hourly solar Radiation data (T. Khatib, and W. Elmenreich, 2015).

Three different routes have been pursued to return in the time domain, the predicting curves. The first and the second, the predicting curves were based on CAY and CAA

complex arrays, where original spectrum have been considered. A third approach was based on a CAY complex array generated with a subset of the original frequencies, minimizing the Mean Squared Error (MSE). The MSE and the predicted array $x_f[n]$ were minimized with an optimization algorithm that embeds a low-pass filter (LPF). LFP iterates the cut-off frequency of the complex array and attenuates signals with the frequencies (k_3) higher than the cut-off frequency as defined in Eq. 3 until the optimal MSE result were obtained. The best complex final array with k_3 spectrum, returned in the time domain thru the IFFT algorithm, the predicting curves (model validation).

$$\min f(k) = \frac{1}{N} \sum_{n=1}^N (x_d[n] - \frac{1}{M} \sum_{k=0}^{M-1} e^{2\pi j \frac{kn}{N}} y_f[k])^2 \quad (3)$$

$$0 \leq f_j[k] \leq \frac{f_c}{2}$$

Finally the performances with R^2 index, which estimates the ratio between the square error and the variance. $R^2=1$ indicates the best performance:

$$R^2 = 1 - \frac{\sum_{n=1}^N (x_d[n] - x_f[n])^2}{\sum_{n=1}^N (x_d[n] - \mu_x)^2} \quad (4)$$

2.2. Detection of climate variable interrelations with different regression analysis

The scope was to define an alternative indirect method to build the predicting curves, starting from one of the variables. As proposed by S. Raschka (2015) an exploratory data analysis was executed to identify the presence of outliers, the distribution of the data, and the relationships between the variables, and then scatterplot was created from the matrix to visualize the pair-wise correlations. To quantify the linear relationship between the variable, a correlation matrix embedding the Pearson product-moment covariance coefficients was defined:

$$P_{x,y} = \frac{\sum_{n=1}^N [(x_d[n] - \mu_x)(y_d[n] - \mu_y)]}{\left[\sum_{n=1}^N (x_d[n] - \mu_x)^2 \right]^{1/2} \left[\sum_{n=1}^N (y_d[n] - \mu_y)^2 \right]^{1/2}} \quad (5)$$

where μ denotes the sample mean of the corresponding variable. The linear dependence between pairs of variables is strictly related to the value of Pearson coefficient within the range -1 and 1. A perfect positive linear correlation is expressed by $P_{x,y} = +1 / -1$, while no correlation if $P_{x,y} = 0$. The relationship among monthly climate variables with the Pearson's coefficient higher than 0.7 has been modeled by using: linear, quadratic and cubic polynomials. For variables with a weak Pearson's coefficient, as proposed by A. Liaw and M. Wienerthe (2002) the random forest method has been used. This method allows dividing a continuous regression curve into a sum of linear functions. The performance of the forest regression was again evaluated with the following parameters: R^2 and MSE.

3. Results

Three FFT-IFFT methods have been utilized to generate the predicting curves, reproducing the climate monthly data and compared the result with ERA5 datasets over the period June 2017 to June 2018. The reference location was: the city of Bremen, where the Latitude is 53.07 and the Longitude is 8.80; both in Decimal Degree. After detecting the frequency domain, the peak frequency of each dataset was identified. As showed in table 1, Radiance, Cloud Cover, Temperature were predictable with a limited spectrum (1,16-2,83 [Hz]), while Wind Speed reached the minimum MSE at a highest cut-off frequency (4,16 [Hz]). The Pearson's coefficient correlation matrix indicated a linear interrelation among the most predictable variables (Radiation, Temperature and Cloud Cover). After generating all the predicting training curves by filtering the frequencies at minimum MSE the R^2 index was measured. As reported in table 1 the best performing curves has been obtained with the filtered frequency dataset for Radiance while for Cloud Cover, Temperature and Wind Speed the average datasets has returned a better extrapolation.

Dataset	Radiance	Cloud Cover	Temp	Wind Speed
R2 test – average all spectrum	0,937	0,226	0,890	0,549
R ² test - all spectrum	0,955	-0,014	0,868	0,172
R ² test - filtered spectrum	0,956	0,196	0,877	0,114
Peak Frequency	1	1	1	1
Cutoff Frequency	1,16	1,16	2,83	4,16
MSE	0,058	0,003	4,025	0,223

Table 1 – Summary of the datasets performances.

An example of test results (Radiance) with a comparison among the three predicting curves is showed in fig.1. The profile of the curve of Temperature reflects a similar behavior. Although the predicting curves of Cloud Cover and Wind Speed did not match the original dataset, tendency of these curves were coherent to the original datasets.

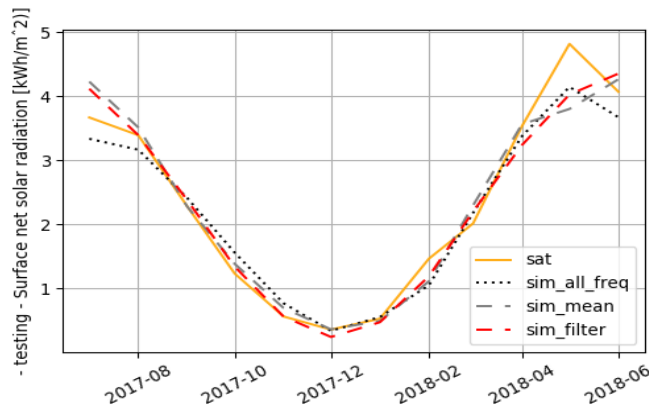


Fig. 1 - Comparison of test curves for Radiance.

After modeling the predicting curves, and visualizing a scattered matrix, the pair-wise correlations between the different variables and the Pearson Coefficients have been measured. The relationship between the Radiation and the other variables is characterized by a value higher than 0.6 ($ssr-t2m = 0.81$, $ssr-tcc = 0.71$, $srr-si10 = 0.63$), which reflects a stronger linear correlation. Looking at these Pearson's correlation coefficients, three different regression models have been implemented. The results delivered linear, quadratic and cubic polynomial regressions (fig. 2). The R^2 (0.65) was the same for all degree of regressions and confirmed the strong correlation among these variables.

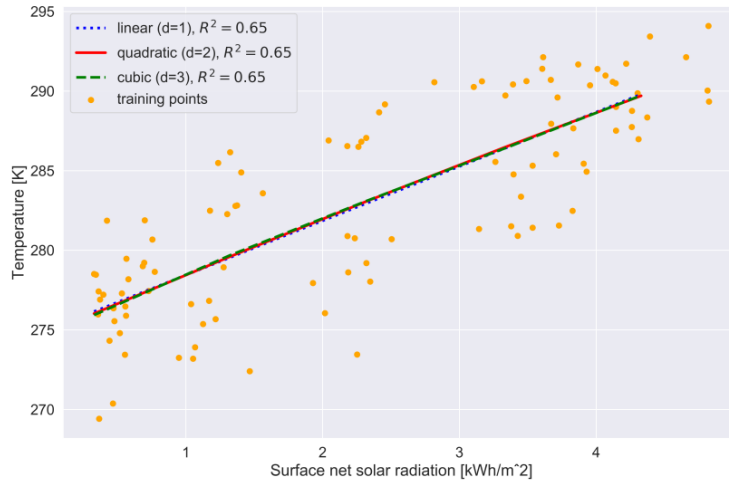


Fig. 2 - Linear, Polynomial regression and performance of two variables with a strong linear interrelation.

For the variables correlated with a lower Pearson coefficient ($tcc-si10$) the random forest regression obtained by subdividing the space into smaller regions and connecting these regions with piecewise linear functions gave a better result: in contrast to the polynomial regression models that returns $R^2=0.30$ with linear, and $R^2=0.34$ with quadratic and cubic regressions, forest tree regression has given $R^2=0.85$.

4. Conclusions

The world is facing massive energy and environment challenges due to global warming and the increase of energy demand. Renewable energy systems play an important role for a sustainable low-carbon energy transition thru microgrid, a major emerging technology concept that enables a tight integration of photovoltaic systems and wind turbines, with residential, commercial, industrial buildings. The design and management of a microgrid has to accomplish several challenging requirements while dealing with uncertainty of the renewable energy sources and the variability of load profiles. Model-based simulation tools are extensively used to identify the best-fit combination of distributed energy sources and the accuracy of input climate variables is pivotal for the quality of the simulations. The European Centre for Medium-Range Weather Forecasts (ECMWF) provides a large number of climate datasets but later works show that since now, their main use is in climate models and weather forecasts. In this paper, we

presented a new application of these climate datasets for improving microgrid simulations. An innovative method based on Fast Fourier Transform combined with Inverse Fast Fourier Transform was used to convert original gridded ECMWF Solar Radiation, Wind Speed, Temperature, and Cloudiness datasets into the frequency domain and then the complex arrays have been transformed back into the time domain by filtering the frequency spectrum. The objective was minimizing the mean square error between the predicted and original climate variables. Three different routes have been utilized to train the algorithm. R^2 index applied to a further testing dataset indicated the resulting performances. Finally the Pearson's correlation coefficient among coupled datasets was used for the choice of the most suitable regression method to generate multiple strings of climate data, starting from a predicted dataset. This innovative method combining FFT-IFFT with linear regression proved to be easy and effective to predict accurate discrete climate variables suitable for microgrid simulations, avoiding errors introduced by historical climate records and observed data.

References

- Aihui Wang, Xubin Zeng, 2015, Global hourly land surface air Temperature datasets: inter-comparison and climate change, *International Journal of Climatology*, 35, 13, pag.3959-3968.
- Andy Liaw and Matthew Wiener, 2002, *Classification and Regression by randomForest*, Vol. 2/3, ISSN 1609-3631, pag.21-22.
- Cooley, James, and Tukey, 1965, "An algorithm for the machine calculation of complex Fourier series," *Math. Comput.* 19, pag.297-301.
- D. Quiggin, S. Cornell, M. T., R. Buswell, 2012, A simulation and optimisation study: Towards a decentralised microgrid, using real world fluctuation data, *Energy*, Volume 41, Issue 1, pag. 549-559.
- E. Andres, Agostaa, 2014, The 18.6-year nodal tidal cycle and the bi-decadal precipitation oscillation over the plains to the east of subtropical Andes, South America. *Int. J. Climatol.* 34, pag.1606-1614.
- Eliassen, E., Machenhauer, B., Rasmussen, E., 1970, On a numerical method for integration of the hydrodynamical equations with a spectral representation of the horizontal fields. Report 2, Institut for Teoretisk Meteorologi, University of Copenhagen.
- E. Kent, S. Fangohr, D. Berry, 2013, A comparative assessment of monthly mean Wind Speed products over the global ocean. *Journal of Climatology* 33, pag.2520–2541.
- M. Wang, Z. Guan, D. Jin, 2018, Two new sea surface Temperature anomalies indices for capturing the eastern and central equatorial Pacific type El Niño-Southern Oscillation events during boreal summer, *International Journal of Climatology*, 38, 11, pag.4066-4076.
- M. Joly, A. Voldoire, 2009, Role of the Gulf of Guinea in the inter-annual variability of the West African monsoon: what do we learn from CMIP3 coupled simulations?, *Int. J. Climatol.* 30, pag.1843–1856.
- Orszag, S., 1970, Transform method for calculation of vector coupled sums: application to the spectral form of the vorticity equation. *J. Atmos. Sci.*, 27, pag.890–895.
- Press, W., Teukolsky, S., Vetterline, W.T., and Flannery, B.P., 2007, *Numerical Recipes: The Art of Scientific Computing*, ch. 12-13. Cambridge Univ. Press, Cambridge, UK.
- S. Amendola, F. Maimone, A. Pasini, F. Ciciulla and V. Pelinod, 2017, A neural network ensemble downscaling system (SIBILLA) for seasonal. *Meteorol. Appl.* 24, pag.157–166
- S. Raschka, *Python Machine Learning*, 2015, pag.280-297.
- T. Khatib, W. Elmenreich, 2015, A Model for Hourly Solar Radiation Data Generation from Daily Solar Radiation Data Using a Generalized Regression Artificial Neural Network, *International Journal of Photoenergy*, Vol. 2015, Article ID 968024, pag.13.

End-of-Pipe Zero Liquid Discharge Networks for different brine water qualities

Fatima Mansour, Sabla Y. Alnouri*

*Department of Chemical and Petroleum Engineering, American University of Beirut,
P.O.Box 11-0236, Riyad El-Solh, Beirut, Lebanon
sa233@aub.edu.lb*

Abstract

More often than not, wastewater generated from any sort of industrial process poses a problem in terms of disposal cost and hazardous environmental impact. Systems that seek to eliminate wastewater discharge from any given process are known as Zero Liquid Discharge (ZLD) systems. Such systems, often composed of a combination of different technologies, aim to minimize wastewater volume and maximize the amount of water that can be recovered. Economically speaking, it is challenging to alter existing processes in a way that can achieve zero discharge. End-of-pipe ZLD systems provide an intermediate solution, whereby additional units can be added, forgoing the need for structural change in the existing process. In addition, environmental discharge standards can be satisfied. This paper presents an overarching ZLD network structure and model that can be customized to yield a cost-effective end-of-pipe ZLD discharge system based on user specified data and conditions. In particular, this paper focuses on the design of different End-of-pipe ZLD systems using brine wastewater data from two different industries: i) wastewater from a coal seam gas plant, and ii) wastewater from a steel plating industry.

Keywords: Brine, Zero-Liquid-Discharge, Wastewater

1. Introduction

Increasing water scarcity and a growing water crisis worldwide have heightened the search for alternative water sources (Subramani and Jacangelo, 2014). Although desalination technologies are highly sought after to amend water scarcity, the brine they generate has also evolved to be a weighty problem (Morillo et al., 2014). Brine is the main by-product of many desalination process, and is always characterized by a high content of dissolved salts and a high salinity. As such, ZLD systems are gaining more attention, as they possess the ability to reduce wastewater discharge, generate recovered product water, and allow for compliance with strict environmental and wastewater disposal regulations. The optimal option for brine discharge depends on a number of factors, mainly brine quantity, quality, and cost (Giwa et al., 2017). Because of this, ZLD systems tend to be customized for each system based on individual system characteristics (Tillberg, 2004). As such, long term brine management has become of utmost importance, particularly with increasing environmental scrutiny and decreasing water supplies. Existing brine disposal methods, such as surface water discharge, deep well injection, and land application, do not eliminate the problem, but attenuate its impact. That and increasingly stringent environmental regulations have propelled the search for more suitable alternatives, mainly ZLD methods. Zero liquid discharge (ZLD) technologies have been gaining more attention as a means for brine minimization. The introduction of

these options has encouraged their integration as end-of-pipe solutions to brine disposal (Subramani and Jacangelo, 2014). Moreover, the water quality generally plays a vital role in the design of any wastewater handling system (Alnouri et al. 2016). To provide a more generic methodology through which users can easily determine the best ZLD scheme for a certain system, this paper proposes an MINLP optimization model in which an economic objective, has been utilized to minimize system design costs, whilst selecting an optimal brine treatment system based on user input.

2. Methodology

The proposed model has been devised based on a ZLD superstructure that is illustrated in Figure 1 below. The ZLD network proposed consists of four different technology sets: chemical processing (set P), thermal (set T), membrane (set M), and brine processing (set B). The chemical processing technologies generally requires a chemical feed stream and results in the production of some salt product, aside from the concentrated brine produced. On the other hand, thermal and membrane technologies take in concentrated brine, and produce product water and further concentrated brine. Brine processing technologies use its feed of concentrated brine to produce salt and product water. The system is designed such that the entering feed water first undergoes chemical processing. Placing the chemical processing blocks first provides a starting point for treatment by removing salts and “softening” the brine for further treatment. The treated water stream can then move to either the thermal or membrane technology blocks, or to both of them. A portion of the streams leaving these two bins is recycled to the start of the system. A recycle stream is included in the design for enhanced system performance. The recycle is split from the concentrated brine leaving the thermal technology block, and another from the concentrated brine leaving the membrane technology block. These two streams then converge to join the original feed stream. The remaining brine enters the brine processing block. This block comes last because it essentially separates the salt from the water, thus resulting in water and salt production.

In accordance with the requirements for a specific system, a selection of technologies must be assessed in each block. The proposed approach selects the optimal technology in each block, or forgoes certain blocks altogether (mainly thermal or membrane), depending on mass balance consistency and other user specified requirements. Each technology comes with its own set of specifications, such as capacity limits and feed water characteristics (e.g. permissible inlet TDS and hardness content). Furthermore, each technology must have a specified water recovery, in addition to component rejection values that have been accounted for and included in system calculations. The system is designed such that different requirements can be met in terms of required product water yield and allowed purge quantities. Constraints can be placed on these values, and the overall ZLD scheme may be assessed based on those input parameters. The splits between technologies within a block, between different blocks, and for recycle and purge purposes can all be controlled by the user and specified to meet any particular standards. Hence, the constraints placed on the system can be specified according to one of the following forms: i) capacity constraints (the flowrate a particular technology can withstand), ii) composition constraints (the inlet or outlet composition limit to a particular technology), iii) and product water production (where the user specifies a certain requirement in terms of how much product water must be generated, as a percentage of the feed flow).

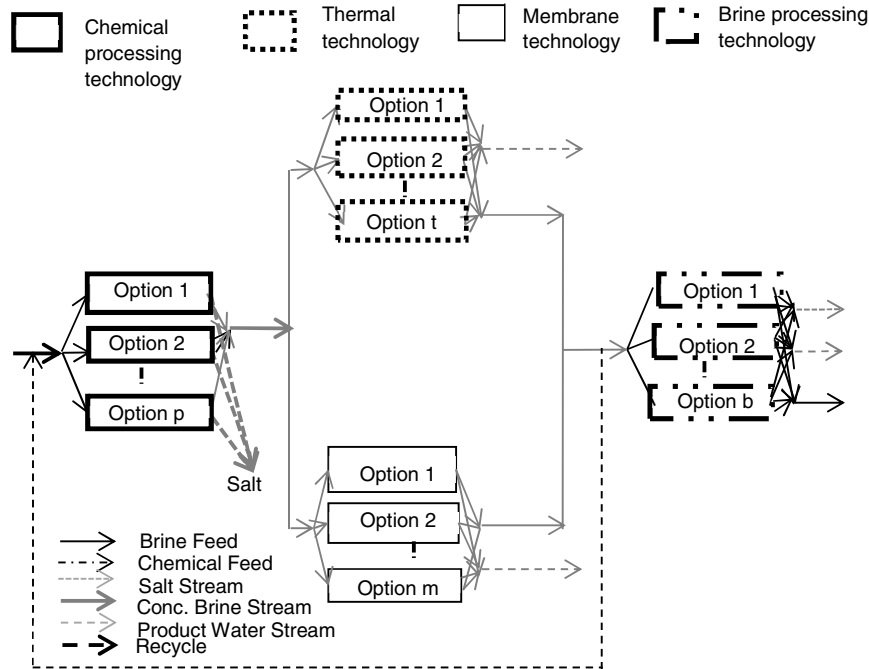


Figure 1. General ZLD superstructure scheme

3. Mathematical Formulation

The mathematical formulation of the proposed optimization model falls under the general form of a Mixed Integer Non-Linear problem, where a cost objective function ($f(x)$) is subjected to various equality and inequality constraints:

$$\min f(x) \tag{1}$$

$$h_i(x) = 0, \forall i \in I = \{1, p\} \tag{2}$$

$$g_j(x) \leq 0, \forall j \in J = \{1, m\} \tag{3}$$

Eq. (1) represents the objective function, $f(x)$, which in the case of this work, is to minimize the overall cost of the ZLD system. The overall cost covers both capital and operating costs. This is where the nonlinearity arises; the cost equations are derived from data sets collected from different literature sources (Mickley, 2008); each technology unit has two cost functions: one for operating costs and another for capital costs. It should be noted that energy requirements are embedded in the operating cost models. Moreover, the total system cost is determined by summing the operating and capital costs of the technologies selected. The central variable in this model (x) is the split fraction vector, and it is of a continuous type. Hence, the split ratios for the flows between technology blocks, for individual feed flows between technologies within each block, and for the amount to be recycled, are all variables. The objective is subjected to two sets of constraints. The first set, $h(x)$, consists of equality constraints (Eq. (2)); these constraints

cover the mass and component balances of the different flowrates and material throughout the system. The mass balance equations take into account technology specifications, particularly salt rejection and water recovery. The second set, $g(x)$, pertains to inequality constraints (Eq. (3)). These constraints can be of several types: i) production and performance requirements, which refer to imposing a minimum or maximum amount of product (product water or salt) or waste (concentrated brine to be purged) to be generated, ii) capacity constraints, which place a limit of the feed flow allowed into a certain limit and/or a limit on the recycle flow, and iii) composition constraints, which place a restriction on the amount of a specific component allowed into (or out of) a technology (such as salinity). Aside from the constraints imposed for the mathematical consistency and practicality, the number and nature of constraints can be tailored to represent any reasonable user imposed constraints.

4. Case Study Illustration

This case study features two types of industrial wastewater: (1) wastewater generated from a steel plating mill and (2) wastewater from a coal seam gas plant. Each of these feed water types has different characteristics and would be expected to require different treatment methods. The main difference showcased for the purpose of this case study is TDS content, as provided in Table 1. In terms of technology appropriation, a handful of the commonly used ZLD technologies are selected for each block, as summarized in Table 2 below.

Table 1. Feed water Parameters, adapted from

Feed water Type	Flow (m ³ /h)	TDS (ppm)	Reference
Coal seam gas wastewater	100	62,450	(Pramanik et al., 2017)
Steel Plating Mill Wastewater	100	2,400	(Chimeng, 2014)

Table 2. Technology Selection

Chemical Processing	Thermal	Membrane	Brine Processing
Lime Softening	Multi-Effect Distillation	Brackish Water Reverse Osmosis (BWRO)	Brine Crystallizer
		Seawater Reverse Osmosis (SWRO)	Evaporation Pond

As noted above, each technology comes with its own set of characteristics and constraints. An overall constraint is imposed such that 95% of the feed must be converted to product water. Aside from this constraint, there are capacity constraints (maximum inlet feed flow) on all of the selected technologies. The BWRO technology has a feed composition constraint in that the maximum allowed Total Dissolved Solids (TDS) into the unit is 6000 mg/L, whereas the brine concentrator can concentrate its feed stream up to 300,000 mg/L, placing a maximum on the allowed exit TDS. All of these values, in addition to each technology's water recovery (γ) and salt rejection (θ) values, are obtained from the

literature and used to characterize the system, as summarized in Table 3. The “what’sBest9.0.5.0” LINDO Global Solver for Microsoft Excel 2010, on a laptop with Intel® Core™ i7-2620M, 2.7 GHz, 8.00 GB RAM, 64-bit Operating System, was used.

Table 3. Summary of system parameters and constraints, (Masnoon and Glucina, 2011)^a, (Mickley, 2008)^b, (Burbano and Brandhuber, 2012)^c, (Tillberg, 2004)^d

Sets	Technology	Flow capacity (L/h)	γ	θ	TDS
Set T	Multi-Effect Distillation (MED)	625,000	0.3 ^a	0.99 ^b	NA
	Brine concentrator	158,987	0.95 ^c	0.9 ^b	300,000 ^d (exit)
Set M	SWRO	5,333,333	0.5 ^b	0.99 ^b	NA
	BWRO	4,083,333	0.7 ^b	0.99 ^b	6000 ^b (inlet)
Set P	Lime softening	NA	NA	0.5 ^b	NA
Set B	Evaporation pond	157,725	NA	NA	NA
	Brine crystallizer	11,354	0.95 ^c	0.85 ^b	NA

The ZLD schemes illustrating the results generated from the solver simulations for each scenario are shown in Figures 2 and 3, respectively. In the first scenario, after the chemical processing unit, 5% of the concentrated brine is purged from the system. The solver only takes 95% of the feed into the thermal technology block, because that is all that is needed to satisfy the product water requirement (95% of the feed), purging the remaining 5% to reduce costs (as the cost functions depend on flow). In the thermal technology block, the concentrator technology is selected as the optimal technology, whereas in the brine processing block, the crystallizer is selected. This scheme train is of significance because the brine concentrator and brine crystallizer are the typical technologies most commonly implemented to achieve ZLD (Mickley, 2008).

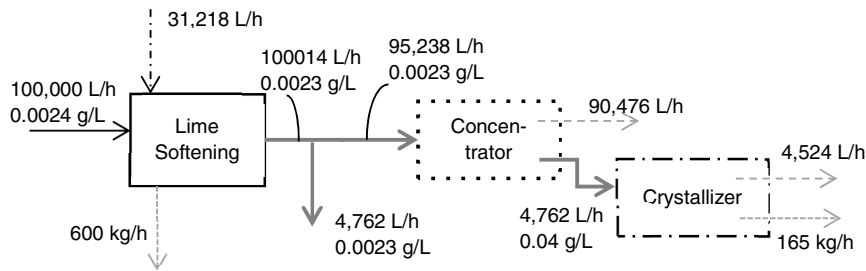


Figure 2. ZLD scheme for steel plating mill wastewater feed

The MED option is selected as a result of the exit TDS constraint being placed on the brine concentrator. Because of the higher inlet TDS in this scenario (62,450 versus 2,400) mixed with the recycled concentrated brine, the brine entering the thermal technology block has high salinity. Concentrating it further renders the exit TDS over the 0.3 composition limit placed on the concentrator, yielding MED as the only feasible choice. A recycle stream appears, where over 90% of the concentrated brine is exiting the MED unit is recycled back and mixed with the original feed. This option is feasible because the product water constraint (yielding 95% of the feed as product water) is already satisfied; and with the objective of minimizing cost, recycling becomes economical, instead of

moving the entire flow to the brine processing block. In the brine processing block, both technologies are included in the scheme, due to the capacity constraint placed on the brine crystallizer (allowing a maximum of 11,354 L/h inlet flow). Consequently, the rest of the concentrated brine is re-diverted to the solar pond.

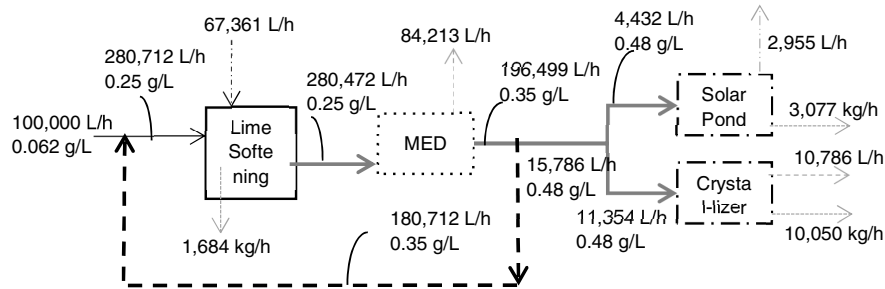


Figure 3. ZLD scheme for coal seam gas wastewater feed

5. Conclusions

The proposed assessment approach provides a simple and effective means of optimally designing ZLD systems, based on cost effectiveness. ZLD systems were found to depend on numerous factors, including but not limited to: the quality and quantity of the brine feed stream, the technologies that have been incorporated into the different technology blocks and their respective design parameters and constraints. In addition, any user-specified product water production or waste limit requirements can be incorporated.

Acknowledgment

The authors would like to acknowledge the financial support received from the University Research Board (Award# 103187; Project# 23308) at the American University of Beirut.

References

- A. Burbano, P. Brandhuber, 2012. Demonstration of Membrane Zero Liquid Discharge for Drinking Water Systems. Water Environment Research Foundation.
- A. Giwa, V. Dufour, F. Al Marzooqi, M. Al Kaabi, M., S. W. Hasan, 2017. Brine management methods: Recent innovations and current status. *Desalination*, 407, 1-23.
- A. Subramani, J. G. Jacangelo, 2014. Treatment technologies for reverse osmosis concentrate volume minimization: A review. *Separation and Purification Technology*, 122, 472-489.
- F. Tillberg, 2004. ZLD-systems An Overview. Stockholm: Department of Energy Technology, Royal Institute of Technology.
- J. Morillo, J. Usero, D. Rosado, H. El Bakouri, A. Riaza, A. and F. J. Bernaola, 2014. Comparative study of brine management technologies for desalination plants. *Desalination*, 336, 32-49.
- M. Mickley, 2008. Survey of High-Recovery and Zero Liquid Discharge Technologies for Water Utilities. Alexandria, VA: WateReuse Foundation.
- S. Masnoon, K. Glucina. 2011. Desalination: Brine and Residual Management. Global Water Research Coalition.
- S. Y. Alnouri, P. Linke, S. Bishnu, M.M El-Halwagi, 2016, Synthesis and Design Strategies of Interplant Water Networks using Water Mains with Quality Specifications. *Comput. Aided Chem. Eng.*, 38, 655-660

An Advanced Data-Centric Multi-Granularity Platform for Industrial Data Analysis

Marco S Reis,^{a,*} Tiago J. Rato^a

*^aCIEQPQPF, Department of Chemical Engineering, University of Coimbra, Rua Silvio Lima, 3030-790, Coimbra, Portugal
marco@eq.uc.pt*

Abstract

Data collected in industrial processes are often high-dimensional, with dynamic and multi-granular characteristics that need to be properly accounted for in order to extract useful information for high level tasks, such as process monitoring, control and optimization. While the first two characteristics are already well addressed by state-of-the-art analytic methods, multi-granularity has received far less attention from the scientific community. Furthermore, data aggregation offers a suitable solution to handle the data deluge in Big Data scenarios, avoiding the loss of information of subsampling and multirate approaches. In this paper, we highlight the main aspects of multi-granularity data and present a novel multi-granularity framework that successfully addresses two fundamental problems: (i) handling multi-granularity data in a rigorous and consistent way; (ii) creating optimal multi-granularity structures for predictive modeling, even when raw data are available at a single granularity.

Keywords: Multi-granularity, Soft sensors, Batch processes, Continuous processes, Process Analytical Technology.

1. Introduction

Among the defining characteristics of industrial data, high-dimensionality and process dynamics are the most well-known and widely explored. They are typically handled through the use of projection-based (or latent variable) methods such as Principal Component Analysis (PCA) (Jolliffe, 2002) and Partial Least Squares (PLS) (Geladi et al., 1986) and their dynamic extensions with time-shifted variables (Ku et al., 1995, Kaspar et al., 1993, Rato et al., 2013). Alongside with these characteristics, multi-granular (or multiresolution) structures are often present in data. However, multi-granularity is often ignored and wrongly treated as a multirate problem, which is not the case. In the multirate case the recorded values regard instantaneous (pointwise) observations taken at regular sampling times. Conversely, in the multi-granularity case the recorded values contain information about the process with different levels of granularity (different resolutions) due to the aggregation of data during successive periods of time where high resolution data are merged and combined in order to produce a single low resolution observation per aggregation period. Another source of granularity can be found in situations where variables represent measurements made on composite samples collected during a certain time period (e.g., production lot, working shift, etc.), and therefore the recorded values regard specific windows of time. These windows of time are here defined as the variable's "time support". This characteristic makes multi-granular data sets fundamentally different from their multirate counterparts. Thus, they require the use of dedicated analytical methodologies that

simultaneously account for high-dimensional, dynamic and multi-granular characteristics, which, until now, were not available.

To achieve the aforementioned goal, two main classes of multi-granular (or multiresolution; these terms are here used interchangeably) modelling approaches must be defined. These classes, as well as their application scope are summarized in Figure 1. The first class of methodologies addresses the case where data already presents a multi-granularity structure. Consequently, the goal of these methodologies is to properly account for the relationships caused by the multi-granularity structure and obtain models that are more parsimonious and able to accommodate this reality. On the other hand, the second class of methodologies relates to the case where raw data is available at a single-granularity (i.e., all variables have the same resolution). In this case, the goal is to change the native granularity of each variable to an optimal granularity level that maximizes the data analysis performance. By doing so, the modelling framework also becomes more flexible, as well as able to smooth noisy variables and to remove redundant information. For these reasons, multi-granularity models are also more parsimonious, accurate and interpretable than single-granularity models.

For the sake of space, only the second class of methodologies are discussed in this paper. As for the first class of methodologies (handling multi-granularity data structures), we refer to reader to (Reis et al., 2006a, Reis et al., 2006b, Rato et al., 2017), where applications to process monitoring and predictive modelling are covered.

The rest of this paper is organized as follows. In Section 2, the modelling framework used for selecting optimal multi-granular structures is described. Afterwards, in Section 3, the application of this methodology is exemplified for (i) continuous processes, (ii) batch processes and (iii) spectroscopy data. Finally, the main conclusions of this work are summarized in Section 4.

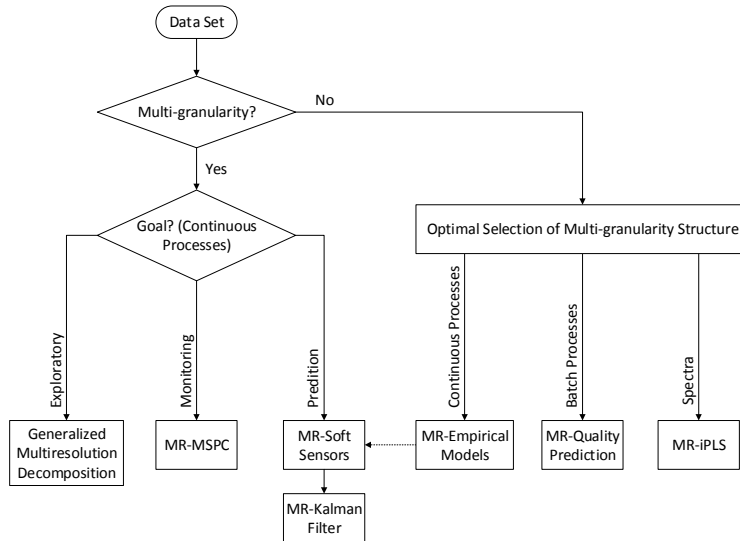


Figure 1 Organogram of the multi-granularity framework and its application scope.

2. Multi-granularity parsimonious models

To introduce the concepts behind the multi-granularity models, let us consider that a variable at a given granularity is represented by $x_{i,t}^{(q_i)}$, where i is the variable index, t is the time index and q_i is an integer defining the variable's granularity level (note that different variables may be at distinct granularities). Without loss of generality, the multi-granularity structure is assumed to follow a dyadic tree with a time support of 2^{q_i} . That is, variables at the granularity level q_i are set to be an average over 2^{q_i} time instants in the finest time domain.

For the class of modelling methodologies discussed in this paper, it is considered that all predictor and response variables are originally available at level 0 (finest granularity or highest resolution). Therefore, multi-granularity is introduced by the modelling methodology, being the optimal granularity level determined by the selection algorithm described below. Furthermore, the approach used to change the predictors' granularity can be adapted to the specificities of each type of data. For instance, in the case of continuous processes, the changes in granularity are performed over moving windows (to preserve process dynamics), while for batch processes they are applied over non-overlapping windows (to accommodate for asynchronous batches and reduce the number of observations).

The multi-granularity selection algorithm used to find the optimal granularity of the predictors is based on the standard stepwise forward algorithm for variable selection with an additional search over the granularity dimension. This search is constrained to fall between the native granularity of the variables (0) and a maximum granularity level defined by the user (q_{max}). From our experience, a maximum granularity level of $q_{max} = 5$ is usually a good starting point, when no further information about the process is available.

In general terms, the multi-granularity stepwise forward selection algorithm starts by choosing an initial model by fitting tentative models for each combination of variables and granularities (i.e., for each combination of i and q_i). In each case, a vector of Cross-Validation Root Mean Squared Error (CV-RMSE) is computed using Monte-Carlo sampling. Afterwards, the combination leading to the lowest median CV-RMSE is selected to build the initial reference model. In the following step, the algorithm proceeds to an "adding" stage, where each combination of variables and granularities (except for the variables already in the model) is tentatively added to the reference model and compared against it using the CV-RMSE values, through a pairwise Wilcoxon rank sum statistical test (Wilcoxon, 1945). Finally, the algorithm performs a "removal" stage to tentatively remove variables from the model that become redundant after the "inclusion" stage. These "inclusion" and "removal" stages are repeated until no further improvement in the CV-RMSE is achieved. Following these steps, the output of the algorithm is a multi-granularity model with the best subset of predictors at their optimal granularity.

3. Applications

3.1. Continuous processes

Based on the algorithm shortly described in Section 2, Rato et al. (2018a) proposed a modelling framework for building multiresolution empirical models for continuous processes (MR-EMC). To illustrate the advantages of MR-EMC, the results obtained for a simulated distillation column using the model described in (Skogestad et al., 2005)

will be presented. This system is composed by a column with 41 stages and returns the compositions and temperatures in all stages. For this comparison, standard PLS, Dynamic PLS (DPLS) and MR-EMC models were used to estimate the distillate composition based on the temperature readings. To assess the consistency of the results, 100 replicates were made. Each replicate was composed by 1,000 observations for training the models and another 1,000 observations for testing their performance using the Mean Squared Error (MSE). In Figure 2, the pairwise differences between the MSEs obtained by PLS and DPLS are compared against those of MR-EMC. From this figure, it is clear that PLS presents the worst performance as it only uses the native granularity of the variables and has no information about process dynamics. When time-shifted variables are added, a significant improvement is observed (DPLS). Nevertheless, MR-EMC is still the best methodology since its MSEs are generally lower than those obtained with PLS and DPLS. These results demonstrate that selecting the optimal granularity for the predictors plays a major role in model accuracy. Furthermore, it was also observed that the MR-EMC models were easier to interpret since the selected combinations of variables and granularities were closely related to the true dynamic dependencies of the process.

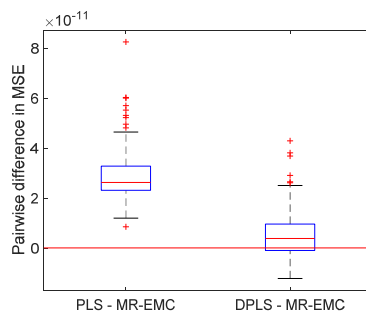


Figure 2 Pairwise differences of the MSE over 100 replicates of the distillation column case study. For reference, the variance of the response is 1.37×10^{-9} .

3.2. Batch processes

A multiresolution quality prediction (MRQP) framework for predicting the end-batch quality by exploiting the structured correlation in both the time and variables dimensions was originally proposed by Gins et al. (2018) and later on extended by Rato et al. (2018c) to account for processes with different operational phases. The selection algorithm is similar to the one presented in Section 2, but now observations are also included as predictors (batch-wise unfolding). Furthermore, the batch is divided in stages in order to allow for a finer modelling of the variables importance. Thus, this methodology can effectively select the key process variables and the prominent operational phases affecting the end-batch quality. Adjusting the granularity of the variables also reduces the number of observations, which can significantly decrease the number of predictors when batch-wise unfolding is applied. This approach was tested with several systems, including simulated and real world processes. For the real world case, regarding an industrial batch polymerization process, the improvement achieved in prediction (*PRESS*) with respect to the standard Multiway PLS approach (Nomikos et al., 1995) was of 54 % (Gins et al., 2018).

3.3. Spectroscopy

The interval PLS (iPLS) algorithm proposed by Nørgaard et al. (2000) is typically applied to compare the performance of a full-spectrum model to that of local models based on subintervals of equal length. However, as this approach does not directly select the most relevant wavebands, sequential approaches based on forward (FiPLS) or backward (BiPLS) algorithms have been suggested (Xiaobo et al., 2007). Still, these methodologies are unable to optimally aggregate the original signal and denoise/merge redundant information within the interval, which ultimately reduces their prediction capabilities. To overcome this limitation, Rato et al. (2018b) proposed a multiresolution interval PLS (MR-iPLS) methodology that also selects the optimal granularity for each interval. Again, the selection algorithm is similar to that presented in Section 2, but since there is no time dimension, the changes in granularity are applied over non-overlapping intervals of wavelengths.

To exemplify the advantages of MR-iPLS against the standard iPLS models, the data set given in (Kalivas, 1997) is here used for comparison purposes. This data set is composed by near infrared (NIR) spectra (with a total of 401 wavelengths) for 60 gasoline samples with known octane numbers. In this study, the samples were randomly divided into a training data set with 40 samples and a testing data set with the remaining 20 samples. The models were fit on the training data set using 12 intervals with 32 wavelengths and one interval with 17 wavelengths. The independent testing data set was then used to evaluate the prediction performance of each model through the MSE, leading to the results presented in Table 1. These results clearly show that the FiPLS model has the worst performance due to its inability to overcome local optima. On the other hand, BiPLS provides better results due to the exclusion of irrelevant intervals. Nevertheless, it is noticeable that using MR-iPLS to optimize the granularity of the selected intervals, a model with even lower MSE is obtained. In this case, the 9 intervals selected by MR-iPLS were all placed at a coarser granularity level ($q=5$). Consequently, instead of using the original 288 wavelengths in these intervals, only their averages are included in the model, which reduces the number of predictors to 9.

Table 1 MSE and number of predictors included in each model for the spectroscopy case study.

	PLS	FiPLS	BiPLS	MR-iPLS
MSE	0.0409	0.0451	0.0410	0.0381
Number of predictors	401	160	256	9

4. Conclusions

The presence of multi-granularity structures in industrial data limits the application of current data analysis methodologies since they are neither able to accommodate for this aspect, nor to take advantage of the intrinsic relationships. Furthermore, even when data is available at a single-granularity, it is not guaranteed that the native granularity of the predictors is the most appropriate one for process modelling. To address this situation, a set of multi-granularity modelling frameworks that simultaneously select the best subset of predictors to be included in the model along with the optimal granularity for each predictor have been proposed for several types of industrial data. In all the data scenarios considered, results show that the multi-granularity methodologies perform consistently better than their single-granularity counterparts, while leading at the same time to more parsimonious and interpretable models.

Acknowledgements

The authors acknowledge financial support through project 016658 (references PTDC/QEQ-EPS/1323/2014, POCI-01-0145-FEDER-016658) co-financed by the Portuguese FCT and European Union's FEDER through the program "COMPETE 2020".

References

- P. Geladi, B. R. Kowalski, 1986, Partial Least-Squares Regression: a Tutorial, *Analytica Chimica Acta*, 185, 1-17.
- G. Gins, J. F. M. Van Impe, M. S. Reis, 2018, Finding the optimal time resolution for batch-end quality prediction: MRQP – A framework for multi-resolution quality prediction, *Chemometrics and Intelligent Laboratory Systems*, 172, 150-158.
- I. T. Jolliffe, 2002, *Principal Component Analysis*, New York, Springer.
- J. H. Kalivas, 1997, Two data sets of near infrared spectra, *Chemometrics and Intelligent Laboratory Systems*, 37, 2, 255-259.
- M. H. Kaspar, W. Harmon Ray, 1993, Dynamic PLS modelling for process control, *Chemical Engineering Science*, 48, 20, 3447-3461.
- W. Ku, R. H. Storer, C. Georgakis, 1995, Disturbance detection and isolation by dynamic principal component analysis, *Chemometrics and Intelligent Laboratory Systems*, 30, 1, 179-196.
- P. Nomikos, J. F. MacGregor, 1995, Multivariate SPC Chart for Monitoring Batch Processes, *Technometrics*, 37, 1, 41-59.
- L. Nørgaard, A. Saudland, J. Wagner, J. P. Nielsen, L. Munck, S. B. Engelsen, 2000, Interval Partial Least-Squares Regression (iPLS): A Comparative Chemometric Study with an Example from Near-Infrared Spectroscopy, *Applied Spectroscopy*, 54, 3, 413-419.
- T. J. Rato, M. S. Reis, 2013, Fault detection in the Tennessee Eastman benchmark process using dynamic principal components analysis based on decorrelated residuals (DPCA-DR), *Chemometrics and Intelligent Laboratory Systems*, 125, 15, 101-108.
- T. J. Rato, M. S. Reis, 2017, Multiresolution Soft Sensors (MR-SS): A New Class of Model Structures for Handling Multiresolution Data, *Industrial & Engineering Chemistry Research*, 56, 13, 3640–3654.
- T. J. Rato, M. S. Reis, 2018a, Building Optimal Multiresolution Soft Sensors for Continuous Processes, *Industrial & Engineering Chemistry Research*, 57, 30, 9750–9765.
- T. J. Rato, M. S. Reis, 2018b, Multiresolution Interval Partial Least Squares: A Framework for Waveband Selection and Resolution Optimization, Under Submission.
- T. J. Rato, M. S. Reis, 2018c, Optimal selection of time resolution for batch data analysis. Part I: Predictive modeling, *AIChE Journal*, 64, 3923-3933.
- M. S. Reis, P. M. Saraiva, 2006a, Generalized Multiresolution Decomposition Frameworks for the Analysis of Industrial Data with Uncertainty and Missing Values, *Industrial & Engineering Chemistry Research*, 45, 6330-6338.
- M. S. Reis, P. M. Saraiva, 2006b, Multiscale Statistical Process Control with Multiresolution Data, *AIChE Journal*, 52, 6, 2107-2119.
- S. Skogestad, I. Postlethwaite, 2005, *Multivariable Feedback Control: Analysis and design*, Chichester, Wiley.
- F. Wilcoxon, 1945, Individual Comparisons by Ranking Methods, *Biometrics Bulletin*, 1, 6, 80-83.
- Z. Xiaobo, Z. Jiewen, L. Yanxiao, 2007, Selection of the efficient wavelength regions in FT-NIR spectroscopy for determination of SSC of 'Fuji' apple based on BiPLS and FiPLS models, *Vibrational Spectroscopy*, 44, 2, 220-227.

Optimal Operation and Control of Fluidized Bed Membrane Reactors for Steam Methane Reforming

Alejandro Marquez-Ruiz^{a*}, Jiaen Wu^b, Leyla Özkan^a, Fausto Gallucci^b, Martin Van Sint Annaland^b

^a *Department of Electrical Engineering, Eindhoven University of Technology, 5612 AJ, Eindhoven, The Netherlands*

^b *Department of Chemical Engineering and Chemistry, Eindhoven University of Technology, 5612 AZ, Eindhoven, The Netherlands*

a.marquez.ruiz@tue.nl

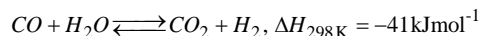
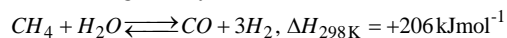
Abstract

This work presents the optimal operation and control of a Fluidized Bed Membrane Reactor (FBMR) for Steam Methane Reforming (SMR). First, a nonlinear distributed parameter dynamic model is developed. Next, the optimal operation of the system is studied by solving a dynamic optimization problem that maximizes the conversion and separation in the reactor. Based on the optimization result, reduced order linear models are developed and used in the design of conventional and model based controllers. The performance of these controllers are tested considering the variation in the inlet concentration of the feed to the reactor and the initial conditions.

Keywords: Fluidized Bed Membrane Reactors, Steam Methane Reforming, Optimal Operation, Model Based Controllers.

1. Introduction

Hydrogen is one of the most important chemicals used in the chemical industry, and lately, it has gained particular attention due to the wide range of applications also as an energy carrier. There are several technologies available for the production of hydrogen; however, the conventional steam methane reforming (SMR) is currently still the most common and economical way to produce hydrogen. The conventional SMR process consists of two main reactions given by:



In order to intensify this process and enhance the yield of hydrogen and shift the reaction equilibrium in the direction of producing hydrogen, new reactor concepts have been developed and investigated. The Fluidized Bed Membrane Reactor (FBMR) is one of the most promising membrane reactors for integrated reforming/dehydrogenation, separation and purification (Rahimpour et al. 2017). In the FMBR, a bundle of hydrogen-selective membranes are immersed into the fluidized catalytic bed in order to carry out the separation and reaction steps simultaneously. Such reactor concepts can reduce capital costs and improve process efficiency, but at the cost of losing degrees of freedom in the operation. Despite the substantial amount of work done on process design based on steady state modelling of FBMR's the study of operational aspects such as controllability, stability, and operational feasibility have not been investigated as extensively. Only a limited number of works is available with the application of control theory for a fluidized

bed reactor (FBR). However, these controllers cannot always be applied to an FBMR, because the intensified FBMR exhibits a quite different dynamic behaviour due to small equipment but same or larger process efficiency. Considering the impact of the intensification on the operation, the control design of a FBMR is very relevant.

In this work, we have studied the optimal operation and control of an FBMR for SMR. First, a dynamic model extending the steady-state models proposed by Medrano et al. (2018) is described. Next, the optimal operation of the system is studied. To this end, a dynamic optimization problem that maximizes conversion and separation in the reactor is proposed. Based on the result obtained from the optimization problem, and the dynamic model, linear models of the system have been developed. However, as the linear model is infinite dimensional (the dynamic model is given by a set of Nonlinear Partial Differential Equations), and control design based on these models is challenging, model reduction techniques have been applied. Finally, with the reduced linear model, low-level and Model Predictive controllers have been designed. The performance of these controllers has been tested in simulation in case of variations in the inlet composition of the feed to the reactor.

2. Dynamic Modelling of FBMR

Consider a FBMR where pure hydrogen is recovered via palladium-based membranes inserted into the fluidized bed (Gallucci et al. 2008). The dynamic model obtained in this work is an extension of the model proposed by Medrano et al. (2018) by including accumulation terms in the gas phase mass (bubble/wake and emulsion phases) and energy balances yielding the following set of Partial Differential Equations (PDEs),

$$\frac{\partial}{\partial t} \begin{bmatrix} (f_{bw}C_{i,bw}) \\ (f_eC_{i,e}) \\ (\rho C_p f_{bew}T) \end{bmatrix} = -\frac{\partial}{\partial z} \begin{bmatrix} (f_{bw}u_bC_{i,bw}) \\ (f_eu_eC_{i,e}) \\ (\rho C_p f_{bew}uT) \end{bmatrix} + \begin{bmatrix} \xi_i + r_{i,bw}f_{bw}(1-\varepsilon_{mf}) + S_{mb} \\ -\xi_i + r_{i,e}f_e(1-\varepsilon_{mf}) + S_{me} \\ \sum_{k=1}^p \sum_{i=1}^m (-\Delta H_{r,k})r_{i,k}f_k(1-\varepsilon_{mf}) \end{bmatrix} + \begin{bmatrix} 0 \\ 0 \\ \frac{4}{d}H_J(T_J - T) \end{bmatrix} \quad (1)$$

$$\forall i = \{CH_4, CO_2, CO, H_2O, H_2\}$$

where ξ_i , $S_{\{mb,me\}}$ are the mass transfer rates between the bubble and emulsion phases,

and the membrane, and $r_{i,\{bw,e\}}$ are the reaction rates. The model given by Eq. (1) is

subject to a set of algebraic equations which are not included in this paper due to space limitations. However, a summary of the hydrodynamics and mass transfer correlations used in this work is reported in Medrano et al. (2018).

2.1. Discrete Model

In order to solve the dynamic model, the spatial derivatives of Eq. (1) are replaced by a backward differences approximation such that the model can be written as a set of ODEs,

$$\frac{d}{dt} \begin{bmatrix} (f_{bw}C_{i,bw}^j) \\ (f_eC_{i,e}^j) \\ (\rho C_p f_{bew}T^j) \end{bmatrix} = -\frac{1}{\Delta z} \begin{bmatrix} \Delta(f_{bw}u_bC_{i,bw}^j) \\ \Delta(f_eu_eC_{i,e}^j) \\ \Delta(\rho C_p f_{bew}uT^j) \end{bmatrix} + M \begin{bmatrix} \xi_i^j \\ S_i^j \\ r_i^j \end{bmatrix} + \begin{bmatrix} 0 \\ 0 \\ \frac{4H_J}{d}(T_J - T) \end{bmatrix}, \forall j=1, \dots, N \quad (2)$$

where Δ is defined as $\Delta C_i^j = C_i^j - C_i^{j-1}$, N is the number of sections in which the reactor is divided, and M is a matrix related to the mass transfer and reaction rates. After some algebraic manipulations Eq. (2) can be expressed as: $\dot{x} = f(x, u, d)$, $y = g(x, u)$, where $x = [C_{i,bw}^j, C_{i,e}^j, T^j]^T \in \mathbb{R}^{11N}$, $y = [X_{CH_4,out}, C_{H_2,out}]^T \in \mathbb{R}^2$ and $u = [F, T_J]^T \in \mathbb{R}^2$ are the states, manipulated, and controlled variables respectively, with F the feed flow of the reactor, T_J the jacket temperature, and $X_{CH_4,out} = C_{CH_4,in}^{-1}(C_{CH_4,in} - C_{CH_4,out})$ the methane conversion. In addition, $d = [C_{i,bw}^{in}, C_{i,e}^{in}, T^{in}]^T \in \mathbb{R}^{11}$ are the disturbances of the system.

3. Optimal Operation of FBMR

The main objective of the FBMR is to maximize both the conversion of methane and the separation of the hydrogen throughout the membrane. By defining $X_{CH_4}^j \in [0,1]$ as the conversion of methane and $S_{H_2}^j \in [0,1]$ as the hydrogen separation factor along the reactor, we formulate the following optimization problem to achieve these objectives:

$$u_{opt} = \arg \min_u \int_{t_0}^{t_f} \left(\sum_{j=1}^N \omega \|1 - X_{CH_4}^j\|_2^2 + (1 - \omega) \|1 - S_{H_2}^j\|_2^2 \right) dt \quad (3)$$

subject to: $\dot{x} = f(x, u, d)$, $y = g(x, u)$, $x \in \mathbf{X}$, $u \in \mathbf{U}$

Where $\omega \in [0,1]$ is a weighting parameter. In this optimization problem, the feed flow F and the jacket temperature T_J are the decision variables. From the practical point of view, the objective function of problem (3) is selected because it takes a minimum value when the raw material and the hydrogen produced are completely consumed and separated. Finally, the problem (3) is solved by parametrizing u and converting Eq. (3) into a Nonlinear Programming problem (NLP). The results of the optimization problem are shown in Figure 1.

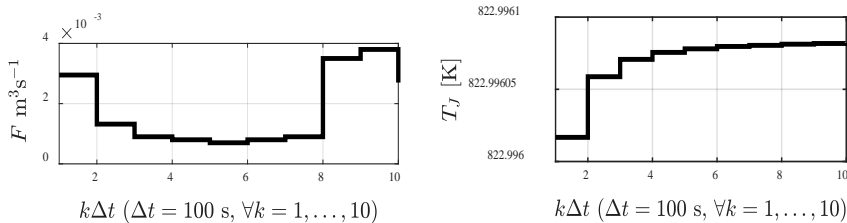


Figure 1. Optimal Trajectories for the inlet feed flow and the jacket temperature.

Notice that in Figure 1, T_J does not change significantly. That means, during the normal operation (no disturbances), this variable must remain constant around 823 K. However, it is important to clarify that the controllers can still manipulate T_J , to reject disturbances and to keep the system in the optimal trajectory.

4. Control Design for FBMR

In this paper, two control techniques are used to keep the operation of the FBMR around the optimal trajectory presented in Section 3, MPC and PID. To design these controllers, a linear model of the process must be obtained.

4.1. Linear Model and Model Reduction

The linear model of the FBMR is obtained by linearizing $\dot{x} = f(x, u, d)$, $y = g(x, u)$ around the optimal operating profiles using Taylor series expansion and considering only the first order terms as follows,

$$\begin{aligned} \dot{x} &= Ax + Bu + B_d d, A = f_x(x, u)|_{x^*, u^*}, B = f_u(x, u)|_{x^*, u^*}, B_d = f_d(x, u)|_{x^*, u^*} \\ y &= Cx + Du, C = g_x(x, u)|_{x^*, u^*}, D = g_u(x, u)|_{x^*, u^*} \end{aligned} \quad (5)$$

where $x \in \mathbb{R}^{11N}$, $y \in \mathbb{R}^2$, and $u \in \mathbb{R}^2$. In this paper, the spatial domain of the reactor is divided into 100 sections, resulting in 1100 number of states. The controllability analysis shows the system has uncontrollable states. These two facts, a large number of states and uncontrollable states, make the design and implementation of model-based controllers for the FBMR very difficult. A good solution to this issue is to eliminate the uncontrollable states. This also reduces the number of states. To this end, a model reduction technique called balance truncation (Gugercin and Antoulas, 2004) is implemented in the FBMR model, and briefly described in Table 1.

Table1: Mathematical formulation of the reduced order model

Full order Model	Reduced Order Model
$G(s) : \begin{cases} \dot{x} = Ax + Bu + B_d d \\ y = Cx + Du \end{cases}, x \in \mathbb{R}^{11N}$	$\tilde{G}(s) : \begin{cases} \dot{\tilde{x}} = \tilde{A}\tilde{x} + \tilde{B}u + \tilde{B}_d d \\ y = \tilde{C}\tilde{x} + \tilde{D}u \end{cases}, \tilde{x} \in \mathbb{R}^n, n \leq 11N$
$\tilde{x} = Tx, \tilde{A} = TAT^{-1}, \tilde{B} = TB, \tilde{B}_d = TB_d, \tilde{C} = T^{-1}C, \tilde{D} = D$, where T is computed using reachability and observability Gramians of $G(s)$. It is important to highlight that \tilde{x} does not preserve the physical meaning of x , because $G(s)$ is not unique.	

Figure 2 shows the steady state concentration profile of the nonlinear, linear and the reduced order models for CH₄, H₂O, CO, CO₂, and H₂ in the emulsion phase. In Figure 2, it can be observed that the reduced order model with only 11 states provides a good approximation of the linear and the nonlinear model.

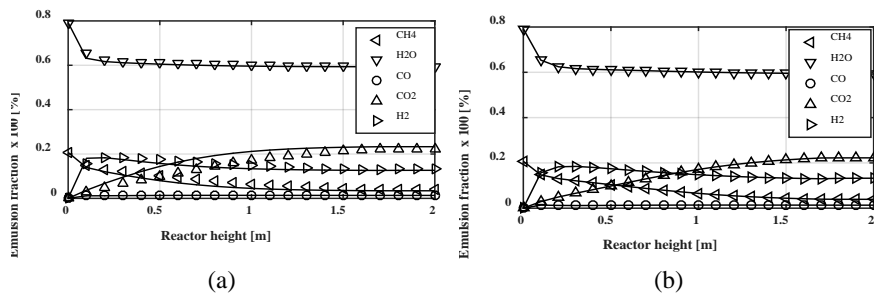


Figure 2: Models comparison: concentration of CH₄, H₂O, CO, CO₂, and H₂ in the emulsion phase in steady state for: (a) the nonlinear (—) and linear ($\Delta, \nabla, \triangleright, \triangleleft, \circ$) models. (b) Linear (—) and reduced order ($\Delta, \nabla, \triangleright, \triangleleft, \circ$) models.

4.2. PID Control

We present the PID control design in Table 2. As the PID controller is a SISO control technique, the Relative Gain Array ($\Lambda(j\omega)$) method is used in this work to calculate the best input-output pairing for the process.

Table 2: Mathematical formulation of the PID including RGA

Model	PID
$y(s) = \tilde{G}(s)u(s)$ $\Lambda(j\omega) = \tilde{G}(j\omega) * \tilde{G}(j\omega)^{-T} = \begin{bmatrix} -0.0028 & 1.0028 \\ 1.0028 & -0.0028 \end{bmatrix}$	$u_i(s) = \left(K_p + \frac{K_i}{s} + K_d s \right) e_i(s)$ $e_i(s) = y_{ref} - y_i(s)$

Based on the RGA the input-output pairing must be $T_J - X_{CH_4,out}$ and $F - C_{H_2,out}$. Additionally, the transfer function $\tilde{G}(s)$ is identified based on the step response of the reduced order model. The results of this controller are presented in Section 4.4.

4.3. Model Predictive Control (MPC)

MPC has been widely adopted by the industrial process control community and has been implemented successfully in many applications. MPC can handle constraints, which often have a significant impact on the quality and safety in process operations. To design predictive controllers, a discrete time model of the process must be obtained. To this end, a Zero-Order Hold discretization method is used. In Table 3, the discrete time version of the reduced order model is described.

Table 3: Mathematical formulation of the discrete time model

Reduced Order Model	Discrete Time Model
$\tilde{G}(s): \begin{cases} \dot{\tilde{x}} = \tilde{A}\tilde{x} + \tilde{B}u + \tilde{B}_d d \\ y = \tilde{C}\tilde{x} + \tilde{D}u \end{cases}$	$\tilde{G}(z): \begin{cases} \tilde{x}_{k+j+1} = \tilde{A}_k \tilde{x}_{k+j} + \tilde{B}_k u_{k+j} + \tilde{B}_{k,d} d_{k+j} \\ y_{k+j} = \tilde{C}_k \tilde{x}_{k+j} + \tilde{D}_k u_{k+j} \end{cases}$
The notation $k + j \triangleq (k + j)\Delta t$ where Δt is the sampling time	

The MPC control problem can be written as,

$$u_{MPC} = \arg \min_{\{u_{k+j}\}_{j=0}^{H_p-1}} \left\| x_{k+H_p} \right\|_P^2 + \sum_{j=0}^{H_p-1} \left\| x_{k+j} \right\|_Q^2 + \left\| u_{k+j} - u_{opt} \right\|_R^2 \quad (6)$$

Subject to:

$$\tilde{x}_{k+j+1} = \tilde{A}_k \tilde{x}_{k+j} + \tilde{B}_k u_{k+j} + \tilde{B}_{k,d} d_{k+j}, \quad y_{k+j} = \tilde{C}_k \tilde{x}_{k+j} + \tilde{D}_k u_{k+j}, \quad x_{k+j} \in \mathbf{X}_k, \quad u_{k+j} \in \mathbf{U}_k$$

where H_p is the prediction horizon, and \mathbf{X}_k and \mathbf{U}_k are convex polyhedrons. The optimization problem (6) can be solved efficiently converting Eq. (6) into a Quadratic Programming (QP) problem.

4.4. MPC and PID comparison

In order to test the performance of the controllers for the FBMR, two experiments have been carried out: step changes in the disturbances of the process at $t = 220s$, and different initial conditions. Figure 3 shows the comparison between the MPC and PID controllers.

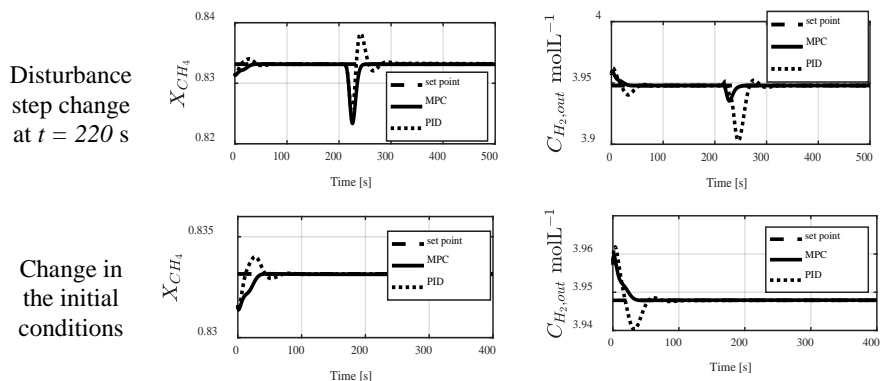


Figure 3: Controllers Comparison: Closed-loop trajectories of the outputs, MPC (—) and PID (···) controllers.

Clearly, from Figure 3, the performance of the MPC is better than the one of PID. Of course, solving an MPC problem in real time is more complex; however, the constraint handling is an advantage. In this case, the inlet flow rate should be kept above minimum fluidization velocity.

5. Conclusions

In this paper, the optimal operation and control of an FBMR for SMR are studied. A dynamic model of the process is obtained, and an offline dynamic optimization problem is proposed to maximize the conversion of methane and separation factor in the FBMR. Based on the optimal operation, and the dynamic model, a reduced order linear model is developed using balance truncation methods. Finally, PID and MPC controllers are designed, and their performance tested in simulations considering variation in the inlet concentration of the feed to the reactor and initial conditions.

References

- S. Gugercin, A. Antoulas, 2004, A survey of model reduction by balanced truncation and some new results, *International Journal of Control* 77.8, 748-766.
- F. Gallucci, M.V.S. Annaland, J.A.M. Kuipers, 2008. Autothermal reforming of methane with integrated CO₂ capture in a novel fluidized bed membrane reactor. Part 1: experimental demonstration. *Topics in catalysis*, 51(1-4), p.133.
- M. R. Rahimpour, F. Samimi, A. Babapoor, T. Tohidian, S. Mohebi, 2017, Palladium membranes applications in reaction systems for hydrogen separation and purification: A review. *Chemical Engineering and Processing: Process Intensification*, 121, 24-49.
- J. A. Medrano, I. Potdar, J. Melendez, V. Spallina, D.A. Pacheco-Tanaka, M. van Sint Annaland, F. Gallucci, 2018, The membrane-assisted chemical looping reforming concept for efficient H₂ production with inherent CO₂ capture: Experimental demonstration and model validation. *Applied Energy*, 215, 75-86.

Optimal design of experiments for the identification of kinetic models of 5-hydroxymethylfurfural hydrogenation

Andrea Bortoli^{a,b}, Fabrizio Bezzo^a and Federico Galvanin^{b,*}

^a*CAPE-Lab - Computer-Aided Process Engineering Laboratory, Department of Industrial Engineering, University of Padova, via Marzolo 9, 35131 Padova (PD), Italy*

^b*Department of Chemical Engineering, University College London (UCL), Gower St., WC1E 7JE London, United Kingdom*

*corresponding author: f.galvanin@ucl.ac.uk

Abstract

The increasing issues about the use of fossil raw materials advocate for an expanding utilization of biomass-based fuels and chemicals. Among the bio-based furan compounds, the 5-hydroxymethylfurfural (HMF) has received considerable attention in the chemical industry since it can be hydrogenated to 2,5-dimethylfuran (DMF) that is a valuable alternative fuel. The identification of a suitable kinetic model, where all the non-measurable kinetic parameters can be reliably estimated, is crucial to pursue the process optimization. In this work, the kinetic models currently available in literature for the HMF hydrogenation process are investigated to underline their strengths and weaknesses using a sensitivity-based identifiability analysis. The application of identifiability analysis techniques allows to define a set of fully identifiable kinetic models to be used for statistically reliable predictions. Furthermore, the use of design of experiments techniques leads to the characterization of design space regions that maximize the quality of the statistics related to the different estimates.

Keywords: 5-hydroxymethylfurfural, identifiability analysis, kinetic models

1. Introduction

Diminishing fossil fuel reserves and growing concerns about global warming indicate that sustainable sources of energy are needed in the near future (Roman-Leshkov et al. (2007)). Thus, the interest toward *renewable fuels* is rapidly growing and the new biomass-derived fuels seem to be an alternative suitable solution, clean and environmental safe, to fossil fuels (Demirbas (2010)) used for vehicles. However, for fuels to be useful in transportation sector, they must have specific physical properties that allow for efficient distribution, storage and combustion. While these properties are fulfilled by non-renewable petroleum-derived liquid fuels, the low energy density, high volatility and tendency to absorb water, are the reasons that bring the researchers to keep looking for a more efficient substitute to currently existent alternative fuels. The catalytic production of 2,5-dimethylfuran (DMF) from 5-hydroxymethylfurfural (HMF) seems to be a potential answer. The use of a catalytic process leads indeed to the identification of a route for transforming abun-

dant carbon-neutral renewable biomass resources into a liquid fuel suitable for the transportation sector (Parikka (2004)), with the final result of a diminished reliance of world's economy on petroleum derivatives and an increased environmental safety. Since HMF hydrogenation is a relatively new process, a well validated kinetic model capable of giving reliable predictions of the process, has not been defined yet: the identification procedure is complex and, in the full range of expected process conditions, a structural identifiability analysis on the existing kinetic models available in literature has never been proposed. Different assumptions and mechanisms lead to different kinetic model structures and determine the overall model complexity: from the simple power law to more complex structures involving adsorption coefficients (Gawade et al. (2016); Gyngazova et al. (2017); Luo et al. (2015); Jain and Vaidya (2016), Grilc et al. (2014)). In this paper an identification analysis is carried out on one of the aforementioned kinetic models, and a correlation study is carried out to underline potential parametric identifiability issues. Finally, model-based design of experiments (MBDoE) techniques are employed to define the most informative experiments to be performed in a batch reactor system.

2. Methodology

2.1. Procedure for the identification of HMF hydrogenation kinetic models

The block flow diagram of the proposed procedure for the study of the HMF hydrogenation kinetic models, is given in Figure 1. As a first step, a set of candidate kinetic models

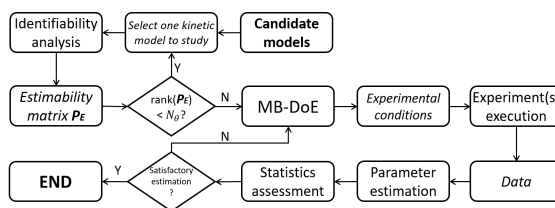


Figure 1: General procedure for the model identification.

is retrieved from the literature available. On each candidate, the identifiability analysis based on the study of the correlation between parameters is conducted by exploiting the local sensitivities. Once a set of identifiable kinetic models is found, MBDoE is applied to generate the optimal experimental conditions meant to maximize the Fisher Information Matrix (FIM) trace (Fisher (1935)). The results of the two analyses determine whether the kinetic models gathered at the beginning are affected by structural or practical unidentifiability issues. Moreover, they allow to define the most suitable regions of the experimental design space in which experiment must be carried out to maximize the quality of the statistics related to each estimate.

2.2. Identifiability analysis and MBDoE

Model identifiability procedures are used to recognize in advance structural and practical weaknesses related to models structure and application conditions. Structural identifiability is a property of the model structure and depends on the specific form of the differential-algebraic equations used to describe the phenomenon. Once an identifiable

model is available, the problem moves to the reliable estimation of its non-measurable parameters: to reduce the weight of this procedure, in terms of time and resources, MB-DoE techniques can be used to select the best experiments to be performed among a set of possible conditions (Galvanin et al. (2016)). With the sensitivity analysis, the local sensitivities for any m -th measurable output are evaluated perturbing one-at-time each N_θ non-measurable parameter and the result is a $n_m \times N_\theta$ sensitivity matrix. By repeating the analysis for each sampling time, it is possible to build a $n_{sp}n_m \times N_\theta$ *estimability matrix* and it can be used as an index of the model identifiability condition. A model can be classified as structurally identifiable if $rank(\mathbf{P}_E) < N_\theta$ (Shaw, 1999). This condition is satisfied when each column of the matrix \mathbf{P}_E is independent on the others. Once the identifiability study has been performed, the sensitivities can be used to calculate the FIM trace and assess the amount of information available for each parameter that requires estimation (see (4.3)).

$$Tr[\mathbf{H}]_{kl} = Tr \left[\sum_{k=1}^{N_\theta} \sum_{i=1}^{N_{exp}} \sum_{j=1}^{N_m} \left[\frac{1}{\sigma_{ij}^2} \left(\frac{\partial \hat{y}_{ij}}{\partial \theta_k} \frac{\partial \hat{y}_{ij}}{\partial \theta_l} \right) \right] \right] \cong Tr[\mathbf{V}_\theta^{-1}] \quad (1)$$

where $Tr[\mathbf{H}]_{kl}$ represents the kl -th element of a metric function (trace) of the FIM and \mathbf{V}_θ is the variance-covariance matrix. Notice that, once the FIM is available for a kinetic model, according to Bard (1974) the variance-covariance matrix can be approximated to the FIM inverse. While the FIM does not take into account the correlation between parameters, the variance-covariance matrix does and allows to figure out the best experimental conditions capable of maximizing the estimates quality. It is possible to demonstrate that by improving the fitting of the model, the quality of the approximation improves as well. The expected correlation between model parameters can be computed from the elements of \mathbf{V}_θ through the correlation matrix \mathbf{C} , whose elements are:

$$c_{ij} = \frac{\mathbf{V}_{\theta,ij}}{\sqrt{\mathbf{V}_{\theta,ii}\mathbf{V}_{\theta,jj}}} \quad (2)$$

Notice that the correlation matrix is a function of the experimental conditions: by perturbing the design variables also the correlation, hence the model identifiability, changes.

3. Case study: kinetic model and design space

For lack of space, only the study of one among kinetic model of Gawade et al. (2016), among the most promising and complex, is reported. In this kinetic model, from now on called M1, the dual-site Langmuir-Hinshelwood-Hougen-Watson (LHHW) theory is used to describe the adsorption and desorption mechanisms of the various species. The differential balances for the species are shown in the following. A = HMF, B = bis-hydroxymethylfuran, D = DMF, E = 2,5dimethyltetrahydrofuran, W = water.

$$\frac{dC_A}{dt} = \frac{k_1 K_A C_A \sqrt{K_{H_2} p_{H_2} w}}{[1 + K_A C_A + K_B C_B + K_D C_D + K_E C_E][1 + \sqrt{K_{H_2} p_{H_2} + K_W C_W}]} \quad (3)$$

$$\frac{dC_B}{dt} = \frac{[k_1 K_A C_A - k_2 K_B C_B] \sqrt{K_{H_2} p_{H_2} w}}{[1 + K_A C_A + K_B C_B + K_D C_D + K_E C_E][1 + \sqrt{K_{H_2} p_{H_2} + K_W C_W}]} \quad (4)$$

$$\frac{dC_D}{dt} = \frac{[k_2 K_B C_B - k_3 K_D C_D] \sqrt{K_{H_2} p_{H_2} w}}{[1 + K_A C_A + K_B C_B + K_D C_D + K_E C_E][1 + \sqrt{K_{H_2} p_{H_2} + K_W C_W}]} \quad (5)$$

$$\frac{dC_E}{dt} = \frac{k_3 K_D C_D \sqrt{K_{H_2} p_{H_2} w}}{[1 + K_A C_A + K_B C_B + K_D C_D + K_E C_E][1 + \sqrt{K_{H_2} p_{H_2} + K_W C_W}]} \quad (6)$$

where C_i are the concentrations and K_i are the adsorption coefficients of the various species, k_i are the kinetic constants of the different reactions, w is the catalyst loading in g/L and p_{H_2} is the hydrogen partial pressure in atm.

3.1. Definition of design space

For the study of this transformation in a batch system, initial concentrations of HMF and DMF are considered as the most meaningful design variables to be investigated. To the aim of reducing the computational expenditure of the study, the Latin Hypercube Sampling is used to select 10 couplets of initial concentrations uniformly distributed in the entire range of concentrations (see Table 1). To study the effect of a limited number of measurements on the collected information, hence on the quality of the estimates, only 10 samplings are simulated and their allocation is evenly spaced along the experiment duration.

Table 1: Values of HMF and DMF initial concentrations.

Exp.	1	2	3	4	5	6	7	8	9	10
C_{HMF}^0 [M]	0.1556	0.0667	0.0000	0.1333	0.0889	0.2000	0.0222	0.1778	0.1111	0.0444
C_{DMF}^0 [M]	0.0667	0.0222	0.0444	0.0000	0.0889	0.2000	0.1111	0.1333	0.1556	0.1778

4. Kinetic model identification results

4.1. Identifiability analysis results

In Table 2 it is possible to appreciate that at least three couples of parameters are totally correlated and $\text{rank}(\mathbf{P}_E) = 6 < 9 = N_\theta$. Moreover, although some minor changes, by varying the sampling points schedule adopted, the three total correlations do not disappear and the kinetic model remains structurally unidentifiable. To solve the correlation problem,

Table 2: Correlation matrix for the kinetic model M1 based on the sampling distribution S1: values and colormap.

R	k_1	k_2	k_3	K_A	K_B	K_D	K_E	K_{H_2}	K_W
k_1	1.000								
k_2	0.703	1.000							
k_3	-0.020	-0.058	1.000						
K_A	0.999*	0.687	-0.020	1.000					
K_B	0.700	1.000*	-0.059	0.685	1.000				
K_D	-0.027	-0.070	1.000*	-0.027	-0.071	1.000			
K_E	-0.679	-0.860	-0.008	-0.664	-0.858	0.003	1.000		
K_{H_2}	0.782	0.991	0.008	0.769	0.990	-0.004	-0.868	1.000	
K_W	-0.563	-0.904	-0.062	-0.553	-0.904	-0.049	0.841	-0.891	1.000
r_{crit}	1	3	1	0	2	0	0	0	-
	-1.00	-0.75	-0.50	-0.25	0	+0.25	+0.50	+0.75	+1.00

since the non-linearity of the system is high, a simplified version of the kinetic model is proposed.

4.2. Simplified version of the kinetic model M1 (M1.2)

The purpose of this simplified version is to by-pass the identifiability issues previously highlighted in order to end up with a simpler version whose non-measurable parameters would be easier to estimate in a statistically reliable way. The new kinetic model is:

$$-\frac{dC_A}{dt} = \frac{k_1 C_A \sqrt{K_{H_2} p_{H_2}} w}{1 + \sqrt{K_{H_2} p_{H_2}}} \quad (7)$$

$$\frac{dC_B}{dt} = \frac{[k_1 C_A - k_2 C_B] \sqrt{K_{H_2} p_{H_2}} w}{1 + \sqrt{K_{H_2} p_{H_2}}} \quad (8)$$

$$\frac{dC_D}{dt} = \frac{[k_2 C_B - k_3 C_D] \sqrt{K_{H_2} p_{H_2}} w}{1 + \sqrt{K_{H_2} p_{H_2}}} \quad (9)$$

$$\frac{dC_E}{dt} = \frac{k_3 C_D \sqrt{K_{H_2} p_{H_2}} w}{1 + \sqrt{K_{H_2} p_{H_2}}} \quad (10)$$

where the nomenclature is analogous to the one used with M1. The comparison of the concentration profiles obtained from the process simulation using the original kinetic model M1 and the simplified version M1.2, allows to quantify the magnitude of the approximation. No substantial differences are present such that the two kinetic models are equivalent: a simpler kinetic model, whose parameters are not affected by correlation issues, can still represent accurately the hydrogenation process.

4.3. Model-based information analysis

In Figure 2 the information and covariance analysis results are illustrated for a sequence of 10 experiments to be performed. The figure shows the cumulative information as given by the trace of FIM and the trace of the variance-covariance matrix \mathbf{V}_θ for 10 in-silico experiments. The conclusions are that conditions of simulations 2 and 4 lead to the high-

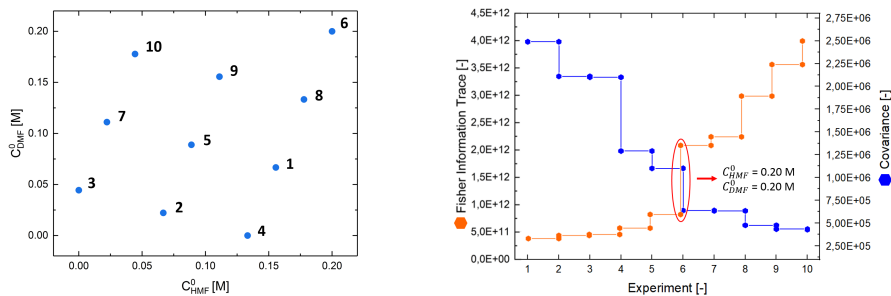


Figure 2: Profiles of Fisher information trace and variance-covariance matrix trace for the kinetic model M1.2 (T = 383 K, $P_{H_2} = 5$ atm)

est covariance reduction while conditions of simulation 6 allow to obtain the greatest increment in the information content.

5. Conclusions

In this paper a sensitivity-based identifiability analysis has been applied to kinetic models of HMF hydrogenation developed from batch reaction data. Through the study of the correlation matrix and its evolution for different values of the design variables, it has been possible to detect and classify the presence of identifiability issues for the kinetic models. Given the high complexity of the kinetic model proposed by Gawade et al. (2016), a simplified version of the same model has been suggested to overcome the impossibility to estimate the full set of kinetic parameters for this model. On the newly proposed model, the information analysis results highlighted that high initial concentrations of HMF and DMF lead to higher amounts of information while low initial concentrations lead to a greater covariance reduction. To conclude, the work presented here represents a first step toward the identification of a more complete kinetic model that contemplate the explicit dependency of reaction rates on both temperature and pressure. It highlights how to obtain reliable predictions on concentration, an extremely complex representation of the chemistry at the basis of the process is not required: kinetic models with many parameters are likely to be unidentifiable and not suitable to be validated through simple kinetic experiments.

References

- Bard, Y., 1974. *Nonlinear Parameter Estimation*. Academic Press.
- Demirbas, A., 2010. Fuels from Biomass. In: *Biorefineries. Green Energy and Technology*. Springer, London, pp. 33–73.
- Fisher, R. A., 1935. *The design of experiments*. Oliver & Boyd, Oxford, England.
- Galvanin, F., Cao, E., Al-Rifai, N., Gavriilidis, A., 2016. A joint model-based experimental design approach for the identification of kinetic models in continuous flow laboratory reactors. *Computers and Chemical Engineering* 95, 202 – 215.
- Gawade, A. B., Tiwari, M. S., Yadav, G. D., 2016. Biobased Green Process: Selective Hydrogenation of 5-hydroxymethylfurfural to 2,5-dimethylfuran under Mild Conditions Using Pd-Cs_{2.5}h_{0.5}pw_{12o40}/K-10 Clay. *Acs Sustainable Chemistry & Engineering* 4 (8), 4113–4123.
- Grilc, M., Likožar, B., Levec, J., 2014. Hydrodeoxygenation and hydrocracking of solvolysed lignocellulosic biomass by oxide, reduced and sulphide form of NiMo, Ni, Mo and Pd catalysts. *Applied Catalysis B: Environmental* 150-151, 275–287.
- Gyngazova, M. S., Negahdar, L., Blumenthal, L. C., Palkovits, R., 2017. Experimental and kinetic analysis of the liquid phase hydrodeoxygenation of 5-hydroxymethylfurfural to 2,5-dimethylfuran over carbon-supported nickel catalysts. *Chemical Engineering Science* 173, 455–464.
- Jain, A. B., Vaidya, P. D., 2016. Kinetics of Catalytic Hydrogenation of 5-Hydroxymethylfurfural to 2,5-bis-hydroxymethylfuran in Aqueous Solution over Ru/C. *International Journal of Chemical Kinetics* 48 (6), 318–328.
- Luo, J., Arroyo-Ramirez, L., Wei, J., Yun, H., 2015. Comparison of HMF hydrodeoxygenation over different metal catalysts in a continuous flow reactor. *Applied Catalysis a-General* 508, 86–93.
- Parikka, M., 2004. Global biomass fuel resources. *Biomass and Bioenergy* 27 (6), 613–620.
- Roman-Leshkov, Y., J Barrett, C., Y Liu, Z., A Dumesic, J., 2007. Production of Dimethylfuran for Liquid Fuels from Biomass-Derived Carbohydrates. *Nature* 447, 982–5.

Iterative Medium-Term Production Scheduling of an Industrial Formulation Plant

Vassilios Yfantis^{a,*}, Thomas Siwczyk^a, Matthias Lampe^b, Nicolai Kloye^b, Manuel Remelhe^b and Sebastian Engell^a

^a*Process Dynamics and Operations Group, Department of Biochemical and Chemical Engineering, TU Dortmund University, Emil-Figge-Str. 70, 44227 Dortmund, Germany*

^b*Bayer AG, Kaiser-Wilhelm-Allee 1, 51368 Leverkusen, Germany*
vassilios.yfantis@tu-dortmund.de

Abstract

In this contribution, a discrete-time medium-term production scheduling model of an industrial formulation plant for crop protection chemicals is presented. As the optimization model has to provide feasible solutions in a real-world environment, all relevant processing characteristics, as e. g. sequence- and unit-dependent changeovers, timing relations between different units and processing tasks or shift patterns must be represented in order to yield feasible and implementable schedules. In order to cope with the computational complexity of the problem, an iterative scheme is employed in which the production orders are scheduled in a sequential fashion. After each iteration a set reduction step is performed, removing all infeasible unit allocations from the feasible set of the next iteration. The proposed framework is tested on a realistic industrial case study.

Keywords: Production scheduling, MILP Model, Formulation Plants, Optimization

1. Introduction

Scheduling in the process industry describes the allocation of limited resources to manufacture several products over a given time horizon (Méndez et al., 2006). The increased global competition increases the need to generate good production schedules fast and efficiently. In order to satisfy varying customer demands, a key feature of the production systems is a high flexibility, e. g. by multipurpose lines and intermediate storage. This flexibility results in a high complexity of scheduling problems. Due to this inherent complexity, scheduling without optimization support is challenging (Harjunkoski et al., 2014). Rigorous mathematical programming-based solution approaches can find optimal schedules for suitably formulated models. However, for the use of optimization based scheduling algorithms in an industrial environment good schedules must be generated within reasonable response times, but the schedules do not necessarily have to be strictly optimal. A way to shorten the computation time is the combination of exact and heuristic methods. This contribution presents a hybrid approach combining a detailed MILP model and a sequential scheduling heuristic for the fast generation of (sub-) optimal schedules for a formulation plant.

2. Case Study

The formulation plant for the production of crop protection chemicals which is considered in this contribution is depicted in Fig. 1. After an initial raw material pre-processing step which mainly includes the preparation of the active ingredient (AI) and solvents, a standardization (mixing)

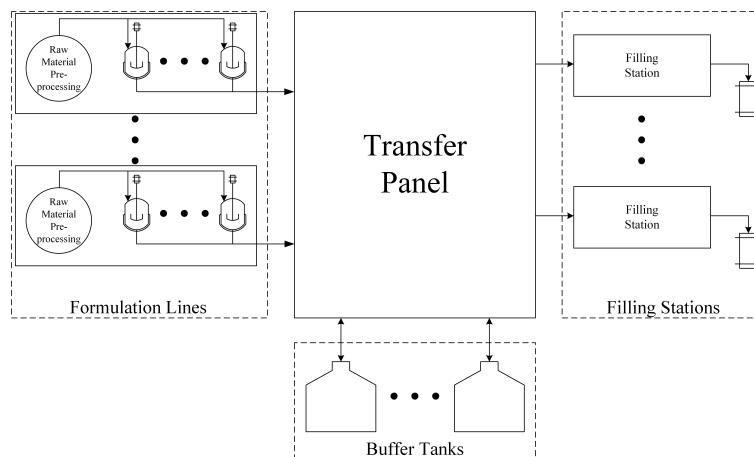


Figure 1: Schematic representation of an industrial formulation plant.

operation is performed in one of several identical standardization tanks within the formulation line, which process batches of a fixed and unit specific size. After a minimum standardization time has elapsed, the finished product can be sent to a filling station where it is filled with an order and unit specific flowrate, resulting in the final product. Since the plant includes fewer filling stations than standardization tanks and the filling stations operate on a shift system with two working and one non-working (night) shift, the filling step constitutes the bottleneck of the production. In order to utilize the full capacity of the plant, the formulation lines and filling stations are decoupled through the use of buffer tanks for finite intermediate storage. The transfer times between the standardization and buffer tanks can be neglected, while the transfer times between the different tanks and the filling stations depend on the flowrate of the latter, since the tanks are gradually drained by the connected filling stations. The objective of the optimization is to satisfy all customer orders over a given time horizon, while minimizing the makespan. The due dates usually lie beyond the scheduling horizon and are considered here.

3. Solution Approach

In order to solve the scheduling problem, a hybrid approach is chosen in which an MILP optimization model is combined with a heuristic. Both elements of the scheduling framework are presented in the following sections.

3.1. MILP Model

The optimization model is based on a discrete representation of time (Méndez et al., 2006), in which a set of orders I are processed in the available units J over a scheduling horizon $T_H = \{1, \dots, H, H + 1\}$, while the makespan is to be minimized. The units can be split into three subsets, the standardization tanks of the formulation lines J^{FL} , the filling stations J^{FS} and the buffer tanks J^{ST} . The subset of units that can process order $i \in I$ is denoted by J_i . The same notation is used for the units of the subsets, except for the buffer tanks, for which $J_i^{\text{ST}} = J^{\text{ST}}$, $\forall i \in I$ holds. The set L denotes the formulation lines, each of which contains a set of standardization tanks $J_l^{\text{FL}} \subset J^{\text{FL}}$, $\forall l \in L$. The decisions taken during the optimization are the start times of processing or storage of material corresponding to order i in unit j (standardization and buffer tank respectively) at time t , expressed by the binary variable W_{ijt} . The release of material from a tank is similarly expressed through the binary variable W_{ijt}^R . The start of a filling process is expressed by the binary

variable X_{ijkt} , where the index $k \in K$ contains information on the filling time (see constraints (5)-(7) below). The amount of material being sent to or being released from processing or storage is modeled through the continuous variables B_{ijt} and B_{ijt}^R . The amount of material stored in a buffer tank at each time point is tracked through the variable B_{ijt}^{ST} . The model contains a large number of constraints, only some of which can be discussed in this paper.

$$\sum_{t \in T_H} \sum_{j \in J_i^{FS}} B_{ijt} \geq D_i, \forall i \in I \quad (1)$$

$$B_{ij(t+1)}^{ST} = B_{ijt}^{ST} + B_{ijt} - B_{ijt}^R, \forall i \in I, j \in J^{ST}, t \in T_H \setminus \{H+1\} \quad (2)$$

$$\sum_{j \in J_i^{FL}} W_{ijt}^R \cdot B_j + \sum_{j' \in J^{ST}} B_{ij't}^R = \sum_{j'' \in J_i^{FS} \cup J^{ST}} B_{ij''t}, \forall i \in I, t \in T_H \quad (3)$$

$$B_{ijt}^{ST} \leq V_j^{\max}, \forall i \in I, j \in J^{ST}, t \in T_H \quad (4)$$

$$\frac{B_{ijt}}{F_{ij}} \leq Y_{ijt} < \frac{B_{ijt}}{F_{ij}} + 1, \forall i \in I, j \in J_i^{FS}, t \in T_H \quad (5)$$

$$\sum_{k \in K} X_{ijkt} \cdot p_k = Y_{ijt}, \forall i \in I, j \in J_i^{FS}, t \in T_H \quad (6)$$

$$\sum_{k \in K} X_{ijkt} \leq 1, \forall i \in J_i^{FS}, t \in T_H \quad (7)$$

$$W_{ijt} + \sum_{t'=t}^{t+p_{ij}-1} W_{ij't'}^R \leq 1, \forall i \in I, j \in J_i^{FL}, t \in T_H \quad (8)$$

$$W_{ijt}^R + X_{ij'kt} + \sum_{t'=t}^{t+p_k+co_{it'}-1} \sum_{j' \in J_i^{FL} \cup J^{ST}} W_{ij't'} \leq 2, \quad (9)$$

$$\forall i \in I, j \in J_i^{FL} \cup J^{ST}, j' \in J_i^{FS}, k \in K, t \in T_H$$

$$W_{ijt}^R + W_{ij't} + \sum_{t'=t}^{t+co_{it'}-1} \sum_{j' \in J^{ST}} W_{ij't'} \leq 2, \forall i \in I, j \in J_i^{FL}, j' \in J^{ST}, t \in T_H \quad (10)$$

$$W_{ijt} + \sum_{t'=t}^{t+p_{ij}^e+co_{it'}-1} \sum_{j' \in J_i^{FL} \setminus \{j\}} W_{ij't'} \leq 1, \forall i \in I, l \in L_i, j \in J_i^{FL}, t \in T_H \quad (11)$$

$$W_{ijt}^R + X_{ij'kt} + \sum_{t'=t+1}^{t+p_k-1} W_{ij't'}^R \leq 2, \forall i \in I, j \in J^{ST}, j' \in J_i^{FS}, k \in K, t \in T_H \quad (12)$$

$$X_{ijkt} + \sum_{t'=t+1}^{t+p_k+co_{it'}-1} \sum_{k' \in K} X_{ij'kt'} \leq 1, \forall i \in I, j \in J_i^{FS}, k \in K, t \in T_H \quad (13)$$

$$C_{\max} \geq X_{ijkt} \cdot (t + p_k), \forall i \in I, j \in J_i^{FS}, k \in K, t \in T_H \quad (14)$$

Constraints (1) ensure that at least the ordered amount corresponding to order i , D_i is produced within the scheduling horizon. An inequality constraint is employed due to the fixed batch sizes B_j in the standardization tanks, which could lead to infeasibilities if the ordered amount had to be met exactly. Constraints (2)-(3) model the material balances around the buffer tanks and the transfer panel respectively. The amount stored in a buffer tank is limited by the maximum capacity V_j^{\max} (4). A major challenge for the discrete-time formulation of the scheduling problem are the variable filling times which depend on the amount to be filled, B_{ijt} , and the order and unit

specific flowrate F_{ij} . Constraints (5) emulate the ceiling function through the non-negative integer variable Y_{ijt} ($= \lceil B_{ijt}/F_{ij} \rceil$). Constraints (6)-(7) capture the information on the filling time (in time intervals) through the binary variable $X_{ijk\ell}$, by selecting the corresponding filling time p_k , with $p_1 = 0$, $p_2 = 1, \dots, p_{|K|} = 2 \cdot p^s$, where $2 \cdot p^s$ is the maximal duration of a filling process, corresponding to two consecutive shifts. The plant exhibits a complex timing behavior due to the interconnection of and the material transfer between the various units. These timing relations are modeled through the timing constraints (8)-(13). The formulation of Méndez et al. (2006) is used, which exhibits stronger relaxations than the commonly used big-M constraints. Constraints (8) enforce the minimum standardization time p_{ij} . If material is sent from a standardization or buffer tank to a filling station, the next standardization or storage can only start after the filling has been completed and an additional changeover time $co_{i'j}$ between the two orders has elapsed (9). As material transfer between a standardization and a buffer tank is assumed to be instantaneous, only a changeover is required for the standardization tank, if such a material transfer is executed (10). Each formulation line contains multiple identical standardization tanks, but only one raw-material pre-processing line. Therefore processing can not start in all tanks of a line simultaneously. After one standardization has started, the charging time p_{ij}^c , during which the tank is filled and a line changeover time $co_{i'l}$ have to elapse before a standardization can start in another tank of the same line (11). Two consecutive releases from a buffer tank are constrained by the filling time of the station to which material is sent (12). Lastly, the filling time and a changeover time have to elapse between two filling operations (13). The makespan of the schedule is used as the objective function. It is modeled by the constraints (14), where C_{\max} is set to be larger than the end of all filling operations.

3.2. Iterative Scheduling and Set Reduction

Solving the optimization problem for a realistic set of orders simultaneously leads to a computationally intractable model size, even when using state-of-the-art MILP solvers. A way to deal with this limitation is to employ iterative scheduling (see e. g. Georgiadis et al. (2018)) in which the different orders are scheduled sequentially, while all decisions associated to previously scheduled orders are fixed. The main requirement for this approach is that the generated schedule represents a feasible solution of the original problem, i. e. that the constraints modeling the (timing) interactions of different orders in the model are satisfied. One way to ensure this feasibility is to include all variables and constraints of the model up to the order scheduled in the current iteration, while fixing all variables associated to the previous orders. In this way, each solution is guaranteed to be feasible together with the results of the previous iterations. However, a drawback of this approach is the increasing model size as the iteration progresses, since more variables and constraints are added to the model, resulting again in a computationally intractable approach. In order to maintain feasibility, we propose the implicit inclusion of the previously scheduled orders through a feasible set reduction. As the allocation and timing decisions of the preceding orders remain fixed, the time points can be identified which would result in an infeasible assignment in the current iteration. They can directly be derived from the timing constraints (8)-(13). The idea is demonstrated for constraints (13):

$$X_{i'jkt} = 1 \Rightarrow \{t - co_{i'j+1} + 1, \dots, t, \dots, t + p_k, \dots, t + p_k + co_{i'j} - 1\} \subset T_{ij}^1.$$

If a filling process of a previously scheduled order i' started at time point t , the time points corresponding to the processing time in addition to the preceding and subsequent changeovers would lead to infeasible assignments of the current order i . The set T_{ij}^1 includes all infeasible time points for order i in unit j . The infeasible time points for the other units are derived in a similar fashion from their respective timing constraints. For the scheduling of order i , all infeasible assignments due to previous allocations are eliminated through the constraints

$$\sum_{\forall t \in T_{ij}^1} W_{ijt} + W_{ijt}^R = 0, \forall j \in J_i^{\text{FL}} \cup J_i^{\text{ST}} \quad (15)$$

$$\sum_{\forall t \in T_{ij}^I} X_{ijkt} = 0, \forall j \in J_i^{\text{FS}}. \quad (16)$$

The time points corresponding to a non-working shift of the filling stations can also easily be added to the infeasible set. Due to the time consuming material transfer from the tanks and the variable filling time, the end of an operation is not solely determined by the variables associated to one unit. In order to still maintain feasibility, it must be guaranteed that each processing task finishes before the start of the next infeasible time points. This is achieved by identifying the feasible time points T_{ij}^{F} and splitting them into disjoint continuous sets $T_{ij}^{\text{F},s} \subset T_{ij}^{\text{F}}$

$$T_{ij}^{\text{F}} = T_H \setminus T_{ij}^{\text{I}} = \bigcup_{\forall s} T_{ij}^{\text{F},s}, T_{ij}^{\text{F},s} \cap T_{ij}^{\text{F},s'} = \emptyset, \forall s, s'. \quad (17)$$

It is ensured by additional constraints that an operation that starts within a feasible subset is finished until the end of that set.

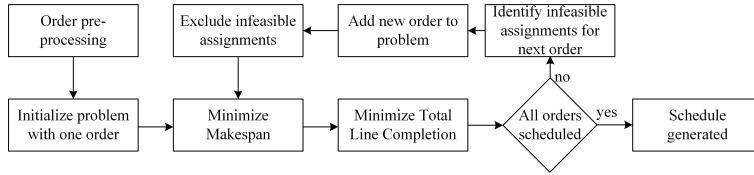


Figure 2: Algorithmic framework for the solution of the scheduling problem.

4. Computational Considerations and Results

Test runs showed a drawback associated to the minimization of the makespan. As only the maximum completion time affects the objective value of the optimization, standardizations that could finish earlier exhibit unnecessary waiting times. This leads to an underutilization of the available production capacity, as more time points are excluded from the feasible set of the next iteration. In order to resolve this limitation, the optimization is performed in two steps. In the first step the makespan C_{\max} is minimized. In the second step the completion times of the formulation lines C_l are added to the model through constraints (18)

$$C_l \geq W_{ij}^R \cdot t, \forall l \in L_i, j \in J_i^{\text{FL}}, t \in T_H. \quad (18)$$

The total line completion time is then minimized, while ensuring that the makespan stays below that of the first stage (C_{\max}^*)

$$\min \sum_{\forall l \in L_i} C_l, C_{\max} \leq C_{\max}^*. \quad (19)$$

The test runs also showed that the computation time of each iteration strongly depends on the ordered amount D_i and the resulting number of batches that have to be scheduled. The computational effort can be decreased by splitting large orders into multiple artificial smaller orders, which are then also scheduled sequentially. The splitting can be performed in a pre-processing step according to a specified maximum number of standardizations that are allowed to be scheduled in each iteration. The complete proposed framework is illustrated in Fig. 2. It was tested for a plant consisting of 7 formulation lines, each with 3 standardization tanks, 8 filling stations and 5 buffer tanks. In total 20 different orders were scheduled over a one week horizon, with a time interval length of one hour. At most 5 standardizations were scheduled in each iteration. The framework was implemented in Julia 0.6.1.1 (Bezanson et al., 2017) with IBM ILOG CPLEX 12.7.1 as an MILP solver on a MS Windows 7 desktop PC (Intel Core i7-4790S CPU @ 3.20 GHz,

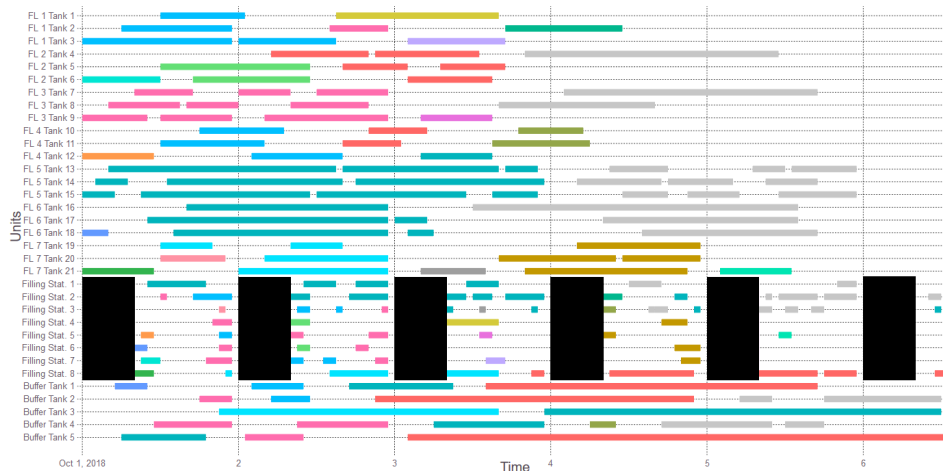


Figure 3: Gantt generated with the proposed scheduling framework.

16 GB RAM). Even for small instances, including just a few orders, no feasible solutions could be obtained due to the model size and complexity and the resulting failed model initialization due to memory limitations. Using the proposed approach the problem was solved in 38 minutes, where a relative gap tolerance of 5 % was used in each iteration. The generated Gantt-chart with a makespan of 133 h is shown in Fig. 3. The black regions in the charts of the filling stations represent non-working shifts. Although the schedule still exhibits unnecessary waiting times and release postponements in the standardization tanks, it finishes more than one day prior to the end of the scheduling horizon. It should also be noted that solving all iterations to global optimality (0 % gap) resulted in a nearly identical schedule, where the overall makespan was improved by only one hour, but the solution required 4.5 hours of computation time. This further underlines the good tradeoff between optimality and computation time that is achieved with the proposed framework.

5. Conclusion

In this contribution an approach for the fast generation of feasible and good schedules that includes an MILP model and a set reduction approach was proposed. The results show that good schedules can be found within relatively short computation times. This is preferable over the time consuming search for an optimal schedule in an industrial environment. Since the scheduling problem is solved in an iterative fashion, the quality of the schedule strongly depends on the sequence in which the orders are scheduled. Therefore further improvements can be achieved by employing a sorting of the orders in the pre-processing step, either through a prioritization of orders according to specified criteria, or based upon operational considerations provided by planners and operators.

References

- J. Bezanson, A. Edelman, S. Karpinski, V. B. Shah, 2017. Julia: A fresh approach to numerical computing. *SIAM Review* 59 (1), 65–98.
- G. P. Georgiadis, C. Ziogou, G. Kopanos, M. Garcia, D. Cabo, M. Lopez, M. C. Georgiadis, 2018. Production scheduling of multi-stage, multi-product food process industries. In: *Computer Aided Chemical Engineering*. Vol. 43. pp. 1075–1080.
- I. Harjunkoski, C. T. Maravelias, P. Bongers, P. M. Castro, S. Engell, I. E. Grossmann, J. Hooker, C. Méndez, G. Sand, J. Wassick, 2014. Scope for industrial applications of production scheduling models and solution methods. *Computers & Chemical Engineering* 62, 161–193.
- C. Méndez, J. Cerdá, I. E. Grossmann, I. Harjunkoski, M. Fahl, 2006. State-of-the-art review of optimization methods for short-term scheduling of batch processes. *Computers & Chemical Engineering* 30 (6-7), 913–946.

On the Solution of the Smoluchowski Coagulation Equation Using a Conservative Discretization Approach (CDA)

Menwer Attarakih^{a,b,*} and Hans-Jörg Bart^{b,c}

^a*The University of Jordan, Scjool of Engineering, Department of Chemical Engineering, 11942 Amman, Jordan*

^b*Chair of Separation Sciences and Technology, The University of Kaiserslautern, 67653 Kaiserslautern, Germany*

attarakih@yahoo.com

Abstract

The continuous Smoluchowski coagulation equation, which is known as the population balance equation (PBE) for particle coagulation, is a nonlinear integro-partial differential equation with no general analytical solution. In this work, we are concerned with extending our discrete formulation of the PBE for particle breakage using a Conservative Discretization Approach (CDA) (Attarakih et al., 2004) to solve the Smoluchowski coagulation equation coupled with particle growth. The method is based on introducing auxiliary functions to modify the discrete loss and formation terms in the discrete PBE. These are then uniquely determined by exactly reproducing two arbitrary chosen integral quantities from the continuous PBE. The CDA is validated using many test cases with known analytical solutions including coupled particle coagulation and growth dynamics as a simplified model for a batch crystallizer. The discrete approximate solutions for the number concentration function is found to converge with an order $O(1/M)$ where M is the number of grid points.

Keywords: CDA, Population Balances, Coagulation, Smoluchowski.

1. Introduction

The continuous nonlinear Smoluchowski coagulation equation (also known as the population balance equation for particle coagulation) is an integro-partial differential equation with no general analytical solution. It finds many applications in process system engineering and on individual unit operation level in pharmaceutical and chemical processes with mono and multivariate number density functions. This equation can describe the system behaviour up to any degree of detail which is necessary for understanding many single processing units such as crystallizers, turbulent flame reactors, polymerization reactors, bubble phase reactors, and extraction columns (Attarakih and Bart, 2014, Ramkrishna, 2014, Ferreira et al., 2017). In spite of the intensive research in the last decades, which is concerned with fast numerical solvers based on the moment methods, numerical solutions which are able to conserve particle integral properties suffer from losing the particle size distribution. The latter is required in industrial particulate systems where it is used to determine mechanical and physiochemical system properties, for online control purposes (Attarakih et al., 2012, Attarakih and Bart, 2014), to evaluate the negative particle fluxes at zero particle size as in the case of droplet evaporation (Vie et al., 2013) and to accommodate time varying boundary conditions in age-structured models of hematological disease (Foley and

Mackey, 2009). When numerical solutions are concerned, our successful discrete formulation of the population balance equation for particle breakage using a Conservative Discretization Approach (CDA) (Attarakih et al., 2004) laid down a solid foundation for the solution of the highly nonlinear and stretched (w.r.t. particle property space) Smoluchowski coagulation equation. The discrete set of equations is derived by treating the number of particles in each size subdomain as a single particle with known fixed position. Starting from a discrete and consistent initial number density, these particles are allowed to coagulate with a given probability and frequency to produce particles of large sizes. Prior to coagulations events, the newly born particles are allowed to adjust their local positions within each subdomain such that two selected integral properties are conserved. This is called internal consistency of the discrete Smoluchowski coagulation equation w.r.t the continuous one. Similar to our CDA for particle breakage, this internal consistency is enforced by introducing a set of two unique and general auxiliary functions (formation and loss auxiliary functions) that are uniquely determined by matching the integral properties obtainable from the discrete set against those from the continuous Smoluchowski equation. These auxiliary discrete functions are converted into matrices which are computed offline and thus placing no new computational burden during the time evolution of the particle-particle coagulation events. The computed matrices depend on the particle grid structure and are functions only of the arithmetic mean volume (mass) of the coagulating pair of particles and the representative volume in which the coagulated pair falls.

2. Discretization of Smoluchowski Equation using the CDA

The Conservative Discretization Approach (CDA) for droplet breakage (Attarakih et al., 2004) when applied to the Smoluchowski coagulation equation with particle growth provides not only the discrete number concentration function, but also its zero and third moments (or any two prior selected population integral properties). The key idea behind the CDA is to constraint the integral particle properties derived from the discrete Smoluchowski coagulation by those derived from its continuous counterpart. This not only reduces the number of ODEs to be solved, but also increases the accuracy of both the calculated particle size distribution and its desired moments. Following these lines, one can introduce auxiliary functions to the formation and loss terms in a hope to force the discrete Smoluchowski coagulation to conserve two desired integral properties of the particle size distribution:

$$\frac{dN_i(x; t)}{dt} = \sum_{k=0}^i \sum_{j=k}^i [\alpha_{k,j} \Psi_{k,j}^i] (1 - \frac{1}{2} \delta_{k,j}) \omega_{k,j} N_k N_j - N_i \sum_{j=0}^{M-1} \eta_{i,j} \omega_{i,j} N_j + S_i \quad (1)$$

In this equation N_i is the total number concentration in the i th subdomain that is defined as $V_i = [v_{i-1/2}, v_{i+1/2})$, $i = 0, 1, \dots, M$ with a representative particle diameter

$d_i^* = \sqrt[3]{v_i^*}$ where v_i^* is the arithmetic mean of the V_i . subdomain boundaries and M is the total number of subdomains. The coagulation binary interaction matrix (Ψ^i) records the occurrence of successful coagulation events between pair of particles from two subdomains of labels (k and j). The summation $\sum (\Psi^i) = 1, \forall i$ is required to conserve the mass of the newly born particles by coagulation. The physical meaning of this constraint is that no newly born particle by coagulation can exist at the same time in

more than one subdomain. The definition of the elements of this matrix are similar to that presented in Attarakih et al. (2009). The two new auxiliary functions α and η are introduced in the respective formation and loss terms to conserve exactly any two targeted population integral properties. For the conservation of zero and third moments w.r.t. particle diameter, these functions are given by:

$$\alpha_{k,j} = \frac{1}{2\chi_{k,j} - 1}, \quad \eta_{i,j} = \frac{\chi_{i,j}}{2\chi_{i,j} - 1}, \quad \chi_{k,j} = \frac{\sum_{i=1}^M v_{i-1}^* \Psi_{k,j}^i}{v_k^* + v_j^*} \quad (2)$$

Note that $\chi_{k,j}$ is in the order of one and can be smaller than one if the summation of the volumes of the coagulating particles from the subdomains (k,j) is greater than v^* in the i th subdomain, equals to one when their volume is exactly the same as v^* in the i th subdomain or greater than one otherwise. These functions do not depend on the particle coagulation frequency and probability but depend only on the grid structure. For example, when the grid is linear in terms of particle diameter $\chi_{k,j} = 1$ and hence both α and η are unity. In this case the discrete Smoluchowski coagulation equation is reduced to the special case of Hidy (1965) where all the integral particle properties are correctly predicted; however, at the expense of drastic increase of the number of ODEs.

The discrete term S_i on the r.h.s of Eq.(1) takes into account the discrete particle breakage which conserves total number and volume concentrations (Attarakih et al., 2004) plus the discrete growth term which is derived using the same concept used in deriving Eq.(1). This derivation is constrained by the conservation of total number and volume concentrations and is given by:

$$S_i^g = H_i(d_i^*, r)(g(d_i^*)N_i - rg(d_{i-1}^*)N_{i-1}) \quad (3)$$

Where $g(d)$ is the particle growth rate, r is the ratio between two consecutive discrete particle diameters ($r = [d_{\max}/d_{\min}]^{(1/M)}$ for geometric grid spanning the domain $d \in [d_{\min}, d_{\max}]$) and the function H is a simple function of d^* and r . The convective flux (w.r.t. particle diameter) in Eq.(3) is a conservative modified first-order upwind scheme which conserves exactly total volume and number concentrations and guarantees the positivity of the reconstructed number concentration function. To this end, the system of Eqs.(1 to 3) presents a consistent discrete model for the numerical solution of the Smoluchowski coagulation equation coupled to particle breakage and growth. To the best of the authors' knowledge, this is the first complete and consistent discrete model for the solution of the population balance equation which takes into account all the possible particle mechanisms including particle nucleation which can be easily added as a birth source term in the first subdomain.

3. Numerical Results and Discussion

3.1. Numerical Analysis

The proposed CDA for Smoluchowski coagulation equation is validated in the first step against well-known analytical solutions. These solutions depend on the coagulation frequency where particle coagulation in a suspension may occur through variety of mechanisms such as Brownian motion, turbulent diffusion and laminar shear (Hidy and Brock, 1970). From physical and analytical point of view, the Brownian motion and turbulent diffusion are the two popular mechanisms. For Brownian coagulation, ω

depends on the sizes of the two coagulating particles. When one particle is in the continuum regime, the coagulation frequency is given by the Smoluchowski kernel:

$$\omega(v, v') = \omega_0(v + v')(v^{-1} + v'^{-1}) \quad (4)$$

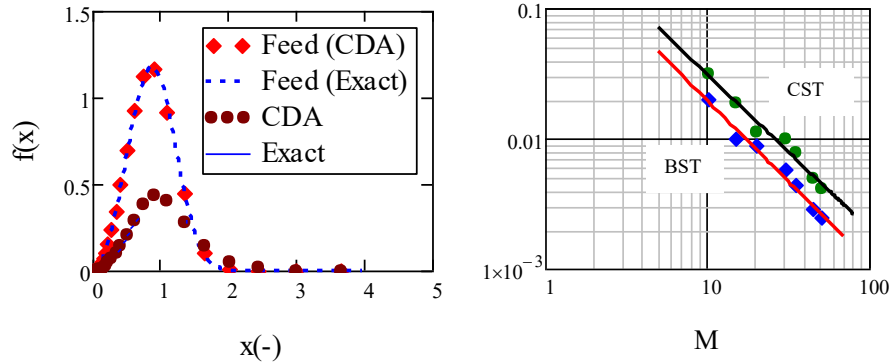


Figure 1: (Left). Solution of Smoluchowski equation with constant kernel particle aggregation (ω_0) in CST using the CDA. (Right). Convergence of the CDA based on the RMSE using $\omega = \omega_0$ in batch and continuous stirred tanks. $d_{\min} = 0.01$, $d_{\max} = 4$, $\tau = 4$, $M = 30$, the feed PSD is $3x^2 \exp(-x^3)$ and the I.C. is zero.

In the initial stage of coagulation of a monodispersed suspension the coagulation frequency is essentially size independent. It has been suggested that ω_0 is a good approximation to ω if the Knudsen numbers ($Kn = 2\lambda/d$) of both coagulating particles are less than 0.1 even for the case of polydispersed suspension. On the other hand, for turbulent diffusion particle coagulation, ω can be approximated by $\omega = \omega_0(v + v')$. These are obviously the only two physically realistic kernels for which analytical solutions of the Smoluchowski equation were derived.

Figure (1, Left) shows the CDA solution as compared to the analytical one (Hounslow, 1990) for constant particle coagulation in a CST (Continuous Stirred Tank) with residence time $\tau = 4$ (dimensionless). Using only 30 subdomains (evolved on a geometric grid) and using AdamsBDF (Adams method with backward differentiation formulas) as an ODE solver, the system of ODEs (Eq.(1)) were integrated from zero initial condition until steady state. As can be seen from this figure, the numerical solution is very accurate with a very high precision reproduction of the first and third moments of the particle size distribution, thanks to the auxiliary functions ($\alpha_{k,j}$, $\eta_{k,j}$).

This convergence of the CDA was tested for both CST and BST as shown in Figure (1, Right) using uniform grids ($d_{\min} = 0$ and $d_{\max} = 4$) and the RMSE (Root Mean Squared Error) based on the difference between the CDA and the analytical solutions using the same discrete predefined grid points where a 10-point grid solution results in less than 0.1 RMSE and still conserves total volume and number concentrations. It is clear that the convergence of the CDA is in the $O(1/M)$ for both cases. When the geometric grid was used ($d_{\min} = 0$ and $d_{\max} = 4$), the CDA is more accurate than that of the uniform grid with even faster rate of convergence. This increased accuracy is expected since the geometric grid results in new born particles with volumes that are

very close to the representative volumes in each subdomain. This hypothesis is elucidated by careful examination of the $\chi_{k,j}$ elements which were very close to unity.

3.2. Batch Crystallizer: Coupled size dependent growth and coagulation

In this section, particle growth and coagulation in a batch stirred tank (BST) is used as a simplified model for a batch crystallizer where the particle size distribution (PSD) depends on time and particle size. In a batch crystallizer, the initial seeds used are carried by the evolution of the PSD and becomes part of it.

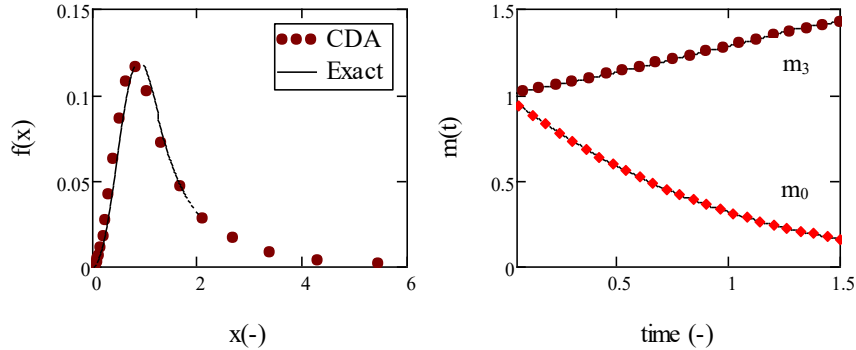


Figure (2): (Left). Solution of Smoluchowski equation with sum kernel particle aggregation and linear particle growth in BST using the CDA. (Right). Prediction of the zero and third moments of PSD using CDA. $d_{min} = 0.005$, $d_{max} = 6$, $\tau = 1.5$, $M = 30$, initial condition $f(x) = 3x^2 \exp(-x^3)$.

The growth rate of crystals $g(x)$ expresses the rate of change of particle volume due to deposition of material on the particle surface. When the Knudsen number ($Kn = 2\lambda/d$) is less than 0.1, the rate of deposition is predicted by the classical continuum diffusion theory (Hidy and Brock, 1970). In this regime the growth rate is given by $g(x) = (1/3)g_0\alpha^\gamma$ where $\gamma = 3$. The rate determining step for deposition, based on this growth rate, is the chemical reaction that takes place throughout the volume of the particle. In this case study, we confined our attention to the case when $\gamma = 1$ where the growth is linearly proportional to particle diameter. By combining linear particle growth and sum kernel ($\omega = \omega_0(v + v')$) particle coagulation, which is induced by turbulent diffusion, one can use the analytical solution of Ramabhadran et al. (1976). This analytical solution is challenging and is complicated by the product of exponential function and modified Bessel function of the first kind. The exponential part is a manifestation of the exponential initial condition ($f(x) = 3x^2 \exp(-x^3)$). Figure (2, Left) shows the predicted PSD using our CDA with 30 subdomains using a geometric grid w.r.t. particle diameter where $\Lambda = g_0/\omega_0 = 0.25$ and $\tau = 1.5$. This means that the dominant mechanism in this example is particle coagulation. This results in a reduction of particle number concentration with little volume growth as shown in Figure (2, Right). In this figure, not only the PSD was accurately predicted, but also the total number and volume concentrations. The conservation of the zero and third moments of the source term is not affected by the number of grid points, but by the discrete form of the initial condition or the inlet feed distribution. This shows the advantage of the CDA when compared to other discrete methods which require very fine grids. The computational time of the CDA is less than that of the fixed-pivot technique which support our previous CPU time analysis for the case of particle breakage (Attarakih et al, 2004).

4. Summary and Conclusions

The numerical analyses of the present CDA show two desirable properties: Firstly, the simplicity of the source term structure (composed of simple summations) which can be easily programmed thanks to the explicit form of the two auxiliary functions and the interaction matrix in which the footprint of the successful coagulation events is saved. Secondly, the two selected conserved integral quantities (e.g total number and volume concentrations) are exactly conserved irrespective of the number of discrete equations. This presents a major advantage over the existing consistent discrete methods (e.g. Fixed-pivot technique). Accordingly, the reconstructed number concentration function converges to the exact solution with exponential decay in terms of the RMSE as function of grid points. As a final conclusion, the CDA is a general discrete formulation framework not only for the Smoluchowski coagulation equation, but also for other deterministic integral equations including simultaneous particle breakage, growth and nucleation in batch and continuous particulate systems and can be easily extended to bivariate population balances.

References

- M. Attarakih and H.-J. Bart, 2014, Solution of the population balance equation using the differential maximum entropy method (DMaxEntM): An application to liquid extraction columns. *Chem. Eng. Sci.*, 108, 123-133.
- M. Attarakih, H. B. Jildeh, M. Mickler and H. J. Bart, 2012, The OPOSPM as a nonlinear autocorrelation population balance model for dynamic simulation of liquid extraction columns. *Comp. Aided Chem. Eng.*, 31, 1216-1220.
- M. Attarakih, C. Drumm and H.-J. Bart, 2009, Solution of the population balance equation using the sectional quadrature method of moments (SQMOM). *Chem. Eng. Sci.*, 64, 742--752.
- M. Attarakih, H.-J. Bart and N. M. Faqir, 2004, Solution of the droplet breakage equation for interacting liquid-liquid dispersions: A conservative discretization approach. *Chemical Engineering Science*, 12, 2547-2565.
- G. S. Ferreira, P.L. Lage and L. F. L. R. Silva, 2017, Extension and convergence analysis of the univariate direct quadrature spanning tree method. *Powder Tech.*, 322, 301-313.
- C. Foley and M. C. Mackey, 2009, Dynamic hematological disease: A review. *J. Math. Biol.*, 58, 285-322.
- G. M. Hidy, 1965, On the theory of the coagulation of noninteracting particles in brownian motion. *J. Coll. Sci.*, 20, 123-144.
- G. M. Hidy and J. R. Brock, 1970, *The Dynamics of Aerocolloidal Systems*, Pergamon Press, Oxford, England.
- M. J. Hounslow, 1990, A discretized population balance for continuous systems at steady state. *AIChE J.*, 36, 106-116.
- T. E. Ramabhadran, T. W. Peterson and J. H. Seinfeld (1976). Dynamics of aerosol coagulation and condensation. *AIChE Journal*, 22, 840-851.
- D. Ramkrishna and M. R. Singh, 2014, Population Balance Modeling: Current Status and Future Prospects, *Annu. Rev. Chem. Biomol. Eng.*, 5, 123-146.
- A. Vie, F. Laurent and M. Massot, 2013, Size-velocity correlations in hybrid high order moment/multi-fluid methods for polydisperse evaporating sprays: Modeling and numerical issues. *J. Comp. Phys.*, 237, 177-210.

Multi-product reactive distillation process for higher acrylates production

Mihai Daniel Moraru,^{a,b,*} Anton Alexandru Kiss,^{c,d} Costin Sorin Bildea^b

^a*Department of Process Technology and Development, Hexion, Seattleweg 17, 3195 ND Pernis, The Netherlands*

^b*Department of Chemical and Biochemical Engineering, University Politehnica of Bucharest, Str. Gh. Polizu 1-7, 011061 Bucharest, Romania*

^c*School of Chemical Engineering and Analytical Science, The University of Manchester, Sackville Street, Manchester M13 9PL, United Kingdom*

^d*Sustainable Process Technology Group, Faculty of Science and Technology, University of Twente, PO Box 217, 7500 AE Enschede, The Netherlands*

mihai.moraru@hexion.com

Abstract

Higher acrylates are used in special applications. However, production at high capacity in continuous reactive distillation (RD) systems, throughout the whole year of only one acrylate, may be hindered by a low market and periodic demands. Thus, for the asset to be fully utilized, one may consider to build a multi-product reactive distillation system. This is a preliminary study that shows what four higher acrylates (i.e., isoamyl acrylate, cyclohexyl acrylate, 2-ethylhexyl acrylate and *n*-decyl acrylate) have in common to be considered candidates for producing them in the same column, and the methodology to design such a multi-product RD column. The systemic design method uses PSE tools to achieve the design, based solely on thermodynamics and equilibrium information.

Keywords: conceptual design, higher alcohols, process intensification, simulation

1. Introduction

Acrylates are essential chemicals used as precursors in the production of polyacrylates which are employed in a range of industries (e.g. packaging, consumer goods, and construction, automotive) and a variety of applications (e.g. coatings, paints, resins, adhesives, textiles, personal care). Acrylates with a high number of carbon atoms are more preferred in special applications. Reports state that the acrylate market was valued at B\$ 6.86 in 2016, aiming to reach B\$ 9.88 in 2022 (www.marketsandmarkets.com).

Conventional processes using strong homogeneous catalysts (i.e., acid sulfuric) are only briefly presented in the open literature (Ohara et al., 2003). A few new conceptual processes using solid-based catalysts for the synthesis of some higher-acrylates and methacrylates have been also developed, showing a high potential in overcoming the well-known drawbacks of conventional processes: corrosion, product purification, and disposal of spent catalyst, which usually lead to high operating and maintenance costs, and increasing difficulty to comply with environmental regulations (Kiss et al., 2015).

This work considers a generic perspective, by investigating the technical feasibility of producing four industrially important higher-acrylates by esterification employing the

same reactive distillation (RD) process using solid catalysts. The pure component properties are estimated using group contribution methods (due to lack of experimental data in literature), followed by studying key thermodynamic properties relevant for process design. Chemical equilibrium is determined by minimizing the Gibbs energy of the system to indicate the maximum conversion possible. A preliminary RD column design is proposed using an equilibrium model. An additional separation step may be required for the recovery of one reactant (alcohol) while the limiting reactant (acrylic acid) has a conversion close to 100%. The design can be refined later, by including the reaction rate, when kinetics data is available in literature.

2. Higher acrylates and key physical properties

A higher acrylate is produced in the reaction of acrylic acid (AA) with an alcohol which has a number of carbon atoms higher than 4, following the chemical reaction:

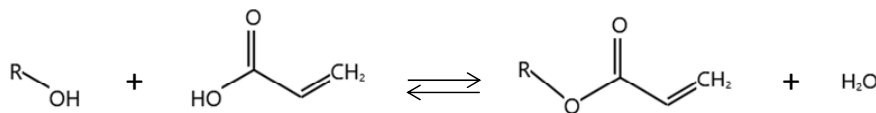
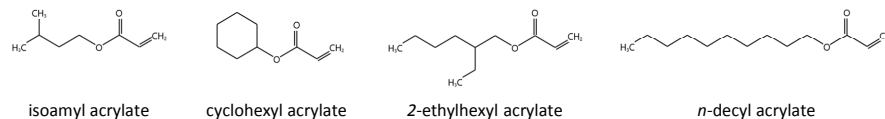


Table 1 presents some basic properties for the four acrylates presented in this study. Two of the acrylates (*i*-AA and 2-EHA) present some branching, one of them (CHA) has a cyclohexane ring, while the remaining (*n*-DA) is a linear acrylate. All have a relatively high molecular weight and normal boiling point.

Table 1. Basic physical properties of some high acrylates

Acrylate [†]	MW [g/mol]	<i>T</i> _b [°C]	DHFORM [‡] [kJ/mol]	DGFORM [‡] [kJ/mol]
isoamyl acrylate (<i>i</i> -AA)	142.2	163.8	-398.82	-208.49
cyclohexyl acrylate (CHA)	154.2	206.6	-382.42	-173.18
2-ethylhexyl acrylate (2-EHA)	184.3	232.4	-458.61	-183.23
<i>n</i> -decyl acrylate (<i>n</i> -DA)	212.3	278.6	-488.18	-163.95

[†]chemical structures:



[‡]DHFORM and DGFORM are the ideal gas enthalpy and energy of formation (25 °C) estimated using the Property Constant Estimation System (PCES) of Aspen Properties.

All these acrylate systems have in common important characteristics that make them candidates to be produced in the same reactive distillation system:

- From the view point of process structure, each acrylate is the highest boiler in its system and is obtained as bottom products (note that water is the lowest boiler component). In addition, all acrylate systems present heterogeneous minimum boiling azeotropes containing water in high concentration (Table 2), making thus possible to eliminate the water in the same way, in the overhead of the column: the vapors are condensed; the condensate undergoes a liquid-liquid split; the organic phase is refluxed to the column, while the water is removed from the process.

- From a mass balance perspective, similar acrylate systems catalyzed by solid catalysts present very similar space-time-yields ($t_{\text{product}}/t_{\text{cat}}/h$): 0.65 for isobutyl acrylate (Moraru et al., 2018), 1.28 for *n*-butyl acrylate (Moraru and Bildea, 2017) and 1.57 for 2-ethylhexyl acrylate (Moraru and Bildea, 2018).
- From a heat balance perspective, all reactions are slightly endothermic, having similar reaction enthalpy (Table 2). Hence, these three main factors are good indicators that the higher acrylates can be produced in the same RD column.

Table 2. Azeotropy and reaction enthalpies of the four acrylate systems

Physical property	<i>i</i> -AA	CHA	2-EHA	<i>n</i> -DA
Azeotrope comp. / [% wt.]				
water/alcohol	50.21/49.79	70.18/29.82	80.87/19.13	96.15/3.85
water/acrylate	53.58/46.42	79.34/20.66	89.45/10.55	97.45/2.55
water/alcohol/acrylate	48.36/43.17/8.47			96.43/3.55/0.02
Enthalpy of reaction (liquid phase, 25 °C) / [kJ/mol]	15.9	16.4	27.0	35.2

3. Chemical equilibrium

Slightly endothermic / exothermic equilibrium esterification reactions are known as perfect candidates to be performed in RD systems (Kiss, 2018). As the equilibrium is shifted towards the products formation by removing water, very high or even complete per-pass conversions can be achieved. Hence, studying the chemical equilibrium gives basic info which is used in the conceptual design of the RD system. Figure 1 shows the equilibrium conversion of AA as function of temperature for several acrylate systems.

Firstly, take the *n*-butyl acrylate (*n*-BA) system. The *n*-BA (*Lit*) profiles, triangles and circles, represent calculated data using two equations taken from published literature, which were in turn derived from experimental data (see the right-lower corner). The *n*-BA (*Aspen Database*) profile is obtained by calculating K_{eq} from Gibbs free energies, for which parameters (for *n*-BA) are available in the Aspen database; although for the low temperatures the agreement is not perfect, it improves for the temperature range of practical interest (over 60 °C) where the reaction rates are higher.

Secondly, consider the 2-EHA system. The 2-EHA (*Lit*) profile uses an equation based on experimental data (see the right-lower corner). The 2-EHA (*PCES*) is obtained by calculating K_{eq} from Gibbs free energies, for which the necessary parameters (for 2-EHA) are estimated using the PCES of Aspen Properties. In this case, the agreement is very good. Thus, one may conclude that the accuracy of the predictive thermodynamic models based on group contributions is reasonable.

For the other three acrylates (*i*-AA, CHA and *n*-DA), the parameters to calculate K_{eq} are estimated by PCES. All reactions are slightly endothermic. Analyses based on experimental data are preferred, but when neither equilibrium data nor the required parameters in the Aspen database are available, then one must rely on group contribution methods to estimate the missing parameters. Results presented in Figure 1 also demonstrate that reasonable conversions can be obtained for all the alcohols considered here. However, the chemical equilibrium sets an upper bound on the achievable conversion. This can be overcome by removing one reactant (water) from the reaction mixture due to formation of the low-boiling azeotrope, and/or by performing the reaction with an excess of one reactant, achieved by refluxing the alcohol-rich organic phase from the top decanter.

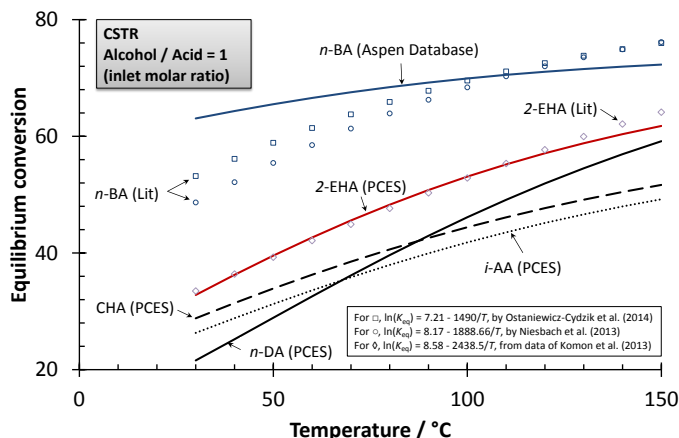


Figure 1. Equilibrium conversion for acrylic acid esterification with different alcohols, for an alcohol / acid feed molar ratio of 1.

4. Conceptual process design

For the acrylates to be all produced in the same equipment, the design has to take into account those conditions, specific to each acrylate, in which the RD is feasible. These conditions are represented here by the shaded area of the P - T diagram showed in Figure 2 (left). The diagram is constructed using four distinct P - T areas, one for each acrylate. For illustration purposes, the right-lower corner shows how this feasibility area is constructed for 2-EHA, using the vapor pressure of the highest (acrylate) and lowest (water/alcohol azeotrope) boilers in this specific system. The area covering all acrylates spans over a large range of conditions: 60–190 °C and 0.1–6 bar. The temperature bounds come from the interval in which the reaction can be performed: the minimum temperature at which the reaction rate becomes fast enough and the maximum temperature the catalyst can withstand. The maximum pressure (about 6 bar) is given by the boiling temperature of most volatile acrylate (i.e. *i*-AA), which should be achieved by using HP steam (240 °C). The minimum pressure constraint (0.1 bar) arrives from the need of using cooling water for condensing the low boiling water-alcohol azeotropes.

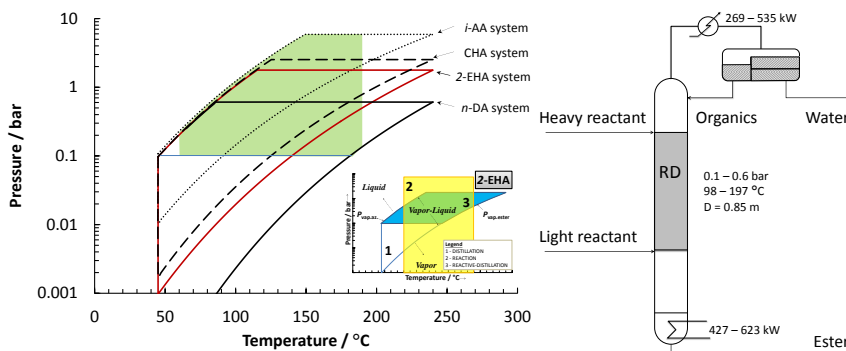


Figure 2. Pressure-Temperature conditions considered in design of the reactive distillation system (left) and reactive distillation column including the main sizes and process data (right)

Based on this feasibility window, one can conclude that it will be difficult to design a column that operates at constant pressure and similar temperature intervals, and produces all four acrylates; basically, to operate in that region where the individual feasibility windows overlap. One approach is to set the column pressure depending on the acrylate produced, and verify that the operating temperature in the column is not higher compared to the temperature the catalyst can withstand. Of course, the temperature should not be too low either. Previous studies for higher acrylates produced in reactive distillation systems (Niesbach et al., 2013) showed that above 100 °C, the reaction rate is high enough to be industrially attractive.

5. Column design

The design of the RD column that is able to produce all acrylates consists of two steps:

1. For each acrylate, design one RD column (i.e., theoretical stages and diameter) that meets certain specifications.
2. For all acrylates, select the RD column with the highest number of theoretical stages determined in the previous step, average the diameter of all columns and rate all acrylate processes in this specific column.

Each acrylate-specific design aimed to have the same production rate, and obtain a product with a purity of at least 99.5 %wt. This design step is iterative, and starts by selecting a top-pressure in the column, followed by the number of trays in each section, and for hydrodynamic reasons, a minimum reflux ratio. Then, the number of stages in each zone was varied and aimed at reducing them until the product purity cannot be achieved anymore. If the pressure can be further reduced (but still being able to use cooling water in the condenser), then a new iteration starts; if not, then the design stops and all variables of interest are recorded. Table 3 presents the results of step 1. Based on these results, in step 2 the number of stages specific to *i*-AA column are considered (i.e., the tallest column) and the diameter is calculated by averaging the column diameters. Then, each acrylate process is rated in this specific column.

The results of step 2 are given in Table 4. Start with the *i*-AA process; since the column diameter is with 0.1 m larger, the reflux had to be increased from 4 to 5.5 (again, from hydrodynamic reasons); no further modifications are required. For the CHA process, only the number of stages is updated; the hydrodynamics presents no issues since the column diameter is only 0.05 m larger; the same holds for the 2-EHA process. For the *n*-DA process, the production capacity is reduced to cope with the decrease in diameter from 0.98 to 0.85 m.

Table 3. Key design and operating parameters for each acrylate produced in individual columns

Parameter	<i>i</i> -AA	CHA	2-EHA	<i>n</i> -DA
$N_R N_{RXN} N_S$	1 4 4	1 3 2	1 3 2	1 4 2
$D_{column} / [m]$	0.74	0.80	0.85	0.98
$F_{acrylate} F_{water} / [kg/h]$	2524 330	2525 305	2535 247	2526 215
Reflux / [kg/h]	1322	1225	990	860
Purity acrylate water / [% wt.]	99.5 96.3	99.5 96.3	99.5 99.6	99.9 99.6
$Q_R Q_C / [kW]$	519 508	546 465	486 340	503 320
$P_{top} P_{bottom} / [bar]$	0.6 0.609	0.3 0.306	0.2 0.203	0.1 0.104
$T_{top} T_{bottom} / [^{\circ}C]$	96 146	99 161	110 172	129 193

Table 4. Key design and operating parameters for each acrylate produced in the same column

Parameter	<i>i</i> -AA	CHA	2-EHA	<i>n</i> -DA
$N_R N_{RXN} N_S$			1 4 4	
$D_{column} / [m]$			0.85	
$F_{acrylate} F_{water} / [kg/h]$	2524 330	2539 306	2537 247	2123 181
Reflux / [kg/h]	1814	1224	988	722
Purity acrylate water / [% wt.]	99.5 96.4	99.5 96.4	99.5 99.9	100 99.7
$Q_R Q_C / [kW]$	623 535	553 471	488 341	427 269
$P_{top} P_{bottom} / [bar]$	0.6 0.606	0.3 0.305	0.2 0.207	0.1 0.115
$T_{top} T_{bottom} / [^{\circ}C]$	99 145	98 161	109 173	129 197

6. Conclusions

Using a PSE methodology based on physical properties and chemical equilibrium data (estimated or reported in the literature), this study shows that higher acrylates are good candidates to be produced in the same reactive distillation column. A follow-up study should reiterate this design based on reaction kinetics and mass transfer considerations.

Acknowledgements

CSB kindly acknowledges the financial support of the European Commission through the European Regional Development Fund and of the Romanian state budget, under the grant agreement 155/25.11.2016 Project POC P-37-449 (ASPiRE). AAK is thankful for the Royal Society Wolfson Research Merit Award.

References

- A. A. Kiss, A. J. B. ten Kate, E. Conte, 2015, Continuous process for the esterification of an alpha, beta-unsaturated carboxylic acid and an alcohol, Patent No. WO/2015/018773.
- A. A. Kiss, 2018, Novel catalytic reactive distillation processes for a sustainable chemical industry, *Top. Catal.*, DOI: 10.1007/s11244-018-1.
- T. Komon, P. Niewiadomski, P. Oracz, M. E. Jamroz, 2013, Esterification of acrylic acid with 2-ethylhexan-1-ol: Thermodynamic and kinetic study. *Appl. Catal.*, A. 451, 127-136.
- M. D. Moraru, D. A. Berinde, C. S. Bildea, 2018, Design, control and economics of a process for isobutyl acrylate production. *Comput. Aided Chem. Eng.* 43, 711-716.
- M. D. Moraru, C. S. Bildea, 2017, Process for n-butyl acrylate production using reactive distillation: Design, control and economic evaluation. *Chem. Eng. Res. Des.* 125, 130-145.
- M. D. Moraru, C. S. Bildea, 2018, Reaction-separation-recycle processes for 2-ethylhexyl acrylate production: Design, control, and economic evaluation, *Ind. Eng. Chem. Res.* 57, 2609-2627.
- A. Niesbach, H. Kuhlmann, T. Keller, P. Lutze, A. Gorak, 2013, Optimisation of industrial-scale n-butyl acrylate production using reactive distillation. *Chem. Eng. Sci.* 100, 360-372.
- T. Ohara, T. Sato, N. Shimizu, G. Prescher, H. Schwind, O. Weiberg, K. Marten, H. Greim, 2003. Acrylic acid and derivatives, in: *Ullmann's Encyclopedia of Industrial Chemistry*.
- A.M. Ostaniewicz-Cydzik, C.S.M. Pereira, E. Molga, A.E. Rodrigues, 2014, Reaction Kinetics and Thermodynamic Equilibrium for Butyl Acrylate Synthesis from n-Butanol and Acrylic Acid. *Ind. Eng. Chem. Res.* 53, (16), 6647-6654.

Stochastic nonlinear model predictive control of a batch fermentation process

Eric Bradford^{a*} and Lars Imsland^a

^a*Engineering Cybernetics; NTNU; O. S. Bragstads plass 2D, Trondheim 7034, Norway*
eric.bradford@ntnu.no

Abstract

Nonlinear model predictive control (NMPC) is an attractive control approach to regulate batch processes reliant on an accurate dynamic model. Most dynamic models however are affected by significant uncertainties, which may lead to worse control performance and infeasibilities, considering the tendency of NMPC to drive the system to its constraints. This paper proposes a novel NMPC framework to mitigate this issue by explicitly taking into account time-invariant stochastic uncertainties. Parametric uncertainties are assumed to be given by so-called polynomial chaos expansions (PCE), which constitutes a flexible approach to depict arbitrary probability distributions. It is assumed that at each sampling time only noisy output measurements are available. The proposed procedure uses a sparse Gauss-Hermite sampling rule to formulate an efficient scenario-based NMPC algorithm based on the PCE, while a stochastic nonlinear filter is employed to update the PCE given the available measurements. The framework is shown to be effective on a challenging semi-batch fermentation process simulation case study.

Keywords: Chemical process control, Polynomial chaos, Nonlinear filters, Model-based control

1. Introduction

Batch processes are commonly used in many chemical sectors, including pharmaceuticals, bulk chemicals and biotechnology. Batch processes are operated at unsteady state and are highly nonlinear, which motivates the use of nonlinear model predictive control (NMPC). The performance of the NMPC algorithm depends strongly on the accuracy of the dynamic model used and inherent uncertainties may lead to constraint violations and worse control actions. If we assume these uncertainties to be given by known probability distributions, stochastic NMPC (SNMPC) methods can be used (Mesbah, 2016). The main difficulty in SNMPC lies in propagating stochastic uncertainties through nonlinear system models. Several SNMPC algorithms have been proposed using different methods to propagate stochastic uncertainties:

- Unscented transformation sampling (Bradford and Imsland, 2018a)
- Polynomial chaos expansions (Fagiano and Khammash, 2012)
- Markov Chain Monte Carlo (Maciejowski et al., 2007)
- Gaussian processes (Bradford and Imsland, 2018b)
- Quasi Monte Carlo methods (Bradford and Imsland, 2017)
- Particle filters (Sehr and Bitmead, 2017)

Most work in SNMPC assumes full state feedback, which is uncommon for real processes. Instead, the measurements made at each sampling time are both noisy and incomplete. In this paper we therefore propose to use a nonlinear filter to update the stochastic uncertainties at each sampling time. The uncertainties are represented by so-called polynomial chaos expansions (PCE), which allow for complex probability distributions to be given by polynomials of simpler stochastic variables. In addition, we suggest to efficiently formulate the SNMPC problem using a sparse Gauss-Hermite quadrature rule. The framework is verified on a fermentation case study.

2. Problem formulation

We aim to control a discrete-time nonlinear equation system with stochastic uncertainties:

$$\mathbf{x}(t+1) = \mathbf{f}(\mathbf{x}(t), \mathbf{u}(t), \boldsymbol{\theta}(\boldsymbol{\xi})), \quad \mathbf{x}(0) = \mathbf{x}_0(\boldsymbol{\theta}(\boldsymbol{\xi})) \quad (1)$$

$$\mathbf{y}(t) = \mathbf{h}(\mathbf{x}(t), \boldsymbol{\theta}(\boldsymbol{\xi})) + \mathbf{v} \quad (2)$$

where k is the discrete time, $\mathbf{x} \in \mathbb{R}^{n_x}$ are the system states, $\mathbf{u} \in \mathbb{R}^{n_u}$ denote the control inputs, $\boldsymbol{\theta}(\boldsymbol{\xi}) \in \mathbb{R}^{n_\theta}$ are time-invariant uncertainties, $\boldsymbol{\xi} \in \mathbb{R}^{n_\xi} \sim \mathcal{N}(\mathbf{0}, \mathbf{I})$ describe standard normally distributed random variables parametrizing the PCE of $\boldsymbol{\theta}$, $\mathbf{f}: \mathbb{R}^{n_x} \times \mathbb{R}^{n_u} \times \mathbb{R}^{n_\theta} \rightarrow \mathbb{R}^{n_x}$ represents the nonlinear dynamic system, $\mathbf{y} \in \mathbb{R}^{n_y}$ denote the measurements, $\mathbf{h}: \mathbb{R}^{n_x} \times \mathbb{R}^{n_\theta}$ are the output equations and $\mathbf{v} \in \mathbb{R}^{n_y} \sim \mathcal{N}(\mathbf{0}, \boldsymbol{\Sigma}_v)$ is the measurement noise assumed to be zero mean multivariate normally distributed with known covariance matrix $\boldsymbol{\Sigma}_v$. The initial condition $\mathbf{x}(0)$ may also be uncertain and hence is a function of $\boldsymbol{\theta}(\boldsymbol{\xi})$.

The time-invariant uncertainty described by $\boldsymbol{\theta}$ are assumed to be given by a known truncated PCE:

$$\theta_i(\boldsymbol{\xi}) = \sum_{0 \leq |\boldsymbol{\alpha}| \leq m} a_j^{(i)} \phi_{\boldsymbol{\alpha}_j}(\boldsymbol{\xi}) = \mathbf{a}_i^T \boldsymbol{\Phi}(\boldsymbol{\xi}) \quad (3)$$

where each component $\theta_i(\boldsymbol{\xi})$ is given by an individual polynomial series with multivariate polynomials $\phi_{\boldsymbol{\alpha}_j}(\boldsymbol{\xi})$ with coefficients $a_j^{(i)}$. We summarise the coefficients as $\mathbf{A} = [\mathbf{a}_1, \dots, \mathbf{a}_{n_\theta}]$. The multivariate polynomials are given by products of univariate polynomials $\phi_{\boldsymbol{\alpha}_j} = \prod_{i=1}^{n_\xi} \phi_{\alpha_{j_i}}(\xi_i)$ with $\phi_{\alpha_{j_i}}(\xi_i)$ being univariate polynomials of ξ_i of degree α_{j_i} . The vector $\boldsymbol{\Phi}(\cdot) = [\phi_1(\cdot), \dots, \phi_L(\cdot)]^T$ contains the multivariate polynomials of the expansions, m denotes the order of truncation and $|\boldsymbol{\alpha}| = \sum_{i=1}^{n_\xi} \alpha_i$. Each polynomial series consists of $L = \frac{(n_\xi + m)!}{n_\xi! m!}$ terms and $\mathbf{a}_i \in \mathbb{R}^L$ represents a vector of coefficients of these terms. The univariate polynomials are given by Hermite polynomials:

$$\phi_j(\xi_i) = (-1)^j \exp\left(\frac{1}{2}\xi_i^2\right) \frac{d^j}{d\xi_i^j} \exp\left(-\frac{1}{2}\xi_i^2\right) \quad (4)$$

3. Gauss-Hermite nonlinear model predictive control

Once the uncertainties are defined as PCE as shown in section 2, we aim to exploit this information together with the dynamic equation system in Eq.(1) to formulate an optimal control problem (OCP) to be solved iteratively. To achieve this we use Gauss-Hermite quadrature rules to create several realizations of $\boldsymbol{\theta}$ from its PCE representation to formulate a scenario-based MPC problem. The Gauss-Hermite quadrature rules can be seen to give an approximation to the integral:

$$\mathbb{E}[f(\boldsymbol{\xi})] = \int_{-\infty}^{\infty} f(\boldsymbol{\xi}) p(\boldsymbol{\xi}) d\boldsymbol{\xi}, \quad p(\boldsymbol{\xi}) = \prod_i \exp(-\xi_i^2) / \sqrt{\pi} \quad (5)$$

where $\boldsymbol{\xi}$ is a standard normally distributed random variable and $\mathbb{E}[\cdot]$ is the expectation operator.

The Gauss-Hermite quadrature rules accomplish this by creating deterministic samples of $\boldsymbol{\xi}$ with corresponding weights. The approximations of expectation and variances of a function $f(\boldsymbol{\xi})$ are:

$$\mu_f = \mathbb{E}[f(\boldsymbol{\xi})] \approx \sum_{q=1}^{N_q} w_q f(\boldsymbol{\xi}_q), \quad \sigma_f^2 = \mathbb{E}\left[(f(\boldsymbol{\xi}) - \mu_f)^2\right] \approx \sum_{q=1}^{N_q} w_q (f(\boldsymbol{\xi}_q) - \mu_f)^2 \quad (6)$$

where $\boldsymbol{\xi}_q$ and w_q are given by the quadrature rule with overall N_q points. The Gauss-Hermite rule used in this work was taken from Jia et al. (2012), which is a sparse Gauss-Hermite quadrature rule. These require less samples than the full Gauss-Hermite rules for the same order of accuracy.

Using Chebyshev's inequality probability constraints can be robustly reformulated involving only the mean and variance of the random variable. Let γ be a generic random variable, then

$$\mathbb{P}(\gamma \leq 0) \geq 1 - \varepsilon \implies \kappa_\varepsilon \sigma_\gamma + \hat{\gamma} \leq 0, \quad \kappa_\varepsilon = \sqrt{(1 - \varepsilon)/\varepsilon} \quad (7)$$

where $\varepsilon \in (0, 1) \subset \mathbb{R}$ is the probability that γ exceeds 0, $\hat{\gamma}$ and σ_γ^2 are the mean and variance of γ respectively.

The optimal control problem to be solved can subsequently be stated as follows using the Gauss-Hermite quadrature rule with N_q points, the dynamic system in Eq.(1), the PCE representation of $\theta(\cdot)$ and the initial condition at time t given as a function of $\theta(\cdot)$ as $\mathbf{x}_t(\theta(\cdot))$:

$$\begin{aligned} & \underset{\mathbf{U}}{\text{minimize}} && \sum_{q=1}^{N_q} w_q J(\mathbf{x}^{(q)}(0), \mathbf{U}, \xi_q) \\ & \text{subject to} && \mathbf{x}^{(q)}(k+1) = \mathbf{f}(\mathbf{x}^{(q)}(k), \mathbf{u}(k), \theta(\xi_q)) && \forall (k, q) \in \mathbb{N}_k \times \mathbb{N}_q \\ & && \mu_{g_{jk}} + \kappa_\varepsilon \sigma_{g_{jk}} \leq 0, \quad \kappa_\varepsilon = \sqrt{(1 - \varepsilon)/\varepsilon} && \forall (j, k) \in \mathbb{N}_g^{(k)} \times \mathbb{N}_{k+1} \\ & && \mu_{g_{jk}} = \sum_{q=1}^{N_q} w_q g_j^{(k)}(\mathbf{x}^{(q)}(k), \theta(\xi_q)) && \forall (j, k) \in \mathbb{N}_g^{(k)} \times \mathbb{N}_{k+1} \\ & && \sigma_{g_{jk}} = \sum_{q=1}^{N_q} w_q \left(g_j^{(k)}(\mathbf{x}^{(q)}(k), \theta(\xi_q)) - \mu_{g_{jk}} \right)^2 && \forall (j, k) \in \mathbb{N}_g^{(k)} \times \mathbb{N}_{k+1} \\ & && \mathbf{u}(k) \in \mathbb{U} && \forall k \in \mathbb{N}_k \\ & && \mathbf{x}^{(q)}(0) = \mathbf{x}_t(\theta(\xi_q)) && \forall q \in \mathbb{N}_q \end{aligned} \quad (8)$$

where $\mathbb{N}_k = \{0, \dots, N-1\}$, $\mathbb{N}_{k+1} = \{1, \dots, N\}$, $\mathbb{N}_g = \{1, \dots, n_g^{(k)}\}$, $\mathbb{N}_q = \{1, \dots, N_q\}$, N is the time horizon, $\mathbf{U} = \{\mathbf{u}(0), \dots, \mathbf{u}(N-1)\}$, the objective is given by the expectation of a nonlinear function $J(\mathbf{x}_q(0), \mathbf{U}, \xi_q)$ approximated by the Gauss-Hermite rule, \mathbb{U} represents the constraints on $\mathbf{u}(k)$ and $\mathbf{x}^{(q)}$ represents the state vector for each sampling point q . The chance constraints are approximated by Chebyshev's inequality given in Eq.(7) as nonlinear functions $g_j^{(k)}(\mathbf{x}^{(q)}(k), \theta(\xi_q))$ constrained robustly to be less than 0 with a probability of ε .

4. Polynomial chaos expansion filter

The PCE filter updates θ given the noisy measurements available from Eq.(2) and was first proposed in Madankan et al. (2013). It has further been applied for linear stochastic MPC in Mühlfordt et al. (2016). Let $D_t = \{\mathbf{y}(1), \dots, \mathbf{y}(t)\}$ be the measurements collected up to time t . Bayes's rule can be employed to update θ recursively using the previous PCE of θ :

$$p(\theta|D_t) = \frac{p(\mathbf{y}(t)|\theta)p(\theta|D_{t-1})}{p(\mathbf{y}(t)|D_{t-1})} \quad (9)$$

where $p(\theta|D_{t-1})$ is the prior distribution of θ given observations up to time $t-1$, $p(\mathbf{y}(t)|\theta)$ is the likelihood $\mathbf{y}(t)$ is observed given θ at time t . We defined $p(\mathbf{y}(t)|\theta) = \mathcal{N}(\mathbf{h}(\mathbf{x}(t), \theta), \Sigma_v)$ as standard normal distribution in Eq.(2) with mean $\mathbf{h}(\mathbf{x}(t), \theta)$ and covariance Σ_v .

If we take both sides of Eq.(9) times $\prod_{j=1}^{n_\theta} \theta_j^{r_j}$ and integrate over both sides we obtain:

$$M_{\mathbf{r}}^+ = \frac{\int \prod_{j=1}^{n_\theta} \theta_j^{r_j} p(\mathbf{y}(t)|\theta)p(\theta|D_{t-1})d\theta}{p(\mathbf{y}(t)|D_{t-1})} \quad (10)$$

where $M_{\mathbf{r}}^+ = \int \prod_{j=1}^{n_\theta} \theta_j^{r_j} p(\theta|D_t)d\theta$ and let $k = \sum_{j=1}^{n_\theta} r_j$. Now $M_{\mathbf{r}}^+$ refers to the various k -th order moments with respect to the updated distribution of θ , $p(\theta|D_t)$.

In our case the distribution of $\theta(\xi)$ depends on its PCE coefficients \mathbf{A} and hence these need to be updated, see Eq.(3). We can approximate the distribution of $p(\theta(\xi)|D_{t-1})$ using sampling, since it is assumed that ξ follows a standard normal distribution. Let $\theta_t(\xi)$ denote the PCE of θ at time t with coefficients \mathbf{A}_t . Applying a sample estimate to Eq.(10) with a sample design of size N_s given by $\{\xi_1, \dots, \xi_{N_s}\}$, where $\xi_i \sim \mathcal{N}(\mathbf{0}, \mathbf{I})$ we obtain the following:

$$M_{\mathbf{r}}^{(s)+} = \frac{1}{\alpha N_s} \sum_{i=1}^{N_s} \prod_{j=1}^{n_{\theta}} (\theta_{t-1}(\xi_i))_j^{r_j} p(\mathbf{y}(t)|\theta_{t-1}(\xi_i)) \quad (11)$$

where $M_{\mathbf{r}}^{(s)+}$ is the sample approximation of the RHS of Eq.(10) of the posterior moments and $\alpha = \frac{1}{N_s} \sum_{i=1}^{N_s} p(\mathbf{y}(t)|\theta(\xi_i))$. The sample design was created using Latin hypercube sampling and the inverse transform of the standard normal distribution.

To update the coefficients \mathbf{A}_{t-1} of θ_{t-1} to \mathbf{A}_t to represent θ_t we use moment matching. It is possible to determine closed-form expressions of moments of PCE expansions as given in Eq.(3) in terms of their coefficient, see Dutta and Bhattacharya (2010). The difference between these and the sample estimate of the posterior moments is then minimized to update the coefficients:

$$\hat{\mathbf{A}}_t = \arg \min_{\mathbf{A}_t} \sum_{k \leq m} \|M_{\mathbf{r}}^+(\mathbf{A}_t) - M_{\mathbf{r}}^{(s)+}\|_2^2 \quad (12)$$

where $k = \sum_{j=1}^{n_{\theta}} r_j$ was defined as the order of the moments and hence m defines the total order of moments we want to match. $M_{\mathbf{r}}^+(\mathbf{A}_t)$ denotes the moments of the PCE expansion as a function of the coefficients \mathbf{A}_t and $\hat{\mathbf{A}}_t$ are the updated coefficients to match the posterior moments.

5. Case study

The overall framework is summarised in Algorithm 1 for receding horizon SNMPC. First it is initialized by specifying the problem, including initial coefficients of the PCE expansion of θ .

Algorithm 1: Output feedback SNMPC

Input : $\hat{\mathbf{A}}_0, \Sigma_{\mathbf{v}}, \mathbf{f}(\cdot), \mathbf{h}(\cdot), \mathbf{x}_0(\theta)$

for each sampling time $t = 0, 1, 2, \dots$ **do**

1. Determine $\mathbf{x}_t(\theta_t(\xi))$ using $\mathbf{f}(\cdot, \cdot, \theta_t(\xi))$ recursively from an updated initial condition $\mathbf{x}(0) = \mathbf{x}_0(\theta_t(\xi))$.
2. Solve SNMPC problem with $\theta_t(\xi)$ and $\mathbf{x}_t(\theta_t(\xi))$ and obtain optimal control actions.
3. Apply first part of the control actions to the plant.
4. Measure $\mathbf{y}(t+1)$.
5. Apply the PCE filter to update $\theta_t(\xi)$ to $\theta_{t+1}(\xi)$ by determining the coefficients $\hat{\mathbf{A}}_{t+1}$.

end

The case study aims to control a fermentation bioreactor using Algorithm 1. Fermentation is an important process in the biochemical and pharmaceutical industries. Uncertainties are often considerable and disregarding these may lead to inadequate performance. In this paper we consider a semi-batch bioreactor with the inlet substrate flowrate as the control variable. The two variables that are considered uncertain are the inlet concentration of the substrate $C_{S,in}$ and the kinetic parameter μ_{\max} . The dynamic model was taken from Petersen and Jørgensen (2014) and describes the fermentation of a single cell protein using *Methylococcus Capsulatus*:

$$\dot{V} = F \quad (13a)$$

$$\dot{C}_X = -FC_X/V + \exp[\mu_{\max}(\xi)] \frac{C_S}{K_S + C_S + C_S^2/K_I} \quad (13b)$$

$$\dot{C}_S = -F(C_S - \exp[C_{S,in}(\xi)]/V - \gamma_S \exp[\mu_{\max}(\xi)]) \frac{C_S}{K_S + C_S + C_S^2/K_I} \quad (13c)$$

where V is the volume of the reactor in m^3 , F is the feed rate of substrate in m^3/h , C_X and C_S are the concentrations of biomass and substrate respectively in kg/m^3 . The uncertain parameters are assumed to be given as a PCE in terms of standard normally distributed variables ξ , which were log-transformed to ensure positiveness. This defines $\mathbf{f}(\cdot)$ in Eq.(1) with $\mathbf{x} = [V, C_X, C_S]^T$, $u = F$ and $\theta(\xi) = [\mu_{\max}(\xi), C_{S,in}(\xi)]^T$. The parameter values are $\gamma_S = 1.777$, $K_S = 0.021\text{kg}/\text{m}^3$ and $K_I = 0.38\text{kg}/\text{m}^3$. The corresponding output equation is given as follows:

$$\mathbf{y} = \mathbf{K}\mathbf{x} + \mathbf{v}, \quad \mathbf{K} = \text{diag}([1, 0, 1]), \quad \mathbf{v} \sim \mathcal{N}(\mathbf{0}, \text{diag}([3 \times 10^{-4}, 3 \times 10^{-4}])) \quad (14)$$

The respective initial PCE expansions are given as, which defines $\hat{\mathbf{A}}_0$ and $\theta_0(\xi)$:

$$\mu_{\max}(\xi) = \log(0.37) + 0.04\xi_1 + 0.02(\xi_1^2 - 1) + 0.0067(\xi_1^3 - 3\xi_1) \quad (15)$$

$$C_{S,in}(\xi) = \log(1.00) + 0.04\xi_2 + 0.02(\xi_2^2 - 1) + 0.0067(\xi_2^3 - 3\xi_2) \quad (16)$$

The objective was set to minimize the batch time with a chance constraint to produce a minimum concentration of biomass of $10\text{kg}/\text{m}^3$ with a probability of 0.05 with 10 control intervals in a shrinking horizon implementation. The input F was constrained between $0\text{kg}/\text{h}$ and $10\text{kg}/\text{h}$.

6. Results, discussion and conclusions

Firstly the simulation was run by setting the parameters of the plant model to $[\mu_{\max}, C_{S,in}] = [0.41, 1.05]$. The results of this are shown in Fig. 1. Next the initial parameter PCE of μ_{\max} and $C_{S,in}$ given in Eq.(15) and Eq.(16) were sampled 100 times randomly and used to simulate the "true" system according to Eq.(13), for which the results are given in Fig. 2. In each case Algorithm 1 was then used to control these systems in closed-loop to verify the performance given the objective and constraints outlined in the previous section. $N_s = 200$ samples were used for the PCE filter, see section 4.

In Fig. 1 it can be seen that given the measurement available at $t = 1$ the initial distribution at $t = 0$ moves towards the correct value. With several more updates it then converges to a sharp distribution at $t = 10$ due to the relatively low measurement noise. The last row highlights the working of the algorithm: The lower left plot shows that less and less time is necessary to reach the required biomass concentration due to the better estimates available of the uncertain parameters, i.e. it becomes possible to reduce the sampling times as it becomes less and less conservative. In the second graph we see that the biomass reaches nearly exactly $10\text{ kg}/\text{m}^3$ at the final time with the control inputs shown in the last graph.

In Fig. 2 we see that the batch times of the Monte Carlo simulations vary significantly with batch times ranging from 70h to 140h, with most batch times around 110h. In the last two graphs it can be seen that the required biomass of $10\text{ kg}/\text{m}^3$ was reached in most simulations despite the uncertainties present, however in about 7% of the scenarios this was not achieved. This is due to the parameter update being overconfident from the limited number of samples used. In particular, it can be seen that two scenarios do not reach even $4\text{ kg}/\text{m}^3$, which happens if the parameters converge to the wrong value due to the limited number of samples used.

In conclusion a novel framework has been proposed by employing PCE to describe parametric uncertainties and exploiting this uncertainty description in a sparse Gauss-Hermite MPC formulation taking into account these uncertainties efficiently. Noisy measurements were used at each sampling time to update the PCE of the uncertain parameters and reduce the inherent uncertainties present significantly. It could be shown that the algorithm is able to achieve the required biomass in 93% of the scenarios, however the parameter update may be overconfident using 200 samples.

Acknowledgements

This project has received funding from the European Union's Horizon 2020 research and innovation programme under the Marie Skłodowska-Curie grant agreement No 675215.

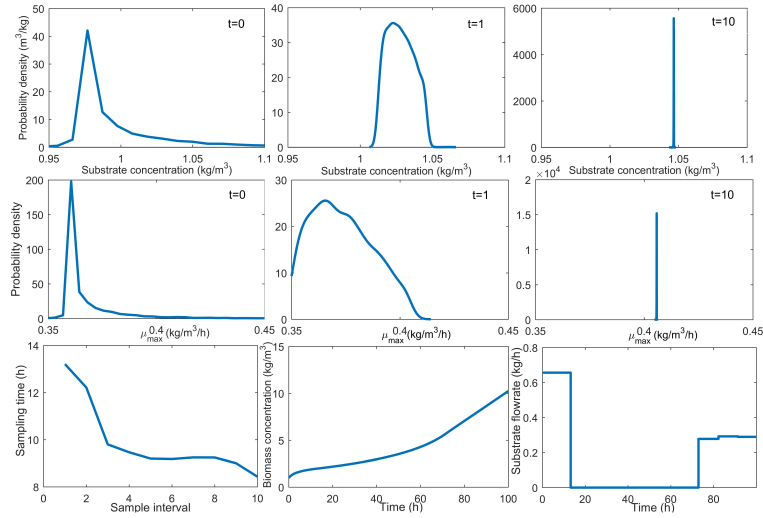


Figure 1: Run of Algorithm 1 with $[\mu_{\max}, C_{S,in}] = [0.41, 1.05]$. The first two graph rows show the evolution of the marginal distribution of the inlet substrate concentration and μ_{\max} at $t = 0$, $t = 1$ and $t = 10$. The last graph row shows the trajectories of the sampling time, biomass concentration and substrate flowrate.

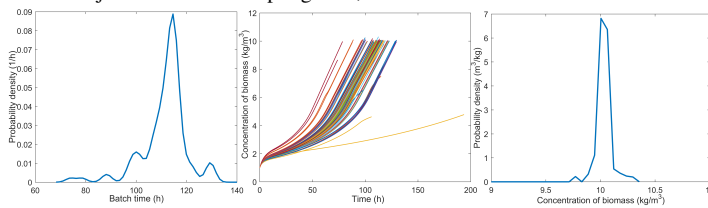


Figure 2: From left to right: Probability density function of batch times, biomass concentration trajectories and probability density function of final biomass concentrations

References

- E. Bradford, L. Imsland, 2017. Expectation constrained stochastic nonlinear model predictive control of a batch bioreactor. *Computer Aided Chemical Engineering* 40, 1621–1626.
- E. Bradford, L. Imsland, 2018a. Economic Stochastic Model Predictive Control Using the Unscented Kalman Filter. *IFAC-PapersOnLine* 51 (18), 417–422.
- E. Bradford, L. Imsland, 2018b. Stochastic Nonlinear Model Predictive Control Using Gaussian Processes. In: 2018 European Control Conference (ECC). IEEE, pp. 1027–1034.
- P. Dutta, R. Bhattacharya, 2010. Nonlinear estimation with polynomial chaos and higher order moment updates. In: American Control Conference (ACC), 2010. IEEE, pp. 3142–3147.
- L. Fagiano, M. Khammash, 2012. Nonlinear stochastic model predictive control via regularized polynomial chaos expansions. In: 51st IEEE Conference on Decision and Control (CDC). IEEE, pp. 142–147.
- B. Jia, M. Xin, Y. Cheng, 2012. Sparse-grid quadrature nonlinear filtering. *Automatica* 48 (2), 327–341.
- J. M. Maciejowski, A. L. Visintini, J. Lygeros, 2007. NMPC for complex stochastic systems using a Markov chain Monte Carlo approach. In: *Assessment and Future Directions of Nonlinear Model Predictive Control*. Springer, pp. 269–281.
- R. Madankan, P. Singla, T. Singh, P. D. Scott, 2013. Polynomial-chaos-based Bayesian approach for state and parameter estimations. *Journal of Guidance, Control, and Dynamics* 36 (4), 1058–1074.
- A. Mesbah, 2016. Stochastic model predictive control: An overview and perspectives for future research.
- T. Mühlpfordt, J. A. Paulson, R. D. Braatz, R. Findeisen, 2016. Output feedback model predictive control with probabilistic uncertainties for linear systems. In: American Control Conference (ACC), 2016. IEEE, pp. 2035–2040.
- L. N. Petersen, J. B. Jørgensen, 2014. Real-time economic optimization for a fermentation process using Model Predictive Control. In: 13th European Control Conference (ECC). IEEE, pp. 1831–1836.
- M. A. Sehr, R. R. Bitmead, 2017. Particle model predictive control: Tractable stochastic nonlinear output-feedback MPC. *IFAC-PapersOnLine* 50 (1), 15361–15366.

Control structure design for a CO_2 -refrigeration system with heat recovery

Adriana Reyes-Lúa^a, Glenn Andreassen^b, Lars F. S. Larsen^c, Jakob Stoustrup^b and Sigurd Skogestad^{a*}

^a*Norwegian University of Science and Technology, Department of Chemical Engineering (NTNU), 7491 Trondheim, Norway*

^b*Aalborg University, Department of Electronic Systems, Fr. Bajers Vej 7C, 9220 Aalborg, Denmark*

^c*Danfoss A/S, Refrigeration and Air conditioning, 6430 Nordborg, Denmark*

**sigurd.skogestad@ntnu.no*

Abstract

In this work, we analyze a generic supercritical CO_2 -refrigeration system with parallel compression, based on systems used for supermarket use. In order to maximize energy efficiency, this system has a “heat-recovery” function, in which part of the heat rejected at high pressure and temperature can be recovered to provide heating. Operating conditions and active constraints are strongly affected by seasonal requirements and ambient temperature. Thus, it is necessary to find a control structure that satisfies operational constraints and maintains (near-)optimal operation with different sets of active constraints. In this paper, we use a systematic procedure to define such control structure.

Keywords: constrained operation, self-optimizing control, PID control, control structure

1. Introduction

An appropriately designed control structure should maintain (near-) optimal operation, also when there are disturbances which cause the system to operate under conditions different than the design point. Optimal operation of a process in the presence of disturbances could be maintained using optimization-based control. However, in some cases, it is possible to design and implement advanced PI(D)-based control structures that also maintain optimal operation when constraints are reached (Skogestad, 2000; Reyes-Lúa et al., 2018). The advantage of such a PI(D)-based control structure compared to optimization-based control is simpler tuning and independence of an explicit model for every system (Forbes et al., 2015).

CO_2 -refrigeration systems with parallel compression is environmentally attractive. Finding optimal design and operating conditions is an ongoing area of research (Gullo et al., 2018). In order to maximize energy efficiency, some systems have a “heat recovery” function, in which part of the heat rejected at high pressure and temperature can be recovered to provide heating (e.g. district heating or tap water) (Sawalha, 2013). The available energy can be increased by operating the cooler at a higher pressure, at the expense of a higher compression work. In this work, we design a PI(D)-based control structure for the studied CO_2 -refrigeration system.

2. Description of the CO_2 -refrigeration system with heat recovery

A flow diagram of the analyzed CO_2 -refrigeration cycle with parallel compression and heat recovery is shown in Fig. 1, and the pressure-enthalpy diagram is shown in Fig. 2. The main function of this system is to provide cooling (\dot{Q}_{ev}) and maintain the desired cabinet temperature (T_{cab}) via heat exchange in the evaporator, which operates at low pressure (P_l). Low-pressure CO_2 in vapor phase is compressed to high-pressure (P_h) and temperature supercritical CO_2 , which may be used to heat tap water in the heat recovery section. Excess heat (\dot{Q}_{gc}) is rejected to the ambient air in the gas cooler.

High-pressure CO_2 is expanded to an intermediate (sub-critical) pressure (P_{IP}) in the high-pressure valve (V_{hp}). Vapor and liquid CO_2 are separated in the liquid receiver. The evaporator valve (V_{ev}) regulates the flow of liquid CO_2 from the receiver to the evaporator. By opening and closing V_{hp} and V_{ev} , we regulate the refrigerant charge (mass) at the high and low pressures. Vapor CO_2 from the liquid receiver is recycled to the high-pressure side either via parallel compression ($K2$) or the intermediate pressure valve (V_{IP}) and the main compressor ($K1$). The total compression work can be reduced by utilizing the parallel compressor instead of the intermediate pressure valve and the main compressor.

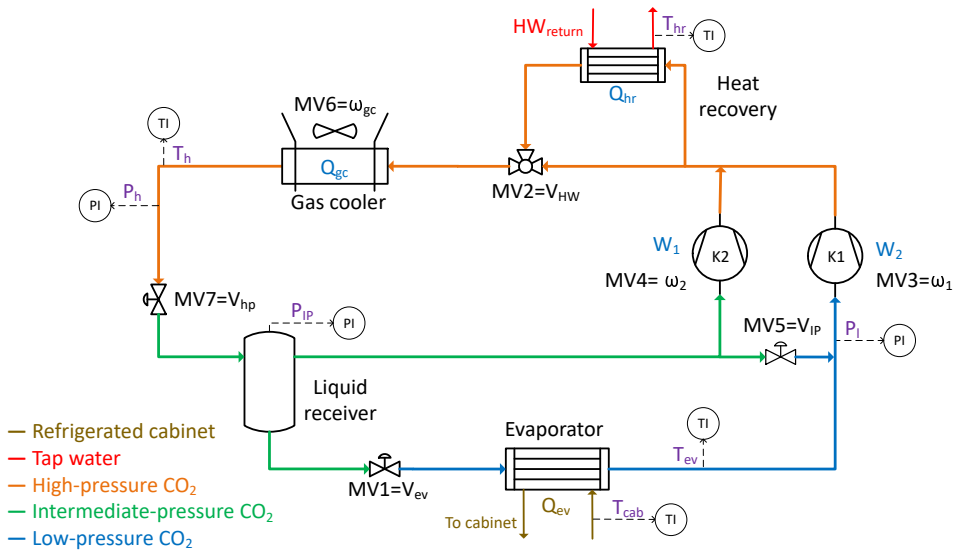


Figure 1: CO_2 -refrigeration system with parallel compression and heat recovery. There are seven available manipulated variables (MV).

2.1. High-side pressure

In the supercritical region, there is no saturation condition and the pressure is independent of the temperature. From the control point of view, this means that it is necessary to control the high pressure (P_h), since it influences the gas cooler exit enthalpy (and evaporator inlet enthalpy). In other words, P_h will determine specific refrigeration capacity. As P_h is determined by the relationship between refrigerant charge, inside volume and temperature in the high-pressure side, we can actively control it using V_{hp} (Kim et al., 2004).

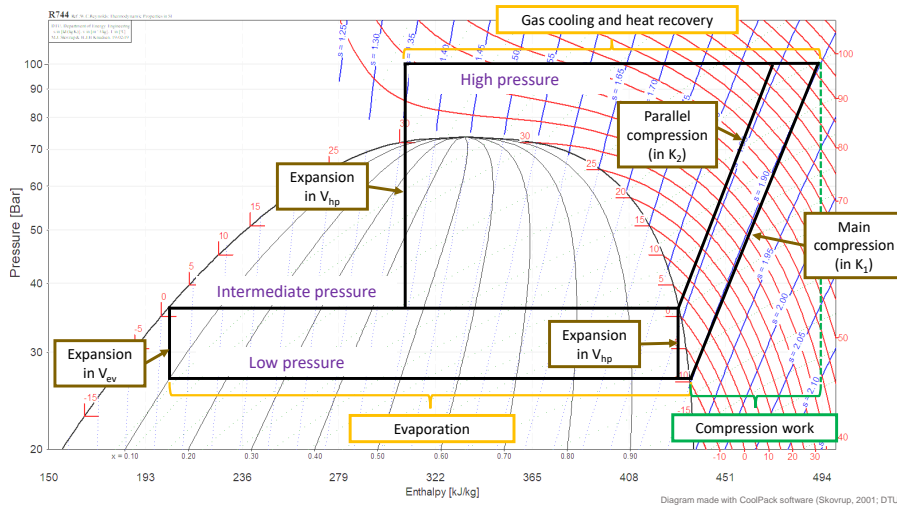


Figure 2: Pressure-enthalpy diagram of CO_2 -refrigeration system with parallel compression.

It is relevant to analyze the effect of high pressure on the coefficient of performance (COP). In the case of a refrigeration system, it is defined as the ratio between cooling and compression work ($COP = \dot{Q}_{ev}/W_s$). As the isentropic compression line in the pressure-enthalpy diagram (blue lines in Fig. 2) is linear, compression work will linearly increase as P_h increases. On the other hand, in the supercritical region the isotherm (red lines in Fig. 2) becomes steeper with pressure, reducing the capacity enhancement from a given increase in pressure. For this reason, the COP reaches a maximum above which the added capacity no longer fully compensates for the additional work of compression. Thus, there is an optimal high pressure that maximizes COP (Nekså, 2002).

We should also note that in the supercritical region, at a fixed pressure, a small change in refrigerant exit temperature can produce a large change in gas cooler exit enthalpy (and evaporator inlet enthalpy), making COP very sensitive to the gas cooler refrigerant exit temperature. Previous studies (Liao et al., 2000; Jensen, 2008; Sawalha, 2013) are in line with this and have shown that the optimal set-point for the high pressure (P_h) should be corrected by the outlet temperature of the gas cooler (T_h).

2.2. Heat-recovery section

Part of the heat rejected at high pressure can be recovered to provide hot water in the heat recovery section. Heat is rejected at gliding temperature, as supercritical CO_2 is cooled. This way, the temperature profile of the CO_2 matches the heating-up curve of water, giving reduced thermodynamic losses and high efficiency (Kim et al., 2004). As it can be deduced from Fig. 2, increasing the high pressure increases the available heat for recovery, at the expense of a higher compression work. Additionally, the available heat for recovery in the supercritical region is much higher than with sub-critical CO_2 .

3. Design of the PI(D)-based control structure

In this section, we apply part of the systematic plantwide control procedure proposed by Skogestad (2000) to design a self-optimizing control structure which maintains (near-) optimal operation, also in the presence of disturbances. The first step of the procedure is to define the operational objective. Here, we want to maximize the coefficient of performance (COP), subject to the system itself and operational constraints:

$$\begin{aligned} \min_u \quad & -COP(u, x, d) = -(\dot{Q}_{ev} + \dot{Q}_{hr}) / (W_1 + W_2) \\ \text{s.t.} \quad & f(u, x, d) = 0 \quad \text{system equations (model)} \quad (1a) \\ & g(u, x, d) \leq 0 \quad \text{operational and physical constraints} \quad (1b) \\ & e(u, x, d) = 0 \quad \text{set-points} \quad (1c) \end{aligned}$$

where x are the internal states, u are the degrees of freedom, and d are the disturbances.

Physical constraints in Eq. (1b) are related to pressure (P_i), motor velocities (ω_i) and valve openings (z_i), specifically: $P_i \leq P_i^{max} \forall i$, $(P_{IP} - P_i)^{min} \leq (P_{IP} - P_i)$, $\omega_j^{min} \leq \omega_j \leq \omega_j^{max} \forall j$, and $z_k^{min} \leq z_k \leq z_k^{max} \forall k$. The most important set-point in Eq. (1c) is to supply enough cooling (\dot{Q}_{ev}) to maintain $T_{cab} = T_{cab}^{sp}$. Additionally, we would like to supply enough heating (\dot{Q}_{hr}) to maintain $T_{hr} = T_{hr}^{sp}$.

The next step is to determine the steady-state optimal operation. In order to do this we:

- *Identify steady-state degrees of freedom:* The analyzed system has seven available manipulated variables, MVs in Fig. 1: $u = [\omega_1, \omega_2, \omega_{gc}, z_{Vev}, z_{Vhp}, z_{VHW}, z_{VIP}]^T$. These degrees of freedom can be used to achieve optimal operation. Note that ω_2 and z_{VIP} are not independent, as either would have a similar effect in P_{IP} .
- *Identify important disturbances and their expected range:* In this case study, important disturbances (d) are cooling demand (\dot{Q}_{ev} , corresponding to T_{cab}^{sp}), and heating demand (\dot{Q}_{hr} , corresponding to T_{hr}^{sp}). The range for both is $\dot{Q}_i^{min} \leq \dot{Q}_i \leq \dot{Q}_i^{max}$.
- *Identify active constraints regions:* Once that the disturbances and their range are specified, the active constraints regions are found. This can be done by optimization or using engineering insight (Jacobsen and Skogestad, 2011). There are three relevant operating regions:
 1. *"Unconstrained" case:* corresponding to spring/fall operation.
 2. *Maximum heating:* corresponding to winter, when $\dot{Q}_{hr} = \dot{Q}_{hr}^{max}$.
 3. *Maximum cooling:* corresponding to summer, when $\dot{Q}_{ev} = \dot{Q}_{ev}^{max}$.

In every case, cooling requirements ($T_{cab} = T_{cab}^{sp}$) must be met. If possible, heating requirements ($T_{hr} = T_{hr}^{sp}$) should also be met. We do not consider $\dot{Q}_{ev} = \dot{Q}_{ev}^{min}$, as it corresponds to shut-down. $\dot{Q}_{hr} = \dot{Q}_{hr}^{min}$ is included in the "unconstrained" and maximum cooling cases. Then, we will design a control structure that works for the three relevant cases mentioned above. Fig. 3 shows the proposed control structure. The procedure to design this control structure is explained below.

For each region, each steady-state degree of freedom (MV) needs to be paired with a controlled variable. First, we pair active constraints. Then, for the remaining degrees of freedom, we identify self-optimizing controlled variables. These are usually a combination of measurements found by optimization. When designing control structures for systems with changing active constraint regions, it is useful to organize constraints in a priority list (Reyes-Lúa et al., 2018). Physical constraints (Eq. (1b)) have the highest priority. Regarding set-points (Eq. (1c)), $T_{cab} = T_{cab}^{SP}$ has a higher priority than $T_{hr} = T_{hr}^{SP}$.

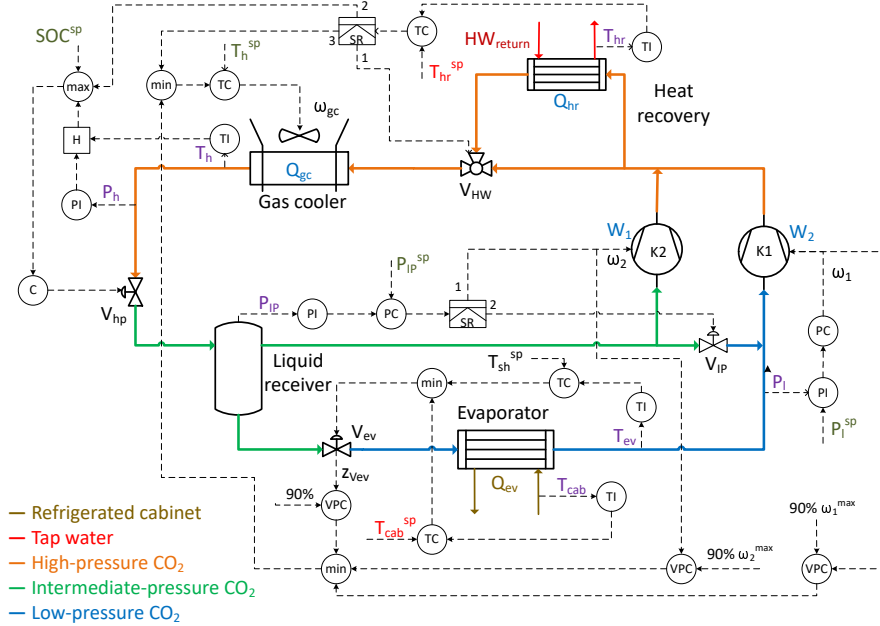


Figure 3: Control structure for the CO₂-refrigeration system with heat recovery.

3.1. "Unconstrained" case

This is the base case and we can satisfy every constraint. We use $MV1=V_{ev}$ to control T_{cab} , and $MV2=V_{HW}$ to control T_{hr} . The set-points are given by the operator. In order to assure that the evaporator is not over-flooded, we include a controller for the evaporator outlet temperature (T_{sh}). We have five remaining unconstrained degrees of freedom, two of which are not independent (ω_2 and V_{IP}). We pair these degrees of freedom as follows:

1. $MV3=\omega_1$ controls P_i . P_i^{SP} is found by optimization (self-optimizing variable).
2. The parallel compressor ($MV4=\omega_2$) and $MV5=V_{IP}$ are used to control the pressure in the liquid receiver (P_{IP}). The set-point defined by optimization and may be a self-optimizing variable. Normal operation is using ω_2 , but when the flow is too low, we use V_{IP} . We can implement this with a split-range controller.
3. $MV6=\omega_{gc}$ controls T_h (outlet of the gas cooler). T_h^{SP} is defined by optimization.
4. $MV7=V_{hp}$ controls P_h . As explained in Section 2.1, the set-point is a linear combination (H) of P_h and T_h , which is a self-optimizing variable (Jensen, 2008).

3.2. Maximum heating

When V_{HW} becomes fully open, we must switch the manipulated variable to continue controlling T_{hr} . This is handled using split-range control with selectors. First, we switch to V_{hp} as manipulated variable and increment the available heat for recovery by increasing P_h . To implement this, we include a selector for the set-point of the high-pressure controller. Once we reach P_h^{max} , we get additional capacity for the heat-recovery section by increasing T_h , using ω_{gc} as manipulated variable. This will increase mass flow through the compressors and, as consequence, the discharge temperature.

If we continue to increase T_h , at some point liquid in the low-pressure section may be insufficient and V_{ev} will reach its maximum opening. Alternatively, the compressors could reach maximum capacity due to the increased mass flow. To prevent this, we implement valve-positioning controllers (VPC) with a *min* selector, which will prevent T_h from increasing in such a way that either the valve or the compressors ($z_{V_{ev}}$, ω_1 or ω_2) saturate.

3.3. Maximum cooling

As cooling requirements increase, $z_{V_{ev}}$ will open and reach $z_{V_{ev}}^{max}$. The valve positioning controller for V_{ev} will adjust T_h (and indirectly P_h) such that the system reaches Q_{ev}^{max} .

4. Final remarks

Using a systematic procedure, we designed a PI(D)-based control structure for a CO_2 -refrigeration system, that maintains (near-)optimal steady-state operation, also with changes in the set of active constraints. We should point out that pairing on the low-pressure side could be different (e.g. controlling T_{cab} with the main compressor, and P_l with V_{ev}). The final decision would consider system dynamics. It is important to mention that we can usually reach the same steady-state control objectives we reach with split-range controllers by using valve-positioning control or different controllers with different set-points.

References

- M. G. Forbes, R. S. Patwardhan, H. Hamadah, R. B. Gopaluni, Jan 2015. Model Predictive Control in Industry: Challenges and Opportunities. IFAC-PapersOnLine 48 (8), 531–538.
- P. Gullo, K. M. Tsamos, A. Hafner, K. Banasiak, Y. T. Ge, S. A. Tassou, Dec 2018. Crossing CO_2 equator with the aid of multi-ejector concept: A comprehensive energy and environmental comparative study. Energy 164, 236–263.
- M. G. Jacobsen, S. Skogestad, Oct 2011. Active Constraint Regions for Optimal Operation of Chemical Processes. Industrial & Engineering Chemistry Research 50 (19), 11226–11236.
- J. B. Jensen, 2008. Optimal operation of refrigeration cycles. Phd thesis, NTNU, Norway.
- M.-H. Kim, J. Pettersen, C. W. Bullard, 2004. Fundamental process and system design issues in CO_2 vapor compression systems. Progress in Energy and Combustion Science 30 (2), 119–174.
- S. Liao, T. Zhao, A. Jakobsen, Jun 2000. A correlation of optimal heat rejection pressures in transcritical carbon dioxide cycles. Applied Thermal Engineering 20 (9), 831–841.
- P. Nekså, Jun 2002. CO_2 heat pump systems. International Journal of Refrigeration 25 (4), 421–427.
- A. Reyes-Lúa, C. Zotică, S. Skogestad, Jul 2018. Optimal Operation with Changing Active Constraint Regions using Classical Advanced Control. In: 10th ADCHEM. IFAC, Shenyang, China.
- S. Sawalha, Jan 2013. Investigation of heat recovery in CO_2 trans-critical solution for supermarket refrigeration. International Journal of Refrigeration 36 (1), 145–156.
- S. Skogestad, Oct 2000. Plantwide control: the search for the self-optimizing control structure. Journal of Process Control 10 (5), 487–507.

A PLSR Model for Consumer Preference Prediction of Yoghurt from Sensory Attributes Profiles

Kexin Bi^a, Dong Zhang^b, Zifeng Song^a, Tong Qiu^{a*}, Yizhen Huang^{b*}

^a*Department of Chemical Engineering, Tsinghua University, 100084 Beijing, China*

^b*COFCO Nutrition Health Research Institute, 102209 Beijing, China*

* *Corresponding author's E-mail: qiuotong@tsinghua.edu.cn and 1289803467@qq.com*

Abstract

Consumer preference investigations are extremely emphasized in marketing management strategy for food enterprises. In this communication, a partial least squares regression (PLSR) model for consumer preference prediction from sensory attributes profiles is developed and three brands of yoghurt are exemplified to demonstrate the accuracy and practicability of the method. The model also provides the importance ranking of the analysed sensory variables, which may give a guidance for industrial production and sensory experiment design. Drawing on the results of PCA and hierarchical clustering analysis, the variable filtering process of PLSR is proved to be theoretically correct.

Keywords: Sensory attributes, Consumer preference, PLSR, Yoghurt

1. Introduction

Yoghurt is one of the most important commodities in people's daily life. Odour compounds, such as proteins, amino acids, fats, sugars, organic acids,^[1] make a solid contribution in the sensory attributes of dairy. The consumer preferences for yoghurt are directly affected by their sensory quality. For dairy companies, consumer preferences for yoghurt data are essential to market competitiveness. Dairy products should be designed and improved according to consumer demand.^[2] However, the data related to consumer is usually hard to be obtained, because the large-scale consumer preferences survey is unfeasible to carry out for new products^[3] and the consumer preferences in different regions have significant differences in the flavor of dairy products.

Thus, a data-driven consumer preference prediction model is urgently needed by dairy companies. And in recent years, several researchers have focused on the sensory profiling of dairy products and proposed various correlation models to forecast the consumer overall likings. Bouteille et al^[4] applied principal component analysis (PCA) to construct internal mapping between Temporal Dominance of Sensations (TDS) curves and liking scores or freshness sensation scores to evaluate plain yoghurts and yoghurt-like product. Oliveira et al^[5] analyzed the relevancy between check-all-that-apply (CATA) frequency and overall linking by threshold statistics and advised the dairy companies to reduce the sugar addition in milk. Farah et al^[6] utilized cluster analysis and multiple factor analysis to associate data from CATA test and acceptance test for overall impression and identified two significantly different clusters of yoghurts', whey-based beverages' and fermented milks' consumers. However, these models were lack of generalization ability and hard to deal with high dimensional data, making the model feeble in practicality and versatility.

To improve the overall performance of the model, a novel correlation model with PLSR was proposed to predict the consumers' overall liking of dairy products from sensory attributes profiles. The PLSR model could not only obtain the prediction value from multicollinear variables, but also filter out the key sensory attributes and classify the samples with its principal components. In consideration of the characteristics of data as well as the need in enterprise production, reducing the number of variables without affecting the accuracy of result fitting was also realized to reduce the cost of subsequent experiments.^[7]

In summary, this communication intended to use the analytical sensory evaluation team to perform sensory evaluation on yoghurt samples and use multivariate statistical analysis methods to profile the sensory evaluation of different samples' flavors, which provided guidance for the improvement of sensory quality.

2. Sensory evaluation and data profiling method

2.1. Sensory data collection

The sensory attributes data was obtained by evaluators' rating of each sample. Through the training^[8] of sensory sensitivity and expressive ability, a total of ten sensory experts were invited to complete the sensory evaluation. After tasting the series of flavored yoghurt samples, these experts were asked to describe all the sensations from the aspects of sight, smell and taste. The evaluation process is carried out in an independent evaluation room. Then the descriptors were screened through preliminary collation and multivariate statistical analysis methods, and the sensory attributes descriptors of the flavored yoghurt were finally determined.^[9]

For the selected sensory attributes descriptors, each sensory expert would give the flavor intensities for a specific sample using a 10-point linear scale. The left end of the linear scale is extremely weak, and the right end is extremely strong. The evaluator can select any value from 0 to 10 as the attributes intensity evaluation value.

Consumer preference rating is an output variable in this study. Fifty heavy consumers of yoghurt products in Beijing were invited to the sensory lab to fill the overall liking questionnaires. The consumer preference test also adopted the 0 (extremely weak) to 10 (extremely strong) scoring mechanism.

2.2. Data characterization analysis

After the data collection process, we obtained a set of data including thirty-three kinds of yoghurt with different storage conditions evaluated by ten sensory experts on twenty-one sensory attributes and fifty consumers on overall likings. Due to the complexity of the input and output data, it's better to find out the data characterization before fitting.

For sensory attributes data, there were three brands of yoghurt stored under eleven different conditions that were evaluated by experts. So the input data could be summarized with a 33*21 matrix, where 33 (3*11) was the quantity of samples and 21 was the quantity of sensory attributes. To extract the key information of the data, Principal component analysis (PCA)^[10] was applied to search for the relationship between the high-dimensional sensory attributes profiles. To profile the variable multicollinearity of yoghurt odour, the scoring plot of two PCs was generated and displayed in Figure 1.

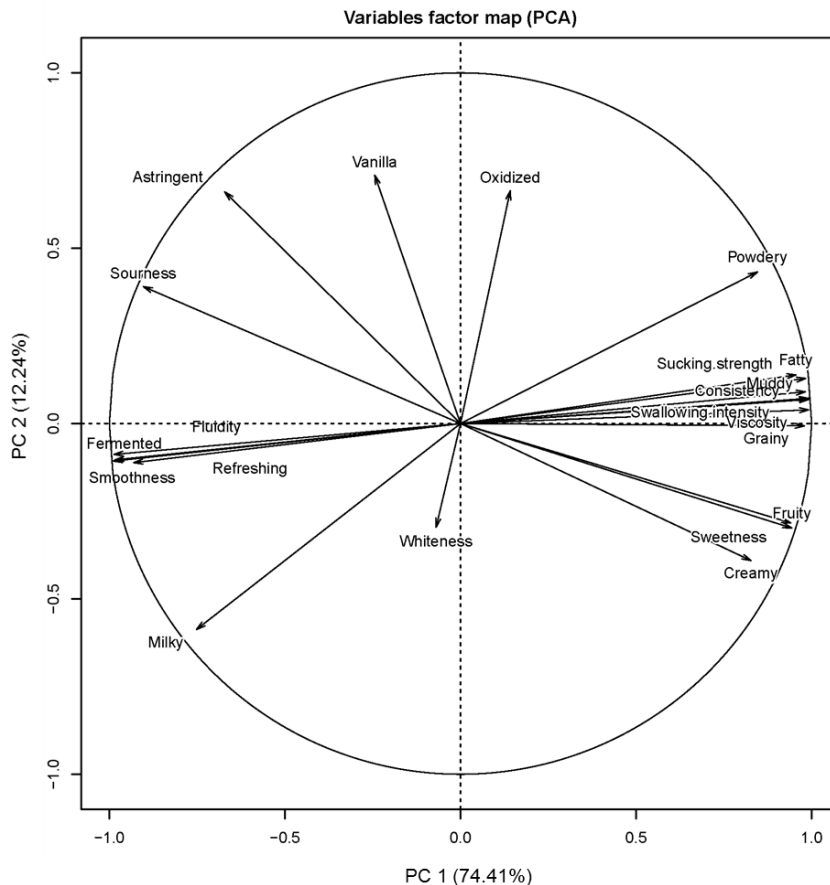


Figure 1. 2-PCs scoring plot of yoghurt sensory attributes variables

As shown in Figure 1, there were several overlapped variables in the scoring plot, which might contain the almost same information for result fitting and interfere the accuracy of regression analysis. However, only utilizing several PCs to predict the consumers overall liking might lose plenty of information. So a regression model with the function of variable filtering was needed.

2.3. PLSR model for preference prediction

The partial least squares regression (PLSR) was proposed by Wold^[11] in 1979, and it was feasible to solve the multivariate regression problem with independent multivariate correlation. This model projected the predicted variables to a new space, so that the difference between the dependent variables was minimized. Then compared to PCA regression method, PLSR also considered the contribution of the input data for the output data, so the correlation during the regression process could be guaranteed.^[12] What's more, an importance ranking of sensory attributes could be obtained from the regression process, which could tell the enterprise how to improve the products.

Thus, through the overall liking assignment and PLSR model building with training data, a complete consumer preference prediction of yoghurt from sensory attributes profiles could be applied for dairy companies or sensory labs.

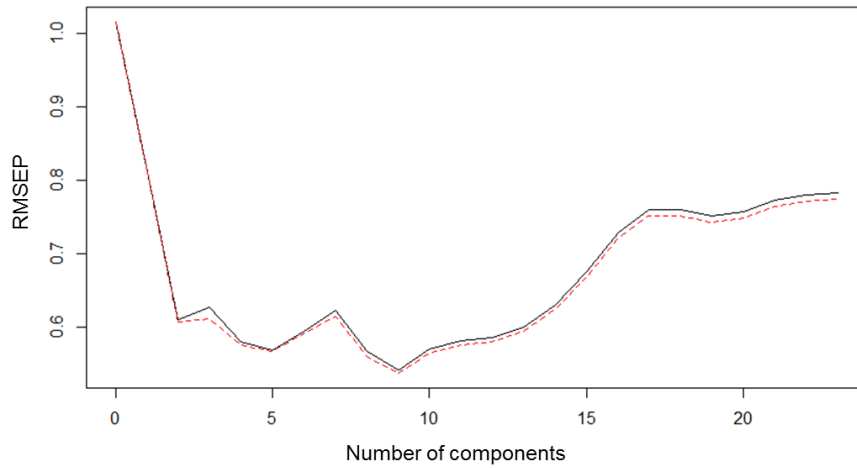


Figure 2. The fluctuation trend of RMSEP value affected by the number of components

3. Result and discussion

To execute the PLSR process, the quantity of variables that were employed to complete regression modeling should be determined. As shown in Figure 2, by analyzing the root-mean-square error of prediction influenced by the number of components, a total of nine variables were finally picked up. The cumulative contribution rate of the nine selected variables reached the value of 94.52%, which gave a relatively comprehensive explanation of the origin input data.

Then the PLSR model was built on the R-3.4.1 and simulated on an Inter Core i7 processor of 2.80 GHz to predict the average liking scores of thirty-three collected samples. Figure 3 displayed the calculation results compared to actual data. Obviously, the calculation process demonstrated low relative errors that were below 10%.

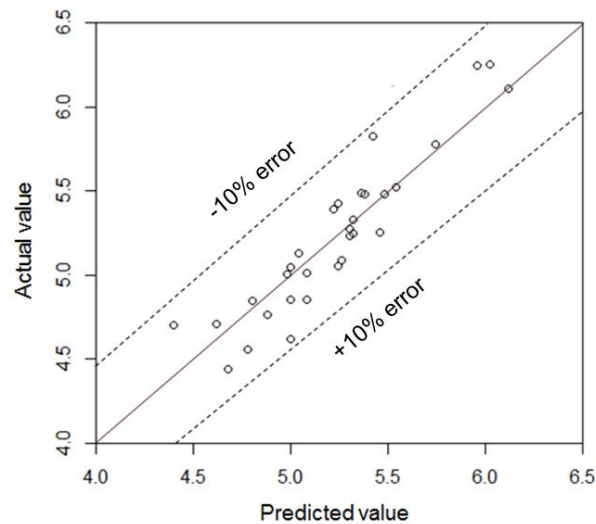


Figure 3. Comparison of predicted and actual value of consumers' preference rating.

Table 1. Properties and corresponding objective functions in simulated annealing algorithm

Variables	+/- Correlation	Relevant significance
Sweetness	+	>95%
Grainy	-	>90%
Sourness	+	>85%
Oxidized	-	>85%
Smoothness	+	>85%
Swallowing intensity	-	>80%

In addition to the overall liking information, the PLSR simulation process also provided the correlation properties of each variables. Table 1 listed top six sensory attributes with high relevant significance of the selected nine variables, and all these relevant significances were larger than 80%, showing a strong relationship between sensory attributes and consumers preference rating value.

From Table 1, a dairy enterprise could obtain the product improvement plan for a typical brand of yoghurt, such as properly increasing the sweetness, sourness, smoothness and decline the grainy, oxidized, swallow intensity as much as possible. What's more, the PLSR process could give the sensory labs a reasonable streamlined solution to design the sensory attributes test. As shown in Figure 4, though PCA showed that there were several variables expressing the similar information in the 2-PC space, the PLSR only picked up two key attributes (Smoothness, Swallowing intensity) for regression process. And PLSR could found out some attributes with high relevant significance, such as oxidized, which didn't own a good variance explanation in PCA result.

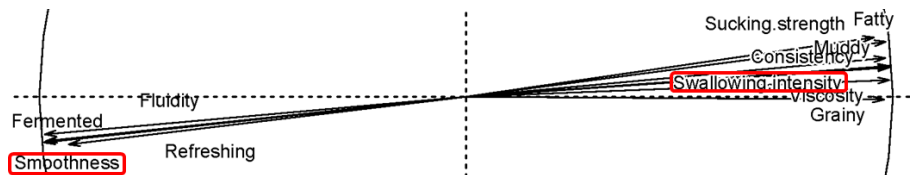


Figure 4. The sensory attributes with similar information in 2D PCA scoring plot

Finally, to demonstrate the description ability of the selected sensory attributes, a hierarchical clustering analysis was carried out. As shown in Figure 5, utilizing the selected sensory attributes as independent variables could clearly classify the three brands (670, 395, 481) of yoghurt, though the storage condition were different (1 to 5 for the storage month, R for Room temperature, H for high temperature, L for low temperature). This result demonstrated the correction of the sensory attributes selection from PLSR because these variables owned the ability to describe a specific brand of yoghurt.

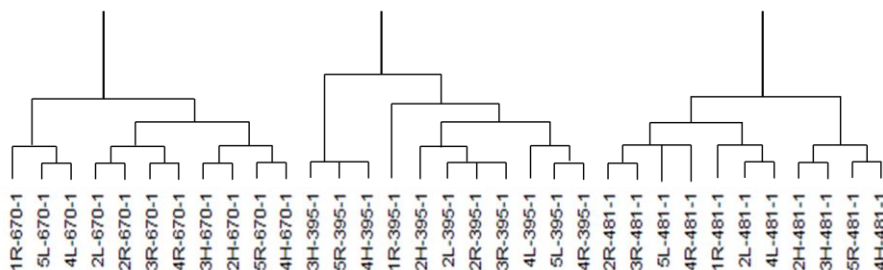


Figure 5. The hierarchical clustering analysis result using selected sensory attributes from PLSR

4. Conclusion

A PLSR model was developed to make connection between the collected sensory attributes profiles from trained sensory experts and the consumer preference rating. The accuracy and practicability of the method was demonstrated by the regression process of three brands of yoghurt. Besides, nine key sensory variables were selected by PLSR process and the correlation parameters between sensory variables and overall liking could give a reasonable advice for dairy enterprise to improve the yoghurt products. And the sensory labs could also update the experimental scheme according to the importance ranking of the sensory descriptors to save the overall consumption of the sensory evaluation.

Accurate and fast prediction of consumer preference can bring huge profits for food enterprise. The theory reliability of the PLSR method proposed in this work provides feasibility to applied the prediction model in other types of food. Hopefully, the utility of R based programs make the model easier to be applied as plug-in for Industrial Internet and promote the benefits for food industry.

Acknowledgements

The authors gratefully acknowledge the National Natural Science Foundation of China for its financial support (Grant No. U1462206).

References

- [1] Cheng, H. (2010). Volatile flavor compounds in yogurt: a review. *Critical reviews in food science and nutrition*, 50(10), 938-950.
- [2] Grunert, K. G., Bech-Larsen, T., & Bredahl, L. (2000). Three issues in consumer quality perception and acceptance of dairy products. *International Dairy Journal*, 10(8), 575-584.
- [3] Krishna, A. (2012). An integrative review of sensory marketing: Engaging the senses to affect perception, judgment and behavior. *Journal of consumer psychology*, 22(3), 332-351.
- [4] Bouteille, R., Cordelle, S., Laval, C., Tournier, C., Lecanu, B., This, H., & Schlich, P. (2013). Sensory exploration of the freshness sensation in plain yoghurts and yoghurt-like products. *Food Quality and Preference*, 30(2), 282-292.
- [5] Oliveira, D., Reis, F., Deliza, R., Rosenthal, A., Giménez, A., & Ares, G. (2016). Difference thresholds for added sugar in chocolate-flavoured milk: Recommendations for gradual sugar reduction. *Food Research International*, 89, 448-453.
- [6] Farah, J. S., Araujo, C. B., & Melo, L. (2017). Analysis of yoghurts', whey-based beverages' and fermented milks' labels and differences on their sensory profiles and acceptance. *International Dairy Journal*, 68, 17-22.
- [7] Lawless, H. T., & Heymann, H. (2010). *Sensory evaluation of food: principles and practices*. Springer Science & Business Media.
- [8] Murray, J. M., Delahunty, C. M., & Baxter, I. A. (2001). Descriptive sensory analysis: past, present and future. *Food research international*, 34(6), 461-471.
- [9] Giboreau, A., Dacremont, C., Egoroff, C., Guerrand, S., Urdapilleta, I., Candel, D., & Dubois, D. (2007). Defining sensory descriptors: Towards writing guidelines based on terminology. *Food quality and preference*, 18(2), 265-274.
- [10] Mackiewicz, A., & Ratajczak, W. (1993). Principal components analysis (PCA). *Computers and Geosciences*, 19, 303-342.
- [11] Gerlach, R. W., Kowalski, B. R., & Wold, H. O. (1979). Partial least-squares path modelling with latent variables. *Analytica Chimica Acta*, 112(4), 417-421.
- [12] Helland, I. S. (2001). Some theoretical aspects of partial least squares regression. *Chemometrics and Intelligent Laboratory Systems*, 58(2), 97-107.

Coordination of multiple production and utility systems in a multi-leader multi-follower Stackelberg game

Ludger Leenders^a, Kirstin Ganz^a, Björn Bahl^a, Maike Hennen^a and André Bardow^{a,b,*}

^a*Institute of Technical Thermodynamics, RWTH Aachen University, Aachen, Germany*

^b*Institute of Energy and Climate Research - Energy Systems Engineering (IEK-10), Forschungszentrum Jülich GmbH, Jülich, Germany*
andre.bardow@itt.rwth-aachen.de

Abstract

Large industrial sites typically consists of multiple production and utility systems. To minimize overall cost, these systems need to coordinate the operation. The problem resulting can be stated as a multi-leader multi-follower Stackelberg game. Thus, we propose a method which coordinates the operation across multiple production systems (leaders) and on-site utility systems (followers). The proposed method performs iterative feedback loops between production and utility systems. The coordination between the production and utility systems is performed by load- and time-dependent energy costs. The proposed method is applied to a case study with two production systems and two utility systems. The proposed method saves 7.3 % in total cost compared to the common separated and unidirectional optimization between each production system and the corresponding utility system. Thus, in summary, we provide an efficient method to enable cost optimization across multiple production and utility systems to reduce site-wide energy cost.

Keywords: Utility System, Production System, Multi-Leader Multi-Follower

1. Motivation

In large industrial sites, multiple production and utility systems are operated on-site. Usually, these systems are operated by different companies or business units. Thus, operational optimization is commonly performed individually and sequentially: First, the production systems schedule their production plan and determine the corresponding energy demand. Subsequently, the energy demand is supplied by the utility system corresponding to each production system. Consequently, there is no feedback between the systems and suboptimal overall cost arise. In this paper, we assume that operation for minimal overall cost is desired.

In principle, operation for minimal overall cost can be achieved by an integrated optimization problem of all production and utility systems. Such an integrated optimization has already been proposed for one production and utility system (Agha et al., 2010). The integrated optimization led to significant cost savings compared to sequential optimization. However, an integrated optimization is often practically prohibited, if the systems are operated by different companies. In such cases, the systems are not allowed to exchange their system knowledge. Maxeiner et al. (2017) therefore allocate shared resources by a

central site manager. The problem is solved by an iterative solution approach via price-based coordination. In their case study, a production system with 3 semi-batch reactors is considered. However, the starting times of the reactors are predefined and not scheduled. In the iterations, the degrees of freedom are the inputs and number of intervals. A central coordinator can be avoided by a multi-leader multi-follower Stackelberg game, where the production systems are the leaders and the utility systems are the followers.

A single-leader multi-follower Stackelberg game has been solved iteratively by Yu and Hong (2016) for a smart grid with one utility company (leader) and multiple customers (follower). Besides profit maximization of the leader and cost minimization of the followers, the method flattens the load profile. Maharjan et al. (2013) solve a multi-leader multi-follower Stackelberg game of a smart grid also by an iterative solution approach for a single time step. The exchanged information between leader and follower are the energy price and the energy demand. Ramos et al. (2018) solve a multi-leader single-follower and a single-leader multi-follower Stackelberg game for design of eco-industrial parks with continuous production systems. Thus, no production scheduling is required. The Stackelberg games are formulated as bilevel problems which are solved by replacing the followers' optimization problem by the Karush-Kuhn-Tucker reformulation. Yue and You (2017) propose an algorithm to solve a mixed-integer linear bilevel problem for the design and operation of supply chains in single-leader single-follower Stackelberg games. The above reviewed literature consider continuously operated or pre-scheduled production systems and shows the benefits of coordination by Stackelberg games. In an earlier publication, the authors therefore proposed a coordination method for a single batch production and a single utility system in a single-leader single-follower Stackelberg game (Holters et al., 2018). This paper extends the coordination method to multiple production and utility systems in a multi-leader multi-follower Stackelberg game. This extension allows to capture the complexity of actual industrial sites.

2. Coordination of multiple production and utility systems

In this section, we present a coordination method for multiple production and utility systems in a multi-leader multi-follower Stackelberg game. The method aims at minimizing energy and production cost for all production systems. In the method, all systems optimize themselves and the results are coordinated. The coordination uses only public information. Thus, the coordinating authority can be any participating production or utility system. A central site-manager or authority to handle non-public information is not required.

The method consists of 4 steps to optimize and to coordinate production and utility systems (Figure 1). In step ①, each production system schedules its production, assuming constant energy prices. The resulting energy demand is used as input for step ②. In step ②, the utility systems are scheduled. The utility systems coordinate the amount of energy provided by each utility system (Section 2.1). In step ②, load- and time-dependent energy costs are calculated (Holters et al., 2018) and passed to the production systems. The load- and time-dependent energy costs are the input for step ③. In step ③, the production systems re-schedule their production now using the load- and time-dependent energy costs (Section 2.2). The resulting energy demand is passed to the utility systems to finally schedule the utility systems (step ④). Thus, in step ④, the utility systems schedule their final operation to calculate the final energy cost. Step ④ performs the same computations as step ②. Steps ②, ③ and ④ use inner algorithms, which are explained in the following Sections 2.1 and 2.2.

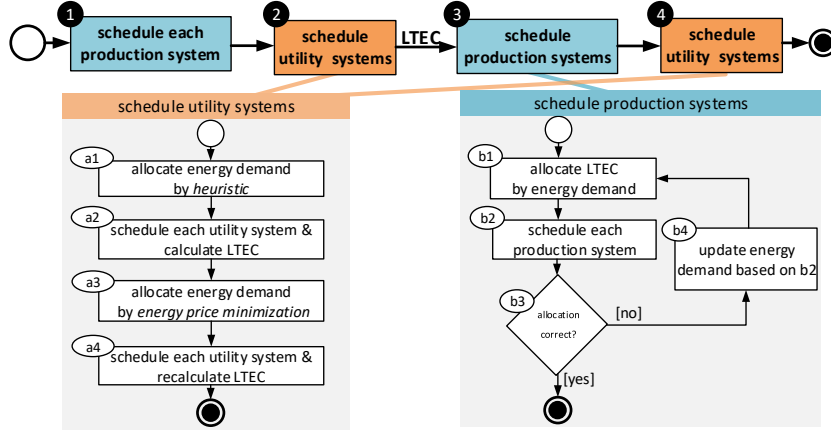


Figure 1: Method to solve the multi-leader multi-follower Stackelberg game by coordination between multiple production and utility systems. Two inner algorithms are employed to schedule utility systems (step ②+④) and schedule production systems (step ③). LTEC: load- and time-dependent energy costs

2.1. Schedule utility systems, step ②+④

In step ② and step ④, the utility systems are scheduled to fulfill the energy demand of the production systems. The amount of energy supplied by each utility system is determined by minimizing the energy price of each energy form e . The coordination of the utility systems is performed in four steps (Figure 1; a1-a4): In step a1, the energy demand of each energy form is allocated to all utility systems based on the maximum capacity of each utility system (=heuristic). An energy price minimization is not possible here, because load- and time-dependent energy costs are not calculated before. In step a2, the utility systems schedule their operation for the allocated energy demand from step a1 and each utility system calculates its load- and time-dependent energy costs. The load- and time-dependent energy costs approximate for each time step the resulting energy costs for changes in the energy demand. For this approximation, the operation of each utility system is scheduled for 2 selected increased energy demands and 2 selected decreased energy demands. The selected energy demands represent loads, at which the supply structure of the utility system needs to change, i.e., an additional unit needs to be switched on or a running unit can be switched off. Between these energy demands, the corresponding energy costs are interpolated to calculate the load- and time-dependent energy costs.

In step a3, the energy price of each energy form e is minimized (Eq. 1) using the load- and time-dependent energy costs of each utility system to allocate the energy demand to the utility systems. This optimization problem is performed by the coordinating authority:

$$\min_{V_{i,e}, C_{i,e}, x} c_e^{\min} \quad (1)$$

$$\text{s.t.} \quad \sum_{i \in US} V_{i,e}^{\text{supply}} = V_e^{\text{demand}} \quad (2)$$

$$c_e^{\min} \geq \frac{C_{i,e}}{V_{i,e}}, \forall i \in US \quad (3)$$

$$A(V_{i,e}, C_{i,e}, x)^T \leq b \quad (4)$$

The objective (Eq. 1) is to minimize the energy price c_e^{min} of each energy form e . The energy supply $V_{i,e}^{supply}$ of the utility systems i needs to fulfill the energy demand V_e^{demand} (Eq. 2). The energy price c_e^{min} is the maximum of the energy prices $C_{i,e}/V_{i,e}$ of all utility systems (Eq. 3). $C_{i,e}$ are the absolute energy cost for provided energy form e by utility system i , which are part of the load- and time-dependent energy costs. All additional constraints are given in Eq. 4, i.e., calculation of $C_{i,e}$ from load- and time-dependent energy costs as function of $V_{i,e}$. x summarizes all additional variables. The energy price minimization allocates the energy demand to the utility systems.

In step a4, each utility system re-schedules its operation to fulfill the newly allocated energy demand and calculates the corresponding load- and time-dependent energy costs. The load- and time-dependent energy costs of all utility systems are cumulated. For step ②, the cumulated load- and time-dependent energy costs and the energy cost are the output and provide the input of step ③. For step ④, the output is the cost to fulfill the final energy demand.

2.2. Schedule production systems, step ③

In step ③, the scheduling of the production systems is coordinated. The scheduling of the production systems is coordinated in 4 steps (Figure 1; b1-b4):

In step b1, the cumulated load- and time-dependent energy costs from step ② are allocated to the production systems. In the allocation of load- and time-dependent energy costs, each section of the piecewise linear load- and time-dependent energy costs (Section 2.1) is split and allocated to the production systems. In the first iteration of the inner algorithm, the load- and time-dependent energy costs are allocated equally to the production systems. In further iterations, the energy demand from the previous iteration is used for allocation to the production systems. In step b2, each production system uses the allocated load- and time-dependent energy costs from step b1 to schedule its production and calculate the energy demand. In step b3, the allocation of cumulated load- and time-dependent energy costs in step b1 is checked by the coordinating authority. If the sum of all energy cost calculated by each production system with the allocated load- and time-dependent energy costs is not equal to the energy cost for the overall energy demand calculated by the cumulated load- and time-dependent energy costs, the algorithm is repeated. If the energy costs are equal, the algorithm terminates. The output of step ③ is the energy demand of all production systems.

3. Case study

3.1. Description

In the case study, an industrial site is considered with 2 production systems and 2 utility systems. The production systems are based on literature examples from Kondili et al. (1993) and Kallrath (2002). Here, we added electricity and heat demands. The product demand is fixed at the time horizon of 30 h. The utility systems are based on the model by Voll et al. (2013). The utility system for the production system from Kondili et al. (1993) has 3 boilers (4000 kW, 1500 kW, 500 kW) and 2 identical combined-heat-and-power engines (1500 kW). The utility system for the production system from Kallrath (2002) has 2 boilers (3000 kW, 1000 kW) and 1 combined-heat-and-power engine (3000 kW). For both utility systems equal prices are assumed to buy (0.16 €/kWh) and purchase (0.1 €/kWh) electricity and buy gas (0.06 €/kWh) from the public grid. All optimization

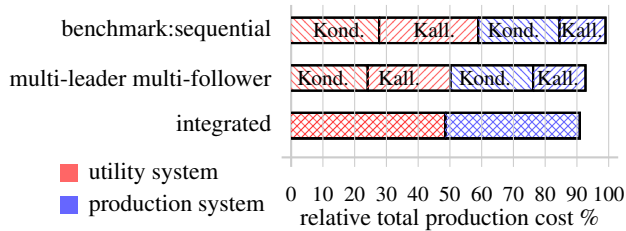


Figure 2: Cost in the case study for the different approaches: The common sequential approach between each production system and the corresponding utility system (benchmark: sequential = 100 %), the multi-leader multi-follower Stackelberg game solved by the proposed coordination method (multi-leader multi-follower) and the integrated optimization of all systems (integrated). Kond.:Kondili; Kall.:Kallrath

problems are formulated in GAMS 24.7.3. The scheduling problems of production and utility systems (MILP) are solved with CPLEX 12.6.3.0, the energy price minimization problems (MINLP) (Eq. 1-4) are solved with DICOPT and CONOPT 3.17A.

3.2. Results

The case study is solved using the proposed method to coordinate multiple production and utility systems in a multi-leader multi-follower Stackelberg game. The results of the method are compared with the common practice to optimize sequentially each production system and the corresponding utility system, and the ideal benchmark, integrated optimization of all systems (Holters et al., 2017). The integrated optimization is solved in 728 s, the proposed method solves the problem in 1477 s.

The proposed method saves 7.3 % of the total production cost compared to the sequential approach (Figure 2). Compared to the integrated optimization, the method increases the cost by only 1.8 % (Figure 2). Thus, the costs from the proposed method are close to the costs from the ideal benchmark. Costs are saved for energy (14.8 %) while production cost increase slightly (3.4 %, Figure 2). However, overall, the production systems as the leaders still benefit, because they have to cover all cost for the energy supply.

In the proposed method, the energy demand of the production systems changes compared to the sequential approach (Figure 3): The peak demands are reduced for electricity (-25.1 %) and increased for heat (+8.5 %). The overall electricity demand also decreases (-17.7 %) and the heat demand increases (+8.0 %). Thus, the production schedules switched to processes with heat demand, because heat can be generated cheaper than electricity. Furthermore, the share of electricity from the public grid decreases (sequential 31.9 %; multi-leader multi-follower 8.2 %). Thus, utilization of on-site utility systems is increased by better coordination between production and utility system scheduling.

Uncertainty in energy demands, electricity prices and gas prices is not considered in the proposed method, but would be an important extension for practical adaption. To explore the sensitivity of the approach to data, we generated 10 instances with variations of ± 20 % around the original energy demands of the production systems by latin-hypercube sampling. For the instances, the proposed method reduces cost by 9.2 % compared to the sequential optimization and is again close to the integrated optimization which saves 10.2 % . Thus, the proposed method saves even more cost than in the nominal case study. In general, the cost savings depend on the actual energy demand of production systems.

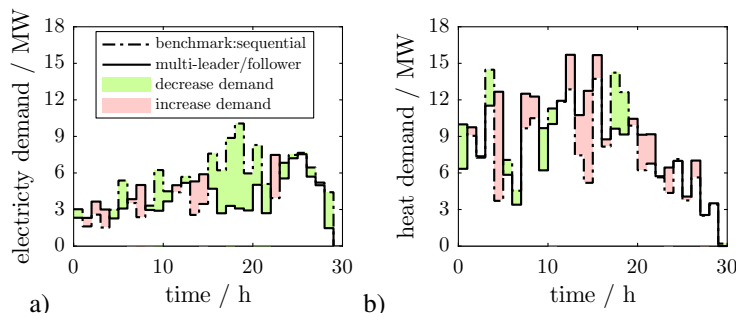


Figure 3: Energy demand of the production systems for the sequential approach and for the proposed method to coordinate the multi-leader multi-follower Stackelberg game.

4. Conclusion

A coordination method is proposed to reduce the overall cost of multiple production and utility systems in a multi-leader multi-follower Stackelberg game. The coordination method employs load- and time-dependent energy costs in one feedback iteration. In a case study, the coordination method reduces overall cost by 7.3 % compared to the common sequential approach. These cost savings are obtained by a revised production schedule, leading to slightly increased production cost (3.4 %), but significantly decreased energy cost (14.8 %). A computational study of 10 instances shows the general benefit of the proposed method.

Acknowledgments

This study was funded by the 'Europäischer Fond für regionale Entwicklung (EFRE)' (EFRE-0800289). The support is gratefully acknowledged.

References

- M. H. Agha, R. Thery, G. Hêtreux, A. Hait, J. M. L. Lann, 2010. Integrated production and utility system approach for optimizing industrial unit operations. *Energy* 35 (2), 611–627.
- L. Holters, B. Bahl, M. Hennen, A. Bardow, 2018. Playing Stackelberg games for minimal cost for production and utilities. In: *Proceedings of ECOS 2018*.
- L. Holters, B. Bahl, M. Lampe, M. Hennen, A. Bardow, 2017. Integrated synthesis of batch plants and utility systems. *Comp. Aided Chem. Eng.* 40, 625 – 630.
- J. Kallrath, Aug 2002. Planning and scheduling in the process industry. *OR Spectrum* 24 (3), 219–250.
- E. Kondili, C. Pantelides, R. Sargent, 1993. A general algorithm for short-term scheduling of batch operations - I. MILP formulation. *Comp. & Chem. Eng.* 17 (2), 211–227.
- S. Maharjan, Q. Zhu, Y. Zhang, S. Gjessing, T. Basar, 2013. Dependable Demand Response Management in the Smart Grid: A Stackelberg Game Approach. *IEEE Transactions on Smart Grid* 4 (1), 120–132.
- L. S. Maxeiner, S. Wenzel, S. Engell, 2017. Shared resource allocation in the process industries via price-based coordination for systems with discrete decisions. *Comp. Aided Chem. Eng.* 40, 1897 – 1902.
- M. A. Ramos, M. Rocafull, M. Boix, D. Aussel, L. Montastruc, S. Domenech, 2018. Utility network optimization in eco-industrial parks by a multi-leader follower game methodology. *Comp. & Chem. Eng.* 112, 132 – 153.
- P. Voll, C. Klaffke, M. Hennen, A. Bardow, 2013. Automated superstructure-based synthesis and optimization of distributed energy supply systems. *Energy* 50, 374–388.
- M. Yu, S. H. Hong, 2016. Supply-demand balancing for power management in smart grid: A stackelberg game approach. *Applied Energy* 164, 702 – 710.
- D. Yue, F. You, 2017. Stackelberg-game-based modeling and optimization for supply chain design and operations: A mixed integer bilevel programming framework. *Comp. & Chem. Eng.* 102, 81 – 95.

A point estimate method-based back-off approach to robust optimization: application to pharmaceutical processes

Victor N. Emenike^{1,a,b}, Xiangzhong Xie^{1, a,b}, Ulrike Krewer^{a,b} and René Schenkendorf^{a,b,*}

^a*Institute of Energy and Process Systems Engineering, TU Braunschweig, Franz-Liszt-Straße 35, 38106 Braunschweig, Germany*

^b*Center of Pharmaceutical Engineering, Franz-Liszt-Straße 35A, 38106 Braunschweig, Germany
r.schenkendorf@tu-braunschweig.de*

Abstract

In this contribution, we propose estimating the means and variances required for calculating back-off terms by using the point estimate method (PEM) as a highly efficient sampling strategy in robust process design. As case studies, we consider an upstream pharmaceutical process which involves the synthesis of 2-hydroxy-ketones via enzyme-catalyzed carbonylation and a downstream pharmaceutical process that includes the continuous crystallization of ibuprofen. We show that the proposed PEM-based back-off approach is significantly faster than conventional Monte Carlo brute-force sampling methods while maintaining robust solutions with low approximation errors. In general, the efficient PEM-sampling strategy guarantees the analysis and the robust design of complex (bio)pharmaceutical process chains.

Keywords: pharmaceutical manufacturing, robust optimization, back-off approach, enzyme catalysis, ibuprofen crystallization

1. Introduction

The pharmaceutical industry has a substantial impact on the social and economic welfare of the individual and society. For the industry to continue producing high-quality and effective drugs even in the face of economic constraints, rising population and diseases, regulatory bodies and industry leaders alike have stipulated Quality by Design (QbD) as an essential paradigm. At the heart of QbD are mathematical models which are crucial for analyzing, optimizing, monitoring and controlling pharmaceutical processes (Emenike et al., 2018a,b). These models need to be properly calibrated to ensure that they reflect the physical processes they represent (Schenkendorf et al., 2018). In calibrating these models, a crucial issue that has to be dealt with is the presence of model and parameter uncertainties. A possible way to robustify processes under uncertainty is by using the back-off approach. This approach involves tightening violated constraints and shrinking the feasible region by introducing margins called back-offs. By so doing, the worst-case realization of a given process will still be feasible despite variations in the constraints (Shi et al., 2016). Moreover, these back-offs are usually calculated offline, and thus, do not lead to additional complexity of the optimization problems. Typically, Monte Carlo simulations are used to estimate the statistical moments (i.e., means and variances) required for calculating back-offs (Shi et al.,

¹These authors contributed equally.

2016). However, for these means and variances to be accurately estimated, numerous Monte Carlo simulations are usually required. Thus, this could lead to high computational costs especially when a single Monte Carlo simulation of the process is computationally expensive.

Alternatively, these statistical moments can be approximated efficiently by using the point estimate method (PEM). It has been shown that the PEM is a computationally efficient and relatively accurate sampling strategy for estimating statistical moments (Schenkendorf, 2014; Xie et al., 2018b). Recently, we proposed a systematic robust optimization framework that combines the elementary process functions methodology, global sensitivity analysis, and the back-off approach (Emenike et al., 2019). A key contribution in Emenike et al. (2019) was a new back-off algorithm that uses the PEM instead of Monte Carlo simulations. We showed that the proposed PEM-based back-off approach is at least 10 times faster than the conventional Monte Carlo-based back-off approach while maintaining the quality of robust solutions. Maußner and Freund (2018) used cubature rules in lieu of Monte Carlo simulations and came to similar conclusions.

In this contribution, we build upon our original work (Emenike et al., 2019) by applying the novel algorithm in the presence of correlated parameter uncertainties and show that the robustification algorithm is not limited to upstream processes but is a versatile tool for whole pharmaceutical process chains. To this end, we apply the novel algorithm to an upstream pharmaceutical process that involves the synthesis of 2-hydroxy-ketones via enzyme-catalyzed carbonylation and a downstream pharmaceutical process that includes the crystallization of ibuprofen. Details of the algorithm and the results for the case studies are presented in sections 2 and 3, respectively.

2. Methodology

A major advantage of the back-off approach to dynamic optimization under uncertainty is that its formulation is of similar complexity as the nominal dynamic optimization problem. The robust optimization problem (Problem 1) with time-varying back-offs $\mathbf{b}(t)$ is given as:

$$\begin{array}{ll} \underset{\mathbf{x}(\cdot), \mathbf{u}(\cdot), \mathbf{z}(\cdot)}{\text{minimize}} & \Phi(\mathbf{x}(t_f)) \end{array} \quad (1a)$$

$$\text{subject to} \quad \dot{\mathbf{x}}(t) = \mathbf{f}(\mathbf{x}(t), \mathbf{z}(t), \mathbf{u}(t), \bar{\mathbf{p}}), \quad \forall t \in \mathcal{T}, \quad (1b)$$

$$\mathbf{g}(\mathbf{x}(t), \mathbf{z}(t), \mathbf{u}(t), \bar{\mathbf{p}}) = \mathbf{0}, \quad \forall t \in \mathcal{T}, \quad (1c)$$

$$\mathbf{h}(\mathbf{x}(t), \mathbf{z}(t), \mathbf{u}(t), \bar{\mathbf{p}}) + \mathbf{b}(t) \leq \mathbf{0}, \quad \forall t \in \mathcal{T}, \quad (1d)$$

$$\mathbf{x}(t_0) = \mathbf{x}_0, \quad (1e)$$

$$\mathbf{u}(t) \in \mathcal{U}, \quad (1f)$$

on the time horizon $\mathcal{T} := [t_0, t_f] \subset \mathbb{R}$, where \mathbf{x} , \mathbf{u} , \mathbf{z} represent states, controls, and algebraic variables, respectively. \mathbf{g} and \mathbf{h} represent the equality and inequality constraints, respectively. As we can see from Problem 1, the dynamic optimization with back-offs is optimized at the nominal parameter vector $\bar{\mathbf{p}}$. Here, the time-varying back-offs $\mathbf{b}(t)$ in Eq. 1d are included as margins to shrink the feasible region of the dynamic optimization problem and thus, making the optimal operating conditions robust.

As pointed out by Shi et al. (2016), the solution from Problem 1 is not guaranteed to be optimum, unless the back-offs are insensitive to the decision variables. Therefore, an iterative approach is proposed to update the back-offs with the optimal design from the last iteration. The solution from Problem 1 and back-offs are consistently improved and can be exported once the back-offs converge. We depict the details regarding the iterative algorithm in Fig. 1. Moreover, we use the PEM instead of Monte Carlo simulations used by Shi et al. (2016) to derive the statistical moments required to calculate the back-offs. The PEM utilizes a relatively small number of deterministic

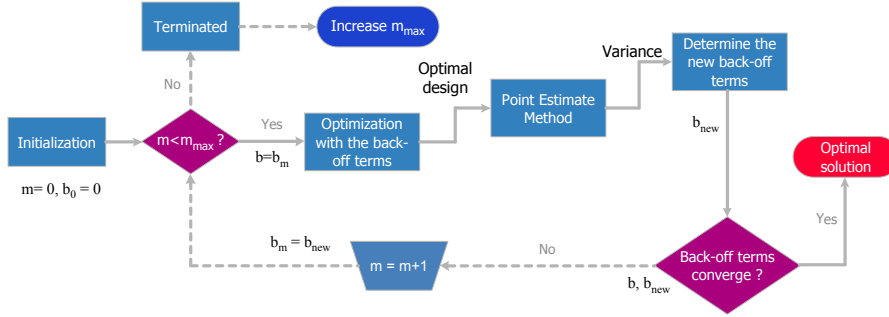


Figure 1: Computational scheme for the point estimate method-based back-off approach for robust optimization, where m is the iteration index.

samples to compute the statistical moments of system states and thus, facilitates an efficient back-off algorithm. For more details regarding the PEM, please refer to Xie et al. (2018b) and Emenike et al. (2019).

3. Case studies

3.1. Enzyme-catalyzed carboligation

First, we consider an upstream pharmaceutical process that involves an enzyme-catalyzed carboligation between propanal (A) and benzaldehyde (B) to form 2-hydroxy-ketones (BA) and benzoin (BB). Here, we aim to maximize the formation of the target product BA under the correlated parameter uncertainties specified in Xie et al. (2018a). The mechanistic model for this reaction is given as:

$$\dot{\mathbf{x}}(t) = \mathbf{f}(\mathbf{x}(t), \mathbf{z}(t), \mathbf{u}(t), \mathbf{p}) = \begin{bmatrix} \frac{u_A \cdot C_A^{\text{in}}}{V} - \frac{C_A}{V} (u_A + u_B) + r_A \\ \frac{u_B \cdot C_B^{\text{in}}}{V} - \frac{C_B}{V} (u_A + u_B) + r_B \\ -\frac{C_{BA}}{V} (u_A + u_B) + r_{BA} \\ -\frac{C_{BB}}{V} (u_A + u_B) + r_{BB} \\ -\frac{C_E}{V} (u_A + u_B) + r_E \\ u_A + u_B \end{bmatrix}, \quad (2)$$

where C_i is the concentration of species i ; r_A, r_B, r_{BA}, r_{BB} , and r_E are the reaction rates for A, B, BA, BB, and E, respectively; u_A and u_B are the controlled feed rates; and C_A^{in} and C_B^{in} are the inlet feed concentrations of A and B, respectively. For details on the model and model parameters, we refer to Emenike et al. (2019). First, forward simulations by using 10,000 Monte Carlo simulations were performed on the nominal problem to determine which constraints were violated, and it was found that only the inequality constraint bounding C_{BB} was violated. Therefore, we focus on robustifying only the C_{BB} inequality constraint as shown in Eq. (3):

$$0 \leq C_{BB}(t) \leq 2.78 \text{ mM} - b(t), \quad \forall t \in \mathcal{T}, \quad (3)$$

where 2.78 mM is the solubility limit of BB, $\mathcal{T} := [t_0, t_f] \subset \mathbb{R}$, and final time, $t_f = 300$ min. By applying the robust optimization strategy presented in Section 2 and aiming to satisfy Eq. 3 at a probability of 99.90%, we see in Table 1 that the PEM-based back-off algorithm is able to achieve this after just one iteration of the algorithm.

Table 1: Comparison of the point estimate method-based algorithm with the Monte Carlo-based back-off algorithm for robust dynamic optimization in comparison to the nominal case.

Scenarios	$C_{BA}(t_f)$ mM	Violation probability [%]	CPU time [s]
Nominal	3.60	57.65	4
PEM-based back-off	3.48	0.16	114
Monte Carlo-based back-off	3.49	0.13	2626

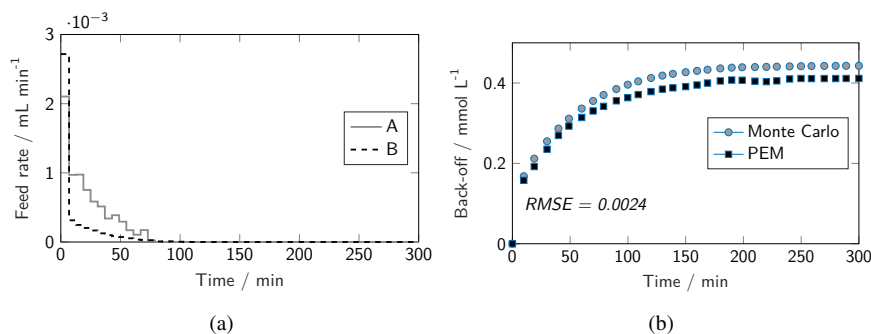


Figure 2: Results for the upstream pharmaceutical process: enzyme-catalyzed carboligation. (a) robust controls. (b) comparison between PEM and Monte Carlo simulations.

Moreover, this was achieved at a computation time that is 23 times faster than the conventional Monte Carlo-based back-off algorithm which was used as a benchmark for our algorithm (see Table 1). This speed-up is mainly due to the lower number of PEM sample points ($2 \times 13^2 + 1 = 339$) in comparison to the 10,000 Monte Carlo sample points. It is also possible to further reduce the PEM points by using a global sensitivity analysis as shown in Emenike et al. (2019). It can be seen in Fig. 2b that the time-varying back-offs calculated by both approaches are close with a marginal root-mean-square prediction error (RMSE) of 0.0024. This low RMSE validates the accuracy of our PEM-based approach. Furthermore, we note that the probability of violation and the maximum $C_{BA}(t_f)$ obtained are very close for both approaches, thus, suggesting that our PEM-based back-off approach is very accurate for the case study considered. The robust controls (see Fig 2a) lead to a maximum concentration of 3.48 mmol L⁻¹ which is 3.33% lower than the nominal value. This marginal decrease shows that the novel approach is not adversely conservative while ensuring robustness. Therefore, these results demonstrate that the PEM-based back-off strategy is very efficient and useful for the enzyme-catalyzed carboligation considered in this work.

3.2. Crystallization of ibuprofen

Second, we consider the continuous crystallization of ibuprofen in a plug-flow crystallizer (PFC) as a representative downstream pharmaceutical process. The crystal size distribution (CSD) n was chosen as an important key performance indicator for QbD. A population balance equation in combination with mass balance equations in liquid and solid phase was used to predict the evolution of the CSD along the PFC. To reduce the computational complexity, we discretized the PFC model to ordinary differential equations by using the classical method of moments. The resulting moment-based model for PFC is given in Eqs. (4) to (6):

$$\frac{d\mu_0}{dz} = \frac{B}{v} \quad (4)$$

$$\frac{d\mu_l}{dz} = \frac{BL_0^l}{v} + \frac{kG\mu_{l-1}}{v} \quad l = 1, \dots, 5 \quad (5)$$

Table 2: The mean value of mass-based mean crystal size d_{43} and the probability of a constraint violation (supersaturation) from the nominal design and the robust design with the PEM-based back-offs.

Scenarios	$\mathbb{E}(d_{43})$	Violation probability [%]
Nominal	109.3	48
PEM-based back-off	108.8	3

$$\text{Liquid: } \frac{\partial C}{\partial z} = -\frac{k_v \rho_s}{v} (BL_0^3 + 3G\mu_2), \quad (6)$$

where z is the axis coordinate of the PFC, m; L_0 is the nuclei size, m; v is the superficial velocity of slurry along the PFC, m s^{-1} ; k_v and ρ_s are the shape factor and the crystal density, kg m^{-3} , and C is the mass of solute per kg slurry, kg kg^{-1} . μ_k is the k th moment which is used to describe the major information in CSD and defined with Eq. (7). B and G are the nucleation rate, $\#\text{kg}^{-1} \text{s}^{-1}$, and the growth rate, m s^{-1} , which describe the kinetics of the crystallization of ibuprofen and are determined by the degree of supersaturation S , as shown in Eqs. (8) and (9):

$$\mu_l = \int_0^{\infty} L^l n dL, \quad l = 0, \dots, 5 \quad (7)$$

$$B = k_{b_0} S(T) \quad (8)$$

$$G = k_{g_0} \exp\left(\frac{T}{T_g}\right) S(T) \quad (9)$$

This case study aims to maximize the mass-based mean crystal size d_{43} (i.e., the ratio between μ_4 and μ_3) by manipulating the temperature along the PFC. There is an inequality constraint in the design which restricts the supersaturation of ibuprofen in the solution below the primary nucleation threshold to ensure no primary nucleation occurs. Several other inequality constraints on the yield of product and temperature gradient are also satisfied but not discussed in what follows, as they are not violated even in the presence of parameter uncertainties. Rashid (2011) estimated the values of the kinetic parameters k_{b_0} , k_{g_0} , and T_g with designed experiments and showed the estimated values are not accurate and associated with uncertainty. The parameter uncertainties are then described by Gaussian distributions and thus, are taken into account in the robust design of the PFC in this work.

For the nominal design, the parameter uncertainties are neglected. The obtained d_{43} is $109.3 \mu\text{m}$ (see Table 2). However, the inequality constraint on supersaturation is violated with a probability of 48% due to parameter uncertainties. The violation probability of inequality constraint is determined with 10,000 evaluations of the PFC model with the random samples generated from the probability distributions of kinetic parameters. The PEM-based back-off strategy introduced in Section 2 is then implemented to design a robust PFC tolerant to the parameter uncertainties, where the target violation probability of the inequality constraint is set to smaller than 1%. Results from the iterative back-off approach are depicted in Fig. 3. As we can see in Fig. 3a, the tolerance factor ε_{tol} , which represents the difference between the back-offs in the adjacent iterations, converges within 10 iterations. The resulting time-varying back-offs are plotted in Fig. 3b, in which the supersaturation is shrunk more in the middle and less on both sides of the PFC to mitigate the effect of parameter uncertainties. According to the results listed in Table 2, the d_{43} from the robust design decreases slightly when compared to the value from nominal design. The probability of constraint violation decreases to 3%. Thus, the process robustness is increased at the cost of a deteriorated performance. Although the back-off approach increases the robustness of the process significantly, the obtained violation probability 3% is still three times larger than the target value of 1%. The reason for this is that the back-offs calculated with the variances of system states are actually not accurate when their probability distributions are asymmetric, as shown in Fig. 3c.

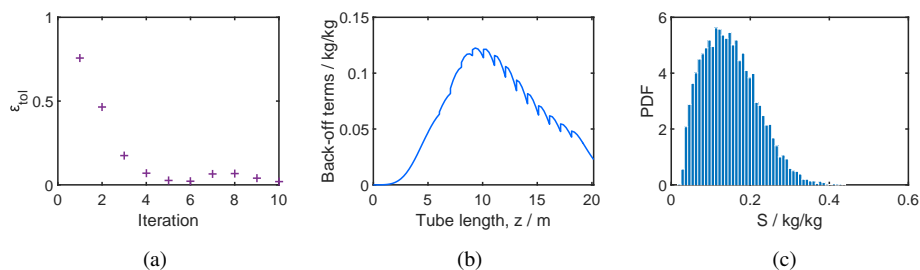


Figure 3: Results for the downstream pharmaceutical process: continuous crystallization of ibuprofen. (a) Convergence plot of the back-off terms. (b) value of the time-varying back-off terms at the last iteration. (c) probability distribution of supersaturation S at location $z = 11$ m of the PFC.

4. Conclusions

In this work, we proposed a PEM-based back-off approach for the robust design of upstream and downstream pharmaceutical processes. First, the approach was implemented for the design of a fed-batch reactor for enzyme-catalyzed carboligation in the presence of parameter correlations and uncertainty. The results showed that the proposed PEM-based back-off approach is significantly faster than the conventional Monte Carlo-based back-off approach while achieving high accuracy of the robust solutions. The method was also applied to the design of continuous crystallization of ibuprofen in the presence of uncertainties in the kinetic parameters. This approach also lowered the value of constraint violation and significantly improved the robustness of the process. However, the probability of a constraint violation is still three times higher than the given target value due to the asymmetric probability distribution of system states. Future work will include non-Gaussian probability distributions for robust process design.

Acknowledgements

X. Xie acknowledges funding from the “Promotionsprogramm μ -Props” by MWK Niedersachsen. V. Emenike and X. Xie acknowledge the support from the International Max Planck Research School for Advanced Methods in Process and Systems Engineering, MPI Magdeburg.

References

- V. N. Emenike, R. Schenkendorf, U. Kreuer, 2018a. A systematic reactor design approach for the synthesis of active pharmaceutical ingredients. *European Journal of Pharmaceutics and Biopharmaceutics* 126, 75–88.
- V. N. Emenike, R. Schenkendorf, U. Kreuer, 2018b. Model-based optimization of biopharmaceutical manufacturing in *Pichia pastoris* based on dynamic flux balance analysis. *Computers & Chemical Engineering* 118, 1–13.
- V. N. Emenike, X. Xie, R. Schenkendorf, A. C. Spiess, U. Kreuer, 2019. Robust dynamic optimization of enzyme-catalyzed carboligation: A point estimate-based back-off approach. *Computers & Chemical Engineering* 121, 232–247.
- J. Maußner, H. Freund, 2018. Optimization under uncertainty in chemical engineering: Comparative evaluation of unscented transformation methods and cubature rules. *Chemical Engineering Science* 183, 329–345.
- M. A. Rashid, 2011. Crystallization engineering of ibuprofen for pharmaceutical formulation. PhD dissertation, Queensland University of Technology.
- R. Schenkendorf, 2014. A general framework for uncertainty propagation based on point estimate methods. Second European Conference of the Prognostics and Health Management Society, PHME14, Nantes, France.
- R. Schenkendorf, X. Xie, M. Rehbein, S. Scholl, U. Kreuer, 2018. The impact of global sensitivities and design measures in model-based optimal experimental design. *Processes* 6 (4), 27.
- J. Shi, L. T. Biegler, I. Hamdan, J. Wassick, 2016. Optimization of grade transitions in polyethylene solution polymerization process under uncertainty. *Computers and Chemical Engineering* 95, 260–279.
- X. Xie, R. Ohs, A. Spiess, U. Kreuer, R. Schenkendorf, 2018a. Moment-independent sensitivity analysis of enzyme-catalyzed reactions with correlated model parameters. *IFAC-PapersOnLine* 51 (2), 753 – 758.
- X. Xie, R. Schenkendorf, U. Kreuer, 2018b. Toward a comprehensive and efficient robust optimization framework for (bio)chemical processes. *Processes* 6 (10), 183.

From peak power prices to seasonal storage: Long-term operational optimization of energy systems by time-series decomposition

Nils Baumgärtner^a, David Shu^b, Björn Bahl^a, Maike Hennen^a and André Bardow^{a,b,*}

^a*Institute of Technical Thermodynamics, RWTH Aachen University, Aachen, Germany*

^b*Institute of Energy and Climate Research - Energy Systems Engineering (IEK-10),*

Forschungszentrum Jülich, Jülich, Germany

andre.bardow@ltt.rwth-aachen.de

Abstract

Long-term operation of energy systems is a complex optimization task. Often, such long-term operational optimizations are solved by direct decomposing the problem into smaller subproblems. However, direct decomposition is not possible for problems with time-coupling constraints and variables. Such time-coupling is common in energy systems, e.g., due to peak power prices and (seasonal) energy storage. To efficiently solve coupled long-term operational optimization problems, we propose a time-series decomposition method. The proposed method calculates lower and upper bounds to obtain a feasible solution of the original problem with known quality. We compute lower bounds by the Branch-and-Cut algorithm. For the upper bound, we decompose complicating constraints and variables into smaller subproblems. The solution of these subproblems are recombined to obtain a feasible solution for the long-term operational optimization. To tighten the upper bound, we iteratively decrease the number of subproblems. In a case study for an industrial energy system, we show that the proposed time-series decomposition method converges fast, outperforming a commercial state-of-the-art solver.

Keywords: large-scale MILP, seasonal storage, network charges, emission targets

1. Introduction

In industry, energy is often supplied by on-site energy systems. The efficiency of on-site energy systems can be significantly improved by optimizing operation. Operational optimization typically results in mixed-integer linear programming (MILP) problems. These MILP problems are proven to be weakly NP-hard, and thus computationally challenging for large problems sizes (Goderbauer et al., 2019).

In the operation of energy systems, the number of variables results directly from the number of considered time steps, and thus long-term operational optimization leads to many variables. An intuitive solution approach is to solve the time steps independently, i.e., use direct decomposition. However, such direct decomposition is only possible without time-coupling constraints and variables (Bradley et al., 1992). In practice, time-coupling constraints and variables are common for energy systems, e.g., by peak power prices, seasonal storage systems, annual emission limits or net connection fees. To cope with time-coupling constraints in the optimization of energy systems, various solution methods have been proposed (Tab.1). A first class of methods is based on simplification of

Table 1: Solution methods for long-term operational optimizations of energy systems with time-coupling constraints and variables

Approach/Idea	Literature	Strengths (+)/Limits (-)
Model simplifications	(Piacentino and Cardona, 2008), (Yokoyama, 2013)	+ easily applicable – limited model scope
Non-deterministic	(Eglese, 1990), (Kavvadias and Maroulis, 2010)	+ allow parallelization + generic – no quality measure
Decomposition	(Yokoyama and Ito, 1996), (Al-Agtash and Su, 1998), (Rong et al., 2008), (Nasrolahpour et al., 2016), (Wang et al., 2016)	+ allow parallelization + generic + provide quality measure – slow convergence – complex formulation

component models to reduce the complexity of the optimization, rendering the full optimization problem solvable even with time-coupling constraints and variables. However, model simplification limits the accuracy of the results. Second, non-deterministic methods, such as genetic algorithms, are therefore employed to solve large-scale problems. While these non-deterministic approaches can generate good solutions for difficult problems and often allow for parallelization, they are unable to evaluate the quality of the proposed solution (Hanne and Dornberger, 2017). Therefore, mathematical decomposition methods have been nested to treat both time-coupling constraints and variables in MILP optimizations, e.g., column generation, Lagrangian, and Benders (Wang et al., 2016). However, despite the successful application of mathematical decomposition methods to energy system problems, some challenges remain: Column generation often suffers from slow convergence in practice (Desrosiers and Lübbecke, 2011a). The formulation and implementation of Branch-and-Price is complex (Desrosiers and Lübbecke, 2011b). Lagrangian methods require a good choice of multipliers for fast convergence. However, the selection of Lagrangian multipliers is difficult leading to a large variety of methods (Conejo et al., 2006). Benders decomposition suffers from slow convergence due to a high number of slow iterations. Improvements for the convergence of Benders decomposition have been proposed but their formulation and implementation is complex (Rahmaniani et al., 2017).

In this work, we propose a time-series decomposition-based solution algorithm for solving long-term operational optimization problems. The proposed time-series decomposition handles both time-coupling constraints and variables in the operational optimization. The method combines the strengths of the approaches in literature (Tab.1) using an exact model, is easily applicable, allows for parallelization and shows fast convergence.

2. Time-coupling constraints and variables in operational optimization

To illustrate the complexity of operation optimization problems with time-coupling constraints and variables, we state a generic operational problem for energy systems as mixed-integer linear programming (MILP) problem.

$$\min_{\dot{V}_{n,t}, \delta_{n,t}, \dot{V}_{\text{grid}}^{\max}, V_{n,t}, x} \text{OPEX} = \sum_{t \in \mathcal{T}} \left(\Delta t_t \sum_{n \in \mathcal{E}} c_{n,t}^o \frac{\dot{V}_{n,t}}{\eta_n} \right) + c_p \cdot \dot{V}_{\text{grid}}^{\max} + c_{\text{net}} \cdot \sum_{t \in \mathcal{T}} \dot{V}_{\text{grid},t} \quad (1)$$

$$\text{s.t.} \quad \sum_{n \in \mathcal{C} \setminus \mathcal{C}_{\text{stor}}} \dot{V}_{n,t} + \sum_{n \in \mathcal{C}_{\text{stor}}} (\dot{V}_{n,t}^{\text{out}} - \dot{V}_{n,t}^{\text{in}}) = \dot{E}_t, \quad \forall t \in \mathcal{T}, \quad (2)$$

$$A_1 \dot{V}_{n,t} + \tilde{A}_1 \delta_{n,t} \leq b_1, \quad \forall t \in \mathcal{T}, \forall n \in \mathcal{C}, \quad (3)$$

$$A_2 (\dot{V}_{n,t}, \delta_{n,t}, x)^T \leq b_2, \quad \forall t \in \mathcal{T}, \forall n \in \mathcal{C}, \quad (4)$$

$$V_{n,t} + \Delta t_t \cdot (\dot{V}_{n,t}^{\text{in}} - \dot{V}_{n,t}^{\text{out}}) = V_{n,t+1}, \quad \forall t \in \mathcal{T}, \forall n \in \mathcal{C}_{\text{stor}} \quad (5)$$

$$|\dot{V}_{\text{grid},t}| \leq \dot{V}_{\text{grid}}^{\text{max}}, \quad \forall t \in \mathcal{T}, \quad (6)$$

$$c_i = \begin{cases} c_i^{\text{high}} & , \text{if } \frac{\sum_{t \in \mathcal{T}} \dot{V}_{\text{grid},t} \cdot \Delta t_t}{V_{\text{grid}}^{\text{max}}} \leq 2500h \\ c_i^{\text{low}} & , \text{otherwise} \end{cases} \quad \text{for } i = \{\text{net}, p\} \quad (7)$$

$$\sum_{t \in \mathcal{T}} \left[(\dot{V}_{\text{grid},t} \cdot c_{t,\text{el}}^{\text{CO}_2}) + \sum_{n \in \mathcal{C}} \left(\frac{\dot{V}_{n,t}}{\eta_n} \cdot c_{t,\text{gas}}^{\text{CO}_2} \right) \right] \leq C_{\text{CO}_2}^{\text{max}}, \quad (8)$$

$$\delta_{n,t} \in \{0, 1\}; x \in \mathbb{R}^a \times \{0, 1\}^{\tilde{a}}; \dot{V}_{n,t} \in \mathbb{R}; V_{n,t}, \dot{V}_{\text{grid}}^{\text{max}} \in \mathbb{R}^+.$$

Operational expenses *OPEX* are defined as the sum of the output power $\dot{V}_{n,t}$ of every component $n \in \mathcal{C}$ in every time step t divided by the efficiency η_n and multiplied by the specific operation cost $c_{n,t}^o$ and the duration Δt_t of a time step (Eq.1). A further contribution to *OPEX* (Eq.1) are the network charges C_{net} , which result from the electricity consumption $\sum_{t \in \mathcal{T}} \dot{V}_{\text{grid},t}$ multiplied by network charges $c_{\text{net}}^{(\text{low/high})}$ that depend on the utilization time. The peak power $\dot{V}_{\text{grid}}^{\text{max}}$ multiplied by a peak power price c_p results in additional *OPEX* (Eq.1). As constraint, the component's output power $\dot{V}_{n,t}$ plus the net energy output of the storage units $\dot{V}_{n,t}^{\text{out}} - \dot{V}_{n,t}^{\text{in}}$ has to meet the energy demand \dot{E}_t at every time step t (Eq.2). Further (in)equalities with the coefficient matrices A_1 , \tilde{A}_1 , and the vector b_1 determine the component's binary on/off status $\delta_{n,t}$ and the current part-load performance (Eq.3). Additional constraints are summarized in the surrogate coefficient matrix A_2 , including all other variables of the original problem represented by the vector x (Eq.4). The future storage level $V_{n,t+1}$ is coupled to the current storage level $V_{n,t}$ by the net energy input of the storage units $\dot{V}_{n,t}^{\text{in}} - \dot{V}_{n,t}^{\text{out}}$. Thus, the storage balance equation couples the entire time series (Eq.5). The peak power $\dot{V}_{\text{grid}}^{\text{max}}$ is the maximum electricity exchanged with the grid. Thus, $\dot{V}_{\text{grid}}^{\text{max}}$ is a time-coupling variable for the entire time series (Eq.6). The dependency of prices $c_i^{(\text{low/high})}$ on the utilization time is both a of coupling constraint and variable for the entire time series (Eq.7). Often, annual emission limits $C_{\text{CO}_2}^{\text{max}}$ have to be obeyed. Emission limits represent a coupling constraint for the entire time series (Eq.8). To solve such long-term operational problems despite time-coupling (Eq. 5-8), we propose a time-series decomposition method.

3. Time-series decomposition for long-term operational optimization

A time-series decomposition method is proposed to generate feasible solutions of long-term operational optimization problems with known solution quality. The decomposition method provides lower and upper bounds in a parallel computing mode.

For the lower bound, we relax all binary variables ($\delta_{n,t}, x \in \{0, 1\}$) of the operational problem (Eq.1-8), thereby converting the complex MILP into an LP, which can be solved efficiently. This solution of the relaxed problem serves as first lower bound. Subsequently, the Branch-and-Cut procedure starts by branching on binary variables and cutting off branches which cannot improve the solution (IBM Cooperation, 2016).

The upper bound is obtained by four steps (Fig. 1):

- (i) Initial heuristic to initialize the number of subproblems
- (ii) Decomposition of time-coupling constraints and variables
- (iii) Optimizing subproblems in parallel computing mode
- (iv) Combining subsolutions to upper bound

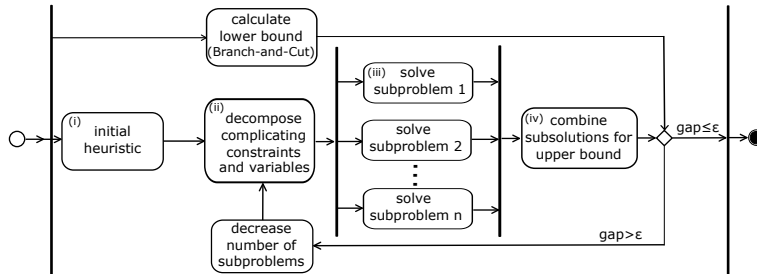


Figure 1: Overview of the proposed time-series decomposition method to create feasible solutions of operational optimization problems with known solution quality.

Using the lower and upper bound, we calculate a solution quality ε and check if the desired optimality gap is satisfied.

$$\varepsilon = \frac{\text{upper bound} - \text{lower bound}}{\text{upper bound}}. \quad (9)$$

If the optimality gap is not satisfied, we iteratively decrease the number of subproblems. In the following, we present the details of steps (i), (ii), and (iv) of the proposed time-series decomposition.

Step (i): Initial heuristic

Initialization of the decomposition method requires an initial number of subproblems. To identify a good estimate for this initial number, a heuristic is employed, aiming at minimal calculation time for the first decomposition. In the heuristic, we consider a wide range for the possible number of subproblems. For each number, we decompose the problem but solve only the first subproblem. The decomposition and solution time is recorded and extrapolated to the full number of subproblems. The number of subproblems resulting in the minimum extrapolated solution time is selected as the initial number of subproblems.

Step (ii): Decomposition of time-coupling constraints and variables

We decompose complicating constraints and variables into smaller subproblems. The decomposition is generic and conducted automatically based on the type of time-coupling constraint or variable:

- (1) For storage-like constraints (Eq. 5), we fix start and end values for each subproblem to ensure feasibility. The fixed values are adapted in the next iteration.
- (2) Time-coupling variables like (Eq. 6-7) are replaced by independent copies in every subproblem, resulting in independent subproblems, e.g., net connection fees and peak power prices are calculated for each subproblem independently.
- (3) For time-coupling constraints like the emission limits in Eq. (8), a fraction of the limit is allocated to each subproblem. This fraction is computed for each subproblem by independent minimization of the emissions within each subproblem.

- (4) To improve performance, we extend each subproblem by aggregated time steps and the peak demands of all other subproblems. Thus, in each subproblem, a small part of the long-term operational optimization is solved with the full accuracy of the time series and the rest with low accuracy.

Step (iv): Combining subsolutions to upper bound

The solutions of the subproblems are combined to a feasible solution for the original problem. For this, the independent copies of variables in the subproblems (2) are resubstituted and the added aggregated time steps (4) are deleted. The solution of the final iteration is used to warmstart the original problem to further enhance solution quality.

4. Case study

The proposed decomposition method is applied to a long-term operational problem based on Baumgärtner et al. (2018). We investigate an industrial energy system with three units of each boilers, compression chillers, absorption chillers, and heat exchangers, one combined heat and power engine, a photovoltaic system, an inverter station, a battery, and one storage tank for each hot and cold water. We consider one year of operation with a two-hourly resolution for demands of process heat, hot and cold water, electricity, as well as solar radiation, and electricity grid prices. The original operational problem contains $1.2 \cdot 10^6$ equations and $6 \cdot 10^5$ variables (incl. $2 \cdot 10^5$ binaries) with $3 \cdot 10^6$ nonzero elements. The resulting long-term operational problem is highly coupled due to the storage and battery systems, an annual emission limit, peak power prices and net connection fees (Eq.1-8). To validate the computational results, we repeat the calculation for 5 instances generated by statistical noise ($\pm 5\%$) on the data. As benchmark, we solve the original synthesis problem directly with CPLEX without any decomposition.

In the initial heuristic (step (i)), the original problem is decomposed into 219 subproblems. The size of the subproblems is iteratively increased until the desired optimality gap of 2 % is satisfied with a decomposition into 20 subproblems.

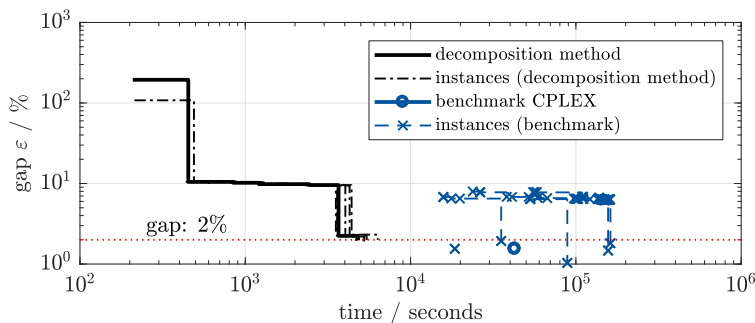


Figure 2: Gap ϵ of the proposed decomposition method and the benchmark CPLEX as function of the solution time. The required optimality gap of 2 % is marked in dotted red.

The decomposition method finds a feasible solution, with cost deviating less than 2 % from optimality, in 5,207 s on average (Fig. 2). The average computational time of the benchmark is 16 times larger (83,952 s) to obtain solutions of equal quality. On average, after 203 s, the proposed time-series decomposition method generates a first feasible solution, whereas on average the benchmark requires 175 times longer (35,617

s) to provide a feasible solution. Thus, the proposed decomposition method outperforms the benchmark in all instances by over an order of magnitude.

5. Conclusions

The long-term operational optimization of energy systems leads to computationally challenging optimization problems. In this paper, we propose a time-series decomposition method providing feasible solutions with known quality. The method decomposes the original problem into smaller subproblems, which are efficiently solved in parallel.

The proposed method requires only simple problem reformulations for creating subproblems and recombines their solutions to a feasible solution of the complete problem while still representing a rigorous decomposition. The proposed method is applied to a long-term industrial operational problem, including time-coupling constraints and variables due to storage systems, emission limits, peak power prices, and net connection fees. The proposed method provides fast convergence, outperforming commercial solvers by more than an order of magnitude.

References

- S. Al-Agtash, R. Su, 1998. Augmented Lagrangian approach to hydro-thermal scheduling. *IEEE Trans. Power Syst.* 13 (4), 1392–1400.
- N. Baumgärtner, R. Delorme, M. Hennen, A. Bardow, 2018. Design of low-carbon utility systems: Exploiting time-dependent grid emissions for climate-friendly demand-side management. submitted to a journal.
- S. P. Bradley, A. C. Hax, T. L. Magnanti, 1992. *Applied mathematical programming*, 19th Edition. Addison-Wesley, Reading, Mass.
- A. J. Conejo, E. Castillo, R. García-Bertrand, R. Mínguez, 2006. *Decomposition techniques in mathematical programming: Engineering and Science Applications*. Springer-Verlag, Berlin, Heidelberg.
- J. Desrosiers, M. Lübbecke, 2011a. *Branch-Price-and-Cut Algorithms*. John Wiley & Sons.
- J. Desrosiers, M. E. Lübbecke, 2011b. *Branch-price-and-cut algorithms*. Wiley Interscience, Hoboken, NJ.
- R. W. Eglese, 1990. Simulated annealing: A tool for operational research. *Eur. J. Oper. Res.* 46 (3), 271–281.
- S. Goderbauer, M. Comis, F. J. Willamowski, 2019. The synthesis problem of decentralized energy systems is strongly NP-hard. *Comput. Chem. Eng.*, doi.org/10.1016/j.compchemeng.2019.02.002.
- T. Hanne, R. Dornberger, 2017. *Computational intelligence in logistics and supply chain management*. Vol. 244 of *Internat. Ser. Oper. Res. Management Sci.* Springer, Switzerland.
- IBM Cooperation, 2016. *IBM ILOG and CPLEX Optimization and Studio and CPLEX User's and Manual and Version 12 and Release 7*.
- K. C. Kavvadias, Z. B. Maroulis, 2010. Multi-objective optimization of a trigeneration plant. *Energy Policy* 38 (2), 945–954.
- E. Nasrolahpour, S. J. Kazempour, H. Zareipour, W. D. Rosehart, 2016. Strategic sizing of energy storage facilities in electricity markets. *IEEE Trans. Sustain Energy* 7 (4), 1462–1472.
- A. Piacentino, F. Cardona, 2008. EABOT – Energetic analysis as a basis for robust optimization of trigeneration systems by linear programming. *Energy Convers. Manag.* 49 (11), 3006–3016.
- R. Rahmani, T. G. Crainic, M. Gendreau, W. Rei, 2017. The Benders decomposition algorithm: A literature review. *Eur. J. Oper. Res.* 259 (3), 801–817.
- A. Rong, R. Lahdelma, P. B. Luh, 2008. Lagrangian relaxation based algorithm for trigeneration planning with storages. *Eur. J. Oper. Res.* 188 (1), 240 – 257.
- Q. Wang, J. D. McCalley, T. Zheng, E. Litvinov, 2016. Solving corrective risk-based security-constrained optimal power flow with Lagrangian relaxation and Benders decomposition. *Inz. J. Elec. Power.* 75, 255–264.
- R. Yokoyama, 2013. Optimal operation of a gas turbine cogeneration plant in consideration of equipment minimum up and down times. *J. Eng. Gas. Turbine Power* 135 (7), 071801.
- R. Yokoyama, K. Ito, 1996. A revised decomposition method for MILP problems and its application to operational planning of thermal storage systems. *J. Energ. Resour.* 118 (4), 277–284.

Real-Time Optimisation of Closed-Loop Processes Using Transient Measurements

Jack Speakman* and Grégory François

*School of Engineering, The University of Edinburgh, Edinburgh EH9 3FB, UK
jack.speakman@ed.ac.uk*

Abstract

Real-time optimisation (RTO) has the ability to boost the performance of a process whilst satisfying a set of constraints by using process measurements to refine the model-based optimal operating conditions towards plant optimality. Modifier adaptation (MA) is a methodology of RTO which can find the optimal operating point of a process even in the presence of plant-model mismatch. This work presents an extension to MA through the combination of two established frameworks. This new combined framework allows for the optimisation of a controlled process using transient measurements whilst using a steady-state open-loop model. In conjunction, an investigation into model-based gradient estimation methods of the controlled process using the open-loop model was undertaken and a correction has been proposed, which allows for the use of limited controller information in gradient estimation using the neighbouring extremals method.

Keywords: Real-time optimisation, Modifier adaptation, Transient measurements, Plant-model mismatch, Model-based gradient estimation

1. Introduction

The optimisation of chemical processes is vital for improving the economic profile, whilst ensuring the meeting of safety and environmental objectives, in the face of increasing global competition and tightening regulations. Process optimisation is typically carried out using a model to calculate the operating conditions which maximise the performance of the process. Fully accurate models are not possible to obtain due to uncertainties, noise, and simplifications, resulting in sub-optimal operation. Real-time optimisation (RTO) solves this through the use of measurements from the process to adjust the operating point towards the true optimal solution.

Modifier adaptation (MA) is an approach to RTO which adds input-affine modifier terms to the cost and constraints (Marchetti et al., 2009), and measurements of the process are used to iteratively update these modifiers. The main advantage of MA lies in the mathematically proven capacity to converge to a KKT point of the process, even in the presence of plant-model mismatch, a case for which the standard two-step approach (Jang et al., 1987) typically fails (Forbes et al., 1994). Recently, an extension to MA has been proposed allowing for the optimisation of a controlled plant using an open-loop model (François et al., 2016), which is mathematically proven to reach a plant KKT point upon convergence. Such cases occur for complex plants using built-in control systems while the model has been developed in the lab. This article aims to extend this framework to allow for the use of transient measurements, and for the use of model-based gradient estimation methods when there is a difference in degrees of freedom between the model and the plant. This paper will state the mathematical optimisation problem, with a brief overview of MA; both extensions will be described, followed by a proposition of the KKT converging nature of the combined framework and associated proof. Finally this new framework will be demonstrated in a case study of a CSTR.

2. Problem formulation

2.1. Steady-State Optimisation Problem

The optimisation of a continuous process consists of finding the inputs (\mathbf{u}) which minimise the cost (ϕ) whilst satisfying a set of constraints (g_j). These functions are assumed to be known for a measured output (\mathbf{y}_p), in practice this is modelled by $\bar{\mathbf{y}} = \mathbf{H}(\mathbf{u}, \boldsymbol{\theta})$, resulting in two problems:

Plant Optimisation Problem	Model Optimisation Problem
$\mathbf{u}_p^* = \arg \min_{\mathbf{u}} \Phi_p(\mathbf{u}) := \phi(\mathbf{u}, \mathbf{y}_p)$ $s.t. \quad G_{p,j}(\mathbf{u}) := g_j(\mathbf{u}, \mathbf{y}_p) \leq 0$	$\mathbf{u}^* = \arg \min_{\mathbf{u}} \Phi(\mathbf{u}, \boldsymbol{\theta}) := \phi(\mathbf{u}, \bar{\mathbf{y}}(\mathbf{u}, \boldsymbol{\theta}))$ $s.t. \quad G_j(\mathbf{u}, \boldsymbol{\theta}) := g_j(\mathbf{u}, \bar{\mathbf{y}}(\mathbf{u}, \boldsymbol{\theta})) \leq 0$

Where $\boldsymbol{\theta}$ are the uncertain model parameters, $(\cdot)_p$ refers to the plant and $j = 1, \dots, n_g$. If there is plant-model mismatch (i.e. $\bar{\mathbf{y}} \neq \mathbf{y}_p$), the solution to Problem 2 will not match that of Problem 1.

2.2. Standard Modifier Adaptation

Standard MA adds correction terms to the model cost and constraints to reconcile the gradient of the plant and model problems with respect to the inputs at the current operating point, which requires the plant cost and constraints to be measured or estimated from the plant input and outputs.

$$\mathbf{u}_{k+1}^* = \arg \min_{\mathbf{u}} \Phi_m(\mathbf{u}, \boldsymbol{\theta}) := \Phi(\mathbf{u}, \boldsymbol{\theta}) + \boldsymbol{\lambda}_k^{\Phi, u}(\mathbf{u} - \mathbf{u}_k^*)$$

$$s.t. \quad G_{m,j}(\mathbf{u}, \boldsymbol{\theta}) := G_j(\mathbf{u}, \boldsymbol{\theta}) + \varepsilon_k^{G_j} + \boldsymbol{\lambda}_k^{G_j, u}(\mathbf{u} - \mathbf{u}_k^*) \leq 0, \quad j = 1, \dots, n_g$$

Where ε and $\boldsymbol{\lambda}$ are the zeroth and first order correction terms, defined as follows:

$$\varepsilon_k^{G_j} = G_{p,j}(\mathbf{u}_k^*) - G_j(\mathbf{u}_k^*, \boldsymbol{\theta})$$

$$\boldsymbol{\lambda}_k^{\Phi, u} = \nabla_{\mathbf{u}} \Phi_p(\mathbf{u}_k^*) - \nabla_{\mathbf{u}} \Phi(\mathbf{u}_k^*, \boldsymbol{\theta})$$

$$\boldsymbol{\lambda}_k^{G_j, u} = \nabla_{\mathbf{u}} G_{p,j}(\mathbf{u}_k^*) - \nabla_{\mathbf{u}} G_j(\mathbf{u}_k^*, \boldsymbol{\theta}), \quad j = 1, \dots, n_g$$

This problem is shown to only converge at a KKT point of the plant (Marchetti et al., 2009). This is a key result from MA and is highly sought after from the extensions to MA.

3. Recent Advances

3.1. Controlled Plant, Open-loop model

Standard MA requires the same degrees of freedom between the model and the process. An extension to MA was proposed which allows for the use of an open-loop model in the optimisation of a process which operates in closed-loop with different degrees of freedom (\mathbf{r}) than the model (François et al., 2016), as illustrated in Figure 1a. This framework has three possible methods of implementation depending on whether the optimisation and modifiers are in terms of \mathbf{u} or \mathbf{r} :

$$\text{UR:} \quad \mathbf{u}_{k+1}^* = \arg \min_{\mathbf{u}} \Phi_{m,k}(\mathbf{u}) := \Phi(\mathbf{u}) + \boldsymbol{\lambda}_k^{\Phi, r}(\mathbf{y}(\mathbf{u}) - \mathbf{r}_k)$$

$$s.t. \quad G_{m,j,k}(\mathbf{u}) := G_j(\mathbf{u}) + \varepsilon_k^{G_j} + \boldsymbol{\lambda}_k^{G_j, r}(\mathbf{y}(\mathbf{u}) - \mathbf{r}_k) \leq 0, \quad j = 1, \dots, n_g$$

$$\text{UU:} \quad \mathbf{u}_{k+1}^* = \arg \min_{\mathbf{u}} \Phi_{m,k}(\mathbf{u}) := \Phi(\mathbf{u}) + \boldsymbol{\lambda}_k^{\Phi, u}(\mathbf{u} - \mathbf{u}_k)$$

$$s.t. \quad G_{m,j,k}(\mathbf{u}) := G_j(\mathbf{u}) + \varepsilon_k^{G_j} + \boldsymbol{\lambda}_k^{G_j, u}(\mathbf{u} - \mathbf{u}_k) \leq 0, \quad j = 1, \dots, n_g$$

$$\text{RR:} \quad \mathbf{r}_{k+1}^* = \arg \min_{\mathbf{r}} \Phi_{m,k}(\mathbf{r}) := \Phi(\mathbf{r}) + \boldsymbol{\lambda}_k^{\Phi, r}(\mathbf{r} - \mathbf{r}_k)$$

$$s.t. \quad G_{m,j,k}(\mathbf{r}) := G_j(\mathbf{r}) + \varepsilon_k^{G_j} + \boldsymbol{\lambda}_k^{G_j, r}(\mathbf{r} - \mathbf{r}_k) \leq 0, \quad j = 1, \dots, n_g$$

Where $\boldsymbol{\lambda}_k^{\Phi, r}$ and $\boldsymbol{\lambda}_k^{G_j, r}$ are the difference between the plant and model gradients with respect to \mathbf{r}

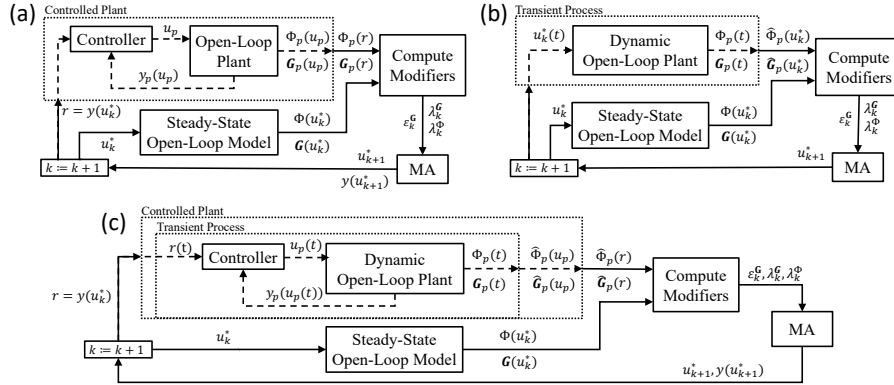


Figure 1: Framework schematics. (a) Closed-loop. (b) Transient. (c) Combined.

3.2. Transient Measurements

Standard MA, and the framework described above in Section 3.1, wait until steady-state before calculating the next operating point, ignoring all the transient information between operating points. Therefore, an extension to standard MA was developed that uses these transient measurements to update the operating points before steady-state is achieved (François and Bonvin, 2014), as illustrated in Figure 1b, resulting in a faster convergence to the process optimum. This method estimates the steady-state value as the current measured value ($\hat{y}_p = y_p(t)$) and performs MA with these values, which was proven by François and Bonvin to reach a KKT point of the process upon convergence, *but only when the process is operated in open-loop*.

3.3. Gradient Estimation Methods

The gradient of the process cost and constraints with respect to the degrees of freedom at \mathbf{u}_k^* is required to calculate $\boldsymbol{\lambda}$. This cannot be directly measured, but must be inferred from process measurements. This paper will implement two different gradient estimation techniques and extend these to work in the case of a difference in degrees of freedom between the model and the process. The first technique, multiple units (MU) (Srinivasan, 2007), uses the finite differences method by running $n_u + 1$ identical units in parallel, offsetting each unit from the current operating point.

The second method, neighbouring extremals (NE) (Gros et al., 2009), is a model-driven approach which takes the difference between the model and process outputs, and relates it to the parametric uncertainty of the model. This can be used when structural plant-model mismatch is present with imperfect accuracy. This can be written mathematically as follows, where $f = \Phi, G_1, \dots, G_j$:

$$\nabla_{\mathbf{u}_p} f_p \approx \nabla_{\boldsymbol{\theta}}^2 f(\nabla_{\boldsymbol{\theta}} \mathbf{H})^+ (\mathbf{y}_p - \mathbf{y}_0) + (\nabla_{\mathbf{u}\mathbf{u}}^2 f - \nabla_{\boldsymbol{\theta}\boldsymbol{\theta}}^2 f(\nabla_{\boldsymbol{\theta}} \mathbf{H})^+ \nabla_{\mathbf{u}} \mathbf{H})(\mathbf{u}_p - \mathbf{u}_0) \quad (10)$$

4. Transient MA of Controlled Processes using Open-Loop Models

The frameworks outlined in the previous section are combined hereafter into a single concise framework, allowing for the use of transient measurements in the optimisation of a controlled process using a steady-state open-loop model, as shown in Figure 1c. A proposition and proof using method UR is given, but similar arguments can be made using method UU and method RR.

Proposition 1. *If upon convergence, the estimates of the process ($\hat{\Phi}_p, \hat{\mathbf{g}}_p, \widehat{\nabla_r \Phi}_p, \widehat{\nabla_r \mathbf{G}}_p$), estimated via a function of the transient measurements ($\mathbf{u}_p(t), \mathbf{y}_p(t)$), approach their true values, then the operating point $\mathbf{r}_\infty = \mathbf{y}(\mathbf{u}_\infty)$ is a KKT point of the process.*

Proof. If the algorithm converges, i.e. $\mathbf{u}_\infty = \lim_{k \rightarrow \infty} \mathbf{u}_k$, then \mathbf{u}_∞ must be steady. Hence, $\mathbf{r}_\infty = \mathbf{y}(\mathbf{u}_\infty)$, and the plant must also be steady. Therefore, the steady-state estimates approach their true values, as stated in the proposition. The gradient of the process, along with steady state estimation of the modifier $\lambda_\infty^{\phi,r}$, can be combined and rearranged into the following:

$$\frac{\partial \phi_{m,\infty}^r}{\partial \mathbf{u}} \left(\left(\frac{\partial \mathbf{y}}{\partial \mathbf{u}} \right)^+ \frac{\partial \mathbf{y}}{\partial \mathbf{u}} \right) = \frac{\partial \phi_p}{\partial \mathbf{r}} \left(\frac{\partial \mathbf{y}}{\partial \mathbf{u}} \right) \quad (11)$$

The same can be applied to $\frac{\partial g_{m,j,\infty}^r}{\partial \mathbf{u}}$. From the definition of the zeroth order term $\mathcal{E}_\infty^{g,j,r}$, the following can be stated: $g_{m,j,\infty}^r(\mathbf{u}_\infty) = G_{p,j}(\mathbf{r}_\infty)$. Hence, as the modified problem is optimised such that \mathbf{u}_∞ is a KKT point, satisfying the following:

$$\frac{\partial \phi_{m,\infty}^r}{\partial \mathbf{u}} + \mathbf{v} \frac{\partial g_{m,\infty}^r}{\partial \mathbf{u}} = \mathbf{0} \quad (12)$$

It follows that the operating point of the plant must be a KKT point since the following must be valid:

$$\frac{\partial \Phi_p}{\partial \mathbf{r}} + \mathbf{v} \frac{\partial \mathbf{G}_p}{\partial \mathbf{r}} = \mathbf{0} \quad (13)$$

$$\mathbf{G}_p(\mathbf{r}_\infty) \leq \mathbf{0} \quad (14)$$

$$\mathbf{v} \mathbf{G}_p(\mathbf{r}_\infty) = \mathbf{0} \quad (15)$$

Hence, \mathbf{r}_∞ is a KKT point of the closed-loop plant. \square

The above proposition and proof are similar to those from the original frameworks, an in-depth proof of each can be found in the respective papers (François and Bonvin, 2014; François et al., 2016). The estimates must be correct at steady state, this is achieved in the same manner as in (François and Bonvin, 2014), by setting them equal to the current transient value, i.e. $\hat{\phi}_p = \phi_p(t)$.

Model-driven gradient estimation methods, such as NE, applied to an open-loop model will obtain an estimate for the open-loop process ($\nabla_{\mathbf{u}_p} \phi_p$). The method described above requires an estimate of the gradient of the process cost and constraints with respect to the controller setpoints ($\nabla_{\mathbf{r}} \phi_p$). Therefore, the gradients must be remapped by multiplying by $\frac{\partial \mathbf{u}_p}{\partial \mathbf{r}}$. However, this relationship is often unknown for complex plants using built-in control systems (whereby the supplier does not provide full information) or when advanced controllers are implemented (e.g. MPC), hence an estimation must be made using some limited information about the controller.

5. Case Study

The methods discussed above have been simulated on the Williams-Otto reactor (Williams and Otto, 1960), which is a benchmark case for MA problems. The open-loop plant follows a three reaction system ($A + B \rightarrow C$, $B + C \rightarrow P + E$, $C + P \rightarrow G$). Whilst the open-loop model follows a 2 reaction system ($A + 2B \rightarrow P + E$, $A + B + P \rightarrow G$). These are illustrated in Figure 2 and the systems of dynamic equations are described in Table 1.

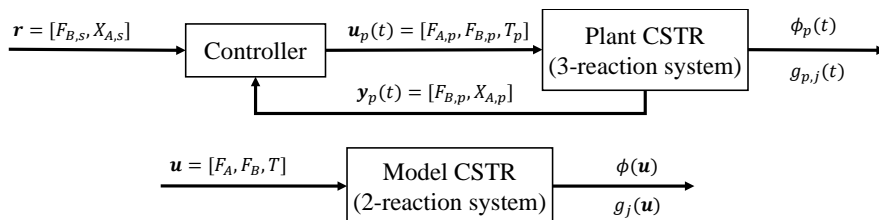


Figure 2: Block flow diagram of controlled plant and open-loop model

Table 1: Dynamic systems for the plant and the model

Plant	Model (steady)
$\frac{dX_A}{dt} = \frac{F_{A,in}}{\rho V} - k_1 X_A X_B - \frac{F}{\rho V} X_A$	$\frac{F_{A,in}}{\rho V} - k_1^* X_A X_B^2 - k_2^* X_A X_B X_P - \frac{F}{\rho V} X_A = 0$
$\frac{dX_B}{dt} = \frac{F_{B,in}}{\rho V} - k_1 X_A X_B - \frac{F}{\rho V} X_B$	$\frac{F_{B,in}}{\rho V} - 2k_1^* X_A X_B^2 - k_2^* X_A X_B X_P - \frac{F}{\rho V} X_B = 0$
$\frac{dX_C}{dt} = 2k_1 X_A X_B - 2k_2 X_B X_C - k_3 X_C X_P - \frac{F}{\rho V} X_B$	-
$\frac{dX_P}{dt} = k_2 X_B X_C - \frac{1}{2} k_3 X_C X_P - \frac{F}{\rho V} X_P$	$k_1^* X_A X_B^2 - k_2^* X_A X_B X_P - \frac{F}{\rho V} X_P = 0$
$\frac{dX_E}{dt} = 2k_2 X_B X_C - \frac{F}{\rho V} X_E$	$2k_1^* X_A X_B^2 - \frac{F}{\rho V} X_E = 0$
$\frac{dX_G}{dt} = \frac{3}{2} k_3 X_C X_P - \frac{F}{\rho V} X_G$	$3k_2^* X_A X_B X_P - \frac{F}{\rho V} X_G = 0$

Where the X_i is the mass fraction of component i, F_i is the mass flowrate of component i, k are the reaction rates, and $\rho V = 2105$ kg is the mass holdup. The values for the parameters of the model are the same as in François et al. (2016). There are 2 cases for the model, with differing parameters, case I and case II, both described in the above paper.

The inputs to the open-loop plant and model are the flowrates of both A and B, and the temperature ($\mathbf{u} = [F_A, F_B, T]$). The controller on the open-loop plant has been designed to reduce and change the nature of the degrees of freedom of the system, with the setpoints being $\mathbf{r} = [F_{B,s}, X_{A,s}]$. This is done by introducing an unmodelled ratio controller on the two input flowrates such that $F_{B,p}/F_{A,p} = 2.4$. Further, the temperature is controlled via a proportional controller of the concentration in component A, $T = T_0 + K_P(X_{A,s} - X_{A,p})$, with $T_0 = 120$ °C and $K_P = -1000$. Also, there is an offset in the flowrate of B, $F_{B,p} = F_{B,s} + 2$, introducing additional uncertainty. In practice better controllers would certainly be designed and implemented but the main point of this article is about when the actual controller is unknown and not about its performances. The objective and constraint functions can be written as follows:

$$\phi(\mathbf{u}, \mathbf{y}(\mathbf{u})) = -(1143X_P F + 25.92X_E F - 76.23F_{A,in} - 114.34F_{B,in}) \quad (16)$$

$$g_1(\mathbf{u}, \mathbf{y}(\mathbf{u})) = X_A - 0.09 \quad (17)$$

$$g_2(\mathbf{u}, \mathbf{y}(\mathbf{u})) = X_G - 0.6 \quad (18)$$

The model optimum, ϕ , for the two cases are -140 and -161 respectively, whilst the process optimum, ϕ_p , is -212. Initially the algorithms were tested using the MU gradient estimation method, which provides perfect estimations with identical units. Figures 3 and 4 show that the new framework approaches the plant optimum more rapidly than for steady-state to steady-state operation.

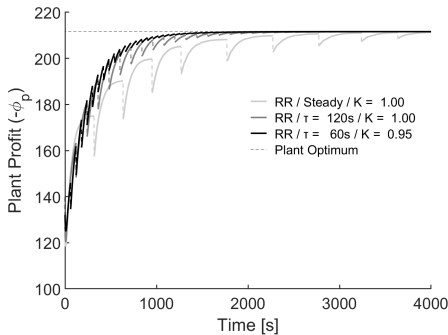


Figure 3: Plant profit for RR Algorithm with MU gradient estimation

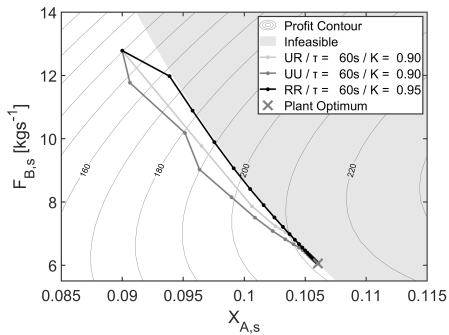


Figure 4: Controller setpoints for MU gradient estimation

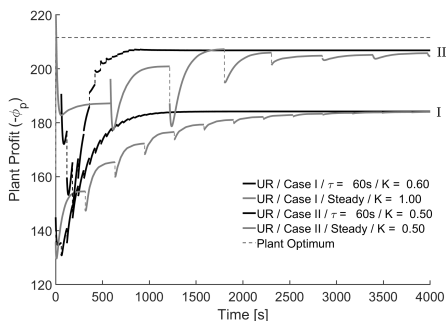


Figure 5: Plant profit for UR Algorithm with NE gradient estimation

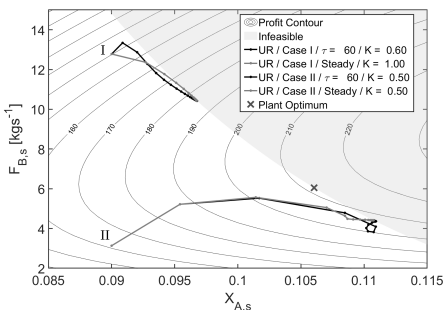


Figure 6: Controller setpoints UR Algorithm with NE gradient estimation

The algorithms were then tested using NE gradient estimation with some controller knowledge. The assumed knowledge is that the flowrates have a fixed, but unknown, ratio control, which is approximated as the flow ratio of the model's previous operating point $\partial F_{A,p} / \partial F_{B,s} = F_{A,k}^* / F_{B,k}^*$. Also, the mass fraction of A is purely controlled by T, however the control law is unknown. This was approximated as $\partial T / \partial X_{A,s} = (\partial X_{A,s} / \partial T)^+$, at the previous operating point. As can be seen in Figures 5 and 6, both cases converge to sub-optimal points on the edge of the feasible region, at a ϕ value of -184 and -207 respectively. This is expected for a model-based gradient estimation technique, which is based on a linearisation of the steady-state nominal model.

6. Conclusion

This paper has proposed that the combination of two established frameworks within modifier adaptation, namely the use of transient measurements and the use of an open-loop model in optimising a controlled process, will reach a KKT point of the process if the algorithm converges. This is backed up with a mathematical proof and case study, resulting in a method which can use transient measurements to optimise a controlled plant with only a steady-state open-loop model. An extension to a model-based gradient estimation technique was proposed to allow for use of the open-loop model to estimate the gradient of the controlled process by transforming the estimate to be with respect to the setpoints using limited controller knowledge. This did not converge to a KKT point of the plant, since NE is a model-linearisation-based gradient estimation technique. However, this did approach a point which is on the edge of the feasible region, while significantly reducing the loss in plant optimality with minimal information about the structure of the controller.

References

- J. Forbes, T. Marlin, J. F. MacGregor, 1994. Model adequacy requirements for optimizing plant operations. *Comp. Chem. Eng.* 18, 497–510.
- G. François, D. Bonvin, 2014. Use of transient measurements for the optimization of steady-state performance via modifier adaptation. *Ind. Eng. Chem. Res.* 53 (13), 5148–5159.
- G. François, S. Costello, A. Marchetti, D. Bonvin, 2016. Extension of modifier adaptation for controlled plants using static open-loop models. *Comp. Chem. Eng.* 93, 361 – 371.
- S. Gros, B. Srinivasan, D. Bonvin, 2009. Optimizing control based on output feedback. *Comp. Chem. Eng.* 33 (1), 191 – 198.
- S.-S. Jang, B. Joseph, H. Mukai, 1987. On-line optimization of constrained multivariable chemical processes. *AIChE J.* 33 (1), 26–35.
- A. Marchetti, B. Chachuat, D. Bonvin, 2009. Modifier-adaptation methodology for real-time optimization. *Ind. Eng. Chem. Res.* 48 (13), 6022–6033.
- B. Srinivasan, 2007. Real-time optimization of dynamic systems using multiple units. *Int. J. of Rob. and Nonlin. Cont.* 17 (13), 1183–1193.
- T. Williams, R. Otto, 1960. A generalized chemical processing model for the investigation of computer control. *AIEE Trans.* 79, 483–473.

A Financial Accounting based Model of Carbon Footprinting: Built Environment Example

Alex Veys^a, Virginia Acha^b, Sandro Macchietto^{a,*}

^a *Department of Chemical Engineering, Imperial College London, South Kensington Campus, London SW7 2AZ, UK*

^b *Imperial Business School, Imperial College London, South Kensington Campus, London SW7 2AZ, UK*

* *s.macchietto@imperial.ac.uk*

Abstract

The built environment contributes up to 50% of the UK's carbon emissions. Most buildings' analyses focus on the "carbon operating cost" of buildings rather than the embodied "carbon capital cost" and do not take into account a building lifespan. In this paper a new carbon accounting framework is presented modelled on financial accounting principles, with a carbon balance sheet and profit and loss. It is argued that it is illogical to discount future emissions of carbon but that it is reasonable to depreciate carbon assets and liabilities. Like Value Added Tax (VAT) accounting in financial transactions, the proposed carbon accounting method enables a proper, explicit and transparent allocation of carbon assets and liabilities to multiple agents in complex supply chains over distinct temporal, spatial and organisational boundaries.

The approach is demonstrated by applying the model to two energy-efficient buildings of the UK National Energy Foundation, a new Light-Weight building and an older High Thermal Mass one, designed for a lifespan of 50 and 150 years, respectively. The analysis shows that cement based materials, metal and insulation are the major carbon liabilities, with concrete foundations the main structural component responsible. On an operating carbon basis, the newest building produces the least CO₂. In aggregate, the new building is more efficient with an annual carbon cost, including depreciated carbon capital costs, of ~14 tonnes of CO₂/year, vs. ~21 tonnes of CO₂/year for the longer lasting building. The best discounted annual capital carbon cost was for a (notional) building constructed by increasing the lifetime of the 50-year building to 150 years. However, in all buildings the discounted carbon capital cost was less than 11% of the total operating costs, showing that improvements in operating efficiency (carbon P&L) are the most important contribution to carbon emissions.

Keywords: CO₂ accounting model, built environment, building lifetime; construction techniques comparison, CO₂ efficiency assessment.

1. Introduction

We are regularly reminded of the need to radically cut emissions of CO₂ and other greenhouse gases (in this paper, collectively called "carbon" as a shortcut). Whether the cost of carbon externalities is better included through a carbon tax on products and services, or a regulatory framework with permits allocation and trading is hotly debated. Whatever the solution, the amount of carbon emitted will need to be counted and

attributed, so that individuals and organisations may be held accountable for their contribution. This is more easily said than done, as most products and services involve multiple materials, parts, suppliers, distributors and end users in highly complex supply chains, across intersecting geographical, national, regulatory, business entity and legal boundaries, to name a few. To properly allocate carbon origination, use, transfer and cost requires agreed, transparent and easily applied carbon accounting mechanisms. While this seems like a daunting problem, it has been addressed and solved in other areas. In particular, most governments have found ways to tax whatever we, as individuals or corporates, produce, earn, trade, spend, or consume (with exclusions, allowances, progressive or regressive rates, etc.) in ways that are (broadly) socially accepted. One such mechanism taxes the “value added” in each step by each entity.

Conventional material and energy balances over a set system boundary and temporal timeframe define their accrual or depletion within the system (Fig. 1, left). The financial state of a system is similarly defined by a set of money balances, done according to conventional principles or rules, and incorporated in three key documents, a Balance Sheet (assets and liabilities at a given time), Profit and Loss (flows in/out from activities between balance sheets) and Cash Flow (covering the same time frame as the P&L but for cash only). Their relationship is schematically shown in Fig. 1, right. Three similar balances and documents were developed to account for carbon assets (value held) or liabilities (value due), flows and cost over defined physical, organisational and temporal boundaries. The value of carbon added (VCA) by a material flow or process, the overall total embodied carbon, EC (sum of all VCAs contributions up to a given time and carried forward) and the overall life cycle impact, LCC of a product or service (adding up all contributions from cradle to grave) are defined. The latter is similar to the values produced by a life cycle analysis, LCA. Entries from single activities or flows are aggregated into the carbon accounting reports (balance sheet, P&L).

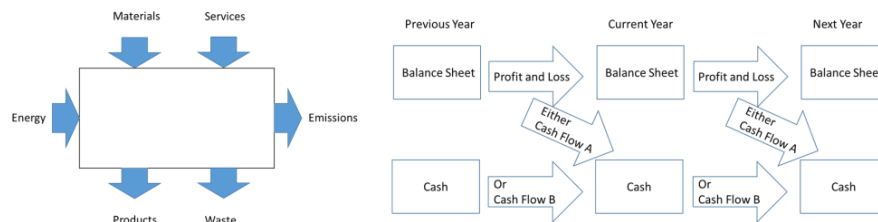


Figure 1. Flows over a physical boundary (e.g. a building), left. Relationship between key financial accounting reports over organisation (e.g. a company) and temporal boundaries (e.g. 1 year), right.

1.1. Carbon accounting and buildings

Half of humanity lives in cities. In the UK, the built environment contributes up to 50% of carbon emissions. The UK construction industry consumes over 420 Mt of materials, 8Mt of oil and releases over 29 Mt of carbon dioxide annually, including a significant quantity of new materials disposed as waste (Hammond and Jones, 2008). Capital cost, not just economic but also in terms of the carbon embodied in materials and construction costs (“carbon capital”) required to achieve such objectives is also important. Some estimate suggest that the embodied energy in domestic buildings might be ten times the annual operating energy requirements and in commercial

buildings the ratio could be as high as 30:1 (Rawlinson and Weight, 2007). Most buildings' analyses and construction regulations focus on the "carbon running cost" of buildings rather than the "carbon capital cost" and do not take into account a building lifespan, which our method proposes to do. Finally, building design, construction, and use involve many entities, each of which will likely be required in the future to produce detailed, non-overlapping, mutually consistent carbon accounting reports. Counting and attributing carbon assets and liabilities is particularly challenging.

Traditional Life Cycle Analysis (LCA) does not account for temporal information and assumes a fixed horizon, often 100 years, with results sensitive to the chosen horizon. More recent advances addressed this aspect. Levasseur et al., 2010 proposed a Dynamic LCA (DLCA), of which there are versions related to the timing of processes, other to the proximity to the time horizon in the study scope. Collinge et al., 2018 applied two static and four time-resolved DLCA models to the analysis of two energy efficient buildings, however only to the buildings operating (use) phase. Pan et al., 2018 proposed a fundamental rethinking of system boundaries for the carbon emissions of buildings to include temporal, spatial, functional and methodological dimensions based on 12 variables. In spite of progress, a recent review of methodologies and applications for the carbon footprint of buildings (Fenner et al., 2018) concluded that there is no internationally accepted method for measuring, reporting, and verifying GHG emissions from existing buildings in a consistent and comparable way and indicated the need for a clear, accessible and consistent method.

Given the long lifetime of a building, financial concepts such as discounting (for future events) and depreciation (for past events) must be considered. A discount factor implicitly values carbon emitted in the future at lower price than emitted now. For example, the future cost of permits in a trading scheme, or the future cost of abatement technologies may decrease. As this is controversial and impossible to estimate on a long timescale (and arguably it is immoral to discount current liabilities to future generations), no discounting was applied. Depreciation is a measure of cost or value of an asset that has been consumed during a period. For carbon accounting purposes, assets should be written down at the faster of a model that estimates the decay of CO₂ in the atmosphere (such as the Bern model used in IPCC reports, Schimel et al., 1997) or the straight line that takes its value to zero at the end of its life, while liabilities should be depreciated over the lifetime of a product. Here, assets and liabilities were aggregated into net assets, depreciated at the shorter of the Bern rule or the lifetime of the building.

For all materials we used the ICE (Inventory of Carbon and Energy) database (Hammond and Jones, 2008). Together with relevant properties (e.g. thermal conductivity, density, specific heat) ICE gives the embodied energy and carbon of construction materials, by main groups, for Typical, Primary and Recycled material, with ranges and accuracy estimates. Values are qualified as being cradle to (factory) gate, to (building) site or to grave. At the project time, ICE1.5a contained records for 1400 construction materials, of which 22 (main materials only) were used (and cross checked against other sources). For each material the embodied carbon in ICE does not include an initial asset contribution, so an adjustment was made for biomass based materials. For example, manufacturing of softwood timber takes ~0.47KgCO₂/Kg, but assuming ~50%_w of Primary wood is carbon drawn from the atmosphere, the initial carbon asset of softwood timber becomes -1.354KgCO₂/Kg. All timber products end up with a negative initial embodied carbon value.

2. Case study: Carbon accounting for buildings with different lifetime

The UK National Energy Foundation (NEF) was set up in 1990 to “provide help to improve energy efficiency in residential buildings”. In addition to providing advice to companies and large corporations, they prepare inspectors for statutory home energy efficiency assessment and the UK National Home Energy Rating scheme. NEF is housed in two main buildings (Fig. 3), built to demonstrate energy efficiency practices. The Phase 1 building with $\sim 1,000\text{m}^2$ net floor area, finished in 1999, was designed based on a High Thermal Mass concept (to store heat and maintain the building’s temperature) using conventional materials, with a lifespan of 150 years. It features amongst other devices a steel frame with brick outer skin, insulated cavity and poured concrete inner skin, a high thermal mass insulated roof, massive concrete highly insulated raft floor, internal light shelves to boost daylight and a 500W PV array. The Phase 2 building with $\sim 450\text{m}^2$ net floor area, finished in 2004, was designed based on a Lightweight Building concept using a timber frame and minimal use of concrete, with a lifespan of 50 years. It features amongst other devices a Ground Source Heat Pump (GSHP) driven by mains electricity feeding a 3 zone underfloor heating systems, solar hot water, eight Sunpipes to boost daylight and a 6.5kW rooftop PV array.



Figure 3. NEF Buildings Phase 1 and 2.

2.1. Carbon analysis

A carbon balance sheet was calculated for the two buildings, comprising carbon “capital” assets (carbon embedded in the building materials, positive or negative, discounted over the expected lifetime of the building) and annual carbon contributions from “operating” costs. As the two buildings are rather different, for ease of comparison calculations were also done for a notional building of the same dimension and plans as the Phase 2 building, but built with the more durable construction materials of Phase 1. This is denoted as Phase 2.1 building. The net carbon assets in each structure, based on detailed construction plans, drawings, records and material samples provided by NEF, are summarised in Fig. 4 by main type of materials used (left) and construction element (right). Some numerical values are shown in Table 1 (left). The embodied carbon in Phase 1 Building is rather evenly distributed between foundations, floors, roofs and walls, while in the Phase 2 building over 95% is in foundations and floors, with the lightweight walls and roof hardly contributing. “Operating” carbon was calculated from a detailed analysis of energy suppliers and use in the buildings (Fig. 5). Table 1(right) summarises the buildings capital, operating and total discounted annual carbon.

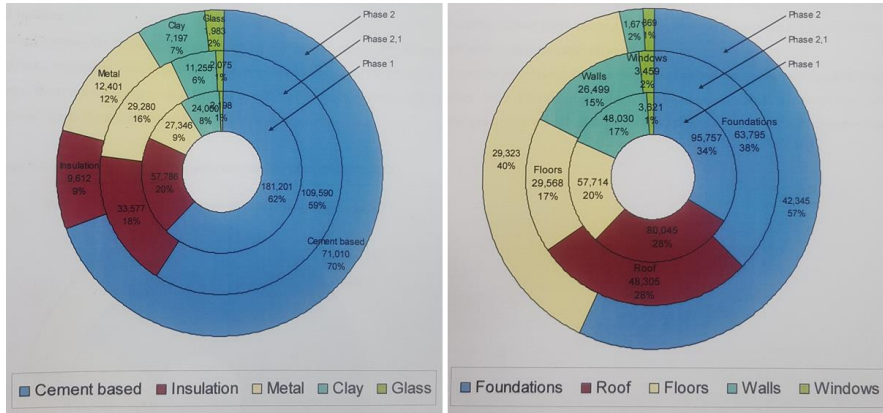


Figure 4. Liabilities in KgCO₂ for NEF Buildings Phase 1, Phase 2.1 and Phase 2 by main materials (left) and main building structure (right).

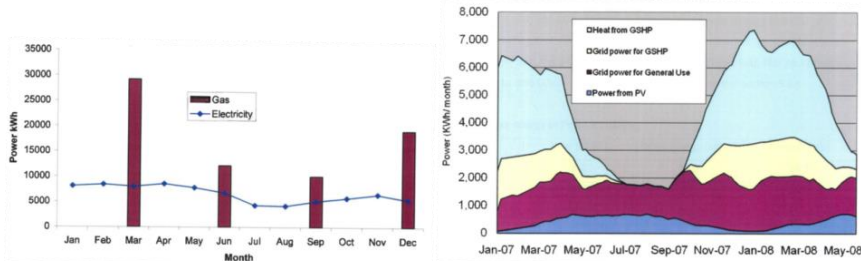


Figure 5. Energy used (kWh): Monthly average for Phase 1 building (left); usage profile for Phase 2 building over 17 months (right).

Table 1. Liabilities [KgCO₂] of Phase 1, Phase 2.1 and Phase 2 buildings by main materials and structure - errors based on estimated uncertainties of data sources (left); Summary of Carbon Opex, Capex and discounted overall P&L in annual terms (right).

Material	Phase 1		Phase 2.1		Phase 2	
	Footprint (kg CO2)	Std. Dev (kgCO2)	Footprint (kg CO2)	Std. Dev (kgCO2)	Footprint (kg CO2)	Std. Dev (kgCO2)
Timber Plywood	-10,971	5,485	-6,192	3,096	-25,427	12,714
Timber Chipboard	-11,776	5,888	-7,722	3,861	-1,069	535
Timber softwood	-1,226	613	-1,150	575	-6,362	3,181
Polyethylene Pipe 16	0	0	0	0	210	63
Plaster	497	248	274	137	0	0
Vapour Barrier	0	0	0	0	1,259	378
...						
Plasterboard	1,690	845	1,263	631	3,085	1,543
Aluminium	2,649	530	2,533	507	0	0
glass soda lime	2,196	836	2,075	789	1,963	753
Insulation ExPoly	0	0	0	0	3,984	1,195
Breeze Block	16,500	4,950	9,103	2,731	0	0
Steel Beams	24,697	7,409	16,409	4,923	0	0
Zinc	18,143	5,443	10,338	3,101	12,206	3,662
Insulation Celotex	57,786	8,668	33,165	4,975	0	0
Brick	24,000	7,200	13,241	3,972	7,197	2,159
Concrete	162,515	48,754	99,425	29,827	59,334	17,800
Total	290,000	52,000	170,000	32,000	71,000	23,000
rounded to nearest:	10,000	1,000	10,000	1,000	1,000	1,000
by STRUCTURE	Phase 1	Phase 2.1	Phase 2			
Foundations	95,757	63,795	42,345			
Roof	80,045	63,795	7,024			
Floors	57,714	29,568	29,323			
Walls	48,030	26,499	1,671			
Windows	3,621	3,459	869			
Supports	1,534	1,139	41			
GSHP	0	0	728			

	Phase 1	Phase 2.1	Phase 2	2/1 over 2
Operating Carbon (annual P&L)				
Energy (Heat)				
GSHP (Renewable)				
Grid GSHP (Carbon)				
Gas (Carbon)				
Gas (Carbon)	70,400	40,800	19,869	8,069
Energy (General)				
PV (Renewable)				
Grid (General)	52,900	23,100	15,994	5,053
Total Heat	70,400	40,800	27,958	46%
Total General Elec	52,900	23,100	21,047	10%
Carbon Energy	123,300	63,900	24,083	165%
Renewable Energy			24,922	
Total Operating Energy	123,300	63,900	49,005	30%
Factor				
Gas	0.206	0.206	0.206	
Electricity	0.523	0.523	0.523	
Carbon from				
Gas	14,502	8,405		
Electricity	27,667	12,081	12,595	
Total Operating Carbon	42,169	20,486	12,595	63%
Capital Expenditure (Completion B/S)				
Construction Carbon	290,000	170,000	68,000	
Waste at start	10%	10%	10%	
Waste at end	1%	1%	1%	
Lifetime	150	150	150	
Total Capital Carbon (annual depreciation)	2,146	1,258	1,510	-17%
Carbon ratio: Capex / (Capex + Opex)	4.8%	5.8%	10.7%	
Annual footprint (P&L including depreciation)	44,315	21,744	14,105	54%

3. Conclusions

The Phase 1 energy efficient building, built with traditional materials, embodied ~290 tonnes of “capital” CO₂ (with an estimated error of 52 tonnes), vs 71 tonnes (+/- 23 tonnes) for the Phase 2 building and 190 tonnes (+/- 32) for the notional 2.1 building. The lightweight, 50-year lifetime Phase 2 building was found to be the most carbon efficient even when carbon embodied in the longer lasting building was discounted over a much longer period. The carbon Capex of all buildings being low relative to their carbon operating costs, the impact of depreciation over longer or shorter building lifetimes was limited. However, it increased from 5% to 11% of discounted annual costs from Phase 1 to Phase 2. As buildings become more efficient, carbon capital cost becomes more important. Further details of method and case study are in Veys (2008).

The proposed (financial-inspired) carbon accounting method enables the assessment of carbon investments with distinct lifetimes. It also enables the attribution, holding and transfer of arising carbon assets/liabilities to multiple agents in a complex supply chain over distinct temporal, spatial and business boundaries. As for VAT tax accounting, it is sufficient for each organisation, product or service to include in its carbon balance sheet just the net liabilities arising between accounting periods from its carbon P&L flows.

Acknowledgements

The authors wish to thank the UK National Energy Foundation for providing the case study, data, information and many useful discussions, and Bath University for access to the ICE database.

References

- Collinge W.O., H. J. Rickenbacker, A. E. Landis, C. L. Thiel and M. M. Bilec, 2018, Dynamic Life Cycle Assessments of a Conventional Green Building and a Net Zero Energy Building: Exploration of Static, Dynamic, Attributional, and Consequential Electricity Grid Models, *Environ. Sci. Technol.*, 52, 11429–11438
- Fenner A. E., C. J. Kibert, J. Woo, S. Morque, M. Razkenari, H. Hakim and X. Lu, 2018, The carbon footprint of buildings: A review of methodologies and applications, *Renewable and Sustainable Energy Reviews*, 94, 1142–1152
- Hammond, G. P. and C. I. Jones, 2008, Embodied energy and carbon in construction materials, *Proceedings of the Institution of Civil Engineers - Energy*, 161 (2) 87-98.
- Levasseur A., P. Lesage, M. Margni, L. Descenes and R. Samson, 2010, Considering Time in LCA: Dynamic LCA and Its Application to Global Warming Impact Assessments, *Environ. Sci. Technol.*, 44, 3169–3174
- Pan W., K. Li and Y. Teng, 2018, Rethinking system boundaries of the life cycle carbon emissions of buildings, *Renewable and Sustainable Energy Reviews*, 90, 379–390
- Rawlinson S. and D. Weight, 2006, Sustainability: embodied carbon. *Building Magazine*, 12 October 2007, 88–91.
- Veys A., 2008, A Financial Accounting based Model of Carbon Footprinting using an Example in the Built Environment, *MSc Thesis*, Imperial College London.
- Schimel D., M. Grubb, F. Joos, R. Kaufmann, R. Moss, W. Ogana, R. Richels, T. Wigley, 1997, Stabilization of Atmospheric Greenhouse Gases: Physical, biological and Socio-economic Implications, pp. 1-48 in *IPCC Technical Paper III*, IPCC, Geneva.

Fouling and Cleaning of Plate Heat Exchangers for Milk Pasteurisation: A Moving Boundary Model

Abhishek Sharma and Sandro Macchietto

Department of Chemical Engineering, Imperial College London

South Kensington Campus, London SW7 2AZ, UK

s.macchietto@imperial.ac.uk

Abstract

Plate heat exchangers (PHEs), widely used in the food industries, use large amounts of energy. Fouling reduces their thermal and hydrodynamic performance, and requires periodic cleaning (often after few hours), with productivity losses. Cleaning uses large amounts of water and produces wastes. Improving productivity, minimising energy, water and wastes, while ensuring effective pasteurization is of high interest and can be supported by simulation models. Current models describing the dynamic behaviour of PHEs with fouling typically rely on simplified assumptions, with limited predictive ability. More detailed models based on Computational Fluid Dynamics (CFD) are very computationally expensive for complete PHEs, not always better at fitting experimental data, and practically infeasible to use for operations optimisation and control.

A 2D distributed, dynamic model described by Guan and Macchietto (2018) for a single PHE channel, is extended to enable the modelling of full PHEs with multiple plates arranged in any design configuration (e.g. with parallel, countercurrent, mixed parallel-countercurrent flow). The model is validated here for two such arrangements (A1 and A2) against experimental results. Four milk fouling models are assessed: two deposition mechanism (due to aggregate or denatured proteins), each with/without deposit re-entrainment. No single model was found capable of describing both arrangements. A1 was predicted best by models with aggregate proteins deposition, A2 with fouling by denatured proteins.

A dynamic model for cleaning of fouled surfaces was integrated with the moving boundary model and validated against experimental data. This enabled for the first time in the literature the simulation of Cleaning-in-Place (CIP) procedures, establishing the duration of cleanings, and the seamless simulation of entire single and multiple heating-CIP cycles, with either pre-set or condition-based termination conditions for each phase. It is shown there is large scope for optimising the performance and productivity of overall heating-CIP cycles, and an optimal operation is demonstrated for arrangement A1.

Keywords: energy recovery, plate heat exchanger, fouling, cleaning, dairy processes, dynamic model

1. Introduction

PHEs, widely used in milk production, suffer from rapid fouling, requiring frequent cleaning (every 5-10 hr) of the equipment to recover thermal and hydraulic performance. A PHE productivity (kg milk processed/day) clearly depends on the time out for cleaning. Modelling provides a way to predict the extent of fouling and optimise the operation of

exchangers individually and in networks, aiming at more efficient processes. Many studies have dealt with modelling of PHEs for milk pasteurisation. Some used a set of differential and algebraic equation models developed from mechanistic mass, energy and reaction balances to capture the fouling dynamics (e.g. Georgiadis et al., 1998a, Jun and Puri, 2006), others used a Computational Fluid Dynamics (CFD) approach. The former is faster but typically needs simplifying assumptions associated with lack of detailed knowledge of underlying phenomena, leading to poor predictive ability. CFD incorporates better the effects of detailed geometry on fluid dynamics, but is computationally very expensive (often days of CPU), even when (other) simplifying assumptions are made, e.g. by focusing on a single channel, fixing temperatures (thus decoupling thermal and hydraulic aspects), or decoupling hot and cold sides (e.g. Bouvier et al. 2014). Cleaning has been much less investigated, and complete detailed models for simulation, monitoring, control and optimisation of full heating and cleaning cycles for PHEs are still not available.

Guan and Macchietto (2018) proposed an advanced dynamic, moving boundary deposition model for a single PHE channel, building on Shell and Tube exchangers work (e.g. Georgiadis et al., 1998b, Diaz Bejarano et al., 2016). The model includes spatially varying, temperature dependent fluid properties, a detailed description of deposition rates over time, and thermal and hydraulic behaviour coupled to deposit layer formation. The result is a more predictive model which is computationally rather inexpensive. However, the Guan and Macchietto (2018) model only describes a single channel, not a complete PHE. A complete PHE model is developed here, with multiple models for aggregation and deposition of milk, and is validated against experimental data for the heating phase, for two quite different PHE design and flow arrangements (Fig.1). A dynamic model of cleaning of a fouled PHE was also integrated and validated. The overall model is then used to simulate and optimise for the first time full Heating and Cleaning in Place (CIP) cycles. Details of the work in this paper are given in Sharma (2018).

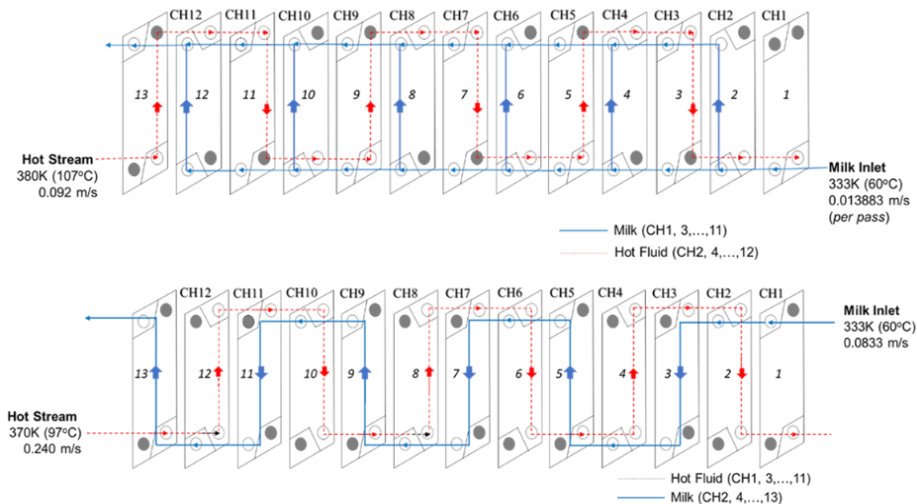


Figure 1. PHE arrangements A1 (top) and A2 (bottom). (Guan & Macchietto, 2018)

2. Models of PHE, Fouling and Cleaning

The thermo-hydraulic model of a single PHE channel (dynamic, 2D-distributed, characterising deposit growth at any point on plates using a moving boundary) detailed in Guan & Macchietto (2018) was used, with a few changes. Temperature dependent physical properties were modified for both heating and milk fluids (De-Jong, 1997, Gut and Pinto, 2003). A correlation between Nusselt, Reynolds and Prandtl numbers, Eq. 1, that better fits the conditions in the PHEs studied (Cavero, 2013) was used.

$$Nu(x) = 0.0902 Re(x)^{0.663} Pr(x)^{0.333} \quad \forall i = L, R \quad (1)$$

Milk fouling depends on denaturation and/or aggregation of the β -lactoglobulin protein but the exact kinetics is uncertain. Four different literature fouling models, differing in respect of source (aggregated or denatured proteins) and re-entrainment, were used here: i) Fouling with aggregate proteins (Model A); ii) with aggregate proteins and entrainment (Model AE); iii) with denatured proteins (Model D) and iv) with denatured proteins and entrainment (Model DE). All are represented by Eq. (2), but with different parameters:

$$\frac{d\delta}{dt} = \beta \frac{\lambda_d}{h_f^0} k_d C^n - k_\tau \delta \quad (2)$$

δ is the deposit thickness, λ_d its thermal conductivity, h_f^0 the heat transfer coefficient in clean conditions, k_d the deposition rate constant, k_τ the re-entrainment rate constant, and β an adjustable constant. k_d is represented in the Arrhenius form. C is the aggregate protein concentration in models A, AE, and the denatured protein concentration in models D, DE. Models A and D parameters are taken from Georgiadis & Macchietto (2000) and De-Jong (1997), respectively. $k_\tau = 0$ in models A, D and $k_\tau = 1.3 \cdot 10^{-3}$ /s in models AE, DE (Fryer & Slater, 1985). The proportionality constant β is fitted to data in each case, as it depends on geometry (e.g. plate corrugations) and operating conditions.

For extension to a whole PHE, a hierarchical model structure was used (Fig. 2). Each channel inherits the single channel fouling model. Channels are linked in a parent PHE model according to its specific arrangement configuration. Connectivity conditions ensure proper connection of temperature, heat flux and flow between adjacent channels. Adiabatic heat flux boundary condition were used for the end plates. A Heating phase is considered, followed by a CIP comprising three phases (Washing with water, Cleaning with hot detergent solution, and Rinsing with water). Heating (the fouling producing phase) is modelled as described above. Mechanical displacement from Washing and Rinsing is very difficult to capture, so a fixed time duration was assumed, with no effects on the deposit. Cleaning was implemented by integrating the model of Bird & Fryer (1992) into the moving boundary model (with deposit removal at each point of a plate as in Eq.2) and validated (Sharma, 2018). We can then simulate a single Heating-CIP cycle, multiple cycles or other operation sequences. The termination of each phase may be based on fixed elapsed time, or some other conditions being achieved (condition-based).

The final DAE system (comprising 16, 15 and 7 equations for the thermal, fouling and CIP models, respectively) was implemented in gPROMS (2018). Differential equations were discretised with a second order backward difference for flow in positive x-direction, second order forward difference for flow in negative x-direction, and a central second order scheme in the y-direction (across deposit), with 20 and 8 differential elements in the x- and y-directions, based on mesh independency tests. For a full Heating-CIP cycle this results after discretisation in 43,485 equations (33,523 for the model + 9,962 initial conditions), with computing times for simulation of ~ 5 minutes.

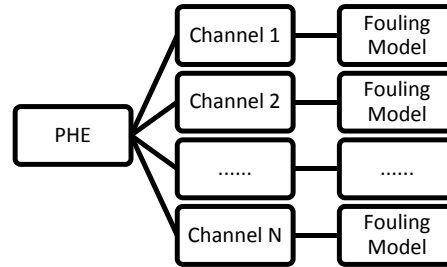


Figure 2. Hierarchical decomposition of solution models. Equipment topology is set in “PHE”

3. Results, Validation and Discussion

Arrangements A1 and A2 were simulated with geometry and operating conditions in Georgiadis & Macchietto (2000), starting from a clean PHE. Figure 3 shows the deposit distribution for A1 after 6.7 hrs of heating. The deposit depth increases along the channel length and is asymmetrical for plates at either side of a channel, due to different plate temperatures. The deposition profiles reflect the calculated bulk protein concentration profiles (not shown). Model responses were validated against experimental fouling data (collected deposit mass in each channel) reported in Georgiadis & Macchietto (2000), with good results. Errors are mostly under 10% for A1 (Fig. 4) and 20% for A2 (not shown). Errors in the initial channels are larger as there is little deposit there due to the low temperatures. There is a very small drop in milk exit temperature by the end of the heating phase (0.1 °C). For A1 (parallel channels), ΔP in a single channel (11) rises from 3.98 kPa when clean to 4.11 kPa. For A2 (parallel-countercurrent channels), ΔP across the PHE goes from 26.6 kPa to 29 kPa. The deposited mass for A1 are better predicted by fouling models A, AE, those for A2 by fouling models D, DE, maybe due to different dependence of deposition on protein aggregation and denaturation with geometry, flow and temperature. The large range in β , used as a fitting parameter by all authors in Fig. 4, confirms that the milk fouling kinetics in the literature warrants further investigation.

A complete Heating-CIP procedure is defined, with a Heating phase with termination condition based on reaching an overall critical deposit mass of 16 g/m² (Georgiadis and Macchietto, 2000), followed by Washing for 3 minutes, then Cleaning until < 0.01 g deposit is on each plate, with a final Rinse phase of 3 minutes. Fig. 5 shows the evolution of deposited mass over two cycles operated according to this procedure, for A2 with fouling model D. After Heating, the deposit mass of 3-6 g on each plate is effectively reduced by CIP to the set low level, the bottleneck being the plate with highest deposit. With a looser termination criterion of 0.1 g of deposit per plate, cleaning times are almost halved (from 0.31h to 0.15h for A1 and 0.30h to 0.15h for A2), decreasing the cycle time and increasing productivity (cycles/day). Care must be taken to ensure this is still safe and acceptable in terms of the milk product quality. With the Cleaning termination condition at the lower, safer level, the Heating time was varied, while maintaining the deposited mass under the critical mass specified. A plot (Fig. 6) of cleaning costs and throughput vs cycle time for arrangement A1 (here with fouling model A, to demonstrate the framework flexibility) shows that the largest productivity is obtained with the longest possible cycle time (7.2 h), as more fouling in the Heating phase is not offset by the longer time required for Cleaning dirtier plates.

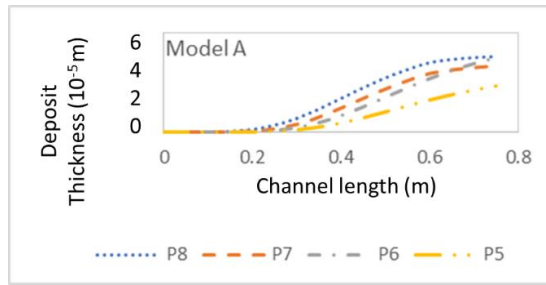


Figure 3. Deposit thickness distribution on A1 plates along channel length after 6.7h of heating

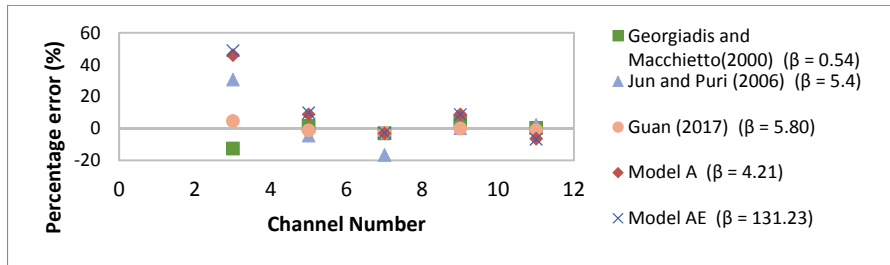


Figure 4. Error in deposited mass in each channel for four milk fouling models (arrangement A1)

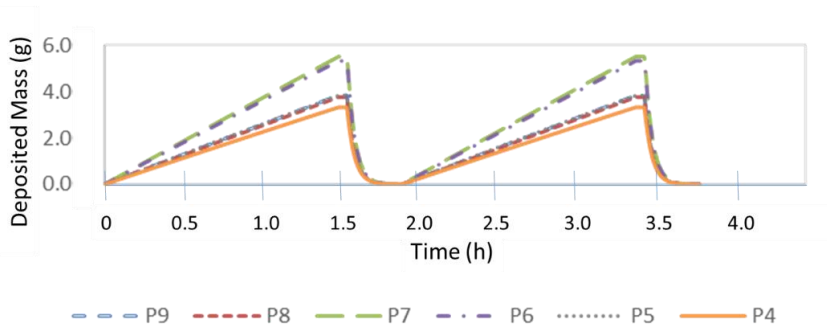


Figure 5. Evolution of deposited mass over two Heating-CIP cycles (A2, fouling model D)

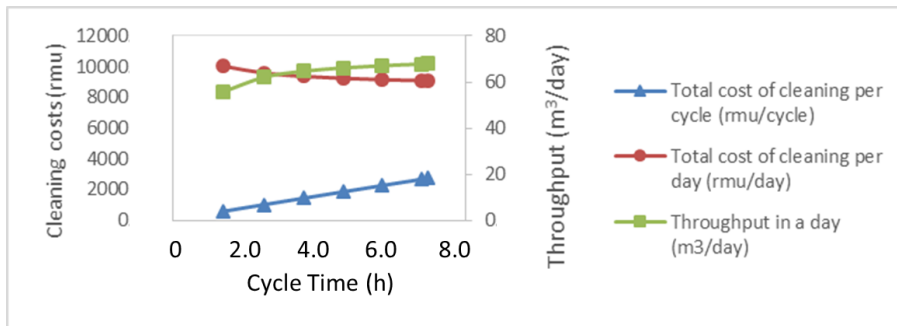


Figure 6. Cost of cleaning and throughput for various cycle times (A1, fouling model A)

4. Conclusions

The novel method presented allows us to easily and flexibly model PHEs of different configurations (e.g. with parallel, countercurrent, mixed parallel-countercurrent flow) and with various fouling, re-entrainment and cleaning models. This was demonstrated for two configurations which were implemented and validated. As far as we are aware, this is the first model describing in detail both fouling deposition and removal in PHEs. Results show that a good match to experimental data is achieved for two PHEs used for milk pasteurisation, in low computation time. It was demonstrated that the model may be used to study and optimise the dynamic operation of a complete PHE, including typical heating and cleaning policies. Its ability to predict deposit distribution on the plates will be also useful for monitoring and control.

References

- Bird, M. R. and Fryer, P. J., 1992. An analytical model for cleaning of food process plant.. Food Engineering in a computer climate, ICHIME Symposium Series , Issue 126, pp. 325-330.
- Bouvier, L, A. Moreau, G. Ronse, T. Six, J. Petit, G. Delaplace, 2014. A CFD model as a tool to simulate β -lactoglobulin heat-induced denaturation and aggregation in a plate heat exchanger, *Journal of Food Engineering*, 136, 56-63.
- Cavero, C., 2013. Análise dinâmica de um processo contínuo de pasteurização em trocadores de calor a placas, PhD Thesis: University of São Paulo.
- De Jong, P., 1997. Impact and control of fouling in milk processing. *Trends in Food Science & Technology*. 8 (12), 4011-405.
- Diaz-Bejarano, E., Coletti, F. and Macchietto, S., 2016. A new dynamic model of crude oil fouling deposits and its application to the simulation of fouling-cleaning cycles. *AIChE J.* 62 (1), 90-107.
- Fryer, P. J. and Slater, N. K. H., 1985. A direct simulation procedure for chemical reaction fouling in heat exchangers. *The Chemical Engineering Journal*, 31 (2) 97-107.
- Georgiadis, M. C. and Macchietto, S., 2000. Dynamic modelling and simulation of plate heat exchangers under milk fouling. *Chemical Engineering Science*. 55 (9), 1605-1619.
- Georgiadis, M. C., Rotstein, G. E. and Macchietto, S., 1998a. Modelling and simulation of complex plate heat exchanger arrangements under milk fouling. *Comp. Chem. Engrng*, 22., S331-S338.
- Georgiadis, M. C., Rotstein, G. E. and Macchietto, S., 1998b. Optimal design and operation of heat exchanger arrangements under milk fouling. *AIChE J.* 44 (9), 2099-2111.
- gPROMS, 2018. Process Systems Enterprise Limited, www.psenderprise.com,
- Guan, S. and Macchietto, S., 2018. A Novel Dynamic Model of Plate Heat Exchangers Subject to Fouling. *Computer Aided Chemical Engineering*, Vol 43 Part B, 1679-1684.
- Gut, J. A. and Pinto, J. M., 2003. Modeling of plate heat exchangers with generalized configurations. *International Journal of Heat and Mass Transfer*, Volume 46, p. 2571–2585.
- Jun, S. and Puri, V. M., 2006. A 2D dynamic model for fouling performance of plate heat exchangers. *Journal of Food Engineering*. 75 (3), 364-374.
- Sharma, A., 2018. MSc Thesis, Imperial College London.

Scale-up Modeling of a Pharmaceutical Antisolvent Crystallization via a Hybrid Method of Computational Fluid Dynamics and Compartmental Modeling

Merve Öner,^a Stuart M. Stocks,^b Jens Abildskov,^a Gürkan Sin,^{a*}

^aProcess and Systems Engineering Center, Department of Chemical and Biochemical Engineering, Technical University of Denmark, 2800 Kgs. Lyngby, Denmark

^bLEO Pharma A/S, Industriparken 55, 2750 Ballerup, Denmark

gsi@kt.dtu.dk

Abstract

In this work, a model of a 218 L scale pharmaceutical antisolvent crystallization process was developed. The model is based on a hybrid method of computational fluid dynamics (CFD) and compartmental modeling. In the model, the mixing behaviour of the bulk fluid at two different impeller speeds was obtained from CFD simulations. The compartmental map of the crystallizer was extracted from CFD results based on a hypothesis driven compartmentalization approach. A novel dynamic compartment model was developed to capture the fluid dynamics during the feeding of the antisolvent into the crystallizer and implemented in MATLAB/Simulink environment. Developed model takes into account the changes in compartmental volume, solvent concentrations and density and it assumes a dynamic flow between compartments during the filling. Dynamic compartment model can be also applied in other areas of modeling practices in chemical engineering instead of steady-state compartment models such as fed batch fermentation.

Keywords: Pharmaceutical crystallization, dynamic compartmental modeling, scale-up, computational fluid dynamics (CFD)

1. Introduction

The performance of crystallization process changes significantly dependent on the scale. Upon scale-up, the influence of the fluid dynamics and mixing on the process kinetics becomes important and variations in the crystal size distribution (CSD), purity and morphology often occur and that impacts the product quality and the performance of further downstream processes (Wei, 2010). Several experimental studies on the antisolvent crystallization system demonstrated the strong dependency of obtained CSD on the operation conditions such as crystallizer scale, impeller speed (mixing intensity), antisolvent addition rate and mode of addition such as direct or reverse. Often variations in these operating conditions directly effects the mixing of the solvent with antisolvent, so called the composition of the solvent mixtures (Woo et al., 2006). Homogeneous mixing in a short time is difficult to achieve in the large-scale crystallizer by making no concessions to the cost of the operation or product stability e.g. high impeller speed to promote mixing increases power input and leads to crystal attrition. When the mixing is inhomogeneous, it leads to local variations of important process variables such as solute

and antisolvent concentration, supersaturation, particle concentration in the large scale geometry (Woo et al., 2006, Green, 2002). Since the crystallization kinetics such as nucleation and growth are strongly influenced by those process variables, the crystallization occurs at different kinetic rates in the vessel depending on the local variation profile. Many published studies that focused on aiding the optimization and control of crystallization processes are based on a well-mixed assumption (Nagy et al., 2008). Even though an optimum operation condition is determined after several experiments at well-mixed laboratory scale, this might not be valid for the scaled-up system, since the mixing behaviour and related local variation can be significantly different. Therefore, understanding and predicting the mixing behaviour in the large scale crystallizers is an effective strategy and crucial for the improvement of the process performance. Fluid dynamics of the large scale and related limitations of the chemical system should be always taken into account in tandem with the interactions of thermodynamics and kinetics between solute-solvent system in modeling of large-scale crystallizers, in order to support reliable design, optimization and control.

This study presents an approach to develop a predictive model for an antisolvent crystallization process scale-up of an active pharmaceutical ingredient (API) that is based on a hybrid method of computational fluid dynamics (CFD) and dynamic compartment modeling. Reliable and detailed mixing information of the fluid system obtained from non-reactive CFD simulations is used as a guidance to build up compartments. The mixing dynamics of the antisolvent addition into the solution is modelled with a dynamic compartment model in which the volumes of the compartments and fluxes in-between changes over time. The compartmental model, where crystallization kinetics are coupled with fluid dynamics, is implemented in MATLAB/Simulink. While compartmental modeling is a well applied technique in many areas of modeling practices in chemical engineering, there is no known application on the pharmaceutical antisolvent crystallization process. Besides, developed compartmental models in the literature always assume the volume of the compartments as constant, which is not the reality during addition of a second liquid into the solution as in the antisolvent crystallization. Therefore, this work presents also a pioneer approach for the dynamic compartmentalization method based on author's knowledge. Additionally, developed model can be applied to other processes where the volume changes can not be ignored e.g. fed batch fermentation.

2. Hybrid Model Development

2.1. Crystallizer geometry

A 218 L crystallizer vessel from a previous work was used for the model development of the large scale antisolvent crystallization system. The vessel has 0.640 m of internal diameter and 0.740 m height. A three-blade marine type impeller of 0.300 m diameter is placed in the vessel with a 0.270 m clearance from the vessel bottom. The diameter of the impeller shaft is 0.040 m. Four baffles are located with 0.009 m distance from the vessel wall (Öner et al., 2018). The initial liquid height in the crystallizer before antisolvent addition is 0.455 m, which equals to 126.1 L of the liquid volume.

2.2. Mixing characterization via CFD simulations

The mixing behaviour of the single-phase liquid in the crystallizer was predicted by solving the representative Navier-Stokes equations through transient CFD simulations

performed with a commercial CFD software ANSYS CFX release 17.1. A turbulent fluid flow in the crystallizer was created by the impeller rotation at a speed of 40 rpm and 100 rpm. The standard $k-\epsilon$ turbulence model was used. The crystallizer volume was divided into two domains: a rotating domain and a stationary domain. The rotating domain is a cylindrical zone with 0.330 m diameter and 0.100 m height that contains the impeller and rotates at the impeller speed. The stationary domain contains the remaining zone. The frozen rotor approach was chosen to model the rotation of the impeller in terms of frame change model between the intersections of the two domains. The rotating and the stationary domains were discretized into 118,895 elements of tetrahedron mesh and 1,037,970 elements of hexahedron mesh, respectively (Öner et al., 2018). Several monitor points at different locations in the crystallizer were placed to monitor the time evolution of the fluid velocity. When the fluid velocity remained constant at all these monitor points (reached the steady state), the simulation was ended and the transient average value of the flow velocity components was used in further compartmentalization procedure.

2.3. Compartmentalization

The aim of the compartmentalization approach is to describe the imperfect mixing by defining the large scale fluid system as a network of finite-number interconnected ideally-mixed sub-volumes that contain no or negligible gradients (Wells and Ray, 2006, Nauha et al., 2018). The compartmental zones can be decided based on several criteria such as flow pattern, gradients of temperature and concentration, solid distribution or local energy dissipation (Kougoulos et al., 2006). In the last decade, CFD has been immensely utilized as a standard tool to study the mixing behaviour and its limitations on the chemical systems in detail. A coarser mesh of CFD cells can be created through compartmental models that facilitates the prediction of fluid dynamics and can be coupled with complex reaction kinetics in a simplified simulation environment in a computational cost efficient manner (Nauha et al., 2018, Nørregaard et al., 2018). The compartmental zones can be identified by processing the fluid dynamics information obtained from CFD simulations using a manual or automatic zoning technique (Bezzo and Macchietto, 2004). In this work, the mixing behavior in the crystallizer volume was firstly predicted by means of CFD simulations. The compartmental zones were identified based on a novel hypothesis-driven compartmental model approach that includes the analyzing of axial and radial bulk flow velocities at different locations in the crystallizer. The boundaries of the compartments were defined at the locations, where there is a change in the flow direction in radial and axial components of the velocity. A unidirectional flow was considered for each surface of compartments (Nørregaard et al., 2018).

2.4. Modeling and simulation of antisolvent crystallization process

Antisolvent crystallization of acetylsalicylic acid (aspirin) from ethanol (solvent) and water (antisolvent) was chosen as a case study. Previously published solubility and kinetic data in the literature were used (Lindenberg et al., 2009). The initial solution in the crystallizer has a volume of 126.1 L and contains the weight fraction of 0.25 w/w water and 0.75 w/w ethanol at 35 °C. The initial supersaturation was 1.05. After addition of the seed, the crystallization started with feeding the antisolvent, water into the solution at a rate of $2.3 \cdot 10^{-5} \text{ m}^3/\text{s}$ for 4000 s. When the antisolvent addition is completed, the final volume in the crystallizer is 218 L and contains 0.60 w/w water. The density change of the liquid mixture upon addition of the antisolvent was also taken into account and dynamically calculated during the simulation.

3. Results and Discussion

3.1. Mixing simulation via CFD and compartmentalization

The mixing characteristics of 218 L liquid flow at two different impeller speeds of 40 rpm and 100 rpm were studied with CFD simulations and is shown in Figure 1 (right). The obtained results show that there is much higher liquid flow circulation around the impeller region and the bottom of the vessel compared to top region in the vessel. After analyzing the three components of the bulk flow velocities at different locations in the vessel, total six compartments were detected and the compartmental map is illustrated in Figure 1 (left). The volume of each compartments (at $t = t_{\text{final}}$) and the volumetric flow rate between compartments (at $t = t_{\text{final}}$) are listed in Table 1. It should be noted that at the beginning of the antisolvent crystallization, while compartment 5 and 6 were completely full, compartment 3 and 4 were empty, and compartment 1 and 2 contained some amount of liquid. As the antisolvent was added to the vessel, firstly the empty volumes were filled in time. During the filling. It was assumed that the volumetric flow rate between compartment 1 and compartment 2 was constant until the compartments were full with liquid, then it started to increase dynamically up to final volumetric flow rate, during the filling of the compartment 3 and compartment 4, since additional flow, $Q_{4 \rightarrow 1}(t)$ entered to the system. The volumetric flow rates between empty compartments were activated after the volume of the compartments below was full. The volumetric flowrate between compartment 3 and 4, $Q_{3 \rightarrow 4}(t)$ as well as between compartment 2 and 3, $Q_{2 \rightarrow 3}(t)$ was also increased dynamically as filling of top zones started. These fluid data were used as input in the compartmental modeling of the antisolvent crystallization in the next section.

3.2. Compartmental model simulation

Antisolvent crystallization kinetics coupled with the fluid dynamics was simulated by means of compartmental modeling. The dynamics of the compartment volumes and accumulated antisolvent amounts in each compartment during the addition of antisolvent into the crystallizer at an impeller speed of 40 rpm are illustrated in Fig. 2 (top). During the antisolvent addition, it was assumed that antisolvent feed was entered from top of the vessel into both compartment 1 and compartment 2 with a volumetric flow rate proportional to their volumes, since the compartments are open volume systems and added liquid will increase the the liquid height at the same amount.

Table 1. Volumetric flow rates between compartments and the volume of the compartments.

Impeller speed	Volumetric Flow Rate [m ³ /s]						
	Q _{1→2}	Q _{2→3}	Q _{3→4}	Q _{4→1}	Q _{2→5}	Q _{5→6}	Q _{6→1}
40 rpm							
t = t ₀	0.0101	0	0	0	0.0101	0.0101	0.0101
t = t _{final}	0.0127	0.0026	0.0026	0.0026	0.0101	0.0101	0.0101
100 rpm							
t = t ₀	0.0326	0	0	0	0.0326	0.0326	0.0326
t = t _{final}	0.0400	0.0074	0.0074	0.0074	0.0326	0.0326	0.0326
	Volume [m ³]						
Time	C1	C2	C3	C4	C5	C6	
t = t ₀	0.0351	0.0270	0	0	0.0200	0.0440	
t = t _{final}	0.0560	0.0430	0.0240	0.0310	0.0200	0.0440	

When these compartments were filled, the antisolvent was fed into the top compartments of 3 and 4. However, the filling of compartment 3 and 4 introduced the new flow from compartment 4 into 1, and increased flow were between the compartment 1 and 2 that explains the increasing mass of antisolvent as illustrated in the Fig. 2 (top). Local variations of the antisolvent fraction shown in Fig. 2 (bottom) affect locally the crystallization growth and nucleation kinetics due to the differences in the supersaturation profiles.

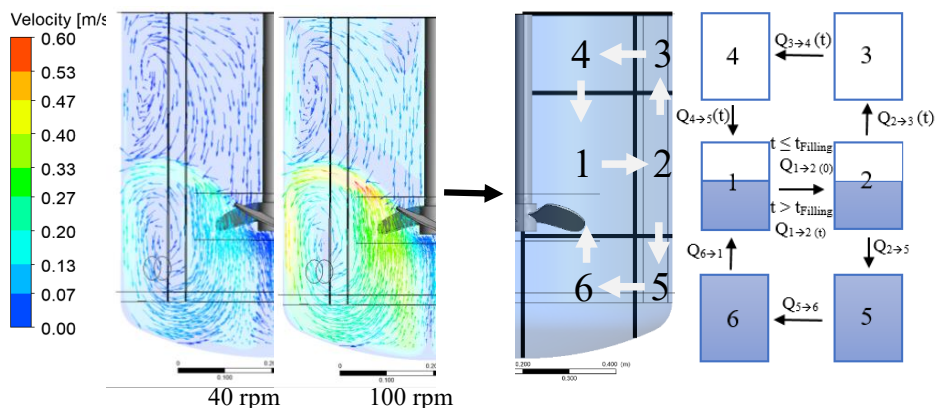


Figure 1. Flow velocity and the mixing behavior at different impeller speed (left) and compartmental map (right).

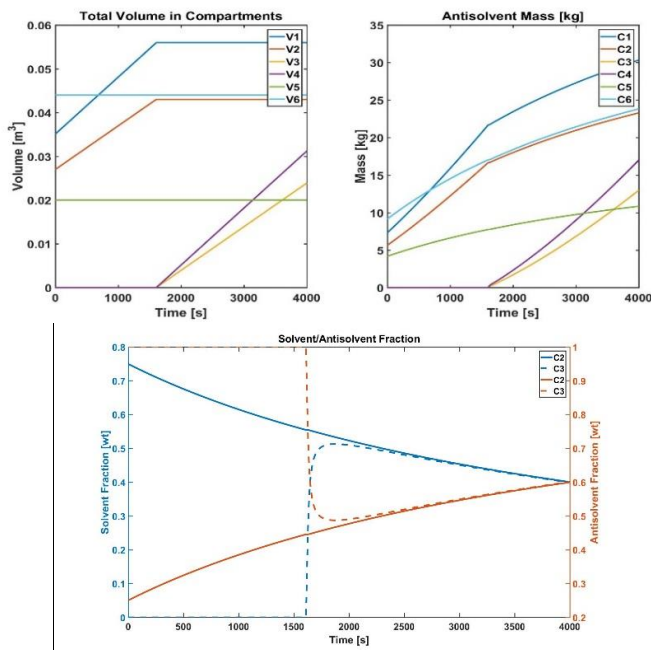


Figure 2. Compartment volumes (top-left), accumulated antisolvent amounts (top-right) and solvent fractions (bottom) during addition of antisolvent into the crystallizer.

4. Conclusions

A model of a large scale pharmaceutical antisolvent crystallization process was developed based on a hybrid approach of computational fluid dynamics and compartmental modeling. Fluid dynamics of bulk fluid mixing at two different impeller speeds were studied via CFD simulations. Compartmental zones were determined based on the flow velocities obtained from CFD simulation through a hypothesis driven compartmentalization approach. A dynamic model was incorporated for predicting the volume changes of the compartments and dynamic exchange flows in-between. The crystallization of aspirin from ethanol (solvent) and water (antisolvent) was simulated for each compartment that interchanges liquid flows and related properties such as density, solvent/antisolvent weight fraction as well as particles. Future work will focus on the refinement of the compartmental map in two ways. First, analyzing the third component of flow velocity in circumferential direction will enable the addition of the antisolvent from a more specific feed point. Second, CFD simulations with different bulk fluid volumes will be performed in order to study the fluid dynamics of antisolvent addition and evolution of the compartmental map in more detail.

References

- F. Bezzo and S. Macchietto, 2004, A general methodology for hybrid multizonal/CFD models, Part II: Automatic zoning, *Computers & Chemical Engineering*, 28, 513-525.
- D. Green. In *Handbook of Industrial Crystallization*, 2nd ed.; A. S. Myerson, Ed.; Butterworth-Heinemann: Boston, 2002; pp 181-200.
- C. Lindenberg, M. Krättli, J. Cornel and M. Mazotti, 2009, Design and optimization of a combined cooling/antisolvent crystallization process, *Crystal Growth & Design*, 9, 2, 1124-1136.
- E. Kougoulos, A.G. Jones and M. Wood-Kaczmar, 2006, A hybrid CFD compartmentalization modeling framework for the scaleup of batch cooling crystallization process, *Chem. Eng. Comm.*, 193, 1008-1023.
- E. K. Nauha, Z. Kálal, J. M. Ali, V. Alopaeus, 2018 Compartmental modeling of large stirred tank bioreactors with high gas volume fractions, *Chemical Engineering Journal*, 334, 2319-2334.
- A. Nørregaard, C. Bach, U. Krühne, U. Borgbjerg, K. V. Gernaey, 2018, Hypothesis-driven compartment model for stirred bioreactors utilizing computational fluid dynamics and multiple pH sensors, *Chemical Engineering Journal*, 356, 161-169.
- M. Öner, C. Bach, T. Tajssoleiman, G. S. Molla, M. F. Freitag, S. M. Stocks, J. Abildskov, U. Krühne, G. Sin, 2018. Scale-up modeling of a pharmaceutical crystallization process via compartmentalization approach, *Computer Aided Chemical Engineering*, 44, 181-186.
- Z. K. Nagy, M. Fujiwara, R. D. Braatz, 2008, Modeling and control of combined cooling and antisolvent crystallization processes, *Journal of Process Control*, 18, 856-864.
- G. J. Wells, W. H. Ray, 2006, Methodology for modeling detailed imperfect mixing effects in complex reactors, *AIChE Journal*, 51, 1508-1520.
- H. Y. Wei, 2010, Computer-aided design and scale-up of crystallization process: Integrating approaches and case studies, *Chemical Engineering Research and Design*, 88, 1377-1380.
- X. Y. Woo, R. B. H. Tan, P. S. Chow, R. D. Braatz, 2006, Simulation of mixing effects in antisolvent crystallization using a coupled CFD-PDF-PBE approach, *Crystal Growth & Design*, 6, 6, 1291-1303.

Design and Operation Optimization for Water and Power Cogeneration System by Reverse Osmosis and Renewable Energy Technologies

Yousef Saif,^a Muhammad Rizwan,^a Ali Almansoori,^{a*} Ali Elkamel,^{a,b}

^a*Department of Chemical Engineering, Khalifa University of Science and Tehnology, The petroleum Institute, Abu Dhabi, P.O.Box 2533, UAE*

^b*Department of Chemical Engineering, University of Waterloo, Waterloo, ON N2L 3G1, Canada*

ali.almansoori@ku.ac.ae

Abstract

In this study, the integration of renewable energy resources (RES) with reverse osmosis (RO) system is investigated to examine optimal design and operation of integrated water and power system over a planning time horizon. The supplied power from RES is assumed to be consumed by RO system for water production. Normally, model parameters vary over time such as water salinity, temperature, wind speed, solar radiation. Therefore, the proposed optimization problem is based on a multiperiod mixed integer nonlinear programming (MINLP) model. The MINLP model features two design and operation layers. The first layer includes design variables and constraints which are independent of time. These variables provide the capital investment requirements, and feasibility boundaries for the operation layer. The second layer involves time dependent variables and constraints to provide optimal operation and cost for the integrated system. The optimal results from the MINLP model will provide optimal system configuration and equipment size for the integrated system. Furthermore, the results will give optimal operation for the integrated system over the planning time horizon. A case study for seawater RO desalination system integrated with wind technology will be analyzed to show the application for the MINLP model.

Keywords: Renewable energy, reverse osmosis, water and power cogeneration, MINLP, multieperiod model.

1. Introduction

Water scarcity is a serious future challenge for sustainable development. Projection of water demand exhibits increasing trends due to global population growth accompanied with industrial expansions. The global water desalination market was valued at US\$ 13.31 billion in 2016 and is expected to register robust growth reaching US\$ 26.81 billion by 2025 (Hexa Research, 2017). Reverse osmosis (RO) is expected to witness the fastest growth because of its lower energy consumption rate. Growing demand for pure water is projected to boost the market for RO technology, and it is estimated to be worth US\$ 15.43 billion by 2025. Nowadays, the generation of clean power from renewable energy sources (RES) is practical such as using wind, solar radiation, hydropower, and others (Ellabban et al., 2014). RES are abundant, moderately inexpensive, and without negative environmental impact compared to traditional fossil

fuels. The application of RES as power sources for desalination technologies have witnessed considerable increase from 2% in 1998 to 23% in 2016 (REN21, 2016).

Several techno-economic studies presented research problems which examined the feasibility of RES technologies as clean energy sources for RO desalination operation. A study investigated the possible integration of photovoltaic solar technology for RO desalination operation (Monnot et al., 2018). The study showed the positive effect of RO configuration selection on the overall optimal cost. Nafey and Sharaf (2010) analyzed different solar Rankine cycle with different working fluids to find minimum treatment desalination cost by RO technology. Gökçek and Gökçek (2016) presented techno-economic study for small scale seawater RO desalination driven by wind turbines in Turkey. The aim from the study is to find the best capacity of wind turbines for reduced cost of power and water production, and reduced emission compared with grid connected system. Gökçek (2018) examined a hybrid energy system (e.g., wind, solar, diesel engine) for small scale seawater desalination in Turkey. The study results showed that a hybrid energy system provides the lowest energy and water cost.

RO desalination network has been studied extensively by many researchers to find the optimal RO configuration in desalination applications (Saif et al., 2008; Sassi and Mujtaba, 2011; Saif et al., 2014). To the best of our knowledge, the integration of RES with RO design and operation through multiperiod optimization model is not available in the literature. Therefore, the main contribution of this work is the development of integrated model for the design and operation of RES and RO integrated system for water and power production in order to satisfy water demand. The proposed optimization model is a multiperiod mixed integer nonlinear program (MINLP). The optimization model is composed by two layers. The design layer is independent of time, and it reflects the required capacities of the process equipment and capital cost. The second operation layer gives decision variables which represent the required operation of process equipment under different time periods with different values of the model parameters. In addition, the operation decision variables are constrained by the selected values for the design variables, and provide the required operation cost. In the following section, the research methodology is briefly described. The third section describes the MINLP formulation. The fourth section presents the results for seawater desalination case study integrated with wind technology. In the last section, the conclusions from this research study are detailed.

2. Methodology

Figure 1 shows the energy and water sections for the proposed research problem. It is assumed that a planning time horizon (T) is given with discrete time intervals. Within these intervals, economic and technical data for the integrated system is available. The objective is to find optimal size of power and RO equipment, and equipment operation to satisfy water demand in every time periods while minimizing total annual cost. The results from the mathematical programming formulation provide optimal RO network configuration (e.g., number of RO passes, pressure vessels, and RO modules), auxiliary equipment (e.g., high pressure (HPP) and booster (BP) pumps, pressure exchangers (PE)), stream assignments within the network, and operation over time for water section. In addition, the results provide optimal selection of RES equipment and their operation over time under minimum total annualized cost. The following section provides the mathematical programming formulation.

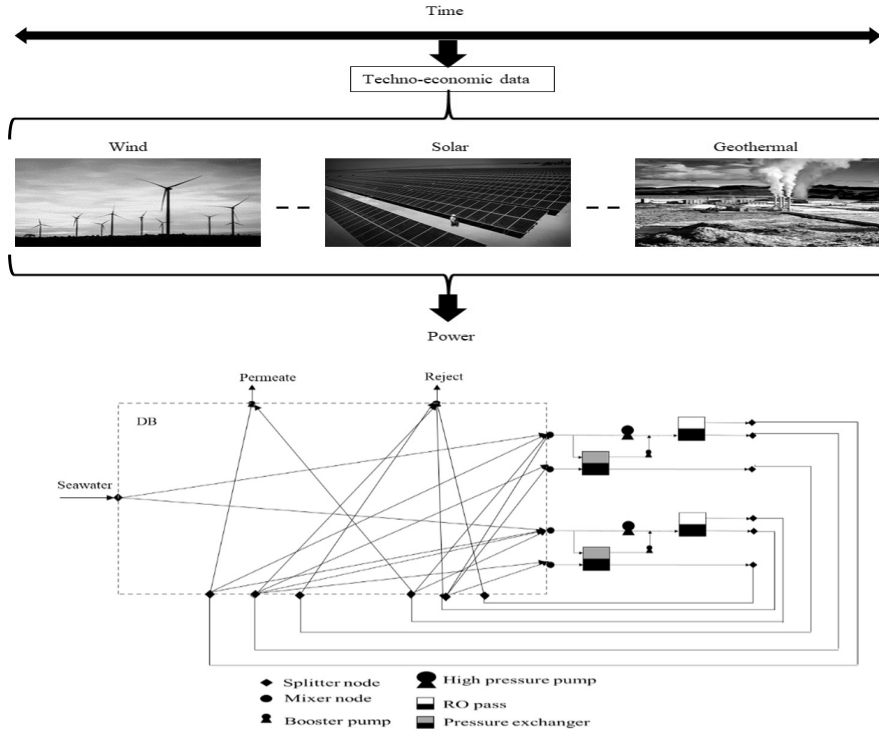


Figure 1. RES-RO integrated system representation under time variant input parameters.

3. MINLP model

The objective function of the MINLP model is to minimize the total annual cost (TAC) which is composed of the annualized capital and operation cost. The annualized capital cost (cc) of equipment (Q) represents the RO passes with their auxiliary equipment, and the RES equipment, and op represents the operation cost for the process equipment over the planning time horizon. Eq. (1) gives the total annual cost.

$$TAC = \sum_Q cc_Q + \sum_{Q,T} op_{Q,T} \quad (1)$$

The higher layer design variables (xe) are assumed to be independent of time. These design variables give operation limit for the lower operation variables (xo) as given by Eq.(2). Examples of design variables are surface area, flow, pressure, temperature, etc.

$$xp_{Q,T} \leq xe_Q \quad \forall Q,T \quad (2)$$

Every RO pass produces water (wp). Water production is related to the selected number of RO modules (mr), RO pressure vessels (pr), applied pressure (p), and osmotic pressure difference (opd) between the reject and permeate side, and the pressure drop ($drop$) as given by Eq.(3). Water permeability is represented by the decision variable

wpr which is a function of reject side physical properties (e.g., salinity, temperature, viscosity, etc.). It should worth pointing out that concentration polarization effects are considered in the MINLP formulation to give better estimation of total dissolved solid (TDS) concentration at the membrane wall. In the water section (Fig. 1), there are stream splitting and mixing in the distribution box (DB). Therefore, total water and TDS balance are required over time for the splitter and mixer nodes which give nonconvex terms.

$$wpr_{RO,T} = wpr_{RO,T} mr_{RO} pr_{RO} (p_{RO,T} - drop_{RO,T} - opd_{RO,T}) \quad \forall RO, T \quad (3)$$

The energy system involves several RES. These RES have different sources of energy for power production. The power production (pwp) from RES are related to the selected number (NU) and size (SZ) of a given technology and the power that can be produced from a single unit (Q) as given by Eq. (4). Examples of power production models from single RES equipment can be found elsewhere (Maleki, 2018). The design variable is a binary variable (y) which indicates existence of a given technology and size. In addition, another binary variable is given in Eq.(4) which indicates if an RES is under operation at time interval T. Therefore, the total energy production from all RES is assumed to be consumed by RO auxiliary equipment for water demand constraint at every time period. The following section provides results for the RO seawater desalination integrated with wind technology in Tunisia.

$$pwp_{RES,NU,SZ,T} = y_{RES,NU,SZ,T} y_{RES,NU,SZ} Q_{RES,T} \quad \forall RES, NU, SZ, T \quad (4)$$

4. Case Study

Table 1 shows input data for the MINLP model to represent a case study of Tunisia (Cherif and Belhadj, 2011). The planning time is assumed to be one year with monthly discrete values. In addition, this case study represents a small scale design problem for power and water cogeneration. Table 2 shows RO membrane properties (e.g., FilmTec SW30HR-380 from Dow chemical company), and Table 3 shows different small scale wind turbines (e.g., from AEOLOS manufacturer).

Table 1. Water demand, seawater properties, and air conditions over year.

Periods, month	T1	T2	T3	T4	T5	T6	T7	T8	T9	T10	T11	T12
TDS, ppt	21	33	34	35	36	36	36	36	38	35	35	35
Seawater temp, °C	12.9	13	17	19	20.6	25.1	28	34	30	23	19	16
Air temp, °C	12	13.4	15.7	18.0	21	25	27.6	28.6	26.9	23.3	18.5	14.3
Wind speed, m/s	7.9	8	8.3	8.4	8.4	8.4	7.8	7.6	7.9	7.6	7.8	8.4
Water demand, kg/s	0.69	0.87	0.98	1.13	1.15	1.2	1.2	1.23	1.13	0.93	0.75	0.67

The optimal solution for the energy section show TAC of US\$ 6504. Furthermore, the optimal selected capacity for the wind turbine is four wind turbines of 5 kW capacity. The total generated power is 94.7 kW for seawater desalination every year. This power

is consumed for seawater desalination in order to satisfy water demand over the year. The TAC for the RO section is US\$ 5681. Therefore, the combined water and energy TAC is US\$ 12,185.

Table 2. RO module specifications

Active area (m ²)	35.3
Module length (m)	1.016
Feed space (mm)	0.737
Equivalent diameter (mm)	0.935
Feed flowrate range (m ³ /h)	0.8-16
Maximum operating pressure (MPa)	8.3
Water permeability (kg/m ² s MPa)	2.7×10 ⁻³
TDS permeability (kg/m ² s)	2.3×10 ⁻⁵
Module cost (\$)	1000

Table 3. Wind turbine specifications.

	Wind turbine 1 (WT1)	Wind turbine 2 (WT2)
Maximum power (kW)	2.6	7
Rated power (kW)	2	5
Cut in speed (m/s)	2	2.5
Rated wind speed (m/s)	10	10
Survival wind speed (m/s)	50	55
Generator efficiency (%)	96	96
Rotor height (m)	2.8	5.3
Cost (\$)	5605	14309

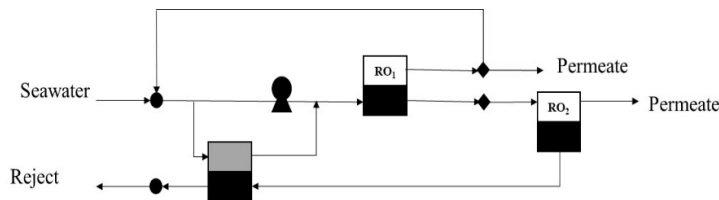


Figure 2. Optimal configuration for the RO plant.

Figure 2 shows the optimal configuration for the RO plant. It features two RO passes with permeate recycling. The recycled permeate stream is periodic when it is necessary to dilute the seawater feed stream. The mixed stream is divided into two streams for pressurization in the HPP and the PE units. Then these streams are processed in the first RO pass with two pressure vessels and single RO module. The reject from the first RO pass flows through the second RO pass with one pressure vessel and dual RO modules to increase water recovery. The permeate streams from the first and second RO passes are combined to satisfy water demand.

5. Conclusions

This study presented a multiperiod MINLP for water and power production by RO and RES technologies. The model formulation is composed of two layers which represent the design and operation of the integrated system. The first layer provides optimal

solution for the RO network configuration, optimal selection of RES equipment sizes, and capital cost. The second layer provides the required operation for the integrated system to satisfy water demand by RO technology, power production by RES technologies, and the required operation cost for the integrated system. A case study in Tunisia was analysed to show the application of the optimization model. Future work will be focused on integrating more RES technologies for improvement of the power cost and production, and examining membrane fouling effects on the desalination energy requirement.

References

- A. Maleki, 2018, Design and optimization of autonomous solar-wind-reverse osmosis desalination systems coupling battery and hydrogen storage by an improved bee algorithm, *Desalination*, 435, 221-234.
- A.S. Nafey, M.A. Sharaf, 2010, Combined solar organic Rankine cycle with reverse osmosis desalination process: Energy, exergy, and cost evaluations. *Renewable Energy*, 35, 2571-2580.
- H. Cherif, J. Belhadj, 2011, Large scale time evaluation for energy estimation of standalone hybrid photovoltaic-wind system feeding reverse osmosis desalination unit, *Energy*, 36, 6058-6067.
- Hexa Research, 2017, Water desalination market size and forecast, by technology (reverse osmosis, multi-stage filtration, multi-effect distillation), by source (seawater, brackish water, wastewater), and trend analysis, 2014 – 2025.
- K.M. Sassi, I.M. Mujtaba, 2011, Optimal design and operation of reverse osmosis desalination process with membrane fouling, *Chemical Engineering Journal*, 171, 582-593.
- M. Monnot, G. D. M. Carvajal, S. Laborie, C. Cabassud, R. Lebrun, 2018 , Integrated approach in eco-design strategy for small RO desalination plants powered by photovoltaic energy, *Desalination*, 435 , 246–258.
- O. Ellabban, H. Abu-Rub, F. Blaabjerg, 2014, Renewable energy resources: current status, future prospects and their enabling technology, *Renewable and Sustainable Energy Reviews*, 39, 748-764.
- REN21, 2016, Renewable energy Policy Network for the 21st century, *Renewables 2014, Global Status Report*.
- Y. Saif, A. Almansoori, A. Elkamel, 2014, Optimal design of split partial second pass reverse osmosis network for desalination applications, *AIChE Journal*, 60, 520-532.
- Y. Saif, A. Elkamel, M. Pritzker, 2008, Global optimization of reverse osmosis network for wastewater treatment and minimization, *Industrial and Engineering Chemistry Research*, 47, 3060-3070.

Modelling of bubble column hydrodynamics using CFD and SQMOM as a population balance solver

Jan Schäfer^a, Mark W. Hlawitschka^a, Menwer Attarakih^{a,b*} and Hans-Jörg Bart^a

^a*Chair of Separation Science and Technology, TU Kaiserslautern, 67663 Kaiserslautern, Germany*

^b*School of Engineering, Chem. Eng. Dept., The University of Jordan, 11942-Amman, Jordan*

jan.schaefer@mv.uni-kl.de

Abstract

The complex interactions between the turbulent flow field, bubble size distribution, mass transfer and chemical reactions make the design of bubble column reactors a challenging task. Especially at broad bubble size distributions the commonly used QMOM is not able to track the different velocities of small and large bubbles, while the classes methods are limited due to a high computational load. In this work, we extended our CFD-Sectional QMOM (SQMOM) (Drumm et al., 2008) to model and simulate bubbly gas flow in a rectangular column. For this purpose, we established a setup to measure, in 18 different zones of a rectangular bubble column, the bubble size distribution, the bubble velocity and bubble orientation. The coalescence and breakage model parameters are extracted in a parameter study using the software Dakota for a single case. A satisfactory agreement between local values of three experimentally investigated flow rates and simulations are found without further adjustment of the parameters. This work enables therefore a characterization of heterogeneous bubbly regimes including breakage and coalescence as found in industrial reactive bubble columns.

Keywords: Bubble movement, Local bubble size distribution, Sectional Quadrature Method of Moments, Population balance equation

1. Introduction

In many process engineering fields, dispersed systems are used to enhance momentum, heat and mass transport in either liquid-liquid, gas-liquid, solid-liquid or solid-gas phases. The generation of mono or multivariate size distributions depends not only on the particle generation and the internals of the apparatus, but also on the operational conditions. These include throughput and energy input. Among these multiphase apparatuses is the bubble column reactor, which is used in chemical and biochemical processes to bring a gas phase in contact with a fluid phase to enhance mass transfer and chemical reactions through maximizing the available interfacial area concentration. The complex interactions between the turbulent flow field, bubble size distribution, mass transfer and chemical reactions make the design of the reactors a challenging task (Hlawitschka et al., 2016). In this regard, population balance models coupled to computational fluid dynamics (CFD) have become a suitable tool to investigate bubbly gas flows where the evolution of full bubble size distribution can be modelled. This is because the experimental evidence shows

that broad distributions developed along bubble column reactors due to bubble breakage, coalescence and growth which could not be ignored (Hlawitschka et al., 2016). Unfortunately, the main population balance CFD modelling tools are based, on the one hand, on the Quadrature Method Of Moments (QMOM) which fail to predict the bubble column hydrodynamics due to averaging the whole distribution. On the other hand, classes methods which can follow the full bubble size distribution are inaccurate, especially when a small number of classes are used to reduce the expensive computer computational cost. For this reason, the Sectional Quadrature Method of Moments (SQMOM) (Attarakih et al., 2009) is used, which is a combination of both approaches (discrete and moment methods) to overcome these drawbacks and enable the simulation of BSD with difficult shapes, like a bimodal distribution.

1.1. Numerical framework

The SQMOM is implemented to the multiphaseEulerFoam solver of the toolbox OpenFOAM (version 4.1). The solver is an Euler-Euler multiphase approach and treats each phase as interpenetrating continua. The multiphase approach enables a direct implementation of the primary and the secondary particle concept of the SQMOM, where the primary particles represent the discrete sections and the secondary particles are responsible to account for the interactions between the sections.

The hydrodynamics inside the bubble column is basically simulated using the Navier-Stokes equations for each phase:

$$\frac{\partial \alpha_n}{\partial t} + \vec{u}_n \cdot \nabla \alpha_n + \nabla \cdot (\vec{u}_{comp}(1 - \alpha_n)) = \alpha_n S_\alpha \quad (1)$$

$$\frac{\partial}{\partial t} (\alpha_n \rho_n \vec{u}_n) + \nabla \cdot (\rho_n \alpha_n \vec{u}_n \vec{u}_n) = -\alpha_n \nabla p - \nabla \cdot (\alpha_n \tau_n) + \alpha_n \rho_n \vec{g} + \vec{F}_{D,n} + \vec{F}_{VM,n} \quad (2)$$

The phase fraction of a phase n is denoted by α , the density of each phase by ρ , and the velocity \vec{u} . In addition, the solver multiphaseEulerFoam includes an interface sharpening term, which includes the interface compression velocity:

$$\vec{u}_{comp} = C_\alpha |\vec{u}| \frac{\nabla \alpha}{|\nabla \alpha|} \quad (3)$$

A value of C_α enables the reconstruction of the interface of large bubbles. However, the dynamic switching between particles accounted by PBM and resolved particles is not resolved until now and we apply a value of $C_\alpha = 0$.

The hydrodynamic interactions between the phases like drag, lift, virtual mass, etc. are accounted by the respective forces. The drag force $F_{D,n}$ is determined by the equation of Tomiyama et al. (1998):

$$C_D = \max \left(\min \left(\frac{16}{Re} (1 + 0.15 Re^{0.687}), \frac{48}{Re} \right), \frac{8}{3} \frac{Eo}{(Eo + 4)} \right) \quad (4)$$

The Reynolds number Re and the Eötvös number EO are calculated by:

$$Re = \frac{\rho_c d_{32} |\vec{u}_c - \vec{u}_d|}{\mu_c} \text{ and } EO = \frac{g(\rho_c - \rho_d) d_{32}^2}{\sigma_c} \quad (5)$$

The virtual mass force $\vec{F}_{VM,n}$ uses a constant value of $C_{VM} = 0$:

$$\vec{F}_{VM,n} = \alpha_n^* \rho_n C_{VM} \left(\frac{Du_n^*}{Dt} - \frac{Du_n}{Dt} \right) \quad (6)$$

The superscript * describes the interacting other phase.

As turbulence model, the model Smagorinsky turbulence model is applied. For the calculation of the energy dissipation, the following equation is applied:

$$\varepsilon = \frac{\mu_{eff,c}^3}{\rho_c^3 (C_S \Delta)^4} \quad (7)$$

C_S is a model constant with a value of 0.167. The cubic root of the cell volume is Δ .

1.1.1. SQMOM

The Sectional Quadrature Method of Moments (SQMOM) and its variants was introduced by Attarakih et al. (2009). The SQMOM calculates the change of the moments using the primary and secondary particle based concept. The primary particles correspond to the classes of a distribution, the secondary particles involve the interactions such as coalescence and breakage, based on the Quadrature Method of Moments concept. The moment of order k of the primary particle i , falling in the bubble size interval $[L_{i-1/2}, L_{i+1/2}]$, can be calculated as follows:

$$m_{ki} = \int_{L_{i-1/2}}^{L_{i+1/2}} (L_i)^k n(L, x, t) dL \approx \sum_{j=1}^{N_{sp}} (w_{ji}(x, t) L_{ji}^k(x, t)) \quad (8)$$

Four moments are sufficient to represent each section. Thereby, each section moves with its own velocity. The two equal weights and abscissas can be calculated by the moments m_0 , m_1 and m_3 :

$$L_{1,2} = m_1 \pm \frac{1}{\sqrt{3}} \sqrt{\frac{m_3}{m_1} - m_1^2} \quad (9)$$

$$w_{1,2} = \frac{1}{2} m_0 \quad (10)$$

The transport equation for each section can therefore be calculated as:

$$\frac{\partial}{\partial t} (\alpha_i \rho_i m_k^{<i>}) + \nabla \cdot (\alpha_i \rho_i m_k^{<i>} \vec{u}_i) = \alpha_i \rho_i S_k^{<i>} \quad (11)$$

The source terms S for breakage and coalescence are described in Drumm et al. (2008). In this work, the breakage from Alopaeus et al. (2002) and coalescence from Coualalou

and Tavlarides (1977) and Prince and Blanch (1990) are applied. The breakage frequency is:

$$g(L) = C_1 \varepsilon^{1/3} \operatorname{erfc} \left(\left[C_2 \frac{\sigma}{\rho_c \varepsilon^{2/3} L^{5/3}} + C_3 \frac{\mu_d}{(\rho_d \rho_c)^{1/2} \varepsilon^{1/3} L^{4/3}} \right]^{1/2} \right) \quad (12)$$

and the coalescence frequency is given by:

$$a(L, L^*) = C_4 \varepsilon^{1/3} (L + L^*)^2 (L^{2/3} + L^{*2/3})^{1/2} \eta(L, L^*) \quad (13)$$

The coalescence efficiency is:

$$\eta(L, L^*) = \exp \left(-C_5 \frac{\mu_c \rho_c \varepsilon}{\sigma_c^2} \left(\frac{LL^*}{L + L^*} \right) \right) \quad (14)$$

The parameters described in literature are $C_1 = 6$, $C_2 = 0.04$ and $C_3 = 0.01$, $C_4 = 0.88$ and $C_5 = 6 \cdot 10^9$ (Buffo et al., 2013). There every system shows slight influences to coalescence and breakage, the model parameters were optimized using the optimization toolbox Dakota.

2. Experimental and numerical setup

A pseudo rectangular bubble column with a dimension of 0.18x0.04x1 m is filled with water up to a level of 0.6 m. Gas is introduced at the center of the column through a needle sparger with 5 needles in a row. The pitch of each needle is 1.5 cm and needle inner diameter is 1 mm. The gas superficial velocity was adjusted to 6 and 10 mm/s. A high speed camera (Imaging Solutions, IDT NX-8 S2) was placed in front of the column to track the bubbles in 18 sections of the column. Images were taken at a frame rate of 500 images per second, which in general allows a detection of bubble movement. The images were automatically analysed in regard to bubble size, bubble shape and orientation using the OpenCV toolbox. The inlet diameter was determined from these experiments, by determine the diameter distribution close to the inlet. For the case of 6 mm/s, the inlet diameter was 6.7 mm/s in average and for the case of 10 mm/s, the inlet diameter is 6.3 mm. The numerical representation of the bubble column (1) consists of a hexahedral mesh with 28x5x120 cells. The dispersers is simplified by a planar surface with an area of 50 mm x 6 mm. Also in the simulation, the air phase above the water level is accounted for.

3. Results

For the case the superficial velocity of 6 mm/s, the model parameters were optimized to obtain a good fit of the bubble size distributions (Figure 2), while for symmetry reasons, only the left zones and middle zones of the bubble column are presented. The optimization resulted in parameters for $C_1 = 2$ and $C_4 = 0.1$. The other parameters were kept equal to the values, described in the numerical framework section. The average diameter obtained from experiments is 6.0 mm and the simulation results in an average diameter of 6.0 mm. The bubble regime is breakage dominated. In a second step, we applied the parameters to the case of higher superficial velocity of 10 mm/s. It can be seen, that the simulation fits well to the experimental results (Figure 3). The bubble size changes from 6.3 mm to

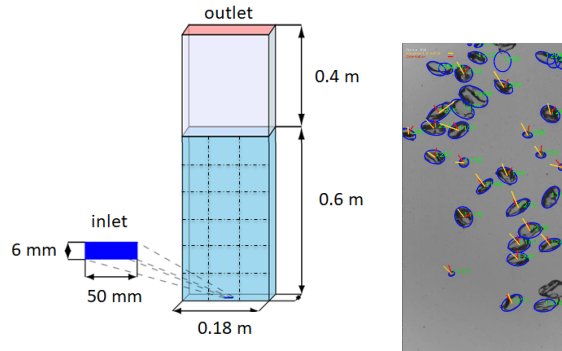


Figure 1: Numerical representation of the experimental setup with the 18 measurement zone for the bubble size detection (left) and example of the bubble size detection (right).

5.7 mm in average. The simulation predicts a diameter of 5.9 mm in average. A clear shift to smaller bubble sizes can be seen from the sections. Especially close to the wall, the smaller sized bubbles dominate the flow regime, while in the center of the column, larger bubbles can be seen. This effect is enhanced at higher velocities.

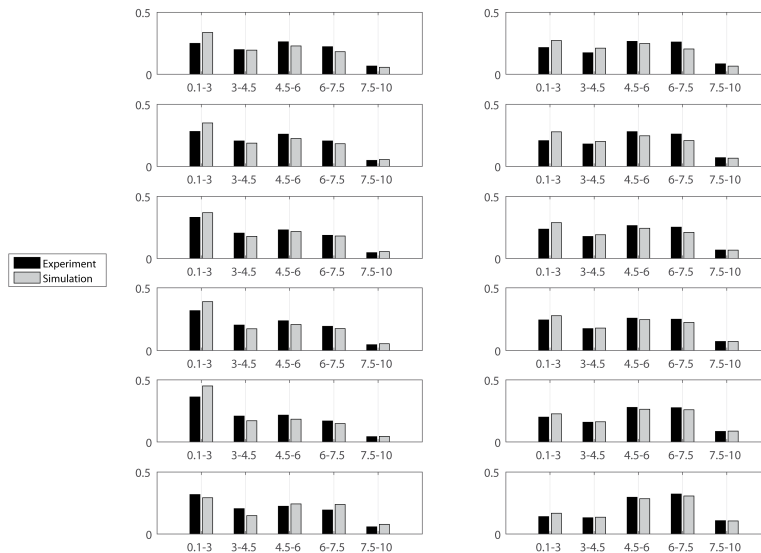


Figure 2: Bubble size distribution in each section at a superficial velocity of 6 mm/s.

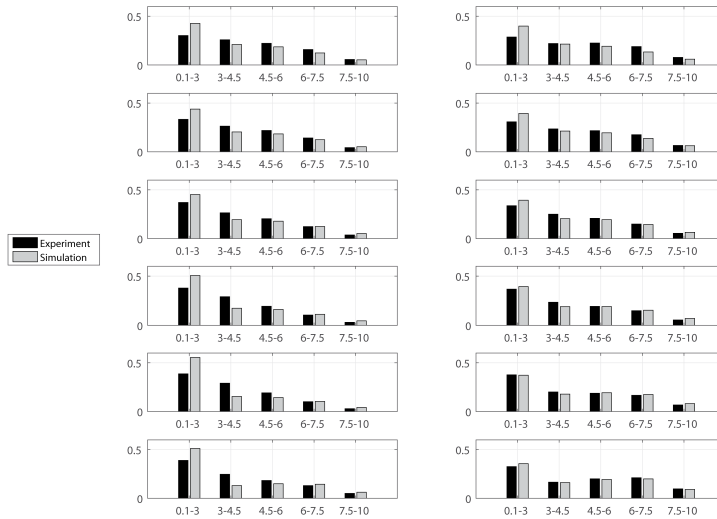


Figure 3: Bubble size distribution in each section at a superficial velocity of 10 mm/s .

4. Conclusion

In this work, we presented a method to model polydisperse systems coupled with an open source toolbox (OpenFOAM) to predict the local size distribution in a pseudo rectangular bubble column. We validated the SQMOM population balance solver to experimental data obtained by a high speed camera and automated data processing. The SQMOM is able to track the bubble size distribution by combining the advantages of the classes method with the ones of the quadrature method of moments. For the still inevitable calibration of the coalescence and breakage parameters, the toolbox Dakota was successfully applied. The computational performance can be flexibly adapted by adding or removing primary particles, leading in the second case to a reduced order model (OPOSPM).

References

- V. Alopaeus, J. Koskinen, K. I. Keskinen, J. Majander, 2002. Simulation of the population balances for liquid-liquid systems in a nonideal stirred tank. Part 2: parameter fitting and the use of the multiblock model for dense dispersions. *Chem Eng Sci* 57, 1815–1825.
- M. M. Attarakih, C. Drumm, H.-J. Bart, 2009. Solution of the population balance equation using the sectional quadrature method of moments (SQMOM). *Chem Eng Sci* 64, 742–752.
- A. Buffo, D. L. Marchisio, M. Vanni, P. Renze, 2013. Simulation of polydisperse multiphase systems using population balances and example application to bubbly flows. *Chem Eng Res Des* 91, 1859–1875.
- C. A. Coualoglou, L. L. Tavlarides, 1977. Description of interaction processes in agitated liquid-liquid dispersions. *Chem Eng Sci* 32, 1289–1297.
- C. Drumm, M. Attarakih, S. Tiwari, J. Kuhnert, H.-J. Bart, 2008. Implementation of the sectional quadrature method of moments in a CFD code. 6th International Conference on CFD in Oil & Gas, Metallurgical and Process Industries, SINTEF/NTNU, Trondheim, Norway, 10-12 June 2008.
- M. W. Hlawitschka, J. Schäfer, M. Hummel, C. Garth, H.-J. Bart, 2016. Populationsbilanzmodellierung mit einem Mehrphasen-CFD-Code und vergleichende Visualisierung. *Chem Ing Tech* 88, 1480–1491.
- M. J. Prince, H. W. Blanch, 1990. Bubble coalescence and break-up in air-sparged bubble columns. *AIChE J.* 36, 1485–1499.
- A. Tomiyama, I. Kataoka, I. Zun, T. Sakaguchi, 1998. Drag Coefficients of Single Bubbles under Normal and Micro Gravity Conditions. *JSME international journal. Ser. B, Fluids Therm Eng* 41, 472–479.

Single-shooting optimization of an industrial process through co-simulation of a modularized Aspen Plus Dynamics model

Mikael Yamane-Nolin^{a,*}, Anton Löfgren^a, Niklas Andersson^a, Bernt Nilsson^a, Mark Max-Hansen^b and Oleg Pajalic^b

^a*Lund University, Naturvetarvägen 14, 221 00 Lund, Sweden*

^b*Perstorp AB, Industriparken, 284 80 Perstorp, Sweden*

mikael.yamane-nolin@chemeng.lth.se

Abstract

The Python Module Coupler (PyMoC) is a tool for co-simulation of Aspen Plus Dynamics modules that together make up an overall process flowsheet. The tool requires only user input in the form of file paths to Aspen Plus Dynamics modules, and it is able to automatically make the required connections there between, and keep track of the simulation whilst updating the streams regularly. This contribution briefly discusses the implementation and mechanisms of PyMoC, and then applies it to a multi-module, single-shooting constrained optimization problem, where an industrial set-up consisting of an evaporator system coupled to a distillation column is studied. This serves as a showcase of PyMoC's functionality and usability, as well as its potential in serving as a helpful tool for practitioners of model-based studies who could benefit from modularizing their models. Utilizing PyMoC for this purpose, the optimization results indicate that the operating costs induced from the steam consumption can be reduced by 54% compared to a nominal operating case, but a holistic, full-process study is necessary to understand the full set of possibilities, causes, and effects.

Keywords: Python, Aspen Plus Dynamics, co-simulation, optimization, PyMoC

1. Introduction

Model-based studies have a wide range of important uses, and can help practitioners save both time and money, whilst improving quality and safety of a process (Oppelt et al., 2015). Especially dynamic model-based studies have many different applications due to their capabilities of investigating not only steady-state conditions but also transient patterns (Skorych et al., 2017). Thus, performing such studies, e.g. single-shooting optimization, plays an important role in improving production processes in order to satisfy demands regarding e.g. environmental aspects whilst increasing production capacity.

When modeling and simulating large, complex flowsheets, there are advantages to be found in dividing the overall model into smaller sub-modules (i.e. modularization), such as simplifying the addition of complementing models and opening up possibilities for parallel work-flows (Felippa et al., 2001). It also makes overview easier if the models would follow existing P&IDs. Modularization is furthermore a solution to convergence issues that large-scale complex process flowsheet models may suffer from (Lin et al., 2017), which would otherwise obstruct model-based studies.

However, modularization comes with its own challenges, as there will thus be a need to connect and co-simulate the modules, which poses a challenge in itself (Andersson, 2016). Doing so manually is obviously not feasible considering the sheer number of spatial and temporal connections necessary for continuous simulation. Commercially available tools such as the AspenTech Operator Training Simulator (OTS) could be used, but the lack of publications utilizing the OTS for model-based studies (Ahmad et al., 2016) supports the conclusion that this tool may not be appropriate to use for such studies. To this end, a tool called the Python Module Coupler (PyMoC) has been developed to help practitioners with co-simulation of modules developed in Aspen Plus Dynamics (APD), utilizing the process flowsheeting software as the engine for calculations. The Python implementation of PyMoC allows for advanced model-based studies by automating connections and data transfer through the application of a naming convention and a zero-order hold analogy (ZOHA), respectively.

In this contribution, PyMoC has been used to optimize a multi-module model of an oscillating polyalcohol separation process, consisting of a two-stage evaporator system and a methanol distillation column. PyMoC will first be introduced briefly, before the modules and the optimization problem is presented, followed by results and conclusions.

2. The Python Module Coupler - PyMoC

PyMoC is based on the COM enabled interface first presented in Nolin et al. (2017), and works by taking as input the paths of the APD files that are to be co-simulated, and then automatically connects these and co-simulates them. The nature of its Python implementation further simplifies customizing model-based studies and applying useful 3rd party software. In this section, two of the main mechanisms behind the function of PyMoC are briefly explained; (i) the naming convention, and (ii) how the transfer of data between modules is performed during runtime.

2.1. The naming convention

In order to minimize the amount of work required by the user, connections between modules are made automatically. This is based on a naming convention, i.e. streams with identical stream names are connected. PyMoC automatically recognizes which stream is the source and the destination, based on the ‘Fixed’/‘Free’ stream variable property used within APD. This means that the user only needs to make sure that the streams to be connected are named identically during modeling. See figure 1 for an illustrative example, where the streams ‘FEED’ will be connected with the algorithm recognizing that the Module A stream is the source to the destination in Module B. The naming convention is also used for deciding which results that are to be presented. The user may provide an *interesting stream-name prefix*, which the algorithm will use to recognize for which streams the user wants results. This is practical especially for large systems, as the user can name the interesting streams with that prefix instead of naming specific streams, and the stream results will be extracted automatically for all interesting streams. Using figure 1 as an example again with e.g. “I-” as the prefix, streams I-IN, I-V, and I-L will have their results extracted automatically.

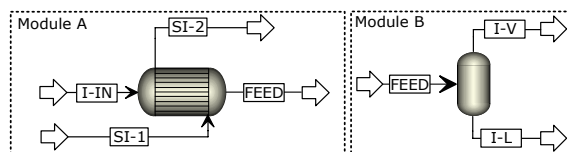


Figure 1: An illustrative example for the naming convention.

2.2. Data transfer using zero-order hold

A zero-order hold (ZOH) strategy, which has recently been successfully applied for the control of chromatographic separation (Sellberg et al., 2017), is utilized to transfer data between modules, and is essentially a piece-wise constant method. It works by taking the output of the source stream and setting that as the input of a destination stream, keeping this constant over a simulation time horizon, τ . The length of the simulation time horizon is chosen by the user, who should consider the trade-off between accuracy and speed - a smaller τ gives more frequently updated modules, increased accuracy since modules can work with fresher data, as well as longer run-times. The main advantage is the simple implementation, and the main disadvantage is that the sudden step-changes to a variable may introduce discontinuities, something of which the user needs to be aware.

3. Optimization of a modularized model using PyMoC

The problem entails optimizing the two parts of the polyalcohol separation system modeled in two independent flowsheets in order to grant the aforementioned advantages of modularization. The modules are described here, followed by the formulation of the optimization problem.

3.1. The models

The modularized process is presented schematically in figure 2. The evaporator system module has been presented in Nolin et al. (2018). The methanol distillation column was modeled using standard blocks of *RADFRAC*, *MHEX*, and *FLASH2* in Aspen Plus and then converted to Aspen Plus Dynamics, since the evaporator system was oscillating with propagations into the distillation system. The default controllers added during the conversion to an APD model were kept. An important aspect to note of both processes is that the separation was driven by steam at different pressures, inducing different process costs. Furthermore, of special interest are the streams named PROD and MEOH in figure 2, representing the target product stream of the main component in each module.

The distillation module shares four connections with the evaporator module, all of which drawn from the top of process units in the evaporator module, thus containing the most volatile components at each instance. These streams are passed through a 'translation module' (TM in figure 2) since the evaporation and distillation modules do not share identical Aspen Property Definition files. The difference there-between, c.p., is that formaldehyde was excluded from the distillation module component/property sets during modeling (and subsequently also the Maurer reactions (Hasse and Maurer, 1991) of the evaporator system), as its presence was assumed to be negligible. Essentially, this means that the distillation module cannot handle formaldehyde since its component/property sets do not contain the component. The translation module makes sure that formaldehyde is bypassed, but that the rest of the stream states (in terms of temperatures, pressures, mass flows, and compositions) are transferred from the evaporation to the distillation module. The translation module consists of one *SEP* block per stream, with the singular task of separating formaldehyde into a bypass stream, available for use if necessary later on.

3.2. The optimization problem

The steam consumption was one of the major cost-drivers in a nominal operating case of the overall, oscillating process. Thus, the goal of the optimization was to minimize the steam consumption cost incurred during daily operation while managing process and product demands (which are averaged due to the process oscillations captured in the modules). These demands entail the evaporation module product stream (PROD in figure 2) purity and mass flow, as well as the mass flow and methanol concentration in the top stream of the distillation column (MEOH in figure 2). In

addition to these constraints, another constraint on the minimum mass flow rate from the top of the distillation column was set at half of the nominal run mean value, to keep the column from running dry. This gives a total of five inequality constraint functions. Furthermore, each simulation included a pre-processing simulation period of 12 simulation hours to have any potential (cyclic) steady-state established before the optimization run. The problem was approached by employing a single-shooting strategy with $\tau = 0.1h$, and formulated as unbounded optimization subject to non-linear constraints:

$$\begin{aligned} & \underset{u}{\text{minimize}} && \phi(u) = \sum_{i=1}^2 \frac{c_i}{u_{i,nom}} \cdot u_i \\ & \text{w.r.t.} && u_1 = w_{steam, evap} \in \mathbb{R} \\ & && u_2 = w_{steam, dist} \in \mathbb{R} \\ & \text{s.t.} && \text{Modularized flowsheet model} \\ & && C_1 = \bar{w}_{PROD} - C_{w_{PROD}} \geq 0 && C_2 = \bar{P}_{PROD} - C_{P_{PROD}} \geq 0 \\ & && C_3 = \bar{w}_{MEOH} - C_{w_{MEOH}} \geq 0 && C_4 = \bar{P}_{MEOH} - C_{P_{MEOH}} \geq 0 \\ & && C_5 = w_{MEOH, min} - C_{w_{MEOH, min}} \geq 0 \end{aligned}$$

where w is mass flow rate, P is purity, \bar{x} denotes the average of a variable over the time period, subscripts *PROD* and *MEOH* refer to the streams thus named (figure 2) $u_{i,nom}$ is the decision variable values, and c_i is a price factor relating the mass flow of steam to the incurred cost thereof; $c_1 = 1$ and $c_2 = 0.7$, reflecting the cost ratio between the two steam pressure levels. C_{ij} , $i = (w, P)$, $j = (PROD, MEOH)$ denote the respective values of the *mean constraints*, while $C_{w_{MEOH, min}}$ denotes the constraint value for the minimum flow rate in the MEOH stream. The problem was solved by utilizing the scientific computing package *SciPy*'s implementation of the optimization algorithm Constrained Optimization By Linear Approximation (COBYLA), using the nominal point of the simulation as initial values for the decision variables, and running the model as part of the constraint function rather than the objective function.

4. Results and discussion

The objective value for the nominal run, $\phi(u_{nom}) = 1.7$, represents a normalized hourly steam consumption cost. By reducing u_1 by 69% and u_2 by 33%, the optimization was able to reduce the objective value by 54% to $\phi(u_{opt}) = 0.78$, whilst successfully satisfying the constraints. The

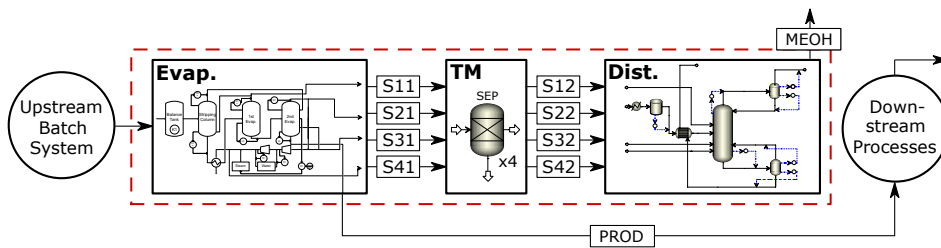


Figure 2: A schematic of the modularized process model, marked by the dashed box; the evaporator system ("Evap.") is described in Nolin et al. (2018), whilst the translation module ("TM") and the distillation column ("Dist.") are introduced in this contribution. Note the target product streams PROD and MEOH. The decision variables, i.e. the steam streams, are fully embedded in each module.

latter can be seen in figures 3 and 4, as the mean of variables in the optimal run is greater than the respective mean constraint; the same is true for the minimum flow constraint regarding \bar{w}_{MEOH} .

To gain insight into the dynamic behavior of the process, the PROD and MEOH stream results (i.e. w and P) of the nominal run as well as the optimal run are presented together with their mean values and the relevant constraints in figures 3 and 4, respectively. The results have been scaled to be centered around the mean constraint for each variable, rendering the results as dimensionless quantities. Neither graph show sudden, discontinuous responses at the start/end of the simulation time horizons, suggesting that the ZOHA strategy has not created any significant discontinuities.

As can be seen in figure 3, the mass flow and purity for the product stream vary somewhat during the nominal run, as previously reported in Nolin et al. (2018), and such is still the case for the optimal run. The size (i.e. difference between minimum and maximum) of the oscillations in the mass flow have been reduced by 27%, which should lead to simplified control and mitigated effects downstream. Furthermore, the optimal solution will effectively lower the purity by almost 2 percentage units. Together, the increased production rate as measured by w_{prod} and the decreased purity as measured by P_{prod} indicate that the optimal solution essentially produces more of a less concentrated product stream. It is therefore possible that increased costs will be incurred downstream to evaporate any excess water. Exactly how these interact with each other and how they in combination will affect downstream processes may require further studies.

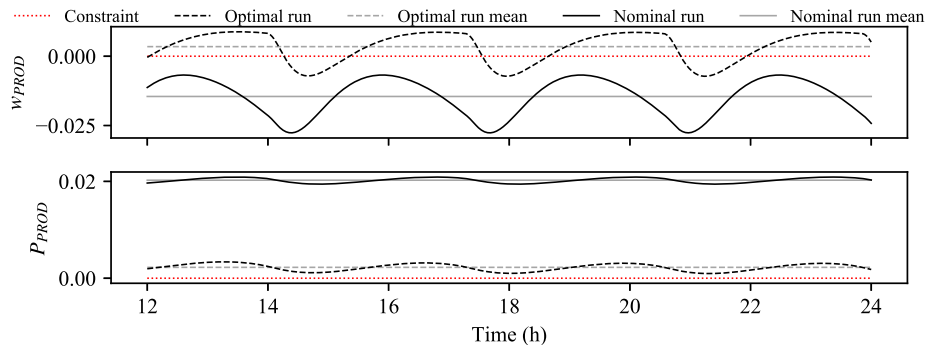


Figure 3: The PROD stream results from the nominal and optimal runs.

The mass flow results for the MEOH stream presented in figure 4 show that the optimal run yields massive oscillations over cycles, with a “jittery” model response, the latter of which presumably caused by the fast dynamics of a pressure controller at the top of the distillation column. The content of this stream is primarily used as fuel for the process, and the effects of propagations here will thus presumably not propagate to the same extent as will oscillations in the PROD stream, even though they are relatively large. Furthermore, the purity of the MEOH was increased significantly in the optimal run. This, combined with the reduced steam consumption for both modules, is further support for the natural conclusion that less water is evaporated in the evaporator module, and subsequently less water is passed on to the distillation column via the top-drawn streams.

5. Conclusions

The optimization shows that it is possible to reduce steam costs by 54 % compared to the nominal case whilst adhering to process demands. However, this may be a globally suboptimal solution

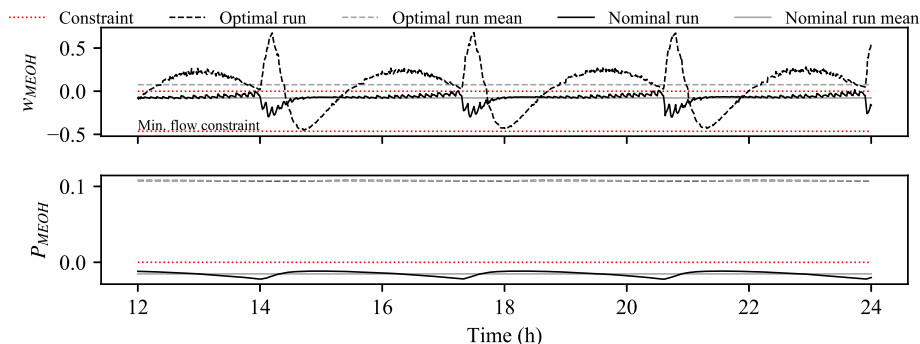


Figure 4: The MEOH stream results from the nominal and optimal runs; note the additional constraint regarding minimal mass flow rate.

when looking at the full process, since less water is evaporated in the investigated modules. This leads to as of now uncertain consequences downstream, but it is possible that the savings in the evaporator and distillation modules presented in the current work may be negated by increased costs downstream. As such, it is imperative to perform a holistic investigation of the full process to prepare for improved decision-making. However, the current work shows that, for the investigated systems, reducing the steam consumption whilst still adhering to production and product demands is indeed possible. Furthermore, oscillatory propagations from any module to other parts of the process need to be studied further. Negative effects thereof are especially necessary to study, and these can potentially be mitigated through an optimal control trajectory optimization possibly combined with improved tuning of the relevant controllers. PyMoC should be a useful tool to use for the former, due to the nature of its Python implementation as well as the implementation of the ZOHA strategy for data transfer.

References

- Ahmad, Z., Patle, D. S., Rangaiah, G., 2016. Operator training simulator for biodiesel synthesis from waste cooking oil. *Process Safety and Environmental Protection* 99, 55 – 68.
- Andersson, C., 2016. Methods and tools for co-simulation of dynamic systems with the functional mock-up interface. Ph.D. thesis, Lund University.
- Felippa, C. A., Park, K., Farhat, C., 2001. Partitioned analysis of coupled mechanical systems. *Computer Methods in Applied Mechanics and Engineering* 190 (24), 3247 – 3270, advances in Computational Methods for Fluid-Structure Interaction.
- Hasse, H., Maurer, G., 1991. Vaporliquid equilibrium of formaldehyde-containing mixtures at temperatures below 320 k. *Fluid Phase Equilibria* 64, 185 – 199.
- Lin, Z., Wang, J., Nikolakis, V., Ierapetritou, M., 2017. Process flowsheet optimization of chemicals production from biomass derived glucose solutions. *Computers & Chemical Engineering* 102, 258 – 267.
- Nolin, M., Andersson, N., Nilsson, B., Max-Hansen, M., Pajalic, O., 2017. Unbiased selection of decision variables for optimization. In: Espuña, A., Graells, M., Puigjaner, L. (Eds.), *27th European Symposium on Computer Aided Process Engineering*, Vol. 40 of *Computer Aided Chemical Engineering*. Elsevier, pp. 253 – 258.
- Nolin, M., Andersson, N., Nilsson, B., Max-Hansen, M., Pajalic, O., 2018. Analysis of an oscillating two-stage evaporator system through modelling and simulation: An industrial case study. Accepted for publication in *Chemical Engineering Transactions*, vol. 69.
- Oppelt, M., Wolf, G., Urbas, L., 2015. Life cycle simulation for a process plant based on a two-dimensional co-simulation approach. Vol. 37 of *Computer Aided Chemical Engineering*. Elsevier, pp. 935 – 940.
- Sellberg, A., Holmqvist, A., Magnusson, F., Andersson, C., Nilsson, B., 2017. Discretized multi-level elution trajectory: A proof-of-concept demonstration. *Journal of Chromatography A* 1481, 73 – 81.
- Skorych, V., Dosta, M., Hartge, E.-U., Heinrich, S., 2017. Novel system for dynamic flowsheet simulation of solids processes. *Powder Technology* 314, 665 – 679, special Issue on Simulation and Modelling of Particulate Systems.

Process Dynamic Analysis and Control Strategy for COGEN option Used for Flare Utilization

Monzure-Khoda Kazi,^a Fadwa Eljack,^{a,*} Saad Ali Al-Sobhi,^a Nikolaos Kazantzis,^b Vasiliki Kazantzi,^c

^a*Qatar University, Department of Chemical Engineering, College of Engineering, Doha P.O. Box-2713, Qatar*

Fadwa.Eljack@qu.edu.qa

^b*Worcester Polytechnic Institute, Department of Chemical Engineering and Center for Resource Recovery and Recycling, 100 Institute Road, Worcester, MA 01609, USA*

^c*University of Applied Sciences / TEI of Thessaly, Department of Business Administration, Business School, Larissa 41110, Greece*

Abstract

The aim of this work is to develop suitable process dynamic analysis and control strategies for implementing cogeneration unit (COGEN) as a flare utilization alternative to handle unexpected disturbances from unknown and uncertain flare sources. The developed steady state and dynamic simulations using Aspen Plus and Aspen Plus Dynamics allow the design of pressure and temperature controllers that demonstrate good performance. The simulation software and its built-in controller tuning option are used to create the dynamic modelling framework, and to perform controller installation and design. Finally, the proposed process dynamic analysis and control strategies are evaluated using an illustrative regulatory case study. It included disturbance rejection capability assessment in the presence of unexpected pressure load disturbances as well as temperature excursions from desirable operating conditions. The simple designed controller and its automated monitoring systems offered means of evaluating COGEN as a flare utilization alternative, while providing insights in to the techno-economic performance of the system.

Keywords: COGEN systems, Flare utilization, Dynamic process analysis, Simulation and control.

1. Introduction

Emissions from industrial flaring contribute to the accumulation of GHG in the environment and consequently to global warming. Thus, there is a need to develop an effective flare mitigation strategy and operational implementation plan that could reliably contribute to a systematic reduction of flare emissions while at the same time allow a further usage of otherwise unutilized flared streams as potentially valuable energy sources. Previous experience and research findings have demonstrated the utility of systematic process systems engineering (PSE) approaches for recovering and utilizing hydrocarbon streams typically flared during abnormal process operations (Kamrava et al., 2015, Kazi et al., 2018). These approaches have shown promising results and opportunities for substantial emissions reduction, enhanced energy recovery and cost-effective performance through the use of modular systems, such as cogeneration (COGEN) unit and thermal membrane distillation (TMD) systems (Elsayed et al., 2014, Kazi et al., 2016).

However, the prevailing design philosophy and most of the associated mathematical models for flare recovery/utilization in the pertinent literature rely on a set of design steady state conditions. Therefore, PSE research studies for flare recovery system analysis and control purposes conducted with the aid of a comprehensive, insightful and computationally tractable dynamic process modelling framework remain relatively limited and deserve further attention (Dinh et al., 2016, Eljack et al., 2014, Wang et al., 2016).

It should be pointed out, that abnormal situations encountered in process industries represent major sources of flaring when the process of interest deviates significantly from what is deemed the normal and acceptable operating conditions range. Consequently, these process deviations from the desirable performance profile are quite concerning since they often lead to financial losses as well as poor environmental records. The key challenge in abnormal situation management is to provide the operating team with tools that will enable them to avoid or minimize the impact of abnormal conditions. At the same time, if some portion of the unburned hydrocarbon streams is recovered and utilized under stable and robust conditions, significant techno-economic-environmental benefits could emerge by appropriately minimizing the associated waste streams. In this regard, the employment of classical yet comprehensive process control strategies could offer a potentially interesting solution option since satisfactory performance characteristics can be complemented by insightful cost-effective practical implementation strategies. Indeed, such strategies tend to be well received by plant personnel and engineering management teams resulting in greater plant operational efficiency through robust abnormal situation management approaches.

Based on preliminary results reported in Kazi et al. (2016), the present research work considers a COGEN unit as a flare mitigation alternative technology where by the dual process requirement of power and heating can be satisfied using a mixture of fresh fuel (natural gas) and unburned hydrocarbon streams. In particular, a systematic dynamic modelling approach is followed that leads to the development of a process analysis framework and control strategies focusing on the flare utilization section/component of the COGEN unit and the partial replacement of fresh fuel feed in order to enhance process system overall techno-economic-environmental performance. The primary objective of the proposed control strategies is the design, tuning and use of PI and PID controllers for a standard regulation problem, namely for smoothly driving key pressure and temperature variables in the combustion unit of the flare utilization section to desirable set-point values in the presence of various unexpectedly occurring disturbances that cause excursion patterns from operationally desirable steady states in flare systems. Therefore, within such a context, the COGEN unit can be used to recover some of the unburned hydrocarbon streams and utilize them to produce some value added products thus enhancing overall environmental and economic performance.

2. Methodology

The Aspen Plus V9 and Aspen Plus Dynamics software packages have been used for the development of a dynamic modelling framework focusing on the behaviour of the whole COGEN unit that encompasses the flare utilization section/component. First, open-loop (manual mode) tune-up is introduced based on an appropriately validated First Order Plus Dead Time (FOPDT) dynamic process modelling framework. Then, comprehensive closed-loop dynamic response tests are carried out for controller tuning and stability characterization purposes. The required steps for controller installation and controller design have been performed using the same software and its built-in controller tuning option. A succinct step-by-step graphic depiction of the methodology followed in this manuscript is presented in Fig. 1.

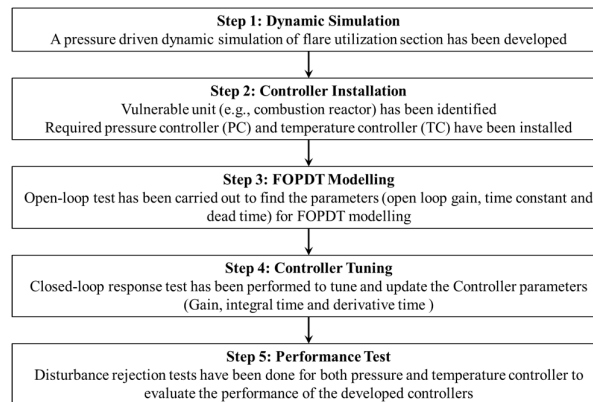


Figure 1. Methodology to develop PC and TC strategies using Aspen Plus Dynamics

3. Development of steady state and dynamic models

In this work, functional baseline steady state and dynamic models have been developed for the entire COGEN unit (see Fig. 2). Special focus was placed on the development of a pressure driven dynamic model for the flare utilization section in order to identify the vulnerable unit and the requisite action plan for reliable pressure or temperature monitoring (see dashed box in Fig. 2). Here, in the pressure controller case the pressure of the combustion reactor (CR) represents the process variable (PV), the set point value is set at 50 bar while the operating variable (OP) is the pressure maintained by the combustion stream valve (CSV). In the temperature controller case, PV is the temperature of CR, the set point value is the steady state temperature 2104 °C and the OP variable is the flow of the cooling medium.

4. Controller design and performance

4.1. Open-loop (manual mode) tune up for FOPDT dynamic modelling

A rather standard open-loop test has been performed to identify and quantitatively capture key unknown complex process dynamics through a first-order plus dead time model-postulate. The response profile of the main process variables is used to estimate meaningful open-loop gain (K_P), time constant (τ_P), and dead time (θ_P) values for the given process. The estimated model parameter values of the installed pressure and temperature controllers are shown in Fig. 3. Specifically, a step up by 5% of the output range method has been used which is a built-in method/feature in Aspen Plus Dynamics software.

4.2. Closed-loop dynamic response tests and controller tuning

The closed-loop Auto Tuning Variation (ATV) test better describes the controlled process and offers more reliable estimates of the tuned-up controller parameters (Kamal et al., 2016). In the present work, using the “Tyreus–Luyben” tuning rule (Luyben et al., 1997), a set of controller parameter values: $K_C = 6.71$, $\tau_I = 1.98$ min, and $\tau_D = 0.0$ min were calculated for a “PI”-type pressure controller. Furthermore, using the “Ziegler–Nichols” tuning rule, the following set of controller parameter values: $K_C = 1586.209$, $\tau_I = 3.75$ min, and $\tau_D = 0.6$ min were calculated for a “PID”-type temperature controller. It should be noted that temperature control loops within the specific controlled process system’s structure typically generate oscillatory behaviour. Therefore, different controller tuning methods were tested to induce

stable responses and appealing controlled process economic and environmental performance profiles. Moreover, temperature measurements can be noisy and the derivative action can lead to a deterioration of the noise-to-signal ratio and process control quality. To remedy this situation, a filtered PID controller or cascade control loop option is advisable.

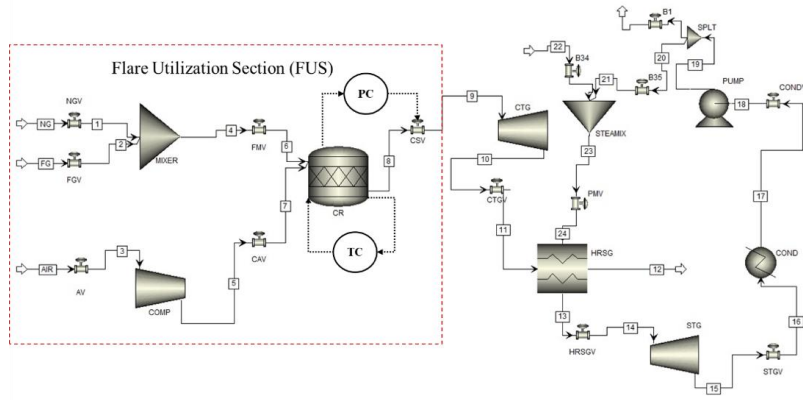


Figure 2. Developed process flow diagram of COGEN unit and its flare utilization section

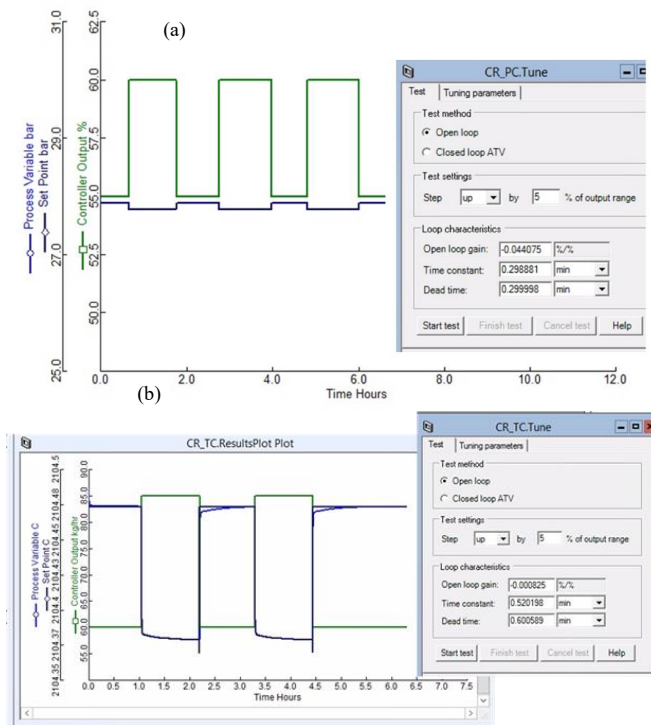


Figure 3. Open-loop response test for FOPDT modelling: (a) PC and (b) TC

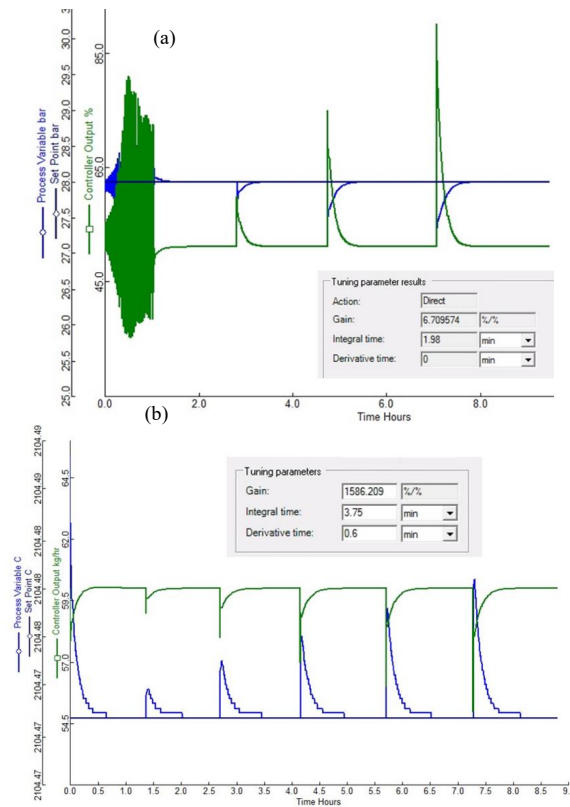


Figure 4. Closed-loop profiles under disturbance rejection (process regulation) test: (a) PC response and (b) TC response

4.3. Regulation Problem: Disturbance rejection test and controller performance evaluation

The regulatory capabilities of the aforementioned pressure and temperature controllers were tested under various disturbances in an effort to evaluate their respective performance during abnormal process operations and upsets. For testing the PI pressure controller, pressure has been changed deliberately from 50 bar to 60 bar, 75 bar and 90 bar at certain time instants to generate a pattern of unexpected occurring output disturbances. From Fig. 4a, it can be inferred that the PI controller successfully brought the pressure variable to its set point value in an offset-less, smooth and stable manner thus rejecting the disturbance effect while inducing desirable dynamic characteristics in the closed-loop response profile. Please note that unfiltered strong fluctuation behavior was observed in the beginning as the controller was not activated during that period. These fluctuations may have occurred due to coupling effects of the installed controllers, an issue which was later adequately addressed by the specific controller's action. Similar satisfactory behavior was observed in the PID temperature controller case where the cooling fluid flow rates were varied to create a pattern of occurrence of sudden disturbances, suggesting that each time the proposed PID controller was able to mitigate the disturbance effect and accomplish the primary regulatory objectives as delineated in the previous case (see Fig. 4b).

5. Techno-economic-environmental performance analysis

Within the context of the present study and the steady state process simulation framework, standard heat/energy integration allows the calculation of the heating utility of the COGEN system which was found to be 52.18 MW as well as power utility that was found to be 105.50 MW. Furthermore techno-economic-environmental performance assessment for the designed COGEN unit with the proposed controllers installed was conducted within the framework presented in (Kazi et al., 2016) where the optimal sizing of the COGEN as a flare mitigation alternative was also pursued. It was found that the proposed configuration of the COGEN unit can lead to savings of 0.18 million USD annually realized by the associated carbon tax savings and can also generate 0.25 million USD annual income from power/heat generation by utilizing the flare during process upsets.

6. Conclusion

A dynamic modelling framework for the flare utilization component of a COGEN system was first developed on the basis of which process dynamic analysis, techno-economic-environmental performance assessment as well as controller design and tuning were also pursued. Simple and practical control strategies were proposed capable of successfully regulating pressure and temperature in the presence of various disturbances as well as inducing appealing performance characteristics for the controlled process. Finally, within the above context, it was demonstrated that there is indeed ample scope to use COGEN as a potentially viable flare mitigation technique by utilizing unburned hydrocarbon streams while generating heat (52.18 MW), power (105.50 MW) as well as annual tax savings (0.18 million USD).

Acknowledgment

This paper was made possible by NPRP grant No 10-0205-170347 from the Qatar National Research Fund (a member of Qatar Foundation). The statements made herein are solely the responsibility of the author[s].

References

- H. Dinh, F. Eljack, S. Wang, Q. Xu, 2016, Dynamic simulation and optimization targeting emission source reduction during an ethylene plant start-up operations, *Journal of Cleaner Production*, 135, 771-783.
- F. Eljack, M. M. El-Halwagi, Q. Xu, 2014, An Integrated approach to the simultaneous design and operation of industrial facilities for abnormal situation management, In *Computer Aided Chemical Engineering*, Mario R. Eden, J. D. S.; Gavin, P. T., Eds. Elsevier, 34, 771-776.
- N. A. Elsayed, M. A. Barrufet, M. M. El-Halwagi, 2014, Integration of thermal membrane distillation networks with processing facilities, *Industrial & Engineering Chemistry Research*, 53, (13), 5284-5298.
- K. Al-Malah, 2016, Apen Plus®: Chemical Engineering Applications, Wiley & Sons, Inc., DOI: 10.1002/9781119293644.
- S. Kamrava, K. J. Gabriel, M. M. El-Halwagi, F. Eljack, , 2015, Managing abnormal operation through process integration and cogeneration systems, *Clean Technologies and Environmental Policy*, 17, (1), 119-128.
- M.-K. Kazi, F. Eljack, N. A. Elsayed, M. M. El-Halwagi, 2016, Integration of energy and wastewater treatment alternatives with process facilities to manage industrial flares during normal and abnormal operations: Multiobjective extendible optimization framework, *Industrial & Engineering Chemistry Research*, 55, (7), 2020-2034.
- M.-K. Kazi, F. Eljack, M. Amanullah, A. M.N. AlNouss, V. Kazantzi, 2018, A process design approach to manage the uncertainty of industrial flaring during abnormal operations. *Computers & Chemical Engineering*, 117, 191-208.
- S. Wang, J. Zhang, S. Wang, Q. Xu, , 2016, Dynamic simulation for flare minimization in chemical process industry under abnormal operations. *Current Opinion in Chemical Engineering*, 14, 26-34.
- M. Luyben, W. Luyben, 1997, Essentials of process control, McGraw-Hill.

Satellite based Vegetation Indices variables for Crop Water Footprint Assessment

Haile Woldesellasse^a, Rajesh Govindan^a, Tareq Al-Ansari^{a*}

Division of Sustainable Development, College of Science and Engineering, Hamad Bin Khalifa University, Qatar Foundation, Doha, Qatar

**talansari@hbku.edu.qa*

Abstract

The global population has quadrupled over the last century. This has increased the global food demand and water sector. In the state of Qatar, the annual freshwater extraction from aquifers is four times the rate of natural recharge, and the depletion is driven by agriculture which represents only 1.6% of the total land area of Qatar, providing approximately 8-10% of domestic food consumption and contributing 0.1% to the domestic GDP. Considering the need for the sustainable intensification of food production systems, satellite technology has the ability to provide a frequent monitoring mechanism enabling the availability of physically-based spatial information useful for reliable environmental monitoring studies. The objective of this research paper is to assess the demand side water footprint of crops using satellite-driven technology in order to optimise the supply side irrigation requirements. The key vegetation indices, such as Normalized Difference Vegetation Index (NDVI) and Normalized Difference Water Index (NDWI) estimated from the remotely acquired information from the Landsat satellite is used for the water footprint assessment. Finally, the water resources demand in agriculture is met by optimising the water supplied from the various decentralized treated sewage effluent plants (TSE). A mixed integer non-linear programming (MINLP) formulation was used to model the spatially-dependent demands, and the TSE plants allocated 80% and 20% of their capacity to fields 1 and 2 respectively. The findings of this paper are promising and a high correlation of -0.93 is found between NDVI and crop water demand, demonstrating that satellite images can be used to monitor the crop vegetation development. vegetation stress can be differentiated using NDVI, thereby demonstrating its applicability for agricultural and water sectors.

Keywords: Crop water footprint, NDVI, NDWI, Satellite remote sensing.

1. Introduction

It is expected that global food production will need to increase to meet the demands of a growing population. Going forward, it is important increase global food production within a sustainable development framework which optimises the use of resources and in consideration of the relationship between energy, water and food (EWF) resources (Al-Ansari et al. 2016). Considering food security, and the need to enhance agriculture production, many countries within the Middle East are facing challenges related to the sustainable provision of water required for enhanced agriculture products. Agricultural production is heavily reliant on available water resources, of which excessive exploitation has contributed towards the depletion of groundwater and salt intrusion. The majority of

farms in the Arabian Peninsula which is characterised by a hyper arid climate depend on irrigation rather than rain fed Haddadin (2002). Considering water scarcity, there is a need to develop methods like water footprint to adequately monitor water consumption. The water footprint (WF) of a crop is defined as the amount of water consumed for crop production, where blue and green water footprint represents irrigation and rain water usage respectively. Moreover, the WF concept can be used to understand international trading of water known as virtual water (Romaguera et al. 2010). Remote sensing has been used within agriculture and hydrology studies to monitor environment conditions. In this study, remote sensing data is used for the assessment of water footprint of crops in a Qatar case study, as an extension of the work previously conducted by the authors (Woldesellasse et al., 2018). It focuses on developing a neural network model which predicts water demand of alfalfa crops over a period of one year. The novelty is demonstrated using macro-scale water demand estimations from satellite imagery as inputs for optimising water supply in the field, linking irrigation systems and decentralized treated sewage effluent (TSE) plants. The study details the location of the plants, the crop water demand (m^3/ha) and the total amount of water is calculated by multiplying the area of the fields with the crop water demand.

2. Vegetation indices for water footprint estimation

The WF is defined as the sum of the volume of fresh water (blue, green and grey) used to produce the product along its supply chain (Hoekstra et al. 2009). A global study conducted between 1995 – 1999 determined the WF of crops based on crop yields and crop water requirement per country (Allen et al. 1998), Hoekstra and Hung (2005). The model assumes an ideal crop condition such as, optimal soil moisture conditions, disease free, single cropping pattern, well-fertilized and grown in large fields with 100% coverage. In a similar study, Liu et al., 2009 provided the blue and green components of water use for different agricultural crops during the period between 1998-2002 and at a spatial resolution of 30 arc minutes. The input datasets for their model includes, maps of harvested area, climatic data from CRU, soil parameters, and crop fertilizer application obtained from statistical reports. The limitations of the study include coarse data resolution, and an optimum ideal soil water conditions is considered in the study.

Remote sensing techniques can be a useful tool to overcome these limitations by providing high spatial, temporal and spectral resolution data using advanced image classification methods. A global assessment of crop WF using remote sensing techniques was conducted by (Romaguera et al. 2010). The study proposed an approach driven by remote sensing techniques for retrieving the global actual irrigation using evapotranspiration, precipitation, and surface runoff as an input dataset. The Satellite instruments used for estimating these parameters include Meteosat and Climatic Prediction Center Morphing Technique (CMORPH) simultaneously. In agriculture, spectral information is used to characterise the biophysical features of plants using vegetation indices. Vegetation indices are a unitless radiometric measures which are calculated by using two or more bands in the wavelength range of VIS, NIR and SWIR. (Rouse et al., 1974) proposed the most commonly used index known as Normalized Difference Vegetation Index (NDVI). It is calculated as the ratio of the reflectance difference and sum of the NIR and Red bands. Green plants strongly absorb the blue and red bands because of the chlorophyll and simultaneously exhibited a strong reflectance in the NIR region. The value of NDVI ranges between -1 to 1, where below zero values

indicate clouds and water, the positive values close to zero indicate bare soil, and higher positive values indicate vegetation. Sparse vegetation ranges from 0.1 to 0.5, and dense vegetation is illustrated by the value starting 0.6 and above (Stancalie et al. 2014).

The NDVI index is used for the application of many vegetative studies, including crop yield estimation, drought monitoring, monitoring of crop conditions, their developmental stage and biomass estimation (Stancalie et al. 2014). Thus, the information provided by different satellite instruments contribute to effective monitoring and management of agriculture, grasslands, forestry and above all help to understand the way the ecosystem works and its interactions with the atmosphere and human activities. Similarly, Normalized Difference Water Index (NDWI) can be used to provide an indication of the water content in leaves, through monitoring the humidity of the vegetation cover. The value of NDWI ranges from -1 to 1, with the green vegetation lies in the range of -0.1 to 0.4 (Gu et al. 2007). In retrieving the vegetation water content information, the combination of the two spectral bands eliminates the variation in information due to the leaf internal structure and dry matter content.

3. Methodology

The first part of the methodology consists of analysing satellite images acquired from Landsat 7 for the year 2002. NDVI and NDWI are calculated to assess the crop vegetation and water stress of crop over the given time period. NDVI is calculated using the Red and Near Infrared channels, which are Band 3 and 4 respectively using the GIS tool. The vegetation phase displays a seasonal pattern in terms of WF which depends on its water intake and temperature. Under ideal condition, where there is an abundance of water available within minimal evapotranspiration (ET), crops display green vegetation characteristics. Therefore, NDVI and NDWI are high because the corresponding water content of the crop is high. Alternatively, high temperature increases the ET and crop water stress, thereby lowering the NDVI and NDWI. The correlation of NDVI with crop water demand (m³/ha) and temperature is also assessed to check the interaction between them. The total water demand of the fields, *D*, is then calculated by multiplying the crop water demand by the area of the fields. This study considers the optimisation of water supplied from the treated sewage effluent (TSE) plants to meet the water demand of the alfalfa fields, *D*, considered in (Woldesellasse, Govindan and Al-Ansari 2018). The water is pumped from the TSE plants and is stored at optimum locations (x,y) prior to its distribution to the alfalfa fields. The objective of the nonlinear optimisation is to minimize the cost of water distribution. The Non-Linear Programming sequence used to allocate the water irrigated to the fields is detailed below:

Constraint:

$$\begin{aligned}
 q_{11} + q_{12} &= 1 \\
 q_{21} + q_{22} &= 1 \\
 C_1 \cdot q_{11} + C_2 \cdot q_{21} &\geq D_1 \\
 C_1 \cdot q_{12} + C_2 \cdot q_{22} &\geq D_2 \\
 q_{11}, q_{12}, q_{21}, q_{22} &\geq 0
 \end{aligned}$$

Objectives - Minimise:

$$(C_1 \cdot q_{11} \cdot r_{11} \cdot Cost_{11} + C_2 \cdot q_{21} \cdot r_{21} \cdot Cost_{21} + C_1 \cdot q_{12} \cdot r_{12} \cdot Cost_{12} + C_2 \cdot q_{22} \cdot r_{22} \cdot Cost_{22})$$

Where, C_i is the capacity of the two TSE, D_i is the demand of the two fields, q_{ij} indicates the fraction of water transported from source plants to alfalfa fields, $Cost_{ij}$ is the cost of water distribution, and r_{ij} is the length of transportation from the TSE to the alfalfa fields.

4. Results and Discussion

The state of a crop is monitored using a timeseries measurement of NDVI. Figure 2 illustrates the change in colour of the circular fields throughout the year, whilst surrounding areas remain almost constant. The values range from 0 to 1, indicated by the colour bar ranging from dark blue to red. Winter is the period where the temperature is cool in arid regions such as Qatar, and harvesting is most of the time during this period. Generally, the winter months demonstrate a high NDVI compared to the summer months. The highest NDVI recorded is 0.646 in January and lowest 0.194 in June.

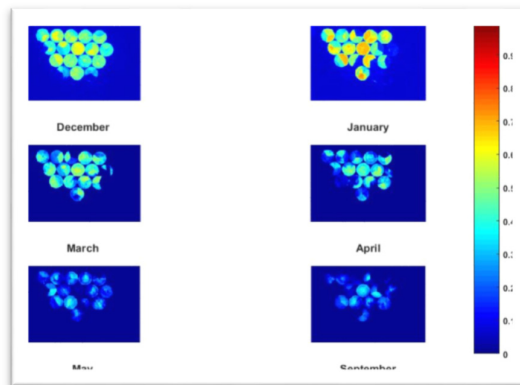


Figure 2. Normalized Difference Vegetation Index (NDVI).

Furthermore, the field images illustrated in Figure 2 can be better interpreted through a comparison with Figure 3, where the NDVI is plotted against temperature and crop water demand. The objective is to ascertain the correlation between vegetation indices and the crop water demand, and to ultimately utilise satellite information to allocate water to agricultural fields. In Figure's 3a and 2b, NDVI displays an inverse relationship with temperature and crop water demand. This is due to the fact that the greenness of a crop is affected by its water stress. Since precipitation is sporadic in arid regions, agricultural fields are irrigated using water from underground or TSE. The analysis clearly illustrates the effect of hot temperature and low precipitation on agriculture, in which the NDVI fluctuates between high to low scores during the low and high temperature respectively. However, it should be noted that a low NDVI does not always imply water stress, as the field can also be a just harvested bare ground. NDVI is an indicator of the water content in the leaves of crops. During dry season, the vegetation state is affected due to water stress, and vegetation index, i.e. NDVI contributes towards monitoring of droughts as the two bands used for calculation are responsive to changes in water content. In this study the NDVI is calculated for the same area using the data acquired from Landsat satellite. The result is illustrated in Figure 4, where NDVI behaves similar to NDVI as it is

responsive to the crop water demand and temperature, and thereby can be used as a good indicator of water footprint.

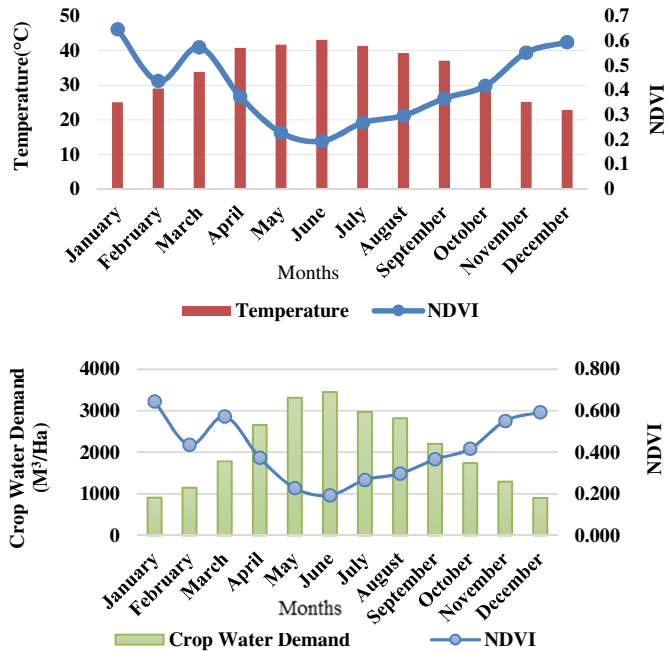


Figure 3. Comparison of (a) NDVI and temperature, b) NDVI and Crop Water Demand.

In general NDVI is high throughout the year except, during the winter-summer transition months or summer months where temperature is very high, and where ET exceeds the normal range. Therefore, during these periods, NDVI falls below 0.2 as illustrated in Figure 4. Overall, the results demonstrate consistency with the previous study done. A high correlation of -0.93 is determined between NDVI and the crop water demand, from which it can be concluded that remote sensing instruments can be used for agricultural applications, including for the assessment of the crop water demand. Considering the optimisation framework applied in this study, the TSE plants (Doha West and Doha South) with a capacity of $7.37 \times 10^6 \text{ m}^3$ and $7.20 \times 10^6 \text{ m}^3$ respectively. Outcomes of the study conclude that 80% of the water production in each plant is distributed to field 1, the remaining 20% of the water capacity in each plant is distributed to field 2.

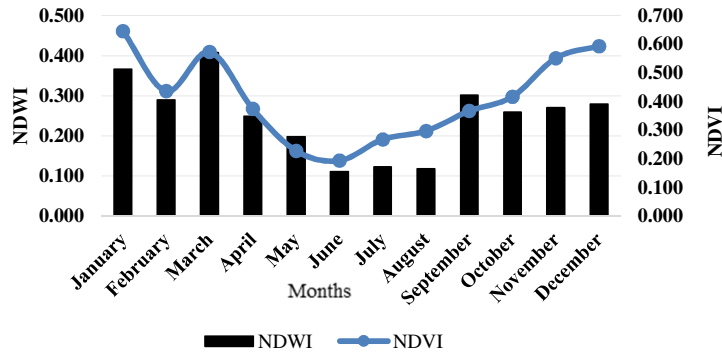


Figure 4. Comparison of NDVI and NDWI.

5. Conclusions

In this study, the correlation between vegetation indices and crop WF is assessed and an inverse relationship is found. This is a good indicator of vegetation phase. The results are further confirmed by considering both the NDVI and NDWI, and their interactions with temperature and ultimately the WF. Finally, the study concludes that satellite images can be used as input data to allocate water irrigated to agricultural fields.

References

- Al-Ansari, T., A. Korre, Z. Nie & N. Shah. 2016. Integration of biomass gasification and CO₂ capture in the LCA model for the energy, water and food nexus. In *Computer Aided Chemical Engineering*, 2085-2090. Elsevier.
- Allen, R. G., L. S. Pereira, D. Raes & M. Smith (1998) FAO Irrigation and drainage paper No. 56. *Rome: Food and Agriculture Organization of the United Nations*, 56, e156.
- Gu, Y., J. F. Brown, J. P. Verdin & B. Wardlow (2007) A five-year analysis of MODIS NDVI and NDWI for grassland drought assessment over the central Great Plains of the United States. *Geophysical Research Letters*, 34.
- Haddadin, M. J. (2002) Water issues in the Middle East challenges and opportunities. *Water Policy*, 4, 205-222.
- Hoekstra, A. Y., A. K. Chapagain, M. M. Aldaya & M. M. Mekonnen (2009) Water footprint manual. *State of the Art*, 1-131.
- Hoekstra, A. Y. & P. Q. Hung (2005) Globalisation of water resources: international virtual water flows in relation to crop trade. *Global environmental change*, 15, 45-56.
- Romaguera, M., A. Y. Hoekstra, Z. Su, M. S. Krol & M. S. Salama (2010) Potential of using remote sensing techniques for global assessment of water footprint of crops. *Remote Sensing*, 2, 1177-1196.
- Stancalie, G., A. Nertan, L. Toullos & M. Spiliotopoulos. 2014. Potential of using satellite based vegetation indices and biophysical variables for the assessment of the water footprint of crops. In *Second International Conference on Remote Sensing and Geoinformation of the Environment (RSCy2014)*, 92290K. International Society for Optics and Photonics.
- Woldesellasse, H., R. Govindan & T. Al-Ansari. 2018. Role of analytics within the energy, water and food nexus—An Alfalfa case study. In *Computer Aided Chemical Engineering*, 997-1002. Elsevier.

Modelling of extractive heterogeneous-azeotropic distillation in dividing wall column

Andras Jozsef Toth,^{*,a} Daniel Fozer,^a Tibor Nagy,^a Eniko Haaz,^a Judit Nagy,^b
Peter Mizsey,^{a,c}

^a*Department of Chemical and Environmental Process Engineering, Műegyetem rkp. 3., Budapest, 1111, Hungary*

^b*Department of Building Services and Process Engineering, Műegyetem rkp. 3., H-1111, Budapest, Hungary*

^c*Department of Fine Chemicals and Environmental Technology, Egyetemváros C/1 108., Miskolc, 3515, Hungary*

ajtoth@envproceng.eu

Abstract

The distillation based separation can be extremely complex if highly non-ideal mixtures are to be separated. In spite of different successfully applied unit operations there is always a possible way to improve the distillation technique and widen its toolbar. A novel improvement in this area is the development of the extractive heterogeneous-azeotropic distillation (EHAD). For the sake of the demonstration of the efficient use of EHAD in Dividing wall columns (DWC), two quaternary mixtures are selected for separation: Water – Ethanol – Ethyl acetate – Acetone and Water – Ethanol – Ethyl acetate – Ethylene glycol. There are real waste mixtures from pharmaceutical industry. It must be mentioned, extractive heterogeneous-azeotropic distillation method has never been investigated in dividing wall columns.

Conventional distillation column sequences and dividing wall columns are selected for comparison. Rigorous steady-state simulations are carried out using ChemCAD flowsheet simulation software. Number of trays, heat duties and Total Annual Cost (TAC) of the systems are optimized. It can be concluded, the application of the EHAD in DWCs allows also the simplification of the separation schemes and the separation reduces the energy requirements of the distillation and opens new horizons for the separation of non-ideal mixtures saving energy, money and natural resources. Using DWCs the reboiler duties can be reduced with 20% and the appropriate separation can be reached with one less column.

Keywords: extractive heterogeneous-azeotropic distillation, dividing wall column, non-ideal mixtures, flowsheet simulator

1. Introduction

The highly non-ideal mixtures can be quite often found in fine chemical industries, where the separation of the usually azeotropic mixtures are complicated with the high product purity descriptions. Szanyi et al. (2004a, b) introduced a novel kind of distillation, the extractive heterogeneous-azeotropic distillation (EHAD) that has been proved as a powerful and efficient separation method for the separation of highly non-ideal liquid mixtures. The recovery of solvents from industrial aqueous solutions has particular

interest and moreover the water can be also recycled (Szabados et al., 2018). The EHAD combines the advantages of the heterogeneous-azeotropic and extractive distillations (see Fig. 1). Heteroazeotropic distillation exploits the differences in volatility and liquid-liquid phase split by linking a distillation column and a phase separator. Therefore, it may also be interpreted as hybrid separation process. The heterogeneous-azeotropic option assumes that water is present in the mixture and limited immiscibility exists (Toth et al., 2016).

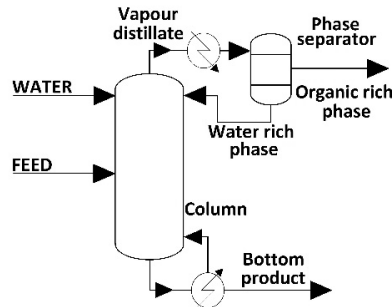


Fig. 1 The extractive heterogeneous-azeotropic distillation (EHAD) (Toth et al., 2016)

The EHAD differs from the heteroextractive distillation since no new azeotrope is formed, namely the extractive agent/entrainer is water and this component is already present in the mixtures to be separated (Toth et al., 2017). Moreover, the extractive and relative volatility changing effect of the autoentrainer/extractive agent is fully utilized and therefore the extractive effect takes place in the whole column (Szanyi et al., 2004b).

Dividing wall columns (DWCs) are today's alternative of sustainable distillation technology. Using DWCs in a distillation sequence significantly increases the number of possible arrangements. These options are worth to be considered as DWCs proved to be attractive in terms of energy consumption. Favourable energy consumption of DWCs is caused by the energy integration technique, thermal coupling (Tarjani et al., 2018). There are numerous feasible partition constructions of a DWC in the literature, but it is a common trend to investigate the properties of the original structure introduced by Asprion and Kaibel (2010) with the partition in the middle. As a systematic approach (Rong, 2011) suggests a strong connection between the conventional sequences and the DWCs with upper (DWCU) and lower (DWCL) partitions (see Fig. 2). DWCU can be considered as an alternative of the conventional direct sequence and DWLC as an alternative of the conventional indirect sequence.

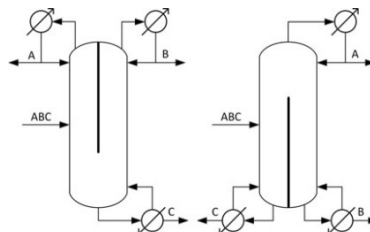


Fig. 2 DWC with Upper partition (DWCU, left) and DWC with Lower partition (DWCL, right) (Tarjani et al., 2018)

The most significant advantage of a DWC is the potential cost saving. Using a DWC can lead to cost savings up to 30% (Sangal et al., 2012) as it only requires one distillation column instead of two ones considering the separation of a three component mixture. On the other hand, thermodynamic efficiency can be increased by avoiding the remixing effect (Kiss et al., 2012). In such a way both investment and operational costs can be reduced compared to the conventional sequences (Tarjani et al., 2018).

Recent studies investigate these complex arrangements and the interest in DWCs begins to increase. Several design methods (Ramírez-Corona et al., 2015; Van Duc Long and Lee, 2012) and applications for azeotropic, extractive and reactive distillation are also developed (Yildirim et al., 2011). It has to be mentioned, EHAD has never been examined in DWC. Therefore, the aim of this work is to investigate the applicability of DWC construction in the case of extractive heterogeneous-azeotropic distillation method considering the separation of quaternary mixtures.

2. Material and methods

Two quaternary mixtures are selected for comparison: Water (Component 1) – Ethanol (2) – Ethyl acetate (3) – Acetone (4) as Mixture I and Water (1) – Ethanol (2) – Ethyl acetate (3) – Ethylene glycol (4) as Mixture II. Table 1 shows the binary and ternary azeotropes of the selected mixtures. The target of this study to create a separation process based on extractive heterogeneous-azeotropic distillation to split the compounds of these mixtures. The limit value for the composition is determined, which is min. 99.5 m/m%, except Ethanol (96 m/m%) and Ethyl acetate (96 m/m%).

Table 1 Binary and ternary azeotropes of the investigated mixtures (Szanyi, 2005)

Azeotrope type	Mixture I	Mixture II	Boil. T [°C]	Azeotropic composition [m/m%]
Binary	(1) - (2)		78	4-96
	(1) - (3)		71.3	8.3-91.7
	(2) - (3)		71.5	29.6-70.4
Ternary	(1) - (2) - (3)		70.3	8.0-8.7-83.3

ChemCAD flowsheet operator program is applied for comparison of column types. Trayed SCDS columns and UNIQUAC method is used for the calculation of the vapor-liquid equilibrium (VLE) as an equilibrium model. The optimal number of trays and heating requirements can be determined (Toth et al., 2017). First, the optimal number of trays are calculated in conventional case and then this value is used in simulation of DWC case.

3. Results and discussion

Fig. 3 and Fig. 4 show the separation alternatives of Mixture I. The separation of Mixture II in conventional and in dividing wall columns can be compared in the case of Fig. 5 and Fig. 6. The achieved product purities can be seen in flowsheet figures. First column can separate the non-azeotropic compounds of the mixtures (Acetone or Ethylene glycol) and the EHAD separation is carried out in the second column in conventional column cases. It can be seen DWCL construction is used in non-conventional case. Column II, III and IV symbolize the DWC construction in Fig. 4 and Fig. 6.

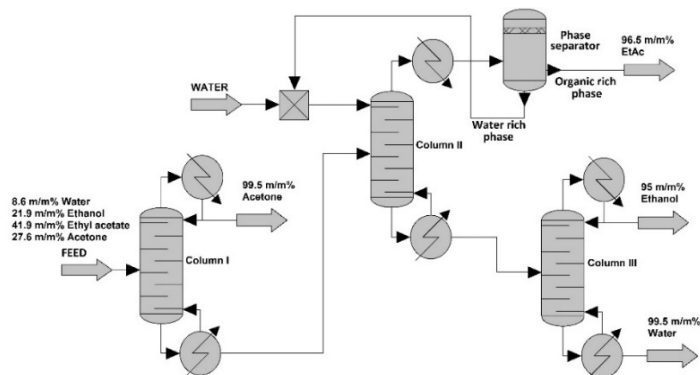


Fig. 3 Separation of Mixture I in conventional column

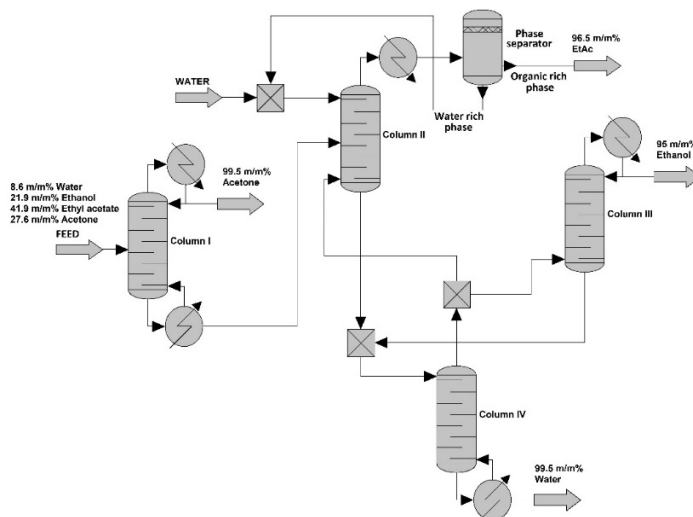


Fig. 4 Separation of Mixture I in dividing wall column (CII, CIII, CIV)

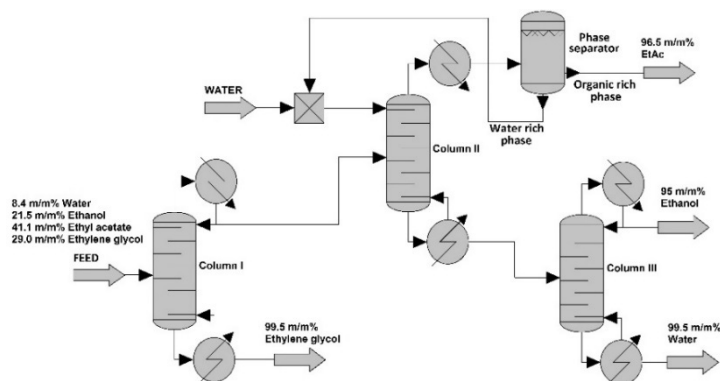


Fig. 5 Separation of Mixture II in conventional column

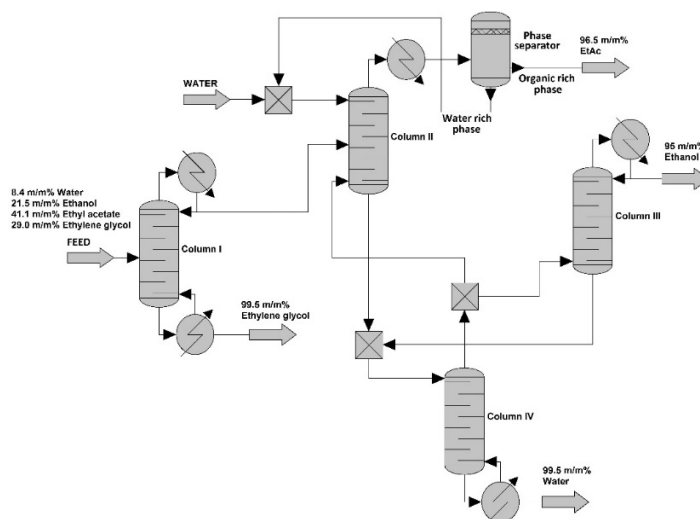


Fig. 6 Separation of Mixture II in dividing wall column (CII, CIII, CIV)

Total Annual Cost (TAC) of the optimized process is calculated according to the cost correlations of Douglas (1988) with current M&S index (1605). Investment costs of the distillation depend on different parameters, for e.g.: heat duty, the sizes of the column, and purity of the products. The operating costs contain the annual costs of the steam and water consumption. 8000 hours/year continuous operation is selected for the calculation of the operating cost. 10-year amortization of capital cost is assumed for the total cost estimation. The mixtures are selected for the comparison for 1000 kg/h feed stream. Valve trays are used in flowsheet simulator (Toth et al., 2017). Table 2 shows the comparison of two column constructions.

Table 2 Comparison of column constructions

	Mixture I		Mixture II	
	Conv.	DWC	Conv.	DWC
Feed water [kg/h]		600		800
Total number of trays [-]		70		80
Reboiler duty [MJ/h]	3343	2740	3837	3252
Total Annual Cost (TAC)	3206	2565	3540	2761

It can be seen the reboiler duty values are in accuracy with TAC and the DWC constructions have lower heat duties.

4. Conclusions

The applicability of extractive heterogeneous-azeotropic distillation is tested on two non-ideal mixtures in flowsheet simulator environment. Two column constructions are investigated and compared: (i) conventional columns, (ii) dividing wall column. It can be concluded both structures are capable for separation of quaternary mixtures. The application of dividing wall column results in cheaper solutions and less energy consumption than conventional column case, which means that DWC can be efficacious

tool for separation of highly non-ideal mixtures. Average 17% reduction can be reached in reboiler duty values and the Total Annual Cost can be reduced by up to 21%.

Acknowledgments

This paper was supported by the János Bolyai Research Scholarship of Hungarian Academy of Sciences, ÚNKP-18-4-BME-209 New National Excellence Program of Ministry of Human Capacities, NTP-NFTÖ-18-B-0154, OTKA 112699 and 128543. This research was supported by the European Union and the Hungarian State, co-financed by the European Regional Development Fund in the framework of the GINOP-2.3.4-15-2016-00004 project, aimed to promote the cooperation between the higher education and the industry.

References

- N. Asprion, G. Kaibel, 2010, Dividing wall columns: Fundamentals and recent advances, *Chem Eng Process* 49, 139-146.
- J. M. Douglas, 1988, *Conceptual design of chemical processes*. McGraw-Hill, New York.
- A. A. Kiss, S. J. Flores Landaeta, C. A. Infante Ferreira, 2012, Towards energy efficient distillation technologies – Making the right choice, *Energy* 47, 531-542.
- N. Ramirez-Corona, N. Ek, A. Jiménez-Gutiérrez, 2015, A method for the design of distillation systems aided by ionic liquids, *Chem Eng Process* 87, 1-8.
- B.-G. Rong, 2011, Synthesis of dividing-wall columns (DWC) for multicomponent distillations—A systematic approach, *Chem Eng Res Des* 89, 1281-1294.
- V. K. Sangal, V. Kumar, I. M. Mishra, 2012, Optimization of structural and operational variables for the energy efficiency of a divided wall distillation column, *Comput Chem Eng* 40, 33-40.
- E. Szabados, A. Jobbagy, A. J. Toth, P. Mizsey, G. Tardy, C. Pulgarin, S. Giannakis, E. Takacs, L. Wojnarovits, M. Mako, Z. Trocsányi, A. Tungler, 2018, Complex Treatment for the Disposal and Utilization of Process Wastewaters of the Pharmaceutical Industry, *Peri Poly Chem Eng* 62, 76-90.
- A. Szanyi, 2005, Separation of non-ideal quaternary mixtures with novel hybrid processes based on extractive heterogeneous-azeotropic distillation, BME, Budapest, PhD Thesis.
- A. Szanyi, P. Mizsey, Z. Fonyo, 2004a, Novel hybrid separation processes for solvent recovery based on positioning the extractive heterogeneous-azeotropic distillation, *Chem Eng Process* 43, 327-338.
- A. Szanyi, P. Mizsey, Z. Fonyo, 2004b, Optimization of nonideal separation structures based on extractive heterogeneous azeotropic distillation, *Ind Eng Chem Res* 43, 8269-8274.
- A. J. Tarjani, A. J. Toth, T. Nagy, E. Haaz, N. Valentinyi, A. Andre, D. Fozer, P. Mizsey, 2018, Thermodynamic and Exergy Analysis of Energy-Integrated Distillation Technologies Focusing on Dividing-Wall Columns with Upper and Lower Partitions, *Ind Eng Chem Res* 57, 3678-3684.
- A. J. Toth, E. Haaz, T. Nagy, R. Tari, A. J. Tarjani, D. Fozer, A. Szanyi, K.-A. Koczka, L. Racz, G. Ugro, P. Mizsey, 2017, Evaluation of the accuracy of modelling the separation of highly non-ideal mixtures: extractive heterogeneous-azeotropic distillation, in: *España, A., Graells, M., Puigjaner, L. (Eds.), Comput Aided Chem Eng*. Elsevier, pp. 241-246.
- A. J. Toth, A. Szanyi, K.-A. Koczka, P. Mizsey, 2016, Enhanced Separation of Highly Non-ideal Mixtures with Extractive Heterogeneous-azeotropic Distillation, *Sep Sci Technol* 51, 1238-1247.
- N. Van Duc Long, M. Lee, 2012, Dividing wall column structure design using response surface methodology, *Comput Chem Eng* 37, 119-124.
- O. Yildirim, A. A. Kiss, E. Y. Kenig, 2011, Dividing wall columns in chemical process industry: A review on current activities, *Sep Purif Technol* 80, 403-417.

A Discrete-time MILP Formulation for the Optimal Scheduling of Maintenance Tasks on Oil and Gas Wells and Surface Facilities

Victoria G. Achkar^{a,b}, Vanina G. Cafaro^{a,b*}, Carlos A. Méndez^{a,b}, Diego C. Cafaro^{a,b}

^a*INTEC (UNL-CONICET), Güemes 3450, 3000 Santa Fe, Argentina*

^b*Facultad de Ingeniería Química (UNL), Santiago del Estero 2829, 3000 Santa Fe, Argentina*

vcafar@fiq.unl.edu.ar

Abstract

Onshore oil and gas exploitation areas are usually composed of a numerous set of wells geographically distributed. The extraction of oil and gas requires complex and expensive equipment, including production devices and surface facilities. To keep efficiency sufficiently high, wells need regular maintenance. In this work, we address the scheduling of maintenance tasks on oil and gas wells and surface facilities. The main challenge is to determine the assignment and sequencing of operations combined with vehicle routing decisions, also accounting for preemption and precedence constraints. The goal is to maximize the use of available resources and also minimize both the production loss and the risk of failure in every well, using a mixed integer linear programming (MILP) formulation. We solve three case studies with increasing complexity to finally assess the model performance in real-size problems of the Argentine oil and gas industry.

Keywords: oil and gas wells, maintenance tasks, optimization, scheduling.

1. Introduction

Maintenance operations over oil and gas fields are usually performed by a specialized fleet of heterogeneous vehicles and crews. These activities comprise safety, environmental protection and regulatory tasks; as well as preventive, predictive and corrective maintenance. Sometimes, depending on the task to be performed, the production of the well needs to be interrupted yielding losses of profits. In practice, tasks are grouped into workorders, and there are many costs associated to the length of an order, related to the production loss and the risk of failure of the well. The more extended the order over the time horizon, the higher the costs of this order. Also, delays on the start time of interventions may cause substantial production losses.

The challenge of this problem is twofold. On the one hand, maintenance tasks should be assigned to crews, each of them having its own capabilities. A task can only be performed by certain crews, and the shifts of the crews widely vary, requiring time coordination. Crews have to travel from well to well and sometimes this time can be relevant (e.g., hours). On the other hand, every task should be precisely scheduled to account for precedence constraints, over a short-term time horizon. A task does not need to be scheduled immediately after the preceding one, but it certainly cannot be

scheduled earlier. There are also both preemptive and non-preemptive tasks. A preemptive task can be interrupted once the shift is over and be continued later. In contrast, a non-preemptive task must necessarily be started and completed within the same day. Complex tasks usually do not allow for interruptions.

To the best of our knowledge, very few works in the literature have focused on the optimal operation of onshore oil and gas wells using multiple heterogeneous resources. Several works have tackled the maintenance planning problem, but most of them are just focused on the most expensive resource: the workover rig (Aloise et al., 2006; Duhamel et al., 2012; Fernández Pérez et al., 2018). The rig planning problem can be seen as the scheduling of jobs (workovers) on parallel heterogeneous machines (rigs), including routing decisions to move the equipment from well to well. However, these problems do not address the whole set of operations, nor preemption and precedence constraints. On the other hand, continuous-time and precedence-based models have proved to be an effective choice when sequence-dependent changeovers are to be considered (Méndez et al., 2006; Castro et al., 2018). However, they would present severe difficulties to manage crews with different shifts. As a result, we propose a discrete-time formulation (Kondili et al., 1993) distinguishing between active and idle periods for every crew. The main contribution of this work is the development of an efficient discrete-time formulation that is able to manage: a) oil and gas well maintenance tasks; b) heterogeneous resources; c) different work shifts; d) preemptive and non-preemptive tasks; e) precedence constraints; f) risk of failure and production losses; and g) crew's travelling time.

2. Problem Statement and Mathematical Model

Our mathematical formulation is based on Kondili's discrete-time approach with predefined fix-size time periods. We introduce six major sets, being I : operations, O : orders, J : crews, T : time periods, D : days and C : locations. The model solution generates a maintenance schedule for every active crew over the planning horizon minimizing operating costs. Figure 1 summarizes the main components of the model and their features.

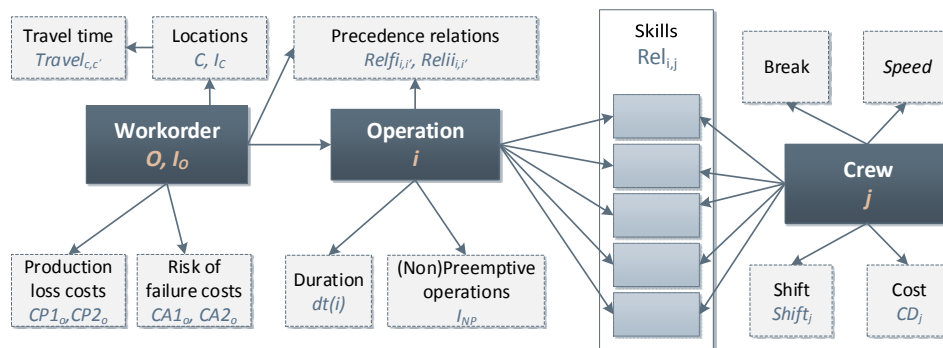


Figure 1: Graphical description of the model

As seen in Figure 1, a maintenance workorder o consists on the set of operations i included in the subset I_o . Each operation $i \in I_o$ requires specific skills and equipment, thus being necessary to assign a crew that is capable of performing that task. Crews are heterogeneous: their specific skills are derived from matching technical capabilities of

the crew and technical requirements of the operations. We define the subset $Crew_i$ to represent the crews with the skills to perform operation i ($j \in Crew_i \subset J$) and the subset $Task_j$ for the operations that can be performed by crew j ($i \in Task_j \subset I$). The binary parameter Rel_{ij} is equal to one if $j \in Crew_i$, and zero otherwise. Additionally, the subset $Shift_j$ includes the periods within the work shift of crew j ($t \in Shift_j \subset T$). Crews have different work shifts and breaks. Shifts are difficult to manage because they widely vary for every crew (not only the start and end times but also the number of working days per week).

The binary variable $W_{i,j,t}$ takes value 1 if operation i is assigned to crew j and starts on time period t . Eq. (1) states that every task should be accomplished by a single crew over the time horizon.

$$\sum_{j \in Crew_i} \sum_{t \in Shift_j} W_{i,j,t} = 1 \quad \forall i \in I \quad (1)$$

In turn, no operation can start until the assigned crew has finished its previous task. This implies that, if the crew starts performing a given operation i at period $t' < t$, the start time of any other operation is forbidden in any time t for at least dt units of time after the start of the task i . This requirement is expressed by Eq. (2).

$$\sum_{i \in Task_j} \sum_{\substack{t' = t - dt_i + 1 \\ t' \in Shift_j}}^t W_{i,j,t'} \leq 1 \quad \forall j \in J, t \in Shift_j \quad (2)$$

Note that constraint (2) is only binding for operations assigned to the same crew j and evaluates just the active periods of that crew, i.e. $\{t - dt_i + 1, t - dt_i + 2, \dots, t\} \in Shift_j$.

Moreover, Eq. (3) determines the value of variable $WF_{i,j,t}$, stating that the end of the operation i occurs just when the time given by its length (dt_i) has gone, that is $dt_i - 1$ periods after it has started. Note that no operation can be completed after the end of the time horizon.

$$W_{i,j,t} = WF_{i,j,t+dt_i-1} \quad \forall i \in I, j \in Crew_i, t \in Shift_j, t \leq |T| - dt_i + 1 \quad (3)$$

Precedence and concurrence constraints determine that a task cannot start until the previous one has finished (end-start relation), or that a task cannot start until the previous one has started (start-start relation). These relations are represented using two binary matrices $Rel_{i,i'}$ and $Rel_{ii,i'}$, respectively. Their elements are equal to one in case the relationship between i and i' is enforced. Eq. (4) accounts for such relations, usually by linking tasks within the same order.

$$TI_{i'} \geq TF_i \quad \forall (i, i') | Rel_{i,i'} = 1 \quad TI_{i'} \geq TI_i \quad \forall (i, i') | Rel_{ii,i'} = 1 \quad (4)$$

$$TI_i = \sum_{j \in Crew_i} \sum_{t \in Shift_j} W_{i,j,t} * (t - 1) * slot \quad TF_i = \sum_{j \in Crew_i} \sum_{t \in Shift_j} WF_{i,j,t} * t * slot$$

Finally, we introduce the notion of preemptive tasks within the equations developed by Kondili et al. (1993). Preemption allows for task splitting when there is a break. Castro et al. (2018) and Peteghem et al. (2010) introduced this concept into their model formulations by making modifications in some constraints. Instead, we propose to simply reduce the time domain to a subset, which only includes the available periods for

each crew, as shown in Figure 2. In this figure, each cell is a time period. Striped cells are unavailable periods, grey cells represent ongoing operations, and white cells are idle periods.

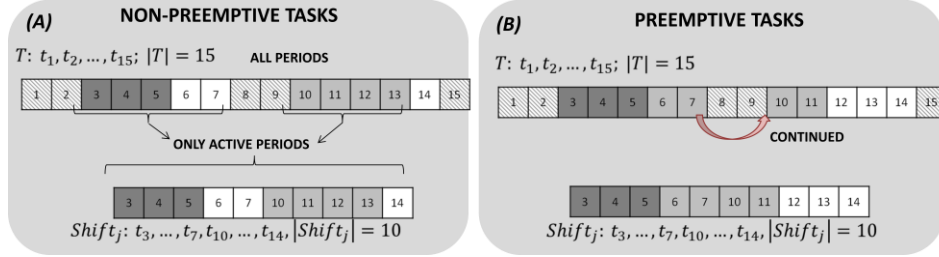


Figure 2: Shifts, preemptive and non-preemptive tasks definition.

As mentioned in the introduction section, non-preemptive constraints enforce that a task must start and end within the same day, mainly due to safety issues. I_{NP} represents the subset of non-preemptive operations. Variables $X_{i,j,d}$ and $XF_{i,j,d}$ in Eq. (5) are equivalent to $W_{i,j,t}$ and $WF_{i,j,t}$ but considering days instead of single time periods.

$$X_{i,j,d} = XF_{i,j,d} \quad \forall i \in I_{NP}, j \in Crew_i, d \in D \quad (5)$$

Following the changeover time concept introduced by Kondili et al. (1993), a travelling matrix is here proposed. We assume that the operations set I can be partitioned into disjoint sets I_c according to the locations c where each task is to be performed. The travelling time between location c and c' is represented by the parameter $travel_{c,c'}$. Thus we introduce a mathematical constraint stating that if two operations i' and i located in different sites c' and c are assigned to the same crew in the same day, and i' is scheduled earlier than i , then the end of operation i' cannot be distanced from the start of i less than $travel_{c',c}$ periods. This can be written in terms of the following linear inequality (6).

$$W_{i,j,t} + \sum_{\substack{t'=t-travel_{c',c} \\ t' \in Shift_j \cup T_d}}^{t-1} WF_{i',j,t'} \leq 1 \quad (6)$$

$$\forall j \in J, d \in D, t \in Shift_j \cup T_d, c \neq c', (i \neq i') \in Task_j, i \in I_c, i'$$

The MILP problem goal is given by Eq. (7), where important cost components are to be minimized. Variable MK is the completion time of the last task over the planning horizon, CD_j is the hourly fixed cost for crew j , $CP1_o$ and $CP2_o$ are production losses, $CA1_o$ and $CA2_o$ are risks-of-failure costs (in USD per hour), while $TLOT_o$ and $TFOT_o$ are the initial and completion times of order o . Note that the crew cost CD_j is paid even if the crew is not used by the scheduler. Since crews are outsourced, these costs must be paid until the end of the last operation.

$$\begin{aligned} Min \quad z = & MK \sum_{j \in J} CD_j + \sum_{o \in O} CA1_o * TLOT_o + \sum_{o \in O} CA2_o * (TFOT_o - TLOT_o) \\ & + \sum_{o \in O} CP1_o * TFOT_o + \sum_{o \in O} CP2_o * (TFOT_o - TLOT_o) \end{aligned} \quad (7)$$

3. Case Studies and Results

To evaluate the computational performance of the proposed model we solve three real-world case studies with increasing complexity from the Argentine oil and gas industry. Table 1 summarizes the model size and total operating cost in the solution of every case study. The MILP is implemented in GAMS using the solver CPLEX 24.6.1, on an Intel® XEON® CPU.

Table 1: Model size and optimization results for every case study

Case Study	$ I $	$ O $	$ J $	$ T $	CPU time (s)	Makespan (h)	Total Cost (USD)
1	28	4	24	96	1.8	33.5	102,939.3
2	45	6	24	96	4.8	34.5	109,936.5
3	73	19	34	96	16.6	42.0	154,947.0

The three cases comprise the same exploitation area and a planning horizon of two days. Note that the first example involves a total of 28 tasks (4 orders) and 24 crews, and takes less than 2 CPU seconds to be solved. The second example includes 45 tasks (6 orders) with the same number of crews, and is solved to optimality in less than 5 CPU seconds. Finally, the third case study comprises 73 tasks (19 orders) taking more than 3 times the CPU time consumed by the second case study. Figure 3 depicts the Gantt chart of the optimal solution to Case Study 1, in which tasks within the same order have the same colour. It comprises 4 workorders for repairing leaks in aqueducts and pipelines. For this purpose, specialized crews with skills to dig and weld, among other more general tasks, are needed. We can easily observe precedence and concurrence relations such as in the workorder o_3 starting with task i_{15} , assigned to crew j_{19} . Tasks i_{16} and i_{17} have end-start relations with task i_{15} , and a start-start relation among themselves. At noon, crews stop for lunch break. In fact, tasks i_4 , i_{23} and i_{24} are interrupted for lunch and resumed later. After lunch, crew j_{11} starts performing task i_{18} (end-start relation with i_{17}) and when i_{18} is completed, i_{19} and i_{20} can also be executed. Once crew j_9 completes task i_{20} , crew j_{18} can perform task i_{21} . Furthermore, workorder o_2 (starting with task i_8) is the only one associated to production losses since the beginning of the time horizon. For that reason, task i_8 starts as soon as possible. In contrast, workorder o_1 (starting with i_1) yields production losses while it is being executed. Hence, once started, it is forced to end as soon as possible. Note that tasks i_{28} and i_7 must be performed during the second day, by crews j_{18} and j_{19} , respectively. Finally, i_8 , i_{18} and i_{25} are non-preemptive tasks.

4. Conclusion

A novel discrete-time MILP model for planning general maintenance tasks on oil and gas wells and surface facilities has been proposed to simultaneously optimize scheduling and routing decisions. The main contribution of our work is the inclusion of travelling times, precedence and concurrence relations, preemptive and non-preemptive operations, different work shifts and heterogeneous crews. Real-world case studies from the Argentine oil and gas industry have been efficiently solved in reasonable computational times. The optimal solutions yield the allocation of up to 34 resources to 73 operations, in less than 20 seconds. Future work will focus on the development of solution strategies to manage the exponential complexity of larger size problems, including more tasks, crews and locations, over longer time horizons.

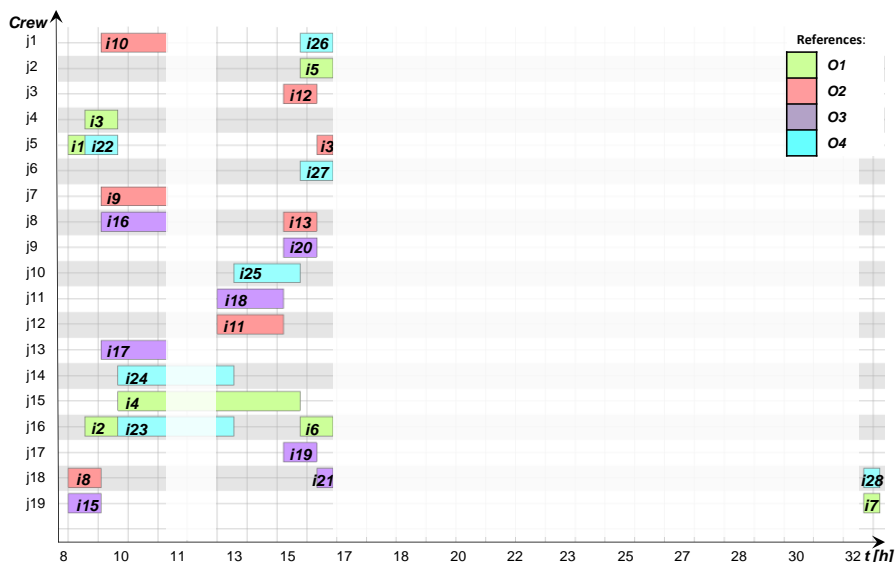


Figure 3: Gantt chart of the optimal solution for Case Study 1

References

- DJ. Aloise, D. Aloise, CTM. Rocha, CC. Ribeiro, JC. Ribeiro Filho, LSS. Moura, 2006, Scheduling workover rigs for onshore oil production, *Discrete Applied Mathematics*, 154(5), 695–702. doi: 10.1016/j.dam.2004.09.021.
- PM. Castro, IE. Grossmann, Q. Zhang, 2018, Expanding scope and computational challenges in process scheduling, *Computers & Chemical Engineering*, 114, pp. 4–42. doi: 10.1016/j.compchemeng.2018.01.020.
- PM. Castro, I. Harjunoski, IE. Grossmann, 2018 Expanding RTN discrete-time scheduling formulations to preemptive tasks, *Computer Aided Chemical Engineering*, 1225–1230. doi: 10.1016/B978-0-444-64241-7.50199-3.
- C. Duhamel, A. Cynthia Santos, L. Moreira Guedes, 2012, Models and hybrid methods for the onshore wells maintenance problem, *Computers & Operations Research*, 39(12), 2944–2953. doi: 10.1016/j.cor.2012.02.026.
- MA. Fernández Pérez, F. Oliveira, S. Hamacher, 2018, Optimizing Workover Rig Fleet Sizing and Scheduling Using Deterministic and Stochastic Programming Models, *Industrial & Engineering Chemistry Research*, 57(22), 7544–7554. doi: 10.1021/acs.iecr.7b04500.
- E. Kondili, CC. Pantelides, RWH Sargent, 1993, A general algorithm for short-term scheduling of batch operations—I. MILP formulation, *Computers & Chemical Engineering*, 17(2), 211–227. doi: 10.1016/0098-1354(93)80015-F.
- CA. Méndez, J. Cerdá, IE. Grossmann, I. Harjunoski, M. Fahl, 2006, State-of-the-art review of optimization methods for short-term scheduling of batch processes, *Computers & Chemical Engineering*, 30(6–7), 913–946. doi: 10.1016/j.compchemeng.2006.02.008.
- V. Peteghem, M. Van and Vanhoucke, 2010, A genetic algorithm for the preemptive and non-preemptive multi-mode resource-constrained project scheduling problem, *European Journal of Operational Research*. Elsevier B.V., 201(2), 409–418. doi: 10.1016/j.ejor.2009.03.034.

Optimization of an Integrated First- and Second-Generation Ethanol Production Plant with Focus on Hydrolysis Parameters

Roymel R. Carpio^a, Roberto C. Giordano^b, Argimiro R. Secchi^{a,*}

^a*Chemical Engineering Program, Universidade Federal do Rio de Janeiro (UFRJ), Rio de Janeiro - RJ, 21941-914, Brazil*

^b*Chemical Engineering Department, Universidade Federal de São Carlos (UFSCar), São Carlos - SP, 13565-905, Brazil*
arge@peq.coppe.ufrj.br

Abstract

Despite there are many studies regarding optimization of biorefineries in the literature, most of them modelled the hydrolysis reactor as a stoichiometric reactor with a predetermined conversion. This simplification implies loss of accuracy and lack of prediction capability, because it does not account for the dependency of hydrolysis yield with important parameters such as enzyme load, solids fraction and reaction time. In this work a kinetic model of the hydrolysis reactor is combined within the whole integrated biorefinery simulation to address this gap. The process modelling and simulation was made in EMSO. Two configurations of the second-generation ethanol (E2G) production process were simulated: the first one considering the xylose biodigestion and the second one implementing the xylose fermentation. The optimization problems involved the maximization of the Net Present Value, taking four key parameters of E2G process as decision variables. The ethanol production increase was incorporated as a constraint of the optimization problem, which was varied in a range of values to obtain optimal configurations for different scenarios. No configuration was economically feasible for the realistic economic scenario considered in the studies. However, the xylose fermentation configuration presented better economic performance than the xylose biodigestion as overall.

Keywords: Sugarcane biorefinery, Modelling and optimization, Economic feasibility.

1. Introduction

The increasing energy demands and the public pressure to decrease greenhouse gas emissions, linked to the governments concern about energy security, are shifting the global energy matrix towards renewable energy technologies (Longati et al., 2018). In this sense, sugarcane biorefineries play an important role producing both biofuel and bioelectricity. Despite the several researches and industry efforts to turn second-generation ethanol production process feasible, this technology is still not consolidated and requires studies to be more sustainable and profitable (Junqueira et al., 2017).

There are many studies regarding optimization of biorefineries in the literature. For a summary of relevant works, we recommend the review of Bechara et al. (2018). However, most of them modelled the hydrolysis reactor as a stoichiometric reactor with a predetermined conversion. This simplification implies loss of accuracy and lack of

prediction capability, because it does not account for the dependency of hydrolysis yield with important parameters such as enzyme load, solids fraction and reaction time. In this work we combined a kinetic model of the hydrolysis reactor within the whole integrated biorefinery simulation to address this gap.

2. Methodology

2.1. Process modelling and simulation

The biorefinery was modelled based on a standard autonomous Brazilian distillery, with a process capacity of 500 t/h of sugarcane (Costa et al., 2016). 35 t/h of sugarcane straw are brought from the field to be burnt in the boiler. The sugarcane and sugarcane straw compositions were in correspondence to Longati et al. (2018). The modelled biorefinery can produce first-generation ethanol (E1G) from sugarcane juice, second-generation ethanol (E2G) from bagasse, and electricity in an integrated process. Two different configurations of the biorefinery were modelled: (1) considering the xylose biodigestion and (2) executing the xylose fermentation. The main data used in the simulation of the biorefinery are shown in Table 1. An overall description of the process follows.

Table 1. Main data used in the biorefinery simulation (TC: ton of sugarcane).

Parameter	Value	Reference
Cleaning energy demand (kWh/TC)	5	Furlan et al. (2013)
Sugar recovery in mill (wt %)	96	Oliveira et al. (2018)
Mill energy demand (kWh/TC)	16	Bechara et al. (2016)
Sugar concentration for fermentation (⁰ Brix)	20	Furlan et al. (2013)
Glycose fermentation yield (%)	90.5	Oliveira et al. (2018)
Anhydrous ethanol purity (wt %)	99.5	Oliveira et al. (2018)
Pre-treatment solid fraction (wt %)	10	Oliveira et al. (2018)
Pre-treatment pressure (bar)	17.4	Oliveira et al. (2018)
Pre-treatment hemicellulose conversion (%)	46.53	Oliveira et al. (2018)
Hydrolysed bagasse fraction (wt %)	5-95	Bechara et al. (2016)
Hydrolysis solid fraction (wt %)	10-20	Angarita et al. (2015)
Hydrolysis Enzyme loading (FPU/g of cellulose)	5-60	Angarita et al. (2015)
Hydrolysis Residence time (h)	12-72	Angarita et al. (2015)
Xylose concentration for fermentation (g/L)	60	Longati et al. (2018)
Xylose fermentation yield (%)	66.5	Furlan et al. (2013)
Boiler steam pressure (bar)	65	Oliveira et al. (2018)
Boiler efficiency based on LHV (%)	86	Longati et al. (2018)
Turbines isentropic efficiency (%)	80	Oliveira et al. (2018)
Electric generator efficiency (%)	95.8	Oliveira et al. (2018)
Biodigester COD removal (%)	74	Ribeiro et al. (2017)
Methane production (L/kg-COD-removed)	290	Ribeiro et al. (2017)

The bagasse obtained after milling is divided in two fractions. The first one is fed in the boiler and the second one is used for E2G production. The bagasse diverted to E2G production undergoes a liquid hot water pre-treatment. After that, the liquid fraction, rich in xylose is separated from the solid fraction containing the cellulose. The xylose liquor could be used in biogas production by biodigestion or in ethanol production by fermentation. On the other hand, the solid fraction containing cellulose is fed to the

enzymatic hydrolysis. The kinetic model of hydrolysis reactor proposed by Angarita et al. (2015) was used to access the dependency of hydrolysis yield on enzyme load, solid fraction and reaction time. The coupling of this kinetic model into the whole steady state simulation was made as described in Carpio et al. (2018a).

After hydrolysis reaction, the remained solid fraction (mostly lignin) is sent to the boiler and the liquid fraction (glycose liquor) is mixed to the 1G treated juice and undergoes the traditional stages of E1G. The cogeneration system includes a boiler, a back-pressure turbine and a condensing one, and produces steam and electricity to supply process demands. The electricity surplus is sold to the grid. EMSO software (Soares and Secchi, 2003) was used to perform the modelling and simulation of the biorefinery. The components and thermodynamic packages used in this work were the same of Longati et al. (2018).

2.2. Economic analysis

The economic analysis was also implemented in EMSO, coupled to the process model. This allows instant calculation of economic indexes for any feasible operational condition simulated, without requiring external or auxiliary sheet calculations. The main economic premises considered in this study are shown in Table 2.

Table 2. Main premises considered in the economic analysis.

Parameter	Value	Reference
Ethanol selling price (US\$/m ³)	584.61	MAPA (2018)
Electricity selling price (US\$/MWh)	71.19	CCEE (2018)
Sugarcane costs (US\$/t)	22.15	UDOP (2018)
Straw cost (US\$/t)	15	Bechara et al. (2016)
Enzyme cost (US\$/t)	1250	Bechara et al. (2016)
Fresh water cost (US\$/t)	0.06	Bechara et al. (2016)
Refrigeration cost (US\$/kW)	0.04	Bechara et al. (2016)
Operation time (h/year)	42000	Furlan et al. (2013)
Project life time (years)	25	Longati et al. (2018)
Construction period (years)	1	Furlan et al. (2013)
Tax Rate (%)	34	Longati et al. (2018)
Discount rate (%)	10	Bechara et al. (2016)
Depreciation strategy (%/year)	10	Longati et al. (2018)

The capital cost (CAPEX), operating costs (OPEX), cash flows (CF) and net present value (NPV) were calculated based on the methodology of Peters et al. (2003). The main equipment purchase costs were estimated from the literature (Humbird et al., 2011) and were updated and scaled according to Peters et al. (2003). The minimum ethanol selling price (MESP) corresponds to the ethanol selling price that makes NPV equal to zero.

2.3. Process optimization

The objective function of the optimization problems was the maximization of the NPV. Some key parameters of hydrolysis were selected as decision variables: hydrolysed bagasse fraction, enzyme loading, solids loading and residence time. The increasing on total ethanol production due to E2G was incorporated as an inequality constrain. The Surrogate Assisted Optimization (SAO) framework proposed by Carpio et al. (2018b)

was applied for estimating an initial global solution of the optimization problems. After that, the Sequential Quadratic Programming (SQP) algorithm was used for refining the solution.

3. Results and discussion

Figure 1 shows the resulting Pareto set of NPV and MESP for different values of the constraint. The economic indexes of both configurations become worse when increasing the constraint value. It means that the additional income obtained by a larger ethanol production does not compensate the investment and operational cost involved in the E2G production process for the realistic economic scenario. This finding is in agreement with the results achieved by Bechara et al. (2016), Junqueira et al. (2017) and Longati et al. (2018).

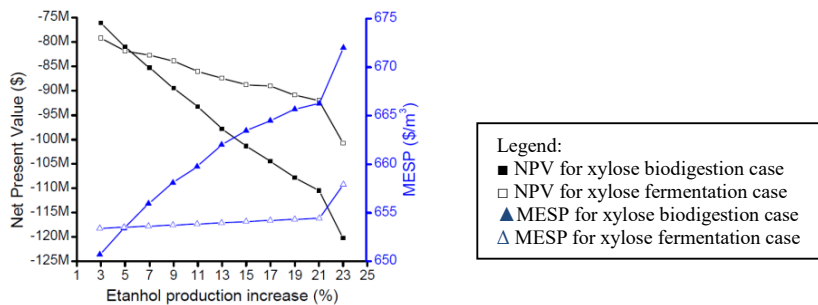


Figure 1. Pareto curve of NPV and MESP for ethanol production increase.

As overall, the economic indexes of the xylose fermentation case are better than the xylose biodigestion case. In addition, the sensitivity of the Pareto curve for xylose fermentation case is lower than for the xylose biodigestion case. It is worth mentioning the existence of knee points, for which NPV and MESP witness a greater change, at the higher values of the constraint. This behaviour is better understood by analysing the optimal values of decision variables shown in Figure 2.

The hydrolysed bagasse fraction (Fig. 2A) rises almost linearly with the constraint increase until approximately 19 %. After that value, this variable rises more gradually because it is close to the maximum value of bagasse that can be diverted to E2G without affecting the steam requirements of the biorefinery. In the case of enzyme loading (Fig. 2B), the optimal values are between 12 and 16 FPU/g. Notice that for constraint values higher than 21 % the enzyme loading rise abruptly. This behaviour is due to the impossibility of an additional increase on the hydrolysed bagasse fraction for that condition. Consequently, it is necessary to increase the enzyme loading for producing more ethanol and meet the constraint.

The optimal values for solids loading (Fig. 2C) of both configurations are mostly above 15 %. For the xylose fermentation case there is a clear tendency of increasing the solids loading as the constraint increases as well. This behaviour is justified by the higher steam demand of this configuration. Therefore, it is necessary to increase the solids loading for decreasing the steam demand and allowing a higher hydrolysed bagasse

fraction. Optimal values for residence times (Fig. 2D) were mostly between 68 and 72 hours. The oscillatory behaviour of the residence time is due to the cost of hydrolysis reactors being a discrete variable that changes in steps, because the total required volume is attained by adding fixed-volume hydrolysis reactors. Consequently, there are some operating conditions where the additional ethanol produced by increasing the residence time does not compensate the cost of a new hydrolysis reactor, leading to optimal resident times below 72 hours.

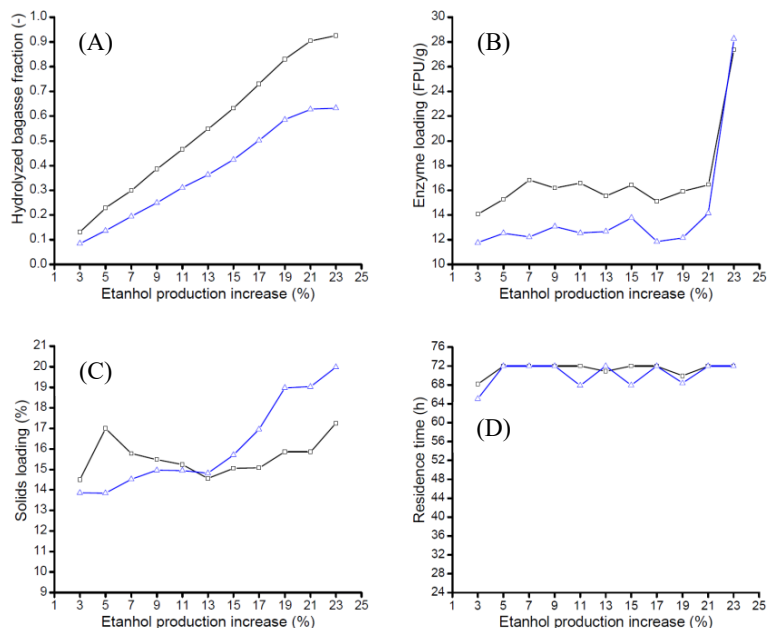


Figure 2. Optimal values of decision variables for: □ xylose biodigestion and △ xylose fermentation.

4. Conclusions

No configuration was economically feasible for the realistic economic scenario considered in this study. However, the xylose fermentation case presented better economic performance than the xylose biodigestion as overall, and particularly for high cellulosic ethanol rates. It is possible to increase the ethanol production up to 23 % in both configurations due to E2G process. However, ethanol production increase greater than 21 % leads to significant deterioration of economic indexes. Most of the optimal configurations were achieved for enzyme loading between 12 and 16 FPU/g, solids loading in the range of 14 and 17 % and residence times above 68 hours.

Acknowledgements

Financial support from CAPES (grant #9003-14-2), from CNPq (grant #302893/2013-0) and from FAPERJ (grant #E012018-236117) are gratefully acknowledged.

References

- J. Angarita, R. Souza, A. Cruz, E. Biscaia, A. Secchi, 2015, Kinetic modeling for enzymatic hydrolysis of pretreated sugarcane straw, *Biochemical Engineering Journal*, 104, 10-19.
- R. A. Bechara, A. Gomez, V. Saint-Antonin, J.-M. Schweitzer, F. Maréchal, 2016, Methodology for the optimal design of an integrated first and second generation ethanol production plant combined with power cogeneration, *Bioresource Technology*, 214, 441-449.
- R. A. Bechara, A. Gomez, V. Saint-Antonin, J.-M. Schweitzer, F. Maréchal, A. Ensinas, 2018, Review of design works for the conversion of sugarcane to first and second-generation ethanol and electricity, *Renewable and Sustainable Energy Reviews*, 91, 152-164.
- R. R. Carpio, F. F. Furlan, R. C. Giordano, A. R. Secchi, A kriging-based approach for conjugating specific dynamic models into whole plant stationary simulations, 2018a, *Computers & Chemical Engineering*, 119, 190-194.
- R. R. Carpio, R. C. Giordano, A. R. Secchi, Enhanced surrogate assisted framework for constrained global optimization of expensive black-box functions, 2018b, *Computers & Chemical Engineering*, 10.1016/j.compchemeng.2018.06.027.
- CCEE, 2018, Public auction electricity prices, Electric Energy Commercialization Chamber, www.ccee.org.br.
- C. B. B. Costa, E. Potrich, A. J. G. Cruz, 2016, Multiobjective optimization of a sugarcane biorefinery involving process and environmental aspects, *Renewable Energy*, 96, 1142-1152.
- F. F. Furlan, R. T. Filho, F. H. Pinto, C. B. Costa, A. J. Cruz, R. L. Giordano, R. C. Giordano, 2013, Bioelectricity versus bioethanol from sugarcane bagasse: is it worth being flexible?, *Biotechnology for Biofuels*, 6 (1), 142.
- D. Humbird, R. Davis, L. Tao, C. Kinchin, D. Hsu, A. Aden, P. Schoen, J. Lukas, B. Olthof, M. Worley, D. Sexton, D. Dudgeon, 2011, Process design and economics for biochemical conversion of lignocellulosic biomass to ethanol, Tech. rep., NREL/TP-5100-47764.
- T. L. Junqueira, M. F. Chagas, V. L. R. Gouveia, M. C. A. F. Rezende, M. D. B. Watanabe, C. D. F. Jesus, O. Cavalett, A. Y. Milanez, A. Bonomi, 2017, Techno-economic analysis and climate change impacts of sugarcane biorefineries considering different time horizons, *Biotechnology for Biofuels*, 10 (1), 50.
- A. A. Longati, A. R. Lino, R. C. Giordano, F. F. Furlan, A. J. Cruz, 2018, Defining research & development process targets through retro-techno-economic analysis: The sugarcane biorefinery case, *Bioresource Technology*, 263, 1-9.
- MAPA, 2018, Brazilian annual ethanol exports, Ministry of Agriculture, Cattle and Supply, www.agricultura.gov.br.
- C. M. Oliveira, L. V. Pavo, M. A. Ravagnani, A. J. Cruz, C. B. Costa, 2018, Process integration of a multiperiod sugarcane biorefinery, *Applied Energy*, 213, 520-539.
- M. S. Peters, K. D. Timmerhaus, R. E. West, 2003, *Plant design and economics for chemical engineers*, 5th Edition, Vol. 5, McGraw-Hill.
- F. R. Ribeiro, F. Passos, L. V. A. Gurgel, B. E. L. Bata, S. F. de Aquino, 2017, Anaerobic digestion of hemicellulose hydrolysate produced after hydrothermal pretreatment of sugarcane bagasse in UASB reactor, *Science of The Total Environment*, 584, 1108-1113.
- R. P. Soares, A. Secchi, 2003, EMSO: A new environment for modelling, simulation and optimisation, *Computer Aided Chemical Engineering*, Vol. 14, pp. 947-952.
- UDOP, 2018, Sugarcane prices, Union of Biofuel Producers, www.udop.com.br.

Optimization of seaweed-based biorefinery with zero carbon emissions potential

Rofice Dickson,^a Jay Liu^{a,*}

^aDepartment of Chemical Engineering, Pukyong National University, Busan, 48547, Korea

jayliu@pknu.ac.kr

Abstract

The superstructure-based optimization was proposed to determine optimal pathway of biorefinery, producing bioethanol. In general, the bioethanol process produces a large number of waste streams such as carbon dioxide, wastewater, and residual solid from fermentation. To utilize the aforementioned waste streams, processes such as succinic acid (SA), microalgae (MA), wastewater treatment (WWT) networks, and solid processing were integrated with bioethanol process. Based on the superstructure, technoeconomic and environmental mixed integer non-linear model was formulated and implemented in GAMS (25.0.2). The aim of the present contribution was to determine a more economically and environmentally viable process design than a standalone process. These goals were achieved by two objective functions; maximize net present (NPV) value and minimize carbon dioxide emissions (CE). To account uncertainties in process parameters, sensitivity analysis was also performed. The result indicated minimum ethanol selling price (MESP) of integrated design is about 34% lower than that of a standalone bioethanol process with more than 90% reduction in CE.

Keywords: Superstructure optimization, process synthesis, biofuels, macroalgae

1. Introduction

Development of biofuel production from renewable sources like biomass has gained significant attention due to growing energy demand, depleting fossil fuel reserves, and increasing environmental concerns such as greenhouse gas emissions. Among various biomass feedstocks, brown algae, as a 3rd generation feedstock, is considered as a promising candidate due to its sustainable cultivation, high sequestration efficiency, and absence of ethical issues such as food competition. Furthermore, brown algae contain high carbohydrates contents, at 32-60%, dry weight, and lack of lignin (Roesijadi et al., 2010). Taking into consideration the benefits of brown algae and its versatile chemical composition, this study will focus on biofuel production from brown alga *Saccharina japonica* (SJ) as a potential feedstock.

In the literature, several bench-scale experimental studies were conducted to produce biofuels from the carbohydrates of SJ via fermentation pathway. Reith et al. (2009) utilized the carbohydrate contents of SJ and obtained ethanol yields of 0.254 kg ethanol/kg of dry feed. Based on this yield, Fasahati et al. (2015) determined the economic viability of bioethanol production from SJ and calculated MESP of 2.39 \$/gal at 80,000 t/y plant capacity. Recently, Dickson et al. (2018) conducted an optimal design of SJ-based biorefinery by using a superstructure approach to report the values of the MESP and the maximum seaweed price (MSP).

Despite the promising yields and economics, bioethanol processing produces numerous waste streams and byproducts, and is water intensive. It is reported that medium-sized biorefinery, processing 2 to 3.5 mt/y sugarcane produces 110 to 193 kt/y of CE during fermentation (Bonfim-Rocha et al., 2018). Similarly, stillage from the distillation column has high values of chemical oxygen demand, biochemical oxygen demand, and minerals. Water consumption in bioethanol plants ranges from 3 to 15 gal of water per gal of ethanol. Disposal of these waste streams without treatment can cause severe environmental issues such as contribution to global warming, deoxygenation of water reservoirs, discoloration, odors, eutrophication, acidification, and other problems. In the literature, however, little attention has been paid to simultaneously reduce all waste streams from bioethanol processing.

Based on the presented challenges and research gap, this study is the first to simultaneously integrate processes such as SA, MA, unreacted solid processing, and WWT networks with bioethanol processing. The goal of this study is to utilize all waste components from SJ biorefinery by designing an economical and environmentally friendly process by taking a superstructure approach. To achieve these goals, two objective functions were employed in the optimization: NPV and CE. The novelty of this work includes a large number of process alternatives to find the optimal design under different objective functions.

2. Methodology

2.1. Problem statement

The optimization problem is defined as determining the optimal design for macroalgae-based biorefinery, which has maximum process economics as well as minimum detrimental effects on the environment.

2.2. Superstructure development

To design an environmentally friendly biorefinery, a superstructure is developed by adding large number of design alternatives into the conventional bioethanol process. The superstructure given in Figure 1 is capable of utilizing all components of seaweed and waste streams from the bioethanol process. Seven major sections are included in the superstructure: feed pre-treatment, enzymatic hydrolysis and fermentation, enzyme production, CO₂ utilization, harvesting, purification, and WWT.

The biorefinery process starts with the feed pre-treatment. The Feed can either be pre-treated with acid thermal hydrolysis (ATH) or hot water wash (HWW). The resulting treated feed then sent to the enzymatic hydrolysis and fermentation section, where carbohydrates are converted into glucose and ultimately to ethanol. There are two alternatives for obtaining enzymes for saccharification and fermentation. Enzymes can be manufactured on-site or they can be purchased. The outlet streams from the saccharification and fermentation section consist of the gaseous, liquid, and solid product stream. The gaseous products primarily consist of CO₂ and sent to CO₂ utilization section. Two design alternatives considered for CO₂ utilization are MA production and SA production. Based on the work of Bai et al. (2015), SA production from SJ is promising and can occur by consuming glucose and CO₂ in the presence of *E. Coli*. Glucose required for the SA fermentation is provided from the saccharification and fermentation section by splitting a part of glucose to CO₂ utilization section. As glucose split for the SA production will decrease the bioethanol production, therefore,

upper bound on SA production is applied. In an alternative method, CO₂ can be utilized to produce microalgae. MA can be cultivated either in open ponds or photobioreactors.

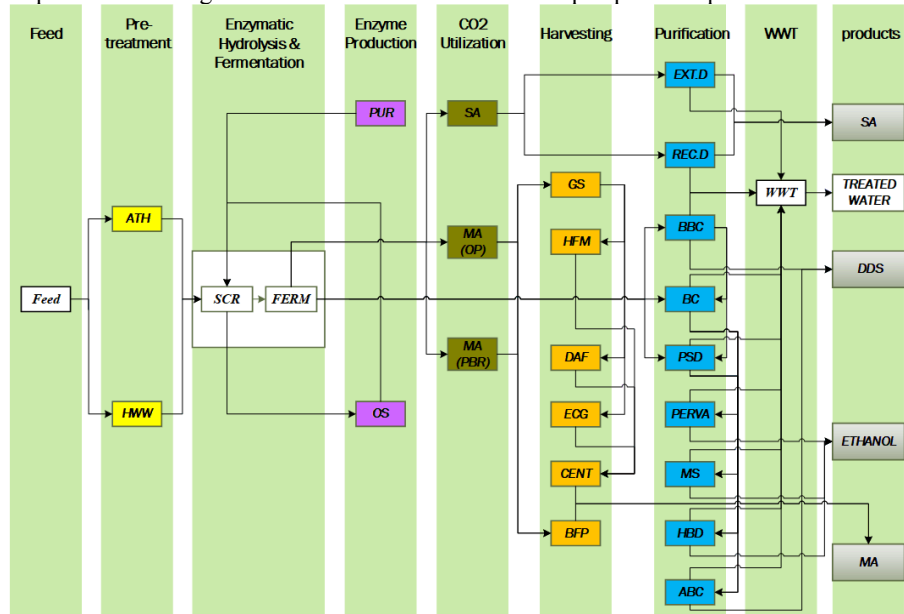


Figure 1. Superstructure for *Saccharina japonica* based biorefinery.

In harvesting section, five design alternatives are considered for MA harvesting and dewatering. The MA are harvested in gravity settler, which can be dewatered either by hallow filter membranes, diffused air flocculation, or electrocoagulation followed by centrifugation. Alternatively, belt filter press can be implemented at the outlet stream of gravity settler. The final concentration of MA from all dewatering alternative is 20 wt.%. The operating data considered for MA production is based on the work of Davis et al. (2011). In the purification section, various streams coming from the fermentation and CO₂ utilization section are processed to their desired level of purity. For example, SA can be purified either by extractive distillation or reactive distillation processes. Unreacted solids from the fermenter can be processed either before the beer column or after the beer column. Furthermore, solid processing can be performed either by centrifuge or belt filter press. As ethanol purification is an energy-intensive process, therefore, multiple design alternatives are considered in superstructure to select optimal topology for its purification. In general, two pathways included in the superstructure are conventional unit operations and novel technologies such as hybrid distillation (HD). The conventional unit operations consist of beer column, rectification column, and molecular sieves (zeolite beds) or pervaporation membranes (cross-linked vinyl alcohol). However, HD includes the combination of distillation columns and pervaporators in series. Furthermore, ethanol purification in the beer column is energy intensive. Therefore, to reduce the energy consumption, the beer column has two design alternatives: a single distillation column and pressure swing distillation (PSD). To reduce freshwater consumption, a complete WWT network incorporated into the superstructure that will treat and recycle wastewater from various process units. Process wastewater is treated using anaerobic digestion, aerobic digestion, and reverse osmosis. The treated water is assumed to be pure and is recycled to the process.

2.3. Objective function and assumptions

The objective function used for this optimization problem are maximization of the net present value (NPV) and minimization of CE, and are defined by:

$$NPV = \sum_{n=0}^{20} \frac{NCF_n}{(1+r)^n}, \quad (1)$$

$$CE = \sum_k F_{k,CO_2}, \quad (2)$$

where NCF_n is non-discounted cash flow for the year n , and r is the discount rate. F_{k,CO_2} is the mass flow rate of CO_2 in the outlet stream k . Various assumptions considered in techno-economic analysis include 20 years project life, 10% discount rate, straight-line depreciation method over 7 years, 30% tax rate, and two-year construction time. The chemical composition of SJ reported by Roesijadi et al. (2010) was used in this work.

2.4. Optimization scenarios

Four optimization scenarios were studied to determine a sustainable biorefinery design. The scenario-1 is a base case design, which consists of traditional bioethanol process. In this scenario, all alternatives related with the utilization of CO_2 were excluded, and the optimization problem was solved with respect to maximizing NPV. The results obtained from this scenario will set targets for further improvements in the process. In scenario-2, all alternatives related to CO_2 utilization were activated and the problem was solved by maximizing the NPV. In addition, there was a restriction that only alternative can be selected for the utilization of CE. In scenario-3, all conditions were similar to that for scenario-2 except objective function which was the minimization of CE. In scenario-4, the synergistic effect of both CO_2 utilization processes was studied by removing the restriction to select only one alternative. The objective function was the maximization of NPV, whereas the second objective function was applied as a constraint in which net CE obtained from the scenario-3 was applied as an upper bound.

3. Results and discussion

The optimal topology obtained for bioethanol production and solid processing in scenario-1 consist of HWW, on-site enzyme production, ethanol purification by PSD and HD, and solid purification after the beer column. The same pathway was obtained in the rest of the scenarios for bioethanol production and solid processing. The products obtained in this scenario are bioethanol and DDS, and their production are presented in Table 1. Results indicated that NPV of this scenario is \$38 MM.

Table 1. Mass balance summary.

Scenario	Ethanol yield (gal/t)	Ethanol (Mgal/y)	DDS (kton/y)	MA (kt/y)	SA (kt/y)	CO2 Produced (kt/y)	Net CE (kt/y)
1	83.94	51.37	314.80	0	0	148.7	148.7
2	73.51	44.99	275.67	0	15.30	129.6	121.8
3	83.94	51.37	314.80	62.13	0	148.7	14.9
4	73.51	44.99	275.67	50.91	15.30	129.6	12.9

In scenario-2, SA production was selected to utilize CE. The products obtained in this scenario are bioethanol, DDS, and SA, and their production are presented in Table 1. Only 6% of CO_2 is utilized in this scenario due to the upper bound on the SA

production. The NPV of this scenario is \$134 MM. This improvement is attributed to the high selling price of SA, which is almost 5.5 times higher than the current wholesale price of ethanol.

In scenario-3, MA production was selected as an optimal process for the utilization of CO₂. The production rate of products obtained in this scenario are shown in Table 1. Results indicated that ~90% of CO₂ is utilized. The NPV of this scenario is \$101 MM.

In scenario-4, both SA and MA production were selected for the utilization of CO₂. The production levels of products obtained in this scenario are given in Table 1. Results indicated that ~90% of CO₂ is utilized. The NPV of this scenario is \$180 MM.

3.1. Optimal design

The comparison of all scenarios highlights that process topology obtained in the scenario-4 is both economically and environmentally superior, and therefore, selected as an optimal design. The optimal design shown in the Figure 2 has water consumption of 6.31 gal/gal of ethanol. The total capital investment, total manufacturing cost, and utility cost of optimal design are \$377 MM, \$153 MM, and \$25 MM, respectively. The total capital investment of optimal design is 55% more than that for a standalone process.

3.2. Minimum and maximum selling price of products and seaweed

The estimated MESP of optimal design is 1.31 \$/gal, which is ~34 times lower than that of scenario-1. Similarly, minimum selling price of DDS, SA, MA are 0.002 \$/kg, 1.52 \$/kg and 0.256 \$/kg. The calculated MSP is 0.127 \$/kg.

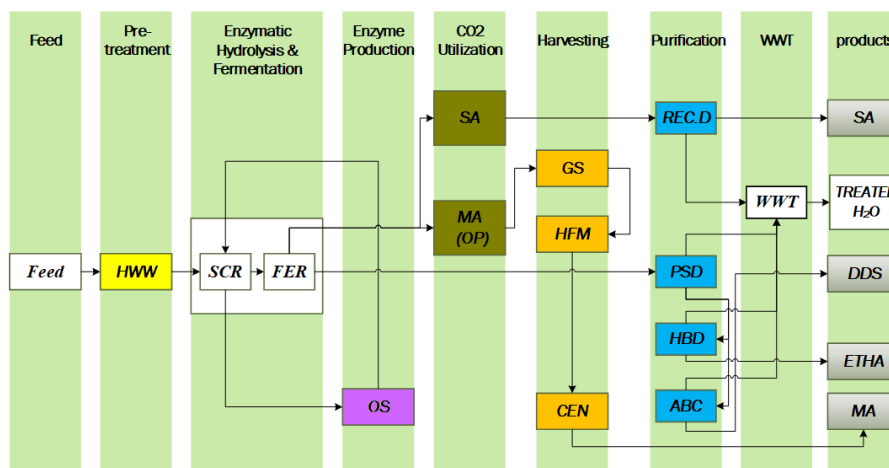


Figure 2. Optimal structure for bioethanol process

3.3. Sensitivity analysis

Sensitivity analysis was performed to evaluate the impact of key model parameters on MESP. Results presented in Figure 3 indicated that total capital investment, product selling prices, seaweed price, and IRR are the most dominant parameters that effect MESP.

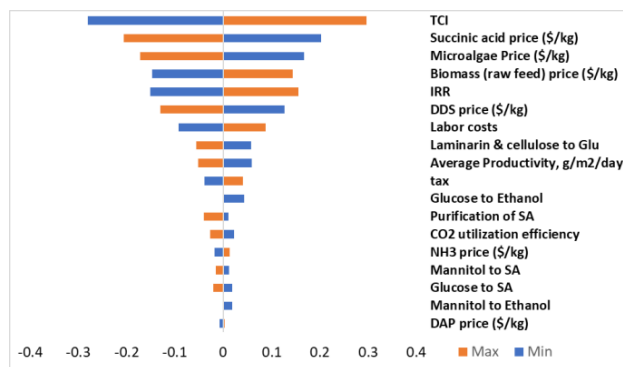


Figure 3. Sensitivity tornado chart for MESP.

4. Conclusion

A process synthesis framework for the optimization of the bioethanol process as well as optimization of CE was proposed. Multiple scenarios were studied based on different optimization criteria to determine the optimal topology. The result indicated that biofuel production from SJ is viable, at MESP of 1.31 \$/gal. The proposed framework is an important decision tool for systematically analysing optimal structure for bioethanol process and reducing various pollutants.

5. Acknowledgments

This research was supported through the Basic Science Research Program of the National Research Foundation of Korea (NRF) funded by the Ministry of Science and ICT (2017R1A2B4004500).

6. Reference

- Bai, B., Zhou, J. min, Yang, M. hua, Liu, Y. lan, Xu, X. hui, Xing, J. min, 2015. Efficient production of succinic acid from macroalgae hydrolysate by metabolically engineered *Escherichia coli*. *Bioresour. Technol.* 185, 56–61.
- Bonfim-Rocha, L., Gimenes, M.L., Bernardo de Faria, S.H., Silva, R.O., Esteller, L.J., 2018. Multi-objective design of a new sustainable scenario for bio-methanol production in Brazil. *J. Clean. Prod.* 187, 1043–1056.
- Davis, R., Aden, A., Pienkos, P.T., 2011. Techno-economic analysis of autotrophic microalgae for fuel production. *Appl. Energy* 88, 3524–3531.
- Dickson, R., Ryu, J.-H., Liu, J.J., 2018. Optimal plant design for integrated biorefinery producing bioethanol and protein from *Saccharina japonica*: A superstructure-based approach. *Energy* 164, 1257–1270.
- Fasahati, P., Woo, H.C., Liu, J.J., 2015. Industrial-scale bioethanol production from brown algae: Effects of pretreatment processes on plant economics. *Appl. Energy* 139, 175–187.
- Reith, H., Huijgen, W., Hal, J. van, 2009. Seaweed potential in the Netherlands. *ECN Biomass, Coal*.
- Roesijadi, G., Jones, S.B., Zhu, Y., 2010. Macroalgae as a Biomass Feedstock : A Preliminary Analysis. *Analysis* 1–50.

Optimal design for integrated macroalgae-based biorefinery via mixed alcohol synthesis

Rofice Dickson,^a Peyman Fasahati,^b Jay Liu^{a,*}

^a*Department of Chemical Engineering, Pukyong National University, Busan, 48547, Korea*

^b*Department of Chemical Engineering and Biological Engineering, University of Wisconsin-Madison, Madison, WI 53706, USA*

jayliu@pknu.ac.kr

Abstract

A novel superstructure is developed for the biochemical conversion of macroalgae to mixed alcohols (MAs). With reference to environmental sustainability of manufacturing process, microalgae production processes are integrated to utilize CO₂ into useful products. Wastewater treatment network was modelled in the process synthesis framework to reduce freshwater consumption. Based on the superstructure, techno-economic mixed integer linear programming model was formulated. The objective function was maximization of the net present value (NPV). The results indicated that biofuel production from macroalgae is economically viable. The minimum selling price of ethanol, heavier alcohols, dry distillery solids, and microalgae are calculated to be 1.26 \$/gal, 2.3 \$/gal, 0.05 \$/kg, and 0.114 \$/kg, respectively. The maximum seaweed purchasing price is calculated to be 113 \$/ton. Furthermore, optimal design has achieved 90% reduction in CO₂ emissions (CE). Sensitivity analysis showed that the selling price of heavier alcohols and purchasing price of macroalgae are the most sensitive parameters to minimum ethanol selling price (MESP).

Keywords: Superstructure optimization, process synthesis, biofuels, macroalgae, volatile fatty acids

1. Introduction

Increasingly high energy prices, volatility of the global oil market, and consistent pressure to reduce greenhouse gases are major challenges within the transportation sector. To address these challenges, energy policies and goals are set by The United States and European Union, which have stimulated global interest in finding sustainable alternatives for replacing crude-oil derivatives (Zittel and Schindler, 2007).

Macroalgae, more specifically brown algae, as the third-generation biomass, are promising feedstock candidates for the biofuel production. Cultivation of macroalgae is considered sustainable, as it requires no arable land, irrigation water, or fertilizer. Among brown alga species, *Saccharina japonica* is extensively studied due to its high carbohydrate content, lack of lignin, and extensively available feedstock (Jiang et al., 2016). Therefore, this study focuses on the biofuel production using *Saccharina japonica* as feedstock.

There are three general pathways to produce biofuels: biochemical, chemical, and thermochemical. With reference to *Saccharina japonica*, arguments supporting

biochemical conversion are the most favourable due to its ability to process feedstock with high moisture content and mild operating conditions in comparison to the alternative pathways. In general, biochemical pathway can produce MAs including ethanol, butanol, and propanol. The biochemical pathway is divided into two alternative pathways: volatile fatty acid platform (VFAP) and sugar platform (SP). In the former, volatile fatty acids (VFAs) are produced by using anaerobic digestion (AD) of the feed using a mixed culture bacterial ecosystem, which can be further processed to produce MAs. In the latter, only bioethanol is produced by extracting sugars from the biomass. Dickson et al. (2018) used a superstructure-based approach to evaluate the economics of bioethanol production from *Saccharina japonica* through SP. They estimated the MESP of 1.97 \$/gal at a plant scale of 612,000 t/y. On the other hand, techno-economic evaluation of biofuel production from VFAP at industrial scale is still limited and should be systematically evaluated in order to determine an optimal biochemical pathway.

In the literature, various bench scale experimental studies demonstrated that VFAP has higher carbon yield (g MAs/g dry feed) than the SP (Pham et al., 2012). This high yield is mainly due to the ability of mixed anaerobic bacteria to utilize all components of the biomass, including carbohydrates, proteins, and lipids, whereas in the case of SP merely carbohydrates contents of biomass are converted to bioethanol (Fasahati and Liu, 2015). Despite the promising yields, the effective and economically viable separation technologies for dehydration of the aqueous VFAs are a major obstacle to industrial scale application of VFAP. This is mainly due to the close boiling point of water and acetic acid, which makes their separation difficult as well as energy intensive by distillation. Another challenge associated with biochemical route is the massive production of CO₂ during fermentation of biomass. A potential method to mitigate direct CE from VFAP is microalgae-based biological utilization. According to Davis et al. (2016), one kilogram of microalgae consumes 1.93 kg of CO₂, which make it a suitable candidate to reduce CE from MAs production.

Based on the presented arguments, this study introduces an optimization-based process synthesis framework for MAs processes that will directly analyse the techno-economic, and environmental trade-offs using a large-scale mixed-integer linear programming model. The proposed framework simultaneously optimizes the topology of MAS manufacturing process as well as determine the optimal strategy to utilize CE produced during fermentation.

2. Methodology

2.1. Problem statement

The optimization problem is defined as determining the optimal design for MAs production process from the given set of alternatives, which has maximum process economics as well as minimum detrimental effects on the environment.

2.2. Overall process description

MAs production process starts with the partial AD of brown algae in the presence of iodoform inhibitor, at 30 PPM concentration (Granda et al., 2009). The operating conditions of AD are 5 days of retention time at 13 wt.% solid loading and 35 °C (Pham et al., 2012). The overall efficiency ranges from 0.307-0.412 g VFAs/ g dry feed. The outlet stream from the digester consists of solid, liquid, and gaseous products. Products

from the digester are sent to flash drum to separate light gases such as hydrogen and carbon dioxide from the solid and the liquid products. Light gases in the vapor stream of flash drum are then sent to pressure swing adsorption to separate hydrogen from carbon dioxide, the former can be utilized during hydrogenation of VFAs to MAs. Solids are then separated from the liquid products by using solid separation technologies such as mechanical separator followed by drying. About 20 wt.% of solids are sent back to digester as an inoculum and nutrient source, while remaining fraction can be sold as animal feed called dry distillery solids. Liquid stream from the solid separation area is sent to VFAs recovery section, where VFAs are recovered at 99.9 wt.% using extraction column, rectification column, decanter, and stripping column. The concentrated VFAs are then hydrogenated for the synthesis of mixed alcohols. The hydrogenation process is a gas phase process, which takes place at 290 °C and 60 bars in the presence of cobalt catalyst to give a high alcohol yield of 97 wt.%. The catalyst consumption as well as hydrogen requirement are 0.46 mg catalyst/ kg MAs, and molar ratio of 2.1:1 (H₂/VFA), respectively. The hot effluent of the hydrogenation reactor is cooled and sent to the two flash drums operating in series to recover vapours, which are recycled to the hydrogenation reactor. The bottom stream of the final flash drum consists of 25 wt.% water, 42 wt.% ethanol, 19 wt.% propanol, and 12 wt.% butanol, and is sent to the alcohol recovery unit. Herein, MAs are dehydrated by the molecular sieves, and sent to the alcohol distillation column to separate ethanol from butanol and propanol. The 99.9 wt.% purity of ethanol is obtained in the overhead stream of distillation column. Propanol and butanol are obtained in the bottom stream of column and considered as co-products.

2.3. Superstructure development

Design alternatives are added in the previously mentioned baseline process to develop a superstructure. The superstructure is shown in Figure 1 and consists of six sections: (1) fermentation and solid processing, (2) volatile fatty acids recovery, (3) hydrogenation, (4) mixed alcohols recovery, (5) utilization of carbon dioxide, and (6) wastewater treatment. The proposed superstructure contains fourteen design alternatives at various processing stages. The general mathematical model is similar to one reported in our previous work (Dickson et al., 2018). The design alternatives for solid processing include mechanical separator and centrifuge. As dehydration is energy intensive, five design alternatives are considered for recovering VFAs and MAs. VFAs can be recovered either by classical extraction/distillation processes or hybrid pervaporation (PV). The classical methods for recovering VFAs are similar to that described in Section 2.2. In PV, pervaporator is integrated into the classical process, which increases the concentration of VFAs from 5 wt.% to 10 wt.% by removing ~50 wt.% of the total water flow. Removal of this large amount of water directly impacts the process economics. Likewise, MAs can be dehydrated by three design alternatives to achieve a desired level of purity for their applications as a fuel. Dehydration can be performed by either molecular sieves, pervaporator, or vapor permeation. In all design alternatives, the target purity of ethanol is 99.5 wt.%.

To reduce CE, seven design alternatives are considered for microalgae cultivation and harvesting. Microalgae can be cultivated either in open ponds or photobioreactors. For its harvesting and dewatering, five design alternatives are considered. The microalgae are harvested in gravity settler, which can be dewatered either by hollow fiber membranes, diffused air flocculation, or electrocoagulation followed by centrifugation. Alternatively belt filter press can be implemented at the outlet stream of gravity settler. The final concentration of microalgae from all dewatering alternative is 20 wt.%. The

operating data and equipment costs considered for microalgae production are based on the work of (Davis et al., 2016).

A complete wastewater treatment network is incorporated that will treat and recycle wastewater from various process units including distillation columns, blowdown from the cooling tower, and blowdown from the boilers. Process wastewater is treated using anaerobic digestion, aerobic digestion, and reverse osmosis. The treated water is assumed to be pure and is recycled to the process.

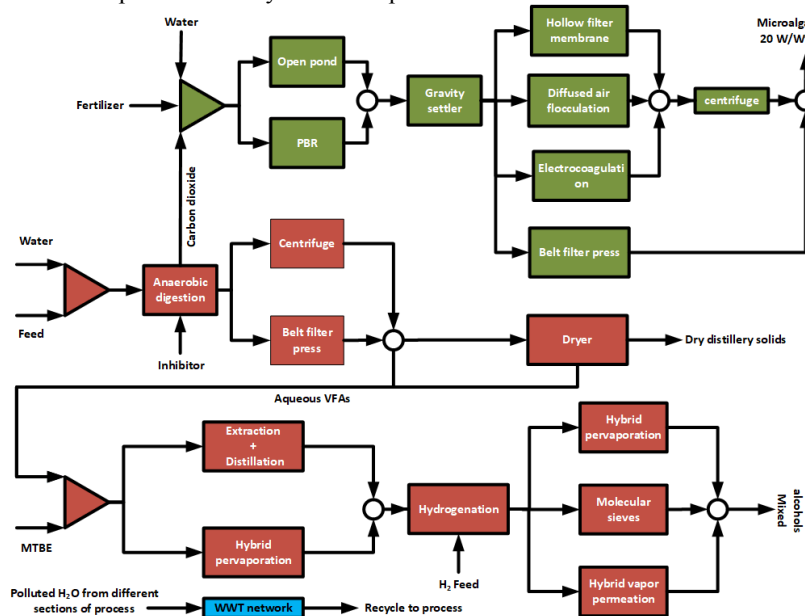


Figure 1. Superstructure for producing mixed alcohol from *Saccharina japonica*.

2.4. Objective function and assumptions

The objective function used for this optimization problem is maximization of the NPV and given in Eq. (1)

$$NPV = \sum_{n=0}^{20} \frac{NCF_n}{(1+r)^n}, \quad (1)$$

where NCF_n is non-discounted cash flow for the year n , and r is the discount rate. Various assumptions considered in techno-economic analysis include: 20 years project life, 10% discount rate, straight line depreciation method over 7 years, 30% tax rate, and two-year construction time. The chemical composition of *Saccharina japonica* reported by Roesijadi et al. (2010) was used in the simulation. An efficiency of 0.35 g VFA/g of dry biomass is considered in AD. The selling prices of products such as ethanol, heavier alcohols, DDS, and microalgae considered in this study to calculate process revenue were 0.72 \$/kg, 1.13 \$/kg, 0.13\$/kg, and 0.5 \$/kg, respectively. Likewise, costs of raw materials such as brown algae, MTBE, cooling H₂O, chilled H₂O, H₂, LP steam, and electricity were 68 \$/t, 1100 \$/t, 0.013 \$/t, 1 \$/t, 1.5 \$/t, 12.68 \$/t, and 0.0622 \$/kWh, respectively.

3. Results and discussion

The proposed process synthesis framework was implemented in GAMS (25.0.2) to determine optimal process design for MAs production process and CE utilization. The digester receives 612,000 t/y dry feed for biofuel production. The optimal manufacturing process for MAs synthesis shown in Figure 2 consists of AD, solid separation by belt filter press and dryer, VFAs dehydration by the extraction followed by distillation, hydrogenation, and MAs dehydration by molecular sieves followed by distillation. For CO₂ utilization, microalgae cultivation in open pond, harvesting by gravity settler, and dewatering by hollow filter membranes followed by centrifugation were selected as an optimal strategy. The products obtained from the biorefinery are ethanol, butanol, propanol, DDS, and microalgae. Their production rates are 32 mgal/y, 8 mgal/y, 14 mgal/y, 258 kt/y, and 49 kt/t, respectively. The NPV, TCI, TCOM, and utilities costs are \$124.7 MM, \$328 MM, \$31 MM, \$141.7 MM, respectively. By integrating microalgae process to MAs manufacturing process, CE are decreased from 117 kt/y to 11kt/y. The cost of integration of microalgae process into the MAs manufacturing is \$72 MM.

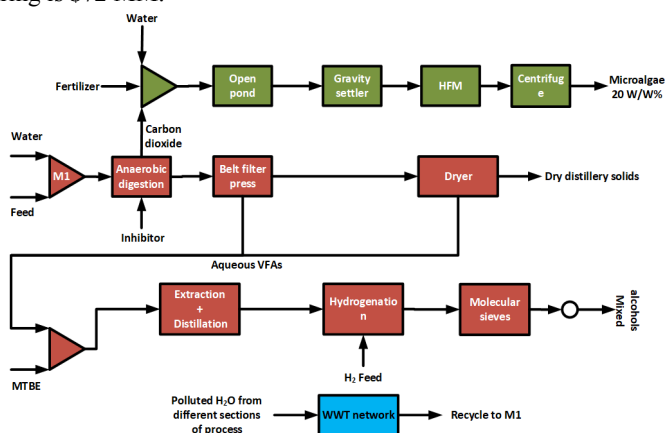


Figure 2. Optimal structure for mixed alcohol manufacturing process.

3.1. Minimum and maximum price of products and seaweed

The minimum selling price of products can be defined as the selling price of products that makes the NPV equal to zero. The estimated MESP of optimal design is 1.26 \$/gal at the current whole sale price of all products. Similarly, minimum selling price of higher alcohols, DDS, and microalgae are 2.3 \$/gal, 0.05 \$/kg, and 0.114 \$/kg. The maximum seaweed price (MSP) can be defined as the purchasing price of seaweed that makes the NPV equal to zero. The estimated MSPP of optimal design is 111 \$/ton, which is 1.63 times more than that of base case price.

3.2. Sensitivity analysis

Sensitivity analysis was performed to evaluate the effect of selling and purchasing prices of products and seaweed, respectively. Each sensitivity parameter was varied by $\pm 10\%$ from the base value. The result of sensitivity analysis is presented as a tornado charts in Figure 3. Result indicated selling price of heavier alcohols and seaweed price are most dominant parameter that effect MESP.

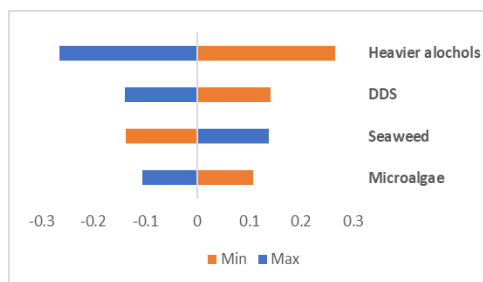


Figure 3. Sensitivity tornado chart for MESP.

4. Conclusion

An optimization-based framework for the MAs process synthesis as well as optimization of CE was proposed in this study. A rigorous techno-economic objective function (NPV) was used to investigate various economic parameters such as minimum selling price of products and MSP. The result indicated that biofuel production by VFAs route is viable; however, some challenges such as biomass price and its availability should be addressed before implementation of such biorefineries.

5. Acknowledgement

This research was supported through the Basic Science Research Program of the National Research Foundation of Korea (NRF) funded by the Ministry of Science and ICT (2017R1A2B4004500).

6. Reference

- Davis, R., Markham, J., Kinchin, C., Grundl, N., Tan, E.C.D., Humbird, D., 2016. Process Design and Economics for the Production of Algal Biomass: Algal Biomass Production in Open Pond Systems and Processing Through Dewatering for Downstream Conversion.
- Dickson, R., Ryu, J.-H., Liu, J.J., 2018. Optimal plant design for integrated biorefinery producing bioethanol and protein from *Saccharina japonica*: A superstructure-based approach. *Energy* 164, 1257-1270.
- Fasahati, P., Liu, J.J., 2015. Impact of volatile fatty acid recovery on economics of ethanol production from brown algae via mixed alcohol synthesis. *Chem. Eng. Res. Des.* 98, 107-122.
- Granda, C.B., Holtzapple, M.T., Luce, G., Searcy, K., Mamrosch, D.L., 2009. Carboxylate platform: The MixAlco process part 2: Process economics. *Appl. Biochem. Biotechnol.* 156, 107-124.
- Jiang, R., Ingle, K.N., Golberg, A., 2016. Macroalgae (seaweed) for liquid transportation biofuel production: What is next? *Algal Res.* 14, 48-57.
- Pham, T.N., Nam, W.J., Jeon, Y.J., Yoon, H.H., 2012. Volatile fatty acids production from marine macroalgae by anaerobic fermentation. *Bioresour. Technol.* 124, 500-503.
- Roesijadi, G., Jones, S.B., Zhu, Y., 2010. Macroalgae as a Biomass Feedstock : A Preliminary Analysis. *Analysis* 1-50.
- Zittel, W., Schindler, J., 2007. Crude oil the supply outlook.

Global Optimization of Counter Current Gasketed Plate Heat Exchanger

Natália Martins,^a Peam Cheali,^b André Costa,^{a,*} and Miguel Bagajewicz^c

^a*Rio de Janeiro State University (UERJ), Rua São Francisco Xavier, 524, Maracanã, CEP 20550-900, Rio de Janeiro, RJ, Brazil*

^b*Enserypower, 1339 Pracharad I, Bangsue, Bangkok, 10310, Thailand*

^c*School of Chemical, Biological and Materials Engineering, University of Oklahoma, Norman, Oklahoma, 73019, USA*

andrehc@uerj.br

Abstract

This paper presents a mathematical programming approach for the design of counter current gasketed plate heat exchangers. The objective function corresponds to the minimization of the heat transfer area and the set of constraints includes the thermofluid-dynamic equations for evaluation of film coefficients and pressure drops, the heat transfer rate equation, and bounds on velocities and pressure drops. We also consider discrete geometric options. The expressions of the objective function and constraints are reformulated into a linear form, without loss of rigor, i.e. the solution of the linear problem is exactly the same of the original one. Therefore, problems related to nonconvergence or multiple local optima with different values of objective function are avoided. An example of a typical design task is employed to illustrate the performance of the proposed approach.

Keywords: Optimization, Plate heat exchangers, Design

1. Introduction

Shell-and-tube heat exchangers are the main type of thermal equipment employed in chemical process plants. However, gasketed plate heat exchangers can be a better option in several thermal tasks. Despite its limitations for more severe operational conditions, plate heat exchangers present several advantages, e.g. film coefficients are higher, cleaning procedures are easier, they are less prone to fouling problems, etc. The design optimization problem seeks to identify the plate heat exchanger associated to the minimum area, according to the available pressure drops for both streams. In our case, the design variables are the number of plates and the plate size. There is no phase change along the heat transfer surface. The thermofluid-dynamic model is based on Kakaç et al.(2012), particularly employing the equations describe in Rao et al. (2005).

2. Problem Formulation

The heat exchanger model is composed of a set of nonlinear equations, encompassing the the heat transfer rate equation, correlations for the evaluation of the heat transfer coefficients and pressure drops, and performance constraints (in the presentation of the model here, the parameters are identified by a symbol ^ on top).

2.1. Heat transfer rate equation

The heat transfer rate equation is:

$$Q = UA_{req} \Delta \hat{T}_{lm} \quad (1)$$

where U is the overall heat transfer coefficient, A_{req} is the required area and $\Delta \hat{T}_{lm}$ is the logarithmic mean temperature difference. The expression of the overall heat transfer coefficient is:

$$U = \frac{1}{1/h_h + \hat{R}f_h + \hat{t}/\hat{k}w + \hat{R}f_c + 1/h_c} \quad (2)$$

where $\hat{R}f$ is the fouling factor, \hat{t} is the plate thickness, $\hat{k}w$ is the thermal conductivity of the plate material.

2.2. Convective heat transfer coefficients

The Nusselt number can be evaluated from the Reynolds and Prandtl numbers through the following correlation, where the index sSt represents the hot and cold streams ($sSt \in \{h,c\}$):

$$Nu_{sSt} = \hat{C} Re_{sSt}^{\hat{a}} \hat{Pr}_{sSt}^{\hat{b}} \quad (3)$$

where the Reynolds number is expressed in relation to the hydraulic diameter:

$$Re_{sSt} = G_{sSt} \hat{D}_{hyd} / \hat{\mu}_{sSt} \quad (4)$$

The expressions of mass flux is:

$$G = \frac{\hat{m}_{sSt} / (Nch / 2)}{\hat{b} Lw} \quad (5)$$

where \hat{m}_{sSt} is the mass flow rate, Nch is the total number of channels, and \hat{b} is the flow channel gap.

2.3. Pressure drops

The pressure drop encompasses the head loss in the flow channels and in the distribution plate orifice:

$$\Delta P_{sSt} = f_{sSt} \frac{(Lp + Dp)}{\hat{D}_{hyd}} \frac{G_{sSt}^2}{2\hat{\rho}_{sSt}} + 1.4 \frac{[\hat{m}_{sSt} / (\pi Dp^2 / 4)]^2}{2\hat{\rho}_{sSt}} \quad (6)$$

where Dp f_{sSt} is the Darcy friction factor:

$$f_{sSt} = \hat{K} Re_{sSt}^{-\hat{n}} \quad (7)$$

2.4. Performance constraints

The heat transfer area must be higher the required area according to a previously established “excess area” parameter:

$$A_{req} \leq A[100 / (100 + \hat{A}_{exc})] \quad (8)$$

where the heat transfer area depends on the plate features and the total number of plates:

$$A = \hat{\phi}LwLp(Nt - 2) \quad (9)$$

where $\hat{\phi}$ is the enlargement factor of the plate. The pressure drop of both fluids and flow velocities must be bounded according to the available values for both streams:

$$\Delta P_{sSt} \leq \Delta \hat{P}_{sSt}^{max} \quad (10)$$

$$\hat{v}^{min} \leq G_{sSt} / \hat{\rho}_{sSt} \leq \hat{v}^{max} \quad (11)$$

2.5. Objective function

The heat transfer area must be higher the required area according to a previously The objective function corresponds to the minimization of the heat transfer area:

$$\min A \quad (12)$$

3. Discrete Options

It is important to observe that the design variables are discrete; therefore, its representation in the model formulation is associated to a set of binary variables, as follows:

$$Nt = \sum_{snt=1}^{sntmax} p\hat{N}t_{snt} yNt_{snt} \quad (13)$$

$$Lp = \sum_{sp=1}^{spmax} p\hat{L}p_{sp} yP_{sp} \quad (14)$$

$$Lw = \sum_{sp=1}^{spmax} p\hat{L}w_{sp} yP_{sp} \quad (15)$$

where Nt is the total number of plates (discrete options $p\hat{N}t_{snt}$ associated to the binary variables yNt_{snt}), Lp and Lw are the plate effective length and width (discrete options $p\hat{L}p_{sp}$ and $p\hat{L}w_{sp}$ associated to the binary variables yP_{sp}). Since one of the options must be selected in the solution, these constraints are complemented by:

$$\sum_{snt=1}^{sntmax} yNt_{snt} = \sum_{sp=1}^{spmax} yP_{sp} = 1 \quad (16)$$

4. Problem Reformulation

The reformulation of the problem to a linear structure employs the procedure applied by Gonçalves et al. (2017) for the optimization shell-and-tube heat exchangers. This approach involves three steps: (i) Substitution of the binary representation of the discrete design variables (Eq. (13-16)) in the heat exchanger model equations and objective function (Eq. 1-12), (ii) Reorganization of the resultant mathematical expressions in a product of binaries, and (iii) Substitution of the product of binaries by a set of linear inequalities.

The procedure is illustrated here through the substitution of the design variables in Eq. (5) by their corresponding representation using binary variables as follows:

$$G_{sSt} = \frac{[2\hat{m}_{sSt} / \sum_{snt=1}^{sntmax} (p\hat{N}t_{snt} - 1)yNt_{snt}]}{(\hat{b} \sum_{sp=1}^{spmax} p\hat{L}w_{sp}yP_{sp})} \quad (17)$$

Due to the nature of the binary variables and the fact that only one option can be selected (Eq. (16)), this expression is equivalent to the following representation using product of binaries:

$$G_{sSt} = \frac{2\hat{m}_{sSt}}{\hat{b}} \sum_{snt=1}^{sntmax} \sum_{sp=1}^{spmax} \frac{1}{p\hat{L}w_{sp} (p\hat{N}t_{snt} - 1)} yNt_{snt} yP_{sp} \quad (18)$$

Substituting the product of binaries by a continuous nonnegative variable $w_{snt,sp}$, together with the inclusion of a set of auxiliary inequalities, Eq. (18) can be substituted by the following set of linear relations:

$$G_{sSt} = \frac{2\hat{m}_{sSt}}{\hat{b}} \sum_{snt=1}^{sntmax} \sum_{sp=1}^{spmax} \frac{1}{p\hat{L}w_{sp} (p\hat{N}t_{snt} - 1)} w_{snt,sp} \quad (19)$$

$$w_{snt,sp} \leq yNt_{snt} \quad (20)$$

$$w_{snt,sp} \leq yP_{sp} \quad (21)$$

$$w_{snt,sp} \geq yNt_{snt} + yP_{sp} - 1 \quad (22)$$

5. Mixed-Integer Linear Programming Formulation

The application of the procedure described above yields the following linear design problem (complemented by Eqs. (10,11, 16, 19-22):

$$\min \sum_{snt=1}^{sntmax} \sum_{sp=1}^{spmax} \hat{\phi} pNt_{snt} pLw_{sp} pLp_{sp} w_{snt,sp} \quad (23)$$

subject to:

$$\hat{Q}_c \left\{ \sum_{sSt}^{sntmax} \sum_{snt=1}^{spmax} \left[\frac{\hat{D}hyd^{\hat{a}-1}}{\hat{C} \hat{k}_{sSt} \hat{p}r_{sSt}^{\hat{b}}} \left(\frac{\hat{b} \hat{\mu}_{sSt}}{2 \hat{m}_{sSt}} \right)^{\hat{a}} p \hat{L} w_{sp} (p \hat{N}t_{snt} - 1)^{\hat{a}} w_{snt,sp} + \hat{R}f_{sSt} \right] + \frac{\hat{t}}{\hat{k}w} \right\} \leq \left(\sum_{snt=1}^{sntmax} \sum_{sp=1}^{spmax} p \hat{N}t_{snt} p \hat{L} w_{sp} p \hat{L} p_{sp} w_{snt,sp} \right) \Delta \hat{T}_m \left(\frac{100}{100 + \hat{A}_{exc}} \right) \quad (24)$$

$$\Delta P_{sSt} = \left(\frac{\hat{K}}{2 \hat{D}hyd \hat{\rho}_{sSt}} \right) \left(\frac{\hat{b} \hat{\mu}_{sSt}}{2 \hat{m}_{sSt} \hat{D}hyd} \right)^{\hat{n}} \left(\frac{2 \hat{m}_{sSt}}{\hat{b}} \right)^2 \sum_{snt=1}^{sntmax} \sum_{sp=1}^{spmax} \left[p \hat{L} w_{sp} (p \hat{N}t_{snt} - 1) \right]^{\hat{n}-2} \left(p \hat{L} p_{sp} + p \hat{D} p_{sp} \right) w_{snt,sp} + \left(\frac{11.2 \hat{m}_{sSt}^2}{\hat{\rho}_{sSt} \pi^2} \right) \sum_{sp=1}^{spmax} \left(\frac{1}{p \hat{D} p_{sp}^4} \right) y P_{sp} \quad (25)$$

6. Numerical Results

The performance of the proposed approach is illustrated through the design of a plate heat exchanger for the thermal task described in Table 1, based on Kakaç and Liu (2002). The thermal conductivity of the plate material is 17.5 W/m°C) and the plate thickness is 0.6 mm. The hydraulic diameter associated to the heat exchanger is 4.8 mm, the enlargement factor of the area is 1.25 and the plate gap is 3 mm. The available pressure drop is 600 kPa for both streams. The fouling factor is 5·10⁻⁵ m²K/W for the hot stream and it is null for the cold stream. The flow velocity must be between 0.4 m/s and 2.0 m/s for both streams. The minimum excess area is assumed equal to 10%.

The search space corresponds to 10 plate sizes with widths from 0.4 m to 1.3 m and lengths from 1.1 m to 2.0 m, associated to increments of 0.1 m. Additionally, an extra plate size is inserted in the search space based on a solution proposed by Kakaç et al. (2012) with width and length equal to 0.63 m and 1.35 m. The number of plates in the search space vary from 50 to 150 plates. The corresponding set of port diameters corresponds to an area of each port equivalent to 3% of the total area of the plate. The parameters associated to the correlations employed from Rao et al. (2005) are $\hat{C} = 0.218$, $\hat{a} = 0.65$, $\hat{b} = 1/3$, $\hat{K} = 21.41$, $\hat{n} = 0.301$.

Table 1: Stream data for the optimization problem.

Stream	m (kg/s)	T_i (°C)	T_o (°C)	ρ (kg/m ³)	Cp (J/kg°C)	μ (mPa·s)	k (W/mK)
Hot	140	65	45	985	4183	0.509	0.645
Cold	140	22	42	995	4178	0.766	0.617

The solution obtained using the proposed design optimization procedure is compared in Table 2 with the solution based on Kakaç et al. (2012) for the same task.

Table 2: Stream data for the optimization problem.

Solution	A (m ²)	A _{req} (m ²)	N _t	L _p (m)	L _w (m)	U (W/m ² °C)	ΔP hot (kPa)	ΔP cold (kPa)
Proposed solution	102.06	92.54	96	1.35	0.63	5503	490	546
Literature	111.63	95.54	105	1.35	0.63	5330	424	471

The results in Table 2 indicate that the optimization found a solution with a smaller area, associated to a reduction of 8.6% in relation to the solution found in the literature data. The plate size is identical in both solutions, but the solution obtained using the proposed procedure has a smaller number of plates (i.e. the solution from the literature has more plates than necessary for a given excess area of 10%).

7. Conclusions

This paper presented a mathematical programming formulation for the optimization of countercurrent plate heat exchangers. Starting from a set of nonlinear equations of the heat exchanger modelling, mathematical manipulations are applied to yield a mixed-integer linear programming problem. Therefore, the global optimum of the design solution can be found without any drawbacks associated to nonconvergence issues. Due to the flexibility of the proposed approach other thermal tasks could also be addressed using the same mathematical scheme (e.g. vaporization or condensation). Possible obstacles to extend the proposed approach would be presence of thermofluidynamic models based on mathematical relations with variables that cannot be explicitly represented in relation to the design variables.

Acknowledgments

André L. H. Costa would like to thank the National Council for Scientific and Technological Development (CNPq) for the research productivity fellowship (Process 311225/2016-0) and the Rio de Janeiro State University through the Prociência Program.

References

- C.O. Gonçalves, A.L.H. Costa, M.J. Bagajewicz, 2017, Shell and Tube Heat Exchanger Design Using Mixed-Integer Linear Programming, *AIChE Journal*, 63, 6, 1907-1922.
- S. Kakaç, H. Liu, A. Pramuanjaroenkij, 2012, *Heat Exchangers: Selection, Rating, and Thermal Design*, CRC Press.
- B.P. Rao, B.Sunden, S.K. Das, 2005, An Experimental and Theoretical Investigation of the Effect of Flow Maldistribution on the Thermal Performance of Plate Heat Exchangers, *Transactions of the ASME*, 127, 332-343.

Efficient robust nonlinear model predictive control via approximate multi-stage programming: A neural networks based approach

Wachira Daosud^a, Paisan Kittisupakorn^b, Miroslav Fikar^c, Sergio Lucia^d and Radoslav Paulen^{c,*}

^a*Department of Chemical Engineering, Faculty of Engineering, Burapha University, Chonburi 20131, Thailand*

^b*Department of Chemical Engineering, Faculty of Engineering, Chulalongkorn University, Bangkok 10330, Thailand*

^c*Faculty of Chemical and Food Technology, Slovak University of Technology in Bratislava, Bratislava 812 37, Slovakia*

^d*Laboratory of Internet of Things for Smart Buildings, Technische Universität Berlin, Einstein Center Digital Future, Berlin 10587, Germany*
radoslav.paulen@stuba.sk

Abstract

Multi-stage nonlinear model predictive control (msNMPC) is a robust control strategy based on the description of the uncertainty propagation through a dynamic system via a scenario tree and is one of the least conservative approaches to robust control. The computational complexity of the msNMPC, however, grows with respect to the number of uncertainties and with respect to the length of the prediction horizon. This paper presents a new approach, where the optimal cost-to-go function is approximated after a specific point in time, here in particular by neural networks, so the independent branches do not have to be optimized but are approximated. The optimization might be casted over the robust horizon only, which reduces the computational burden, but still guarantees robust satisfaction of the constraints. Moreover, this approach allows to consider any length of the prediction horizon for the same computational cost. The neural network models are trained offline using the optimal profiles in all branches of the scenario tree. The potential of the proposed approach is demonstrated by simulation studies on a semi-batch reactor.

Keywords: Nonlinear model predictive control, robust control, neural networks.

1. Introduction

Robust nonlinear model predictive control (NMPC) methods aim at overcoming the limitations of conventional NMPC w.r.t. the influence of model errors and presence of uncertainty. Very popular are min-max approaches (Witsenhausen, 1968) despite that these approaches are quite conservative because they ignore the fact that new measurements will be available in the future and that the future control actions can be adapted accordingly. Another possibility to formulate the NMPC controller within the framework of stochastic optimization. Such a formulation leads to a multi-stage NMPC (msNMPC) (Lucia et al., 2013), which has shown very promising results

Acknowledgements: Support from the SAIA, n.o., the national scholarship programme of the Slovak Republic and the Slovak Research and Development Agency under the project APVV 15-0007 are gratefully acknowledged.

for challenging nonlinear examples. Nevertheless, the main disadvantage of the msNMPC lies in solving a large-scale optimization problem. The size of the optimization problem grows exponentially with the length of the prediction horizon and with the number of uncertainties. To overcome this problem, deep neural networks (NNs) (LeCun et al., 2015) were proposed to approximate the NMPC policy (Lee and Lee, 2005) or the msNMPC policy (Karg and Lucia, 2018).

A neural networks-based (NN-based) msNMPC is investigated in this paper. The NNs are used to approximate the optimal cost-to-go functions of different scenarios. Then, after a specific point in time, the independent branches do not have to be optimized but are approximated using the NNs, which results in the reduction of the computational burden, that the approach retains the same robustness guarantees as the standard msNMPC. To demonstrate the potential of the proposed strategy, simulation tests are performed and the control performance of the approach is compared to standard NMPC and msNMPC approaches.

2. Multi-stage NMPC

Multi-stage NMPC is a robust NMPC strategy that is based on the description of the uncertainty propagation through a dynamic system by a tree of discrete scenarios (Lucia et al., 2013). Each branch of the tree represents an evolution of the system states under a certain realization of the uncertainty. The main advantage of this formulation is that the availability of information provided by the future measurements is taken into account, so that the future control inputs depend on the future knowledge and can be adapted w.r.t. the expected realizations of the uncertainty.

The optimization problem to be solved at each sampling instant using the msNMPC reads as:

$$\min_{x_{k+1}^j, u_k^j, \forall (j,k) \in I_{N_p}} \sum_{i=1}^N \omega_i \overbrace{\left(\sum_{k=0}^{N_p-1} L(x_{k+1}^j, u_k^j) + \phi(x_{N_p}^j) \right)}^{J_i(x_0)}, \quad \forall x_{k+1}^j, u_k^j \in S_i, \quad (1a)$$

$$\text{s.t. } x_{k+1}^j = f(x_k^{p(j)}, u_k^j, d_k^{r(j)}), \quad \forall (j, k+1) \in I_{N_p}, \quad (1b)$$

$$g(x_{k+1}^j, u_k^j) \leq 0, \quad \forall (j, k+1) \in I_{N_p}, \quad (1c)$$

$$u_k^j = u_k^l \text{ if } x_k^{p(j)} = x_k^{p(l)}, \quad \forall (j, k), (l, k) \in I_{N_p}, \quad (1d)$$

where, at stage $k+1$ and position in the tree j , the state vector x_{k+1}^j depends on $x_k^{p(j)}$, u_k^j and $d_k^{r(j)}$, i.e., the parent state vector, the vector of control inputs, and the realization of the uncertainty, respectively, via the system dynamics equations (1b). The scenario tree originates at the root node x_0 and is defined with the same number (s) of branches at each node, given by $d_k^{r(j)} \in \{d_k^1, d_k^2, \dots, d_k^s\}$, and with the index set I_{N_p} . Constants N , N_p are the number of scenarios and the length of the prediction horizon, respectively. The functions $L(\cdot)$ and $\phi(\cdot)$ denote stage and terminal costs, respectively. The constraints on inputs and states are denoted by $g(\cdot)$. Parameter $\omega_i \geq 0$ is a weighting coefficient of the i th scenario (S_i) and is chosen based on the relative importance of the scenario while $\sum_{i=1}^N \omega_i = 1$. The constraints (1d) are non-anticipativity constraints, which denote that all the control inputs that branch at the same parent node must be equal. The branching of the tree stops at a certain point, which is denoted as the robust horizon of the length N_r , which can be set to 1 or 2 in practice (Lucia et al., 2013). Note that after N_r , all the scenarios become independent.

3. Neural networks-based multi-stage NMPC

The size of the optimization problem grows exponentially with the length of the prediction horizon and with the number of uncertainties. The main idea of this work is to use NNs (LeCun et al., 2015; Daosud et al., 2017; Kittisupakorn et al., 2017) to approximate the optimal cost-to-go

function of the individual scenarios such that the contribution of the independent scenarios can be approximated after the robust horizon when solving (1). This allows simultaneously for efficient real-time execution, for robust constraint satisfaction, and for an efficient training of NNs, since only an optimization over a single branch is needed therein. The NN is trained to give an approximate cost $\tilde{J}_i^*(x_{k,p}, W, b)$ of the scenario S_i , where $x_{k,p}$ is a training point for which (1) is solved. The optimal weights (W) and biases (b) for each neuron are found via

$$\min_{W,b} \sum_{p=1}^{N_t} (J_i^*(x_{k,p}) - \tilde{J}_i^*(x_{k,p}, W, b))^2, \quad (2)$$

where N_t is the number of data pairs $(J_i^*(x_{k,p}), x_{k,p})$.

The NN-based msNMPC then approximates the problem (1) as:

$$\min_{x_{k+1}^j, u_k^j, \forall (j,k) \in I_{N_c}} \sum_{i=1}^N \omega_i \left(\sum_{k=0}^{N_c-1} L(x_{k+1}^j, u_k^j) + \tilde{J}(x_{N_c}^j) \right), \quad x_{k+1}^j, u_k^j \in S_i, \quad (3a)$$

$$\text{s.t. Eqs. (1b)–(1d),} \quad \forall (j, k+1) \in I_{N_c}, \quad (3b)$$

$$g_{SS}(x_{k+1}^j) \leq 0, \quad \forall (j, k+1) \in I_{N_c}, \quad (3c)$$

where $N_c \in \{N_r, \dots, N_p - 1\}$ is the length of the reduced prediction horizon and functions $g_{SS}(\cdot)$ represent the so-called safe sets (Rosolia and Borrelli, 2017), which constrain the states such that these are in the range of the data in the training set of the NNs. In practice, construction of suitable safe sets can be cumbersome, so one can then decide to drop the safe sets entirely from the formulation (3) or replace them with tightened $g(\cdot)$. This however requires tuning of N_c by increasing it to guarantee recursive feasibility of the problem. This path is examined in this study.

4. Case study

We use a challenging case study from the chemical engineering domain, i.e., a semi-batch reactor that is equipped with a cooling jacket, where the cooling jacket inlet temperature is controlled by a thermostat (Thangavel et al., 2015). An exothermic reaction of A and B produces C. The model includes mass balances for the reactor content (expressed through reactor volume V and species concentrations c_A , c_B , and c_C) and energy balances of the reaction mixture, the reactor jacket and the thermostat (expressed using the temperature of the reaction mixture T , cooling jacket T_J , and jacket inlet temperature $T_{J,in}$). The control inputs are the feed rate of the component B and the set point of jacket inlet temperature, summarized in $u = (\dot{V}_{in}, T_{J,in,set})^T$. The detailed mathematical model with all parameters and considered constraints can be found in Thangavel et al. (2015).

The control goal is to maximize the concentration of C in the fixed batch time $t_f = 1,800$ s. Thus, a shrinking-horizon strategy is used and the sampling time is taken as 120 s. The constraints on T and V must be respected despite a $\pm 30\%$ uncertainty in the reaction enthalpy H and in the reaction rate k , with nominal values $H_{nom} = -355 \text{ kJ mol}^{-1}$ and $k_{nom} = 3.35 \times 10^{-7} \text{ m}^3 \text{ mol}^{-1} \text{ s}^{-1}$.

5. Results

The dynamic optimization problems are solved using orthogonal collocation on finite elements using CasADi (Andersson et al., 2012). The nonlinear programs are solved via Ipopt (Wächter and Biegler, 2006). The plant response is simulated using a 4th-order Runge-Kutta scheme. All the results are obtained on a workstation with Intel i7 running at 2.4 GHz with 8 GB RAM.

Neural networks with several hidden layers (deep NNs) are employed due to the theoretical evidence of outperforming the shallow NNs (Safran and Shamir, 2016). For the approximation of

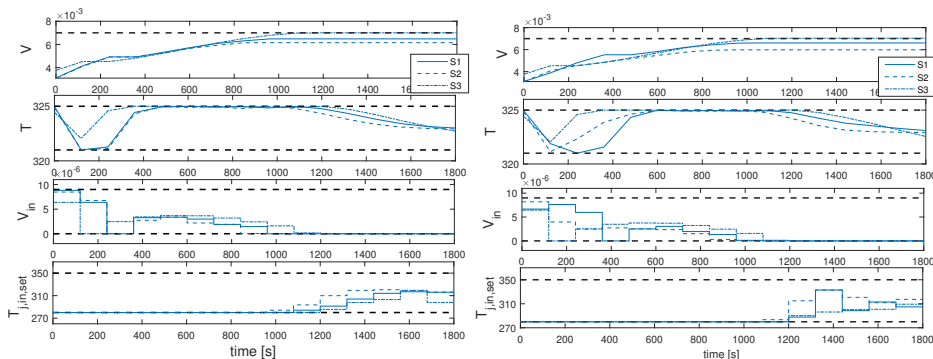


Figure 1: Input/state trajectories for $[S_1, S_2, S_3]$; Left: standard NMPC, right: NNs-based NMPC.

Table 1: Performance comparison standard NMPC vs. NNs-based NMPC for $[S_1, S_2, S_3]$.

Algorithm	$c_C(t_f)$ [mol m^{-3}]	Cons. viol. [$\text{m}^3 \text{s}^{-1}$]	Cons. viol. [K s^{-1}]
standard NMPC	[379.1, 470.8, 525.9]	$[0, 0, 1.03] \times 10^{-6}$	$[0, 6.48, 0] \times 10^{-8}$
NNs-based NMPC	[378.3, 470.0, 526.5]	$[0, 0, 1.64] \times 10^{-5}$	$[0, 0, 9.39] \times 10^{-4}$

cost-to-go functions, a state vector $x = (V, c_A, T, T_j, T_{j,in}, t)^T$ is used as an input to the NN, which represents the minimal number of states (all other states can be obtained as combinations of these states) and the current time t is considered due to the problem nature (batch, shrinking horizon).

The NNs are trained with the data generated for 360 batches, where the initial conditions are randomly varied, w.r.t. the ones in Thangavel et al. (2015), between $\pm 5 \text{K}$, $\pm 5 \times 10^{-4} \text{m}^3$, and $\pm 50^\circ \text{C mol m}^{-3}$ for the temperatures, volume, and concentration of A, respectively. 75 % of the 34,560 data points is used for training and the remaining 25 % for testing. The structure of NN is selected based on the MSE criterion (Kittisupakorn et al., 2009). The activation function is the tanh function. The number of hidden nodes is varied between 2–34. The resulting structure of the NNs consists of 2 hidden layers with different number of nodes for different scenario (S_i).

We compare the performance of the standard NMPC and NNs-based NMPC for some selected scenarios. Figure 1 shows trajectories of constrained states and control inputs in $S_1 = (H_{min}, k_{min})$, $S_2 = (H_{nom}, k_{nom})$, and $S_3 = (H_{max}, k_{max})$. The optimal solution tries to feed B as much as possible at the beginning of the batch. Then the feed rate is adjusted to respect the temperature constraints. At these phases cooling is maximal. Towards the end of the batch, feeding is stopped since either maximal volume is reached or any further feeding only dilutes the reaction mixture and decreases the final concentration of C. At this phase, cooling is adjusted to respect the constraints on T . It can be seen that the use of the NNs-based NMPC results in similar state and input trajectories as the standard NMPC. Both control methods result in similar final concentrations of C (see Tab 1), while the constraint violations occur only marginally, due to numerical reasons. The average CPU times per sampling time are 0.35 s and 0.14 s for standard and NN-based NMPC, respectively.

For the msNMPC, we use $N_r = 1$. Nine scenarios are considered with all the combinations of extremal and nominal values of the uncertain parameters. As we do not use safe sets in this work, a tuning has to be done for the value of N_c . The tuning procedure is illustrated in Fig. 2, where state and input trajectories resulting from the use of NN-based msNMPC are shown for different values of N_c under the most extreme scenario (H_{min}, k_{max}), i.e., the most exothermic and the fastest reaction. As the NN-based msNMPC is myopic from its nature, large constraint violations can occur if N_c is too small. While the msNMPC would be initialized with $N_p = 15$, the NN-based

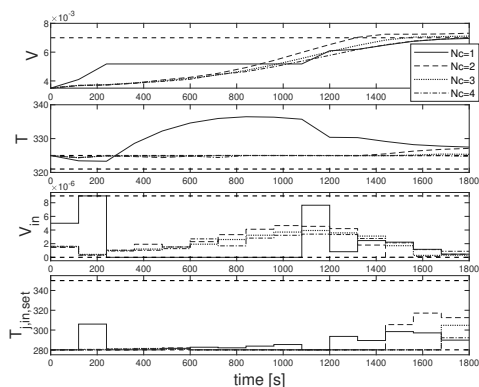


Figure 2: Input/state profiles using the NN-based msNMPC for (H_{min}, k_{max}) and different N_c .

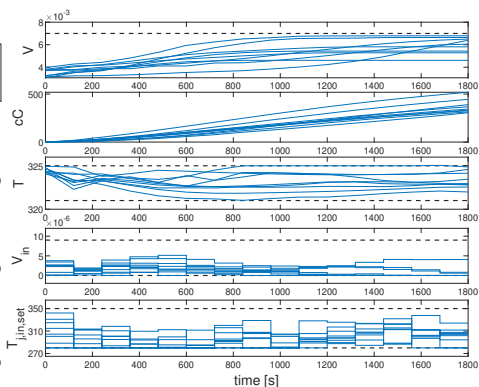


Figure 3: Input/state profiles using the NN-based msNMPC for the 9 scenarios.

Table 2: Performance comparison msNMPC vs. NN-based msNMPC averaged over 9 scenarios.

Algorithm	$c_c(t_f)$ [mol m^{-3}]	Cons. viol. [$\text{m}^3 \text{s}^{-1}$]	Cons. viol. [K s^{-1}]
msNMPC	354.4	3.72×10^{-10}	1.36×10^{-2}
NN-based msNMPC	371.5	3.50×10^{-4}	0

msNMPC is able to robustly satisfy the constraints with $N_c = 4$.

Figure 3 shows the state and input trajectories resulting from the use of the NN-based msNMPC in all 9 scenarios. The trajectories show great similarity with the trajectories obtained by msNMPC.

The performance comparison averaged over the 9 scenarios considered is shown in Tab. 2 for msNMPC and NN-based msNMPC. Use of both algorithms results in certain minor constraint violations while the control performance is better when using NN-based msNMPC, which is attributed to slightly greater constraints violations. The optimization problems solved by the msNMPC have at most 5,686 optimization variables and are solved in average in 2.19 s, while NN-based msNMPC requires 0.95 s of CPU time in average for solving optimization problems with at most 1,528 variables.

Figure 4 shows input and state trajectories obtained using NN-based msNMPC for 40 batches with different values of the uncertain parameters being randomly generated with uniform distribution ($\pm 30\%$) around the nominal values. It can be seen that the performance is satisfactory for all batches and that the constraints are consistently respected, though with minor violations. The msNMPC and NN-based msNMPC achieve the maximum concentration of product C as 313.6 mol m^{-3} and 297.6 mol m^{-3} , respectively. The 5% performance loss of NN-based NMPC is attributed to the interpolation inaccuracy of the neural networks and represents the price to pay for the computational efficiency.

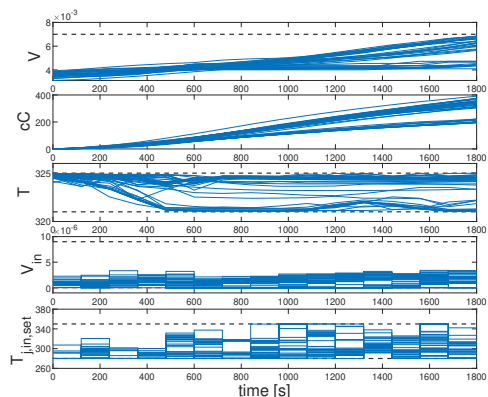


Figure 4: Input/state trajectories for 40 batches with random uncertainties (NN-based msNMPC).

The developed NN-based msNMPC scheme shows a great promise regarding an efficient implementation of the robust NMPC schemes. The results obtained on the challenging case study are encouraging, despite the fact that certain portion of performance must be given up for robust constraint satisfaction. This aspect can be further improved when safe sets are used. Another way of performance improvement, which we will concentrate on in our further studies, is the reduction of the sampling time. Our preliminary results show that using NN-based msNMPC and safe sets, one can reduce the sampling time up to 12 s and N_c to 1, while the CPU time reduces to 0.8 s in the worst case. Note that the use of msNMPC here requires 15 s for execution in the worst case.

6. Conclusions

Non-conservative robust NMPC control methods, such as msNMPC, are challenged by a large computation burden. To deal with this problem, an NN-based msNMPC is proposed. The idea pursued is to simplify the optimization problems of the msNMPC by approximating the cost-to-go functions of independent scenarios (after the robust horizon of the msNMPC). In this work, neural networks are used for this purpose. The results show that the proposed approach obtains similar results compared to the msNMPC, which is demonstrated on a challenging case study from chemical engineering domain. Most importantly, the NN-based msNMPC shows superior performance in terms of computational time. Thus the presented approach is a promising method of real-time implementation of msNMPC in case of complex control problems with long prediction horizons, large number of parametric uncertainties and short sampling times. Our future work will consist in improving the closed-loop performance of the proposed approach by the use of safe sets.

References

- J. Andersson, J. Åkesson, M. Diehl, 2012. Casadi: A symbolic package for automatic differentiation and optimal control. In: Recent advances in algorithmic differentiation. Springer, pp. 297–307.
- W. Daosud, J. Thammasato, P. Kittisupakorn, 2017. Neural network based modeling and control for a batch heating/cooling evaporative crystallization process. *Eng J* 21 (1), 127–144.
- B. Karg, S. Lucia, 2018. Efficient representation and approximation of model predictive control laws via deep learning. arXiv preprint arXiv:1806.10644.
- P. Kittisupakorn, P. Somsong, M. A. Hussain, W. Daosud, 2017. Improving of crystal size distribution control based on neural network-based hybrid model for purified terephthalic acid batch crystallizer. *Eng J* 21 (7), 319–331.
- P. Kittisupakorn, P. Thitiyasook, M. Hussain, W. Daosud, 2009. Neural network based model predictive control for a steel pickling process. *Journal of Process Control* 19 (4), 579–590.
- Y. LeCun, Y. Bengio, G. Hinton, 2015. Deep learning. *Nature* 521 (7553), 436.
- J. M. Lee, J. H. Lee, 2005. Approximate dynamic programming-based approaches for inputoutput data-driven control of nonlinear processes. *Automatica* 41 (7), 1281–1288.
- S. Lucia, T. Finkler, S. Engell, 2013. Multi-stage nonlinear model predictive control applied to a semi-batch polymerization reactor under uncertainty. *Journal of Process Control* 23 (9), 1306–1319.
- U. Rosolia, F. Borrelli, 2017. Learning model predictive control for iterative tasks: a computationally efficient approach for linear system. *IFAC-PapersOnLine* 50 (1), 3142–3147.
- I. Safran, O. Shamir, 2016. Depth-width tradeoffs in approximating natural functions with neural networks. arXiv preprint arXiv:1610.09887.
- S. Thangavel, S. Lucia, R. Paulen, S. Engell, 2015. Towards dual robust nonlinear model predictive control: A multi-stage approach. In: American Control Conference 2015. pp. 428–433.
- A. Wächter, L. T. Biegler, 2006. On the implementation of an interior-point filter line-search algorithm for large-scale nonlinear programming. *Mathematical programming* 106 (1), 25–57.
- H. Witsenhausen, 1968. A minimax control problem for sampled linear systems. *IEEE Transactions on Automatic Control* 13 (1), 5–21.

Optimal design of multi-stage depressurization systems using dynamic modelling

Juan Quattordio^a, Sander Groenendijk^a, Robert Kedzierski^a, Hans Göebel^{a,*}

^a Fluor, Taurusavenue 155, Hoofddorp 2132 LS, The Netherlands

hans.goebel@fluor.com

Abstract

High pressure process facilities like hydrocrackers and solvent deasphalting units in most cases are equipped with a system to quickly discharge the inventory in case of an emergency, and by doing so reduce the pressure to safe values in a short amount of time. Multi-stage depressurization is usually applied to cope with additional boundary conditions, such as high reliability and the limited capacity of the downstream flare system. In this paper, a design development is described using detailed dynamic simulation studies to come to an optimal design of such a system. The result of the work described is a structured design procedure for use on large scale design projects.

Keywords: depressurization, dynamic simulation, solvent deasphalting unit, hydrocracker

1. Introduction

Process facilities handling vapor or LPG at high pressures are in most cases equipped with a system to quickly discharge the inventory in case of an emergency in order to reduce the pressure and by doing so reducing the risk of fire and explosion and consequential damages.

Typical examples of this are: Hydrotreaters, Hydrocrackers and LPG plants.

The example presented in this study is related to an Solvent Deasphalting Unit, which uses LPG as solvent for the liquid-liquid extraction of the asphalt components in the crude oil vacuum distillation residue. [Sattarin, 2006]

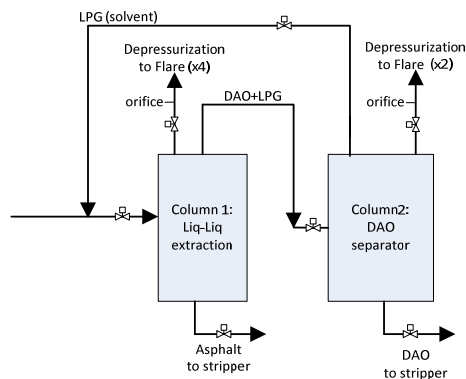


Figure 1: block flow diagram of SDA unit

The target of the system depressurization design is typically to reduce the pressure to 8 bar or 50% of the operating pressure, whichever lower in a period of 15 minutes time. [API, 2014]

For some designs this can be solved with readily available tools like the Aspen HYSYS depressurization module, or the HYSYS blowdown module [AspenTech, 2018]. An example of this is the depressurization of a hydrocracker: for this unit the depressurization calculations can be solved in a relatively simple way by means of the standard utilities. A typical hydrocracker example is shown on figures 2A and 2B.

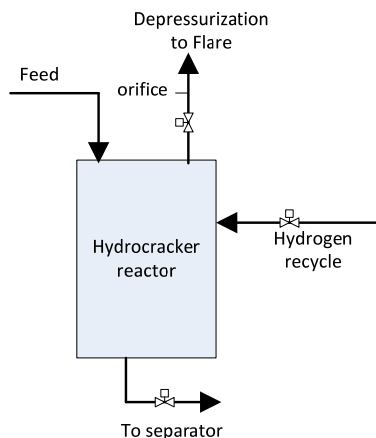
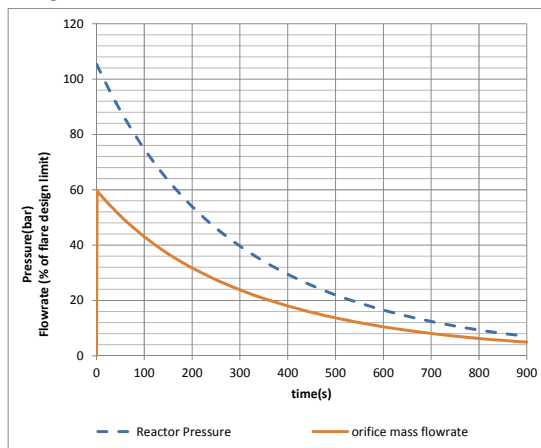


Figure 2A

Figure 2A: the figure shows a typical block flow diagram of a Hydrocracker unit reactor. Figure 2B: a typical depressurization curve for a hydrocracker reactor is shown. The fluid is depressurized from an initial pressure of 105 barg to a final pressure of 7 barg in 15 minutes. As can be observed, this can be achieved in one step, via a single valve. The calculation has been done with the HYSYS blowdown module.

Figure 2B



The depressurization calculation of the system becomes more difficult when, as in the case of SDA process, dealing with liquid LPG at supercritical conditions, since a single valve design would imply a too high initial peak, which in turn would have a significant economic impact in the flare system design i.e. flare header and flare stack will increase in size. In the case of connecting to existing flares, it would imply to exceed the flare system capacity.

In order to cope with this constraint, multistage depressurization is applied.

2. A dynamic simulation study applied to a depressurization system

The design procedure of the SDA unit multistage depressurization system is discussed when using HYSYS dynamic simulation. Additionally, the benefits of this method compared with the standard HYSYS depressurizing utilities are highlighted.

2.1 Definition of the system

The evaluated system consists of two columns containing liquid LPG at high pressure (see Figure 1), which will be depressurised in parallel. In order to reduce the peak flowrate released to the flare, multiple valves are installed i.e. 4 on-off valves for the first column and 2 on-off valves for the second. The depressurized fluid is sent to flare via the flare header and knock out drum, which allows the liquid LPG collected during the depressurization case.

2.2 Staggered Depressurization Scenarios (multistage depressurization)

In industrial plants, the flare has a maximum capacity of gas that it can burn off. Exceeding this capacity can result in incomplete combustion and high pressure built-up exceeding the design conditions of the system. The soot produced in incomplete combustion could potentially block the flare. Hence, the flow of flammable gases to the flare needs to be limited below the maximum capacity.

In a standard depressurizing setup, peak flow is reached at the start, when the pressure is highest.

To reduce the peak flow, pressure is often relieved from a vessel stepwise: multiple valves, with smaller openings than the original single valve, are connected to the vessel. These valves are opened at different times. In this way, the initial peak flow that would be present in the original single valve setup, is distributed over several peaks. Consequently, the pressure can be decreased by the same amount in the same time as in the non-staggered case, without exceeding the maximum flare capacity. This is called staggered depressurization.

This method is also applied to plants with a high amount of equipment, where multiple units are usually connected to the same flare. This can create a high total flow to the flare. This total flow can be reduced by using a stepwise method, similar as described above for a single vessel. A staggered pressure relief scenario is created for the multiple vessel system by opening the valves of the several units at different times.

2.3 Sectionalizing

Sectionalizing is applied in order to limit the inventory release in the case of leakage, e.g. if only one column needs to be depressurized. This can reduce for some design cases the required capacity of the emergency depressurization system, considering that the case of all sections depressurizing at once is not a case for flare header sizing.

However, the study case is a particular case in which the flare capacity is limited since an existing flare is considered, and additionally the case of both sections depressurizing at the same time has to be considered.

One major drawback is the greatly increased number of valves required for this setup. More valves require higher investment cost, more maintenance and more chance of leakage to the flare. However, for this case increasing the amount of valves cannot be avoided, in order not to exceed the flare design limit constraint.

2.4 Control valve versus restriction orifice

There are typically two alternatives to control the emergency depressurization i.e. via a control valve or by means of a combination of on-off valve and a restriction orifice.

This study has been performed considering a combination of on-off valves and restriction orifices.

The benefit of this configuration is to avoid the risk of freezing because of low temperatures (as low as -40°C), caused by LPG depressurization. That may cause malfunctioning of closing the control valve that has been opened for depressurization.

With the proposed scheme the on-off valve will be able to close since the low temperatures will occur downstream the RO. The restriction orifice is installed at a safe distance downstream the on-off valve, so that the low temperature can dissipate without risk of freezing in the on-off valve.

2.5 Computational setup

This study is executed in Aspen HYSYS, using the full dynamic simulation capabilities. HYSYS also offers two other methods to simulate depressurization, the Depressuring Utility and the Blowdown Module, which are easier to use, but allow less detail in the model.

The thermodynamic model used in each depressuring case is the Peng-Robinson equation of state. Being HYSYS' most enhanced model, Peng-Robinson is especially suitable for the fluid considered in this study, with a wide range of T and P applicability and its extensive binary coefficients database.

For the modelling of the system, adiabatic vessels are considered.

2.6 Valve characteristics and hydraulics

2.6.1 On-off valves

On-off valves opening time is included in the simulation. A valve model was used with a cv-percentage opening characteristic taken from vendor information. For the actuator, a linear characteristic was taken with different values for the time to fully open the valve for individual valves. Note that in the HYSYS depressurization and blowdown utilities (and many other simplified calculation modules), on-off valves are considered instantaneously opened, which is a simplification of the method which leads to a higher peak than actual flow, and to a shorter depressurization time than actual.

2.6.2 Flare system

A level control was implemented for flare knock-out drum in the model. Having the level control keeps a low level to minimize evaporation in the KO vessel in the model. In reality, the KO vessel does not have a level control, but a quick evaporation is unlikely because of the limited surface area between gas and liquid. In the depressurization curves, the mass flow in and out of the KO vessel is shown.

Hydraulic restrictions were added to the system in order to model the hydraulics of the downstream system. The input to these restrictions was based on the detailed hydraulic calculations available for the existing system.

2.7 Simulation results

The main results of the depressurization study done with HYSYS dynamic simulation can be observed in Figure 3. In Figure 4, the results of the depressurizing tool are shown.

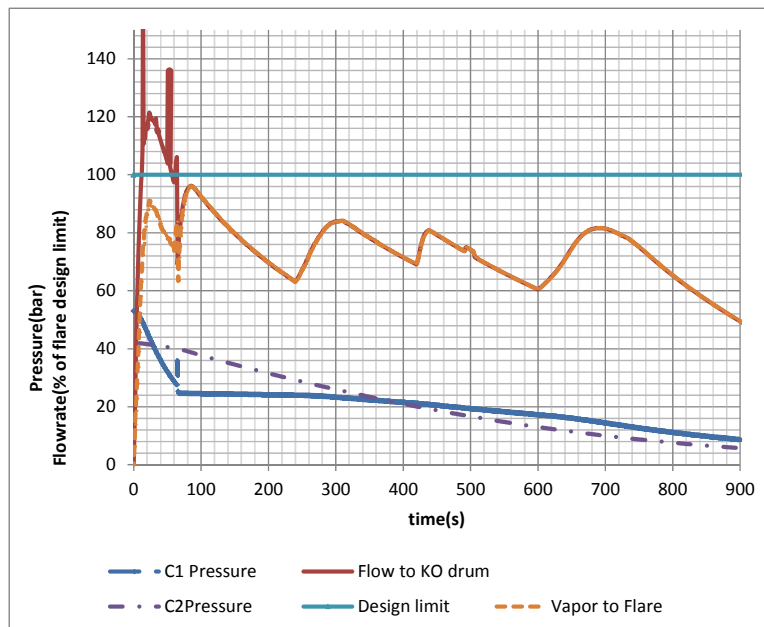


Figure 3: full dynamic simulation, pressure evolution and peak flowrate

As can be observed in the Figure 3, the C1 and C2 pressures are reduced to recommended levels while the depressurizing flowrate is within the capacity of the flare system.

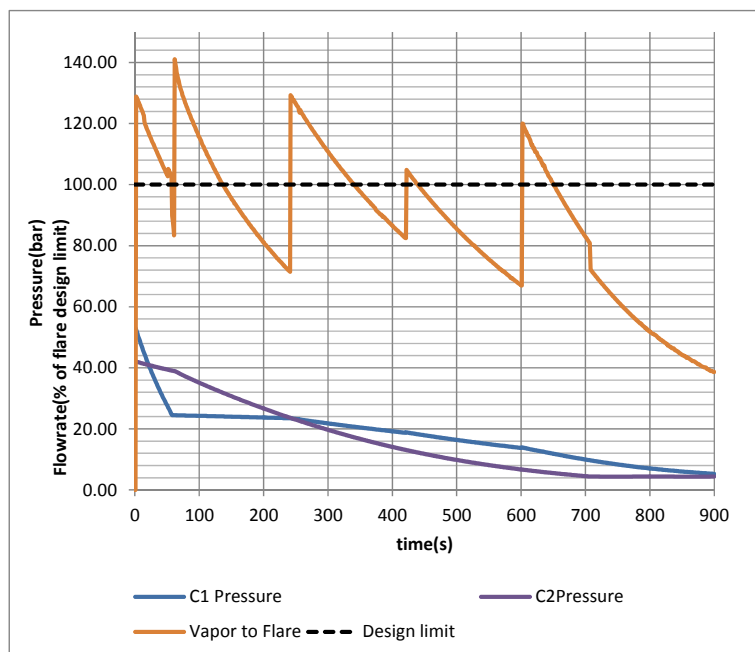


Figure 4: simplified dynamic simulation using depressurization utility, pressure evolution and peak flowrate

Figure 4 shows that, when applying the depressuring utility, the design of the flare system is exceeded when the same orifice sizes and opening times are considered respect to the full dynamic simulation approach. The main reason for such a discrepancy is that depressurization utility does not take into account limitations like hydraulics, opening time of on-off valves and positive impact of a flare knock-out drum.

3. Conclusions

When dealing with complex depressurization systems with additional constraints respect to standard designs, a full dynamic simulation is a tool to be considered since, despite being more time consuming to build if compared with the HYSYS depressurization utility and blowdown module, its results are more accurate, take into account the influence of more parameters and can better represent the actual system behaviour, leading to an optimal design of the depressurization system.

4. References

Sattarin, Manzar & Modarresi, Hassan & Talachi, Hossaien & Teymori, Mohammad. (2006). Solvent deasphalting of vacuum residue in a bench-scale unit. *Petroleum & Coal*. 48. 14-19.

API recommended practice 521, sixth edition, January 2014, Guide for Pressure-Relieving and Depressuring Systems.

AspenTech (2018): www.aspentech.com

Innovative mapping method for screening reactive distillation designs

Rahma Muthia,^a Megan Jobson,^a Anton A. Kiss^{a,b*}

^a*School of Chemical Engineering and Analytical Science, The University of Manchester, Sackville Street, Manchester, M13 9PL, United Kingdom*

^b*Sustainable Process Technology, Faculty of Science and Technology, University of Twente, PO Box 217, 7500 AE Enschede, The Netherlands*

tony.kiss@manchester.ac.uk

Abstract

Reactive distillation (RD) technology offers key benefits in many chemical processes, including energy savings and costs reduction. Prior to its application in industry, screening, addressing technical feasibility and economic viability, must be performed at the conceptual design level. But these tasks can be challenging and time-consuming since detailed models are usually needed. To overcome this complexity, we provide a mapping method to quickly assess the applicability of RD. The mapping method overlays key parameters of a real system, i.e. relative volatilities (α) and chemical equilibrium constant (K_{eq}), onto pre-calculated graphs indicating the RD performance, i.e. the reflux ratio (RR) vs number of theoretical stages (NTS) based on generic cases. The mapping method focuses on quaternary systems ($A + B \rightleftharpoons C + D$). A case study (methyl lactate hydrolysis) is used to demonstrate the approach. Three scenarios are presented, applying different characteristic volatility values; each scenario gives rise to a different RD applicability map for equilibrium constants in the range 0.01 to 10. The findings are validated against results of rigorous process simulation and optimisation. The most accurate scenario is that in which α sets are calculated for mixtures with molar compositions 99% C / 1% A, 50% A / 50% B, 1% B / 99% D, respectively. The results show that the mapping approach allows the prediction of number of theoretical stages and reflux ratio to be estimated within 10% of the optimum values.

Keywords: reactive distillation, mapping method, applicability graph.

1. Introduction

Reactive distillation (RD) is an important intensification technology that offers multiple advantages: 1. an improved chemical process (i.e. higher conversion and selectivity), 2. energy savings, 3. costs reduction, and 4. inherently safer designs (Shah et al., 2012). This technology has received industrial interest for over 30 years; and for example the production of methyl acetate and ethers using RD is commercially well established (Stankiewicz, 2003). Within the same time frame, studies have been performed to intensify operation of a wider range of chemical processes, such as (trans-)esterification, hydrolysis, (de-)hydration and alkylation (Kiss, 2017).

In spite of the promising applications offered by RD, the complexity of designing RD columns has hindered industrial application of the technology. Simpler approaches are needed to guide design engineers and support design decision making as to whether RD

is an applicable unit (Segovia-Hernández et al., 2015). Recent work has aimed to provide such guidance, via a mapping approach that facilitates screening of RD application (Muthia, Reijneveld, et al., 2018). The method uses RD applicability graphs which plot reflux ratio (RR) vs number of theoretical stages (NTS) and aid go/no-go screening of proposed RD operations considering the maximum acceptable values for NTS and RR. The mapping method is currently limited to use in quaternary reactions (Muthia, van der Ham and Kiss, 2018). This paper presents an extended development of the method and highlights the importance of using appropriate characterisation of the relative volatilities in the column to predict RD applicability.

2. Mapping method

Figure 1 (left) shows the RD configuration used in this study. The column is assumed to operate at atmospheric pressure, with negligible pressure drop, and to achieve vapour-liquid and reaction equilibria at each stage. The reactive section is located between the inlets of the lighter and heavier reactants; reaction and separation occur simultaneously in this section. Further separation takes place in the rectifying and stripping sections, to achieve the targeted product purities. It is assumed that equal molar flows of the reactants are fed to the column as saturated liquids.

The RD column, with any configuration, is simulated using Aspen Plus v8.6. For a given NTS, a sensitivity analysis is carried out in which the number of stages in the rectifying, reactive and stripping sections is varied. A generic case is defined, in which the boiling order of the reactants and products and the type of reaction are defined (e.g. $A + B \rightleftharpoons C + D$). The method assumes that the generic cases have ideal vapour-liquid equilibrium behaviour (neither azeotropes formation nor liquid split) and constant key parameters, i.e. all relative volatilities (α) and chemical equilibrium constant (K_{eq}). The optimisation tool within Aspen Plus is used in order to minimize the reflux ratio, where the purity of both products is specified as a constraint. Multiple (flat) optimal solutions are obtained for each choice of NTS which correspond to multiple column designs that can meet the specifications. For a given number of theoretical stages, the lowest value of the reflux ratio defines a boundary to the region in which RD is feasible – this is known as the applicability area, as shown in Figure 1 (right).

Figure 1 (right) depicts the boundary lines of two RD applicability areas, corresponding to two different K_{eq} s. Only on and above each boundary line, the RD technology is applicable, i.e. the targeted product purities are achieved. The two dashed curves are the lower bounds belonging to two generic cases, i.e. with K_{eq} s equal to 1 and 2.

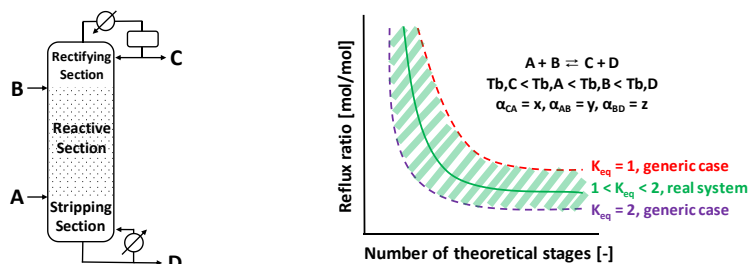


Figure 1. RD column configuration (left); RD boundary lines of generic and real systems (right)

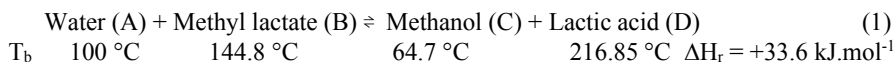
The boundary lines of the generic cases are used to predict the RD applicability of a specific, real system. Firstly, key process parameters are calculated (a set of α values and the value of K_{eq}) for the real system. Then the user seeks the two boundary lines, one with a higher K_{eq} value and one with a lower K_{eq} . This allows the user to estimate the position of the boundary line for the real system. For example, for a real system with $1 < K_{eq} < 2$, its boundary line is predicted to lie between the two generic boundary lines, within the shaded area shown in Figure 1 (right). Later, rigorous simulations will be carried out to confirm that the actual boundary line of the real system – indicated by the solid line – is indeed well predicted by the neighbouring generic boundary lines.

In classic distillation, short-cut methods, such as the Fenske and Underwood methods, are used to estimate the minimum number of theoretical stages (NTS_{min}) and minimum reflux ratio (RR_{min}). The α value may be that of the feed or considered as an average α along the column based on the composition of the top and the bottom streams, and the results of the Fenske and Underwood design calculations can be relatively sensitive to which approach is adopted. The approximation quality is significantly affected by the nonideality of the mixtures involved. Greater errors are in general obtained in more nonideal systems (Smith, 2016). Therefore, it is crucial to use an appropriate representation of the set of α values in the column when applying simple distillation design methods. In the context of RD, this study evaluates different representations of α sets in the development of the mapping method. The work assumes that the characteristic value of the equilibrium constant, K_{eq} , should be calculated at the average boiling point (T_b) of the two reactants, as the temperature profile in the reactive section is typically confined to the within the range of the reactant boiling temperatures.

The generic boundaries are created by extensive series of calculations. The vast number of possible combinations of α sets and K_{eq} values implies that an infinite number of boundary lines for generic cases can be obtained. Therefore, the range of K_{eq} is limited to a pragmatic range from 0.01 to 10 (i.e. 0.01, 0.02, 0.05, 0.1, 0.2, 0.5, 1, 2, 5, 10) that aims to cover the range of reactions with potential for practical RD application. In addition, the lower bound is chosen to the set of results corresponding to a number of theoretical stages that is twice the minimum ($NTS=2 \cdot NTS_{min}$), in which the reflux ratio is up to 10% higher than the lowest reflux ratio on the boundary line. These choices are based on heuristics for estimating the optimal number of stages for classic distillation.

3. Case study

This study focuses on the quaternary reaction ($A + B \rightleftharpoons C + D$), where $T_{b,C} < T_{b,A} < T_{b,B} < T_{b,D}$), which has been explored widely for RD applications. Due to space limitations, only the case study of methyl lactate hydrolysis is presented, as shown in Eq. (1).



The activity coefficients are calculated by UNIFAC-HOC and a correlation between temperature and chemical equilibrium constant is shown in Eq. (2), where T is in K (Sanz et al., 2004). An azeotrope exists at 99.8°C with a molar composition of 97% water and 3% methyl lactate. In this study, the targeted purity of products ≥ 99 mol%.

$$\ln(K_{eq}) = 2.6 - (1954.2 / T) \quad (2)$$

4. Method development and validation

Table 1 presents three scenarios, applying different definitions for the characteristic α sets. For all scenarios, α_{AB} is for a 50/50 mol% mixture of the reactants, corresponding to the equimolar feed of reactants. In Scenario 1 (S1), α_{CA} and α_{BD} are calculated using the compositions of the top and the bottom streams, respectively. Scenario S2 aims to consider volatilities within the column, and not just at its extremities; therefore, the characteristic α_{CA} and α_{BD} are calculated 50/50 mol% binary mixtures. Scenario S3 calculates α_{CA} and α_{BD} at compositions (1/99% CA and 99/1% BD mixtures) that are only expected to occur if K_{eq} is very low, leading to very low conversion. In this case, a single RD column is unlikely to be appropriate.

Table 1. Characterisation of α sets

Scenario	Representation of α set		
	α_{CA}	α_{AB}	α_{BD}
S1	2.5 (99/1 mol%)		6.5 (1/99 mol%)
S2	3.6 (50/50 mol%)	5.5 (50/50 mol%)	11.7 (50/50 mol%)
S3	7.5 (1/99 mol%)		14 (99/1 mol%)

The dashed boundary lines in Figure 2, Figure 3 and Figure 4 (left) represent generic cases for S1, S2 and S3, respectively. Note that the solid line in each graph, which is the actual boundary line for the case study, is added later, after performing rigorous simulation for validation purposes.

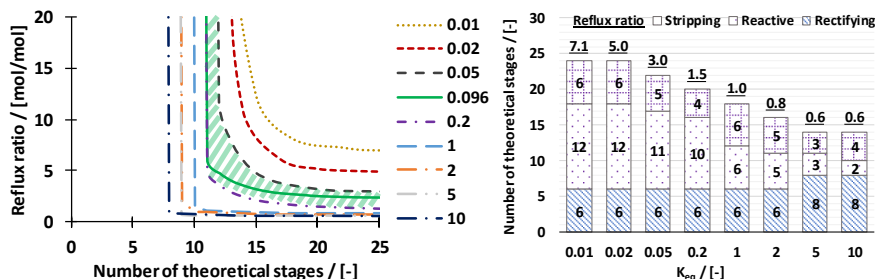


Figure 2. RD applicability areas (left); their RD configurations at $NTS=2-NTS_{min}$ (right) for S1

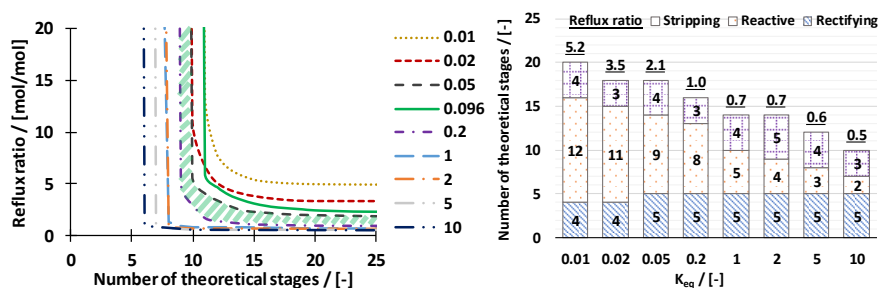


Figure 3. RD applicability areas (left); their RD configurations at $NTS=2-NTS_{min}$ (right) for S2

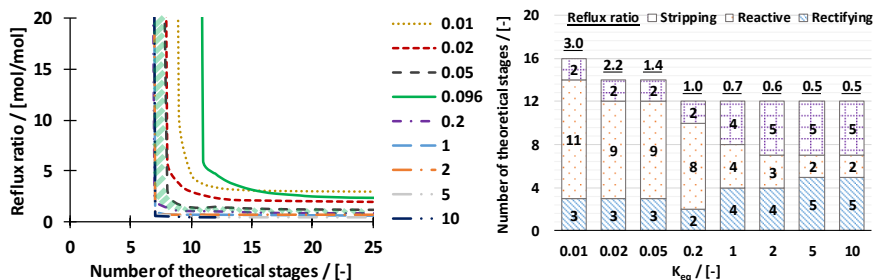


Figure 4. RD applicability areas (left); their RD configurations at NTS=2-NTS_{min} (right) for S3

The size of RD applicability areas of the generic cases increases from S1, S2, to S3, respectively: the increasing ease of separation between reactants and products (shown in Table 1), leads to lower reflux ratios for any number of stages. This observation is in agreement with the resulting RD configurations, presented in Figures 2, 3 and 4 (right). In each system, fewer reactive stages are needed for higher K_{eq} values, since the reaction performance is improved. Conversely, more separation stages are needed because fewer reactive stages achieve less simultaneous separation.

For the particular conditions of the case study, K_{eq} is 0.096, calculated using Eq. (2). A premise of the mapping method is that the actual boundary line will lie between neighbouring generic boundary lines, i.e. within the shaded areas in Figure 2, Figure 3 and Figure 4 (left). Rigorous simulations of the case study provide the actual boundary line, indicated by the solid line. It may be seen that the generic boundary lines predict its location well only in S1, i.e. the effectiveness of the mapping method is sensitive to the approach used to characterise volatilities in the column.

Figure 5 (left) illustrates how the generic results can be used to design a particular RD column using linear interpolation to estimate number of theoretical stages and reflux ratio, for $K_{eq} = 0.096$. The number of rectifying, reactive and stripping sections can be estimated using the same approach. Multiple designs configurations exist; two RD configurations of neighbouring generic cases (with K_{eq} values close to the actual value) are considered, i.e. K_{eq} values of 0.05 and 0.2. Figure 5 (right) shows the actual (simulated) RD configuration and configurations predicted using linear interpolation for S1, S2 and S3. Table 2 quantifies the goodness of fit in terms of the differences in NTS and RR, relative to that of the actual case. S1 is in good agreement with the generic results, with deviations below 10%.

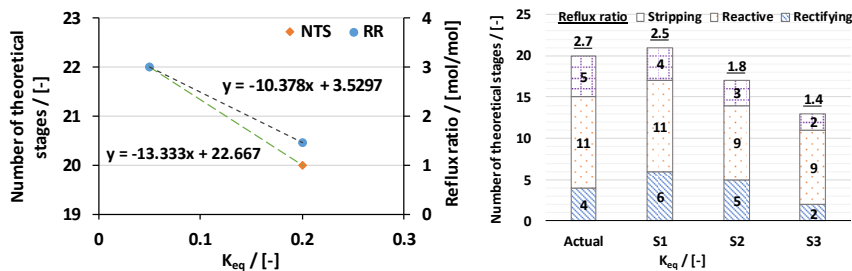


Figure 5. NTS and RR predictions for S1 (left); Predicted and actual RD configurations (right)

Table 2. Comparison of linearly interpolated and actual NTS and RR values

Scenario	NTS			RR		
	Actual	Predicted	Deviation	Actual	Predicted	Deviation
S1	20	21	5%	2.7	2.5	8%
S2	20	17	15%	2.7	1.8	33%
S3	20	13	35%	2.7	1.4	48%

5. Conclusions

The mapping method aims to help engineers to carry out relatively quick initial evaluation of potential RD applications. The approach uses characteristic relative volatilities and chemical equilibrium constant of a real system to screen the RD designs based on generic RD applicability graphs. This study highlights the importance of having the appropriate characterisation of relative volatilities sets to predict the RD applicability and validates the approach by comparing predictions to rigorous simulation results. The relative volatilities sets should be calculated for total feed, top product and bottom product conditions. The approach enabled prediction of NTS and RR for the case study with deviations of less than 10%.

Acknowledgements

RM gratefully acknowledges full fund support from LPDP (Indonesia Endowment Fund for Education). AAK is thankful for the Royal Society Wolfson Research Merit Award.

References

- A. A. Kiss, 2017, Process intensification by reactive distillation, Process Synthesis and Process Intensification: Methodological Approaches, 143-181, Boston, De Gruyter.
- R. Muthia, A. G. T. Reijneveld, A. G. J. van der Ham, A. J. B. ten Kate, G. Bargeman, S. R. A. Kersten, A. A. Kiss, 2018, Novel method for mapping the applicability of reactive distillation, Chemical Engineering and Processing: Process Intensification, 128, 263-275.
- R. Muthia, A. G. J. van der Ham, A. A. Kiss, 2018, Preliminary economic ranking of reactive distillation processes using a navigation method, Computer Aided Chemical Engineering, 43, 827-832.
- M. T. Sanz, R. Murga, S. Beltrán, J. L. Cabezas, J. Coca, 2004, Kinetic study for the reactive system of lactic acid esterification with methanol: methyl lactate hydrolysis reaction, Industrial & Engineering Chemistry Research, 43, 2049-2053.
- J. G. Segovia-Hernández, S. Hernández, A. B. Petriciolet, 2015, Reactive distillation: A review of optimal design using deterministic and stochastic techniques. Chemical Engineering and Processing: Process Intensification, 97, 134-143.
- M. Shah, A. A. Kiss, E. Zondervan, A. B. de-Haan, 2012, A systematic framework for the feasibility and technical evaluation of reactive distillation processes, Chemical Engineering and Processing: Process Intensification, 60, 55-64.
- R. Smith, 2016, Separation of Homogeneous Fluid Mixtures I – Distillation, Chemical Process Design and Integration, 155-158, United Kingdom, John Wiley & Sons Ltd.
- A. Stankiewicz, 2003, Reactive separation for process intensification: an industrial perspective, Chemical Engineering and Processing, 42, 137-144.

Filter-based Constraints to Easier Plant Feasibility in Modifier Adaptation Schemes

A. Papasavvas^a and G. Francois^a

^a*School of Engineering, Institute for Material and Processes, The University of Edinburgh, Edinburgh EH93FB*

A.Papasavvas@sms.ed.ac.uk

Abstract

Output modifier adaptation (MAy) is an iterative model-based real-time optimization (RTO) method with the proven ability to reach, upon converge, the unknown plant optimal steady-state operating conditions despite structural and parametric plant-model mismatch and disturbances. However, as such, feasibility of the iterates cannot be guaranteed before convergence is achieved. This issue can be mitigated with additional modelling and/or experimental efforts, which is costly and sometimes cannot be envisaged, especially for large-scale systems. In this article, MAy is compared to one of its most recent extensions, namely “KMAy”, which is shown to have more favorable sufficient conditions for feasibility of the iterates. A simulation study, performed on the Williams-Otto reactor – a standard benchmark case study for RTO algorithms – illustrates that KMAy is safer for practical applications.

Keywords: Real-time optimization, modifier adaptation, feasibility.

1. Introduction

Plant operators often manipulate the degrees of freedom of industrial processes to maximize performances, while trying to enforce the satisfaction of safety and quality constraints. However, such experience-based decision methods often lead to sub-optimal operations. Real-time optimization (RTO) methods use both the available model and measurements in the decision-making process. Output modifier-adaptation (MAy-Marchetti et al. (2016), Papasavvas et al. (2019)) has been recently proposed as an extension of Modifier Adaptation (MA) schemes (Marchetti et al., 2016). Basically, MAy uses all real-time plant measurements to implement input-affine corrections on the modelled input-output mapping to improve the prediction of the cost and constraints, while preserving the proven ability of MA schemes to reach upon convergence the true plant optimal inputs.

One challenge to push MAy further is to provide, at least, the same level of feasibility guarantees as experience-based decision methods. Indeed, forcing the satisfaction of the plant constraints typically requires global knowledge of the plant behaviour (Bunin et al., 2013; Marchetti et al., 2017), which is unfortunately rarely the case. In this paper, the focus is on a recent extension of MAy, i.e. “KMAy” (Papasavvas and François, 2019). This method is shown to offer better feasibility guarantees than other MA algorithms without requiring more data or knowledge. On the basis of this study, a simple method for improving most MA algorithms is proposed.

The paper is organized as follows. After a brief review of MAy and KMAy in Section 2, these schemes are compared in Section 3 w.r.t. their ability to enforce plant feasibility. These results are illustrated by means of simulated chemical reactor in Section 4, and Section 5 concludes the paper.

2. Real-Time Optimization via Modifier Adaptation

Plant optimal operating conditions $\mathbf{u}_p^* \in \mathbb{R}^{n_u}$ are such that they minimize the operating cost $\phi(\mathbf{u}, \mathbf{y}_p(\mathbf{u})) \in \mathbb{R}$ while satisfying the constraints $\mathbf{G}(\mathbf{u}, \mathbf{y}_p(\mathbf{u})) \leq \mathbf{0} \in \mathbb{R}^{n_g}$, where $\mathbf{y}_p(\mathbf{u}) \in \mathbb{R}^{n_y}$ is the input-output mapping of the plant, i.e. the relationship between the operating conditions and the steady-state measured outputs of the plant. Finding \mathbf{u}_p^* when only an approximate model of the plant $\mathbf{y}(\mathbf{u})$ is available, is generally not possible with standard model-based optimization methods but becomes handy with RTO algorithms like MAy. The main idea behind MAy is to use plant measurements to iteratively modify the model-based optimization problem so that its first order conditions of optimality match those of the plant optimization problem at each operating point \mathbf{u}_k . It is proven that the true plant optimum is the only possible fixed point of MAy despite structural plant-model mismatch (Papasavvas et al., 2019). MAy can be summarized as follows:

Output Modifier Adaptation (MAy): At the k^{th} iteration, \mathbf{u}_k is applied to the plant until steady state is reached, and the modified input-output mapping is modified: $y_{i,m,k}(\mathbf{u}) := y_i(\mathbf{u}) + \varepsilon_k^{y_i} + (\boldsymbol{\lambda}_k^{y_i})^\top (\mathbf{u} - \mathbf{u}_k)$, where $\varepsilon_k^{y_i} := y_{i,p}(\mathbf{u}_k) - y_i(\mathbf{u}_k)$ and $\boldsymbol{\lambda}_k^{y_i} := \nabla_{\mathbf{u}} y_{i,p} \big|_{\mathbf{u}_k} - \nabla_{\mathbf{u}} y_i \big|_{\mathbf{u}_k}$ are the 0th- and 1st-order modifiers, respectively, and $\nabla_{\mathbf{u}}(\cdot)$ is the gradient operator w.r.t. \mathbf{u} . Then, the following optimization problem is solved to derive the model-based optimal inputs \mathbf{u}_{k+1}^* :

$$\mathbf{u}_{k+1}^* := \arg \min_{\mathbf{u}} \Phi_{\text{MAy},k}(\mathbf{u}) := \phi(\mathbf{u}, \mathbf{y}_{m,k}(\mathbf{u})) \quad (2.1)$$

$$\text{s.t.} \quad \mathbf{G}_{\text{MAy},k}(\mathbf{u}) := \mathbf{g}(\mathbf{u}, \mathbf{y}_{m,k}(\mathbf{u})) \leq \mathbf{0}, \quad (2.2)$$

The next iterate \mathbf{u}_{k+1} is obtained by applying the following filter:

$$\mathbf{u}_{k+1} := \mathbf{u}_k + \mathbf{K}(\mathbf{u}_{k+1}^* - \mathbf{u}_k), \quad (2.3)$$

with $\mathbf{K} \in \mathbb{R}^{n_u \times n_u}$ a filter gain matrix, typically diagonal with $K_{i,i} \in (0, 1]$, $\forall i \in [1, n_g]$.

The filter of (2.3) is used here to enable asymptotic stability and to avoid excessive corrections (Marchetti et al. (2016)) but its implementation is indeed risky: *Figure 1 illustrates that this filter can lead MAy to generate the next inputs where the model predicts infeasibility! This is due to the fact that the filter of (2.3) picks \mathbf{u}_{k+1} in the segment $[\mathbf{u}_k, \mathbf{u}_{k+1}^*]$, while the model predicts that the constraint is not satisfied in the red-shaded area. Of note is that this is a major common weakness to standard MA algorithms using a similar filter.* To avoid this, the following extension of MAy can be used:

Output Modifier Adaptation Extension (KMAy): Apply MAy until equation (2.1), and solve the following problem instead of (2.1)-(2.3):

$$\mathbf{u}_{k+1} := \arg \min_{\mathbf{u}} \Phi_{\text{KMAy},k}(\mathbf{u}) := \Phi_{\text{MAy},k}(\mathbf{v}_k(\mathbf{u})) \quad (2.4)$$

$$\text{s.t.} \quad \mathbf{G}_{\text{KMAy},k}(\mathbf{u}) := [\mathbf{G}_{\text{MAy},k}(\mathbf{v}_k(\mathbf{u}))^\top, \mathbf{G}_{\text{MAy},k}(\mathbf{u})^\top]^\top \leq \mathbf{0}, \quad (2.5)$$

$$\mathbf{v}_k(\mathbf{u}) := \mathbf{K}^{-1}(\mathbf{u} - \mathbf{u}_k) + \mathbf{u}_k. \quad (2.6)$$

As seen in (2.5), KMAy duplicates the model-based constraints, which are in turn also

checked at what would be the next iterate as the filter (2.3) is here implemented by means of equation (2.6). Note that loss of constraint qualification upon convergence could be expected with the duplication of the constraints, but it has been recently shown that if linear constraint qualification holds for MAy, then Mangasarian Fromowitz qualification holds for KMAy, while KMAy also leads to model adequacy conditions that are less difficult to satisfy compared to MAy (Papasavvas and François, 2019). Since model-based feasibility is checked at both at $\mathbf{v}_k(\mathbf{u}_{k+1})$ and \mathbf{u}_{k+1} , KMAy will generate a \mathbf{u}_{k+1} where modelled constraints are satisfied, while MAy will not, as illustrated in Figure 1. Selecting \mathbf{u}_{k+1} such that the modified model predicts feasibility also at the next iterate does not guarantee, per se, plant feasibility. However, KMAy should outperform MAy in most cases, especially when the model provides a reasonable prediction of the plant constraints.

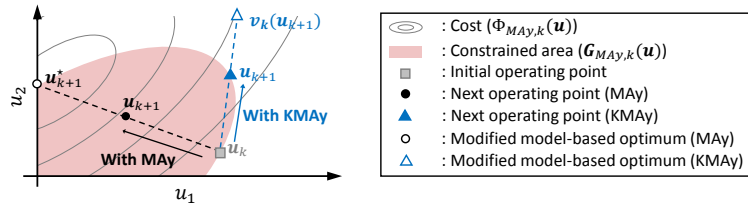


Figure 1: A 2D optimization problem solved with MAy and KMAy.

3. Comparison between MAy and KMAy from a Feasibility Perspective

In this section, we compare the ability of MAy and KMAy to generate feasible iterates or sequences of feasible iterates. To do so, the following definitions are required:

Definitions:

- $\mathcal{U} \subseteq \mathbb{R}^{n_u}$ is the set of feasible inputs for the subset of known constraints (i.e., not subject to modelling errors). The *known* constraints functions only depend of \mathbf{u} , e.g., input bounds: $\mathbf{u}^L \leq \mathbf{u} \leq \mathbf{u}^U$. $\mathcal{F}_p \subseteq \mathcal{U}$ denotes the set of feasible inputs for the plant.
- A *model* is an object m in the universe of models \mathcal{M} : $m \in \mathcal{M}$.
- $\forall k$, $\mathcal{C}_{\text{KMAy}}^k$ denotes the set of inputs that satisfy the constraints (2.5) and $\mathcal{C}_{\text{MAy}}^k$ denotes the set of inputs generated by the application of the filter of (2.3) to any input satisfying the constraint (2.2). This can be rewritten as: $\mathcal{C}_{\text{KMAy}}^k := \{\mathbf{u} \in \mathbb{R}^{n_u} \mid \mathbf{G}_{\text{KMAy},k}(\mathbf{u}) \leq \mathbf{0}\}$ and $\mathcal{C}_{\text{MAy}}^k := \{\mathbf{u} \in \mathbb{R}^{n_u} \mid \mathbf{G}_{\text{MAy},k}(\mathbf{K}^{-1}(\mathbf{u} - \mathbf{u}_k) + \mathbf{u}_k) \leq \mathbf{0}\}$, respectively. In other words, \mathcal{C}_X^k are the sets of candidate inputs \mathbf{u}_{k+1} that can be generated by MAy or KMAy for $X \in \{\text{MAy}, \text{KMAy}\}$.
- $\forall k$ and for each $X \in \{\text{MAy}, \text{KMAy}\}$, $\mathcal{S}_X^k \subseteq \mathcal{M}$ are the sets of models m such that the candidate inputs \mathbf{u}_{k+1} are feasible for the plant, i.e., $\mathcal{S}_X^k := \{m \in \mathcal{M} \mid \mathcal{C}_X^k \subseteq \mathcal{F}_p\}$. From the definition of \mathcal{S}_X^k , it is clear that $m \in \mathcal{S}_X^k$ is a *sufficient condition for the plant feasibility at the next iterate*.

For any given $\mathbf{u}_k \in \mathcal{F}_p$ and given a model $m \in \mathcal{M}$, the following proposition states that KMAy is more likely to lead to $\mathbf{u}_{k+1} \in \mathcal{F}_p$ than MAy:

Proposition 1 $\forall k$, the set of models satisfying the sufficient condition for plant feasibility at $k+1$ with MAy is a subset of the set of models satisfying it with KMAy, i.e., $\mathcal{S}_{\text{MAy}}^k \subseteq \mathcal{S}_{\text{KMAy}}^k$.

Proof. \mathbf{u}_{k+1} (generated by $X \in \{\text{MAy}, \text{KMAy}\}$) is in \mathcal{C}_X^k and is feasible for the plant

when $m \in \mathcal{S}_X^k$, since, as said before, $m \in \mathcal{S}_X^k$ is a sufficient condition for plant feasibility at the next iterate. Since KMAy includes the same constraints as MAy *together with additional constraints*, $\mathcal{C}_{\text{KMAy}}^k \subseteq \mathcal{C}_{\text{MAy}}^k$. In other words, the duplication of the constraints with KMAy shrinks the set of candidate inputs \mathbf{u}_{k+1} compared to MAy. Finally, $\mathcal{C}_{\text{MAy}}^k \subseteq \mathcal{F}_p \Rightarrow \mathcal{C}_{\text{KMAy}}^k \subseteq \mathcal{F}_p$ while $\mathcal{C}_{\text{KMAy}}^k \subseteq \mathcal{F}_p \not\Rightarrow \mathcal{C}_{\text{MAy}}^k \subseteq \mathcal{F}_p$. Thus, $\mathcal{S}_{\text{MAy}}^k \subseteq \mathcal{S}_{\text{KMAy}}^k$. \square

Indeed, Proposition 1 implies that any model satisfying the aforementioned sufficient condition for feasibility with MAy also satisfies it for KMAy, while the opposite does not hold. Thus, from the point of view of the feasibility of the iterates, KMAy should be preferred to MAy, since the chances that \mathbf{u}_{k+1} is in \mathcal{F}_p are higher.

Next, we go one step further and show that $\mathcal{C}_{\text{KMAy}}^k$ can be manipulated through the filter gain K in a way that plant feasibility of \mathbf{u}_{k+1} is guaranteed if a *local assumptions* about the model m holds. The observation that a reduction of the value of K leads to the aforementioned shrinkage of $\mathcal{C}_{\text{KMAy}}^k$ on \mathbf{u}_k is key to this result.

Assumption 1: Assume that at iteration k , there exists a subset \mathcal{D}_k of \mathcal{U} , i.e., $\mathcal{D}_k \subseteq \mathcal{U}$, in which the modified model provides pessimistic predictions of the plant feasibility, i.e., the constraints of the modified model upper-bound the constraints of the plant: $\mathcal{D}_k := \{\mathbf{u} \in \mathcal{U} | G_{i,\text{MAy},k}(\mathbf{u}) \geq G_{i,p}(\mathbf{u}), \forall i \in [1, n_g]\}$. Assume that $\mathbf{u}_k \in \mathcal{D}_k^o$ the interior of \mathcal{D}_k .

These assumptions are likely to hold since at \mathbf{u}_k the modified-model and the plant have identical local first-order properties thanks to the affine corrections of the model. Note that one way to enforce the satisfaction of this assumption over a larger area around \mathbf{u}_k would be to amend the model so that the modelled constraints are local upper bounds of the plant constraints, similarly to what has been proposed in Marchetti et al. (2017). Contrary to what is suggested in (Marchetti et al., 2017), such modifications would only be performed here at a *local* level and will not necessitate more than the available measurements. Pessimistic predictions of the plant constraints should always be a favorable case, since pessimistic predictions are such that $G_{i,\text{MAy},k}(\mathbf{u}) \geq G_{i,p}(\mathbf{u})$, while the optimization problems aims at enforcing $G_{i,\text{MAy},k}(\mathbf{u}) \leq \mathbf{0}$, but it is shown hereafter that only KMAy can take advantage of this situation.

Theorem 1 *If (i) Assumption 1 holds, and (ii) \mathcal{U} is bounded, then there exist diagonal filters $\mathbf{K} = \mathbf{K}\mathbf{I}_{n_u}$ such that $\mathcal{C}_{\text{KMAy}}^k \subseteq \mathcal{F}_p$ and, in turn, such that $\mathbf{u}_{k+1} \in \mathcal{F}_p$.*

Proof. Assumption 1 allows to define the biggest ball $\mathcal{B}(\mathbf{u}_k, r) \subseteq \mathcal{D}_k$, centered at \mathbf{u}_k of radius r . Notice that $r > 0$ because $\mathbf{u}_k \in \mathcal{D}_k^o$. Now we show that the distance $\|\mathbf{u}_{k+1} - \mathbf{u}_k\|_2$ can be manipulated through K such that $\mathbf{u}_{k+1} \in \mathcal{B}(\mathbf{u}_k, r)$. By definition, $\mathbf{u}_{k+1} \in \mathcal{U}$, $\mathbf{v}_k(\mathbf{u}_{k+1}) \in \mathcal{U}$, and $\|\mathbf{u}_{k+1} - \mathbf{u}_k\|_2 := \|\mathbf{u}_k + K(\mathbf{v}_k(\mathbf{u}_{k+1}) - \mathbf{u}_k) - \mathbf{u}_k\|_2 = K\|\mathbf{v}_k(\mathbf{u}_{k+1}) - \mathbf{u}_k\|_2 \leq K \max_{\mathbf{u} \in \mathcal{U}} \{\|\mathbf{u} - \mathbf{u}_k\|_2\}$. According to (ii) \mathcal{U} is bounded, so $\max_{\mathbf{u} \in \mathcal{U}} \{\|\mathbf{u} - \mathbf{u}_k\|_2\} \in \mathbb{R}$. Therefore, $\forall K$ such that $K \leq r / (\max_{\mathbf{u} \in \mathcal{U}} \{\|\mathbf{u} - \mathbf{u}_k\|_2\})^*$, the inequality $\|\mathbf{u}_{k+1} - \mathbf{u}_k\|_2 \leq r$ holds, and $\mathbf{u}_{k+1} \in \mathcal{B}(\mathbf{u}_k, r) \subseteq \mathcal{D}_k$. Given that the feasibility is checked** at $\mathbf{u}_{k+1} \in \mathcal{D}_k$ and that the model provides pessimistic predictions of the plant constraints in \mathcal{D}_k , it follows that $\mathbf{u}_{k+1} \in \mathcal{F}_p$. \square

Despite the fact that the set \mathcal{D}_k is unknown in practice, Theorem 1 shows that reducing K in KMAy is a very simple way to increase the chances to have $\mathbf{u}_{k+1} \in \mathcal{D}_k$ and, thus,

*Since $r > 0$, satisfying this inequality does not requires to have $K \rightarrow 0$.

**This difference between MAy and KMAy is the reason why a similar theorem can not be stated for MAy.

to make RTO iterations safer. Interesting enough is that in (Papasavvas and François, 2019), it is shown that *reducing* K is also the way to relax the model adequacy condition for KMAy. Also, it has to be noticed that a similar result cannot be obtained from MAy, mainly because model-based feasibility is not checked at the filtered inputs. In fact, when the conditions (i) and (ii) hold, the iterate \mathbf{u}_{k+1} can be brought arbitrarily close to \mathbf{u}_k if K is taken small enough. However, with MAy, the feasibility being not checked at \mathbf{u}_{k+1} , the fact that the model is pessimistic in \mathcal{D}_k is ignored and changing K so that $\mathbf{u}_{k+1} \in \mathcal{D}_k$ is not helpful for feasibility with MAy. As illustrated on Figure 1, reducing K with MAy would also bring \mathbf{u}_{k+1} closer to \mathbf{u}_k , but on the segment $[\mathbf{u}_{k+1}^*, \mathbf{u}_k]$, while it is ignored that this segment lies in set the of infeasible inputs (red-shaded area) for the modified-model.

4. Case study

Williams-Otto Reactor: The continuous stirred-tank reactor described in (Williams and Otto, 1960) is considered. 3 reactions take place in reality: (i) $A + B \rightarrow C$, (ii) $C + B \rightarrow P + E$, and (iii) $P + C \rightarrow G$; but the models only considers two (different) reactions (Marchetti et al., 2017; Forbes et al., 1994). So there is structural plant-model mismatch.

A and B are fed separately, with mass flowrates of F_A and F_B ([kg/s]), respectively. P and E are the desired products, C is an intermediate product and G is an undesired by-product. The reactor is operated isothermally at T_R ($^{\circ}C$). Steady-state mass balances can be found in Zhang and Forbes (2000). The model-based optimization problem of (Marchetti et al., 2017) is considered, where $\mathbf{u} = [F_A, F_B, T_R]^T$ and $\mathbf{y} = [X_E, X_P, X_G]^T$ are the inputs and outputs, respectively, and X_i denotes the concentration of species i . The goal is to maximize profit at steady state, and both inputs and X_G are constrained:

$$\max_{\mathbf{u}} \quad \phi(\mathbf{u}, \mathbf{y}) = (1143.38X_P + 25.92X_E)(F_A + F_B) - 76.23\alpha F_A - 114.34\beta F_B \quad (4.1)$$

$$\text{s.t.} \quad g(\mathbf{y}) = X_G - 0.08 \leq 0, \quad F_A \in [3, 4.5], \quad F_B \in [6, 11], \quad T_R \in [80, 105]. \quad (4.2)$$

The two parameters $\alpha \in \mathbb{R}$ and $\beta \in \mathbb{R}$ are used to simulate market fluctuations. Also, note that $g(\mathbf{y})$ is a concave constraint (Marchetti et al., 2017).

Three different market regimes are considered: mode 1: (1.1, 1.1), mode 2: (0.85, 1), and mode 3: (1, 0.9), with different pairs of α and β values (in brackets). For the two mode transitions mode 1 \rightarrow mode 2 and mode 2 \rightarrow mode 3, MAy and KMAy have been applied and constraints violations have been analyzed for different filter values of the diagonal filter $\mathbf{K} = K\mathbf{I}_{n_u}$. Other transitions have been simulated with similar conclusions.

Simulation Results: Note that the optimal operating conditions activating the concave constraint (4.2) for each mode, the segment that joins the optimal operating points of two different modes always lies in the infeasible part with MAy. Therefore, constraint violations will clearly be likely to occur with MAy similarly to what is illustrated in Figure 1. Both problems are indeed comparable, i.e., “sliding around a concave constraint” with KMAy or going potentially through it with MAy. Figures 2 and 3 show a large difference between the maximal constraint violations observed with MAy and KMAy for different K values. As expected, using KMAy always leads to less violations.

5. Conclusion

In this article, a weakness that is common to all MA-inspired RTO algorithms using a filter has been identified. Two recent MA extensions are compared and it is argued that KMAy

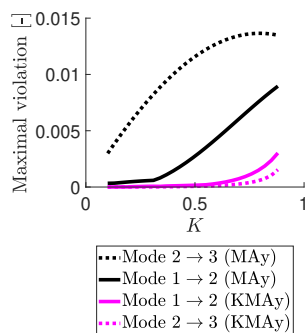


Figure 2: Maximal constraint violations with MAy and KMAy, for two different market variations.

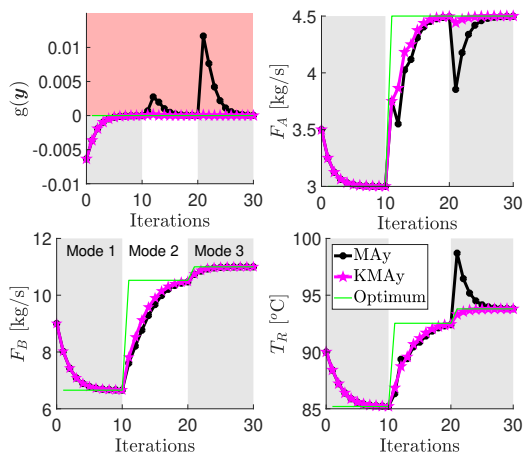


Figure 3: Simulation results for $K = 0.5$.

is safer than MAy, in the sense that less, or smaller, constraints violations can be expected. Sufficient conditions for plant feasibility have been compared for the two algorithms and it has been shown that they are in favor of KMAy. It has been proven that, under certain conditions, a filter value can always be found such that plant feasibility can be enforced at the next iteration with KMAy, while this is not the case with MAy and it indeed appears that most MA algorithms would benefit from a formal implementation of the filter at the level of the optimization problem. Future research could include an analysis of the potential effects of such an integration to most MA-inspired RTO methods. Also, the conditions for the existence of \mathcal{D}_k in Assumption 1, though beyond the scope of this article, should be investigated. Finally, the main benefit of the integration of the filter into the KMAy formulation (with the relaxation of model adequacy conditions, (Papisavvas and François, 2019)) being to prevent the generation of operating conditions where the modified model predicts infeasibility, future research should investigate how this double model-based feasibility check could, in practice, enforce plant feasibility under moderate assumptions about the nature of plant-model mismatch.

References

- G. A. Bunin, G. François, D. Bonvin, 2013. Sufficient conditions for feasibility and optimality of real-time optimization schemes - I. Theoretical foundations. ArXiv:1308.2620.
- J. F. Forbes, T. E. Marlin, J. F. MacGregor, 1994. Model adequacy requirements for optimizing plant operations. *Comp. Chem. Eng.* 18 (6), 497–510.
- A. G. Marchetti, T. Faulwasser, D. Bonvin, 2017. A feasible-side globally convergent modifier-adaptation scheme. *J. Process Contr.* 54, 38–46.
- A. G. Marchetti, G. François, T. Faulwasser, D. Bonvin, 2016. Modifier adaptation for real-time optimization – Methods and applications. *Processes* 4 (55), 1–35.
- A. Papisavvas, G. François, 2019. Filter-based additional constraints to relax the model adequacy conditions in modifier adaptation. (Accepted) In *Proc. IFAC International Symp. DYCOPS*. Florianopolis.
- A. Papisavvas, A. Marchetti, T. de Avila Ferreira, D. Bonvin, 2019. Analysis of output modifier adaptation for real-time optimization. *Comp. Chem. Eng.* 121, 285–293.
- T. J. Williams, R. E. Otto, 1960. A generalized chemical processing model for the investigation of computer control. *AIEE Trans.* 79, 458.
- Y. Zhang, J. F. Forbes, 2000. Extended design cost: A performance criterion for real-time optimization systems. *Comp. Chem. Eng.* 24, 1829–1841.

An optimization model for a biorefinery system based on process design and logistics

Christos Galanopoulos^a, Aristide Giuliano^b, Diego Barletta^{b*}, Edwin Zondervan^a

^a*Institute for Environmental Science and Technology (UFT), University of Bremen, Leobener Straße D, Bremen 28359, Germany*

^b*Dipartimento di Ingegneria Industriale, Università degli Studi di Salerno, Via Giovanni Paolo II 132, I-84084 Fisciano SA, Italy*

dbarletta@unisa.it

Abstract

Design of biorefineries has been often addressed by process flowsheet optimization tools without adequately considering the relevant supply chain network. In this work, an integrated optimization algorithm including the biorefinery process flowsheet structure and biobased supply chain network was developed. A superstructure of different process pathways for a biorefinery co-producing ethanol, ethyl levulinate and electricity is built on the base of up-to-date technologies. The bio-based supply chain model was implemented to address the transportation, the inventory management and the size of the biorefinery. Mixed Integer Linear Programming (MILP) was used as a modeling approach. The efficiency of the algorithm was demonstrated by applying it to a case study consisting of a wheat straw supply chain network for bioproducts demand in Germany. The algorithm reached convergence after three iterations providing a final optimal number of biorefineries distributed in different regions of the country corresponding to a maximum Net Present Value.

Keywords: biorefinery, superstructure, bio-based supply chain, optimization, MILP

1. Introduction

A biorefinery is an industrial facility that is capable of producing multiple products from a wide variety of biomass sources. Decision-making tools and tailor-made approaches allow the appropriate exploitation of the potential of each type of biomass in power generation, heat and cooling application and as a transportation fuel (Láinez-Aguirre et al., 2015). Design of biorefineries has been often addressed by process flowsheet optimization tools without adequately considering the relevant supply chain network (Belletante et al., 2016). In particular, the optimal plant size does not depend simply on the economies of scale, but also on the biomass feedstock availability and the topology of the territory affecting logistics (transportation and storage) costs (Giuliano et al., 2018). On the other hand, works aiming at the supply chain level consider literature data or approximate correlations to estimate biorefinery technical performance, capital and operating expenditure (Galanopoulos et al., 2017). In this work, an integrated optimization algorithm including the biorefinery process flowsheet structure and the biomass and bioproduct supply chain network is developed. An original superstructure of alternative process pathways for a biorefinery co-producing biofuels and fuel additives like ethanol “EtOH”, ethyl levulinate “EL” (from levulinic acid and ethanol) and electricity is built on the basis of more recent technologies from literature.

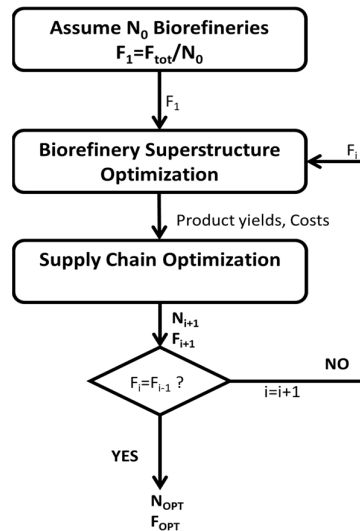


Figure 1: Graphical representation of the integrated optimization algorithm.

The bio-based supply chain model is implemented to address the logistics network, the transportation, the inventory management. The aim of the work was concentrated also on the optimal size of each biorefinery to build in a Germany region.

2. Methodology

The algorithm used to optimize the biorefinery system is presented in Figure 1. Assuming N_0 biorefineries of the same size F_1 initially, where F_1 is obtained dividing the total available biomass by N_0 , the process optimization model for a single biorefinery fed by F_1 is used to optimize the flowsheet by maximizing the Net Present Value (NPV) of the single biorefinery by a MILP approach (Giuliano et al., 2015). Product flowrates, capital costs, operating costs of the single biorefinery are obtained and these data are used as input to the supply chain optimization model by Galanopoulos et al. (2018). The total system of biorefineries is then optimized by maximizing the total NPV including the supply chain costs. As a result, an updated N_i value and a new set of F_i values are obtained removing the constraints of biorefineries with equal size. The new F_i is then used for the process optimization model applied to each biorefinery of different size. In this way, the relevant process flowsheets, product flowrates, capital costs and operating costs are updated. Optimal biomass allocation, product flowrates, costs are obtained in order to design the biobased system. Convergence is achieved when the number of biorefineries and all the flowrates of feedstock for each biorefinery are the same as those obtained from the previous iteration. Finally, N_{opt} and F_{opt} are obtained.

2.1. Process Optimization Modelling

The process optimization model is based on a multiproduct lignocellulosic biorefinery superstructure. The model is obtained by Mixed Integer Linear Programming and it consists in the mathematical description of all biorefinery processes (Giuliano et al.,

2016). The original optimization mathematical model is a MINLP with integer variables for the selection of alternative technologies, after a discretization method for each non-linear variable, the model is rearranged as a MILP, in order to find the global optimal solution (Giuliano et al., 2014).

2.2. Supply Chain Modelling

Biomass is cultivated and collected at the harvesting site of each district. Then, it is either stored or transported to a biorefinery of a region where the conversion to products takes place. Similarly, the bioproducts are then transported to the demand sites to satisfy the demand. The goal is to develop a piece-wise linear model that includes the capital costs of the biorefineries. A detailed description of the supply chain network can be found in Galanopoulos et al. (2018).

3. Case study description

In Germany, the creation of a supply chain network based on cereal straw seems profitable. According to S2Biom report on cost supply (S2Biom, 2017), Germany is the second country in Europe with the highest production of cereal straw (22 Mt_{DRY}/y). The country is divided into 16 regions to quantify the distances in a cereal straw supply chain network in Germany. The distance between each region is evaluated using Google Maps. For the distance inside one region, the Manhattan Distance calculation ($8r/3\pi$) is used by considering that the regions are circles. To have a sustainable supply chain, 30% of all cereal straw produced in each region is assumed to be used for biorefinery purposes. Moreover, a seasonality similar to the growth of wheat is assumed. The products of the cereal straw biorefinery are bioethanol, ethyl levulinate and excess electricity. According to Wang et al. (2012), bioethanol and ethyl levulinate can be used as biofuel and fuel additive respectively for diesel/biodiesel. Ethyl levulinate was obtained by levulinic acid and ethanol equimolar reaction (Nandiwale et al., 2014), while the percentage of demand covered by the ethyl levulinate was set lower than the demand covered by the biofuel ethanol in order to obtain a similar covered demand for both products. The produced electricity can be sold to the grid. The demand of biofuel and of fuel additive is assumed equal to 10 % of the diesel demand for both products.

Table 1: Economic parameters used in the model.

Economic parameter	Value
Wheat straw cost (€/t)	100
Ethyl levulinate price (€/kg)	3.73
Ethanol price (€/kg)	0.694
Electricity price (€/MWh)	145
Biomass transportation cost (fix €/t) + (variable €/t km)	2.64 + 0.15
Bioproduct transportation cost (fix €/t) + (variable €/t km)	2.4 + 0.17

4. Results

To develop the biomass supply chain model and process optimization model, the Advanced Interactive Multidimensional Modelling (AIMMS) software, version

4.21.5.583 64-bit, was used. CPU time to solve the supply chain model was equal to about 1 hour, for the process optimization was equal to about 30 minutes. For the process optimization the model got linear about 200 nonlinear variables. Data collected from the topology of Germany were used to find the total available wheat straw (WS). The initial number of biorefineries was assumed equal to three, because, by previous studies (Galanopoulos et al., 2018), Germany could contain about three biorefineries, considering the territory topology and availability of wheat straw in full Germany. Consequently, three biorefineries fed with 2,203,200 t/y of biomass were initially considered in the process optimization. The results of the iterative calculations are reported in Table 2. The two models converge after three iterations of the algorithm. The results show that the optimal solution is a decentralized production by means of nine biorefineries, eight with a capacity of 698,400 t/y of biomass and only one with a capacity of 871'200 t/y. Yields to products were constant for all iterations and all the biorefineries with different sizes because of constraints on covered product demands. The optimal number of biorefineries derived from a trade off between capital costs and transportation costs.

Table 2: Results of the iterations of the algorithm.

	Iteration number		
	I	II	III
<i>Process optimization results</i>			
Assumed number. of biorefineries for process optimization	3	13	9
Total straw used/total straw available (%)	100	100	98
EtOH yield (% of feedstock)	8	8	8
EL yield (% of feedstock)	10	10	10
Revenues (M€/y)	3'119	2'993	2'919
Biorefinery Operating Costs (M€/y)	1'093	1'193	1'149
Capital Costs (M€)	4'155	4'585	4'167
<i>Supply chain optimization results</i>			
Calculated number of biorefineries from supply chain optimization	13	9	9
Total straw used/total straw available (%)	100	98	98
Ethanol yield (% of feedstock)	8	8	8
Ethyl Levulinate yield (% of feedstock)	10	10	10
Revenues (M€/y)	2'993	2'919	2'919
Biorefinery Operating Costs (M€/y)	1'162	1'149	1'149
Capital Costs (M€)	4'418	4'167	4'167
Wheat straw production cost (M€/y)	845	800	800
Wheat straw & products transportation costs (M€/y)	341	337	337
NPV (M€)	30	43	43

Table 3: Biorefinery size (Mt/y of feedstock) distribution for each iteration of process optimization. Iterat. = iteration.

Iterat	Number of biorefineries												
	1	2	3	4	5	6	7	8	9	10	11	12	13
I	2.2	2.2	2.2	-	-	-	-	-	-	-	-	-	-
II	0.9	0.8	0.8	0.7	0.7	0.5	0.5	0.4	0.3	0.3	0.2	0.0	0.0
III	0.8	0.7	0.7	0.7	0.7	0.7	0.7	0.7	0.7	0.7	-	-	-

In particular, the first iteration assuming only three biorefineries implied high transportation costs for the wheat straw. Therefore, next the supply chain optimization provided a result consisting in a decentralized production with 13 biorefineries with feedstock rate spanning between 0.05 and 0.94 Mt/y (Table 3). More accurate evaluation of the capital costs of smaller biorefineries, by process optimization of single plants, determined that the four smallest biorefineries, processing less than 0.3Mt/y, were deleted in the next iteration of the supply chain optimization. The straw production costs are lower in the second and third iteration compared to the first one because only 98% of available wheat straw is used as feedstock. Moreover, the transportation costs in the first iteration are almost the same with the ones in the second and third iteration as more wheat straw is used. The final result shows an increase of NPV up to 43 M€. Figure 2 shows the localization of the final biorefineries in the Germany's territory. The largest biorefinery (871'200 t/y) resulted in Rhineland-Palatinate region (dashed line in Figure 2) because WS is harvested in North West and West of Germany and from the topology results since there are no biorefineries in all its neighbour regions.



Figure 2: Biorefineries location in the map from the final iteration of the algorithm.

5. Conclusions

In this work, an integrated methodology to consider both the supply chain optimization and the process optimization was proposed. The developed MILP algorithm was tested on a biobased system transforming cereal straw into biofuels, ethanol and ethyl levulinate, in Germany. The algorithm efficiency was successfully demonstrated. In fact, three iterations were sufficient to reach the convergence of the algorithm to the optimal solution consisting in nine biorefineries located in different regions of Germany. This decentralized production resulted from a trade off between capital costs and transportation costs in a big territory. In fact, by increasing the number of biorefineries capital costs increase while biomass and bioproducts transportation costs decrease. The optimal solution derived from the maximization of the NPV.

References

- S. Belletante, L. Montastruc, S. Negny, S. Domenech, 2016. Design of a Multiproduct Lignocellulosic Biorefinery through the Process Modelling of a Feasible Superstructure. *Comput. Aided Chem. Eng.* 38, 595–600.
- C. Galanopoulos, D. Barletta, E. Zondervan, 2018. A decision support platform for a bio-based supply chain: Application to the region of Lower Saxony and Bremen (Germany). *Comput. & Chem. Eng.* 115, 233–242.
- C. Galanopoulos, A. Odierna, D. Barletta, E. Zondervan, 2017. Design of a wheat straw supply chain network in Lower Saxony, Germany through optimization. *Comput. Aided Chem. Eng.* 40, 871–876.
- A. Giuliano, D. Barletta, I. De Bari, M. Poletto, 2018. Techno-economic assessment of a lignocellulosic biorefinery co-producing ethanol and xylitol or furfural. *Comput. Aided Chem. Eng.* 43, 585–590.
- A. Giuliano, R. Cerulli, M. Poletto, G. Raiconi, D. Barletta, 2016. Process Pathways Optimization for a Lignocellulosic Biorefinery Producing Levulinic Acid, Succinic Acid, and Ethanol. *Ind. Eng. Chem. Res.* 55, 10699–10717.
- A. Giuliano, R. Cerulli, M. Poletto, G. Raiconi, D. Barletta, 2014. Optimization of a Multiproduct Lignocellulosic Biorefinery using a MILP Approximation. *Comput. Aided Chem. Eng.* 33, 1423–1428.
- A. Giuliano, M. Poletto, D. Barletta, 2015. Process Design of a Multi-Product Lignocellulosic Biorefinery. *Comput. Aided Chem. Eng.* 37, 1313–1318. <https://doi.org/10.1016/B978-0-444-63577-8.50064-4>
- J.M. Laínez-Aguirre, M. Pérez-Fortes, L. Puigjaner, 2015. Strategic Planning of Biomass Supply Chain Networks for Co-combustion Plants. *Comput. Aided Chem. Eng.* 36, 453–474.
- K.Y. Nandiwale, P.S. Niphadkar, S.S. Deshpande, V. V. Bokade, 2014. Esterification of renewable levulinic acid to ethyl levulinate biodiesel catalyzed by highly active and reusable desilicated H-ZSM-5. *J. Chem. Technol. Biotechnol.* 89, 1507–1515.
- S2Biom Project Report D1.8 Atlas with regional cost supply biomass potentials for EU 28, Western Balkan Countries, Moldavia, Turkey and Ukraine, 2017. https://s2biom.wenr.wur.nl/doc/S2Biom_D1_8_v1_1_FINAL_19_04_2017_CP.pdf
- Z. Wang, T. Lei, L. Liu, J. Zhu, X. He, Z. Li, 2012. Performance investigations of a diesel engine using ethyl levulinate-diesel blends. *BioResources* 7. (4), 5972-5982.

Design of smart liquid-liquid extraction columns for downstream separations of biopharmaceuticals using deep Q-learning algorithm

Soonho Hwangbo¹, Merve Öner¹, Gürkan Sin^{1,*}

¹*Process and Systems Engineering Center (PROSYS), Department of Chemical and Biochemical Engineering, Technical University of Denmark, Building 229, DK-2800 Kgs. Lyngby, Denmark*
gsi@kt.dtu.dk

Abstract

We propose smart liquid-liquid extraction columns of biopharmaceuticals using deep Q-learning algorithm. In this contribution, we demonstrated the application of the tool for design of liquid-liquid extraction process for concentration of API from fermentation broth. To this end, we present the following; 1) development of property model to describe solubility of API in different solvents using the nonrandom two-liquid segment activity coefficient model, 2) design the liquid-liquid extraction process for different solvent candidates commonly used in pharma industries, 3) application of deep Q-learning algorithm to optimize liquid-liquid extraction control, and 4) perform sensitivity analysis to study effect of feed fraction of API on the performance. We have validated the developed property process modelling by comparing the existing experimental data and the characteristics of diverse solvents and using sensitivity analysis. We expect that the results from this study would contribute to further development the general framework of downstream separation for the future by extending to more downstream separation processes.

Keywords: Property process modelling, liquid-liquid extraction, deep Q-learning, control, biopharmaceuticals.

1. Introduction

The global pharmaceuticals industry enjoyed years of favorable growth –total revenues generated in 2011 were in excess of \$698 billion representing an annual growth rate of 6.7% between 2007 and 2011. The industry now finds itself facing a number of challenges including a changing health care landscape, expiring patents and generic competition, pricing pressures, and a persistent economic slowdown (Fernandes 2015). One of the feasible solutions to overcome the current situation is to develop a smart modelling tool for design and synthesis of downstream separation for biopharmaceuticals. Liquid-liquid extraction (LLE), which is also called solvent extraction, is the main process that is much employed during the downstream separation. In LLE process, a liquid feed of two or more components is faced with a second liquid phase containing solvent (Seader, Henley et al. 1998). Therefore, the use of proper solvents is an inevitably important issue to obtain high yield of active

pharmaceutical ingredients (APIs) and achieve great crystalline form from the product performance's point of view. The property process modelling such as the solubility, which is a chemical property referring to the ability for a given substance called solute to dissolve in solvents, can explicitly affect the general feasibility of the LLE process. As part of development of a general framework of a smart modelling tool for downstream separation process for biopharmaceuticals, this study aims to develop the property process modelling and design one of the commonly used separation step for concentration of API by using an in-silico tool and reinforcement learning. In the reinforcement learning section, a deep Q-learning algorithm to control the LLE process considering Markov decision process and deep neural networks has been investigated (Henderson, Islam et al. 2018). Sensitivity analysis of API has been simulated and the general framework of a smart LLE column for downstream separation has been proposed.

2. Problem statement

Figure 1 illustrates the overall framework of this study. Property process modelling based on thermodynamic model is developed and the LLE process is designed using the results from the property process modelling. The property process modelling is able to be constructed by either conducting experiments or applying thermodynamic models. However, the research on the property process modelling of various compounds via thermodynamic models have been actively studied because the experiments costs time and resources. Nonrandom two-liquid segment activity coefficient (NRTL-SAC) model was selected for the purpose of solubility modeling and Aspen Properties was employed to regress segment parameters. Reinforcement learning was applied to conduct process operation optimization in the LLE process to optimize process operation.

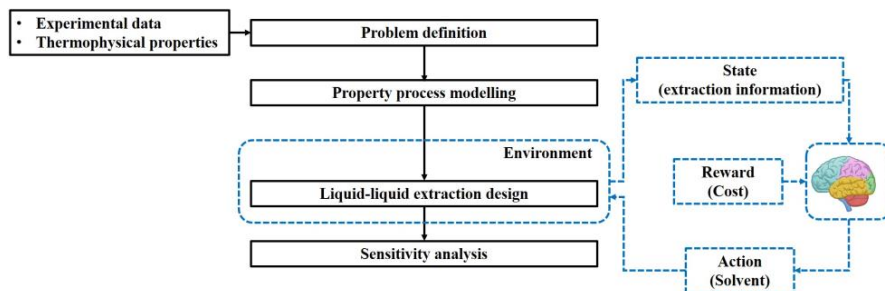


Figure 1. Overall framework of a smart liquid-liquid extraction process for downstream separation of biopharmaceuticals.

Deep Q-learning algorithm, which is one of the most dominant reinforcement learning tools, was employed to implement to design optimal control strategies (Mnih, Kavukcuoglu et al. 2015, Gu, Lillicrap et al. 2016). The LLE process corresponds to the environment and discloses LLE column information towards a deep Q-learning agent. The main role of the deep Q-learning agent optimizes parameters of the value function, which is taken into account as deep neural networks, to obtain the reward as much as

possible that is the operating cost in this research. The deep Q-learning agent makes an action to manipulate information of solvents and finally the environment is newly characterized by the action. Sensitivity analysis of APIs with distinct solvents that were selected by the property process modelling has been performed.

3. Property process modelling and the LLE column design

Aforementioned thermodynamic models such as universal functional activity coefficient (UNIFAC), conductor-like screening model for real solvent (COSMO-RS), conductor-like screening model-segment activity coefficient (COSMO-SAC), NRTL-SAC correspond to liquid-phase non-ideality of organic nonelectrolytes (Chen and Crafts 2006). In this study, the NRTL-SAC model has been selected and utilized to construct the property process modelling. General mathematical expression at stages in the LLE process consists of differential equations. Solute concentrations in the raffinate phase (x_i) and the extract phase (y_i) are derived by the raffinate flowrate (R), the extract flowrate (E), backmixing coefficients (α and β), mass transfer (Q_{x_i}), and fractional holdup (h_{x_i} and h_{y_i}) and mass transfer is determined by mass transfer coefficient (K_{x_i}), interfacial area coefficient (a_i), and equilibrium concentration (x_i^*) (Eqs. (3) and (4)) (Mjalli 2005).

$$\frac{dx_i}{dt} = \frac{[(1 + \alpha)R_{i+1}x_{i+1} + \alpha R_{i-1}x_{i-1} - (1 + 2\alpha)R_i x_i - Q_{x_i}]}{h_{x_i}} \quad (1)$$

$$\frac{dy_i}{dt} = \frac{[\beta E_{i+1}y_{i+1} + (1 + \beta)E_{i-1}y_{i-1} - (1 + 2\beta)E_i y_i + Q_{x_i}]}{h_{y_i}} \quad (2)$$

$$Q_{x_i} = K_{x_i} a_i V (x_i - x_i^*) \quad (3)$$

The equilibrium concentration of solute is numerically connected with the mole fraction of the solute (x^{SAT}), which is able to be calculated by the entropy of fusion of the solute ($\Delta_{fus}S$), the activity coefficient of the solute (γ^{SAT}), and the melting point (T_m) (Eq. (4)) (Chen and Song 2004).

$$\ln x^{SAT} = \frac{\Delta_{fus}S}{R} \left(1 - \frac{T_m}{T} \right) - \ln \gamma^{SAT} \quad (4)$$

The LLE process can be designed with inherent input data. In this LLE process, we mainly assume that the number of stages is 10, the system temperature is the room temperature, the reactor is adiabatic, and liquid-liquid coefficient form is calculated by the defined property method. As the feed composition, we have considered a stream after solid-liquid removal of the fermentation broth which results in a water rich (rather

dilute) stream containing API with typical concentration levels. For confidentiality purposes, the identity of the API cannot be disclosed.

4. Off-policy control with deep Q-Learning

General reinforcement learning includes five components, each of which is state, state transition probability matrix, action, reward, and discount factor. State illustrates the current environment and the transition from the previous state to the next state depends on actions from the agent. All the actions are based on a policy contained in the agent and the ultimate goal of reinforcement learning is to figure out the optimal policy to maximize rewards during both exploration and exploitation. In the case of off-policy learning, experience generated from old policies can be reused and the agent learns about multiple policies while following one policy. Off-policy Q-learning converges to the optimal action-value function, and provides the optimal control solution. The general definition of the action-value function ($Q(S, A)$) is the expected return obtained by starting from the current state (S), taking an action (A), and then following the current policy (π) (Eq. (5)). Reward (R) and another state (S') are observed by taking action from the existing state using policy derived from the existing action-value function. Then, the current action-value function is updated toward a better action-value function (Eq. (6)).

$$Q_{\pi}(s, a) = E_{\pi}[G_t | S_t = s, A_t = a] \quad (5)$$

$$Q(S, A) \leftarrow Q(S, A) + \alpha \left(R + \gamma \max_{a'} Q(S', a') - Q(S, A) \right) \quad (6)$$

Action-value functions in this study were considered by deep neural network and the concept of experience replay was taken into account to enhance the performance of training agent. Extraction information such as flowrates of materials, molar ratio, operating temperature, and pressure represents the state of the environment and the deep Q-learning agent exports actions such as solvent flowrate to control the LLE extraction. The LLE process operation method under the optimal control strategies can be suggested with the minimization of the operating costs.

5. Results and discussion

Validation of the property process modelling and sensitivity analysis of the API mole fraction with the amounts of solvents have been performed. Figure 3 describes the predicted solubility of API with various single solvents and one binary solvents. Acetone, acetonitrile, 1-butanol, methyl tert-butyl ether (MTBE), 1,4-dioxane, ethanol, ethyl acetate, n-heptane, methyl isobutyl ketone (MIBK), isobutanol, isopropyl alcohol (IPA), and methanol were used as single solvent and the predicted mole fraction of API dissolved in those solvents shows a considerably linearity with the experimental solubility (Figure 2(A)). In the case of the binary solvents, the patterns between the predicted and the experimental values are alike but there exist visually differences until 20% of water in the binary solvents because the experiment had been conducted over the unsteady room temperature (Figure 2(B)).

The deep Q-learning algorithm has been performed to conduct process operation optimization. Designed LLE process as the environment in the deep Q-learning world

manifests a total of 5 characteristics in a state which are flowrates, molar ratio, operating temperature, and pressure in the LLE process. The deep Q-learning agent has received state information and been trained via deep neural networks. In this research, two deep neural networks have been used in order to account for behaviour action-value function and target action-value function. We assumed that the internal structure of those deep neural networks are identical, with three hidden layers. The behaviour action-value function is related to an exploring policy able to extend the range of control optimality. The target action-value function is associated with the optimal policy which should be finally determined with maximizing rewards, in other words, minimizing the operating costs of the LLE process. The action of the deep Q-learning agent has been assumed as solvent information and the total of 20,000 episodes for training have been executed. The total operating costs were approximately reduced by 4.66% compared to the existing LLE process. The more real data, the better robustness and feasibility would be anticipated.

Sensitivity analysis using Aspen Plus indicates that the types of solvents play an important role in the LLE process. 94%(w/w) water in the feed stream and the room temperature in the system were assumed in the sensitivity analysis. The range between the minimum value and the maximum value of the API mole fraction in the extract stream of the LLE process is infinitesimal because used solvents (acetone, acetonitrile, 1,4-dioxane, ethanol, and methanol) are miscible with water. The API mole fraction exponentially decreases according to an increase of the quantity of solvents because used solvents (1-butanol, MTBE, ethyl acetate, MIBK, and isobutanol) are immiscible with water. Changing the number of stages in the LLE process, adding different solvents or replacing single solvents with binary solvents would be implemented with respect to sensitivity analysis.

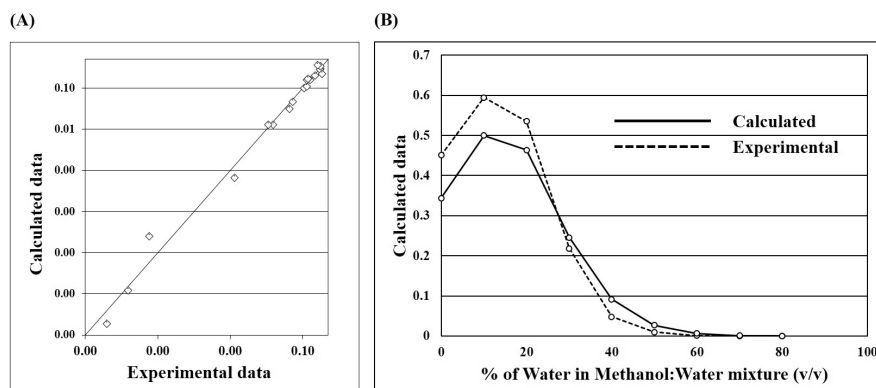


Figure 2. Solubility results from the property process modelling using thermodynamic model. (A): Solubility of API in single solvents. (B): Solubility of API in different volume fraction of water in methanol/water solvents.

6. Conclusions

An in-silico tool for the property process modelling and the LLE process has been studied and developed by using simulation tools and artificial intelligence software. We have demonstrated the application for a fermentation broth containing an API with

dilute concentration (<5% wt). The main conclusions of this study are as follows: 1) NRTL-SAC model and parametric regression in Aspen Properties are able to describe solubility of API in different solvents quite satisfactorily, 2) the LLE process has been designed considering a class of solvents commonly used in pharmaceutical industry which enabled fast screening of LLE design candidates, 3) reinforcement learning such as deep Q-learning in this study has been conducted to implement the LLE process operation optimization, and 4) sensitivity analysis has been performed to clarify the connection and impact between solvents and API. Future works will extend the analysis of LLE design under uncertainty of experimental data in particular property measurements and modelling to enable robust design and solvent screening (Frutiger, Jones et al. 2018). Moreover, the LLE column design technique implemented in this study would be applied for the development of a general downstream separation framework tool able to be extended to other relevant downstream separation steps including crystallization process and chromatographic separation to offer a complete design of biopharmaceutical separation.

Acknowledgment

We would like to thank the Danish Council for Independent Research (DFF) for financing the project under the grant ID: DFF-6111600077B.

References

- Chen, C.-C. and P. A. Crafts (2006). "Correlation and prediction of drug molecule solubility in mixed solvent systems with the nonrandom two-liquid segment activity coefficient (NRTL-SAC) model." *Industrial & engineering chemistry research* **45**(13): 4816-4824.
- Chen, C.-C. and Y. Song (2004). "Solubility modeling with a nonrandom two-liquid segment activity coefficient model." *Industrial & engineering chemistry research* **43**(26): 8354-8362.
- Fernandes, P. (2015). "The global challenge of new classes of antibacterial agents: an industry perspective." *Current opinion in pharmacology* **24**: 7-11.
- Frutiger, J., M. Jones, N. G. Ince and G. Sin (2018). From property uncertainties to process simulation uncertainties—Monte Carlo methods in SimSci PRO/II process simulator. *Computer Aided Chemical Engineering*, Elsevier. **44**: 1489-1494.
- Gu, S., T. Lillicrap, I. Sutskever and S. Levine (2016). *Continuous deep q-learning with model-based acceleration*. International Conference on Machine Learning.
- Henderson, P., R. Islam, P. Bachman, J. Pineau, D. Precup and D. Meger (2018). *Deep reinforcement learning that matters*. Thirty-Second AAAI Conference on Artificial Intelligence.
- Mjalli, F. S. (2005). "Neural network model-based predictive control of liquid-liquid extraction contactors." *Chemical engineering science* **60**(1): 239-253.
- Mnih, V., K. Kavukcuoglu, D. Silver, A. A. Rusu, J. Veness, M. G. Bellemare, A. Graves, M. Riedmiller, A. K. Fidjeland and G. Ostrovski (2015). "Human-level control through deep reinforcement learning." *Nature* **518**(7540): 529.
- Seader, J. D., E. J. Henley and D. K. Roper (1998). "Separation process principles."

Process design and techno-economic analysis of a pineapple wine production plant under the context of the Choco-Colombia region

Juan Fernando Murcia Palacios^{a*}, Rolando Barrera^a, Edwin Zondervan^b.

^a *Grupo CERES-Agroindustria & Ingeniería, Universidad de Antioquia UdeA, Calle 70 No. 52-21, Medellín, Colombia*

^b *University of Bremen, Leobener Str. 6, Bremen, 28359, Germany*

**fernando.murcia@udea.edu.co*

Abstract

Pineapple surplus in the region of Choco-Colombia, the selection process that involves its commercialization and being a rapidly perishable fruit, causes serious losses for farmers. Due to the high content of sugars, it is anticipated that discarded fruit juice can be used as a substrate for the development of bioprocesses to obtain value-added products on an industrial scale. A new model for a 1600 ton / year pineapple wine production plant has been developed with Aspen Plus® v10.0 (Aspentech, Cambridge, MA). It is observed that the cost of the raw material and the fixed manufacturing costs have the greatest impact on the operating cost with 29 and 28% respectively, the capital cost are estimated in US\$ 15.52 million, on the other hand the plant generates 2210 tons of pineapple bagasse as solid waste and emits of 162.3 tons of CO₂ per year.

Keywords: modeling, simulation, techno-economic analysis, pineapple wine

1. Introduction

About 4 thousand tons of pineapple are wasted every year in the Choco region [1]. Thanks to governmental programs that have encouraged the cultivation of this fruit, in recent years the production of pineapple in the region went from 2,737 tons in 2007 to more than 8,000 tons in 2015[2]. However, such an increase in pineapple production leads to a simultaneous increase in waste generation due to the selection and elimination of components during processing. Most pineapples are eaten fresh; nevertheless, only the first-quality fruit is selected for later distribution to the markets. Therefore, fruit that does not comply with these characteristics is left to rot on farms or is sold at very low prices [1]. Although some alternatives to fresh consumption (jams, concentrates, nectars, purées, etc.) are being implemented, a high percentage of the production is still left in the fields as a waste[3]. These practices create both an ecological and an economic problem, because large amounts of organic matter have to be recycled and money must be spent on agrochemicals, labour, and machinery for both the fruit that is consumed and the fruit that is disposed of, but all the costs are borne by the fruit that is consumed. Thus, higher prices and environmental contamination result from fruit surplus[4].

Several alternatives have been proposed and implemented in some countries, mainly transformations by fermentation, with wine, vinegar and other compounds as value-added products. Despite several laboratory-scale experimental investigations of pineapple wine

production, little information is available on the economics of semi-industrial or industrial production [1, 5-7]. In this work, both modeling and simulation are used to evaluate the process of transformation of pineapple juice into wine. To the best of author's knowledge, a techno-economic evaluation to the transformation of pineapple juice into wine under the context of Choco-Colombia region has not been reported so far. Aspen Plus® v10.0 was used to model and simulate the process, then the model was used to estimate the capital and operating costs, as well as the emissions of the plant.

2. Model description

Using the Aspen Plus® software a process flowsheet is presented in Fig. 1. The diagram shows the fundamental operations of the plant: the extraction of the juice, the clarification, fermentation, ageing, filtration and bottling, the process is simulated and the material and energy flows of each operation and the sizing of the equipment can be determined. Based on these values, the purchase costs of the equipment are estimated and with data from the literature assume the values corresponding to the operating costs of each unit. Currently such models (of non-conventional operations) and the related data for evaluation are not at hand. In this work we offer this valuable information. From the design and simulation, the economic analysis of the plant is presented.

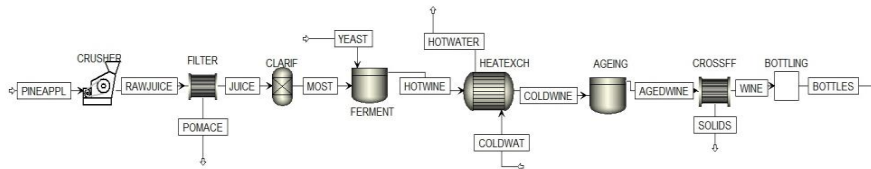


Figure 1. Aspen Plus® process flowsheet of the pineapple wine manufacturing plant

3. Outline of Process Technology

Pineapples are mechanically peeled, cored and crushed for juice extraction. The ripeness of the pineapple is judged from the sugar content in the juice; it is assumed that the pineapple juice has a 22°Brix index. Pineapple pomace is considered as a waste and the cost for its final disposal is included in the value of the raw material. Fermentation tanks made of stainless steel are used and the fermentation time is set at 15 days. Pineapple juice of a 22°Brix index when fully fermented with yeast will produce wine with an ethanol percentage of 11.5% at a rate of 1L of wine/kg of juice [8]. The fermentation is an exothermic process and the temperature in the fermentation tank must be maintained below 30°C. Therefore, cooling is required. The storage of pineapple wine results in biochemical- and physicochemical reactions that improve organoleptic characteristics and facilitate its clarification. In this case, the pineapple wine is aged for 6 months, before being bottled. Pineapple wine is stored in stainless steel tanks of 150ton capacity at 20°C, which requires cooling. Then, pineapple wine is filtered to remove all suspended particles before bottling. A suitable technology is a cross flow microfiltration. The aged and clarified pineapple wine is packaged in 0.75 L capacity glass bottles, using a high speed bottling machine at a speed of up to 5000 bottles/h.

4. Economic assessment

The economic assessment includes the purchase prices of the raw material, labor cost, industrial services, capital costs and the tentative value of sale of the finished product, the

economic analysis of the production plant. Additionally, a plant lifetime of 27 years is considered, three years lower compare with a similar project using grapes, due to immediate pineapple availability. It is assumed that 50% of the required capital is covered by a loan with interest of 8% for 15 years, with a discount rate of 4%. The annual depreciation is estimated from the modified accelerated cost recovery system (MACRS) method described in Maroulis and Saravacos [9], in which, the machinery depreciates in 7 years. It assumes a production capacity equal to the installed capacity during the life time of the project. Finally, a 35% tax rate on profits is considered.

5. Results and Discussion

A flow chart of the process including the unit operations considered during the transformation of pineapple juice into wine is shown in Fig. 2. The values are based on 1000 kg of raw material. In the same diagram the requirements of the industrial services are presented in MJ. Also, Table 1 lists the material and energy requirements of the wine manufacturing plant, based on the material and energy diagram in Figure 2. The annual data corresponds to 320h/y. Labour refers only to production workers that is obtained by the counting method, both supervision and technical support are obtained by the factorial method both methods described in Maroulis and Saravacos [9].

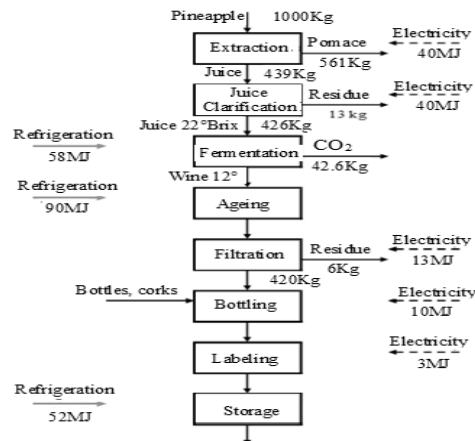


Figure 2. Material and energy balances of the pineapple wine manufacturing plant

In the extraction of the juice, pineapple peel and core are considered as residue, and the yield of this operation is taken from the literature with a value close to 44% of pulp juice per each kilogram of pineapple. In this operation, 13kg of waste is generated for each ton of pineapple, which means that from 1 ton of pineapple that enters the process only 426kg reaches the fermenter, which generates a loss of raw material close to 60%. Therefore, a strategy that generates value to these lignocellulosic wastes using superstructure optimization approach, which will be addressed in future work[10, 11].

Based on the juice input flows it the size of the fermenters should be 40 m³ of stainless steel capacity. The pineapple juice of 22 ° Brix index was inoculated with activated dry yeast (ADY) at the rate of 0.15kg / ton, and was transformed into pineapple wine with

approximately 12% ethanol with a yield close to 1L of wine / kg of juice. The carbon dioxide generated during the reaction at a rate of 0.1kg CO₂ / L juice of 22 ° Brix.

On the other hand, as can be seen in Figure 1, 0MJ of electricity is required for each ton of pineapples for juice extraction, 40MJ for clarification, 13 MJ for filtration, 10 MJ for bottling and 3MJ in the labelling. While the refrigeration requirements are made in the stages of fermentation with 58MJ, aging with 90MJ and storage with 52MJ. It should be noted that water consumption is not considered during the cleaning of both the raw material and the equipment, nor the sterilization process.

Table 1. Material and Energy Requirements of the Pineapple Wine Manufacturing Plant

		<u>Per product</u>		<u>Hourly basis</u>		<u>Annual</u>	
<u>Product</u>							
Pineapple wine		1.00	kg/kg	5.00	t/h	1 600	t/y
<u>Raw material</u>							
Pineapples	Fr.	2.38	kg/kg	11.9	t/h	3 810	t/y
Bottles	Fg.	0.75	kg/p	6667	p/h	2. 133 333	p/y
<u>Utilities</u>							
Electricity	Fe.	0.05	kWh/kg	0.26	MW	82	MWh/y
Refrigeration	Fz.	0.13	kWh/kg	0.66	MW	212	MWh/y
<u>Labour</u>							
Manpower	M.	6.4	h/t	32.0	p	10 240	h/y

Capital costs and operating costs calculations are based on the short methods detailed in Maroulis and Saravacos [9], the size and cost of the equipment are estimated and the results are summarized in Table 2. The required capitals along with the appropriate assumptions are presented in Table 3.

Table 2. Equipment Cost Estimation of the Pineapple Wine Manufacturing Plant

<u>Equipment</u>	<u>Qty</u>	<u>Size unit</u>	<u>Cost, Thousands US\$</u>
1. Fermentation tanks	20	40 ton	1000
2. Storage tanks	10	150 ton	1000
3. Crusher	1	5 ton/h	150
4. Screw press	1	5 ton/h	150
5. Heat exchanger	1	5 ton	150
6. Microfiltration	1	1 ton/h	150
7. Bottling machine	1	5 ton/h	400
			3000

It should be noted that for the economic analysis the purchase price of equipment had to be considered, these prices were updated taking by assuming a Lang factor of 4.5 because it is a new construction for food processing and to be located in an area with difficult access conditions. Although a centralized plant is considered in this work to reduce the cost of transporting the raw material, since more than 60% of the pineapple transported does not end up in the final product local storing might reduce costs significantly. In addition, it is assumed that the plant is close to the fields, the maximum distance is assumed to be 50km. In addition, losses are not considered due to the manipulation of the raw materials.

For the costs calculations the following assumptions are made: the annual operating time is 4 weeks per year, 5 days per week, 2 shifts per day and 8 hours per shift, product rate 4 ton/h, a labour cost of US \$ 2.5 / h was assumed, which is representative of the unskilled

workers in the Colombian context, raw material US\$0.3/kg, a value three times higher than the price farmers normally receive when selling second and third quality pineapples, packaging material US\$ 0.3/p, electricity cost US\$ 0.11/kWh, cooling water cost US\$ 0.01/kWh. and the results are presented in Figure 3. From figure 3, it is observed that the cost of the raw material is the one that has the greatest impact on the cost analysis, so if the farmers are directly involved in the pineapple wine production the cost of the raw material could decreased and the profitability of the plant could be higher.

Tabla 2. Capital Cost Estimation of the Pineapple Wine Manufacturing Plant

Purchased Equipment Cost	Ceq	3.00	M\$
Lang Factor	fL	4.50	-
Fixed Capital Cost	CF	13.50	
Working Capital Cost	CW	2.02	
Total Capital Cost	CT	15.52	M\$

The estimated profitability data is shown in Table 4. An internal rate of return of 23% is attractive for this type of investment. In that sense, this model can be the first step of a tool for helping processing decisions in the pineapple wine production sector. Although first result look promising, further research is needed to determine for example the amount of pineapple wine that can be diverted for the production of vinegar or premium-quality brandy.

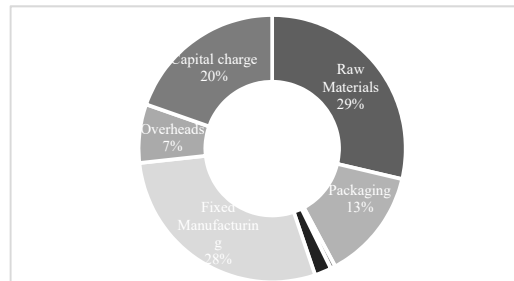


Figure 3. Operating cost estimation of the wine manufacturing plant per unit of product.

Table 4. Profitability of the Pineapple Wine Manufacturing Plant.

Profitability			
Sales Income	S	6.73	M\$/y
Manufacturing Cost	CM	3.81	M\$/y
Gross Profit	Pg	2.92	M\$/y
Net Present Value	VPN	19.23	M\$
Own Capital Cost	Co	7.59	M\$
Capital Return Ratio	CRR	2.53	-
Internal Rate of Return	IRR	0.23	-

6. Conclusions

A techno-economic analysis of a plant that transforms pineapple juice into wine as the main product was carried out. The higher capital costs are related to the size of the

fermentation and aging tanks, and the bottling machine. The emissions are primarily the residue or bagasse of the pineapple, which can be arranged in the field or be processed to obtain other products of interest. Moreover, this model can be the first step of a tool for helping processing decisions, making possible to vary the amount of raw material that can be transformed into pineapple wine, giving the flexible enterprise the advantage to better adapt to changes in demands that occur in the market. We are aware that this result may be significantly affected by the size of the plant, raw materials and products prices, or the volume of production and deserves a sensitivity analysis, which will be addressed in future work.

Acknowledgments

Juan Fernando Murcia Palacios express his acknowledgements to the Departamento Administrativo de Ciencia, Tecnología e Innovación (Colciencias) call 647 – 2014

References

- Murcia Palacios, J.F., *Ensayos para la producción de etanol utilizando Ananas comosus de rechazo*, in *Escuela de Ingeniería*. 2013, Universidad Pontificia Bolivariana: Medellín. p. 61.
- MADR, *Red de Información y Comunicación del Sector Agropecuario Colombiano (Spanish)*, M.d.A.y.D. Rural, Editor. 2018.
- Grewal, H., H. Tewari, and K. Kalra, *Vinegar production from substandard fruits*. *Biological wastes*, 1988. **26**(1): p. 9-14.
- Hidalgo, C., E. Mateo, and A.B. Cerezo, *Technological process for production of persimmon and strawberry vinegars*. *International Journal of Wine Research*, 2010. **2010**(1): p. 55-61.
- Roda, A., et al., *Effect of pre-treatments on the saccharification of pineapple waste as a potential source for vinegar production*. *Journal of Cleaner Production*, 2016. **112**: p. 4477-4484.
- Tropea, A., et al., *Bioethanol production from pineapple wastes*. *Journal of Food Research*, 2014. **3**(4): p. 60.
- Roda, A., et al., *Vinegar production from pineapple wastes—Preliminary saccharification trials*. *Chem. Eng. Trans*, 2014. **37**.
- Maroulis, Z.B. and G.D. Saravacos, *Food process design*. Vol. 126. 2003: CRC Press.
- Maroulis, Z.B. and G.D. Saravacos, *Food plant economics*. 2007: CRC Press.
- Nawaz, M., et al., *Design of an optimal biorefinery*, in *Computer Aided Chemical Engineering*. 2011, Elsevier. p. 371-376.
- Giuliano, A., et al., *Techno-economic assessment of a lignocellulosic biorefinery co-producing ethanol and xylitol or furfural*, in *Computer Aided Chemical Engineering*. 2018, Elsevier. p. 585-590.

A dynamic model for automated control of directed self-assembly of colloidal particles at low densities

Baggie W. Nyande, Yu Gao & Richard Lakerveld*

*Department of Chemical and Biological Engineering, The Hong Kong University of Science and Technology, Clear Water Bay, Hong Kong S.A.R.
kelakerveld@ust.hk*

Abstract

Directed self-assembly of colloidal particles is a promising route for the fabrication of advanced materials with novel properties. However, the formation of defect-free non-periodic structures is difficult to achieve without active control. Dynamic models can determine optimal input trajectories of manipulated variables during directed self-assembly. This paper presents a dynamic model for the simulation of particle trajectories in a microfluidic device in the presence of an electric field with time-varying properties, which can be used to predict the dynamic development of the particle density distribution. The model is based on first principles and has been experimentally validated at low particle densities. It has great promise to be used for model-based control of directed self-assembly of colloidal particles.

Keywords: Directed self-assembly, Model-based control, dynamic modelling, dielectrophoresis

1. Introduction

Self-assembly is defined as the spontaneous and reversible association of molecules or particles into organized structures (Whitesides and Grzybowski, 2002). The self-assembly of desired structures can be directed by external fields such as flow, magnetic or electric fields. Such directed self-assembly provides a promising bottom-up route for the fabrication of advanced materials with micro- and nanoscale structures that may unlock novel optical, mechanical and electrical properties. The control of particle densities is necessary for the formation of defect-free non-periodic structures when specific features need to be self-assembled (Solis et al., 2010). However, controlling a local density of colloidal particles is challenging due to the stochastic nature of the particles, potential lack of local actuation and the highly nonlinear process behaviour. Controls based on free energy landscapes (Tang et al., 2016) and model-free feedback control have been implemented for the electric field assisted crystallization of colloidal particles (Jurez and Bevan, 2012) and for the defect-free alignment of colloidal particles (Gao and Lakerveld, 2018). The use of dynamic models in an open-loop or closed-loop model-based control framework offers the potential to better control the local colloidal particle density, which can ultimately minimize the occurrence of defects for non-periodic structures. However, the development and experimental validation of dynamic models that are favourable for online implementation for control of local particle density within a directed self-assembly process are in their infancy.

Directed self-assembly of micro and nano-sized particles are inherently stochastic even in the absence of measurement noise and unknown perturbations (Ulissi et al., 2013), therefore the dynamics of directed self-assembly processes are typically described with probabilistic models such as the Fokker-Planck equation (Komaee and Barton, 2016) for systems with continuous states or

master equations (Lakerveld et al., 2012) for discrete-state continuous-time Markov processes. The use of master equations is limited to systems with a relatively low number of states. The full set of master equations may become computationally intractable if all states are considered due to the curse of dimensionality. In addition to the computational challenges, experimental validation of probabilistic models is difficult. Therefore, the utilization of existing dynamic models for automated control of directed self-assembly processes remains challenging.

The objective of this work is to develop and validate a dynamic model that describes the dynamic development of the particle density distribution within a microfluidic device in the presence of electric fields that can be used for control purposes. The model is deterministic and describes the prevailing dielectrophoretic and drag forces based on first principles. The model is validated with experiments. In future work, the proposed dynamic model can be extended to include noise from Brownian motion. This model can be a suitable basis for the development of novel open and closed-loop model-based control approaches for directed self-assembly of colloidal particles in microfluidic devices.

2. Approach

2.1. Microfluidic device and self-assembly system

The colloidal particles (silica, diameter of $2\ \mu\text{m}$) are suspended in DI water. The suspension is contained in a microfluidic device, which consists of two transparent electrodes (one patterned with photoresist and the other unpatterned) arranged in a parallel-plate configuration (see Fig. 1). The patterned electrode ($2\ \text{cm} \times 2\ \text{cm}$) is fabricated by spin-coating a 25–45 nm thick indium-tin oxide (ITO) coated glass with positive photoresist (400 nm) through standard photolithographic techniques. The two electrodes are separated by a $750\ \mu\text{m}$ thick silicone rubber spacer (Grace Bio-Labs Bend, Oregon). About $23\ \mu\text{L}$ suspension of silica particles is pipetted into a hole that is punched in the silicone double-adhesive rubber spacer. Electric wire leads are connected to the top and bottom electrodes. AC electric fields with a frequency between 300 kHz and 1 MHz and a peak-to-peak voltage between 2V and 10V are applied to the electrodes via a function generator (33500B, Keysight Technologies). Particles are allowed to settle in the device for about 10 minutes at the beginning of each experiment so that the effect of gravity on particle motion can be neglected. The particle assembly in the cell is continuously observed with an optical microscope (Nikon Ni-U) equipped with a digital camera (Nikon Digital Sight Qi2). Images captured by the CCD camera at a rate of 2 frame/s are analysed using image processing functions in MATLAB 2017a to obtain particle positions as a function of time in an automated fashion.

When non-uniform AC fields are applied to the microfluidic device, the particles and medium experience forces of electrical origin including dielectrophoresis (DEP) and AC electro-osmosis (ACEO). DEP is the electrically induced movement of uncharged dielectric particles in the presence of a non-uniform electric field. For two electrodes separated at a certain distance, the minimum electric field occurs at an equidistance to both electrodes which coincides with the center of the photoresist layer in our experimental setup. The maximum electric field occurs at the edges of the photoresist (Gao and Lakerveld, 2018). The direction of the particle motion is determined by the relative polarizability of the particles and the suspending medium. Particles that are more polarizable than the medium are drawn towards regions of electric field maxima (pDEP). Alternatively, particles with lower polarizability compared with the medium are directed to regions of lower electric field (nDEP). ACEO on the other hand, arises from the interaction of ions in the electrical double layer formed close to the surface of the electrodes and the tangential component of the applied electric fields. At the high AC frequencies applied in our experiments, there is insufficient time for the double layer to form, thus there is no resultant fluid flow to drive the particles (Squires and Bazant, 2004). Therefore only DEP is considered in our model development.

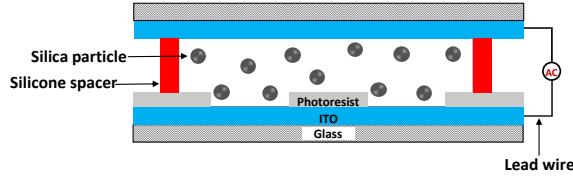


Figure 1: Schematic drawing of the microfluidic device

2.2. Model development

The dynamic trajectories of the colloidal particles in the microfluidic device in the presence of electric fields is described by a force balance over the individual particles. The translational motion of a colloidal particle in a fixed frame of reference is governed by the momentum equation:

$$m \frac{d\vec{v}}{dt} = -6\pi\eta a \vec{v} + \pi a^3 \epsilon_m \text{Re}(f_{CM}) \nabla |E|^2. \quad (1)$$

The first term on the right-hand side of Eq. (1) is the Stokes drag force acting on the particles where \vec{v} is the velocity of the particle at any given instant of time. The directed self-assembly of the colloidal particles is carried out at a frequency above the charge relaxation frequency of the ions in the electrical double layer; therefore, ACEO effects are assumed negligible. Since ACEO is not considered, the fluid velocity is assumed to be zero, a is the radius of the particle, η denotes the dynamic viscosity of the medium, m represents the mass of the particle. The effects of Brownian motion and particle-particle interactions are not considered in the model and are subject of future work.

The second term on the right-hand side of Eq. (1) is the dielectrophoretic force (Bakewell and Morgan, 2001) acting on the colloidal particles in nonuniform AC fields. The DEP force depends on the gradient of the electric field, $\nabla |E|^2$, the permittivity of the medium, ϵ_m and the real part of the Clausius-Mossotti function, $\text{Re}(f_{CM})$. The Clausius-Mossotti function is defined in Eq. (2) with respect to the complex permittivity of the medium, ϵ_m^* and particles, ϵ_p^* :

$$f_{CM} = \left(\frac{\epsilon_p^* - \epsilon_m^*}{\epsilon_p^* + 2\epsilon_m^*} \right). \quad (2)$$

The complex permittivity is defined as $\epsilon^* = \epsilon - (j\sigma/\omega)$, where σ represents the electrical conductivity of the medium and particles, ω is the angular frequency of the electric field applied. The Clausius-Mossotti function is frequency-dependent and dictates the direction of the DEP force. For example, when the particles are more polarizable than the medium, the real part of the Clausius-Mossotti function is positive and the colloidal particles experience pDEP. Parameter values used in the simulations are obtained from literature (Yeh and Juang, 2017) and are shown in Table 1. The gradient of the electric field is obtained from the Laplace equation for electric potential, ϕ according to Eq. (3).

$$\nabla^2 \phi = 0, E = -\nabla \phi. \quad (3)$$

The Laplace equation is a mixed boundary problem which involves a boundary condition for the applied voltage on the electrode surface and a zero-flux condition in the direction normal to the electrode plane. The solution of the mixed boundary Laplace equation is computed by the finite element method using COMSOL Multiphysics to obtain the gradient of the electric field norm as function of position in the microfluidic device as shown in Fig. 2a, which completes the dynamic model.

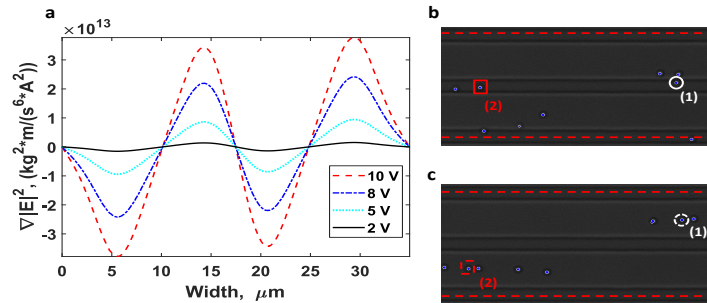


Figure 2: (a) FEM simulation of the gradient of electric field norm squared at different voltages (b) Initial positions of particles for an experiment at low particle density. (c) Particle positions after a step change from no electric field to an AC field of 1 MHz and 10 V for 32.5 s.

Table 1. Parameter values used in simulations

Parameter	ϵ_p	ϵ_m	σ_p	σ_m
Value	$3.363 \times 10^{-11} F/m$	$6.947 \times 10^{-10} F/m$	$2.56 \times 10^{-3} S/m$	$1.23 \times 10^{-2} S/m$

The model is used to simulate the dynamics of the colloidal particles in the microfluidic device with results for a step change in frequency and voltage (from 0 to 1 MHz and 0 to 10V, respectively) shown in the following section.

3. Results and Discussion

3.1. Simulation and validation of particle trajectories for a low particle density

In order to validate the predictive capabilities of the dynamic model, the model is first used to predict the trajectories of single particles in an experimental system with low particle density (see Fig. 2b), which facilitates easy particle tracking. Simulations of the single particle trajectories are performed using the initial particle positions obtained from the experiment. Under the experimental conditions, the electric-field minima for the system are located in the middle of the photoresist layer while the center of the ITO layer forms (indicated with red dashed lines in Fig. 2b and 2c) a potential barrier to particle motion. The predicted trajectories of two selected particles (indicated with circles and squares as particle (1) and (2), respectively, in Fig. 2b and 2c) obtained from simulation are shown in Fig. 3. Furthermore, the experimentally obtained particle trajectories are shown for comparison. The predicted particle trajectories from simulation are generally consistent with the experimental particle trajectories. The model slightly overestimates the response time when a step change in AC frequency and voltage is applied compared to the experimental trajectories. Nevertheless, the model predictions are satisfactory when considering that no fitting parameters have been used and the effects of Brownian motion have been neglected.

The performance of the model under pDEP conditions has also been tested, which is not shown here due to space limitations. The predicted particle trajectories when pDEP is the dominant electrokinetic phenomenon are also consistent with the experimentally observed particle trajectories. Therefore, it is concluded that the model can predict individual particles trajectories well at least in dilute systems when either nDEP or pDEP is the dominant electrokinetic phenomenon.

3.2. Simulation and validation of particle density distribution

The performance of the dynamic model at high overall particle density is investigated in this section. The particles are initially randomly distributed (see Fig. 4a) but are directed towards the

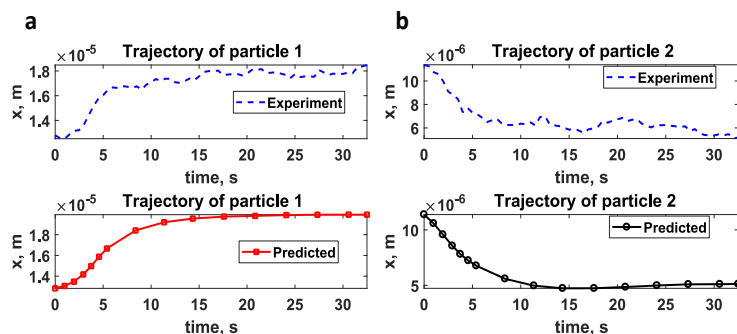


Figure 3: Experimental and predicted trajectories of particles (1) and (2) in Fig. 2b and 2c

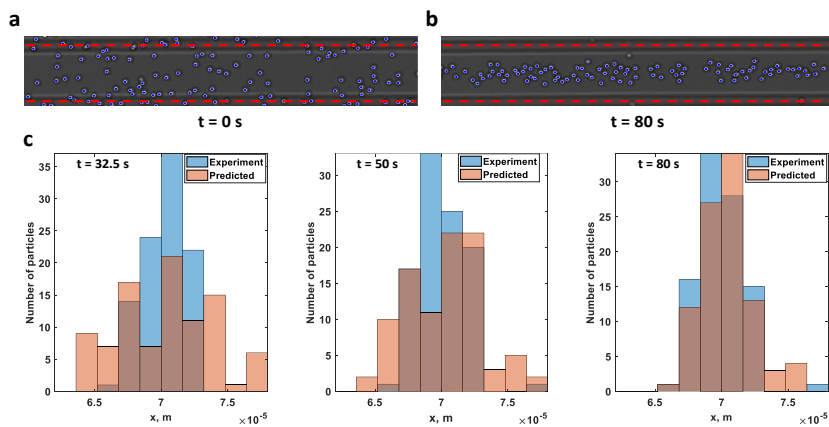


Figure 4: Particle density (a) at the start of experiment (b) when AC fields of 10 V at 1 MHz are applied for 80 s. (c) experimental and predicted particle distribution in the microfluidic device at 32.5 s, 50 s and 80 s respectively.

middle of the photoresist layer by an nDEP force acting on the particles as shown in Fig. 4b. Simulations of the particle density distribution are based on the initial particle positions of Fig. 4a. The experimental and predicted density distributions at different times are shown in Fig. 4c for comparison. It can be seen that the density distributions of the experimental system show less variation with time compared to the distributions obtained from the model. In addition, the dynamics of the model seem slower in comparison with experiments. It can also be observed that the accuracy of the model initially increases with time. However, simulations at longer times for which experimental results are not available indicate that all the particles accumulate in the center of the photoresist layer after about 400 s which is physically not possible in the experimental system because of the high overall density. The error between the model predictions and experiments may be the result of particle-particle interactions. Particle-particle interactions would have to be added to the model to predict such long-term behaviour more accurately.

4. Conclusion

A dynamic model based on the dielectrophoretic and drag forces acting on colloidal particles is presented to predict the dynamic trajectories of particles during directed self-assembly in a mi-

crofluidic device. The combined trajectories of all particles in a system can predict the dynamic development of the particle density distribution, which is of practical importance for assembling defect-free small-scale structures. The model predictions of the particle trajectories at low particle densities are in good agreement with experiments. The model is based on first principles and is computationally tractable for online implementation to develop novel control approaches for directed self-assembly. The model can be extended in future work by considering Brownian motion and particle-particle interactions from induced dipole forces (Mittal *et al.*, 2008) and electrostatic forces that result from the particles acquiring a negative surface charge density in water. The electrostatic forces between the colloidal particles can be obtained from the DLVO theory.

Acknowledgements

The work described in this paper was supported by a grant from the Research Grants Council of the Hong Kong Special Administrative Region, People's Republic of China (Project No. 16214617).

References

- D. J. Bakewell, and H. Morgan, 2001. Measuring the frequency dependent polarizability of colloidal particles from dielectrophoretic collection data. *IEEE Transactions on Dielectrics and Electrical Insulation*, 8(3), 566-571.
- Y. Gao and R. Lakerveld, 2018. Feedback control for defect-free alignment of colloidal particles. *Lab on a Chip*.
- J.J. Jurez and M. A. Bevan, 2012. Feedback Controlled Colloidal Self-Assembly. *Advanced Functional Materials* 22 (18): 3833-39.
- A. Komae and P. I. Barton, 2017. Potential canals for control of nonlinear stochastic systems in the absence of state measurements. *IEEE Transactions on Control Systems Technology*, 25(1), pp.161-174.
- R. Lakerveld, G. Stephanopoulos, and P. I. Barton, 2012. A Master-Equation Approach to Simulate Kinetic Traps during Directed Self-Assembly. *Journal of Chemical Physics* 136 (18).
- M. Mittal, P. P. Lele, E. W. Kaler, and E. M. Furst, 2008. Polarization and interactions of colloidal particles in ac electric fields. *The Journal of chemical physics*, 129(6), 064513.
- E. O. P. Solis, P. I. Barton, and G. Stephanopoulos, 2010. Controlled Formation of Nanostructures with Desired Geometries. 1. Robust Static Structures. *Ind. Eng. Chem. Res.*, 7728-45.
- T. M. Squires, and M. Z. Bazant, 2004. Induced-charge electro-osmosis. *Journal of Fluid Mechanics* 509: 217-252.
- X. Tang, B. Rupp, Y. Yang, T. D. Edwards, M. A. Grover, M. A. Bevan, 2016. Optimal feedback controlled assembly of perfect crystals. *ACS Nano* 10 (7): 6791-98.
- Z. W. Ulissi, M. S. Strano and R. D. Braatz, 2013. Control of nano and microchemical systems. *Computers & Chemical Engineering*, 51, pp.149-156.
- G. M. Whitesides, and B. Grzybowski, 2002. Self-assembly at all scales. *Science* 295 (5564): 2418-2421.
- C. K. Yeh and J. Y. Juang, 2017. Dimensional analysis and prediction of dielectrophoretic crossover frequency of spherical particles. *AIP Advances*, 7(6), 065304.

Towards Model-Based Optimization for Quality by Design in Biotherapeutics Production

Alireza Ehsani^a, Chrysoula Dimitra Kappatou^b, Adel Mhamdi^b, Alexander Mitsos^b, Andreas Schuppert^{a,c}, Sebastian Niefenfuhr^{a,*}

^a*Bayer AG, 51368 Leverkusen, Germany*

^b*RWTH Aachen University, AVT – Aachener Verfahrenstechnik, Process Systems Engineering, Forckenbeckstrasse 51, 52074 Aachen*

^c*Joint Research Center for Computational Biomedicine; RWTH Aachen University, Pauwelsstrasse 19, 52074 Aachen, Germany*

sebastian.niefenfuhr@bayer.com

Abstract

Quality by Design (QbD) is the concept of designing a process by gathered knowledge to fulfill desired quality of the product. This requires monitoring and controlling product quality throughout process development. In biotherapeutics production, glycosylation is one of the major quality attributes. In general, the glycoform generated by the cell glycosylation machinery is highly dependent on the cell performance and the variations in its surrounding. Mathematical modelling of this machinery can facilitate process understanding, describe the complexity of different layers of cellular metabolism and enable model-based optimization of product formation.

In this work, we investigate possible feeding scenarios utilizing a calibrated model to help understanding the possible effects of process changes in the paradigm of QbD for biotherapeutics. Our QbD objective is to maximize product yield while satisfying product quality given by criteria on the protein glycosylation pattern. For this we use a mechanistic model comprised of three major layers (scales) including bioreactor dynamics, intracellular reaction network and kinetic reactions inside Golgi apparatus. We apply design of experiments method followed by *in silico* experiments using the mechanistic model to identify optimal feeding profiles and evaluate the respective formed glycopatterns. In a future step, these predictions can be experimentally tested. Thereby, in a series of steps, a model can be developed to be used for model-based optimization.

Keywords: Biotherapeutics, Quality by Design, Mathematical Modelling, Optimization

1. Introduction

Variations in product quality are generally caused by changes in the production process. In order to be able to ensure that the product quality variations lie within pre-defined ranges, a systematic approach is needed. This approach should be able to incorporate knowledge of the process and effects of critical factors on product quality. This is called QbD, where the key elements are the critical process parameters (CPPs), the critical quality attributes (CQAs), the design space, and the quality target product profile (QTPP) (ICH Q8). The implementation of QbD needs, first, a definition of the intended

product properties to define QTPP. Through process knowledge, regulatory guidelines and literature, CQAs can be identified. To identify the sensitive parameters (i.e. CPPs) affecting the QTPP, often an initial experimental design for screening is conducted in the wet-lab. The CPPs should be monitored and controlled to ensure the process produces the desired quality.

In biotherapeutics production considered in this work, bioactivity, stability and *in vivo* circulatory half-life are examples for QTPP. One of the most important CQAs is the protein glycosylation pattern, since it highly affects the respective QTPPs. Human-like glycosylation is important for correct functionality of glycoproteins. Usually, well known CPPs for mAb CQAs include cultivation parameters (e.g., pH, dissolved oxygen, temperature) and medium composition (e.g., carbon and nitrogen sources, vitamins, trace elements).

An important step in the QbD process is to determine the design space for the CPPs. The design space as defined in (ICH Q8) is “*the multidimensional combination and interaction of input variables and process parameters that have been demonstrated to provide assurance of quality. Working within the design space is not considered as a change. Movement out of the design space is considered to be a change and would normally initiate a regulatory post-approval change process*”. Description of the design space provides flexibility of the manufacturing process in the defined ranges.

To determine the design space, additional experiments are needed within the boundaries of the CPPs. Statistical design of experiments (DoE) helps in a systematic planning of such experiments in order to identify the effects of variations of CPPs on CQAs. In the paradigm of QbD, the traditional one-factor-at-a-time designs are no longer efficient since a holistic understanding of the system at hand is aimed for.

Combination of DoE methods for process development and model-based simulations within the QbD context can provide an estimate of the critical QbD elements before running time consuming and cost intensive experiments. In addition, it can help in assessing the points in parameter boundaries where performing real experiments face limitations.

As pursued in this work, model-based optimization for QbD in biotherapeutics production, the optimization of the cell culture process in regard to product quality requires systematic analysis of the glycosylation throughout the cell line and process development. The biosynthesis of glycans is a result of a complex network of metabolic and enzymatic reactions that are influenced by many factors, including the host cell line as well as the upstream and downstream bioprocesses (Sha et al. 2016). Mathematical modelling of the system provides better understanding on the product quality variations. Initial computational models (Umana and Baily 1997) approximated the Golgi apparatus as a series of continuously stirred tank reactors where reactions generate potential glycan structures. Hossler et al. (2007) started to adopt the Golgi maturation model and used plug flow reactors in series to mimic the change in enzyme concentrations along the Golgi apparatus. Follow-up models were developed to simulate antibody glycosylation specifically, and particular attention was paid to the nucleotide sugar donor level to link glycosylation to cellular metabolism (Jedrzejewski et al. 2014). The mechanistic models which link glycosylation to cellular metabolism are state of the art (Jedrzejewski et al. 2014, Sou et al., 2017).

In this work, we utilize the current state-of-the-art modelling approach in combination with DoE methods to assess and understand the process response. This is done as a first step towards a model-based approach of a QbD workflow. Before performing the experiments in wet-lab, the resulting responses are checked against observations taken from literature. The results of these *in silico* studies give first insights about the system's outcome and need to be later tested experimentally. Finally, the predictive nature of mechanistic models can be used for control of the glycosylation process and pave the way towards quality-based optimization of therapeutic production bioprocesses.

2. Modelling and Identification Approach

2.1. Mathematical Model of Cell Culture and Protein Glycosylation

We use our previous mechanistic model (Ehsani et al. 2017). It includes three layers (i) extracellular, (ii) intracellular dynamics coupled with (iii) glycosylation reactions inside Golgi apparatus. The model equations are solved using ODE15s in MATLAB R2017b. We perform a global sensitivity analysis (Wang et al. 2003) by evaluating 105 samples in the range of 50%-200% of the nominal values of the parameters nominal values. By calculating first order global sensitivity indices, we can fix 97 parameters, out of 133, to their nominal values. We use a scatter search optimization algorithm (Egea et al. 2009) to estimate the remaining parameter values and fit model outputs with experimental data of hybridoma batch culture taken from Jedrzejewski et al. (2014).

2.2. Design of Experiments

We conduct two rounds of design of experiments using Box-Behnken design (MATLAB Statistics Toolbox) as a response surface method, each one followed by *in silico* experiments. The design goals are, first, finding the strategy to maximize protein titer and second taking this strategy as starting point to adjust glycosylation pattern.

In the first DoE round, three factors (decision variables), namely glucose and glutamine feeding concentrations and the number of feed boluses are incorporated. Three levels of each factor are considered, which corresponds to low, middle, and high for the concentrations and one, two or three number of boluses. The boundaries of 5-15 mM and 2-6 mM are used for glucose (Glc) and glutamine (Gln) respectively, according to the feeding strategies reported for hybridoma cell by Pörtner et al. (2004). With this input, a set of 15 experiments are designed that are then performed *in silico* to examine the effects of different feeding strategies on process performance.

The values for the fed-batch process that results in the maximum value of response (protein titer) are selected as starting point to perform the second round of DoE. In this case, four factors, namely N-acetylglucosamine, fucose, galactose and sialic acid, in three levels within the boundaries of 1-10 mM, 1-8 mM, 5-20 mM and 1-5 mM are assessed using Box-Behnken design followed again by *in silico* experiments.

2.3. Identify Feeding Strategies by Optimization of Response Surface Function

We use the outcomes of the designed set of experiments in previous section to fit a second-order function as response surface (R). This function (Eq. (1)) is composed of

intercept (β_0), linear terms ($\beta_1, \beta_2, \beta_3$), cross product terms ($\beta_{12}, \beta_{13}, \beta_{23}$) and squared terms ($\beta_{11}, \beta_{22}, \beta_{33}$).

$$R = \beta_0 + \sum \beta_1 \text{Glc} + \sum \beta_2 \text{Gln} + \sum \beta_3 \text{No. Feed} + \sum \beta_{12} \text{Glc Gln} + \sum \beta_{13} \text{Glc No. Feed} + \sum \beta_{23} \text{Gln No. Feed} + \sum \beta_{11} \text{Glc}^2 + \sum \beta_{22} \text{Gln}^2 + \sum \beta_{33} \text{No. Feed}^2 \quad (1)$$

We use numerical optimization function *fmincon* (MATLAB Optimization Toolbox) to calculate the optimum point of the response function (Eq. 1) within the boundaries of its variables as mentioned in previous section.

After performing two DoE rounds and *in silico* experiments, we find the optimal values for supplementation of both nucleotide sugars and nutrients for maximizing the response function. This approach can be extended in our future research using dynamic optimization in the whole space of decision variables.

3. Results and Discussion

In this section, we briefly present the results obtained in the considered case study.

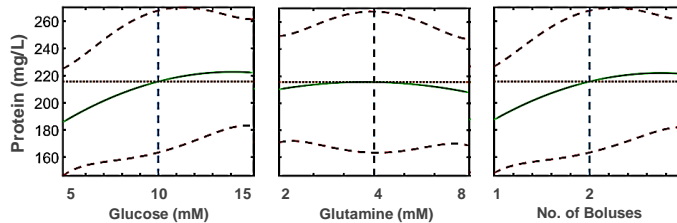


Figure 1. The projection of the response function (protein titer) with respect to the different levels of glucose and glutamine concentration and number of bolus feeds. Dashed lines show the protein titer in min/max levels; solid line shows the protein for medium values of the other factors.

We show the changes in response function (protein titer) in different levels of decision variables from the first DoE round in Figure 1. The toxic effect of ammonia in the culture is assumed to be the limiting factor when overfeeding occurs. In order to avoid overfeeding, the simulated culture stops, when ammonia accumulation reaches 4 mM.

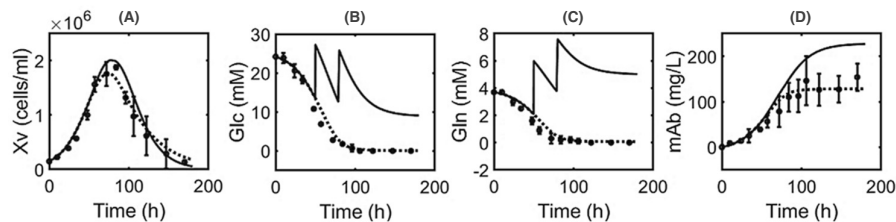


Figure 2. Batch (dashed line) and fed-batch (solid line) simulation results of (A) cell density, (B) glucose and (C) glutamine dynamics and (D) protein titer. Experimental data are shown with solid circles.

As shown in Figure 1 the optimum feeding strategy is two feeds with 13.4 mM glucose and 3.9 mM glutamine concentration. This fed-batch strategy results in a maximum cell density of $2e+6$ cells/ml and 218.6 mg/L protein titer. Supplementing cell culture media by glucose and glutamine provides major nutrients and energy sources for growth and

protein production. We show in Figure 2 the dynamics of cell density and the concentrations of glucose, glutamine and protein in batch and the selected fed-batch process with maximum protein titer in first round of *in silico* experiments.

Coupling glycosylation to the metabolic model provides the opportunity to assess the effects of supplementation on product quality and helps in making further improvements in the process. Figure 3 shows the differences between eight important glycosylation patterns in batch and fed-batch processes. Generally, there is a shift from accumulation of unmaturing early structures (high mannoses like M5) to more complex structures: The glycosylation pattern of batch culture shows the presence of more than 10% Mannose-5 glycans which in monoclonal antibodies should be normally less than 10% (Blondeel and Aucoin, 2018).

In the fed-batch culture providing enough glucose and glutamine caused conversion of this early structure to more complex glycans. M3Gn2F is the most popular structure in monoclonal antibodies with around 40% (Blondeel and Aucoin, 2018). The fraction of this structure in fed-batch compared to batch culture is about 2.5 fold higher. This results in improved quality, albeit not sufficiently. Further quality improvement could be achieved possibly through supplementing N-Acetylglucosamine. In average, the amount of galactosylation is between 10-40% depending on the glycoprotein (Blondeel and Aucoin, 2018). As shown in Figure 3 the galactosylated (M3Gn2FG /M3Gn2FG2) content is also increased in fed batch but not in the same rate as M3Gn2F increased. This arises from the fact that the cell is producing more glycosylated protein having enough glucose available, while the intracellular biosynthesis rate of galactose is limited by the cell's capacity. Therefore, Galactose supplementation can increase the galactosylated content.

In the second DoE round, we assessed further supplementation of nucleotide sugars using Box-Behnken design in 46 *in silico* experiments. According to the results the optimum glycosylation pattern can be achieved by adding 15 mM Galactose and 6 mM N-acetylglucosamine in 3 boluses. These predictions are in well agreement with literature reports where the most effective and popular supplementation strategy to increase galactosylated content is to feed N- acetylglucosamine 7-10 mM and galactose 10-20 mM (Blondeel and Aucoin, 2018). This feeding strategy also increased the sialylated content to about 2% which improves plasma half-life of the glycoprotein (Sha et al., 2016).

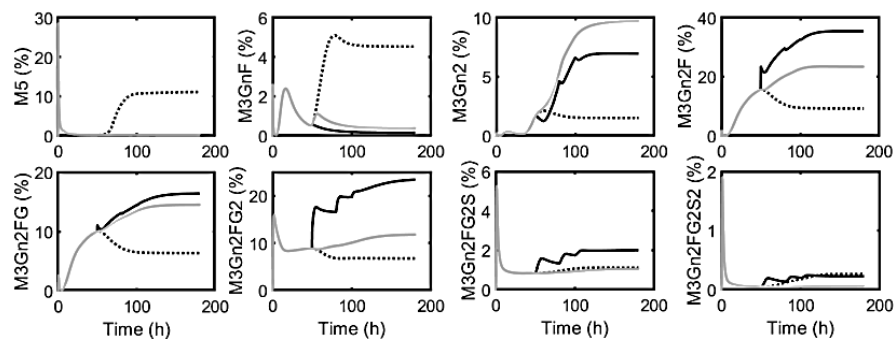


Figure 3. Batch (dashed line), fed-batch with (dark solid line)/ without (light solid line) nucleotide sugars supplementation, simulated dynamics of eight important glycan structures. M: mannose, Gn: N-acetylglucosamine, F: fucose, G: galactose, S: N-acetylsialic

4. Conclusions

Implementation of QbD requires detailed characterization of the process and thorough exploration of the various conditions that can affect the quality. In this work, we use a mechanistic model of cell culture and glycosylation to identify biological meaningful feeding strategies and pave the way towards quality-based optimization of glycoforms. We proposed adjustment of CQA (glycosylation) by supplementing nutrients (nucleotide sugars) and the qualitative behavior of our model showed agreement with reported literature data.

5. Acknowledgements

This work has received funding from the European Union's Horizon 2020 research and innovation program under the Marie Skłodowska-Curie grant agreement no.675251.

References

- S. Sha, C. Agarabi, K. Brorson, D. Lee, S. Yoon, N-Glycosylation Design and Control of Therapeutic Monoclonal Antibodies, *Trends Biotechnol.*, 34, 10, 835-846, 2016.
- P. Umana, JE. Bailey, A mathematical model of N-linked glycoform biosynthesis, *Biotechnol. Bioeng.*, 55, 890-908, 1997.
- P. Hossler, BC. Mulukutla, WS. Hu, Systems analysis of N-glycan processing in mammalian cells, *PLoS ONE*, 2(8), e713, 2007.
- PM. Jedrzejewski, IJ. del Val, A. Constantinou, A. Dell, SM. Haslam, KM. Polizzi, C. Kontoravdi, 2014, Towards controlling the glycoform: a model framework linking extracellular metabolites to antibody glycosylation, *Int. J. Mol. Sci.*, 15, 4492-4522
- A. Ehsani, S. Niedenfuehr, T. Eissing, S. Behnken, and A. Schuppert, How to Use Mechanistic Metabolic Modeling to Ensure High Quality Glycoprotein Production. *Computer Aided Chemical Engineering*, 40: 2839-284, 2017.
- JA. Egea, E. Balsa-Canto, M. García, J. Banga, Dynamic Optimization of Nonlinear Processes with an Enhanced Scatter Search Method, *Ind. Eng. Chem. Res.*, 48, 4388-4401, 2009.
- SW. Wang, PG. Georgopoulos, G. Li , H. Rabitz, Random Sampling–High Dimensional Model Representation (RS–HDMR) with Nonuniformly Distributed Variables: Application to an Integrated Multimedia/Multipathway Exposure and Dose Model for Trichloroethylene, *The J. Phys. Chem.*, 107, 23, 4707-4716, 2003.
- R. Pörtner, JO. Schwabe, B. Frahm. Evaluation of selected strategies for fed-batch cultures of a hybridoma cell line. *Biotechnology Appl Bioc.* 40: 47–55, 2004.
- E. Blondeel, M. Aucoin, Supplementing glycosylation: A review of applying nucleotide-sugar precursors to growth medium to affect therapeutic recombinant protein glycoform distributions, *Biotechnology Advances*, 36, 1505-1523, 2018.
- ICH and FDA Guidance for Industry, Q8(R2) Pharmaceutical Development, November 2009. <https://www.fda.gov/downloads/drugs/guidances/ucm073507.pdf>
- S. N. Sou, P. M. Jedrzejewski, K. Lee, C. Sellick, K. M. Polizzi, and C. Kontoravdi, Model-based investigation of intracellular processes determining antibody Fc-glycosylation under mild hypothermia, *Biotechnol. Bioeng.*, 114: 1570-1582, 2017.

Population Balance Equation Applied to Microalgae Filtration

Pui Ying Lee^a, Keat Ping Yeoh^a, Chi Wai Hui^{a,*}

^aDepartment of Chemical and Biological Engineering, The Hong Kong University of Science and Technology, Clear Water Bay, Hong Kong SAR

**kehui@ust.hk*

Abstract

In this paper, a mathematical model is developed for microalgae filtration by applying Population Balance Equation. The main objective is to investigate the impacts of cell size distribution and filter average pore size on filtration efficiency and their interrelationships. The results of using standard filters with different pore sizes are compared and discussed. Experiments of microalgae filtration on *Chlorella* cells are performed to provide size distribution information of the cell cultures to validate the model. Behaviours of cells at different sizes during the harvesting process are examined and the obtained data is combined with the mathematical model to evaluate the harvesting efficiency along with operation time and filter depth. The model could be extended to predict the size specific filtration efficiency of microalgae under different operation conditions, which potentially helps determine the process parameters for optimization purposes.

Keywords: Microalgae harvesting, Filtration, Population Balance Equation

1. Introduction

Biofuel, as a renewable energy, is an alternative to the traditional fossil fuel. One of its bio-resources is microalgae, which is regarded to be promising with high lipid content and high photosynthetic efficiency. Microalgae harvesting has been the bottleneck of the whole microalgae production process since it accounts for 20-30 % of the cost (Danquah et al., 2009). Therefore, maximizing the harvesting efficiency as well as capacity and meanwhile minimizing the cost are of critical importance to the development of a scale-up process for industrial purposes.

Filtration is a commonly employed harvesting method for microalgae because of its high efficiency as well as stable operation conditions without using chemicals. Although research efforts have been dedicated to investigate the efficiency of microalgae filtration, few modelling works have been done to understand the relationships between different physical parameters. Previous studies usually consider the algal culture, which contains different cell sizes, as a whole for performance evaluations (Wicaksana et al., 2012; Zhao et al., 2017). However, not many concerns have been raised towards the interdependence of cell size distribution and the corresponding cell recovery although size distribution is a critical factor of the filtration process.

The main objective of this study is to apply Population Balance Equation (PBE) to simulate the microalgae filtration process. This equation has been commonly used in chemical engineering processes to describe evolutions of particle populations. There are few studies employing PBE for modelling microalgae growth (Pahija et al., 2017) and harvesting processes of sedimentation and centrifugation (Lee et al., 2018). So far there is no significant research contribution to the application of PBE to model the microalgae filtration process and to study the impact of cell size distributions or characteristics. In this study, a PBE model is proposed for investigating microalgae filtration efficiency, which derives additional size specific information of the cells during the process.

2. Methodology

Applying Population Balance Equation to microalgae filtration, a model is proposed with the aim to study size dependent recovery and filtration coefficient of the process. Experimental data is used to evaluate the process efficiency and to validate the mathematical model.

2.1. Population Balance Equation model

One of the simplified forms of PBE for studying particle size distributions commonly includes two terms as follow:

$$\frac{\partial n(t, d)}{\partial t} + \frac{\partial [G \cdot n(t, d)]}{\partial d} = 0 \quad (1)$$

The first term on the left side denotes changes in particle number density with time, while the second term represents the change with particle size, in which n is number density, t is time and G is particle growth rate. To model the microalgae filtration process, Eq. (1) is modified into the following form in this study:

$$\frac{\partial n(t, h, d)}{\partial t} + v \frac{\partial [1 - \phi(h, d)] \cdot n(t, h, d)}{\partial h} = 0 \quad (2)$$

The first term is similar to that in Eq. (1), while the second term is revised to be the cell number density change with h , which denotes traveling distance of cells inside the filter medium. ϕ is defined as filtration coefficient, so that the fluid velocity v times $[1 - \phi(h, d)]$ together gives the cell velocity inside the filter medium. The larger the coefficient, the smaller the cell velocity compared to fluid velocity, resulting in higher harvesting efficiency of microalgae. First order upwind discretization scheme is used to generate numerical solutions for Eq. (2).

Since the model parameters i.e. cell number density, cell size, time, filter depth and flux can be easily measured, the filtration coefficient can be back-calculated for evaluations of the process efficiency. In addition, the main purpose of the model application in this paper is to compare and study the impacts of different filter mediums on cell size distributions during microalgae filtration.

2.2. Experiments

Chlorella is a common green spherical microalgae species and the cell size ranges from 3 μm to 9 μm . In this study, an experimental setup of dead end vacuum filter with filter diameter of 50 mm is used to separate the cells from the cultivation medium. To

evaluate the impacts of filter pore size on the harvesting process, standard polypropylene filters with different average pore sizes of 6, 8, 10, 15 and 20 μm are used. Each run of the experiment filters 10 mL microalgae solution for 1 min and the filtrate's optical density (OD) as well as size distribution are measured. In every sampling, 1.5 mL filtrate is transferred by an electronic pipette to a photospectrometer for OD measurement to obtain the solution concentration. Meanwhile, a micropipette is used to take 10 μL filtrate for imaging under a microscope and the images are processed and analysed by a computer software to give cell size distribution information. A calibration curve of the relationship between cell concentrations and OD is experimentally attained prior to conducting the filtration experiments.

3. Result

Performances of filtration is commonly evaluated by the change in liquid concentration after the process. In this study, the filtration efficiency is defined as the percentage change in optical density, which is proportional to the cell number density, from the original algal solution to the collected filtrate. The overall filtration efficiency represents the percentage change in cell number density of the solution as a whole without taking the specific change of cells at each size into consideration. After the experiments and data analysis, the overall filtration efficiencies of microalgae filtrations with different filter mediums are obtained. With the previously mentioned calibration curve, the cell number densities of the filtrate samples can be derived from the OD measurements. By fitting the cell size distribution results into the proposed PBE model, the filtration coefficient ϕ defined in the model can be derived.

As shown in Figure 1, the filtration efficiency is inversely proportional to pore size as expected and the relationship is observed to be almost linear. Although the pore size of from 15 to 50 μm are obviously larger than the cell size range of 3 to 9 μm , considerable amounts of cells are captured. Therefore, concerns are raised towards size selectivity of the microalgae filtration process and the mechanisms behind. With an original mean cell size of 5.381 μm , Figure 2 shows the mean filtrate cell size, which drops with decreasing filter pore size. From the pore size of 6 μm to 15 μm , it is observed that smaller mean pore size filters can effectively capture smaller size cells since the cells cannot penetrate through the narrow pores. However, a drop of mean captured cell size is observed at 20 μm pore size, implying that an increasing number of small cells are captured even though the pores become larger. This data briefly indicates the tendencies of the filters to capture cells at different sizes.

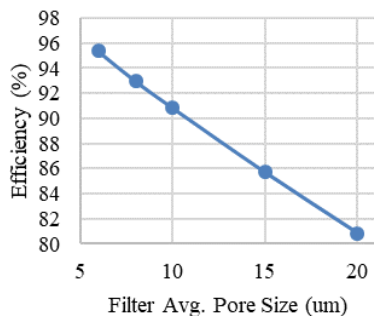


Figure 1. Impact of filter pore size on the overall cell harvesting efficiency

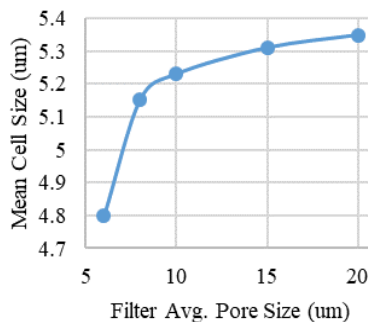


Figure 2. Impact of filter pore size on the mean filtrate cell size

Analysing size distributions of the captured cells can give additional information of microalgae filtration for studying the changes in mean cell size during the process. Figure 3 presents the size distributions of captured cells after the filtration experiments. It agrees with the previous findings that the number density of microalgae in the filtrate generally decreases when a filter with smaller pores is used. Applying Population Balance Equation to simulate the filtration process, the harvesting efficiencies of microalgae cells at each size changing along with time and travelling distance throughout the process are investigated. After numerical simulations of the developed PBE model with size distribution data from the experiments, the size specific filtration coefficients of microalgae filtered by medium of different pore sizes are obtained as shown in Figure 4.

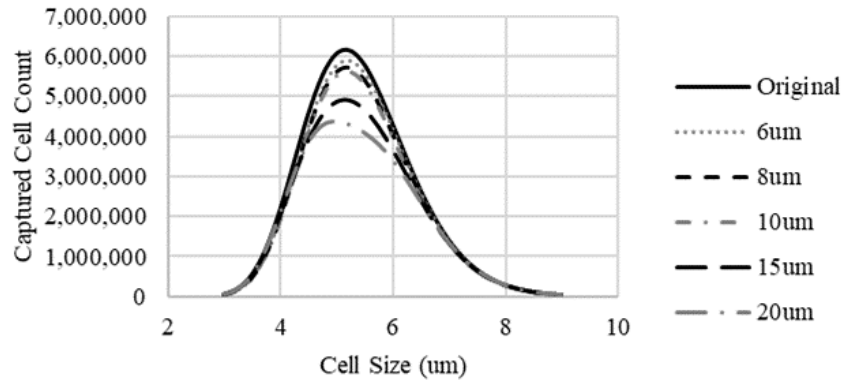


Figure 3. Size distributions of captured cells with different mean filter pore sizes

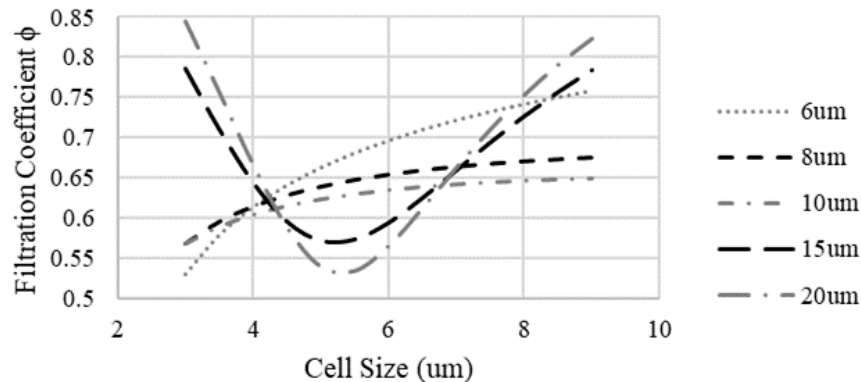


Figure 4. Derived size specific filtration coefficients of microalgae from the PBE model

Two different patterns are observed for smaller pore sizes (6, 8 and 10 um) and larger pore sizes (15 and 20 um). For small pore sizes of 6, 8 and 10 um, the coefficient increases with cell size, indicating that larger cells are more favourable to be captured. Among the three curves, the 6um pore size curve has the steepest slope, which means it is more sensitive to cell size and its selectivity for large cells is higher. For large pore sizes of 15 and 20 um, convex curves are observed, indicating that both large and small cells are more favourable to be captured. The 20 um pore size curve is comparatively

steeper, such that the filter captures small and large cells better but oppositely it captures middle size cells worse than 15 μm pore size filter.

4. Discussion

Comparing the overall filtration efficiencies of the tested standard filters, the filters with smaller pore size are generally more effective in capturing the microalgae cells. Studying the pattern of the derived size specific filtration coefficients gives additional insights of the process size selectivity as well as the filtration mechanisms behind. It is shown in Figure 4 that 6, 8 and 10 μm filters demonstrate similar size selectivity patterns, which the direct interception mechanism is essentially dominant. 6 μm filter gives the best overall filtration efficiency, but its performances for capturing 3 and 3.5 μm cells are the worst. For 15 and 20 μm filters, although their resulted changes in mean captured cell size are different, their derived filtration coefficients give similar patterns. The capture of more large cells can again be explained by the direct interception mechanism. Meanwhile, the tendency of capturing more small cells by larger pore filters shows that other mechanisms which are selective towards small cells are dominant. Particularly, the mechanism of electrostatic effect favours the capture of small cells since microalgae cell surface is known to be negatively charged and it is enhanced with increasing charge intensities of the cells. The convex pattern implies that in addition to direct interception, electrostatic effect is also affecting the process size selectivity. This is in alignment with the literature finding of a minimum filtration efficiency at a certain particle size in micron scale when the pore size to particle size ratio becomes large (O'Melia and Ali, 1978; Yao et al., 1971), confirming the results of this study.

With the PBE model, the actual size selectivity of the filters are derived. If only the overall filtration efficiency or mean cell size is considered, a very brief conclusion of the filters' capturing tendencies may be drawn. For example, although 15 μm filter apparently tends to capture more large cells than small cells as shown in Figure 2, it actually tends to capture both small and large cells as shown in Figure 4. Its size selectivity pattern is also quite different from those of 6, 8 and 10 μm filters, which this information is obtained by the model simulation. The new modelling approach to examine the size specific performance of microalgae harvesting derives additional information of the process size selectivity. This is useful for understanding the interrelationship between process parameters and cell characteristics, including cell size and surface charge.

5. Conclusion

A Population Balance Equation model is developed for modelling microalgae filtration, which is a common harvesting process in microalgae production. The model effectively describes changes in cell number densities with cell size, filter pore size, filtration time together with filter depth during the process. Filtration experiments are carried out on *Chlorella* cells by using filters different pore sizes. Experimental data, including the overall filtration efficiency, mean filtrate cell size and size distribution, are processed and analysed from a size specific approach. The results are combined with the developed mathematical model to study the impacts of cell size distribution and filter pore size on the filtration performance as well as their interrelationships. Furthermore,

size specific capturing of the cells is investigated for a clearer picture of the process size selectivity.

The derived size specific filtration coefficient provides insights to anticipate the effectiveness of different filter mediums for the filtration process. Instead of analysing the cell culture as a whole, this model focuses on size selective properties of microalgae filtration. The PBE model can also be extended to study and predict microalgae size distributions throughout the filtration process with different parameters or set ups. Meanwhile, it is beneficial for the determination of process parameters, such as filter pore size, material, thickness and filtration time for specific size selective separation purposes as well as process optimization.

References

- MK. Danquah, L. Ang, N. Uduman, N. Moheimani, GM. Forde, 2009, Dewatering of microalgal culture for biodiesel production: exploring polymer flocculation and tangential flow filtration, *Journal of Chemical Technology and Biotechnology* 84, 7, 1078-1083
- PY. Lee, E. Pahija, Y. Liang, KP. Yeoh, CW. Hui, 2018, Population balance equation applied to microalgae harvesting, *Proceedings of the 28th European Symposium on Computer Aided Process Engineering*, Graz, Austria
- C.R. O'Melia, W. Ali, 1978, The role of retained particles in deep bed filtration, *Proceedings of the 9th International Conference*, Stockholm, Sweden, 167-182
- E. Pahija, Y. Liang, CW. Hui, 2017, Determination of microalgae growth in different temperature condition using a Population Balance Equation, *Chemical Engineering Transactions* 6, 721-726
- F. Wicaksana, AG. Fane, P Pongpairoj, R. Field, 2012, Microfiltration of algae (*Chlorella sorokiniana*): Critical flux, fouling and transmission, *Journal of Membrane Science* 387-388, 83-92
- K.M. Yao, M.T. Habibiyan, C.R. O'Melia, 1971, Water and wastewater filtration: Concepts and applications, *Environmental Science and Technology* 5, 11, 1105-1112
- F. Zhao, H. Chu, Z. Yu, S. Jiang, X. Zhao, X. Zhou, Y. Zhang, 2017, The filtration and fouling performance of membranes with different pore sizes in algae harvesting, *Science of the Total Environment* 587-588, 87-93

Optimisation of Aqueous Two-Phase Systems

Emma Chandler^a, Robert Falconer^a and Solomon Brown^{a,*}

^a*Department of Chemical and Biological Engineering, University of Sheffield, Sheffield, S1 3JD, United Kingdom*
s.f.brown@sheffield.ac.uk

Abstract

Aqueous two-phase extraction (ATPE) is a liquid-liquid extraction (LLE) technique which is viable as a continuous protein purification unit operation for the manufacture of therapeutic proteins. A shift from batch to continuous manufacturing in this industry has been encouraged by regulatory bodies, including the Food and Drug Administration (FDA), as it is expected to increase the quality and consistency of the product and decrease manufacturing costs.

For ATPE to compete with current batch protein purification procedures, a multi-stage operation can be used to achieve a high purity and yield. However, there is a lack of reliable modelling techniques in the design of multi-stage ATPE; as a result, its design and operation is often reliant on both individual expertise and trial and error. To reduce this, there is a need to develop modelling techniques to aid in system design. In this study we present a modified equilibrium binary separation method to predict an optimal number of stages in a multi-stage system. The model is validated against data, for both traditional LLE and ATPE, in a counter-current multi-stage operation [Rosa et al., 2009a, Warade et al., 2011]. The model is then applied to a case study separation of phycocyanin from lysozyme using PEG-phosphate ATPE. The model is successfully used to predict a suitable design of a counter-current multistage system to optimise purity and yield of the target protein. The approach provides the basis with which to design general ATPE-based continuous downstream processes incorporating extraction, back-extraction and washing steps.

Keywords: Aqueous two-phase extraction, equilibrium binary separations, multi-stage optimisation.

1. Introduction

Aqueous two-phase extraction (ATPE) has been demonstrated to be capable of being a valuable alternative protein purification technique to chromatography [Rosa et al., 2010]. The unit operation is cheap relative to chromatography and, unlike chromatography, it is geared towards continuous manufacturing. Continuous manufacturing, as opposed to the traditional batch manufacturing techniques used in biomanufacturing, has been encouraged by regulatory bodies such as the FDA as it is seen as a way to reduce costs, increase manufacturing capacity and increase the consistency of the product quality [Konstantinov and Cooney, 2014]. A move to continuous manufacturing will require either a rethinking or replacement of the current downstream purification operations. However, these new manufacturing techniques still need to compete with the current manufacturing techniques as well as meet the high purity standards required of the regulatory bodies of this industry [Azevedo et al., 2009].

Currently, there are two major drawbacks to ATPE as a unit operation: the low purity / yield achieved in a single stage operation, and the lack of understanding of the phase forming mechanisms [Rito-Palomares, 2004, Ruiz-Ruiz et al., 2012]. The number of different parameters which

control the phase separation and protein partitioning mean that the process optimisation is achieved through trial and error, which is both time consuming and expensive. Modelling strategies have been employed to identify key performance parameters, such as the concentration of the phase forming material (polymer(s) and salt(s)) used, and reduce the experimental workload [Rosa et al., 2007, Mao et al., 2010, Patel et al., 2018]. However, the specifics of optimising system selection still requires extensive experimental work and experience. Multi-stage techniques have been used extensively in the process industries when a separation technique is simple and cost effective but provides low purity and / or yield. In PEG-Salt ATPE the economics of the process can be further improved through using the multistage technique of back extracting the target protein into the less expensive salt rich phase, so that the more expensive polymer rich phase can be recycled [Rosa et al., 2013].

A common method for the stage-wise optimisation of equilibrium binary separations is McCabe Thiele. It was originally used to determine the number of stages for binary distillation and is still widely used in this application [Richardson et al., 2002]. The method has been demonstrated to be suitable for traditional liquid-liquid extraction (LLE) by Warade et al. [2011]. In this study a single operating line was used to optimise the number of stages for a specified purity in multi-stage counter current systems. The method was also demonstrated to be suitable for ATPE when it was applied by Rosa et al. [2009b,a], who also used a single operating line to optimise the number of stages for a required yield in ATPE. They also utilised equilibrium curves of different fractions of Chinese Hamster Ovary (CHO) cell media to predict the success of their extraction from Immunoglobulin G (IgG) [Rosa et al., 2009b]; however, the number of stages for extraction was not determined. In both cases, a single component is considered in the model the target component. In terms of traditional LLE, there are often only two components and by considering one, the other component can be inferred as one phase forming component is the target compound and the other is the contaminant. However, in ATPE, the phases are formed by the phase forming components (i.e. polymer(s), salt(s) and water) and the partitioning of the contaminants (protein, cells and solutes) is determined by the phase forming components and the environmental conditions. As such by considering only the target protein, the contaminants cannot be inferred in ATPE, and only the yield of the system can be evaluated.

This paper uses equilibrium binary separations to evaluate and optimise multi-stage ATPE. The model is validated using the experimental data in Warade et al. [2011], (counter-current multi-stage traditional LLE) and in Rosa et al. [2009a], (counter-current multi-stage ATPE). In this paper the models in Rosa et al. [2009a] and Warade et al. [2011] are interpreted for a counter-current multi-stage ATPE to evaluate both contaminants and target protein in a model separation of phycocyanin from lysozyme using a PEG phosphate ATPE. Equilibrium curves were constructed for both the target protein, phycocyanin, and the contaminant. The required number of stages to achieve the desired purity and yield were predicted using the model. Through alteration of the operating line, the system could be evaluated in other operational configurations, for instance co-current, cross-current, etc.

The work is structured as follows, Section 2 presents the model formulation developed, Section 3 presents the results from validating the model followed by the results from the model separation of phycocyanin from lysozyme and Section 4 discusses the conclusions from this work.

2. Model Formulation

In this work, we present a model for the multi-stage ATPE which incorporates the separation behaviour in each stage and that may then be used as a basis for optimisation. The model firstly assumes that while the phases are semi-miscible, the phases are treated as immiscible; this is a common assumption for ATPE. The process is isothermal so an energy balance is not used [Mistry et al., 1996, Rosa et al., 2009b,a]. It was assumed that perfect mixing was achieved

at each stage and the phases are operated in equilibrium. In ATPE, several components must be considered and can be divided into the phase forming materials (polymer(s), salt(s) and water), and the protein / particulates / cells which are to be partitioned (the contaminants and target protein / cells / particulates). The partitioning of the protein is assumed to be a result of the phase forming materials. The concentration of the phase forming components and the phase volumes are assumed to be constant across the system [Rosa et al., 2009b,a]. The binary separation evaluated is the target protein from the contaminants.

Assuming X is the phase which the component / solute should be removed from and Y is the target phase, the volumes of the phases are V_X and V_Y respectively. A mass balance across an entire counter-current process can be written as:

$$V_X X_0 + V_Y Y_{n+1} = V_X X_n + V_Y Y_1 \quad (1)$$

Likewise, material balances for stage i can be written as:

$$V_X X_{i-1} + V_Y Y_{i+1} = V_X X_i + V_Y Y_i \quad (2)$$

Using equations (1) and (2) we can pose the stage-wise optimisation of the multi-stage ATPE as follows:

$$\max X_N \leq X_{Target}^w \quad (3)$$

Where X_{Target} is the required concentration in phase X . If optimising for yield, X is the bottom phase and the solute / component to be considered is the target solute / component. If optimising for purity, X is the top phase and the solute / component to be considered is the contaminant solute / component. To determine the first step a mass balance across the entire system is used:

$$Y_1 = Y_{n+1} - \frac{V_X}{V_Y} (X_n - X_0) \quad (4)$$

Each stage is then evaluated as follows:

$$\left. \begin{aligned} X_i &= f(\text{equilibrium line}), \\ Y_{i+1} &= Y_i - \frac{V_X}{V_Y} (X_i - X_{i-1}), \end{aligned} \right\} \quad i = 1, \dots, n \quad (5)$$

Where f is the function determined for the equilibrium line. The line is determined by piecewise linear function between the equilibrium points. To determine equilibrium points, a model separation of phycocyanin from lysozyme was carried out using a PEG-phosphate ATPE. Two equilibrium curves were generated; one for phycocyanin and one for lysozyme. Protein concentration was determined using ultraviolet visible spectroscopy.



Figure 1: Depiction of a multi-stage counter current operation.

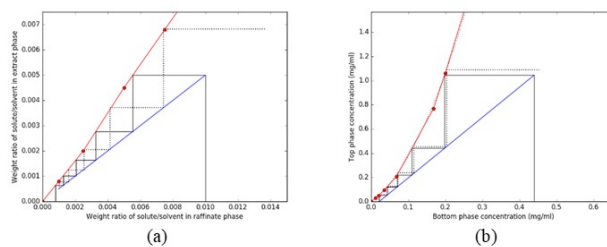


Figure 2: (a) McCabe Thiele diagram generated from data in Warade et al. [2011]. (b) McCabe Thiele diagram generated from data from Rosa et al. [2009a]. The dotted lines represent the stage results from the original authors. The solid line shows the results from the model in this paper.

3. Case Study

Figure 1 shows a schematic representation of the multistage counter current system where Y_i is the concentration of the phase component / solute in the target phase (% w/w) or (mg /ml) of stage i , for stages 1 to n , and X_i is the concentration of the phase component / solute (% w/w) or (mg /ml) in the opposing phase of stage i , for stages 1 to n .

The model developed above is first applied to traditional LLE and ATPE. The fit is shown above, Figure 2 (a) shows a result for traditional LLE and (b) shows a result for ATPE. It should be noted that in this model, the stages were counted off from the feed as opposed to from the target composition and so the predicted compositions are slightly different; however, the results for the number of stages were the same as the original authors.

Figure 3 shows the McCabe Thiele diagram for achieving > 99 % yield of phycocyanin using a counter-current multi-stage PEG-phosphate system. It can be seen from Figure 3 that the equilib-

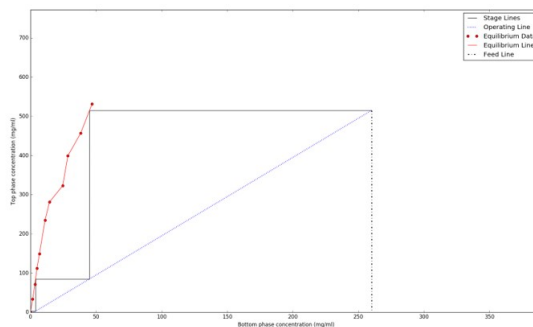


Figure 3: McCabe diagram for phycocyanin in the model PEG-phosphate ATPE.

Table 1: Stage results for lysozyme in the model PEG-phosphate ATPE.

Stage	Bottom phase (mg/ml)	Top phase (mg/ml)
1	8.91	0.503
2	0.161	0.00885

rium curve is a linear for phycocyanin before the concentration of 110 mg/ml. It is predicted that three stages were required to achieve a yield of > 99 % of phycocyanin.

Similarly, Table 1 shows the results for the concentration (mg/ml) of the contaminant, lysozyme, in each phase for each stage. The model was set up to remove > 99 % of lysozyme from the target phase using a counter-current multi-stage PEG-phosphate system, in this case two stages were required to achieve this.

4. Conclusion

In conclusion, ATPE is a developing, cheaper alternative protein purification technique which is disadvantaged by the low purity and yield achieved in a single step and the extensive experimental work required in system development and optimisation. Multi-stage operation can be used to achieve the high purities and yields required in the biopharmaceutical industry. The work has shown that the use of an equilibrium binary separation model is a viable technique in evaluating different multi-stage ATPE. The model was validated using experimental data in the literature and a case study on the purification of phycocyanin from lysozyme was carried out. It was shown that a yield of > 99 % and a purity of > 99 % could be achieved using three and two stages respectively in a counter current ATPS of PEG - phosphate. The work evaluates the different proteins separately in terms of protein concentration in each of the phases. This approach simplifies the model greatly and removes some of the complexity which is associated with ATPS, thereby further increasing the accessibility of the process.

In the future, the model could be used to optimise the stages for not only extraction protocols, but also back extraction and washing protocols as a repeating unit in a superstructure. In back extraction, conditions would be selected, usually through the addition of NaCl, to push the target protein into the salt phase. This is easier to deal with down-stream and allows the recycling of the more expensive polymer phase. For this, only a single equilibrium curve for the target protein under the new extraction protocols would be required. The washing protocol would also require a single equilibrium curve and would require looking at removal of any remaining contaminants in the salt phase, once the target protein has been extracted there, using a fresh polymer phase. Using this method, the model can be used to investigate and develop more complicated multi-stage operational techniques. Modification of the operation line can be used to investigate different multi-stage modes of operation i.e. cross current, co-current, counter-current procedures.

References

- A. M. Azevedo, P. a. J. Rosa, I. F. Ferreira, and M. R. Aires-Barros. Chromatography-free recovery of biopharmaceuticals through aqueous two-phase processing. *Trends in Biotechnology*, 27(4):240–247, 2009.
- K. B. Konstantinov and C. L. Cooney. White Paper on Continuous Bioprocessing. May 20-21, 2014 Continuous Symposium. *Journal of pharmaceutical sciences*, pages 1–8, 2014.
- L. N. Mao, J. K. Rogers, M. Westoby, L. Conley, and J. Pieracci. Downstream antibody purification using aqueous two-phase extraction. *Biotechnology Progress*, 26(6):1662–1670, nov 2010.
- S. L. Mistry, A. Kaul, J. C. Merchuk, and J. A. Asenjo. Mathematical modelling and computer simulation of aqueous two-phase continuous protein extraction. *Journal of Chromatography A*, 741(2):151–163, 1996.
- N. Patel, D. G. Bracewell, and E. Sorensen. Dynamic modelling of aqueous two-phase systems to quantify the impact of bioprocess design, operation and variability. *Food and Bioproducts Processing*, 107:10–24, jan 2018.
- J. F. J. F. Richardson, J. H. J. H. Harker, J. R. Backhurst, and J. M. J. M. Coulson. *Coulson and Richardson's chemical engineering. Vol. 2, Particle technology and separation processes*. Butterworth-Heinemann, 2002. ISBN 9780080490649.

- M. Rito-Palomares. Practical application of aqueous two-phase partition to process development for the recovery of biological products. *Journal of Chromatography B: Analytical Technologies in the Biomedical and Life Sciences*, 807(1):3–11, 2004.
- P. Rosa, A. Azevedo, I. Ferreira, S. Sommerfeld, W. Bäcker, and M. Aires-Barros. Downstream processing of antibodies: Single-stage versus multi-stage aqueous two-phase extraction. *Journal of Chromatography A*, 1216(50):8741–8749, dec 2009a.
- P. A. Rosa, A. M. Azevedo, and M. R. Aires-Barros. Application of central composite design to the optimisation of aqueous two-phase extraction of human antibodies. *Journal of Chromatography A*, 1141(1):50–60, feb 2007.
- P. A. J. Rosa, A. M. Azevedo, S. Sommerfeld, A. Mutter, M. R. Aires-Barros, and W. Bäcker. Application of aqueous two-phase systems to antibody purification: a multi-stage approach. *Journal of biotechnology*, 139(4):306–13, feb 2009b.
- P. a. J. Rosa, I. F. Ferreira, a. M. Azevedo, and M. R. Aires-Barros. Aqueous two-phase systems: A viable platform in the manufacturing of biopharmaceuticals. *Journal of Chromatography A*, 1217(16):2296–2305, 2010. ISSN 00219673. doi: 10.1016/j.chroma.2009.11.034. URL <http://dx.doi.org/10.1016/j.chroma.2009.11.034>.
- P. a. J. Rosa, A. M. Azevedo, S. Sommerfeld, M. Mutter, W. Bäcker, and M. R. Aires-Barros. Continuous purification of antibodies from cell culture supernatant with aqueous two-phase systems: From concept to process. *Biotechnology Journal*, 8(March):352–362, 2013.
- F. Ruiz-Ruiz, J. Benavides, O. Aguilar, and M. Rito-Palomares. Aqueous two-phase affinity partitioning systems: Current applications and trends. *Journal of Chromatography A*, 1244:1–13, 2012.
- A. Warade, R. Gaikwad, R. Sapkal, and V. Sapkal. Simulation of Multistage Countercurrent Liquid-Liquid Extraction. *Leonardo Journal of Sciences*, (20):79–94, 2011.

Integrated Process and Controller Design Software Tool – ProCACD

Jialiang Wang^a, Peng Ji^a, Xi Chen^{a,b,*}, Anjan Tula^c, Rafiqul Gani^{a,c}

^a *College of Control Science and Engineering, Zhejiang University, Hangzhou, China*

^b *National Center for International Research on Quality-targeted Process Optimization and Control, China*

^c *PSE for SPEED, Skyttemosen 6, Allerød, DK-3450, Denmark*

*: xi_chen@zju.edu.cn

Abstract

The field of Process system engineering (PSE) is constantly developing with the availability of advanced computational resources. Since 1960s, process simulation has been one of the most successful story in using computer aided methods and tools in the field of chemical engineering. Nowadays, several software tools are available for process simulation, process optimization, process synthesis and design. However, the current software in PSE is mainly focussed on processes without consideration of controller design or validation. The gap between process design and controller design seems to be increasing, which may lead to suboptimal solutions especially for closed-loop systems. Therefore, there is always a demand for integrating the process design with consideration of the controller design; even though the development of such software tool has not been well addressed so far, or are industry specific. In this paper, a model-based integrated process and controller design software tool called ProCACD (computer aided controller design) is presented along with a case study to design controllers and optimize controller parameters for a system of three-tanks-in-series with recycle.

Keywords: computer aided controller design, process simulation, PID tuning.

1. Introduction

Nowadays sustainable and efficient processes are needed in chemical industry to address the grand challenges of resource depletion, energy consumption and environmental impacts (Roh et al., 2016). Therefore, identification, design and development of appropriate processes are important for the industry to remain competitive. During the last decades, many researchers have developed computer aided software tools to address different aspects of process development, including Aspen for process simulation and control, ProCAFD (Tula et al., 2017) for process synthesis, GAMS (Biegler, 2018) for process optimization, etc. However, it seems that not much work has been done in the area of software development of simultaneous process design and control, though a trend towards considering process design and control aspects simultaneously has been proposed. Several methodologies have been developed for addressing the interactions between process design and process control (Mansouri et al., 2015). At first, researchers focus on the controllability of process systems. Controllability metrics based on open and closed-loop stability analysis were developed (Yi & Luyben, 1997). However, controllability metrics are used mostly in either steady state or linear dynamic models, and the uncertain link between the value of the measure

and the plant design may cause trouble. Thus, methods to overcome the limitation of controllability metrics appeared. These methods can be classified into two types. One type is based on multi-objective optimization (Gebreslassie et al., 2012). The other type is based on dynamic optimization (Diangelakis et al., 2017). Lagging behind the advance of method development for integration of process design and control, the software development is quite scarce. The objective of process design is to identify the types of tasks/operations that need to be performed, the corresponding design of the operation/equipment, their configuration, mass/energy flows, etc. (Tula et al., 2015). And the main objective of process control is to design control system to achieve optimal closed-loop dynamic performance (Yuan et al., 2012). Solving these two problems independently may lead to suboptimal solutions. A key to integrating the process design and controller design is to model them in a unified structure. Embedded with the previously developed modelling tool-box MoT (Fedorova et al., 2015), an integrated controller design software tool, ProCADC, is proposed in this work.

2. Architecture of ProCADC

2.1. MoT based Model-objects

ProCADC is a *c#* based software tool developed in Visual Studio. The process and control models are generated in ProCADC through the modelling tool-box MoT, where model developers define equations and set necessary variable values. In this work, a generic model object approach is implemented where a unified model is used to represent both open-loop and closed-loop processes for all possible pairings and all controller types (P, PI, PID, etc). As shown in Figure 1, one model-object can have several different configurations in ProCADC. While using the model-objects, the user should select the manipulated variables (MVs) and controlled variables (CVs) according to the real process, and then select the controller type and pairing based on his system. ‘*MV_i*’ and ‘*CV_i*’ are used to name the *i*th selected MVs and CVs, respectively.

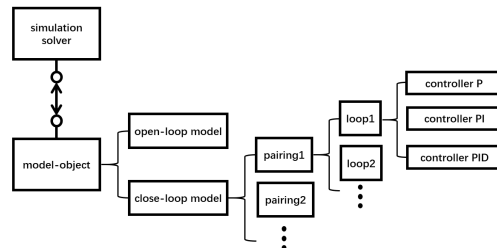


Figure 1: Different configurations of model-object

The controller equations part is the most essential part for model developers to establish a model-object with different kinds of controller configurations. Keywords ‘*ol*’, ‘*clp*’, ‘*clpi*’, and ‘*clpid*’ are kept to denote logic configurations of open-loop control, closed-loop P control, closed-loop PI control, and closed-loop PID control, respectively. Additionally, to denote the pairing between MVs and CVs, another keyword, “*Pairm_n*” is adopted to denote if a pairing exists between the *m*th MV and *n*th CV. An example template is given as follows to describe the controller equations of a process containing two MVs and two CVs.

$$Error1 = CV1 - CV1SP \quad (1)$$

$$Error2 = CV2 - CV2SP \quad (2)$$

$$\frac{dAE1}{dt} = Error1 \tag{3}$$

$$\frac{dAE2}{dt} = Error2 \tag{4}$$

$$MV1 = MV1 * oI1 + \tag{5}$$

$$[(P1 * Error1 + MV1Star) * cIp1 + (P1 * Error1 + I1 * AE1 + MV1Star) * cIpi1] * Pair1_1 + [(P1 * Error2 + MV1Star) * cIp1 + (P1 * Error2 + I1 * AE2 + MV1Star) * cIpi1] * Pair1_2$$

$$MV2 = MV2 * oI2 + \tag{6}$$

By properly setting the logic variables, this template can represent different controller type and the pairing structure between MVs and CVs. It should be noted that the need for process understanding is very essential for an efficient design. The process model together with the controller model template, called as MoT based model-object in this project, can be used to design, analyze and verify controller design and application.

2.2. Process Analysis and Controller Design

An overview of the 5-staged method is presented in Figure 2, which describes the main architecture of the ProCADC software as follows.

1.Problem Definition	2.View Model Variable	3.Open-Loop Run	4.Controller Configuration	5.Closed-Loop Run
<i>Inputs:</i> Generic MoT model-object <i>Outputs:</i> Configured process model	<i>Inputs:</i> Configured process model <i>Outputs:</i> Detailed variable information of the model	<i>Inputs:</i> Configured open-loop process model Data of initial variable values <i>Outputs:</i> Data of model simulation results	<i>Inputs:</i> Configured open-loop process model <i>Outputs:</i> Best pairing of the model Tuned Controller parameters results	<i>Inputs:</i> Tuned Controller parameters results <i>Outputs:</i> Data of configured closed-loop model simulation results

Figure 2: Process Analysis and Controller Design Method (in ProCADC)

Problem Definition: The main objective of this step is to define the configuration of the loaded generic MoT model-object. Configuration includes open-loop or closed-loop model, number of closed-loops as well as the pairing status and the selection of controller type (P, PI, or PID) for each loop.

View Model Variable: In this step, the configured process model defined in Problem Definition is elaborated through a table showing all the model variable details. If closed-loop option is chosen in Problem Definition step, an additional table showing the pairing of each loop is added.

Open-Loop Run: This step is used for the open-loop option in Problem Definition, where the configured open-loop process model variable details are listed in a table allowing users to set the initial input variable values so that open-loop simulations can be performed.

Controller Configuration: This is an essential step for finding the best pairing structure and tuning of the controller parameters for a closed loop process model. Here we connect Tai-ji PID tuning system through a web-API deployed in public cloud (www.taijipid.com). This web-based technology can conduct system identification and PID parameter tuning based on supplied simulation data. Additionally, the relative gain is calculated to find the best pairing by using the identified transfer function model. Once the best pairing is found, it is possible to tune the PID controller parameters. The related flow-diagram is shown in Figure 3. The MoT first generates open-loop data

through simulations. The generated simulation data is transformed to equal time interval data using the cubic spline interpolation algorithm embedded in ProCADC. Then the transformed simulation data is exported to Tai-ji PID tuning system, which analyses the process through transformed simulation data and conducts system identification as well as tuning of the controller parameters.

Closed-Loop Run: In this step, the tuned controller parameters are used for the configured close loop process model simulation. The software also allows the user to modify the controller parameters and add disturbances in this step. Eventually, the software provides a graph, in which, different closed-loop simulations are compared. The integration of process and controller design is achieved through model analysis in terms of sensitivity of process variables to controller variables.

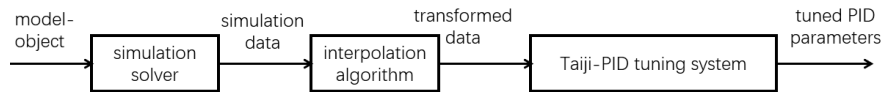


Figure 3: Flowsheet of Controller Tuning step

3. Case Study

The application of ProCADC is highlighted using a recycled three-tanks-in-series process model stored in a MoT-based model-object. The process is shown in Figure 4(a). Variables A1, A2 and A3 represent the cross-sectional area of the three tanks. Variables h1, h2 and h3 represent the liquid level of three tanks. Variables alpha1, alpha2 and alpha3 represent the valve opening values. Variables Fin, F1, F2 and Fout represent the inlet and outlet flowrate of the tanks. Variable purge represents the outlet flowrate of the whole system. The candidate control variables and manipulated variables are also marked in the figure with bracketed CV and MV, respectively. ProCADC helps users to find the best pairing, design controllers for the process, and tune controller parameters.

In the first step, Problem Definition, a user starts from introducing the MoT model, followed by a selecting options between open-loop or closed-loop analysis. If open-loop option is chosen in Problem Definition step, then in step 2, View Model Variable, a table will be automatically generated to list all the variables in this model; there follows an Open-Loop Run step, where the user can conduct open-loop simulations through the tank model. While if the closed-loop option is chosen in Problem Definition, further an initial configuration among CVs and MVs and selection of controller type will be prompted. Then in the second step, View Model Variable, ProCADC automatically creates another table listing the user's configuration information. Afterwards, the Open-Loop Run step is skipped and ProCADC goes straight to the Controller Configuration option, where the best pairing between CVs and MVs is found and the controller parameters are tuned accordingly.

The recycled three-tanks-in-series process model consists of 3 CVs and 3 MVs. Thus, there is a total of 6 different pairings if a user wants to control all the three liquid levels. It also means that the model has 6 different closed-loop configurations. ProCADC can find the best configuration using relative gain method through three steps. First, transfer function matrix is obtained with the generated open-loop simulation data. Then, relative gain matrix is calculated according to the transfer function matrix. Last, the best pairing is obtained by analysing the relative gain matrix. In this case, the best configuration is

shown in Figure 4(b), where valve opening of the outlet stream of each tank is used to control each tank level, which agrees with the process understanding.

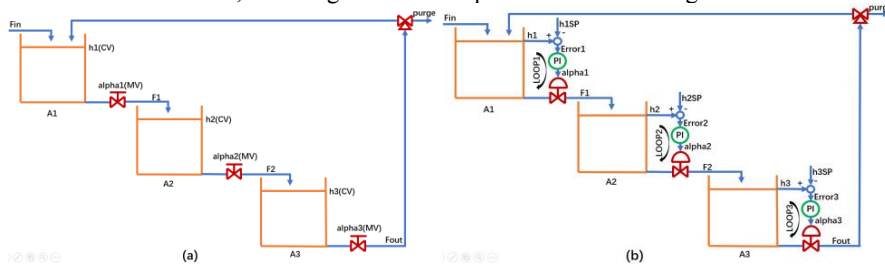


Figure 4: A case study of recycled three-tanks-in-series

(a) The original process flowsheet; (b) The process flowsheet with best pairing controller design.

Based on this closed-loop configuration, ProCACD further tunes the PID controller parameters in Controller Configuration step. After finishing Controller Configuration step, the data, including the tuned controller parameters, is stored and transferred to the Closed Loop Run step, where users can conduct closed-loop simulations. Figure 5 shows the comparison of the simulation results of CVs with the tuned controller parameters and the initial controller parameters which were obtained manually according to experiences. The simulation results indicate that the controllers perform well both in disturbance rejection and set point tracking using the tuned controller parameters. Here, the value of the integral time square error (ITSE) is used to quantitatively analyze control performance. At time 0, users give a set point step change of h_1 from 1 to 2. The ITSE value of h_1 using the tuned parameters is 0.31, much less than the ITSE value 0.62 using initial parameters. From the simulation result of h_1 , we can also see that the tuned parameters perform both less overshoot and less adjusting time, indicating a better set point tracking. As for h_2 and h_3 , the step change of h_1 could be regarded as a disturbance to them. The ITSE values of h_2 and h_3 using the tuned parameters are 0.19 and 0.23, respectively, less than the ITSE values of 0.26 and 0.33 with initial parameters. From the simulation results of h_2 and h_3 , it can also be seen that the tuned parameters bring less oscillation amplitude and less adjusting time, thus a better disturbance rejection. At 10 second time, a disturbance step change of F_{in} from 0.1 to 0.2 is introduced. The ITSE values of h_1 , h_2 and h_3 using the tuned parameters are 0.15, 0.26 and 0.31, respectively, less than the ITSE values of 0.28, 0.31 and 0.37 with the initial parameters. As shown in Figure 5, the tuned parameters perform less oscillation amplitude and less adjusting time than the initial setting, which again demonstrates better disturbance rejection. Further integration of the process design and controller design can be achieved through analyzing the sensitivity of process variables to controller variables, e.g., how the recycle ratio from the final tank outlet to the first tank affects the process dynamics and what the optimal recycle ratio should be designed.

4. Conclusions

In this work, a computer-aided method and associated software is developed to integrate modelling-simulation tools with controller design, analysis and verification tools. Interfacing with the modelling toolbox MoT, ProCACD helps users to design controllers from an open-loop process model with designated candidate CVs and MVs. The best pairing among the CVs and MVs can be detected. PID controller parameters can be well tuned. Good performance in disturbance rejection and set point tracking is

demonstrated through a case study involving control of liquid levels of a recycled three-tanks-in-series process model. As a summary, the model-based analysis tool provides a good understanding of the process and through it, a good design of the controller configuration and the controller parameter tuning can be achieved. In the future, an extensive library of process models and control strategy such as model predictive control (MPC) will also be implemented. On the basis of this work, a simultaneous process and controller design will be developed.

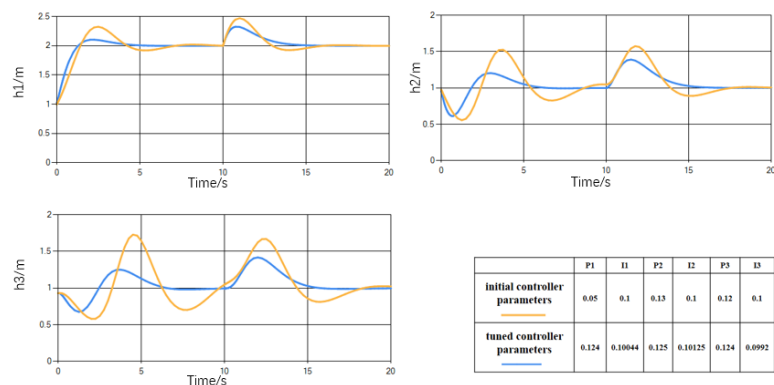


Figure 5: Comparison simulation results using different controller parameters

Acknowledgements

The authors gratefully acknowledge the financial support of NSFC-Zhejiang Joint Fund for the Integration of Industrialization and Informatization (No. U1509209).

References

- L. T. Biegler, 2018, New directions for nonlinear process optimization, *Current Opinion in Chemical Engineering*, 21, 32-40.
- N. A. Diangelakis, B. Burnak, J. P. Katz, E. N. Pistikopoulos, 2017, Process Design and Control optimization: A simultaneous approach by multi-parametric programming, *AIChE J*, 63(11), 4827-4846.
- M. Fedorova, G. Sin, R. Gani, 2015, Computer-aided modelling template: Concept and application, 83, *Computers & Chemical Engineering*, 232-247.
- B. H. Gebreslassie, Y. Yao, F. You, 2012, Design under uncertainty of hydrocarbon biorefinery supply chains: multiobjective stochastic programming models, decomposition algorithm, and a comparison between cvar and downside risk, *AIChE J*, 58(7), 2155-2179.
- S. S. Mansouri, M. Sales-Cruz, J. K. Huusom, J. M. Woodley, R. Gani, 2015, Integrated Process Design and Control of Reactive Distillation Processes, *IFAC-PapersOnLine*, 48, 8, 1120-1125.
- K. Roh, R. Frauzem, R. Gani, J. H. Lee, 2016, Process systems engineering issues and applications towards reducing carbon dioxide emissions through conversion technologies, *Chemical Engineering Research and Design*, 116, 27-47.
- Tai-ji PID. <http://www.taijipid.com>.
- A. K. Tula, M. R. Eden, R. Gani, 2015, Process synthesis, design and analysis using a process-group contribution method, *Computers & Chemical Engineering*, 81, 245-259.
- A. K. Tula, R. Gani, M. R. Eden, 2017, New Method and Software for Computer-Aided Flowsheet Design and Analysis, *Computer Aided Chemical Engineering*, 40, 649-654.
- C. K. Yi, W. L. Luyben, 1997, Design and control of coupled reactor/column systems—Part 1. A binary coupled reactor/rectifier system, *Computers & Chemical Engineering*, 21, 1, 25-46.
- Z. Yuan, B. Chen, G. Sin, R. Gani, 2012, State-of-the-art and progress in the optimization-based simultaneous design and control for chemical processes, *AIChE J*, 58(6), 1640-1659.

Computational Fluid Dynamics of Rectangular Monolith Reactor vs. Packed-Bed Column for Sorption-Enhanced Water-Gas Shift

Vlad C. Sandu^{a,*}, Ionela Dumbrava^a, Ana-Maria Cormos^a, Arpad Imre-Lucaci^a,
Calin C. Cormos^a, Paul D. Cobden^b, Robert de Boer^b

^a*Faculty of Chemistry and Chemical Engineering, Babeş-Bolyai University, Arany Janos 11, Cluj-Napoca RO-400028, Romania*

^b*ECN part of TNO, Westerduinweg 3, Petten 1755 LE, The Netherlands*

vcsandu@chem.ubbcluj.ro.

Abstract

Sorption-enhanced water-gas shift (SEWGS) process is very attractive for an energy efficient pre-combustion CO₂ capture, as it enables direct conversion of syngas into separate streams of H₂ and CO₂ at high temperatures and pressures. Using advanced computational fluid dynamics (CFD) methods, quantitative performance differences were assessed for rectangular channel monolith structures versus regular packed-bed structures when used for pre-combustion CO₂ capture. Published data of breakthrough capacities at different pressures for CO₂ and H₂O were used to validate a multicomponent adsorption isotherm. A COMSOL 1D model was developed to describe CO₂ adsorption in a fixed-bed reactor, filled with adsorbent pellets, to confirm the accuracy of the results compared to the existing studies, after which a 2D model was built simulating the adsorption step of a SEWGS process inside of a monolith reactor channel. Model predictions display an increase in productivity of adsorption in the case of monolith structures versus conventional packed-bed columns. Results will be used to improve the performance of experimental monolith structures undergoing SEWGS.

Keywords: CFD, CO₂ adsorption, isotherm, SEWGS

1. Introduction

Developing energy efficient low carbon applications is of great importance today as an active way of combating the climate change (IPCC, 2014). Sorption-enhanced water-gas shift (SEWGS) is a pre-combustion carbon capture and storage (CCS) process which combines the water-gas shift (WGS) reaction (Eq. (1)) with in situ adsorption of CO₂ (Eq. (2)) at 300-500 °C and 10-40 bar. Steam can also be adsorbed (Eq. (3)).



A SEWGS process consists of a series of reactors capable of CO₂ adsorption, operated in pressure cycles, similar to the cycles of a PSA, as to enable the periodic loading and regeneration of the sorbent. By using multiple reactors, the process can be characterized as a continuous one, allowing the constant production of separate H₂ and CO₂ streams. In the adsorption step of the cycle, syngas is fed into a reactor where the CO and steam react to produce CO₂ and H₂. The sorbent material takes up the CO₂ and a hot high pressure, H₂ rich product stream is directly produced, ready to be used as gas turbine fuel for power generation. SEWGS enables a direct conversion of syngas into separate hot streams of H₂ at feed pressure and CO₂ at regeneration pressure, making the process attractive for pre-combustion CCS and reduction of GHG emissions (van Selow et al., 2009).

Hydrotalcite based adsorbents are valuable for SEWGS, as they demonstrate high thermal stability, fast sorption kinetics and high CO₂ selectivity. The clay layered structure collapses at high temperatures, transitioning to a well dispersed mixed metal oxide with a higher surface area because of porosity formation. The impregnation of the oxide with K₂CO₃ increases the sorbent's capability to adsorb basic species. The potassium-promoted hydrotalcite (K-HTC) has two roles in SEWGS, catalyzer for the WGS reaction and sorbent for reversibly adsorbing CO₂. After adsorption, during K-HTC regeneration, the CO₂ released is sufficiently pure to be stored (Sikander et al., 2017).

Traditionally, columns filled with granulated adsorbent pellets are used in a SEWGS process, however, in this work, the columns are replaced with innovative 3D printed monolith reactors built of K-HTC material, as packed-bed reactors show significant bottleneck due to the restrictions regarding flow-rate inside the reactor, pressure drops and adsorption kinetics (Govender and Friedrich, 2017). A graphical representation of a monolith structure with square channels is presented in Figure 1.

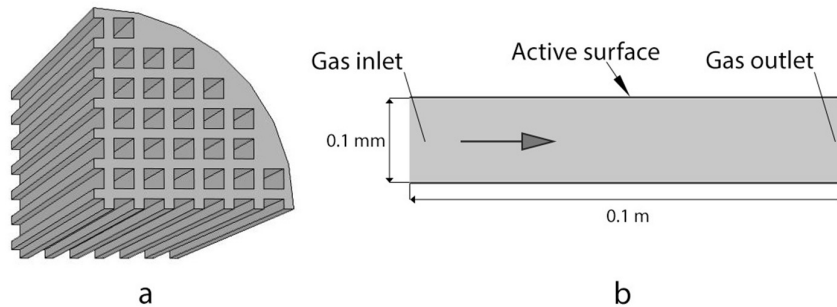


Figure 1. a – 3D schematic representation of a monolith reactor with square channels; b – 2D representation of the channel geometry used in the monolith reactor model.

Models simulated in COMSOL Multiphysics are used in order to further add improvements to experimental monolith structures. If successful, a significant size reduction of SEWGS for syngas processing with CO₂ capture will be possible while maintaining the same productivity.

2. Model development

This paper is evaluating the high-temperature, high-pressure adsorption step of a SEWGS process in which the columns, normally filled with K-HTC pellets that act as sorbents, are replaced by monolith reactors that are made entirely of adsorbent K-HTC material. Using COMSOL Multiphysics, a 1D model was developed to simulate, in space and time, the adsorption process of CO₂ in a packed-bed reactor. A reactor model published by Reijers et al. (2009) was used for validation. Following, a 2D COMSOL Multiphysics model was developed to simulate the adsorption step of SEWGS for CO₂ inside a single rectangular channel of a monolith reactor.

2.1. Adsorption isotherms

Adsorption isotherms are used to describe the quantity of adsorbate on the surface as a function of its pressure at constant temperature. Boon et al. (2014) used experimentally obtained breakthrough data to fit a multicomponent adsorption isotherm for the system and obtained good results with two double isotherms, deriving a model that takes into account surface and nanopores contributions for the adsorption of CO₂ and H₂O at high pressures.

2.2. Model parameters and assumptions

For the 1D fixed-bed reactor model, process parameters are taken from literature (Reijers et al., 2009), so as to add validity to the predictions and enable proper comparison. Although the monolith structure contains around 500 channels, the 2D model simulates the adsorption of CO₂ inside a single rectangular channel, in order to reduce hardware computation requirements. The geometry of the model is seen in Figure 1b. The parameters for the fixed-bed reactor model and the rectangular channel reactor model are presented in Table 1.

Table 1. Model specific parameters

Parameter	Fixed-bed model	Monolith model	Parameter	Common values	
Length	0.2 m	0.1 m	Bed density	533	kg m ⁻³
Tube diameter	0.016 m	-	Particle density	922	kg m ⁻³
Bed height	0.02 m	-	Feed temperature	673.15	K
Width	-	1e-4 m	k _{LDF}	0.1	s ⁻¹
Feed velocity	0.0056 m s ⁻¹	0.035 m s ⁻¹			
Feed pressure	101,325 Pa	25e5 Pa			
Porosity	0.4	0.44			

Simplifying assumptions are common for both models. These include a uniform distribution of sorbent activity, laminar fluid flow, dispersion does not occur, heat transfer is not considered and the LDF mass transfer coefficient is constant.

2.3. Process phenomena

For the fixed-bed model, the phenomena occurring are convection-diffusion of the bulk phase and diffusion-adsorption of CO₂, which are solved with a convection-diffusion equation (Eq. (5)) and a porous media transport equation (Eq. (6)).

$$\frac{\partial c_i}{\partial t} + \nabla \cdot (-D_i \nabla c_i) + u \cdot \nabla c_i = R_i \quad (5)$$

$$(\varepsilon_p + \rho k_{p,i}) \cdot \frac{\partial c_i}{\partial t} + \left(c_i - \frac{\rho}{(1 - \varepsilon_p)} \cdot c_{p,i} \right) \frac{\partial \varepsilon_p}{\partial t} + \nabla \cdot \Gamma_i + u \cdot \nabla c_i \quad (6)$$

For the 2D monolith reactor channel model, mass transport in the bulk is solved by using Eq. (5), while adsorption of CO₂ is solved through the material balance on the active surface of the walls inside the channel (Eq. (7)). The surface concentration of CO₂, c_s , is described using Eq. (8) with terms for the linear driving force mass transfer coefficient and adsorption isotherm. The way through which mass transport and surface adsorption are coupled is by setting the adsorption rate as an outward flux in the boundary condition for Eq. (5).

$$\frac{\partial c_s}{\partial t} + \nabla \cdot (-D_s \nabla c_s) = r_{ads} \quad (7)$$

$$\frac{\partial q_{CO_2}}{\partial t} = k_{LDF} \cdot (q_{CO_2}^* - q_{CO_2}) \quad (8)$$

3. Results and discussions

3.1. Breakthrough capacities for CO₂ and H₂O

For validation of the adsorption isotherms, published data (Boon et al., 2014) regarding breakthrough capacities for CO₂ and H₂O were plotted as a function of pressure, with pressure values of up to 24 bar. The data points in Figure 2 show pure component breakthrough capacities measured for CO₂, while Figure 3 shows the capacities for steam. The lines are drawn based on the isotherm developed from the full dataset and the symbols are the measured data.

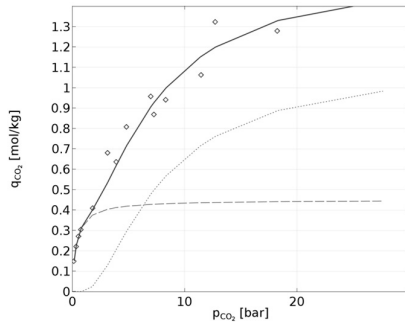


Figure 2. CO₂ breakthrough capacities vs CO₂ partial pressure (diamonds), predicted capacity (line), surface contribution (dashed line), nanopore contribution (dotted line).

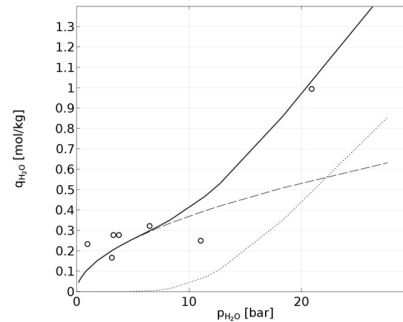


Figure 3. Pure H₂O breakthrough capacities versus H₂O partial pressure (circles), predicted capacity (line), surface contribution (dashed), nanopore contribution (dotted line).

The capacities for CO₂ seen in Figure 2 follow a two-step adsorption mechanism. The first step is due to surface sites and adds contribution up to 0.4 mol kg⁻¹, while the additional adsorption at partial pressures over 3 bar is attributed to nanopores. Steam behaves similarly to CO₂. In Figure 3, at partial pressures under 12 bar, the

experimental capacities show a surface contribution of about 0.3 mol kg^{-1} , while the point above 20 bar might indicate an additional nanopore adsorption mechanism.

3.2. Fixed-bed reactor model describing CO_2 adsorption

In regards to the validation of the fixed-bed reactor model, Figure 4 shows the breakthrough curve calculated by the COMSOL 1D model compared to existing published data (Reijers et al., 2009). The results seem to be in agreement with their predictions, as the breakthrough times are within close range and the curves present similar profiles for identical process parameters.

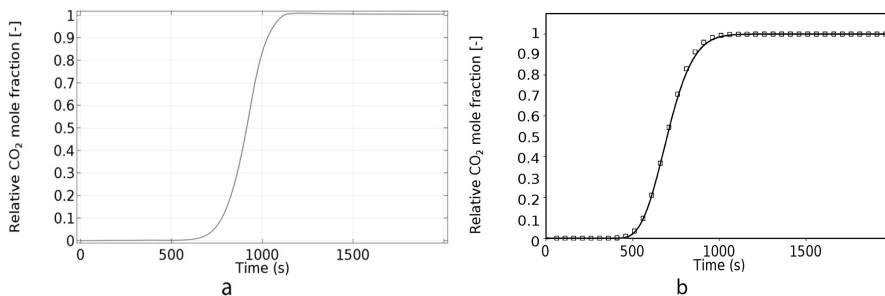


Figure 4. CO_2 mole fraction at the reactor outlet relative to CO_2 mole fraction of the feed gas calculated by the COMSOL 1D. a – breakthrough curve calculated by the COMSOL Multiphysics model; b – breakthrough curves calculated by the MATLAB model (line) and from the analytical solution (symbols) (Reijers et al., 2009).

3.3. Monolith reactor model describing CO_2 adsorption in a single rectangular channel

The breakthrough curve predicted by the 2D monolith reactor model, in which the adsorption of CO_2 takes places at the surface of the walls inside the rectangular channel, can be seen in Figure 5. Comparing the time of breakthrough and its profile with existing data predicted by fixed-bed reactor models, it can be assumed that a monolith reactor would provide a better adsorption of CO_2 .

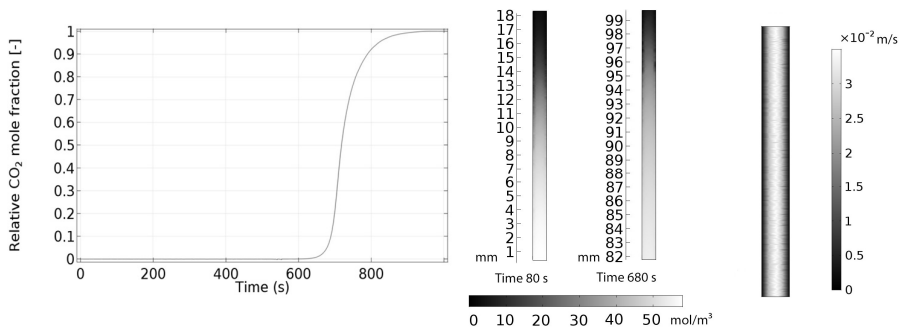


Figure 5. CO_2 mole fraction at the reactor outlet relative to CO_2 mole fraction of the feed gas calculated by the COMSOL 2D monolith reactor model.

Figure 6. CO_2 surface concentration at different times calculated by the COMSOL 2D monolith reactor model and surface velocity profile along the reactor.

4. Conclusions

Using the published data regarding breakthrough capacities of CO₂ and H₂O, a multicomponent adsorption isotherm has been successfully validated. The isotherm accounts for surface adsorption at lower partial pressures and nanopore contributions at higher values of partial pressures.

A 1D model of a fixed-bed reactor has been developed using COMSOL Multiphysics, with the purpose of validation based on published data. Using the multicomponent isotherm and the linear driving force approximation, the adsorption of CO₂ was successfully simulated, as breakthrough predictions agree with other predictions found in literature.

Finally, a 2D monolith reactor model describing adsorption of CO₂ occurring at the surface of a single channel's walls was developed. Although validation is not possible at the moment due to lack of experimental data, assessing the time of breakthrough and its profile leads to the conclusion that a monolith structure would provide better adsorption.

Acknowledgements

This work was supported by a grant of the Romanian National Authority for Scientific Research and Innovation, CCCDI - UEFISCDI, project number COFUND-ACT ERANET – 3D-CAPS (contract number: 87/2017): "Three Dimensional Printed Capture Materials for Productivity Step-Change", within PNCDI III.

References

- J. Boon, P.D. Cobden, H.A.J. van Dijk, C. Hoogland, E.R. van Selow and M. van Sint Annaland, 2014, Isotherm model for high-temperature, high-pressure adsorption of CO₂ and H₂O on K-promoted hydrotalcite, *Chem. Eng. J.*, 248, 406-414.
- S. Govender and H.B. Friedrich, 2017, Monoliths: a review of the basics, preparation methods and their relevance to oxidation, *Catalysts*, 7, 2, 62.
- IPCC, 2014, Climate change 2014: Synthesis report. Contribution of working groups I, II and III to the Fifth Assessment Report of the Intergovernmental Panel on Climate Change, IPCC: Geneva, Switzerland.
- H.T. Reijers, J. Boon, G.D. Elzinga, P.D. Cobden, W.G. Haije and R.W. van den Brink, 2009, Modelling study of the sorption-enhanced reaction process for CO₂ capture. I. Model development and validation, *Ind. Eng. Chem. Res.*, 48, 15, 6966-6974.
- E.R. van Selow, P.D. Cobden, P.A. Verbraeken, J.R. Hufton and R.W. van den Brink, 2009, Carbon capture by sorption-enhanced water-gas shift reaction process using hydrotalcite-based material, *Ind. Eng. Chem. Res.* 48, 9, 4184-4193.
- U. Sikander, S. Sufian and M.A. Salam, 2017, A review of hydrotalcite based catalysts for hydrogen production systems, *Int. J. Hydrogen Energy*, 42, 31, 19851-19868.

Review of override control methods

Jan Schuurmans^{a,*}

^aDotX Control Solutions, Oudeweg 91, office B.1-1, Haarlem 2031CC, the Netherlands

j.schuurmans@dotxcontrol.com

Abstract

This paper focusses on potential issues with override control. We show that, in the presence of stochastic disturbances, the existing methods can fail due to frequent switching from one controller to the other. Based on the analysis of the cause of the problem, we propose a simple solution and demonstrate its applicability on a test setup involving a Siemens PLC and software.

Keywords: override control, PID, constrained output control, cascade control

1. Introduction

In some cases, the control must adjust a manipulated variable to control one process variable at setpoint while maintaining other process variable(s) within limits. In practice, this problem, sometimes referred to as the output constrained control problem, is often solved with the use of PID controllers. Scientific literature on this subject usually focusses on stability and performance in the presence of deterministic disturbances (Glattfelder 1988, Lopez 1996). To the knowledge of the author, the case of stochastic disturbances has not been considered so far. This paper analyses two common methods to handle output constraints and shows that they face potential problems in the presence of stochastic disturbances. Based on the analysis of the cause of the problem, we propose a simple solution and demonstrate its applicability on a test setup involving a standard Siemens PLC.

The paper is structured as follows. Section 2 defines the output constraint problem in full detail. Section 2 and 3 present two common solutions (override control and cascade control, respectively) to the output constraint problem, using PID controllers, and shows that these solutions may not work in the presence of stochastic disturbances. Section 4 analyses the problem and presents solutions. Finally, section 5 presents the conclusions.

2. Description of the output constraint problem

The main question of this paper, is: are the existing constraint handling methods (using PID controllers) capable of handling stochastic disturbances, and if not, can we fix the problem? This section describes this main question in more detail.

We assume that the process is described by the following model:

$$y_1 = G_1(s) m + d_1, \quad y_2 = G_2(s) m + d_2 \quad (1)$$

with m the manipulated variable, y_i ($i = 1$ or 2) process variable, d_i disturbance variable, $G_i(s)$ a transfer function as a function of the Laplace variable s .

This paper considers both deterministic and stochastic disturbances. The deterministic disturbances provide immediate insight in the dynamic behaviour, the stochastic disturbances are more common in practice.

The output constrained control challenge is defined in words as follows. Control y_1 as closely as possible to setpoint s_1 , while the second process variable y_2 should not cross some limit (that we assume, without loss of generality, to be a high limit y_{2max}). When we are dealing with stochastic disturbances, it makes sense to try to ensure that the chance of exceeding the limit y_{2max} is less than some predefined percentage. The controllers are assumed to be PID controllers equipped with a Tracking Mode option. Although the exact equations are usually not provided by commercial manufacturers, we shall assume, for clarity of the paper, that this means that the PID controllers can be represented by $m_i = C_i(s)e_i + b_i$, with $C_i(s)$ a PID controller in the Standard Form:

$$C_i(s) = K_{p,i} \left(1 + \frac{1}{T_{i,i}s} + T_{d,i}s \right) e_i \quad (2)$$

Furthermore, $e_i = s_i - y_i$, and b_i is a bias term, defined by $b_i = \frac{1}{T_t s} (m - m_i)$ with m the manipulated input. If the i -th PID is active, i.e. if $m = m_i$, the bias term disappears. Otherwise, in Tracking mode, the controller's output can be written as:

$$m_i = \frac{T_t s}{T_t s + 1} C_i(s) e + \frac{1}{T_t s + 1} m \quad (3)$$

and clearly, m_i tracks m for frequencies below $\omega < 1/T_t$

Basically, the Tracking mode ensures that the output of the controller that is not active 'tracks' the output of the controller that is active, to avoid a bump when switching. The exact equations for the Tracking mode method are not essential for the results in this paper.

In the next sections, we consider different control solutions. To simulate them, we shall simulate one specific process model, according to:

$$G_1(s) = \frac{1}{3s + 1} e^{-0.2s}, \quad G_2(s) = \frac{2}{4s + 1} e^{-s}$$

The disturbances vary according to:

$$d_1(s) = w_1 + d_d, \quad d_2(s) = w_2 + d_d$$

with w_1 and w_2 independent normally randomly distributed white noise, with variance 1, and d_d a deterministic disturbance component, starting at time $t = 0.4$ and changing stepwise to -2 at $t = 100$ s.

The setpoint for controller C_1 is $s_1 = -0.1$ and we assume that at $t = 0$, the system is in steady state. The maximum on output y_2 is $y_{2max} = 2$, and we wish to reduce the chance of y_2 exceeding y_{2max} to less than 2.5%. In order to allow comparison between different control options, we adopt the following control parameters for the controllers C_1 and C_2 :

$$K_{p1} = 5.25, \quad T_{i1} = 1.6, \quad T_{d1} = T_{d2} = 0, \quad K_{p2} = 0.7, \quad T_{i2} = 4$$

These settings were chosen based on the tuning rules as presented in (Skogestad 2001) and results in well damped and fast response under normal conditions (i.e. no switching between controllers). We have chosen not to use D-action for reasons of simplicity.

Given these control parameter settings, and the stochastic disturbance w_2 as defined above, the standard deviation (σ_2) of y_2 will be close to $\sigma_2 = 1$, if C_2 is either

active or not during the entire simulation period. This implies that if we choose the setpoint s_2 as 0 or slightly lower, we can expect that the output constraint on y_2 can be met in ‘steady state conditions’, i.e. at all times outside the transients caused by the deterministic variations in d_d . Therefore, we select setpoint $s_2 = y_{2max} - 2\sigma_2 = 2 - 2 = 0$, since the chance of exceeding $2\sigma_2$ is less than 2.5% for a normal distribution.

The override control solutions, as described in this paper, were tested on a hardware in the loop setup, as shown in Figure 1. In this setup, the process model was simulated using the PID Tuner software described in its manual (Schuurmans 2018). The control output (m) was calculated by the Siemens S7 1200 PLC, programmed with an override control solutions as described in the manual of the PLC (Simatic 2018). The controllers C_1 and C_2 were realised with the PID Compact blocks.

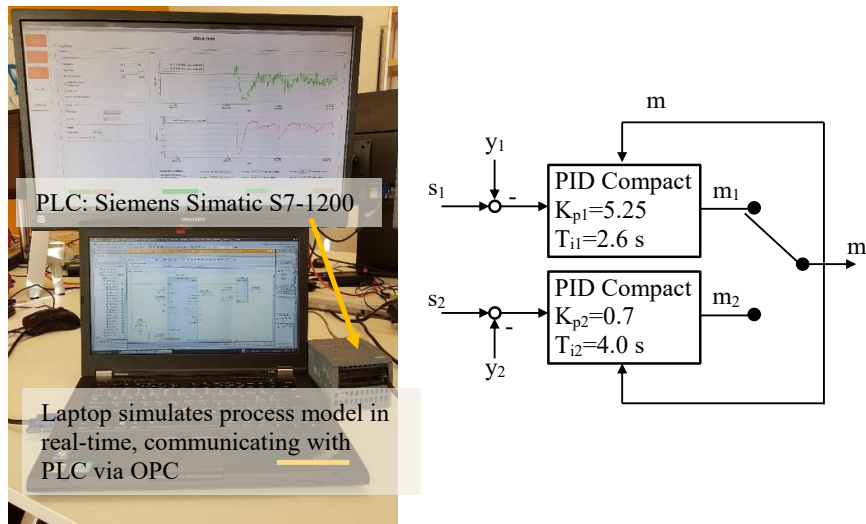


Figure 1 Photo of the Hardware in the Loop setup (left) and diagram of the control setup (right).

3. Override control

One method to handle the output constraint is Override control (Shinsky 2005). In override control, the controller with minimal (or maximal) manipulated variable is selected, i.e. $m = \min(m_1, m_2)$. In other words, control switches to C_2 if (and only if) $m_2 < m_1$. For this method, it is clear how to set the control parameters. Indeed, the PID settings as presented in section 1 work well in the absence of stochastic disturbances, see Figure 2. This figure shows both the simulated response according to our assumed PID formulas (solid lines) and the actual PID Compact (dashed lines); the responses differ slightly, but in essence the behaviour agrees. Control switches correctly from C_1 to C_2 at $t=100$ s.

However, in case of stochastic disturbances, frequent switching between controllers take place, and this results in a problematic performance (solid lines in Figure 3). The Mean Squared Error (MSE) of y_1 , defined as $MSE_1 = \frac{1}{n} \sum_{i=0}^n e_1(t)^2$ increases to 9 (with n = number of samples), whereas MSE equals just 1.2 if C_1 is active all the time.

4. Cascade control

In case of cascade control, the PID controller C_1 adjusts the setpoint of the second PID controller (s_2). By constraining the setpoint of s_2 , according to $s_2 \leq y_{2\max}$, the output y_2 can be expected to satisfy the output constraint.

A disadvantage of this method is that the controller C_1 cannot be tuned optimally on the basis of the process model given by Eq. 1, but, instead, it must be tuned on the basis of the closed-loop dynamics given by $y_2 = \frac{G_2}{1+C_2G_2} s_2$. In many cases, these closed-loop dynamics are slower than the open-loop dynamics. This problem can be overcome using cleverly chosen filters, as was shown in (Lestage 1999). Nevertheless, this solution copes with the same issues as Override control, in the presence of stochastic noise, and similar results as shown in Figure 3 apply to this control solution.

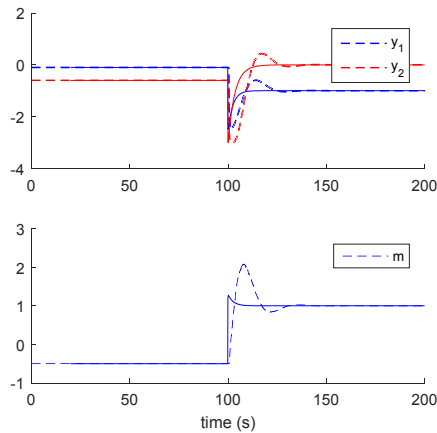


Figure 2 Simulated (solid) and measured response of the PID Compact (dashed).

5. Analysis of the problem and solutions

Override control and (cleverly chosen) cascade control boil down to the same solution, where control switches from C_1 to C_2 or vice versa. In case of stochastic disturbances, the switching may occur too frequently, resulting in lousy performance. We can analyse the switching conditions more closely. The controller that is not active, is in tracking mode. Let us, for example, assume that C_1 is active and C_2 is in tracking mode. In that case, the switching condition can be written as $C_1 e_1 > C_2 e_2$. The same condition applies when the second controller is active. Hence, the condition for switching from one controller to the other can be expressed in terms of a condition on controller deviations (e_i), weighed by the controller transfer function. Similar switching conditions, but with different 'weighting transfer functions' can be derived for cascade control, and in case of different PID implementations (such as the PID in velocity form). In the presence of noisy control deviation signals (e_i) with mean values that differ less than the variations, frequent switching will take place.

To resolve this issue, we can change the switching conditions such that switching takes only takes place when meaningful. Changing the switching conditions does not alter the stability (proofs) of the control systems, see for instance the stability proofs as

presented in Glattfelder (1988, 2004) and Lopez (1996). We therefore defined a continuous ‘switching’ parameter α , according to

$$\frac{d\alpha}{dt} = K_{\alpha 1}(e_1 - e_2) - K_{\alpha 2}(\alpha - \alpha_c) \quad (4)$$

with $\alpha_c = \text{sat}(\alpha)$, i.e. $\alpha_c = \alpha$ if $\alpha_{\min} < \alpha < \alpha_{\max}$, $\alpha_c = \alpha_{\min}$ if $\alpha \leq \alpha_{\min}$ and $\alpha_c = \alpha_{\max}$ if $\alpha \geq \alpha_{\max}$.

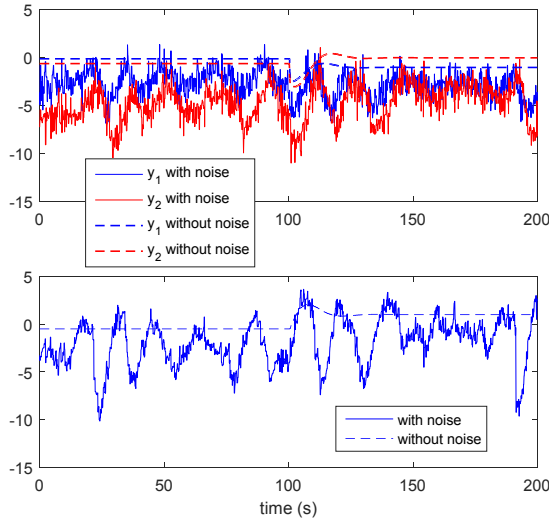


Figure 3 Measured response with stochastic disturbances (solid lines) and without (dashed) when using the Siemens PID Compact. In the case of stochastic disturbances, control switches frequently.

The parameter α is driven to ‘one side’ as long as there is a difference between e_1 and e_2 . Control switches to C_1 if $\alpha_c > 0.45$. Control switches to C_2 if $\alpha_c < -0.45$.

For sufficiently small gain $K_{\alpha 1}$, it will not switch too frequently. The gain $K_{\alpha 2}$ feeds back on saturations of α , and basically provides anti-windup. The parameters were chosen as $\alpha_{\min} = -0.5$, $\alpha_{\max} = 0.5$, $K_{\alpha 1} = 3$, $K_{\alpha 2} = -3$.

Figure 4 shows the results when we changed the switching conditions in the PLC to the conditions depending on α_c described here. Clearly, control switches only when it makes sense, from controller C_1 to C_2 at $t=100$ seconds in the simulation. As a result, the MSE of the deviations of y_1 from setpoint have reduced from 9 to 1.76 (compared to the results shown in Figure 3), while the percentage of y_2 samples crossing the limit $y_{2\max}$ is within specifications at 1.9% (outside the transients due to the deterministic disturbance change at $t = 100$, so outside the time span $t = 100$ to 130 s).

6. Conclusions

Returning to the main question posed in this paper, if the existing constraint handling methods (using PID controllers) are capable of handling stochastic disturbances, and if not, if we can fix the problem, the answer to the first question is ‘no’. This answer was based on an analysis of the existing methods, both on paper and in experiments. Analysis showed that the problem was due to too frequent switching from one controller to the other. By changing the switching conditions this problem can be overcome though.

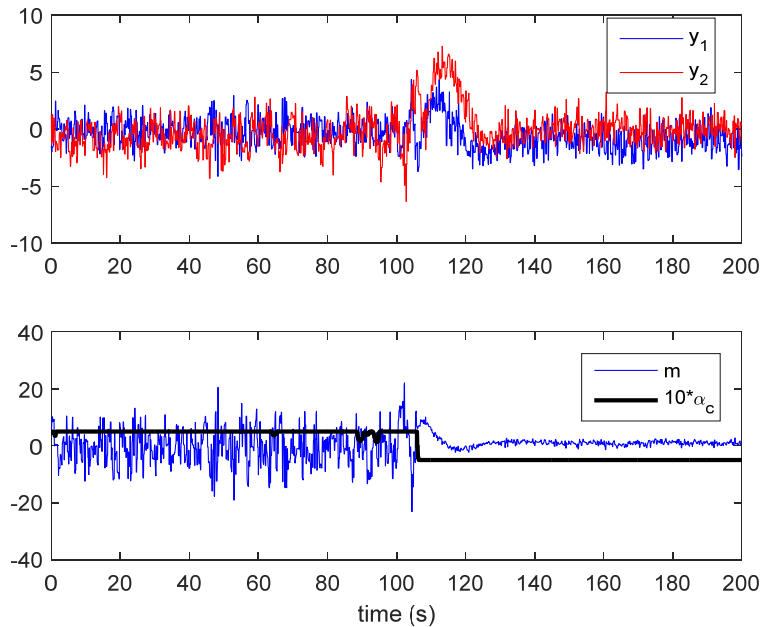


Figure 4 Results with override control with adjusted switching conditions applied to the Siemens PID Compact. Now, control switches from C_1 to C_2 at $t=100$ s only.

References

- A.H. Glattfelder and W. Schaufelberger, Stability of discrete override and cascadelimiter single loop control systems. *IEEE Transactions on Automatic Control* 33, 1988
- A.H. Glattfelder, W. Schaufelberger, 'A path from antiwindup to override control, *IFAC Nonlinear Control Systems*, 2004
- R. Lestage, Improved constrained cascade control for parallel processes, *Control Engineering Practice*, Volume 7, Issue 8, August 1999, Pages 969-974
- A.A. Lopez, J.A. Joseph, 'On the stability of override control systems', LAAS-CNRS, Toulouse France, Rapport N° 98304, 1996
- A.I. Ribic, M.R., Design and Tuning of PID Override Control System Based on Signal Filtering, *International Symposium on Industrial Electronics INDEL 2014*, 2014
- J. Schuurmans, T.Zabel 'PID Tuner', manual, www.pid-tuner.com, 2018
- F.G. Shinskey, J.P. Shunta, J.E. Jamison, chapter 2.28 Selective, Override, and Limit Controls, *Instrument Engineers' Handbook, Volume Two: Process Control and Optimization*, 4th edition, 2005
- Simatic, S7-1200, S7-1500, PID Control, Function manual, Version 10, 2018
- S. Skogestad, 'Probably the best simple PID tuning rules in the world', *AICHE Annual meeting*, 2001

Development of a biorefinery scheme to produce biofuels from waste cooking oil

Araceli Guadalupe Romero-Izquierdo^a, Fernando Israel Gómez-Castro^a, Claudia Gutiérrez-Antonio^b, Rogelio Cruz Barajas^c, Salvador Hernández^a

^a*Departamento de Ingeniería Química, División de Ciencias Naturales y Exactas, Campus Guanajuato, Universidad de Guanajuato, Noria Alta s/n, Guanajuato, Guanajuato, 36050, México.*

^b*Facultad de Química, Universidad Autónoma de Querétaro, Centro Universitario, Av. Cerro de las Campanas s/n Col. Las Campanas, Santiago de Querétaro, Querétaro, 76010, México. claudia.gutierrez@uaq.mx*

^c*Instituto Tecnológico de Ciudad Madero, Av. 1° de Mayo y Sor Juana Inés de la Cruz Col. Los Mangos, Ciudad Madero, Tamaulipas, 89440, México.*

Abstract

Biofuels are a promissory alternative to satisfy the world energy demand, and its production can be performed in a biorefinery scheme; however, few researches have been reported under this concept. According to the open literature, the raw material used to obtain renewable fuels represents roughly 60-80% of total annual cost. Thereby, the exploitation of a low-price feedstock into a biorefinery scheme is a good strategy to improve the production cost of the renewable fuels, and mitigate the environmental impact related with the processing. In this work, a biorefinery scheme using waste cooking oil (WCO) is presented, aiming to obtain biodiesel and biojet fuel simultaneously as main products. The modelling of the biorefinery scheme is performed in the process simulator Aspen Plus. The biodiesel is obtained through esterification and transesterification with ethanol, adding the refining zone to recover the ethanol; biojet fuel is produced through the hydrotreating process. The biorefinery is evaluated in terms of economic and environmental indicators, whose are compared with previously reported assessments for the separate production processes. Reductions on the processing cost and CO₂ emissions are expected regarding each individual process.

Keywords: waste cooking oil, biorefinery scheme, biofuels

1. Introduction

The depletion of fossil resources is a huge economic and environmental issue concerning the modern society, due to population growth, and the increase of energy demand. Since last decade, scientific and technological efforts have been focused on the development of novel alternatives to take advantage of renewable resources. Second and third generation raw materials have been used to produce a broad range of renewable products, mainly biofuels. However, its processing cost is high along with the price of renewable fuels. Recent studies on alternative biofuels have reported the use of agricultural wastes and waste cooking oil as promising feedstock to produce renewable products, diminishing the processing cost (Dewan et al, 2013; Gasca-González et al, 2018). The production of biofuels can be performed in a biorefinery scheme, which is a processing plant wherein

biomass is converted into a broad range of renewable products; its processing routes are designed according to biomass nature and composition. Regarding petroleum refineries, a biorefinery splits the raw material in useful fractions, which are taken as internal raw material to generate the desired products (Sadhukhan et al, 2014). Therefore, due to integral and multiple use of the feedstock selected, the price of the obtained renewable products could be competitive with its fossil counterparts. On the other hand, in the transport sector the demand of diesel and jet fuel has expanded significantly, and so its environmental impact (Grote et al, 2014). Thus, the use of biodiesel and biojet fuel has been recognized as a promising strategy to diminish the generated environmental impact and partially cover the demand. Regarding biodiesel production, several techniques have been proposed to diminish its energy consumption, related costs, and improve the biodiesel yield (Hajjari et al, 2017). However, conventional processing route through esterification and transesterification reactions is commonly chosen due to its low cost (Gasca-González et al, 2018). Furthermore, the biojet fuel is an emergent biofuel, which can be produced through few processing pathways that are certified by ASTM (Gutiérrez-Antonio et al, 2018); one of them is the hydrotreating process, which is the most mature technology due to similarity with the petro-refineries (Gutiérrez-Antonio et al, 2016). Recently, advances into process operation such as novel catalyst to improve biojet fuel yield and strategies of process intensification have been proposed. In this work, a biorefinery scheme using waste cooking oil (WCO) is presented, aiming to obtain biodiesel and biojet fuel as main products. The biorefinery scheme is modelled in the process simulator Aspen Plus. The biodiesel is obtained through esterification and transesterification with ethanol; while the biojet fuel is produced through the hydrotreating process, generating green diesel and naphtha as co-products. The economic and environmental indicators for the biorefinery process are calculated, and they are compared with the previously reported assessments for biodiesel and biojet fuel individual production processes. The main contribution of this work relies on the proposal and assessment of a biorefinery scheme to convert WCO into biofuels, employing both, conventional and intensified technologies, and establishing a base structure for future enhancements.

2. Process modelling

The WCO is classified as a hazardous waste, which has severe effects on urban waste water and, thus, on fresh water bodies, due to its inadequate disposal (Hajjari et al, 2017). In Mexico were recollected 5,596,032.97 L of WCO in 2015, in agreement with government data (SEMARNAT, 2004; SEDEMA, 2015). Thus, the proposed biorefinery scheme, showed in Figure 1, has been designed to process 5,596,032.97 L/year of WCO; moreover, the scheme considers two stages of heating at 65°C and impurities removal by sedimentation as pre-treatment for the WCO. At the end of these pre-treating stages, 20% of the total volume of WCO was removed as water and suspended solids. The average density for WCO was assumed as 0.91 g/ml. Thus, 2,004.88 kg/h were processed through simulations in Aspen Plus V.8.0. The WCO composition has been considered as 94 wt% triglycerides and 6 wt% FFA; also, according to Gasca-González et al (2018) the FFA profile in wt% is: palmitic acid (12.3%), oleic acid (24%), linoleic acid (56.6%), and linolenic acid (7.1%). It is important to highlight that several efforts to recollect the WCO have been implemented in the country; however, a well-defined supply chain has not been established yet. In the biorefinery scheme, the total WCO recollected in 2015 is divided in half after pre-treatment in order to produce biodiesel and biojet fuel; this percentage

was chosen as the base scenario after a preliminary analysis to determine the proportion which allows the higher gross profit. The biodiesel process starts conditioning the WCO at 70°C, operation temperature for the esterification process. Ethanol is fed with molar ratio ethanol:oil, 6:1 and 1 wt% of sulfuric acid as catalyst; processed into a batch module. Next, the reaction products are fed to a neutralization reactor, wherein Na₂CO₃ was used to remove H₂SO₄ catalyst as Na₂SO₄ salt. The amount of Na₂CO₃ was stoichiometrically calculated regarding the H₂SO₄. The removal of Na₂CO₃ salt was realized by a filter. At once, the output stream is feeding to the transesterification reactor operated at 70°C, adding NaOH (1 wt%) as catalyst. Fresh ethanol is added to complete the 6:1, ethanol:oil molar ratio. The reaction is done into a batch module reactor. The stream leaving the transesterification reactor is feeding to decanter module, wherein two streams are splittling. In the first one, the separated biodiesel (FAEE) is fed to the washing column, operating with water (50 wt% regard FAEE); and then the excess of water is eliminated in an evaporator. The FAEE yield was 92.37%. The second stream leaving the decanter module is introduced to a neutralization reactor with H₃PO₄ (stoichiometrically calculated regarding NaOH). The Na₃PO₄ salt generated was removed by a filter. The stream leaving the neutralization reactor was rich in ethanol and water; this stream was feeding to distillation train, which includes 3 distillation columns to recover the ethanol. In the first one, the ethanol was concentrated near to the azeotropic point. In the second one, a glycerol stream was fed in 1.3:1 mass ratio, glycerol:mixture (ethanol + water). The azeotropic point was overcome and the ethanol mol purity was 99.76%. Finally, the last distillation column was used to separate water from glycerol; mole purity of 99.99% was reached for glycerol. The glycerol used to break the azeotropic point was generated as co-product in transesterification process; only 0.64% of fresh glycerol was purchased from external source to cover the glycerol/mixture ratio. The recovered ethanol and glycerol were cooled down to 25°C and recirculated to the process. It is worth to mention that the ethanol was used as alternative reactant to methanol, since it can be produced from renewable feedstock; also, is lower toxic than methanol. UNIQUAC was the thermodynamic method used to model the reaction and conditioning zones of the biodiesel process; also, the refining FAEE zone (distillation train) were modelled by NRTL method. The reaction kinetics for esterification and transesterification reactions were reported by Gasca-González et al (2018). Regarding the biojet fuel process, the WCO and hydrogen were conditioned at 380 °C and 30 bar, and fed into the hydrotreating reactor, which operates with NiMo/USY@Al-SBA-15 as catalyst. The volume ratio hydrogen:WCO was 500:1. The operation conditions, conversion, yield and distribution of products were reported by Zhang et al (2018). It is important to emphasise that the catalyst used is bifunctional, thus, the hydrotreating and hydrocracking /hydroisomerization reactions were carried out in the same equipment. Three products are obtained from the hydrotreating reactor: naphtha, biojet fuel and green diesel. A distillation train conformed by two distillation columns was designed to separate each product. The thermodynamic method used to model the conditioning of reactants and reactor zone was Peng-Robinson; while the distillation train was modelled using BK10 method. The naphtha selectivity was of 41%, biojet fuel 36% and green diesel of 84%. It is worth to mention that the biojet fuel is composed by 79.4 wt% of lineal paraffins, 1.9 wt% cycloparaffins, and 18.7 wt% aromatic compounds. Figures 2 and 3 show the biodiesel process from WCO and biojet fuel process from *Jatropha curcas* oil reported by Gasca-González et al (2018) and Gutiérrez-Antonio et al (2016), respectively. It is worth to mention that the processing structure for the biorefinery scheme has been constructed based on each individual process.

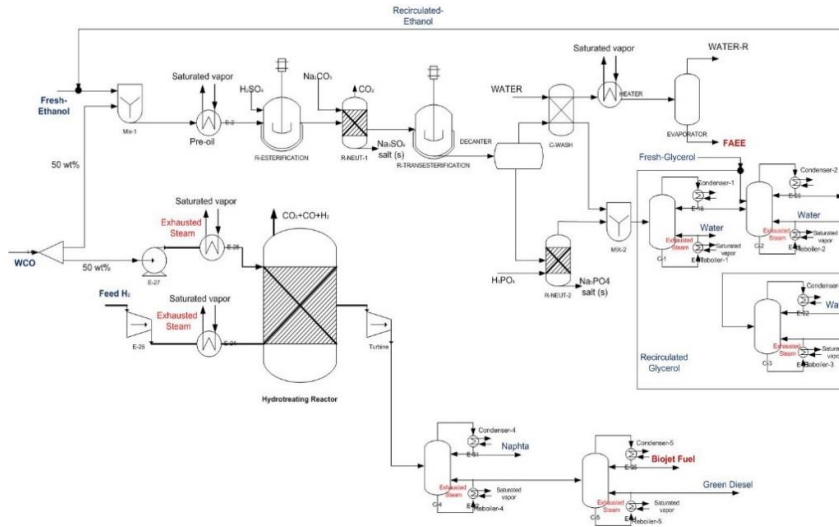


Figure 1. Proposed biorefinery scheme.

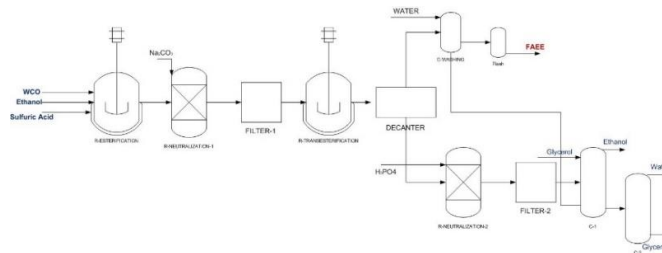


Figure 2. Biodiesel individual process extracted from Gasca-González et al (2018).

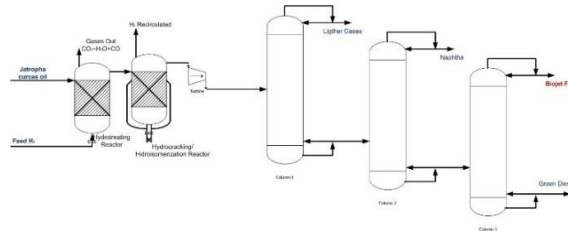


Figure 3. Biojet fuel individual process extracted from Gutiérrez-Antonio et al (2016).

3. Results

In this section, results for the proposed biorefinery scheme are presented. The TAC was obtained by Guthrie-Ulrich method (Turton et al, 2012), which take into account cost equipment, utilities cost (heating and cooling), raw materials (hydrogen and ethanol) and additional reagents (neutralisation reagents and glycerol). This estimation does not consider the cost of the heterogeneous catalyst for hydrotreating, filters cost and cost for removal equipment of $\text{CO}_2\text{-CO}$. Likewise, the biorefinery generates 20.4 kW of electricity; thus, its sale was considered, after covering the internal demand. In Table 1

the TAC and total CO₂ emissions per year are presented. The raw material cost represents 61.7% of TAC; also, the utilities cost is high. Regarding total CO₂ emissions, those related to the generation of vapor used in the process and those released by the hydrotreating reactor are considered. The CO₂ emissions by electricity are not considered, since the internal demand is covered by the energy produced in the biorefinery. Thus, the major CO₂ emissions are generated due to vapor production, considering a natural gas boiler with efficiency of 80%.

Table 1. TAC and total kg CO₂ emissions /year for proposed biorefinery scheme.

<i>Utilities Cost (\$USD/year)</i>	<i>Equipment Cost (\$USD/year)</i>	<i>Raw Material Cost (\$USD/year)</i>	<i>Electricity Sale Cost (\$USD/year)</i>	<i>Total Annual Cost, TAC (\$USD/year)</i>
\$1,158,967.54	\$1,858,623.10	\$4,826,117.42	\$19,490.04	\$7,824,218.02
<i>Used vapor (kg CO₂/year)</i>	<i>CO₂ Release by hydrotreating process (kg CO₂/year)</i>		<i>Total Emissions (kg CO₂/year)</i>	
7,347,269,188.12	1,346,683.54		7,348,615,871.66	

The comparison between the biorefinery and individual processes is made in terms of two economic indicators and two environmental indicators. The economic indicators are defined as TAC per mass unit and TAC per energy unit of main biofuel produced. The environmental indicators are defined as kg CO₂ per mass unit and kg CO₂ per energy unit of main biofuel produced. In the individual processes, the main products are biodiesel and biojet fuel, respectively; while in the biorefinery process, the sum of biodiesel and biojet fuel are considered as the main products. The proposed indicators show, in Table 2, that the biorefinery has a higher cost than biodiesel individual process, but lower than the biojet individual process. In addition, the minimum value of kg CO₂ is reached by the biorefinery scheme, regarding to each individual process; this reduction in CO₂ emissions and cost could be attributed to the use of the free-of-charge WCO, the use of bifunctional hydrotreating catalyst, and the biorefinery concept.

Table 2. Proposed economic and environmental indicators.

Indicators		Biodiesel process (Gasca-González et al, 2018)	Biojet fuel process (Gutiérrez-Antonio et al, 2016)	Biorefinery (This work)
TAC/kg biofuel	(USD/kg)	0.7651	29.915	0.7471
TAC/kJ release	(USD/kJ)	0.0006	0.021	0.0005
kg CO₂/ kg biofuel	(kg CO ₂ /kg)	4.0828	1769.48	0.1294
kg CO₂/ kJ biofuel	(kg CO ₂ / kJ)	0.0030	1237	0.0001

4. Conclusions

A biorefinery scheme to transform WCO into biodiesel and biojet fuel as main products has been presented. The total WCO recollected in Mexico for 2015 was the processing goal; 92.37 % yield to biodiesel and 36 % selectivity to biojet fuel were obtained in this scheme. The TAC per unit of mass or energy from biorefinery process was better than the

biojet fuel individual process reported; while, the total kg CO₂ emissions per mass or energy obtained were better than each individual process. Thus, the biorefinery scheme could be a promissory alternative to use WCO to produce biofuels.

5. Acknowledgments

Financial support provided by CONACyT, grants 239765 and 279753, for the development of this project is acknowledged.

References

- A. Dewan, J.P. Raftery, Z. Li, M.N. Karim, 2013, Biofuel from waste agricultural product and lignocellulosic biomass, *IFAC Proceedings Volumes*, 46, 18, 178-186.
- R. Gasca-González, F.I. Gómez-Castro, A.G. Romero-Izquierdo, E. Zenón-Olvera, C. Gutiérrez-Antonio, 2018, Design of a low-cost process for the production of biodiesel using waste cooking oil as raw material, *Computer Aided Chemical Engineering*, 43, 1529-1534.
- J. Sadhukhan, K. Siew-Ng, E. Martínez-Hernández, 2014, *Biorefineries and Chemical Processes: design, integration and sustainability analysis*, 1, 20-30.
- M. Grote, I. Williams, J. Preston, 2014, Direct carbon dioxide emissions from civil aircraft, *Atmospheric Environment*, 95, 214-224.
- M. Hajjari, M. Tabatabaei, M. Aghbashlo, H. Ghanavati, 2017, A review on the prospects of sustainable biodiesel production: a global scenario with an emphasis on waste-oil biodiesel utilization, *Renewable and Sustainable Energy Reviews*, 72, 445-464.
- C. Gutiérrez-Antonio, F.I. Gómez-Castro, J.A. De Lira-Flores, S. Hernández, 2017, A review on the production processes of renewable jet fuel, *Renewable and Sustainable Energy Reviews*, 79, 709-729.
- C. Gutiérrez-Antonio, A.G. Romero-Izquierdo, F.I. Gómez-Castro, S. Hernández, A. Briones-Hernández, 2016, Simultaneous energy integration and intensification of the hydrotreating process to produce biojet fuel from *jatropha curcas*, *Chemical Engineering and Processing: Process Intensification*, 110, 134-145.
- S. Semarnat, 2014, Subsecretaría de Gestión para la Protección Ambiental, Dirección General de Gestión Integral de Materiales y Actividades Riesgosas, México. Consulted (10-September-2018), Web site: https://apps1.semarnat.gob.mx:445/dgeia/informe_resumen/08_residuos/cap8.html#5
- S. Sedema, 2015, Inventario de Residuos Sólidos CDMX, Consulted (10-September-2018), Web site: <https://www.sedema.cdmx.gob.mx/storage/app/media/IRS-2015-14-dic-2016.compressed.pdf>
- Z. Zhang, Q. Wang, H. Chen, X. Zhang, 2018, Hydroconversion of waste cooking oil into bio-jet fuel over a hierarchical NiMo/USY@Al-SBA-15 Zeolite, *Chemical Engineering Technology*, 41,3, 590-597.
- R. Turton, R.C. Bailie, W.B. Whiting, J.A. Shaeiwitz, D. Bhattachayya, 2012, *Analysis, synthesis and design of chemical processes*, 4th edition, Prentice Hall, New Jersey, 951-982.

A novel process monitoring approach based on Feature Points Distance Dynamic Autoencoder

Feifan Cheng^a and Jinsong Zhao^{a,b,*}

^a*State Key Laboratory of Chemical Engineering, Department of Chemical Engineering, Tsinghua University, Beijing 100084, China*

^b*Beijing Key Laboratory of Industrial Big Data System and Application, Tsinghua University, Beijing 100084, China*
jinsongzhao@tsinghua.edu.cn

Abstract

For chemical industry, safety is always primary. A safe and reliable systems are required to ensure the safety of chemical plants. Many data-driven process monitoring methods have been developed and successfully applied to various processes. Autoencoder is an unsupervised learning algorithm, which can extract the features automatically from the unlabelled data. However, one limitation of autoencoder is that it does not consider any temporal dependency of the data. And autoencoder can not be ensured to get various meaningful features from the raw data. In this work, we proposed Feature Points Distance Dynamic Autoencoder (FPDDAE) to capture the temporal dependency and encourage the autoencoder to get meaningful features. The FPDDAE is constructed by the recurrent neural network (RNN), RNN can capture the time dependency of the process by adding a recurrent hidden state whose activation at each time is dependent on that of the previous time. To make the data points as near as possible in feature space, we define a penalty term \mathcal{FPD} that measures the average distance between any two points in feature space. The penalty term \mathcal{FPD} is a constraint to encourage the FPDDAE to learn meaningful features. A simple nonlinear simulation example is used to illustrate how the proposed method works. The proposed method is applied to the Tennessee Eastman process (TEP) to demonstrate its performance.

Keywords: Process monitoring; Dynamics; Deep learning; Alarm management.

1. Introduction

For chemical industry, safety is always primary. Names like Bhopal or Piper Alpha, are well-known not only for causing a lot of death but also for the damage to the environment (Drysdale and Sylvester-Evans, 1998; Sen and Egelhoff, 1991). A safe and reliable systems are required to ensure the safety of chemical plants. With the wide application of distributed control system (DCS) and large number of variables are measured and stored, many data-driven process monitoring methods have been developed and successfully applied to various processes.

Data-driven process monitoring methods can be roughly divided into statistical methods and artificial intelligent methods, although there are many connections between them. Some typical statistical methods include principal component analysis (PCA) (Wise et al., 1990), partial least squares (PLS) (Kruger and Dimitriadis, 2008), independent component analysis (ICA) (Lee et al., 2004), Fisher discriminant analysis (FDA) (He et al., 2005), statistics pattern analysis (SPA) (He and Wang, 2011) and their variations. Due to the dynamics and nonlinearity of the chemical

process data, statistical methods have a lot of limitations when they are applied to the process monitoring.

For artificial intelligent based process monitoring methods, significant progress has been made in recent years, especially for the deep learning (DL) methods. DL methods were originally proposed as feature selection and classification methods. There is one limitation of most deep learning methods that they need large amount of labelled data and usually they do not perform well with limited data (Zhang and Zhao, 2017; Wu and Zhao, 2018). Autoencoder is an unsupervised learning algorithm, which can extract the features automatically from the unlabelled data. However, one limitation of autoencoder is that it does not consider any temporal dependency of the data. And autoencoder can not be ensured to get various meaningful features from the raw data (Jia et al., 2018). The feature extraction process of an autoencoder can be regarded as the dot produce results between its weight matrix composed by a set of basis vectors and raw data. In this paper, we proposed Feature Points Distance Dynamic Autoencoder (FPDDAE) to solve the above problems. We use the recurrent neural network (RNN) to construct the autoencoder. RNN can capture the time dependency of the process by adding a recurrent hidden state whose activation at each time is dependent on that of the previous time. To make the data points as near as possible in feature space, we define a penalty term \mathcal{FPD} that measures the average distance between any two points in feature space. The penalty term \mathcal{FPD} is a constraint to encourage an autoencoder to learn meaningful features.

The remainder of the paper is organized as follows. In section 2, the autoencoder and RNN are briefly reviewed. Section 3 introduces the proposed FPDDAE method. In addition, a simple nonlinear simulation example is used to demonstrate how the proposed method work. In section 4, the proposed method is applied to the TEP model to demonstrate its performance. Conclusions are given in section 5.

2. Autoencoder and recurrent neural network

2.1. Autoencoder

An autoencoder consists of encoder and decoder. Given unlabeled data $\{\mathbf{x}_m\}_{m=1}^M$, the function \mathbf{f} is called encoder and will calculate a feature vector \mathbf{h}_m from \mathbf{x}_m :

$$\mathbf{h}_m = \mathbf{f}(\mathbf{x}_m) \quad (1)$$

The decoder reconstructs $\hat{\mathbf{x}}_m$ from the feature vector \mathbf{h}_m by a mapping function \mathbf{g} :

$$\hat{\mathbf{x}}_m = \mathbf{g}(\mathbf{h}_m) \quad (2)$$

The set of parameter θ of the encoder and decoder are learned simultaneously on the task of reconstructing as well as possible the original input data. The aim of an autoencoder is to minimize the reconstruction error. This minimization is usually carried out by stochastic gradient descent in the training of Multi-Layer-Perceptrons (MLPs). The reconstruction error is as followed:

$$\mathcal{L}_{AE} = \frac{1}{2M} \sum_{m=1}^M \|\hat{\mathbf{x}}_m - \mathbf{x}_m\|_2^2 \quad (3)$$

2.2. Recurrent neural network

A recurrent neural network (RNN) is an extension of a conventional feedforward neural network, which is able to handle a variable-length sequence input. The reason that RNN can handle time series is that RNN has a recurrent hidden state whose activation at each time is dependent on that of the previous time. Long short-term memory units (LSTMs) are one type of RNN, which make each recurrent unit to adaptively capture dependencies of different time scales. LSTMs have cell and forget gate to modulate the flow of information. The structure of LSTMs is showed in figure 1.

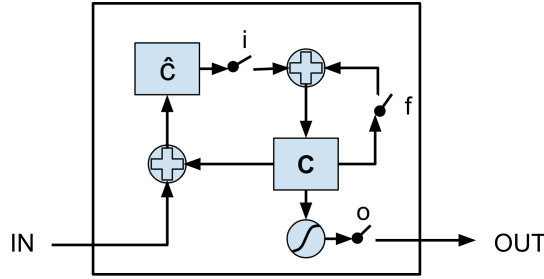


Figure 1: The structure of LSTMs.

3. Feature Points Distance Dynamic Autoencoder

We use \mathbf{X}_t to denote a window (with window width w) of process measurements of n variables as below:

$$\mathbf{X}_t = [\mathbf{x}_{t-w+1}, \mathbf{x}_{t-w+2}, \dots, \mathbf{x}_t]^T = \begin{bmatrix} x^{(1)}(t-w+1) & x^{(2)}(t-w+1) & \dots & x^{(n)}(t-w+1) \\ x^{(1)}(t-w+2) & x^{(2)}(t-w+2) & \dots & x^{(n)}(t-w+2) \\ \vdots & \vdots & \ddots & \vdots \\ x^{(1)}(t) & x^{(2)}(t) & \dots & x^{(n)}(t) \end{bmatrix} \quad (4)$$

LSTMs are used as the neural network layers of FPDDAE to capture the time dependency among the process variables. The encoder \mathbf{f}_L consists of two layers of LSTMs and calculates the feature vector \mathbf{h}_t from \mathbf{X}_t :

$$\mathbf{h}_t = \mathbf{f}_L(\mathbf{X}_t) \quad (5)$$

The decoder reconstructs $\hat{\mathbf{X}}_t$ from the feature vector \mathbf{h}_t by a mapping function \mathbf{g}_L :

$$\hat{\mathbf{X}}_t = \mathbf{g}_L(\mathbf{h}_t) \quad (6)$$

The penalty term \mathcal{FPD} is the measure of the average distance between any two points in feature space. The historical data of normal operation is easily obtained in the industry. The process monitoring model is often built from the data at normal state. Therefore, it is meaningful to make points in feature space as near as possible when training the model. The penalty term \mathcal{FPD} is defined as followed:

$$\mathcal{FPD} = \frac{1}{M-w} \sum_{i=1}^{M-w} \sum_{j=1}^i \|\mathbf{h}_i - \mathbf{h}_j\|_2^2 \quad (7)$$

The cost function of FPDDAE is made up of reconstruction error and \mathcal{FPD} . The β regular parameter controlling the weight between the reconstruction error and the penalty term \mathcal{FPD} . The cost function is as followed:

$$\mathcal{L}_F = \frac{1}{2(M-w)} \sum_{i=1}^{M-w} \|\hat{\mathbf{X}}_t - \mathbf{X}_t\|_2^2 + \beta \frac{1}{M-w} \sum_{i=1}^{M-w} \sum_{j=1}^i \|\mathbf{h}_i - \mathbf{h}_j\|_2^2 \quad (8)$$

The FPDDAE is trained by minimizing the cost function \mathcal{L}_F . The structure of FPDDAE is showed at figure 2. The \mathcal{L}_F is used as the monitoring scores. A threshold of monitoring scores is estimated by the empirical method. If test samples are faulty, when they are projected onto the FPDDAE model, which was trained using normal samples, the resulted monitoring scores would be higher than the threshold.

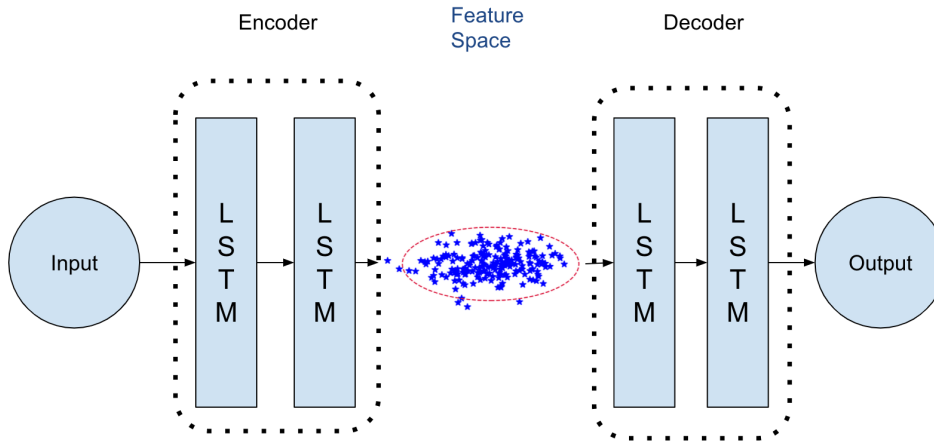


Figure 2: Structure of FPDDAE.

3.1. A simple nonlinear example

A simple nonlinear simulation example is as followed:

$$x_2 = x_1^2 + e \quad (9)$$

where x_1 is a random variable that follows a uniform distribution between $[-0.5, 0.5]$, and e is a random variable that follows a normal distribution with variance 0.02. A total of 15000 normal samples is simulated with 10000 samples for training and 5000 samples for validation. Two groups of testing samples (faults A and B) are simulated, each group with 5000 samples. Figure 1 shows the scatter plot of the normal and faulty samples. Both autoencoder and FPDDAE are trained by normal data. The results of autoencoder and FPDDAE at training process are compared in figure 3. From the figure 3 (b)-(d), the average distance of data points decreases in the FPDDAE method. The normal data and faulty data are clearly separated in the feature space. However, as showed at figure 3 (e)-(f), the normal data and faulty data can not be separated clearly by using an autoencoder. The proposed method FPDDAE can deal with the nonlinearity and capture the meaningful features.

4. Case study

In this section, the benchmark Tennessee Eastman model process simulator is used to demonstrate the performance of the proposed method. Compared with the small nonlinear simulation model in the previous section, the TEP is a much larger nonlinear system. The model consists of five major units: a reactor, condenser, compressor, separator, and stripper (Downs and Vogel, 1993). The process contains 12 manipulated variables and 41 measured variables. The measured variables contain 22 process variables sampled every 3min, and 19 quality variables sampled with dead time and time delays. In this case study, 22 process variables and 12 manipulated variables are used for the process monitoring. Here we compare PCA, DPCA, KPCA, autoencoder and FPDDAE. For all the methods, 960 samples of normal state is used as the training data set. The validation data set is made up of 480 samples of normal state. Each fault consists of 960 samples, and the fault is introduced at 161 samples. The upper control limits correspond to the 99% confidence level for all the methods.

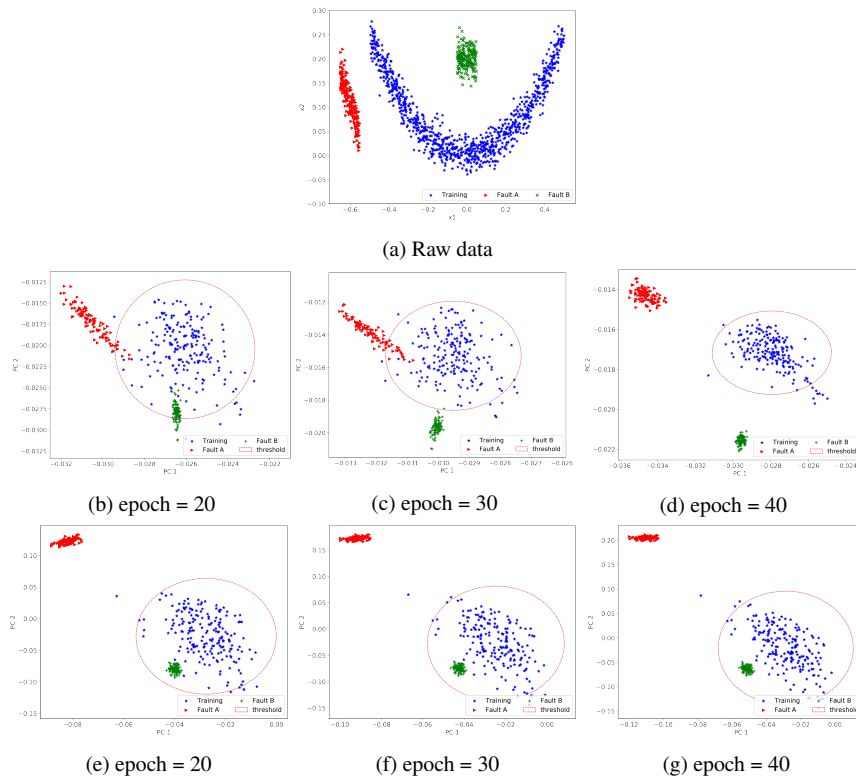


Figure 3: Scatter plot of normal and faulty data. Raw data: (a). FPDDAE: (b) , (c) , (d) . Autoencoder: (e) ,(f) , (g).

The fault detection rates of different methods for all faults are listed in Table 1. It is suggested that faults 3,9 and 15 are difficult to detect and may have been corrected by the control mechanism, so they are not consider here (Lee et al., 2006). In the case study, PCA, KPCA and DPCA don't perform well on six faults (Fault 5, 10, 16, 19, 20, 21). In comparison, the proposed FPDDAE method have a higher detection rate than other methods.

5. Conclusion

In this paper, we proposed a new cost function to make the points in the feature space as near as possible. Based on this new cost function, we proposed FPDDAE for the process monitoring. FPDDAE can capture the temporal dependency and encourage the autoencoder to get meaningful features. Compared with the traditional methods like PCA, FPDDAE can deal with nonlinearity and dynamics. The performance of the proposed FPDDAE is compared with other methods on a small nonlinear example and the benchmark Tennessee Eastman process. The results show that FPDDAE can detect the faults more efficiently than other methods. The temporal dependency is captured by the LSTMs.

This work highlights that the unsupervised deep learning methods can be adapted for process monitoring. Various meaningful features can be captured by using the different cost functions. For

Table 1: Fault Detection Rates of PCA, DPCA, KPCA, AE and FPDDAE for TEP

Fault	PCA		DPCA		KPCA		AE	FPDDAE
	T^2	SPE	T^2	SPE	T^2	SPE	SPE	scores
1	99.1	99.6	99.1	99.6	99.2	99.8	99.0	99.3
2	98.5	98.5	98.5	98.4	98.2	98.8	97.8	98.4
4	5.2	97.2	3.8	100.0	7.8	99.1	99.4	99.9
5	23.5	26.0	23.4	32.5	23.1	25.0	60.6	88.5
6	98.8	100.0	98.6	100.0	18.6	99.5	99.4	99.6
7	39.2	100.0	61.0	100.0	99.0	100.0	99.8	99.8
8	96.2	96.9	96.9	97.5	96.9	96.1	98.5	97.8
10	30.5	21.8	25.9	34.9	36.0	22.2	79.5	91.3
11	19.9	68.6	17.0	85.2	32.0	58.4	98.8	99.0
12	97.6	96.0	98.6	97.2	98.0	92.5	99.6	100.0
13	93.2	95.2	93.9	95.5	94.0	94.8	94.1	94.3
14	79.5	100.0	91.6	100.0	97.8	99.9	99.6	99.8
16	12.5	16.6	9.5	30.2	18.2	17.6	73.1	94.3
17	72.8	91.2	74.1	95.6	74.4	93.5	96.8	98.3
18	89.1	90.0	88.5	90.4	23.6	90.6	89.0	95.9
19	0.2	20.4	0.4	48.5	0.4	6.9	90.9	97.6
20	28.6	43.8	27.6	57.4	29.4	44.9	88.6	89.1
21	31.0	43.2	34.5	47.2	31.5	44.4	50.4	70.6

future work, determining the value β regular parameter needs further research.

References

- J. J. Downs, E. F. Vogel, 1993. A plant-wide industrial process control problem. *Computers & chemical engineering* 17 (3), 245–255.
- D. Drysdale, R. Sylvester-Evans, 1998. The explosion and fire on the piper alpha platform, 6 July 1988. a case study. *Philosophical Transactions Mathematical Physical and Engineering Sciences* 356 (1748), 2929–2951.
- Q. P. He, S. J. Qin, J. Wang, 2005. A new fault diagnosis method using fault directions in fisher discriminant analysis. *AIChE journal* 51 (2), 555–571.
- Q. P. He, J. Wang, 2011. Statistics pattern analysis: A new process monitoring framework and its application to semiconductor batch processes. *AIChE journal* 57 (1), 107–121.
- F. Jia, Y. Lei, L. Guo, J. Lin, S. Xing, 2018. A neural network constructed by deep learning technique and its application to intelligent fault diagnosis of machines. *Neurocomputing* 272, 619–628.
- U. Kruger, G. Dimitriadis, 2008. Diagnosis of process faults in chemical systems using a local partial least squares approach. *AIChE Journal* 54 (10), 2581–2596.
- J.-M. Lee, S. J. Qin, I.-B. Lee, 2006. Fault detection and diagnosis based on modified independent component analysis. *AIChE journal* 52 (10), 3501–3514.
- J.-M. Lee, C. Yoo, I.-B. Lee, 2004. Statistical process monitoring with independent component analysis. *Journal of Process Control* 14 (5), 467–485.
- F. Sen, W. G. Egelhoff, 1991. Six years and counting: Learning from crisis management at bhopal. *Public Relations Review* 17 (1), 69–83.
- B. M. Wise, N. Ricker, D. Veltkamp, B. R. Kowalski, 1990. A theoretical basis for the use of principal component models for monitoring multivariate processes. *Process control and quality* 1 (1), 41–51.
- H. Wu, J. Zhao, 2018. Deep convolutional neural network model based chemical process fault diagnosis. *Computers & Chemical Engineering* 115, 185–197.
- Z. Zhang, J. Zhao, 2017. A deep belief network based fault diagnosis model for complex chemical processes. *Computers & Chemical Engineering* 107, 395–407.

A comparison of the performance of multi-objective optimization methodologies for solvent design

Ye Seol Lee^a, Edward Graham^a, George Jackson^a, Amparo Galindo^a and Claire S. Adjiman^{a*}

^a*Department of Chemical Engineering, Centre for Process Systems Engineering, Imperial College London, South Kensington Campus, London SW7 2AZ, United Kingdom*
c.adjiman@imperial.ac.uk

Abstract

In this work, we present a systematic comparison of the performance of five mixed-integer non-linear programming (MINLP) multiobjective optimisation algorithms on a computer-aided solvent design problem. The five methods are designed to address the nonconvexity of the problem, with the aim of generating an accurate and complete approximation of the Pareto front. The approaches includes: a weighted sum approach with simulated annealing (SA), a weighted sum approach with multi level single linkage (MLSL), the sandwich algorithm with SA, the sandwich algorithm with MLSL and the non dominated sorting genetic algorithm-II. These five combinations of optimisation techniques are applied to the design of a solvent for chemical absorption of carbon dioxide (CO₂). The results shows that the sandwich algorithm with MLSL can efficiently generate diverse Pareto points leading to a construction of more complete Pareto front.

Keywords: multiobjective optimisation, CAMD, MINLP, global search

1. Introduction

Computer-Aided Molecular Design (CAMD) is a promising technique that can accelerate the discovery of new molecules, such as solvents, refrigerants, and pharmaceutical products, by making it possible to explore *in silico* a very large space of possibilities. In the field of CAMD, numerous mathematical methods have been developed to handle the complexities that arise from the large number of molecules that can be formed from the combination of a given set of atom groups and from the inherent non-linearity and non-convexity of structure-property and process models. Many of the methods proposed to date have been based on an optimisation framework and have made use of single objective Mixed-Integer Non-Linear Programming (MINLP) to achieve better economic criteria or property targets. However, in many cases, it is beneficial to consider multiple conflicting objectives that cannot easily be combined together in a single metric. Multi-Objective Optimisation (MOO) is thus receiving increasing attention in the CAMD area. Papadopoulos and Linke (2006) proposed a multi-objective molecular design technique linked with a process synthesis framework, extending it (Papadopoulos et al., 2013) to the design of binary working fluid mixtures in organic Rankine cycles and (Papadopoulos et al., 2016) to the design of solvent for CO₂ capture. Burger et al. (2014) adapted the sandwich algorithm to the design of a solvent for a CO₂ physical absorption process. Her-ring and Eden (2015) also successfully introduced MOO with a genetic algorithm to the

molecular design problem. Although the mixed-integer nature of molecular design MOO problems presents specific challenges, there has been no systematic analysis to compare the performance of MOO algorithms for CAMD applications.

In this work, we present a comparative analysis of the performance of three main MINLP MOO approaches, the weighted sum (WS), the sandwich algorithm (SD) (Rennen et al., 2011), and the non-dominated sorting algorithm-II (NSGA-II) (Deb et al., 2000). To increase the likelihood of identifying the globally optimal Pareto front, we make use of the simulated annealing version of WS (Marcoulaki and Kokossis, 2000), which has been previously applied to MOO CAMD (Papadopoulos et al., 2016). We also put forward a simulated annealing version of the sandwich algorithm, and multi-start approaches for the both WS and SD. This results in 5 combinations of algorithmic options, which are applied to the design of a solvent for the chemical absorption of CO₂. Algorithmic performance is compared based on reliability and efficiency criteria.

2. Optimisation methodology

In this section, we describe the methodologies for MINLP MOO that are used in this work. The WS and SD rely on a scalarisation of the multiple objective functions as a single aggregated objective function. NSGA-II, on the other hand, falls into the category of ‘evolutionary algorithms’. The NSGA-II can in principle solve a broader range of MOO problems as it is a derivative-free method, but the accuracy of the resulting approximation cannot be guaranteed.

2.1. Weighted sum method

WS is the most widely used scalarisation method in MOO. It is formulated as $\min \sum_{i=1}^p \lambda_i f_i$ (p : # of objectives), where $\sum_{i=1}^p \lambda_i = 1$. The weights, λ_i are positive real values. The method is that it is easy to implement and the scalarised problem is of the same degree of difficulty as the original MOO problem. However, the weights have to be assigned beforehand and a large perturbation in weights does not always lead to a corresponding change in the objectives. As a result, the generated Pareto points are strongly dependent on expert knowledge and this might lead to points that are biased. Alternatively, weight vectors can be randomly generated to try and obtain a sufficient coverage of the Pareto front.

In our study, the weights are randomly chosen from the uniform distribution to achieve multiple search directions.

2.2. Sandwich algorithm

The basic idea behind the algorithm is that inner and outer approximations of the Pareto set are constructed iteratively until the difference (error) between the two approximations falls below a given tolerance. This approach can help to reduce the number of solutions of the scalarised problem that need to be obtained to construct a good approximation of the Pareto front (Rennen et al., 2011). In this study, the tolerance of error is taken as 10^{-3} .

2.3. Global phase for WS and SD

A challenge in applying WS and SD to nonconvex MOO problems is ensuring that the global solution of each scalarised problem is identified, as local solutions are dominated

Table 1: Algorithmic parameters for MLSL, GA, and NSGA-II

(a) Literature source of parameters			(b) Heuristic parameters	
Parameters		Source	Parameters	value
R_k	Critical distance	Kucherenko et al.,(2005)	Cooling parameter (SA)	0.8
Encoding	Tree-structure	Zhou et al. (2016)	No. of initial points (MLSL)	100
Fitness	Gaussian-like	Liu et al. (2018)	No. of population (NSGA-II)	150
Operators	Mutation, crossover	Zhou et al. (2016)	No. of generations (NSGA-II)	500
Selection	Tournament	Liu et al. (2018)	Mutation fraction (NSGA-II)	0.2
Stopping	No. of generations	Table (1b)	Crossover fraction (NSGA-II)	0.8

solutions of the MOO rather than Pareto-optimal points. In this work, Multi-Level Single Linkage (MLSL) (Kucherenko and Sytsko, 2005) and Simulated Annealing (SA) (Maroulaki and Kokossis, 2000) are used. The MLSL method is based on the simple idea of enumerating all the local minima by starting a local minimization procedure at a set of starting points generated by a Sobol' sequence, combined with a clustering method in which the local search procedure is applied to a sample point, only if there is no other sample point within some critical distance (R_k) which has a lower objective function value. In the SA algorithm, the analogy of the heating and slow cooling of a metal so that a uniform crystalline state can be achieved is adopted to guide the search for an optimal point. The key algorithmic feature of SA is that it encourages a more extensive exploration of the search space, thereby increasing likelihood of global solution. The parameters were carefully chosen based on the statistical experiment and the values are listed in Table 1.

2.4. Non-dominated Sorting Genetic Algorithm-II (NSGA-II)

The NSGA-II algorithm (Deb et al., 2000) is a particular form of genetic algorithm (GA) and is one of the most widely-used MOO evolutionary algorithms. NSGA-II is directly applicable to MOO as it uses an explicit diversity-preserving mechanism based on a crowding distance metric to generate uniformly distributed Pareto points. Furthermore, it makes use of elite-preserving operators to give "elite genes" an opportunity to survive in the next generation. To implement the NSGA-II into a solvent design, one needs to specify a suitable set of heuristic parameters. These parameters are specified in Table 1.

3. Comparative methodology

A CAMD application based on the design of a solvent for the chemical absorption CO_2 is introduced in Section 3.1 as an example that can be used to evaluate the performance of each method. The formulation is based on the recent work of Papadopoulos et al. (2016), who considered an extensive list of property criteria for MOO. The performance of the selected algorithms is analysed based on the criteria, as discussed in Section 3.2.

3.1. Objectives and constraints

Four of solvent properties considered by Papadopoulos et al. (2016) are selected as objective functions in this study, namely, liquid density (ρ), heat capacity (C_p), saturated vapour pressure (P_{vap}), and relative energy difference (RED). Several other performance criteria are considered as constraints: a) the normal melting point (T_m), to ensure that the solvent is in the liquid phase at the lowest process operating temperature, b) the normal

Table 2: property constraints

Physical properties, $\mathbf{g}(\mathbf{n})$	Bounds
ρ (g/cm ³)	[0.6,1.5]
RED	(0, 6.5]
T_b (K)	[393, 550]
T_m (K)	[273,313]
σ (dyn/cm) at 25°C	[25, 60]
μ (cP) at 40°C	(0,60]

Table 3: Solvent design space

Functional groups	Bounds
CH ₂ -N<, -CH ₂ -N<, CH ₂ -NH-, -CH ₂ -NH-, >CH-NH-, -CH ₂ -NH ₂ ,	$n_{total} = 13$
>CH-NH ₂ , ≥C-NH ₂ ,	$n_{tot, amine} = 5$
CH ₃ -, -CH ₂ -, >CH-, >C<, -OH	

boiling point (T_b) to avoid excessive evaporation at absorber operating conditions, c) the viscosity (μ) to ensure ease of transport and d) the surface tension (σ), to promote mass transfer performance. The property targets and performance criteria are summarised in Table 2. The SAFT- γ Mie group contribution equation of state (Papaioannou et al., 2014) is used to predict ρ , C_p , P_{vap} , and T_b . The Group Contribution (GC) methods are used for T_m , σ , RED (Hukkerikar et al., 2012) and μ (Hsu et al., 2002). A set of 13 functional groups ($n_i, i=1, \dots, N, N=13$) shown in Table 3 including 8 amine molecular groups are selected as molecular building blocks based on the applicability of the in property prediction methods used and knowledge of the problem (Papadopoulos et al., 2016). The mathematical formulation of the solvent design problem for CO₂ capture by chemical absorption is described as follows:

$$\begin{aligned}
 & \min_{\mathbf{n}} C_p, P_{vap}, RED \\
 & \max_{\mathbf{n}} \rho_{solvent} \\
 & \text{s.t. } \mathbf{g}(\mathbf{n}) \leq 0 \\
 & \sum_{i=1}^N (2 - v_i) n_i - 2m = 0, \\
 & \sum_{j \in G_a} n_j - n_{tot, amine} \leq 0, \quad (G_a : \text{amine groups}), \quad \sum_{i=1}^N n_i - n_{total} \leq 0
 \end{aligned} \tag{1}$$

where $\mathbf{g}(\mathbf{n})$: inequality constraints of the physical properties, v_i : valence of each group, m : structural parameter ($m=1$ for acyclic)

3.2. Algorithmic performance measures

In this study, three measures for comparing the performance of the algorithms are used: 1) average CPU times (CPU_{avg} , seconds); 2) the number of Pareto points found (N_{Pareto}); 3) hypervolume indicator (HV) (Zitzler et al., 2003). The CPU_{avg} is calculated by averaging the time taken to generate one point on the Pareto front. An algorithm with a lower value of this criterion is preferable. The number of unique Pareto optimal solutions obtained by algorithm is also considered. The algorithm with the highest value of this metric provides a more complete and diverse representation of the Pareto front. The hypervolume indicator represents the volume in the objective space that is covered by a set of Pareto points and a corresponding reference point (Zitzler et al., 2003). The indicator can provide a measure of closeness to the real Pareto set as well as of the diversity of the points.

4. Results and Discussion

In this section, we compare the relative performance of five algorithms: the WS with MLSL (WSML), WS with SA (WSSA), SD with MLSL (SDML), SD with SA (SDSA), and non-dominated sorting genetic algorithm-II (NSGA-II). All algorithms under comparison were implemented in MATLAB 2017a and interfaced with gPROMS Model Builder, which provides a standard MINLP solver. All computations were run under 64-bit Windows 10 on a single Intel i7-6700 3.4GHz processor core and with 8 GB of memory.

Table 4 summarises the performance of the global search methods, SA and MLSL in combination with WS and SD method. WS combined with the local MINLP solver is used as a base case. The simulation data correspond to a set of 100 different weight vectors: an identical set of weight vectors was assigned to each algorithmic options. The results in Table 4 demonstrate that the WSML outperforms the WSSA such that the higher hypervolume can be achieved within the same cost of CPU time. This clearly indicates that the MOO algorithm with MLSL is more efficient. However, for both WSML and WSSA, only a small number of chemical structures (Pareto points) has been identified. This confirms that different weight vectors do not always lead to different solutions. As can be seen in the results of SDML and SDSA, systematically assigned weights also cannot generate different Pareto points for each iteration although the methods result in a larger set of Pareto points than WS. This is mainly due to the fact that the mapping of the weights into objective space assume that the feasible region is continuous. As a result, the assigned weights may result in same Pareto point as the problem is MINLP.

Table 5 summarises simulation results under a fixed CPU time (48 h) with respect to the performance measures. In the comparison between five combinations of algorithmic options, SDML produces the best results for two criteria, hypervolume and the number of Pareto points. The reason is that the SDML can deterministically guide the direction of the weight vector in a sequence of iterations, which increases the possibility of finding different Pareto points. This results largely imply that more difference in molecular structures and physical properties can be seen in the Pareto optimal set generated by SDML. In Table 5, the NSGA-II exhibits a relatively lower hypervolume than other tested methods although it generated a larger number of Pareto points within the allowed CPU time. This implies the accuracy of the Pareto front generated is not satisfactory when using NSGA-II with the parameters in Table 1.

Table 4: Comparison of global search methods

Metric	Base	WSML	WSSA	SDML	SDSA
No. of iterations	100	100	100	100	100
N_{Pareto}	20	12	14	54	50
HV	3.436	3.689	3.539	4.891	4.724
CPU _{avg} (s)	23	809	22106	818	17837

Table 5: Comparison of WSML, SDML, and NSGA-II algorithms

Metric	WSML	SDML	NSGA-II
CPU time (fixed, h)	48	48	48
N_{Pareto}	26	74	100
HV	3.982	5.832	0.672

5. Conclusion

In this paper, five different MOO algorithms have been compared by assessing their specific performance on a solvent design problem. To increase the probability of finding the true Pareto front, two different global search algorithms were combined with two scalarisation based methods. The algorithms were tested using a solvent design problem with four objective functions. For the global search phase, comparative results have highlighted the efficiency of the MLSL algorithm. In comparison to WSML and NSGA-II, SDML been found to have the best performance as it can generate a better distributed Pareto fronts in a given time frame, as indicated by the number of Pareto points generated and the hypervolume achieved. In a future work, the application of the methodologies will be extended to different size of CAMD problems to generalised the performance of the methods beyond the solvent design for the CO₂ removal.

Acknowledgements

The authors gratefully acknowledge financial support from the Engineering and Physical Sciences Research Council (EPSRC) of the UK (grants EP/M507878/1, EP/J003840), innovation programme under Grant Agreement No.727503 (ROLINCAP), and Centre for Process Systems Engineering Research Committee of Imperial College London via Roger Sargent scholarship.

References

- J. Burger, N. Asprion, S. Blagov, R. Böttcher, U. Nowak, M. Bortz, R. Welke, K.-H. Küfer, H. Hasse, 2014. Multi-Objective Optimization and Decision Support in Process Engineering - Implementation and Application. *Chemie Ing. Tech.* 86 (7), 1065–1072.
- K. Deb, A. Pratab, S. Moitra, 2000. Mechanical Component Design for Multiple Objectives Using Elitist Non-dominated Sorting GA. *Proc. Parallel Probl. Solving from Nat. VI Conf. (i)*, 859–868.
- R. H. Herring, M. R. Eden, 2015. Evolutionary algorithm for de novo molecular design with multi-dimensional constraints. *Comput. Chem. Eng.* 83, 267–277.
- H.-C. Hsu, Y.-W. Sheu, C.-H. Tu, 2002. Viscosity estimation at low temperatures ($T_r < 0.75$) for organic liquids from group contributions. *Chem. Eng. J.* 88, 27–35.
- A. S. Hukkerikar, B. Sarup, A. Ten Kate, J. Abildskov, G. Sin, R. Gani, 2012. Group-contribution+(GC+) based estimation of properties of pure components: Improved property estimation and uncertainty analysis. *Fluid Phase Equilib.* 321, 25–43.
- S. Kucherenko, Y. Sytsko, 2005. Application of deterministic low-discrepancy sequences in global optimization. *Comput. Optim. Appl.* 30 (3), 297–318.
- X. Liu, Y. Zhao, P. Ning, H. Cao, H. Wen, 2018. Modified Structural Constraints for Candidate Molecule Generation in Computer-Aided Molecular Design. *Ind. Eng. Chem. Res.* 57 (20), 6937–6946.
- E. Marcoulaki, A. Kokossis, 2000. On the development of novel chemicals using a systematic optimisation approach. Part II. Solvent design. *Chem. Eng. Sci.* 55 (13), 2547–2561.
- A. I. Papadopoulos, S. Badr, A. Chremos, E. Forte, T. Zargiannis, P. Seferlis, S. Papadokonstantakis, A. Galindo, G. Jackson, C. S. Adjiman, 2016. Computer-aided molecular design and selection of CO₂ capture solvents based on thermodynamics, reactivity and sustainability. *Mol. Syst. Des. Eng.* 1 (3), 313–334.
- A. I. Papadopoulos, P. Linke, 2006. Efficient integration of optimal solvent and process design using molecular clustering. *Chem. Eng. Sci.* 61 (19), 6316–6336.
- A. I. Papadopoulos, M. Stijepovic, P. Linke, P. Seferlis, S. Voutetakis, 2013. Toward Optimum Working Fluid Mixtures for Organic Rankine Cycles using Molecular Design and Sensitivity Analysis. *Ind. Eng. Chem. Res.* 52 (34), 12116–12133.
- V. Papaioannou, T. Lafitte, C. Avendaño, C. S. Adjiman, G. Jackson, E. A. Müller, A. Galindo, 2014. Group contribution methodology based on the statistical associating fluid theory for heteronuclear molecules formed from Mie segments. *J. Chem. Phys.* 140 (5).
- G. Rennen, E. R. Van Dam, D. Den Hertog, 2011. Enhancement of sandwich algorithms for approximating higher-dimensional convex pareto sets. *INFORMS J. Comput.* 23 (4), 493–517.
- T. Zhou, S. Engineering, M. Reviewers, K. S. Prof, R. G. Prof, Z. Qi, 2016. Systematic Methods for Reaction Solvent Design and Integrated Solvent and Process Design (August).
- E. Zitzler, L. Thiele, M. Laumanns, C. M. Fonseca, V. G. Da Fonseca, 2003. Performance assessment of multiobjective optimizers: An analysis and review. *IEEE Trans. Evol. Comput.* 7 (2), 117–132.

Real-time feasible model-based crystal size and shape control of crystallization processes

Botond Szilagy^a, Zoltan K. Nagy^{a,b*}

^a Davidson School of Chemical Engineering, Purdue University, West Lafayette, IN 47907-2100, USA

^b Department of Chemical Engineering, Loughborough University, Loughborough, LE11 3TU, UK;

zknagy@purdue.edu

Abstract

The simultaneous control of crystal size and shape is particularly important in fine chemical and pharmaceutical crystallization. These two quantities influence the dissolution rate and bioavailability of final drug products, and also contribute to the manufacturability and efficiency of downstream operations. Numerous practical issues are associated with the implementation of an industrially relevant crystal size and shape control algorithm, such as the limited number of commercially available measurement devices and tight productivity constraints. Model-based control algorithm is required to address these problems, which, however, brings an additional challenge: the high computational demand of the applicable process simulation.

In this work we show that the model predictive control, relying on measurements coming from routinely applied, commercially available process analytical technology (PAT) tools may be feasible. The algorithm is based on GPU accelerated full 2D population balance model (PBM) solution, which does not require external computation units (i.e. cloud computing). The state estimation, which is a crucial part of any robust model-based control system, is carried out by fitting the model, through the re-adjustment of some model parameters, on the measured FBRM count, PVM based mean aspect ratio (AR) and solute concentration, in real time. Artificial neural network (ANN) based soft-sensor is employed to simulate the most likely mean AR of the bivariate crystal size distribution (2D CSD) calculated by the PBM, which is compared then to the mean AR measured by the *in-situ* imaging tool, as a part of real-time parameter re-adjustment.

Keywords: crystallization, model predictive control, real time control, crystal shape

1. Introduction

The size and shape of crystalline active pharmaceutical ingredients (APIs), in addition to the purity and polymorphic form, impact both the downstream operations (filtration, drying *etc.*) and some of physical properties (dissolution rate, flowability *etc.*). Consequently, simultaneous size and shape control of particles during solution crystallization has gained more attention from both academic and industrial perspectives (Nagy and Braatz, 2012). The size control in crystallization processes is a well-studied field, but simultaneous size and shape control has gained more attention only in the recent years, due to two major factors: (1) the lack of real-time crystal shape measurement tools and (2) limitations by computational power for the (often required) model-based control.

Numerous variables can be manipulated to control crystal shape, including the supersaturation (through temperature or antisolvent addition), facet-specific growth rate

inhibitor concentration, stirring power or internal/external milling (breakage). The most convenient is to manipulate supersaturation, which influences the crystal shape through the different supersaturation dependencies of facet-specific growth and dissolution rates. Although model free shape control was already successfully achieved by these simple principles, the productivity and yield is far under the industrially desired levels. Model-based shape control approaches, which can directly involve productivity and yield constraints, were not implemented so far, mainly due to the aforementioned limitations.

In this work we propose a real-time feasible nonlinear model predictive control (NMPC) algorithm, with growing horizon state estimator (GHE). The system is based on full 2D PBM (with nucleation, growth and dissolution) to describe the entire 2D CSD, not only its moments. ANN based soft-sensor model is applied to quickly approximate the most likely measurable AR distribution (ARD) in conjunction with a GPU accelerated bi-dimensional FVM solver, already presented in the literature (Szilágyi and Nagy, 2018). In this paper we show that the NMPC is real-time feasible and it has no practical limitations from the standpoint of measurement system, since it relies on routinely applied concentration, chord-length distribution (CLD) and ARD measurements, which is a significant novelty of this work. For brevity, we will analyse the performance and calculation time requirement of GHE and NMPC individually. In the feasibility analysis we assume 4 hours batch crystallization of rod-like crystals and 5 minutes sampling time. The timings were obtained on a Dell Alienware machine with Intel i7-7700 CPU, 2400 MHz main memory clock speed, and nVidia GeForce GTX 1060m GPU.

2. The process model and the soft-sensor

The process model and simulation procedure was described in details in the literature (Szilágyi and Nagy, 2018), thus here we give only a brief overview. Assuming that the crystals are characterized by the length (L_1) and width (L_2) size dimensions, denoted by the $(L_1, L_2) \rightarrow \mathbf{L}$ size vector, and the crystal population is described by the $n(\mathbf{L}, t)$ bivariate size density function, the 2D PBE governing the variation of 2D CSD is:

$$\frac{\partial n(\mathbf{L}, t)}{\partial t} + \sum_{i=1}^2 G_i \frac{\partial n(\mathbf{L}, t)}{\partial L_i} = B \delta(\mathbf{L} - \mathbf{L}_n) \quad (1)$$

B is the nucleation rate, and G_i denotes the size-independent growth rates along the length and width axes. Eq.(1) has $n(\mathbf{L}, t=0) = n_0(\mathbf{L})$ initial and $n(\mathbf{L} = \infty, t) = 0$ boundary conditions. The initial condition is given by the seed distribution, whereas the boundary condition expresses that the crystals must have finite size. The first term in Eq. (1) describes the temporal evolution of the 2D CSD, the second term is for the growth. The right hand side is the nucleation term. The solute mass balance is written as:

$$\frac{dc}{dt} = -k_v \rho_c \left(\iint G_1 L_2^2 n(\mathbf{L}, t) d\mathbf{L} + 2 \iint G_2 L_1 L_2 n(\mathbf{L}, t) d\mathbf{L} \right) \quad (2)$$

with the $c(t=0) = c_0$ initial condition. Here, k_v is the volume shape factor, whereas ρ_c is the crystal density. Since the temperature is manipulated variable, energy balance is not required for model closure.

The applied kinetic rate equations are listed in Table 1. The equations were compiled based on the literature data for potassium dihydrogen phosphate (KDP) (Eisenschmidt et al., 2015; Gunawan et al., 2002). Since the activation energies and supersaturation exponents are from separate works, the rate constants were modified so to bring the growth and dissolution rates in reasonable domain. The nucleation parameters were modified to give reasonable nucleation rate with the applied growth rate expressions.

Table 1. Kinetic rate equations applied in this work. σ is the absolute supersaturation.

Mechanisms	Expression (for length)	Expression (for width)
Nucleation [#m ³ s]	$B = 3 \cdot 10^{12} \sigma^{5.24}$	
Growth [$\mu\text{m/s}$]	$G_1 = 6.04 \cdot 10^6 \sigma^{1.74} \exp\left(-\frac{39100}{RT}\right)$	$G_2 = 2.42 \cdot 10^5 \sigma^{1.48} \exp\left(-\frac{37100}{RT}\right)$
Dissolution [$\mu\text{m/s}$]	$D_1 = 2.72 \cdot 10^5 \sigma^1 \exp\left(-\frac{26800}{RT}\right)$	$D_2 = 8.18 \cdot 10^5 \sigma^1 \exp\left(-\frac{29700}{RT}\right)$

The model equations were solved with a high-resolution finite volume method (HR-FVM) on non-uniform grid involving GPU acceleration. This allows up to two orders of magnitude speedup compared to a standard serial *C* implementation, which makes the simulation capable of real-time optimization (for timing details see the literature Szilágyi & Nagy, 2018). The advantage of the GPU acceleration, beyond enabling NMPC, is that it provides the computational power on site for low investment cost, eliminating the need for supercomputers or cloud-services, which are both undesired in industrial environment.

It is known that the *in-situ* imaging based shape measurement underestimates the real AR due to random spatial orientation of the crystals. To calculate the most likely measurable AR of a crystal, a geometrical model-based technique was proposed, that constructs the ARD of the single 2D crystal by mapping all possible two dimensional projections of the crystal. Then, using large number of $ARD = f(\mathbf{L})$ pairs, an ANN is trained to give the most likely ARD of an arbitrary sized (\mathbf{L}) crystal. The most likely ARD of the 2D CSD is then approximated in real time as a weighted sum of individual ARDs corresponding to the HR-FVM grid sizes, returned by the ANN, where the weighting factor is the $n(\mathbf{L}, t)$.

3. Growing horizon state estimator (GHE)

There are two major reasons that require the utilization of already available measurement data. Firstly, the system states (2D CSD and concentration) are required in NMPC optimization as initial condition of the simulation. While the concentration can be measured, the 2D CSD generally not. Therefore, the 2D CSD must be estimated from the available measurements, but for robustness (e.g. with respect to sensor communication errors), the concentration is often estimated, too. Secondly, there are often uncertainties related to seed loading, and the crystallization kinetics is known to be sensitive to process conditions (through disturbances from impurities, mixing energy *etc.*), which is a typical plant-model mismatches (PMMs) that leads to sub-optimal control.

The basic idea of the NMPC is that if the system states are accurate and the model describes well the process, the process output can be predicted, hence, optimized. Our GHE is based on the same principle: the parameters that capture the main sources of PMM are identified, then used as decision variables for fitting the model to the measured data in the estimation horizon (from zero to the actual process time) in real-time. Once the updated model parameters become available, process simulation is carried out from the initial time to the actual process time, which gives the system states.

In a batch crystallization process, the parameters related to nucleation and growth kinetics as well as the seed loading generally exhibit the most batch-to-batch variability, thus are ideal candidates for decision variables in the GHE optimization. Denoting the vector of model parameters by ψ , listed in Table 2, the following GHE objective is proposed:

$$O_{GHE}(\psi) = \sum_i (c_{m,i} - c_{s,i})^2 + w \sum_i (AR_{m,i} - AR_{s,i})^2 + u \sum_i \frac{(N_{m,i} - N_{s,i})^2 (N_{m,i}^2 + N_{s,i}^2)}{N_{m,i}^2 N_{s,i}^2} \quad (3)$$

Subscript “*m*” and “*s*” are for measured and simulated quantities, N_m is the FBRM count and N_s is the simulated number density normalized to $N_m(t = 0)$. The values w and u are weighting factors. The first part of the objective is for the fitting of concentrations, the second is for the ARs. It can be shown that the count term is considerably more sensitive to the correct capturing of the nucleation point than to the actual value of final count. This enables to reliably use the FBRM for nucleation detection.

Table 2. Initial values and bounds of decision variables of GHE optimization as well as the performance of state estimator in parameter re-adjustment

ψ_i	Seed v.f.	k_b^*	b	k_{g1}^*	g_1	k_{g2}^*	g_2
Starting point	$1.21 \cdot 10^{-3}$	$3.0 \cdot 10^{12}$	5.24	$6.04 \cdot 10^6$	1.74	$2.42 \cdot 10^5$	1.48
Actual parameters	$1.43 \cdot 10^{-3}$	$1.1 \cdot 10^{12}$	5.30	$2.91 \cdot 10^6$	1.72	$1.38 \cdot 10^5$	1.44
Lower bound	$8.5 \cdot 10^{-4}$	$7.1 \cdot 10^{11}$	5.08	$2.72 \cdot 10^6$	1.68	$1.32 \cdot 10^5$	1.43
Upper bound	$1.6 \cdot 10^{-3}$	$1.2 \cdot 10^{13}$	5.40	$1.31 \cdot 10^7$	1.80	$4.49 \cdot 10^5$	1.52
Readjusted parameters	$1.38 \cdot 10^{-3}$	$7.8 \cdot 10^{11}$	5.15	$2.94 \cdot 10^6$	1.71	$1.38 \cdot 10^5$	1.44

*In the GHE the $\log(k)$ was readjusted rather than the nominal value, to improve the optimization performance

A recent study suggested that in such a GHE, the kinetic parameters move within the confidence intervals of the off-line parameter estimation (Szilágyi et al., 2018). Hence, the bounds for kinetic parameters are set to the 95 % confidence interval limits available from the off-line parameter estimation. The bounds of the seed loading may be chosen arbitrarily, based on the accuracy and precision of the balance, for instance. The nominal values of ψ , as well as the (assumed) bounds are listed in Table 2.

To improve the convergence, the decision variables were scaled ($\psi \rightarrow \psi_s$), using scale parameters (χ) that normalizes the initial values to 1. The i^{th} element of vector χ is:

$$\chi_i = \frac{1}{\psi_i} \rightarrow \psi_{s,i} = \psi_i \times \chi_i \quad (4)$$

The optimization was solved in Matlab using the interior-point algorithm (implemented in the *fmincon* inner optimization routine). The iteration limit was set to 13. It worth

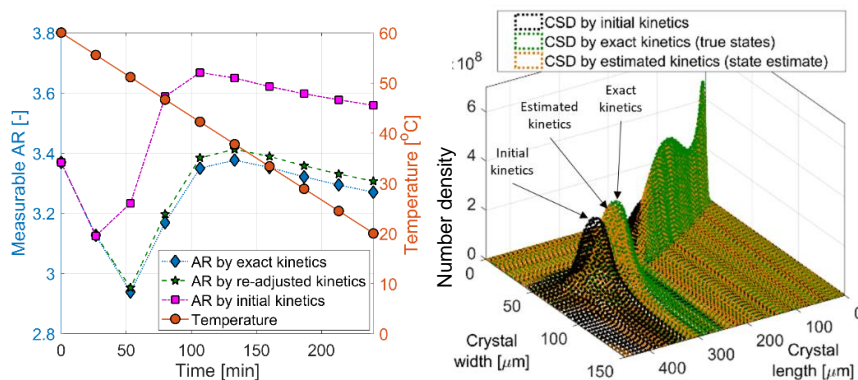


Figure 1. State estimator performance: fitting the model on measured ARs (the concentrations and counts are not plotted for brevity) as well as the estimated and exact 2D CSD. The calculation time was 115 s.

noticing that in the demonstration (Figure 1) we assumed that the estimation horizon is the same as the batch time. Therefore, this GHE operates on the longest possible time frame, so the 115 s timing gives the maximum calculation time requirement. According to Table 1 and Figure 1, the estimator readjusted successfully the model parameters, and was able to estimate the actual system states with acceptable accuracy.

4. The real time optimization problem and provisionally results

The NMPC is a repeated real-time optimization of the control signal in every sampling instance, using the estimated system states and the updated model parameters. Hence, the calculation time, i.e. the NMPC optimization and the state estimation time, must fit into the sampling time. The 5 minutes sampling time is a reasonable choice for the dynamics of a usual crystallization processes.

For the sake of simplicity, the batch NMPC problem is formulated as end-point (product property) optimization. The decision variables are the vector of temperatures in the control horizon, i.e. the current time to the final time, which time frame is shrinking as the batch evolves. We defined the temperature profiles by 12 discrete temperature points, which translates to 10 decision variables (the initial and final temperature are fixed).

$$O_{NMPC}(T) = w_1 AR_{prod}^2 + w_2 F_{idx}^2 + w_3 \left(\frac{n_{t_{final}}}{n_{t_{initial}}} \right)^2 + w_4 \sum_i (t_{i+1} - t_i) \frac{(T_{i+1} - T_i)^2}{(t_{i+1} - t_i)^2} \quad (5)$$

The first term of objective function is to minimize the product AR, the second term minimizes the fine index (i.e. volume fraction of crystals under a threshold sphere-equivalent diameters, here set to $L_f = 100 \mu\text{m}$), the third term is for the ratio of final to initial number density (zero moment), whereas the last term is to ensure smooth temperature profile. The values of weight factors (w_i , $i=1, \dots, 4$) define the relative importance of sub-objectives. Setting all values to 0, except w_1 , leads to pure AR minimization NMPC, w_2 controls minimization of fines in the product, whereas w_3 is for the nucleation minimization, or, indirectly crystal size maximization.

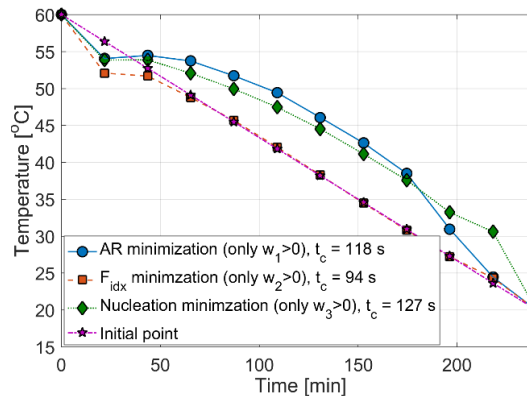


Figure 2. Optimal temperature profiles calculated for different objectives and the corresponding. All timing is an average of three run.

Although there is an AR term in the Eq.(5), the AR can be manipulated only within the attainable AR domain. The attainable size and shape domains are delimited by the crystallization kinetics and process parameters (temperature profile, seed properties *etc.*) (Vetter et al., 2014; Acevedo and Nagy).

In the optimization constraints are imposed on the heating and cooling rates (0.5 °C/min both) and for minimal and maximal temperatures (60 and 15 °C). The initial and final temperatures are fixed for yield to 60 and 20 °C. The optimization was solved using a sequential quadratic programming approach in the *fmincon* routine of Matlab. Provisional optimization results and timings are presented in Figure 2. The development of the NMPC control algorithm from its main components is associated with numerous challenges to ensure robustness and stability (Mayne et al., 2000).

5. Conclusions

In this paper a full 2D PBM based NMPC was presented for batch crystallization processes. In the study it was shown that the system is real-time feasible and implementable using commercially available monitoring systems and locally available, low cost GPUs as efficient accelerators for improved optimization times. Another enabling invention used in this work was the fast, approximate, ANN based soft-sensor, which takes the 2D CSD calculated by the PBM and transforms it to the most likely measurable ARD (mean AR), which is measured by the most common, commercially available imaging based PAT tools. Due to brevity, we analyzed separately the feasibility and performance of the NMPC and GHE optimizations only; both simulations revealed that, using the accelerated computation, fast soft-sensor and the search-space delimited by the constraints, all the calculations can be done within the 5 minutes sampling time on a standard computer, which is reasonable for many industrial crystallization processes.

6. Acknowledgements

The financial support of the International Fine Particle Research Institution is acknowledged gratefully.

7. References

- Acevedo, D., Nagy, Z.K., 2014. Systematic classification of unseeded batch crystallization systems for achievable shape and size analysis, *J. Cry. Gro.*, 394, 97-105.
- Eisenschmidt, H., Voigt, A., Sundmacher, K., 2015. Face-specific growth and dissolution kinetics of potassium dihydrogen phosphate crystals from batch crystallization experiments. *Cryst. Growth Des.* 15, 219–227.
- Gunawan, R., Ma, D.L., Fujiwara, M., Braatz, R.D., 2002. Identification of Kinetic Parameters in Multidimensional Crystallization Processes. *Int. J. Mod. Phys. B* 16, 367–374.
- Mayne, D.Q., Rawlings, J.B., Rao, C. V., Scokaert, P.O.M., 2000. Constrained model predictive control: Stability and optimality. *Automatica* 36, 789–814.
- Nagy, Z.K., Braatz, R.D., 2012. Advances and New Directions in Crystallization Control. *Annu. Rev. Chem. Biomol. Eng.* 3, 55–75.
- Szilágyi, B., Borsos, Á., Pal, K., Nagy, Z.K., 2018. Experimental implementation of a Quality-by-Control (QbC) framework using a mechanistic PBM-based nonlinear model predictive control involving chord length distribution measurement for the batch cooling crystallization of l-ascorbic acid. *Chem. Eng. Sci.* doi: 10.1016/J.CES.2018.09.032.
- Szilágyi, B., Nagy, Z.K., 2018. Aspect Ratio Distribution and Chord Length Distribution Driven Modeling of Crystallization of Two-Dimensional Crystals for Real-Time Model-Based Applications. *Cryst. Growth Des.* doi:10.1021/acs.cgd.8b00758.
- Vetter, T., Burcham, C.L., Doherty, M.F., 2014. Regions of attainable particle sizes in continuous and batch crystallization processes. *Chem. Eng. Sci.* 106, 167–180.

Automated open-loop control of directed self-assembly with multiple electrokinetic actuators in microfluidic devices

Yu Gao, Richard Lakerveld*

*Department of Chemical and Biological Engineering, The Hong Kong University of Science and Technology, Clear Water Bay, Hong Kong S.A.R
kelakerveld@ust.hk*

Abstract

Directed self-assembly provides a novel processing route for the manufacture of structured materials. Future processes based on self-assembly will need to be equipped with suitable automated process controls for improving performance. Closed-loop control has been applied to directed self-assembly with one or two actuators when real-time and non-invasive observation is feasible. However, such observation may be challenging in practice. Furthermore, multiple actuators may have to be used for the self-assembly of complicated structures. In this work, an automated open-loop control method for directed self-assembly using multiple actuators is developed and tested experimentally. The method relies on a novel design of microelectrodes to assemble a specific number of particles in a desired area in a microfluidic device. An empirical model is developed to determine an optimal sequence of control actions. The experimental results show that the number of particles after the implementation of the open-loop control is close to the targeted number.

Keywords: directed self-assembly, open-loop control, modelling, electrokinetics

1. Introduction

Self-assembly is the spontaneous association of small molecules or particles into structures, which provides a novel processing route for the manufacture of materials with structures at the micro/nano-scale. Future manufacturing processes based on self-assembly will need to be equipped with suitable automated process controls to compensate for design uncertainty and to reject disturbances. Local actuation is required to fabricate specific structural features or to heal defects, which can be enabled by the introduction of external fields to direct the self-assembly (Ulissi et al., 2013; Paulson et al., 2015). Electric fields are of particular interest for local actuation due to their noninvasiveness and flexibility in manipulating particles according to a diverse set of electrokinetic phenomena that can be induced (Oh et al., 2009). Feedback control has been implemented for directed self-assembly to effectively assemble colloidal structures using one or two electrokinetic actuators when real-time observation is feasible (Juárez et al., 2012; Tang et al., 2016; Gao and Lakerveld, 2018). However, to enhance control performance or to assemble more complicated and possibly non-periodic structures, multiple actuators have to be used systematically to direct the self-assembly process. Such control is challenged by the stochastic nature of self-assembly, nonlinear process behavior and also by the design of the actuators. In case a system would not allow for real-time and non-invasive observation, an open-loop strategy has to be considered

based on a suitable mathematic model (Komaee and Barton, 2016). Model-based control methods are particularly interesting for nonlinear systems when multiple actuators are available. However, experimental studies on the performance of such control methods for directed self-assembly are limited.

In this work, a novel automated open-loop control method for directed self-assembly of colloidal particles using multiple actuators to induce various electrokinetic phenomena in a microfluidic device is developed and characterized experimentally. The control objective is to adjust the particle densities of two neighbouring regions. Firstly, a triple-parallel microelectrode is fabricated to provide multiple actuators in the microfluidic device for directing the self-assembly process over the two neighbouring regions. The multiple-electrode actuators can be manipulated flexibly to exhibit four types of system state. By engineering the different electrokinetic interactions within the four states, particles can either be transferred between two regions or be maintained in individual regions. Subsequently, an open-loop control strategy based on an input-output model is designed to transfer a specific number of particles from one region to the other. Finally, the open-loop control is implemented experimentally for performance assessment.

2. Microfluidic design and system characterization

The microfluidic cell and the microelectrode design are illustrated in Figure 1. A suspension of microspheres (radius $1\mu\text{m}$) is placed between two transparent ITO-coated glass slides that act as electrodes. After approximately 20 minutes, the particles settle to form a two-dimensional system on the bottom electrode, where the ITO is patterned such that three actuators are available. The space between the adjacent actuators is defined as the density control area (see Figure 1B). Each actuator is connected independently to a channel of a function generator (33500B, Keysight Technologies) to apply AC electric fields. An optical microscope (Nikon, Ni-U) equipped with a digital camera (Nikon Digital Slight Qi2) and automated image analysis (Matlab, The Mathworks) are used to observe the positions of all particles in real time with a typical image processing time of 1s.

Four types of system state form the basis of the process model (see Figure 2), which can be realized with different combinations of the electric fields parameters (i.e. voltage v , frequency f) applied to the three actuators. These states are referred to as stabilization, shifting, collection and transfer. The transitions between the four states enable the transfer of particles between regions, which are dynamically modelled (Gao and Lakerveld, 2018). During the stabilization step (see Figure 1(A)), negative dielectrophoresis (nDEP) at a high field frequency is induced, which directs the particles towards an electric field minimum (Gao and Lakerveld, 2018). The particles cannot cross the middle actuator, which can be understood from a COMSOL simulation of the field strength distribution (see Figure 1(A)). The particles all accumulate near the field minimum, which allows for easier transfer in the next step, as the distance towards the middle actuator is similar for all particles. Note that the particles form chains due to their induced dipoles at this frequency. In the shifting step (Figure 1(B)), the voltage on the left actuator is increased and the voltage on the right actuator is decreased, which shifts the electric field minima.

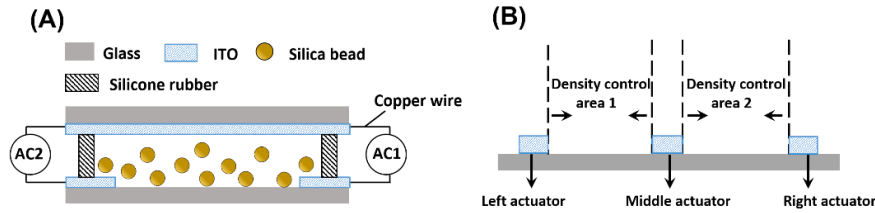


Figure 1. (A) Schematic design of the microfluidic device. (B) Illustration of the bottom electrode including density control areas and multiple actuators.

The shift causes the particles in the left control area to move closer to the middle actuator while the particles in the right control area move further away. In the collection step (Figure 1(C)), electroosmotic flow (EOF) at a low frequency is generated using only the middle actuator. The induced flow carries the particles from the left control area towards the middle actuator. Finally, in the transfer step (Figure 1(D)), the nDEP is induced again to transfer the particles collected at the middle actuator to the right control area. The electric field strength has been shaped such that only the particles on the middle actuator will be transferred to the right control area. The electric field parameters for each step are summarized in Table 1.

Table 1. Electric field parameters for the four types of state in Figure 2

	Left actuator		Middle actuator		Right actuator	
	f/kHz	v/volt	f/kHz	v/volt	f/kHz	v/volt
Stabilization	100	5	100	1	100	5
Shifting	100	8	100	1	100	1
Collection	-	-	5	0.5	-	-
Transfer	100	8	100	1	100	1

3. Model development and open-loop control design

To design an open-loop control strategy for transferring a specific number of particles from the left to the right control area, the dynamics of the collection step has to be modelled. To describe the dynamics of the collection step, two sets of experiments involving all four steps were conducted and the location of all particles as function of time were documented using optical microscopy and automated image analysis. Figure 3(A)-(B) shows the change in the number of particles that are present in the left control area during the collection step as function of time. The dynamic evolution of the change in the number of particles in the left control area with time can be modelled empirically using a fifth-order polynomial for both experiments. By taking the average of the two fifth-order polynomial models, the empirical model for simulating the collection dynamics is constructed as follows:

$$n(t) = 0.0000049t^5 - 0.00054t^4 + 0.02t^3 - 0.23t^2 + 0.81t + 0.057 \quad (1)$$

where n represents the change of particle number in the left control area and t represents the implementation time of the collection step. Based on the four-step control framework and the empirical model for simulating the dynamics of the collection step, automated

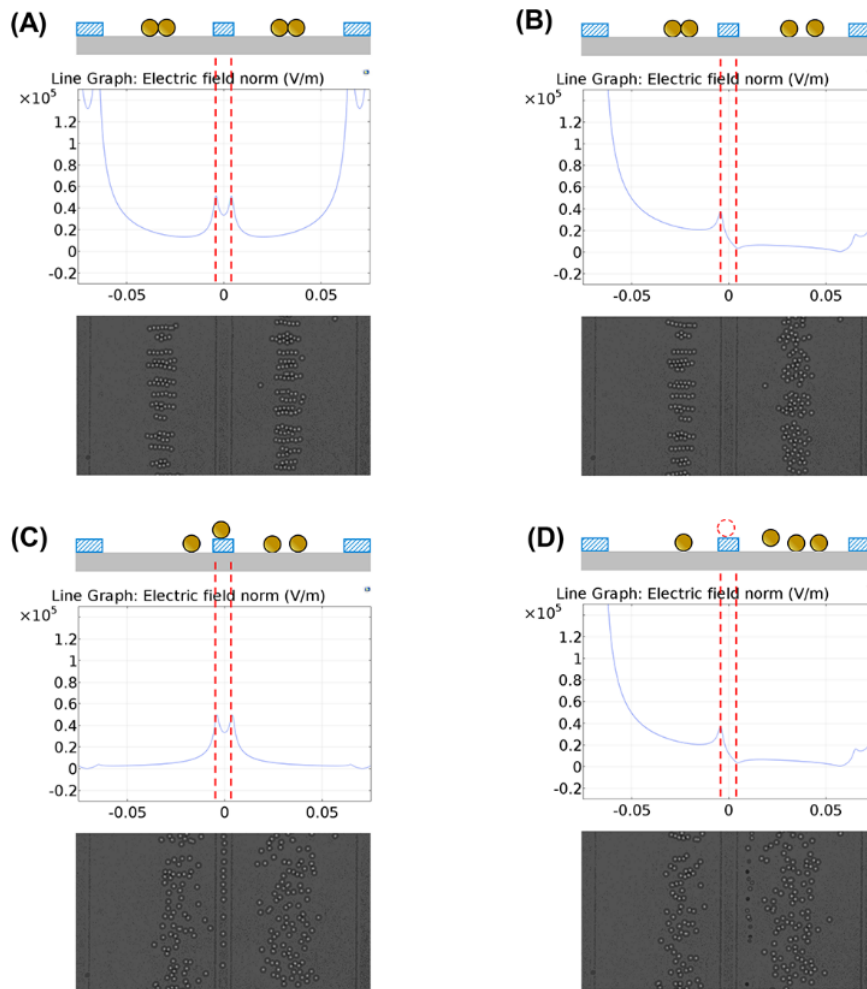


Figure 2. Illustration of the four types of system state with different electric field parameters. (A) Stabilization. (B) Shifting. (C) Collection. (D) Transfer. For each state, the top figure shows a schematic illustration of the locations of the particles. The middle figure shows the electric field strength distribution on the electrode surface from COMSOL simulation. The bottom figure shows a representative microscopy image.

open-loop control strategies can be designed to relocate a specific number of particles from the left density control area to the right density control area. The four steps are implemented sequentially and in an automated fashion using Matlab and an interface between Matlab and the function generator. To relocate a specific number of particles, the desired execution time for the collection step is estimated using the empirical model. Two open-loop strategies were designed and implemented for relocating 14 and 22 particles, corresponding to a transfer time of 21s and 25s, respectively.

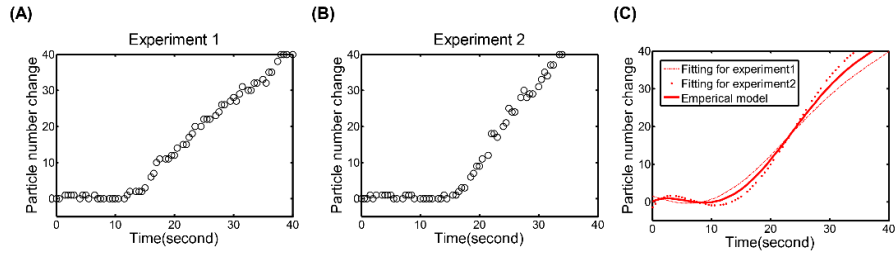


Figure 3. (A)–(B) The change in the number of particles in the left control area with respect to time during the collection step in an open-loop experiment. (C) Empirical model describing the dynamics of the collection step.

4. Control strategy implementation and performance assessment

The dynamic development of the particle number on the middle actuator for the two experiments with open-loop control is illustrated in Figure 4. Note that the different steps from the four-step control framework are labelled differently. It can be seen that 11 and 21 particles are relocated from the left to the right control area, respectively, which are equal to number of particles collected on the middle actuator (see Figure 4). The relocated particle numbers are close to the intended number of particles to be transferred (14 and 22, respectively) set as objective for the open-loop control strategy, which demonstrates the effectiveness of the proposed open-loop control strategy. The small deviation in the number of relocated particles can be due to the stochastic nature of the self-assembly process, which cannot be avoided in this type of system, or due to the inaccuracy of the process model.

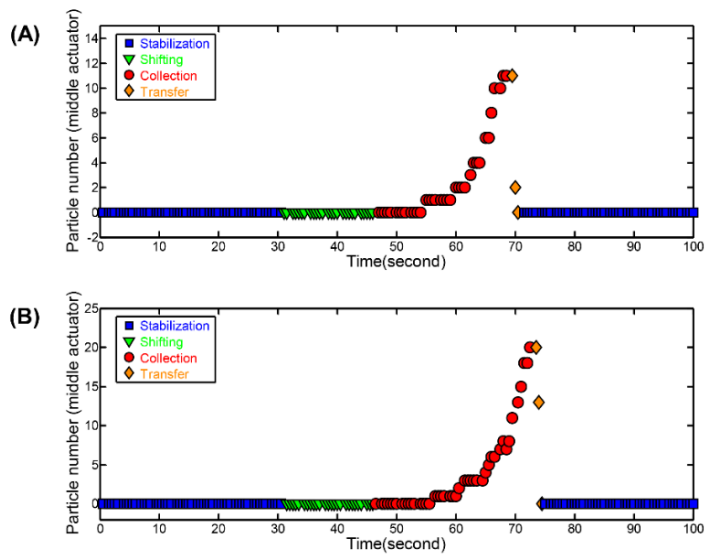


Figure 4. Dynamic change of the particle number on the middle actuator. (A) Open-loop control for relocating 15 particles. (B) Open-loop control for relocating 22 particles.

5. Conclusions and outlook

An automated open-loop control method for directed self-assembly using multiple actuators has been developed and experimentally validated in a microfluidic device. The method is illustrated with the control objective of transferring a specific number of particles from one control area to an adjacent control. The control approach has two main elements. First, a four-step framework can be utilized by engineering the different interactions between the particles and the electric fields. Second, an empirical model is used to describe the dynamics of the most critical step in that framework. The dynamic model is used to estimate the optimal actuation time for a given number of particles that need to be transferred to a different control area. The performance of two open-loop control experiments shows that the actually number of transferred particles is close to the targeted value. Since the involved interactions are generic, the approach can be applied to other small-scale objects such as nanoparticles or biological cells. Therefore, future work may focus on specific applications. The current framework may also provide a foundation for more comprehensive approaches to shape the particle density distributions over multiple control areas, which is needed for assembling complicated structures at the micro/nano-scale (Lakerveld et al., 2012; Solis et al., 2010). Finally, future work will involve using first principles for the development of the process model to improve the predictive capability of the model.

This work is financially supported by Hong Kong Research Grant Council No.16214617

References

- Y. Gao, R. Lakerveld, 2018, Feedback control for defect-free alignment of colloidal particles, *Lab on a Chip*, 18, 2099-2110
- Y. Gao, R. Lakerveld, 2018, Feedback control for shaping density distributions of colloidal particles in microfluidic devices, submitted
- J. Juárez, P. Mathai, J. Liddle, M. Bevan, 2012, Multiple electrokinetic actuators for feedback control of colloidal size, *Lab on a Chip*, 12, 20, 4063-4070
- A. Komae, P. Barton, 2016, Directed self-assembly of linear nanostructures by optimal control of external electrical fields, arXiv preprint arXiv: 1603.00113
- R. Lakerveld, G. Stephanopoulos, P. Barton, 2012, A master-equation approach to simulate kinetic traps during directed self-assembly, *The Journal of chemical physics*, 136, 18, 184109
- J. Oh, R. Hart, J. Capurro, H.M. Noh, 2009, Comprehensive analysis of particle motion under non-uniform AC electric fields in a microchannel, *Lab on a Chip*, 9, 1, 62-78
- J. Paulson, A. Mesbah, X. Zhu, M. Molaro, R. Braatz, 2015, Control of self-assembly in micro- and nano-scale systems, *Journal of Process Control*, 27, 38-39
- E. Solis, P. Barton, G. Stephanopoulos, 2010, Controlled Formation of Nanostructures with Desired Geometries. 2. Robust dynamic paths, *Industrial&Engineering Chemistry Research*, 49, 17, 7746-7757
- X. Tang, B. Rupp, Y. Yang, T. Edwards, M. Grover, M. Bevan, 2016, Optimal Feedback Controlled Assembly of Perfect Crystals, *ACS nano*, 10, 7, 6791-6798
- Z. Ulissi, M. Strano, R. Braatz, 2013, Control of nano and microchemical systems, *Computers and Chemical Engineering*, 51, 149-156

A network model-based optimisation analysis for the utilisation of CO₂ in Qatar's chemical industries

Ali Attiq Al-Yaeeshi, Tareq Al-Ansari*, Rajesh Govindan

Divison of Sustainable Development, College of Science and Engineering, Hamad Bin Khalifa University, Qatar Foundation, Doha, Qatar

*talansari@hbku.edu.qa

Abstract

A continuous increase of anthropogenic greenhouse gas (GHG) concentrations in the atmosphere since the industrial revolution has been attributed to global climate change. Mitigation technologies, such as CO₂ Capture and Utilisation (CCU) is promising where by it can reduce the global environmental footprint of CO₂. In addition, CCU adds value to the producers by enabling the increase of exports of economically valuable products to the global markets. The objective of this study is to assess the integration of CO₂ utilisation in the existing processes and technologies to create economic opportunities within the State of Qatar. The study considers CO₂ capture and subsequent utilisation as chemical feedstock for several industrial applications. The methodology includes the development of a geospatial (network) optimisation model that comprehensively models the CCU infrastructure, from the CO₂ sources to sinks considering pipeline transportation routes in order to maximise the economic benefits of CO₂ utilisation. The methodology is primarily based on a techno-economic assessment and single-objective linear programming of the proposed CO₂ utilisation network which includes Methanol, Urea and Gas-to-Liquid industries. It considers the economic life cycle of the network at the plant-level and modelling the economic objective in terms of the net present value (NPV) and internal rate of return (IRR), implemented within a multi-period optimisation formulation. The results demonstrate that by applying back-testing using the market prices of value-added products, mainly for the urea, methanol, gasoline, diesel and wax for the period of 2005 - 2018, the optimal solution of the distribution and utilisation of CO₂ within the industrial network changes reach to 5.99 Mt/y, whilst considering the revenue functions as the network objectives vary from 1.17 to 3.99 Billion US dollar per year.

Key words: CO₂ Utilisation, Linear Programming, Methanol, Urea, GTL, NPV, IRR

1. Introduction

It is widely accepted that emissions of greenhouse gases (GHGs) have contributed towards global warming. Carbon Capture and Storage (CCS) and Carbon Capture and Utilisation (CCU) are considered promising technologies to control CO₂ emissions. CCU programs avoid the need to store CO₂ in underground storage sites which in many cases remain under research and development. Incidentally, CCU enables the creation of an ecosystem which encourages the recycling of CO₂ and conversion into value-added products, such as urea, methanol, cement, and other well-known applications in addition to its possible utilisation for enhanced oil recovery (EOR). Pérez-Fortes et al. (2016)

evaluated through a techno-economic analysis the potential to combine hydrogen with captured CO₂ from a coal power plant to produce Methanol product. Although, the system demonstrated a reduction in CO₂ emissions, the project was deemed financially unattractive due to the high price of hydrogen in relation to the market price of Methanol. Anantharaman et al. (2013) pointed out that most of the studies consider average steady-state flow of CO₂ from the source into the capture unit, as opposed to variable amounts of CO₂, which impacts the operations as well as the cost at the sink. The study concluded that to optimize the cost of capturing system, the trade-off between the CO₂ capture cost and the payment of the emissions cost or tax should be established. This will lead to the deployment of an optimal investment of the capturing system and assure steady state of the CO₂ mitigation profile. However, considering multiple sinks may overcome the cost of the CO₂ capture system and ensure the steady state of the CO₂ flow, according to King et al. (2013). They indicated that the CO₂ utilisation network comprising EOR sinks could be economically attractive taking into consideration low energy prices associated with the overall operations. The objective of this study is to evaluate the optimum pathways for network integration of CCU options, considering existing processes and technologies within the State of Qatar in order to create new economic opportunities. It considers a single CO₂ capture system located at the source with the highest CO₂ emissions, thereby reducing the CAPEX and OPEX of the required compression system and pipeline network. The methodology developed considers an optimisation framework utilising Linear Programming (LP) in order to determine the sinks that maximizes revenues/profits based on CO₂ allocations and market prices of value-added products. This approach was applied to the fertilizer, methanol and GTL plants located in Mesaieed and Ras Laffan industrial zones in Qatar.

2. Source and Sink Data for CCU system

The system considered comprises of a single CO₂ source, namely Qatar Gas (QG), and five potential sinks that have been identified for the economic utilisation of CO₂, namely: Qatar Fertilizer Company (QAFCO); two plants in Qatar Fuel Additives Company (QAFAC), one utilising natural gas, whilst the other utilising hydrogen; Oryx GTL; and Pearl GTL, all located in the Mesaieed and Ras Laffan industrial zones. The optimisation model was developed where the objective is to develop a profitable allocation plan for up to 25 years (assumed as the operating lifetime of the project) to maximize the total CO₂ captured and utilised, thereby achieving maximum economic benefits from all the sinks. The related costs for these include the capital cost of capture system and plants, including the equipments at the sinks, CO₂ compression and transportation, and other operating costs.

2.1. CO₂ Source Data

The CO₂ emissions from Qatar Gas is approximately 35.8 Mt/year (Sayeed, 2016). The capture of CO₂ is presumed to be via chemical absorption using amine solvents operating at 90% efficiency in which the assumed cost of the capture system is \$40/t of CO₂ (Hildebrand, 2009). The estimated capital cost of the capture system is \$169 million.

2.2. CO₂ Compression and Transport Data

Compression is needed to overcome the pressure drop in pipelines and to meet sinks pressure requirements. The unit cost of compression and transportation per 100 km of the pipeline is approximately \$1.5/tCO₂ (Herzog et al., 2004). In this study, the total cost of compression and transport to both QAFAC and QAFCO is approximately \$0.5 million,

which is also the same for both Pearl GTL and Oryx GTL plants located in Ras Laffan. Considering that the distance between Messaid and Ras Laffan industrial zones is 100km, the capital cost was estimated according to the API 5L X60 and diameter 20”.

2.3. CO₂ Sinks Data

Utilisation in GTL Plant (Pearl GTL and Oryx GTL)

In addition to the sinks considered by the authors in the previous study (Al-Yaeshi, *et al.*, 2018), CO₂ can also be utilised within the GTL plants through the integration with the Fischer-Tropsch process (Rafiee *et al.*, 2017), where the captured CO₂ is supplied into an auto-thermal reformer (ATR). For the case of Qatar, a CO₂ network consisting of both the Pearl GTL and Oryx GTL can be developed with an uninterrupted supply of pure CO₂ at the required flow rate and pressure. Furthermore, recycling some unreacted syngas to the reforming and F-T synthesis units can increase process efficiency and significantly reduce CO₂ emissions. In addition, the process can increase the output of products of gasoline, diesel, and wax therefore increasing plant revenue.

3. Methodology

The methodology developed in this work study is an extension of the previous models by Al-Yaeshi, *et al.* (2018), where the optimised allocation was based on average prices of products in the CO₂ utilisation network. For this study, the LP formulation considers CO₂ allocation from QG to QAFCO, QAFAC with NG, QAFAC with H₂, Oryx GTL and Pearl GTL constrained by their utilisation capacities. The aim is to optimise the allocation in response to price variabilities of value-added products at the sinks, thereby maximising the overall revenue of the CO₂ utilisation network.

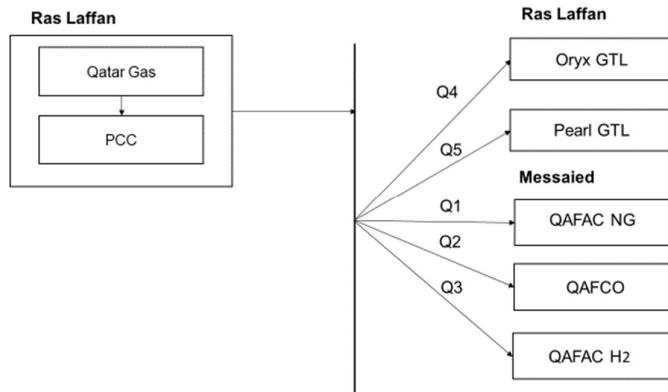


Figure 1 Proposed CO₂ utilisation network in Qatar

The decision variables used in the LP formulation are indicated in Figure 1. A detailed nomenclature of model parameters considered per industry within the CO₂ utilisation network are listed below:

Parameters related to Qatar Gas

- η : efficiency of CO₂ capture system = 0.9.
- e : CO₂ emissions rate = 15 Mt/year.
- C_1 : cost factor incurred through CO₂ capture = $\eta \times e \times \$40/\text{t CO}_2$.

Parameters related to QAFAC (natural gas), QAFACO and QAFAC (Hydrogen), are available in (Al-Yaeshi et al., 2018). In this study, Revenue period formulation is added:

- R : Revenue factor from methanol = $\sum_{k=0}^n \left(\eta \times e \times q \times \frac{\$m}{t} \right)$, where n is the number of years, m is the price of the product and q is Amount of CO₂ required (kt/year) for each sink hence. In this work q is 0.6, 1.01, and 1.82 for R_2 (QAFAC NG), R_3 (QAFACO) and R_4 (QAFAC H₂) respectively

Parameters related to Oryx GTL

- D_5 : pipeline distance from Qatar Gas = 5km.
- C_{51} : CAPEX of Reactors and utilities = \$2000 million.
- C_{52} : cost factor incurred through CO₂ transportation = $\eta \times e \times (d_5/100) \times \$1.5/\text{t CO}_2$
- R_5 : revenue factor from Oryx GTL = $\sum_{k=0}^n \left(\eta \times e \times \left((0.0006c^2 - 0.2945c + 7662.5) * \frac{\$w}{t} + (-0.0006c^2 + 1.1319c + 1431.1) * \frac{\$d}{t} + (-0.0003c^2 + 0.2786c + 1237.1) * \frac{\$g}{t} \right) \right)$
- Where n is the number of years and w , d , and g are the price of wax, diesel and gasoline respectively. In each formula, c is the desired production rate for product

Parameters related to Pearl GTL

- D_6 : pipeline distance from Qatar Gas = 5km.
- C_{61} : CAPEX of Reactors and utilities plant = \$6000 million.
- C_{62} : cost factor incurred through CO₂ transportation = $\eta \times e \times (d_3/100) \times \$1.5/\text{t CO}_2$
- R_6 : revenue factor from Pearl GTL = $\sum_{k=0}^n \left(\eta \times e \times \left((0.0006c^2 - 0.2945c + 7662.5) * \frac{\$w}{t} + (-0.0006c^2 + 1.1319c + 1431.1) * \frac{\$d}{t} + (-0.0003c^2 + 0.2786c + 1237.1) * \frac{\$g}{t} \right) \right)^n$

Where n , c , w , d , and g are the years, desired production rate of products, prices of wax, diesel and gasoline respectively.

In addition to the reduction in CO₂ emissions, the main purpose is to optimize CO₂ allocations in order to maximize the economic returns within the utilisation network. Hence, the economic objective is given by:

$$\text{Maximize } \{Q_1 \times (R_2 - C_{11} - C_{21} - C_{22} - C_{23}) + Q_2 \times (R_3 - C_{11} - C_{31} - C_{32}) + Q_3 \times (R_2 - C_{11} - C_{41} - C_{42}) + Q_4 \times (R_4 - C_{11} - C_{51} - C_{52}) + Q_6 \times (R_5 - C_{11} - C_{61} - C_{62})\}$$

subject to,

$$Q_1 + Q_2 + Q_3 + Q_4 + Q_5 \leq I,$$

$$Q_1 \times \eta \times e \leq 0.60 \times 10^6,$$

$$Q_2 \times \eta \times e \leq 1.01 \times 10^6,$$

$$Q_3 \times \eta \times e \leq 1.83 \times 10^6,$$

$$Q_4 \times \eta \times e \leq 0.36 \times 10^6,$$

$$Q_5 \times \eta \times e \leq 2.19 \times 10^6,$$

$$Q_1 \times (R_2 - C_{11} - C_{21} - C_{22} - C_{23}) \geq 0 \text{ (profit constraint QAFAC using natural gas)}$$

$$Q_2 \times (R_3 - C_{11} - C_{31} - C_{32}) \geq 0 \text{ (profit constraints - QAFAC)}$$

$$Q_3 \times (R_2 - C_{11} - C_{41} - C_{42}) \geq 0 \text{ (profit constraint - QAFAC using hydrogen).}$$

$$Q_4 \times (R_4 - C_{11} - C_{51} - C_{52}) \geq 0 \text{ (profit constraints for Oryx GTL) and}$$

$$Q_6 \times (R_5 - C_{11} - C_{61} - C_{62}) \geq 0 \text{ (profit constraints for Pearl GTL).}$$

In addition, the economic feasibility of the optimised network was evaluated using the Net Present Value (NPV) concept. The construction period and capital investment were assumed to occur in the first year, and the project life 15 years and the interest rate is 10%. The Internal rate of Return (IRR) is defined as the discount rate i at which the NPV equals to zero, and Profit to investment ratio (PIR) are part of the economic evaluation, hence;

$$NPV(t, n) = \sum_{t=0}^n (CF_t / (1 + i)^t)$$

where CF is the cash flow, t is the year of the cash flow, i is the discount rate, and n is the total number of years.

$$NPV \geq 0 \text{ before year } 15^{th}; \text{ IRR} \leq 20\%; \text{ PIR} \geq 0$$

4. Results

Table 1 indicates the optimum values for CO₂ allocations when the profit constraint is relaxed, i.e. the net revenue is maximised in the CCU network. Consequently, this also increases the annual rate of CO₂ utilisation by the sinks in the network.

Table 1. The profit constraints are relaxed.

Decision Variables (fractional amount of CO ₂ from Qatar Gas)	% CO ₂ Allocation
Q ₁	0.045
Q ₂	0.075
Q ₃	0.14
Q ₄	0.027
Q ₅	0.16

The modelling results illustrate that when the CCU network optimisation is applied, a clear benefit is achieved in terms of generating revenues at the sinks, whilst reducing CO₂ emissions. The total CO₂ captured and transported to the sinks is 6.71 Mt/y, out of the annual emissions rate of 15 Mt/y, which corresponds to a 44.7% emissions reduction. As such, the model indicates that the CCU network is considered economically attractive when the prices of products, namely urea, methanol, wax, diesel and gasoline increases. Although it was expected that the main driver of the allocations are the product prices at the sinks, the allocation results in Table 1 were found to be constant for the period between 2005 – 2018. Furthermore, the economic evaluation yielded positive returns, as given below:

NPV = 4.43 Billion USD as the positive pay back starting between 2012 and 2013 (after 8 years)

PIR = 0.385

IRR = 16%

5. Conclusion

The modelling and analysis presented in this paper considers CCU technology to enhance the production of value-added products at the sinks such as methanol, urea, wax, diesel and gasoline, whilst reducing CO₂ emissions at the sources. The approach demonstrates the potential economic benefit of a proposed CCU network in Qatar whilst considering the market prices of value-added products. The price fluctuations of these products, however, does not significantly change the allocations in the CCU network, and as such the revenue maximisation by the network was directly linked to crude oil and commodities prices. In addition, the economic feasibility of the network was also demonstrated by evaluating NPV, PIR and IRR which demonstrated a positive indication based on the optimal allocation for each sink although 40 % of CO₂ captured utilised. Future work will consider detailed environmental assessment in order to quantify CO₂ emissions in the network at the plant-level.

6. References

- A. Attiq Al-Yaeshi, T. Al-Ansari, R. Govindan, (2018), Computer Aided Chemical Engineering, The potential for carbon dioxide capture and utilization within the State of Qatar, 28th European Symposium on Computer Aided Process Engineering, pp.1499-1504
- A. N. Hildebrand, (2009). Strategies for Demonstration and Early Deployment of Carbon Capture and Storage: A Technical and Economic Assessment of Capture Percentage. Retrieved from:
http://sequestration.mit.edu/pdf/AshleighHildebrand_Thesis_May09.pdf
- C. W. King, G. Gulen, S. Cohen, and V. Nuñez-Lopez, (2013). The system-wide economics of a carbon dioxide capture, utilization, and storage network: Texas Gulf Coast with pure CO₂-EOR flood, Environ. Res. Lett. 8 (2013) 034030 (16pp) ENVIRONMENTAL
- Herzog, H. and Golomb, D., 2004. Carbon capture and storage from fossil fuel use. Encyclopedia of energy, 1(6562), pp.277-287.
- M. Pérez-Fortes, A.B. Dumitriu, E. Tzimas, (2014). CO₂ Utilization Pathways: Techno-Economic Assessment and Market Opportunities. Energy Procedia 63 (2014) 7968 – 7975
- QAFCO, 2014. Sustainability Report, Available from:
<http://www.qafco.qa/Satellite?blobcol=urldata&blobheader=application%2Fpdf&blobheadername1=Content-Disposition&blobheadername2=MDT-Type&blobheadervalue1=inline%3B+filename%3DSustainability+report+2014+Final.pdf&blobheadervalue2=abinary%3B+charset%3DUTF-8&blobkey=id&blobtable=MungoBlobs&blobwhere=1372606173378&ssbinary=true> [Accessed 10 Novmeber]
- R. Anantharaman, S. Roussanaly, S.F. Westman and J. Husebye, (2013). Selection of optimal CO₂ capture plant capacity for better investment decisions. Energy Procedia 37 (2013) 7039 – 7045 GHGT-11
- S. Mohammed (2016), Qatar's National Emission Inventory Report, Figshare, Available from; <http://creativecommons.org/licenses/by/4.0/> [Accessed [February 2018]

A Framework for Multi-level Life Cycle Analysis of the Energy System

Emre Gençer,^{a,*} Francis M. O'Sullivan^a

^aMIT Energy Initiative, Massachusetts Institute of Technology, 77 Massachusetts Avenue, Cambridge, MA, 02139, USA

emregencer@mit.edu

Abstract

The energy sector is undergoing a major transformation that is characterized by greater convergence of power, transportation, and industrial sectors and inter-sectoral integration. The existing techniques and tools are unable to accurately estimate the environmental impact of this paradigm shift. To develop a realistic understanding of these dynamics, we have developed a modeling framework that is designed to explore the emissions impacts of all relevant technological, operational, temporal, and geospatial characteristics of the evolving energy system. The tool is built as a MATLAB app that encapsulates MATLAB models, databases, and integrated process simulations. A modular framework constitutes the underlying analytical engine that covers all the life stages of major energy conversion pathways. The current version of the tool contains more than 900 individual pathways, which are responsible for ~80% of US greenhouse gas (GHG) emissions. Here we present an overview of the tool, the modeling approach and example results of case studies investigating electric power system.

Keywords: Life cycle analysis, multi-level analysis, energy systems modeling, computational tool, process simulation

1. Introduction

The global energy sector faces the grand challenge of meeting the increasing demand while profoundly reducing greenhouse gas emissions. Today's energy sector is responsible for approximately 80% of the world's total GHG emissions, and the electricity sector is the largest single emitting sector with 33% share. Industrial processes constitute 22% of emissions, while the transportation sector is responsible for 16% (Annual Energy Outlook 2018, 2018). Moving forward, the evolution of energy systems is characterized by greater convergence of power, transportation, and industrial sectors and inter-sectoral integration. Existing techniques and tools are unable to accurately estimate the environmental consequences of this paradigm shift. Understanding the implications of these dynamics requires novel tools that provide deep systems-level insights (Majumdar and Deutch, 2018). To address this pressing need, we have developed a modeling framework that is specifically designed to explore the emissions impacts of all relevant technological, operational, temporal, and geospatial characteristics of the evolving energy system.

The tool is built as a MATLAB app that encapsulates MATLAB models, databases, and integrated process simulations. A modular framework constitutes the underlying analytical engine that covers all the life stages of major energy conversion pathways. The

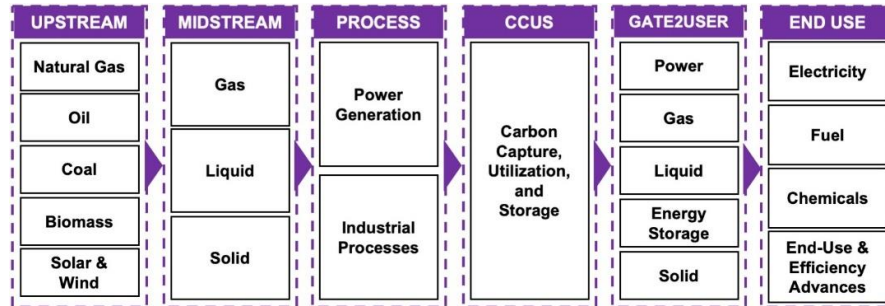


Figure 1 Summary of the contents of the tool. All major conventional and renewable energy pathways with their associated end-uses covering more than 85% of GHG emission sources in the US are represented.

first version of the tool contains more than 900 individual pathways (Figure 1), which are responsible for ~80% of US greenhouse gas (GHG) emissions. For the GHG emission hot spots, such as power plants and some chemical conversion pathways, detailed process simulation capabilities have been incorporated for in-depth analysis. In addition to performing pathway-level life cycle analysis (LCA), a central aspect of this analytical framework is the ability to assess key systems interactions and couplings. The system-level analysis is enabled by the embedded power systems and vehicle fleet models that captures market dynamics and explore dynamics of technology adoption and usage.

This paper focuses on the overview of the tool, the modeling approach as well as the results of case studies investigating electric power system. We demonstrate how the changes in the operational variability of natural-gas fired power plants impacts the system-wide emissions. Specifically, the operation of NG power plants in the evolving power system that significantly reduces plant performance and increases the emissions footprint of NG power generation. Example results of analysis of power plant dispatch profiles and detailed life cycle analysis of the US power grid using high resolution plant level simulation models and incorporation of publicly available US-wide generation and emissions data are presented (U.S. EPA, 2018a, 2018b).

2. Methodology

A crucial aspect of this analytical framework is the ability to assess key systems interactions and couplings. This allows transition options to be comprehensively assessed on the same basis. To allow performing such comprehensive analyses, we have built a flexible and modular programming architecture specifically designed to evolve as the complex energy system restructures.

The modular approach composed of four main compartments at the very high-level: User input, Control panel, Life stage modules, and Model output. To initiate the computation the necessary input parameters such as selection of complete value chain, specifications of power grid mix, geographical location, and temporal resolution should be provided by user. Control panel module constitutes the core of the tool that takes user inputs and communicates with relevant life stage modules to send and receive information as shown in Figure 2(a). The results from each life stage module are adjusted and combined in accord with the user selections given by Eq. (1). The energy consumption by fuel type is used as the basis for calculations. The efficiency of each stage is accounted for in the

overall calculation denoted by ℓ . EF_i represents the emission factor from each stage given in the stage specific unit and χ is the conversion factor to adjust to the final unit. The results calculated as the sum of contribution from each stage is returned as output in desired unit and format.

$$EF = \sum_{i=1}^6 (EF_i \times \chi_i) \prod_{j=1}^i 1_j \quad (1)$$

Each life stage module consists of sub-modules. Depending on options selected, different sets of submodules are activated in parallel with the real-world operation. For example, the bituminous coal upstream operation includes all steps of extraction described by the processes involved coupled with fuels and electricity consumed. The midstream and gate2user stages are characterized by the phase of the flow. Process step is represented with high resolution to include all feedstocks and energy flows. The detailed information and data are collected from published LCA literature, reports, publicly available tools and life cycle inventory databases such as technology baselines reports (DOE NETL, 2015), GREET model (Wang, 2011), ecoinvent database.

2.1. Modeling Approach

The described programming architecture and linked modules are implemented in MATLAB. We have augmented MATLAB's capabilities by integrating with Aspen Plus process simulation software (Gençer and Agrawal, 2017a). This approach allows complementing life cycle analysis with process simulation capabilities to capture the performance and emission changes arising from technological and operational variations. It is computationally very expensive and unnecessary to simulate every process for all potential conditions. However, the developed architecture provides a platform to implement simulations of process units with high emission rates, critical for the system design, or sensitive to externalities.

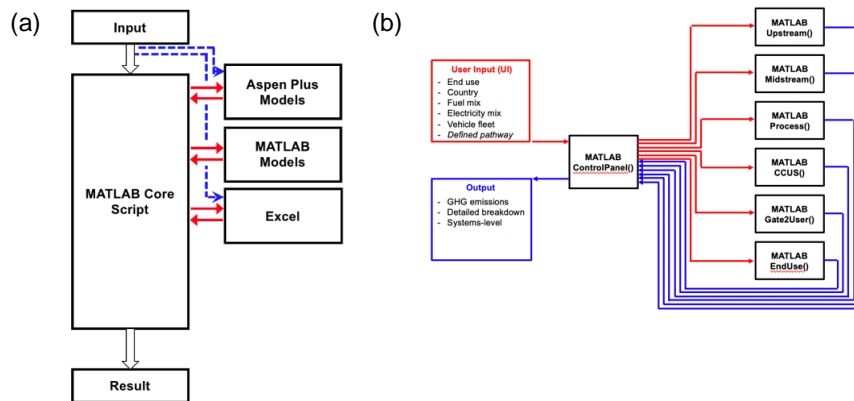


Figure 2 (a) The tool is developed in MATLAB with the added capabilities of communicating with various modeling programs such as Aspen Plus. (b) The modular structure: control panel connecting to primary life stage modules.

Figure 2(a) depicts the communication between MATLAB Core Script and auxiliary components: MATLAB Models, Aspen Plus Models, and Excel models and databases.

As needed, the tool can be equipped with more programming platforms. MATLAB is used to develop life stage modules, each one of which has its unique structure. Each module is composed of numerous custom developed MATLAB functions. Functions are designed to minimize the repetition of same scripts and framed clearly separate different tasks.

Natural gas fired power plants play a critical role in the evolving electric power system

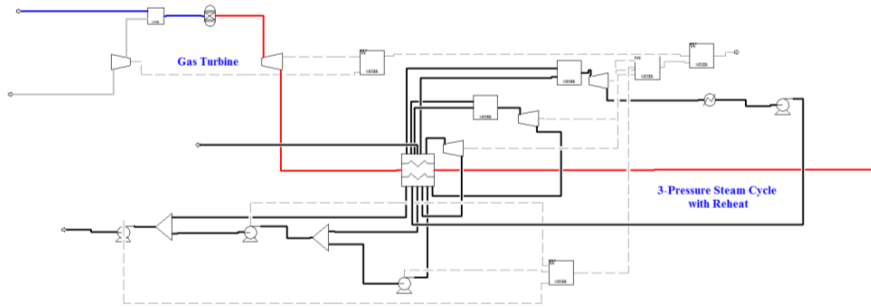


Figure 3 Process flow diagram of natural gas combined cycle unit simulated in Aspen Plus to match the performance of GE's 7FA model.

both as a lower carbon intensity alternative to coal power plants, and as balancing capacity for variable renewable energy sources. Power plant performance is sensitive to parameters such as percent loading, ambient temperature and relative humidity. To have a representative characterization of power generation units, we have developed Aspen Plus simulations for the most widely used combined cycle and gas turbine units. The performance of models is validated using the manufacturer's catalogs (Chase and Kehoe, 2013). Simulations represents steady-state operation at various conditions including percent loading (Gençer and Agrawal, 2017b).

3. System Boundaries

Pathway level analysis constitutes the backbone of the computation engine. The platform is capable of calculating all the combinations of modules, presented in Figure 1, that form a meaningful pathway. The individual pathways can be further expanded with the addition of new modules. Cradle-to-grave system boundary for every complete pathway is set and the selections are limited to allowed components. System boundary for coal-to-electricity pathway is shown

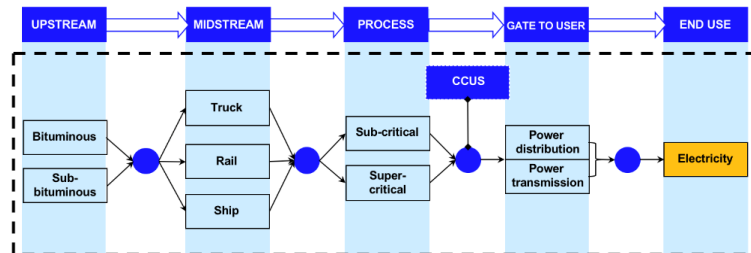


Figure 4 Coal-to-electricity pathway system boundary.

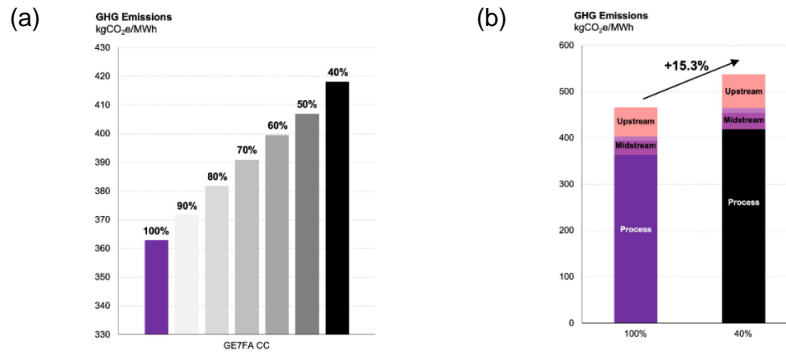


Figure 5 (a) GHG emissions from the flue gas of NGCC for varying loadings. (b) Cradle-to-grave life cycle emissions of shale gas-to-power pathway for 100 % and 40 % of the nameplate capacity of NGCC unit.

in Figure 4. For every life stage, there are multiple options that can be selected such as the coal type (bituminous or subbituminous), the transportation method of coal (truck, rail, or ship). Combination of these alternatives can also be specified.

3.1. Representation of Systems

Pathway-level analysis provides valuable insights however, understanding system wide emissions impact is critical. The presented modular framework is designed to perform systems-level calculations. A system is defined as a collection of individual pathways. This approach allows performing high resolution LCA based upon detailed individual pathways embedded. System can be as small as two pathways and as large as a city or a region. To determine the minimum emission option, the problem can be optimized using genetic algorithm (Gençer et al., 2015; Liu and Bakshi, 2018).

4. Results

The model can be run in pathway level or systems-level modes. The pathway level calculations are performed to estimate the life cycle GHG emissions in a given system boundary. The impact of cycling for NGCC plants is explored. Simulation results for 40 % to 100 % loading relative to nameplate capacity for a NGCC unit is shown in Figure 5(a). The emission rate increases from 362 kgCO₂/MWh to 419 kgCO₂/MWh when the power output is reduced to 40 %. The emission impact of this variation is propagated to

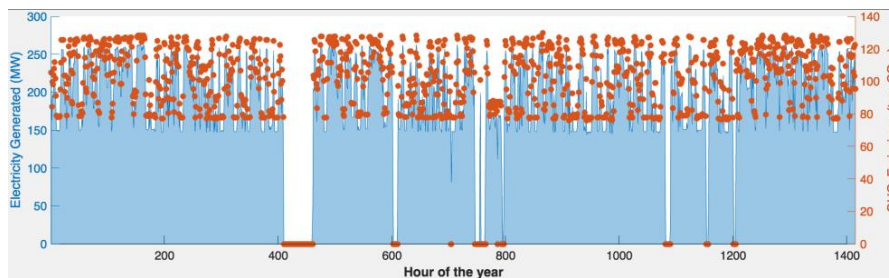


Figure 6 Hourly LCA based on observed load profile of a NGCC unit in California.

all life cycle stages of the supply chain. Cradle-to-grave life cycle analysis for the two extreme cases are performed and results are summarized in Figure 5(b). The emission intensity increases by 15.3 % relative to operation at peak efficiency. Using the embedded hourly generation profiles of thermal generation units a life cycle emissions of generators in the US has been calculated. Results for a combined cycle unit in California (Dynergy Moss Landing Power Plant Unit 1A) is shown in Figure 6, the area graph shows the hourly electricity generation and dots are the calculated full life cycle emissions in tCO₂e. For this particular unit, we observe more than 40% fluctuations in total emissions. While one reason for this change is the lower net generation, the other reason is higher emission intensity operation due to operation at off peak mode.

5. Conclusions

The adoption of a holistic approach is increasingly important to accurately characterize the energy system. Here, we have demonstrated a novel tool to integrate the systems aspect for the conventional life cycle analysis. The underlying analytic engine constitutes of numerous individual energy pathways. The developed tool provides a consistent platform to estimate LCA of all components of the energy sector. Furthermore, the system representation is embedded into the tool for power and transportation sectors. LCA of power generation at hourly generator level resolution is estimated by integrating calculated performances from process simulations.

6. References

- Annual Energy Outlook 2018. 2018.
- Chase DL, Kehoe PT. GER-3574G - GE Combined-Cycle Product Line and Performance. Schenectady, NY: 2013.
- DOE NETL. Cost and Performance Baseline for Fossil Energy Plants. vol. 1a. 2015.
- Gençer E, Agrawal R. Strategy to synthesize integrated solar energy coproduction processes with optimal process intensification. Case study: Efficient solar thermal hydrogen production. *Comput Chem Eng* 2017a;105:328–47. doi:10.1016/j.compchemeng.2017.01.038.
- Gençer E, Agrawal R. Synthesis of efficient solar thermal power cycles for baseload power supply. *Energy Convers Manag* 2017b;133:486–97. doi:10.1016/j.enconman.2016.10.068.
- Gençer E, Tawarmalani M, Agrawal R. Integrated Solar Thermal Hydrogen and Power Coproduction Process for Continuous Power Supply and Production of Chemicals. vol. 37. 2015. doi:10.1016/B978-0-444-63576-1.50076-5.
- Liu X, Bakshi BR. Extracting Heuristics for Designing Sustainable Built Environments by Coupling Multiobjective Evolutionary Optimization and Machine Learning. *Comput Aided Chem Eng* 2018;44:2539–44. doi:10.1016/B978-0-444-64241-7.50418-3.
- Majumdar A, Deutch J. Research Opportunities for CO₂ Utilization and Negative Emissions at the Gigatonne Scale. *Joule* 2018;2:805–9. doi:10.1016/j.joule.2018.04.018.
- U.S. EPA. Emissions & Generation Resource Integrated Database (eGRID) 2018a.
- U.S. EPA. Air Markets Program Data 2018b.
- Wang M. GREET Model: The Greenhouse Gases, Regulated Emissions, and Energy Use in Transportation Model. 2011.

Contract Settlements for Exchanging Utilities through Automated Negotiations between Prosumers in Eco-Industrial Parks using Reinforcement Learning

Dan E. Kröhling, Ernesto C. Martínez*

INGAR (CONICET-UTN), Avellaneda 3657, Santa Fe, S3002 GJC, Argentina

ecmarti@santafe-conicet.gov.ar

Abstract

Peer-to-peer trading of utilities (heating, cooling and electric power) in an eco-industrial park (EIP) is key to realize significant economic and environmental benefits by exploiting synergistic co-generation and surplus trading. A crucial aspect of this symbiotic scheme is that each selfish company (prosumer) will participate in exchanging utilities to increase its own profits depending on its internal load. In this paper, an automated negotiation approach based on utility tokens is proposed to incentivize participation in a market of prosumer peers for trading surpluses in an EIP. During each negotiation episode, a pair of prosumers engage in a bilateral negotiation and resort to a learned policy to bid, concede and accept/reject using both private information and environmental variables. Contract negotiation revolves around agreeing (or not) on the price expressed in tokens of a utility profile. The time-varying value of the utility token accounts for contextual variables beyond the control of each prosumer. Simulation results demonstrate that reinforcement learning allows finding Nash equilibrium policies for smart contract negotiation in a blockchain environment.

Keywords: automated negotiation, blockchain, reinforcement learning, smart contracts.

1. Introduction

An EIP mainly consists of distributed co-generation (e.g. heating, cooling and electric power), shared storage systems and flexible/distributed demand/supply of intermediate products and waste materials (Chertow, 2007; Nair et al., 2016). A key aspect of this symbiotic scheme is that each potential partner company will only participate in exchanging utilities through loans or credits with the motivation of increasing its own profits. The selfish nature of each prosumer thus results in a conflict of interest which, if not resolved, may give rise to the failure of the EIP (Chew et al, 2009; Tan, et al., 2016). It is argued here that the Blockchain approach based on a distributed ledger (Sikorski et al., 2017) and smart contracts (Kristides and Devetsikiotis, 2016) can be used to foster decentralized, peer-to-peer automated negotiations between prosumer companies that want to trade their utility surplus with other peers in the park. Considering heterogeneous prosumer preferences, which are private information, each peer company (represented by a software agent) should learn to negotiate how to bid and what to accept in utility contract settlements by properly accounting for its context including weather, scheduled utility loads, season, oil prices, mood of the economy, etc. The strategic behavior of a prosumer (proactive consumer actively managing its consumption and production of different types of utilities) in EIPs depends significantly

on the influence of these environmental conditions or contextual variables on its negotiation policy, since they affect not only a given agent preferences and decision-making policies, but also those of other agents. A novel context-driven approach for policy learning in automated peer-to-peer negotiations between prosumers of an EIP is proposed. Reinforcement learning (Sutton and Barto, 2018) is key to learn negotiate utility contracts via simulation by properly accounting for most relevant environmental variables, other peer negotiation policies, their models and contextual information, which provides each prosumer agent a competitive edge while incentivizing its participation in an EIP near to Nash equilibrium conditions with other prosumers.

2. Peer-to-peer negotiations of utility contracts

Utility prosumers are agents that both consume and may produce different types (heating, cooling and electric power) of utilities in an EIP. Each prosumer company is assumed to be equipped with one or more utility generation means (e.g. a boiler, solar panel, freezer, heating/quenching streams, etc), has a scheduled profile load and, possibly, a temporary surplus for some of its internal generated utilities and extra needs for other utilities. Peer-to-peer local trading of such surpluses by taking advantage of material and energy integration in an EIP gives rise to unique opportunities to lower emissions and reduce energy costs.

Each company in the EIP is modeled as a software agent, $i \in N$, where N is the set of engaged prosumer agents in the peer-to-peer utility market of the EIP at time t . It is assumed that, depending on the utility needs for their scheduled load and surplus, if any, each agent negotiates buying/selling utility profiles and their prices in tokens (τ_t). For example, in Fig. 1 agent A , at time t , seeks an agreement with agent O_3 to sell part of its heating power. Concurrently, agent A aims to buy renewable electric power from agent O_1 and some cooling from agent O_2 . The context for these negotiations is private information (X_i) and environmental variables (Y_j). The specific type for an agent i is summed up in state variable v^i , known as “necessity”, whereas its external context is given by a “risk” ρ^i . Each agent necessity accounts for the needs and surplus derived from capacity slacks and scheduled usage loads. In turn, risk accounts for the different factors that may influence the current and future values of the token $\tau_t, \tau_{t+1}, \dots, \tau_{t+H}$.

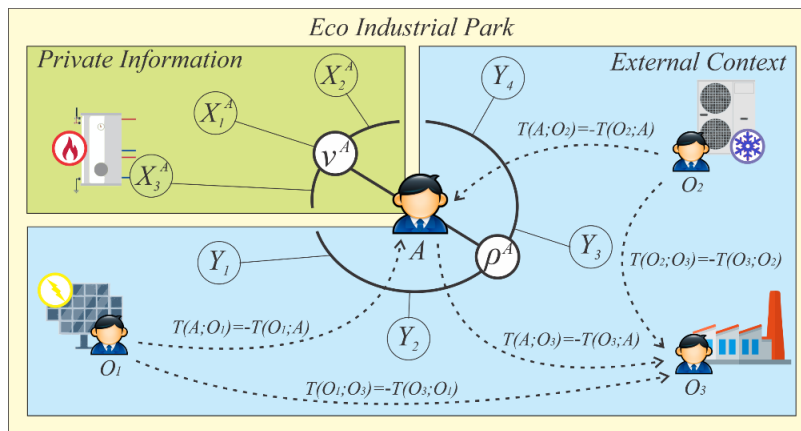


Fig. 1. Peer-to-peer negotiation setting at time t for utility surpluses in an EIP.

From the point of view of a central EIP authority, the exchange utility problem requires maximizing the overall value of surplus traded assuming perfect information about both public variables and private prosumer types, that is, their necessities and risks as follows

$$\text{Max } \sum_u \sum_t \sum_i T_t^u(i; -i) \quad (1)$$

subject to:

$$T_t^u(i) + T_t^u(-i; i) - T_t^u(i; -i) \geq NCT_t^u(i) \quad \forall i, u, t \quad (2)$$

$$T_t^u(i) + T_t^u(-i; i) - T_t^u(i; -i) - NCT_t^u(i) = MCT_t^u(i) - SCT_t^u(i) \quad \forall i, u, t \quad (3)$$

$$T_t^u(i; -i) \leq SCT_t^u(i) \quad \forall i, u, t \quad (4)$$

$$T_t^u(i), T_t^u(i; -i), NCT_t^u(i), MCT_t^u(i), SCT_t^u(i) \geq 0 \quad \forall i, u, t \quad (5)$$

where each variable represents:

- $T_t^u(i)$, the total amount of utility u in tokens traded by agent i at time t .
- $T_t^u(-i; i)$, the amount of u in tokens bought by i to all other agents $-i$ at time t .
- $T_t^u(i; -i)$, the amount of u in tokens sold by i to all other agents $-i$ at time t .
- $NCT_t^u(i)$, the overall power of u in tokens required by i in t to fulfil its necessity.
- $MCT_t^u(i)$, the max power of utility u in tokens that i could produce at time t .
- $SCT_t^u(i)$, the surplus capacity of u in tokens that i is ready to sell at time t .

The problem aims to maximize the number of tokens (utilities) traded between agents. This gives rise to a maximization of the EIP's social welfare while minimizing the surplus capacity loss over time, considering the maximum power per agent, its internal generation and scheduled usage. The assumption of a perfectly informed central authority is unrealistic in the selfish, competitive environment of any EIP. Prosumers are reluctant to provide their private information when behaving strategically.

3. Learning to negotiate

Bilateral negotiations between two agents using a discrete timeline will be used. The alternating offers protocol is used throughout. We will use a technique widely known, namely Reinforcement Learning (or RL) (Sutton and Barto, 2018). Prosumers in an EIP will learn to negotiate better by simulating negotiation episodes against each other using the Q -Learning algorithm and accumulate their experience rewards in a decision policy. A prior work on prosumers' negotiation can be found in (S. Chakraborty et. al., 2018).

The Q -Learning algorithm consists of a function that estimates the expected cumulative rewards for future time steps in negotiation episodes given the actual state s_t each agent is in, if it chooses for a certain action a . Which action to take is determined by the negotiation policy π derived from the Q -values. At the end of each episode, an agent receives the reward r which allows updating Q -values. To this aim, the learning rule is:

$$Q(s_t; a_t) = Q(s_t; a_t) + \alpha * [r_{t+1} + \gamma * \max_a Q(s_{t+1}; a_t) - Q(s_t; a_t)] \quad (6)$$

Each state for the i th prosumer agents is defined by the tuple:

$$s = (v, \rho) \quad (7)$$

where v and ρ , as defined before, are the necessity and risk associated with the perceived state by an agent, including the token value and its utility needs/surplus.

Each action during the negotiation episode, on the other hand, will be defined by:

$$a = (RV, \beta) \quad (8)$$

where RV is the reserve value of the negotiation, that is, the worst agreement an agent is willing to accept, and β is the concession rate, or the way it concedes in negotiations.

The Q -learning algorithm hyper-parameters, as defined commonly in the literature, are set to $\alpha = 0,1$ and $\gamma = 0,9$. ε , that measures how much our agent will take random actions to explore different options, starts at 1 and slowly decreased towards 0. Next, we define the way our agents compute necessities and risks out of their context, considering time t as one entire trading day. Necessities will be given by:

$$v_t^b = 0.5 * g_t(e_t + p_t) + 0.3 * g_{t+1}(e_{t+1} + p_{t+1}) + 0.2 * g_{t+2}(e_{t+2} + p_{t+2}) \quad (9)$$

$$v_t^s = su_t \quad (10)$$

For the buyer, g_t is the probability of rescheduling production tasks at time t ; e is the amount of energy needed for the period and p is the maximum utility power required. For the seller, su_t is the surplus utility capacity or power it has available to trade. The risk may be similar for both agents, but, as defined, when the risk is low, the buyer is in a stronger position, whereas when the risk is high, the seller is in a stronger position.

$$\rho_t = season_t * \tau_t \quad (11)$$

where $season_t$ represents the variability of demand and τ_t , the price of the token.

4. Simulation results

4.1. The nature of the negotiation learning process

In Fig. 2 is presented the learning experienced by prosumer agents via simulating negotiation episodes against each other. It is worth noting the random nature of the learning process in negotiation episodes as it is shown in the 10000 simulated outcomes and the rewards obtained by the agents. This is mainly due to a rather unknown context and private information our agents must deal with. Simulations with diverse environmental contexts were conducted, varying utility or maxim power needed, possibility of rescheduling tasks, seasonality influence and the token price. The average trend highlights how negotiating agents increasingly obtain better deals as simulations makes room for learning to concede and accept. From the sparsity of rewards obtained it seems contextual information influence less to the seller than to the buyer. In the latter, greater risks are at stake when a contract is not settled in due course.

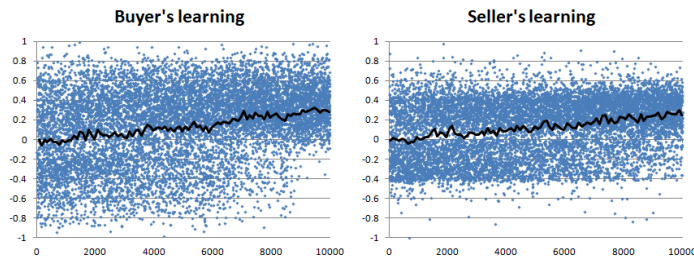


Fig. 2. Agents learning via simulation of negotiation episodes.

4.2. Reward functions

In Fig. 3, the functions used for rewarding negotiation outcomes of prosumer agents are shown. In the graph of the buyer's rewards when agreements are reached, it can be clearly perceived the importance of considering the risk ρ involved in the negotiation (the price τ of the token and the seasonality), given its reward function. On the other hand, it is very important for this agent to consider its necessity ν when it decides not to agree, as rewards strongly depend on such private information and the possibility of rescheduling tasks and changing the utility load by levelling power peaks.

Similarly, for an agent in the role of a seller, its necessity and risk should be taken almost equally into account when deciding to agree the terms of an offer, but the agent deems better considering mainly its perceived risk when not agreeing. Such a reasoning helps illustrate the importance of correctly designing a reward function for guiding negotiation agents about what to bid, when to concede, what to accept or reject in contract settlements by considering what is at stakes in different scenarios.

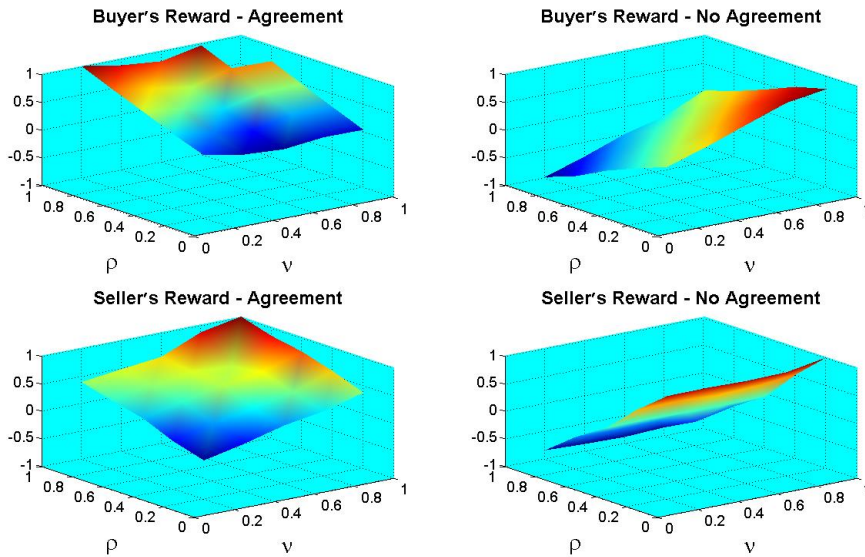


Fig. 3. Rewards for prosumer agents in different environmental contexts.

4.3. Agents' policies

In Fig. 4, the policies learned by prosumer agents are shown. Given ν and ρ , agents behave differently depending on their role (buyer or seller). From a buyer's point of view, it will concede more slowly (β) and less (RV) as its perceived risk is higher, but it will concede faster and more as its necessity increases. From a seller's point of view, it will concede more slowly and to a lesser extent as its perceived risk is higher. Conversely, it will concede more quickly and to a lesser extent as its (internal) necessity increases. Having a near optimal policy for negotiating smart contracts is key for automating utility exchanges and incentivizing prosumer to participate in a peer-to-peer market. Social welfare in industrial parks is heavily dependent on negotiation policies that generate win-win deals that lower capital costs and carbon emissions.

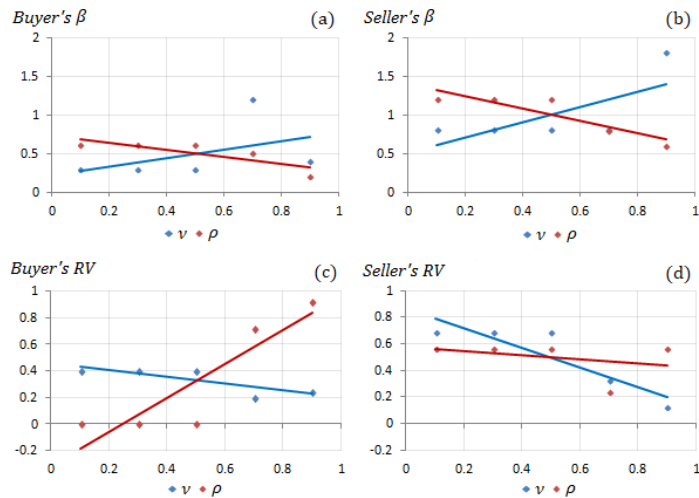


Fig. 4. Behavior of negotiation agents in different scenarios.

5. Conclusions

The importance of learning to negotiate utility surpluses in eco-industrial parks where prosumers do have private information has been addressed. Simulation results highlight that reinforcement learning is key to learn negotiation policies based on each agent internal necessity and the perceived risk in its environment. The proposed approach can be readily implemented using the Blockchain technology, industrial internet of things and smart contracts to enforce the agreed upon terms automatically.

References

- S. Chakraborty et al., 2018, Energy Contract Settlements through Automated Negotiation in Residential Cooperatives, IEEE International Conference on Communications, Control, and Computing Technologies for Smart Grids, DOI: 10.1109/SmartGridComm.2018.8587537.
- M. Chertow, 2007, Uncovering Industrial Symbiosis, J. Industrial Ecology, 11, 1, 11-30.
- I. M. L. Chew et al., 2009, Game theory approach to the analysis of inter-plant water integration in an eco-industrial park, J. Cleaner Production, 17, 18, 1611–1619.
- K. Kristides and M. Devetsikiotis, 2016, Blockchains and Smart Contracts for the Internet of Things, IEEE Access, 4, 2292 – 2303.
- S. K. Nair et al., 2016, Shared and practical approach to conserve utilities in eco-industrial parks, Computers and Chemical Engineering, 93, 221–233.
- J. J. Sikorski et al., 2017, Blockchain technology in the chemical industry: Machine-to-machine electricity market, Applied Energy, 195, 234-246.
- R. S. Sutton and A. G. Barto, 2018, Reinforcement Learning – An Introduction, The MIT Press, Cambridge, MA, USA.
- R. R. Tan, et al., 2016, An optimization-based cooperative game approach for systematic allocation of costs and benefits in interplant process integration, Chemical Engineering Research and Design, 106, 43-58.

Integration of Max-Plus-Linear Scheduling and Control

Risvan Dirza^a, Alejandro Marquez-Ruiz^a, Leyla Özkan^a and Carlos S. Mendez-Blanco^a

^a*Department of Electrical Engineering, Eindhoven University of Technology, 5612 AJ, Eindhoven, The Netherlands*

A.Marquez.Ruiz@tue.nl

Abstract

In this paper, we investigate the Max-Plus-Linear (MPL) representation for the integration of scheduling and control problem. This is an attractive approach because the MPL representation can result in a convex scheduling problem. Using this representation, we have formulated the integration of scheduling and control problem considering the corresponding transitions time for each processing time. Furthermore, the MPL representation is combined with the sequential decomposition method (SDM) (Chu and You (2012)) in order to solve the integrated problem. The final result is a formulation that preserves the convexity of the original scheduling problem. Finally, the performance of the new formulation is tested on a simple case study and compared with the traditional method.

Keywords: Integration, Scheduling, Control, Max-Plus-Linear Systems

1. Introduction

Scheduling and control are complementary tasks for optimizing chemical process operations. Traditionally, these tasks have been implemented separately in a sequential way. Scheduling problems, whose solutions provide the optimal production sequence and production times, do not in general consider the dynamic behavior of the processes. The inclusion of such dynamics in the scheduling problem is called the integration of scheduling and control, and it has shown important economic benefits for the overall performance of the process. Despite the advantages of the integration, several challenges have been also reported. Nevertheless, the most critical issues are the modeling approach used in the scheduling problem and the computational aspects. Both topics are strongly related.

There are several approaches to model the scheduling problem i.e. the state-task network (STN) or resource-task network (RTN). These modeling options lead to transforming the integration of scheduling and control into an MINLP problem which is relatively computationally expensive (Chu and You (2012), Subramanian et al. (2012)). An attractive approach to avoid the MINLP formulation is modeling the scheduling problem using the MPL representation (Schutter and van den Boom (2001), van den Boom et al. (2018)). There are a lot of advantages of the MPL representation. The most remarkable one is that the scheduling problem can be transformed into a convex optimization problem. In addition, the MPL representation has not been investigated for the integration of scheduling and control problem.

In this paper, we assume a perishable goods scheduling problem and no disturbances affecting the completions of the tasks. Based on these assumptions, we propose an approach to formulate an integrated problem of MPL scheduling and control, and methods to solve the problem.

This paper is organized as follows. In Section 2, preliminaries related to the control problem and the MPL system are presented. Section 3 presents the formulation of the integration of scheduling and control using the MPL representation. The details on the new proposed methods to solve the integrated problem are presented in Section 4. The proposed formulation and solutions are demonstrated on a simple case study and compared in Section 5. Finally, the conclusion is given in Section 6.

2. Preliminaries

2.1. Max-Plus Linear (MPL) system

The MPL utilizes timed-discrete event system (timed-DES) in the modeling of time (Schutter and van den Boom (2001)). A max-plus-algebraic (MPA) model, called MPL system, can represent timed-DES with no concurrency, where we assume no capacity constraint and each unit starts working as soon as all parts or conditions are available. The general form of MPL scheduling model is as follows:

$$\check{x}_i(k) = \check{A}_i \otimes \check{x}_i(k-1) \oplus \check{B}_i \otimes \check{u}_i(k); \quad \check{y}_i(k) = \check{C}_i \otimes \check{x}_i(k) \quad (1)$$

where $\check{A}_i \in \mathbb{R}_\varepsilon^{n_{x_i} \times n_{x_i}}$, $\check{B}_i \in \mathbb{R}_\varepsilon^{n_{x_i} \times n_{u_i}}$, and $\check{C}_i \in \mathbb{R}_\varepsilon^{n_{y_i} \times n_{x_i}}$ are system matrices configured by all units contributing in production line i . \otimes is equal to operator "+" and \oplus is equal to operator "max". In Eq.(1), the components of the input, the output, and the state are event times, and the counter k is an event cycle counter. For a process system, $\check{u}_i(k)$ would typically represent the time instants at which raw material is fed to the system for the $(k+1)^{th}$ time, $\check{x}_i(k)$ represent the time instants at which the unit start processing the k^{th} batch of intermediate products, and $\check{y}_i(k)$ represent the time instants at which the k^{th} batch of finished products leaves the system (completion time).

2.2. Control Problem

We consider a batch reactor as a plant model equipped with controllers to reach an optimum set point. The controller(s) of each unit, i.e. MPC or PID can be expressed in general as: $u = K(x, t_s)$, where u , x and t_s are the input, states and the transition time of a processing unit, respectively. For example, a PI controller can be expressed as: $u = K_P(Cx - y^{sp}) + K_I \int (Cx - y^{sp})$, where y^{sp} is the optimal set point of a processing unit given by the Real-Time Optimization (RTO). The parametrization of the controller(s) in terms of the transition time can be done because the tuning parameters are a function of t_s . In the planning layer, where the planning decisions are taken, a set of transition times has been determined based on the historical data. This set is expressed as: $\tilde{t}_s^{(l)} = \{t_s^{(1)}, \dots, t_s^{(n_l)}\}$, where l is the index of the reachable transition time.

The presence of transition time influences the accuracy of the scheduling policy. Thus, the controller is also responsible for reaching and tracking the given transition time that is regulated by controller parameters $\Omega_{i,ii}^{(l)}$ (e.g. $\Omega_{i,ii}^{(l)} = \{K_P, K_I\}$ for PI controller), where

i is the production line and ii is the index of the unit contributing in line i . The controller parameters can minimize the difference between given transition time and the transition time obtained by an off-line simulation $\bar{t}_{s_{i,ii}}^l$. This simulation is only executed once at the beginning and it requires the dynamic behavior of the closed-loop control system that depends on three parameters: the initial condition value $y_{0_{i,ii}}$, the set point $y_{i,ii}^{sp}$, and the controller parameters $\Omega_{i,ii}^{(l)}$ (Chu and You (2012)). Moreover, it also depends on three numerical parameters: the tolerable bound width of steady output condition $b_{i,ii}$ [in %], sampling time T_s , and the prediction horizon $N_{MPC_{i,ii}}$ for MPC controller. Thus, $\bar{t}_{s_{i,ii}}^{(l)} = f(\Omega_{i,ii}^{(l)}, y_{i,ii}^{sp}, y_{0_{i,ii}}, b_{i,ii}, T_s, N_{MPC_{i,ii}})$. After minimizing this difference, we assign the optimal controller parameters $\Omega_{i,ii}^{(l)} \rightarrow \Omega_{i,ii}^{(l)*}$. Thus, we have the following set of controller parameters $\tilde{\Omega}_{i,ii}^{(l)} = \{\Omega_{i,ii}^{(1)*}, \dots, \Omega_{i,ii}^{(n_i)*}\}$. From the same calculation, we can also estimate the set of transition cost $\tilde{\delta}_{i,ii}^{(l)} = \{\delta_{i,ii}^{(1)}, \dots, \delta_{i,ii}^{(n_i)}\}$. This computation is part of Algorithm (1).

Data: Historical data, Closed-loop system dynamic model

Result: $u_{i,ii}^*(t)$

Get transition set: $\{\tilde{t}_{s_{i,ii}}^{(l)}, \tilde{\Omega}_{i,ii}^{(l)}, \tilde{\delta}_{i,ii}^{(l)}\} \leftarrow$ Execute simulation (Off-line computation) ;

$k = 1$;

while $k \leq$ the total amount of production cycles **do**

procedure: Execute selection algorithm for all units ii (see Tab. (1));

Identify the relation of $\{\tilde{t}_{s_{i,ii}}^{(l)}, \tilde{\delta}_{i,ii}^{(l)}\}$;

Get $\{t_{s_{i,ii}}^{(l)*}(k), \Omega_{i,ii}^{(l)*}(k)\}$;

Update (Integrated) MPL scheduling model (Eq. (3)): $t_{s_{i,ii}}^{(l)}(k) \leftarrow t_{s_{i,ii}}^{(l)*}(k)$;

Get $\check{u}_i^*(k) \leftarrow$ Solve Eq. (5);

Controller $\leftarrow \{\check{u}_i^*(k), \Omega_{i,ii}^{(l)*}(k)\}$;

Get $u_{i,ii}^*(t) \leftarrow$ Solve control problem from $t = \check{u}_i^*(k)$ to $t = \check{y}_i^*(k) - t_{ei,n_s}$;
 (i, n_s indicates the last unit in the production line i);

$k = k + 1$;

end

Algorithm 1: Sequential Decomposition Method

3. Integration of Scheduling and Control using MPL Systems

3.1. Batch scheduling problem

Batch scheduling problems typically have decision variables i.e. starting time. Currently, many scheduling problems are represented in the conventional algebra. This study focuses on the MPL scheduling problem called due date perishable goods which is a convex optimization problem (Schutter and van den Boom (2001)). If the due dates for the finished products are known, every difference between the due dates and the actual output time instants has to be penalized. Hence, the suitable cost criterion takes the following form: $J(k) = \otimes_{j=1}^{N_p} \otimes_{i=1}^{n_p} |\check{y}_i(k+j|k) - \check{r}_i(k+j|k)|$; where $\otimes_{q=1}^Q$ is equal to $\sum_{q=1}^Q$, N_p is the length of prediction horizon and \check{r} is the expected completion time. The standard

MPC for the MPL systems scheduling problem is introduced as follows:

$$\min_{\hat{\mathbf{u}}_i(k)} J(k) \quad (2)$$

where $\hat{\mathbf{u}}_i(k) = [\check{u}_i(k|k) \ \dots \ \check{u}_i(k+N_p|k)]^\top$ and Eq. (2) is subject to: MPL scheduling model shown in Eq. (1) and scheduling linear constraint for N_p horizon, time as a non-decreasing input, and starting time constraint regulation. A well-developed MPC theory for MPL system has also been introduced (Schutter and van den Boom (2001)). Moreover, the study of MPL convexity has been conducted.

3.2. Integrated scheduling model

In a stand-alone scheduling problem, the transition time is assumed to be '0'. The presence of transition time cannot be ignored; therefore, the decision variables of scheduling problem should cope with the existence of the transition time. The scheduling problem requires information of the reachable transition time from all control problems, while a control problem in each cycle needs the optimal transition time and the set-points. As an additional information, the control layer interacting with scheduling layer can be a local, a supervisory control or the combination of both.

For simplicity reasons, this study considers a single product that is manufactured cyclically in a processing unit for a certain processing time $t_{p_i,ii}$ so that the completion time of product satisfies the due date at every cycle given by the planning layer.

In MPL model, we can modify Eq.(1) to facilitate the existence of transition, filling time $t_{f_i,ii}$ and emptying time $t_{e_i,ii}$ and represent the integrated MPL scheduling model as follows, where the filling and emptying times are usually constant:

$$\check{x}_i(k) = \check{A}_i(t_{s_i,ii}^{(l)}) \otimes \check{x}_i(k-1) \oplus \check{B}_i(t_{s_i,ii}^{(l)}) \otimes \check{u}_i(k); \quad \check{y}_i(k) = \check{C}_i(t_{s_i,ii}^{(l)}) \otimes \check{x}_i(k) \quad (3)$$

To accommodate an economic objective, we introduce a total cost ω consisting of due date deviation penalty cost ω_1 , total production costs ω_2 , and total transition costs ω_3 related to $\delta_{i,ii}^l$. The relationship between $\tilde{t}_{s_i,ii}^{(l)}$ and $\tilde{\delta}_{i,ii}^{(l)}$ will define the approach to minimize ω .

$$\omega = \omega_1 \otimes \omega_2 \otimes \omega_3 \quad (4)$$

4. Proposed algorithms

By means of off-line computation explained in Section 2.2, we obtain a set containing achievable transition times, their associated controller parameters, and transition costs: $\{\tilde{t}_{s_i,ii}^{(l)}, \tilde{\Omega}_{i,ii}^{(l)}, \tilde{\delta}_{i,ii}^{(l)}\}$. In general, the integrated problem can be solved either sequentially or simultaneously. In this study, we utilize SDM, illustrated in Fig. (1) and described in Algorithm (1).

SDM consists of two steps in order to solve two main problems. The first problem is determining the element inside $\tilde{t}_{s_i,ii}^{(l)}$ leading to the most (economically) optimal result (see Eq. (4)) by selecting the associated controller parameters. The idea of selection algorithm which is described in Tab. (1) consist of three cases. The solution for case (#1) is Conventional Sequential Method (CSM) and (#2) is Integration Method (IM) proposed

$\tilde{\delta}_{i,ii}^{(l)}$ vs $\tilde{t}_{s_i,ii}^{(l)}$	(#1) Monotonically non-decreasing	(#2) Random	(#3) Monotonically non-increasing
Key appr.	$t_{s_i,ii}^{(l)*} \leftarrow t_{s_i,ii}^{(l)}$	$t_{s_i,ii}^{(l)*} \leftarrow t_{s_i,ii}^{(l)}$	$t_{s_i,ii}^{(l)*} (t_{s_i,ii}^{(n_l)}, \check{r}_i, y_i, t_{f_{i,ii}}, t_{p_{i,ii}}, t_{e_{i,ii}})$

Table 1: The key approach of selection algorithms: to determine the most economically optimal transition set based on the relation of $\tilde{\delta}_{i,ii}^{(l)}$ vs $\tilde{t}_{s_i,ii}^{(l)}$.

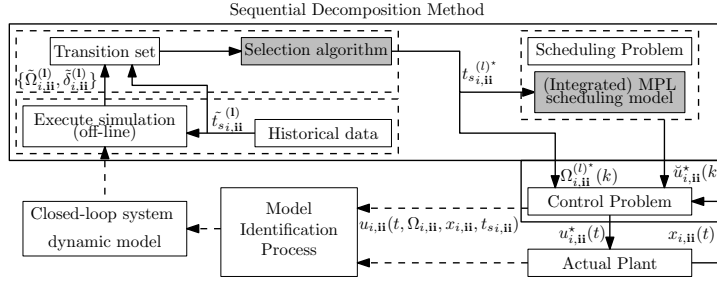


Figure 1: Illustration of SDM

in Chu and You (2012). Meanwhile, the solution for case (#3) is Constrained Deterministic Min-Max Method (CDM) inspired by Necoara et al. (2009) with some modifications incorporating threshold time to avoid penalty cost. Once we obtain the optimal transition time $t_{s_i,ii}^{(l)*}$ and its index $(l)^*$, we can determine the associated control parameters $\Omega_{i,ii}^{(l)*}$ required for the controllers.

The second problem is determining the scheduling policy that considers the information provided by the solutions of the first step. By utilizing the SDM, where we incorporate $t_{s_i,ii}^{(l)*}$ in the integrated MPL scheduling model (3), we preserve the convexity of the problem (see problem (2) as the integrated MPL scheduling problem (5)). Once we solve the integrated MPL scheduling problem, the (integrated) scheduling policy is determined.

$$\min_{\hat{\mathbf{u}}_i(k)} J(k) = \min_{\hat{\mathbf{u}}_i(k)} \bigotimes_{j=1}^{N_p} \bigotimes_{i=1}^{n_p} |\check{y}_i(k+j|k) - \check{r}_i(k+j|k)| \quad (5)$$

subject to (for details of notations, please see Schutter and van den Boom (2001)):

- Scheduling dynamic for N_p horizon: $\hat{\mathbf{y}}_i(k) = \mathcal{H}(\hat{t}_{s_i,ii}^{(l)*}) \otimes \hat{\mathbf{u}}_i(k) \oplus \mathcal{G}(\hat{t}_{s_i,ii}^{(l)*}) \otimes \check{x}_i(k)$
- Scheduling linear constraint for N_p horizon: $\mathcal{D}_i \hat{\mathbf{u}}_i(k) + \mathcal{F}_i \hat{\mathbf{y}}_i(k) \leq \hat{\mathbf{h}}_i(k)$
- Time as non-decreasing input: $\Delta \check{u}_i(k+j) \geq 0$ for $j = 0, \dots, N_p - 1$
- Starting time constraint regulation: $\Delta \check{u}_{i-} \leq \Delta \check{u}_i(k+j) \leq \Delta \check{u}_{i+}$

5. Case Study

We consider a simple case study, comprising a single processing unit of an input refinement problem for temperature control of a nonlinear chemical batch reactor. It is assumed that the reactor has a cooling jacket whose temperature is directly manipulated (Lee et al. (2000)). The control objective of this case study is to reach and control the reactor temperature at certain fixed set-point ($y^{sp} = 30^\circ\text{C}$) for a certain period ($t_p = 40$ sec) by means of

inlet coolant temperature. Moreover, the scheduling objective is that the heating process should be completed cyclically.

Fig. (2) shows the monotonically non-increasing relation between $\tilde{\delta}_{i,ii}^{(1)}$ and $\tilde{t}_{si,ii}^{(1)}$. In Fig. (3), the simulation result shows that the (integrated) MPL model requires less computation time than the traditional one in more accurate (frequent) sampling time, indicating similar result for longer processing time, $t_p \gg 40$ sec (even for less frequent sampling). Moreover, the MPL can be computationally efficient for a large-scale interconnected system. In terms of the performance, both MPL model and the traditional one yield the same trajectory. Unlike stand-alone model, Fig. (4) shows that the integrated MPL scheduling model is able to eliminate delay because it considers the transition time in the model.

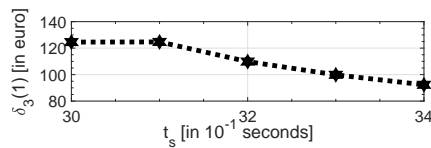


Figure 2: Monotonically non-increasing relation

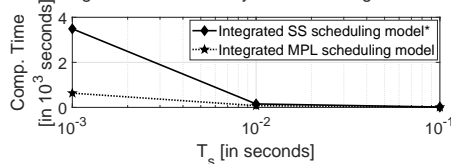


Figure 3: Computation time to solve integrated scheduling problem in different sampling time (T_s).

* refer to Subramanian et al. (2012).

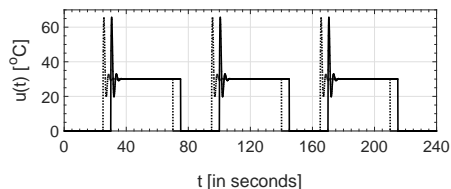
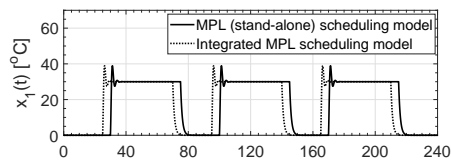


Figure 4: Trajectories performance; Due dates \rightarrow [76 146 216]

6. Conclusion

In this paper, a new formulation for an integrated scheduling and control problem using MPL representation is proposed. Based on this formulation, the SDM sets the optimal (integrated) scheduling policy. Finally, the proposed formulation and solution are tested in simulation on a temperature control and scheduling of a nonlinear chemical batch reactor. Future work could include incorporating uncertainties and capacity constraint, investigating simultaneous solution method and the extension to other type of scheduling problems.

References

- Y. Chu, F. You, 2012. Integration of scheduling and control with online closed-loop implementation: Fast computational strategy and large-scale global optimization algorithm. *Computers and Chemical Engineering* 47, 248 – 268.
- J. Lee, K. Lee, W. Kim, 2000. Model-based iterative learning control with a quadratic criterion for time-varying linear systems. *Automatica* 36, 641 – 657.
- I. Necoara, B. D. Schutter, T. van den Boom, H. Hellendoorn, 2009. Robust control of constrained max-plus-linear systems. *Int. J. robust and nonlinear control* 19, 218 – 242.
- B. D. Schutter, T. van den Boom, 2001. Model predictive control for max-plus-linear discrete event systems. *Automatica* 37, 1049 – 1056.
- K. Subramanian, C. Maravelias, J. Rawlings, 2012. A state-space model for chemical production scheduling. *Computers and Chemical Engineering* 47, 97 – 110.
- T. van den Boom, H. de Bruijn, B. D. Schutter, L. Özkan, 2018. The interaction between scheduling and control of semi-cyclic hybrid systems. *IFAC PapersOnLine* 51-7, 212 – 217.

Nonlinear dynamic analysis of chemical engineering processes described by differential-algebraic equations systems

Ataíde S. Andrade Neto^{a,*}, Argimiro R. Secchi^a and Príamo A. Melo^a

^a*Chemical Engineering Program, COPPE, Universidade Federal do Rio de Janeiro, Brazil*
ataide@peq.coppe.ufrj.br

Abstract

Chemical processes are subject to parametric variation due to, among others things, desired changes in process conditions, instrumentation malfunction or unpredicted disturbances. The outcome of these adversities is plural, the entire system may collapse or the output variables might not be affected at all. Thus, the theoretical analysis of processes prone to nonlinear responses plays a key role in design and operation of chemical plants either for safety or economic purposes. Because of the widespread use in the last couple decades of the differential-algebraic equations (DAE) approach in chemical processes modeling, the development of computational algorithms and tools specifically designed for the analysis of DAE systems becomes necessary, specially for high-index cases. In this work, we present a novel and index-free approach for the nonlinear dynamic analysis of mathematical models based on DAEs. A methodology for the direct detection of Hopf bifurcation points based on an optimization procedure, in which we rewrite the necessary condition for the Hopf bifurcation point occurrence as a constrained optimization problem was developed. In this approach, we do not compute the generalized eigenvalues of the system, but their Hurwitz determinants using a new algorithm for the computation of characteristic polynomials of matrix pencils based on the La Budde's method. The resulting optimization problem was solved with a hybrid global optimization technique, coupling particle swarm (PSA) and active-set (ASA) algorithms. The parametric continuation of steady-state branches was conducted with the pseudo arc-length method and the stability analysis based on the spectral theory for linear matrix pencils. As an illustrative example we evaluate the dynamic behavior of a reactive flash drum formulated as an index-2 DAE system. The results show that the proposed methodology can handle DAE systems of high index in a fast and accurate way.

Keywords: Hopf bifurcation, differential-algebraic equations, stability analysis.

1. Introduction

Since the advent of calculus, the mathematical modeling of dynamic physicochemical processes has been based on ordinary and partial differential equations, with a very few exceptions (notably, the works of Lagrange on constrained mechanics dated from 1788 and Kirchhoff on electric circuits from 1847). However, with the growing studies on the differential-algebraic equations systems, started in the early 1970s, and also because their vast applicability this paradigm has been changing. Several authors have already pointed out numerous advantages of working directly with DAE; but we reinforce that formulating differential-algebraic models in many practical applications occurs naturally, specially in chemical engineering, as thermodynamic and equilibrium constraints, which are all imposed by algebraic equations, may be directly incorporated in

the process modeling. Because of this feature, the DAE approach is largely exploited by the majority of dynamic simulation software used in the context of Computer Aided Process Engineering (CAPE).

Regarding the dynamic analysis of chemical processes, we can safely say that it is a well-developed field for systems governed by ordinary differential equations (ODE) or discrete maps, specially the bifurcation theory which contemplates the study of dynamic systems under variation in their evolution laws. From a historical point of view, it is possible to recognize the importance of the bifurcation theory developed for ODE as a fundamental tool for nonlinear analysis. Unfortunately, for systems described by DAE, the same is not true. Because it is a rather new topic compared to ODE systems, computational algorithms and tools specifically designed for DAE have not evolved so steadily yet. It is noticed, nevertheless, that some works in the literature have already addressed the bifurcation analysis for DAE systems using either classical algorithms for differential equations or extensions of them for index-1 systems (Clausbruch et al., 2006), which are far much simpler than high-index DAE.

Although it is possible to reduce some high-index DAE to index-1 systems, this can be a tedious error-prone procedure and, in many cases, the solution of the reduced system may significantly differ from that of the original problem due to the well-known drift-off effect. Additionally, Harney et al. (2013) showed that the stability analysis of the reduced system may not represent the stability of the higher-index system from which it is derived, often being necessary to apply some stabilization methodologies, which has been developed for DAEs in Hessenberg form of size 2.

Knowing beforehand the precise location where nonlinear phenomena, such as bifurcation points, occur is of great importance in real-life applications, as not only safety but also economic issues may be avoided. Also, because the DAE approach is the current paradigm in the theoretical analysis of chemical processes, computational methods that efficiently handle DAE systems becomes necessary. Driven by this, we present, in this work, a novel and index-free approach for the direct computation of Hopf bifurcation points (HBPs), without the necessity of applying index reduction algorithms or stabilization procedures.

2. Theoretical framework

2.1. Linearization of differential-algebraic equations systems

The core of bifurcation theory of nonlinear system inevitably falls back to the dynamic analysis of linear ones. Because of that, the fundamental question one may ask is if there exist a linearized DAE system with the same qualitative behavior around fixed points of its nonlinear counterpart. Reich (1995) proved that the existence of such systems depends on some conditions which will be presented in the sequence.

Consider the nonlinear index- ν DAE system in the fully implicit form

$$f(x(t), \dot{x}(t); p) = 0 \quad (1)$$

with $f: \mathbb{R}^n \times \mathbb{R}^n \times \mathbb{R}^m \mapsto \mathbb{R}^n$ and $p \in \mathbb{R}^m$ a vector of time-invariant parameters. A linearization of f around a fixed point x_e in the form

$$B(p)\dot{y}(t) = A(p)y(t) \quad (2)$$

where $A = \nabla_x f^T(x_e, 0; p)$, $B = \nabla_{\dot{x}} f^T(x_e, 0; p)$ and $y = x - x_e$, will exist only if the original DAE in Eq. (1) is regular (or solvable) and fulfill the following conditions:

$$\text{rank} [\nabla_{\dot{x}} f^T(x, \dot{x}; p)] = \text{constant for all } t \quad (3a)$$

$$\text{rank} [\nabla_x f^T(x_e, 0; p)] = n \quad (3b)$$

$$\text{rank} [\nabla_x g_V^T(x_e, 0; p)] = n \quad (3c)$$

in which $g_v(x, \dot{x}; p)$ is a derivative-array obtained by stacking the vector f with all the equations that arise in an index reduction procedure. According to Campbell (1995), those conditions are simple to evaluate and often observed in physical systems.

2.2. Stability in DAE systems

Several authors have shown that the stability of a linear DAE is closely related to the spectrum, $\sigma(A, B)$, of the matrix pair (A, B) as defined in Eq. (2) (see Reich (1995) for a detailed overview on this subject). The spectrum of a DAE have exactly n_d finite values; the other $n - n_d$ values is said to be at the infinity. Here, n_d represent the number of Dynamics Degree of Freedom (DDoF) and n the dimension of the system. If all the finite values in $\sigma(A, B)$ lie in the left complex half-plane, then, the fixed point is stable.

2.3. Detection of Hopf bifurcation points

Hopf bifurcation points can be detected by an indirect method by tracing a branch of steady state solutions of an ODE system, usually done by homotopy continuation methods, while monitoring the eigenvalues of Jacobian matrix at the fixed points. When a single pair of eigenvalues crosses the imaginary axis a trapping method, such as the bisection or the secant method, can be used to refine the HBP. This procedure, despite being effective and easily extended to handle DAE systems, has a high computational cost. Alternatively, HBPs can be calculated directly. The first successful algorithm for the direct computation of Hopf bifurcation points in ODE systems was presented by Griewank and Reddien (1983) by formulating a set of $3n + 2$ equations that algebraically determines these points. Later, Reich (1995) extended this algorithm to the DAE systems.

We present a different approach in which instead of an augmented algebraic system, we solve a constrained nonlinear optimization problem. The main advantage of this method is that we do not restrict the Hopf bifurcation points search to a single parameter of the model. In fact, our algorithm works for any number of parameters. Also, we do not compute the spectrum of the DAE system, but its $n_d - 1$ Hurwitz determinants, D_k .

The Hurwitz determinants can be calculated from the normalized characteristic polynomial:

$$P(\lambda; p) = \det(\lambda B - A) / \bar{a}_{n_d}(p) = a_0(p) + a_1(p)\lambda + a_2(p)\lambda^2 + \dots + \lambda^{n_d} \quad (4)$$

by building the Hurwitz matrix:

$$L(p) = \begin{bmatrix} a_1(p) & a_0(p) & 0 & \dots & 0 \\ a_3(p) & a_2(p) & a_1(p) & \dots & 0 \\ a_5(p) & a_4(p) & a_3(p) & \dots & 0 \\ \vdots & \vdots & \vdots & \ddots & \vdots \\ 0 & 0 & 0 & \dots & 1 \end{bmatrix} \quad (5)$$

then, evaluating its first $n_d - 1$ principal subdeterminants:

$$D_k(p) = \det(L_k) = \det \begin{bmatrix} l_{1,1} & \dots & l_{1,k} \\ \vdots & \ddots & \vdots \\ l_{k,1} & \dots & l_{k,k} \end{bmatrix} \quad (6)$$

where $a_i = \bar{a}_i / \bar{a}_{n_d}$ and $\bar{a}_i(p)$ are the coefficients of $\bar{P}(\lambda; p) = \det(\lambda B - A)$; $L \in \mathbb{R}^{n_d \times n_d}$, $L_k \in \mathbb{R}^{k \times k}$, $D_k \in \mathbb{R}$ and $k = 1, 2, 3, \dots, n_d - 1$.

Extending the theorem of Liu (1994) for DAE systems, a Hopf bifurcation point arises when:

$$a_0 > 0, D_1 > 0, D_2 > 0, \dots, D_{n_d-2} > 0, D_{n_d-1} = 0 \quad (7)$$

This allows us to formulate the following constrained optimization problem:

$$\begin{aligned} \min_{p \in \mathbb{P}^m, x \in \mathbb{R}^n} S(p) &= D_{n_d-1}^2 \quad \text{subject to:} \\ a_0 > 0, D_1 > 0, \dots, D_{n_d-2} > 0 & \quad (8) \\ f(x, \dot{x}; p) &= 0 \end{aligned}$$

where $\mathbb{P}^m \subseteq \mathbb{R}^m$ is a selected parametric space and $S: \mathbb{P}^m \mapsto \mathbb{R}$. The global minimum of this problem ($S(p) = 0$) is always a Hopf bifurcation point.

2.4. Characteristic polynomials of matrix pencils

A general matrix pair (A, B) can be decomposed by Householder reflections into the form $A = QHZ$ and $B = QTZ$ where Q and Z are orthogonal, H upper Hessenberg and T upper triangular $n \times n$ matrices. Then,

$$\lambda B - A = \lambda QTZ - QHZ \Rightarrow \lambda Q^T QTZZ^T - Q^T QHZZ^T = \lambda T - H \quad (9)$$

Solving $\det(\lambda T - H)$ is numerically more efficient than solving $\det(\lambda B - A)$, because it can be rapidly evaluated by the following recursion formula derived from the La Budde method (Rehman and Ipsen, 2011):

$$\bar{P}_i(\lambda; p) = (\gamma_i \lambda - \alpha_i) \bar{P}_{i-1}(\lambda; p) + \sum_{k=1}^{i-1} \left[(t_{i-k,i} \lambda - h_{i-k,i}) \bar{P}_{i-k-1}(\lambda; p) \prod_{m=i-k}^{i-1} \beta_m \right] \quad (10)$$

with $\bar{P}_0(\lambda; p) = 1$ and $\bar{P}_1(\lambda; p) = \gamma_1 \lambda - \alpha_1$; $i = 2, 3, \dots, n$. The coefficients α_i and β_i are, respectively, the diagonal and the subdiagonal of H ; γ_i the diagonal of T ; $t_{i,j}$ and $h_{i,j}$ are the (i, j) -elements of T and H ; $\bar{P}_n(\lambda; p) = \bar{P}(\lambda; p) = \det(\lambda T - H) = \det(\lambda B - A)$.

3. Results

In order to evaluate the proposed methodology, it was applied to a benchmark model in chemical engineering. Consider the index-2 system describing the chemical reaction $A \rightarrow B \rightarrow C$ conducted in reactive flash drum:

$$f(x, \dot{x}; p) = \begin{bmatrix} \dot{x}_A - x_{Af} + x_A \left[\ell + K_A \phi + D_{a1} \exp\left(\frac{-g_1}{u+1}\right) \right] \\ \dot{x}_B - x_{Bf} + x_B \left[\ell + K_B \phi + D_{a2} \exp\left(\frac{-g_2}{u+1}\right) \right] - x_A D_{a1} \exp\left(\frac{-g_1}{u+1}\right) \\ \dot{u} - 1 + u + \phi \delta - Q - H_1 D_{a1} x_A \exp\left(\frac{-g_1}{u+1}\right) - H_2 D_{a2} x_B \exp\left(\frac{-g_2}{u+1}\right) \\ K_A x_A + K_B x_B + K_C x_C - 1 \\ x_A + x_B + x_C - 1 \\ \ell + \phi - 1 \end{bmatrix} = 0 \quad (11)$$

where x_A , x_B and x_C are molar fractions, u the dimensionless temperature and ϕ and ℓ the vapor and liquid fractions; the vector of search parameters is $p^T = [D_{a1}, D_{a2}, g_1, g_2, \delta, Q, H_1, H_2]$. The feeding compositions x_{Af} and x_{Bf} were set to 0.8 and 0.2, respectively, and the equilibrium constants $K_i = P_i^{\text{sat}}/P_{\text{ref}}$. The saturation pressure was modeled by the Antoine equation

$$P_i^{\text{sat}} = \exp \left[\alpha_i + \frac{\beta_i}{(u+1)T_{\text{ref}} - \gamma_i} \right] \quad (12)$$

for some reference chemical species with the following parameters: $\alpha^T: [21.3, 23.2, 25.1]$; $\beta^T: [-2428.2, -3835.2, -6022.2]$; $\gamma^T = [35.4, 45.3, 25.3]$. The reference temperature and pressure were set to 298 K and 101,325 Pa.

The optimization problem in Eq. (8) for the model described by Eq. (11) was solved using a hybrid approach by coupling the particle swarm (PSA) and active-set (ASA) algorithms. The PSA was applied at the start of the optimization procedure until a predetermined value of the objective function was reached, $S(p_m) = \varepsilon_m$. Then, the ASA was called to refine the solution to $S(p_f) = \varepsilon_f$, where ε_f is a predefined tolerance. This technique can be more efficient and effective for non convex problems with high number of optimization variables. In Table 1, we present a comparison between the hybrid approach and the standalone algorithms in terms of number of successful attempts and spent computational time that support this assertion. All simulations were done with Matlab on a 8GB RAM, Intel CORE-i7 laptop running Linux. With the exception of the standalone ASA, the PSA and the hybrid approaches were able to attain the global minimum in every scenario.

An appropriated selection of \mathbb{P}^m is necessary for the success of the optimization. The vectors $L^T = [0, 0, 0, 0, 0, 0, 0, 0]$ and $U^T = [10, 10, 10, 10, 100, 10, 100, 100]$ represent feasible values for all the parameters, as they are dimensionless groupings resulting from the combination of physical properties and operating conditions, therefore, they were chosen to bound the set \mathbb{P}^m . As a result of the optimization problem, we found that a Hopf bifurcation point occurs at:

$$x^T = [0.2920, 0.3469, 0.0681, 0.7466, 0.3611, 0.2534]$$

$$p^T = [8.6807, 9.9707, 6.7821, 3.8784, 15.5261, 1.3430, 35.9778, 99.8517]$$

The periodic solutions arising at this HBP are stable, as can be seen in the phase diagram and the time series in Fig. 1. Another HBP was found at $Q = 2.1741$, using Q as the single search parameter while fixing all other parameters. In this case, the arising periodic solutions were found to be unstable.

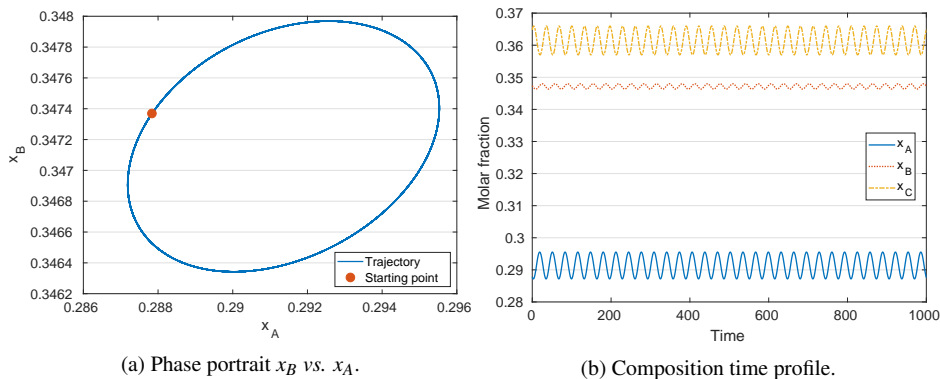


Figure 1: Simulation in the neighborhood of Hopf bifurcation point at $Q = 1.3430$, the stable case. Total simulation time $t = 1000$.

The pseudo arc-length method was applied in order to make the one-parameter steady-state continuation of the model in Eq. (11). The resulting bifurcation diagram of this procedure is presented in Fig. 2.

Table 1: Average performance of optimization algorithms[†].

Parameters	PSA ^{††}	ASA ^{††}	Hybrid ^{††}
all	129.0/4	-/10	12.1/0
D_{a1}, Q	53.1/0	1.9/0	13.6/0
D_{a1}, δ	56.6/0	1.9/0	12.9/0
Q	51.1/0	1.8/0	11.5/0

[†] $\varepsilon_m = 0.099$; $\varepsilon_f = 10^{-8}$; random initial guess;

^{††} Time (s) / Number of failures in 10 attempts.

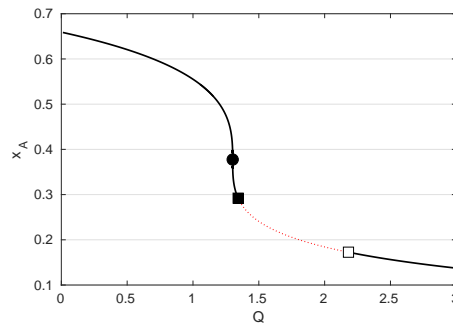


Figure 2: Bifurcation digram for the model in Eq. (11) using Q as the continuation parameter. Solid line: stable branch; dotted line: unstable branch; ■: HBP around stable periodic solutions; □: HBP around unstable periodic solutions; ●: bifurcation point.

4. Conclusion

A novel methodology for the direct computation of Hopf bifurcation points in differential-algebraic equations systems was presented. This strategy is based on the formulation of the constrained optimization problem in Eq. (8) with multiple search parameters. With the proposed methodology, we were able to find the occurrence of HBPs in a benchmark model with up to eight search parameters in a fast and accurate manner.

Acknowledgments

This work was supported by the National Council for Scientific and Technological Development (CNPq) grant numbers 302893/2013-0 and 152572/2016-3. This study was financed in part by the Coordenação de Aperfeiçoamento de Pessoal de Nível Superior - Brasil (CAPES) - Finance Code 001.

References

- K. E. Brenan, S. L. Campbell, L. R. Petzold, 1996. Numerical Solution of Initial-Value Problems in Differential-Algebraic Equations. Society for Industrial and Applied Mathematics (SIAM), Philadelphia, PA.
- S. L. Campbell, 1995. Linearization of daes along trajectories. *Zeitschrift für angewandte Mathematik und Physik ZAMP* 46 (1), 70–84.
- B. C. Clausbruch, E. C. Biscaia, P. A. Melo, 2006. Stability analysis of differential-algebraic equations in AUTO_DAE. Vol. 21 of *Computer Aided Chemical Engineering*. Elsevier, pp. 297 – 302.
- A. Griewank, G. Reddien, 1983. The calculation of hopf points by a direct method. *IMA Journal of Numerical Analysis* 3 (3), 295–303.
- D. Harney, T. Mills, N. Book, 2013. Numerical evaluation of the stability of stationary points of index-2 differential-algebraic equations: Applications to reactive flash and reactive distillation systems. *Computers & Chemical Engineering* 49, 61 – 69.
- I. Hyaneq, J. Zacca, F. Teymour, W. H. Ray, 1995. Dynamics and stability of polymerization process flow sheets. *Industrial & Engineering Chemistry Research* 34 (11), 3872–3877.
- W. Liu, 1994. Criterion of hopf bifurcations without using eigenvalues. *Journal of Mathematical Analysis and Applications* 182 (1), 250 – 256.
- M. Mangold, A. Kienle, E. Gilles, K. Mohl, 2000. Nonlinear computation in diva — methods and applications. *Chemical Engineering Science* 55 (2), 441 – 454.
- R. Rehman, I. C. F. Ipsen, 2011. La Budde’s Method for Computing Characteristic Polynomials. ArXiv e-prints.
- S. Reich, 1995. On the local qualitative behavior of differential-algebraic equations. *Circuits, Systems and Signal Processing* 14 (4), 427–443.
- B. Simeon, 2017. On the History of Differential-Algebraic Equations. Springer International Publishing, Cham, pp. 1–39.
- R. P. Soares, A. R. Secchi, 2005. Direct initialisation and solution of high-index DAE systems. Vol. 20 of *Computer Aided Chemical Engineering*. Elsevier, pp. 157 – 162.

Life Cycle Assessment of Petroleum Coke Gasification to Fischer-Tropsch Diesel

Ikenna J. Okeke, Thomas A. Adams II*

*Department of Chemical Engineering, McMaster University, 1280 Main St. W,
Hamilton, ON, Canada, L8S 4L8.*

tadams@mcmaster.ca

Abstract

This work presents a novel study on the life cycle assessment of Fischer-Tropsch diesel (FTD) production via petroleum coke (petcoke) gasification with and without carbon capture and sequestration (CCS). A detailed analysis which focuses on evaluating and quantifying the well-to-wheel (WTW) environmental impacts of converting petcoke to FTD and its subsequent combustion is discussed. The overall process inventory includes mass and energy balances data from our Aspen Plus model, the US Life Cycle Inventory Database, and the GREET model. Life cycle impact assessment (LCIA) categories of the petcoke-derived diesel (PDD) were calculated using TRACI 2.1 v1.04 in SimaPro 8.5.0.0 which is compared against both conventional petroleum and oil-sands derived diesel. In addition, two different plant locations in Canada (Alberta and Ontario) which respectively have very high and low electricity grid emissions were considered as they are representative of grid emissions across the world. Results of the analysis showed an overall reduction in fossil fuel depletion of up to 80% and 83% for Alberta and Ontario respectively when compared to the fossil derived diesel. When operated with CCS, the WTW GHG emissions were 7% lower than conventional petroleum diesel and 18% lower than oil-sands diesel for the plant located in Ontario. However, when located in Alberta, the WTW GHG emissions were 49% higher than conventional petroleum diesel and 30% higher than oil-sands diesel. This is due to the significant electricity requirement for the PDD process and the vast differences in carbon intensities of the Ontario and Alberta grids. Overall, the other impact categories for the PDD process showed to be significantly lower than the petroleum and oil-sand derived diesel.

Keywords: Petroleum coke, Fischer-Tropsch, Life cycle assessment, CO₂ Capture.

1. Introduction

Petroleum coke (“petcoke”) is regularly produced as a by-product of crude oil refining, especially from heavy crudes commonly produced in Canada. While some forms of petcoke are useful for steel making or other speciality purposes, it is often stockpiled in large quantities as a waste product. Although the stockpiled petcoke can be combusted for heat or electricity generation, it is more carbon intensive than coal, and this along with other environmental concerns makes combustion undesirable or even prohibited by government regulation. Hence, instead of the traditional stockpiling practice, petcoke can also be converted to liquid fuels both as a means of disposal and to help meet increasing fuels demand.

Recent studies have shown the technical and economic feasibility and the high fuel, energy, and carbon efficiencies of converting petcoke to chemicals and fuels (Salkuyeh et al. 2015, Okeke et al. 2018). Although several studies have presented the life cycle assessment (LCA) of other synthetic fuels processes such as gas-to-liquids (Forman et al. 2011), coal-to-liquids (Jaramillo et al. 2009), and biomass-to-liquids (Xie et al. 2011) processes, to the knowledge of the authors, no work has reported the LCA study of petcoke conversion to liquid fuels. Therefore, this study presents the first-of-a-kind detailed cradle-to-grave LCA of petcoke gasification to FTD so as to ascertain the environmental feasibility of this petcoke disposal approach.

2. Life cycle methodology and process description

2.1. Goal, scope, and boundaries

The goal of the LCA study is to evaluate the environmental impacts associated with the production of FTD from petcoke gasification operating with or without CCS. The scope covered in this analysis includes all the direct and indirect material and energy inputs with its associated output and emissions in the entire life cycle of the PDD process. The energy allocation method was employed for the distribution of emissions between diesel and gasoline fuels produced. Overall, the WTW system boundaries comprise of the cradle to plant exit gate emissions, the diesel fuel transportation and distribution (T&D), and the diesel combustion in a compression ignition direct injection (CIDI) vehicle as shown in Figure 1. The WTW inventory was normalized to 1 MJ_{PDD} combusted which is compared against conventional petroleum and oil-sands derived diesel (GREET, 2017). The impact categories considered were: ozone depletion potential (ODP), global warming potential (GWP), smog formation (SF), acidification potential (AP), eutrophication potential (EP), carcinogenic potential (CP), non-carcinogenic potential (NCP), respiratory effects (RE), ecotoxicity potential (ETP), and fossil fuel depletion (FFD).

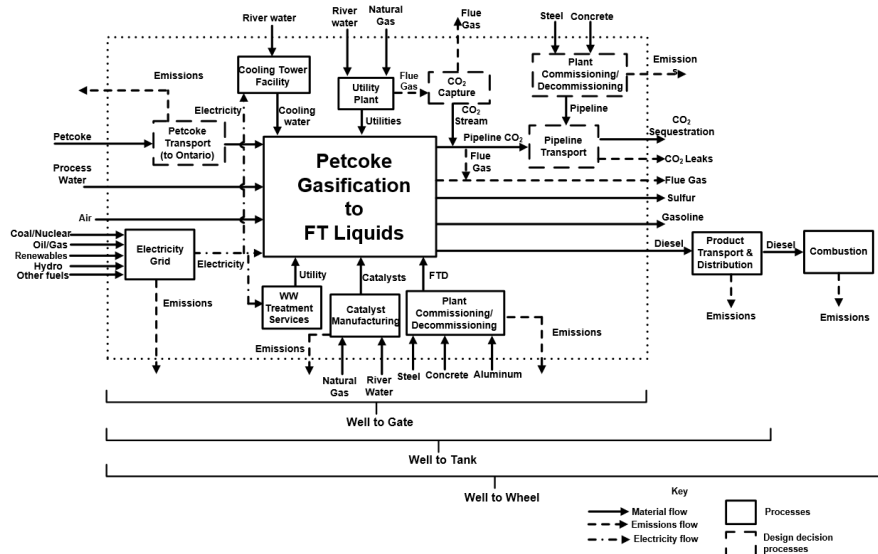


Figure 1: Complete WTW system boundary of the PSG designs studied

2.2. Process description

Figure 1 shows the system boundary for the WTW LCA of the PDD process which is based on our prior design (Okeke et al. 2018). Depending on the case, stockpiled petcoke at the refinery yard in Fort McMurry, Alberta is either directly sent to a petcoke standalone gasification (PSG) plant nearby, or, transported by train 3114 km to Sarnia, Ontario. The petcoke undergoes pre-processing prior to being fed to the petcoke E-gas gasifier operated with 99.5% pure oxygen from an air separation unit. Syngas is produced at 1426°C and 56 bar with the syngas cooling provided by boiler feed water sent through the radiant tubes, thereby, producing high-pressure steam (HPS).

The gasifier is designed for a carbon conversion of 99% (Amick 2000) while slag is collected which consists of unconverted carbon and trace metals such as nickel and vanadium (Basu 2006). An adiabatic water-quench saturation temperature of 200°C is employed to remove the entrained slag in the syngas while ammonia is removed from the syngas based on its high solubility in water to tolerable limits in order to avoid downstream catalyst deactivation (Pendyala et al. 2017). Water-gas shift and COS hydrolysis are employed to raise the H₂/CO ratio and convert COS to H₂S respectively.

Acid gases such as H₂S and CO₂ are removed from the syngas using the pre-combustion based MDEA solvent. The two-stage removal process is employed: H₂S removal in an H₂S absorber and CO₂ capture (for the CCS design) in a CO₂ absorber enhanced with piperazine. The absorbed H₂S is sent to the Claus unit for sulfur production while the captured CO₂ is compressed to 153 bar and sent via CO₂ pipeline to sequestration site. The minimum energy requirements for the overall system was determined by performing a heat exchanger network design (Okeke et al. 2018) of which all the required utilities and its associated emissions were considered.

FTD is produced by converting the syngas in a cobalt aluminium-based catalyst filled slurry reactor operating at 240°C and 30 bar. The slurry reactor design configuration consists of a once-through conversion of 80% CO and a chain growth probability, α , of 0.92. Up to 90% of the unconverted syngas was recycled to the FT reactor while the other portion is combusted primarily to produce HPS needed in the plant and the remaining HPS is sold. The boiler flue gas is emitted to the atmosphere which accounts for the direct process emission. The mass and energy balance results for the petcoke-to-liquids portion of the life cycle were determined and described in the prior work (Okeke et al. 2018) and incorporated within the present work. The system electricity demand is supplied from the local electricity grid, with the environmental impacts of the Alberta and Ontario grids considered (Environment and Climate Change Canada 2018).

Transportation of the PDD from the plant location to a bulk terminal for subsequent distribution to refueling stations was carried out using a combination of barge, pipeline, and rail for the transportation and truck for distribution based on the GREET model data (GREET, 2017). The subsequent combustion emissions of 1 MJ of PDD is evaluated in a CIDI vehicle with an assumed fuel consumption of 27.5 miles per gallon. In this analysis, we considered four cases, which were PSG plants with and without CCS, located either in Alberta or Ontario.

3. Results and discussion

Table 1 shows the plant gate-to-gate (GTG) process life cycle inventory of the PSG design with and without CCS. Both PSG processes were designed to consume the same amount of petcoke per FTD produced. However, a 27% increase in electrical consumption for the plant with CCS is observed due to the parasitic energy load of the CCS technology compared to the design without CCS.

Table 1. The total GTG life cycle inventory for the petcoke to diesel process.

Inventory	PSG-CCS	PSG
<i>Input flows (kg)</i>		
Petcoke	0.091	0.091
Petcoke transport, by train (t-km)	0.283	0.283
Catalyst, aluminium-based	6.11×10^{-5}	6.11×10^{-5}
Air	0.483	0.483
Process water	0.148	0.143
Cooling water, cooling tower	35.677	28.518
Waste water treatment (m ³)	1.81×10^{-4}	1.77×10^{-4}
LP steam generation (GJ)	5.67×10^{-4}	2.86×10^{-4}
MP steam generation (GJ)	-2.83×10^{-6}	-2.83×10^{-6}
HP steam generation (GJ)	-3.65×10^{-4}	-3.65×10^{-4}
Fired heat (GJ)	9.55×10^{-6}	9.55×10^{-6}
Electricity consumed (MW)	9.98×10^{-4}	7.88×10^{-5}
<i>Output flows (kg)</i>		
<i>Products flow (MJ)</i>		
Diesel	1	1
Gasoline	0.371	0.371
Sulfur (kg)	5.19×10^{-3}	5.2×10^{-3}
Sequestered CO ₂ (kg)	0.177	0
<i>Emissions flow (kg)</i>		
Carbon monoxide	0	8.06×10^{-5}
Carbon dioxide	7.09×10^{-3}	0.186
Water (g)	1.57×10^{-2}	1.65×10^{-2}
Argon	1.51×10^{-3}	1.52×10^{-3}
Nitrogen	6.32×10^{-2}	6.33×10^{-2}
Nitrogen oxides	8.92×10^{-6}	8.92×10^{-6}

Similarly, there is an approximately 50% and 20% reduction in heating and cooling water requirements when the plant is operated with no CCS. Comparing the direct emissions of both plants, the GHG emissions for the design with CCS were 71 tCO₂eq/MJ_{PDD} while the design without CCS emits up to 186 tCO₂eq/MJ_{PDD}. This amounts to a 162% increase in GWP and defeats the overall goal of alternative sources of fuel with reduced environmental impacts. Therefore, it can be concluded that it is not environmentally desirable to dispose petcoke by converting it to diesel without using CCS. The complete WTW environmental impacts of the PDD plants operating with or without CCS for the 2

locations studied compared against the conventional petroleum and oil-sands derived diesel with the oil-sands diesel as the reference process is shown in Figure 2.

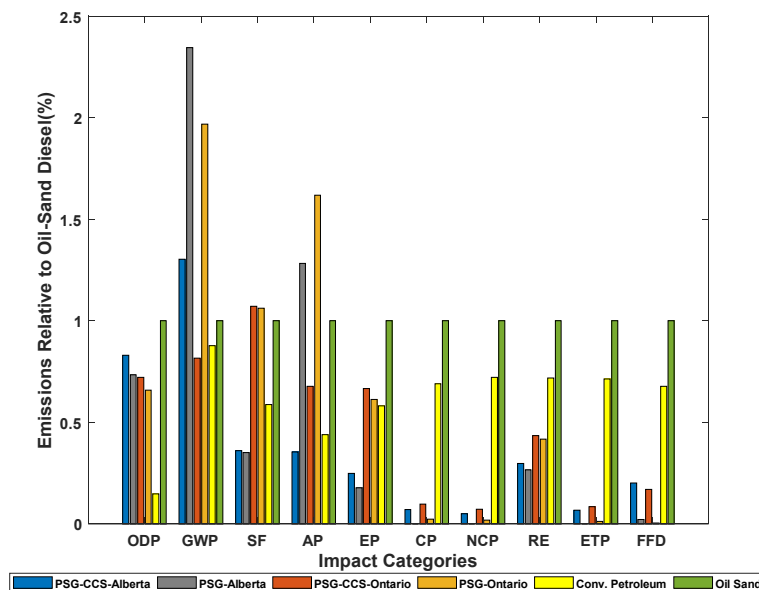


Figure 2: WTW life cycle impact categories relative to oil-sands derived diesel. The “Alberta” cases are cases where the PSG plant is located at the source of the petcoke stockpile. The “Ontario” cases indicate that the stockpiled petcoke is transported to Ontario for conversion. “Conv. Petroleum” is for diesel fuel from conventional oil.

Analyzing the performance of the plants when located in Alberta, it can be observed from Figure 2 that the GWP for the PSG plant with CCS is 49% and 30% higher than the petroleum and oil-sands derived diesel processes respectively. Such a huge GHG emission above the reference processes is due to the high carbon-intensive electricity grid in Alberta. Without CCS, the GHG emissions rises as high as 167% and 135% above the petroleum and oil-sands derived diesel respectively. Comparing the GWP of the plants when located in Alberta and Ontario, there is a significant 37% and 16% reduction in GHG emissions for the Ontario plants with and without CCS respectively. Furthermore, this Ontario plant showed up to 7% and 18% reductions in GHG emissions when operated with CCS compared to the conventional and oil-sands derived diesel plants respectively. When the economics (Okeke et al. 2018) and GHG emissions reductions of the PSG design operated with CCS are considered, there is an incentive in constructing the plant. Although the GWP is higher in Alberta, its SF, AP, EP, RE, and ETP are 66%, 48%, 63%, 32%, and 20% lower than that of the Ontario plant respectively. These increased impacts are linked to the train transit emissions during petcoke transportation to Ontario. It is noteworthy to mention that the impacts of ODP, CP, and NCP are not significant but were presented for completeness purposes and thus, not discussed. Finally, FFD at Alberta is 19% higher than in Ontario because of Alberta’s grid high dependence on fossil energy. However, its FFD is still 70% and 80% lower than that of the conventional petroleum and oil-sands derived diesel processes respectively.

4. Conclusions

A novel WTW study on the LCA of PDD operating with or without carbon capture at different locations in Canada was presented and compared against conventional petroleum and oil-sands derived diesel. It was found that the GHG emissions of the PSG with CCS plant at Alberta and Ontario were 137 and 86 tCO₂eq/MJ_{PDD} respectively. This implies that the plant can compete favorably with the status quo refinery GHG emission if its sited in locations with grid emissions like that of Ontario. Similarly, it is generally preferable to transport petcoke from Alberta to Ontario to take advantage of its lower grid carbon intensity than to gasify petcoke at the source in Alberta. Also, the extent of FFD for the design at Alberta and Ontario are between 70-80% and 75-83% lower compared to the conventional and oil-sands derived diesel respectively. Overall, it can be concluded that disposing petcoke via diesel production is an avenue to be considered when GHG emissions and FFD are a concern.

Although this work focused on the WTW LCA of petcoke only gasification operated with or without CCS, in our future work, we will explore the WTW environmental impacts of other designs such as combining petcoke gasification and natural gas reforming to FTD so as to ascertain the technology which has the most reduced impact on the eco-system.

5. Acknowledgments

Support for this research is made possible through funding from an NSERC Discovery grant (RGPIN-2016-06310).

References

- P. Amick, (2000), Gasification of petcoke using the e-gas technology at wabash river. 2000 Gasification Conference, Houston, Texas.
- P. Basu, (2006), Combustion and gasification in fluidized beds, CRC press.
- Environment and Climate Change Canada, (2018). "E-Tables-Electricity-Canada-Provinces-Territories." Retrieved 30-06-2018, from <http://data.ec.gc.ca/data/substances/monitor/national-and-provincial-territorial-greenhouse-gas-emission-tables/E-Tables-Electricity-Canada-Provinces-Territories/?lang=en>.
- G. S. Forman, T. E. Hahn, and S. D. Jensen, (2011), "Greenhouse gas emission evaluation of the GTL pathway." *Environmental science & technology* **45**(20): 9084-9092.
- Jaramillo, P., et al. (2009). "Greenhouse gas implications of using coal for transportation: Life cycle assessment of coal-to-liquids, plug-in hybrids, and hydrogen pathways." *Energy Policy* **37**(7): 2689-2695.
- I. J. Okeke and T. A. Adams II (2018), "Combining petroleum coke and natural gas for efficient liquid fuels production." *Energy*, 163, 426-442.
- V. R. R. Pendyala, W. D. Shafer, G. Jacobs, M. Martinelli, D. E. Sparks, and B. H. Davis, (2017), "Fischer–Tropsch synthesis: effect of ammonia on product selectivities for a Pt promoted Co/alumina catalyst." *RSC Advances* **7**(13): 7793-7800.
- Salkuyeh, Y. K. and T. A. Adams II (2015), "Integrated petroleum coke and natural gas polygeneration process with zero carbon emissions." *Energy* **91**: 479-490.
- X. Xie, M. Wang, and J. Han, (2011), "Assessment of fuel-cycle energy use and greenhouse gas emissions for Fischer–Tropsch diesel from coal and cellulosic biomass." *Environmental science & technology* **45**(7): 3047-3053.
- REET 2017, The Greenhouse Gases, Regulated Emissions, and Energy Use in Transportation Model. (available at: <http://reet.es.anl.gov/>)

Superstructure Optimization for the Production of Fuels, Fertilizers and Power using Biomass Gasification

Ahmed AlNouss,^{a,b} Gordon McKay,^b Tareq Al-Ansari^{b,*}

^aDepartment of Chemical Engineering, College of Engineering, Qatar University, Doha, Qatar

^bDivision of Sustainable Development, College of Science and Engineering, Hamad Bin Khalifa University, Qatar Foundation, Doha, Qatar

Abstract

The production of renewable fuels and decreasing the dependency on fossil fuels is an integral component of sustainable development.

As the production and utilization of petrochemicals represent an extremely important economic pillar of modern society, there exists an impetus to identify alternative routes of production in order to conserve finite resources. Furthermore, there is an additional necessity to utilize waste to produce value-added products in order to reduce greenhouse gas (GHG) emissions. Biomass, a CO₂ neutral energy source, serves as a potential basis for the production of fuels, which would have otherwise been produced from natural gas. The gasification of biomass produces a hydrogen-rich syngas, which can be utilized in the petrochemical industry to produce ammonia and methanol or processed through the Fischer-Tropsch synthesis to produce liquid fuels. In this study, the utilization strategy of biomass gasification feedstock for the poly-generation of different products is environmentally and economically evaluated. The potential production volumes of fuels and green chemicals are increased by the addition of multiple biomass sources, and thereby gaining potential positive scale effects, and by the optimization of the gasification process, in terms of operating conditions and feed blending to yield high-quality syngas. This forms a superstructure network of multiple biomass feedstocks (sources) and multiple potential applications (sinks) that can be optimized to yield the most economical and environmental-friendly production configuration. The base model developed is an oxygen-steam gasification process of different feedstocks available in the State of Qatar to generate H₂-rich syngas that is utilized in the production of value-added products: methanol, urea, power through integrated biomass gasification combined cycle (IBGCC) and Fischer-Tropsch liquids (FTL). The results of the optimization problem demonstrated the domination of urea generation with an overall net cost objective function of \$ 0.096 per kg of biomass input and an overall net emissions objective function of 0.83 kg of CO₂-e emitted per kg of biomass input. The manure based biomass is more suitable than sludge and date pits in the resulting optimum blending option for this utilization technique.

Keywords: Biomass Gasification, Sustainability, Optimization, Superstructure, Decision Making.

1. Introduction

Converting carbon-based wastes to valuable chemicals and energy through thermochemical conversion ranging from biomass and forestry residues to pet coke, have various advantages over conventional processes. Some of these advantages are the reduction of environment harmful emissions and the ability to produce electricity independently of an external power source (Mahinpey and Gomez, 2016). Biomass, waste or otherwise is a resource which can be processed into various chemicals and fuels. Biomass gasification (BG) is one process by which biomass can be converted into value added products, therefore mitigating polluting waste disposal strategies whilst simultaneously generating useful products such as bio-fuels, bio-char, syngas, power, heat, and fertilizer. Through the production of syngas, it creates flexible pathways by which advanced biofuels can be produced, e.g., methanol, di-methyl ether or Fischer-Tropsch diesel (Andersson, 2013). The high energy source feedstock into the BG process can include, wood waste, agricultural waste, municipal solid waste (MSW), sewage treatment waste, and food waste (Kumar and Shukla, 2016). BG technology can reduce the generated carbon to hydrogen (C/H) ratio resulting in a higher calorific value content and a favourable H₂ fraction. Syngas, the main product from BG consists of carbon monoxide (CO), hydrogen (H₂), methane (CH₄) and carbon dioxide (CO₂). It is an important element in the production of environment-friendly fuels and chemicals and in the generation of power. However, various types of contaminants are associated with syngas production such as tars, sulphur inorganic compounds, particulates and nitrogenous compounds. The properties and quality of the gasification product and its associated contaminants depend on the gasifying agent, feedstock material and dimensions, reactor conditions and design, presence of sorbent and catalyst (Sikarwar et al., 2016).

Anderson et al. evaluated a techno-economic analysis of methanol and ammonia production from BG and the co-gasification of pyrolysis oil and black liquor. The results demonstrated that the recovery of a bark boiler can be replaced by a biomass gasifier. This will improve the overall energy system efficiency and economic performance of green chemical production compared to the traditional mill operation (Andersson, 2013). Sara et al. carried out a techno-economic analysis on small scale biomass gasification and purification system for the production of hydrogen and power. A sensitivity analysis was conducted in order to study the effect of hydrogen production cost on capital cost, operating cost and process efficiency. The results indicated that costs cannot be reduced to a favourable level by only increasing the efficiency of the process unless the portable purification unit cost goes down (Sara et al., 2016). AlNouss et al. studied the utilization of multiple biomass sources to find the optimal blends for the generation of different value-added products. The objective was to maximize the production of syngas while constraining the H₂ to CO ratio with a specific application value. The results demonstrated a variation in the biomass blends for the different applications with a domination for date pits biomass in most cases (AlNouss et al., 2018). The literature is rich with other studies, which used similar pathways in identifying the top value added products generated from biomass. In this study, the utilisation strategy of biomass gasification for the poly-generation of different products is evaluated from economic and environmental perspectives to identify optimal poly-generation routes. An Aspen Plus model simulating oxygen-steam gasification technology is utilised to generate the optimal characteristics for each utilisation technique.

2. Model development

In order to efficiently utilize the biomass feedstock in a poly-generation system which produces value-added products, it is essential to use advanced system models. Hence, Aspen Plus software is utilized in this study to simulate the different generation technologies. An oxygen-steam gasification process is simulated in order to generate the optimal characteristics for each utilization technique. The optimization problem is built on the basis of superstructure representation with multiple biomass sources and multiple application sinks. The ultimate goal is to utilize the optimal blends of biomass feedstock in achieving optimal polygeneration routes of different utilization techniques as illustrated in Figure 1. The main focus of this study is the production of methanol, urea, power and Fischer-Tropsch liquids (FTL) from biomass.

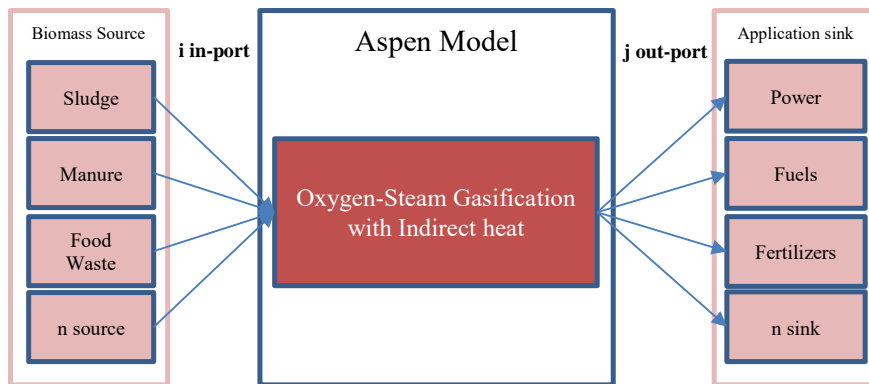


Figure 1: Superstructure representation of the biomass gasification to value added products

The first objective of the optimization problem is to maximize the production of syngas from the different biomass feedstocks, whilst constraining the specific H₂ to CO ratio of each generation technique. This was conducted partially by (AlNouss et al., 2018) and it is expanded here to capture the other optimization objectives. The H₂ to CO ratios considered the products are H₂:CO = 2 for Fischer-Tropsch liquids, H₂:CO = 3 for ammonia/urea, and (H₂ – CO₂):(CO+CO₂) = 2 for methanol. There is no specific ratio used for the generation of power through IBGCC. The formulation of the first objective function is presented in equations 1 and 2.

$$\text{Maximize} \quad \sum_{i=1}^n x_i * \text{Syngas} \quad \forall i \in \text{Biomass Sources} \quad \text{eq. (1)}$$

$$\text{Subject to} \quad \sum_{i=1}^n x_i = 1 \quad \& \quad \frac{y_{H_2+Syngas}}{y_{CO*Syngas}} = \text{Application unique} \quad \text{eq. (2)}$$

Where, Syngas is the molar flowrate of the generated H₂-rich synthesis gas, yH₂ & yCO are molar fractions of hydrogen and carbon monoxide and x is the blending fraction of each biomass feedstock.

The optimal biomass feedstock blends are then utilized in Aspen Plus to estimate the economic and environmental indicators of each utilization technique. The estimation is executed by means of the economic and energy activated analyses of Aspen Plus. These analyses are interfaces to the full software; Aspen Process Economic Analyser (APEA)

and Aspen Energy Analyser (AEA). The economic and environmental outputs are used in a multi-objective optimization problem with the aim of maximizing the economic benefit and minimizing the environmental impact for the poly-generation routes. Therefore, the second and third objective functions are formulated based on the net profit and net emissions of each utilization technique multiplied by the fraction of H₂-rich syngas produced, as illustrated in equations 3 through 5.

$$\text{Maximize} \quad \sum_{i=1}^4 x_i * \text{Net Profit}_i \quad \text{eq. (3)}$$

$$\text{Minimize} \quad \sum_{i=1}^4 x_i * \text{Net Emissions}_i \quad \text{eq. (4)}$$

$$\text{Subject to} \quad \sum_{i=1}^4 x_i = 1 \quad \text{eq. (5)}$$

Where x is the specific fraction of syngas and i is the index notation for each process from 1 to 4 according to table 1. The breakdown of the profit and emission equations are illustrated in Eq. 6 through 8.

$$\text{Net Profit}_i = \frac{\text{Revenue}_i - \text{TAC}_i}{(\text{Annual Biomass input})_i} \quad \text{eq. (6)}$$

$$\text{TAC}_i = \text{CC}_i \frac{i(1+i)^n}{(1+i)^n - 1} + \text{OC}_i \quad \text{eq. (7)}$$

$$\text{Net Emission}_i = \frac{(\text{Stream Emissions})_i + (\text{Utility Emissions})_i}{(\text{Hourly Biomass input})_i} \quad \text{eq. (8)}$$

Where, TAC is the total annualized cost, CC is the capital cost, OC is the operating cost, i is the interest rate evaluated as 20% and n is the project life evaluated as 20 years.

As the capacity of the biomass-based value added products is below the established infrastructure worldwide, therefore the upper limit was set to 1. For the minimum limit, the production capacity of each technique based on natural gas (NG) were collected and a fraction of each based on the total NG utilized in Qatar is generated as demonstrated in Table 1 (Alfadala and El-Halwagi, 2017). The results of the optimization problem is a Pareto front demonstrating the most attractive poly-generation route for the generation of value-added products.

Table 1: Fraction of maximum limit of each utilization technique

	MMTPY	Fraction
(1) Ammonia	3.8	0.032
(2) Methanol	1	0.0085
(3) FTL	0.04	0.00032
(4) Power	4.93	0.042
Total Fractions		0.083
Total NG	117.6	

Therefore, the limits of the specific fraction are summarized in equations 6 through 9.

$$0.032000 \leq x_1 \leq 1 \text{ for Ammonia production technique}$$

$$0.008520 \leq x_2 \leq 1 \text{ for Methanol production technique}$$

$$0.000032 \leq x_3 \leq 1 \text{ for Fischer-Tropsch liquids production technique}$$

$$0.042000 \leq x_4 \leq 1 \text{ for power generation technique}$$

3. Results and discussion

Considering that the biomass feedstock is optimized in order to determine the optimum blended feedstock. The results of the biomass feedstock blends optimization are illustrated in Figure 2. An economic and environmental evaluation is done to quantify capital cost, operating cost and revenue along with the environmental emissions from streams and utilities for the optimal feedstock blends, determined. Table 2 summarizes the main results from the evaluation.

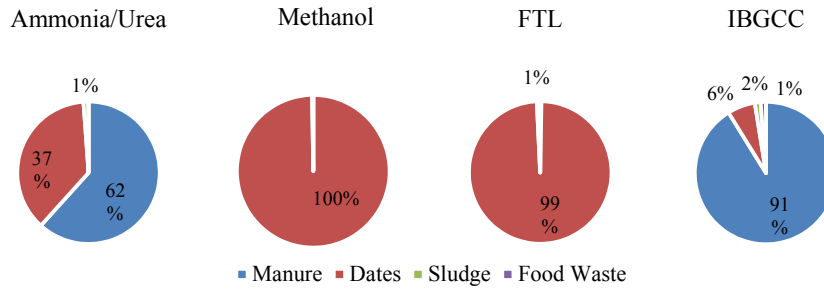


Figure 2: Biomass feedstock blending options for the different utilization techniques

The resulting optimized blends demonstrated a domination of date pits biomass for the methanol and liquid fuels options. Whereas, a domination of manure biomass is determined for the IBGCC alternative and 62:37 ratio of manure to date pits is accomplished for the ammonia/urea option. The economic and environmental results are used in a multi-objective optimization problem with the aim of maximizing the economic benefit and minimizing the environmental impact. The results of the optimization problem revealed the domination of ammonia/urea generation technique with around 95 % of the generation. The overall net cost objective function for the ammonia/urea production technique is \$ 0.096 per kg of biomass input and the overall net emissions objective function is 0.83 kg of CO₂-e emitted per kg of biomass input. The rest of the distribution indicated around 4% for the IBGCC power generation and around 1% for methanol production technique.

Table 2: Results of economic and environmental evaluation

	Ammonia/ Urea	Methanol	FTL	IBGCC
Total Capital Cost [\$]	2.4x10 ⁷	2.5x10 ⁷	1.9x10 ⁷	1.5x10 ⁸
Total Operating Cost [\$ /y]	9.7x10 ⁶	9.7x10 ⁶	6.0x10 ⁶	3.7x10 ⁷
Revenue [\$ /y]	5.2x10 ⁶	6.0x10 ⁶	3.0x10 ⁶	1.1x10 ⁷
Total Annualized [\$ /y]	1.5x10 ⁷	1.5x10 ⁷	9.8x10 ⁶	6.6x10 ⁷
Net Cost per Input [\$ /kg]	9.6x10 ⁻²	2.4x10 ⁻¹	4.5x10 ⁻¹	9.6x10 ⁻²
CO ₂ Emissions (Streams) [kgCO ₂ -e /h]	9.2x10 ³	6.8x10 ³	3.1x10 ³	6.8x10 ⁴
CO ₂ Emissions (Utilities) [kgCO ₂ -e /h]	8.3x10 ¹	9.8x10 ²	4.1x10 ²	4.6x10 ³
Total CO ₂ Emissions [kgCO ₂ -e/h] per input	8.3x10 ⁻¹	1.9x10 ⁰	2.0x10 ⁰	1.1x10 ⁰

The results can be plotted in a Pareto front curve in order to inform decision making regarding the optimum biomass utilization technique. The Pareto curve resulting from the optimization of the different utilization techniques is illustrated in Figure 3.

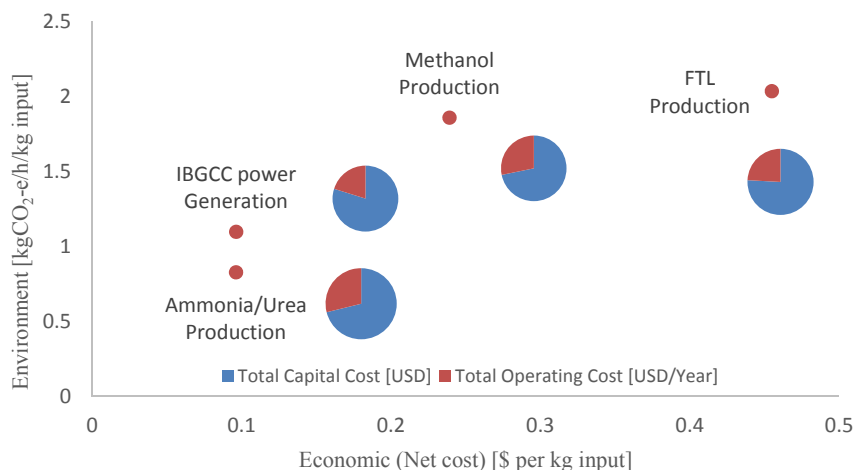


Figure 3: Pareto Curve of the optimization problem

4. Conclusions

The growing demand for global energy has motivated the utilization of renewable sources such as biomass in the generation of green fuels and chemicals. This study considers the development of a superstructure representation to capture the various biomass feedstocks and utilization techniques for the generated H₂-rich syngas through gasification. The results demonstrated the enhanced urea production as the most attractive technique in the poly-generation route.

Acknowledgment

The authors acknowledge the support of Qatar National Research Fund (QNRF) (a member of Qatar Foundation) by GSRA grant No GSRA4-1-0518-17082.

References

- A. AlNouss, G. McKay, and T. Al-Ansari, 2018, Optimum Utilization of Biomass for the Production of Power and Fuels using Gasification, *Computer Aided Chemical Engineering*, 43, 1481-86.
- J. Andersson, 2013, Techno-economic analysis of integrated biomass gasification for green chemical production, Luleå tekniska universitet.
- S. Kumar, and S. Shukla, 2016, A Review on Recent Gasification Methods for Biomethane Gas Production, *International Journal of Energy Engineering*, 6, 1A, 32-43.
- N. Mahinpey, and A. Gomez, 2016, Review of gasification fundamentals and new findings: Reactors, feedstock, and kinetic studies, *Chemical Engineering Science*, 148, 14-31.
- H.R. Sara, B. Enrico, V. Mauro, D.C. Andrea, and N. Vincenzo, 2016, Techno-economic Analysis of Hydrogen Production Using Biomass Gasification -A Small Scale Power Plant Study, *Energy Procedia*, 101, 806-13.
- V.S. Sikarwar, M. Zhao, P. Clough, J. Yao, X. Zhong, M.Z. Memon, N. Shah, E.J. Anthony, and P.S. Fennell, 2016, An overview of advances in biomass gasification, *Energy & Environmental Science*, 9, 10, 2939-77.

Parameter Estimation for Thermal Runaway of Li-ion cells: a Gaussian Process approach

Robert Milton^a, Peter Bugryniec^a and Solomon Brown^{a,*}

^a*Department of Chemical and Biological Engineering, University of Sheffield, Sheffield, S1 3JD, United Kingdom*
s.f.brown@sheffield.ac.uk

Abstract

Lithium ion (Li-ion) cells are the most prominent electrochemical energy storage device in today's world as they are utilised in many applications across many scales. However, Li-ion cells can suffer from a severe safety issue known as thermal runaway (TR). This process is due to exothermic chemical decomposition of a cell's components. Being able to understand and model this process is essential for the development of safer batteries. Lithium iron phosphate (LFP) cells are known to have the safest chemistry of Li-ion cells. However, TR models developed for LFP cells have not been validated and when compared to new experimental work are shown to be inaccurate. Hence, the development of an accurate and validated LFP TR model is the focus of present research.

Classical TR modelling of Li-ion cells utilises four Arrhenius equations to predict the reaction rate of these reactions and in turn the heat generated. However, the development of a TR model (via parameter estimation) is difficult due to 1) the large range some of the parameters of the Arrhenius equation can take i.e. several 10s order of magnitude between literature values for a given reaction, 2) the complex interaction between different parameters within an Arrhenius equation, and 3) the effect of the heat generated by each reaction on the others. Given this, direct minimisation of the root mean squared error (RMSE) between simulated and experimental results has proven to be difficult, with optimized parameters unable to represent important experimental features.

As such, an approach is developed in which the viable parameter space is defined and sampled using a pseudo-random sampling. The error of the heuristic fit (RMSE) is then emulated by a Gaussian Process, further refined by Global Sensitivity Analysis. The result is an emulator providing predictions (with attached uncertainties a part of the process) as a function of a reduced number of combined parameters. This is a reduction in model order achieved by a novel, optimal rotation of input basis.

Keywords: Li-ion, thermal runaway, Gaussian Processes, parameter estimation

1. Introduction

Lithium ion (Li-ion) cells are a prominent electrochemical energy storage device, being utilised in many applications across many scales from mobile phones, to electric vehicles and grid scale energy storage (Placke et al., 2017). However, Li-ion cells can suffer from a severe safety issue known as thermal runaway (TR) (Wang et al., 2012). The hazard of TR is one of an uncontrollable temperature rise of a cell, due to heat generation from the exothermic chemical decomposition of a cell's components (Melcher et al., 2016), that can lead to catastrophic failure and result in fire and explosion. Hence, understanding the TR process is essential for the development of safer batteries.

Significant research has gone into studying the safety of Li-ion cells of various chemistries under various abuse methods, which has shown that the Lithium iron phosphate (LFP) cathode is the safest (Liu et al., 2016; MacNeil et al., 2002). Additionally, much research has gone into modelling the TR of cells (e.g. Hatchard et al., 2001; Coman et al., 2017), as this is more cost effective and safer than iterating cell and battery design experimentally. Previous work utilises Accelerating Rate Calorimetry (ARC) to determine the initial reaction kinetics of the SEI and cathode reactions (Richard and Dahn, 1999a) and inverse modelling techniques for parameter estimation of reaction kinetics for cell components (Richard and Dahn, 1999b) and full cells (Ren et al., 2018; Liu et al., 2018). Ren et al. (2018) determine parameters values through Kissinger and nonlinear fitting methods of DSC data. Fundamental thermal abuse experiments of ARC, DSC and oven exposure are used to validate such models. However, TR models developed for LFP cells (Peng and Jiang, 2016) have not been validated and when compared to new experimental work (Bugryniec et al., 2018) are shown to be inaccurate. Hence, the development of an accurate and validated LFP TR model is the focus of present research.

The classical theory of TR attributes the heat generation to four chemical reactions, the solid electrolyte interphase, negative electrode, positive electrode and electrolyte reactions (Richard and Dahn, 1999a). The heat generation of these reactions is commonly modelled utilising Arrhenius equations (Hatchard et al., 2001), characterized by the activation energy, frequency factor and heat of reaction, which we refer to here as the “reaction parameters” (12 parameters in total, 3 for each of the 4 individual reactions). However, preliminary work has shown that direct minimisation of the root mean squared error (RMSE) between simulated and experimental results is difficult, with optimized parameters unable to represent important experimental features.

In order to address this, in this paper we develop an approach for estimating the parameters through the development of a Gaussian Process (GP) emulator. To increase the efficiency of the optimization the dimensionality reduction method is applied, which utilises both an appropriate kernel and a Global Sensitivity Analysis (GSA).

This work is organised as follows: Section 2 presents a description of the full model that is applied to simulate TR. Section 3 describes the approach to model order reduction using GPs and GSA, while Section 4 presents the application of this approach to estimating the parameters of TR in fully charged 18650 LFP cells. Section 5 presents the conclusions drawn.

2. Full Order Model

The full order model is constructed in *COMSOL Multiphysics 5.2a* (<https://uk.comsol.com/>) and simulates the thermal runaway behaviour of an 18650 LFP cell under an ARC heat-wait-seek (HWS) test. ARC is considered as it operates in such a manner that the cell experiences near adiabatic conditions. Hence, with no heat exchange to or from the ARC, the temperature rise of a cell is entirely due to self-heating and can be entirely attributed to the decomposition reactions, while the model can be simplified to a zero heat loss simulation, reducing the amount of uncertainty by eliminating the variable for heat transfer between the cell and its surroundings.

The cell is modelled by a 1 dimensional asymmetric line along the radius of the cell comprised of 102 finite elements. The geometry is simplified by considering the multilayer jelly roll (i.e. the electrodes, separators and current collectors) as a single homogeneous material with averaged thermo-physical properties. Heat transfer in the model assumes a solid body throughout and considers conduction within the cell and convection at the cell's surface. Convection is only considered during the HWS part of the ARC simulation, upon self-heating detection the heat transfer coefficient is set to zero to simulate adiabatic conditions.

The governing equations for the heat generated by the decomposition reactions follows that outlined by Kim et al. (2007). Wherein the rate of each reaction follows an Arrhenius relation, while

the power generated by each reaction is the product of the specific heat of reaction, specific weight and reaction rate. In this work, the model geometry simulates a single domain for the jelly roll, with each decomposition reaction applied over the entire jelly roll domain, there would result in an over-estimate of heat generated. As such, to take account of this fact, the heat generated by each decomposition equation is scaled by a factor equal to the proportion of jelly roll that the reaction actually occurs in.

3. Model Order Reduction

To describe the dependence of RMSE on the reaction parameters we adopt the notation

$$\begin{aligned} y &\propto \text{RMSE} \\ \mathbf{x} &\propto (A_{ne}, A_{pe}, E_{a,ne}, E_{a,pe}, H_{ne}, H_{pe}) \end{aligned} \quad (1)$$

where each variable is offset and scaled to have zero mean and unit variance. Without loss of generality RMSE is represented as the scalar response f to input vector \mathbf{x} plus independent noise e of zero mean

$$y(\mathbf{x}) = f(\mathbf{x}) + e \quad (2)$$

Our first assumption is that y and e are normally distributed at any fixed \mathbf{x} , rendering this model as a GP, which is a cheap and versatile emulator.

The significance of each input dimension to the GP is readily discerned by an Automated Relevance Determination (ARD) kernel. However, this restricts the orientation of relevant dimensions to the fixed axes of \mathbf{x} . As an alternative, we develop an approach employing the GP simply as an emulator facilitating global sensitivity analysis (GSA) via the Sobol' indices (Sobol', 2001). Using an arbitrary basis to calculate the Sobol' indices furnishes a very practical method for optimizing the rotation of input dimensions.

Essentially, optimization is then a two-stage process: 1) a GP emulator is optimized, then GSA using the emulator rotates the input basis; 2) this rotated basis is then used in a new emulator. Ultimately this yields an emulator that only significantly depends on a dimensionally reduced basis.

3.1. Gaussian Process Emulator

The emulator takes a $(1 \times M)$ row vector \mathbf{x} and returns a Gaussian random variable

$$y(\mathbf{x}) \sim \mathcal{N}[\tilde{f}(\mathbf{x}), \Sigma_y] \quad \text{where} \quad \tilde{f}(\mathbf{x}) = k(\mathbf{x}, \mathbf{X})(k(\mathbf{X}, \mathbf{X}) + \sigma_e^2 \mathbf{I})^{-1} \mathbf{y} =: \sigma_f^{-2} k(\mathbf{x}, \mathbf{X}) \tilde{\mathbf{y}} \quad (3)$$

whose mean $\tilde{f}(\mathbf{x})$ is learned from training data $\mathbf{y} = f(\mathbf{X}) + \mathbf{e}$. Standard Bayesian inference has been used to express the mean prediction in terms of the $(N \times 1)$ observed responses \mathbf{y} to $(N \times M)$ training inputs \mathbf{X} . At the heart of this lies the kernel function $k: \mathbb{R}^{I+M} \times \mathbb{R}^{J+M} \rightarrow \mathbb{R}^I \times \mathbb{R}^J$, expressing the correlation between responses to input samples of sizes $(I \times M)$ and $(J \times M)$. In this paper, of course, the number of input dimensions is $M = 6$ throughout. This work exclusively uses the ARD kernel (Wipf and Nagarajan, 2007):

$$k(\mathbf{x}', \mathbf{x}) := \sigma_f^2 \exp\left(-\frac{(\mathbf{x} - \mathbf{x}') \Lambda^{-2} (\mathbf{x} - \mathbf{x}')^\top}{2}\right) \quad (4)$$

where Λ is an $(M \times M)$ diagonal positive definite lengthscale matrix. The work which follows would be vastly complicated by any other kernel. However, this choice can be entirely justified from the assumption that the similarity function $k(\mathbf{x}', \mathbf{x})$ is differentiable at $\mathbf{x} = \mathbf{x}'$, together with original assumption that RMSE is normal (see Rasmussen and Williams, 2005, for further standard details).

3.2. Global Sensitivity Analysis

In this section an $(M \times 1)$ sample datum \mathbf{u} is drawn from a standardized normal test distribution

$$\mathbf{u} \sim \mathcal{N}[(\mathbf{0})_M, (\mathbf{I})_{M \times M}] \quad \text{where} \quad (\mathbf{I})_{M \times M} \text{ is the } (M \times M) \text{ identity matrix.} \quad (5)$$

This provides input to the emulator upon rotation by row orthogonal matrix Θ

$$\mathbf{x} := \mathbf{u}^\top \Theta \quad \text{eliciting response} \quad \tilde{f}(\mathbf{x}) = \tilde{f}(\mathbf{u}^\top \Theta) \quad (6)$$

GSA proceeds by conditioning on several fixed components of rotated input \mathbf{u} . The variance of $\tilde{f}(\mathbf{u}^\top \Theta)$ due to the first m components of \mathbf{u} is

$$D_{\mathbf{m}} := \mathbb{E} \left[\mathbb{E} [\tilde{f}(\mathbf{u}^\top \Theta) | (\mathbf{u})_{\mathbf{m}}]^2 \right] - \mathbb{E} [\tilde{f}(\mathbf{u}^\top \Theta)]^2 \quad (7)$$

The ARD kernel affords analytic expressions for these quantities, after some algebra. Firstly

$$\mathbb{E} [\tilde{f}(\mathbf{u}^\top \Theta)] = \mathbf{g} (\mathbf{1})_N \quad (8)$$

where $\mathbf{1}$ is a vector of ones, and \mathbf{g} is the $(1 \times N)$ (Θ -independent) row vector

$$\mathbf{g} := |\Lambda^{-2} + \mathbf{I}|^{-1/2} \sum_{n=1}^N (\tilde{\mathbf{y}})_n (\mathbf{I})_{n \times N} \exp \left(- \frac{(\mathbf{X})_{n \times M} (\Lambda^2 + \mathbf{I})^{-1} (\mathbf{X})_{n \times M}^\top}{2} \right) \quad (9)$$

the modulus of a matrix signifying, as usual, its determinant. Then

$$D_{\mathbf{m}} = \frac{\mathbf{g} \mathbf{W}_{\mathbf{m}} \mathbf{g}^\top}{|2(\Sigma)_{\mathbf{m} \times \mathbf{m}} - (\Sigma)_{\mathbf{m} \times \mathbf{m}}^2|^{1/2}} - \mathbf{g} (\mathbf{1})_{N \times N} \mathbf{g}^\top \quad (10)$$

where $\mathbf{W}_{\mathbf{m}}$ is the $(N \times N)$ symmetric matrix with components

$$\begin{aligned} (\mathbf{W}_{\mathbf{m}})_{n \times o} := & \exp \left(\frac{-(\mathbf{T})_{n \times \mathbf{m}} (\Sigma)_{\mathbf{m} \times \mathbf{m}}^{-1} (\mathbf{T})_{n \times \mathbf{m}}^\top - (\mathbf{T})_{o \times \mathbf{m}} (\Sigma)_{\mathbf{m} \times \mathbf{m}}^{-1} (\mathbf{T})_{o \times \mathbf{m}}^\top}{2} \right) \\ & \exp \left(\frac{+((\mathbf{T})_{n \times \mathbf{m}} + (\mathbf{T})_{o \times \mathbf{m}}) (\Phi)_{\mathbf{m} \times \mathbf{m}}^{-1} (\Sigma)_{\mathbf{m} \times \mathbf{m}}^{-1} ((\mathbf{T})_{n \times \mathbf{m}}^\top + (\mathbf{T})_{o \times \mathbf{m}}^\top)}{2} \right) \end{aligned} \quad (11)$$

and

$$\begin{aligned} \mathbf{T} &:= \mathbf{X} (\Lambda^2 + \mathbf{I})^{-1} \Theta^\top \\ \Sigma &:= \Theta (\Lambda^{-2} + \mathbf{I})^{-1} \Theta^\top \\ \Phi &:= \Theta (\Lambda^{-2} + \mathbf{I})^{-1} (2\Lambda^{-2} + \mathbf{I}) \Theta^\top \end{aligned} \quad (12)$$

These $D_{\mathbf{m}}$ are then maximized using gradient descent, for $m = 1, 2, \dots$ in turn.

4. Results

In this section, the methodology developed above is applied to the estimation of the reaction parameters described in Section 2 for experimental ARC data of fully charged 18650 LFP cells during HWS testing. In order to provide the input data for applying the GP approach the parameter space is sampled using a standard Latin hypercube method. These inputs are then filtered for simulations in which physically incorrect reaction initiation temperatures are obtained.

Optimization of the Sobol' indices via GPs reveals that two directions account for less than 0.15% of RMSE variance in total. There is also a clear principal direction, composed mainly of H_{pe} , which accounts for at least 35% of RMSE variance on its own. The variance is therefore (almost) entirely captured in four dimensions, which could potentially be reduced to just two dimensions by accepting some loss of fidelity.

The optimal two-dimensional parameter subspace is shown as a contour plot in Fig. 1, alongside the least relevant two-dimensional parameter subspace. Fragmentation or noise in these plots indicates uncaptured variance in RMSE. Ideally, the optimal subspace exhibits a smooth contour plot. By the Bayesian measure of fit (log likelihood), the Sobol' optimized GP model improves 19% over an unrotated ARD kernel, and 37% over the optimal isotropic one.

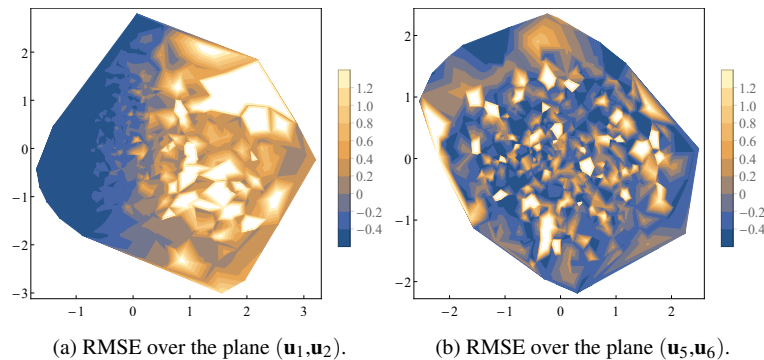


Figure 1: Contour plots of normalized RMSE over (a) the two most significant directions and (b) the two least significant directions.

A GP has been fit to the two most relevant directions ($\mathbf{u}_1, \mathbf{u}_2$) alone, selecting a somewhat regularized local optimum with noise variance of 0.36. This GP was searched for minimum predicted RMSE, and combined with mean values for the irrelevant coordinates to produce a set of optimal reaction parameters (ROM).

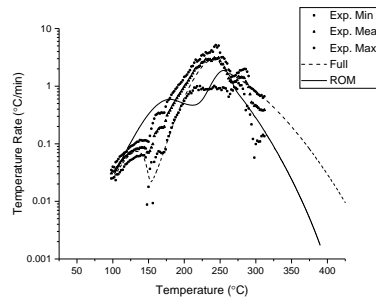


Figure 2: Comparison of predictions obtained with reaction parameters selected by reduced model (ROM) optimization, heuristic full model optimization, and experimental data.

Fig. 2 presents the variation of the temperature rate with temperature according to simulation and experiment. The reaction parameters used for simulation have been optimized by ROM, and independently by a costly heuristic full model optimization. Clearly the ROM optimized model is no substitute for full optimization at this stage, but it does lie within experimental range over most of the domain, and reflects the gross features of the experimental plots reasonably well.

5. Conclusions

In this work a GP approach for the estimation of reaction parameters for the simulation of thermal runaway in Li-ion batteries was presented. The method uses a GSA-based dimensionality reduction to increase the efficiency of the optimization process.

When applied to data obtained from the experimental testing of 18650 LFP cells, comparison of the reduced-dimension GP emulators showed that the difference in predictions between the four- and six-dimensional emulators was negligible. For optimization purposes nearly all the useful information resides in just two-dimensions. Future work will investigate less robust, but potentially more precise, high variance (low noise) GP solutions, and analyze the robustness of the reduced approach.

6. Acknowledgements

This work is financially supported by the Engineering and Physical Sciences Research Council (EPSRC) under grant number (EP/P026214/1) and in the form of the Energy Storage and its Applications Centre for Doctoral Training (EP/L016818/1).

References

- P. J. Bugryniec, J. N. Davidson, D. J. Cumming, S. F. Brown, 2018. Pursuing safer batteries: thermal abuse of lifepo₄ cells, manuscript submitted for publication.
- P. T. Coman, E. C. Darcy, C. T. Veje, R. E. White, 2017. Modelling Li-Ion Cell Thermal Runaway Triggered by an Internal Short Circuit Device Using an Efficiency Factor and Arrhenius Formulations. *Journal of The Electrochemical Society* 164 (4), A587–A593.
- T. D. Hatchard, D. D. MacNeil, A. Basu, J. R. Dahn, 2001. Thermal Model of Cylindrical and Prismatic Lithium-Ion Cells. *Journal of The Electrochemical Society* 148 (7), A755–A761.
- G. H. Kim, A. Pesaran, R. Spotnitz, 2007. A three-dimensional thermal abuse model for lithium-ion cells. *Journal of Power Sources* 170 (2), 476–489.
- X. Liu, Z. Wu, S. I. Stolarov, M. Denlinger, A. Masias, K. Snyder, 2016. Heat release during thermally-induced failure of a lithium ion battery: Impact of cathode composition. *Fire Safety Journal* 85, 10–22.
- X. Liu, Z. Wu, S. I. Stolarov, M. Denlinger, A. Masias, K. Snyder, 2018. A Thermo-Kinetic Model of Thermally-Induced Failure of a Lithium Ion Battery: Development, Validation and Application. *Journal of Electroanalytical Society* 165 (11), A2909–A2918.
- D. D. MacNeil, Z. Lu, Z. Chen, J. R. Dahn, 2002. A comparison of the electrode/electrolyte reaction at elevated temperatures for various Li-ion battery cathodes. *Journal of Power Sources* 108 (1-2), 8–14.
- A. Melcher, C. Ziebert, M. Rohde, H. J. Seifert, 2016. Modeling and simulation of the thermal runaway behavior of cylindrical Li-ion cells-computing of critical parameters. *Energies* 9 (4), 1–19.
- P. Peng, F. Jiang, 2016. Thermal safety of lithium-ion batteries with various cathode materials: A numerical study. *International Journal of Heat and Mass Transfer* 103, 1008–1016.
- T. Placke, R. Kloepsch, S. Dühnen, M. Winter, 2017. Lithium ion, lithium metal, and alternative rechargeable battery technologies: the odyssey for high energy density. *Journal of Solid State Electrochemistry* 21 (7), 1939–1964.
- C. E. Rasmussen, C. K. I. Williams, 2005. *Gaussian Processes for Machine Learning* (Adaptive Computation and Machine Learning series). The MIT Press.
- D. Ren, X. Liu, X. Feng, L. Lu, M. Ouyang, J. Li, X. He, 2018. Model-based thermal runaway prediction of lithium-ion batteries from kinetics analysis of cell components. *Applied Energy* 228, 633–644.
- M. N. Richard, J. R. Dahn, 1999a. Accelerating Rate Calorimetry Study on the Thermal Stability of Lithium Intercalated Graphite in Electrolyte I. Experimental. *Journal of The Electrochemical Society* 146 (6), 2068–2077.
- M. N. Richard, J. R. Dahn, 1999b. Accelerating Rate Calorimetry Study on the Thermal Stability of Lithium Intercalated Graphite in Electrolyte. II. Modeling the Results and Predicting Differential Scanning Calorimeter Curves. *Journal of The Electrochemical Society* 146 (6), 2078–2084.
- I. M. Sobol', 2001. Global sensitivity indices for nonlinear mathematical models and their monte carlo estimates. *Mathematics and Computers in Simulation* 55, 271–280.
- Q. Wang, P. Ping, X. Zhao, G. Chu, J. Sun, C. Chen, 2012. Thermal runaway caused fire and explosion of lithium ion battery. *Journal of Power Sources* 208, 210–224.
- D. Wipf, S. Nagarajan, 2007. A new view of automatic relevance determination. In: *Proceedings of the 20th International Conference on Neural Information Processing Systems. NIPS'07*. Curran Associates Inc., USA, pp. 1625–1632.

Techno-Economic-Environmental Study for Recovery of Novel Water Source within a Power Plant - Desalination Complex

Ahmed AlNouss, Fadwa Eljack *

*Department of Chemical Engineering, College of Engineering, Qatar University,
Doha, Qatar*

fadwa.eljack@qu.edu.qa

Abstract

The global water supply is at an already critical level; around 3.9 billion people (47% of the world population) will be subject to water stress in 2050, according to the Organization for Economic Co-operation and Development (OECD). Unless advanced and alternative technology solutions are applied, construction of desalination facilities will continue to rise, leading to higher CO₂ emissions. While desalination allows for the production of water from highly saline sources, it is considered an energy intensive process that is largely powered by fossil fuel sources. The natural interconnections between water and energy known as water-energy nexus has been widely recognized for desalination facilities; yet, there are tremendous amounts of cooling water that are still needed for condensing steam in the thermoelectric Rankine cycle to produce electricity; and large amounts of energy are typically required to transport and treat the water. For example, over 45 thousand cubic meter per hour of water are required to run a 500 MW power plant, for cooling and other process requirements. Moreover, large amounts of water vapour exit in the effluent flue gas from the combustion process. The amount of water that can be recovered from the flue gas is sufficient to substantially reduce the need for freshwater make-up. This represents a promising opportunity to exploit synergies among water and energy systems specifically for arid regions.

In this paper, the aim is to identify suitable water recovery (dehydration hybrid) technologies that are capable of maximizing the recovery of water from flue gas in gas fired power plant-desalination plant coupled system. Specifically, compression and cooling, quenching, membrane separation and absorption alternatives are studied. The capacity of the power plant, the capacity of the desalination plant, fuel consumption of the power plant and energy requirement of the desalination facility are known. This work studies the technical, environmental and economic competing objectives when integrating the dehydration hybrid technology within the desalination-power plant complex. In this paper, the results for all the considered alternatives will be presented in terms of water recovery, energy savings, emissions reduction and economic indicators. The integrated low pressure quenching water recovery alternative has shown promising results, with up to 42% water recovery, while the integrated low pressure absorption alternative has demonstrated the highest figure in energy savings and emissions reduction with around 37%. These results can aid the decision on the suitable water recovery alternative to be used in the integrated energy-water complex.

Keywords: Energy-Water Nexus, Desalination, Flue gas, Gas-fired power plant, Techno-Environmental-Economic Analysis.

1. Introduction

Fossil-based power plants consume vast quantities of water for heat rejection, fuel preparation, power augmentation, emissions control, and cycle makeup purposes. At the same time, global water resources are becoming scarcer especially in the arid areas which necessitates more efficient and inexpensive water production processes. Although dehydration is done extensively in natural gas processing, water recovery from power plant flue gas is a new concept. Liquid desiccant dehumidification can be used to remove 64-68% water from the flue of a coal fired power plant (Martin et al., 2016). Condensing boilers can be used in the coal fired power plant to recover water and almost 15% of energy (Chen et al., 2012). Thermal membrane condensers can be used to recover heat and water from flue gasses from coal fired power plant (Wang et al., 2012). Although water recovery from coal fired power plants have been studied, gas fired combined cycle power plants are yet to get significant attention. To offset these observed escalating consumption rates, a new system must be developed to meet partial water demand of power plants. Recovering substantial portion of the water vapour present in the flue gas can act as potential source of water. The recovered water is of a quality similar to the desalinated water from reverse osmosis (RO) systems. This water can be used for various plant needs as recovered or can receive minimal treatment so that it can be used as direct-cycle makeup (Copen et al., 2005). Recently, a simultaneous heat and water recovery from flue gas was experimentally studied using membrane condensation. Different operating parameters such as fluid flowrates and temperatures were tested against process performance (Zhao et al., 2017). The results from the study can potentially guide through optimising the operational performance of membrane condensation technology for water and heat recovery. Until the moment, all the power plants in Qatar use natural gas (NG) as source of fuel and all the power plants, except one, are coupled with desalination plants to reduce the heating requirement of the desalination plant. This set up gives an opportunity to integrate the available heat in flue gas to desalination plant. Apart from desalination plants, Qatar does not have an alternative source of fresh water. With a booming economy, the need for fresh water is increasing every day in Qatar. In 2013, 70.6 Million m³ of fresh water was consumed for industrial and domestic use in Qatar. Power plants in Qatar exhausts 30 Million m³ of water vapour every year. With proper design, this water can be captured and integrated with desalination plants to supplement fresh water production. In addition, the heat recovered from flue gas would be integrated with the desalination plant to reduce their economic implications and environmental impacts (TokyYasir, 2018).

The aforementioned preliminary studies have shown the feasibility of a technology to recover water from industrial gases as novel sources of water. Water from flue gas, if cost-effectively separated as fresh water, is expected to have major impact on overall fresh water generation and usage capacities in Qatar and the world. It can be reused for industrial and agricultural purposes. The water management strategies will enable encapsulating water sources from flue gas and desalination for integration. In an earlier study, (TokyYasir, 2018) examined a case of combined cycle power plant that uses both gas turbine and steam turbine to produce electricity to show the applicability of recovering water from flue gas. Specifically, compression and cooling, quenching, membrane separation and absorption alternatives are studied as potential technologies for flue gas dehydration. Detailed modelling and simulation using Aspen HYSYS V9 was done for the potential flue gas dehydration technologies. Each simulated process has multiple processing steps. For example, pressurized feed absorption has 3 steps:

compression, cooling, and absorption. Process simulation results were validated by comparison with published actual plant data in terms of energy demand. From this recent research project, a feasible source of fresh water was identified and a suitable technology was synthesized. Simulations showed that, by quenching almost 75% of the available water in the flue gas of a natural gas fired combined cycle power plant can be captured. By energy integration with a desalination plant, the energy demand for quenching was reduced by more than 50%. For further reduction in capital cost, the flow can be divided into multiple streams and other technologies like membrane filtration and adsorption can be tested in order to check for enhanced water capture to cost intensity ratio. The primary aim of this study is to valorise novel suitable water recovery technologies that are capable of maximizing the recovery of water from flue gas in gas fired power plant-desalination plant coupled system. The capacity of the power plant, the capacity of the desalination plant, fuel consumption of the power plant and energy requirement of the desalination plant are known. The study looks over the technical, environmental and economic competing objectives when integrating the dehydration hybrid technology within the desalination-power plant complex.

2. Model Development

Given the capacity of the desalination facility, its water and energy needs, the product specification or water properties, and the amount of available recovered water from hybrid dehydration technology, the aim is to develop a multi-objective optimization approach to assess the process performance targets and economic indicators. The developed optimization method and simulation track and assess the environmental impact due to the addition of the proposed hybrid water recovery technology/system. The developed tool provides flexibility in the design of water networks considering varying water quality feed, and varying objectives of utilizing the recovered water. The outcome of the presented tool is a two objectives diagram to help the decision maker in understanding the competing trade-offs in the integrated gas fired power plant/desalination plant/ and the studied water recovery technology.

The detailed simulations of the flue gas dehydration technologies using Aspen HYSYS V9 are integrated with gas fired power plant-desalination plant coupled system. Desalination process simulation models for multi-flash separation (MSF) and reverse osmosis (RO) membrane separation are considered for this study and are also developed using Aspen HYSYS along with the gas fired power plant. Figure 1 illustrates the overall configuration of the system. Each simulated process has multiple processing steps. For absorption, glycol package is used to dehydrate the flue gas stream from the power plant. The cooling alternative is a series of chiller coolers, expanders and two phase separators to recover the water from flue gas. Combining the cooling and absorption gives another alternative to be studied where the flue gas is first cooled, expanded and purified before entering the glycol absorption. Compression and cooling option adds a compression unit to the cooling system. Whereas the quenching alternative looks at recycling part of the water to the two phase separation unit to increase the separation. Finally, the membrane system utilizes the membrane unit extension modelled in Aspen HYSYS to purify the flue gas stream and recover its water content. The systems are tested under high and low operating pressures (LP and HP) to evaluate the impact on the performance of the dehydration alternative.

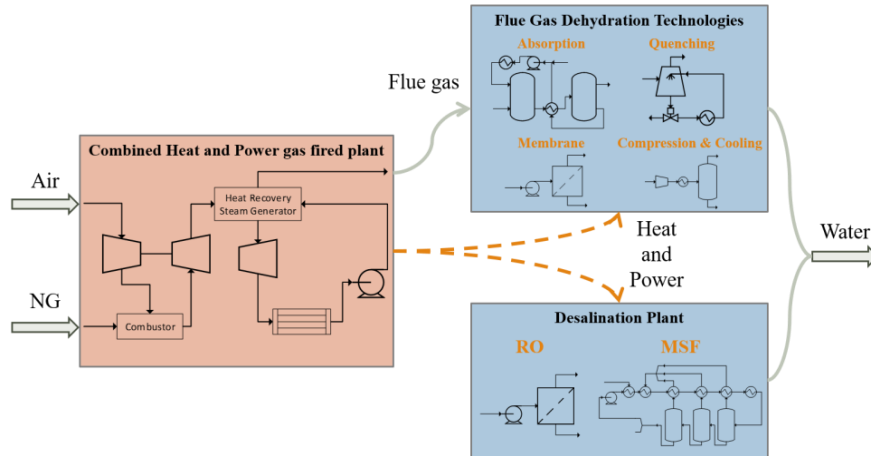


Figure 1: Overall configuration of the flue gas dehydration coupled with CHP-desalination plant
The main characteristics for the simulation models of the flue gas dehydration technologies and desalination plants are summarized in Tables 1.

Table 1: Main characteristics of the flue gas dehydration technologies and desalination plants

System	Water Recovery (%)	Water Purity (%)
LP absorption (1)	2.9	99.55
HP quenching (2)	37.9	99.95
LP quenching (3)	41.2	99.99
Compression and cooling (4)	29.9	99.99
HP cooling and absorption (5)	40.8	99.56
LP cooling and absorption (6)	38.8	99.95
Membrane separation (7)	29.4	99.91
RO desalination	15.8	99.88
MSF desalination	24.6	99.88

In addition, the characteristics of the combined heat and power (CHP) gas fired plant are highlighted in table 2.

Table 2: Main characteristics of combined heat and power (CHP) gas fired plant

CHP plant property	Value	Unit
NG feed (mainly methane)	8.3	kmol/s
Air feed (21% O ₂ , 79% N ₂)	79.4	kmol/s
Exhaust temperature	100	°C
Power generated	4.5	GW

After the simulation of the different flue gas dehydration configurations in Aspen HYSYS, the built-in activated economic analysis is utilized to quantify the capital and operating costs. In addition, the activated energy analysis capabilities of Aspen HYSYS are utilized to estimate the potential heat integration between the different units in the

integrated water-energy system along with the emissions of carbon dioxide equivalent. The different performance indicators are then optimized to generate a two objectives diagram of the different flue gas dehydration configurations emphasizing the environmental and economic performance. The objective of the optimization approach is to minimize the economic parameter estimated as the levelized cost of water (LCOW) expressed in Eq. (1), in addition to the environmental parameter estimated as the emissions of carbon dioxide equivalent expressed in Eq. (3).

$$LCOW \left(\frac{\$}{m^3} \right) = \frac{(Capital\ Cost \cdot CRF) + Operating\ Cost}{rate\ of\ water\ recovery \cdot operating\ hours} \quad \text{Equation (1)}$$

Taking the discount rate (r) equal to 20% and plant useful life (n) equal to 25 years,

$$CO_2\ emission\ rate\ in\ [CO_2 - e] = Q\ EF\ \eta\ GWP \quad \text{Equation (2)}$$

Where, CRF is the capital recovery factor calculated in Eq. (3), Q is the energy calculated for each utility type (energy per time), EF is the emission factor associated with each utility type (kg CO₂ per energy), η is the CO₂ energy source efficiency factor associated with each utility type, and GWP is the global warming potential of CO₂ considered to be 1 on this study. The annual operating hours considered for this study are 8760.

$$CRF = \frac{r(1+r)^n}{[(1+r)^n]-1} \quad \text{Equation (3)}$$

3. Results

The results for all the considered alternatives are presented in terms of energy savings, emissions reduction and economic indicators. Figure 2 illustrates the energy savings across the heat integration for each of the integrated flue gas dehydration system. The figure indicates a higher saving for the alternatives containing the MSF desalination plant compared to the RO ones. Nevertheless, the overall costs associated with MSF is double that of RO. The low pressure absorption option coupled with CHP and MSF units demonstrates the highest percentage of saving among the different alternatives with around 37%.

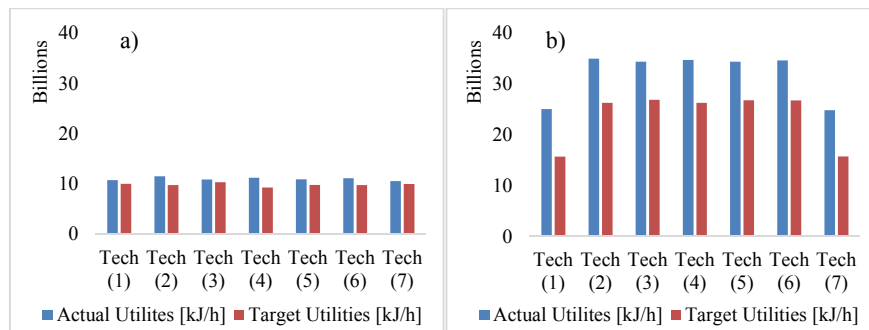


Figure 2: Energy savings among the different flue gas dehydration systems coupled with CHP for a) RO and b) MSF options

The ultimate outcome of the developed tool is a two objectives diagram to help the decision maker in understanding the competing trade-offs in the integrated gas fired power plant/desalination plant/ and the studied water recovery technology. Figure 3 illustrates the resulting economic-environmental diagram for the different integrated

flue gas dehydration systems. It can be concluded from the figure that the alternatives with RO units have lower emissions compared to the ones using MSF units. In particular, the low pressure absorption and cooling alternative demonstrated the lowest LCOW with around 0.27 $\$/\text{m}^3$ and 5.45×10^5 kg/h in terms of $\text{CO}_2\text{-e}$. Whereas, the compression and cooling alternative demonstrated the lowest emissions in terms of $\text{CO}_2\text{-e}$ with around 5.19×10^5 kg/h and 0.38 $\$/\text{m}^3$ in terms of LCOW.

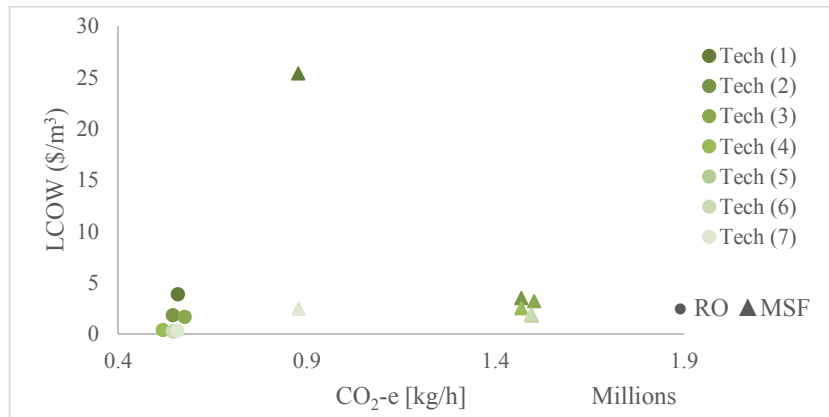


Figure 3: Economic-environmental results for the different flue gas dehydration systems coupled with CHP and RO or MSF

4. Conclusions

Water recovery from flue gas can have a major impact on overall fresh water generation and usage capacities in Qatar and the world. This study examined the techno-economic-environmental evaluation of different flue gas dehydration alternatives when integrated with gas fired power plant-desalination plant coupled system. The generated economic-environmental diagram demonstrated a much lower environmental impact for the options utilizing RO unit.

Acknowledgment

The authors acknowledge the support of Qatar University by the internal grant No QUCD-CENG-2018-2.

References

- Q. Chen, K. Finney, H. Li, X. Zhang, J. Zhou, V. Sharifi, and J. Swithenbank, 2012, Condensing boiler applications in the process industry, *Applied Energy*, 89, 1, 30-36.
- J. Copen, T. Sullivan, and B. Folkedahl, 2005, Principles of flue gas water recovery system,
- C.L. Martin, B.C. Folkedahl, D.J. Dunham, and J.P. Kay, 2016, Application of liquid desiccant dehumidification to amine-based carbon capture systems, *International Journal of Greenhouse Gas Control*, 54, 557-65.
- A. TokyYasir, 2018, Techno-Economic and Environmental Performance of Water Capture Technologies for Gas Fired Power Plants in Qatar, Qatar University.
- D. Wang, A. Bao, W. Kunc, and W. Liss, 2012, Coal power plant flue gas waste heat and water recovery, *Applied Energy*, 91, 1, 341-48.
- S. Zhao, S. Yan, D.K. Wang, Y. Wei, H. Qi, T. Wu, and P.H.M. Feron, 2017, Simultaneous heat and water recovery from flue gas by membrane condensation: Experimental investigation, *Applied Thermal Engineering*, 113, Supplement C, 843-50.

Molecular tracking: A novel approach for multicomponent distillation column design

Nima Nazemzadeh^a, Isuru A. Udugama^b, Michael A. Taube^c, Jens Abildskov^b,
Seyed Soheil Mansouri^{b,*}

^a*Department of Chemistry, Materials and Chemical Engineering “G. Natta”, Politecnico di Milano, Piazza Leonardo da Vinci 32, 20133 Milano, Italy*

^b*Process Systems Engineering Research Centre, Chemical and Biochemical Engineering Department, Technical University of Denmark, DK-2800 Lyngby, Denmark*

^c*S&D Consulting LLC, 1227 Jackson Blvd, Houston Texas 77006, USA*
seso@kt.dtu.dk

Abstract

This paper proposes a new systematic methodology to design a distillation column with middle products (side-draw) for ideal ternary mixtures, where the middle boiling component is present at trace concentrations. The method uses a molecular tracking concept, which uses a probability function based on the thermodynamic properties of the system. The probability function expresses the possibility of upward/downward movement of a single molecule on a tray inside a column. The advantage of this method compared to other existing methods is in its capability to quickly and efficiently provide a feasible solution without relying on rigorous optimization or trial/error approaches. In addition, the inherently graphical nature of the methodology allows engineers to get an intuitive understanding of the movement of the often-complicated middle product. The methodology is demonstrated on an ideal ternary mixture of benzene and p-xylene with toluene as the trace middle boiler, where the results obtained through the molecular tracking were validated against a rigorous process simulation.

Keywords: molecular tracking, side-draw distillation, design, multi-component distillation

1. Introduction

Separation of mixtures through distillation is an established practice in many industries from petrochemicals to bio-manufacturing processes. Despite being the standard-choice for many separations, distillation typically consumes about 60 % of total required energy of chemical industries (Ma et al. 2018). Nonetheless, distillation contributes to about 3% of the total U.S national energy consumption (Seader et al., 1999). As a result, both industrial and academic practitioners have invested considerable efforts in reducing the amount of energy required to operate these units (Kraller et al., 2016), one avenue of which has been the process intensification route. One simple forms of distillation intensification at the unit operation level and in presence of trace component in the system is the replacement of sequential distillation columns by using a single side-draw distillation column. The parametric study in industrial distillation carried out by (Tedder et al., 1978) asserts that for all ternary mixtures where a low middle product purity is acceptable, a side-draw distillation should be considered as one of the possible

configurations. Early stage design of distillation columns with side-draw is challenging due to lack of a simple and reliable method to efficiently obtain the (near) optimal feed and side draw locations. Today, side draw distillation columns are designed by either a trial/error or rigorous mathematical formulation, both of which are time consuming and resource intensive endeavors. This work attempts to address this through a systematic design methodology with integration of several concepts and tools including molecular tracking at its core.

2. Molecular tracking

Molecular tracking is a probability-based concept, based on the thermodynamic properties of the system. The concept evaluates the probability of a single molecule to move upwards into the vapor phase or downward into the liquid phase at a given stage of a column. The mixture existing on each stage of a distillation unit splits into vapor and liquid flows with specific vapor and liquid concentrations. The liquid moves downward to the lower tray and the vapor moves upward to the upper tray. Hence, in order to evaluate the molecules probability of moving upward or downward, the function has to be defined over the flowrates of every component on each stage. The probability function as shown in Eq. (1) can be derived (Maat, 2017). The function is defined as the ratio between the existing vapor flowrate of a component over the total outlet flowrate of the same component as expressed below:

$$\beta_i^n = \frac{y_i^n V_i^n}{y_i^n V_i^n + x_i^n L_i^n} \quad (1)$$

Here, β is the probability function, x and y are liquid and vapor compositions respectively. The variables L and V are liquid and vapor internal molar flows and i denotes the component and n is the stage number inside the column.

In molecular tracking concept, a single molecule (typically of the middle key) is tracked from the moment it enters the feed tray by comparing the output of a random number generator function with the calculated system probability value from Eq. (1). If the random number lies within the range $(0, \beta_i^n)$ the molecule is considered to have moved to the vapor phase and hence up to the stage above. This operation is repeated until the molecule leaves the column from one of the outlet streams. Figure (1) illustrates the concept of molecular tracking applied to the heavy key, light key as well as the middle boiling components. As shown in the figure, the light key component has a tendency to move directly towards the top of the column while the heavy key component has a tendency to move directly towards the bottom of the column. However, the middle boiling trace component tends to spend several steps in the middle of the column before eventually exiting the column. From a thermodynamic point of view, the tray with maximum number of hits for the middle boiling component identifies the most probable location for the side-draw as this is the location where the probability of the middle boiling molecules travelling with the vapor or liquid phases is the same (i.e. β of middle boiling component is 50%)

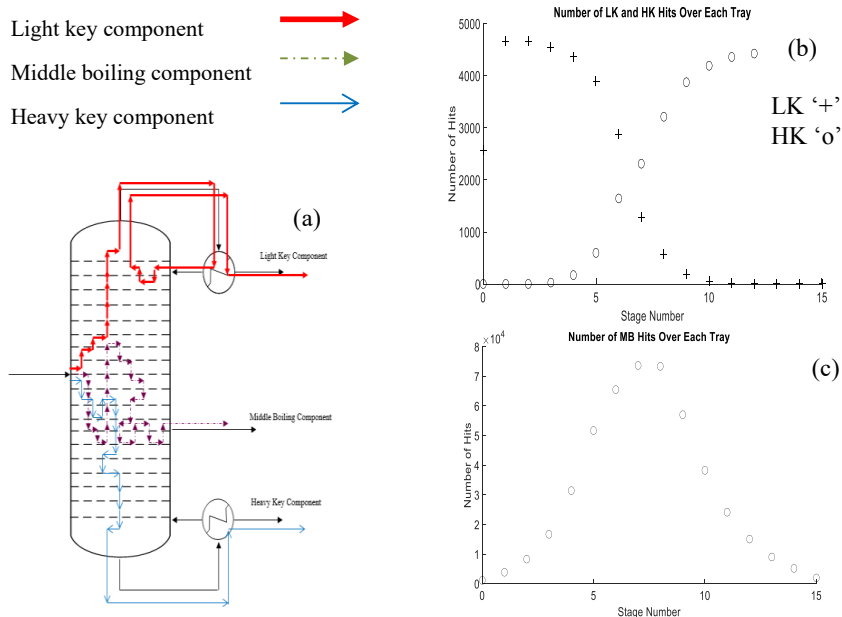


Figure 1: (a) Schematic of a side-draw distillation column with representative molecular pathways, (b) Number of hits of light key and heavy key components, (c) Number of hits of trace component versus stage number

3. Systematic design methodology based on molecular tracking

Here, a systematic hierarchical framework for designing a side-draw distillation column for a ternary mixture, with a middle boiling component at infinite dilution is proposed. In this methodology, the information of a distillation process for the hypothetical binary mixture of key components is used to design the side-draw column for the real mixture. In this work, the design methodology is presented systematically in Figure (2), and the corresponding case study is illustrated in the next section.

Methodology This methodology determines the number of stages, feed and side-draw location based on the specifications of the system. Specifications required to design the column are light key component purity in distillate and heavy key component purity in bottom stream. The reflux ratio of the final configuration of the column is implicitly calculated when the column model is solved.

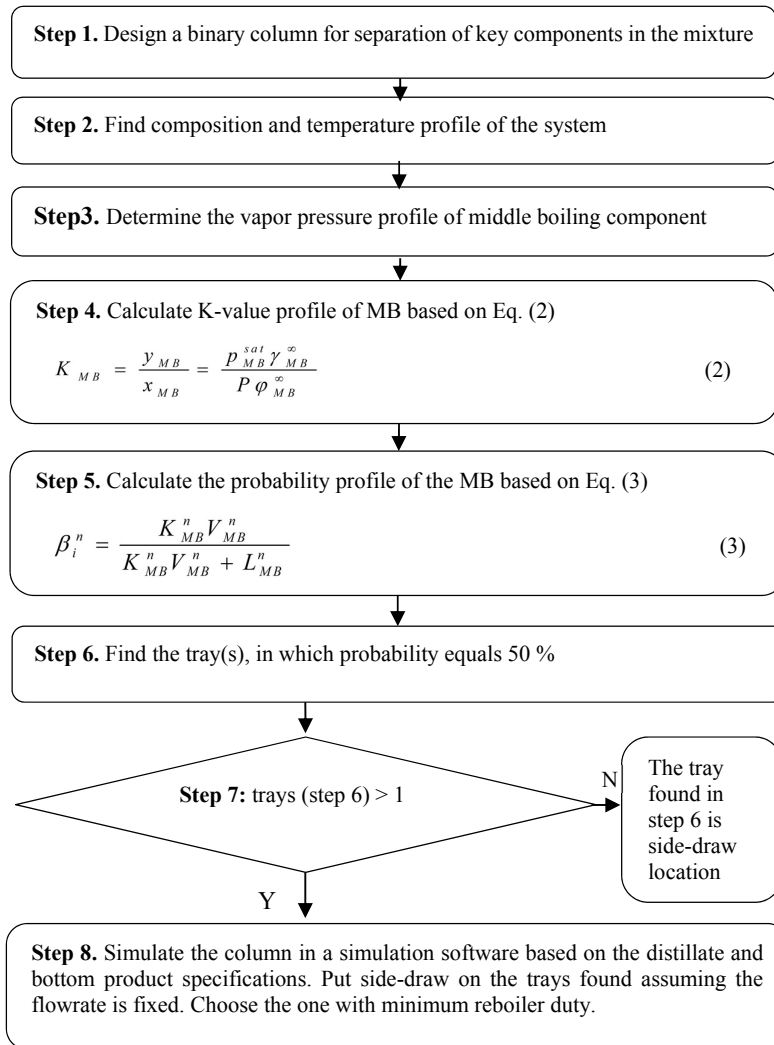
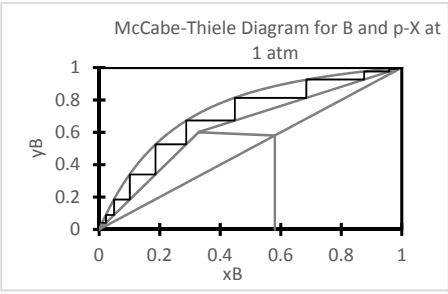
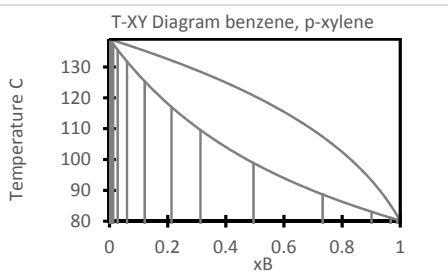
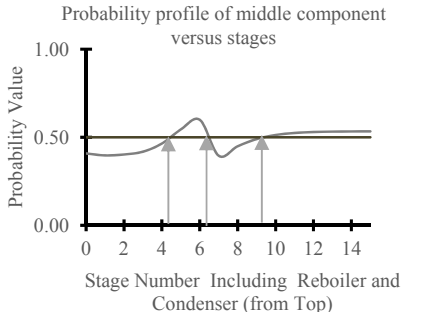
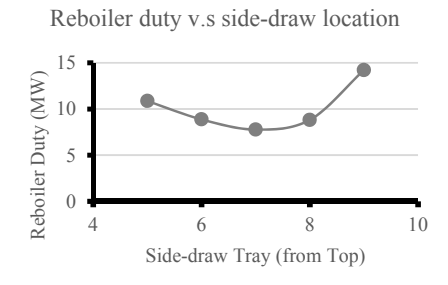


Figure 2: Workflow of methodology

4. Case study

The application of the design methodology is highlighted through a benzene and p-xylene mixture with trace amounts of toluene as an impurity. The separation process is considered isobaric at 1 atm. A comparison is carried out between this method and driving force based method for designing a side-draw column at the end of this section. The results of each step of design methodology are listed in Table (1). The outcome configuration of this algorithm shows that feed has to be located at tray 6 and side-draw has to be located at tray 7.

Table 1: Data sheet of benzene, p-xylene case study

Action	Feed: (B 58 %, T 1,000 ppm p-X 41.9 %)
<p>Steps 1, 2</p> <ol style="list-style-type: none"> Design the column, using driving force approach. $N = 14$, $N_F = 6$ Determine composition profile and temperature profile. 	 
<p>Steps 3-7</p> <ol style="list-style-type: none"> Calculate p_{MB}^{sat} profile. Calculate K_{MB} profile. Determine probability profile. Find trays in which probability is 50 %. 	
<p>Steps 7, 8</p> <ol style="list-style-type: none"> Simulate the column <p>Optimum Side-draw location is tray 7. $Q_{reboiler}^{MT} = 7.77 MW$ $Q_{condenser}^{MT} = 12.01 MW$</p>	

This information has been validated against a rigorous process simulation in step 7 and 8. Comparing the rigorous process simulation results for the molecular tracking is able to

narrow down the possible most energy efficient tray location for a column with a side draw purely based on thermodynamic properties (in this case to three options) and with the aid of process simulation narrow down the answer to the most energy efficient one that is illustrated in Table (1) at steps 7 and 8.

When comparing these results with driving force method proposed by Erik Bek-Pedersen and Gani (2004), the maximum driving force occurs at $D_x = 0.4$ (D_x is the liquid composition of light key component at maximum driving force) between benzene and toluene. The joint driving force diagram shows $D_s = 0.35$ (D_s is the liquid composition of light key component when two binary driving force diagrams intersect). Algorithm D2 on that paper shows that feed should be introduced at tray 5 while, side-draw should be introduced at tray 9. The simulation of this configuration in HYSYS. It can be clearly seen that molecular tracking proposes much more efficient configuration compared to driving force based method.

Conclusions

A systematic methodology to design side-draw columns for ideal ternary mixtures, where the middle component is at trace concentration level is proposed. The methodology is based on a probability function expressed in terms of thermodynamic properties of the system. The column is first designed for the key components in the mixture, and then the side-draw location is deterministically found. The side-draw is located at the stage, which the middle component (trace component) is indifferent to move either upward or downward. A case study of benzene, p-xylene and trace amount of toluene has been examined in this work. The design configuration of molecular tracking has shown less energy demand compared to the corresponding configuration of driving force. Considering that it is possible to find the side-draw location analytically by using trial/error approach, the real scope of molecular tracking is to design a dividing wall column by finding the location of dividing wall.

References

- C. Maat TPC Group, 2017, Molecular tracking- a new way to analyze distillation columns, Oral Presentation, AIChE 2017 Spring Meeting – Kister Distillation Symposium, San Antonio, Texas, United States of America
- D. Seader, E.J. Henley, D.K. Roper, 1999, Distillation of binary mixtures, Separation process principles, Second Edition, Page 252, John Wiley and Sons Inc., United States of America.
- D.W. Tedder, D.F. Rudd, 1978, Parametric studies in industrial distillation: Part I. Design comparisons, AIChE J. 24.
- E. Bek-Pedersen, R. Gani, 2004, Design and synthesis of distillation systems using a driving-force-based approach, Chem. Eng. Process. Process Intensif. 43.
- Kraller, M. A.; Udugama, I. A.; Kirkpatrick, R.; Yu, W.; Young, B. R., 2016, Side Draw Optimisation of a High-Purity, Multi-Component Distillation Column. Asia-Pacific J. Chem. Eng., 11 (6)
- Y. Ma, Y. Luo, S. Zhang, X. Yuan, 2018, Simultaneous optimization of complex distillation systems and heat integration using pseudo-transient continuation models, Comput. Chem. Eng. 108.

Improved Design of Experiments for Identification of MIMO Systems

Kurt E. Häggblom

Åbo Akademi University, Faculty of Science and Engineering, Biskopsgatan 8, Turku FI-20500, Finland

khaggblom@abo.fi

Abstract

A problem in the identification of MIMO systems is that the system outputs in an identification experiment may be strongly correlated if the inputs are perturbed by uncorrelated signals, as is standard practice. Such a correlation reduces identifiability.

A set of methods to design input perturbations that minimize the sample correlation between the outputs has previously been proposed. These methods require an initial model for the design. In this paper, a data-based design method is proposed. Data are obtained from preliminary experiments with the system to be identified. Besides being preferable from a practical point of view, the data-based approach makes it easier to handle some numerical issues that gave problems in the model-based approach.

A design method that minimizes the input or output peak value subject to desired output variances with no output correlation is presented. A model of an ill-conditioned distillation column is used to illustrate the method.

Keywords: System identification, Multivariable systems, Ill-conditioned systems, Experiment design, Data-based design.

1. Introduction

The quality of the data is of utmost importance in the identification of multiple-input multiple-output (MIMO) systems. The standard approach of perturbing all inputs simultaneously by uncorrelated signals tends to produce correlated outputs. For ill-conditioned systems this correlation is very strong. Such data may jeopardize identifiability (Koung and MacGregor, 1992).

A design method that addresses the output distribution was proposed by Häggblom (2017a, 2018b). The method can produce uncorrelated outputs, which is considered good for identifiability. A drawback of the method is that it requires an initial model of the system. A short overview of related design methods is given in Häggblom (2017a).

In this paper, a completely data-based method is introduced for the same purpose of obtaining uncorrelated outputs. Data are obtained from one or more preliminary experiments with the system to be identified. It is possible, for example, to use the data from a standard identification experiment with uncorrelated inputs to design a better experiment. Additional properties such as input and output peak values can be minimized in addition to correlation handling.

An ill-conditioned distillation column model is used for illustration of the methods.

2. Problem formulation

Experiment design for identification of MIMO systems is considered. The system has n inputs $u(k)$ and n outputs $y(k)$, sampled at time instants $k = 1, \dots, n_s$, where n_s is the total number of sample points. The variables are related by a dynamic relationship

$$y(k) = G(q)u(k), \quad (1)$$

where $G(q)$ is a matrix of pulse transfer operators defined through the shift operator q . This relationship is assumed to be initially unknown. It is not implied that a model of this form is to be identified.

The input design for the identification experiment is facilitated by the use of an n -dimensional perturbation signal $\xi(k)$. This signal is typically a random binary signal (RBS), a pseudo random signal (PRBS), or a multi-sinusoidal signal (MSS). The correlation between the individual signals $\xi_i(k)$, $i = 1, \dots, n$, should preferably be small (ideally non-existent). In practice, this is achieved by constructing each ξ_i from a base sequence ξ_0 , of length N , by shifting it (approximately) $(i-1)N/n$ positions in a circular way. As suggested by Ljung (1999), more than one period of the sequences may be used to give a total sequence length $n_s = n_p N$, where n_p is the number of periods.

The input $u(k)$ to be applied in the identification experiment is given by a linear transformation

$$u(k) = T\xi(k), \quad (2)$$

where T is a constant matrix determined in the input design with the aim of making the output samples $y_i(k)$, $k = 1, \dots, n_s$, $i = 1, \dots, n$, uncorrelated with $y_j(k)$, $j \neq i$.

The output correlation depends on the output covariance matrix, which for an $n \times n$ system is defined by $n(n+1)/2$ parameters. This suggests that the same number of adjustable elements of T is sufficient to produce uncorrelated outputs. Thus, T can be a triangular or symmetric matrix, for example. If more elements are used, it is possible to optimize some quantity besides output correlation. In this paper, minimization of the peak values $\max_{i,k} |y_i(k)|$ and $\max_{i,k} |u_i(k)|$ is considered.

3. Input design

Applying the input $u(k)$, $k = 1, \dots, n_s$, to a system yields an $n_s \times n$ matrix of sampled outputs Y , where the k th row and i th column of Y holds the sample $y_i(k)$. Given the perturbation sequence $\xi(k)$, $k = 1, \dots, n_s$, it is desired to choose T in Eq. (2) to give Y specified properties. In particular, the covariance matrix $P = \text{cov}(Y)$ is desired to be diagonal, which means no correlation between the outputs. Assuming the variances $\text{var } y_i = 1$ are desired, the objective is to obtain $P = I$.

Assume it is known that the single input $u_i(k) = \xi_j(k)$ produces an output matrix Y_ℓ , $\ell = i + (j-1)n$. If the system is linear, applying an input $u_i(k) = T_{ij}\xi_j(k)$ would then

produce the output matrix $T_{ij}Y_\ell$. If Y_ℓ is known for every combination of $u_i(k)$ and $\xi_j(k)$, applying the input $u(k)$ given by Eq. (2) would then produce the output

$$Y = \sum_{i=1}^n \sum_{j=1}^n T_{ij}Y_\ell, \quad \ell = i + (j-1)n, \quad (3)$$

where T_{ij} is the element of T in row i and column j .

To streamline the notation needed further below, the vector

$$x = \text{vec}(T) \quad (4)$$

is introduced. The vectorization results in $x_\ell = T_{ij}$, where $\ell = i + (j-1)n$. Equation (3) is then replaced by

$$Y = \sum_{\ell=1}^{n^2} x_\ell Y_\ell. \quad (5)$$

The output covariance matrix becomes

$$P = \sum_{\ell_1=1}^{n^2} \sum_{\ell_2=1}^{n^2} x_{\ell_1} x_{\ell_2} P_{\ell_1 \ell_2}, \quad (6)$$

where $P_{\ell_1 \ell_2} = \text{cov}(Y_{\ell_1}, Y_{\ell_2})$ is the matrix of covariances between Y_{ℓ_1} and Y_{ℓ_2} . Thus, $P_{\ell_1 \ell_2}$ can be calculated when Y_{ℓ_1} and Y_{ℓ_2} are known.

The task of the input design is now to determine the vector x to obtain $P=I$. The nonlinearity of Eq. (6) is a difficulty, however. To overcome this, Eq. (6) can be linearized and solved iteratively. The linearization is

$$P = \sum_{\ell_1=1}^{n^2} \sum_{\ell_2=1}^{n^2} (\tilde{x}_{\ell_1} x_{\ell_2} + x_{\ell_1} \tilde{x}_{\ell_2} - \tilde{x}_{\ell_1} \tilde{x}_{\ell_2}) P_{\ell_1 \ell_2}, \quad (7)$$

where \tilde{x} is the previous value of x in the iteration procedure.

4. Obtaining data

Data for the design is generated by one or more experiments with the system to be identified. The most reliable method is to make an experiment with every combination $u_i(k) = \xi_j(k)$, $i = 1, \dots, n$, $j = 1, \dots, n$, one at a time. This results in n^2 experiments, each one yielding a matrix of sampled outputs Y_ℓ , $\ell = i + (j-1)n$, needed in the input design.

For $n > 2$, this is a lot of experiments, and even for $n = 2$, four experiments might be undesirable. An alternative is to make just n experiments with $u_i = \xi_j$, $i = 1, \dots, n$ and j arbitrary (e.g., $j = i$ or $j = 1$). For each experiment, a pulse-response model $G(q)$ satisfying Eq. (1) can be determined in a simple way. This makes it possible to simulate all combinations $u_i = \xi_j$ to obtain the required output data matrices.

It is possible to take this one step further, and make only one experiment with $u(k) = \xi(k)$. Here, all inputs are perturbed simultaneously. If the components $\xi_i(k)$, $i = 1, \dots, n$, are essentially uncorrelated with one another, it is possible to determine the n pulse-response models above and proceed in the same way. This kind of experiment is the standard identification experiment recommended in textbooks (e.g., Ljung 1999; Isermann and Münchhof, 2011), but here the data is used to design a better experiment.

5. Solution procedures

In the case of a structurally constrained T (which is a user choice) with $n(n+1)/2$ free elements such that T is not structurally singular, Eq. (6) can be solved directly to obtain a solution that yields $P=I$. However, there are multiple solutions because of the quadratic nature of Eq. (6). Moreover, various column and row permutations of T can be applied. For a triangular structure, there are $(n!)^2$ permutations; for a symmetric or skew-symmetric structure, there are $n!$ permutations of each.

To avoid the nonlinearity of Eq. (6), an iterative application of Eq. (7) can be used. It is then convenient to use an optimization framework to obtain a solution. Using the YALMIP toolbox (Löfberg, 2004) in conjunction with MATLAB makes it easy to formulate the problem as

$$\max_{x \in X} \lambda, \text{ s.t. (7) and } \lambda I \leq P \leq I, \quad (8)$$

where X denotes the allowed structures of x (and T). This procedure does not eliminate multiple solutions. Generally, the solution depends on the starting value \tilde{x} in Eq. (7).

If T is constrained to a lesser degree, an unconstrained T being the typical case, Eq. (6) and (7), with $P=I$, are underdetermined with respect to x . This makes it possible to optimize some other property besides correlation. Minimization of the peak values $\max_{i,k} |y_i(k)|$ and $\max_{i,k} |u_i(k)|$ are very relevant choices.

Minimization of $\max_{i,k} |y_i(k)|$, later referred to as $\min Y_{\max}$, can be formulated as

$$\min_{x \in X} r, \text{ s.t. (5), (7), } P=I, \text{ and } -r \leq Y \leq r. \quad (9)$$

In the case of perturbation signals that switch between two levels, as e.g. PRBS inputs, minimization of $\max_{i,k} |u_i(k)|$ can be accomplished by minimization of T_∞ (Häggblom, 2018a, 2018b). This minimization can be formulated as

$$\min_{x \in X} r, \text{ s.t. (7), } P=I, \text{ and } \sum_{j=1}^n |T_{ij}| \leq r, \quad i = 1, \dots, n. \quad (10)$$

Because these optimizations are completely data based, they are also non-convex. This means that there is no guarantee that the obtained solution is a global optimum. Hence, many starting values \tilde{x} should be tried. Fortunately, the differences between the best local optima tend to be small.

6. Case study

An ill-conditioned distillation column model introduced by Skogestad and Morari (1988) is used to illustrate the input design methods. This model was also used for input design in Häggblom (2017b, 2018b). The model is a state-space model

$$\begin{aligned} \dot{x}(t) &= Ax(t) + Bu(t), \\ y(t) &= Cx(t) \end{aligned}, \quad A = \begin{bmatrix} -\frac{1}{194} & 0 \\ 0 & -\frac{1}{15} \end{bmatrix}, \quad B = \begin{bmatrix} 1 & -1 \\ 0 & 1 \end{bmatrix}, \quad C = \begin{bmatrix} \frac{87.8}{194} & \frac{1.4}{15} \\ \frac{108.2}{194} & -\frac{1.4}{15} \end{bmatrix}. \quad (11)$$

In this case study, the sampling time is $T_s = 1$ and a PRBS with minimum switching time $T_{sw} = 4$ and sequence length $N = 255$ is used as perturbation.

For a triangular T structure, including all permutations of columns and rows, eight solutions were found (two for each permutation) by the optimization in Eq. (8). The ones with the smallest peak values $\max |y| \equiv \max_{i,k} |y_i(k)|$ and $\max |u| \equiv \max_{i,k} |u_i(k)|$ are

$$\min Y_{\max} : T = \begin{bmatrix} 1.4863 & 0 \\ 1.4652 & 0.0866 \end{bmatrix} \Rightarrow \max |y| = 2.5940, \quad \max |u| = 1.5567 \quad (12)$$

$$\min T_{\infty} : T = \begin{bmatrix} 0 & 1.5012 \\ -0.0820 & 1.4646 \end{bmatrix} \Rightarrow \max |y| = 2.9594, \quad \max |u| = 1.5466 \quad (13)$$

For a symmetric or skew-symmetric T , including all permutations, eight solutions were found (two for each permutation). The ones with the smallest peak values are

$$\min Y_{\max} : T = \begin{bmatrix} 1.0439 & 1.0875 \\ 1.0875 & 1.0179 \end{bmatrix} \Rightarrow \max |y| = 2.7250, \quad \max |u| = 2.1315 \quad (14)$$

$$\min T_{\infty} : T = \begin{bmatrix} 1.0628 & -0.9897 \\ 0.9897 & -1.0542 \end{bmatrix} \Rightarrow \max |y| = 2.7367, \quad \max |u| = 2.0525 \quad (15)$$

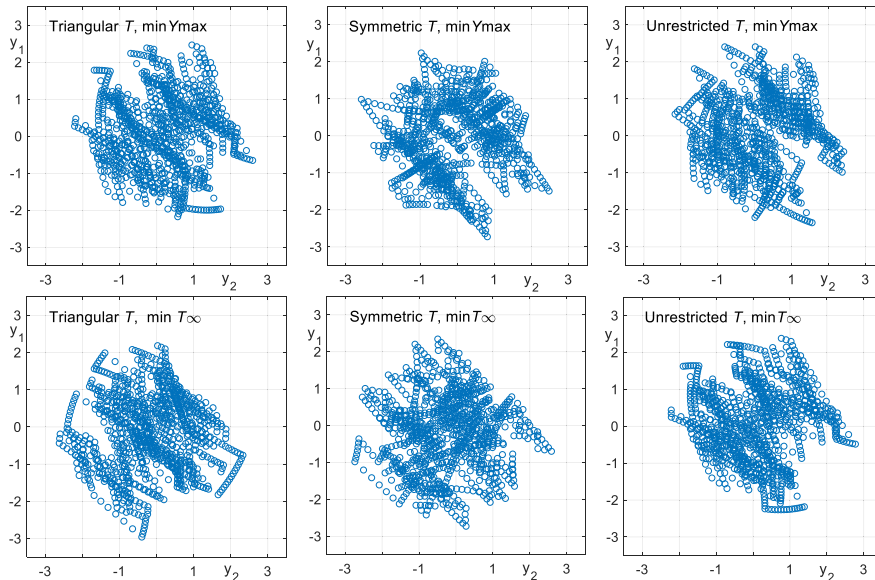


Figure 1. Scatter plots of output distributions.

Minimization of the peak values with an unrestricted T matrix using the formulations in Eqs (9) and (10) gave the following results:

$$\min Y_{\max} : T = \begin{bmatrix} 1.4568 & 0.3367 \\ 1.4189 & 0.4116 \end{bmatrix} \Rightarrow \max|y| = 2.4079, \max|u| = 1.8305 \quad (16)$$

$$\min T_{\infty} : T = \begin{bmatrix} -0.0363 & 1.4769 \\ 0.0432 & 1.4700 \end{bmatrix} \Rightarrow \max|y| = 2.7726, \max|u| = 1.5132 \quad (17)$$

As can be seen, a triangular type of T matrix is a good choice for obtaining a small input peak value, whereas a symmetric type of T matrix is not good. A small output peak value requires minimization of Y_{\max} with an unrestricted T matrix.

Figure 1 shows scatter plots of the output distributions of the various designs.

7. Conclusions

A data-based method for design of experiments for identification of MIMO systems was described. The required data can be obtained from some preliminary experiment(s) with the system. The input design, which is easy to carry out with standard optimization software, yields uncorrelated outputs. This is considered good for identifiability. In addition, input and output peak values can be minimized subject to desired output variances with no output correlation. It is an advantage in process operation to obtain desired output variances with input and output peaks as small as possible. The method works with any kind of standard perturbation signals used in system identification.

References

- K.E. Häggblom, 2017a, A new optimization-based approach to experiment design for dynamic MIMO identification, *IFAC PapersOnline*, 50 (1), 7582–7587.
- K.E. Häggblom, 2017b, Design of optimal experiments for dynamic MIMO identification, *Proc. 27th European Symp. on Computer Aided Process Design — ESCAPE 27*, Barcelona, Spain, 319–324.
- K.E. Häggblom, 2018a, Input designs to obtain uncorrelated outputs in MIMO system identification, *Proc. 13th Int. Symp. on Process systems Engineering — PSE 2018*, San Diego, CA, USA, 637–642.
- K.E. Häggblom, 2018b, Easy ways to design inputs to obtain uncorrelated outputs in MIMO system identification, *IFAC PapersOnline*, 51 (15), 227–232.
- R. Isermann and M. Münchhof, 2011, *Identification of Dynamic Systems*, Springer: Berlin and Heidelberg, Germany.
- C.-W. Kung and J.F. MacGregor, 1992, Design of identification experiments for robust control. A geometric approach for bivariate processes, *Ind. Eng. Chem. Res.*, 32 (8), 1658–1666.
- L. Ljung, 1999, *System Identification: Theory for the User*, Prentice Hall: Upper Saddle River, NJ, USA.
- J. Löfberg, 2004, YALMIP, A toolbox for modeling and optimization in MATLAB, *Proc. IEEE Int. Symp. on Computer Aided Control Systems (CACSD)*, Taipei, Taiwan, 284–289.
- S. Skogestad and M. Morari, 1988, Understanding the dynamic behavior of distillation columns, *Ind. Eng. Chem. Res.*, 27 (10), 1848–1862.

Nonlinear Model Predictive Control of Haemodialysis

Tianhao Yu^{a,b}, Vivek Dua^{a,*}

^a *Department of Chemical Engineering, Centre for Process Systems Engineering, University College London, London WC1E 7JE, United Kingdom*

^b *Current address: University of Surrey, Guildford GU2 7XH, United Kingdom*

*Corresponding author: v.dua@ucl.ac.uk

Abstract

Haemodialysis is a blood treatment technique used for patients whose kidneys are not working normally. A number of Linear Model Predictive Control (LMPC) formulations for controlling haemodialysis have been proposed in the literature. In this paper, a Nonlinear Model Predictive Control (NMPC) formulation is proposed that instead of using an approximated linear model takes into account the nonlinear model for haemodialysis. One of the key advantages of the NMPC formulation is that it gives more comprehensive control of the haemodialysis process. Four manipulated variables are considered: the blood flow out of the body, the blood flow returned from the dialysis machine to the body, the dialysate rate and the sodium concentration of the inlet blood flow. By manipulating these variables, the fluid volumes and the toxin clearance are monitored and controlled. The results show that a better control performance for the blood volumes and toxin clearance is obtained while the blood and dialysate flow rates are held at a relatively low level, which is expected to reduce the risk of adverse reactions for the patients.

Keywords: Haemodialysis, Model Predictive Control, Optimisation

1. Introduction

Human kidney functions as a crucial organ which balances electrolytes and volumes of body fluid, and filters toxin content out of the blood before the blood returns to heart. Approximately 20% of the blood is processed by kidneys which amounts to 1800 litres per day (Lote 2013). Haemodialysis refers to a blood treatment process that removes toxins and waste for patients with severe renal failure. In order to achieve normal functions of the kidney, the haemodialysis treatment typically takes 3 to 5 hours per week for one patient (Pierce, Tubing, and Cassettes 2008).

The blood and dialysate flowrates are normally considered as two key variables during the treatment process. A trade-off arises when determining the two variables: increasing the two flowrates will generally shorten the required treatment time period, but will result in higher risk of adverse reactions for the patients including headache and muscle cramps. Therefore, finding the optimum operating conditions for haemodialysis becomes a complex optimisation problem. Currently the haemodialysis treatment is usually performed by nurses under empirical operating conditions.

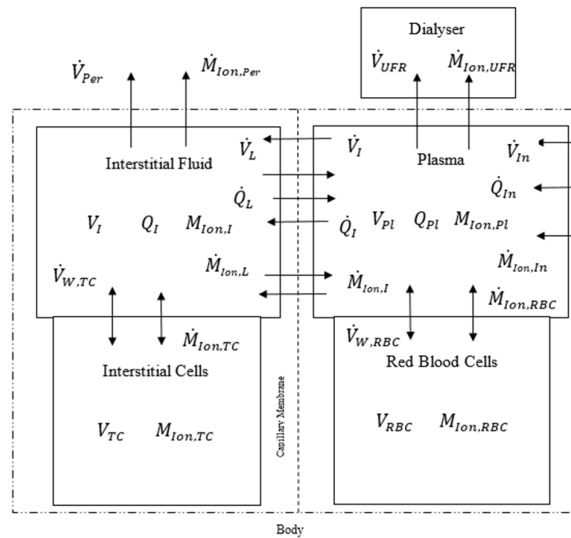


Figure 1.1: Mathematical model describing the haemodialysis process where four compartments are separated.

Eck and Dua (Eck and Dua 2016) performed simulation of the haemodialysis process based on the relevant mathematical model describing the dynamic behaviours of haemodialysis proposed by Gyenge et al. (1999) and Canete and Huang (2010). In the LMPC formulations proposed in the literature, the controlled variables include the relative blood volume (RBV), heart rate (HR) and systolic blood pressure (SBP). These variables are controlled by manipulating the ultrafiltration rate (UFR), the rate at which the fluid is being removed from the patient's body but the objectives regarding toxin clearance and excess water were not considered. In this work an NMPC approach taking into account the nonlinear model of the haemodialysis process, incorporating toxin clearance and excess water, is proposed.

2. Methodology

2.1. Mathematical model

A mathematical model describing the dynamic behaviour of the haemodialysis has been developed in order to achieve the desired optimisation. The model used in this paper is derived based on studies by Gyenge et al. (1999) and Canete and Huang (2010), as well as the modifications by Eck and Dua (2016). The proposed model divides the human body into four individual compartments and one dialyser compartment, as presented in Figure 1.1. The four compartments consist of two extracellular compartments: the red blood cells and the interstitial cells, as well as two intracellular compartments including the blood plasma and interstitial fluid, which are separated by the capillary walls. From Figure 1.1 it can be observed that the interstitial cells are connected to the interstitial fluid while the red blood cells are connected to the plasma compartment. The dialyser only connects to the plasma compartment, which indicates that the plasma compartment is the only compartment that is directly affected by external elements. V refers to the

volumes of the compartments (L), M represents the ion contents (kg), \dot{M} is the ion flux (kg/h) and Q denotes the protein content (kg). The subscripts denote the different compartments and components including ions and toxins.

The development of the mathematical model takes the assumptions into consideration that the four compartments are perfectly mixed and homogeneous, and all proteins have the similar physical and chemical properties as albumin. The model contains theoretical and empirical correlations from literatures such as mass balances, ion distribution and concentration gradients. The state variables of the haemodialysis treatment process are described by simultaneous ordinary differential equations (ODEs) representing the interconnected compartments as shown in Figure 1.1. The values of the parameters are taken from literature (Chapple et al. 1993).

2.2. Orthogonal collocation on finite elements (OCFE)

When solving the mathematical model symbolic and numerical methods are considered. The symbolic method is not suitable due to the complexity of the model. Orthogonal collocation on finite elements (OCFE) is a numerical method for solving ODEs and is widely applied to chemical and biomedical engineering systems. The method minimises the difference between the Lagrange interpolation and the actual solution on predetermined collocation points. The OCFE method is used to both simulate the haemodialysis process and solve the control problem based on the proposed mathematical model.

2.3. Nonlinear model predictive controller setup

The objective function of the NMPC formulation is defined as follows:

$$\min_{u,z} E_{MPC} = \sum_{t=0}^{H_p} Q_z (z_c^{pred}(t_i) - z_c^{sp}(t_i))^2 + \sum_{t=0}^{H_c} Q_u (u(t_i) - u^{ref}(t_i))^2 \quad (1)$$

The objective function minimises the differences between the controlled predictive state variables $z_c^{pred}(t)$ and the set point $z_c^{sp}(t)$ over the prediction horizon H_p . In the objective function the volumes of plasma and interstitial cells compartments, the total body fluid volume and the urea contents are selected as controlled predictive state variables. The objective function also minimises the deviation of the input variables $u(t)$ from a reference value $u^{ref}(t)$ over the control horizon H_c . As mentioned above, four input (manipulated) variables are proposed: the blood flow out of the body, the blood flow returned from dialysis machine to the body, the dialysate rate and the sodium concentration of the inlet blood flow. Q denotes the penalty ratios which can be modified to adjust the controller performance. The total simulation time is set to 210 minutes since normal haemodialysis treatment time is 3 to 5 hours. In order to apply the OCFE method, the simulation time period is divided into 210 elements with 2 internal collocation points in each element. The prediction horizon is set to 5 timesteps while each timestep represents 1 minute. The values of the parameters and the initial conditions of the variables are taken from the literature assuming a 70-kg patient (Xie et al. 1995). The bounds and set points for the variables are given in Table 2.1.

Table 2.1: Values of variables in the NMPC set up

Variable	Units	Lower Bound	Upper Bound	Maximum Change	Set Point	
Manipulated Variables	$J_{B,Out}$	ml/min	0.0	800.0	25.0	0.0
	$J_{B,In}$	ml/min	0.0	800.0	25.0	0.0
	J_D	ml/min	0.0	800.0	25.0	0.0
	$[Na]_{J_{B,In}}$	mmol/l	96.6	179.4	-	139.7
Controlled Variables	V_{Total}	L	-	-	-10; +5	40.74
	V_{PI}	ml	320	32000	-	3200
	V_I	ml	840	84000	-	8400
	$Urea_{Ex}$	mmol	-	-	-	0.0

3. Results and discussion

3.1. Model validation

The mathematical model has to be firstly validated before implementation of the NMPC. The results of infusion simulation are compared with the experimental results obtained by Manning and Guyton (1980) who performed experiments in which dogs were infused with RS in an amount equivalent to 5%, 10, and 20% of the actual body weight. The results of dialysis simulation regarding the toxin concentrations were in good comparison with the experimental data obtained by Ziofcko (2000). The experimental data consists of the urea, uric and creatinine blood concentrations, which were obtained by measuring the dialysate and blood toxin concentrations 11 times in a 210-minute interval. The data was taken from a 58-kg bodyweight patient who experienced a dialyzing treatment lasting 3 hours and 30 minutes, 3 times a week. Two examples of comparison between the simulation results and experimental data, the blood volume change for infusion and the urea concentration change for dialysis simulation, are given in the top two plots in Figure 3.1. The comparisons show a good agreement which indicates that the model can be considered as a valid representation of the haemodialysis process.

3.2. NMPC

Figure 3.1 presents the change of the values of the objective function E_{MPC} . It can be observed that the initial value of 2.82 rapidly declines towards 0 in 18 minutes and is kept around the desired value of zero. Concerning the fluid volume change for the total body, it falls from 41.72 L to the set point of 40.73 L in 25 minutes. Afterwards, the total fluid volume is controlled around the desired level until the completion of simulation.

The graph shown in Figure 3.1 shows the change of total urea content in both the extracellular and intracellular compartments. It can be observed that the NMPC controller is able to achieve approximately 60% urea clearance, which satisfies one of the purposes of the haemodialysis process.

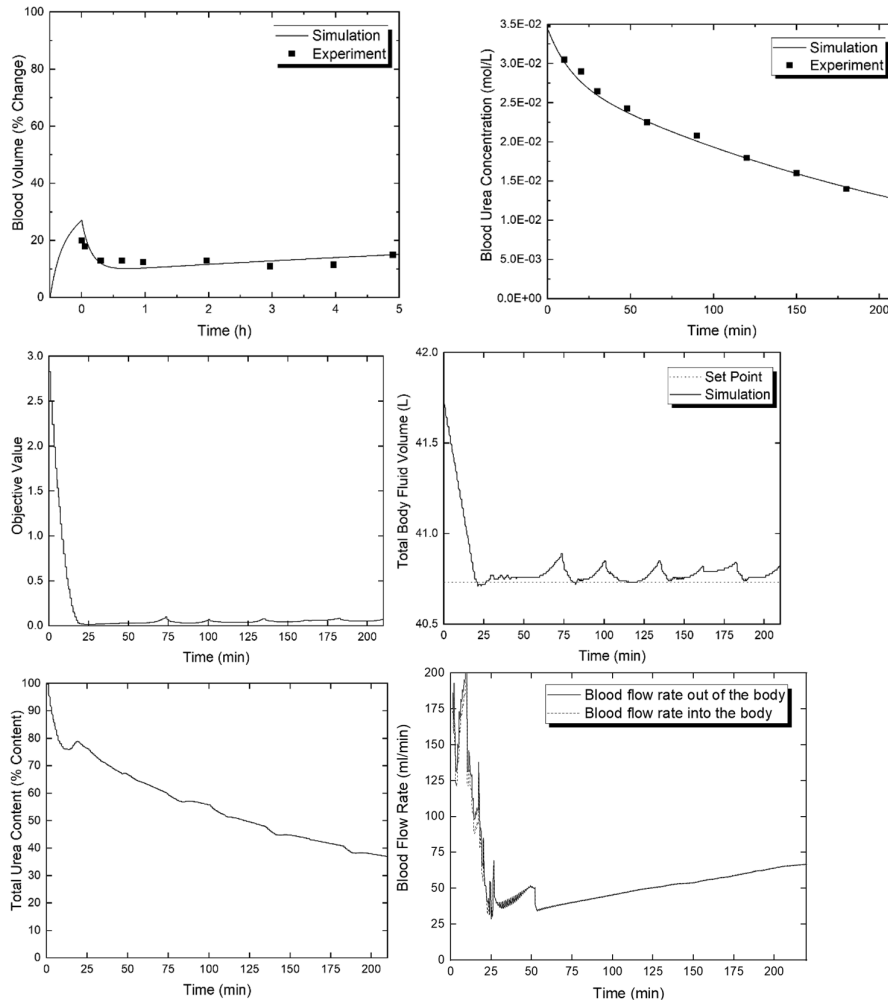


Figure 3.1: Results for NMPC of haemodialysis.

The dynamic behaviours of the blood flow rate out of the body and returned to the body are also plotted in Figure 3.1. From the graph the values of the two manipulated variables follows each other very closely during the entire horizon. This is due to the inequality constraint embedded in the NMPC: $0 \leq J_{B,Out} - J_{B,In} \leq 10$. The difference between the two blood flow rates also represent the ultrafiltration rate. The blood flow rates rapidly fall to their set points of zero in 25 minutes and from minute 50 on, the blood flowrates gradually increases and become stable eventually. In the previously developed Linear Model Predictive Controller (LMPC) by Javed et al. (2009, 2010), the systolic blood pressure (SBP) was controlled by manipulating the relative blood volume (RBV) and heart rate (HR) and the haemodialysis objectives regarding the toxin clearance and excess water content were not considered. In this paper, the NMPC controller successfully demonstrated that the desired toxin clearance can be achieved

while the flowrates are maintained at a relative low level to ensure the side effects will not occur. The NMPC controller also controls the sodium concentration to avoid hypotension.

4. Conclusions

A non-linear model predictive controller (NMPC) for haemodialysis treatment is proposed in this work. The developed mathematical model which describes the dynamic behaviours of haemodialysis is validated by comparing the simulation results with previously reported experimental data. The implementation of NMPC on haemodialysis gives promising results. The total body fluid volume is maintained around its set point and the blood flowrates are kept at a low level. As mentioned above, increasing the blood and dialysate flowrates will generally enhance the efficiency of haemodialysis and shorten the treatment time period, but may result in adverse reactions. The proposed NMPC controller is able to reduce the risk of side effects by controlling the flowrates. At the same time, it achieves desired goals of haemodialysis: clearance of toxins and filtration of excess water. Comparing to the Linear Model Predictive Control (LMPC) proposed in literatures (Javed et al. 2009, 2010), the NMPC gives more comprehensive control and could be considered as a more reliable controller due to the good control performance. Future work could include personalised therapy and clinical validation of the controller.

5. References

- Chapple, C., B. D. Bowen, R. K. Reed, S. L. Xie, and J. L. Bert. 1993. "A Model of Human Microvascular Exchange: Parameter Estimation Based on Normals and Nephrotics." *Computer Methods and Programs in Biomedicine* 41(1):33–54.
- Eck, Thomas and Vivek Dua. 2016. "Control Relevant Modelling for Haemodialysis." Pp. 949–954 in *Computer Aided Chemical Engineering*. Vol. 38.
- Fernandez de Canete, J. and P. Del Saz Huang. 2010. "First-Principles Modeling of Fluid and Solute Exchange in the Human during Normal and Hemodialysis Conditions." *Computers in Biology and Medicine* 40(9):740–750.
- Gyenge, CC; Bowen, BD; Reed, RK; Bert, JL. 1999. "Transport of Fluid and Solutes in the Body II. Model Validation and Implications." *Am J Physiol* 277(3 Pt 2):H1228–H1240.
- Javed, F., A. V Savkin, G. S. H. Chan, P. M. Middleton, P. Malouf, E. Steel, J. Mackie, and T. M. Cheng. 2009. "Modeling and Control of the Heart Rate and Blood Volume Responses to Hemodialysis." *2009 IEEE International Conference on Control and Automation* 625–630.
- Javed, Faizan, Andrey V. Savkin, Gregory S. H. Chan, and James D. Mackie. 2010. "Modeling and Model Predictive Control of Hemodynamic Variables during Hemodialysis." Pp. 4673–4678 in *Proc. of the IEEE Conf. on Decision & Control*.
- Lote, Christopher J. 2013. *Principles of Renal Physiology*.
- Pierce, Thermo Scientific, Dialysis Tubing, and Dialysis Cassettes. 2008. "Dialysis : An Overview." *Thermo Scientific*.
- Xie, S. L., R. K. Reed, B. D. Bowen, and J. L. Bert. 1995. "A Model of Human Microvascular Exchange." *Microvascular Research* 49(2):141–162.

Machine Learning of Molecular Classification and Quantum Mechanical Calculations

Jie-Jiun Chang¹, Jia-Lin Kang^{2*}, David Shan-Hill Wong^{1*}, Cheng-Hung Chou¹,
Hsuan-Hao Hsu³, Chen-Hsuan Huang³ and Shang-Tai Lin^{3*}

*1 Department of Chemical Engineering, National Tsing Hua University,
Hsinchu, Taiwan*

*2 Department of Chemical and Material Engineering, Tam Kang University,
New Taipei City, Taiwan 30013*

*3 Department of Chemical Engineering, National Taiwan University, Taipei,
Taiwan*

e-mail: conlinkang@gmail.com, dshwong@che.nthu.edu.tw, stlin@ntu.edu.tw

Abstract

In this paper, a machine learning method is proposed to extract molecular features as floating-point numbers in a high dimensional space from the language-like description Simplified Molecular Input Line Entry Specification (SMILES). Principle component analysis showed that this method can successfully classify alkanes and alcohols and also the chain lengths of the molecular by their location in a three-dimensional feature space. A neural network model is build using the location of a compound in this high dimensional space as input to predict the “sigma-profile”, the charge distribution of the molecule near a perfect infinite conductor, which is calculated by quantum mechanics. The sigma-profile can be used in the COSMOSAC model for predicting thermodynamic properties such as activity coefficient. Preliminary results showed that an accurate neural work model with generalization ability can be developed.

Keywords: Machine Learning, Word embedding, COSMO-SAC, Sigma profile..

1. Introduction

One of the popular ways of generalized correlations of thermodynamic properties, developed over four decades ago, is the use of group contribution methods (Joback and Reid 1987, Fredenslund et al. 1975). Such methods required expert suggestions of the functional dependence of the predicted properties and regression of binary interaction parameters using large amount of data. In the last two decades, a priori, or first principle approach that used quantum mechanical calculations to predict thermodynamic properties has been developed (Klamt 1995, Lin and Sandler 2002). In the COSMO method, quantum mechanical calculations is used to predict the charge distribution of a molecule near an infinite conductor, known as the sigma σ -profile, which can be used to predict thermodynamic properties of mixtures (e.g. COSMO-SAC). Substantial effort needs to be expended in producing the σ -profile. Database of σ -profiles of a limited number of compounds was provided 0. Yet it is desirable that a fast surrogate generation method be developed to alleviate the load of first principle calculations.

Machine learning (ML) is the use of computer and statistics to learn from data with minimum human intervention. In other words, ML tries to identify the functional relation between an input and an output from a set of data, given that such a functional relation exists. Sigma profile can be considered as a function of molecular structure since it is uniquely defined. Yet there are many ways to represent molecular structure ranging from aforementioned group contribution method to text-based description such as Simplified Molecular Input Line Entry Specification (SMILES, Weininger, 1998) or .mol file () or even three dimensional representation (Humphrey et al. 1996). Recent development in machine learning has been able to convert word-based content into vector space (Mikolov et al 2013). In this paper, a machine learning method is proposed to convert word-based molecular features from SMILES into a floating-point vector space representation, and used it to develop a neural network to generate σ -profiles.

2. Method

2.1. Molecular recognition using SMILES and word embedding

The SMILES format encoded molecular structure clearly with a short ASCII string. It is able to read the structures like chain length, double bond (=), triple bond (#) and aromatic ring (c1ccccc1) easily. With this link between molecules and nature language, we can use machine learning language model to extract molecular features.

The SMILES format is presented as word, which is not readable by machine. To translate the word to inputs of network, i.e. vectors, we build a “dictionary”. In this dictionary, every elements and symbols can be transformed to a specific number. Then we can translate the SMILES format data to sequences of numbers. However, these number sequences are just encoding, and do not represent “characteristic” or feature of the molecules. Word embedding solve this problem by projecting translated sequence into a high-dimensional vector using a neural network.

In order to that the transformation is able to truly recognize molecule features, the high dimensional output of the embedding layer is collapsed by a dense-layer with 1 output. About 1372 true compounds are used and tagged 0, or “true-compound”. Another 1372 compounds with randomly created SMILES file are tagged 1 as “false” or “fake-compound”. Supervised learning are used until the recognizer network can accurately distinguish between the two classes. 274 true compounds and the same amount of fake-compound are used as test set.

2.2. Sigma profile predictor

The high dimensional output of are then used as input into a Long short-term memory (LSTM), which is commonly used in nature language recognition is used (), with hyperbolic tangent activation function and 4-layer back-propagation network with rectified linear unit (RELU) activation function. It is trained with 1096 compounds while 279 were used as test data. The overall network structure is shown in Figure 1.

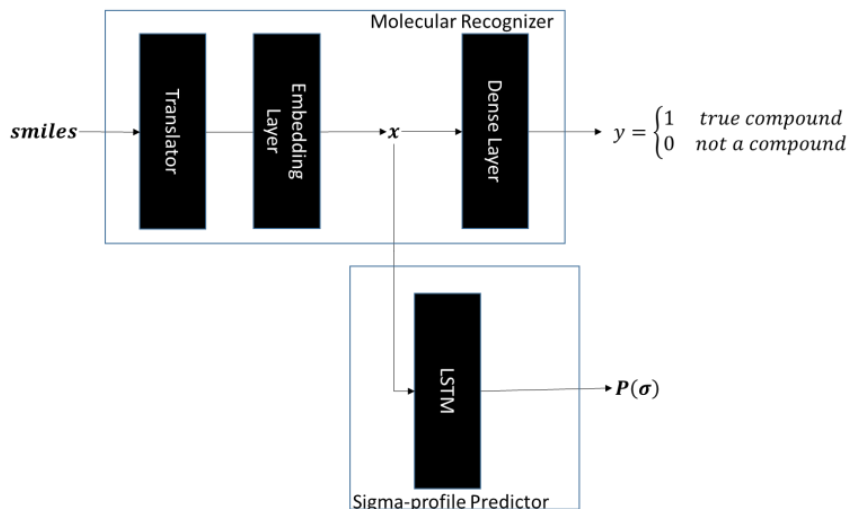


Figure 1 : Overall network structure

3. Results

3.1. Recognizer and Molecular Classification

Table 1 showed the training performance of our recognizer. There is a limited number of false positive, i.e. fake compound recognized as true, are found because we may have 2 accidentally generated a true compound. There is no “false negative”, i.e. true compound recognized as fake.

Table 1: Performance of the Recognizer

	True Compound	Fake Compound
Training Data		
Output 0	1372	1
Output 1	0	1371
Test Data		
Output 0	274	1
Output 1	0	273

Hence principle component analysis (PCA) (Joliffe 2011) was performed to help visualize how molecules are distributed in the high dimensional space. Figure 2(a) showed that the first 3 PCs account for about 80% of the variation. Furthermore Figure 2 (b) to 2(d) if we locate homologues of normal paraffins, straight chain alcohols and acids, they are arranged in an orderly manner, indicating that the embedding is able to transform the text-based SMILES input into a distance-relevant high dimensional space that can be used for molecular recognition and classification.

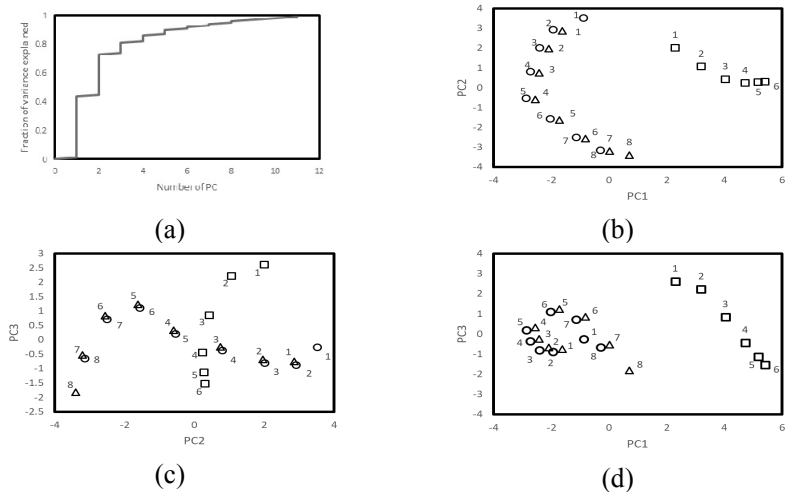


Figure 2: PCA projection of the high dimensional feature space

3.2. Sigma-profile prediction

Figure 3 showed the best model we obtained with different training set. Out of 274 test data, the average R^2 is 0.96, 179 has a R^2 of over 0.95, the worst R^2 is 0.79. Figure 4a and 4b showed ML predictions sigma profile for two compounds with $R^2=0.99$ 0.79 respectively. Even when the actual agreement is inferior, the trend of the sigma-profile is consistent.

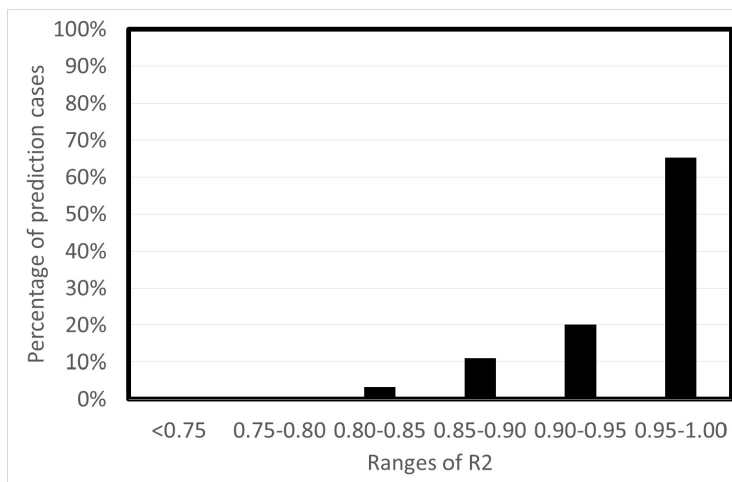


Figure 3 Distribution of prediction accuracy

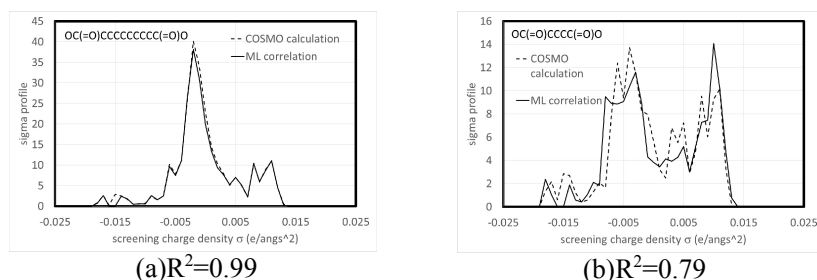


Figure 4: Sigma profile correlations of (a) OC(=O)CCCCCCCC(=O)O, $R^2=0.99$

3.3. Prediction of infinite dilution coefficients

Figure 5a and 5b compare the infinite dilution coefficients obtained using sigma profiles predicted by ML and sigma profiles using quantum mechanical calculations in water and n-hexane respectively. Fair agreements were obtained between two types of sigma profiles. However, it was found that the ML model over-predicts the infinite dilution activity coefficient in water when they are much less than 1; and under-predicts the infinite dilution activity coefficient in n-hexane when is much greater than 1. This indicates that ML correlation is biased towards non-polar compounds. Improvement of model can be achieved by refined sampling of training data.

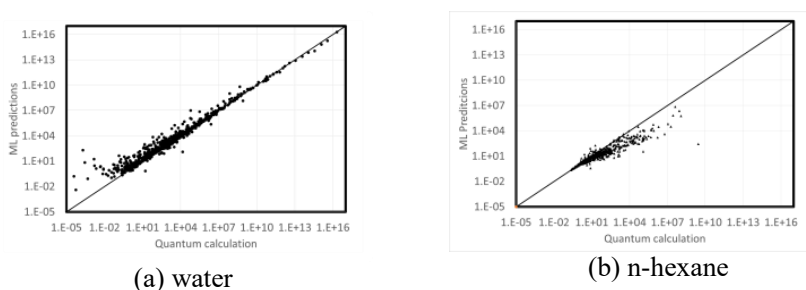


Figure 5: Prediction of infinite dilution coefficients

4. Conclusion

The above results serve as a preliminary demonstration that molecular classification and prediction of sigma-profile, results of quantum calculations, using text-based molecular description is possible. A recognizer was trained using word-embedding network, and a LSTM transformation network. The network gave no false negative and very few false positive. PCA analysis showed that the transformed space can be used as for molecular feature representation and classification. Use this space as input, we showed that fairly accurate prediction of sigma-profile can be developed. Optimization of network structure have not yet been considered. The promising results suggest that extension of this approach to a more extensive data base should be a valuable for a

priori property prediction and molecular design. Refinement of neural network structure, better sampling of data and the use of other molecular representation should also be investigated.

References

- Dalby, A., Nourse, J. G., Hounshell, W. D., Gushurst, A. K., Grier, D. L., Leland, B. A., & Laufer, J. (1992). Description of several chemical structure file formats used by computer programs developed at Molecular Design Limited. *Journal of Chemical Information and Computer Sciences*, 32(3), 244-255.
- Fredenslund, A., Jones, R. L., & Prausnitz, J. M. (1975). Group-contribution estimation of activity coefficients in nonideal liquid mixtures. *AIChE Journal*, 21(6), 1086-1099.
- Hochreiter S. and Schmidhuber J.. (1997) Long short-term memory. *Neural Computation*, 9(8):1735–1780.
- Humphrey, W., Dalke, A., & Schulten, K. (1996). VMD: visual molecular dynamics. *Journal of Molecular Graphics*, 14(1), 33-38.
- Joback, K. G., & Reid, R. C. (1987). Estimation of pure-component properties from group-contributions. *Chemical Engineering Communications*, 57(1-6), 233-243.
- Jolliffe, I. (2011). Principal component analysis. In International encyclopedia of statistical science (pp. 1094-1096). Springer, Berlin, Heidelberg.
- Klamt, A. (1995). Conductor-like screening model for real solvents: a new approach to the quantitative calculation of solvation phenomena. *The Journal of Physical Chemistry*, 99(7), 2224-2235.
- Lin, S. T., & Sandler, S. I. (2002). A priori phase equilibrium prediction from a segment contribution solvation model. *Industrial & engineering chemistry research*, 41(5), 899-913.
- Mikolov, T., Chen, K., Corrado, G., & Dean, J. (2013). Efficient estimation of word representations in vector space. *arXiv preprint arXiv:1301.3781*.
- Mullins, E., Oldland, R., Liu, Y. A., Wang, S., Sandler, S. I., Chen, C. C., ... & Seavey, K. C. (2006). Sigma-profile database for using COSMO-based thermodynamic methods. *Industrial & engineering chemistry research*, 45(12), 4389-4415.
- Weininger D. SMILES, a chemical language and information system. 1. Introduction to methodology and encoding rules. *Journal of Chemical Information and Modeling*. 1998, 28, 31–36.

Comparative CFD analysis of thermal energy storage materials in photovoltaic/thermal panels

Aya Al-Hmoud^a, Daniel Sebastia-Saez^a, Harvey Arellano-Garcia^{a,b,*}

^a*Department of Chemical and Process Engineering, University of Surrey, Guildford GU2 7XH, United Kingdom*

^b*LS Prozess- und Anlagentechnik, Brandenburgische Technische Universität Cottbus-Senftenberg, D-03046 Cottbus, Germany*

h.arellano-garcia@surrey.ac.uk

Abstract

Photovoltaic/thermal systems are a novel renewable energy approach to transform incident radiation into electricity and simultaneously store the excess thermal energy produced. Both sensible and latent heat storage materials have been investigated in the past for thermal storage; with desert sand having been recently considered as an efficient and inexpensive alternative. In this work, we use a transient Computational Fluid Dynamics simulation to compare the performance of desert sand to that of well-established phase-change materials used in photovoltaic/thermal systems. The simulation gives as a result the temperature profiles within the device as well as the time evolution of the charge/discharge cycles when using PCMs. The results show the suitability of desert sand as a thermal storage material to be used in photovoltaic/thermal systems.

Keywords: photovoltaic/thermal system, phase change material, thermal energy storage, CFD, charge/discharge cycle.

1. Introduction

Amongst the different renewable energy technologies available, photovoltaic systems are currently one of the best positioned to be fully implemented in order to tackle the global carbon mitigation challenge. An important drawback however is their low efficiency, which results in only a fraction of the incident energy being converted into electricity, while the rest of the incident energy is lost to the surroundings in the form of heat (Preet, 2018). Nonetheless, this energy loss may lead to a temperature rise which can jeopardise the structure of the photovoltaic (PV) cell, ultimately causing a decrease in its lifetime. With the cooling of the PV panel being crucial, an alternative technology called photovoltaic thermal (PV/T) systems has emerged to allow for co-generation of both electricity and thermal energy. In PV/T systems, the heat loss can be stored by increasing the temperature of a material layer, i.e. a thermal energy storage (TES) medium, placed underneath the absorber. The thermal energy stored in this manner can subsequently be passed on to a liquid or gas stream. PV/T systems give way thus to increased general efficiency relative to photovoltaic cells cooled by natural convection (Preet, 2018). It is necessary then to determine the best material for the TES module to maximise the performance of the PV/T configuration. Sensible heat TES media and phase change materials (PCM) are the options available.

Sensible TES media store sensible heat as a function of their specific heat capacity, whereas PCMs allow for extra energy storage by undergoing phase change. PCMs can therefore pave the way to increased efficiencies and overnight use thanks to slow energy release after the external source of heat ceases to be applied. Moreover, the use of PCMs in conjunction with PV cells allows for effective control of the working temperature of the cell by damping any fluctuations (Alva et al., 2017; Sardarabadi et al., 2017; Ma et al., 2017). Regarding sensible heat storage, silicon carbide (SiC) and natural desert sand have also received attention recently because their particulate material gives way to enhanced heat transfer. Desert sand has also the advantage of presenting high availability and extraordinary resistance to agglomeration, being capable of withstanding temperatures of up to 1000°C.

Research on the use of desert sand as a TES medium began in the 1980s (Flamant, 1982), and has been taken up recently because the use of costless local materials is considered a key factor to reduce the levelised energy cost of CSP systems (Schlipf et al., 2015). A comprehensive assessment of the thermal and morphological properties of different types of desert sand from the United Arab Emirates was reported in the literature (Diago et al., 2018; Iniesta et al., 2015). They used these data to further develop a combined solar receiver/storage system (similar to that proposed by Flamant et al., 2013) using desert sand as TES medium.

The scope of the work presented here is to further develop the use of desert sand by presenting a transient CFD approach to compare the performance of sand and some well-established PCMs (including capric/palmitic acid, salt hydrate, and n-octacosane) in a PV/T configuration. A similar configuration has been reported by Mousavi et al. (2018), who run a steady-state 2-D CFD model to carry out a parametric study and exergy analysis of the system including different PCMs. The objective of this work, in contrast, is to assess the performance of desert sand in the same PV/T configuration by using a transient 3-D approach, and establish a comparison with various PCMs. The thermal efficiency of the system, temperature distributions within both the water channel and the surrounding thermal storage matrix, and the heating-cooling cycles of both n-octacosane and sand-based systems are simulated to quantify the suitability of desert sand as an effective material to be used in PV/T systems. As of today, to the best of our knowledge the use of desert sand in PV/T systems remains unexplored, and thus this article presents the first steps in that direction. The article begins with the description of the computational methodology employed (Section 2), and follows with a systematic grid convergence assessment for the main output variables from the simulation, i.e. temperature and density of the phase change material, before discussing the results in section 3 and presenting the concluding remarks in section 4.

2. Modelling methodology and grid convergence study

The computational domain is depicted in Figure 1, and consists of a copper pipe containing a water stream embedded in a rectangular PCM block exposed to the radiation from the sun. An additional layer, placed on top of the PCM, is included in the model in order to represent the absorber layer. The computational domain mimics, then, the configuration presented by Browne et al. (Browne et al., 2015; 2016), but only one of the copper pipes has been considered here for computational economy reasons. The schematic illustration showcases the dimensions and the different layers of the three-dimensional computational domain used in this work. The top wall of the absorber layer (the one which is not in contact with the PCM layer) is modelled as a constant heat

source wall in order to mimic the incident sunrays. A PCM matrix is placed directly underneath. A granular material is defined in the PCM matrix in those cases where desert sand was considered. Water enters the copper pipe with a specific mass flow rate and temperature (mass flow inlet boundary condition with 0.002 kg/s) and abandons the domain through a pressure outlet boundary. Adiabatic walls are specified as boundary conditions on the rest of the boundaries. The simulations were performed using the commercial software ANSYS Fluent v19.1. The options Solidification/Melting and Energy were switched on along with the laminar option for turbulence. The steady state solver was implemented to obtain the results in Figures 2, 3 and 4. Under-relaxation factors were kept at default values. Further simulations were run by using the transient solver, in order to monitor the time evolution of temperature difference between the water inlet and outlet. To do so, the heat flux wall boundary condition was switched on and off each other 4,000 s flow time in order to mimic the charge/discharge cycles of the PCM matrix.

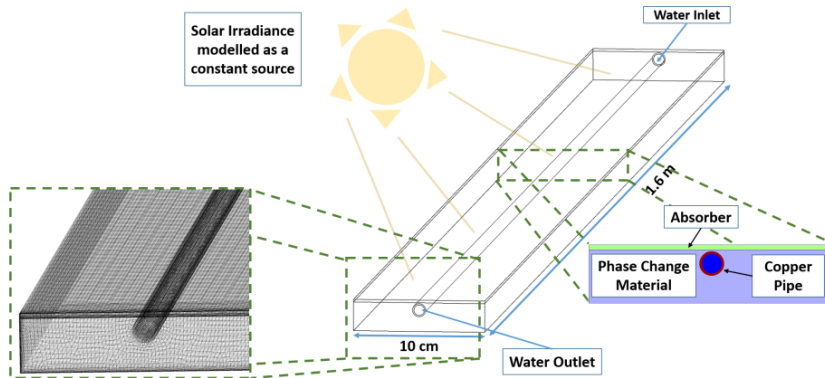


Figure 1: Schematic illustration of the computational domain including boundary conditions, dimensions and a detail of the numerical grid.

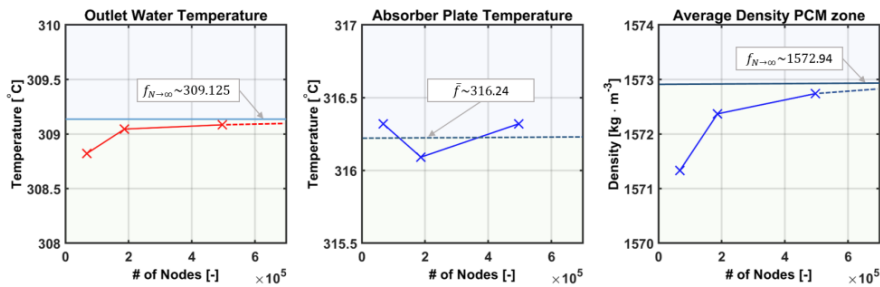


Figure 2: Results of the grid convergence test.

A systematic grid convergence assessment has been performed by applying the Richardson extrapolation method (Roache, 1994), which allows to quantify the numerical error caused by the space discretization relative to the estimated solution of the conservation equations at zero grid spacing. A coarse (67,488 nodes), medium (186,951), and a fine mesh (496,824) were used to perform the grid convergence study. The results are reported in Figure 2, where the extrapolated value at zero grid spacing is

also represented in those cases that showed convergence (outlet water temperature and the density of the PCM zone). Oscillatory behaviour is observed for the average absorber plate temperature; this possibility is also covered in the literature (Ali et al., 2009). The order of magnitude of the maximum value observed for the grid convergence index (see its definition in Roache, 1994) using the fine and the medium mesh was 10^{-4} . This means a deviation obtained with the different grids of up to 0.01%.

3. Results and discussion

The steady state solver was initially used to check the temperature fields across the device upon a range of solar irradiance values (from 150 to 1,200 W/m^2) and using different options as PCM. The two plots on the top part of Figure 3 depict the temperature difference between the average temperature at successive cross-sections along the pipe and the temperature at inlet conditions (25°C). Similar values are obtained for n-octacosane and desert sand, proving the latter as a valid material in order to harvest the excess energy produced in the PV/T panel and transfer it to a working fluid. The colour maps on the bottom part of Figure 3 shows the temperature distribution in a plane parallel to the absorber and containing the symmetry axis of the pipe upon a solar irradiance of 1,200 W/m^2 . The results show that the temperature attained by the liquid at the outlet boundary and the maximum temperature of the TES matrix do not match (~ 315 K against ~ 366 K) when using n-octacosane (a PCM). A longer domain would therefore be needed in order to fully avail the energy stored by the PCM. Conversely, they are close when using sand as TES medium (~ 315 K against ~ 319 K). This suggests that there is an advantage in using desert sand instead of n-octacosane because a smaller quantity of TES medium is required to fully avail the incident solar irradiance.

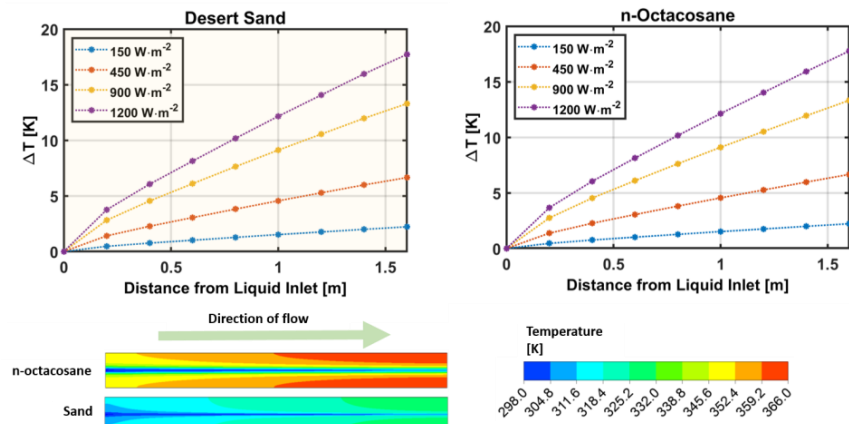


Figure 3: Temperature profiles in the symmetry axis of the copper pipe (top two graphs) and colour maps of the temperature distribution within the PCM matrix (bottom part of the figure) for n-octacosane and sand.

Figure 4 on the other hand shows the effect of the solar irradiance on the PCM solid fraction (left-hand side graph) for several materials. A visualization of the boundary delimiting the liquid and the solid fraction is included (right-hand side plot) for the case of n-octacosane. The graph on the left-hand side allows the reader to establish which PCM is more advantageous depending on the solar irradiance. Among the materials

used in our simulations, n-octacosane needed a solar irradiance of 600 W/m^2 to begin melting (subsequently storing latent heat), whereas capric-palmitic acid underwent full phase change for the entire range of solar irradiances tested in the present study. The results contained in Figure 4 allow the user of the present model to calculate the amount of latent heat that a given PCM can store for solar irradiances between 150 and $1,200 \text{ W/m}^2$ and different materials.

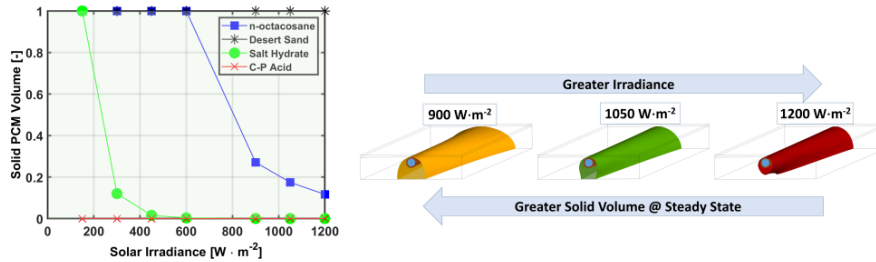


Figure 4: Relationship between the PCM solid fraction and the solar irradiance (left-hand side graph). Visualization of the PCM n-octacosane melted volume at steady state as a function of the solar irradiance (right-hand side). In the latter, the water outlet is visible, whereas the inlet is hidden by the solid portion of the PCM.

Finally, Figure 5 shows the transient charge/discharge cycle of the PCM material n-octacosane relative to the behavior of desert sand, which does not undergo phase change. This transient solution was obtained by using the results at steady-state as the initial values. In the beginning the heat flux was switched off, mimicking the conditions that the panel would have at night. In the case of desert sand, one can observe that heat has been retained during approximately $4,500 \text{ s}$ (1.25 hours), after which there is no water temperature difference between inlet and outlet. The PCM, however, retains heat during more time by virtue of the phase change process. The results in Figure 5, however, prove as expected that the use of a PCM is more convenient than granular desert sand in those applications where heat needs to be released overnight.

4. Final remarks

A 3-D CFD model has been developed in order to compare the suitability of different materials to be used as thermal energy storage (TES) media in photovoltaic/thermal panels, including desert sand and different phase change materials (PCM).

Better heat transfer to the water stream occurs at steady state with desert sand than with n-octacosane (one of the PCMs studied), leading to a reduction on the volume of TES needed to fully avail the thermal energy excess. Moreover, since the 3-D model presented here calculates the solid volume fraction of PCM upon given conditions, the user can determine which PCM is best to be used for a particular value of the solar irradiance and to estimate the latent heat stored. The transient configuration proves as a useful tool to study the charge/discharge cycles of the thermal energy storage materials, and thus provides a value of the energy a particular TES medium can release and for how long.

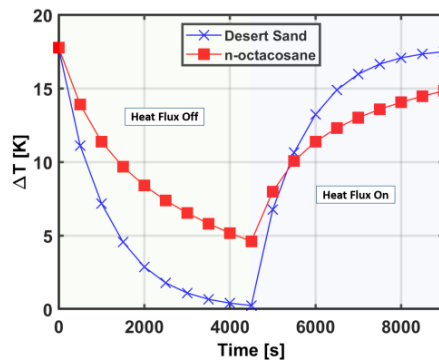


Figure 5: Time evolution of the inlet-outlet water temperature difference.

References

- M.S.M. Ali, C.J. Doolan, V. Whitley, 7th International Conference on CFD in the minerals and process industries (CSIRO), Melbourne, Australia, December 2009.
- G. Alva, L. Liu, X. Huang, G. Fang, 2017, Thermal energy storage materials and systems for solar energy applications, *Renew. Sust. Energ. Rev.*, 68(1), 693–706.
- M.C. Browne, K. Lawlor, A. Kelly, B. Norton, S. J. McCormack, 2015, Indoor characterisation of a photovoltaic/thermal phase change material system, *Energ. Proced.*, 70, 163–171.
- M.C. Browne, D. Quigley, H.R. Hard, S. Gilligan, N.C.C. Ribeiro, N. Almeida, S.J. McCormack, 2016, Assessing the thermal performance of phase change material in a photovoltaic/thermal system, *Energ. Proced.*, 91, 113–121.
- M. Diago, A.C. Iniesta, A. Soum-Glaude, N. Calvet, 2018, Characterization of desert sand to be used as a high-temperature thermal energy storage medium in particle solar receiver technology, *Appl. Energ.*, 216, 402–413.
- G. Flamant, 1982, Theoretical and experimental study of radiant heat in a solar fluidized-bed receiver, *AIChE J.*, 28(4), 529–535.
- G. Flamant, D. Gauthier, H. Benoit, J.-L. Sans, R. Garcia, B. Boissiere, R. Ansart, M. Hemati, 2013, Dense suspension of solid particles as a new heat transfer fluid for concentrated solar thermal plants: On-sun proof of concept, *Chem. Eng. Sci.*, 102, 567–576.
- A.C. Iniesta, M. Diago, T. Delclos, Q. Falcoz, T. Shamim, N. Calvet, 2015, Gravity-fed combined solar receiver/storage system using sand particles as heat collector, heat transfer and thermal energy storage media, *Energ. Proc.*, 69, 802–811.
- T. Ma, J. Zhao, J. Han, 2017, A parametric study about the potential to integrate phase change material into photovoltaic panels, *Energ. Proced.*, 142, 648–654.
- S. Mousavi, A. Kasaeian, M. Behshad, S. Mohammad, H. Jahangir, 2018, Numerical investigation of the effects of a copper foam filled with phase change materials in a water-cooled photovoltaic/thermal system, *Energ. Convers. Manage.* 163, 187–195.
- S. Preet, 2018, Water and phase change material based photovoltaic thermal management systems: A review, *Renew. Sust. Energ. Rev.*, 82(1), 791–807.
- P.J. Roache, 1994, Perspective: A method for uniform reporting of grid refinement studies. *J. Fluids Eng.*, 116(3), 405–413.
- M. Sardarabadi, M. Passandideh-Fard, M.-J. Maghrebi, M. Ghazikhani, 2017, Experimental study of using both ZnO/ water nanofluid and phase change material (PCM) in photovoltaic thermal systems, *Sol. Energ. Mat. Sol. C.*, 161, 62–69.
- D. Schlipf, P. Schicktzanz, H. Maier, G. Schneider, 2015, Using sand and other small grained materials as heat storage medium in a packed bed HTTESS, *Energ. Proced.*, 69, 1029–1038.

Development of a Model-Based Quality-by-Control Framework for Crystallization Design

Ayşe Eren,^a Botond Szilágyi,^a Justin Quon,^b Masashi Furuta,^b Charles Papageorgiou,^b Zoltán K. Nagy^{a*}

^a*Davidson School of Chemical Engineering, Purdue University, 610 Purdue Mall, West Lafayette 47907, United States*

^b*Takeda Oncology, 40 Landsdowne St, Cambridge 02139, United States*

erena@purdue.edu

Abstract

The work proposes a combination of model-free and model-based quality-by-control (mfQbC and mbQbC) paradigms as a general framework for the optimal crystallization design with the aim of minimization of fines and agglomerates in the product. This framework provides an improved alternative to the current industrial practice, by the combined use of feedback control and mathematical models for rapid design of robust crystallization processes. The implementation of the proposed mbQbC framework enhanced the prediction of crystallization events and was able to achieve better control of the crystallization processes by providing controlled heating/cooling cycles, for deagglomeration and fines destruction. The information for parameter estimation and optimization calculations was collected from the experiments in mfQbC part, which additionally also provided a rapid design of robust operating conditions, which subsequently in the mbQbC approach were improved to achieve optimal operation.

Keywords: Optimization, modelling, control, crystallization, design.

1. Introduction

Batch crystallization is used substantially in purification of the active pharmaceutical ingredients (APIs) in the pharmaceutical industries. Particle size has a significant effect on the quality of drugs and on the efficiency of downstream processes such as filtration, milling, centrifugation, drying, granulation, and tableting (Rawlings et al., 1993). A narrow crystal size distribution (CSD) at the desired mean crystal size is crucial for efficient downstream processes and desired critical quality attributes (CQAs) of the final product, therefore crystallization control strategies such as model-based control approaches, automated direct nucleation control (ADNC), supersaturation control (SSC) or temperature control (T-control) have been developed to achieve desired CSD (Simon et al., 2018). Current industrial practice for the design of operating conditions generally uses a quality-by-design (QbD) framework, based on exploring the design space by experimentation, which can be time consuming even with a well thought experimental design. More recently, a novel and faster alternative, the quality-by-control (QbC) framework has been introduced as a new paradigm that uses feedback control (model-free or model-based) to automatically find the optimum operating profiles that lead to the manufacturing of final product with desired CQAs, rather than applying open-loop experimentation.

The new sequential QbC approach proposed consists of the combination of the mfQbC approach where first closed loop feedback control is used to automatically identify the design space and feasible region of operation, while also providing a robust, although probably suboptimal, operating procedure. This is followed by the implementation of a mathematical model that uses the information from experimental part for parameter estimation and model-based optimization to provide an optimal refined operating procedure. The experimental control strategy provides the first important step of improving the product quality and phase diagram information of the system. MbQbC provides the ability to predict crystallization phenomena or to enhance the control of crystallization processes. Worlitschek (2004) showed that a developed deterministic model for solution thermodynamics, crystal growth, and nucleation enhanced the control of the crystallization of paracetamol from ethanol. After optimization, the determined cooling profile was good enough to obtain the desired monomodal particle size distribution and supersaturation. Hermanto, Braatz et al. (2010) showed that an integrated batch-to-batch and nonlinear model predictive control (B2B-NMPC) strategy based on a hybrid model can be used to control the polymorphic transformation of L-glutamic acid. Nagy (2009) showed that a lower model-free approach can be used to operate the system in the phase diagram in combination with a higher-level model-based approach to maintain product uniformity. Acevedo et al. (2017) showed that model-based design can also be used for the design of model-free direct nucleation control (DNC) for the optimal operation in the case of continuous crystallization.

A critical step of model-based approaches is the parameter estimation of the crystallization kinetics, which requires the solution of the population balance equations (PBE) of the crystallization model. For efficient parameter estimation, model-based optimization, and real-time model predictive control, it is imperative to have fast and accurate solution. Various techniques have been proposed for the solution of PBEs, including analytical solution-based approaches, such as method of moments, quadrature method of moments, or method of characteristics, or direct numerical solutions such as finite volume method (FVM) or Monte-Carlo simulations, which have also been applied along with the solution of the optimization problem (Omar and Rohani, 2017). In this work, the model-free and model-based QbC approaches were combined for the optimal design of crystallization systems with the aim of minimization of fine formation and agglomeration of paracetamol (PCM) crystals, as the model compound. Although PCM is well-studied, only the parameters for the nucleation and growth kinetics have been determined so far. This work will be the first study that estimates all kinetic parameters for the primary and secondary nucleation, growth, dissolution, agglomeration and deagglomeration mechanisms for the crystallization of PCM by developing a novel QbC framework combining model-free and model-based techniques.

2. Experimental Methods, Model Development, Parameter Estimation, and Process Optimization

Four types of batch experiments were performed to understand the system dynamics, seed production and for crystallization kinetics parameter estimation of the crystallization of paracetamol (PCM) from isopropyl alcohol (IPA). Seeded linear cooling and heating experiments were used for determination of the crystal count during secondary nucleation. These were followed by several direct nucleation control (DNC) experiments with different cooling/heating rates to keep the crystal count within certain thresholds.

DNC experiments provided the information about the primary and secondary nucleation curves in the phase diagram. After determining the metastable zone width (MSZW) according to these curves, a seeding point and set point were selected for the SSC experiments. The temperature data generated from SSC experiment gave the cooling profile required to operate below the secondary nucleation curve (e.g. growth zone) in the phase diagram. The cooling curve provided was approximated by a sequence of three linear cooling ramps and was used in an open-loop temperature control experiment to show that the simplified profile can produce similar product. Data from all experiments were used to estimate nucleation, growth, agglomeration, dissolution and de-agglomeration kinetic parameters. UV/Vis spectrophotometer, focused beam reflectance measurement (FBRM), and Particle Vision Measurement (PVM) were used as PAT tools to measure concentration, particle count, morphology and size. In addition, Malvern Mastersizer 3000 and Nikon SMZ1500 microscope were used for offline characterization of size distribution and crystal morphology.

A mathematical model is required for mbQbC that describes the crystal birth, growth, and death due to nucleation, growth, agglomeration, dissolution, and de-agglomeration. A 1D Population Balance Model (PBM) with size-independent growth and dissolution, including size-dependent agglomeration and de-agglomeration kernels (1) was used to model the system for the supersaturated and desaturated regions along with corresponding mass balances equations (2).

$$\frac{\partial n(L, t)}{\partial t} + G \frac{\partial n(L, t)}{\partial L} = B\delta(L - L_m) - \int_0^{\infty} \beta(t, L, \lambda)n(L, t)n(\lambda, t)d\lambda + \frac{1}{2} \int_0^L \frac{\beta(t, (L^3 - \lambda^3)^{1/3}, \lambda)}{(L^3 - \lambda^3)^{2/3}} \times n(t, (L^3 - \lambda^3)^{1/3})n(t, \lambda)d\lambda, \text{ if } \sigma > 0 \quad (1)$$

$$\frac{\partial n(L, t)}{\partial t} - D \frac{\partial n(L, t)}{\partial L} = \int_L^{\infty} b(L|\lambda)S(\lambda)n(t, \lambda)d\lambda - S(L)n(t, L), \text{ if } \sigma < 0$$

$$\frac{dC}{dt} = \begin{cases} -k_v \rho_c \left(3G \int_0^{\infty} L^2 n(L, t) dL \right), & \text{if } \sigma > 0 \\ k_v \rho_c \left(3D \int_0^{\infty} L^2 n(L, t) dL \right), & \text{otherwise} \end{cases} \quad (2)$$

$$B = B_p + B_b, B_p = k_p \sigma^p, B_b = k_b \sigma^b A_c, G = k_g \sigma^g \exp\left(-\frac{E_A}{RT}\right), \beta(\lambda, L) = k_{ag} F(\lambda^3 + L^3), D = k_d (-\sigma)^d, S(\lambda) = k_{br} F(\lambda^3) \quad (3)$$

The model was solved by using the high-resolution FVM (HR-FVM) during parameter estimation and optimization calculations. Parameter estimation calculations were done to estimate 10 parameters in the crystallization events (3) which are also used in PBEs. The equations are given for primary and secondary nucleation, growth, agglomeration, dissolution, and de-agglomeration, respectively. Size dependent de-agglomeration and agglomeration selection functions F are described by hyperbolic tangent functions using the crystal crystals sizes for both cases. Optimizations were carried out for the temperature profile (T-profile), in three steps: a) first a preliminary stochastic global optimization of a crude T-profile defined by 10 discrete temperature points was performed to provide a good starting point for the b) gradient-based optimization (sequential quadratic programming-SQP) for refinement of the solution and c) SQP-based

optimization of a smoother T-profile (defined by 20 discrete temperatures), using as starting point the outcome of b). For global optimization, a custom implementation of Covariance Matrix Adaptation Evolution Strategy (CMA-ES) was applied. The objective function (4) was defined to minimize each term: the product fine index, product agglomeration index, sharpness of T-profile and agglomerates index during the crystallization, respectively. The weight factors (w_i) were set by preliminary optimizations so to ensure that the sub-objective values are in the same order of magnitude around the optimum. Note that changing the values of weight factors also changes the optimal solution. This is a subjective decision, which is taken based on detailed process understanding. In Eq. (4) N_A is the number of agglomerates, L is the length of the crystals, n is the population density. The product fine index is the ratio of the number of fine crystals to the total number of crystals in the product CSD; the product agglomeration index is the ratio of the agglomerates in the same product CSD. Sharpness of the T-profile was defined as the gradient of the profile to be minimized for smoother operation and the last term is defined as the total number of agglomerated crystal fraction during the crystallization rather than only in the product CSD.

$$OF = 100 \left[\frac{\int_0^{L_f} L^3 n(L, t = t_f) dL}{\int_0^{L_{max}} L^3 n(L, t = t_f) dL} \right]^2 + w_1 100 \left[\frac{N_A(t = t_f)}{\int_0^{L_{max}} n(L, t = t_f) dL} \right]^2 + w_2 \sum_{i=2}^N (t_i - t_{i-1}) \left(\frac{T_i - T_{i-1}}{t_i - t_{i-1}} \right)^2 + w_3 100 \int_0^{t_f} \left[\frac{N_A(t)}{\int_0^{L_{max}} n(L, t) dL} \right]^2 dt \quad (4)$$

3. Results and Discussion

The experiments performed in the mfQbC framework were seeded cooling crystallization, DNC, followed by SSC, and a T-control experiments. The benefits of this procedure are to obtain detailed information about the system's phase diagram/operating zone, as well as to produce the product obtained from the close-loop SSC experiment by a more practical, simplified cooling crystallization (T-control). Volume-based crystal size distribution and microscopy images showed that similar products were achieved. Data from each controlled experiment was used as input for the parameter estimation calculations in the model-based approach.

Param.	Value	Dev.	Units
k_p	10.35	± 0.71	$\#/m^3s$
p	2.63	± 0.21	-
k_b	$1.19 \cdot 10^6$	$\pm 0.25 \cdot 10^6$	$\#/m^3s$
b	0.88	± 0.05	-
k_g	$4.56 \cdot 10^{15}$	$\pm 0.65 \cdot 10^{15}$	m/m^3s
g	1.61	± 0.11	-
E_A	89044	± 7184	kJ/mol
k_d	1.95	± 0.03	m/m^3s
k_{ag}	$1.46 \cdot 10^{-14}$	$\pm 0.25 \cdot 10^{-14}$	$\#/m^3s$
k_{br}	$1.08 \cdot 10^{-2}$	$\pm 0.11 \cdot 10^{-2}$	$\#/m^3s$

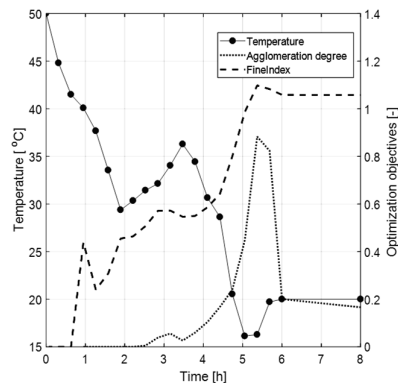


Fig. 1. (a) Estimated kinetic parameters; (b) Optimum temperature profile and the evolution of the agglomeration degree and fine index during the optimum operation.

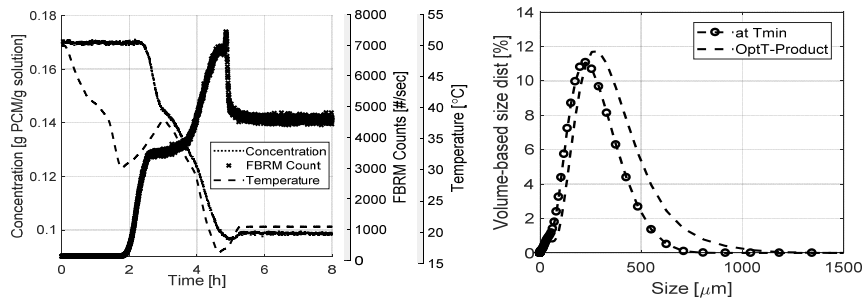


Fig. 2. (a) Experimental results of the optimum temperature profile; (b) Volume-based size distribution of the crystals from the minimum temperature point and the end of the same experiment.

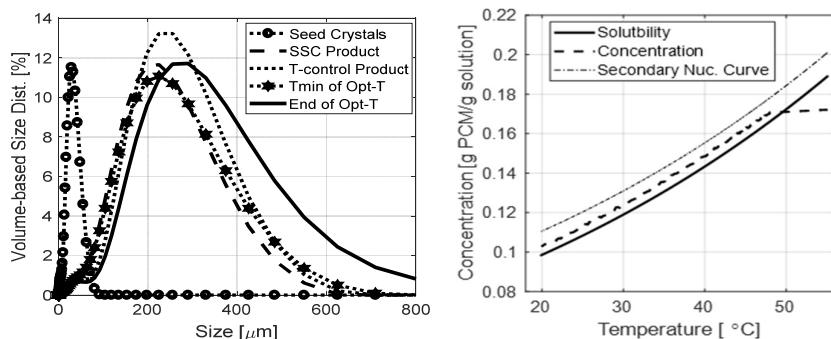


Fig. 3. (a) Volume-based size distribution of the seed crystals used and products from SSC and T-control experiments; (b) Operation profile of SSC experiment in growth region.

The combined framework is designed so that the two parts to be complementary to each other. Collected data from mfQbC was used in parameter estimation and optimization calculations in mbQbC. Estimated parameters (Fig. 1) were used in the model for optimization calculations. The optimum temperature profile (T-opt) was obtained by the three step optimization calculations as described. The resulting profile exhibited two heating cycles including a small heating ramp at the end. T-opt was tested by an unseeded cooling crystallization experiment. Results show that the model predicts the nucleation accurately, and the system is heated before detectable nucleation by FBRM counts. Although the system was in the heating region the primary nucleation still occurred, but the first heating cycle was able to slow down the nucleation event. In addition, the 4 °C heating at the end was efficient to destroy fine crystals and to induce de-agglomeration. During the experiment, two samples were taken at the minimum temperature point and at the end to understand the effect of the last heating cycle. Microscopy images and the size distributions of the samples before and after this heating cycle showed that this small heating ramp (4 °C) was enough for de-agglomeration and elimination of fine crystals (Fig. 2), which could be observed by the corresponding FBRM peak before the decrease in the counts (2,500 counts/sec), respectively. The strength of fine elimination and de-agglomeration of the T-opt by predicting nucleation correctly can be emphasized by the comparison of the products from SSC, T-control and T-opt experiments. The size distribution (Fig.3) shows that, T-opt product contains more larger crystals and less fines. The model-free direct design approach provided automatically a T-profile from SSC

experiment that was implemented easily using a simple T-control experiment. While this is easy to develop and implement, this may not be the optimum operating profile especially for systems that tend to agglomerate or produce significant number of fines due to attrition, breakage or some secondary nucleation. The model-based optimization provided a T-profile that reinforces fine dissolution and de-agglomeration (Fig. 3). The shift in the distribution of the end-sample from the T-opt experiment shows that fines elimination is significant when compared to samples from other experiments or different time moment of the same experiment.

4. Conclusions

A new hybrid (model-based and model-free) QbC framework for crystallization design was developed that can predict the crystallization process and keep the measured CQAs at their desired values, while using feedback control approaches efficiently. This framework was developed to provide the optimum operating procedure for crystallization systems. The model could even predict the primary nucleation time and apply heating cycle before detectable nucleation. The experimental validation of the approach demonstrated that the desired fine dissolution was achieved, agglomerated index was significantly decreased and the mean crystal size of the CSD could be increased accordingly, indicating the potential benefits of the new approach as a novel and efficient design of crystallization systems governed by complex phenomena.

Acknowledgements

Financial support from Takeda Pharmaceuticals Int. Co. is gratefully acknowledged.

References

- Acevedo, David, Yang Yang, Daniel J. Warnke, and Zoltan K. Nagy. 2017. "Model-Based Evaluation of Direct Nucleation Control Approaches for the Continuous Cooling Crystallization of Paracetamol in a Mixed Suspension Mixed Product Removal System." *Crystal Growth and Design* 17 (10): 5377–83. doi:10.1021/acs.cgd.7b00860.
- Hermanto, Martin, Richard Braatz, and Min-Sen Chiu. 2010. "Integrated Batch-to-Batch and Nonlinear Model Predictive Control for Polymorphic Transformation in Pharmaceutical Crystallization." *AIChE Journal* 57 (4): 1008–19. doi:10.1002/aic.
- Nagy, Zoltan K. 2009. "Model Based Robust Control Approach for Batch Crystallization Product Design." *Computers and Chemical Engineering* 33 (10): 1685–91. doi:10.1016/j.compchemeng.2009.04.012.
- Omar, Hecham M., and Sohrab Rohani. 2017. "Crystal Population Balance Formulation and Solution Methods: A Review." *Crystal Growth & Design* 17 (7): 4028–41. doi:10.1021/acs.cgd.7b00645.
- Rawlings, James B., C.W. Sink, and S.M. Miller. 1993. "Control of Crystallization Processes." *Handbook of Industrial Crystallization*, 201–30. doi:10.1016/B978-075067012-8/50011-2.
- Simon, Levente L., Elena Simone, and Kaoutar Abbou Oucherif. 2018. *Crystallization Process Monitoring and Control Using Process Analytical Technology. Computer Aided Chemical Engineering*. 1st ed. Vol. 41. Elsevier B.V. doi:10.1016/B978-0-444-63963-9.00009-9.
- Worlitschek, Jörg, and Marco Mazzotti. 2004. "Model-Based Optimization of Particle Size Distribution in Batch-Cooling Crystallization of Paracetamol." *Crystal Growth and Design* 4 (5): 891–903. doi:10.1021/cg034179b.

DEM Study of a Mixer for Core Manufacturing System

Jiwon. Roh,^{a,b} Junghwan. Kim,^{a,*} Man Sig. Lee,^a Il. Moon,^b

^a*Korea Institute of Industrial Technology, 55 Jongga-ro, Jung-gu, Ulsan 44413, South Korea*

^b*Yonsei University, 50 Yonsei-ro, Seodaemun-gu, Seoul 03722, South Korea*

kjh31@kitech.re.kr

Abstract

A core is a special, preformed part of a casting which is essential for complex and delicate shapes in the casting process. Around 95% of sand and 5% of binder are mixed as the raw material for manufacturing the core. Organic binders exhibit a high performance but generate contaminants and toxic gases since they are composed of toxic chemicals, and therefore, the trend in popular types of binder is evolving from organic to inorganic. In this context, we focus on the development of a discrete element model (DEM) model for the mixer in the core manufacturing process using an inorganic binder. We validate the developed model by comparing it with an actual horizontal mixer system. The actual mixer has dimensions of 1.36 m in length and 0.17 m in diameter. When the process is simulated once under the same operating conditions, the actual process run time is the same as the simulation run time. Based on this model, we carry out case studies by varying conditions such as the length of the mixer, and location of injection nozzle. As per our DEM study, the mixer length can be reduced by more than 20% relative to the existing design. We also suggest alternative mixer designs by optimizing the location of the injection nozzle.

Keywords: Core, Inorganic Binder, DEM, Mixer.

1. Introduction

Casting is a manufacturing process in which molten metal is poured into a mould of desired shape and allowed to solidify. The core is the part of the mould which fills the empty space of the mould forming internal cavities in the casting process. Most moulds are made of sand. To fix the mould, a binder is added to the sand. In this regard, although organic binders are currently prevalent worldwide, they generate harmful gases such as benzene and formaldehyde. Further, air bubbles form when the molten metal solidifies, thereby deteriorating the quality of the product. In addition, since an organic binder is for single use only, a considerable amount of waste is discharged. However inorganic binders are eco-friendly because they can be reused and they do not emit harmful substances.

Despite industrial research on inorganic binders, very few manufactures have attempted to address the issue of core manufacturing based on inorganic binders. For core manufacture, it is important to mix a minimum amount of inorganic binder evenly with sand mould and simultaneously ensure excellent fluidity in the mixed state. Existing core manufacturing has relied on empirical manipulation. In order to produce a high

quality core, it is necessary to optimize the core manufacture process and analyse whether the process has led to appropriate mixing. Against this backdrop, in this study, we developed a computational fluid dynamics (CFD) mixing model and carried out simulations using the discrete element method (DEM) for core manufacturing. The DEM computes the flow of segmented fluid based on molecular dynamics. It is a numerical analysis method suitable for micro-mechanical behaviour calculations of particles or granular materials. Further, based on an intuitive representation of how individual particles collide with each other, contact stiffness can be used to express the interaction between the grid and the particles. Our simulation results were validated through experiment and the results can be applied directly to improve the actual process.

2. Experiments

The experimental horizontal mixer system used for our investigations consisted of a hopper with a pile of sand and a steel cylindrical vessel with a length of 1.36 m, and diameter of 0.17 m. Paddle impellers were positioned along a rotating shaft which was aligned along the centre of the stationary vessel. This shaft-impeller was connected to a motor. The paddle impellers on the shaft were arranged in various angled patterns as shown in Figure 1. Figure 2 illustrates the dimensions of the mixer considered in the study. In all our experiments, spherical sand particles with an average particle size of 0.15 mm and density of 550 kg/m^3 were used. This mixer operated at a rotational speed of 50 RPM. The inorganic binder used in the experiments comprised a mixture of silica calcium and sodium oxide.

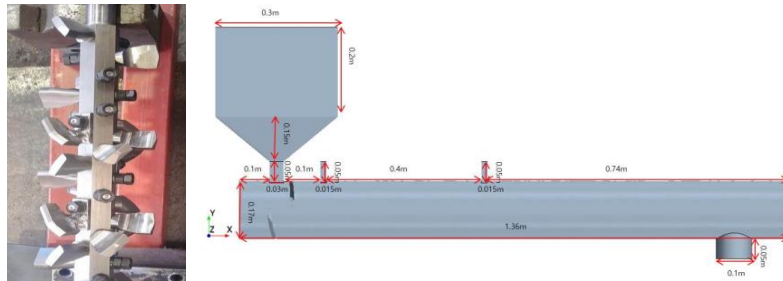


Figure 1. Paddle Impeller shaft in mixer Figure 2. Geometry and dimensions of mixer

2.1. Mixing quality of Mixer

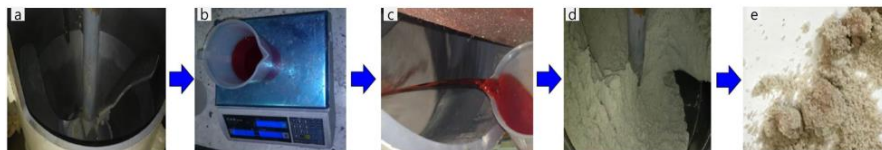


Figure 3. Experiment process (a)Cleaning of mixer (b)Measurement of red dye (c)Pouring of dye into the mixer (d)Mixing with sand and binder (e)Estimating on experiment result

Figure 3. indicates the experimental procedures for mixing quality test. Red coloured particles were stacked in the hopper, to evaluate the mixing performance. We note from the figure that the red colour is hardly visible in the mixture after mixing; i.e. the mixer affords an even mix

2.2. Fluidity test results

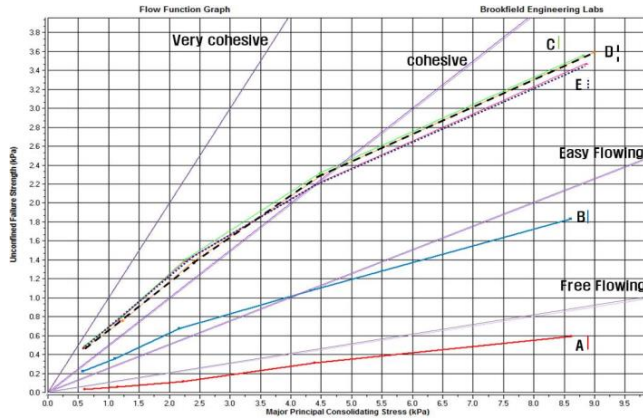


Figure 4. Fluidity graph of mixture for various binder content values

In Figure 4, curves A, B and C lying curves between the cohesive curve and the easy flowing ranges satisfy the appropriate fluidity condition. Among the three corresponding binder content values, we chose the binder with the lowest content (Curve C, 2%) in our experiments.

3. Simulations

Next, we constructed the simulation model using the experimental data. All the DEM and CFD simulations were performed with the use of STAR CCM+ (SIEMENS).

3.1. Numerical approach

In general, CFD simulations are based on continuum models. However, DEM is a discrete approach which accurately models the micromechanics of granular material. Further, the continuum model considers the entire material as one mass, whereas each particle is a unique quantity in DEM. The governing equations of the particle translational and rotational motions can be expressed as the following Newton's equations.

$$m \frac{dv}{dt} = \sum F_g + F_c + F_{fluid} \quad (1)$$

$$I \frac{d\omega}{dt} = \sum (M^T + M^r) \quad (2)$$

Here, m, v, I, ω represent the mass, velocity, moment and angular velocity of a particle, respectively. Further, $F_g, F_c, F_{fluid}, M^T, M^r$ denote the force due to gravity, contact force between particles, fluid force, torque produced at the point of contact, and rolling friction force corresponding to particle-particle and particle-wall contacts, respectively. Here, we note that the choice of the time step is critical in DEM simulations. The time step has to be set to sufficiently small value to ensure numerical stability and accuracy, and it is limited by the time taken for a Rayleigh wave to propagate across the surface of the sphere from one pole to the opposite pole.

Table 1. Binder content of corresponding to each curve in Figure 4

Data name	Binder content
A	0%
B	1%
C	2%
D	3%
E	4%

In order to determine the optimal binder ratio for the mixing process, we examined the fluidity of the mixture as a function of the binder content.

$$\tau = \pi \frac{R_{\min}}{v_{\text{Rayleigh}}} \tag{3}$$

In the above equation, $\tau, R_{\min}, v_{\text{Rayleigh}}$ represent the time-step, minimum particle radius and surface wave speed, respectively. The τ value is set to 30%. The Rayleigh velocity is solved internally, however, it depends on the material properties, particularly the Poisson's ratio and Young's modulus. Thus, we have

$$\tau_2 = 2.94 \left(\frac{5\sqrt{2}\pi\rho}{4} \frac{1-u^2}{E} \right)^{0.4} \frac{R_{\text{particle}}}{\sqrt[5]{v_{\text{impact}}}} \tag{4}$$

Here, $\rho, u, E, v_{\text{impact}}, R_{\text{particle}}$ denote the particle density, Poisson's ratio, Young's modulus, impact velocity and particle radius, respectively. Upon assumption of the Hertzian contact theory, the duration of impact of two perfectly elastic spheres needs to be equal to a minimum of 10time-steps to estimate the collision accurately.

3.2. Model setup

Our simulation geometry was the same as that shown in Figure 2. The material properties of the particle were set as follows; Poisson's ratio = 0.35 and Young's modulus = 5MPa. The simulation consisted of more than 2 million polyhedral meshes. The

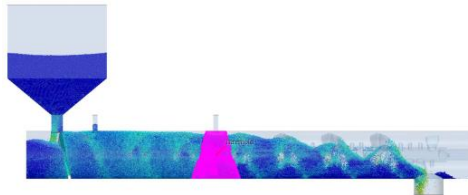


Figure 5. Simulation using The field function

Lagrangian multiphase interaction was used in this model. To simulate the mixing of the binder with the sand, we set the field function assuming that the binder is coated on the particle surface. The field function was declared such that the particle size after coating was 5% larger than that before coating. The field function was applied to the particles which existed in the area lying in the angular range of 0.3° below the injector, as depicted in Figure 5.

3.3. Simulation Results

We analysed the mixing results in 20 internal regions in the mixer. Figure 6 shows the model wherein the injector position is changed from 0 to 0.5 along the x-axis. Figure 7, shows the analysed regions of the mixer. In order for the blue region in Figure 7 to be distinguished in the grayscale mode, the blue area corresponding to coating degree = 0 was indicated by X.

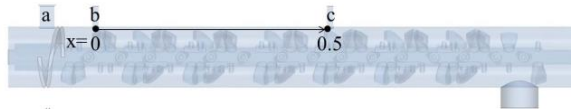


Figure 6. Model representing position of binder injector (a) Sand inlet (b) Initial injector position (c) Final injector position



Figure 7. A model division into coloured regions as per degree for mixing analysis



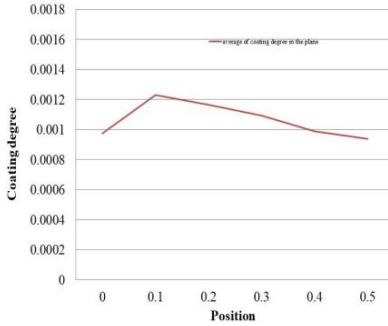


Figure 8. Coating degree as function of injector position

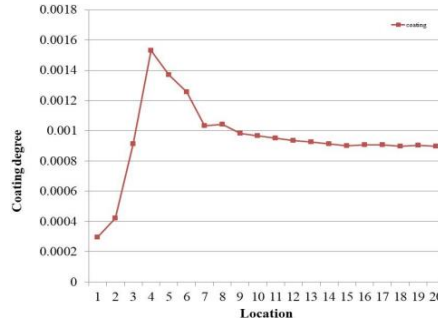


Figure 9. Coating degree as per location along mixer length

Figure 8 depicts the coating degree at the outlet as a function of the injector position Figure 6. When the injector is located at the zero point, the particle velocity tends to become low, thus leading to poor coating. Otherwise, the coating degree is satisfactory when the injector is close to the zero. The curve indicates that the overall coating difference is not large with change in the injector position. Therefore, the location of the injector is not a main consideration in the mixing process. Figure 9 shows the degree of coating obtained at each of the 20 segments shown in Figure 7. The coating degree increase up to location # 5, which is directly under the binder injection nozzle. However, the slope of curve is nearly zero beyond location #15, which indicates that the coating is well mixed and exhibits uniform distribution, and thus, further mixing is not necessary. The coating degree was determined as the average particle data along the vertical cross section of the mixer Figure 11. The data were calculated as per Figure 8 at and each position shown in Figure 9.

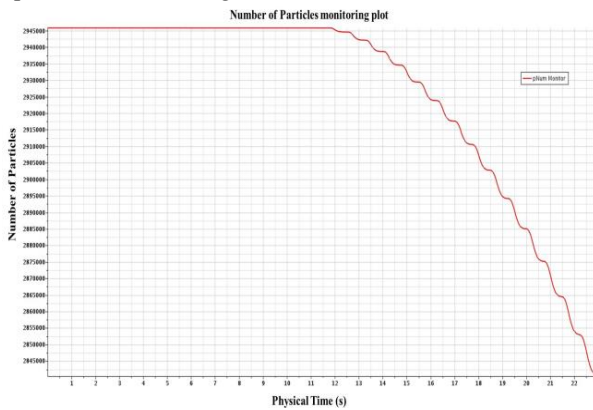


Figure 10. Number particles in mixer as function of time

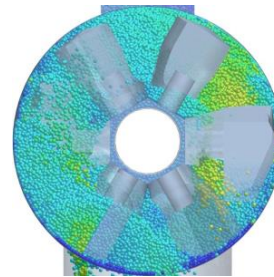


Figure 11. Particle coating degree along vertical cross section of mixer

The residence time in the mixer was defined as the start time at which the particle number began decreasing due to particles exiting the outlet. The residence time in this simulation was 12 seconds Figure 10. This value is the same as the corresponding experimental values, which result validates the reliability of the simulation.

4. Conclusions

We investigated the mixing performance of a horizontal mixer via experiments and DEM simulations. The results of the simulations and experiments were found to be in good agreement. The performance of the mixer was subsequently evaluated as a function of the mixer length and injection nozzle position. In addition, the flow pattern of particles was examined based on the particle size, and coating degree.

Our findings indicate that, the total length of the cylindrical vessel can be reduced to 70% of the original length; the particles were already uniformly distributed inside the mixer at a position 1.09 m away from the particle inlet along the x axis of Figure 2. When the injector of the binder nozzle was located close to the inlet along the x-axis, the mixing quality tended to improve, but the difference in the mixing quality as a function of the subsequent nozzle position was not large. When the particles were mixed with the binder close to the inlet, there was increased stacking and adhering of particles to the impeller. Further, we determined that minimized cleaning load improves the process operating conditions, while ensuring high mixing quality. Therefore, the injector should be located in the midpoint of the mixer along the x-axis.

We plan to focus on varying the vessel fill level, increasing the impeller rotational speed, and the DEM solving time in our follow up studies. We believe that our findings will significantly contribute to industrial manufacturing processes.

Acknowledgement

This study has been conducted with the support of the Korea Institute of Industrial Technology as "Development of Global Optimization System for Energy Process (kitech EE-18-0017)".

References

- A. Yaraghi, M. Ebrahimi, F. Ein-Mozaffari, A. Lohi, 2018, Mixing assessment of non-cohesive particles in a paddle mixer through experiments and discrete element method (DEM), *Advanced Powder Technology*, 29, 11, 2693-2706
- C. J. Coetzee, 2014, Discrete and continuum modelling of soil cutting, *Computational Particle Mechanics*, 1, 4, 409-423
- A. Mariotti, C. Galletti, R. Mauri, M. V. Salvetti, E. Brunazzi, 2018, Steady and unsteady regimes in a T-shaped micro-mixer: Synergic experimental and numerical investigation, *Chemical Engineering Journal*, 341, 414-431
- W. Cai, G. R. McDowell, G. D. Airey, 2013, Discrete element modelling of uniaxial constant strain rate tests on asphalt mixtures, *Granular Matter*, 15, 163-174
- Z. You, M. ASCE, W. G. Buttlar, 2004, Discrete Element Modeling to Predict the Modulus of Asphalt Concrete Mixtures, *J. Mater. Civ. Eng.*, 16, 2, 140-146
- Z. You, 2003, development of a micromechanical modeling approach to predict asphalt mixture stiffness using the discrete element method, *Doctoral Thesis*
- SIEMENS product lifecycle management software, 2016, Introduction to particle modeling using the discrete element method
- EDEM, 2018, What is dem- an introduction to the discrete element method, webinar

Automatic synthesis of distillation processes for the separation of azeotropic multi-component systems

Thulasi Sasi^a, Jonas Wesselmann^a, Hanns Kuhlmann^a and Mirko Skiborowski^{a,*}

^a*TU Dortmund University, Department of Chemical and Biochemical Engineering, Laboratory of Fluid Separations, Emil-Figge-Strasse 70, D-44227 Dortmund, Germany*
mirko.skiborowski@tu-dortmund.de

Abstract

The synthesis of distillation processes for azeotropic systems is a complex task for which commercial simulation software mainly offers a graphical analysis of residue curve maps for ternary (sub)systems or an iterative evaluation based on tedious simulation studies. The current work presents a novel algorithmic approach that aims at an automatic synthesis of distillation-based separation processes for azeotropic systems. Building only on a thermodynamic model of the multi-component mixture, split feasibility at both limiting operating conditions of total reflux and reversible distillation are considered. Possible process variants including the integration of suitable recycle streams are automatically generated and stored in a tree structure and the incorporation of an efficient pinch-based shortcut method provides initial estimates of the required energy demand of the generated process variants. The application of the proposed method is illustrated for the separation of a four and five component azeotropic mixture, which allow comparison with previous publications.

Keywords: conceptual design, flowsheet optimization, azeotropic distillation

1. Introduction

Conceptual process design is of imminent importance in process development, since the choices made in this early stage account for about 80% of the final cost of the entire process (Biegler et al., 1997). Due to the reliability and robustness, distillation still represents the default choice in fluid separation processes. However, the evaluation of split feasibility and the synthesis of alternative separation processes presents a significant challenge for the separation of azeotropic multi-component mixtures. While finding the optimal process configuration for the separation of a zeotropic mixture is a combinatorial problem, for which all alternative sequences can be generated automatically and only the computational demand increases with an increasing number of components (Agrawal, 2003), the feasibility of certain splits for azeotropic mixtures is governed by the location of the azeotropes and the emanating distillation boundaries. Only few methods for the generation of a distillation-based separation of azeotropic mixtures have been proposed. None of them was designed to be fully automatic and none is available in a commercial software tool. Wahnschafft et al. (1993) have developed a synthesis tool called *Split*, which is based on a black-board architectural model for developing separation processes. Although their work provides significant insight into the use of recycles for separation processes, its application for automatic sequencing is limited. A major simplification is the initial grouping of binary *separation tasks*, before selecting applicable separation methods. Rooks et al. (1998) have devised a generalized algorithm to synthesize separation sequences based on the creation of adjacency and reachability matrices, similar to the proximity and reachability matrix proposed by Poellmann and Blass

(1994). Feasible splits are further identified based on the so called *common saddle test*, which checks if the residue curves (RC) for the top and bottom products approach a common saddle. This feasibility check is fully algorithmic, very efficient and allows for the identification of feasible splits considering total reflux operation. However, as pointed out by Thong and Jobson (2001a), it excludes a lot of feasible splits especially for azeotropic mixtures. In a series of articles, Thong and Jobson (2001a,b,c) and Thong et al. (2004) developed an alternative approach, which builds on the evaluation of a linear approximation of the operating leaves/manifolds for rectifying and stripping section to determine split feasibility. Furthermore, the generation of sequences with the possibility of internal recycles is developed on the basis of the split feasibility test in combination with the topological analysis of distillation regions on the basis of the adjacency and reachability matrices. While the developed method is very sophisticated, the considered linear approximation of the operating manifolds is equivalent to the rectification bodies at total reflux (Bausa et al., 1998), such that feasibility is also determined primarily for total reflux operation. Another algorithmic approach was presented by Wasylkiewicz (2006) and was even available for some time in ASPEN *Distil*, which is however no longer part of the software. The tool was also based on the identification of the topological distillation regions in order to identify feasible products and propose potential recycle streams. The latest effort on an algorithmic feasibility test was proposed by Brüggemann and Marquardt (2011). Opposite to all previous approaches this test is based on the concept of pitchfork distillation boundaries (PDB), which represent the distillation boundaries for reversible, rather than total reflux distillation. It was not applied in the synthesis of alternative variants, but rather for the optimization of fixed process flowsheets with shortcut models (Brüggemann and Marquardt, 2011). While the test implements a sophisticated homotopy continuation algorithm and bifurcation analysis, the identification of valid solutions in case of intersecting branches presents a significant challenge.

While currently no tools exist that consider both limiting operating modes, reversible distillation and total reflux operation, several studies showed that a simultaneous consideration can extend the range of feasible splits for distillation (Wahnschafft et al., 1992; Krolkowski, 2006; Kraemer et al., 2009). The current article fills this gap by proposing such a feasibility test and illustrates how an automatic generation of process variants for the separation of azeotropic multi-component systems can be accomplished. Feasible splits are determined based on the highest purity products w.r.t. the different modes of operation and validated through application of the rectification body method (RBM) (Bausa et al., 1998), which does not only indicate the intersection of rectifying and stripping profiles, but also provides an estimate of the energy requirements for the single splits. The developed methodology is introduced in Section 2 and illustrated for two representative case studies in Section 3, before some conclusions and an outlook are presented in Section 4.

2. Methodology

The general concept of the developed methodology is illustrated in Figure 1 and is composed of three consecutive steps. First, a topological analysis of the given mixture is performed based on the thermodynamic property models. The computation of all azeotropes allows for a characterization of all singular points (SP) (Skiborowski et al., 2016), which present the basis for further computation of pinch lines (PL) as well as the adjacency and reachability matrices (Rooks et al., 1998). The latter is used for the computation of the topological distillation region (DR) and distillation boundaries (DB), as well as the compartments for each DR (Thong and Jobson, 2001a), which are stored as ordered subsets of the SP. The second step computes feasible splits based on the generated topological information in combination with the computation of RC and PL, as well as the RBM, and stores the resulting information in a tree structure. Different branches of the tree, which are generated sequentially, can finally be converted to respective column sequences. After specifying the initial feed stream, possible sequences are generated based on a recursive algorithm, which evaluates the products of each split as new feed streams on a subsequent layer, until the desired products are obtained or no further splits are feasible. The results are stored

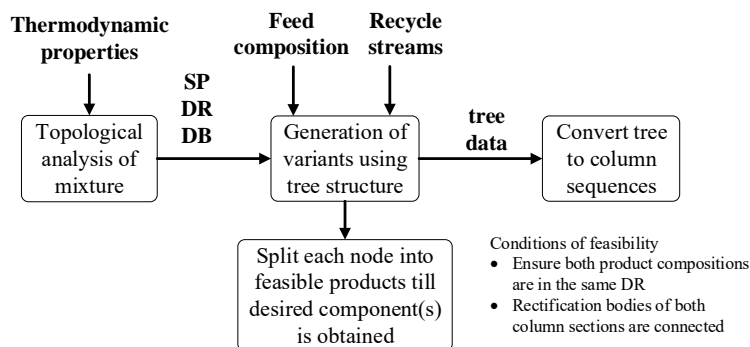


Figure 1: Schematic overview of the methodology for distillation process synthesis

in a tree-like structure, which links the feed and products via a number of nodes. These nodes represent the single splits that are located on different branches, which can subsequently be translated into corresponding column sequences. Figure 2 presents an exemplary illustration, which also indicates the consideration of a recycle stream and the translation of a branch (shaded) into the corresponding column sequence. Each layer of the tree is composed of alternative splits, for which distillate and bottom product result that each are potentially processed as feed streams on individual sub layers. For each feed stream that is to be separated, the topological DR is determined, by evaluating the terminals of the RC and PL passing through the feed composition. The RC is computed using the Runge-Kutta method and the PL is computed using continuation and bifurcation methods as described in more detail in the article of Skiborowski et al. (2016).

Subsequently all SP of the feed DR are considered as possible products and a split feasibility test is performed in order to evaluate if a sharp split is feasible, or if a DB is limiting the separation. For the latter, the highest possible purity (HPP) of the opposing product on the DB is determined, based on a bisection along the mass balance line, monitoring the terminals of the RC and PL. As long as the terminals are equivalent for both products, they are located within the same DR, while the change of any terminal indicates the transition to another DR. The transition point for the PL marks a point on the PDB, while the transition of the RC marks the corresponding location of the simple distillation boundary (SDB). This test can be performed efficiently for any number of components, and directly provides information on differences between the feasibility at total reflux and reversible distillation thus circumventing the complexities of the pitchfork bifurcation analysis proposed by Brüggemann and Marquardt (2011). Starting the bisection based on the potential sharp separation, product compositions located in a different DR than the feed composition, so-called curved boundary processes, are automatically identified as feasible splits in case the terminals of the RC and PL through the products are equivalent.

The determination of HPP products is essential for the final step of the split evaluation, which is the computation of the minimum energy duty (MED) based on the RBM (Bausa et al., 1998). The general idea of the RBM is to check for the intersection of the tray-to-tray profiles of the stripping and the rectifying section, which is also considered as the sufficient criteria for split feasibility. In order to do this efficiently, the RBM uses linear approximations of the manifolds of possible tray-to-tray profiles based on respective pinch points for specific reflux and reboil ratios. The underlying assumption of an infinite number of equilibrium trays per section mandates the specification of HPP products. Therefore, the initial split feasibility test provides the necessary product specifications for a reliable application of the RBM that furthermore determines an MED estimate, which indicates if the column profiles of both sections intersect. The MED can further be used to rank the different sequences, which are generated by the algorithm.

In case the desired products are located outside the feed distillation region and curved boundary

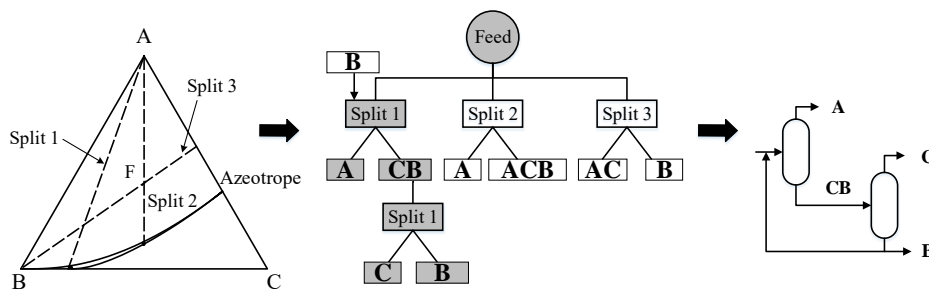


Figure 2: Exemplary illustration of the tree structure and a derived column sequence for the separation of an (A)cetone-(C)hloroform-(B)enzene mixture

splits are not feasible, recycle options can be included in the evaluation on demand. Hereby, the different SP are considered as internal recycle in order to reach the preferred DR, i.e. the DR with the desired product (Wasykiewicz, 2006). In order to limit the number of options, potential recycle streams can be defined upfront. Necessary recycle ratios to shift the mixed feed to the preferred DR are again determined based on a bisection that aims at the maximization of the recovery of the desired product. After the variant generation, it needs to be checked if the necessary amount of the recycled stream is generated in the corresponding sequence. In the exemplary illustration of Figure 2, the possible recycle of benzene enables a full separation of acetone, as also demonstrated in the manual analysis of Wahnschafft et al. (1992). If only a fraction of a stream that is not a desired product is recycled, a post-processing step evaluates the feasibility of a full recycle, as will be illustrated in the subsequent case study. The methodology is implemented in a computer-based tool, which is primarily coded in Matlab and C-coded subroutines for thermodynamic property calculations and computation of all SP, RC and PL, which are available as open source code¹.

3. Case Studies

The application of the developed methodology is illustrated for the separation of a quaternary and a quinary mixture. The first case study considers the separation of an equimolar mixture of acetone, chloroform, benzene and toluene (ACBT). The mixture exhibits a maximum boiling azeotrope between acetone and chloroform and a respective DB, for which SDB and PDB deviate considerably, as illustrated in Figure 3. This mixture and possible separation sequences have been analysed in multiple studies (Thong and Jobson, 2001c; Kraemer et al., 2009) and the results of the proposed algorithm are further compared with the MED computations of Kraemer et al. (2009), who build up on the results of the process synthesis performed by Thong and Jobson (2001c). Figure 4 illustrates a combination of the four configurations (a-d) that were considered by Kraemer et al. (2009) and the highest ranked three configurations (b,d,e) of the

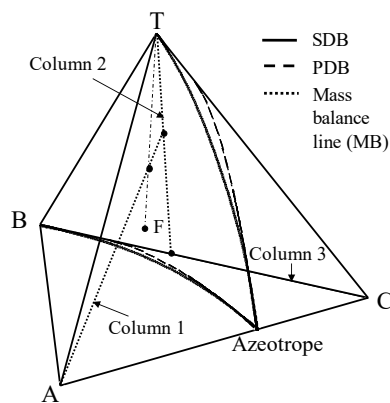


Figure 3: Illustration of the ACBT system and MB of variant (b) (cf. Fig. 4)

¹Softwaresammlung Prozesssynthese (<http://www.avt.rwth-aachen.de/cms/AVT/Forschung/Software/iptu/Softwaresammlung-Prozesssynthese/>)

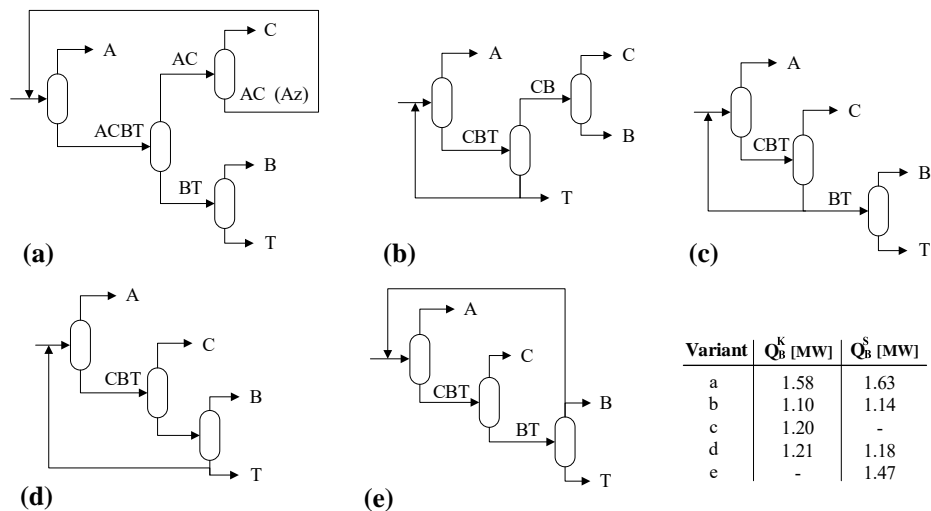


Figure 4: Alternative flowsheets for the separation of an equimolar mixture of acetone-chloroform-benzene-toluene (ACBT) along with their corresponding minimum reboiler duties

total 18 configurations, which are generated by the proposed synthesis method for the same feed and thermodynamic model as used by Kraemer et al. (2009). From the four variants considered by Kraemer et al. (2009), only variant (c) is not generated by the proposed method, since at current state only SP are considered as valid recycle streams. However, comparing the results in the embedded table it becomes apparent that the remaining three variants are evaluated with comparable MED by the current method (Q_B^S) and the approach by Kraemer et al. (2009) (Q_B^K) and that variant (b) is considered as lowest MED variant in both evaluations. The differences can be explained by different recycle rates, as Kraemer et al. (2009) perform a minimization of the MED for each process, applying the PDB criteria of Brüggermann and Marquardt (2011). While they report computational times of ~ 1000 s for each variant, the synthesis and ranking of the 18 variants in the current method is performed in less than 60 s.

To further illustrate the applicability of the method, the separation of a 25 mol-% acetone, 40 mol-% chloroform, 25 mol-% methanol, 5 mol-% ethanol and 5 mol-% benzene (ACMEB) mixture, as analysed in the article of Wasylkiewicz (2006), is studied. The quinary mixture exhibits six binary, two ternary and a quaternary azeotrope. The topological analysis identifies four distillation regions, with each of them containing four to six compartments. As in the study of Wasylkiewicz (2006), purified ethanol and benzene are to be separated from the feed. While overall nine process variants are generated by the proposed synthesis method, only the variant illustrated in Figure 5 allows for a full recovery of both products in only three columns. Herein, methanol is used as internal recycle, which enables a full separation of ethanol in the second column. However, the post-processing step shows that the introduced methanol stream cannot be fully recovered from the third column. In fact, the generated process variant is equivalent to the one proposed by Wasylkiewicz (2006). However, Wasylkiewicz (2006) proposed operation of the third column at lower pressure, which then enables a

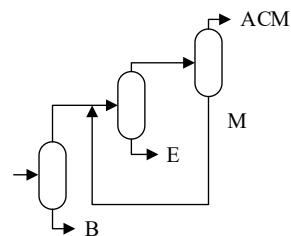


Figure 5: Process variant for ACMEB case study.

closed methanol recycle. Thus, the case study illustrates the capability of the proposed method to automatically generate feasible process configuration for this complex multi-component system, but also illustrates that further extensions, e.g. for the consideration of pressure variations, are required to further extend the search space.

4. Conclusion and outlook

The current article introduces a fully automated method for the synthesis of distillation processes for the separation of homogeneous azeotropic mixtures. The method is not restricted to any number of components and incorporates a general feasibility test, which examines both limiting operational modes for distillation, total reflux as well as reversible distillation. The integration of the rectification body method further checks for an intersection of the rectifying and stripping profiles and provides an estimate of the minimum energy duty that is used for a direct ranking of the generated variants. The only requirements for the application of the method is a reliable thermodynamic model of the multi-component mixture. The current implementation further allows for an automatic consideration of the singular points as internal recycle streams. Future work will focus on the extension of the method towards alternative and more complex recycle options, pressure variations, as well as other process options, like extractive and heteroazeotropic distillation for heterogeneous mixtures. Furthermore, an automatic evaluation of different options for energy-integration, as proposed by Skiborowski (2018), is considered as future post-processing step.

References

- Agrawal, R., 2003. Synthesis of multicomponent distillation column configurations. *AIChE J.* 49 (2), 379–401.
- Bausa, J., Watzdorf, R. v., Marquardt, W., 1998. Shortcut methods for nonideal multicomponent distillation: I. simple columns. *AIChE J.* 44 (10), 2181–2198.
- Biegler, L. T., Grossmann, I. E., Westerberg, A. W., 1997. Systematic methods for chemical process design. Prentice Hall, Old Tappan, NJ (United States).
- Brüggemann, S., Marquardt, W., 2011. Conceptual design of distillation processes for mixtures with distillation boundaries: I. computational assessment of split feasibility. *AIChE J.* 57 (6), 1526–1539.
- Brüggemann, S., Marquardt, W., 2011. Conceptual design of distillation processes for mixtures with distillation boundaries. ii. optimization of recycle policies. *AIChE J.* 57 (6), 1540–1556.
- Kraemer, K., Kossack, S., Marquardt, W., 2009. Efficient optimization-based design of distillation processes for homogeneous azeotropic mixtures. *Ind. Eng. Chem. Res.* 48 (14), 6749–6764.
- Krolkowski, L. J., 2006. Determination of distillation regions for non-ideal ternary mixtures. *AIChE J.* 52 (2), 532–544.
- Poellmann, P., Blass, E., 1994. Best products of homogeneous azeotropic distillations. *Gas Sep. Purif.* 8 (4), 194–228.
- Rooks, R. E., Julka, V., Doherty, M. F., Malone, M. F., 1998. Structure of distillation regions for multicomponent azeotropic mixtures. *AIChE J.* 44 (6), 1382–1391.
- Skiborowski, M., 2018. Fast screening of energy and cost efficient intensified distillation processes. *Chem. Eng. Trans.* 69, 199–204.
- Skiborowski, M., Bausa, J., Marquardt, W., 2016. A unifying approach for the calculation of azeotropes and pinch points in homogeneous and heterogeneous mixtures. *Ind. Eng. Chem. Res.* 55 (24), 6815–6834.
- Thong, D. Y.-C., Jobson, M., 2001a. Multicomponent homogeneous azeotropic distillation 1. assessing product feasibility. *Chem. Eng. Sci.* 56 (14), 4369–4391.
- Thong, D. Y.-C., Jobson, M., 2001b. Multicomponent homogeneous azeotropic distillation 2. column design. *Chem. Eng. Sci.* 56 (14), 4393–4416.
- Thong, D. Y.-C., Jobson, M., 2001c. Multicomponent homogeneous azeotropic distillation 3. column sequence synthesis. *Chem. Eng. Sci.* 56 (14), 4417–4432.
- Thong, D. Y.-C., Liu, G., Jobson, M., Smith, R., 2004. Synthesis of distillation sequences for separating multicomponent azeotropic mixtures. *Chem. Eng. Process.: Process Intensification* 43 (3), 239–250.
- Wahnschafft, O. M., Koehler, J. W., Blass, E., Westerberg, A. W., 1992. The product composition regions of single-feed azeotropic distillation columns. *Ind. Eng. Chem. Res.* 31 (10), 2345–2362.
- Wahnschafft, O. M., Le Rudulier, J. P., Westerberg, A. W., 1993. A problem decomposition approach for the synthesis of complex separation processes with recycles. *Ind. Eng. Chem. Res.* 32 (6), 1121–1141.
- Wasykiewicz, S. K., 2006. Synthesis of separation systems for azeotropic mixtures: Preferred distillation region. *Comput.-Aided Chem. Eng.* 21, 1033–1038.

Development of Guidelines for Optimal Operation of a Cogeneration System

Jia-Lin Kang^a, Hsu-Hung Chang^b, Shyan-Shu Shieh^c, Shi-Shang Jang^{b*},

Jing-wei Ko^d, Hsiang-Yao Sun^d

^a *Department of Chemical and Material Engineering, Tamkang University,
New Taipei City, 25137, Taiwan, ROC*

^b *Department of Chemical Engineering, Tsinghua University, Hsinchu,
30031, Taiwan, ROC*

^c *Department of Occupational Safety and Health, Chang Jung Christian
University, 71101, Taiwan 30031, Taiwan, ROC*

^d *Refining and Manufacturing Research Institute, CPC Corporation,
Taiwan, ROC*

ssjang@mx.nthu.edu.tw

Abstract

Guidelines for optimal operation strategy of cooling water temperature are presented to find the maximum net electrical energy of a cogeneration system for turbine generators (TGs) and cooling towers (CTs). In this study, a real cogeneration plant in Taiwan, consisting of variable-frequency drive fan-based CTs and a generator, was chosen as a case study. Statistical linear models were used to build TGs and CTs. A multi-linear model was established to approach a nonlinear system in the cooling tower using a physically meaningful index, the cooling capability index, as an indicator of data clustering. The results showed that the cooling capability index was a good clustering index for the CTs. The cooling tower multi-linear model regressed by the clustering data performed well in predicting the cooling water outlet temperature. The simulated case verified that the online operating guidelines were consistent with real plant data and that it has the ability to find the optimal cooling water temperature. Two cases of plant test prove that the online operating guidelines can assist operators in operating cooling water temperature to the maximum net electrical energy.

Keywords: cooling capability index, multi-linear model, online operating guide, net electrical energy

1. Introduction

Steam turbine generators (TGs) are widely used in the chemical and energy industries, and optimization of the energy efficiency of a generator is an important issue in industrial energy conservation. In general, low-pressure vapor at the outlet of the generator is introduced into the condenser in order to increase the vacuum, thus increasing power generation. On the other hand, the supplied cooling water requires additional fan power in the cooling towers (CTs) to maintain a low water temperature. (Pan et al., 2011) Due

to the fact of the complexities in TG-CT systems, the optimization of these power generation processes is still an active area among the researchers (Hajabdollahi et al., 2012; Bornman et al., 2016; Li et al., 2018).

Cooling tower and generator modeling are essential to finding the optimal operating conditions. Models of CTs can be divided into theoretical models and data-driven models. The modeling of CTs and TGs using theoretical models to investigate the potential optimization of operating conditions have been reported in many papers (Zhao et al., 2008; Zhao and Cao, 2009; Ganjehkaviri et al., 2015; Hafdhi et al., 2015). However, the construction of theoretical models requires sufficient knowledge and is time consuming. Thus, constructions of such models cannot provide optimal conditions in a short period. Data-driven models were adopted in a few studies to shorten the modeling time and to investigate the interaction between steam TGs and the CW temperature of CTs to find the optimal operating conditions. Furthermore, the optimal operating condition between steam TGs and the CW temperature of CTs was rarely discussed and verified. Pan et al. (Pan et al., 2011; Pan et al., 2013) used the LMN method to establish a multi-linear model for cogeneration systems with two-speed fans. The model results suggested adjusting the CW temperature to achieve the optimization. The multi-linear model obtained by LMN via clustering had high prediction performance for the cooling water temperature, but the physical meaning of each cluster is unknown, such that operators cannot trust the model to implement on plants. Therefore, it is desirable to use a physically meaningful method to cluster the data to guide the operator in adjusting the cooling water temperature. On the other hand, the optimum operation strategy of fans was determined by the arrangement of fan speed modes for two-speed fans but it is not the ideal optimization method for variable-frequency fans. Furthermore, with an automatic clustering approach in LMN, the model may become rather unstable and need retune frequently.

According to the above previous works, we found the following problems remained unsolved. (1) there exist many disturbances in the TG-CT systems, such as steam unstable steam flow, changing humidity as well as environmental temperature. Empirical models are basically not making sense to these changes. (2) First principle models are difficult to obtain due to the lack of trustworthy physical parameters. (3) The optimal conditions are changing from time to time due to the change of the system parameters mentioned above.

The purpose of this study was to tackle the above difficulties by constructing models of TGs with variable-frequency fans using a physical clustering index. Multi-linear model for variable-frequency fans was built. Online operating guidelines based on the models of TGs and CTs were presented to find the optimal cooling water temperature and maximum net electrical energy of the cogeneration system with some physically meaningful plant tests. The rest paper is organized as follows. Section 2 presents details of the modeling and optimal approach, including the TG model, the multi-linear model of CTs, and an optimal strategy named online operating guidelines. Results of a simulated case and plant tests are discussed in Section 3 to demonstrate the feasibility of the online operating guidelines, and a summary of findings is given in the concluding section.

2. Methodology

2.1 Cooling Tower Modeling with Multi-linear Model

Wang et al. (2013) presented a cooling capability index, γ , which can describe the cooling capability of a CT in terms of effective power utilization. The definition of γ is

$$\gamma = \frac{F_{CW} C_p \Delta T_{CW}}{W_{fan}} \quad (1)$$

In this study, the cooling capability index was adopted as a clustering index for regressing the CT multi-linear model. The format of the multi-linear model is a set of the following equations:

$$T_{CW,out} = a_0 + a_1 T_{CW,in} + a_2 H_{R,in} + a_3 T_{air,in} - a_4 W_{fan} \quad (2)$$

In the multi-linear model, the reciprocal of a_4 ($1/a_4$, kW/°C) is physically representative of the required fan power consumption per unit CW outlet temperature change, $\Delta \widehat{W}_{fan}$.

2.2 Last Stage Turbine Generator Modeling

The enthalpy of the steam at the last stage of the TG can be simplified and regressed as follows:

$$H_{steam@the\ last\ stage\ of\ TG} = b_0 + b_1 T_{CW,out} + b_2 F_{steam} \quad (3)$$

2.3 Online Operating Guidelines

The procedure is shown in Figure 1. The optimal CW outlet temperature cannot be over maximum temperature, T_{max} because that will cause the vacuum in the condenser is not enough, leading the TG tripped. The procedure will give two online operating guidelines of the ΔE_{net} and W_{fan} . According to these two online operating guidelines, operators can find the optimal CW outlet temperature and corresponding fan power consumption.

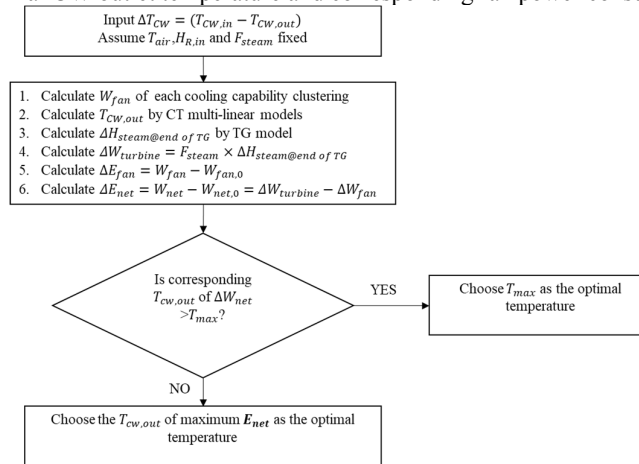


Figure 1 Procedure of operating guidelines for CW temperature

3. Results and Discussion

3.1 Plant Description

In this study, real cogeneration plant in Taiwan, consisting of a variable-frequency drive fan-based cooling tower and a generator, was chosen as a case study to demonstrate model establishment and the online operating guidelines according to the last stage TG and CT models. As Figure 2 shows, the cogeneration plant consists of a TG, a three-cell CT in which every cell has a fan, and a condenser. The range of the fan power is approximately 0–200 kW. The total supplied cooling water of the cooling towers is 5400 T/H. High-pressure steam is introduced into a TG, which in turn drives a power generator to produce electric power.

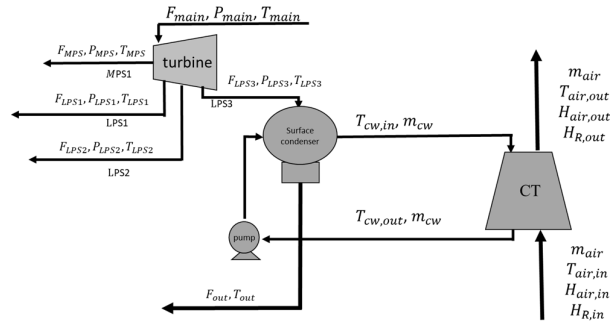


Figure 2 Schematic of a typical cogeneration plant.

3.2 Cooling Tower Model

The CT data presented in this study were divided into nine clusters ($\alpha = 1$ to 9) according to the range of the γ . Every eight intervals of γ starting from the smallest value of γ served as a cluster. The range of the minimum γ_α was from 67 to 75; the range of the maximum γ_α was from 133 to 141. These nine clusters were used to regress the multi-linear model. The R^2 of each linear model is above 0.97.

3.3 Last Stage Turbine Generator Model

The enthalpy of the steam at the last stage of the TG correlation is regressed as the following:

$$H_{\text{steam@the last stage of TG}} = 2506 + 1.78T_{CW,out} + 0.2F_{\text{steam}} \quad (4)$$

The R^2 of the correlation is 0.99.

3.4 Demonstration with a Simulated Case

Figure 3 shows the online operating guidelines of the relative net electrical energy, ΔE_{net} . The values are 29.70 °C and 30.25 °C for the two cases of ΔT_{CW} , respectively. The trends of the ΔE_{net} calculated by historical data were consistent with the trend of the online operating guideline of the ΔE_{net} . As Figure 3(a) shows, the optimal CW outlet temperature is approximately 32.7 °C for the CT. However, the CW outlet temperature can only be increased to 34 °C if the optimal temperature cannot be found during the increase in the cooling water outlet temperature, as Figure 3(b) shows, because the T_{max} of the CW outlet temperature is 34 °C in this case study.

3.5 Plant Test

Figure 5 shows the plant test results and online operating guidelines of the case 2. The online operating guidelines were given based on 24.9 °C of T_{air} and 59.9 % of H_{air} . The initial CW outlet temperature was 29.1 °C. However, because the cooling capability index was 155 at this condition, which beyond the range of the CT multi-linear model, the online operating guidelines at this condition were obtained by extrapolation. According to the online operating guidelines, the CW outlet temperature must be raised to increase the net electrical energy. Thus, the CW outlet temperature was raised to 31.4 °C. The final ΔE_{net} increased by 21.75 kW. Compared with Case 1, Case 2 had greater ΔE_{net} because the

CW outlet temperature was operated at the lower temperature, which required the larger fan power consumption. As the CW outlet temperature increased, the fan power consumption dropped dramatically, leading to the energy saving benefit appear. The results of cases 1 and 2 showed that the net electrical energy can be increased by the online operating guidelines and the final ΔE_{net} of the plant tests are close to the final ΔE_{net} of the online operating guidelines. These results prove that the online operating guidelines using the TG model and the CT multi-linear model are feasible.

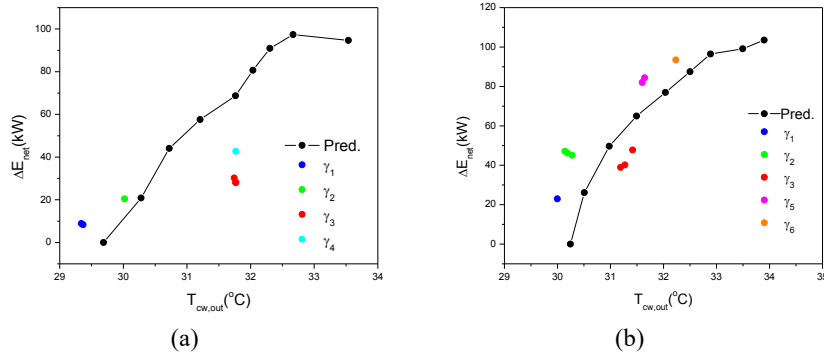


Figure 3 The agreement of the relative net electrical energy between multi-linear model and measurement using the conditions of (a) $T_{air,in}$: 28.5~29 °C, $H_{R,in}$: 78~79.5%, and F_{steam} : 30~32 (T/H), and (b) $T_{air,in}$: 30~32 °C, $H_{R,in}$: 70~73%, and F_{steam} : 35~36 (T/H)

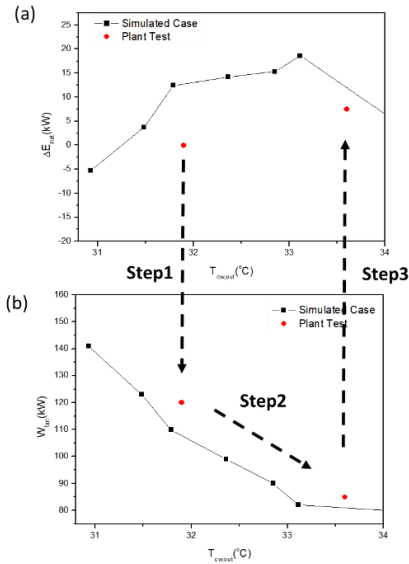


Figure 4 Measured data of (a) cooling water outlet temperature, and (b) fan power consumption for Case 1.

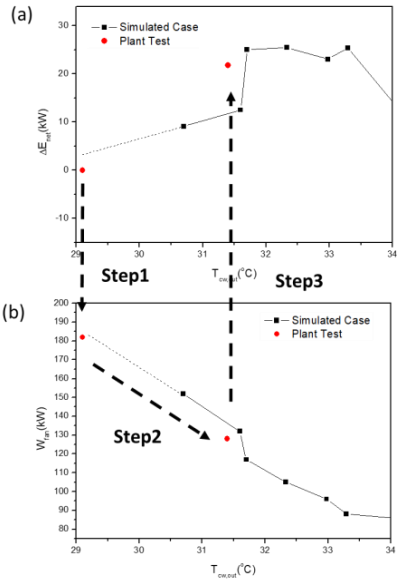


Figure 5 Measured data of (a) cooling water outlet temperature, and (b) fan power consumption for Case 2

4. Conclusions

In this study, we presented an optimal operation method for finding the maximum power generation for cogeneration systems by using a CT multi-linear model and a TG model. An online operating guidelines were used to determine the optimal CW outlet temperature to achieve maximum net electrical energy. In the demonstration, the online operating guidelines were consistent with historical data and that it had the ability to find the optimal CW temperature. Two cases of the plant test based on the online operating guidelines showed that the final ΔE_{net} increased by 7.5 and 21.75 kW, respectively. The difference of ΔE_{net} between Case 1 and Case 2 is mainly caused by the different initial CW outlet temperatures. The ΔE_{net} of plant test and ΔE_{net} of the online operating guidelines were close to prove that the online operating guidelines can be practically applied.

Acknowledgment

The authors acknowledged the financial support provided by Refining and Manufacturing Research Institute, CPC Corporation through the grant EEA-0615001.

References

- Bornman, W., Dirker, J., Arndt, D.C., Meyer, J.P., 2016. Operational energy minimisation for forced draft, direct-contact bulk air cooling tower through a combination of forward and first-principle modelling, coupled with an optimisation platform. *Energy* 114, 995-1006.
- Ganjehkaviri, A., Jaafar, M.M., Hosseini, S., 2015. Optimization and the effect of steam turbine outlet quality on the output power of a combined cycle power plant. *Energy Conversion and Management* 89, 231-243.
- Hafidhi, F., Khir, T., Yahyia, A.B., Brahim, A.B., 2015. Energetic and exergetic analysis of a steam turbine power plant in an existing phosphoric acid factory. *Energy conversion and management* 106, 1230-1241.
- Hajabdollahi, F., Hajabdollahi, Z., Hajabdollahi, H., 2012. Soft computing based multi-objective optimization of steam cycle power plant using NSGA-II and ANN. *Applied Soft Computing* 12, 3648-3655.
- Li, X., Wang, N., Wang, L., Kantor, I., Robineau, J.-L., Yang, Y., Maréchal, F., 2018. A data-driven model for the air-cooling condenser of thermal power plants based on data reconciliation and support vector regression. *Applied Thermal Engineering* 129, 1496-1507.
- Pan, T.-H., Shieh, S.-S., Jang, S.-S., Wu, C.-W., Ou, J.-J., 2011. Electricity gain via integrated operation of turbine generator and cooling tower using local model network. *IEEE Transactions on Energy Conversion* 26, 245-255.
- Pan, T.-H., Xu, D., Li, Z., Shieh, S.-S., Jang, S.-S., 2013. Efficiency improvement of cogeneration system using statistical model. *Energy conversion and management* 68, 169-176.
- Wang, J.-G., Shieh, S.-S., Jang, S.-S., Wu, C.-W., 2013. Discrete model-based operation of cooling tower based on statistical analysis. *Energy conversion and management* 73, 226-233.
- Zhao, B., Liu, L., Zhang, W., 2008. Optimization of cold end system of steam turbine. *Frontiers of Energy and Power Engineering in China* 2, 348-353.
- Zhao, H., Cao, L., 2009. Study on the optimal back-pressure of direct air-cooled condenser in theory, *Power and Energy Engineering Conference, 2009. APPEEC 2009. Asia-Pacific. IEEE*, pp. 1-4.

On the Optimization of Production Scheduling in Industrial Food Processing Facilities

Georgios P. Georgiadis^{a,b}, Chrysovalantou Ziogou^b, Georgios Kopanos^a, Borja Mariño Pampín^c, Daniel Cabo^d, Miguel Lopez^d, Michael C. Georgiadis^{a,b,*}

^a*Department of Chemical Engineering, Aristotle University of Thessaloniki, Thessaloniki 54124, Greece*

^b*Chemical Process and Energy Resources Institute (CPERI), Centre for Research and Technology Hellas (CERTH), PO Box 60361, 57001, Thessaloniki, Greece*

^c*FrinSA del Noroeste S.A., Avenida Ramiro Carregal Rey – Parcela 29, Ribeira, La Coruña, Spain*

^d*ASM Soft S.L., Crta de Bembrive 109, Vigo, Spain*

mgeorg@auth.gr

Abstract

This work presents the development and application of an efficient solution strategy for the optimal production scheduling of a real-life food industry. In particular, the case of a canned fish production facility for a large-scale Spanish industry is considered. Main goal is to develop an optimized weekly schedule, in order to minimize the total production makespan. The proposed solution strategy constitutes the basis to develop an efficient and robust approach for this complex scheduling problem. A general precedence Mixed-Integer Linear Programming (MILP) model is utilized for all scheduling-related decisions (unit allocation, timing and sequencing). To solve the scheduling problem in a computational time accepted by the industry, a two-step decomposition algorithm is employed. Salient characteristics of the canned fish industry are aptly modelled, while valid industry-specific heuristics are incorporated. The suggested solution strategy is successfully applied to a real study case, corresponding to the most demanding week of the plant under study.

Keywords: production scheduling, food industry, MILP, decomposition

1. Introduction

Market trends and competitiveness has steered food industry towards large production volumes, complex alternative recipes and an increasing product portfolio, making production scheduling a challenge. The current industrial practice imposes scheduling-related decisions to be mainly derived by managers and operators, hence the overall plant performance is subject to their experience. Computer-aided scheduling tools can significantly improve these decisions by proper consideration of all involved parameters and therefore significantly enhance production scheduling (Harjunkski, 2016). As a result, productivity is improved, while customers remain satisfied and profits increase. Acknowledging the importance of optimized production scheduling, the scientific community has widely studied the topic over the last 30 years, introducing numerous scheduling models (Méndez et al., 2006). However, most of these works consider small-

scale study cases. This is mainly attributed to the fact that production scheduling is an NP-hard problem, therefore large complex instances can become intractable. The scientific community has widely recognised the lack of applications to real industrial cases (Harjunkoski et al., 2014). Recently some attempts have been made to close the existing gap between theory and industrial practice. In (Kopanos et al., 2010), the authors studied a real-life yoghurt production facility using a novel mixed discrete and continuous MILP model. Furthermore, Baumann and Trautmann, (2014) proposed a hybrid MILP method for make-and-pack processes using a decomposition strategy and a critical-path improvement algorithm. Moreover, Aguirre et al., (2017) combined a novel MILP model that incorporates TSP (Travelling Salesman Problem) constraints, with a rolling horizon algorithm. In this work a solution strategy is proposed that deals with scheduling problems of large-scale industrial food production facilities. In particular, an MILP model is proposed to optimize the production schedule, while a two-step decomposition algorithm is utilized to solve the problem in an acceptable computational time.

2. Problem statement

In this work, the canned fish production in a real-life industrial facility is examined. Specifically, the production process of Frinsa del Noroeste S.A., located in Ribeira, Spain, is investigated using real process data. The plant is capable of producing more than 400 codes, and it is one of the largest canned fish industries in Europe. The facility comprises of multiple stages, including both batch and continuous processes (Fig. 1). The raw materials arrive in the facility in the form of frozen fish blocks, and as such they need to be unfrozen in the thawing chambers. Then, the blocks are chopped in the appropriate size and filled in the cans alongside with all other ingredients (brine, olive oil etc.) required by the recipe. In the next stage, the sealed cans are sterilized in order to ensure the microbiological quality of the final products. Finally, the cans are packaged in their final form (6-pack, 12-pack, boxes etc.) and are stored in the warehouse, to be later distributed in the market.

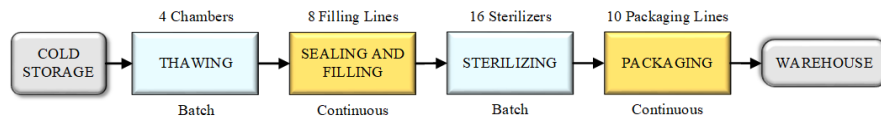


Figure 1: Facility layout

The plant under consideration can be identified as a multiproduct, multistage facility with both batch (thawing, sterilizing) and continuous (sealing and filling, packaging) processes each utilizing multiple parallel units. Additionally, the large production demand and high production flexibility increases significantly the plant's complexity. The thawing stage is oversized compared to the processing capacity of all other stages, therefore it is a valid assumption to omit it from this study. Unfortunately, no clear bottlenecks exist, and as such all other processing stages need to be modelled. The short-term scheduling horizon of interest is 5 days, whereas all units are available 24 hours per day. Sequence-dependent changeovers are considered. All design and operating constraints of the facility, such as a limited waiting time between stages to ensure microbiological integrity, are taken into account. The objective is to minimize the total production makespan, while ensuring demand satisfaction.

3. Mathematical framework

The key scheduling decisions to be made are related to: a) the number of product batches required to satisfy the incoming orders, b) the allocation of product batches to units in every processing stage, c) when will the process of each batch in every stage start and finish and d) in what relative sequence. A typical industrial practice in most food industries, imposes the operation of the intermediate batch processes in their maximum capacity. Utilizing the batch stage to its fullest, leads to reduction of changeovers between products and a general increase in the plant's productivity. Thus, the number of batches of each product required to satisfy the demand is calculated a priori, based on the given demand, the inventory levels and the capacity of the sterilization chambers.

3.1. MILP model

The suggested MILP model is based on the general precedence framework. Due to lack of space, only a brief description of the model is presented:

$$\sum_{j \in (S_{s,j} \cap PJ_{p,j})} \bar{Y}_{p,b,s,j,n} = 1 \quad \forall p \in I_p^{in}, b \in PB_{p,b,n}, n \in I_n^{in} \quad (1)$$

$$L_{p,b,s,n} + \sum_{j \in (S_{s,j} \cap PJ_{p,j})} (fs_{p,b,j,n}^{time} \cdot \bar{Y}_{p,b,s,j,n}) = C_{p,b,s,n} \quad \forall p \in I_p^{in}, b \in PB_{p,b,n}, n \in I_n^{in} : s = 1 \quad (2)$$

$$C_{p,b,s,n} + W_{p,b,s,n} = L_{p,b,s+1,n} \quad \forall p \in I_p^{in}, b \in PB_{p,b,n}, n \in I_n^{in} : s < 3 \quad (3)$$

$$L_{p',b',s,n} \geq C_{p,b,s,n} + ch_{p',j}^{time} - M \cdot (1 - X_{p,p',n}) - M \cdot (2 - \bar{Y}_{p,b,s,j,n} - \bar{Y}_{p',b',s,j,n}) \quad (4)$$

$$\forall p \in I_p^{in}, p' \in I_{p'}^{in}, b \in PB_{p,b,n}, b' \in PB_{p',b',n}, j \in (PPJ_{p,p',j} \cap SJ_{s,j}), n \in I_n^{in} : p < p', s \neq 2$$

$$L_{p',b',s,n} > C_{p,b,s,n} - M * (1 - \bar{X}_{p,b,p',n}) - M * (2 - \bar{Y}_{p,b,s,j,n} - \bar{Y}_{p',b',s,j,n}), \quad (5)$$

$$\forall p \in I_p^{in}, b \in PB_{p,b,n}, p' \in I_{p'}^{in}, b' \in PB_{p',b',n}, j \in (PPJ_{p,p',j} \cap S_{s,j}), n \in I_n^{in} : p < p', s = 2$$

$$C_{p,b,s+1,n} - L_{p,b,s,n} \leq Q_p \quad \forall p \in I_p^{in}, b \in PB_{p,b,n}, n \in I_n^{in} : s = 1 \quad (6)$$

$$C_{p,b,s,n} \leq 24 \quad \forall p \in I_p^{in}, b \in PB_{p,b,n}, n \in I_n^{in} : s = 3 \quad (7)$$

$$C_{p,b,s,n}^{max} \geq C_{p,b,s,n} \quad \forall p \in I_p^{in}, b \in PB_{p,b,n}, n \in I_n^{in} : s = 3 \quad (8)$$

Constraints (1) guarantee that all product batches p,b to be scheduled on day n will be processed by exactly one unit j in every stage s , using the binary allocation variable $\bar{Y}_{p,b,j,n}$. Constraints (2) impose the timing constraints in the sealing and filling stage. More specifically, they state that the completion of the sealing and filling task for every product batch to be scheduled in every day $C_{p,b,s,n}$ is equal to the starting time of the task $L_{p,b,s,n}$ plus the required processing time $fs_{p,b,j,n}^{time}$. Similar constraints are used for the sterilization and packing stages. To synchronize the stages, constraints (3) are employed. The continuous variable $W_{p,b,s,n}$ defines the waiting time between each stage. The sequencing

constraints between product batches in every stage are portrayed in constraints (4) and (5). Two general precedence variables are introduced, $X_{p,p',n}$ and $\bar{X}_{p,b,p',b',n}$, alongside a big-M parameter. The first precedence variable defines the sequencing of product batches in the continuous stages (sealing and filling and packing), while the latter in the batch stage (sterilization). Notice, that the batch sets b, b' are not used in the first precedence variable, since a single campaign policy is followed in the continuous stages. This way the binary variables are significantly decreased, thus the computational complexity of the problem is reduced. In particular, constraints (4) state that if a product p is processed prior to p' on day n ($X_{p,p',n} = 1$) and both product batches are processed in the same unit j ($\bar{Y}_{p,b,j,n} = \bar{Y}_{p',b',j,n} = 1$), then the starting time of p', b' must be greater than the completion time of p, b plus any required changeover $ch_{p,p',j}^{time}$. Similarly, constraints (5) impose the sequencing constraints in the sterilization stage. Constraints (6) enforce the waiting time between the sealing and filling stage and the sterilization stage to be less than a specific limit Q_p . This limit ensures the microbiological integrity of the final product. To ensure that the daily scheduling horizon is not violated, constraints (7) are used. The objective of the model is the minimization of the total production makespan C_{max} and is expressed by constraints (8).

3.2. Decomposition algorithm

The complexity of the examined plant is such that an exact method cannot solve the scheduling problem in reasonable time. Therefore, a two-step decomposition algorithm is employed to split the initial problem into several tractable subproblems. First, the weekly scheduling problem is decomposed in a temporal manner into 5 daily scheduling subproblems. Then, an order-based decomposition is utilized to solve the daily scheduling problem for a specific number of products in each iteration. Fig. 2. illustrates the flowchart of the proposed solution strategy. At first the batching subproblem is solved to translate the product orders into batches. Afterwards, the number of orders to be scheduled in each iteration are set. Then, the MILP is solved for the specified subproblem area (day and number of products) and only the binary variables (unit allocation, sequencing) are fixed. When all orders are scheduled for a given day, all variables are fixed, and the algorithm continues to the next day. Finally, when all days are considered, the complete schedule is generated.

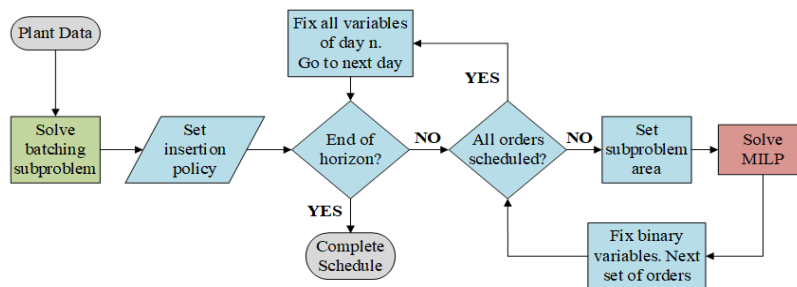


Figure 2: Solution strategy

4. Results

An industrial study case using real data from the Frinsa production plant is presented. In total 136 final products are to be scheduled, corresponding to a real weekly demand from a period with the most intensive production. To solve this complex case, the proposed solution strategy is utilized. In each iteration the daily schedule for half of the product-orders was chosen to be optimized. The MILP model was implemented in GAMS 25.1 and solved in an Intel Core i7 @3.4Gz with 16GB RAM, using CPLEX 12.0. Optimality is reached for all iterations of the suggested solution strategy. Figure 3 illustrates the complete schedule generated for all units of every processing stage. Each color corresponds to a batch or lot of a product-code.

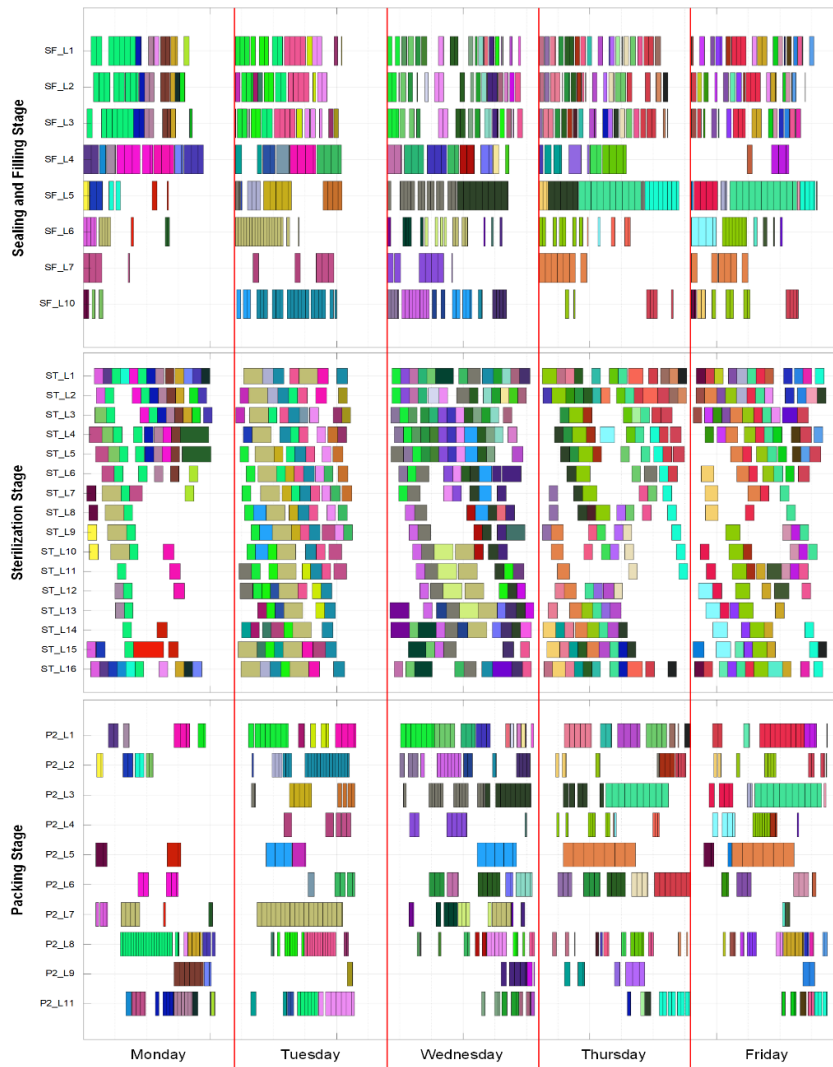


Figure 3: Gantt chart of units of all processing stages

Compared to the real weekly schedule proposed by Frinsa, the optimized schedule of the proposed strategy illustrates interesting results. To satisfy the given demand, the manually derived schedule by Frinsa, requires the addition of a shift on Sunday evening, while the optimized schedule satisfy all orders within 5 days. Moreover, the total CPU time for the solution of the problem is approximately 1 hour and it is acceptable by the company.

5. Conclusions

This work presents the optimization-based production scheduling of a large-scale real-life food industry. More specifically, all major processing stages of a canned fish production facility have been optimally scheduled. The industrial problem under consideration illustrates significant complexity, due to the mixed batch and continuous stages, each having numerous shared resources, the large number of final products and the various operational, design and quality constraints. This make-and-pack structure (one or multiple batch or continuous processes followed by a packing stage) is typically met in most food and consumer packaged goods industries, hence, the presented solution strategy can be easily implemented in other industrial problems. It has been shown that the suggested solution strategy can optimally schedule even the most demanding weeks of the examined industry in acceptable time, leading to reduction of overtime production. The proposed strategy can be the core for a computer-aided scheduling tool that can facilitate the decision-making process for the production scheduling of food industries. Current work focuses on the introduction of cost related objectives, as well as, the incorporation of uncertainty in product demands.

Acknowledgements

The work leading to this publication has received funding from the European Union's Horizon 2020 research and innovation programme under grant agreement No 723575 (Project CoPro) in the framework of the SPIRE PPP.

References

- Aguirre, A.M., Liu, S., Papageorgiou, L.G., 2017. Mixed Integer Linear Programming Based Approaches for Medium-Term Planning and Scheduling in Multiproduct Multistage Continuous Plants. *Ind. Eng. Chem. Res.* 56, 5636–5651.
- Baumann, P., Trautmann, N., 2014. A hybrid method for large-scale short-term scheduling of make-and-pack production processes. *Eur. J. Oper. Res.* 236, 718–735.
- Harjunoski, I., 2016. Deploying scheduling solutions in an industrial environment. *Comput. Chem. Eng.* 91, 127–135.
- Harjunoski, I., Maravelias, C.T., Bongers, P., Castro, P.M., Engell, S., Grossmann, I.E., Hooker, J., Méndez, C., Sand, G., Wassick, J., 2014. Scope for industrial applications of production scheduling models and solution methods. *Comput. Chem. Eng.* 62, 161–193.
- Kopanos, G.M., Puigjaner, L., Georgiadis, M.C., 2010. Optimal Production Scheduling and Lot-Sizing in Dairy Plants : The Yogurt Production Line. *Ind. Eng. Chem. Res.* 49, 701–718.
- Méndez, C.A., Cerdá, J., Grossmann, I.E., Harjunoski, I., Fahl, M., 2006. State-of-the-art review of optimization methods for short-term scheduling of batch processes. *Comput. Chem. Eng.* 30, 913–946.

A Systematic Parameter Study on Film Freeze Concentration

Jan-Eise Vuist^a, Maarten Schutyser^{a,*} and Remko Boom^a

^a*Food Process Engineering Wageningen University, P.O. Box 17, 6700 AA, Wageningen, The Netherlands*

maarten.schutyser@wur.nl

Abstract

Film freeze concentration is an alternative method to concentrate aqueous streams compared to suspension freeze concentration. Major advantage is that the equipment is less complex and thus capital costs are in principle lower. In our research we investigated especially how hydrodynamics, applied freezing temperatures and solution properties influence inclusion of solutes in ice and ice yield during film freeze concentration. For this we carried out both lab-scale experiments and CFD simulations. Model solutions of sucrose and maltodextrin were concentrated in a stirred vessel by growth of an ice layer at the bottom freezing plate. For varying stirring speeds, feed concentrations and freezing plate temperature profiles we determined the solute inclusion in the grown ice and the ice yield. When increasing stirrer speeds a decreasing amount of solute included in ice was found at constant freezing plate temperature. This can be explained because the transport of the solute molecules in the boundary layer is diffusion limited. An increase in shear above the surface reduces the thickness of this layer and therefore less solute is included in ice at high shear rates. CFD simulations were carried out to describe the hydrodynamics near the surface and to relate the shear rate to the impeller Reynolds number. Moreover, the CFD simulations could explain the increased solute inclusions for higher concentrations of sucrose as higher viscosities lead to significant reduction of shear rates close to the ice layer. The CFD simulations will facilitate easier translation of the obtained results for a differently designed film freeze concentration system. Sucrose and maltodextrin appeared to behave very similar with respect to inclusion behaviour, which may be explained from their similar diffusivities. Ice growth rate is found another important factor and is very much influenced by applied freezing temperatures. Our experiments showed that there is a critical ice growth rate. If this ice growth rate is exceeded more solutes will be included in the ice layer. In this case the solute molecules will not have the chance to move away from the ice boundary. The next step in our research is modelling of the ice growth rate as function of the freezing plate temperature to optimise both ice yield and solute inclusion.

Keywords: freeze concentration, solute inclusion, modelling

1. Introduction

Concentration of aqueous food streams is a routine operation in food industry to increase their shelf-life and to reduce their transportation volume. To concentrate these streams multiple techniques are available based on evaporation, physical separation or freeze concentration. While thermal evaporation is the most common industrial technique and is readily applicable to many streams, such as dairy or sugar, it has drawbacks for streams containing heat-sensitive components as reviewed by Sánchez et al. (2009).

Heat-sensitive components such as proteins and flavours either become damaged by the heat-treatment or may be stripped away with the water from the product stream. Both phenomena result in a loss of product quality. During freeze concentration, these components are exposed only to low temperature and therefore minimally damaged. Because freeze concentration produces minimal thermal damage, it is considered a mild concentration technique.

Freeze concentration can be performed in two main modes: suspension freeze concentration and film freeze concentration. During suspension freeze concentration the ice is formed in suspension. The ice growth and the degree of supercooling are maintained by continuously seeding the suspension with fresh crystals. The ice crystals are then washed and melted in a continuous washing filter. This technique is commercially available and has applications in the fruit juice and beer industry. During film freeze concentration the ice crystal(s) are grown on the wall of a heat exchanger. Growing the ice crystals on the wall eliminates the need for a washing filter and reduces the complexity of the unit operation. This article will focus on the film freeze concentration process.

The objective of this study is to study the relationship between inclusion behaviour of solutes and the hydrodynamic conditions near the growing ice layer during film freeze concentration. Sucrose and maltodextrin are selected as the model solute components. To study their inclusion behaviour, a custom build freeze cell is used. Previous studies by Miyawaki et al. (1998) have often used progressive freeze concentration set-ups, which are optimized for studying solute partitioning behaviour at the ice water interface. In this study we chose for a different set-up that provides more realistic hydrodynamic conditions. This is especially relevant for scaling-up the film freeze concentration process. Previous studies by Jusoh et al. (2009) already indicated that hydrodynamic conditions in the liquid are relevant to inclusion behaviour. To gain more insight into this, we used a computational fluid dynamics (CFD) model to describe the hydrodynamic conditions near the ice-liquid boundary. The outcomes of this model are linked to the observed inclusion behaviour during the freeze concentration experiments.

2. Material and Methods

2.1. Experimental

The film freeze concentration experiments were conducted in a small-scale test apparatus designed after Genceli et al. (2007). The test apparatus was constructed from an acrylic cylinder with 90 mm internal diameter. The bottom of the cylinder was constructed out of a stainless steel chamber, which was cooled using a cooling fluid. The vessel was equipped with a pitched two-bladed stirrer. To monitor the temperature during the experiments, we placed thermocouples in the vessel at 1, 2, and 5 mm from the bottom surface, one thermocouple at 10 mm below the liquid surface and two thermocouples were placed in the in- and outgoing liquid flow. All thermocouples (type T) were connected to 24-bit data logger (National Instruments, cDAQ-9214, ± 0.01 °C relative accuracy, USA).

Sucrose and maltodextrin solutions with various concentrations were used as feed solutions. The sucrose ($342.30 \text{ g mol}^{-1}$) was obtained from Sigma-Aldrich (BioXtra, >99.5 %) and the maltodextrin DE12 ($\approx 3423.0 \text{ g mol}^{-1}$) from Roquette Freres (Glucidex 12). The feed solutions were pre-cooled to 4 °C before use. To determine the sucrose concentration in the sample, we used a refractometer (Anton Paar, Abbemat 500, Austria). To determine

the maltodextrin concentration, we heated the pre-weighed solutions overnight in an oven at 105 °C and weighed the samples afterwards. The solutions were reused for a maximum of 5 days and separate solutions were used for experiments on the same day.

At the start of the freeze concentration experiments, a droplet (100 μL) of pure water was deposited on the freeze plate. This ice droplet prevented the initial super cooling. Initial supercooling will cause fast initial freezing and very strong inclusion of solutes at the beginning of the freezing process and can even lead to ice crystals forming in suspension rather than on the freeze plate. When the droplet was completely frozen, the feed solution was introduced through a filling port at the top of the cylinder. Only when the liquid submerged the stirrer blades, the stirring was started to prevent major inclusions of air in the solution. The experiments were stopped after a half hour. At the end of the experiment the liquid was removed from the cylinder and the ice was melted. Both fractions were weighted and their contents analysed. All experiments were carried out in duplicate.

2.2. Modelling

A COMSOL Multiphysics 5.3a model was used to estimate the fluid flow induced by the stirrer near the bottom of the cylinder. The fluid flow is described by the Navier-Stokes equation (Batchelor (2000)). The model used a geometry similar to the experimental set-up. For the outer walls and the bottom walls of the cylinder a no-slip boundary condition was applied. A symmetry boundary condition was applied to the fluid surface. The behaviour at the fluid surface is assumed to have no influence on the ice formation. To simulate the stirring a rotating material coordinate system was used. The wall condition for the stirrer is equal to the rotational speed of the material coordinate system and the wall condition for the outside and bottom wall the rotational speed is equal to 0.

The system was simulated for stirring rates of 50 and 150 rpm ($\text{Re} = 703$ to 9845) with laminar flow model and a turbulent $\kappa - \varepsilon$ model was used for the simulation of 500 rpm ($\text{Re} = 7030, 20674, 32818$ respectively for 36, 18, 6 wt% solutions). For the wall treatment the built-in wall functions of COMSOL Multiphysics 5.3a were used. The mesh is based on the physics induced sequence with the fine settings.

Three sugar solutions were simulated at their freezing points. The density of the sucrose solutions was estimated by calculating mass fraction average. The viscosity of the solution was measured with a rheometer (Anton Paar MCR-301, geometry: DG26.7/200/AL, Austria) using a shear rate sweep in the range of $1\text{-}100 \text{ s}^{-1}$. The freezing point of the solutions was determined using the melting curve from differential scanning calorimetry (TA Instruments DSC-250, USA). The variables are summarised in table 1. These values are similar to the ones observed by Bubnick and Werner (1995).

3. Results

3.1. Ice formation

Table 1: Used constants for CFD simulations

Solution [wt% Sucrose]	ρ [kg m^{-3}]	η [mPa s]	T_{fp} [$^{\circ}\text{C}$]
6	1021	2.1	-0.3
18	1072	3.6	-1.9
36	1156	11.1	-4.5

The ice yield of film freeze concentration was compared for different stirrer rates and cold wall temperatures. The ice yield showed little dependence on the stirrer rate. A clear dependence was found on the cold wall temperature. The lower temperatures yielded more ice because the driving force for heat transfer is higher. There was a slight dependence on the solution concentration due to the freezing point depression at higher sucrose concentrations (figure 1).

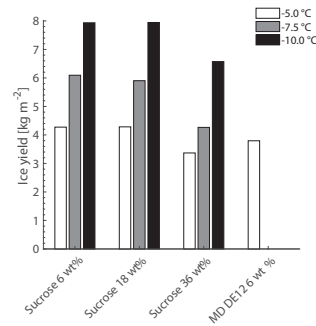


Figure 1: Effect of applied freeze plate temperature and solute concentration on the ice formation after freezing for a half hour. Ice yield for sucrose and maltodextrin DE12 solution averaged over the stirrer speeds.

3.2. Sucrose and Maltodextrin inclusion

The effective solute inclusion (equation 1) versus the Reynolds numbers were compared for the same conditions as in figure 1 (figure 2). The solute inclusion decreased at increasing Reynolds numbers for all different solutions and cold wall temperatures. No major differences between the solutions could be found at Reynolds number below 10,000, the laminar regime. At Reynolds numbers above 10,000, differences were clear between the different solutions and the different cold wall temperatures. The 18 wt% sucrose solutions showed more inclusion than the 6 wt% sucrose solutions. The 6 wt% maltodextrin solution showed a similar behaviour to the 6 wt% sucrose solution. A lower cold wall temperature increased the amount of inclusions due to an increased freezing rate.

$$K[-] = \frac{C_S[\text{wt}\%]}{C_L[\text{wt}\%]} \quad (1)$$

An increase of the stirrer speed increases the shear above the ice surface which improves the transport of the solute away from the ice-liquid boundary and therefore reduces the diffusion limitation of the freeze concentration. The solute inclusion will increase at lower cold wall temperatures. For a constant cold wall temperature, the freezing initially proceeds much faster than later. This implies that the inclusion rate in the initial stages is larger than later. Thus, by adjusting the cold wall temperature such, that it starts not too cold and gradually cools further, we may avoid the initial large amount of inclusions.

If one compares the freezing of solutions with different solutes, one observes that solutions with maltodextrin show less inclusion. We expect that this is because of the larger

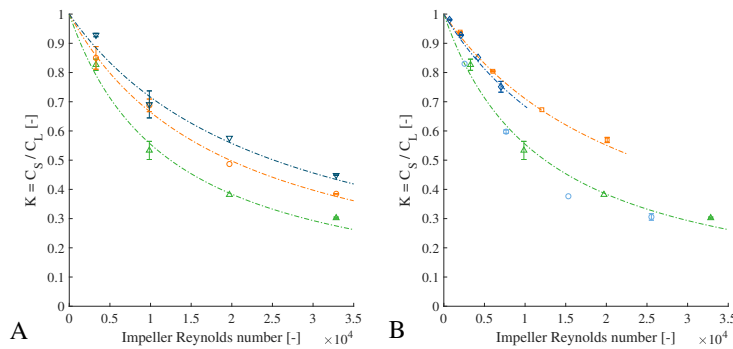


Figure 2: Effect of impeller Reynolds number on the effective solute inclusion. A.) 6 wt% sucrose at Δ -5.0 °C; \circ -7.5°C; ∇ -10.0°C below the freezing point of the solution. B.) Δ , 6 wt% sucrose; \square , 18 wt% sucrose; \diamond , 36 wt% sucrose; \circ 6 wt% maltodextrin DE12 at -5.0 °C. The error bars indicate standard deviation. The lines fitted to guide the eye.

molecular weight, giving rise to less melting point depression, hence a larger equilibrium concentration at a given freezing temperature, a stronger concentration gradient towards the solution and therefore faster diffusion from the freezing surface.

3.3. Fluid flow modelling

The shear rates present at the bottom of the cylindrical device was derived from the CFD simulations. The bottom surface, was taken from the result (figure 3). From this the average shear rate was calculated and compared to the Reynolds number ($Re = \frac{\rho ND^2}{\mu}$), with ρ in $kg \cdot m^{-3}$, N in s^{-1} , D in m , and μ in $Pa \cdot s$. The shear rate increased with increasing Reynolds number. Higher shear rates near the surface leads to a reduction of the thickness of the boundary layer. A thinner boundary layer will aid the transport from the solute away from the ice-water boundary and thus will lead to a solute inclusion close to the equilibrium between the ice and the solution. The diffusion through the boundary layer is the rate-limiting step in the freeze concentration process. The simulations show that there is a correlation between the surface shear rate and the impeller Reynolds number found for the vessel. This correlation is specific for our geometry. This correlation is a useful tool for translation of the found results to a pilot scale set up.

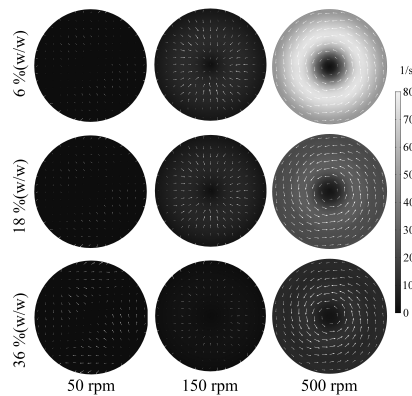


Figure 3: Shear rate magnitude in the freeze cell, from simulation. The arrows indicate the direction of the shear.

Higher viscosities of the sucrose solutions will diminish the intensity of the fluid flow

near the ice surface. The lower fluid flow will lead to higher rate of inclusions due to the aforementioned effects. To reach similar inclusion rates the stirrer speed needs to be increased proportionally. The increase in viscosity during a longer and larger freeze concentration process leads to a decrease in performance of the process.

4. Conclusion

In this study the inclusion behaviour of sucrose and maltodextrin during film freeze concentration was found to be closely linked with the stirrer speed and the ice growth rate. Fluid flow simulations showed that there is a direct link to the hydrodynamic conditions above the ice surface. The transport of the solute molecules in the boundary layer is diffusion limited and therefore an increase in shear above the surface reduces the thickness of this layer. The ice growth rate is the other important factor. Our experiments showed that there is a critical ice growth rate. Lewis et al. (2015) showed if the ice growth rate is exceeded more solute will be included in the ice layer. In this case the solute molecules will not have the chance to move away from the ice boundary. At a high enough stirrer speed and a sub critical ice growth rate the inclusions will reach a minimum dictated by a phase partitioning equilibrium as found by Jusoh et al. (2009). To improve the process and decrease the inclusions, experiments with a decreasing cold wall temperature will be carried out.

5. Acknowledgements

This work is an Institute for Sustainable Process Technology (ISPT) project. Partners in this project are TNO, Royal Cosun and Akzo Nobel.

References

- G. K. Batchelor, 2000. *An Introduction to Fluid Dynamics*. Cambridge University Press, Cambridge, United Kingdom.
URL <http://ebooks.cambridge.org/ref/id/CB09780511800955>
- Z. Bubnick, E. Werner, 1995. *Sugar technologists manual : chemical and physical data for sugar manufacturers and users TT -, 8th Edition*. Bartens, Berlin, Germany.
- F. E. Genceli, M. Lutz, A. L. Spek, G.-J. Witkamp, dec 2007. Crystallization and Characterization of a New Magnesium Sulfate Hydrate MgSO₄·11H₂O. *Crystal Growth & Design* 7 (12), 2460–2466.
URL <https://doi.org/10.1021/cg060794e>
- M. Jusoh, R. Yunus, M. Hassan, dec 2009. Performance Investigation on a New Design for Progressive Freeze Concentration System. *Journal of Applied Sciences* 9 (17), 3171–3175.
URL <http://www.scialert.net/abstract/?doi=jas.2009.3171.3175>
- A. Lewis, M. Seckler, H. Kramer, G. Van Rosmalen, 2015. *Industrial crystallization: Fundamentals and applications*. Cambridge University Press, Cambridge, United Kingdom.
- O. Miyawaki, L. Liu, K. Nakamura, sep 1998. Effective partition constant of solute between ice and liquid phases in progressive freeze-concentration. *Journal of Food Science* 63 (5), 756–758.
URL <http://doi.wiley.com/10.1111/j.1365-2621.1998.tb17893.x>
- O. Miyawaki, L. Liu, Y. Shirai, S. Sakashita, K. Kagitani, jul 2005. Tubular ice system for scale-up of progressive freeze-concentration. *Journal of Food Engineering* 69 (1), 107–113.
URL <http://linkinghub.elsevier.com/retrieve/pii/S0260877404003528>
- J. Sánchez, Y. Ruiz, J. M. Auleda, E. Hernández, M. Raventós, aug 2009. Review. Freeze concentration in the fruit juices industry. *Food Science and Technology International* 15 (4), 303–315.
URL <http://journals.sagepub.com/doi/abs/10.1177/1082013209344267>

A Stacked Auto-Encoder Based Fault Diagnosis Model for Chemical Process

Yi Qiu, Yiyang Dai*

*College of Chemistry and Chemical Engineering, Southwest Petroleum University,
Chengdu 610500, China*

daiyiyang1984@163.com

Abstract

Fault detection and diagnosis (FDD) is one of the key technologies to ensure the safe operation of chemical processes. With the widespread application of automation technology in chemical plants and the era of big data, data-based methods have become a hot research topic in the field of fault diagnosis. How to effectively extract the fault characteristics from the data and determine the cause of the fault is the key to help the operator deal with the abnormal conditions. Stack auto-encoder is a deep learning model with strong feature extraction and generalization capabilities. This paper proposes a SAE-based chemical process fault diagnosis model and applies it to Tennessee Eastman process. The performance of the SAE-based model is illustrated by comparison with the results of other methods.

Keywords: fault diagnosis, chemical engineering, stacked auto-encoder, neural network.

1. Introduction

With the development of science and technology, the chemical production process has become increasingly large-scale and complicated. When an abnormal situation occurs in the system, if it cannot be discovered and dealt with in time, it will cause huge economic losses and even casualties. Therefore, fault detection and diagnosis (FDD) have important application significance for chemical process.

Since Beard (1971) proposed the concept of fault diagnosis, many scholars have conducted related research in the field of fault diagnosis. Venkatasubramanian et al. (2003) classify fault diagnosis methods into three general categories according to models: quantitative model-based methods, qualitative model-based methods, and process history data based (data-driven) methods. With the widespread use of automation technology in the process industry, researchers can easily obtain a large amount of process history data. Therefore, the data-based FDD method has become a hot research topic in the field of fault diagnosis.

There are two types of FDD methods based on historical data. One type is statistical methods, such as principal component analysis (PCA), independent component analysis (ICA), kernel principal component analysis (KPCA), partial least squares (PLS) and their derivatives. The other type is pattern recognition methods, such as artificial neural networks (ANN), support vector machines (SVM), and so on. However, with the large-scale and complicated development of chemical units, the application of statistical methods and traditional pattern recognition methods will be limited by high-

dimensional data and high-correlation data. Since Hinton & Salakhutdinov (2006) proposed deep learning, the development and application of artificial intelligence technology has achieved great success in the past decade. Today, artificial intelligence is widely used in computer science, finance, and natural language processing. Zhang & Zhao (2017) proposed a chemical process fault diagnosis model based on deep belief network (DBN). Wu & Zhao (2018) proposed a chemical process fault diagnosis model based on convolutional neural network (CNN). The application of artificial intelligence technology in the field of chemical process fault diagnosis has also shown excellent performance.

In this paper, we propose a chemical process fault diagnosis model based on stack auto-encoder (SAE) and apply it to the fault diagnosis of Tennessee Eastman Process (TEP). The remainder of this paper is organized as follows: A brief introduction to SAE is given in Section 2. Section 3 shows a SAE-based fault diagnosis model. In section 4, The SAE-based model is applied in the TE process. Finally, we conclude the paper and describe some work in the future.

2. Stacked Auto-Encoder

The auto-encoder (AE) is proposed by Rumelhart et al. (1986), which is a typical single hidden layer neural network. The stack auto-encoder (SAE) is a modified model proposed by Hinton & Salakhutdinov (2006) based on the auto-encoder. SAE is an important deep learning model and it is a deep neural network essentially.

2.1. Structure of SAE

A SAE with 5 hidden layers is shown in Fig. 1. Structurally, the SAE consists of a coder layer (Layer-1 to Layer-4) and a decoder layer (Layer-4 to Layer-7), which assume a symmetrical structure. Each two adjacent layers from left to right is an AE, the weighted connections of neurons exist between each two adjacent layers.

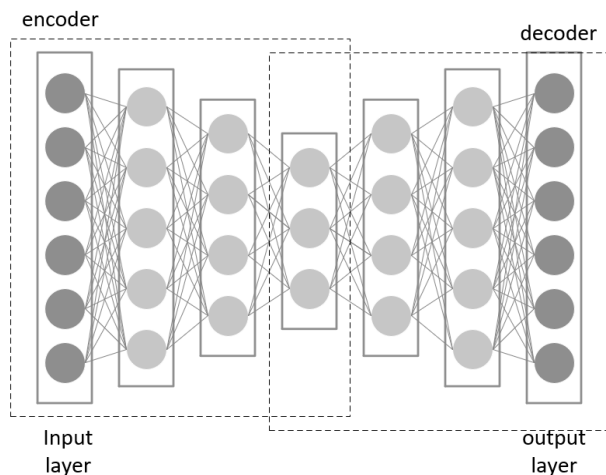


Fig. 1 Structure of a SAE with 5 hidden layers

Because the network structure of SAE has multiple hidden layers, it can well represent complex high-dimensional functions and has powerful feature extraction capabilities.

2.2. Training of SAE

The SAE training process consists of the following two stages: Pre-training stage and fine-tuning stage. The first stage is to initialize the weight of the deep neural network by means of layer-by-layer unsupervised learning (unsupervised greedy algorithm). The layer-by-layer greedy algorithm can effectively avoid the network falling into local optimum. The second stage is to fine-tune the model produced in the previous step by supervised learning (such as backpropagation algorithm).

For a training set x containing m samples, each of the data passes through the encoder to obtain a characteristic expression of the hidden layer, as shown in Eq. (1).

$$y^{(i)} = f_{\theta}(x^{(i)}) = s(Wx^{(i)} + b) \quad (1)$$

Where $\theta = (W, b)$ is the network parameter, W is the weight, b is the bias term, and s is the activation function.

The reconstructed vector is obtained by the $y^{(i)}$ input decoder, as shown in Eq. (2).

$$z^{(i)} = g_{\theta'}(y^{(i)}) = s(W'y^{(i)} + b') \quad (2)$$

Where $\theta' = (W', b')$, $W' = W^T$.

In order to prevent the model from over-fitting, a penalty term (regularization) needs to be added. The cost function is shown in Eq. (3).

$$J = \frac{1}{m} \sum_{i=1}^m \left(\frac{1}{2} \|z^{(i)} - x^{(i)}\|^2 \right) + \frac{\lambda}{2} \|W\|^2 \quad (3)$$

Where λ is the regularization parameter.

Iterative calculation is performed by the gradient descent method, and the optimal weight is obtained when the cost function is the minimum. In each iteration, the update process of the weight W and the bias term b as shown in Eq. (4) and Eq. (5).

$$W \leftarrow W - \alpha \frac{\partial J}{\partial W} \quad (4)$$

$$b \leftarrow b - \eta \frac{\partial J}{\partial b} \quad (5)$$

Where η is the learning rate.

After the pre-training stage, the weight of the pre-training model is iterated and updated again using the backpropagation algorithm until the error between the predicted label and the input label is lower than the expected value. Finally, the best weights and bias terms for each layer of AE are obtained.

3. Fault diagnosis model

According to the training process of SAE, we constructed a SAE-based chemical process fault diagnosis model. The fault diagnosis model is shown in Fig. 2, which includes the offline stage and the online stage. 80% of the historical data is used as training data, and its corresponding label is generated. The model is trained using the training set and its corresponding labels, and the remaining data is entered into the model for testing. Compare the test results to the label, and apply the model to online-stage if it performs well. If the model has a low correct rate on the test set, the parameters should be changed for retraining.

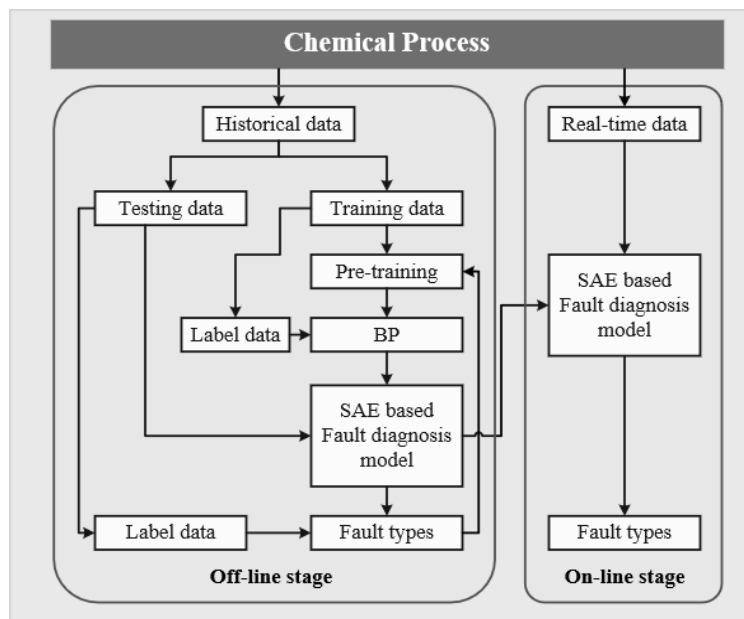


Fig 2. The framework of the SAE based fault diagnosis model

4. Application to Tennessee Eastman process

In order to verify the performance of the model which is proposed in this paper. The dataset of Tennessee Eastman (TE) process is applied to the SAE-based fault diagnosis model. The results are compared to some other FDD methods.

4.1. TE process

TE process is a simulation based on the actual chemical industry process, which was proposed by Downs & Vogel (1993). TE process includes 12 manipulated variables and 41 measured variables. Since the 12th manipulated variable is a constant, the diagnosis model involves a total of 52 variables. There are 20 faults in TE process.

All simulation data come from <http://web.mit.edu/braatzgroup/links.html>. There are 2 sets in this data set. Each set contains 21 sets of data, which are normal state data and 21 types of fault state data. The first dataset was first simulated in the normal state for 1

hour, and simulation was continued for 24 hours after adding the disturbance. The second dataset was first simulated in the normal state for 8 hours, and simulation was continued for 40 hours after the disturbance was added. The sampling period for both sets of data is 3 minutes, so the dataset includes 30,260 samples.

4.2. Diagnosis results and comparison

We conducted comparative experiments by setting different hyperparameters. A multivariate hyperparameter set was obtained through experiments. The SAE model includes 6 layers of neurons, and the number of neurons in each layer is 52, 100, 50, 50, 100, 21. The number of pre-trainings is 200, the size of each batch in pre-training stage and fine-tuning stage is 89, the learning rate is 1, and the regularization parameter is 0.0000005.

The performance of the model is usually evaluated by the fault diagnosis rate (FDR). p_i is the count of type i samples that are classified to type i .

$$FDR_i = \frac{P_i}{\text{total count of type } i \text{ samples}} \quad (6)$$

The comparison of diagnosis performance with several statistical methods and traditional pattern recognition methods is shown in Table 1.

Table 1 Diagnosis performance comparison of different methods. (a) based partitioning PCA (Wang et al., 2016); (b) based dynamic ICA (Hsu et al., 2010); (c) based designing a hierarchical neural network (Eslamloueyan, 2011); (d) based support vector machines (Yélamos et al., 2009); (e) based SAE (proposed in this paper).

FDR (%)	(a)	(b)	(c)	(d)	(e)
Fault01	99.8	100.0	97.0	95.0	98.2
Fault02	98.8	99.0	98.0	100.0	99.6
Fault03	13.6	2.0	53.0	0.0	34.6
Fault04	86.5	97.0	95.0	57.0	96.3
Fault05	100.0	100.0	96.0	64.0	99.2
Fault06	99.5	100.0	100.0	93.0	100.0
Fault07	100.0	100.0	100.0	100.0	100.0
Fault08	98.3	98.0	60.0	100.0	95.3
Fault09	13.4	1.0	29.0	0.0	37.8
Fault10	64.4	82.0	47.0	53.0	89.2
Fault11	77.1	54.0	48.0	21.0	74.3
Fault12	99.3	100.0	46.0	0.0	94.7
Fault13	94.6	95.0	32.0	91.0	94.0
Fault14	100.0	100.0	67.0	0.0	95.2
Fault15	16.9	2.0	66.0	0.0	84.9
Fault16	49.0	82.0	37.0	88.0	82.6
Fault17	96.3	90.0	72.0	68.0	92.4
Fault18	91.3	90.0	94.0	82.0	90.0
Fault19	39.4	81.0	52.0	16.0	86.3
Fault20	54.0	88.0	67.0	100.0	86.4
Average	74.6	78.1	67.8	56.4	86.5

5. Conclusions and prospects

With the widespread use of automation technology in chemical processes, it has become increasingly convenient for researchers to access historical data. Many new data-based methods have been applied to the study of chemical process fault diagnosis. In the increasingly complex chemical process, SAE has strong feature extraction and generalization capabilities. This paper proposes a SAE-based chemical process fault diagnosis model, and uses the data generated by the TE process for model construction and training, the average fault diagnosis rate reaches 86.5%. Compared to traditional shallow neural networks, deep learning requires a larger training sample to present its advantages. Therefore, our next work is to simulate the TE process to get more data. Then, the key variables are divided according to the relevance of the variables.

Acknowledgement

The authors gratefully acknowledge financial support from the National Natural Science Foundation of China (NSFC) (No. 21706220).

References

- Beard, Vernon, R., 1971. Failure accommodation in linear systems through self-reorganization.
- Eslamloueyan, R., 2011. Designing a hierarchical neural network based on fuzzy clustering for fault diagnosis of the Tennessee - Eastman process. *APPL SOFT COMPUT*, 1407-1415.
- GuozhuWang, JianchangLiu, YuanLi, ChengZhang, 2016. Fault diagnosis of chemical processes based on partitioning PCA and variable reasoning strategy☆. *CHINESE J CHEM ENG*, 869-880.
- Hinton, G.E.H.C., Salakhutdinov, R.R., 2006. Reducing the Dimensionality of Data with Neural Networks. *SCIENCE*, 504-507.
- Hsu, C.C.C.E., Chen, M., Chen, L., 2010. A novel process monitoring approach with dynamic independent component analysis. *CONTROL ENG PRACT*, 242-253.
- Rumelhart, D.E., Hinton, G.E., Williams, R.J., 1986. Learning representations by back-propagating errors. *NATURE*, 533-536.
- Venkatasubramanian, V.V.C.P., Rengaswamy, R.R.C.E., Yin, K., Kavuri, S.N., 2003. A review of process fault detection and diagnosis Part I: Quantitative model-based methods. *Computers and Chemical Engineering*, 293-311.
- Vogel, J.J.D.A., 1993. A plant-wide industrial process control problem. *Computers and Chemical Engineering*, 245-255.
- Wu, H., Zhao, J., 2018. Deep convolutional neural network model based chemical process fault diagnosis. *COMPUT CHEM ENG*, 185-197.
- Yélamos, I., Escudero, G., Graells, M., Puigjaner, L., 2009. Performance assessment of a novel fault diagnosis system based on support vector machines. *Computers and Chemical Engineering*, 244-255.
- Zhang, Z.Z.Z., Zhao, J.Z.J., 2017. A deep belief network based fault diagnosis model for complex chemical processes. *COMPUT CHEM ENG*, 395-407.

Simulation-based reinforcement learning for delivery fleet optimisation in CO₂ fertilisation networks to enhance food production systems

Rajesh Govindan, Tareq Al-Ansari*

Division of Sustainable Development, College of Science and Engineering, Hamad Bin Khalifa University, Qatar Foundation, Doha, Qatar

*talansari@hbku.edu.qa

Abstract

As part of the drive for global food security, all nations will need to intensify food production, including those situated in hyper arid climates. The State of Qatar is one such example of a national system that whilst it is presented with environmental challenges, seeks to enhance food security. There is a consensus that CO₂ fertilisation of agricultural systems has the potential to enhance their productivity. In this paper, the authors present a novel study that involves the development of a simulation model of a GIS-based CO₂ fertilisation network comprising of power plants equipped with CO₂ capture systems, transportation network, including pipeline and roadways, and agricultural sinks, such as greenhouses. The simulation model is used to specifically train the CO₂ distribution agent in order to optimise the logistical performance objectives of the network, namely delivery fulfilment and network utilisation rates. The Pareto non-dominating solutions correspond to an optimal CO₂ delivery fleet size of around 1-2 trucks for an average year in the simulation example considered.

Keywords: CO₂ fertilisation, Simulation, Logistics, Reinforcement Learning

1. Introduction

With the changing climate and growing population, there exists a global drive towards the intensification of food production. Those countries particularly situated in hyper arid regions that seek to boost their agricultural productivity are faced with the challenges pertaining to the sustainable usage of their land, energy and water resources. As such, the importance of understanding the relationship between food security and the natural environment is recognised, as agricultural productivity essentially depends on the condition of the latter. This introduces the notion of ‘sustainable intensification’, which is related to the need to meet the nutritional demands of a growing population without furthering the depletion of resources and degradation of the environment (Godfray and Garnett, 2014). To this effect, there has been much discussion on the effect of elevated levels of CO₂ in the atmosphere on agricultural productivity. The consensus is that it is possible to obtain higher crop yields because CO₂ is an essential compound in the photosynthesis process where its carbon content is utilised to form carbohydrates. Furthermore, increasing the concentrations of CO₂ inhibits the loss of water, also known as transpiration, due to increased resistance from leaf stomata. The natural fertilisation of crops using CO₂ offsets the effects of increasing temperature and decreasing soil moisture (Lawlor and Mitchell, 1991). Moreover, CO₂ fertilisation of plants not only

results in increases in dry matter production but is also accompanied by improvements of water utilisation efficiency (WUE) (Kimball and Idso, 1983).

Previously, the authors developed a GIS-based EWF nexus model to explore the potential of enhancing agricultural productivity through CO₂ fertilisation at the farm level (Al-Ansari *et al.*, 2018). It was noted that, the approach is promising from an environmental perspective, as the emission reduction that can be potentially achieved by the CO₂ fertilization network is between 0.5 - 1 Mt/year considering the integration of capture technology for both CCGT and BIGCC, with the potential benefit of saving precious water resource at the agricultural fields. However, the overall viability must also depend on the economic feasibility of the transport network. As such, there is a requirement of using a combination of pipelines and roadways (using trucks) for the transportation of CO₂ from the source to the sink. It is likely that a dedicated CO₂ fertilisation network for enhancing agricultural productivity could either remain underutilised or sometimes unable to meet the demands of new greenhouses that are expected to be built, and hence, extended studies are necessary to address such logistical issues. Furthermore, increasing utilisation reduces the amount of net traffic (in vehicle kilometres) needed to transport a given quantity of freight (in tonne-kilometres), which in turn corresponds to decreased energy consumption and reduced CO₂ emissions from transportation itself (McKinnon, 2010).

The objective of the research presented in this paper is to develop a network simulation model comprising of spatially-distributed and autonomous learning agents representing sub-systems participating in a national-scale CO₂ supply chain logistics problem. For the purposes of illustration in this study, the business logic to enable agent simulation representing CO₂ distribution centres and greenhouses, was implemented. The authors posed the logistics problem as non-linear and multi-objective optimisation model using Markov Decision Processes (MDP) framework. This allows to determine the optimal solution representing the size and routing behaviour of a fleet of delivery trucks that transport CO₂ from the distribution centres in order to simultaneously fulfil the demand at various greenhouse locations (dependent on seasonal weather conditions) and improve the network utilisation rate.

2. Available data and assumptions

The information was derived from multimodal datasets for Qatar, each of which provides spatial information for: (a) distribution of land use for farming activities; (b) distribution of solar irradiance; (c) the locations of the major sources of CO₂ emissions; and (d) possible modes of CO₂ transport, namely pipelines and road transport. A meta-heuristic formalism was previously introduced by the authors which helped in determining the promising locations for new greenhouse developments as illustrated in Fig 1 (Al-Ansari *et al.*, 2018). This served as the basis for setting up the CO₂ fertilisation network simulation model in the current study. It should, however, be noted that the locations of CO₂ distribution centres were assumed to be at the intersections of pipelines and roadways for simplification purposes and are not necessarily optimised.

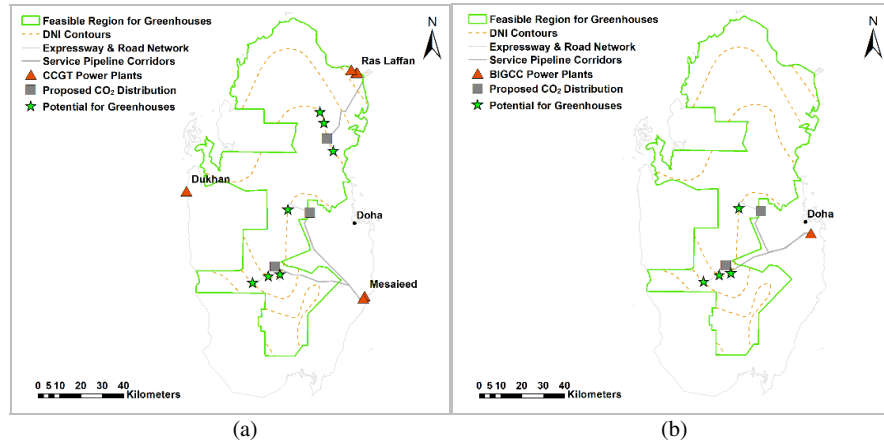


Fig 1. Optimised locations of greenhouses in the State of Qatar for the case of CO₂ captured from: (a) CCGT plants; and (b) BIGCC plants (After Al-Ansari *et al.* (2018)).

3. Methodology

3.1. CO₂ fertilisation network simulation

The network simulation model was setup using the Java-based AnyLogic® platform. The necessary spatial information was used in order to accurately capture the road networks in Qatar, which is used by the fleet in the model to transport CO₂ between the distribution centre and greenhouses, as illustrated in Fig 2.

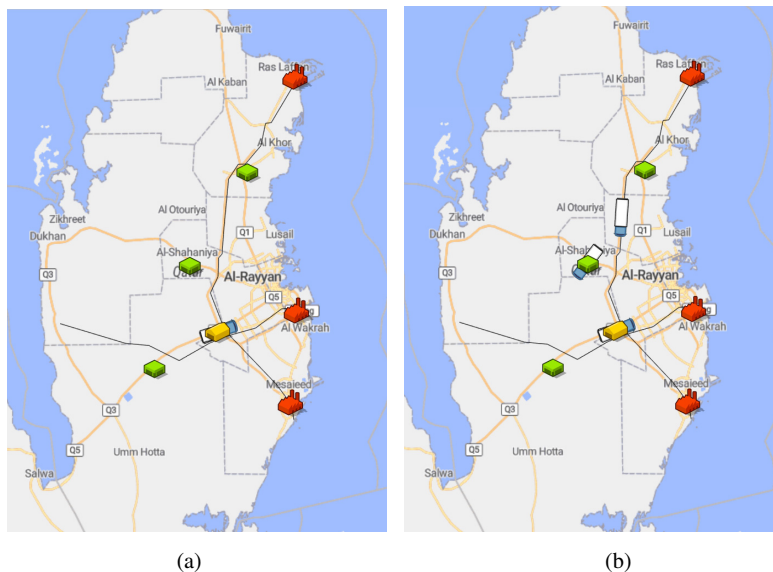


Fig 2. Spatial simulation of the CO₂ fertilisation network indicating power plants; CO₂ distribution centre; and greenhouses for: (a) initial state of the fleet; (b) moving state of the fleet during simulation.

The simulation period corresponds to one year capturing the essential variability in the average seasonal temperatures, *i.e.* minimum, maximum and mean temperatures, at different locations in Qatar. The business logic for the agents representing greenhouses was implemented using the modified form of Hargreaves original equation for evapotranspiration (ET), which uses local weather data, such as the temperatures and solar irradiance distribution data, given by (Hargreaves and Samani, 1985):

$$ET = k \times 2.3 \times 10^{-4} \times (T_{\max} - T_{\min})^{0.5} \times (T_{\text{avg}} + 17.8) \times R_a \quad (1)$$

Where, k is a factor which varies from 0.79 – 1.02. Increasing ET values (in mm) is an indicator of increasing CO₂ demand, and thus a maximum allowable water loss was assumed as the trigger condition for greenhouses to place an ‘order’ for more CO₂ from the distribution centre. Currently, this amount of CO₂ is assumed to be fixed, and the stock is fully utilised before a new order can be placed; no monetary transaction is associated with the placement of an order.

Meanwhile, at the distribution centre, the business logic for fleet management is illustrated by the process diagram in Fig 3. The ‘seizing’ of a truck from the fleet resource pool occurs whenever a demand trigger (order) is received. On the other hand, the ‘loading’ and ‘unloading’ times are assumed to be stochastic.

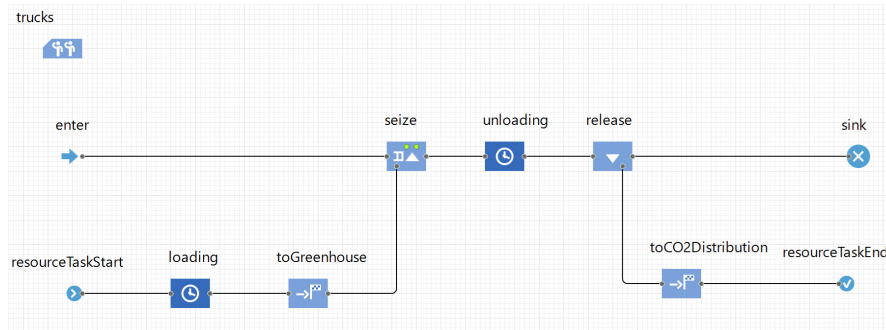


Fig 3. The process model setup in AnyLogic® representing the business logic for fleet resource pool management at the CO₂ distribution centre.

3.2. Fleet optimisation using Reinforcement Learning

The classical formalism of Markov Decision Process (MDP) was implemented to aid the learning feature in the agent representing the CO₂ distribution centre. More specifically, a temporal difference learning approach called Q-learning was used to maximise the expected cumulative value of an action (a) taken under a given state (s) of the agent during the simulation period of one year. More formally, the network objectives, namely order fulfilment time and utilisation rate, are modelled as Bellman Eq 2 and 3 (Sutton and Barto, 1998) to give the optimal policy for all states and actions in Eq 4 (Sutton and Barto, 1998):

$$Q(S_t = s, A_t = a) = E[r + \gamma V(S_{t+1} = s') | S_t = s, A_t = a] \quad (2)$$

$$V(S_t = s) = E[r + \gamma V(S_{t+1} = s') | S_t = s] \quad (3)$$

$$Q_*(S_t = s, A_t = a) = \max\{Q_x(S_t = s, A_t = a)\}, \forall s \in S, a \in A \quad (4)$$

Where ‘r’ is the immediate reward signal for an action ‘a’ in state ‘s’; γ is the discount factor whose value lies between 0 (short-term minded or greedy agent) and 1 (long-term minded agent), which indicates the importance the optimisation gives towards future rewards. Finally, the update of the action value function (Q) from a given time step to the next is given by (Sutton and Barto, 1998):

$$Q(S_{t+1} = s, A_{t+1} = a) \leftarrow Q(S_t = s, A_t = a) + \dots \alpha \left[r + \gamma \max_{a'} \{Q(S_{t+1} = s', A_{t+1} = a')\} - Q(S_t = s, A_t = a) \right] \quad (5)$$

4. Results and discussion

One of the performance metrics used by the agent (and receiving the corresponding reward signal) is the time it takes for the distribution centre to fulfil an order depends on both the speed of the truck (assumed constant) and the route it takes (assumed initially stochastic). The other performance metric used by the agent is the fleet utilisation rate. Q-learning was performed with respect to these performance metrics over the simulation period of one year.

The results obtained from the multi-objective optimisation using the Q-learning approach listed in Table 1 demonstrates that there exist Pareto non-dominating solutions for the optimal fleet size for the CO₂ distribution centre. It is therefore expected that the optimal fleet size is around 1-2 trucks for the simulation example considered. However, it is important to note that the study carried out thus far is a small network for the purposes of illustrating the technique, and does not consider the entire CO₂ fertilisation network, such as the power stations (see Fig 2).

Table 1. Objective function values using the Q-learning approach for various fleet sizes.

Size of the fleet	Order fulfilment time of the network (orders per day)	Utilisation rate in the network (%)
1	2.1	65
2	2.34	36
3	2.33	23
4	2.47	19
5	2.39	15

5. Conclusions

The study discussed in this paper provides an illustrative example of how simulation-based optimisation can aid in making large-scale logistical decisions for network-based applications having economic implications. With the recent advent of artificial intelligence, non-linear, multi-objective and sequential decision-making techniques such as reinforcement learning is useful in solving hard problems whose objective functions do not have closed form analytical representations, such as the CO₂ fertilisation network for the enhancement of agricultural productivity.

It is envisaged that the results obtained have important implications for planning the expansion of greenhouse networks, particularly for the State of Qatar, where self-sustenance and food security has become a priority. In this regard, it has been considered that both the environmental and economic dimensions are equally important. As such, the utilisation of waste streams such as CO₂ emissions for growing crops not only provides for food security, but also enhances the efficiencies of energy and water utilisation as highlighted in the research carried out by the authors.

With regards to the limitations of the current work, only a single agent has been considered thus far and hence there is scope to extend the work to develop multiple learning agents in large-scale network optimisation. The business logic considered are also likely to be simplified for the current illustration, and hence the simulator requires incorporating agent functions for real world scenarios, *e.g.* in multi-echelon supply chains where dynamic distribution of resources, inventory and supply risk management and long-term supply chain planning and development are some of the core problems to be generally solved.

References

- Al-Ansari, T., Govindan, R., Korre, A., Nie, Z. and Shah, N., 2018. An energy, water and food nexus approach aiming to enhance food production systems through CO₂ fertilization. In *Computer Aided Chemical Engineering*, 43, 1487-1492, Elsevier.
- Godfray, H.C.J. and Garnett, T., 2014. Food security and sustainable intensification. *Phil. Trans. R. Soc. B*, 369(1639), 20120273.
- Hargreaves, G.H. and Samani, Z.A., 1985. Reference crop evapotranspiration from temperature. *Applied engineering in agriculture*, 1(2), 96-99.
- Lawlor, D. W. and Mitchell, R. A. C., 1991, The effects of increasing CO₂ on crop photosynthesis and productivity: a review of field studies, *Plant, Cell and Environment*, 14, 807-818.
- Kimball, B., and Idso, S., 1983, Increasing atmospheric CO₂ effects on crop yield, water use and climate, *Agricultural Water Management*, 7, 55-72.
- McKinnon, A., 2010. Green logistics: the carbon agenda. *Electronic Scientific Journal of Logistics*, 6(1).
- Sutton, R.S. and Barto, A.G., 1998. Reinforcement learning. MIT Press Cambridge, MA.

Exergoeconomic Analysis for a Flexible Dry Reforming Power Plant with Carbon Capture for Improved Energy Efficiency

Szabolcs Szima*, Calin-Cristian Cormos

Babes-Bolyai University, Faculty of Chemistry and Chemical Engineering, Arany Janos 11, Cluj-Napoca, RO-400028, Romania

szima@chem.ubbcluj.ro

Abstract

Dry reforming of methane is an innovative alternative method for the production of hydrogen that uses CO₂ for the reforming process, thus lowering the carbon emissions of the plant. With the rise of renewable energy sources (solar, wind), the difference between the power supply and demand within the grid increased heavily, making flexibility of power plants more important for costs and emissions reduction. This paper presents the exergoeconomic analysis performed on the dry reforming technology designed for flexible power and hydrogen co-generation with carbon capture. The examined power plants' output is 450 MW net power with the possibility of hydrogen production of 200 MW_{th} (based on lower heating value). The CO₂ capture rate is 90 % (a part being used in the reforming process). The energy efficiency of the plant is 50 %, the exergy destruction rate is 370 MW and the specific capital cost of the plant is 1,295 M€/MW. The goal of this work is to offer an alternative to conventional steam reforming, improve the process of dry reforming by finding and improving the components of the system that contribute the most to the destruction of exergy and present a new flexible power plant that can produce both power and hydrogen. The evaluated design concepts were simulated using process flow modeling software and the mass & energy balances were used for the exergoeconomic analysis to improve the overall performance of the plant.

Keywords: dry methane reforming, flexible power plant, exergy analysis, exergoeconomic analysis,

1. Introduction

As atmospheric CO₂ concentrations are on the rise, a shift can be expected in global energy sources from conventional power sources to renewable ones, like solar and wind. This transition generates a stress on the electric grid as renewable energy sources power output depend heavily on the weather. The flexibility of a power system describes the ability of the system to balance out predictable and unpredictable changes on the supply or on the demand side. Cruz et al., (2018a) presents an extensive review on this issue and discusses potential options to ease the integration of renewable sources. Alemany et al., (2018) proposes the storing of electric energy during high production intervals. Several storing possibilities were proposed in the literature, the use of chemicals being heavily discussed (Chiuta et al., 2016).

With the rise of carbon capture technologies, the amount of available CO₂ is expected to increase in the future and as storage can be geographically limiting, the use of captured

CO₂ can be an alternative. Dry methane reforming uses CO₂ for the reforming of methane in the process of obtaining syngas. Several studies have been published in the past year on the subject (Salkuyeh et al., 2017). Aramouni et al. (2018) did a comprehensive review on catalysts and identified carbon deposition as the major issue in deploying the technology. As the carbon ratio is high in the reactor, carbon deposition on the catalyst is a barrier that needs solving. Developing new highly active catalysts is one of the approaches in resolving this issue.

In the current global context, as energy consumption is constantly on the rise while carbon mitigation is becoming more important a stalemate situation will be reached. In order to comply with the strict emissions reductions, set either large-scale carbon capture deployment is needed or a shift will be necessary towards energy carriers with a lower carbon footprint. Hydrogen is one promising alternative to fossil fuels, however this is conditioned to an adequate supply-chain. Hydrogen is obtained from natural gas reforming (48 %), petroleum refining (30 %) and coal gasification (18 %) (Cruz et al., 2018b). In order for hydrogen to be a viable option, either these technologies have to be redesigned with lower CO₂ emissions or a new, carbon-free way has to be implemented for its production. One option is water hydrolysis, however this technology is too expensive. Flexible power plants with carbon capture producing hydrogen can be an alternative to supply the necessary hydrogen.

This paper investigates the thermodynamic performance of dry methane reforming for the co-production of power and hydrogen through exergy analysis and offers a glance into the economics of the process. The plant is divided into four subunits, gas reforming, syngas processing, CO₂ capture and purification and the power island. A model of the plant is implemented in Aspen Plus process simulator to obtain the mass and energy balance of the process. Each division is evaluated separately in the analysis to better understand and identify the least efficient units.

2. Evaluation methodology

The plant was designed based on the general structure of a steam-methane reforming system, as presented in Figure 1. The gas reforming unit consists mainly of the reforming reactor, the syngas processing unit contains the water-gas shift reactors and the steam generator. The carbon capture unit is a gas-liquid absorption system using MDEA solution. Part of the captured CO₂ is recycled to the reforming unit, while the rest is sent to a storage site. The power island is designed using a Mitsubishi Hitachi Power Systems M701G2 series gas turbine combined cycle with the following specifications: 334 MW net power output, 39.5 % net power efficiency. The heat and energy balances from the process flow simulator are at the basis of the economic calculations of the plant.

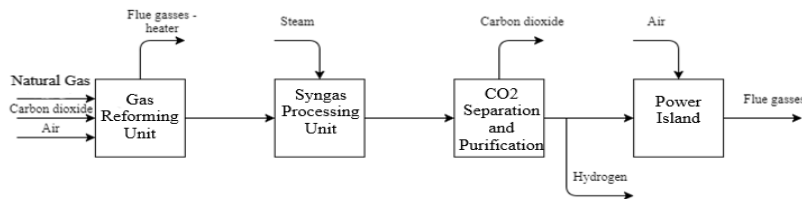


Figure 1. Simplified process flow diagram

The reactions describing the process of dry reforming are presented in Table 1. The reforming reaction is highly endothermic; hence 153 MW_{th} energy is necessary for the reforming reactor (this is provided by the burning of additional natural gas). The reverse-WGS reaction has a great impact on the final equilibrium and being endothermic, it is highly favored. Coke formation, the major issue in the case of dry reforming can be described by the last four reactions in the table, one of them being highly favored also because of its endothermic nature. In the process simulator, equilibrium reactors were considered, as equilibrium conditions can be easily achieved in these conditions.

Table 1. Governing reaction for dry reforming of methane

Reaction number	Name	Equation	ΔH_{298K} (kJ* mol^{-1})
Main reaction			
1	Dry methane reforming	$\text{CH}_4 + \text{CO}_2 \leftrightarrow 2\text{CO} + 2\text{H}_2$	+ 247
Side reaction			
2	Reverse water-gas-shift	$\text{CO}_2 + \text{H}_2 \leftrightarrow \text{CO} + \text{H}_2\text{O}$	+ 41.0
Coke formation			
3	Decomposition of methane	$\text{CH}_4 \leftrightarrow \text{C} + 2\text{H}_2$	+ 74.9
4	Disproportionation of CO	$2\text{CO} \leftrightarrow \text{C} + \text{CO}_2$	- 172.4
5	Hydrogenation of CO ₂	$\text{CO}_2 + 2\text{H}_2 \leftrightarrow \text{C} + 2\text{H}_2\text{O}$	- 90.0
6	Hydrogenation of CO	$\text{H}_2 + \text{CO} \leftrightarrow \text{H}_2\text{O} + \text{C}$	- 131.3

Exergy analysis is a powerful tool for energy analysis of a system. By its definition, exergy is the maximum theoretical useful work obtained if a system S is brought into thermodynamic equilibrium with the environment by means of processes in which the S interacts only with this environment (Cruz et al., 2018b). In contrast to mass and energy laws, exergy is destroyed in a system due to irreversibility. A system is in equilibrium with its surroundings when there is no difference in temperature, pressure or chemical composition. In the present work, thermodynamic and chemical exergy was calculated with respect to the reference conditions (Table 2).

Table 2. Reference environment for exergy calculations

Thermo-mechanical exergy		Chemical exergy	
Parameter	Value	Component	Molar fraction
Temperature	18°C	N ₂	0.7651
Pressure	1 atm	O ₂	0.2062
		H ₂ O	0.0190
		Ar	0.0094
		CO ₂	0.0003

The temperature and pressure data were used for the calculation of the thermodynamic exergy and the chemical composition for the chemical exergy. In both cases, atmospheric parameters were considered as a reference. For the calculation of the exergy flow and the exergy efficiency in the system, equations (1) and (2) were used.

Parameters were obtained from the exergy balance of the system. Simulation was performed using Aspen Plus process simulator.

$$E_f = E_p + E_d + E_l \quad (1)$$

$$\varepsilon = E_p / E_f \quad (1)$$

E_f - exergy flow; E_p - exergy of product; E_d - exergy destruction; E_l - exergy lost

The estimation of the capital costs for each unit were performed using capital cost correlations found in the literature (Cormos et al., 2017) based on the simulation results. On-site utility costs, owners' cost and land purchasing costs were estimated as 20 %, 15 % and 5 % of the total installed cost of the plant. Specific capital requirements were also calculated to ease comparison between technologies.

3. Results and discussion

Table 3. Exergy analysis results

	Exergy flow in (MW)	Exergy flow out (MW)	Exergy destruction (MW)	Exergy efficiency
Gas reforming unit	933.88	888.70	63.32	91.37 %
Syngas processing	888.70	863.20	33.47	93.72 %
CO ₂ separation and purification	863.20	819.75	12.34	95.70 %
Power island	819.75	476.30	260.04	57.99 %

69 t/h of natural gas is required (900 MW_{th}) for the plant. The reforming, the water gas shift and the CO₂ capturing unit, all operate at 32 bar, whereas the gas turbine inlet pressure is at 19 bar. An expander is introduced to facilitate this pressure drop. The recovered energy is 2.3 MW. Combined with the gas turbine and the steam turbine the gross electric output is 476 MW_e. The ancillary energy for the system totals to 26 MW_e. This equals a net power output of 450 MW_e with a net electric efficiency of 50 %.

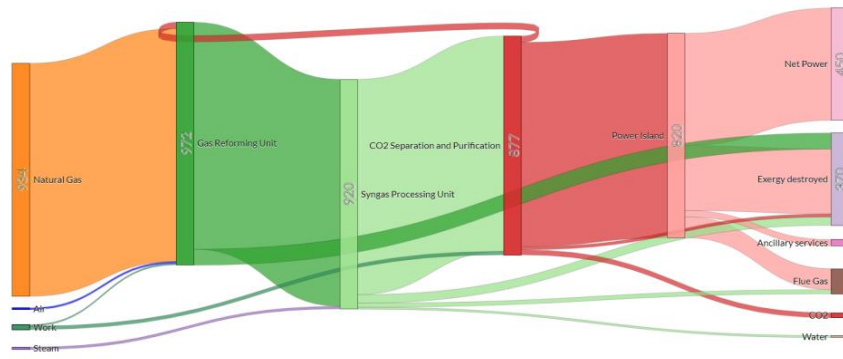


Figure 2. Exergy flow diagram for the process

The stream leaving the carbon capture unit is rich in hydrogen. With the addition of a pressure swing adsorption unit, the plant can produce high purity H₂ during low power demand offering a higher degree of flexibility to the system.

The results of the exergy analysis are presented in Figure 2 and Table 3. 934 MW exergy is introduced into the system with the natural gas stream. In the gas reforming unit with the compression of CO₂ another 38 MW of exergy is added. As a significant amount of heat is required for the endothermic reforming reaction, more than 60 MW of exergy is destroyed; the rest is fed into the Syngas processing unit (20 MW of exergy is transferred from the gas reforming unit to the syngas processing unit in the flue gasses stream leaving the heater). The syngas processing unit is significantly more efficient with an exergy efficiency of 93 %. The carbon capture unit is the most efficient, that is in part because 60 % of the captured CO₂ is recycled to the reforming unit. As expected, most of the exergy is destroyed in the power island; this is the subsystem with the highest grade of irreversibility, because of combustion. Energy and exergy analysis show similar results, the exergy analysis resulting lower efficiencies for the plant.

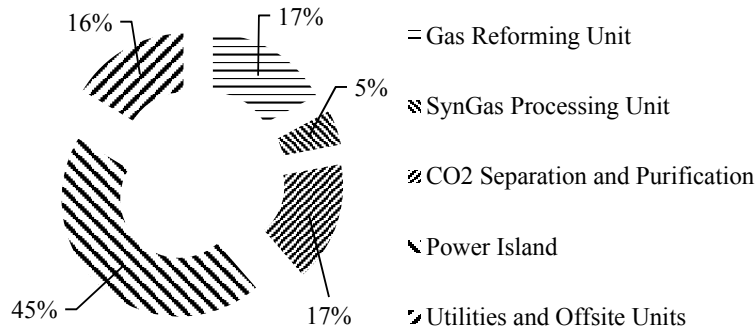


Figure 3. Share of each subsystem in the total capital cost

Figure 3 presents the obtained costs share in the total capital cost requirement for each subsystem. The most expensive unit, the power islands' cost was estimated at 219 M€, the gas reforming unit at 83 M€, the CO₂ separation and purification unit at 80 M€. The syngas processing unit had the lowest cost, this was estimated at 24 M€. To obtain the total installed cost of the plant, utilities and offsite units capital costs were also added, these were estimated as 20 % of each units' cost resulting in 80 M€. The obtained costs for the proposed power plant are higher than in the case of a NGCC plant without carbon capture, however its comparable to the costs of a NGCC power plant with post-combustion capture.

Table 4. Capital cost data for the plant

Total Installed Cost	MM Euros	486.18
Total Investment Cost	MM Euros	583.41
Gross Power production	MWe	476.30
Net Power Production	MWe	450.30
Total Investment Cost per kWe (gross)	MM Euro / MWe	1,224.88
Total Investment Cost per kWe (equiv.)	MM Euro / MWe	1,295.60

Both exergy and economic analyses point to the power island as the unit that's improvement can have the highest positive impact on the plant. Exergy analysis shows, that the burning and boiling processes are responsible for this, however these are intrinsically low efficiency units. This calls for improvements to be made in other parts of the plant.

4. Conclusions

This paper presents the dry methane reforming technology as an alternative reforming process incorporated into a power plant for flexible operation. During low electricity demand, this can produce hydrogen for better efficiency. The system underwent a rigorous exergy analysis to better understand and to locate the least efficient units. Overall efficiencies for the two reforming systems are comparable, meaning dry reforming is a viable alternative for steam reforming if the issue of carbon deposition is addressed. The analysis also presented the effect of individual unit on the overall efficiency of the system simplifying the process of improvement. The highest grade of irreversibility was observed in the case of the power generation and reforming unit. Exergy analysis shows that most of the exergy is destroyed in the burner and in the boiler. The paper also presents an insight into the economics of the proposed flexible power plant, the power generation unit having the highest cost, the gas reforming and the CO₂ capturing unit having similar costs and the syngas processing unit having the lowest cost.

Acknowledgement

This work was supported by a grant of Ministry of Research and Innovation, CNCS – UEFISCDI, project ID PN-III-P4-ID-PCE-2016-0031: "*Developing innovative low carbon solutions for energy-intensive industrial applications by Carbon Capture, Utilization and Storage (CCUS) technologies*", within PNCDI III.

References

- J.M. Alemany, B. Arendarski, P. Lombardi, P. Komarnicki, 2018, Accentuating the renewable energy exploitation: Evaluation of flexibility options, *International Journal of Electrical Power & Energy Systems*, 102, 131–151
- N.A.K. Aramouni, J.G. Touma, B.A. Tarboush, J. Zeaiter, M.N. Ahmad, 2018, Catalyst design for dry reforming of methane: Analysis review, *Renewable and Sustainable Energy Reviews* 82, 2570–2585
- S. Chiuta, N. Engelbrecht, G. Human, D.G. Bessarabov, 2016, Techno-economic assessment of power-to-methane and power-to-syngas business models for sustainable carbon dioxide utilization in coal-to-liquid facilities, *Journal of CO₂ Utilization*, 16, 399–411
- A.-M. Cormos, C.-C. Cormos, 2019, Techno-economic evaluations of post-combustion CO₂ capture from sub- and super-critical circulated fluidised bed combustion (CFBC) power plants, *Applied Thermal Engineering*, 127, 106–115
- M.R.M. Cruz, D.Z. Fitiwi, S.F. Santos, J.P.S. Catalão, 2018, A comprehensive survey of flexibility options for supporting the low-carbon energy future, *Renewable and Sustainable Energy Reviews*, 97, 338–353
- P.L. Cruz, Z. Navas-Anguita, D. Iribarren, J. Dufour, 2018, Exergy analysis of hydrogen production via biogas dry reforming, *International Journal of Hydrogen Energy*, 43, 11688–11695
- Y. Khojasteh Salkuyeh, B.A. Saville, H.L. MacLean, 2017, Techno-economic analysis and life cycle assessment of hydrogen production from natural gas using current and emerging technologies, *International Journal of Hydrogen Energy*, 42, 18894–18909.

Structured millichannel multiphase reactors

J. Ruud van Ommen^{*}, John Nijenhuis, Johan T. Padding

*Delft University of Technology, TU Delft Process Technology Institute & e-Refinery,
Delft, the Netherlands*

j.r.vanOmmen@tudelft.nl

Abstract

This paper examines the use of millichannels in designing multiphase reactors. We give a general analysis based on dimensionless numbers, followed by an illustration of this approach to catalytic packed-bed reactors. Finally, we discuss how such reactors can play an important role of increasing the number of electrocatalytic processes in the chemical industry. The increased degrees of freedom gives these reactors clear advantages over thermocatalytic non-structured reactors, as well as over electrocatalytic processes.

Keywords: electrocatalysis, fixed beds, degrees of freedom, reactor engineering

1. Introduction

The classical approach of randomly organized catalyst beds (either fixed or fluidized) is often outperformed by carefully designed channels or structures in which the reactions take place (Gascon et al., 2015). In recent years, microreactors have received enormous attention in academic research because they offer excellent mass and heat transfer performance, and provide a powerful tool for process intensification (Yao et al., 2015). However, their sub-mm channel diameters typically imply laminar flow, which is for many applications not optimal. Other drawbacks are high pressure drop and tendency to fouling. Moreover, a huge number of parallel channels or devices is needed to reach reasonable production volumes. Millireactors – reactors with structures and features in the mm range rather than the sub-mm range – have the potential to combine the best of both worlds: imposing a structure that enhances heat and mass transfer, while their somewhat larger feature size reduces capital and operating costs.

In this study, we explore the benefits and limitations of applying millichannel-based systems for multiphase reactions. We give a brief literature overview, and present a few cases. The interaction between reactor and catalyst will be discussed, as well as the interplay between chemistry and flow behavior. For example, we will show how filling millichannels with small particles leads to partially structured fixed beds, with attractive performance concerning mass transfer, heat transfer, and pressure drop. We will also discuss how millichannel reactors can contribute to the transition to electrochemical processes, in which the presence of sufficient electrode surface together with the ability to removed produced gases will be key. We conclude that millireactors can provide an attractive option for a range of applications in the chemical and pharmaceutical industry, giving a good compromise between physiochemical performance and cost-effectiveness.

2. Advantages of millistructured reactors

The reason why millistructured reactors offer advantages over microstructured reactors can be appreciated by estimating magnitudes of key dimensionless numbers for two

Table 1. Important dimensionless numbers for flow reactors. We use the hydraulic diameter d_h as characteristic length scale. For channels filled with particles, replace d_h by d_p .

Dimensionless number
$Re = \rho U d_h / \mu$
$Nu = \alpha d_h / \lambda = Nu(Re, Pr)$
$Sh = h d_h / D = Sh(Re, Sc)$
$Pr = c_p \mu / \lambda$
$Sc = \mu / (\rho D)$

archetypal systems: (1) An empty flow reactor of hydraulic diameter d_h and length L . (2) A flow reactor of the same dimensions, but filled with catalytic particles of diameter d_p , leading to an average porosity ε . We will consider flow of two types of fluids through these reactors, one gas-like and one liquid-like, for which we will use the physical properties of air and water at 20 °C temperature and 1 atm pressure.

A significant enhancement of mixing by convective flow is commonly experienced for sufficiently high Reynolds number Re (dimensionless numbers are defined in Table 1). Similarly, convective flows enhance the heat transfer coefficient h . A significant enhancement of heat transfer is possible for $Re > 100$. Similar

conclusions may be drawn for mass transfer, with the roles of Nu and Pr replaced by the Sherwood and Schmidt numbers Sh and Sc (Hayhurst, 2000).

The differential pressure drop necessary to reach significant convective improvement of mixing and heat and mass transfer becomes prohibitive for small channels. For example, for an empty structured channel of hydraulic diameter d_h , the pressure drop associated with wall friction can be described by the Darcy-Weisbach equation (Romeo et al., 2002):

$$\frac{\Delta p}{L} = f \frac{\rho U^2}{2 d_h} \quad (1)$$

where f is the dimensionless friction factor. For a smooth straight channel and $Re < 10^3$, $f = 64/Re$. For other channels and higher Re , f is larger and depends on the roughness characteristics of the channel. Fig. 1 shows $\Delta p/L$ as a function of d_h for liquid-like (black solid line) and gas-like (black dashed line) fluids at $Re = 100$, assuming $f = 64/Re$. At this fixed Re , U decreases like $1/d_h$, leading to $1/d_h^3$ scaling of the required pressure drop: for $d_h = 0.1$ mm, the pressure drop to reach $Re=100$ is already substantial, approximately 10 bar/m, while for $d_h = 1$ mm the necessary pressure drop is a more manageable: 0.01 bar/m.

For a channel filled with catalytic particles of diameter d_p , the differential pressure drop can be described by the Ergun equation (Ergun, 1952):

$$\frac{\Delta p}{L} = 150 \frac{(1 - \varepsilon)^2 \mu U}{\varepsilon^3 d_p^2} + 1.75 \frac{1 - \varepsilon \rho U^2}{\varepsilon^3 d_p} \quad (2)$$

The first part is dominant in the laminar regime $Re < 1$, the second part in the turbulent regime $Re > 10^3$. Figure 1 shows $\Delta p/L$ as a function of d_p for liquid-like (red solid line) and gas-like (red dashed line) fluids at $Re = 100$ and $\varepsilon=0.5$. At fixed Re , both laminar and turbulent terms scale like $1/d_p^3$. Under these conditions, for $d_p = 0.1$ mm, the pressure drop necessary to reach $Re=100$ is enormous, approximately 1000 bar/m, while for $d_p = 1$ mm, the necessary pressure drop is much more reasonable, approximately 1 bar/m.

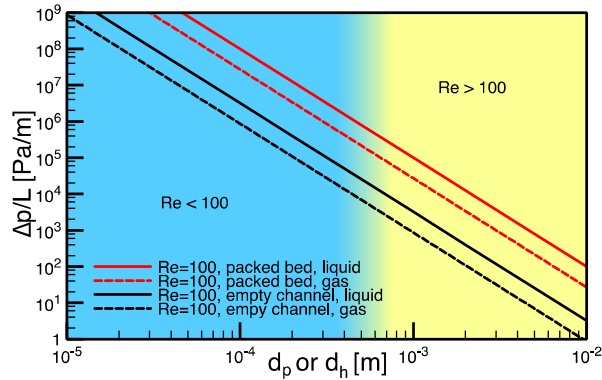


Figure 1. Pressure drop necessary to reach $Re=100$ as a function of hydraulic or particle diameter. Red: packed bed ($\epsilon = 0.5$), black: empty channel. Solid lines: liquid-like fluid, dashed lines: gas-like fluid. Blue: microchannel regime, yellow: millichannel regime.

Pressure drop is not the only important consideration. Smaller reactors are also more prone to contaminants and agglomerates getting stuck in corners of the channel or pore space. Moreover, it is important to tune the residence time in the channel to optimize reaction yield or selectivity. The average residence time is $\tau = \epsilon L/U$. At fixed Re , this leads to $\tau/L = \rho d_h/(\mu Re)$ or $\tau/L = \rho \epsilon d_p/(\mu Re)$, for the two respective systems. In the regime where inertial flow enhancement becomes relevant ($Re > 100$), reaching sufficiently long residence times requires sufficiently wide channels or sufficiently large particles.

3. Filling channels with particles

Although we have highlighted a number of clear advantages in the previous paragraph, a concern with applying structured reactors for catalytic applications is often that the catalyst holdup (i.e., the volumetric fraction of catalyst) is typically much lower than in randomly packed beds (Vervloet et al., 2013). Even if one takes into account that the catalyst effectiveness in packed beds is often below 1, still the productivity per reactor volume will be typically lower. A hybrid form of the two approaches can yield us the best of both worlds: using a system of structured channels, that are filled with particles (Calis et al., 2001, Dautzenberg and Angevine, 2004). The advantage of filling channels with particles that are of the same order of magnitude as the channel diameter is that the particle packing also becomes regular; see Fig. 2. In this way, we obtain a porosity that is importantly lower than the one for a randomly packed bed, which is 0.36 (Torquato et al., 2000). This has the advantage of a much lower pressure drop at a given particle size and fluid velocity. Alternatively, one can use higher fluid velocities and/or smaller particles to increase catalyst effectiveness and productivity of the system.

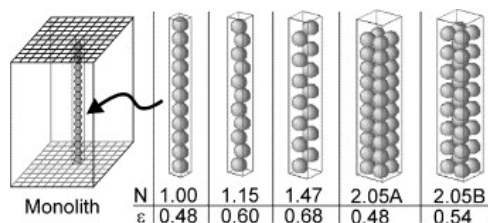


Figure 2. Packings obtained by filling small channels with particles. The aspect ratio (N) and porosity (ϵ) are given. Please note that for certain values of N , such as 2.05, multiple arrangements are possible (From: (Romkes et al., 2003), © Elsevier).

When the ratio of tube diameter over particle diameter becomes around 3 or larger, then the chance of getting a regular packing like in Fig. 1 strongly reduces (Calis et al., 2001). However, even in this case that are still advantages compared to regular packed beds with N typically about 104. At the wall of a packed bed, the porosity is higher than in the centre of a bed. For a channel with N around 10, the wall region covers a large part of the bed, leading to an overall porosity that is importantly lower than 0.36. Again, this has the advantage of lower pressure drop.

Vervloet et al. (2013) showed that for channels with a triangular cross-section of 7.7 mm, filled with particles of 2 mm ($N=3.8$), no regular packing was obtained. Still, the porosity was 0.50 (as opposed to 0.38 which was experimentally obtained for a randomly packed bed in the same study). Moreover, the heat transfer coefficient for transfer from fluid to wall (especially important for strongly exothermal reactions) was double that of a packed bed, and comparable to that of structured packings with empty channels. This shows that filling structures with particles can lead to large advantages in terms of pressure drop and heat transfer, and by analogy also mass transfer. An additional practical advantage is that one can still use the same catalyst particles as in conventional packed beds, i.e., no novel catalyst preparation procedure is required. particles.

4. Use in electrochemical processes

There is a broad consensus that the chemical industry will have to make a transition to renewable feedstocks. An important route will be to use electrochemical processes, driven by electricity from sustainable sources, to produce hydrogen from water, hydrocarbons from CO_2 and water, and ammonia from nitrogen and water. This will require novel reactor designs, with special attention to the structured design of electrodes. Although there is progress in electrochemical flow reactors, scalable macro- and micro-reaction environments need to be developed involving e.g. gas-liquid electrolyte flow (Walsh and Ponce de León, 2018).

In gas producing electrochemical cells a gas-liquid mixture is produced which impacts on energy consumption in terms of increased Ohmic resistance in the electrolyte. This is largely due to bubbles which hinder the mass transport of ionic species or block the electrode surface, and thereby reduce the effective electrode reaction sites i.e. by sticking to the electrode and/or forming a bubble curtain (Scott, 2018).

Traditionally, parallel plate structures are used in a wide range of electrochemical synthesis applications, where gas diffusion electrodes (GDEs) and Membrane Electrode Assemblies (MEAs) are used to reduce mass transfer limitations (Merino-Garcia et al.,

2016). Gas evolution and bubble formation at electrodes plus the coalescence of these bubbles leads to the formation of a heterogeneous electrolyte system with low conductivity, higher resistance and higher cell voltage, with corresponding electrical energy losses. The temporary or permanent occupancy of the electrode surface or the electrolyte volume by gas bubbles leads to a reduced performance (Ziogas et al., 2009). Bubble disengagement is therefore key.

In electrochemical rotating cylinder reactors, a high flow rate is induced such that the electrochemical process is enhanced by convective transport. In order to obtain the mass and charge transfer from the solution to the surface of the electrodes, an optimum flow field is essential (Tomasoni et al., 2007). Nonetheless, enhancement in mass transfer to a rotating cylinder electrode depends to a large extent upon micro turbulence at the electrode surface and is at the expense of high shear losses (Scott, 2018). Other forms of flow or turbulence promoters are also used to improve gas bubble disengagement. In general, it is observed that Ohmic voltage losses and overpotentials can only be reduced to a limited extent due to practical limitations of e.g. a higher pressure drop. Gas evolution reactions occur in the three-phase (gas–liquid–solid) interface formed at the electrode when a potential is applied with a magnitude greater than the equilibrium potential. The nucleation, growth and detachment of bubbles are affected by surface tensions of gas–liquid, gas–solid and liquid–solid (Scott, 2018).

The use of fluid flow to promote greater electrochemical reaction rates by increased mass transfer to surfaces is well known and commonly practiced in flow electrolyzers. However, the approach has limited success since the scalability of these microflow systems is an issue, and has not led to a compact scalable cell design, as in flat plate electrode stacks. Since bubbles are transported more easily through millichannels than through microchannels, Taylor flow in millichannel electrochemical cells would be beneficial since; a) the bubbles naturally drive the flow, b) a still narrow channel inhibits coalescence of bubbles, c) it leads to more homogeneous behaviour of the electrolyte, and d) the flow induces transportation of products away from the reaction surface. Furthermore, millichannel Taylor flow systems could lead to better scalability and a compact cell design.

The electrodes in electrochemical reactors automatically introduce a certain degree of structuring; this can be combined with other functions of the structure. Moreover, introducing structure gives more degrees freedom, and thus the possibility to solve potentially conflicting design criteria.

5. Conclusions

Millichannels have clear advantages over traditional, non-structured reactors, both in thermocatalytic and electrocatalytic processes. Analysis based on dimensionless numbers shows that the use of millichannels has important advantages over microchannels. The potential drawback of too low catalyst holdup can be overcome by filling the channels with particles. Also in electrocatalytic processes millichannels reactors can play an important role: the walls can act as electrode, while the channel configuration prevents problems with gas bubbles encountered in other types of electrocatalytic reactors.

References

- Calis, H. P. A., Nijenhuis, J., Paikert, B. C., Dautzenberg, F. M. & Van Den Bleek, C. M. 2001. CFD modeling and experimental validation of pressure drop and flow profile in a novel structured catalytic reactor packing. *Chemical Engineering Science*, 56, 1713-1720.
- Dautzenberg, F. M. & Angevine, P. J. 2004. Encouraging innovation in catalysis. *Catalysis Today*, 93-95, 3-16.
- Ergun, S. 1952. Fluid flow through packed columns. *Chem. Eng. Prog.*, 48, 89-94.
- Gascon, J., Van Ommen, J. R., Moulijn, J. A. & Kapteijn, F. 2015. Structuring catalyst and reactor - An inviting avenue to process intensification. *Catalysis Science and Technology*, 5, 807-817.
- Hayhurst, A. N. 2000. The mass transfer coefficient for oxygen reacting with a carbon particle in a fluidized or packed bed. *Combustion and Flame*, 121, 679-688.
- Kang, T. G. & Anderson, P. D. 2014. The Effect of Inertia on the Flow and Mixing Characteristics of a Chaotic Serpentine Mixer. *Micromachines*, 5, 1270-1286.
- Merino-Garcia, I., Alvarez-Guerra, E., Albo, J. & Irabien, A. 2016. Electrochemical membrane reactors for the utilisation of carbon dioxide. *Chemical Engineering Journal*, 305, 104-120.
- Romeo, E., Royo, C. & Monzón, A. 2002. Improved explicit equations for estimation of the friction factor in rough and smooth pipes. *Chemical Engineering Journal*, 86, 369-374.
- Romkes, S. J. P., Dautzenberg, F. M., Van Den Bleek, C. M. & Calis, H. P. A. 2003. CFD modelling and experimental validation of particle-to-fluid mass and heat transfer in a packed bed at very low channel to particle diameter ratio. *Chemical Engineering Journal*, 96, 3-13.
- Scott, K. 2018. Process intensification: An electrochemical perspective. *Renewable and Sustainable Energy Reviews*, 81, 1406-1426.
- Swamee, P. K. & Jain, A. K. 1976. Explicit equations for pipe-flow problems. *ASCE J Hydraul Div*, 102, 657-664.
- Tomasoni, F., Thomas, J. F., Yildiz, D., Van Beeck, J. & Deconinck, J. Transport phenomena in an electrochemical rotating cylinder reactor. *WIT Transactions on Engineering Sciences*, 2007, 153-162.
- Torquato, S., Truskett, T. M. & Debenedetti, P. G. 2000. Is random close packing of spheres well defined? *Physical Review Letters*, 84, 2064-2067.
- Vervloet, D., Kapteijn, F., Nijenhuis, J. & Van Ommen, J. R. 2013. Process intensification of tubular reactors: Considerations on catalyst hold-up of structured packings. *Catalysis Today*, 216, 111-116.
- Wakao, N., Kaguei, S. & Funazkri, T. 1979. Effect of fluid dispersion coefficients on particle-to-fluid heat transfer coefficients in packed beds. Correlation of nusselt numbers. *Chemical Engineering Science*, 34, 325-336.
- Walsh, F. C. & Ponce De León, C. 2018. Progress in electrochemical flow reactors for laboratory and pilot scale processing. *Electrochimica Acta*, 280, 121-148.
- Yao, X., Zhang, Y., Du, L., Liu, J. & Yao, J. 2015. Review of the applications of microreactors. *Renewable and Sustainable Energy Reviews*, 47, 519-539.
- Ziogas, A., Kolb, G., O'connell, M., Attour, A., Lopicque, F., Matlosz, M. & Rode, S. 2009. Electrochemical microstructured reactors: Design and application in organic synthesis. *Journal of Applied Electrochemistry*, 39, 2297-2313.

Systematic decision-support methodology for identifying promising platform technologies towards circular economy

Dominic Silk, Beatrice Mazzali, Isuru A. Udugama, Krist V. Gernaey, Manuel Pinelo, John Woodley, and Seyed Soheil Mansouri

*Process and Systems Engineering Centre, Department of Chemical and Biochemical Engineering, Technical University of Denmark, DK-2800 Kgs. Lyngby, Denmark
seso@kt.dtu.dk*

Abstract

This work presents a systematic computer-aided decision-support framework to tackle challenges faced when attempting to identify and develop resource recovery projects. The framework is hierarchical and has been developed to facilitate the industries' transition towards more sustainable production, providing users with the opportunity to evaluate and support decisions on not only a financial basis, but also from a comprehensive techno-economic and sustainability angle. To this end, the framework collects relevant aspects within the sustainability field and addresses concepts such as circular economy, waste management and 'legacy' compounds to name some of the more pertinent topics. The proposed methodology is generic and can be applied to a wide variety of potential resource recovery projects. The application of the framework is highlighted through two case studies, phosphorus recovery from a phosphate-based wastewater stream; and monosaccharide recovery from wheat straw liquor.

Keywords: Sustainability, Decision-support framework, Technology readiness level (TRL), Resource recovery, Circular Economy

1. Introduction

For over 200 years, the world economy has been built upon a linear economic model, leading for never before seen economic and societal transformation (Hayward et al., 2013). However, this human induced change has led to unprecedented global environmental degradation and rapid resource depletion, together with an unprecedented climate impact. The proposed countermeasure to this impending catastrophe is the circular economy model. In this model, resources are no longer extracted and discarded but instead products and revenues are generated from what in a linear economy would be considered waste. In this context, resource recovery, being the facilitating process to enhance attainable resource value and avoid resource deployment, perfectly fits the proposed paradigm shift. Today, the use of resource recovery is widely expressed in various industrial processes, including applications related to the dairy industry (Udugama et al., 2017) and biodiesel refining (Mansouri et al., 2019). In petrochemical operations, waste reintegration is also practiced widely (Mansouri et al., 2017). Consequently, resource recovery can be observed as a key missing element required to close an imperfect production cycle. Resource recovery project implementation enables companies to achieve several sustainable development

goals, such as responsible production and consumption, whilst improving their product portfolio and reducing dependency on external players in the supply chain.. Historically, little importance has been placed upon resource recovery, namely due to resource abundance, absence of reliable opportunity identification methods, and ease of waste treatment regulation compliance. In the domain of process systems engineering, this multi-dimensional and multi-scale problem has been an area of active interest with works on techno-economic sustainability analysis looking to address parts of these requirements (Gargalo et al., 2014, Gargalo et al., 2016, Hoseinzade et al., 2019). However, while these frameworks and methodologies can be adopted to perform a somewhat detailed analysis they do not consider the overall role of techno-economics and customer readiness feasibility in the pursuit of resource recovery technology deployment in an industrial context.

Based on the above considerations, the authors have identified the need to develop a methodology to manage the multi-faceted and multi-disciplinary intricacies of deploying resource recovery concepts, with focus placed on employing separation technology for recovering resources. The proposed methodology not only explicitly takes into consideration the techno-economics aspects but also implications of technology development and customer readiness in implementing resource recovery projects as well as taking implicitly taking into account the environmental impact of recovering a resources in both early and late stage of the decision making process. The proposed a decision-support methodology is intended to employed in introducing the resource recovery paradigm within traditional organisations and provide them the necessary tools to transition to a circular economy.

2. Methodology

The framework is decomposed into five segments, each defined by a characteristic question. Figure 1. illustrates the overall work flow of the methodology.

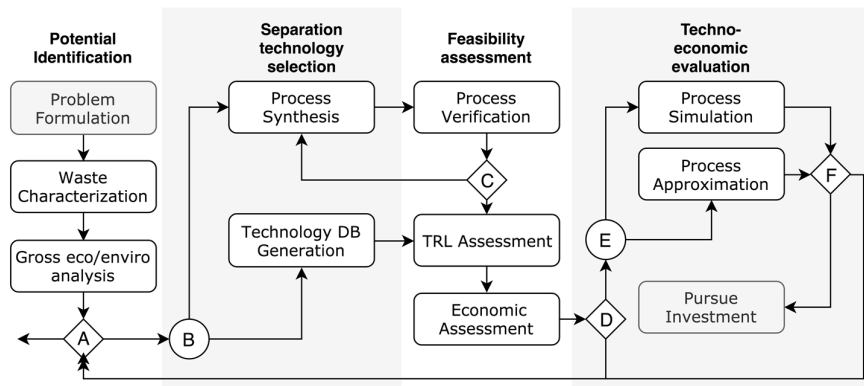


Figure 1. Schematic representation of the workflow of the methodology. Grey framework steps indicate input/output.

2.1 Step 1: Problem formulation. The first and most instrumental task of framework construction is the problem definition. It is here that the aim, objectives, and scope of the design problem are outlined mathematically. The objective function is formulated to fit the user's agenda, and demonstrates the desired outcome of the design problem. The subsequent algorithms are structured in a broad to narrow manner intended to thin the field of candidates that do not satisfy the objective function early on. This approach facilitates swift progression through the framework, especially in instances that manual input is required.

2.2 Step 2: Potential identification. The first screening phase, potential identification, preliminarily assesses whether resource recovery is relevant in the context of the stream studied and objective function set by the user. To account for all intentions, the gross sustainability potential is applied, providing a quantitative assessment of financial, environmental, and societal aspects. The information required in this section is easily attainable via the waste characterization algorithm, facilitating the rapid and efficient evaluation of many cases. The objective of this section is to identify valuable resources that can potentially justify the economic, environmental and societal aspects that are vital in implementing a resource recovery project and acts as a preliminary screening mechanism. Note: The gross sustainability potential in this step implicitly takes into account the overall environmental impact of recovering given resource, as such in a situation a pollutant or a "legacy" compound is captured, this will be reflected in the gross sustainability potential calculation. If a full circular economy model is desired, the potential identification step can be bypassed as all raw-materials are utilized irrespective of their value, generating no waste.

2.3 Step 3: Separation technology selection. In the next step of the framework, viable separation technologies for the recovery of the stream constituents are identified. Such technologies can then be sequenced to provide a physical feasible process synthesis for the recovery of the afore-determined target components. Separation task flowsheets should be furnished by process synthesis techniques where applicable, with the remainder subjected to technology database generation and manual pairing. A feedback loop is integrated with the feasibility assessment step to facilitate revisions of tasks that are not technically viable.

2.4 Step 4: Feasibility assessment. In the case of process synthesis, physically feasible flowsheets are automatically generated. This can be problematic as some tasks may be unsuitable or impractical, thus a feasibility assessment is carried out in the next step. This ensures that only technologically feasible flowsheets progress through the framework, each task is verified against openly available industrial implantations as well as academic literature where the concept of technology Readiness Level is applied. Preliminary financial viability is also assessed at this stage, by comparing the streams process revenue (Gross sustainability potential) to its estimated capital cost (Tsagkari et al., 2016). The payback period is then calculated and must surpass the user specified threshold to progress through the framework.

2.5 Step 5: Techno-economic evaluation. Now that basic technological and financial feasibility is proven, further granularity must be obtained to form a foundation for investment. If the user intends only on an order of magnitude estimate of the Net

Present Value, process approximation methods should also be applied to determine the associated operating costs. For more detailed assessments, process simulation is suggested. Once simulated, the model can be applied to determine recoveries, equipment costs, and operational expenses, ultimately resulting in improved NPV accuracy. If financially satisfactory, the framework is concluded with application of the WAR algorithm application to ensure environmental compliance. At this point the user should have a clear picture as to whether or not to pursue investment.

Note: the application of WAR algorithm as a part of this step implicitly takes into account the environmental impacts of a given resource recovery solution. The detailed economic analysis conducted will also account for the economic impact (marginal cost of abatement) which takes into account the environmental impact of reducing/eliminating a polluting compound.

3. Case studies

The application of the above framework is demonstrated through two case studies: phosphorus recovery from a phosphate-based wastewater stream; and monosaccharide recovery from wheat straw liquor. Besides the Biofuel and waste water treatment operations, the framework applicability is far reaching, providing potential in various other industries, such as petrochemicals and pharmaceuticals,

3.1 Monosaccharide recovery

In the case study the intention is to recover economically viable components from a wheat straw process stream (30,000 ton/yr), thereby improving economic potential and reducing waste, this was identified by applying step 1. Applying the potential identification, it was found that xylose (241/m³) and arabinose (\$236/m³) are the two most lucrative components in the waste stream. Applying step 2, a feasible process was synthesized for the case study where thermodynamic insights for process synthesis were used (Jakslund et al., 1995). The feasibility assessment step required five passes for an adequate flowsheet to be produced, as depicted in figure 2.

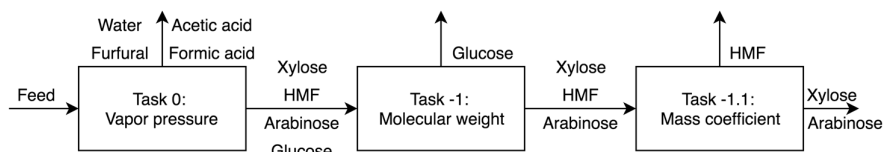


Figure 2. Output of step 2, final separation task flowsheet for monosaccharide extraction case study, generated by TaskGen software

Separation technologies were then paired to the successful separation tasks, resulting in a flowsheet consisting of detoxification via evaporation, glucose removal with nanofiltration, and monosaccharide purification with an ion exchange resin. Applying step 4 it was confirmed that the process sequence is a feasible one. In step 5, the recovery rates of the target components were then determined via process simulation, as seen in Table 1. Finally, the financial feasibility of the case was evaluated subject to uncertainty analysis, providing the results seen in Table 2.

Table 1: Results from process simulation in the techno-economic evaluation step

Target	Flow	Recovery
Xylose	16.36 kg/hr	56.5%
Arabinose	86.79 kg/hr	43.6%

Table 1: Results in million USD from the techno-economic evaluation step (10% DR).

Case	Present value	Capital cost	Development cost	Net Present value
Mono	39.1	-8.2	-11.0	19.6

Based on the results of the demonstration of the proposed methodology, the conventional bio-ethanol production process could be feasibly diversified with the recovery of supplemental products, prior to the fermentation process.

3.2 Phosphorus recovery

In this case, the framework was applied to a wastewater stream containing phosphate. Applying step 1, the problem is formulated as follows: “Given a pre-treated waste water stream of 14 mg/l of phosphate in water, 550000 m³/day, return a feasible separation technique to recover the desired resource, maximizing the resource recovery net present value meanwhile minimising the environmental impact”.

For step 2, potential identification, the user obtains an overview of the compound details to evaluate the most valuable resource on which the analysis can be carried forward. In this step, the gross sustainability potential and environmental impact was computed for both phosphorus and water. For phosphorous, the environmental influence and geopolitical considerations were significant factors behind the decision to target the resource for recovery. In this case, the geopolitical influence draws from the location of the case study, New Zealand, where Phosphorous-shortage has been increasing problem over the years (Cordell et al., 2014). Based on this consideration and on the higher phosphorus environmental impact value, phosphorus has been selected as the resource to be further analysed in the framework. The subsequent application of step 3, via technology database generation, illustrated that there are many potential phosphorus recovery pathways, but the application of step 4 illustrated that Crystallisation of phosphorus to struvite, using magnesium hydroxide was the only technologically mature and hence feasible pathway. The pathway was subjected to preliminary financial feasibility assessment by applying the capital cost estimation technique (Tsagkari et al., 2016). This yielded an estimated capital cost of USD 576 Million and a yearly process revenue of USD 0.62 Million. Based on this finding the financial infeasibility of the project is evident, and that the recovery of phosphorus in the form of struvite crystal is not a process to consider for implementation. Resultantly, the framework iterates back to step 2, to pick the next most feasible separation pathway. However, as no other technology meets the maturity requirement, the case exits the framework unsuccessfully.

5. Conclusions

In this work, a systematic computer aided framework has been developed to systematically evaluate the techno-economic and environmental potential of a resource

recovery initiative. The merit of the developed framework was then demonstrated on two practical case studies where the framework was able to systematically identify resource recovery potential, and synthesize first pass separation process designs. The diverse nature of the case study waste stream composition illustrates the generic structure, thus versatility of the framework. Analysis of the first case study demonstrated the framework's ability to identify and develop solutions in the presences of multiple target resources, and facilitate generation of lucrative technically feasible separation pathways. This established the frameworks applicability in the context of handling realistic waste streams, often containing numerous significant constituents. In the second case study, the framework facilitated the "weeding out" of numerous process technologies that illustrated phosphorus recovery potential, but were not currently at a sufficient technology readiness for industrial implementation. This illustrated the value of the multi-faceted approach undertaken by the framework, as feasible yet technologically underdeveloped solutions are quickly discarded in favour of the development of solutions that are of a sufficient technology development streamlining the long and resource intensive development phase.

Acknowledgments

This work partially received financial support from the Carlsberg Foundation of Denmark (Grant Number CF17-0403)

References

- Cordell, D., Mikhailovich, N., Mohr, S., Jacobs, B., White, S. (2014) 'Austalian sustainable phosphorus futures'. Rural industries research and development. 14, pp 1-59.
- Gargalo C. L., Carvalho A., Gernaey K.V., Sin G., (2016), 'A framework for techno-economic & environmental sustainability analysis by risk assessment for conceptual process evaluation', *Biochemical Engineering Journal*, Volume 116, pp. 146-156.
- Gargalo C. L., Carvalho A., Matos H.A., Gani R., (2014), 'Techno-Economic, Sustainability & Environmental Impact Diagnosis (TESED) Framework', *Computer Aided Chemical Engineering*, Volume 33, pp. 1021-1026.
- Hayward, R., Lee, J., Keeble, J., McNamara, R., Hall, C., Cruse, S., Gupta, P., Robinson, E., (2013) 'The UN Global Compact-Accenture CEO Study on Sustainability 2013', *UN Global Compact Reports*. 5(3), pp. 1-60.
- Hoseinzade L., Adams T.A., (2019), 'Techno-economic and environmental analyses of a novel, sustainable process for production of liquid fuels using helium heat transfer', *Applied Energy*, Volume 236, pp. 850-866.
- Mansouri S.S. et al. (2019) Economic Risk Analysis and Critical Comparison of Biodiesel Production Systems. In: Tabatabaei M., Aghbashlo M. (eds) *Biodiesel. Biofuel and Biorefinery Technologies*, vol 8. Springer, Cham
- Mansouri, S. S., Udugama, I. A., Mitic A., Flores-Alsina X., Garney K. V., (2017) 'Resource recovery from bio-based production processes: a future necessity?', *Current Opinion in Chemical Engineering*. 18, pp. 1-9.
- Udugama, I. A., Mansouri S.S., Mitic A., Flores-Alsina X., Garney K. V., (2017) 'Perspectives on Resource Recovery from Bio-Based Production Processes: From Concept to Implementation', *Processes*, 5(3), p. 48.
- Jakslund C. A, Gani,R., and Lien K.M. (1995), "Separation process design and synthesis based on thermodynamic insights," *Chem. Eng. Sci.*, vol. 50, no. 3, pp. 511-530.
- M. Tsagkari, J. L. Couturier, A. Kokossis, and J. L. Dubois, "Early-Stage Capital Cost Estimation of Biorefinery Processes: A Comparative Study of Heuristic Techniques," *ChemSusChem*, vol. 9, no. 17, pp. 2284-2297, 2016.

Variations of the shrinking core model for effective kinetics modeling of the gas hydrate-based CO₂ capture process

Hossein Dashti,^a Daniel Thomas,^b Amirpiran Amiri,^{b,*} Xia Lou^a

^a*Department of Chemical Engineering, WA School of Mines: Minerals, Energy and Chemical Engineering, Curtin University, Kent Street, Bentley WA 6102, Australia*

^b*European Bioenergy Research Institute (EBRI), School of Engineering and Applied Science, Aston University, Birmingham, B4 7ET, United Kingdom*

a.p.amiri@aston.ac.uk

Abstract

The hydrate-based carbon dioxide (CO₂) capture (HBCC) process has been widely studied for CO₂ separation and sequestration. This paper aims to conduct a model-based investigation of the kinetics of the HBCC process. A variation of the shrinking core model (SCM) was developed for the analysis of this heterogeneous system under varying boundary conditions. The results revealed that while CO₂ diffusion through the hydrate layer is the dominant controlling mechanism, for a realistic scenario in which a time-dependent bulk gas concentration exists, the model results would better match the experimental data if the effects of the reaction rate were incorporated into the diffusion-based model. Sensitivity analysis showed that increasing the diffusivity through the hydrate layer significantly decreases the full conversion time of the water. Moreover, the effect of temperature change was investigated, and it was found that lower temperatures slow the hydrate growth rate. The model was demonstrated to be a computationally effective and time-efficient predictive tool that does not require high-speed computers for large-scale (reactor) applications.

Keywords: gas hydrate, CO₂ capture, shrinking core model

1. Introduction

Gas hydrates are solid clathrates comprising gas molecules (guests) such as CO₂, nitrogen (N₂), hydrogen (H₂), methane (CH₄) encased in a cage of water molecules (H₂O) connected to each other by hydrogen bonds. Hydrates form under specific thermodynamic conditions, including low temperature and high pressure. The small and nonpolar CO₂ gas forms hydrate structure I at temperatures lower than 283 K and pressures lower than 4.5 MPa (Sloan and Koh, 2008). CO₂ hydration under 203 K and 0.08 MPa has also been reported (Falabella, 1975). The potential of gas hydrate technology to capture CO₂ from flue gases has sparked research interest in investigating different aspects of this novel technology (Dashti and Lou, 2018; Dashti et al., 2015). Early research mostly focused on the experimental investigation of CO₂ hydrate formation and methods to improve the hydration kinetics and separation efficiency. In recent years, studies focused on understanding gas hydrate formation kinetics have increased (Yin et al., 2018). Many of these studies have been based on the methane hydrate formation process, and the kinetic model reported by Englezos et al. (1987) has been frequently used (Englezos et al., 1987).

This model follows the modeling approach for crystal growth from solution (Karpiński, 1980) and divides hydrate particle growth into two steps: 1) diffusion of the dissolved gas from the bulk solution to the hydrate-liquid interface and 2) the hydrate formation reaction at the interface. According to Lederols et al. (1996), gas hydrate formation is similar to the crystallization process, which is governed by nucleation followed by the rapid growth of hydrates; both are controlled by kinetics and mass and heat transfer phenomena (Lederhos et al., 1996).

The unreacted shrinking core model (SCM) has been widely used for solid reactions in which the intrinsic reaction rate is much higher than the mass transfer rate (Amiri et al., 2013; Amiri et al., 2015). This paper applies a modified SCM to model the CO₂ hydrate formation process assuming a single mechanism for a better understanding of gas hydrate formation kinetics.

2. Modeling methodology

2.1. Base model with a constant boundary condition

A variation of SCM with the steady boundary condition was applied to the CO₂ hydrate formation case study. In a batch reactor, however, the composition of the bulk gas surrounding the reactive particle is significantly dynamic, which conflicts with the boundary condition assumption in a mechanistic model.

In the typical SCM paradigm, the gas-solid reaction initiates at the outer surface of a solid particle and then moves towards the particle core, leaving a product layer behind. The unreacted core radius shrinks with time until full conversion of the solid particles to products, as shown in Figure 1. The model can be adopted to describe the CO₂ hydrate formation process, which includes three steps. Assuming effective agitation leading to the formation of water droplets that interact with CO₂ to form gas hydrates, the whole process involves (i) CO₂ diffusion through the gas film surrounding the hydrate particle to reach the particle's surface; (ii) CO₂ diffusion through the hydrate shell to reach the unreacted core (water) surface; and (iii) reaction of CO₂ with water (Eq. (1)) at the hydrate-liquid interface or unreacted core surface. The overall reaction can be expressed using Eq. (1):



where n is the hydrate number, 5.75 (Sun and Kang, 2016); r_h represents the overall hydrate formation rate; C_{CO_2} is the CO₂ concentration at the water-hydrate interface; and k is the reaction rate constant for reaction (1).

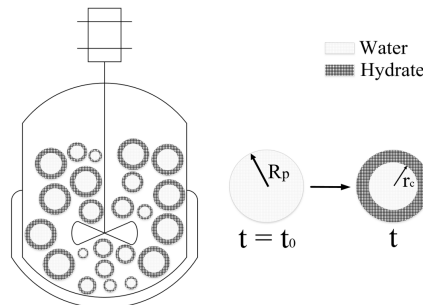


Figure 1: Schematic diagram of the CO₂ hydrate formation in a well-mixed batch reactor (Left) and a shrinking core hydrate particle (Right)

To build a comprehensive model, the system is first analyzed step by step, assuming that the analyzed step is rate limiting. The results are then compared with the experimental data. According to Eq. (1) and Figure 1 (right), for a liquid droplet with a spherical geometry, water conversion (X_{H_2O}) and the unreacted water core radius (r_c) can be correlated as follows:

$$X_{H_2O} = 1 - \left(\frac{r_c}{R_p} \right)^3 \quad (2)$$

where R_p is the particle radius. Assuming a rigid hydrate shell and constant R_p , step (ii) and step (iii) occur instantaneously. There is a linear relationship between the conversion rate and time (Eq. (3)).

$$t = \frac{\rho_{H_2O} R_p}{3n k_g C_{CO_2}^b} X_{H_2O} \quad (3)$$

where ρ_{H_2O} is the molar density of water and k_g and $C_{CO_2}^b$ are the mass transfer coefficient of CO₂ through the gas layer surrounding the hydrate particle and the molar concentration of CO₂ in the gas bulk, respectively. Similarly, the conversion rate and rate relationship for step (ii) rate limiting and step (iii) rate limiting can be expressed by Eqs. (4) and (5), respectively.

$$t = \frac{\rho_{H_2O} R_p^2}{6n D_e C_{CO_2}^b} [1 - 3(1 - X_{H_2O})^{\frac{2}{3}} + 2(1 - X_{H_2O})] \quad (4)$$

$$t = \frac{\rho_{H_2O} R_p}{n k C_{CO_2}^b} [1 - (1 - X_{H_2O})^{\frac{1}{3}}] \quad (5)$$

where D_e is the CO₂ diffusion coefficient in the hydrate layer.

2.2. Base model with a varying boundary condition

The base model presented earlier is based on the constant partial pressure of CO₂ in the bulk gas, $p_{CO_2}^b$. However in a closed system, when CO₂ capture in the hydrate cages is exceedingly fast, $p_{CO_2}^b$ declines with time. Given that the partial pressure of CO₂ in the bulk gas is the boundary condition in solving the mass transfer differential equations, the CO₂ concentration profile inside the particle, C_{CO_2} , might be influenced by the transient CO₂ partial pressure in the batch reactor. The base model for the hydrate layer diffusion-dominated case, step (ii), is extended. Eq. (6) defines the rate of CO₂ capture:

$$\frac{dN_{CO_2}}{dt} = -4\pi r^2 D_e \frac{dC_{CO_2}}{dr} \quad (6)$$

in which N_{CO_2} is the number of moles of CO₂. The steady-state assumption and integration yield Eq. (7) and Eq. (8):

$$\frac{dN_{CO_2}}{dt} \int_{r_c}^{R_p} \frac{dr}{r^2} = -4\pi D_e \int_0^{C_{CO_2}^b} dC_{CO_2} \quad (7)$$

$$\frac{dN_{CO_2}}{dt} \left(\frac{1}{r_c} - \frac{1}{R_p} \right) = -4\pi D_e C_{CO_2}^b(t) \quad (8)$$

Instant N_{CO_2} can be presented as a function of $r(t)$ according to Eq. (9):

$$\frac{1}{n} dN_{CO_2} = 4\pi \rho_{H_2O} r_c^2 dr_c \quad (9)$$

CO₂ concentration in bulk gas is the boundary condition for Eq. (6) and is related to the CO₂ partial pressure in the reactor by Eq. (10):

$$C_{CO_2}^b(t) = \frac{p_{CO_2}^b(t)}{RT} \quad (10)$$

Eq. (9) and (10) are substituted in Eq. (8) and integrated across the hydrate layer, resulting in Eq. (11):

$$\frac{R_p^2 \rho_{H_2O} RT}{6nD_e} \left[1 - 3(1 - X_{H_2O})^{\frac{2}{3}} + 2(1 - X_{H_2O}) \right] = \int_0^t p_{CO_2}(t) dt \quad (11)$$

which describes the correlation between water conversion and CO₂ partial pressure changes and allows monitoring of the time-dependent mass diffusion resistance based on the reactor pressure readings. Similarly, the governing equations for the reaction control case with a varying boundary condition have been derived and are given below:

$$\frac{R_p \rho_{H_2O} RT}{nk} \left(1 - (1 - X_{H_2O})^{\frac{1}{3}} \right) = \int_0^t p_{CO_2}(t) dt \quad (12)$$

Combining Eq. (11) with Eq. (12), a model considering both the diffusion step (ii) and the reaction step (iii) is produced according to Eq. (13):

$$\frac{R_p \rho_{H_2O} RT}{n} \left[\frac{R_p}{6D_e} \left[1 - 3(1 - X_{H_2O})^{\frac{2}{3}} + 2(1 - X_{H_2O}) \right] + \frac{1 - (1 - X_{H_2O})^{\frac{1}{3}}}{k} \right] = \int_0^t p(t) dt \quad (13)$$

The right-hand side of Eq. (13) presents the measured time-dependent CO₂ partial pressure inside the reactor. This must be provided practically, making the presented model a semi-empirical model.

3. Results and Discussion

3.1. Controlling mechanism identification

The models derived based on the individual mechanisms (Eqs. 3, 4, 5) were compared against a set of experimental data obtained from batch reaction vessel experiments at 203 K and 0.08 MPa (Falabella, 1975). As shown in Figure 2(A), for the model based on step (ii), diffusion through the hydrate layer best fits the data. The model developed based on gas film control (step (i)) predicts a linear relationship between conversion and time that departs greatly from the experimental data. This is not surprising and is consistent with the assumptions of Englezos et al. (1987) (Englezos et al., 1987). Judgments about the dominant mechanism become critically challenging when comparing the modeling results based on the intrinsic reaction with those based on the diffusion controlling model. While both models follow the practically observed non-linear clathrate conversion trend, the diffusion-dominated model seems more appropriate. This is more obvious at the early stages of the process, from zero to 55% conversion, because the reaction on the water-hydrate interface occurs after gas diffusion through the hydrate layer. At higher conversion ranges, above 55%, both models reasonably predict the experimental data. It can be concluded that while diffusion through the formed hydrate predominantly controls the hydration progress rate, the inherent reaction kinetic role is not negligible. The former becomes more significant when considering the depleting CO₂ partial pressure in the bulk gas surrounding the particle that occurs in a batch reactor.

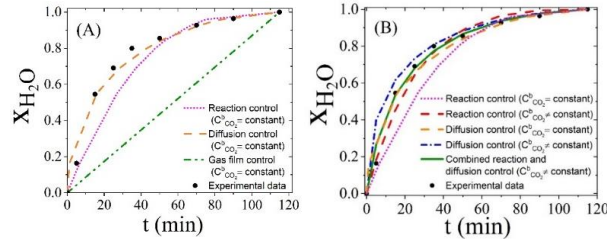


Figure 2: Comparisons of (A) the single-mechanism model prediction with the experimental data for constant bulk concentration and (B) the single- and combined-mechanism model predictions against the experimental data for constant ($C_{CO_2}^b = \text{constant}$) and varying bulk concentration ($C_{CO_2}^b \neq \text{constant}$)

The assumptions, including the single mechanism control and constant CO₂ partial pressure in bulk gas, used in the base model derivation may be responsible for the observed deviation between the modeled and experimental results in Figure 2(A). The model was improved by accounting for combined mass transfer and reaction kinetics rates, both of which are influenced by the depleting CO₂ fraction in the surrounding gas. Figure 2(B) presents the prediction results for (i) the hydrate diffusion control model with varying CO₂ concentration in the bulk gas (Eq. (11)), (ii) the intrinsic reaction control model with varying CO₂ concentration in the bulk gas (Eq. (12)), and (iii) the combined model under a transient CO₂ concentration (Eq. (13)) and compares these results with the experimental data (Falabella, 1975). The results of the combined model fall between the hydrate layer diffusivity and reaction control results, thus improving the prediction results compared with the experimental data.

3.2. Model analysis

Due to the role of the diffusion rate demonstrated earlier, the accuracy of the diffusion coefficient estimation is of critical importance for model fidelity. The diffusivity of CO₂ in hydrates has been reported to be in the range of 1×10^{-16} m²/s to 2×10^{-14} m²/s (Liang et al., 2016). The effect of CO₂ diffusivity on the CO₂ hydrate conversion time was investigated as shown in Figure 3(A). The total conversion time increases dramatically with decreasing diffusivity because at lower diffusivity values, the diffusion of the gas into the inner layer of the gas hydrate shell is slower. As a result, it takes longer to form the gas hydrate particle and consequently reach the end of the conversion time.

In further analysis of the model, the effects of the gas hydrate formation temperature on the completion time were investigated. As shown in Figure 3(B), the effect of the temperature changes on the completion time is not as significant as the effects of the diffusivity on the completion time. At lower temperatures, CO₂ hydrate formation is faster. For example, at 250 K and 298 K, the completion times are approximately 107 min and 130 min, respectively.

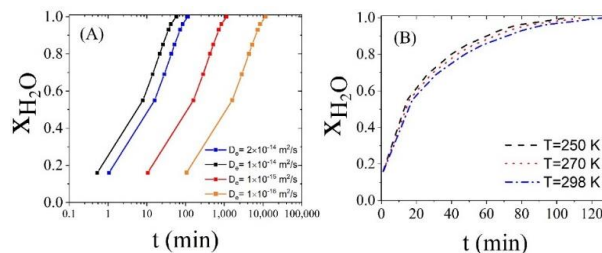


Figure 3: Effects of (A) CO₂ diffusivity and (B) hydrate formation temperature change on the conversion time

4. Conclusions

The purpose of the present study was to determine the dominant controlling mechanism during gas hydrate formation using a novel variation of SCM. The primary model was proposed based on a constant concentration of CO₂ in the bulk gas. The model was further improved by considering the transient CO₂ concentration in the bulk gas, which is a more realistic case. While the diffusion-based model reasonably predicts the CO₂ hydration rate under a constant bulk gas concentration condition, for the realistic scenario in which the bulk gas varies with time, the model must consider the reaction control role as well. The proposed model was successfully used to quantify the effects of the CO₂ diffusivity and the operating temperature on conversion.

References

- A. Amiri, A.V. Bekker, G.D. Ingram, I. Livk, N.E. Maynard, 2013, A 1-D non-isothermal dynamic model for the thermal decomposition of a gibbsite particle, *Chemical Engineering Research and Design*, 91, 485-496.
- A. Amiri, G.D. Ingram, N.E. Maynard, I. Livk, A.V. Bekker, 2015, An unreacted shrinking core model for calcination and similar solid-to-gas reactions, *Chemical Engineering Communications*, 202, 1161-1175.
- H. Dashti, X. Lou, 2018, Gas hydrate-based CO₂ separation process: Quantitative assessment of the effectiveness of various chemical additives involved in the process, Springer International Publishing, Cham, pp. 3-16.
- H. Dashti, L. Zhehao Yew, X. Lou, 2015, Recent advances in gas hydrate-based CO₂ capture, *Journal of Natural Gas Science and Engineering*, 23, 195-207.
- P. Englezos, N. Kalogerakis, P.D. Dholabhai, P.R. Bishnoi, 1987, Kinetics of formation of methane and ethane gas hydrates, *Chemical Engineering Science*, 42, 2647-2658.
- B.J. Falabella, 1975, A Study of Natural Gas Hydrates, University of Massachusetts Amherst, Ann Arbor, p. 180.
- P.H. Karpiński, 1980, Crystallization as a mass transfer phenomenon, *Chemical Engineering Science*, 35, 2321-2324.
- J.P. Lederhos, J.P. Long, A. Sum, R.L. Christiansen, E.D. Sloan, 1996, Effective kinetic inhibitors for natural gas hydrates, *Chemical Engineering Science*, 51, 1221-1229.
- S. Liang, D. Liang, N. Wu, L. Yi, G. Hu, 2016, Molecular mechanisms of gas diffusion in CO₂ hydrates, *The Journal of Physical Chemistry C*, 120, 16298-16304.
- E.D. Sloan, C.A. Koh, 2008, Clathrate Hydrates of Natural Gases, third ed., Taylor & Francis Group, New York.
- Q. Sun, Y.T. Kang, 2016, Review on CO₂ hydrate formation/dissociation and its cold energy application, *Renewable and Sustainable Energy Reviews*, 62, 478-494.
- Z. Yin, M. Khurana, H.K. Tan, P. Linga, 2018, A review of gas hydrate growth kinetic models, *Chemical Engineering Journal* 342, 9-29.

Multi-objective optimization approach to design and planning hydrogen supply chain under uncertainty: A Portugal study case.

Diego Câmara,^{a,*} Tânia Pinto-Varela,^a Ana Paula Barbósa-Povoá^a

^a*Centro de Estudos de Gestão-IST, Instituto Superior Técnico, Universidade de Lisboa, Av. Rovisco Pais, Lisboa 1049-001, Portugal*

diegofelipe@tecnico.ulisboa.pt

Abstract

The progress of the current energy infrastructure to a new pattern, where hydrogen plays an important role has been increasing the interest of industrial communities, as well as, academics. This is mainly associated with sustainability goals where reducing environmental impacts is a target while guaranteeing economic benefits. In this context, the development of hydrogen optimized global supply chains (SC) that can support industrial processes through renewable energy sources is to be pursued. In this paper, we explore this challenge and a multi-objective, multi-period, stochastic Mixed Integer Linear Programming (MILP) problem for design and planning a hydrogen SC is developed. Uncertainty over the availability of primary energy sources (PES) is considered through the definition of set scenarios. A Portuguese case is explored, from where it is concluded that the reduction in global warming potential is very small when compared to the increase in cost.

Keywords: Hydrogen supply chain, Renewable energy source, Multi-objective optimization, Uncertainty in primary energy sources.

1. Introduction

The use of fuels with low emissions has been recently highlighted as one of the trends to mitigate environmental impacts. In this set, the use of hydrogen as a fuel has been considered an alternative with significant potential to integrate a more sustainable energy matrix, especially in the transportation sector (Almansoori et al., 2011). Hydrogen has become a key element for governments under pressure of emission constraints and environmental laws. Despite this, there is still no appropriate infrastructure available and uncertainties are one of the main drawbacks to the development of the hydrogen economy as the case of primary energy sources (PES) availability.

Different approaches to formulating a hydrogen SC have been appearing in the literature, as an attempt to determine if hydrogen is a competitive option, as an energetic vector, while mitigating the high capital investment, this is the case of the study of Ogumerem et al. (2017), in which the oxygen co-produced from the electrolysis is further processed and sold to generate revenue. In the process of designing a hydrogen SC, forecasts associated with demand, price, and type of energy sources are the main uncertainty sources. But the existent literature studies have mainly focused on demand uncertainty and a few addressed cost uncertainty. To the author's knowledge, none explored uncertainty associated with the availability of PES, which are required for the hydrogen production technology.

Considering the aforementioned, a model to determine strategic and planning decisions taking into account uncertainty on the PES availability is here explored. A MILP is developed, considering a multi-period model and two objective functions: minimization of cost and minimization of global warming potential (GWP) in the SC network. A scenario-based tree approach is defined where scenarios describe the possible PES availability. The ϵ -constraint method with lexicography optimization is implemented and the results of several non-dominated solutions from the Pareto curve are characterized.

2. Problem definition

The hydrogen SC can include diverse echelons, depending on the specifications and needs of each application. The problem in this paper considers three main echelons: primary energy sources, production plants, and storage facilities. The links between the different echelons are guaranteed through a multimodal transportation network to satisfy the hydrogen demand. Hydrogen production can use a wide diversity of energy sources, from this, were considered only renewables energies, and based on the hydrogen production technologies selection. The hydrogen produced is stored in storage facilities according to its physical form (gaseous or liquid). In order to satisfy the demand, importation is also allowed. In sum the problem in the study can be described as follows:

Given:

- A set of potential locations to install hydrogen production units as well as storage facilities;
- type of production and storage facilities;
- the maximum and minimum capacities for flows, production, and storage;
- primary energy source availability;
- global warming potential for each transportation mode;
- regional delivery distances;
- operating and capital costs;
- the initial existent number of production plants and storage facilities;
- customer's demand.

Determine:

- the number, location, size, capacity, and technologies of hydrogen production plants and storage facilities;
- the network planning with all flows, rates of hydrogen and primary energy sources consumption, production rates and average inventory of materials.

So as to:

- minimize the cost of the supply chain and the GWP.

GWP, stands for the global warming potential and is taken as an environmental indicator of the overall effect related to emissions of greenhouse gases (CO₂-equiv).

3. Model main characteristics

As mentioned above the model developed is a multi-objective, multi-period, stochastic Mixed Integer Linear Programming (MILP) where two main objectives are considered: minimization of cost and minimization of global warming potential (GWP). A set of constraints are defined considering: network expansion; PES availability, demand requirements, production, storage capacities, and transportation capacities; mass balances and importation needs. The demand is assumed to have a profile over the long-term planning horizon, and it follows an s-shape pattern, according to a hydrogen market penetration factor (Almansoori et al., 2009). Uncertainty in the PES availability is

characterized using a dynamic scenario tree approach as detailed in the following section. A ϵ -constraint method with lexicography optimization is implemented to avoid weak (dominated) solutions.

3.1 The scenario tree approach

To model PES uncertainty a dynamic scenario tree is considered formed by nodes and arcs. Every node represents a state of the random parameter, in our case the PES availability, at a given time point, which evolves over the planning horizon. A scenario comprises a sequence of nodes, and arcs, from the first time point to the last one. The probability of a scenario is given by the product of the probability of each arc between the root and leaf nodes (Lima et al, 2018). Fig. 1 depicts a scenario tree example with 8 scenarios, in which two branches leave, from the root node until the last node.

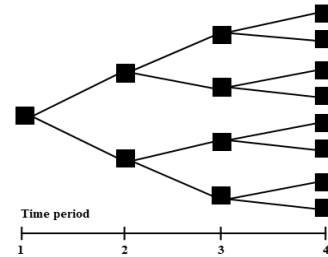


Figure 1 - Scenario tree example.

4. Case study

The design and planning of a hydrogen supply chain in Portugal is taken as case-study. An administrative segmentation of Portugal has been used to obtain a realistic path between districts with the existing main roads and truck lines and to estimate the potential demand from local population statistics (De-León Almaraz e al., 2014).

Four renewable energy sources are considered: wind power, solar power, hydroelectric and biomass. In production terms, two types of production technologies are assumed: electrolyzes and biomass gasification. Hydrogen is produced in liquefied form. Two transportation modes are used, a tanker truck and a railway tanker. Cryogenic storage is assumed.

To estimate the hydrogen demand was assumed the current number of private and light vehicles in Portugal, the average distance travelled, and fuel economy hydrogen (kg H₂/km) to calculate the total equivalent hydrogen demand. Furthermore, the demand equivalent was treated based on the penetration factor in each time period, in this case, 5 years per stage, in a horizon of 15 years of network planning. The hydrogen penetration factor starts at 5% in the first period, growing to 25% in the second period, and it reaches 50% in the third period.

To generate the scenarios considering the PES uncertainty availability an S-shape PES trajectory is considered, then a scenario tree of the form shown in Fig. 2 was obtained. Three time periods and nine distinctive scenarios are considered. The scenarios were structured from current energy data and considering variability over time, reaching a maximum growth of 11% in a scenario in the last time period compared to the initial information. The probabilities of occurrence of each scenario are given in Table 1, assuming a pessimist, a neutral and an optimistic scenario in each time period after the first one. The first time period has a deterministic PES profile. The model was solved through GAMS 25.1.1, using CPLEX 12.0, in a two Intel Xeon X5680, 3.33 GHz computer with 24 GB RAM. The time presented in table 3 is the sum of the execution times of the 10 points of the Pareto border.

Table 1 - Probabilities of occurrence.

Scenarios“w”	Probabilities
w1	6,25 %
w2	12,5 %
w3	6,25 %
w4	12,5 %
w5	25,0 %
w6	12,5 %
w7	6,25 %
w8	12,5 %
w9	6,25 %

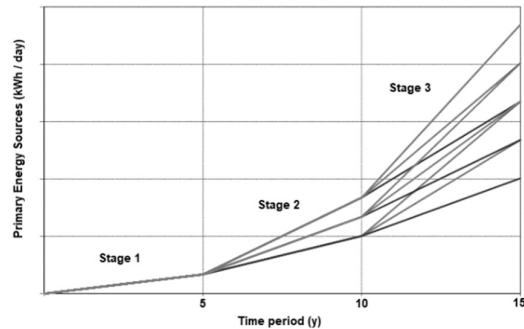


Figure 2 - S-shape scenario tree of PES.

5. Results and Discussion

The results are summarised in the Pareto frontier represented in Figure 3. In order to detail its analysis, three points of the curve are selected as identified in Figure 3. The extreme points 1 and 10 corresponds respectively to the maximum values of GWP and total daily cost. The solution from the middle, point 7, was selected to evaluate the differences with the other selected solutions.

Table 2 depicts the topology, total costs and GWP of the three solutions. Comparing the point 1 and the point 10 solutions it can be seen an increase of 17 times in cost, and a reduction of 0.94, about 6%, in the GWP impact. Moreover, by comparing the lowest cost solution, point 1, and the middle solution, point 7, there is an 8-fold increase in the total daily cost of the network, while the reduction of the GWP is about a ratio 0,96, which indicates a reduction approximately 4%. This shows that the reduction in total GWP is very small when compared to the necessary increment in costs.

Thus, despite the high variability in the supply chain cost, a small impact in the GWP value was obtained, which is justified by the type of PES selected and its respective production technology. In point 10 biomass was selected as the primary energy source, while point 1 presents the selection of two types of production technologies, electrolyzes and biomass gasification, therefore having as energy sources not only biomass but integrating the other ones, such as solar power, wind power and hydroelectric.

These choices are justified by the fact that biomass has the lowest price compared to other energy sources, but biomass gasification is a less environmental friendly production technology when compared to electrolysis.

Related to the network decisions it is possible to observe that the number of production plants increases from 8 to 17 from point 1 to 10. These results are justified by the incremental use of biomass as the energy source that has associated lower technologies capacities. Since the demand variability is unchanged, the number of storage facilities remains the same for all solutions.

In sum the obtained results suggest decentralized SC topologies for lower values of GWP (point 10), with smaller capacities, and where the demand for hydrogen is supplied locally by production plants. On the contrary, when the objective is the minimization of costs a centralized topology is obtained (point 1), where higher capacities are installed.

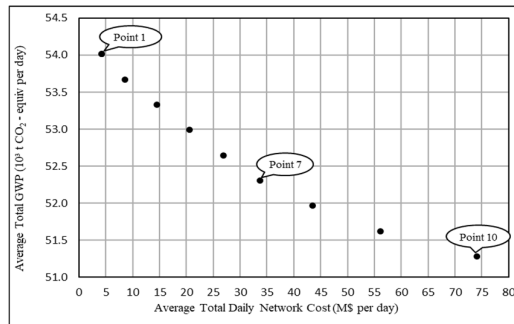


Figure 3 - Optimal solutions in the Pareto curve.

Table 2 – Comparison of multiperiod solutions topologies

Point in Pareto Frontier	1	7	10
Total number of production plants	8	13	17
Total number of storage facilities	54	54	54
Total number of transportation units	1283	200	405
Average Total Daily Network Cost (M\$ per day)	4.19	33.67	74.11
Average GWP Production plants (10^3 t CO ₂ - equiv per day)	18.09	16.44	15.40
Average GWP Storage facilities (10^3 t CO ₂ - equiv per day)	35.85	35.85	35.85
Average GWP Transportation modes (10^3 t CO ₂ - equiv per day)	0.075	0.014	0.034
Average Total GWP (10^3 t CO₂ - equiv per day)	54.02	52.31	51.28

Considering point 1 it can be analyzed through Figure 4 the topology evolution over time. As demand increases, the number of production plants and storages facilities increases accordingly, in the same regions, to satisfy the increment of local demand. Production plants are strategically centralized disseminated along Portugal territory.

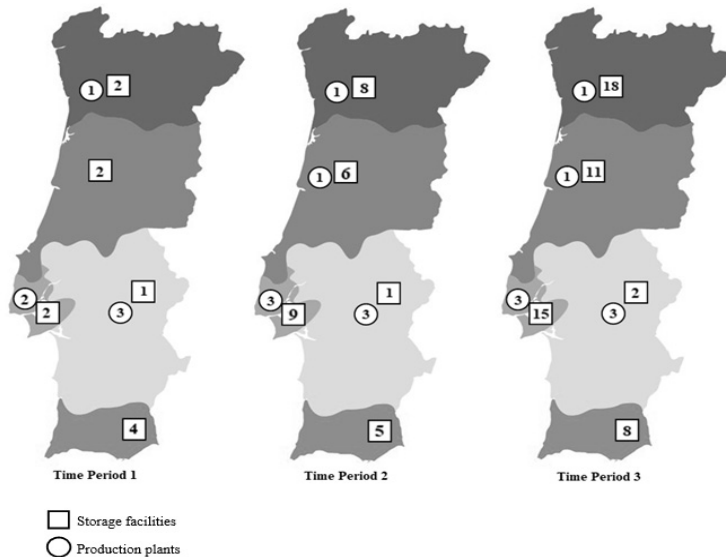


Figure 4 – SC topology evolution over the multi-period solution (point 1)

Table 3 – Computational results for the multi-objective optimization

Continuous variables	Binary variables	Constraints	CPU (s)	GAP (%)
8252	1621	10457	122	0

6. Conclusion

In this work, a MILP model to support the decision maker in the design and planning of hydrogen supply chains is developed. The model considers variability in renewable energy sources and integrates a set of constraints describing the supply chain characteristics. Economic and environmental objectives are considered.

The model is applied to the design and plan of a hydrogen supply chain in Portugal. When a cost objective is at stake a centralized network is obtained when compared to a decentralized supply chain when an environmental objective is considered.

It was also concluded that the reduction in total GWP is very small compared to the necessary increment in costs.

As future work is intended to explore other sources of uncertainty in the model and thus analyze their impact in the SC network. It is also expected to integrate the risk component as an objective function into the model.

References

- Almansoori, A., & Shah, N. (2009). Design and operation of a future hydrogen supply chain : Multi-period model. *International Journal of Hydrogen Energy*, 34(19), 7883–7897. <https://doi.org/10.1016/j.ijhydene.2009.07.109>
- Almansoori, A., & Shah, N. (2011). Design and operation of a stochastic hydrogen supply chain network under demand uncertainty. *International Journal of Hydrogen Energy*, 37(5), 3965–3977. <https://doi.org/10.1016/j.ijhydene.2011.11.091>
- De-León Almaraz, S., Azzaro-Pantel, C., Montastruc, L., & Domenech, S. (2014). Hydrogen supply chain optimization for deployment scenarios in the Midi-Pyrénées region, France. *International Journal of Hydrogen Energy*, 39(23), 11831–11845. <https://doi.org/10.1016/j.ijhydene.2014.05.165>
- De-León Almaraz, S., Azzaro-Pantel, C., Montastruc, L., Pibouleau, L., & Senties, O. B. (2013). Assessment of mono and multi-objective optimization to design a hydrogen supply chain. *International Journal of Hydrogen Energy*, 38(33), 14121–14145. <https://doi.org/10.1016/j.ijhydene.2013.07.059>
- Lima, C., Relvas, S., & Barbosa-póvoa, A. (2018). Stochastic programming approach for the optimal tactical planning of the downstream oil supply chain. *Computers and Chemical Engineering*, 108, 314–336. <https://doi.org/10.1016/j.compchemeng.2017.09.012>
- Ogumerem, G. S., Kim, C., Kesisoglou, I., Diangelakis, N. A., & Pistikopoulos, E. N. (2017). A Multi-objective Optimization for the Design and Operation of a Hydrogen Network for Transportation Fuel. *Chemical Engineering Research and Design*, 1–14. <https://doi.org/10.1016/j.cherd.2017.12.032>

Global Uncertainty and Sensitivity Analysis for Robust Design of a Rotary Kiln Process

Thomas B. Iversen,^a Gürkan Sin,^{a,*}

^aProcess and Systems Engineering Center (PROSYS), Department of Chemical and Biochemical Engineering, Technical University of Denmark, Søtofts Plads Building 229, 2800 Kgs. Lyngby, Denmark

*gsi@kt.dtu.dk

Abstract

In this contribution, we present and evaluate a systematic framework for comprehensive uncertainty and sensitivity analysis of a model used for design of Rotary Kiln processes. We consider two sources of uncertainties, namely operational (such as measurement errors, feedstock composition, etc.) and model (key assumptions in the model used for design equations) parameter uncertainty. As model outputs for evaluation we considered the impacts of these uncertainties on key process design metrics, specifically the minimum required rotary kiln length and the conversion degree of limestone. The results revealed that the operational sources of uncertainty lead to a higher uncertainty in process design metric (e.g. standard deviation of the computed length is 6.1 m) compared to the model parameter uncertainty (standard deviation of the computed length is 4.5 m). In order to achieve a robust process design, one needs to dimension the length of the reactor with 187 m so that all particles will be converted with 100 % efficiency with 95 % confidence. Ignoring these sources of uncertainty will lead to suboptimal process performance with the degree of conversion of limestone reduced to 97 %. Among input uncertainty considered, the global sensitivity analysis revealed measurement errors of temperature sensors as the most influential parameters. Overall the results encourage application of comprehensive sensitivity and uncertainty analysis methods for robust design of rotary kiln processes.

Keywords: Uncertainty, Sensitivity, Rotary Kiln, Monte Carlo simulation, Morris Screening, Sobol's method.

1. Introduction

A rotary kiln is a physically large process unit used in cement production where limestone is decomposed into calcium oxide which forms the basis of cement clinker particles under high temperatures. The modelling of rotary kilns are well documented in literature. Mujumdar et al. 2007 developed an iteration based rotary kiln simulator (RoCKS), which integrates models for a pre-heater, calciner, kiln and clinker cooling that agreed well with observations in industry. The model takes complexities in reactions and heat transfers with different sections into account by coupling multiple models with common boundaries regarding heat and mass communications. Other work (Ngadi and Lahlaoui, 2017) neatly demonstrates an experimentally proven kiln model being applied for screening of combustion fuel used for kilns, and how it may impact the production. This contribution coupled modelling of reactions and heat transfer in the bed region and another model for combustion and heat transfer in the freeboard region.

While modelling of these processes with varying degree of complexity has been performed, proper uncertainty and sensitivity analysis of these models have not been given due importance/consideration. As the use of computer aided process engineering tools increases, the need for robust uncertainty and sensitivity analysis frameworks becomes more important. There are several frameworks of uncertainty and sensitivity analysis applied for different problems, from good modelling practice (Sin et al, 2009) to process design and product design (Frutiger et al 2016). These frameworks typically include the following steps (0) problem statement, (i) identification of input sources of uncertainties, (ii) sampling (iii) Monte Carlo simulations and (vi) sensitivity analysis. The purpose of this work is to perform a systematic uncertainty and sensitivity analysis of rotary kiln process design in order to address the following: (1) Given a certain base case design, what is the impact of uncertainties in the model and measurements on the key process design metrics (minimum required reactor length and degree of conversion), and, (2) given a certain source of uncertainties, what is the robust design to ensure process performance with 95 % confidence.

2. Modelling of the Physical System

The overall goal of the rotary kiln model evaluated here is to determine the minimum required rotary kiln length to process 115,000 tons of limestone annually. The design model is built on a number of mechanisms and processes (Mujumdar et al., 2007), including a spherical particle model, a shrinking core model with three resistances (gas film, ash layer, and reaction at core), a steady state energy balance, and a counter-current gas-particle flow in kiln. The model accounts for changes in flue gas compositions, which affects the heat transfer coefficient and the particle core temperature.

Table 1: Summary of equations used in rotary kiln. Parameters marked up red are used in uncertainty analysis.

Equation	Description
$\frac{dX_i}{dt} = -\frac{3h_p}{\Delta H \rho R_i} \left(\frac{\lambda(1-X_i)^{1/3}(T_g - T_c)}{h_p R_i(1-(1-X_i)^{1/3}) + \lambda(1-X_i)^{1/3}} \right)$	Conversion rate (X) of particle size i . h_p is the energy transfer coefficient, R is the particle radius, λ is the heat diffusion coefficient, and T_c is the particle core temperature. This is used to find the conversion for the drying and calcination, which uses enthalpies (ΔH), densities (ρ) and heat diffusion coefficients. Heat of reaction is used for calcination and the heat of vaporization is used for drying.
$h_p = 23.7G^{0.67} \left(\frac{A_{KW}}{A_p} \right)$	The heat transfer coefficient is dependent on the gas mass velocity (G) and the fraction of particles consuming heat.
$\log_{10}(P_i) = A - \frac{B}{C + T_c}$	Antoine's equation is used to find the temperature at the unreacted core of the particle.
$\left(\frac{A_{KW}}{A_p} \right) = \begin{cases} 0.0686 & \text{for } t < \tau_1 \\ 0.1744 & \text{for } \tau_1 < t < \tau_2 \\ 0.5194 & \text{for } \tau_2 < t \end{cases}$	Increased effective area when particles are fully reacted. τ_i is the time required to fully convert a particle size i . A represents the area of the kiln wall (denoted KW) and particles (denoted P).
$G_i(X) = G_0 + m_K[(1-X_1) + (1-X_2) + (1-X_3)]$	A measure of the gas mass velocity. Throughout the kiln, the amount of gas changes accordingly to the calcination and drying.
$L = \frac{NDS t}{0.19}$	Used to find total kiln length, L . t is the residence time of the particles, D is kiln diameter, S is the inclination, and N is the rotational speed.

The model also accounts for discrete particle distributions, where fully reacted particles are assumed to no longer consume heat (Dam-Johansen K, 2018). The conceptual model is shown in Figure 1 and the equations are shown in Table 1 (Levenspiel, O., 1999). The model and the framework for the sensitivity and uncertainty analysis have been implemented in Matlab[®] (Mathworks) while additional sensitivity analysis has been performed using Polynomial Chaos Expansion (PCE) with UQlab (ETH Zurich).

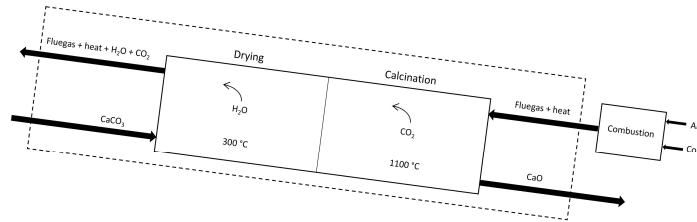


Figure 1: Defined rotary kiln system that have been modelled (stippled lines). Heat is produced through combustion of coal, which flows counter-current of the limestone. The wet limestone is first dried, where water vapor is added to the flue gas composition. Thereafter, the calcination reaction forms calcium oxide particles and carbon dioxide gas. The gas is added to the flue gas composition.

3. Methodology for Uncertainty and Sensitivity Analysis

The framework for uncertainty and sensitivity analysis (Sin et al, 2009) used here is illustrated in Figure 2. Input uncertainty is first determined (Table 2), which is used to make a sample based on the input data (Figure 3a). Each parameter set in this sample is then used in the model to create a set of output data (Figure 3b). The output data can be evaluated accordingly to ambitions (uncertainty/sensitivity metrics etc.), which can be visualized and/or ranked to draw conclusions. In this work, input uncertainty in operational (Table 2) and model (highlighted in bold and red in Table 1) parameters are evaluated.

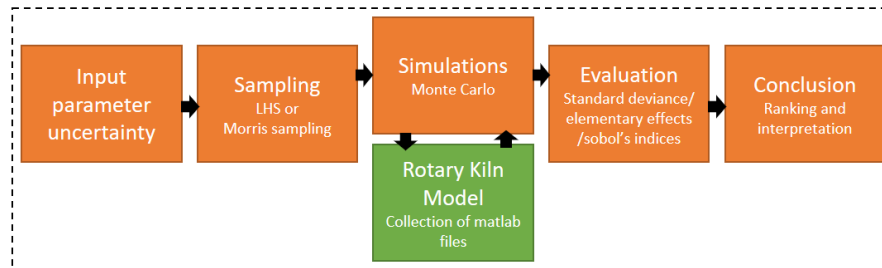


Figure 2: Overview of framework for uncertainty/sensitivity analysis according to Sin et al., 2009.

Table 2: Input uncertainty for operational parameters used in uncertainty and sensitivity analysis.

Parameter	Description	(Mean)	Unit	(Std.dev)
		μ		σ
$T_{g,d}$	Temperature in drying section	573	K	12.76
$T_{g,c}$	Temperature in calcination section	1,373	K	12.76
m_{CaCO_3}	Mass feed of limestone	115,000	t/yr	293.37
m_{Coal}	Mass feed of coal	9,547	t/yr	24.35
N	Rotational speed of kiln	1/3	1/min	1.70E-4
S	Inclination of rotary kiln	52.6	mm/m	8.06E-4

4. Results and Discussion

4.1. Uncertainty Analysis

The model output uncertainty is based on input uncertainty of parameters relevant for controlling the kiln operation, as shown in Table 2. Input space was sampled using Latin Hypercube Sampling (LHS) to generate 4,000 samples shown in Figure 3a. These samples are simulated using the model through Monte Carlo simulations (Figure 3b). Thereafter, the uncertainty related to the model output data were evaluated. Figure 3c and 3d present the model output results in cumulative distribution functions (CDF) of the kiln length and conversion rate for a fixed length. The figure shows that the operational uncertainty gives the highest output uncertainty. Therefore, taking the input uncertainties into account, to ensure a robust design, one needs to dimension the length of the reactor with 187 meters so that in 95 % of uncertainty realization (hence confidence) that all particles will be converted with 100 % efficiency.

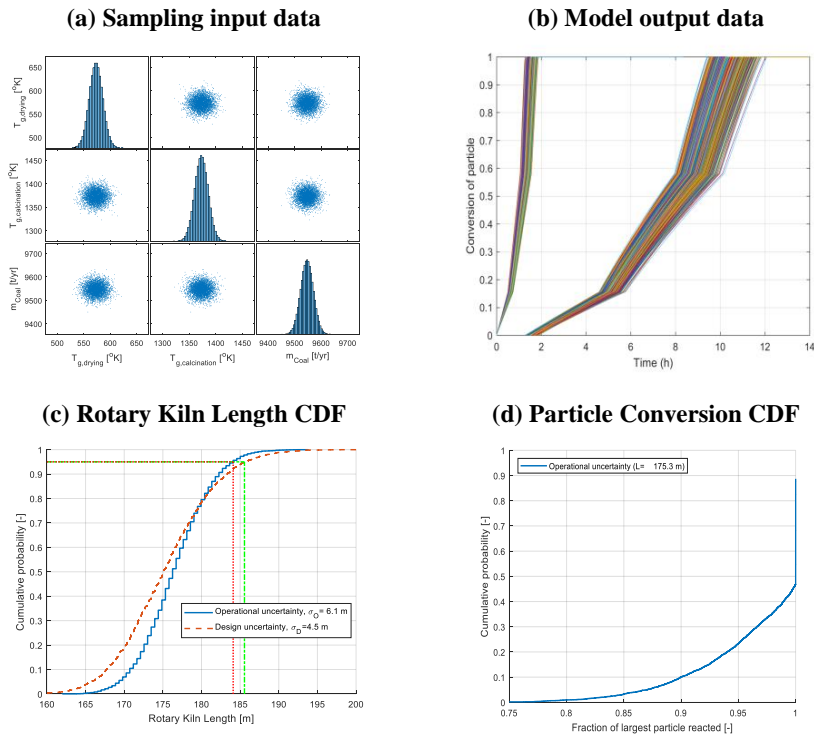


Figure 3: Input (a) and output (b) data using operational input uncertainty according to Table 2. Cumulative distribution function (CDF) of length (c) and average conversion with a fixed length (d) from uncertainty analysis. For the length, both operational and design uncertainty is included.

If the length is kept at 175 meters (base case design obtained by assuming no uncertainty), all but the largest particle in the particle distribution would be 100 % converted. However, it was found that the largest particle would on average be 97.15 %

(Figure 3d) converted. The latter particle consists of 35 w% of the limestone fed to the kiln, which amounts to roughly 1,147 tons of unreacted limestone annually wasted.

4.2. Sensitivity Analysis

Given that the output uncertainty is highest with operational sources of uncertainty, a global sensitivity analysis is performed on 6 operational parameters. To this end, two global sensitivity analysis techniques are used: Morris screening (Sin et al. 2009) and Sobol’s method through Monte Carlo sampling and PCE-based method (Al et al. 2018).

4.3. Morris Screening

Morris Screening is a global sensitivity method that systematically varies one parameter at a time at randomly selected points in the input space. The input parameter change is then evaluated based on how much it changes the output, and stored as Elementary Effects (EE). By doing a sufficient amount of these local sensitivity measures, the mean value and standard deviation of the elementary effects provides a global context to the sensitivity analysis (Sin et al, 2009). Figure 4 show EE of the operational parameters, where high frequency at low values represents a non-influential parameter (low mean and standard deviance). Conclusions from this Morris screening is that N and S are insignificant, and the temperature is the most influential parameter.

4.4. Sobol’s Method

Sobol’s method determines the sensitivity of parameters on model output based on the decomposition of variance. Sobol’s method produces two sensitivity measures, main effect (S_i) and total effect (S_{Ti}) respectively. Thus, S_i describes how much, on average, the model output variance could be reduced by if parameter i could be fixed. S_{Ti} is the expected variance when all parameters except i are fixed. While S_i is used to prioritize parameters relative to each other, S_{Ti} is used as a measure to determine non-important parameters. Table 3 show the results from Sobol’s method. The table show which of the parameters are most influential for this model, where the parameter with rank 1 is the most sensitive. Notably, the results are well in accordance with the Morris screening results. All values should to be positive, where negative numbers can be described as a consequence of numerical approximation.

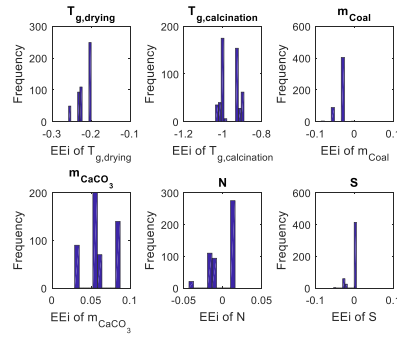


Figure 4: Morris screening result. High frequency of EE near 0 corresponds to low sensitivity.

Table 3: Sobol indices for sensitivity analysis of operational parameters on the model output.

Parameter	S_i	S_{Ti}	$S_{i,PCE}$	$S_{Ti,PCE}$	Rank
Temperature in drying section	0.0463	0.0487	0.0490	0.0491	2
Temperature in calcination section	0.9470	0.9447	0.9467	0.9468	1
Mass feed of limestone	0.0001	0.0018	0.0011	0.0012	4
Mass feed of coal	0.0030	0.0040	0.0030	0.0031	3
Rotational speed of kiln	-0.0027	0.0005	0.0000	0.0000	5
Inclination of rotary kiln	-0.0014	0.0002	0.0000	0.0000	6
SUM	0.9924	0.9998	0.9999	1.0001	N.A.

5. Conclusions

This work demonstrates successful application of uncertainty and sensitivity analysis in the model-based design and analysis of a rotary kiln process. The results showed that there are significant uncertainties, and that the uncertainty attached to operational uncertainty (standard deviation equal to 6.1 m) gives higher model length output uncertainty compared to the design uncertainty (standard deviation equal to 4.5 m). This means that in order to counter the effect of the operational uncertainty, one needs to dimension the length of the reactor with 187 m so that in 95 % of confidence one can ensure that all particles will be converted with 100 % efficiency. If the length is kept at 175 m which corresponds to the base case design, the largest particle would on average be 97.15 % converted. Taking the annual capacity into account (115,000 t limestone/y), this amounts to 1,147 t of unreacted limestone wasted annually.

Moreover, global sensitivity analysis indicated the following as the most influential parameters from the operational uncertainty (in descending order): temperature in calcination zone (1) and drying zone (2), the mass flow of limestone (3) and coal (4), the kiln rotational speed (5), and inclination of the kiln (6). Based on the input uncertainty, the four latter parameters can be seen as non-influential for the model output variance. Overall, the results show a high model output based on the input uncertainty, which highlights the importance of including detailed uncertainty and sensitivity analysis in model development. The results encourage application of comprehensive sensitivity and uncertainty analysis to improve robustness of rotary kiln process design.

References

- K.S. Mujumdar, K.V. Ganesh, S.B. Kulkarni, and V.V. Ranade. Rotary cement kiln simulator (rocks): Integrated modeling of pre-heater, calciner, kiln and clinker cooler. *Chemical Engineering Science*, 62:2590–2607, 2007.
- Levenspiel, O. (1999) *Chemical Reaction Engineering*. 3rd Edition. John Wiley & Sons, New York, 54.
- Dam-Johansen, K (2018), Lecture notes Industrial reaction engineering, DTU Chemical Engineering, spring 2018 semester, Lyngby, Denmark.
- Sin G, Gernaey KV, Lantz AE. Good modeling practice for PAT applications: Propagation of input uncertainty and sensitivity analysis. *Biotechnology progress*. 2009 Jul;25(4):1043-53.
- Ngadi, Z., & Lahlaoui, M. L. (2017). Impact of Using Alternative Fuels on Cement Rotary Kilns: Experimental Study and Modeling. *Procedia Engineering*, 181, 777–784.
- Frutiger, J., Andreasen, J., Liu, W., Spliethoff, H., Haglind, F., Abildskov, J. and Sin, G., 2016. Working fluid selection for organic Rankine cycles–Impact of uncertainty of fluid properties. *Energy*, 109, pp.987-997.
- Al, R., Behera, C. R., Zubov, A., & Sin, G. (2018). Systematic framework development for the construction of surrogate models for wastewater treatment plants. In *Computer Aided Chemical Engineering* (Vol. 44, pp. 1909-1914). Elsevier.

A novel scenario aggregation framework based on network community detection methods.

Sergio Medina-González, Ioannis Gkioulekas, Vivek Dua, Lazaros G. Papageorgiou*

*Centre for Process Systems Engineering, Department of Chemical Engineering,
University College London, Torrington Place, London WC1E 7JE, United Kingdom.*

l.papageorgiou@ucl.ac.uk

Abstract

Development of fast, robust and reliable computational tools capable of addressing the process management under uncertain conditions, is an active topic in the current process systems engineering literature. In fact, scenario reduction strategies (for example SCENRED and OSCAR) have acquired a lot of attention to overcome the traditional issues associated to large-scale scenario-based problems. Thus, this work proposes a novel scenario-reduction alternative (henceforth known as SCANCODE approach) by combining Graph Theory to construct a network and community detection methods to identify the clusters within the network. The capabilities and limitations of the proposed approach were tested through the two-stage MILP optimisation of a bio-based energy network under raw material availability and energy demand uncertainties. For comparison purposes, the same problem was solved using the sets of scenarios obtained with SCENRED and OSCAR. This comparison demonstrates the quality of SCANCODE approach while states the potential benefits of the proposed approach over the current alternatives.

Keywords: Scenario aggregation, Graph Theory, Community detection.

1. Introduction

The explicit consideration of the inherent uncertainty in a process system is becoming a key aspect for improving system performance and guaranteeing feasible operation. Two-stage programming and robust optimisation are the most used mathematical formulations/techniques to solve problems affected by uncertain conditions in which the conditions are modelled through a sufficiently large set of scenarios with their associated probability. Even though these formulations aid to effectively represent the whole uncertainty space, they are highly demanding in terms of computational effort. In order to address this critical challenge, scenario reduction strategies such as SCENRED and OSCAR have been successfully and extensively used during the recent past (Feng and Ryan, 2013; Li and Floudas, 2016). Essentially, both approaches identify a small amount of scenarios that minimise the total distance between them and the original uncertainty space; however, in the case of OSCAR, the effect of the input disturbances over the output performance is also considered. Despite being very effective, proximity might not be the best criterion to define clusters and more importantly, cluster centroids, since a lot of information associated to the pairwise relations is lost. Such information could be used as a metric to define and evaluate the quality of the clusters centroids.

Consequently, in this work an integrated framework of Graph Theory and network community detection methods is proposed. On one hand, Graph Theory is used to construct a network out of a large set of data using the pairwise information to determine connections. Disregarding the high-dimensionality or different distribution of the raw data set, the obtained network is composed essentially by a set of vertices (representing the scenarios) connected by edges if and only if the correlation of those vertices is equal to or higher than a desired value (threshold). On the other hand, any suitable algorithm can be used to extract a set of communities out of the network using a modularity function as quality metric (Xu et al., 2007). Several community detection methods are available in the literature including Girvan-Newman, Tyler-Wilkinson and Louvain algorithms among others (Javed et al, 2018). Individually, Graph Theory and community detection methods have been applied to different data management applications such as the worldwide web, collaboration networks and biological systems (Newman and Girvan, 2004). However, to the best authors' knowledge, they have never been used together in a scenario reduction framework.

The capabilities of the proposed approach were tested by comparing its performance against the ones obtained by the traditional SCENRED and OSCAR approaches, while using the two-stage MILP bio-based energy management problem described in Medina-González et al., (2017) as a comparison test bed.

2. Solution strategy

The proposed approach consists of four parts: Parameter initialisation/declaration, network construction, cluster generation and centroid identification. A detailed explanation of these elements is presented.

2.1. Parameter initialisation.

In this step, a sufficiently large set of scenarios is defined to represent the process's uncertainties. In order to create an interconnected structure out of this data set (i.e. a network), the pairwise relationship between vertices are modelled and collected in an adjacency matrix ($A_{i,j}$) using any suitable correlation metric. Finally, in order to reduce the network complexity, the connections quality might be assess using a tolerance value (threshold that lies between 0 and 1).

2.2. Network construction.

Using the above defined parameters, the quality of the network connectivity ($A_{i,j}$) is adjusted, by replacing any connectivity values that do not satisfy the minimum threshold condition by zero (non-connection state), hence obtaining a strongly connected network. Notice that even though the threshold definition is independent of the correlation value, it affects the network density, which might lead to an impractical solution. For example, low threshold values lead to "perfectly connected" networks and therefore the whole system is considered as a unique cluster, while large threshold values produce nodes that are considered as isolated clusters. Thus, a systematic threshold definition rule is vital.

2.3. Cluster/community generation.

This part of the algorithm aims to identify the communities that lead to the most efficient network division. Essentially, a community is a local area/group of vertices

densely connected between them and loosely (or not at all) connected with other groups. In order to assess the quality of these communities, the modularity metric (Q) can be used which represents the number of edges that fall within communities/modules minus the expected number of edges that should fall into communities in an equivalent network configuration with edges being placed randomly (Newman and Girvan, 2004). The general formulation of the community detection problem is presented in Eq. (1), where the partition that yields the maximum modularity for a target network is sought.

$$Q = \sum_m \left[\frac{L_m}{L} - \left(\frac{D_m}{2L} \right)^2 \right] \quad (1)$$

From Eq. (1), the first term $\frac{L_m}{L}$ represents the ratio of edges that fall into module m in relation with the total number of links in the network (L), while the second one represents the expected fraction of links that would fall in module m if they were randomly generated. Particularly, D_m is the total random degree in each module m and the difference in these terms indicate how “non-random” cluster m is.

2.4. Centroid identification.

For each one of the obtained communities/clusters, their centroids are identified by selecting the vertex with the highest centrality criteria value. For simplicity, three different criteria are suggested, however more options might be found in the literature:

- Degree. Represents the number of connections of each vertex.
- Betweenness. Accounts for the paths passing through a vertex.
- Closeness. Distance of a vertex against all the others within a cluster.

The general SCANCODE algorithm is presented next:

0. Initialise a defined amount of scenarios that represent the process uncertainties as well as a threshold value ($Th = [0, 1]$) in order to establish the connections between vertices.
 - a. Generate the adjacency matrix (A_{ij}) by calculating the correlation between each pair of vertices.
1. Let the value in A_{ij} be zero if the correlation value is below the defined threshold ($A_{ij} < Th$) and create the network by using the new data in the adjacency matrix.
2. Identify the community arrangement that maximises the modularity metric using any available algorithm/method.
3. For each cluster, identify the scenario with the highest value in the desired centrality metric.

3. Illustrative example

Due to space limitations and since the scope of the paper is to describe and test the proposed approach, the mathematical formulation of the case study is omitted and the interested readers are referred to Medina-González et al., (2017). However, for

continuity purposes a brief description of the case study is included. The problem was formulated as a MILP problem that maximises the economic benefit of a biomass-based energy SC system through the management of its design and operations. The model considers nine districts (fc), and all of them can be simultaneously biomass suppliers, energy generation and market sites. 40 different biomass states (s), six available technologies (tec) and 79 activities (act) were considered across a monthly discretization (t) of a year horizon. Cassava Rhizome (CR) was used as a raw material for energy production, while its availability and the total energy demand ($As(s,fc,t)$ and $dem(s,fc,t)$ respectively) were considered as uncertainty sources. A total of 153 uncertain parameters are considered since As and dem are defined only for the first and last raw material state respectively while for As , only five time periods are considered (length of the CR production season). Without loss of generality, 100 equiprobable scenarios were randomly generated for each uncertain parameter using a normal distribution with the average values presented in Table 1 and a 30% standard deviation.

Table.1. Mean values for uncertainty conditions at each district.

District	fc_1	fc_2	fc_3	fc_4	fc_5	fc_6	fc_7	fc_8	fc_9
Demand (MJ)	1942	4055	15250	19363	2684	3198	913	3884	4169
Availability (kg)	12.75	24.38	81.1	122.18	16.22	22.07	5.27	21.08	28.15

4. Results and discussion

Using the Pearson correlation and three thresholds values (0.91 ; 0.92 and 0.93) the adjacency matrices and the associated networks were constructed as described in section 2. Then, the Louvain algorithm was used to detect the communities within each network. Essentially, Louvain is a two-step algorithm that maximises the modularity metric, in which for a given network, the first step assigns nodes into clusters only if that increases the modularity value, whereas the second step creates a new network where each node represents a cluster from the previous step. These two steps are iterated until no further modularity improvement is possible (Blondel et al., 2008). After applying the Louvain algorithm for this problem, a total of 9, 13 and 31 communities were identified for each threshold respectively. Analysing the obtained networks (Figure 1), it is evident that the density is inversely proportional to the threshold value. Particularly, the larger the threshold values, the more isolated scenario clusters are produced, whereas for small values a very densely connected network is obtained which compromises the definition of cluster centroids. Such a behaviour confirms the undesirable properties in the reduced set of scenarios for the extreme threshold points and stresses the need for a metric that represents a balanced rate between number of clusters and network density.

For the three generated networks, their centroids were identified using *degree* as centrality metric. The probability of each cluster centroid is represented by the aggregation of the original probabilities of all the elements within their respective cluster, while the original uncertainty parameters information was kept. Finally, the MILP problem was implemented in GAMS 24.7 and solved for each one of the reduced sets of scenarios using CPLEX 12.6.3 to a relative optimality gap of 5%.

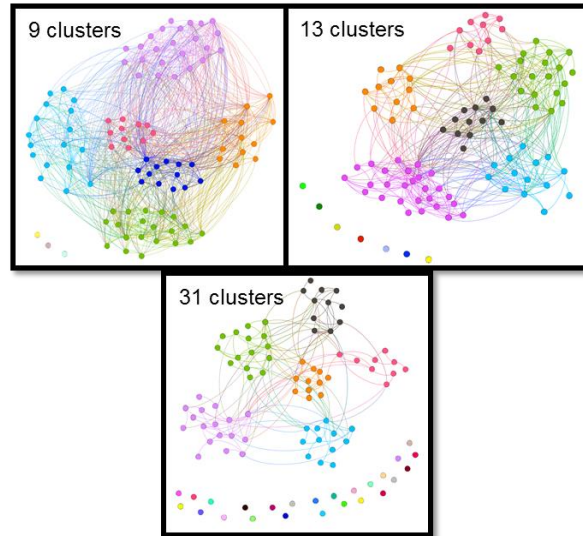


Figure 1. Networks and clusters for different thresholds values.

In order to illustrate the effectiveness of the proposed approach, SCENRED and OSCAR (the two most used scenario reduction approaches) were used as a comparison reference. The resulting set of scenarios from the three methods represent the input data to solve the MILP problem. Table 2 shows the optimal results for each case.

Table 2. Results for the optimisation of MILP problem.

	<i>Size/modules(m)</i>	<i>ExpProfit (€)</i>	<i>PostProcess Profit (€)</i>	<i>Gap (%)</i>	<i>CPUtime (s)</i>
FULL-SPACE	100	345,198	---	--	131,607
<i>Th= 0.91</i>		<i>Modularity (Q=0.205214)</i>			
OSCAR	9	346,642	345,231	0.4085	1,101
SCENRED	9	348,304	342,374	1.7322	1,193
SCANCODE	9	357,655	345,500	3.5183	1,137
<i>Th= 0.92</i>		<i>Modularity (Q=0.32264)</i>			
OSCAR	13	343,475	345,115	0.4752	1,459
SCENRED	13	349,373	345,500	1.1211	1,512
SCANCODE	13	348,142	345,115	0.8771	1,495
<i>Th= 0.93</i>		<i>Modularity (Q=0.43473)</i>			
OSCAR	31	346,051	345,115	0.2711	7,765
SCENRED	31	348,562	345,115	0.9987	7,812
SCANCODE	31	344,156	343,545	0.1779	7,818

Table 2, displays a significant dispersion between the expected performances (*ExpProfit*) for the reduced set of scenarios and the full-space (no reduction), since the scenarios in the reduced set may be different for each cluster and strategy. Therefore, a post-process analysis was performed in order to promote a fair comparison (*PostProcessProfit*). To derive those values, the first stage decisions obtained after optimising the MILP problem using the reduced set, were fixed for the full-space problem. The gap between the expected value and its associated post-process outcome was also calculated, confirming that the three approaches approximate the profit (variation <4%) and

proving that SCANCODE is a feasible alternative to the current scenario reduction approaches. Despite this small gap, the approximation error for SCENRED and SCANCODE increases as a function of the reduction degree while in the case of OSCAR, a relatively steady gap was obtained despite the level of reduction. Such a behaviour is due to the consideration of both, the original uncertain parameters and their effect over the expected performance. Nonetheless, obtaining such information implies a pre-processing task, which hinders its application to large-scale problems. In any case, further research seeking the reduction of the approximation gap in SCANCODE is crucial for its further application in real-life problems with large sized scenario sets.

5. Conclusions

This paper proposes a novel scenario reduction/aggregation framework that integrates Graph Theory and community detection methods. Numerical results demonstrate that the proposed strategy is as efficient as other well-studied techniques for identifying a reduced and representative set of scenarios. Additionally, the well-structured cluster definition used in the proposed approach justifies its potential applications to large-scale networks considering many uncertainty scenarios (of several orders of magnitude). Despite the efficiency of SCANCODE, some opportunity areas have been identified that will improve its performance. Particularly, further work is focused on combining this strategy with other data-management techniques to identify the most efficient relation between the number of clusters and the quality of the uncertainty space.

Acknowledgements

The authors would like to thank the financial support received from the UK Engineering and Physical Sciences Research Council (under the project EP/M027856/1) as well as the UK Leverhulme Trust under grant number RPG-2015-240.

References

- Blondel, V. D., Guillaume, J.L., Lambiotte, R. and Lefebvre, E. 2008. Fast unfolding of communities in large networks, *Journal of Statistical Mechanics: Theory and Experiment*, (10).
- Feng, Y. and Ryan, S.M. 2013. Scenario construction and reduction applied to stochastic power generation expansion planning. *Computers & Operations Research*, 40, 9-23.
- Javed, M.A., Younis, M.S., Latif, S., Qadir, J. and Baig, A. 2018. Community detection in networks: A multidisciplinary review. *Journal of Network and Computer Applications*, 108, 87-111.
- Li, Z. and Floudas, C.A. 2016. Optimal scenario reduction framework based on distance of uncertainty distribution and output performance: II. Sequential reduction, *Computers & Chemical Engineering*, 84, 599-610.
- Medina-González, S., Graells, M., Guillén-Gosálbez, G., España, A., and Puigjaner, L. 2017. Systematic approach for the design of sustainable supply chains under quality uncertainty, *Energy Conversion and Management*, 149, 722-737.
- Newman, M.E.J. and Girvan, M. 2004. Finding and evaluating community structure in networks. *Physical Review*, 69, 1-15.
- Xu, G., Tsoka, S., and Papageorgiou, L.G. 2007. Finding community structures in complex networks using mixed integer optimisation, *The European Physical Journal B*, 60, 231-239.

Towards development of a decision support tool for conceptual design of wastewater treatment plants using stochastic simulation optimization

Resul Al, Chitta Ranjan Behera, Krist V. Gernaey, Gürkan Sin*

Process and Systems Engineering Center (PROSYS), Department of Chemical and Biochemical Engineering, Technical University of Denmark, Building 229, 2800 Kgs. Lyngby, Denmark

gsi@kt.dtu.dk

Abstract

Available treatment technologies for wastewater are diversifying as the industry is undergoing a paradigm shift from considering wastewater as a waste to treat to an increasingly valuable source for energy production and resource recovery. With the purpose of addressing the problem of determining optimal plant network for wastewater treatment plants, we develop a new decision support tool (SPDLab) relying on a novel simulation optimization based process synthesis framework and a library of rigorous process models. The capabilities of SPDLab are demonstrated with a case study for designing an energy surplus WWTP. The Benchmark Simulation Model No. 2 (BSM2) (Gernaey et al., 2014) plant layout is populated with additional options for primary treatment technologies, such as a rotating belt filter with or without polymer addition, and mainline treatment options including also fixed film activated sludge (IFAS) technology. A side stream treatment with partial nitrification-Anammox process is also included in the superstructure. Results obtained show that the combination of efficient carbon recovery with main stream Anammox and anaerobic digester produces the most net energy among the investigated alternatives.

Keywords: Process synthesis and design, wastewater treatment plant design, simulation-based optimization, Monte Carlo simulation.

1. Introduction

The design of domestic wastewater treatment plants (WWTPs) has seen an unprecedented shift since the inception of the widely used activated sludge process. The priority for a design engineer was mainly to ensure effective removal of organic pollutants from wastewater. However, with the ever growing demands on the WWTP, such as population growth leading to increased pollutant loads, stringent environmental laws, demand for energy neutrality and contributing to circular economy, the layout of WWTP looks more gigantic than ever. The WWTP design intricacy has been further exacerbated by the remarkable innovation and availability of novel treatment technology (both matured and emerging) in the market. Therefore, given the steadily growing number of competing treatment technologies and ever-ambitious performance goals, the need for the use of simulation, optimization, and systematic process synthesis methodologies for engineering design of WWTPs is becoming more pronounced among design professionals.

Accurate modelling of highly complex biological processes in WWTPs require use of rigorous (non-linear) bio-process models such as ASM1 (Henze et al., 2006), ADM1 (Batstone et al., 2002), etc. Such models remain too complex for use in traditional process synthesis approaches such as superstructure optimization using mathematical programming due to the highly nonlinear process equations (Chen et al., 2018). The main

contribution of this paper is the development and application of a new simulation optimization-based process synthesis approach to explore more rigorously alternative WWTP networks using a model library of high-fidelity mechanistic bio-process models. For this purpose, a decision support tool for sustainable process synthesis and design, SPDLab, has been developed to assist design professionals with the implemented methodology. SPDLab provides computational tools for interfacing with complex bio-process models implemented in a Simulink environment and searches for an optimal plant layout configuration for the given design objective. The process synthesis methodology consists of three major steps. First, a superstructure containing all different design configurations is created using combinatorial synthesis and expert knowledge approach (Bozkurt et al., 2015). Second, design degrees of freedoms of each configuration are investigated with Monte Carlo simulations and promising configurations are selected for the third step, which imposes user-defined effluent quality constraints to rank and select optimal plant layouts with preliminary design.

2. Methodology

Simulation is an established tool for evaluating and predicting the performance of complex engineering systems. Stochastic simulation optimization, also referred to as simulation optimization, uses simulation to find values of decision variables that will optimize the system's key performance indicators (KPI) of interest, which are obtained by performing stochastic simulations like Monte Carlo simulations. Promoted by recent advancements in computing power, simulation optimization allows one to work with arbitrarily complex simulation models, eliminating the need to keep model complexity to mathematically tractable forms as required by deterministic optimization frameworks (Pasupathy et al., 2011). A step-by-step overview of the proposed simulation optimization based process synthesis and design methodology is shown in Table 1.

Table 1: Overview of proposed methodology for early stage design of WWTPs.

Step 1	Generation of a superstructure containing all the different plant layouts using combinatorial synthesis and expert knowledge
Step 2	Design space exploration of each alternative plant layout with Monte Carlo simulations
Step 3	Ranking and selection of optimal plant layouts

2.1. Step 1: Superstructure generation

A superstructure is postulated to represent all practical plant layouts, which can be selected as an alternative plant design by the decision support tool, using combinatorial synthesis together with expert knowledge. Combinatorial synthesis allows exhaustive exploration of all different combinations of technologies whereas expert knowledge is used to exclude layouts with an infeasible sequence of treatment units from further investigation.

2.2. Step 2: Design space exploration

For each treatment technology, there exist several design degrees of freedom, such as the volume ratio of aerobic and anaerobic tanks in an activated sludge system, which needs to be selected by the designer and significantly affects the plant performance. Therefore, to achieve desired effluent quality levels, one often needs to explore these design degrees of freedom for every different technology. For this purpose, design-related parameters of each technology included in a given layout are gathered in a global parameter space, i.e. the design space, which is then sampled using a uniform space filling sampling design such as Latin hypercube sampling (LHS). The resulting design space is explored with Monte Carlo simulations to identify promising plant layouts which will provide optimized performance results by also satisfying imposed effluent constraints.

2.3. Step 3: Ranking and selection (R&S)

Among the methods developed for solving simulation-based optimization problems are ranking and selection (R&S), black-box search methods, surrogate model based methods, and sample path approximation, etc. For a detailed review of these methods, the work of Xu et al. (2015) can be consulted. For problems with a finite number of solutions in the search space, such as optimal plant layout among the alternatives contained in the superstructure, R&S procedures can be directly applied to find the most promising plant layout for the given design objective. To further assist the decision-maker in identifying promising layouts, results of Monte Carlo simulations are exposed to the performance constraints to filter out infeasible solutions and then ranked according to the design objective.

3. A decision support tool for process design of WWTPs: SPDLab

3.1. The model library and the user interface

The SPDLab model library (shown in Figure 1) encompasses models representing both conventional and emerging treatment technologies. The primary clarifier works based on gravity settling and is modelled as presented in Gernaey et al. (2014), whereas the rotating belt filter, which is an emerging technology, works based on cake filtration and sieving and is modelled as presented in Boiocchi et al. (2018), and Behera et al. (2018).

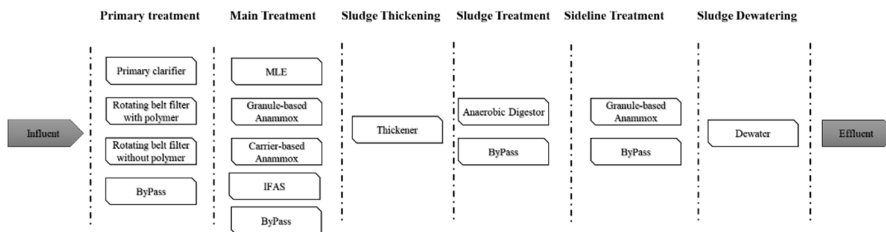


Figure 1: The model library of SPDLab is shown for different treatment steps in WWTPs.

For mainstream nutrient removal the Modified Ludzack-Ettinger (MLE) system is used based on the ASM1 principle (Gernaey et al., 2014). Anammox based nutrient removal for both mainstream and side stream is modelled using a one-dimensional biofilm concept. The integrated fixed-film activated sludge (IFAS) system is a retrofitted version of the MLE system, where the aerobic tanks are filled with carrier in order to enhance the nitrogen loading rate. For sludge treatment, the anaerobic digestion (AD) system is modeled using the ADM1 (Batstone et al., 2002). The sludge thickening and dewatering are modeled using the approach of Gernaey et al., (2014). To design each unit, several widely used design parameters such as sludge retention time (SRT), hydraulic retention time (HRT), surface over flow rate (SOR), nitrogen removal rate (NRR), recycle ratio (RR), carrier filling etc. are used while sampling the design space using LHS. Figure 2 shows the SPDLab’s user interface, which was developed in the Simulink modelling environment.

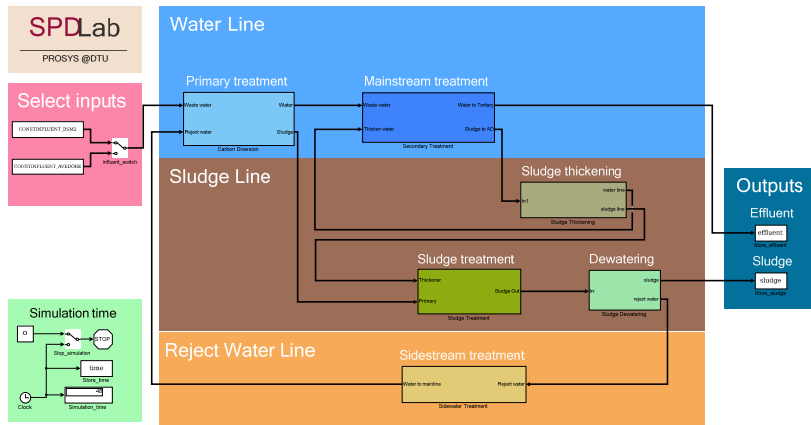


Figure 2: The main user interface of the decision support tool

3.2. A case study: Designing an energy surplus WWTP

The main objective of this case study is to illustrate the proposed methodology outlined in Table 1. To this end, a scenario is considered where the primary objective is to build an energy surplus WWTP for a benchmark municipal wastewater stream (Gernaey et al., 2014) with a plant capacity of 100,000 PE. Figure 3 depicts the synthesis problem along with the design flows and the effluent quality limits imposed in the case study.

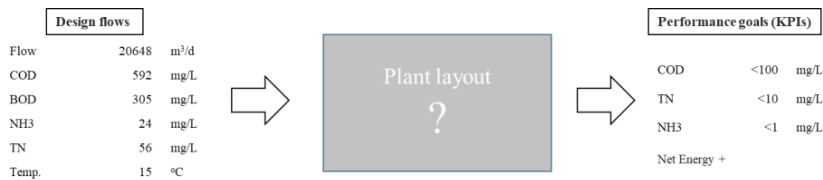


Figure 3: Design flows and performance goals considered in the case study.

4. Results and discussion

Following the proposed methodology, a total of 80 different plant layouts were generated in step 1 with a combinatorial synthesis approach, and step 2 explored automatically the generated design space of each layout with Monte Carlo simulations using a LHS of size 100. Results are shown for net energy production of feasible designs in Figure 4. Furthermore, the solutions are screened and ranked (see Figure 5) by enforcing the effluent quality limits (COD < 100 mg/L, TN < 10 mg/L and NH₄⁺ < 1 mg/L) and the plant KPIs such as methane gas production, aeration energy demand and sludge production, etc., are calculated for each design. Besides, the net energy is calculated by subtracting the aeration energy consumption from the energy produced via the methane gas. The energy modelling at this stage is kept intentionally simple as the primary objective of this work is to assess the methodology.

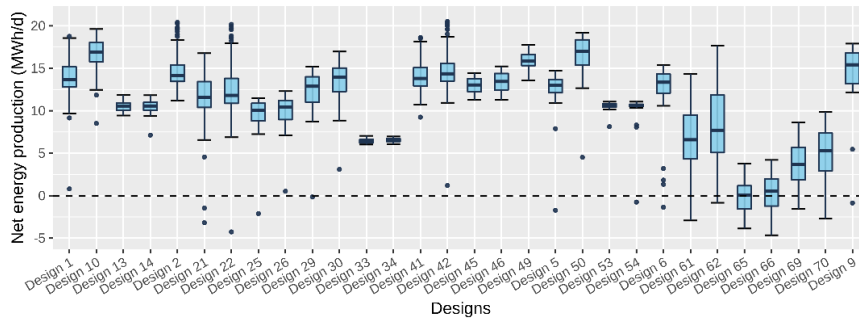


Figure 4: Comparing net-energy production of all potential plant layouts.

The top five feasible designs selected by the tool for building an energy surplus WWTP are shown in Table 2, which picks main stream Anammox as an efficient carbon recovery technology together with an AD unit. This combination also agrees well with the available process knowledge, i.e., increasing biogas production by diverting more carbon to the AD unit and then treating the low COD/TN load wastewater with Anammox technology. In this way the aeration energy demand can be reduced significantly as the Anammox process needs significantly less oxygen compared to the conventional activated sludge process (Morales et al., 2015).

Table 2: Top 5 promising plant layouts selected by SPDLab for energy surplus WWTP design.

Selected Configuration	Aeration Energy (kWh/d)	Methane Production (kWh/d)	Net Energy (kWh/d)
PC – Anx_carrier – Thickener – AD – Dewater	3662	19452	15790
RBF w/ polymer – Anx_carrier – Thickener – AD – Dewater	3795	18987	15192
PC – Anx_granule – Thickener – AD – Dewater	3721	18109	14388
PC – Anx_carrier – Thickener – AD – Dewater – Anx_granule_side	3546	17777	14231
PC – Anx_granule – Thickener – AD – Dewater – Anx_granule_side	3880	18018	14138

5. Conclusions

This paper presented a new methodology and a tool for process synthesis and preliminary design of WWTP networks using simulation optimization. The tool is targeted at exploring alternative WWTP designs for a given wastewater stream and design objective/constraints. The case study results demonstrate that SPDLab can provide decision makers with valuable insights during the early-stage design of WWTP networks with its rigorous search and advanced visualization capabilities for identifying promising

plant layout configurations. Furthermore, development of a fully-fledged commercial decision support tool allowing also for multi-objective design optimization, extension of the model library to newly arising treatment technologies, and integration of other early stage design tools, such as sustainability analysis, are planned as future work.

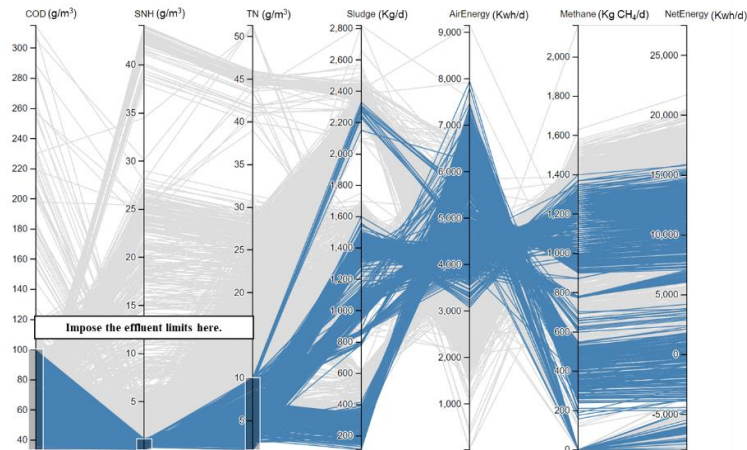


Figure 5: Comparison of all feasible designs after imposing effluent quality constraints.

Acknowledgements: The authors acknowledge funding from the EU Horizon 2020 research and innovation programme under the Marie Skłodowska-Curie grant agreement no.675251 as well as the funding from the Water Joint Programming Initiative under the PIONEER_STP project.

References

- C.R. Behera, D. Santoro, K.V. Gernaey, G. Sin, 2018, Organic carbon recovery modeling for a rotating belt filter and its impact assessment on a plant-wide scale, *Chemical Engineering Journal*, 334, pp.1965-1976.
- D.J. Batstone, J. Keller, I. Angelidaki, S.V. Kalyuzhnyi, S.G. Pavlostathis, A. Rozzi, W.T.M. Sanders, H. Siegrist, V.A. Vavilin, 2002, The IWA anaerobic digestion model no 1 (ADM1), *Water Science and Technology*, 45(10), pp.65-73.
- H. Bozkurt, A. Quaglia, K.V. Gernaey, G. Sin, 2015, A mathematical programming framework for early stage design of wastewater treatment plants, *Environmental Modelling & Software*, 64, 164–176.
- J. Xu, E. Huang, C.H. Chen, L.H. Lee, 2015, Simulation Optimization: A Review and Exploration in the New Era of Cloud Computing and Big Data, *Asia-Pacific J. Oper. Res.*, 32, 1550019.
- K.V. Gernaey, U. Jeppsson, P.A. Vanrolleghem, and J.B. Copp, 2014, *Benchmarking of control strategies for wastewater treatment plants*, IWA Publishing.
- M. Henze, W. Gujer, T. Mino, M.C.M. van Loosdrecht, 2000, *Activated Sludge Models ASM1, ASM2, ASM2d and ASM3*, IWA Scientific and Technical Report 9, IWA Publishing, London.
- N. Morales, Á.V. del Río, J.R. Vázquez-Padín, R. Méndez, A. Mosquera-Corral, J.L. Campos, 2015, Integration of the Anammox process to the rejection water and main stream lines of WWTPs, *Chemosphere*, 140, pp.99-105.
- R. Boiocchi, F. Giaccherini, F. Khan, C. DeGroot, A. Sherratt, D. Santoro, *Dynamic Modelling And Validation Of A Rotating Belt Filter For Primary Wastewater Treatment*, 4th ecoSTP conference, Ontario, Canada.
- X. Chen, R. Al, C.R. Behera, G. Sin, 2018, *Process Synthesis, Design, and Control of Wastewater Treatment Plants*, Elsevier Reference Module in Chemistry, Molecular Sciences and Chemical Engineering, pp. 1–14.

Optimization of semi-permeable membrane systems for biogas upgrading

Diego Filipetto^a, Federico Capra^{a,b}, Francesco Magli^{a,b}, Manuele Gatti^{a,b},
Emanuele Martelli^{a,*}

^a*Politecnico di Milano, Department of Energy, Via Lambruschini 4, 20156 Milano, Italy
Milano*

^b*LEAP s.c.a r.l. – Laboratorio Energia e Ambiente Piacenza, Via N. Bixio 27/C, 29121,
Piacenza, Italy*

* *emanuele.martelli@polimi.it*

Abstract

This work focuses on the optimization of a biogas upgrading process consisting of three CO₂-permeable membranes. A 1-D membrane model, capable of handling multi-component gas mixtures, is formulated as a set of differential algebraic equations and validated against experimental data. The model is used within a sequential algorithm to solve the simulation of the three-stage system. The key design variables (i.e., areas of each membrane module, stream pressures and recycle mass flow rates) are optimized using the recently developed MO-MCS algorithm, a derivative-free optimizer suitable for multi-objective problems. Results show that the Pareto-optimal solutions have a total plant cost in the range 720-770 €/Nm³/h of feed) and an energy efficiency of 87.7-89.2%.

Keywords: Biogas upgrading, membrane separation, black-box optimization, multi-objective optimization

1. Introduction

Biomethane is produced through the purification of biogas, a mixture of CH₄, CO₂ and other contaminants (e.g., H₂S, NH₃ and siloxanes) which is originated by the anaerobic digestion of biomass. Such biogas purification process is typically called “biogas upgrading”. Among the available upgrading technologies (e.g. water scrubbing, amines, PSA), CO₂-permeable membranes appear as a promising option, especially for medium-low size plants (250-500 Nm³CH₄/h), owing to their good separation efficiency, modularity, straightforward operation and maintenance, and low installation costs. However, since a single membrane stage cannot achieve high purity and recovery of the desired product (CH₄), it is advantageous to adopt integrated configurations which combine multiple modules placed in series and/or parallel, entailing recycle streams. Due to the presence of multiple design variables, optimization-based design approaches have been adopted by several authors. For example, Scholz et al. (2015) proposed a structural-optimization approach employing a flexible superstructure of possible process layouts. The modelling and optimization problems are solved together as a single MINLP, according to the equation oriented process optimization approach. Also, the choice of the optimal membrane material according to an economic criterion is tackled with the same approach. Gabrielli et al. (2017) adopt the black-box approach, combining a genetic algorithm with a 1-D model of the membrane modules, to minimize the compression energy and the required membrane area by selecting the optimal process layout.

This work investigates the numerical optimization of the most promising integrated membrane-based configuration found by Scholz et al. (2015) for biogas upgrading. First, the 1-D model proposed by Gabrielli et al. (2017) for co-current hollow-fiber membranes is extended to handle multi-component gas mixtures. Then, the model is validated with the experimental data available in Pan et al. (1986) and integrated into a modular Matlab algorithm to solve the overall process simulation. Finally, the key design variables (i.e., areas of each membrane module, stream pressures and recycle mass flow rates) are optimized using the recently developed MO-MCS algorithm (Capra et al., 2018), a model-based derivative-free optimizer for multi-objective problems.

2. Process description

The process configuration considered in this work is shown in Figure 1. A gas dryer and a bed of activated carbon, not shown in the figure, are placed upstream of the membrane system to remove H_2O and H_2S (and other contaminants) respectively. Then, sulphur-free dried biogas (stream 0) is mixed at atmospheric pressure with the recycle stream (stream 6), pressurized by the first compressor, and fed to the first membrane unit (stage A). The retentate flow (stream 2) can be further compressed (compressor 2, included in case $Pressure_{stage\ B} > Pressure_{stage\ A}$) and sent to the second membrane unit (stage B). Since the permeate flow of the first stage (flow 1P) may include a certain amount of CH_4 , it is advantageous to perform a selective recycle including a third membrane unit (stage C) downstream of it. The permeate of stage C is expected to be nearly pure CO_2 with a very low content of CH_4 , while the retentate stream (stream 5) can be mixed with stream 2P and recycled back to the process inlet (stream 6). According to Scholz et al. (2015), with the proper selection of the membrane material, this configuration combines high purity of the produced biomethane ($96\%_{mol}$), high recovery of CH_4 ($> 95\%$) and a good balance between energy consumption and investment cost.

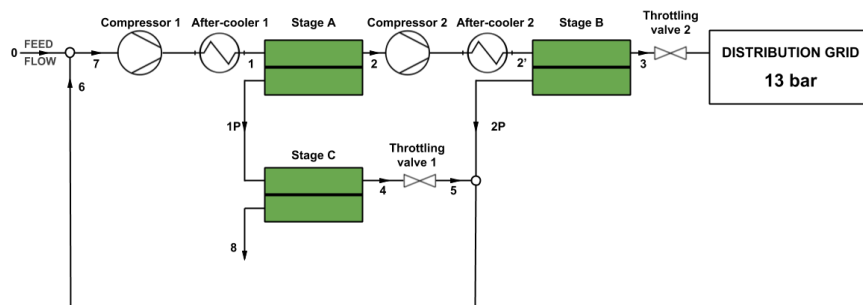


Figure 1. Scheme of the integrated membrane configuration considered in this study.

As far as the membrane material is concerned, we selected a dense polymer, specifically polyaramid (PA), on the basis of the results found by Scholz et al. (2015) and Havas in (2017). According to Scholz et al. (2015), this commercially available material can be assembled in hollow-fibers modules featuring a CO_2 permeance of 200 gpu and a CO_2/CH_4 selectivity of 20.

The main process data (dry biogas composition and pressure) and specifications (grid injection requirements and membrane material properties) are reported in Table 1 and can be considered representative of an anaerobic digestion plant fed with chicken-manure.

Table 1. Assumptions and specifications for the process.

Biogas flow rate	11.75	mol/s
Dry biogas CH_4 content	56%	% _{mol}
Dry biogas CO_2 content	44%	% _{mol}
Biogas feed pressure	1	bar
Grid injection pressure	13	bar
Max biomethane oxygen content	< 0.6%	% _{mol}
Max biomethane CO_2 content	< 3%	% _{mol}
Biomethane HHV range	34.95 ÷ 45.28	MJ/Sm ³
Wobbe index range	47.31 ÷ 52.33	MJ/Sm ³
Relative density range	0.5548 ÷ 0.8	-
Membrane CO_2 permeance (polyaramide, Havas and Lin, 2017)	$6.8 \cdot 10^{-8}$	mol/(s · Pa · m ²)
Membrane CO_2/CH_4 selectivity (polyaramide, Havas and Lin, 2017)	20	-

3. Problem statement

The objective of this work is to identify the set of Pareto-optimal solutions which exhibit the minimum total plant cost and maximum process efficiency. More in detail, the optimization problem can be stated as follows: “Given the biogas specifications and the membrane material properties, determine the set of Pareto-optimal design solutions which minimize the total upgrading plant cost (TPC) while maximizing the primary energy efficiency η_{PE} (chemical power of biomethane/total primary energy consumed by the process) and meet the specifications on the produced biomethane (minimum CH_4 fraction, allowed ranges of HHV, Wobbe index, etc)”. The primary energy efficiency is computed as the ratio between the primary energy contained in biomethane (given by the product between mass flow rate of biomethane and its LHV) and the primary energy input of the process (i.e. the primary energy contained in biogas plus the equivalent primary energy consumed by the upgrading process to operate compressors and other auxiliaries, etc).

The independent optimization variables of the selected process configuration are the areas of the three modules and the pressure ratios of the two compressors and the pressure of the permeate side of stage A membrane. Given the limited amount of independent optimization variables, the black-box approach has been selected to tackle the multi-objective optimization problem. MO-MCS, a recently developed multi-objective model-based derivative-free algorithm (Capra et al., 2018), optimizes the independent design variables and, for each sampled solution, the process simulation is executed and the total plant cost is assessed.

4. Membrane module model

We propose an extension for multi-component gas mixtures of the 1-D model originally formulated by Gabrielli et al. (2017) for the membrane separation of binary gas mixtures. The peculiarity of such model is the use of dimensionless parameters and variables which attenuate the numerical problems arising in the solution of the set of differential equations.

$$\frac{d\Psi}{d\zeta} = \frac{m_1}{y'_1} (x_1 - \beta y'_1) \quad (1)$$

$$\frac{dx_i}{d\zeta} = \frac{m_i}{\Psi y'_i} (x_i - y'_i)(x_i - \beta y'_i) \quad \forall i = 1, \dots, C - 1 \quad (2)$$

$$0 = y'_1(x_j - \beta y'_j) - \alpha_{1j} y'_j (x_1 - \beta y'_1) \quad \forall j = 2, \dots, C \quad (3)$$

$$0 = \sum_{i=1}^C y'_i - 1 \quad (4)$$

$$\Psi|_{\zeta=0} = 1 \quad (5)$$

$$x_i|_{\zeta=0} = x_i^{FEED} \quad \forall i = 1, \dots, C \quad (6)$$

As described in Gabrielli et al. (2016), ζ is the non-dimensional variable representing the axial coordinate, $\Psi(\zeta)$ is the non-dimensional total molar flow rate on the retentate side (the ratio between the flow rate at point ζ and the one in the feed), $x_i(\zeta)$ is the molar fraction of the permeate bulk flow, and y'_i is the molar fraction at the membrane interface. The parameter β is the ratio between the permeate and retentate pressure, α_{1j} is the membrane selectivity of the j -th component with respect to the most permeable component (CO_2 in this application). The parameter m_i is defined as:

$$m_i = \frac{Q_i p^F A}{\delta U^F} \quad (8)$$

Where Q_i denotes the permeability of the i -th gas species, p^F is the feed pressure, A is the membrane area, δ is the membrane thickness and U^F is the total feed molar flow rate. Eq. (1) is the balance of total gas moles on the retentate side and it relates the variation of the total dimensionless flow on the retentate side Ψ with the total molar flux across the membrane. Eq. (2) relates the axial variation of concentration of species on the permeate side with the molar flux across the membrane. Eq. (3) expresses the membrane fluxes of the different gas species with respect with that of CO_2 ($i = 1$). Eq. (4) imposes that the sum of the molar fractions on the membrane interface is equal to one, while Eq. (5) and (6) are boundary conditions. Eq. (1-6) define a set of Differential Algebraic Equations (DAE) which is solved in Matlab® v. 2018-a with the *ode15s* algorithm.

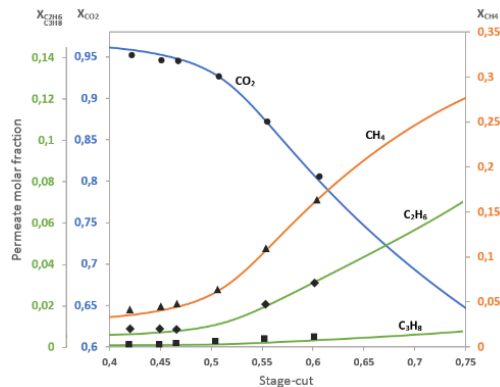


Figure 2. Validation of the module model with the experimental data of Pan et al. (1986).

The permeability of the various species have been validated against the experimental data provided by Pan et al. (1986) for stage cuts of the membrane comprised between 0.4 and 0.6. Figure 2 shows that the model fits well the experimental data, with maximum discrepancies in the permeate molar fractions limited to 1%.

5. Process simulation and optimization

The process flowsheet is solved using a sequential-modular approach with tearing. The optimal precedence ordering consists in calculating the units in this sequence: inlet gas mixer (0+6), first compressor, membrane stage A, second compressor, membrane stage B and stage C, valve and the mixer (5+2P). It is important to note that the system of DAE described in Section 4 is solved for each membrane module. The recycle stream 6 has been selected for tearing and the tear stream properties (i.e., molar flow rates of the gas species) is updated with the direct substitution. All the membrane stages operate at a constant temperature of 40 °C and any enthalpy change related to the Joule-Thomson effect or non-ideal mixing has been neglected with limited loss of accuracy, as suggested by the literature. Test cases have shown that convergence of the tear stream is reached in a few iterations (10-30, corresponding to 15-40 s of computational time) not justifying the adoption of more sophisticated algorithms (because the maximum eigenvalue of the Jacobian of the overall simulation function is in the range 0.2-0.3). After the process simulation has reached convergence, the total plant cost (overall capital expenditure) and the primary energy efficiency are computed considering literature data for the cost of the units (for the membranes we considered a lumped-cost of the equipment of 50 €/m²) and the performance of small size reciprocating compressors.

It is worth noting that the output of the process simulation (i.e., TPC and η_{PE}) are in general noisy and non-smooth due to the round-off errors and convergence tolerances of the algorithms which are called to solve the DAE and the process simulation. Moreover, the problem may feature multiple minima. For these reasons, gradient-based optimization algorithms are not suitable and it is necessary to adopt global-search, black-box algorithms. Recently, Capra et al. (2018) have proposed a model-based, derivative-free, algorithm which uses a local model of the black-box function so as to save computationally expensive evaluations. The algorithm is an extension of the MCS algorithm (Huyer & Neumaier 1999) to the multi-objective case. It allows for well-spaced Pareto fronts thanks to the integration of the Normalized Normal Constraint method (Messac et al. 2003). In MO-MCS the search for the Pareto optimal points is assigned to the available workers (cores) so as to reach the maximum possible parallelization of computations.

6. Results

The process optimization has been performed considering three different limits on the CH₄ slip (fraction of CH₄ which is lost to the process and goes together with the vented CO₂): no slip limit, 2% and 1%. The three Pareto fronts returned by MO-MCS are shown in Figure 3. The required computational time to obtain a Pareto front is 3 hours on a workstation with Intel® Core™ i7-3770 CPU @ 3.40 GHz and 4 cores. Their optimality have been double-checked repeating the optimization with different setup of MO-MCS and performing sensitivity analyses. The biomethane specification constraints are active for all Pareto-optimal points. Figure 3 indicates that setting a limit of 2% on the CH₄ slip does not penalize the achievable efficiency and it does not lead to a considerable increase of TPC. Instead, 1% CH₄ slip calls for 40% higher recycle flow rates causing an

appreciable increase of compressors costs and power consumption. For the case with slip $< 2\%$, the total membrane area is approximately 1500 m^2 for the maximum efficiency design and 950 m^2 for the minimum total plant cost. Another interesting result is that no Pareto-optimal solution employs the intermediate compressor (compressor 2).

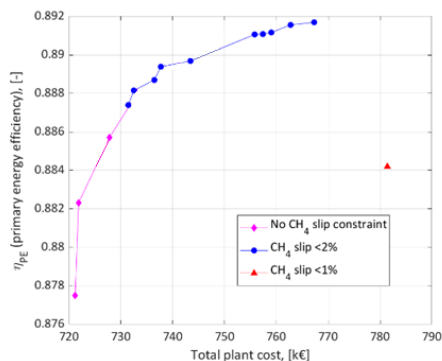


Figure 3. Pareto fronts returned by MO-MCS for three different limits of CH₄ slip.

7. Conclusions

The proposed 1-D model is suitable for multi-component gas mixtures and it can be efficiently adopted in sequential process simulation codes as well as derivative-free optimization algorithms, such as MO-MCS. The application to a biogas upgrading process with increasingly tight specifications has shown that the proposed approach is able to return very good approximations of the Pareto-front within a reasonable computational time. Optimization results indicate that the considered membrane process can achieve primary energy efficiency figures in the range 87.7%-89.2% with specific total plant costs ranging from 720-770 €/Nm³/h of feed).

Acknowledgements

Politecnico di Milano acknowledges the Social Energy project (CUP E59J18000000009) funded by Regione Lombardia, while LEAP is grateful to the Gobiom project (CUP E82F16001020007, funded by Regione Emilia Romagna) which has set the basis for the membrane model development.

References

- P. Gabrielli, M. Gazzani, M. Mazzotti, 2017, On the optimal design of membrane-based gas separation processes, *Journal of Membrane Science*, 526, 118–130
- M. Scholz, M. Alders, T. Lohaus, M. Wessling, 2015, Structural optimization of membrane-based biogas upgrading processes, *Journal of Membrane Science*, 474, 1–10
- C.Y. Pan, 1986, Gas separation by high-flux, asymmetric hollow-fiber membrane, *AIChE Journal*, 32(12), 2020–2027
- D. Havas, H. Lin, 2017, Optimal membranes for biogas upgrade by removing CO₂: High permeance or high selectivity?, *Separation Science and Technology*, 52(2), 186–196
- F. Capra, M. Gazzani, L. Joss, M. Mazzotti, E. Martelli, 2018, MO-MCS a Derivative-Free Algorithm for the Multiobjective Optimization of Adsorption Processes, *Industrial & Engineering Chemistry Research*, 57, 9977-9993

A Fuzzy Analytic Hierarchy Process (FAHP) Approach to Multi-Objective Optimisation of Oil Palm Value Chains

John Frederick Tapia, Sheila Samsatli*

Department of Chemical Engineering, University of Bath, Claverton Down, Bath, United Kingdom, BA2 7AY

**S.M.C.Samsatli@bath.ac.uk*

Abstract

The economic potential of palm oil and palm-based biomass can be realised through oil palm's very high vegetable oil yield and the wide variety of high-value products that can be derived from it. This potential can be maximised through streamlined oil palm value chains (OPVCs) which involve considering different environmental impacts alongside the economic benefits. Multi-objective optimisation aids in the development of a strong value chain by generating valuable planning insights based on the most appropriate set of impact weights. However, a typical approach in assigning impact weights is arbitrary or based on rough estimates. This study develops a decision framework to support planning and designing OPVCs. The decision framework is a novel approach of integrating a fuzzy analytic hierarchy process (FAHP) to the multi-objective optimisation of OPVCs. This enables descriptive judgments to be converted into numerical weights. An optimal design is then generated based on these weights. A case study based on Malaysian palm oil biomass scenario is presented to illustrate the decision tool. This could help develop better policies in the future through a systematic approach in dealing with sustainability issues in the palm oil industry.

Keywords: Value chain modelling, fuzzy analytic hierarchy process, palm oil biomass, environment-food-energy-water (EFEW) nexus.

1. Introduction

Palm oil is regarded as the world's main source of vegetable oil due to its excellent yield and low land requirement (Corley, 2003). The current status of vegetable oil industry is such that the replacement of palm oil is economically infeasible as alternative crops would likely require more land to produce the same yield as oil palm. However, several issues arise with palm oil plantations such as negative impacts of land use change, biodiversity losses and waste generation. In a typical palm oil mill, around four tons of waste materials are generated for every ton of palm oil produced. Bio-conversion technologies can transform these wastes into high-value products such as energy, fuels and other valuable products. To maximize the benefits from these transformations, a strong value chain is required. It is formed by a network of conversion technologies, logistical infrastructures and associated activities to convert low-value waste materials into high-value products (Jarvis and Samsatli, 2018). The development of a strong value chain requires rigorous planning and design considering the presence of multiple sustainability factors and the guidance of expert

recommendations. In this study, a systematic decision framework based on multi-objective optimisation and multi-criteria decision analysis (MCDA) approaches are developed to address these barriers in planning and design of oil palm value chains (OPVCs).

Recent PSE works on palm oil and palm-based systems presented methods to aid planning and designing systems such as integrated biorefineries and supply chains (Ng and Ng, 2013). Optimisation models on large-scale palm oil systems have been developed considering plantation management (Foong et al., 2019) and EFB valorisation (Abdulrazik et al., 2017). These models addressed specific problems focusing on maximising economic gains. None of the recent and relevant studies focused on large-scale palm oil systems addressed multi-objective and multi-criteria decision making simultaneously. Thus, in this paper a fuzzy analytic hierarchy process (FAHP) approach is integrated with a multi-objective mixed integer linear program (MOMILP) for OPVCs considering environmental and economic impacts weighted through expert judgement. Using FAHP to quantify verbal judgements as numerical weights has been demonstrated in a wide range of applications in sustainable technologies (Promentilla et al., 2018) and in multi-objective molecular design (Ooi et al., 2017). The rest of this paper is organised as follows. Section 2 gives a brief description of the decision framework and the models used are described in Section 3. Then, the framework is illustrated using the Malaysian palm oil industry case with results given in Section 4. Finally, conclusions and future works are given in Section 5.

2. Decision Framework

The FAHP approach to multi-objective optimisation of OPVCs is summarised in Figure 1. First, the optimal solution of the value chain based on the best economic potential, the minimum climate change impact and the minimum water impact are determined. This is to identify the factor to normalise the objectives when aggregated into a single objective. Then, the weights of each impact are obtained using FAHP approach based on four criteria, namely, short-term benefit, long-term benefit, policy development and social acceptance. Finally, an optimal solution based on the weights generated by FAHP is obtained.

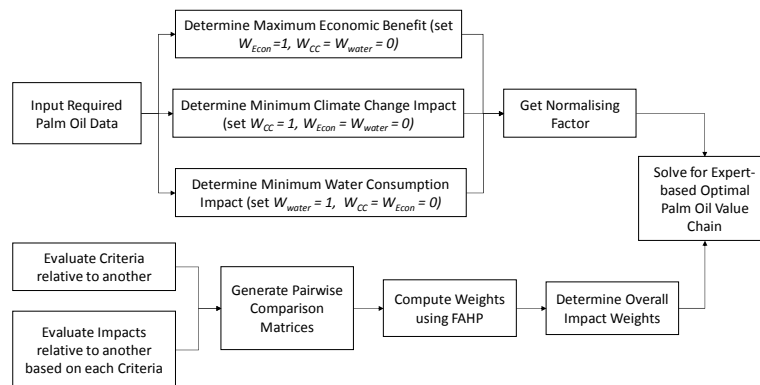


Figure 1: Decision framework for multi-objective optimization of OPVCs with FAHP. The weights of each impact objective are determined based on a decision structure with four criteria.

3. Optimisation Models

3.1. Multi-Objective Oil Palm Value Chains

The MOMILP model is summarized below with an aggregated objective function subject to the following key constraints:

$$\min \sum_{i,p} W_i (NF_i) (IU_{i,p} + FIP_{i,p}^{OM} + VIP_{i,p}^{OM} + IP_{i,p}^{Cap} + IT_{i,p}^{OM} + II_{i,p}^{OM}) \quad (1)$$

$$RU_{r,z,s,y,p} + RP_{r,z,s,y,p} + RT_{r,z,s,y,p} + RI_{r,z,s,y,p} \geq D_{r,z,s,y,p} (D_r^{\min}) \quad (2)$$

$$RU_{b,z,s,y,p} \leq AE_{b,z} YFE_p Y_{b,z,s,y} + Y_{b,z,s,y} \sum_{p'} YF_{p,p'} AI_{b,z,p'} \quad (3)$$

$$RP_{r,z,s,y,p} = \sum_c (PROD_{c,z,s,y,p})(CONV_{r,c,p}) \quad (4)$$

$$RT_{r,z,s,y,p} = \sum_{t,z'} TR_{t,r,z',z,s,y,p} - \sum_{t,z'} TR_{t,r,z',z,s,y,p} \quad (5)$$

Eq. (1) defines the weighted objective function, including impacts from utilization, production, transportation and import of resources. Eq. (2) ensures the satisfaction of demands by balancing net resource utilisation, production, transportation and import. The constraint on the available oil palm biomass (Eq. (3)) is based on the area available for plantation, the biomass yield and the expansion of land at each time period. Resources are produced through conversion technologies with rates and conversion factors given in Eq. (4). Finally, the net rate of transportation of resources is denoted by Eq. (5). For brevity, only these main constraints in the model are shown. More details on how the impacts are defined and the other constraints in the model can be found in related works (Samsatli and Samsatli, 2018; Samsatli et al., 2015).

3.2. Fuzzy Analytic Hierarchy Process (FAHP)

The outline of the procedure to determine the impact weights to be used for the multi-objective optimization model is as follows:

1. The decision structure is developed based on a hierarchical structure in which three impacts are evaluated using four criteria. For each criterion, the relative importance of each impact is determined by qualitative expert judgment. Qualitative judgements are given as either “equally”, “slightly more”, “moderately more”, “strongly more” or “very strongly more” important than the other with equivalent triangular fuzzy number (TFN) of <1, **1**, 1>, <1.2, **2**, 3.2>, <1.5, **3**, 5.6>, <3.0, **5**, 7.9> and <6.0, **8**, 9.5>, respectively. These judgments are based on a calibrated fuzzy scale derived from a survey with large number of respondents and applied in prioritisation of green technologies (Promentilla et al., 2018). Note that if an impact is less preferred than another, the reciprocal values are used.
2. The criteria set for the decision structure are then evaluated by pairwise comparison to obtain the relative importance of one criterion with respect to the others. The same fuzzy scales are used in this step.

3. The priority weights, w_i are calculated based on the nonlinear fuzzy preference programming model described by Promentilla et al. (2018). The model maximizes the degree of satisfaction λ with the given fuzzy triangular number $\langle l_{ij}, m_{ij}, u_{ij} \rangle$:

$$\max \lambda \quad (6)$$

$$a_{ij} - l_{ij} \geq \lambda(m_{ij} - l_{ij}) \quad a_{ji} - l_{ji} \geq \lambda(m_{ji} - l_{ji}) \quad \forall (i, j) | i < j \quad (7)$$

$$u_{ij} - a_{ij} \geq \lambda(u_{ij} - m_{ij}) \quad u_{ji} - a_{ji} \geq \lambda(u_{ji} - m_{ji}) \quad \forall (i, j) | i < j \quad (8)$$

$$a_{ij} = w_i / w_j \quad a_{ji} = w_j / w_i \quad \forall (i, j) | i < j \quad (9)$$

$$\sum_i w_i = 1 \quad (10)$$

4. The final impact weights, W_i to be used for multi-objective optimization of oil palm value chains is given using the weighted sum of the priority weights of each impact i for each criterion k , w_{ik} . The criteria are also assigned with weights denoted by s_k using step 2:

$$W_i = \sum_k s_k w_{ik} \quad \forall i \quad (6)$$

4. Malaysian Oil Palm Value Chain Case Study

A case study based on the Malaysian palm oil industry is used to illustrate the decision framework. It is supposed that it is necessary to convert palm-based biomass materials such as palm oil mill effluent (POME), palm kernel shell (PKS) and empty fruit bunch (EFB) and to develop the value chain for the Peninsular Malaysia for the next 32 years.

To illustrate the generation of impact weights, supposed that an expert provides judgement based on future directions needed for the industry. The weights generated from FAHP are summarised in Table 1. The importance given to environmental impacts (i.e. climate change and water impacts) is higher than the economic benefits that can be generated from the value chain. Using these weights, the optimal value chain is presented in Figure 2. In this case, pathways to consider for the conversion of EFB lead to the production of energy products such as gasoline, jet fuel and diesel. On the other hand, POME is treated to produce usable water and undergoes anaerobic digestion to produce biogas. Pathways for PKS lead to generation of electricity used both internally and externally.

Table 1: Impact Weights Generated from FAHP

	Short-Term Benefits (0.038)	Long-Term Benefits (0.361)	Policy Development (0.361)	Social Acceptance (0.241)	Total
Economic Benefits	0.500	0.059	0.333	0.450	0.269
Climate Change Impact	0.250	0.471	0.333	0.300	0.372
Water Impact	0.250	0.471	0.333	0.250	0.360

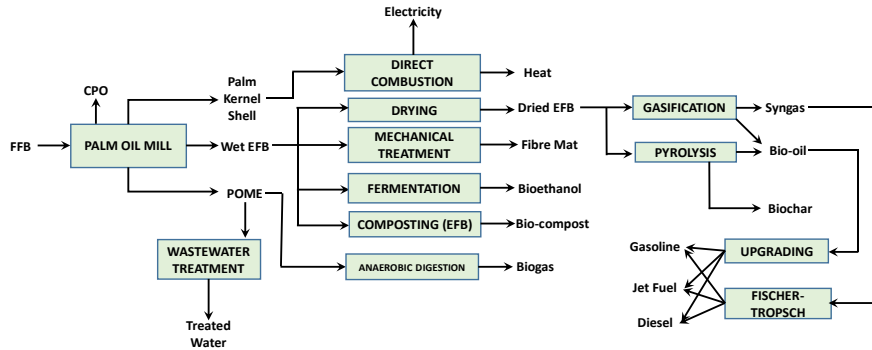


Figure 2: Optimal Value Web Pathways for Malaysian Palm Oil Industry

The resulting rate of production of palm oil per region, shares of energy distribution of palm-based biomass after conversion and the number of investments in units are shown in Figure 3. Three regions, namely Perak, Pahang and Johor contribute to the majority of the production having a total production of more than 3 MT of palm oil. Then, palm-based biomass materials are converted to different energy products, the majority of which is syngas. Biogas is also produced in the value chain to add value to palm oil mill effluent produced. The optimal solution also suggests investment in the beginning of the planning period and at the time period where most palm oil mills will retire. A summary of the results is shown in Table 2. The trade-offs between economic gains, climate change impact and water impact is balanced through expert judgment. Profit reduction of 8.93% is needed in order to achieve 31% less water impact and 11% less climate change impact if the expert judgment is to be incorporated as weights in the OPVC model. The contribution of FAHP in multi-objective planning of OPVC is that qualitative objectives are considered in the model. The decision framework can also provide scenarios for minimum climate change impact in which the highest attainable reduction up to 17% of the carbon footprint and 60% of the total water impact.

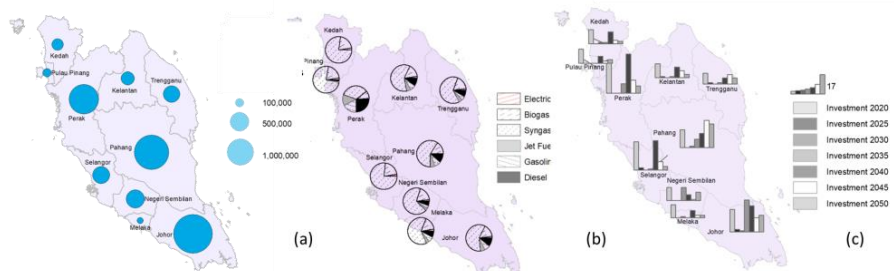


Figure 3: Results of the Malaysian case study: (a) palm oil production (t/y), (b) energy products from palm-based biomass and (c) conversion unit investment at each time period.

Table 2: Summary of scenarios for Malaysian oil palm value chain

Scenarios	Profit (billion MYR)	Climate Change Impact (Mt CO ₂ equivalent)	Water Impact (million m ³ utilised H ₂ O)
Maximum Profit	414	426	12,923
Minimum Climate Change Impact	369	353	12,086
Minimum Water Impact	324	422	5,337
Expert-based Solution	377	375	8,932

5. Conclusions

A fuzzy analytic hierarchy process (FAHP) approach has been applied to multi-objective optimisation to generate an expert-based optimal plan of oil palm value chains. These weights, converted from verbal judgment by using FAHP, are used to generate an expert-based oil palm value chain design. A balance between economic gains, climate change impact and water pollution impact is obtained. Future work includes extending the case to incorporate biodiversity losses due to land use change.

6. Acknowledgement

The authors would like to thank the Newton Fund and the Engineering and Physical Sciences Research Council for financial support of this work through the BEFEW project (Grant No. EP/P018165/1) and the Science & Technology Facilities Council (STFC) ODA Institutional Award.

References

- Abdulrazik, A., Elsholkami, A., Elkamel, A., & Simon, L., 2017, Multi-products productions from Malaysian oil palm empty fruit bunch (EFB): Analyzing economic potentials from the optimal biomass supply chain, *Journal of Cleaner Production*, 168, 131-148.
- Corley, R. H. V., & Tinker, P. B., 2003, The origin and development of oil palm industry, in *The Oil Palm*, 4th ed, Blackwell Science Ltd.
- Foong, S. Z. Y., Goh, C. K. M., Supramaniam, C. V., & Ng, D. K. S., 2019. Input–output optimisation model for sustainable oil palm plantation development, *Sustainable Production and Consumption*, 17, 31-46.
- Jarvis, S., & Samsatli, S., 2018, Technologies and infrastructures underpinning future CO₂ value chains: A comprehensive review and comparative analysis, *Renewable and Sustainable Energy Review*, 85, 46-68.
- Ooi, J., Promentilla, M. A. B., Tan, R. R., Ng, D. K. S., Chemmangattuvalappil, N., 2017, A fuzzy analytic hierarchy process approach for multi-objective molecular design problem. *Computer Aided Chemical Engineering*, 40, 967-972.
- Promentilla, M. A. B., Janairo, J. I. B., Yu, D. E. C., Pausta, C. M. J., Beltran, A. B., Huelgas-Orbecido, A. P., Tapia, J. F. D., Aviso, K. B., Tan, R. R., 2018, A stochastic fuzzy multi-criteria decision-making model for optimal selection of clean technologies, *Journal of Cleaner Production*, 183, 1289-1299.
- Samsatli, S., & Samsatli, N. J., 2018. A multi-objective MILP model for the design and operation of future integrated multi-vector energy networks capturing detailed spatio-temporal dependencies, *Applied Energy*, 220, 893-920.
- Samsatli, S., Samsatli, N. J., & Shah, N., 2015. BVCM: a comprehensive and flexible toolkit for whole-system biomass value chain analysis and optimisation - mathematical formulation, *Applied Energy*, 147, 131-160.

Numerical Simulation of Forced Convection in a Microchannel with Realistic Roughness of 3D Printed Surface

Seyed Alborz Manavi^a, Eugeny Y. Kenig^{a,b,*}

^a*Chair of Fluid Process Engineering, Faculty of Mechanical Engineering, Paderborn University, Paderborn 33098, Germany*

^b*Gubkin Russian State University of Oil and Gas, Moscow, Russian Federation.*
eugeny.kenig@upb.de (E.Y. Kenig)

Abstract

This study aims at exploring the thermo-hydraulic performance of 3D printed micro heat exchangers. We performed CFD simulations of single-phase laminar fluid flow and heat transfer in a microchannel with rough surface and compared the results with those obtained in a smooth channel. The model was based on the Navier-Stokes and energy equation. These equations were implemented and solved in the STAR-CCM+ commercial software. The Reynolds number was varied in the range 100-500, while two values of Pr number, 0.71 and 6.0, were chosen. The height of the channel varied between 0.2 and 0.5 mm. The micro-geometry of the surface roughness representing a completely random configuration was reproduced by a 3D scanner. Our results demonstrate that decreasing channel height leads to rising heat transfer rate and pressure drop. At the height of 0.2 mm, a significant rise in pressure drop is evidenced, which indicates a critical height limit for designing such microchannels.

Keywords: 3D printing, Heat transfer, stochastic roughness, 3D scanner, microchannel

1. Introduction

The demand for enhancement of heat exchanger performance is ever increasing (Haarlemmer and Pigourier, 2016). Such enhancement is challenging when manufacturing constrains become a significant factor, especially for micro and mini heat exchangers. Additive manufacturing (3D printing), an innovative type of fabrication, offers enormous design freedom and great potential to outperform conventional methods of manufacturing. Consequently, this technology has been exploited by various industries, such as aerospace, automotive, medical and fluid process engineering, in particular regarding microfluidic devices (Femmer et al., 2016). Moreover, 3D printed objects are characterized by a certain surface roughness resulting from the fabrication process; such rough surface can be used as a passive method to increase the efficiency of heat exchangers. This beneficial combination of both variability and inherent roughness justifies a new study route toward improving heat exchangers performance.

It is worth noting that at the moment, 3D printed micro heat exchangers are still in an early development stage. This is the reason why just a limited number of publications on this topic can be found in the open literature. Few recent works are focused on the

Nomenclature						
$Re = \frac{\rho V_m D_h}{\mu}$	Reynolds number		V_m (m/s)	Mean velocity	μ (Pa/s)	Dynamic viscosity
$Nu_{ave} = \frac{h_m D_h}{k}$	Average number	Nusselt	D_h (m)	Hydraulic diameter	T_b (K)	Bulk temperature
\dot{q} (W/m ²)	Heat flux normal to the surface		ρ (Kg/m ³)	Density	T_s (K)	Surface temperature
k (W/(mK))	Thermal conductivity		$h_m = \frac{q_m}{T_s - T_b}$ (W/(m ² K))			Mean heat transfer coefficient

design flexibility aspect of 3D printing allowing manufacturing of uniquely formed micro heat exchangers. For example, Arie et al. (2017) conducted an experimental and a numerical study which mainly aimed to compare the performance of a manifold microchannel with heat exchangers with conventional surfaces. Air-water manifold finned microchannels (with a manifold as a flow distributor positioned above the microchannels) were fabricated using one of the additive manufacturing methods, namely, direct metal laser sintering (DMLS). Thanks to the ability to build objects layer-by-layer, the authors could fabricate manifold and microchannel segments together as one united construction and eliminated the bonding process.

Ferster et al. (2017) performed an experimental study on the microchannel pin fin arrays fabricated by DMLS. Various geometries of pin fins, such as star-formed, triangular and dimpled sphere, with different spacing and number of pin fins, were built and their influence on the friction factor and heat transfer was analysed. One work, which considered the effect of the inherent surface roughness due to 3D printing on the performance of a heat exchanger has been recently published by Saltzman et al. (2018). They replicated a crossflow heat exchanger with 20×9.25×11.5 cm dimensions using laser-based powder bed fusion process. The additively manufactured heat exchanger was characterised by a lower weight and significantly rougher surfaces. The authors reported that the additively manufactured heat exchanger showed around 10% improvement in the overall heat transfer, whereas the pressure drop was doubled.

The necessity of surface roughness modelling in microchannels originates from its great potential to improve the micro heat exchanger efficiency, which is still an open problem. Moreover, experimental studies on such a small scale are characterized by measurement uncertainties which represent an interfering factor for the experiments beside surface roughness. Numerous studies contributed to the modelling of surface roughness in microchannels by setting different geometries, e.g. regular configurations, such as wavy sinusoidal one (Wang and Chen, 2002), triangular, square and irregular or random geometries (Guo et al., 2015). In the latter work, the authors used random functions like the Gauss function and the Fractal model to create random roughness.

In this study, we created the roughness geometry of a printed surface by a 3D scanner. This geometry is very close to the reality and thus it can be called realistic roughness. For this realistic roughness, we performed a fundamental numerical investigation of forced convection laminar flow in a microchannel. The results are presented for a variety of channel heights and Reynolds numbers, thus yielding valuable data on pressure drop and heat transfer characteristics in a 3D printed micro heat exchanger.

2. Physical model

The initially studied geometry was a 3D printed flat plate (Figure 1a). The scanning results yield the mean roughness depth equal to $85\ \mu\text{m}$. This geometry was then

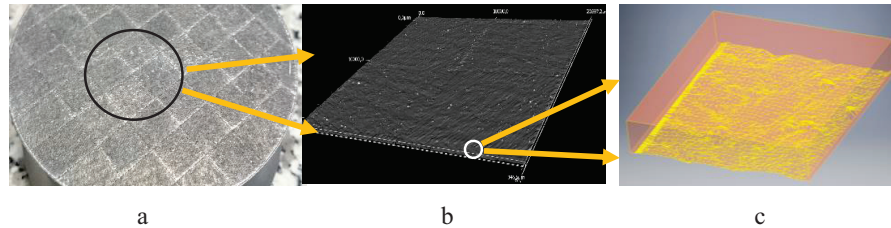


Figure 1. The steps of creating the geometry of stochastic roughness of 3D printed flat plate for CFD simulation: examined sample from 3D printing (a); scanning result of the selected area (b); prepared geometry for CFD study (c)

exported in CAD format (Figure 1b) which is readable by a corresponding software tool (Autodesk Inventor). The obtained surface geometry is represented by very small surfaces, which form the detailed roughness structure. To reduce computational effort, a small part of the surface was selected to perform the simulations (Figure 1c). The next step was to form the geometry of the CFD computational domain. This was done by adding side walls and an upper cover to the element. This configuration shown in Figure 1c was used for the CFD simulations.

3. CFD-based modelling

Three-dimensional fully developed steady-state laminar flow with constant physical properties in a microchannel with rough surface was studied. Finite volume approach implemented in STAR-CCM+ was applied in order to simulate the fluid flow and heat transfer in the duct. Periodic boundary condition was set at the inlet and outlet boundaries of the channel. In this way, the velocity profile is repeated after the channel length, so that after reaching convergence the whole periodic domain represents a hydraulically developed region. Thermally fully developed flow is characterized by a constant heat transfer coefficient. In STAR-CCM+, the temperature profile at the outlet is scaled and then used as the inlet profile, in such a way that the heat transfer coefficient remains constant for the whole domain. The bottom (rough) wall was maintained at a constant temperature, and the other walls were assumed to be adiabatic. No-slip boundary condition was assumed at all the walls. Figure 2 shows the geometry of the investigated microchannel element.

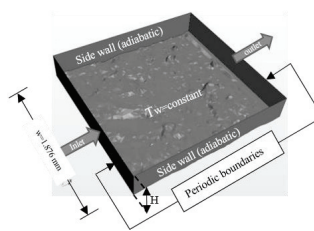


Figure 2. Periodic computational domain of microchannel and boundary conditions

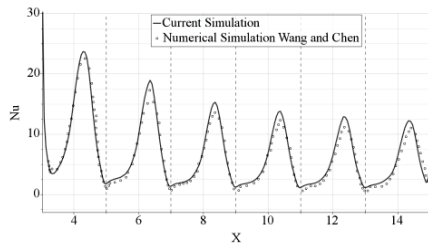


Figure 3. Local Nusselt number along the length of wavy channel

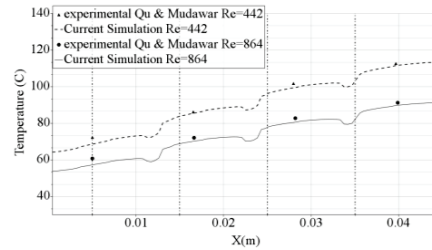


Figure 4. Wall temperature along the channel length obtained from our simulations and empirical data from Qu and Mudawar (2002)

A direct validation of the simulation results was not possible because of missing data on such geometry. Therefore, we selected and modelled two other configurations from the literature sufficiently close to the studied original geometry. The numerical simulation of fluid flow in a wavy duct reported by Wang and Chen (2002) at $Re=300$ and $Pr=6.93$ was replicated. In their work, the geometry of wavy wall was considered as a kind of roughness. Further model validation was carried out using the heat transfer experiment in a microchannel conducted by Qu and Mudawar (2002). The wall temperature was estimated along the channel length and compared with that obtained from Qu and Mudawar (2002) at $Re = 442$ and $Re = 864$. The validation results are shown in Figures 3 and 4. In both cases, a good agreement between the numerical and experimental data was achieved.

The primary mesh independency test was performed with respect to the heat transfer parameter (average Nusselt number). As can be seen from Table 1, the relative difference between the two finest grids are less than 1%. Additionally, a study of the velocity profile (Figure 5) along the channel height revealed that the grid setting with 3,322,691 cells is sufficient for the whole simulation studies, yielding a reasonable compromise between computational time and accuracy.

Table 1. Mesh independency results for Nu_{ave}

Number of cells	Nu_{ave}
1,502,520	5.051
3,322,691	5.040
7,877,453	5.037

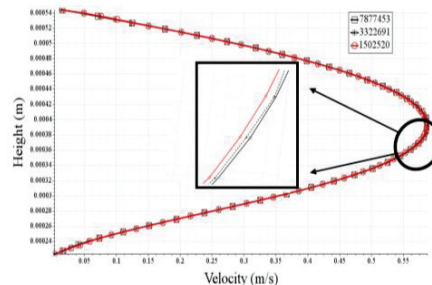


Figure 5. Velocity profile along the height of the channel

The effect of channel height on the pressure drop and average Nusselt number for various Re values between 100 to 500 and $Pr = 6$ are presented in Figures 6 and 7. As the channel height decreases, both Nusselt number and pressure drop increase. However, pressure drop change between 0.3 and 0.2 mm is much more intensive than the corresponding Nusselt number change, while this is true for all studied flow rates.

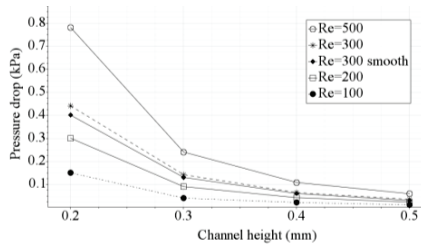


Figure 6. Pressure drop in rough channel versus channel height for $Pr=6$

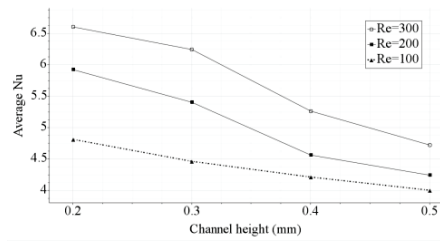


Figure 7. Average Nusselt number in rough channel versus channel height for $Pr=6$

Figure 7 demonstrates that the effect of the channel height on pressure drop is much more significant than the effect of surface roughness. For instance, for $Re=300$ and $H=0.3\text{mm}$, the roughness results in just 10% increase, whereas the channel height variation causes substantially larger changes.

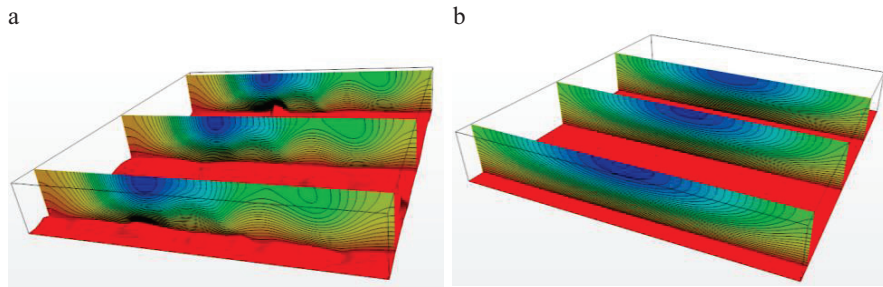


Figure 8. Isothermal line distribution in a rough (a) and a smooth (b) channel at $Re=200$ and $H=0.3\text{ mm}$

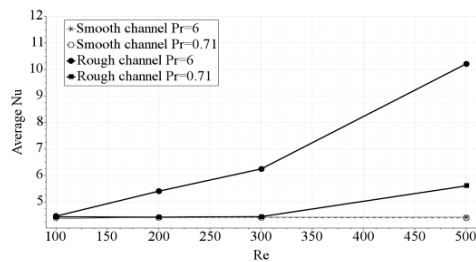


Figure 9. Nusselt number in a rough and a smooth channel as function of Reynolds number at $H=0.3\text{ mm}$

Figure 8 depicts the effect of stochastic surface roughness on the isothermal lines in a smooth and rough channel for $Pr=6$. They are shown in three different cross-sections normal to the flow direction. The isothermal lines in a smooth channel (Figure 8b) reveal regular structure throughout the whole channel. By contrast, in the channel with rough surface (Figure 8a), the stochastic geometry of the roughness perturbs the regular fluid behaviour leading to irregular configuration of isothermal lines. As the result, the interactions between hotter and colder layers become more intensive, which facilitates heat transfer. Another impact of the random roughness on the fluid flow can be seen in a shift of the cold fluid core position away from the top wall centreline visible in Figure 8a,

unlike in the smooth channel, in which it is placed in the centreline of top wall with a symmetric configuration.

The influence of surface roughness on the average Nusselt number is illustrated in Figure 9 for two Prandtl numbers. As expected, for smooth channels, the average Nusselt number remains nearly constant for both Prandtl numbers. For a rough channel at $Pr = 6$, the average Nusselt number increases with increasing Reynolds number. For the fluid with Prandtl number below one, the Nusselt number dependence on Reynolds number is less pronounced, especially for small Reynolds numbers. However, starting from a certain Reynolds number value, the effect of surface roughness on the heat transfer rate becomes significant.

4. Conclusions

The CFD-based study of fluid flow and heat transfer in a microchannel with realistic roughness of 3D printed surface was carried out. The 3D scanner was used to create the geometry of the roughness on microscale. The simulations of a fully developed laminar flow were performed for smooth and rough channels with a height varying between 0.2 and 0.5 mm. Random roughness results in an increase of both the average Nusselt number and pressure drop, while for the smallest studied channel height, the largest pressure drop and the highest average Nusselt number are found. This helps to estimate the critical channel height value, 0.2 mm, for the heat exchanger design. The use of 3D printing in manufacturing of micro heat exchangers offers design flexibility along with the possibility to reach a high thermal performance due to the surface roughness.

Acknowledgement

The authors gratefully acknowledge the technical support of the Direct Manufacturing Research Center (DMRC) at Paderborn University. Calculations were performed with resources provided by the Paderborn Center for Parallel Computing.

References

- M. A. Arie, A.H. Shoostari, V.V. Rao, S.V. Dessiatoun, M.M. Ohadi, 2017, Air-side heat transfer enhancement utilizing design optimization and an additive manufacturing technique. *Journal of Heat Transfer*. ASME, 139, 3, 031901-1.
- T. Femmer, I. Flack, M. Wessling, 2016, Additive manufacturing in fluid process engineering, *Chemie Ingenieur Technik*, 88, 5, 535-55.
- K.K. Ferster, K.L. Kirsch, K.A. Thole, 2017, Effects of geometry, spacing, and number of pin fins in additively manufactured microchannel pin fin arrays. *Journal of Turbomachinery*, ASME, 140, 011007-1.
- L. Guo, H. Xu, L. Gong, 2015, Influence of wall roughness models on fluid flow and heat transfer in microchannels, *Applied Thermal Engineering* 84 ,399-408.
- G.W. Haarlemmer, J. Pigourier, 2008, Towards a new generation heat exchanger models, *Computer Aided Chemical Engineering*, 25, 763-768.
- W. Qu, I. Mudawar, 2002, Experimental and numerical study of pressure drop and heat transfer in a single-phase micro-channel heat sink, *International Journal of Heat and Mass Transfer* 45, 2549–2565.
- D. Saltzman, M. Bichnevicius, S. Lynch, T.W. Simpson, E.W. Reutzel, C. Dickman, R. Martukanitz, 2018, Design and evaluation of an additively manufactured aircraft heat exchanger. *Applied Thermal Engineering*, 138, 254–263.
- C.C. Wang, C.K. Chen, 2002, Forced convection in a wavy-wall channel, *International Journal of Heat and Mass Transfer* 45 ,2587–2595.

Morris screening for FMECA of valve failure modes on offshore gas reinjection

Emil Krabbe Nielsen^{a,b}, Jérôme Frutiger^b and Gürkan Sin^{b,*}

^a*Department of Electrical Engineering, Technical University of Denmark, Elektrovej 326, Kgs. Lyngby 2800, Denmark*

^b*Department of Chemical Engineering, Technical University of Denmark, Søtofts Plads 227, Kgs. Lyngby 2800, Denmark*
ekrani@elektro.dtu.dk

Abstract

FMECA is commonly used as a tool for assessing the consequences of different failure modes of a component and the criticality of the consequences. Traditionally failure modes are generated using a one-factor-at-a-time method. In this study, we propose extensions to the FMECA procedure in which failure modes are sampled using statistical sampling techniques, and their effects are evaluated under a wide range of operating conditions. Morris's efficient sampling technique is used for generating failure mode effect analysis scenarios. The scenarios are evaluated in a K-Spice simulator with a model of an offshore gas reinjection system in the Danish North Sea. The impact of the failure modes on the process performance and process safety is evaluated under varying process conditions. The extended methodology enables fast screening of the effects of the failure mode under different realistic process conditions. This provides a more comprehensive and global assessment of the consequences for process safety and reliability in the chemical industry.

Keywords: Failure Mode Effect and Criticality Analysis, Morris screening, Gas reinjection

1. Introduction

For safety-critical systems, tools like Failure Mode, Effects and Criticality Analysis (FMECA), and Hazard and Operability Study (HAZOP) are important in reliability analysis as well as Quantitative Risk Assessment (QRA) studies to ensure an inherently safe design and safe operation of the system. For modern chemical process plants, a model is a requirement in the design phase. This model should be exploited, not just to ensure mass, energy and momentum balances of the system, and to optimize productivity, but also to ensure the safety of the system. In a previous study Enemark-Rasmussen et al. (2012), simulations are performed according to a single defined operational setpoint to evaluate failure modes. However as the economical experimental designs proposed by Morris (1991) are available and computational power increases, such evaluations should be carried out by rigorously investigating the influence of failure modes under a range of potential variation of the process conditions.

In this work we propose a quantitative approach to analyse the effects of failure modes of a control valve under a range of process conditions. Four failure modes of control valves on offshore oil and gas platforms have been identified, which will be simulated under varying process conditions. The method is more time consuming and computationally expensive than conventional approaches, especially as the number of process conditions, components and failure modes increases with system complexity. To avoid an excessively time consuming method, the process conditions, and

the failure modes are sampled by using a random and economically efficient sampling method: Morris screening. Morris screening is a discrete sampling method, and allows for evaluation of different and completely unrelated failure modes in one study.

2. Process system

The approach is applied to an offshore gas reinjection system of Mærsk, that has been modelled in K-Spice based on design and operation data in Enemark-Rasmussen et al. (2012). The purpose of the gas reinjection system is to maintain the well pressure for enhanced oil recovery. The feed of gas from upstream is controlled by a control valve. In the reinjection system the gas is first cooled by a heat exchanger, supplied with sea water. The cooling rate is controlled by a control valve, at the outlet of the heat exchanger. Next, the gas enters the scrubber to avoid vapour in the gas being reinjected to the well. Production of liquids from the scrubber is undesired, however a control valve releases the liquid to a flare, if the level becomes too high. A compressor sucks the gas from the scrubber, after which the gas is either reinjected to the wells or recycled. The gas is recycled to avoid the compressor from surging. Surging is undesirable, however so is recycling the gas as it limits the productivity. An anti-surge controller controls the setpoint of four control valves, one for the gas feed, two for the gas recycling and one for the gas reinjection, to ensure a steady flow through the compressor. The system is modelled in K-Spice as shown in Figure 1. K-Spice, a dynamic process simulator for the oil and gas industry, is used for process design and engineering verification. It features parameterised process models for oil and gas processing.

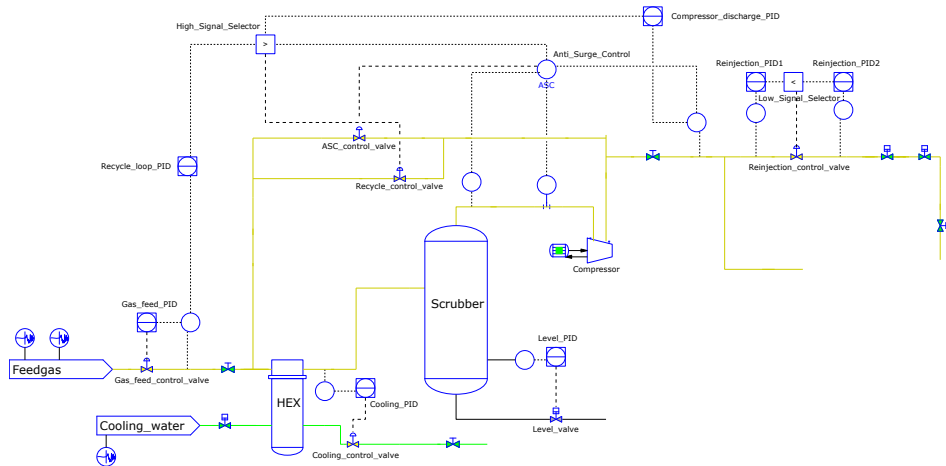


Figure 1: Offshore gas reinjection system.

Various different failure modes have previously been simulated in K-spice for this system by Enemark-Rasmussen et al. (2012). However common for all simulations was the use of only a single set of process conditions according to the design specifications. The process conditions before and after introducing the failure mode was used to calculate the sensitivity of the process to assess the criticality of each failure mode using a one-factor-at-a-time approach. In this study, we use a global sampling based approach to assess the criticality of the consequences, and focus the study on four failure modes of one control valve evaluated under a range of process conditions.

The effort to document the occurrence of failure modes for valves, pumps etc. is extensive in the oil and gas industry, however the level of detail on reported failure modes is very sparse (Management, 2002; Peters and Sharma, 2003). In this study, the valve opening P , and the valve opening and

closing time t_{open} and t_{close} are used for implementing four different failure modes for the gas feed control valve. When implementing the failure mode, the manipulated parameter is fixed for the remaining simulation from t_{fm} to t_{end} . Apart from the failure modes, the sampled initial process conditions are the temperature T_{gas} and the pressure P_{gas} of the feed gas, and additionally the feed temperature T_{cool} of the sea water used for cooling.

The values of the sampled initial conditions is determined by a discrete cumulative distribution function (CDF). The variation in percentage for the conditions are as follows: $T_{gas} = 5\%$, $P_{gas} = 4\%$ and $T_{cool} = 4\%$. As described by Sin et al. (2009), it can be used to determine the minimum and maximum values of a uniform distribution discretized into $p = 4$ levels, around a mean or nominal value of operation. The nominal operation is defined here as: $T_{gas} = 44.5^\circ\text{C}$, $P_{gas} = 121$ bar and $T_{cool} = 30^\circ\text{C}$. Gaussian noise is added to the process conditions as measurement noise and varies during the simulation. The standard deviation σ_{noise} in Table 3 defines the normal distribution of the noise, around the values sampled by Morris screening for θ_{1i} , θ_{2i} and θ_{3i} as mean. The noise is randomly sampled and added by K-Spice as part of the simulation.

3. Procedure

First a set of k process conditions including the failure mode is sampled as the input $\theta_i = [\theta_{1i}, \theta_{2i} \dots \theta_{ki}]$ for the simulation for $i = 1, 2 \dots n$ simulations. The n number of sampled sets are then simulated in K-Spice. All simulations start with a sampled set of initial process conditions θ_{1i} , θ_{2i} and θ_{3i} at time $t_{start} = 0$ s. These conditions are used throughout the entire simulation. To allow the system to stabilize under the set of process conditions specified by the sampling, the simulation is run for 1200 seconds. At time $t_{fm} = 1200$ s the failure mode (FM) θ_4 is introduced. Next, the simulation is run for 7200 seconds until $t_{end} = 8400$ s after which the simulation is stopped, and the simulation output for every simulation $Y_{ij} = [y_{1ij}, y_{2ij} \dots y_{mij}]$ for $j = [10, 20 \dots t_{end}]$ is recorded by sampling every ten seconds. Here, j denotes a point in the time series of the m th output signal from the i th simulation. The steps, inputs and outputs of the procedure is shown in Table 3.

#	Step	Input	Output
1	Morris screening	$r=40, k=4, p=4, \Delta = 2/3$, CDF	θ_i
2	Load initial conditions in simulation i	$\theta_{1i}, \theta_{2i}, \theta_{3i}$	
3	Run simulation i until $t_{fm} = 1200$ s	$\sigma_{Noise} = [5, 2.5, 2.5]$	
4	Introduce failure mode	θ_4	
5	Run simulation i until $t_{end} = 8400$ s		Y_{ij}
6	Sensitivity analysis	θ_i, Y_{ij}	EE_i

Table 1: Procedure for sampling, simulating and analysing.

4. Experiment and sample design

Morris screening is a global sensitivity analysis method that employs a one-factor-at-a-time (OAT) approach for producing experimental designs. OAT analysis is performed for a number of randomly sampled nominal values in the design space. The analysis is based on the mean and standard deviation of the elementary effects, EE_i for the input i to determine how sensitive the outputs are to changes in the inputs $i = 1, 2, \dots$. For these experiments $k = 4$ input parameters are sampled at $p = 4$ levels. Typically, the number of repetitions needed for Morris screening is in the range of $r = [10, 50]$ (Sin et al., 2009), and based on the required number of elementary effects F_i to be calculated. For this study $r = 40$ is used, however only five elementary effects are shown. Based on this, the number of samples are $n = r(k + 1) = 40(4 + 1) = 200$ Sin et al. (2009). The elementary effects are calculated based on changes to the inputs, defined by the step size $\Delta = p/[2(p - 1)] = 4/[2(4 - 1)] = 2/3$ for a uniform distribution of the sampling space. These

steps are used for performing local sensitivity analysis, however when averaging the mean of the elementary effects, the method can be used in a global context. The sampled probabilities in unit hyperspace $[0, 1]$ have been converted to real values by using their inverse discrete and cumulative probability distribution function. The values of the resulting four levels are shown in table 4.

Level	T_{gas} (θ_1)	P_{gas} (θ_2)	T_{cool} (θ_3)	Failure mode (FM) (θ_4)
1	28.6 °C	116.2 bar	17.9 °C	Valve seized at current position P
2	39.2 °C	119.4 bar	26.0 °C	Valve fail open at $P = 1\%$
3	49.8 °C	122.6 bar	34.0 °C	Valve fail close at $P = 99\%$
4	60.4 °C	125.8 bar	42.1 °C	Stiction $3t_{close}$ & $3t_{open}$

Table 2: Design space.

5. Results

For each simulation i , the output Y_{ij} is a time series with j samples in time, corresponding to the sampled input θ_i . A selection of the process signals from the simulations are shown in Figure 2. The average of all 200 samples for each time step j is plotted for each output, along with a lower and upper safety limit. The limits are an average of the 200 process signals for each output from time t_{start} to t_{fm} , multiplied by $\pm 25\%$. In general the control system is capable of maintaining the temperature close to nominal operating conditions as can be seen on plot 1-5 in Figure 2. However, under some conditions, the temperature exceeds the upper limit at the gas outlet, and in the recycle loop. The plots 6-9 shows a stable pressure under the majority of process conditions, although it drops below the lower limit to nearly 0 bar under some conditions. This does however not pose a safety risk. Plot 10 shows that the amount of recycled gas varies a lot between 0 and 200 kg/h, and under some specific conditions the recycled amount approaches 300 kg/h. In general the productivity is stable, but it drops close to 0 kg/h under some conditions. The surge rate, defined as $\frac{\int \text{Time surging } dt [s]}{\text{Time [s]}}$, varies a lot initially, as expected, and in time splits up into four distinct bands, for which two of them increases over time, one remains constant and one decreases over time.

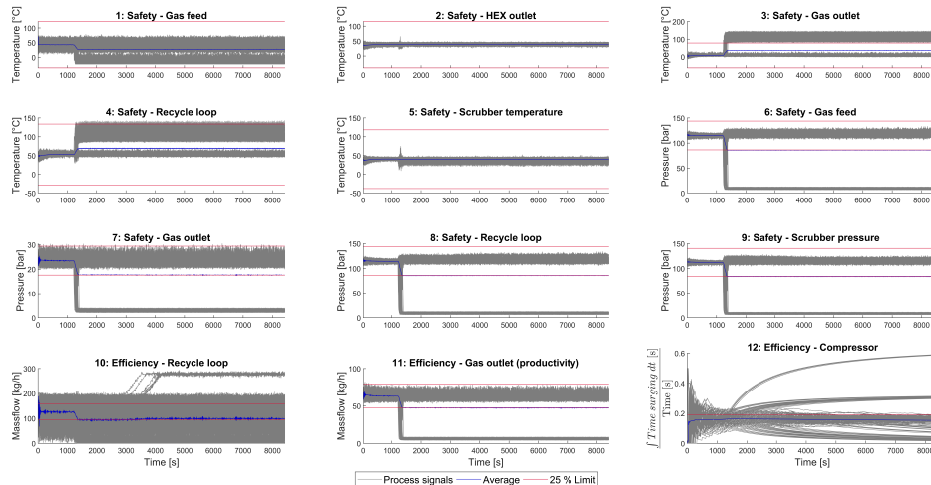


Figure 2: A selection of process signals for output Y_{ij} from the $n = 200$ samples.

The plots in Figure 3 of each output as a function of each input shows that failure mode two is the sole cause of the high temperatures for the gas outlet and recycle loop, independent of the process conditions. The plot also shows, that failure mode two is the sole reason for the pressure drop in the gas reinjection system, as only very little new gas is supplied. On the contrary, failure mode four consistently produces high pressure with almost no variation. The amount of recycled gas drops close to 0 kg/h for failure mode two as only a small amount of gas is supplied to the system. Failure mode three causes the high amount of recycled gas for a gas feed pressure of 125.8 bar. As previously mentioned, the productivity is stable, which is true for all process conditions, except those including failure mode two. Failure mode two results in three bands of surging, resulting in both the lowest and highest amount of time surged in total. The plots do however not show any unique set of conditions producing these bands. The variation in the amount of time surged is very low for both failure mode one and four as opposed to two and three.

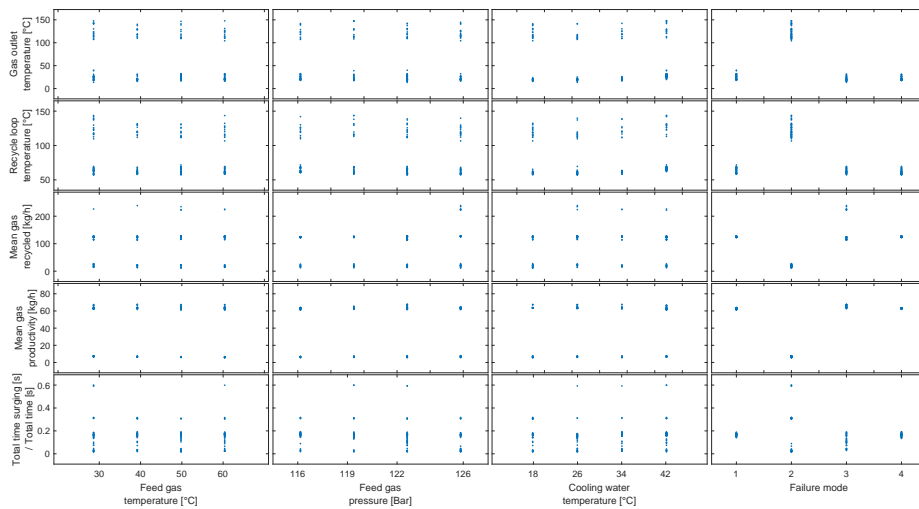


Figure 3: Matrix plot of model output Y_i as a function of model input θ_i .

The most significant elementary effect has the highest average, and a high standard deviation is an indication of interactions or non-linearity (Morris, 1991). The elementary effects for some of the critical outputs are shown in Figure 4. The wedge in the figure can be used as an indication of significance, and is calculated as the mean of samples of the elementary effects: $\hat{d}_i = \pm 2SEM_i$. The standard error of mean, SEM_i is calculated as the variance S_i of the elementary effects of input sample i divided by the square root of repetitions r : $SEM_i = \frac{S_i}{\sqrt{r}}$. If an elementary effect is outside of the wedge it is considered significant, and insignificant if inside (Morris, 1991).

A change in failure mode can be considered as the most influential input parameter on the gas outlet temperature, recycle loop temperature, amount of gas recycled and the gas productivity, but shows no significance on the amount of time surged. This result for the total surge rate contradicts the observations from Figure 3. The values in Figure 4 are averaged elementary effects based on all changes to the respective input parameter. This can lead to ambiguous results and for this reason these results cannot be interpreted alone. The gas feed pressure change should also be considered significant for the increase in gas outlet temperature, and a change in temperature of the cooling feed is significant for an increase in temperature in the recycle loop. The mean of the total surge rate shown in Fig. 4 indicates no significant inputs, as the standard error of the mean SEM_i is quite large due to the high variance S_i of elementary effects. The estimated mean μ^* of the distribution of absolute values of the elementary effects is however useful for Type II errors when the variance

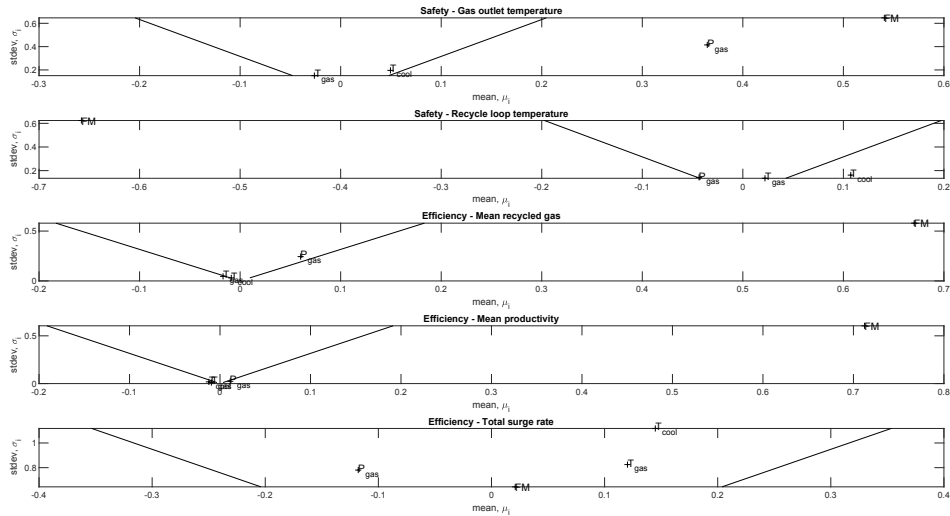


Figure 4: Elementary effects of outputs.

is both negative and positive (Campolongo et al., 2007). It reveals that the failure mode is the most significant parameter for the variation of the surge rate as $\mu^* = 5.70$ for FM, $\mu^* = 5.51$ for T_{cool} , $\mu^* = 4.02$ for T_{gas} and $\mu^* = 3.98$ for P_{gas} .

In general, the standard deviation of the elementary effects of the failure mode is quite large for all outputs except for the surge rate. However as this input parameter is not continuous, but merely four completely different parameters in itself, a high standard deviation is expected and should thus be either interpreted with caution or disregarded.

6. Conclusion

Morris screening has been used for analysing failure modes of a valve under varying process conditions in simulations of an offshore gas reinjection system. The analysis showed that only the temperature at the gas outlet and in the recycle loop could compromise the safety, caused by the gas feed valve closing. In general the results showed that within the studied range of variation the process conditions are insignificant, and that the effect of the failure modes is independent of the process conditions. The efficiency of the plant was also examined, and in general the productivity was stable, except for when the valve closes, and the gas feed is shut off. Additionally, the closed valve impacts the amount of time which the compressor surged both negatively and positively. In case of an open valve, the recycling rates increased, but only under high pressure.

References

- F. Campolongo, J. Cariboni, A. Saltelli, 2007. An effective screening design for sensitivity analysis of large models. *Environmental modelling & software* 22 (10), 1509–1518.
- R. Enemark-Rasmussen, D. Cameron, P. B. Angelo, G. Sin, 2012. A simulation based engineering method to support hazop studies. In: *Computer aided chemical engineering*. Vol. 31. Elsevier, pp. 1271–1275.
- S. I. Management, 2002. OREDA: Offshore Reliability Data Handbook, 4th Edition. OREDA Participants.
- M. D. Morris, 1991. Factorial sampling plans for preliminary computational experiments. *Technometrics* 33 (2), 161–174.
- J. Peters, R. Sharma, 2003. Assessment of valve failures in the offshore oil & gas sector. Health and Safety Executive.
- G. Sin, K. V. Gernaey, A. E. Lantz, 2009. Good modeling practice for pat applications: Propagation of input uncertainty and sensitivity analysis. *Biotechnology progress* 25 (4), 1043–1053.

Optimization of a large-scale biorefinery problem by decomposition

Varun Punnathanam^a and Yogendra Shastri^{a,*}

^a*Indian Institute of Technology Bombay, India*
yshastri@che.iitb.ac.in

Abstract

The biorefinery system based on agricultural residue primarily consists of feedstock procurement and processing which need to be taken into consideration together in order to obtain a globally optimal design. This generally results in large-scale mixed integer linear programming (MILP) models that scale rapidly based on the number of technology and location options, resulting in highly complex and challenging optimization problems. This work considers a case study based on setting up a biorefinery system for the state of Maharashtra (India), and employs the Dantzig-Wolfe decomposition based approach to solve this problem. An approximation strategy is proposed to handle the binary variables of the problem. Our approach results in up to 92% reduction in computational time, and leads to a near linear increase in computational time as a function of the problem size. The proposed approach may be used to solve other large-scale optimization problems with a similar structure of various fields.

Keywords: Large-scale optimization, biorefinery, Dantzig-Wolfe decomposition

1. Introduction

A biorefinery is a plant which converts biomass into biofuels as well as other products. In the Indian context, biorefineries must largely rely on a variety of agricultural residues which can have varying compositions. Additionally, their availability is distributed and seasonal, due to which it may be required to collect them from large distances. The biorefinery problem primarily involves two aspects. Process synthesis is a large part of the problem, where the designer develops pathways to interconnect specific raw materials to products of interest. While there might be a myriad of possible pathways (Gong et al., 2016), the designer is required to identify a pathway which would optimize a specific objective, such as maximizing the profit generated by the industry. The selection of a process synthesis pathway is coupled with the design of an optimal supply chain network (Sun et al., 2018), which forms another significant part of the problem. As the raw materials can be procured from multiple sources, the selection of the raw material source as well as the quantity of raw material to be procured from individual sources can greatly impact the economics of the plant. In addition, there can be multiple potential locations for setting up one or more biorefineries. The biorefinery problem is generally formulated as a mixed integer linear programming (MILP) problem, and can potentially be very large in size, consisting of well over a hundred thousand variables and constraints.

In this work, we considered a biorefinery model described in literature (Vikash and Shastri, 2017) which incorporates a single fixed biorefinery and accounts for both feedstock procurement as well as processing. We have extended this model to consider the possibility of setting up multiple biorefineries, and to also optimize the locations of the biorefineries among several potential lo-

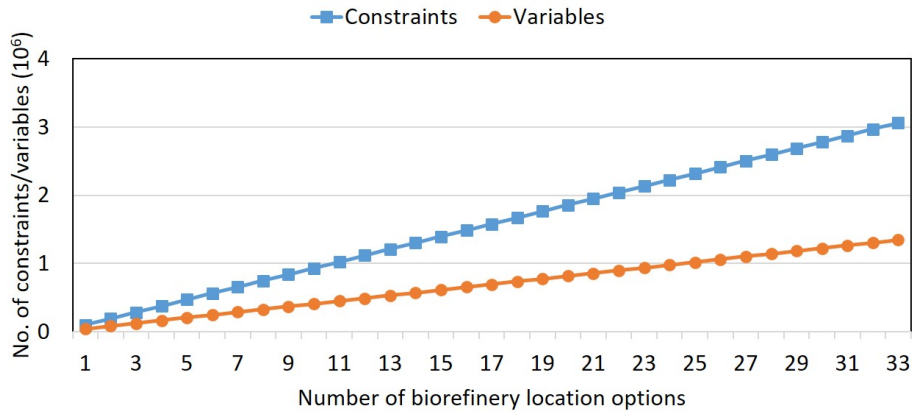


Figure 1: Increase in problem size with increase in potential number of biorefinery locations

cations. Figure 1 shows how the size of this MILP problem varies based on number of potential biorefinery locations. Depending on the specifics, we can expect the size of such a problem to increase rapidly with increase in model details. The full sized problem has more than 3 million constraints and 1.3 million variables including over 6500 binary variables, leading to enormous computational requirements. A popular method for solving large problems is to decompose them into smaller sub-problems which are easier to solve. These sub-problems are iteratively solved by employing certain strategies (Conforti et al., 2014) to ultimately obtain the optimal or near optimal solution to the original monolith problem. The constraint matrix for our biorefinery problem has a block diagonal structure except for a few constraints, which is a very favourable structure for employing Dantzig-Wolfe decomposition (DWD) (Dantzig and Wolfe, 1960).

We therefore propose a DWD based methodology to solve our large-scale biorefinery problem. The following section outlines the formulation of the optimization model. Section 3 presents the proposed solution methodology. The simulation results in terms of reduction in computational time requirement are discussed in Section 4. We conclude this report in Section 5 by mentioning some of the future directions for this work.

2. Problem formulation

The biorefinery problem from literature (Vikash and Shastri, 2017) integrated the biomass procurement and processing aspects into a single model, but considered the location of the biorefinery to be fixed. We expanded this model to consider multiple potential biorefinery locations, thereby drastically increasing the size of the model as shown in Figure 1. The revised model considers a second generation biorefinery which produces ethanol. The superstructure of the problem is conceptually shown in Figure 2 with the number of choices corresponding to each block mentioned in parenthesis.

A specific case study for the production of ethanol for the state of Maharashtra, India (Vikash and Shastri, 2017) is considered. The time horizon is taken to be one year, which is divided into 12 time periods. There are 14 varieties of biomass (N_B) which can be sourced from 33 biomass availability sites (N_H) corresponding to 33 district centroids within Maharashtra. There are potentially 33 locations (corresponding to the 33 district centroids) (N_L) where one or more biorefineries can be located. The biomass is transported via trucks, and can be stored at inventories located at the biorefinery facilities. Regarding the selections involving technological stages within each biore-

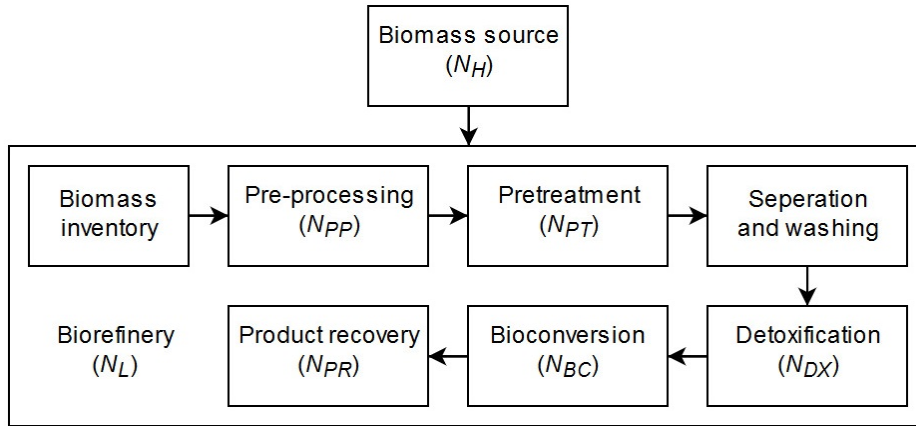


Figure 2: Biorefinery problem structure

finery, $N_{PP} = 1$, $N_{PT} = 8$, $N_{DX} = 4$, $N_{BC} = 4$ and $N_{PR} = 3$. All the necessary data for the problem is reported in literature (Vikash and Shastri, 2017). The objective of the optimization problem is to minimize the total annualized cost (TAC) while meeting a specific monthly demand of ethanol. The problem variables and constraints include:

- Binary variables corresponding to selection of biorefinery location(s), biomass type to be processed at each time period at each biorefinery and the various technological selections within each biorefinery.
- Continuous variables corresponding to the flow of biomass to biorefineries, the size of biomass storage facility at each biorefinery, the amount of biomass stored at each time period for each biorefinery and the flow of intermediate products within the biorefinery.
- Constraints corresponding to the overall biomass availability and demand for ethanol at each time period, economic cost calculations and limiting the selections of processing technologies within each biorefinery, and mass balance constraints within each biorefinery at each time period.

The biorefinery optimization problem can be concisely represented as follows:

$$\min \sum_t^L (C_{\text{Total CAPEX},t} + C_{\text{Variable OPEX},t} + C_{\text{Fixed OPEX},t})$$

subject to [individual biorefinery specific constraints]

$$\sum_t^L f_{b,h,t} \leq F_{b,h,t} \quad \forall b, h, t \in B, H, T$$

$$\sum_t^L e_{l,t} \geq D_t \quad \forall t \in T$$

where, C, f, F, e and D are the annualized cost, flow of biomass, availability of biomass, ethanol production and demand for ethanol, respectively. B, H, T and L corresponds to the set of biomass types, biomass sources, time periods and potential biorefinery locations, respectively. The constraints mentioned as "individual biorefinery specific constraints" correspond to the distribution of

biomass and intermediate products between processing stages, limiting the selections of processing technologies and maintaining the biomass inventory balance within a biorefinery. Thus, these are the process synthesis constraints focusing on process selection. We don't individually specify them for the sake of brevity. The problem in this form is referred to as the integrated problem.

3. Decomposition based solution approach

The Dantzig-Wolfe decomposition (DWD) (Dantzig and Wolfe, 1960) is a well known technique for solving problems in which the constraints have a block diagonal structure consisting of disjoint sets of variables linked by connecting or complicating constraints. In this section, we discuss the decomposition of the biorefinery problem such that DWD may be employed. Subsequently, we provide a detailed description on the proposed solution methodology for solving the biorefinery problem. In order to employ DWD, the biorefinery problem described in the previous section is decomposed in the following manner. Each individual biorefinery is modelled as a sub-problem, while the biomass supply and ethanol demand constraints connect the sub-problems and hence are part of the master problem. At iteration $i \in I$, the master problem is given as

$$\begin{aligned}
 \min_{\lambda} \quad & \sum_l^L \sum_1^i (\bar{C}_{\text{Total CAPEX},l}^i + \bar{C}_{\text{Variable OPEX},l}^i + \bar{C}_{\text{Fixed OPEX},l}^i) \lambda_l^i \\
 \text{subject to} \quad & \sum_l^L \sum_1^I \bar{f}_{b,h,l,t}^i \lambda_l^i \leq F_{b,h,t} & \forall b, h, t \in B, H, T \\
 & \sum_l^L \sum_1^I \bar{e}_{l,t}^i \lambda_l^i \geq D_t & \forall t \in T \\
 & \sum_1^i \lambda_l^i = 1, & \forall l \in L \\
 & \lambda_l^i \geq 0 & \forall i \in I, \forall l \in L
 \end{aligned}$$

where, \bar{C} , \bar{f} and \bar{e} denotes corresponding vertices obtained by solving sub-problems.

At iteration $i \in I$, sub-problem $l \in L$ has the following structure

$$\begin{aligned}
 \min_{\hat{X}_l} \quad & (C_{\text{Total CAPEX},l} + C_{\text{Variable OPEX},l} + C_{\text{Fixed OPEX},l}) - \\
 & \left(\sum_{b,h,t}^{B,H,T} \mu_{1,b,h,t}^i f_{b,h,l,t} + \sum_t^T \mu_{1,t}^i e_{l,t} \right) - \mu_2^{l,i} \\
 \text{subject to} \quad & [\text{individual biorefinery specific constraints}] \\
 & \hat{X}_l \geq 0
 \end{aligned}$$

where, \hat{X}_l denotes all the variables specific to sub-problem l , μ_1^i is the dual variables corresponding to the master constraints and $\mu_2^{l,i}$ is the dual variable corresponding to the l^{th} convexity constraint in the master problem.

Figure 3 describes our approach for solving the decomposed problem. The first step is to define the master problem and sub-problem models, following which DWD is employed. Iterations corresponding to DWD terminates when (i) none of the sub-problem solutions correspond to a negative reduced cost, (ii) DWD exceeds the maximum number of iterations or (iii) change in objective function value over past few iterations is lower than a specified tolerance. In our implementation, we considered that the objective function value should change by at least 1% over 5 iterations. For the sake of brevity, we do not describe the implementation DWD as it is well documented in literature (Kalvelagen, 2003). For problems involving integer variables, the decomposition method

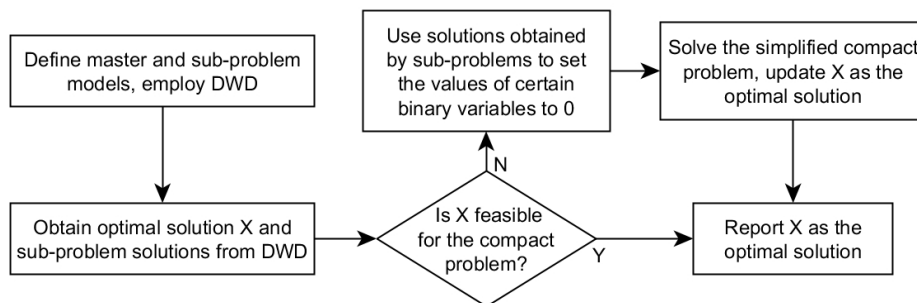


Figure 3: Flowsheet of the solution methodology

which we employ generates the lower bound for the problem, as the integrality of these variables are not guaranteed. Hence, if the solution obtained by DWD is feasible, this is reported as the final solution. On the other hand, if this is not feasible, we utilize the solutions obtained by the sub-problems over DWD iterations to simplify the integrated problem. This is done by filtering out certain selections (setting corresponding binary variable to 0) in the following manner. We identify the sub-problem solutions corresponding largest two λ for each sub-problem l . Subsequently, we filter out the processing technology selections (such as preprocessing, pretreatment, detoxification, bioconversion, fermentation strains and product recovery technologies) which do not appear in the solutions identified earlier. For instance, if the solutions corresponding to the largest and second largest λ for a particular biorefinery location selects pretreatment technologies Dilute Acid Hydrolysis and Lime Pretreatment, respectively, then all other pretreatment technologies are not considered in the simplified problem. The last step is to solve this simplified integrated problem using the standard CPLEX® solver in order to obtain the final optimal solution. Note that this method does not guarantee optimality, although we expect it to produce solutions reasonably close to optimality. In short, our approach is effectively to solve a decomposed problem in order to filter out options for various processing selections which seem to be sub-optimal, thus greatly reducing the complexity of the integrated problem. Subsequently, this simplified MILP problem is solved by standard procedures.

4. Results and discussion

This section presents the improvement in performance obtained by employing the decomposition based method as opposed to solving the integrated problem using the standard CPLEX® solver. The integrated and decomposed biorefinery problem models and the solution methodology were coded in GAMS®. The sub-problems and master problem at each iteration was solved using the standard CPLEX® solver. We do not describe the optimal solution in detail as the focus of our work is the solution methodology and the resulting reduction in computational time.

Figure 4 compares the performance of our approach with that of solving the integrated problem. Although solving the integrated problem requires lesser time for smallest three problem sizes ($N_L = 1$ to $N_L = 3$), the decomposition based approach is significantly faster for all the remaining cases ($N_L = 4$ to $N_L = 33$). For the $N_L = 18$ case, we observe a 92% reduction in computational time. Furthermore, this reduction in computational time is associated with no compromise in the optimal objective function value. It was observed that on employing the decomposition based approach, almost all of the computational time was utilized for solving the sub-problems, with the simplified integrated problem requiring comparatively negligible time. This is reflected in the fact that the computational time requirement for the decomposition based approach appears to be

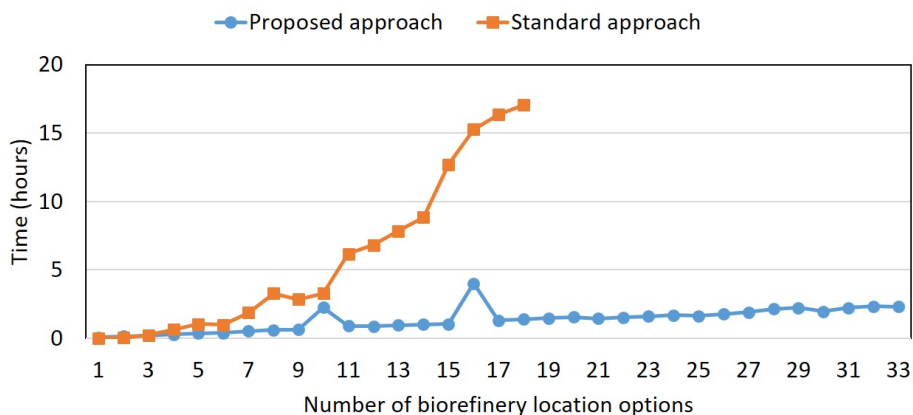


Figure 4: Comparison of computational time requirement of the proposed approach and solving the integrated problem

a linear function of the number of biorefinery options. In comparison, the time taken to solve the integrated problem seems to increase exponentially with increase in the number of biorefinery location options. For the largest problem size ($N_L = 33$), the optimal solution determined by implementing the decomposition based approach corresponded to setting up a single biorefinery located at the Beed district centroid. Ethanol was largely produced by using sugarcane bagasse and wheat based biomass at a price of INR 52.72 per litre.

5. Conclusion

We solve a large-scale biorefinery problem which considers both biomass procurement and process synthesis within each biorefinery. Although this results in a very large optimization problem, its inherent structure allowed us to employ DWD. We developed a DWD based approach and employed it to solve the biorefinery problem. As a result, we obtained up to 92% reduction in computational time while obtaining the same optimal objective function value. This allows us expand the biorefinery model such that it describes the real-world scenario more accurately. In addition, this approach may be tested on similarly structured problems in various fields.

References

- M. Conforti, G. Cornuéjols, G. Zambelli, 2014. Integer programming. Vol. 271. Springer.
- G. B. Dantzig, P. Wolfe, 1960. Decomposition principle for linear programs. *Operations Research* 8 (1), 101–111.
URL <http://dx.doi.org/10.1287/opre.8.1.101>
- J. Gong, D. J. Garcia, F. You, 2016. Unraveling optimal biomass processing routes from bioconversion product and process networks under uncertainty: an adaptive robust optimization approach. *ACS Sustainable Chemistry & Engineering* 4 (6), 3160–3173.
- E. Kalvelagen, 2003. Dantzig-Wolfe Decomposition with GAMS. Amsterdam Optim. Model. Group LLC, Washington, DC, USA.
- F. Sun, M. M. Aguayo, R. Ramachandran, S. C. Sarin, 2018. Biomass feedstock supply chain design – a taxonomic review and a decomposition-based methodology. *International Journal of Production Research* 0 (0), 1–34.
URL <https://doi.org/10.1080/00207543.2018.1475766>
- P. V. Vikash, Y. Shastri, 2017. Economic optimization of integrated lignocellulosic biorefinery. In: A. España, M. Graells, L. Puigjaner (Eds.), 27th European Symposium on Computer Aided Process Engineering. Vol. 40 of Computer Aided Chemical Engineering. Elsevier, pp. 2503 – 2508.

Planning of Supply Chains Threatened by Extreme Events: Novel Heuristic and Application to Industry Case Studies

Michael Ehrenstein^a, Chi-Hsiang Wang^b and Gonzalo Guillén-Gosálbez^{a,*}

^a*Centre for Process Systems Engineering, Imperial College London, London SW7 2AZ, United Kingdom*

^b*CSIRO Land and Water, Bayview Dr., Clayton, VIC 3168, Australia*
g.guillen05@imperial.ac.uk

Abstract

Chemical supply chains are a crucial component in the ongoing supply of large population centres. Unfortunately, episodes of extreme weather have, in recent years, revealed vulnerabilities in global supply networks to high-impact events. With a possible increase in both frequency and intensity of these events due to climate change, supply chains are at risk of disruption now more than ever, with potentially dire economic, societal, and environmental consequences. Acknowledging that the direct application of stochastic programming can quickly lead to very large CPU times, we propose an algorithm that combines the sample average approximation method with a selection heuristic for extreme event scenarios. Our method allows to analyse the tradeoff between economic performance and disruption risk, identifying supply chain configurations which are more resilient against extreme events. We demonstrate the effectiveness of this methodology in multiple case studies, showing how it identifies near optimal solutions in short CPU times.

Keywords: supply chains, optimization, stochastic programming, climate change, extreme events

1. Introduction

Supply chains today have evolved to become an integral and indispensable part of the global economy. What started out centuries ago as small scale, local trade networks, has evolved into an interconnected system spanning all inhabited continents. Along with unprecedented scale and reach, today's supply chains involve more stakeholders than ever: Owners and operators with direct financial stakes, customers depending on an ongoing supply of essential goods such as food and medicine, and local and national governments tasked to supply their populace with water, gas, and other utilities.

As the value and importance of supply chains has increased, so has the academic interest in making them more efficient, with the fields of chemical engineering and operations research at the forefront. Much work done on the optimisation of supply chains has been deterministic, meaning that full information on the state of current and future parameter values is presupposed. In recent years however, optimisation of supply chains under uncertainty has become an active and important field of research, illustrating the importance of reflecting the uncertainty of everyday real-world processes in an accurate manner. In this context, the main focus in the literature has been to hedge against what we call "operational uncertainties", e.g. fluctuations in price, demand, or raw material availability. Significantly less attention has been given to uncertain events of higher

impact, but lower probability of occurrence. Extreme weather events, device failures, and black-outs (just to name a few) can all have potentially dire consequences for supply chains and the people that rely on them. This has been evidenced by periods of extreme weather affecting supply chains in recent years, like the 2011 Thailand floods, or the 2017 Atlantic hurricane season. And with recent findings projecting an increase in either frequency and/or intensity of such events due to climate change, the need for adequate methods to contribute to the resilience of such crucial systems is clear.

2. Problem statement

In this work, we will consider a multi-echelon supply chain similar to the one shown in Figure 1. We start with a number of potential and existing locations for production, storage, and sale of multiple products. Additionally, prices of materials and final products, costs of production, storage, and transport, as well as the cost of establishing new infrastructure are given. All production and storage locations may be disrupted by an extreme event with a certain probability of occurrence. The goal of this analysis is to determine the optimal supply chain configuration in terms of economic performance and risk, while considering said disruptions.

When applying a scenario-based, stochastic programming approach to such a task, the issue of problem size quickly becomes apparent. For example, a supply chain comprised of 10 disruptable units, along with 5 customer zones which can vary in demand between low, medium, and high, results in a set of $2^{10} \cdot 3^5 = 2.5 \cdot 10^5$ scenarios. While numerous methods exist to reduce the size of the problem to solve, these approaches often perform poorly when faced with disruption uncertainties, which are based on more heavy-tailed distributions than conventional operational uncertainties. The following section introduces a method to solve this problem efficiently.

3. Methodology

3.1. Two-stage stochastic programming

The method we propose to solve the issues mentioned above is based on two-stage stochastic programming (Birge and Louveaux, 1997), as well as the sample average approximation (SAA) method (Kleywegt et al., 2001). Two-stage stochastic programming, along with robust optimisation (Ben-Tal and Nemirovski, 2001), is one of the most common methods used to handle parameter uncertainty in mathematical programming, and usually relies on the partitioning of the underlying uncertainty into discrete realisations, or scenarios. Variables are partitioned into "first stage" and "second stage" variables. First stage variables are calculated before the realisation of any uncertainties and correspond to "here-and-now" decisions, such as initial capital investments. Second stage variables on the other hand are calculated after the uncertainties are revealed ("wait-and-see" decisions), and allow the model to take recourse, or corrective action. These second stage variables correspond to operational decisions, such as production rates and inventory levels.

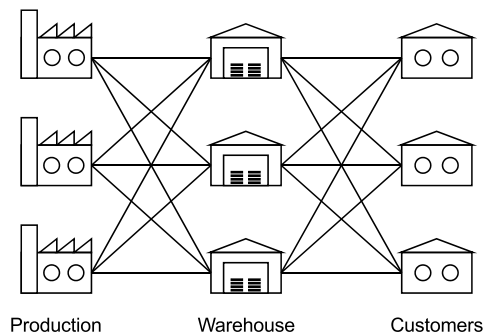


Figure 1: Example of a three-echelon supply chain (production, warehouse, customers), with transport connections linking adjacent echelons.

3.2. Modeling disruptions

Applying stochastic programming, we can now introduce extreme event disruption into the supply chain model. These models typically contain constraints on the maximum available capacity for production or storage, of the form

$$prod_s \leq cap^{max} \tag{1}$$

where $prod_s$ is the current production level, and cap^{max} is the maximum production capacity. By introducing a disruption parameter ϕ_s , which can take a value between 0 and 1 for every scenario, we can vary the amount of capacity available for production, depending on the disruption scenario:

$$prod_s \leq \phi_s \cdot cap^{max} \tag{2}$$

Assuming independence between disruption events, as well as binary disruption (disrupted, or not) with probability p , we can now construct a scenario set encompassing all units. For instance, let us consider a supply chain made up of two units, A and B. Four combinations of scenarios are possible here: 1. No disruption, 2. A disrupted, 3. B disrupted, 4. A & B disrupted. Assuming the disruption probability to be p and independent, the probability for each scenario will be: 1. $(1 - p)^2$, 2. $(1 - p)p$, 3. $p(1 - p)$, 4. p^2 .

3.3. Sample average approximation

Our approach to improve the tractability of large supply chain problems is further based on the sample average approximation method, which is a Monte Carlo approach to reduce the problem size of large stochastic programs. When solving a conventional two-stage stochastic program, all first and second stage variables, as well as the full scenario space, are taken into account. The sample average approximation method on the other hand partitions the problem into two sub-problems, each of which is simpler to solve than the parent problem: First, the problem is solved using a random subset of N scenarios instead of the full scenario space. Next, the value of all first stage variables is fixed, and the problem is solved again using the full scenario space, ensuring feasibility of the solution in all scenarios. These two steps are now repeated K times, with a new independent sample of N scenarios chosen in each iteration. Finally, the best of the K candidate solutions is selected to approximate the true optimal solution. Figure 2 compares the SAA method to a two-stage stochastic programming model, in terms of scenarios and variables taken into account.

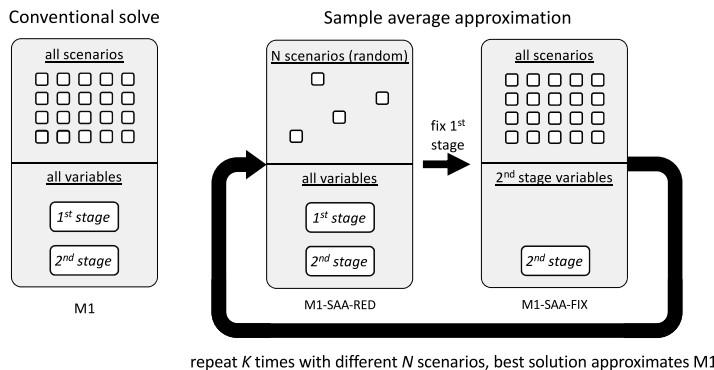


Figure 2: Illustration of the sample average approximation method (right), compared to a conventional two-stage stochastic programming solve.

3.4. Two-stage problem reduction

Based on these methods, we introduce the two-stage problem reduction (TSPR) algorithm, in which we follow the SAA, but apply a heuristic to formulate the sub-problems in a novel way. This heuristic capitalises on our knowledge of the structure of the disruption scenarios, as shown above. Specifically, instead of selecting N scenarios at random, we select scenarios with disruption of zero, one, and all units.

Exploiting our aprioristic knowledge of the scenario set allows the TSPR algorithm to approximate the true solution of the stochastic program after a single iteration, as opposed to K iterations in the SAA method. Furthermore, the TSPR method avoids the need to set parameter values (N and K), thereby simplifying implementation. Figure 3 illustrates this process.

3.5. Risk management and multiobjective optimisation

When assessing the risk posed by extreme event disruption to supply chains, it is of importance to analyse the results beyond the expected economic performance, and to obtain information on the variability of the objective function in the uncertain parameter space. This can be achieved by implementing risk metrics in the optimisation model, which allow for the assessment of the performance of the supply chain in different scenarios. We employ the downside risk (DR) and worst case (WC) metrics (Sabio et al., 2014), though in principle others like the conditional value-at-risk can be implemented. The DR is calculated by comparing the performance of the supply chain in each scenario to a predefined cut-off Ω . Each scenario that falls under the cut-off is penalised by the product of this shortfall and the respective probability of occurrence. The WC metric on the other hand is obtained simply by taking the performance of the worst scenario. Once a metric is implemented in the optimisation model, multiobjective optimisation, for instance by way of the epsilon-constraint method (Ehrgott, 2005), can be employed to investigate the trade-offs between economic performance and risk of the supply chain, yielding a set of Pareto-optimal solutions. Figure 4 illustrates the process of combining the TSPR method with multiobjective optimisation from start to finish.

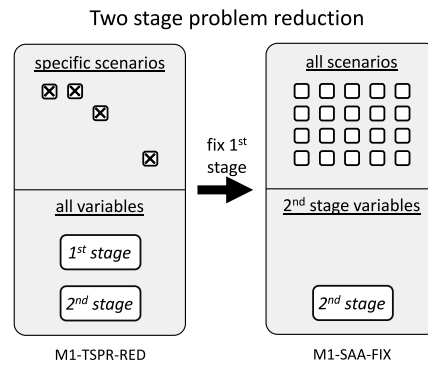


Figure 3: Illustration of the TSPR method. Compared to the sample average approximation, predetermined scenarios are selected for the first solve, and no iterations are performed.

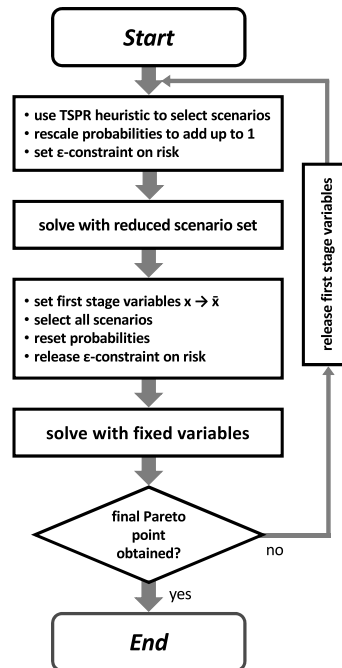


Figure 4: Combining the TSPR method with risk metrics and multiobjective optimisation.

Table 1: Comparing multiobjective optimisation of the petrochemical supply chain in terms of TSPR time reduction, difference in economic performance, and hypervolume measure.

Objectives	Time reduction	max E[profit] diff.	HV diff.
E[profit] vs. WC	93 %	0.0 %	3.2%
E[profit] vs. DR	99 %	0.0 %	0.0%

4. Case studies

4.1. Petrochemical supply chain

We demonstrate the capabilities of this methodology through its application to two case studies. The first is based on earlier work by Ruiz-Femenia et al. (Ruiz-Femenia et al., 2013), who investigated the trade-offs between environmental impact and economic performance in the design of a petrochemical supply chain in Europe.

In our case, the supply chain is made up of three echelons, with four potential locations for production plants, seven for warehouses, and four markets. The potential disruption of all plants and warehouses results in 2048 scenarios. The model seeks to optimise the supply chain's profit, and one of the risk metrics outlined above, while making decisions on production and storage capacities, transportation volumes, and inventory levels. We generated ten Pareto-optimal solutions using the epsilon-constraint method, both using the full scenario space, and the TSPR method. In order to adequately compare the two sets of solutions in each case, the hypervolume (HV) (Zitzler and Thiele, 1998) indicator was employed. This measure quantifies the area enclosed by the obtained solutions, and a reference point, as illustrated in Figure 5. The solutions obtained using the full scenario set are compared to the TSPR solutions in Table 1.

A significant reduction in solution time is evident, while at the same time the Pareto solutions of the TSPR run are close (WC) or near identical (DR) to their optimal counterparts.

4.2. Hydrogen supply chain

The TSPR method was further applied to the optimisation of a hydrogen supply chain for vehicle use in the UK, based on work by Almansoori and Shah (Almansoori and Shah, 2006). The model in our case has 9 regions, in each of which production and storage facilities can be established, along with a set customer demand. 512 disruption scenarios are considered, and the full-space solution is again compared to the TSPR solution for both the profit-WC and the profit-DR trade-off. A summary of the results can be found in Table 2, again showing that the TSPR method is able to achieve results close to the optimal case, while reducing the solution time significantly.

5. Conclusion

We addressed the problem of the design and risk management of optimal multi-echelon supply chains threatened by rare event disruptions, which to our knowledge had not been adequately

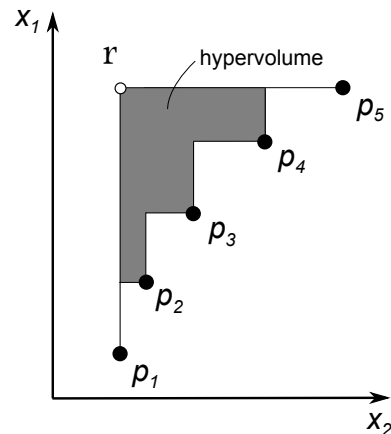


Figure 5: Illustration of the hypervolume (grey) enclosed by points p and the reference point r.

Table 2: Comparing multiobjective optimisation of the hydrogen supply chain in terms of TSPR time reduction, difference in economic performance, and hypervolume measure.

Objectives	Time reduction	max E[profit] diff.	HV diff.
E[profit] vs. WC	96 %	0.0 %	0.2%
E[profit] vs. DR	98 %	0.0 %	6.6%

addressed in the current literature. Combining the SAA algorithm with a selection heuristic, the TSPR methodology was developed to reduce the computational effort required to solve these types of problems. The effectiveness of the TSPR method was demonstrated through application to two supply chain case studies from the literature, achieving close to optimal results in significantly reduced time.

6. References

- Almansoori, A., & Shah, N. (2006). Design and Operation of a Future Hydrogen Supply Chain. *Chemical Engineering Research and Design*, 84, 423-438.
- Ben-Tal, A., & Nemirovski, A. (2001). *Lectures on modern convex optimization: analysis, algorithms, and engineering applications* (Vol. 2): Siam.
- Birge, J. R., & Louveaux, F. (1997). *Introduction to stochastic programming*. In: Springer, New York.
- Ehrgott, M. (2005). *Multicriteria Optimization*: Springer-Verlag New York, Inc.
- Kleywegt, A. J., Shapiro, A., & Homem-de-Mello, T. (2002). The Sample Average Approximation Method for Stochastic Discrete Optimization. *SIAM Journal on Optimization*, 12, 479-502.
- Ruiz-Femenia, R., Guillén-Gosálbez, G., Jiménez, L., & Caballero, J. (2013). Multi-objective optimization of environmentally conscious chemical supply chains under demand uncertainty. *Chemical Engineering Science*, 95, 1-11.
- Sabio, N., Pozo, C., Guillén-Gosálbez, G., Jiménez, L., Karuppiah, R., Vasudevan, V., Sawaya, N., & Farrell, J. T. (2014). Multiobjective optimization under uncertainty of the economic and life-cycle environmental performance of industrial processes. *AIChE Journal*, 60, 2098-2121.

Optimal Maintenance Scheduling for Washing of Compressors to Increase Operational Efficiency

Frederik Schulze Spüntrup^a, Giancarlo Dalle Ave^{b,c}, Lars Imsland^{a,*} and Iiro Harjunkoski^b

^a*Department of Engineering Cybernetics, Norwegian University of Science and Technology, 7491 Trondheim, Norway*

^b*ABB Corporate Research Germany, 68526 Ladenburg, Germany*

^c*Technical University Dortmund, 7491 Dortmund, Germany*
lars.imsland@ntnu.no

Abstract

The need for simultaneously decreasing carbon emissions and increasing operational profit motivates gas turbine and gas compressor operators to understand, minimize and control performance deterioration. Fouling is one of the most prevalent deterioration problems. This work addresses the causes and effects of fouling and investigates an approach to give decision-support on the questions if, how often and when compressor washing should be conducted. Integration with other maintenance actions is also considered. In this work, a discrete time-scheduling approach that follows the Resource Task Network framework is developed and formulated as a Mixed Integer Linear Program. A novel enumerator formulation makes this method simpler and easier to extend for different maintenance types than existing methods. Degradation is included in a linearized way for a case study from the Oil and Gas industry. Results indicate that washing scheduling is beneficial for the profit. This study gives the foundation for decision-support regarding additional investments in existing production systems, amortization, and supplies optimal maintenance schedules for various applied maintenance types.

Keywords: Maintenance scheduling, asset degradation, energy efficiency

1. Introduction and Background

Degradation of assets is an omnipresent phenomenon in the process industries where the lifetime of a plant easily reaches 30-50 years. Deterioration of assets is inevitable. Over the lifecycle of an equipment its efficiency will decrease and it will degrade up to a level where it cannot be operated any longer or the operating company decides to take countermeasures. According to Diakunchak (1992) compressor fouling constitutes 70-85% of the performance loss caused by deterioration in gas turbines. With the latest IPCC report on achieving the maximum 1.5°C average temperature increase goal it is important to avoid any unnecessary waste of energy.

While the literature identifies performance degradation and declares washing as an appropriate countermeasure (Stalder, 2001), there is not much work done on the decision when to perform the washing procedure. The contribution of this work is to include the efficiency degradation of assets into the decision on when to perform maintenance tasks.

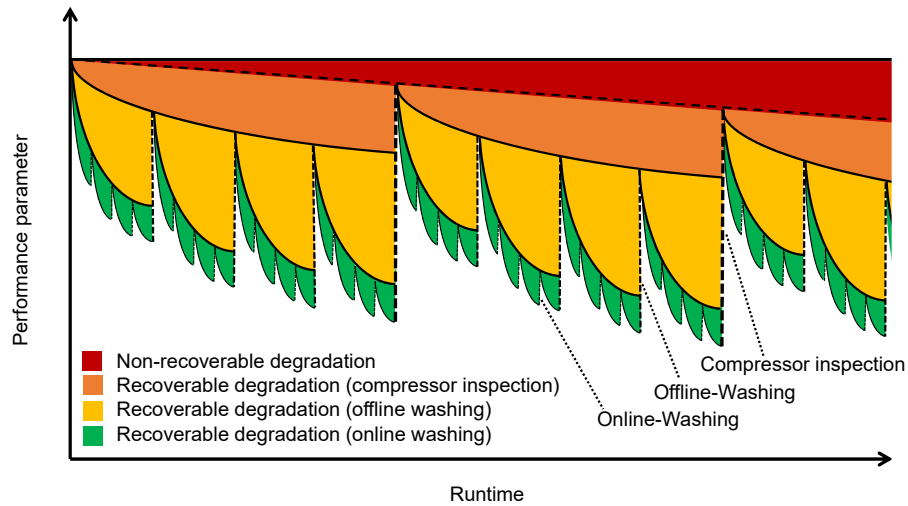


Figure 1: Example of the different types of degradation in a compressor and different types of maintenance to restore efficiency.

Kurz and Brun (2001) describe the degradation of gas turbine systems. Different mechanisms affect the degradation process: Increased tip clearance (Khalid et al., 1999) and changes in the airfoil geometry (Singh et al., 1996) are interlinked with the effect of non-recoverable degradation. Recoverable degradation, which can be (partially) reversed by specific methods (e.g. washing) is described as changes in the airfoil surface quality (Elrod et al., 1990). Kurz and Brun (2012) reported significant deterioration of different gas turbines, ranging between 2 and 12 % after one year of operation.

Hovland and Antoine (2006) optimise the power generation by applying parameter estimation via Kalman filtering combined with a hybrid dynamic model. Model predictive control is used with this hybrid dynamic model and compared to fixed washing schedules.

Xenos et al. (2016) investigate an air separation plant. Optimal operation and the maintenance of compressor networks are part of the developed MILP model. Online and offline washing are considered as part of the condition-based maintenance approach. The degradation is considered in three different cases: low, medium and high degradation. They are based on a study of industrial data. Offline-washing is not considered to be done during non-performance-related maintenance actions or regular shutdowns of the equipment. The degradation in the case study causes an increase in electrical power consumption of 2 % per month, which leads to high saving potential.

This paper addresses optimal scheduling of maintenance actions to increase operational efficiency. Section 2 presents the problem statement of this work. Even though this problem is common in many kinds of process industries, we will focus on a case study of an offshore compressor fleet of an oil and gas company, which is introduced in Section 3. A short overview of the mathematical formulation of the scheduling approach is given in Section 4. The results of the maintenance scheduling are illustrated and discussed within

the different subcases in Section 5. The conclusion gives an overview of the findings of this work and shows possible directions for future work.

2. Problem Statement and Case Study

The problem considered in this paper investigates how often online and offline washing in the context of other maintenance types should be conducted to optimally countermeasure deterioration effects and efficiency loss in compressors due to fouling. Furthermore, the actual benefit of washing can not always be determined beforehand. This information is important for the decision-making process; if a washing system should be installed on existing assets or not.

The case study that is used is inspired by a real fleet of compressors. In order to assess the performance of the formulation, the case study is analyzed with varying grid coarseness and time horizon length. For the length of the scheduling horizon a duration of 1-3 months was chosen, as this resembles the need for ahead-scheduling of maintenance workers and the ordering of specific resources such as spare parts or other supplies in most companies.

Table 1: Notation of the scheduling formulation

Index/Set	Description	Continuous Variable	Description
i	Task	$C_{rc,t}$	Enumerator
j	Unit	$G_{rc,t}$	Goodness of unit
t	Time Interval	K	Profit/Cost term
R	Resource	$\mu_{i,t}$	Discrete interaction
R_c	Resource (asset)	Binary Variable	Description
T_S	Time (Scheduling)	$N_{i,t}$	Maintenance task i starts at t
I	Maintenance tasks	Parameters	Description
		D_{rc}	Degradation factor
Superscript	Description	Superscript	Description
$NonRecov$	Non-recoverable degradation	$ROnW$	Recoverable degradation (Online Washing)
$RInsp$	Recoverable degradation (Inspection)	$ROffW$	Recoverable degradation (Offline Washing)
Min	Minimum	Max	Maximum

3. Mathematical Modeling

The scheduling model is designed as a discrete-time model. While the exact starting times of maintenance actions depend on other external factors such as weather conditions or the changeover between two shifts, it is not important to work with a continuous-time model. A generic approach based on the Resource-Task Network (RTN) framework (Pantelides, 1994) is applied. The notation of the model is shown in Table 1.

The central element of the scheduling approach is the inherent goodness of every asset. This goodness is affected by degradation and therefore the efficiency decreases over time.

As depicted in Figure 1 the efficiency of the compressor is decreasing over time. There are different terms for the various types of degradation and there are 5 distinctive maintenance modes that have particular effects. Different counters for each type of degradation are used to calculate the time passed since the last maintenance has taken place. Every conducted maintenance resets one or multiple counters, which are used to model the degradation in a linear fashion. The goodness degradation is defined as follows:

$$G_{r_c,t} = C_{r_c}^{initial} - D_{r_c}^{NonRecov}(C_{r_c,t}^{GN} - 1) - D_{r_c}^{RInsp}(C_{r_c,t}^{RInsp} - 1) - D_{r_c}^{ROffW}(C_{r_c,t}^{ROffW} - 1) - D_{r_c}^{ROnW}(C_{r_c,t}^{ROnW} - 1), \forall r_c \in R_c, t \in T_S \quad (1)$$

The enumerators are each formulated in a comparable way. As an example, the enumerator $C_{r_c,t}^{ROnW}$ for counting the time intervals since the last online washing is introduced:

$$C_{r_c,t}^{ROnW} \geq C_{r_c,t-1}^{ROnW} + 1 - M \sum_{i_{r_c}}^{I_{OnW}} N_{i,t}, \forall r_c \in R_c, t \in T_S \quad (2)$$

$$C_{r_c,t}^{ROnW} \leq C_{r_c,t-1}^{ROnW} + 1, \forall r_c \in R_c, t \in T_S \quad (3)$$

$$C_{r_c,t}^{ROnW} \leq 1 + M(1 - \sum_{i_{r_c}}^{I_{OnW}} N_{i,t}), \forall r_c \in R_c, t \in T_S \quad (4)$$

$$C_{r_c,t}^{ROnW} \geq 1, \forall r_c \in R_c, t \in T_S \quad (5)$$

The enumerator for the Remaining Useful Life of the assets works in a similar fashion. However, it is reset by a short-term maintenance I_{SM} that does not restore the goodness but fixes operational problems with the asset. The formulation is not shown in this paper. In a real-world application a continuous input from a Condition Monitoring System would be required.

The resource balance describes that every active maintenance task $N_{i,t}$ is consuming a specific amount of resources $\mu_{i,t}$ from the initial amount of resources R_0 , including the compressors and the maintenance personnel. When a task is concluded, these resources are released again for the following time interval.

$$R_{r,t} = R_{initial} - \sum_i^I N_{i,t} \mu_{i,t}, \forall r \in R, t \in T_P \quad (6)$$

The target of the optimization is to maximize the profit, calculated by the production profit from each compressor, multiplied by the goodness of the compressor in each time interval minus the cost for maintenance.

$$\max z = K_{profit} \sum_{plat}^{r_c} G_{r_c,t} - K_i \sum_i \sum_t^{T_S} N_{i,t} \quad (7)$$

Table 2: Results of the washing scheduling for a fleet size of 10 compressors. (Legend: H - Time Horizon, G - Grid Size, Off - Offline Washing, On - Online Washing)

Case	H: 1 month, G: 4 hours			H: 2 month, G: 4 hours		
	On	Off	On+Off	On	Off	On+Off
Improvement ¹	0.97%	0.13%	1.07%	2.06%	1.50%	3.30%
MIP-Gap	0.72%	0.46%	0.61%	7.03%	4.45%	2.24%
CPU-s ²	1800	1800	1800	1800	1800	1800

Case	H: 1 month, G: 8 hours			H: 2 months, G: 8 hours		
	On	Off	On+Off	On	Off	On+Off
Improvement ¹	1.29%	0.38%	1.28%	1.88%	0.84%	2.71%
MIP-Gap	0.26%	0.01%	0.28%	3.42%	2.91%	1.19%
CPU-s ²	1800	1411	1800	1800	1800	1800

¹Improvement is calculated as the ratio between the case with solely regular maintenance types, but without any washing.

²The computation was terminated after a maximum of 1800 s or when the MIP-Gap was below a threshold of 0.01%.

4. Results and Discussion

Four different cases with fixed fleet size, but varying time horizon and grid size were solved using GAMS 24.8.4/CPLEX 12.7.1.0. The calculations are carried out as follows: Each case has the information that two different maintenance actions (long overhaul and short maintenance, e.g. change of a broken seal) must be conducted within the time horizon. This information could come in a real-world implementation e.g. from a higher level planning system. Furthermore, a specific combination of washing actions (online, offline or combined) can be conducted. The optimization problem tries to optimize production profit by recovering degradation of the compressors at the right time.

The improvement is calculated by comparing the three different scenarios for each case against the base-scenario in which no washing is performed, just the basic maintenance such as long overhauls and short-term maintenance. The quotient of the objective function for a specific scenario and the base scenario indicate the improvement.

The results of four different cases with three scenarios each are shown in Table 2. While the specific values of the objective function represent the entire production profit within the time horizon (see Eq. 7), the actual values of the production profit are not insightful. As the size of the optimization problem is larger the longer the time horizon is and the finer the grid size is, the scheduling algorithm is terminated prematurely in all cases at 1800 seconds. Therefore, the result shows the minimum improvement, as further calculation might improve the objective function. More exhaustive calculations may be conducted in a follow-up study.

The results show that the algorithm is able to improve the operating profit. The improvement ranges between 0.4% and 3.3%. Several trends can be observed: The longer the time horizon is, the more improvement can be observed. As the overall degradation (non-recoverable plus all recoverable degradation) is set to 5% per year, this makes sense, as smaller decreases in the efficiency do not necessarily justify conduction of washing, while

on a longer time horizon washing is more economically viable. With fixed computational time, the gap between the best bound of the problem and the integer solution is dependent on the time horizon and the grid size and is thus scaling with the problem size.

5. Conclusion

A novel maintenance scheduling approach was presented in this work. The model differs from other work, as it combines the information about the asset degradation via an enumerator-approach into the decision-making for several types of maintenance actions, especially washing actions.

Degradation is considered to be a combination of recoverable degradation, non-recoverable degradation and the decreasing remaining useful lifetime of an asset. Results show that the scheduling of the proposed compressor washing in addition to other maintenance types is able to improve the production profit by up to 3.3% compared to operations without the compressor washing. Next to the fact that the scheduling model can give help to optimize the operation of process networks, it can be used as a decision-support tool. By comparing the possible saving introduced through new maintenance types, e.g. washing, a maximum capital investment for the amortization within a specific timeframe can be calculated.

Future work will investigate a multi-time-scale model that integrates both long-term planning and short-term scheduling of maintenance.

6. Acknowledgment

Financial support is gratefully acknowledged from the Marie Skłodowska Curie Horizon 2020 EID-ITN project “PROcess NeTwork Optimization (PRONTO)”, Grant agreement No 675215.

References

- Diakunchak, I. S., 1992. Performance Deterioration in Industrial Gas Turbines. *Journal of Engineering for Gas Turbines and Power* 114 (2), 161.
- Elrod, W. C., King, P. I., Poniatowski, E. M., 1990. Effects of Surface Roughness, Freestream Turbulence, and Incidence Angle on the Performance of a 2-D Compressor Cascade. Volume 1: Turbomachinery, V001T01A061.
- Hovland, G., Antoine, M., 2006. Scheduling of gas turbine compressor washing. *Intelligent Automation and Soft Computing* 12 (1), 63–73.
- Khalid, S. A., Khalsa, A. S., Waitz, I. A., Tan, C. S., Greitzer, E. M., Cumpsty, N. A., Adamczyk, J. J., Marble, F. E., 1999. Endwall Blockage in Axial Compressors. *Journal of Turbomachinery* 121 (3), 499–509.
- Kurz, R., Brun, K., 2001. Degradation in Gas Turbine Systems. *Journal of Engineering for Gas Turbines and Power* 123 (1), 70.
- Kurz, R., Brun, K., 2012. Fouling Mechanisms in Axial Compressors. *Journal of Engineering for Gas Turbines and Power* 134 (3), 032401–032401.
- Pantelides, C. C., 1994. Unified framework for optimal process planning and scheduling. In: *Proc. Second Conf. on Foundations of Computer Aided Operations*. pp. 253–274.
- Singh, D., Tabakoff, W., Mechanics, E., 1996. Simulation of Performance Deterioration in Eroded Compressors. *ASME. Turbo Expo: Power for Land, Sea, and Air Volume 1*; 1–8.
- Stalder, J.-P., 2001. Gas Turbine Compressor Washing State of the Art: Field Experiences. *Journal of Engineering for Gas Turbines and Power* 123 (2), 363.
- Xenos, D. P., Kopanos, G. M., Ciccotti, M., Thornhill, N. F., 2016. Operational optimization of networks of compressors considering condition-based maintenance. *Computers and Chemical Engineering* 84, 117–131.

Turbulent flow modeling in continuous oscillatory flow baffled reactor using STAR CCM+

Nikola Kljajić, Branislav Todić, Danijela Slavnić, Nikola Nikačević*

Faculty of Technology and Metallurgy, University of Belgrade, Karnegijeva 4, Belgrade 11000, Serbia

nikacevic@tmf.bg.ac.rs

Abstract

A detailed transient tridimensional CFD model of the turbulent flow of liquid phase inside of 26 mm diameter continuous oscillatory baffled reactor (COBR) was developed using STAR CCM+ software. The model considered a large number of COBR cavities separated with single-orifice baffles. The CFD model was validated using residence time distribution experiments with several flowrates and frequencies. Different from previous studies, flow oscillations in our work were generated using a membrane pump, which enabled lower amounts of backflow. Simulations were used to analyse flow patterns and mixing for several values of inlet flowrate and oscillation frequencies.

Keywords: continuous oscillatory flow baffled reactors, process intensification, CFD modeling.

1. Introduction

Oscillatory flow baffled reactors are a successful example of process intensification in chemical engineering. They have been shown to provide improved performance in a number of process operations, including crystallization, polymerisation, adsorption, reaction etc. (Jolliffe et al., 2018). Typically, continuous oscillatory baffled reactors (COBRs) are made up of a number of equally spaced single-orifice baffles inside a tube. However, other designs (e.g. helical and double-helical ribbons) have been used as well. The main characteristic of COBRs is the enhancement of mixing by using flow oscillations, which periodically collide with baffles forming vortices. The intensity of mixing in COBRs is dependent on the oscillation amplitude and frequency, as well as reactor geometry. The application of these continuous reactors can lead to significant improvements in productivity, investment and operating cost savings, as well as better reaction control, for slow processes typically performed in batch systems. Initial studies with COBRs explained the mechanisms of oscillatory flow mixing by using a number of experimental approaches. Ni et al. (2002) presented the first 3-D CFD model which solved Navier–Stokes equations (i.e. without stream function) for oscillatory Reynolds numbers covering both symmetric and asymmetric flows. Due to computational complexity the model included only a few cavities (i.e. cells between baffles), and was validated with particle image velocimetry (PIV) experiments in oscillatory baffled column (OBC) with fixed baffles. Several other later CFD works also focused on a smaller number of cavities due to similar reasons (Hamzah et al., 2012).

In this study, the transient 3D CFD model of the turbulent flow of liquid inside of single-orifice baffled tube reactor was developed using K-Epsilon turbulence model and STAR CCM+ software. In order to provide a full picture of the flow inside the entire

reactor, the model included a large number of cavities (total of 29). This enabled direct experimental validation using residence time distribution studies, conducted for several sets of input oscillation frequency and amplitude. Backflow created during generation of flow oscillations was minimized by feeding the fluid to the reactor using a membrane pump with a non-return valve. Furthermore, by using a membrane pump, there is no need for an oscillator in addition to the regular pump (net flow), used in many previous studies (i.e. more cost effective). Detailed analysis of velocity streamlines, vorticity, turbulent viscosity, and kinetic energy is used to provide insights into fluid flow and mixing flow inside of COBR with this design.

2. Methodology

2.1 Experimental setup and procedures

Experiments were performed in a 2 m long reactor with an internal diameter of 26 mm. Single-orifice baffles were placed along the reactor tube, equally spaced at 1.5 times the internal diameter of the tube. The primary stream was generated by the dosing membrane pump and carried fluid oscillatory movement. The control unit of this pump allows the volume and frequency of strokes to be adjusted. The process fluid was water at atmospheric pressure and temperature. The tracer used in experiments was a solution of methylene blue in the concentration of 2.0 g/l. The pulse-response method was used to examine the liquid flow pattern in the COBR. The samples were taken from the 29th cavity, placed 1.03 m downstream of the injecting point. The absorbance of samples was determined using a UV-VIS spectrophotometer. Details of the experimental setup and procedures can be found in Slavnic et al. (2017).

2.2 3D COBR model development

The 3D COBR model was defined using Simcenter STAR-CCM+ 12.04 software. The reactor geometry was drawn using SolidWorks 2011 CAD software and imported into STAR CCM+. Reactor dimensions corresponded to our experimental setup. Due to the reactor symmetry, only one horizontal half of the full volume was modelled, in order to speed up the computing time. The reactor geometry was split up into regions, which define boundaries and regions of interest. Surface and volume mesh was generated using Polyhedral and Prism Layer Meshers, respectively. To ensure higher precision, denser mesh settings were used in boundaries around the baffles. A higher computational speed was achieved by decreasing the density of meshes around tube walls.

The reactor model includes balance equations for momentum, mass and energy, as well as continuity equations. The balance equations used can be presented as:

$$\frac{\partial \rho}{\partial t} + \nabla \cdot [\rho(\bar{v} - v_g)] = 0 \quad (1)$$

$$\frac{\partial(\rho\bar{v})}{\partial t} + \nabla \cdot [\rho\bar{v}(\bar{v} - v_g)] = -\nabla \cdot \bar{p}I + \nabla \cdot (T + T_r) + f_b \quad (2)$$

where ρ is fluid density, t time, \bar{v} and \bar{p} are mean velocity and pressure, v_g referent velocity, I identity tensor, T viscous stress tensor, T_r Reynolds stress tensor and f_b is resultant of the body forces. Unsteady state turbulent flow of multi-component non-reacting liquid was modelled using the K-Epsilon turbulence model:

$$\frac{\partial(\rho k)}{\partial t} + \nabla \cdot (\rho k \bar{v}) = \nabla \cdot \left[\left(\mu + \frac{\mu_t}{\sigma_k} \right) \nabla k \right] + P_k - \rho(\varepsilon - \varepsilon_0) + S_k \quad (3)$$

$$\frac{\partial(\rho \varepsilon)}{\partial t} + \nabla \cdot (\rho \varepsilon \bar{v}) = \nabla \cdot \left[\left(\mu + \frac{\mu_t}{\sigma_\varepsilon} \right) \nabla \varepsilon \right] + \frac{1}{T_e} C_{\varepsilon 1} P_\varepsilon - C_{\varepsilon 2} f_2 \rho \left(\frac{\varepsilon}{T_e} - \frac{\varepsilon_0}{T_0} \right) + S_\varepsilon \quad (4)$$

where μ is dynamic viscosity, μ_t is turbulent eddy viscosity, σ_k , σ_ε , $C_{\varepsilon 1}$, $C_{\varepsilon 2}$ model coefficients, P_k , P_ε terms which define generation of kinetic energy k and dissipation of turbulent energy ε , f_2 dampening function, S_k , S_ε source terms, T_e large-eddy time scale and T_0 specific time scale.

Inlet boundaries for base and tracer fluid were defined as oscillatory and impulse functions, respectively. The inlet of base fluid was defined using a data matrix generated in Matlab based on experimental measurements of the inlet flow. Schematic representation of base fluid oscillatory flow at the inlet is shown in Figure 1. The inlet of the tracer is defined as an impulse of flow with the volume of 2 ml in the 0.5 s interval, which replicates the syringe injection of tracer into the reactor.

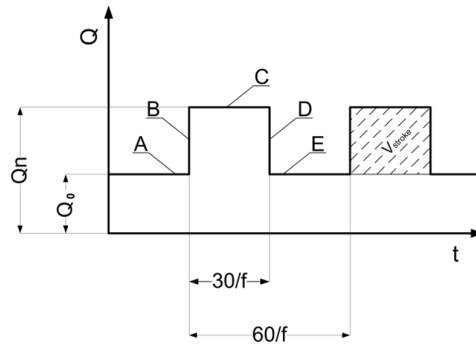


Figure 1 - Schematic representation of base fluid oscillatory flow at the reactor inlet (A, B, C, D and E represent specific moments during each oscillation). Notes: f – pump frequency; Q_0 – base flowrate; Q_n – total flowrate;

3. Results and discussion

3.1 Model validation

Reliable design, scale-up and control of COBRs are conditioned by fluid flow accurate representation. One of the most effective experimental approaches for defining non-ideal flow is still the investigation of residence time distribution (RTD) of fluid elements, realized through tracer experiments and population-based analysis. In order to validate our CFD model, comparison with experimental RTD under a range of conditions was performed. Three tracer experiments covered a range of net flow Reynolds numbers ($Re_n = 142, 453$ and 678), oscillatory Reynolds numbers ($Re_o = 670, 1644$ and 2458) and frequencies ($f = 0.5, 1$ and 2 s^{-1}).

By solving the material balance for the tracer component in STAR CCM+, and integrating (spatially) molar fractions at the outlet plane, we are able to calculate the residence time probability distribution (i.e. E-curve). Comparison of E-curves for two of the experiments is shown in Figure 2 and depicts a very good agreement between the CFD model and experiments. E-curve from the third experiment (not shown in Figure

2) also matched well with the CFD model. We also compared the resulting E-curve obtained by using the axial-dispersion (AD) model, based on the empirical correlation for Peclet number (Slavnic et al., 2017). Figure 2 shows that in the range of high Re_n values, CFD model considerably outperforms the AD model. Albeit slower to solve and with a significantly higher computational cost, an additional benefit of the CFD model is it provides a more detailed picture of the fluid flow inside of COBRs. This is valuable for further process intensification considerations of such reactors.

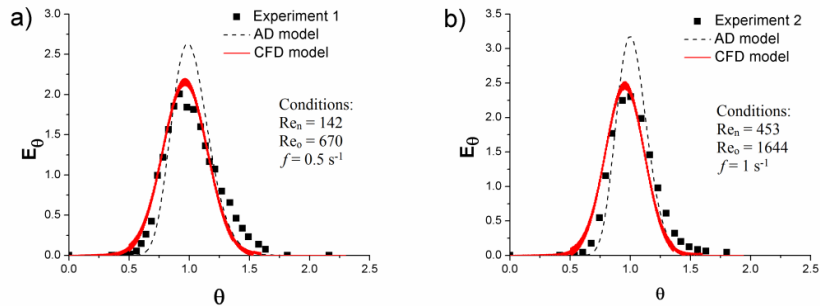


Figure 2 – Comparison of RTD for CFD model with the experimental and AD model results: a) Experiment 1; b) Experiment 2.

Recently, Kimuli et al. (2017) performed a similar investigation, where a CFD model (using STAR CCM+ software) with a large number of cavities was developed and validated using RTD experiments. However, they focused on lower values of Re_n (i.e. laminar flows with $Re_n = 8.4$ and 21.2) and smaller meso-scale reactors (5 mm internal diameter). Mazubert et al. (2016) also used commercial CFD software to simulate laminar liquid flow through meso-scale COBRs with multiple designs of baffles. Several previous studies, which focused on turbulent flow, performed simulations for a small number of cavities (i.e. one to three) (Nogueira et al., 2013).

Our results show that the developed CFD model can be used to predict turbulent liquid flow in larger-scale COBRs and that such model can provide more reliable information compared to the more traditional models, such as the AD model.

One of the critical parameters which can affect the solutions of CFD models in various simulations is mesh refinement and its convergence. To that end, we conducted simulations with several mesh densities (i.e. lower and higher densities) in order to choose optimal mesh density, which both do not extensively affect the final results and does not slow down the simulations. Results with the optimized mesh density were within 2% of those obtained with a very fine mesh.

3.2 Analysis of turbulent flow in COBR

The mechanism of oscillatory flow mixing in COBRs was examined in the literature. However, previous studies focused on experiments where flow oscillations were generated by either a piston which periodically moves the entire fluid volume inside the reactor or mechanical periodic movements of baffles inside the reactor tube or movements of the entire reactor (i.e. column). These approaches result in a significant amount of backflow, and are in addition costly in terms of additional equipment and devices. In our experiments, input flow oscillations are generated by a dosing membrane

pump which supplies the reactor with the fluid. In this type of design, fluids' forward flow rate is significantly higher than the backflow rate, due to the use of a non-return valve positioned after the pump. Thus, the mechanism of oscillatory flow mixing warrants a further evaluation for this case.

Simulation results were analysed in terms of velocity streamlines and intensity, vorticity, turbulent viscosity and kinetic energy for several key moments during each oscillation (marked A – E in Figure 1). Figure 3 shows the velocity streamlines for two sets of conditions. At higher inlet flowrates and oscillation frequency ($Re_n = 678$ and $Re_o = 2458$), velocity streamlines show that before the stroke of the oscillatory wave (period A), there is a recirculation of flow and mixing. Fluid energy is insufficient to be transported into the next or previous cavity, but is mixed inside of the current one. When the oscillatory component of flow is active (periods B, C and D), there is no considerable radial flow mixing and fluid energy is used for its transport through the reactor. At that time the flow core is formed by fluid moving through the baffle openings at higher velocities. However, a small fraction of fluid circumvents the baffles and moves along the tube walls at significantly lower velocities, due to loss of energy from the collision with the rings and wall friction (laminar flow). At the period after the stroke of the oscillatory flow wave (period E), inertial forces are decreased and there is intense (radial) fluid mixing. It is at this time turbulent eddies are formed, and their concentration is highest in the volume right behind the baffles. At lower flowrates and oscillation frequency ($Re_n = 142$ and $Re_o = 670$), the behaviour is quite different and fluid mixing is not pronounced in periods A-D. In this case, intense mixing only occurs in period E after the oscillatory flow wave impact.

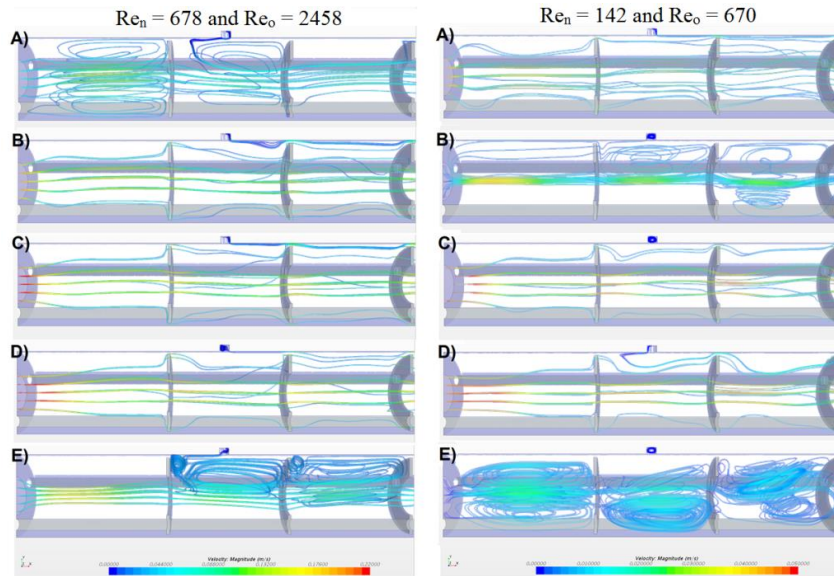


Figure 3 – Velocity streamlines at higher inlet flowrates and oscillation frequency (left figure) and lower flowrates and oscillation frequency (right figure) for characteristic time periods (periods A – E shown in Figure 2).

In both cases (high and low flowrates and oscillation peak velocities), observed vorticity before the oscillatory flow wave (period A) is minimal. This is due to the low backflow

in our system. At the stroke start, during and right after the wave impact (B, C and D), vorticity increases in areas of fluid collision with the baffles. After the impact (period E), vortices spread within the same cavity, but decrease in intensity. The values of turbulent viscosity show the turbulent transport is dominant in both cases and the laminar layer only exists close to the walls. The laminar layer width for high and low inlet flowrates and oscillation frequency case is 0.5 – 2 and 2 – 4 mm, respectively.

4. Conclusions

3D CFD model of the oscillatory flow of liquid in turbulent regime inside of COBR was developed using STAR CCM+ software. The model included a large number of cavities and was validated by direct comparison to RTD experiments for several flowrates and oscillation frequencies. The developed CFD model was shown to outperform the classical AD model, based on literature correlation for Peclet number. The analysis of velocity streamlines, vorticity and turbulent viscosity, obtained with minimal backflow related to the generation of oscillations, revealed specific findings about fluid mixing inside of COBR with this particular design. Recirculation of fluid flow occurs when the oscillatory component of flow is not active, but its intensity can be affected by manipulating the magnitude and frequency of the flow. Turbulence is most intense in moments before and after the fluid wave collision. Higher frequencies and flowrates intensify the momentum transfer and cause for a higher fraction of reactor volume to be used in turbulent fluid mixing.

Acknowledgements

This work was realized within the framework of national projects funded by the Ministry of Education, Science and Technological Development of the Republic of Serbia [III 46001, III 46010 and 172022]. Branislav Todić would like to gratefully acknowledge the financial support of the Joint Japan-Serbia Center for the Promotion of Science and Technology and the ITO Foundation for this research.

References

- A. A. Hamzah, N. Hasan, M. S. Takriff, S. K. Kamarudin, J. Abdullah, I. M. Tan, W. K. Sern, 2012, "Effect of oscillation amplitude on velocity distributions in an oscillatory baffled column (OBC)", *Chem. Eng. Res. Des.*, 90, 1038-1044.
- H. G. Jolliffe, D. I. Gerogiorgis, 2018, "Process modelling, design and techno-economic evaluation for continuous paracetamol crystallisation" *Comput-Aided Chem. Eng.*, 43, 1637-1642.
- E. N. Kimuli, I. I. Onyemelukwe, B. Benyahia, C. D. Riellya, 2017, "Characterisation of axial dispersion in a meso-scale oscillatory baffled crystalliser using a numerical approach", *Comput-Aided Chem. Eng.*, 40, 223-228.
- A. Mazubert, D.F. Fletcher, M. Poux, J. Aubin, 2016, "Hydrodynamics and mixing in continuous oscillatory flow reactors—Part I: Effect of baffle geometry", *Chem. Eng. Process.*, 108, 78-92.
- X. Ni, H. Jian, A.W. Fitch, 2002, "Computational fluid dynamic modelling of flow patterns in an oscillatory baffled column", *Chem. Eng. Sci.*, 57, 2849 – 2862.
- X. Nogueira, B. J. Taylor, H. Gomez, I. Colominas, M. R. Mackley, 2013, "Experimental and computational modeling of oscillatory flow within a baffled tube containing periodic-tri-orifice baffle geometries", *Comput. Chem. Eng.*, 49, 1-17.
- D. Slavnic, L. Zivkovic, A. Bjelic, B. Bugarski and N. M. Nikacevic, 2017, "Residence time distribution and Peclet number correlation for continuous oscillatory flow reactors", *J. Chem. Technol. Biotechnol.*, 92, 2178–2188.

Overpotentials in Water Electrolysis: In-Silico Comparison of PEM-cell and GAP-cell performance

Luisa C. Brée^a, Tobias Schiek^a and Alexander Mitsos^{a,*}

^a*Aachener Verfahrenstechnik - Process Systems Engineering, RWTH Aachen University, Aachen, Germany*
amitsos@alum.mit.edu

Abstract

Many studies focus on the performance of electrochemical reactors and very often result in presenting a polarization curve.

Modeling and simulation can simplify the examination of overpotentials, which reduce process performance, and thus help finding an improved electrolyzer for an envisaged application. Moreover, they are useful for optimization of the design and operation at process level.

Herein, we develop a mechanistic, dynamic model for electrochemical water splitting and compare two established cell setups, the PEM-cell and the GAP-cell, in order to assess the performance and optimization potentials of these processes. We model ohmic overpotentials and mass transport limitations in order to show their impact on energy losses, especially towards higher cell potentials. Further, we consider the formation of gas bubbles which have been identified as major source of undesired overpotentials at high current densities. We model this decrease of the effective electrode area via geometrical considerations using experimental investigations of bubble dynamics, including the formation, growth, and detachment of single hydrogen bubbles during electrolysis carried out by Yang et al. (2015).

A parameter estimation results in a good match of the experimental data and the simulation results. For the GAP-cell, the contribution of different overpotentials to the whole electrolyzer performance is determined with high accuracy.

We use the model to show reachable current densities, cell efficiencies and dominant loss terms of the reactor setups and thus indicate optimization possibilities and potentials.

Keywords: water electrolysis, rigorous modeling and simulation, overpotential distribution, performance comparison

1. Introduction

Electrolyzers face increasing overpotentials towards high cell potentials reducing the energy efficiency of the reactor. At elevated cell potentials, the reactors even tend to reach a limiting current density with high energy losses due to mass transport limitations or electrode coverage by evolving product gases. Therefore, an optimal operating point balances high product formation and high energy losses. Additionally, different concepts of electrolyzer setups exist with specific dominating overpotentials, such that depending on the type of application, one or the other setup must be selected. Therefore, the most beneficial combination of setup and cell potential should be found for an envisaged application.

To simplify this search, research activities in the field of electrochemical cell modeling is extensive and numerous models exist for various applications, setups or even individual components. These models vary in their level of detail, including 0D, 1D, 2D or even 3D models, the number

of assumptions taken into account, etc. For instance Wu (2016) presents a review on transport and performance modeling of PEM fuel cells.

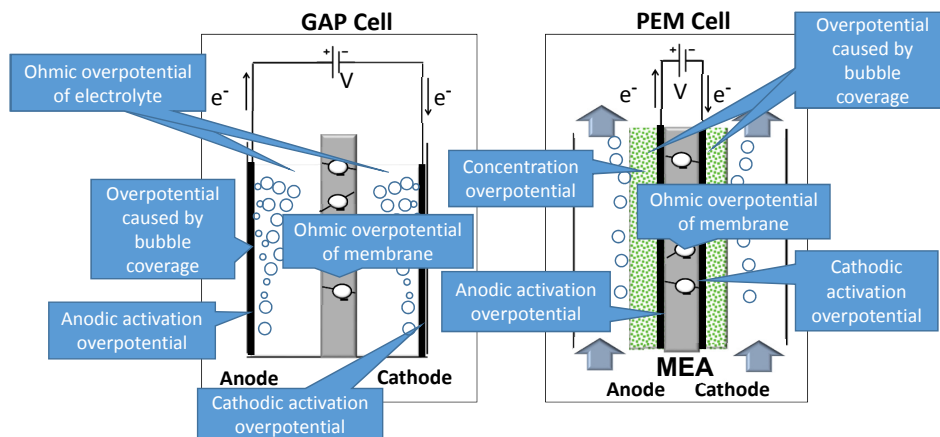


Figure 1: Scheme of both reactor setups with overpotentials taken into account in the model.

A classic application of electrolysis is water splitting. Here, the oxygen evolution reaction (OER) occurs at the anode and the hydrogen evolution reaction (HER) at the cathode. There are (among others) two established cell setups for water electrolysis: The older and more common is the alkaline GAP-cell, where an aqueous ionic solution as liquid electrolyte is present. The newer setup is the Proton Exchange Membrane (PEM) electrolysis. Here a solid polymer like Nafion is used as a membrane and electrolyte at the same time (see Fig. 1).

In order to assess the performance and optimization potentials of these processes, we develop dynamic models for water electrolysis in an electrochemical membrane reactor (ecMR) with both cell setups. Dynamic models allow the analysis of control-strategies or demand side management, though, for the herein presented results the dynamics are not needed. The models take into account all important overpotentials mostly via state-of-the-art equations found in literature. We introduce a new model for simulating the overpotential due to bubble formation.

The models are validated with experimental data from literature and unknown parameters are determined. Simulations are then executed to characterize the behaviour of each setup. Knowing the influence of relevant loss terms, individual optimization approaches can be developed for each setup.

2. Modeling

We develop dynamic models for potentiostatic electrochemical water splitting in a PEM-cell and a GAP-cell for unpressurised reactors at room temperature based on mass balances, transport equations and electrochemical kinetics. This results in models considering the overpotentials shown in Figure 1. Additionally, we assume ideal gases, 100 % Faradaic efficiency, fully hydrated membranes, no cross-over of gases and a uniformly distributed current across the cell.

In a PEM-cell the reactants need to pass through the porous gas diffusion layers (GDL) to reach the electrode-membrane interface, the products need to be removed from this site of the electrochemical reaction. We describe the transport through the GDL via mass balances with diffusion by Fick's law. In a GAP-cell, the electrodes are immersed in an ionic solution. Here, we model mass transport through the electrolyte via mass balances taking into account diffusion and migration, as

well as ionic equilibria with pH-calculation. Mass transport limitations causes the concentration of reactants to decrease and of products to increase leading to concentration overpotentials at the electrodes' surfaces.

We relate the molar consumption and production rates of the electrochemical reactions to the cell's current density by Faraday's law. The effect of changing concentrations on the concentration overpotential is then calculated via the Nernst equation (Newman and Thomas-Alyea, 2004).

The electrochemical reactions are induced by activation overpotentials. We calculate this activation loss via the Butler-Volmer equation (Newman and Thomas-Alyea, 2004) and use experimental results for nonlinear regression to estimate the reaction specific transfer coefficients α and exchange current densities j_0 .

Ohmic overvoltages are caused by the resistance to the flow of electrons or ions by the electrolyte, the electrodes and their various interconnectors. According to Ohm's law, we correlate the ohmic overvoltage linearly proportional to the current by the conductivity factor.

In water electrolysis, a water flux through the membrane occurs, which is governed by: (i) electro-osmotic drag, (ii) diffusion driven by a concentration gradient and (iii) convection if a pressure gradient is present. In this study, no pressure gradient is considered.

The physical blocking of the electrodes in both setups by the gaseous reaction products is named as major source for undesired overpotentials according to Yang et al. (2015), though, no modeling approach could be found in literature. Therefore, we describe a first approach to model this effect:

Influence of electrode coverage by product gases The gas bubbles are formed at the surface of the electrode where they grow until the uplift force exceeds the surface forces binding the bubbles to the electrodes. During the time span τ from formation till detachment, the gas bubbles reduce the effective surface of the electrode that can be used for electrochemical reactions.

$$\eta_{ohm_{el}} = \frac{R_{0_{el}} I_{total}}{A_{rel}} \quad (1)$$

<p style="text-align: center;">GAP</p> $A_{rel,GAP} = \frac{A_0 - A_{cov}}{A_0}$ $A_{cov} = \frac{\pi d_{contact}^2}{4} number_{bub}$ $number_{bub} = \frac{V_{gas}}{\bar{V}_{bub}}$	<p style="text-align: center;">PEM</p> $A_{rel,PEM} = \frac{V_0 - V_{gas}}{V_0}$ $V_0 = x \cdot A_{PEM} \cdot \varepsilon$
---------------------------------------------------------------------------------------------------------------------------------------------------------------------------------------------	-----------------------------------------------------------------------------------------------------------------------------------

$$V_{gas} = \dot{V}_{gas} \tau \quad (3)$$

$$\dot{V}_{gas} = \frac{\dot{n}_{gas} R_{ig} T}{p} \quad (4)$$

For modeling the overpotential due to bubble formation, we introduce a dimensionless variable A_{rel} into the ohmic relationship of the electrode's overpotential as shown in Eq. (1). A_{rel} describes the fraction of the total electrode surface, which can still be used for electrochemical reactions, and is calculated according to Eq. (2) comparing the original electrode surface A_0 to the covered electrode surface A_{cov} for the GAP-cell and for the PEM-cell via comparing the product gas volume in the catalyst layer V_{gas} and the inner reactive pore volume of the GDL $V_{0,GDL}$. This allows to introduce a linear relationship between the resistance and the (un)covered area with an infinite resistance when the whole surface is covered by bubbles. $R_{0_{el}}$ is the electrode's electric resistance when fully surrounded by water. This resistance is the product of the specific electric resistance of the electrode's material and a geometric factor. For determining A_{cov} , we calculate the number of bubbles $number_{bub}$ using the total volume of produced gas V_{gas} and the mean volume of a single bubble $\bar{V}_{bub} = 0.45e^{-12} \text{ m}^3$ which was calculated by averaging time dependent bubble radii measured by Yang et al. (2015). The mean diameter of the contact area $d_{contact} = 80 \mu\text{m}$ is taken from the same data and probably a parameter dependent on \bar{V}_{bub} .

Using the ideal gas law (4), we calculate the volume flows of the evolving gases \dot{V}_{gas} from the electrochemical consumption and production rates giving the total volume of gas bubbles bound to the electrode via Eq. (3). The simplified assumption of spherical bubbles is justified as the con-

tact angles between bubble and surface were small with values between 5° and 15° (Yang et al., 2015). V_0 for the PEM-cell is calculated using the GDL's porosity ε , its thickness x and the cross sectional area of the PEM-cell A_{PEM} .

3. Results

In Figure 2 we show the results of the parameter estimations comparing simulated and experimentally determined polarization curves for both reactor setups (upper row) as well as an analysis of the prevailing overpotentials (lower row). The estimated parameters are listed in Table 1. Note that τ for the PEM-cell is estimated as the value from literature holds for electrodes freely immersed in a liquid. The assumption of a constant membrane's proton conductivity is based on a well hydrated membrane due to the electro-osmotic drag. Especially for the GAP-cell it has to be noted, that the Butler-Volmer parameters correlate strongly and therefore, could not be identified.

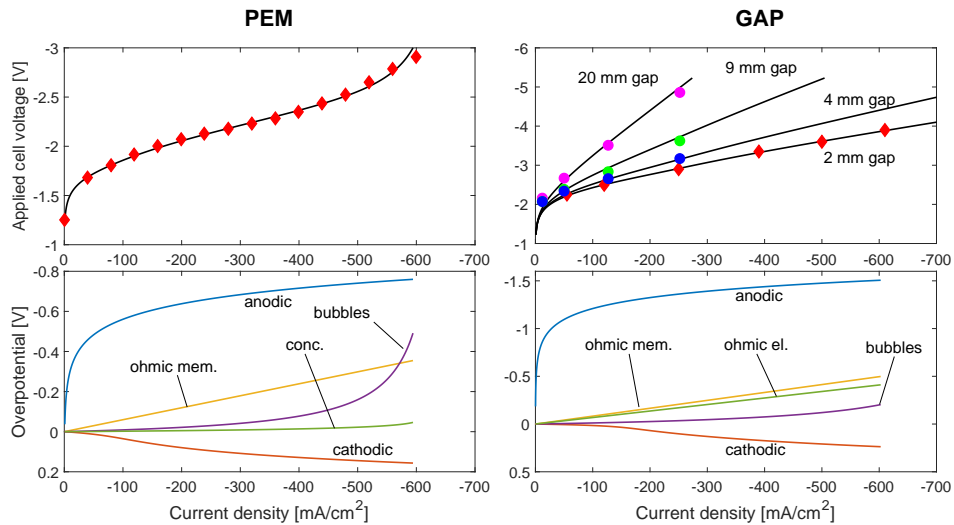


Figure 2: Top row: Polarization curves (black line: simulation results; Red diamonds: experimental data by Dedigama et al. (2014) for PEM-cell and by Phillips et al. (2017) for GAP-cell used for parameter estimation; Blue/green/purple circles: experimental data by Phillips et al. (2017) used for model validation). Bottom row: Overpotentials depending on current density for PEM-cell and GAP-cell with 2 mm gap. (shown: anodic activation; cathodic activation; ohmic overpot. of membrane; ohmic overpot. of electrolyte; concentration overpot.; overpot. caused by gas bubbles).

PEM-cell With parameter estimation, we achieve a good match of the experimental and simulated data for the PEM-cell, even for high applied cell voltages (Figure 2, upper row, left). Close to the onset potential, the cell behaviour depends almost completely on the anodic activation overpotential (see Figure 2, lower row, left). This is caused by a high activation energy of the water splitting reaction which is a consequence of a non-optimized platinum electrode used in the experiments. A catalyst optimized for the OER reaction could lower this loss term significantly.

The current density shows the characteristic exponential rise governed by the reaction kinetics which turns into a linear section governed by ohmic overpotentials. The ohmic overpotential exhibits a fairly high influence compared to standard PEM-cells. Simulations with the same model with a typical value for fully hydrated Nafion membranes of $9.4 \frac{\text{S}}{\text{m}}$ results in a significantly lower ohmic overvoltage of 0.12 V at $600 \frac{\text{mA}}{\text{cm}^2}$.

The concentration overpotential is low, indicating a sufficient transport of reactants through the

Table 1: Estimated model parameters. α : transfer coefficient; j_0 : exchange current density; D_{H_2O} : diffusion coefficient; κ : proton conductivity; an : at anode; cat : at cathode; mem : in membrane; el : in liquid electrolyte

Symbol	Value PEM (*)	Value GAP(*)	Unit
α_{an}	0.89(± 0.01)	0.92(± 2.2)	–
α_{cat}	0.15(± 0.02)	0.08(± 2.82)	–
$j_{0,an}$	7.16(± 1.61)	0.66(± 131)	A·m ⁻²
$j_{0,cat}$	657(± 118)	1286(± 48780)	A·m ⁻²
τ	0.036(± 0.001)	–	s
$D_{H_2O,mem}$	$1.1 \cdot 10^{-10}$ ($\pm 1.86 \cdot 10^{-10}$)	$9.62 \cdot 10^{-11}$ (± 0.99)	m ² ·s ⁻¹
κ_{mem}	2.98(± 0.1)	–	S·m ⁻¹

(*90% confidence interval)

GDL. Towards higher current densities the gradient of the current density curve increases going over to an asymptotic course due to increased gas production and an exponential rise of the overvoltage caused by gas bubbles.

To reach higher current densities with the PEM-cell, the removal of gases through the GDL has to be improved. While the study by Dedigama employs a GDL with a porosity of 0.4, porosities over 0.5 are available on the market. Another possibility is the employment of water vapour instead of liquid water. Here, bubble formation can be avoided but this has to be contrasted with a much lower water concentration.

The efficiencies calculated with the PEM-model for the experimental setup by Dedigama are fairly low. At a typical current density for industrial applications of 500 $\frac{mA}{cm^2}$ the efficiency is only 46 %. Simulating the same model with a membrane conductivity elevated to the literature value of 9.4 $\frac{S}{m}$ causes a small improvement to 50%. At a lower current density of 200 $\frac{mA}{cm^2}$ the cell efficiency reaches 61 %, which is significantly lower than typical values shown by state of the art PEM-electrolyzers located around 76 % (Bertuccioli et al. (2014)) at the same current density. To reach desired efficiency values in the range of 80 % or higher, the utilization of an optimized catalyst material is mandatory.

Alkaline GAP-cell We validate the GAP-cell model with experimental investigations by Phillips et al. (2017) who varied the inter-electrode gap (the distance between anode and cathode) between 2 mm and 20 mm. We use the experimental results of the 2 mm cell for parameter estimation and achieve a good match of the simulated and experimentally determined polarization curve as shown in Figure 2 (upper row, right).

The ecMR investigated by Phillips shows a relatively high onset potential of 1.75 V due to the non optimized stainless steel electrodes used for the experiments. The current density rises exponentially. Around 2.5 V the curve reaches a linear section as the ohmic overpotential gains increasing influence on the ecMR's performance. The overvoltage caused by evolving gas bubbles is negligible at low and medium current densities and rises with a fast growing gradient at elevated current densities. However, at 600 $\frac{mA}{cm^2}$ the overvoltage is still rather small with a value of 0.20 V. Changing the inter-electrode gap-widths in the model, while keeping the estimated parameters constant we show that the simulations could be extrapolated to higher gap-widths (Figure 2, upper row, right, circles).

Comparison The course of the anodic activation overpotentials of both reactor setups is similar, the absolute value, however, is about twice as high as for the GAP-cell. This indicates that the chosen stainless steel electrodes in the GAP-cell experiments have a significantly lower catalytic activity for the OER than the platinum electrode employed in the PEM-cell experiments. Even though different cathodes were also employed, this influence seems negligible, as the cathodic activation overpotentials reach similar values for PEM and GAP-cell. The ohmic overpotential of

the membrane used in the GAP-cell experiments shows a higher value than the Nafion membrane in the PEM-cell. The maximum total ohmic overvoltage of the GAP-cell at $600 \frac{\text{mA}}{\text{cm}^2}$ of 0.90 V is much higher than the ohmic overvoltage of the PEM-cell due to the additional ohmic resistance caused by proton movement in the electrolyte, only present in the GAP-cell.

For comparison purposes, we refer to a third study by Siracusano et al. (2017) which introduces an optimized PEM-cell. Instead of the typical Nafion membrane Aquivion was used as membrane material, which offers a higher proton conductivity along with a lower thickness. The second and most important improvement was the implementation of an $\text{Ir}_{0.7}\text{Ru}_{0.3}\text{O}_x$ catalyst for the OER. In simulations with these adjustments, the limiting current density remains the same, though high current densities are reached much faster with a competitive energy efficiency of 76 % at $200 \frac{\text{mA}}{\text{cm}^2}$.

4. Conclusion

In order to assess the performance and optimization potentials of different reactor setups for water electrolysis, we develop mechanistic, dynamic models for a PEM-cell and a GAP-cell. The models, based on mass balances, transport equations and electrochemical kinetics are mostly based on state-of-the-art equations found in literature. We introduce a new model for simulating the influence of evolving gas bubbles on the reactor's performance.

The models are validated with chosen experiments from literature. We determine unknown parameters by estimation under consideration of reasonable upper and lower bounds. A good match of simulated and experimental data is achieved. We show that the GAP-cell model is able to be extrapolated to different gap widths.

We investigate the reactor setups with regard to reachable current densities, cell efficiency and dominant loss terms. For the chosen experimental setups we show that high anodic activation overpotentials due to poor catalytic activity of the anodic electrode for the OER limit the performance in both cases. Another major limitation for the PEM-cell is the formation of bubbles. A higher GDL porosity and the change from a liquid to a gaseous inlet stream could be possible solutions.

Acknowledgements The study was conducted under the project Sustainable Chemical Synthesis (SusChemSys), which is co-financed by the European Regional Development Fund (ERDF) and the state of North Rhine-Westphalia, Germany. The authors gratefully acknowledge the financial support of the Kopernikus-project SynErgie by the Federal Ministry of Education and Research (BMBF) and the project supervision by the project management organization Projektträger Jülich (PtJ). We are also grateful to Kristina Baitalov for valuable discussions.

References

- Bertuccioli, L., Chan, A., Hart, D., Lehner, F., Madden, B., Standen, E., 2014. Study on development of water electrolysis in the eu. Final report in fuel cells and hydrogen joint undertaking.
- Dedigama, I., Ayers, K., Shearing, P. R., Brett, D. J., 2014. An experimentally validated steady state polymer electrolyte membrane water electrolyser model. *International Journal of Electrochemical Science* 9 (5), 2662–2681.
- Newman, J., Thomas-Alyea, K., 2004. *Electrochemical systems*, chapter 8: Models for electrode kinetics. John Wiley & Sons, 212–213.
- Phillips, R., Edwards, A., Rome, B., Jones, D. R., Dunnill, C. W., 2017. Minimising the ohmic resistance of an alkaline electrolysis cell through effective cell design. *International Journal of Hydrogen Energy* 42 (38), 23986–23994.
- Siracusano, S., Baglio, V., Van Dijk, N., Merlo, L., Aricò, A. S., 2017. Enhanced performance and durability of low catalyst loading pem water electrolyser based on a short-side chain perfluorosulfonic ionomer. *Applied Energy* 192, 477–489.
- Wu, H.-W., 2016. A review of recent development: Transport and performance modeling of pem fuel cells. *Applied Energy* 165, 81–106.
- Yang, X., Karnbach, F., Uhlemann, M., Odenbach, S., Eckert, K., 2015. Dynamics of single hydrogen bubbles at a platinum microelectrode. *Langmuir* 31 (29), 8184–8193.

Study on the formation of chemical wave patterns for the *Belousov–Zhabotinsky* reaction system

Jiali Ai,^a Wei Sun,^a Chi Zhai^{a*}

^a*College of Chemical Engineering, Beijing University of Chemical Technology, North Third Ring Road 15, Chaoyang District, Beijing, 100029, China*

Abstract

The *Belousov–Zhabotinsky* (BZ) reaction system is famous because it can generate self-organized patterns, also known as “chemical waves”. Pattern formation out of an initially homogeneous system is seemingly violating the 2nd-law of thermodynamics (order is produced out of disorder), while in fact, the BZ reaction is an open, far-from thermodynamic equilibrium system, where instability is the cause of morphogenesis and Hopf bifurcation of the reaction kinetics can generate self-oscillatory state trajectories. In this paper, the evolution of the BZ reaction in a two dimensional diffusion system is studied by the numerical computation methods, for the purpose of reconstructing the chemical wave patterns. The similarity of the chemical waves to many complex systems in biology, ecology and engineering makes current study potentially significant. With the study of the pattern formation, we hope provide some thoughts on complex system theory, thermodynamics of the self-oscillatory reaction system, and numerical computation methods on complex patterns, etc.

Keywords: far-from thermodynamic equilibrium, instabilities, reaction-diffusion system, Hopf bifurcation.

1. Introduction

As early as 1950s, Turing (1952) has studied the possibility of morphogenesis out of a diffusive-reactive system. While, Pattern formation out of an initially homogeneous system is seemingly violating the 2nd-law of thermodynamics (order is produced out of disorder), and is contradictory to the “equilibrium hypothesis” of the classic thermodynamics. Hence, instabilities may be the reason of morphogenesis, and since then, nonlinear dynamic theory has been introduced to study nonequilibrium systems. Prigogine (1978) expanded the domain of thermodynamics and developed the dissipative structure theory. By his theory, far from thermodynamic equilibrium may be the source of order (also means entropy decrease), and when the system is open and far from thermodynamic equilibrium, fluctuation could make the system unstable and self-organized patterns may form instead.

It is obvious that BZ reaction is a dissipative structure system because time-symmetric breaking bifurcation has taken place. In fact, various types of bifurcations may be the source of bio-complexity (Kitano, 2002). As for the BZ reaction kinetics, Hopf bifurcation causes the equilibrium point being unstable, changing stability via a pair of purely imaginary eigenvalues, and giving birth to a self-oscillator in the dynamic system, while the cooperative action of reaction and diffusion causes the (distributive) system to generate chemical-waves. As is shown in Fig. 1, when the 2-dimensional system is properly meshed, every “dot” on the picture can be viewed as a homogeneous subset,

and they are identical because they all follow relation of BZ reaction kinetics. One can view the dots as agents who behave self-oscillatory state trajectories (or, change color periodically), and each dot exchanges information with its neighbor by following the Fick's law of diffusion, then, mass transfer by diffusion causes time-delay, hence as a whole, all dots exhibit chemical wave patterns.



Fig. 1. Pattern of the diffusive *Belousov-Zhabotinsky* reaction.

Traditionally, one can adopt numerical simulation method to solve a mathematical model, ie, a reaction-diffusion system, established on a chemical wave physical background in a specific reaction system on a computer. Since a set of partial differential equations are obtained for this BZ reaction system, often a finite elements method is adopted, which meshes the 2-dimension reaction region into subsets, each is assumed to be homogeneous at very short time interval; while each subset correlates to its neighbors by diffusion law. Therefore, one can summarize that, for the formation of a complex pattern as shown in Fig. 1, identical agents are distributed in 2-dimensional reaction field, and by diffusion law, these agents transfer information to one another, which is coherent to the idea of “cooperative information consensus” (Olfati-Saber, et al, 2007) in computer science terminology. Hence, the formation of chemical wave is studied by a decomposed procedure: the property of agent first, then, information exchange between agents.

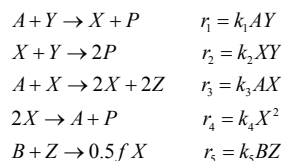
The algorithm of cellular automata (CA) is introduced in this study; this method is a parallel, temporally and spatially discrete one proposed by Von Neumann (1966). The basic idea of CA computation is that the agent should follow specific dynamics which is comparatively independent to the environment, and each agent will exchange information with its nearest neighbors by a few rules. Different from the traditional way of thinking, the CA adopts a bottom-up computing strategy, which uses simple unit changes and unit interaction to show the changes of complex systems, reflecting a systematic and integrated way of thinking. As to the development of the CA algorithm, Conway developed a program called a life game using a cellular automaton. After that, Wolfram gave a more systematic explanation of the cellular automata, classifying the cellular automata according to the dynamic behavior (Tyson, et al, 1980), and further expanding the original one-dimensional system to two-dimensional one (Wang et al, 2018).

Since CA computation provides a framework of studying the complex system, namely, decomposing the system into time-dependent independent agents and locally information exchange in a special scale. Hence, for the study of chemical waves, the

following section is focused on the property of the BZ reaction kinetics, then, information exchange rules between agents, followed by the exhibition of CA simulation, at last, the conclusion remarks are provided.

2. The BZ reaction kinetics: a self-oscillator

Many models have been developed for BZ reaction kinetics, and the Oregonator is adopted here because it describes the self-oscillatory behavior properly, 5 species are identified and their reaction relations are provided as follows,



Species identification with respect to the Field-Koros-Noyes (FKN) mechanism (Field, 1972) are $X = \text{HBrO}_2$, $Y = \text{Br}^-$, $Z = \text{Ce(IV)}$, $A = \text{BrO}_3$, $B = \text{Organic species}$, $P = \text{HOBr}$, and f is an adjustable stoichiometric factor. In fact, this is the reduction reaction of bromide iron, the overall reaction is $A + B \rightarrow P$, while X , Y and Z are the intermediate species. The reactant species A and B are normally presented in much higher concentrations than the dynamic intermediate species X , Y and Z , and when A and B are viewed as constants, and a dynamic model is developed out of the Oregonator,

$$\begin{cases}
 X' = k_1 AY - k_2 XY + k_3 AX - 2k_4 X^2 \\
 Y' = -k_1 AY - k_2 XY + 0.5fk_5 BZ \\
 Z' = 2k_3 AY - 0.5fk_5 BZ
 \end{cases} \quad (1)$$

From the viewpoint of dynamic system theory, nonlinearity of the intermediate terms (X , Y , Z) brings about a Hopf bifurcation where increasing one of the parameters beyond the critical point may cause a self-oscillatory structure to emerge. By properly normalizing of Eq. (1), bifurcation analysis can be implemented, and one can find that the working point ($f = 0.53$) is at the self-oscillatory region, as is shown in Fig.2.

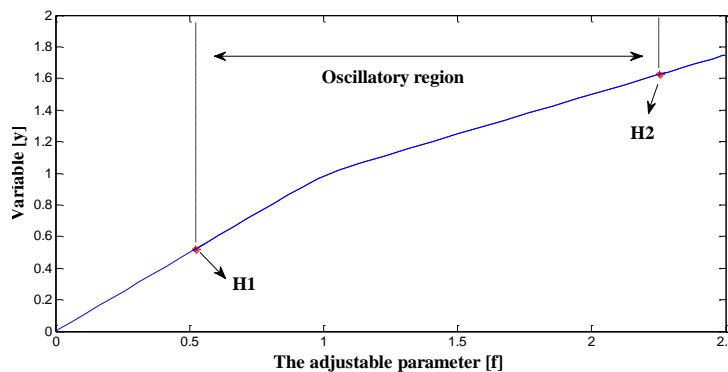


Fig. 2. Numerical continuation and bifurcation of the Oregonator with varying f .

3. Cellular automation and the results

A complete cellular automaton consists of four parts: cells, cellular space, neighbors, and local rules, where the cell is the self-oscillator, the neighbors and the local rules are the interaction ones and their properties nearest to the considered cell, and space related to the mesh space and cell numbers.

To determine the local rules, the property of the oscillator needs to be re-investigated. Here, the Tyson model is used, which is the normalization of the Oregonator,

$$\begin{cases} \varepsilon a' = (qc - ac + a - a^2) \\ b' = a - b = g(a, b) \\ \delta c' = (-qc - ac + 2fb) \end{cases} \quad (2)$$

Since $\varepsilon \ll \delta \ll 1$, one can get that $-qc - ac + 2fb \approx 0$. Substitute this relation to the 1st-formula of Eq. (2), and the right hand side of this formula becomes $f(a, b)$. To determine the local rules, the nullclines is drawn on the (a, b) plane, as is shown in Fig.3.

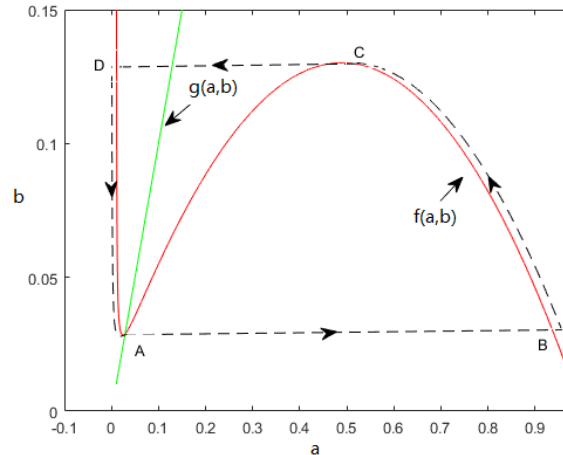


Fig. 3 The nullclines of the Tyson model.

The dashed line indicates the actual trajectory of the change of the state. At the intersection of the two zero lines is the only equilibrium point of the system, and is the equilibrium point of the local asymptotic stability. When the equilibrium is subjected to small disturbances, the medium can return fast; but once the disturbance exceeds a certain threshold, the change in the medium will pass through the excitation period, then, the drift period before it can finally return to the equilibrium state. In detail, the local rules are given in Fig. 4.

For the neighbors, the extended Moor type neighboring is selected. Since the diffusive character is decided by neighboring, one can select a weight *mask* to represent the effect of the distance on the cell. It can be seen from the simulation comparison that the *mask* has a good approximation to the diffusion coefficients, as is shown in Fig. 5.

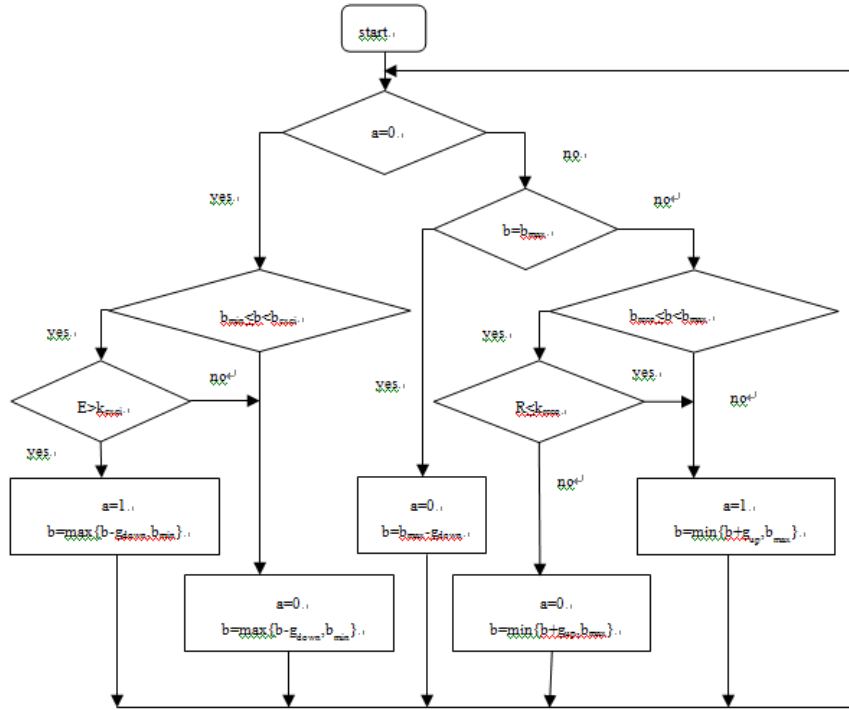
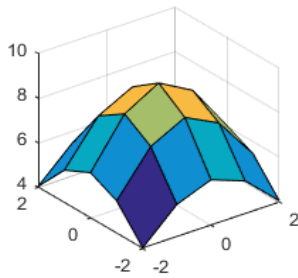
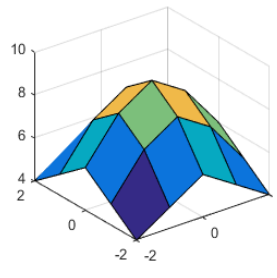


Fig 4. CA block diagram



(a) actual diffusion coefficient effect



(b) mask

Fig 5. Comparison the mask and the diffusion coefficient.

With all the preceding work done, one can implement the CA computation. The result of the simulation on MATLAB is shown at Fig6.

4. Conclusions

By CA computation, the spiral wave is generated, as shown in Fig. 6, which simulates reasonable well the pattern of the diffusive BZ reaction shown in Fig. 1 Therefore, the

formation of complex system (such as the chemical waves) usually undergoes two scales of evolution: on time scale, the agents exhibit unique dynamic behavior, i.e., in the case of chemical waves, the reaction kinetics exhibits self-oscillatory state trajectories; on the spacial scale, an agent exchanges information with its neighbors by some kind of local rules, i.e., in current case, identical agents behave mass transfer with their neighbors by diffusion law. As a whole, chemical waves propagate in time and space. Through the deconstructing procedure, one can conclude that the formation of complex chemical wave patterns is caused by agents obeying typical local rules, and this analyzing structure may aid the exploration of other complex systems in biology, ecology and engineering.

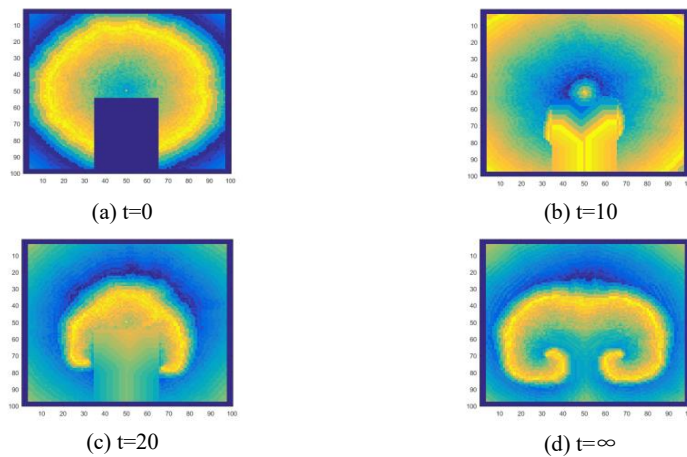


Fig. 6 Spiral wave solution of the cellular automaton.(where t means time steps).

References

- Turing A.M., 1952. The Chemical Basis of Morphogenesis, *Biological Sciences*, 237(641), 37-72.
- Kitano H., 2002, Systems biology: a brief overview. *Science*, 295, 5560, 1662-1664.
- Prigogine, I., 1978. Time, structure, and fluctuations. *Science*, 201(4358), 777-785.
- Olfati-Saber, R., Fax, J.A., Murray R.M. Consensus and cooperation in networked multi-agent systems. *Proceedings of the IEEE*, 2007.
- Von Neumann J. 1966, Theory of self-reproducing automata. University of Illinois Press.
- Field, R. J., Koros, E., Noyes, R. M., 1972. Oscillations in chemical systems. II.. *Journal of the American Chemical Society*, 94(25), 8649-8664.
- Tyson J.J., Fife P.C. 1980, Target patterns In a realistic model of the Belousov-Zhabotinskii reaction. *Chem. Phys.* 73, 2224-2237.

Efficient design of intensified extractive distillation processes based on a hybrid optimization approach

Kai Fabian Kruber^a, Tamara Grueters^a, Mirko Skiborowski^{a,*}

*^aTU Dortmund University, Department of Biochemical and Chemical Engineering,
Laboratory of Fluid Separations, Emil-Figge-Straße 70, 44227 Dortmund, Germany*

mirko.skiborowski@tu-dortmund.de

Abstract

Solvent-based separation processes, such as extractive distillation, show large potential for the separation of azeotropic mixtures. However, these processes are rather complex to design and optimize since the overall process performance depends strongly on the choice and amount of solvent and can only be evaluated for a process flowsheet with closed recycles. It is important to note that the potential for heat integration also depends strongly on the solvent choice. Consequently, a successive selection of a suitable solvent followed by process design and optimization and finally energy integration likely results in suboptimal choices. In order to allow for direct optimization of an extractive distillation process, including solvent selection and different means for energy integration, the current study proposes the use of a hybrid evolutionary-deterministic algorithm. The application is demonstrated for the separation of an azeotropic acetone-methanol mixture, considering six solvent candidates and up to four alternative means for energy integration. The results illustrate the existence of a multitude of suboptimal local solutions and demonstrate the capability of the proposed method to effectively overcome these limitations.

Keywords: hybrid optimization, evolutionary algorithm, solvent selection, energy integration

1. Introduction

The design of efficient separation processes is one of the key challenges for conceptual process design, as it accounts for almost 50 % of the overall process costs (Blahušiak et al., 2018). A considerable challenge, especially in the scope of a transition to bio-renewable feedstocks, is the separation of azeotropic mixtures (Skiborowski et al., 2013). Solvent-based separation processes, such as extractive distillation, are popular solutions for which process design is, however, a rather complex task. A key design decision is the choice of a suitable solvent that facilitates the desired separation and can be efficiently recovered. Since the choice of a suitable solvent is of major importance for the feasibility and performance of the separation process, a variety of computer-aided methods have been developed in order to support the solvent selection. Methods for computer-aided molecular design (CAMD), like the multi-level generate and test procedure by Harper and Gani (2000), screen solvents based on thermodynamic criteria, such as capacity and selectivity. The set of selected solvents can further be refined by a model-based evaluation of the process performance, for which shortcut methods and rigorous flowsheet optimization can be applied in a hierarchical fashion (Kossack et al., 2008, Kruber et al., 2018). Herein, the combination with a quantum mechanics-based property prediction

allows for the screening of thousands of solvent candidates based on computationally efficient shortcut methods (Scheffczyk et al., 2016).

While similar methods have been proposed for several solvent-based separation processes, the investigation of energy integration is generally considered as a potential post-processing step, similar to the classical hierarchical approach to process design (Douglas, 1985). In the case of distillation-based separation processes, there are various options for energy integration, which need to be considered (Kiss et al., 2012). Especially for solvent-based processes, such as extractive or heteroazeotropic distillation, energy integration can have a considerable effect on the screening of potential solvents, as e.g. indicated in the recent study by Waltermann et al. (2018). Thus, simultaneous evaluation of energy integration and solvent selection should be performed in order to identify the optimal process design and best solvent. While this task can in principle be formulated as a mathematical programming problem, the solution to this problem is specifically complex. In order to enable an automated evaluation that overcomes suboptimal solutions, the current work proposes of the combination of hybrid evolutionary-deterministic optimization approach (Skiborowski et al., 2015a) with a tailored polylythic modeling and solution approach, considering rigorous MESH models (Waltermann et al., 2018). To the best of the author's knowledge, this is the first approach that enables an optimization-based design of an extractive distillation process with simultaneous consideration of solvent selection and energy and mass integration. The methodology is described in Section 2, while the case study for acetone-methanol separation and the obtained results are discussed in Section 3. Finally, Section 4 provides a brief conclusion and outlook on future work.

2. Methodology

In order to solve the highly complex process design problem, it is formulated as a mixed integer nonlinear programming problem (MINLP), which is solved by a two-level hybrid evolutionary-deterministic optimization approach. The concept of this approach, which also qualifies as a so-called memetic optimization algorithm, was introduced by Skiborowski et al. (2015a). The specific difference to other memetic algorithms, like the sophisticated method of Urselmann and Engell (2010), is the distinct feature that a full MINLP is solved by the gradient-based solver on the lower level. Thereby the search-space of the evolutionary algorithm (EA) is reduced significantly. The subsequent subsections provide a brief description of the hybrid optimization approach and describe the performed extension for additional means for energy integration.

2.1. Hybrid optimization approach

As indicated in Figure 1, the hybrid approach is a nested combination of an EA and a local deterministic optimization. The local deterministic optimization is performed in order to evaluate the fitness of the individuals in each generation of the EA. However, the genome of each individual is not representing all design degrees of freedom (DDoF) of the process optimization problem. Only discrete decisions that significantly affect the size and complexity of the design problem and initial values for setting up the superstructure model for the local deterministic optimization are optimized by the EA. In the initial optimization of an extractive distillation process presented by Skiborowski et al. (2015a), the EA handled the choice of solvent, as this determines the structure and parameterization of the thermodynamic models, as well as the maximum number of equilibrium trays per column and the feed tray. In the current study, the conventional

process without energy integration (CONV) and additional four means for energy integration are considered, which are thermal coupling (TC), integration of both columns into a dividing wall column (DWC), direct heat integration (HI) and vapor recompression (VRC). As each of them requires modifications of the superstructure model, the type of energy integration is also introduced as DDoF optimized by the EA. This information extends the genome and is used for setting up the MINLP problem, which is to be solved by the local deterministic optimization.

2.2. Local deterministic optimization

The local optimization builds on a superstructure formulation, derived from the information of the genome that is to be evaluated in the EA. The superstructure is based on a rigorous MESH model with up to 190 equilibrium trays in total and a number of binary decisions w.r.t. the allocation for the feed, boil-up and recycle streams. The solution of this highly nonlinear MINLP is achieved via a polyolithic modeling approach that integrates implicit functions for VLE and enthalpy computations (Skiborowski et al., 2015b) and the solution of a series of successive relaxed NLP problems with additional NCP-functions. The necessary extensions for the optimization of the energy-integrated process variants are further described in the articles of Waltermann et al. (2016, 2018). Each of the variants builds on the initialization of the basic process variant, while specific modifications of the superstructure model are automatically introduced in a sequence of refinement steps and embedded optimization problems.

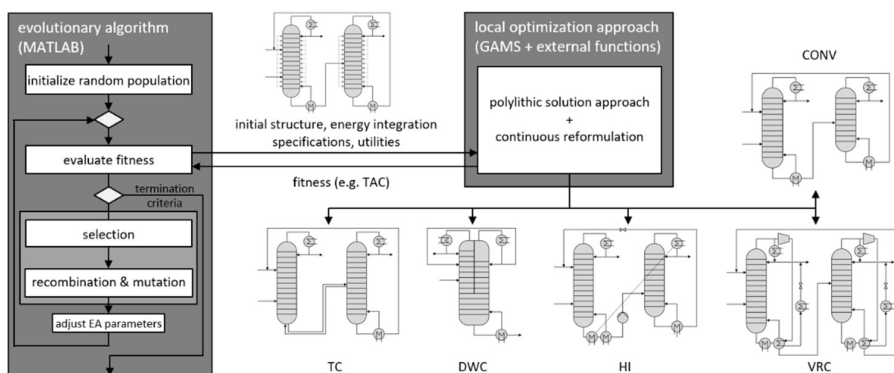


Figure 1: Scheme of hybrid optimization approach (based on Skiborowski et al. 2015)

3. Results

In order to illustrate the capabilities and the need for the developed optimization approach, the well-investigated separation of acetone and methanol is considered. Kossack et al. (2008) determined chlorobenzene, dimethyl sulfoxide (DMSO), ethanol, p-xylene, water and mesitylene as suitable solvent candidates based on an initial CAMD screening. Previous investigations showed that the hybrid optimization approach can reliably overcome local optima that might result in a sub-optimal solvent selection for the extractive distillation process (Skiborowski et al., 2015a), while the energy integration might again result in an alternative ranking of the different solvents (Waltermann et al., 2018). The objective of the current study is, therefore, to evaluate whether the extended hybrid optimization approach can reliably determine the optimal solvent choice for an

extractive distillation process with the considered options for energy integration. The optimal process design is determined w.r.t. the total annualized costs (TAC).

The same thermodynamic properties, as well as feed and product specifications that were used by Kossack et al. (2008) and Skiborowski et al. (2015a) are used in the current study. Only the economic process model was updated w.r.t. more recent cost indices and utility prices, which nevertheless has a recognizable effect on the results. Considering the previous investigation of the energy integrated process variants by Waltermann et al. (2018), the HI and VRC variant are not considered for the solvent DMSO, due to the significant pressure increase required for heat integration. Since the necessary pressure shift can be evaluated based on simple flash calculations for known product compositions, the complex optimization of the energy integrated variants should generally be avoided to save unnecessary computational load. For the current study, a (μ, λ, κ) -selection with 50 individuals and 15 parents with a maximum age of 6 generations is used, while an initial population size of 150 individuals is considered, covering all combinations of solvents and means of energy integration. The algorithm terminates in case the TAC of the best individual does not improve by more than 10 €/y, which is less than 0,005% of the best solution, in 3 consecutive generations. The optimization problem was solved on a HP Z820 workstation with two Intel Xeon E5-2660 CPUs and an evaluation of up to 24 individuals in parallel by means of a multi-threading approach. Four independent runs, with a mean computation time of 5.5 h, confirmed the best solution with a maximum deviation of less than 1% in TAC.

Figure 2 compares the lowest TAC of all process configurations, solvents and considered

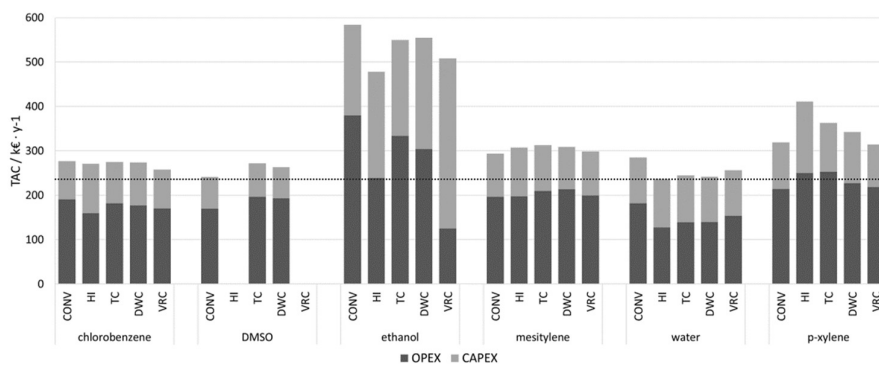


Figure 2: TAC of the best individuals of four independent runs considering OPEX and CAPEX

energy integration options. For each bar, the share of annual operating (OPEX) and capital expenditures (CAPEX) is illustrated. Interestingly, energy integration is only beneficial for ethanol and water. Depending on the product of the extractive distillation column, the potential decreases with increasing solvent boiling temperature. While ethanol results in the highest TAC, water becomes the favorable solvent in the HI variant and outperforms chlorobenzene and DMSO, which are superior in comparison to the basic sequence. Waltermann et al. (2018) obtained similar results in a local optimization study based on the embedded deterministic optimization approach. The results of the hybrid optimization approach further allow for an analysis of the sensitivity of the local optimization w.r.t. the initialization.

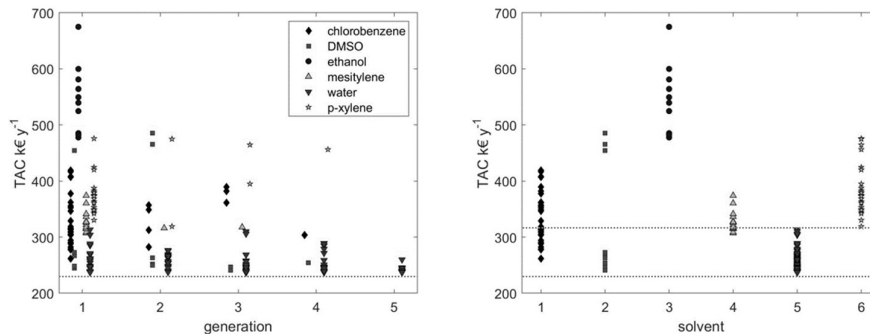


Figure 3: Evolution of the fitness over the generations (left) and variation for solvents (right)

Figure 3 summarizes the evolution of the fitness over the generations (left) and the distribution of the costs for all evaluations of each solvent (right) for a single run. The results indicate the capability of the hybrid optimization approach to quickly find a very good solution and confirm this in a few generations for which an increasing number of individuals focus on the preferred solvent and process variant. On the other side, the large variations in the TAC determined for the single solvents highlights the dependence of the results on the consideration of energy integration and the specifications of the initial superstructure, both of which are modified by the EA in the hybrid optimization approach. While the best individual for water outperforms all other solvents, a suboptimal solution may instead favor any of the remaining solvents (see dotted lines in Fig. 3 right), except ethanol, which can be discarded clearly.

Figure 4 further illustrates the distribution of the fitness of the evaluated individuals in the respective run in terms of OPEX and CAPEX (left) and a magnified illustration of the most effective water-based separation processes. Additional lines of constant TAC are introduced to highlight the existence of almost equivalent process designs with alternative DDof. Thus, although a single objective optimization is performed, specific trade-offs of the different cost shares are automatically determined in the hybrid optimization approach. The illustration also highlights the concentration of solutions in close vicinity to the best performing process options (<5% higher TAC).

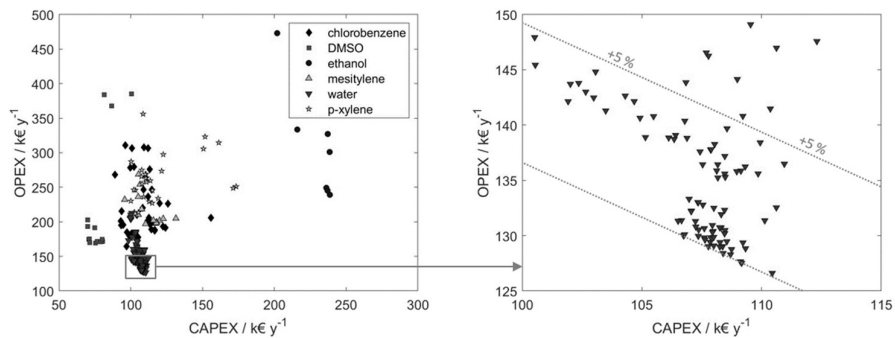


Figure 4: Cost distribution for all individuals (left) and for the best-performing processes utilizing water for a single run

4. Conclusion

The current work presents the purposeful extension of a previously introduced hybrid optimization approach and illustrates its capabilities for the optimal selection of solvents and the design of intensified separation processes. The investigated case study addresses the design of energy integrated extractive distillation columns and illustrates that superior solvent choices and process designs may easily be missed based on the limitation to a single locally optimal solution. The presented hybrid optimization approach effectively overcomes these limitations and increases the confidence in the determined optimization results. It furthermore provides information on possible trade-off solutions with similar TAC, but variations in CAPEX and OPEX, without the need for multi-objective process optimization. The fully algorithmic implementation should furthermore allow for an extension of the search space to an increased number of solvents and therefore enable integration with a CAMD approach that provides the necessary thermodynamic property predictions. However, as indicated for the case of DMSO, apparently infeasible or inferior process variants should be discarded directly to save unnecessary computational load. The transfer of the approach to other solvent-based separation processes requires the development of reliable deterministic optimization strategies, as well as the adaption of the EA and will be part of future work.

References

- Blahušiak, M., Kiss, A.A., Babic, K., Kersten, S.R.A., Bargeman, G., Schuur, B., 2018, Insights into the selection and design of fluid separation processes, *Sep. Purif. Technol.*, 194, 301-318
- Douglas, J.M., 1985, A hierarchical decision procedure for process synthesis, *AIChE J.*, 31(3), 353-362
- Harper, P.M., Gani, R.: A multi-step and multi-level approach for computer aided molecular design, *Comp. Chem. Eng.*, 2000, 24, 677-683.
- Kiss, A.A., Flores Landaeta, S.J., Infante Ferreira, C.A., 2012. Towards energy efficient distillation technologies – Making the right choice. *Energy* 47 (1), 531-542.
- Kossack, S., Kraemer, K., Gani, R., Marquardt, W., 2008, A systematic synthesis framework for extractive distillation processes, *Chem. Eng. Res. Des.*, 86 (7), 781-792
- Kruber, K., Scheffczyk, J., Leonhard, K., Bardow, A. and Skiborowski, M. 2018, A hierarchical approach for solvent selection based on successive model refinement, *Comp. Aided Chem. Eng.*, 43, 325-330
- Scheffczyk, J., Redepenning, C., Jens C.M., Winter B., Leonhard, K., Marquardt, W., Bardow, A., Massive automated solvent screening for minimum energy demand in hybrid extraction-distillation using COSMO-RS. *Chem. Eng. Res. Des.* 2016;115:433-42.
- Skiborowski, M., Harwardt, A., Marquardt, W., 2013, Conceptual design of distillation-based hybrid separation processes, *Annu. Rev. Chem. Biomol. Eng.*, 4, 45-68.
- Skiborowski, M., Rautenberg, M., Marquardt, W., 2015a, A Hybrid Evolutionary-Deterministic Optimization Approach for Conceptual Design, *Ind. Eng. Chem. Res.*, 54(41), 10054-10072.
- Skiborowski, M., Harwardt, A., Marquardt, W., 2015b, Efficient optimization-based design for the separation of heterogeneous azeotropic mixtures. *Comput. Chem. Eng.*, 72, 34-51.
- Urselmann, M.; Engell, S., 2010, Optimization-based design of reactive distillation columns using a memetic algorithm. *Comp. Aided Chem. Eng.*, 2010, 28,1243-1248.
- Waltermann, T., Skiborowski, M., 2016, Efficient optimization-based design of energetically intensified distillation processes, *Comp. Aided Chem. Eng.*, 38, 571-576.
- Waltermann, T., Grueters, T., Skiborowski, M., 2018, Optimization of extractive distillation – integrated solvent selection and energy integration, *Comp. Aided Chem. Eng.*, 44, 187-192.

Flux Balance Analysis Incorporating a Coarse-grained Proteome Constraint for Predicting Overflow Metabolism in *Escherichia Coli*

Hong Zeng,^a Aidong Yang^{a,*}

^a*University of Oxford, Parks Road, Oxford OX1 3PJ, United Kingdom*

aidong.yang@eng.ox.ac.uk

Abstract

Flux balance analysis (FBA) and its dynamic extension DFBA are typical constraint-based modelling tools in systems biology. They have been widely used for *in silico* analysis of intracellular metabolic flux distributions. The objective of this work is to use FBA and DFBA to predict quantitatively the extent of overflow metabolism in *E. coli* under a wide range of growth conditions. In light of the recently validated proteome allocation theory, we developed a coarse-grained constraint to represent the competition of the limited proteomic resource between energy biogenesis and biomass synthesis. Incorporating such constraint to FBA renders accurate predictions of the onset of overflow metabolism and the rates of acetate production at increased growth rates for various wild-type *E. coli* strains. On top of this, we further use DFBA to investigate how the production of a foreign protein affects the growth physiologies of recombinant *E. coli*. Simulation results show that the incorporation of proteomic burden and the tuning of cellular energy demand via strain-specific growth data are key to an accurate prediction. Although several limitations remain to overcome, this work provides a starting point of using FBA-based model as an efficient predictive tool to guide metabolic decisions to address issues such as reducing acetate production and enhancing protein productivity.

Keywords: *Escherichia coli*, overflow metabolism, resource allocation, recombinant protein production, genome-scale model

1. Introduction

Flux balance analysis (FBA) is a widely adopted modelling tool in metabolic engineering and systems biology for predicting intracellular metabolic fluxes (Orth et al., 2010). As a constraint-based modelling approach, the outcome of FBA depends on the constraints incorporated in the optimisation problem being solved. In addition to the built-in mass and energy balances, several constraints have been proposed to account for the previously proposed notion of constrained cellular resources (Molenaar et al., 2009) via quantifying the enzymatic cost of individual reactions (Nilsson et al., 2017). These constraints have been shown to improve efficiently the growth rate prediction by FBA. However, most of these models require extensive information of enzyme kinetics for thousands reactions involved in the metabolic network. In this work, we propose a coarse-grained constraint to represent the limit of cellular proteome resources and their allocation over (a small number of) energy pathways and the biomass synthesis flux, based on the recently-developed proteome allocation theory (PAT) for explaining the overflow metabolism in *E. coli* (Basan et al., 2015). We named this new constraint as the PAT constraint. Due to

its coarse-grained nature, the PAT constraint introduces only a small number of parameters (independent of the scale of the metabolic model), which can be estimated using experimentally determined growth data. In particular, we have focused on the prediction of acetate production at high growth rates, a phenomenon commonly referred to as the overflow metabolism, which represents not only a waste of substrate carbon but also leads to low cell density and low product yield (Eiteman and Altman, 2006) due to acid toxicity. In this paper, we describe the modelling approach and the results of simulation experiments that have been carried out to obtain the predicted growth phenotype of various wild-type and recombinant *E. coli* under a wide span of growth conditions. Comparisons are made with the experimental data in terms of (i) the steady state acetate-growth rate profile and steady state biomass yield-growth rate profile for wild-type *E. coli* and (ii) the biomass accumulation, substrate consumption, acetate accumulation and protein production of batch cultures of recombinant *E. coli*. Future perspective in terms of using the modelling framework developed in this work to guide metabolic decisions for efficient microbial protein production processes is illustrated in the end of the result section.

2. Methodology

Following the philosophy of multi-scale modelling, we propose to construct a FBA model that combines (i) detailed stoichiometry and topology of the cellular metabolic network and (ii) a concise global regulation rule to govern an accurate flux prediction. More specifically, a genome-scale metabolic model was adopted, and a coarse-grained PAT constraint was constructed at pathway level (on the contrary to reaction level constraints adopted in previous studies) to depict the constrained proteome to be allocated between energy biogenesis and biomass synthesis. The energy pathways discussed here are fermentation (involving glycolysis, acetate pathways and oxidative phosphorylation) and respiration (comprising glycolysis, tricarboxylic acid cycle and oxidative phosphorylation). Biomass synthesis flux includes primarily catabolic reactions, anabolic reactions and ribosomal reactions for the synthesis and assembly of biomass building blocks

2.1. PAT Constraint

Based on the recently published proteome allocation theory (Basan et al., 2015), we proposed the following coarse-grained proteomic constraint:

$$w_f^* v_f + w_r^* v_r + b^* \lambda + \phi_{recP}^* \leq 1 \quad (1)$$

where v_f , v_r and λ are the fermentation, respiration and biomass synthesis flux, respectively; w_f^* , w_r^* and b^* are the proteomic cost parameters denoting the fractions of proteome required per unit fermentation, respiration and biomass synthesis flux, respectively; ϕ_{recP}^* represents the portion of proteome used for the synthesis of foreign proteins in recombinant strains, i.e. $\phi_{recP}^* = 0$ for wild-type strains. The equal sign of Eq. (1) is expected to hold in fast-growing conditions (e.g. overflow region) where the cell growth is limited predominantly by proteome resources; in other growth conditions this constraint is relaxed by the less-than sign. Eq. (1) is referred to as the PAT constraint.

2.2. Genome-scale modelling

The genome-scale metabolic model *iAF1260* (Feist et al., 2007), integrated with the PAT constraint was used in FBA simulations to obtain the steady state growth rate and metabolic flux distribution for *E. coli* at different growth conditions. The generic optimization problem solved in FBA is formulated as:

Maximise growth rate λ , subject to

$$\begin{aligned} \text{(i) } S\mathbf{v} &= \mathbf{0} \\ \text{(ii) } \mathbf{v}^L &\leq \mathbf{v} \leq \mathbf{v}^U \\ \text{(iii) } w_f^*v_f + w_r^*v_r + b^*\lambda + \phi_{recP}^* &\leq 1 \end{aligned} \tag{2}$$

where S comprises the reaction stoichiometry defined by the *iAF1260* model; \mathbf{v} is a column vector containing intracellular metabolic fluxes with upper and lower bound set by \mathbf{v}^L and \mathbf{v}^U ; the third constraint of Eq. (2) is the PAT constraint that depicts the global proteome allocation rule. The dynamic framework (DFBA) is achieved by coupling the standard FBA with a set of ordinary differential equations (ODEs) describing the dynamic extracellular environment:

$$\frac{dX}{dt} = \lambda X \tag{3}$$

$$\frac{dG}{dt} = -v_{glc}X \tag{4}$$

$$\frac{dA}{dt} = v_{ac}X \tag{5}$$

$$\frac{dP}{dt} = v_{recP}X \tag{6}$$

where X , G , A and P are the concentrations of biomass, glucose, acetate and recombinant protein in the bioreactor, respectively. The growth rate λ , glucose uptake flux v_{glc} , acetate production flux v_{ac} and protein synthesis flux v_{recP} are obtained from the solution of FBA. Dynamic simulation is carried out by exchanging information between FBA and ODEs at a number of time intervals: FBA is performed at the beginning of every time interval to give steady state flux distribution; the values of the fluxes of interest are then passed to the ODEs to update the outer environment state. This procedure is repeated until the entire time duration has been simulated.

3. Results

3.1. Predicting overflow metabolism for wild-type *E. coli*

Experimental data from the literature (Extended Data Figure 1, Basan et al., 2015) was used to estimate three PAT constraint parameters, namely w_f^* , w_r^* and b^* . FBA was then

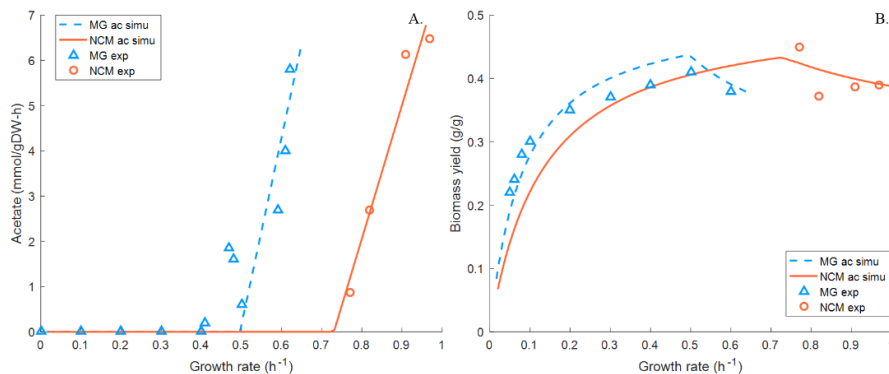


Figure 1: Comparison between model predictions and experimental data

performed to obtain the steady state acetate production rate for wild-type *E. coli* MG1655 and NCM3722 under aerobic-glucose conditions. The predicted acetate production rate is in good agreement with the experimental results (Figure 1A), which validates the suitability of using the concise pathway-level proteome allocation constraint as the global regulatory rule to guide the prediction of the overflow metabolism in a FBA model.

Furthermore, we calculated the simulated biomass yield on glucose (g biomass produced per g glucose consumed). Interestingly, we found that the accuracy of the biomass yield prediction is closely related to the cellular energy demand (i.e. overall ATP production rate at steady state). When FBA was performed with the default energy demand given in the *iAF1260* model, considerable inconsistency was observed between the simulation results and the experimental data for both MG and NCM strains. Such deviation indicates that the carbon utilization in the model is not consistent with the real case. In FBA models, carbon balance is dictated by three aspects: (i) the assumed biomass content of the cell; (ii) the endogenous structure of the metabolic network and (iii) the energy demand for supporting cell maintenance and growth. In *iAF1260*, the first aspect is determined by experimentally measured dry cell composition of *E. coli*; the metabolic network is obtained by well-developed *E. coli*-specific biochemical characterization. Only the last aspect is constructed with assumptions and is reported with $\pm 50\%$ uncertainty. Therefore, we decided to modify the default energy demand using experimentally determined strain-specific growth data. Subsequently, the prediction of biomass yield (Figure 1B) became highly coincided with the experimental values without compromising the accuracy in the prediction of the onset and extent of the overflow metabolism.

3.2. The effect of recombinant protein production

Having validated the efficiency of using the PAT constraint to guide the prediction of overflow metabolism in wild-type *E. coli*, we further investigated the impact of recombinant protein production on the overall growth physiologies. According to the proteome allocation theory, the production of a foreign protein should occupy a certain fraction of the proteome. Therefore, we added a recombinant protein sector (ϕ_{recP}^* in Eq. (1)) to the wild-type PAT constraint. We also added the synthesis reaction of the recombinant protein (in this case green fluorescent protein, GFP) to the model. DFBA was performed to simulate the dynamic cell growth in a batch culture. During the analysis, we found that the introduction of ϕ_{recP}^* alone is not sufficient to render satisfied predicted

results. Strong deviations were observed for both cell growth, glucose consumption, acetate accumulation and protein production when comparing with the experimental data. Based on the experience gained in the wild-type case, we considered that in this case it is likely that the energy demand again plays an important role. We thus co-estimated ϕ_{recP}^* and the maintenance energy (ATPM) simultaneously, and found that with $\phi_{recP}^* = 0.1333$ and ATPM = 32.6 mmol/gDW-h, the dynamic simulation results were in excellent agreement with the experimental data (Figure 2A). It is worth noting that the default ATPM of wild-type *E. coli* in iAF1260 is 8.39 mmol/gDW-h, which is significantly lower than the new ATPM determined for GFP-producing *E. coli*. The strong increase in maintenance energy for recombinant *E. coli* is consistent with previously proposed notion of “metabolic burden of recombinant protein production” (Wu et al., 2016). Our model suggests that the production of GFP provokes not only proteomic burdens on the allocation of cellular proteome resources, but also a significant increase in the overall energy demand, which is potentially used for plasmid maintenance, protein secretion and degradation of the misfolded protein. Building on the aforementioned findings on the impact of PAT constraint (with ϕ_{recP}^*) and energy demand on the growth predictions for GFP-producing *E. coli*, we further considered the potential of using the model to support the enhancement of protein productivity. According to the proteome allocation theory, the production of extra proteins, a desirable process from the engineering point of view, reduces the portion of proteome attainable to energy pathways and biomass synthesis, thus leads to more severe overflow phenomenon that gives rise to undesirable products such as acetate.

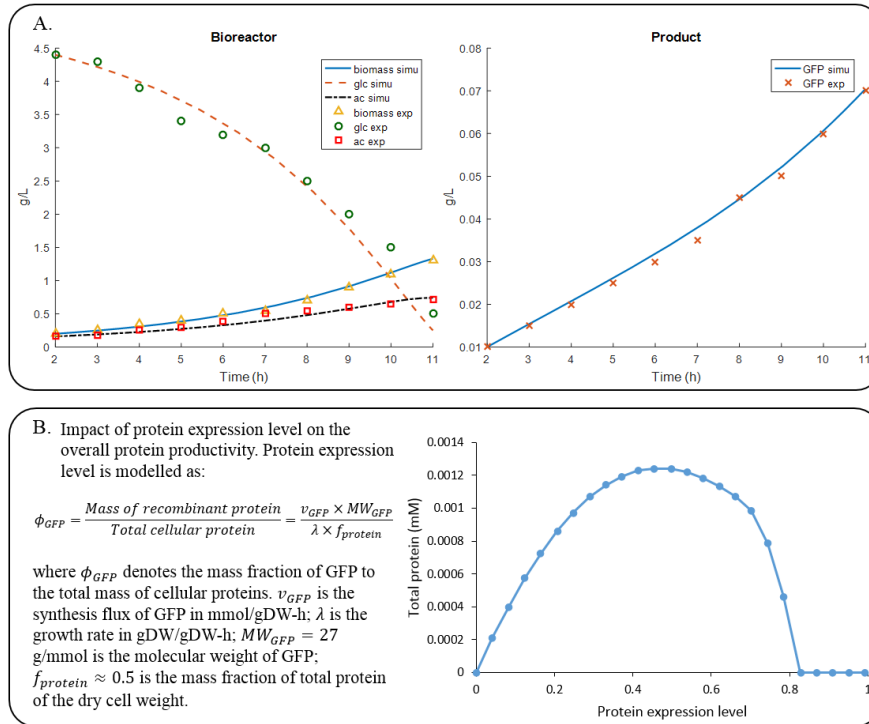


Figure 2: Modelling recombinant protein production and potential application

Investigating this trade-off, we performed further DFBA simulations with different protein production levels (while all the other conditions were kept identical between simulations), attempting to find an optimal expression level with highest GFP produced at the end of a batch culture (Figure 2B). Simulation results show the predicted existence of an optimal protein expression level ($\phi_{recP}^* \sim 0.5$), which offers a preliminary indication of the potential use of the proposed model for guiding metabolic engineering decisions. However, several limitations need to be resolved for the development of a fully predictive tool: (i) it is still unclear how the *in vivo* protein expression system is linked to the modelled proteomic burden ϕ_{recP}^* ; (ii) a robust and reliable quantification of the protein expression level (currently quantified by mass fraction of the recombinant protein) remains unresolved; and (iii) how different protein expression levels affect the substrate uptake kinetics and the energy demand is still to be quantified.

4. Conclusions

This work shows that the incorporation of a coarse-grained proteome constraint into a genome-scale metabolic model can produce accurate prediction of the overflow metabolism in wild-type *E. coli* as well as predict key growth physiologies of a batch culture of recombinant *E. coli*. Although several limitations remain to overcome, the proposed modelling approach provides a basis of using FBA as an efficient predictive tool to guide metabolic engineering decisions to address issues such as reducing acetate production and enhancing the productivity of recombinant proteins.

References

- Basan, M., Hui, S., Okano, H., Zhang, Z., Shen, Y., Williamson, J.R., Hwa, T., 2015. Overflow metabolism in *Escherichia coli* results from efficient proteome allocation. *Nature* 528, 99–104.
- Eiteman, M.A., Altman, E., 2006. Overcoming acetate in *Escherichia coli* recombinant protein fermentations. *Trends Biotechnol.*
- Feist, A.M., Henry, C.S., Reed, J.L., Krummenacker, M., Joyce, A.R., Karp, P.D., Broadbelt, L.J., Hatzimanikatis, V., Palsson, B.Ø., 2007. A genome-scale metabolic reconstruction for *Escherichia coli* K-12 MG1655 that accounts for 1260 ORFs and thermodynamic information. *Mol. Syst. Biol.* 3.
- Molenaar, D., van Berlo, R., de Ridder, D., Teusink, B., 2009. Shifts in growth strategies reflect tradeoffs in cellular economics. *Mol Syst Biol* 5.
- Nilsson, A., Nielsen, J., Palsson, B.O., 2017. Metabolic models of protein allocation call for the kinetome. *Cell Syst.* 5, 538–541.
- Orth, J.D., Thiele, I., Palsson, B.Ø., 2010. What is flux balance analysis? *Nat. Biotechnol.* 28, 245–248.
- Wu, G., Yan, Q., Jones, J.A., Tang, Y.J., Fong, S.S., Koffas, M.A.G., 2016. Metabolic Burden: Cornerstones in Synthetic Biology and Metabolic Engineering Applications. *Trends Biotechnol.* 34, 652–664.

A Quality-by-Control Approach in Pharmaceutical Continuous Manufacturing of Oral Solid Dosage via Direct Compaction

Qinglin Su,^a Sudarshan Ganesh,^a Dan Bao Le Vo,^a Anushaa Nukala,^a Ysasvi Bommireddy,^b Marcial Gonzalez,^b Gintaras V. Reklaitis,^a Zoltan K. Nagy^{a,*}

^a*Davidson School of Chemical Engineering, Purdue University, West Lafayette, IN 47907, United States*

^b*School of Mechanical Engineering, Purdue University, West Lafayette, IN 47907, United States*

znagy@purdue.edu

Abstract

The pharmaceutical industry has been undergoing a paradigm shift towards continuous manufacturing, under which novel approaches to real-time product quality assurance have been investigated. A new perspective, entitled Quality-by-Control (QbC), has recently been proposed as an important extension and complementary approach to enable comprehensive Quality-by-Design (QbD) implementation. In this study, a QbC approach was demonstrated for a commercial scale tablet press in a continuous direct compaction process. First, the necessary understanding of the compressibility of a model formulation was obtained under QbD guidance using a pilot scale tablet press, Natoli BLP-16. Second, a data reconciliation strategy was used to reconcile the tablet weight measurement based on this understanding on a commercial scale tablet press, Natoli NP-400. Parameter estimation to monitor and update the material property variance was also considered. Third, a hierarchical three-level control strategy, which addressed the fast process dynamics of the commercial scale tablet press was designed. The strategy consisted of the Level 0 built-in machine control, Level 1 decoupled Proportional Integral Derivative (PID) control loops for tablet weight, pre-compression force, main compression force, and production rate control, and Level 2 data reconciliation of sensor measurements. The effective and reliable performance, which could be demonstrated on the rotary tablet press, confirmed that a QbC approach, based on product and process knowledge and advanced model-based techniques, can ensure robustness and efficiency in pharmaceutical continuous manufacturing.

Keywords: Quality-by-Design, Quality-by-Control, Continuous manufacturing, Process control, pharmaceutical

1. Introduction

The recent approval of four drug products using continuous manufacturing technologies, e.g., Orkambi (lumacaftor/ivacaftor) in 2015, Prezista (darunavir) in 2016, Verzenio (abemaciclib) and Symdeko (tezacaftor/ivacaftor) in 2018, by United States Food and Drug Administration (US FDA) is a strong evidence of the on-going paradigm shift from batch to continuous manufacturing in the pharmaceutical industry. The US FDA Quality-

by-Design guidance has also been widely acknowledged in providing directions with respect to product and process knowledge development, such as identifying critical process parameters (CPPs) in process design and linking critical material attributes (CMAs) to critical quality attributes (CQAs) (Yu et al., 2014). Control strategies that include specification of the drug substance, excipients, and drug products as well as controls for each step of the manufacturing process are also considered as important elements of the QbD concept. In addition to designing quality into the product during the early stages of drug development, the quality attributes must also be automatically and consistently controlled, in the presence of process uncertainties and disturbances, during drug manufacturing (Lee et al., 2015). This recognition has led to a call for Quality-by-Control, particularly in continuous manufacturing, consistent with the current Industry 4.0 or smart manufacturing approaches. The proposed QbC idea consists of the design and operation of a robust manufacturing system that is achieved through an active process control system designed in accordance with hierarchical process automation principles, based on a high-degree of quantitative and predictive understanding of product and process.

Our previous work has investigated the characterization of the compressibility of a model formulation, consisting of Acetaminophen (API, 10.0%), Avicel Microcrystalline Cellulose PH-200 (excipient, 89.8%), and SiO₂ (lubricant, 0.2%), using a Natoli BLP-16 tablet press (Su et al., 2018). System dynamics and hierarchical process control development for a direct compression line were also undertaken for this pilot scale tablet press. In this study, we demonstrate the use of the proposed QbC approach in transferring the product and process understanding generated with the Natoli BLP-16 to the commercial scale, Natoli NP-400, tablet press. The rest of the manuscript will first discuss the QbC concept, followed by a brief introduction of the features of the tablet press in a continuous direct compression process. The advantages of a QbC approach in continuous tablet manufacturing will be presented in the result and discussion section. Concluding remarks and considerations for future work are given at the end of the manuscript.

2. Quality-by-Control

In traditional batch manufacturing quality attributes of products are tested at the end of each batch manufacturing step, following the so-called Quality-by-Testing (QbT) approach, as shown in Figure 1. Under the QbD guidance, systematic understanding of drug quality, including identification of CMAs and CPPs, is developed and monitoring is employed to assure that the quality attributes are met. The QbD approach is also very important to advancing the adoption of continuous manufacturing. However, assurance of quality in the continuous manufacturing mode in addition requires the use of QbC concepts to actively drive reduction in the variance of quality attributes, in the presence of process disturbances, raw material property variations, or uncertainties introduced as a result of scale up or technology transfer. The QbC approach builds on QbD by employing quantitative and predictive product and process knowledge in the form of models of appropriate fidelity, together with process analytical technology (PAT), to actively and robustly control the CQAs at the specified levels by adjusting CPPs, thus, achieving real-time quality assurance. The on-going trend towards Industry 4.0 or smart manufacturing also demands a high-level automation in process operation and quality control, which is fully consistent with the QbC approach.

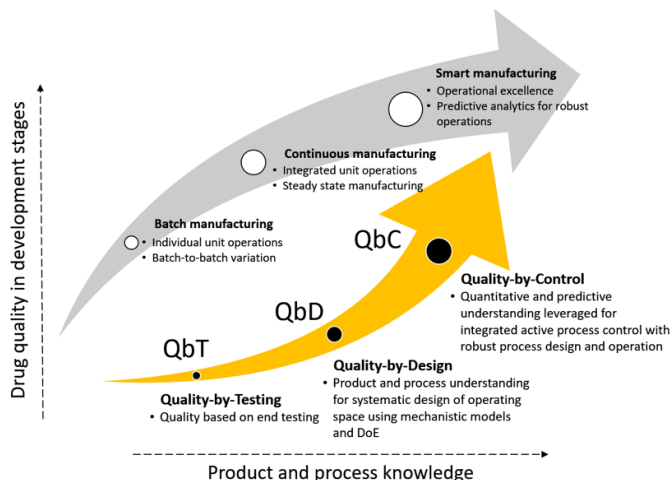


Figure 1. The systematic progression in quality assurance via QbT, QbD, and QbC.

3. Continuous tablet manufacturing

3.1. Continuous direct compaction

The continuous direct compression process under study consists of two Schenck AccuRate PureFeed® AP-300 loss-in-weight feeders which continuously feed the API and excipient ingredients into a Gericke GCM-250 continuous blender. A Schenck AccuRate DP4 micro feeder adds the lubricant into the powder blend exiting the continuous blender, which is then conveyed directly to a rotary tablet press (Su et al., 2017). The tablet press is a multi-stage process, in which each station undergoes the recurring major steps of die filling, metering, pre-compression, main-compression, tablet ejection and take-off, as shown in Figure 2. The tablet weight can be controlled by changing the dosing position subject to the variation of powder bulk density or filling time due to change in turret speed and/or feeder rotation speed. A Natoli BLP-16 tablet press (16 stations with flat-head punches) was employed in our previous work to characterize the formulation compressibility while a commercial scale Natoli NP-400 (22 stations with concave-head punches) was used in the present work for continuous tablet manufacturing. The two tablet presses are also different in size and design of hopper and feed frame, which may result in differences in powder bulk density at the die table.

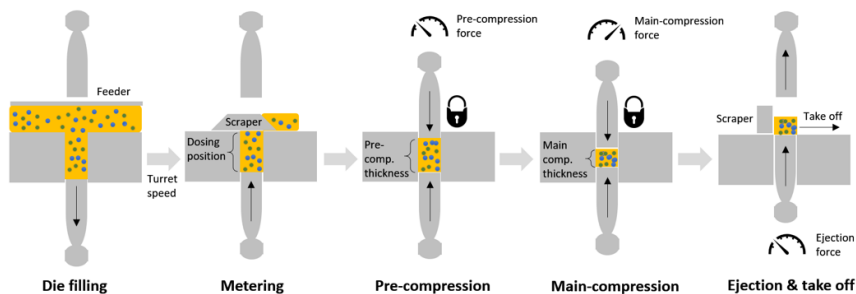


Figure 2. Major steps in a Natoli rotary tablet press.

3.2. Formulation compressibility

The classical Kawakita model was employed to characterize the formulation compressibility in the Natoli BLP-16 tablet press (Su et al., 2018), as shown in Figure 3,

$$\frac{CF}{1 - \rho_c / \rho_r} = \frac{CF}{a} + \frac{\pi D^2 / 4}{ab} \quad (1)$$

$$\rho_r = \frac{4W_t}{\pi D^2 \rho_t T} \quad (2)$$

where CF is the main compression force, kN; ρ_c is the critical relative density, ρ_r the calculated in-die relative density from tablet weight W_t , and ρ_t the known a priori true density of the powder, g/cm³; parameters a and b (MPa) are interpreted as the maximum degree of compression and the reciprocal of the pressure applied to attain the maximum degree of compression, respectively; D is the diameter of the die (mm) and T (mm) is the minimum in-die tablet thickness pre-set by the main compression thickness for B tooling punches with flat cylindrical punch surfaces.

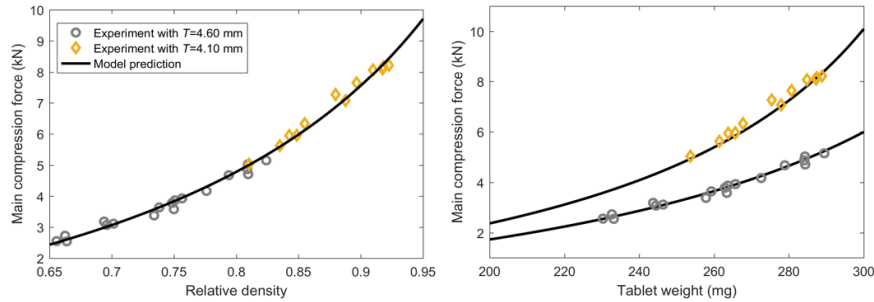


Figure 3. Compressibility characterization by a classical Kawakita model.

3.3. Hierarchical control system

A three-level hierarchical control system, shown in Figure 4, was developed based on the product and process understanding developed using the Natoli BLP-16 tablet press (Su et al., 2018) and was transferred to the NP-400 tablet press. The CQA and CPP measurement data were collected using an Emerson DeltaV DCS system to support the process control system design following the ISA 95 standard (Su et al., 2017). Specifically, the vendor built-in machine control at Level 0 manipulates the dosing position, pre-compression thickness, main compression thickness, and turret speed. At Level 1, the DCS system employs four PID controllers, controlling the tablet weight, pre-compression force, main compression force, and production rate by manipulating the above four Level 0 variables, respectively. A Level 2 data reconciliation module was implemented which serves to reconcile the tablet weight measured by an in-house adapted load cell with the main compression force measurement using the constraints imposed by the Kawakita model, Eqs. (1) and (2) (see Su et al., 2018). Specifically, the model parameter ρ_c was continuously re-estimated and updated during data reconciliation to account for variation in the powder bulk density due to material property changes (particle size, water content) or differences in equipment scale (hopper and feed frame, etc.) that also results in changes in powder bulk density at die table.

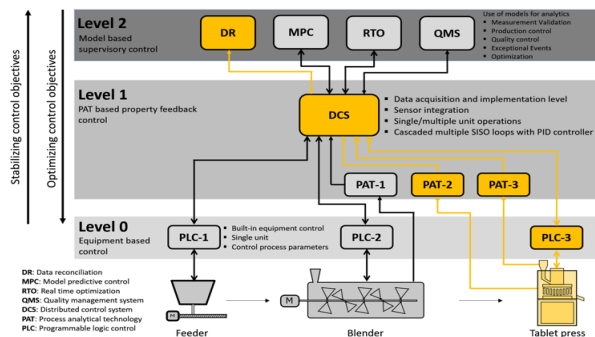


Figure 4. A hierarchical three-level process control for direct compaction.

4. Results and discussion

With a QbC approach based on a quantitative model of compressibility, the Level 2 data reconciliation approach was able to reduce the uncertainty in real-time tablet weight measurement from the load cell for both tablet presses (see the reconciled measurement matched the at-line measurement of tablet weight), as shown in Figure 5. More importantly, the model parameter of critical density (which is related to powder bulk density) in the Kawakita equation (1), which was first estimated from BLP-16 runs, was readily updated from NP-400 tablet press real-time data. The shift in the critical density which was observed in the transfer from BLP-16 to NP-400 may be a result of changes in the bulk density at the die table due to different scale of hopper and different feed frame design. Assurance of model validity and parameter updating are the common concerns in most technology transfers and these results demonstrate that these concerns can be managed within a QbC approach. The high-level understanding of the process dynamics of the tablet press and resulting control structure design, such as the pairing of the control input and output variables, were readily transferable from the pilot to a larger scale press. Specifically, the control structure in which tablet weight was controlled by manipulating the dosing position and the production rate was controlled by adjusting turret speed (the feed frame stirrer speed also changes accordingly), resulted in effective control performance of both tablet presses. Both tablet presses could reach their tablet weight set points steadily. For instance, as shown in Figure 5, when the production rate was increased at 600 s from 3 kg/hr to 5 kg/hr after start-up of the NP-400 tablet press or reduced at 1000 s from 5 kg/hr to 4 kg/hr, the tablet weight was maintained at nearly constant levels.

5. Conclusions and future work

A Quality-by-Control approach was implemented in a continuous tablet manufacturing process based on the product and process understanding gained through the previous Quality-by-Design studies on a pilot unit. Compared to rigid process operation within a predefined design space, active process control response to common process variations, disturbances, or uncertainties can be automatically achieved under the QbC paradigm in a quantitative and predictive way to maintain consistent product quality. The systematic implementation of a hierarchical process control system in continuous direct compression process was highlighted, leveraging QbD understanding of the product and process to achieve robust and efficient process operations and real-time quality control of oral solid dosages. Future efforts in systematic sensor network maintenance, control performance

monitoring and continuous improvement should be pursued to further advance QbC implementation.

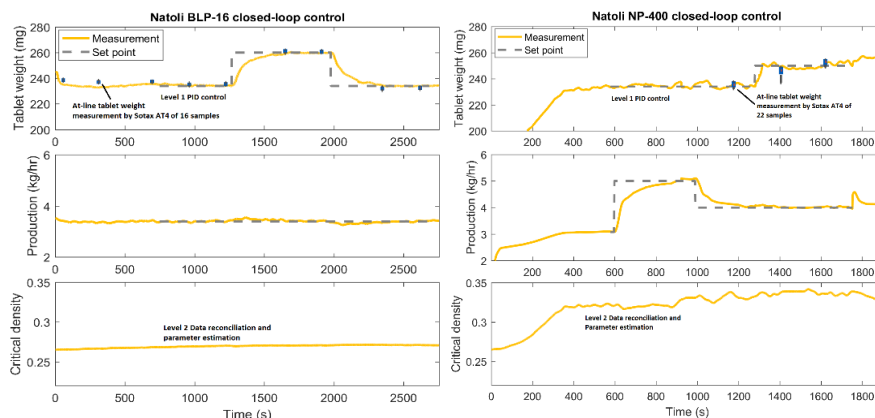


Figure 5. Control performance of Natoli BLP-16 and NP-400 tablet press.

Acknowledgement

Funding for this project was made possible, in part, by the Food and Drug Administration through grant U01FD005535. Views expressed by authors do not necessarily reflect the official policies of the Department of Health and Human Services; nor does any mention of trade names, commercial practices, or organization imply endorsement by the United States Government. This work was also supported in part by the National Science Foundation under grant EEC-0540855 through the Engineering Research Center for Structure Organic Particulate Systems. Purdue Process Safety and Assurance Centre (P2SAC) and technical support from Douglas Voss of Natoli are also appreciated.

References

- L. X. Yu, G. Amidon, M. A. Khan, S. W. Hoag, J. Polli, G. K. Raju, J. Woodcock, 2014, Understanding pharmaceutical quality by design. *The AAPS Journal*, 16(4), 771-783.
- S. L. Lee, T. F. O'Connor, X. Yang, C. N. Cruz, S. Chatterjee, R. D. Madurawe, J. Woodcock, 2015, Modernizing pharmaceutical manufacturing: from batch to continuous production. *Journal of Pharmaceutical Innovation*, 10(3), 191-199.
- Q. Su, S. Ganesh, M. Moreno, Y. Bommireddy, M. Gonzalez, G. V. Reklaitis, Z. K. Nagy, 2018, A perspective on Quality-by-Control (QbC) in pharmaceutical manufacturing. *Computer and Chemical Engineering*. Under review.
- Q. Su, Y. Bommireddy, M. Gonzalez, G. V. Reklaitis, Z. K. Nagy, 2018, Variation and risk analysis in tablet press control for continuous manufacturing of solid dosage via direct compaction, *Computer Aided Chemical Engineering*, 44, 679-684.
- Q. Su, M. Moreno, A. Giridhar, G. V. Reklaitis, Z. K. Nagy, 2017, A systematic framework for process control design and risk analysis in continuous pharmaceutical solid-dosage manufacturing, *Journal of Pharmaceutical Innovation*, 12, 327-346.
- Q. Su, Y., Bommireddy, Y. Shah, S. Ganesh, M. Moreno, J. Liu, M. Gonzalez, N. Yazdanpanah, T. O'Connor, G. V. Reklaitis, Z. K. Nagy, 2018, Data reconciliation in the Quality-by-Design (QbD) implementation of pharmaceutical continuous tablet manufacturing. Submitting.

Targeting of sustainable chemical processes using data envelopment analysis: application to liquid fuels for transportation

Daniel F. Rodríguez-Vallejo,^a Ángel Galán-Martín,^a Gonzalo Guillén-Gosálbez^{a,*} Benoît Chachuat^a

*^aDepartment of Chemical Engineering, Centre for Process System Engineering, Imperial College London, South Kensington Campus, London SW7 2AZ, United Kingdom
g.guillen05@imperial.ac.uk*

Abstract

In this paper we proposed a framework aimed to improve the sustainability of chemical processes based on the combination of data envelopment analysis and process system engineering tools. Given a set of chemical process alternatives, each characterised by techno-economic and environmental performance indicators, the framework discerns between efficient (optimal) and inefficient (suboptimal) processes in the sense of these indicators. We develop an approach to quantifying the closest targets for an inefficient process to become efficient, while avoiding unattainable targets by accounting for thermodynamic limitations in that process in terms of mass and energy flow constraints. We demonstrate the capabilities of the framework through a case study that involves the assessment of a methanol production process with CO₂ captured from power plants and H₂ derived from fossil fuels, in comparison to ten fuel alternatives. We find that this methanol fuel is presently suboptimal in comparison with other fuels. Making it competitive would require a significant reduction in hydrogen price, which is unrealistic in the short term. Alternatively, the methanol fuel could become competitive upon combining H₂ derived from fossil fuels with sustainably produced H₂ via wind-powered electrolysis.

Keywords: data envelopment analysis, chemical process targeting, sustainability, practical closest targets, process synthesis.

1. Introduction

The development of more sustainable chemical processes with good performance in the three sustainability pillars (i.e. economic, environmental and social) has recently attracted growing interest in the process systems engineering literature (Azapagic and Perdan, 2014). A wide range of methods for process design have been put forward, either based on heuristics or super-structure optimisation. These approaches often focus on optimising profit as unique criterion while disregarding other environmental and social indicators (Yuan and Eden, 2016). Furthermore, they are often based on a given chemical route and do not compare flowsheets based on alternative reaction pathways, which can be sometimes radically different. Last but not least, in the process of identifying the optimal solution to the problem, suboptimal alternatives are discarded without providing any analysis on why they underperform compared to others and on how they could be improved so as to become competitive. This piece of information, however, is highly

relevant and insightful for those developing new chemical routes that are at present suboptimal but could become competitive via targeted improvements. The sustainability assessment is further complicated by the existence of multiple indicators on the basis of which the process design alternatives need to be compared against each other.

Acknowledging these gaps in the literature, this work presents a framework that combines data envelopment analysis (DEA) (Cook and Seiford, 2009) with process systems engineering tools (Grossmann and Guillén-Gosálbez, 2010), with a view to improving the sustainability of chemical processes and products, and supporting decision-makers towards more sustainable design solutions. We demonstrate the capabilities of the framework on a real case study assessing eleven transportation liquid fuels: a new methanol process obtained from CO₂ captured from power plants and H₂ from fossil fuels, and ten existing alternatives.

2. Methodology

The proposed DEA framework comprises three steps, which are detailed next.

2.1. Step 1. Simplified input-output model representation

The first step consists of gathering information from a detailed process simulation of the candidate design in order to develop a simplified input-output model representation to be used in the DEA model in Step 2. In essence, this model relates a set of elementary mass and energy flows Z_f ($f = 1 \dots F$) to the key performance indicators (KPIs), treated either as inputs $x_{\ell,i}(Z_1, \dots, Z_F)$ or outputs $y_{\ell,j}(Z_1, \dots, Z_F)$ of the decision making unit (DMU). For instance, Z_f could comprise the flows of raw materials and utilities in connection to DMU inputs, or products and emissions in connection to DMU outputs. In turn, thermodynamic limits in the system can be enforced by restricting the flows, e.g. in the form of inequality constraints $g(Z_1, \dots, Z_F) \leq 0$, and these restrictions are then reflected on the KPIs. For instance, these constraints could represent the minimum amount of raw materials and energy that the process would consume under the assumption of a 100 % yield and a full heat integration of streams to meet the minimum utility requirements dictated by a composite curve.

2.2. Step 2. Enhanced closest-target DEA model

In this step the simplified input-output model from Step 1 is combined with a closest-target DEA model. Our enhanced DEA model projects inefficient DMUs onto the efficient frontier by minimising the distance to target (according to a given metric), while accounting for the thermodynamic limits of the process so as to prevent unrealistic targets. A certificate of infeasibility for this model is an indication that the candidate design may not be projected onto the efficient frontier within the design envelope dictated by the thermodynamic limits. The model takes the form of a mixed-integer program, either linear (MILP) or nonlinear (MINLP) depending on the nature of the simplified input-output model. This step is divided into three sub-steps.

2.2.1. Step 2.1 Definition of attributes

The attributes are classically labelled as inputs or outputs according to whether they are to be maximised (DMU outputs) or minimised (DMU inputs). A tailored approach to

sustainability assessment in process synthesis and design entails the selection of a single DMU output, corresponding to the functional unit in LCA; while all of the economic, environmental and social indicators are normalized in reference to the functional unit.

2.2.2. Step 2.2 Characterization of the efficient frontier

Given a set of n DMUs $k = 1 \dots K$, each consuming m inputs $x_{k,i}$ ($i = 1 \dots I$) and generating n outputs $y_{k,j}$ ($j = 1 \dots J$), the question about whether or not a DMU ℓ is efficient can be answered via the solution of the following LP model (Galán-Martín et al. 2016):

$$\max \theta_\ell^* = \sum_{j=1}^J v_j y_{\ell,j}^* \quad (1)$$

$$\text{s.t. } \sum_{i=1}^I u_i x_{\ell,i}^* \quad (2)$$

$$\sum_{j=1}^J v_j y_{k,j} - \sum_{i=1}^I u_i x_{k,i} \leq 0 \quad k = 1 \dots K, k \neq \ell \quad (3)$$

$$u_i, v_j \geq 0, \quad i = 1 \dots I, j = 1 \dots J \quad (4)$$

where u_i and v_j denote the linear weights of outputs and inputs, which are treated as variables to be optimised; and the relative efficiency score θ_ℓ^* indicates whether the DMU ℓ is efficient ($\theta_\ell^* = 1$) or inefficient ($\theta_\ell^* < 1$) in comparison to the other DMUs. The best-practice or efficient frontier consists of the subset $E \subset \{1, \dots, K\}$ of all efficient DMUs and may be used as a benchmark to define improvement targets for the inefficient units.

2.2.3. Step 2.2 Target setting with thermodynamic limits

In the second step, the simplified input-output model from Step 1 is combined with a closest-target DEA model, based on the work by Aparicio et al. (2007). Our enhanced DEA model projects inefficient DMUs onto the efficient frontier by minimising the distance to target (according to a given metric), while accounting for the thermodynamic limits of the process so as to prevent unrealistic targets. A certificate of infeasibility for this model is an indication that the candidate design may not be projected onto the efficient frontier within the design envelope dictated by the thermodynamic limits. The model takes the form of a mixed-integer program, either linear (MILP) or nonlinear (MINLP) depending on the nature of the simplified input-output model. The targets for an inefficient DMU $\ell \notin E$ are computed by solving the model represented by Eqs. (5)-(15).

$$\min \sum_{f=1}^F \left| \frac{Z_f - Z_f^{\text{ref}}}{Z_f^{\text{ref}}} \right| \quad (5)$$

$$\text{s.t. } \sum_{k \in E} \lambda_k x_{k,i} = x_{\ell,i}(Z_1, \dots, Z_F), \quad i = 1 \dots I \quad (6)$$

$$\sum_{k \in E} \lambda_k y_{k,j} = y_{\ell,j}(Z_1, \dots, Z_F), \quad j = 1 \dots J \quad (7)$$

$$g(Z_1, \dots, Z_F) \leq 0 \quad (8)$$

$$\sum_{j=1}^J v_j y_{k,j} - \sum_{i=1}^I u_i x_{k,i} + d_k = 0, \quad \forall k \in E \quad (9)$$

$$d_k \leq M(1 - b_k), \forall k \in E \quad (10)$$

$$0 \leq \lambda_k \leq Mb_k, \forall k \in E \quad (11)$$

$$b_k \in \{0,1\}, \forall k \in E \quad (12)$$

$$d_k \geq 0, \forall k \in E \quad (13)$$

$$u_i \geq 1, i = 1 \dots I \quad (14)$$

$$v_j \geq 1, j = 1 \dots J \quad (15)$$

The main degrees of freedom in this model are the modified mass and energy flows Z_f in order to make the DMU ℓ efficient. The objective function in Eq. (5) minimises relative deviations between Z_f and the original flows Z_f^{ref} . The improvement targets are enforced in Eqs. (6)-(7), where λ_k are the weights assigned to each efficient DMU (belonging to the reference set E). These targets are constrained by thermodynamic limits in the system via the generic inequality constraints in Eq. (8). The linear constraints in Eq. (9) combined with the big-M constraints in Eqs. (10) and (11) determine the peer group of the DMU ℓ . A binary variable b_k equal to 1 indicates that the DMU k belongs to the peer group, in which case $d_k = 0$ and $\sum_{j=1}^J v_j y_{k,j} = \sum_{i=1}^I u_i x_{k,i}$, and the corresponding weight λ_k can be adjusted freely (provided that the constant M is set to a large enough positive value). Otherwise, having b_k equal to 0 forces $\lambda_k = 0$ when the DMU k does not belong to the peer group of the DMU ℓ (Aparicio et al., 2007).

3. Case study in liquid fuels for transportation

We illustrate the capabilities of the enhanced DEA framework through the sustainability assessment of liquid fuels for transportation, which could be potentially employed in the automotive fleet powered by internal combustion engines. Our main objective is to assess methanol produced from H_2 derived from fossil fuels, and compare it with ten alternative transportation liquid fuels including gasoline, bio-gasoline, Fischer-Tropsch naphtha from natural gas, ethanol produced from three different sources (i.e. corn, sugarcane, switchgrass), liquid hydrogen produced from three sources (i.e. natural gas, coal, biomass), and methanol employing electrolysis powered by wind as a source of H_2 . The methanol production process of interest is based on the work by Gonzalez-Garay and Guillen-Gosalbez (2018). If this process were found to be inefficient, a further objective is to quantify practical improvement targets that would make it competitive. The scope of our analysis follows a well-to-wheel (WTW) approach, which is further decomposed into well-to-pump (WTP) and pump-to-wheel (PTW) contributions (Greet, 2016). Two indicators are used to assess the performance of the liquid fuels: the total driving cost (DC) and the global warming potential (GWP) per driven mile. Both indicators are defined as inputs to be minimised, while the output is set to 1 driven-mile.

4. Results and discussion

The results in Figure 1 show that four fuels are efficient ($\theta_\ell^* = 1$), namely gasoline, EtOHsc-85, Bio-gasoline and 85-MeOH_{re} and therefore, they constitute the efficient frontier which in turn may be used as a benchmark to define the improvement targets for

our fuel of interest 85-MeOH_{re}. Gasoline shows the lowest price, but the second highest GWP, being overcome only slightly by FT-naphtha. Ethanol from sugarcane has a very similar cost to gasoline, but a lower GWP. Bio-gasoline and methanol based on H₂ from renewable electrolysis are the cleaner fuels, showing the lowest GWP. On the other hand, ethanol from corn or switchgrass, hydrogen-based fuels, and our fuel of interest (85-MeOH_f) are all deemed inefficient. The comparison confirms that liquid H₂ from coal, natural gas and biomass perform significantly worse than the other fuels, both in terms of DC and GWP. This is principally due to the high cost and energy consumption associated to the transport and storage stages (IEA, 2013). Observe also that our fuel 85-MeOH_f shows the second highest DC, just behind methanol employing renewable electrolysis as source of H₂ (85-MeOH_{re}). For the targets definition, we consider three cases: 1) H₂ flow defined as variable; 2) H₂ cost as variable (flows defined as constant); and 3) H₂ produced from two different sources, namely fossil fuels and wind-powered electrolysis. Case 1 is proved to be infeasible. Therefore, our fuel 85-MeOH_f cannot be projected onto the efficient frontier by modifying the sole flow of H₂ subject to the stoichiometric limit defined by the reaction that governs the process (Gonzalez-Garay and Guillen-Gosalbez 2018). In Case 2 (see Figure 1), it is found that 85-MeOH_f could reach the target defined by its peers, 85-EtOH_{sc} and Bio-gasoline, on the efficient frontier, but this would call for a 60% reduction in H₂ price, down to 1.17 US\$/kg. In practice however, such a large drop is unlikely given the current state-of-the-art in H₂ production technology (Gonzalez-Garay and Guillen-Gosalbez, 2018). In case 3, 85-MeOH_f could also reach the target defined by its peers, 85-MeOH_{re} and Bio-gasoline, on the efficient frontier, by allowing for a mix of H₂ from fossil fuels and wind-powered electrolysis. This projection increases DC by 7.9 % and reduces GWP by 9.4 % with respect to their initial values, which is enabled by: (i) the reduction of the total H₂ flow to the stoichiometric lower bound which represents a decrease of 14.5 % compared with the initial H₂; and (ii) the use of a 26-74 % mix of H₂ from fossil fuels and wind-powered electrolysis, respectively, which suggests that our fuel 85-MeOH_f may only become competitive upon substituting a majority of the H₂ feedstock from fossil fuels by a more sustainable production route, despite the resulting increase in fuel price.

5. Conclusions

This paper has presented a systematic framework for improving the sustainability of chemical processes, based on the synergistic combination between DEA and process synthesis tools. Our approach improves the capabilities of standard DEA models and process targeting methodologies by providing realistic targets for suboptimal processes. Its main advantages are four-fold: (i) Applicability in the presence of multiple sustainability KPIs; (ii) Discernment between the efficient and inefficient options among a set of candidate designs, thereby defining an efficient frontier; (iii) Identification of quantitative targets for the inefficient process, which are at a minimum distance of the best-practise frontier in terms of mass and energy flow modifications; and (iv) Definition of realistic targets that account for the thermodynamic limits of the underlying process, by embedding a (simplified) model of the sustainability KPIs in terms of the process mass and energy flows into the enhanced closest-targets DEA model.

The application of the DEA framework to the case study reveals that for the methanol fuel 85-MeOH_f the current price of H₂ is a major impediment to its competitiveness, the sole reduction of the H₂ flow from fossil fuels does not allow to reach the best-practise frontier when the stoichiometric limits are taken into account. However, if flexibility is introduced in the H₂ source by mixing H₂ from fossil fuels and wind-powered electrolysis,

it is found that 85-MeOH_f could indeed become competitive due to a reduction in GWP despite an increase in its DC.

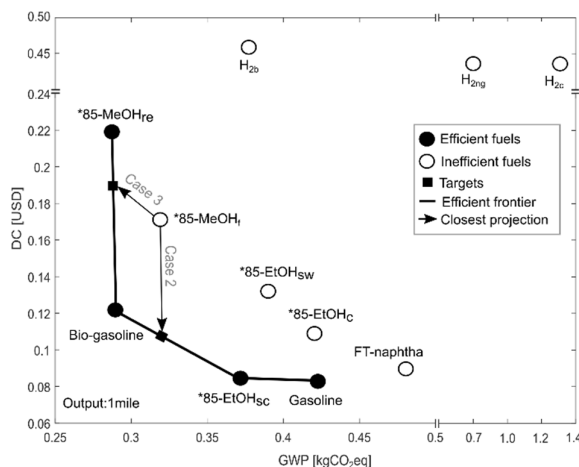


Figure 1. Results of the enhanced DEA framework applied to the transportation fuels case study (*Fuels blending 15 % of regular gasoline).

References

- Aparicio, Juan, José L. Ruiz, and Inmaculada Sirvent. 2007. "Closest Targets and Minimum Distance to the Pareto-Efficient Frontier in DEA." *Journal of Productivity Analysis* 28 (3): 209–18. doi:10.1007/s11123-007-0039-5.
- Azapagic, Adisa, and Slobodan Perdan. 2014. "Sustainable Chemical Engineering: Dealing with 'Wicked' Sustainability Problems." *AIChE Journal* 60 (12). Wiley Online Library: 3998–4007.
- Centre for Transportation Research-Energy Systems Division. 2016. "GREET."
- Cook, Wade D., and Larry M. Seiford. 2009. "Data Envelopment Analysis (DEA) - Thirty Years On." *European Journal of Operational Research* 192 (1): 1–17. doi:10.1016/j.ejor.2008.01.032.
- Galán-Martín, Ángel, Gonzalo Guillén-Gosálbez, Laurence Stamford, and Adisa Azapagic. 2016. "Enhanced Data Envelopment Analysis for Sustainability Assessment: A Novel Methodology and Application to Electricity Technologies." *Computers & Chemical Engineering* 90. Elsevier Ltd: 188–200. doi:10.1016/j.compchemeng.2016.04.022.
- Gonzalez-Garay, Andres, and Gonzalo Guillen-Gosalbez. 2018. "SUSCAPE: A Framework for the Optimal Design of SUSTainable Chemical Processes Incorporating Data Envelopment Analysis." *Chemical Engineering Research and Design* 137. Institution of Chemical Engineers: 246–64. doi:10.1016/j.cherd.2018.07.009.
- Grossmann, Ignacio E., and Gonzalo Guillén-Gosálbez. 2010. "Scope for the Application of Mathematical Programming Techniques in the Synthesis and Planning of Sustainable Processes." *Computers and Chemical Engineering* 34 (9). Elsevier Ltd: 1365–76. doi:10.1016/j.compchemeng.2009.11.012.
- International Energy Agency (IEA). 2013. "Production of Alternative Transportation Fuels: Influence of Crude Oil Price and Technology Maturity," 46.
- Yuan, Zhihong, and Mario R. Eden. 2016. "Superstructure Optimization of Integrated Fast Pyrolysis-Gasification for Production of Liquid Fuels and Propylene." *AIChE Journal* 62 (9): 3155–76. doi:10.1002/aic.15337.

Design and Planning of Agri-Food Supply Chains

Lourenço Cruz^a, João Pires-Ribeiro^a and Ana Barbosa-Póvoa^{a,*}

^a*CEG-IST, Universidade de Lisboa, Av. Rovisco Pais 1, 1049-001 Lisboa, Portugal*
apovoa@tecnico.ulisboa.pt

Abstract

This paper develops a mixed-integer linear programming (MILP) formulation to support the design and planning of agri-food supply chains (AFSC). The model focuses on the strategic-tactical decisions of capacity definition, selection of processing technologies, and the establishment of product flows to achieve expected net present value (ENPV) maximisation. Within the model, AFSC-specific characteristics are modelled as is the case of product perishability, flexible storage strategies, and reverse logistics operations. Supply and demand uncertainty is considered using a stochastic scenarios tree. The model is tested via the application of a case study from an existing sugar beet processing supply chain in The Netherlands.

Keywords: agri-food supply chain, perishability, reverse logistics, uncertainty

1. Introduction

With a growing world population and worldwide problems such as water scarcity and desertification, providing food on a global level will continue to be a challenge, one to which AFSC need to adapt to, cemented on solid drivers for change. Within the major drivers, sustainability concerns should be highlighted. Awareness for environmental impacts is currently on the rise, with a considerable portion of consumers beginning to adapt their consumption habits to reflect such concerns. Social concerns are also becoming generalised. These concerns, which span from supporting locally-grown products to investing in local job creation, lead customers to preferring a closer proximity to farms and markets, as well as paying more attention to the origin of their products. Naturally, this pushes supply chains (SC) towards a more local (decentralised) configuration and puts emphasis on product freshness and traceability. Finally, the access to ever-evolving technologies pushes changes and sector improvement at an increasing rate where uncertainty has to be dealt at both demand and supply sides.

This context creates a high level of complexity when designing and planning AFSC, that imply the development of decisions in tools, where AFSC characteristics are accounted for, so as to support the decisions makers in their decision making process.

In this paper we explore this need and a MILP modelling approach is proposed. This has a strategic-tactical breadth and focuses on defining technology and storage capacity for each AFSC facility, accounting for processing pathway selection, and definition of product flows between entities while considering the main ASFC characteristics as are product perishability, flexible storage strategies, reverse logistics operations, under a context where uncertainty on demand and supply exist.

The paper is structured as follows: Section 2 performs a literature review of papers addressing the design and planning of AFSC with quantitative methods. In Section 3, the major problem characteristics are introduced and briefly explained. In Section 4, the modelled objective is analysed, and novelties introduced explained. Section 5 highlights the details of the case study used to assess model performance. In Section 6, the results of the application of the case study are presented and discussed. Finally, Section 7 uses all previously gathered knowledge to arrive at conclusions and suggest future research directions.

2. Literature Review

The number of papers focusing on the design and planning of AFSC using quantitative models has been steadily increasing (Tsolakis et al., 2014), mostly due to the ever-increasing relevance of the topic on a worldwide scale. Sustainability is one of the most important current concerns. However, most authors still primarily address economic objectives, with just two publications addressing environmental sustainability without simultaneously pursuing economic goals (Banasik et al., 2017; Pipatprapa et al., 2016).

Among SC characteristics, a major focus is verified in centralised SC, against fewer which explicitly focus on decentralised configurations. This is particularly concerning, as decentralisation strategies may be a solution for current environmental and social challenges. In fact, decentralisation allows for the reduction of transportation costs and emissions, and supports local food production and job creation (Bosona and Gebresenbet, 2011; Accorsi et al., 2018). Apart from this, most studies have also addressed forward-oriented SC exclusively, in which reverse logistics are not considered. With current sustainability and waste reduction concerns on the rise, it is expected that the role of reverse and closed-loop SC will only increase (Barbosa-Póvoa et al., 2018). In light of this paradigm, the work of Banasik et al. (2017) must be highlighted, as it focuses on closing the loops in AFSC with the use of multi-objective optimisation.

In the literature is also clear that AFSC possess a series of characteristics which render them unlike any other, reason for which specific tools need to be devised for these SC. Among these, the high level of uncertainty verified in both supply and demand must be highlighted. Naturally, the inclusion of uncertainty modelling is an important trait when evaluating currently-proposed methodologies. Disregarding uncertainty drives models away from reality and, consequently, limits their applicability. When accounting for supply and demand uncertainty, it is clear that attention has been given to demand uncertainty. With fewer publications contributing with both demand and lead time uncertainty considerations (Galal and El-Kilany, 2016). Apart from recognising which authors address AFSC with uncertainty-encompassing approaches, the analysis of which methods have been used to model uncertainty is also interesting. Stochastic models are the more popular approach towards incorporating uncertainty in models.

To support solving some of the knowledge gaps identified throughout the literature review, this paper develops a generic model to assist decision makers on the design and planning of AFSC. The model achieves this goal by incorporating underexplored characteristics in the existing literature, such as reverse logistics, integration of both supply and demand uncertainty, as well as perishability and flexible storage strategies.

3. Problem Characteristics

A generic AFSC is here considered and it consists of five echelons: suppliers, which ensure the supply of raw materials; factories/processors, which use raw materials to manufacture products; warehouses/ distributors, which store products for posterior sale and distribute them to retailers; retailers, where products are sold to end consumers; and reprocessors, which receive wasted products from the remaining SC and produce other valuable products from them, which are then sold to end consumers. The different production processes are represented as technologies, which have associated production costs and bills of materials. To model supply and demand uncertainty, a stochastic scenario tree was established. Each tree node is associated to a randomised occurrence probability and has associated supply and demand variation rates. The problem can be described as follows:

Given: A set of products (raw materials, intermediate products, and final products); a set of technologies, which convert raw materials to intermediate and final products with associated operating costs, material inputs, and outputs; a set of entities (suppliers, processors, distributors, markets, and reprocessors) with associated locations and transportation costs, associated technology capacity, associated storage capacity, and associated demand.

Select the: Technology capacity to use in each entity in each time period; stored quantity in each entity in each time period; product flows between entities in each time period.

Subject to: Inventory/storage constraints; technology constraints; transportation constraints; demand constraints; supply constraints; reprocessing constraints; uncertainty-encompassing constraints.

4. Model Formulation

This section describes the modelled objective and puts emphasis on the differences operated from the modelling approach first proposed by Cardoso et al. (2013), which has been taken as basis for this work.

Equation 1 corresponds to the objective of ENPV maximisation, where the ENPV is expressed as a function of the cash flows ($CF_{s,t}$) of each time period (and scenario), corresponding interest rate (ir) and the probability of occurrence of each stochastic node.

$$\max ENPV = \sum_{t \in T} prob_s \times \frac{CF_{s,t}}{(1 + ir)^t} \quad (1)$$

Supply uncertainty has been pinpointed as one of the areas in which research is lacking. AFSC frequently show mismatches between supply and demand due to high lead times. To mimic this condition, the supply is a theoretical value (for instance, the total production from the arable land of a farm), which never truly corresponds to the effective supply that comes from it, due to inevitable losses. To mitigate such uncertainty, to the maximum expected production capabilities are then taken fractions corresponding to the various sources of loss and uncertainty that affect AFSC, Equation 2. This equation agglomerates all sources of waste in farms to obtain the total spoiled quantity in a given time period ($SQ_{p,v,t}$). The first element on the right hand side, takes into account what is produced ($W_{v,p,s,t}^{out1}$) and immediately spoiled ($imwf_{p,v}$) on each facility; the second element considers the mismatch between supply and demand and the spoilage created by

excessive supply ($p_{p,v,t}^{farm}$); finally the third element considers the spoilage ($lostsf_{p,v,t}$) in inventory ($INV_{v,p,s,t}$) along the supply chain.

$$\sum_{p \in raw(p)} SQ_{p,v,t} = \sum_{p \in raw(p)} (W_{v,p,s,t}^{out1} \times imwf_{p,v}) + \sum_p p_{p,v,t}^{farm} + \quad (2)$$

$$\sum_{p \in raw(p)} (INV_{v,p,s,t} \times lostsf_{p,v,t}) \quad \forall v \in v_{sup} \wedge p \in P_{raw} \wedge (s,t) \in \mathcal{E}S \quad (3)$$

The inclusion of reverse logistics is also of extreme relevance since it is able to generate value with otherwise disposable products. The production of the reprocessors ($W_{i,v,p,s,t}^{out}$) is considered in Equation 4, as a function of the waste input ($W_{i,v,p,s,t}^{in}$) taking into account both the raw material requirements necessary to produce the new product ($qmat_{p,p'}$) and what can be used from reprocessed products ($reprof_{p,v}$).

$$W_{i,v,u,s,t}^{in} \times reprof_{v,u} = \sum_{p \in raw(p)} (W_{i,v,p,s,t}^{out} \times qmat_{u,p}) \quad (4)$$

5. Case Study and results

The case study here described is based on the work by Jonkman et al. (2018), a schematic of the SC is presented in Figure 1. The case study was divided in three different scenarios, all with specific changes meant to be addressed comparatively to assess the applicability of the model to a realistic context. The different scenarios are structured as follows: **Case A**: the expansion of an existing AFSC is considered, in which storage is allowed solely in warehouses, and under supply and demand uncertainty; **Case B**: the expansion of the same AFSC is considered, but storage is allowed in every echelon, and under supply and demand uncertainty; **Case C**: the expansion of the same AFSC is considered, in which storage is allowed in every echelon, under supply and demand uncertainty, and including a reprocessing echelon where reverse logistics operations are allowed.

The SC includes two processing facilities (factories), and two potential processing facilities, one equipped with conventional technology, and one with a small scale bio-refinery technology. The processing echelon is served by 43 suppliers. The distribution echelon includes 4 facilities, and serves a total of 17 markets. For the third scenario, the reprocessing echelon corresponds to facilities in which reprocessing technologies are installed.

As final results, an ENPV of €3074961.95, 3080248.23, and 4053404.26 were obtained for Cases A, B, and C, respectively. The economic performance between Cases A and B is not remarkably different, as the added storage capacity throughout the SC can help prevent product wastage, but only up to a certain level, as product perishability prevents keeping high inventory levels. Still, as can be seen, this added storage capacity does impact the economic performance positively, even if not in a striking manner. However, the same does not hold true for Case C, in which a considerably higher economic performance is

Table 1: Economic and service level results

	Case A	Case B	Case C
ENPV (€)	3074961.95	3080248.23	4053404.26
Unmet demand (%)	9.8	7.6	6.5

achieved due to the additional sales unlocked by the existence of reverse logistics, Table 1.

In fact, the addition of reverse logistics does provide a very meaningful increase in the maximum registered ENPV, a finding which goes well in line with what is seen in the literature review. The appropriate response to the subsequent additions of AFSC characteristics also translates the correct behaviour of the model when addressing the AFSC context, one of the desired goals of this work.

It can also be seen that the capital investments increase from one case to the next, as the addition of flexible storage capacity and one entire reprocessing echelon do come at a cost (approx. 1M€ from Cases A and B to C). However, and as previously mentioned, the additional investment does bear significant economic compensation.

It is interesting to note that the model behaves similarly for all three cases in terms of storage capacity. As far as technology is concerned, it should be highlighted that the model chooses to operate processing capacity increases in already-existing factories rather than opening a new facility. Contrasting, the alternative bio-refinery configuration is indeed installed, in all cases, to satisfy demand for products not generated by the standard technology alternative.

It is important to recognise how the improved economic performance of the model impacts customer service, with unmet demand being a good performance indicator. Before further analysis, it should be noted that a minimum percentage of demand satisfaction of 90% is imposed to the model. It can be seen that in Case A the minimum percentage is barely achieved (90.20% demand satisfaction). An increase in demand satisfaction is registered between Cases A and B, as the additional scattered storage capacity in Case B reduces waste cost, by 26%, and improves demand fulfilment, by 2%. Finally, an additional small increase in demand satisfaction (1%) is seen between Cases B and C, as the reverse logistics activities provide further waste reduction and generate resources that can be applied to other productive activities, thus positively impacting the available quantities for sale. Case C is also where waste costs are reduced to the maximum with reductions of 68% and 57% if compared with Case A and Case B, respectively.

6. Conclusions

In the present work a quantitative model is proposed to support the design and planning of AFSC via an optimisation approach, focused on the strategic and tactical decision levels.



Figure 1: Location of the facilities within the sugar beet SC. Suppliers are marked in blue, existing processors in red, the potential conventional processor in green, the potential bio-refinery processor in purple, warehouses/distributors in brown, and markets/retailers in orange.

The satisfactory performance of the model in an AFSC context solves a set of clearly identified knowledge gaps. Firstly, the model is an important step towards encompassing both supply and demand uncertainty in the AFSC sector, traits deemed essential for the appropriate applicability of the model to real-world cases. Secondly, the model incorporates reverse logistics, which have been identified as powerful tools in the optimisation of both the economic and environmental performance of AFSCs and that, so far, had been understudied. Finally, the model includes specific under-explored AFSC characteristics such as product heterogeneity and a flexible storage strategy.

Despite providing several improvements when compared to non AFSC-specific models, the current model can still be subject to several improvements. At first, it should be noted that the model here developed incorporates one single economic objective, a trait which fails to meet current Triple Bottom Line (TBL) optimisation concerns. Secondly, more attention can also be given to the stochastic scenarios tree used to model uncertainty. The proposed scenarios tree seems appropriate to the modelled context, but the application of a larger set of possible scenarios could help improve on the model's realism.

Acknowledgements: The authors acknowledge the support provided by FCT and P2020 under the project PTDC/EGE-OGE/28071/2017 e Lisboa - 01-0145-FEDER-28071

References

- R. Accorsi, G. Baruffaldi, R. Manzini, A. Tufano, 2018. On the design of cooperative vendors' networks in retail food supply chains: a logistics-driven approach. *International Journal of Logistics Research and Applications* 21 (1), 35–52.
- A. Banasik, A. Kanellopoulos, G. D. Claassen, J. M. Bloemhof-Ruwaard, J. G. van der Vorst, 2017. Assessing alternative production options for eco-efficient food supply chains using multi-objective optimization. *Annals of Operations Research* 250 (2), 341–362.
- A. P. Barbosa-Póvoa, C. da Silva, A. Carvalho, 2018. Opportunities and challenges in sustainable supply chain: An operations research perspective. *European Journal of Operational Research* 268 (2), 399–431.
- T. G. Bosona, G. Gebresenbet, 2011. Cluster building and logistics network integration of local food supply chain. *Biosystems Engineering* 108 (4), 293–302.
- S. R. Cardoso, A. P. F. D. Barbosa-Póvoa, S. Relvas, 2013. Design and planning of supply chains with integration of reverse logistics activities under demand uncertainty. *European Journal of Operational Research* 226 (3), 436–451.
- N. M. Galal, K. S. El-Kilany, 2016. Sustainable agri-food supply chain with uncertain demand and lead time. *International Journal of Simulation Modelling* 15 (3), 485–496.
- J. Jonkman, A. P. Barbosa-povoa, J. M. Bloemhof, 2018. Integrating harvesting decisions in the design of agro-food supply chains, *under revision*.
- A. Pipatprapa, H.-H. Huang, C.-H. Huang, 2016. A Novel Environmental Performance Evaluation of Thailand's Food Industry Using Structural Equation Modeling and Fuzzy Analytic Hierarchy Techniques. *Sustainability* 8 (3), 246.
- N. K. Tsolakis, C. A. Keramydas, A. K. Toka, D. A. Aidonis, E. T. Iakovou, 2014. Agrifood supply chain management: A comprehensive hierarchical decision-making framework and a critical taxonomy. *Biosystems Engineering* 120, 47–64.

Production scheduling of semi-continuous milk processing facility

Utkarsh Konge^a and Sivakumar Subramanian^{a,*}

^a*TCS Research and Innovation, Tata Research Development and Design Centre, Tata Consultancy Services, Pune 411013, India*

**sivakumar.subramanian1@tcs.com*

Abstract

Production scheduling of a semi-continuous multi-product plant with multiple units working in series or parallel mode is a challenging problem. Furthermore, characteristics like limited inventory and single continuous packing campaigns add to its complexity. In this work, an MILP formulation with continuous time representation is implemented to maximize the production of a milk processing facility. Unlike the batch processes where the batch sizes in the time intervals are the key variables, in the semi-continuous process considered, the time duration for which the process is active in each time interval becomes the key variable. A schedule which maximizes the production is generated for each day so that a minimum market requirement is satisfied for each product. The results obtained can further be used to find the bottlenecks and help improve the productivity of the facility.

Keywords: MILP, Scheduling, Semi-continuous Process, Dairy Plant Scheduling

1. Introduction

High competition in process industries has led manufacturers to prioritize optimization of existing production operations. This is where optimal scheduling of the facility plays an important role. Harjunkski et al. (2014) presented the impact of optimal scheduling for various industries. The case presented in Bongers and Bakker (2008) saw a significant increase in production due to optimal scheduling. This motivated a rich set of literature showcasing scheduling optimization in food industry. Most of the production plants in food processing industry work in semi-continuous mode as the production is flexible and production equipment can be utilized more efficiently. As discussed by van Elzakker et al. (2012) characteristics like multi-stage production, limited inventory, intermediate cleaning, and single continuous packing campaigns are representative of a typical FMCG industry. These characteristics were modelled for a semi-continuous ice-cream manufacturing process. Kopanos et al. (2010) discussed the scheduling of yoghurt production in detail. In both works, the stages of pasteurization, standardization, and homogenization were considered as a single stage. The schedule for downstream stages is thrown over the wall to this stage.

Most of the milk derivatives like ice-cream, yoghurt, milk powder and so on, have pasteurized and standardized milk as a precursor. This makes it imperative to schedule the process of pasteurization and standardization of milk. Bilgen and Dogan (2015) optimized the production planning of a milk pasteurization facility which comprised of raw milk tanks, pasteurization unit, intermediate storage tanks and so on. The work presented in this paper aims at developing optimal schedule for a similar semi-continuous process with characteristics like limited intermediate storage and single

continuous packing campaign. The model is expressed as an MILP formulation with continuous representation of time. A decomposition method is implemented to solve the problem in a reasonable time. Results obtained were used to find the bottlenecks of the process and improve the process further.

2. Problem Statement

Bylund (2003) discussed the pasteurization process in detail. It depicts the significance of various process components like milk silos, intermediate storage tanks, pasteurizer, standardization unit and so on. The semi continuous dairy plant, considered based on the discussion in Bylund (2003), is shown in Figure 1. This production facility converts raw milk into standardized milk, which is then converted into Stock Keeping Units (SKU). Raw milk is received in the silos at the beginning of each day. It is then processed in a pasteurization unit which operates in continuous mode. In a standardization unit, cream is separated from the raw milk in a continuous mode and collected in separate Cream Storage Tanks. The pasteurization unit and standardization unit work in continuous mode consecutively. Hence, these are considered as a single unit in the process. Apart from cream, the standardization unit produces standardized milk. This standardized milk is then stored in the intermediate storage tanks which is then converted into SKUs by the packaging lines. Changing the operation from one fat content to other on the pasteurizer stage can be done without any additional setup time or intermediate cleaning. As there are various types of intermediate products based on the fat content, multiple storage tanks are required to avoid mixing. The packaging lines operate in continuous mode with feed from the intermediate tanks. Typically, packaging lines can process multiple types of SKUs with different rates. Additional setup time or intermediate cleaning may be required while changing the mode from one SKU to other on the packaging lines. In Kopanos et al. (2010), typical daily production line shutdowns are modelled due to hygienic requirements. Similar shutdowns are modelled in the presented facility where the packaging lines are allowed to run only for 18 hours a day. At the end of the scheduling horizon (week) the levels of all the intermediate products are constrained to be zero. The objective of the scheduling problem is to maximize the total production subject to continuous single product packing campaign, limited intermediate storage and some minimum production of each SKU.

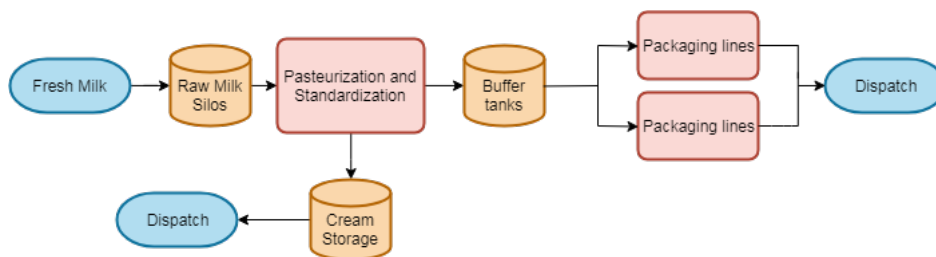


Figure 1: Schematic overview of a milk processing plant

3. Formulation

The key decision variables in this optimization problem are: (i) the start time of each stage in the production line, (ii) the amount of each SKU to be produced on each day of the week and on each packaging line, (iii) the order in which the SKUs and the intermediate products are processed. To keep track of the levels of intermediate products, a continuous time formulation is implemented. The start and completion times of products on the pasteurization stage and the packaging lines

are considered as events for the formulation. A slot is created between two events and since the processes are continuous, the time for which each stage is active in a slot is a key variable too. The binary variables denoting the start and end of a particular process for a specific product in the given slot are used to find the slots in which the process is active. The time of processing in each slot can be equated to this slot length. Let $\Delta t_{i,l,p,k}$ denote the time for which a process line p was active processing product i in slot l on day k . Let $s_{i,l,p,k}$ and $f_{i,l,p,k}$ be the binary variables denoting the start and end of this process in slot l respectively. The relation between these variables are captured in constraints (1)-(3). The variable $S_{l,k}$ denotes the starting time of slot l on day k . M is large value compared to $\Delta t_{i,l,p,k}$. $nslots$ is the total number of slots given.

$$\Delta t_{i,l,p,k} \geq S_{l+1,k} - S_{l,k} - M \times (1 - \sum_{lm \in \{1,2,3,\dots,l\}} (s_{j,lm,p,k} - f_{j,lm,p,k})) \quad (1)$$

$$\Delta t_{i,l,p,k} \leq S_{l+1,k} - S_{l,k} + M \times (1 - \sum_{lm \in \{1,2,3,\dots,l\}} (s_{j,lm,p,k} - f_{j,lm,p,k})) \quad (2)$$

$$\Delta t_{i,l,p,k} \leq M \times \left(\sum_{lm \in \{1,2,3,\dots,l\}} (s_{j,lm,p,k} - f_{j,lm,p,k}) \right) \quad (3)$$

$$\forall i \in Products, p \in ProcessLines, l \in slots \setminus \{nslots\}, k \in Days$$

The levels of each intermediate product is updated at each event so that the input from the pasteurization stage adds to the level at previous event and the output to the packaging lines reduces it. The total capacity of intermediate storage is limited. To model this, the storage amount is divided into various bins. The parameters U_{cap}^r and L_{cap}^r are the upper and lower bounds of the bins respectively. Computation of these bounds is explained with an example here. Consider three tanks each with capacity of 1000 kg. The index r will run from 1 to 3 (total number of tanks). The set of parameters is as shown in constraints (4).

$$\{(L_{cap}^1, U_{cap}^1), (L_{cap}^2, U_{cap}^2), (L_{cap}^3, U_{cap}^3)\} = \{(0, 1000), (1000 + \varepsilon, 2000), (2000 + \varepsilon, 3000)\} \quad (4)$$

Here ε is a small value compared to tank capacity. A binary variable keeps track of the bin in which the level of each intermediate product lie in each slot on each day. Now, to implement the maximum capacity constraint, the sum of U_{cap}^r for the bins in which the levels lie, is constrained to be less than or equal to the maximum capacity. Let the binary variable denoting whether the level of intermediate product j is in bin r in slot l for day k be $z_{j,r,l,k}$. The constraints capturing the relations are equations (5) and (6). The constraints (7) ensure that the levels are in exactly one bin for a given intermediate product, slot and day. The variable $R_{j,l,k}$ represents the amount of intermediate product j at the start of slot l on day k . $MPast$ is a large value as compared to $R_{j,l,k}$. I is the set of intermediate products.

$$R_{j,l,k} \geq L_{cap}^r - MPast \times (1 - z_{j,r,l,k}) \quad \forall j \in I, r \in bins, l \in slots, k \in Days \quad (5)$$

$$R_{j,l,k} \leq U_{cap}^r + MPast \times (1 - z_{j,r,l,k}) \quad \forall j \in I, r \in bins, l \in slots, k \in Days \quad (6)$$

$$\sum_{r \in bins} z_{j,r,l,k} = 1 \quad \forall j \in I, l \in slots, k \in Days \quad (7)$$

Since raw milk has a very short shelf-life, all the milk procured on a particular day must be pasteurised and stored in the intermediate storage. The input stream of the pasteurizer, which is converted into intermediate products with different fat content, has a constant flowrate. But the output flowrate depends on the type of intermediate product being produced. Cream is produced as a side product and stored in storage tanks of limited capacity. The pasteurized milk can be kept overnight in the tanks and used for production on the following day. For the first day of the

Intermediate Product	Output flowrate (kg/h)
Z1 (Low fat)	2199.5
Z2 (Medium fat)	2256.6
Z3 (High Fat)	2348.1

Table 1: Pasteurizer output flowrates of intermediate products

week, it is assumed that the tanks are empty at the beginning of the day. Packaging lines can start packing the products only when some buffer time has elapsed after the start of pasteurization of the corresponding intermediate product. Sequence dependent changeover is implemented on the packaging lines. When a product is assigned to a particular packaging line, some minimum amount of it has to be processed on the line. To maintain the hygiene of the plant, the fillers or the packaging lines are allowed to run only for 18 hours a day. Finally, the constraints ensuring meeting of the market demand and the mass balance between the intermediate products and the SKUs are enforced. Apart from these constraints, the regular scheduling constraints like non-preemptive assignment of units and sequencing of the products are enforced.

3.1. Decomposition

For the given case, the scheduling for the whole week turned out to be a difficult problem to solve due to the size of the problem. Hence, the problem was divided into smaller problems by decomposing the temporal dimension. In each of the smaller sub-problem, scheduling optimization was carried out for just one day with the objective of maximizing the production. Through the constraints of the model, it was ensured that the daily production of each product was more than the daily average requirement to satisfy the weekly target. The level of each intermediate product at the end of the day was recorded and was used to initialize the level of each intermediate product at the start of the following day. The sub-problems are solved for all the seven days of the week. A schematic of the decomposition method is given in Figure 2. The advantage of such a decomposition is that if in the optimal schedule for a day, the initial levels of the intermediate product are equal to the levels at the end of the day, then the problem need not be solved for the next day as it would have the same optimal schedule.

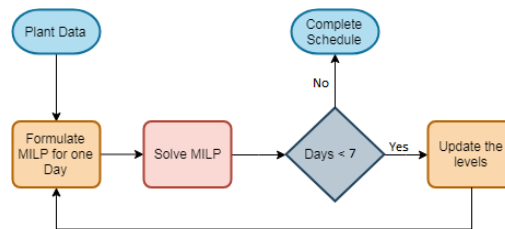


Figure 2: Decomposition strategy

4. Results and Discussion

The problem was formulated in Pyomo 5.5.1 (Hart et al. (2017), Hart et al. (2011)) and solved using COIN-OR Cbc (Forrest et al. (2018)). For one day of scheduling, the MILP formulation consisted of 1281 variables and 2726 constraints and was solved within 120 seconds on a system with i5-2400 (3.10 GHz) processor and 10 GB RAM. The continuous time representation consisted of 20

SKU	Rates (kg/h)		Intermediate Product	Min Req.(kg)	Optimal production (kg)
	S1	S2			
A	600	540	Z3	30000	32899
B	900	600	Z2	20000	20000
C	-	600	Z1	15000	15000
D	540	540	Z1	7500	7500
E	720	780	Z3	15000	22399
F	600	-	Z2	2500	2500

Table 2: Packaging Rates, Minimum and Optimal production

events. The input flow rate of the pasteurization stage is 2400 kg/h. The output flow rates of various intermediate products are given in Table 1. The maximum capacity of the Raw Milk silos is 15000 kg. There are four intermediate storage tanks each with capacity of 5000 kg. The facility has two packaging lines namely S1 and S2. The packaging rates for the SKUs on each line are given in Table 2 along with the corresponding intermediate product. The sequence dependent changeover for the packaging lines ranges from 0.25 to 0.5 h. The minimum required quantity and the optimal production of the products are given in the last column of Table 2. The products A and E are produced more than the minimum required value (9 % and 49 % more, respectively). Rest of the products met their demands exactly. The excess production of A and E can be explained by the fact that both A and E are produced with the intermediate product with the highest flow rate (Z3). This ensures high availability of intermediate product required for the production. The packaging rate of product E is high on both the packaging lines. Thus, more of this product can be processed in less time. Figure 3 depicts the optimal schedule for one day. Figure 4 depicts the time profile of quantities of intermediate products stored in the intermediate tanks. As the initial and final levels of all the intermediate products is same, the same schedule is optimal for all the days.

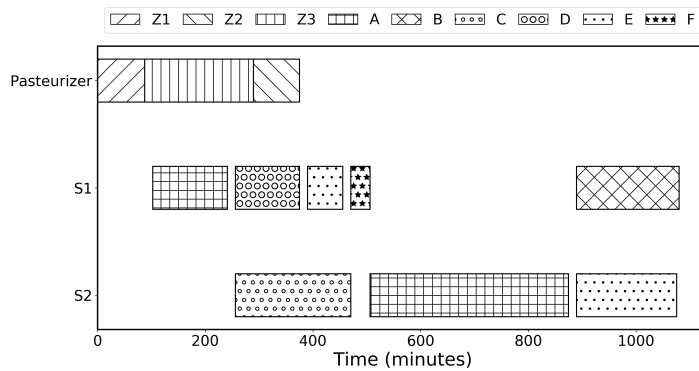


Figure 3: Gantt Chart of the schedule

As evident from the Figure 3, the packaging lines S1 and S2 are not being used to the fullest as there is some idle time apart from the sequence dependent changeover. This can be attributed to low capacity of the raw milk silos. This is explained even by Figure 4 in which the levels of all the intermediate products drop to zero at the end of the day. To improve the utilization of S1 and S2, the capacity of raw milk silo, in other words, the procurement of raw milk, should be increased. Additional optimization simulations can be performed to find the capacity of silos which enable

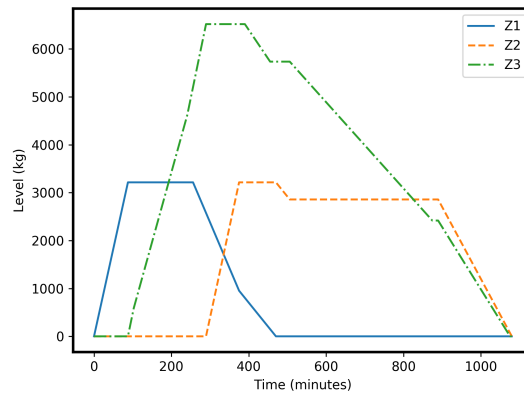


Figure 4: Levels of intermediate products

the packaging lines to be utilized to the fullest.

5. Conclusion

An MILP model was formulated for a semi-continuous milk processing facility. The process characteristics typical of an FMCG industry were successfully modelled. A decomposition algorithm was developed, implemented, and successfully tested. An optimal schedule was obtained using an open source solver. The results obtained were used to draw insights to further improve the performance of the plant. The framework developed here provides a good foundation to simulate additional scenarios and to further increase the throughput of the plant by varying the silo capacity. This naturally transitions into simultaneous synthesis and scheduling optimization problem.

References

- B. Bilgen, K. Dogan, 2015. Multistage Production Planning in the Dairy Industry: A Mixed-Integer Programming Approach. *Industrial & Engineering Chemistry Research* 54 (46), 11709–11719.
- P. M. Bongers, B. H. Bakker, 2008. Validation of an Ice cream factory operations model. In: ESCAPE 18 proceedings.
- G. Bylund, 2003. Dairy processing handbook. Tetra Pak Processing Systems AB.
- J. Forrest, T. Ralphs, S. Vigerske, LouHafer, B. Kristjansson, jpfasano, EdwinStraver, M. Lubin, H. G. Santos, rlougee, M. Saltzman, Jul. 2018. coin-or/Cbc: Version 2.9.9.
- I. Harjunkoski, C. T. Maravelias, P. Bongers, P. M. Castro, S. Engell, I. E. Grossmann, J. Hooker, C. Méndez, G. Sand, J. Wassick, 2014. Scope for industrial applications of production scheduling models and solution methods. *Computers & Chemical Engineering* 62, 161 – 193.
- W. E. Hart, C. D. Laird, J.-P. Watson, D. L. Woodruff, G. A. Hackebeil, B. L. Nicholson, J. D. Siirola, 2017. Pyomo—optimization modeling in python, 2nd Edition. Vol. 67. Springer Science & Business Media.
- W. E. Hart, J.-P. Watson, D. L. Woodruff, 2011. Pyomo: modeling and solving mathematical programs in Python. *Mathematical Programming Computation* 3 (3), 219–260.
- G. M. Kopanos, L. Puigjaner, M. C. Georgiadis, 2010. Optimal Production Scheduling and Lot-Sizing in Dairy Plants: The Yogurt Production Line. *Industrial & Engineering Chemistry Research* 49 (2), 701–718.
- M. A. H. van Elzakker, E. Zondervan, N. B. Raikar, I. E. Grossmann, P. M. M. Bongers, 2012. Scheduling in the FMCG industry: An Industrial Case Study. *Industrial & Engineering Chemistry Research* 51 (22), 7800–7815.
- A. S. Wallerand, R. Voillat, F. Maréchal, 2016. Towards optimal design of solar assisted industrial processes: Case study of a dairy. Tech. rep., University of Ljubljana.

Fast Bypass Selection Method during the Heat Exchanger Network Synthesis

Rupu YANG,^{a*} Cong Toan Tran,^a Assaad Zoughaib^a

^a*CES-MINES ParisTech, PSL Research University, CES (Center for Energy efficiency of Systems), 5, rue Léon Blum, 91120 Palaiseau, France*

rupu.yang@mines-paristech.fr

Abstract

This paper provides a new and fast method to select bypass during the heat exchanger network (HEN) synthesis stage. An indicator, namely disturbance over utility (DoU), was introduced to measure the maximum simultaneous disturbance rejection ability over the utility consumption. Together with a physical distance study, they can select the bypass placement fast and efficiently. DoU can select preferable heat exchangers to place bypass, and compare different HENs. For a given HEN with specified bypass strategies, the higher the DoU is, the larger the disturbance rejection ability per unit utility consumption, which was solved by a non linear programming (NLP) model. The physical distance study utilizes the structural information to discard potential inverse response and compare response time of different bypasses. The method has been applied into two alternative HENs, illustrating the process to select better HEN and find preferable bypass placement strategies. The main goal of this work is to contribute to HENs synthesis, by proposing a fast and efficient bypass selection method to decide the control structure.

Keywords: heat exchanger network synthesis, bypass selection, simultaneous disturbance, inverse response, time response

1. Introduction

The operational performance of HEN is largely dependent on the control structure, which deserves to be set up at design stage (Escobar et al., 2013). The manipulation of HEN is usually achieved through the operation of bypass and utility when the system is facing disturbance. While the number of utility is often not adequate to meet the HEN control requirement, thus bypasses are required in the HEN, and they usually denoted as manipulated variables (MVs). A challenging work is how to find optimal bypass placement strategy considering the simultaneous disturbance rejection, utility consumption and dynamic performance fast and efficiently.

During the past decades, many approaches were put forward to select the bypass for HENs by studying the trade-off between disturbance rejection ability, investment cost and dynamic performance. For explicit disturbance, flexibility index is widely accepted as the criteria to iterate the synthesis stage, along with checking the disturbance range individually (Yan et al., 2001)(Escobar et al., 2013). Chen and Hung (2004) agreed that the individual disturbance cannot guarantee the feasibility of the network when simultaneous disturbance occurs. The simultaneous disturbance analysis is especially important when disturbances are not explicit, for example, the HEN integrated with renewable energy systems. For a given HEN, the disturbance rejection is actually the heat load redistribution process limited by the constraints in MVs and the utility cost.

The disturbance rejection ability is a static problem, while the dynamic part is mainly about the control problems and time response, and it largely depends on the control strategy and specific controller. The following discussion is based on decentralized control scenario with PID as controller, which is the most commonly selection for HENs. Escobar et al. (2013) applied PID controller in MATLAB to study the dynamic performance of different bypass selections without consideration of the potential inverse response. In decentralized control scenario, the presence of right half plane (RHP) zeros might evoke the inverse response, and lead to control difficulty which ought to be avoided (Skogestad and Postlethwaite, 2005). The presence of inverse response in HENs comes from different downstream pathways with contrary effect on the same controlled variable (CV). The time response is the time delay between two stable conditions when MV functions, and the faster the better. Lersbamrungsuk and Srinophakun (2009) introduced the structural time delay (physical distance from MV to CV) to represent time response. We employ the same idea to compare different bypass placement strategies.

In this context, we aim to propose a fast and efficient method to select control structure during the HEN design. The method employs disturbance-over-utility (DoU), coupling with RGA-number, inverse response and physical distance to find a preferable bypass selection. The calculation of DoU involves optimization, while the whole method is trying to locate a good result by integrating static and dynamic criteria.

2. Bypass selection process

Figure 1 presents the integration of bypass selection in HEN sequential design process. In this paper we focus only on the control structure selection step. To reach the preferable bypass placement strategies, RGA-number and DoU will help to select preferable heat exchangers to place bypass, then potential inverse response and physical closeness will be employed to evacuate the most appealing bypass. RGA-number has been widely accepted as an efficient tool to quantify the interaction between different control loops and here it is also calculated with the same method as (Chen and Hung, 2004) (Escobar et al., 2013).

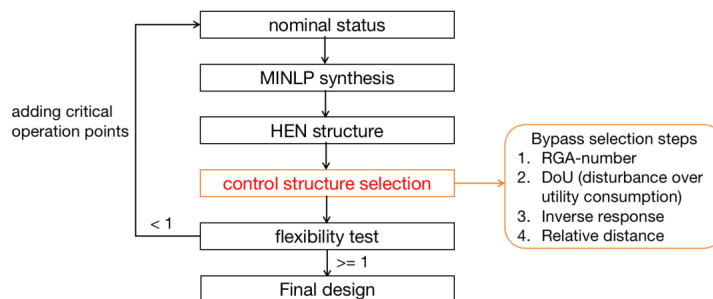


Figure 1: Bypass selection during the HEN synthesis

2.1 NLP model to calculate DoU

The HEN model regards the heat exchanger (HX) as the knot throughout each process stream, and for each stream there are '2*number of knots + 1' stages of temperature by assuming that bypass is on every side of all HXs. The simplified thermal effectiveness

method (Knut W. Mathisen, 1994) was selected to describe the energy balance of HX. The method is based on the simple relationship between the thermal effectiveness of the cold and the hot side (P^c and P^h) as in equation (4). With the constraint that P^c and P^h are within 0 and 1. For each heat transfer process, the heat transfer between two streams can be described as following:

$$P^h [i, j, k, l] = \frac{1 - \exp(-N_{tu}^h [i, j, k, l](1 - R^h [i, j, k, l]))}{1 - R^h [i, j, k, l] \exp(-N_{tu}^h [i, j, k, l](1 - R^h [i, j, k, l]))} \quad (1)$$

$$R^h [i, j, k, l] = CP_h [i, j, k, l] / CP_c [i, j, k, l] \quad (2)$$

$$N_{tu}^h [i, j, k, l] = UA [i, j, k, l] / CP_h [i, j, k, l] \quad (3)$$

$$P^c [i, j, k, l] = R^h [i, j, k, l] P^h [i, j, k, l] \quad (4)$$

$$P^h [i, j, k, l] = (T [i, 2k - 1] - T [i, 2k]) / (T [i, 2k - 1] - T [j, 2l - 1]) \quad (5)$$

$$P^c [i, j, k, l] = (T [j, 2l] - T [j, 2l - 1]) / (T [i, 2k - 1] - T [j, 2l - 1]) \quad (6)$$

Where i, j stand for the hot and cold stream of a HX; k, l stand for the order of knot that the HX lies in each stream; CP_h, CP_c are the heat capacity flow of hot and cold streams separately, U is the heat transfer coefficient, A is the transfer area; and T is the temperature. DoU is depicted as equation (7), d_i is the disturbance item, $d_{i,o}$ is the nominal value of that disturbance, and $W_{utility}$ is the utility consumption. The product can be interpreted as the volume by which the system can operate normally, the larger the DoU the better the disturbance rejection ability of HEN and utility consumption. It helps to select preferable HXs to place bypass and can also act as controllability indicator of HEN.

$$DoU = \text{Max} \left(\prod \left| \frac{d_i}{d_{i,o}} - 1 \right| / W_{utility} \right) \quad (7)$$

The constraint information to reach DoU is as following:

$$MV_y \in (0, 1) \quad (8)$$

$$CV_x \in (CV_{x,o} - \alpha, CV_{x,o} + \alpha) \quad (9)$$

$$W_{utility} \leq \text{load}_{i,\text{max}} \quad (10)$$

$CV_{x,o}$ is the nominal value of CV_x , α represents the allowable range of CV.

2.2 Potential inverse response

Inverse response is a typical obstacle to achieve preferable control performance (Skogestad and Postlethwaite, 2005). It possibly occurs when there are different downstream pathways from a MV to a CV, and especially when those effects arrive at different velocity with contrary trend. Firstly, an algorithm will find the possible downstream pathway for a MV-CV pairing and the relationship between them. Then if the longest pathway dominates the integral effect and is contrary to the effect of other pathways, the inverse response will highly come out. By definition, the pathway length is the number of physical steps required from MV to CV. Refer to Figure 2 as example, when bypass at hot side of HX3 is changed, there are two downstream paths to affect $y1$ dotted curves illustrating.

Path 1: 3H->4H->4C->2C-> $y1$, (4), +

Path 2: 3H->3C->1C->1H->2H->2C-> $y1$, (6), -

where H and C stand for hot and cold side of HX; the number in the bracket stands for the pathway length. When the bypass increases, positive effect “+” means that the corresponding path will increase y_1 while negative effect “-” means that it will decrease y_1 . In this example, path 1 is shorter physically, and if the effect of path 2 dominates the final variance of y_1 , the inverse response is expected to present. The integral effect can be read from bypass gain matrix directly.

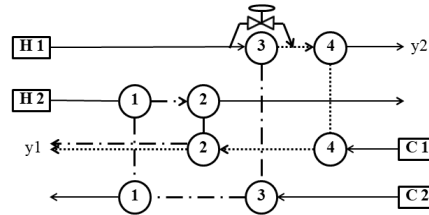


Figure 2: Example of two downstream paths with opposite effect

2.3 Physical distance

The physical distance of certain control pairings can be represented by the longest downstream path among the selections. Taking Figure 2 as example again, compare two pairings P1 and P2 as shown in Table 1. For P1, path 2 is the longest one that requires 6 steps, which dominates the time response and requires 6 steps. For P2, path 2 dominates the time response and only requires 4 steps. Thus P2 is preferable in term of time response aspect. The above inverse response detection and physical distance study is carried out with a program in Python automatically.

Table 1: Result of physical distance of two pairings

P1, 3H-y1/4H-y2	P2, 2H-y1/4H-y2
Path 1: 3H->4H->4C->2C->y1, (4), +	Path 1: 2H->2C->y1, (2), -
Path 2: 3H->3C->1C->1H->2H->2C->y1, (6), -	Path 2: 4H->4C->2C->y1, (4), -
Path 4: 4H->4C->2C->y1, (3), -	Path 3: 4H->y2, (1), +
Path 3: 3H->4H->y2, (2), +	
Path 5: 4H->y2, (1), +	

3. Case study

The case study that involves two hot streams and two cold streams is a classical case discussed in many studies (Yan et al., 2001)(Escobar et al., 2013) (Masoud et al., 2016). The two alternative designs consist of three HXs and two coolers, as shown in Figure 3. The pinch method aims to reach the maximum energy recovery and leads to HEN1, while the superstructure approach aims to find the minimum total annualized cost leads to HEN2. The heat capacity flow of each stream is 10, 15, 20, 30 (kW/K) separately, heat transfer coefficient is 0.16 (kW/(m²·K)) and their supply and target temperatures are also listed in the Figure 3. The four stream outlet temperatures are CVs with ± 1 K allowable operational range. In addition to two utilities acting as MVs, two bypasses are required to help the system to reject disturbance, and inlet temperature variation of C1 and C2 are expected disturbance with unknown range.

RGA-number in Table 2 was calculated from the gain matrix result in Table 1. Pairings E1E3 and E2E3 are both perfect pairings in two structures according to the interpretation of RGA-number. The DoU results are presented in Table 3, the pairing

E1E3 in both structures get the largest DoU value which represents structure's maximum disturbance rejection region under the same utility cost. It can also be concluded that HEN1 is better than HEN2. Then physical distance result can help to select desirable bypass shown in Table 4 (pairing 1H3H means bypass at hot side of exchanger 1 and 3 will control y_1 and y_2 separately). For all the pairings there exist three paths from MV to CV, while they all present the same change direction as bypass fluctuate, regardless of inverse response. Pairings 1C3H and 1C3C share the same longest path which is smaller than other choices, and 1C3C present smaller integral distance than 1C3H. Therefore, 1C3C in HEN1 is the best bypass selection both in static and dynamic aspects.

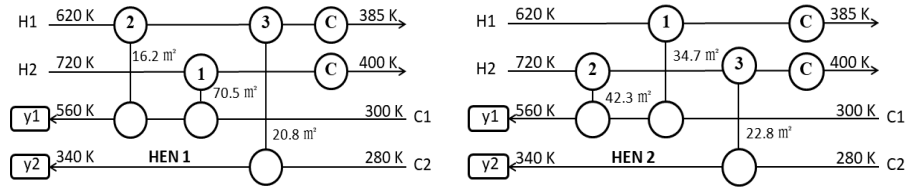


Figure 3: HENs in case study

Table 2: Gain matrix of HEN

	HEN1			HEN2		
	E1	E2	E3	E1	E2	E3
C1	-0.0376	-0.0511	0	-0.0259	-0.0501	0
C2	-0.0051	0.0195	-0.0331	-0.0081	0.0167	-0.0333

Table 3: RGA result

HEN1, pairings	RGA-number	HEN2, pairings	RGA-number
E1E2	1.0488	E1E2	1.9362
E1E3	0	E1E3	0
E2E3	0	E2E3	0

Table 4: DoU result

HEN1, pairings	DoU*1,000	HEN2, pairings	DoU*1,000
E1E3	63.3	E1E3	62.6
E2E3	62.6	E2E3	62.3

Table 5: Physical distance analysis

Pairings	Pathway	Longest path	Integral distance
1H3H (1H-y1,3H-y2)	P1: 1H->1C->2C->y1, - P2: 3H->3C->y2, - P3: 1H->1C->2C->2H->3H->3C->y2,-	P3 (6)	11
1H3C	P1: 1H->1C->2C->y1, - P2: 3C->y2, - P3: 1H->1C->2C->2H->3H->3C->y2, -	P3 (6)	10
1C3H	P1: 1C->2C->y1, - P2: 3H->3C->y2, - P3: 1C->2C->2H->3H->3C->y2, -	P3(5)	9
1C3C	P1: 1C->2C->y1, - P2: 3C->y2, - P3: 1C->2C->2H->3H->3C->y2, -	P3(5)	8

4. Conclusion

The work provides a new method to select bypass during HENs synthesis, considering the simultaneous disturbance analysis and prediction of dynamic performance with pure static calculation. The method proposed an indicator DoU to represent the maximum disturbance rejection region over utility consumption, it can be used to compare the operability of different HENs, and select preferable exchangers to control HEN. A physical distance method is used to reject the potential inverse response and compare the response time of various bypass selections. The case study had shown the applicability of the method, they can reach optimal result quickly and efficient since only in static calculation is required. It deserves to be mentioned that the static result cannot guarantee the desirable dynamic performance, and a dynamic study is required to confirm the solution found by the method. Finally, it can be seen that implementing the method directly in the synthesis step is possible, and that allows designing HEN by considering simultaneously a main objective (energy consumption or cost) and disturbance rejection ability.

5. Acknowledgments

The authors are very grateful for the grants from China Scholarship Council (CSC).

References

- Chen, C., Hung, P., 2004. Simultaneous Synthesis of flexible heat-exchange networks with uncertain source-stream temperatures and flow rates. *Industrial & Engineering Chemistry Research* 43(18), 5916–5928.
- Escobar, M., O.Treirweiler, J., E.Grossmann, I., 2013. Simultaneous Synthesis of Heat Exchanger Networks with Operability Considerations: Flexibility and Controllability. *Computers & Chemical Engineering* 55, 158–180.
- Knut W. Mathisen, 1994. Integrated design and control of heat exchanger networks. Ph.D. Thesis. University of Trondheim - NTH, Norway.
- Lersbamrungsuk, V., Srinophakun, T., 2009. Structural Controllability Evaluation for Heat Exchanger Networks, in: *Proceedings of the 7th Asian Control Conference*. 835–840.
- Masoud, I.T., Abdel-Jabbar, N., Qasim, M., Chebbi, R., 2016. Methodological framework for economical and controllable design of heat exchanger networks: Steady-state analysis, dynamic simulation, and optimization. *Applied Thermal Engineering*. 104, 439–449.
- Skogestad, S., Postlethwaite, I., 2005. *Multivariable feedback control: analysis and design*, chapter 5, Chichester, New York, Brisbane, Toronto, Singapore, John Wiley & Sons.
- Yan, Q.Z., Yang, Y.H., Huang, Y.L., 2001. Cost-effective bypass design of highly controllable heat-exchanger networks. *AIChE Journal*. 47(10), 2253–2276.

Integrating Oil Refineries and Bio-refineries: Upgrading Acetone, Butanol and Ethanol to High- Value Products

Elham Ketabchi, Laura Pastor-Perez, Tomas Ramirez Reina, Harvey Arellano-Garcia*

*Department of Chemical and Process Engineering, University of Surrey, Guildford,
GU27XH, United Kingdom*

**h.arellano-garcia@surrey.ac.uk*

Abstract

In this work, an integration systems approach connecting an oil refinery and a bio-refinery is proposed. These plants can be connected through various pathways such as on-site power generation, utility systems and syngas production with the feed of refinery residue, bio-oil and other streams. One important pathway that is the focus in this work represents the production of chemicals produced via biomass sources into the petrochemical and transportation industry as valuable products. Focusing on the latter route of integration, the upgrading of Acetone, Butanol and Ethanol produced by sugar fermentation via bacterial species, has been chosen as a pathway to produce valuable products that could be utilised in both the chemical sector and the transportation industry. There is little current literature regarding this upgrading process, making it a relatively novel option of producing valuable products.

The reaction systems studied consist of the self-condensation of the alcohols and cross condensation of alcohols and acetone using active metals supported on basic supports as catalysts at high temperatures and pressure in a batch reactor. Moreover, catalysts syntheses were conducted successfully to verify the proposed integration approach. The results have shown an outstanding performance for the catalysts in terms of conversion and selectivity, having conversions as high as 90%. The catalysts have also proven to yield valuable products with broad market options in the chemical Industry. In conclusion, this route has shown promising results in terms of providing valuable C₂-C₁₅ products, useful for both the petrochemical industry and the transportation sector while using economically favourable catalysts in comparison with previous studies.

Keywords: Integration, oil refinery, bio-refinery, ABE, long-chain hydrocarbons.

1. Introduction

One of the main issues that many manufacturing sectors such as oil refineries are facing is that they are not performing as efficient as the past due to various factors. These factors could be environmental, economic, etc. A main factor that should be considered for oil refineries is their dependency on crude oil, the main feedstock of the process. Following this, the price fluctuation in crude oil has a direct impact on this industry. The price increase will force a rise in the search for fossil fuel substitutes from renewable and sustainable sources becoming a driving factor towards cheaper feedstocks, such as biomass. Another major factor impacting the oil refinery that should be taken into account

represents the strict environmental regulations that have raised the cost of producing clean fuels (Fahim, M. F., Alsahhaf, T. A., & Elkilan, 2010)(Leffler, 2008). As global energy consumption increases, as does the production of greenhouse gases like CO₂. The latter increase has caused the scientific community to look towards the “green” production of fuels and chemicals that were once dependant entirely on fossil fuels. The depletion of fossil fuels has also prompted interest in the production of fuels and chemicals that are compatible with petroleum liquids such as biomass-based products. Similar processes and approach to the refining industry that could be combined with the existing refining processes can be seen in bio-refineries. Using non-fossil fuel-based feedstocks, the bio-refinery produces low-value fuels and high-value materials and chemicals. Biomass conversion such as the production of ethanol and butanol through ABE (Acetone, Butanol and Ethanol) fermentation (Gupta and Demirbas, 2010) in which sugar is fermented using the bacteria genus *Clostridium* (Qureshi *et al.*, 2010)(Qureshi and Ejezi, 2008), is a well-recognized drop-in fuel option. Following upgrading and conversion, the products from the ABE mixture are compatible with fuel or chemicals, making the process an attractive option for the transportation and chemicals industry.

The focus of this work is to produce chemicals through the upgrading of ABE and to incorporate it in the proposed integration system aiming to decrease both dependency on fossil fuel and reduce greenhouse gas emissions. This process has been carried out previously in literature but with strong emphasis on the utilisation of noble metal-based catalysts. Amongst the noble metals, Pd has been proven to work better when compared to other noble metals such as Pt, Rh, Ru and Ir (Goulas *et al.*, 2017). Although they have performed efficiently towards converting ABE to valuable products, the economic aspect of these catalysts should also be considered as the process of ABE production is an expensive process in itself (Bildea *et al.*, 2016). Therefore, one of the main aims of this work is to be able to achieve valuable products whilst using economically viable catalysts based on transition metals.

2. Methodology

The integration system proposed, presented in Figure 1, depicts various routes to connect the oil refinery with bio-refining processes. These connections are through utility

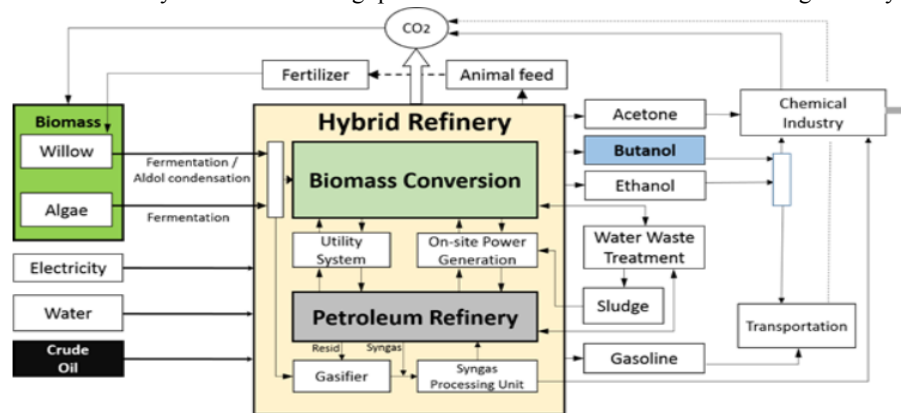


Figure 1. Schematic of proposed integration routes between an oil refinery and bio-based processes.

systems, on-site power generation, production of ABE through biomass fermentation and further upgrading to chemicals and many more. Focusing on the latter route, the fermentation of sugar in this case, produces a mixture of acetone, butanol and ethanol. These products can either be transformed into pyrolysis oil through the pyrolysis unit or used to produce bio-fuels via self-condensation of the alcohols and cross condensation of the alcohols with acetone, known as upgrading, that can also blend with the gasoline produced from the oil refinery. This will form part of the whole picture that is provided through experimental work which can be directly applied to the integration system.

This process as can be seen in Figure 1 starts from using sugar as an input to the ABE fermentation unit while bacterial species such as *Clostridium acetobutylicum* ferment sugar producing the ABE mixture. This is then combined with extractive fermentation using a water-immiscible solvent of glyceryl tributate. Following this, a series of distillations occur separating the extractant phase from the ABE mixture (Sreekumar *et al.*, 2015). The ABE mixture obtained will then go through an upgrading process leading to the production of longer chained hydrocarbons.

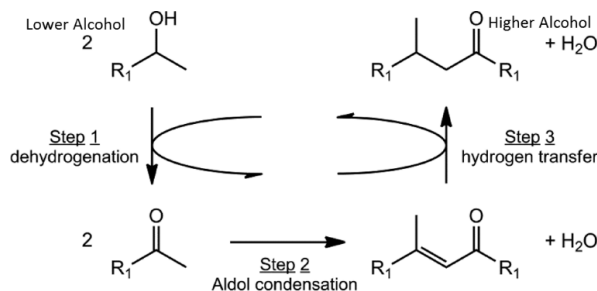


Figure 2. Guerbet reaction pathway adapted from (Shimura *et al.*, 2013)

The upgrading reactions have been carried out in the laboratory using the mixture of reactants with the same molar ratio of 3:6:1 acetone:butanol:ethanol, as representative composition obtained from the sugar fermentation reactor. The reaction was then carried out in a pressure vessel at high temperature and pressures using an activated transition metal on basic support with the condition of purging air trapped in the reactor with N_2 to ensure an oxygen-free atmosphere. This upgrading reaction requires active catalysts which have been synthesised using the wet impregnation method that have also been proven successful through various characterisation methods such as XRD, BET, TPR, TGA, Raman, etc. The reaction route, also known as the Guerbet reaction, forms branched or unbranched products which is demonstrated in Figure 2. This reaction typically consists of three steps being the dehydrogenation of a primary alcohol, then a base catalysed aldol coupling reaction followed by the hydrogenation of an α,β -unsaturated aldehyde (Chakraborty *et al.*, 2015). Most industrial Guerbet reactions have been carried out over homogenous catalysts, usually corrosive bases using a soluble metal complex producing Guerbet alcohols. Throughout the process water is produced that must be removed by the addition of a desiccant such as CaO (Patel *et al.*, 2015). However, due to the disadvantages of these catalysts, mainly being their corrosive nature, heterogenous catalysts have been chosen in this reaction using a basic support and transition metal active phases.

Following the reaction, the products were analysed using a GC-MS for quantification and identification purposes. Using the results obtained from this, the conversion and selectivity were calculated using the following equations:

$$ABE \text{ Conversion (\%)} = \frac{n_{Initial ABE} - n_{Unreacted ABE}}{n_{Initial ABE}} \times 100 \quad (1)$$

$$Selectivity (\%) = \frac{n_{Initial ABE}}{n_{Initial ABE} - n_{Unreacted ABE}} \times 100 \quad (2)$$

Where n is the number of total moles of reactants or product.

3. Results and Discussions

The catalysts have demonstrated exceptional results in terms of conversion and selectivity rates both having values up to 90%. They have also been successfully synthesised proven by the characterisation methods which due to space limitations are not presented in this paper. The BET analysis has shown the mesoporosity of the samples while also depicting the textural properties of the catalysts. The XRD has also clearly shown the presence of the metals and the support giving information about the crystal structure of the powder samples. The Raman spectroscopy carried out also proved the presence of the elements in each catalyst while providing information about the bonding structure of the sample. Due to the nature of the upgrade, which includes hydrogen transferring, the redox properties of the catalysts must be a relevant factor therefore TPR was carried out.

TGA conducted has demonstrated the weight loss and/gain occurring while heating the sample. This also demonstrates carbon loss associated with organic compounds attached to the samples after reaction which is a good indication that the reaction has proceeded successfully.

In terms of the products obtained, a range of hydrocarbons from C₂-C₁₅ was identified using the GC-MS. The quantification of the products was carried out by establishing GC response factors of the main products identified, by the injection of samples with known concentrations prepared using standards. Following this, the conversion and selectivity was then calculated using Equations 1 and 2 which can be seen in table 1 and Figure 4.

Table 1. Selectivity of products in the range of C₂-C₁₅ with the corresponding catalysts

Catalyst	Selectivity (%)	
	C ₂ -C ₇	C ₈ -C ₁₅
Active catalyst 1	60	5
Active catalyst 2	90	4
Active catalyst 3	43	14

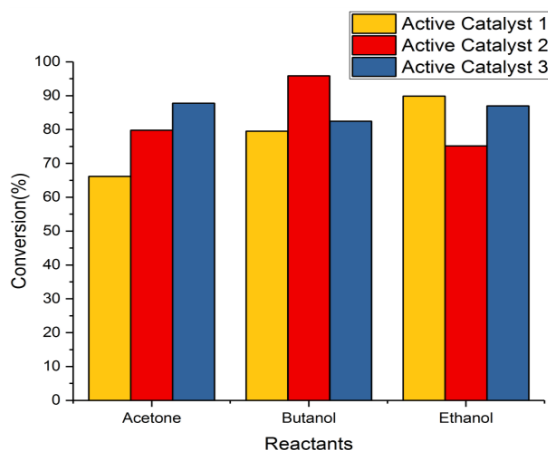


Figure 3. Demonstrating conversion of reactants individually with the corresponding catalyst

As demonstrated in Figure 3, all the catalysts are active in this upgrading reaction displaying very high conversion levels. As demonstrated in this figure, catalyst 1 is more selective towards ethanol conversion while catalyst 2 converts more butanol in comparison with the rest. This could be due to the fact that the catalysts are favorable towards the cross condensation of alcohols and acetone i.e. catalyst 1 is promoting the reaction between ethanol and acetone as well as ethanol dimerization (Zhu *et al.*, 2017) while the second catalyst is more favorable towards the reaction between butanol and acetone.

Using the data obtained and Equation 2, the selectivity was calculated considering all products in all concentrations presented in Table1. Catalyst 2 shows outstanding selectivity towards hydrocarbons in the range of C₂-C₇. However, catalyst 3 with the high conversion of 84.5% has demonstrated high selectivity in comparison with the others regarding the range of C₈-C₁₅ which depending on the application of the products could also be the desired catalyst. Catalyst1 has also shown promising results with high conversions of 82.92% while favoring the products of C₂-C₇. However, the aforementioned catalyst demonstrated higher ability to push the reaction towards the production of higher carbon number chemicals, as high as C₁₅, when compared to the other catalysts.

Overall, among the catalysts, the second catalyst especially exhibits an excellent performance of 88.92% conversion and performing with the highest selectivity and yield amongst the selected products that were in significant concentrations.

Further details about the catalyst will be discussed in the presentation.

4. Conclusions

The successfully synthesized catalysts proven through various characterization techniques have performed effectively in terms of producing valuable range of chemicals from biomass-based sources. All catalysts have been able to convert the ABE reactants to the long chain hydrocarbons with significantly high conversion levels while also demonstrating reasonable selectivity towards the identified added value products.

Catalyst 2 has been chosen as the best performing catalyst in terms of conversion and selectivity. Nevertheless, the third catalyst has demonstrated notable performance to produce longer chain hydrocarbons and the first catalyst was able to push the reaction towards the production of the highest carbon number hydrocarbon in comparison to the rest.

Finally, taking all of this into account, it has been shown that this route delivers valuable chemicals that can facilitate the integration of a bio and a traditional refinery. One of the key parameters to be optimized is the catalytic reaction to obtain high value chemicals from ABE. This work showcases that transition metal-based catalysts are effective materials for this process and open new avenues for research in the catalysts design towards an optimized ABE upgrading pathway.

References

- Bildea, C. S. *et al.* (2016) 'Enhanced Down-Stream Processing of Biobutanol in the ABE Fermentation Process', *Computer Aided Chemical Engineering*, 38, pp. 979–984. doi: 10.1016/B978-0-444-63428-3.50168-5.
- Chakraborty, S. *et al.* (2015) 'Highly Selective Formation of n-Butanol from Ethanol through the Guerbet Process: A Tandem Catalytic Approach', *Journal of the American Chemical Society*, 137(45), pp. 14264–14267. doi: 10.1021/jacs.5b10257.
- Fahim, M. F., Alsahhaf, T. A., & Elkilan, A. E. (2010) *Fundamentals of Petroleum Refining*. Edited by Ist. Oxford: Elsevier.
- Goulas, K. A. *et al.* (2017) 'ABE Condensation over Monometallic Catalysts: Catalyst Characterization and Kinetics', *ChemCatChem*, 9(4), pp. 677–684. doi: 10.1002/cctc.201601507.
- Gupta, R. and Demirbas, A. (2010) *Gasoline, Diesel and Ethanol Biofuels from Grasses and Plants*. 1st edn. Cambridge, England: Cambridge University Press.
- Leffler, W. L. (2008) *Petroleum Refining in Nontechnical Language*. 4th edn. Tulsa, Oklahoma: PenWell.
- Patel, A. D. *et al.* (2015) 'Analysis of sustainability metrics and application to the catalytic production of higher alcohols from ethanol', *Catalysis Today*, 239, pp. 56–79. doi: 10.1016/j.cattod.2014.03.070.
- Qureshi, N. *et al.* (2010) 'Production of butanol (a biofuel) from agricultural residues: Part II - Use of corn stover and switchgrass hydrolysates', *Biomass Bioenergy*, 34(4), pp. 566–571.
- Qureshi, N. and Ejezi, T. (2008) "'a superior biofuel" production from agricultural residues (renewable biomass): recent progress in technology', *Biofuels, Bioprod. Biorefin*, 2(4), pp. 319–330.
- Shimura, K. *et al.* (2013) 'Self-coupling of secondary alcohols by Ni/CeO₂ catalyst', *Applied Catalysis A: General*. Elsevier B.V., 462–463, pp. 137–142. doi: 10.1016/j.apcata.2013.04.040.
- Sreekumar, S. *et al.* (2015) 'Production of an acetone-butanol-ethanol mixture from *Clostridium acetobutylicum* and its conversion to high-value biofuels', *Nature Protocols*, 10(3), pp. 528–537. doi: 10.1038/nprot.2015.029.
- Zhu, Q. *et al.* (2017) 'Upgrade of Solvent-Free Acetone-Butanol-Ethanol Mixture to High-Value Biofuels over Ni-Containing MgO-SiO₂ Catalysts with Greatly Improved Water-Resistance', *ACS Sustainable Chemistry and Engineering*, 5(9), pp. 8181–8191. doi: 10.1021/acssuschemeng.7b01837.

Dynamic transitions in a reactive distillation column for the production of silicon precursors

Salvador Tututi-Avila^{a*}, Nancy Medina-Herrera^b, Luis Ricardez-Sandoval^c and Arturo Jiménez-Gutiérrez^d

^a *Facultad de Ciencias Químicas, Universidad Autónoma de Nuevo León, Av. Universidad S/N Ciudad Universitaria, 66455, San Nicolás de los Garza, N.L., México.*

^b *Facultad de Agronomía, Universidad Autónoma de Nuevo León, Francisco Villa S/N, ExHacienda el Canadá, General Escobedo, N.L., México.*

^c *Department of Chemical Engineering, University of Waterloo, 2NL 3G1, Waterloo, Ontario, Canada.*

^d *Departamento de Ingeniería Química, Instituto Tecnológico de Celaya, Av. Tecnológico y García Cubas S/N, 38010, Celaya, Gto., México.*

salvador.tututiavl@uanl.edu.mx

Abstract

The production of energy from solar cells is being considered as one key technology of the future. The remarkable growth in this market is primarily based upon solar cells made from polycrystalline silicon, which is typically produced via chemical vapor deposition of dichlorosilane or silane. Different technologies including reactive distillation have been considered for the production of polycrystalline silicon precursors. In the reactive distillation process, the trichlorosilane disproportionation reaction takes place producing monochlorosilane, dichlorosilane and silane. Steady state studies have reported that different silane products can be obtained by adjusting the operating condition of the reactive column. However, dynamic transitions from one product to another that can meet product quality specifications during operation still remains as a key challenge. This work investigates a feasible strategy for the dynamic transition and production of three silanes in a reactive distillation column. Results from this study show that there is a feasible dynamic transition from silane to monochlorosilane, then to dichlorosilane, and then back to monochlorosilane and silane. Temperature control and equipment sizing were identified as key design and operating variables to accomplish those transitions.

Keywords: reactive distillation; silane; solar cell; optimal transitions; dynamic transition; process control

1. Introduction

The need for additional renewable energy resources has led to the development of new green technologies that can aid to meet global energy demands in the coming decades. Solar energy technology has received special attention from industry and the scientific community mainly because of its positive impact on the environment. In this context, solar cells have emerged as one of the preferred technologies to produce clean energy; thus, the global market for this technology has been growing every year. Semiconductor industries use ultra-high purity polysilicon as the main raw material to produce solar cells. Polysilicon is synthesized using volatile silicon hydride. The most common silicon

hydride is silane; however, dichlorosilane or monochlorosilane can also be employed (Ceccaroli and Lohne, 2010). The first process used to produce polysilicon was the Siemens process, which is based on thermal decomposition of trichlorosilane; however, this process has been recently replaced by others because of the higher energy requirements of the Siemens process. Two industrial-scale alternative technologies used nowadays are the Union Carbide process and the Ethyl corporation process. In the latter, silane is used as the main precursor for polysilicon production (Ceccaroli and Lohne, 2010).

The trichlorosilane disproportionation process conveys three reversible reactions, which involve five components including dichlorosilane and monochlorosilane. The latter compounds are of particular interest because of their wide application in the semiconductor industry as well as the thin-film solar photovoltaic industry (Mochalov, 2016). The intensified reactive distillation process has been considered as an attractive process to produce silane, dichlorosilane and monochlorosilane with low energy consumption (Medina-Herrera et al., 2017). The pressure, distillate to feed ratio and reflux ratio in the reactive column have been reported as key variables that directly determine the desired silane product specifications. Optimal steady-state operation for the production of the three different silane products has also been reported (Medina-Herrera et al., 2017). Similarly, controllability studies showing that temperature control is a key feature for this process have also been reported (Medina-Herrera et al., 2017). On the other hand, studies on the dynamic transitions in the reactive column that can maintain dynamic feasibility and that comply with the product specifications are very limited (Ramírez-Márquez et al., 2016). Previous studies have shown that dynamic transitions impact process performance and the logistics of multi-product systems (Koller and Ricardez-Sandoval, 2017; Patil et al. 2015). The aim of this work is to present a systematic method that specifies the way in which the reactive distillation column needs to be operated in closed-loop to achieve dynamically feasible transitions for three trichlorosilane products, i.e. silane, monochlorosilane and dichlorosilane.

2. Steady-State: Reactive Distillation Column

The trichlorosilane decomposition process consists of three reversible reactions, i.e.



This reaction mechanism, along with the kinetic parameters reported by Huang et al. (Huang et al., 2013), were used in this work to carry out both steady state and dynamic the simulations. The Radfrac rigorous distillation model of AspenPlus® process simulator was used for modelling the reactive distillation column.

In a previous study, a sensitivity analysis was performed to identify suitable conditions for the production of the silane products considered in this work (Medina-Herrera et al., 2017). That study suggested that the production of the different silane products could be achieved with appropriate pressure conditions and distillate to feed (D/F) ratio. Table 1 shows the parameters specified for the optimal steady-state operation of the reactive distillation unit reported in Medina-Herrera et al. (2017). The specifications obtained

from that analysis aimed to minimize the total annual cost by considering equal production of the three different products during the year.

Table 1. Optimal steady-state parameters, reactive distillation column (Medina-Herrera et al., 2017).

	Silane Production	Monochlorosilane Production	Dichlorosilane Production
Number of stages	89	89	89
Feed stage	42	42	42
Feed flowrate of SiHCl ₃ (kmol/h)	10	10	10
Reactive Zone (Stage to Stage)	29-72	29-72	29-72
Purity of product in D1 (mol%)	99.5	99.5	99.5
Distillate to feed ratio	0.25	0.333	0.5
Reflux ratio	34.9	38.9	11.3
Operating pressure (atm)	4.9	2.3	1
Column diameter (m)	0.73	0.73	0.73
Holdup of Reactive Section (m ³)	0.068	0.068	0.068
Q _c (kW)	292	712	375
Q _R (kW)	333	739	387

3. Transient Analysis

In order to carry out the dynamic analysis, the reflux drum tank was sized taking into account the inventories for the different silane products. As shown in Table 1, the production of the monochlorosilane requires a higher vapor flow rate; therefore, the column's specifications for monochlorosilane were used to determine the size of the reflux drum. Once the steady state simulation converged, the simulation was exported to Aspen Dynamics. Rigorous hydraulics were considered for all simulations. Hold-up was evaluated at steady-state assuming a residence time of 2.5 second per stage (Huang et al., 2013). When dynamic transitions are considered, internal mass flows and therefore the residence time, will change accordingly, but under the assumption that hold-up on the reactive trays remains the same. The overall hold-up for the reactive zone is reported in Table 1. Ideal trays were assumed for the column.

Identification of the critical process variables in the transient domain was carried out by a degrees of freedom analysis. Due to their relevance for the dynamic operation, the pressure and D/F ratio were considered as part of the degrees of freedom in the analysis. Also, the liquid level in the reflux drum was controlled with the reflux flowrate. For this analysis, the heuristic rule of using reflux flowrate to control the level of the drum for reflux ratios higher than three was considered. Column hydraulics plays an important role on the dynamic simulations, since temperature and composition profiles inside the column are likely to change when disturbances enter into the process. Therefore, a key variable that should be taken into account for dynamic simulations is temperature. This variable needs to be controlled to promote production of the desired product. Furthermore, temperature control is required to avoid thermal degradation of the catalyst.

A sensitivity analysis was carried out to determine the most sensitive column trays for each silane product under changes in the reboiler duty (Luyben, 2006). For that purpose, changes of +/- 0.1% in the reboiler duty and in the reflux ratio were performed. The results from the temperature tray profiles allowed the identification of the trays with largest deviation in temperature. The trays that resulted with the largest temperature change were selected as controlled variables (Luyben, 2006). The results of the sensitivity analysis that show the tray selection for each individual silane product are presented in Table 2.

Table 2. Identification of the most sensitive stage for the production of silanes and PI tuning parameters for their controllers.

Production	Stage	PI tuning parameters	
Silane	79	P=4.7	I=9.2 min
Dichlorosilane	69	P=1.1	I=14.5 min
Monochlorosilane	63	P=0.9	I=11.8 min

Temperature, pressure and D/F ratio control loops were taken into account to develop the following dynamic analysis procedure for the production of the silane products. In order to meet the desired operating conditions of each silane production, pressure, D/F and controlled tray temperature should be changed progressively. It was decided to implement setpoint ramps, as opposed to step ramps, to prevent abrupt changes that could lead to process instabilities. Therefore, setpoint ramps were imposed for distillate to feed ratio, pressure and the temperature controllers simultaneously while monitoring the reflux drum level. Figure 1 shows the control configuration of the reactive column as implemented in Aspen Dynamics to carry out the dynamic transitions, which was based upon an implementation for disturbance rejection strategies, with the tuning parameters for temperature controllers reported in Table 2. It is important to note that pressure changers were configured in order to develop pressure driven simulations.

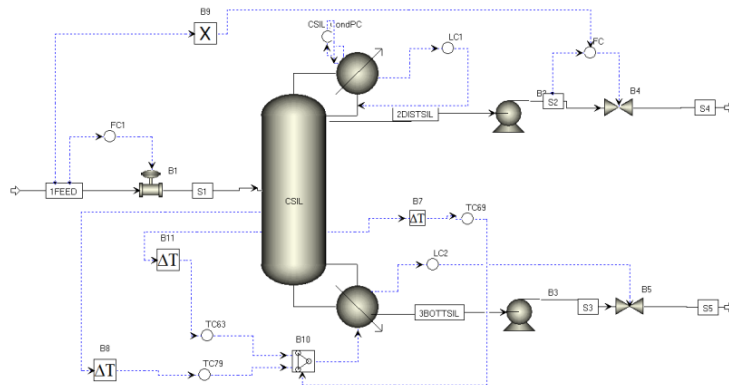


Figure 1. Control configuration of the reactive column for the dynamic transitions.

As three different products can be produced independently for each design in the reactive distillation column, six possible routes can be followed to change from the production of a silane product to another. Those possible transitions are: silane to monochlorosilane, monochlorosilane to dichlorosilane, dichlorosilane to monochlorosilane, monochlorosilane to silane, silane to dichlorosilane and dichlorosilane to silane. In order to implement the procedure described above for all the different transitions, a selector

structure was implemented in the simulation. The selector model was configured so that the appropriate temperature stage in the loop was set as active for the desired transition.

4. Results

Dynamic transitions using the methodology described above were tested for all the different combinations. Figure 2 shows the liquid composition profiles for the production of monochlorosilane from dichlorosilane. Ramp set points of 20 h were configured in the column's pressure, D/F ratio and temperature controllers. As shown in Figure 2, it takes around 60 hours to obtain a high purity stream of monochlorosilane. This figure also shows that the dynamic setpoint changes imposed in pressure, and D/F ratio and temperature are tracked properly.

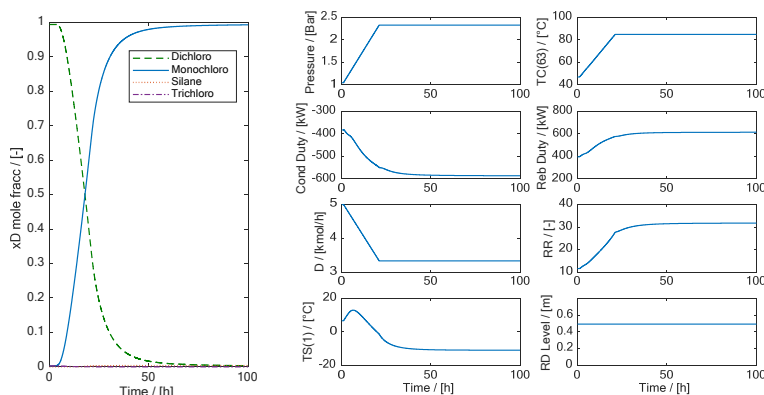


Figure 2. Column profiles for the transition of Dichlorosilane to Monochlorosilane in the distillate.

When the setpoint ramps in the controlled variables were applied for the other five transitions, it was observed that all of them were feasible in terms of reaching the desired new steady state for the corresponding silane products. Nevertheless, when the transitions silane to dichlorosilane and dichlorosilane to silane were tested, monochlorosilane was initially produced thus affecting the time to reach the final silane product (dichlorosilane). This behaviour is due to the nature of the reaction mechanism. Because of its impact on the process operating costs, another important result is that related to the column heat duty. Figure 2 also shows that higher energy requirements are needed for the dichlorosilane to monochlorosilane transition. This result agrees with the results reported in Table 1, which showed that higher energy requirements were needed for the production of monochlorosilane. Table 3 reports the overall transition times for the different silane products. Even when all transitions were successful to reach the desired set points for the products, an economic analysis should be used to assess the impact of the transition times observed for each case to quantify the impact of production losses during such time periods.

Table 3. Transition time for the different silane productions.

Transition	Time (h)	Transition	Time (h)
Dichlorosilane to monochlorosilane	62.6	Dichlorosilane to silane	94.5
Monochlorosilane to Silane	67.8	Silane to monochlorosilane	100
Silane to dichlorosilane	100	Monochlorosilane to dichlorosilane	61.2

5. Conclusions

This work explored the feasibility of implementing dynamic transitions for the production of three high-value silane products. Operating points obtained from steady-state calculations for the production of three silane products were used as target values for each transition. A control policy based on ramps for the controlled variables was implemented for the six possible transitions considered in this study. The results showed that such a control strategy was effective to yield feasible transitions from a silane product to another. The most critical transition was that from silane to dichlorosilane and viceversa. This was mostly due to the production of monochlorosilane as an intermediate product, which affected the length of the dynamic transition between these two products. An effective transition policy should avoid this condition; that is, given that the three products are desired to be produced, the production of either silane or dichlorosilane should be preceded by the production of monochlorosilane.

References

- B. Ceccaroli, L. Otto, 2010, "Solar Grade Silicon Feedstock." In Handbook of Photovoltaic Science and Engineering, John Wiley & Sons, Ltd, 169–217.
- X. Huang, D. Wei-Jie, Y. Jian-Min, X. Wen-De, 2013, "Reactive Distillation Column for Disproportionation of Trichlorosilane to Silane: Reducing Refrigeration Load with Intermediate Condensers." *Industrial & Engineering Chemistry Research* 52(18): 6211–20.
- W. Luyben, 2006, "Evaluation of Criteria for Selecting Temperature Control Trays in Distillation Columns." *Journal of Process Control* 16(2): 115–34.
- N. Medina-Herrera, S. Tututi-Avila, A. Jiménez-Gutiérrez, J. Gabriel Segovia-Hernández, 2017, "Optimal Design of a Multi-Product Reactive Distillation System for Silanes Production." *Computers & Chemical Engineering*: 1–10.
- L. A. Mochalov, 2016, "Preparation of Silicon Thin Films of Different Phase Composition from Monochlorosilane as a Precursor by RF Capacitive Plasma Discharge." *Plasma Chemistry and Plasma Processing* 36(3): 849–56.
- C. Ramírez-Márquez, 2016, "Dynamic Behavior of a Multi-Tasking Reactive Distillation Column for Production of Silane, Dichlorosilane and Monochlorosilane." *Chemical Engineering and Processing: Process Intensification* 108: 125–38.
- R. W. Koller, L. A. Ricardez-Sandoval, 2017, "A dynamic optimization framework for integration of design, control and scheduling of multi-product chemical processes under disturbance and uncertainty." *Computers & Chemical Engineering*, 106: 147-159.
- B. P. Patil, E. Maia, L. A. Ricardez-Sandoval, 2015, "Integration of scheduling, design, and control of multiproduct chemical processes under uncertainty." *AIChE Journal*, 61(8): 2456-2470.

Adjoint system method in shape optimization of some typical fluid flow patterns

Alexis Courtais^{a,*}, François Lesage^a, Yannick Privat^b, Pascal Frey^c and Abderazak Latifi^a

^a*Laboratoire Réactions et Génie des Procédés, CNRS, Université de Lorraine, Nancy, France*

^b*Institut de Recherche Mathématique Avancée, CNRS, Université de Strasbourg, Strasbourg, France*

^c*Laboratoire Jacques-Louis Lions, CNRS, Sorbonne Universités, Paris, France*
alexis.courtais@univ-lorraine.fr

Abstract

In this paper a shape optimization approach based on the Hadamard geometric optimization method is developed. Four case studies representing typical fluid flow patterns in fluid dynamics, i.e. flow around an obstacle, flow in a 90 ° or 180 ° elbow pipe and flow in a dyadic tree, are considered. Low velocities are imposed at the inlet of each case study in order to operate in laminar flow regime. The objective is to determine the shape that minimizes the energy dissipated by viscous friction subjected to the Navier-Stokes equations and to iso-volumic constraint. The required gradients of the performance index and constraint with respect to the shape are computed by means of the adjoint system method. The momentum equations are implemented and solved using the OpenFOAM CFD software, and the solver "adjointShapeOptimizationFoam" is modified in order to compute the solution of the resulting optimization problems. The optimal shapes obtained in the four case studies are in very good agreement with the available literature works. Moreover, they allow a significant reduction of the dissipated energy ranging from 10.8 to 53.3 %.

Keywords: Shape optimization, Adjoint system, Energy dissipation, CFD, OpenFOAM

1. Introduction

Chemical industry is more than ever constrained to invest in research and innovation to remain competitive. This competitiveness necessarily requires the development of more flexible, intensified, efficient and compact processes. The shape of the units involved in these processes is very often critical to their efficiency and represents major scientific, technical and technological challenges. Shape optimization is a technology that is quite appropriate to meet these challenges. It consists of a set of techniques and methods allowing to find the best shape of an object that optimizes a cost function or a performance index while satisfying given constraints. Originally, shape optimization has been developed for aerodynamic industry and particularly for aircrafts. More recently, it has been used in chemical engineering to determine the optimal shape of a pipe (Henrot and Privat, 2010) or microchannels (Tonomura et al., 2010).

This paper presents the development of a shape optimization approach based on adjoint system method. The latter is used to derive the shape gradient needed in the optimal shape determination. OpenFOAM software is used as CFD solver for the flow model, i.e. the Navier-Stokes equations, and adjoint system equations.

2. Case studies and modeling

The optimization approach developed in this paper is tested on four 2D case studies: flow around an obstacle, flow in a 90 ° or 180 ° elbow pipe and flow in a dyadic tree. Each initial domain, Ω_0 , of the case studies is presented on Fig. 1. The boundary $\partial\Omega$ of the domain Ω is given by $\partial\Omega = \Gamma_{in} \cup \Gamma_{out} \cup \Gamma_{lat} \cup \Gamma$, where

- Γ_{in} is the inlet of the domain on which a quadratic velocity profile is imposed. Thus, the laminar flow is already developed at the inlet boundary (Eq (1c)).
- Γ_{out} is the outlet of the domain on which the normal component of the stress tensor is equal to zero (Eq (1e)).
- Γ_{lat} is the fixed edge of the domain on which a no-slip condition is applied (Eq (1d)).
- Γ is the free boundary of the domain, i.e. the unknown of the shape optimization problem. Moreover, it is the boundary that will evolve over the iterations of the optimization algorithm. A no-slip condition is applied on this boundary (Eq (1d)).

In each case, the velocity is set to a value leading to Reynolds numbers lower than 500, thus ensuring that the flow is laminar. The condition of zero absolute pressure is imposed at the outlet boundary. The system of Navier-Stokes equations describing the fluid flow is given as

$$\left\{ \begin{array}{ll} -\nu\Delta\mathbf{U} + (\mathbf{U} \cdot \nabla)\mathbf{U} + \nabla p = 0 & \text{in } \Omega \\ \nabla \cdot \mathbf{U} = 0 & \text{in } \Omega \\ \mathbf{U} = \mathbf{U}_{in} & \text{on } \Gamma_{in} \\ \mathbf{U} = 0 & \text{on } \Gamma_{lat} \cup \Gamma \\ \sigma(\mathbf{U}, p) \cdot \mathbf{n} = 0 & \text{on } \Gamma_{out} \end{array} \right. \quad \begin{array}{l} (1a) \\ (1b) \\ (1c) \\ (1d) \\ (1e) \end{array}$$

In the above system, $\sigma(\mathbf{U}, p)$ is the stress tensor, given by :

$$\sigma(\mathbf{U}, p) = 2\nu\varepsilon(\mathbf{U}) - p\mathbf{I} \quad \text{with} \quad \varepsilon(\mathbf{U}) = \frac{1}{2}(\nabla\mathbf{U} + (\nabla\mathbf{U})^T), \quad (2)$$

where ν is the fluid kinematic viscosity, \mathbf{I} the identity matrix, \mathbf{U} and p respectively the velocity and the absolute pressure of the fluid and $\varepsilon(\mathbf{U})$ the strain tensor.

3. Shape optimization formulation

3.1. Optimization problem

In this work, the objective is to determine the shape of the four aforementioned case studies that minimizes the energy dissipated by the fluid due to the work of viscous forces. Such a criterion is relevant in practice since the energy dissipated is directly related to pressure losses. The performance index is therefore defined as

$$J(\Omega) = 2\nu \int_{\Omega} |\varepsilon(\mathbf{U})|^2 dx \quad (3)$$

This optimization problem is subjected to Navier-Stokes equations (1) and to the volume constraint given by Eq. (4). It is solved using the adjoint system method.

$$C(\Omega) = \mathcal{V}(\Omega) - \mathcal{V}(\Omega_0) = 0 \quad (4)$$

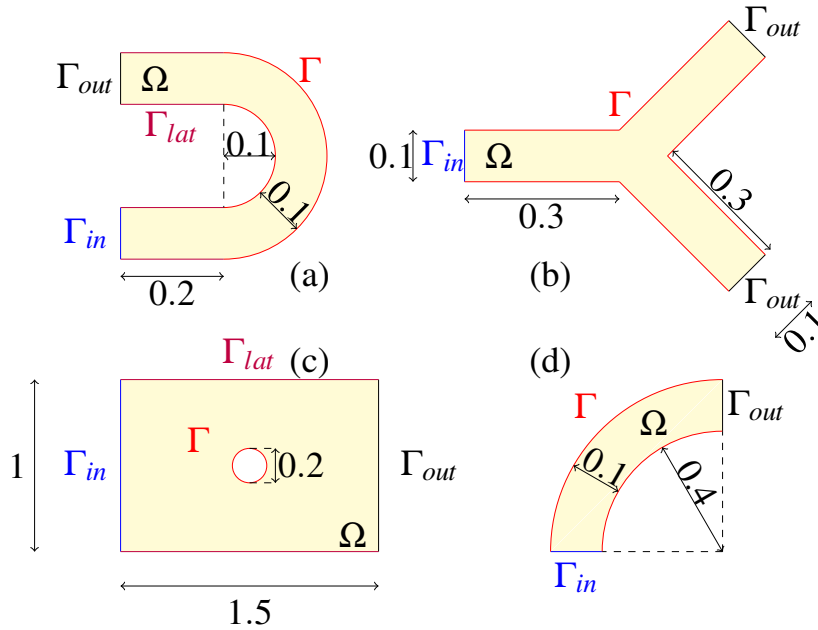


Figure 1: Initial shapes of the four case studies, (a) flow in a 180° elbow pipe, (b) flow in a diadryc tree, (c) flow around an obstacle, (d) flow in a 90° elbow pipe.

3.2. Adjoint system method

The shape optimization approach developed involves the differentiation with respect to the domain also called derivative in the sense of Hadamard (Allaire, 2007; Henrot and Pierre, 2005). It consists in moving all the meshpoints according to the following induction formula

$$\Omega_{i+1} = (\mathbf{X} + t\mathbf{V})(\Omega_i) \quad (5)$$

where \mathbf{X} is the vector of meshpoints coordinates at iteration i , t the method's step and \mathbf{V} is the vector field describing the mesh displacement. The objective of the method is to compute t and \mathbf{V} .

Let us introduce the lagrangian functional defined as

$$\mathcal{L}(\Omega) = J(\Omega) + \lambda C(\Omega) = 2\nu \int_{\Omega} |\varepsilon(\mathbf{U})|^2 dx + \lambda (\mathcal{V}(\Omega) - \mathcal{V}(\Omega_0)) \quad (6)$$

where λ is the Lagrange multiplier.

On the other hand, let $\mathbf{V} : \mathbf{R}^d \rightarrow \mathbf{R}^d$ be a regular vector field. The derivative of the Lagrangian $\mathcal{L}(\Omega)$ in the direction of \mathbf{V} is defined by (Henrot and Privat, 2010)

$$\mathcal{L}'(\Omega)(\mathbf{V}) = \langle d\mathcal{L}(\Omega), \mathbf{V} \rangle = \lim_{t \rightarrow 0} \frac{\mathcal{L}(\Omega_t) - \mathcal{L}(\Omega)}{t}, \quad \text{with} \quad \Omega_t = (\mathbf{X} + t\mathbf{V})(\Omega). \quad (7)$$

To implement the shape optimization algorithm, it is necessary to express the Lagrangian derivative in the following form

$$\mathcal{L}'(\Omega)(\mathbf{V}) = \int_{\partial\Omega} (G + \lambda)(\mathbf{V} \cdot \mathbf{n}) \quad (8)$$

where G is the shape gradient, i.e. a function defined on the boundary of the domain Ω depending on \mathbf{U} but not on the vector field \mathbf{V} . Under this form, it will be easy to determine a new mesh choice leading to a decrease of the Lagrangian. The adjoint method is based on the introduction of an adjoint state (\mathbf{U}_a, p_a) . Straightforward computations (see (Henrot and Privat, 2010) for more details) lead to the following shape derivative of the Lagrangian functional expressed as

$$\mathcal{L}'(\Omega)(\mathbf{V}) = \int_{\partial\Omega} (2\nu(\varepsilon(\mathbf{U}) : \varepsilon(\mathbf{U}_a) - \varepsilon(\mathbf{U}) : \varepsilon(\mathbf{U})) + \lambda)(\mathbf{V} \cdot \mathbf{n}) d\sigma \quad (9)$$

Thus, the shape gradient is given by

$$G = 2\nu(\varepsilon(\mathbf{U}) : \varepsilon(\mathbf{U}_a) - \varepsilon(\mathbf{U}) : \varepsilon(\mathbf{U})) \quad (10)$$

where \mathbf{U}_a is the velocity of the adjoint state (\mathbf{U}_a, p_a) defined as the solution of the following equations

$$\begin{cases} -\nu\Delta\mathbf{U}_a + (\nabla\mathbf{U})^T\mathbf{U}_a - \nabla\mathbf{U}_a\mathbf{U} + \nabla p_a = 2\nu\Delta\mathbf{U} & \text{dans } \Omega & (11a) \\ \nabla \cdot \mathbf{U}_a = 0 & \text{dans } \Omega & (11b) \\ \mathbf{U}_a = 0 & \text{sur } \Gamma_{in} \cup \Gamma_{lat} \cup \Gamma & (11c) \\ \sigma(\mathbf{U}_a, p_a)\mathbf{n} + (\mathbf{U} \cdot \mathbf{n})\mathbf{U}_a = 4\nu\varepsilon(\mathbf{U})\mathbf{n} & \text{sur } \Gamma_{out} & (11d) \end{cases}$$

known as adjoint system equations. Finally, the mesh displacement \mathbf{V} is computed by solving the following system

$$\begin{cases} -\Delta\mathbf{V} + \mathbf{V} = 0 & \text{dans } \Omega & (12a) \\ \mathbf{V} = 0 & \text{sur } \Gamma_{in} \cup \Gamma_{out} \cup \Gamma_{Lat} & (12b) \\ \nabla\mathbf{V}\mathbf{n} = -(G + \lambda)\mathbf{n} & \text{sur } \Gamma & (12c) \end{cases}$$

4. Implementation of the optimization algorithm

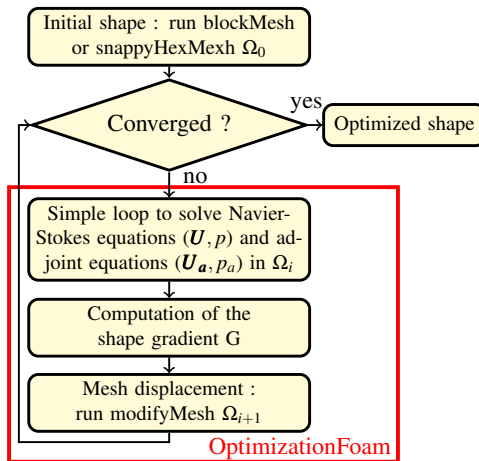


Figure 2: Shape optimization algorithm

The CFD equations are implemented using C++ language within OpenFOAM software (Weller et al., 1998). The latter is a free and open source software which allows to solve partial differential equations (Navier-Stokes and adjoint equations Eq. (1) and (11)) using finite volume method. OpenFOAM supplies a solver which solves the Navier-Stokes and an adjoint system for topologic optimization. This solver is named "adjointShapeOptimizationFoam". The latter is modified and enriched in order to implement the optimization algorithm and determine the best shape in each of the four considered case studies. The algorithm is detailed in Fig.2. At each iteration, a test of the quality of the mesh is carried out through the aspect ratio. In 2D, the aspect ratio is defined as the ratio of its longer side to its shorter side. If the ratio is too large, i.e. higher than 5, the domain is remeshed.

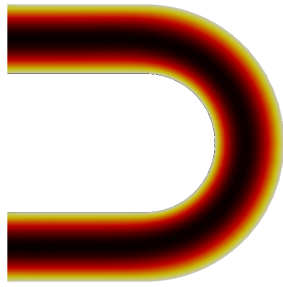


Figure 3: Initial shape of the 180 ° elbow

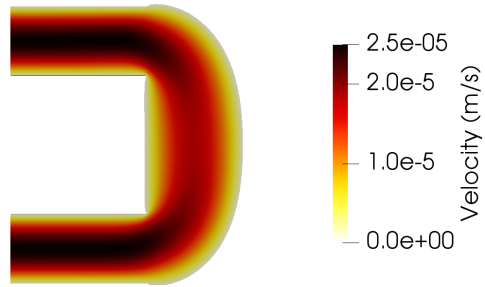


Figure 4: Optimized shape of the 180 ° elbow

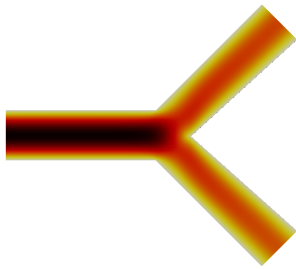


Figure 5: Initial shape of the dyadic tree

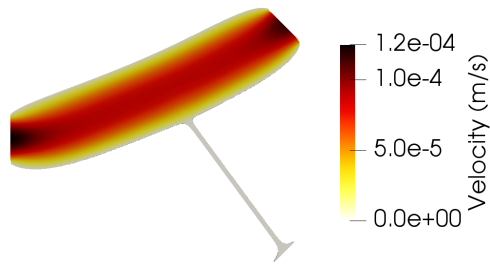


Figure 6: Optimal shape of the dyadic tree

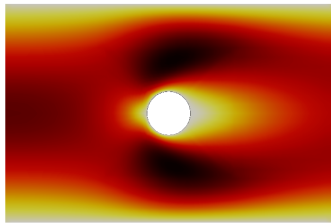


Figure 7: Initial shape of the obstacle

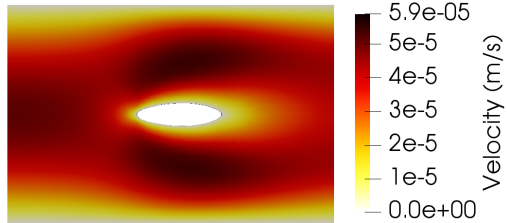


Figure 8: Optimal shape of the obstacle



Figure 9: Initial shape of the 90 ° elbow

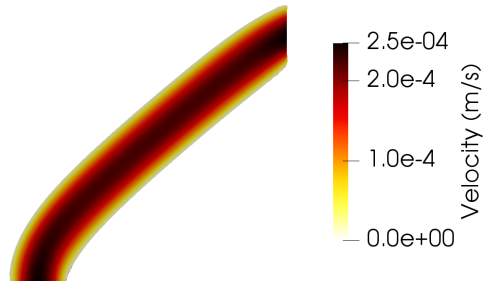


Figure 10: Optimal shape of the 90 ° elbow

5. Main results

Initial shapes and velocity distributions are presented in Figs. 3, 5, 7 and 9, and optimized shapes are shown in Figs. 4, 6, 8 and 10. In each case, moving the free boundary allows a reduction

Table 1: Performances of the optimization approach

Case	Iterations	Simulation time	Reduction of dissipated energy	Reduction of pressure losses
180 ° elbow	300	40 min	30.7 %	33.3 %
Dyadic tree	550	1 h 01	53.3 %	40.4 %
Obstacle	200	9 mn 14	10.8 %	15.4 %
90 ° elbow	80	2 mn 30	27 %	24 %

of the velocity distribution due to an increase in the width of the channel (for the elbows and the dyadic tree) or to a decrease of the width of the obstacle. Thus, the reduction of the velocity and the increase of the section lead to a reduction of the velocity gradient and, consequently, to a reduction of the performance index. All the optimal shapes obtained in this study are in very good agreement with the literature works (Tonomura et al., 2010; Dapogny et al., 2017).

The performances of the optimization approach for each case study are presented in Table 1. Depending on the case, a significant reduction of the dissipated energy is observed, between 10.8 and 53.3 %. Since the energy dissipated by the fluid and the pressure drops are related, a decrease of pressure losses is also observed in similar proportions, i.e. between 15.4 and 40.4 %. The dyadic tree case is the most costly in terms of computation time. Indeed, the geometry in that case undergoes huge changes, and therefore, one has to finely remesh many times. In this case, the flow seems to privilege one of the two branches. The small one cannot be removed because the outlet is a fixed boundary and the geometric algorithm cannot modify the topology of the domain.

From a numerical point of view, the case "flow around an obstacle" is the most difficult to implement. Indeed, the initial Lagrange multiplier must be properly chosen in order to avoid the removal of the obstacle which would result in wrong simulations due to invalid meshes. To overcome this problem, the initial Lagrange multiplier λ_0 is set to a value higher than the absolute value of shape gradient G .

6. Conclusion

In this work, a shape optimization approach has been developed and implemented within OpenFOAM software. Four case studies representing typical fluid flow patterns in fluid dynamics were considered. The objective was to determine the shape that minimizes the energy dissipated by viscous friction while meeting the volume constraint and satisfying the momentum equations. A significant reduction of pressure losses was observed in each case study which will result in important energy savings. The coming works will focus on shape optimization of a mass or heat exchangers and the mixing in a stirred tank.

References

- G. Allaire, 2007. Conception optimale de structures . Vol. 58 of *Mathématiques et Applications*. Berlin: Springer.
- C. Dapogny, P. Frey, F. Omnès, Y. Privat, 2017. Geometrical shape optimization in fluid mechanics using freefem++. *Structural and Multidisciplinary Optimization*, 1-28.
- A. Henrot, M. Pierre, 2005. Variation et optimisation de formes. Vol. 48 of *Mathématiques et Applications*. Springer-Verlag, Berlin.
- A. Henrot, Y. Privat, 2010. What is the optimal shape of a pipe? *Archive for Rational Mechanics and Analysis*, 196 (1), 281–302.
- O. Tonomura, M. Kano, S. Hasebe, 2010. Shape optimization of microchannels using cfd and adjoint method. *Computers and Chemical Engineering*, 28, 37-42.
- H. G. Weller, G. Tabor, H. Jasak, C. Fureby, 1998. A tensorial approach to computational continuum mechanics using object-oriented techniques. *Computers in physics* 12 (6), 620–631.

Dynamics and control of a heat pump assisted azeotropic dividing-wall column (HP-A-DWC) for biobutanol purification

Iulian Patraşcu,^a Costin Sorin Bîldea,^a Anton A. Kiss,^{b,c,*}

^a*University “Politehnica” of Bucharest, Polizu 1-7, Romania*

^b*School of Chemical Engineering and Analytical Science, The University of Manchester, Sackville Street, Manchester, M13 9PL, United Kingdom*

^c*Sustainable Process Technology Group, Faculty of Science and Technology, University of Twente, PO Box 217, 7500 AE Enschede, The Netherlands*

tony.kiss@manchester.ac.uk

Abstract

Recently, the butanol purification from acetone-butanol-ethanol mixture was achieved in one azeotropic dividing-wall column requiring 2.7 MJ/kg butanol, which represents just 7.5% of the energy content of butanol. Compared to a conventional separation sequence, this design allows 60% energy savings due to heat integration and use of a heat pump. This work considers the dynamics and control of the process. The basic regulatory control can provide stability for small and short-time disturbances, but the process shuts down if the disturbances persist. By adding a reboiler and a condenser, better control becomes possible. As a result, the process can handle large and persistent disturbances in feed rate and composition, achieving good control of product purity.

Keywords: Dividing-wall column, optimal design, heat integration, process control.

1. Introduction

The biobutanol is considered a competitive fuel over ethanol, being characterized by low water miscibility, flammability and corrosiveness. In the upstream fermentation process, biobutanol is obtained with a concentration lower than 3%wt. Using gas stripping technology, the acetone-butanol-ethanol (ABE) mixture reaches 4.5 %wt. acetone, 18.6 %wt. butanol and 0.9 %wt. ethanol (Xue et al., 2013). In downstream processing, these components can be separated by distillation, reverse osmosis, adsorption, liquid-liquid extraction, pervaporation and others (Abdehagh et al., 2014).

For large scale plants, distillation remains the most promising technique. Significant energy savings can be achieved by employing novel configurations (such as dividing-wall column) and heat integration facilitated by heat pumps (Kiss, 2013; Luo et al., 2015; Kiss and Infante Ferreira, 2016). A novel heat pump assisted azeotropic dividing-wall column (A-DWC) was suggested for the ABE separation, allowing up to 60% energy savings compared to a conventional separation sequence (Patrascu et al., 2017, 2018). The present work considers the dynamics and controllability of this highly-integrated process. For this purpose, a rigorous pressure-driven simulation is developed in Aspen Plus Dynamics. After few design modifications, the process proves to be controllable by using only conventional control loops.

2. Problem statement

Fewer equipment units can drive the ABE separation by combining three distillation columns in a single A-DWC, while using heat integration and vapor recompression (VRC) technologies can further reduce the energy requirement. This highly integrated design delivers large energy savings of up to 60% but must be also operable. However, combining all these technologies in a single process can reduce the flexibility of the process due to fewer degrees of freedom, raising difficulties in the controllability of the process. In this paper the dynamics of the process is investigated by testing the stability and introducing minor design changes which offer two new variables to be manipulated.

3. Process design

Patrascu et al. (2018) proposed a heat-integrated VRC-assisted A-DWC for ABE separation (Figure 1). The A-DWC contains two stripping and one fractionation sections. The feed-side stripping section (DWC-L) separates the most plentiful component (water) with high purity in bottom. In the fractionation section, the light components (acetone, ethanol and some water) are obtained as distillate, while the butanol-water azeotrope is routed to a side stream, and cooled for decantation. Here, the distillation boundary is crossed and breaking the butanol-water azeotrope is achieved. The aqueous phase is sent to DWC-L for water purification and the organic phase sent to the second stripping section (DWC-R) for butanol purification. The top vapor stream is compressed from 1 bar to 5.8 bar (60 °C to 150 °C) and used to drive the reboiler from DWC-L and to preheat the fresh feed, and the organic and aqueous phases, before being returned to the column. Performing this heat integration, the energy requirement is reduced by 69% compared to a simple A-DWC column. The purity of water product is 99.8 %wt. and the purity of butanol product is 99.4 %wt. (Figure 2). A small amount of water is present in distillate due to the ethanol – water azeotrope.

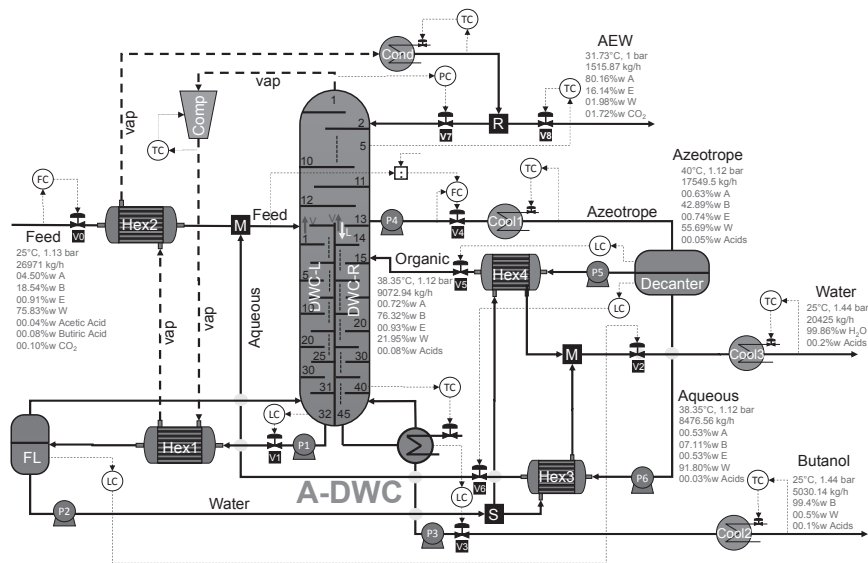


Figure 1. Heat-integrated VRC-assisted A-DWC for ABE separation

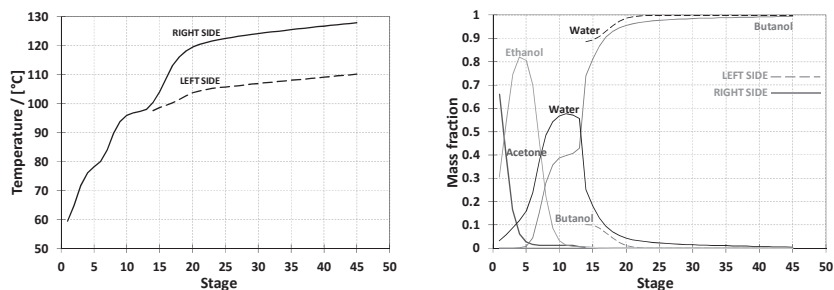


Figure 2. Temperature (left) and mass composition (right) profiles

4. Process dynamics

A dynamic simulation is built in Aspen Plus Dynamics. Two RADFRAC units are used to model the water removal section (DWC-L) and the combined fractionation (AEW) and butanol purification (DWC-R) sections. The reboiler on the water-removal side is represented as a HEATX (counter-current heat exchanger) followed by a FLASH. Several pumps and valves are provided, as required by the pressure-driven simulation. The basic control loops of flow rate, liquid level, pressure and temperature are shown in Figure 1. The column pressure is controlled with the reflux flow rate, which is subcooled at 31 °C. Besides the inventory control loops, the temperature on stage 5 of the fractionation section is controlled by manipulating the valve position of the distillate stream; the temperature on stage 40 of the butanol-purification section (DWC-R), is controlled by manipulating the reboiler duty; the temperature of the compressed vapor (to not exceed 150 °C) is controlled by the compressor brake-power.

The dynamic of the process is tested by changing the feed flow rate (by $\pm 5\%$ for 10 minutes and by $\pm 5\%$ for one hour), as shown in Figure 3. The control structure can successfully reject small and non-persistent disturbances (top diagrams). However, when the disturbance persists (bottom diagrams), the stream entering the column cools down, and the pressure and the temperature in column drop. As a result, less vapours are sent to the fractionation section and to the compressor. In the meantime, the stage 40 temperature controller located on the butanol-purification section tries to compensate the disturbance by increasing the reboiler duty. This affects the temperature of stage 5, so the top temperature controller closes the distillate stream valve. Further, the pressure controller closes the valve from the reflux stream, trying to increase the column pressure. However, the vapours flow is too small. Although the compressor brake-power is available as a variable to be manipulated, this action would increase the temperature of the compressed vapours above 150 °C, which is not allowed for safety reasons. Therefore, another manipulated variable is needed.

When the feed flow rate is decreased by 5% and the disturbance persists for a long time (Figure 3, bottom diagrams) the feed enters the column at higher temperature. In this case, more vapours are sent to fractionation section and more vapours are compressed, leading to a continually temperature increase in the water-removal section. As a result, more water is vaporized and eventually reaches the butanol product stream. Such disturbance could be rejected by controlling the temperature of the stream entering the column, but no manipulated variable is available.

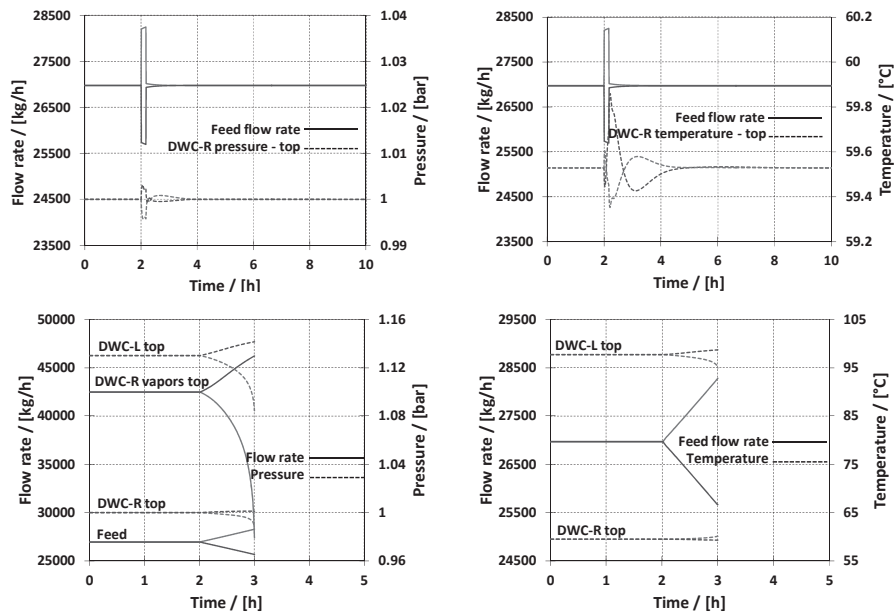


Figure 3. Stability test of the basic control structure for 5% disturbance in feed flow rate (10 min. top, 1 hour bottom)

5. Process control

To overcome these control difficulties, two new variables to be manipulated were added (Figure 4). The first one is a small additional duty on the reboiler of the water-removal section, which represents 10% of the energy required. The second one is an additional cooler placed on the compressed vapor stream, between the reboiler and the feed preheating. These variables are used in new control loops, namely: a) temperature control of the preheated feed, by manipulating the duty of the additional cooler; and b) temperature on stage 25 in water-removal section (DWC-L), by manipulating the additional reboiler duty.

In addition, a valve-position controller has the task to keep the additional duty at its steady state value by changing the set point of the temperature controller of compressed vapor stream (a low-select block ensures that the setpoint does not exceed 150 °C). This controller is essential when the feed flow rate is decreased because if less energy is required, the additional duty will remain at steady state value by reducing the temperature of the compressed vapours. The additional duty will increase only when more energy is required. By introducing these controllers, the process can handle large feed flow rate disturbances for long time.

Other dynamic simulation results (not shown here) indicate that the transient regime takes about 5 hours. As the feed rate changes, the water purity and the mass fraction of water in the distillate are practically unaffected, while the butanol purity deviates by only 0.1 %wt. from the design value. When the fraction of butanol in the feed stream changes (from 18.6 %wt. to 17 %wt. or 20 %wt.) the behaviour is similar: water and

distillate composition is practically unchanged, while the concentration of the butanol product deviates by about 0.1 %wt. from the design value. The performance of the control system is excellent, considering that only temperature measurements were used.

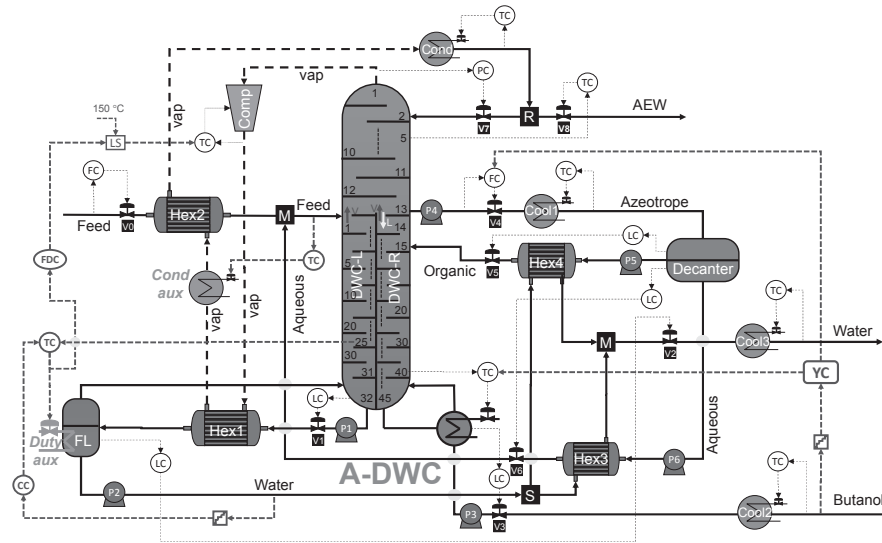


Figure 4. Control structure of the heat-pump assisted A-DWC

Finally, the performance of the new control structure can be improved by introducing two concentration controllers for maintaining the products (water and butanol) quality (Figure 4). The slow dynamics of these measurement was taken into account by using the Aspen Plus Dynamics sensor model with 5 minutes sampling period and 5 minutes dead time. Figure 6 and Figure 6 show dynamic simulation results for the control structure employing the concentration controllers, for feed flow rate and concentration disturbances, respectively.

The deviation of butanol purity from the steady state value is quite small. Eventually, 4 hours after the disturbance, the butanol purity comes back to the design value (99.4 %wt.). Water purity is practically unchanged, while the mass fraction of water in the distillate is acceptable.

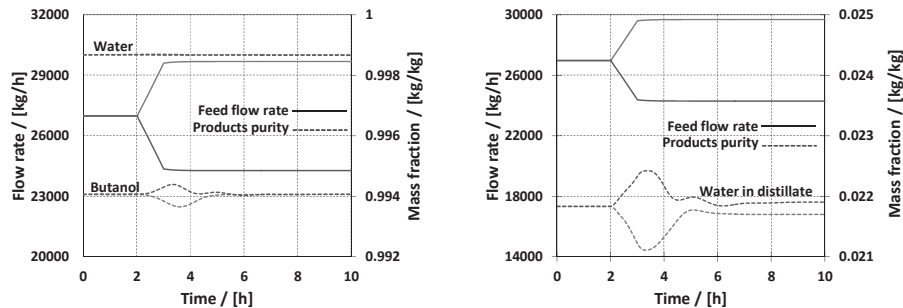


Figure 5. Performance of the control structure for 10% disturbance in feed flow rate

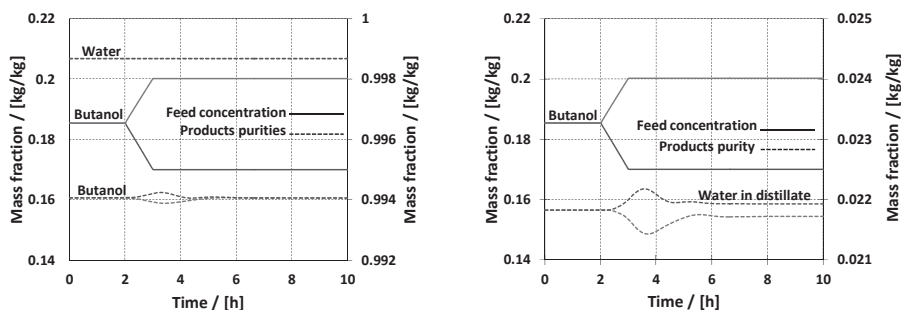


Figure 6. Performance of the control structure for feed concentration disturbances

6. Conclusions

The basic control structure of the A-DWC can reject small and short-time disturbance, but the process shuts down when the disturbance persists. Adding an additional reboiler and a condenser on the feed side stripping section provides two new variables to be manipulated. This change in the main design reduces the energy savings of 60% by only 4%. This is small penalty to pay, as the control structure performs successfully when disturbances of 10% in the flow rate and butanol concentration occur in the fresh feed.

Acknowledgements

The financial support of the European Commission through the European Regional Development Fund and of the Romanian state budget, under the grant agreement 155/25.11.2016 Project POC P-37-449 (ASPiRE), is kindly acknowledged. AAK is thankful for the Royal Society Wolfson Research Merit Award.

References

- N. Abdehagh, F. H. Tezel, J. Thibault, 2014, Separation techniques in butanol production: Challenges and developments, *Biomass and Bioenergy*, 60, 222-246.
- A. A. Kiss, Novel applications of dividing-wall column technology to biofuel production processes, 2013, *Journal of Chemical Technology and Biotechnology*, 88, 1387-1404.
- A. A. Kiss, C. A. Infante Ferreira, 2016, *Heat pumps in chemical process industry*, CRC-Press, Taylor & Francis Group.
- H. Luo, C. S. Bildea, A. A. Kiss, 2015, Novel heat-pump-assisted extractive distillation for bioethanol purification, *Industrial & Engineering Chemistry Research*, 54, 2208-2213.
- I. Patraşcu, C. S. Bildea, A. A. Kiss, Eco-efficient butanol separation in the ABE fermentation process, 2017, *Separation and Purification Technology*, 177, 49-61.
- I. Patraşcu, C. S. Bildea, A. A. Kiss, Eco-efficient downstream processing of biobutanol by enhanced process intensification and integration, 2018, *ACS Sustainable Chemistry & Engineering*, 6, 5452-5461.
- C. Xue, J-B. Zhao, F-F. Liu, C-G. Lu, S-T. Yang, F-W. Bai, 2013, Two-stage in situ gas stripping for enhanced butanol fermentation and energy-saving product recovery, *Bioresource Technology*, 135, 396-402.

Integrated white-box models for designing freezing processes of human induced pluripotent stem cells considering diversity within a container

Yusuke Hayashi,^{a,*} Ikki Horiguchi,^b Masahiro Kino-oka,^b Masahiko Hirao,^a
Hirokazu Sugiyama^a

^a *Department of Chemical System Engineering, The University of Tokyo, 7-3-1 Hongo, Bunkyo-ku, 113-8656, Tokyo, Japan*

^b *Department of Biotechnology, Osaka University, 2-1, Yamadaoka, Suita, 565-0871, Osaka, Japan*

y-hayashi@pse.t.u-tokyo.ac.jp

Abstract

This work presents a novel combination of white-box models that describes heat transfer, mass transfer, and intracellular ice formation during freezing of human induced pluripotent stem (hiPS) cells. The models can be applied to the design of freezing processes for hiPS cells considering the diversity in cell quality within a container. In the case study, two design variables were defined, i.e., the cooling rate of a programmed freezer as an element of {1.0, 1.2, ..., 3.8, 4.0 K/min} and the diameter of a vial as an element of {5, 50, 150 mm}. The objective functions were defined as the maxima of cell volume change and intracellular ice crystal volume as the proxy for the cell survival rate. The Pareto optimal solutions were obtained as 5 mm as the vial diameter with all considered cooling rates; given a threshold of the ice crystal volume, the feasible range of the cooling rate was strongly influenced by the diameter of the vial.

Keywords: Regenerative medicine, Cells, Cryopreservation, Numerical simulation, Multiobjective process design

1. Introduction

Regenerative medicine is the future technology that aims to heal or restore human tissues and organs damaged by age, disease, or trauma, back to the original condition (Mao and Mooney, 2015). Human induced pluripotent stem (hiPS) cells are considered as one of the promising sources of regenerative medicine products because of various advantages compared to the conventional sources. Towards industrialization of hiPS cells, freezing processes are essential in order to transport, distribute, and preserve the cells. However, hiPS cells are known to be sensitive to damages caused by freezing (Hunt, 2011), which could lead to undesired deviation of cell quality in the process. Several authors tackled the design of the freezing process by experiments using a programmed freezer (Li et al., 2018) or cryoprotective agents (Xu et al., 2014). However, it is yet to design reasonably the freezing process based on the fundamental understanding of physicochemical mechanisms.

In this work, we present a set of white-box models that describes heat transfer, mass transfer, and intracellular ice formation during freezing of hiPS cells. The novelty of this work is that the three models are integrated in such a way that the diversity in cell quality

inside a container can be evaluated, which would enable precise design of freezing processes.

2. Freezing process of hiPS cells

2.1. Manufacturing process of hiPS cells

Figure 1 shows the manufacturing process of hiPS cells. First, somatic cells are derived from a donor. Second, the somatic cells are converted to hiPS cells by introducing specific genes to the cells. Third, the number of hiPS cells is increased by cultivation. Finally, hiPS cells are differentiated to the target cells. It is estimated that a hiPS-based liver would require 10^{10} units of the cells, suggesting the importance of homogeneous cell quality. The freezing process is required to transport hiPS cells to the next process with protecting the cells from degeneration. In the freezing process, hiPS cells filled in a container named as vial with a cryoprotective agent are cooled in a programmed freezer as shown in Figure 2.

2.2. Damages to hiPS cells during freezing

As cooling progresses, extracellular water including a cryoprotective agent begins to freeze. At this point of time, the intracellular water is not yet frozen but remains in the supercooled state. Osmotic pressure difference between the inside and the outside of the cells occurs because the osmotic pressure of supercooled water is higher than that of frozen water. The pressure difference causes the dehydration of hiPS cells, decrease of the cell volume, and ultimately a damage to the cells (Mazur et al., 1972). Along with the further progress of cooling, intracellular water is eventually frozen, and ice crystals grow in the cell. The volume of intracellular ice crystals affects the degree of the additional damage to the cells (Mazur et al., 1972).

2.3. Formulation of the optimization problem

The optimization problem was defined as shown in Eq. (1):

$$\min \begin{cases} \Delta V_{\text{cell}}^{\max}(B, d_v) \\ V_{\text{ice}}^{\max}(B, d_v) \end{cases} \quad \text{s.t.} \quad \begin{array}{l} B \in \{1.0, 1.2, \dots, 3.8, 4.0\} \\ d_v \in \{5, 50, 150\} \end{array} \quad (1)$$

where $\Delta V_{\text{cell}}^{\max}$ [m^3] is the maximum cell volume change inside a vial, V_{ice}^{\max} [m^3] is the maximum intracellular ice crystal volume inside a vial, B [K min^{-1}] is the cooling rate of a programmed freezer, and d_v [mm] is the diameter of a vial. The final objective of the

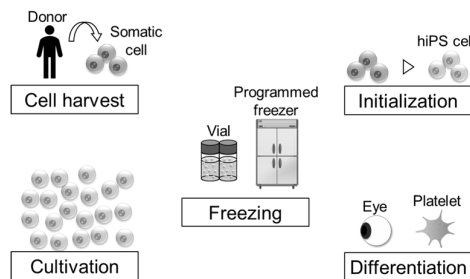


Figure 1 Manufacturing process of hiPS cells

design is to determine the decision variables that could maximize the survival rate of cells after the entire freezing process. Based on the analysis presented in section 2.2, we considered the cell volume change due to the osmotic pressure difference and the formation of intercellular ice crystal as the key factors for the cell survival (Mazur et al., 1972).

3. Construction of the white-box models

3.1. Heat transfer model

Considering that the primary mode of heat transfer in a vial is conduction rather than convection, we adopted the following equations to calculate the temperature inside a vial (Hu and Argyropoulos, 1996):

$$\frac{\partial T}{\partial t} = \alpha_w \left(\frac{\partial^2 T}{\partial r^2} + \frac{1}{r} \frac{\partial T}{\partial r} \right) \quad (2)$$

$$\frac{\partial T}{\partial t} = \alpha_{ice} \left(\frac{\partial^2 T}{\partial r^2} + \frac{1}{r} \frac{\partial T}{\partial r} \right) \quad (3)$$

$$\frac{\partial T}{\partial t} = \alpha_v \left(\frac{\partial^2 T}{\partial r^2} + \frac{1}{r} \frac{\partial T}{\partial r} \right) \quad (4)$$

where T [K] is the temperature, t [s] is the time, α [$\text{m}^2 \text{s}^{-1}$] is the thermal diffusion coefficient, r [m] is the radial distance from the center of a vial, and the subscripts of w, ice, and v represent water, ice, and vial, respectively. According to Hu and Argyropoulos (1996), the position of the solid-liquid interface from the center of a vial δ [m] can be calculated as follows:

$$\frac{\rho_{ice} \Delta H_f}{M_{ice}} \frac{d\delta}{dt} = k_{ice} \left(\frac{\partial T}{\partial r} \right)_{r=\delta} - k_w \left(\frac{\partial T}{\partial r} \right)_{r=\delta+d\delta} \quad (5)$$

where ρ [kg m^{-3}] is the density, ΔH_f [J mol^{-1}] is the molar heat of fusion of ice, M [kg mol^{-1}] is the molar mass, and k [$\text{J s}^{-1} \text{m}^{-1} \text{K}^{-1}$] is the thermal conductivity.

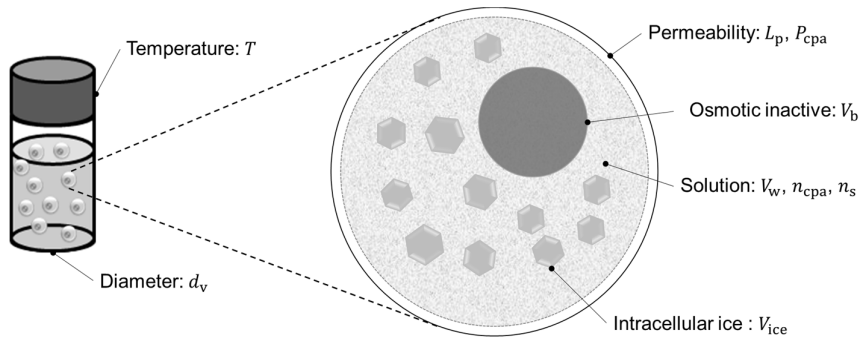


Figure 2 Schematic representation of the freezing process (adapted from Fadda et al., 2010)

3.2. Mass transfer model

Transmembrane mass transport by the osmotic pressure difference was modelled using the following equations (Xu et al., 2014):

$$\frac{dV_{\text{cell}}}{dt} = -\frac{L_p A_{\text{cell}} RT}{v_w} \left[\frac{\Delta H_f}{R} \left(\frac{1}{T_0} - \frac{1}{T} \right) - \ln \left\{ \frac{V_w}{V_w + v_w (\mu_s n_s + n_{\text{cpa}})} \right\} \right] \quad (6)$$

$$\frac{dn_{\text{cpa}}}{dt} = \frac{(C_{\text{ex}} + C_{\text{in}})(1 - \sigma)}{2} \frac{dV_{\text{cell}}}{dt} + A_{\text{cell}} P_{\text{cpa}} (C_{\text{ex}} - C_{\text{in}}) \quad (7)$$

where V [m^3] is the volume, L_p [$\text{m s}^{-1} \text{Pa}^{-1}$] is the water permeability, A [m^2] is the surface area, R [$\text{J mol}^{-1} \text{K}^{-1}$] is the gas constant, v [$\text{m}^3 \text{mol}^{-1}$] is the partial molar volume, μ [-] is the dissociation constant, n [mol] is the molar amount, C [mol m^{-3}] is the cryoprotective agent concentration, σ [-] is the reflection coefficient, P_{cpa} [m s^{-1}] is the cryoprotective agent permeability. The subscripts of cell, 0, s, cpa, in, and ex represent cell, reference, salt, cryoprotective agent, intracellular, and extracellular, respectively. According to Xu et al. (2014), the cell membrane permeability coefficients of L_p and P_{cpa} are temperature-dependent and can be calculated using the following equations:

$$L_p = L_{p0} \exp \left[-\frac{E_w}{R} \left(\frac{1}{T} - \frac{1}{T_0} \right) \right] \quad (8)$$

$$P_{\text{cpa}} = P_{\text{cpa}0} \exp \left[-\frac{E_{\text{cpa}}}{R} \left(\frac{1}{T} - \frac{1}{T_0} \right) \right] \quad (9)$$

where E [J mol^{-1}] is activation energy.

3.3. Crystal growth model

Nucleation of ice in a cell occurs by two different mechanisms: homogeneous nucleation (HOM) and heterogeneous nucleation (HET). HET is further categorized into two types: surface-catalysed nucleation (SCN) that occurs at cell membrane and volume-catalysed nucleation (VCN) that occurs inside a cell. The nucleation rate of ice in a cell was modelled using the following equations (Zhao et al., 2014):

$$J_{\text{ice}} = \begin{cases} 0 & (T_m < T) \\ I^{\text{HOM}} V_w + I^{\text{SCN}} A_{\text{cell}} + I^{\text{VCN}} V_w & (T \leq T_m) \end{cases} \quad (10)$$

where J [s^{-1}] is the nucleation rate, I [$\text{s}^{-1} \text{m}^3$ or $\text{s}^{-1} \text{m}^2$] is the nucleation rate per unit, and the subscript of m represents melting point.

In order to estimate ice crystal growth under non-isothermal conditions, the radius of intracellular ice crystals was modelled using the following equations (Fadda et al., 2010; Karlsson et al., 1994):

$$r_{\text{ice},i} = \begin{cases} 0 & (0 \leq N_{\text{ice}} < 1) \\ \sqrt{\int_{\tau_i}^t \gamma_{\text{ice}}^2 D_{\text{av}} dt} & (1 \leq N_{\text{ice}}) \end{cases} \quad (11)$$

where r_{ice} [m] is the radius of an ice crystal, N_{ice} [-] is the number of intracellular ice crystals, γ_{ice} [-] is the non-dimensional ice crystal growth parameter, τ [s] is the starting time of ice crystal formation, and D_{av} [m² s⁻¹] is the average water diffusion coefficient. According to Fadda et al. (2010), the total volume of intracellular ice crystals V_{ice} can be calculated using the following equation.

$$V_{ice}(r) = \sum_{i=1}^{N_{ice}} \frac{4}{3} \pi r_{ice,i}^3 \quad (12)$$

4. Results and discussion

Figure 3 shows the relationship between the design variables, i.e., cooling rate B and the diameter d_v , and the objective functions, i.e., the maximum intracellular ice crystal volume V_{ice}^{max} and the maximum cell volume change ΔV_{cell}^{max} . The calculation results at $d_v = 5$ mm are the most favourable, and thus all values of B at $d_v = 5$ mm are the Pareto optimal solutions to the problem defined in Eq. (1). The graph shows that the change of ΔV_{cell}^{max} due to the difference in B and d_v is less significant than that of V_{ice}^{max} , and thus in practice, ΔV_{cell}^{max} could be ignored. Focusing on the results of V_{ice}^{max} , the values of B and d_v should be as small as possible. In case a threshold of V_{ice}^{max} is given, e.g., 8 μm^3 , the volume of a human mitochondrion, Figure 3 indicates that the largest possible B would differ depending on d_v , i.e., dimensionality. In the literature, the ideal cell volume changes and ice crystal growth have been simulated for a type of mouse cells during the freezing process (Karlsson et al., 1994) by considering mass transfer and crystal growth. With a focus on hiPS cells, this study integrated heat transfer (see Eqs. (2-5)) in addition, so that the dependence of the cell quality on the intra-container dimensionality can be quantified, which is the novelty of this work.

A solver adopted solving partial differential equations was the Crank-Nicolson method and the algorithm was implemented in Python 3.6. The total CPU time that the results shown in Figure 3 was obtained was about 8 hours, using Intel(R) Core(TM) i5-6500 CPU@3.2 GHz with 8 GB RAM memory.

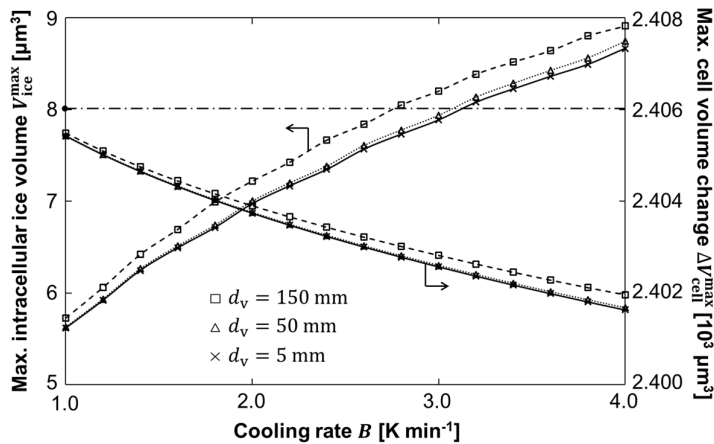


Figure 3 Relationship between cooling rate and volume change or ice crystal volume

5. Conclusions and outlook

We presented the white-box models that are applicable to dynamic and simultaneous simulation of heat transfer, mass transfer, and intracellular ice formation. The three models are integrated in such a way that the diversity in cell quality inside a container can be evaluated, which would enable precise design of freezing processes. We applied the models to calculate the change of the cell volume and the formation of the intracellular ice crystal that are considered to affect the survival rate of the hiPS cells. The Pareto optimal solutions were obtained as 5 mm as the vial diameter with all considered cooling rates; given a threshold of the ice crystal volume, the feasible range of the cooling rate was influenced by the diameter of the vial. The result implies the significance of the intra-container dimensionality in considering cell quality, which was made possible by the proposed models for the first time. In future, we will conduct dynamic optimization of the process parameters by quantifying the temperature distribution inside the freezer, and by evaluating the productivity of the entire process.

Acknowledgement

This study was supported by the Japan Agency for Medical Research and Development (AMED) in the project “Development of cell manufacturing and processing system for industrialization of regenerative medicine” (No. P14006).

References

- S. Fadda, A. Cincotti, G. Cao, 2010, The effect of cell size distribution during the cooling stage of cryopreservation without CPA, *AIChE J.*, 56, 2173–2185
- H. Hu, S. A. Argyropoulos, 1996, Mathematical modelling of solidification and melting: a review, *Model. Simul. Mater. Sci. Eng.*, 4, 371–396
- C. J. Hunt, 2011, Cryopreservation of Human Stem Cells for Clinical Application: A Review, *Transfus. Med. Hemother.*, 38, 107–123
- J. O. M. Karlsson, E. G. Cravalho, M. Toner, 1994, A model of diffusion - limited ice growth inside biological cells during freezing, *J. Appl. Phys.*, 75, 4442–4455
- R. Li, G. Yu, S. Azarin, A. Hubel, 2018, Freezing Responses in DMSO-Based Cryopreservation of Human iPS Cells: Aggregates vs. Single Cells, *Tissue Eng. Part C Methods*, 24, 289–299
- A. S. Mao, D. J. Mooney, 2015, Regenerative medicine: Current therapies and future directions, *Proc. Natl. Acad. Sci.*, 112, 14452–14459
- P. Mazur, S. P. Leibo, E. H. Y. Chu, 1972, A two-factor hypothesis of freezing injury: Evidence from Chinese hamster tissue-culture cells, *Exp. Cell Res.*, 71, 345–355
- Y. Xu, L. Zhang, J. Xu, Y. Wei, X. Xu, 2014, Membrane permeability of the human pluripotent stem cells to Me2SO, glycerol and 1,2-propanediol, *Arch. Biochem. Biophys.*, 550–551, 67–76
- G. Zhao, H. Takamatsu, X. He, 2014, The effect of solution nonideality on modeling transmembrane water transport and diffusion-limited intracellular ice formation during cryopreservation, *J. Appl. Phys.*, 115, 1–13

Heat-Integrated Reactive distillation processes to produce Ethyl Levulinate: Design and Optimization including Environmental, Safety and Economics Aspects

J.A. Vazquez-Castillo,^{a,*} G.Contreras-Zarazúa,^b J.G. Segovia-Hernandez^b

^a*Faculty of Chemical Sciences Autonomous University of Chihuahua, Circuito Universitario 8, Campus II, Chihuahua, Chih. 31125,*

^b*Department of Chemical Engineering University of Guanajuato, Noria Alta S/N, Guanajuato, Gto., 36000, Mexico.*

vazquezcastillo@gmail.com

Abstract

This study provides optimally designed reactive distillation (RD) processes for the production of ethyl levulinate, taking into account costs, environmental impact and safety. The thermally coupled RD process is the most appealing with major energy savings in the range of 9.6-54.3% lower than other RD processes, reduced environmental impact in the range of 5.7-51% lower ECO 99 index value and similar process safety less than 2% difference compared to other RD processes considered. The lower energy requirement of the thermally coupled process was reflected in the lowest energy use to produce ethyl levulinate (1.667 GJ/ton.).

Keywords: Ethyl Levulinate, Reactive Distillation, Cost and Safety of chemical processes, Multi-objective optimization.

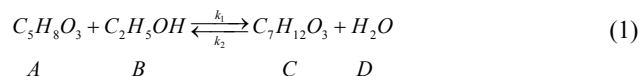
1. Introduction

Ethyl Levulinate (EL) is a valuable chemical whose utilization is extended in multiples industries, EL distinguishes as a product with the potential to be used as a replacement of the fuel additives such as Methyl Tert-Butyl Ether (MTBE) y el Tert-Amyl Methyl Ether (TAME), the industry related with the production of ethyl Levulinate can be considered in its infancy however the forecast for the ethyl Levulinate demand indicates that 49.1 tons will be demanded by the year 2022 with a worth value in the market of 11.8x10⁶ USD (Grand View Research, 2017). An appealing route to avoid the use of harmful solvents and larger amounts of energy is the reaction between the levulinic acid with ethanol to obtain ethyl Levulinate (Fernandes et al., 2012), however, this route is limited by the equilibrium of the reaction, in order to overcome the limitation, the implementation of Reactive Distillation is relevant, even more the heat integration and thermally coupling of these designs adds significant improvements to be consistent with the philosophy of seek for sustainable processes.

In this work, the evaluation of the TAC, the ECO 99 and the Individual Risk (IR) of proposals of processes based on heat integrated and thermally coupled reactive Distillation to produce Ethyl Levulinate is introduced, as these proposals involve the handling of organic compounds, which are the most common source of fires and explosions in industry, in addition to the traditional economic and sustainable evaluation, a quantitative risk analysis is highly desirable.

2. Methodology

Ethyl Levulinate is produced through the reaction of the Levulinic Acid with Ethanol, the reaction is showed in the Eq. (1).



From the Equation 1: A=Levulinic Acid; B= Ethanol; C=Ethyl Levulinate; D=Water.

The kinetics equation and the kinetic parameters were taken from a previous work by Tsai, 2014. In this work the Hayden-O'Connell model was selected as the thermodynamic model to properly estimate the vapor-liquid equilibrium. The binary interaction parameters of the components were taken from a previous work by Resk et al. (2014). Four different reactive distillation configurations are studied; the alternatives and the schemes of these configurations are shown in Figure 1 these consist in: Conventional Reactive Distillation Process (CRDP); Thermally Coupled Reactive Distillation (TCRD); Reactive Distillation With heat Integration (RDHI) and Reactive Distillation with Thermally Coupled and heat Integration (THRD). All of the sequences consist of a reactive distillation column (RDC) and two separation columns RC-1 and RC-2. The first separation column, RC-1, performs the separation of the by-product water from the main product, ethyl levulinate (EL) and the unreacted Levulinic Acid (LA), in the second separation column, RC-2, the separation of the Ethyl Levulinate and the Levulinic Acid is carried out, the Levulinic Acid is returned to the RDC column. In all cases, the feed flow of Ethanol and fresh Levulinic Acid were 100 kmol/h. The topology of these processes was taken from the previous work by Novita et al. (2017), however, in this work a rigorous multi-objective optimization algorithm is implemented, and three key factors are simultaneously evaluated, even more through the optimization strategy would help to contrast and eventually to carry out the selection of the optimal designs in terms of multiple objectives as the proposed in this work.

The total annual cost has been computed using the Guthrie methodology. Five years was assumed as a payback period, whereas carbon steel is considered as construction material for the process equipments. The operating costs included cooling utilities, heating utilities, and 8400 hours of yearly operation for each alternative have been considered. The ECO 99 is used to calculate the environmental impact. This approach is based on the evaluation of three impact categories: human health, ecosystem quality, and resources depletion. This method has been successfully implemented in the environmental evaluation of chemical processes (Quiroz-Ramirez et al 2017). According to the importance of three major impact categories the weighting for ECO 99 was realized as follows: damages to human health and damage to ecosystem quality are of equal importance, thus these were equally weighted while the damage to the resources was considered to be half of importance in weighting. The individual risk is an index used to quantify the safety of a process and it is calculated through a quantitative risk analysis where the damage caused by an accident is identified and quantified. For the cases of study seven possible incidents have been identified, these are divided in two categories. Instantaneous incidents are: Boiling liquid expanding vapour explosion (BLEVE), unconfined vapour cloud explosion (UVCE), flash fire and toxic release, whereas the continuous release incidents are: jet fire, flash fire and toxic release. The calculations of the individual risk were carried out for a reference distance

of 50 m, the complete set equations to calculate the IR is showed by Medina-Herrera et al. 2014.

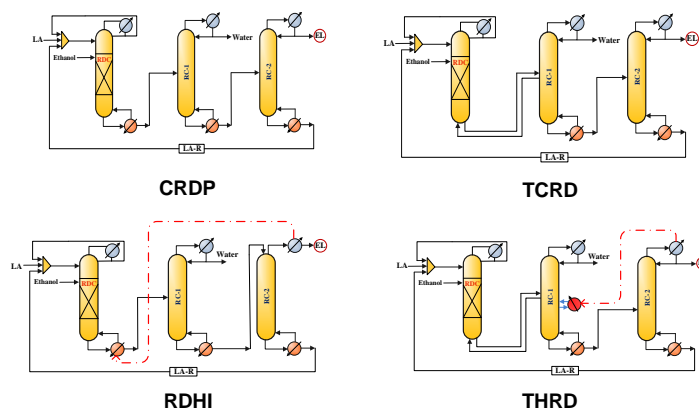


Figure 1. Reactive distillation processes to produce Ethyl Levulinate.

The multi-objective optimization problem was solved using the mathematical technique called Differential Evolution with Tabu List (DETL) by Sharma, S., & Rangaiah, G. P. (2010). The values of the parameters required by DETL method are: Population size (NP): 200 individuals, Generations Number (GenMax): 500, Tabu List size (TLS): 100 individuals, Tabu Radius (TR): 0.01, Crossover fractions (Cr): 0.8, Mutation fractions (F): 0.3. The DETL method together with objective function were implemented in a hybrid platform involved, which linked Aspen Plus™ and Microsoft Excel™ through Visual Basic™. The design variables for the different processes are offered in the Table 1.

Table 1. Design variables for the processes separation of furfural.

Decision Variables	CRDP	TCRD	RDHI	THRD
Number of stages, RDC	X	X	X	X
Number of reactive stages	X	X	X	X
Heat duty of RDC, kW	X		X	
Distillate flow, kmol h ⁻¹	X	X	X	X
Diameter of RDC, m	X	X	X	X
Number of stages, RC-1	X	X	X	X
Feed stage, RC-1	X	X	X	X
Reflux ratio of RC-1	X	X	X	X
Interlinking flow, kmol h ⁻¹		X		X
Bottom flow of RC-1, kmol h ⁻¹	X	X	X	X
Diameter of RC-1, m	X	X	X	X
Withdrawal side stage of RC-1				X
Side flow of RC-1, kmol h ⁻¹				X
Number of stages, RC-2	X	X	X	X
Feed stage, RC-2	X	X		X
Reflux ratio of RC-2				X
Bottom flow of RC-1, kmol h ⁻¹	X	X	X	X
Heat duty of RC-2, kW	X	X		
Diameter of RC-2, m	X	X	X	X

Total number of variables	15	15	13	17
---------------------------	----	----	----	----

Finally, the overall optimization problem can be mathematically expressed as in Eq. (2) and Eq. (3):

$$\min Z = \{TAC; ECO\ 99; IR\} \quad (2)$$

$$\text{Subject to: } \begin{aligned} y_{i,F} &\geq x_{i,F} \\ w_{i,F} &\geq u_{i,F} \end{aligned} \quad (3)$$

The objective functions are restricted to satisfy the purity ($y_{i,F}$) and molar flowrate ($w_{i,F}$) especifications of Ethyl Levulinate and Water. The purity required for Ethyl Levulinate (EL) and Water was 99.5 mol%.

3. Results

The Pareto charts obtained for all of the reactive distillation processes at the end of the optimization process are offered in the Figure 2. Each point in the graphics represents a solution or design that meets the purity requirements with the best values of the three objective functions under evaluation.

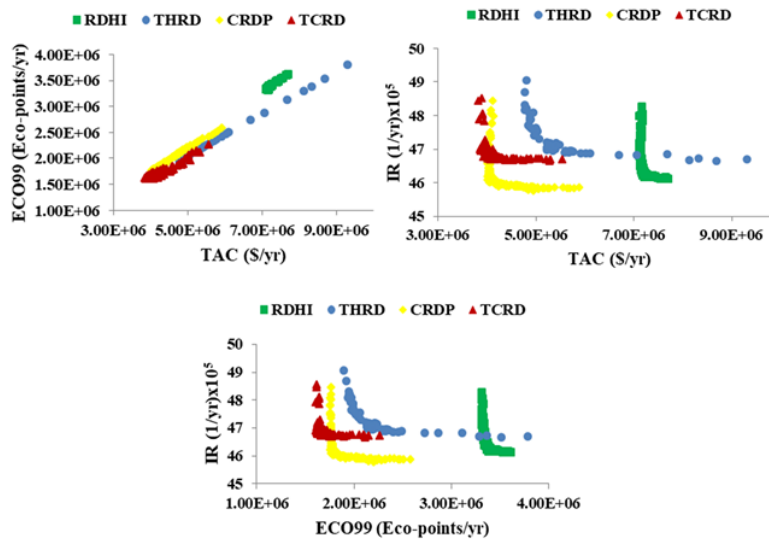


Figure 2. Pareto charts of the RD processes.

The shape of the Pareto TAC vs ECO99, in the Figure 2, is explained relating the influence of total energy consumed by each process and the amount of steel required to build the equipments in the ECO 99 calculation. The Pareto front of IR vs TAC for all the processes exhibits a trend of opposite objectives for IR and TAC, this behaviour indicates that the selection of a design with the lowest TAC, it necessarily causes the value of IR to increase, therefore, the solutions that offer the best trade-offs between the two objectives are those located in the curve zone of the Pareto Chart for these sequences; the Pareto front of IR vs ECO 99, the shape of the Paretos of all the processes exhibits a similar trend as the IR vs TAC Pareto for these same sequences. In the optimal designs of all the sequences, the larger reflux ratios and reboiler duties the higher utilization of heating services and electricity for cooling services, these larger values have a direct contribution in the increment of the ECO 99 values. According to

the behaviour of the Paretos of the objective functions IR vs ECO 99 and IR vs TAC, which is the same behaviour for both combinations of indexes, it is possible to assert that the best optimal designs of the processes CRDP, THRD and TCRD are found in the zone of the Pareto that compensates both objectives, this is the curve zone as explained above. Therefore, the selection of a design that compensates the IR index with the TAC, this choice directly equilibrates the IR index with the ECO 99. The Table 2 provides the design variables of the selected designs of the Pareto charts of the processes.

Table 2. Design variables of optimal designs of reactive distillation processes.

Design Variables	CRDP	TCRD	RDHI	THRD
<i>Topology of columns</i>				
Number of stages, RDC	83	93	48	58
Number of reactive stages, RDC	2-45	2-63	2-23	2-37
Number of stages, RC-1	26	23	32	19
Number of stages, RC-2	31	34	16	16
Feed stage, RC-1	13	15	21	15
Feed stage, RC-2	21	27	1	14
Withdrawal side stage, RC-1	—	—	—	14
Diameter of RDC, m	1.009	1.334	1.04	1.17
Diameter of RC-1, m	1.170	1.036	1.13	1.60
Diameter of RC-2, m	1.080	1.090	1.07	1.88
<i>Operating conditions</i>				
Top pressure (atm)	1	1	1	1
Distillate flow, kmol h ⁻¹	493.73	441.58	532.464	342.606
Tray holdup, l	44.004	76.951	46.687	59.442
Reflux ratio of RC-1	0.5371	0.5819	0.9651	1.152
Reflux ratio of RC-2	—	—	—	0.7045
Heat duty of RDC, kW	3019.1	0	10211.3	0
Heat duty of RC-1, kW	2738.9	4830.7	3226.57	6750.52
Heat duty of RC-2, kW	1698.8	1839.3	1122.45	2052.30
Interlinking flow, kmol h ⁻¹	—	151.44	—	272.922
Side flow of RC-2, kmol h ⁻¹	—	—	—	24.7091
Bottom flow of RC-1, kmol h ⁻¹	118.68	119.813	117.416	125.435
Bottom flow of RC-2, kmol h ⁻¹	18.7575	19.9172	17.4219	25.6693
Temperature bottom, RDC (°C)	118.95	117.70	117.94	117.15
Temperature bottom, RC-1 (°C)	227.31	232.07	227.47	228.638
Temperature bottom, RC-2 (°C)	247.83	267.91	230.42	235.69
<i>Molar flowrates of process streams</i>				
Ethyl Levulinate stream, kmol h ⁻¹	99.5081	99.877	99.5036	99.7631
Water stream, kmol h ⁻¹	99.6249	99.990	99.5128	99.9929

Continue Table 2

Purity of EL product and by-product water (mol%)

Ethyl Levulinate	0.9964	0.9998	0.9951	0.9999
Water	0.9957	0.9981	0.9950	0.9979

Performance indexes

Energy per ton. of EL produced (GJ/ton. EL)	1.8712	1.6676	3.6539	2.2033
Utilities cost (million \$/yr)	3.8125	3.7141	6.9426	5.0005
Equipment cost (million \$)	0.2544	0.2305	0.2767	0.2218
TAC (million \$/yr)	4.0670	3.9447	7.2193	5.2224
Eco99 (million Eco-points/yr)	1.7803	1.6592	3.3916	2.1465
IR (1/yr)*10 ⁵	45.994	46.766	46.1502	46.962

4. Conclusions

The multi-objective optimization taking into account simultaneously the total annual cost, environmental impact and process safety, revealed that the thermally coupled reactive distillation (TCRD) process has the lowest energy use (1.667 MJ/kg EL) with major energy savings (9.6-54.3% lower than other RD processes), reduced environmental impact (5.7-51% lower ECO 99 index value) and similar process safety (less than 2% difference compared to other RD processes considered). Thus, the TCRD process is suggested as the best process alternative to produce ethyl levulinate, although there is room for further selection of other feasible RD processes where other tradeoffs among the indicators may be devised.

References

- Grand View Research. Ethyl Levulinate Market Worth \$11.8 Million by 2022. (2016). <http://www.grandviewresearch.com/press-release/global-ethyl-levulinate-market>.
- Fernandes, D. R., Rocha, A. S., Mai, E. F., Mota, C. J., & Da Silva, V. T. (2012). Levulinic acid esterification with ethanol to ethyl levulinate production over solid acid catalysts. *Applied Catalysis A: General*, 425, 199-204.
- Tsai C. Y., Kinetic Behavior Study on the Synthesis of Ethyl Levulinate over Heterogeneous Catalyst (2014), Master Thesis, NTUST, Taiwan.
- Resk, A. J., Peereboom, L., Kolah, A. K., Miller, D. J., & Lira, C. T. (2014). Phase Equilibria in systems with levulinic acid and ethyl levulinate. *Journal of Chemical & Engineering Data*, 59(4), 1062-1068.
- Novita, F. J., Lee, H. Y., & Lee, M. (2017). Energy-efficient design of an ethyl levulinate reactive distillation process via a thermally coupled distillation with external heat integration arrangement. *Industrial & Engineering Chemistry Research*, 56(24), 7037-7048.
- Medina-Herrera, N., Jiménez-Gutiérrez, A., & Mannan, M. S.; Development of inherently safer distillation systems. *Journal of Loss Prevention in the Process Industries*, 2014, 29, 225-23
- Quiroz-Ramírez, J. J., Sánchez-Ramírez, E., Hernández-Castro, S., Segovia-Hernández, J. G., Ponce-Ortega, J. M.; (2017). Optimal planning of feedstock for butanol production considering economic and environmental aspects, *ACS Sustainable Chemistry & Engineering*, 5(5), 4018-4030.
- Sharma, S., & Rangaiah, G. P. (2010). A hybrid multi-objective optimization algorithm. In 5th International Symposium on Design, Operation, and Control of Chemical Processes (pp. 1494-1503)

An Explicit Online Resource-Task Network Scheduling Formulation to Avoid Scheduling Nervousness

Giancarlo Dalle Ave^{a,b}, Mert Alici^a, Iiro Harjunoski^{a,*} and Sebastian Engell^b

^a*ABB Corporate Research Center Germany*

^b*Process Dynamics and Operations Group, Technische Universität Dortmund*
Iiro.Harjunoski@de.abb.com

Abstract

Scheduling is a decision-making process that is often based on the assumption of nominal operating conditions. In reality, scheduling is a dynamic process and uncertainties often arise during the execution of a schedule. One way to handle uncertainty in schedule is via reactive scheduling, or rescheduling. Rescheduling accounts for uncertainty by revising the existing agenda in response to real-time events. The downside to frequent revisions of the schedule is that it often leads to scheduling nervousness. In this work, a novel set of constraints based on the Resource-Task Network (RTN), coupled with a region-based penalty approach is proposed to combat scheduling nervousness. Results show that the approach is able to produce more stable schedules, while still giving rescheduled agendas the flexibility needed to pursue the original scheduling objective.

Keywords: Resource-Task Network (RTN), Scheduling Nervousness, Rescheduling

1. Introduction

Scheduling is a decision-making process that plays a central role in almost any type of industrial production facility where tasks need to be processed on a set of resources. The production in these facilities needs to be appropriately planned in order to prioritize the tasks and to ensure that the equipment, material, utilities, personnel and other resources are available at the plant when they are needed (Harjunoski et al., 2014). There exist several mathematical programming-based scheduling formulations that can be roughly divided into discrete- and continuous-time models, each of which have different strengths and weaknesses. One such mathematical programming-based scheduling formulation that has received significant attention is the the Resource-Task Network (RTN) model (Pantelides, 1994). The RTN model, particularly the discrete-time RTN model, is a generic scheduling framework that has been shown to be applicable to many different industries including stainless steelmaking (Castro et al., 2013), and petrochemical production (Wassick and Ferrio, 2011).

Most scheduling approaches are predictive techniques that deal with the generation of production plans while assuming a given set of tasks and resources. However, industrial environments are dynamic and unplanned events often disrupt the planned schedule. There are two main classes of approaches to accommodate these unplanned events, scheduling under uncertainty, and reactive/online scheduling. Scheduling under uncertainty aims at accounting for uncertain parameters *a priori* by building a production plan with some slack that is directly incorporated into the schedule (Gupta et al., 2016). Reactive or online scheduling on the other hand accounts for uncertainty by revising the existing agenda in response to real time events. Rescheduling approaches are the most common dynamic scheduling approaches in manufacturing (Ouelhadj and Petrovic, 2008).

The drawback to frequent revisions of the schedule is that they lead to what is known as scheduling

nervousness. Scheduling nervousness is an important aspect of online scheduling and is one of the reasons scheduling is not as widespread in industry as it could be (Henning, 2016). In this direction, Méndez and Cerdá (2004) proposed an iterative MILP framework to repair schedules by limited reallocation and reordering of operations defined by user-controlled sets. Other work in the area includes that of Novas and Henning (2010) who propose a domain knowledge-based rescheduling framework using constraint programming.

In this work, a novel method is proposed to avoid scheduling nervousness with minimal domain-specific knowledge. This is accomplished by using a set of general constraints to compare subsequent rescheduling iterations. Zones are defined in which subsets of these constraints are enforced more or less strictly than in other zones. Deviations from the existing schedules are penalized between iterations in a multi-objective optimization approach. The goal of this approach is to provide the subsequent scheduling iteration flexibility to respond to a disturbance, but in a way that minimizes the impact to the shop floor.

2. Methodology

The proposed approach is based on the discrete-time RTN framework to make it generic and easy to adapt to various applications. The RTN model represents the entire schedule as a set of resources (R) and tasks (I). In this formulation, tasks represent operations that need to be performed, which consume and produce sets of resources. Examples of resources in this case include raw materials, final products, and processing units. In the discrete-time RTN, the scheduling horizon (H) is divided into a set of δ sized intervals (T). The resource availability over the time grid is controlled by the variable $R_{r,t}$ which is modified by the execution of a task ($i \in I$) with a duration of τ_i time slots. These tasks are characterized by two sets of variables, the binary variable $N_{i,t}$ and the continuous variable $\xi_{i,t}$. The binary variables couple the execution of the task i with time point $t \in T$ and are associated with the discrete-interaction of a resource ($\mu_{i,r,\theta}$). For example, the execution of a reaction task always consumes a reactor regardless of the amount of product reacted. Conversely, the continuous variable $\xi_{i,t}$ indicates the amount handled by the task and is not considered in this work as batching functions are often handled by higher level planning functions (Harjunkoski et al., 2014) and are treated as inputs to the problem. External interactions with the scheduling system are modeled using the variable $\pi_{r,t}$. Examples of external interactions include raw material deliveries, product shipments, or equipment breakdowns. The modified resource balance that is considered in this work can then be seen in Eq. (1), while Eq. (2) limits the excess capacity of a resource.

$$R_{r,t} = R_{r,t-1}^{\neq 0} + \pi_{r,t} + \sum_i \sum_{\theta=0}^{\tau_i} \mu_{i,r,\theta} N_{i,t-\theta} \quad \forall r \in R, t \in T \quad (1)$$

$$R_{r,t}^{\min} \leq R_{r,t} \leq R_{r,t}^{\max} \quad \forall r \in T, t \in T \quad (2)$$

When using the RTN, tasks are often aggregated together into a single binary variable in order to reduce the problem size. For example, if five orders of a product have been requested, it is possible to treat each order as an individual task which will execute once, or to treat the orders as a single task which must execute five times. This aggregation however creates problems when accounting for scheduling nervousness as it is uncertain which specific order an active binary is referring to. Therefore, in this work, non-aggregated tasks are considered. The same logic applies to aggregated resources, especially to equipment resources.

2.1. Additional Model Constraints

In order to define the constraints necessary to combat scheduling nervousness some additional notation and sets will be used. When a reschedule is performed at time $t^{\text{resched}} < H$ the set of all

tasks that have not yet been started is represented by $I^{resched}$. Additionally, tasks that have been assigned to a specific processing unit in the current iteration of the schedule will be denoted by I^u , where $u \in U$ represents a single unit in the set of all processing units. All units at a single production stage ($k \in K$) are referred to using U_k . The start time of a task ST_i^σ is given by Eq. (3), where the index σ is used to refer to a particular iteration of the schedule. Similarly, the end time of a task is given by Eq. (4). In the rescheduling problem, the new version of the agenda that is going to be calculated is given by σ while $\sigma - 1$ refers to the current in progress agenda. Lastly, each task that will be rescheduled ($i \in I^{resched}$) on a specific machine could potentially be directly preceded by a task ($i' \in I_i^{predecessor}$) and/or succeeded by a task ($i' \in I_i^{successor}$) both of which will have at most one member. Note that it is possible for the predecessor i' of a task to be already executed, or currently in progress, which implies it is not possible to reschedule this task ($i' \notin I^{resched}$). If a task has no direct predecessors or successors the corresponding sets will be empty. For example, tasks A, B and C are scheduled one after another on a specific machine. Task A has no predecessors but has task B as a successor. On the other hand, task B has task A as a predecessor and task C as a successor while task C has no successors but task B as a predecessor.

$$ST_i^\sigma = \sum_{t \in T} N_{i,t}^\sigma \cdot t \tag{3}$$

$$ET_i^\sigma = \sum_{t \in T} N_{i,t}^\sigma \cdot (t + \tau_i) \tag{4}$$

Scheduling nervousness is generally associated with three different components, the reallocation of tasks between units, the changing of task timings, and the reordering of tasks. Constraints (5) to (7) are proposed in order to account for these concerns:

$$1 - \sum_{t \in T} N_{i,t}^\sigma - S_i^{machine} = 0 \quad \forall u \in U, i \in I^u \cap I^{resched} \tag{5}$$

$$ET_{i'}^{\sigma-1} - \sum_{u \in U_k} ST_i^\sigma + S_i^{backwards} \geq 0 \quad \forall i \in I^{resched}, i' \in I_i^{predecessor} \tag{6}$$

$$\sum_{u \in U_k} ET_i^\sigma - ST_{i'}^{\sigma-1} + S_i^{forward} \geq 0 \quad \forall i \in I^{resched}, i' \in I_i^{successors} \tag{7}$$

Eq. (5) penalizes the reallocation of tasks by summing up the binary variables corresponding to the execution of the task on the same machine as the previous scheduling iteration. If the task occurs on the same machine no value is assigned to the machine change slack variable ($S_i^{machine}$), else the slack takes a value of one. Constraints (6) and (7) together are then used to address the issues of task timing and sequencing. Each of these constraints penalizes changes in the timing of a task relative to the execution of either the tasks predecessor (Eq. (6)) or successor (Eq. (7)) in the previous iteration of the schedule. If a task should change places, large values of the slack variable will be needed to accommodate this. This also implicitly penalizes the deviations in the individual task timings within a certain range. This is because, if a task is planned to occur between two neighbouring tasks it can occur anytime in this range with the same total slack variable value. If a task is moved outside this range, a larger sum of slack variables will be incurred. It is worth mentioning at this point that these constraints will be penalized in the objective function according to the preferences of the scheduler. For example, if it is not a problem to move tasks forward from their planned time slot it may only be desirable to penalize backwards changes in the task timings. Some of these penalty function combinations may involve some additional constraints (for example, a penalty on the absolute value of a slack variable), however a detailed description of all these combinations is outside the scope of this paper. A general method to determine these penalties based on the timings of the tasks relative to the rescheduling point will be outlined below.

The objective function can be seen in in Eq. (8), where OF represents the original scheduling objective function, C_i^s represents the coefficient for the corresponding slack variable, and λ is a weight parameter to balance the two objectives. The set SI refers to the set of the slack variables.

$$\min \quad \lambda OF + (1 - \lambda) \sum_{s \in SI} C_i^s \cdot S_i^s \quad (8)$$

2.2. Overall Framework to Address Scheduling Nervousness

The goal of rescheduling is to restore feasibility to the schedule and to reduce the effect that a disturbance has on the quality of the scheduling solution. In the near future of a rescheduling point it is undesirable to have large changes. Due to interactions with the longer-term planning systems it is also desirable to minimize the propagation of a disturbance to the long-term result. A three time region approach is therefore proposed; in the short-term after a reschedule ($t^{reschedule} < t^{ShT}$) any changes to the schedule are very undesirable due to operational concerns. Changes in the medium-term ($t^{ShT} < t^{MedT}$) have the most freedom and should be utilized to restore optimality to the schedule and to ensure that disturbances do not propagate to the long-term. In order to prevent tasks switching from the medium-term into the short-term Eq. (9) will be used with the slack variable ($S^{regionChange}$) as an additional penalty being appropriately added to the objective function. Note that pushing tasks backwards from the medium-term to the long-term is sometimes necessary if a large scheduling disturbance occurs and therefore is not penalized. In the long-term, changes to the schedule are undesirable due to the need to meet planning targets. If a scheduling disturbance occurs it should ideally be dealt with before it propagates enough to impact long-term planning targets.

$$\sum_{u \in U_k} ST_i^\sigma + S^{regionChange} \geq t^{ShT} \quad (9)$$

Tasks in the three regions will each have a set of constraints and corresponding penalties applied to them. The pseudocode for how these penalties are applied can be seen in Figure 1.

Data: Update $I^{resched}$ based on $ST_i^{\sigma-1}$ and $t^{resched}$
foreach $i \in I^{resched}$ **do**
 if $ST_i^{\sigma-1} \leq t^{ShT}$ **then**
 Apply constraints (5) to (7)
 Set C_i^s to a high value
 else if $t^{ShT} < ST_i^{\sigma-1} \leq t^{MedT}$ **then**
 Apply constraints (5) to (7), and (9)
 Set C_i^s to a low value
 else
 Apply constraints (6) and (7)
 Set C_i^s to a medium value
 end
end

Figure 1: Pseudocode outlining the definition of the different regions.

Based on the soft nature of all the constraints, there still is the potential to switch sequence and machines, however, due to the nature of the penalty terms, tasks in the near term are less likely to switch than tasks in the medium-term. Comparing this algorithm and constraint setup to earlier work (Novas and Henning, 2010) this roughly corresponds to tasks in the near-term being only allowed to shift timing on the same machine (*Shift-JumpAT*), while tasks in the medium- and long-term can be more easily reordered and shifted to other machines (*ReassignAT*). The added benefit of this algorithm is that it is possible for any task to be moved, both in respect to time or to the resources used if this a large enough change in the original scheduling objective function, and

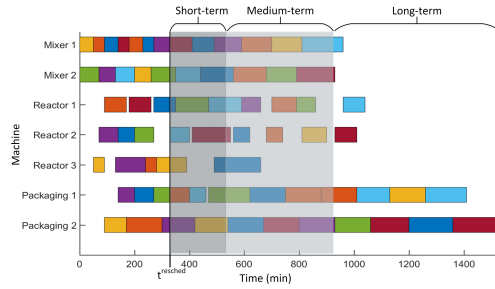


Figure 2: Initial schedule for the problem (objective = 39030 min).

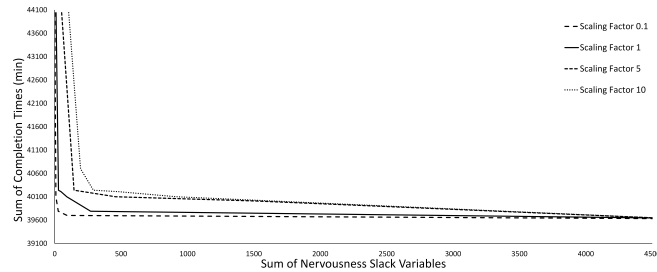


Figure 3: Pareto front illustrating the trade-off between scheduling stability and the original problem objective (sum of completion times).

that less expert knowledge is required as these regions need to be defined only on a time-basis, instead of a task-by-task basis.

3. Results

The aforementioned methodology is applied to the plant layout described in Harjunoski and Bauer (2017). The first iteration of the schedule based on the minimization of the sum of completion times objective can be seen in Figure 2.

In this scenario, Reactor 2 needs to be maintained for two hours and rescheduling is performed at that point in time ($t^{resched} = 320min$). The length of the short- and medium-term regions are two and four hours respectively. The penalties (C_i^S) are 100 for the short-term region, 1 for the medium-term region, and 10 for the long-term region. There is a trade-off between the emphasis placed on scheduling stability versus the emphasis placed on the original scheduling objective. In order to analyze the effect of these parameters on the schedule a Pareto front is generated for a few scaling factors of these penalties. This can be viewed in Figure 3. Logically, the Pareto front shows that the more emphasis that is placed on scheduling stability, the larger the loss of optimality from the original scheduling objective. It is interesting that the lines seem to be very region-based, with nervousness dominating in one area and the original objective dominating in the other with little room in between. This indicates that several tasks need to be rearranged before a sufficiently large improvement in the original objective function is obtained.

Lastly a qualitative analysis of the results is performed. The Gantt charts for a complete reschedule ($\lambda = 1$) are compared with the values for a reschedule with large emphasis placed on nervousness ($\lambda = 0.1$), which can be seen in Figure 4. From the left Gantt chart it can be seen that the complete reschedule produces a vastly different result from the first iteration, with many changes being made in all three regions of the schedule. On the other hand, the reschedule with emphasis on stability produces a schedule with very similar sequence to the first iteration, but with a few modification

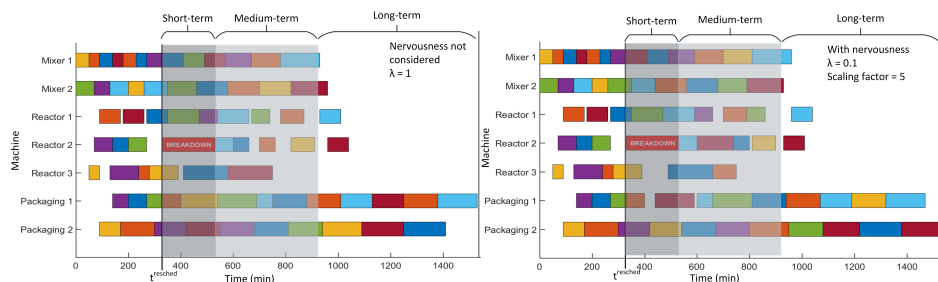


Figure 4: Gantt charts for the complete reschedule (left) compared to a reschedule with a large emphasis placed on nervousness (right).

being made in the medium-term region of the schedule. The more emphasis that is placed on the original scheduling objective, the more the resulting optimal solution reflects the solution obtained from the complete reschedule.

4. Conclusions and Future Work

In this work, a novel set of constraints and a corresponding region-based penalty method was proposed in order to combat scheduling nervousness. Results showed that the proposed method is able to produce the desired stability between scheduling iterations while still providing for sufficient flexibility to restore the quality of the resulting schedule. Additionally the trade-off between the original scheduling objective and the stability of the solution was explored. Results show that the stability of the solution is maintained for many different penalty values until the inertia to overcome these changes is surpassed by a sufficient improvement in the objective function. Future work will investigate the affect of the sizes of the regions on the optimal solution and stability as well as test the overall closed-loop performance of such an approach. Additionally, the constraints proposed focus on the stability between two subsequent iterations. It would be interesting to also investigate the effect of a bigger look-back period.

Acknowledgments: Financial support is gratefully acknowledged from the Marie Skłodowska Curie Horizon 2020 EID-ITN project “PRONTO” (Grant agreement No 675215).

References

- P. M. Castro, L. Sun, I. Harjunkoski, 2013. Resourcetask network formulations for industrial demand side management of a steel plant. *Industrial and Engineering Chemistry Research* 52 (36), 13046–13058.
- D. Gupta, C. T. Maravelias, J. M. Wassick, 2016. From rescheduling to online scheduling. *Chemical Engineering Research and Design* 116, 83 – 97.
- I. Harjunkoski, R. Bauer, 2017. Industrial scheduling solution based on flexible heuristics. *Computers and Chemical Engineering* 106, 883 – 891.
- I. Harjunkoski, C. T. Maravelias, P. Bongers, P. M. Castro, S. Engell, I. E. Grossmann, J. Hooker, C. Méndez, G. Sand, J. Wassick, 2014. Scope for industrial applications of production scheduling models and solution methods. *Computers and Chemical Engineering* 62, 161 – 193.
- G. P. Henning, 2016. Realistic rescheduling: is it achievable? FOCAP0 2016.
- C. A. Méndez, J. Cerdá, 2004. An milp framework for batch reactive scheduling with limited discrete resources. *Computers and Chemical Engineering* 28 (6), 1059 – 1068.
- J. M. Novas, G. P. Henning, 2010. Reactive scheduling framework based on domain knowledge and constraint programming. *Computers and Chemical Engineering* 34 (12), 2129 – 2148.
- D. Ouelhadj, S. Petrovic, Oct 2008. A survey of dynamic scheduling in manufacturing systems. *Journal of Scheduling* 12 (4), 417.
- C. Pantelides, 1994. Unified frameworks for the optimal process planning and scheduling. In: *Proceedings of the Second Conference on Foundations of Computer Aided Operations*.
- J. M. Wassick, J. Ferrio, 2011. Extending the resource task network for industrial applications. *Computers and Chemical Engineering* 35 (10), 2124 – 2140.

A systemic approach for agile biorefineries

Michelle Hougbe^a, Anne-Marie Barthe-Delanoë^a, Stéphane Négny^a

^aLaboratoire de Génie Chimique, Université de Toulouse, CNRS, INPT, UPS, Toulouse, France

annemarie.barthe@ensiacet.fr

Abstract

Biorefineries is one of the main pathways towards energy transition. However, they are challenged by demand and supply variability. Moreover, the standalone and highly specialized biomass processing system has to face several internal and external constraints. To tackle this unstable ecosystem, it is necessary to provide agility in terms of both physical structure and organization. In this context, the ARBRE project proposes to redesign the biorefinery, at local scale, by introducing a collaborative network of stakeholders and the servitization of the biomass processing steps, and by integrating digital concepts from Industry 4.0. This paper proposes a framework to design agile biorefinery with a systemic approach by modelling the knowledge about the system and its environmental characteristics through a metamodel.

Keywords: Agility, Biorefinery, Collaboration, Industry 4.0, Virtual Organization, Meta-modelling

1. Introduction and motivations

Despite an increase of biomass processing projects these last years, the development of biorefineries is significantly slowed down because of several constraints.

First, the biorefinery concept is similar to the oil refinery principles [1]. Thus, the four major steps of the whole biomass processing are performed into a unique plant. Each step of the process requires specific devices, and specific operating conditions, according to the chosen biomass and the targeted bioproduct. In case of any changes regarding the biomass (type, quantity, quality, etc.) or the bioproduct, this physical, centralized, standalone and highly specialized plant cannot function at all. Adaptation to changes would require building a new plant, which is unrealistic considering investment and operational costs. Then biorefineries face high variability due to several constraints as: the external parameters influencing the availability of the biomass (seasonality, crop rotation), the natural biomass degradation or else the impurities inside the biomass feedstock (e.g. weeds, silica, minerals or soil). Therefore, this huge variability challenges the biomass supply leading to production irregularities. Additional challenging factors are the supply spreading and the geographic dispersion of both biomass feedstocks and biorefineries, increasing the nervousness of this supply chain.

All the aforementioned hurdles underline the need to design the biorefinery with its entire ecosystem to take into account uncertainties. This disruptive way to design biorefineries should be done on both the physical structure (equipment and apparatus) and the organisation (supply chain) to provide the required agility to face uncertainties.

Thus, our goal is to answer to the following research question: “How can biorefineries development be fostered with required agility to cope this unstable environment?” In the literature, biorefineries are analysed at different scales: molecular, equipment, process and supply chain scale [2]. Nevertheless, designing the biorefinery with a systemic approach, from the harvest to the final customer, as an agile collaborative network, is a new approach. This is the goal of our proposal.

2. State of art of agility in chemical process industry

Agility is used as well as a concept, a paradigm, a tool or else a method to qualify a professional sector or a means of production, in a context of changing, volatile and uncertain environment, characterized by the globalization and a production customization for customers. This concept was defined by several authors in the last years and leans on major development axis: responsiveness, flexibility, information and communications technology, and adaptability [3]. A relevant definition of agility that could be applied to the biorefinery system has been proposed by [4] as the ability of a system to “lead as quickly as possible, on the one hand, to the detection of its mismatch to a given context, on the other hand, to the set up of the required adaptation”.

In the manufacturing industry literature, the expression “agile manufacturing” has been the subject of extensive researches for the last two decades. Whereas, in the process and the chemical industry areas, a few articles address about the agility issue. They often deal with subjects partially related to agility (as defined above) as flexible process, reconfigurable manufacturing, responsiveness system, modular production, with a technological or a chemical approach, at microscopic or mesoscopic scales. Considering the whole biomass processing system, at the macroscopic scale, including both the chemical process and the environment, the entire biomass supply chain is then taken into account for the biorefinery design. Existing researches on this topic consider agility as the optimization criteria to design a standalone plant. but this standalone centralized plant cannot cope with the adaptation requirements to be considered as agile.

To switch from this centralized biomass processing paradigm, a few research works focus on decentralization by creating a collaborative network. [2] restrains its network to two stakeholders and assesses the decentralization based only on the cost of the transportation. Regarding [5], the concept of virtual biorefinery deals with a “loose coupling of decentralized stakeholders” where the biomass processing is dispatched according to the optimal biomass supply chain. In this work, the pre-treatment step is separated from the chemical process treatment. Within a service economy approach, the servitization aims to make the transition from material products (tangible) to global services (intangible). It enables to develop full services leaning on existing resources (equipment, devices, workforce...) and a know-how. A type of servitization, Product-Service System, has been studied by [6] in a manufacturing company in an organizational and a collaborative way. This type of work does not yet address the biomass processing. However, because of the high number of farmers involved in cooperatives, it could be economically attractive to enhance this collaborative behaviour with the share of the investment into apparatus and skilled workforce.

Plus, Information and Communication Technologies have a predominant position into agricultural and industrial sectors. They can provide a huge amount of data about weather forecast, crop state, device monitoring (e-farming) or market (economics) that are

relevant to support decision making about biomass processing. Among new technologies, Complex Event Processing could support data collection and analysis by detecting patterns over a stream of data [7]. It could be used to study the variability of the entire ecosystem: territory, weather, stakeholders and complex biomass chemical treatment.

3. ARBRE: A collaborative software platform to design and monitor agile biorefineries

The part aims to present the methodological framework enabling to design and monitor agile biorefineries as a collaborative network, using stakeholders' services and reusing existing apparatus. Moreover, it can enhance the territorial anchorage of the biomass processing by choosing a local scale (biomass supply radius of fifty kilometres). This framework will be implemented as a decision support system (software platform) available for the biomass processing stakeholders, from farmers to customer.

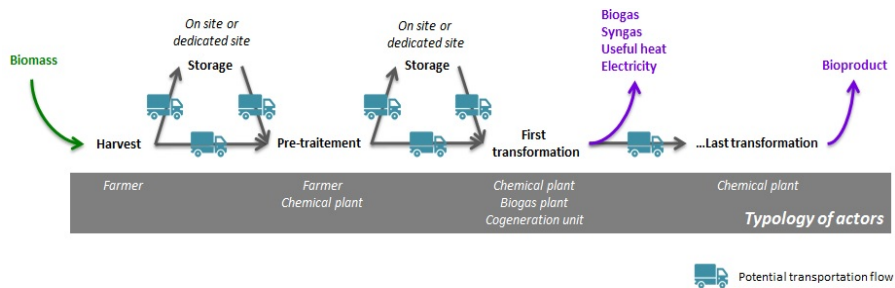


Figure 1: Agile biorefinery concept

The agile biorefinery concept leans on two main axes. Within a systemic approach, the first axis considers that the chemical process could be performed not into a unique standalone plant but among a network of several existing plants and locations. Thus, the chemical process is decentralized. Each processing step is servitized. When a change occurs into the system (context, stakeholder, etc.), each actor of the biomass supply chain could propose a service matching the consequent need for adaptation. This service could address one or several steps of the biomass processing. The process is then easily reconfigured. Then, the collaboration between the stakeholders creates the biorefinery as a virtual enterprise, relevant to the biomass to process, the targeted bioproduct and the context. The role of each stakeholder and/or the choice of the process (steps, apparatus) can evolve according to the occurring changes: biomass, bioproducts (type, purity, quantity), context (weather, market, etc.). This agile biorefinery will use existing equipment, devices and workforce, which is highlighting the concept of “virtual biorefinery” as an agile collaborative process. The second axis focuses on the biomass processing itself. To design this process according to the available input, the targeted output and the system constraints, it is possible to combine knowledge management with a technological approach. The objective is to match a typology of services proposed by the stakeholders (farmers, chemical industry, cogeneration unit, local authority) with a typology of biomass processing steps, while taking into account constraints such as the location, the price, etc.

4. The agile biorefinery metamodel

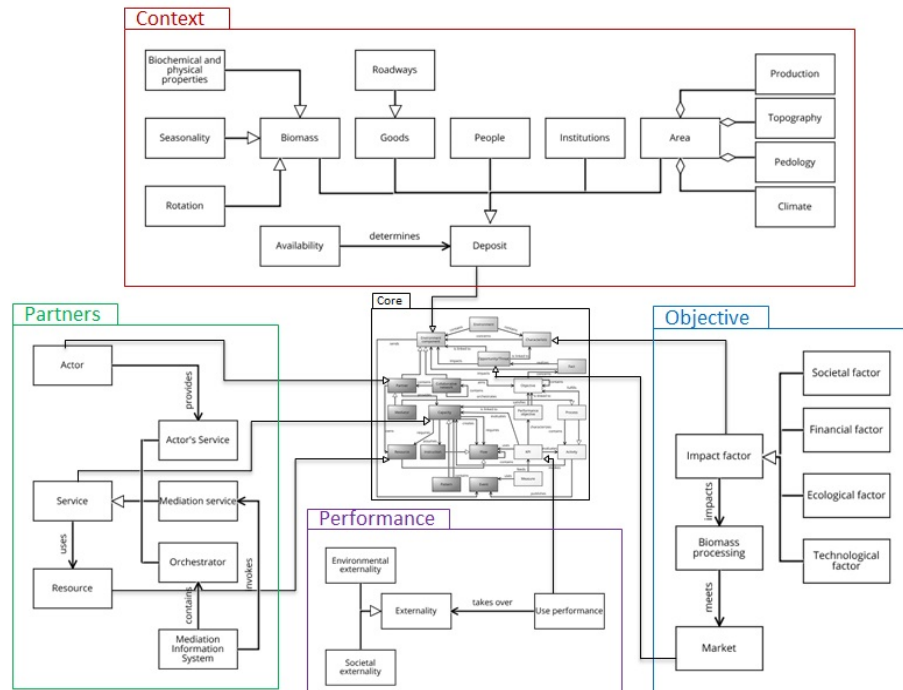


Figure 2: Agile biorefinery metamodel

4.1. The CORE metamodel as support

The Model Driven Engineering (MDE) approach provides a better understanding of complex systems, as biorefineries, thanks to a high level of abstraction. This engineering practice is focused on the model, which is at the heart of the process. It defines the modelling language. In this way, it is adapted to define the required and relevant data about the agile biorefinery system. To this end, we used the CORE metamodel as defined into [8]. Organized in layers, the core of this metamodel represents any collaborative situations, by including general concepts categorized into four main packages: the context (what is the environment?), the partners (who are the actors and their services?), the collaboration objectives and the performance. Then, each successive layer defines a business domain, which inherits concepts from the core. Besides, in this way, it has been successfully used in various application domains as crisis or business organization. So, based on this CORE metamodel, a specific layer has been extended to model the agile biorefinery. Each concept and link have been defined in this application area. They are generic enough to be adapted to any type of agile biorefinery and specialized enough to be relevant to the biomass processing domain. This agile biorefinery metamodel has to be instantiated with real data, in order to ensure the validity of the obtained model and so the relevancy of the concepts.

4.2. The “Context” package

The context enables to determine the characteristics of the collaborative environment. The deposit concept is the entry point. It inherits from the environment component concept from the CORE package. Its availability (related to the quantity) is crucial to start a collaboration. Therefore, the deposit is about the organic deposit usable which does not include: the organic matter needing to return to the ground, the unusable organic matter and the organic matter already involved into a chemical transformation process. It contains biomass, which is specified by biochemical and physical properties (chemical composition, humidity, shape, size), a seasonality (biomass capacity to be productive and harvested over one or several seasons) and the crop rotation (crop diversification including intermediate crops). The deposit is set on an area owing topographic, soil and climate features, with a given kind of production (intensive, organic, reasoned). The good concept is related to the required equipment ensuring the proper management of the deposit. This one is specified with the roadways concept, enabling to determine the accessibility to the deposit (fields path, paved road). The deposit concept embodied the people concept, essential for the public acceptability issues. Institutions concept, as political and decision-making bodies, are key players to provide public aids and subsidies. The context is crucial to characterize the environment where the collaboration takes place.

4.3. The “Actor” package

Partners constitute the collaborative network. They participate actively in the biomass processing. In the servitization context, actors from the collaborative network bring information about their ability to provide a service, according to their existing resources (material, human, special skills) and their constraints. They inherit from the CORE partner package. The proposed services ensure one or several biomass processing and transformation steps. Moreover, Mediation Information System (MIS) coordinates the collaborative process, from the data collection until the conversion to information, as an orchestra conductor. It makes connections and shares information among all the actor services. The whole collaboration partners aim to reach a common goal.

4.4. The “Objective” package

The objective package defines a target for the agile biorefinery. This concept inherits from the objective concept from the CORE package. The main purpose is to process the biomass, by meeting the market. The market determines the supply, the demand and the competitive requirements between stakeholders. However, impact factor concept can foster or disadvantage the biomass processing. This concept highlights issues about the agile biorefinery operation. It encompasses criteria about sustainability (social, economic and environmental) and the system’s evolution capabilities. It is specified into four types of impact factors: the societal factor concept relates to the impacts on the extended community organization (annoyances); the financial factor concept relates to process, equipment and maintenance work cost evolution (trend in price for biomass); the ecologic factor concept concerns changes about living beings and their environment which can affect the biomass processing (biodiversity trend); the technological factor concept gathers innovations and evolutions about devices, processes and methods that could affect also the biomass processing. Achievements enable to assess the performance.

4.5. The “Performance” package

Agile biorefinery performances are measured thanks to Key Performance Indicators (KPI) about the overall result of the collaboration and also each service used. To this end, the use performance concept inherits from KPI concept, in the CORE metamodel. KPIs ensure positive or negative impact of the agile biorefinery on a societal level as economic drive or job development (measurable with meetings and surveys) and on an environmental level as pollution (measurable with sampling program and measurement campaign in the environment).

5. Conclusion and future work

To increase the development of biorefineries, it is crucial to take into account its whole ecosystem, which is marked by a high variability. Agility represents an innovative way in the chemical and process engineering to reconfigure easily the biomass transformation process, according to the constraints and the stakeholders. Being aware of environmental, economic and human factors enables to keep the system functional (operational) and relevant. Thus, the ARBRE project proposes to transform and decentralize the biomass transformation process, leading to a collaboration-based biorefinery. In this paper, the metamodel supporting the characterization of the agile biorefinery has been presented. It defines the concepts and the links between them, enabling to model the environment of the collaboration according to: the context, the actors, the objectives and the performances. The next step of the ARBRE project will focus on the instantiation of the proposed biorefinery metamodel into a model, prior to its use for collaborative process deduction. This will be achieved with real data provided by local authorities from Southern France (interviews, feasibility study, etc.).

Acknowledgements

This research work is funded by the French Research Agency regarding the research project ARBRE (Agility for BioRefinerieEs)[Grant ANR-17-CE10-0006], 2017-2021. The authors would like to thank the project partners for their advice and comments regarding this work.

References

- [1] B. Kamm, P. R. Gruber, et M. Kamm, « Biorefineries—Industrial Processes and Products », in *Ullmann's Encyclopedia of Industrial Chemistry*, American Cancer Society, 2016, p. 1-38.
- [2] D. Yue, F. You, et S. W. Snyder, « Biomass-to-bioenergy and biofuel supply chain optimization: Overview, key issues and challenges », *Computers & Chemical Engineering*, vol. 66, p. 36-56, juill. 2014.
- [3] A. Soepardi, P. Pratikto, P. B. Santoso, et I. P. Tama, « An updated literature review of agile manufacturing: classification and trends », *International Journal of Industrial and Systems Engineering*, vol. 29, n° 1, p. 95-126, janv. 2018.
- [4] A.-M. Barthe, « Prise en charge de l'agilité de workflows collaboratifs par une approche dirigée par les événements », Université de Toulouse, École Nationale Supérieure des Mines d'Albi-Carmaux conjointement avec l'INSA de Toulouse, 2014.
- [5] B. Rapp et J. Bremer, « Paving the Way towards Virtual Biorefineries », *Green Technologies: Concepts, Methodologies, Tools and Applications*, p. 1901-1921, 2011.
- [6] S. Dahmani, X. Boucher, et S. Peillon, « Industrial Transition through Product-Service Systems: Proposal of a Decision-Process Modeling Framework », in *Collaborative Systems for Reindustrialization*, 2013, p. 31-39.
- [7] O. Etzion et P. Niblett, *Event Processing in Action*, 1st éd. Greenwich, CT, USA: Manning Publications Co., 2010.
- [8] F. Bénaben, M. Luras, S. Truptil, et N. Salatgé, « A Metamodel for Knowledge Management in Crisis Management », in *2016 49th Hawaii International Conference on System Sciences (HICSS)*, 2016, p. 126-135.

Closed-loop dynamic real-time optimization of a batch graft polymerization reactor

Ryad Bousbia-Salah^a, François Lesage^a, Miroslav Fikar^b, Abderrazak Latifi^{a,*}

^aLaboratoire Réactions et Génie des Procédés, CNRS – ENSIC, Université de Lorraine, 1 rue Grandville, 54001, Nancy Cedex, France

^bFaculty of Chemical and Food Technology, Slovak University of Technology in Bratislava, Radlinskeho 9, 81237 Bratislava, Slovakia

**Abderrazak.Latifi@univ-lorraine.fr*

Abstract

In a recent work (Bousbia-Salah et al, 2018), dynamic real-time optimization (D-RTO) of a batch reactor where polymer grafting reactions take place is experimentally implemented within open-loop control. This paper constitutes the continuation of the work and presents the experimental implementation of closed-loop D-RTO in the same reactor. The objective is to determine and to apply the online reactor temperature profile that minimizes the batch period while meeting terminal constraints on the overall conversion rate and grafting efficiency. The computed and measured optimal profiles of temperature, overall conversion rate and grafting efficiency exhibit a good agreement and show also that the terminal constraints are satisfied.

Keywords: Dynamic real-time optimization, Closed-loop control, Polymer grafting batch reactor, Experimental implementation

1. Introduction

Dynamic real-time optimization (D-RTO) is the most suitable technology to successfully handle uncertainty and changing conditions in the operation of plants particularly those that are never in steady-state (Rawlings et al, 2011; Ellis et al, 2013 and 2014). It makes use of the online available measurements to maximize a process performance index while meeting environmental and operating constraints (e.g. terminal specifications, temperature limits...). The results from the optimization problem can be directly applied to the process or sent to a lower level where a (e.g. MPC) control law is designed to apply to the process the optimal profiles of decision variables.

In a recent study (Bousbia-Salah et al, 2018), we considered a batch reactor where polymer grafting reactions take place. The objective was to determine the reactor temperature profile that minimizes the batch period while meeting terminal constraints on the overall conversion rate and grafting efficiency. The resulting optimal temperature profile was then experimentally implemented within the reactor in open-loop control. Although the results showed a good agreement between the computed and the measured profiles, the implementation was not able to handle the possibly disturbances or model mismatch. Closed-loop control is therefore needed in order to overcome this problem.

In the present paper, the D-RTO approach developed in (Bousbia-Salah et al, 2018) is experimentally implemented within the same batch polymerization reactor, but in closed-loop control with the help of an efficient moving horizon observer designed to estimate unmeasured states of the system.

2. Grafting polymerization

When styrene is added to ground tire rubber (GTR) particles, it can be located inside and/or outside them, depending on the styrene/GTR ratio. The latter is kept below 2 so that styrene is completely located inside GTR particles where it polymerizes in two types of polymerization. The first type is the polymerization of styrene itself leading to polystyrene (PS) chains which are not linked to GTR particles. These PS chains are called free PS. The second type is the polymerization of styrene from the rubber chains and the resulting PS chains are attached (grafted) to the rubber ones. These PS chains are designated as GTR-g-PS. The resulting material is GTR particles inside which there are free PS and GTR-g-PS. The main objective is to minimize the amount of free PS in the PS/GTR-g-PS while maximizing the amount of GTR-g-PS in order to allow recycling a maximum of GTR with the best properties, especially the impact strength (Yu, 2015).

This objective is taken into account here through constraints on the grafting efficiency (GE) and the styrene conversion rate (X). GE is defined as the ratio between the amount of grafted PS and that of the total PS (grafted PS + free PS).

3. Formulation of the D-RTO problem

The dynamic optimization problem that is solved within the D-RTO approach may be formulated as

$$\min_{T(t), t_f} J = t_f \quad (1)$$

$$\text{Subject to } \dot{x} = f(x, T) \text{ with } x(t_k) = \hat{x}_k \text{ and } t \in [t_k, t_f] \quad (2)$$

$$GE(t_f) \geq GE_f \quad (3)$$

$$X(t_f) \geq X_f \quad (4)$$

$$T \leq T_{max} \quad (5)$$

where the reactor temperature $T(t)$ and the batch period t_f are the decision variables and x is the vector of state variables. GE and X are the measured process outputs and GE_f and X_f are their desired final values. T_{max} is the reactor temperature upper bound.

The model equations are derived after obtaining the moment rates of the polymer chains. Moreover, the model consists of a system of 20 non-linear ODEs involving 24 unknown kinetic parameters.

The process model equations (2) are derived after obtaining the moment rates of the polymer chains. Moreover, the model consists of a system of 20 non-linear ODEs involving 24 unknown kinetic parameters. (Yu, 2015).

The optimization problem is solved over a shrinking horizon using the control vector parametrization (CVP) method (Goh and Teo, 1988). The latter is based on the approximation of decision variables by means of piece-wise constant functions over the optimization horizon taken equal to 3. The vector of time-independent parameters is then given by $p^T = (T_1, T_2, T_3, t_f)$.

The resulting non-linear programming problem is solved by means of a gradient-based method where the gradients are computed through the integration of sensitivities at each iteration of the optimizer. The equations of sensitivities are defined as

$$\dot{s} = \frac{\partial f}{\partial x} s + \frac{\partial f}{\partial p} \text{ with } s(t_k) = 0 \quad (6)$$

where $s(t) = \frac{\partial x(t)}{\partial p}$ are the sensitivities of the vector of state variables with respect to the vector of parameters p . Note that Eqs.(6) are integrated from t_k to t_f at each iteration of the optimization solver.

The D-RTO approach proceeds then as follows. Starting from the real process to which the optimal decision variables are applied at a sampling time t_k , the outputs as well as inputs are used to estimate the state vector \hat{x}_k that will be used as the initial condition for the next optimization at the sampling time t_{k+1} . The corresponding initial condition for the sensitivities is always taken equal to zero. The estimation \hat{x} of x is carried out by means of a moving horizon estimator (MHE) in a closed-loop control (Michalska and Mayne, 1995; Robertson and Lee, 1995) using input and output variables.

4. Experimental rig and measurements

4.1. Experimental rig

The polymerization reactions take place in a stirred batch reactor equipped with a condenser, a temperature control device and a sample collection system. The substances involved in the reactions are GTR particles of 800 μm in diameter, styrene (monomer) and two initiators, i.e. benzoyl peroxide (BPO) and dicumyl peroxide (DCP). Hydroquinone (HQ) and chloroform are used for the measurements of the conversion rate and the grafting efficiency.

2.2. Conversion measurement

The conversion of monomer is measured by a gravimetric method. Samples are taken from the reactor and weighed. A known amount of hydroquinone is added in to stop the polymerization. Then they are put into a Halogen Moisture Analyzer and the temperature is raised to 170°C and kept at this temperature for 10 min. The residual monomer could completely evaporate and the remaining material is composed of free PS, GTR-g-PS and HQ.

4.2. Grafting efficiency measurement

Samples taken from the reactor are put in chloroform to measure the grafting efficiency of the polymerization of styrene inside GTR particles. The free PS and HQ are soluble in chloroform, while GTR and/or GTR-g-PS are not. After at least 6 hours during which the samples are shaken many times, the solvent is removed using filter paper. The free PS and HQ are in the solvent, and the non-soluble portion in the filter paper is GTR or GTR-g-PS.

5. D-RTO implementation

The algorithm used to implement the closed-loop D-RTO is detailed below (Bousbia-Salah, 2018).

1. Initialize the iteration number and time: $k = 0$ and $t_k = 0$.
2. Solve the optimization problem (1-5) for T_1, T_2, T_3 and t_f .
3. Apply the first temperature T_1 during 60 minutes and set $t_k := t_k + 60\text{min}$ and $k := k + 1$.
4. Take a reaction mixture sample from the reactor for conversion rate measurement.
5. Apply the second temperature T_2 while the measurement is being performed, i.e. 30 minutes (time required for measurement). Set $t_k := t_k + 30\text{min}$ and $k := k + 1$.

6. Use the measured conversion rate to estimate the state \hat{x}_k .
7. Repeat the steps (2) to (6) until t_f is reached and stop the reaction.

It is noteworthy that since the dynamics of the polymerization reaction is relatively slow, manual temperature control is found to be sufficient to achieve reasonable accuracy. On the other hand, as mentioned above, the conversion rate is measured in 30 minutes, whereas the measurement of GE needs much more time and takes about 6 hours. The implementation is carried out for $GE_f = 60\%$ and $X_f = 85\%$.

Figures 1, 2 and 3 show the temperature, monomer conversion and grafting efficiency profiles, respectively. They compare the computed optimal profiles and the measured ones in the reactor. The temperature profile exhibits a regular increase in order to fulfill the required monomer conversion rate and grafting efficiency. This regular increase is meaningful since at constant temperature, the conversion rate increases with time whereas the grafting efficiency decreases. Therefore the temperature should increase with time in order to achieve the desired conversion rate but not too much in order to guarantee the specified terminal value of grafting efficiency.

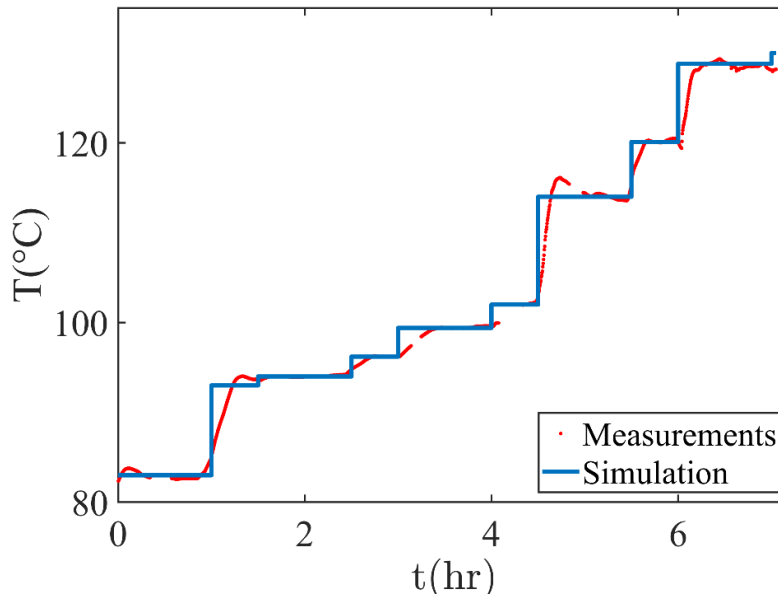


Figure 1: Optimal profiles of reactor temperature for $GE_f = 60\%$ and $X_f = 85\%$.

Figures 2 and 3 show the time-varying process outputs, i.e. conversion rate and grafting efficiency, respectively, with two different profiles. The estimated profile using the moving horizon state observer, and the measured one. It can be seen that the computed terminal inequality constraints on both process outputs are satisfied and are almost the same as the measured ones. This very good agreement between the computed and measured profiles can be explained by the absence of disturbances and a very good quality of the process model.

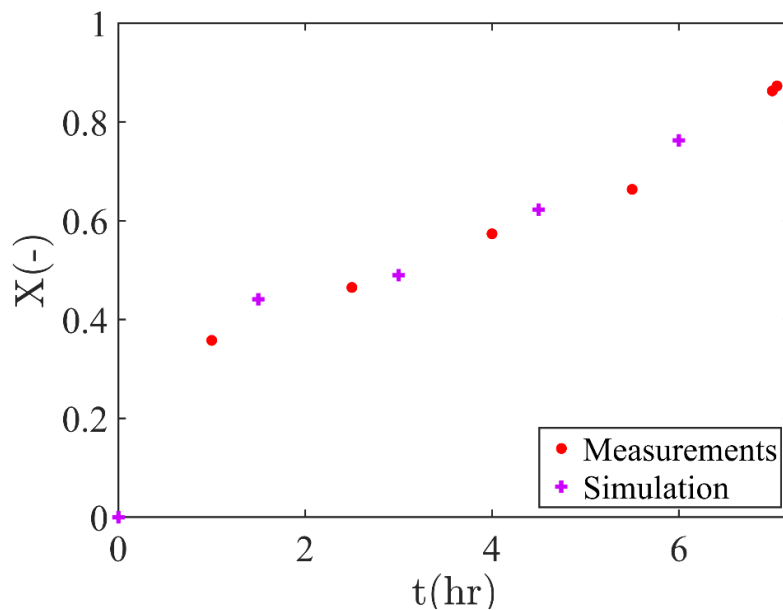


Figure 2: Time-varying profiles of the conversion rate for $GE_f = 60\%$ and $X_f = 85\%$.

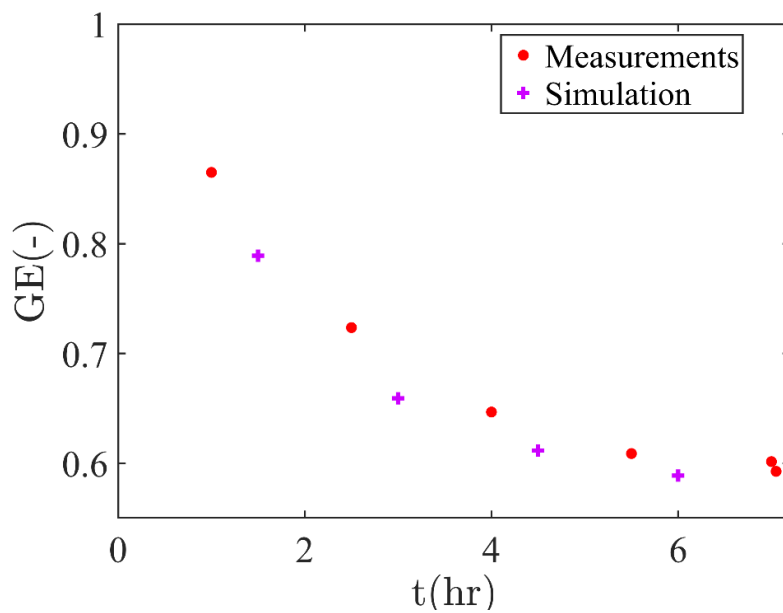


Figure 3: Time-varying profile of the grafting efficiency for $GE_f = 60\%$ and $X_f = 85\%$.

6. Conclusions

The closed-loop control results presented in this paper showed that dynamic real-time optimization is a suitable technology for online dynamic optimization of the grafting polymerization reactor considered here. It allowed to determine and implement online the temperature profile that minimizes the batch period under terminal constraints on monomer conversion and grafting efficiency using an optimization horizon of 3. The results show very good agreement between the computed and measured profiles of temperature, monomer conversion and grafting efficiency. Moreover, the computed and measured terminal constraints are fully satisfied. On the other hand, the stability of the computed optimal temperature is guaranteed since the process considered is of the batch type and the shrinking optimization horizon covers the whole operational time. The current works deal with the development of Raman spectroscopy to measure online the monomer conversion rate in order to improve the experimental implementation of the closed-loop control at the laboratory scale prior to its implementation within a reactor at industrial scale.

References

- R. Bousbia-Salah, F.Lesage, G.H. Hu, M.A.Latifi, 2018, Experimental implementation of dynamic real-time optimization in a graft polymerization reactor, *Computer - Aided Chemical Engineering*, 43, 829 – 834, 2018.
- R. Bousbia-Salah, 2018, Optimisation dynamique en temps-réel d'un réacteur de polymérisation par greffage, PhD Thesis, Université de Lorraine, Nancy, France.
- M.Ellis, H.Durand, P.D. Christofides, 2014, A tutorial review of economic model predictive control methods, *Journal of Process Control*, 24, 1156 – 1178.
- M.Ellis, M.Heidarinejad, P.D.Christofides, 2013, Economic model predictive of nonlinear singularly perturbed systems, *Journal of Process Control*, 23, 743 – 754.
- C.J. Goh, K.L. Teo, 1988, Control parametrization: A unified approach to optimal control problems with general constraints, *Automatica*, 24, 3-18.
- H. Michalska, D. Q. Mayne, 1995, Moving horizon observers and observer-based control, *IEEE Transactions on Automatic Control*, 40, 995-1006.
- J.B.Rawlings, D.Angeli, C.N. Bates, 2012, Fundamentals of economic model predictive control, In *Proceedings of the 51st IEEE Conference on Decision and Control*, 3851 – 3861, Manui, Hawaii, USA.
- D.G. Robertson, J.H. Lee, 1995, A least squares formulation for state estimation, *Journal of Process Control*, 5, 291-299.
- N.Yu, 2015, Etude de la cinétique de polymérisation radicalaire du styrène dans un réseau tridimensionnel et application à la valorisation de pneus usagés, PhD Thesis, Université de Lorraine, Nancy, France.

Optimizing Return on Investment in Biomass Conversion Networks under Uncertainty Using Data-Driven Adaptive Robust Optimization

Jack Nicoletti, Chao Ning, Fengqi You

Cornell University, Ithaca, New York 14853, USA

Abstract

Bioconversion networks provide a means of turning raw biomass feedstock into useful biochemicals and fuels. These networks can display not only how crops and plants can be converted into bioproducts, but also how organic waste and other unconventional feedstocks can be used to create useful products as well. In order to determine the economic feasibility of the conversion pathways in these networks, an economic measure of design profitability such as return on investment must be used. Given a bioconversion network containing 216 technologies and 172 materials/compounds, we propose a two-stage adaptive robust mixed integer fractional programming model capable of measuring the economic success of bioconversion technology pathways. The proposed approach yields the processing pathways with optimal return on investment subject to minimum demand and maximum capacity constraints.

Keywords: adaptive robust optimization, return on investment, biomass conversion

1. Introduction

One of the primary goals of any business is to maximize the profit of their operations. In the context of bioconversion, if a plant cannot produce biofuels or industrial chemicals at a price even to or lower than the market price for that product, then the plant will not operate at a profit (Dodds et al., 20017; Yue et al. 2014; Gallezot, 2012). One way to measure the profitability and economic sustainability of any process is to calculate its return on investment (ROI), which is calculated in this work as the net yearly earnings of the process over the total capital investment. While work has been done to consider the cost of a bioconversion network under budgeted demand and price uncertainty (Garcia et al., 2015), in practice these facilities will only be built if they are proven to be profitable. A network that ignores the selling prices of the products that it creates could risk being economically infeasible (Sahinidis, 2004). It is necessary to ensure that a model is constructed such that the selling prices of the products are taken into consideration when deciding whether a bioconversion pathway is optimal (Lipinsky, 1981). Furthermore, with the increasing prevalence of historical data used in forecasting and planning decisions, it is quite useful to consider the uncertainty in feedstock price to be dependent on the historical price.

In this work, the biomass conversion network is optimized using a two-stage adaptive robust optimization method (Ben-Tal et al., 2009), with the first stage representing decisions made during the construction and planning phase and the second stage representing decisions made continuous during the day-to-day operation of the processing network (Ning and You, 2017). In this formulation, both the demand for products and price of biomass feedstocks are taken as uncertain parameters. Latent uncertainty realizations in collected data are identified using principal component analysis, and a

kernel density estimator is used to form probability distributions of the projected uncertainty data given by principal component analysis like previous works (Ning and You, 2018). The resulting solution provided by this two-stage problem will be robust to worst-case instances of demand and price. Finally, the return on investment objective leads to an Adaptive Robust Mixed-Integer Fractional Program (ARMIFP) that can be solved using the Parametric Algorithm. This framework is then applied to an expanded bioconversion network, with the case study included in this work focusing on the upgrading and conversion of organic waste material to useful biomaterial.

2. Model Formulation

2.1. Return on Investment as an Objective

Return on Investment (ROI) is a key economic metric for measuring the payoffs of long-term investments (Gong et al., 2017). For the bioconversion network, return on investment was calculated as a ratio of the net revenue over the total capital cost of investment in the required processing and upgrading technologies. The net profit is expressed as the total revenue generated by selling units of bioproduct S_i , minus the cost of both the feedstock purchased P_i and the cost of operating the technology at a given operating level, W_j . The denominator is the total cost of building a plant of specified capacity Q_j . Overall, the objective function to be maximized is as follows:

$$\frac{\sum_{i \in I} c_{4,i} S_i - \sum_{i \in I} c_{3,i} P_i - \sum_{j \in J} c_{2,j} W_j}{\sum_{j \in J} c_{1,j} Q_j^{sf}} \quad (1)$$

where sf represents the scaling factor for technology j , $c_{4,i}$ represents the selling price of bioproduct i , and $c_{1,j}$, $c_{2,j}$, and $c_{3,i}$ represent parameters for economic evaluation as given in previous works (Gong et al., 2016). The first term of the numerator represents the profit from selling a specific quantity of bioproduct i at the market price. The second term represents the cost associated with buying a specific quantity of feedstock i . The last term in the numerator represents the cost associated with operating technology j . Upon inspection, it becomes clear that the decision variable for operating level W_j must be in the range of zero to the total capacity of the technology, Q_j . The denominator represents the cost associated with building technology j at a specific total capacity.

2.2. Two-Stage Adaptive Robust Optimization Formulation

Traditional robust optimization problems are static, meaning that all decisions are made at the same time and are final. However, in practice it is known that decision makers will make recourse decisions based on market conditions, risk tolerance, and many other factors. To ensure that the model accurately reflects the ability of a decision maker to act in real time, the model must allow for decisions to be made in multiple time frames. The solution is a two-stage adaptive robust optimization (ARO) formulation, which provides multiple advantages over static robust optimization (Shi et al., 2016). First, ARO leads to solutions that are less conservative than static robust solutions, as the solution can “adapt” to the uncertainty realizations. Additionally, ARO allows for “here and now” decisions to be made during the planning and construction of the bioconversion network as well as “wait and see” decisions to be made during the real-time operation of the facilities. In the bioconversion network, “here and now” decisions involve binary variables Y_j representing the decision to use technology j as well as continuous variables Q_j representing the

capacity of technology j . Meanwhile, the “wait and see” variables that can be chosen in the second stage are the operating level of each technology W_j , the amount of feedstock purchased P_i , and the amount of product sold S_i .

The resulting two stage adaptive-robust optimization model considers uncertainty in both feedstock price and demand. Furthermore, the model allows for selection and capacity decisions to be made before uncertainty realization while also allowing for operational, purchasing, and sale decisions to be made after uncertainty has been realized. The model also employs nonlinear functions to evaluate the technology capital costs associated with the first-stage decisions. Furthermore, the model allows for the building of backup technologies that can sit idle and guard against uncertain demand fluctuations.

The overall bioconversion optimization model is shown as follows:

$$\max_{Y, Q} \min_{c_3 \in U_2, d \in U_1} \max_{W, P, S} \frac{\sum_{i \in I} c_{4,i} S_i - \sum_{i \in I} c_{3,i} P_i - \sum_{j \in J} c_{2,j} W_j}{\sum_{j \in J} c_{1,j} Q_j} \quad (2)$$

$$\text{s.t.} \quad a_{1,j} Y_j \leq Q_j \leq a_{2,j} Y_j, \quad \forall j \in J \quad (3)$$

$$W_j \leq Q_j, \quad \forall j \in J \quad (4)$$

$$P_i - S_i + \sum_{j \in J} a_{3,i,j} W_j = 0, \quad \forall i \in I \quad (5)$$

$$P_i \leq b_i, \quad \forall i \in I \quad (6)$$

$$S_i \geq d_i, \quad \forall i \in I \quad (7)$$

$$W_j, P_i, S_i \geq 0, \quad \forall i \in I, j \in J \quad (8)$$

$$Y_i \in \{0, 1\}, \quad \forall i \in I \quad (9)$$

$$U_1 = \left\{ d_i \left| \begin{array}{l} d_i = d_i^0 + \sum_k p_{ik} (\xi_k^L \cdot z_k^- + \xi_k^U \cdot z_k^+), \quad \forall i \\ \sum_k (z_k^- + z_k^+) \leq \Phi^{\text{dem}}, \quad z_k^- + z_k^+ \leq 1, \quad 0 \leq z_k^-, z_k^+ \leq 1 \end{array} \right. \right\} \quad (10)$$

$$U_2 = \left\{ c_{3,i} \left| \begin{array}{l} c_{3,i} = c_{3,i}^0 + \sum_l r_{il} (\beta_l^L \cdot \delta_l^- + \beta_l^U \cdot \delta_l^+), \quad \forall i \\ \sum_l (\delta_l^- + \delta_l^+) \leq \Phi^{\text{pri}}, \quad \delta_l^- + \delta_l^+ \leq 1, \quad 0 \leq \delta_l^-, \delta_l^+ \leq 1 \end{array} \right. \right\} \quad (11)$$

where Eq. (2) represents the fractional objective, and Eq. (3) enforces first-stage capacity constraints. Eqs. (4), (5), and (7) enforce operational level, supply, and demand level constraints, respectively. Eq. (5) enforces a mass balance constraint, Eqs. (8) and (9) ensure non-negativity of continuous variable and range for binary variables, respectively. Eqs. (10) and (11) represent the data-driven uncertainty sets that are used in this work, with (10) representing the demand uncertainty set and (11) representing the feedstock price uncertainty set.

3. Solution Algorithm

The chosen approach for solving the computationally expensive ARMIFP is a combination of the parametric algorithm (Zhong et al. 2014) and a decomposition-based method. The parametric algorithm is first employed to handle the fractional term in the ARMIFP. We then break the MINLP into master problem and subproblem and solves these problems iteratively to obtain converging upper and lower bounds on the correct

solution (Takeda et al. 2008). The proposed solution algorithm works as follows. First, the decomposition algorithm solves the master problem with feasibility cuts. The optimal value is used to update the lower bound on the optimal solution. Next, the subproblem is solved to obtain the optimal solution. This optimal value is then used to update the upper bound. The subproblem also generates cuts for the master problem, which are then added to the feasibility cut set. The uncertain demand and uncertain feedstock price are then changed to reflect the addition of the cuts in the set as well. The inner loop will terminate when the upper and lower bounds converge. The inner loop returns the current numerator and denominator to the outer loop. The outer loop will terminate when the numerator of the objective minus the denominator times the current multiplier value equals zero. When the outer loop does converge, the resulting multiplier value will be the optimal return on investment of the bioconversion system. Pseudocode for the algorithm is given in Fig. 1.

Algorithm. Parametric algorithm and column-and-constraint algorithm

```

1: Set  $k \leftarrow 0, tol \leftarrow 10^{-3}, r \leftarrow 0$  and  $\zeta$ ;
2: while  $N^* - r \cdot D^* \geq tol$ 
   |  $iter \leftarrow iter + 1, LB \leftarrow -\infty, UB \leftarrow +\infty, m \leftarrow 0$ 
3:   while  $|UB - LB| > \zeta$  do
4:     |  $m \leftarrow m + 1$ 
5:     | Solve (MAS) to obtain  $mo^*, N^*, D^*$  and  $Q^*$ ;
6:     | Update  $LB \leftarrow \max\{LB, mo^*\}$ ;
7:     | Solve (SUB) to obtain  $so^*$ ;
8:     | Update  $UB \leftarrow \min\left\{UB, -r \cdot \sum_j c_{1,j}(Q_j^*)^{q_j} + so^*\right\}$ ;
9:     |  $M \leftarrow M \cup \{m\}$ ;
10:    |  $d_{i,m} = d_i^0 + \sum_k p_{ik}(\xi_k^L \cdot z_k^- + \xi_k^U \cdot z_k^+), \forall i$ 
11:    |  $c_{3,i,m} = c_{3,i}^0 + \sum_l r_{il}(\beta_l^L \cdot \delta_l^- + \beta_l^U \cdot \delta_l^+), \forall i$ 
12:    | Create second-stage variables with respect to index  $m$ ;
13:   | end
14:   |  $r \leftarrow \frac{N^*}{D^*}$ ;
15: end
16: return  $UB$ ;

```

Figure 1. Pseudocode for the proposed nested solution algorithm

4. Case Study

In the case study, the demands for bioproducts were chosen to showcase the capabilities of some of the new bioconversion pathways. As explained in the introduction, one novel contribution of this work was the expansion of the bioconversion network to include organic and inorganic waste material as alternative potential feedstocks. In this example, the demands and uncertainty set for raw biogas, methane, and pectin were given.

When the solution algorithm presented in previous sections was executed, the processing network displayed in Fig. 2 was constructed. To make pectin, orange peel waste was treated using microwave hydrodiffusion. This process yields pectin as well as small amounts of essential oils (EO) and phenolic compounds (TPC). Meanwhile, to satisfy demand for methane, landfill methane extraction techniques can be used on various types

of municipal solid waste landfills. Finally, to satisfy the demand for biogas, multiple types of animal manure and anaerobic digestion (AD) methods were used.

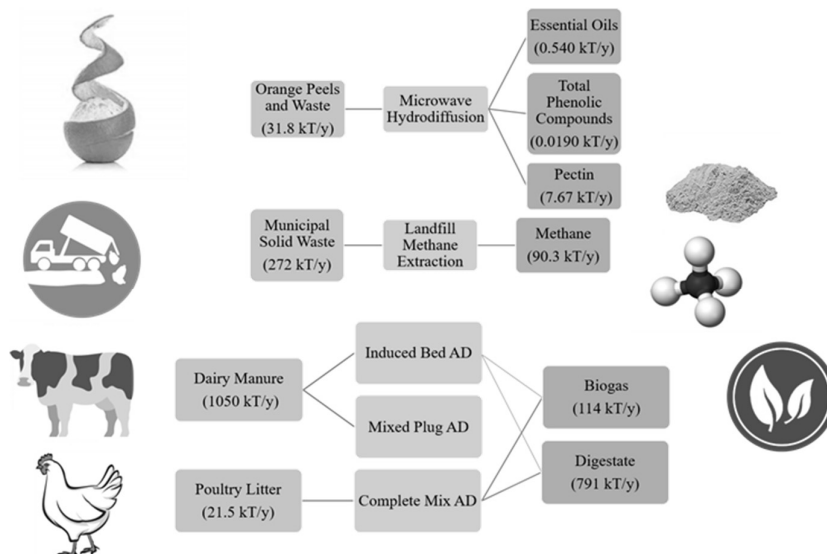


Figure 2. Process diagram displaying the conversion of waste materials to useful biofuels and other bioproducts. The amounts produced by each process vary widely based on average demand for each product.

For dairy manure, the best way to product biogas was through induced bed and mixed plug anaerobic digestion. To process poultry litter, however, the most efficient was to produce biogas was using a complete mix anaerobic digestion system. The other main by-product of anaerobic digestion, digestate, was also produced in large quantities along with the biogas. We also find that one of the processing pathways was built to operate at maximum capacity, while the others were built to ensure demand satisfaction. The biogas and methane production pathways are producing at demand-satisfying levels, while the orange peel processing pathway to produce pectin is operating at maximum capacity. Maximum pectin production implies that for the current input price, making pectin using microwave hydrodiffusion is profitable. In the aggregate processing network, the total cost was \$277.6 M/y, with the cost being split between capital cost (\$170.5 M/y) and operating cost (\$107.1 M/y). The purchase cost for this case was assumed to be zero because the feedstocks for each pathway are waste products, which are assumed to have negligible or zero cost associated with obtaining them. The overall return on investment of the alternative feedstock processing pathway was 6.2%.

5. Conclusions

In this work, we developed a two-stage adaptive robust optimization model to maximize return on investment of a bioconversion network. We focused on uncertainty in feedstock price and bioproduct demand. Feedstock price was derived from historical data, leading to a data-driven uncertainty set for feedstock price that was constructed using the machine learning techniques. Furthermore, we also investigated the economic feasibility of using organic waste and other waste material as feedstock. The two-stage adaptive robust

optimization problem with return on investment maximization is a MILFP which cannot be solved directly due to its multi-stage and fractional objective components. The case study focused on the production of useful chemicals from waste material. The result of the case study was a network that satisfied demand for all bioproducts and had a return on investment of 6.2%. Overall, the proposed solution method was able to quickly and efficiently identify optimal processing pathways for the bioconversion network.

References

- Ben-Tal, A., El Ghaoui, L., Nemirovski, A. (2009). Robust optimization: Princeton University Press.
- Ben-Tal, A., Nemirovski, A. (2002). Robust optimization - methodology and applications. *Mathematical Programming*, 92, 453-480.
- Dodds, D. R., Gross, R. A. (2007). Chemicals from Biomass. *Science*, 318, 1250-1251.
- Garcia, D. J., You, F. (2015). Multiobjective Optimization of Product and Process Networks: General Modeling Framework, Efficient Global Optimization Algorithm, and Case Studies on Bioconversion. *AIChE Journal*, 61, 530-551.
- Garcia, D. J., You, F. (2015). Network-Based Life Cycle Optimization of the Net Atmospheric CO₂-eq Ratio (NACR) of Fuels and Chemicals Production from Biomass. *ACS Sustainable Chemistry & Engineering*, 3, 1732-1744.
- Gallezot, P. (2012). Conversion of biomass to selected chemical products. *Chemical Society Reviews*, 41, 1538-1558.
- Gong, J., Garcia, D. J., You, F. (2016). Unraveling Optimal Biomass Processing Routes from Bioconversion Product and Process Networks under Uncertainty: An Adaptive Robust Optimization Approach. *ACS Sustainable Chemistry & Engineering*, 4, 3160-3173.
- Gong, J., You, F. (2017). Optimal processing network design under uncertainty for producing fuels and value-added bioproducts from microalgae: Two-stage adaptive robust mixed integer fractional programming model and computationally efficient solution algorithm. *AIChE Journal*, 63, 582-600.
- Lipinsky, E. S. (1981). Chemicals from biomass: petrochemical substitution options. *Science*, 212, 1465-1471.
- Ning, C., You, F. (2017). Data-Driven Adaptive Nested Robust Optimization: General Modeling Framework and Efficient Computational Algorithm for Decision Making Under Uncertainty. *AIChE Journal*, 63, 3790-3817.
- Ning, C., You, F. (2018). Data-driven decision making under uncertainty integrating robust optimization with principal component analysis and kernel smoothing methods. *Computers & Chemical Engineering*, 112, 190-210.
- Ning, C., You, F. (2018). Data-driven stochastic robust optimization: General computational framework and algorithm leveraging machine learning for optimization under uncertainty in the big data era. *Computers & Chemical Engineering*, 111, 115-133.
- Sahinidis, N. V. (2004). Optimization under uncertainty: state-of-the-art and opportunities. *Computers & Chemical Engineering*, 28, 971-983.
- Shi, H., You, F. (2016). A computational framework and solution algorithms for two-stage adaptive robust scheduling of batch manufacturing processes under uncertainty. *AIChE Journal*, 62, 687-703.
- Takeda, A., Taguchi, S., Tütüncü, R. H. (2008). Adjustable Robust Optimization Models for a Nonlinear Two-Period System. *Journal of Optimization Theory and Applications*, 136, 275-295.
- Yue, D., You, F., Snyder, S. W. (2014). Biomass-to-bioenergy and biofuel supply chain optimization: Overview, key issues and challenges. *Computers & Chemical Engineering*, 66, 36-56.
- Zhong, Z., You, F. (2014). Globally convergent exact and inexact parametric algorithms for solving large-scale mixed-integer fractional programs and applications in process systems engineering. *Computers & Chemical Engineering*, 61, 90-101.

Improving the prediction of multi-component tablet properties from pure component parameters

Hikaru G. Jolliffe^{a*}, Foteini Papathanasiou^b, Elke Prasad^a, Gavin Halbert^a, John Robertson^a, Cameron J. Brown^a, Alastair J. Florence^a.

^a *EPSRC Centre for Innovative Manufacturing in Continuous Manufacturing and Crystallisation, University of Strathclyde, Technology and Innovation Centre, 99 George Street, Glasgow G1 1RD, United Kingdom.*

^b *Strathclyde Institute of Pharmacy & Biomedical Sciences, University of Strathclyde, 161 Cathedral St, Glasgow G4 0RE, United Kingdom.*

hikaru.jolliffe@strath.ac.uk

Abstract

Direct compaction tableting, a widely used secondary downstream processing operation, has recently received significant research attention. Experimental data can be used to fit model parameters for the prediction of single-component tablet thickness and hardness with good agreement, and this has been done for two components (Avicel[®] PH-101 and Pharmatose[®] 50M). These pure component parameters have then been used to predict multicomponent tablet properties, with the use of novel modified parameter averaging calculations improving predictions. Furthermore, a relation has been developed to estimate the required gap between tablet press punch faces for multicomponent tablets based on the gaps required for pure components; a quick and efficient way to estimate the necessary equipment settings to generate the desired compaction forces is a useful tool.

Keywords: direct compaction, tablet prediction, optimisation.

1. Introduction

Continuous Pharmaceutical Manufacturing (CPM) is a promising alternative to the current paradigm of batch production, and mathematical modelling and simulation is a useful tool within the methodology of CPM (Lee et al., 2015). The final step in many production process is final product formulation. In the case of solid dosage forms such as tablets the critical quality attributes include tablet tensile strength and thickness; appropriate dissolution rates are also crucial (Velasco et al., 1999). Currently, time-consuming design-of-experiment (DOE) approaches are commonly used to determine the necessary conditions to achieve the required tablet properties, and the need for cost-effective R&D methodologies brings process modelling and simulation to the forefront of initial stages of process option evaluation (Diab and Gerogiorgis, 2018).

In the present work, we predict the properties of multicomponent tablets using parameters determined from pure component compaction data; a model by Gavi and Reynolds (2014) has been used to fit the parameters for tablet compaction. The use of pure component parameters in the prediction of multicomponent tablet properties entails the use of some form of mixing or averaging rule, and the appropriateness of currently implemented rules are analysed, with novel modifications made where necessary.

2. Compaction experiments

Experiments (Papathanasiou, 2018) were performed for varying tablet weights (200, 250 or 300 mg) and components (microcrystalline cellulose: Avicel® PH-101; α -lactose monohydrate: Pharmatose® 50M). Tablet thickness and hardness were recorded for a range of compaction forces. Tablet masses were also measured after ejection (due to material flowability, there was always some variation from target tablet mass, approximately $\pm 2\%$). For each compaction force, experiments were performed 10 times (*i.e.* 10 tablets were produced). In addition to the above experiments being done for pure components, a similar set of experiments were done for binary tablets of lactose and cellulose, to allow the assessment of binary tablet predictions.

The pure component experiments showed the expected trends, such as hardness increasing with increasing compaction force, and thickness decreasing with increasing compaction force (routine data not shown due to space constraints – available in the work of Papathanasiou, 2018). Cellulose achieves significantly higher hardness values (up to 450 N for 250 mg tablets) than lactose (up to approximately 50 N), which is unsurprising as Avicel® PH was introduced with direct compaction in mind. The hardness values achieved with the mixtures fall between those of pure cellulose and pure lactose, as one might expect.

3. Compaction model

The compaction model used here is one developed by Gavi and Reynolds (2014), and is also included in the FormulatedProducts module of the gPROMS software package (henceforth called gFormulate), produced by Process Systems Enterprise (PSE, 2018). The model has several key equations. The first computes the tablet relative density ρ^* (Equation 1). Here, ρ_0^* is the relative density at zero compaction pressure (taken to be the tapped density of the powder), P is compaction pressure (MPa) and K is the compressibility constant (a dimensionless fitting parameter). Tablet ρ^* values can be calculated from the compressed tablet densities and the true density of the material (ρ^{cryst} , determined experimentally with a gas pycnometer). Equation 1 is used first in the calculations – the model is sequential. With relative density calculated, tablet thickness h is then calculated for known ρ^{cryst} , mass M , and diameter d (Equation 2; assumes flat-faced cylinders) (Fell and Newton, 1970).

Another key equation is that governing tensile strength, σ (Equation 3). Here, σ_0 is the tensile strength at zero porosity (*i.e.* a fitting parameter corresponding to the theoretical maximum possible compaction, units of MPa), k_b is the bonding capacity (also a dimensionless fitting parameter), and ε is tablet porosity (Equation 4). The three key parameters, then, are the compressibility constant (K), the tensile strength at zero porosity (σ_0) and bonding capacity (k_b). Experimentally, tensile strength can be calculated from hardness via Equation 5, where F is the compaction force in kN.

$$\rho^* = \rho_0^* P^{1/K} \quad (1)$$

$$h = \frac{M}{\rho^* \rho^{cryst}} \frac{4}{\pi d^2} \quad (2)$$

$$\sigma = \sigma_0 e^{-k_b \varepsilon} \quad (3)$$

$$\varepsilon = 1 - \rho^* \quad (4)$$

$$\sigma = \frac{2 F}{\pi h d} \quad (5)$$

4. Pure component parameter estimation

Comprehensive experimental data allows for parameters to be fitted for use in empirical and data-driven models. In this work, the parameters being fitted are compressibility constant (K), tensile strength at zero porosity (σ_0) and bonding capacity (k_b).

The pure component experimental data were imported into gFormulate, where a digital flowsheet of the process was created. The control variables are compaction pressure P and tablet weight M , while the key measured variables are tablet thickness h and hardness H (the diametrical load which causes tablet failure). With three fitted parameters and four variables (two control, two measured), the problem was straightforward, and computationally undemanding; the parameters themselves (for cellulose/Avicel[®] PH-101 and lactose/Pharmatose[®] 50M) are given in Table 1.

5. Multi-component tablet property prediction

Pure component parameters that reliably predict single-component tablets have been determined. The subsequent use of these for multi-component tablet property prediction has been investigated, which entails the use of some form of averaging or mixing rule for the model parameters K , σ_0 and k_b . Doing this by pre-compaction component volume fractions is one option (Equation 6) (Gavi and Reynolds, 2014). Results for mixtures of lactose-cellulose indicate that while predictions for hardness are good at lower compaction forces, there is a trend of over-prediction which becomes more evident at higher compaction forces (Fig. 1). However, this trend is not present for pure components, *i.e.* pure lactose and pure cellulose tablets are predicted reasonably well, with no significant hardness over-prediction at higher compaction forces (Fig. 1B). This implies the potential for prediction improvement from using alternative parameter averaging/mixing rules.

The volume fractions of the components after compaction (as opposed to prior) can be estimated by assuming they compact at similar rates as when they are a pure component (*i.e.* a 25 % volume reduction for pure material i when subjected to a given force implies a 25 % reduction for component i when a mixture is subjected to the same force), and can be computed via Equation 7 (Reynolds et al., 2017).

Table 1. Optimal pure component parameter values for Avicel[®] PH-101 and Pharmatose[®] 50M.

Component	Tensile strength at zero porosity		Bonding capacity		Compressibility constant	
	σ_0 (MPa)	99% CI	k_b (-)	99% CI	K (-)	99% CI
Avicel [®] PH-101	12.0067	±1.9080	7.5847	±0.6362	4.2008	±0.1372
Pharmatose [®] 50M	1.6789	±0.3212	11.6020	±0.8704	9.0901	±0.2130

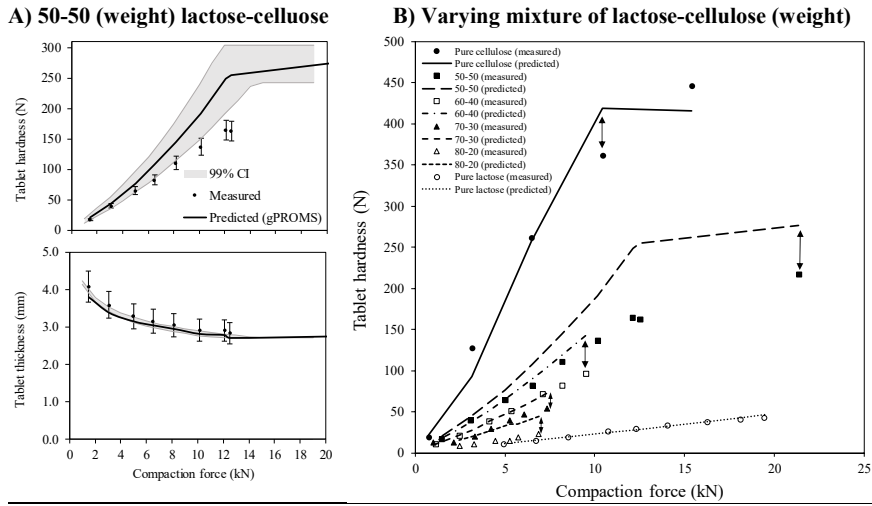


Figure 1. Predicted (Gavi and Reynolds, 2014) vs measured 250 mg tablet hardness and thickness for varying mixtures of lactose-cellulose. For each substance, the predicted curves use the same respective set of parameters. The parameters can be found in Table 1. Arrows in B are a visual aid, to indicate which predicted curve corresponds with which experimental data set.

$$p_{mix} = \sum_{i \in C} \varphi_i p_i, \quad p = \{K, \sigma_0, k_b\} \quad (6)$$

$$\varphi'_i = \frac{m_i / (1 - \varepsilon_i) \rho_i^{crys}}{\sum_{i \in C} m_i / (1 - \varepsilon_i) \rho_i^{crys}} \quad (7)$$

$$\sigma_{Tab} = \prod_{i \in C} \sigma_i^{\varphi'_i} \quad (8)$$

The Reynolds et al. (2017) model then use Equation 8 to compute the tensile strength of multicomponent tablets. In essence, tensile strengths for each component are calculated on a pure basis, then averaged using Equation 8. However, this approach relies on the components being of similar particle size (Reynolds et al., 2017). For applications where the particle sizes are different, such as in this work (Avicel® PH-101 has an average particle size of 50 μm , Pharmatose® 50M has an average size of 360 μm), an alternative approach is required.

The approach used in this work is to use Equation 6 to average the compressibility constant K as before, then use Equation 7 to compute component volume fractions in the compact (φ'_i), and then use these volume fractions to average the post-compaction tensile strength (σ_0) and bonding capacity (k_b) parameters (Equation 9) for use with Equation 3.

$$\sigma_{0mix} = \sum_{i \in C} \varphi'_i \sigma_{0i}, \quad k_{bmix} = \sum_{i \in C} \varphi'_i k_{bi} \quad (9)$$

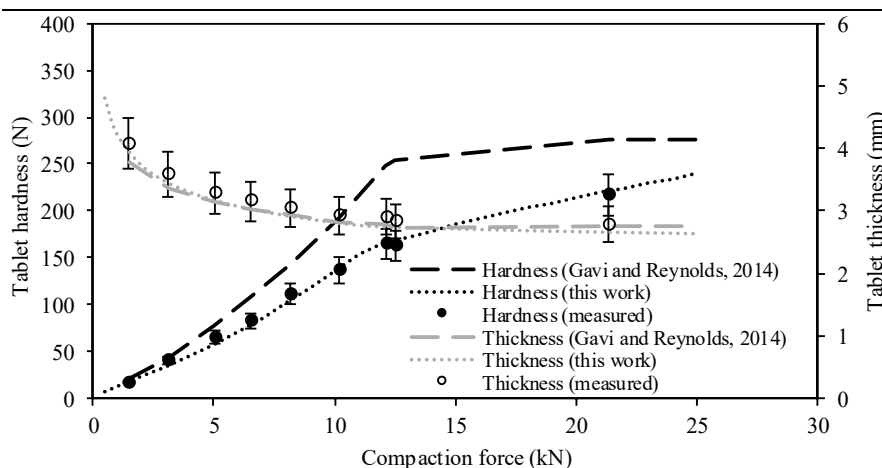


Figure 2. Predicted vs measured (experimental) 250 mg tablet hardness and thickness for 250mg lactose-cellulose tablets (50-50 by weight), illustrating prediction improvements from using post-compaction volume fractions to weight the pure component parameters.

This approach results in improved predictions (Fig. 2). Compared with the previous method (Fig. 1, Fig. 2 dashed lines) the improvements are evident, especially for tablet hardness. While predictions using the previous method agreed with measured data at lower compaction forces, the method outlined in here produces predictions which match the experimental data across the entire range of compaction forces.

The main variable in the compaction model used here is, as with many compaction models, the pressure applied (or the force in some cases) (Equation 1). However, in tablet presses there frequently is not a setting or dial for pressure, but a way to set the distance to which the punch faces compact the material (punch gap, PG); knowing what pressure or force is required might not be immediately useful to a user in the lab. We have taken the compaction force and PG data, and have been able to determine a relation between them, adjusted for tablet weight. An example of this for cellulose is given in Fig. 3A. This variable, which we have called the gap-mass factor γ , has units of mm/g. When plotted against compaction pressure as in Fig. 3A, a power law relation (Equation 10) can be determined for the curved portion corresponding to lower compaction pressures; the horizontal portion, corresponding to the limit of zero porosity, is less useful as there is no improvement in tablet properties at these compaction pressures. This fitting of the curved portion will result in two parameters a and b for a given pure component, and we have then used a mass fraction (m_i)-based mixing rule (Equation 11) to estimate what PG might be required for a binary tablet of given weight M . The predicted PG values are in good agreement with the experimentally required values for binary tablets, with the difference being of a similar order of magnitude as tablet thickness (Fig. 3B). Such a relation is envisaged to be useful to users wishing to apply a certain compaction force.

$$\gamma_i = a_i P^{b_i} \quad (10)$$

$$PG = M \sum_{i \in C} m_i \gamma_i \quad (11)$$

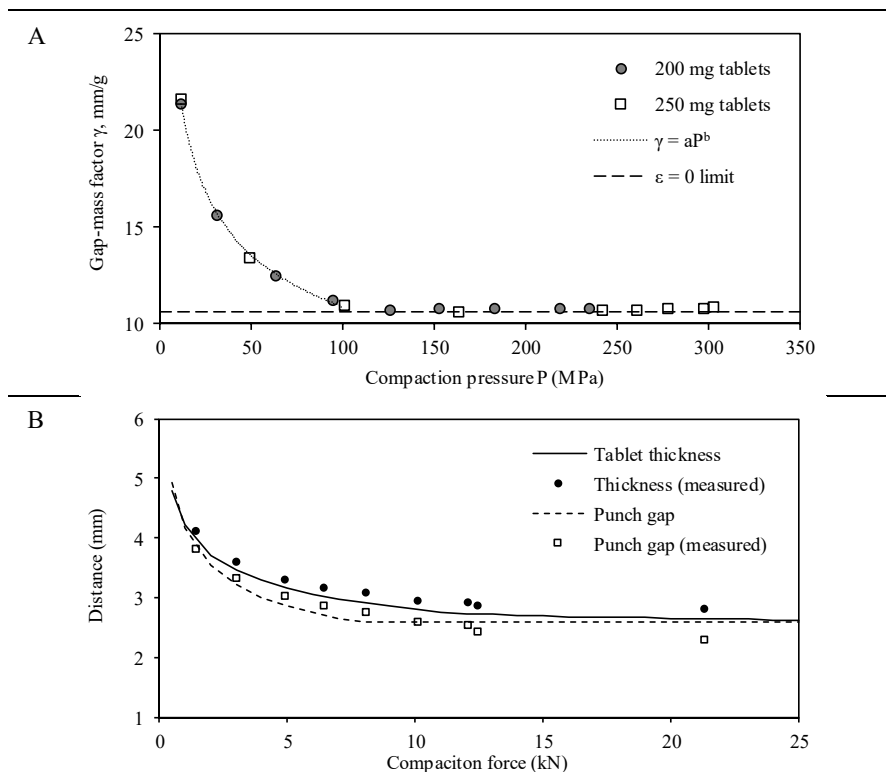


Figure 3. A) Punch gap-compaction pressure relation for Avicel® PH-101. Data points have been normalized by dividing punch gap values (mm) by tablet weights (g). B) Prediction from pure component data of required punch gap values of multicomponent tablets (Equations 10–11).

6. Conclusions

Pure component parameters can be fitted with good statistical results. The use of these pure parameters for the prediction of multicomponent tablet properties is possible, and predictions have been improved by a novel use of model equations. In addition, a relation between tablet press punch gap values and applied compaction pressures has been developed, which predicts necessary punch gaps with good accuracy.

References

- Diab, S & Gerogiorgis, DI, 2018. *Ind. Eng. Chem. Res.* 57, 9489–9499.
- Fell, JT, Newton, JM, 1970. *J. Pharm. Sci.* 59, 688–691.
- Gavi, E, Reynolds, GK, 2014. *Comput. Chem. Eng.* 71, 130–140.
- Lee, SL, O’Connor, TF, Yang, X, Cruz, CN, Chatterjee, S, Madurawee, RD, Moore, CMV, Yu, LX, Woodcock, J, 2015. *J Pharm Innov.* 10, 191–199.
- Papathanasiou, F, 2018. (Masters Thesis). University of Strathclyde.
- Reynolds, GK, Cambell, JI, Roberts RJ, 2017. *Int J Pharm.* 531, 215–224.
- PSE, 2018. gPROMS Formulated Products. www.psenterprise.com (accessed 10.30.18).
- Velasco, MV, Ford, JL, Rowe, P, Rajabi-Siahboomi, AR, 1999. *J. Control. Release* 57, 75–85.

Targeting material exchanges in industrial symbiosis networks

Ana Somoza-Tornos, Valeria Giraldo-Carvajal, Antonio Espuña, Moisès Graells *

Chemical Engineering Department, Universitat Politècnica de Catalunya, EEBE, C/ Eduard Maristany 16, 08019 Barcelona, Spain

moises.graells@upc.edu

Abstract

Industrial symbiosis plays an important role in the process industry, where an effective management of resources can bring both economic and environmental benefits. Traditionally, the design and extension of eco-industrial parks has been mainly based on intuition and experience; yet, the number of actors involved, the number of flows to manage and the different nature of the materials and energy exchanged lead to complex problems that can benefit from the use of systematic decision-making methods. The aim of this contribution is to produce useful tools to identify the most favourable synergies and transformations for a process network. The proposed model has been tested on a case study that consists of an ethylene and chlorine based eco-industrial park. Results confirm the capabilities of the proposed targeting methodology to match sources and sinks of resources.

Keywords: Industrial symbiosis, process networks, targeting, eco-industrial parks, optimization, sustainability.

1. Introduction

In the last years, there has been a growing awareness of the importance of applying circular economy approaches to close material, energy and water cycles (Merli et al., 2018). With their focus on closing loops in industrial processes, Industrial Symbiosis (IS) principles have been widely applied in many specific sectors (van Ewijk et al., 2018; Deschamps et al., 2018). A shared concern is engaging industries to join: the more participants are involved, the better environmental performance is achieved.

However, current eco-industrial parks (EIP) and resource exchange designs are mainly ad-hoc Industrial Symbiosis approaches, based on identifying opportunities through expert analysis. These strategies, even after a systematic local search, usually lead to sub-optimal solutions. In light of this, there is a need of systematic methods aimed at coping with the complexity of the problems by exploring only feasible and promising alternatives. Previous works have focused on the development of tools for transformation companies that might make profit of connecting sources and sinks of resources, and thus reducing the final waste involved (Somoza-Tornos et al., 2017 and 2018).

The aim of this work is to develop efficient targeting methods that identify the most promising synergies for industrial symbiosis while discarding infeasible links. A material network is designed to model the exchange of materials that become profitable

for the involved actors (sources, transformers and sinks). Conservation laws and thermodynamic constraints are used to discern between the resulting alternatives.

2. Problem statement

The system under study is illustrated in Figure 1.

The targeting problem can be stated as follows: Given a set of waste streams j that could be potentially treated to satisfy the raw materials demand of streams k ; a set of chemical reactions that may take place between the i products composing the mentioned streams: and other available data, including complete economic data, technical constraints and thermodynamic parameters. The decisions to be made comprise the amount of waste processed by the system, whether or not it is transformed, the requirements of external feeds or demands, how the products are distributed to satisfy the needs of customers and which side products have to be disposed.

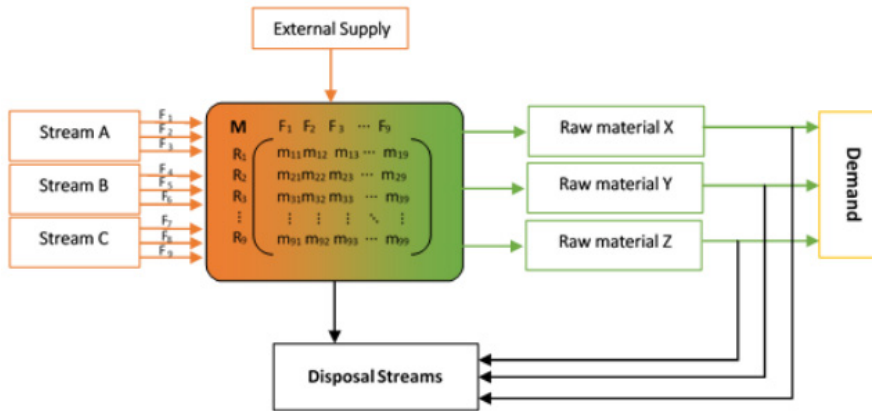


Figure 1. Material network scheme.

3. Mathematical formulation

The problem is formulated as a MILP that finds the optimal synergies between waste producers and raw materials consumers.

The total inlet to the system includes waste streams W_{ji} and potential supply of products required to complete the transformation ES_i (Eq. (1)).

$$\sum_j W_{ji} + ES_i = F_i^{in} \quad \forall i \quad (1)$$

Eq. (2) defines the mass balance of the system considering the inlet, outlet and generation terms, the last one calculated through stoichiometric coefficients R_{mi} and the extent of the reaction F_m^{gen} .

$$F_i^{in} + \left(\sum_m R_{mi} \cdot F_m^{gen} \right) = F_i^{out} \quad \forall i \quad (2)$$

The result of the transformation F_i^{out} is then divided in two, the amount sent to customers F_{ki}^{tm} and the side products that are unassigned F_{li}^d (Eq. (3)). This balance is

completed with the introduction of the term F_i^{ed} to represent the external demand that new partners may have.

$$F_i^{out} = \sum_k F_{ki}^{rm} + \sum_l F_{li}^d + F_i^{ed} \quad \forall i \quad (3)$$

z_k is defined in Eqs. (4),(5) as a binary variable that takes a value of 1 if the amount sent to the customers, F_{ki}^{rm} , is greater than the demand.

$$D_{ki} \cdot z_k \leq F_{ki}^{rm} \quad \forall k, i \quad (4)$$

$$F_{ki}^{rm} - D_{ki} \leq M \cdot z_k \quad \forall k, i \quad (5)$$

Hence, when the demand is surpassed, the profit of selling C_k it is penalized with a cost for the excess of delivery C_k^d .

$$f_k^1 \leq M \cdot z_k \quad \forall k \quad (6)$$

$$f_k^1 \leq (\sum_i D_{ki} \cdot C_k) - C_k^d \cdot \sum_i (F_{ki}^{rm} - D_{ki}) \quad \forall k \quad (7)$$

On the contrary, when demand is not covered, only the amount sent to the customer must be taken into account for the profit calculation.

$$f_k^2 \leq M \cdot (1 - z_k) \quad \forall k \quad (8)$$

$$f_k^2 \leq (\sum_i F_{ki}^{rm} \cdot C_k) \quad \forall k \quad (9)$$

The energy balance of the system is calculated as in Eq. (10), where Q_m^{exc} denotes the amount of energy added or extracted from the system.

$$(\sum_i R_{m,i} \cdot F_m^{gen} \cdot H_i) = Q_m^{exc} \quad \forall m \quad (10)$$

Binary variable y_m is defined in Eqs. (11),(12) to differentiate processes that require heating or cooling and apply costs accordingly.

$$Q_m^{exc} \leq M \cdot y_m \quad \forall m \quad (11)$$

$$-Q_m^{exc} \leq M \cdot (1 - y_m) \quad \forall m \quad (12)$$

Eqs. (13),(14) apply when heat is extracted from the system, and cost parameter CQ_{out} is considered.

$$f_m^3 \leq M \cdot y_m \quad \forall m \quad (13)$$

$$-f_m^3 \leq Q_m^{exc} \cdot CQ_{out} \quad \forall m \quad (14)$$

Conversely, when heat is added to the system, the cost is calculated through Eqs. (15),(16).

$$f_m^4 \leq M \cdot (1 - y_m) \quad (15)$$

$$-f_m^4 \leq -Q_m^{exc} \cdot CQ_{in} \quad (16)$$

The objective function to be maximized is the economic balance shown in Eq. (17). It considers the profit obtained from satisfying the demand of current companies and potential new partners. Aggregated cost parameters associated with the different transformation routes are considered at this step. These aggregated costs, including capital and operational costs plus indirect costs like transportation and management, must be estimated according to the specific circumstances, and the sensibility of the results to these estimations must be adequately assessed.

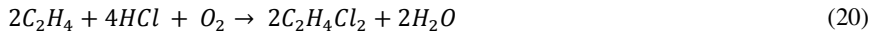
$$OF = - \left(\sum_i \sum_l F_{li}^d \cdot C_l \right) - \left(\sum_i \sum_j W_{j,i} \cdot C_j \right) - \left(\sum_m F_m^{gen} \cdot C_m^R \right) - \left(\sum_i ES_i \cdot C_i^{es} \right) + \left(\sum_i F_i^{ed} \cdot C_i^{ed} \right) + \sum_k f_k^1 + \sum_k f_k^2 - \left(\sum_m f_m^3 + \sum_m f_m^4 \right) \quad (17)$$

The resulting model for the targeting can be posed as follows:

$$\begin{aligned} \text{TSym} \quad & \min [\text{OF}] \\ \text{s.t.} \quad & \text{Eqs. (1)-(17)} \end{aligned}$$

4. Case study

The capabilities of the model are illustrated in a case study consisting of an eco-industrial park based on ethylene and chlorine, with 10 available waste streams and 7 demands of raw material have been defined. The considered compounds include acetic acid, benzene, chlorine, vinyl chloride, ethanol, ethylbenzene, ethylene, ethylene dichloride, ethylene oxide, hydrochloric acid, oxygen, tetrachloroethylene, trichloroethylene, vinyl acetate and water. Eqs. (18)-(26) show the reactions that the park would consider can take place between the components by a transformation company.



5. Results

The resulting MILP problem, featuring 1209 equations, 1064 continuous variables and 159 binary variables, has been modeled in GAMS 23.8.2 and solved with CPLEX 12.4.

Four different scenarios have been defined to examine the chances of incorporating new participants in the symbiotic network. These new participants can either be a source of waste or raw materials consumers, all presenting their own capacity limitations.

- Base case of the existing eco-industrial park (EIP)
- New companies could join the EIP and offer new sources of waste
- New partners could join the EIP and take advantage of generated waste
- New companies could both as a source and sink of resources

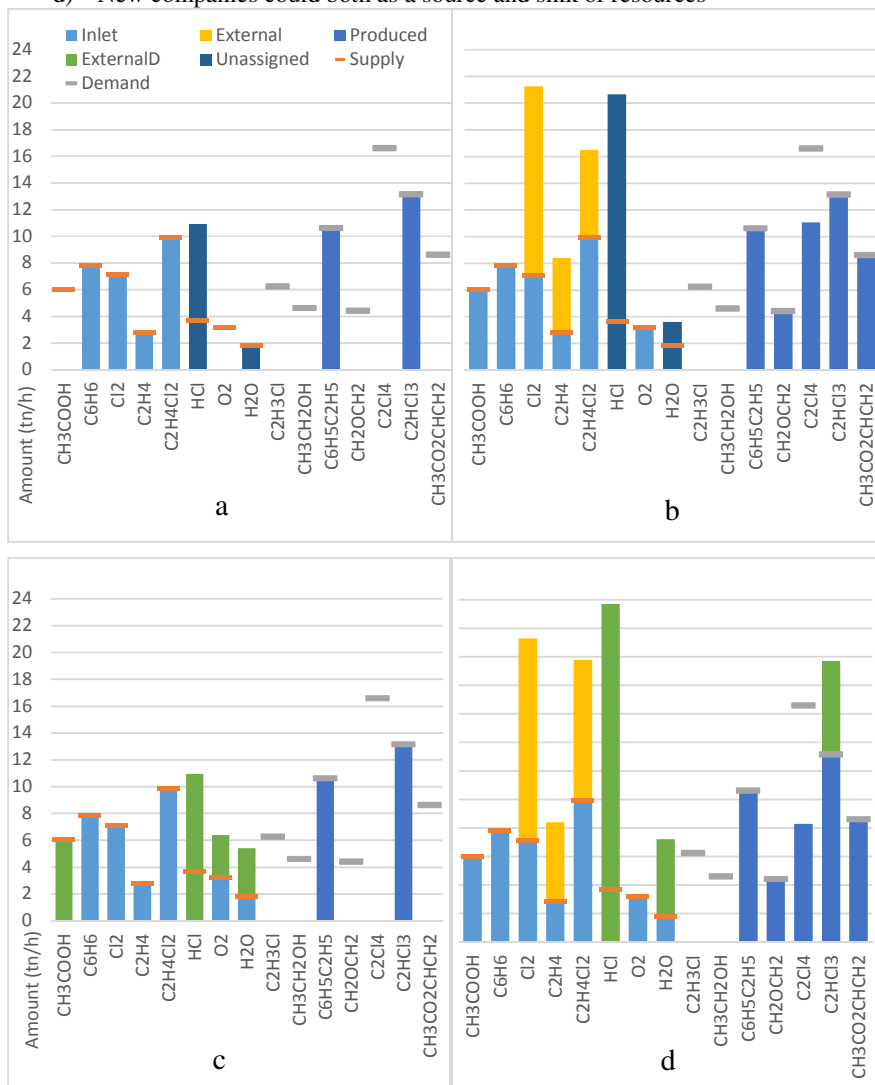


Figure 2. Waste usage and raw materials satisfaction for scenarios a, b, c, d.

Figure 2.a depicts the waste usage and the raw materials demand satisfaction for the existing EIP. The first case, where no external supply is available, is constrained by the limit in the waste supply. Reactions (22) and (26) are active to produce ethylbenzene and trichloroethane. The lack of ethylene does not allow acidic acid to be used in reaction (25) and there are sources of an excess of HCl and water that is not reused. Figure 2.b shows the effect of finding new partners that may be a source of waste. By

adding new producers of chlorine, ethylene and ethylene dichloride to the park, more of the demands are internally covered and thus the external requirements of raw materials are reduced. Transformations (19), (24) and (25) would have to be activated to produce ethylene oxide, tetrachloroethylene and vinyl acetate, thus increasing the amount of waste processed and the profit of the entire complex. This would increase even more the excess of side products. In Figure 2.c the opposite case is represented, where new partners would only be interested in raw materials production. As the waste supply was limiting the base case, only the side products in excess can be used, resulting in a reduced grow of the EIP. When these limitations are overcome in Figure 2.d, the most promising ways of making the EIP grow are identified, and so are the transformations that the policy-makers should foster.

6. Conclusions

This work has addressed the development of a tool to identify the most promising routes to match sources and sinks of resources, even when a transformation step is required. This will help to reduce the complexity of the analysis required during the synthesis and design of industrial processing networks. Hence, the model offers policy-makers a method to systematically identify and assess opportunities for increasing the integration of process networks in industrial complexes. Thus, Administrations may use their resources to incentive partners that will ensure economically feasible synergies with the ultimate goal of reducing waste. An adequate reformulation of the objective function may also allow these companies to identify their opportunities, and even the different members of the industrial network the best cooperation opportunities (multi-objective approach). Future work will also focus on the application of combined targeting-synthesis methodologies to systematically analyse in detail the resulting proposals.

Acknowledgements

Financial support received from the Spanish "Ministerio de Economía, Industria y Competitividad" and the European Regional Development Fund, both funding the research Projects AIMS (DPI2017-87435-R) and PCIN-2015-001/ELAC2014/ESE0034 is fully acknowledged.

Ana Somoza-Tornos thankfully acknowledges financial support received from the Spanish "Ministerio de Educación, Cultura y Deporte" (Ayuda para la Formación de Profesorado Universitario - FPU15/02932).

References

- J. Deschamps, B. Simon, A. Tagnit-Hamou, B. Amor (2018). Is open-loop recycling the lowest preference in a circular economy? Answering through LCA of glass powder in concrete. *J. Clean. Prod.* 185 14-22.
- R. Merli, M. Preziosi, A. Acampora (2018). How do scholars approach the circular economy? A systematic literature review. *J. Clean. Prod.* 178, 703-722.
- A. Somoza-Tornos, M. Graells, A. Espuña (2018). Evaluating the effect of separation and reaction systems in industrial symbiosisComp. *Aided Chem. Engng* 43, pp. 749-754.
- A. Somoza-Tornos, M. Graells, A. Espuña (2017). Systematic Approach to the Extension of Material Exchange in Industrial Symbiosis. *Comp. Aided Chem. Engng* 40-B, pp.1927-1932.
- S. van Ewijk, J. Y. Park, M. R. Chertow (2018). Quantifying the system-wide recovery potential of waste in the global paper life cycle. *Resour. Conserv. Recycl.* 134, 48-60.

Total Organic Carbon Prediction with Artificial Intelligence Techniques

Eda Goz^{a*}, Mehmet Yuceer^b, Erdal Karadurmus^c

^aAnkara University, Faculty of Engineering, Dept. of Chemical Engineering, Ankara 06100, Turkey

^bInonu University, Faculty of Engineering, Dept. of Chemical Engineering, Malatya 44280, Turkey

^cHitit University, Faculty of Engineering, Dept. of Chemical Engineering, Çorum 9200, Turkey

esemizer@eng.ankara.edu.tr

Abstract

This study used the Extreme Learning Machine (ELM), Kernel Extreme Learning Machine (KELM) and Artificial Neural Network (ANN) models with a feed-forward neural network structure and partial least squares (PLSR) methods to estimate total organic carbon. In order to develop models, on-line data measured at five-minute time intervals were collected through one year (2007-2008) from the online-monitoring stations which were built near the River Yeşilırmak in Amasya in North-Eastern Turkey. These stations were the first practice in Turkey. Twelve parameters as luminescent dissolved oxygen (LDO), pH, conductivity, nitrate nitrogen (NO₃-N), ammonium nitrogen (NH₄-N), total organic carbon (TOC), chloride, orthophosphate, temperature, turbidity, suspended solid and flow rate were measured at the on-line monitoring stations. To predict the total organic carbon, four input variables, pH, conductivity, dissolved oxygen and temperature were selected. Moreover, the data were also collected at the central office in Ankara via a General Packet Radio Service (GPRS) channel. The validity of models was tested by using statistical methods in MATLAB including correlation coefficients (R), mean absolute percentage error (MAPE%) and root mean square error (RMSE). The best result was obtained in the presence of KELM with a radial basis function (RBF) kernel. $R_{\text{test}}=0.984$, $\text{MAPE}_{\text{test}}=3.01$, $\text{RMSE}_{\text{test}}=0.9676$. Additionally, $R_{\text{train}}=0.995$, $\text{MAPE}_{\text{train}}=1.58$ and $\text{RMSE}_{\text{train}}=0.532$. Among the other two algorithms ANN provided better results than ELM and PLSR.

Keywords: Artificial Neural Network, Extreme Learning Machine, On-line monitoring, River water quality

1. Introduction

Rivers play a vital role not only as sources of drinking water but also basic elements in sustainable development especially in industrial and agricultural activities. Additionally, rivers and streams also serve as the lifelines of the population staying in the basins. Increased anthropogenic and other effects cause substantial increase in river pollution. Water quality in rivers has also been changed by environmental factors, but the main reason for water contamination is known to be caused by human activities. Especially in agricultural activities such as usage of chemical fertilizers, animal feeding and mining, combustion of fossil fuels affect the quality of all natural water bodies the most. Destruction of wetlands, point or diffuse pollution sources, large amounts of industrial

waste discharge and the exponential increase of population growth have also affected water quality within environmental factors. In the last decades, monitoring of water quality from several rivers by regular measurements has received increasing demand. In this context, a real-time monitoring station, as the first practice in Turkey, was built near the River Yeşilırmak in Turkey. The system involved two in-situ on-line analysis stations in River Yeşilırmak and a central monitoring office at Ankara University. Pollutant parameters of luminescent dissolved oxygen (LDO), pH, conductivity, nitrate nitrogen ($\text{NO}_3\text{-N}$), ammonium nitrogen ($\text{NH}_4\text{-N}$), TOC, o-phosphate, chloride, temperature, turbidity, suspended solid and flow rate were measured at five-minute intervals at the on-line monitoring stations. The data were collected at the central office in Ankara via General Packet Radio Service (GPRS). In these parameters, measurement of total organic carbon was the most expensive -about eight-fold of the total amount of LDO, conductivity, pH and temperature- parameter, therefore, various models for prediction of TOC was proposed in this study. Various types of river water quality models such as parametric, statistical and deterministic models were proposed in the literature. The use of water quality models is inevitable in explaining some problems like nonlinearity, subjectivity and cause-effect relationships between water quality variables and water status. However, deterministic modelling approaches for water quality parameters need a lot of information on various hydrological processes and several different units of input data to arrive the results, while these methods have been seen to be very effortful and time-consuming. Artificial intelligence methods have some advantages over semi empirical or deterministic models due to the fact that they contain a set of input data without assumption, and they are also able to map the nonlinear relationships that are characteristics of aquatic ecosystems. For these reasons ANNs, which are artificial intelligence methods, have widespread use in hydrological processes and modelling river water quality. Moreover, ANNs are used to forecast of water quality parameters, as well as determining the uncertainty of contaminant source and nonlinearity of water quality data. Csabragi et al. (2017) applied a neural network structure on dissolved oxygen levels in the River Danube. Within this context, four models were used. In order to estimate dissolved oxygen, multivariate linear regression, multilayer perceptron neural network, radial basis function network and general regression neural network models were developed. Another dissolved oxygen prediction study was carried out by Olyaei et al. (2017). In their study, they used two types of ANN structures, namely multi linear perceptron and radial basis functions. Moreover, linear genetic programming and support vector machine (SVM) were also proposed to estimate dissolved oxygen levels in the River Delaware. An extreme learning machine technique was used to predict dissolved oxygen concentration with and without water quality parameters by Heddami and Kisi (2017). Their study compared a standard extreme learning machine with a sigmoid activation function (S-ELM), an extreme learning machine with a radial basis function (R-ELM), an on-line sequential ELM (OS-ELM), and an optimally pruned extreme learning algorithm (OP-ELM). Temperature, specific conductance, turbidity and pH were used as the input variables. In the study without water quality parameters, year, month, day and month numbers were used as predictors. Using extreme learning machines for river water quality parameters is quite limited in literature.

We compared three data-driven approaches to predict TOC concentration from data collected from real-time monitoring stations. Extreme learning machine (ELM), kernel extreme learning machine (KELM) and artificial neural network (ANN) modelling methods were used to predict TOC. TOC is one of the most important pollution parameters in the topic of river water quality and measurement of this parameter is more

expensive than measuring other parameters. This state is important to reduce the costs of building stations. According to the results of our statistical analysis, KELM was better than the artificial neural network and ELM.

2. Data collection and modelling studies

A real-time central river monitoring system was built to monitor river pollution. The system involved two in-situ on-line monitoring stations. One of the stations was positioned in the Aynalı Cave region after the sewage system and Tersakan stream, while the other one was stationed at the Administration of Hydraulic Works' Durucasu station which had a 26.876 km distance from the first station and after the yeast factory. Furthermore, a central monitoring office was designated at Ankara University. The data were collected in a database at the station. The data were transferred from the stations to the central office in Ankara through a GPRS transmission channel as shown in Figure 1 and continuously monitored and displayed in different formats.

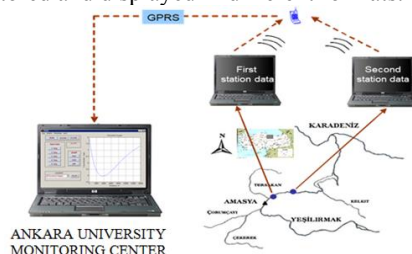


Figure 1. The locations of the on-line measurement stations and the data collection process

The study area has various pollution sources such as industrial, domestic, municipal and agricultural run-off. Real-time data were measured at five-minute time intervals for the parameters of luminescent dissolved oxygen (LDO), pH, conductivity, nitrate nitrogen ($\text{NO}_3\text{-N}$), ammonium nitrogen ($\text{NH}_4\text{-N}$), TOC, o-phosphate, chloride, temperature, turbidity, suspended solid and flow rate.

2.1 Modelling Studies

2.1.1 Artificial Neural Network

An artificial neural network is a type of artificial intelligence technique, and it was inspired by the learning algorithm of the human brain. An ANN is composed of a large number of processing elements with their connections, and it has three distinctive layers, namely input, hidden and output layers as shown in Figure 2.

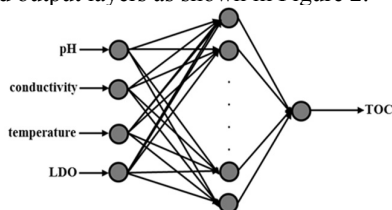


Figure 2. Artificial neural network structure

These layers are called the basic elements of architecture and known as nodes/neurons. Connection of nodes is achieved with synapses, and each node has a weight factor. In an

artificial neural network design, signals are passed through the neurons, and simultaneously, the weights and transfer functions are modified, and this process is repeated until a broad output is reached. The numbers of neurons numbers in each layer is determined depending on the structure of the problem.

In this study, we used data for the one-year period of 2007-2008. Especially outlier detection, which was coded in MATLAB, was carried out to sort out the data that deviated from the normal value. The 70% and 30% of the remaining data were used for training and testing respectively. At the stage of artificial neural network modelling, a feed-forward neural network architecture was designed. Feed-forward neural networks have been shown to be an effective neural design for forecasting water quality parameters. The numbers of neurons in the input layer, hidden layer and output layer determined as 4, 25 and 1 respectively. In the training network, number of iterations, degree of training, number of neurons were determined by using a trial and error approach as in training of most network architectures. The transfer function was selected as tangent-sigmoid, and in the training of the network, a Bayesian Regularization Backpropagation (*'trainbr'*) algorithm was used. *trainbr* is a network training function that updates the weight and bias values based on the Levenberg-Marquardt optimization. It minimizes a combination of squared errors and weights, and then, determines the correct combination to produce a network which generalizes well. This process is known as Bayesian regularization.

2.1.2 Extreme Learning Machine

Extreme Learning Machine has become a new method developed in recent years (Huang et al. 2006). In the proposed method, learning algorithms, hidden node weights and biases randomly assigned and need not to be tuned, as well as output weights, are calculated by a simple inverse operation. Due to these properties and less human intervention, ELM provides an extremely fast learning speed and better generalization capability in comparison to traditional learning algorithms. However, ELM is not capable of managing large amounts of data with a high number of dimensions. The number of nodes of the ELM that was required was higher than those of traditional algorithms. So, in this study, we used five different activation functions and numbers of neurons in the ELM. These activations functions were triangular radial basis (*'tribas'*), radial basis (*'radbas'*), hard limited (*'hardlim'*), sigmoidal (*'sigmoid'*) and sinusoidal (*'sine'*) functions. In the KELM, the RBF kernel and linear kernel functions were used as activation functions in the presence of different numbers of neurons. The schematic representation of the extreme learning machine is given in Figure 3.

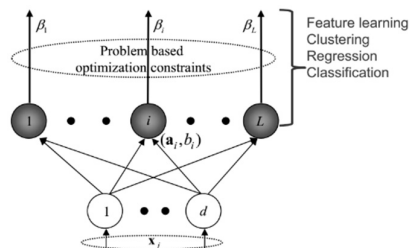


Figure 3. ELM architecture

The algorithm of ELM is given in the following steps (Ding et al. 2014)

Input: a training set $(x_i, t_i) \in R^n \times R^m$ ($i = 1, 2, \dots, N$), activation function and number of neurons in the hidden layer (N); Output: the output weights, β (the output weights between the hidden and output layers which is calculated with Moore Penrose inversion as given in the last step)

Step 1: Randomly assign the parameters of the hidden layer

Step 2: Calculate the output matrix of the hidden layer

Step 3: Calculate the output weight $\beta = H^+ T$

According to these steps, we may say that ELM includes two phases: in the first phase, the hidden layer is initialized by ELM so that the input data can be mapped into a feature space. In the second phase, solution of β (linear parameters) is calculated by Moore Penrose inversion.

2.1.3 Kernel Extreme Learning Machine

In the kernel-based extreme learning approach, kernel functions are used as activation functions in the hidden nodes. In KELM, feature mapping is unknown, and the kernel matrix of ELM based on Mercer's condition can be defined. There are many types of Kernel functions that can be used. The most commonly used one of these are gaussian kernel, linear kernel, hyperbolic tangent kernel, radial basis function and polynomial kernel functions. In this study, RBF kernel and Linear Kernel functions were used.

2.1.4 Partial Least Square Regression (PLSR)

Partial least square regression is a generalization form of multiple linear regression. In this method, collinear, correlated, noisy and numerous X-variables can be analyzed according to this several response variables Y can also be simultaneously modelled.

3. Results and Discussion

In this study, three different artificial intelligence techniques were used to determine total organic carbon in the River Yeşilırmak. For this purpose, we used five different activation functions and numbers of neurons in ELM. These activation functions were triangular radial basis, radial basis, hard limit, sigmoidal and sinusoidal functions. The best result in ELM was obtained in the presence of the tribas activation function, and the number of neurons in the hidden layer was 350. In KELM, RBF kernel and linear kernel functions were used as activation functions in the presence of different numbers of neurons. In this study, 150 neurons were used, and a radial basis function was selected. The artificial neural network test was carried out with 4, 25 and 1 neurons in the input, hidden and output layers respectively.

The kernel-based extreme learning machine provided the best result. A kernel-based extreme learning machine is a powerful learning algorithm in comparison to an extreme learning machine and an artificial neural network. In fact, the ELM technique has many advantages, but ELM is not capable of managing data with high numbers of dimensions. In this case, ELM needs more nodes than traditional learning algorithms. In KELM, kernel functions were used instead of activation functions as shown in Table 1. Moreover, for KELM, it was not needed to choose the number of hidden neurons, and feature mapping was not needed to be known. KELM had the same generalization, but it was more stable than ELM. The performances of the models were tested by the results of statistical analysis as correlation coefficient (R), root mean square error (RMSE) and

mean absolute percentage error (MAPE%). The results of the statistical analyses are given in Table 1.

Table 1. Statistical performance indices of the modelling techniques

Modelling techniques	Activation Function	Number of Neurons	Training			Test		
			RMSE	MAPE (%)	R	RMSE	MAPE (%)	R
Kernel ELM	RBF Kernel	150	0.532	1.58	0.995	0.968	3.01	0.984
ELM	Triangular Basis	350	1.374	6.40	0.967	1.764	8.22	0.947
ANN	Tangent Sigmoid	25	1.430	6.09	0.966	1.430	6.48	0.965
PLSR	--	--	3.638	20.23	0.750	3.647	20.31	0.740

4. Conclusion

In this study, three different artificial intelligence techniques were used to predict the total organic carbon concentration in the River Yeşilırmak in Turkey. Actually, the River Yeşilırmak is the most important water resource considering its agricultural potential and other human activities. 12 river water quality parameters were monitored in two on-line measurement stations, but among these monitoring total organic carbon raised the cost considerably. For this reason, prediction of total organic carbon from the other parameters that are cheaper than directly measuring TOC significantly reduced the cost of building stations. The results showed that the kernel-based extreme learning machine is a good tool to predict TOC concentration. This may be explained by the reduction of the cost of measuring stations with the developed algorithm. The extreme learning machine worse than Kernel ELM due to data size, and this method required a higher number of neurons than the traditional ANN algorithm as shown in Table 1. Although the generalization ability of a kernel ELM is the same as ELM, a kernel ELM has good stability. Additionally, PLSR algorithm has the worst scenario. In the next time, other ELM and different kernel ELM structures will be used to predict river water quality parameters.

Acknowledgment

This study was supported by TUBITAK (Project Number: 105G002).

References

- A. Csabragi, S. Molnar, P. Tanos, J. Kovacs, 2017, Application of Artificial Neural Networks to the Forecasting of Dissolved Oxygen Content in Hungarian Section of the River Danube, *Ecological Engineering*, 100, 63-72
- E. Olyaie, H.Z. Abyaneh, A.D. Mehr, 2017, A Comparative Analysis among Computational Intelligence Techniques for Dissolved Oxygen Prediction in Delaware River, *Geoscience Frontiers* 8, 3, 517-527
- G.B. Huang, Q.Y. Zhu and C.K. Siew, 2006, Extreme Learning Machine: Theory and Applications, *Neurocomputing* 70, 1-3, 489-501
- S. Ding, X. Xu, R. Nie, 2014, Extreme Learning Machine and applications, *Neurocomputing and Applications*, 25, 3-4, 549-556
- S. Heddad, O. Kisi, 2017, Extreme Learning Machines: A New Approach for Modeling Dissolved Oxygen (DO) Concentration with and without Water Quality Variables as Predictors, *Environmental Science and Pollution Research*, 24, 20, 16702-16724

On the Design and Implementation of a Process Modelling Language for Uncertainty

Pedro I. O. Filho^a and Eric S. Fraga^{a,*}

^a*Centre for Process Systems Engineering, Department of Chemical Engineering, University College London, WC1E 7JE, London, United Kingdom*
e.fraga@ucl.ac.uk

Abstract

A modelling framework focusing on the treatment of uncertainty is proposed. The framework is based on Julia, given that it is an open-source, modern, computationally efficient language (scripted but with just-in-time compilation) providing support for the design of domain specific languages via abstract types, multiple dispatch, operator overloading and full Unicode support. The framework provides a concise and natural syntax, allowing for a traditional mathematical notation. For instance, users can write $t = 700 \pm (3\delta)$ (uncertainty range), $X \sim \mathcal{N}(\mu, \sigma^2)$ (probability distribution) or $F_0 = V^3 + [21.3, 21.7]$ (interval arithmetic) without having to compromise between speed and code readability. A case study on the scale-up of an Aerosol-Assisted Chemical Vapour Deposition (AACVD) process is presented to exemplify the use of the framework.

Keywords: Modelling language, uncertainty, process modelling.

1. Introduction

The formulation of engineering processes has different stages. Importantly, uncertain parameters can be found from the synthesis and design through to the process operation. The ubiquity of uncertainty can be explained by its many sources, such as conceptual modelling errors (wrong or incomplete assumptions, simplifications, wrong equations); unknown consequences that depend on future events; imprecise decision-maker preferences; etc. Therefore, treating uncertainty is a key element in process modelling. Even though process simulation systems (e.g. Aspen, Hysys, gPROMS) and/or modelling systems (e.g. GAMS, AIMMS, AMPL) have made it easier for practitioners to apply process systems engineering methodologies to industrial applications, the treatment of uncertainty is not always straightforward. There is, therefore, a necessity of further research on the development of tools aimed at the modelling of uncertainty.

This paper proposes a framework characterised by methods and operators which allow users to easily write down models with intrinsic parameter uncertainty or distributed quantities and evaluate these models. Such a framework has the final goal of becoming a computational modelling language for incorporating uncertainty in mathematical modelling and also supporting communication with currently available modelling and simulation systems. The next sections present the background in uncertainty modelling; introduce the framework, and present examples to show the ease with which models can be developed. This includes a case study on the scale-up of an Aerosol-Assisted Chem-

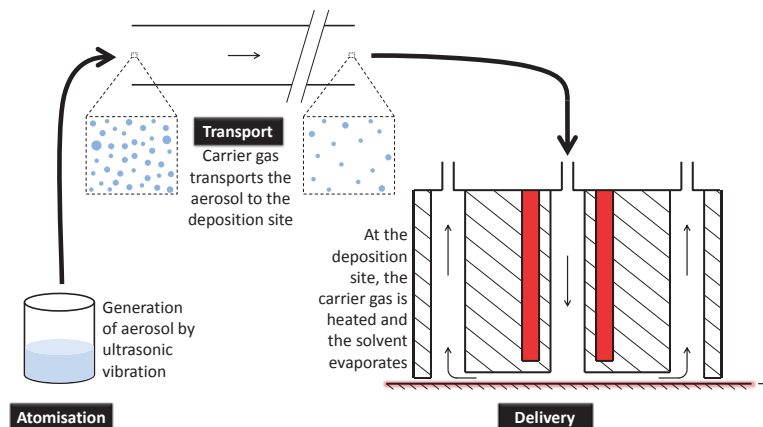


Figure 1: Schematics of the AACVD process, including the atomisation of the solution containing the reactants, the aerosol transport, the chemical deposition and the film formation.

ical Vapour Deposition (AACVD) process. Such a process, schematically represented in Figure 1, can be summarised as a deposition method employed to produce high-quality, high-performance, solid materials. The process is often applied in the semiconductor industry to produce thin films, such as Transparent Conducting Oxides, used from personal digital devices through to solar panels.

2. Uncertainty in Computational Models

Uncertainty is ubiquitous in process design, given that there is always imperfect or unknown information where it is impossible to exactly describe all the parameters. Some of them may have a single exact value, which cannot always be known with precision, for example, transfer coefficients. Other parameters are themselves inherently distributed due to variability or heterogeneity, for example, the sizes of droplets generated by ultrasonic vibration. Both cases can be mathematically represented using the same approach, namely, probability theory. The strengths of this approach are exemplified by how straightforward it becomes to quantify and understand how likely different outcomes are and to visualise potential scenarios. There are a number of quantities which help decision makers to understand the impacts of uncertain variables, such as the mean, variance, skewness, upper and lower quantile values, confidence intervals, etc. Such information can also be represented graphically, using probability density functions or cumulative distribution functions. Once the uncertain parameters are modelled, all the pertinent information should be automatically provided by a computational tool focused on uncertainty representation.

The modelling of uncertainty is essential in process design and optimisation, evidenced by Grossmann et al. (2016), who also shared some challenges in the field. In particular, they showed how important it is to develop tailored solution strategies, which can be facilitated when there is a framework that allows easy prototyping, especially with specific tools dedicated to representing uncertainty. Additionally, when dealing with uncertainty, running simulations helps to rationalise and explain the results from models. That can be done, for example, incorporating Monte Carlo experiments and the associated statistical

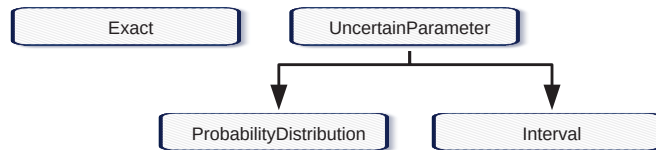


Figure 2: Current type hierarchy of the Uncertainty.jl framework.

methods into the stochastic models. A modelling language focused on the treatment of uncertainty would, therefore, be helpful to facilitate writing, running, maintaining and sharing computational models.

3. Uncertainty.jl

This paper introduces the Uncertainty.jl framework, a high-level interface to represent uncertainty in process modelling, built to address some of the challenges previously mentioned. The framework is user-friendly and straight forward to be employed, aiming therefore at users who are not experts in computer programming. It was written in Julia¹ for a number of reasons. Firstly, Julia is a high-level, high-performance, dynamic language, which allows both large-scale computation and flexible prototyping without having to simultaneously use two or more languages; for example, many engineers use MATLAB (high-level, but slow) and C (fast, but low-level) at the same time. On the other hand, Julia is a high-level language and yet has been shown to at least approach the performance of C (Bezanson et al., 2017). Finally, the users of Uncertainty.jl can also join the large and active community of Julia and have access to a vast and growing number of packages focused on scientific computing, which they can employ and, when necessary, extend.

Chen and Grossmann (2017) outlined the current trend of allowing modellers direct access to model objects, which are easily created using Uncertainty.jl within Julia. This facilitates code sharing and the generation of models that are more readable and easier to validate. However, the main advantage is the use of Julia's multiple dispatch feature, allowing the overloading of generic functions using different type signatures (Zappa Nardelli et al., 2018). This gives a greater expressive power, since additional code can be written in a concise and clear style. Function calls will be dispatched to the relevant method, according to the type signature.

Another advantage of using multiple dispatch is how straight forward it becomes to extend any of the Julia packages already available. For example, Algorithm 1 shows how Uncertainty.jl extended the ODEProblem function, from the package DifferentialEquations.jl (Rackauckas and Nie, 2017). It now became possible to input uncertain parameters, which can be intervals or probability distributions, before solving the differential equations. Uncertainty.jl currently has the object hierarchy shown in Figure 2, which takes advantage of Julia's multiple dispatch. This allows, for example, that the appropriate ODEProblem method will be called according to the types of the input variables as follows: if the uncertain variables are all of the Interval type, Latin hypercube sampling will be used to generate samples. If there is a mix of intervals and probability distributions, a random

¹<https://julialang.org/>


```

1 Size = 500
2 Range = [0, 20]
3 X = ProbabilityDistribution(Size, Range)
4 k = 7
5 X ~  $\chi^2(k)$ 

```

```

X ▾ ProbabilityDistribution
  > x → Float64[500]
    minimum → 0.00
    maximum → 20.0
  > P → Float64[500]
    mean → 7
    percentile25 → 4.25...
    median → 6.35...
    percentile75 → 9.04...

```

Figure 3: Definition of a random variable with 500 entries ranging from 0 to 20 and following a chi-squared distribution with 7 degrees of freedom. The output of line 5 is shown on the grey section, at the right-hand side. Screenshot from Atom editor.

sampling will be performed. The differential equations are then solved using the generated samples from the uncertain variables, according to their distributions. The output will itself be a distribution built from the solutions of the ODEs. The relevant statistics are also automatically provided. The framework also includes methods to perform sensitivity and uncertainty analysis for the whole model or its parts.

```

1  $\delta = 20$ 
2  $x = 700 \pm 36$ 
3  $y = x + [20, 50]$ 
y ▾ Interval
  min → 660
  max → 810

```

Figure 4: Example of consecutive operations using interval arithmetic. The final output is in grey, at the bottom. Screenshot from Atom editor.

Figure 4. Additionally, the operator \pm was also defined, acting on real numbers to produce an interval, which can then be used in any further interval arithmetic operations. Finally, independent model evaluations, including the solution of differential equations, are intrinsically compatible with parallel computing, easily done in Julia.

4. Case Study: Aerosol-Assisted Chemical Vapour Deposition

In the context of the AACVD process, the first step is to atomise a solution containing the reactants, generating the aerosol that will be transported to the reaction chamber. As seen in Figure 1, the aerosol is characterised by droplets of different sizes, which should be accounted for by the models, since the droplet sizes impact the loss of aerosol during transport and the solvent evaporation in the reactor. Details about the modelling and experimental validation of the aerosol transport system, accounting for the distributed nature of the droplet sizes, were previously presented by Filho et al. (2017). Subsequently, the uncertainty and sensitivity analysis of the overall AACVD system, including the aerosol generation, transport and delivery to the reaction chamber was performed by Filho et al. (2018). Finally, when the aerosol reaches the reaction chamber, the solvent evaporates and chemical reactions take place, resulting in the film formation. Equation 1 represents

Algorithm 1 Overloading the function ODEProblem from the DifferentialEquations.jl package. The function generateSamples identifies which parameters are exact and creates samples for the uncertain parameters.

Input: set of differential equations \mathbf{f} ; initial condition \mathbf{u}_0 ; time interval \mathbf{t}_{span} ; set of exact and uncertain parameters $\mathbf{allParameters}$.

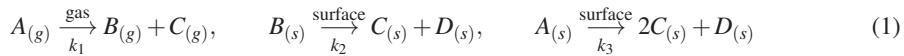
Output: inferred probability distribution and its properties using the solutions of the ODEs system.

```

1      function ODEProblem(f, u0, tspan, allParameters)
2          samples := generateSamples(allParameters);
3          sol := {};
4          for each exactParameters ∈ samples do
5              prob := ODEProblem(f, y0, tspan, exactParameters);
6              sol := sol ∪ {solve(prob)};
7          end for
8          distribution := inferDistribution(sol);
9      return distribution;

```

general chemical reactions, where the film is formed mainly by the component D:



Although these equations are general, Vallerio et al. (2016) used them specifically for the production of high-grade polysilicon, using monosilane as the reactant. Performing mass balances, the dynamic model equations for the CVD reactor is shown in Equation 2:

$$\frac{dC_i^g}{dt} = \frac{\dot{F}_{in}}{V} \cdot C_i^{in} - \frac{\dot{F}_{out}}{V} \cdot C_i^g - h_{m,i} \cdot \frac{A}{V} \cdot (C_i^g - C_i^s) - k_j \cdot C_i^g \quad (2)$$

where C_i^g [mol/m³] and C_i^{in} [mol/m³] are, respectively, the gas phase concentration and the inlet feed concentration of component i ; C_i^s [mol/m³] is the volumetric concentration of component i on the surface of the glass, whose thickness grows with time, t [s]; \dot{F}_{in} [m³/s] and \dot{F}_{out} [m³/s] are, respectively, the inlet and outlet volumetric flow rates; k_j [units vary] is the kinetic constant of reaction j , in the gas phase or on the surface; $h_{m,i}$ [m/s] is the gas to solid phase mass transfer coefficient of component i ; V [m³] is the volume in which the gas phase reactions take place; and A [m²] is the glass surface area in contact with the gas.

```

1      (k1, μ, σ2) = (ProbabilityDistribution(), 25, 4)
2      (k2, Range2) = (ProbabilityDistribution(), [150, 250])
3      (k3, Range3) = (ProbabilityDistribution(), [0.03, 0.05])
4
5      k = [k1 ~  $\mathcal{N}(\mu, \sigma^2)$ , k2 ~  $\mathcal{U}(\text{Range}_2)$ , k3 ~  $\mathcal{U}(\text{Range}_3)$ ]
6      h = [Interval(100, 300), Interval(4, 20), Interval(20, 50)]

```

Figure 5: Defining the uncertain parameters, namely the three reaction kinetic constants and the three mass transfer coefficients, before solving the system of ODEs.

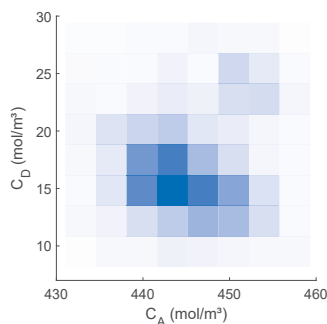


Figure 6: Plot showing the likelihood regions of the concentrations of components A and D, given the uncertainties in the model parameters. The darker the region, the more likely it is to represent reality.

The reaction rate constants and the mass transfer coefficients are usually quantified experimentally or using correlations from the literature. Such coefficients are known for their uncertainties and can be represented using probability distributions. Figure 5 shows how straight forward it is to define uncertain variables using `Uncertainty.jl`. Once k and h are defined, they can join any additional exact parameters to be the input for the `ODEProblem` function, which will return a distribution. Figure 6 shows a plot exemplifying how the information from the output can be visualised. Using similar visualisation tools and the statistics returned by `Uncertainty.jl`, users can understand what the most likely values of the variables are and make educated decisions.

5. Conclusions and Future Work

This paper introduced `Uncertainty.jl`, a user-friendly environment for the modelling of uncertainty. The examples provided, the case study on AACVD and the obtained solutions demonstrated the viability of this prototype language. Much more is required, especially in terms of incorporating existing methods for handling uncertainty. Future work will address, for example, the representation of model uncertainty. It will also facilitate and encourage the use of Machine Learning in the context of process modelling, from additional Monte Carlo algorithms through to defining and learning models using inference algorithms and probabilistic programming. Finally, `Uncertainty.jl` aims at supporting optimisation algorithms and the communication with the most established modelling platforms, such as GAMS, AMPL and gPROMS.

Acknowledgements: The authors acknowledge the support provided by Conselho Nacional de Desenvolvimento Científico e Tecnológico (CNPq) and EPSRC (EP/L017709/1).

References

- J. Bezanson, A. Edelman, S. Karpinski, V. B. Shah, 2017. Julia: a fresh approach to numerical computing. *SIAM Review* 59 (1), 65–98.
- Q. Chen, I. Grossmann, 2017. Recent developments and challenges in optimization-based process synthesis. *Annual Review of Chemical and Biomolecular Engineering* 8, 249–283.
- I. E. Grossmann, R. M. Apap, B. A. Calfa, P. García-Herreros, Q. Zhang, 2016. Recent advances in mathematical programming techniques for the optimization of process systems under uncertainty. *Computers & Chemical Engineering* 91, 3–14.
- P. I. O. Filho, P. Angeli, E. S. Fraga, 2018. Modelling under uncertainty for process design and scale-up of an industrial AACVD. *Computer Aided Chemical Engineering* 44 (1), 253–258.
- P. I. O. Filho, D. B. Potter, M. J. Powell, C. J. Carmalt, P. Angeli, E. S. Fraga, 2017. Probability density functions for droplet sizing in aerosol transport modelling. *Computer Aided Chemical Engineering* 40 (1), 2245–2250.
- C. Rackauckas, Q. Nie, 2017. `DifferentialEquations.jl` – a performant and feature-rich ecosystem for solving differential equations in Julia. *Journal of Open Research Software* 5 (1), 1–10.
- M. Vallerio, D. Telen, L. Cабianca, F. Manenti, J. Van Impe, F. Logist, 2016. Robust multi-objective dynamic optimization of chemical processes using the sigma point method. *Chem. Eng. Science* 140, 201–216.
- F. Zappa Nardelli, J. Belyakova, A. Pelenitsyn, B. Chung, J. Bezanson, J. Vitek, 2018. Julia subtyping: a rational reconstruction. *Proceedings of the ACM on Programming Languages* 2 (1), 1–27.

Simulation of Food Waste Pyrolysis for the Production of Biochar: A Qatar Case Study

Samar Elkhailifa,^a Ahmed AlNouss,^{a,b} Tareq Al-Ansari,^a Hamish R Mackey,^a
Prakash Parthasarathy,^a Gordon Mckay^{a,*}

^aDivision of Sustainable Development, College of Science and Engineering, Hamad Bin Khalifa University, Qatar Foundation, Doha, Qatar

^bDepartment of Chemical Engineering, College of Engineering, Qatar University, Doha, Qatar

gmckay@hbku.edu.qa

Abstract

One-third of the edible parts of food produced for human consumption is lost or wasted globally, amounting to 1.3 billion tonnes per year. Food waste contains many constituents, which makes it a promising source for fuels and chemicals production. Moreover, the State of Qatar, which is situated in a hyper arid region is characterized by a disproportionate distribution of resources. It is rich in natural energy resources, but suffers from water scarcity and its natural environment does not encourage food production. Qatar's economy continues to expand rapidly and faces a number of environmental challenges which include the management and disposal of wastes that are generated by industrial and domestic activities. As such, the pyrolysis of biomass waste and food waste specifically is a viable option to transform waste, which would have otherwise been disposed into the natural environment, into value-added products which can be utilized to enhance resource efficiency, especially water. In this work, the pyrolysis of different food waste has been simulated using Aspen Plus software to produce value-added biochar products. The pyrolysis of food waste in steady-state mode has been studied using a yield reactor, in the 300–600 °C temperature range, by feeding five types of food waste with different ultimate and proximate properties. In addition, the optimum feedstock is identified in which the objective is to optimize food waste blends for maximizing solids to syngas ratio. The optimization results indicated an increase in the yield of the solid biochar product from 36.56% to 41.81%, while both the ash and carbon content decreased slightly. These findings open the doors to the transformation of food waste into value-added biochar via pyrolysis. Furthermore, the produced chars can be utilized in carbon sequestration when applied as soil amendment and as precursors for higher value-added products such as adsorbents.

Keywords: Food Waste, Pyrolysis, Biochar, Simulation, Optimization

1. Introduction

With the predicted increase in population to 9.8 billion by 2050 according to UNO, the world is inevitably facing multiple dilemmas. Human and industrial activities are responsible for the creation of most types of waste. Urban and industrial wastes need to be managed sustainably if we are to avoid serious, lasting effects such as global warming. Furthermore, food waste is generated in abundance globally with estimated losses of 1.3

billion tonnes per year (Gustavsson et al., 2011) and hence it constitutes an attractive source for the recovery of energy and the production of value-added products (e.g. fuels and chemicals).

Pyrolysis is a promising thermochemical conversion method (Panwar et al., 2012; White et al., 2011) that transforms biomass into value-added products. In this process, biomass is heated to temperatures greater than 400 °C, under the partial presence of/or the complete absence of oxygen (Laird et al., 2009). The main products of the process are bio-oil, bio-gas, and biochar. There is a wide range of applications of the highly porous material and their composites that are produced by pyrolysis, which include their use as supercondensers, catalytic support materials, and adsorbents (Gordienko et al., 2017).

Many soils suffer from water deficiency and low soil fertility (Basso et al., 2013; Koide et al., 2015). Therefore, it is essential to improve soil fertility in order to achieve food security. Biochar, a product of the thermochemical conversion of biomass, can be implemented into soils as an enhancer that improves the fertility and quality of agricultural soils while enhancing the sustainability of biomass and crop production (Zhang et al., 2016).

The use of Aspen Plus in simulating the pyrolysis of waste streams, particularly municipal green waste, was previously demonstrated (Kabir et al., 2015). In their pyrolysis study, they investigated the production of bio-fuel from Australian municipal green waste (MGW) and then validated the simulation results against experimental results. The objective of this paper is to simulate the pyrolysis of different food wastes that are available in the State of Qatar using Aspen Plus software with the aim of producing a value-added biochar product. The pyrolysis of food waste in steady-state mode has been studied using a yield reactor, in the 300–600 °C temperature range, by feeding five types of food waste with different ultimate and proximate properties. The food waste includes banana peel, mango endocarp, orange peel, tea waste and cooked rice.

2. Methodology

2.1. Data: Proximate and Ultimate Analysis

The problem formulated in this study is based on experimental data obtained from the literature for food items that are available in the state of Qatar. Table 1 summarizes the proximate and ultimate analyses of the different food wastes considered here.

Table 1: Proximate and ultimate analyses of biomass (food waste) feedstocks

	Banana peel	Mango endocarp	Orange peel	Tea waste	Cooked rice
Moisture (wt. %) ^c	10.36 ^{*a}	4.760 ^{*a}	9.910 ^{*a}	12.00 ^{*a}	64.44 ^{*b}
Proximate analysis (wt. %) ^c					
Volatile matter	78.90	63.81	55.86	64.17	62.50
Fixed carbon	10.82	33.19	41.14	30.09	37.05
Ash	10.28	3.000	3.000	5.740	0.4500
Ultimate analysis (wt. %) ^c					
C	35.65	40.06	41.13	45.81	43.28
H	6.190	5.530	5.630	5.120	8.040
N	1.940	0.2900	0.5800	2.450	1.530
O	45.94	51.12	49.66	40.88	46.44
S	0.0000	0.0000	0.0000	0.0000	0.2600
Cl	0.0000	0.0000	0.0000	0.0000	0.0000
Ash	10.28	3.000	3.000	5.740	0.4500
LHV (MJ/kg) (dry basis)	17.33	11.64	12.08	12.66	17.33

	Banana peel	Mango endocarp	Orange peel	Tea waste	Cooked rice
Reference	(Kabenge et al., 2018)	(Lam et al., 2016)	(Lam et al., 2016)	(Yadav et al., 2016)	(Liu et al., 2016)

*a Air-dried basis, *b As received basis, *c Total dry-basis

2.2. Modelling and Simulation

2.2.1. Model Development

The base model developed in this work and used in the generation of the carbon-rich biochar solid is based on the pyrolysis of different feedstocks. Moreover, the simulation software is composed of several unit operation blocks which are models of specific process operations (e.g. reactors). The blocks were placed on a flowsheet through the specification of material and energy streams. The pyrolysis of food waste in this study is modelled based on the assumptions of steady state, kinetic-free equilibrium model, isobaric process, neglected pressure drops, and neglected tar formation. Moreover, the RYield reactor type was used to convert the feed material into its constituent elements (i.e. pyrolysis part of the modelling) through using the calculator block formulation from (AlNouss et al., 2018), while the nonstoichiometric Gibbs free energy equilibrium-based splitter model was used for solid yield separation.

2.2.2. Simulation of the Results

A computational model has been developed in this study to simulate this process using Aspen Plus software. Aspen Plus is a process-oriented software that facilitates calculation of physical, chemical and biological parameters (Puig-Arnau et al., 2010). It can handle solid, liquid and vapour phases in the process. The process simulator does not have a built-in pyrolysis model; however it contains a number of built-in unit block models which enable the realistic specification of processes (Kabir et al., 2015). A pyrolysis process diagram is presented in Figure 1. An Aspen Plus model was developed based on this pyrolysis process flow diagram. The function of each block is summarized in Table 2.

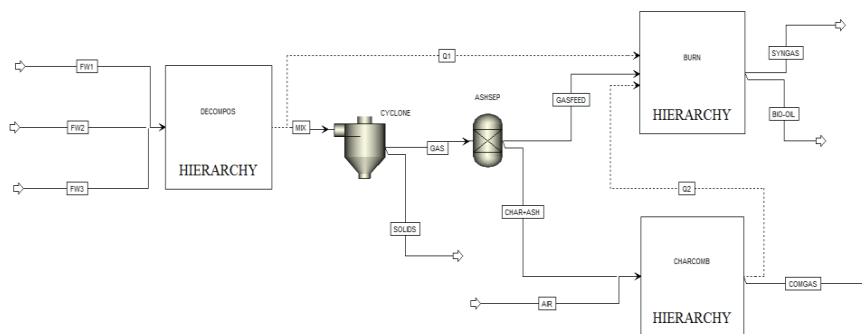


Figure 2: Aspen plus flowsheet of the food waste pyrolysis

Table 2: Summary of the functions of each block in the developed Aspen flowsheet

Block ID	Aspen name	Description
DECOMP	RYield	Converts the non-conventional attributes into conventional components
CYCLONE	Cyclone	Simulates the separation of bio-char using cyclone

Block ID	Aspen name	Description
ASHSEP	Sep	Separates gases from ash and small part of carbon by specifying split fraction
CHARCOMB	Stoic	Simulates combustion of carbon and ash to provide heat
BURN	RGibbs	Simulates the separation of syngas and bio-oil using flash separator and further syngas pyrolysis through Gibbs reactor restricting chemical equilibrium

2.2.3. Process Optimization

After the development of the pyrolysis model, the five food waste feedstocks were optimized to determine the optimum blended stream. The objective of the optimization problem is to maximize the solids to syngas ratio. The optimization equations are as below:

$$\text{Maximize } \frac{\text{Solid}}{\text{Syngas}} \quad \text{Eq. (1)}$$

$$\text{Subject to } \sum_{i=1}^n x_i = 1 \forall i \in \text{BiomassSources} \quad \text{Eq. (2)}$$

Where, Solid is the molar flowrate of the generated biochar, Syngas is the molar flowrate of the generated H₂-rich synthesis gas, and x is the blending fraction of each biomass feedstock.

3. Results and Discussion

The developed model has been tested against data provide in Table 1 in order to find the optimum blended feedstock. The results before and after the optimization are presented in Table 3 and Table 4 respectively.

Table 3: Results for Biomass Feedstock Blending without optimization at original moisture content

Total Biomass Input (kg/h)	5000 (1000 each biomass)		
LHV (MJ/kg) Input (dry basis)	12.94		
	Solids	SYN	Oil
Output (kg/h)	1828	3172	0.3700
N ₂	0.0000	52.38	0.0000
O ₂	0.0000	1871	0.0000
H ₂ O	0.0000	1015	0.0000
S	0.0000	0.9400	0.0000
H ₂	0.0000	232.5	0.0000
C	1628	0.0000	0.3700
ASH	199.8	0.0000	0.0000
% Yield (kg/kg input)	36.56	63.43	0.0100
Energy Requirement (T=500 °C)	DECOMP	CHARCOMB	BURN
Heat Flow (kJ/h)	31.08	2.900	-28.40

It could be noticed that the use of Cyclone has driven almost all the carbon and ash to the solid biochar flow. In addition, the reported composition of syngas is before utilizing it for further pyrolysis through Gibbs free energy.

Furthermore, a restriction on the modelling terms of the maximum amount of any of the feeds used has been identified. The results are highlighted in Table 4. The model results

demonstrated almost an equal amount of the 4 feed waste streams (2 through 5) as optimum blend. This reflects the amounts of carbon and ash per pure feed stream that these streams contain. Where, Banana peel contains around 41% (carbon+ ash), Mango endocarp (41%), Orange peel (40%), Tea Waste (45%) and cooked rice (16%). From this analysis it is clear that cooked rice has the lowest Carbon and Ash content and the highest moisture content and it is not of an interest.

Table 4: Results for Biomass Feedstock Blending with optimization at original moisture content

Total Biomass Input (kg/h)	3984.90				
Biomass Blends	FW1	FW2	FW3	FW4	FW5
	24.70%	25.10%	25.10%	25.10%	0.0000%
LHV (MJ/kg) Input (dry basis)	12.48				
	Solids	SYN	Oil		
Output (kg/h)	1666	2318	0.4400		
N ₂	0.0000	46.66	0.0000		
O ₂	0.0000	1699	0.0000		
H ₂ O	0.0000	369.3	0.0000		
S	0.0000	0.0200	0.0000		
H ₂	0.0000	203.1	0.0000		
C	1469	0.0000	0.4400		
ASH	196.7	0.0000	0.0000		
% Yield (kg/kg input)	41.81	58.18	0.0100		
Energy Requirement (T=500 °C)	DECOMP	CHARCOMB	BURN		
Heat Flow (kJ/h)	26.12	2.310	-24.79		

According to the results, prior to optimization, a percentage by weight of biochar obtained is 36.56 % w/w. The results of the optimization then improve to reach a yield of 41.81 % w/w biochar when a total food waste input of 3984.90 kg/h and a contribution of ~25 % w/w of each food waste except cooked rice is implemented. With respect to the ash and carbon contents of the produced biochars through the simulation, it can be observed that there is a slight reduction in their quantities (see Table 3 and Table 4).

With drying all the food waste streams to a maximum of 9.000 % moisture content and still restricting the flow of each food waste to 1000, the results showed equal distribution for all the feedstock. The drying energy requirement for the different food wastes were estimated at 0.1500, 0.0000, 0.0400, 0.0700 and 7.170 kJ/h, respectively. When releasing the restriction on the flow of each food waste to high number (~10⁵), the optimization yields a feed of only Tea waste. This can be explained since it contains the highest Carbon and Ash content and with the releasing of the feed constraint, it has dominated the result.

4. Conclusion

In this work, the pyrolysis of different food waste feedstocks is simulated using Aspen Plus software in order to obtain biochar products at optimum conditions. While producing the value-added products, the objective is to optimize the food waste blends for maximizing solids to syngas ratio. The base model developed in this work used in the generation of the carbon rich biochar solid is based on the pyrolysis of different feedstocks with different ultimate and proximate properties and that are available in the State of Qatar. The results of the optimization indicated an increase in the yield of the solid biochar product from 36.56 % w/w (1000 kg/h of each of the food wastes as initial input) to 41.81 % w/w (food waste input of 3984 kg/h and ~25 % w/w of each food waste except cooked rice), while both the ash and carbon content decreased slightly. These findings are promising because they open doors to the transformation of the abundant amounts of food waste that are available globally into value-added biochar via pyrolysis.

Furthermore, the produced chars can be utilized in carbon sequestration when applied as soil amendment and as precursors for higher value-added products such as adsorbents.

Acknowledgment

The authors would like to express their gratitude to Hamad Bin Khalifa University and Qatar Foundation for the provision of support during this project. The authors thank the Supreme Committee for Legacy and Development in Qatar for the further support of this research and development programme.

References

- A. AlNouss, G. McKay, and T. Al-Ansari, 2018, Optimum Utilization of Biomass for the Production of Power and Fuels using Gasification, *Computer Aided Chemical Engineering*, 43, 1481-86.
- A.S. Basso, F.E. Miguez, D.A. Laird, R. Horton, and M. Westgate, 2013, Assessing potential of biochar for increasing water-holding capacity of sandy soils, *GCB Bioenergy*, 5, 2, 132-43.
- M. Gordienko, D. Belous, A. Tyrtysnikov, I. Mitrofanov, N. Menshutina, and E. Lebedev, 2017, Prediction of structure changes of organic-silica aerogels during pyrolysis, *Computer Aided Chemical Engineering*, 40, 181-86.
- J. Gustavsson, C. Cederberg, U. Sonesson, R.v. Otterdijk, and A. Meybeck, 2011, Global food losses and food waste: extent, causes and prevention, Food and Agriculture Organization of the United Nations (FAO).
- I. Kabenge, G. Omulo, N. Banadda, J. Seay, A. Zziwa, and N. Kiggundu, 2018, Characterization of Banana Peels Wastes as Potential Slow Pyrolysis Feedstock, *Journal of Sustainable Development*, 11, 2, 14-24
- M. Kabir, A. Chowdhury, and M. Rasul, 2015, Pyrolysis of Municipal Green Waste: A Modelling, Simulation and Experimental Analysis, *Energies*, 8, 8, 7522.
- R.T. Koide, B.T. Nguyen, R.H. Skinner, C.J. Dell, M.S. Peoples, P.R. Adler, and P.J. Drohan, 2015, Biochar amendment of soil improves resilience to climate change, *GCB Bioenergy*, 7, 5, 1084-91.
- D.A. Laird, R.C. Brown, J.E. Amonette, and J. Lehmann, 2009, Review of the pyrolysis platform for coproducing bio-oil and biochar, *Biofuels, Bioproducts and Biorefining*, 3, 5, 547-62.
- S. S. Lam, R. K. Liew, X. Y. Lim, F. N. Ani, and A. Jusoh, 2016, Fruit Waste as Feedstock for Recovery by Pyrolysis Technique, *International Biodeterioration and Biodegradation*, 113, 325-333
- H. Liu, J. E. X. Ma, and C. Xie, 2016, Influence of Microwave Drying on the Combustion Characteristics of Food Waste, *Drying Technology*, 34, 12, 1397-1405.
- N.L. Panwar, R. Kothari, and V.V. Tyagi, 2012, Thermo chemical conversion of biomass – Eco friendly energy routes, *Renewable and Sustainable Energy Reviews*, 16, 4, 1801-16.
- M. Puig-Arnavat, J.C. Bruno, and A. Coronas, 2010, Review and analysis of biomass gasification models, *Renewable and Sustainable Energy Reviews*, 14, 9, 2841-51.
- J.E. White, W.J. Catallo, and B.L. Legendre, 2011, Biomass pyrolysis kinetics: A comparative critical review with relevant agricultural residue case studies, *Journal of Analytical and Applied Pyrolysis*, 91, 1, 1-33.
- D. Yadav, L. Barbora, L. Rangan, and P. Mahantaa, 2016, Tea Waste and Food Waste as a Potential Feedstock for Biogas Production, *Environmental Progress & Sustainable Energy*, 35, 5, 1247-1253
- C. Zhang, L. Zhou, P. Chhabra, S.S. Garud, K. Aditya, A. Romagnoli, G. Comodi, F. Dal Magro, A. Meneghetti, and M. Kraft, 2016, A novel methodology for the design of waste heat recovery network in eco-industrial park using techno-economic analysis and multi-objective optimization, *Applied Energy*, 184, 88-102.

The robust pooling problem

Johannes Wiebe^{a,*}, Inês Cecílio^b and Ruth Misener^a

^a*Department of Computing, Imperial College London, 180 Queen's Gate, SW7 2AZ London, UK*

^b*Schlumberger Cambridge Research, Cambridge, UK*
j.wiebe17@imperial.ac.uk

Abstract

The pooling problem is a widely studied case study in global optimization. To date, it has largely been treated deterministically, neglecting the influence of parametric uncertainty. This work introduces a robust optimization formulation of the standard pooling problem with uncertain component concentrations. The quality constraints in which these uncertain parameters occur are non-linear and non-convex in the decision variables — something which has rarely been explored in the context of robust optimization. The resulting reformulation is a global optimization problem with the complexity determined by the selected uncertainty set. We compare the computational performance of three commonly used uncertainty sets on 14 pooling problem instances and demonstrate how accounting for uncertainty changes the optimal solution.

Keywords: robust optimization, global optimization, pooling problem

1. Introduction

The widely studied pooling problem has applications in oil and gas refining, water systems, supply chains, and more (Misener et al., 2011). It consists of optimizing material flow through a network of sources, pools, and terminals. Due to bilinear mixing terms at the pools it is non-linear and non-convex and is known to be NP-hard (Alfaki and Haugland, 2013). The pooling problem has frequently been used as a case study in global deterministic optimization (e.g. Floudas and Visweswaran, 1990; Meyer and Floudas, 2004; Quesada and Grossmann, 1995; Tawarmalani and Sahinidis, 2004; Wicaksono and Karimi, 2008; Gounaris et al., 2009; Misener and Floudas, 2010; Alfaki and Haugland, 2013; Baltean-Lugojan and Misener, 2018). Parameters of the pooling problem can be subject to uncertainty. In particular, the concentrations of components and pollutants entering the system can be subject to measurement errors and/or fluctuations over time. These concentrations will have a large effect on product quality at the terminals, which is often subject to constraints. Violating these constraints can have a negative impact on profit, health and safety, or the environment.

Nonetheless, to the best of our knowledge, only Li et al. (2011, 2012b) and Li et al. (2012a) have considered uncertainty in the pooling problem to date. Li et al. (2011) consider component concentration uncertainties for the extended pooling problem and pooling network synthesis. They utilize a two-stage stochastic programming approach: the first stage determines the number of sources, pools, and product terminals developed and the connections between them. The second stage assumes the uncertainty has been realized and optimizes the pooling network production. Li et al. (2012b) propose a decomposition strategy for solving the stochastic program. Li et al. (2012a) apply robust optimization to demand uncertainty in the standard pooling problem. An advantage of the robust approach is that the increase in problem complexity is moderate and no decomposition is required (Grossmann et al., 2016).

This work applies robust optimization to uncertain component concentrations in the quality constraints of the standard pooling problem. The process systems engineering community has recently been increasingly interested in applying robust optimization to chemical processes (e.g. Gounaris et al., 2013; Zhang et al., 2015; Janak and Floudas, 2005; Vujanic et al., 2016; Li and Ierapetritou, 2008; Ning and You, 2017; Shang and You, 2018). Most of these applications have been limited to linear models. The work by Li et al. (2012a) on the pooling problem is an early exception to this, even though the uncertain demand constraints considered are still linear. In fact, robust optimization in general is largely focused on problems which are convex in the decision variables and concave in the uncertain parameters (Ben-Tal et al., 2015). While concavity in the uncertain parameters is necessary for robust optimization reformulation, the restriction on convexity is largely due to a focus in the robust optimization literature on applications which are solvable in polynomial time. “Robust optimization” problems which are non-convex in the decision variables and non-concave in the uncertain parameters can generally only be addressed with semi-infinite programming.

In this work, we are interested in constraints which are non-convex in the decision variables but concave in the uncertain parameter, as is the case for the quality constraints in the standard pooling problem. Robust optimization reformulation can be applied to these constraints, but the result is a global optimization problem. In Section 2, a robust formulation for the standard pooling problem is derived. Section 3 demonstrates the computational complexity of the resulting problem for box, ellipsoidal, and polyhedral uncertainty sets and how the optimal flows in the network change when varying degrees of uncertainty are considered.

2. A robust pooling formulation

We consider the q-formulation of the standard pooling problem (Haverly, 1978) in which the uncertain component concentrations only occur in the quality constraints. This formulation is favorable for robust optimization because the uncertain parameters do not occur in any equality constraints. The robust counterpart of the uncertain quality constraint is

$$\sum_{\substack{l:(l,j) \in T_Y \\ i:(i,l) \in T_X}} \tilde{C}_{i,k} \cdot q_{i,l} \cdot y_{l,j} + \sum_{i:(i,j) \in T_Z} \tilde{C}_{i,k} \cdot z_{i,j} \begin{cases} \geq P_{j,k}^L \left(\sum_{l:(l,j) \in T_Y} y_{l,j} + \sum_{i:(i,j) \in T_Z} z_{i,j} \right) \\ \leq P_{j,k}^U \left(\sum_{l:(l,j) \in T_Y} y_{l,j} + \sum_{i:(i,j) \in T_Z} z_{i,j} \right) \end{cases}, \forall j, k, \tilde{C}_{i,k} \in \mathcal{U}_p, \quad (1)$$

where $\tilde{C}_{i,k}$ is the uncertain concentrations of component k in source i , $P_{j,k}^L$ and $P_{j,k}^U$ are their lower and upper limits at pool j respectively, and \mathcal{U}_p is the uncertainty set. The decision variables are $q_{i,l}$, the fraction of flow to pool l from source i , $y_{l,j}$, the flow from pool l to terminal j , and $z_{i,j}$, the direct flow from source i to terminal j . The sets T_X, T_Y, T_Z describe the connections between sources, pools and terminals. By introducing the indicator function

$$\mathbb{1}(s \in S) = \begin{cases} 1 & s \in S \\ 0 & s \notin S \end{cases}$$

and rearranging, we can bring eqn. 1 into standard form

$$\sum_i \tilde{C}_{i,k} a_{i,j} \begin{cases} \leq b_{j,k}^U \\ \geq b_{j,k}^L \end{cases}, \quad \forall j, k, \tilde{C}_{i,k} \in \mathcal{U}_p,$$

where

$$a_{i,j} = \sum_{l:(l,j) \in T_Y} \left[\mathbb{1}((i,l) \in T_X) y_{l,j} q_{i,l} \right] + \mathbb{1}((i,j) \in T_Z) z_{i,j}, \text{ and} \quad (2)$$

$$b_{j,k}^{U/L} = P_{j,k}^{U/L} \left(\sum_{l:(l,j) \in T_Y} y_{l,j} + \sum_{i:(i,j) \in T_Z} z_{i,j} \right). \quad (3)$$

We define the uncertainty set \mathcal{U}_p as

$$\mathcal{U}_p = \left\{ \tilde{C}_{i,k} = C_{i,k} + \hat{C}_{i,k} \xi_{i,k} \mid \|\xi_k\|_p \leq r \right\},$$

where $\xi_k = (\dots, \xi_{i,k}, \dots)^T$, $C_{i,k}$ is the nominal value of $\tilde{C}_{i,k}$, and $\hat{C}_{i,k}$ its maximum deviation. For $p = 1$ this corresponds to a polyhedral, for $p = 2$ to an ellipsoidal, and for $p = \infty$ to a box uncertainty set. For each set, standard robust optimization reformulation techniques can be used to obtain the deterministic equivalent of the robust counterpart:

$$\sum_i C_{i,k} a_{i,j} + r[\dots] \leq b_{j,k}^u \quad \forall j,k \quad (4a)$$

$$- \mu_{i,j} \leq a_{i,j} \leq \mu_{i,j} \quad \forall i,j \quad (4b)$$

$$\left(\lambda_{j,k}^u \geq \hat{C}_{i,k} \mu_{i,j} \right) \quad \forall i,j,k \quad (4c)$$

where $[\dots]$ is $\sum_i \hat{C}_{i,k} \mu_{i,j}$ for $p = \infty$, $\sqrt{\sum_i \hat{C}_{i,k}^2 \mu_{i,j}^2}$ for $p = 2$, and $\lambda_{j,k}^u$ for $p = 1$ and constraint 4c is only needed for $p = 1$. Substituting eqn. 2 for $a_{i,j}$ and simplifying gives

$$r[\dots] \leq b_{j,k}^u - \sum_{\substack{l:(l,j) \in T_Y \\ i:(i,l) \in T_X}} C_{i,k} \cdot q_{i,l} \cdot y_{l,j} - \sum_{i:(i,j) \in T_Z} C_{i,k} \cdot z_{i,j} \quad \forall j,k \quad (5a)$$

$$- \mu_{i,j} \leq \sum_{l:(l,j) \in T_Y} q_{i,l} y_{l,j} + z_{i,j} \leq \mu_{i,j} \quad \forall (i,j) \in T_Z \quad (5b)$$

$$- \mu_{i,j} \leq \sum_{l:(l,j) \in T_Y} q_{i,l} y_{l,j} \leq \mu_{i,j} \quad \forall (i,j) \notin T_Z \quad (5c)$$

$$\left(\lambda_{j,k}^u \geq \hat{C}_{i,k} \mu_{i,j} \right) \quad \forall i,j,k \quad (5d)$$

where $[\dots]$ is defined in the same way as above.

While the box and ellipsoidal uncertainty set both add $\mathcal{O}(|i| \cdot |j|)$ constraints, the polyhedral set adds $\mathcal{O}(|i| \cdot |j| \cdot |k|)$ constraints. An advantage of the polyhedral set, however, is that the problem remains bilinear, while the ellipsoidal set introduces a square root, which can be problematic numerically. Squaring each side of eqn. 5a avoids this, but the squared constraint is only equivalent if the nominal quality constraints (eqn. 1 with $\tilde{C}_{i,k}$ replaced by $C_{i,k}$) are added, increasing the total number of constraints once again.

3. Results

The robust formulation outlined above was applied to 14 instances from the literature (Adhya et al., 1999; Foulds et al., 1992; Ben-Tal et al., 1994; Haverly, 1978; Audet et al., 2004). The model was implemented in GAMS 25.1.2 and solved using ANTIGONE 1.1 (Misener and Floudas, 2014) on an i7-6700 CPU with 8×3.4 GHz and 16GB RAM. Each instance was solved for 30 values of r using the box, ellipsoidal, and polyhedral uncertainty set with a time limit of 1 hr, a tolerance of 10^{-6} , and $\hat{C}_{i,k} = C_{i,k}$.

Fig. 1 shows the performance of each uncertainty set as a function of its size r for four representative instances. As expected, the fraction of the nominal objective value achieved decreases as

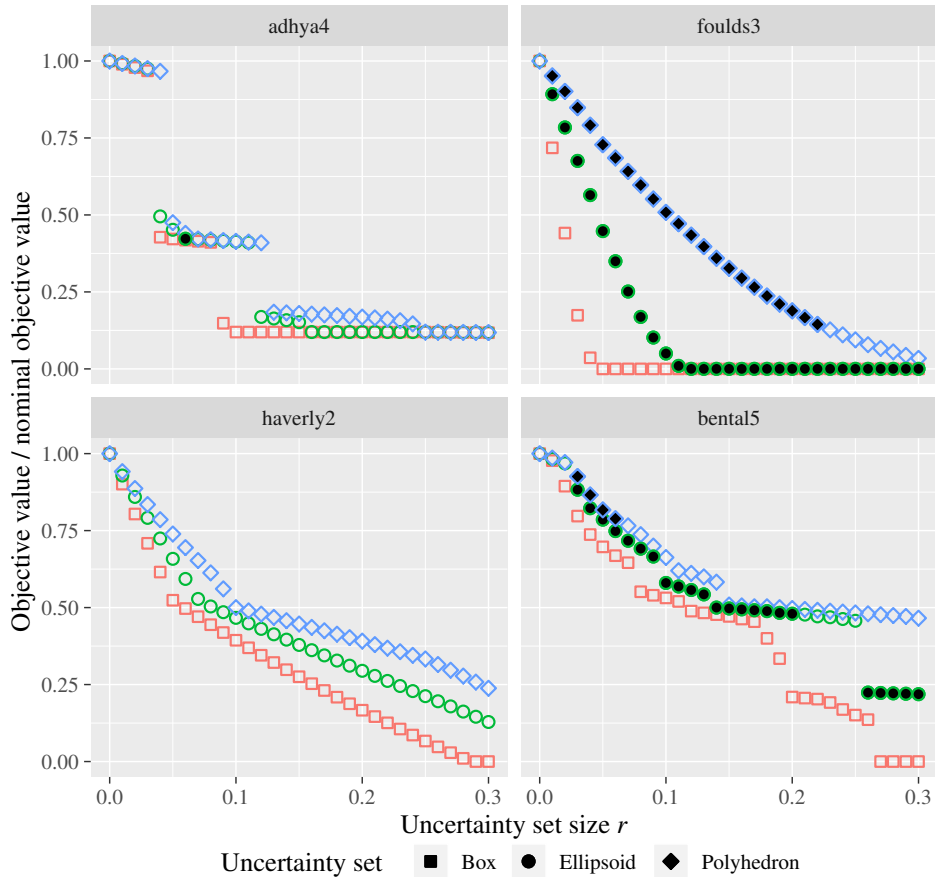


Figure 1: Objective value (relative to nominal case) for different uncertainty set types and sizes for four literature instances. Points filled black were not solved to global optimality within 1 hr.

the uncertainty set size r is increased. Since the polyhedral set is always smallest and the box set always largest, they consistently achieve the best and worst objective value respectively. For points filled in black the model could not be solved to optimality within 1 hr. Table 1 shows the fraction of instances solved for each uncertainty set. While the box uncertainty set could be solved for all instances, the polyhedral and especially the ellipsoidal cannot, due to the increased number of constraints for these formulations. The consistency between solutions which have and have not been solved globally indicates however, that in a lot of cases the global optimum (or a solution close to it) may have already been found though it has not been certified. For those instances which could be solved to optimality, Table 1 shows the median time taken across instances. While the box and polyhedral uncertainty set have very similar median times, the ellipsoidal set shows a moderate increase. The solution times for the box and polyhedral set are generally very close to the nominal case. As in linear robust optimization, the ellipsoidal set increases the complexity of the nominal problem, while the box and polyhedral set largely retain it.

Fig. 2 shows the obtained solutions for three different values of r for instance Adhya1 (Adhya et al., 1999) using a polyhedral set. The width of the arrows between nodes indicates the fraction of flow from/to each pool. Edges from a source to a pool are also labeled with this fraction, while edges from a pool to a terminal are labeled with the absolute flow. In the nominal case ($r = 0$),

Uncertainty set	% instances solved	median time [s]
Box	100	0.14
Ellipsoid	66	1.42
Polyhedron	83	0.15

Table 1: Percentage of instances solved to global optimality within 1 hr time limit for different uncertainty set types.

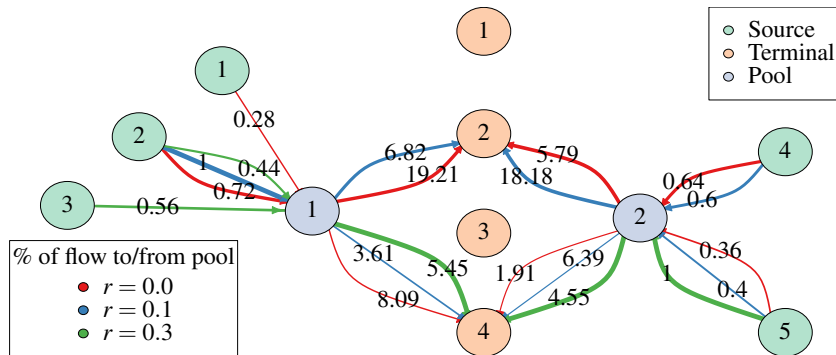


Figure 2: Active source, pools, and terminals for three different uncertainty set sizes r using instance Adhya1 with the polyhedral uncertainty set. The width of the arrows shows the percentage of flow to/from each pool.

both product 2 and 4 are produced. As r is increased, hedging against more uncertainty, the total amount of products 2 and 4 produced remains constant, but the fraction coming from pool 1 increases drastically. The utilization of sources largely remains the same, with the exception of source 1. Once r is increased past 0.14, the quality of product 2 cannot be guaranteed anymore for all possible realizations of the uncertainty. This leads to a jump in the expected profit from 446.2 to 65.9. Similar jumps can be seen in Fig. 1 for instances Adhya4 and Bental5. In this regime, both sources 1 and 4 are replaced by source 3. All of this shows that optimal solution is clearly very dependent on how much uncertainty one wants to hedge against. In practice, the size of the uncertainty set therefore has to be determined based on the risk aversion of the decision maker.

4. Conclusion

Applying robust optimization to the non-convex pooling problem leads to a global optimization problem with increased complexity compared to the nominal case. The tractability of the resulting reformulation with global optimization solvers is highly dependent on the selected uncertainty set. While simple box uncertainty sets hardly increase computational time, more advanced ellipsoidal and polyhedral sets are more difficult to solve. The relevance of optimization under uncertainty is supported by the significant changes in the solution observed when different degrees of uncertainty are taken into account.

5. Acknowledgements

This work was funded by the Engineering & Physical Sciences Research Council (EPSRC) Center for Doctoral Training in High Performance Embedded and Distributed Systems (EP/L016796/1), an EPSRC/Schlumberger CASE studentship to J.W. (EP/R511961/1, voucher 17000145), and an EPSRC Research Fellowship to R.M. (EP/P016871/1).

References

- N. Adhya, M. Tawarmalani, N. V. Sahinidis, 1999. A Lagrangian Approach to the Pooling Problem. *Industrial & Engineering Chemistry Research* 38 (5), 1956–1972.
- M. Alfaki, D. Haugland, 2013. Strong formulations for the pooling problem. *Journal of Global Optimization* 56 (3), 897–916.
- C. Audet, J. Brimberg, P. Hansen, S. L. Digabel, N. Mladenović, 2004. Pooling Problem: Alternate Formulations and Solution Methods. *Management Science* 50 (6), 761–776.
- R. Baltean-Lugojan, R. Misener, 2018. Piecewise parametric structure in the pooling problem: from sparse strongly-polynomial solutions to NP-hardness. *Journal of Global Optimization* 71 (4), 655–690.
- A. Ben-Tal, D. den Hertog, J.-P. Vial, 2015. Deriving robust counterparts of nonlinear uncertain inequalities. *Mathematical Programming* 149 (1-2), 265–299.
- A. Ben-Tal, G. Eiger, V. Gershovitz, 1994. Global minimization by reducing the duality gap. *Mathematical Programming* 63 (1-3), 193–212.
- C. Floudas, V. Visweswaran, 1990. A global optimization algorithm (GOP) for certain classes of nonconvex NLPsI. *Theory. Computers & Chemical Engineering* 14 (12), 1397–1417.
- L. R. Foulds, D. Haugland, K. Jörnsten, 1992. A bilinear approach to the pooling problem.
- C. E. Gounaris, R. Misener, C. A. Floudas, 2009. Computational Comparison of PiecewiseLinear Relaxations for Pooling Problems. *Industrial & Engineering Chemistry Research* 48 (12), 5742–5766.
- C. E. Gounaris, W. Wiesemann, C. A. Floudas, 2013. The Robust Capacitated Vehicle Routing Problem Under Demand Uncertainty. *Operations Research* 61 (3), 677–693.
- I. E. Grossmann, R. M. Apap, B. A. Calfa, P. García-Herreros, Q. Zhang, 2016. Recent advances in mathematical programming techniques for the optimization of process systems under uncertainty. *Computers and Chemical Engineering* 91, 3–14.
- C. A. Haverly, 1978. Studies of the behavior of recursion for the pooling problem. *ACM SIGMAP Bulletin* (25), 19–28.
- S. L. Janak, C. A. Floudas, 2005. Advances in robust optimization approaches for scheduling under uncertainty. *Computer Aided Chemical Engineering* 20 (C), 1051–1056.
- J. Li, R. Misener, C. A. Floudas, 2012a. Scheduling of crude oil operations under demand uncertainty: A robust optimization framework coupled with global optimization. *AIChE Journal* 58 (8), 2373–2396.
- X. Li, E. Rmagan, A. Tomaszgard, P. I. Barton, 2011. Stochastic pooling problem for natural gas production network design and operation under uncertainty. *AIChE Journal* 57 (8), 2120–2135.
- X. Li, A. Tomaszgard, P. I. Barton, 2012b. Decomposition strategy for the stochastic pooling problem. *Journal of Global Optimization* 54 (4), 765–790.
- Z. Li, M. G. Ierapetritou, 2008. Robust Optimization for Process Scheduling Under Uncertainty. *Industrial & Engineering Chemistry Research* 47 (12), 4148–4157.
- C. A. Meyer, C. A. Floudas, 2004. Trilinear Monomials with Mixed Sign Domains: Facets of the Convex and Concave Envelopes. *Journal of Global Optimization* 29 (2), 125–155.
- R. Misener, C. A. Floudas, 2010. Global Optimization of Large-Scale Generalized Pooling Problems: Quadratically Constrained MINLP Models. *Industrial & Engineering Chemistry Research* 49 (11), 5424–5438.
- R. Misener, C. A. Floudas, 2014. ANTIGONE: Algorithms for coNTinuous / Integer Global Optimization of Nonlinear Equations. *Journal of Global Optimization* 59 (2-3), 503–526.
- R. Misener, J. P. Thompson, C. A. Floudas, 2011. APOGEE: Global optimization of standard, generalized, and extended pooling problems via linear and logarithmic partitioning schemes. *Computers & Chemical Engineering* 35 (5), 876–892.
- C. Ning, F. You, 2017. A data-driven multistage adaptive robust optimization framework for planning and scheduling under uncertainty. *AIChE Journal* 63 (10), 4343–4369.
- I. Quesada, I. Grossmann, 1995. Global optimization of bilinear process networks with multicomponent flows. *Computers & Chemical Engineering* 19 (12), 1219–1242.
- C. Shang, F. You, 2018. Distributionally robust optimization for planning and scheduling under uncertainty. *Computers and Chemical Engineering* 110, 53–68.
- M. Tawarmalani, N. V. Sahinidis, 2004. Global optimization of mixed-integer nonlinear programs: A theoretical and computational study. *Mathematical Programming* 99 (3), 563–591.
- R. Vujanic, P. Goulart, M. Morari, 2016. Robust Optimization of Schedules Affected by Uncertain Events. *Journal of Optimization Theory and Applications* 171 (3), 1033–1054.
- D. S. Wicaksono, I. A. Karimi, 2008. Piecewise MILP under- and overestimators for global optimization of bilinear programs. *AIChE Journal* 54 (4), 991–1008.
- Q. Zhang, I. E. Grossmann, C. F. Heuberger, A. Sundaramoorthy, J. M. Pinto, 2015. Air separation with cryogenic energy storage: Optimal scheduling considering electric energy and reserve markets. *AIChE Journal* 61 (5), 1547–1558.

A model identification approach for the evaluation of plant efficiency

Keivan Rahimi-Adli^{a,b,*}, Patrick D. Schiermoch^a, Benedikt Beisheim^{a,b}, Simon Wenzel^b and Sebastian Engell^b

^aINEOS Manufacturing Deutschland GmbH, Alte Str. 201, 50769 Köln, Germany

^bProcess Dynamics and Operations Group, Department of Biochemical and Chemical Engineering, TU Dortmund University, Emil-Figge-Str. 70, 44227 Dortmund, Germany
keivan.rahimi-adli@ineos.com

Abstract

Regulations and the public expectations on improving efficiency, reducing the carbon footprint and lowering the environmental impact drive the process industry towards improved operation and the development of new technologies. The efficiency of an existing production plant depends on a variety of factors like capacity utilisation, raw material quality, ambient temperature or operational performance. Identifying the influence of these factors on the performance of the plant helps to take suitable measures to drive it towards a more efficient operation. One approach to assess the resource efficiency potential of a plant is the comparison of the actual performance with the best possible operation under the given circumstances. This work presents a surrogate modelling approach for the identification of the best possible operation based on historical data. The surrogate model is compared to a more detailed rigorous model and advantages and possible shortcomings of the surrogate approach are discussed based on real production data at INEOS in Köln.

Keywords: Surrogate models, plant efficiency, energy management systems, model detail level, model identification

1. Introduction

The process industry is constantly developing methods for the evaluation of their resource consumption and the identification of possible improvement potentials. In cases where there are no structural changes of the process planned, on the one end this can be achieved by implementing Advanced Process Control (APC) solutions, which is time consuming and expensive. On the other end, there are well-trained operators who are often able to realize a significant fraction of the APC saving potential, if information on the magnitude of the performance gaps is accessible and the experience about how to improve the operational efficiency can be used. The international standard ISO50001:2011 demands the use of energy performance indicators (EnPI) which have to be compared with an energy baseline. The idea of the Best Demonstrated Practice (BDP), as shown in Fig. 1, is similar and provides the operators with a performance reference model which represents the most resource efficient and stable production at a specific instance of non-influenceable

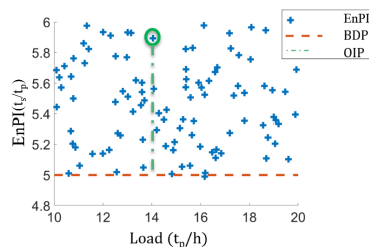


Figure 1: Illustrative example of the BDP concept

circumstances, as e.g. plant load. By comparing the real-time EnPI, which is defined as the specific steam consumption at a particular point in time in this example, with its BDP, the operational improvement potentials (OIP) can be identified (NAMUR WG 4.17, 2017).

2. BDP Model

The level of detail of the BDP models can vary from rigorous models to simple input-output models. The accuracy and the extrapolation capability of rigorous models are advantageous. However, the time and effort needed to develop these models is usually high. On the other end of the scale are input-output models based on linear regression which cannot always represent the complexities of the chemical processes properly.

An alternative to these two types of models are surrogate models (see e.g. Cozad et al. (2014)). In this modelling approach the process data is used to fit a model to the observations. The development of such models requires considerably less effort compared to the development of rigorous models and they are able to capture the plant behaviour better than linear regression models. Furthermore, the evaluation of the surrogate models is easier which makes them attractive for large scale optimisation (Søndergaard, 2003). On the downside, the validity of the surrogate models is limited to the range of the data that is used for their fitting and the results of the model for extrapolated data must be used with care.

2.1. Surrogate modelling procedure

This section briefly discusses the approach to surrogate modelling of the BDP curves that has been developed and implemented at INEOS in Köln. A detailed description of the procedure can be found in Beisheim et al. (2018). As depicted in Fig. 2, the method consists of five general steps. The first step is the acquisition of measurement data. The goal of this step is to collect representative and reliable measurements of the performance of the plant, where aspects as e.g. removal of gross errors, stationarity, selection of suitable sampling times and removal of abnormal operation windows have to be considered.

The second step is the preprocessing of the data. The goal of this step is to remove outliers, classify the data and to standardise. For the latter mean centring and unit variance scaling is used. Data standardisation is useful for the clustering of the data, which is explained in the next step.

The third step of the method is data clustering. The goal of this step is to reduce the large amount of the measurement data into a much smaller number of a few representatives of different operating regimes, which are then used for model fitting. In this work, the `kmeans++` algorithm (Arthur and Vassilvitskii, 2007) is applied, which is an extension of the `kmeans` algorithm (MacQueen et al., 1967). The distance metric used for clustering is the Euclidean distance of the data from the cluster centres and therefore it is sensitive to the magnitude of the data and is prone to the assignment of a higher influence on a variable with a higher magnitude. As the important factor to consider in this work is the effect of the variation of the non-influenceable factors on the resource efficiency, the data is pre-processed by the subtraction of the mean of each variable and dividing the values by the standard deviation. The `kmeans++` algorithm requires the number of the clusters as an input. The clustering algorithm assigns a centre to each cluster that represents the average of the points in that cluster. As the goal of the BDP model is to calculate the most efficient operational domain, the cluster centres are not used as representative values. Instead, a percentile analysis for each cluster

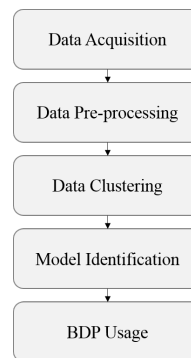


Figure 2: Steps of the BDP modelling procedure

is performed:

$$\mathbf{r}_j = \frac{1}{|\mathcal{R}_j|} \sum_{\mathbf{x} \in \mathcal{R}_j} \mathbf{x} \quad (1)$$

$$\mathbf{x} \in \mathcal{R}_j \quad \forall \quad P_{j,n} \leq \text{EnPI}(\mathbf{x}) \leq P_{j,m} \quad (2)$$

$$\mathcal{R}_j \subseteq \mathcal{X} \quad (3)$$

$$\text{EnPI}_{\mathcal{R}_j} = \frac{1}{|\mathcal{R}_j|} \sum_{\mathbf{x} \in \mathcal{R}_j} \text{EnPI}(\mathbf{x}), \quad (4)$$

where \mathcal{R}_j denotes the set of points which are assigned to the cluster j , $|\mathcal{R}_j|$ is its cardinality and \mathbf{r}_j is the cluster centre. $P_{j,n}$, $P_{j,m}$ are the lower and upper percentile bounds for cluster j . These bounds are used to select achievable good operation points as representatives, $\text{EnPI}_{\mathcal{R}_j}$, for each cluster. The chosen percentiles are tuning factors and can be modified for each case.

The surrogate model development is an adapted ALAMO approach (Cozad et al., 2014). It generates simple and accurate models from simulated or experimental data. In order to overcome the drawbacks of linear regression models, ALAMO selects a combination of transformed inputs using simple basis functions that fit the responses with an acceptable accuracy. The set of basis functions are defined by the user and ALAMO selects the most suitable ones and their respective parameters as a result of an optimisation. The details of the implemented adapted version of the ALAMO approach can be found in Beisheim et al. (2018). The model is fitted by solving an optimisation problem formulated as:

$$\min_{\beta, y} \sum_{i=1}^N e_i \quad (5)$$

$$\text{s.t.} \quad e_i \geq z_i - \sum_{j \in \mathcal{B}} \beta_j X_{ij} \quad i = 1, \dots, N \quad (6)$$

$$e_i \geq \sum_{j \in \mathcal{B}} \beta_j X_{ij} - z_i \quad i = 1, \dots, N \quad (7)$$

$$\sum_{j \in \mathcal{B}} y_j = B \quad (8)$$

$$-U_j(1-y_j) \leq \sum_{i=1}^N X_{ij} \left(z_i - \sum_{j \in \mathcal{B}} \beta_j X_{ij} \right) \leq U_j(1-y_j) \quad j \in \mathcal{B} \quad (9)$$

$$\beta^l y_j \leq \beta_j \leq \beta^u y_j \quad j \in \mathcal{B} \quad (10)$$

$$y_j = \{0, 1\} \quad j \in \mathcal{B}, \quad (11)$$

where z_i are the values of the responses, X is the matrix of the transformed inputs and β is the coefficient vector of X . \mathcal{B} is the set of the basis functions and B is the number of the maximum allowed terms of the model. The binary variables y_j are equal to 1 if their respective basis function is selected. β^u , and β^l are the upper and lower bounds for the coefficient vector. N is the number of the samples and the indices i and j correspond to the samples and the basis functions respectively. The optimisation is done repeatedly for increasing values of B and the suitable level of complexity is decided based on the modified corrected Akaike Information Criterion (AIC_c). Eq. 9 is an additional constraint, which as described in Beisheim et al. (2018) uses the relaxed bounds U_j to convert the problem formulation into an MILP.

2.2. Application to production data at INEOS in Köln

In this section, the surrogate BDP modelling approach introduced in Sec. 2.1 is applied to two sections of the ethylene oxide production plant at INEOS in Köln and the results are compared to

the results of a rigorous model. All of the plots and information in this section are presented in the scaled space due to the confidentiality of the data.

2.2.1. Surrogate approach

The algorithm described in Sec. 2.1 is used with $[1, x^{\pm[1,2,3]}, \exp(x)]$ as basis functions. The first example is a section of the plant which processes the products from the ethylene oxide reactor. The upper and lower percentile limits, $P_{j,n}$ and $P_{j,m}$ are defined as 5 and 10 respectively. As a result of discussions with plant personnel, the production load (\dot{m}_p) is defined as the only non-influenceable factor and is used to calculate the resource efficiency of the specific steam consumption ($\text{EnPI}_{s,1}$). The number of the clusters is defined as 16. The algorithm results in a model with two basis functions:

$$\text{EnPI}_{s,1} = -3.1902\dot{m}_p^2 + 1.4843 \exp(\dot{m}_p) \quad (12)$$

Fig. 3 depicts the results of the model fitting. Each data cloud (shown by coloured points) represents a cluster and the circles and the + signs represent the cluster centres and the percentile centres that are used for model fitting. As mentioned in Sec. 2, extrapolation of the model should be avoided. Therefore, the range of validity of the model is defined as the range between the minimum and maximum of the percentile centre values, and the data outside of this range are shown with dark diamonds.

The second investigated section is the ethylene oxide reactor. Both the main and the side reactions are exothermic and the produced heat is used for steam generation. The heat of reaction of the side reaction is significantly higher than the heat produced by the main reaction. Therefore, the reduction of the catalyst selectivity increases the steam production. Considering this fact, the load of the reactor ($\dot{m}_{p,r}$) and the catalyst selectivity (S) which is available as a measurement, are used as non-influenceable factors for modelling the resource efficiency of the steam production ($\text{EnPI}_{s,2}$). As the number of non-influenceable factors in this case is higher than the previous one, the number of the clusters is increased to 30. The other modification in this case is the choice of the percentile limits. Considering that this case is about the modelling of the production of steam, so higher values are preferable, the BDP is defined as the highest possible amount of steam production. Therefore the lower and upper percentile limits are defined as 90 and 95 respectively. The algorithm identifies a model, shown in Fig. 4, using three basis functions as:

$$\text{EnPI}_{s,2} = -0.0669\dot{m}_{p,r}^3 - 5.7478S + 3.0651 \exp(S). \quad (13)$$

A conservative method for the definition of the domain of validity of regression models in higher dimensions is the "Convex Hull" of the input variables (Brooks et al., 1988). This method is used here to calculate the validity bounds of the model. The importance of the validity range is more obvious in this example compared to the previous model. It can be seen that outside of the convex hull, the model diverges from the data and should not be trusted.

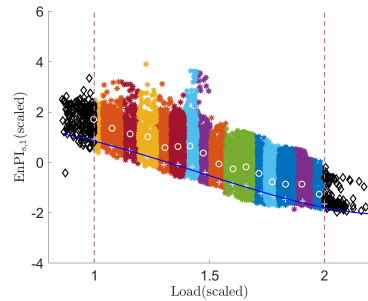


Figure 3: Surrogate BDP model of the product processing section of the ethylene oxide plant

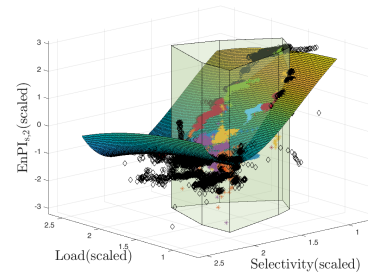


Figure 4: Surrogate BDP model of the steam production of the ethylene oxide reactor

2.2.2. Rigorous approach

In this section, a more detailed model of the ethylene oxide reactor is developed that is based on physico-chemical principles and measurement data. This model is then used to make a comparison between the detailed model and the proposed surrogate modelling approach and to identify the advantages and shortcomings of each. The model is based on the energy balance around the reactor as follows:

$$\frac{\partial Q}{\partial t} = \bar{C}_{p,in} \dot{n}_{in} T_{in} - \bar{C}_{p,out} \dot{n}_{out} T_{out} - \dot{Q}_{cool} + \sum_i (-\Delta H_{R,i} r_i) - \dot{Q}_{loss}, \quad (14)$$

where the left hand side of the equation is set to zero due to the assumed stationarity of the process. The first two terms on the right hand side of the equation represent the amount of the heat entering and leaving the reactor with the material streams. $\bar{C}_{p,j}$, \dot{n}_j , T_j denote average specific heat capacity of the gas mixture, mole flow and temperature at position j . $\sum_i (\Delta H_{R,i} r_i)$ represents the produced heat of reaction, \dot{Q}_{cool} is the heat transferred from the reactor to the cooling fluid inside the jacket and \dot{Q}_{loss} is the amount of heat that is transferred to the environment.

\bar{C}_p is calculated as the weighted average of the values $C_{p,j}$ of the different components using the volumetric percentage values available in the plant, where the dependencies of the values of $C_{p,j}$ of the components on the temperature are determined based on the Shomate equation (Linstrom and Mallard, 2018). The molar flow \dot{n}_{in} is not measured, but can be calculated based on the volumetric flow rate and the ideal gas law. The situation for \dot{n}_{out} is more complex, as there is no direct flow measurements at the output of the reactor. However, using the composition measurements and the change of the volumetric percentage of an inert gas present in the mixture, this flow can be estimated.

The values of $\Delta H_{R,i}$ for each reaction are known and $\sum_i (-\Delta H_{R,i} r_i)$ is calculated using this information together with the selectivity measurement and the estimation of the ethylene conversion based on its volumetric percentage at the inlet and outlet flows. \dot{Q}_{cool} is assumed to be equal to the amount of the heat required for the production of steam.

Considering the above mentioned assumptions, the value of \dot{Q}_{loss} can be calculated from eq. 14. \dot{Q}_{loss} can also be described as:

$$\dot{Q}_{loss} = k(T_{cf} - T_{amb}), \quad (15)$$

where T_{cf} and T_{amb} are equal to the cooling fluid and ambient temperature, and k is the heat transfer coefficient. Assuming that k remains constant for an unchanged setup (physical structure, cooling fluid etc.), its value can be estimated based on eq.15.

Eq. 14 is rearranged and \dot{Q}_{cool} , and thus the amount of steam produced is calculated based on the energy balance. Fig. 5 depicts the real steam production together with the values that are calculated based on the surrogate BDP model and the detailed model at two different time windows. The x-axis and the y-axis represents the time and the resource efficiency of steam production $\text{EnPI}_{s,2}$.

From Fig. 5a it can be seen that the surrogate model predicts a higher steam production rate compared to the real data and the detailed model. As the result of a deeper investigation it became clear that the conversion of ethylene in the reactor is lower in this period, which is not considered by the surrogate model and thereby deviates from reality. It is expected that the addition of conversion as a new non-influenceable factor to the surrogate model improves the accuracy of its prediction. Results from a second interesting time window are presented in Fig. 5b. Here it can be seen that the amount of produced steam predicted by the detailed model is significantly higher after a period of time. The reason is, that the heat exchanger that is used for steam production has a limit for the heat removal. Therefore, as a result of the decrease of the catalyst selectivity and the increase of the amount of heat produced by the reaction, the heat removal system is not able to convert all of the heat into steam, and this heat is lost in an extra heat exchanger against a large stream of cooling

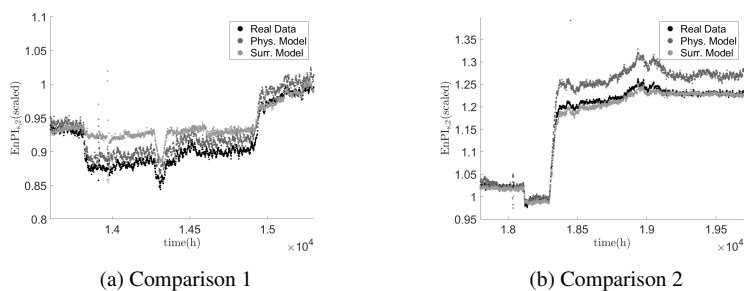


Figure 5: Comparison of the physical and the surrogate BDP models against production data

water. This limitation is identified with the help of the rigorous model, which is not possible with a surrogate BDP model.

3. Conclusions

In this work a surrogate and a more detailed modelling approach were used to calculate the BDP of production plants. It was observed that the surrogate modelling approach has a good performance in fitting the BDP data and requires a considerably lower modelling effort compared to more rigorous models. The proposed surrogate modelling approach is flexible and does not require a large effort. The time spent for the development of the surrogate model of the reactor was approximately 20 % of time that was needed for the development of the rigorous model. However, the range of trustworthiness of surrogate models is limited to the range of the observed data. Therefore, the performance of the models cannot be trusted beyond the data used for fitting them. Also, as discussed above for the situation depicted in Fig. 5b, deviations of the observed BDP from the possible best performance cannot be detected using a surrogate model and improvements of the plant that realize the potential cannot be deduced.

Acknowledgment

The project leading to this publication has received funding from the European Union's Horizon 2020 research and innovation programme under grant agreement No 723575 (CoPro) in the framework of the SPIRE PPP.

References

- D. Arthur, S. Vassilvitskii, 2007. k-means++: The advantages of careful seeding. In: Proceedings of the eighteenth annual ACM-SIAM symposium on Discrete algorithms. Society for Industrial and Applied Mathematics, pp. 1027–1035.
- B. Beisheim, K. Rahimi-Adli, S. Krämer, S. Engell, 2018. Energy performance analysis of continuous processes using surrogate models. Submitted to Energy, Manuscript No. EGY-D-18-07030.
- D. G. Brooks, S. S. Carroll, W. A. Verdini, 1988. Characterizing the domain of a regression model. *The American Statistician* 42 (3), 187–190.
- A. Cozad, N. V. Sahinidis, D. C. Miller, 2014. Learning surrogate models for simulation-based optimization. *AIChE Journal* 60 (6), 2211–2227.
- P. Linstrom, W. Mallard, 2018. Nist chemistry webbook, nist standard reference database number 69, national institute of standards and technology data.
- J. MacQueen, et al., 1967. Some methods for classification and analysis of multivariate observations. In: Proceedings of the fifth Berkeley symposium on mathematical statistics and probability. Vol. 1. Oakland, CA, USA, pp. 281–297.
- NAMUR WG 4.17, 2017. Resource efficiency indicators for monitoring and improving resource efficiency in processing plants. NAMUR Recommendation 162, NAMUR, NAMUR, Leverkusen, Germany.
- J. Søndergaard, 2003. Optimization using surrogate models-by the space mapping technique. Ph.D. thesis, Technical University of Denmark.

Risk-conscious approach to optimizing bioenergy investments in the Brazilian sugarcane industry

Victoria M. Mutran^{a,b}, Celma O. Ribeiro^a, Claudio O. A. Nascimento^a and Benoît Chachuat^{b,*}

^a*Escola Politécnica da Universidade de São Paulo, São Paulo, Brazil*

^b*Centre for Process Systems Engineering, Imperial College London, London, United Kingdom*

b.chachuat@imperial.ac.uk

Abstract

Deciding price policies in order to attract new investments on renewable energy generation remains a challenge to many public policy-makers. This is particularly relevant to the Brazilian sugarcane industry, which has experienced a significant reduction in new bioenergy projects in recent years. Since investment costs thereof are expressive, a producer's willingness to increase energy generation is highly dependent on market conditions. Herein, we propose an optimization model based on portfolio theory to assess different price policies for attracting investment, where historical variations in sugar, ethanol and spot-market electricity prices are accounted for. Results obtained on a representative case study highlight the significant role played by regulated market prices in mitigating financial risks in the sugarcane business. The analysis enables a better understanding of investors' behavior according to their aversion to risk. It could support policy-makers with more effective pricing in the regulated market to keep promoting bioenergy generation.

Keywords: sugarcane, bioenergy, portfolio optimization, risk analysis, CVaR

1. Introduction

The Brazilian sugarcane industry is an example of a successful concerted public effort towards reducing a country's dependency on fossil fuels. In addition to its contribution to the energy sector with ethanol production, sugarcane mills now play an important role in the national electricity matrix. Cogeneration with bagasse—the fibrous residue after sugarcane stalks are crushed to extract their juice—currently holds a share of about 7% of the installed capacity in Brazil. Albeit significant, this share is still far from the industry's full potential, since less than half of all Brazilian mills are currently exporting electricity to the grid. All of Brazil's sugarcane mills are self-sufficient in energy through the use of bagasse for cogeneration of steam and power, but a majority still operates with low efficiency. Because the investment costs for new technologies to improve energy generation are high, a producer's willingness to invest is very sensitive to the market conditions and the prices practiced by the power sector.

Electricity in Brazil may be sold in either one of two ways: the free market and the regulated market. The former consists of a spot market, whereby prices are highly sensitive to the local weather conditions. The latter presents long-term contracts (e.g. over 20-25 years) with a determined rate (tariff) for the supplied power, in the form of power auctions organized by the Brazilian government. Since the free market is inherently high risk, new projects for renewable energy generation are usually enabled by the regulated market. However, the Brazilian government is yet to propose effective policies to incentivize the production of bioelectricity, withholding many producers from

wanting to bear the costs for modernizing their cogeneration systems and connect to the distribution network to sell electricity (Hofsetz and Silva, 2012). The absence of new installed capacity of bioelectricity into the Brazilian matrix in 2019 illustrates this trend perfectly.

Several studies have analyzed scenarios to increase power generation from the sugarcane bagasse. Grisi et al. (2012) applied an optimization model to decide the best economical combinations of sugar, bioethanol, biogas and electricity for production in a sugarcane mill. They highlighted the role of the regulated market in incentivizing sales of surplus power and showed that these sales could increase profits significantly. However, their assessment did not account for price risks, nor did it consider investments on new technologies to increase power production.

Accounting for risks in production and investment decisions is paramount in the sugarcane sector, especially since sugar, ethanol and spot electricity prices have been historically volatile. Hence, recent studies have applied Portfolio Theory to assess production decisions in the sugarcane sector (Carpio and Souza, 2017; Dutenkefer et al., 2018), but technological routes on bioenergy generation in the sugarcane sector have not been assessed yet in light of price risks, to the best of our knowledge.

This paper presents a risk-conscious assessment of investments on bioelectricity projects in sugarcane mills, through the application of a portfolio optimization strategy. Detrimental price scenarios are accounted for by means of the Conditional-Value-at-Risk (CVaR), a single tail risk-measure which is amenable to a fully linear optimization formulation using historical price data. The main objective of the analysis is to gain a better understanding of the role played by price policies on the increase of surplus power generation in the sugarcane sector, while accounting for the impact of bioelectricity sales on the sugar-ethanol business.

The proposed model is presented in Sec. 2. The case study of a generic sugarcane mill is introduced in Sec. 3, whereby investment decisions are assessed with regards to different scenarios of regulated market prices for electricity. The results of this case study are presented and discussed in Sec. 4, and final conclusions are drawn in Sec. 5.

2. Methodology

Our approach consists of modeling the production decisions related to the use of resources in the sugarcane mill and optimizing the trade-off between annual profit and risk in order to assess investments in new bioelectricity capacity.

2.1. Process Model

Production decisions in sugarcane processing plants generally relate to using available resources to produce a range of products that yield the largest economic profit. The resources comprise juice, bagasse, molasse and vinasse, denoted by the set $I = \{\text{ju, bag, mol, vin}\}$, whereas the products consist of sugar, ethanol, fertilizer, free electricity and regulated electricity denoted by $J = \{\text{su, et, fert, free, reg}\}$.

Assuming a predetermined amount of sugarcane to be crushed during the season, denoted here by the parameter Ca , and given a yield of juice extracted in the milling process, a producer needs to choose the amount that will be sent to both sugar and ethanol processes at the onset of the season:

$$r_{\text{ju, su}} + r_{\text{ju, et}} = \gamma_{\text{ju}} Ca \quad (1)$$

where the decision variable $r_{i,j}$ denotes the amount of each resource $i \in I$ used for the production of product $j \in J$; and γ_i is the yield of resource i . The product (sugar) and byproduct (molasse) in

the sugar production process are described by:

$$x_{\text{su}} = \theta_{\text{ju,su}} r_{\text{ju,su}} \quad (2)$$

$$r_{\text{mol,et}} = \gamma_{\text{mol}} x_{\text{su}} \quad (3)$$

where the decision variable x_j denotes the amount of product j ; and $\theta_{i,j}$ are process conversion parameters describing the average yields from resource i to product j . Both juice and molasse can be used as inputs to the ethanol generation process, whereas vinasse, a residue of ethanol distillation, is widely used as a fertilizer in sugarcane plantation areas:

$$x_{\text{et}} = \theta_{\text{ju,et}} r_{\text{ju,et}} + \theta_{\text{mol,et}} r_{\text{mol,et}} \quad (4)$$

$$r_{\text{vin,fert}} = \gamma_{\text{vin}} x_{\text{et}} \quad (5)$$

$$x_{\text{fert}} = \theta_{\text{vin,fert}} r_{\text{vin,fert}} \quad (6)$$

Lastly, but not least importantly, the main residue from the milling process, bagasse, is used in all of Brazilian sugarcane mills as a fuel for thermal, mechanical and electrical energy through the use of power-steam cogeneration systems. Our main objective herein is to assess investments to upgrade bioelectricity from bagasse according to various free and regulated electricity price scenarios. Technological routes to increase energy recovery from bagasse are discussed by Dantas et al. (2013), who identify the use of condensation turbines within a Rankine cycle plant as the most competitive alternative for generating surplus electricity. Accordingly, we consider both a traditional Rankine cycle (base-scenario) and a Rankine cycle with a condensation turbine (improved scenario), so the surplus electricity available for commercialization in the sugarcane mill is such that:

$$x_{\text{free}} + x_{\text{reg}} \leq G_{\text{base}} z_{\text{base}} + G_{\text{imp}} z_{\text{imp}} \quad (7)$$

$$z_{\text{base}} + z_{\text{imp}} = 1 \quad (8)$$

where $z_k \in \{0, 1\}$ is the investment decision variable; G_k is a parameter for the annual surplus electricity expected in each configuration $k \in K$ of the cogeneration process, with the set $K = \{\text{base, imp}\}$; and the surplus electricity production is separated into free and regulated market sales, which present different prices and risks.

2.2. Portfolio Optimization

The goal of the model is to enable risk-conscious decisions regarding product mix and investment in the sugarcane industry. We assume that product prices are the only source of uncertainty, so the optimization model chooses the best production portfolio to maximize profits in the case of detrimental price scenarios. Consequently, the decisions are based on historical records for sugar, ethanol and spot market electricity prices. Such information from past scenarios is used to robustify decisions against potential future short-falls, on account of historical market fluctuations. The validity of our results therefore relies on the assumption that future market conditions can be captured by such historical price records over several years.

As risk measure, we apply the Conditional-Value-at-Risk (CVaR), a coherent and convex, one-tailed measure. Following Rockafellar and Uryasev (2000), CVaR is amenable to a tractable, fully linear formulation, and optimizing CVaR has been shown to indirectly optimize other risk measures such as variance and Value-at-Risk (VaR) as well. Thus, given $q = 1 \dots Q$ historical price observations, $p_{j,q}$ and production costs, c_j for each product $j \in J$, alongside investment costs, $\$k$ for each technology $k \in K$, the proposed portfolio optimization model may be stated as:

$$\max_{x, z, P_q, u_q} \left\{ \underbrace{\frac{1}{Q} \sum_{q=1}^Q P_q}_{=: \text{EP}}, \underbrace{\alpha - \frac{1}{Q(1-\beta)} \sum_{q=1}^Q u_q}_{=: \text{CVaR}} \right\}$$

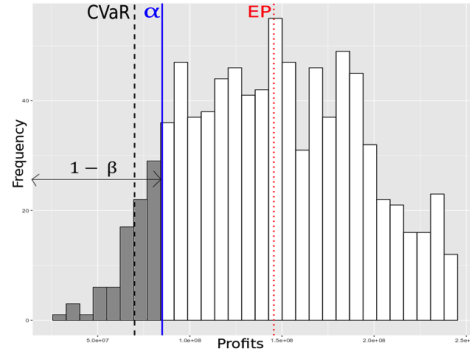
s.t. Model (1)–(8)

$$\forall q = 1 \dots Q,$$

$$P_q = \sum_{j \in J} (p_{j,q} - c_j) x_j - \sum_{k \in K} \$_k z_k$$

$$P_q \geq \alpha - u_q$$

$$u_q \geq 0$$



where P_q are auxiliary variables denoting the profit in each scenario $q = 1 \dots Q$; α is a decision variable corresponding to the VaR at confidence level β ; and $u_q, q = 1 \dots Q$ are auxiliary variables introduced in the formulation in order to reduce it to a linear problem. Note that this is a bi-objective optimization problem, seeking a trade-off between expected profit (EP) and risk (CVaR). Also note that minimizing risk comes to maximizing the CVaR in our formulation. We apply the ε -constraint approach to construct the Pareto frontier here (Miettinen, 1999).

3. Case Study

A case study is defined based on a generic sugarcane plant in order to demonstrate the proposed portfolio optimization model for product mix and investments decisions in the sugarcane sector. This plant processes 3 million tonnes of sugarcane per year, an average-size plant in Brazil. The initial configuration of the cogeneration system is a traditional Rankine cycle running with a 67 bar boiler at 520°C and generating an average surplus electricity of 53 kWh per tonne of sugarcane processed. As the investment alternative, we consider the addition of a condensation turbine that increases surplus power generation to an average of 83 kWh per tonne.

The parameters used in the model are taken from the literature. Production and investment costs are from Grisi et al. (2012) and Dantas et al. (2013), respectively, while process yields and waste generation rates are derived from the Open Sugarcane Process Simulation Platform (Castro et al., 2018). The selling prices of sugar, ethanol and spot market electricity correspond to historical price records at a weekly frequency between 2002 and 2018. These prices are all expressed for the same base-year (2010 US\$) by discounting the effect of inflation, before using them to estimate the expected profit and risk.

Since the regulated market does not present price variations within the contracted supply period, and since those prices are set during the energy auctions prior to making the investments, a sensitivity analysis is performed to assess how different price policies practiced by the government could affect investment and production decisions in the sugarcane sector. The range of regulated market prices used in this analysis is US\$50-100 per MWh, based on the average prices practiced in Brazilian renewable energy auctions over the past 10 years. The results obtained are presented and discussed in the following section.

4. Results and Discussion

The model predicts two distinct investment behaviors within the range of regulated electricity prices investigated in the sensitivity analysis (US\$50-100 per MWh): one when the price in the regulated market is lower than or equal to the expected price of the free market, and the other one when it is higher. This is expected since the regulated prices are not subject to variations and

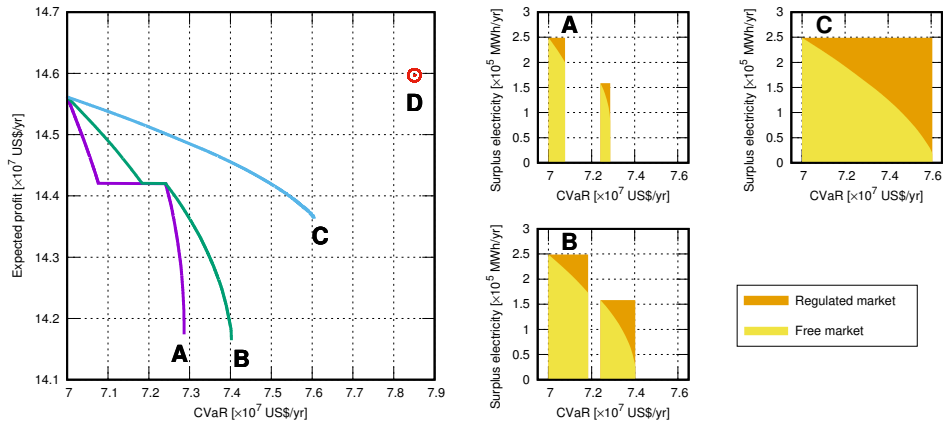


Figure 1: Efficient frontiers and annual surplus electricity sales in the free and regulated markets for different regulated price scenarios. **A**: US\$50/MWh; **B**: US\$60/MWh; **C**: US\$70/MWh; **D**: US\$80/MWh.

are essentially risk-free. Consequently, when regulated prices are greater than the expected value of prices in the free market, a decision-maker will always choose to sell to the regulated market. Given the expected free market price of US\$78 per MWh, this latter behavior is clearly seen in Fig. 1 (scenario **D**).

For lower prices practiced in the regulated market (scenarios **A–C**), there is a tendency for producers to prefer selling at spot market price. As price policies of renewable energy auctions in Brazil become more efficient, they attract sales to the regulated market and thereby generate more interest in investing towards surplus energy generation. Notice that for low regulated market prices, such as US\$50–60 per MWh, only a risk-inclined investor would choose to invest in new bioelectricity projects, aiming most of their surplus electricity sales to the free market. This analysis corroborates the results of two auctions performed by the Brazilian government in 2011, with average prices of US\$52 and US\$57 per MWh, which led to significantly less contracted energy compared with the subsequent auctions in 2013, with average prices of US\$65 and US\$68 per MWh.

Another relevant aspect of this analysis is the disparity of portfolio choices for different risk levels. For lower prices in the regulated market in particular (scenarios **A–B**), a risk-inclined decision aiming to maximize the expected profit only, presents significant difference with a risk-averse decision. For instance, for the regulated market price of US\$60 per MWh, a risk-inclined optimization model would recommend investing in a condensation turbine and selling all of the surplus electricity to the free market, a particularly risky strategy with regard to short-falls.

The efficient frontiers for all four price scenarios is shown on the left plot in Fig. 1. Recall that in our bi-objective optimization formulation, increasing the CVaR reduces risk. Therefore, the risk-neutral scenarios originate from the left and have the greatest expected profits, while risk-averse scenarios are on the right. The three frontiers for which regulated market prices are lower than the expected price in the free market (scenarios **A–C**) all originate from the same point, where a risk-inclined producer would sell all of its surplus electricity to the free market. For regulated price scenarios in the range of US\$50–60 per MWh, the Pareto frontier presents a significant jump because the decision to invest is not made until the risk level is quite high. Below this threshold, the investment is not made, but surplus power is sold entirely to the free market. The sales decisions only change among prices in this range when risk starts playing a more important role than expected profit in the investor's decisions. Regulated prices of US\$70 per MWh or

higher are sufficiently attractive to promote the investment, and we no longer observe a jump in the Pareto frontier. There is furthermore a clear tendency for risk-averse profiles to prefer the regulated market in all of the regulated price scenarios.

There is also a notable gain in efficiency as the prices in the regulated market increase. Although it is expected, this result is interesting as it shows a change in the trade-off between risk and profit among the scenarios. Clearly, raising the regulated market price reduces the gap between the expected profits in risk-averse and risk-inclined strategies. This shows how long-term electricity contracts may play a relevant role as a strategy to mitigate price risks of other products in the sugarcane business.

Finally, as far as assisting price policies to attract more bioelectricity investments is concerned, the sensitivity analysis of the portfolio decisions allows a better understanding of the regulated market prices that would be attractive to sugarcane producers. The results obtained with the cost conditions of the case study suggest that a price range between US\$65-70 per MWh would raise the interest of risk-averse investors in implementing a condensation turbine to increase their surplus electricity generation. Naturally, there are other market aspects that may influence a producer's willingness to invest, such as economic and political uncertainties in Brazil. However, by evidencing the impact of long-term energy contracts on reducing the overall price risks of the sugarcane business and proposing economically attractive prices for the energy auctions, policymakers are more likely to succeed in increasing the share of bioelectricity in the national matrix.

5. Conclusions

This paper has presented a portfolio optimization model to address investment decisions in the Brazilian sugarcane sector. Price risks are accounted for by means of the Conditional-Value-at-Risk, in combination with historical price records of sugar, ethanol and spot market electricity, to enable risk-conscious decisions that are robust to potential shortfalls. A sensitivity analysis has been conducted for a variety of regulated market prices and risk-aversion profiles. Results obtained on a representative case study confirm that the decision to invest on bioenergy projects is highly sensitive to the price policies practiced in the regulated market, evidencing also the importance of bioelectricity sales on the economic performance of sugarcane mills. Typical optimal solutions also present a large sensitivity towards the level of risk, which confirms the need to account for market price variations in the analysis. The developed risk-conscious optimization framework therefore provides a more robust tool to assist policy-makers and to incentivize bioenergy projects in the Brazilian sugarcane industry.

Acknowledgements: The authors thank São Paulo Research Foundation (FAPESP) under grants 2015/50684-9, 2017/17530-3 and 2018/08255-1 for student scholarships and financial support.

References

- L. Carpio, F. Souza, 2017. Optimal allocation of sugarcane bagasse for producing bioelectricity and second generation ethanol in Brazil: Scenarios of cost reductions. *Renewable Energy* 111, 771–780.
- R. E. N. Castro, R. M. B. Alves, A. Hawkes, C. A. O. Nascimento, 2018. Open Sugarcane Process Simulation Platform. *Computer Aided Chemical Engineering* 44, 1819–1824.
- G. Dantas, L. Legey, A. Mazzone, 2013. Energy from sugarcane bagasse in Brazil: An assessment of the productivity and cost of different technological routes. *Renewable & Sustainable Energy Reviews* 21, 356–364.
- R. M. Dutkenfer, C. O. Ribeiro, V. M. Mutran, E. E. Rego, 2018. The insertion of biogas in the sugarcane mill product portfolio: A study using the robust optimization approach. *Renewable & Sustainable Energy Reviews* 91, 729–740.
- E. F. Grisi, J. M. Yusta, R. Dufo-Lopez, 2012. Opportunity costs for bioelectricity sales in Brazilian sucro-energetic industries. *Applied Energy* 92, 860–867.
- K. Hofsetz, M. Silva, 2012. Brazilian sugarcane bagasse: Energy and non-energy consumption. *Biomass & Bioenergy* 46, 564–573.
- K. Miettinen, 1999. *Nonlinear Multiobjective Optimization*. Springer.
- R. T. Rockafellar, S. Uryasev, 2000. Optimization of Conditional Value-at-Risk. *Journal of Risk* 2, 21–41.

Modeling and Multi-Objective Optimization of Syngas Fermentation in a Bubble Column Reactor

Elisa M. de Medeiros,^{a,b,*} John A. Posada,^a Henk Noorman,^{a,c} Rubens Maciel Filho^b

^a*Department of Biotechnology, Delft University of Technology, van der Maasweg 9, Delft 2629 HZ, The Netherlands*

^b*School of Chemical Engineering, University of Campinas, Av. Albert Einstein 500, Campinas 13084-852, Brazil*

^c*DSM Biotechnology Center, PO Box 1, Delft 2600 MA, The Netherlands*

E.MagalhaesdeMedeiros@tudelft.nl

Abstract

Ethanol may be produced from waste materials via a thermochemical-biochemical route employing gasification and syngas fermentation by acetogenic bacteria. This process is considered promising, but commercialization might be hindered by sub-optimal choices of design and operating conditions. In the present work, process systems engineering (PSE) techniques were applied for the optimization of a large-scale syngas fermentation bioreactor. Starting with the development of a dynamic model for a bubble column reactor with gas recycle, the multiple system outputs were studied with Principal Component Analysis to assist in the definition of relevant objective functions, and artificial neural networks were used to approximate the steady-state responses with fast and accurate functions. This framework was then used to conduct a multi-objective optimization aiming at maximizing the ethanol production rate, lower heating value efficiency and ethanol titer, while also minimizing acetic acid titer and reactor volume.

Keywords: bioethanol, syngas fermentation, multi-objective optimization, neural networks, principal component analysis

1. Introduction

Syngas fermentation is a biological process in which facultative autotrophic bacteria called acetogens convert CO, H₂ and CO₂ into cell mass, acids and alcohols. Most wild-type strains produce acetic acid and ethanol –and this is the focus of this work–, but other carboxylic acids and higher alcohols may also be obtained (Wainaina et al., 2018). Since syngas may be produced from the gasification of a diversity of feedstocks, including various waste materials, and syngas fermentation is conducted under mild conditions, this process has been gaining growing attention alongside other conversion pathways for waste to fuels and chemicals. Nonetheless, bench-scale experiments reported in the literature are often marked by difficulties with low productivity and unsatisfactory product selectivity. Moreover, modeling and optimization studies on this process are scarce in the literature, which makes it difficult to conduct appropriate economic and environmental assessments. This work therefore aims to fulfill part of this demand by presenting a bubble column model and a multi-objective optimization (MOO) framework using neural network surrogate models. The ultimate goal is to

provide insights into the process conditions and reactor design that enhance reactor performance and demonstrate how the proposed methods may be used for this purpose.

2. Syngas bioreactor model

2.1. Dynamic bubble column

The bubble column reactor (BCR) hydrodynamic model is based on the Axial Dispersion Model described by Deckwer (1992) and it considers the following main assumptions: (i) isothermal operation; (ii) axial dispersion is neglected in the gas phase; (iii) in the liquid phase substances are carried differentially by convective and dispersive flows; (iv) volumetric mass transfer coefficient ($k_L a$), gas hold-up (ε_G) and liquid dispersion coefficient (D_L) are constant throughout the column; (v) atmospheric pressure at the top of the column. The system consists of 13 types of state variables distributed in space: the concentrations [mol/m^3] of 6 chemical species ($i = \text{CO}, \text{H}_2, \text{CO}_2, \text{ethanol or EtOH}, \text{acetic acid or HAc}, \text{and H}_2\text{O}$) distributed in the gas ($C_{G,i}$) and liquid ($C_{L,i}$) phases, and cell biomass ($C_{L,x}$) which is present in the liquid phase. It is therefore described by $13N$ ordinary differential equations, where N is the number of discretization points considered. The general governing equations are formulated in Eqs. (1)-(3), where x is the spatial variable and u_G is the superficial gas velocity calculated at each point from a mole balance, as the gas expands due to reduced hydrostatic head or shrinks due to consumption by the cells. The hydrodynamic parameters $k_L a$ and ε_G are calculated using correlations by Heijnen and van't Riet (1984) and Deckwer et al. (1974), and a indicates the column operation mode: -1 if counter-current (present case), 1 otherwise. The saturation concentrations $C_{L,i}^*$ and $C_{G,i}^*$ are calculated using Henry's law constants and vapor pressures at 36°C . In Eqs. (1)-(3), the boundary conditions ($x = 0$ and $x = L$) follow the model by Deckwer (1992), and the spatial derivatives are calculated using 1st and 2nd order finite differences.

$$\frac{\partial C_{G,i}}{\partial t} = -\frac{u_G}{\varepsilon_G} \cdot \frac{\partial C_{G,i}}{\partial x} - \frac{C_{G,i}}{\varepsilon_G} \cdot \frac{\partial u_G}{\partial x} - \frac{\dot{n}_{MT}}{\varepsilon_G} \quad (1)$$

$$\frac{\partial C_{L,i}}{\partial t} = -\frac{a u_L}{(1-\varepsilon_G)} \cdot \frac{\partial C_{L,i}}{\partial x} + D_L \frac{\partial^2 C_{L,i}}{\partial x^2} + \frac{\dot{n}_{MT}}{(1-\varepsilon_G)} + v_i C_{L,x} \quad (2)$$

$$\frac{\partial C_{L,x}}{\partial t} = -\frac{a u_L}{(1-\varepsilon_G)} \cdot \frac{\partial C_{L,x}}{\partial x} + D_L \frac{\partial^2 C_{L,x}}{\partial x^2} + \frac{\dot{n}_{MT}}{(1-\varepsilon_G)} + (\mu - k_d) C_{L,x} \quad (3)$$

$$\dot{n}_{MT} = k_L a_i (C_{L,i}^* - C_{L,i}), \quad i = \text{CO}, \text{H}_2, \text{CO}_2 \quad (4a)$$

$$\dot{n}_{MT} = -k_L a_i (C_{G,i}^* - C_{G,i}), \quad i = \text{EtOH}, \text{HAc}, \text{H}_2\text{O} \quad (4b)$$

The biokinetic variables v_i , μ and k_d refer to the specific secretion or production rate [$\text{mmol}\cdot\text{g}^{-1}\cdot\text{h}^{-1}$] of each component i , the specific biomass growth rate [h^{-1}] and the biomass decay rate [h^{-1}]. This kinetic model considers ethanol and acetic acid formation as well as cell growth, using CO/H_2 as energy sources and CO/CO_2 as carbon sources. The parameters that are used in the calculation of these variables were adjusted using experimental data obtained in a continuous stirred-tank reactor with high ethanol concentration, and the detailed modeling and statistical analysis are at the moment unpublished but under submission to a scientific journal (de Medeiros et al., Forthcoming).

2.2. Steady-state surrogate models

Steady-state solutions were generated by integrating the BCR ODE system over a sufficiently long time range using the MATLAB stiff solver *ode15s*. However, this procedure was proved very computationally expensive for some choices of process parameters, specifically when very low dilution rates were used in combination with high recycle ratios, with some case scenarios taking as long as three minutes to be solved. Since the multi-objective evolutionary algorithm requires a large number of objective function evaluations, the objectives were approximated with fast surrogate models. Similar strategies have been adopted before for a variety of chemical processes employing different types of models, such as artificial neural networks (ANNs) (Chambers and Mount-Campbell, 2002) and Kriging models (Quirante and Caballero, 2016). In the present work, multi-layer feedforward ANNs were trained with Bayesian regularization backpropagation to approximate responses that would be relevant for the optimization, namely: the concentrations of ethanol and acetic acid at the column outlet and the lower heating value (LHV) efficiency η_{fuel} , the latter being defined as the ratio between the total ethanol LHV and the total energy input considering syngas LHV and heat intake associated with the power consumed in the gas compressor. ANN architectures were selected after several tries, with the final ANNs containing two hidden layers with 10 to 20 neurons per hidden layer depending on the case. The data set used for ANN training and validation consisted of 2,780 points comprising random combinations of the operating and design parameters considered as model inputs (and optimization decision variables): dilution rate (D [h^{-1}]), fresh gas residence time (GRT [min]), gas recycle ratio (RR), column height (L [m]), and column aspect ratio (L/d_c). For the gas compressor, the power consumption was calculated in Aspen plus as function of the gas composition and flow rate at the top of the column, and the pressure at the bottom; Aspen Simulation Workbook was employed to facilitate the automatic execution of all considered scenarios. The output of the ANNs is depicted in Fig. 1 against the rigorous solutions (i.e. obtained with integration of the ODE system), where for each response the results are normalized with relation to the minimum and maximum values of the corresponding rigorous response.

3. Formulation of MOO problem

3.1. Decision variables and fixed conditions

The MOO problem aims at finding optimal combinations of the decision variables described in Sec. 2.2 within the following pre-defined ranges: $0.001 \leq D \leq 0.1$; $5 \leq GRT \leq 50$; $0 \leq RR \leq 0.8$; $10 \leq L \leq 30$; $3 \leq L/d_c \leq 6$. Some variables are fixed in this study but should be analyzed in connection with other unit operations in future studies of the global process. These are: the fresh syngas composition (fixed at 60% CO, 35% H₂, 5% CO₂), which is affected by the choices of design and operating conditions in the gasifier; and liquid inlet composition (considered pure water), which could contain small amounts of acetic acid if distillation waste streams are recirculated within the process. Cell recycle is also considered with a fixed purge fraction of 10% of the cells.

3.2. Selection of objectives using Principal Component Analysis

Process performance often needs to be measured by multiple criteria which are conflicting, such that a decision must be made based on Pareto-optimal solutions. Nonetheless, a too large number of objectives might bring unnecessary complexity to the problem, both in terms of computational effort and interpretation of the results. With

that in mind, the multivariate technique of Principal Component Analysis (PCA) can be employed to uncover relationships among objectives and reduce the dimensionality of the problem (Sabio et al., 2012). In a nutshell, this is achieved by finding a new coordinate system that explains the variance in the original data set using a smaller dimensionality. In this study, PCA was applied to a set of 8 potential objectives calculated from the BCR model results at various conditions. Fig. 2 shows the coefficients (loadings) of the two first principal components (PC), which together explain nearly 87% of the data variance. These coefficients represent the contribution of the original variables to the PCs, thereby pointing out aligned or opposing tendencies. From this analysis, the gas conversions X_{CO} and X_{H_2} were removed from the MOO since their tendencies are well captured by the LHV efficiency η_{fuel} . The other efficiency, η_{total} , considers the LHV of both ethanol and unconverted syngas. Since ethanol production is accompanied by CO_2 formation, this efficiency has an opposite trend to the conversions, eventually reaching 1 if no ethanol is formed; hence it was also removed from the analysis. The minimization objective functions were then defined with the 5 remaining metrics: (i) $OF_1 = -Prod$ (ethanol production rate); (ii) $OF_2 = -\eta_{fuel}$; (iii) $OF_3 = -C_{L,EtOH}$; (iv) $OF_4 = C_{L,HAc}$; (v) $OF_5 = V_R$ (reactor volume). Apart from the production rate and LHV efficiency that ideally would be maximized, the definition of objectives OF_3 and OF_4 takes into account possible energy expenses in downstream operations, and OF_5 is aimed at reducing CAPEX.

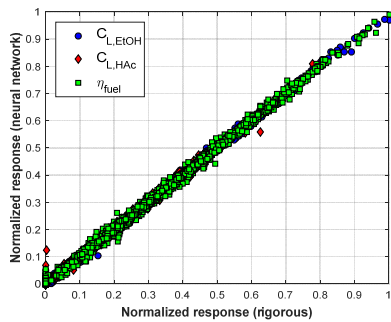


Figure 1. Validation of neural networks

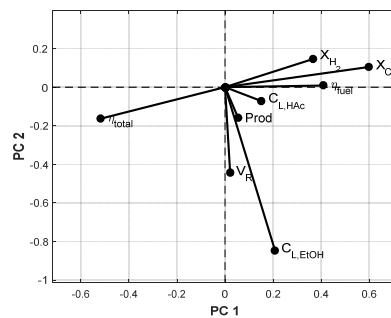


Figure 2. Principal Component Coefficients

4. Generation and analysis of the Pareto front

The Pareto front was generated in MATLAB using a hybrid algorithm that starts with multi-objective genetic algorithm (MOGA) and shifts to a local goal attainment method once the solution is near the optimum front. The short evaluation times due to the adoption of neural networks made it possible to test the hybrid MOGA with different population sizes, with and without the hybrid search. Fig. 3 presents the pairwise projections of the Pareto front, specifically for the objective OF_1 (maximization of ethanol production rate) against the other four objectives. These plots can be used to delineate a range of desirable and feasible operation; for example, it is not convenient to aim at production rates higher than 2,700 kg/h, since this would require reactor vessels of at least 1,500 m³ which might be unpractical in real operation. It can also be noted that, for the current system, the highest LHV efficiencies are achieved at lower EtOH production rates, which makes sense since higher gas conversions are obtained when the

gas residence time is longer (lower gas velocity), thus leading to smaller mass transfer coefficients and reaction rates. The ethanol titer is bounded to a maximum 30 g/L for a large range of production rates, with increasing formation of undesirable acetic acid, while low production rates can lead to over 50 g/L ethanol with almost zero by-product. The normalized values of the parameters are shown in Fig. 4 for sub-sets selected from the boundary dashed lines depicted in Fig. 3, where it can be seen how the optimal parameters adapt to the objective functions. An ultimate decision would need to consider the relevance of these objectives on the outcome of the global process; for example, a lower production rate that is compensated by a more concentrated broth might in some cases be more advantageous than the other way around. Either way, the current results may be used to define an optimal region where the LHV efficiency is higher than 30%, the ethanol titer is higher than 20 g/L, the acetic acid titer is lower than 10 g/L, and the reactor volume is less than 1,500 m³; the decision variables in this region are in the range: $0.02 \leq D \leq 0.03$; $32 \leq GRT \leq 50$; $0.56 \leq RR \leq 0.8$; $27.8 \leq L \leq 29.4$; $3.8 \leq L/dC \leq 4.7$.

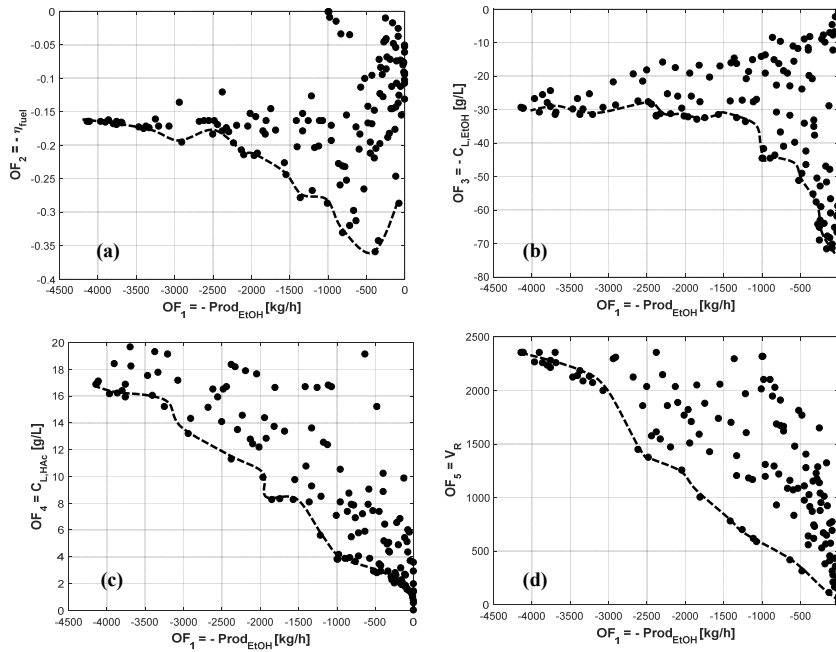


Figure 3. Pareto front 2-D Projections: (a) $OF_1 \times OF_2$; (b) $OF_1 \times OF_3$; (c) $OF_1 \times OF_4$; (d) $OF_1 \times OF_5$

5. Conclusions

In this study a modeling and optimization framework was built for syngas fermentation in bubble column reactors. First a spatial dynamic model was created to predict the concentrations of the chemical species and cells along the reactor in the gas and liquid phases; and the most relevant responses were approximated by artificial neural networks to reduce computational effort, so that objective functions could be evaluated efficiently during the multi-objective optimization search. We demonstrated how Principal Component Analysis can be used to reduce the complexity of the MOO problem

without losing significant information. Although further studies are needed connecting the bioreactor to other unit operations, the five-objective Pareto front generated in this study can be used to pre-define an optimal range of process conditions and reactor size.

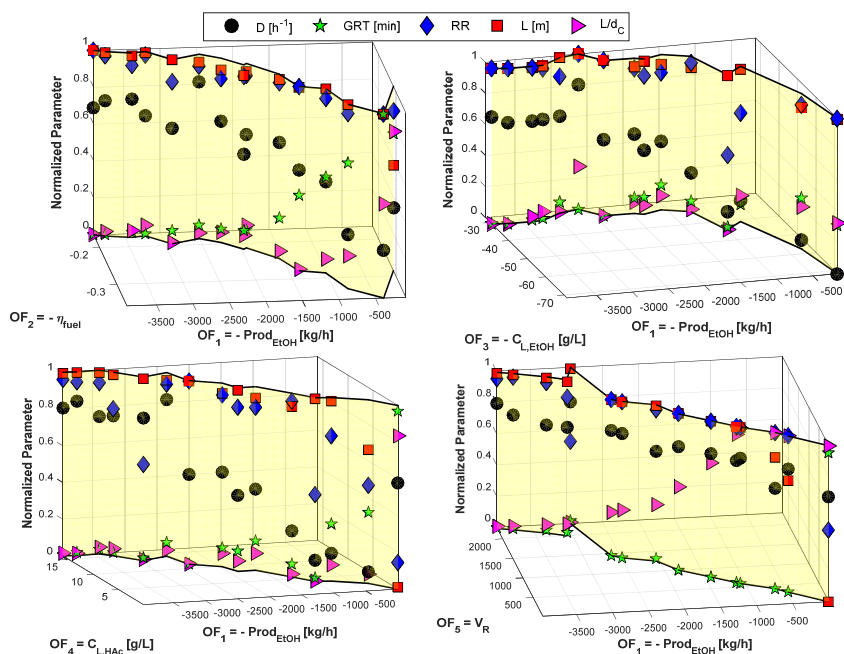


Figure 4. Selected Points from the Pareto Front Projected in 2-D vs Normalized Parameters

References

- Chambers, M., Mount-Campbell, C. A., 2002. Process optimization via neural network metamodeling. *Int. J. Prod. Econ.* 79, 93–100.
- Deckwer, W. -D., Burckhart, R., Zoll, G., 1974. Mixing and mass transfer in tall bubble columns. *Chem. Eng. Sci.* 29, 2177–88.
- Deckwer, W. -D., 1992. *Bubble Column Reactors*. Chichester, New York: Wiley.
- Heijnen, J. J., van't Riet, K., 1984. Mass transfer, mixing and heat transfer phenomena in low viscosity bubble column reactors. *The Chemical Engineering Journal* 28, B21–B42.
- de Medeiros, E., Posada, J. A., Noorman, H., Maciel Filho, R. Dynamic modeling of syngas fermentation in a continuous stirred tank reactor: multi-response parameter estimation with statistical analysis. (Forthcoming).
- Quirante, N., Caballero, J. A., 2016. Optimization of a sour water stripping plant using surrogate models. *Computer Aided Chemical Engineering* 38, 31–36.
- Sabio, N., Kostin, G., Guillén-Gosálbez, G., Jiménez, L., 2012. Holistic minimization of the life cycle environmental impact of hydrogen infrastructures using multi-objective optimization and principal component analysis. *Int. J. Hydrogen Energ.* 37, 5385–5405.
- Wainaina, S., Horváth, I. S., Taherzadeh, J., 2018. Biochemicals from food waste and recalcitrant biomass via syngas fermentation: A review. *Bioresour. Technol.* 248, 113–121.

Production of chemicals from syngas: an enviro-economic model-based investigation

Andrea Bernardi^a, Jose E. A. Graciano^a and Benoît Chachuat^{a,*}

^a*Centre for Process Systems Engineering, Department of Chemical Engineering, Imperial College London, SW7 2AZ, UK*

b.chachuat@imperial.ac.uk

Abstract

Syngas has traditionally been derived from fossil fuels, but alternative production routes have attracted significant interest recently, such as syngas from biomass gasification, electrolysis of water, or electrocatalytic reduction of CO₂. The composition of the produced syngas can vary drastically, in addition to presenting large price differences. The main contribution of this paper is a systematic, model-based comparison of three syngas conversion technologies, namely methanol, DME and Fisher-Tropsch syntheses, for a range of syngas compositions. The key performance indicators in this comparison are the break-even price of syngas, the carbon efficiency, and the energy return on energy investment. The results suggest that DME synthesis is the most promising technology both economically and in terms of carbon efficiency, while methanol synthesis presents the best energy efficiency.

Keywords: methanol, DME, Fisher-Tropsch, process simulation, techno-economic analysis, carbon efficiency, energy efficiency

1. Introduction

Syngas – a gas mixture made primarily of CO and H₂ – provides a flexible feedstock for a variety of chemical syntheses, including methanol (MeOH) and dimethyl ether (DME) production and higher hydrocarbons via Fischer-Tropsch (FT) synthesis. A majority of the syngas worldwide is currently produced from fossil hydrocarbon feedstock and carries a large environmental burden. In response to this, alternative routes to syngas generation have received significant attention, including biomass gasification, co-generation of CO and H₂ via electrochemical and solar routes, and catalytic reduction of CO₂ into CO (Foit et al., 2017). Many of these sustainable syngas production processes are at a much lower technological readiness level compared with syngas from fossil feedstock, and their integration within existing plants may not be so straightforward because the obtained syngas composition can vary drastically depending on the feedstock or selected route. There is also significant uncertainty about the projected price of sustainable syngas in a scaled-up production. This cursory analysis suggests that there exist significant opportunities for better integration and optimization across syngas production and conversion processes.

A number of research studies have been conducted on this topic in recent years. Trippe et al. (2013) compared direct DME synthesis and FT synthesis, using syngas from biomass gasification. They assumed that the syngas composition could be varied with-

out incurring a penalty, and therefore considered optimal $H_2:CO_x$ ratios of 1 for direct DME synthesis and of 2 for the FT synthesis. They furthermore used simplified models (Gibbs reactor) of the DME and FT reactors to conduct the assessment. Hankin and Shah (2017) compared methanol and DME syntheses (both direct and indirect) using CO_2 and H_2 as feedstock. They considered different layouts, including electrocatalytic cells (SOECs) and a separate water-gas-shift reactor prior to the reactor in order to adjust the $CO:CO_2:H_2$ ratio for each conversion technology, and they also used equilibrium models in their assessment.

The main objective of this paper is to conduct an assessment of alternative technologies for the production of fuels/chemicals from syngas, by accounting for different $H_2:CO_x$ ratios. Our focus is on three syngas conversion processes, namely FT, MeOH and indirect DME synthesis. Direct DME synthesis was not included in the analysis due to its much lower optimal syngas composition ($H_2:CO_x$ ratio close to 1; see Peng et al. (1999)) compared with the other three processes. A distinctive feature of our analysis is that it relies on detailed kinetic models of the various syntheses, which were calibrated against experimental data. We furthermore consider process flowsheets that are flexible enough to operate under different syngas compositions, not merely at the optimal syngas composition. Finally, the technologies are assessed in terms of their environmental and energy efficiency, alongside their economic performance.

2. Methodology

State-of-the-art process flowsheets for FT, MeOH, and DME syntheses are simulated using Aspen Plus[®] (FT, DME) and Aspen Hysys[®] (MeOH). Both simulation environments are also used to conduct the techno-economic analysis, using the information provided by the detailed models, which include mass and energy balances, thermodynamic properties and kinetics. Specifically, the kinetic rate expressions are taken from the works of Todic et al. (2013), Graaf et al. (1988) and Bercic and Levec (1993) for FT, MeOH and DME, respectively. All of these models have been calibrated against experimental data from dedicated measurement campaigns.

The influence of the syngas composition is analyzed by simulating each process with different $H_2:CO_x$ inlet ratios in the range of 1.6–2.4 and a fixed $CO:CO_2$ ratio of 10, as shown in Table 1. The molar flow rate, pressure and temperature are kept constant at 8000 mol.hour⁻¹, 24 bar and 80°C, as well the concentration of inerts (N_2 , H_2O and CH_4) that are inherent to the syngas production process.

Three key performance indicators (KPIs) are used to assess and compare the syngas conversion processes. The *break-even price* (BEP) indicator represents the highest price we should be willing to pay for syngas in order for the conversion process to remain economically feasible, here considering a process life-time of 30 years and in the price scenario of Europe 2017. The *carbon efficiency* (CE) indicator accounts for the fraction of carbon from the syngas that ends up in the fuel products. Lastly, the *energy return on energy investment* (EROI) is the amount of energy in the products divided by the amount of energy provided to the process, considering chemical, thermal and electrical energy all together. An important difference between the MeOH, DME and FT processes is that the latter is a net producer of electricity, a saleable co-product that can improve both the BEP and EROI indicators.

Table 1: Molar composition of the different syngas streams used in the process simulation

x_i [mol%]	$H_2:CO_x$				
	1.6	1.8	2	2.2	2.4
H_2	59.7%	62.4%	64.7%	66.7%	68.5%
CO	33.9%	31.5%	29.4%	27.5%	25.9%
CO_2	3.4%	3.1%	2.9%	2.8%	2.6%
N_2, H_2O, CH_4	1.0%	1.0%	1.0%	1.0%	1.0%

Fischer-Tropsch liquids synthesis. The FT plant considered herein is based on the work of Graciano et al. (2018a,b), which comprises six main units: Fischer-Tropsch reaction, water-gas shift (WGS), upgrading, separation, Rankine cycle, and gas turbines (top row of Fig. 1). In the proposed arrangement, the syngas is mixed with H_2 surplus from the WGS unit to adjust the $H_2:CO$ ratio to 2 (unless this ratio is already higher than 2). Then, the mixture feeds into the slurry bubble FT reactor filled with cobalt catalyst, producing the paraffin and olefin that compose the synthetic oil (synoil). This synoil is sent to the separation section to be fractionated into gasoline, kerosene, diesel, and wax products. The upgrading unit is responsible for converting both heavy synoil and recycled wax into lighter and more valuable fractions. The unconverted syngas from the FT unit passes through a WGS unit that converts part of the CO into H_2 , before feeding into the FT reactor and the upgrading unit. The thermal energy produced by the exothermic FT reactions is recovered by the Rankine cycle unit and converted into electricity, while the gas turbine unit produces additional electricity by burning the tail gas from the WGS unit.

Methanol synthesis. The MeOH plant is simulated based on the process flowsheet developed by Van-Dal and Bouallou (2013) (middle row of Figure 1). This process comprises only two units: methanol reaction and separation. The former mainly consists of a compressor train and an adiabatic reactor filled with a fixed amount of copper-based catalyst and operating at 78 bar. The latter comprises a sequence of two flash drums and a distillation column, which separate the unconverted syngas and purify the methanol product to the product grade (AA grade), respectively. A heat integration analysis of the process reveals that the heat produced in the reactor is sufficient to cover the process needs, so no external heating utility is needed. By contrast, cooling water and electricity are still required and need to be supplied by external sources.

We consider two alternative copper-based catalysts with the objective to compare their effect on the methanol synthesis. The kinetic data of the first catalyst (Catalyst I) is taken from Van-Dal and Bouallou (2013), which relies on the model by Bussche and Froment (1996). The kinetic data for the second catalyst (catalyst II) is taken from Ng et al. (1999) work, which have been used to calibrate the model by Graaf et al. (1988). The amount of catalyst was adjusted in such a way that a conversion close to the equilibrium is obtained at the reactor outlet; the corresponding amounts of catalyst I and II are 44.7 and 26.6 tons, respectively.

Dimethyl ether synthesis. The process flowsheet for indirect DME production comprises two steps, methanol synthesis and methanol dehydration (middle and bottom rows of Figure 1). The methanol produced from a given syngas composition is mixed with the recycle

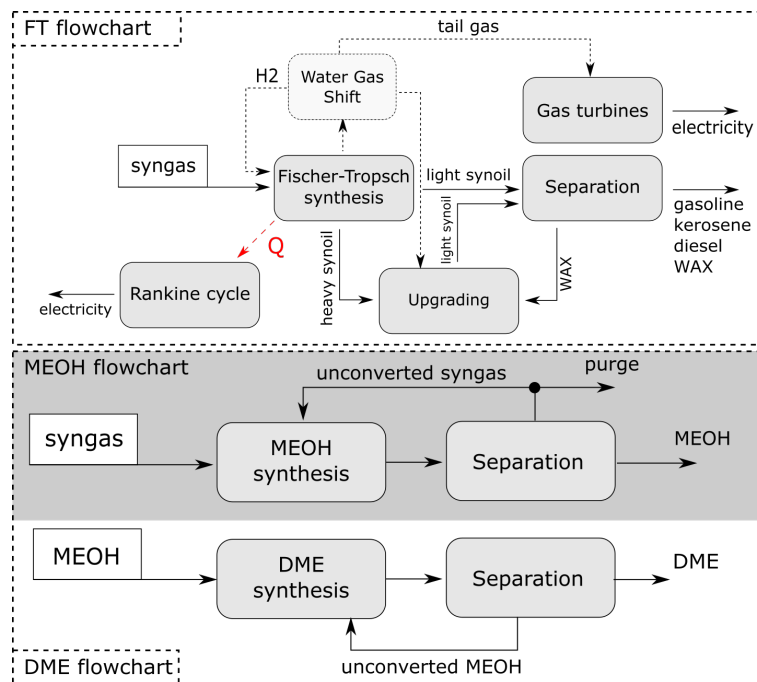


Figure 1: Schematic diagrams for the FT process (top), MeOH process (middle), and DME process (bottom)

stream and heated up to 275°C in a furnace, before entering a jacketed tubular reactor to undergo DME synthesis. Then, the unreacted methanol is separated from the produced water and DME by a train of two distillation columns and recycled back to the reactor. Because water is the only impurity present in the recycle stream, a purge stream is not necessary here.

The kinetic model used in the simulation was initially calibrated against data from a double bed reactor fed with syngas and producing methanol and DME. The model was also tested against experimental data of DME synthesis from methanol, showing a good agreement with the experimental data (Bernardi et al., 2019).

3. Results and discussion

The process simulation results are summarized on Fig. 2. A first observation is that the H₂:CO_x ratio of the syngas has a large effect on the three KPIs, which all pass through a maximum in the investigated range 1.6-2.4.

Economic performance. We start by noting that the catalyst choice has a great effect on the economic performance of the MeOH process, both in terms of capital and operating costs. The catalyst may also modify the optimal syngas composition. The FT process is found to be economically superior to the MeOH process for both catalysts, albeit the MeOH process with catalyst II becomes competitive with the FT process for H₂:CO_x > 2. Thereafter, catalyst II is selected to produce methanol in the first step of indirect DME production due to its superior economic performance compared to catalyst

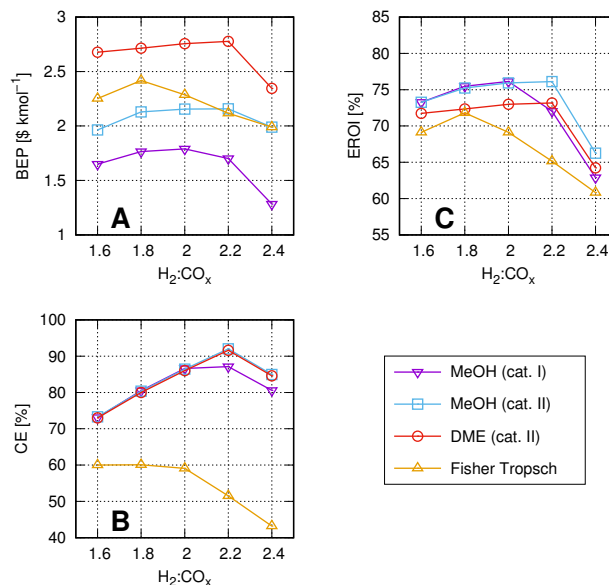


Figure 2: Comparison between MeOH, DME and FT processes in terms of break-even price (A), carbon efficiency (B), and energy efficiency (C)

I. DME is found to be the most profitable product by a large margin, for all analyzed H₂:CO_x ratios even considering a conservative price for the DME (e.g. Chinese market). These results are in agreement with Trippe et al. (2013), who predicted a slightly better economic performance for gasoline from DME compared with gasoline from FT.

Carbon conversion efficiency. The FT process presents the lowest carbon efficiency, around 60% for H₂:CO_x ≤ 2 and decreasing to about 40% thereafter. This decline is attributed to the H₂ recycle needed for adjusting the H₂:CO = 2 at the FT reactor inlet. By contrast, the CE of the MeOH process is consistently over 70%, and it presents a maximum above 90% with catalyst II at the H₂:CO_x ratio of 2. The effect of catalyst selection on the CE is rather low; the main difference being noticeable for H₂:CO > 2 due to catalyst I requiring a larger recycle stream. Lastly, there is hardly any difference in CE between the MeOH and DME processes, due to the near-100% conversion of the methanol dehydration in DME synthesis.

Energy efficiency. The most favorable EROI is consistently obtained for the MeOH process, and passes a maximum of about 75% for both catalysts around H₂:CO_x = 2. (Recall that the EROI calculation accounts for the chemical energy of the syngas feed, so the resulting EROI may not be greater than 100%.) A fast decline in the EROI is observed for larger H₂:CO_x ratios, due to the increase in the recycle flowrate of unconverted syngas. Unlike CE, the EROI indicator is lower in the DME process than in its MeOH counterpart alone, a consequence of the extra process complexity and exergetic losses. Finally, the FT process presents the worst performance in terms of EROI. At its optimal syngas ratio H₂:CO_x = 1.8, it has a similar performance as the DME process nevertheless. This behavior is again explained by the higher complexity of the FT plant in comparison with the other two processes, which results in larger exergetic losses overall.

4. Conclusions

This paper has presents a systematic, model-based comparison between different syngas conversion technologies for the production of liquid transportation fuels. Our results show that the production of DME is the most attractive technology in both economic and carbon efficiency terms, while methanol synthesis has the best performance in terms of energy efficiency. It is also noteworthy that the techno-economic analysis provides quantitative price targets for novel syngas generation technologies. Our current investigations aim at completing the sustainability assessment by looking at additional environmental impacts and comparing different geographical locations (UK, US, South America and China).

Acknowledgements: This paper is based upon work supported by the Engineering and Physical Sciences Research Council (EPSRC) under Grant EP/N010531/1 and EP/P016650/1 “Flexible routes to liquid fuels from CO₂ by advanced catalysis and engineering”. Financial support from Shell and FAPESP through the “Research Centre for Gas Innovation - RCGI” (FAPESP Proc. 2014/50279-4), ANP (Brazil National Oil, Natural Gas and Biofuels Agency) through the R&D levy regulation, and CNPq Brasil (Conselho Nacional de Desenvolvimento Científico e Tecnológico - Proc. 200470/2017-5) is gratefully acknowledged.

References

- G. Bercic, J. Levec, 1993. Catalytic dehydration of methanol to dimethyl ether – Kinetic investigation and reactor simulation. *Industrial & Engineering Chemistry Research* 32 (11), 2478–2484.
- A. Bernardi, L. Gomoescu, J. Wang, C. C. Pantelides, D. Chadwick, B. Chachuat, 2019. Kinetic model discrimination for methanol and DME synthesis using Bayesian estimation. *IFAC-PapersOnLine* (to appear).
- K. M. V. Bussche, G. F. Froment, 1996. A steady-state kinetic model for methanol synthesis and the water gas shift reaction on a commercial Cu/ZnO/Al₂O₃ catalyst. *Journal of Catalysis* 161 (1), 1–10.
- S. R. Foit, I. C. Vinke, L. G. J. de Haart, R.-A. Eichel, 2017. Power-to-syngas: An enabling technology for the transition of the energy system? *Angewandte Chemie International Edition* 56 (20), 5402–5411.
- G. Graaf, E. Stamhuis, A. Beenackers, 1988. Kinetics of low-pressure methanol synthesis. *Chemical Engineering Science* 43 (12), 3185–3195.
- J. E. Graciano, B. Chachuat, R. M. Alves, 2018a. Conversion of CO₂-rich natural gas to liquid transportation fuels via trireforming and Fischer-Tropsch synthesis: Model-based assessment. *Industrial & Engineering Chemistry Research* 57 (30), 9964–9976.
- J. E. Graciano, B. Chachuat, R. M. Alves, 2018b. Enviro-economic assessment of thermochemical polygeneration from microalgal biomass. *Journal of Cleaner Production* 203, 1132–1142.
- A. Hankin, N. Shah, 2017. Process exploration and assessment for the production of methanol and dimethyl ether from carbon dioxide and water. *Sustainable Energy & Fuels* 1 (7), 1541–1556.
- K. L. Ng, D. Chadwick, B. Toseland, 1999. Kinetics and modelling of dimethyl ether synthesis from synthesis gas. *Chemical Engineering Science* 54 (15-16), 3587–3592.
- X. Peng, A. Wang, B. Toseland, P. Tijm, 1999. Single-step syngas-to-dimethyl ether processes for optimal productivity, minimal emissions, and natural gas-derived syngas. *Industrial & Engineering Chemistry Research* 38 (11), 4381–4388.
- B. Todici, T. Bhatelia, G. F. Froment, W. Ma, G. Jacobs, B. H. Davis, D. B. Bukur, 2013. Kinetic model of Fischer-Tropsch synthesis in a slurry reactor on Co-Re/Al₂O₃ catalyst. *Industrial & Engineering Chemistry Research* 52 (2), 669–679.
- F. Trippe, M. Fröhling, F. Schultmann, R. Stahl, E. Henrich, A. Dalai, 2013. Comprehensive techno-economic assessment of dimethyl ether (DME) synthesis and Fischer-Tropsch synthesis as alternative process steps within biomass-to-liquid production. *Fuel Processing Technology* 106, 577–586.
- E. S. Van-Dal, C. Bouallou, 2013. Design and simulation of a methanol production plant from CO₂ hydrogenation. *Journal of Cleaner Production* 57, 38–45.

Application of cyclic operation to acetic / water separation

Catalin Patrut^a, Elena Catalina Udrea^a, Costin Sorin Bildea^{a*}

*^aUniversity "Politehnica" of Bucharest, Polizu 1-7, 011061 Bucharest, Romania
s_bildea@upb.ro*

Abstract

Acetic acid is an important bulk chemical, used as raw material in the production of vinyl acetate, terephthalic acid, acetate esters and acetic anhydride. All these processes include a step for separating the acetic acid from water, both high-purity and high-recovery of acetic acid being required. Although acetic acid and water do not form an azeotrope, the separation is difficult due to the tangent pinch present on the pure water end. A common industrial practice to overcome the tangent pinch is to add an entrainer and, therefore, to use heterogeneous azeotropic distillation. This work investigates the applicability of cyclic distillation to this difficult separation. A mathematical model is presented and used for sizing and optimization considering the total annual cost as objective function and the number of trays, feed tray location, and the duration of vapor-flow period as decision variables.

Keywords: Water, Acetic Acid, Cyclic distillation.

1. Introduction

Acetic acid is an important chemical, produced by methanol carbonylation, acetaldehyde oxidation and the oxidation of butane and/or naphtha fractions. All these processes contain a step for separating the acetic acid from water. Although acetic acid and water do not form an azeotrope, the separation is difficult due to the tangent pinch present on the pure water end. In this contribution, the applicability of cyclic distillation for separation of 10780 kg/h mixture of water (71%wt) and acetic acid (29%wt) is investigated. The required separation performance is given as purities of the acetic acid (99.3 %wt) and water (99.4 %wt) products.

Cyclic operation of distillation columns is attractive for difficult separations, being already used for kerosene fractionation (petrochemical industry) and ethanol concentration (food industry). Cyclic operation of distillation columns (Patrut et al., 2014) consists of a vapour flow period and a liquid flow period, as shown in Figure 1. During the vapor flow period, the liquid remains stationary on the tray while the vapour is flowing upwards through the column. During the liquid flow period, the vapor flow is stopped, reflux and feed are supplied to the column, and the liquid holdup is dropped from each tray to the tray below. This mode of operation can be achieved by using perforated trays, without downcomers, combined with sluice chambers located under each tray.

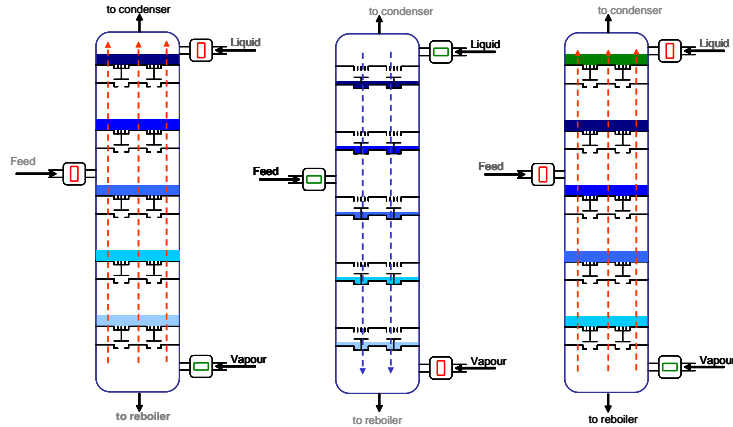


Figure 1. Schematics illustrating the working principle of cyclic distillation: (a) vapor-flow period; (b) liquid flow-period; (c) beginning of a new vapor-flow period.

2. Mathematical model

The model of the cyclic distillation column (Patrut et al., 2014) is derived under the following assumptions: ideal stages (vapor-liquid equilibrium is reached); equal heat of vaporization; perfect mixing on each stage; negligible vapor holdup; saturated liquid feed. No assumptions are made here regarding the linearity of vapor-liquid equilibrium, negligible or constant pressure drop, infinite reboiler holdup or zero condenser holdup.

The vapor-flow period: For each component, $j = 1, NC$, the following equations describe the evolution of species holdup on each tray:

$$\text{Condenser: } \frac{dM_{1,j}}{dt} = V \cdot y_{2,j} \quad (1)$$

$$\text{Trays: } \frac{dM_{k,j}}{dt} = V(y_{k+1,j} - y_{k,j}); \quad k = 2, NT - 1 \quad (2)$$

$$\text{Reboiler: } \frac{dM_{NT,j}}{dt} = -V \cdot y_{NT,j} \quad (3)$$

For each tray, $k = 1, NT$, the following relationships describe the liquid-vapor equilibrium:

$$P_k \cdot y_{k,j} - x_{k,j} \cdot \gamma_{k,j}(x_1, \dots, x_{NC}, T_k) \cdot P_j^{vap}(T_k) = 0 \quad (4)$$

$$x_{k,j} = \frac{M_{k,j}}{\sum_j M_{k,j}}; \quad \sum_j y_{k,j} - 1 = 0 \quad (5)$$

For each tray, $k = 3, NT$, the pressure is calculated based on the vapor flow rate and the amount of liquid on the tray above:

$$P_2 = P_{cond} + \Delta P_{cond} ; \quad P_k = P_{k-1} + \Delta P(M_{k-1}, V) \quad (6)$$

The state of the system at the beginning of the vapor-flow period is the same as the state at the end of the liquid-flow period:

$$\mathbf{M}(t = 0) = \mathbf{M}^{(L)} \quad (7)$$

The state of the system at the end of the vapor flow period is found by integrating the equations (1)-(7)

$$\mathbf{M}^{(V)} = \mathbf{M}(t = t_{vap}) \quad (8)$$

The liquid-flow period: for each component, $j = 1, NC$, the following equations give the stage holdup at the end of the liquid-phase period:

$$\text{Condenser:} \quad M_{1,j}^{(L)} = M_{1,j}^{(V)} - (D + L) \cdot x_{1,j}^{(V)} \quad (9)$$

$$\text{Trays, rectifying section:} \quad M_{2,j}^{(L)} = L \cdot x_{1,j}^{(V)} ; \quad M_{k,j}^{(L)} = M_{k-1,j}^{(V)} , \quad k = 2, NF \quad (10)$$

$$\text{Feed tray:} \quad M_{NF+1,j}^{(L)} = M_{NF,j}^{(V)} + F \cdot x_{F,j} \quad (11)$$

$$\text{Trays, stripping section:} \quad M_{k,j}^{(L)} = M_{k-1,j}^{(V)} , \quad k = NF + 2, NT - 1 \quad (12)$$

$$\text{Reboiler:} \quad M_{NT,j}^{(L)} = M_{NT,j}^{(V)} - B \cdot x_{NT,j}^{(V)} + M_{NT-1,j}^{(V)} \quad (13)$$

Equations (1) - (6) and (9) - (13) can be written in the following condensed form, where $\Phi^{(V)}$ and $\Phi^{(L)}$ are mappings relating the state at the start and the end of the vapor- and liquid-flow periods, respectively.

$$\left(M^{(V)}, x^{(V)} \right) = \Phi^{(V)}(M, x) \quad (14)$$

$$\left(M^{(L)}, x^{(L)} \right) = \Phi^{(L)}(M, x) \quad (15)$$

Periodicity condition requires:

$$\left(M^{(L)}, x^{(L)} \right) = \Phi^{(L)} \circ \Phi^{(V)} \left(M^{(L)}, x^{(L)} \right) \quad (16)$$

A straightforward solution of equation (16) can be obtained by considering an initial state and applying relationships (14) and (15) until the difference between two iterations becomes small. However, the convergence can be accelerated by applying numerical methods suitable for algebraic equations (for example Newton).

The fugacity and activity coefficients have been calculated using the NRTL activity model for the vapor-liquid phase and Hayden O'Connell (HOC) fugacity coefficient model for the vapor phase. The parameters for the NRTL and HOC models have been regressed from the NIST TDE database using Aspen Plus.

3. Results and discussion

In order to size and to determine the most efficient column from an economical point of view, the operating characteristics of the cyclic distillation systems have been studied. It

is observed that, for a fixed number of trays, the required vapor flow-rate (which is directly related to the energy requirements) depends on the chosen feed tray. The variation of the required vapor flow-rate with the chosen feed tray for a column with 20 trays is presented in Figure 2.

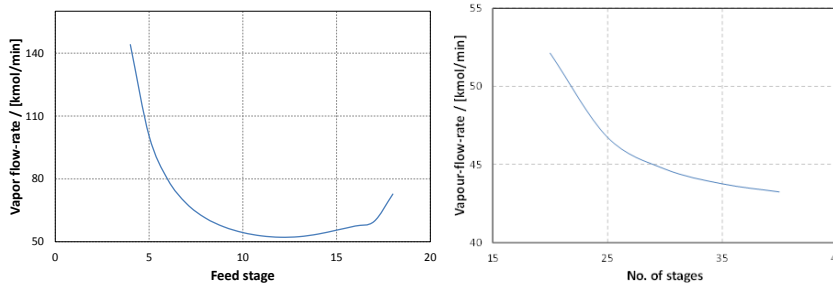


Figure 2. Dependence of the vapor flow-rate with the feed tray for a 20 trays column (left); Variation of the vapor flow-rate with the number of trays (right)

The influence of the number of trays on the vapor flow-rate has been investigated by calculating the vapor flow-rate for columns with 20, 25, 30, 35 and 40 trays, fed at the optimal feed tray. The variation of the vapor flow-rate with the number of trays is represented in Figure 2 (right). The vapor flow-rate decreases with the increase of the number of trays, which indicates the existence of an optimum number of trays. The flow-rate decreases sharply between 20 and 25 trays, followed by a slower decrease between 25 and 40 trays. The variation of the total annual cost (calculated with well-known correlations) with the number of trays is shown in Figure 3.

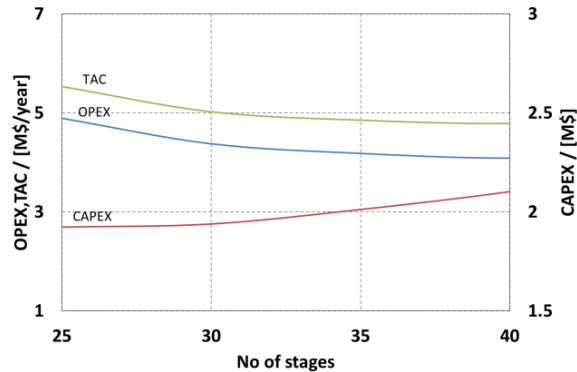


Figure 3. Total annual cost for the water acetic acid through cyclic distillation column

The total annual cost decreases with the increase of the number of trays. However, the decrease between 35 and 40 trays is very small. For practical reasons, a column with 35 trays is further studied. The variation of the required vapor flow-rate with the bottoms product purity is shown in Figure 4.

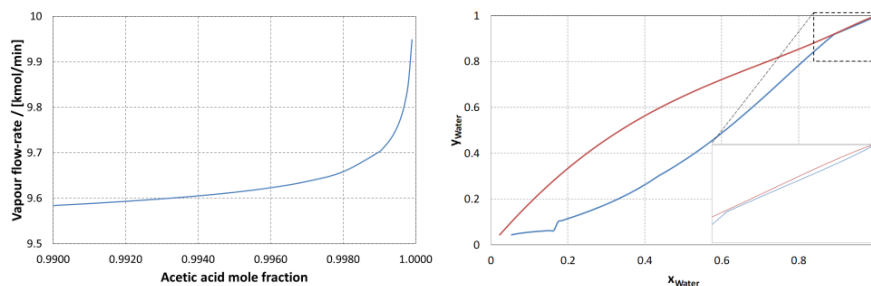


Figure 4. Variation of the vapour-flow-rate with the bottoms stream purity (left); Equilibrium and operating curves for a 35 tray cyclic distillation column (right)

The equilibrium and operating curves for the 35 trays column are shown in Figure 4 (right). In the tangent pinch region, the equilibrium and operation curves are very close to each other, as in conventional distillation. The mass balance of the cyclic distillation column is shown in Table 1. The characteristics of the column are shown in Table 2.

Table 1. Mass balance of the water - acetic acid cyclic distillation column

Stream	Feed	Distillate	Bottoms
Flow-rate / [kmole/h]	477.31	424.76	52.55
Water mole fraction	0.8919	0.9982	0.0230
Acetic acid mole fraction	0.1081	0.0018	0.9770
Water mass fraction	0.7100	0.9940	0.0070
Acetic acid mass fraction	0.2900	0.0060	0.9930

Table 2. Characteristics of the water – acetic acid cyclic distillation column

Number of trays	35
Feed tray	25
Diameter / [m]	3.7
Height / [m]	22.2
Reboiler duty / [kW]	17037
Condenser duty / [kW]	12957

It should be noted that the water / acetic acid separation can be also performed by azeotropic distillation, using *i*-butyl acetate as entrainer. The acetic acid / water mixture and *i*-butyl acetate are fed to the first column. High-purity acetic acid is obtained as bottoms product, while the water – *i*-butyl acetate azeotrope is obtained in the distillate. The 2-phase azeotrope mixture is separated in a decanter. The organic phase is returned into the first column as reflux. The aqueous phase is fed into the second column, where high-purity pure water is produced as bottoms product and water – *i*-butyl acetate azeotrope is produced as distillate (Li et al., 2014).

Table 3 compares the economics of cyclic distillation, conventional distillation and azeotropic distillation alternatives, for an operating time of 8000 h/year and a payback period of 3 years.

Table 3. Cost summary for the water / acetic acid separation by different methods

	Cyclic distillation	Conventional distillation	Azeotropic distillation	
			Acetic acid column	Water column
Column / [k\$]	806	1318	305	19.6
Trays / [k\$]	142	280	45	1.2
Reboiler / [k\$]	758	1129	515	64.7
Condenser / [k\$]	397	521	605	10.1
CAPEX / [k\$]	2102	3248	1470	95.6
Cooling water / [k\$/y]	269	412	178	0.3
Steam / [k\$/y]	3817	4527	1914	125.6
OPEX / [k\$/y]	4087	4938	2092	125.9
Total annual cost / [k\$/y]	4787	6021	2582	158

4. Conclusion

Separation of the acetic acid / water mixture in a distillation column operated in a cyclic manner appears to be economically competitive for the cases when impurification with a solvent is not acceptable. For comparison, when the separation is performed by conventional distillation, the optimal column has 70 trays, requires 6.03 kWh/kg acetic acid, for a total annual cost of 6200 k\$/y. Azeotropic distillation (for example, using isobutyl acetate as entrainer) is cheaper (2.9 kWh/kg acetic acid, 2800 k\$/y). Even though possible from a theoretical point of view, separation of water and acetic acid through binary distillation is unpractical. A very large number of trays is required in the rectifying section, to overcome the tangent pinch formed by the two components. Through cyclic operation, the number of trays is reduced to half and slightly lower energy consumption (therefore a lower total annual cost) is required for the same distillate purity and a higher purity of the bottoms product.

References

- J. Hayden, J. P. O'Connell, 1975, A generalized method for predicting second virial coefficients, *Ind. Eng. Chem. Process Des. Dev.*, vol. 14, no. 3, pp. 209-216.
- K.L. Li, I.L. Chien, C.L. Chen, Design and optimization of acetic acid dehydration process, *The 5th international symposium of advanced control industrial processes*, Hiroshima (2014).
- C. Patrut, C. S. Bildea, I. Lita, A. A. Kiss, 2014, Cyclic distillation - Design, control and applications, *Separation and purification technology*, vol. 125, pp. 326-336.
- H. Renon, J. Prausnitz, 1968, Local compositions in thermodynamic excess functions for liquid mixtures, *AIChE Journal*, vol. 14, no. 1, pp. 135-144.

Control analysis of batch reactive distillation column with intermittent fed

C F. Rodriguez-Robles,^{a,*} S. Hernandez-Castro,^a H. Hernandez-Escoto,^a J. Cabrera-Ruiz,^a F. O. Barroso-Muñoz,^a J. E. Terrazas-Rodriguez^b

^a*Universidad de Guanajuato, Noria Alta s/n Col. Noria Alta, Guanajuato, Guanajuato.*

^b*Universidad Veracruzana, Av. Universidad Veracruzana, Paraiso, Coatzacoalcos, Veracruz, 96538, Mexico.*

cf.rodriguezrobles@ugto.mx

Abstract

This work addresses control issues of a batch reactive distillation for the production of methyl lactate via esterification reaction. The particular challenge of this classic process intensification case lies on that reactant is lighter than product and is easier to be taken away from the reaction, in such a way the conversion of loaded reactant is shrunk; to overcome this drawback, excess of reactant is typically added in the reactive zone. In order to guarantee a high conversion, a practical control approach is proposed: maintaining the maximum allowed temperature of the reaction through reboiler duty, and intermittently feeding the reactant excess, which is driven by maintaining a fixed amount of reactant in reboiler. The controllers for this two-point control configuration are conventional PI linear. The results in a simulation framework show that a reactant conversion greater than 90 % is reached with ease.

When the product is the lightest component in the mixture, the equilibrium reactions are favoured because the products are removed as the reaction proceeds; as a result, conversion is increased; however, when a reactant is the lightest component there are problems causing low conversion, and to overcome the problem, excess of such a reactant is fed in the reactive zone. Control strategy (one and two-point control) is proposed such a practical solution and novel conversion control is explored to ensure a 90% conversion. Also, the maximum temperature of the process is 393,15 K. The temperature in reboiler is satisfactorily controlled using the reboiler duty as the input control. The conversion set point (90 %) is reached with an intermittent fed of excess reactant, in this loop the control input is the feed.

Keywords: batch reactive distillation, batch distillation control, lactic acid.

1. Introduction

Reactive distillation is one of the most representative cases of process intensification (reaction and separation in one equipment), where equilibrium reactions are favoured because the products are removed as the reaction proceeds; as a result, conversions are increased and energy is saved. Nevertheless, in some reactions, certain reactants can be the lighter components, leading to low conversion because they are taken out from the reaction zone. In order to overcome this problem, it is necessary to use an excess of reactant to support the advance of the reaction; one example of this case come up in the

the esterification reaction between alcohols and carboxylic acids, such as methanol and lactic acid yielding methyl acetate and water.

A typical control structure of a continuous reactive distillation column uses the reactants feed to control the temperature in a selected stage. However, in a batch reactive distillation, the control strategy is different, one-point control can regulate temperature, but is not sufficient to guarantee conversion; then, using a two-points control configuration is resorted to (Sørensen and Skogestad, 1994). Moreover, the reactive system is another important factor due the physical properties.

Methyl acetate can be produced by reactive distillation. Figure 1 shows the reactive batch distillation with an inlet to allow intermittent reactant feed. The reaction is carried out in the reboiler, during which the methanol (MeOH) and water (W) are evaporated but condensed in the top accumulator, while the methyl acetate (ML) remain in the reboiler with the lactic acid (LA) and the methanol flow is fed into the reboiler, and the initial load of reactants as well. Aqar et al. (2016) studied the production of ML in a batch reactive distillation to optimize the LA conversion following an optimal control approach: When the column operates in total reflux, the maximum LA conversion achieved 62 %, and with the control system implemented, using the reflux ratio (RR) and the methanol flow as control inputs, the achieved conversion was greater than 90%. The result showed that the RR must be low to extract the water from the reboiler; however, the temperature profile was not shown in such study.

In the open literature there are a few works about control of batch reactive distillation: Sørensen and Skogestad (1994) demonstrated that one-point control strategy is enough to have a good control in the column for a typical case of reactive batch distillation where the products are the lighter components and reaction zone is in the reboiler. On this framework of designing a control system to guarantee a high conversion of reactant, controllability analysis in batch distillation is possible by linearized model, but if the model has high nonlinear behaviour large deviations could be presented and multiple points are necessary to know how controllability changes during the process (Biller and Sørensen, 2002). In this work, the nonlinear model of a batch reactive distillation column is rather used and the controllability is set by evaluating the performance of the proposed control system using one and two-points control strategy.

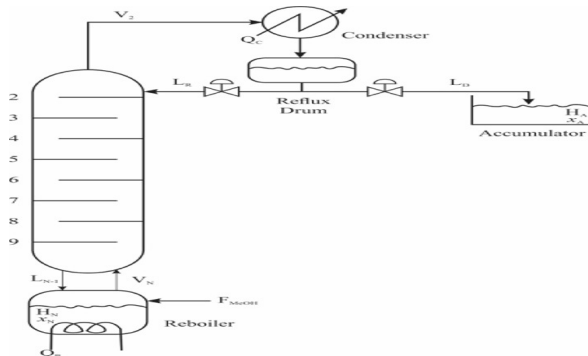


Figure 1. Batch reactive distillation with intermittent fed.

2. Method

Two control configuration are considered: (i) one-point control, and (ii) two-points control. In the one-point one, methanol inflow is manipulated to control the reboiler level; in this control scheme, the reboiler duty is kept constant at its maximum value. In the case of two-points control, two pairs were analysed. In the first structure, the reboiler duty was manipulated to control the reboiler temperature and the methanol feed was selected as input to control the bottom level. In the second structure, the heat duty supplied to the reboiler was used to control the reboiler temperature and the methanol feed flow was the input to control the LA conversion.

2.1. Reactive case study

In this work, the esterification of methanol with LA in a batch reactive distillation column was considered (Saenz et al. 2004). The initial load of LA and methanol was 100 mole (H_{N0}) in the reboiler, an equimolar mixture. Saenz et al. (2004) studied the kinetic of reaction LA and methanol to produce ML and water: they proposed different kinetics using Amberlyst 15 (Supelco) resin. The maximum temperature was 393,15 K to avoid desulfonation.

2.2. Model

An equilibrium model (total mass balances, component mass balances, equilibrium, summation, energy balances) is used for the distillation column and the condenser holdup is constant assuming a perfect control through flow distillate. The number of stages (NT) in the column was 10 including the condenser and reboiler and accumulator (Figure 1). The maximum reboiler duty was fixed at 7200 kJ h⁻¹, the maximum reboiler level was 157 moles (around 0,009 m³). The process configuration and process features were recalled from Aqar et al. (2016), and the dynamic model followed Sørensen and Skogestad (1994) with a lineal tray hydraulic. The thermodynamically model UNIQUAC was used to calculate the Vapour–Liquid Equilibrium. A summary of column process conditions is shown in Table 1. The amount of catalyst used was 2% of the total grams of the mixture.

Table 1. Operation parameters in the column.

Maximum reboiler duty	7200 kJ h ⁻¹
Maximum temperature in reboiler	373.15 K
Column pressure	100,325 N m ²
Hydraulic time constant	100(RR) s
Initial holdup on the trays	$[0.25(H_{N0})]/(NT-2)$
Initial liquid flow	10 % of initial charge (H_{N0})
Condenser holdup	$0.25(H_{N0})$

Hydraulic time constant was a function of RR and the condenser holdup was 2.5 % of the initial charge of the mixture. The vapour flow V2 is equal to the vapour flow VN.

2.3. Control strategies

To ensure reactant (methanol) in excess during the whole process, the initial reboiler level was kept constant and this will be the one-point control strategy. Control strategies summary are given in Table 2. Sørensen and Skogestad (1994) used the reboiler heat duty to control the reboiler temperature. So, it is possible to use the methanol reactant and the reboiler temperature in the next two-point control strategy.

Table 2. Control Strategies Summary.

Strategy	Control Input	Control Output
One-point Control	Methanol Flow	Reboiler Level
Two-point Control (a)	Reboiler Duty	Reboiler Temperature
	Methanol Flow	Reboiler Level
Two-point Control (b)	Reboiler Duty	Reboiler Temperature
	Methanol Flow	LA Conversion

In the first two-point control configuration (a), the level both and temperature in reboiler will be controlled. The temperature is the control output to avoid desulfonation of the resin and oligomerization of LA (Thotla and Mahajani, 2009). Another way to ensure the LA conversion is to control it directly with a SP equal or greater of 90 %. The two-point control strategy (b) used the methanol flow to control the LA conversion. In the two-point control strategies (a) and (b), the reboiler temperature is controlled with the reboiler duty. Proportional Integral (PI) controllers were used. A parametric tuning was employed through the equation (1), selecting the parameters that requires less control effort for the system. Where u_0 is the initial value of the control input at time zero.

$$effort = \int_{t_0}^{t_f} (u - u_0)^2 dt \quad (1)$$

3. Results

In this section, the simulation results will be presented. The control parameters for the PI-controllers used in the simulations are shown in the Table 3. The reboiler level is RL. For the one-point control, the reboiler duty was kept to its maximum value.

Table 3. Control parameters used in the PI controllers.

One-point Control	$K_p = 1 \text{ kmol}^{-1}$	$\tau_I = 10 \text{ h}$	$RL \rightarrow F_{MeOH}$
Two-point Control (a)	$K_p = 0.1 \text{ kmol}^{-1}$	$\tau_I = 10 \text{ h}$	$RL \rightarrow F_{MeOH}$
	$K_p = 100 \text{ kmol}^{-1}$	$\tau_I = 10 \text{ h}$	$T_{NT} \rightarrow Q_R$

Table 2. Control parameters used in the PI controllers.

	$K_p = 100 \text{ kmol}^{-1}$	$\tau_I = 10 \text{ h}$	$X_{LA} \rightarrow F_{MeOH}$
Two-point Control (b)			
	$K_p = 200 \text{ kmol}^{-1}$	$\tau_I = 10 \text{ h}$	$T_{NT} \rightarrow Q_R$

The reboiler level control presented a poor performance caused by the use of maximum value of reboiler duty in the whole operation; this is observed in Figure 2. Reboiler level SP was the initial charge of the mixture (100 mol).

In the one-point control, the final LA conversion is 63 % because the system reached the equilibrium as in the reflux total operation; the RR was 0.3 for this case. In the two-point control strategy (a), the level and temperature in reboiler were controlled. The RR value was 0.3. The system has good control performance still the LA conversion is 65.2%. The control output response and reboiler composition profile are given in Figure 3.

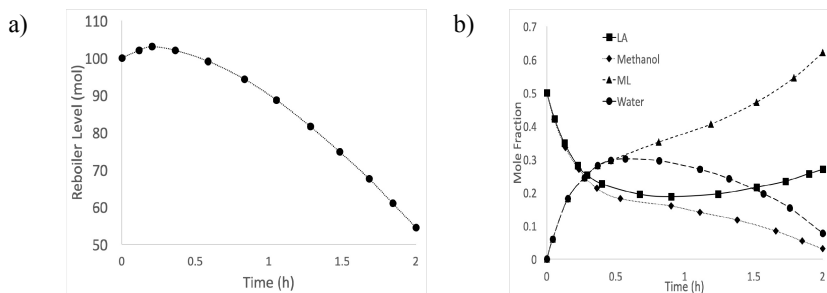


Figure 2. a) control output response SP: 100 mol. b) Reboiler composition profiles for the one-point control strategy.

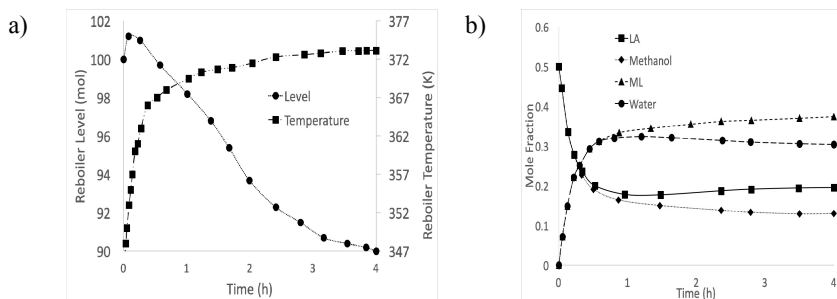


Figure 3. a) control output response; SP1= 100 mol, SP2= 373.15 K. b) Reboiler composition profiles for the two-point control (a) strategy.

In the two-point control strategy (b), the reboiler temperature was controlled satisfactorily while the LA conversion reaches the 96 % at the 6 h of operation with a RR = 0.1 and SP of 99 %. The ML mole composition at the final time (15 h) was 0.7,

the methanol composition remains constant throughout the operation and the total amount of methanol flow was 397.75 mol.

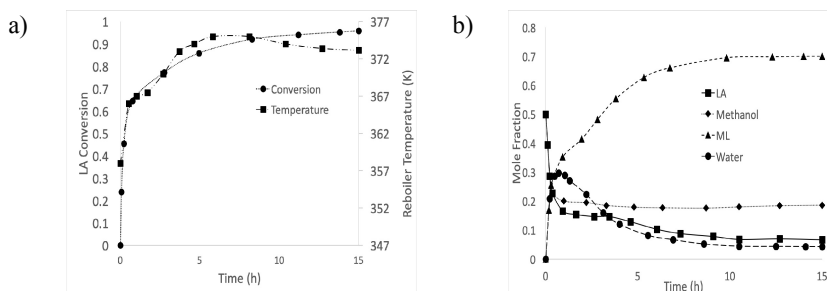


Figure 4. a) control output response b) Reboiler composition profiles for the two-point control (a) strategy.

4. Conclusions

The reboiler temperature in the reactive batch distillation was effectively controlled with two-point control (a), but it did not improve the LA conversion compared with the total reflux operation condition. Although considering temperature and reboiler level as control outputs did not raise LA conversion, reboiler temperature and LA conversion as control output did. The temperature specification was achieved using the two-point control strategy (b). Conversion control is a good option to improve the conversion in a batch reactive distillation. Even though the PI controller has shown good performance, in order to reduce the time operating a nonlinear controller is needed.

Acknowledgements

C. F. Rodriguez-Robles acknowledges the scholarship granted by CONACYT for the accomplishment of their graduate studies.

References

- D. Y. Aqar, N. Rahmanian, and I. M. Mujtaba, 2016, Methyl lactate synthesis using batch reactive distillation: Operational challenges and strategy for enhanced performance, *Separation and Purification Technology* 158, 193-203.
- N. C. T. Biller, E. Sørensen, 2002, Controllability of reactive batch distillation columns, *Computer Aided Chemical Engineering* 10, 445-450.
- M. T. Sanz, R. Murga, S. Beltrán, J. L. Cabezas, J. Coca, 2004, Kinetic study for the reactive system of lactic acid esterification with methanol: methyl lactate hydrolysis reaction. *Industrial & engineering chemistry research* 43 (9), 2049-2053.
- E. Sørensen, S. Skogestad, 1994, Control strategies for reactive batch distillation, *Journal of Process Control* 4 (4), 205-217.
- S. Thotla, S. Mahajani, 2009, Reactive distillation with side draw, *Chemical Engineering and Processing: Process Intensification* 48 (4), 927-937.

New Methodology for Bias Identification and Estimation – Application to Nuclear Fuel Recycling Process

Amandine Duterme^{a*}, Marc Montuir^a, Binh Dinh^a, Julia Bisson^b, Nicolas Vigier^c, Pascal Floquet^d, Xavier Joulia^d

^a*CEA Marcoule, Nuclear Energy Division, Research Department on Processes for Mining and Fuel Recycling, 30207 Bagnols-sur-Cèze, France*

^b*ORANO, La Hague Plant, Technical Department, 50444 Beaumont-Hague, France*

^c*ORANO, La Défense, Technical Department – R&D, 92400 Courbevoie, France*

^d*Laboratoire de Génie Chimique, Université de Toulouse, CNRS, INP, UPS, Toulouse, France*

amandine.duterme@cea.fr

Abstract

This paper focuses on the data reconciliation technique (DR) in case of numerous biases. DR improves the degree of confidence in available information and generates consistent data. The inventory and analysis of the plant data (position and type of sensors ...) enable an evaluation of the process redundancy. Classical Gross Error Detection and Identification (GED) techniques delete the biased variables, decreasing the redundancy. This leads to information loss and possibly an inability to apply DR. The methodology proposed here combines DR, based on a reduced model, and rigorous simulations to locate and estimate multiple biases and to make data consistent in case of inter-connected flows. This methodology is applied to the nuclear fuel recycling process within the scope of a state estimation tool built on a process simulation code.

Keywords: simulation, nuclear fuel treatment, data reconciliation, bias estimation.

1. Introduction

A measurement intrinsically possess uncertainty that prevents straightforward closure of mass and energy balances. In the data reconciliation (DR) methodology, accuracy is given to the measurements by exploiting redundancies in process data and physical constraints, from steady-state mass balances (Simpson et al., 1991) to nonlinear dynamic constraints (Liebman et al., 1992).

There are two main approaches to dealing with gross errors that impact DR. The first uses Gross Error Detection and Identification (GED) methods (Narasimhan and Jordache, 2000) and sequentially deletes the biased variables from the DR. The redundancy, which implies the ability of DR to correct the measurements in order to satisfy the process constraints, is reduced. However, performances of DR and GED are still limited in disrupted cases, such as multiple flows between two units, numerous gross errors, and the position and magnitude of gross errors (Corderio do Valle et al. 2018). The second

approach, not discussed in this study, modifies the objective function of DR to mitigate the effect of gross errors (Fuente, M.J. et al. 2015).

A new methodology for a nonlinear system is proposed here, combining the DR approach, based on a simplified model, and simulations, based on a first-principle model. It prevents the removal of the biased variables from the measurement set. The bias estimation is performed by the rigorous model, which enables the maximum redundancy to be kept. With a set of consistent input data generated by DR, the simulation can precisely estimate key indicators.

2. Methodology

Graph theory can be used to classify data in order to distinguish observable (measured or calculable) data from non-observable data. Among observable data, three categories can be defined: redundant data (deleting this measurement does not change the system observability), non-redundant and measured data, non-measured data. The redundant data are reconciled.

The n measurement vector X^B is linked to the true value of the measured variables X^T , the random error ε^B (assumed to be independent, with a zero mean and normally distributed), and the gross error B , here, the bias, by the following equation:

$$X^B = X^T + \varepsilon^B + B \quad (1)$$

Data reconciliation consists of minimizing an objective function constrained by a set of constraints f :

$$\underset{X^R, B}{\text{Min}}((X^B - B) - X^R)^T V^{-1} ((X^B - B) - X^R) \quad (2)$$

$$\text{s.t. } f(X^R, \theta) = 0$$

where X^R is the n reconciled values vector, V the (n, n) covariance matrix of the measured data, and θ the parameters of the system. X^R are the best estimates of process variables, in the sense of the maximum likelihood. A study of the redundant variables, depending on the process topology and the number of independent equations, enables the determination of the ability of the DR to calculate a consistent set of reconciled data.

A global approach is to solve the DR with the rigorous model as constraints and simultaneously estimates the reconciled values X^R and the biases B . In most industrial applications, the entire first-principle model of the process, named rigorous model thereafter, cannot be directly used as the constraints f for the DR. This is generally due to implementation difficulties, such as code interfaces, and complex numerical estimation of the gradient of the constraints. The methodology proposed performs bias estimation outside the DR by an iterative strategy. It divides the problem into two sub problems: the rigorous model estimates the biases while the DR solves Eq. (2), in regards of X^R only, with a reduced model as constraints. This simplified model is made up of a selection of linear and nonlinear equations specially chosen in order to exploit all information available from the measurements. In particular, it contains the total mass balance and, depending on the case study, some partial mass balances and equations for the calculation of physical properties and fluid phase equilibria.

Figure 1 displays the new methodology. First, a map of the process (list of fluxes, units, sensors, uncertainties etc.) is built offline to generate the redundancy graph. The second

step makes use of process expertise to identify bias locations, concerning measurements on internal or output fluxes. An initial simulation, based on the rigorous model, with input fluxes raw measurements X_{in}^B as input data, gives a first estimation for the biases $B^{C(0)}$. As regards the vector of the calculated bias B^C , each element is null except for the identified biased output variables. These elements are equal to the difference between the biased measurements X_{out}^B and the rigorous simulation calculated outputs X_{out}^C .

The DR is then solved iteratively with respect to X^R only, the values of biases $B^{C(i)}$ being considered fixed. Therefore, the process redundancy is unreduced by biases. To solve the nonlinear steady-state DR problem, this study uses the Fmincon function of Scilab software. The uncertainty for reconciled values is estimated at each DR solution by uncertainty propagation (Narasimhan and Jordache, 2000).

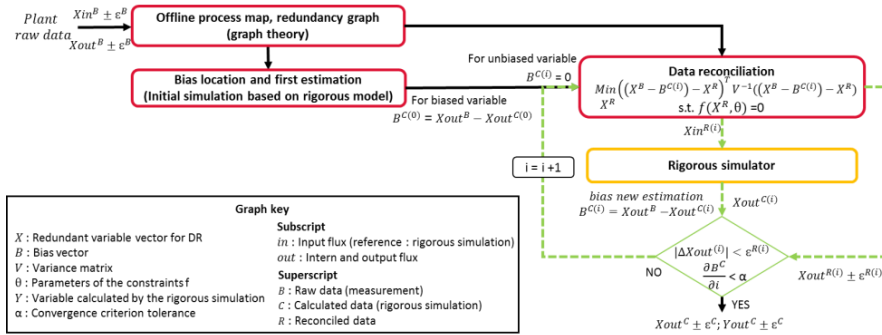


Figure 1: Bias identification and estimation methodology

At iteration i , the reconciled values of the input fluxes $X_{in}^{R(i)}$ are transferred to the rigorous simulator. The reconciled and calculated output flow information, $X_{out}^{R(i)}$ and $X_{out}^{C(i)}$ respectively, are compared. If the difference $|\Delta X_{out}^{C-R(i)}|$ between them is smaller than the uncertainties of reconciled data, the DR gives consistent values for rigorous model equations in the case of Lipschitz continuity around the solution. New bias values $B^{C(i)}$ are estimated with the last rigorous calculation. The best estimation of the bias values is reached when the biases between two iterations are constant. If these two criteria are not respected, bias information given to the DR is not satisfactory. The new bias values $B^{C(i)}$ are given to the DR for the next step. The iterations continue until the bias value estimation enables consistent data to be reached. The final DR is performed with fully known bias information, and has a minimal objective function value.

3. Case study

The methodology proposed in this paper is applied to the PUREX process and uses the PAREX simulation code developed and validated by the CEA (Dinh et al., 2008). This process carries out the treatment of spent nuclear fuel. Spent fuel contains the elements of interest, uranium and plutonium, and the waste, i.e. fission products. TBP (tributyl-phosphate) is the extractive molecule used to recover and purify uranium and plutonium through interconnected liquid-liquid extraction steps. For the final products, very specific features in terms of purity as well as extraction efficiency are required. In order to reach the necessary high performances, the metal loading of the solvent (metal mass flowrate in the solvent for a specific TBP mass flowrate) must be precisely controlled. This ratio is a sensitive parameter which deeply impacts the process state (Bisson et al., 2016). Therefore, DR aims to reduce uncertainty on this key process indicator by giving reliable

input data to the rigorous simulator PAREX. It is based on first-principle models notably taking into account the partitioning of the species, the transfer, and chemical kinetics.

This study deals with an extraction-stripping step of the PUREX process where many sensors are implemented, and can be separated into two categories. Major consideration is given to a specific set of sensors essential for operation, control, and to respect the safety regulations (multiple sensors, regular checking, preventive maintenance, etc.). They are listed as reference information for the industrial plant. The secondary sensors are not used for process control or for industrial safety. They give additional information, increasing redundancy, which can help process state estimation. Some of this additional data can have biases non-detectable with previously-acquired data. A scenario is defined in order to encounter identified causes of GEDI performance loss (Corderio do Valle et al., 2018): the biases concern flows connecting the same two units, and their suppression leads to the system being non-redundant.

The initial graph of the PUREX process (Figure 2a) contains information about flows (directed arcs) and units (nodes). The redundancy graph (Figure 2b) is free of internal non-measured physical quantities: arcs depict constraints linking measurements of interest from one unit to the other. The measured variables used in the DR problem are volumetric flowrates, densities for each arc, temperature, and uranium, plutonium, nitric acid and TBP composition for specific arcs. The six identified biases are all located on internal and output flowrates measured by secondary sensors.

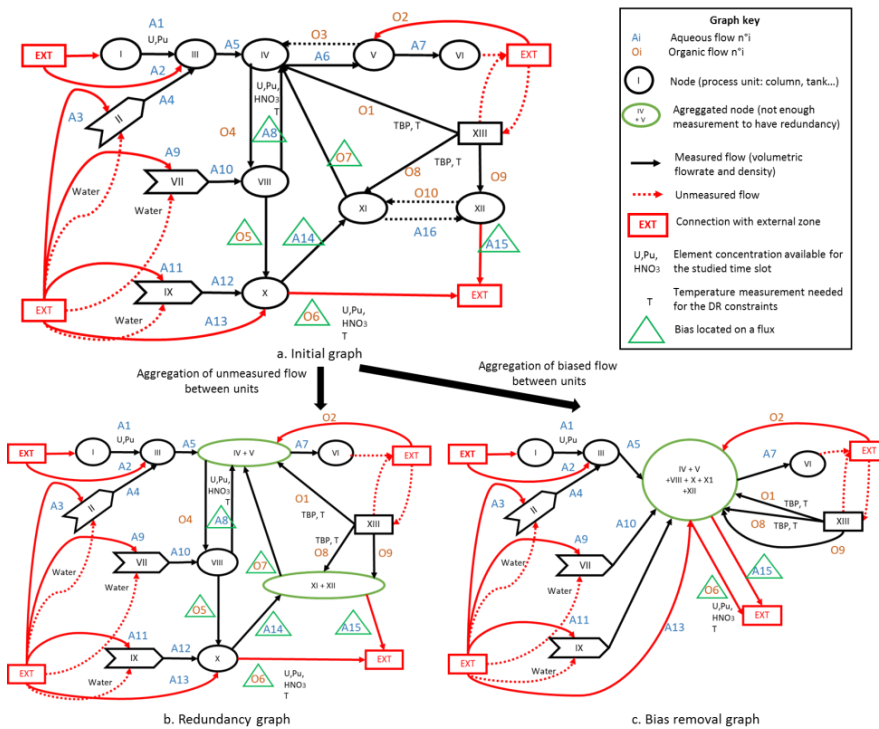


Figure 2: Graphs of an extraction-stripping step of the PUREX process.

For the classical GEDI methodology, each time a bias is detected, the redundancy decreases (Narasimhan and Jordache, 2000). The bias removal graph (Figure 2c) shows this loss of redundancy: DR cannot be applied on the aggregated node (IV+V+VIII+X+XI+XII), as only the calculation of the biases on output flowrates is possible in this scenario. In addition, classical GEDI techniques cannot locate a bias within two-way arcs between two units, such as between IV and VIII.

4. Results

The first bias estimation $B^{C(0)}$ was obtained by the comparison between measured internal and output flow-rates and the initial PAREX calculation. Four iterations were needed to obtain consistent bias estimations B^C and the minimum of the objective function. As soon as all biases can be considered constant, the iterations stop ($|B^{C(4)} - B^{C(3)}| < \alpha$, with $\alpha = 10^{-4}$ the tolerance of the convergence criterion). Note that the bias values are considerably higher than the measurement uncertainty in this scenario; therefore their contribution must be isolated.

All redundant data (80 variables), biased and unbiased, are reconciled. Figure 3 displays the differences ΔX_{out}^{B-R} between some of the measured X_{out}^B and reconciled X_{out}^R values and their corresponding uncertainties. The differences $\Delta X_{out}^{B-C(0)}$ and ΔX_{out}^{B-C} between the measured X_{out}^B and, respectively, initial $X_{out}^{C(0)}$ and final X_{out}^C PAREX values, are also laid out.

The differences $\Delta X_{out}^{B-C(0)}$ result from input measurement uncertainty. For flowrate A7, flowrate O4, and density A8, the reconciled values are closer to the PAREX calculations than the measured values, highlighting the consistency of the final data set. Moreover, the uncertainty of the reconciled values is smaller than the measurement uncertainty.

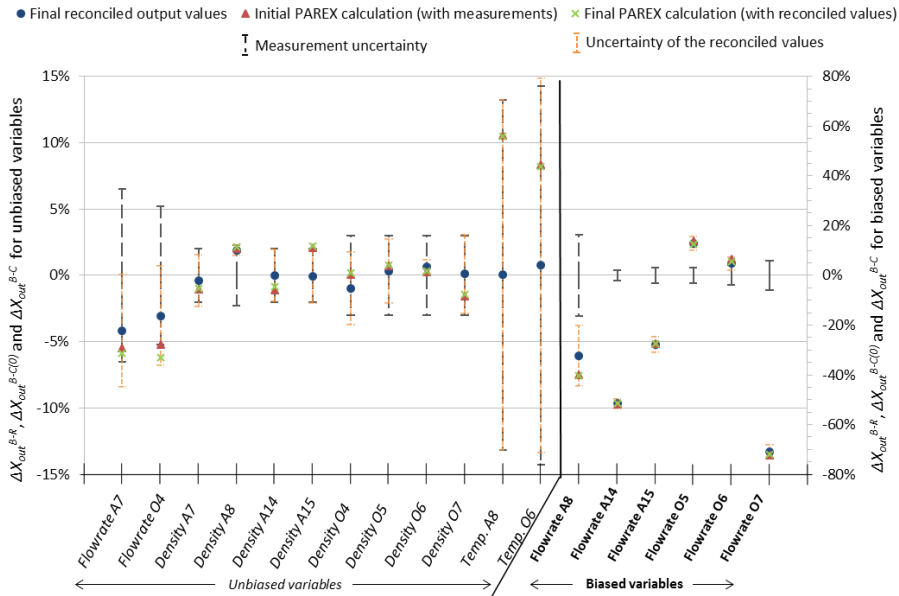


Figure 3: Comparison between measured, reconciled, and PAREX calculated outputs.

Concerning density A8 and density O6, the uncertainties of the reconciled values are very small and surround the reconciled and calculated values. These densities are linked to uranium and plutonium concentrations through a density equation. The analytical concentration measurement methods are more precise than the density sensors. Thus, the uncertainty propagation through the constraints enables the X_{out}^R to be more precise.

Concerning the other unbiased variables, mostly linked by mass balances, the reconciled X_{out}^R values are only slightly different from the measured X_{out}^B values. The two PAREX simulations give very similar results. This reflects the low sensitivity of these physical quantities to the change in the inputs from measured to reconciled values.

As PAREX input data are reconciled, accuracy is given to process indicators estimation. For instance, the uncertainty of the TBP mass flowrate is reduced by half (measurement uncertainty: 5.26 %, uncertainty of the reconciled value: 2.81 %). The uncertainties of uranium and plutonium mass flowrates are also reduced (from 2.8 % to 2.0 %), which leads to a better estimation of the metal loading in the solvent.

5. Conclusions

In classical GEDI methods, each bias decreases the redundancy of the system. The new methodology is based on nonlinear DR in which the biases are fixed and estimated by a rigorous model, with the reconciled values as input data. Therefore, the redundancy is not modified. For the bias estimation to be precise, the rigorous code and the DR iterate until the bias values offer a consistent set of reconciled data. This methodology enables explicit and implicit constraints for a DR problem to be addressed.

The proposed methodology was applied with success to a spent nuclear fuel treatment process. As a tool to reduce uncertainty in nuclear matter management within the plant, combining data reconciliation and the PAREX code could help in process monitoring and control.

References

- J. Bisson, B. Dinh, P. Huron, C. Huel, 2016, PAREX, a numerical code in the service of La Hague plant operations, *Procedia Chemistry*, 32, 117-124.
- E. Corderio do Valle, R. De Araújo Kalid, A. Resende Secchi, A. Kiperstok, 2018, Collection of benchmark test problems for data reconciliation and gross error detection and identification, *Computers and Chemical Engineering*, 111, 134-148.
- B. Dinh, P. Baron, J. Duhamet, 2008, Treatment and recycling of spent nuclear fuel, monograph of CEA DEN, the PUREX process separation and purification operations, 55-70.
- M. Fuente, G. Gutierrez, E. Gomez, D. Sarabia, C. de Prada, 2015, Gross error management in data reconciliation, *IFAC-PapersOnLine*, 48, Issue 8, 623-628.
- M. Liebman, T. Edgar, L. Lasdon, 1992, Efficient data reconciliation and estimation for dynamic processes using nonlinear programming techniques, *Computers & chemical engineering*, 16, 963-986.
- S. Narasimhan, C. Jordache, 2000, *Data reconciliation and gross error detection: an intelligent use of process data*, Gulf Publishing Co.
- C. Pantelides, J. Renfro, 2013, The online use of first-principles models in process operations: review, current status and future needs, *Computers & chemical engineering*, 51, 136-148.
- D. Simpson, V. Voller, M. Everett, 1991, An efficient algorithm for mineral processing data adjustment, *International Journal of Mineral Processing*, 31, 73-96.

Reinforcement Learning for Batch-to-Batch Bioprocess Optimisation

P. Petsagkourakis^a, I. Orson Sandoval^b, E. Bradford^c, D. Zhang^{a,d,*} and E.A. del Rio-Chanona^{d,*}

^a*School of Chemical Engineering and Analytical Science, The University of Manchester, M13 9PL, UK*

^b*Instituto de Ciencias Nucleares, Universidad Nacional Autónoma de México, A.P. 70-543, C.P. 04510 Ciudad de México, Mexico*

^c*Department of Engineering Cybernetics, Norwegian University of Science and Technology, Trondheim, Norway*

^d*Centre for Process Systems Engineering (CPSE), Department of Chemical Engineering, Imperial College London, UK*

dongda.zhang@manchester.ac.uk, a.del-rio-chanona@imperial.ac.uk

Abstract

Bioprocesses have received great attention from the scientific community as an alternative to fossil-based products by microorganisms-synthesised counterparts. However, bioprocesses are generally operated at unsteady-state conditions and are stochastic from a macro-scale perspective, making their optimisation a challenging task. Furthermore, as biological systems are highly complex, plant-model mismatch is usually present. To address the aforementioned challenges, in this work, we propose a reinforcement learning based online optimisation strategy. We first use reinforcement learning to learn an optimal policy given a preliminary process model. This means that we compute diverse trajectories and feed them into a recurrent neural network, resulting in a policy network which takes the states as input and gives the next optimal control action as output. Through this procedure, we are able to capture the previously believed behaviour of the biosystem. Subsequently, we adopted this network as an initial policy for the "real" system (the plant) and apply a batch-to-batch reinforcement learning strategy to update the network's accuracy. This is computed by using a more complex process model (representing the real plant) embedded with adequate stochasticity to account for the perturbations in a real dynamic bioprocess. We demonstrate the effectiveness and advantages of the proposed approach in a case study by computing the optimal policy in a realistic number of batch runs.

Keywords: Reinforcement Learning, Batch Process, Recurrent Neural Networks, Bioprocesses

1. Introduction

There has been a global interest in using sustainable bio-production systems to produce a broad range of chemicals and substitute fossil derived synthetic routes (Harun et al., 2018). Bioprocesses exploit microorganisms to synthesise platform chemicals and high-value products by using different means of resources (Jing et al., 2018). Compared to a traditional chemical process, a biochemical process is highly complex due to the intricate relationships between metabolic reaction networks and culture fluid dynamics (del Rio-

Chanona et al., 2018). As a result, it is difficult to construct accurate dynamic models to simulate general large-scale biosystems, and plant-model mismatch is inevitable. Furthermore, bioprocess dynamics are often stochastic due to the underlying metabolic pathways which are sensitive to even mild changes in operating conditions (Zhang and Vassiliadis, 2015; Thierie, 2004). Therefore, developing control and optimisation strategies for bioprocesses remains an open challenge. Given these critical limitations in physical models, in this work we propose a data-driven approach to address this challenge.

We must seek a strategy that can handle both the system's stochasticity and plant-model mismatch. It is here that we have opted to use *reinforcement learning* and more specifically, *policy gradients*, the rationale behind this is next explained. Reinforcement learning (RL) addresses the problem of solving nonlinear and stochastic optimal control problems (Bertsekas, 2000). Two main branches have been established on how to solve dynamic optimisation problems via RL. The first one is based on *dynamic programming* (DP), hence termed approximate dynamic programming (ADP). DP relies on the Hamilton-Jacobi-Bellman equation (HJBE), the solution of which becomes intractable for small size problems with nonlinear dynamics and continuous state and control actions. Hence, past research has relied on using ADP techniques to find (approximate) solutions to this type of problem (Sutton and Barto, 2018). The second branch, is to use *policy gradients* which directly obtain a policy by maximising a desired performance index. This approach is well suited for problems where both the state and control space are continuous. We have therefore adopted this approach for this work. Policy gradient methods are further explained in Section 2.2.

Finally, to address plant-model mismatch, we have applied a data-driven approach. Although there are knowledge-based modelling strategies such as iterative learning (Moore et al., 2006), here we propose a fully data-driven method that can learn from the true dynamics of the system while incorporating previous knowledge.

2. Preliminaries

In this section we introduce important concepts for the proposed work.

2.1. Recurrent Neural Network

Recurrent neural networks, (RNNs) (Rumelhart et al., 1986), are tailored to address sequential data. RNNs produce an output at each time step and have recursive connections between hidden units. This allows them to have a "memory" of previous data and hence be well suited to model time-series. Thus, it could be said that RNNs are essentially simulating a dynamic system for a given set of parameters. In this work, RNNs are applied to parameterise the stochastic policy.

2.2. Policy Gradient Methods

A particular family of RL methods that do not require an explicit estimate of the value of state-action pairs are called *policy gradient methods*. These methods rely on a parametrised policy function $\pi_{\theta}(\cdot)$ that returns an action a given a state of the system s and a set of intrinsic parameters θ . In the case of stochastic policies, the policy function returns the defining parameters of a probability distribution over possible actions, from which the

actions are sampled:

$$a \sim \pi_{\theta}(a|s) = \pi(a|s, \theta) = p(a_t = a | s_t = s, \theta_t = \theta). \quad (1)$$

In this work, an RNN is used as the parametrised policy, which takes states and past controls as inputs and returns a mean and a variance from which a control is drawn. In this setting, the exploitation-exploration trade-off is represented explicitly as the variance of the underlying distribution of the policy. Deterministic policies may be approached as a limiting case where variance fades upon convergence. Let a sequence of H states and actions be called an *episode* τ . An episode τ is a sequence of states and actions generated by following the current policy, $\tau \sim p(\tau|\theta)$. The reward function ($R(\cdot)$) may be estimated over K episode samples:

$$\hat{R}(\theta) = \mathbb{E}_{\theta} [R(\tau)] = \int_{\tau} p(\tau|\theta) R(\tau) d\tau \approx \frac{1}{K} \sum_{k=1}^K R(\tau^{(k)}). \quad (2)$$

The objective of policy gradient methods is to maximise a reward function $\hat{R}(\theta)$ by using gradient ascent techniques over a continuously differentiable policy. The evolution of the intrinsic parameters at each optimisation step m is given by

$$\theta_{m+1} = \theta_m + \alpha_m \nabla_{\theta} R|_{\theta=\theta_m}. \quad (3)$$

Differentiable policies guarantee smooth changes over sufficiently small variations of the parameters.

2.3. REINFORCE Algorithm

The REINFORCE (Williams, 1992) algorithm approximates the gradient of the policy to maximise the expected reward with respect to the parameters θ without the need of a dynamic model of the process. For this, it is necessary to take advantage of the gradient of a logarithm and a decomposition of the likelihood of an H step episode τ under a policy π_{θ} (Sutton and Barto, 2018; Peters and Schaal, 2008),

$$p(\tau|\theta) = p(s_0) \prod_{h=0}^H p(s_{h+1}|s_h, a_h) \cdot \pi_{\theta}(a_h|s_h), \quad (4)$$

to express approximate the desired gradient as

$$\begin{aligned} \nabla_{\theta} \hat{R}(\theta) &= \int_{\tau} R(\tau) p(\tau|\theta) \nabla_{\theta} \log p(\tau|\theta) d\tau \approx \frac{1}{K} \sum_{k=1}^K R(\tau^{(k)}) \nabla_{\theta} \log p(\tau^{(k)}|\theta) \\ &\approx \frac{1}{K} \sum_{k=1}^K R(\tau^{(k)}) \sum_{h=1}^H \nabla_{\theta} \log \pi_{\theta}(a_h^{(k)}|s_h^{(k)}). \end{aligned} \quad (5)$$

The variance of this estimation can be reduced with the aid of an action-independent baseline b without introducing bias. A simple but effective baseline is the expectation of reward under the current policy, approximated by the mean over the sampled paths:

$$b = \hat{R}(\theta) \approx \frac{1}{K} \sum_{k=1}^K R(\tau^{(k)}), \quad (6)$$

$$\nabla_{\theta} \hat{R}(\theta) \approx \frac{1}{K} \sum_{k=1}^K \left(R(\tau^{(k)}) - b \right) \sum_{h=1}^H \nabla_{\theta} \log \pi_{\theta} \left(a_h^{(k)} | s_h^{(k)} \right). \quad (7)$$

This selection increases the log likelihood of an action by comparing it to the expected reward of the current policy.

3. Reinforcement Learning for Bioprocess Optimisation under Uncertainty

In this work, during Stage 1, we assume a preliminary model has been constructed to approximate the real system's dynamics. This approximate model can be used to generate a large size of episodes (different control actions subject to probability) for each training epoch (an epoch corresponds to a specific set of RNN parameter values) to *initially* design a control policy network that produces the model identified optimal policy. Hence the control policy is an RNN which takes states (including time to termination) and past controls as inputs and returns a mean and a variance from which a control action is drawn.

During Stage 2 (real plant optimal control), the policy network is directly updated using the real system (the plant) in a *batch-to-batch* framework. Accuracy of the control policy (*i.e.* the RNN) is therefore consolidated during an online implementation. The stochastic control policy is a RNN that represents a conditional probability distribution π_{θ} . The RNN predicts the mean and standard deviation of the next action through a deterministic map using the measurements (the previous states s_i , a sequences of previous actions (a_i) with $i \in \{-N, \dots, -1\}$) and the time that is left for the end of the batch process. This proposed stochastic control policy is trained using the REINFORCE algorithm (see Section 2). This algorithm aims to maximise a given reward (*e.g.* concentration of target product at the final time), with the mean value of this reward being employed as a baseline during the update of RNN parameter values (see Eq. 6 & 7). The use of a baseline has been proven to be advantageous as long as it is independent of the control actions (Sutton and Barto, 2018).

Initially (Stage 1), the policy network is trained *off-line* using an available approximate model. The algorithm runs for several epochs and episodes until convergence. The network is then adopted to generate initial optimal policies for the real system (the plant, simulated by a model complex process model which is not available for RNN construction)(Stage 2). Methods used in the REINFORCE algorithm usually require a large number of episodes and epochs, therefore a good initial solution is paramount so that Stage 2 (which is assumed to be done in the actual plant) can be completed with few batch-to-batch runs. In order to keep the problem realistic, only a small number of batches is utilised in Stage 2 to refine the policy network.

4. Computational Case Studies

The proposed methodology is applied to a fed-batch bioreactor, where the objective is to maximise the concentration of target product (y_2) at the end of the batch time, using light and an inflow rate (u_1 and u_2) as control variables. The plant (real photo-production system) is simulated using the following equations:

$$\frac{dy_1}{dt} = -(u_1 + 0.5 u_1^2)y_1 + 0.5 \frac{u_2 y_2}{(y_1 + y_2)} \quad \frac{dy_2}{dt} = u_1 y_1 - 0.7 u_2 y_1 \quad (8)$$

where u_1 , u_2 and y_1 , y_2 are the control variables and the outlet concentrations of the reactant and product, respectively. The batch operation time course is normalised to 1.

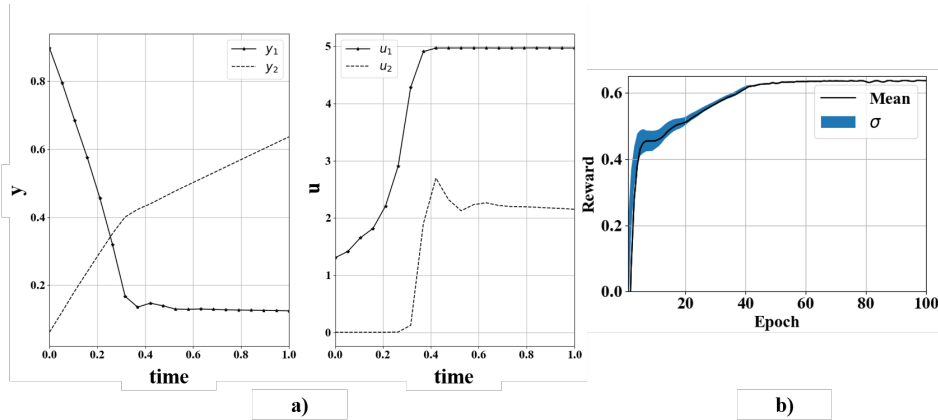


Figure 1: (a) The time trajectories produced by the trained policies. (b) The reward computed for the approximate model.

Additionally, a random disturbance is assumed, which is given by a Gaussian distribution with mean value 0 and standard deviation 0.02. It is assumed that only the following approximate model (simplified from the complex model) is known, and the preliminary training is performed based on this model to construct the control policy network, whilst the real system model is unknown due to the complexity of the process mechanisms.

$$\frac{dy_1}{dt} = -(u_1 + 0.5 u_1^2)y_1 + u_2 \quad \frac{dy_2}{dt} = u_1 y_1 - u_2 y_1 \quad (9)$$

Initially, 100 epochs and 800 episodes are generated from the simplified model to search the optimal control policy that maximises the reward for Eq. 9. Control variables are constrained to be in $[0, 5]$. The control policy RNN is designed to contain 3 hidden layers, each of which comprising 15 neurons embedded by a hyperbolic tangent activation function. Adam (Kingma and Ba, 2014) is employed to compute the network parameter values. It should be mentioned that the reward computed after convergence is almost the same in comparison to the result given by the optimal control problem (OCP) at Stage 1. The maximum rewards for RL and OCP are 0.637 and 0.640, respectively. The reward for its epoch is depicted in Figure 2b) and the process trajectories after the final update of the policy network are shown in Figure 2a). This policy is then used to initialise the REINFORCE algorithm for the plant's RL (Stage 2), where 25 episodes are used (*i.e.* 25 real plant batches). The solution after only 4 epochs is 0.575 whilst the stochastic-free optimal solution identified using the *unknown* (complex) model of the plant is 0.583. The reward of this epoch is depicted in Figure 1b) and the process trajectories after the last epoch are depicted in Figure 1a).

5. Conclusions

In this work we show that by adapting reinforcement learning techniques to uncertain and complex bioprocesses we are able to obtain a near optimal policy for a stochastic system where the true dynamics are unknown. Furthermore, we obtain this result in a realistic scenario where only a modest number of batch runs is used. We emphasise that

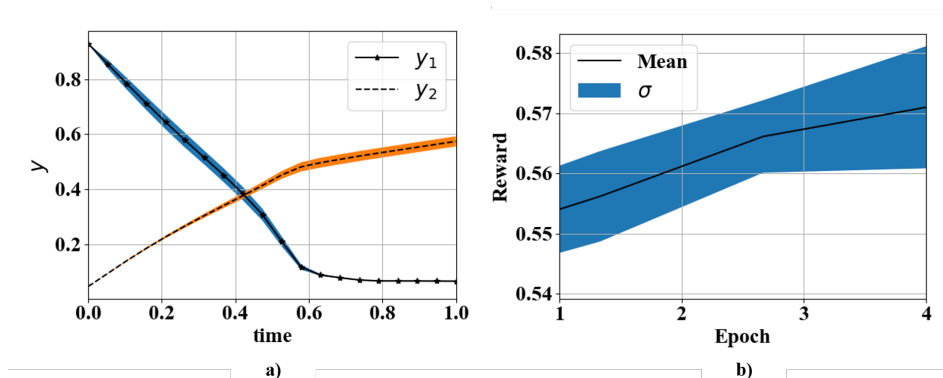


Figure 2: (a) The time trajectories produced by the real plant. (b) The reward computed by the updated training using the plant ("real" system) for each epoch.

we assume no process structure and embed both stochasticity and plant-model mismatch into the considered system, the optimisation of which is generally known to be intractable. Future work will focus on more complex case studies and exploring other RL methods, such as bias reduction and sample efficiency strategies.

References

- D. P. Bertsekas, 2000. *Dynamic Programming and Optimal Control*, 2nd Edition. Athena Scientific.
- E. A. del Rio-Chanona, J. L. Wagner, H. Ali, D. Zhang, K. Hellgardt, 2018. Deep learning based surrogate modelling and optimization for microalgal biofuel production and photobioreactor design. *AIChE Journal*, in press.
- I. Harun, E. A. Del Rio-Chanona, J. L. Wagner, K. J. Lauenstein, D. Zhang, K. Hellgardt, aug 2018. Photocatalytic Production of Bisabolene from Green Microalgae Mutant: Process Analysis and Kinetic Modeling. *Industrial & Engineering Chemistry Research* 57 (31), 10336–10344.
- K. Jing, Y. Tang, C. Yao, E. A. del Rio-Chanona, X. Ling, D. Zhang, feb 2018. Overproduction of L-tryptophan via simultaneous feed of glucose and anthranilic acid from recombinant *Escherichia coli* W3110: Kinetic modeling and process scale-up. *Biotechnology and Bioengineering* 115 (2), 371–381.
- D. P. Kingma, J. Ba, 2014. Adam: A Method for Stochastic Optimization. *ArXiv:1412.6980*.
- K. L. Moore, Y. Chen, H. Ahn, Dec 2006. Iterative learning control: A tutorial and big picture view. In: *Proceedings of the 45th IEEE Conference on Decision and Control*. pp. 2352–2357.
- J. Peters, S. Schaal, 2008. Reinforcement learning of motor skills with policy gradients. *Neural networks* 21 (4), 682–697.
- D. E. Rumelhart, G. E. Hinton, R. J. Williams, 1986. Learning representations by back-propagating errors. *Nature* 323, 533.
- R. Sutton, A. Barto, 2018. *Reinforcement Learning: An Introduction*, second edition Edition. MIT Press.
- J. Thierie, feb 2004. Modeling threshold phenomena, metabolic pathways switches and signals in chemostat-cultivated cells: the Crabtree effect in *Saccharomyces cerevisiae*. *Journal of theoretical biology* 226 (4), 483–501.
- R. J. Williams, 1992. Simple statistical gradient-following algorithms for connectionist reinforcement learning. *Machine learning* 8 (3-4), 229–256.
- D. Zhang, V. S. Vassiliadis, nov 2015. *Chlamydomonas reinhardtii* Metabolic Pathway Analysis for Biohydrogen Production under Non-Steady-State Operation. *Industrial & Engineering Chemistry Research* 54 (43), 10593–10605.

A new index for chemical process design considering risk analysis and controllability

Nancy Medina-Herrera,^{a*} Salvador Tututi-Avila,^b Arturo Jiménez-Gutierrez^c

^a *Universidad Autonoma de Nuevo León, Agronomy School, Francisco Villa s/n, Ex Hacienda el Canadá, General Escobedo, N.L, 66451, MEXICO*

^b *Universidad Autónoma de Nuevo León, Department of Chemical Engineering, Av. Universidad s/n, Ciudad Universitaria, San Nicolas de los Garza, NL, 66451, MEXICO*

^c *Department of Chemical Engineering, Instituto Tecnológico de Celaya, Av. Tecnológico s/n, Celaya, Gto. 38010 MEXICO*

nancy.medinahr@uanl.edu.mx

Abstract

Safety and controllability are two important items that complement the economic analysis commonly done during a process design. Such factors are typically carried out once the process has been designed. Although some approaches have been proposed to include controllability properties from the design stage of the process, safety is still addressed after the design has been completed, so that safety devices are added to mitigate the consequences of potential accidents. Inherent safety is the most effective risk management approach, since actions can be taken to avoid accidents instead of mitigating their consequences. However, inherent safety is not a straightforward procedure, nor universal, and sometimes in conflict with other properties or parameters of the process. This manuscript describes a new index to account for inherent safety and controllability. The combination of a conditions number that accounts for controllability and a distance likely to cause death that emerges from the application of a quantitative risk analysis for the process was used as a basis. Three mathematical relationships were explored in the search for a suitable combination of such indices. The procedure was applied to a case study dealing with a distillation system design. Results show how the values obtained from the proposed index can give an initial assessment of the combined effect of risk and controllability as part of the design of a process.

Keywords: controllability, design, inherent safety, risk analysis.

1. Introduction

The concepts associated with inherent safety provide an effective tool for risk management. Inherent safety relies on the principles of elimination, minimization, moderation, substitution and simplification. The objective of inherent safety is to avoid risk instead of diminishing its consequences. The effectiveness of inherent safety depends on the stage of the plant life it is applied, being the design stage the most effective. The decisions based on inherent safety must be evaluated carefully, since inherent safety principles sometimes show conflicts among them. For instance, the minimization principle states that a process is safer when hazardous materials inventory is reduced, but dynamic performance might work against safety if inventory is reduced. Thus, it is important to assess safety in early stages of process design including this type of self-

conflicting behavior. Recently, a comprehensive review of process safety indices has been published (Roy et al., 2016). From this collection, some highlighted indexes are discussed here. Dow Fire & Explosion Index (DF&EI) was the first proposed index to account for safety in the mid-60's. There have been several works to assess inherent safety since it was defined in the 80's. The first index related to inherent safety was proposed by Heikkila et al (1996). This index is similar to DF&EI and considers two main parts of the process: chemicals properties and process conditions. Khan and Amyotte (2004) have published an integrated inherent safety index, named I2SI. This index is more complex and considers process control within inherent safety.

Most of the indices published so far are semi-quantitative, but many times weight factors are used to rank their importance. This semi-quantitative characteristic results in different processes with similar conditions so that material properties may get the same rating, which is not totally accurate. A quantitative risk analysis (QRA) has been shown as a proper tool to account for safety (Medina-Herrera et al., 2014). A QRA performs a more detailed study and provides a more exact risk measurement because probabilities and consequences are considered (AIChE, 2000).

The Morari resilience index (MRI) can be used to discriminate among process alternatives; the larger its value, the more controllable the process is. Another important index is the condition number (CN) related to system sensitivity against input disturbances. Small values are desired. Another important index is the relative gain array number (RGA_{No}) which gives information about the controlled and manipulated variables in the frequency domain; pairings with low RGA_{No} values are preferred. All these indices provide a good basis to account for controllability, but a suitable approach to include both controllability and process safety is needed.

In this work, we propose a quantitative approach for process design that accounts for inherent safety considering both risk and controllability. In terms of risk, we use a QRA approach to obtain a distance likely to cause death, which relates to material inventory. For controllability, we test two indices, namely the condition number and the relative gain array. From a set of design candidates, the indices are normalized, and three mathematical relationships between risk and controllability are explored.

2. Safety Indices Calculation

2.1. Design approach

A set of initial designs (P) is considered to evaluate the performance of each design using the proposed indexes. Once the candidates are set, they are subjected to a combined controllability and QRA analysis. The approach is carried out using ASPEN Tech and MATLAB as software tools. In Aspen Plus steady state simulations are carried out, simulations are then exported to Aspen Dynamics, and the results are transferred to MATLAB, where indexes are computed.

2.2. Controllability analysis

In terms of controllability, a singular value decomposition procedure is carried out, from which the condition number CN_i is evaluated. Regularly, a matrix of gain is obtained for the process at zero frequency and a singular value decomposition analysis is carried out. In this work, we followed the methodology proposed by Gabor and Mizsey (2008) to

make calculations using a linearized state-space model system of every candidate i . The linearized state space model can be obtained with the Control Design Interface module. The methodology also computes MRI and $RG_{A_{No}}$.

2.3. Quantitative risk analysis

QRA was implemented to assess the risk of a chemical inside process, following the methodology described in Medina-Herrera et al. (2014). The methodology is based on frequency and consequences analyses. First, catastrophic scenarios are identified from potential failures within the system using a bow tie procedure, and frequencies are calculated from literature data on failures. Then, a consequence analysis is performed for every catastrophic scenario previously identified. In brief, the consequences analysis implies quantification of the amount of material released, dispersion calculations, characterization of the scenario, and finally quantification of consequences. The models for consequence analysis were taken from CCPS Guidelines for Quantitative Risk Analysis in Chemical Process (AIChE, 2000). After the application of QRA, DD_i is obtained, which represents the distance of affectation such that there is a 50% chance of death in case of a catastrophic event. DD_i was selected because it can be calculated as measurement of risk even when layout is not yet defined, in an early design stage.

2.4. Normalization

After controllability and risk indices are individually evaluated, a normalization procedure is needed, since such indices have values with different orders of magnitude, and they also depend on the system of units.

When the set P was evaluated and controllability and risk indicators were obtained for each candidate i , a normalization procedure was used taking as a basis the highest value of each index, DD_i and CN_i , within the set P , that is,

$$\left. \begin{aligned} DD_N^i &= \frac{DD^i}{\text{Maximum}(DD^i)} \\ CN_N^i &= \frac{CN^i}{\text{Maximum}(CN^i)} \end{aligned} \right\} \forall i \in P \quad (1)$$

As a result, the normalized indices are bound between zero and one, and they can be subject to numerical comparison on a consistent basis.

2.5. Basic mathematical relationships: Indices

After the indicators are obtained with similar orders of magnitude, they can be used to rank process alternatives from controllability and risk considerations. Even when the relationship between such items is complex, we can establish that they are related to the process safety. Facing the lack of knowledge about the relationship between controllability and risk to assess safety, we followed the methodology by Ni et al. (2010) to create indices with two different inputs, and derived three basic mathematical relationships. As a result, a proposed safety index, SI, was developed, and three versions of such an index were created. The objective of testing three different relationships is aiding in the analysis to understand whether risk and controllability are additive, factored or follow a balanced relationship.

The first version SI_1 is the addition of both criteria, distance likely to cause death (DD_N) and condition number (CN_N).

$$SI_1 = DD_N + CN_N \quad (2)$$

The second version, SI_2 , is the product of both inputs,

$$SI_2 = DD_N * CN_N \quad (3)$$

For both additive and product relationships, the smaller the value of the index, the safer the process is.

The third version we explore is a fraction given by the distance likely to cause death divided by the condition number (see Eq. (4)). In this case, a value close to one means that the process is balanced from both controllability and safety considerations, which may not necessarily be desirable. A value higher than one would indicate that risk is a more important criterion than controllability, and vice versa.

$$SI_3 = DD_N / CN_N \quad (4)$$

These three versions arise from the lack of knowledge on the relationship between risk and controllability. It deemed convenient to calculate and evaluate all three alternatives for an initial insight into behavior of the proposed index.

3. Case Study and Results

The case study was taken from the CCPS Example of the guidelines for chemical process quantitative risk analysis (AIChE, 2000). The distillation system is a single column that separates n-hexane and n-heptane. The feed stream has 60,120 kg/h of a binary mixture with 58%wt of n-hexane. The purity specification for the top product is 0.9 on a weight basis, with a flowrate of 36,000 kg/h. The column has 16 equilibrium stages and the top pressure is 4.9 atm. The internal diameter calculated by ASPEN Plus was 2.7 meters. The residence time for sump was fixed at 6 minutes, and for reflux drum at 12 min using a 2D=L rule for tank dimensions. The QRA performed with the CCPS Guidelines has been used to analyze process risk. The objective of this example is to describe the methodology for the proposed index calculations along with the analysis of results. The hydraulic variables considered for this example were diameter and residence time for the reflux drum and sump. Such hydraulic variables affect both criteria, controllability and risk. In order to define the set of designs P , we took the CCPS design as the base case, which has a diameter of 2.71m and 12 and 6 min of residence time on the reflux drum and sump. Other designs were considered by varying the diameter from half the base diameter to three times that value, such that $D = [0.5D_{base}, 0.75D_{base}, D_{base}, 1.5D_{base}, 2D_{base}, 3D_{base}]$ where $D_{base}=2.71m$. As for the residence time, a range was fixed from 1 minute to 20 minutes, assuming equal values for both tanks. It should be noted that the base case assumes residence times of 12 and 6 minutes. When the diameter was varied, the designs were set with a residence time of 10 min for reflux drum and sump, and when residence time was varied, the diameter was kept fixed at 2.71m (in that case, the residence time was the same for reflux drum and sump).

The results obtained are illustrated in Figure 1. We can observe that there is no significant difference using CN_N or $RGAN_{NoN}$ for the controllability component. We also observe that for the range analyzed, the trend seems not to be linear. The index presents almost the same value from 0.5 times diameter to the base diameter; after that point, increasing the diameter has a more pronounced effect on the three forms of the safety index, which means that increasing the diameter to improve controllability conflicts with the safety parameter. The safest design is the base case, according to SI_1 and SI_2 . The design with three times diameter (3D) is more balanced between controllability and risk, as given from the results of SI_3 , while for the base design controllability has a higher weight than risk ($SI_3 < 1$), which means that changing the diameter is not recommended for an inherently safer process. In part b, we observe that the contribution of the two controllability indicators used here is similar for the three safety indices. It is important to notice that for this variation range (1min -20 min) the trend seems to be linear. From SI_1 and SI_2 , a residence time of 1 minute is the safest option. From the results of SI_3 , the same trend is observed; decreasing residence time has a lower impact on risk with respect to the effect on controllability. Residence time has therefore an important effect on safety, as given from the risk evaluations conducted here.

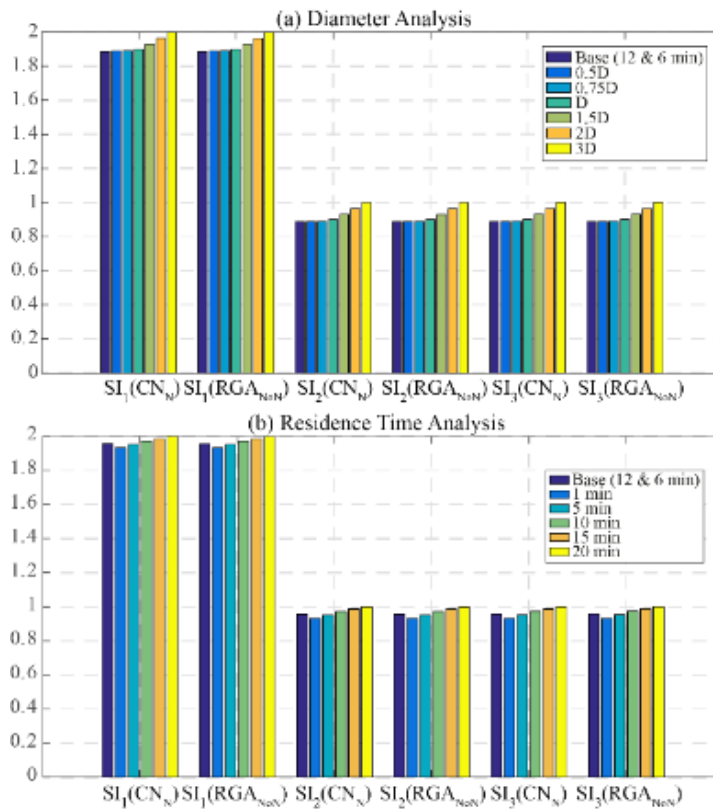


Figure 1. CCPS case study Results of Proposed Indexes for analysis of (a) changes of diameter and (b) changes of residence times

Conclusion

A combined index that accounts for risk and controllability has been described. After normalizing the individual indices chosen for each item between zero and one, three types of relationships were explored. The results of the application to a case study taken from the CCPS publication showed that implementing the minimization principle of inherent safety can lead to a conflict with controllability properties, which calls for a careful consideration of risk and controllability during the design stage of a process. The approach given in this work attempts to contribute in that direction. It is worthy of mention that there is not a general guideline whether reducing inventory, which is called for from the minimization principle of inherent safety, is a correct policy when controllability is considered. The results of the application to the case study show this type of conflict. It is important to notice that this methodology has been implemented in case studies on steady state and it has not been implemented in an intrinsically dynamic system, such as a batch process. Further work is needed to consolidate these initial efforts towards the development of a useful index that combines risk and controllability and that can be used during the design stage of a chemical process.

References

- AICHe, A. I. of C. E. (2000). *Guidelines for Chemical Process Quantitative Risk Analysis*. (C. for C. P. Safety, Ed.) (2nd ed.). New York, New York.
- Gabor, M., & Mizsey, P. (2008). A Methodology To Determine Controllability Indices in the Frequency Domain. *Industrial & Engineering Chemistry Research*, 47(14), 4807–4816.
- Heikkilä, A.-M., Hurme, M., & Järveläinen, M. (1996). Safety considerations in process synthesis. *Computers & Chemical Engineering*, 20(Supplement 1), S115–S120.
- Khan, F. I., & Amyotte, P. R. (2004). Integrated inherent safety index (I2SI): A tool for inherent safety evaluation. *Process Safety Progress*, 23(2), 136–148.
- Medina-Herrera, N., Grossmann, I. E., Mannan, M. S., Jimenez-Gutierrez, A., & Jiménez-Gutiérrez, A. (2014). An approach for solvent selection in extractive distillation systems including safety considerations. *Industrial & Engineering Chemistry Research*, 53(30), 12023–12031.
- Medina-Herrera, N., Jiménez-Gutiérrez, A., & Grossmann, I. E. (2014). A mathematical programming model for optimal layout considering quantitative risk analysis. *Computers & Chemical Engineering*, 68, 165–181. <https://doi.org/10.1016/j.compchemeng.2014.05.019>
- Medina-Herrera, N., Jiménez-Gutiérrez, A., & Mannan, M. S. (2014). Development of inherently safer distillation systems. *Journal of Loss Prevention in the Process Industries*, 29, 225–239. <https://doi.org/http://dx.doi.org/10.1016/j.jlp.2014.03.004>
- Ni, H., Chen, A., & Chen, N. (2010). Some extensions on risk matrix approach. *Safety Science*, 48(10), 1269–1278. <https://doi.org/http://dx.doi.org/10.1016/j.ssci.2010.04.005>
- Roy, N., Eljack, F., Jiménez-Gutiérrez, A., Zhang, B., Thiruvenkataswamy, P., El-Halwagi, M., & Mannan, M. S. (2016). A review of safety indices for process design. *Current Opinion in Chemical Engineering*, 14, 42–48. <https://doi.org/10.1016/j.coche.2016.07.001>

A primal bounding approach for multistage stochastic programs of resource-constrained planning and scheduling with stochastic task success

Zuo Zeng, Selen Cremaschi*

*Department of Chemical Engineering, Auburn University, Auburn, AL 36849, USA
selen-cremaschi@auburn.edu*

Abstract

Resource-constrained planning and scheduling problems under stochastic task success, which are common in chemical industries, lend themselves well to being modelled using multistage stochastic programming (MSSP) because most projects involve a series of tasks that needs to be completed in stages and that may or may not be successful. However, these MSSP models rapidly grow and quickly become computationally intractable for real world problems. This paper presents three alternative ways to estimate objective function values in a general primal bounding framework for MSSP models of resource-constrained planning and scheduling with stochastic task success. The framework extends the concept of expected value solution. We apply the proposed framework with alternative objective function estimation approach to instances with varying project sizes (i.e., 3-, 4-, 5-, and 6- projects) with up to 4096 scenarios. The framework yields primal bounds within 1.01% of the true solutions for all tested cases with a reduction in solution times up to four orders of magnitude.

Keywords: multistage stochastic programming, primal bound, endogenous uncertainty, resource constrained planning, probabilistic task success

1. Introduction

This paper considers resource-constrained planning and scheduling problem with project selection and execution under uncertainties, where the development of projects will be extended or terminated depending on the results of success or failure of associated tasks (Honkomp, 1998). Each project requires a variety of the shared limited resources for completing the required tasks associated with it. If a project fails, it is abandoned, the resources that were originally assigned to that project become available and the return associated with that project is not realized. In these planning problems, the decisions are which projects to pursue and the best way to assign the resources to the chosen projects to maximize the returns. The uncertainties associated with the tasks are resolved once these tasks are in execution or are completed, which makes them endogenous. One approach for modeling and solving these problems is multistage stochastic programming.

Multistage stochastic programming (MSSP) is a scenario-based approach that considers recourse actions in multiple stages after observing uncertainties. Uncertainties are represented by scenarios, which usually are obtained as the Cartesian product of all possible outcomes of uncertain parameters. In explicit formulation, the decision variables are defined independently for each scenario, and non-anticipativity constraints (NAC) are added to prevent the current stage decisions from anticipating future realizations of

uncertain parameters. Size of a MSSP model, especially with endogenous uncertain parameters, grows rapidly with the number of uncertain parameters and their outcomes leading to both space and time complexities. In general, the solution approaches for these problems rely on heuristic or approximation approaches, and it has been shown that moderate-size problems can be solved to optimality. Example approaches are rolling-horizon heuristic approach (Colvin and Maravelias, 2009), sample average approximation (SAA) algorithm (Solak et al., 2010), decision-rules based approximation (Vayonos et al. 2011), improved Lagrangean decomposition framework (Gupta and Grossmann, 2014), sequential scenario decomposition approach (Apap and Grossmann, 2017), branch and bound algorithm (Brianna and Cremaschi, 2017), a generalized knapsack decomposition algorithm (Brianna and Cremaschi, 2015; Zeng et al., 2018), and absolute expected value solution (AEEV) framework (Zeng and Cremaschi, 2019).

In this paper, we investigate three approaches to estimate the expected objective function value to be used in the AEEV framework for generating tight primal bounds and implementable solutions for large-scale planning and scheduling problems under stochastic task success and. We present this approach using clinical-trial planning problem (Colvin and Maravelias, 2008), which is summarized in §2. AEEV framework and the proposed approaches to estimate the expected objective function value are presented in §3. The problem instances and the solutions obtained by three alternatives are given, compared and discussed in §4. Finally, we present concluding remarks in §5.

2. Clinical Trial Planning Problem

Under limited resources, the goal of clinical-trial planning is to maximize the expected net present value (ENPV) by determining which clinical trials of drugs to start and when to start them (Colvin and Maravelias, 2008). The endogenous uncertainty is in the outcomes of clinical trials. If a drug fails a clinical trial in a phase, it is abandoned. The observation of a clinical trial outcome depends on whether and when it has been started. There are three clinical trials, $J = \{PI, PII, PIII\}$, that must be completed for a drug under limited resources before the drug can generate revenue, rev_i^{max} . Drug $i \in I$ has known required resources ρ_{ijr} , cost C_{ij} , and fixed duration τ_{ij} associated with clinical trial j . There is a random variable, Ω_i , associated with each uncertain parameter for drug i , and its support is $\{PI-F, PII-F, PIII-F, \text{ and } PIII-P\}$. Here, PI-F, PII-F, PIII-F correspond to drug i failing in clinical trials PI, PII, and PIII, and PIII-P indicates that drug i has successfully passed all clinical trials (Colvin and Maravelias, 2008). The scenario set, S , is constructed as the Cartesian product of uncertain parameter outcomes. The planning horizon is discretized $t = 1, 2, 3 \dots T$ (period t starts at time $t - 1$ and ends at time t).

A slightly modified MSSP formulation (Colvin and Maravelias, 2008) for this problem is given in Eqns. (1) – (8). The MSSP model uses a binary variable $X_{i,j,p,s}$ which is equal to 1 if clinical trial (i, j) is started at time t in scenario s . Two continuous variables, $Y_{i,j,p,s}$ and $Z_{i,j,p,s}$, are bounded between 0 and 1, where $Y_{i,j,p,s}$ turns 1 if drug i completes clinical trial j by the beginning of time period t in scenario s , and $Z_{i,j,p,s}$ becomes 1 if drug i completes clinical trial $j - 1$ by time period p and has not started clinical trial j . Losses are represented by two penalty terms: γ_i^D (loss of market) and γ_i^L (loss of patent life).

$$\max ENPV = \sum_s p_s (Rev_s + FRev_s - Cst_s) \quad (1)$$

$$Cst_s = \sum_{i,j,t} cd_t C_{i,j} X_{i,j,t,s} \quad \forall s \quad (2)$$

$$Rev_s = \sum_i success_{i,s} \left\{ \sum_t \left\{ rev_t^{max} X_{i,P_{II},t,s} - \gamma_t^D (Z_{i,P_{II},t,s} + Z_{i,P_{III},t,s}) - \gamma_t^L (t + \tau_{i,P_{III}}) X_{i,P_{III},t,s} \right\} \right\} \quad \forall s \quad (3)$$

$$FRev_s = \sum_i success_{i,s} \left\{ \sum_j rev_{i,j}^{open} f_{i,j} Z_{i,j,|T|,s} \right\} + \sum_i success_{i,s} \left\{ \sum_{j \in \{P_{II}, P_{III}\}} \sum_{t > |T| - \tau_{i,j}} rev_{i,j,t}^{run} f_{i,j+1} X_{i,j,t,s} \right\} \quad \forall s \quad (4)$$

$$f(X_{i,j,t,s}, Y_{i,j,t,s}, Z_{i,j,t,s}) \leq 0 \quad \forall i, j, t, s \quad (5)$$

$$h(X_{i,j,t,s}, Y_{i,j,t,s}, Z_{i,j,t,s}) = 0 \quad \forall i, j, t, s \quad (6)$$

$$X_{i,1,1,s} = X_{i,1,1,1} \quad \forall i, s \quad (7)$$

$$-\sum_{t' \leq t} Z_{i^{s,s'}, j^{s,s'}, t', s} \leq Y_{i,j,t,s} - Y_{i,j,t,s'} \leq \sum_{t' \leq t} Z_{i^{s,s'}, j^{s,s'}, t', s} \quad \forall i, j, (s, s') \in \Psi, t > 1 \quad (8)$$

The objective function is represented by Eqns. (1) – (4), including the probability of scenario s (p_s), the costs Cst_s , current revenue Rev_s , and future revenue $FRev_s$. Current and future revenue depends on the outcome of uncertain parameter, $success_{i,s} \in \{0,1\}$, which is equal to 1 for drug i successfully passing all clinical trials in s , 0 otherwise. The total cost is discounted using the time discounting factor cd_t (Eq. (2)). The parameter $f_{i,j}$ (Eq. (4)) represents the fraction of the revenue that would be realized by completing all remaining trials at the end of the planning horizon. Inequalities, Eq. (5), and equalities, Eq. (6), are scenario specific constraints, which include resource and clinical trial sequencing constraints. Constraints (7) and (8) are NACs. The model grows rapidly due to the increases in number of candidate drugs, scenario size, which results in exponential growth in size of NACs (Eqns. (7) and (8)). It is important to note that for this type of planning problems that has uncertain task outcomes, the uncertain parameters are only incorporated in the objective function (Eqns. (3) and (4) in clinical trial planning model) because the outcomes of clinical trials only impact the ENPV in objective function.

3. Absolute Expected Value Solution (AEEV) framework

The framework generates and solves a series of deterministic sub-problems (DSPs) based on the observation of uncertainties and yields a feasible solution for the original MSSP model. Future unknown information is assumed to be at its expected value, and here-and-now decisions are made based on the current available information and expected values of future events. The uncertainties are observed after here-and-now decisions are made, and recourse actions are determined for each observed uncertain outcome. The AEEV framework repeats this process of making decisions with current and expected future information, observing uncertainties, and taking recourse actions until the end of the planning horizon. Details of the framework can be found in Zeng and Cremaschi (2019).

In resource-constrained planning and scheduling under stochastic task success, there are no recourse actions. The AEEV framework starts by making decision 1 by solving DSP_{1,1}, where indices (1,1) are the indices of sub-problems and time. In DSP_{1,1}, which is generated at the beginning of the planning horizon (Figure 1), all uncertain parameters take their expected values. After decision 1 is implemented, uncertainties associated with decision 1 are observed (observation 1). Based on observation 1, new sub-problems are

generated and solved to determine decisions, and associated uncertainties are observed. This process continues until the end of the planning horizon.

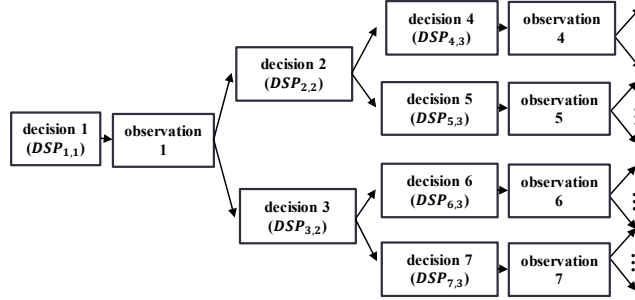


Figure 1. Traditional decision-making process under uncertainty for resource-constrained planning and scheduling under stochastic task success and the AEEV framework

Scenario tree observed for MSSP under endogenous uncertainty depends on decisions made, unlike the scenario tree for MSSP under exogenous uncertainty, which is fixed. AEEV framework works efficiently especially with endogenous uncertainties, where only partial scenarios and uncertainties can be observed in the planning horizon. The framework has a scenario-free structure and only generates and solves the necessary deterministic problems based on the realized outcomes, where the non-anticipativity is implicitly enforced. The objective function value obtained by AEEV framework is a valid primal bound for MSSP models with complete recourse.

3.1. The formulation of deterministic sub-problems (DSPs)

We use clinical trial planning model to illustrate the DSP formulation (Eqns. (9) – (15)) in AEEV framework. In DSPs, the scenario index and NACs are removed from the MSSP model, and the uncertain parameter values are set to their expected values ($E[\text{success}_i]$ in Eqns. (11) and (12)). The realizations of clinical trial outcomes until the current time period are incorporated in set F_n , where n is the sub-problem index. For failure outcomes, the values of the decision variables associated with subsequent trials are set to zero in F_n . Because the MSSP model contains uncertain parameters only in its objective function, scenario-specific constraints in DSPs are identical to the ones in the MSSP model.

$$\max \text{ENPV} = \text{Rev} + \text{FRev} - \text{Cst} \quad (9)$$

$$\text{Cst} = \sum_{i,j,t} cd_t C_{i,j} X_{i,j,t} \quad (10)$$

$$\text{Rev} = \sum_i E[\text{success}_i] \left\{ \sum_t \left\{ \text{rev}_i^{\max} X_{i,P_{II},t} - \gamma_i^D (Z_{i,P_{II},t} + Z_{i,P_{III},t}) - \gamma_i^L (t + \tau_{i,P_{III}}) X_{i,P_{III},t} \right\} \right\} \quad (11)$$

$$\begin{aligned} \text{FRev} = \sum_i E[\text{success}_i] & \left\{ \sum_j \text{rev}_{i,j}^{\text{open}} f_{i,j} Z_{i,j,|T|} \right\} \\ & + \sum_i E[\text{success}_i] \left\{ \sum_{j \in \{P_I, P_{II}\}} \sum_{t > |T| - \tau_{i,j}} \text{rev}_{i,j,t}^{\text{run}} f_{i,j+1} X_{i,j,t} \right\} \end{aligned} \quad (12)$$

$$f(X_{i,j,t}, Y_{i,j,t}, Z_{i,j,t}) \leq 0 \quad \forall i, j, t \quad (13)$$

$$h(X_{i,j,t}, Y_{i,j,t}, Z_{i,j,t}) = 0 \quad \forall i, j, t \quad (14)$$

$$X_{i,j,t} \in F_n \quad \forall i, j, t \quad (15)$$

3.2. Three alternative ways to estimate objective function values in DSPs

In the MSSP model, $success_{i,s}$ is an uncertain parameter indicating if drug i passed all clinical trials in scenario s . The expected value of this parameter in MSSP model is $\sum_{s \in S} p_s success_{i,s}$, where p_s is the probability of scenario s . There is no scenario index in DSPs, and the uncertain parameter is replaced with an approximate expected value ($E[success_i]$, Eqns. (11) and (12)). Here, we propose three alternative ways to estimate this approximate expected value:

- (1) A1: take $E[success_i] = \sum_{s \in S} p_s \cdot success_{i,s}$ at the initial time period, and it is fixed throughout the planning horizon.
- (2) A2: take $E[success_i] = \sum_{s \in S} p_s \cdot success_{i,s}$ at the initial time period, and update $E[success_i]$ based on the realized outcomes of clinical trial for the drug.
- (3) A3: update $E[success_i] = \sum_{s \in DSP} p_s \cdot success_{i,s}$, where $E[success_i]$ is calculated based on the scenario groups that belong to the sub-problem DSP.

The values of $E[success_i]$ in $DSP_{1,1}$ are equal to each other for all three approaches.

4. Case Study

We applied the AEEV framework to generate primal bounds for the clinical-trial planning problem with 3-, 4-, 5-, and 6-products, and three clinical trials with different planning horizon lengths. The complete parameters of the instances can be found in Brianna and Cremaschi (2017). We also solved the corresponding MSSP models to compare the objective function values obtained using A1, A2, and A3 by the AEEV framework. The models and algorithms were implemented in Pyomo and solved using CPLEX 12.6.3 to 0.1% optimality gap on a standard node of Auburn University Hopper Cluster. The MSSP and AEEV framework solution results are presented in Tables 1 and 2, respectively.

Table 1. Partial parameters of the clinical trial planning instances and the MSSP solution

Instance	Trials	Time Periods	Scenarios	ENPV	Soln. Time (CPUs)
3-prod	3	12	64	1193	12
4-prod	3	6	256	1700	20
5-prod	3	6	1,024	2087	1776
6-prod	3	6	4,096	2460	104,541

Table 2. The relative gap and solution times of AEEV framework using three alternative expected value estimation approaches (A1, A2, and A3)

Instance	Relative Gap from MSSP solution			Solution Time (CPU s)		
	A1	A2	A3	A1	A2	A3
3-prod	0.75%	0.08%	0.76%	6	6	6
4-prod	0.00%	0.00%	0.00%	4	5	4
5-prod	0.43%	1.01%	0.58%	8	7	6
6-prod	0.65%	0.81%	0.82%	55	54	52

Table 1 reveals the exponential growth in scenario size with the number of drugs and the corresponding growth in MSSP solution times. As can be seen from Table 2, the AEEV framework yields the optimum solution for 4-product instance and the largest relative gap is 1.01% for 5-product instance obtained by A2. The solution times seems to grow super-

linearly but not exponentially. A1 performs better among all except for 3-product case with relative large 0.75% gap. Considering the fast solution time, we would recommend taking the best feasible solution from all three approaches, which we can summarize relative gaps as 0.08%, 0.00%, 0.43%, 0.65% for 3-, 4-, 5-, and 6-product instances.

5. Conclusion

This paper contributes three alternative objective function estimation approaches for AEEV framework to obtain primal bounds for MSSP of resource constrained planning and scheduling problems with stochastic task success. In such problems, the uncertain parameters are only incorporated in objective function, and scenario specific constraints can be readily transferred to deterministic models. Using all three approaches, the AEEV framework obtains the best feasible bounds within 0.65% of the true optimal for all instances of the clinical trial planning problem. The AEEV framework and the proposed objective function estimation approaches can be used to obtain feasible solutions and tight primal bounds for MSSPs under endogenous uncertainties where the model has complete recourse, and the AEEV framework do not suffer from space and time complexities. It should be noted that the AEEV framework may yield infeasible solutions if the MSSP model does not have complete recourse.

6. Acknowledgements

This work was financially supported RAPID Manufacturing Institute, the U.S.A and was completed in part with resources provided by the Auburn University Hopper Cluster.

References

- Apap, R. M., & Grossmann, I. E. (2017). Models and computational strategies for multistage stochastic programming under endogenous and exogenous uncertainties. *Comput. Chem. Eng.*, 103, 233-274.
- Honkomp, S. J. (1998). PhD Dissertation, Purdue University
- Christian, B., & Cremaschi, S. (2017). Variants to a knapsack decomposition heuristic for solving R&D pipeline management problems. *Comput. Chem. Eng.*, 96, 18-32.
- Christian, B., & Cremaschi, S. (2015). Heuristic solution approaches to the pharmaceutical R&D pipeline management problem. *Comput. Chem. Eng.*, 74, 34-47.
- Colvin, M., & Maravelias, C. T. (2008). A stochastic programming approach for clinical trial planning in new drug development. *Comput. Chem. Eng.*, 32(11), 2626-2642.
- Colvin, M., & Maravelias, C. T. (2009). Scheduling of testing tasks and resource planning in new product development using stochastic programming. *Comput. Chem. Eng.*, 33(5), 964-976.
- Gupta, V., & Grossmann, I. E. (2014). A new decomposition algorithm for multistage stochastic programs with endogenous uncertainties. *Comput. Chem. Eng.*, 62, 62-79.
- Solak, S., Clarke, J. P. B., Johnson, E. L., & Barnes, E. R. (2010). Optimization of R&D project portfolios under endogenous uncertainty. *Eur. J. Oper Res.*, 207(1), 420-433.
- Vayanos, Phebe, Daniel Kuhn, and Berç Rustem. (2011). Decision rules for information discovery in multi-stage stochastic programming Decision and Control and European Control Conference (CDC-ECC), 2011 50th IEEE Conference on. IEEE
- Zeng, Z., Christian, B., & Cremaschi, S. (2018). A generalized knapsack-problem based decomposition heuristic for solving multistage stochastic programs with endogenous and/or exogenous uncertainties. *Ind. Eng. Chem. Res.*, 2018, 57 (28), pp 9185-9199.
- Zeng, Z., & Cremaschi, S. (2019). A general primal bounding framework for large-scale multistage stochastic programs under endogenous uncertainties. *Chemical Engineering Research and Design*, 141, 464-480.

Rigorous Bayesian Inference VS New Approximate Strategies for Estimation of the Probability Distribution of the Parameters of DAE Models

Francesco Rossi,^{a,*} Linas Mockus,^a Gintaras Reklaitis^a

^a*Purdue University, Forney Hall of Chemical Engineering, 480 Stadium Mall Drive, West Lafayette, IN 47907-2100, United States*

frossi@purdue.edu

Abstract

This manuscript assesses the accuracy and computational efficiency offered by three different strategies for the estimation of probability distributions, applied to DAE systems. Specifically, two approximate PDF estimation techniques, named ODMCMC and PDFE&U, are compared to Bayesian Markov-chain Monte Carlo (BMCMC), using a simulation-based approach. The results of our analysis show that ODMCMC and PDFE&U offer a good trade-off between accuracy and computational efficiency, thus are excellent choices for time-critical PDF estimation tasks.

Keywords: Uncertainty quantification, Bayesian inference, optimization, drug delivery.

1. Introduction

The application of statistical techniques to the quantification of model uncertainty is a new paradigm, which has recently emerged due to the growing interest of industry and of the PSE community in stochastic optimization, robust design, real-time quality control and quantitative risk assessment. As an example, strategies for uncertainty quantification have been applied in areas such as robust process and product design (Mockus et al., 2011), drug delivery (Láinez et al., 2011) and stochastic dynamic optimization (Rossi et al., 2016).

Typically, model uncertainty quantification comes down to the estimation of the joint probability distribution (PDF) of some key uncertain parameters of the model, which often consists of a system of differential-algebraic equations (DAEs). To solve this type of PDF estimation problem, we usually rely on Bayesian inference methods such as Bayesian Markov-chain Monte Carlo (Green and Worden, 2015), which are well-established but also extremely computationally demanding. Therefore, it is important to investigate and develop new approximate PDF estimation strategies, which offer a good trade-off between accuracy and computational efficiency, and to validate them against state-of-the-art Bayesian inference approaches.

To that end, this contribution considers two approximate PDF estimation strategies plus a conventional one, and compares them to identify the most suitable method for solving PDF estimation problems, in which the underlying model is a DAE system. The approximate PDF estimation methods, analysed in this manuscript, include: (I) a novel Bayesian Markov-chain Monte Carlo algorithm, where sampling is performed by optimization (ODMCMC); and (II) a likelihood-free approach, recently proposed by

Rossi et al. (2018), which relies on a combination of parameter estimation, projection techniques and maximum likelihood estimation (PDFE&U). On the other hand, the conventional Bayesian inference strategy, included in this analysis, is standard Bayesian Markov-chain Monte Carlo (BMCMC). Note that we do not include Variational Inference (Beal, 2003) in our study because Yao et al. (2018) recently showed that this type of technique performs satisfactorily only for 28 % of all the problems they considered (over 200).

The comparison of approximate and conventional PDF estimation algorithms is performed by analysing both their computational efficiency and their outputs, i.e. their PDFs, using well-known statistical indicators (expectation, variance and quantiles) and the concept of confidence/credible region. The DAE model, selected for this study, is a pharmacokinetic (PB/PK) model for the administration of Gabapentin.

The rest of the paper is organized as follows: first, we introduce the rationale of PDFE&U and ODMCMC, with particular emphasis on the latter; then, we report the most significant results of our analysis on the accuracy and computational performance of PDFE&U, ODMCMC and BMCMC; finally, we discuss the most relevant consequences of these analyses.

2. Fundamental features of ODMCMC and PDFE&U

ODMCMC and PDFE&U are approximate strategies for estimation of the probability distribution of the uncertain parameters of a nonlinear system, using experimental data and (optionally) an existing PDF of the parameters (a so-called prior). These algorithms are designed for maximum computational efficiency, thus can easily handle DAE models, unlike conventional Bayesian inference frameworks. This section describes their features, novelties and implementation rationale.

ODMCMC is a novel type of Markov-chain Monte Carlo algorithm, in which sampling is performed by optimization. Specifically, this method does not make use of conventional random strategies to sample the posterior PDF (e.g. Metropolis-Hastings, Gibbs and No-U-Turn samplers), which only accept about 30 % of all the samples analysed. On the other hand, it selects optimal posterior samples by iterative solution of small-scale, multi-objective optimization problems, which measure the degree of optimality of every single sample based on two indices, namely, its linear and angular distances from all the other samples and its posterior probability density. This innovative sampling approach can efficiently identify samples, which uniformly span only those regions of the uncertainty space that are associated with high values of posterior probability density. Therefore, it allows us to approximate the posterior PDF with fewer samples and, consequently, to save computational resources. In addition, unlike conventional random samplers, it allows reliable and efficient approximation of complex, multi-modal posterior PDFs.

The rationale of ODMCMC is summarized in Figure 1. The algorithm is comprised of two phases, called Phase I and Phase II, of which the second is executed in an iterative fashion until convergence is reached. Phase I involves first computation of all the modes of the posterior PDF via multi-start optimization methods (step A), and then division of the uncertainty space into a user-supplied number of regions (step B), selected such that every one of them encompasses an appropriate interval of values of posterior probability density (further details cannot be reported due to space limitations).

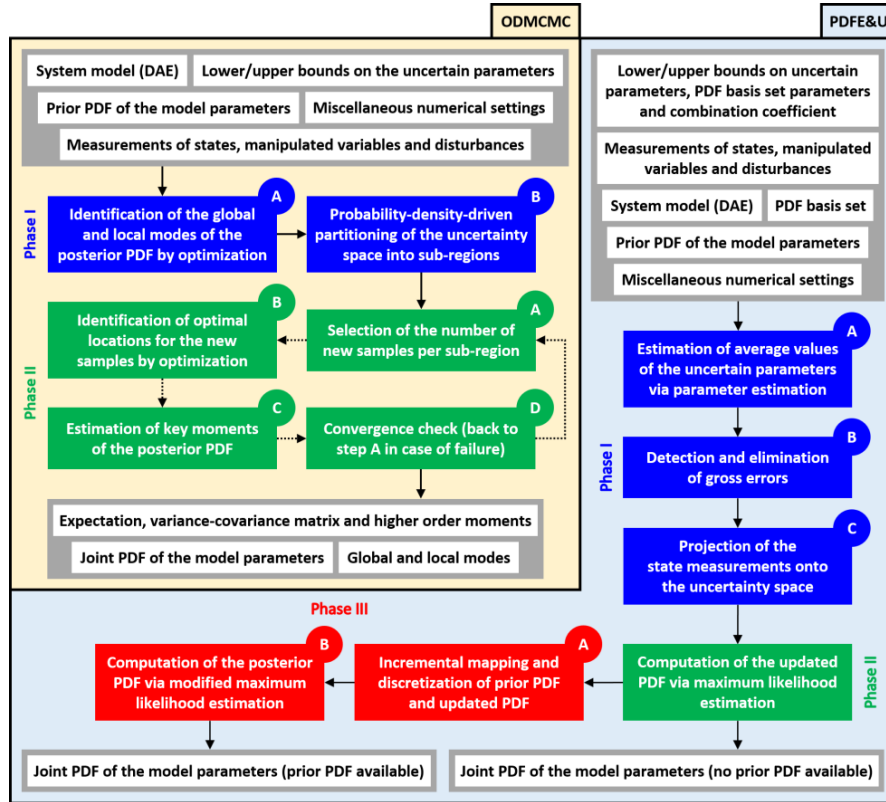


Figure 1: Architecture of ODMCMC and PDFE&U.

Phase II involves iterative execution of steps A, B and C in series, until the variation in the first, second and third order moments of the posterior PDF over two consecutive iterations is smaller than some predefined error tolerance (step D). In step A, we compute the number of samples that must be added to every region of the uncertainty space in the current iteration, using an estimate of the algorithm convergence rate calculated by error extrapolation. Step B involves solution of several multi-objective optimization problems (one problem per region) via goal programming, which allow identification of the optimal locations of the new samples. All of these optimization problems are independent of each other, thus can be solved in parallel to improve the overall computational efficiency of the algorithm. Finally, in step C, we estimate the first, second and third order moments of the posterior PDF, using the samples selected up to the current iteration. These calculations rely on simple formulas, derived by discretization of well-known integral expressions, utilized to compute the moments of continuous probability distributions.

Before moving on, two final remarks are in order. First, note that ODMCMC technically requires identification of all the modes of the posterior PDF (Phase I – step A) via multi-start optimization. However, this requirement can be relaxed without affecting the accuracy of the algorithm, but at the cost of longer computation time. Second, note that the bottleneck for computational efficiency in ODMCMC is

represented by step A of Phase I and step B of Phase II, which are both parallelizable. Therefore, ODMCMC exhibits very good scalability features, unlike many conventional Bayesian inference strategies.

After introducing ODMCMC, we offer a brief description of the principal features of PDFE&U (the reader is invited to refer to Rossi et al. (2018) for further details). This is an innovative likelihood-free algorithm that relies neither on Bayes theorem nor on any sampling techniques to approximate the posterior PDF. In particular, it first projects the available experimental data (specifically the state measurements) onto the uncertainty space, by solving several small-scale, dynamic optimization problems. Then, it utilizes maximum likelihood estimation to convert the data projections into a new PDF, called the updated PDF. Finally, it combines updated and prior PDFs to compute a posterior. This sampling-free, two-stage strategy for estimating the posterior PDF offers a significant computational advantage over conventional Bayesian inference approaches. In addition, it allows PDFE&U to easily handle correlated/non-Gaussian measurement errors, features which make it difficult to apply standard Bayesian inference.

The rationale of PDFE&U is shown in Figure 1. The algorithm is composed of three phases, called Phase I, Phase II and Phase III, each of which involves one or more steps. However, due to space limitations, we only discuss step C of Phase I, which is the core of PDFE&U. In this step, we project every state measurement onto the uncertainty space by solving several small-scale, dynamic optimization problems, thus obtaining a set of “samples”. This operation is conceptually the inverse of the problem of propagation of a probability distribution through a DAE system. It is the most computationally demanding task of PDFE&U but can be fully parallelized because all the dynamic optimization problems, previously mentioned, are independent of each other. As a consequence, the overall computational efficiency of PDFE&U is not negatively impacted.

Before moving on to our case study, it is important to comment on the implementation of both ODMCMC and PDFE&U. Both rely on the sequential approach, but the first has been implemented in a MATLAB[®] script while the second has been coded in C++, utilizing the BzzMath library as numerical engine (Buzzi-Ferraris and Manenti, 2012). In addition, the implementation of PDFE&U exploits parallel computing while that of ODMCMC currently allows only serial execution. All of this information will be useful for purposes of computational performance analysis (see the next section).

3. General assessment of ODMCMC, PDFE&U and BMCMC

The computational performance and accuracy offered by PDFE&U, ODMCMC and by a well-established implementation of BMCMC, i.e. Stan (Carpenter et al., 2017), have been analysed using a PB/PK model, which simulates the response of a patient to the administration of Gabapentin. Specifically, this case study involves estimation of the joint probability distribution of the 10 uncertain parameters of this PB/PK model, comprised of 34 nonlinear DAEs. The data set, used in this PDF estimation problem, includes about 150 data points, and consists of measurements of drug concentration in plasma and urine.

The results of the aforementioned PDF estimation problem are summarized in Figure 2 and Figure 3. Specifically, Figure 2 reports the most important statistical properties of the 10 uncertain model parameters, computed by PDFE&U, ODMCMC and Stan

(BMCMC + Random Effects). On the other hand, Figure 3 shows the 95 % credible regions of drug concentration in a patient’s blood stream, predicted by both PDFE&U and ODMCMC.

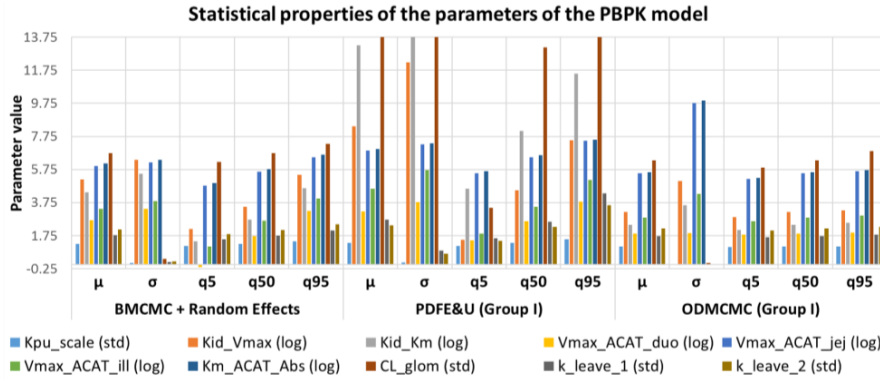


Figure 2: Statistical analysis of the PDFs computed by PDFE&U, ODMCMC and Stan (some quantities are reported in log-scale to improve the chart readability; μ , σ and qX stand for expectations, standard deviations and X % quantiles).

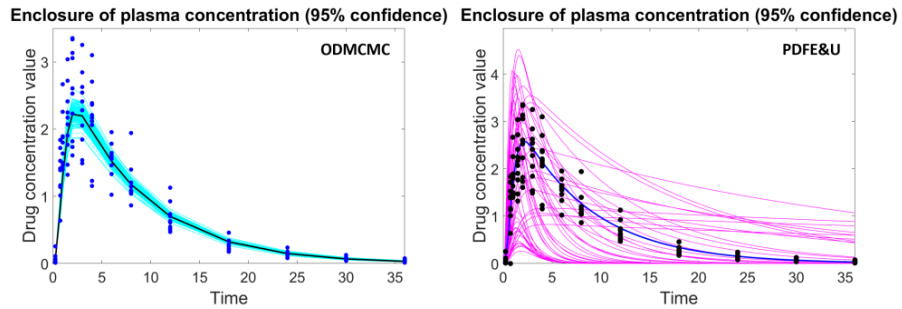


Figure 3: Predicted enclosures of the profiles of drug concentration in a patient’s blood stream at 95% confidence level (the black/blue dots are the experimental data; the black/blue curves represent the profiles of drug concentration in the blood stream of the average patient).

Both Figure 2 and Figure 3 confirm that PDFE&U tends to overestimate variance but provides decent estimates of the central tendency measures and of the qualitative properties of the PDF (specifically variance ratios), at a very attractive computational cost (Table 1).

Table 1: Computational performance of PDFE&U, ODMCMC and Stan.

Case study	Model size	Number of uncertain parameters	Time elapsed for solving a single PDF estimation problem [h]		
			PDFE&U	ODMCMC	Stan
Administration of Gabapentin	34 DAEs	10	0.3 – 0.6 ^a	≈ 40 ^b	≈ 120 ^a

^a Simulations performed with custom C++ codes; ^b Simulation performed with MATLAB® R2018a

On the other hand, ODMCMC proves to be more accurate than PDFE&U (Figure 2) in terms of both variance and central tendency measure estimates, but also demonstrates to be slightly less computationally efficient (since ODMCMC has been implemented in a MATLAB[®] script, its computational time, shown in Table 1, must be divided by at least a factor of 20). In addition, it tends to underestimate variance, as shown in Figure 3.

4. Conclusions

The results of the case study, discussed in the previous section, suggest that both ODMCMC and PDFE&U provide a favourable trade-off between accuracy and computational efficiency, by comparison to Bayesian Markov-chain Monte Carlo methods. This allows us to conclude that ODMCMC and PDFE&U are more suitable for time-critical applications, where the PDF estimation task must be completed as soon as possible (e.g., in stochastic dynamic optimization, robust data reconciliation and robust soft-sensor systems). Conversely, Bayesian Markov-chain Monte Carlo is more accurate and reliable, and is more suitable for offline, detailed PDF estimation studies.

In the near future, we are planning to improve and augment both ODMCMC and PDFE&U, with the aim of reducing the gap in accuracy between these two strategies and BMCMC without negatively affecting their computational efficiency.

References

- M.J. Beal, 2003, Variational algorithms for approximate Bayesian inference, London: University of London, UK.
- G. Buzzi-Ferraris, F. Manenti, 2012, BzzMath: library overview and recent advances in numerical methods, *Computer Aided Chemical Engineering*, 30, 1312-1316.
- B. Carpenter, A. Gelman, M.D. Hoffman, D. Lee, B. Goodrich, M. Betancourt, M. Brubaker, J. Guo, P. Li, A. Riddell, 2017, Stan: A probabilistic programming language, *Journal of Statistical Software*, 76, 1-32.
- P.L. Green, K. Worden, 2015, Bayesian and Markov chain Monte Carlo methods for identifying nonlinear systems in the presence of uncertainty, *Philosophical Transactions A*, 373, 20140405.
- J.M. Láinez, G. Blau, L. Mockus, S. Orçun, G.V. Reklaitis, 2011, Pharmacokinetic based design of individualized dosage regimens using a Bayesian approach, *Industrial and Engineering Chemistry Research*, 50, 5114-5130.
- L. Mockus, J.M. Láinez, G. Reklaitis, L. Kirsch, 2011, A bayesian approach to pharmaceutical product quality risk quantification, *Informatika*, 22, 537-558.
- F. Rossi, L. Mockus, F. Manenti, G. Reklaitis, 2018, Assessment of accuracy and computational efficiency of different strategies for estimation of probability distributions applied to ODE/DAE systems, *Computer Aided Chemical Engineering*, 44, 1543-1548.
- F. Rossi, G. Reklaitis, F. Manenti, G. Buzzi-Ferraris, 2016, Multi-scenario robust online optimization and control of fed-batch systems via dynamic model-based scenario selection, *AIChE Journal*, 62, 3264-3284.
- Y. Yao, A. Vehtari, D. Simpson, A. Gelman, 2018, Yes, but did it work?: evaluating variational inference, arXiv preprint arXiv: 1802.02538.

This page intentionally left blank

29TH EUROPEAN SYMPOSIUM ON COMPUTER AIDED CHEMICAL ENGINEERING

PART B

Edited by
**ANTON A. KISS, EDWIN ZONDERVAN
RICHARD LAKERVELD AND LEYLA ÖZKAN**



COMPUTER-AIDED CHEMICAL ENGINEERING, 46



ELSEVIER

29TH EUROPEAN SYMPOSIUM ON
COMPUTER AIDED PROCESS
ENGINEERING

PART B

This page intentionally left blank

29TH EUROPEAN SYMPOSIUM ON COMPUTER AIDED PROCESS ENGINEERING

PART B

Edited by

Anton A. Kiss

*The University of Manchester, United Kingdom
Manchester, M13 9PL*

Edwin Zondervan

*University of Bremen, Germany
D. Bremen, 28359*

Richard Lakerveld

*The Hong Kong University of Science and Technology
Clear Water Bay, Kowloon, Hong Kong*

Leyla Özkan

*Eindhoven University of Technology, The Netherlands
Postbus 513, 5600 MB*



ELSEVIER

Amsterdam – Boston – Heidelberg – London – New York – Oxford
Paris – San Diego – San Francisco – Singapore – Sydney – Tokyo

Elsevier
Radarweg 29, PO Box 211, 1000 AE Amsterdam, Netherlands
The Boulevard, Langford Lane, Kidlington, Oxford OX5 1GB, UK
50 Hampshire Street, 5th Floor, Cambridge, MA 02139, USA

Copyright © 2019 Elsevier B.V. All rights reserved.

No part of this publication may be reproduced or transmitted in any form or by any means, electronic or mechanical, including photocopying, recording, or any information storage and retrieval system, without permission in writing from the publisher. Details on how to seek permission, further information about the Publisher's permissions policies and our arrangements with organizations such as the Copyright Clearance Center and the Copyright Licensing Agency, can be found at our website: www.elsevier.com/permissions.

This book and the individual contributions contained in it are protected under copyright by the Publisher (other than as may be noted herein).

Notices

Knowledge and best practice in this field are constantly changing. As new research and experience broaden our understanding, changes in research methods, professional practices, or medical treatment may become necessary.

Practitioners and researchers must always rely on their own experience and knowledge in evaluating and using any information, methods, compounds, or experiments described herein. In using such information or methods they should be mindful of their own safety and the safety of others, including parties for whom they have a professional responsibility.

To the fullest extent of the law, neither the Publisher nor the authors, contributors, or editors, assume any liability for any injury and/or damage to persons or property as a matter of products liability, negligence or otherwise, or from any use or operation of any methods, products, instructions, or ideas contained in the material herein.

British Library Cataloguing in Publication Data

A catalogue record for this book is available from the British Library

Library of Congress Cataloging-in-Publication Data

A catalog record for this book is available from the Library of Congress

ISBN (Part B): 978-0-128-19940-4

ISBN (Set) : 978-0-128-18634-3

ISSN: 1570-7946

For information on all Elsevier publications visit our website at <https://www.elsevier.com/>

		Working together to grow libraries in developing countries
www.elsevier.com • www.bookaid.org		

Publisher: Joe Hayton

Acquisition Editor: Kostas Marinakis

Editorial Project Manager: Kelsey Connors

Production Project Manager: Paul Prasad Chandramohan

Designer: Greg Harris

Typeset by SPi Global, India

Contents

189. Deterministic Global Process Optimization: Flash Calculations via Artificial Neural Networks
Artur M. Schweidtmann, Dominik Bongartz, Wolfgang R. Huster and Alexander Mitsos 1129
190. An MILP model for safe multi-floor process plant layout
Jude O. Ejeh, Songsong Liu and Lazaros G. Papageorgiou 1135
191. A Generalized, Nonsmooth Operator for Process Integration
Caroline J. Nielsen, and Paul I. Barton 1141
192. Analysis of Process Alternatives for Energy-Efficient Bioethanol Downstream Processing
Dinis S. Nunes, José F.O. Granjo, Belmiro P.M. Duarte and Nuno M.C. Oliveira 1147
193. An Efficient MILP-Based Decomposition Strategy for Solving Large-Scale Scheduling Problems in the Offshore Oil and Gas Industry
Natalia P. Basán, Mariana E. Cóccola, Alejandro García del Valle, Carlos A. Méndez 1153
194. A Blockchain Framework for Containerized Food Supply Chains
Dimitrios Bechtsis, Naoum Tsolakis, Apostolos Bizakis, Dimitrios Vlachos 1159
195. System-Level Optimisation of Combined Power and Desalting Plants
Houd Al-Obaidli, Sarah Namany, Rajesh Govindan, Tareq Al-Ansari 1165
196. Computer-aided Design of Solvent Blends for the Cooling and Antisolvent Crystallisation of Ibuprofen
Oliver L. Watson, Amparo Galindo, George Jackson, Claire S. Adjiman 1171
197. Modeling of multi-effect desalination process operated with thermosolar energy applied to the northeastern Brazil
Diego P.S Cunha, Vanessa V. Gomes, Karen V. Pontes 1177
198. Flexible and efficient solution for control problems of chemical laboratories
Tibor Nagy, Florian Enyedi, Eniko Haaz, Daniel Fozer, Andras Jozsef Toth and Peter Mizsey 1183
199. Process model validation and analysis for intensification of an industrial scale process
Renata Chinda, Rotjana Ponsatorn, Amata Anantpinijwatna, Fernando P. Pessoa, John M. Woodley and Seyed Soheil Mansouri 1189

200. Towards a systematic framework for the synthesis of operable process intensification systems – application to reactive distillation systems
Yuhe Tian, Iosif S. Pappas, Baris Burnak, Justin Katz, Styliani Avraamidou, Nikolaos A. Diangelakis and Efstratios N. Pistikopoulos 1195
201. A Model based analysis in applying Anderson–Schulz–Flory (ASF) equation with CO₂ Utilisation on the Fischer Tropsch Gas-to-liquid Process
Ali Attiq Al-Yaeshi, Ahmed AlNouss, Gordon McKay, Tareq Al-Ansari 1201
202. Consequential Life Cycle Analysis for Food-Water-Energy-Waste Nexus
Yanqiu Tao, Fengqi You 1207
203. A stochastic environmental model to deal with uncertainty in life cycle impact assessment
Andreia Santos, Ana Barbosa-Póvoa, Ana Carvalho 1213
204. BIOPRO-Sim: A benchmark simulation model for bio-manufacturing processes
Giorgio Colombo, Isuru A. Udugama, Krist V. Gernaey, Seyed Soheil Mansouri 1219
205. Facilitating learning by failure through a pedagogical model-based tool for bioprocesses
Simoneta Caño de Las Heras, Björn Gutschmann, Krist V. Gernaey, Ulrich Krühne and Seyed Soheil Mansouri 1225
206. Data-Based Robust Model Predictive Control Under Conditional Uncertainty
Chao Shang, Wei-Han Chen, Fengqi You 1231
207. Development of the Texas A&M Superfund Research Program Computational Platform for Data Integration, Visualization, and Analysis
Rajib Mukherjee, Melis Onel, Burcu Beykal, Adam T. Szafran, Fabio Stossi, Michael A. Mancini, Lan Zhou, Fred A. Wright, Efstratios N. Pistikopoulos 1237
208. Scalable manufacturing of nanostructured materials by atomic layer deposition in fluidized bed reactors
J.Ruud van Ommen, Fabio Grillo, Johan Grievink 1243
209. The Optimization of Heliostat Canting in a Solar Power Tower Plant
Nao Hu, Yuhong Zhao, JieQing Feng 1249
210. Effect of Non-Ideal Kinetics on Hybrid Reactive Distillation Models for Selectivity Engineering
Deepshikha Singh, Antanim Dutta, Ankur Gaur, Shabih Ul Hasan 1255

211. Modelling Paraffin Wax Deposition Using Aspen HYSYS and MATLAB <i>Ana M. Sousa, Henrique A. Matos, Maria J. Pereira</i>	1261
212. Integrated Design of Solvents and Processes based on Reaction Kinetics from Quantum Chemical Prediction Methods <i>Christoph Gertig, Kai Leonhard and André Bardow</i>	1267
213. Green Supply Chain: Integrating Financial Risk Measures while Monetizing Environmental Impacts <i>Cátia da Silva, Ana Paula Barbosa-Póvoa, Ana Carvalho</i>	1273
214. Optimal distributed load allocation and resource utilisation in evaporation plants <i>Maria P. Marcos, Jose L. Pitarch, Christian Jasch and Cesar de Prada</i>	1279
215. Optimisation and control of a distributed energy resource network using Internet-of-Things technologies <i>Evgenia Mechleri, Tim Sidnell, Bogdan Dorneanu, Harvey Arellano-Garcia</i>	1285
216. Centralised versus localised supply chain management using a flow configuration model <i>Bogdan Dorneanu, Elliot Masham, Evgenia Mechleri, Harvey Arellano-Garcia</i>	1291
217. Novel refrigeration cycle configurations for performance improvements in LNG processes at small scale <i>Fernando Almeida-Trasvina and Robin Smith</i>	1297
218. Modelling and optimal operation of a natural gas fired natural draft heater <i>Richard Yentumi, Bogdan Dorneanu, Harvey Arellano-Garcia</i>	1303
219. Molecular Modelling of Co-processing Biomass Pyrolysis Oil with Vacuum Gasoil in an Oil Refinery Fluid Catalytic Cracking Unit <i>Mohamed Al Jamri, Robin Smith, Jie Li</i>	1309
220. A Chance-Constrained Nonlinear Programming Approach for Equipment Design Under Uncertainty <i>Javier Tovar-Facio, Yankai Cao, José M. Ponce-Ortega, Victor M. Zavala</i>	1315
221. Involving the Water-Energy-Food Nexus in Integrating Low-Income and Isolated Communities <i>Brenda Cansino-Loeza, J. Betzabe González-Campos, José María Ponce-Ortega</i>	1321
222. Sustainable Strategic Planning for a National Natural Gas Energy System Accounting for Unconventional Sources <i>Esbeydi Villicaña-García, J. Betzabe González-Campos, José María Ponce-Ortega</i>	1327

223. Engineering success: What does it take to get PSE technologies used?
Sandro Macchietto 1333
224. Integration of Consumer Preferences and Heuristic Knowledge
in the Design of Formulated Products: Application to a Cosmetic
Emulsion
*Javier A. Arrieta-Escobar, Fernando P. Bernardo, Alvaro Orjuela,
Mauricio Camargo, Laure Morel, Laurent Wendling* 1339
225. An improved approach to scheduling multipurpose batch processes
with conditional sequencing
Nikolaos Rakovitis, Jie Li, Nan Zhang 1345
226. On-grid Hybrid Power System and Utility Network planning to supply
an Eco-Industrial Park with dynamic data
*Florent Mousqué, Marianne Boix, Stéphane Négny, Ludovic Montastruc,
Serge Domenech* 1351
227. Economic Study of the Urea Alcoholysis Process for Dimethyl Carbonate
Production
*Juan Javaloyes-Antón, Daniel Vázquez, Juan D. Medrano-García,
José A. Caballero* 1357
228. Evaluating the Benefits of LNG Procurement through Spot Market
Purchase
Mohd Shahrukh, Rajagopalan Srinivasan, I.A.Karimi 1363
229. Effect of Ambient Conditions on Boil Off Gas Generation in LNG
regasification terminals
Philips Prince Pokkatt and Rajagopalan Srinivasan 1369
230. Electroencephalogram based Biomarkers for Tracking the Cognitive
Workload of Operators in Process Industries
Mohd Umair Iqbal, Babji Srinivasan, Rajagopalan Srinivasan 1375
231. Optimal design of biomass supply chains with integrated process design
Theodoros Damartzis, François Maréchal 1381
232. Modelling Full Cycles of Carbonation-Calcination for Calcium Looping
Process Simulation
*Miguel Abreu Torres, Paula Teixeira, Rui M. Filipe, Luis Domingues,
Carla I. C. Pinheiro, Henrique A. Matos* 1387
233. Determination of the optimal distribution of active centers in a
multifunctional catalyst pellet using global searching combined with
reduced-order modeling approach
Katarzyna Bizon, Gaetano Continillo 1393

234. Sequential and Simultaneous Optimization Strategies for Increased Production of Monoclonal Antibodies
Chrysoula D. Kappatou, Oktay Altunok, Adel Mhamdi, Athanasios Mantalaris, Alexander Mitsos 1399
235. An MPCC Reactive Distillation Optimization Model for Multi-Objective Fischer–Tropsch Synthesis
Yizu Zhang, Cornelius M. Masuku and Lorenz T. Biegler 1405
236. Operating regime model based multi-objective sensor placement for data reconciliation
Gyula Dorgo, Mate Haragovics and Janos Abonyi 1411
237. Optimisation of the integrated water – energy systems: a review with a focus in Process Systems Engineering
Christiana M. Papapostolou, Georgios T. Tzanes, Emilia M. Kondili 1417
238. Techno-economic analysis of alternative reactive purification technologies in the lactic acid production process
Roberto Gasca-González, Oscar A. Prado-Rubio, Fernando I. Gómez-Castro, Javier Fontalvo-Alzate, Eduardo S. Pérez-Cisneros, Ricardo Morales-Rodriguez 1423
239. Life cycle assessment of Jatropha jet biodiesel production in China conditions
Haoyu Liu, Tong Qiu 1429
240. Optimal design of post combustion CO₂ capture processes based on phase-change solvents
Panagiotis Kazepidis, Athanasios I. Papadopoulos, Panos Seferlis, Felipe A. Perdomo, Amparo Galindo, George Jackson, Claire S. Adjiman 1435
241. Optimization of a hydroformulation process in a thermomorphic solvent system using a commercial steadystate process simulator and a memetic algorithm
Tim Janus, Maximilian Cegla, Sabine Barkmannb and Sebastian Engell 1441
242. Exergy analysis for energy integration in a bioethanol production process to determine heat exchanger networks feasibility
J. Cristóbal García-García, Jaime D. Ponce-Rocha, Danahe Marmolejo-Correa, Ricardo Morales-Rodriguez 1447
243. ProCAFD: Computer-aided Tool for Sustainable Process Synthesis, Intensification and Hybrid solutions
Anjan K.Tula, Mario R. Eden, Rafiqul Gani 1453

244. Component based development of computer-aided tools for different applications
Anjan K.Tula, Mario R. Eden, Rafiqul Gani 1459
245. Fouling Modelling in Crude Oil Heat Exchanger Networks using Data Reconciliation and Estimation of Unmeasured Process Variables
José Loyola-Fuentes, Megan Jobson and Robin Smith 1465
246. Novel Methodology for Cogeneration Targeting with Optimum Steam Level Placement
Julia Jimenez, Adisa Azapagic, Robin Smith 1471
247. A multi-objective multi-period optimization of carbon integration networks in industrial parks
Dhabia M. Al-Mohannadi, Patrick Linke, Nialy Shah 1477
248. Life-Cycle Environmental Impact Assessment of the Alternate Subsurface Intake Designs for Seawater Reverse Osmosis Desalination
Abdulrahman H. Al-Kaabi, Hamish R. Mackey 1483
249. Optimization of biofuel supply chain design via a water-energy-food nexus framework
Dulce Celeste López-Díaz, Luis Fernando Lira-Barragán, José Maria Ponce-Ortega, Mahmoud M. El-Halwagi 1489
250. Reduced model-based global optimisation of largescale steady state nonlinear systems
Min Tao, Jie Li and Constantinos Theodoropoulos 1495
251. A multiscale model approach for cell growth for lipids and pigments production by *Haematococcus pluvialis* under different environmental conditions
Alessandro Usai, Jon Pittman, and Constantinos Theodoropoulos 1501
252. Advanced Model Design Based on Intelligent System Characterization And Problem Definition
Edrisi Munoz, Elisabet Capon-Garcia, Luis Puigjaner 1507
253. Improved problem constraints modeling based using classification
Elisabet Capón-García, Edrisi Munoz, Luis Puigjaner 1513
254. Bioethanol Production with Cyanobacteria by a Two-Stage Fermentation Strategy
Romina Lasry Testa, Claudio Delpino, Vanina Estrada, M. Soledad Diaz 1519
255. Application of plate heat exchangers into heat exchanger networks retrofit with fixed structure
Kexin Xu, Robin Smith 1525

256. Ecosystem Services Valuation and Ecohydrological Management in Salt Lakes with Advanced Dynamic Optimisation Strategies
A.G. Siniscalchi, C. Garcia Prieto, E.A. Gomez, A. Raniolo, R.J. Lara, M.S. Diaz 1531
257. Life cycle design of indoor hydroponic horticulture considering energy-water-food nexus
Yasunori Kikuchi, Yuichiro Kanematsu, Tatsuya Okubo 1537
258. A Data-Driven Robust Optimization Approach to Operational Optimization of Industrial Steam Systems under Uncertainty
Liang Zhao, Chao Ning, Fengqi You 1543
259. Probabilistic Design Space
Linas Mockus, Gintaras Reklaitis, Ken Morris, David LeBlond 1549
260. Modeling Impacts of Tracking on Greenhouse Gas Emissions from Photovoltaic Power
Ian Miller, Emre Gençer, Francis M. O'Sullivan 1555
261. Process Intensification and Miniaturization of Chemical and Biochemical Processes
Filip Strniša, Tomaž Urbič, Polona Žnidaršič-Plazl and Igor Plazl 1561
262. Clustering alternative product formulations using graphs
Fernando P. Bernardo, Javier A. Arrieta-Escobar 1567
263. Recent Advances in Graph-Based Abstractions for Modeling and Simulating Complex Systems
Jordan Jalving and Victor Zavala 1573
264. Synthesis technology for failure analysis and corrective actions in process systems engineering
Ákos Orosz, Ferenc Friedler 1579
265. Spatio-Temporal Control of Nutrient Pollution from Organic Waste
Yicheng Hu, Gerardo Ruiz-Mercado and Victor Zavala 1585
266. Optimal design and planning multi resource-based energy integration in process industries
Shabnam Morakabatchiankar, Fernando D. Mele, Moisés Graells, Antonio Espuña 1591
267. Predictive LCA - a systems approach to integrate LCA decisions ahead of design
Paraskevi Karka, Stavros Papadokostantakis, Antonis Kokossis 1597

268. From renewable energy to ship fuel: ammonia as an energy vector and mean for energy storage
Francesco Baldi, Alain Azzi and François Maréchal 1603
269. Heat-integrated water allocation network design: a novel hyperstructure and sequential solution strategy for industrial applications
Maziar Kermani, Ivan Kantor, Adriano Ensinas and François Maréchal 1609
270. Giving added value to products from biomass: the role of mathematical programming in the product-driven process synthesis framework
Aleksandra Zderic, Alexandra Kiskini, Elias Tsakas, Cristhian Almeida Rivera, Edwin Zondervan 1615
271. Energy System Modelling in support of the Energy Transition
Jan van Schijndel, Karin Griffioen, Levi Ikele, Andreas ten Cate 1621
272. Are renewables really that expensive? The impact of uncertainty on the cost of the energy transition
Xiang Li, Stefano Moret, Francesco Baldi and François Maréchal 1627
273. Bottom-up method for potential estimation of energy saving measures
Anna S. Wallerand, Ivan Kantor and François Maréchal 1633
274. Analysis of the Tri-Reforming of Methane in a Membrane Reactor
Samuel S. Q. Jardim, José E. A. Graciano and Rita M. B. Alves 1639
275. Design of a novel sour water stripping unit
Umer Zahid, Ali Al-Qadri, Baqer Al-Mousa, Ali Al-Nasser, Usama Ahmed 1645
276. Techno-economic Assessment of Future Generation IGCC Processes with Control on Greenhouse Gas Emissions
Usama Ahmed, Umer Zahid 1651
277. Modelling of Microfluidic Devices for Analysis of Radionuclides
Miguel Pineda, Panagiota Angeli, Takehiko Tsukahara and Eric S. Fraga 1657
278. Comparative analysis of gasification and reforming technologies for the syngas production
Hussain A Alibrahim, Siddig SeedAhmed, Usama Ahmed, Umer Zahid 1663
279. Generating Efficient Wastewater Treatment Networks: *an integrated approach comprising of contaminant properties, technology suitability, plant design, and process optimization*
Kirti M. Yenkie, Sean Burnham, James Dailey, Heriberto Cabezas, Ferenc Friedler 1669

280. Model-based decision-support for waste-to-energy pathways in New South Wales, Australia
Koen H. van Dam, Bowen Feng, Xiaonan Wang, Miao Guo, Nilay Shah and Stephen Passmore 1675
281. Optimal Oversizing and Operation of the Switchable Chlor-Alkali Electrolyzer for Demand Side Management
Kosan Roh, Luisa C. Brée, Karen Perrey, Andreas Bulan and Alexander Mitsos 1683
282. A process systems engineering approach to designing a solar/biomass hybrid energy system for dairy farms in Argentina
Carolina Alvarez C. Blanchet, Antonio M. Pantaleo and Koen H. van Dam 1689
283. Describing CO₂-Absorbent Properties in AspenPlus®
Jasper A. Ros, Derk W. F. Brilman, Ida M. Bernhardsen and Hanna Knuutila 1695
284. Challenges in Decision-Making Modelling for New Product Development in the Pharmaceutical Industry
Catarina M. Marques, Samuel Moniz, Jorge Pinho de Sousa 1701
285. Extension of a Particle Filter for Bioprocess State Estimation using Invasive and Non-Invasive IR Measurements
Julian Kager, Vladimir Berezinskiy, Robert Zimmerleiter, Markus Brandstetter and Christoph Herwig 1707
286. Design of Multi Model Fractional Controllers for Nonlinear Systems: An Experimental Investigation
G Maruthi Prasad, A Adithya and A Seshagiri Rao 1713
287. Modelling and Simulation of Supercritical CO₂ Oil Extraction from Biomass
Rui M. Filipe, José A. P. Coelho, David Villanueva-Bermejo, Roumiana P. Stateva 1719
288. Immune system modelling in case of a septic shock
Jean Tallon, Françoise Couenne, Claire Bordes, Melaz Tayakout-Fayolle, Fabienne Venet, Guillaume Monneret, Patrice Nony, François Gueyffier 1725
289. More power to the individual modeller using ontologies
Heinz A Preisig, Arne Tobias Elve and Sigve Karolius 1731
290. Optimal Operation and Control of Heat-to-Power Cycles: a New Perspective using a Systematic Plantwide Control Approach
Cristina Zotică, Lars O. Nord, Jenő Kovács and Sigurd Skogestad 1737

291. Relative Optimality Index for Evaluation of the Approximate Methods for Synthesis of Flexible Processes under Uncertainty
Klavdija Zirngast, Zdravko Kravanja, Zorka Novak Pintarič 1743
292. Process Systems Engineering from an industrial and academic perspective
Anton A. Kiss, Johan Grievink 1749
293. Optimisation of the integrated water – energy systems: a review with a focus in Process Systems Engineering
Christiana M. Papapostolou, Emilia M. Kondili, Georgios T. Tzanes 1755
294. Time Resolved Sensitivity & Identifiability Analysis for Directed Parametrization of Highly Dynamic Models
Sven Daume, Julian Kager and Christoph Herwig 1761
295. Synthesis of Solar Heat Network for Preheating of Industrial Process Streams
Ben Abikoye, Lidija Čuček, Adeniyi Isafiade, Zdravko Kravanja 1767
296. Novel strategies for predictive particle monitoring and control using advanced image analysis
Rasmus Fjordbak Nielsen, Nasrin Arjomand Kermani, Louise la Cour Freiesleben, Krist V. Gernaey and Seyed Soheil Mansouri 1773
297. Integrating Simulation and Optimization for Process Planning and Scheduling Problems
Miguel Vieira, Samuel Moniz, Bruno Gonçalves, Tânia Pinto-Varela, Ana Paula Barbosa-Póvoa 1779
298. On Robustness of Mixed-Integer reformulations of Generalized Disjunctive Programs
Miloš Bogataj, Zdravko Kravanja 1785
299. A Comparison of Data Reconciliation Tools for Modelling Heat Recovery
Petar Sabev Varbanov, Jun Yow Yong, Jiří Jaromír Klemeš, Zdravko Kravanja 1791
300. Process design meets sustainability: overview on the use of modelling tools for process design and sustainability assessment at Corbion
Van Bochove G., Cruz L., Morao A., Rugerio C 1797
301. Assessment of the dominant factors during hydroprocessing stabilization
Ngoc Yen Phuong Cao, Benoit Celse, Denis Guillaume, Isabelle Guibard, Joris W.Thybaut 1803

302. New MINLP Formulations for Flexibility Analysis for Measured and Unmeasured Uncertain Parameters <i>María Paz Ochoa, Ignacio E. Grossmann</i>	1809
303. Mathematical process modelling past, present and future – a personal perspective <i>J.P. Schmal</i>	1815
304. The use of optimization tools for the Hydrogen Circular Economy <i>M. Yáñez, A. Ortiz, B. Brunaud, I.E. Grossmann, I. Ortiz</i>	1821
Author Index	1827

This page intentionally left blank

Deterministic Global Process Optimization: Flash Calculations via Artificial Neural Networks

Artur M. Schweidtmann^a, Dominik Bongartz^a, Wolfgang R. Huster^a and Alexander Mitsos^{a*}

^a*Process Systems Engineering (AVT.SVT), RWTH Aachen University, Aachen 52074, Germany
amitsos@alum.mit.edu*

Abstract

We recently demonstrated the potential of deterministic global optimization in a reduced-space formulation for flowsheet optimization. However, the consideration of implicit unit operations such as flash calculations is still challenging and the solution of complex flowsheets incorporating such operations can be intractable. We show that the solution of flash equations can be integrated in global optimization via artificial neural networks (ANNs). Thus, flash calculations are no longer performed within the flowsheet optimization. Instead, flash equations are solved offline and then learned using ANNs. ANNs have been used successfully in the literature to learn flash equilibria but have not yet been included in deterministic global optimization for this task. We embed the ANNs in a hybrid model and use deterministic global optimization to solve it. In addition, we utilize deterministic global optimization to calculate a guaranteed worst-case accuracy of ANNs compared to a rigorous model. We demonstrate the proposed approach on an illustrative five-component vapor-liquid equilibrium flash using our in-house solver MAiNGO.

Keywords: Reduced-space, McCormick relaxations, Guaranteed accuracy, Flowsheet

1. Introduction

The optimization of process flowsheets is still a major challenge after many years of important advances in process systems engineering. Flowsheet optimization problems typically result in nonlinear programs (NLPs) that exhibit nonconvexities and multiple local optima. In contrast to local and stochastic global solution methods, deterministic global optimization methods are guaranteed to identify global optima, making them a desirable solution method.

In the previous literature, deterministic global optimization of flowsheet problems has mostly been performed using general-purpose global solvers and an equation-oriented modeling approach (also known as full-space). However, when complex processes are considered, this leads to large-scale optimization problems. In addition, the equation-oriented modeling approach necessitates bounds on all modeling variables which can be difficult to determine. An alternative to this is a hybrid between the equation-oriented and a sequential modular approach where the branch-and-bound solver operates only in a subset of the model variables (also known as a reduced-space approach) (Byrne and Bogle (2000); Balendra and Bogle (2009)). Similar reduced-space approaches have long been used for simulation and local optimization (e.g., Tolsma et al. (2002); Poth et al. (2003)). We recently demonstrated the potential of reduced-space for deterministic global flowsheet optimization (Bongartz and Mitsos (2017)) and hybrid flowsheet problems with artificial neural networks (ANNs) embedded (Schweidtmann and Mitsos (2018); Rall et al. (2019)). Therein and herein, we use our in-house solver MAiNGO (Bongartz et al. (2018)) which in turn relies on propagation of McCormick relaxations (McCormick (1976)) through external functions (Mitsos et al.

(2009); Chachuat et al. (2015))

However, a particular challenge of realistic flowsheet optimization problems lies in the consideration of accurate thermodynamic calculations and complex unit operations because these often include implicit functions and complex calculations. In the reduced-space formulation, these can lead to additional variables, equality constraints, and weak McCormick relaxations (Stuber et al. (2015); Schweidtmann et al. (2019); Bongartz and Mitsos (2019)). A possible solution to this is to substitute complex model parts by surrogate models. This can essentially reduce the number of optimization variables and equality constraints that the B&B algorithm branches on because the surrogate models are called as external functions (Schweidtmann and Mitsos (2018)). In some cases, the McCormick relaxations of surrogate models are even tighter than the ones of the substituted model (Schweidtmann et al. (2019)).

Machine learning surrogate models have been used extensively in the previous process systems engineering literature (Lee et al. (2018)), e.g., for embedding them in hybrid process models (e.g., Caballero and Grossmann (2008); Mistry et al. (2018); Rall et al. (2019)) or black-box optimization of simulations (e.g., Wilson and Sahinidis (2017); Boukouvala et al. (2017)). In addition, multiple works have addressed the learning of single species thermodynamic properties (e.g., Chouai et al. (2002); Laugier and Richon (2003)) and vapor-liquid equilibrium compositions (e.g., Sharma et al. (1999); Sözen et al. (2004); Şencan et al. (2006); Nentwich and Engell (2016); Keßler et al. (2017)) demonstrating that ANNs are capable of learning those properties accurately. In our previous organic Rankine cycle case study, we have showed that substituting an implicit Helmholtz thermodynamic model for ethanol by ANNs leads to favorable solution times for the optimization because of a reduction in the number of optimization variables and equality constraints as well as tighter relaxations (Schweidtmann et al. (2019)). However, many chemical engineering applications include flash calculations which do not lend themselves as naturally to a reduced-space formulation and may require a number of variables and constraints to remain in the optimization problem (Bongartz and Mitsos (2019)). ANNs for thermodynamic equilibrium equations have not yet been included in deterministic global optimization. Further, the previous literature does not provide guarantees on the accuracy of trained ANNs but mostly indicates their performance on a finite test set.

We propose to learn thermodynamic equilibrium via ANNs in order to include them subsequently in deterministic global optimization problems. The method learns the solution of flash calculations retrieved from a nonsmooth model that describes not only the two-phase region, but also single-phase output streams (Sahlodin et al. (2016); Watson et al. (2017)). Furthermore, we compute a guarantee on the worst-case performance of ANNs compared to an analytical model using deterministic global optimization. The method is illustrated on a five-species nonideal mixture.

2. Flash calculations & illustrative case study

Many chemical flowsheets include flash separations that are assumed to be in equilibrium. Herein, we consider a vapor-liquid equilibrium (VLE) flash: Given an inlet stream flow rate (F) and its molar fractions (\mathbf{z}), the flash calculation determines the outgoing flow rates of the liquid stream (L) and vapor stream (V) with their corresponding molar fractions \mathbf{x} and \mathbf{y} , respectively. The flash has two degrees of freedom that are either specified by design or are optimization variables. In this work, we use temperature (T) and pressure (p) as the degrees of freedom because intensive properties are advantageous for data-driven modeling (see Section 4).

The flash model consists of balance equations for overall molar flow rates Eqn. (1), component flow rates Eqn. (2), the isofugacity equation Eqn. (3), and the closure relation Eqn. (4) (c.f., Watson et al. (2017)):

$$F - L - V = 0 \quad (1)$$

$$F \cdot z_i - L \cdot x_i - V \cdot y_i = 0 \quad i = 1, \dots, N \quad (2)$$

$$f_i^V(p, T, \mathbf{y}) - f_i^L(p, T, \mathbf{x}) = 0 \quad i = 1, \dots, N \quad (3)$$

$$\text{mid} \left(V/F, \sum_{i=1}^N (x_i - y_i), V/F - 1 \right) = 0 \quad (4)$$

where N is the number of components and f_i^V, f_i^L are the fugacities of component i in the vapor and liquid phase, respectively. Note that herein we use the nonsmooth closure relation proposed by Watson et al. (2017) which is based on the commonly used closure relation $\sum_{i=1}^N (x_i - y_i) = 0$ and which can model both two-phase and single-phase outlet streams. We use the flash model Eqns. (1) - (4) to generate data for training the ANNs (Section 3) and as a reference model for comparison to the data-driven approach (Sections 4 & 5). Note that we use the isofugacity equation Eqn. 3 and thus cannot guarantee stable states because we want to avoid a bilevel problem which arises when the Gibbs free energy is minimized as an embedded optimization problem. However, the proposed approach can in principle be applied to these as well.

For illustration, we consider a five-species mixture of hydrogen (H_2), carbon dioxide (CO_2), carbon monoxide (CO), methanol ($MeOH$), and water (H_2O). We assume ideal gas/liquid phases, use Henry's law for the supercritical species H_2 , CO_2 , and CO being dissolved in liquid methanol and water, and use model parameters and the solvent mixing rule from AspenPlus. The case study is described in more detail in Bongartz and Mitsos (2019) where rigorous, not hybrid, flash models with the common closure relation were optimized.

3. Training of the artificial neural networks

In order to generate the training data set, we create a Latin hypercube of 20,000 points on $z_i \in [0, 1], T \in [300, 512]$ K, $p \in [1, 66.5]$ bar with $\sum_{i=1}^N z_i = 1$. Then, we simulate the fully specified flash model Eqns. (1) - (4) in MAiNGO. Herein, we use an inlet stream flow rate of 1 kmol/s without loss of generality. As we use the nonsmooth closure relation Eqn. 4, data on the complete box-constrained input domain is feasible.

For training, the input vector of the ANNs is set to $(z_{H_2}, z_{CO_2}, z_{CO}, z_{MeOH}, T, p)^T$ and the output vector is set to $(x_{H_2}, x_{CO_2}, x_{CO}, x_{MeOH}, \beta)^T$ with $\beta = V/F$. The training is conducted in MATLAB using Bayesian regularization backpropagation because we observed that regularization leads to tighter relaxations and favorable performance in subsequent optimization studies. However, the comparison of training algorithms is not within the scope of this work. All outputs are learned using individual ANNs with two hidden layers with ten nodes each. Furthermore, the hyperbolic tangent activation function is used in the hidden and output layers as we know from physical understanding that our outputs are bounded.

4. Optimization of hybrid flash model

In this section, the learned ANNs are embedded in an hybrid optimization problem that is solved using our deterministic global solver MAiNGO. In particular, the ANNs are used to compute $x_{H_2}, x_{CO_2}, x_{CO}, x_{MeOH}, \beta$ and the remaining mole fractions and flows are obtained by solving overall and component molar balances. This gives a hybrid flash model where the equilibrium is learned via ANNs and the balances are given by mechanistic equations. This allows for applying the hybrid model to any given input flow rate. All problems were solved on an Intel(R) Core(TM) i7-4790 CPU with 3.60 GHz, 16 GB RAM, and Windows 7 64 bit operating system.

For the illustrative case study, we consider an inlet stream of $F = 1$ kmol/s with the composition $\mathbf{z} = (0.644, 0.195, 0.025, 0.072, 0.064)^T$. The objective of the problem is to identify $T \in [300, 512]$ K and $p \in [1, 66.5]$ bar that maximize the amount of methanol recovered in the liquid phase, i.e., $\min -L \cdot x_{MeOH} / (F \cdot z_{MeOH})$, subject to the purity constraint $x_{CO_2} \leq 0.01$.

As shown in Table 1, the solution point of the hybrid ANN model is close to the one of the rigorous model. The optimal point of the illustrative problem is at the lower temperature boundary, intermediate pressure, and results in a two-phase outlet stream. The solution time of the hybrid

Table 1: Problem size and solution statistics of the illustrative flash case study (relative optimality tolerance 10^{-3}). In the table we use the following abbreviations: Var.: number of optimization variables, Eq.: number of equality constraints, Ineq.: number of inequality constraints, CPU: computational time, Iter.: number of iterations, T : temperature, p : pressure, Obj.: objective value.

Formulation	Problem size			Performance		Solution point		
	Var.	Eq.	Ineq.	CPU [s]	Iter.	T [K]	p [bar]	Obj. [%]
Rigorous flash	6	4	1	3.74	2,195	300	16.7	93.2
Hybrid flash	2	0	1	0.59	347	300	16.5	93.7

model gives a considerable speedup as it takes less than 16% of the solution time of the rigorous model. One reason for the speedup is the smaller problem size of the hybrid model, i.e., the B&B algorithm has to branch only on the two degrees of freedom and requires less iterations. In contrast, the optimization problem including the rigorous flash model has four additional optimization variables and equality constraints because the model is not explicit in the degrees of freedom (c.f. *ideal flash formulation* in Bongartz and Mitsos (2019)).

5. Guaranteed accuracy of the artificial neural networks

When ANNs and other surrogate models are used in decision-making processes, trust in the accuracy of their predictions is a major concern. Typically, ANNs are trained on a large set of training data and subsequently validated on an independent test set. However, even in cases where accurate fits are obtained on both the training and test set, there is no guarantee that the model gives reasonably good predictions on the whole input or even out of the sampled training domain because of the universal approximator theorem (e.g., Hornik et al. (1989)). This means that an ANN of sufficient size can in principle represent any continuous function - also unphysical functions between training and test points. Previous works addressed this problem, e.g., Wilson and Sahinidis (2017) use an adaptive sampling technique where they iteratively select new training points by maximization of the error between the surrogate model and the underlying simulation used for data generation using a stochastic black-box solver. However, the stochastic solution approach does not provide a guaranteed worst-case accuracy.

In this section, we propose a method that computes a guaranteed accuracy of ANNs for cases where an algebraic formulation of the underlying model used for data generation is available. In particular, we maximize a norm of an error between the underlying model for data generation and our surrogate model on a compact input domain using deterministic global optimization. Any upper bound of this maximization problem provides a guarantee on the worst-case performance of the surrogate model.

For illustration, we maximize the squared distance of the component molar liquid streams of the rigorous flash model and the previously trained ANN. This problem is reformulated to an equivalent minimization problem as the optimization literature usually formulates minimization problems:

$$\min \quad -\|(\mathbf{L}_{\text{ANN}} - \mathbf{L}_{\text{Rig flash}})\|_2^2 \quad (5)$$

subject to the rigorous flash model Eqns. (1) - (4) and the hybrid flash model where $\mathbf{L}_{\text{Rig flash}} = L_{\text{Rig flash}} \cdot \mathbf{x}_{\text{Rig flash}}$ is the liquid molar flow rate vector from model Eqns. (1) - (4) and \mathbf{L}_{ANN} is the vector of corresponding predictions computed by the hybrid flash model. Herein, we compare component molar flow rates and not mole fractions because they are a relevant measure for the error for both the two-phase and the single-phase case. Given inlet mole fractions of $\mathbf{z} = (0.644, 0.195, 0.025, 0.072, 0.064)^T$ and a total inlet stream of $F = 1$ kmol/s, the optimization problem Eqn. (5) is solved for the degrees of freedom $T \in [300, 512]$ K and $p \in [1, 66.5]$ bar.

The solution point with the largest squared distance that has been found in the B&B algorithm is $2.05 \cdot 10^{-4} \text{ kmol}^2/\text{s}^2$ at $T^* = 315 \text{ K}$, $p^* = 1.1 \text{ bar}$ with $\mathbf{L}_{\text{Rig flash}}^* = (1.2 \cdot 10^{-7}, 1.2 \cdot 10^{-6}, 6.4 \cdot 10^{-9}, 1.3 \cdot 10^{-3}, 5.0 \cdot 10^{-3})^T$ and $\mathbf{L}_{\text{ANN}}^* = (1.3 \cdot 10^{-6}, 1.6 \cdot 10^{-5}, 1.8 \cdot 10^{-7}, 5.0 \cdot 10^{-3}, 1.9 \cdot 10^{-2})^T$ in kmol/s . This solution is near the phase boundary, i.e., $\beta = 0.994$, indicating that inaccuracies of the ANNs are higher near the phase boundary. Also, the solution point is near the box constraints of the training data indicating that it is sensible to extend the training set outside the actually used input domain. However, the result also shows the worst-case absolute inaccuracies are relatively small. The lower bound of the problem gives a guaranteed worst-case performance of $1.41 \cdot 10^{-3} \text{ kmol}^2/\text{s}^2$. Herein, an absolute optimality gap of $1.21 \cdot 10^{-3} \text{ kmol}^2/\text{s}^2$ remains after the maximum solution time of 43,200 CPU seconds showing that the guaranteed accuracy optimization problem is much harder to solve than the optimization of the hybrid flash model in Section 4.

6. Conclusion

We propose a hybrid modeling approach that learns thermodynamic equilibria of multicomponent mixtures via ANNs for subsequent deterministic global process optimization. The ANNs learn liquid equilibrium mole fractions and the vapor-to-feed ratio from a set of data covering both two-phase and single-phase regions. Then, we combine the ANNs with rigorous balance equations to form a hybrid flash model. An illustrative five-component flash case study shows that the hybrid flash model can be optimized in less than 16% of the CPU time necessary to optimize a rigorous flash model. Finally, deterministic global optimization is used to compute a guaranteed worst-case accuracy of the ANNs compared to a rigorous flash simulation.

The considerable speedup of the optimization does, however, come at the cost of offline data generation and training of the ANNs (on the order of minutes to hours). Thus, the hybrid modeling of a single flash calculation does not seem practical unless the optimization problem needs to be solved very quickly. However, it is expected that the substitution of several flash calculations in larger flowsheet problems will give much larger speedups due to the exponential worst-case runtime of B&B algorithms. Furthermore, this work presents a first step towards the learning and subsequent deterministic global optimization of complete separation columns. This is a promising future work because the reduced-space optimization of rigorous column models requires tear variables and flash calculation on every stage whereas an ANN could learn the column as a whole.

The computation of a guaranteed worst-case performance of ANNs is also a relevant contribution because it can be used as a rigorous tool to identify regions in the input domain with large errors, choose new training points accordingly, or select a suitable network architecture/complexity. In addition, the method allows us to use ANNs as a model reduction technique with guaranteed accuracy in the future.

Acknowledgments: The authors gratefully acknowledge the financial support of the Kopernikus project SynErgie by the German Federal Ministry of Education and Research (BMBF) and the project supervision by the project management organization Projektträger Jülich (PtJ). The authors gratefully acknowledge funding by the BMBF within the Kopernikus Project P2X: Flexible use of renewable resources exploration, validation and implementation of ‘Power-to-X’ concepts. We thank Tim Kerkenhoff and Nils Graß for their help on the data generation and implementation.

References

- S. Balendra, I. D. L. Bogle, 2009. Modular global optimisation in chemical engineering. *Journal of Global Optimization* 45 (1), 169–185.
- D. Bongartz, A. Mitsos, 2017. Deterministic global optimization of process flowsheets in a reduced space using McCormick relaxations. *Journal of Global Optimization* 20 (9), 419.
- D. Bongartz, A. Mitsos, 2019. Deterministic global flowsheet optimization: between equation-oriented and sequential-modular methods. *AIChE Journal* 65 (3), 1022–1034.

- D. Bongartz, J. Najman, S. Sass, A. Mitsos, 2018. MAiNGO – McCormick-based Algorithm for mixed-integer Nonlinear Global Optimization. Tech. rep., Process Systems Engineering (AVT.SVT), RWTH Aachen University. URL <http://permalink.avt.rwth-aachen.de/?id=729717>
- F. Boukouvala, M. F. Hasan, C. A. Floudas, 2017. Global optimization of general constrained grey-box models: new method and its application to constrained PDEs for pressure swing adsorption. *Journal of Global Optimization* 67 (1-2), 3–42.
- R. Byrne, I. Bogle, 2000. Global optimization of modular process flowsheets. *Industrial & engineering chemistry research* 39 (11), 4296–4301.
- J. A. Caballero, I. E. Grossmann, 2008. An algorithm for the use of surrogate models in modular flowsheet optimization. *AIChE journal* 54 (10), 2633–2650.
- B. Chachuat, B. Houska, R. Paulen, N. Perić, J. Rajyaguru, M. E. Villanueva, 2015. Set-theoretic approaches in analysis, estimation and control of nonlinear systems. *IFAC-PapersOnLine* 48 (8), 981–995. URL <http://omega-ic1.bitbucket.org/mcpp/>
- A. Chouai, S. Laugier, D. Richon, 2002. Modeling of thermodynamic properties using neural networks. *Fluid Phase Equilibria* 199 (1-2), 53–62.
- K. Hornik, M. Stinchcombe, H. White, 1989. Multilayer feedforward networks are universal approximators. *Neural Networks* 2 (5), 359–366.
- T. Keßler, N. Mertens, C. Kunde, C. Nentwich, D. Michaels, S. Engell, A. Kienle, 2017. Efficient global optimization of a novel hydroformylation process. In: *Computer Aided Chemical Engineering*. Vol. 40. Elsevier, pp. 2113–2118.
- S. Laugier, D. Richon, 2003. Use of artificial neural networks for calculating derived thermodynamic quantities from volumetric property data. *Fluid Phase Equilibria* 210 (2), 247–255.
- J. H. Lee, J. Shin, M. J. Reaiff, 2018. Machine learning: Overview of the recent progresses and implications for the process systems engineering field. *Computers & Chemical Engineering* 114, 111–121.
- G. P. McCormick, 1976. Computability of global solutions to factorable nonconvex programs: Part i convex underestimating problems. *Mathematical Programming* 10 (1), 147–175.
- M. Mistry, D. Letsios, R. Misener, G. Krennrich, R. M. Lee, 2018. Optimization with gradient-boosted trees and risk control. *arXiv preprint arXiv:1803.00952*.
- A. Mitsos, B. Chachuat, P. I. Barton, 2009. McCormick-based relaxations of algorithms. *SIAM Journal on Optimization* 20 (2), 573–601.
- C. Nentwich, S. Engell, 2016. Application of surrogate models for the optimization and design of chemical processes. In: *2016 International Joint Conference on Neural Networks (IJCNN)*. IEEE.
- N. Poth, D. Brusis, J. Stichlmair, 2003. Rigorous optimization of reactive distillation in gams with the use of external functions. In: *Computer Aided Chemical Engineering*. Vol. 14. Elsevier, pp. 869–874.
- D. Rall, D. Menne, A. M. Schweidtmann, J. Kamp, L. von Kolzenberg, A. Mitsos, M. Wessling, 2019. Rational design of ion separation membranes. *Journal of Membrane Science* 569, 209 – 219.
- A. M. Sahlodin, H. A. Watson, P. I. Barton, 2016. Nonsmooth model for dynamic simulation of phase changes. *AIChE Journal* 62 (9), 3334–3351.
- A. M. Schweidtmann, W. R. Huster, J. Lütjhe, A. Mitsos, 2019. Deterministic global process optimization: Accurate (single-species) properties via artificial neural networks. *Computers & Chemical Engineering* 121, 67 – 74.
- A. M. Schweidtmann, A. Mitsos, 2018. Deterministic global optimization with artificial neural networks embedded. In Press: *Journal of Optimization Theory and Applications*.
- A. Şencan, K. A. Yakut, S. A. Kalogirou, 2006. Thermodynamic analysis of absorption systems using artificial neural network. *Renewable Energy* 31 (1), 29–43.
- R. Sharma, D. Singhal, R. Ghosh, A. Dwivedi, 1999. Potential applications of artificial neural networks to thermodynamics: vapor–liquid equilibrium predictions. *Computers & Chemical Engineering* 23 (3), 385–390.
- A. Sözen, M. Özalp, E. Arcaklioğlu, 2004. Investigation of thermodynamic properties of refrigerant/absorbent couples using artificial neural networks. *Chemical Engineering and Processing: Process Intensification* 43 (10), 1253–1264.
- M. D. Stuber, J. K. Scott, P. I. Barton, 2015. Convex and concave relaxations of implicit functions. *Optimization Methods and Software* 30 (3), 424–460.
- J. E. Tolsma, J. A. Clabaugh, P. I. Barton, 2002. Symbolic incorporation of external procedures into process modeling environments. *Industrial & engineering chemistry research* 41 (16), 3867–3876.
- H. A. Watson, M. Vikse, T. Gundersen, P. I. Barton, 2017. Reliable flash calculations: Part I. nonsmooth inside-out algorithms. *Industrial & Engineering Chemistry Research* 56 (4), 960–973.
- Z. T. Wilson, N. V. Sahinidis, 2017. The ALAMO approach to machine learning. *Computers & Chemical Engineering* 106, 785–795.

An MILP model for safe multi-floor process plant layout

Jude O. Ejeh^a, Songsong Liu^b and Lazaros G. Papageorgiou^{a,*}

^a*Centre for Process Systems Engineering, Department of Chemical Engineering, University College London, Torrington Place, London WC1E 7JE, United Kingdom;*

^b*School of Management, Swansea University, Bay Campus, Fabian Way, Swansea SA1 8EN, United Kingdom;*

Abstract

In this work, a mixed integer linear programming (MILP) model is presented to obtain the optimal layout of a multi-floor chemical process plant with minimum risk in fire and explosion scenarios. Layout decisions determine the spatial arrangement of process plant equipment on available land area considering the equipment interconnections, dimensions, costs, general operability, as well as associated structures and auxiliary units. Optimal decisions ought to strike a balance between risk and cost savings. Previous attempts to include safety considerations in the layout decision making process have been restricted to minimise connection and risk costs alone, with some unrealistic assumptions on safety distances for mostly single floor layout cases. The model presented adopts the Dow's Fire & Explosion system to quantify risk in order to determine the optimal multi-floor plot layout simultaneously with more realistic constraints for safety distance calculations. The optimal layout design obtained minimises costs attributed to the installation of connecting pipes, pumping, area-dependent construction of floors, land purchase, as well as the risk associated with fire and explosion events by inherent and passive strategies.

Keywords: multi-floor plant layout; safety; optimisation; MILP

1. Introduction

Right from conceptualisation to plant decommissioning, it is quite important that safety assessments be carried out for every aspect of a chemical process plant design project (Khan and Amyotte, 2004). Improper safety considerations at each stage of design or operation can result in fatalities, injuries, disruption of production activities within the plant and its neighbouring environment. Amidst a range of factors that contribute towards the overall safety levels, a study has shown that 79% of process plant accidents were attributed to design errors, the most critical being poor layout (Kidam and Hurme, 2012). Layout design determines the spatial arrangement of chemical process plant units considering their interconnections based on pre-defined criteria. These units may be process vessels in which unit operations are carried out, storage facilities, work centres or departments, and their spatial arrangement affect capital and operating costs, efficiency of plant activities, and of particular concern to this work, the overall safety levels within the plant and the immediate environment. From an optimisation point of view, safety considerations in layout designs have been considered in the past. While a great deal of research has

focused on the economic aspects alone - piping, construction and operating costs associated for a layout configuration, an ideal plant layout design ought to establish a balance between risks and costs. In a recent review, Roy et al. (2016) outlined available safety metrics for process design and their level of application. One of the key indices applicable to layout design with numerical quantification is the Dow Fire and Explosion Index (F&EI). The Dow F&EI was developed by American Dow Chemical Company (American Institute of Chemical Engineers, 1994) and is currently a widely applied method for hazard evaluation of chemical and industrial processes (Wang and Song, 2013). It estimates the hazards of a single unit based on the chemical properties of the material(s) within it, and the potential economic risk such equipment poses to itself and neighbouring structures with or without the installation of protection devices. A similar concept was adopted by Penteado and Ciric (1996) in a mixed integer non-linear programming (MINLP) model where financial risks associated with potential events from process units were modelled as cost functions with an overall objective to minimise the net present cost of a single floor layout. The choice of safety devices was also made available to reduce the associated risk levels. Patsiatzis et al. (2004) proposed a mixed integer linear programming (MILP) model solely based on the Dow F&EI to minimise the total cost associated with connecting process units by pipes, financial risks and the purchase and installation of protection devices. Other research activities have built on these to include multi-floor considerations (Park et al., 2018), human risk considerations, and in more recent times by employing the Domino Hazard Index (López-Molina et al., 2013).

In this work, an MILP model is proposed to address the multi-floor process plant layout problem with safety considerations, which are quantified using the Dow F&EI. Readers may consult the Dow's F&EI Hazard Identification guide (American Institute of Chemical Engineers, 1994) for detailed steps to calculate this metric. The proposed model will minimise the total cost attributed to pipe connections, pumping, floor construction, land purchase, installation of protection devices and financial losses in the event of an accident, which prior to this work has not been simultaneously addressed. Safety distances between equipment items are also modelled in a new way - from the opposing boundaries of equipment items as compared to the midpoints as previously done in order to better capture the actual distances between equipment for risk quantifications. Tall equipment items spanning through consecutive floors are also considered with the model determining the optimal number of floors and the equipment floor and spatial arrangements.

In the rest of the paper, the problem description is outlined in section 2. In section 3 the mathematical model is proposed and its computational performance is shown with a relevant case study in section 4. Final remarks are given in section 5.

2. Problem Description

The problem is as follows: *Given* a set of process plant units ($i \in I$), their dimensions - length (l_i), breadth (d_i) and height (h_i) - and connectivity network with space and unit allocation limitations, a set of potential floors for layout with respective floor height (FH), a set of pertinent equipment item ($i \in I^{pe}$), a set of protection device configurations available for each pertinent item ($p \in P_i$), with associated costs (C_{ip}^p) and loss control credit factor if installed on an equipment item; *determine* the total number (NF) and area of floors (FA), the protection device configuration, p , to be installed on each pertinent equipment item, and the plot layout *so as to* minimise the total plant layout and safety costs.

It is assumed that the geometries of all process plant equipment are rectangles, with horizontal connection distances taken as the rectilinear distance from the geometrical centres in the x-y plane. Vertical connection distances are taken from a design-specified height on each equipment. For safety considerations, all rectilinear distances are taken from the boundaries of equipment items to evaluate the probability, magnitude and impact of an incident. Equipment items are allowed to rotate by 90° and those with heights greater than the floor height can extend through consecutive floors but must start from the base of a floor.

3. Mathematical Formulation

The mathematical formulation constitutes an extension of model A.1 in Egeh et al. (2018) for the multi-process plant layout problem and by Patsiatzis et al. (2004). All constraints in model A.1 (Egeh et al., 2018) apply with the following modifications/additions. First of all, the distance constraints written for connected equipment items ($f_{ij} = 1$) (Patsiatzis et al., 2004), are further written for pairs of items (i, j) including a pertinent item, $i \in I^{pe}$, and any other item j , i.e., $\zeta = \{(i, j) : i \in I^{pe}, j \neq i\}$.

For safety considerations, the rectilinear distances between equipment items taken from the geometrical centres no longer seem to be a valid assumption. This is especially true for process plants having large and/or tall equipment items where rectilinear distances from the geometrical centres may have a high value but the equipment items are physically close to each other. A more valid assumption will be to calculate the separation distances from the equipment boundaries as illustrated in Figure 1, as an event on a pertinent item i can emanate at any point within the item up to its boundaries.

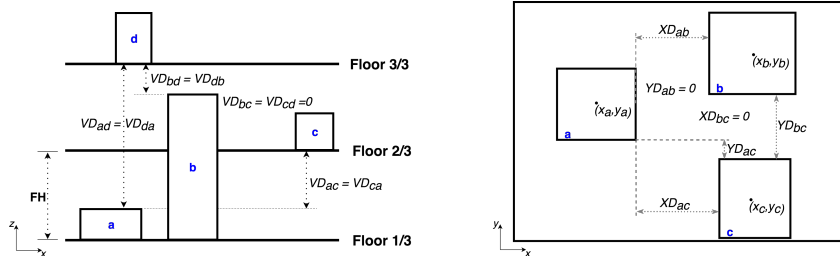


Figure 1: Vertical and horizontal safety distances between equipment items

For vertical separation distances between any two equipment items i and j (VD_{ij}), the distance is taken from the top of j to the bottom of i if i is on a higher floor than j , and if the reverse is the case, from the top of i to the bottom of j . However, if both i and j are on the same floor, i.e., $N_{ij} = 1$, the vertical separation distance is taken to be zero. The conditions stated above are modelled by Eqs. (1) - (3) where S_{ik}^s is a binary variable with a value of 1 if item i starts at floor k , and η_{ij}^u and η_{ij}^d are positive variables evaluated by Eqs. (4) - (6).

Horizontal separation distances are also calculated from the item boundaries in the x and y planes as XD_{ij} (Eqs. (7) - (11)) and YD_{ij} (Eqs. (12) - (16)) respectively (Figure 1). A value of zero is assigned to these distances if the opposing boundaries of an item i is not strictly to the right or left (in the x plane), or above or below (in the y plane) j . That is, items i and j overlap at any point on either the x or y plane. The binary variable W_{ij}^{x0} is

assigned a value of 1 if item i is strictly to the right or left of item j or 0 otherwise. The same applies for W_{ij}^{yo} if item i is strictly above or below j . The relative distances between items i and j in the x plane are represented by R_{ij} and L_{ij} if i is to the right of j , and if i is the left of j respectively. A_{ij} and B_{ij} represent the relative distances in the y plane if i is above j , and if i is below j respectively. $E2_{ij}$ is a non-overlapping binary variable and BM is a large number (Patsiatzis et al., 2004). Given these modifications, the total safety distance, TD_{ij}^s , between equipment items i and j is then calculated by Eq. (17).

$$VD_{ij} \leq FH \sum_k (k-1)(S_{jk}^s - S_{ik}^s) - h_i + \eta_{ij}^u + BM \cdot N_{ij} \quad \forall (i, j) \in \zeta \quad (1)$$

$$VD_{ij} \geq FH \sum_k (k-1)(S_{jk}^s - S_{ik}^s) - h_i + \eta_{ij}^u - BM \cdot N_{ij} \quad \forall (i, j) \in \zeta \quad (2)$$

$$VD_{ij} \leq BM \cdot (1 - N_{ij}) \quad \forall (i, j) \in \zeta \quad (3)$$

$$\eta_{ij}^u - \eta_{ij}^d = 2FH \sum_k (k-1)(S_{ik}^s - S_{jk}^s) + h_i - h_j \quad \forall (i, j) \in \zeta \quad (4)$$

$$\eta_{ij}^u \leq BM \cdot W_{ij}^z \quad \forall (i, j) \in \zeta \quad (5)$$

$$\eta_{ij}^d \leq BM \cdot (1 - W_{ij}^z) \quad \forall (i, j) \in \zeta \quad (6)$$

$$x_i - x_j + 2L_{ij} \geq \left(\frac{l_i + l_j}{2} \right) - BM(1 - W_{ij}^{xo}) \quad \forall (i, j) \in \zeta \quad (7)$$

$$XD_{ij} \leq R_{ij} + L_{ij} - \left(\frac{l_i + l_j}{2} \right) + BM(1 - W_{ij}^{xo}) \quad \forall (i, j) \in \zeta \quad (8)$$

$$XD_{ij} \geq R_{ij} + L_{ij} - \left(\frac{l_i + l_j}{2} \right) - BM(1 - W_{ij}^{xo}) \quad \forall (i, j) \in \zeta \quad (9)$$

$$XD_{ij} \leq BM \cdot W_{ij}^{xo} \quad \forall (i, j) \in \zeta \quad (10)$$

$$W_{ij}^{xo} \geq 1 - E2_{ij} |_{j>i} - E2_{ji} |_{i>j} \quad \forall (i, j) \in \zeta \quad (11)$$

$$y_i - y_j + 2B_{ij} \geq \left(\frac{d_i + d_j}{2} \right) - BM(1 - W_{ij}^{yo}) \quad \forall (i, j) \in \zeta \quad (12)$$

$$YD_{ij} \leq A_{ij} + B_{ij} - \left(\frac{d_i + d_j}{2} \right) + BM(1 - W_{ij}^{yo}) \quad \forall (i, j) \in \zeta \quad (13)$$

$$YD_{ij} \geq A_{ij} + B_{ij} - \left(\frac{d_i + d_j}{2} \right) - BM(1 - W_{ij}^{yo}) \quad \forall (i, j) \in \zeta \quad (14)$$

$$YD_{ij} \leq BM \cdot W_{ij}^{yo} \quad \forall (i, j) \in \zeta \quad (15)$$

$$W_{ij}^{yo} \geq E2_{ij} |_{j>i} + E2_{ji} |_{i>j} \quad \forall (i, j) \in \zeta \quad (16)$$

$$TD_{ij}^s = XD_{ij} + YD_{ij} + VD_{ij} \quad \forall (i, j) \in \zeta \quad (17)$$

The area of exposure and maximum probable property damage cost constraints are as described in Patsiatzis et al. (2004) using the modified total distance, TD_{ij}^s .

The objective function (Eq. (18)) is the minimisation of the total cost attributed to connection, pumping, land purchase, construction, financial risk and the installation of protective devices. The financial risk is evaluated from the actual maximum probable property damage cost (Ω_i) (Patsiatzis et al., 2004) and μ_{ip} is a binary variable with a value of 1 if protection device configuration p is to be purchased and installed on pertinent item $i \in I^{pe}$. C_{ij}^c , C_{ij}^v , C_{ij}^h , LC , $FC1$ and $FC2$ represent the connection cost, vertical pumping cost, horizontal pumping cost, area-dependent land purchase cost, fixed floor construction

cost and area-dependent floor construction cost respectively.

$$\begin{aligned} \min \sum_i \sum_{j \neq i: f_{ij}=1} [C_{ij}^c TD_{ij} + C_{ij}^v D_{ij} + C_{ij}^h (R_{ij} + L_{ij} + A_{ij} + B_{ij})] + FC1 \cdot NF \\ + FC2 \sum_s AR_s \cdot NQ_s + LC \cdot FA + \sum_i \Omega_i + \sum_{i,p \in P_i} C_{ip}^p \cdot \mu_{ip} \end{aligned} \quad (18)$$

4. Case study

The model proposed was applied to an Ethylene oxide plant (Figure 2) (Patsiatzis et al., 2004). Six protection device configurations are made available for installation, with the first configuration having no protection device purchased or installed. Full details for the configurations, the characteristic protection devices in each, and the associated cost and loss control credit factor can be found in Patsiatzis et al. (2004). The model was solved to global optimality using GAMS modelling system v25.0.2 with the CPLEX v12.8 solver on an Intel® Xeon® E5-1650 CPU with 32GB RAM. It had 260 discrete and 386 continuous variables with 894 equations, and obtained a total cost value of 480,114.4 rmu in 33s.

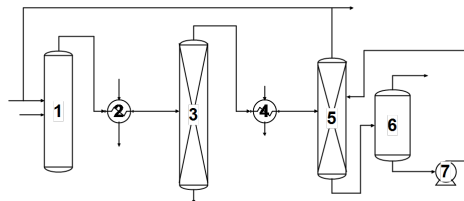


Figure 2: Flow diagram of Ethylene Oxide plant

Figure 3 shows the optimal layout plot with safety considerations. With the inclusion of fire and explosion scenarios, an additional floor is required compared to the layout results without safety considerations (Ejeh et al., 2018). Out of the total cost of 480,114.4 rmu, 175,000 rmu was attributed to the installation of protection devices, 187,535.4 to financial risks and 117,579.0 rmu to connection, pumping and construction costs. The latter cost quota is much larger when compared to the case without safety considerations, 66,262 rmu (Ejeh et al., 2018), owing to additional separation distances between equipment items, a larger floor area (30m × 30m compared to 20m × 20m), as well as the cost of the additional floor constructed.

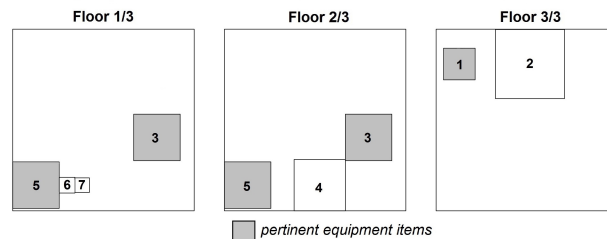


Figure 3: Optimal layout results

For the case where safety was not considered and no protection device was installed, the financial risk was calculated, based on the layout results obtained in Ejeh et al. (2018), to

be 935,820.9 rmu. In the optimal solution with safety considerations, protection devices were installed on all the pertinent equipment items - 1, 3 and 5 - to reduce the probability and magnitude of an incident. The total cost of purchase and installation was 175,000 rmu, with a reduced financial risk of 187,535.4 rmu. Hence, the cost of protection devices, financial risk, and other layout costs combined is much less for the case where safety is considered and protection devices are installed than if they were not. This provides for a more informed balance between cost savings and financial risks.

5. Concluding remarks

An MILP model (extended from Ejeh et al., 2018 and Patsiatzis et al., 2004) was proposed for the multi-floor process plant layout problem considering connection, pumping, construction, financial risk and protection device installation costs in fire and explosion scenarios. The model successfully described tall equipment items spanning through multiple floors with more accurate safety distance calculations obtained from the boundaries of neighbouring equipment items within similar floors and on different floors. The proposed model was applied to a 7-unit case study having 3 pertinent equipment items and 6 protection device configurations. 3 floors were obtained for the optimal solution, with a larger floor area and total cost compared to the same case without safety considerations. Overall, the proposed model is proved to be able to optimise the installation of protection devices and significantly reduce the risk associated with fire and explosion, resulting in a substantial decrease in probable property damage cost, much higher than the required additional safety device purchase, installation, connection, pumping and construction costs. Future work will seek to apply the model to larger case studies with more complex connection networks.

Acknowledgement

JOE acknowledges the financial support of the Petroleum Technology Development Fund (PTDF).

References

- American Institute of Chemical Engineers, 1994. Dow's Fire & Explosion Index Hazard Classification Guide. Vol. 7. John Wiley & Sons, Inc., Hoboken, NJ, USA.
- J. O. Ejeh, S. Liu, M. M. Chalchooghi, L. G. Papageorgiou, 2018. Optimization-Based Approach for Process Plant Layout. *Ind. Eng. Chem. Res.* 57 (31), 10482–10490.
- F. I. Khan, P. R. Amyotte, 2004. Integrated Inherent Safety Index (I2SI): A Tool for Inherent Safety Evaluation. *Process Saf. Prog.* 23 (2), 136–148.
- K. Kidam, M. Hurme, 2012. Design as a Contributor to Chemical Process Accidents. *J. Loss Prev. Process Ind.* 25 (4), 655–666.
- A. López-Molina, R. Vázquez-Román, M. S. Mannan, M. G. Félix-Flores, 2013. An Approach for Domino Effect Reduction Based on Optimal Layouts. *J. Loss Prev. Process Ind.* 26 (5), 887–894.
- K. Park, D. Shin, W. Won, 2018. Risk Based 3-Dimensional and Multifloor Plant Layout Optimization for Liquefied Natural Gas (LNG) Liquefaction Process. *Korean J. Chem. Eng.* 35 (5), 1053–1064.
- D. I. Patsiatzis, G. Knight, L. G. Papageorgiou, 2004. An MILP Approach to Safe Process Plant Layout. *Chem. Eng. Res. Des.* 82 (5), 579–586.
- F. D. Penteado, A. R. Ciric, 1996. An MINLP Approach for Safe Process Plant Layout. *Ind. Eng. Chem. Res.* 35 (4), 1354–1361.
- N. Roy, F. Eljack, A. Jiménez-Gutiérrez, B. Zhang, P. Thiruvengataswamy, M. El-Halwagi, M. S. Mannan, 2016. A Review of Safety Indices for Process Design. *Curr. Opin. Chem. Eng.* 14, 42–48.
- J. Wang, W.-H. Song, 2013. Fire and Explosion Index Calculation Method Incorporating Classified Safety Measure Credits. *J. Loss Prev. Process Ind.* 26 (6), 1128–1133.

A Generalized, Nonsmooth Operator for Process Integration

Caroline J. Nielsen^{a,*} and Paul I. Barton^a

^a*Massachusetts Institute of Technology, 77 Massachusetts Ave., Cambridge, MA 02139, USA*
cjn1994@mit.edu

Abstract

This work presents a novel, generalized method for solving resource targeting problems for process integration. The approach uses nonsmooth systems of two equations per resource to simulate the process under optimal resource reuse. The resulting equation system, including process models, is solved using new advances in the automatic generation of LD-derivatives to supply generalized derivative elements to nonsmooth equation-solving methods. Therefore, this method can be used to solve for process variables in addition to resource targets and retains the same number of equations regardless of the number of resource sources and sinks in the problem. An illustrative example of combined mass and water integration is included to demonstrate the strengths and flexibility of this approach.

Keywords: Process integration, Targeting, Process design, Nonsmooth equations

1. Introduction

Process integration methods have been widely proposed and utilized to minimize resource use through optimal reuse. These approaches were initially considered for heat recovery in heat integration problems (Linnhoff and Flower, 1978) and were then extended to the recovery of materials in mass exchange networks (MENs) and water allocation problems (El-Halwagi and Manousiouthakis, 1989; Dhole et al., 1996). In recent years, integration methods have also been applied beyond these traditional areas to new problems, such as hydrogen allocation, carbon planning, and even inventory problems (Alves and Towler, 2002; Munir et al., 2012; Castillo and Mahalec, 2013). There is a significant body of work on solving these integration problems; however, although the underlying integration problem is the same for each application, the existing solution methods are specific to one resource type and not immediately generalizable.

Process integration problems consist of two stages, first, determining the minimum attainable fresh and waste resource flows, and second, designing a resource conservation network that can approach these targets. The focus of this work is the former resource targeting problem. By eliminating the network design step and avoiding simultaneous superstructure approaches that scale poorly with problem size, resource targeting is able to consider resource usage and constraints efficiently when screening and optimizing plant designs.

The simplest class of targeting approaches are graphical pinch analysis and cascade (also

referred to as transshipment) formulations. These approaches are easy to use and physically intuitive, but are applicable to only a limited number of scenarios and are usually unable to solve for process variables. Therefore, they cannot be used to simulate systems with known resource targets or for simultaneous process integration and optimization. To address these limitations for heat integration, Navarro-Amoros et al. (2013) proposed a cascade-type model that uses disjunctions to determine temperature intervals. Alternatively, Duran and Grossmann (1986) developed a "pinch location method," which avoids the construction of temperature intervals by using an optimization formulation with nonsmooth inequalities that is solved using smoothing approximations or as a disjunctive program (Grossmann et al., 1998). However, all of these approaches either require approximations or solving nonconvex MINLPs, and they scale either cubically or quadratically with the number of hot and cold streams in the problem.

To avoid approximations and improve scaling, Watson et al. (2015) reformulated the inequalities in the pinch location method to create a simple system of nonsmooth equations to simulate heat integration systems. In this work, we extend the approach of Watson et al. to develop compact nonsmooth operators that can be applied beyond heat integration to the general integration problem. The result is a solution method that scales well with problem size, requires only equation-solving approaches, and can solve for process variables while simultaneously considering the integration of multiple resources.

2. Problem Statement

Consider a set of resource types under consideration for integration, T . Using the notation for general resource integration presented by Foo (2013), for each resource type $n \in T$, there exists a fresh resource supply, $R_{SR,n}$, and a waste resource flow, $r_{SK,n}$, a set of sources, SR_n , with constant states $S_{i,n}$ that change in quality from $Q_{i,n}^{in}$ to $Q_{i,n}^{out}$, and a set of sinks, SK_n , with states $s_{j,n}$ that change in quality from $q_{j,n}^{in}$ to $q_{j,n}^{out}$. The source and sink states determine the extent to which a resource transfer $R_{i,n}$ or $r_{j,n}$ will affect the quality according to $R_{i,n} = S_{i,n}\Delta Q_{i,n}$ or $r_{j,n} = s_{j,n}\Delta q_{j,n}$ respectively, and the quality is selected such that higher values indicate higher purity resources.

Table 1: State and qualities for common integration types.

Integration Type	Quantity	Quality	State
Heat	heat transfer rate	temperature	heat capacity flow rate
Mass	contaminant mass load flow rate	concentration in reference stream	scaled solvent mass flow rate
Water	water mass flow rate	negative cumulative contaminant mass load flow rate	inverse contaminant concentration, sorted by increasing concentration

The states and qualities for common integration problems are given in Table 1. Note that for mass integration problems, concentrations and flow rates are transformed to their corresponding values in a specified reference stream using equilibrium relations. Additionally, in water allocation problems, the sources and sinks must be sorted by increasing

concentration, and the qualities are the negative of the cumulative contaminant flow rates of the sources or sinks in this order to ensure that high purity water flows have higher quality values.

Given this system, we want to be able to solve the following problem for a selection of unknowns from the vector of process variables, \mathbf{x} , and the $|T|$ vectors of resource utilities, $\mathbf{y}_n = (R_{SR,n}, r_{SK,n})$:

$$\begin{aligned} \mathbf{0} &= \mathbf{h}(\mathbf{x}, \mathbf{y}_1, \dots, \mathbf{y}_{|T|}), \\ \mathbf{y}_n &= \underset{\mathbf{y}_n, R_{1,n}, \dots, R_{K_n-1,n}}{\operatorname{argmin}} R_{SR,n}, \quad \forall n \in T, \\ \text{s.t. } 0 &= R_{SR,n} - R_{1,n} + \sum_{i \in SR_{1,n}} S_{i,n} \Delta Q_{1,n} - \sum_{j \in SK_{1,n}} s_{j,n} \Delta q_{1,n}, \\ 0 &= R_{k-1,n} - R_{k,n} + \sum_{i \in SR_{k,n}} S_{i,n} \Delta Q_{k,n} - \sum_{j \in SK_{k,n}} s_{j,n} \Delta q_{k,n}, \quad \forall k \in \{2, \dots, K_n - 1\}, \\ 0 &= R_{K_n-1,n} - r_{SK,n} + \sum_{i \in SR_{K_n,n}} S_{i,n} \Delta Q_{K_n,n} - \sum_{j \in SK_{K_n,n}} s_{j,n} \Delta q_{K_n,n}, \\ 0 &\leq R_{k,n}, \quad \forall k \in \{1, \dots, K_n - 1\}. \end{aligned}$$

This problem consists of a process model, \mathbf{h} , dependent on resource utilities and process variables, and embedded resource minimization problems parametric in the process variables. These minimization problems are constrained by resource balances and feasibility constraints for resource transfer. While a number of formulations of these constraints have been presented in the literature, for the sake of example, here we use the transshipment formulation of Papoulias and Grossmann (1983), which ensures that resource flows, $R_{k,n}$, are positive from high to low quality between the K_n quality intervals that have quality changes $\Delta Q_{k,n} = \Delta q_{k,n}$.

3. Operator Formulation

Our approach to solving the general integration problem is using explicitly nonsmooth equations to express the solutions of the embedded minimization problems. This formulation results in two equations per resource n in addition to the process model. Neglecting the index n for clarity, these two equations can be written as

$$0 = \sum_{i \in SR} S_i (Q_i^{in} - Q_i^{out}) - \sum_{j \in SK} s_j (q_j^{out} - q_j^{in}) + R_{SR} - r_{SK}, \quad (1)$$

$$0 = \min_{p \in P} \{ RBP_{SK}^p - RBP_{SR}^p \} + r_{SK}, \quad (2)$$

where P is the finite index set of pinch point candidates and

$$\begin{aligned} RBP_{SR}^p &:= \sum_{i \in SR} S_i [\max\{0, Q^p - Q_i^{out}\} - \max\{0, Q^p - Q_i^{in}\} \\ &\quad - \max\{0, Q^{min} - Q^p\} + \max\{0, Q^p - Q^{max}\}], \quad \forall p \in P, \\ RBP_{SK}^p &:= \sum_{j \in SK} s_j [\max\{0, (Q^p - \Delta Q_{min}) - q_j^{in}\} \\ &\quad - \max\{0, (Q^p - \Delta Q_{min}) - q_j^{out}\} + \max\{0, (Q^p - \Delta Q_{min}) - q^{max}\} \\ &\quad - \max\{0, q^{min} - (Q^p - \Delta Q_{min})\}], \quad \forall p \in P, \end{aligned}$$

where $Q^{min,max}$ and $q^{min,max}$ are the minimum and maximum qualities across the sources or the sinks, respectively, ΔQ_{min} is the minimum feasible quality difference for resource transfer to occur, and the source qualities at the potential pinch points are

$$Q^p = \begin{cases} Q_i^{in}, & \forall p = i \in SR, \\ q_j^{in} + \Delta Q_{min}, & \forall p = j \in SK. \end{cases}$$

Here, Equation 1 is the overall resource balance, and Equation 2 is the resource balance below potential resource transfer pinch points. Equation 2 uses a simple nonsmooth expression to ensure that the resource balance is nonnegative below all potential pinch points and zero below at least one of these potential pinch points, i.e. resource transfer is always feasible and at least one pinch point exists to ensure optimality. The expressions for $RBP_{SR,SK}^p$ are the cumulative source and sink resources below the potential pinch point quality. The nonsmooth max terms capture the position of the inlet and outlet qualities of the source or sink in relation to the potential pinch point quality. Nonphysical extensions to the cumulative resource quantities are also included, which avoid additional singular regions or infinite solutions by ensuring the difference between the source and sink resource balances is always defined.

These two equations replace the embedded minimization problem for each resource and we solve the resulting system of equations with a nonsmooth equation solving method such as the semismooth or LP Newton methods (Facchinei et al., 2014). In the past, these methods have been limited by the ability to calculate useful generalized derivative elements automatically. However, using recent work by Khan and Barton (2015), we calculate LD-derivatives using a vector forward mode of automatic differentiation which computes elements of the B-subdifferential for piecewise differentiable functions. Therefore, we are able to automatically compute generalized derivative elements to achieve local quadratic convergence for these nonsmooth equation-solving methods.

4. Example: Dephenolization and recycling of aqueous wastes

Adapting the problem presented by El-Halwagi (2012), we consider an oil recycling facility that uses steam strippers to remove sulfur and other light compounds from the oil streams. The main contaminant of concern in the stripper condensates is phenol, which can be removed through transfer to the oil streams in a MEN. Here, we consider the possibility of reuse of the stripper condensate after dephenolization to reduce both fresh water consumption and wastewater production. We wish to determine the minimum attainable fresh and waste water flow rates as well as the phenol concentrations and water flow rates throughout the system. We require that no external utilities are used in the MEN and that the concentrations of the two stripper condensates are the same when they exit the MEN. We also assume that there are phenol concentration limits in the boilers that limit the inlet concentrations to the strippers and that the mass of phenol transferred in the strippers is constant. (This assumption can be replaced by more complex stripper models if desired.) The parameters for this system are given in Table 2.

To solve this problem, we used two integration operators, one for the allocation of water and one for the mass exchange of phenol. We obtained the sorted mass fractions required to determine the states and qualities for the water allocation problem using a simple bubble sort algorithm. Because this algorithm applies a fixed number of min

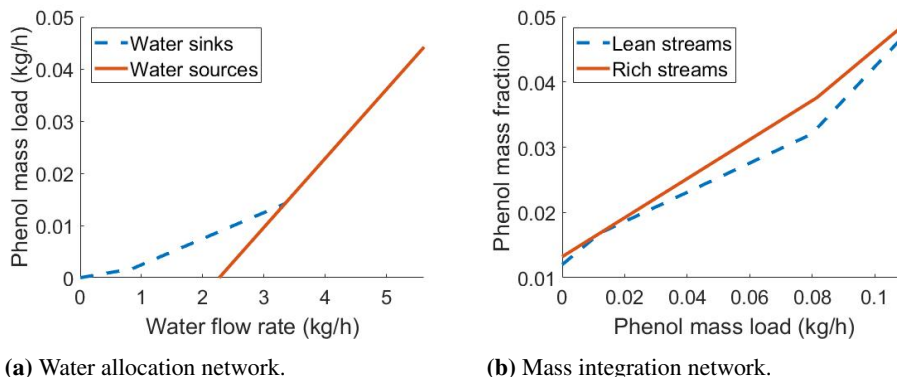
Table 2: System parameters for dephenolization example.

Stream	Flow rate (kg/h)	Inlet mass fraction	Outlet mass fraction
Lube Oil	5	0.005	0.015
Gas Oil	3	0.010	0.030
Stripper 1 steam	2.5	0.005	z_2
Stripper 2 steam	z_1	0.002	z_4
Stripper 1 wastewater	2.50	z_2	z_3
Stripper 2 wastewater	z_1	z_4	z_5
Fresh water	z_6	-	-
Wastewater	z_7	-	-

Stripper 1 mass load: 0.11 kg/h
Stripper 2 mass load: 0.03 kg/h

Equilibrium relation for lube oil: $y = 2.00x_1$
Equilibrium relation for gas oil: $y = 1.53x_2$
Minimum MEN concentration difference: $\varepsilon = 0.001$

and max functions for a given input size, it allows us to automatically calculate LD-derivatives for the sorting process that can be supplied to nonsmooth equation-solving methods (Watson et al., 2015). In addition to the integration operators, we also included process equations describing the constant mass transfer in the strippers and equating the MEN water outlet concentrations. The result was a nonsmooth system of 7 equations which we solved for 7 unknowns using a semismooth Newton method to give $\mathbf{z} = (0.84, 0.049, 0.013, 0.038, 0.013, 2.27, 2.27)$. For a range of initial guesses, the semismooth Newton method quickly converged to the solution in 3 to 9 iterations. The mass and water composite curves for this solution are given in Figure 1 and demonstrate that our solution method produces the optimal pinch behavior.

**Figure 1:** Composite curves for the optimized dephenolization system.

5. Conclusions

We have developed an approach for solving process integration problems using compact, nonsmooth operators. These operators are generalizable to the integration of any resource and can be combined to simultaneously consider multiple resources coupled by a process model. These operators also only require equation-solving methods, can solve for process variables, and are only two equations per resource regardless of the number of sources and sinks in the problem. As a result, we have formulated a readily adaptable approach that significantly reduces problem complexity and can provide computationally tractable solutions to a wide variety of large-scale integration problems.

6. Acknowledgments

We are grateful to the OCP Group for providing financial support for this research and to the Université Mohammed VI Polytechnique - MIT Research Program for supporting and facilitating this collaboration.

References

- J. J. Alves, G. P. Towler, 2002. Analysis of Refinery Hydrogen Distribution Systems. *Industrial Engineering and Chemistry Research* 41, 5759–5769.
- P. A. C. Castillo, V. Mahalec, 2013. Inventory Pinch Algorithm for Gasoline Blend Planning. *AIChE Journal* 59 (10), 3748–3766.
- V. R. Dhole, N. Ramchandani, R. Tainsh, M. Wasilewski, 1996. Make your process water pay for itself. *Chemical Engineering* 103 (1), 100–103.
- M. A. Duran, I. E. Grossmann, 1986. Simultaneous optimization and heat integration of chemical processes. *AIChE Journal* 32 (1), 123–138.
- M. M. El-Halwagi, 2012. *Sustainable Design Through Process Integration*. Elsevier.
- M. M. El-Halwagi, V. Manousiouthakis, 1989. Synthesis of Mass Exchange Nextworks. *AIChE Journal* 35 (8), 1233–1244.
- F. Facchinei, A. Fischer, M. Herrich, 2014. An LP-Newton method: nonsmooth equations, KKT systems, and nonisolated solutions. *Mathematical Programming* 146, 1–36.
- D. C. Y. Foo, 2013. *Process Integration for Resource Conservation*. Taylor & Francis Group.
- I. Grossmann, H. Yeomans, Z. Kravanja, 1998. A rigorous disjunctive optimization model for simultaneous flowsheet optimization and heat integration. *Computers and Chemical Engineering* 22, S157–S164.
- K. A. Khan, P. I. Barton, 2015. A vector forward mode of automatic differentiation for generalized derivative evaluation. *Optimization Methods and Software* 30 (6), 1185–1212.
- B. Linnhoff, J. R. Flower, 1978. Synthesis of heat exchanger networks: I. Systematic generation of energy optimal networks. *AIChE Journal* 24 (4), 633–642.
- S. M. Munir, Z. A. Manan, S. R. W. Alwi, 2012. Holistic carbon planning for industrial parks: a waste-to-resources process integration approach. *Journal of Cleaner Production* 33, 74–85.
- M. A. Navarro-Amoros, J. A. Caballero, R. Ruiz-Femenia, I. E. Grossmann, 2013. An alternative disjunctive optimization model for heat integration with variable temperatures. *Computers and Chemical Engineering* 56, 12–26.
- S. A. Papoulias, I. E. Grossmann, 1983. A structural optimization approach in process synthesis - II: Heat recovery networks. *Computers and Chemical Engineering* 7 (6), 707–721.
- H. A. J. Watson, K. A. Khan, P. I. Barton, 2015. Multistream heat exchanger modeling and design. *AIChE Journal* 61 (10), 3390–3403.

Analysis of Process Alternatives for Energy-Efficient Bioethanol Downstream Processing

Dinis S. Nunes^a, José F.O. Granjo^{a*}, Belmiro P.M. Duarte^{a,b} and Nuno M.C. Oliveira^a

^a*CIEPQPF, Department of Chemical Engineering, University of Coimbra, Rua Sílvio Lima — Polo II, 3030-790 Coimbra, Portugal*

^b*Coimbra Polytechnic-ISEC, Dept. Chemical & Biological Engineering, Portugal*
josegranjo@eq.uc.pt

Abstract

This work addresses the production of gasohol using gasoline as a separation agent, an alternative approach to processes that recover and dehydrate ethanol before its blending with gasoline. Experimental data was used to build the thermodynamic model used to predict phase equilibrium and thermophysical properties. Two configurations for the direct manufacture of E10 gasohol were analyzed. Process I is extraction-based whereas Process II is extractive distillation-based. The processes were compared with each other in terms of energy needs as well as with a state-of-art process where ethanol dehydration is performed with molecular sieves (Process MS). The results show that Processes I and II are energetically favorable, and consume, after process optimization and heat integration, 30% less heat than Process MS, for ethanol concentrations in fermentation broths between 2 and 10 wt%. Furthermore, estimated ethanol separation costs are approximately \$0.19/kg-ethanol for a 5 wt% feed.

Keywords: Ethanol separation; Gasohol direct production; Process design; Heat integration; Techno-economic analysis

1. Introduction

The pursuit of alternative sources of energy prompted global research and industrial developments of biofuels. Ethanol (produced from diverse sources) falls into this class and is typically marketed in blends with gasoline (as gasohol) for road transport vehicles. The downstream processing of fuel-grade ethanol involves the removal of the solids fraction and secondary products from the broth, followed by concentration and dehydration to prevent phase separation in fuel systems. This step is energy-intensive because of the need of separating the water, and challenging by the existence of a binary azeotrope in the ethanol/water mixture which hinders the economic performance of the process.

Several separation systems are described in literature for the recovery and dehydration of ethanol, including pressure-swing distillation (Black, 1980), liquid-liquid extraction (Neves et al., 2011), salt-effect distillation (Zeng and Li, 2015), and azeotropic, extractive and dividing-wall distillation operations (Singh and Rangaiah, 2017). Kubička et al. (2013) describes an arrangement coupling a distillation pre-concentration step followed by molecular sieves, which adsorb the reminiscent water out of ethanol with great energy efficiency. Configurations including membrane separation units (e.g., pervaporation, vapor permeation) for water removal in the vicinity of azeotrope mixture after a previous ethanol concentration step were also successfully implemented (Vane, 2008).

All the aforementioned configurations have a common feature. They are designed to produce anhydrous ethanol. However, this approach may be economically sub-optimal if the product is to be marketed as a blend with gasoline rather a pure fuel or chemical. Another option is to consider hydrocarbon streams to be incorporated from diverse sources in ethanol separation systems, or simply pre-blending gasoline with ethanol on-site. Potential opportunities for heat and process integration could arise, besides the utilization of hydrocarbon cuts as solvents for water elimination.

Schemes for the direct production of gasohol were developed in previous contributions wherein gasoline fractions work as solvents in extraction columns where the final product is obtained from a concentrated aqueous solution of ethanol (Kyle, 1981; Stacey et al., 2016) or as entrainers in extractive distillation systems (Black, 1980; Chianese and Zinamosca, 1990). Estimates indicate achievable energy savings of 17–68% for both methods compared with classical azeotropic distillation methods. Nevertheless, no rigorous process simulation is provided to quantify in detail the operating conditions, materials and energy requirements (Stacey et al., 2016); besides the process optimization and heat integration were not addressed (Black, 1980; Kyle, 1981; Chianese and Zinamosca, 1990). Noticeably, a techno-economical analysis of processes that incorporate gasoline fractions in ethanol separation can benefit potential users and complement existing references.

Consequently, this work examines the production of gasohol using gasoline as a separating agent, focusing on techno-economic aspects involving different process designs and comparing their performance to the benchmark. We developed a modeling framework to describe accurately phase equilibria and thermophysical properties of mixtures (Section 2). Subsequently, two main configurations were simulated in Aspen Plus[®], analyzed at base case conditions (i.e., close to the ones reported in the literature). Specifically, they are compared against each other and with a benchmark alternative – Process MS – regarding the energy consumption for achieving ethanol concentrations in broth in 2–10 wt% (Section 3). Next, process optimization and pinch analysis were carried out to estimate the minimum energy needs for both processes (Section 4). Moreover, heat exchanger networks (HENs) were also optimally designed for minimum total cost using systematic strategies, with the ethanol production cost estimated and compared with those reported in literature. Finally, the paper closes in Section 5 with a summary of the main findings.

2. Modeling framework

The scope of analysis is the separation of ethanol, where a simplified broth composition is assumed, i.e., the secondary products and solids were previously removed. Therefore, the components in the stream are water, ethanol, and gasoline. The latter may be modeled as an assay with different cuts of hypothetical components or as a single hypothetical component, with the pure and mixing thermophysical parameters estimated from petroleum distillation-curves. However, classical equations-of-state are usually inadequate to describe liquid phase non-idealities of mixtures containing polar components, like water and ethanol (Carlson, 1996). Consequently, gasoline was considered as a single pseudo-component, wherein pure thermophysical properties are estimated using a distillation-curve ASTM D86 presented in Andersen et al. (2010) and the API methods (Aspentech, Inc., 2016). Phase equilibrium is modeled considering the vapor as an ideal gas and non-ideality in liquid phase is modeled with NRTL model (Renon and Prausnitz, 1968).

2.1. Data regression

The binary interaction parameters of NRTL model were fitted to an experimental data set collected from several works containing 40 tie-lines of the ternary water-ethanol-gasoline system, plus 23 points of VLE and 9 of excess molar enthalpy for the binary ethanol-gasoline. The fitting strategy followed here is similar to that in Granjo et al. (2014), where data points were weighted uniformly and phase stability conditions were explicitly included in the mathematical formulation. Regression results show a good agreement between experiments and model predictions, since the global

Table 1: NRTL parameters for water(1)-ethanol(2)-gasoline(3). $\tau_{ij} = a_{ij} + b_{ij}/T$, $\alpha_{ij} = \alpha_{ji}$.

i	j	a_{ij}	a_{ji}	b_{ij}/K	b_{ji}/K	α_{ij}
1	2 [†]	3.8173	-1.3047	-263.33	-0.62597	0.10000
1	3	17.881	9.0361	-2773.7	-1495.0	0.24115
2	3	-0.20257	-0.27569	515.11	722.30	0.4837

[†]1-2 pair fixed. Values from NISTV100 NIST-IG database (Aspentech, Inc., 2016).

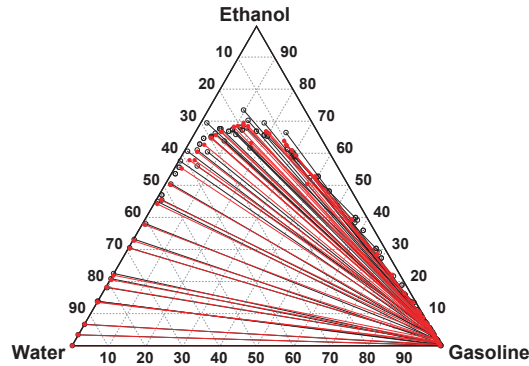


Figure 1: Experimental (black, empty) and predicted (red, filled) tie-lines (wt %).

average relative deviation (ARD) is 5.3% with an ARD of 0.7% in tie-line predictions (check Figure 1).

3. Process simulation & benchmark

Two processes described in literature are used for benchmark. In Process I, the broth stream is pre-concentrated up to the vicinity of the azeotropic concentration (~ 90 wt% ethanol), and then fed to an extraction column, with the gasohol leaving the extract while raffinate goes to a gasoline recovery distillation column (Kyle, 1981). Process II is similar to Process I, but the extraction column is replaced by an extractive distillation arrangement where the product leaves in the bottoms and the distillate is decanted (Black, 1980). Processes I and II are represented in Figure 2 and Figure 3, respectively. To assess the thermal efficiency, energy requirements of Processes I and II were estimated for ethanol concentrations in feed within 2–10 wt%. It was considered a continuous processing plant with an hourly capacity of approximately 2 tonnes of ethanol (dry mass) and 8322 h/y of operation.

For a comparative analysis, energy needs were calculated for a liquid saturated feed with 2–10 wt% ethanol and (i) a *Single Column* system comprising an ethanol/water distillation column operating at 1 atm, with total condenser and producing a distillate with 93.5 wt% ethanol; (ii) a *Double Column* system consisting on a stripping column followed by a concentration distillation column (with total condenser), both at 1 atm and producing a distillate with 93.5 wt% ethanol; and (iii) Process MS involving a dehydration step with molecular sieves preceded by a double-column distillation system. The total number of stages (NT) and the feed stage (NF) in D101 and D102 were estimated with the approximate methods of Fenske-Underwood-Gilliland, whereas the reboiler duties and reflux ratio were optimized to find the minimum energy consumption. NT_{D101} and NF_{D101} in Single Column/Process I are 30 and 12, respectively. NT_{D101} , NT_{D102} , and NF_{D102} in Double Column/Process II/Process MS are 26, 34, and 20, respectively. The operating conditions of D102 and the extraction column in Figure 2 are similar to the ones in Kyle

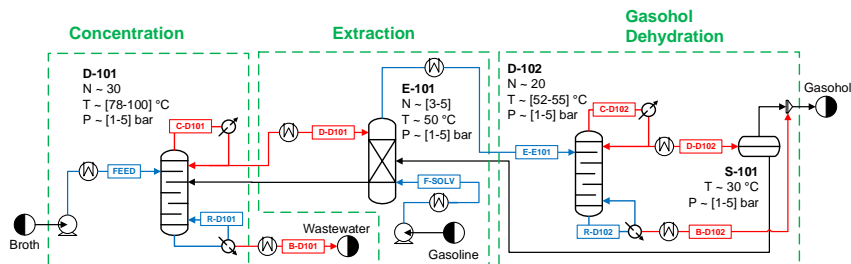


Figure 2: Process flowsheet diagram of Process I.

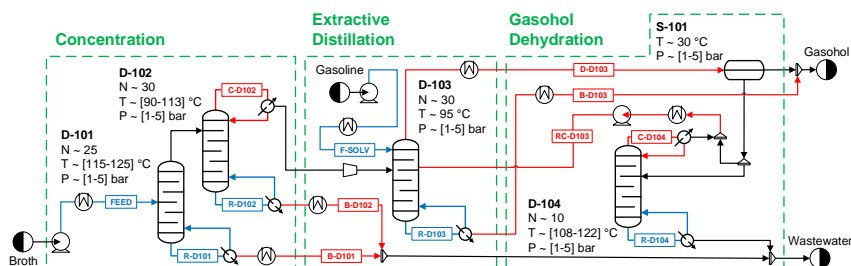


Figure 3: Process flowsheet diagram of Process II.

(1981), whereas the conditions D103 and D104 of Figure 3 are similar to the ones reported in Black (1980).

Figure 4 shows that Processes I and II are energy-efficient, since their heat duties to produce E10 gasohol at base case conditions are, respectively, within 5.1–14.1 MJ-heat/kg-ethanol and 4.8–13.8 MJ-heat/kg-ethanol for ethanol concentrations in feed between 10 wt% and 2 wt%. This means that Process I requires on average 0.9 MJ-heat/kg-ethanol of heat to produce E10 gasohol from near-azeotropic composition, while Process II needs about 1.6 MJ-heat/kg-ethanol. These figures are competitive with those reported in Singh and Rangaiah (2017) considering other technologies (0.7–5.1 MJ-heat/kg-ethanol). Both processes also compare well with Process MS, since molecular sieves are reported to spend 1–2 MJ-heat/kg-ethanol to produce 99.5 wt% ethanol from ethanol/water azeotropic distillates (Vane, 2008).

4. Process optimization and heat integration

Once the performance of Processes I and II at base case conditions were found, the goal is to determine the operating conditions that minimize the total hot utilities consumption. For such a purpose a mathematical program was formulated and then solved in Aspen Plus® V10 using BOBYQA (Powell, 2009), where reboiler duties and reflux ratios of all distillation columns in Processes I and II were optimized to minimize energy consumption. The total number of stages, feed stages and operating pressures remain fixed. Afterwards, pinch analysis was carried out with ASPEN Energy Analyzer to find the theoretical minimum energy usage for both processes with $\Delta T_{\min} = 10^\circ\text{C}$. Dashed lines in Figure 4 show that modifications in operating conditions and heat integration can significantly reduce the energy needs of Processes I and II to 3.8–14.0 MJ-heat/kg-ethanol and 3.5–12.2 MJ-heat/kg-ethanol, respectively, for ethanol concentrations in broth between 10 wt% and 2 wt% which represent energy savings up to 30% compared to Process MS. Practically, the lower energy consumptions are due to (i) the reduction in heat requirements for solvent recovery; and (ii) the heat integration between the pre-concentration distillation columns and the gasoline

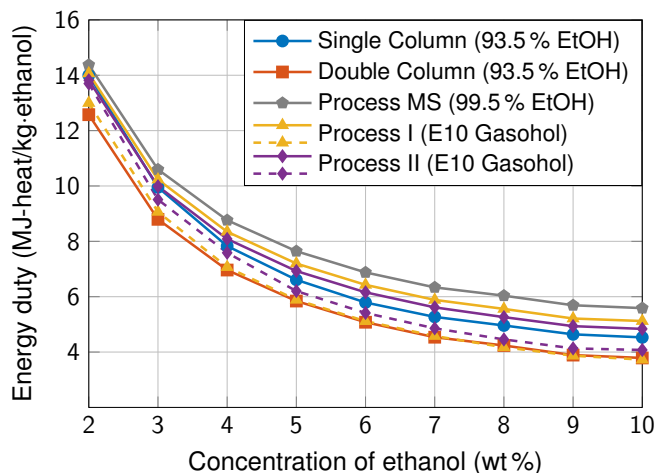


Figure 4: Energy duty vs. ethanol concentration in feed for the various process configurations. Dashed lines represent the Processes I and II optimized for minimum energy requirements.

recovery/extractive distillation columns.

4.1. HEN optimal design and ethanol production cost

Now we consider the plant capacity and the optimal operating conditions obtained before, and design optimal HENs for both processes. A concentration of 5 wt% of ethanol in the broth is used for demonstration. The optimal design of HENs for minimum total cost was determined with Aspen Energy Analyzer, which uses a sequential procedure where superstructures similar to those proposed by Yee et al. (1990) are built and solved as MILP problems to provide feasible HENs satisfying the heat load distributions. Finally, ethanol production cost was estimated from capital and manufacturing costs for a 15 years life plant. Figure 5 shows the optimal HEN found for Process I. It is observed that the overhead vapor and the bottom streams of D-101 (respectively, C-D101 and B-D101) are the main heat sinks and are used to heat the feeding stream, pre-heat the solvent and in the reboiler of D-102. Regarding the production costs, Processes I and II have similar figures (respectively, \$0.17/kg-ethanol and \$0.19/kg-ethanol) and they are in the lower decile of the costs range indicated by Singh and Rangaiah (2017), i.e. \$0.03–3.65/kg-ethanol. However, a fair comparison in this case is hard due to the different concentrations of ethanol in the fermentation broths and the set of assumptions used in techno-economic analyzes.

5. Conclusions

This contribution addresses the direct production of gasohol where gasoline is employed as separating agent. It is demonstrated that Processes I and II are energetically favorable relatively to Process MS, especially after optimization and heat integration. Specifically, total energy savings can reach up to 30% for ethanol concentrations in feed within 2–10 wt%. The results show that these alternative processes can be very competitive (production costs ca. \$0.19/kg-ethanol) when gasoline can blend on ethanol production site or the integration with a petrochemical plant is possible. The capital costs involved are potentially low as the retrofitting of existing distillation facilities would require a limited number of modifications. Future works may include the simultaneous optimization and heat integration of multi-effect and/or dividing-wall distillation systems seeking for further decrease of energy and capital costs.

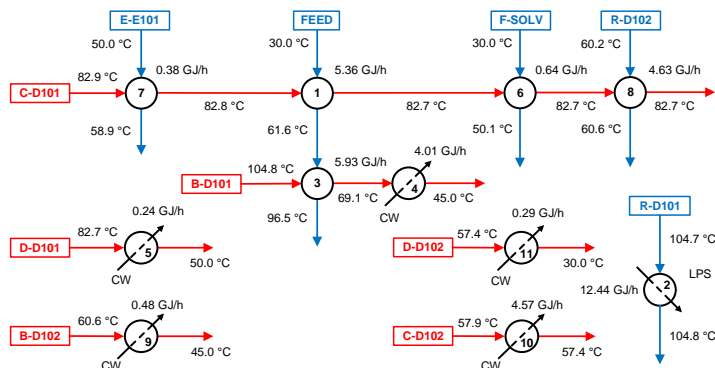


Figure 5: Heat exchanger network of Process I. (CW) cooling water. (LPS) low pressure steam.

6. Acknowledgments

This work was carried out under the Project *inactus* – innovative products and technologies from eucalyptus, Project N. ° 21874 funded by Portugal 2020 through European Regional Development Fund (ERDF) in the frame of COMPETE 2020 n°246/AXIS II/2017 for the post-doctoral grant of José F.O. Granjo and under the Project “MultiBiorefinery - Multi-purpose strategies for broadband agro-forest and fisheries by-products valorisation: a step forward for a truly integrated biorefinery” (POCI-01-0145-FEDER-016403) for the research grant of Dinis S. Nunes.

References

- V. F. Andersen, J. E. Anderson, T. J. Wallington, S. A. Mueller, O. J. Nielsen, 2010. Distillation Curves for Alcohol–Gasoline Blends. *Energy Fuels* 24 (4), 2683–2691.
- Aspentech, Inc., 2016. Aspen physical property system V9, Bedford, MA, USA.
- C. Black, 1980. Distillation modeling of ethanol recovery and dehydration process for ethanol and gasohol. *Chem Engng Prog* 76 (9), 78–85.
- E. C. Carlson, 1996. Don't gamble with physical properties for simulations. *Chem Engng Prog* 92 (10), 35–46.
- A. Chianese, F. Zinamosca, 1990. Ethanol dehydration by azeotropic distillation with a mixed-solvent entrainer. *Chem Eng J* 43 (2), 59–65.
- J. Granjo, N. Oliveira, J. Coutinho, 2014. Systematic parameter estimation for equilibria data with thermodynamic consistency metrics and phase stability. In: *CHEMPOR 2014*, September 10-12th, Porto, Portugal.
- D. Kubička, I. Kubičková, J. Čejka, 2013. Application of molecular sieves in transformations of biomass and biomass-derived feedstocks. *Catalysis Reviews* 55 (1), 1–78.
- B. G. Kyle, 1981. Low energy process of producing gasoline-ethanol mixtures, U.S. Patent 4297172 A.
- C. M. Neves, J. F. Granjo, M. G. Freire, A. Robertson, N. M. Oliveira, J. A. Coutinho, 2011. Separation of ethanol–water mixtures by liquid–liquid extraction using phosphonium-based ionic liquids. *Green Chem* 13 (6), 1517–1526.
- M. J. D. Powell, 2009. The BOBYQA algorithm for bound constrained optimization without derivatives. Tech. Rep. DAMTP 2009/NA06, Department of Applied Mathematics and Theoretical Physics, Cambridge University.
- H. Renon, J. M. Prausnitz, 1968. Local compositions in thermodynamic excess functions for liquid mixtures. *AIChE J* 14 (1), 135–144.
- A. Singh, G. P. Rangaiah, 2017. Review of technological advances in bioethanol recovery and dehydration. *Ind Eng Chem Res* 56 (18), 5147–5163.
- N. T. Stacey, A. Hadjitheodorou, D. Glasser, 2016. Gasoline preblending for energy-efficient bioethanol recovery. *Energy Fuels* 30 (10), 8286–8291.
- L. M. Vane, 2008. Separation technologies for the recovery and dehydration of alcohols from fermentation broths. *Biofuels*, *Bioprod Biorefin* 2 (6), 553–588.
- T. F. Yee, I. E. Grossmann, Z. Kravanja, 1990. Simultaneous optimization models for heat integration — I. Area and energy targeting and modeling of multi-stream exchangers. *Comput Chem Eng* 14 (10), 1151–1164.
- L. Zeng, Z. Li, 2015. A new process for fuel ethanol dehydration based on modeling the phase equilibria of the anhydrous $MgCl_2$ + ethanol + water system. *AIChE J* 61 (2), 664–676.

An Efficient MILP-Based Decomposition Strategy for Solving Large-Scale Scheduling Problems in the Offshore Oil and Gas Industry

Natalia P. Basán,^a Mariana E. Cóccola,^a Alejandro García del Valle,^b Carlos A. Méndez^{a,*}

^a*INTEC (UNL – CONICET), Güemes 3450, Santa Fe, 3000, Argentina*

^b*University of A Coruña, C/ Mendizábal s/n, Ferrol, 15403, Spain*

cmendez@intec.unl.edu.ar

Abstract

This paper presents a MILP-based decomposition algorithm for solving large-scale scheduling problems with assembly operations in flexible flow shop environments. First, a rigorous mixed-integer linear (MILP) formulation based on the general precedence notion is developed for the problem under study. Then, the MILP model is embedded within a decomposition algorithm in order to accelerate the resolution of large-size industrial problems. Finally, the proposed solution approach is tested on several examples derived from a real-world case study arising in a company that builds vessels for the offshore oil and gas industry.

Keywords: flexible flow shop, scheduling problem, assembly operations, MILP model, decomposition strategy.

1. Introduction

The flexible flow shop scheduling problem (FFSP) is a generalization of the classical flow shop problem (FSP), wherein all products follow the same flow processing line but all of them may not visit all processing stages. When some stage on the line performs an assembly operation, the problem is known as FFSP-A. Generally, the objective is to minimize the completion time of all products (makespan). This type of scheduling problem appears in many industrial applications such as automotive industry, paint companies, and shipbuilding industry, between others.

The FFSP-A is strongly NP-hard (Pinedo, 2016). Consequently, real-world industrial problems lead to intractable model sizes when rigorous mathematical formulations are used. To overcome this drawback, this work presents a decomposition algorithm that allows finding high quality solutions with low computational effort even for large-size instances. The decomposition approach first obtains a good schedule (constructive stage), by using an insertion method, and then improves it (improvement stage) by executing partial rescheduling actions. All decisions in the iterative procedure are taken by solving a MILP model featuring a reduced search space. Specifically, the mathematical formulation used in this paper was developed applying the general precedence notion, but other alternative approaches can be considered too. The applicability and efficiency of the solution strategy is tested by solving a challenging real-world problem dealing with the construction of a ship for the development of marine resources, specifically for the offshore oil and gas industry.

2. Mathematical formulation

The FFSP-A problem consists of a set of products $i \in I$ ($i = 1, 2, \dots, |I|$) processed through several consecutive operation stages $s \in S$ ($s = 1, 2, \dots, |S|$) with parallel identical units $k \in K_s$ working in parallel at each stage s . The subset S_i identifies all stages processing product i , while the parts $i' \in I$ that integrates a product i are defined by the subset SA_i . The subset $S^a \subseteq S$ contains all stages performing assembly operations. The final products obtained on the line are identified by subset I^f ($I^f \subset I$). Either the non-intermediate storage (NIS) policy or the unlimited intermediate storage (UIS) policy between stages can be adopted. When a NIS strategy is used, each processing unit becomes intermediate storage if its processing has finished and the next step is not available yet.

The problem constraints can be mathematically modelled using any of the continuous-time formulations that have been published in the literature for the short-term scheduling of multistage batch plants (Méndez, Henning and Cerdá, 2001). Particularly, the MILP model developed in this work and presented follow is based on the general precedence notion. It is worth to remark that some changes have been incorporated to the original proposal in order to consider the assembly operations. As shown Eq. (1), the main goal is to minimize the total time required to obtain the final products.

$$\text{minimize } MK \quad (1)$$

$$\sum_{k \in K_s} Y_{ik} = 1 \quad \forall i \in I, s \in S_i \quad (2)$$

$$Tf_{is} \geq Ts_{is} + tp_{is} \quad \forall i \in I, s \in S_i \quad (3)$$

$$Ts_{is} = Tf_{i(s-1)} \quad \forall i \in I, s \in S_i, (s-1) \in S_i, s > 1 \quad (4a)$$

$$Ts_{is} \geq Tf_{i(s-1)} \quad \forall i \in I, s \in S_i, (s-1) \in S_i, s > 1 \quad (4b)$$

$$Ts_{is} \geq Tf_{i'(s-1)} \quad \forall i \in I, i' \in SA_i, s \in S^a, s \in S_i, (s-1) \in S_{i'} \quad (5)$$

$$Ts_{i's} \geq Tf_{is} - M(1 - W_{ii's}) - M(2 - Y_{ik} - Y_{i'k}) \quad (6)$$

$$\forall i \in I, i' \in I, s \in S_i, s \in S_{i'}, k \in K_s, i < i'$$

$$Ts_{is} \geq Tf_{i's} - MW_{ii's} - M(2 - Y_{ik} - Y_{i'k}) \quad (7)$$

$$\forall i \in I, i' \in I, s \in S_i, s \in S_{i'}, k \in K_s, i < i'$$

$$MK \geq Tf_{is} \quad \forall i \in I, s \in S_i: s = |S| \quad (8)$$

Eq. (2) defines the allocation constraint. Binary variable Y_{ik} takes 1 as value when product i is processed in unit k ; otherwise, it is set to zero. Eq. (3) computes the ending

time Tf_{is} of product i at stage s as its starting time Ts_{is} plus the associated processing time pt_{is} . The storage police between two consecutive stages is represented by Eq. (4a) for NIS or Eq. (4b) for UIS. Constraint (5) determines that the assembly of a product i in stage $s \in S^a$, with $s \in S_i$, must begin after its associated sub-assemblies $i' \in SA_i$ have completed their processing in the previous stage. Eqs. (6) and (7) define the sequencing constraints on a same unit k . Binary variable $W_{ii's}$ is the general precedence variable in stage s . Finally, Eq. (8) states a lower bound for the variable MK to be minimized.

3. The MILP-based decomposition algorithm

The computational efficiency of the full space approach presented in the above section or any other rigorous formulation is rapidly deteriorated when increasing the problem size. For industrial applications, the solvers report solutions with a high GAP after several CPU hours. This weakness can be overcome by solving the mathematical model several times but considering a reduced search space at each iteration. Even though this solution strategy does not guarantee the optimality of the solution found, it allows reporting practical solutions with reasonable computational time.

The decomposition method presented here is based on the strategy of first obtaining an initial solution (*constructive stage*), to then gradually enhance it by applying several rescheduling iterations (*improvement stage*). Both algorithmic stages have as core the general precedence MILP model presented previously. At this point, it is worth mentioning that other alternative mathematical formulations (Méndez *et al.*, 2006) may also be easily adapted to the proposed decomposition strategy.

The general structure of the algorithm is given in Figure 1. Note that a feasible initial scheduling solution is obtained from inserting order by order in the constructive stage. Then, an iterative enhancement-based technique is used to improve the current solution. The assignment and sequencing decisions are left free only for the product that is being rescheduled in each improvement iteration, which significantly reduces the optimization search space. When no improvements are obtained for the objective function, the current solution is reported as the best solution for the problem under study.

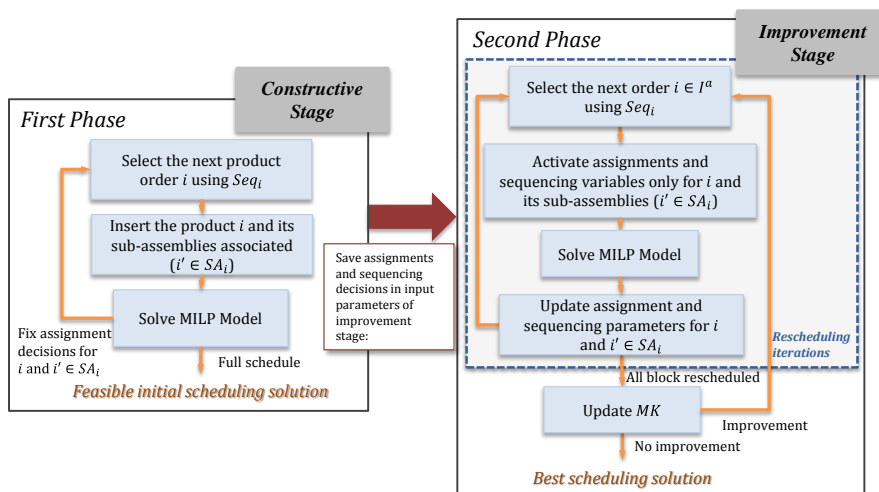


Figure 1: Overview of the iterative MILP-based algorithm.

3.1. First phase: Constructive step

The first phase of decomposition algorithm aims at generating an initial full schedule with low computational effort. The constructive method is based on the insertion technique presented by Kopanos et al. (2010) for solving large-scale pharmaceutical scheduling problems. These authors propose to insert (schedule) the products one-by-one in an iterative mode. As the FFSP-A problem includes assembly operations, it is needed that a product $i \in I^f$ and its sub-assemblies $i' \in SA_i$ will be inserted and scheduled at each iteration. Every time the MILP model (1)-(8) is solved, the binary variables Y_{ik} and $W_{ii's}$ for the new products scheduled are fixed at their optimal values.

One key point to consider in the constructive stage is to define the order in which the products will be inserted. The insertion criterion should be determined according to the problem features (Roslöf et al., 2001, 2002), for example, it can follow the lexicographic order or is based on a specific sequence. The aim should always be to find a good initial scheduling solution in a short computational time.

The constructive stage procedure ends when all products have been scheduled. Next, the initial solution is sent to the next algorithmic phase (improvement stage) using the parameters sY_{ik} and $sW_{ii's}$, which indicate the assignment and sequencing decisions taken by the constructive stage.

3.2. Second phase: Improvement step

Taking as starting point the assignments sY_{ik} and sequencing decisions $sW_{ii's}$ obtained as initial solution in the constructive step, this second phase applies the strategy of rescheduling each product $i \in I$ in a sequential way to try to improve the current solution. In other words, reassignment and reordering decisions are iteratively taken for each product i and its sub-assemblies $i' \in SA_i$. The improvement stage is executed sequentially until no improvement can be achieved to the makespan.

A boolean parameter $active_i$ is used for determining the subset of products i that can be rescheduled at each iteration. Thus, the MILP formulation (1)-(8) will active only the binary variables Y_{ik} and $W_{ii's}$ for products i with $active_i = true$. For other products, only timing decisions can be made. Reassignment to other units is not allowed for products with parameter $active_i$ set to false. Furthermore, their relative position in the processing sequence remains unchanged. This decomposition strategy allows reducing the number of binary variables of the mathematical formulation with regards to the full space approach, reducing drastically the CPU time needed to solve the model. Note that solving the full space approach is equivalent to set $active_i = true \forall i \in I$.

Every time a rescheduling action is executed, the current solution is updated. Once the rescheduling step was applied for all products, the procedure checks the makespan achieved. If the solution found is better than the best solution obtained until that moment, the algorithm updates the makespan and goes to execute the improvement step for all products again. Otherwise, the algorithm ends and reports the current solution as the best solution found for the problem under study.

4. Computational results

The MILP-decomposition algorithm is applied for the solution of a complex case study arising in a shipbuilding company, which constructs ships for the development of

marine resources, specifically for the offshore oil and gas industry. This real-world FFSP-A problem involves 7 processing stages, each one with K_s processing units working in parallel, as is shown in Figure 2. A ship is built using dozens of blocks of specific size. A block is the largest construction unit of a ship. In turn, each block is assembled from one or more sub-blocks, which are composed of steel plates according to the design drawing for the ship. Both blocks and sub-blocks are considered intermediate products in the ship, which contains other components such as pipes, supports, and electronic equipment. From Figure 2, it follows that stage s_1 - s_2 process sub-blocks, which are then assembled in stage s_3 to form the block. The last processing stages on the line (s_4 - s_6) perform operations on the blocks, which are finally transported and positioned in a dry dock (*stage* s_7) for assembling the ship. Note that this manufacturing process includes two assembly stages: in the first one, each block is constructed by one or more sub-blocks while in the second one the mounting of these blocks is carried out to build the ship.

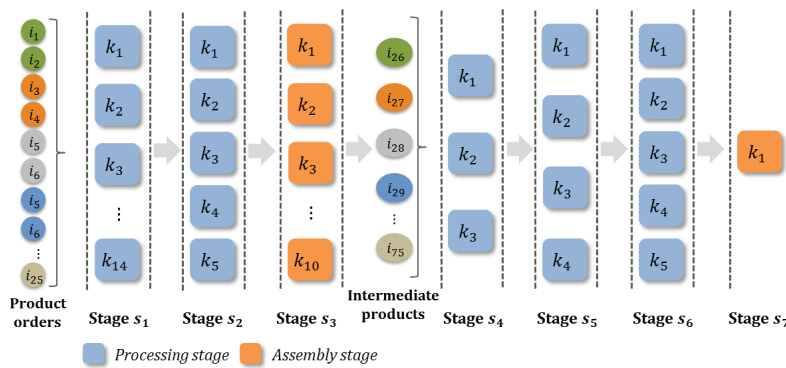


Figure 2: FFSP-A process – case study.

From the original case study, 10 problem instances were derived in order to test the computational performance of the decomposition algorithm when facing different problem sizes. Alternative storage policies, UIS and NIS, were considered for each problem size. Moreover, it is assumed that the blocks are formed by two sub-blocks. All experimental studies were implemented in GAMS 24.9.2 with CPLEX 12.6.3.0 as MIP solver and run on a PC with four-core Intel Xeon X5650 Processor (2.6 GHz). Besides, the termination criterion imposed for the solution of all problem instances has been either 0 % optimality gap or 3600 sec of CPU time.

Table 1 presents a comparison of both the results reported by MILP model and those reached by the decomposition algorithm. The expression $N \times M$ refers to a ship constructed with N blocks and M sub-blocks. The smallest problem addressed involves 10 sub-blocks and 5 blocks, while the biggest one deals with a ship built with 50 sub-blocks and 25 blocks. From Table 1, it follows that when the amount of blocks exceeds the number of 5, the full space approach does not find the optimal solution within the time limit specified, reporting a high integrality GAP for all examples. Instead, near-optimal solutions, sometimes the optimal one, are found by the solution strategy for all problem instances in few seconds of CPU time. For the more complex instance, P.10, the algorithm finds a solution of 270.5 days after 56.6 seconds, reaching an improvement of 16.5% with regards to the solution reported by the MILP model after 3600 seconds of CPU time.

Table 1: Comparison between exact MILP formulation and MILP-based algorithm statistic.

Problem	Size $N \times M$	Storage policy	MILP Model			MILP-based strategy			Enhanced solution (%)
			MILP solution	GAP (%)	CPU Time (s)	Initial solution	Best solution	Total CPU (s)	
P.01	5×10	UIS	126.3	0	2.3	144.0	126.3	2.3	0
P.02	5×10	NIS	126.3	0	2.2	144.4	126.3	2.1	0
P.03	10×20	UIS	160.1	12.7	3600	176.3	162.9	11.1	-1.7
P.04	10×20	NIS	161.4	13.4	3600	177.9	167.8	6.8	-3.8
P.05	15×30	UIS	207.0	25.9	3600	239.1	205.8	16.3	0.6
P.06	15×30	NIS	210.6	27.2	3600	241.9	206.5	24.1	1.9
P.07	20×40	UIS	231.1	27.8	3600	248.8	221.0	37.6	4.4
P.08	20×40	NIS	240.2	30.6	3600	255.4	228.6	41.2	4.8
P.09	25×50	UIS	287.8	37.3	3600	301.1	262.8	49.8	8.7
P.10	25×50	NIS	323.8	44.3	3600	298.3	270.5	56.6	16.5

5. Conclusions

A MILP-based iterative solution algorithm for solving industrial-scale FFSP-A problems has been presented in this work. The procedure was based on a MILP scheduling formulation rely on the general precedence notion. The performance of the proposed methodology has been deeply evaluated by solving several instances derived from a real-world case of study. Computational results showed that high-quality solutions can be efficiently found by the algorithm in short computational time, outperforming the rigorous optimization approach.

References

- Kopanos G. M., Méndez C. A., Puigjaner L., 2010, MIP-based decomposition strategies for large-scale scheduling problems in multiproduct multistage batch plants: A benchmark scheduling problem of the pharmaceutical industry, *European Journal of Operational Research*, 207(2), 644–655.
- Méndez C. A., Cerdá J., Grossmann I.E., Harjunkski I., Fahl, M., 2006, State-of-the-art review of optimization methods for short-term scheduling of batch processes, *Computers and Chemical Engineering*, 30(6–7), 913–946.
- Méndez C. A., Henning G. P., Cerdá J., 2001, An MILP continuous-time approach to short-term scheduling of resource-constrained multistage flowshop batch facilities, *Computers & Chemical Engineering*, 25(4–6), 701–711.
- Pinedo M. L., 2016, *Scheduling: Theory, Algorithms, and Systems*. Fifth Edit, Scheduling: Theory, Algorithms, and Systems. Fifth Edit. New York: Springer.
- Roslöf J., Harjunkski I., Björkqvist J., Karlsson S., Westerlund T., , 2001, An MILP-based reordering algorithm for complex industrial scheduling and rescheduling, *Computers & Chemical Engineering*, 25(4–6), 821–828.
- Roslöf J., Harjunkski I., Westerlund T., Isaksson J., 2002, Solving a large-scale industrial scheduling problem using MILP combined with a heuristic procedure, *European Journal of Operational Research*, 138(1), 29–42.

A Blockchain Framework for Containerized Food Supply Chains

Dimitrios Bechtsis,^{a,d,e*} Naoum Tsolakis,^{a,b} Apostolos Bizakis,^{a,c} Dimitrios Vlachos^{a,c}

^a*Laboratory of Statistics and Quantitative Analysis Methods, Industrial Management Division, Department of Mechanical Engineering, AUTH, Greece*

^b*Centre for International Manufacturing, Institute for Manufacturing, Department of Engineering, School of Technology, University of Cambridge, United Kingdom*

^c*TREDIT SA Engineering/Consulting, Thessaloniki, Greece*

^d*Department of Automation Engineering, Alexander Technological Educational Institute of Thessaloniki, Greece*

^e*Center for Interdisciplinary Research and Innovation (CIRI-AUTH), Balkan Center, Buildings A & B, Thessaloniki, Greece.*

dimbec@autom.teithe.gr

Abstract

Global agricultural trade flows demonstrated a three-fold growth during the past decade particularly in emerging economies. At the same time, global food scandals in conjunction with the spillover effects in economy and society highlight the unreliability of existing food tracking systems and the inefficiency in monitoring food quality and fraud incidents across global food supply chains (SCs). Blockchain technology (BCT), which has already been successfully applied on the financial industry to validate critical transactions, seems to be a promising option. This research investigates a two-stage containerized food SC by implementing a demonstrator application at the Hyperledger Fabric framework. The study findings indicate that on one hand BCT has entered its maturity phase while on the other hand its adoption in food SC operations could add significant value by authenticating critical parameters and providing enhanced traceability. At the same time, BCT enabled by other digital technologies could allow for the optimization of global food SCs. Thus, BCT constitutes a promising digital technology that provides the capability to food SC stakeholders to securely share information, enhance process control and traceability and prevent potential risks.

Keywords: container handling, food supply chain, blockchain, traceability.

1. Introduction

Global agricultural trade flows are valued at about USD 1.7 trillion annually (FAO, 2017), demonstrating a three-fold growth during the past decade, particularly in emerging economies. At the same time, wastage/losses of perishable products along with global food scandals and in conjunction with associated spillover effects in economy and society, highlight the unreliability of existing food tracking systems and the inefficiency in monitoring food quality and fraud incidents across farm-to-fork food supply chains (SCs). To that end, blockchain constitutes a promising digital technology

that provides food SC stakeholders the capability to securely share information and prevent potential risks. To this effect, the financial technology (FinTech) industry provides solutions, such as the blockchain technology (BCT), that could (Christidis and Devetsikiotis, 2016): (i) provide a sustainable, robust and secure option for promoting synergies and reliable information sharing across SCs; (ii) minimize time consuming actions that comply with continuously changing legislation; (iii) reduce the need for trusted third parties; and (iv) introduce the use of smart contracts. Despite the prospects of BCT in end-to-end SC operations, a framework describing data requirements for containerized food SCs, particularly in case of maritime logistics, is still lacking.

In this regard, this research first provides a systematic literature review for mapping the blockchain landscape and proposes a blockchain framework for containerized food SCs. The framework contributes to the SC management research by establishing a blockchain infrastructure that employs smart interconnected devices across network echelons and further provides the capability to food SC stakeholders to securely share information, enhance process control and traceability, and prevent potential risks to containerized food SCs. A pilot case study in Greece is presented for the shipping container industry transporting perishable food products in refrigerated containers. The smart containers enable the uninterrupted communication with the blockchain backbone and allow the continuous and reliable storage of critical information. The case particularly focuses on critical maritime logistics processes involved in, namely: (i) preannouncement phase; (ii) port of origin storage yard; (iii) origin vessel; (iv) sea transport; (v) destination vessel; (vi) port of destination storage yard; and (vii) last mile logistics. To that end, our analysis captures key data requirements from key involved stakeholders, namely line shipping companies, terminal operators and port authorities (Lee and Song, 2017).

2. Blockchain Technology in Food Supply Networks

Global food trade has increased the total transportation time and distance from the farmer to the end consumer. In addition, fresh and processed food is vulnerable to hygiene and safety risks at all food SC echelons, thus rendering the farm-to-fork assessment of the products' quality very challenging. Aung and Chang (2013) stated that the transition of the food industry to a global value network necessitates traceability systems and faster response times to prevent food scandals. Wahyuni et al. (2018) identified risks across end-to-end food SCs by analyzing a case study for the fish industry. Across the entire spectrum of food SC operations, all stakeholders are responsible for preventing any biological and chemical contamination. Stakeholders are encouraged to use Information and Communication Technologies (ICTs) for advanced control, and monitor all 'source-make-deliver' processes to safeguard perishable products and eliminate quality variations from the stringent food safety requirements.

BCT could signal a digital transformation to the food SC landscape, affect key SC objectives (e.g. cost, quality, speed, risk reduction, flexibility) and increase transparency and accountability (Kshetri, 2018). Caro et al. (2018) presented AgriBlockIoT, a practical implementation of BCT using the Ethereum and the Hyperledger. Internet of Things (IoTs) devices capture and directly transmit data to the BCT ecosystem, while sensors ensure the automated execution of smart contracts. Tse et al. (2018) introduced BCT to the food industry in China to tackle food safety issues, as it provides a permanent record for each transaction and a replacement for traditional paper tracking systems. The authors also included an Administration and Regulator level at their

implementation in order to help government track, monitor and audit the food SC. Finally, Tian et al. (2017) identified the emerging role of ICTs to the SC ecosystem and focused on an innovative decentralized BCT for implementing a real-time food tracing system based on Hazard Analysis and Critical Control Points and the IoTs.

3. Business Processes in Containerized Food Supply Chains

In order to analyze the critical business processes in containerized food SCs, this research explores the illustrative real-world case study of an end-to-end food SC. In particular, we study a Greek Third-Party-Logistics provider, located in the city of Thessaloniki, offering services for containerized food. The investigated case study takes into consideration the following business processes – farming-processing-distribution – where all retrieved critical information is stored in a BCT structure to ensure the product quality. The main focus of the Third-Party-Logistics provider is on logistics processes involved in maritime containerized global transportation through using reefers.

The end-to-end perspective of the investigated case study enables integrated data gathering and ensures visibility and traceability across all food SC stages. We recognize that the gathered data across the food SC under investigation can be segmented in two categories: (i) critical data that are considered as input to a BCT framework; and (ii) supporting data that are considered as informative metadata. We claim that the identification of these data categories supports the viable development of BCT software as the required resources (e.g. storage capacity, energy consumption) are minimized.

3.1. Farming and Processing

In a typical food SC ecosystem, the agricultural commodities are being collected by the farmer and are then forwarded downstream the SC to the retailer and the final consumers. Every farmer is characterized by primary production focus (Farmer ID and metadata) at a specific geolocation of a field (Field ID and metadata) in the farm (Farm ID and metadata). Furthermore, the farming processes involved include sowing, cultivation and harvesting of agricultural commodities. At each process it is necessary to retain critical information and transactions, including: quality of the seeds (Seed ID and metadata); cultivation practices (Cultivation Type IDs and metadata); used fertilizers (Fertilizer ID and metadata); environmental conditions during the growth of the product (environmental metadata). IoTs devices are vital for the uninterrupted communication of the SC software and BCT with the farming infrastructure. At a second stage, food and beverages processing industry utilizes the inbound agricultural materials as input to manufacture processed foods and distribute the final products to wholesalers. Critical data include: industry's ID; food processing methods; ingredients and preservatives; processed food ID and all relevant metadata. Industry 4.0 technologies enable the direct communication of the manufacturing environment (equipment and machinery) with the infrastructure and BCT.

3.2. Distribution

Wholesalers are responsible for the distribution of the final products to retailers. At the distribution process transportation conditions are critical as they could tamper the quality of food products, particularly in the case of perishable goods. Refrigerated containers store agricultural products and with the use of smart sensors a 24/7 link for informing the ICTs and BCT of the SC is ensured. The distribution of agri-commodities from the wholesaler to retailers involves three major entities: (i) port of origin; (ii) shipping line for maritime freight; and (iii) port of destination.

3.3. Port of Origin

At the port of origin, the process begins with the preannouncement phase. The list of export containers to enter the Container Terminal is required for the communication between the shipping agent who handles the container and the port authority, and it must be submitted before the arrival of each container (48h in advance). Port authorities use this list to plan the transport of the container by examining the origin, content, port of destination, Verified Gross Mass as well as space availability at the port, and the required temperature limits for preserving the agricultural products. The port's handling equipment (e.g. forklift, and straddle carrier) is used for transferring the container boxes close to the dock in order to be positioned in the vessels by Gantry Cranes based on specific EDI messages (container loading list). Containers are categorized according to: (i) port of destination; (ii) agent responsible for transportation (i.e. primary or secondary); (iii) container's properties (i.e. Verified Gross Mass, container size – 20, 40, 45, high-cube); (iv) load (e.g. barrels, parcels, boxes); (v) container type (e.g. reefer); (vi) hazard type (e.g. non-flammable gas, organic peroxides, oxidizing substances, substances demonstrating fire hazard, mass explosion hazard); and (vii) payment responsible. Once the refrigerated container is at the storage yard it is plugged at the power supply in order to maintain appropriate temperature while at the same time it communicates its status to the information communication infrastructure. The final responsibility of the port of origin is the ship loading from the origin vessel with the use of straddle carriers. Port employees are equipped with personal digital assistant devices to confirm the execution of every individual task. It is critical to continuously monitor containers, in an automated manner, to track container flows.

3.3.1. Shipping Line for Maritime Freight

Once a container is correctly loaded at the ship, the port has no further obligations and the ship has to fulfil the consignment. Provided that a refrigerated container is safely loaded, it must be plugged in to the ship's power supply. The ship's operator manually establishes the correct temperature at the reefer and ensures that it properly operates during shipment. The Electronic Data Interchange message that presents the exact position of every container in the ship is generated in order to inform all stakeholders. The reverse process then takes place as the container arrives at the port of destination. The CORPAR order for unloading containers, along with the determination of the containers' exact position, is executed to complete the unloading process.

3.3.2. Port of Destination

At the destination port, and prior to the arrival of the ship, port authorities use the bill of lading in order to plan the handling of the inbound containers by examining their origin, content and destination as well as space availability at the port and temperature requirements for preserving the transported food products. Bills of lading are submitted in either Electronic Data Interchange or Extensible Markup Language formats and contain attributes such as: quantity; weight; type of hazards; type of container (e.g. size, reefer); state information (e.g. temperature tolerance limits). Port authorities review the bill of lading and proceed to the appropriate preparatory activities. In case a specific product is on the bill of lading, the port receives the container and temporarily stores it at the destination warehouse. Containers are stored according to their load, destination or transportation agent. In the case of reefer containers, a power supply is necessary for ensuring appropriate storage conditions. The port operator is responsible for the reefer and the temperature settings which should be clearly stated at the bill of lading. Selected containers could be moved for customs control where all the obligatory custom

declaration forms are checked and then the container is moved for a short-term storage to the destination storage yard. All transport information during last mile logistics must be monitored to safeguard the quality of the delivered products.

4. Digital Transformation: Blockchain Framework

Modeling the containerized food SC processes enables the digital transformation of the shipping industry and provides added value to the SC (Scholliers, 2016). Food value networks are sensitive to time critical parameters and to the transportation and storage conditions of the agricultural commodities. Perishable products should be delivered to the consumers without losing their organoleptic and nutritional properties and this could be safeguarded by the use of innovative information technology-based solutions. The proposed framework enables the integration of BCT from a farm-to-fork perspective, with special focus on the business model of containerized food SCs. Every step of the process is designed in order to provide all the obligatory and critical data to the sequential blocks of the BCT framework. The blockchain architecture could follow a public (Ethereum) or a private (Hyperledger) scenario and blockchain nodes are responsible for safeguarding the information flow of the SC and ensure data integrity. In tandem with IoTs devices (e.g. radio-frequency identification) and autonomous vehicles in industrial environments that can operate on a 24/7 basis (Bechtsis et al., 2018), communication with the blockchain allows real-time information and data sharing among all stakeholders, hence increasing traceability and trust. Finally, a demonstrator working model is implemented at the Hyperledger Fabric framework. The use case scenario involves a two-stage Distributor and Retailer SC business model that includes Assets (Product, Driver, Container, Truck), Transactions (Product Transportation Steps) and Events (Distributor and Retailer Updates). The Business model for all entities was implemented at the Hyperledger Composer and was tested using the Hyperledger’s Playground interface. Every participant could receive credentials for joining the network either by simply communicating with other peers or by creating a distinct node. The proof of concept scenario used the levelDB for the immutable transaction log and CouchDB for storing metadata. Further research is needed for developing a full scale SC tool that will implement the proposed containerized food SC framework (Figure 1).

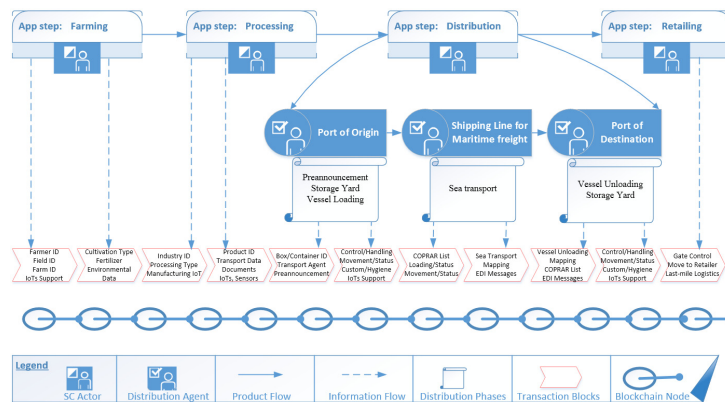


Figure 1. Blockchain Framework for Containerised Food SCs

5. Conclusions

The study findings indicate that BCT is in its maturity phase as it has been successfully applied on the FinTech processes. Digital technologies and the blockchain framework focus on critical transactions provide added value to SC operations and promote optimization techniques to global organizational challenges. The proposed framework integrates operations of the various partners across a global containerized food supply chain on a single secure information sharing process implemented on a farm-to-fork blockchain platform. A working model of a two stage SC was implemented on Hyperledger Fabric as a proof of concept demonstrator. The cost of developing/operating or leasing this platform, which is closely related to the volume of exchanged data, as well as the additional costs (sensors, IoTs devices) for collecting the necessary information will be the key parameter for documenting the feasibility (under business terms) of this system for a supply network.

References

- M. M., Aung, and Y. S., Chang, 2014, Traceability in a food supply chain: Safety and quality perspectives, *Food Control*. Elsevier Ltd, 39(1), pp. 172–184
- D., Bechtsis, N., Tsolakis, D., Vlachos, and J.S., Srari, 2018, Intelligent Autonomous Vehicles in digital supply chains: A framework for integrating innovations towards sustainable value networks, *Journal of Cleaner Production*, 181, pp. 60–71
- M. P., Caro, M.S., Ali, M., Vecchio, R., Giaffreda, 2018, Blockchain-based traceability in Agri-Food supply chain management: A practical implementation', in 2018 IoT Vertical and Topical Summit on Agriculture - Tuscany, IOT Tuscany 2018, pp. 1–4
- K., Christidis, and M., Devetsikiotis, 2016, Blockchains and Smart Contracts for the Internet of Things, *IEEE Access*, 4, pp. 2292–2303
- FAO, 2017, Trade and Food Standards. Rome: Food and Agriculture Organization of the United Nations and the World Trade Organization
- J. F., Galvez, J. C., Mejuto, and J., Simal-Gandara, 2018, Future challenges on the use of blockchain for food traceability analysis, *TrAC - Trends in Analytical Chemistry*. Elsevier Ltd, 107, pp. 222–232
- N., Kshetri, 2018, 1 Blockchain's roles in meeting key supply chain management objectives, *International Journal of Information Management*. Elsevier, 39(December 2017), pp. 80–89
- C.Y., Lee, and D.P., Song, 2017, Ocean container transport in global supply chains: Overview and research opportunities, *Transportation Research Part B: Methodological*, 95, pp. 442–474
- J., Scholliers, A., Permala, S., Toivonen, H., Salmela, 2016, Improving the Security of Containers in Port Related Supply Chains, *Transportation Research Procedia*. Elsevier B.V., 14, pp. 1374–1383
- F., Tian, 2017, A supply chain traceability system for food safety based on HACCP, blockchain and Internet of Things, in *Proc. of the ICSSSM*, pp. 1–6
- D., Tse, B., Zhang, Y., Yang, C., Cheng, H., Mu, 2017, Blockchain application in food supply information security, in 2017 IEEE International Conference on Industrial Engineering and Engineering Management (IEEM), pp. 1357–1361
- H. C., Wahyuni, W. Sumarmi, and I. A., Saidi, 2018, Food safety risk analysis of food supply chain in small and medium enterprises (case study: Supply chain of fish), *International Journal of Engineering and Technology(UAE)*, 7(2.14 Speci), pp. 229–233

System-Level Optimisation of Combined Power and Desalting Plants

Houd Al-Obaidli,^a Sarah Namany,^a Rajesh Govindan,^a Tareq Al-Ansari^{a,*}

^aDivision of Sustainable Development, College of Science and Engineering, Hamad Bin Khalifa University, Qatar Foundation, Doha, Qatar

**talansari@hbku.edu.qa*

Abstract

Nations in the Gulf Cooperation Council (GCC) utilise their vast oil and natural gas resources in order to satisfy the demand for water and power, which continues to increase due to population and economic growth. The abundance in fossil fuels and relatively low O&M costs make fuel-based technologies a de-facto choice when planning new power or desalting facilities which are proven to have the lowest levelized cost compared to other alternatives. However, energy intensive desalination systems have contributed to high greenhouse gas (GHG) emissions and increased costs. Recently, several facilities have been designed to include renewable energy in order to mitigate GHG emissions and improve the overall environmental welfare. This study evaluates different power and desalting configurations using both fossil-based and renewable energy sources to determine an optimal configuration that minimises CO₂ emissions at a relatively low levelized cost. Using the current utilities infrastructure in Qatar as a basis, six configurations were devised where three of them mimic current configurations and three were proposed. The technologies selected were limited to existing configurations: open cycle gas turbine (OCGT), combined cycle gas turbine (CCGT), multi-stage flash (MSF), and seawater reverse osmosis (SWRO), and three renewable technologies concentrated solar power (CSP), solar PV, and biomass integrated gasification combined cycle (BIGCC). At a system-level, optimisation of levelized costs vs global warming potential (GWP) was conducted using a stochastic programming framework. The findings conclude that current configurations are suboptimal and the infusion of renewable energy sources (RES) into the combined power and desalting plant (CPDP) infrastructure significantly improves CO₂ emissions with a reduction ranging between 52% and 67% and overall system levelized cost decrease between 8% and 32%.

Keywords: Portfolio optimisation, renewable energy, stochastic processes, levelized costs, environmental impact.

1. Introduction

Economic and population growth in the Middle-East since the hydrocarbon boom has increased the industrial and urban demand for water and energy resources. By 2030, water demand globally is expected to rise by 25%, with a 50% increase in energy (Madani et al., 2015). Considering the demand for both, water and power, the countries in the GCC bordering the Arabian Gulf, are reliant on co-generation power desalting plants (CPDP) which produce two useful utilities: electricity and freshwater. In fact, 44% of the global desalination capacity is located in the Middle-East and North Africa

(Voutchkov, 2016). Desalination is an energy intensive process in which associated emissions are a function of the input energy, i.e. natural gas, oil, etc.

The State of Qatar, a peninsula located in the heart of the Arabian Gulf, suffers from freshwater scarcity as it is located in a hyper arid region with renewable groundwater rate equivalent to 58 million m³ annually (Darwish, 2014). It exhibits a similar development profile to those witnessed by the rest of the region and in terms of its energy resources, Qatar possess approximately 25.4 trillion m³ of gas reserves and its annual output of liquefied natural gas is 77 million tons per year (Qatargas, 2018). Technology advancements in the provision and supply of natural gas, in addition to the fact that it is considered the cleanest of fossil fuels has enhanced the position of natural gas as an energy resource. In fact, natural gas, it is the sole driver of power generation in Qatar and has witnessed increasing demand in the global market, therefore offering further opportunities for the export of natural gas and associated products. Several utility plants based on affordable and clean natural gas have been constructed in Qatar in order to satisfy water and electricity increasing needs as illustrated in Table 1. The State of Qatar aims to diversify the energy mix and reduce GHG emissions through the integration of alternative and renewable energy and desalination technologies. This study serves as a guideline for decision makers offering a comparative tool for identifying an optimal mix of power and water systems minimizing environmental and economic impacts.

Table 1. List of CPDP facilities in Qatar (Kahramaa, 2017).

Plant	OCGT (MW)	CCGT (MW)	MSF (MIGD)	SWRO (MIGD)
RAF A	497			
RAF A1			45	
RAF A2			36	
RAF A3				36
RAF B	609		33	
RAF B1	376.5			
RAF B2	567		30	
RLPC		756	40	
Q Power		1,025	60	
RGPC		2,730	63	
M Power		2,007		
UHPC		2,520	76.5	60
Total	2,049.5	9,038	383.5	96

In terms of portfolio optimisation, Bhattacharya and Kojima (2012) examined the increase of renewable energy contribution in the energy supply portfolio for Japan utilizing mean-variance portfolio (MVP) optimisation. Fuss et al. (2012) examined the adoption of renewable energy and carbon-saving technologies across different socioeconomic scenarios. Cucchiella et al. (2012) analysed the electricity market in Italy using MVP, and reviewed a set of optimal portfolios with different energy mixes. The study concluded that it is necessary to include renewable energy into the portfolio to mitigate the high investment risk in this market. Lucheroni and Mari (2014; 2015; 2016) used stochastic levelized cost of energy (LCOE) theory to determine the optimal power generation portfolio for different scenarios. Govindan et al. (2018) estimated the LCOE for CCGT using stochastic modelling and applied it into a portfolio optimisation of different energy and water technology mixes as part of energy, water and food

(EWF) Nexus studies. Namany et al. (2018) expanded on the work by Govindan et al. (2018) and Al-Ansari et al. (2015; 2017) by applying a game theoretic approach using a Stackelberg duopoly model to the EWF Nexus. The study considered a CCGT competing against bio-energy with carbon capture and storage (BECCS). Darwish et al. (2014, 2015) provided a techno-economic analysis of different CPDP to improve energy and water security in Qatar in a cost-effective manner. The aim of this paper is to evaluate the integration of RES, consisting of PV, BIGCC and CSP, into the existing utilities infrastructure in terms of CO₂ emissions and levelized costs by applying stochastic modelling and multi-objective genetic algorithm optimisation.

2. Methodology

Using a stochastic optimisation framework that considers fluctuation in natural gas prices, this study models diverse power and desalting scenarios using a combination of renewable and non-renewable energy sources to identify the optimal configuration with the lowest levelized and environmental impact. The utilities infrastructure is segregated by typical configurations of CPDP as illustrated in Table 2. There are 3 existing configurations observed based on 2 power technologies OCGT and CCGT and 2 water desalination technologies MSF and SWRO. Typically, configurations tend to improve over time transitioning to a more reliable and efficient technology as was obvious from the transition of legacy OCGT systems in favour of CCGT and from expensive and energy intensive MSF to SWRO. Three new technologies were selected based on suitability for the environment in the Middle-East, CSP, PV and BIGCC.

Table 2 List of Current CPDP Configurations.

Configuration	OCGT	CCGT	MSF	SWRO
1	1.0		1.0	
2		1.0	1.0	
3		1.0	0.63	0.37

Figure 1 illustrates a comparison of the 7 technologies together with the 3 existing configurations. The aforementioned technologies form the baseline and will be used for comparison with 3 additional scenarios that are based on a portfolio optimisation using stochastic modelling of natural gas prices, thus providing a representation for natural gas price volatility. The model was based a mean gas price and a standard deviation as predicted by Govindan et al. (2018).

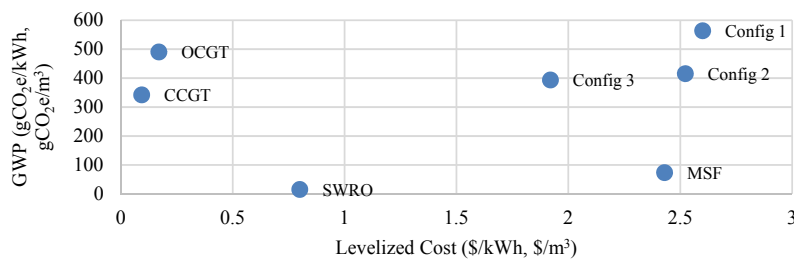


Figure 1. Current Water and Power Technologies and CPDP Configurations.

A multi-objective genetic-algorithm (GA) model was developed for the 7 technologies representing 7 decision variables with the aim of minimizing both the overall levelized costs of the system and GWP. Levelized costs and GWP factors per technology were selected from literature as described in Table 3. Subsequently, two optimisation objectives are formulated for the levelized costs and GWP respectively:

$$\text{Minimize } \sum_i c_i x_i \quad (1)$$

$$\text{Minimize } \sum_i e_i x_i \quad (2)$$

Where, c represents the levelized cost factors, and e represents the emission factors per technology.

The optimisation was subject to a number of constraints:

$$x_{OCGT} + x_{CCGT} + x_{CSP} + x_{PV} + x_{BIGCC} = 1 \quad (3)$$

$$x_{MSF} + x_{SWRO} = 1 \quad (4)$$

$$0 \leq x_i \leq 0.5 \quad (5)$$

Several iterations will be run to ensure a representative sample is obtained and the median pareto front will be selected for comparison with the existing configurations.

Table 3 Levelized Costs and GWP Factors per Technology.

Technology	Levelized Cost (\$/kWh, \$/m ³)	Source	GWP (gCO ₂ e/kWh, gCO ₂ e/m ³)	Source
OCGT	0.17	NREL OpenEI	490	IPCC (2014)
CCGT	0.093	Govindan (2018)	341.56	Al-Ansari (2017)
MSF	2.43	Darwish (2015)	73.35	Darwish (2015)
SWRO	0.8	Darwish (2015)	14.67	Darwish (2015)
CSP	0.16	NREL OpenEI	27	IPCC (2014)
PV	0.215	Al-Ansari (2017)	33.79	Al-Ansari (2017)
BIGCC	0.1	NREL OpenEI	230	IPCC (2014)

3. Results and Discussion

Thirty iterations were run using the GA model and a representative sample was obtained as illustrated in Figure 2. The median pareto front (Figure 3) is selected for comparison with the different configurations. Figure 4 illustrates the three manually selected points from the pareto front in comparison to the existing configurations. It is evident that current configurations are suboptimal although the more recent installations following configuration 3 display significant improvement and do approach the optimal solution in the right direction. However, without the integration of RES, the configurations will continue to be suboptimal and increasing share in the portfolio should be assigned to

CSP, BIGCC, and PV. Using configuration 5 as a representative proposed configuration and the comparison to existing configurations reveal that configuration 5 displayed an improvement in GWP of 67%, 55%, and 52% in relation to configurations 1, 2, and 3 respectively. A similar comparison using levelized costs showed an improvement of 32%, 30%, and 8%. All 3 proposed configurations exhibited a significant share of renewables and a large reduction of natural gas-driven technologies from 100% to a range between 10% and 20%. Water desalination technologies on the other hand had an equal share in the portfolio due to the given constraints in the optimisation problem formulation.

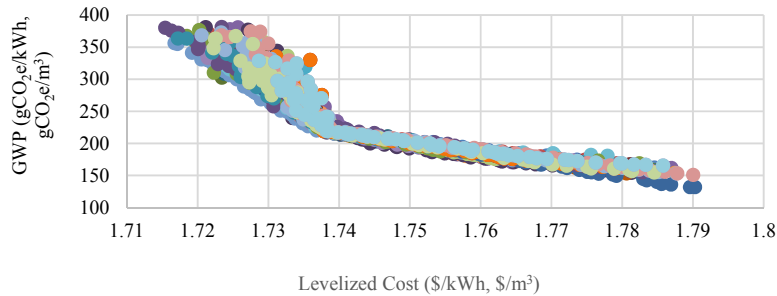


Figure 2. Pareto front for 30 iterations.

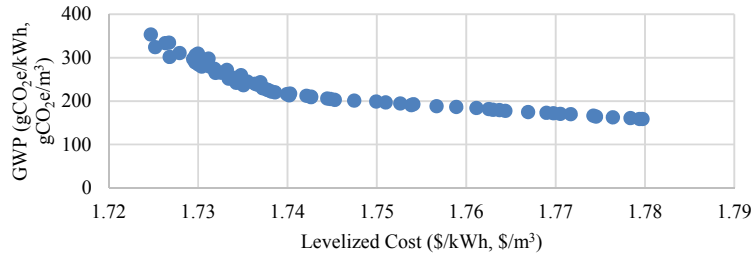


Figure 3. Median Pareto front.

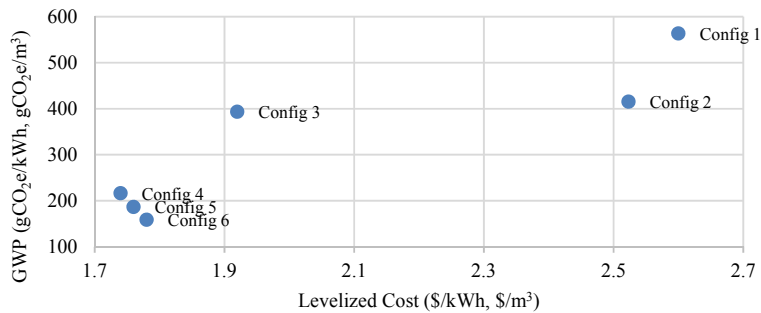


Figure 4. Comparison between 3 optimal configurations with existing ones.

4. Conclusions

In this paper, current CPDP configurations in Qatar are compared to a set of proposed configurations using non-conventional RES such as CSP, PV and BIGCC. Using stochastic modelling of natural gas prices and a multi-objective GA optimisation, it is concluded that the 3 current configurations evaluated are suboptimal. The optimal configurations are represented by a significant share of RES technologies which decrease both CO₂ emissions and levelized costs. Considering, water desalination, since there are only two technologies and both are constrained not to exceed a 50% share, the load is distributed to both of them equally. In the event that the constraint is removed, SWRO would dominate due to its significantly low levelized cost and GWP factors. However, such a scenario is not possible due to the large installed base of MSF units in Qatar. Similarly, gas-driven power generation units with a huge installed base, are also somewhat difficult to upgrade to RES. Meanwhile, RES integration can be considered for future network expansions or upgrade projects. Future research can consist of the integration of additional RES technologies such as nuclear, wind and geothermal and further evaluation of less-common water desalination technologies such as multiple-effect distillation (MED), membrane distillation (MD) and mechanical vapor-compression (MVC).

References

- T. Al-Ansari, A. Korre, Z. Nie, and N. Shah, 2016, Integration of Biomass Gasification and CO₂ Capture in the LCA Model for the Energy, Water and Food Nexus, *Computer Aided Chemical Engineering*, 38, 2085-2090.
- , 2017, Integration of Greenhouse Gas Control Technologies within the Energy, Water and Food Nexus to Enhance the Environmental Performance of Food Production Systems, *Journal of Cleaner Production*, 162, 1592-1606.
- M. Darwish, 2014, Qatar water problem and solar desalination, *Desalination and Water Treatment*, 52(7–9), 1250–1262.
- M. Darwish, H. Abdulrahim, A. Hassan, 2015, Realistic Power and Desalted Water Production Costs in Qatar, *Desalination and Water Treatment*, 57, 4296-4302
- R. Govindan, T. Al-Ansari, A. Korre, N. Shah, 2018, Assessment of Technology Portfolios with Enhanced Economic and Environmental Performance for the Energy, Water and Food Nexus, *Computer Aided Chemical Engineering*, 43, 537-542.
- Kahramaa, 2017, *Statistics Report 2016*, Kahramaa Publications.
- K.Madani, 2015, *Using Game Theory to Address Modern Resource Management Problems*, Grantham Briefing note 2, Imperial College London.
- S. Namany, T. Al-Ansari, R. Govindan, 2018, Integrated Techno-economic Optimisation for the Design and Operations of Energy, Water and Food Nexus Systems Constrained as Non-cooperative Games, *Computer Aided Chemical Engineering*, 44, 1003–1008.
- Qatargas, 2018, *Global Energy Supplier*, Retrieved from <https://www.qatargas.com/english>
- N. Voutchkov, 2016, *Desalination – Past, Present and Future*, Retrieved from <https://www.iwa-network.org>

Computer-aided Design of Solvent Blends for the Cooling and Anti-solvent Crystallisation of Ibuprofen

Oliver L. Watson^a, Amparo Galindo^a, George Jackson^a, Claire S. Adjiman^{a,*}

^a*Department of Chemical Engineering, Centre for Process Systems Engineering, Imperial College London, South Kensington Campus, London SW7 2AZ, U.K.*

c.adjiman@imperial.ac.uk

Abstract

We present a general computer-aided mixture/blend design (CAM^bD) formulation for the design of optimal solvent mixtures for the crystallisation of pharmaceutical products. The proposed methodology enables the simultaneous identification of the optimal process temperature, solvent and anti-solvent molecules, and solvent mixture composition. The SAFT- γ Mie equation of state is used for the first time in the design of crystallisation solvents; based on an equilibrium model, the formulation considers both the crystal yield and solvent consumption. This design formulation is implemented in gPROMS and successfully applied to the crystallisation of ibuprofen, showing that this more general approach to crystallisation design can be used effectively to optimise the desired metrics.

Keywords: Crystallisation, CAM^bD, SAFT, solvent mixture design.

1. Introduction

The majority of pharmaceutical products are delivered to patients in solid form, such as tablets or aerosols. During their manufacture, crystallisation is particularly important in determining the properties of the crystalline form of the drug, which can impact downstream processing and ultimately the *in vivo* efficacy of the pharmaceutical product (Variankaval et al., 2008). Solvent-based crystallisation is commonly employed; as such, the effect of solvent choice is wide-reaching. Thermodynamically, the impact of this decision will manifest itself as changes to the solubility of the Active Pharmaceutical Ingredient (API), and thus as differences in two key performance indicators: the yield of API; and the mass of solvent required to complete the crystallisation. Currently, the selection of solvents for the crystallisation of newly discovered drug molecules is often performed via time-consuming and expensive experiments (Brown et al., 2018). Due to the material constraints inherent in early drug development, alongside the short timeframes required to maximise active patent life, the full range of solvent mixtures and process conditions cannot be completely explored.

With the aim of guiding experiments towards optimal candidate molecules, the application of Computer Aided Molecular Design (CAMD) in solvent selection and design has been explored (Achenie et al., 2003; Gani, 2004) over the last decades, thus facilitating faster development of crystallisation processes (Karunanithi et al., 2006). Karunanithi et al. (2005) proposed a decomposition-based approach, whereby smaller, successive subproblems are posed and solved to avoid being overwhelmed by the number of potential solutions. Most existing methodologies follow a similar approach; a specific

crystallisation technique is utilised, process operating conditions are fixed, and the problem is then focused on the selection of a single solvent. More integrated problems, in which cooling and anti-solvent effects are treated simultaneously and solvent mixtures are considered, have not yet received attention. This is likely due to the complexity of formulating and solving a mixed-integer optimisation problem to represent these design choices; such problems result in challenging non-convex feasible regions for the continuous variables, in addition to the combinatorial solution space. More recently, the use of Generalised Disjunctive Programming (GDP) within the CAM^bD framework has been proposed to design optimal solvent mixtures that maximise solubility (Jonuzaj et al., 2016; Jonuzaj and Adjiman, 2017); optimal mixtures were shown to outperform pure compounds.

In view of the potential limitations highlighted in the current CAMD framework for solvent selection, a more comprehensive CAM^bD formulation for the design of crystallisation solvent systems is proposed here. This is developed via a general methodology, whereby the identities of solvent and anti-solvent molecules are optimised, in conjunction with their compositions and the process operating conditions, to maximise the crystal yield. This design formulation is implemented in gPROMS and successfully applied to the design of the solvent-based crystallisation of ibuprofen.

2. Crystallisation design

2.1. Problem definition

The CAM^bD problem is based on a generic formulation for the design of a crystallisation solvent system, whereby optimal solvent and anti-solvent molecules (s_1 and s_2 respectively), their compositions and the process temperatures are identified to maximise the performance objective, taken here to be the API crystal yield. Hence, the design considers both the initial state, where all the API is dissolved in the solvent blend, and the final state, where the system has reached an equilibrium between the crystalline API product and the remaining API dissolved in the final solvent mixture. By using solvent blends in both the initial and final states, the anti-solvent can serve a dual purpose. The enhanced solubility often exhibited by solvent mixtures (Granberg and Rasmuson, 2000) can first be exploited in the initial state, followed by a large reduction in API solubility in the final state after further addition of anti-solvent. Moreover, the proposed formulation enables simultaneous cooling and anti-solvent crystallisation, allowing the design to incorporate the benefits of both techniques simultaneously.

2.2. Model formulation

The formulation is based on an equilibrium model, where the SAFT- γ Mie equation of state (EoS) (Papaioannou et al., 2014) is used to calculate the activity coefficients required to determine the solubility of the API molecule in the solvent mixture in the initial and final states; Hutacharoen et al. (2017) have shown recently that this thermodynamic platform can provide high quality predictions of solubility. Furthermore, because anti-solvent crystallisation is dependent on both solvent and anti-solvent remaining in a single liquid phase, a miscibility function is included in the formulation to ensure the solubility of the binary solvent pair at the initial and final stages. Whilst this only guarantees the phase stability of the binary solvent mixture, calculation of the stability of the ternary mixture would lead to a more challenging problem. The addition of the API is assumed

not to significantly affect the calculated phase stability – this is then validated after a solution to the design problem is found.

In addition, whilst the selected solvent and anti-solvent must remain in the liquid phase throughout the crystallisation process, how this requirement is implemented into the formulation can affect the optimisation outcome. It is often chosen to design a cooling crystallisation by fixing the initial and final temperatures, and thus to exclude any solvents with melting or boiling temperatures which lie within those operating limits (Karunanithi et al., 2006). Whilst this is likely chosen to reduce the complexity of the problem – operating temperature is no longer a manipulated variable of the CAM³D problem, and consequently solvent candidates only need to be screened once – this method may also limit the results by screening out powerful yet volatile solvents or anti-solvents. With the approach proposed here, the optimal process temperature and solvent molecules are selected simultaneously, highlighting potentially interesting solvent mixtures regardless of volatility. A liquid range constraint is thus included for all solvent molecules.

The key model equations are provided in Table 1, where the crystal yield, Y_{API} , is defined as the difference in the number of moles of API dissolved in the liquid phase, n_{API}^L , between the initial state (subscript 0) and final state, relative to the number of moles dissolved in the initial state before crystallisation. The solubility of the API of equilibrium, x_{API}^* , is related to the activity coefficient of the API at equilibrium, γ_{API}^* , the enthalpy of melting of the API, ΔH_{API}^m , the melting temperature of the API, T_{API}^m , and the operating temperature of the system, T ; R is the ideal gas constant. When determining the phase stability of the binary solvent mixture, the partial derivative of the chemical potential of the anti-solvent in the binary mixture, $\mu_{s_2}^{s_1,s_2}$, is calculated with respect to the mole fraction of the anti-solvent in the binary mixture, $x_{s_2}^{s_1,s_2}$, at fixed temperature and pressure, and must be non-negative for the solvents to be miscible.

Table 1: Key model equations.

Description	Equation
Objective function: Maximise crystal yield	$\max Y_{API} = \frac{n_{API,0}^L - n_{API}^L}{n_{API,0}^L}$
Solid-liquid equilibrium model	$\ln x_{API,0}^* + \ln \gamma_{API,0}^* = \frac{\Delta H_{API}^m}{R} \left(\frac{1}{T_{API}^m} - \frac{1}{T_0} \right),$ $\ln x_{API}^* + \ln \gamma_{API}^* = \frac{\Delta H_{API}^m}{R} \left(\frac{1}{T_{API}^m} - \frac{1}{T} \right)$
Miscibility constraint	$\left(\frac{\partial \mu_{s_2,0}^{s_1,s_2}}{\partial x_{s_2,0}^{s_1,s_2}} \right)_{T_0,P} \geq 0, \quad \left(\frac{\partial \mu_{s_2}^{s_1,s_2}}{\partial x_{s_2}^{s_1,s_2}} \right)_{T,P} \geq 0$

3. Case study: maximising the crystal yield of ibuprofen

3.1. Problem description

Ibuprofen is a widely-used pharmaceutical compound known for its anti-inflammatory properties. The objective of the design problem examined here is to identify an optimal solvent mixture and corresponding process conditions required to maximise the crystal

yield of the API, ibuprofen. In addition to this, it is important to investigate how the choice of solvent and temperatures affects the overall solvent consumption for the crystallisation, whereby a lower consumption is preferable. Solvents are selected from a list of eight candidate molecules, compiled from low-toxicity solvents with parameters available in the SAFT- γ Mie framework (Dufal et al., 2014). To understand the effects of the process temperature on the design problem, six design scenarios are run; in each, the upper temperature limit is different, ranging from 290 K to 330 K, whilst the lower temperature limit is always fixed at 290 K and the solvent consumption was not constrained. These specifications are summarised in Table 2.

3.2. Results and discussion

The formulation is implemented in gPROMS version 5.1.1.55066, using gSAFT to perform calculations using the SAFT- γ Mie EoS. The results of the design problems pertaining to the integrated cooling and anti-solvent method are summarised in Figure 1, and the comparison between cooling, anti-solvent, and the integrated approach are given in Table 3. For all problem solutions, the stability of the ternary system is confirmed using gSAFT within gPROMS.

As can be seen in Figure 1, the combination of cooling and anti-solvent crystallisation, utilising solvent mixtures, leads to a high crystal yield, which is fractionally increased by relaxing the upper temperature limit. Furthermore, the solvent consumption improves simultaneously with the objective function as the upper temperature limit is increased, leading to increasingly environmentally benign design. This is largely due to an increase in the ratio of solvent to anti-solvent in the initial solvent mixture, meaning a smaller mass of anti-solvent is required to drive forward the crystallisation to the final state. Interestingly, the optimal process temperature of the initial state is not always equal to the upper temperature limit. When the maximum temperature is fixed at 320 K, the optimal initial temperature found is 319.15 K, as a solvent liquid range constraint becomes active near the boiling point of acetone. Additional optimisations confirm that this result remained optimal up to an upper temperature limit of 323 K. Maximising the temperature range, $T_{\max} - T_{\min}$, is thus not always optimal and this emphasises the importance of employing a general formulation.

In addition to the combined cooling and anti-solvent crystallisation approach, problems involving only cooling or anti-solvent crystallisation are solved, as summarised in Table 3. Although the solvent consumption decreases when using cooling crystallisation, a much lower crystal yield is obtained. Anti-solvent crystallisation allows one to achieve a similar result to the integrated approach, but the crystal yield is marginally lower and the solvent consumption is higher. Here, Y_{API} is the crystal yield of the ibuprofen, and χ_s is the solvent consumption of the crystallisation, defined as the total mass of solvent mixture used in the final state, normalised by the mass of crystalline API produced.

Table 2: Problem specifications.

Description	Model inputs
Components in the mixture	API, s_1 , s_2
Candidate molecules	water, acetone, ethanol, 1-propanol, 1-butanol, 1-pentanol, n-pentane, n-heptane 28 potential binary solvent pairs
Temperature limits	$T_{\min} / \text{K} = 290$, $T_{\max} / \text{K} = \{290, 300, 310, 320, 325, 330\}$

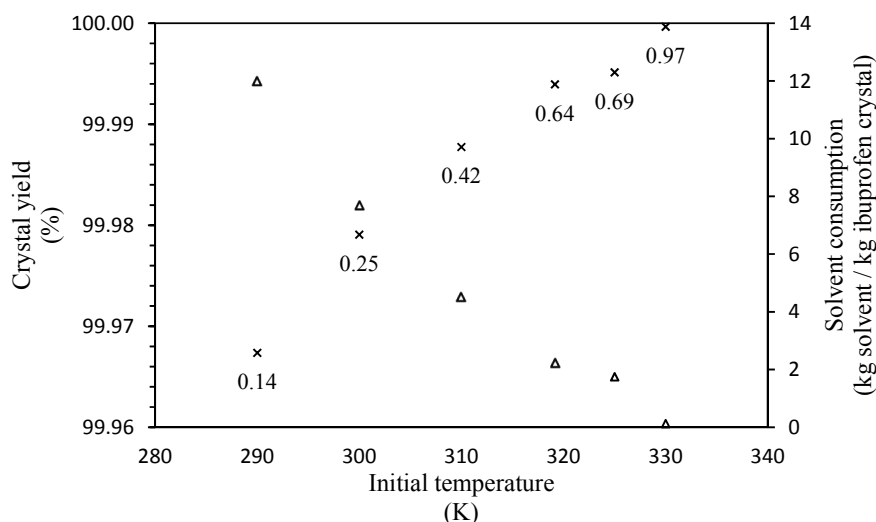


Figure 1: Optimised crystal yield of ibuprofen for different initial operating temperatures. The final temperature for all crystallisations was 290 K, whilst the upper temperature limit is changed per design, which in turn affects the initial operating temperature. The × symbol indicates the percentage crystal yield (left axis), whilst the Δ symbol refers to the solvent use, normalised by the mass of API crystal produced (right axis). For points below 320 K, the solvent mixture is formed with acetone and water, whereas above this temperature the mixtures comprise of ethanol and water. The data points are labelled with the mole fraction of anti-solvent in the initial binary solvent mixture.

Table 3: Comparison of the integrated methodology to standalone methods.

Case	Solvent selection	T_0 /K	T /K	$x_{s,0}^{s_1,s_2}$	$x_s^{s_1,s_2}$	Y_{API} %	χ_s /(g/g)
Integrated	s_1 : Acetone s_2 : Water	310	290	s_1 : 0.5809 s_2 : 0.4191	s_1 : 0.0253 s_2 : 0.9747	99.99	4.329
Anti-solvent	s_1 : Acetone s_2 : Water	310	310	s_1 : 0.5814 s_2 : 0.4186	s_1 : 0.0264 s_2 : 0.9736	99.97	4.506
Cooling	s_1 : Acetone s_2 : Water	310	290	s_1 : 0.4249 s_2 : 0.5751	s_1 : 0.4249 s_2 : 0.5751	95.28	0.705

4. Conclusions

A general formulation for the design of optimal solvent blends for the crystallisation of pharmaceuticals is presented, based on a (CAM^bD) framework. With this general approach the optimal solvent and anti-solvent molecules, their compositions and the process temperatures required to maximise the crystal yield of a given API can be identified simultaneously. The general formulation is successfully applied to the crystallisation of ibuprofen, where the optimal solvent mixture is determined for several operating temperatures. The simultaneous design of the solvent mixture and operating temperature lead to improved results compared to those achieved when the temperature range is fixed. Better results are also found for the integrated cooling and anti-solvent crystallisation technique compared to standalone methods. A ranked list of potential

solvent mixtures can be generated using the proposed methodology, with the overall aim to guide experiments rapidly towards high performance crystallisation systems.

Acknowledgements: The authors gratefully acknowledge financial support from the EPSRC DTP grant (Grant Ref: EP/R513052/1), and the EPSRC and the Future Continuous Manufacturing and Advanced Crystallisation Research Hub (Grant Ref: EP/P006965/1) for funding this work. The Molecular Systems Engineering Group also appreciated support from the EPSRC (grants GR/T17595, GR/N35991, EP/E016340 and EP/J014958), the Joint Research Equipment Initiative (JREI) (GR/M94426), and the Royal Society-Wolfson Foundation refurbishment scheme.

References

- L. E. K. Achenie, R. Gani, V. Venkatasubramanian, 2003, *Computer aided molecular design: theory and practice*, Elsevier, Amsterdam, The Netherlands.
- C. J. Brown, T. McGlone, S. Yerdele, V. Srirambhatla, F. Mabbott, Gurung R, M. L. Briuglia, B. Ahmed, H. Polyzois, J. McGinty, F. Perciballi, 2018, Enabling precision manufacturing of active pharmaceutical ingredients: workflow for seeded cooling continuous crystallisations, *Molecular Systems Design & Engineering*, 3, 518-549.
- S. Dufal, V. Papaioannou, M. Sadeqzadeh, T. Pogiatis, A. Chremos, C. S. Adjiman, G. Jackson, A. Galindo, 2014, Prediction of thermodynamic properties and phase behavior of fluids and mixtures with the SAFT- γ Mie group-contribution equation of state, *Journal of Chemical & Engineering Data*, 59, 10, 3272-3288.
- R. Gani, 2004, Chemical product design: challenges and opportunities, *Computers & Chemical Engineering*, 28, 12, 2441-2457.
- R. A. Granberg, Å. C. Rasmuson, 2000, Solubility of paracetamol in binary and ternary mixtures of water acetone toluene, *Journal of Chemical & Engineering Data*, 45, 3, 478-483.
- P. Hutacharoen, S. Dufal, V. Papaioannou, R. M. Shanker, C. S. Adjiman, G. Jackson, A. Galindo, 2017, Predicting the solvation of organic compounds in aqueous environments: from alkanes and alcohols to pharmaceuticals, *Industrial & Engineering Chemistry Research*, 56, 38, 10856-10876.
- S. Jonuzaj, P. T. Akula, P. Kleniati, C. S. Adjiman, 2016, The formulation of optimal mixtures with generalized disjunctive programming: A solvent design case study, *AIChE Journal*, 62, 5, 1616-1633.
- S. Jonuzaj, C. S. Adjiman, 2017, Designing optimal mixtures using generalized disjunctive programming: Hull relaxations, *Chemical Engineering Science*, 159, 106-130.
- A. T. Karunanithi, L. E. K. Achenie, R. Gani, 2005, A new decomposition-based computer-aided molecular/mixture design methodology for the design of optimal solvents and solvent mixtures, *Industrial & Engineering Chemistry Research*, 44, 4785-4797.
- A. T. Karunanithi, L. E. Achenie, R. Gani, 2006, A computer-aided molecular design framework for crystallization solvent design, *Chemical Engineering Science*, 61, 4, 1247-1260.
- V. Papaioannou, T. Lafitte, C. Avendaño, C. S. Adjiman, G. Jackson, E. A. Müller, A. Galindo, 2014, Group contribution methodology based on the statistical associating fluid theory for heteronuclear molecules formed from Mie segments, *The Journal of Chemical Physics*, 140, 5, 054107.
- N. Variankaval, A. S. Cote, M. F. Doherty, 2008, From form to function: Crystallization of active pharmaceutical ingredients, *AIChE Journal* 54, 7, 1682-1688.

Modeling of multi-effect desalination process operated with thermosolar energy applied to the northeastern Brazil

Diego P.S Cunha^a, Vanessa V. Gomes^a, Karen V. Pontes^a

^a*Universidade Federal da Bahia, Rua Prof. Aristides Novis 02, Salvador-BA, 40210-630, Brazil*
diego.cunha@ufba.br

Abstract

Desalination is one of the possible solutions to the world's potable water scarcity. In order to make the process feasible and sustainable, use of renewable energy is a very useful option. The multi-effect desalination (MED) process linked with solar energy is one of the most thermodynamically efficient and the one with lower cost by produced potable water. In this context, the present work focuses on modelling a MED process with thermosolar energy applied to the local conditions of northeastern Brazil. This region suffers from water scarcity but, on the other hand, shows the highest levels of solar radiation in Brazil. Despite that, the literature still lacks a study concerning the technical viability of operating a desalination process with solar energy in this semi-arid region. The steady-state model is based on mass and energy balances and empirical correlations from literature to calculate the enthalpy of water and brine as well as boiling point elevation and latent heat. The model is firstly validated against simulated results from the literature regarding the Plataforma Solar de Almeria. The results have shown that the implementation of a solar desalination plant in Northeast Brazil is technically feasible. The obtained model is useful for further process optimization towards minimization of investment and operational costs and to facilitate access to potable water in arid regions with high solar incidence.

Keywords: Desalination, MED, Solar, Brazil

1. Introduction

The need of potable water increases proportionally to the world's population growth; however, the planet's water sources are mostly salty water and the fresh water sources are scarce. According to Al-Rawajfeh et al. (2017), more than two billion people currently suffer from lack of water and until 2025 this number will rise to more than four billion people. One possible solution to increase the fresh water availability is the salty water desalination, since salty water is abundant through oceans and seas. Desalination is a process that aims to remove the excess of salt, microorganisms and some particles present on seawater or brackish water. According to Byrne et al (2015), this process may be accomplished in different ways, the most commercially used are: reverse osmosis (RO), multi stage flash desalination (MSF) and multi-effect desalination (MED).

Energy cost is one of the factors which has strong impact on desalination process total cost (Ghobeity and Mitsos, 2014; Shatat et al, 2013). The energy used by the main desalination industries comes predominantly from fossil fuels, which are responsible for increasing the release of carbon dioxide to the atmosphere, contributing to the greenhouse

effect (Sirola, 2012). Due to this energy cost and carbon dioxide emission, a renewable and abundant energy source, like solar energy, would offer some benefits. Solar energy can be used as electric or thermal energy source.

MED and RO are the cheapest desalination processes and their costs in large scale commercial plants are around 1 USD/m³ (Shatat et al, 2013). On the other hand, when comparing desalination costs using renewable energies, Alkaisu et al. (2017) report that MED process with solar thermal energy has the lowest cost by m³ (2.5-3 USD/m³) while RO process with solar electric energy has a cost of 12.5-16.8 USD/m³. RO process requires mainly electrical energy and MED mainly thermal energy. El-Dessouky et al. (1998) also affirm that MED process has more operation flexibility, being able to operate from 0 to 100% of plant capacity, and presents shorter start time and less specific investment cost.

Considerable efforts have been made for the research of MED desalination plants coupled with solar energy. Desalination plant of Plataforma Solar de Almeria (PSA), in Spain, for example is one of those plants. It is a desalination plant composed of 14 effects with a design capacity of 72 m³/day. This plant has been modeled by several authors. Hatzikioseyan et al. (2003) develop a stationary model aiming to evaluate plant performance regarding energy consumption. Roca et al. (2012) develop a dynamic model to optimize distillate production. De La Calle et al. (2014) focus on thermal transient behavior of a MED plant's first cell, which is main responsible for plant energy consumption. In Turkey, Yilmaz and Söylemez (2012) simulate a stationary MED plant in Turkey regions using wind and solar energy. It has 12 effects and capacity of 1m³/day. Simulation results show that, although both energies are intermittent, solar energy is more stable than wind. In Jordan, Bataineh (2016) analyzes a stationary MED desalination plant combined with thermo compressor coupled with solar energy. It has 12 effects, capacity of 43,000 m³/day, 1,080,000 m² of solar collectors and a gas boiler back up to continuous operation. In this scenario, results show that solar energy can supply almost 70% of energy demanded for this plant. Bataineh (2016) also affirms that MED desalination plants powered by solar energies are able to produce more than 35 L/m²/day in regions with solar radiation above 4.8 kWh/m²/day.

The Northeast of Brazil is a semi-arid region where 11 million people suffers from fresh water scarcity (Rocha and Soares, 2015), although brackish water on underground wells is available. According to Fichter et al. (2017), the Northeast of Brazil has great potential to use solar energy because it presents solar radiation above 6 kWh/m²/day. Despite the investments and studies on desalination process in Middle East and North Africa, Brazil is still giving it first steps. Up to author's knowledge, there is no technical feasibility study of MED processes coupled with solar energy applied to the irradiation and water demand of the Brazilian semi-arid region. This paper, therefore, analyzes the technical feasibility of a MED desalination plant coupled with solar energy in Bom Jesus da Lapa (BA), a city in Northeast of Brazil. The study is based on a stationary model, validated with data from literature, considering different scenarios of solar radiation during the year.

2. Methodology

The desalination process model is based on Hatzikioseyan et al. (2003), which represents the PSA. Figure 1 represents the process layout which comprises the solar collectors and the MED process. In order to maintain plant's operation during night hours, the

water heated by collectors feeds two tanks which are perfectly insulated and store the thermal energy. The hot water tank supplies the MED plant and the cold water returns to the cold-water tank.

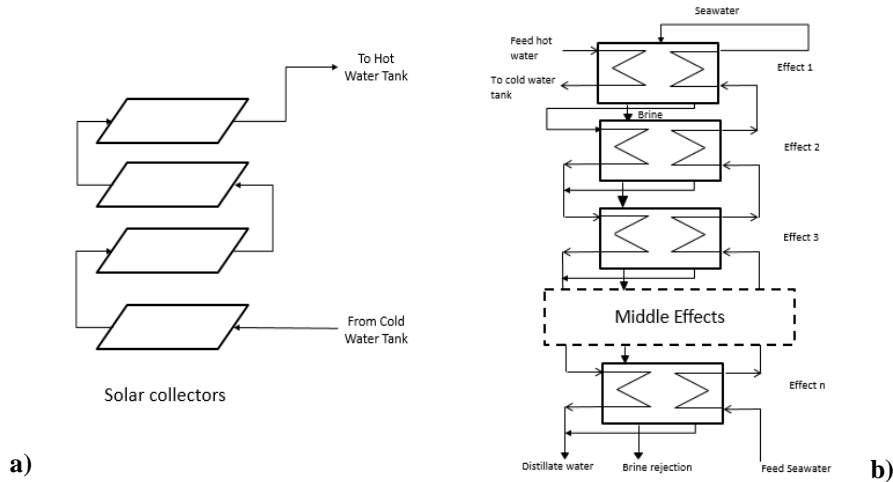


Figure 1 – Schematic of process layout: a) Solar collectors b) MED desalination plant.

Additionally to the mass and energy balance presented by Hatzikioseyan et al. (2003), the following assumptions and equilibrium relations are considered in the present model:

- The temperature difference between saturated vapor and non-evaporated brine in equilibrium at an effect is obtained by the boiling point elevation (BPE), following Aly and El-Fiqi (2003);
- The mass production of saturated vapor at an effect is estimated by the latent heat of vaporization λ according to Roca et al. (2012);
- The enthalpy of brine and liquid water follows Sharqawy et al. (2010) model, which was validated here with experimental data from Chou (1968), presenting deviations up to 4 %;
- The vapor enthalpy follows Khademi et al. (2009), which was validated here with experimental data from Smith et al. (1996), presenting deviation up to 1 %;

Solar collectors' model was developed accordingly to Al-Ajlan et al. (2003), which focus on flat plate collectors to heat water. The water outlet temperature is computed based on the geometry of the collectors and on the following input variables: solar radiation, ambient temperature, water mass flow rate and inlet temperature. The stationary model was implemented in MOSAIC modeling (MOSAIC, 2018) and solved in MATLAB®.

The base case for simulation has the same number of effects (14) and distillate production capacity (72 m³) as the PSA. The brackish water is fed at 30 °C and 0.3 bar with 7 g/L of salt, considering the average brackish water salinity in Brazilian semi-arid region (Menezes et al, 2011). According to Palenzuela et al. (2011), the hot water flow rate to the first stage (Figure 1b) is 12 L/s, whose inlet and outlet temperatures are 74 °C and 70 °C, respectively. Considering the average water consumption recommended by the World Health Organization guideline, that is 50-100 L per person per day (United Nations, 2018),

and the population from Bom Jesus da Lapa, which is around 60,000 people, the plant nominal capacity could supply approximately 2% of the population's fresh water need. The daily average solar radiation data from Bom Jesus da Lapa (BA) was collected by the RETScreen software (RETScreen, 2018) and is about 5.7 kWh/m²/day, while at Almeria this value is about 4.9 kWh/m²/day. The daily average solar radiation data considers a daily cycle with 24h but in Bom Jesus da Lapa (BA) the sun shines during 12h. Therefore, the average solar radiation considered for simulation is the double of the collected data.

3. Results and discussion

Figure 2a compares the model prediction with simulated data from Hatzikioseyan et al. (2003). Results show good fit of data as deviations up to 1% were obtained. Furthermore, the predicted total condensate water production is 5017.4 L and the predicted total brine production is 2982.6 L presenting deviations of 0.3% and 0.6%, respectively. Figure 2b shows the temperature and brine salinity profile along the desalination effects. The temperature decreases due to decreasing pressure in order to enable an efficient flash evaporation and brine salinity increases due to evaporation and production of fresh water.

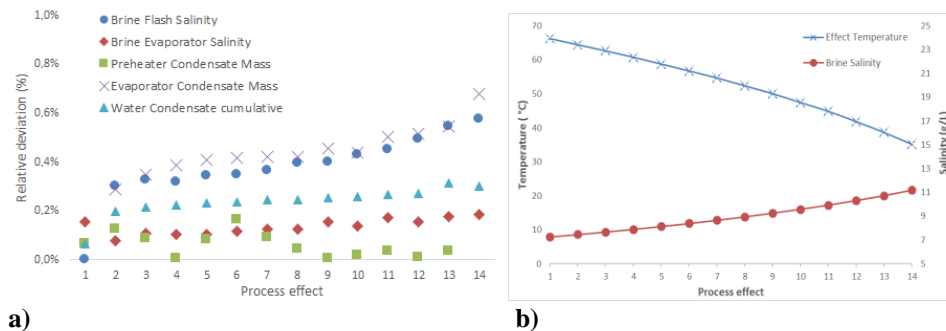


Figure 2: a) Validation of MED model: deviations of the model predictions against the data reported by Hatzikioseyan et al. (2003); b) Profile of temperature and brine salinity along process effects.

The solar collectors' model also presents good fit with Al-Ajlan et al. (2003), with deviations up to 0.7%. The collectors' area needed to supply thermal energy to the MED base case is about 2929 m², which is 9.6% higher than the PSA. According to Bataineh (2016), though, the Almeria's plant has a gas boiler back-up system which can supply up to 30% of desalination thermal energy needs, what can explain the lower collectors' area in the PSA. Table 1 shows the required area for the solar collectors for MED plants with different capacities. It further shows the percentual of the population which would be benefited by the desalination plant.

The daily solar radiation at Bom Jesus da Lapa (BA) varies every month of the year according to Figure 3. Considering the solar area of the base case 2,929 m², the collectors' hot water temperature and the distillate production for the varying solar radiation are shown in Figure 3. The average distillate production is 24.5 L/m²/day for an average solar radiation of 5.7 kWh/m²/day. Although Bataineh (2016) affirms that MED plants coupled with solar energies are able to produce more than 35 L/m²/day in regions with solar radiation above 4.8 kWh/m²/day, another source of energy, besides solar energy, is used. Furthermore, the plant studied by Bataineh (2016) is a large scale plant combined with thermo compressor system which may increase desalination energy efficiency.

Therefore, the distillate production obtained for Bom Jesus da Lapa is acceptable and cannot be directly compared with the value reported by Bataineh (2016).

Table 1 : Sensibility analysis of water production and solar collectors' area.

Water Production capacity(m ³ /day)	Solar Area(m ²)	City's population supplied (%)
72	2,929	2 %
144	6,182	4 %
288	12,365	8 %
576	23,628	16 %

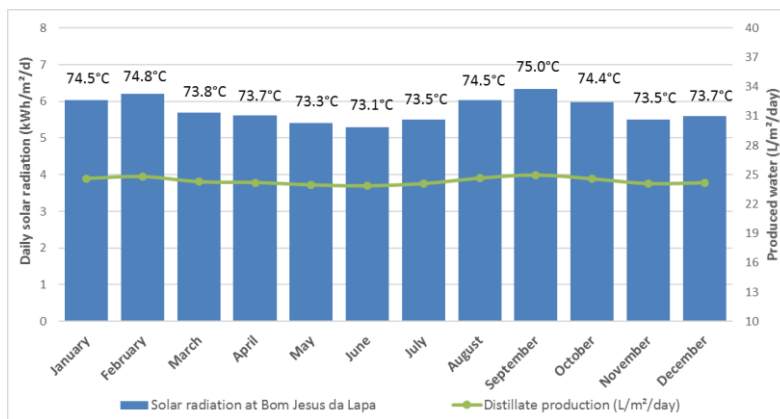


Figure 3 – Model Results and solar radiation data

4. Conclusions

This paper developed a model for a MED plant operated with thermosolar energy, which was successfully validated with data from literature. The model was used to evaluate the technical feasibility of the process in the northeastern Brazil, where the population suffers from water scarcity. The results show that is possible to produce fresh water using solar energy due to the high irradiation rates. Further studies might focus on the economic feasibility analysis to implement this MED desalination plant in Bom Jesus da Lapa (BA).

Acknowledgements

The authors would like to thank CAPES (Coordenação de Aperfeiçoamento de Pessoal de Nível Superior) and CNPq (Conselho Nacional de Desenvolvimento Científico e Tecnológico) for the financial support.

References

- S.A. Al-Ajlan, H. Al Faris, H. Khonkar, 2003. A simulation modeling for optimization of flat plate collector design in Riyadh, Saudi Arabia. *Renewable Energy*, v. 28, n. 9, p. 1325–1339.
- A. Al-Rawajfeh, S. Jaber, H. Etawi, 2017. Desalination by renewable energy: A mini review of the recent patents. *Hemijaska industrija*, v. 71, n. 05, p. 451–460.
- A. Alkaisi, R. Mossad, A. Sharifian-Barforoush, 2017. A Review of the Water Desalination Systems Integrated with Renewable Energy. *Energy Procedia*, v. 110, n. December 2016, p. 268–274.

- N.H. Aly, A.K. El-Fiqi, 2003. Thermal performance of seawater desalination systems. *Desalination*, v. 158, n. 1–3, p. 127–142.
- K.M. Bataineh, 2016. Multi-effect desalination plant combined with thermal compressor driven by steam generated by solar energy. *Desalination*, v. 385, p. 39–52.
- J.C. Chou, 1968. Thermodynamic properties of aqueous sodium chloride solutions from 32 to 350°F, PhD thesis, Oklahoma State University.
- A. De la Calle, J. Bonilla, L. Roca, P. Palenzuela, 2014. Dynamic modeling and performance of the first cell of a multi-effect distillation plant. *Applied Thermal Engineering*, v. 70, n. 1, p. 410–420.
- H. El-Dessouky, H.M. Ettouney, A.L. Imad, 1998. Steady-state analysis of the multiple effect evaporation desalination process. *Chemical Engineering Technology*, v. 21, p. 15–29.
- A. Ghobeity, A. Mitsos, 2014. Optimal design and operation of desalination systems: New challenges and recent advances. *Current Opinion in Chemical Engineering*, v. 6, p. 61–68.
- A. Hatzikioseyan, R. Vidali, P. Kousi, 2003. Modeling and thermodynamic analysis of a Multi-Effect Distillation (MED) plant for seawater desalination. *National Technical University of Athens journal (NTUA)*.
- M.H. Khademi, M.R. Rahimpour, A. Jahanmiri, 2009. Simulation and optimization of a six-effect evaporator in a desalination process. *Chemical Engineering and Processing: Process Intensification*, v. 48, n. 1, p. 339–347.
- J.S. Menezes, V.P. Campos, T.A.C. Costa, 2011. Desalination of brackish water for household drinking water consumption using typical plant seeds of semi arid regions. *Desalination*, v. 281, p. 271–277.
- P. Palenzuela, D. Alarcón, J. Blanco, E. Guillén, M. Ibarra, G. Zaragoza, 2011. Modeling of the heat transfer of a solar multi-effect distillation plant at the Plataforma Solar de Almería. *Desalination and Water Treatment*, v. 31, n. 1–3, p. 257–268.
- RETScreen. “Natural Resources Canada.”, 2018, <http://www.nrcan.gc.ca/energy/software-tools/7465>, Accessed September 2018.
- L. Roca, L.J. Yebra, M. Berenguel, A. de la Calle, 2012. Dynamic modeling and simulation of a multi-effect distillation plant. p. 883–888.
- R. Rocha, R.R. Soares, 2015. Water scarcity and birth outcomes in the Brazilian semiarid. *Journal of Development Economics*, v. 112, p. 72–91
- M.H. Sharqawy, J.H. Lienhard, S.M. Zubair, 2010. Thermophysical properties of seawater : a review of existing correlations and data. *Desalination and Water Treatment*, v. 16, n. 1–3, p. 354–380.
- M. Shatat, M. Worall, S. Riffat, 2013. Opportunities for solar water desalination worldwide: Review. *Sustainable Cities and Society*, v. 9, p. 67–80.
- J.J. Siirola, 2012. A Perspective on Energy and Sustainability. In: I.A. Karimi, R.B.T. Srinivasan-Computer Aided Chemical Engineering (Eds.). 11 International Symposium on Process Systems Engineering. [s.l.] Elsevier. v. 31p. 1–7
- J.M. Smith, H.C. Van Ness, M.M. Abbott. *Introduction to Chemical Engineering Thermodynamics*. 5. ed.
- United Nations. “The human right to water and sanitation”, 2018, http://www.un.org/waterforlifedecade/pdf/human_right_to_water_and_sanitation_media_brief.pdf, Accessed October 2018.
- I.H. Yilmaz, M.S. SÖYLEMEZ, 2012. Design and computer simulation on multi-effect evaporation seawater desalination system using hybrid renewable energy sources in Turkey. *Desalination*, v. 291, p. 23–40.

Flexible and efficient solution for control problems of chemical laboratories

Tibor Nagy^{a*}, Florian Enyedi^a, Eniko Haaz^a, Daniel Fozer^a, Andras Jozsef Toth^a and Peter Mizsey^{a,b}

^a*Dept. of Chemical and Environmental Process Engineering, Budapest University of Technology and Economics, Budafoki út 8. F II. ,Budapest H-1111, Hungary*

^b*Department of Fine Chemicals and Environmental Technologies, University of Miskolc, H-3515, Miskolc, Egyetemváros, Hungary*
tibor.nagy@mail.bme.hu

Abstract

In chemical laboratories there are always a permanent need to apply flexible, target oriented and efficient control solutions and data acquisition. Traditional equipment and methods utilized are however either time consuming or relatively expensive causing chemical laboratories often to be either not equipped with proper data acquisition and control systems or the installed setup is not easily reconfigured etc... Our aim is to show a simple and promising example that provides flexible and efficient control solution in chemical laboratories.

Keywords: distillation column control, fixed-, variable reflux

1. Introduction

Automation and process control is carried in increasing depth since the 50's. With such solution, operation of plants has become more precise, cost efficient and more safe. In smaller scales, such as chemical laboratories where various processes are investigated, reconfigured and developed, processes are regulated either manually or with high relative investment. Our choice for control as a demonstration is a distillation column that is particularly important since it is such a separation process that includes the common control problems and challenges that may occur in operation Luyben (1989). These common problems are found as a cause of high difference of time constants of process variables (*PV*), delay, process stiffness, interacting loops etc. studied by Morari et al. Grosdidier et al. (1985). Some of the mentioned problems and challenges occur only in MIMO (multiple input multiple output) control while others are also appear also in SISO systems. In our case we investigate a SISO (single input single output) case of column bottom and head temperature control that is in direct function of the product purity. With various control solutions and setup, cost-efficient and flexible operation can be carried out in laboratory sizes as well.

2. Methods and experimental Setup

In our work we define two cases:

- case A: purifying chlorobenzene from impurities

- case B: separating n-heptane and hexane

The column (see figure 1) for case A glass wall distillation column with the height of 30 cm height of Mellapak structured packing from Sulzer Chemtech and for case B it is built of two packed stages filled with random glass raschig ring type packings. In both cases the top of the column includes a gas vapor separator below the condenser. The condensed liquid is driven out of the column to a glass valve that is able vary the reflux ratio based on its on/off time ratio. The glass valve is driven by a 24 V solenoid valve and mosfet structure driven by the controller digital output. Preliminary tests showed, that the minimal time of stay/state should set to be at least 2 seconds. For normal operation we set the periodic time to be 10 seconds.

The reboiler of the distillation column is a 750 ml triple neck type round-bottom flask filled to with 500 ml of the initial liquid mixture. The heat is applied at the bottom by a heating basket by Bovimex MBO that is powered by 50 Hz 230 V AC and actuated with a solid state relay (SSR) that is regulated by the digital output of the Arduino board with the periodic time of 2 seconds. As the solid state relay is only capable of cutting power at 0 V crossings of the power source, 2 seconds is chosen as time period so the minimal resolution of the power adjustment is 1%.

In case of distillation, the temperature measurement should be particularly precise as in such case it is the process variable (PV) that gives the basis of the quality of control. In the investigated scenario, the temperature range is set to 0-200 °C with a precision range of +/- 0.1 °C. In order to satisfy these, RTD PT100 temperature sensors are applied with two approaches. The measured signal is either applied to a MAX31865 temperature sensor amplifier DAC from Adafruit or is sent to a signal transmitter to form 4-20 mA analog signals. In case of the utilization of MAX31865, in order to receive the most accurate signals the measured resistance is continually compared to a lookup table including resistance and temperature value pairs of DIN 43760/IEC 751 standard. The thermometer verification is carried out by the boiling of penthane at atmospheric pressure (36.1 °C) and as the steady state is achieved, the thermometer oscillates within +/- 0.1 °C range. In case of the analog signal processing two point temperature verification is carried out, by adjusting the range minimum and span of the transmitter.

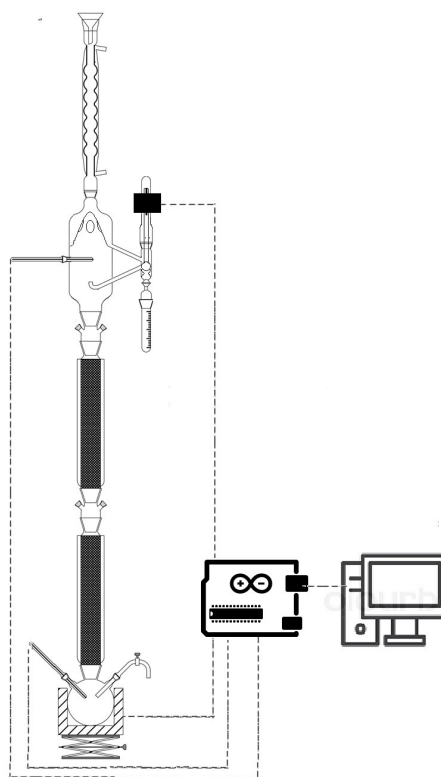


Figure 1: Distillation column and control scheme

The microcontrollers utilized are Arduino UNO and Due that are particularly popular for process control studies Rubio-Gomez et al. (2019). In case of analog signal input the transmitted signal is converted to 0-3 V to match the controller input range. These analog input reads are then refined with running average that takes 200 samples and gives two digital signals/second. Such frequency of data acquisition in such system is sufficient and will not cause stability problems. In case of digital input, SPI communication is utilized. Output signals are connected to the digital output pins with PWN. The Arduino is programmable by integrated development environment (IDE) with a PC by defining the variables of the different input and output pin-s, setpoints and generating the control algorithm etc. In other cases it is also possible to retransmit the Arduino's I/O and perform the data acquisition and control at a higher level.

As for controller tuning, different methods are available. In order to test the built system and closed loop a number of tuning methods and setups are investigated, these are:

- PID applying step response (open Z-N tuning) tuning
- PID applying Matlab PID tuner
- Cohen Coon method

2.1. Open Loop Ziegler-Nichols Method

The Ziegler-Nichols Method is one of the best known tuning methods, that is based on an open loop step-response function of time (Ziegler (1942)). The produced response function is approached by a first order transfer function with dead time. Applying the extracted parameters (K , τ and D_s) heuristic tables are utilized for tuning.

2.2. Cohen Coon method

The Cohen Coon tuning method also approximates the process with a first order element with dead time, but it is calculated differently (Cohen and Coon (1953)). Some literature favor the Cohen Coon method as it is more flexible with dead time compared to the Z-N method. To determine the tuning parameters just like with Z-N method, tuning tables are used.

2.3. Matlab PID tuner

Matlab PID tuner is an application of Matlab software that allows the instant tuning of a processes. The tuner application includes process identification in which the One pole + delay model is used. The application automatically calculates the linear model of the process and it provides interactive tuning where performance and robustness can be balanced. In our case the control loop is tuned for both performance and robustness to have only a moderate overshoot and after damping to settle on the new setpoint.

2.4. Model based control

A model based composition control is carried out with the model mixture of n-heptane and hexane. The internal model is divided to a reflux plan and the reflux control part. In order to achieve the planned product purity the number of theoretical plate (NTP) for the column is measured. In order to keep the composition of the distillate constant, the slope of the distillation working line must change in time and thus the reflux ratio changes as

well. The reflux control part executes the process including startup, setting the correct reflux ratio to the corresponding reboiled temperature and the shut down procedure.

3. Results

In figure 2 the temperature response of the step change of 50% can be observed that is applied to demonstrate a startup. The initial temperature is room temperature and the final value settled at ~ 120 °C. The tendency of the function shows dead time of ~ 5 minutes, while the rising time has an inflection at 26 minutes and the final value is reached at ~ 32 minutes.

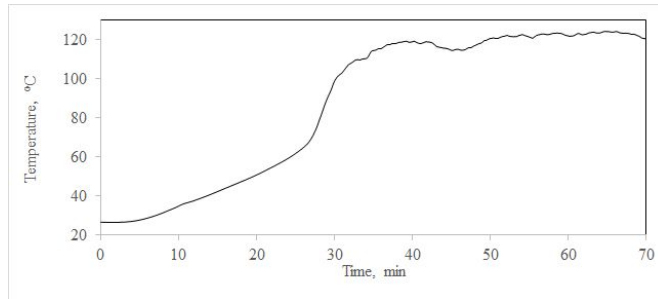


Figure 2: Response of the open loop distillation column

Based on the step response, the different tuning method show different control qualities for the column bottom temperature control (see figure 3).

Table 1: Evaluation of different tuning methods

rating parameter	Open Z-N Method	Cohen-Coon method	MATLAB PID Tuner
rise time [min]	82	23	17,5
maximal overshoot [°C]	2.65	18.2	10,6
settling time [min]	183	61.5	90
steady state error [°C]	(-0.1) - (+0.4)	(+0.2) - (+0.6)	± 0.5
ISE	5041300	2956470	2187620

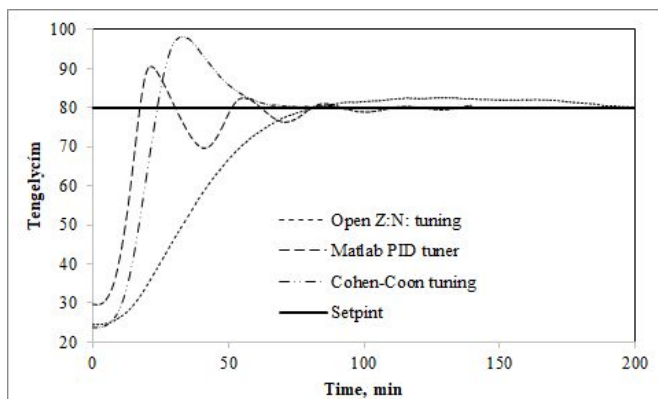


Figure 3: Column bottom temperature control with different tuning methods

The bang-bang control of the top product is shown on figure 4 for purifying chlorobenzene from impurities. In the figure the top temperature of the column and the reboiler is shown in the function of time. A results show a typical startup and operation procedure, where the dead time of the column top temperature is roughly over 15 min. As the column reaches the steady state within the target temperature range the reflux valve starts its operation with a reflux ratio of 3. It can be observed, that as product is taken away from the system, the bottom temperature starts rising as the composition changes in the reboiler.

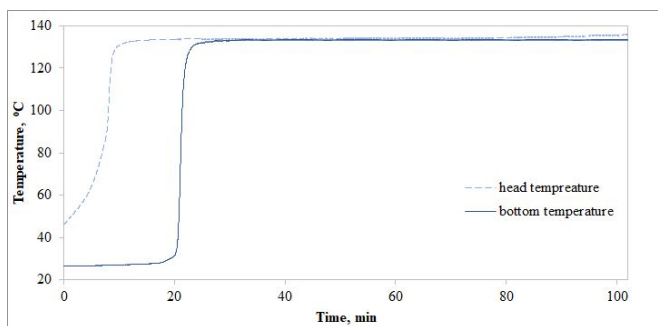


Figure 4: onoff control

The case of varying reflux composition control is shown in figure 5. The figure shows the case of separating n-hapten from hexane. The top and the bottom temperature and the reflux ratio in the function of time. After the steady state is established the reflux ratio is adjusted according to the calculated reflux plan to maintain the desired product purity. At the reflux ratio of 14 the product rate becomes so small, that the system shuts the reflux valve and the heating off, shutting the process down.

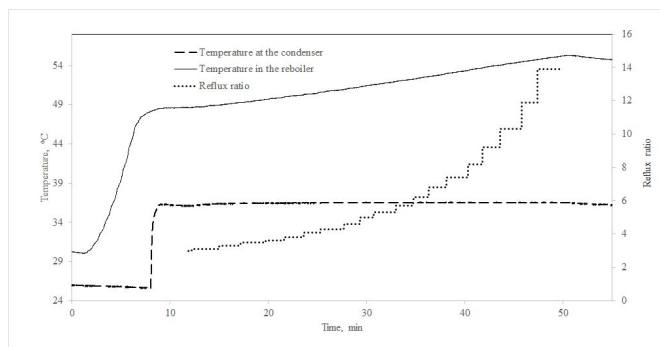


Figure 5: Variable reflux ratio control

4. Conclusions

There is permanent demand for target oriented and flexibly operated apparatus in chemical laboratories for efficient research activities. This challenge can be overcome by the utilization of microcontrollers. In many cases the additional knowledge for implementing such devices make such solution time consuming and effort intensive, while professional out of the box devices prices are high. Increasing popularity of microcontrollers these barriers are constantly stretched and by now user-friendly solutions are available. Applying such solution data acquisition and process control at laboratory scale is made practical and easy and cost efficient. As for demonstration in a chemical laboratory, batch distillation process is investigated with various cases of SISO control. In these cases The column bottom and head temperature is controlled either by the reboiler duty or the reflux ratio. Including on-line in-situ data acquisition, process analysis and controller tuning is carried out. The control structure is also investigated applying on-off, PID, and model based control strategies.

5. Acknowledgement

This publication was supported by the János Bolyai Research Scholarship of the Hungarian Academy of Sciences, ÚNKP-18-4-BME-209 New National Excellence Program of the Ministry of Human Capacities, NTP-NFTÁŰ-18-B-0154, OTKA 112699 and 128543. This research was supported by the European Union and the Hungarian State, co-financed by the European Regional Development Fund in the framework of the GINOP-2.3.4-15-2016-00004 project, aimed to promote the cooperation between the higher education and the industry.

References

- G. Cohen, G. Coon, 1953. Theoretical consideration of retarded control. *Trans. ASME* 75, 827–834.
- P. Grosdidier, M. Morari, B. R. Holt, 1985. Closed-loop properties from steady-state gain information. *Industrial & Engineering Chemistry Fundamentals* 24 (2), 221–235.
- W. L. Luyben, 1989. *Process Modeling, Simulation and Control for Chemical Engineers*, 2nd Edition. McGraw-Hill Higher Education.
- G. Rubio-Gomez, L. Corral-Gomez, J. A. Soriano, A. Gomez, F. J. Castillo-Garcia, 2019. Vision based algorithm for automated determination of smoke point of diesel blends. *Fuel* 235, 595 – 602.
- N. B. Ziegler, J.G & Nichols, 1942. Optimum settings for automatic controllers. *Transactions of the ASME* 64.: 759–768.

Process model validation and analysis for intensification of an industrial scale process

Renata Chinda^{a,§}, Rotjana Ponsatorn^{b,§}, Amata Anantpinijwatna^b, Fernando P. Pessoa^c, John M. Woodley^d and Seyed Soheil Mansouri^{d,*}

^a*Department of Chemical Engineering, Federal University of Rio de Janeiro, Av. Athos da Silveira Ramos, 149, CT, Sala E-207, 21941-909, Rio de Janeiro - RJ, Brazil*

^b*Department of Chemical Engineering, Faculty of Engineering, King Mongku's Institute of Technology Ladkrabang, Chalongkrung Rd., Ladkrabang, Bangkok, TH-10520*

^c*SENAI CIMATEC, Av. Orlando Gomes, 1845, Salvador - Ba, Brazil*

^d*Department of Chemical and Biochemical Engineering, Technical University of Denmark, Building 229, Søtofts Plads, DK-2800 Kgs. Lyngby, Denmark*

§ *Authors contributed equally to this work.*

**seso@kt.dtu.dk*

Abstract

Adopting reliable process models is one of the main requisites for wide spread use of process models in industry for design, control, operation and troubleshooting purposes. Validating a model against operational conditions is a plausible way to guarantee assurance and reproducibility of model outputs. Economic and sustainability analysis together with process intensification (PI) can provide feasible solutions for industrial hot-spot identification and removal. In this work, an industrial scale urea plant was modelled and simulated in a commercial process simulator. More than thirty different industrial process parameters were statistically analysed and used to perform the model validation. Economic and sustainability analyses were performed and the main hot-spots were identified. Process intensification at phenomena-level was employed to obtain more sustainable intensified process flowsheets. The results show that economic and environmental factors can be improved to reliable extent since the process model is closely replicating the reality in the base case and it fits well with industrial data.

Keywords: industrial data validation, process intensification, sustainable solutions.

1. Introduction

Modelling and simulation plays an important role in the development of chemical engineering systems. For laboratory, pilot or even industrial scale, computer aided solutions are one of the most cost effective tools available and, sometimes, the only option for engineering judgments. In order to guarantee the accuracy of these judgments it is necessary that the computational models correspond very well to the industrial data. Then, they can also be a good tool for real improvements through analysis like economic, sustainability, Life Cycle Assessment (LCA) and even reaching Process Intensification in order to achieve a more sustainable process.

This paper is on demonstrating the importance of validating simulations against real industrial data to make development of more advanced modelling approaches and even intensified solutions for existing chemical process possible.

2. Process description and modelling

The base case studied in this paper is the production of urea through CO_2 stripping. This process is divided into five blocks: Synthesis, Evaporation, Desorption and Hydrolysis, Recirculation and Prilling, as it can be seen in Fig. 1.



Figure 1: Simplified block diagram for the urea production process.

The principal section of this process is the Synthesis where reactions between NH_3 and CO_2 to produce ammonium carbamate and urea take place. The product of this section goes to Evaporation section to concentrate the urea and then it is sent to the Prilling. The remaining unconverted reactants are processed and recovered in the Hydrolysis and Desorption sections and, before they are sent again to Synthesis section, pressure and temperature need to be adjusted in the Recirculation step. The main equipment in each section are: Synthesis – pool condenser, reactor, stripper and scrubber; Evaporation – Pre-evaporator, 1st and 2nd evaporator; Desorption and Hydrolysis – adsorber, desorber I and II; Recirculation – rectifying column and condenser; Prilling – prilling tower. The reactions occurring at this process and considered in this paper are the well known ammonia and carbon dioxide producing ammonium and this one dehydrating in urea and, finally, the biuret formation, which presents a lack in literature of the area and it occurs from the condensation of two urea molecules resulting in biuret and ammonia. This process was modelled assuming steady state conditions, SR-POLAR for thermodynamic representation, production of biuret in the Pool Condenser, Reactor, Stripper and in all the Evaporators. Kinetics models were taken from Chinda et al. (2017).

3. Process validation

The experimental data used for validating the simulation was provided by an industrial urea plant in Brazil. A statistical analysis based on dispersion was performed with the plant capacity in order to exclude data that may have been taken in transient process conditions. For this, it was considered that coefficient of variation to be less than 1.5% would reflect stability in operation of the industrial plant. Statistical concepts such as arithmetic mean and standard deviation sample to calculate the variation coefficient were employed. Using this criteria it was found that the set of points at steady state available for validating the simulation was in range capacity from 86.45% to 98.21%. Validation of the simulation was performed by calculating the difference between industrial and simulated data and dividing it per industrial data.

A total of 37 different process parameters were evaluated following this criteria, among them stream temperature, steam generation, mass fraction composition for CO_2 , NH_3 , urea, H_2O and biuret, CO_2 conversion in the reactor and stripper efficiency. For all evaluated mass fractions, the deviation between the value predicted by the simulation

and the real value obtained from industrial data were less than 5%, while for steam generation and streams temperature the deviation was less than 8%. Fig. 2(a) shows the comparison between mass fraction for each component in the outlet of the reactor and the stripper. While in Fig 2(b) it is possible to see no deviation tendency for the 10 points evaluated in the steam generated in the Pool Condenser and in the outlet temperature of the Stripper liquid phase corresponding to the production capacity of the urea plant.

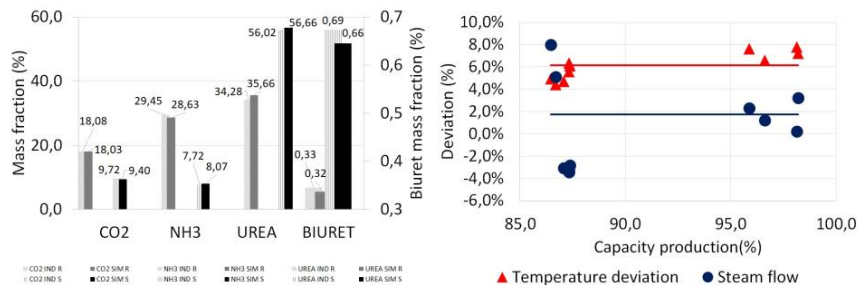


Figure 2 (a): Comparison between mass fraction composition in the outlet of the reactor and the liquid outlet of stripper. **(b)** Deviation analysis of the simulation data for the steam generation in the Pool Condenser and outlet temperature of the Stripper.

4. Process performance analysis & Hot-spots identification

Economic analysis was performed using ICAS-ECON. Sustainability analysis was carried out using the framework by Carvalho et al. (2008), Mansouri et al. (2013), and Tallis (2002); and for LCA analysis UK Government GHG conversion factors and IPCC emission factors were used.

4.1 Economic, life cycle assessment and sustainability analysis

The economic and life cycle assessment as a part of the performed analysis provide evidence that the main drivers for operating costs in urea production process are, heating (56.06 %), cooling (9.43 %) and electricity (34.51%). The analysis also showed that the rectifying column, the pre-evaporator, the 1st evaporator and the CO₂ compressor have the large utility cost, around 89.52% collectively. Furthermore, CO₂ compressor also has the largest carbon footprint because of its high-energy consumption, around 40.95 Wh.

The sustainability analysis performed in this study is a set of calculated closed- and open- paths. The method calculates and ranks as a set of mass and energy indicators, from the data obtained from steady-state simulation validated with industrial data. The main sustainability indicators are given in Table 1; and their corresponding paths are given in Fig. 2.

Table 1: Base case more expressive economic and sustainability indicators.

Path	Compound	MVA (10 ³ \$ /year)	TA (10 ³ \$ /year)	EWC (10 ³ \$ /year)	AF (10 ³ \$ /year)	MJ energy/kg product	kg product/kg raw material	Total kg CO ₂ Equivalent
OP150	H ₂ O	-11	-177.204	166.427	-			
CP284	H ₂ O	-	-	47.220	0.030	2.18	0.75	0.20
CP1	NH ₃	-	-	36.148	0.295			

Note: MVA – mass value added, TVA – total value added, EWC – energy to waste cost, CO₂ equivalent, carbon footprint, OP – open path, CP – closed path.

It can be seen in the Table 1, that water in the OP150 water is losing its value as it exits the process through this path. On the other hand, on the CP284 it is possible to see a high flow of water being recycled resulting in high loads of energy and waste/use of utilities for raw material recovery. The same also applies to ammonia in CP1 and water in the CP284. Fig. 3 shows a task-based flowsheet with the main closed- and open-paths.

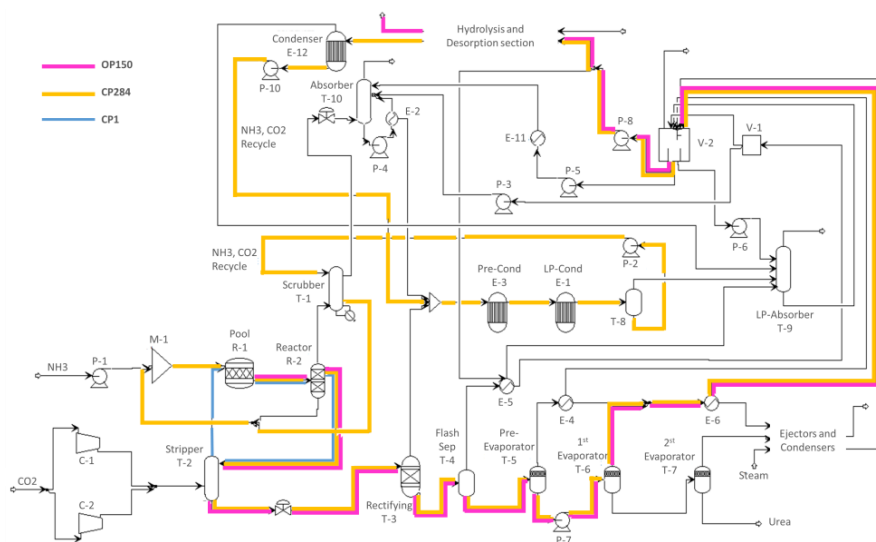


Figure 3: Base-case design for Synthesis, Evaporation and Recirculation sections for the production of urea, including process bottlenecks, closed- and open-paths.

4.2 Process hot-spots identification

The hot-spots identified based on the results of the economic, LCA and sustainability analysis are present in Table 2 and indicates the necessity of reducing the utility consumption. Utility is highly demanded in Evaporation and Recirculation sections. Thus, the Process Intensification was focused just in these sections.

Table 2: Urea Process hot-spots.

Hot-Spots	Design targets	Improvement solution
Limiting equilibrium	Un-reacted raw materials	-Reduction in number of unit operations
High energy consumption and/or demand	products recovery	- Improvement in sustainability and LCA factors

5. Process Intensification

Process Intensification was performed using a multi-stage framework according to (Babi et al, 2015) and (Garg et al, 2018). The base case was translated in a task-based flowsheet in order to identify Phenomena Building Blocks (PBB's), and generate Simultaneous Phenomena Building Blocks (SPB's). The total number of SPB's calculated were 16278, for 11 PBB's. Since, not all of them are feasible, following connectivity rules, it was found possible only 70 SPB's. The identified feasible SPB's are combined to form basic structures and then they were translated into unit-operations, as reactive distillation as it can be seen in Fig. 4.

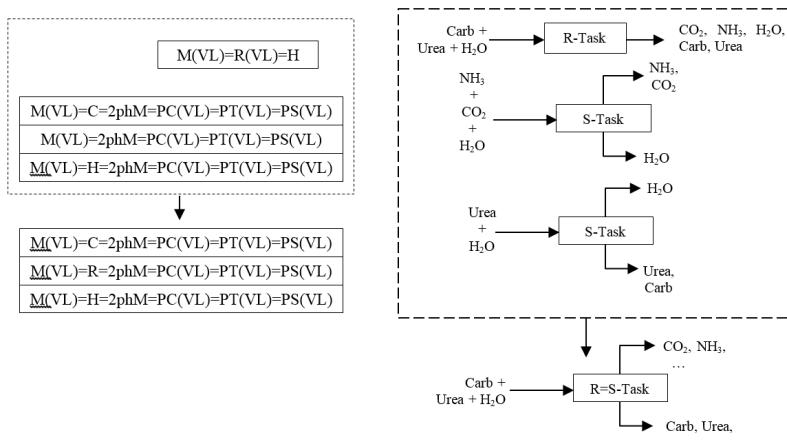


Figure 4: Basic structures combined into intensified unit operations: reactive distillation.

Finally, two intensified flowsheet alternatives are generated, as shown in Fig. 5 for Evaporation and Recirculation sections. Alternative 1 is the combined basic structure translated into Pervaporation membrane, while in Alternative 2 it is translated to Vapour permeation membrane.

The two process alternatives offer superior performance in terms of all indicators to the base case process, given that the best process alternative is the pervaporation membrane option (alternative 1). The energy consumption per one unit of urea is significantly reduced (53.48%) as well as utility cost (42.27%). The hot utilities (steam/hot water) and cold utilities (cooling water) usage were reduced to 68.63% and 29.15%, respectively. In addition, the carbon footprint, HTPI and GWP were reduced to 41.63%, 1.51% and 1.39%, respectively.

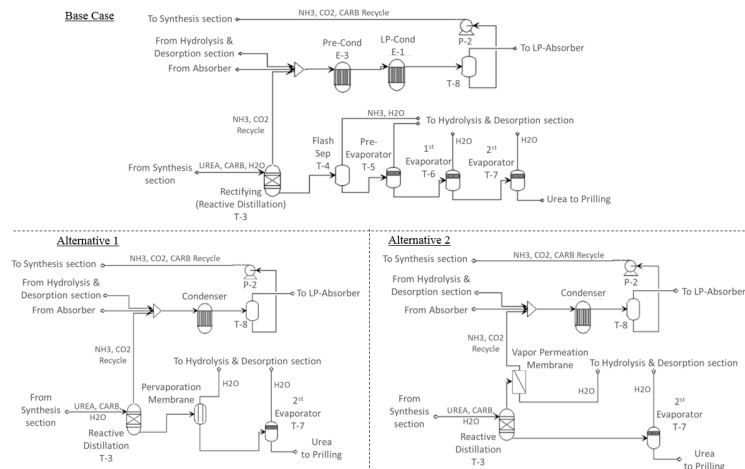


Figure 5: Base case and intensified flowsheet analysis.

5. Conclusions

Modelling and simulation of a urea plant was performed and validated with industrial data. Hot-spots were identified through economic and sustainability analyses. For Evaporation and Recirculation sections two feasible intensified alternatives were proposed using membranes. The pervaporation membrane unit for the separation of H₂O/Urea shows itself as the most sustainable one. The validation step with industrial data was an essential factor to perform a reliable and realistic study in order to suggest improvements to the process.

Acknowledgments

R.C. would like to acknowledge CAPES (Coordenação de Aperfeiçoamento de Pessoal de Nível Superior – Finance Code 001) and R.P. would like to acknowledge KMITL (King Mongkut's Institute of Technology Ladkrabang) for the research grants.

References

- Babi, D.; Holtbruegge J.; Lutze P.; Gorak, A.; Woodley, J.; Gani, R.. Sustainable Process Synthesis-Intensification. *Comput. Chem. Eng.* 2015, 81, 218-244.
- Carvalho, A.; Gani, R.; Matos, H. Design of sustainable chemical processes: Systematic retrofit analysis generation and evaluation of alternatives. *Process Saf. Environ. Prot.* 2008, 86, 328–346.
- Chinda, R., Yamamoto, C., Lima, D., & Pessoa, F. (2017/July). Modeling and Simulating the Synthesis Section of an Industrial Urea Plant: Analyzing the Biuret Formation. *UreaKnowHow.com*.
- Garg, N.; Kontogeorgis G.; Woodley, J.; Gani, R. A Multi-stage and multi-level Computer Aided Framework for Sustainable Process Intensification. *Proceedings of the 28th European Symposium on Computer Aided Process Engineering*. Graz, Austria.
- Mansouri, S.S.; Ismail, M.I.; Babi, D.K.; Simasatitkul, L.; Huusom, J.K.; Gani, R. Systematic sustainable process design and analysis of biodiesel processes. *Processes* 2013, 1 (2), 167-202
- Tallis, B., Sustainable Development Progress Metrics, IChemE Sustainable Development Working Group, IChemE, Rugby, UK, 2002.

Towards a systematic framework for the synthesis of operable process intensification systems - application to reactive distillation systems

Yuhe Tian^{a,b}, Iosif S. Pappas^{a,b}, Baris Burnak^{a,b}, Justin Katz^{a,b}, Styliani Avraamidou^{a,b}, Nikolaos A. Diangelakis^{a,b} and Efstratios N. Pistikopoulos^{a,b,*}

^a*Artie McFerrin Department of Chemical Engineering, Texas A&M University, College Station, TX 77843, United States*

^b*Texas A&M Energy Institute, Texas A&M University, College Station, TX 77843, United States*
stratos@tamu.edu

Abstract

We present a systematic framework for the design and operability/safety optimization of process intensified systems, with specific focus on reactive distillation processes. This framework is based on a phenomenological process intensification/synthesis approach (i.e., Generalized Modular Representation Framework) which first identifies promising intensified tasks and then translates them to equipment-based flowsheet alternatives. Flexibility analysis is integrated with the synthesis model to ensure that resulting design configurations are operable under varying operating conditions. To systematically account for inherent safety performance, risk assessment criteria are included as process constraints involving failure frequency and consequence severity criteria. A case study on the production of methyl tertiary butyl ether is presented to highlight the potential of the proposed approach in deriving inherently operable and safe intensified reactive separation systems.

Keywords: Process intensification, Reactive distillation, Generalized Modular Representation Framework, Operability analysis, Risk assessment

1. Introduction

In recent years, process intensification (PI) has attracted burgeoning interest in the chemical engineering research community and the chemical/energy industry due to its potential for drastic improvements in process productivity, efficiency, and profitability (Tian et al., 2018). The integration of multiple processing tasks into a single unit (e.g., combined reaction/separation processes) is one of the major PI pathways towards the development of breakthrough technologies. Reactive distillation (RD), a classic intensified invention, is showing significant energy and cost savings over conventional reactor-distillation counterparts (between 15 and 80 %) (Harmsen, 2007). Recent works for the synthesis of reactive separation systems have been leveraging phenomenological representation methods to systematically generate intensified process options from a lower-aggregated level without the pre-postulation of plausible unit-operation-based flowsheets which may hinder the discovery of novel solutions (Tula et al., 2017; da Cruz and Manousiouthakis, 2017; Demirel et al., 2017). However, these efforts mainly focus on steady-state design

at nominal operating conditions. The operational performances in these units under uncertainty and disturbances are mostly neglected, whereas their highly integrated schemes often decrease the degrees of freedom of the online decision maker, adversely affecting the process safety and limiting the operability of the systems (Baldea, 2015). Therefore, a holistic synthesis approach is required for the delivery of reactive distillation systems with guaranteed operability and safety performances at the early design stage.

In this work, we introduce a systematic framework for intensified process synthesis, which is based on the phenomenological Generalized Modular Representation Framework (GMF) with embedded process operability and safety assessment criteria. The rest of the paper is organized as follows. In Section 2, the proposed framework is presented in detail. Section 3 showcases this approach on a distillation-based reactive separation process for methyl tertiary butyl ether (MTBE) production. Finally, conclusions and directions for future work are discussed in Section 4.

2. Synthesis framework for Process Intensification

To address the synthesis of operable PI systems, we propose an integrated framework as depicted in Figure 1, with its stepwise procedure described in what follows:

Step 1: Process Intensification/Synthesis Representation via Generalized Modular Representation Framework – GMF, originally introduced by Papalexandri and Pistikopoulos (1996), represents chemical processes with two sets of phenomenological building blocks, namely the pure heat exchange module and the multifunctional mass/heat exchange module. Utilizing Gibbs free energy-based driving force constraints to characterize mass/heat transfer feasibility, GMF characterizes various (intensified) tasks (e.g., separation, reaction, combined separation/reaction) by optimizing physical and chemical driving forces to exploit the “ultimate” thermodynamic design space. The synergistic integration of multiple phenomena are automatically explored via superstructure optimization (Ismail et al., 2001) without a pre-postulation of plausible (and possibly myriad) tasks.

Step 2: Process Operability/Safety Analysis – Flexibility test is applied to identify the critical operating conditions when the resulting design configuration is operated under an expected range of the uncertainty. As for the consideration of inherent safety, risk assessment criteria (Nemet et al., 2017), which account for equipment failure frequency and consequence severity at the release of entire intrinsic hazards existing in the process, are included as constraints in the synthesis model to enable systematic generation of inherently safer design options instead of iterative evaluation in a posterior manner.

Step 3: Process Synthesis/Optimization – In this step, an integrated GMF-operability-safety synthesis strategy is developed in the formulation of a mixed integer nonlinear

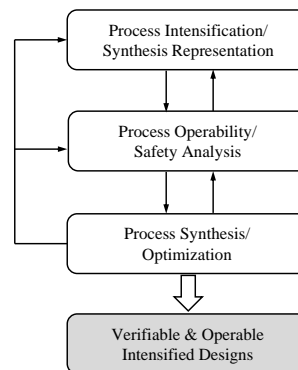


Figure 1: Proposed framework for the synthesis of operable process intensification systems (adapted from Tian et al. (2018)).

programming (MINLP) problem, as shown in Table 1. The Generalized Benders Decomposition (GBD) method (Geoffrion, 1972) is utilized for the solution of this optimization problem and is implemented in the General Algebraic Modeling System (GAMS) (Rosenthal, 2016). The primal NLP subproblem is solved with solver CONOPT and the master MIP problem with CPLEX. The optimization results will deliver optimal GMF-based design configurations with desired operability and safety performances.

Step 4: Operable Intensified Designs Verified via Steady-State & Dynamic Simulation – The resulting GMF configurations are translated to corresponding equipment-based flow-sheet alternatives and validated with steady-state simulation. To integrate steady-state and dynamic operation, “high-fidelity” dynamic models are developed to fully capture and analyze the system dynamics. This allows for further design and control optimization studies (Pistikopoulos et al., 2015; Diangelakis et al., 2017). Closed-loop validation is finally performed, with necessary iterations between different steps to ensure the delivery of consistent and verifiable operable intensification systems throughout the framework.

Table 1: Mathematical model for GMF-flexibility-safety synthesis – an indicative list.

GMF Synthesis Model	
Mass balance	$f^{LI}x_i^{LI} + f^{VI}x_i^{VI} - f^{LO}x_i^{LO} - f^{VO}x_i^{VO} + \sum v_i \times r \times M_{cat} = 0$
Energy balance	$f^{LI}h_i^{LI} + f^{VI}h_i^{VI} - f^{LO}h_i^{LO} - f^{VO}h_i^{VO} + \sum \Delta H_{reac} \times r \times M_{cat} = 0$
Driving force constraints	$G2_i = \ln \left[\frac{\gamma_i^L x_i^L P_{tot}^{sat,L}}{\phi_i^V x_i^V P_{tot}} \right] + \sum_i \sum_k \left[\frac{v_{ik} \Delta G_i^f}{RT} + v_{ik} \ln(\phi_i^V x_i^V P_{tot}) \right] \frac{\partial \varepsilon_k}{\partial n_i^f}$
Phase defining	liq: $\sum_i K_{eq,i} x_i \leq 1$, vap: $\sum_i x_i / K_{eq,i} \leq 1$
Kinetic model	$r = k [\prod a^\alpha - \frac{1}{K_a} \prod a^\beta]$, $k = A \exp(-Ea/RT)$
Thermodynamic model	$\gamma_i = \gamma(x_i, T, P)$, $P_i^{sat} = P^{sat}(T)$
Structural interconnection	$y_{e+1} - y_e \leq 0$, $y_e - [\sum y_{ne}^{LL} + \sum y_{ee}^{LL} + \sum y_{ee}^{CL} \leq 0]$
Flexibility Analysis	
	$\max_{V_\theta \in U(V_\theta)} \min_{V_z} \max_{j \in J_f} f_j(V_\theta, V_d, V_x, V_z) \leq 0$ s.t. $h(V_\theta, V_d, V_x, V_z) = 0$
Risk Assessment	
Consequence severity	$Severity_{i,e} = W_{i,e} \times O_e^1 \times O_e^2 \times O_e^3 / S_{risk}$
Risk evaluation	$Risk_{i,e} = freq_{e,fail} \times Severity_{i,e}$
Objective Function	
Total annualized cost	$Cost_{obj} = Cost_{cooling} + Cost_{heating} + Cost_{module}$

* Nomenclature: G = Gibbs free energy, O = factors accounting for process conditions, S = limit value for hazardous properties, W = quantity of hazardous substances present, y = binary variable, V_θ = uncertain parameters, V_d = design variables, V_x = state variables, V_z = control variables; Superscripts: LI = GMF module liquid inlet stream, VI = vapor inlet stream, LO = liquid outlet stream, VO = vapor outlet stream, LL = interconnecting liquid stream; Subscripts: e = module, i = component, k = reaction, n = feed stream.

3. Case study: MTBE production

In this section, the proposed framework is tested on a reactive separation system for the production of methyl tertiary butyl ether (MTBE) (Ismail et al., 2001). The case study aims to demonstrate the integration of operability/safety criteria at the early synthesis level as well as the potential of systematically deriving multiple intensified design options with different operational and cost performances for decision-making.

3.1. Problem statement

MTBE can be produced via the catalytic reaction of methanol (MeOH) and isobutylene (IB4) in the liquid phase using an ion-exchange resin as catalyst (e.g., Amberlyst 15 (Rehfinger and Hoffmann, 1990)). The production task is to obtain liquid MTBE at a rate of at least 197 mol/s with a purity higher than 98 mol%. Raw material availability (i.e., methanol and butene feed streams with given composition, flowrate, and temperature) is taken from Hauan et al. (1995). Additionally, an uncertainty range of ± 10 mol/s is considered for the methanol feed flowrate. Given the hazardous properties of the substances in this process, manifold process risks (i.e., toxicity, flammability, explosiveness) need to be considered for a holistic evaluation of inherent safety performance. The synthesis objective is to identify a flowsheet alternative to meet the MTBE production specifications with minimum total annualized cost (TAC) and desired operability/safety performance.

3.2. Synthesis with operability and safety considerations

In this case study, a maximum of 10 GMF mass/heat exchange modules and 20 pure heat exchange modules are allowed for the representation/synthesis of this process. The separation and/or reaction task taking place in each mass/heat exchange module is not postulated *a priori*, but to be determined through the superstructure optimization driven by the minimization of total annualized cost.

A nominal GMF configuration without flexibility or safety considerations is first synthesized as a reference design. The resulting MINLP model has 14,594 constraints, 8,098 continuous variables, as well as 734 binary variables. The optimal solution, shown in Fig. 2, features reactive distillation column at a total annualized cost of $\$1.7 \times 10^6$ /y. In this nominal design configuration, two pure heat exchange modules are selected as reboiler/condenser, while two reactive separation modules are used as reaction zone to produce MTBE, two separation modules as stripping section to separate unreacted methanol/isobutylene back to reaction zone, and another one as rectification section to transfer n-butene to distillate.

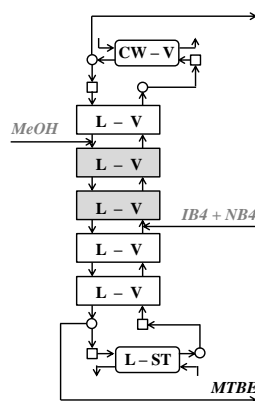


Figure 2: Nominal design.

Flexibility analysis is then applied to test if the nominal GMF configuration can be operated under the uncertainty of methanol feed flowrate, which identifies a critical point at the higher flowrate extreme value. On the other hand, inherent safety performance is improved by reducing the overall process risk by at least 20 % than that seen in the nominal design. The resulting design alternative, as shown in Fig. 3(a), utilizes four mass/heat exchange modules. Thus in this case, the enhancement of process safety is achieved by minimizing the unit size.

However, a comparatively more “risky” component is observed in Fig. 3(a) - i.e. the second reactive separation module (numbered from top to bottom) takes up more than 1/3 of overall process risk. To avoid the safety concerns resulting from a single module, the individual module risk is constrained to be less than 30 % of the overall process risk. The new optimal design configuration is illustrated in Fig. 3(b). The afore-mentioned module

is bypassed to alleviate its mass/heat transfer burden, thus introducing more degrees of freedom to enhance the system's flexibility and operability performances. The detailed design and operating parameters can be found in Table 2.

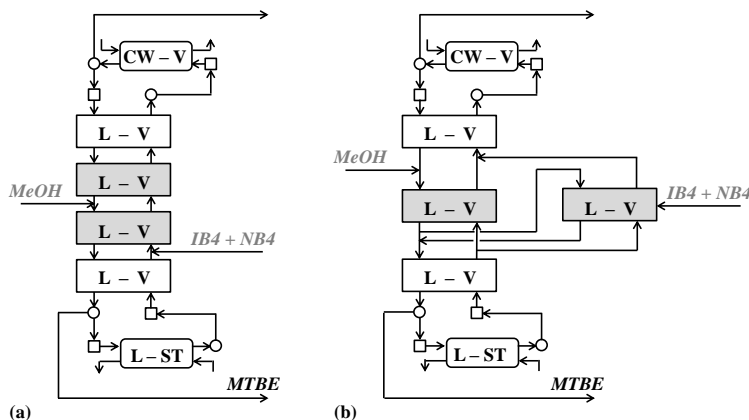


Figure 3: Flexible & inherently safer design configurations.

(a) Operable design I, (b) Operable design II

3.3. Steady-state & dynamic simulation and validation

Having generated the optimal and operable GMF configurations for the MTBE production (Fig. 3), in this step we identify and validate the corresponding equipment-based flow-sheet using steady-state simulation. Each GMF separation module is translated to two distillation trays in Aspen Plus® RADFRAC column (Aspen, 1981-2018), while each GMF reactive separation module to three reactive distillation trays. Therefore, the first operable design is verified as a 13-tray RD column, while the other one as a 10-tray RD column integrated with an additional 3-tray side-column. Table 2 provides a summary of quantitative validation between GMF and Aspen simulation on design/operating variables. “High-fidelity” dynamic models (Schenk et al., 1999) are also developed for the reactive distillation systems (Fig. 3) in gPROMS ModelBuilder® (PSE, 1997-2018), consisting of a system of differential and algebraic equations (DAE) for the description of component molar and energy balances for each tray, the partial reboiler and the total condenser, reaction kinetics, phase equilibrium, etc. The developed dynamic systems will be utilized for the derivation of receding horizon control policies (Pistikopoulos et al., 2015) to guarantee the optimal operation of the proposed designs.

Table 2: GMF quantitative validation with Aspen simulation.

	Nominal Design		Operable Design I		Operable Design II	
	GMF	Aspen	GMF	Aspen	GMF	Aspen
Column pressure (atm)	5.46	6.00	7.85	7.95	9.48	8.20
Reflux ratio	1.70	2.10	1.70	2.50	1.70	3.30
Reboiler duty (kW)	7.5×10^3	6.6×10^3	8.4×10^3	9.6×10^3	8.9×10^3	2×10^4
Condenser duty (kW)	2.3×10^4	2.2×10^4	2.3×10^4	2.4×10^4	2.3×10^4	3.4×10^4
Module/Tray Number	7	15	6	13	6	13
Bottom product flowrate (mol/s)	197.0	197.0	197.0	197.0	197.0	197.0
Product purity (MTBE mol/mol)	0.98	0.98	0.98	0.98	0.98	0.98
TAC ($\times 10^4$ \$/y)	171.1		182.4		190.2	

4. Conclusion

In this paper, we have presented a systematic framework to efficiently address the combinatorial PI design space and to integrate steady-state synthesis, dynamic analysis, and operability assessment to deliver validated operable intensification designs. It is shown, through an MTBE reactive separation example, that operability considerations may result in significant structural and operating changes of the process optimal solutions. Ongoing work addresses simultaneous design and control studies on the resulting MTBE reactive distillation configurations to close the loop under dynamic operating conditions.

5. Acknowledgement

We acknowledge the financial support from the Texas A&M Energy Institute, Shell Oil Company, RAPID SYNOPSIS Project (DE-EE0007888-09-03), and the NSF (Grant no. 1705423) under the project titled SusChEM: An integrated framework for process design, control and scheduling [PAROC].

References

- Aspen, 1981-2018. Aspen technology, inc. <https://www.aspentech.com/en/products/engineering/ Aspen-plus>.
- M. Baldea, 2015. From process integration to process intensification. *Computers & Chemical Engineering* 81, 104–114.
- F. E. da Cruz, V. I. Manousiouthakis, 2017. Process intensification of reactive separator networks through the ideas conceptual framework. *Computers & Chemical Engineering* 105, 39–55.
- S. E. Demirel, J. Li, M. F. Hasan, 2017. Systematic process intensification using building blocks. *Computers & Chemical Engineering* 105, 2–38.
- N. A. Diangelakis, B. Burnak, J. Katz, E. N. Pistikopoulos, 2017. Process design and control optimization: A simultaneous approach by multi-parametric programming. *AIChE Journal* 63 (11), 4827–4846.
- A. M. Geoffrion, 1972. Generalized benders decomposition. *Journal of optimization theory and applications* 10 (4), 237–260.
- G. J. Harmsen, 2007. Reactive distillation: the front-runner of industrial process intensification: a full review of commercial applications, research, scale-up, design and operation. *Chemical Engineering and Processing: Process Intensification* 46 (9), 774–780.
- S. R. Ismail, P. Proios, E. N. Pistikopoulos, 2001. Modular synthesis framework for combined separation/reaction systems. *AIChE Journal* 47 (3), 629–649.
- A. Nemet, J. J. Klemeš, I. Moon, Z. Kravanja, 2017. Safety analysis embedded in heat exchanger network synthesis. *Computers & Chemical Engineering* 107, 357–380.
- K. P. Papalexandri, E. N. Pistikopoulos, 1996. Generalized modular representation framework for process synthesis. *AIChE Journal* 42 (4), 1010–1032.
- E. N. Pistikopoulos, N. A. Diangelakis, R. Oberdieck, M. M. Papathanasiou, I. Nascu, M. Sun, 2015. PAROC – an integrated framework and software platform for the optimisation and advanced model-based control of process systems. *Chemical Engineering Science* 136, 115–138.
- PSE, 1997-2018. Process systems enterprise. *gproms*. <https://www.psenterprise.com/products/gproms>.
- A. Rehfinger, U. Hoffmann, 1990. Kinetics of methyl tertiary butyl ether liquid phase synthesis catalyzed by ion exchange resin – i. intrinsic rate expression in liquid phase activities. *Chemical Engineering Science* 45 (6), 1605–1617.
- R. E. Rosenthal, 2016. GAMS: A user's guide.
- M. Schenk, R. Gani, D. Bogle, E. Pistikopoulos, 1999. A hybrid modelling approach for separation systems involving distillation. *Chemical Engineering Research and Design* 77 (6), 519–534.
- Y. Tian, S. E. Demirel, M. F. Hasan, E. N. Pistikopoulos, 2018. An overview of process systems engineering approaches for process intensification: State of the art. *Chemical Engineering and Processing-Process Intensification* 133, 160–210.
- A. K. Tula, D. K. Babi, J. Bottlaender, M. R. Eden, R. Gani, 2017. A computer-aided software-tool for sustainable process synthesis-intensification. *Computers & Chemical Engineering* 105, 74–95.

A Model based analysis in applying Anderson–Schulz–Flory (ASF) equation with CO₂ Utilisation on the Fischer Tropsch Gas-to-liquid Process

Ali Attiq Al-Yaeshi,^a Ahmed AlNouss,^{a,b} Gordon McKay,^a Tareq Al-Ansari^{a,*}

^a *Division of Sustainable Development, College of Science and Engineering, Hamad Bin Khalifa University, Qatar Foundation, Doha, Qatar*

^b *Qatar University, College of Engineering, Department of Chemical Engineering, Qatar*

talansari@hbku.edu.qa

Abstract

Industrial emissions of CO₂ have observed a rapid increase since the industrial revolution and is accepted as a major contributor towards global warming. Despite the low market demand for the captured CO₂, carbon capture and storage has not seen commercial deployment due to questions regarding economic feasibility. As such, carbon capture and utilisation (CCU) is considered as an alternative and commercially viable CO₂ reduction approach, which can contribute effectively to the economy and environment. In CCU systems, captured CO₂ is utilised as a feedstock in other processes which require CO₂. This includes the synthesis of chemicals and materials such as Fischer-Tropsch Gas-to-liquid (GTL) production. The purpose of this paper is to evaluate the production of LPG, gasoline, diesel and wax using a Fischer-Tropsch (FT) GTL process model utilising mainly synthetic and captured CO₂ as a raw material. The aim is to assess the effects of reforming methods, recycle ratio of syngas mixture on the process efficiency. The reforming unit of this study includes both; auto-thermal reforming (ATR) and steam-methane reforming (SMR), to form synthesis gas (syngas). Moreover, the application of the Anderson–Schulz–Flory (ASF) equation on the product distribution of FT synthesis is studied to investigate the growth probability of hydrocarbons (α) affected by CO₂ utilisation. This GTL process is modelled using Aspen HYSYS software, and mainly includes a feeding unit, a reforming unit, an FT synthesis unit, upgrading and separation units and recycling units. The unreacted syngas mixture is recycled to the FT synthesis unit to enhance process efficiency and reduce the required amount of fresh feed. This work indicates that the optimal application of ASF with CO₂ captured can increase the production rates of paraffin's and olefins depending on the variation of α and H₂/CO. Initial results demonstrated promising results for an SMR case with around 27% and 4% increase in CO and H₂ production; respectively, when introducing CO₂ with around 38% mass flowrate of natural gas. The ATR case demonstrated less potential with only 9% increase in CO production when introducing the same flow rate of CO₂. The findings of this study include the effect of this increase on the production of fuel liquids such as gasoline and diesel and the optimization of ASF and H₂/CO ratio when introducing the captured CO₂. These results can have a positive impact on enhancing the overall process efficiency and reduce significantly the environmental impact.

Keywords: CO₂ Utilisation, ASF, Auto-Thermal Reforming, Steam-Methane Reforming, Gas-to-Liquid.

1. Introduction

Conversion of gas to liquids in what is known as (GTL) through the Fischer-Tropsch process has increased in production globally comparing to 2010 by 150% in 2015 and is expected to reach 500% by 2025 after commissioning of large scale plants in South Africa and Uzbekistan (EIA, 2017). The main purpose of the GTL process is to convert natural gas (NG) into synthesis products mainly hydrogen and carbon monoxide and subsequently to refined products such as LPG, gasoline, diesel and wax. GTL products contribute effectively to the environmental performance due to the low sulphur and aromatic fuels derived from the process as synthetic fuels. In addition, the process has low emissions of carbon monoxide, nitrogen oxides, hydrocarbons, and other components. Hence, synthetic fuels (GTL products) are considered green fuels, which have an added benefit of reducing the dependence on conventional fuels (Shell, 2018). Although the process is considered as environment-friendly, the GTL process with the Fischer Tropsch Synthesis (FTS) reaction has a very high cost breakeven value when compared to the conventional refinery product (Wood *et al.*, 2012). The GTL process consists of five main sections: pre-reforming, reforming, FT synthesis, upgrading and product fractionation. Upon conversion of the NG into syngas through different reforming technologies, the syngas is converted to liquid hydrocarbons in the FT reactor. These liquid hydrocarbons are then processed in the upgrading unit using hydrogen and separated as refined products in a fractionation column. There are different types of reformers used for syngas production. The main reformers include; Steam Methane Reforming (SMR) and Partial Oxidation Reformer (POX). However, some other reforming units can be used, such as dry methane reforming (DMR) and Auto Thermal Reforming (ATR) (Baltrusaitis and Luyben, 2015). The cost and the efficiency of producing a stable molecule pair of CO and H₂ (syngas) form a challenge to these techniques. As part of the GTL process, CO₂ can be utilised as a raw material or as part of recycling process to shift the chemical equilibrium in the aforementioned reformers and upgrade syngas quality. As such, the process design parameters, which need to be considered include: reactor/process design, effect of operating conditions, and the amount of CO₂ where each element is affecting the overall efficiency of the hydrocarbon products distribution including H₂/CO ratio of syngas and catalyst selectivity. The economic feasibility for CO₂ utilisation in the GTL process was studied by Zhang *et al.* (2014) based on two models. The first model to feed fresh CO₂ to the reforming unit and the FT synthesis unit to produce the required hydrocarbons. The second model considered fresh CO₂ as a direct feed to the FT synthesis unit only. The study targeted the process CAPEX and OPEX, and it was concluded that the two processes are environmentally friendly and economically feasible at large-scales. Rafiee *et al.* (2017) explored feeding captured CO₂ into the GTL plants' SMR or ATR processes. The economic feasibility demonstrates a benefit for both the emitters and consumers considering low project costs. Applied a multi-objective optimization which considered minimising of CO₂ emissions, while maximising carbon efficiency and mass flow of wax was demonstrated (Panahi *et al.*, 2018). The results indicated a high wax production rate and carbon efficiency, albeit with higher CO₂ emission than the base case.

The objective of this work is to evaluate the production of LPG, gasoline, diesel and wax using a GTL process model utilizing mainly FT synthetic and captured CO₂ as raw materials. The aim is to assess the effects of reforming methods and recycle ratio of syngas mixture on the process efficiency. The reforming units considered in this study include both; ATR and SMR, to form syngas. Moreover, the application of the Anderson–

Schulz–Flory (ASF) equation on the product distribution has been studied to investigate the growth probability of hydrocarbons (α) affected by CO₂ utilisation.

2. Process model of GTL

In addition to the sinks considered by the authors in the previous study (Al-Yaeshi, et al., 2018), the system considered is comprised a single CO₂ source and multiple GTL plants located in close proximity. The optimization model is developed for each GTL plant based on different reformer technologies, where the objective function is to maximise the total CO₂ utilised taking into consideration the highest production of LPG, gasoline, diesel and wax. This can ensure lower harmful emissions to the environment and increased economic benefits. Hence, it is important to assess the efficiency of integrating the CO₂ into SMR and ATR and compute the enhancements in the output production. The data are related to a specific CO₂ source; namely from Qatar Gas (QG), and multiple GTL sinks for CO₂ utilisation; namely Oryx GTL, and Pearl GTL in the Ras Laffan industrial zone.

2.1. GTL Process Technology

The feed consisting of NG and steam with O₂ in the case of ATR enters a Gibbs Reactor, where NG is reformed to mainly CO and H₂. The syngas produced is first purified from water and then sent to the FT section to produce the higher carbon molecules. The effluent from the FT reactor is purified in a 3-phase separator to remove water and recycle back the unreacted CO and H₂ for what's known as Tail gas. The high hydrocarbon content stream is sent to the upgrading section, where the higher molecules are cracked with H₂ into smaller ones. The cracked effluent is finally sent to the fractionation unit where the unreacted H₂ is first recycled to the hydrocracking unit and the product is distilled into LPG, gasoline, diesel, and wax. Part of the wax is recycled back to the upgrading unit to increase the efficiency of the section (Figure 1).

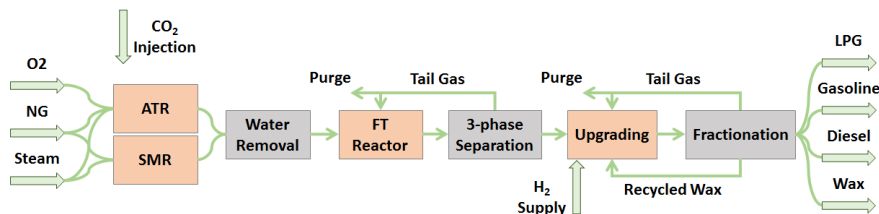


Figure 1: Process flow diagram of GTL plant

2.2. CO₂ Source Data

Emissions of CO₂ from Qatar Gas is approximately 35.8 Mt/year (Sayeed, 2016). The capturing of CO₂ is processed by chemical absorption using amine solvents, with the maximum achievable capture removal efficiency of 90%. The captured CO₂ is transferred through a pipeline connected to Pearl GTL and Oryx GTL plants.

2.3. CO₂ Sinks Data (Pearl GTL and Oryx GTL)

The Pearl GTL is the largest GTL plant on the global scale. Utilising ATR technology, it produces LPG, naphtha, kerosene, diesel and base oils. It is supplied with 1.6 billion cubic feet per day of lean methane-rich gas from the Qatar north gas field. The capacity of plant 260,000 bbl/day divided as 120,000 bbl/day upstream products and 140,000 bbl/day GTL

products (Shell, 2018). Oryx GTL utilizes ATR technology and is supplied with 330,000 cubic feet per day of lean methane-rich gas from the Qatar North gas field to produce 34,000 barrels per day of liquids with 24,000 barrels of GTL diesel, 9,000 barrels of naphtha and 1,000 barrels of liquefied petroleum gas (QP, 2018).

3. Methodology

This study develops a simulation model of a GTL plant which integrates CO₂ as raw feed to attain optimal production of hydrocarbon products based on integrated SMR and ATR reformers. The model assumes the captured CO₂ is pure and reaches the sinks at the required pressure of the GTL process at a given capacity which is not exceeded. The simulation is developed using Aspen HYSYS-V9 using the parameters listed in Table 1.

Table 1. Model parameters

Parameter	NG	Steam (ATR)	O ₂ (ATR)	Steam (SMR)
Flow (T/d)	1.54 x 10 ⁴	6.49 x 10 ³	1.72 x 10 ⁴	4.87 x 10 ⁴
T (C)	25	500	144	500
P (bar)	1	25	25	25
	Reformer	FT	Hydrocracking	Fractionator
T (C)	1050	250	345	Top P: 1 bar
P (bar)	23	24	80	Bottom P :1.5 bar
	1 st Purge (ATR)	2 nd Purge (ATR)	1 st Purge (ATR)	2 nd Purge (ATR)
%	5	5	8	1

The scenarios considered vary depending on plant capacity, reformer types, and feed rate of CO₂ into Oryx GTL and Pearl GTL. It is considered that the plant capacity for the two trains is 34000 bbl/day with 15372 ton/d of NG feed flow rate with molar steam to carbon ratio (S/C) of 0.4, and oxygen to carbon ratio of 0.6 in the case of ATR. However, the steam to carbon ratio in the case of SMR will increase to a ratio of 3 with zero oxygen while the NG will remain the same. The CO₂ injection to the ATR/SMR reformer has been varied between 500-2500 ton/d to examine its effect on the production rates of the refined products compared to the ATR case with zero CO₂ feed. The target is for the H₂/CO ratio to be in the acceptable range and to maximise the production. The main constraint used in the model is the appropriate ratio of H₂: CO which does not exceed a ratio of 2 in the case of ATR (Aasberg-Petersen et al., 2003) and 3 in case of SMR (Rafiee et al., 2017) without CO₂ injection, to ensure optimal synthesis gas after the reformers. A carbon mass balance has been applied to estimate the FT products distribution according to the Anderson-Schulz-Flory model, illustrated in Eq. (1) (Krishna and Sie, 2000).

$$W_n = Cn (1 - \alpha)^2 \alpha^{n-1} \quad \text{Eq. (1)}$$

Where, W_n is weight fraction of a particular product characterized by the carbon number (Cn) and chain growth probability (α).

4. Results

The results demonstrated a higher rates of refined products with the addition of CO₂ for both cases. In the base case of the ATR reformer with zero injection of CO₂, an H₂/CO ratio of 2.15 is achieved after the ATR reformer, and a ratio of 3.1 is achieved before the

FT reactor. These ratios were reduced significantly with the addition of CO₂ to the system. As illustrated in Figures 2a and 3a, the H₂/CO ratio before the FT reactor performance declined. Furthermore, production rates of LPG, gasoline, diesel and wax demonstrated increasing trends. Moreover, the SMR reformer indicated a high production of LPG and wax in comparison with the base reference case of ATR and conversely to gasoline and diesel, where the results demonstrated a substantial decrease. Furthermore, it can be deduced that in case of the ATR the total production of the refined products is larger in comparison to the SMR. Furthermore, the CO₂ rate to the system has a significant impact on the H₂/CO ratio after the SMR and before the FT reactor as illustrated in Figure 2b. This contributes positively to the overall process as it will reduce the needed purge rate and increase the production rates of refined products.

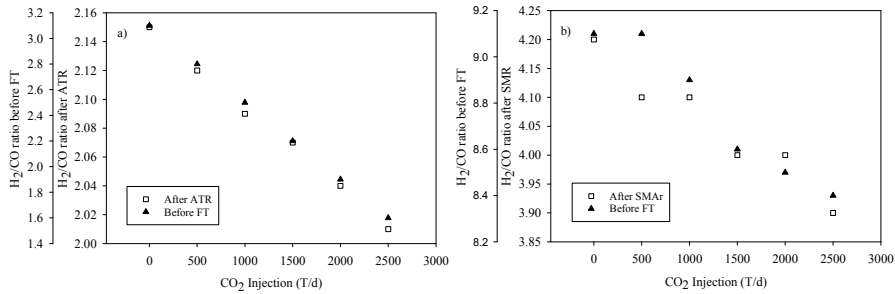


Figure 2: Impact of CO₂ injection on H₂/CO ratio in a) ATR and b) SMR

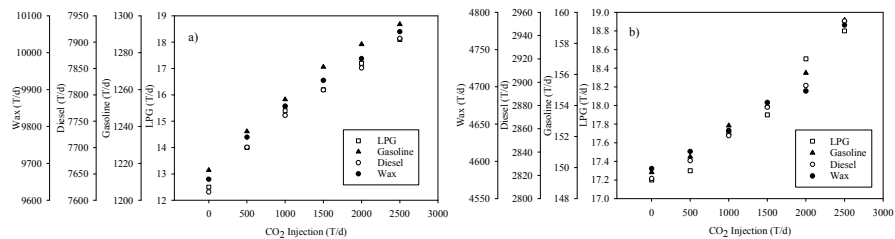


Figure 3: Production trend of refined products in a) ATR and b) SMR with CO₂ injection rates

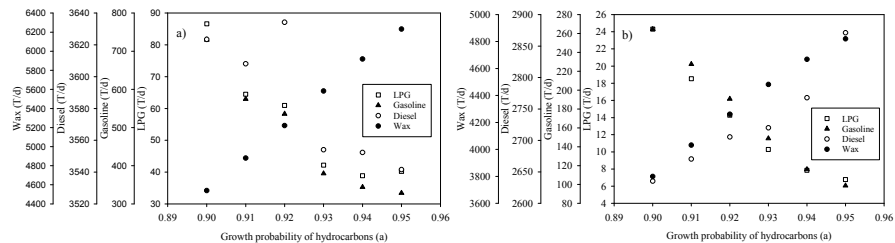


Figure 4: Impact of (α) in a) ATR and b) SMR on production trend of refined products

The study of varying growth probability of hydrocarbons is conducted to examine the effect on production rates and to identify the optimal location of α. The results of the ATR case, illustrated in Figure 4a, indicate an increasing trend for the wax with the increase in α, while the three remaining products illustrated a declining trend. The diesel production indicated a peak around 0.92α at approximately 3630 T/d. The SMR case demonstrated a

declining trend in the production of LPG and gasoline with the increase of α . Whereas, the production rates of diesel and wax demonstrated an increasing trend with a peak value of around 0.95α in the case of Diesel.

5. Conclusion

The study demonstrates the suitability of integrating CO₂ into GTL plants in order to increase production rates of finished products, reduce rogue CO₂ emissions and to generate economic benefits. The GTL plants considered in this study consist of two different reforming operations, ATR and SMR. The base reference considered is the ATR with zero CO₂, after which the injection of CO₂ is studied at varying rates between 500-2500 tonne per day to monitor the refined production rates. The results demonstrated a significant enhancement, however the LPG and wax in the case of the SMR are larger than the base reference case, although the purge and the H₂/CO is higher for the case after the reformer and before the FT reactor. Future studies should include the computation of net emissions of CO₂, and the economic viability considering process steam and heat energy requirements.

References

- A. Attiq Al-Yaeshi, T. Al-Ansari, R. Govindan, 2018, Computer Aided Chemical Engineering, The potential for carbon dioxide capture and utilization within the State of Qatar, 28th European Symposium on Computer Aided Process Engineering, pp.1499-1504.
- A. Rafiee, M. Panahi, and K.R. Khalilpour, 2017, CO₂ utilization through integration of post-combustion carbon capture process with Fischer-Tropsch gas-to-liquid (GTL) processes, Journal of CO₂ Utilization, 18, 98-106.
- C. Zhang, K.-W. Jun, K.-S. Ha, Y.-J. Lee, and S.C. Kang, 2014, Efficient Utilization of Greenhouse Gases in a Gas-to-Liquids Process Combined with CO₂/Steam-Mixed Reforming and Fe-Based Fischer-Tropsch Synthesis, Environmental Science & Technology, 48, 14, 8251-57.
- D.A. Wood, C. Nwaoha, and B.F. Towler, 2012, Gas-to-liquids (GTL): A review of an industry offering several routes for monetizing natural gas, Journal of Natural Gas Science and Engineering, 9, 196-208.
- EIA, 2017, Global gas-to-liquids growth is dominated by two projects in South Africa and Uzbekistan, U.S. Energy Information Administration, International Energy Outlook 2017, Accessed 14/11/2018, <https://www.eia.gov/todayinenergy/detail.php?id=33192>
- J. Baltrusaitis, and W.L. Luyben, 2015, Methane Conversion to Syngas for Gas-to-Liquids (GTL): Is Sustainable CO₂ Reuse via Dry Methane Reforming (DMR) Cost Competitive with SMR and ATR Processes?, ACS Sustainable Chemistry & Engineering, 3, 9, 2100-11
- K. Aasberg-Petersen, T.S. Christensen, C. Stub Nielsen, and I. Dybkjær, 2003, Recent developments in autothermal reforming and pre-reforming for synthesis gas production in GTL applications, Fuel Processing Technology, 83, 1, 253-61.
- M. Panahi, A. Rafiee, S. Skogestad, and M. Hillestad, 2012, A Natural Gas to Liquids Process Model for Optimal Operation, Industrial & Engineering Chemistry Research, 51, 1, 425-33.
- M. Panahi, E. Yasari, and A. Rafiee, 2018, Multi-objective optimization of a gas-to-liquids (GTL) process with staged Fischer-Tropsch reactor, Energy Conversion and Management, 163, 239-49.
- QP, 2018, Subsidiaries and joint venture details Accessed 14/11/2018, <https://www.qp.com.qa/en/QPActivities/Pages/SubsidiariesAndJointVenturesDetails.aspx?aid=3>
- R. Krishna, and S.T. Sie, 2000, Design and scale-up of the Fischer-Tropsch bubble column slurry reactor, Fuel Processing Technology, 64, 1, 73-105.
- Shell, 2018, Shell qatar project and sites https://www.shell.com.qa/en_qa/projects-and-sites/pearl-gtl.html
- S. Mohammed (2016), Qatar's National Emission Inventory Report, Figshare, Available from; <http://creativecommons.org/licenses/by/4.0/> [Accessed February 2018]

Consequential Life Cycle Analysis for Food-Water-Energy-Waste Nexus

Yanqiu Tao, Fengqi You

Cornell University, Ithaca, New York, 14853, USA

Abstract

Animal manure, as a type of unavoidable organic wet biomass waste, contains abundant nutrients, moisture and pathogen, therefore how to properly handle them has become an arising problem. Opposite to the severe challenge, dairy manure can be viewed as stably supplied feedstocks for biorefinery, which is invariant to seasonal and climate change and is of huge quantities. In this study, to thoroughly explore the potential to treat manure as biorefinery feedstocks, we select three promising thermo-chemical technologies, namely slow pyrolysis, fast pyrolysis and hydrothermal liquefaction and quantify their corresponding environmental impacts. We adopt a consequential life cycle assessment (LCA) approach, and successfully capture the environmental impact both attributed to the target process and consequential to the affected processes and markets. Lastly, we compare the consequential environmental impact with the attributional environmental impact and find consequential LCA advantageous to capture environmental impact without overestimation.

Keywords: wet biomass, dairy manure, pyrolysis, hydrothermal liquefaction, consequential life cycle assessment

1. Introduction

Organic wastes treatment is recognized as one of the most challenging issues in the systems engineering of food-water-energy nexus (FWEN) (Garcia et al., 2016). For example, animal manure, as one main type of unavoidable organic wastes, is rich in nutrients, bacteria and aerobic organics, hence it causes severe degradation of water and soil quality and makes contribution to greenhouse gas emission if being composted or landfilled (Yue et al., 2014). However, if handled properly, manure wastes can be converted to value-added products, for example biochar, biogas and bio-oil, which may bring both environmental and economic benefits (Garcia and You, 2017).

To address this issue, we specifically focus on the treatment of dairy manure wastes in this study. The environmental impact of three promising technologies for organic waste conversion, namely slow pyrolysis, fast pyrolysis and hydrothermal liquefaction, are evaluated and compared. To assess the environmental impacts, we adopted a cradle-to-grave analysis technique named life cycle assessment (LCA). The methodology of LCA involves four steps: goal and scope definition, life cycle inventory analysis (LCI), life cycle impact assessment (LCIA) and interpretation. The first step, goal and scope definition, includes the definition of the goal of LCA, the functional unit, system boundary, allocation procedures, type of methodology, life cycle impact category and assumptions. The second step LCI involves compilation and quantification of LCI data such as mass and energy flow rates. Next, LCI data is assigned to life cycle impact categories such as global warming potential (GWP) and multiplied by the

characterization factors of corresponding impact categories. Eventually the environmental impact indicators are obtained and interpreted during the final step. Notably, interpretation does not only happen in the end, but is conducted iteratively in every step of LCA.

LCA approach can be classified into two types: attributional LCA (ALCA) and consequential LCA (CLCA). The conventional ALCA takes a “snapshot” of existing conditions by only taking into account the environmental impacts of direct physical flows attributed to the life cycle of the products (Yang 2016). One underlying assumption of ALCA in which supply of inputs are unlimited implies the absence of both market effects and indirect environmental impacts. Therefore, ALCA is not suitable for situations where market effects and those indirect environmental impacts are not negligible, which accounts for the vast majority of the real world cases. Furthermore, another assumption, fixed input/output coefficients, eliminates possibilities for ALCA to capture any change in decision making to targeted processes.

In contrary to ALCA, by involving market constraints, CLCA is capable of capturing consequential environmental impacts in response to changes all through the targeted processes. CLCA systematically identifies the affected processes that change its production in response to the changes in both demand for inputs and supply for outputs, and sequentially expands its system boundary by including those indirectly affected processes. Several frequently-used methods to quantify the indirect environmental impacts are scenario analysis, simple partial equilibrium (PE) model, sophisticated PE model and computable general equilibrium (CGE) model (Garcia and You 2018). Considering model resolution, model maturity and the viability of the plan to incorporate CLCA into an optimization framework, it is the most appropriate to integrate the simple PE model in our CLCA study. Simple PE model relies on the microeconomic concepts of price elasticity of demand and supply, and it is confined to only one or a few economic sectors. While in reality, economic consequences can be passed on through multiple levels of markets, intuitively in this study, we aim to identify and analyze no more than two levels of markets and no more than one affected technology. Considering the inherently interrelated nature of FWEN, the CLCA approach is more reliable and may contribute to the improvement of systems engineering of more sustainable production, consumption, and distribution processes in the FWEN (Gong and You 2017).

2. System boundary, assumptions, and consequence identification

The goal of this consequential LCA is to assess the consequential life cycle environmental impacts of three thermo-chemical technologies: slow pyrolysis, fast pyrolysis and hydrothermal liquefaction (HTL), and make a comparison between the attributional and consequential environmental impacts. Pyrolysis is a thermo-chemical process that converts the waste biomass into a series of value-added products: product gas, bio-oil and biochar in the absence of oxygen (Zhang et al. 2014). Pyrolysis can be categorized as slow pyrolysis and fast pyrolysis, according to the heating rate and residence time (Gebreslassie et al., 2013). Particularly, the product yields vary with temperature, where the slow pyrolysis produces more product gas, biochar and less bio-oil, while the fast pyrolysis leads to more oil product (Goyal et al, 2008). Notably, by taking into account its capability of more than 100-year carbon sequestration and fertilizer use efficiency improvement, biochar is especially valuable from an

environmental point of view (Roberts 2010). Hydrothermal liquefaction converts biomass into bio-oil, product gas, hydro-char and aqueous phase product at moderate temperature in water (Gong et al. 2014). Therefore, this process does not need the energy-intense drying process and may serve as an ideal approach to handle wet biomass (Gollakota et al, 2018).

The functional unit is defined as treatment of 1 t fresh dairy manure. System boundary for the slow and fast pyrolysis is shown in Figure 1. In both processes, we start from collection of 1 t fresh dairy manure, transport it to anaerobic digestion (AD) and solid-liquid separation (SLS) (Aguirre-Villegas and Larson 2017). The avoided emission resulted from the AD-derived biogas is not included in the system boundary. Then, the pre-treated feedstock is transported to the biorefinery and undergone thermal-drying prior to being pyrolyzed. The heat is assumed to be supplied by high pressure steam, which is vaporized using natural gas (Gong et al., 2014). The resulting wastewater is sent to a wastewater plant for treatment and recycling. The biochar from pyrolysis is used as a soil amendment, which is then transported and applied to soil. Product gas will be used to generate electricity, and bio-oil will be converted to gasoline and diesel after being hydrotreated and hydrocracked. System boundary for the HTL is shown in Figure 2. After AD and SLS, the digested dairy manure is transported to the biorefinery and sent to the HTL reactor directly. The resulting bio-oil will be converted to gasoline and diesel, gas will be emitted directly, hydro-char will be applied to soil as P, K fertilizer. Additionally, the aqueous phase is treated by anaerobic digestion and used for algae cultivation (Zhou et al. 2015).

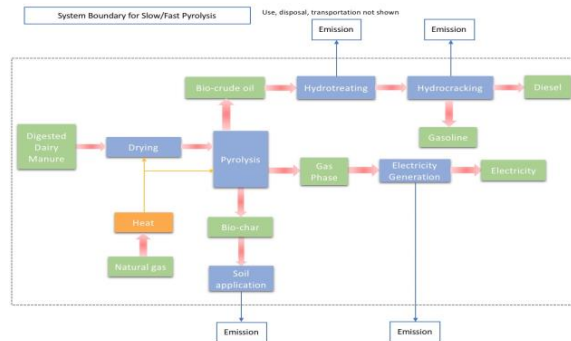


Figure 1. System boundary for slow and fast pyrolysis

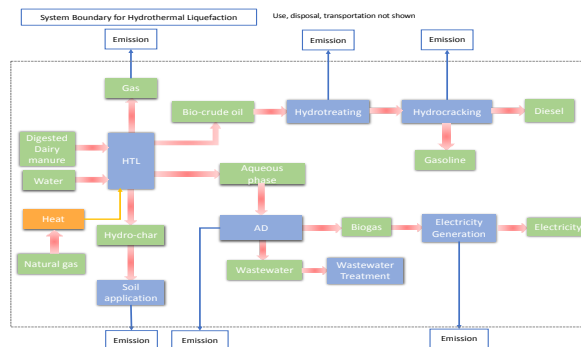


Figure 2. System boundary for hydrothermal liquefaction

While feedstocks are consumed, products are generated, the biorefinery interacts with the feedstock and product markets and breaks the current market equilibrium. The change in supply and demand in the feedstock and product market lead to change in the price and quantity, and eventually shifts to a new market equilibrium. This will also consequentially affect the market equilibrium in the downstream market. Therefore, it is important to identify the affected markets and capture the changes. There are five markets directly interacting with the target process: (1) Gasoline market. As an additional supply of gasoline is introduced into the market, the demand for fossil-based gasoline decreases, and the market reaches a new equilibrium. (2) Diesel market. The diesel market experiences the same trend as the gasoline market. (3) Electricity market. We assume that the price elasticity of demand is zero, and thus the increase in supply of electricity from the target process can be completely absorbed by other electricity suppliers. (4) Biochar market. The biochar market is very small and expanding, so we will not model the market behavior of biochar. Instead, we will only account for its improved fertilizer use efficiency and avoided soil emission during soil application. (5) Natural gas market. The natural gas will be consumed as a feedstock to generate heat for vaporization. The increased demand for natural gas will lead to increased price, and thus consequentially increased demand in other fossil-based fuels in the downstream market of heat generation. Two other modifications we made are: (1) Hydro-char. Because the hydro-char is sold as a substitute for P, K fertilizer, it will in fact avoid emissions during the use and disposal of the P and K fertilizers. (2) Dairy manure. Since the dairy manure market is absent, we will only calculate the avoided manure composting emissions.

3. Life cycle assessment results

Following the steps of consequential LCA, we obtain results as shown in Figure 3. The 100-year global warming potential (GWP) generated from consequential analysis for the treatment of fresh dairy manure using slow pyrolysis, fast pyrolysis and HTL are: 26.6, 34.7 and 15.7 kg CO₂ eq., respectively. HTL has the overall best performance with respect to the 100-year GWP. The energy-intensive process involved in the slow and fast pyrolysis process, thermal-drying, contributes to a large portion of the environmental burden. Moreover, the natural gas market accounts for a large part of the GWP, and this is mainly because the demand for natural gas consumed in our processes is fulfilled by the substitution of fossil-based fuel, which puts much consequential environmental burden on the target process. In contrary, the consequential GWP associated with the products are all negative, especially for the electricity. This result confirms that the products from these three technologies are truly environmental friendly. Attributional LCA is also conducted for comparison, the result is shown in Figure 4 and 5. The attributional LCA shows a similar trend that HTL has the best performance among the three technologies, except that the net GHG emissions are significantly higher. The 100-year GWP value of slow pyrolysis, fast pyrolysis and HTL are 85.9, 89.2 and 52.7 kg CO₂ eq., respectively. Since the attributional approach overlooks a series of consequences, it overestimates the overall environmental impacts of each target process.

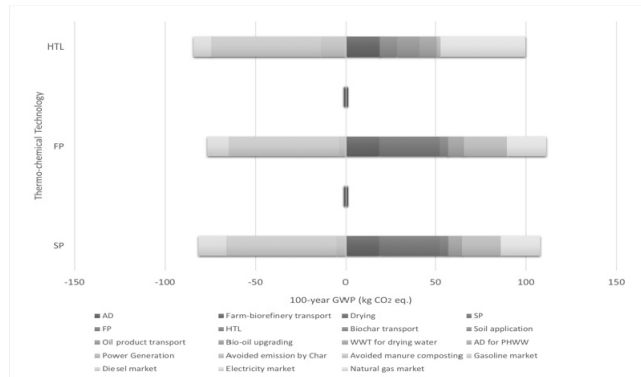


Figure 3. CLCA environmental impacts evaluated by 100-year GWP

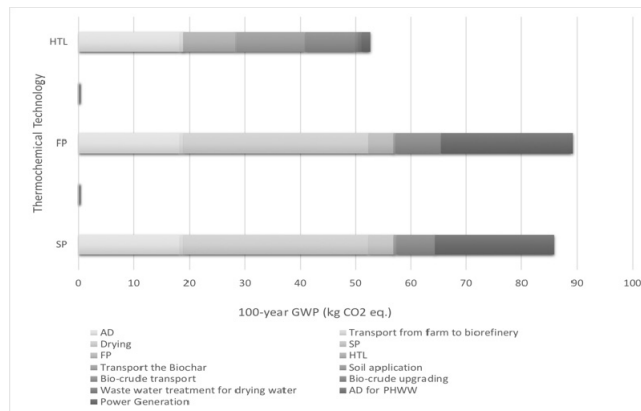


Figure 4. ALCA environmental impacts evaluated by 100-year GWP

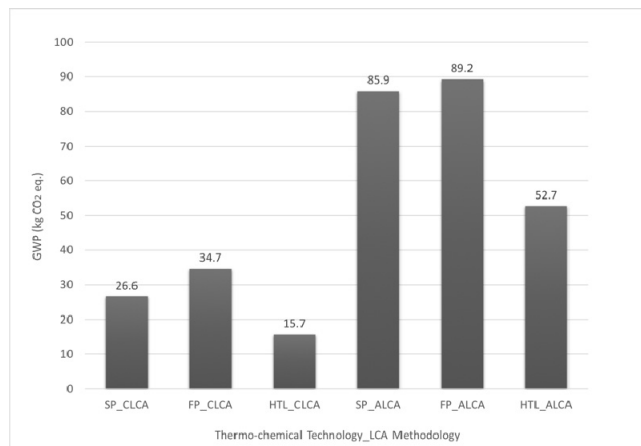


Figure 5. Comparison of ALCA and CLCA using 100-year GWP

4. Conclusion

We conducted attributional and consequential life cycle analysis for three types of thermo-chemical conversion of dairy manure. In both ALCA and CLCA, HTL showed the best environmental performance with respect to the 100-year GWP. Moreover, by including consequential environmental impacts associated with the affected processes and downstream markets, CLCA leads to a much lower GWP than ALCA does. In the future, we will further extend our research to consequential life cycle optimization and broaden the scope of our study by integrating spatial analysis tools and uncertainty analysis.

References

- H.A. Aguirre-Villegas, R.A. Larson, 2017, Evaluating greenhouse gas emissions from dairy manure management practices using survey data and lifecycle tools. *Journal of Cleaner Production*, 143, 169-179.
- D.J. Garcia, F. You, 2016, The water-energy-food nexus and process systems engineering: A new focus. *Computers & Chemical Engineering*, 91, 49-67.
- D.J. Garcia, F. You, 2017, Systems engineering opportunities for agricultural and organic waste management in the food-water-energy nexus. *Current Opinion in Chemical Engineering*, 18, 23-31.
- D.J. Garcia, F. You, 2018, Addressing global environmental impacts including land use change in life cycle optimization: Studies on biofuels. *Journal of Cleaner Production*, 182, 313-330.
- B.H. Gebreslassie, M. Slivinsky, B. Wang, et al., 2013, Life cycle optimization for sustainable design and operations of hydrocarbon biorefinery via fast pyrolysis, hydrotreating and hydrocracking. *Computers & Chemical Engineering*, 50, 71-91.
- A. Gollakota, N. Kishore, S. Gu, 2018, A review on hydrothermal liquefaction of biomass. *Renewable & Sustainable Energy Reviews*, 81, 1378-1392.
- J. Gong, F. You, 2014, Global Optimization for Sustainable Design and Synthesis of Algae Processing Network for CO₂ Mitigation and Biofuel Production Using Life Cycle Optimization. *AIChE Journal*, 60, 3195-3210.
- J. Gong, F. You, 2014, Optimal Design and Synthesis of Algal Biorefinery Processes for Biological Carbon Sequestration and Utilization with Zero Direct Greenhouse Gas Emissions: MINLP Model and Global Optimization Algorithm. *Industrial & Engineering Chemistry Research*, 53, 1563-1579.
- J. Gong, F. You, 2017, Consequential Life Cycle Optimization: General Conceptual Framework and Application to Algal Renewable Diesel Production. *ACS Sustainable Chemistry & Engineering*, 5, 5887-5911.
- H. Goyal, D. Seal, R. Saxena, 2008, Bio-fuels from thermochemical conversion of renewable resources: a review. *Renewable & Sustainable Energy Reviews*, 12, 504-517.
- K.G. Roberts, B.A. Gloy, S. Joseph, et al., 2009, Life cycle assessment of biochar systems: estimating the energetic, economic, and climate change potential. *Environmental Science & Technology*, 44, 827-833.
- Y. Yang, 2016, Two sides of the same coin: consequential life cycle assessment based on the attributional framework. *Journal of Cleaner Production*, 127, 274-281.
- D. Yue, F. You, S.W. Snyder, 2014, Biomass-to-bioenergy and biofuel supply chain optimization: Overview, key issues and challenges. *Computers & Chemical Engineering*, 66, 36-56.
- Q. Zhang, J. Gong, M. Skwarczek, et al., 2014, Sustainable Process Design and Synthesis of Hydrocarbon Biorefinery through Fast Pyrolysis and Hydroprocessing. *AIChE Journal*, 60, 980-994.
- Y. Zhou, L. Schideman, M. Zheng, et al., 2015, Anaerobic digestion of post-hydrothermal liquefaction wastewater for improved energy efficiency of hydrothermal bioenergy processes. *Water Science and Technology*, 2139.

A stochastic environmental model to deal with uncertainty in life cycle impact assessment

Andreia Santos,^{a,*} Ana Barbosa-Póvoa,^a Ana Carvalho^a

^aCentro de Estudos de Gestão do IST (CEG-IST), Av. Rovisco Pais, 1049-001 Lisbon, Portugal

andreia.d.santos@tecnico.ulisboa.pt

Abstract

Life cycle assessment (LCA) is the most applied methodology to compare the environmental impacts of different products and processes. As uncertainty may be present in the first three steps of an LCA an uncertainty analysis should be considered allowing higher confidence in the results. However, few LCA studies include this analysis and when it is included is mostly applied to the LCI step of an LCA. Thus, the goal of this study is to develop a methodology to apply uncertainty analysis on the characterization factors used at the midpoint level in the LCIA step. The methodology employs Monte Carlo simulation as the stochastic modelling technique. A case study comparing the use of softwood and hardwood in the production of unbleached Kraft pulp is utilised to better explain the application of the developed methodology. As main results it can be concluded that the use of softwood as a raw material is overall worse for the environment than the use of hardwood when considering the production of unbleached Kraft pulp.

Keywords: Life Cycle Assessment, Uncertainty, Monte Carlo, ReCiPe, Pulp Production

1. Introduction

Life cycle assessment (LCA) is a four-step methodology for calculating the environmental impact of a product or service. The first step of this methodology, goal and scope definition, consists of defining the main objectives of the study, the functional unit (a representative element of the system being study), and system boundary. In the next step, life cycle inventory (LCI), all the flows that go in (e.g. raw materials and electricity) and out (e.g. emissions and solid waste) of the system are collected. The third step, life cycle impact assessment, consists in categorizing and characterizing the life cycle environmental impact of the system under study by converting the flows collected in the previous step into environmental impact using different parameters such as characterization factors. There are several LCIA methods that consider different categories and parameters. In the last step, results interpretation, the LCA study results are analysed and interpreted to identify the hotspots (areas to be prioritized for action) of the system and suggest possible improvements (ISO 14000 2006).

The aforementioned methodology is the most used to support environmental decision making and for this reason, the reliability of LCA results is of extreme importance. As uncertainty is always present in LCA (Björklund 2002), an adequate uncertainty analysis should accompany LCA studies to help decision makers having more confidence in the results. A literature review was conducted to understand how uncertainty in LCA has been addressed and it was concluded that uncertainty analysis has been increasingly included in LCA studies usually in the form of sensitivity analysis but also through Monte Carlo simulation and scenario analysis. Furthermore, uncertainty in the LCIA step is

rarely treated and there is no clear guidance on how to take uncertainty into account. For these reasons, the main goal of this work is to develop a methodology capable of addressing the uncertainty associated with the characterization factors applied in the LCIA step by exploring Monte Carlo simulation. The developed methodology is applied to a case-study to show its usability in the decision-making process.

2. Methodology

The methodology followed in this study comprises three main steps:

Step 1 – Case Study Description

The first step of the methodology consists in applying the first two steps of an LCA to the case study in analysis.

Step 2 – Environmental Impact Assessment

In this step, the third step of an LCA, Life Cycle Impact Assessment, is deterministically and stochastically applied to the case study under analysis. To deterministically apply the LCIA, a deterministic environmental assessment model was developed in Excel considering the LCIA method ReCiPe 2008 with Hierarchist perspective (Goedkoop, et al. 2013), which considers 18 midpoint categories that can be further aggregated into three endpoint categories. After being normalized and weighted, these endpoint categories are added to calculate a single score (SS) that reflects the overall environmental impact of the system under study. To stochastically apply the LCIA, Monte Carlo simulation is applied to the deterministic model using the @Risk software (Palisade Corporation 2016). Three main tasks were followed for the stochastic analysis:

- Uncertain Parameters Identification – The characterization factors of 14 out of the 18 midpoint categories have uncertainty associated. The other four midpoint categories, agricultural land occupation, urban land occupation, natural land occupation, and water depletion do not have uncertainty associated.
- Probability Distributions Assignment – From the 14 midpoint categories consider as having uncertain characterization factors, probability distributions should be assigned to the characterization factors of the most impactful midpoint categories (identified using a pareto analysis). The @Risk software was used to fit several probability distributions to the characterization factors available for each impactful midpoint categories. The Akaike Information Criteria statistics was used as a goodness-of-fit statistics to help determine the best fit.
- Simulation Settings Definition – Instead of defining the number of iterations at the beginning of the simulation, the @Risk software should be run in Auto-Stop mode until all results reach an established convergence tolerance (3% and a confidence level of 95% are the default settings). This means that the simulation will stop when the estimated mean of the results simulated is within 3% of its actual value and is accurate 95% of the time.

Step 3 – Results Analysis

The last step of the methodology followed in this study coincides with the last step of the LCA methodology and consists in analysing and comparing the deterministic and stochastic environmental impacts obtained in the prior step.

3. Case-Study

The first stage in wood pulp production (i.e. pulping) consists in growing and harvesting the trees. Then, the trunk of each tree is bucked into logs, which are delivered to mills where they are debarked (bark contains few cellulose fibres, the main component of paper products) and chipped. The next stage consists in separating the cellulose fibres from the other wood components such as lignin (the “glue” that cements the fibres together), extractives (e.g. fats, waxes and alcohols), minerals and other inorganics. This can be done through different processes but the most common is the Kraft (sulphate) process. In this process, the wood chips are pressure-cooked with water and chemicals, sodium hydroxide (NaOH) and sodium sulphide (Na₂S), in a digester. The resulting pulp is screened to remove uncooked wood and washed to remove the spent cooking mixture. Depending on the final product, the pulp can be bleached after being produced due to the brown coloration of the raw pulp caused by the presence of lignin that was not removed during cooking (Bajpai 2012) (Teschke 2011). In Figure 1, the pulp life cycle is represented.

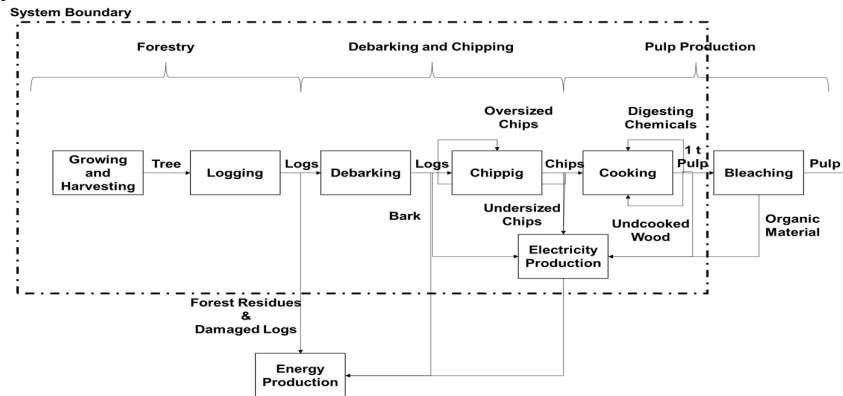


Figure 1 - Pulp life cycle including system boundary and functional unit

The species of the wood used as raw material is one of the characteristics that mostly influences the final properties of the pulp produced. Each tree species can be classified into one of two main families, the hardwoods and the softwoods.

In this paper, two different processes are compared – Case A (production of unbleached Kraft softwood pulp) and Case B (production of unbleached Kraft hardwood pulp). The system boundary considered is cradle-to-gate including the processes within the dashed rectangle in Figure 1 and the functional unit selected is 1 t of unbleached Kraft pulp produced in Europe.

The LCI of each system analysed was retrieved from the ecoinvent v3.3 database (ecoinvent 2018) with consequential system model which was assessed through the software SimaPro 8.4.0 (PRé Consultants 2018).

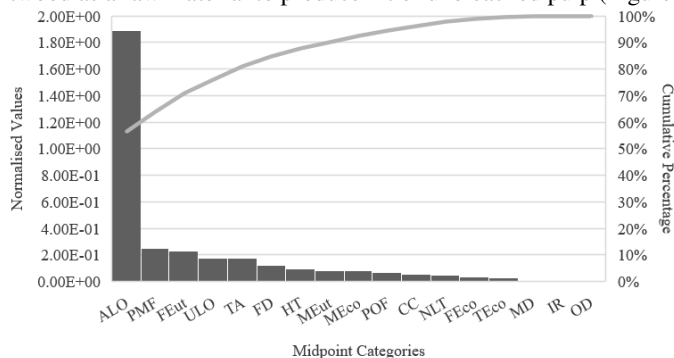
The results obtained through the deterministic and stochastic application of the LCIA to the case study presented are presented and discussed in the next section.

4. Results Analysis

4.1. Deterministic Results

After applying the deterministic environmental assessment model to the case study, it can be concluded that producing 1 t of unbleached Kraft softwood pulp (Case A) results in an

overall environmental impact of about 300 Pt while the same process using hardwood (Case B) results in an overall environmental impact of 238 Pt, which implies that the use of softwood as a raw material is worse for the environment than the use of hardwood. A pareto analysis was conducted considering the normalised results at the midpoint level of using softwood as a raw material to produce 1 t of unbleached pulp (Figure 2).



Agricultural Land Occupation (ALO), Particulate Matter Formation (PMF), Freshwater Eutrophication (FEut), Urban Land Occupation (ULO), Terrestrial Acidification (TA), Fossil Depletion (FD), Human Toxicity (HT), Marine Eutrophication (MEut), Marine Ecotoxicity (MEco), Photochemical Oxidant Formation (POF), Climate Change (CC), Natural Land Transformation (NLT), Freshwater Ecotoxicity (FEco), Terrestrial Ecotoxicity (TEco), Metal Depletion (MD), Ionising Radiation (IR), and Ozone Depletion (OD)

Figure 2 - Pareto analysis conducted considering the results at the midpoint level of Case A

By analyzing Figure 2, five midpoint categories (ALO, PMF, FEut, ULO, and TA) are responsible for about 80% of the overall environmental impact of producing 1 t of softwood unbleached Kraft pulp. Agricultural land occupation is the most contributing midpoint category because this process requires a continuous use of forestry land area. When comparing the results at the midpoint level of Case A and Case B, it can be concluded that the use of softwood as a raw material to produce 1 t of unbleached Kraft pulp has a higher result (worse for the environment) in 14 of the 18 midpoint categories considered in the ReCiPe 2008 method.

4.2. Stochastic Results

From the five midpoint categories identified in Figure 2 as being the most impactful in terms of environmental impact, three have uncertainty in the characterization factors (PMF, FEut, and TA) has previously explained. The simulation ran until the convergence of results previously stipulated was obtained which occurred after 2000 iterations. Several stochastic results were obtained, and Figure 3 presents a summary of these results through box and whisker plots regarding the difference between Case A and Case B. Looking at the right side of Figure 3, it can be concluded that the difference between the single scores will be at least 61.90 Pt and at most 70.53 Pt. There is a 25 % chance that this difference will be lower than 62.05 Pt and higher than 62.35 Pt and a 50 % chance that it will be between these values. The inter-quartile range could be used as a measure of data variability and is calculated through the difference between the third quartile and the first quartile presented in Figure 3. Using this measure and looking at the left side of Figure 3, it can be concluded that the difference between terrestrial acidification shows the lowest variability while the difference between freshwater eutrophication shows the greatest variability.

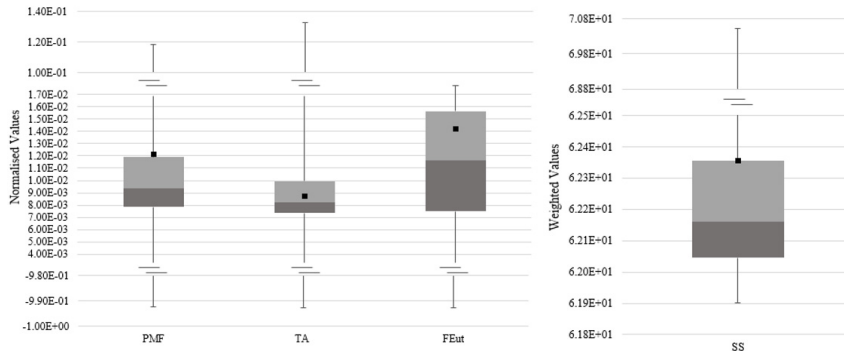


Figure 3 - Box and whisker plots of the difference between the three most impactful midpoint categories (on the left) and single score (on the right) of Case A and Case B

The characterization factor assigned to nitrogen oxides in the PMF midpoint category is the one that most contributes to the variability of the difference between the single scores of Case A and Case B (right side of Figure 3). In the other two most impactful midpoint categories, the characterization factor assigned to the emission of phosphate to the water in the FEut midpoint category and ammonia to the air in the TA midpoint category are the ones that most contributes to the referred variability.

4.3. Results Comparison

The difference between the deterministic single score for Case A and Case B (black square in the right side of Figure 3) and the difference between the value of the three most impactful midpoint categories for Case A and Case B (black squares in the left side of Figure 3) are represented in Figure 3. The comparison of the deterministic and stochastic results allows the following conclusions to be drawn:

1. The deterministic difference between the single score of Case A and Case B is about 62.36 Pt (see square in the right side Figure 3). A positive difference means that Case A is overall worst for the environment than Case B.
2. The difference between the single score of Case A and Case B, in the stochastic scenario, is always positive and ranges from 61.90 Pt and 70.53 Pt (see right side Figure 3), which means that even with uncertainty Case B has always lower environmental impact. Therefore, the confidence in this conclusion is high.
3. The deterministic difference between the single score of Case A and Case B is close to the third quartile of the stochastic results (see right side of Figure 3). This reveals that the deterministic difference between the single score of both cases is overestimated – there is 75 % chance that this difference is actually lower and therefore the overall improvement from Case A to Case B is lower than the initial estimated (62.36 Pt).
4. The deterministic difference between Case A and Case B considering the two of the most impactful uncertain midpoint categories (PMF and FEut) is also close to the third quartile of the stochastic results (see left side of Figure 3), which also points out to an overestimation of the improvements obtained by switching from softwood to hardwood. In the case of terrestrial acidification the deterministic difference between Case A and Case B is closer to the median – the deterministic results obtained for this midpoint category are more robust.
5. These overestimations of results lead to the conclusion that there is a high chance that the environmental impact improvements obtained by switching from the use

of softwood to hardwood to produce unbleached Kraft pulp are smaller than expected.

5. Conclusions

A methodology to address uncertainty in the characterization factors used in the LCIA step of an LCA was proposed and applied to a case study where the use of softwood and hardwood in the production of 1 t unbleached Kraft pulp were compared. From this application it was concluded that the use of hardwood is, overall, better for the environment even when considering the uncertainty associated with the characterization factors at the midpoint level. However, the improvements obtained by switching from softwood to hardwood to produce unbleached Kraft pulp are expected to be smaller than the deterministic assessment revealed. This reinforces the problem with deterministic LCA – it leads to misleading perception regarding the differences between the environmental profile of different products or processes.

Future research should include the application of uncertainty analysis to other LCIA methods besides ReCiPe 2008 along with the study of other parameters such as the normalization and weighting factors.

Acknowledgements

The authors gratefully acknowledge the project funding (POCI-01-0145-FEDER-016733) and PhD grant SFRH/BD/134479/2017.

References

- Z. Allen, Year, Article or Chapter Title, Journal or Book Title, Volume, Issue, Pages
- P. Bajpai, 2012, Brief Description of the Pulp and Paper Making Process, *Biotechnology for Pulp and Paper Processing*, 7-14, Springer, Boston, United States of America
- A. Björklund, 2002, Survey of approaches to improve reliability in lca, *The International Journal of Life Cycle Assessment*, 7, 64–72
- Ecoinvent, 2018, Introduction to ecoinvent Version 3, <https://www.ecoinvent.org/database/introduction-to-ecoinvent-3/introduction-to-ecoinvent-version-3.html> (accessed September 06, 2018)
- M. Goedkoop, R. Heijungs, M. Huijbregts, A. De Schryver, J. Struijs, and R. van Zelm, 2013, ReCiPe 2008 - A life cycle impact assessment method which comprises harmonised category indicators at the midpoint and the endpoint level, Ministerie van Volkshuisvesting, Ruimtelijke Ordening en Milieubeheer, Netherlands
- ISO 14000, 2006, International Organization for Standardization, www.iso.org (accessed December 04, 2017)
- Palisade Corporation, 2016, "@Risk User's Guide.", Ithaca, United States of America
- PRé Consultants, 2018, SimaPro, <https://simapro.com/> (accessed September 06, 2018)
- K. Teschke, A. Keefe, G. Astrakianakis, J. Anderson, D. Heederik, S. Kennedy, K. Torén, 2011, Chapter 72 - Pulp and Paper Industry, *Encyclopaedia of Occupational Health and Safety*, Fourth Edition

BIOPRO-Sim: A benchmark simulation model for bio-manufacturing processes

Giorgio Colombo^a, Isuru A. Udugama^b, Krist V. Gernaey^b, Seyed Soheil Mansouri^{b,*}

^aDepartment of Chemistry, Materials and Chemical Engineering “G.Natta”, Politecnico di Milano, Piazza Leonardo da Vinci 32, 20133 Milano, Italy

^bProcess and Systems Engineering Centre, Department of Chemical and Biochemical Engineering, Technical University of Denmark, Building 229, 2800 Lyngby, Denmark

**seso@kt.dtu.dk*

Abstract

In this work, an end to end bio-pharmaceutical production process of the API lovastatin is developed through a systematic process synthesis and design approach, and then simulated. The developed simulation is intended to be used as benchmark process model as it captures the generic process dynamics of a bio-pharmaceutical process, and as such it is well-suited to use as a test problem to evaluate different processing scenarios in continuous fermentation processes. The synthesis and design of the simulation is realised through a methodology based on two complimentary steps, that can be applied individually or in conjunction, and is adopted to synthesize the upstream and downstream processing pathway. As such, the process model can be operated either as a whole, or as an individual upstream or downstream process. The open loop response of the whole benchmark simulation is presented here.

Keywords: upstream design, process development, benchmark process model, process modelling and simulation.

1. Introduction

Pharmaceutical manufacturing is a highly regulated field, where the regulations together with economics dictate that the process for production of an active pharmaceutical ingredient (API), which is generally synthesized in lab scale for clinical trials, must be quickly scaled up to full scale manufacturing once approval of the drug is granted. As a result, industry in general focuses on batch synthesis processes while downstream purification typically runs in a semi continuous manner, despite the inherent cost of inventory (Plumb, 2005). Due to this limited time for process development as well as the changing of operating regimes, there is a need for accurate benchmark process models. This work focuses on the field of fermentation as previous work in the domain of API continuous manufacturing through traditional organic synthesis has been carried out by Benyahia et al., whose work has then been exploited for control and other purposes (Ramin, Mansouri, Udugama, Benyahia, and Gernaey 2018), Mansouri, Udugama, Huusom, Gernaey, & Benyahia, 2018). In this work we will discuss the synthesis of an end to end benchmark process model for bio-pharmaceutical manufacturing with an emphasis on illustrating how process systems engineering

principles were used to develop the benchmark, in particular the downstream unit operation selection and layout. The dynamic behavior of both upstream and downstream unit operations is illustrated with relevant step test and disturbances in the following sections. The intended uses for this benchmark include but are not limited to process control and process optimization, while the benchmark is also designed so the process can be operated as an end-to-end model or as a separate downstream process model. The benchmark model is developed in Matlab Simulink environment and can be obtained by contacting the corresponding author; while a full manuscript detailing the modeling of each unit operation will be published in the near future.

2. Upstream design

The upstream process is designed through a three-step hierarchical methodology as described below. The feed to the upstream is a liquid mixture with dissolved solid compounds which are lactose, adenine, and cells, responsible for the production of the API lovastatin.

Level 1 (kinetic model selection)

The first step requires the selection of a kinetic model to describe the underlying physical and chemical phenomena occurring during the chemical reaction. Macrokinetic unstructured models are preferred to microkinetic models since they are able to represent the system as a whole, thus being suitable for the purpose of reactor modeling.

Level 2 (batch to continuous)

A subsequent step in the methodology would require the shifting of batch reactor model/operations to continuous reactor operations as the kinetic models are generally developed using batch operations.

Level 3 (choice of upstream design and simulation)

In this stage, the upstream process is modeled and its operating parameters are optimized. One major issue common to many pharmaceutical processes is the dilution of the desired product in the reacting mixture, thus an efficient solution for the upstream design has to be chosen to achieve a tradeoff between the product final titer and productivity, in order to facilitate the downstream recovery and purification operations.

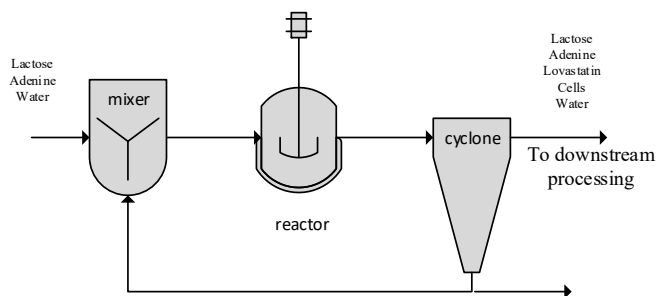


Figure 1: Upstream recirculation process design

These issues are remedied by selecting an upstream process with cell recirculation, embedding a mixer, a continuous reactor and a cyclone for biomass recirculation. The upstream process model has been solved by means of steady state component and total material balance equations to test the effect of a couple of design parameters which are the recirculation factor, defined as the ratio between the recycle flowrate and the outflow from the reactor, and the cell recycle factor characterized as the ratio between biomass concentration in the recycle stream and reactor outlet stream. Figure 2 illustrates the effect of recycling on overall upstream productivity (subplots A and C) and reactor productivity (Subplot B), and is based on the implementation of the upstream process design illustrated in Figure 1 in the Matlab Simulink environment. The highest upstream productivity has been achieved with the largest recycle ratio whereas the opposite is true for the reactor productivity, as indicated by the arrow which points out the direction of increasing recirculation factor. Despite a trade-off between maximum and minimum recycle ratio, a higher recirculation factor is suggested to accomplish a higher final titer of the desired product directed downstream (Subplot D), where the recirculation factor is increasing in the direction of the arrow. It is important to note that the productivity of the overall upstream system (Subplots A and C), benefits from an increase in the amount of cells recycled, namely an increase in the β parameter. The evidence presented by this analysis thus far supports the idea that the upstream design benefits from a high volumetric flow recirculation rate and a large cell recycle.

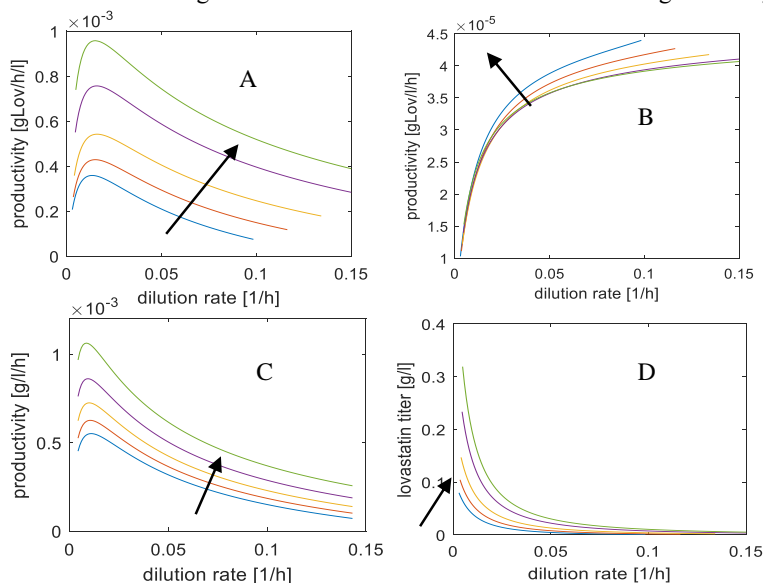


Figure 2: Figure showing overall upstream productivity (Subplot A), reactor productivity (Subplot B), and final titer (Subplot D) upon increasing of the recirculation factor. Subplot C shows changes in the overall upstream productivity with increasing cell recirculation factor β .

3. Downstream process synthesis

The methodology currently adopted in the downstream process synthesis employs physicochemical properties and their relation to separation techniques to develop separation processing pathways. All separation techniques achieve their separation task

by exploiting physicochemical property differences between the separating components. The methodology has been extended, along with the inclusion of new physicochemical properties, including the most frequently used separation technologies in the biopharmaceutical field, which are centrifugation, electrophoresis, size exclusion and reversed phase chromatography, nanofiltration and reverse osmosis. The application of the methodology to the Lovastatin case study results in the processing route depicted in figure 3.

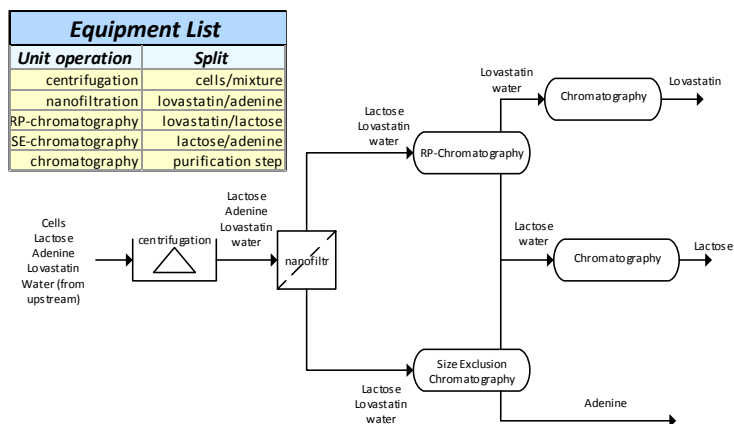


Figure 3: Downstream process synthesis result

4. Process simulation

In this section the upstream (Figure 1) and downstream process (figure 4) are connected and simulated as a continuous process by means of unit operation models either retrieved in the literature or derived from first principles.

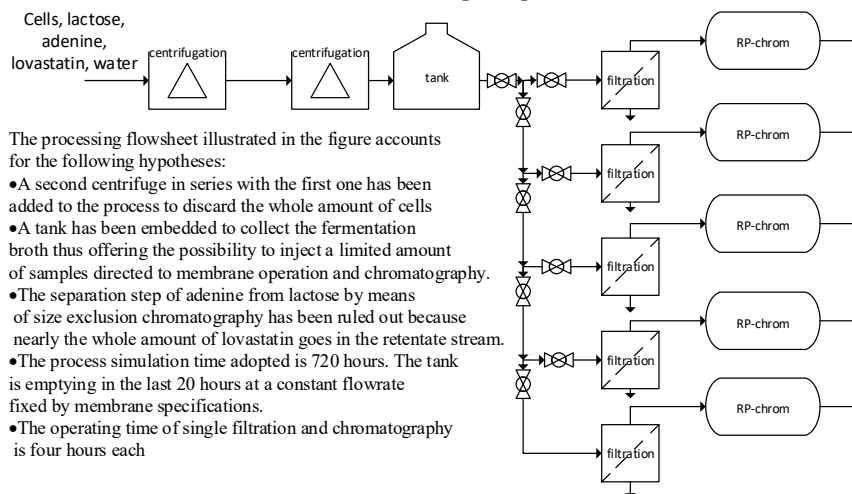


Figure 4: Overview of the downstream benchmark process

Figure 5 highlights the behavior of the four components of interest in the cyclone outlet flow, which is directed downstream for final recovery and purification and is obtained by the benchmark process model (overall process illustrated in figure 1 and 2) developed in the Matlab Simulink environment. The increase of lovastatin (subplot A) and cells concentration (subplot B) comes along with a decreasing concentration of lactose (dashed line, right plot) and adenine (dotted line, right plot). Subplot C of Figure 6 shows the separation of lovastatin from lactose and adenine. Subplots A and C of Figure 6 instead show how sample dilution in the processing mixture decreases as an effect of membrane filtration which contributes to achieving a final product which is more concentrated.

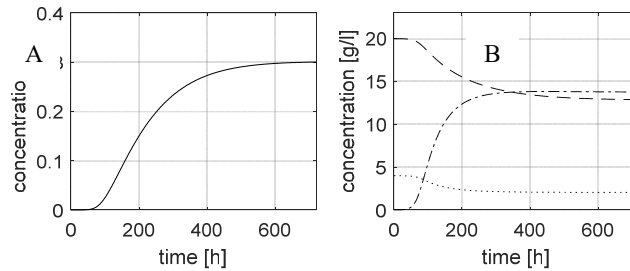


Figure 5: Cyclone concentration of lovastatin (subplot A), cells, lactose and adenine (subplot B)

Please note that no energy integration has been included in the model in view of the fact that reactor temperature is not an issue for the present reaction as reported in the literature (Bizukojc & Ledakowicz, 2007). Besides, the downstream separation technologies employed in the process are isothermal.

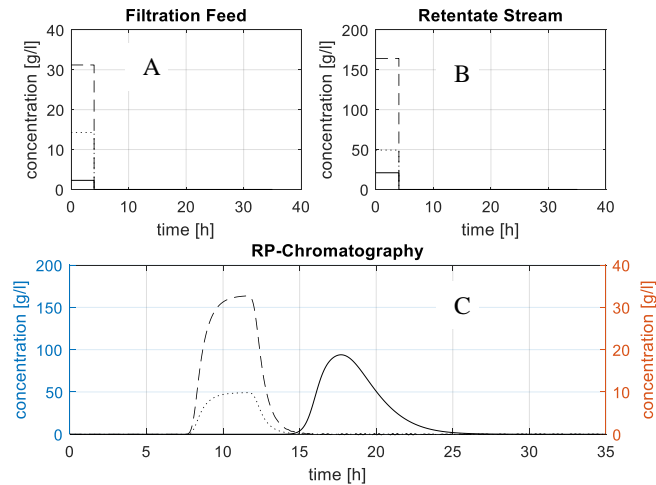


Figure 6: Filtration feed concentration (subplot A), retentate stream concentration (subplot B) and the final chromatogram (Subplot C)

5. Conclusion

It has been successfully demonstrated that such a benchmark simulation has the ability to reproduce component behavior in a fermentation process, therefore representing an alternative to experimental evaluations, which could be time consuming and expensive. Furthermore the benchmark process allows evaluating different scenarios as its flexibility lies in the wide range of operational parameters that can be changed. We do believe the process represents a valid playground to test different control strategies, which would be a future work to be carried out on the presented process flowsheet.

Acknowledgments

This work partially received financial support from Innovation Fund Denmark through the BIOPRO2 strategic research centre (Grant number 4105-00020B). The project also received funding from the Carlsberg Foundation of Denmark (Grant Number CF17-0403)

References

- Benyahia, B., Lakerveld, R., & Barton, P. I. (2012). A Plant-Wide Dynamic Model of a Continuous Pharmaceutical Process. *Industrial & Engineering Chemistry Research*, 51(47), 15393–15412. <https://doi.org/10.1021/ie3006319>
- Bizukojc, M., & Ledakowicz, S. (2007). A macrokinetic modelling of the biosynthesis of lovastatin by *Aspergillus terreus*. *Journal of Biotechnology*, 130(4), 422–435. <https://doi.org/10.1016/j.jbiotec.2007.05.007>
- Mansouri, S. S., Udugama, I. A., Huusom, J. K., Gernaey, K. V., & Benyahia, B. (2018). A shortcut approach for decision-making and operational analysis of an integrated end-to-end continuous pharmaceutical process (pp. 2107–2112). <https://doi.org/10.1016/B978-0-444-64241-7.50346-3>
- Plumb, K. (2005). Continuous processing in the pharmaceutical industry: Changing the mind set. *Chemical Engineering Research and Design*, 83(6 A), 730–738. <https://doi.org/10.1205/cherd.04359>
- Ramin, P., Mansouri, S. S., Udugama, I. A., Benyahia, B., & Gernaey, K. V. (2018). Modelling continuous pharmaceutical and bio-based processes at plant-wide level: A roadmap towards efficient decision-making. *Chimica Oggi/Chemistry Today*, 36(2), 26–30.

Facilitating learning by failure through a pedagogical model-based tool for bioprocesses

Simoneta Caño de Las Heras^a, Björn Gutschmann^b, Krist V. Gernaey^a, Ulrich Krühne^a and Seyed Soheil Mansouri^{a,*}

^a*Process and Systems Engineering Centre (PROSYS), Department of Chemical and Biochemical Engineering, Technical University of Denmark, Søtofts Plads, Building 229, DK-2800 Kgs. Lyngby, Denmark*

^b*Chair of Bioprocess Engineering, Institute of Biotechnology, Technische Universität Berlin, Ackerstraße 76, ACK24, 13355 Berlin, Germany*
seso@kt.dtu.dk

Abstract

Facing uncertain situations and deciding a course of action is an opportunity to help students understand the practical implications of the theoretical knowledge and prepares them for the future challenges as engineers. However, allowing “failures and making wrong decisions” is becoming more and more challenging in industry due to safety and economic reasons and must be essentially allowed in academia. However, in academia it is also very challenging due to limitations in resources and safety concerns. Meanwhile, simulators are generally valuable tools for education that allow an intuitive learning based on action and offer the students an autonomy in their decision-making process. In spite of these advantages, the simulators commonly used in engineering education are meant for commercial purposes and incorporate a rigorous description of the process. Therefore, they are not inherently ready to be deployed in an educational program. This work presents a model-based pedagogical simulation tool, *FermProc*, having a clear objective for use in bio-manufacturing education. The in *FermProc* implemented computer-aided framework devises an active learning design based on the creation and analysis of different realistic and unrealistic scenarios such that students can safely confront common operational problems. Therefore, this model-based tool is intended to provide the users with the experience and the confidence to face and resolve uncomfortable situations encountered while operating a bioprocess.

Keywords: Learning by failure, Educational Simulator, Bioprocess simulator, Decision-making.

1. Introduction

A survey conducted by Nguyen (1998), stated that industry “requires an engineering graduate with an equivalent of a person with 10 years of experience” and “a person with motivation, who is creative, a good team member, risk-taking and decisive”. Up-to-date, the current changing technological landscape makes it even more necessary to provide engineering graduates with these qualities. Most of these attributes are strongly connected to training. However, providing the opportunity for such training can be difficult considering the increasing number of students, the time restrictions, and the available resources. Simulators, with learning based on action and enhancing exploration, can help in fulfilling this need (Balamuralithara and Woods 2009). However, the question to answer is if “simulators can solve the problems we are

interested in?” Even so, the majority of the commercial simulators used in engineering education lack a pedagogical aim in the design; which entails limitations in the learning process. For example, in the case of infeasible operational conditions, commercial simulators are not prepared to provide information about the corresponding inappropriateness. On the other hand, the acquisition of knowledge and skills can be facilitated through an enjoyable experience and considering the new habits and interests of the students (Kiili 2005).

In this work, different approaches inside a model-based software that allows experiencing failure with the support of learning content for bioprocesses are presented. Furthermore, game-based elements are implemented inside the computational tool to encourage an enjoyable experience and the conceptualisation of complex knowledge. Therefore, the current version of the virtual software, *FermProc*, is explained, with its design requirements and advantages for allowing the learning by failure.

2. *FermProc*: A pedagogical model-based tool for bioprocesses

FermProc is a software designed with prime pedagogical objectives based on a previously developed methodology (Caño et al. 2018). Hence, it includes the simulation of mathematical models, as well as the possibility to modify them, learning-hints, questionnaires, mini-games, and the possibility to confront realistic technical problems. Furthermore, the process simulation is developed in an open-source platform, thus offering the possibility for students to access the mathematical models and gain a profound understanding about their complexity.

2.1 Design requirements of FermProc

This model-based tool is based on three pillars: 1) a careful learning design, 2) a motivational approach based on the use of gamification and, 3) the use of template-based models that can be displayed, reused and modified (Fedorova, Sin, and Gani 2015). Template-based modelling is an approach that requires the development of models on divisible pieces that compose a template. Through this approach, a model is decomposed into three sets of equations; i) balance equations, ii) constitutive equations and iii) connection and conditional equations (Cameron and Gani 2011). Each existing concept can be treated as a building block which can be combined with other suitable building blocks to create a new model. Meanwhile, the rational combination of equations to create a new model requires previous knowledge of the user or it can evolve to the creation of an additional process model. In both scenarios, the users can explore and learn about the construction of mathematical models. Furthermore, due to the educational aims, this software provides an organized and versatile learning experience in a user-friendly environment that engages the user in the learning process. This is promoted by the presence of rules and explanation across the tool.

In order to fulfil the design requirements, a relational database is developed in SQLite. This database scheme with the corresponding data types can be seen in Figure 1. The database collects and reuses interrelated rules for a comprehensive modification of the kinetic models (shown in Figure 2). Moreover, it uses the process conditions to correlate an “expert system” with problem and solutions. The problem-solution feature in *FermProc* will be further explained in Section 2.2.

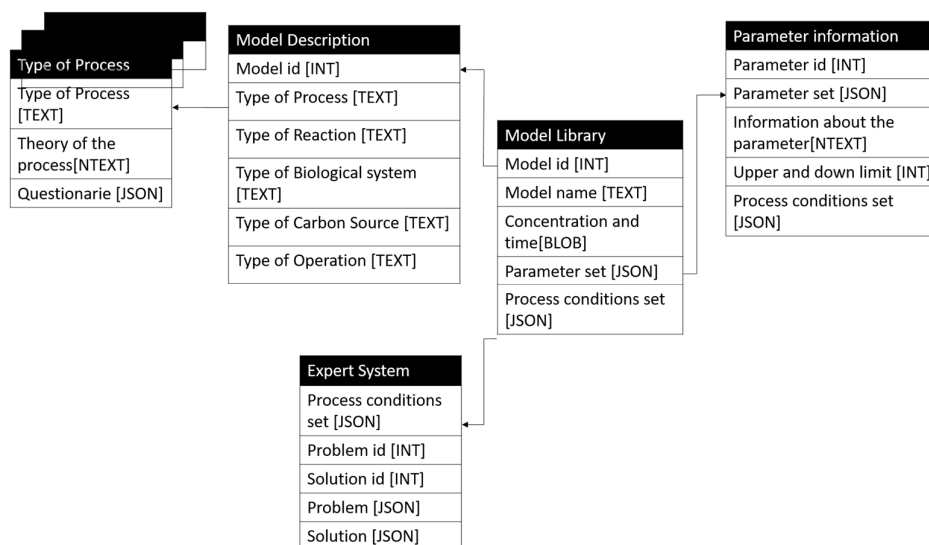


Figure 1. Database scheme with data types.

2.2 Advantages of *FermProc*

FermProc is a platform developed “by students for students” with the support of highly skilled teachers. This is done through involving the students in all the steps of the process as co-designer and co-developers of the computational tool. Therefore, in contrast with other commercial simulators, *FermProc* has clear learning goals. At its current stage, they are the acquisition of i) knowledge for the understanding of the mathematical model associated with a bioprocess, ii) skills in the evaluation of fictional and non-fictional scenarios in a bioconversion and iii) competences in meaningful decision-making across the design of the bioprocess. Moreover, this software has the objective to promote creativity and critical-thinking as it allows to make and take control of mistakes. This is done by the support of theory in every decision taken by the user, the need for applying their knowledge in different scenarios and a continuous assessment of the choices of the user. In the current stage of development, this is put into practice with the modification of the simulated model and other activities implemented as mini-games or multimedia content.

The feature for the modification of a chosen model can be seen in Figure 2. Initially, the model is selected based on a series of questions related to the bioprocess to be simulated. These choices are supported by theoretical content and the structure of the selected model is explained with a visual help or a video. Once the model is selected and solved inside the tool, the user can select a parameter or operational condition from the mathematical model and modify different values in a range depending on the parameter or selected conditions. If the modified value is out-of-range due to, for example, a thermodynamic restriction, the software will display a new window with the theoretical explanation and the corresponding literature reference. This allows enhanced awareness of the feasible range of values and provides a source of information that the users can rely on to intensify knowledge about the applied model.

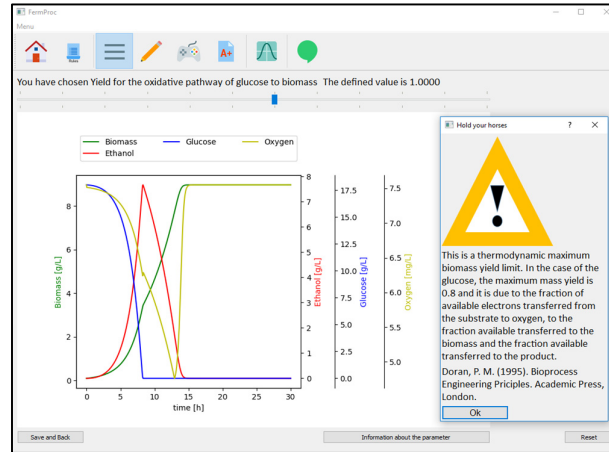


Figure 2. Example of the screen for the modification of the model in FermProc with a popup window that will appear when an out-of-range value is selected.

In addition, other activities are implemented to engage the creativity of the user and to make complex knowledge more approachable with the inclusion of game elements. Some examples of the implemented mini-games inside *FermProc* are:

- A *memory game* for matching combinations of definitions, nomenclature and international units of the parameters involved in a complex fermentation model. With different levels of difficulty, the user starts connecting nomenclature and definition and advances to connect nomenclature and units.
- A “*what is what?*” for the analysis of graphs. The software solves the model, chosen by the user, with different initial model parameter values (1%, 25%, 50% and 100%) and generates a graph for each simulation. Then, the user is required to choose the graph with the highest value of the parameter. In the current state, the parameters are associated with the biomass growth and the choice is made based on the plot of the evolution of the biomass concentration against the time. This system can provide the user with the training for the critical thinking needed to associate the variation of parameters that are not directly represented in the graphs but have an effect in the process. In addition, the understanding of mechanistic models is strongly intensified using this approach.
- An *operational problem*. In this game, the user needs to recognize an operational issue and select a solution from a problem and solution data set. This can be seen in Figure 3 and Figure 4. The operational problem is randomly picked inside a database (in Figure 1) considering the process modelled. For example, in Figure 3, the user is facing a very low *Saccharomyces cerevisiae* growth rate and he/she needs to use the available information about glucose, ethanol, oxygen and the set value temperature and the measured temperature to identified possible problems in the operation

process. In this specific case, the low efficiency of the microorganisms is due to a low fixed temperature value (of 15°C) when yeast has an optimal growth rate at 30°C (Sonnleitner and Käppeli 1986).

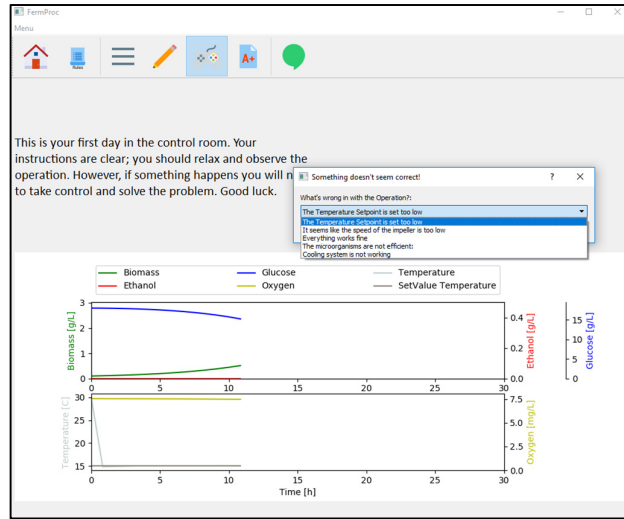


Figure 3. The screen of the first step of the operational problem in which the problem needs to be categorized.

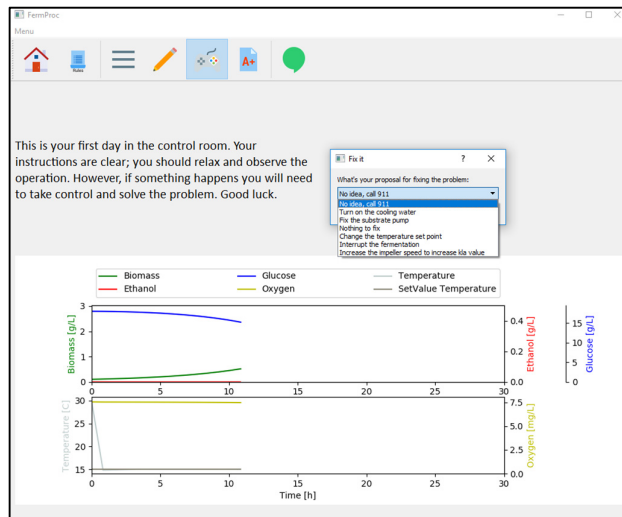


Figure 4. The second step of the operational process mini-game. A solution for the issue needs to be proposed based on the available solutions. Due to lack of space, the screen for the modification of the parameter (such as, like in this case, the change of the temperature setpoint and the choices based on the type of microorganism you are using) hasn't been included in this manuscript

The problem-solution database, that is part of the Figure 1, is created with the experiences gained by industry and academia, and therefore the users can confront real-life situations. It is expected that as the users are solving those operational issues, they are building confidence in its decision-making abilities and developing a skilled mindset with awareness of the most common failures and the capability of solving hand-on problems.

Therefore, *FermProc* is designed considering how to allow meaningful failures and to make choices with the support of a learning design and content. Consequently, as the user goes through the software, he/she develops the abilities to analyse and confront problematic situations and make decisions about the process. It is important to highlight that *FermProc* is still in development and a user experience is planned for summer 2019 to corroborate the design and features of the software.

3. Conclusions

In order to allow students to gain experience without exposing themselves or put the installations at risk and with a limited consumption of time and resources, new and innovative model-based tools need to be developed. In the case of bioprocesses, several technical problems can happen during the operation that will require a fast analysis and critical response. Considering those issues, *FermProc*, which is a model-based tool for the simulation of bioprocesses, is developed. It integrates learning design and game elements. In its current state of development, *FermProc* is prepared to facilitate comprehension of kinetic parameters and their limits. *FermProc* also has implemented other activities such as problem-solution database that will help students to face technical problems while gaining theoretical knowledge in a safe environment.

References

- B. Balamuralithara and P. C. Woods, 2009, "Virtual Laboratories in Engineering Education: The Simulation Lab and Remote Lab" Computer Applications in Engineering Education.
- I. T. Cameron and R. Gani, 2011, Product and Process Modeling: A Case Study Approach. Elsevier B.V., Amsterdam.
- M. Fedorova, G. Sin, and R. Gani, 2015, "Computer-Aided Modelling Template: Concept and Application." Computers and Chemical Engineering, 83: 232-247
- K. Kiili, 2005. "Digital Game-Based Learning: Towards an Experiential Gaming Model." Internet and Higher Education 8(1):13–24.
- S. Caño, et al. , 2018, "A Methodology for Development of a Pedagogical Simulation Tool Used in Fermentation Applications." Computer Aided Chemical Engineering 44:1621–26.
- D. Q. Nguyen, 1998, "The Essential Skills and Attributes of an Engineer: A Comparative Study of Academics, Industry Personnel and Engineering Students." Business 2(1):65–76.
- B. Sonnleitner, and O. Käppeli, 1986, "Growth of *Saccharomyces Cerevisiae* Is Controlled by Its Limited Respiratory Capacity: Formulation and Verification of a Hypothesis." Biotechnology and Bioengineering 28(6):927–37.

Data-Based Robust Model Predictive Control Under Conditional Uncertainty

Chao Shang, Wei-Han Chen, Fengqi You

Cornell University, Ithaca, New York, 14853, USA

Abstract

In this work, a novel data-driven robust model predictive control (RMPC) framework is outlined for optimal operations and control of energy systems, where uncertainty in predictions of energy intensities enters into the process in an additive manner. However, the distribution of prediction errors may be time-varying and depend on other external variables. To appropriately describe the distribution of uncertainty, a novel concept of conditional uncertainty as well as the conditional uncertainty set is proposed, which disentangles the dependence of distribution on external variables and hence reduces the conservatism. In general, the conditional uncertainty set can be modelled by integrating domain-specific knowledge and data collected from previous experience. An example arising from agricultural irrigation control is presented to illustrate the effectiveness of the proposed methodology.

Keywords: Model predictive control, robust optimization, data-based decision-making

1. Introduction

In the past two decades, model predictive control (MPC) has established itself as an enabling technology for optimal control and operation of dynamic complex systems, with uncountable applications in process industries (Morari and Lee, 1999). In the MPC framework, a dynamic process model is adopted to describe future system behaviour, based on which the input sequence is optimized by various MPC algorithms. Despite of its significant success, MPC technology commonly requires heavy manual workload for maintenance, mainly because of model mismatch and random disturbances that drive the system to deviate from its trajectory and affect the control performance (Chu et al. 2015).

To address this issue, robust MPC (RMPC) has been extensively investigated in both academia and industries (Saltık et al., 2018), with representative applications in building control (Zhang et al., 2017), operations of smart grid (Zong et al., 2012), and irrigation systems (Delgoda et al., 2016), where process systems are influenced by various weather and climatic factors in an additive manner, such as solar radiation, wind energy, rainfall, etc. Fortunately, thanks to the development of information technology, forecasts of many climatic factors have become more and more easy to attain nowadays. However, these forecasts themselves are not sufficiently accurate, thereby bringing uncertainties in forecast errors. Consequently, in the associated RMPC scheme, the external disturbance can be decomposed into a known deterministic input arising from forecasts, and the uncertainty representing forecast errors. In existing studies, norm-based uncertainty sets, as a basic ingredient in robust optimization and RMPC, have been adopted to characterize the distribution of uncertain forecast errors.

In this work, we point out the limitations of using traditional norm-based uncertainty sets to deal with forecast errors of energy intensities. In fact, their distributions can be heavily

dependent on some other external variables, e.g. forecast values, thereby showing significant time-varying characteristics. Motivated by this, we make clear such dependence with some concrete examples, and define a new conditional uncertainty set to disentangle the dependence of forecast error on external variables. In this way, primitive uncertainties independent from external variables can be effectively extracted, based on which the time-varying uncertainty distribution can be expressed in a unified manner, thereby significantly reducing the conservatism of RMPC. To determine the distribution of primitive uncertainties in a data-driven way, the use of support vector clustering (SVC)-based uncertainty set (Shang et al., 2017) is recommended. We adopt an example from irrigation control and carry out closed-loop simulations based on real weather prediction and measurement data. Case studies show that the proposed approach can help reducing conservatism of RMPC significantly and safely maintain soil moisture above a certain level with reduced water consumptions.

2. Robust Model Predictive Control under Conditional Uncertainty

2.1 Robust Model Predictive Control

We consider optimal control problems of the following linear system:

$$x_{t+1} = Ax_t + Bu_t + Ev_t + Hw_t, \quad (1)$$

here x_t and u_t are the system state and control input, v_t and w_t are deterministic disturbance and random disturbance, and $\{A, B, E, H\}$ are system matrices of appropriate dimensions (Tatjewski, 2007; Seborg et al. 2010). Given the control horizon N , Compact expression of system dynamics given the control horizon N :

$$\mathbf{x} = \mathbf{A}x_0 + \mathbf{B}\mathbf{u} + \mathbf{E}\mathbf{v} + \mathbf{H}\mathbf{w}, \quad (2)$$

where $\mathbf{x} = [x_1^T, \dots, x_N^T]^T$ is the stacked sequence of future states, and $\{\mathbf{u}, \mathbf{v}, \mathbf{w}\}$ can be defined in a similar way. System constraints can be generally expressed as $\mathbf{C}\mathbf{x} + \mathbf{D}\mathbf{u} \leq \mathbf{f}$. In the presence of uncertainty, future control inputs \mathbf{u} are essentially functions of past disturbance \mathbf{w} , which can be approximately parameterized by affine disturbance feedback (ADF) policy (Ben-Tal et al., 2004; Goulart et al., 2006; Shang et al., 2018):

$$\boldsymbol{\pi}(\mathbf{w}) = \mathbf{P}\mathbf{w} + \mathbf{q}. \quad (3)$$

Here \mathbf{P} has a lower-triangular structure to respect the causality of ADF policy. By optimizing over coefficient matrix \mathbf{P} and vector \mathbf{q} , the formulation of traditional RMPC reads as follows (Saltik et al., 2018):

$$\begin{aligned} & \min_{\boldsymbol{\pi}} J_H(x_0, \boldsymbol{\pi}) \\ & \text{s.t. } \mathbf{x} = \mathbf{A}x_0 + \mathbf{B}\boldsymbol{\pi}(\mathbf{w}) + \mathbf{E}\mathbf{v} + \mathbf{H}\mathbf{w} \\ & \quad \mathbf{C}\mathbf{x} + \mathbf{D}\boldsymbol{\pi}(\mathbf{w}) \leq \mathbf{f}, \quad \forall \mathbf{w} \in \Omega \end{aligned} \quad (4)$$

where $J_H(x_0, \boldsymbol{\pi})$ denotes the loss function to be minimized, and Ω is the uncertainty set to describe the region of uncertainty. The most-used formulations of Ω are typically based on l_1 , l_2 and l_∞ norms, e.g., $\Omega = \{\mathbf{w} \mid \|\mathbf{w}\|_1 \leq \Gamma\}$ (polyhedral), $\{\mathbf{w} \mid \|\mathbf{w}\|_2 \leq \Gamma\}$

(ellipsoidal), and $\{\mathbf{w} \mid \|\mathbf{w}\|_{\infty} \leq \Gamma\}$ (box), where Γ stands for the size parameter (Bertsimas and Sim, 2004). By adopting techniques from robust optimization, one can translate (4) into a tractable optimization problem by introducing auxiliary variables (Ben-Tal et al., 2004).

2.2 Description of Conditional Uncertainty

A potential limitation of (4) lies in that, unnecessarily conservative solutions may be attained because the structure of Ω cannot well describe the distribution of \mathbf{w} . Specifically, in the optimal operations and control of energy systems, it is common that \mathbf{w} and \mathbf{v} represents future predictions and prediction errors of energy intensities. For example, in operations of micro-grid, predictions of wind and solar energies are typically available based on weather forecasts (Zong et al., 2012). In this case, the distribution of prediction errors may exhibit time-varying characteristics. Consider two different cases where predictions of solar energies are made in the daytime and at night. In the daytime, due to varying cloudiness, predictions tend to be uncertain, while at night predictions are much more accurate in the absence of sunlight. Hence, prediction errors in the day time will be more pronounced than those at night. It implies that one cannot use generic uncertainty sets to appropriately tackle such uncertainty, and hence research attentions are required in this vein.

We state that, such uncertainty can be understood as being dependent on some external variables, which can be prediction values in the case of solar energy predictions. This is because prediction values of solar energy will be high in the daytime and be low at night, which embody time-varying information themselves. Our idea is to disentangle the dependence the time-varying uncertainty on the external variables, thereby obtaining the underlying primitive uncertainty whose distribution tends to be time-invariant. Formally, such dependence can be described in the following generative manner:

$$\mathbf{w} = \mathbf{g}(\boldsymbol{\delta}, \mathbf{z}), \quad (5)$$

where $\boldsymbol{\delta}$ and \mathbf{z} denote external variables and the primitive uncertainty, respectively. $\mathbf{g}(\cdot, \cdot)$ is a specific function to be determined. We further assume that with $\boldsymbol{\delta}$ given, there is a one-to-one mapping from \mathbf{w} to \mathbf{z} , which is denoted as:

$$\mathbf{z} = \mathbf{g}^{-1}(\boldsymbol{\delta}, \mathbf{w}). \quad (6)$$

Because of the effect of decoupling $\boldsymbol{\delta}$ from \mathbf{z} , which has a homogeneous distribution, a constant uncertainty set D can be adopted. Recently, a popular and efficient way to parameterize D is to utilize machine learning techniques (Ning and You, 2017, 2018), where SVC induced by the weighted generalized intersection kernel (WGIK) is an appealing one due to its compact representation capability, ease of implementation and robustness to outliers. The typical expression of the SVC-based uncertainty set is given by (Shang et al., 2017):

$$D = \left\{ \mathbf{z} \mid \sum_i \alpha_i \|\mathbf{Q}(\mathbf{z} - \mathbf{z}^{(i)})\|_1 \leq \theta \right\}, \quad (7)$$

where \mathbf{Q} is a weighting matrix, and $\{\mathbf{z}^{(i)}\}$ are historical samples of \mathbf{z} . Parameters $\{\alpha_i\}$ and θ can be obtained by solving a dual quadratic program (Ben-Hur et al., 2001). With the distribution of \mathbf{z} described by D , we can further arrive at the expression of Ω :

$$\Omega = \{ \mathbf{w} \mid \mathbf{w} = \mathbf{g}(\boldsymbol{\delta}, \mathbf{z}), \mathbf{z} \in D \}. \quad (8)$$

We refer to (8) as *conditional uncertainty set*, which is established based on the data-driven uncertainty set D of primitive uncertainty \mathbf{z} .

2.3 Robust Optimal Control with Conditional Uncertainty Set

Because \mathbf{w} can be expressed in terms of \mathbf{z} , the ADF policy can be defined directly on \mathbf{z} , which is $\boldsymbol{\pi}(\mathbf{z}) = \mathbf{P}\mathbf{z} + \mathbf{q}$. Up to now, we can derive the following optimal control problem:

$$\begin{aligned} \min_{\boldsymbol{\pi}} J_H(x_0, \boldsymbol{\pi}) \\ \text{s.t. } \mathbf{x} = \mathbf{A}\mathbf{x}_0 + \mathbf{B}\boldsymbol{\pi}(\mathbf{z}) + \mathbf{E}\mathbf{v} + \mathbf{H}\mathbf{g}(\boldsymbol{\delta}, \mathbf{z}) \\ \mathbf{C}\mathbf{x} + \mathbf{D}\boldsymbol{\pi}(\mathbf{z}) \leq \mathbf{f}, \forall \mathbf{z} \in D \end{aligned} \quad (9)$$

With $\mathbf{g}(\cdot, \cdot)$ appropriately defined, (9) can be regarded as a traditional robust optimization problem and is amenable to a dual reformulation (Shang and You, 2019). Next, an irrigation control example is presented to demonstrate its generality.

3. An Irrigation Control Example

In the context of irrigation control, the irrigation amount is manipulated to keep soil moisture level within a proper range. The water balance in the root zone soil can be mathematically expressed as $x_{t+1} = (1-c) \cdot x_t + u_t + v_t + w_t$, where x_t is the soil moisture level, u_t is the irrigation amount, and $c \cdot x_t$ stands for the amount of runoff and water percolation ($0 < c < 1$) (Delgoda et al., 2016). We assume that $v_t = -e_t + y_t$, where e_t denotes the amount of crop evapotranspiration that is precisely known, and y_t is the predicted rainfall amount. w_t is the rainfall prediction error at stage t . The control goal is to minimize water usage subject to limited water supply $u_t \leq 10$ mm while maintaining soil moisture above a safety level $x_t \geq 30$ mm, because the deficiency in soil moisture can probably lead to crop devastations. Such goal can be easily interpreted by choosing appropriate loss functions and constraints.

To devise a conditional uncertainty set for \mathbf{w} , we first plot in Figure 1 the joint empirical distribution of w_t and y_t ($t = 1$) based on real weather data collected at Des Moines, Iowa. It can be observed that the distribution of w_t is apparently asymmetric and varies with the value of y_t . In particular, when the value of w_t is negative, the ground truth rainfall amount p_t is smaller than predicted, and hence we have $w_t = p_t - y_t \geq -y_t$. By the same token, when the value of w_t is non-negative, the ground truth rainfall amount p_t is larger than predicted but smaller than a maximum p^{\max} , and hence we have $w_t = p_t - y_t \leq p^{\max} - y_t$. Therefore, the ranges of positive and negative parts of w_t rely on the predicted value y_t , which highlight the requirement of employing the conditional uncertainty set. Based on such an observation, we propose to parameterize Ω as follows:

$$\Omega = \left\{ \mathbf{w} \mid \mathbf{w} = \mathbf{G}(\mathbf{y})^+ \mathbf{w}^+ - \mathbf{G}(\mathbf{y})^- \mathbf{w}^-, \mathbf{w}^+ - \mathbf{w}^- \in D, \mathbf{0} \leq \mathbf{w}^+, \mathbf{w}^- \leq \mathbf{1} \right\}. \quad (10)$$

Therefore, $\mathbf{z} = \{\mathbf{w}^+, \mathbf{w}^-\}$ stands for the primitive uncertainty that explains variations within \mathbf{w} . Diagonal coefficient matrices are given by:

$$\mathbf{G}(\mathbf{y})^+ = \text{diag}\{p^{\max} - y_{1,L}, p^{\max} - y_N\}, \quad \mathbf{G}(\mathbf{y})^- = \text{diag}\{y_{1,L}, y_N\}, \quad (11)$$

which help normalizing the primitive uncertainty. To construct D , historical prediction and measurement data have been collected at Des Moines, Iowa from Jun 2016 to Oct. 2016. Since D is essentially a polytope, the above problem is a typical robust optimization problem that allows for a tractable dual reformulation. Here the external variables δ become future rainfall predictions \mathbf{y} . Finally, the optimal control problem (9) becomes:

$$\begin{aligned} & \min_{\boldsymbol{\pi}} J_H(x_0, \boldsymbol{\pi}) \\ & \text{s.t. } \mathbf{x} = \mathbf{A}\mathbf{x}_0 + \mathbf{B}\mathbf{u} + \mathbf{E}\mathbf{v} + \mathbf{H}\mathbf{G}(\mathbf{y})^+ \mathbf{w}^+ - \mathbf{H}\mathbf{G}(\mathbf{y})^- \mathbf{w}^- \\ & \quad \mathbf{C}\mathbf{x} + \mathbf{D}\boldsymbol{\pi}(\mathbf{w}^+, \mathbf{w}^-) \leq \mathbf{f}, \quad \forall \mathbf{w}^+ - \mathbf{w}^- \in D, \quad \mathbf{0} \leq \mathbf{w}^+, \mathbf{w}^- \leq \mathbf{1} \end{aligned} \quad (12)$$

where $\boldsymbol{\pi}(\mathbf{w}^+, \mathbf{w}^-) = \mathbf{P}^+ \mathbf{w}^+ + \mathbf{P}^- \mathbf{w}^- + \mathbf{q}$ stands for the ADF policy. Closed-loop simulations have been executed from May 2017 to Oct. 2017 under open-loop control, certainty equivalent MPC (CEMPC), and the proposed method. The results with respect to monthly irrigation amounts and constraint violation probabilities have been summarized in Tables 1 and 2.

Table 1. Monthly Irrigation Amounts in 2017

	Jun.	Jul.	Aug.	Sep.	Oct.
Open-Loop Ctrl. (mm)	300.00	283.00	226.00	268.00	92.00
CEMPC (mm)	196.64	209.03	141.11	131.12	47.32
RMPC (mm)	198.87	209.55	142.39	132.87	50.11

Table 2. Monthly Violations Probabilities of Soil Moisture Levels in 2017

	Jun.	Jul.	Aug.	Sep.	Oct.
Open-Loop Ctrl. (%)	0.00	0.00	0.00	0.00	0.00
CEMPC (%)	21.67	23.38	15.32	17.50	5.98
RMPC (%)	0.00	0.00	0.00	0.00	0.00

It can be observed that, the open-loop control strategy that determines weekly irrigation schedule in advance, leads to zero probability of soil moisture deficiency along with the greatest water consumptions. In contrast, CEMPC yields the most aggressive control actions, since the least amount of water is used. However, the price is that state constraints are frequently violated, which may heavily compromise crop productivity. The proposed data-based RMPC achieves a satisfactory performance. On one hand, it reduces the water consumption by about 40% compared to open-loop control, which is the state-of-the-art technology. On the other hand, it successfully safeguards soil moisture level constraints. This owes to an appropriate characterization of the uncertainty distribution based on the proposed conditional uncertainty set constructed with historical data. The proposed method can achieve a desirable balance between saving water, and hedging against uncertainty in forecast errors with the aim to reliably avoid potential harm to crop.

4. Conclusions

This paper features a new framework for RMPC under additive conditional uncertainty, where the dependence of original uncertainty on primitive uncertainty is clearly described, based on which data-driven uncertainty sets are constructed to indirectly

characterize the distribution of original uncertainty. The proposed method applies to optimal operations and control of energy systems where predictions of energy intensities are available but inevitably induce uncertain prediction errors. By compactly describing the distribution of uncertainty with the proposed conditional uncertainty set, the conservatism of control actions can be efficiently reduced, which uncovers the value of leveraging big data. A real-world case study based on agricultural irrigation systems is performed to show the effectiveness and merits of the proposed method.

References

- A. Ben-Hur, D. Horn, H. T. Siegelmann, V. Vapnik, 2001, Support vector clustering. *Journal of Machine Learning Research*, 2(Dec), 125–137.
- A. Ben-Tal, A. Goryashko, E. Guslitzer, A. Nemirovski, 2004, Adjustable robust solutions of uncertain linear programs, *Mathematical Programming*, 99, 351–376.
- D. Bertsimas, M. Sim, 2004, The price of robustness. *Operations Research*, 52(1), 35–53.
- Y. Chu, F. You, 2015, Model-based integration of control and operations: Overview, challenges, advances, and opportunities. *Computers & Chemical Engineering*, 83, 2–20.
- D. Delgoda, H. Malano, S. K. Saleem, M. N. Halgamuge, 2016, Irrigation control based on model predictive control. *Environmental Modelling & Software*, 78, 40–53.
- P. J. Goulart, E. C. Kerrigan, J. M. Maciejowski, 2006, Optimization over state feedback policies for robust control with constraints. *Automatica*, 42(4), 523–533.
- M. Morari, J. H. Lee, 1999, Model predictive control: Past, present and future. *Computers & Chemical Engineering*, 23(4-5), 667–682.
- C. Ning, F. You, 2017, Data-Driven Adaptive Nested Robust Optimization: General Modeling Framework and Efficient Computational Algorithm for Decision Making Under Uncertainty. *AIChE Journal*, 63, 3790–3817.
- C. Ning, F. You, 2017, A data-driven multistage adaptive robust optimization framework for planning and scheduling under uncertainty. *AIChE Journal*, 63, 4343–4369.
- C. Ning, F. You, 2018, Data-driven stochastic robust optimization: General computational framework and algorithm leveraging machine learning for optimization under uncertainty in the big data era. *Computers & Chemical Engineering*, 111, 115–133.
- C. Ning, F. You, 2018, Data-driven decision making under uncertainty integrating robust optimization with principal component analysis and kernel smoothing methods. *Computers & Chemical Engineering*, 112, 190–210.
- M. B. Saltik, L. Özkan, J. H. Ludlage, S. Weiland, P. M. Van den Hof, 2018, An outlook on robust model predictive control algorithms: Reflections on performance and computational aspects. *Journal of Process Control*, 61, 77–102.
- D.E. Seborg, D.A. Mellichamp, T.F. Edgar, et al. (2010). *Process Dynamics and Control*: John Wiley & Sons.
- C. Shang, X. Huang, F. You, 2017, Data-driven robust optimization based on kernel learning. *Computers & Chemical Engineering*, 106, 464–479.
- C. Shang, F. You, 2018, Distributionally robust optimization for planning and scheduling under uncertainty. *Computers & Chemical Engineering*, 110, 53–68.
- C. Shang, F. You, 2019, A data-driven robust optimization approach to scenario-based stochastic model predictive control. *Journal of Process Control*, 75, 24–39.
- P. Tatjewski. (2007). *Advanced control of industrial processes: structures and algorithms*: Springer.
- X. Zhang, M. Kamgarpour, A. Georghiou, P. Goulart, J. Lygeros, 2017, Robust optimal control with adjustable uncertainty sets. *Automatica*, 75, 249–259.
- S. Zhao, F. You, 2019, Resilient supply chain design and operations with decision-dependent uncertainty using a data-driven robust optimization approach. *AIChE Journal*, 65, 1006–1021.
- Y. Zong, D. Kullmann, A. Thavlov, O. Gehrke, H. W. Bindner, 2012, Application of model predictive control for active load management in a distributed power system with high wind penetration. *IEEE Transactions on Smart Grid*, 3(2), 1055–1062.

Development of the Texas A&M Superfund Research Program Computational Platform for Data Integration, Visualization, and Analysis

Rajib Mukherjee^{a,b}, Melis Onel^{a,b}, Burcu Beykal^{a,b}, Adam T. Szafran^c, Fabio Stossi^c, Michael A. Mancini^c, Lan Zhou^d, Fred A. Wright^e, Efstratios N. Pistikopoulos^{a,b,*}

^a *Artie McFerrin Department of Chemical Engineering, Texas A&M University, College Station, TX*

^b *Texas A&M Energy Institute, Texas A&M University, College Station, TX*

^c *Molecular and Cellular Biology, Baylor College of Medicine, Houston, TX*

^d *Department of Statistics, Texas A&M University, College Station, TX*

^e *Bioinformatics Research Center, Center for Human Health and the Environment, Department of Biological Sciences, North Carolina State University, Raleigh, NC.*

**stratos@tamu.edu*

Abstract

The National Institute of Environmental Health Sciences (NIEHS) Superfund Research Program (SRP) aims to support university-based multidisciplinary research on human health and environmental issues related to hazardous substances and pollutants. The Texas A&M Superfund Research Program comprehensively evaluates the complexities of hazardous chemical mixtures and their potential adverse health impacts due to exposure through a number of multi-disciplinary projects and cores. One of the essential components of the Texas A&M Superfund Research Center is the Data Science Core, which serves as the basis for translating the data produced by the multi-disciplinary research projects into useful knowledge for the community via data collection, quality control, analysis, and model generation. In this work, we demonstrate the Texas A&M Superfund Research Program computational platform, which houses and integrates large-scale, diverse datasets generated across the Center, provides basic visualization service to facilitate interpretation, monitors data quality, and finally implements a variety of state-of-the-art statistical analysis for model/tool development. The platform is aimed to facilitate effective integration and collaboration across the Center and acts as an enabler for the dissemination of comprehensive ad-hoc tools and models developed to address the environmental and health effects of chemical mixture exposure during environmental emergency-related contamination events.

Keywords: Data analytics, data integration, statistical analysis, collaborative networks.

1. Introduction

The risk of chemical contamination and exposure to hazardous chemicals are elevated during and after natural catastrophic events (*i.e.*, hurricanes) due to the increased mobility of many chemical toxicants. In such situations, the rapid and precise examination of potential sources and pathways of chemical contamination becomes essential: (i) for identifying their adverse health impacts and (ii) for delivering solutions to mitigate such

adverse effects. To this end, Texas A&M Superfund Research Program (TAMU Superfund Research Center, 2018) aims to build both experimental and computational models, methods and tools through exposomics research and data analysis. The program extensively studies the health, economic and social impacts of hazardous complex chemical mixtures after environmental emergencies with Galveston Bay/Houston Ship Channel area being selected as a case study.

TAMU SRP is a cross-disciplinary program and has a tightly integrated structure which governs four main research projects (two environmental and two biomedical research projects). The two environmental projects, namely Project 1 and 2, focus on understanding dynamic exposure pathways under the conditions of environmental emergencies and designing novel broad-acting sorption materials for reducing bioavailability of contaminants. Project 3 and 4, being the two biomedical projects, are studying *in vitro* and *in vivo* hazard, kinetics and inter-individual variability of responses to chemical mixtures and developing *in vitro* multiplex single-cell assays to detect endocrine disruption potential of mixtures. Each of these projects utilizes various experimental methodologies for detecting, assessing, evaluating and characterizing the effects of complex chemical contaminants including Gas Chromatography-Mass Spectrometry (GC-MS), Ion Mobility-Mass Spectrometry (IM-MS), Inductively Coupled Plasma Mass Spectrometry (ICP-MS), Ultraviolet-Visible Spectroscopy (UV-Vis), high-throughput imaging and image analysis. Hence, these four projects generate large quantities of highly diverse datasets, where their maintenance and analysis require a systematic approach through the development of a computational platform.

In addition to the four main research projects, there are three research supporting cores within the TAMU SRP, one of which is the Data Science Core. The Data Science Core serves as the basis for translating the data produced by the four research projects into useful knowledge for the community via data collection, quality control, analysis, visualization and model generation. This Core functions as a hub that collects, processes and integrates the aforementioned diverse datasets over a computational platform to draw specific conclusions via supervised (*i.e.*, regression, classification) and unsupervised (*i.e.*, clustering) analysis. These techniques are widely used in process systems engineering (PSE) including process monitoring (Onel et al., 2018b) and grey-box optimization (Beykal et al., 2018). In this work, we present the TAMU SRP computational platform which aims to promote collaboration across the Center and facilitate dissemination of methods/data across all projects of the program as well as to the wider community. The computational platform is developed as an online tool that specifically uses a relational database for data storage as well as statistical and machine learning techniques to create decision support models, housing both novel computational methodologies and state-of-the-art data analytics techniques. It establishes an accessible front-end interface for the application of the high-performance models and tools developed during collaborations with individual research projects (Onel et al., 2018a). The details of the computational platform are provided in the following sections where its integration and connection with one of the biomedical projects is demonstrated as a motivating example.

2. Computational Platform

The online computational platform is developed in Python environment, whereas the backend functionalities utilize either R or Python environments. The relational database for storing and sharing data across the Center is based on SQLite. A flow diagram of the

platform is shown in Figure 1. The computational platform is developed and implemented in two stages. The first stage entails the dissemination of datasets and methodologies across the Center for supplying a convenient environment for collaboration among all projects. The second stage enables access to the extracted knowledge, models, and tools with the scientific community, government and commercial stakeholders. In this work we will only present the developments of the first stage.

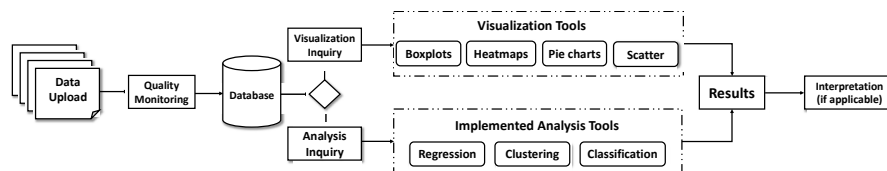


Figure 1. Online computational platform flowchart.

The computational platform first requires a data upload by the user, which is further passed to an initial quality monitoring module. The quality monitoring module checks the dataset for any missing data and/or outliers. Missing data is handled two-fold: (i) Deletion of rows or columns that include missing data, (ii) imputation by k-nearest neighbor (k-NN) methodology (Ramaswamy et al., 2000). This pre-processed data is stored under the relational database for future reference. A summary of this first module is provided as a feedback to the user. Second, the user specifies a type of inquiry, namely visualization and analysis. Currently, four visualization techniques are implemented within the platform including, boxplots, heatmaps, pie charts and scatter plots. Guidelines for selecting the relevant visualization technique is provided online. The generated plots or maps are then displayed on the interface which can be downloaded by the user. Specifically, further interpretation of boxplots, containing the summary of statistics (*i.e.*, median, interquartile range etc.) is provided along with the visuals. Next, the datasets can be analyzed via unsupervised or supervised techniques depending on the purpose of the study. For untargeted analysis, clustering with hierarchical, k-means, and deep learning techniques are utilized. For targeted analysis, where the output of certain experiments is known and used for training models, supervised learning approaches are chosen. Specifically, for the datasets with discrete type of output (or label), classification techniques are used. Current classification techniques include Support Vector Machines (SVM), Random Forest (RF) Algorithm, and logistic regression. Whereas if the output of the dataset is continuous, regression techniques are employed. Here, in addition to SVM and RF Algorithm, interpolation (*i.e.*, Kriging, radial basis functions) and multivariate regression techniques (*i.e.*, linear, quadratic) are employed. The analysis selection is guided by the collaboration between the Data Science Core personnel and individual research projects. Once the data analysis methodology is established for a specific type of data, custom tools are generated and implemented within the platform. This automates the workflow across the Center, minimizes repetitive efforts, thus increasing the overall efficiency.

It is important to note that the large (*i.e.*, exposomics and imaging) datasets generated by the two biomedical research projects under TAMU SRP are in high dimensional space. This necessitates the use of dimensionality reduction techniques along with the aforementioned data analysis methodologies. To this end, numerous dimensionality reduction methodologies are implemented in the computational platform. These include

Principal Component Analysis, Chi-squared test, built-in feature ranking algorithms of RF and in-house developed SVM-based feature selection algorithms (Onel et al., 2018b).

3. Motivating Example

Here, we present a motivating example from TAMU SRP Project 4 to showcase the use of the developed computational platform. This project focuses on understanding the hazardous effects of environmental contaminants and mixtures that may interfere with proper function of the human endocrine system, causing several adverse health effects (*i.e.*, reproductive, developmental, metabolic etc.) due to modulations in hormone nuclear receptors' action. Hence, Project 4 personnel develop single-cell high throughput microscopy experiments with associated image analysis and informatics, thus producing high dimensional imaging data to fingerprint the endocrine disruptor potential of chemicals and environmental mixtures, whereas Data Science Core personnel use the generated data to build predictive models that classifies and quantifies the endocrine disruptor potential. Below, the development of data-driven models that predict potential activity of chemicals on a prototypical target, the estrogen receptor (ER), and their use through the computational platform are described in detail.

In order to establish a framework, 45 known chemical compounds (agonists, antagonists and inactive for the ER) used by the United States Environmental Protection Agency (US EPA) are utilized to determine the effectors of ER action (Judson et al., 2015). The GFP-ER α :PRL-HeLa cell line, and its derivatives, is an engineered model that allows multi-parametric simultaneous measurements of many important features, including, ligand binding, DNA binding, chromatin remodeling and transcriptional output, required for the activation of Estrogen Receptors (ER) (Szafran et al., 2017). This high throughput microscopy assay is used to test the responses to the EPA 45 reference compounds as well as to the control agonist 17 β -estradiol (E2) and antagonist 4-hydroxytamoxifen (4OHT). The effect of these test chemicals can broadly be classified three-fold: (i) agonist (which elicits a positive response of the ER signaling pathway – akin to E2), (ii) antagonist (mimicking a response like 4OHT), or (iii) inactive. By treating the cells with a six-point dose-response of these compounds, high throughput imaging data is generated and analyzed. This yields a data matrix of 180 (4 measurements for each 45 compounds) by 70 descriptors (features). Each descriptor considers various aspects of the ER pathway (*i.e.*, Is the ER level changing? Does ER bind to DNA? How much chromatin remodeling happens? etc.). This dataset is later passed to the Data Science Core for further analysis and for modeling the ER disrupting potential of the tested compounds. The details on model generation and step-by-step use of the developed model within the computational platform are provided below.

Step 1 – Data Quality Monitoring: As an initial step, the quality of the received experimental data is inspected by identifying any potential missing data. In this case study, there are no missing data. The complete dataset is analyzed to detect any potential outliers via hierarchical clustering algorithm with complete linkage methodology and Euclidean distance metric. Identification and removal of outliers is essential in order to ensure accurate model development. The results reveal “Reserpine” as an outlier, which has been removed from further analysis (Figure 2).

Step 2 – Normalization: The goal is to classify the compounds based on agonist/antagonist activity. To achieve this, inactive compounds must be separated prior

to normalization and model building. This is done by using a threshold for the cell population with a visible nuclear spot, signifying ER-DNA binding. Less than 10% of the cell population, that has a visible nuclear spot, are considered to be inactive and removed from further analysis. Then, the dataset is normalized in order to attain a consistent range per feature. Specifically, the order of magnitude of intensity related measurements significantly differ from measurements derived from nucleus shape. Therefore, normalization is performed by using Equation 1.

$$sample_{normalized} = \frac{sample - median(media)}{median(E2) - median(media)} \tag{1}$$

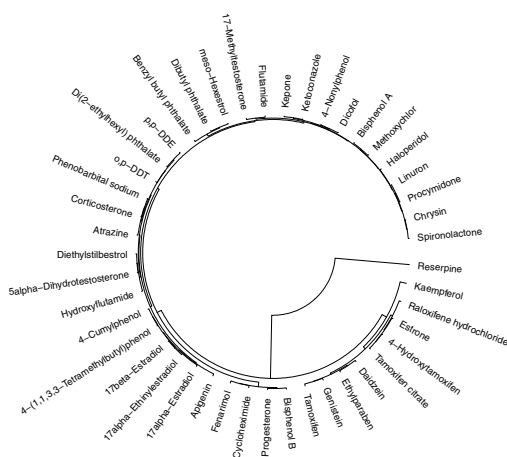


Figure 2. Outlier identification via hierarchical clustering. Reserpine is identified as outlier.

before dimensionality reduction is achieved as 90%, whereas the end-model, the reduced model that use the top 10 informative features, has 92% accuracy.

Step 4 – Automation of Analysis: This end-model is then converted into an executable tool and implemented to the Python based environment of the computational platform.

4. Future directions

Development of the computational platform is an ongoing process. As new data are generated, corresponding tools and models are tailored, updated and incorporated in the platform. Current limitation of the platform is that the analysis only covers the Center projects and datasets. However, access to historical data provided by government agencies is crucial for comparative analysis in TAMU SRP (e.g., ToxCast and Tox21 initiatives). Therefore, additional features will be provided for access to the relevant public data repositories through integration. Finally, one of the main goals of the Data Science Core is to serve as a basis to facilitate TAMU SRP data analysis and understanding. Therefore, training for the use of generated models and tools within the computational platform will be provided in collaboration with the Research Translation and Training Cores.

Step 3 – Predictive Modeling & Dimensionality Reduction: Once the data is pre-processed, cleaned from outliers and normalized, various classification algorithms are applied to build predictive models. In this study, RF algorithm is employed for the classification of agonist/antagonist activity and for identifying important descriptors through the built-in feature ranking property (Breiman, 2001). Tuning is performed and optimal number of trees is identified as 500. Final model is then built with the optimal number of trees by using 5-fold cross-validation. The top 10 informative features achieved during modeling are also reported in Table 1. The model accuracy

Table 1. Top 10 informative features for agonist/antagonist classification.

Rank	Measurement	Rank	Measurement
1	Nucleoplasm GFP Pixel Intensity Variance	6	Ratio of Nuclear Spot to Nucleoplasm GFP Intensity
2	Nuclear GFP Pixel Intensity Variance	7	Nuclear Spot GFP Pixel Intensity Variance
3	Nucleoplasm 90 th Percentile GFP Pixel Intensity	8	Cytoplasm 75 th Percentile GFP Pixel Intensity
4	Nuclear 90 th Percentile GFP Pixel Intensity	9	Nuclear Spot 75 th Percentile GFP Pixel Intensity
5	Nuclear Spot 90 th Percentile GFP Pixel Intensity	10	Cytoplasm 90 th Percentile GFP Pixel Intensity

5. Conclusions

In this study, development of a computational platform for the Texas A&M Superfund Research Center is presented. This platform provides on-demand, intuitive access to the custom-made data analysis tools and models developed for the environmental and biomedical projects within the Center. These analysis techniques are applicable to PSE problems. The ultimate goal is to establish an online data analytics services for rapid decision-making during environmental emergencies. This research is funded by U.S. National Institute of Health grant P42 ES027704 and Texas A&M Energy Institute.

References

- A.T. Szafran, F. Stossi, M.G. Mancini, C.L. Walker, M.A. Mancini, 2017, Characterizing properties of non-estrogen substituted bisphenol analogs using high throughput microscopy and image analysis, *PLoS one*, 12(7), e0180141.
- B. Beykal, F. Boukouvala, C.A. Floudas, N. Sorek, H. Zalavadia, E. Gildin, 2018, Global Optimization of Grey-Box Computational Systems Using Surrogate Functions and Application to Highly Constrained Oil-Field Operations, *Computers & Chemical Engineering*, 114, 99-110.
- L. Breiman, 2001, Random Forests, *Machine Learning*, 45, 1, 5-32.
- M. Onel, B. Beykal, M. Wang, F.A. Grimm, L. Zhou, F.A. Wright, T.D. Phillips, I. Rusyn, E.N. Pistikopoulos, 2018a, Optimal Chemical Grouping and Sorbent Material Design by Data Analysis, Modeling and Dimensionality Reduction Techniques, *Computer Aided Chemical Engineering*, 43, 421-426.
- M. Onel, C.A. Kieslich, Y.A. Guzman, C.A. Floudas, E.N. Pistikopoulos, 2018b, Big Data Approach to Batch Process Monitoring: Simultaneous Fault Detection and Diagnosis Using Nonlinear Support Vector Machine-based Feature Selection, *Computers & Chemical Engineering*, 115, 46-63.
- R.S. Judson, F.M. Magpantay, V. Chickarmane, C. Haskell, N. Tania, J. Taylor, M. Xia, R. Huang, D.M. Rotroff, D.L. Filer, K.A. Houck, M.T. Martin, N. Sipes, A.M. Richard, K. Mansouri, R.W. Setzer, T.B. Knudsen, K.M. Crofton, R.S. Thomas, 2015, Integrated Model of Chemical Perturbations of a Biological Pathway Using 18 *In Vitro* High-Throughput Screening Assays for the Estrogen Receptor, *Toxicological Sciences* 148(1), 137-154.
- TAMU Superfund Research Center (2018). <https://superfund.tamu.edu/> (accessed 9 November 2018).

Scalable manufacturing of nanostructured materials by atomic layer deposition in fluidized bed reactors

J.Ruud van Ommen,^{a,*} Fabio Grillo,^{a,b} Johan Grievink^a

^a*Dept. of Chemical Engineering, Delft Univ. of Technology, Delft, the Netherlands*

^b*Dept. of Materials, ETH Zurich, Zurich 8093, Switzerland*

J.R.vanOmmen@TUDelft.nl

Abstract

Atomic layer deposition (ALD) is a gas-phase coating technique that can be used to coat nanoparticles in a fluidized bed reactor. ALD is based on the alternating supply of two precursors, which makes it an inherent dynamic process. We discuss a multi-scale, multi-phase mass transfer-diffusion-reaction model capable of predicting the evolution of surface coverage of particles at different local operating conditions. The dynamic ALD-reactor model can be extended with operational scenarios. The reactor design combined with the scenarios has many degrees of freedom, yielding ample opportunities to optimize the process with efficient utilization of precursors.

Keywords: particle technology, nanotechnology, fluidization, ALD, nanoparticles

1. Introduction

Nanostructured particles (e.g., core-shell nanoparticles or nano-decorated micro-particles) have high a potential in applications such as catalysis and energy storage, but also in medicine and food. However, from designing products incorporating nanostructuring to produce them in large quantities is not trivial. Gas-phase coating using atomic layer deposition (ALD, a variant of chemical vapour deposition) can be used to provide the surface of a particle with either an ultrathin continuous coating or a decoration of nanoclusters. When carried out in a fluidized bed or a pneumatic reactor, ALD is an attractive way of producing nanostructured particles with excellent scale-up potential (Salameh et al., 2017). Even nanopowders can be treated with this process. This is facilitated by the fact that during fluidization they are not present as individual particles but as very dilute agglomerates of several hundreds of microns.

2. Atomic Layer Deposition in a Fluidized Bed

Atomic layer deposition (ALD) is a gas-phase coating technique that is being increasingly used in the semi-conductor industry to provide microchips with coatings on the order of 1-10 nm. It enables digital control over the amount of deposited material by relying on sequential self-limiting surface reactions. In ALD the compound to be deposited is synthesized directly on the substrate surface instead of being deposited from the vapour phase as in other thin film techniques such as chemical vapor deposition (CVD), from which ALD is derived. The synthesis of the desired compound is typically split into two

steps, each step follow by a purge. Each reaction step involves self-saturating chemisorption reactions between a precursor and the substrate surface. The precursor is provided for a certain period of time, which is typically called the pulse time. The purge step after the precursor pulse is crucial to preserve the self-limiting nature of ALD reactions, as it prevents the intermixing between different precursors, and between precursors and reaction by-products, which might result in uncontrolled deposition. By repeating these steps in a cyclic fashion one can grow the desired material with a resolution set by the amount of material deposited in each cycle referred to as growth per cycle (GPC), which is usually a fraction of a monolayer. This in principle translates into an atomic-level control over the material properties (Van Bui *et al.*, 2017).

Since ALD is a surface-driven process, its use is not limited to wafers and other flat substrates, but it can also be used to obtain conformal coatings on substrates with complex geometries such as high-aspect-ratio structures for electronic devices, porous media and powders (Van Bui *et al.*, 2017, Longrie *et al.*, 2014, Puurunen, 2005). Especially its application to powders is interesting: 70% of the industrial processes involve powders, and there is an increasing demand for nanostructured powders. By applying ALD to a fluidized bed, we have a precise, versatile and scalable way of making such powders.

3. Modelling ALD in a Fluidized Bed Reactor

Fluidized bed ALD is an interesting process from a dynamics point of view, since the fluidized bed dynamics (gas residence time and particle mixing \sim seconds) is combined with very fast ALD reaction kinetics (\ll 1s) and relatively slow precursor pulse times (\sim minutes), in order to provide enough precursor molecules to cover all surface. In order to analyze the interplay between these phenomena, we developed a multiscale model to describe this process (Grillo *et al.*, 2015), which will be briefly recapped here.

Our dynamical model captures the essential features of the coupling between the precursor transport, from the reactor- to the particle-scale, and the kinetics of the ALD surface reactions. During ALD in fluidized bed reactors, the precursor transport takes place on at least three different length scales: (1) from the inlet of the reactor throughout the bulk of the gas phase, (2) from the bulk of the gas phase to the outer surface of the particles, and (3) from the outer surface of the particles to their inner porous structure. We therefore describe the precursor transport via two sub-models: the one describing the transport across the length scales (1-2), which we refer to as the “reactor-scale”, and the second describing the transport within the inner structure of the particles (3), which we refer to as the “particle-scale”. Next to the precursor transport we also account for the precursor consumption arising from the gas-solid reactions taking place on the surface of the particles. In particular, to retrieve the self-limiting nature of ALD surface reactions our model also incorporates the detailed balance of the surface coverage of active sites prescribed by the stoichiometry of the chemistry of choice.

The reactor-scale model is based on the two-phase theory of bubbling fluidization. The latter accounts for the uneven distribution of gas within a fluidized bed of cohesive

powders such as many nanostructured particles. It assumes that the gas flow at the reactor inlet is distributed between two phases: the emulsions phase, characterized by a high density of particles, and the bubble phase, which instead contains only gas. The gas flow in the bubble phase is approximated to be plug flow; the emulsion phase is assumed to be fully mixed. Furthermore, the two phases exchange precursor through interphase mass transfer mediated by both diffusion and convection, and the precursor can reach the particles only in the emulsion phase through mass transfer. The reactor-scale precursor transport model therefore translates into the following system of differential equations:

$$\frac{\partial C_b}{\partial t} + u_b \frac{\partial C_b}{\partial z} = -K_{be}(C_b - C_e) \quad (1)$$

$$\varepsilon_e \frac{dC_e}{dt} = \frac{u_e}{H}(C_{in} - C_e) + \frac{K_{be}\delta}{H(1-\delta)} \int_0^H (C_b - C_e) dz - K_{ga} \frac{6(1-\varepsilon_e)}{d_p} (C_e - C_p|_{r=R_p}) \quad (2)$$

where C_b , C_e , $C_p|_{r=R_p}$, C_{in} , u_b , u_e , ε_e , δ , z , H , K_{be} , K_{ga} are the concentration of precursor in the bubble phase, in the emulsion, at the particles outer surface, at the reactor inlet; the gas velocity in the bubble, and in the emulsion; the gas volume fraction in the emulsion phase; the total volume fraction of the bubble phase; the vertical distance from the inlet of the reactor; the total height of the reactor; the bubble-to-emulsion mass transfer coefficient; and the gas-to-particle mass transfer coefficient, respectively.

The precursor transport at the particle-scale is modeled in terms of diffusion and reaction of dilute species within porous spheres. Nanostructured particles such as nanoparticle agglomerates may present a hierarchical porous structure: pores of different sizes at different length scales. This means that the transport model should take into account that the diffusion rates are a function of the position within the pore network. Nevertheless, if the transport through the pore network is limited along a preferential direction (e.g., the radius of the nanoparticle agglomerate), then its description can be reduced to a diffusion problem within mono-dispersed porous media in spherical coordinates:

$$\varepsilon_p \frac{\partial C_p}{\partial t} = \frac{D_p}{r^2} \frac{\partial}{\partial r} \left(r^2 \frac{\partial C_p}{\partial r} \right) + g(C_p, \boldsymbol{\theta}) \quad (3)$$

$$D_p \frac{\partial C_p}{\partial r} |_{r=R_p} = K_{ga} (C_e - C_p|_{r=R_p}) \quad (4)$$

where C_p , D_p , r , R_p , ε_p , g , $\boldsymbol{\theta}$ are the concentration within the particles, the diffusion coefficient, the radial distance, the radius of the particle, the particle porosity, the reaction term arising from the surface reaction kinetics, and the surface coverage of the active sites, respectively. As already argued in our previous work (Grillo et al., 2015), this treatment is suitable for describing the precursor transport through both nanoparticle agglomerates and nano-porous particles presenting mono-dispersed pores.

The precursor model at the particle scale is coupled to the kinetics of the ALD surface reactions via the evolution of the surface coverage of the active sites:

$$\frac{\partial \boldsymbol{\theta}(r)}{\partial t} = f(C_p(r), \boldsymbol{\theta}, \mathbf{v}) \quad (5)$$

where \mathbf{v} are the reaction rates associated with the surface reactions. The latter balance can assume varying degree of complexity depending on the number and nature of the active sites and of the gas-solid reactions involved in the surface chemistry behind the ALD scheme of choice.

4. Operation

The ALD fluidized bed reactor is by nature operated in a non-stationary way: precursor pulses are alternated with purges by inert gas. Figure 1 gives a schematic of the operation: after loading the reactor with particles, a precursor pulse is given (e.g., a metal precursor), then a purge with inert gas (typically nitrogen) to remove byproducts and possible excess precursor, followed by a pulse of the second precursor (e.g., an oxidizer), and finally again a purge with inert gas. The length of the pulse and purge periods depends on parameters such as surface area of the substrate, concentration of the precursors, and reaction rate. The precursor pulse and purge periods typically last a few minutes.

The precursor pulse and the purge step are characterized by several processes that take place at different time scales. Analyzing the relative order of magnitude of such time scales offers a clue into the scalability and controllability of the process. With regard to the precursor pulse, we already shown through a time scale analysis that all the relevant chemical and physical processes are typically faster than the rate at which the precursor is supplied by as much as five orders of magnitude. This allows one to tailor the precursor pulsing time such that just enough precursor is being supplied to for saturating all the available surface. In other words, no precursor will be wasted.

A key aspect that our model currently does not take into account is the time scale associated with the purging of excess precursor and reaction by-products. In fact, as already pointed out elsewhere (Onn et al., 2018), the purging step in ALD on powders is particularly cumbersome compared to ALD on flat substrates. This is mainly due to two phenomena that slow down the purging process: (1) capillary condensation of precursor within small pores and (2) delayed desorption kinetics caused by the fact that, once desorbed, a molecule has a high probability of adsorbing on another location, either within the porous structure of the same particle or even on other particles within the fluidized bed, before leaving the reactor. The purging dynamics during ALD on powders certainly merits investigation because, on the one hand, the effective purging of unreacted precursor is essential to the self-limiting nature of ALD, and on the other hand excessively long purging times undermine the overall throughput of the process. The model presented here represents a starting point in this regard because it can be readily integrated with a set of equations describing the desorption kinetics of excess precursor.

The amount of precursor to be fed is determined by the surface area in the reactor. Often, it is not possible to exactly know this quantity. In that case, it can be attractive to monitor the outlet of the reactor for a breakthrough of the precursor, e.g. by a mass spectrometer. Since the precursor concentration in the outlet approaches a block wave (Grillo et al., 2015), it is possible to quickly respond to a decrease in precursor concentration.

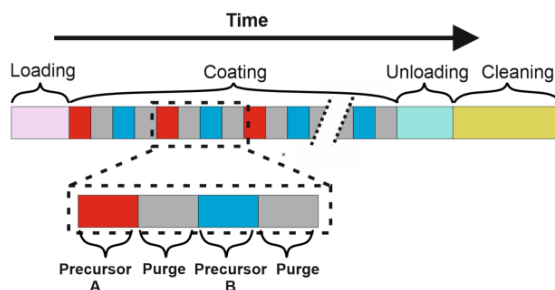


Figure 1. Schematic of the operation of a fluidized bed reactor for ALD

5. Dynamic reactor model with operational scenarios

The reactor operation with its sequence of precursor additions and pulses can be modelled by including the species mass balances, the energy balance, and the transfer and reaction rate equations. The result is a mix of partial differential equations for the bubbly phase, ordinary differential equations for the emulsion phase with algebraic equation for rate laws. The resulting reactor model is written in a compact way, where $x(z,t)$ represents the internal physical state (concentrations, temperature, pressure and fluxes) of all matter (in gas & in solid particles) in the reactor at position z at time t :

$$\frac{\partial x}{\partial t} = f\left(\frac{\partial x}{\partial z}, x; p, d\right) \quad (6)$$

The physical parameters are denoted by p , while d is the set of the reactor design parameters. The model equations are first-order in the spatial derivative of the states as shown in eq. (1). The radial coordinate (r) and the associated concentration dependency in eq. (3) and (4), are assumed to have been approximated by discretization or by orthogonal collocation, considerably extending the number of states at position z .

There is a boundary condition at entrance $z = 0$: $x(0, t) = g(t)$ (7)

as well as an initial condition for $t = 0$: $x(z, 0) = x_0$ (8)

Let this initial condition correspond to a fully fluidized bed in a steady state at the end of the loading, just before any precursor addition will start. The particles are supposed to be in a clean state at $t = 0$.

During the sequence of precursor additions and pulses the model equations remain invariant. It is the inlet boundary condition that changes per addition and pulse. Let the sequence of additions and pulses be denoted by j ($j = 1, 2, \dots, N$), while the starting time of inlet operation j by T_j and it is running till time T_{j+1} . For inlet operation j one has:

Inlet condition: $x_j(0, t) = g_j(t)$ for $T_j < t \leq T_{j+1}$ (9)

Initial condition: $x_j(z, T_j) = x_{j-1}(z, T_j)$ for $0 < z < H$ and $t = T_j$ (10)

The inlet condition reflects the feeding conditions during inlet operation j , while the initial condition for this operation j is equal to the final state at the end of the previous operation $j - 1$. In pulsing intervals the inlet concentrations of precursors are zero.

The product quality at the end of the last operation, pulse $N(Q_N)$ can be related to the process state $x_N(H, T_N)$:

$$Q_N = h(x_N(H, T_N)) \quad (11)$$

Given the operational policies as the set $\{g_j(t), T_j | j = 1, \dots, N\}$ and the initial condition (8) one can simulate the evolution of states $x(z,t)$ over time t by means of (6), (9) & (10). Then it becomes possible to perform sensitivity analyses of the end state, $x_N(H, T_N)$ with respect to the:

- physical parameters (p);
- design parameters (d),
- the starting times of pulses $\{T_j; j=1, \dots, N\}$ and
- piece-wise constant pulse inlet conditions $\{g_j(t) = g_j; j=1, \dots, N\}$.

Furthermore one can analyse operational features such as stability and system time constants by determining the eigenvalues of the Jacobian matrix of the differential equations at reactor exit $z = H$. The ultimate objective is, given a certain product specification (Q_N^*), to obtain an optimum operational policy $\{T_j^*, g_j^*, j = 1, \dots, N\}$ and reactor design (d^*). I.e., an optimum is sought for an economic objective function, while making full use of the precursors. The many degrees of freedom process has, likely make it sustainizable (Jorat & Manousiouthakis, 2018): for the right set of parameters, it can be operated in a sustainable manner.

6 Conclusions

The typically fast kinetics of ALD surface reactions enable the complete uptake of the added precursor, even in the limit of high surface coverages. This has been shown by multi-scale modelling of physical phenomena in the reactor. The same multi-scale model used to analyze the precursor utilization is also amenable to the incorporation of the desorption kinetics of excess precursor. Such extended model can inform the choice of the optimal purging time. The alternation of precursor pulses and purging steps translates into many degrees of freedom. These can be used to optimize the process in line with a given economic objective function, while ensuring nearly full consumption of the supplied precursors. A mathematical model of the reactor with its operational scenarios is formulated as the starting point for such optimizations.

References

- Grillo, F., Kreutzer, M. T. & Van Ommen, J. R. 2015. Modeling the precursor utilization in atomic layer deposition on nanostructured materials in fluidized bed reactors. *Chemical Engineering Journal*, 268, 384-398.
- Jorat, M. & Manousiouthakis, V. 2018. Sustainability identification for infinite-dimensional systems. *AIChE annual meeting*, paper 62c.
- Longrie, D., Deduytsche, D. & Detavernier, C. 2014. Reactor concepts for atomic layer deposition on agitated particles: A review. *Journal of Vacuum Science & Technology A*, 32, 010802.
- Onn, T., Küngas, R., Fornasiero, P., Huang, K. & Gorte, R. 2018. Atomic layer deposition on porous materials: Problems with conventional approaches to catalyst and fuel cell electrode preparation. *Inorganics*, 6, 34.
- Puurunen, R. L. 2005. Surface chemistry of atomic layer deposition: A case study for the trimethylaluminum/water process. *Journal of Applied Physics*, 97, 1-52.
- Salameh, S., Gómez-Hernández, J., Goulas, A., Van Bui, H. & Van Ommen, J. R. 2017. Advances in scalable gas-phase manufacturing and processing of nanostructured solids: A review. *Particuology*, 30, 15-39.
- Van Bui, H., Grillo, F. & Van Ommen, J. R. 2017. Atomic and molecular layer deposition: off the beaten track. *Chemical Communications*, 53, 45-71.

The Optimization of Heliostat Canting in a Solar Power Tower Plant

Nao Hu,^a Yuhong Zhao,^{a*} JieQing Feng^b

^a*College of Control Science and Engineering, Zhejiang University, Hangzhou 310027, China*

^b*State Key Laboratory of CAD&CG, Zhejiang University, Hangzhou 310058, China*

yhzhao@zju.edu.cn

Abstract

In a solar power tower plant, solar radiation is reflected by the heliostat field and concentrated in the receiver at the top of the tower to provide energy for conventional thermodynamic cycle. For the heliostats composed of small facets, heliostat canting, which means applying specific rules for the orientation of single facets, can reduce the size of reflected energy spot and increase the concentration ratio and the optical efficiency of the heliostat field. An optimization based on the paraboloid canting method is presented in this paper. The facets are aligned to fit the paraboloid to get a minimal spillage lost. A two-stage method combining Particle Swarm Optimization (PSO) and direct search method based on quadratic fitting model is designed to solve the optimization problem. The simulation results of two real plants demonstrate that the canting method with the optimal parameter can reduce the spillage lost significantly.

Keywords: Solar power tower plant, Heliostat canting, PSO, Direct searching optimization, Quadratic fitting model.

1. Introduction

Concentrated solar power (CSP) technologies offer promising options for high efficiency solar energy applications. Of all CSP technologies available, the solar power tower (SPT) can achieve higher temperature up to 1000°C and hence higher efficiency (A. Boretti et al, 2017). In a SPT plant, the solar radiation is reflected and gathered by an array of mirrors called heliostat field to the aperture of receivers to form high-temperature steam.

A large heliostat is usually composed of several small flat facets and the power reflected by a flat mirror creates a large energy spot on the receiver plane due to the sun shape and various errors, such as optical, tracking, and positioning. This usually causes spillage lost, that part of the energy spot is out of the receiver area, and reduces the heliostat field efficiency. Therefore, the alignment of facets in a specific orientation on the heliostat frame, usually called heliostat canting, influences the focusing performance of the heliostat significantly. Applying specific rules for the orientation of single facets does not necessarily mean additional cost, since also standard canting methods require precise and controlled orientation of the facets (Buck and Teufel, 2009). On the other hand, the reduction of the spot size can decrease the spillage lost and provide heliostat aiming strategy more operating choices, thus a higher optical efficiency of the heliostat field and a better power distribution on the receiver can be achieved.

For the heliostat with azimuth-elevation tracking, traditional canting methods include on-axis canting and off-axis canting. Jones (1996) investigated the difference of the two strategies and concluded that off-axis canting can achieve slightly higher efficiency but it depends on the appropriate canting date and time. Moreover, dynamic off-axis canting, in which the facets are actively controlled such that the center of each facet is always perfectly focusing, is concerned in simulation and shows a remarkable reduction of spot size (Bonanos and Noone, 2012), but it's complex and costly in practical applications. Another canting method is aligning the facet normals parallel to the corresponding surface normals of a paraboloid. Buck and Teufel (2009) compared the three methods above and paraboloid canting gets the best result. However, no optimization method is employed to ensure the optimal alignment for the entire year in these methods.

An optimization of heliostat canting based on paraboloid pattern is presented to find the minimum annual spillage. In section 2, the Monte Carlo raytracing method is introduced and the optimization model is built. A two-stage method combining PSO and direct search method based on quadratic fitting model is designed to solve the optimization problem in section 3. Section 4 explores the practical applications of the proposed method in two heliostat fields, namely a test small heliostat in Hangzhou, China, and the large heliostat of PS10. Finally, conclusions are drawn and future research is indicated in Section 5.

2. Optimization model

2.1. Flux distribution on the receiver

The calculation of the flux distribution on the receiver surface is fundamental for the design and operation of a solar power tower plant. The sun is a disk rather than a point observed from any place on the earth. Therefore, the incident rays can't be considered parallel but a group of light described by the sun shape. The common way to calculate the flux distribution on the receiver can be divided into two classes, raytracing approaches and analytical approaches. Considering the high accuracy, a raytracing process using Monte Carlo method to address the sun shape is employed in this paper. An empirical sun shape model proposed by Walzel et al (1977) is adopted to evaluate the solar energy flux density $S(\alpha)$ for different values of the solar angle α :

$$S(\alpha) = \begin{cases} S_0 \left[1 - \lambda \left(\frac{\alpha}{\alpha_s} \right)^4 \right], & \alpha \leq \alpha_s \\ 0, & \alpha > \alpha_s \end{cases} \quad (1)$$

where S_0 is a parameter related with the direct normal irradiance, $\lambda=0.5138$ is a constant, $\alpha_s=4.6$ mrad is half the angle of the light cone and the solar angle α is the angle between the vector QP and QO as shown in Figure 1 and P is a point on the solar disk.

Consequently, a large number of rays are produced depending on the probability of the energy flux density by Roulette Wheel Selection Principle. Figure 2 illustrates the flux distribution of the solar disk by random points, where the closer the points appear to the center of the sun, the greater the number of the points is. In the raytracing process, a set of random points are generated on the heliostats and each point reflected a group of sun light illustrated in Figure 2.

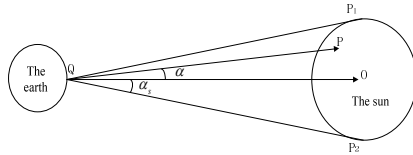


Figure 1 solar disk and solar angle

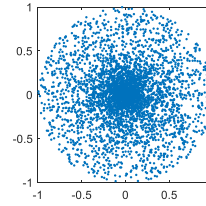


Figure 2 solar flux density

The raytracing method, however, needs huge amount of sun light be traced to get the accurate result and it is a time-costing process. Therefore, a parallel implementation of this process is utilized based on CUDA platform to speed up the simulation.

2.2. Paraboloid canting optimization

As mentioned above, the large reflected flux spot will cause spillage lost. A paraboloid canting method can be applied to improve the situation. The objective of the optimization problem is described as:

$$\min_{a,b} f(a,b) = \sum_{t=1}^{n_s} \sum_{i=1}^{n_f} \left[1 - \frac{E_{t,i}^{in}(a,b)}{E_{t,i}(a,b)} \right] \quad (2)$$

where n_s and n_f are respectively the sample number in a year and the facet number, $E_{t,i}(a,b)$ is the total power reflected by the facet i at sample time t when aligned to fit the paraboloid determined by the parameters (a, b) , and $E_{t,i}^{in}(a,b)$ is the part in the receiver area. The objection function represents the spillage lost of the specific heliostat for an entire year. The facets normal vectors are determined in the way showed in Figure 3. For the facet center at position (x, y, z) in the heliostat coordinate, x and y are predetermined by heliostat size and facet numbers, and z is calculated through the standard paraboloid equation and then the facet normal vector is set to the surface normal vector at this point. There are gaps between adjacent facets to ensure that no collision occurs when applying different canting angles.

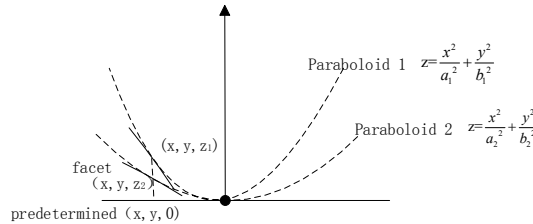


Figure 3 paraboloid canting

More than 500 samples are calculated to ensure the result behave well in the entire year. The sampling interval is three days and five or six uniformly spaced times are chosen in each sampled day according to the day length. The reflected spot at each sample time is obtained by Monte Carlo ray tracing method based on GPU. As the objective function is calculated through raytracing, the derivatives are not available. Also the high time cost of objective function evaluation and the noise of Monte Carlo method bring difficulties to the solving process.

3. Optimization algorithm

A two-stage method combining PSO and direct search method based on quadratic fitting model is designed to solve above optimization problem.

PSO is a metaheuristic as it makes few or no assumptions about the problem being optimized and can search very large spaces of candidate solutions. The output of this algorithm, with parameters selected appropriately can converge to the neighbourhood of the optimum after several iterations. More details about PSO can be found in Bonyadi and Michalewicz (2017). The fitness of swam is evaluated in each iteration and the rate of convergence falls down as the particles move to the neighbourhood of the optimum.

A direct search method with trust region is combined to find the optimal result in the neighbourhood of the preliminary result offered by PSO. The trust region method behaves well in the search of small scale so that the times of objective function evaluation to find the final optimal result can be reduced significantly.

During the iteration, a cheaper model is built around the current optimal point in place of the real expensive one. There are several research and optimization solver (Powell, 2007) using quadratic interpolation model. In this problem, however, due to the noise in the objective function evaluation, the interpolation may not represent the real model well, which leads to a slow convergence process or even to a failure. Thus, the quadratic approximation model, which is more robust to the noise, is used in the trust region. The algorithm procedure is as follows:

Step 1. Initialization: Choose an initial trust region radius $\Delta_0 > 0$ and an approximation set Y with L points derived from PSO. Determine $x_0 \in Y$ such that $f(x_0) = \min_{y \in Y} f(y)$.

Set values for parameters $\eta \in (0, 1)$, $\theta_0 \in (0, 1)$, $\theta_1 \in (1, 2)$, maximal number of iterations k_{max} , error tolerance ε , maximal fitting error E_{max} and upper limit of the cardinality of the approximation set L_{max} . Set $k=0$.

Step 2. Using the current approximation set Y , build the quadratic fitting model $m_k(x)$ and compute the minimal point x_k^+ within the trust region $B_k = \{x_k + s \mid s \in R^n, \|s\| < \Delta_k\}$ such that $m_k(x_k^+) = \min_{x \in B_k} m_k(x)$. Compute $f(x_k^+)$ and the ratio:

$$\rho_k = \frac{f(x_k) - f(x_k^+)}{m_k(x_k) - m_k(x_k^+)} \quad (3)$$

Step 3. Update the approximation set and the trust region radius. For the successful step that $\rho_k > \eta$, include x_k^+ in Y and check the existing points to drop the ones far away from x_k^+ . Set $\Delta_{k+1} = \theta_1 \Delta_k$. For the unsuccessful step that $\rho_k \leq \eta$, add more sample points to Y and set $\Delta_{k+1} = \theta_0 \Delta_k$. The point that maximizes the qualitative index $\delta(x)$ is added to Y until the fitting error is less than E_{max} or the cardinality of the approximation set $L > L_{max}$. $\delta(x)$ is described in Eq. (4).

$$\delta(x) = \sum_{j=1}^L \lambda \|x - x_j\| + (1 - \lambda)(S(x) - S_j(x))^2 \quad (4)$$

where x_j represents existing point in Y , and $\|x - x_j\|$ is the Euclidean norm, which is used to place new points in relatively unexplored region and as far away from the existing points as possible. $S(x)$ is the fitting model built using all points in set Y , $S_j(x)$ is the fitting model built using all points except point x_j . The impact of locating a sample point in the neighbourhood of x_j on $S(x)$ is measured in this way. With the weighting factor $\lambda \in (0,1)$, a new point can be placed to achieve space filling and high impact on the current model, without evaluation of the real objective function.

Step 4. Update the current iteration and check for convergence. For the successful step, set $x_{k+1} = x_k^+$, else $x_{k+1} = x_k$. Increase k by one and go to step 2 until the termination criterion, $k > k_{max}$ or $\|x_{k+1} - x_k\| < \varepsilon$ is satisfied.

The minimal annual spillage lost can be achieved using the optimization method above.

4. Case studies

The optimization is applied to get the canting paraboloid parameter for a test heliostat in Hangzhou, China and different heliostats in PS10, Spain. The two cases represent the small size and large size heliostats respectively, both of which are serving in the existing SPT plant and are two different technologies with their own advantages and disadvantages. Three typical heliostats positions in the PS10 field are considered, the two exactly in the northern direction of the receiver with different distance and the other one located in the northwest.

The optimization results are listed in Table1. The position of heliostat is represented in the coordinates system that x-coordinate points to the east, y-coordinate to north and z-coordinate to the zenith. In order to reveal the influence by the heliostat canting, a receiver size smaller than the actual receiver in the plant is used. It should be noted that the receiver size is also adjusted to get the optimal canting angles in the optimization process though it's fixed in an established plant. Since the spot size of heliostat far away from the receiver and the one in the northwest side is much larger than that of the nearer one and the one exactly in the north, the formers need larger receiver size to obtain acceptable spillage lost. The objective function calculation times in the trust region process and time consumption of the programme running on the computer equipped with NVIDIA GeForce GTX 1080 are also shown in Table 1. The optimal result can be obtained in less than an hour for various heliostats.

Table 1 heliostats parameters and optimization results

Heliostat No.	location	size (m ²)	facets number	receiver size	position	optimal (a, b)	minimal lost	objective evaluation times	time consumption
1	Hangzhou	2	3×3	1.69 m ²	(12, -107, 1.2)	(28, 32)	7.17 %	17	2461 s
2				16 m ²	(0.84, 110, 11)	(25, 23)	14.63 %	18	3018 s
3	PS10	121	7×4	36 m ²	(0.84, 698, 52)	(55, 52)	15.19 %	15	2846 s
4				28 m ²	(139, 138, 15)	(30, 26)	14.22 %	20	2961 s

The reflected spots of the heliostats at 8:00, 12:00 and 16:00 in 26th, April under the circumstances that the facets are aligned in on-axis canting, dynamic off-axis canting and in the paraboloid determined by the optimization result separately are illustrated in Figure 4. Compared with the on-axis canting, the optimal paraboloid canting method

reduces the spot size remarkably. The spot sizes of the optimal paraboloid canting are slightly larger than that of the dynamic off-axis canting which nearly represents an ideal situation. More significant reduction of the spot size can be achieved for the larger heliostat with more facets. Actually, the spillage lost in PS10's origin receiver (168 m²) can be decreased to zero using the optimal canting angle.

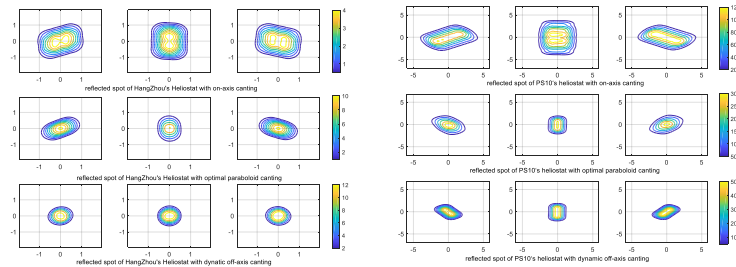


Figure 4 reflected spot of small heliostat (left) and large heliostat (right)

5. Conclusions

An optimization based on the paraboloid canting method is developed in this paper to reduce the reflected spot of the heliostats and improve the annual optical efficiency of the SPT plant. With the combined optimization method, the optimal result can be got at a low time cost, which is helpful when a large number of heliostats are designed in a SPT plant. The further research will be focused on the integrated optimization of the heliostat field and the receiver.

Acknowledgement

This work is supported by the National Natural Science Foundation of China (61772464).

References

- A. Boretti, S.Castelletto, A.Z. Sarim, (2017), Concentrating solar power tower technology: Present status and outlook. *Nonlinear Engineering*. 10.1515/nleng-2017-0171.
- A. M. Bonanos, C J. Noone, A. Mitsos, (2012), Reduction in Spot Size via Off-Axis Static and Dynamic Heliostat Canting, *International Conference on Fuel Cell Science, Engineering and Technology*. 2012: 567-571.
- M. J. D. Powell, (2007), A view of algorithms for optimization without derivatives. *Cambridge Na Reports Optimization Online Digest 2007*, 5: 170-174.
- M. R. Bonyadi, Z. Michalewicz, (2017), Particle Swarm Optimization for Single Objective Continuous Space Problems: A Review, *Evolutionary Computation*, 2017, 25(1): 1-54.
- R. Buck., E. Teufel, (2009), Comparison and Optimization of Heliostat Canting Methods. *Energy Sustainability*, DLR. 131, 1015-1022.
- S. A. Jones, (1996), A comparison of on-axis and off-axis heliostat alignment strategies. *Office of Scientific & Technical Information Technical Reports*.

Effect of Non-Ideal Kinetics on Hybrid Reactive Distillation Models for Selectivity Engineering

Deepshikha Singh, Antaram Dutta, Ankur Gaur, Shabih Ul Hasan*

*Department of Chemical Engineering, Motilal Nehru National Institute of Technology,
Allahabad 211004, India*

shasan@mnnit.ac.in

Abstract

Multi-reaction schemes comprise of highly non-ideal mixtures (such as alcohols, esters, aldehydes, ethers, water, etc.) can be quite often found in fine chemical industries. Previous work [Hasan et al., 2014] has looked at finding the designs for simple and complex hybrid RD columns targeting to obtain the desired selectivity for ideal kinetics and in the present work we extend it to cover non-ideal kinetics. In particular, it is found that in case of non-ideal kinetics the single feed hybrid RD models to be used are strongly dependent on the number of components involved in a multireaction scheme, contrary to our earlier work for ideal kinetics in which the hybrid RD models used were depends on the number of products that undergo further side reactions and is applicable for any number of components. The developed method is applicable to single reactant as well as multi-reactants single-feed hybrid RD columns, provided all the reactants should be saddle in the residue curve map and is limited to four components.

Keywords: Hybrid Reactive Distillation, Non-ideal kinetics, Design, Selectivity

1. Introduction

Reactive Distillation (RD) which is a combination of reaction and distillation in a single functional unit can also be effectively used to obtain desired selectivity in multi-reaction schemes comprises of highly non-ideal mixtures. The present work concerns the design and selection of type of single feed hybrid RD models depending upon whether the given reaction kinetics is ideal or non-ideal. A van de Vusse type hypothetical reaction scheme having ideal and non-ideal kinetics is used as an example, with the capability of the new approach demonstrated in terms of its ability to provide promising designs of hybrid RD models to obtain desired selectivity in multireaction schemes.

2. Design Methodology

The methodology starts with non-reactive distillation column (non-RD) and then introduces the reaction related attributes. For non-RD, we use the concept of visualization of the locus of feed stage compositions (LFSCs) in 3D composition space. For reaction related attributes we view the column as a reactor and relate it to the conventional reactors for which geometric interpretation is well studied through the attainable region approach. Glasser et al. (1987) presented geometrical interpretation of CSTR in terms of process vectors viz. reaction and mixing. In order to know whether a point in the composition space is attainable or not, they derived a condition that the rate vector at that point is collinear with the mixing vector of feed and product stream. The component material balance of CSTR gives the required condition. It must be noted that the reaction takes place at the product composition in the case of CSTR. On the other hand, in an arbitrary reactor (R), if the composition at which reaction takes place is

different than the product composition, then the collinearity condition is no longer valid. The composition at which reaction takes place is dependent on the type of reactor. One can control this composition by introducing separation attributes as is done the case of reactive distillation.

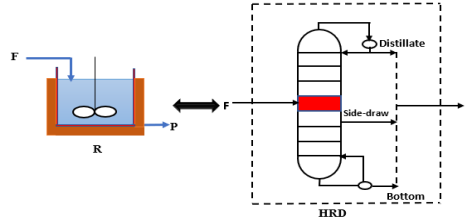


Fig. 1. Analogy between Arbitrary reactor (R) and hybrid RD Column (HRD) with side draw
Now, as shown in Fig.1, let us consider a side draw hybrid column with single reactive stage. It may be noted that the reaction in the column does not take place at a composition corresponding to that of the product (P). The overall product composition is the one obtained by virtually mixing the distillate and bottom streams. The composition of the reactive stage depends on the distillation attributes such as reflux ratio, feed location, number of stages, etc. Therefore, the next exercise is to know – which are the points in the composition space that can be the potential reactive stage composition(s) giving the desired selectivity corresponding to the point of desired product composition. The following section determines the surface of such feasible reactive stage compositions.

2.1. Surface of Reactive Stage Compositions (SRSCs)

Consider an equimolar van de Vusse type reaction scheme Eq. (1) with one reacting component A having all the reactions irreversible, except B to A, with first, second and third reactions are of 1st order while the fourth reaction A to D is of 2nd order. The feed is pure reactant A and the kinetic rate constants are given by $[k_1 k_2 k_3 k_4] = [2 1 1 3]$. The non-ideal kinetics is given by Eq. (2) and for ideal kinetics (Table 1) the value of activity coefficients of all components is taken as unity.



$$[r_A \ r_B \ r_C \ r_D] = [-k_1 \gamma_A x_A^* - k_4 \gamma_A^2 x_A^{*2} + k_2 \gamma_B x_B^*, \ k_1 \gamma_A x_A^* - k_2 \gamma_B x_B^* - k_3 \gamma_B x_B^*, \ k_3 \gamma_B x_B^*, \ k_4 \gamma_A^2 x_A^{*2}] \quad (2)$$

The material balances for components A and B on any arbitrary reactor are given by

$$x_{A,P} - x_{A,0} = \tau \cdot \sum_{k=1}^{nR} r_{k,A}(x^*) \quad (3)$$

$$x_{B,P} - x_{B,0} = \tau \cdot \sum_{k=1}^{nR} r_{k,B}(x^*) \quad (4)$$

where τ is the residence time and nR represents number of reactions

Divide (3) by (2) we get,

$$\frac{x_{B,P} - x_{B,0}}{x_{A,P} - x_{A,0}} = \frac{r_B}{r_A} = \frac{k_1 \gamma_A x_A^* - k_2 \gamma_B x_B^* + k_3 \gamma_B x_B^*}{-k_1 \gamma_A x_A^* - k_4 \gamma_A^2 x_A^{*2} + k_2 \gamma_B x_B^*} \quad (5)$$

where $x_{i,p}$ is the product composition of component i , $x_{i,0}$ is the inlet composition of component i and x^* denotes the compositions at which the reaction takes place in the reactor. The LHS of Eq. (5) is the slope of line joining points A (x_{A0} , x_{B0}) and P (x_{AP} , x_{BP}) as shown in Fig. 2. It should be noted that point P is on ABD plane in Fig. 2 and since Eq. (5) is independent of x_{CP} , its value is not required for plotting the SRSCs.

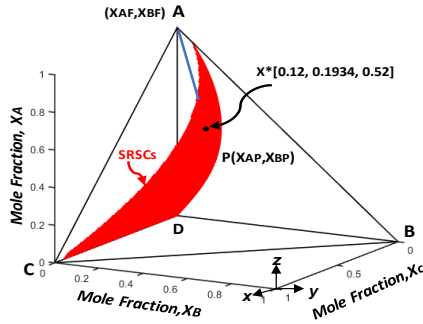


Fig. 2. Surface of reactive stage compositions (SRSCs).

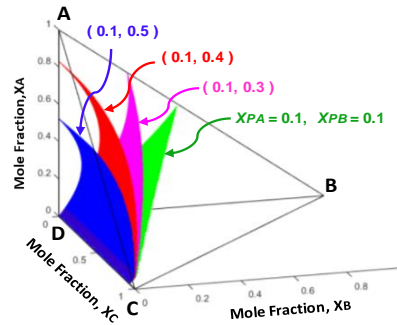


Fig. 3. Shifting of SRSCs with variation in desired selectivity

Hence, for any desired point P in the composition space, Eq. (5) gives a relation between x_A^* and x_B^* . One can plot the SRSCs for the quaternary mixture by taking a meshgrid of $[x_A^*, x_C^*]$ and plot x_B^* compositions [by solving a non-linear equation (Eq. 5) at each point of meshgrid; with γ being calculated by WILSON model] as shown in Fig. 2. Figure 3 indicates that with increase in the desired selectivity keeping conversion fixed, the feasible reactive stage compositions get reduced.

2.2. Effect of non-ideal kinetics and thermodynamic models on SRSCs

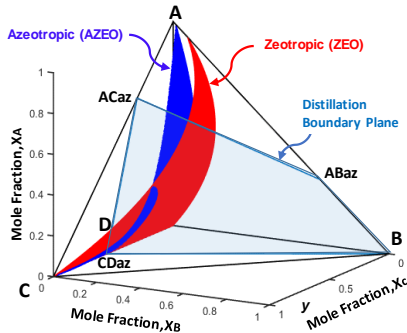


Fig. 4. Effect of non-ideal kinetics on SRSCs for ZEO and AZEO mixtures.

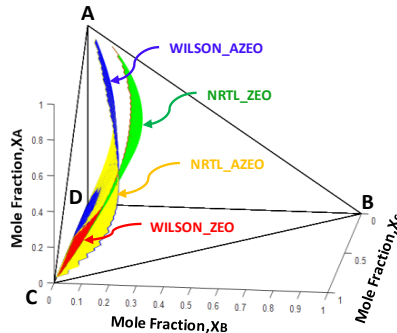


Fig. 5. Effect of thermodynamic models on SRSCs for ZEO and AZEO mixtures.

In case of azeotropic systems, non-ideal vapor-liquid equilibrium and distillation boundaries [for multicomponent azeotropic mixture in Fig.4, see Hasan et al., 2014; Section 4 (Example 3)] are responsible for the contraction of the feasible reactive stage compositions required for the design of hybrid RD column. Figure 4 shows that if non-ideality is present in kinetics as well then these feasible reactive stage compositions reduces further and thereby increase the design complexity for RD systems. Figure 5 indicates that there is no effect of thermodynamic models (WILSON & NRTL) on the surface of reactive stage compositions both for zeotropic as well as azeotropic mixtures.

2.3. Selection of Single Feed Hybrid RD Models

Hasan et al. (2014) proposed a design algorithm for ideal kinetics in which the type of hybrid RD models to be used in order to obtain the feasible design of desired selectivity is strongly dependent on the nature of reaction schemes i.e. whether in a complex reaction scheme one, two or more products undergo further side reaction(s). If one product undergoes further side reaction, then simple hybrid RD column (SHRD) is capable to give desired selectivity and if two product undergoes further side reaction then hybrid RD column with side draw is to be used. In the present example (Eq.1) although only one product undergoes further side reaction, due to the presence of non-ideal kinetics it is found that the desired selectivity is achievable by using simple hybrid RD model in a three component multi-reaction scheme while for four components multi-reaction scheme hybrid side-draw RD model is needed. The design procedure of which is explained in the next section.

2.4. Design Procedure

Consider a simple hybrid side-draw RD column with one reactive stage (Fig. 6a) and a reactor-separator system (Fig. 6b). A systematic methodology that uses intersection of LFSCs with the selected reactive stage composition (X^*) to obtain feasible designs of desired selectivity using hybrid RD column for the reaction scheme given by Eq. (1) is described. The approach presented here exploits the fact that if we split the reaction and distillation attributes of the hybrid RD column (Fig. 6a), then the new configuration (Fig. 6b) gives the same performance as that of a hybrid RD column. If the feed stage in the RD column is the reactive stage, then the column profiles of non-RD and RD column coincide for the same distillation attributes. This would be made clear with the following example.

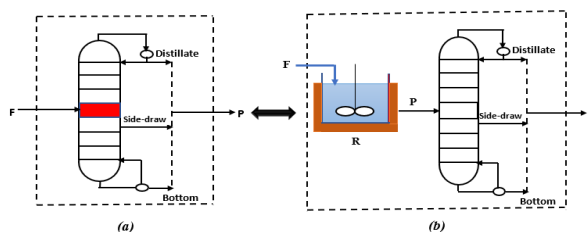


Fig. 6. (a) Hybrid (RD) column. (b) Reactor separator system (Non-RD).

A simplified equimolar van de Vusse type reaction scheme with only one reacting component with rate constants, $[k_1 \ k_2 \ k_3 \ k_4] = [2 \ 1 \ 1 \ 3]$ is chosen as an illustrative example (see Eq. 1). The reaction takes place in the liquid phase and the assumption of constant molar overflow is valid. Following are the proposed step-by-step design procedure to obtain desired selectivity using hybrid RD column with side draw:

Step 1: Select any point P (Fig. 2) according to the desired selectivity of intermediate product, B in the composition space. This point represents the overall output composition of hybrid RD column with side draw (Fig. 6b), obtained by virtually mixing distillate, side draw and bottoms streams. Hence, it can be considered as the feed to Non-RD column in Fig. 6a.

Step 2: Join point P (0.3, 0.275) with A (1, 0) to calculate the slope of line AP, and hence obtain the SRSCs using Eq. (5) as shown in Fig. 2.

Step 3: Select any X^* on the curve of SRSCs as shown in Fig. 2. For the present example we have selected $X^* = [x_A^* \ x_B^* \ x_C^*] = [0.52, 0.1934, 0.12]$.

Step 4: Find the composition of all the components in the hypothetical feed that is sent to the non-RD distillation column (Fig. 6b) by using the material balances given by Eq.

(7), Eq. (8) and Eq. (9). The composition of C is related to the extent to which individual reactions take place, which in turn depends on the Damkohler number (Da) number i.e. the ratio of characteristic liquid residence time to the characteristic reaction time (Eq. 6).

$$Da = \left(\frac{W_{cat} * k_{ref}}{F} \right) \tag{6}$$

We determine Da by applying material balance for either component A (Eq. 7) or component B (Eq. 8) for any arbitrary reactor in which reaction takes place at the selected composition, X^* . Further, by using material balance for component C (Eq. 9), one can find the composition of C in the feed to the distillation column. Composition of D can be obtained by summation equation.

$$x_{A,0} - x_{A,P} + Da \left(\frac{-k_1 \gamma_A x_A^* - k_4 \gamma_A^2 x_A^{*2} + k_2 \gamma_B x_B^*}{k_{ref}} \right) = 0 \tag{7}$$

$$x_{B,0} - x_{B,P} + Da \left(\frac{k_1 \gamma_A x_A^* - k_2 \gamma_B x_B^* + k_3 \gamma_B x_B^*}{k_{ref}} \right) = 0 \tag{8}$$

$$x_{C,0} - x_{C,P} + Da \left(\frac{k_3 \gamma_B x_B^*}{k_{ref}} \right) = 0 \tag{9}$$

Step 5: Specify the number of stages and feed location (say $N=12$, $N_f=7^{th}$ stage) with Reboiler as first stage. Side draw location depends on the volatility of that product whose composition is required to be adjusted through side draw to obtain the desired selectivity; in the present case it is component C. Hence, if the volatility of component C is less than the volatility of the reactant A then the side draw location is below the feed location ($SD=6^{th}$ stage).

Step 6: Find the operating parameters such that the feed stage of Non-RD column coincides with the selected reactive stage composition, X^* . To obtain this intersection draw the family of curves (FOC) representing LFSCs obtained for a range of distillate to feed ratio ($D:F$) and boil-up to feed ratio ($V:F$) ratios by choosing initially some arbitrary value of side draw to feed ratio (say $SD=0.1$) as shown in Fig. 7.

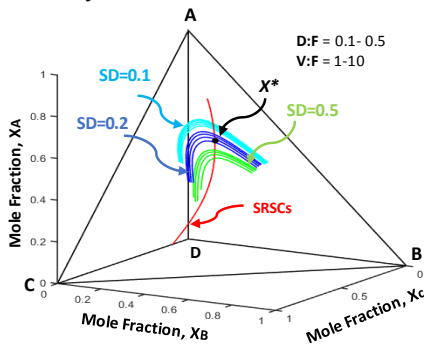


Fig. 7. FOC for a range of $D:F$ at different values of $V:F$ and $S:F$ representing LFSCs.

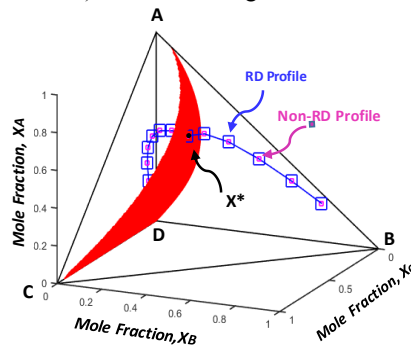


Fig. 8. Identical column profiles in triangular diagram

Range of $D:F$ can be decided based on whether or not one of the LFSCs crosses the curve of SRSCs containing selected reactive stage composition, X^* , while the $V:F$ ratio can start from any small value till the performance becomes insensitive at higher values.

It should be noted that there is one curve that corresponds to the range of $D:F$ at a given value of SD and $V:F$. Now if one considers the range of $V:F$ too then a family of curves can be plotted. Fig. 7 shows three such families for a range of distillate to feed ratio (0.1-0.5) and boil-up to Feed ratio (1-10) at three different values of SD . It can be clearly seen in Fig. 7 that the reactive composition, X^* of interest lies in the vicinity of curves obtained for $SD=0.2$.

Step 7: Next step is to consider the range of side draw to feed ratio, near the value $SD=0.2$ and narrow down the ranges of $D:F$ and $V:F$ ratios based on the results shown in Fig. 7. The values of three operating parameters viz. SD , $V:F$, and $D:F$ at which the exact intersection of feed stage of Non-RD column with the selected reactive stage composition, X^* is found are 0.22, 3.225 and 0.321, respectively. The column profile for Non-RD side draw column in 3D composition space (Fig. 8) is then plotted.

Step8: Obtain the column profile for RD, with the feed as pure A and the feed stage as the reactive stage, using the same design and operating parameters as used for the Non-RD case. The profiles coincide (Fig. 8) to indicate that the design is feasible. Hence, the desired selectivity for the given reaction scheme with non-ideal kinetics is attainable through hybrid side-draw RD column with design specifications given in Table 1.

Table 1. Design specifications for hybrid RD Models for ideal and non-ideal reaction kinetics

Kinetics Type	Ideal Kinetics [Hasan et al., 2014]		Nonideal Kinetics [Present work]	
Reaction Scheme	Eq. (1)		Eq. (1)	
Rate Constants	$[k1\ k2\ k3\ k4] = [2\ 1\ 1\ 3]$		$[k1\ k2\ k3\ k4] = [2\ 1\ 1\ 3]$	
Column configuration	Non-RD SHRD Model	RD SHRD Model	Non-RD Side Draw Model	RD Side Draw Model
Number of components, NC	4	4	4	4
Volatility Order	$B > A > C > D$	$B > A > C > D$	$B > A > C > D$	$B > A > C > D$
Number of stages, N	12	12	12	12
Feed location, Nfl	6 th Stage	6 th Stage	7 th Stage	7 th Stage
Feed flow rate, F	1	1	1	1
Side draw location, Sdl	-	-	6 th Stage	6 th Stage
Feed composition, Xf	(0.30, 0.275, 0.0701, 0.3549)	(1, 0, 0, 0)	(0.3, 0.275, 0.0816, 0.3434)	(1, 0, 0, 0)
Number of reactive stages, Nr	-	1	-	1
Location of Reactive stage, Nrl	-	6 th Stage	-	7 th Stage
Damkohler Number, Da	-	0.3641	-	0.4741
Distillate to feed ratio, $D:F$	0.3775	0.3775	0.321	0.321
Vapor to feed ratio, $V:F$	2.315	2.315	3.225	3.225
Side draw to feed ratio, $S:F$	-	-	0.22	0.22
End Compositions after mixing the distillate and bottom streams	(0.3, 0.275, 0.0701, 0.3549)	(0.30, 0.275, 0.0701, 0.3549)	(0.3, 0.275, 0.0816, 0.3434)	(0.3, 0.275, 0.0816, 0.3434)

3. Conclusions

A combined graphical-simulation algorithm for the design and selection of type of hybrid RD models is developed considering both ideal and non-ideal kinetics. For same reaction scheme, volatility order, and number of components it is found that for ideal kinetics SHRD and for non-ideal kinetics hybrid RD side draw model is capable to obtain the desired selectivity. The next step of the algorithm is to extend its applicability for mixtures (including multiazeotropic) containing more than four components.

References

- D. Glasser, D. Hildebrandt, C. Crowe, 1987, A geometric approach to steady flow reactors: The attainable region and optimization in concentration space, *Ind. Eng. Chem. Res.*, 26, 1803-1810.
 S.U. Hasan, S.M. Mahajani, R.K. Malik, 2014, Selectivity Engineering with Simple and Complex Hybrid Reactive Distillation Columns, *Ind. Eng. Chem. Res.*, 53, 18526-18538.

Modelling Paraffin Wax Deposition Using Aspen HYSYS and MATLAB

Ana M. Sousa^{a*}, Henrique A. Matos^a, Maria J. Pereira^a

^aCERENA, Instituto Superior Técnico, Universidade de Lisboa, Av. Rovisco Pais 1, 1049-001 Lisboa, Portugal

ana.margarida.sousa@tecnico.ulisboa.pt

Abstract

Wax deposition problems are an increasingly important research topic in the oil industry, as wells and pipelines become longer and heavier crude oils are explored. Much has been published within pipelines domain but information about such challenge in wells is much scarcer. Wax deposition is due to the cooling process, which occurs when oil flows from the high-pressure reservoir to the surface. Heat loss, with temperature reduction, induces wax crystallization and the subsequent well plugging. This leads to the decrease of well flowrates, and eventually causes the total blockage.

One of the goals of this work was to determine wax deposition by applying Aspen HYSYS, as a modelling tool and developing a numerical model in Matlab to face some limitations encountered in Aspen HYSYS.

One major accomplishment of the conceived Matlab model was being able to accurately consider internal pipe insulation, the effect of pipe-in-pipe, as well as the underlying geological conditions. Also, two comprehensive engineering solutions, including heating and insulation, were assessed for one oil well with proven wax deposition problems.

In conclusion, Aspen HYSYS is highly recommended for most applications since, beyond showing reliable results, is very versatile, user-friendly and has a vast database of worldwide oils' common properties. However, Aspen HYSYS does not accurately allow estimating wax precipitation curve, nor the Wax Appearance Temperature, given the oil properties. This is quite a hindrance for wax deposition simulations and leads to the need for experimental data.

Keywords: Wax deposition, Paraffinic oil crudes, Flow Assurance.

1. Introduction

Among the naturally occurring hydrocarbons that compose crude oils are the alkanes, or paraffin hydrocarbons, with the chemical formula C_nH_{2n+2} . Groups of normal paraffins, with 16 or more carbon atoms, form crystalline solid substances (designated wax), when the fluid temperature decreases below the wax appearance temperature (WAT). As cooling proceeds, the dissolved paraffins align together and bind a solid crystalline wax structure. Such wax deposits reduce the net internal diameter and consequently affect the crude oil production (Averbuch, 2006).

Developing improved computational models can help to predict upcoming operational problems, by allowing to take preventive measures so that the losses caused by the well shutting down can be avoided (Coutinho et al., 2004).

This article will focus on the prediction of the wax precipitation from crude oils.

2. Methodology

Modelling wax deposition is a complex endeavour because it involves several disciplines, such as: chemistry, thermodynamics and fluid mechanics. In this case, Aspen HYSYS and Matlab were applied to perform the simulations. The modelling approach encompassed the following steps:

- i. Experimental data was collected, so that a broad database of wax deposition measurements was synthesized. Then, using Aspen HYSYS, the experimental conditions were simulated;
- ii. The results were compared with the gathered experimental data. A critical evaluation was performed, validating Aspen HYSYS models;
- iii. Once observing Aspen HYSYS software limitations for the analysis purpose, a Matlab model was considered to overcome them;
- iv. Matlab model was applied to a real case of a well. Finally, the model was used to assess a wide range of possible engineering strategies for avoiding or controlling wax deposition.

3. Aspen HYSYS simulation

3.1. Fluid characterization

Aspen HYSYS was used to simulate 8 published experimental data sets, presented in Rosvold's work (2008). The pipeline system, tested in this experiment, was composed by a horizontal pipe, with 5.31 m of length and an inner diameter of 51.70 mm. The temperature around this pipeline was kept constant and equals to 10 °C. In these experiments, a condensate from the North Sea was used and its wax appearance temperature was 45 °C. The characteristics of each experiment and the wax precipitation curve are referred in the Table 1.

Table 1 – Rosvold's experiments data (Rosvold, 2008)

Lab. tests	Flow rate (m ² /h)	Inlet temp. (°C)	Wax precipitation curve
A	5	20	
B	10	20	
C	15	20	
D	21	20	
E	25	20	
F	21	15	
G	21	30	
H	21	40	

To evaluate the wax deposition behaviour in time, as function of the flow rate and the oil inlet temperature, the graphs shown below were drawn considering the experimental data (Rosvold, 2008).

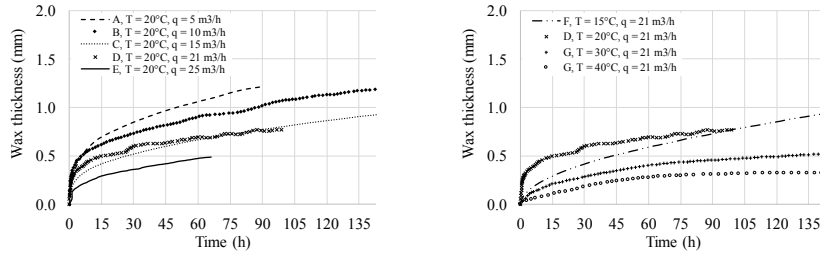


Figure 1 – Temporal evolution of wax deposition thickness for different flow rates and inlet temperatures.

For the same oil inlet temperature, the higher the flow rates are, the lower the wax deposition thickness will be. Maintaining the flow rate constant, the general tendency is to have fewer wax deposits as the temperature is higher.

3.2. Process flowsheet diagram

For this case, the steady-state model was performed in Aspen HYSYS, using the process flowsheet presented in Figure 2.

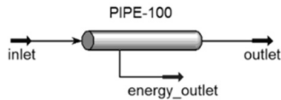


Figure 2 – Process flowsheet to simulate the wax deposition inside a pipe, using Aspen HYSYS

HYSYS contains a tool called pipe segment model, in which two of the following variables are required: inlet pressure, outlet pressure, or flow rate. Once two of these parameters are specified, the third will be computed. Furthermore, geometrical inputs need to be included, such as: length, elevation change, pipe diameter and material.

To calculate pressure and temperature, HYSYS uses an iterative routine to estimate these parameters. Once the inner pressure loop has converged, the outlet temperature is calculated, using the Eq. (1):

$$Q = U \times A \times \Delta T \quad (1)$$

Where, Q is the amount of heat transferred (W), U is the overall heat transfer coefficient ($W/(m^2 \cdot K)$), A is the outer heat transfer (m^2) and ΔT is the log mean temperature difference (K).

The wax equilibrium calculations were performed using the AEA model, given by the Eq. (2):

$$\ln K_i = \frac{\Delta h_i^f}{RT} \left(1 - \frac{T}{T_i^f} \right) + \frac{\Delta C_p}{R} \left[1 - \frac{T_i^f}{T} + \ln \frac{T_i^f}{T} \right] + \int_0^P \frac{V_i^L - V_i}{RT} \partial P \quad (2)$$

Where, K_i is the equilibrium constant, which is the ratio of concentrations of a particular component in the solid and liquid phase, Δh_i^f is the enthalpy of melting, R is the gas constant, T is the temperature, T_i^f is the melting temperature, ΔC_p is the heat capacity difference between solid and liquid, V_i^L is the molar volume, and P is the pressure.

Peng and Robinson Equation of State has been selected for its accuracy and the simplicity (Luo et al., 2014).

3.3. Analyses and Simulation Results

These eight experiments were simulated in Aspen HYSYS to understand the software ability to forecast the wax deposition in real scenarios. The results obtained were synthetized in the Figure 3.

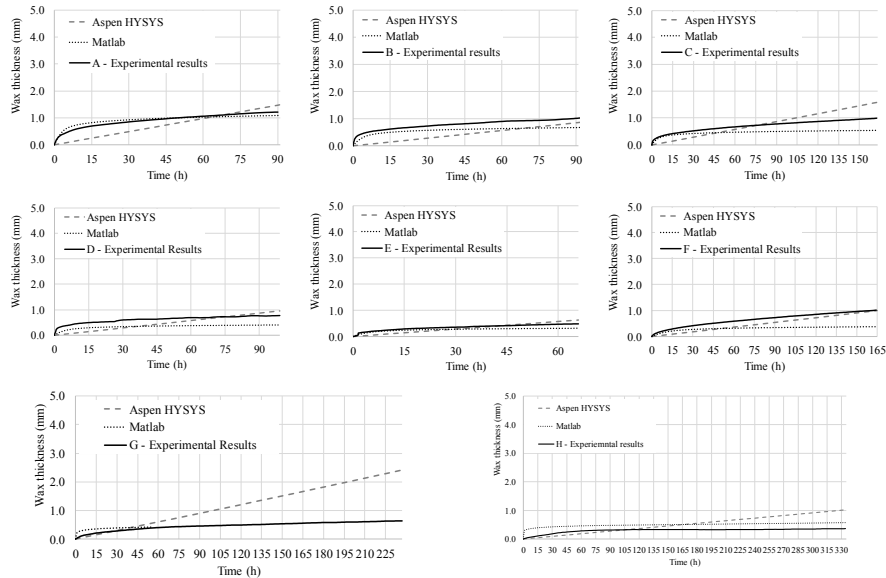


Figure 3 – Aspen HYSYS and MATLAB simulation results and the Rosvold's experimental data

The maximum deviation between the experimental data and the simulated results happened in the experiment G. In this case, the relation between the wax deposition thickness and the inner radius obtained in laboratory experiments was 2.5%, while for the simulated results this relation was 9.3%.

A sensibility test was performed to understand the influence of the overall heat transfer coefficient (OHTC) on the wax deposition thickness. As it was expected for higher OHTC, the estimated wax deposition will be higher. Using the OHTC automatically determined by the software, the results from the simulations and the experimental differed no more than 6 mm.

Doing this sensibility test, it was possible to perceive that Aspen HYSYS has some limitations, namely, the impossibility to include the effect of internal pipe insulation, since only an external one is allowed.

The influence of pressure on the paraffin deposition is negligence when modelling this system, because the fluid pressure was not substantial. Nevertheless, this parameter can be relevant in other cases (Coutinho et al., 2004).

4. MATLAB simulation

4.1. Description and Methodology

MATLAB model most significant accomplishments are the ability to accurately consider internal pipe insulation, the effect of pipe-in-pipe (tubing plus casing), as well as the heat transfer for different geological layers around the well. These are some of the aspects that HYSYS does not allow simulating, yet. The procedure developed in MATLAB to determine the wax deposition inside the well is presented in Figure 4.

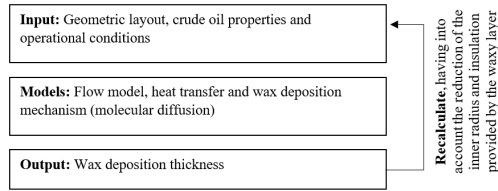


Figure 4 – Methodology to determine the wax deposition

Molecular diffusion, given by Eq. (3), was the chosen mechanism to model wax deposition, due to its most wide acceptance in the bibliography (Huang et al., 2015).

$$\frac{dm_i}{dt} = -\rho \times D_i \times A \times \frac{dw_i}{dT} \frac{dT}{dr} \quad (3)$$

Where, m_i is the mass, D_i is the effective diffusion coefficient, A is the deposition area, w_i is the weight fraction, r is the radial distance and i is the component i .

In order to consider the effect of insulation provided by the wax deposit layer, Eq. (4) was used for computing the overall heat transfer coefficient, U_{in} ($W/(m^2 \cdot ^\circ C)$):

$$\frac{1}{U_{in}} = \frac{r_{in}}{r_{deposit} h_{in}} + \frac{r_{in}}{k_{deposit}} \ln\left(\frac{r_{in}}{r_{deposit}}\right) + \frac{r_{in}}{k_{pipe}} \ln\left(\frac{r_{out}}{r_{in}}\right) + \frac{r_{in}}{r_{out} h_{out}} \quad (4)$$

In this equation, h_{in} is the inside convective heat transfer coefficient ($W/(m^2 \cdot ^\circ C)$), k_{pipe} is the thermal conductivity of the steel pipe, $k_{deposit}$ is thermal conductivity of waxes deposit ($W/(m \cdot ^\circ C)$), h_{out} is the outside convective heat transfer coefficient ($W/(m^2 \cdot ^\circ C)$), $r_{deposit}$ is the distance between the centre and the deposit (m), r_{in} and r_{out} are the inner and outer pipe radius, respectively (m).

4.2. Fluid characteristics

This model considers fluid properties provided by Aspen HYSYS, which were determined by the pseudo-compounds estimated through the TBP curves (Cuadros et al., 2009). Viscosity laboratorial tests were also used to further tune the fluid model.

4.3. Analysis and Simulation results

Firstly, the results from MATLAB model were validated through the comparison with Rosvold’s experimental data. Estimated thicknesses are quite similar to those obtained experimentally, as presented in the Figure 3. There is, however, a slight tendency (of 0.6 mm, in maximum) to underestimate the thickness at the beginning and to overestimate (by no more than 0.3 mm, in maximum) as time progresses. The same MATLAB model was used to simulate one productive well. Also, two comprehensive engineering solutions, including heating and insulation, were assessed for one oil well with proven wax deposition problems. The geometric characteristics of the oil well and the simulated profiles are shown in the Figure 5.

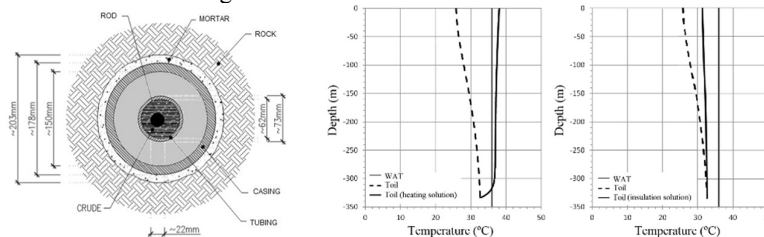


Figure 5 – Well cross section characteristics and MATLAB simulation results for two scenarios

Assessing both scenarios, it is possible to conclude that the only one capable of maintaining crude oil temperature above the WAT is the heating solution. However, this technique can eventually damage the geologic formation (Newberry and Barker, 2013).

5. Conclusions

In conclusion, Aspen HYSYS is highly recommended for most applications since, beyond showing reliable results, is very versatile, user-friendly and has a vast database of worldwide oils' common properties. However, Aspen HYSYS does not allow esteeming wax precipitation curve, nor the wax appearance temperature, given the oil properties. This is quite a hindrance for wax deposition simulations and leads to the need for experimental data. The proposed methodology combines accurate and highly reliable Aspen HYSYS modelling with versatile Matlab programming to provide a novel approach for wax deposition estimation in wells. Allowing the consideration of internal pipe insulation, pipe-in-pipe and the different geological layers around the well effects into the numerical simulations is regarded as a major advantage for this proposal.

On the drawbacks side, both the Aspen HYSYS and the conceived Matlab model do not account for the effect of pressure on the wax precipitation curve nor the inside well pumping system effect onto the wax deposition dynamics. Thus, those are the model current restrictions. While conceived models' reliability and truthfulness has been observed against experimental data where the aforementioned restrictions do not play a major role, further developments on such matters are required for increasing the model applicability towards cases where pumping systems are used and significant pressure in the well lower length is observed. Such developments are ongoing.

6. Acknowledgements

Authors would like to acknowledge Partex Oil&Gas and FCT support through the project UID/ECI/04028/2013 and the PhD grant number SFRH/BD/131005/2017.

References

- Averbuch, D., 2006. Recent developments in the risk management of offshore production systems. *Comput. Aided Chem. Eng.* 21, 39–44. [https://doi.org/10.1016/S1570-7946\(06\)80024-6](https://doi.org/10.1016/S1570-7946(06)80024-6)
- Coutinho, J.A.P., Pauly, J., Daridon, J., 2004. Chapter 10 : Modelling Phase Equilibria in Systems with Organic Solid Solutions. *Comput. Aided Prop. Estim. Process Prod. Des.* 229–249. [https://doi.org/10.1016/S1570-7946\(04\)80012-9](https://doi.org/10.1016/S1570-7946(04)80012-9)
- Cuadros, J.F., Maciel Filho, R., Maciel, M.R.W., Benedito Batistella, C., Medina, L.C., 2009. Evaluation and Application of the Extended TBP Curves in Processing and Refining of Heavy Oil Fractions. *Comput. Aided Chem. Eng.* 26, 195–200. [https://doi.org/10.1016/S1570-7946\(09\)70033-1](https://doi.org/10.1016/S1570-7946(09)70033-1)
- Huang, Z., Zheng, S., Fogler, H.S., 2015. Wax deposition: experimental characterizations, theoretical modeling, and field practices.
- Luo, X., Mistry, K., Okezue, C., Wang, M., Cooper, R., Oko, E., Field, J., 2014. Process Simulation and Analysis for CO₂ Transport Pipeline Design and Operation – Case Study for the Humber Region in the UK. *Computer Aided Chemical Engineering*. Elsevier. <https://doi.org/10.1016/B978-0-444-63455-9.50107-0>
- Newberry, M.E., Barker, K.M., 2013. Formation Damage Prevention Through the Control of Paraffin and Asphaltene Deposition. *SPE*. <https://doi.org/10.2118/13796-MS>
- Rosvold, K., 2008. Wax deposition models. Master Thesis. NTNU.

Integrated Design of Solvents and Processes based on Reaction Kinetics from Quantum Chemical Prediction Methods

Christoph Gertig^a, Kai Leonhard^a and André Bardow^{a,b,*}

^a*Institute of Technical Thermodynamics, RWTH Aachen University, Schinkelstrasse 8, 52062 Aachen, Germany*

^b*Institute of Energy and Climate Research (IEK-10), Forschungszentrum Juelich, Wilhelm-Johnen-Strasse, 52425 Juelich, Germany*
andre.bardow@itt.rwth-aachen.de

Abstract

The choice of the employed solvent often strongly influences the performance of chemical processes. To obtain optimal process designs, we propose a method for the integrated in silico design of solvents and reaction-based processes. The search space of possible solvent molecules is explored by a genetic optimization algorithm which is directly linked to gradient-based process optimization. Thereby, the process performance of the designed solvent is evaluated. While most approaches for such integrated design problems are based on group contribution methods and limited to equilibrium properties, we here propose a quantum mechanics-based approach to capture reaction kinetics. The integrated design method is successfully applied to the design of solvent and process for a carbamate cleavage reaction. The presented method allows for efficient design of a large number of promising solvents within the integrated reaction solvent and process design.

Keywords: computer-aided molecular design, process design, quantum mechanics

1. Introduction

The performance of chemical processes largely depends on the occurring chemical reactions, which are in turn influenced by the choice of solvent (Reichardt, 1990). Thus, the selection of optimal solvents is essential in the design of reaction-based processes. As the number of potential solvents is theoretically unlimited, systematic solvent design methods have been developed. The success of such methods depends on the evaluation of candidate solvents. For a reliable evaluation, first, a sound prediction of solvent impacts on the reactions is essential and second, the objective used for the evaluation should reflect the performance of candidate solvents in the process.

The sound prediction of solvent impacts on reactions has been addressed by several solvent design methods (Papadopoulos et al., 2018). Struebing et al. (2013) calculate reaction kinetics from surrogate models fitted to few data points derived from quantum chemical calculations. Austin et al. (2018) propose a design method where reaction kinetics are predicted for every candidate solvent based on transition state theory and a correction term fitted to experiments. However, in these approaches, solvents are assessed based on reaction rate constants as design objective and the designed solvents are likely different

from those showing optimal performance in the chemical process. The approach proposed by Zhou et al. (2015) overcomes this disadvantage by employing a process model allowing for the process-based assessment of the designed solvents. However, the solvent impact on reaction kinetics is predicted with a simplified model fitted to few available experimental data points, which does not guarantee good extrapolation.

To overcome the limitations of previous approaches, we here propose an integrated reaction solvent and process design approach using a sound prediction of reaction kinetics combined with a process-based assessment of solvents. The required reaction rates are determined by fully predictive, quantum chemistry-based computations. Experimental data is not needed and only used for validation. To reduce the computational effort such that large molecular design spaces can be explored, we separate the computation of solvent-independent and solvent-dependent quantities required for calculating reaction rates. Detailed process optimizations are employed for the process-based solvent assessment. To demonstrate the proposed approach for integrated reaction solvent and process design, we apply it to the case study of a carbamate cleavage process.

2. Approach for the Integrated Reaction Solvent and Process Design

The integrated solvent and process design problem is formulated based on the general computer-aided molecular and process design (CAMPD) problem by Gani (2004):

$$\begin{array}{ll}
 \max_{x,y} f(x,y) & \text{process-based objective} \\
 \text{s.t. } g_1(x,y) = 0 & \text{process model} \\
 g_2(x,y) = 0 & \text{property models} \\
 g_3(y) = 0 & \text{chemical feasibility of molecules} \\
 c_1(y) \leq 0 & \text{constraints on molecular and thermodynamic properties} \\
 x \in X \subset \mathbb{R}^n, y \in Y. &
 \end{array} \tag{1}$$

The process-based objective $f(x,y)$ (e.g., a product yield) depends on n continuous process variables x (e.g., temperatures) contained in the operation range X and on the molecular structure of the inert solvent y contained in the molecular design space Y . The equality constraints $g_1(x,y)$ correspond to the process model (see section 2.2) and the equality constraints $g_2(x,y)$ to models for kinetic and thermodynamic properties (see section 2.1). Constraints $g_3(y)$ ensure feasibility of the molecular structures y , e.g., by ensuring correct valency of all atoms in a molecule. Inequality constraints $c_1(y)$ limit molecular properties like the number of atoms in the molecule as well as thermodynamic properties like boiling points. The solution of the integrated design problem is the combination of the optimal solvent with its optimal process conditions.

2.1. Prediction of Reaction Kinetics and Thermodynamic Properties

Reaction rate constants are predicted based on transition state theory (Eyring, 1935) from the activation barrier ΔG^\ddagger between the reactants and the transition state. The activation barrier ΔG^\ddagger is computed in two steps for a reaction in an inert solvent (Kröger et al., 2017):

1. Geometries of reactants and transition states are optimized and vibrational frequencies are determined with b3lyp and TZVP basis set using the software Gaussian

09 (Frisch et al., 2009). Electronic energies are calculated with DLPNO-CCSD(T) and aug-cc-pVTZ basis set using the software ORCA (Neese, 2018). Next, the activation barrier ΔG^\ddagger in an ideal gas state is computed with the statistical thermodynamics package TAMkin (Ghysels et al., 2010).

2. Solvation effects are accounted for based on Gibbs free energies of solvation G^{solv} of reactants and transition states. We predict G^{solv} using the COSMO-RS method (Eckert and Klamt, 2002) implemented in the COSMOtherm software (Eckert and Klamt, 2017).

Step 1 is the computationally most demanding step, but is independent of the solvent and thus needed only once per reaction. COSMO-RS is also used for predicting normal boiling points and vapor pressures as well as activity coefficients used to fit parameters for the NRTL model (Renon and Prausnitz, 1968). NRTL is used to efficiently compute activity coefficients in process optimization.

2.2. Process Modeling

Process models are formulated as differential-algebraic systems of equations (DAE) based on balance equations. Further, the models contain algebraic equations describing phase equilibria and the NRTL equations. Process models are implemented in MatLab (The MathWorks, Inc., 2015) and solved with the DAE solver ode15s.

2.3. Solution of the Integrated Design Problem

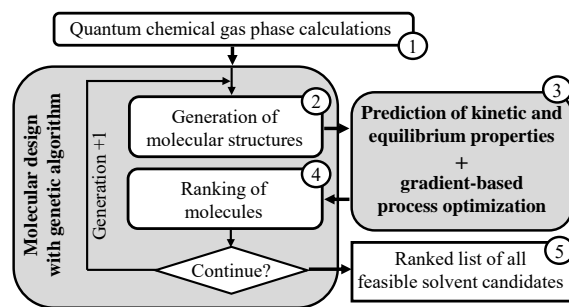


Figure 1: Flowsheet of the solution approach to the integrated design problem.

To solve Problem 1, first, the quantum-chemical gas phase calculations are performed (step 1 in Figure 1). Next, the actual integrated design problem is solved with a hybrid optimization scheme. The molecular structure of the solvent is optimized with the genetic optimization algorithm LEA3D as proposed for non-reactive systems by Scheffczyk et al. (2017). For this purpose, candidate solvent molecules are generated by connecting 3D molecule fragments

from a given library (step 2). Full 3D structural information is maintained in this step. Next, the 3D molecular structures are used to predict kinetic and thermodynamic properties of the resulting reaction systems based on quantum chemistry and to optimize processes with the candidate solvents (step 3). For this purpose, we use gradient-based optimization with `fmincon` in MatLab (The MathWorks, Inc., 2015). Based on the final objective function values of the process optimizations, the candidate solvents are ranked (step 4) and refined (step 2). Steps 2 to 4 are repeated for a predefined number of iterations before a ranked list of all feasible solvents is returned (step 5).

3. Case Study: Thermal Cleavage of Cyclohexyl Carbamate

The thermal cleavage of methyl carbamates to isocyanates and methanol is part of a production route of industrially important isocyanates (Six and Richter, 2000). Carbamate cleavage reactions are strongly endothermic (Leitner et al., 2018) with an unfavorable reaction equilibrium almost completely on the reactants' side. To avoid the fast back-reaction, methanol has to be continuously removed from the reactor. As methanol is volatile at typical reaction temperatures around 200 °C, it can be removed by stripping with an inert gas like nitrogen (Cao et al., 2015). In this work, we consider the cleavage of cyclohexyl carbamate (CHC) in a batch reactor with nitrogen stripping and a flash for recycling flushed out isocyanate and solvent (Figure 2).

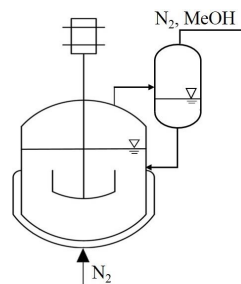


Figure 2: Batch process for CHC cleavage.

3.1. Prediction of Reaction Rate Constants

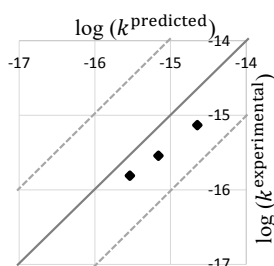


Figure 3: Log-log plot of experimental vs. predicted rate constants.

Alcohols and carbamates have an autocatalytic effect on carbamate cleavage reactions (see e.g., Thiele (1979)). Therefore, we consider the completely non-catalytic cleavage reaction as well as autocatalysis by carbamate and methanol molecules. Suitable experimental data for direct validation of the predictions for the autocatalytic carbamate cleavage is not available in the literature. However, the carbamate cleavage can be considered as reverse reaction of the isocyanate-alcohol reaction (Thiele, 1979). Moreover, different aliphatic isocyanates (Lorenz et al., 1984) and different alcohols (Sardon et al., 2013) have been shown to react with similar rate in isocyanate-alcohol reactions. Thus, we use rate constants determined experimentally by Lorenz et al. (1984) for the reaction of the cycloaliphatic isocyanate group in isophorone diisocyanate with butanol for comparison (Figure 3). The deviation of our predictions from the experimental values is much less than one order of magnitude, which can be considered a very good agreement (Kröger et al., 2017). Moreover, we aim at comparisons of solvents such that several errors cancel. Thus, the chosen prediction methods for rate constants are regarded as suitable for the reactions under consideration in this work.

3.2. Specifications for the Integrated Solvent and Process Design

As process objective $f(x,y)$, the yield of isocyanate is chosen and defined as the final amount of isocyanate divided by the initial amount of carbamate in the reactor. The free process variables x are the temperature T^{flash} in the flash (cf. Figure 2) and the volume flow of nitrogen \dot{V}_{N_2} . We set a constant reactor temperature of $T^{\text{R}} = 200$ °C, a pressure of $p = 4$ bar, a reactor volume $V^{\text{R}} = 1$ m³ and a reaction time of $t^{\text{R}} = 10$ h. A library of 3D fragments is used for the genetic optimization of solvent structures y in 25 generations with a maximum of 40 molecules per generation. Alkanes, aromates, ketones, ethers, esters, nitro- and nitrile compounds are suitable solvents for carbamate cleavage (see

Ephraim et al. (1958) and Merger et al. (1983)) and according fragments are provided. As only inert solvents are desired, protic substances are not considered because they may react with the produced isocyanate. As inequality constraints $c_1(y)$, the number of non-hydrogen atoms in solvent structures y is limited to a maximum of 20 and a minimal normal boiling point of the solvents of 176 °C, which is 10 °C higher than the normal boiling point of the produced isocyanate, is required to prevent solvent evaporation.

3.3. Results of the Integrated Solvent and Process Design

The solution of the integrated solvent and process design problem takes about 6 days using an Intel Xeon CPU E5-1660 v3 @ 3.00 GHz with 16 virtual processor cores. The design results in an optimal process with the inert solvent n-undecane and an isocyanate yield of 68%. The temperature in the flash is $T^{\text{flash}} = 20.5\text{ °C}$ and the nitrogen flow rate is $\dot{V}_{\text{N}_2} = 0.72\text{ m}^3\text{ min}^{-1}$, which is in a similar range as the experimental conditions used by Cao et al. (2015). 176 designed solvents meet all constraints (Figure 4). Interestingly, solvent selection based on equilibrium constants of the cleavage reaction fails (solvent benzaldehyde, 43% yield). The reason is that methanol removal prevents the control of the process by reaction equilibrium. A selection based on the rate constant of carbamate cleavage results in a good solvent (i-icosane, 62% yield), but not in the best solvent. The reason is that a tradeoff between high rate constants and favorable vapor-liquid equilibrium properties is important to achieve maximum product yield. This tradeoff is only captured by integrated solvent and process design, which clearly shows the strength of the proposed approach.

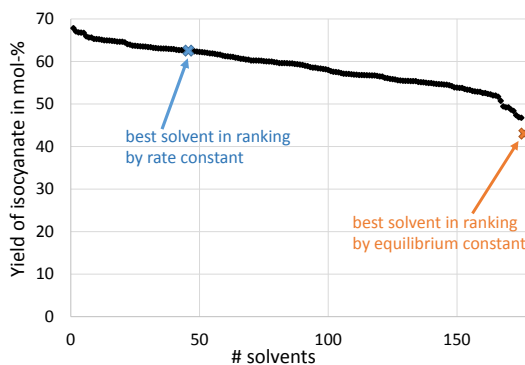


Figure 4: Yields of optimized carbamate cleavage processes for 176 designed feasible solvents.

4. Conclusion

An approach is presented for the integrated design of reaction solvents and processes which overcomes the limits of previous approaches. Our approach uses quantum chemistry-based predictions of reaction kinetics and thermodynamic properties and thus avoids simplified models. The integrated solvent and process design problem is solved with a hybrid optimization scheme combining genetic optimization of solvent structures and gradient-based process optimization. In a case study of a carbamate cleavage process, the strength of the integrated design compared to a solvent selection by equilibrium or rate constants is demonstrated.

Acknowledgements:

We thank the German Federal Ministry of Education and Research for funding of the Project Carbon2Polymers (03EK30442C). Simulations were performed with computing

resources granted by RWTH Aachen University under project rwth0284.

References

- N. D. Austin, N. V. Sahinidis, I. A. Konstantinov, D. W. Trahan, 2018. COSMO-based computer-aided molecular/mixture design: A focus on reaction solvents. *AICHE Journal* 64 (1), 104–122.
- Y. Cao, H. Li, N. Qin, G. Zhu, 2015. Kinetics of the decomposition of dimethylhexane-1,6-dicarbamate to 1,6-hexamethylene diisocyanate. *Chinese Journal of Chemical Engineering* 23, 775–779.
- F. Eckert, A. Klamt, 2002. Fast solvent screening via quantum chemistry: COSMO-RS approach. *AICHE Journal* 48 (2), 369–385.
- F. Eckert, A. Klamt, 2017. COSMOtherm, C3.0, release 1701, COSMOlogic GmbH & Co KG, Leverkusen.
- S. Ephraim, A. Woodward, R. Mesrobian, 1958. Kinetic Studies of the Reaction of Phenyl Isocyanate with Alcohols in Various Solvents. *Journal of the American Chemical Society* 80 (6), 1326–1328.
- H. Eyring, 1935. The Activated Complex in Chemical Reactions. *The Journal of Chemical Physics* 3, 107–115.
- M. J. Frisch et al., 2009. Gaussian 09, Gaussian Inc., Wallingford, CT.
- R. Gani, 2004. Computer-aided methods and tools for chemical product design. *Chemical Engineering Research and Design* 82 (11), 1494–1504.
- A. Ghysels, T. Verstraelen, K. Hemelsoet, M. Waroquier, V. van Speybroeck, 2010. TAMkin: a versatile package for vibrational analysis and chemical kinetics. *Journal of Chemical Information and Modeling* 50 (9), 1736–1750.
- L. C. Kröger, W. A. Kopp, K. Leonhard, 2017. Prediction of Chain Propagation Rate Constants of Polymerization Reactions in Aqueous NIPAM/BIS and VCL/BIS Systems. *The Journal of Physical Chemistry B* 121 (13), 2887–2895.
- W. Leitner, G. Franciò, M. Scott, C. Westhues, J. Langanke, M. Lansing, C. Hussong, E. Erdkamp, 2018. Carbon2Polymer—Chemical Utilization of CO₂ in the Production of Isocyanates. *Chemie Ingenieur Technik* 90 (10), 1504–1512.
- O. Lorenz, H. Decker, G. Rose, 1984. NCO-Prepolymere aus Diisocyanaten mit unterschiedlich reaktiven NCO-Gruppen. *Die Angewandte Makromolekulare Chemie: Applied Macromolecular Chemistry and Physics* 122 (1), 83–99.
- F. Merger, G. Nestler, R. Platz, F. Towae, H. Hellbach, 1983. Verfahren zur Herstellung von Isocyanaten durch thermische Spaltung von Urethanen, DE 3142627, BASF.
- F. Neese, 2018. Software update: the ORCA program system, version 4.0. *Wiley Interdisciplinary Reviews: Computational Molecular Science* 8 (1), 1327.
- A. I. Papadopoulos, I. Tsivintzelis, P. Linke, P. Seferlis, 2018. Computer-Aided Molecular Design: Fundamentals, Methods, and Applications. In: *Reference Module in Chemistry, Molecular Sciences and Chemical Engineering*. Elsevier, <https://doi.org/10.1016/B978-0-12-409547-2.14342-2>.
- C. Reichardt, 1990. *Solvents and solvent effects in organic chemistry*, 2nd Edition. VCH, Weinheim.
- H. Renon, J. M. Prausnitz, 1968. Local compositions in thermodynamic excess functions for liquid mixtures. *AICHE Journal* 14 (1), 135–144.
- H. Sardon, A. C. Engler, J. M. Chan, J. M. García, D. J. Coady, A. Pascual, D. Mecerreyes, G. O. Jones, J. E. Rice, H. W. Horn, et al., 2013. Organic acid-catalyzed polyurethane formation via a dual-activated mechanism: unexpected preference of N-activation over O-activation of isocyanates. *Journal of the American Chemical Society* 135 (43), 16235–16241.
- J. Scheffczyk, L. Fleitmann, A. Schwarz, M. Lampe, A. Bardow, K. Leonhard, 2017. COSMO-CAMD: A framework for optimization-based computer-aided molecular design using COSMO-RS. *Chemical Engineering Science* 159, 84–92.
- C. Six, F. Richter, 2000. Isocyanates, organic. *Ullmann's Encyclopedia of Industrial Chemistry*.
- H. Struebing, Z. Ganase, P. G. Karamertzanis, E. Siougekrou, P. Haycock, P. M. Piccione, A. Armstrong, A. Galindo, C. S. Adjiman, 2013. Computer-aided molecular design of solvents for accelerated reaction kinetics. *Nature chemistry* 5 (11), 952–957.
- The MathWorks, Inc., 2015. MATLAB R2015b.
- L. Thiele, 1979. Isocyanatreaktionen und Katalyse in der Polyurethanchemie. *Fortschrittsbericht. Acta Polymerica* 30 (6), 323–342.
- T. Zhou, K. McBride, X. Zhang, Z. Qi, K. Sundmacher, 2015. Integrated solvent and process design exemplified for a Diels-Alder reaction. *AICHE Journal* 61 (1), 147–158.

Green Supply Chain: Integrating Financial Risk Measures while Monetizing Environmental Impacts

Cátia da Silva^{a*}, Ana Paula Barbosa-Póvoa^a, Ana Carvalho^a

^a*CEG-IST, University of Lisbon, Av. Rovisco Pais, 1049-001 Lisboa, Portugal*

catia.silva@tecnico.ulisboa.pt

Abstract

Nowadays the growing concerns about the environment and society in general led companies to invest in a sustainable development. In this way, companies' design and planning decisions need to encompass simultaneously economic, environmental and social concerns. In addition, considering the complexity associated with market uncertainties, there is the need to consider risk management. This work is developed along this line and proposes a mixed integer linear programming model (MILP) that accounts for the economic and environmental performances in the same objective function by monetizing environmental impacts and simultaneously considering the most popular risk measures in the literature, CVaR. The goal is to maximize the difference between the expected net present value and the environmental impact while minimizing the associated risk. The augmented ε -constraint method is used to generate a Pareto-optimal curve in order to determine the trade-off between the objective functions. Conclusions can be drawn based on decision makers' risk profile as well as how monetization can support the decision maker's decision. A European supply chain case study is explored.

Keywords: supply chain, sustainability, risk management, monetization, uncertainty

1. Introduction

The importance of supply chain (SC) has been well-known for years in both scientific and industrial communities. As supply chain is a complex logistic system that covers the set of all activities from raw materials to final products' sales, it involves a careful and efficient management so that it is possible to obtain satisfactory results for the company. In fact, supply chain management intends to optimize customer value and to achieve a competitive advantage in the market. However, in the past, this optimization only included the economic performance of the supply chain. Taking into account the increasing companies' competitiveness and governmental pressures, SC has extended its goals to consider environmental and social concerns as well (Barbosa-Póvoa et al., 2017). The management of those economic, environmental and social concerns resulted in the appearance of sustainable supply chain (SSC) concept, which is a recognized area by the World Commission on Environment and Development. If managing a supply chain was a difficult task due to the higher number of variables, entities and products that can be included, then including environmental and social concerns makes this difficulty and complexity even greater. Thus, managing sustainable supply chains towards efficient and sustainable objectives is a challenge, especially if this encompasses the design and planning of the chain. Besides sustainability and responsiveness that supply chain management has to obey, risk management is also a current reality that needs to be

accounted when considering the supply chain design and planning problems (Barbosa-Póvoa, 2017). In this way, the typical design and planning models for minimization of supply chain costs need to become more holistic. In fact, the majority of real-world supply chain problems are dynamic, because there are several uncertain factors, like raw material prices, demand, labour costs, among others (Cristonal et al., 2009). For this reason, there is the need to develop risk management tools that efficiently address the uncertainty involved. In the literature, there are several examples of the application of risk measures in supply chain design and/or planning. However, this application is mainly done in the financial area, which means that only the economic performance of the supply chain is assessed. Nevertheless, risk can have impact in multiple dimensions, such as financial, environmental and social aspects and, therefore, that should be accounted when analysing risk in supply chains, particularly in sustainable supply chains. This paper presents a mixed integer linear programming model (MILP) that accounts for the economic and environmental concerns in the same objective function by monetizing environmental impacts and considering a risk measure. The goal is to maximize the difference between economic and environmental performances while minimizing the associated risk.

2. Environmental monetization methodologies

There are several methods to assess environmental impacts. The most used methodology is life cycle assessment (LCA). One of the most controversial phases of LCA is the life cycle impact assessment (LCIA), as it encompasses the assignment of weighting factors by decision-makers and it may be difficult to choose the best method to use. On the LCIA phase, there are methods that assess environmental impacts with scores and others that monetize. According to the European Commission, EPS 2000 is a quite complete method and it has the uncertainties fully specified when compared to other LCIA methods. For this reason, in this study, monetization is performed by using EPS. The environmental impacts are quantified in a monetary unit through EPS, which is mainly derived from future costs (raw material depletion), direct losses (production) and willingness-to-pay WTP (health, biodiversity, and aesthetic values). The WTP values resulted from academic knowledge to proactively reduce environmental impacts (Steen, 1999).

3. Problem description and model characterization

The problem intends to study the design of a generic SC, where raw materials flow from suppliers to factories and final products are obtained. These final products move to warehouses or directly to markets. In addition, at the markets, end-of-life products can be recovered and sent to warehouses or directly to factories to be remanufactured. Taking into account the possible set of locations of SC entities, production and remanufacturing technologies, possible transportation modes between entities, and products within the SC, the main objective is to obtain the SC network structure, supply and purchase levels, entities' capacities, transportation network, production, remanufacturing and storage levels, supply flow amounts, and product recovery levels, in order to maximize profit, minimize environmental impacts, and minimize financial risk. The mixed integer linear programming (MILP) model used to solve this problem is based on da Silva et al. (2018). This model was extended to consider simultaneously two objective functions through the augmented \mathcal{E} -constraint method (Mavrotas, 2009), namely the maximization of the difference between economic and environmental performances, and the minimization of

the financial risk, considering demand uncertainty. The first objective function is represented by Eq. (1), which is the maximization of the difference between the expected net present value (eNPV) and expected environmental impact (eEnvImpact). The economic performance is assessed through the eNPV (represented by Eq (2)), which is obtained through the sum of each node's probability multiplied by the discounted cash flows (CF_{Nt}) in each period t and for each node N at a given interest rate (ir). These CF_{Nt} are obtained from net earnings (difference between incomes and costs). The costs include raw material costs, product recovery costs, production/remanufacturing operating costs, transportation costs, contracted costs with airline or freight, handling costs at the hub terminal, inventory costs, and labour costs. In addition, for the last time period, it is considered the salvage values of the SC (FCI_{γ}). The environmental performance is assessed through the eEnvImpact (represented by Eq. (3)), LCA is performed on the transportation modes, in the technology involved, and on entities installed in the SC boundaries, using EPS 2015 (updated version of EPS 2000). The Life Cycle Inventory is retrieved from the Ecoinvent database (assessed through SimaPro 8.4.0 software). The LCA results are expressed in Environmental Load Units (ELU) and used as input data (ei) in Eq. (3), particularly in the environmental impact of transportation (first term), in the environmental impact of entity (second term), and in the environmental impact of technology (third term). The second objective function is represented by Eq. (4), where it is intended to minimize the financial risk, which is modelled through the adoption of conditional value at risk (CVaR). CVaR evaluates the likelihood of obtaining the difference between eNPV and eEnvImpact lower than value-at-risk (VaR). VaR is the minimum difference between NPV and EnvImpact for a given confidence level (α).

$$\max (eNPV_N - eEnvImpact_N) \quad (1)$$

$$eNPV_N = \sum_N pb_N \left(\sum_{t \in T} \frac{CF_{Nt}}{(1+ir)^t} - \sum_{\gamma} FCI_{\gamma} \right) \quad (2)$$

$$eEnvImpact_N = \sum_N pb_N \left(\sum_{\substack{t \in T \\ (a,m,i,j) \in NetP}} ei_{ac} pw_m d_{ij} X_{majitN} + \sum_{i \in I_f \cup I_w} ei_{ic} YC_i \right. \\ \left. + \sum_{\substack{t \in T, t \in I_f \\ (m,g) \in H}} ei_{mge} pw_m (P_{mgiitN} + R_{mgiitN}) \right) \quad (3)$$

$$\min Risk = \max CVaR_{\alpha} = \max (VaR - \frac{1}{1-\alpha} \sum_N (pb_N \cdot \delta_N)); \delta_N \geq VaR - NPV_N \quad (4)$$

4. Case study

The model is applied to an electronic components' producer located in Italy (Silva et al., 2018). The company's suppliers are located in Verona. Currently, this company owns a factory and a warehouse with enough capacity to meet the demand of their existing clients. These clients are located in three main European markets, namely in Spain, Italy, and Germany. The SC capacity cannot meet a demand increase and four new potential clients induce the company's decision-makers to study different SC possibilities of expansion. Given the locations of the clients, Leeds and Hannover are possible locations for installing new factories, which may lead to significant changes in the transportation modes, particularly for clients that are located outside Europe. Also, other possible warehouse locations close to the markets have to be considered. There are two types of products (fp1 and fp2) that are currently being produced through two technology types.

There are two new technologies available to produce those products. Furthermore, end-of-life products can be recovered and remanufactured into final products. In addition, transportation can be performed only by road or through a combination of road, air and sea transportation modes. There are two types of road transportation available (Truck1 and Truck2) that vary in terms of capacity, investment costs, depreciation rate, variable costs, and vehicle consumption. This work accounts for product's demand uncertainty through a scenario tree approach, due to the fact that this is a method that allows the discretization of stochastic data over the time horizon and can be adjusted during the planning horizon. In this scenario tree (Figure 2), a node N characterizes a possible state and the arcs represent the evolutions it may have. Each node has a specific probability and a path from the root to a leaf node represents a scenario.

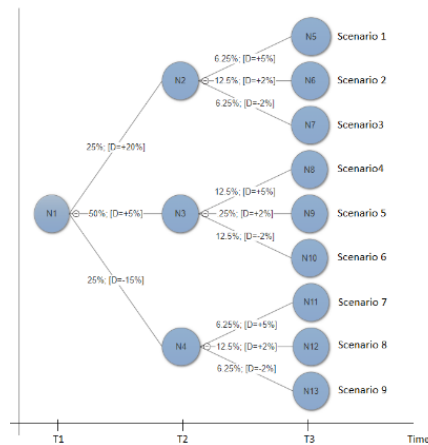


Figure 1 . Scenario tree - values for probability and demand (D) variation are represented

5. Results

Based on the SC reality, two cases are studied to understand the different decisions that can be made, considering the design and planning of the SC. Case A considers a stochastic approach since products demand is uncertain and does not considers a risk measure (risk neutral); while case B considers uncertainty in products' demand and studies the trade-offs between the expected value of (eNPV-eEnvImpact) and the associated financial risk, assessed through CVaR. Case B is analysed for the extreme values, namely the highest and lowest associated risk. Table 1 shows the eNPV and the eEnvImpact obtained in both cases (A and B). For case B, assuming a confidence level of 95%, it is necessary to compute all the scenarios and assess the cumulative distribution function (Figure 2). Thus, VaR is equal to $-40043 \times 10^4 \text{€}$., meaning that, at the end of the time horizon, the difference between eNPV and eEnvImpact for the design and planning of this supply chain is going to be, at least, this value. Thus, it is possible to obtain the Pareto curve assessed through CVaR (Figure 3).

Comparing the different cases, it can be seen that the risk neutral case has an eNPV of $97729 \times 10^4 \text{€}$ and a correspondent eEnvImpact of $218570 \times 10^4 \text{€}$. Regarding case B, the results show that when the difference between eNPV and eEnvImpact increases the related risk also increases. Analysing in detail the extreme points of the Pareto curve, it is visible that the lowest risk decision is associated with the lowest eNPV and the highest eEnvImpact. In contrast, the highest risk decision offers better results for eNPV comparing with the risk neutral case, showing the relevance of considering risk measures.

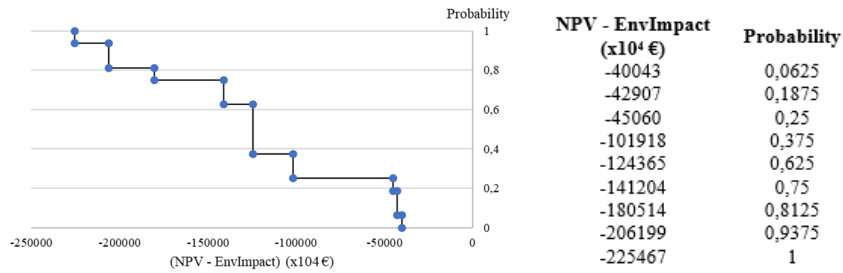


Figure 2. Cumulative distribution function to determine VaR

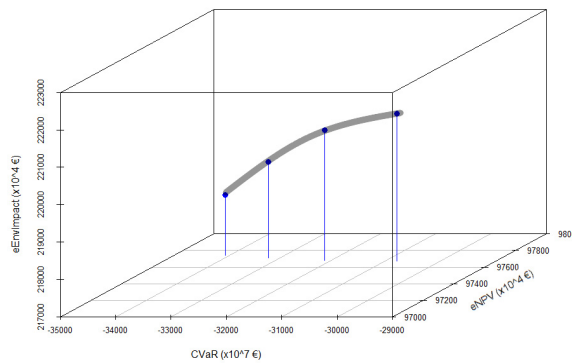


Figure 3. Pareto curve using CVaR risk measure

Table 1. Results for the economic (eNPV) and environmental (eEnvImpact) performances.

	Case A		Case B	
	Risk-neutral	High-risk	Low-risk	
	<i>Stochastic</i>		<i>CVaR</i>	
eNPV (x10⁴)	97729 €	97745 €	97675 €	
eEnvironmental impact (x10⁴)	218570 €	218600 €	220940 €	

Table 2 shows SC structure decisions considering the results depicted in Table 1. It can be seen that there are some changes across the cases A and B. Additionally to the already existent factory, all cases are going to have the same new factories installed. The results also show that in all cases there is the need to expand the existing capacity by opening new warehouses. Regarding suppliers' allocation, it can be seen that in risk neutral and high-risk cases, where environmental impacts are lower, the results show that most factories are supplied by the closest suppliers. This can be explained by the lower environmental impact of transportation. On the other hand, in the low-risk case, all factories are supplied by all suppliers, which results from the balance between the lower costs of raw materials and fewer transportation costs. Regarding transportation, the truck with more capacity (Truck2) is preferred in all cases, since this has a lower environmental impact. In terms of intermodal transportation, sea option is preferred in all scenarios, while air transportation is not used. Going deeper into the results, it can be seen that the network structure of the risk-neutral case is similar to the high-risk case, due to the fact

that both SC entities and transportation modes are the same, with some differences in capacities involved and in the product flows between entities.

Table 2. Summary of the SC decisions considering the different cases

	Case A		Case B	
	Risk-neutral	High-risk	High-risk	Low-risk
Factories	The same in all cases			
Warehouses	The same in all cases			
Suppliers allocation	Factories are supplied in totally by the closest supplier		All factories are supplied by all suppliers	
Production	Most production of fp1 is in the existing warehouse			
	Most production of fp2 is divided between two new warehouses			
Inventory	fp1 and fp2 divided between Verona and Sofia; and most inventory of fp2 kept in Verona		fp1 and fp2 divided between Verona and Sofia	
Transportation	Road	4 Truck1 and 17 Truck2	5 Truck1 and 17 Truck2	5 Truck1 and 18 Truck2
	Air	Not used		
	Sea	Used in all cases		

6. Conclusion

This study aimed to develop an optimization model for the design and planning of a generic SC, where the maximization of the difference between the expected economic and environmental performances was considered against the minimization of financial risk under uncertainty on the products demand. Considering the assessment of risk, CVaR was used. To show the trade-offs between (eNPV – eEnvImpact) and risk, a Pareto optimal curve was developed through the application of the augmented \mathcal{E} -constraint method. It is important to notice that this analysis was only possible, due to the monetization, which was able to quantify the environmental impacts in a monetary unit. This allowed to include in the same objective function both economic and environmental impacts. Furthermore, from the analysis made, it was clear that results are influenced by differences in risk strategies and this proves the importance of risk management in solving real-life problems. For future work, further research should be done on this topic to evolve monetization approaches in order to be a reliable alternative to evaluate environmental impacts. Also, an extension of this work should consider different risk measures and a more comprehensive study of uncertainty so as to even better conclude on its adequacy.

7. Acknowledgements

This work was supported by Portugal 2020, POCI-01-0145-FEDER-016418 by UE/FEDER through the program COMPETE2020 and FCT and Portugal 2020 under the project PTDC/EGE-OGE/28071/2017 and Lisboa - 01-0145-FEDER-28071

References

- A.P. Barbosa-Póvoa, C. da Silva, A. Carvalho, 2017, Opportunities and Challenges in Sustainable Supply Chain: An Operations Research Perspective, *European Journal of Operational Research*, <http://doi.org/10.1016/j.ejor.2017.10.036>
- B. Steen, 1999, A systematic approach to environmental priority strategies in product development (EPS), Version 2000 – General system characteristics, CPM Report 1999:4 CPM, Chalmers University of Technology, Goteborg, Sweden
- M. Cristonal, L. Escudero, J. Monge, 2009, On stochastic dynamic programming for solving large-scale planning problems under uncertainty, *Computers Operation Research*, 36, 2418-28
- C. da Silva, A. P. Barbosa-Póvoa, A. Carvalho, 2018, Sustainable Supply Chain: Monetization of Environmental Impacts, *Computer Aided Chemical Engineering*, 43, 773-778
- G. Mavrotas, 2009, Effective implementation of the ϵ -constraint method in multi-objective mathematical programming problems, *Ap Math Comp*, 213(2), 455-465

Optimal distributed load allocation and resource utilisation in evaporation plants

Maria P. Marcos^{a,b,*}, Jose L. Pitarch^a, Christian Jasch^c and Cesar de Prada^{a,b}

^a*Systems Engineering and Automatic Control Department, EII, Universidad de Valladolid. C/Real de Burgos S/N, Valladolid, 47011, Spain.*

^b*Sustainable Processes Institute (IPS), Universidad de Valladolid.*

^c*Lenzing AG. Werkstraße 2, Lenzing, 4860, Austria*

* maria.marcos@autom.uva.es

Abstract

This work aims to optimise the operation of an evaporation network with shared resources in real time. The goal is minimising the resource utilisation (live steam and cooling water) while satisfying a set of operational constraints. Hence, problems of optimal load allocation of feeds to plants and cooling-water distribution among them arise. The work bases on plants surrogate models, experimentally obtained, and analyses different formulation alternatives of the optimisation from the practical point of view: centralised vs distributed approaches. In particular for the distributed approach, we propose a problem decomposition which allows us to solve the problem in two iterative ways: 1) as two independent optimisations or 2) via price-coordination schemes.

Keywords: decomposition methods, RTO, evaporation network, resource efficiency

1. Description of the case study

Manufacture of viscose fibers in Lenzing AG bases on a continuous spinning process where cellulose pulp transforms into very thin threads. This process performs in an acid bath (“spinbath” from now on) which is progressively degraded. Consequently, it must be continuously recovered. Therefore, a side evaporation process is performed in parallel to remove part of water. For this task, an evaporation network of 15 plants is available to serve in 5 different types of spinbath, where a single plant is formed by several equipment. See Pitarch et al. (2017b) for a deeper description.

Plants efficiency depends on several factors: the evaporation flow removed from the spinbath (plant load) EC , the spinbath temperature T and circulating flow F_s , the fouling state in the heat exchangers and the performance of the cooling system (see Figure 1a). In particular, the more cooling water (shared resource) is provided to the surface condenser, the less live steam consumption (utility) is needed to achieve the evaporation setpoint.

Denote the *specific steam consumption* (SSC) by the live steam usage per unit of evaporated water (Pitarch et al., 2017a). Then, the *absolute steam consumption* (ASC) in each plant is computed by $ASC = SSC \cdot EC$.

This research is funded by the European Union’s Horizon 2020 research and innovation programme under grant agreement No. 723575. The first author also acknowledges the European Social Fund and the “Consejería de Educación de la Junta de Castilla y León”.

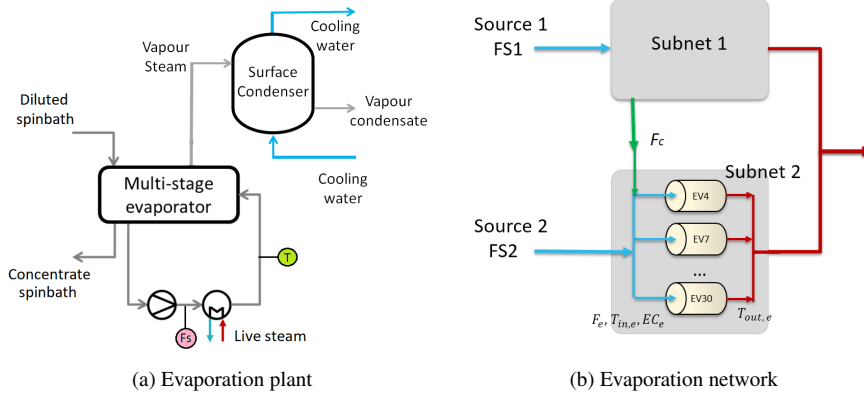


Figure 1: Systems simplified schemes.

Plant surrogate models were developed to estimate the SSC in Kalliski et al. (2019), which, after straightforward manipulations, is found to depend on EC and on the cooling capacity of the surface condenser C_{pow} , as shown in (1). The cooling system performance is also modelled experimentally: the outlet cooling-water temperature of the condensers T_{out} is estimated by a polynomial function up to degree 3 on the cooling-water flow F_w and affine in its inlet temperature T_{in} , as proposed in (Marcos et al., 2018):

$$SSC = \beta_2 \cdot EC + \beta_1 \cdot C_{pow} + \beta_0; \quad C_{pow} = 4.18 \cdot F_w (T_{out} - T_{in}) / 3600 \quad (1)$$

$$T_{out} = \alpha_0 + \alpha_1 F_w + \alpha_2 F_w^2 + \alpha_3 F_w^3 + T_{in} \quad (2)$$

Here, $\theta = \{\beta_0, \beta_1, \beta_2, \alpha_0, \alpha_1, \alpha_2, \alpha_3\}$ are experimental regression parameters.

According to the physical layout of the evaporation network, the plants can be grouped in two subnets, each one directly supplied by an independent water source. The water distribution among plants is done in parallel and, additionally, the exceeding water in Subnet 1 (F_c) can go to Subnet 2 but not backwards (see Figure 1b). Further details on the evaporation network can be found in Palacín et al. (2018); Marcos et al. (2018).

2. Problem formulation

The objective is to allocate feeds to plants and distribute the cooling-water in the network at minimum cost. This cost is a trade-off between the usage of resources: live steam and cooling water, times their respective “prices” (P_s and P_w). Three sets of decision variables are defined: $X_{e,p} \in \{0, 1\}$ to link product p to plant e , $EC_{e,p} \in \mathbb{R}$ defining the evaporation flow of p to be achieved in plant e , and $F_{w,e} \in \mathbb{R}$ defining the water sent to plant e . Further, an additional variable $F_c \in \mathbb{R}$ indicates the flow of water sent from Subnet 1 (SN1) to Subnet 2 (SN2). Hence, for a given set of $e \in \mathcal{E}$ evaporation plants that have to process $p \in \mathcal{P}$ spinbaths, the centralised formulation of the optimisation problem is:

$$\min_{X_{e,p}, EC_{e,p}, F_{w,e}, F_c} J = \sum_e \left(\sum_p ASC_{e,p} \cdot P_s + F_{w,e} \cdot P_w \right) \quad (3a)$$

$$\text{s. t. : } \sum_p X_{e,p} \leq 1 \quad \forall e \in \mathcal{E}; \quad X_{e,p} = 0 \quad (e,p) \in \mathcal{N} \quad (3b)$$

$$\sum_e^{\mathcal{E}} EC_{e,p} \geq SP_p \quad \forall p \in \mathcal{P} \quad (3c)$$

$$\sum_e^{\mathcal{E}_{SN1}} F_{w ee} + F_c \leq FS1; \quad \sum_e^{\mathcal{E}_{SN2}} F_{w e} - F_c \leq FS2; \quad F_c \geq 0 \quad (3d)$$

$$\underline{EC}_{e,p} \cdot X_{e,p} \leq EC_{e,p} \leq \overline{EC}_{e,p} \cdot X_{e,p} \quad \forall e \in \mathcal{E}, \forall p \in \mathcal{P} \quad (3e)$$

$$\sum_p^{\mathcal{P}} X_{e,p} \cdot \underline{F}_{w e} \leq F_{w e} \leq \overline{F}_{w e} \cdot \sum_p^{\mathcal{P}} X_{e,p} \quad \forall e \in \mathcal{E} \quad (3f)$$

$$T_{out e} \leq T_{max} + (1 - \sum_p^{\mathcal{P}} X_{e,p}) \cdot M \quad \forall e \in \mathcal{E} \quad (3g)$$

Where the sets \mathcal{E}_{SN1} and \mathcal{E}_{SN2} ($\mathcal{E} = \mathcal{E}_{SN1} \cup \mathcal{E}_{SN2}$) include the plants belonging to SN1 and SN2 respectively, the set \mathcal{N} represents connections between some plants and spinbaths that are forbidden due to the factory layout, and M is a big enough number.

The problem constraints are: (3b) each plant can only serve in one spinbath loop at a time; (3c) total evaporation demands per spinbath (SP_p) have to be fulfilled; (3d) total water consumption in each subnet has to be lower than the available at the sources (F_s), considering that exceeding water can go from SN1 to SN2 but not backwards; (3e)-(3f) evaporation and water flows are bounded and; (3g) outlet water temperatures have to be lower than a limit (T_{max}), stated by the environmental regulation.

The presence of discrete and continuous variables as well as the nonlinear dependency of (3a) and (2) on them, makes (3) become an MINLP problem.

3. Problem decomposition

In order to avoid the issues that commonly arise with MINLP (slow convergence, high computational demands, etc.), we propose a suitable decomposition of (3) in two local optimisation subproblems, according to the physical layout of the evaporation network. In fact, the overall equipment can be grouped in two sets or networks: 1) the spinbath allocation one, composed by the evaporation plants and the spinbath loops themselves, and 2) the water distribution from the sources to the respective plant surface condensers. Hence, a first local problem can handle the plants load allocation whereas a second one optimises the water distribution. By this decomposition, only the magnitudes EC and C_{pow} are shared between problems 1) and 2).

1. Load-allocation problem:

$$\min_{X_{e,p}, EC_{e,p}} J_1 = \sum_e^{\mathcal{E}} \sum_p^{\mathcal{P}} SSC_{e,p} \cdot EC_{e,p} \cdot P_s \quad \text{s. t.:} \quad (3b), (3c), (3e) \quad (4)$$

In this way, (4) is a mixed integer quadratic programming (MIQP) problem, provided that C_{pow} in (1) is assumed known.

2. Cooling-water distribution problem:

$$\min_{F_{w e}, F_c} J_2 = \sum_e^{\mathcal{E}} (SSC_e \cdot \sum_p^{\mathcal{P}} EC_{e,p} \cdot P_s + F_{w e} \cdot P_w) \quad \text{s. t.:} \quad (3d), (3f), (3g) \quad (5)$$

Thus, assuming that the load allocation ($EC_{e,p}$) is known, (5) is an non linear programming (NLP) problem.

Now, we can solve the original problem in two iterative ways: sequentially as two fully independent optimisations, or in a price-coordination fashion. See next section.

4. Implementation

The above formulated optimisation problems (3), (4) and (5) are coded in Pyomo (Hart et al., 2017). The centralised version (3) uses Bonmin as MINLP solver (Bonami et al., 2008), whereas Gurobi Optimization (2018) is used to solve the MIQP (4) and Ipopt (Wächter and Biegler, 2006) to solve the NLP (5). In order to implement the decomposition approach in an iterative fashion, we propose the following.

4.1. Sequential approach

Take $C_{\text{pow } e}$ as known (computed by (1)-(2) and from given flows $F_{w e}$) and solve (4). Then, from the obtained solution, take the values of $EC_{e,p}$ and solve (5), getting a new set of values $F_{w e}$ to compute the $C_{\text{pow } e}$ and so on. The procedure is formalised in:

Algorithm 1 Sequential optimisation

- 1: Compute the $C_{\text{pow } e}$ from current (measured) $F_{w e}, T_{\text{out } e}, T_{\text{in}}$ and set $\varepsilon = 1$
 - 2: **while** $\varepsilon > 0.001$ **do**
 - 3: Solve (4) and save the computed allocation $EC_{e,p}$
 - 4: Solve (5) using the $EC_{e,p}$ from Step 3 and get a water distribution $F_{w e}, T_{\text{out } e}$
 - 5: Compute $\varepsilon = \sum_e^{\mathcal{E}} \|C_{\text{pow } e} - 4.18F_{w e} \cdot (T_{\text{out } e} - T_{\text{in}})/3600\|_2^2$
 - 6: Update $C_{\text{pow } e} = 4.18F_{w e} \cdot (T_{\text{out } e} - T_{\text{in}})/3600$ with values from Step 4
-

4.2. Distributed approach

In a distributed fashion, we need to decouple problems (4) and (5) to allow a “true” parallel implementation. Thus, we make use of the well-known Lagrangean or price-driven decomposition approaches (Cheng et al., 2007).

Indeed, now $C_{\text{pow } e}$ will be also *local* decision variables in (4) and EC_e will be so in (5) as well¹. Then, we have to add a *coordination* layer to progressively force both sets of magnitudes to be equal in both local optimisations (shared constraints). As usual in Lagrangean decomposition, these constraints will be added as a penalty in the respective objective functions:

$$J_1 = \sum_e^{\mathcal{E}} \left(\sum_p^{\mathcal{P}} SSC_{e,p} \cdot EC_{e,p} \cdot P_s + \frac{1}{2} (p_{11e} (C_{\text{pow } e} - \mathbf{C}_{\text{pow } e}^*)^2 + p_{12e} (\sum_p^{\mathcal{P}} EC_{e,p} - \mathbf{EC}_e^*)^2) \right) \quad (6)$$

$$J_2 = \sum_e^{\mathcal{E}} \left(SSC_e \cdot EC_e \cdot P_s + F_{w e} \cdot P_w + \frac{1}{2} (p_{21e} (C_{\text{pow } e} - \mathbf{C}_{\text{pow } e}^*)^2 + p_{22e} (EC_e - \mathbf{EC}_e^*)^2) \right) \quad (7)$$

¹Note that variables EC_e equivalently replace $\sum_p^{\mathcal{P}} EC_{e,p}$ in (5) to reduce the problem size.

Where $p_{ije} \in \mathbb{R}^+$ are the *shadow prices* for “resource” utilisation and $\mathbf{R}^* := \{\mathbf{C}_{\text{pow } e}^*, \mathbf{EC}_e^*\}$ are the reference values, computed somehow from the local solutions of both optimisations in in the previous iteration. In this way, both problems will be managed by a coordinator which, in each iteration k , will receive the values got for the shared variables $R_e := \{C_{\text{pow } e}, EC_e\}$, and it will update the prices as well as the reference values for the next iteration $k + 1$ according to the following rules:

$$p_{ije}^{[k+1]} = p_{ije}^{[k]} + (R_{ije}^{[k]} - \mathbf{R}^{*[k]})^2 \cdot \mu^{[k]}, \quad R_{ije} \in R, \quad \mathbf{R}^* \in R \quad (8)$$

$$\mu^{[k+1]} = \mu^{[k]} \cdot \lambda; \quad \lambda > 1 \quad (9)$$

$$\mathbf{C}_{\text{pow } e}^{*[k+1]} = C_{\text{pow } e}^{[k]}(2); \quad \mathbf{EC}_e^{*[k+1]} = EC_e^{[k]}(1) \quad (10)$$

Where notation $R_e^{[k]}(i)$ denotes the values of variables R_e , solution of subproblem i at iteration k . Progressive hedging (Rockafellar and Wets, 1991) is used in (9) to update the factor μ in each iteration, via the user-defined parameter λ . The procedure to solve the distributed optimisation is summarized below.

Algorithm 2 Distributed optimisation

- 1: Set \mathbf{R}^* to the current values measured from the plants and $p_{ije} = \varepsilon = 0.1$
 - 2: **while** $\varepsilon > 0.001$ **do**
 - 3: Solve subproblems (4) and (5), and get new values for R_{ije}
 - 4: Compute $\varepsilon = \|R_{ije} - \mathbf{R}^*\|_2^2$
 - 5: Update prices p_{ije} and references \mathbf{R}^* with (8)-(10)
-

Of course, due to the non-convex nature of the problem, global optimality is not guaranteed in either of the implementations, centralised or distributed.

5. Results and discussion

For the sake of comparison/analysis, we have solved the problem from a particular network situation following the three presented ways. Table 1 shows a brief summary.

Table 1: Optimised cost and computational effort for the 3 approaches.

	Total CPU Time (s)	Optimal cost (€/h)	Iterations
Centralised	29.64	962.82	-
Sequential	0.89	964.81	3
Distributed	1.73	964.33	6

We can conclude that the three approaches are able to reach nearly the same (local) optimal solution². However, as expected, the centralised problem elapses more time to reach the solution. This is not a major issue in this application (the execution period for real-time optimisation is about 30 min.) but, it will be so if the problem grows by considering fouling predictions over time or by including more parts of the factory (the water network is larger and also serves to other processes, and there is a heat-recovery network which also interacts with the evaporation one).

²Values $p_{ije}^{[0]} = 0.1$, $\mu^{[0]} = 1$ and $\lambda = 1000$ were set for the distributed approach.

6. Conclusions

In this work we addressed a medium-scale real-time optimisation problem (~ 200 variables, it depends on the approach) on resource efficiency in an industrial evaporation network with shared resources. The proposed approaches will support the operators to take better decisions in real time, thus, improving the operation of the overall network: product-plant allocation and water distribution to the cooling systems.

The plant models are incorporated in three different optimisation schemes, analysing the convenience of the decomposition approaches vs the centralised one. In this case study, the three approaches solve the problem in acceptable CPU time for real-time purposes, although the iterative sequential approach has arisen as the most efficient one. The key is the proposed decomposition for the original centralised problem, which allows us to formulate two effortless independent problems (MIQP and NLP), solved efficiently by modern optimisation algorithms.

Apparently, the price-coordination approach does not have any advantage here: the optimal cost is slightly higher than the one reached by the centralised and it elapses double time than the sequential. This is because the centralised problem is not so large-scale, many constraints are affine in the decision variables, and the advantages of parallel computation cannot be exploited with just two local optimisation subproblems. Nevertheless, this approach will clearly beat the other two if the problem is extended to consider uncertainty in an explicitly way via, for instance, two-stage stochastic optimisation.

References

- P. Bonami, L. T. Biegler, A. R. Conn, G. Cornuéjols, I. E. Grossmann, C. D. Laird, J. Lee, A. Lodi, F. Margot, N. Sawaya, A. Wächter", 2008. An algorithmic framework for convex mixed integer nonlinear programs. *Discrete Optimization* 5 (2), 186–204.
- R. Cheng, J. Forbes, W. Yip, 2007. Price-driven coordination method for solving plant-wide mpc problems. *Journal of Process Control* 17 (5), 429 – 438.
- L. L. C. Gurobi Optimization, 2018. Gurobi optimizer reference manual. <http://www.gurobi.com>.
- W. E. Hart, C. D. Laird, J.-P. Watson, D. L. Woodruff, G. A. Hackebeil, B. L. Nicholson, J. D. Sirola, 2017. *Pyomo—optimization modeling in python*, 2nd Edition. Vol. 67. Springer Science & Business Media.
- M. Kalliski, J. L. Pitarch, C. Jasch, C. de Prada, 2019. Apoyo a la toma de decisión en una red de evaporadores industriales. *Revista Iberoamericana de Automática e Informática industrial* 16 (1), 26–35.
- M. P. Marcos, J. L. Pitarch, C. de Prada, C. Jasch, Oct 2018. Modelling and real-time optimisation of an industrial cooling-water network. In: 2018 22nd International Conference on System Theory, Control and Computing (ICSTCC). pp. 591–596.
- C. G. Palacín, J. L. Pitarch, C. Jasch, C. A. Méndez, C. de Prada, 2018. Robust integrated production-maintenance scheduling for an evaporation network. *Computers & Chemical Eng.* 110, 140 – 151.
- J. L. Pitarch, C. G. Palacín, C. de Prada, B. Voglauer, G. Seyfriedsberger, 2017a. Optimisation of the resource efficiency in an industrial evaporation system. *Journal of Process Control* 56, 1–12.
- J. L. Pitarch, C. G. Palacín, A. Merino, C. de Prada, 2017b. Optimal operation of an evaporation process. In: H. G. Bock, H. X. Phu, R. Rannacher, J. P. Schlöder (Eds.), *Modeling, Simulation and Optimization of Complex Processes HPSC 2015*. Springer International Publishing, Cham, pp. 189–203.
- R. T. Rockafellar, R. J.-B. Wets, 1991. Scenarios and policy aggregation in optimization under uncertainty. *Mathematics of operations research* 16 (1), 119–147.
- A. Wächter, L. T. Biegler, Mar 2006. On the implementation of an interior-point filter line-search algorithm for large-scale nonlinear programming. *Mathematical Programming* 106 (1), 25–57.

Optimisation and control of a distributed energy resource network using Internet-of-Things technologies

Evgenia Mechleri^{*a}, Tim Sidnell^a, Bogdan Dorneanu^a, Harvey Arellano-Garcia^{a,b}

^a*Department of Chemical & Process Engineering, University of Surrey, Guildford, United Kingdom*

^b*LS Prozess- und Anlagentechnik, Brandenburgische Technische Universität Cottbus-Senftenberg, Cottbus, Germany*

e.mechleri@surrey.ac.uk

Abstract

This work investigates the use of variable pricing to control electricity imported and exported to and from both fixed and unfixed distributed energy resource network designs within the UK residential sector. It was proven that networks which utilise much of their own energy and import little from the national grid are barely affected by variable import pricing, but are encouraged to export more energy to the grid by dynamic export pricing. Dynamic import and export pricing increased CO₂ emissions due to feed-in tariffs which encourages CHP generation over lower-carbon technologies such as solar panels or wind turbines.

Keywords: Internet-of-Things, Distribution Energy Resource, Mixed-Integer Linear Programming.

1. Introduction

Most electricity on the UK grid comes from large producers based far from customers, e.g. large offshore wind farms or isolated nuclear plants, leading to enormous volumes of electricity being wasted through transmission losses and step-up/step-down transformers [1]. Distributed Energy Resource (DER) networks have the potential to provide buildings capabilities for self-generation from renewable or low carbon assets and reduce both emissions and energy bills through mitigation of much of these losses [2]. Government incentives make a good case for investing in DER technologies, however large-scale investment into domestic DERs without sensible controls would destabilize the national grid [3]. Internet of Things (IoT) technologies have the potential to better control and optimize DERs, in conjunction with the needs of national electricity grids. This can be done through internet connected controllers which utilize live data on energy prices, generation, consumption, and asset failures, in a way which is aligned with national grid strategies. It also presents the capability to optimize the design and operation of local renewable resources, to cope with predicted changes in weather or disruptive events. The work presented in the following sections focuses on the use of IoT-type integration and communication strategies for the control of residential DERs, as opposed to the control of entire grids, as presented by [4]. With

respect to dynamic pricing, the paper is unique from [5] in that it investigates both demand- and supply-side control. Finally the model builds on the models presented in [6] and [7]. The novelty is in the investigation of the effect of dynamic pricing on the demand- and supply-side control in residential housing scenarios. Section 2 presents the methodology, Section 3 the mathematical formulation, while Section 4 the results and discussion.

2. Methodology

A case study is used to illustrate the approach: a residential house arrangement based on streets in Guildford, Surrey, UK, with 5 houses (Fig.1). The demand profiles for this arrangement are presented in Fig.2

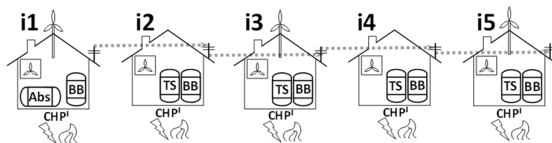


Fig 1. Design of the baseline scenario network

A baseline scenario with a set, pre-designed DER network is used to investigate the effect of dynamic pricing. A simulation is run to optimize the design of the network without IoT control, based on a number of available renewable technologies. The set of technologies installed in the network (*Tech*) could include: absorption chillers (*Abs*), air conditioning units (*AC*), biomass boilers (*BB*), gas boilers (*GB*), combined heat and power generators (*CHPs*), which are fuel cells, internal combustion engines or Sterling cells, gas heaters (*GH*), heating/cooling pipelines, microgrid controllers (*MGCC*), photovoltaic cells (*PV*), thermal storage (*TS*) and wind turbines (*WT*). A second scenario is investigated, where the design of the network is completed with IoT dynamic pricing control strategies. This is done to compare the design and operation of DER networks which have been designed and are yet to be designed.

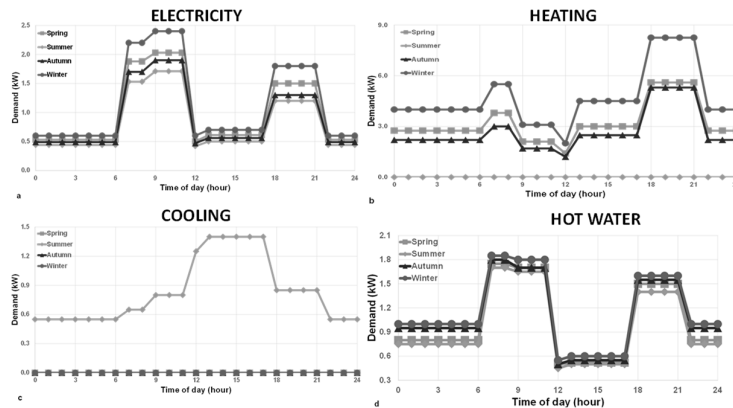


Fig 2. Demand profiles for the network for electricity, heating, cooling and hot water

Real seasonal and hourly variations in supply and demand of the various energy requirements and renewable generating assets are considered for the models. Weather and demand data is split into four seasons ($m1$ – spring, $m2$ – summer, $m3$ – autumn and

$m4$ – winter), which each lasts for three months (Mar-May, Jun-Aug, Sep-Nov, Dec-Feb). Every day is split into six periods ($p1$ – $p6$) in which demand, weather operation and thus energy supply are constant. The concept of dynamic pricing is investigated through the use of Equations (1) and (2), which calculate the price (in British pence per kWh) of electricity from the DER network purchased ($P_{Elec,mp}$) and sold ($P_{SalElec,mp}$) to the grid, respectively. The price is scaled against the average electricity price ($P_{Elec,Avg}$ and $P_{SalElec,Avg}$, for the purchased and sold price, respectively) for the UK residential sector, by dividing the national demand ($NatDemand_{m,p}$) at time of day, p , and season, m , by the yearly average national demand ($NatDemand_{Avg}$).

$$P_{Elec,mp} = P_{Elec,Avg} \cdot NatDemand_{m,p} / NatDemand_{Avg} \quad (1)$$

$$P_{SalElec,mp} = P_{SalElec,Avg} \cdot NatDemand_{m,p} / NatDemand_{Avg} \quad (2)$$

Table1. Cost of imported and exported electricity, per time of day and year

Time period (p)	$p1$	$p2$	$p3$	$p4$	$p5$	$p6$
Time of day	07:00-09:00	09:00-12:00	12:00-13:00	13:00-18:00	18:00-22:00	22:00-07:00
Season, m	Price purchased electricity, $P_{Elec,m,p}$ (pence/KWh)					
Spring, $m1$	31.120	33.660	8.290	10.110	24.870	8.787
Summer, $m2$	25.370	28.350	6.964	8.290	19.900	7.295
Autumn, $m3$	28.190	31.500	7.793	9.285	21.550	8.124
Winter, $m4$	36.480	39.790	9.948	11.610	29.840	9.948
Season, m	Price exported electricity, $P_{SalElec,m,p}$ (pence/KWh)					
Spring, $m1$	9.625	10.390	2.560	3.123	7.680	2.713
Summer, $m2$	7.833	8.755	2.150	2.560	6.144	2.253
Autumn, $m3$	8.703	9.727	2.406	2.867	6.655	2.509
Winter, $m4$	11.260	12.290	3.072	3.584	9.215	3.072

Overall the price of purchased electricity, taken as a time average, is $P_{Elec,Avg} = 16.29$ pence/kWh, while the price of exported electricity is that given by the government incentives, $P_{SalElec,Avg} = 5.03$ pence/kWh. Table 1 shows the calculated values for the imported and exported electricity, for each time period throughout the year.

3. Mathematical model

The model's objective function minimises the total cost of the network, C_{Total} , which is calculated as the sum, for all technologies, of the investment costs, C_{Inv} , annualised over the project lifetime, n (years), and the annual operating and maintenance costs, $C_{O\&M}$, the annual cost of carbon emission taxation, C_{Tax} , the annual cost of imported energy and fuel, C_{Fuel} , minus the annual income, C_{Inc} made from exporting the electricity to the grid, feed in tariffs (FITs) and renewable energy heat incentives (RHIs):

$$C_{Total} = \sum_{Tech} (C_{Inv} + C_{O\&M}) + C_{Tax} + C_{Fuel} - C_{Inc} \quad (3)$$

The annualized investment costs are calculated using a capital recovery factor, CRF based on an interest rate, r (%), and project lifetime, n :

$$CRF = r(1+r)^n / [(1+r)^n - 1] \quad (4)$$

A cost per kW of installed capacity, or cost per meter of piping and wiring was found, for each technology, from literature based on UK case studies and industrial sources, and used to calculate the annualised cost for each technology:

$$C_{Inv,tech} = \sum_i (CRF \times C_{InvTech} \times Max_{Tech,i}) \quad (5)$$

Here, the $Max_{Tech,i}$ is the maximum power generated by the technology in a house i , in a year, and represents the required capacity. The installed capacity must also fall between upper and lower bounds of available technology units. Binary variables are used to decide whether or not a technology is installed in a home.

O&M costs of the technologies are calculated using fixed costs, C_{Fixed} and variable costs, C_{Var} . The costs are defined in £/kWh.

$$C_{O\&M,tech} = \sum_i [(C_{Fixed} \times Max_{Tech,i}) + (C_{Var} \times \sum_{m,p} Gen_{Tech,i,m,p})] \quad (6)$$

C_{Tax} is calculated from the government tax per kg of CO₂ emitted, P_{CO_2} , the carbon intensity of electricity purchased from the grid, CI_{grid} , and carbon intensities of emitting technologies, namely: *GB*, *CHP* and *CH*. All these units consume natural gas, so their intensities are calculated as the carbon intensity of grid gas CI_{Gas} divided by the technology efficiency, η_{Tech} . The intensities are defined in kg CO₂/kWh. The cost of fuel, C_{Fuel} is equal to the volume of gas and electricity purchased multiplied by the respective cost of each technology. The income, C_{Inc} is calculated from FITs per kWh of low carbon heat or electricity generated, $P_{FIT,Tech}$, electricity sales to the grid, $ESal_{Tech,i,m,p}$, and the annual payment for the utilization of a *BB* under the RHI, P_{RHI} . For pipelines and microgrid (*MG*) cables, binary variables are used to indicate connections between homes. An *MG* controller binary, Z_i , is introduced and its existence is decided by the *MG* cable existence. The demands for the house are met with balance equations that match demand with appropriate technologies:

$$Load_{i,m,p} + Additional\ Demand - \sum_j (\beta_{i,j} Q_{j,i,m,p} - Q_{i,j,m,p}) = E_{Grid,i,m,p} + \sum_{tech} Self_{i,m,p} + StorOut_{i,m,p} \quad (7)$$

$Load_{i,m,p}$ represents a generic demand, while *Additional Demand* can come from a unit (e.g., *AC* electricity) which, when installed, adds extra demand. $E_{Grid,i,m,p}$ represents electrical energy imported from the grid, while $Self_{i,m,p}$ is energy generated for self-use by the installed units. *StorOut* is the power available from storage facilities. Q is the power transferred via the *MG* or pipelines from house j to i . This value is subtracted from the demand and vice versa for *QE*. The left side of the equation is the net demand, met by technologies and imports on the right side. β is a loss coefficient, dependent on the cable or pipe lengths between 2 homes. Looped networks are mitigated by the following equation where E is a numerical position of a connected home. A higher order home cannot give energy to lower order homes, only import it from them, while *card* is the value of i .

$$E_j \geq E_i + 1 - [card_i \times (1 - YMG_{i,j})] \quad (8)$$

Moreover, energy flows in one direction along connections, and the energy transferred must be equal to the sum of energies from contributing technologies within the house i .

Finally, the *MG* controller itself uses electricity and therefore has an O&M cost.

The electricity generated in the network which exceeds demand can be sold to the national grid. *CSalGRID* represents the annual income from electricity sales for the network and is calculated as the volume of electricity sold for a given technology and time period multiplied by the length of that time period, the number of days in which in that time period appears, and the number of months in which those days appear. This is summed for all time periods, houses and technologies. To ensure that homes do not become power plants, and are only selling electricity and not generating it for profit, a rule is put in place that states that the total energy sold from all technologies cannot

exceed that generated by all units, minus the demand of the home. The annual electricity cost for energy purchase from the grid, $CPurGrid$, is calculated as the sum for all houses and time periods, of the volume purchased in any given period multiplied by the length of time period and the number of days and months. At any time, a house either buys or sells electricity, not both.

$$PurGRID = \sum_{i,m,p} EGRID_{i,m,p} \times PElec \times day(m) \times hours(p) \times season(m) \quad (9)$$

According to legislation, BB units are not allowed to provide heat to more than one home, and there is also a limitation on the annual heat produced from BB which receive RHI payments. The capacity of the generating units is based on the demands which can come from self-provisions, sales to the grid, storage and transfer to other homes:

$$Self_{tech,i,m,p} + Sal_{tech,i,m,p} + Stor_{tech,i,m,p} + \sum_j Q_{tech,i,j,m,p} = Gen_{tech,i,m,p} \quad (10)$$

Power generation from a unit cannot occur in a house unless the unit is installed.

The money earned through FITs is calculated from the FIT price or electricity generated, $PFIT_{Tech}$.

$$FITPay = \sum_{i,m,p,tech} (EGen_{tech,i,m,p} \times PFITCHP \times day(m) \times hours(p) \times season(m))$$

For the sake of space, only one CHP is permitted in which dwelling. Electricity generation from PV cells is a function of solar irradiance, which varies with the time of day and seasons, the surface area installed (a variable which the model optimizes) and the panel efficiency, a set parameter. The volume of energy in the TS is a function of the volume in the unit in the previous time period, what is sent to the unit, what is withdrawn from the unit for heating and DHW demand, as well as the static loss. A balance is needed to calculate how much energy can be withdrawn and is based on energy provided in the previous time period. It is impractical to have WT in adjacent houses, hence a rule is put in place that there must be at least one house gap between WT installations. Power generated by WT s is not a continuous function of the available wind resource but is instead, a piecewise function dependent on the “rated”, “cut in” and “cut-out” speed for the units available. Finally, a tax is imposed for electricity taken from the grid, which has its own carbon intensity.

4. Results and conclusions

The model is formulated as a MILP and solved using the GAMS CPLEX solver [8]. A summary of models' statistics and solution times is shown in Table 2. The combined variable import and export pricing increase charges both from and to the grid but, overall, profitability is increased. This is due to the extreme differences in volumes of imported and exported energy. While the relative increase in charges from purchased electricity is much higher than the relative increase in sales, the absolute increase in charges is slightly smaller than absolute increase in sales. This is due to the network generating much of its own energy. Carbon emissions per kWh are increased due to increased sales from CHP units which are more economically incentivised by the FIT payments than generation from WT . In the variable network design case study, variable pricing greatly affects the installations made and the operation of the DER network. The network becomes much less dependent on thermal storage (TS) capabilities and a pipeline connection is installed between houses $i4$ and $i5$. The network also becomes less dependent on AC units for cooling demands and the number of absorption chillers (Abs) is increased. This is due to increased CHP sizes which allow Abs to be added and

also the ability to share cold loads through the pipelines. Fig. 3 shows the layout of the newly designed network. In terms of operational effects, dynamic pricing increases environmental impacts, as for the fixed network, due to UK FIT payments encouraging electricity generation from *CHPs* over other renewable assets. Profitability increases more than for the fixed network because the model is able to adjust to the changes in pricing and take advantage of a more economical trading scenario.

Table2. Economic and environmental results of the different case studies

Pricing	Constant	Dynamic	Dynamic
Scenario	Baseline	Fixed	Unfixed
CO ₂ emissions (kg / kWh)	0.0856	+ 1.17 %	+ 25.00 %
Profitability (£ / year)	1,535.81	1,550.80	1,620.83
Investment cost (£)	51,178.72	+ 0.00 %	+ 12.30 %
Sales to grid (£ / year)	1,106.57	+ 2.00 %	+ 47.30 %
Grid purchases (£ / year)	9.85	+ 143 %	- 100 %
Equations	3,810	3,810	10,397
Variables	4,475	4,475	14,983
Binaries	120	120	226
CPU Time (s)	0.14	0.11	160.22

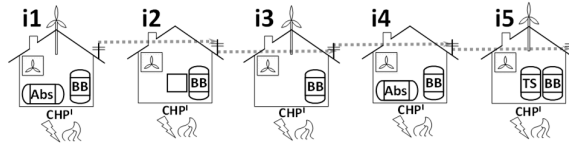


Fig 3. Layout of the newly designed DER network for dynamic import and export pricing

Furthermore, the short times for solving the models is encouraging as it demonstrates that optimization using dynamic pricing control is achievable and the network should be able to respond rapidly and reliably to incoming demand and pricing data, even for time periods in the distant future.

References

- [1] L.B. Nikonowicz, J. Milewski, Virtual Power Plants – general review: structure, application and optimization, *Journal of Power Technologies* 92, 135, 2012;
- [2] S. Acha, A. Mariaud, N. Shah, C.N. Markides, Optimal design of distributed low-carbon energy technologies in commercial buildings, *Energy* 142, 578, 2018;
- [3] A.S. Hasan, L. Cipcigan, N. Jenkins, Optimal battery storage operation for PV systems with tariff incentives, *Applied Energy* 203, 422, 2017;
- [4] B.L. Gowreesunker, S.A. Tassou, The impact of renewable policies on the adoption of anaerobic digesters with farm-fed wastes in Great Britain, *Energies* 9, 1038, 2016;
- [5] G. Xu, W. Yu, D. Griffith, N. Golmie, P. Moulema, Toward integrating distributed energy resources and storage devices in Smart Grid, *IEEE Internet of Things Journal* 4, 192, 2017;
- [6] E.D. Mehleri, H. Sarimveis, N.C. Markatos, L.G. Papageorgious, A mathematical programming approach for optimal design of distributed energy systems at the neighborhood level, *Energy* 44, 1, 2012
- [7] C. Wouters, E.S. Fraga, A.M. James, An energy integrated, multi-grid, MILP (mixed-integer linear programming) approach for residential distributed energy system planning – A South Australian case-study, *Energy* 85, 30, 2015

Centralised versus localised supply chain management using a flow configuration model

Bogdan Dorneanu^a, Elliot Masham^a, Evgenia Mechleri^a, Harvey Arellano-Garcia^{*a,b}

^a*Department of Chemical & Process Engineering, University of Surrey, Guildford, United Kingdom*

^b*LS Prozess- und Anlagentechnik, Brandenburgische Technische Universität Cottbus-Senftenberg, Cottbus, Germany*

h.arellano-garcia@surrey.ac.uk

Abstract

Traditional food supply chains are often centralised and global in nature. Moreover they require a large amount of resource which is an issue in a time with increasing need for more sustainable food supply chains. A solution is to use localised food supply chains, an option theorised to be more sustainable, yet not proven. Therefore, this paper compares the two systems to investigate which one is more environmentally friendly, cost efficient and resilient to disruption risks. This comparison between the two types of supply chains, is performed using MILP models for an ice cream supply chain for the whole of England over the period of a year. The results obtained from the models show that the localised model performs best environmentally and economically, whilst the traditional, centralised supply chain performs best for resilience.

Keywords: supply chain management, flow configuration model, ice cream, centralised versus localised, MILP.

1. Introduction

Food supply chains (FSCs) are complex due to the large amount of actors, but are also unique amongst the supply chains (SCs) due to seasonal production and demand, as well as requiring to operate at refrigerated temperatures to ensure food safety and quality. The traditional FSC require a large amount of resources, which is an issue in a time with increasing need for more sustainable food supply [1, 2]. The majority of the FSC are very global and centralised, a solution designed to minimise the cost of the whole chain and therefore to increase the profits of a company. However, these are not considered sustainable due to the large amount of resource they consume [3]. A theoretical approach has been proposed to make the FSC more sustainable by having it localised [4, 5], a solution where all actors function within the same area. These FSC are seen to be more sustainable since the local customers are using local ingredients and a decrease in CO₂ emissions and resource demand can be achieved [6]. Thus there are significant business trade-offs to consider in deciding on an operational strategy – and some of these trade-offs may be entirely valid between food chains and food transport. Although the localised FSC has been theorised to be more sustainable in environmental terms, this has not been proven through a model, as most existing studies optimise without considering all the chain stages [7, 8]. For comparison of centralised and localised SCs, MILP models have

been developed. To perform this comparison, an ice cream SC model is developed for England, incorporating the use of the 8N configuration neighborhood flow approach [9].

2. The neighbourhood flow approach and the FSC

The model is built for the ice cream SC over a period of one year and consists of 4 different actors. The first set of actors are represented by a total of 16 different suppliers, all with different supply capacities, providing two ingredients. Half of the suppliers will simulate dairy farms, supplying only milk, while the other half will simulate sugar factories, providing the sugar. The second set of actors are the factories where both milk and sugar from the suppliers will use. The milk is transported from suppliers to each factory, where ingredient storage is available, before manufacturing. In the centralised model there is 1 large factory while the localised model considers 8 small factories. All factories make 4 different types of ice cream (SKUs). The third set of actors is represented by the SKU warehouses, which is the location where products are stored during the time the factories are producing more than the demand. In the localised model there will be 8 small warehouses, while the centralised model assumes 3 large ones. Only the product that leaves the factory and needs to be stored will be transported to the warehouse, while the rest is sent directly to the demand centre. The demand centre is the final actor and the customer of the FSC. There is a total of 8 different demand centres where the demand and locations are the same for both the localised and the centralised model. The demand at the centres varies for each type of SKU and across the individual 52 weeks of a year. The movement between the actors of the FSC is summarised in Fig.1.

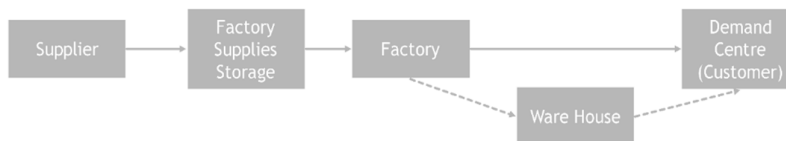


Figure 1: The flow between the actors of the ice cream supply chain

To simulate the locations, the transport of ingredients and ice cream between the actors all the models will use a neighbourhood flow approach with the use of the 8N configuration as set out by [9]. The neighbourhood flow approach requires the use of a grid system which consists of multiple different regions. A region is specified to contain an actor and the ice cream or the ingredients can be transported from one actor to another through flow from one region to another neighbouring region through 4N or 8N flows. If the corresponding actors that send and receive the transported goods are not in neighbouring regions the simulation model will move the goods from one neighbouring region to another and repeat this process until the goods are delivered to the required actors. The size of each region is taken as being 50x50 km, the distance travelled by the goods through 4N neighbourhood flow is 50 km, while for the 8N flow is 70.7 km. the grid system that the neighbourhood flow approach uses has been set up to simulate the whole England in both models, which resulted in a total of 69 different regions of 50x50 km size (Fig.2). In the centralised model all actors required for the SC can be in any region, and the ingredients and products can be transported through any region shown in Fig.2. For the localised models, different local area sizes and location are selected where the different regions of England are designated by double lines in Fig.2. Moreover, in the localised models London and the SE of England are considered to be the same region due

to Greater London's small size, and the practical assumption that some actors may not be present here, such as the farm, the warehouse or the factory.

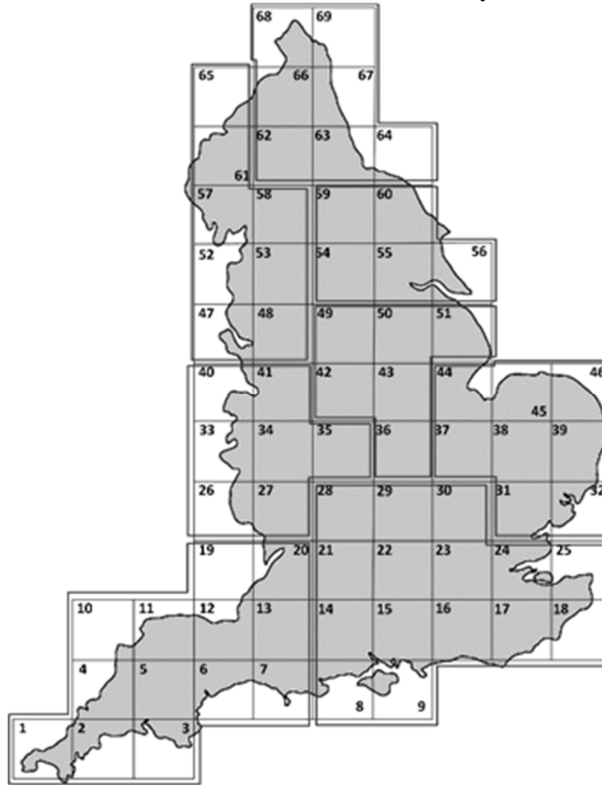


Figure2: Grid system for England, used to simulate the FSC models

3. Mathematical formulation

In all the MILP models developed, the constraints remain the same and only the objective equations differ.

3.1. Model constraints

The amount of ingredients h , being taken from the supplier in region g in week t , cannot exceed the amount of ingredients that are available weekly from the supplier:

$$SupplyUse_{h,g,t} \leq MaxSupply_{h,g} \quad \forall h, g, t \quad (1)$$

The total amount of ingredients h , stored in the factory in region g in week t cannot exceed the factory maximum ingredient storage.

$$INVIng_{h,g,t} \leq INVIngCap_{h,g} \quad \forall h, g, t \quad (2)$$

The amount of ingredients h in the factory storage in region g in week t is equal to the amount of ingredients h that is in the factory storage in the previous week, plus the ingredient delivered from the suppliers minus the amount of ingredients used to produce the SKU in the factory in week t . The set up time and the production time of every SKU

in a factory in region g in week t cannot exceed the maximum weekly production time allowed for each SKU. The ingredients and the SKU should satisfy mass balances for each region g and week t .

3.2. Economic objective equation

The objective of the centralised and localised economic models is to minimise the total economic cost of the whole SC. The costs consists of the factory production costs, $ProdC$, the ingredients purchase, transport, $IngTransC$ and storage, ISC , WHC costs, the SKU storage and transport, $SKUTransC$ costs and a penalty if demand is not met at the demand centres, $DNMPen$:

$$TEC = ISC + ProdC + WHC + IngTransC + SKUTransC + DNMPen \quad (3)$$

3.3. Resilience objective equation

In the resilience model, localised and the centralised SC are tested under disruptive scenario of the supplier not being able to provide ingredients over an 8 week period of high demand. The objective is to minimise the total demand that is not met at the demand centres.

$$DNM = \sum_i \sum_g \sum_t (Demand_{i,g,t} - Retailer_{i,g,t}) \quad (4)$$

To this end, an extra equation is added to the model to calculate the rate of fulfilment for every SKU in every week t for all the demand centres.

3.4. Model parameters

The value of the parameters is chosen to closely match realistic values of an ice cream SC. The total yearly demand is split into weekly demands that match the typical seasonal demand (Fig.3). The weekly demand split into the 4 SKUs, and split between the 8 different demand centres across England. The selection of the regions is based on the population for the localised area. The demand centres and their proportion are localised in regions 6 (10%), 23 (32%), 34 (10%), 37 (11%), 43 (8%), 53 (13%), 55 (10%), 67 (5%). The location and maximum supply available from each supplier is the same for both the localised and centralised models. The availability of supply is assumed constant over the year. Each localised region must have a milk and a sugar supplier. The region with milk suppliers are assumed in locations where the density of dairy farms is high. The milk suppliers are in regions 5 (600 t/wk), 16 (1,550 t/wk), 39 (600 t/wk), 41 (600 t/wk), 49 (500 t/wk), 60 (600 t/wk), 61 (700 t/wk), 63 (300 t/wk), while the sugar supplier are in regions 3 (450 t/wk), 9 (800 t/wk), 31 (350 t/wk), 40 (350 t/wk), 43 (300 t/wk), 56 (300 t/wk), 57 (350 t/wk), 67 (150 t/wk). For the centralised model there will be only one large factory located in region 42, the most central region.

For the localised model there are 8 small factories in regions 25, 52, 44, 35, 13, 54, 51, 62. It is assumed that ice cream consists of 75% of milk and 25% of sugar. The factory maximum ingredients capacity differs for all the 8 different factories in the localised model, and the factory maximum ingredients capacity for the single centralised factory in the centralised model is the sum of all the 8 different localised factories maximum ingredients capacities. The warehouses are located in regions 21 (4,000 t), 34 (2,000 t), and 54 (1,170 t) for the centralised model, and in regions 17 (3,000 t), 57 (1,100 t), 45 (620 t), 26 (590 t), 7 (560 t), 56 (560 t), 50 (475 t), 50 (475 t) and 64 (260 t).

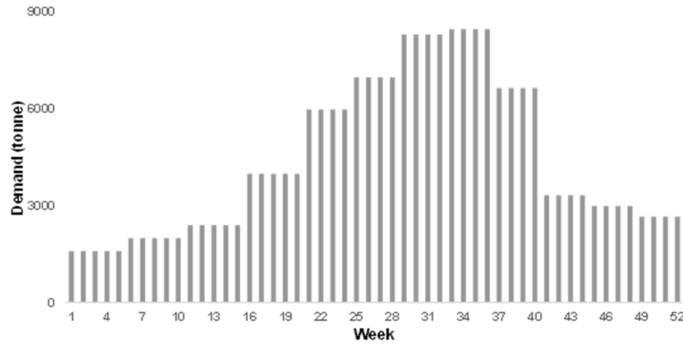


Figure3: The weekly demand profile

Moreover, all the cost parameters (ingredients, transport, manufacturing, storage) are expressed according to the values for the UK. If the SC does not meet the demand there is a penalty defined as the price the ice cream would sell at the demand centre.

4. Results

4.1. Economic results

When the centralised economic model is optimised to minimise the total SC cost, the results was that it would cost a total of £214.3 million over all of the 52 weeks. Since over the 52 weeks the SC handles 231,600 tonnes of ice cream, the cost in terms of every unit of ice cream is £925.25 per tonne of ice cream. When the localised economic model is optimised to minimise the total SC costs, it would cost £213 million over the 52 week period. Since the localised SC handles overall the same amount of ice cream as the centralised one, the cost in terms of unit of ice cream is £919.50 per tonne of ice cream. Fig.4 shows the layout of the economic model for the two types of SC, for week 33.

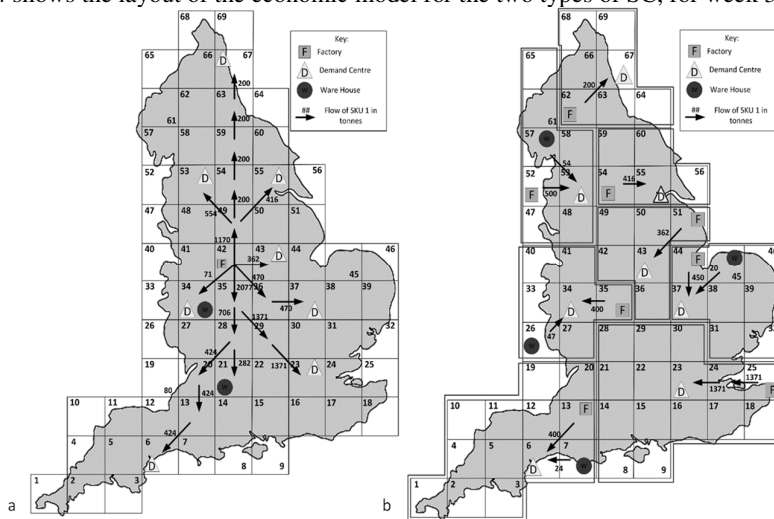


Figure4: Flow of SKU1 in week 33 for the a) centralised SC and b) localised SC

4.2. Resilience results

The disruption scenario assumes that the milk supplier in region 16 is not able to provide any milk over an 8 week period in the high season. In the centralised SC the minimum of the demand not being met achieved is 8,582 tonne of ice cream, with the model specifying the overall weekly fulfilment rate. The resilience index for the centralised SC is 0.932. For the localised SC the minimum demand not being met achieved from the optimised model is 16,485 tonnes of ice cream, with the optimised model specifying the overall weekly fulfilment rates. The resilience index in this case is 0.869. Fig.5 shows the demand profile fulfilment during the SC disruption scenario.

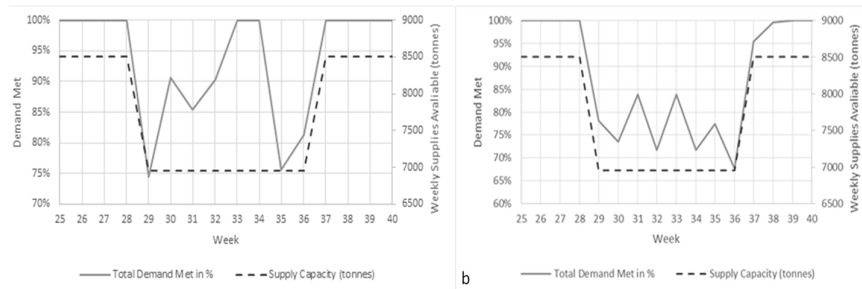


Figure5: Demand profile fulfilment during the SC disruption scenario for the a) centralised and b) localised model;

5. Conclusions

This work describes the development of two MILP models to simulate a centralised and a localised ice cream SC in England over 52 weeks, using the 8N neighbourhood flow configuration. The two SC are compared at economical and resilience level. The localised SC is £1.377 million cheaper than the centralised one due to the shorter transportation distances between the various actors. At resilience level, the centralised SC has a higher resilience index, due to the possibility to being supplied from other regions when one of the suppliers fails to fulfil the demand. Although centralised distribution shows efficiency benefits, the distributed system may have the ability to reduce temporal, geographical and administrative gap between decision makers and the impact of their decisions, reduce the possibility of widespread impacts if production systems fail and avoid the need for long-distance transport infrastructure. Rather than considering the two configurations as alternatives to each other, a sustainability assessment considering economic, environmental and societal situations where complementarities and synergies between centralised and localised FSC occur should be investigated.

References

- [1]. Akkerman, et al., 2010, *OR Spectrum* 32, 863; [2]. Kirwan, et al., 2017, *Journal of Rural Studies* 52, 21; [3]. Mundler & Rumpus, 2012, *Food Policy* 37, 609; [4]. Rothwell, et al., 2016, *Journal of Cleaner Production* 114, 420; [5]. Rahimifad, et al., 2017, *Sustainable Design and Manufacturing*, Springer, 13; [6]. Rauch, et al., 2016, *Journal of Cleaner Production* 135, 127; [7]. Estes, et al., 2018, *International Journal of Production Research* 56, 4418; [8]. Zhu, et al., 2018, *International Journal of Production Research* 56, 5700; [9]. Akgul, et al., 2012, *Biomass and Bioenergy* 41, 55

Novel refrigeration cycle configurations for performance improvements in LNG processes at small scale

Fernando Almeida-Trasvina* and Robin Smith

Centre for Process Integration, School of Chemical Engineering and Analytical Science, The University of Manchester, Manchester M13 9PL, UK

hector.almeidatrasvina@manchester.ac.uk

Abstract

The refrigeration cycles employed in the LNG industry are highly energy-intensive. The costs associated to the shaft work energy required for refrigerant compression usually dominates the overall operating costs of the LNG plant. In this work, four different single mixed refrigerant (SMR) cycle configurations, including the commercial PRICO cycle and the CryoMan cycle, are studied for energy-efficiency improvements in the production of LNG at small scale (i.e. up to 1 million tonnes per annum, MTPA). The cycle configurations are based on structural modifications applied to the PRICO cycle. The four configurations are first optimised to minimise shaft work demand, so analysis is carried out in the scenario in which each cycle fully exploits their corresponding configuration. Additionally, the complexity of the SMR cycles, in terms of number of compression stages is kept similar, so the energy savings can be associated to the structural modifications only. From the four SMR cycles, the CryoMan cycle is the most energy-efficient, achieving saving of around 8.5% compared to the commercial PRICO cycle. The exergy analysis applied to their multi-stream heat exchangers (MSHE) suggests that the structural modifications allow reducing the refrigeration duty at the lowest temperature level to bring energy savings.

Keywords: LNG, small scale, refrigeration cycle, SMR cycles.

1. Introduction

Small scale production of liquefied natural gas (LNG), i.e. up to 1 MTPA, is becoming commercially attractive. To liquefy a natural gas stream (to around -160 °C), energy-intensive refrigeration cycles are usually employed. The shaft work energy required for refrigerant compression strongly dominates the overall operating costs of the LNG plant. Thus, minimising shaft work energy demand of a given cycle configuration leads to minimising operating costs. The PRICO single mixed refrigerant (SMR) cycle is the commercial benchmark SMR cycle for small scale production of LNG.

The energy-efficiency of mixed refrigerant cycles can be improved by structurally modifying its configuration, as shown by Almeida-Trasvina and Smith (2018) for cascade cycles in large scale production of LNG. However, little research has been done in structural modifications to mixed refrigerant cycles for LNG processes at small scale. He et al. (2019) optimised the energy-efficiency of an SMR cycle consisting of two MSHE stages but with a flash unit before the first MSHE unit. Aslambakhsh et al. (2018) optimised the PRICO cycle considering both operating and capital costs. Nguyen et al. (2018) optimised the energy-efficiency of the PRICO cycle for five different

natural gas feeds. Morosuk et al. (2015) analysed the PRICO cycle using exergy analysis for improving its energy-efficiency. Mehrpooya and Ansarinassab (2015) assessed two SMR cycles using an exergoeconomic analysis.

In this paper, the energy-efficiency performance of four different SMR cycles is studied. The SMR cycle configurations are based on structural modifications applied to the PRICO cycle, and are taken from Zheng (2009). The SMR cycles are first optimised in a case study for small scale production of LNG. The complexity of the SMR cycles (in terms of number of compression stages) is kept similar, so differences in energy performance can be associated to their structural modification only. Exergy analysis is applied to each configuration so as to bring insights of how each structural modification allows achieving energy savings.

2. Configuration of the single mixed refrigerant (SMR) cycles

Figure 1 shows the four SMR cycles studied in this paper. The PRICO cycle is shown in Figure 1a. In the MultiStream cycle (Figure 1b), the structural modification consists in splitting the refrigerant stream flow rate into two streams before entering the MSHE, each with an independent evaporating pressure. In the PreFlash cycle (Figure 1c), the structural modification consists in using a flash unit; the resulting refrigerant streams would then have different compositions between each other. In the CryoMan cycle (Figure 1d), the main refrigerant stream is also split into two streams using a flash unit, and the resulting flash outlet streams are partially mixed to create the two refrigerant streams that provide cooling in the MSHE.

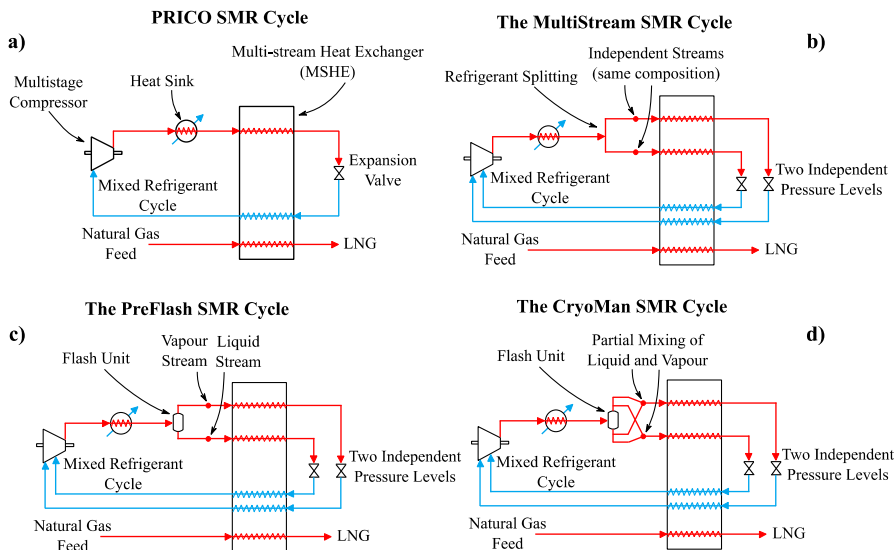


Figure 1. SMR configurations: a) PRICO; b) MultiStream; c) PreFlash; d) CryoMan.

The configurations of the SMR cycles are defined to have a total of three compression stages for refrigerant compression, in order to have similar complexity across the SMR cycles since compressors are major contributors to capital costs and also impact on energy performance (Mokhtab et al., 2014, Ch. 3.2).

3. Optimisation of the SMR cycle configurations

The operating variables of the four SMR cycles are optimised in order to analyse their best performance, i.e. the scenario in which the SMR cycles are fully exploiting their corresponding structural modifications to reduce the energy demand.

All the four SMR cycle configurations are optimised to minimise the specific shaft work energy demand (Equation 1) in a case study to produce LNG at small scale. The data of the natural gas is taken from Fahmy et al. (2016), and is given in Table 1. The natural gas feed flow rate is equivalent to LNG production of 1.0 MTPA. It is assumed that the minimum temperature approach for heat exchange in the MSHE is 2 °C; a maximum pressure ratio of 3.5 has been defined for any compression stage.

$$\frac{W^{Total}}{\dot{m}_{LNG}} = \frac{\sum_{i=1}^n W_i^{Stg}(\phi)}{\dot{m}_{LNG}} \tag{1}$$

The optimisation strategy followed in this work is similar to that employed by Almeida-Trasvina and Smith (2018) for the optimisation of cascade refrigeration cycles for large scale production of LNG. The strategy consists in applying a stochastic algorithm to search the solution space (using Genetic Algorithm) and avoid local optima, and the best solution found is fed to an SQP solver to refine the solution.

Table 1. Natural gas specifications for the case study.

Flow rate [kg·s ⁻¹]	31.71
Inlet pressure [bar]	63.0
Inlet temperature [°C]	25.0
Outlet temperature [°C]	-161.0
Composition [mole fraction]	
Methane	0.98385
Ethane	0.01070
Propane	0.00090
<i>n</i> -Butane	0.00020
CO ₂	0.00005

The results from the optimisation are presented in Table 2. The CryoMan cycle is the most energy-efficient of the four SMR cycles. The CryoMan cycle performance is equivalent to a specific shaft work demand of 28.67 MW·MTPA LNG⁻¹, whereas that of the PRICO cycle is 31.32 MW·MTPA LNG⁻¹. That is, the CryoMan cycle achieved energy savings of around 8.5% compared to the PRICO cycle.

The results in Table 2 suggest that manipulating the refrigerant composition brings energy savings. The modification applied to the PreFlash cycle (i.e. the flash unit) implies splitting the refrigerant stream into two streams that have different composition with respect to each other (unlike with the MultiStream cycle). Energy savings of 3.22% are achieved by the PreFlash cycle compared to the MultiStream cycle.

Table 2. Energy-efficiency comparison between the SMR cycles (relative to PRICO cycle).

	PRICO SMR Cycle	MultiStream SMR Cycle	PreFlash SMR Cycle	CryoMan SMR Cycle
Compression Stages	3	3	3	3
LNG production [MTPA]	1.00	1.00	1.00	1.00
Specific shaft work [MW·MTPA ⁻¹ LNG]	31.32	30.47	29.38	28.67
Energy savings [%]	—	+ 2.71%	+ 6.19%	+ 8.46%

The CryoMan SMR cycle allows manipulating further the refrigerant composition by partially mixing the flash unit outlet streams. Energy savings of around 2.78% are achieved by the CryoMan SMR cycle relative to the PreFlash SMR cycle.

4. Exergy analysis of the SMR cycles

In refrigeration cycles, exergy is defined as the minimum shaft work input (Equation 2) needed to provide refrigeration at a given temperature, assuming a thermodynamically reversible process (Venkatarathnam, 2008, Ch. 1.4). Equation 2 suggests that the exergy increases either as the refrigeration temperature (T_{Evap}) decreases, or as the refrigeration duty (Q_{Evap}) increases. The term in brackets on the right-hand side of the equation is widely known as the Carnot factor. Alternatively, exergy can be expressed as in Equation 3, which implies that the exergy demand is also dependent on the nature of the refrigerant mixture employed (values of enthalpies and entropies).

$$Ex = -W_{rev} = Q_{Evap} \left(\frac{T_{Cond}}{T_{Evap}} - 1 \right) \quad (2)$$

$$Ex = n \left[(h_{out} - h_{in})_{Evap} - T_{Cond} (s_{out} - s_{in})_{Evap} \right] \quad (3)$$

Exergy analysis is applied to the SMR cycles, by plotting the exergy composite curves (from Equation 2) of the MSHE for each SMR cycle. The exergy composite curves are the analogue of the conventional composite curves, but the temperature axis in the latter is replaced by the Carnot factor. The area between the exergy composite curves represents exergy loss, associated to the temperature difference needed for heat transfer.

Figure 2 shows the exergy composite curves for each optimised SMR cycle. As can be implied from Equation 2, the area between the exergy composite curves is minimised at the cold end of the process across the four SMR cycles. Moreover, the overall exergy losses are gradually reduced with each of the structural modifications applied. The exergy losses in the MSHE for the PRICO cycle are equivalent to 2.71 MW, whereas in the CryoMan cycle the exergy losses are equivalent to only 1.13 MW, i.e. the losses are reduced by around 58%.

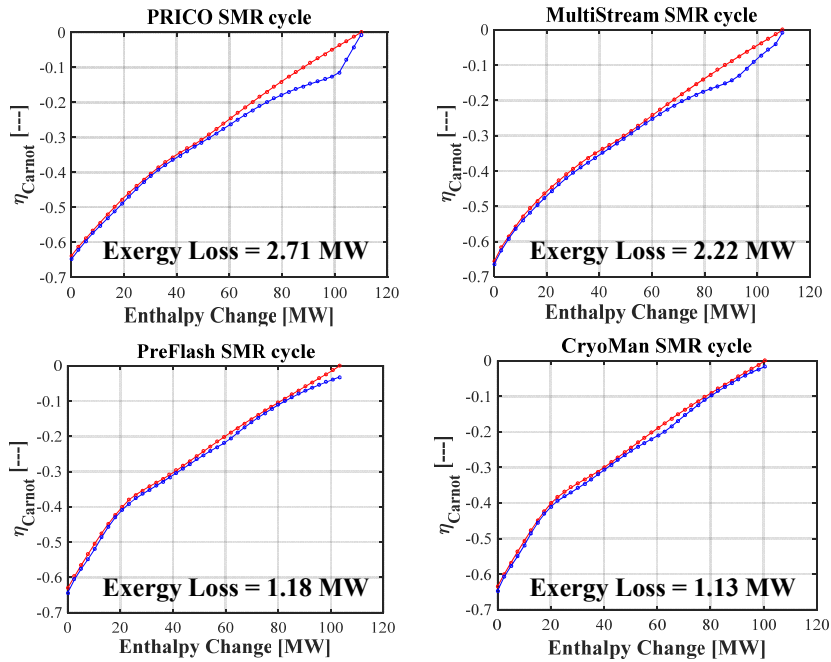


Figure 2. Exergy composite curves of MSHE for each SMR cycle.

The main results from the exergy analysis over the MSHE unit for each SMR cycle are shown in Table 3. The exergy efficiency in Table 3 is defined as the ratio of overall exergy change of the natural gas stream (15.72 MW) to the total shaft work demand for refrigerant compression. The exergy duty in the MSHE is calculated for both composite curves at intermediate temperatures using Equation 3.

Table 3. Summary of exergy performance results for each SMR cycle.

	PRICO SMR cycle	MultiStream SMR cycle	PreFlash SMR cycle	CryoMan SMR cycle
Shaft work demand [MW·MTPA LNG ⁻¹]	31.32	30.47	29.38	28.67
Exergy Duty MSHE [MW]	54.79	53.12	44.06	43.17
Exergy Losses MSHE [MW]	2.71	2.22	1.18	1.13
Exergy Efficiency [%]	50.19	51.59	53.50	54.83

As shown in Table 3, the exergy duty in the MSHE is decreased by around 9.1 MW when the flash unit is introduced, since the refrigerant flow rate in the low pressure stream (at the lowest temperature level) is significantly reduced. Also, the flash unit helps reducing the exergy losses by creating two different refrigerant compositions that yield a reduced area between the composite curves (see Figure 2).

In the CryoMan cycle, partial mixing of the streams leaving the flash unit allows to reduce further the flow rate of the stream at the lowest temperature level, and also to reduce the exergy losses by manipulating the refrigerant composition of each resulting stream. Thus, the exergy demand further reduced, bringing the corresponding savings in shaft work demand.

5. Conclusions

The structural modifications applied to the PRICO cycle were demonstrated to bring significant energy savings – up to 8.46 % with the CryoMan cycle – for configurations with similar level of complexity in terms of number of compression stages, and for the same liquefaction duty. The results from the exergy analysis suggest that structural modifications should be applied with the aim to reduce the refrigeration load at the lowest temperature level. Additionally, creating different refrigerant compositions and manipulating refrigerant flow rates allow minimising the exergy losses in the MSHE.

Further study is still needed on the implications of structural modifications in the configuration of LNG mixed refrigerant cycles. More insights would be useful to further develop and optimise novel LNG refrigeration cycles more systematically.

References

- Almeida-Trasvina, F. & Smith, R. (2018). Design and Optimisation of Novel Cascade Refrigeration Cycles for LNG Production. *In: Friedl, A., Klemeš, J. J., Radl, S., Varbanov, P. S. & Wallek, T. (eds.) Computer Aided Chemical Engineering*. Elsevier. Vol. 43, 621-626.
- Aslambakhsh, A. H., Moosavian, M. A., Amidpour, M., Hosseini, M. & AmirAfshar, S. (2018). Global cost optimization of a mini-scale liquefied natural gas plant. *Energy*, 148, 1191-1200.
- Fahmy, M. F. M., Nabih, H. I. & El-Aziz, M. R. A. (2016). Investigation and performance improvement of the propane precooling cycle in the propane precooled mixed refrigerant cycle liquefaction process. *Industrial & Engineering Chemistry Research*, 55(10), 2769-2783.
- He, T., Liu, Z., Ju, Y. & Parvez, A. M. (2019). A comprehensive optimization and comparison of modified single mixed refrigerant and parallel nitrogen expansion liquefaction process for small-scale mobile LNG plant. *Energy*, 167, 1-12.
- Mehrpooya, M. & Ansarinasab, H. (2015). Exergoeconomic evaluation of single mixed refrigerant natural gas liquefaction processes. *Energy Conversion and Management*, 99, 400-413.
- Mokhatab, S., Mak, J. Y., Valappil, J. V. & Wood, D. A. (2014). *Handbook of Liquefied Natural Gas*. Kidlington, Oxford, UK: Gulf Professional Elsevier, Inc.
- Morosuk, T., Tesch, S., Hiemann, A., Tsatsaronis, G. & Bin Omar, N. (2015). Evaluation of the PRICO liquefaction process using exergy-based methods. *Journal of Natural Gas Science and Engineering*, 27, 23-31.
- Nguyen, T.-V., Rothuizen, E. D., Markussen, W. B. & Elmegaard, B. (2018). Thermodynamic comparison of three small-scale gas liquefaction systems. *Applied Thermal Engineering*, 128, 712-724.
- Venkatarathnam, G. (2008). *Cryogenic Mixed Refrigerant Processes*. New York, NY, USA: Springer Science+Business Media LLC.
- Zheng, X. (2009). *Design and Integration of Refrigeration and Power Systems*. Ph.D. Thesis. Centre for Process Integration, The University of Manchester. Manchester, UK

Modelling and optimal operation of a natural gas fired natural draft heater

Richard Yentumi^{a,b}, Bogdan Dorneanu^b, Harvey Arellano-Garcia^{*b,c}

^a*Department of Engineering & Maintenance, Ghana National Gas Company, Accra, Ghana*

^b*Department of Chemical & Process Engineering, University of Surrey, Guildford, United Kingdom*

^c*LS Prozess- und Anlagentechnik, Brandenburgische Technische Universität Cottbus-Senftenberg, Cottbus, Germany*

h.arellano-garcia@surrey.ac.uk

Abstract

Current industrial trends promote reduction of material and energy consumption of fossil fuel burning, and energy-intensive process equipment. It is estimated that approximately 75% of the energy consumption in hydrocarbon processing facilities is used by such equipment as fired heater, hence even small improvements in the energy conservation may lead to significant savings [1, 2]. In this work, a mathematical modelling and optimisation study is undertaken using gPROMS[®] ProcessBuilder[®] to determine the optimal operating conditions of an existing API 560 Type-E vertical-cylindrical type natural draft fired heater, in operation at the Atuabo Gas Processing Plant (GPP), in the Western Region of Ghana. It is demonstrated that the optimisation results in significant reduction of fuel gas consumption and operational costs.

Keywords: fired heater, tubular heater, mathematical modelling, optimisation, gPROMS.

1. Introduction

Fired heaters, also commonly called furnaces, are a primary source of thermal energy for process heating operations in petroleum refining and chemical plants. They have been studied extensively, both experimentally and theoretically, and previous work [1-3] draws attention to the need of conserve energy, improve energy efficiency and reduce carbon emissions. Notably, most fired heaters models from literature are lumped parameter models with steady-state assumptions, mainly due to the complex thermodynamic mechanisms making the problem computationally expensive to solve [1-3]. For instance, longitudinal and radial variations or temperature gradients of the hot flue gases along the vertical height of the fired heater are normally ignored. The novel approach adopted for this work involves the distributed parameter system modelling of the temperature profiles in the tubular coils and the heat transfer fluid (HTF). The resulting ‘white-box’ model may serve as basis for conducting simulation studies to aid decision-making and to identify the best operating conditions within the specified constraints that minimise the operational costs. The model is applied to a 15.8 MW fired heater (H600) in operation at the GPP. The total heat input is supplied by the combustion reaction of fuel gas and combustion air occurring in 8 sets of floor mounted, upwards firing, gas only pre-mix

main burners. A fuel gas-fired pilot is also supplied to each set of main burners. Aside the need to improve efficiency, significant deviations from the desired HTF supply temperature have on many occasions hampered smooth operation. Currently, there is no validated model of H600 to aid monitoring of thermal efficiency, to identify areas for process improvements and to aid trouble-shooting of process deviations. Furthermore, the current temperature control scheme has been ineffective at rejecting disturbances such as changes in fuel gas pressure.

2. Mathematical model

The mathematical model is applied for each section of H600 (Fig.1), namely convection (CS), shield (SS) and radiant section (RS). A 1D tube coil running through the RS, SS and CS is considered. The axial variation is related to the tube wall and the HTF temperatures, while the flue gas temperature along the sectionalised vertical height of the heater is lumped. The tubes in the SS are assumed isolated from the RS. All tube coils are uniformly heated. The combustion process is assumed to be steady-flow and the CO₂, N₂ and other non-hydrocarbon components of the fuel are ignored in combustion reaction calculations. Key geometrical characteristics of H600 are summarised in Table1.

Table1: Geometry of the fired heater

Parameter	Radiant section	Shield section	Convection section
Number of tubes	88	24	72
Overall length [m]	138.69	21.8	62.94
Outside tube diameter [mm]	114.3	114.3	114.3
Effective tube length [m]	12.192	6.245	6.245
Cold plane surface area [m ²]	217.8	33.27	-
Total heating area (bare) [m ²]	398.46	53.86	-
Total heating area [m ²]	-	-	1946
Orientation of tubes	Vertical	Horizontal	Horizontal
Tube material of construction	ASTM A106 Gr.B	ASTM A106 Gr.B	ASTM A106 Gr.B

2.1. Radiant section/firebox

On a rate basis, the conservation of energy in the fired heater is given by:

$$Q_F + Q_{air} = Q_R + Q_{WL} + Q_G \quad (1)$$

Where Q_F =the total rate of heat released by the combustion of the fuel gas [W]; Q_{air} =the rate of heat flow into the burners in the combustion of air [W]; Q_R =the heat duty of the RS [W]; Q_{WL} =total rate of heat loss through the fired heater walls [W]; Q_G =rate of heat flow out of the RS in the flue gases [W].

$$Q_F = N_B \cdot \left(\min \left(\eta_{MB} \cdot \left(\frac{\dot{m}_{F-MB} \cdot LHVF}{N_B} \right), Q_{MaxHR-MB} \right) + \min \left(\eta_{PB} \cdot \left(\frac{\dot{m}_{F-PB} \cdot LHVF}{N_B} \right), Q_{MaxHR-PB} \right) \right) \quad (2)$$

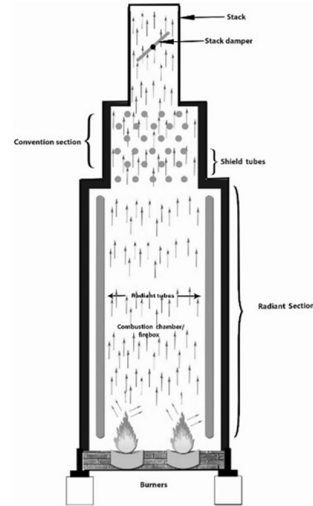


Fig.1: The distinct sections in a box-type style fired heater

With N_B =number of burner in use; η_{MB} , η_{PB} =efficiency of the main/pilot burners; LHV_f =lower heating value of the fuel gas [J/kg]; $Q_{MaxHR-MB}$, $Q_{MaxHR-PB}$ =design maximum rate of heat released per main/pilot burner [W]; \dot{m}_{F-MB} , \dot{m}_{F-PB} =total mass flowrate of fuel gas supplied to main/pilot burners [kg/s]. Based on the ratios of the maximum heat released per pilot burner to the main burner, \dot{m}_{F-PB} is assumed to be 0.0133% of \dot{m}_{F-MB} .

$$Q_{air} = \dot{m}_{act-air} \cdot c_{air} \cdot (T_{air} - T_{ref}) \quad (3)$$

Where $\dot{m}_{act-air}$ =actual mass flowrate of air supplied to burners [kg/s]; c_{air} =mass specific heat capacity of air [J/kgK]; T_{ref} =reference temperature [K]; T_{air} =temperature of air [K].

$$Q_R = F \cdot \sigma \cdot \alpha \cdot A_{cp,r} \cdot (T_{Gr}^4 - T_{w,avg,r}^4) + h_{Gr} \cdot A_{Sr} \cdot (T_{Gr} - T_{w,avg,r}) \quad (4)$$

With F =overall heat exchange factor to allow for both geometry and non-blackbody emissivities of cold and hot bodies; σ =the Stefan-Boltzmann constant [W/m²K⁴]; $A_{cp,r}$ =area of cold plane replacing a bank of RS tubes [m²]; A_{Sr} =total outside area of the RS tubes [m²]; h_{Gr} =convection heat transfer coefficient flue gas-outside of the tube wall [W/m²K]; T_{Gr} =temperature of flue gases leaving RS [K]; $T_{w,avg,r}$ =average temperature of the wall in the RS, calculated as the mean between the temperature at the entrance and the temperature at the exit of the section [K].

$$Q_{WL} = f_{WL} \cdot Q_{in} \quad (5)$$

With f_{WL} =factor of fired heater wall losses; Q_{in} =total rate of heat into the fired heater [W]. The overall enthalpy of the flue gases is expressed as the sum of the product of the molar flow rates and the specific heat capacities of each component gas. Thus:

$$Q_G = \sum n_i \cdot \Delta H_{m,i} \quad (6)$$

With n_i =molar flowrate of component i released by the combustion reaction [kmole/s]; $\Delta H_{m,i}$ =the molar enthalpy change of component i [J/kmole].

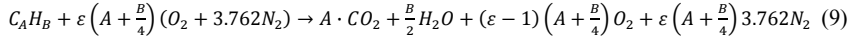
The rate of change and axial variation of the thermal energy per unit length of tube wall and the HTF are given as:

$$\frac{\partial H_{wr}(t,z)}{\partial t} = F \cdot \sigma \cdot \pi \cdot D_o \cdot (T_{Gre}^4 - T_{wr}^4(t,z)) + h_{Gr} \cdot \pi \cdot D_o \cdot (T_{Gre} - T_{wr}(t,z)) - h_{Lr} \cdot \pi \cdot D_i \cdot (T_{wr}(t,z) - T_{Lr}(z,t)) \quad (7)$$

$$\frac{\partial H_{Lr}(t,z)}{\partial t} = -u_{Lr} \cdot \frac{\pi \cdot D_i^2}{4} \cdot H_{Lr}(t,z) + h_{Lr} \cdot \pi \cdot D_i \cdot (T_{wr}(t,z) - T_{Lr}(z,t)) \quad (8)$$

Where H_{Lr} =the enthalpy of the wall in the RS; D_o , D_i =the outer/inner tube diameter [m]; T_{Gre} =the effective radiating gas temperature [K]; T_{wr} =temperature of the wall in the RS [K]; h_{Lr} =convection heat transfer coefficient wall-HTF [W/m²K]; T_{Lr} =temperature of the HTF in the RS [K].

A general balance equation for the combustion of gaseous hydrocarbon fuels with dry excess air is published by [2] in the form:



Where ε = excess air.

While the conservation of mass for the flue gases is expressed as: $\dot{m}_F + \dot{m}_{Air} = \sum \dot{m}_i$ (10).

The composition of the fuel gas is assumed as: 65.59% C1; 17.8032% C2; 12.2454% C3; 0.8817% i-C4; 1.5703% n-C4; 0.1766% i-C5; 0.1303% n-C5; 0.0515% C6+; 0.0231% N₂ and 1.4976% CO₂.

With \dot{m}_F =total mass flowrate of fuel gas [kg/s]; \dot{m}_{Air} =total mass flowrate of air [kg/s]; i =CO₂; H₂O; O₂; N₂. The temperature control valve is modelled as in [8].

For the SS and CS, the heat transfer equations are written as:

$$Q_{section} = Q_{section,in} - Q_{section,out} \quad (11)$$

The rates of heat for the flue gases in and out of the sections are calculated using a third-degree polynomial function for the specific heat in the form: $\bar{C}_p = \alpha + \beta T + \gamma T^2 + \delta T^3$.

For the wall and the HTF, equations like (7) and (8) are used and adapted to the geometries and operating conditions of the CS and SS, respectively.

For each section of the fired heater, the general form of the initial and boundary conditions for the temperature of the wall, T_w and the fluid, T_f are expressed as:

$$T_{L,Section}(0, z) = T_{Lout,Section-1}; \quad T_{w,Section}(0, z) = T_{wout,Section-1}; \quad T_{L,Section}(t, 0) = T_{Lout,Section-1}, \quad \forall t; \quad T_{w,Section}(t, 0) = T_{wout,Section-1}, \quad \forall t \quad (12)$$

The Berman equation [1] is used to determine the convection heat transfer coefficient, h_{GS} in the CS: $h_{GS} = 1.1(h_{CS} + h_{RS})$. The radiant heat transfer coefficient is not considered for the finned tube bank of the CS.

$$h_{CS} = (1.273T_{f,s}^{0.28} \cdot G_{max,s}^{0.6})/D_0^{0.4} \quad (13)$$

With $G_{max,s} = \dot{m}_G/A_{min,s}$ = flue gas max flux [m/s]; $A_{min,s}$ =the minimum cross-section flow area [m²]; $T_{f,s}$ =the film temperature [K].

The film temperature, $T_{f,s}$ and the radiant heat transfer coefficient, h_{RS} are calculated from:

$$T_{f,s} = 0.5(T_{w,avg} + T_{Gr}) \quad (14)$$

$$h_{RS} = 0.2565T_{Gr} - 2.84 \quad (15)$$

For each section of the heater, the convection heat transfer coefficients for the inside tube wall and the HTF, varying with the axial position, are calculated from the relation:

$$h_L(z) = Nu(z) \cdot k_L(z)/D_i \quad (16)$$

While, within the application ranges, the local Nusselt number is calculated from the Gnielinski correlation [5] and the local Darcy friction factor using Petukhov's correlation [6]. The heat transfer coefficient for the RS, h_{Gr} is specified as 11.36 W/m²K as reported by [7]. The thermophysical properties (density, specific heat capacity, thermal conductivity, and kinematic viscosity) of the tube coil material and the HTF, all of which vary with temperature are expressed in polynomial regression forms obtained using curve fitting techniques of the manufacturer's thermal data. The heat capacity relation of ASTM A106 Grade B as a function of temperature could not be obtained from literature and Type 304 stainless steel was used instead [4]. The different sections, RS, SS, CS of H600 are connected by mass and energy flows at their boundaries (see Figure 2).

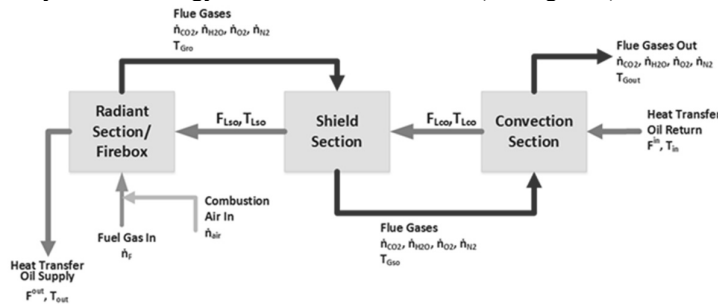


Figure 2: Connectivity between the distinct zones of the fired heater

The parameters for H600, mostly consisting of geometrical quantities are specified in Table 2.

3. Optimisation

Energy consumption in the fired heater is to be optimised to identify the best process operating conditions within the specified constraint that minimise fired heater operational costs. The objective function is formulated as an economic model describing the sum of two key daily operating costs: the fuel gas burned, and the electrical power consumed in pumping the HTF:

$$\min f = (86400 \cdot c_F \cdot \dot{m}_F \cdot LHV_F) + \left(c_E \cdot \frac{F_L^{in} \cdot \rho \cdot g \cdot H_P}{3.6 \cdot 10^6 \cdot \eta_P \cdot \eta_M} \right) \cdot t_r \quad (17)$$

Subject to $25 \leq VT \leq 75$
 $1.0 \leq \varepsilon \leq 1.5$
 $130 \leq F_L^{in} \leq 340$
 $523.15 \leq T_{out} \leq 548.15$

With VT =valve travel [%]; F_L^{in} =total return volumetric flowrate of HTF to fired heater [m³/h]; T_{out} =HTF supply temperature [K]; η_P =pump efficiency=0.75; η_M =motor efficiency=0.85; c_F =fuel cost=6.161 · 10⁻⁹ [\$/J]; c_E =cost of electric power=0.32 [\$/kWh]; g =acceleration due to gravity [m/s²]; H_P =pump head=51 [m]; t_r =pump runtime per day [h]; ρ =average density of the fluid=735.16 [kg/m³]. The lower heating value of the flue gas, LHV_F was considered equal to 46,890 kJ/kg.

Table 2: Parameters for the sections of the heater.

Parameter	Radiant section	Shield section	Convection section
σ , [W/m ² K ⁴]	5.7604 · 10 ⁻⁸	5.7604 · 10 ⁻⁸	-
D_i , [m]	0.1023	0.1023	0.1023
D_o , [m]	0.1143	0.1143	-
Equivalent cold plane area, [m ²]	217.88	33.27	-
Overall exchange factor, F	0.590	0.559	-
Reference temperature, T_{ref} [K]	298.15	298.15	298.15
$Q_{MaxHR-MB}$, [W]	1,472,682	-	-
$Q_{MaxHR-PB}$, [W]	29,307	-	-
Mass per unit length of radiant tube coil, [kg/m]	16.07	16.07	20.5

4. Results and discussion

A plot of HTF temperature versus the axial position and time in the CS, SS, and RS, are illustrated in Figures 3-5, respectively. An overall temperature profile for the HTF is shown in Figure 6.

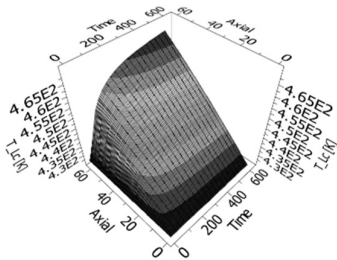


Figure 3: HTF temperature in the CS

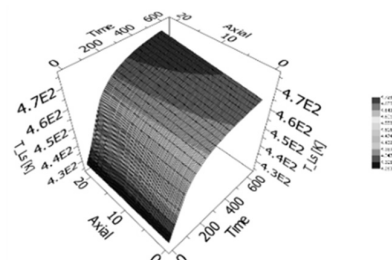


Figure 4: HTF temperature in the

Table 3 shows a summary of the simulation results compared with measured data from the plant. A base case scenario is considered where the daily operating cost is 1,599.81 \$/day, based on a flow of fuel gas of 0.632 kg/s, a HTF return volumetric flow rate of 139.5 m³/h, and a total operating number of burners of 8. The optimisation using the model in gPROMS[®] resulted in an operating cost of \$776.18 \$/day, which equals to

283,305.70 \$/year. Overall, this translates into savings of about \$360,625 \$/year compared with the base case scenario. In percentage terms, savings of about 51.48% could be achieved.

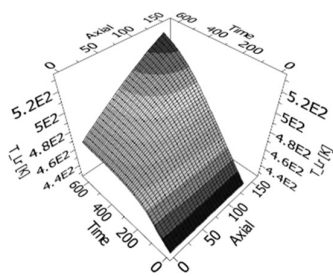


Figure 5: HTF temperature in the RS

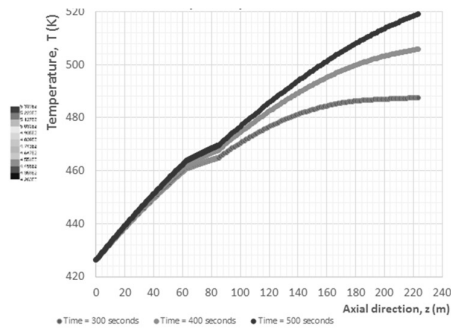


Figure 6: HTF temperature in H600

Table 3: Simulation results at 380 seconds.

Parameter	Predicted	Measured	%Error
Valve travel, VT [%]	50	37.45	-33.51
HTF Supply temperature, T_{out} [K]	505.58	523.95	3.51
Flue gas temperature, T_{Gr} [K]	647.19	758.7	14.7
Average radiant tube wall temperature, [K]	511.84	544.47	5.99
Flue gas temperature at exit of CS, [K]	546.13	520.50	-4.92

For a simulation time of 786 seconds, the optimum supply temperature is identified at 548.4 K. These results demonstrate how a model-based process systems approach can be deployed to achieve optimal operation of the fired heater. However, a more comprehensive study, with a validated model must be carried out before optimal operating conditions can be clearly identified.

5. Conclusions

The simulation results of the heater model indicate that the distributed parameter dynamic model proposed in this work closely approximates the actual process behaviour under varied operating conditions. Potential for significant annual savings have been identified. Furthermore, a parameter estimation and model validation should be performed to ensure good agreement between the model predictions and the actual behaviour of H600.

References

- [1]. H.L. Berman, Fired Heaters, Chemical Engineering, 1978; [2]. J. Baukal, E. Charles, John Zink, 2013, Hamworthy Combustion Handbook – Fundamentals, Vol.1, 2nd Edition, Taylor & Francis Group LLC; [3]. G. Ashbutosh, 1997, Optimise fired heater operations to save money, Hydrocarbon Processing; [4]. J.J. Valencia, P.N. Quested, 2008, Thermophysical properties, ASM Handbook, Vol. 15; [5]. V. Gnielinski, 1976, Int. Chem.Eng. 16, 359; [6]. P. Frank, D.P Dewitt, T.L. Bergman, A.S. Lavine, 2007, Introduction to Heat transfer, 5th Edition, John Wiley & Sons; [7]. R.K. Shah, E.C. Subbarao, R.A. Mashelkar, 1988, Heat transfer equipment design-Advanced Study Institute Book, Hemisphere Publishing Corporation; [8]. ISA Standard 75.01.01-2007 (IEC60534-2-1 Mod), 2007, Flow Equations for Sizing Control Valves

Molecular Modelling of Co-processing Biomass Pyrolysis Oil with Vacuum Gasoil in an Oil Refinery Fluid Catalytic Cracking Unit

Mohamed Al Jamri, Robin Smith, Jie Li *

Centre for Process Integration, School of Chemical Engineering and Analytical Science, The University of Manchester, Manchester M13 9PL, UK

Jie.li-2@manchester.ac.uk

Abstract

Integration of biomass resources in petroleum refining for sustainable production of transportation fuels has gained increased attention in the last few decades (IEA, 2013). One potential integration option is to mix biomass-based pyrolysis oil (BPO) with petroleum gas oil (VGO) and then co-process the blend in oil refinery fluidised catalytic cracking (FCC) units (Naik *et al.*, 2017). It is important to establish the prediction model of product yield and quality with such coprocessing in FCC units. In this work, a novel molecular-level modelling approach is proposed for kinetic modelling of co-processing BPO with VGO in an oil refinery FCC unit. Molecular-level characterisation of BPO and VGO blends using Molecular Type and Homologous Series matrix is first conducted. Then, a novel reaction network is synthesized and a reaction model is developed for the proposed reaction network which considers not only the complex intermolecular interactions between various types of molecular attributes in the feed, but also the interactions between individual molecules and catalyst surface. A hybrid optimisation strategy combining genetic algorithm with deterministic optimisation algorithm is developed to obtain the optimal parameters in the reaction model. The results demonstrate an overall good agreement between measured and predicted yields using the developed kinetic model for VGO: BPO blending ratio of 90:10, C/O ratio between 5 and 8, and reaction temperature of 525°C. PONA composition, oxygen compounds compositions and oxygen content in each product fraction such as gasoline, diesel and gas oil can also be predicted. The effect of different blending ratios of BPO and VGO on oxygenates compositions is demonstrated.

Keywords: Catalytic cracking, Fast pyrolysis oil, biomass, refinery, MTHS matrix.

1. Introduction

Integration of renewable biofuels into transportation sector is gaining increased attention. Several integration options (pyrolysis oil upgrading, fermentation, and gasification/F-T synthesis) have been proposed and investigated for biofuels production (Huber *et al.*, 2006; Petrus and Noordermeer, 2006; Vispute *et al.*, 2010; Serrano-Ruiz and Dumesic, 2011). Among these options, co-processing biomass pyrolysis oil (BPO) with heavy petroleum fractions such as vacuum gasoil (VGO) in the refinery fluid catalytic cracking (FCC) unit arises as a promising option. This is mainly due to the efficiency of pyrolysis processes in phase transformation (up to 70% liquid yield), as well as the low capital investment required as a result of using refinery's economy of scale (Wang *et al.*, 2016).

To evaluate and optimise this co-processing option, it is important to develop mathematical models for product yields and properties prediction in the FCC unit with

such co-processing of BPO and VGO. Although several approaches have been proposed for modelling of conventional FCC units (Feng *et al.*, 1993; Xu *et al.*, 2005; Gomez-Prado, 2009), only limited efforts have been reported for modelling of co-processing BPO with VGO in FCC units (Naik *et al.*, 2017). Conventional modelling approaches cannot be directly applied for modelling of co-processing option due to their inability to accurately characterise oxygenated molecules in the feedstock. Molecular-level characterisation and molecular-level reaction models can be used to overcome the limitations of the previously mentioned approaches. Such techniques are based on detailed description of the sizes and types of the various molecules present in process streams. A detailed molecular-level reaction network that takes into account the various interactions between the molecules themselves and the catalyst (if any) surface is employed to describe the chemical and physical changes that occur inside process units.

In this work, a novel molecular-level modelling approach is proposed for the modelling of co-processing BPO with VGO in an FCC unit. The proposed approach comprises molecular-level characterisation of blended feedstock using Molecular Type and Homologous Series (MTHS) matrix method, as well as molecular-level reaction network for catalytic cracking of hydrocarbons and oxygenated species found in blended feedstock. The proposed reaction network is tuned using a hybrid optimisation strategy combining Genetic Algorithm (GA) and Successive Quadratic Programming (SQP) to guarantee obtaining a reproducible solution in the vicinity of global optimum using a robust search method. The proposed approach is applied for the modelling of a pilot-scale FCC riser used for co-processing catalytic-pyrolysis-derived bio oil with VGO at a blending ratio of 10 wt.%. The results demonstrate an overall good agreement between measured and predicted yields using the developed kinetic model for VGO: BPO blending ratio of 90:10, C/O ratio between 5 and 8, and reaction temperature of 525°C. PONA composition, oxygen compounds compositions and oxygen content in each product fraction such as gasoline, diesel and gas oil can also be predicted. The effect of different blending ratios of BPO and VGO on oxygenates compositions is demonstrated.

2. Methodology

2.1 Process Stream Characterisation

The developed characterisation approach in this work provides detailed molecular-level information compatible with reaction models, efficiently and at low cost. In particular, the proposed method is based on Molecular Type and Homologous Series (MTHS) matrix which uses a 2-D matrix to capture the size and the type of the various molecules present in the stream, simultaneously (see Figure 1). The characterisation methodology used in this work is similar to the methodology presented in a previous work (Al Jamri *et al.*, 2018). The only difference is that in this work VGO and BPO are characterised independent from each other using two matrices. The two matrices are then blended according to the required blending ratio used in the feed stream to the process. In addition, the degrees of freedom (DOF) in the characterisation problem is reduced via introducing Volume Average Boiling Point (VABP) concept. This allowed to reduce the number of DOF from 3 to 2 for each hydrocarbon homologous series, which resulted in total reduction of DOF from 21 to 17 in the characterisation problem of VGO.

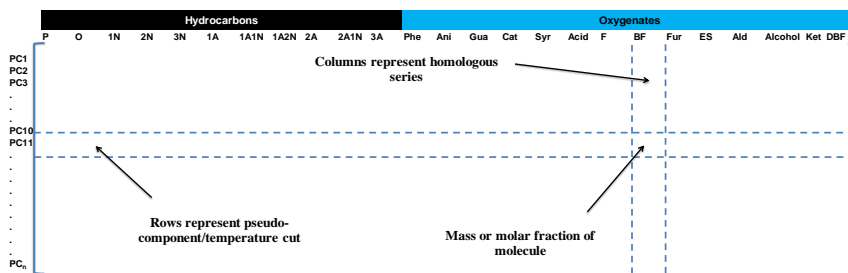


Figure 1 Proposed MTHS Representation Matrix for Characterisation of Mixed Stream

2.2 Reaction Network Modelling Methodology

Modelling of conventional catalytic cracking reaction network is a complex task. The complexity of this problem increases significantly when BPO oxygenated molecules are considered. This is mainly due to the limited information available in literature on bio oil molecules catalytic cracking pathways and kinetics compared to conventional hydrocarbon molecules usually found in petroleum streams. In addition, the already known kinetic behaviour of conventional petroleum fractions maybe affected when BPO is co-processed with VGO in a refinery FCC unit. Therefore, molecular-level reaction network is devised to quantify the effects of introducing oxygenated molecules on the kinetic behaviour of catalytic cracking reactions. The reaction network is synthesised by considering two different categories of molecules: hydrocarbons and oxygenates. Reaction pathways and kinetics for hydrocarbon molecules are deduced from previous work of Gómez-Prado (2009). Model compound studies for catalytic conversion of bio oil oxygenated molecules (Adjaye and Bakhshi, 1995a) are used for the synthesis of bio oil molecules catalytic cracking reaction network. The kinetic expressions and kinetic parameters values used to populate the kinetic network are taken from previous work (Adjaye and Bakhshi, 1995b).

The developed reaction network comprises 328 reaction terms, 299 of which are used for the description of hydrocarbons catalytic cracking reactions. The remaining 29 reactions are used for the representation of catalytic conversion of bio oil oxygenated molecules. The main feature of the proposed reaction network is its ability in predicting the composition of various hydrocarbons (PONA) and oxygenates (Phenolics, aldehydes and ketones, acids and esters, and alcohols) in each liquid product fraction, which can be used to satisfy industrial requirements in monitoring and controlling product quality. In addition, the proposed methodology avoids the need for kinetic parameters re-fitting when feedstock composition and/or blending ratio changes as a result of using molecular-level reaction network.

Kinetic parameters tuning problem is formulated as a non-linear optimisation problem. The objective function considers the absolute difference between measured ($Y_{L,OP}^{msd}$) and model-predicted ($Y_{L,OP}^{PRE}$) products' yields of each lump (L) and operating condition (OP) (see Eq. 1). Different weights (W_L) are used to give similar sizes for each difference between the different product yields.

$$Obj = \sum_{L,OP} W_L \sqrt{(Y_{L,OP}^{msd} - Y_{L,OP}^{PRE})^2} \quad \text{Eq. 1}$$

Kinetic parameters regression problem is solved using hybrid optimisation framework. Both stochastic and deterministic optimisation algorithm are employed in a unified framework (Figure 2). Initially, stochastic search methods (GA) is used to increase the chance of obtaining a solution in the vicinity of global optimum. The solution obtained from GA is fed to the deterministic algorithm (SQP) to improve the quality of the solution. This increases the chance of obtaining a reproducible solution in the vicinity of global optimum. The results obtained using this hybrid optimisation framework show good agreement between predicted and measured products' yields.

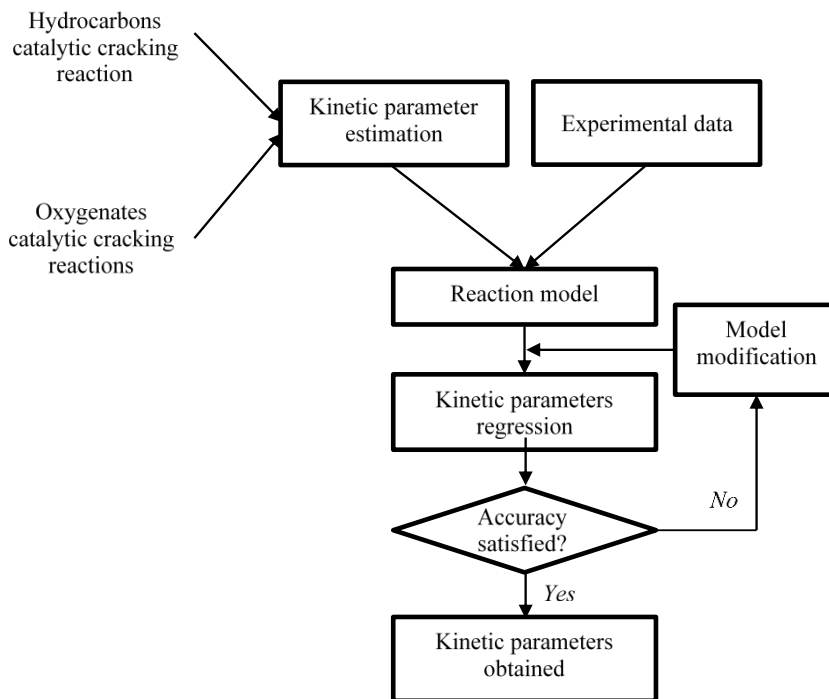


Figure 2 Kinetic Parameters Tuning Problem Solution Algorithm

3. Results and Discussion

The proposed characterisation approach has been tested in the characterisation of a blend of 90:10 VGO:BPO. This blend is used as a feedstock for pilot-plant scale FCC riser (Wang *et al.*, 2016). In this work, BPO stream is characterised independently from VGO. The two characterisation matrices obtained are combined together according to the specified blending ratio and fed to the reaction model. This way, blending ratio in the reaction model can be varied without the need to re-characterise the blended stream. Figure 3A shows the values of relative error when measured bulk properties of VGO are compared to model-predicted values. A maximum error of 5% was found in the prediction of molecular weight (MW) and aniline point (AP). Figure 3B shows a comparison between measured and predicted boiling curve of BPO.

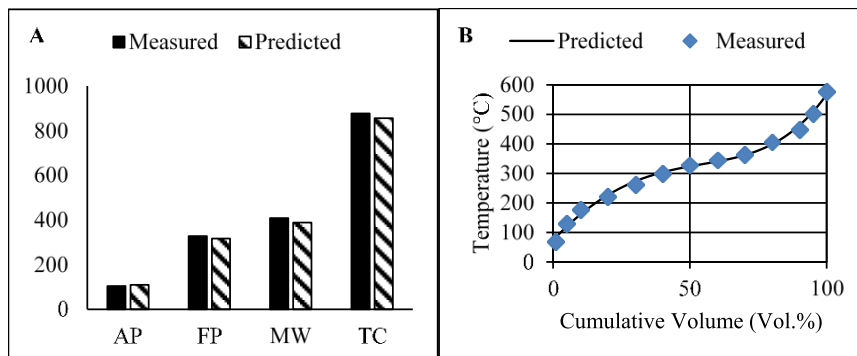


Figure 3 VGO and BPO characterisation results

The compositional matrix obtained is fed to the reaction model, and kinetic parameters tuning is carried out using the proposed hybrid optimisation framework. The results obtained are shown in Figure 4. The value of index of correlation (R^2) for this fitting is found to be 0.933, which indicates good correlation with measured data.

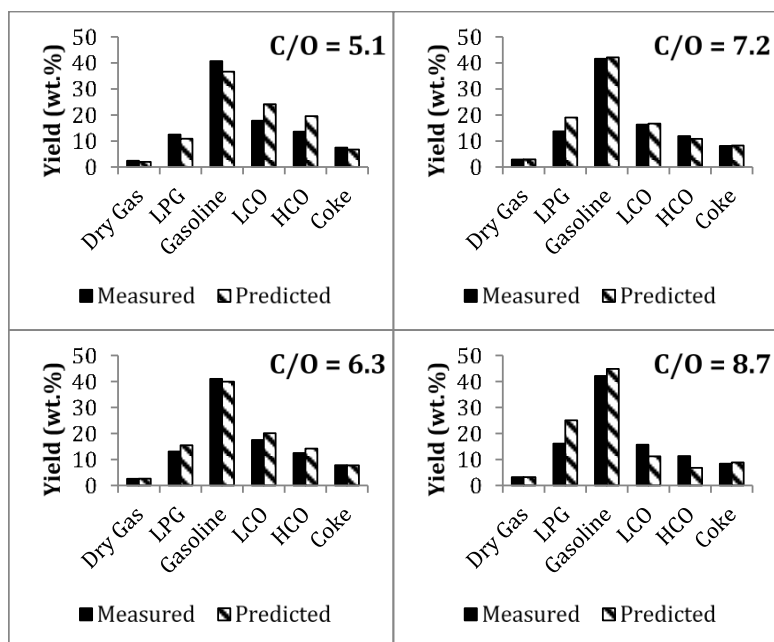


Figure 4 Comparison between Measured and Predicted Yields at different C/O ratio

The novelty of the proposed modelling approach lies in the ability of the developed modelling framework in predicting PONA and oxygenates yields at different blending ratios. Figure 5 shows oxygenates yields in heavy gasoline fractions as a function of blending ratio.

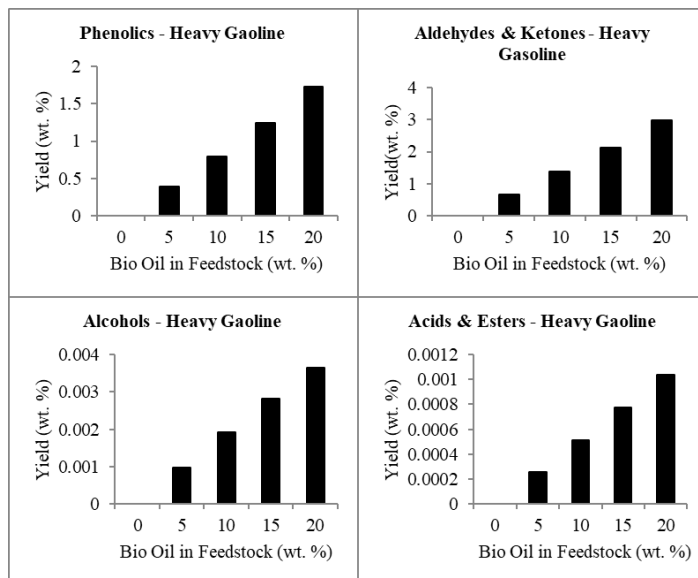


Figure 5 Oxygenates Yields in Heavy Gasoline Fraction at different Blending Ratio

4. Conclusions

A novel approach for molecular-level modelling of co-processing BPO with VGO in an FCC unit is proposed. The methodology comprises a novel characterisation framework in which bulk properties are converted to molecular information using optimisation-based modelling approach. A novel molecular-level reaction network comprising 328 reactions is proposed and used for the modelling of pilot-plant scale FCC riser. The results obtained showed good accuracy when compared to experimentally measured data. The model exhibits ability in predicting the various molecular attributes (hydrocarbons and oxygenates) at different blending ratios.

References

- Adjaye, J. D. and Bakhshi, N. N. (1995a), *Biomass and Bioenergy*, 8(4), pp. 265–277.
- Adjaye, J. D. and Bakhshi, N. N. (1995b), *Fuel Processing Technology*, 45(3), pp. 185–202.
- Feng, W., Vynckier, E. and Froment, G. F. (1993), *Industrial & Engineering Chemistry Research*, 32(12), pp. 2997–3005.
- Gomez-Prado, J. (2009). University of Manchester.
- Huber, G. W., Iborra, S. and Corma, A. (2006), *Chemical Reviews*, 106(9), pp. 4044–4098.
- IEA (2013) *World Energy Outlook 2013*.
- Al Jamri, M., Smith, R. and Li, J. (2018) *28th European Symposium on Computer Aided Process Engineering*. Elsevier (Computer Aided Chemical Engineering), pp. 1439–1444.
- Naik, D. V et al. (2017), *Chemical Engineering Science*, 170, pp. 790–798.
- Petrus, L. and Noordermeer, M. A. (2006), *Green Chem*. The Royal Society of Chemistry, 8(10), pp. 861–867.
- Serrano-Ruiz, J. C. and Dumesic, J. A. (2011), *Energy Environ. Sci*. The Royal Society of Chemistry, 4(1), pp. 83–99.
- Vispute, T. P. et al. (2010), *Science*. American Association for the Advancement of Science, 330(6008), pp. 1222–1227.
- Wang, C., Li, M. and Fang, Y. (2016), *Industrial & Engineering Chemistry Research*, 55(12), pp. 3525–3534.
- Xu, C. et al. (2005), *Fuel*, 84(6), pp. 669–674.

A Chance-Constrained Nonlinear Programming Approach for Equipment Design Under Uncertainty

Javier Tovar-Facio,^a Yankai Cao,^b José M. Ponce-Ortega,^{a*} Victor M. Zavala,^b

^a*Department of Chemical Engineering, Universidad Michoacana de San Nicolás de Hidalgo, Francisco J. Mugica S/N, Morelia 58030, Mexico*

^b*Department of Chemical and Biological Engineering, University of Wisconsin-Madison, 1414 Engineering Dr, Madison 53706, USA*

jmponce@umich.mx

Abstract

In this work there are shown different strategies to cope uncertainty in large-scale chance-constrained nonlinear programs. We present the design of a flare system as a case study. The design of this system is influenced by several uncertain factors, such as the volume and composition of the waste flow stream to be combusted and the ambient conditions. These systems are currently designed based on typical historical values for waste fuel gases and ambient conditions. Consequently, an improperly designed flare can be susceptible to extreme events previously not experienced. Particularly, we use moment matching (MM) when the algebraic form of the moments and the quantile function of the chance constrained (CC) distribution is known, and for more general settings when the distribution cannot be predicted we use the scenario approach (AS), the popular conditional value at risk (CVaR) and the recently proposed sigmoid value at risk (SigVaR). We demonstrate that the SigVaR approximation offers the best results and this approach overcome the conservative results of the AS and CVaR.

Keywords: Uncertainty, design, sigmoid conditional value at risk, flares.

1. Introduction

We study the chance-constrained nonlinear program:

$$\min_{d \in D} \varphi(d) \tag{1a}$$

Subject to

$$\mathbb{P}(f(d, \Xi) \leq \bar{f}) \geq 1 - \alpha \tag{1b}$$

We review exact approaches to handle chance constrained problems (CC-P). We consider the special case in which the algebraic form of the quantile function is known or approximately known, and we propose to use moment matching to compute its parameters. However, there are some cases where the nonlinear chance constrained problems are particularly difficult to solve because nonlinear propagation makes it hard to obtain the distribution of output variables (this case will be analysed in a future work).

To handle more general settings, we consider the use of three different approximations. The first one is the scenario approximation, in this approach we approximate the chance constrain ensuring that the constrain is satisfied for each scenario or with probability of 1, and this implies that the constraint is satisfied for any probability different to one. This is extremely conservative; nevertheless, it let us express the chance constrain using the standard scenario-based stochastic programming formulation. The second approximation is the conditional value at risk, this approximation enables expressing our problem as a common nonlinear optimization problem, but CVaR can be slightly conservative. Moreover, the CVaR approximation does not offer a mechanism to enforce convergence to a solution of CC. The third approximation is the sigmoid value at risk approximation (Cao and Zavala, 2018), which provides a mechanism to determine exact solutions for CC-P.

2. Flare systems

Gas flares are used as safety (relief) devices that are used all over the world to manage abnormal situations in infrastructure systems (natural gas and oil processing plants and pipelines), manufacturing facilities (chemical plants, offshore rigs), and power generation facilities. Abnormal situations include equipment failures, off-specification products, and excess materials in start-up/shutdown procedures. In particular, flares prevent over pressurization of equipment and use combustion to convert flammable, toxic or corrosive vapors to less-dangerous compounds (Sorrels et al., 2017). A proper design of flare systems is vitally important due to it is influenced by several uncertain factors, such as the amount and composition of the waste fuel gases to be combusted and the ambient conditions like wind velocity. An improperly designed flare can be susceptible to extreme events previously not experienced or have as a result an oversized and expensive equipment. Here, it is proposed to use stochastic programming formulations to systematically capture uncertain conditions in the design procedure.

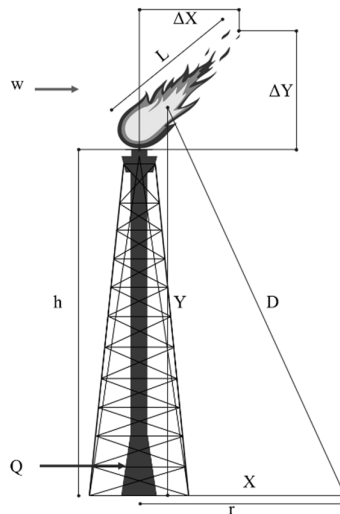


Figure 1. Flare system generic diagram.

3. Physical model

It was formulated a mathematical model for sizing a flare system (see Figure 1). The design goals are to minimize the equipment cost while controlling the thermal radiation level at ground level. It was based on the American Petroleum Institute standard 521 as follows:

The heat released by combustion H (BTU/h) is a function of the random input waste flow Q (lb/h) and the heat of combustion h_c (BTU/lb):

$$H = h_c Q \quad (1)$$

The flame length L (ft) can be calculated as a function of the released heat using an approximation of the form:

$$\log L = a_1 \log H - a_2 \quad (2)$$

The wind speed w (ft/s) is an important environmental factor that affects the tilting of the flame and the distance from the center of the flame. The following correlations capture the flame distortion as a result of the wind speed and the exit velocity:

$$\log \Delta X = \log(a_5 L) + a_6 (\log w - \log U) \quad (3)$$

$$\log \Delta Y = \log(a_7 L) - a_8 (\log w - \log U) \quad (4)$$

The flare stack diameter t (ft) is sized on a velocity basis. This is done by relating this to the Mach number M and the waste flow as:

$$M^2 = \left(\frac{a_3}{t^2} \right) Q^2 \quad (5)$$

The flare tip exit velocity U (ft/s) is function of the flow and the diameter:

$$U = a_4 \frac{Q}{t^2} \quad (6)$$

Here, ΔX and ΔY (ft) are the horizontal and vertical distortions. The distortions are used to compute the horizontal X , vertical Y , and total distance D (ft) to a given ground-level safe point $(r,0)$ as:

$$X = r - \left(\frac{1}{2} \right) \Delta X \quad (7)$$

$$Y = h + \left(\frac{1}{2}\right)\Delta Y \quad (8)$$

$$D^2 = X^2 + Y^2 \quad (9)$$

Here, h (ft) is the flare height. The flame radiation K (BTU/h ft²) is a function of the heat released and the total distance:

$$K = a_9 \left(\frac{H}{D^2} \right) \quad (10)$$

A primary safety goal in the flare stack design problem is to control the risk that the radiation exceeds a certain threshold value \bar{k} (BTU/h ft²) at the ground-level reference point $(r,0)$. This is modelled using the CC:

$$\mathbb{P}(K \leq \bar{k}) \geq 1 - \alpha \quad (11)$$

The objective function is the cost (USD), which is a function of height and diameter:

$$\varphi(t, h) = (a_{10} + a_{11} t + a_{12} h)^2 \quad (12)$$

The height and the diameter play a key role in controlling the radiation at the reference point (i.e., a higher and wider flare reduces the radiation intensity). As a result, there is an inherent trade-off between capital cost and safety that must be carefully handled.

4. Case study

The design was considered of a flare stack that combusts a waste fuel gas flow, Q (see Figure 1). The goal is to design a flare system that minimizes cost and satisfies CC on the thermal radiation using the AS, CVaR, SigVaR, and MM approaches. In this work, the case is presented in which the input flow to the flare stack follows a log-normal distribution (with mean $a = 10,000$ lb/h and standard deviation $b = 3,000$ lb/h to exemplify a distribution with isolated events). All formulations were solved using 1000 random samples for the inlet flow (see Figure 2). The flare design must satisfy a CC on the radiation with a maximum threshold (\bar{k}) of 2,000 BTU/h ft² and with a probability $1 - \alpha = 0.95$. The optimization formulation is an NLP with 9,005 variables that was implemented using the open-source modelling language JuMP (Bezanson et al., 2017) and solved with Ipopt (Wächter and Biegler, 2006).

5. Results

Table 1 presents the optimal cost, diameter, and height for the flare system under the used approaches. The results show that the design of the AS approximation is the most conservative. The design is 64% more expensive than the MM design. This is since the

AS approach does not allow for explicit control of the probability of constraint satisfaction. The CVaR approximation reduces this highly conservatism, but it considerably overdesigns the flare stack. The optimal height obtained with CVaR is 67.70% larger and 20% more expensive than those obtained with MM; therefore, CVaR approximation reduces the extreme conservatism of the AS, but it still overdesigned. Table 1 also presents that the optimal solution of SigVaR and MM are very close. The SigVaR design is only 1% more expensive than the MM approach, and that let to highlight the fact that the SigVaR solution is rightly conservative.

Table 1. Optimal Values for Design Variables

	AS	CVaR	SigVaR	MM
Cost (USD)	233,179	172,329	143,609	142,128
Diameter (ft)	1.70	1.70	1.70	1.70
Height (ft)	179.87	105.08	65.16	63.00

Figure 2 shows the empirical PDFs for the input flow and for the radiation at the optimal solution of the CVaR, SigVaR, and MM approaches. First, it is observed that, for the MM approach, the distribution of the radiation is indeed log-normal. This indicates that the structure of the flare model preserves the log-normal shape of the input flow. It is also observed that the histograms of SigVaR and MM are quite similar, with SigVaR being slightly more conservative. In particular, the tail of the SigVaR distribution is very similar to that of MM (the tail reaches values of 6,000 BTU/h ft² for SigVaR, compared to 6,100 BTU/h ft² with MM). The histogram of CVaR further validates the observation that this approach is very conservative (the tail reaches values of 4,000 BTU/h ft²)

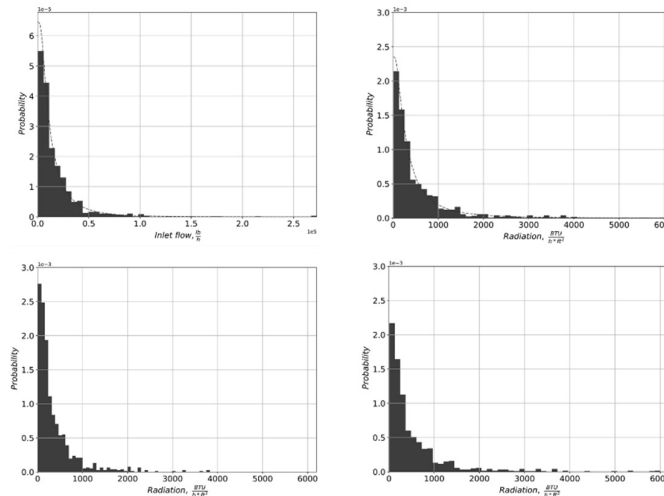


Figure 2. (Top-left) Inlet flow PDF, (top-right) radiation PDF using MM, (bottom-left) radiation PDF using CVaR, and (bottom-right) radiation PDF using SigVaR.

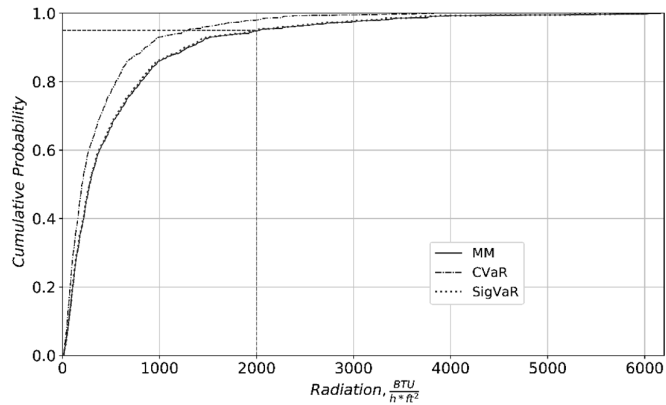


Figure 3. Radiation CDFs using MM, CVaR and SigVaR.

Figure 3 compares the optimal radiation CDFs obtained with CVaR, SigVaR, and MM. It can be seen again that CVaR is very conservative, achieving probability levels for the chance constraint of 98–99% (when 95% is only required). Also, the CDFs for SigVaR and MM overlap for the log-normal case, reinforcing that SigVaR provides good quality approximations and that the distribution of the radiation is indeed log-normal and thus MM is a good approach to solve the problem.

6. Conclusions

An application of moment matching techniques was presented to reformulate chance constraints when the shape of the underlying density function is known. It was also demonstrated the use of conservative approximations, that can be applied to more general setting in which the shape of the density function is unknown. A flare system design study showed that a sigmoid approximation overcomes the conservativeness of the popular conditional value-at-risk and scenario approaches, and it can be an excellent alternative when moment matching is not applicable. The proposed approaches enable the solution of large-scale NLPs with chance constraints.

References

- J. Sorrels, J. Coburn, K. Bradley, and D. Randall, 2017, Air Pollution Control Cost Manual, United States Environmental Protection Agency: Washington, DC.
- American Petroleum Institute (API), 1997. Recommended Practice 521, Guide for Pressure Relieving and Depressuring Systems.
- Y. Cao and V. Zavala, 2018, A sigmoidal approximation for chance-constrained nonlinear programs. Under review (see the following URL: <http://zavalab.engr.wisc.edu/publications/journalpubs/sigvar.pdf?attredirects=0>).
- J. Bezanson, A. Edelman, S. Karpinski, V. Shah, 2017, Julia: A fresh approach to numerical computing. *SIAM Rev*, 59, 65 – 98.
- A. Wächter and L. Biegler, 2006, On the implementation of a primal-dual interior point filter line search algorithm for large-scale nonlinear programming, *Math. Program.*, 106, 25 – 57.

Involving the Water-Energy-Food Nexus in Integrating Low-Income and Isolated Communities

Brenda Cansino-Loeza^a, J. Betzabe González-Campos^b, José María Ponce-Ortega^{a*}

^a *Chemical Engineering Department, Universidad Michoacana de San Nicolás de Hidalgo, Francisco J. Múgica S/N, Ciudad Universitaria, 58060, Morelia, Michoacán, México.*

^b *Institute for Chemical and Biological Research, Universidad Michoacana de San Nicolás de Hidalgo, Morelia, Michoacán 58060, Mexico.*

jmponce@umich.mx

Abstract

This work presents a general mathematical programming model for satisfying water, energy and food needs in isolated and low-income communities involving different process integration approaches. The problem consists in determining the optimal and sustainable configuration to satisfy the energy, water and food demands. Also, the use of waste-to-energy technologies is proposed aiming to obtain valued products from wastes to reduce the environmental impact. A multi-objective analysis is presented considering the consumption of fresh water, the greenhouse gas emissions and the cost of the integrated system as objective functions. As case study, the community with the lowest index of poverty and marginalization from the State of Guerrero in Mexico is presented. The results show that it is possible to satisfy the water, energy and food needs in isolated communities accounting for integrated processes.

Keywords: Water-Energy-Food Nexus, Isolated community, Polygeneration, Optimization, Process integration.

1. Introduction

Water, energy and food are critical resources for meeting the social demands and socioeconomic development of communities and societies around the world (Fuentes-Cortés and Ponce Ortega, 2017). Nevertheless, there are communities that do not have access to energy and, consequently, there is a lack of access to water and food. Many rural communities or small towns still do not have access to these resources mainly due to their geographic location that makes difficult the interconnection with the electrical grid (Sánchez et al., 2015). Moreover, the provision of water from the public network is a big problem. Satisfying the basic needs of inhabitants in isolated communities is a problem that is closely related to the water-energy-food nexus due to the inhabitants consume considerable amounts of resources to meet their demands (Martínez-Guido et al., 2017). Water, energy and food are inextricably interrelated and each of them depends on others (Zhang and Vesselinov, 2017). The water-energy-food nexus is considered to achieve a sustainable development that allows maintaining the security of these resources and promote economic growth without affecting the environment considerably. However, the inadequate management of these resources may also

produce significant environmental impacts. Currently, alternative energy sources have been used to decrease the environmental impact. Also, there have been reported several studies related to the use of renewable energies implemented in isolated communities to generate electric energy (Ahadi et al., 2016). Furthermore, other researches have focused on distributed generation to produce electricity in remote places by isolated systems due to the generation units are close to the consumers and the transmission energy losses are negligible; examples of this type of generation are polygeneration systems, which can be defined as the simultaneous production of two or more energy utilities and products, seeking to take advantage of the maximum potential of the consumed resources. It has been demonstrated that polygeneration systems reduce fuel consumption, operational costs and consequently reduce the environmental impact, which is associated to the greenhouse gas emissions. There are many studies that propose the use of different schemes of distributed generation to meet the energy demands at a household level. Other researches have been focused on integrating different processes to take advantage of the available resources in residential complexes (Nuñez-López et al., 2018). Nevertheless, none of the previous mentioned works have considered the water-energy-food nexus involving a polygeneration system that allows to decrease the use of fresh resources and the environmental impact in an isolated community.

Another important challenge to decrease the environmental impact is planning a sustainable waste management system. In this context, Diaz-Barriga-Fernandez et al. (2017) proposed a multi-objective optimization approach for the strategic planning of a municipal solid waste management system considering recycle, reuse, transportation, separation and distribution of solid wastes. The management of municipal solid waste has been identified as one of the global challenges that must be carefully faced to achieve sustainable goals, recent researches have focused on proposing processes that convert waste-to-energy or valuated products. Matsakas et al. (2018) investigated the conversion of municipal solid waste to energy and chemicals by biological and thermochemical treatments that are among the most used technologies.

However, none of the previous researches has focused on studying different types of solid waste treatments in a low-income municipality to be a community in which their needs can be met through the proper management of their resources and recycled wastes. In addition, no research has been conducted to address the integration of water-energy-food nexus and the management of solid wastes in isolated communities, which can help to reduce the environmental impact and improve the living conditions of the inhabitants. Faced with this problem, it is needed to implement a system capable of integrating the energy-water-food nexus so that the needs of the inhabitants of the isolated community can be met. In this context, a polygeneration system is an attractive option to provide electricity, heating and cooling to the community, satisfying the energy demands making proper management of water and the resources which in turn will facilitate the food production and consequently the access to food.

2. Problem Statement

This work presents a mathematical programming model for the design of a residential polygeneration system in an isolated community considering the water-energy-food nexus (Figure 1). The problem consists in determining the optimal and sustainable configuration to satisfy the energy, water and food demands of the inhabitants. To meet energy demands, the existence of different cogeneration units such as Internal

Combustion Engines, Fuel Cells, Microturbines and Stirling Engines were contemplated. In addition, there was considered the use of renewable energies such as solar collectors, aerogenerators and solar panels to help to satisfy the energy demands of the community. Water demand was satisfied by rainwater collection systems and wells, it was proposed the use of rainwater collection systems for provide water in the community, agriculture activities, cattle activities and gardening. Wastewater generated in the community was sent to blackwater and greywater treatment plants. The treated greywater was used in gardening, cattle and agriculture. Different types of crops and animal production were considered to satisfy the food demands of the inhabitants. The agriculture activities involve the production of peanut, jicama, corn, lemon, mango, papaya, and sorghum, and the livestock activities are related to the bovine, porcine, ovine, goat and bird production. On the other hand, the generated municipal solid wastes are separated in plastic, metal, paper, glass and non-recyclables, the latter can be treated in process plants such as pelletization, incineration, gasification, pyrolysis and anaerobic digestion to obtain pellets, steam, natural gas and pyrolysis oil that can be used as an energy source or can be sold.

The objective functions of the problem are to minimize the consumption of fresh water, the greenhouse gas emissions and the cost (Eq. (1)).

$$OF = \{ \min Cost; \min Water; \min GHGE \} \quad (1)$$

The economic objective function (*Cost*) considers the minimization of the total annual cost associated to satisfy the needs of the community, which includes operating and capital costs for each needed unit and the sales associated with animals, crops, pyrolysis oil, natural gas, biogas, pellets and recyclable products. Additionally, the environmental objective function involves the minimization of fresh water consumption (*Water*) and the minimization of greenhouse gas emissions (*GHGE*) produced by the cogeneration units and the process plants for non-recyclable wastes. To solve this problem, in this paper is proposed the superstructure shown in Figure 1 to satisfy the demand.

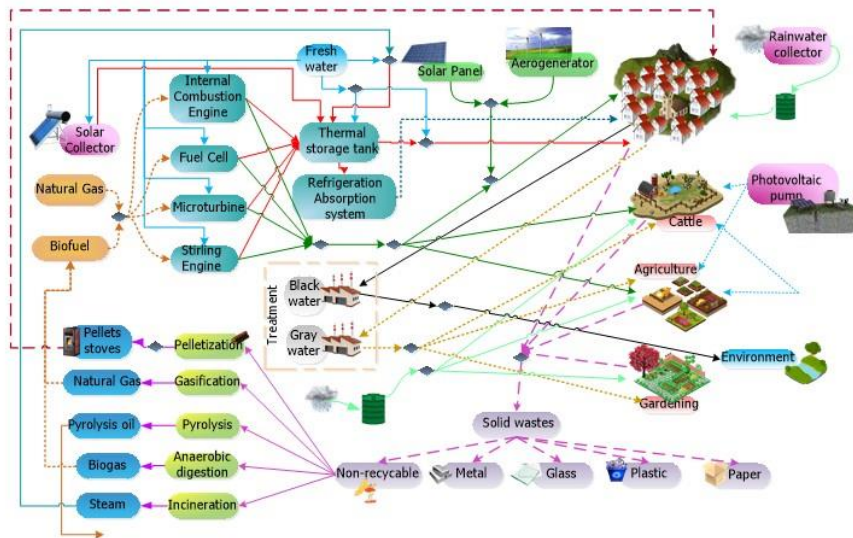


Figure 1. Proposed superstructure.

3. Case Study

There is considered the community of “Cochoapa el Grande”, located in the State of Guerrero in Mexico with coordinates 17° 12' N 98° 27' O as case study, this community has been listed as the municipality with the highest index of poverty and marginalization in the country, mainly due to its geographical location which coincides with a mountainous zone called “Sierra Madre del Sur”. The difficult access to the community as well as the irregular distribution of their localities causes that the water supply of the public network represents a severe problem and consequently agricultural and livestock activities are affected. Therefore, there is difficult access to food. Likewise, there is a lack of electric power, affecting the provision of services that are essential for human, social and economic development. Faced with this problem, there is proposed a polygeneration system capable of integrate energy, water and food demands of this isolated community.

4. Results

The proposed model corresponds to a Mixed-Integer Linear Programming problem and it was implemented in the software GAMS. The mathematical model consists of 3,138 continuous variables, 21 binary variables and 1,561 equations. The points obtained from the functions to minimize water consumption, greenhouse gas emissions and cost are shown in Table 1.

Table 1. Results obtained for each scenario evaluated.

	Min Water	Min GHGE	Min Cost
Cost (\$)	161,000,000	161,000,000	-27,903,000
Water (m ³ /y)	3,060,000	3,088,500	3,178,700
GHGE (t CO ₂ /y)	147,400,000	12,790,000	900,200,000

For the evaluated scenarios, water consumption does not vary significantly between the different solutions. If we compare the minimum consumption of fresh water scenario and the minimum cost scenario, which represents the highest consumption of fresh water, this only increase approximately 4 %. The selected cogeneration technologies for the case of minimizing the consumption of fresh water are represented by a Microturbine, a Fuel Cell and a Stirling Engine, while in the case of minimizing emissions a Fuel Cell is proposed, and in the case of minimizing costs the selected technology was the Microturbine. The case for minimizing the emissions selects the Fuel Cell for power generation. In the case of minimum consumption of fresh water, fuel requirements increase by 28 %. On the other hand, in the case of minimizing costs, 46 % more fuel is required than in the case of minimizing emissions, which causes a greater generation of greenhouse gases. For solid waste management, the processing plants selected in the scenario of minimizing emissions are the pelletization and pyrolysis plants. In the case of minimum consumption of fresh water, the pelletization, pyrolysis and incineration plants are selected, which represents a considerably increase in the GHGE and, in the case of minimizing costs, gasification, incineration and pelletization plants are selected.

Table 2. Results for the multi-stakeholder analysis.

Case	Stakeholder weights			Objectives			% Dis
	COST (\$U.S./y)	WATER (m ³ /y)	GHGE (t CO ₂ /y)	COST (\$U.S./y)	WATER (m ³ /y)	GHGE (t CO ₂ /y)	% Dis
1	4	3	3	-24,770,000	3,063,700	96,820,000	4.75
2	3	4	3	-24,770,000	3,063,700	96,820,000	4.75
3	3	3	4	-24,770,000	3,063,700	96,820,000	4.75
4	2	7	1	-15,080,000	3,060,000	96,820,000	5.42
5	1	2	7	-14,950,000	3,084,100	21,580,000	9.38
6	7	1	2	-26,990,000	3,070,400	96,820,000	6.24
7	8	1	1	-26,990,000	3,070,400	96,820,000	6.24
8	1	8	1	-15,080,000	3,060,000	96,820,000	5.42
9	1	1	8	-24,660,000	3,094,200	12,790,000	10.18

Due to the conditions of the community and because of the lack of processes to generate energy and manage the resources, very high costs are presented, which lead to an exponential increase in greenhouse gas emissions, as well as an increase in the use of water. This can be attributed to the fact that in the case of minimizing costs, it is sought to obtain the maximum production of animals and crops for sale. In the same way, the gasification and pyrolysis plants are selected to make use of the natural gas generated in the gasification plant and thereby reduce the cost associated with the purchase of natural gas and obtain profits from the sale of pyrolysis oil.

Because the objectives are in conflict, the methodology of Multi-stakeholder Optimization is used in this work with the purpose of finding a balance between the objective functions and giving feasible solutions to the problem. In addition, a dissatisfaction analysis is included in each of the proposed feasible solutions. The dissatisfaction of each of the objective functions, as well as the total dissatisfaction for each of the scenarios is presented in Table 2. There were randomly generated weights and it was calculated the percentage of dissatisfaction.

The results obtained in general show that in cases where the objective has a greater weight in the GHGE objective present a greater percentage of dissatisfaction. Moreover, it is possible to obtain better results in cases where the weights are distributed between the three objectives, as Cases 1, 2 and 3, with 4.5% of dissatisfaction, which is the lowest percentage of dissatisfaction of all the evaluated feasible solutions.

5. Conclusions

This paper has presented a multi-objective optimization approach for the optimal design of a polygeneration system applied in a low-income and isolated community. The proposed model is capable to determine the optimal configuration of technologies that meet the demands of water, energy and food of the community accounting for economic and environmental objectives. There were evaluated different scenarios for the

minimum cost of the integrated system, the minimum fresh water consumption and the minimum greenhouse gas emissions generated. To trade-off the proposed objectives, it is presented a multi-stakeholder approach which is capable to find the compromise solution which is the point where the objectives are minimized simultaneously. As case study, it was considered the community of Cochoapa el Grande, which is the community with the lowest human development index of Mexico. There were generated different feasible solutions and it was evaluated the dissatisfaction percentage of each one. The results show that the compromise solution is very close of the Utopian Point, which indicates that is possible to obtain a solution that satisfies almost entirely the minimum of the objectives. It should be noticed that in the generated feasible solutions the dissatisfaction increases when it is assigned a major priority to the GHGE objective. On the other hand, the lowest percentage of dissatisfaction corresponds to the cases in which the priorities are distributed between the three objectives.

6. Nomenclature

<i>OF</i>	Objective functions
<i>GHGE</i>	Greenhouse gas emissions

References

- A. Ahadi, S.K. Kang, J.H. Lee, 2016, A novel approach for optimal combinations of wind, PV, and energy storage system in diesel-free isolated communities. *Applied Energy*, 170, 101-115.
- A.D. Diaz-Barriga-Fernandez, J.E. Santibañez-Aguilar, N. Radwan, F. Nápoles-Rivera, M.M. El-Halwagi, J.M. Ponce-Ortega, 2017, Strategic planning for managing municipal solid wastes with consideration of multiple stakeholders. *ACS Sustainable Chemistry and Engineering*, 5(11), 10744-10762.
- L.F. Fuentes-Cortés, J.M. Ponce-Ortega, 2017, Optimal design of energy and water supply systems for low-income communities involving multiple-objectives. *Energy Conversion and Management*, 151, 43-52.
- J.M. Núñez-López, E. Villicaña-García, B. Cansino-Loeza, E. Rubio-Castro, J.M. Ponce-Ortega, 2018, Involving acceptability in the optimal design of total integrated residential complexes involving the water-energy-waste nexus. *ACS Sustainable Chemistry and Engineering*, 6(6), 7390-7402.
- S.I. Martínez-Guido, J.B. González-Campos, M.M. El-Halwagi, J.M. Ponce-Ortega, 2017, Sustainable optimization of food networks in disenfranchised communities. *ACS Sustainable Chemistry and Engineering*, 5(10), 8895-8907.
- L. Matsakas, Q. Gao, S. Jansson, U. Rova, P. Christakopoulos, 2017, Green conversion of municipal solid wastes into fuels and chemicals. *Electronic Journal of Biotechnology*, 26, 69-83.
- A.S. Sánchez, E.A. Torres, R.A. Kalid, 2015, Renewable energy generation for the rural electrification of isolated communities in the Amazon Region. *Renewable Sustainable Energy Reviews*, 49, 278-290.
- X. Zhang, V.V. Vesselinov, 2017, Integrated modeling approach for optimal management of water, energy and food security nexus. *Advances in Water Resources*, 101, 1-10.

Sustainable Strategic Planning for a National Natural Gas Energy System Accounting for Unconventional Sources

Esbeydi Villicaña-García,^a J. Betzabe González-Campos,^a José María Ponce-Ortega^{a,*}

^aChemical Engineering Department, Universidad Michoacana de San Nicolás de Hidalgo, Av. Francisco J. Múgica S/N, Ciudad Universitaria, Edificio VI, Morelia, Michoacán, 58060, México

jmponce@umich.mx

Abstract

This work presents an optimization model for the strategic planning to satisfy the national demands of natural gas considering unconventional extraction such as shale gas and offshore extraction and conventional ways to produce associated and non-associated natural gas using enhanced gas recovery systems, as well as importation. The model incorporates a multi-objective optimization strategy to obtain trade-offs between economic, environmental and health issues.

A case study from Mexico is presented to show the applicability of the proposed approach to satisfy the increasing national demand of natural gas through different extraction ways. Furthermore, in the presented study, economic, environmental and health factors were evaluated to select the best option. The economic factors consider costs associated with the production and treatment of natural gas, the used fresh water and the costs that involve the transportation of natural gas from its point of extraction to final markets. Regarding to the environmental impact, the fresh water consumption and CO₂ emissions are considered. The occupational health of the involved processes in the production of natural gas is also evaluated, this because workers are continuously exposed to hazardous substances that can cause long-term damage. Results show that it is possible to decrease imports to satisfy the national demands for natural gas only with their own resources, and taking care for the economic, environmental and health issues.

Keywords: Strategic planning, Natural gas, Fresh water, CO₂ emissions, Occupational health.

1. Introduction

Several works have analysed the strategic planning of shale gas to satisfy diverse demands; in this sense, Gao and You (2015) proposed a model for designing a shale gas supply chain accounting for the involved water supply, as well as the economic and environmental impacts.

It should be noticed that a large part of the oil reserves is below the sea. In Mexico, more than 80% of total oil production is provided from the sea. This zone is in the states of Campeche, Yucatán and Quintana Roo, and includes approximately 189,056 square kilometres (PEMEX, 2017). However, this method is very challenging, since it does not

only must deal with extracting oil to the surface by drilling in the sea, without having visibility, but also avoiding the sea contamination with hydrocarbons.

Once the oil is not extracted from the well, means that this is exhausted. However, there are several improved recovery techniques that stimulate the subsoil, these are known as Enhanced Oil/Gas recovery (EOR/EGR), causing the release of oil that is currently contained in the deposit. Li et al. (2018) investigated the natural gas production from fracture-filled methane hydrate reservoirs by the CO₂ replacement method.

Moreover, occupational health deals with all aspects of health and safety in the workplace and it has a strong focus on primary prevention of hazards. The health of the workers has several determinants, including risk factors at the workplace leading to cancers, accidents, musculoskeletal diseases, respiratory diseases, hearing loss, circulatory diseases, stress related disorders and communicable diseases and others (WHO, 2018).

However, it is important to note that the reported approaches for the strategic planning for satisfying the national demands of natural gas have not considered simultaneously conventional and unconventional resources with economic, environmental (associated to emissions and used water) and health implications for the proper analysis. These are important points that must be studied for the correct planning to satisfy the national demands of natural gas for any country, because these are intrinsically related. Therefore, this paper presents a general mathematical model to obtain energy independence from a country to take advantage of its own reserves of fossil fuels through using unconventional extraction methods such as shale gas, offshore extraction, and considering conventional ways to obtain natural gas that the country already has. In addition, in this paper the nexus between environment and health damages together with the economic implications is involved; also, the model considers reducing the consumption of fresh water and generation of CO₂ emissions, considering the configuration that represents the least damage for the workers that dangerous substances present in the extraction and production processes.

2. Problem Statement

Throughout the years, the conventional extraction of fossil fuels has been decreasing but the energy needs have increased; this way, different unconventional forms for the extraction of natural gas have been explored. However, these new ways of extraction have considered the costs and environmental damage mainly associated to emissions of CO₂, but the chronic diseases caused in workers and the implications in the use of fresh water have not been properly addressed since the planning stage.

The objective is to satisfy the national demands of natural gas for a given country.

3. Optimization Model

The proposed mathematical programming model is general, it is based on the superstructure presented in Figure 1, and it involves different forms of unconventional extraction such as shale gas, offshore extraction, and conventional forms; for example, the extraction of associated reservoirs using improved recovery techniques, the conventional extraction of non-associated deposits and even the importation of natural gas. Fresh water and seawater are used for producing natural gas through different

extraction methods. According to the type of extraction, the produced natural gas is separated, and it can be treated to eliminate dangerous substances to health. The natural gas obtained by each extraction method is distributed to the different markets. The model includes costs for producing natural gas, fresh water, treatment and transportation. In addition, the sale of oil obtained in offshore extraction and associated conventional extraction is considered.

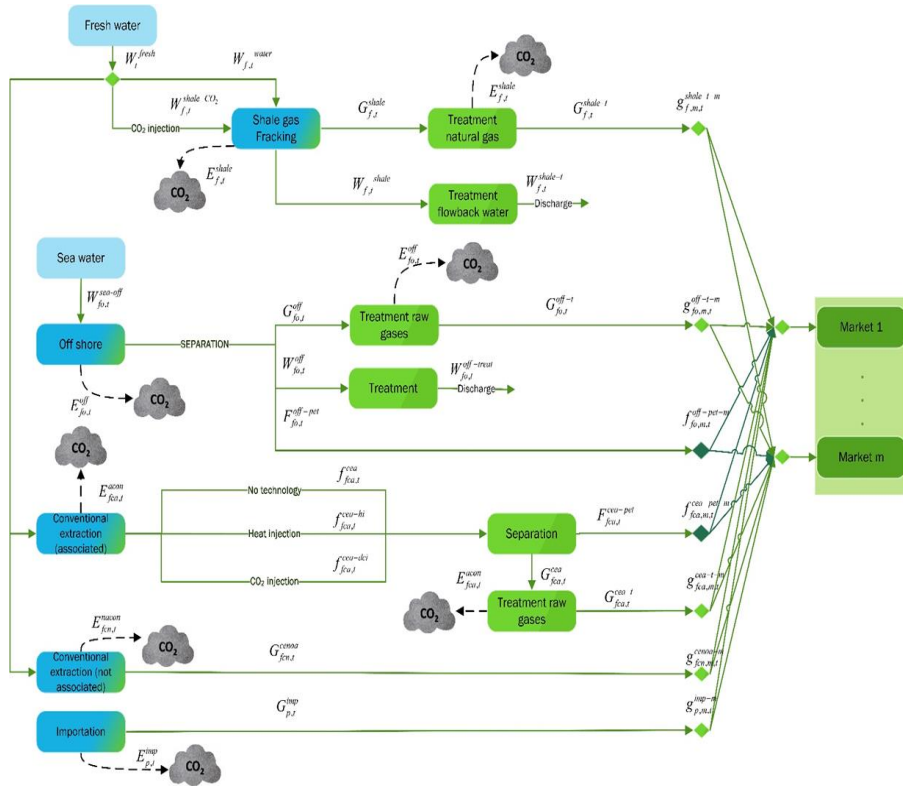


Figure 1. Proposed superstructure

3.1. Profit

The profit is obtained by the sum of the sale of oil and natural gas, minus all the involved expenses:

$$\begin{aligned}
 \text{Profit} = & \text{Sale}^{PET} + \text{Sale}^{NG} - \text{Cost}^{shale-prod} - \text{Cost}^{fresh-shale} - \text{Cost}^{treatment-shale} - \text{Cost}^{off-prod} \\
 & - \text{Cost}^{seawater} - \text{Cost}^{treatment-off} - \text{Cost}^{cea-prod} - \text{Cost}^{fresh-acon} - \text{Cost}^{treatment-cea} - \text{Cost}^{cenoa-prod} \quad (1) \\
 & - \text{Cost}^{fresh-nacon} - \text{Cost}^{imp} - \text{Cost}^{pet} - \text{Cost}^{transp-pet} - \text{Cost}^{transp-ng}
 \end{aligned}$$

3.2. Total fresh water

The total used fresh water is the sum of each flow needed of water in shale, conventional associated and non-associated production:

$$TFW = \sum_f \sum_t W_{f,t}^{shale} + \sum_{fca} \sum_t W_{fca,t}^{fresh-acon} + \sum_{fcn} \sum_t W_{fcn,t}^{fresh-nacon} \quad (2)$$

3.3. Total emissions

The total emissions are the sum of the generated emissions in each process as it follows:

$$TE = \sum_f \sum_t E_{f,t}^{shale} + \sum_{wo} \sum_t E_{wo,t}^{off} + \sum_{wca} \sum_t E_{wca,t}^{acon} + \sum_{wcn} \sum_t E_{wcn,t}^{nacon} + \sum_p \sum_t E_{p,t}^{imp} \quad (3)$$

3.4. Occupational health

Occupational health has been evaluated in each of the options to produce natural gas that are considered in the superstructure. Equation 4 relates natural gas flows for each case multiplied by a factor that shows the relationship of damage between each of the options with respect to the most damaging. It is worth mentioning that shale gas is the one that generates the most health damage for workers who are exposed continuously to the substances present in the process.

$$HD = I^{shale} \cdot \sum_{f,t} G_{f,t}^{shale-t} + I^{off} \cdot \sum_{fo,t} G_{fo,t}^{off-t} + I^{cca} \cdot \sum_{fca,t} G_{fca,t}^{cca-t} + I^{cenoa} \cdot \sum_{fcn,t} G_{fcn,t}^{cenoa-t} + I^{imp} \cdot \sum_{p,t} G_{p,t}^{imp} \quad (4)$$

3.5. Objective functions

The formulation of the mathematical programming model is a multi-objective problem, where the objectives are to maximize the profit, minimize the consumption of fresh water, the total emissions and the health damage, subject to relationships (1-4).

$$ObjectiveFunction = MaxProfit; MinTFW; MinTE; MinHD \quad (5)$$

The model is a mixed integer linear programming model, and this was coded in the software GAMS.

4. Case Study

The consumption of natural gas in any country is of special interest to ensure independence on foreign countries to meet fuel needs. In this context, Mexico was selected as a case study, since this country has natural gas reserves by 31,904.7 billion cubic feet, of which 70.3% is associated natural gas and the rest is not associated. The associated natural gas is the one that is in presence with oil and other compounds in the reservoir and non-associated is because there is only natural gas in the reservoir. In addition, it is important to note that Mexico is in 6th place worldwide with a reserve of unproven but technically recoverable resources of shale gas with 545,000 billion cubic feet (EIA, 2018).

5. Results

The results for optimizing each objective separately are shown in Table 1. It should be noticed that by maximizing the PROFIT, there is a profit of 1.58×10^{10} \$/y, which is 186% higher than the case of minimizing the TFW (fresh water consumption), 2.1% greater than minimizing TE (total emissions) and 2,119% higher with respect to minimizing HD (damage to health).

Table 1. Results for optimizing different objectives separately

	Max PROFIT	Min TFW	Min TE	Min HD
PROFIT (\$/y)	1.58×10^{10}	5.51×10^9	7.11×10^8	7.12×10^8
HEALTH DAMAGE (MMmetric ton CO ₂ e/y)	1,509,500	105,820	0.137	0.137
Importation	22.774	1.091	0.690	0.690
Offshore	0	0.273	0.273	0.272
Shale	1.977	0.818	0	0
Associated	19.389	0	0	0
Non-associated	0.844	0	0	0
TOTAL FRESH WATER (MMm ³ /y)	0.564	0	0.417	0.418
Importation	36.576	0	14.333	14.333
Offshore	0	0	0	0
Shale	0	0	0	0
Associated	2.729	0	0	0
Non-associated	14.464	0	0	0
Natural gas produced (MMcfy)	19.386	0	14.333	14.333
Importation	1,901,853	1,901,847	1,901,853	1,901,843
Offshore	0	1,773,910	1,770,660	1,770,650
Shale	309,142	127,937	0	0
Associated	1,252,970	0	0	0
Non-associated	162,304	0	0	0
	177,437	0	131,193	131,193

On the other hand, health damage provides different scenarios, where this value helps to determine the harmful level of an option; where the higher the value, the greater the damage. In this case, the HD values are quite different. Minimizing TE and HD, there is less damage (0.137), in addition, when TFW is minimized, there is a decrease of 92.9% compared with the case when PROFIT is maximized, which represents the scenario with the greatest damage to health.

The total demand of natural gas in the country is 1,901,888.77 MMcfy; by maximizing PROFIT, 65.9% is satisfied through the production of shale gas, 16.2% with offshore production, 9.3% by associated conventional extraction and 8.5% by non-associated conventional extraction. It is important to highlight that in this scenario, importation is not used and despite having the greatest health damage, emissions and water consumption, it would be no dependence on another country to satisfy the demand for natural gas. When TFW is minimized, 93.3% is satisfied through importation and the rest through offshore production. In the cases when TE and HD are minimized, the results are very similar, 93.1% is imported natural gas and the rest is from the conventional production of non-associated natural gas.

The fresh water required to maximize PROFIT is used to produce shale gas, associated and non-associated natural gas. When TFW is minimized there is no water consumption since everything was satisfied through importation and offshore extraction. On the other hand, for the minimum TE and HD, there is only fresh water consumption due to the production of non-associated natural gas.

The greatest amount of total emissions (millions of tons of CO₂ equivalent per year) occurs when the PROFIT is maximized (22,774), where 85.1% is generated due to shale gas. In the case of minimum TFW (1.091), there is a decrease of 95.2% with respect to the maximum PROFIT scenario; for the minimum TE and HD, the decrease in emissions is 96.9%.

6. Conclusions

This paper has presented a mathematical programming model for the strategic planning to satisfy the national demands of natural gas. The proposed model incorporates non-conventional options, particularly shale gas, which can be used to decrease the imports. Furthermore, in the proposed model, in addition to economic objectives, the minimization for the fresh water consumption, CO₂ emissions and the health damage to the involved workers were considered.

Throughout the presented analysis for the case of satisfying the national demands of natural gas in Mexico, there was determined that is possible to satisfy these demands with a greater profit, less damage, fresh water consumption and emissions of CO₂. Also, occupational health was evaluated showing that when the profit increases, the higher the damage, but the less the damage, the more the dependence with another country because the needed imports. However, it can be noted that the dependence of Mexico (maximizing profit) with another country is reduced because the demand of natural gas can be satisfied with the national production, only by substituting importation with shale gas production and using the conventional reservoirs that already exist.

Finally, the proposed model is general, and it can be applied to different cases with different conditions.

7. References

- EIA, 2018, Energy Information Administration. www.eia.gov. [Accessed March 2018].
- J. Gao, F. You, 2015, Shale gas supply chain design and operations toward better economic and life cycle environmental performance: MINLP model and global optimization algorithm, *ACS Sustainable Chemistry and Engineering* 3(7), 1282-1291. DOI:10.1021/acssuschemeng.5b00122.
- B. Li, T. Xu, G. Zhang, W. Guo, H. Liu, Q. Wang, L. Qu, Y. Sun, 2018, An experimental study on gas production from fracture-filled hydrate by CO₂, and CO₂/N₂ replacement. *Energy Conversion and Management*, 165: 738-747. DOI:10.1016/j.enconman.2018.03.095.
- PEMEX, 2017, Mexican oil. www.pemex.com/saladeprensa/boletines_nacionales/Paginas/2017-043-nacional.aspx, www.pemex.com/ayuda/preguntas_frecuentes/Paginas/reservas_hidrocarburos.aspx. [Accessed May 2017].
- WHO, 2018, World Health Organization. www.who.int/topics/occupational_health/en. [Accessed August 2018].

Engineering success: What does it take to get PSE technologies used?

Sandro Macchietto*

Imperial College London, South Kensington Campus, London SW72AZ, UK

s.macchietto@imperial.ac.uk

Abstract

Over the years there have been many excellent contributions in the ESCAPE conferences to the R component of R&D, but less emphasis on the D element, and even less on the steps required for taking a piece of research to the final users in industry, that is, the technology transfer process itself.

These days, initiatives in tech transfer (variously called “third mission” or “translation” activities) are everywhere. A variety of supporting structures (Enterprise Launch Pads, Spinout Clinics, Tech Launch Prizes, Venture Competitions, Technology Parks, etc.) are implemented in most academic and research establishments. The enterprise climate is possibly at its hottest for many years, the message has been spreading widely, and there are a number of notable successes. However, in my experience, there is still a big gap between theory and practice, only a very small fraction of researchers are involved and there is an enormous untapped potential. Based on 30-year experience of “translation” activities, some more successful than others, a personal overview is presented of what it takes to go from novel research to final use of a technology. It briefly touches on things found working and not, essential and unnecessary (or counter-productive), drawing on the experience of launching and managing two companies in the PSE area (including Process Systems Limited), various interdisciplinary consortia and two applied research centres. Some final comments address how to tweak the odds towards “engineering success by design”.

Keywords: technology transfer, R&D translation, industrial uptake.

1. The numbers

The ESCAPE Conference Series is 29 years old. Assuming ~350-400 papers accepted in each one, altogether over 10,000 papers have been produced and passed a peer review quality test, representing a huge collective investment in research time and resources. No doubt they include a good number of seminal papers presenting highly innovative ideas, results and applications. A quick scan indicates that most contributions address the R component of R&D (not surprisingly, given the nature of the conference), with less emphasis on the D element and even less on the steps required for taking a piece of research to the final users in industry, that is, the technology transfer process itself.

The longevity of the conference is a good indicator of its perceived usefulness to the community. It is however a legitimate question to ask how many of these ideas have actually found their way into industry and are productively used as methods, tools, or embedded in products. Some relevant related questions are: Does good research actually produce good impact? How many good ideas result in eventual industrial uptake and

impact? Is academic recognition (e.g. publication in peer reviewed journals, number of citations) a good indicator of uptake and impact? How long does it take? And the more operative question, are there better mechanisms for “engineering” such success? These questions are complex and the subject of much research in the academic entrepreneurship community. Without pretence to provide a formal answer, some figures and considerations from personal experience are presented in the following.

The *inventive output* of an organisation is typically measured in terms of number of Disclosures (being considered for commercialisation) and Patents (filed and awarded), *technology transfer* performance in terms of Licensing and company Spinoff (formation plus various progress metrics e.g. survival rate, investment capital attracted, employment generated, turnover, growth, acquisition value, etc.). Other mechanism for transferring technology from academia include Consultancy, industrial projects and (in my experience, the main channel) “brain walks” (hiring of students and researchers).

Technology transfer is hard. US Venture capital funds invested \$175bn in the two year technology boom period 1998-2000. Out the myriad companies started, Google, and Amazon are outstanding survivors, but most of the \$175bn was wasted. The average rate of return of VC funds invested in the 2000-2004 period following the Dot.com bust was less than 2% (marginally less than ordinary bank savings). The concept of supporting the transfer of intellectual property (IP) and technologies from academic research into practical use was introduced in the UK in the 1980’s Thatcher years. These days, initiatives in tech transfer (variously called “third mission” or “translation” activities) are everywhere. A variety of supporting structures (Enterprise Launch Pads, Spinout Clinics, Tech Launch Prizes, Venture Competitions, Technology Parks, etc.) are implemented in most academic and research establishments. The enterprise climate is possibly at its hottest for many years.

In the UK, Imperial College has a good reputation for being one of the most active and successful in technology transfer, and has created a quite variegated eco-system to nurture and support enterprise by student and staff along the long path from idea to Exit/IPO (Imperial College London, 2018, p.19). A summary of Imperial’s tech transfer results for the 5 years to 2016-17 is given in Figure 1. A few things are worth noting. The number of yearly start-ups (5-9 per year) is relatively modest (those in the technology and industrial sectors based on IP produced by R&D are even fewer, 1-3 per year, most others being in health and medicine). Only about 20% of Disclosures results in a patent filing, with a conversion rate of ~50% to Patents granted. While a double digit number of new licences were signed each year and over 200 active ones are held, less than half of them (42% in 2016-17) actually generate income, on average of £33K each. Even a cursory thought to patenting, legal, commercial and administrative costs indicated there are no great returns here! Some data on generation rate and cost efficiency are also given in Fig. 1 in the form of ratios. On this basis, in 2016-17 £100m of research generated 92 Disclosures, 19 Patent filed and 11 granted, 2.5 IP based start-up and 4.4 student start-ups. The income from licensing and realisation of participated companies is 2.6% of the research income, a rate of return comparable to keeping the money in the bank. Actually, this performance is pretty good, as most societal and commercial gains do not accrue to the universities. A comparative analysis (Autio and Webb, 2015) of the ability of universities to spin out new ventures and their subsequent growth, found that while the UK entrepreneurial culture is weaker than in the US, after adjusting for population size and economic activity, UK universities are more efficient

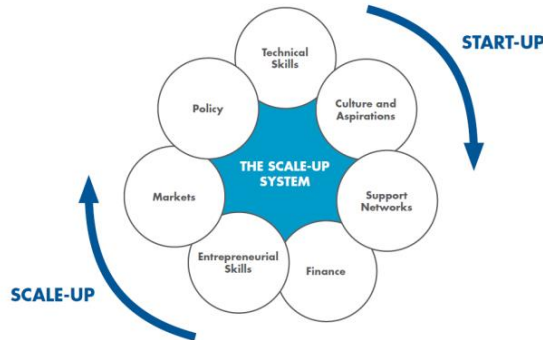
Figure 1. Imperial College Inventive Output Scorecard YE 2016-2017 (extracts from Imperial College London, 2018, p. 20)

Metric	2012-13	2013-14	2014-15	2015-16	2016-17
Inventive Output					
Inventions disclosed	306	323	296	310	332
Patent applications filed	43	57	66	73	68
Patents issued	78	98	47	59	40
Active inventions in portfolio	832	977	1,007	1,021	1,009
Active patents in portfolio	325	373	394	404	429
Licensing Performance					
New licenses signed	29	27	39	39	46
Active licenses held	170	175	193	202	217
Licenses generating income in the period	48	71	74	70	91
Royalty and fee income generated in the period (£m)	£1.3	£1.6	£2.8	£2.1	£3.0
Startup Formation					
IP-based startups formed	5	7	8	6	9
Student-based startups formed	6	8	18	16	16
Ratios					
Research income (£m)	£330	£351	£436	£351	£361
Invention disclosures per £100m of research income	93	92	68	88	92
Patents filed per £100m research income	13	16	15	21	19
Patents issued per £100m research income	24	28	11	17	11
Licensing and realisation income : research income (%)	0.5%	0.4%	1.1%	1.1%	2.6%
IP startups per £100m research income	1.5	2.0	1.8	1.7	2.5
Student startups per £100m research income	1.8	2.3	4.1	4.3	4.4

than German and US ones in generating new ventures (576 spinouts in UK vs. 428 in US per \$ trillion GDP, and 48 vs.16 per \$ billion of tertiary education spending). The UK however was found to lag the US in scale-up performance, due to lower funding (US spinout raised on average 50% more equity) and lower entrepreneurial aspirations, including a number which are good indicators of scalability (Risc Capital, Internationalisation, High Growth and Product and Process Innovation aspirations). Their analysis focused on low-carbon technologies, but also gives useful general data. They identify the ecosystem in Figure 2 as enabling enterprise.

The fraction of academics involved in impact-related activities even in a relatively enterprising place like Imperial is small, with 26%, of total academic staff involved in collaboration with industry, 41% in consulting, 13% in patent ownership and just 4% in IP commercialization (Gann et al, 2016). Patents and IP commercialisation are the least preferred ways by academics to generate impact. Recent emphasis has been more on unleashing students' enterprise juices, with excellent response and good success. This is particularly important. While universities still largely train students for big company employment, they increasingly like to start their own. It is useful to remember that Apple, Facebook, Microsoft, Uber, Spotify and Tesla were all started by university dropouts. Perversely, some universities that have encouraged student enterprise activities in the early years have found that significant numbers do not return to their books, and (in the UK) risk being penalised due to high drop-out rate (e.g. Sheffield University, article in The Times, 14 Nov 2018). Data on UK university technology transfer is provided by the Higher Education Statistical Agency (HESA, 2018), while R&D data by OECD countries are in (OECD, 2018).

Figure 2. Structures and ecosystem which enable enterprise in the UK (Autio and Webb, 2018, p. 4)



2. The practical experience

So much for statistics. If one follows the recommended path, first carries out fundamental research, then does a first prototype and product development, followed by trials, market research and business development. If/when this works, one may address commercialisation. This is often formalised into several sequential “technology readiness levels” (TRLs). In my experience, this has two main pitfalls. First, it may take years. Second, the best people at each stage are often not available for or interested in the next. A Phd or Post-doc who has demonstrated the superior convergence of a new algorithm is usually not interested in (or does not have the skills for) re-implementing it in professional code, with documentation, interfaces, testing, validation, versioning, customisation, applications support, etc. While continuity of funding across the TRLs is always a problem (some agencies fund research, other commercialisation, few the hard bit in between), in my experience a bigger challenge is ensuring continuity in technical expertise and injecting management, financial, commercial expertise at the right time.

Solving many problems: One way to address this is to pursue many related ideas in parallel, in larger projects with a broad research programme, with people of different competences, all at the same time. A multidisciplinary team ensures that each idea is explored from multiple angles and that many other unexpected ideas are generated, especially when industry is also closely involved. An example is represented by the Centre for Process Systems Engineering at Imperial, where from the inception PhDs and MSc researchers worked alongside “development” teams (full time programmers, project managers and industry visitors) on so-called “major projects”, tasked with implementation, consolidation and early validation of the research. Notable outcomes of two of these projects were several “industry-tested” technologies that went into the Process System Enterprise spinoff, and the company formation itself.

Solving the right problem: In the PSE approach, a problem is conceptualised, formulated, analysed and solved. We typically seek an exact (rigorous) solution, using the best solvers, for a complete formulation. However, we often need to make simplifying formulation assumptions (e.g. on size, detail, constraints, nonlinearities) in order to use a solution technique. An alternative approach is to use an approximate solution of a more complete problem formulation. Failure to consider all relevant

problem features is in my experience a key reason limiting the credibility and acceptability of a new method in industry, where “better but feasible” always trumps “optimal but not quite feasible”. Understanding the problems in their full detail and complexity, ideally in the plant or design office, can be a humbling experience! An example from my own research include Batch Processing (Crooks et al., 1992) in the food industry. Key features include multipurpose recipes, multiples sources for the same material that must remain segregated, vessels coupling through shared piping, condition-based cleaning, multi-layered product packaging, and a myriad of other subtle but essential elements. Much of the published work in this area considers such simplified views of the process that make the methods not applicable, whatever the elegance of the combinatorial solution. A more heuristic solution which however captured all required features was successfully applied industrially to scheduling and design of very complex, large scale food productions (e.g. Figure 3, Macchietto, 2005). Similarly, much elegant heat exchanger network (HEN) optimisation work in the literature cannot deal with fouling, very often present. This requires much more detailed, representative models and sophisticated solutions (e.g. Diaz et al., 2016).

Figure 3. Scheduling of beer production in one of the largest UK breweries (26 beer families, 140 pieces of equipment) (Macchietto, 2005)



Solving the problem right: A 90% success rate for a new optimisation method is a very good improvement over methods that only solve 80% of the problems. However, it is not good enough for practical everyday use in industry, as users will spend 90% of their time in dealing with the 10% of failures, and will soon give up. Achieving a 100% rate is not easy, maybe impossible, so should we park the method? A common R&D failure is that too much emphasis is put on performance, and too little on usability. To address this requires analysing, understanding and facilitating user’s workflows, and where benefits and losses (for them) really lie. Not easy without close contact with target users in their environment. For example, Dr. Chen, a brilliant student of mine produced a new, 90% good, nonlinear optimisation algorithm (SRQP, for successive reduced quadratic programming) for his PhD thesis. We spent the next 18 months with BP to make it industry-usable, including adding some obvious (but not easy) items such as meaningful error messages, a range of fail-safe, gently-degrading features, a guide to options and reverse communication for ease of embedding in third party software. As a result, the now robust software was licensed to and used in 4 different commercial simulators, in various on-line control applications, and has been for 20 years, with hardly any modifications, the optimisation workhorse within gPROMS.

Changing the odds: An example combining many of the above features is the UNIHEAT project, a £9.3m collaboration between Imperial College, the Borskov

Institute of Catalysis in Novosibirsk, Russia, BP, the University of Novosibirsk, UNICAT, a Russian company, and the Russian Skolkovo Foundation (Macchietto and Coletti, 2015). It featured large multidisciplinary research teams with adjacent expertise; a dedicated knowledge and technology transfer team; several related projects in parallel; concurrent research, demonstration/prototype development and proof of concept; significant, integrated industrial involvement; very early IP identification and development alongside the research. This turbocharged the whole process. Results obtained in three years, described in the reference, include, in addition to the expected large number of publications in scientific journals, 3 spinoffs and 22 patents filed. Expectations based on the ratios in Fig. 1 would be 0.23 spinoffs (at 2.5/£100m), and 1.9 patent filed (at 20/£100m). Results achieved represents a x10 improvement in R&D productivity, even for a difficult multi-partner project across 7 time zones.

3. Conclusions

Technology transfer is not easy, but a few mechanisms have proved useful to boost it. These include shortening the timescales by working on multiple related developments in multidisciplinary teams, industrial involvement from the beginning, making sure we address the right problems by understanding the solution end use and users, addressing usability as well as performance from the outset, and integrating knowledge and technology transfer professionals and activities with the R&D team. Results on a recent project thus configured show that a large increase in R&D productivity can be achieved.

References

- Autio E and R. Webb, 2015. Engineering Growth: enabling world-class UK entrepreneurship in the low-carbon economy. Imperial College Business School Report for Shell Springboard Awards 2015. <http://www.shellspringboard.org/shell-springboard-imperial-college-study/>
- Crooks, C.A, K Kuriyan and S Macchietto, 1992. "Integration of batch plant design, automation, and operation software tools". Proceedings, ESCAPE I Conference, Elsinore, Denmark, May 24-28.
- Diaz - Bejarano, E., Coletti, F. and Macchietto, S., 2016, A new dynamic model of crude oil fouling deposits and its application to the simulation of fouling - cleaning cycles. *AIChE J.* 62 (1), 90-107.
- HESA, 2018. <https://www.hesa.ac.uk/data-and-analysis/providers/business-community>
- Imperial College London, 2018. Review of Enterprising Activity 2016-17, <http://www.imperial.ac.uk/enterprise/publications/enterprising-activity-2017/> accessed 10.10.2018
- Gann, G., M. Tackett, C. Thorne, 2016. Pathways to Societal Impact, Report, Imperial College London.
- Macchietto, S., 2005. Integrated Batch Processing: A model for advanced manufacturing. Proceedings, APACT 05 Conference, Birmingham, UK, 20-22 April 2005
- Macchietto S. and Coletti F., 2015. Innovation: better together. *The Chemical Engineer*, 893 24-27. (Cover article)
- OECD, 2018. <http://www.oecd.org/innovation/inno/researchanddevelopmentstatisticsrds.htm>

Integration of Consumer Preferences and Heuristic Knowledge in the Design of Formulated Products: Application to a Cosmetic Emulsion

Javier A. Arrieta-Escobar^{a,b*}, Fernando P. Bernardo^c, Alvaro Orjuela^b, Mauricio Camargo^a, Laure Morel^a, Laurent Wendling^d

^a*ERPI (Equipe de Recherche sur les Processus Innovatifs) - University of Lorraine - 8, rue Bastien Lepage, 54010 Nancy Cedex, France*

^b*Department of Chemical and Environmental Engineering- Universidad Nacional de Colombia - Sede Bogotá, Colombia*

^c*GEPSI-PSE Group, CIEPQPF, Department of Chemical Engineering - University of Coimbra, Portugal*

^d*LIPADE (Laboratoire d'Informatique Paris Descartes) - Paris Descartes University - 45 rue des Saints Pères, 75270 Paris Cedex 06, France*

arrietael@univ-lorraine.fr

Abstract

In this work, an optimization-based methodology to design formulated products, incorporating heuristic rules, property models and also quantified customer preferences, is proposed and applied to a skin moisturizer. The relative importance of each product attribute valued by customers is first quantified and then related parameters progressively incorporated in an optimization-based method that generates plausible alternative formulations. The proposed method can be useful to accelerate the selection among alternative formulations, moreover in a benchmarking process.

Keywords: Product design, Consumer assessment, Heuristics, Emulsions, Skin moisturizer

1. Introduction

In the highly competitive market, consumer acceptance has become an important factor in the formulated product design process. Besides key physicochemical properties of the final product, it is of paramount importance to account for the performance of the product as perceived by the final consumer. Therefore, the prediction of acceptability is essential in product development, especially in the domain of cosmetic products, whose performance assessment integrates not only functional but also sensorial characteristics (Wortel and Wiechers, 2000).

Here, a recently proposed methodology (Arrieta-Escobar et al., 2018, 2017) to find a set of plausible product formulations, based on mixed-integer programming and incorporating heuristic rules (modelled as algebraic restrictions), is extended to include the consumer assessment. Starting with a list of attributes directly valued by consumers, the importance level of each of them as well as their interactions are determined from data of usability tests made on an on-market product, by using fuzzy measures (Grabisch, 1995). These consumer parameters can then be incorporated into the optimal design problem formulation, progressively and accordingly to their level of importance but also

depending on the availability of models or heuristics correlating them with product composition. This stepwise procedure may result in a reduction in the number of lab scale tests and alternatives preceding to consumer testing. Our main objective is to illustrate the application of this methodology using a skin moisturizer as a case study.

2. Consumer assessment methodology

In "Affective Engineering" or "Kansei Engineering" approaches, usability tests are made to unveil the subjective and even unconscious perception of the user (Nagamachi, 1995). Recently a methodology to integrate the user's perception and identify the importance and interaction of consumer attributes, based on fuzzy measures was proposed by Camargo et al. (2014). This methodology combines a Hybrid Kansei Engineering approach (Matsubara and Nagamachi, 1997), which uses a prototype or mock-up to elicit the product attributes, with a fuzzy integral analysis, namely the Choquet integral (Choquet, 1954). The main advantage of this approach is the possibility to consider the attributes relevance, based on the user's preferences, and the interactions among them. Here, the aforementioned methodology was adapted for cosmetic emulsions in order to understand the importance level (Shapley index) along with the interactions among the attributes (Murofushi and Soneda indices) using a composite index. The main stages of this methodology are described in detail in the original paper, and here only some aspects will be mentioned in the context of a skin moisturizer example (see Figure 1).

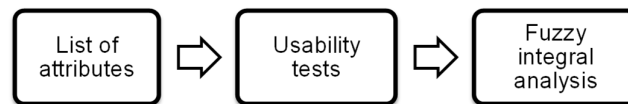


Figure 1: Consumer assessment methodology. Adapted from (Camargo et al., 2014)

Consumer attributes reported in the literature (Parente et al., 2010) are classified in 8 groups (thickness, ease of spreading, stickiness, easy of absorption, freshness, residues, greasiness/oiliness and moisturization) and an on-the-market product (Bioderma® Atoderm Ultra-nourishing Cream) is chosen for the usability test. For that, a questionnaire was prepared, in which the participants were told to apply the product on their arms, and to answer two questions corresponding to each one of the 8 groups of attributes, using a 5-level ordinal scale from “not at all” to “very much” (Osgood, 1959). Two additional questions about product's acceptability allow the algorithm in the fuzzy integral analysis to “learn” how important the attributes were to the overall performance.

3. Skin moisturizer case study

A skin moisturizer can be described as a cosmetic product that provides a healthy skin feeling thanks to the use of moisturizing agents (humectants and emollients), typically delivered in the form of an oil in water (O/W) emulsion, stabilized with a combination of emulsifiers (mostly nonionic surfactants) and thickeners (Barel et al., 2001).

3.1. Ingredients, property models and heuristics

Skin moisturizer emulsifiers are usually a suitable combination of at least two nonionic surfactants (Rieger and Rhein, 1997) used at a minimum level of 2% and up to 5% (Rähse, 2013). The final HLB value of the combination – 1 part of medium HLB (9-15), 3 to 6 parts of high HLB (>16) and 2 to 6 parts of low HLB (<8) – should be between 8 and 15

to assure O/W emulsions. Also, a total surfactants/oil ratio of 1:4 to 1:6 should be kept to stabilize the resulting emulsion (Iwata and Shimada, 2013). The classical empirical HLB model is here adopted: HLB of the surfactant mixture should approximately match the HLB required by the oil mixture: $HLB = RHLB$.

Water-soluble polymers are added as thickeners to provide consistency and stability to the emulsion (Iwata and Shimada, 2013). The primary feeling (consistency at first contact) is correlated to the high viscosity η_1 , perceived on the onset of flow of the product, under low applied stresses. In contrast, the secondary feeling (consistency during spreading) corresponds to a much lower final viscosity η_2 , when the product is being applied under higher stresses (the emulsion has a strong shear-thinning behavior). Composition-viscosity data for polymer thickened aqueous solutions are available, based on which one has constructed linear models of $\log(\eta_1)$ and $\log(\eta_2)$ as a function of polymer concentration and also total content in oils.

Emollients are the main moisturizing agents and improve the spreadability of the product. A proper combination of at least one emollient of high, one of medium, and one of low spreading types, provides the complete profile for a well-performing product (Ansmann et al., 2005). The after-feel provided by the emollients is related to their greasiness value (γ), which can be calculated as a weighted average from individual values (scale from 1 to 5), available for a wide range of products (Mentel et al., 2014). Similarly, the RHLB value of the emollients mixture is estimated from individual values obtained directly from the providers or from other sources (Pensé-Lhéritier, 2016).

All formulations consider a fixed amount of mandatory ingredients, i.e. the humectant (3% Glycerol) and the preservative (0.7% Cosgard®).

3.2. Optimization of the formulation

Table 1 shows the most relevant design variables and a short formulation of the optimization problem. Thirty-six possible ingredients were considered (vector \mathbf{y} and \mathbf{x} have dimension 36): Six emulsifiers, three polymer thickeners, three fatty alcohols and twenty-four emollients. The complete list of adopted heuristics is not here reported. The resulting model is a small MINLP problem, easily solved in less than 1 s using GAMS/BARON.

Table 1. Product design variables and problem formulation.

Binary variables \mathbf{y} (choice of ingredients) and continuous variables \mathbf{x} (wt %)	Problem formulation
Emulsifiers: y_r, x_r Thickening polymers: y_n, x_n Fatty alcohols: y_m, x_m High spreading emollients: y_i, x_i Medium spreading emollients: y_j, x_j Low spreading emollients: y_k, x_k	Find vectors \mathbf{y} and \mathbf{x} that minimize cost, subject to: Heuristics of typical amounts and combinations of ingredients $2.0 \leq \gamma \leq 2.4$ $120 \leq \eta_1 \leq 500$ Pa.s, $0.023 \leq \eta_2 \leq 0.500$ Pa. s $HLB = RHLB$

4. Results and discussion

Thirty-two female users of moisturizers (average age 31 years old) tested the commercial product and completed the questionnaire. Table 2 contains the resulting average scores of each attribute, along with the normalized Shapley, Murofushi and Soneda and composite

indices. Under the latter metric, “ease of absorption” (0.29), “freshness” (0.25) and “residues” (0.20), are the most important attributes. Noteworthy is that these attributes also have the highest values of mutual interactions (Table 2 only shows the sums of the total interactions as normalized interactions).

Table 2. Scores, normalized values of Shapley (relative weights), Murofushi and Soneda (interactions), and composite indices.

Attribute	Symbol	Score	Normalized relative weights	Normalized interactions	Normalized composite index
Thickness	V	0.46	0.13	0.08	0.07
Spreadability	S	0.75	0.04	0.07	0.02
Stickiness	P	0.45	0.15	0.11	0.11
Ease of absorption	A	0.35	0.20	0.22	0.29
Freshness	F	0.31	0.21	0.18	0.25
Residues	R	0.30	0.15	0.20	0.20
Greasiness	G	0.74	0.05	0.06	0.02
Moisturization	H	0.61	0.07	0.08	0.04
Overall performance	C	0.43			1.00

A first basic formulation (Formulation 0) was generated solving the problem specified in Table 1. In this case, 3 of the 8 attributes of Table 2 are already addressed (at least partially): “Thickness” and “Spreadability” (through the imposed viscosity limits, which were determined from sensorial tests on general purpose creams), and also “Greasiness” (through the limits imposed on the greasiness value γ). In a second stage, the “residues” attribute (R) was then chosen as the next attribute to be considered, since, among the remaining 5 attributes, it is the most informative one and the easiest to evaluate (it has by itself a composite index of 0.20 and the highly correlated trio (A+F+R) adds up to 0.74). Formulation 0 and the commercial reference sample were then evaluated in this attribute, with results shown in Figure 2 (left side). The poor performance of Formulation 0 is clear.



Figure 2. “Residues” of the analyzed formulations compared with the commercial sample.

In a third stage, the optimization of product formulation was readdressed, now including an additional heuristic to correct residues excess: add up to 2% of low HLB emulsifier so as to reduce the micro-foam formation (Institute of Personal Care Science, 2016). With this extra restriction (and allowing RHLB to deviate up to one unit from HLB), the optimization resulted in Formulation 1 (also shown in Figure 2 – right side). Both Formulations 0 and 1 are presented in Table 3 and their rheological profiles in Figure 3.

Figure 2 clearly shows that the additional heuristic worked very well, with Formulation 1 presenting a level of white residues very similar to that of the commercial sample.

Regarding rheology, both Formulations 0 and 1 have profiles similar to that of the commercial reference and in agreement with the simple viscosity models adopted in the optimization. Formulation 1 is thus a good candidate to customer satisfaction regarding attributes V, S, R and G (attributes A and F to the extent of their correlation with R too).

Table 3. Computer-generated alternative formulations for skin moisturizers.

Ingredient	Cost (USD/kg)	Formulation 0	Formulation 1
Water A		60.00%	60.00%
Xanthan gum	35	1.10%	1.10%
Cetyl Alcohol	7.4	4.00%	4.00%
Polysorbate 60	15.5	0.50%	0.50%
PEG-100 Stearate	9.8	1.50%	1.50%
Glyceryl Stearate SE	8.9		1.00%
Sorbitan Stearate	12.5	1.30%	0.70%
Isopropyl Myristate	16.7	5.60%	6.80%
Paraffinum Liquidum	12.2	2.70%	3.20%
Persea Grattissima Oil	16.7	1.00%	1.00%
Water B		18.60%	16.50%
Glycerol		3.00%	3.00%
Preservative (Cosgard)		0.70%	0.70%
	Total	100%	100%
	Cost (USD/kg)	2.50	2.77

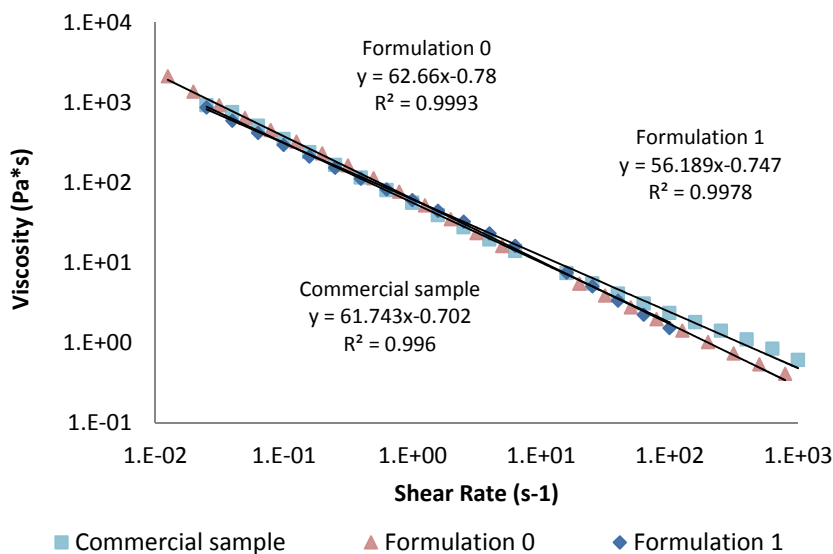


Figure 3. Rheological profile of the two formulations studied and of the commercial sample.

5. Conclusions

We have proposed an optimization-based methodology for the design of formulated products, which incorporates consumer assessment data along with available heuristic rules, and presented a case study of a skin moisturizer. Although not all product attributes were here addressed, the example provided illustrates how the proposed method can guide the selection among alternatives, according to the relative importance given by consumers to different product attributes and available information correlating product performance and acceptance with its composition.

Acknowledgments

This work was financially supported by the Universidad Nacional de Colombia within the framework of the research project QUIPU 202010026994.

References

- A. Ansmann, P. Busch, H. Hensen, K. Hill, H.-U. Krächter, M. Müller, 2005. Personal Care Formulations, in: Handbook of Detergents, Part D, Surfactant Science. CRC Press, Boca Raton FL. 207–260.
- J.A. Arrieta-Escobar, F.P. Bernardo, A. Orjuela, M. Camargo, L. Morel, 2018. Incorporation of Heuristic Knowledge in the Optimal Design of Formulated Products: Application to a Cosmetic Emulsion. *Comput. Chem. Eng.* In press.
- J.A. Arrieta-Escobar, F.P. Bernardo, A. Orjuela, M. Camargo, L. Morel, 2017. An Integrated Methodology for Emulsified Cosmetic Product Formulation Using Integer Programming with Logical Constraints, in: Espuña, A., Graells, M., Puigjaner, L. (Eds.), *Computer Aided Chemical Engineering*. Elsevier B.V., Barcelona, Spain, 985–990.
- A. O. Barel, M. Paye, H.I. Maibach, 2001. *Handbook of Cosmetic Science and Technology*. Marcel Dekker, New York - Basel.
- M. Camargo, L. Wendling, E. Bonjour, 2014. A fuzzy integral based methodology to elicit semantic spaces in usability tests. *Int. J. Ind. Ergon.* 44, 11–17.
- N. Choquet, 1954. Theory of capacities. *Ann. l'Institut Fourier* 5, 131–295.
- M. Grabisch, 1995. Fuzzy integral in multicriteria decision making. *Fuzzy Sets Syst* 69, 279–298.
- Institute of Personal Care Science, 2016. Free formulas/Videos (accessed 3.7.18) URL <https://personalcarescience.com.au/Freeformulas-Videos/FreeVideos-448/>
- H. Iwata, K. Shimada, 2013. *Formulas, Ingredients and Production of Cosmetics*. Springer.
- Y. Matsubara, M. Nagamachi, 1997. Hybrid Kansei Engineering System and design support. *Int. J. Ind. Ergon.* 19, 81–92.
- M. Mentel, S. Wiechers, A. Howe, P. Biehl, J. Meyer, 2014. Senses- A Scientific Tool for the Selection of The Right Emollient. *SOFW* 140, 8–15.
- M. Nagamachi, 1995. Kansei Engineering: A new ergonomic consumer-oriented technology for product development. *Int. J. Ind. Ergon.* 15, 3–11.
- C.E., Osgood, 1959. Semantic Space Revisited. *WORD* 15, 192–200.
- M.E. Parente, G. Ares, A.V. Manzoni, 2010. Application of two consumer profiling techniques to cosmetic emulsions. *J. Sens. Stud.* 25, 685–705.
- A.-M. Pensé-Lhéritier (Ed.), 2016. *Conception des produits cosmétiques : La formulation*, 1st ed. Lavoisier Tec&Doc, Paris.
- W. Rähse, 2013. Design of Skin Care Products, in: Bröckel, P.D.-I.U., Meier, D.W., Wagner, D.-I.G. (Eds.), *Product Design and Engineering: Formulation of Gels and Pastes*. Wiley-VCH Verlag GmbH & Co. KGaA, Weinheim, Germany, 273–313.
- M.M. Rieger, L.D. Rhein (Eds.), 1997. *Surfactants in Cosmetics*, 2nd ed, Surfactants Science Series. Marcel Dekker, New York.
- V. a. L. Wortel, J.W. Wiechers, 2000. Skin sensory performance of individual personal care ingredients and marketed personal care products. *Food Qual. Prefer.* 11, 121–127.

An improved approach to scheduling multipurpose batch processes with conditional sequencing

Nikolaos Rakovitis, Jie Li,* Nan Zhang

*School of Chemical Engineering and Analytical Science, University of Manchester,
Manchester M13 9PL, UK*

Jie.li-2@manchester.ac.uk

Abstract

Scheduling of multipurpose batch processes has gained much attention in the past decades. Numerous models using different mathematical modelling approaches have been proposed. The model size and computational performance largely depend on the number of time points, slots or event points required. Most existing models still require a great number of time points, slots or event points mainly because a consumption task always takes place after its related production tasks regardless of whether it consumes materials from the related production tasks. Although two existing models have been developed to overcome this limitation, they can either lead to real time violation or generate suboptimal solutions in some cases. In this work, we develop an improved unit-specific event-based model in which a consumption task takes place after its related production task only if it consumes materials from the production task. A consumption task starts immediately after its related production task completes only if there is no enough storage for materials produced from the producing task. We also allow production and consumption tasks related to the same state to take place at the same event points. The results show that the proposed model generates same or better solutions than existing models with less number of event points and less computational time.

Keywords: Scheduling, Multipurpose batch process, Mixed-integer linear programming.

1. Introduction

Scheduling of multipurpose batch processes has received much attention during the past three decades (Harjunkoski et. al. 2014). A number of mathematical models have been developed using discrete-time and continuous-time modelling approaches. The continuous-time modelling approaches include slot-based, global event-based, sequence based, and unit-specific event-based approaches. The model size and the computational performance largely depend on the number of time points, slots or event points required. Most existing models still require a great number of time points, slots, or event points to generate the optimal solution since a consuming task must start after the related producing tasks even if it does not consume materials from the producing tasks. In addition, production and consumption tasks related to the same state are not allowed to take place at the same time points, slots, or event points. To tackle these issues, Seid and Majozzi (2012) imposed consuming tasks to take place after related production tasks if materials produced from the production units are used by any related consuming task. However, their model could lead to storage violations in real time. Vooradi and Shaik

(2013) enforced a consuming task to take place after a related production task only if this consuming task uses materials from the specific production task with introduction of a high number of additional binary variables, leading to an intractable model size. Furthermore, materials are not allowed to be stored in a processing unit if it is idle, leading to suboptimality in some cases. These two efforts do not allow production and consumption tasks related to the same state to take place at the same time points, slots, or event points yet. Recently, Shaik and Vooradi (2017) and Rakovitis et al. (2018) did allow related production and consumption tasks to take place at the same event points. They still impose a consuming task must always start after the related producing tasks.

In this work, we develop an improved unit-specific event-based approach for this scheduling problem, which requires less number of event points than existing formulations. We use the definition of recycling tasks from Rakovitis et al. (2018) and allow related non-recycling producing and consumption tasks to take place at the same event points. Furthermore, the proposed model sequence a processing unit which process a consumption task with its related production task, only if it consumes materials from the unit that process that task, and it force the finish time of a consuming task to be equal to the start time of the production task, if materials produced by the producing task are not able to be stored. Finally, we allow processing units to store the materials that were produced during the events that the unit is inactive. The computational results demonstrate that the proposed model generates same or better solutions using less number of event points and less computational time.

2. Problem description

Figure 1 illustrates a multipurpose batch process facility involving S ($s = 1, 2, \dots, S$) states, J ($j = 1, 2, \dots, J$) processing units and I ($i = 1, 2, \dots, I$) tasks. The states include feed materials S^{fed} , intermediates S^{IN} and final products S^{FP} . Each processing unit can process I_j tasks, but process at most one task at a time. Two storage policies including unlimited or finite intermediate storage (UIS or FIS) for intermediate states are considered, while unlimited storage is available for feed materials and products. Unlimited amount of feed materials is assumed during the scheduling horizon. Finally, unlimited wait policy (UW) is considered for all batches. Given production recipes, minimum/maximum unit capacities, processing times, storage policy for each intermediate and the scheduling horizon, the scheduling problem is to determine the optimal allocation of tasks to units, the start and end times of each task, task sequences in a processing unit as well as the inventory profiles in order to maximize productivity.

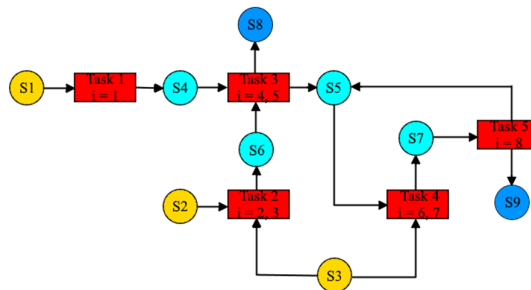


Figure 1 STN representation of a multipurpose batch process facility

3. Mathematical formulation

The mathematical formulation is developed using unit-specific event-based modelling approach because the advantages of this modelling approach have been well established in the literature. In the model, we have similar allocation constraints, capacity constraints, material balance constraints, and duration constraints to those of Rakovitis et al. (2018), which are not presented here. Next, we introduce new features of the proposed model.

3.1. Different tasks in different units

We define continuous variables $bc_{i,i',s,n}$ as material s produced from task i consumed by task i' at event n . Thus, the material consumed should not exceed total available materials.

$$-\sum_{j'} \sum_{i' \in \mathbf{I}_s^C, i' \in \mathbf{I}_j} \left(\rho_{s,i'} \cdot \sum_{n \leq n' \leq n + \Delta n} b_{i',j',n,n'} \right) \leq ST_{s,n-1} + \sum_{i \in \mathbf{I}_s^P} \sum_{i' \in \mathbf{I}_s^C} bc_{i,i',s,n} \quad \forall s \in \mathbf{S}^{IN}, n \quad (1)$$

The amount of materials from i to i' (i.e., $bc_{i,i',s,n}$) should not exceed the production amount of task i or consumption amount of task i' .

$$\sum_{i' \in \mathbf{I}_s^C} bc_{i,i',s,n} \leq \rho_{s,i} \cdot \sum_{n - \Delta n \leq n' \leq n} b_{i,j,n',n} \quad \forall s \in \mathbf{S}^{IN}, i \in \mathbf{I}_s^P, i \notin \mathbf{I}^{\text{Re}}, j, n \quad (2)$$

$$\sum_{i \in \mathbf{I}_s^P} bc_{i,i',s,n} \leq -\rho_{s,i'} \cdot \sum_{n \leq n' \leq n + \Delta n} b_{i',j',n,n'} \quad \forall s \in \mathbf{S}^{IN}, i' \in \mathbf{I}_s^C, j, n \quad (3)$$

$$bc_{i,i',s,n} \leq z_{j,j',s,n} \cdot \rho_{s,i} \cdot B_{i,j}^{\max} \quad \forall s \in \mathbf{S}^{IN}, i \in \mathbf{I}_s^P, i \in \mathbf{I}_j, i' \in \mathbf{I}_s^C, i' \in \mathbf{I}_{j'}, j', j \neq j', n \quad (4)$$

$$T_{s,j,n} \geq Tf_{j,n} - M \cdot \left(1 - \sum_{i \in \mathbf{I}_s^P, i \in \mathbf{I}_j} \sum_{n - \Delta n \leq n' \leq n} w_{i,j,n',n} \right) \quad \forall s \in \mathbf{S}^{IN}, j, n \quad (5)$$

$$T_{s,j,n} \leq Ts_{j',n} + M \cdot \left(2 - \sum_{i' \in \mathbf{I}_s^C, i' \in \mathbf{I}_j} \sum_{n \leq n' \leq n + \Delta n} w_{i',j',n,n'} - z_{j',j,s,n} \right) \quad \forall s \in \mathbf{S}^{IN}, j, j', i \in \mathbf{I}_j, i \in \mathbf{I}_s^P, i \notin \mathbf{I}^{\text{Re}}, n \quad (6)$$

An active consumption task i' should be processed in a unit after the time that state s is available at the previous event n .

$$T_{s,j,n} \leq Tf_{j',n+1} + M \cdot \left(1 - \sum_{i' \in \mathbf{I}_s^C, i' \in \mathbf{I}_j} \sum_{n+1 \leq n' \leq n+1+\Delta n} w_{i',j',n+1,n'} \right) \quad \forall s \in \mathbf{S}^{IN}, j, j', i \in \mathbf{I}_s^P, i \in \mathbf{I}_j, i \notin \mathbf{I}^{\text{Re}}, n < N \quad (7)$$

3.2. Sequencing constraints for limited intermediate storage policies

For FIS states, it should be examined whether the materials produced can be stored.

$$\sum_{i \in \mathbf{I}_s^P, i \in \mathbf{I}_j, i \in \mathbf{I}^{\text{Re}}} \sum_j \rho_{i,s} \sum_{n - \Delta n \leq n' \leq n} b_{i,j,n',n} + ST_{s,n} \leq ST_s^{\max} + \sum_{i \in \mathbf{I}_s^P} \sum_{i' \in \mathbf{I}_s^C} bs_{i,i',s,n} \quad \forall s \in \mathbf{S}^{\text{FIS}}, n \quad (8)$$

If they cannot be stored then they either have to be consumed immediately or stored in the unit, processing consuming task i' at event n , must take a non-zero value.

$$bs_{i',s,n} \leq B_{i,j}^{\max} (x_{i',s,n} + u_{i',s,n}) \quad \forall s \in \mathbf{S}^{FIS}, j, j', i \in \mathbf{I}_s^P, i' \in \mathbf{I}_s^C, n \quad (9)$$

$$x_{i',s,n} + u_{i',s,n} \leq 1 \quad \forall s \in \mathbf{S}^{FIS}, j, j', i \in \mathbf{I}_s^P, i' \in \mathbf{I}_s^C, n \quad (10)$$

$$\rho_{s,i} \cdot \sum_{n-\Delta n \leq n' \leq n} b_{i,j,n',n} \geq \sum_{i' \in \mathbf{I}_s^C} bs_{i',s,n} \quad \forall s \in \mathbf{S}^{FIS}, j, i \in \mathbf{I}_s^P, i \in \mathbf{I}_j, i \notin \mathbf{I}^{\text{Re}}, n \quad (11)$$

$$-\rho_{s,i'} \cdot \sum_{n \leq n' \leq n+\Delta n} b_{i',j',n,n'} \geq \sum_{i \in \mathbf{I}_s^P} bs_{i',s,n} \quad \forall s \in \mathbf{S}^{FIS}, i' \in \mathbf{I}_s^C, j', n \quad (12)$$

If $bs_{i',s,n}$ takes a non-zero value, then the start time of consuming task as well as the finish time of the producing task are enforced to be equal.

$$T_{s,j,n} \leq Tf_{j,n} + M \cdot \left(1 - \sum_{i \in \mathbf{I}_s^P, i \in \mathbf{I}_j, i \notin \mathbf{I}^{\text{Re}}} x_{i',s,n} \right) \quad \forall s \in \mathbf{S}^{FIS}, j, n \quad (13)$$

$$T_{s,j,n} \geq Ts_{j',n} - M \cdot \left(1 - \sum_{i' \in \mathbf{I}_s^C} x_{i',s,n} \right) \quad \forall s \in \mathbf{S}^{FIS}, j, j', i \in \mathbf{I}_s^P, i \in \mathbf{I}_j, i \notin \mathbf{I}^{\text{Re}}, n \quad (14)$$

In order to avoid real time storage violations, between producing and consumption tasks occurring at the previous event the following constraint is introduced.

$$Tf_{j',n+1} \geq Ts_{j,n} - M \cdot \left(1 - \sum_{n+1-\Delta n \leq n' \leq n+1} w_{i',j',n',n+1} \right) \quad \forall s \in \mathbf{S}^{FIS}, j, j', i' \in \mathbf{I}_s^C, i' \in \mathbf{I}_j, n < N \quad (15)$$

3.3. Allow production units to hold materials

We define $us_{j,n}$ as the extra amount of materials stored in a processing unit j at n .

$$ST_{s,n} \leq ST_s^{\max} + \sum_j \sum_{i \in \mathbf{I}_s^P, i \in \mathbf{I}_j} us_{j,n} \quad \forall s \in \mathbf{S}^{FIS}, n \quad (16)$$

The amount of materials stored in a unit at n cannot exceed the amount produced at $n-1$.

$$us_{j,n} \leq \sum_{s \in \mathbf{S}^{FIS}} \sum_{i \in \mathbf{I}_j, i \in \mathbf{I}_s^P} \sum_{n-1-\Delta n \leq n' \leq n} \rho_{i,s} b_{i,j,n',n-1} + us_{j,n-1} \quad \forall j, n > 1 \quad (17)$$

If a unit j holds some material at n , then it cannot process any task at this event.

$$us_{j,n} \leq \left[\max_{i \in \mathbf{I}_j} (B_{i,j}^{\max}) \right] \cdot \left(1 - \sum_{i \in \mathbf{I}_j} \sum_{n-\Delta n \leq n' \leq n} \sum_{n \leq n' \leq n+\Delta n} w_{i,j,n',n'} \right) \quad \forall j, n \quad (18)$$

We define binary variables $xs_{j,n}$ to denote if a unit j holds materials.

$$us_{j,n} \leq \left[\max_{i \in \mathbf{I}_j} (B_{i,j}^{\max}) \right] \cdot xs_{j,n} \quad \forall j, n \quad (19)$$

Finally, if a unit holds some material at n , the finish time of all consuming tasks must be equal to the start time of that unit.

$$T_{s,j,n} \leq Tf_{j,n} + M \cdot (1 - xs_{j,n}) \quad \forall s \in \mathbf{S}^{FIS}, j, i \in \mathbf{I}_s^P, i \in \mathbf{I}_j, n \quad (20)$$

$$T_{s,j,n} \geq Ts_{j',n} - M \cdot \left(2 - xs_{j,n} - \sum_{n \leq n' \leq n + \Delta n} w_{i',j',n,n'} \right)$$

$$\forall s \in \mathbf{S}^{FIS}, j, j', i \in \mathbf{I}_s^p, i \in I_j, i \notin \mathbf{I}^{Re}, i' \in \mathbf{I}_s^c, i' \in I_{j'}, n \quad (21)$$

4. Computational results

We solve five examples including four well-established examples in the literature (Shaik and Floudas, 2009; Li and Floudas, 2010) to illustrate the capability of the proposed model. Both UIS and FIS policies are considered. We also compare the performance of the proposed model with the models of Li and Floudas (2010) (denoted as LF) and Vooradi and Shaik (2013) (denoted as VS). The computational results are given in Tables 1-2. From Tables 1-2, it can be observed that the proposed model reduces the total number of event points required for all examples compared to the LF model. This is because as it is depicted in figure 2 unit J1 is able to process 100 units of intermediate state using the proposed formulation since 50 of them can be temporary stored in the processing unit before being processed by J2, while by using existing formulations only 60 units can be processed since they cannot be stored in the processing unit and the storage capacity is 10. Compared to the VS model, the proposed model reduces the number of event points required for most examples except Examples 2 and 3 because all tasks in these two examples have to be treated as recycling task. The proposed model required less computational time for all examples compared to the LF and VS models especially for Example 3 which is reduced by 55% with UIS policy and 15% with FIS policy. More significantly, the proposed model generates a better solution than LF and VS models for Example 5. This is because a production unit is allowed to store materials produced. Therefore, the amount of materials produced can exceed the storage capacity. The optimal schedule for the proposed model is illustrated in Figure 2.

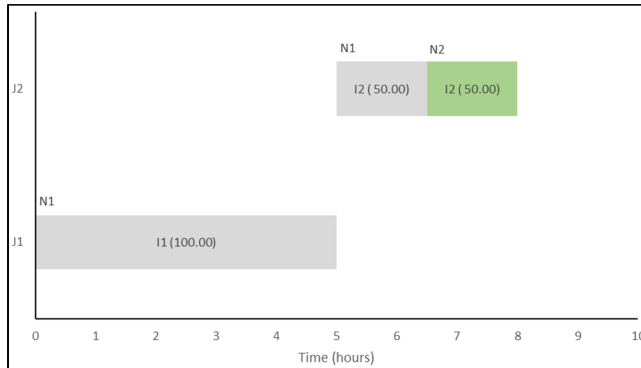


Figure 2 STN representation of a multipurpose batch process facility

5. Conclusions

In this work, an improved unit-specific event-based formulation for multipurpose batch processes has been presented. The proposed model allows related non-recycling production and consumption units to take place at the same event. Furthermore, a unit processing a consuming task is sequenced with a related production task, only if the unit processing the consuming task consumes materials from the unit processing the producing task. Additionally, a consumption task is allowed not to start immediately

after the finish of the related production task if storage is available. Finally, a processing unit is allowed to store materials if it is idle. The results demonstrate that the proposed model is able to generate same or better solutions, using less events, which can significantly reduce the computational time, especially in computationally expensive problems.

Table 1 Comparative results for examples 1-5 with UIS and FIS policy

Ex.	Model	UIS				FIS			
		Event points	CPU time (s)	RMILP	MILP	Event points	CPU time (s)	RMILP	MILP
1	LF ^a	5	0.1	3000.00	2628.19	6	0.2	3973.92	2628.19
	VS ^b	5	0.3	3000.00	2628.19	5	0.2	3000.00	2628.19
	U-S ^c	3	0.1	3000.00	2628.19	3	0.2	3000.00	2628.19
2	LF	6 ^d	3.7	2730.66	1962.69	6 ^d	4.4	2730.66	1962.69
	VS	5	0.2	2436.69	1962.69	5	0.3	2436.69	1962.69
	U-S	5	0.2	2436.69	1962.69	5	0.4	2436.69	1962.69
3	LF	8 ^d	1244	3618.64	2358.20	9 ^d	3600 ^e	3618.64	2345.31 ^f
	VS	7	1179	3369.69	2358.20	7	950	3369.69	2358.20
	U-S	7	546	3369.69	2358.20	7	821	3369.69	2358.20
4	LF	5	0.1	80.0000	58.9870	5	0.1	80.0000	58.9870
	VS	5	0.2	80.0000	58.9870	5	0.2	80.0000	58.9870
	U-S	2	0.2	80.0000	58.9870	2	0.1	80.0000	58.9870
5	LF	3	0.1	500.000	500.000	3	0.1	500.000	300.000
	VS	3	0.1	500.000	500.000	3	0.1	500.000	300.000
	U-S	2	0.1	500.000	500.000	2	0.1	500.000	500.000

^aLi et. al. 2010. ^bVooradi and Shaik 2013. ^cProposed unit-specific model ^d $\Delta n = 1$ ^eRelative gap 7.11%. ^f Suboptimum solution.

References

- I. Harjunkski, C. Maravelias, P. Bongers, P. Castro, S. Engell, I. Grossmann, J. Hooker, C. Méndez, G. Sand, J. Wassick, 2014, Scope for industrial application of production scheduling models and solution methods, *Computers and Chemical Engineering*, 62(5), 161-193
- J. Li, C. Floudas, 2010, Optimal Event Point Determination for Short-Term Scheduling of Multipurpose Batch Plants via Unit-Specific Event-Based Continuous-Time Approaches, *Industrial & Engineering Chemistry Research*, 49(16), 7446-7469
- N. Rakovitis, J. Li, N. Zhang, 2018, A novel modelling approach to scheduling of multipurpose batch processes, *Computer Aided Chemical Engineering*, 44, 1333-1338
- R. Seid, T. Majozzi, 2012, A robust mathematical formulation for multipurpose batch plants, *Chemical Engineering Science*, 68(1), 36-53
- M. Shaik, C. Floudas, 2009, Novel Unified Modeling Approach for Short-Term Scheduling, *Industrial & Engineering Chemistry Research*, 48(6), 2947-2964
- M. Shaik M., R. Vooradi, 2017, Short-term scheduling of batch plants: Reformulation for handling material transfer at the same event, *Industrial & Engineering Chemistry* 56(39), 11175-11185
- R. Vooradi, M. Shaik, 2013, Rigorous unit-specific event based model for short term scheduling of batch plants using conditional sequencing and unit-wait times, *Industrial and Engineering research*, 52(36), 12950-12792

On-grid Hybrid Power System and Utility Network planning to supply an Eco-Industrial Park with dynamic data

Florent Mousqué^a, Marianne Boix^{a*}, Stéphane Négny^a, Ludovic Montastruc^a,
Serge Domenech^a

^a *Laboratoire de Génie Chimique, Université de Toulouse, CNRS, INPT, UPS,
Toulouse, France*

marianne.boix@ensiacet.fr

Abstract

Eco-Industrial Parks (EIP) aim to preserve environment while increasing competitiveness of companies. This paper presents a mathematical Mixed Integer Linear Programming (MILP) model to optimally grassroots design an EIP energy network comprising heat and electricity. In the utility system, heated steam is produced, network is designed by selecting boilers and turbines technologies and interconnection pipes between companies. Simultaneously in the on-grid Hybrid Power System (HPS) composed of wind turbines, solar Photovoltaic (PV) panels, steam turbines and external grid, the model can select which source to use to meet the power demand.

A case study of 10 industries from Yeosu real industrial park with seasonal data is provided to assess the model, first on economic comparison between stand-alone and EIP situation of companies, and secondly to determine which power source is profitable for HPS based on the sale price of electricity on the external power grid.

In conclusion, this model allows the optimal design of the energy network of an EIP with dynamic data and with the objective of minimizing the net present cost.

Keywords: Industrial Ecology, Eco-Industrial Parks, Utility Network, Hybrid Power System, Mathematical Optimization, Renewable Energies.

1. Introduction

Nowadays the risks of human-induced climate change are increasingly pointed out by scientific reports. These reports conclude that limiting global warming would require ambitious mitigation actions while achieving sustainable development which means a development leading to economic, environmental and social benefits (Brundtland et al., 1987). To these objectives, industry has an important role to play because classical linear model (extract, produce, consume, throw) is responsible for overwhelming extraction of natural resources and waste rejection.

Facing these environmental issues, Industrial Ecology (IE) provides an innovative way to produce goods and services based on a circular model (share, reuse, mutualize). Indeed, in these industrial ecosystems, energy and resources consumption are optimized, waste generation is minimized and effluents from one production process are used as raw materials for another (Frosch & Gallopoulos, 1989). An application to this concept are EIP, in which industries gather on a same site and thanks to their vicinity they share and exchange efficiently different flows (material, energy, utilities). Furthermore, while

reducing their environmental impacts they can also achieve greater economic competitiveness. To implement EIP in a sustainable way, companies need methods and optimization tools to design appropriate inter-enterprises exchanges. While an increased number of research projects have been carried out in recent years, Boix et al. (2015) pointed out that only a few deal with energy flow management neither with coupled networks. However, a systemic approach studying interactions between the different flows and optimizing them simultaneously would allow a better synergy between companies.

In the great majority of industrial parks, the facilities to meet energy demand are utility systems producing utilities for processes (i.e. mainly heat, cold streams and compressed air) and HPS that produce electricity using several power sources.

In utility systems, main energy consumption concerns heat, due to its high calorific value and its ability to generate power by rotating turbine. Moreover, in these utility systems, Combined Heat and Power (CHP) is an energy-efficient way to produce simultaneously electricity and thermal energy. Indeed, compared to the separate generation of heat and power, cogeneration can improve energy efficiency between 10 and 40% (Madlener & Schmid, 2003) and thereby reduces CO₂ emissions. Through combined production raises other constraints such as operational planning of production. Yet a large number of publications are dedicated to optimizing the operational management of existing CHP, (Aguilar, 2007; Mitra, 2013) but only a few to design such facilities even less so adapted to EIP context with heat utility exchanges between companies. Afterwards, HPS, as a coupled system, is an efficient way to harness RE sources, relying on complementarity between sources. When it is connected to the external grid it is possible to compensate for the lack of production from other sources purchasing power, it is then called on-grid HPS. In addition, a decentralized production means to reduce reliance on external grid and reinforces the robustness of the power system.

In a previous publication, a study on on-grid HPS to supply electricity in an EIP was carried out using a mathematical LP model for the optimal design of this HPS with dynamic demand, on an hourly basis (Mousqué et al., 2018). This model has the possibility to select power sources to install between wind turbines, solar PV panels, biomass by combustion or also buy electricity from the grid.

To go further, this work extends the previous HPS model by presenting a generic optimization model to the grassroots design of both the utility network and the HPS of an EIP. The first purpose of this article is to assess economic interest that companies can encounter by sharing their heat and power facilities in comparison to their stand-alone situation. Another objective is to discuss which RE or energy-efficient electricity source can be profitable to supply EIP demand. Two optimal solutions are finally discussed depending on the sale price of electricity fixed by politic regulation. These results are obtained on a complex real problem using the proposed approach involving 10 companies in an EIP with real demands taken from Yeosu industrial park (Kim et al., 2010).

2. Problem statement

The aim is to design the exchanges of water, steam and electricity between processes inside a single company as well as exchanges between different companies, during several time steps. A generic superstructure (Figure 1) has been developed in order to show the different components taken into account in the model.

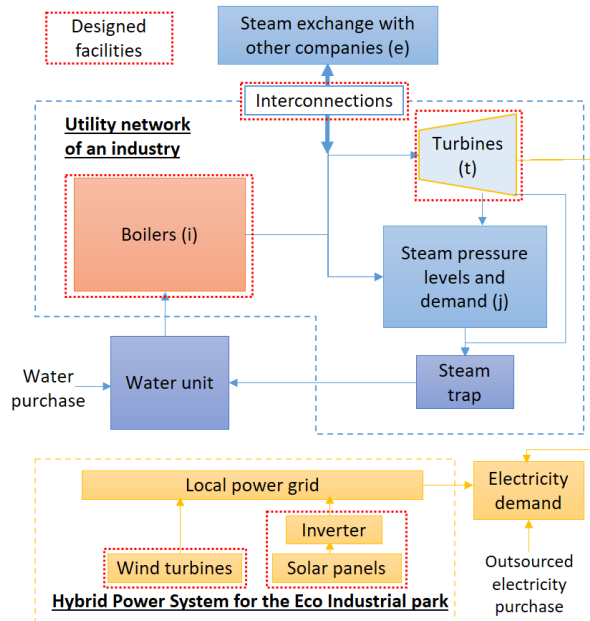


Fig 1. Superstructure of the utility system of an industry and HPS of the EIP.

In a company, steam flows through steam headers, different levels of steam pressure are taken into consideration. Pressure release valves are used to convert higher pressure steam into lower pressure steam by dropping its pressure. Steam is produced by boilers installed in companies. In the case studied in this publication, they are natural gas boilers. Different types of boilers can be installed depending on the maximum production capacity and the level of steam pressure produced. Boiler capacity range is between 50 and 100 % of its maximum power, because in this range boiler has a relatively constant efficiency (Aguilar et al., 2007) and also in seasonal operation it would be a big loss to operate the boiler at a low capacity, which means at a low efficiency level.

These power sources are selected to be RE technologies, i.e. wind turbines and photovoltaic panels, or energy-efficient such as cogeneration by mean of turbines. Data are dynamic with a seasonal variation (one-step for each season). In an EIP configuration, the power production is shared between companies and used to supply their demand. By connecting to external power grid, power can be bought and excess production can be sold. Finally, multi-stage extraction turbines can be selected between three technologies (i.e. 500 kW, 3 MW, and 15 MW). These turbines convert energy contained in high-pressure steam to a lower level of pressure or to condensed water. Higher is the pressure difference, higher the power production.

In this case, the production of renewable energy is considered as an average over a season. This estimate is only possible thanks to the external grid connection. Indeed, periods when production is higher or lower than the average production are supposed to be offset by the purchase or sale of electricity.

Water flow is a closed loop, after consumption from the process, water returns to the water unit, reducing water consumption. Each company has the possibility to buy water at every time step if necessary. Indeed, water losses by evaporating in water unit and steam losses by condensing trap or vent to evacuate overload are included.

3. Generic optimization model

Regarding the superstructure previously shown and the complexity of this model, due to the important numbers of continuous and binary design variables, a large-scale MILP model is developed. Due to its genericity, it is intended to be adaptable to the initial design of new EIP or to the retrofit of existing industrial parks, this last case by setting the initial structure.

The selected objective function is to minimize NPV of the designed utility network and HPS for a project duration considered of 20 years, with a discount factor of 7%. Constraints to model units are based on thermodynamic principles, mass and energy balances. Decision variables are the different possible connexions between units and enterprises characterized by their type (VHS, HS, MS, LS, water...) and their flow and the decision to install or not a boiler and if it is installed which one is chosen? Capital and operational cost for installed boilers, turbines, pipes and the consumption of raw material are thus determined by the decision variables. Raw materials are fuel i.e. natural gas, treated water and electricity, which can be purchased or sold. Binary variables are used to select installed pipes between companies, installed technologies for boilers and turbines and operational state of boilers (i.e. switched on or off).

Given the high capacity of the superheated steam to be transported, losses in the interconnection pipes between the companies are considered negligible. Implemented data for boiler cost and steam pipes comes from economic evaluation manual (Chauvel et al., 2001) and are actualized using OECD Industrial Production Index. Renewable production is supposed to take place in France, with RTE report seasonal production (RTE, 2018) for these sources complete cost are those from ADEME (2016). Price for natural gas is set at 280 €/ton.

This model has 4101 constraints, 5103 variables including 540 binaries and it was solved with IBM ILOG CPLEX Optimizer.

4. Results and discussion

Two studies are conducted: an economic analysis of the case study to determine the interest of a company to take part of an EIP while the second one deals with the design of HPS power sources considering a different price for sale electricity.

This first study will compare Stand-alone and EIP solutions, both with a sale price of 0.05€/kWh which reflects the average price for electricity producer in France. While the second analyse will be a comparison between EIP (0.05) and EIP (0.10), latter case with a price of 0.10 €/kWh, considering politic aids to enhance creation of a local power grid. Detailed costs for these discussed optimal solutions are presented in Table 1.

Table 1

Overall economic comparison between Stand-alone and EIP situation.

Overall cost	Net Present Cost	Boilers cost	Power sources cost			Raw Materials cost				Pipes cost
			Turbines	Solar PV panels	Wind Turbines	Fuel	Water	Electricity purchased	Electricity sold	
Stand-alone	1,097,762 k€	56,294 k€	4,181 k€	- €	- €	1,040,671 k€	3,781 k€	4,311 k€	-11,478 k€	- €
EIP (0.05)	1,048,715 k€	36,186 k€	- €	- €	- €	1,001,113 k€	3,416 k€	4,430 k€	- €	3,569 k€
EIP (0.10)	982,324 k€	55,638 k€	56,647 k€	- €	38,594 k€	1,184,730 k€	3,923 k€	4,431 k€	-366,036 k€	4,396 k€

4.1. Stand alone and EIP (0.05) comparison

Observations show that while cost is slightly different for NPV of the EIP (0.05) (i.e. -4.7 %), for water (i.e. -10.7 %) and for fuel (i.e. -4.0 %), main reduction observed is for the cost of installed boilers (i.e. a reduction of 55.6 %). Additionally in stand-alone situation, the model proposes to invest in turbines, produce electricity and sale it.

This is because single companies have oversized boilers during seasons with lower demand, and this overproduction cannot be valorised. To avoid dumping it, it is profitable to install turbines to value this overproduction. In EIP configuration, cost for installed boilers is significantly reduced. In fact, pipe cost being less expensive than gain resulting from creating interconnections, companies share their production and their demand. This share allows a better size and management of installed boilers. This is observable by an average production ratio of installed boiler at 77% of their maximal production in EIP against 60% in stand-alone. However, on project life span, fuel is the most important cost, and in comparison between cases, only a few difference is observed. More accurate fuel consumption results should be obtained by including boiler inertia on a daily basis.

4.2. Impact of the electricity sale price on the design

Figure 2 shows the optimal solution of the utility network for EIP (0.05) case, with boiler for each company and different pressure level exchanges, highlighting results that this model achieves and its complexity.

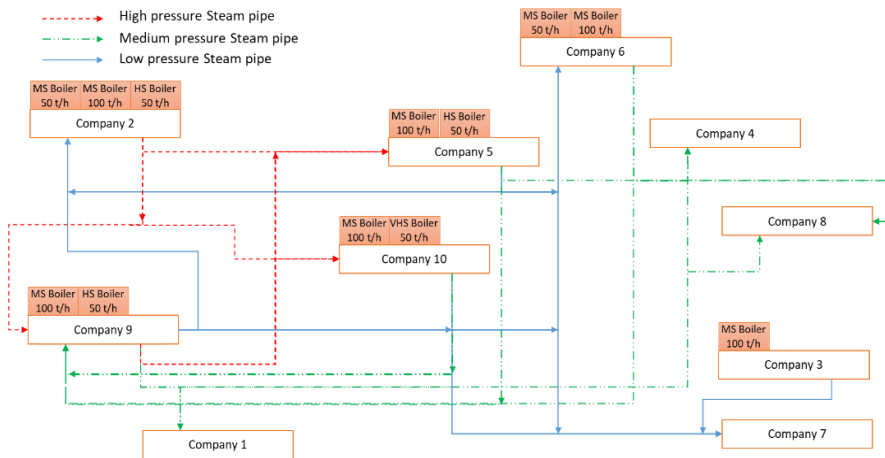


Fig 2. Designed boilers and utility steam exchange network for EIP (0.05).

With a sale price of 0.05 €/kWh neither turbines nor RE are selected, whereas when the sale price increases at 0.10 €/kWh both wind turbines and turbines are selected with three turbines of 15 MW. These choices can be justified with wind turbines and PV panels break-even point, which is calculated as respectively 0.094 €/kWh and 0.125 €/kWh, depending on discount factor and overall production and complete cost of each technology. For turbines, it is also dependent on utility system criteria, such as turbines and boilers technology (i.e. investment cost and efficiency), output pressure steam and if extra steam production is available to value it. However, over the lifespan of the project, the complete discounted cost for the installation of the turbines represents only a relatively

small part. For example, for a 500 kW system operating at nominal power, the cost of the installation is calculated at 0.019 €/kWh. Only based on an economic criterion, external electricity price has been identified as a main parameter to decide which technology to use. Turbines can be considered as an efficient way to value overproduction or overheated steam. Currently, wind turbines are cheaper than PV panels, although the difference is small, the design will depend mainly on the renewable resource available on the site.

5. Conclusion

A model of grass-root design of an EIP utility system and HPS with an economic criterion has been developed to determine the facility to invest in and the exchanges between companies. In this model, the implementation of this EIP represents a slight NPV gain, but a significant reduction in the investment cost of boilers. For HPS, a too low price of outsourced electricity does not foster to create a local grid with cogeneration, wind turbines or PV panels. However, other criteria could be taken into account, such as public subsidies on investment or on sale price to incite such technologies. This mathematical model has validated a first frame to assess capability of MILP to be solved on a real case of 10 companies taken from Yeosu industrial park with dynamic seasonal data. Further improves could be achieved, using this model on a case study with dynamic data on a daily basis (day and night) allowing more accurate results for boiler management, more detailed analyse on RE sources variation production depending on weather conditions. Another interesting point is that due to fuel cost importance, other fuels and boilers technology could be added. Finally using a multi-objective optimization, including environmental objective is another way to explore.

References

- ADEME. (2016). Coûts des énergies renouvelables en France. Edition 2016. France
- Aguilar, O., Perry, S. J., Kim, J.-K., & Smith, R. (2007). Design and optimization of flexible utility systems subject to variable conditions. *Chemical Engineering Research and Design*.
- Boix, M., Montastruc, L., Azzaro-Pantel, C., & Domenech, S. (2015). Optimization methods applied to the design of eco-industrial parks: A literature review. *Journal of Cleaner Production*.
- Brundtland, G., Khalid, M., Agnelli, S., Al-Athel, S., Chidzero, B., Fadika, L.M et al., (1987). *Our Common Future : world commission on environment and development*. Oxford.
- Chauvel, A., Fournier, G., Raimbault, C., & Pigeyre, A. (2001). *Manuel d'évaluation économique des procédés*. Editions Technip. France.
- Frosch, R. A., & Gallopoulos, N. E. (1989). Strategies for Manufacturing, *261(3)*, 144–153.
- Kim, S. H., Yoon, S. G., Chae, S. H., & Park, S. (2010). Economic and environmental optimization of a multi-site utility network for an industrial complex. *Journal of Environmental Management*, *91(3)*, 690–705.
- Madlener, R., & Schmid, C. (2003). Combined Heat and Power Generation in Liberalised Markets and a Carbon-Constrained World. *GAEA - Ecological Perspectives for Science and Society*, *12(2)*, 114–120.
- Mitra, S., Sun, L., & Grossmann, I. E. (2013). Optimal scheduling of industrial combined heat and power plants under time-sensitive electricity prices. *Energy*, *54*, 194–211.
- Mousqué, F., Boix, M., Négny, S., Montastruc, L., Genty, L., & Domenech, S. (2018). Optimal on-grid hybrid power system for eco-industrial parks planning and influence of geographical position. *Computer Aided Chemical Engineering (Vol. 43)*.
- RTE - Réseau de transport d'électricité. (2018). *Panorama de l'électricité renouvelable en 2017*.

Economic Study of the Urea Alcoholysis Process for Dimethyl Carbonate Production

Juan Javaloyes-Antón^{a,*}, Daniel Vázquez^a, Juan D. Medrano-García, José A. Caballero^a

^aInstitute of Chemical Process Engineering. Universito of Alicante, Alicante, Spain

javaloyes.anton@ua.es

Abstract

In this work, we study the techno-economic feasibility of the urea alcoholysis process for the continuous manufacture of dimethyl carbonate. We propose a superstructure for the urea alcoholysis process based on patents and research articles found in literature. In this superstructure, different reaction and separation alternatives have been considered leading to 54 feasible flowsheets. Due to the complexity of some unit operations (reactive distillation columns, azeotropic distillation columns) and the reduce number of alternatives (or at least not prohibitive), we performed an exhaustive search to determine the most profitable flowsheet using Aspen Plus. Results prove the feasibility of this process, as long as a good catalyst is employed in the process.

Keywords: dimethyl carbonate, urea alcoholysis, process simulator, Aspen Plus.

1. Introduction

Dimethyl carbonate (DMC) is a non-toxic chemical that stands out thanks to its versatile use as reagent and solvent. DMC is employed as a substitute of dimethyl sulfate and methyl halides in methylation reactions, and as carbonylation agent to replace phosgene in the production of polycarbonates. DMC could also be used as a fuel additive since it has a higher oxygen content (53%) than the MTBE or TAME. However, the current price of DMC still prohibitively expensive to use as fuel additive (Ryu and Gelbein, 2006).

Different technologies to produce DMC have been studied, although a few of them are industrially exploited (Pacheco and Marshall, 1997). The commercial routes to make DMC that are currently in operation are: the older commercial process based on the phosgenation of methanol; and the greenest processes: liquid phase oxidative carbonylation of methanol (ENIChem), vapor phase oxidative carbonylation of methanol (Covestro and Ube), and transesterification of ethylene carbonate with methanol (Asahi Kasei). In addition, there is a developing process with some promise: the urea alcoholysis.

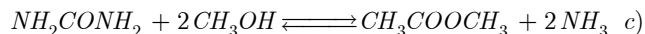
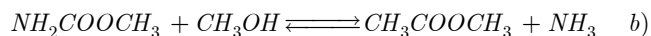
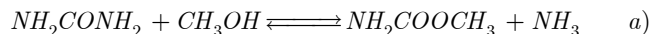
The urea route allows the production of DMC using urea and methanol as raw materials, which are abundant and not especially expensive. It also avoids the use of phosgene, carbon monoxide, nitric oxide and ethylene oxide, which are present in the commercial routes aforementioned. The most promising chemical scheme to obtain DMC from urea and methanol is based on a two-step reaction.

First, urea is converted to the intermediate methyl carbamate (MC) by reaction with methanol (Reaction 1a). Then, the carbamate is further reacted with methanol in the presence of a catalyst to produce DMC (Reaction 1b). The first reaction is thermodynamically favorable. In the work of Wang et al. (2007) it is also noted that a

high conversion of urea to MC can be reached quickly. However, the critical aspect associated with this route is the highly unfavorable equilibrium of the second step reactions, whose equilibrium constant is about $2.08 \cdot 10^{-3}$ at 300 K. This reaction is endothermic, therefore, a positive effect on the equilibrium is observed rising the temperature. Nevertheless, the gain on the equilibrium constant value is not so pronounced as to overcome the problems raised by the reaction thermodynamics, as it is shown in Table 1 (Wang et al., 2007). In addition, the component N-methyl methyl carbonate (NMMC) has been detected as the main byproduct, which is formed from the reaction of DMC with MC.

Beside the unfavorable thermodynamics of Reaction 1b, the synthesis of DMC from urea alcoholysis is a very attractive route since it avoids the hazards of using dangerous compounds, and would allow the synthesis of DMC starting from carbon dioxide, since the co-product ammonia can be recycled to the synthesis of urea ($\text{NH}_3 + \text{CO}_2 \rightarrow \text{urea} + \text{water}$). The commercial success of this route basically depends on the development of an appropriate catalyst to the second reaction step, and the design of suitable reaction arrangements in order to carry out the second step reaction on a large industrial scale.

Remark that a large amount of works in academia and industrial literature can be found about this topic. However, as far as the authors are aware, the academia papers are mainly focus on the study of the reaction mechanisms and catalyst. And the patents, even though they describe the process for large scale production, all the examples that they provide are laboratory scale. Thus, the main aim of this work is to provide a preliminary techno-economic assessment for the urea alcoholysis process, based on the rigorous simulation of possible large industrial scale flowsheets.



Reaction 1. a) Methyl carbamate (MC) formation. b) DMC formation. c) Global reaction.

Table 1. Temperature dependence of the equilibrium constant for reactions 1a and 1b.

T (K)	K – Reaction 1a	K – Reaction 1b
300	203.88	$2.08 \cdot 10^{-3}$
350	120.88	$4.30 \cdot 10^{-3}$
400	86.07	$7.20 \cdot 10^{-3}$
450	70.27	$1.04 \cdot 10^{-3}$
500	62.74	$1.37 \cdot 10^{-3}$
550	58.40	$1.66 \cdot 10^{-3}$
600	57.65	$1.92 \cdot 10^{-3}$

2. Superstructure for the DMC production process from Urea

The superstructure for the DMC production process from urea and methanol given in Figure 1 is considered. This superstructure consists of the following three main sections:

2.1. Reaction and ammonia recovery section

As discussed in the previous section, DMC is produced from the reaction of methanol with urea in a two-step reaction. The first reaction is thermodynamically favorable. However, the second one has a low equilibrium constant. Thus, as other equilibrium reactions (such as the production of diphenyl carbonate from phenol and DMC), Reaction 1b is best carried out in a reactive distillation column (Ryu and Gelbein, 2002). Under these conditions, the following alternatives have been considered. On the one hand, a continuous stirred-tank reactor (R-101) can be used for the production of MC without catalyst. Then the byproduct NH_3 is removed by means of a distillation column (C-101). This column can operate at lower or higher pressure than R-101. Depending on the operating pressure, around 7 or 14 bar respectively, refrigerated water or cooling water will be used in the column condenser as cold utility. C-101 bottoms product is fed to the reactive distillation column C-102, where MC is converted to DMC. This column strips the product DMC and co-product NH_3 from the reaction mixture, shifting the equilibrium to the product side. C-102 can operate with a total or partial condenser. The C-102 overhead stream, containing most of the unreacted MeOH, NH_3 , CO_2 and some DMC is mixed with a stream coming from the distillation section with similar composition, and fed to the C-103 column. In this column, NH_3 is recovered as top product, and the bottom product, containing MeOH and some DMC, is recycled back to the reaction section.

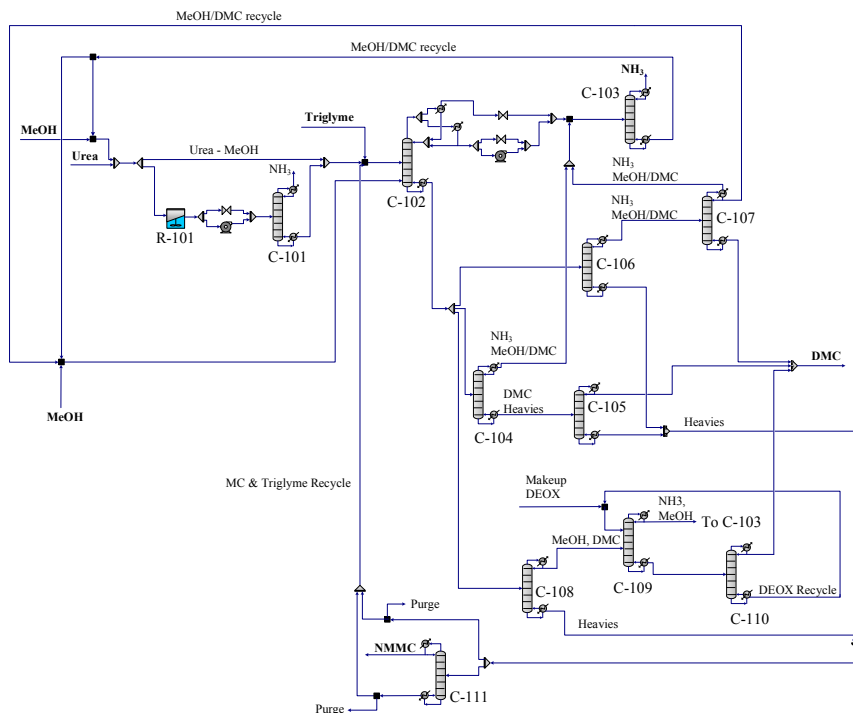


Figure 1. Superstructure for the production of DMC from urea and methanol.

As in the previous ammonia recovery column (C-101), the refrigerant fluid in the condenser of C-103 can be refrigerated water or cooling water depending on the column

operating pressure. On the other hand, reactive distillation column R-102 can be used as the single reactor to carry out the two-step reaction.

The reaction of MC with methanol to DMC takes place in the presence of a catalyst. Different heterogeneous and homogeneous catalyst have been studied so far. In the present work, the homogeneous catalyst triglyme is used according to the US patent 6,392,078 (Ryu and Gelbein, 2002).

2.2. Distillation section

The crude DMC from the bottom product of C-102 is diverted to the distillation section. This stream, containing NH_3 , unreacted MeOH, DMC product and heavier compounds (NMMC, unreacted MC and triglyme) has to be separated into three main streams: high purity DMC product stream, a MeOH recycle stream (which will contain DMC and NH_3), and a stream containing the heavy compounds (NMMC, MC and triglyme).

The binary system MeOH-DMC has a homogeneous azeotrope which makes the separation somewhat more complex. Fortunately, this azeotrope is pressure dependent, increasing the percentage of MeOH with pressure (Romano, 1976). For instance, at one bar the azeotrope composition of MeOH is around to 85 mol%, and at 15 bar around to 96 mol% (Yunhai et al., 2005). This allows for using pressure distillation to improve the MeOH-DMC separation.

Two different sequences are considered in the superstructure shown in Figure 1 based on exploiting this change in the azeotropic composition with pressure. The direct sequence (C-104 and C-105 columns), and the indirect sequence (C-106 and C-107 columns).

In the direct sequence, C-104 column operates at around 12 bars. At higher pressures, the temperature in the reboiler overcomes 240°C , which prevent from using high pressure steam (41 barg, 254°C) as hot utility. The overhead product from C-104 is a mixture of MeOH-DMC close to the azeotrope composition and all the NH_3 in C-102 bottom product, while the bottom product contains DMC and the heavier compounds. The C-104 column bottoms are fed to C-105 distillation column where high purity DMC is obtained as top product. The column bottoms, containing NMMC, MC and triglyme are sent to the catalyst and MC recovery section. C-105 column operates close to atmospheric pressure. In the indirect sequence, the C-106 column splits the bottom product of the reactive distillation column into a stream containing all the NH_3 , MeOH and DMC as top product, and a stream containing the heavier compounds (NMMC, MC and triglyme) as bottom product. The C-106 bottoms are diverted to the catalyst and MC recovery section. The overhead product is fed into the high-pressure C-107 column. In this column (C-107), high purity DMC is obtained from the bottoms, and a mixture of MeOH-DMC close to the azeotrope composition with the NH_3 as top product. The C-106 column operates at atmospheric pressure, and C-107 at 12-16 bar. A third alternative has been considered in the superstructure based on extractive distillation (C-108, C-109 and C-110). For instance, the US Patent No. 5,214,185 (Nishihira et al., 1993) disclosed the separation of the DMC-MeOH mixture by using dimethyl oxalate (DMOX) as solvent, and US Patent No. 6,392,078 (Ryu and Gelbein, 2002) assert that diethyl oxalate (DEOX) has more desirable properties than DMOX. The extractive distillation sequence proposed in Figure 1 can be used either with DMOX and DEOX. Preliminary simulations have shown that both solvents are effective, and in our work we selected DMOX.

2.3. Catalyst and methyl carbamate recovery section

The bottom product of C-105, C-106 or C-108 depending on whether the direct sequence, indirect sequence or extractive sequence is selected respectively, is sent to the catalyst and MC recovery section. In this section, part the undesired product NMMC is removed by means of C-111 column or a purge, in order to control the build-up of this component in the system. If the purge is selected, a bleed of 3-5% is performed in the stream. If the distillation column is selected, most of the NMMC is removed from the system and the performance of the process improves, at the expense of using an additional column.

3. Results

An exhaustive search is performed using the flowsheeting program Aspen Plus to determine the most profitable flowsheet based on raw material, products, and utility costs. Actually, the existence of dominated solutions avoids the need of simulation all 54 alternatives. For instance. The composition specifications of the effluent heavy stream from the distillation section is the same independently of the selected distillation arrangement. If we compare all the alternatives resulting from fixing the direct distillation sequence followed by C-111 column (9 alternatives), with the alternatives resulting from fixing the direct distillation sequence followed by the purge in order to control the build-up of byproduct NMMC (9 alternatives), it is possible to determine that the use of C-111 column gives the best results. Thus, the remaining branches of the decision tree that uses purges to control the amount of NMMC can be cut-off (18 alternatives).

The main results for the best flowsheet are summarized in Table 1. The best flowsheet consists of the following columns: C-102 with partial condenser, C-103 at low temperature, C-104, C-105 and C-111 (Figure 2). The yearly DMC plant production rate was fixed to 52 Kton/y, based on 8,000 operating hours per year. The price for the raw materials and products were taken from different webs (www.icis.com, www.mathanex.com, and www.alibaba.com), and the prices for the utility services from Turton et al. (2008).

Table 1. Results for the best flowsheet simulation

Materials	ton/h	\$/ton	\$MM/y	Utilities	MW	\$/MWh	\$MM/y
Feed stock			22.40	Hot utility			9.30
MeOH	4.97	340.0	13.53	LPS (5 barg)	9.35	50.6	3.78
Urea	4.98	221.5	8.82	MPS (10 barg)	0.05	53.4	0.02
Triglyme	0.01	830.0	0.05	HPS (41 barg)	10.77	63.7	5.49
Products			48.33	Cold utility			0.63
DMC	6.50	830.0	43.16	CW (30°C)	13.17	1.3	0.14
NH3	2.69	240.0	5.17	RW (5°C)	3.91	15.9	0.50
Operating Costs (\$MM/y)							32.32
Product Sales – Feed Costs (\$MM/y)							25.93
Profit Value (\$MM/y)							16.00

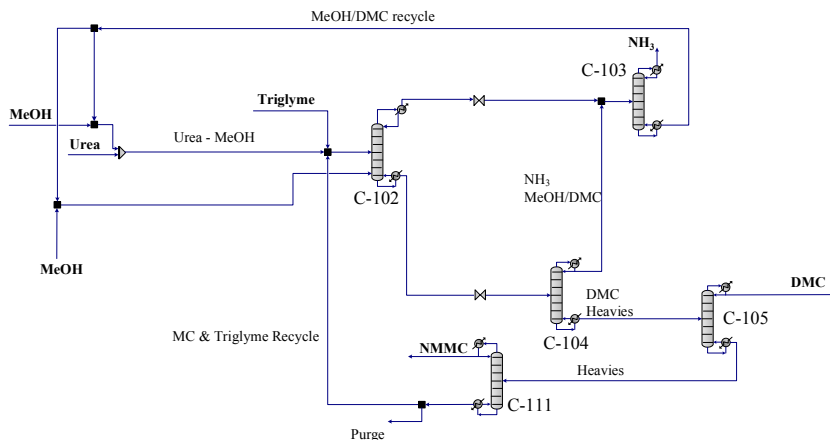


Figure 2. Best flowsheet for the production of DMC from urea and methanol

4. Conclusions

The urea process for making DMC is a promising alternative to the current processes, since it avoids the hazards of using dangerous compounds, and also would allow the synthesis of DMC starting from carbon dioxide. The results of this preliminary techno-economic study show that, if a catalyst that permit overcome the kinetic barriers of the second step reaction is developed in the future, DMC could be synthesized with considerable annual positive cash flows.

Acknowledgments.

The authors gratefully acknowledge the financial support by the Spanish Ministry of Economy, Industry and Competitiveness CTQ2016-77968-C3-02P, FEDER, UE.

References

- Nishihira, K., Yoshida, S., Tanaka, S., 1993. Continuous process for preparing dimethyl c. US Patent 5,214,185.
- Pacheco, M.A., Marshall, C.L., 1997. Review of Dimethyl Carbonate (DMC) Manufacture and Its Characteristics as a Fuel Additive. *Energy & Fuels* 11, 2–29.
- Romano, U., 1976. Recovery of DMC from its azeotropic mixture with methanol. DE Patent 2,607,003.
- Ryu, J.Y., Gelbein, A.P., 2006. Process for making dialkyl carbonates. US 7,074,951 B2.
- Ryu, J.Y., Gelbein, A.P., 2002. Process and catalyst for making dialkyl carbonates. US Patent 6,392,078.
- Turton, R., Baile, R.C., Whiting, W.B., 2008. Analysis, synthesis and design of chemical processes. Pearson Education.
- Wang, M., Wang, H., Zhao, N., Sun, Y., 2007. High-Yield Synthesis of Dimethyl Carbonate from Urea and Methanol Using a Catalytic Distillation Process. *Ind. Eng. Chem. Res.* 46, 2683-2687.
- Yunhai, S., Honglai, L., Kun, W., Wende, X., Ying, H., 2005. Measurements of isothermal vapor-liquid equilibrium of binary methanol/dimethyl carbonate system under pressure. *Fluid Phase Equilib.* 234, 1–10.

Evaluating the Benefits of LNG Procurement through Spot Market Purchase

Mohd Shahrukh,^a Rajagopalan Srinivasan,^a I.A.Karimi,^b

^a*Department of Chemical Engineering, Indian Institute of Technology Madras, Chennai 600036, India*

^b*Department of Chemical and Biomolecular Engineering, National University of Singapore, 119077, Singapore*

raj@iitm.ac.in

Abstract

Natural gas (NG) is liquefied for shipping and storage purposes, this gas in liquid state is known as liquefied natural gas (LNG). The trade of LNG is usually regulated by contracts between suppliers and buyers. Historically long term contracts covering 20-25 years have been used; but more recently, due to emergence of new suppliers and consumers spot market purchases of LNG has also become possible. Nowadays, a consumer can opt to procure LNG via long term contracts or from spot market purchase or a combination of the two. We seek to evaluate the relative benefits of long term versus spot purchases. As a first step, in this paper, we report a mixed-integer linear programming (MILP) model to compare the cost of transportation through long term contracts as against spot market purchase. Several examples are solved; the results show that, in every case, spot market purchase is better compared to long term contracts.

Keywords: LNG, mixed integer linear programming, Long term contracts.

1. Introduction

Consumption of natural gas (NG) has grown steadily in recent years all over the world. Major factors that have contributed to this growth are environmental impact of conventional fossil fuels, abundant availability, and local market liberalization (Pospíšil et al., 2019). Despite NG being the most favored fossil fuel, its transportation to distant markets constitutes a challenge due to its gaseous state. Its liquefied form, liquefied natural gas (LNG), with its 600 time reduction in volume over NG, can be more easily transported using specially designed LNG carriers (Kumar et al., 2011).

Trade of LNG is usually regulated by contracts between suppliers and buyers. Historically, there were only a few buyers and suppliers of LNG. So contracts were generally 20-25 years long and thus provided security of demand and supply to sellers and buyers, respectively. In recent years, new suppliers have emerged, and LNG trade is increasing rapidly. Further, local NG market liberalization in many countries has also triggered many small companies to become LNG consumers. The emergence of these new players, especially small companies in the power sector and fertilizer manufacturers which use the regasified LNG as a feedstock has led to competitive LNG markets, but one characterized by high demand variability. Consequently, there is an increased need felt by regasification terminals to increasingly purchase LNG through short term (i.e., spot) contracts. In this paper, we seek to evaluate the relative benefits of

long term versus spot purchases. Specifically, we develop a mathematical programming to quantify the transportation cost of LNG purchase for a given demand via spot market and long-term contracts.

1.1. Literature Review

In literature, procurement of LNG is considered as a contract (vendor) selection problem, mainly from a buyer's perspective. The problem is formulated from the point of a focal company that needs to procure a certain amount of LNG over a planning horizon. The company can buy LNG from suppliers distributed all over the world. A supplier may offer one or more contract options. Typically, a mathematical model can be used to choose a set of contracts (vendors), which allows the buyer to minimize the procurement cost. Till the 1970's, vendor selection was done using linear weighting model where each vendor was scored on multiple decision criteria and the vendor with maximum score selected. Later on, researchers started using linear programming (LP) for vendor selection (Khalilpour and Karimi, 2011).

Contract selection problems reported in literature are usually from single buyer's perspective. See for examples (Khalilpour and Karimi, 2011) and (Jang et al., 2017). No model has been proposed to make a comparative study between spot market purchase and long term contracts for a set of buyers. In this paper, we therefore develop separate models for the long term and spot purchase of LNG and compare the optimal transportation costs.

2. Problem Statement

Consider a set of buyers and producers of LNG distributed all over the world. Each consumer and producer has its own specific production and consumption profile. Let P ($p=1, 2, \dots, P$) be the total number of producer and C ($c=1, 2, \dots, C$) be the total number of consumers such that $I = P \cup C$. Each site has a storage tank. A heterogeneous fleet of V ships ($v=1, 2, \dots, V$) is used to transport LNG and manage the inventory level at all sites. A site i has J_i identical jetties. Thus, at most J_i number of ships may load/unload at a site. For spot market purchase, ship moves among all sites to maintain inventory level at each site, while for long term contract, ships move only between sites that have contracts with each other.

Initial positions of ships, capacity, loading/unloading rate, material onboard are known. Site to site travel costs, number of sites, production, and consumption profile are also known along with duration of the planning horizon. Sites having long term contracts with each other are known. The aim is to administer the ship movements over the planning horizon so that inventory levels are maintained at all the sites for both spot market purchase as well as for long term contracts.

2.1. Example 1

This example consists of two ships; five ports in which two of them are production sites (Site 1 and Site 2) while three of them are consumption sites (Site 3, 4 and 5). Every port has one jetty at each site. Each port has storage tank with limited capacity. Planning horizon is of 10 days. At time zero both ships are empty. Initially, ship 1 is at Site 1 while ship 2 is at Site 2. Loading/Unloading rate of both the ships at every site is 12t/day. Complete data for this example is shown in Tables 1 and 2. Producer 1 has contract with Consumer 3 while Producer 2 have contract with Consumers 4 and 5.

Table 1: Supply and demand data for Example 1

Site	Type	Initial material (t)	Capacity (t)	Production / Consumption rate (t/day)
1	Producer	2	80	2
2	Producer	6	100	1.25
3	Consumer	3	25	0.5
4	Consumer	2	40	0.5
5	Consumer	5	60	1

Table 2: Travel time and travel cost for ships in Example 1

i→j	Travel time	Travel cost
i1→i2	1.62	38.90
i1→i3	1.75	42.07
i1→i4	2.05	49.21
i1→i5	1.99	47.72
i2→i3	0.16	3.95
i2→i4	0.82	19.76
i2→i5	0.73	17.50
i3→i4	0.95	22.89
i3→i5	0.86	20.64
i4→i5	0.33	7.80

3. Mathematical Model

The proposed model for spot market purchase is based on the model for bulk maritime logistics for the supply and delivery of multiple chemicals reported by (Li et al., 2010). They developed a model for a multinational company (MNC) which has sites distributed globally. The model considers multiple materials such that the product of one site is a raw material for another. The goal of the model was to develop routing and scheduling for a fleet of ships while ensuring the continuity of operation at all sites at minimum transportation costs. (Li et al., 2010)'s model has been simplified for the transportation of LNG by reducing the dimensions of all variables which explicitly considered the multiple materials to one (LNG). These variables denoted storage tank capacity, material unloading, material onboard etc. For long term contracts, this model is modified with additional constraints to model the stipulated contract terms.

3.1. Modeling long term contracts for procuring LNG

Long term contracts are between suppliers and buyers and specify the quality, quantity, payment terms, etc of the product to be delivered to the buyer over a specified period of

time. For modelling long term contracts we consider a set of producers P ($p=1,2,\dots,P$) with each producer having supply contracts with a set of customers L_{cp} ($L_{cp} \subseteq C$). Since producer p has contracted only with customers L_{cp} , ships from p can only move to L_{cp} . Hence we write

$$\sum_{i=1}^P \sum_{j \in L_{cp}} z_{vijk} = 0 \quad 1 \leq v \leq V, 1 \leq k \leq K \quad (1a)$$

$$\sum_{i \in L_{cp}} \sum_{j \in L_{cp}, j \neq i} z_{vijk} = 0 \quad 1 \leq v \leq V, 1 \leq k \leq K \quad (1b)$$

where z_{vijk} is equal to 1 when ship v is at site i in slot k and at site j in slot $k+1$, otherwise it is zero.

3.2. Objective Function

The objective is to minimize total transportation cost over the planning horizon. Let $C_{V_{vij}}$ be the cost of travelling from site i to site j via ship v . Then the objective function can be written as:

$$\sum_{v=1}^V \sum_{i=0}^{I+1} \sum_{j=0, j \neq i}^{I+1} \sum_{k=1}^K C_{V_{vij}} * z_{vijk} \quad (2)$$

Eq.(1a) and Eq.(1b) are specific to the long term contract model; all other equations are common to both the models.

4. Case Studies

We have solved three examples to assess our model. These examples vary in planning horizon, distances between the sites and production and consumption rates. We used Cplex 12.8.0 on a Lenovo idea pad 510 workstation (core i5-7200U, 8GBmemory) for solving these examples running on windows 10. Results of these examples are summarized in Table 3.

4.1. Case Study 1

In this example, Site 2 has contracts with Sites 4 and 5 while Site 1 has a contract with Site 3. Results shows that Ship 1 loads 5.58 t of LNG during $[0,0.465]$ from Site 2 then moves to Site 4 and Site 5 to deliver 4.0 and 1.58 t of LNG at time (in days) 1.28 and 3.53 respectively. Then, it moves to Site 2 again to load 5.48 t of LNG and delivers it to Site 5 from time $[5.581, 6.038]$. Ship 2 loads 0.78 t of LNG from Site 1 during $[0, 0.065]$ and delivers it to Site 3. Then it moves back to Site 1 to load 2.21 t of LNG which is delivered to Site 3. Fig 1 shows the resulting inventory profile of the sites over the planning horizon.

When the same example is solved as a spot market purchase problem, there is a significant reduction in the transportation cost. Here Ship 1 loads 5 t of LNG from Site 2 and delivers it to Sites 4 and 5. Ship 2 loads 1.2 t of LNG from Site 1 during [0,0.1] and delivers it to Site 3 and then moves to Site 2 to load 5 t of LNG which is delivered at Site 5 in between [4.56,4.97]. It then returns to Site 2 to load 2.8 t which is delivered at Site 3 during [5.99, 6.22]. The total transportation cost is therefore reduced by 46.64%. Fig 2 shows the inventory profile of the sites over the planning horizon with spot purchases.

Table 3: Results for examples

Example	Planning Horizon	No. of Voyages	No of Iterations	Time (min: sec: ms)	Optimal Cost
		Spot / Long Term	Spot / Long Term	Spot / Long Term	Spot / Long Term
1	10	7/9	5435k/211k	00:50:40/02:43:29	88.82/146.7
2	15	10/11	8264k/1632k	03:56:82/00:43:26	134.11/136.77
3	25	3/6	10k/13k	00:00:90/00:01:48	127.03/220.76

5. Discussion

We solved two other examples with different parameters (see Table 3). In these examples also, the transportation cost with spot market purchase is less than with the long-term contract. The difference in the transportation costs between the long term and spot purchases increases significantly when the producer and consumer sites are at large distances. These clearly indicate that spot purchases lead to a more optimal usage of the ships – i.e., the same demands can be more effectively met in the absence of long-term contracts. The current model relies on a number of simplifying assumptions. Here, the price of the LNG cargo has not been taken into account. In practice, purchases through long term contracts may have price advantage. The net effect of lower cargo price and a higher transportation cost therefore needs to be evaluated. Also, the current model assumes deterministic values for all parameters; in reality, these would vary based on demand. In future, we aim to develop a model that can incorporate effect of demand variability.

References

- Jang, W., Hong, H.-U., Han, S.H., Baek, S.W., 2017. Optimal Supply Vendor Selection Model for LNG Plant Projects Using Fuzzy-TOPSIS Theory. *J. Manag. Eng.* 33, 04016035. [https://doi.org/10.1061/\(ASCE\)ME.1943-5479.0000474](https://doi.org/10.1061/(ASCE)ME.1943-5479.0000474)
- Khalilpour, R., Karimi, I.A., 2011. Selection of Liquefied Natural Gas (LNG) Contracts for Minimizing Procurement Cost. *Ind. Eng. Chem. Res.* 50, 10298–10312. <https://doi.org/10.1021/ie200275m>
- Kumar, S., Kwon, H.-T., Choi, K.-H., Lim, W., Cho, J.H., Tak, K., Moon, I., 2011. LNG: An eco-friendly cryogenic fuel for sustainable development. *Appl. Energy* 88, 4264–4273. <https://doi.org/10.1016/j.apenergy.2011.06.035>

Li, J., Karimi, I.A., Srinivasan, R., 2010. Efficient bulk maritime logistics for the supply and delivery of multiple chemicals. *Comput. Chem. Eng.* 34, 2118–2128.

<https://doi.org/10.1016/j.compchemeng.2010.07.031>

Pospíšil, J., Charvát, P., Arsenyeva, O., Klimeš, L., Špiláček, M., Klemeš, J.J., 2019. Energy demand of liquefaction and regasification of natural gas and the potential of LNG for operative thermal energy storage. *Renew. Sustain. Energy Rev.* 99, 1–15.

<https://doi.org/10.1016/j.rser.2018.09.027>

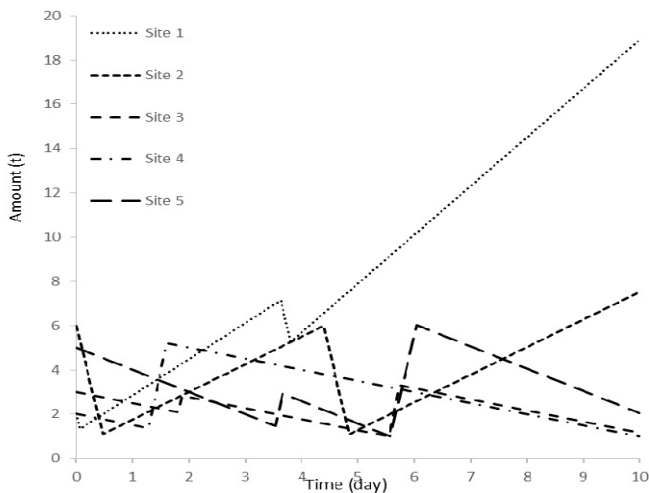


Fig 1: Inventory profile at sites while procuring LNG via Long term contracts

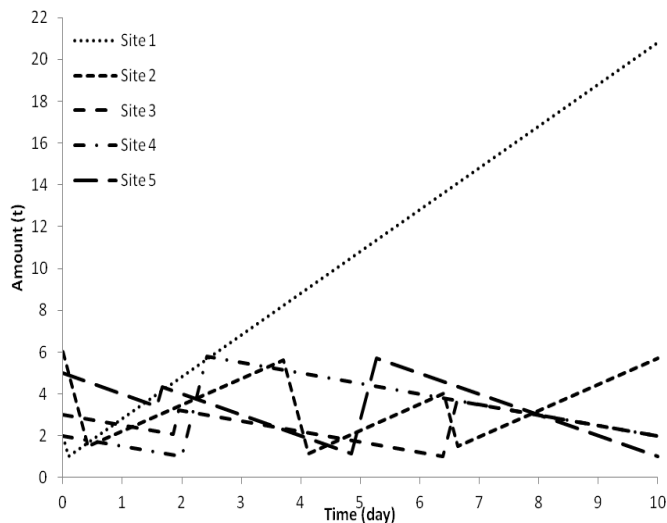


Fig 2: Inventory profile at sites while procuring via spot market purchase.

Effect of Ambient Conditions on Boil Off Gas Generation in LNG regasification terminals

Philips Prince Pokkatt^a and Rajagopalan Srinivasan^a

^a *Department of Chemical Engineering, Indian Institute of Technology Madras, Chennai, 600036, India*

raj@iitm.ac.in

Abstract

Liquefied natural gas has started to establish itself as the fuel of choice across the globe, evident from its sustained growth over the last three decades. As a result, more regasification terminals are coming up every year. Hence, it is critical to develop technologies which make sure the plants are operated efficiently. This paper studies the generation and management of Boil Off Gases (BOG) in LNG regasification terminals. The effect of time varying ambient temperature on the BOG generation is studied, and ways to improve the operational efficiency of BOG compressors are suggested.

Keywords: LNG, Ambient temperature, Regasification, BOG compressor

1. Introduction

As the global population increases, world's energy demand stands to double by the year 2050. Natural gas is believed to have a significant role in driving this rising demand. Gas is the fastest growing hydrocarbon market today. Natural Gas (NG), being the cleanest fossil fuel, has become the fuel of choice in many of the developed and emerging economies. NG demand is expected to grow at an average of 2% per year which is twice the rate of total worldwide energy demand. Natural gas is transported to India as Liquefied Natural Gas (LNG) through specially designed ships known as LNG carriers. Natural gas is converted to liquefied natural gas (LNG) by refrigeration below -162°C; this reduces its volume by 600 times. LNG is imported to the regasification terminal, where it is stored, vaporized and distributed to the customers.

Processes involved in the regasification are energy intensive. Vaporizers, used for conversion of LNG to natural gas uses major share of energy consumption in the plant. Although the storage tanks are provided with extensive insulation, the heat ingress into them cannot be avoided. This leads to the vaporization of LNG producing Boil off Gases (BOG). Excessive buildup of BOG causes surge in the storage tank pressure. For the safe operation of the plant, the tank pressure must be kept much below the designed level of the pressure. Hence, it is imperative that the BOG is timely taken out and either liquefied or sent to distribution line. The pressure in the distribution line is over the range of 75bar which is significantly higher when compared to pressure of the BOG which is nearly 1.17 bar. So, the warm BOG produced are liquefied in the recondenser and sent back into the storage tank, causing the temperature to rise. BOG is transported to the recondenser through BOG compressor. The composition of BOG and LNG is quite different, with the former having more methane and latter having relatively heavier hydrocarbons. The BOG management process is also an energy intensive one.

BOG management is one of the most challenging tasks in the operation of a regasification terminal. Most studies assume a constant BOG rate while devising energy efficient ways to condense BOG and transport them back to the storage tank. In reality, BOG generation is not constant and it fluctuates in the course of a day. For estimating the BOG generation rate, modeling of the storage tank is cardinal and it also enables us to study the dynamics of the regasification terminal, closer to the reality. In the paper, we studied the effect of ambient conditions on the variation in the BOG generation. Further, we also propose methodologies to reduce to energy consumption in the operation of BOG compressors.

2. Various Models of BOG in Literature

BOG management holds a major role in reducing the energy consumption in the plant. Effects of BOG generation often cause ripple effects in other operations in the plant. Different studies have incorporated these effects in their models. The fluctuation in the BOG generation causes change in the level of LNG in the recondenser. (Shin et al., 2008) studied the effect the above occurrence can have on the high pressure LNG pump (which pumps LNG from the recondenser to the vaporizer) e.g. cavitation of the pump and equipment vibration. (Park et al., 2012) proposed a retrofit design the form of intermittent cooling of the BOG before its compression, saving compression costs. But many of those studies like above, were done on the underlying assumption of constant BOG generation. Studies by (Saleem et al., 2018) brought better insights into factors affecting BOG generation, by studying the heat ingress magnitude and convective heat transfer in the LNG storage tank. Most models also assumed that the vapor and liquid phases in the LNG tank are at same temperature and composition. (Effendy et al., 2017) studied the BOG generation in the storage tank by taking into account the temperature and composition variation which exists in the different phases. In their model, the storage tank is considered to be composed of four subsystems, namely, vapor, liquid, flash, recirculation subsystems. Also, the heat leaks from the surroundings to the liquid and vapor subsystems are accounted for separately.

The temperature of the liquid subsystem is governed by the following energy balance:

$$\frac{dT_L}{dt} = \frac{4}{\pi D_T^2 \rho_L h} \left[-\frac{\lambda \dot{m}_e}{C_{p,L}} + (1 - \bar{f}_F) \dot{m}_r (T_v - T_L) + \frac{\dot{Q}_L}{C_{p,L}} \right] \quad (1)$$

$$\dot{Q}_L = U_{side} (\pi D_T h) (T_a - T_L) + U_{bottom} \frac{\pi D_T^2}{4} (T_{bottom} - T_L) + U^* \frac{\pi D_T^2}{4} (T_v - T_L) \quad (2)$$

where T_L is the temperature of liquid phase, D_T is diameter of the storage tank, ρ_L is the density of liquid phase, h is the height of liquid in storage tank, λ is the latent heat of vaporization, \dot{m}_e is the LNG evaporation rate, $C_{p,L}$ specific heat capacity of liquid subsystem, \bar{f}_F is the fraction of liquid phase in the flash subsystem, \dot{m}_r is the rate of recirculation liquid returning back to the tank, T_v is the temperature of the vapor

phase, \dot{Q}_L is rate of heat leak into the liquid subsystem, T_{bottom} is the temperature of bottom of the storage tank, $U_{side}, U_{bottom}, U^*$ are the overall heat transfer coefficients at storage tank shell, bottom and the vapor-liquid interface respectively

The temperature of the vapor subsystem is governed by the following energy balance:

$$\frac{dT_V}{dt} = \frac{\left[\dot{m}_E (T_L - T_V) + (T_F - T_V) (1 - \bar{f}_B) \bar{f}_F \dot{m}_R + \frac{\dot{Q}_V}{C_{p,V}} \right]}{m_V} \quad (3)$$

$$\dot{Q}_V = U_{top} A_{top} (T_a - T_V) + U_{side} (\pi D_T (H - h)) (T_a - T_V) + U^* \frac{\pi D_T^2}{4} (T_L - T_V) \quad (4)$$

where, U_{top} is the overall heat transfer coefficient at top of the storage tank, T_F is the temperature of the flash subsystem, \bar{f}_B is the fraction of boil off stream, \dot{Q}_V is the total heat transfer into vapor phase, $C_{p,V}$ is the specific heat capacity of vapor phase.

Rate of change of mass in the vapor subsystem is governed by the follow equation:

$$\frac{dm_V}{dt} = -\frac{\pi D_T^2}{4} \rho_V \left[\frac{dh}{dt} + \frac{(H - h)}{T_V} \frac{dT_V}{dt} \right] \quad (5)$$

Total amount of BOG generated is given by:

$$\dot{m}_B = \dot{m}_E + \bar{f}_F \dot{m}_R - \frac{dm_V}{dt} \quad (6)$$

where \dot{m}_B is the rate of BOG generation.

As heat leaks into the tank, the LNG boils and the BOG generated has to be managed so that the pressure of the tank remains within the safety limits. This is typically done by a BOG compressor as it transports the vapor into the liquefaction system. BOG compression being energy intensive, it is critical to optimize the operation of the process.

3. Effect of Ambient Conditions on Boil Off Gas Generation

We consider a regasification terminal operated in the holding mode i.e. LNG is not transferred from the carrier ship to the storage tank.

The objective of this paper is to demonstrate the effect of ambient weather conditions on the generation of Boil off Gas (BOG) and optimal operation of BOG compressor in a LNG regasification terminal. The LNG storage tank and recirculation pipeline are modeled by utilizing the model proposed by (Effendy et al., 2017). The regasification

plant modeled has eight storage tanks, and ten cooling lines connecting the jetties to the storage tanks. The storage tank is assumed to be operated in an isobaric regime so that any BOG generated will be evacuated from the tank. The simulation is run for a span of 16 days.

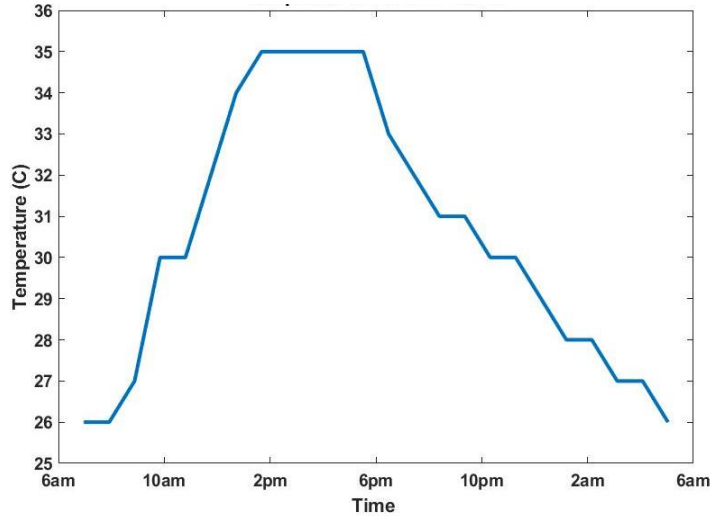


Figure 1: Ambient temperature profile in Hazira, India

In order to understand the effect of ambient temperature, the temperature profile in Dahej, where India's largest regasification terminal is situated was considered. On a typical day in November, the temperature was observed to be rising quickly after sunrise from 26 °C to 35 °C in six hours, then remaining fairly constant at 35 °C for five hours and slowly cooling to 26 °C over twelve hours. The first and last temperature regime fitted for a quadratic and linear fit respectively. It is assumed here that a given day starts at 6 a.m. in the morning (around sunrise).

$$Ambient\ Temperature(K) = \begin{cases} 1 < t_k < 7 \rightarrow 0.107 * x^2 + 0.536 * x + 298 \\ 8 < t_k < 12 \rightarrow 308 \\ 13 < t_k < 24 \rightarrow -0.601 * x + 313.46 \end{cases} \quad (7)$$

The above ambient temperature function was incorporated into the model proposed by Effendy et al. (2017) and the BOG generated thereof was calculated. The variation of BOG generation rate on a given day due to the change in ambient conditions is shown in Figure 2.

Figure 3 shows the BOG generation over a 16-day period for three different conditions – ambient conditions constant at 25 °C, ambient conditions constant at 30.5 °C (median temperature of the profile in Figure 1) and ambient temperature varying as per Figure 1. From this, it can be readily inferred that there is significant fluctuation in the BOG generation over the course of a day, and this fluctuation also depends with the inventory level of the LNG in the tank. The BOG generated is recompressed back to liquid using

compressors – the substantial variation in BOG generation rates described above, therefore, motivate a study of suitable operations regimes for the compressor network.

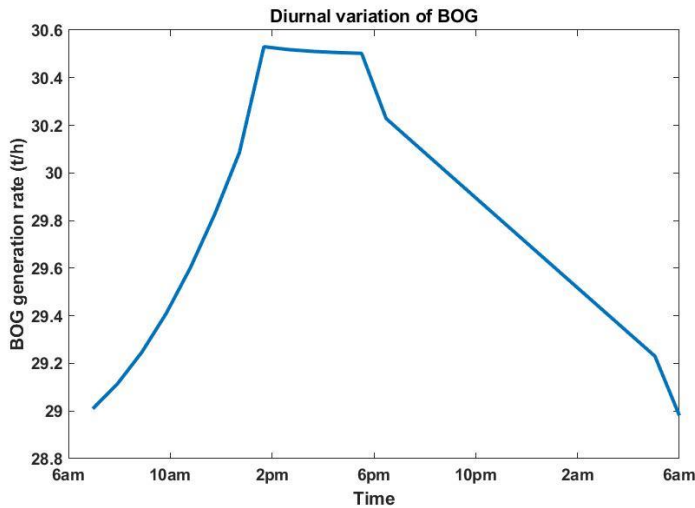


Figure 2: Variation of BOG generation resulting from the ambient conditions in Figure 1

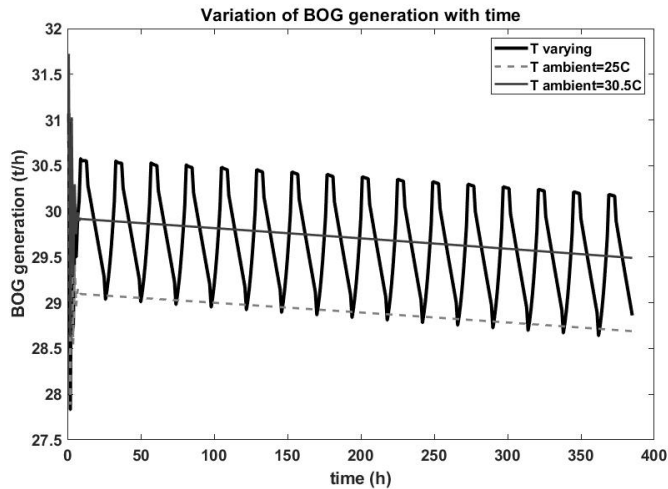


Figure 3: Comparison of BOG generation rate for various ambient models

4. Effect on Compressor Operations

The compression cost can be significantly reduced by improving the operation of the compressor network for processing a specified amount of BOG. (Shin et al., 2007) proposed a method to minimize the power consumption using mixed integer linear problem (MILP) formulation, which improved the operational policies based on safety analysis on the dynamics of the tank pressure. Hence, for reducing the energy

consumption in a regasification terminal, it is important to optimize the operation of the BOG compressors.

In our study of compressor operations, following Shin et al. (2007) we assume that at load levels of 0, 50%, 75%, and 100%, the current requirement by the compressor is 65 A, 115 A, 127 A, and 145 A, respectively. Given the voltage of 6900 V, the corresponding amount of energy consumed is 449 kW, 794 kW, 876 kW, and 1000 kW. Table 1 shows the energy consumed by BOG compressors when operated at different loads. The quantity and quality i.e. the flow rate and enthalpy, of the BOG generated by the LNG train vary depending upon the operating conditions in the plant, as well as on the mode of operation.

As the BOG generation rate changes significantly over time, optimizing the compressors could save significant amounts of energy. A simple analysis reveals a reduction of over 13% on a given day in compressor energy consumption when BOG compressors are operated differently over the course of the day. Further, as evident from Figure 3, the BOG generation profiles are different from day to day depending on the inventory, so the energy optimal mode and the savings potential would also vary on a daily basis and motivates real-time optimization.

5. Conclusions

As the size of LNG regasification plants grow, and multiple LNG trains are connected, the complexity of BOG management also increases. BOG management is a multi-faceted problem requiring study of hydraulics, transient behavior and compressor operations. This paper has demonstrated that the effects of ambient temperature on the rate of BOG generation is significant and motivates daily optimization of compressors' operation modes. Further, we believe such studies would educate new designs of regasification terminals in tropical regions.

References

- Effendy, S., Khan, M.S., Farooq, S., Karimi, I.A., 2017. Dynamic modelling and optimization of an LNG storage tank in a regasification terminal with semi-analytical solutions for N₂-free LNG. *Comput. Chem. Eng.* 99, 40–50. <https://doi.org/10.1016/j.compchemeng.2017.01.012>
- Park, C., Song, K., Lee, S., Lim, Y., Han, C., 2012. Retrofit design of a boil-off gas handling process in liquefied natural gas receiving terminals. *Energy* 44, 69–78. <https://doi.org/10.1016/j.energy.2012.02.053>
- Saleem, A., Farooq, S., Karimi, I.A., Banerjee, R., 2018. A CFD simulation study of boiling mechanism and BOG generation in a full-scale LNG storage tank. *Comput. Chem. Eng.* 115, 112–120. <https://doi.org/10.1016/j.compchemeng.2018.04.003>
- Shin, M.W., Shin, D., Choi, S.H., Yoon, E.S., 2008. Optimal operation of the boil-off gas compression process using a boil-off rate model for LNG storage tanks. *Korean J. Chem. Eng.* 25, 7–12. <https://doi.org/10.1007/s11814-008-0002-9>
- Shin, M.W., Shin, D., Choi, S.H., Yoon, E.S., Han, C., 2007. Optimization of the Operation of Boil-Off Gas Compressors at a Liquefied Natural Gas Gasification Plant. *Ind. Eng. Chem. Res.* 46, 6540–6545. <https://doi.org/10.1021/ie061264i>

Electroencephalogram based Biomarkers for Tracking the Cognitive Workload of Operators in Process Industries

Mohd Umair Iqbal,^a Babji Srinivasan,^a Rajagopalan Srinivasan^{b,*}

^a*Indian Institute of Technology Gandhinagar, Gujarat, 382355, India*

^b*Indian Institute of Technology Madras, Tamil Nadu, 600036, India*

babji.srinivasan@iitgn.ac.in, raj@iitm.ac.in

Abstract

Human errors are a root cause of majority of accidents occurring in the process industry. These errors are often a result of excessive workload on operators, especially during abnormal situations. Understanding and measurement of cognitive workload (overload), experienced by human operators while performing key safety critical tasks, is thus important to the understanding of human errors. Subjective measurements of workload are often not reliable and there is a need for physiological based parameters of workload. In this work, we propose a methodology to measure cognitive load of a control room operator in terms of a biomarker, specifically theta/alpha ratio, obtained from a single electrode EEG signal. Real-time detection of the biomarker can enable minimize errors and improve safety.

Keywords: EEG, human errors, cognitive workload, safety

1. Introduction

With the advancement of technology and enhanced automation, the role of human operators has been shifting more towards monitoring the process operations. However, the disturbances in the process often call for human intervention. It often happens that humans commit errors in either planning or execution of actions; human errors have been a root cause of over 70% of accidents in process industries (Mannan, 2005). This situation is similar in other safety critical domains like aviation, health and nuclear industries. The reason for such errors is often attributed to the high cognitive workload experienced by the operator(s) during abnormal process events (Bhavsar et al., 2015). During these events, the operator uses their mental model of the process (developed during training, prior knowledge about the process, heuristic rules learnt from experience with the process, etc.) to initiate and execute a sequence of steps that would bring the process back to normal operating conditions. However, any mismatch between the plant behaviour and the mental model would result in higher cognitive workload, a common cause for human errors. Therefore, it is imperative to understand the nature and evolution of the mental model of the operators.

Mental models of an operator can be broadly divided into three categories: skill based, rule based and knowledge-based (Reason, 1990). Operators use skill-based models to perform repetitive tasks which do not require any mental effort. For instance, an experienced driver on a traffic free road subconsciously performs driving related

actions. An if-then rule-based mode would be used to tackle some abnormal situations in the process, specifically those that they are well-versed with a priori. Operators resort to a knowledge-based mode when they face a new situation where skill-based and rule-based modes are not available; they therefore need to apply their knowledge to identify suitable actions. However, operators traverse between the three mental modes (Reason, 1990) in the course of handling an abnormal situation. The resulting cognitive workload is different in each of the mental states. Therefore, it is essential to understand, explain and predict the transition among the various mental modes based on cognitive load so that the nature of the human errors can be uncovered and interventions taken to minimize the same. This is the ultimate objective of the research described here.

2. Literature Survey

Cognitive workload is experienced because of the limited working memory capacity of humans (Parasuraman, 2008). A mismatch between this capacity and demands of the process leads to errors which may transform into catastrophic accidents. To understand the underlying cognitive constructs during such mismatch, the nature and extent of cognitive workload needs to be quantified. Physiological parameters offer a potent approach to understand the underpinnings of human behaviour and provide information about the internal state of an individual. One such is Electroencephalogram (EEG) which has been used in diverse fields to understand the mental states of humans and predict stress levels and cognitive load.

EEG involves measurement of electrical activity of the brain using electrodes which are placed on skin. The electrical activity is the result of neural-oscillations occurring in brain due to fluctuations in excitability of neurons in response to stimuli. A raw EEG signal is comprised of various frequency components which are often clubbed into different frequency bands for the purpose of drawing meaningful observations. The commonly used frequency bands are delta (1-4 Hz), theta (4-7 Hz), alpha (8-12 Hz), beta (12-30 Hz), and gamma (30-80 Hz). Alpha and theta band activity have been extensively used for cognitive load measurement. Specifically, alpha activity is associated with idling, arousal and workload. A decrease in alpha activity is associated with increase in arousal, mental load, stress and anxiety (Neurosky, 2015). Conversely, an increase in alpha activity signifies idling or calmness (Pfurtscheller et al., 1996). Lim et. al, (2014) showed a significant increase in alpha activity when the eyes were closed, reflecting relative calm. Theta activity is also associated with attention and internal mental processing (Harmony et al., 1996); hence, an increase in theta activity means more mental effort. The power spectral density of delta waves has been reported to show a positive correlation with mental stress (Awang et al., 2011). Other frequency bands also have some significance e.g. beta waves in optimum condition can help with memory, conscious focus and problem solving (Abhang, 2016); delta waves are associated with adult sleep; and gamma waves with hypertension and high mental activity.

The potential of EEG to predict cognitive workload for dynamic processes has, however, been limited. Nevertheless, these frequency bands in the EEG signal have been used as biomarkers, for instance in the aviation sector involving dynamic tasks. A study by Gentili et. al, (2014) highlight the potential of theta by alpha ratio to measure cognitive workload and degradation of pilot performance when carrying out complex

tasks involving manoeuvring. Theta by alpha ratio is reported to increase with task complexity. A study by Wilson (2002) revealed that the alpha band relative power decreased while delta band relative power increased for pilots, when compared at the same electrode locations in comparison to their pre-flight baseline values, for the majority of cases. These studies highlight the potential of EEG to offer insight into task difficulty and workload. There is, hence, a need to carry out cognitive workload studies in chemical process industries which like aviation offer highly dynamic situations involving high-risk and potential for disasters. The cognitive workload of the plant operators, in the process industry domain, depends on their ability to develop a mental model in a given situation, which is distinctly different from the time space representation of airplane pilots and drivers. Previously, the authors have explored eye-tracking based approaches to understand the cognitive behaviour of control room operators in process plants (Bhavsar et al., 2015). However, to the best of authors' knowledge, there is hardly any work, in this domain, to understand the cognitive workload of operators using EEG. In this paper, we seek to evaluate the potential of EEG biomarkers to discriminate between levels of cognitive load (mental states) and task difficulty.

3. Experimental Methodology

The experiment consists of monitoring a simulated ethanol production plant via a Human Machine Interface (HMI). The process involves an exothermic reaction between ethene and water taking place in a jacketed Continuous Stirred Tank Reactor (CSTR) whose output goes to a distillation column for separation of ethanol product. In case of any disturbance in the plant, the operator needs to take action(s) to bring the process variables to within acceptable limits, using various flow control sliders operable from HMI, as deemed appropriate by the participant. The reader is referred to Iqbal and Srinivasan (2017) for a detailed description of the process.

The study involved 6 post graduate chemical engineering students who performed 8 disturbance rejection tasks after receiving proper training (reading handouts and video training). During the course of the experiment the EEG data was recorded using Neurosky Mindwave+ single electrode headset. Different tasks involved dealing with different abnormalities. Tasks 1 and 2 involved a disturbance in coolant flow rate which resulted in the coolant flow rate crossing the upper alarm limit. Tasks 3 and 4 involved tackling the disturbance in coolant flow rate going outside the lower shutdown limits. Tasks 5 and 6 demanded bringing back the process to within alarm/acceptable limits in response to feed flow rate to CSTR breaching the upper alarm limit. The tasks differed by the magnitude of disturbance which in turn accordingly affected other process variables. Task 7 and 8 involved a disturbance in the feed flowrate going outside the lower alarm limits.

4. Results

An overview of the methodology employed to study the cognitive workload and related constructs is shown in Figure 1. We recorded the operators' EEG during the course of different tasks using an EEG headset and then carried out task-wise Short Time Fourier Transform (STFT) of the recorded raw EEG signal to obtain information in frequency domain. Among various possible biomarkers that have been reported in literature, theta (4-7 Hz) and alpha activity (8-12 Hz) showed promising results, which

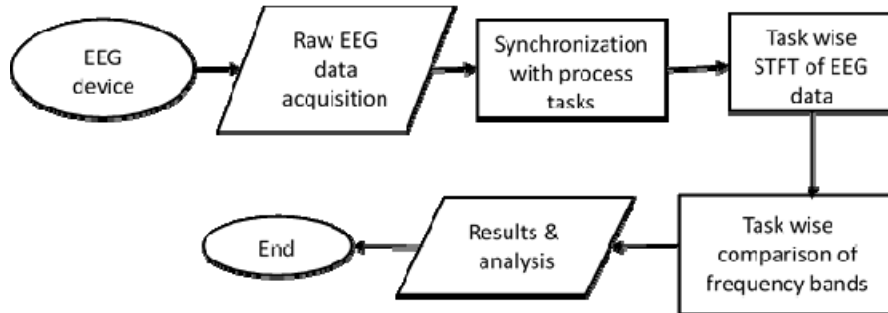


Figure 1: Overview of the methodology

are reported after the detailed description of a typical task in the following paragraph.

A typical task involves a disturbance resulting in a process variable(s) going outside its acceptable limits designated by upper and lower alarm limits. The operator is notified about the disturbance by an alarm entry in the alarm log and by change in colour of the tag(s), representing that variable(s) in the process schematic to red. The operator needs to assess the situation, decide on the appropriate recovery action and then take the action by moving appropriate slider(s) to bring the process variable(s) back to within acceptable limits. If the operator is unsuccessful to bring the process within normal bounds within a short time, the disturbance will result in the process variables crossing the shutdown limits (which is considered as a failure). The operator can see the trend of any process variable on HMI by clicking on the tag corresponding to that variable. The tasks have been designed in such a way that different aspects of cognitive behaviour and workload of operators could be studied; the tasks involve abnormal events (depending on the nature and magnitude of initial disturbance) with single alarm triggered, multiple alarms triggered in slow/quick succession and similar tasks i.e. tasks of varied difficulty as well as tasks of similar difficulty are included in the study.

Consider tasks 1 and 8, the simplest and the most difficult tasks, respectively; Task 1 involves an abnormality in coolant flow rate (through jacket) which does not affect other process variables immediately whereas during Task 8 an initial disturbance in the feed flowrate results in triggering of other alarms (temperature and concentration of CSTR) in quick succession. The comparison of theta/alpha activity of participants for these tasks reveals that the ratio is lower for a majority of simple tasks compared to Task 8, as shown in Figure 2. Out of 6 participants, 4 participants showed higher theta/alpha ratio for Task 8. For those 4 participants the average value is 1.05 for Task 8 compared to 1.03 for Task 1. Only one showed a lower score for Task 8 and for 1 participant it showed a negligible change. We therefore evaluated if this ratio has the potential to differentiate task difficulty and the consequent mental workload.

A comparison of two tasks - 7 and 8 – was therefore performed. Task 8 is a more difficult task compared to Task 7 as it involves a larger disturbance in the feed flowrate. This larger disturbance in feed flowrate in turn results in triggering of multiple alarms (temperature and concentration of CSTR) in quick succession compared to Task 7 (where the deviations are relatively slow), and also involves rapid evolution of process variables to outside shutdown limits. A relative comparison of these two tasks, for all

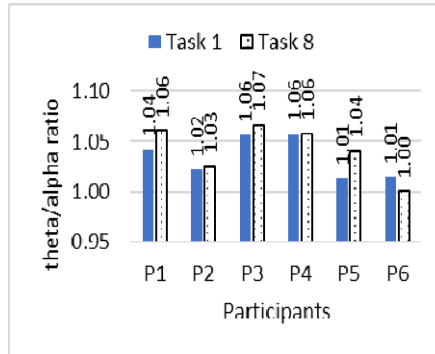


Figure 2 Theta by alpha ratio comparison of Task 1 vs Task 8

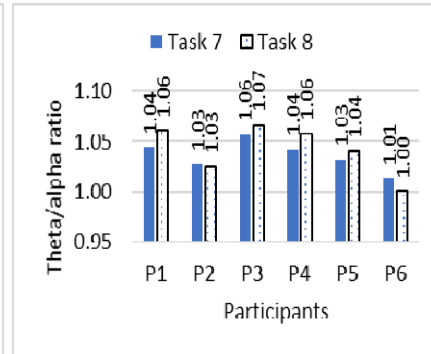


Figure 3 Theta by alpha ratio comparison of Task 7 vs Task 8

the 6 participants revealed that out of the 6 participants, 4 participants showed a higher theta by alpha ratio for task 8. For those 4 participants the average value was 1.05 for Task 8 compared to 1.04 for Task 7. One participant showing negligible change. Thus, theta by alpha ratio can act as a marker to predict the cognitive load as imposed by the task difficulty and as perceived by the participant.

The trend shown by the theta by alpha ratio in our study is in line with the results reported by Gentili et. al, (2014) during their pilot cognitive workload assessment studies. The alpha by theta ratio changes between easy and medium difficulty tasks and between medium & highest difficulty tasks in their study was around 0.05 and 0.08, respectively. The reason for the smaller difference in the values observed in our study can be attributed to the different nature and level of the complexity of the tasks in our study compared to theirs; the nature of the EEG device especially the electrode employed is also known to lead to differences. Our tasks involved control room tasks which would last 2-3 minutes while in their case the operator would carry out each task for 10 minutes. The persistent workload for longer duration experienced by pilots in their study might have invoked different levels of theta and alpha activity compared to our study. Our study is also consistent with the pilot-workload study by Wilson (2002) in terms of alpha activity; the study revealed that alpha activity corresponding to the different electrodes decreases for majority of the electrode positions in comparison to pre-flight base line values, though the differences were not always significant for all the electrodes; alpha activity alters the theta by alpha ratio. Nevertheless, in real control room settings where the disturbances and the remedial procedures can persist for longer time, our biomarker can show more significant differences. Further, more studies need to be carried out to identify the regions of brain which are more important for the cognitive workload determination involving different nature of dynamic tasks involved in process industries. This will help in a holistic understanding of cognitive workload determined using EEG based bio-markers. The tracing of the workload of the operators using biomarkers can help us minimize human errors due to high cognitive workload. If the workload during an unknown disturbance crosses a particular threshold/limit, automatic cues (may be in the form of additional information about the disturbed segment of the process) can be provide to the operator accordingly to minimize the likelihood of error.

5. Conclusions

In this work, we have found that EEG based bio-markers have the potential to help quantify the task difficulty and the consequent cognitive workload on the participants. Our results show that theta by alpha ratio is higher for tasks which are more difficult and impose higher cognitive workload on the participants. This marker can be used to assess training level of the operators before they are asked to monitor a plant. These will ensure their preparedness and feasibility for tasks involving monitoring and control of the processes in highly hazardous chemical process industries. In the future, we plan to measure the cognitive workload using EEG in real-time and also correlate them with markers obtained from our eye-tracking studies. Real time gauging of cognitive workload can help create systems which provide relevant cues to check the workload of operators by providing appropriate support in the form of certain information or otherwise. Multivariate analysis, involving various physiological parameters obtained from EEG and eye-tracking will help arrive at robust indices of cognitive load which will go a long way in understanding and obviating human errors.

References

- Abhang, P. A., Gawali, B. W., & Mehrotra, S. C. (2016). Chapter 3—technical aspects of brain rhythms and speech parameters. *Introduction to EEG-and Speech-Based Emotion Recognition*, 51-79.
- AlZu'bi, H. S., Al-Nuaimy, W., & Al-Zubi, N. S. (2013, December). EEG-based driver fatigue detection. In *Developments in eSystems Engineering (DeSE), 2013 Sixth International Conference on* (pp. 111-114). IEEE.
- Awang, S. A., Pandiyan, P. M., Yaacob, S., Ali, Y. M., Ramidi, F., & Mat, F. (2011). Spectral density analysis: theta wave as mental stress indicator. In *Signal Processing, Image Processing and Pattern Recognition* (pp. 103-112). Springer, Berlin, Heidelberg.
- Bhavsar, P., Srinivasan, B., & Srinivasan, R. (2015). Pupillometry based real-time monitoring of operator's cognitive workload to prevent human error during abnormal situations. *Industrial & Engineering Chemistry Research*, 55(12), 3372-3382.
- Harmony, T., Fernández, T., Silva, J., Bernal, J., Díaz-Comas, L., Reyes, A., ... & Rodríguez, M. (1996). EEG delta activity: an indicator of attention to internal processing during performance of mental tasks. *International journal of psychophysiology*, 24(1-2), 161-171.
- Iqbal, M. U., & Srinivasan, R. (2017). Simulator based performance metrics to estimate reliability of control room operators. *Journal of Loss Prevention in the Process Industries*.
- Lim, C. K. A., Chia, W. C., & Chin, S. W. (2014, August). A mobile driver safety system: Analysis of single-channel EEG on drowsiness detection. In *Computational Science and Technology (ICCST), 2014 International Conference on* (pp. 1-5). IEEE.
- Mannan, S. (Ed.). (2005). *Lees' Loss Prevention in the Process Industries: Hazard Identification, Assessment and Control (Vol. 1)*. Butterworth-Heinemann.
- Neurosky. (2015). Greek Alphabet Soup – Making Sense of EEG Bands (Last assessed: Nov 10, 2018) <http://neurosky.com/2015/05/greek-alphabet-soup-making-sense-of-eeb-bands/>
- Parasuraman, R., Sheridan, T. B., & Wickens, C. D. (2008). Situation awareness, mental workload, and trust in automation: Viable, empirically supported cognitive engineering constructs. *Journal of Cognitive Engineering and Decision Making*, 2(2), 140-160.
- Pfurtscheller, G., Stancak Jr, A., & Neuper, C. (1996). Event-related synchronization (ERS) in the alpha band—an electrophysiological correlate of cortical idling: a review. *International journal of psychophysiology*, 24(1-2), 39-46.
- Reason, J. (1990). *Human error*. Cambridge university press.
- Wilson, G. F. (2002). An analysis of mental workload in pilots during flight using multiple psychophysiological measures. *The International Journal of Aviation Psychology*, 12(1), 3-18.

Optimal design of biomass supply chains with integrated process design

Theodoros Damartzis*, François Maréchal

*Industrial Process and Energy Systems Engineering (IPESE), Ecole Polytechnique
Fédérale de Lausanne (EPFL) Valais, 1951, Sion, Switzerland*

theodoros.damartzis@epfl.ch

Abstract

The current work focuses on the optimal design of biomass supply chains, addressing the conversion of raw materials into useful services. The latter include not only heat and power but also synthetic bio-based fuels (e.g. bio-SNG). Optimally pre-designed processing units representing the conversion facilities responsible for the transformation of biomass are employed. This permits the use of standardized units that act as building blocks within a MILP optimization problem, significantly simplifying the formulation and solution of the problem. These building blocks encompass a variety of transformation options and carry specific information regarding their capacity, total processing cost, overall efficiency and energetic performance. Then, the supply chain design optimization problem aims not only to identify the most suitable conversion plant type but also to determine their location by minimizing the overall cost, expressed as the capital and operating expenses of the processing units as well as the transport costs between the points of operation. The above formulation is applied for the conversion of animal manure to different end products in the district of Brig in southern Switzerland. Results reveal the predominance of large centralized bio-SNG producing units as a consequence of their higher conversion efficiency.

Keywords: supply chain design, bio-SNG, biomass conversion, animal manure.

1. Introduction

The increasing depletion of the fossil-based energy resources as well as the new mandates for the insertion of renewables in the global energy mix are continuously shaping the background for the energy transition. As renewable energy sources are presented to be promising alternatives to the traditional fossil resources, an intensification of the efforts to deploy sustainable biomass-based energy systems is ongoing not only from a strategic decision point of view, but also from an environmental perspective (d'Amore and Bezzo, 2016).

However, the introduction of bioenergy into the existing energy market necessitates not only the efficient design of the processing of raw materials but also the consideration of the spatial interactions of the conversion plants with the supply and demand points (Chomette et al., 2018). A number of recent studies address the issue of the biomass supply chain design. Costa Melo et al. (2018) present a data envelopment analysis approach (DEA) to identify the most suitable transport pathway of wood from Africa to Europe. How and Lam (2017) proposed a novel optimization approach that incorporating principal component analysis (PCA) and analytical hierarchy process

(AHP) to determine the optimal transportation design and processing hub location in an integrated biomass supply chain. The work of Ghaderi et al. (2016) provides a comprehensive review regarding the design of biomass supply chains. In this paper, a large number of published works are compared and a large diversity on modeling approaches is revealed. Focusing more on manure as a source material and the production of bio-SNG, Calderón et al. (2017) provide a framework for the design and optimization of bio-SNG supply chain using an explicit MILP multi-period scheme.

However, one should not forget that the role of process design within the definition of the supply chain is crucial. Thus, a bigger approach is needed that accounts for the integration of process design with the supply chain, highlighting the benefits and revealing potential synergies between the various steps of the conversion path from raw materials to services. Moreover, such a formulation will set the transition from the well-established process design level to the larger scale market level. To account for the role of the design of the processing units in the supply chain, expressed both as the type of conversion plant but also in relation to the output capacity, the current work presents a holistic approach based on the model presented by Chomette et al. (2018) for the design of wet biomass supply chains. To this end, the type and size of the conversion plants will play a decisive role in the formulation of the supply chain. The type of the plant refers to the various sub-processes that are used to convert the raw material to useful products as well as the formulation of the entire process flowsheet, while the size represents the output capacity in energy units. Using optimally designed conversion plants as predefined building blocks permits the synthesis of the entire supply chain through a MILP optimization problem that aims to minimize the total cost, expressed as the sum of the processing and transport expenses. The above formulation is then presented in an illustrative example for Brig, one of the highest manure producing districts of the canton of Valais in Switzerland.

2. Methodology

2.1. Manure conversion and design of the building blocks

The use of animal manure as the raw biomass material offers the possibility of using a plethora of conversion options of variable efficiencies depending on the desired end use as well as the conversion pathway that is followed. The common conversion process is anaerobic digestion, in which manure is converted to biogas through a series of complex (bio-)chemical reactions. The employment of pretreatment options of the raw biomass offers the chance to increase the biogas yield from the digester, inducing however an extra processing cost. Especially in cases where thermal pretreatment is used, extra degrees of freedom appear in the design process, related to the heat exchange between the pretreatment unit and the rest of the process. Biogas, being a mixture of CH_4 and CO_2 in a molar ratio of roughly 60:40 has to undergo through a cleaning and upgrading process to remove traces of impurities like H_2S , NH_3 , siloxanes etc. and increase its methane content, respectively. The final stream of upgraded biogas consists mainly of CH_4 and can be used as bio-SNG for grid insertion or power production in engines or fuel cells. On the other hand, anaerobic digestion leaves an undigested stream that still contains a large portion of the initial carbon content. It is therefore of great interest to extract the latter in order to maximize the efficiency of the overall process. Hydrothermal gasification (HTG) offers the possibility of converting wet organic

streams into methane using high pressure in a complex reactor scheme. The supercritical conditions that prevail within the HTG reactor ensure that the nitrous and phosphoric minerals are released unharmed in the residual output stream. Moreover, the use of catalytic methanation to convert the separated stream of CO_2 from the biogas is another option of further increasing the final bio-SNG yield. The methanation reactor can be fed with hydrogen produced through the electrolysis of water using renewables (e.g. solar power).

Using the MILP optimization framework described in Vigot et al. (2018), a number of possible configurations have been designed, each emphasizing in different process schemes and end products. Figure 1 shows the pareto front correlating the annualized process cost (in Swiss francs) with the overall energy efficiency of the process for a 100 kW unit.

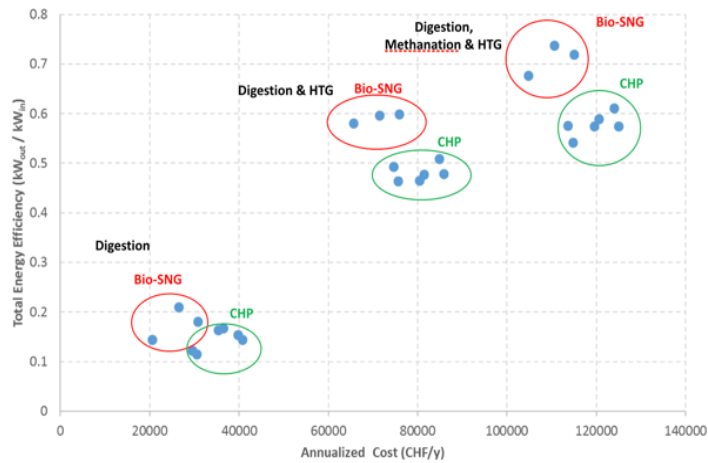


Figure 1. Pareto front of various process designs for manure conversion.

2.2. Employed flowsheets and typical sizes

Three different indicative flowsheets have been chosen to be used in the design of the supply chain, each focusing in a different end product. The employed flowsheets are depicted in Figure 2.

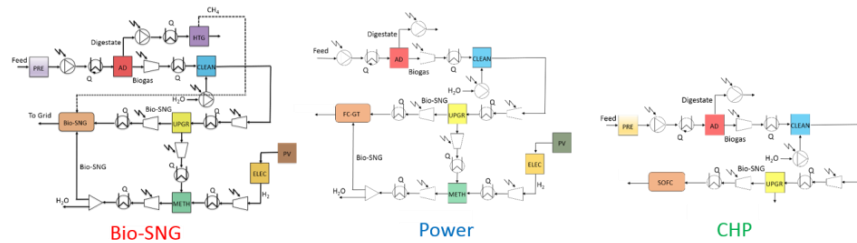


Figure 2. Employed flowsheets for the conversion of manure to different end products.

As already mentioned, the size of the conversion units plays an important part in the supply chain design. The specific costs of each flowsheet expressed as Swiss francs per kW produced is shown in Table 1. The typical sizes are selected with a reference on the raw material supply as well as the existing plants in the application area. The nonlinear dependence of the specific cost with the output capacity of each plant stems from the nonlinear dependence of the process efficiency with the plant dimensions.

Table 1. Specific costs (cost per kW) in Swiss Francs (CHF) of the employed flowsheets

	50 kW	100 kW	250 kW
Bio-SNG	2945.90	2292.54	1830.96
Power	2188.55	1821.40	1605.95
CHP	866.28	709.39	594.17

3. Application - Results

The three types of conversion plants presented in Section 2 together with the three typical sizes are used for the design of a supply chain for manure conversion in the commune of Brig in southern Switzerland. Six source sites have been identified and the corresponding manure potentials are taken from Thees et al. (2017). Using the design framework presented by Chomette et al. (2018), the results are illustrated in Figure 3.

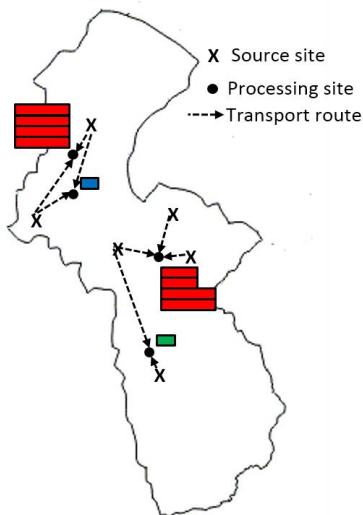


Figure 3. Supply chain results for manure conversion in the district of Brig, Switzerland

The horizontal length of the bars representing the processing units corresponds to the energetic output and specifically, 50 kW for small bars, 100 kW for medium bars and 250 kW for large bars. Similarly, the colors of the units correspond to the type of the plant, namely red for bio-SNG producing plants, blue for power production and green for CHP (also see Figure 2). It is seen that large centralized bio-SNG units are favored over the rest of the options due to the much larger energy efficiency of the process. In other words, these plants are able to convert more effectively a larger capacity of raw materials into bio-SNG. The centralized fashion in the placement is a direct consequence of the larger capital expenses that correspond to this type of conversion (Table 2). On the other hand, one can see that one biomass source is not limited to feeding a single conversion unit as shown in the northern part of the commune. According to the results, heat and power producing plants act as a supplement to the residual manure that is more expensive to be converted to bio-SNG. It has to be noted that this of course depends also on the initial choice of the building blocks. In other words, if an exhaustive investigation was made using all the available conversion options, it would be apparent that the highly efficient designs would be preferentially used over the other options. This of course, will increase the accuracy of the results but also drastically raise the computational effort and is the next step of this research.

4. Conclusions

A study for the design of manure supply chains was presented here. Based on a previous work, the approach involves the use of pre-designed processing plants representing the main steps of the biomass-to-services conversion chain. Such plants come equipped with information on their assigned capacity and type, the first being expressed as the energetic output of the conversion process while the second as the pathway from raw materials to products and are then used within a MILP design optimization framework. The latter is able to perform the spatial allocation by selecting the most suitable conversion type and size of each plant with regard to the supply of raw biomass by minimizing the total cost of the supply chain represented by the sum of the processing and transport costs. Three pre-defined process flowsheets, each accounting for the conversion of manure to different end products and with a different energetic efficiency, as well as three typical plant sizes selected by considering the domain of application are used for the design of the manure supply chain for the district of Brig in Switzerland. According to the model outputs, the conversion to bio-SNG in large plants of centralized fashion seems to be the most economically viable option.

Acknowledgements

This research project is financially supported by the Swiss Innovation Agency Innosuisse and is part of the Swiss Competence Center for Energy Research SCCER BIOSWEET.

References

- A. J. Calderón, P. Agnolucci, L. G. Papageorgiou, 2017, An optimisation framework for the strategic design of synthetic natural gas (BioSNG) supply chains, *Applied Energy*, 187, 929-955.
- G.A. Chomette, Th Damartzis, F. Maréchal, 2018, Optimal design of biogas supply chains, *Computer Aided Chemical Engineering*, 43(A), 669-674, 2018.

- I. Costa Melo, A. Rentizelas, A. J. Paulo Nocera, J.S. Campoli, D.A. do Nascimento Rebelatto, 2018, An assessment of biomass supply chain : a DEA application. *Athens Journal of Sciences*, 5 (2). pp. 125-140.
- F. d'Amore, F. Bezzo, 2016, Strategic optimisation of biomass-based energy supply chains for sustainable mobility, *Computers and Chemical Engineering* 87, 68–81.
- H. Ghaderi, M. S. Pishvae, A. Moini, 2016, Biomass supply chain network design: An optimization-oriented review and analysis, *Industrial Crops and Products*, 94 (30), 972-1000.
- B.S. How, H. L. Lam, 2017, Novel Evaluation Approach for Biomass Supply Chain: An Extended Application of PCA, *Chemical Engineering Transactions*, 61, 1591-1596.
- O. Thees, V. Burg, M. Erni, G., Bowman, R. Lemm, 2017, Biomass potenziale der Schweiz für die energetische Nutzung, *WSL Berichte*, Heft 57.
- M.A. Vigot, Th. Damartzis, F. Maréchal, 2018, Thermoeconomic design of biomass biochemical conversion technologies for advanced fuel, heat and power production, *Computer Aided Chemical Engineering*, 44(A), 1801-1806, 2018.

Modelling Full Cycles of Carbonation-Calcination for Calcium Looping Process Simulation

Miguel Abreu Torres,^a Paula Teixeira,^a Rui M. Filipe,^{b,c} Luis Domingues,^d Carla I. C. Pinheiro,^a Henrique A. Matos^{c*}

^a*Centro de Química Estrutural, DEQ, Instituto Superior Técnico/Universidade de Lisboa, Av. Rovisco Pais 1, Lisboa 1049-001, Portugal*

^b*Instituto Superior de Engenharia de Lisboa/Instituto Politécnico de Lisboa, R. Conselheiro Emídio Navarro 1, Lisboa 1959-007, Portugal*

^c*CERENA, DEQ, Instituto Superior Técnico/Universidade de Lisboa, Av. Rovisco Pais 1, Lisboa 1049-001, Portugal*

^d*Process Systems Enterprise, 5th Floor East, Hammersmith Grove 26-28, London W6 7HA*
henrimatos@tecnico.ulisboa.pt

Abstract

This work is part of a study to develop a multi-scale model of a Ca-looping (CaL) post-combustion process for CO₂ capture that relies on the carbonation reaction of CaO (s) and on the calcination of the resulting CaCO₃ (s) to generate a stream of highly concentrated CO₂ (g).

The literature lacks models that combine the modelling of both reactions with a cyclic structure that accounts for sorbent deactivation and allows for a realistic estimation in the case of incomplete reactions or different reaction media. Therefore, in this work two sub-models are combined to form this novel modelling approach for the simulation of complete carbonation-calcination cycles of the CaL process: The overlapping grain model for the carbonation reaction, and a proposed modified version (mRThPSD) of the rate equation theory for the pore size distribution (PSD) of calcined CaCO₃ (RThPSD) for the calcination.

The cyclic structure accounting for sorbent deactivation present in the proposed model was justified using data from fixed bed reactor experiments which highlights the relationship between loss of superficial area of CaO sorbents and loss of reactivity.

The model was implemented in gPROMS ModelBuilder[®] software and was validated with data from fixed bed reactor experiments for different CaL sorbents. One full CaL cycle was simulated successfully for dolomite, with the model estimating both reactions profiles and changes to the calcinated particle PSD with errors below 3%.

Keywords: Calcium-looping, CO₂ capture, modelling, carbonation, calcination.

1. Introduction

Calcium-looping (CaL) is a post-combustion technique for carbon capture and storage, where the carbonation of CaO (s) is used to capture CO₂ (g) and form CaCO₃ (s), the calcination of which yields a stream of highly concentrated CO₂ (g). CaL is a very

promising candidate for industrial post-combustion CO₂ capture due to the fact that widely available and low-cost natural limestone can be used as a sorbent.

Several carbonation and calcination reaction models can be found in literature, but one complete model that includes both reactions and a cyclic structure accounting for sorbent deactivation during reaction cycling does not exist. An existing model by Zhou et al. (2013) attempts a similar concept by combining the Overlapping Grain Model (OGM) by Liu and Dennis (2012) with an empirical equation that correlates sorbent deactivation with the cycle number. However, the lack of a detailed calcination model restricts it to the experimental conversion loss profile that originated the correlation, and respective temperatures and atmosphere compositions.

This work is part of a study aiming to techno-economically evaluate the implementation of a CaL CO₂ capture process in a Portuguese cement producer's industrial plant based on a multi-scale model of a CaL reactor. Hence there is an urgent need for a model of carbonation and calcination reaction cycles to be used for different reaction temperatures and reaction media, and thus different extents of reaction. By modeling the changes of the sorbent particle's porous structure during calcination using a modified version of the model originally proposed by Li et al. (2016), it is possible to estimate the changes on the sorbent particle's surface area during this reaction, which can be experimentally correlated to the loss of carbonation conversion. By estimating the post-calcination sorbent surface area, one can simulate the loss of carbonation conversion along multiple carbonation-calcination cycles for different extents of both reactions, as well as different temperatures and CO₂ partial pressures.

The objective of this work is to model the complete cycle: the carbonation reaction, the calcination reaction and the subsequent changes on the sorbent porous structure. The model was then implemented and validated in the gPROMS ModelBuilder[®] software. In this work, data from fixed bed reactor experiments are used to validate both sub-models. Experimental data are used to justify the relationship between the loss of superficial area of CaO sorbents and the loss of carbonation conversion, which allows to extend the simulation to multiple reaction cycles.

2. Model Development

To simulate a complete CaL cycle, two different models were combined as sub-models: the OGM by Liu and Dennis (2012) for the carbonation reaction, and a proposed modified version (mRThPSD) of the rate equation theory for the pore size distribution (PSD) of calcined CaCO₃ (RThPSD) by Li et al. (2016) for the calcination reaction.

2.1. Carbonation – Overlapping Grain Model - OGM

The OGM grain model considers that each CaO particle is composed of solid and randomly distributed spherical grains with different sizes. The formation of CaCO₃ during carbonation reaction is assumed to happen at the grain surface, causing the grain's volume to expand concentrically, increasing its radius, and shrinking the radius of the CaO core.

The known two main reaction regimes of carbonation are considered: a kinetic controlled profile for small reaction times and a diffusional regime for longer reaction times. By modelling the particle as an aggregate of dynamic grains with shells of CaCO₃ and allowing for particle porosity, two mechanisms can control the rate of reaction. The

particle porosity allows the inclusion of the diffusion of CO₂ in the porous network, and the layer of CaCO₃ around the grain adds an additional resistance to the transport of CO₂ between the pore and the front of reaction. In addition to the intrinsic reaction rate, these mechanisms contribute to more accurate carbonation simulations.

However, the OGM cannot estimate the maximum conversion for a given cycle and uses the deactivated fraction V_d as an input parameter, calculated as the difference between the theoretical maximum conversion and the experimentally observed conversion, that scales down the conversion estimated by the OGM to achieve the desired maximum conversion. The theoretical maximum conversion X_{Max} is a function of porosity of the initial CaO particle ϵ_0 and of the volumetric expansion coefficient between product and reactant α and can be calculated using Eq. (1).

$$X_{Max} = \frac{\epsilon_0}{(1 - \epsilon_0)(\alpha - 1)} \quad (1)$$

The OGM allows for CaO particles with non-reacting impurities by considering their molar volume in the calculation of α , as defined by Liu and Dennis (2012), thus this value varies between particles – e.g. 2.18 for pure CaO and 1.82 for dolomite. Due to this theoretical maximum conversion, there is an experimental limitation that should be accounted for when attempting to fit the OGM to data from carbonation experiments.

Figure 1 displays a plot of X_{Max} , with values larger than 1 computed as 1; and shows that X_{Max} is increasingly sensitive to the value of ϵ_0 as α decreases. Generically, the porous characteristics of a sample of sorbent particles are not homogeneous, so it might occur that the porosity considered to be characteristic of a given sorbent sample of particles results in lower values of X_{Max} than the experimentally observed maximum conversion, which is of course impossible. As such, when fitting the model to the experimental results, and especially for the samples rich in CaO (e.g. commercial CaCO₃), one should verify that this is not the case. If this condition is not verified, the variability of the sorbent sample porosity should be known and used to increase the value of ϵ_0 in the OGM to ensure that X_{Max} will at least equal the experimental maximum conversion, and only then should the parameter estimation be performed. With the maximum possible ϵ_0 being 1, the difference in sensitivity means samples less pure in CaO (e.g. dolomite) have more possible ϵ_0 values for which $X_{Max} > 1$, and thus it is less likely that the condition is not verified. Nonetheless, it can still happen, since ultimately it is the variability of sample's porosity that is more indicative of the likeliness of the condition not being verified – more likely for batches with high variability and less likely if otherwise.

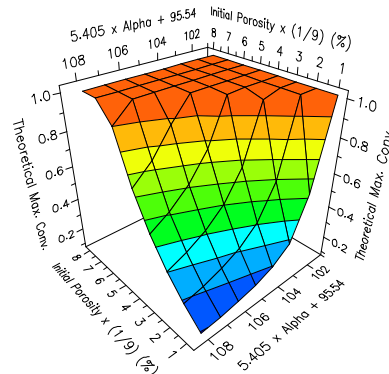


Figure 1 – Plot of the OGM's Theoretical Maximum Conversion (Eq. 1) for Initial Porosity between 0% and 60% and Alpha between 1.01 and 2.20.

2.2. Calcination – A rate equation theory for the PSD of calcined CaCO₃ - RThPSD

The RThPSD models the calcination reaction based on a shrinking core model, where a CaCO₃ core leads to a shell of CaO. It also models the dynamics of the porous structure using a rate equation based on balances to the number of vacancies of various sizes. The original RThPSD considers that two phenomena can change the porous structure during the calcination reaction: the release of CO₂ from the reaction, which creates vacancies by leaving the lattice; and the sintering process, which occurs naturally in CaO due to the high temperatures necessary for calcination.

The model, as presented by Li et al. (2016), has its shortcomings addressed by the modified version, mRThPSD, developed in this work, with the lack of initial conditions for the vacancy distribution being one of those drawbacks. Without these, the parameter values that result from model validation will not accurately represent the decomposition and sintering processes. The original model assumes that the particle is initially a solid with no porosity and that the porous structure present in the final PSD is formed solely from the release of CO₂ and from the sintering of those vacancies, which is not true, since the unreacted CaCO₃ is already porous, as seen in the work of Dennis and Pacciani (2009). The final PSD is thus inextricably linked to the PSD of the unreacted CaCO₃. The mRThPSD model addresses this problem by deriving initial conditions from the PSD of the initial unreacted CaCO₃, through the assumption that the measured total pore volume for a given pore diameter is equal to the total volume of vacancies of that respective size, assuming these vacancies to be spherical. It is also assumed that these vacancies are homogeneously distributed throughout the particle. The initial conditions are calculated with Eq. (2), where $N_{i,k,Initial}$ is the initial number of vacancies of size i in the k^{th} layer, V_{Pore_i} is the porous volume for pore diameter i of the unreacted CaCO₃ in m³g⁻¹, Vol_{R_0} is the particle volume in m³ and k_{layers} is the number of layers. The remaining variables and respective units are found in the original paper by Li et al. (2016).

$$N_{i,k,Initial} = \frac{V_{Pore_i} M_{CaO} Vol_{R_0}}{V_{CaO}^M v_i q^{i-1} k_{layers}}, \forall \kappa \in [1, k_{layers}] \quad (2)$$

Furthermore, in the original model, the area of the solid surface around the vacancies is calculated as the surface area of a sphere of the same diameter. However, sorbents for CaL are typically analyzed using N₂ adsorption-desorption experiments together with the BJH model, where the cylindrical pores assumption, among others, leads to Eq. (3).

Since for a sphere of volume V and radius r , the superficial area S is $3V/r$, assuming the vacancies as spherical when calculating their solid surface area generates values 1.5 larger than using Eq. (3). Since, as reported by Dennis and Pacciani (2009), the total pore surface area plays an important role in the carbonation reactivity of the sorbent, overestimating this property will skew future simulations towards unconservative conversion values. To address this, the mRThPSD assumes that the total surface area of pores of a given size is equal to the superficial area of a cylinder with the same total volume as the vacancies of the same size, calculated by Eq. (3) (SI units).

$$V_{Pore_i} = D_{Avg} S_i / 4 \quad (3)$$

Also, on the proposed mRThPSD the vacancy balance was modified to make the effects of CaCO_3 decomposition and CaO sintering simultaneous. Also, an error was corrected in the vacancy balance where the total volume of vacancies would decrease, which does not occur during calcination, as stated in the work by Li et al. (2016), as no pore straightening mechanism is present. Figure 2 highlights this error by showing the evolution of the total pore volume along the time during simulation with the original balance versus with the modified balance. The decrease in pore volume in the original balance is very apparent in Figure 2, caused by the artificial volume consumption brought on by this error being larger than the vacancy generation. As for the modified balance, it is possible to see that the volume created is conserved, as expected.

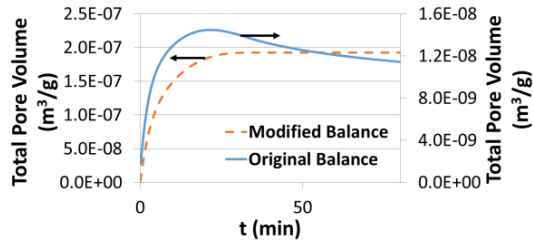


Figure 2 – Total Pore Volume along time using the Original and the Modified Vacancy Balance in the RThPSD model;

3. Results

Experimental data from fixed bed reactor experiments were used to validate both models. The OGM was validated for three different sorbents: commercial CaCO_3 , dolomite, and waste marble powder, a residue from the Portuguese marble industry, shown to have economic potential as a CaL sorbent (Pinheiro et al., 2016). As for the mRThPSD, it is currently only validated for dolomite due to the extensive experimental work required, and its validation with other sorbents is underway. The OGM was able to replicate both reaction regimes for all sorbents with an excellent accuracy, as shown on Figure 3 and by an average error of approximately 2%, for all sorbents. The reaction regimes are highlighted for the dolomite series as line segments i and ii (Figure 3). As for the validation of the mRThPSD, in terms of the estimation of the post-calcination particle's total pore volume, Figure 4 shows a quite satisfactory fitting, considering the complexity of the system. Despite observing that part of the volume allocated to the peak of the mRThPSD post-calcination curve should be located in higher pore diameters, there is an excellent agreement between the estimated and the experimental total pore volume, with a deviation of approximately 3%. As for the calcination conversion profile the proposed

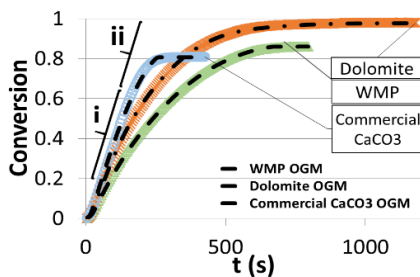


Figure 3 – Validation of the OGM for different sorbents (700 °C, 0.15 bar CO_2). Reaction domains for Dolomite: i – Kinetic Regime, ii – Diffusional Regime;

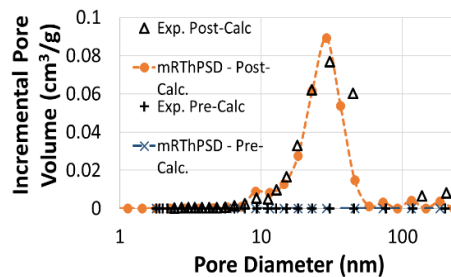


Figure 4 – Validation of the mRThPSD for Dolomite (800 °C, 0% CO_2);

mRThPSD can estimate it precisely, with an average deviation of approximately 1.2% to the experimental results. The fact that the solid's porous structure influences the reaction rate, highlights the necessity of an adequate fitting to the evolution of the particle's PSD, as seen in Figure 4. However, the inclusion of Eq. (3) limits the effect of an imperfect fit to the superficial area, whereas the overestimation of this

property in the original model would result in lower diffusivity values and thus lower reactions rates, hindering the fitting to the conversion profile. As for the cyclic structure of the model, it was implemented using the relationship between the loss of superficial area and sorbent deactivation, shown on Figure 5. This was used to redefine the OGM's deactivated fraction V_d , thus connecting the sub-models. The mRThPSD estimates the total loss of area during calcination, which determines the extent of the following carbonation. Figure 5 shows the importance of using the mRThPSD to model these mechanisms to estimate sorbent deactivation in the case of incomplete reactions, different temperatures and CO₂ partial pressures.

4. Conclusions

A new model that combines carbonation and calcination was implemented in gPROMS ModelBuilder[®]. Both sub-models were successfully validated using data from fixed bed reactor experiments, for three different sorbents, commercial CaCO₃, dolomite, and waste marble powder, a Portuguese marble industry residue, recently shown to have economic potential as an industrial sorbent for CaL. The predicted values have errors below 3% for both sub-models, when compared to experimental results. Only dolomite was used for the validation of mRThPSD and further experimental work with other sorbents is underway. The proposed model contains a cyclic structure accounting for sorbent deactivation, based on the relationship between loss of superficial area of CaO sorbents and loss of reactivity. While only one cycle was simulated in this work, experimental work is underway to validate the cyclic structure for more reaction cycles.

References

- J. S. Dennis, R. Pacciani, 2009, The rate and extent of uptake of CO₂ by a synthetic, CaO-containing sorbent, *Chemical Engineering Science*, 64, 9, 2147–2157.
- Z. S. Li, P. T. Liang, N. S. Cai, 2016, A rate equation theory for the pore size distribution of calcined CaCO₃ in calcium looping, *Faraday Discussions*, 192, 197-216.
- W. Liu, J. S. Dennis, S. Sultan, S. A. T. Redfern, S.A. Scott, 2012, An investigation of the kinetics of CO₂ uptake by a synthetic calcium based sorbent, *Chemical Engineering Science*, 69, 1, 644-658.
- C. I. C. Pinheiro, A. Fernandes, C. Freitas, E. T. Santos, M. F. Ribeiro, 2016, Waste marble powders as promising inexpensive natural CaO-based sorbents for post-combustion CO₂ capture, *Industrial & Engineering Chemistry Research*, 55, 29, 7860–7872.
- Z. Zhou, P. Xu, M. Xie, Z. Cheng, W. Yuan, 2013, Modeling of the carbonation kinetics of a synthetic CaO-based sorbent, *Chemical Engineering Science*, 95, 283-290.

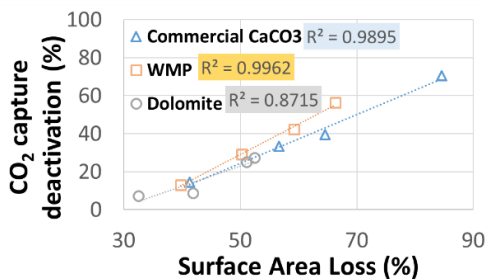


Figure 5 – Sorbent Deactivation (%) Vs. Surface Area Loss (%) for cycles 2, 5, 10 and 20 (from left to right);

Determination of the optimal distribution of active centers in a multifunctional catalyst pellet using global searching combined with reduced-order modeling approach

Katarzyna Bizon^{a,*}, Gaetano Continillo^b

^a*Cracow University of Technology, ul. Warszawska 24, 31-155 Kraków, Poland*

^b*Università degli Studi del Sannio, Piazza Roma 21, 82100 Benevento, Italy*

kbizon@chemia.pk.edu.pl

Abstract

The problem of optimal distribution of two types of catalytic active sites for yield maximization is solved for a spherical porous catalyst pellet. The case where two consecutive chemical reactions with one reversible step following arbitrary kinetics occur under isothermal conditions is investigated numerically using the global searching technique. The constraints given by mass balances of the reactants within the pellet accounting both for internal and external mass transfer resistances are reduced by means of Proper Orthogonal Decomposition combined with Galérkin projection method. The applied computational procedure gives significant savings in calculation time as compared to classical discretization approach based on finite differences. Results demonstrate that particle microstructuring via optimal catalyst distribution within the pellet may constitute a powerful means of multistep process intensification.

Keywords: multifunctional catalyst pellet, numerical optimization, reduced order modeling, proper orthogonal decomposition

1. Introduction

Multifunctional catalyst pellets are a relatively new concept, therefore many issues concerning their performance, design, and feasibility of technological implementation as well as economic aspects remain open. Multifunctionality extended down to the particle level may consist both in the integration of sorptive mass storage and catalytic sites as well as coupling of two or more catalytic active sites in a single particle of the catalyst (Grünewald and Agar, 2004; Lugo and Wilhite, 2016). Due to the reduction of mass transfer resistances both applications may result in the enhancement of process performance, as compared to the processes carried out in reactors that integrate different functionalities solely on the apparatus level.

According to Grünewald and Agar (2004), the enhancement of yield through particle microstructuring depends on many factors including the reaction rate constant and composition of the gaseous phase. The authors demonstrated superiority of some selected non-uniform over the uniform distribution of active sites. However, the analysis was limited to a discrete set of a priori selected particle structures. Moreover, while the optimization of the distribution of a single active component within catalyst

particles was examined thoroughly in the past decades (Morbidelli et al., 2001), there are no reports dealing with optimization of the distribution of multiple active components.

In this work, the optimal distribution of two active centers in terms of the yield is determined for a single isothermal catalyst pellet by means of a global searching technique. In order to increase the efficiency of the numerical algorithm, differential equations describing concentration profiles of the reactants within catalyst pellet are reduced using Galérkin projection onto empirical modes determined via Proper Orthogonal Decomposition.

2. Mathematical model and algorithms

2.1. Model of a single isothermal catalyst pellet

Let us consider as a test case a general multistep chemical reaction:



developing in an isothermal spherical catalyst pellet. Under the assumption that all chemical reactions are first order, the steady-state mass balances in a catalyst written in terms of dimensionless variables are (Bizon, 2017):

$$\frac{d^2 \beta_A}{d\zeta^2} + \frac{2}{\zeta} \frac{d\beta_A}{d\zeta} - f_1 \Phi_1^2 \frac{k_1 \beta_A - k_{-1} \beta_B}{k_1 + k_{-1}} \quad (2a)$$

$$\frac{d^2 \beta_B}{d\zeta^2} + \frac{2}{\zeta} \frac{d\beta_B}{d\zeta} + f_1 \Phi_1^2 \frac{k_1 \beta_A - k_{-1} \beta_B}{k_1 + k_{-1}} - f_2 \Phi_2^2 \beta_B \quad (2b)$$

where $\zeta = r/R_p \in [0,1]$ is the dimensionless radial coordinate with R_p being the dimensional particle radius, $\beta_i = C_i/C_{ref}$ is the dimensionless concentration, whereas f_1 and $f_2 = 1 - f_1$ denote the volume fractions of two types of catalytic active sites which are function of the radial coordinate ζ . If the pore diffusion occur with the same effective diffusion coefficient D_{eff} for all reactants, then Thiele moduli Φ_1 and Φ_2 can be defined, respectively, as (Roberts and Lamb, 1996):

$$\Phi_1 = R_p \sqrt{\frac{k_1 + k_{-1}}{D_{eff}}}; \quad \Phi_2 = R_p \sqrt{\frac{k_2}{D_{eff}}} \quad (3)$$

The boundary conditions associated with Eq. (2) are:

$$\left. \frac{d\beta_A}{d\zeta} \right|_{\zeta=0} = 0; \quad \left. \frac{d\beta_A}{d\zeta} \right|_{\zeta=1} = \text{Bi}(\beta_{bulk,A} - \beta_A(1)) \quad (4a)$$

$$\left. \frac{d\beta_B}{d\zeta} \right|_{\zeta=0} = 0; \quad \left. \frac{d\beta_B}{d\zeta} \right|_{\zeta=1} = \text{Bi}(\beta_{bulk,B} - \beta_B(1)) \quad (4b)$$

where the mass Biot number is defined as $Bi = k_m R_p / D_{eff}$.

2.2. Formulation of the optimization problem

Several indices may quantify the performance of a single catalyst pellet when multiple chemical reactions occur, including effectiveness factor, selectivity or yield. Let us assume that C (Eq. (1)) is the desired product. Following Morbidelli et al. (2001), the yield of product C with respect to reactant A can be defined as the ratio between the actual production rate of C and the consumption rate of A in absence of internal and external transport resistances. Hence, for the yield, the objective function is given by:

$$Y_{CA} = \frac{3 \int_0^1 f_2 k_2 \beta_B \zeta^2 d\zeta}{k_1 - k_{-1}} \quad (5)$$

The optimization problem consists therefore in finding the distribution $f_2(\zeta)$, which maximizes the yield given by Eq. (5) under the constraint given by Eq. (2) and Eq. (4), and the constraints related to the volume fractions of each functionality and to the constant total amount of each catalyst:

$$0 \leq f_2(\zeta) \leq 1 \quad \text{and} \quad 3 \int_0^1 f_2(\zeta) \zeta^2 d\zeta = \nu \quad \text{where} \quad 0 \leq \nu \leq 1 \quad (6)$$

Since the cost function has local minima, the global search algorithm with a scatter-search mechanism for generating start points (Urgay et al., 2007) was applied to solve the optimization problem. The problem was solved directly using the Galérkin projection combined with Proper Orthogonal Decomposition (POD) to transform the boundary value problem given by Eq. (2) into a set of algebraic equations, along with the trapezoidal rule to evaluate the integrals given by Equations (5) and (6). Thus, the adjustable parameters of the problem are the values of the distribution f_2 at the discrete nodes ζ_i , $i = 1, \dots, N$ with $N = 51$.

2.3. Model reduction

Let us consider a steady-state boundary value problem:

$$L(y(x)) + F(y(x)) = 0, \quad x \in [a, b] \quad (7a)$$

$$B_a(y(a)) = A, \quad B_b(y(b)) = B \quad (7b)$$

where L is a linear operator containing spatial derivatives, F is a non-linear function of y whereas B_a and B_b are boundary operators. The approximation of the spatial derivatives by finite differences leads to the transformation of Eq. (7) into the following system of N algebraic equations, where N is the number of discretization nodes:

$$\mathbf{A}\mathbf{y} + \mathbf{G}(\mathbf{y}) = 0 \quad (8)$$

where \mathbf{y} is a state variable vector, \mathbf{A} is a coefficient matrix whereas $\mathbf{G}(\mathbf{y})$ is a vector accounting for the system nonlinearities and non-homogenous boundary conditions. By employing a POD basis (Bizon, 2017) the state variable vector can be represented in a truncated form as:

$$\mathbf{y} \approx \Phi_K \mathbf{c}_K \quad (9)$$

where \mathbf{c}_K are modal coefficients, and Φ_K are K leading POD modes, $K \leq N$ determined by solving the eigenvalue problem:

$$\mathbf{C}\Phi = \Lambda\Phi \quad \text{where} \quad \mathbf{C} = \frac{1}{M} \mathbf{Y}\mathbf{Y}^T \quad (10)$$

with the autocorrelation matrix \mathbf{C} calculated from M solutions of the system given by Eq. (8) for various values of the selected model parameters. Introduction of the truncated state variable (9) into the system (8) and its projection onto the basis yield the following reduced order model consisting of K algebraic equations:

$$\Phi_K^T \mathbf{A} \Phi_K \mathbf{c}_K + \Phi_K^T \mathbf{G} (\Phi_K \mathbf{c}_K) = 0 \quad (11)$$

3. Results and discussion

Table 1 reports the values of the model parameters employed in the numerical simulations. The values of dimensionless concentration of reactant A and intermediate product B in the bulk gas were set respectively to $\beta_{bulk,A} = 1$ and $\beta_{bulk,B} = 0$. In terms of the entire tubular reactor, such boundary conditions can be interpreted by assuming that the considered particle is located in the vicinity of the reactor inlet.

Table 1. Main model parameters used in the numerical simulations

Parameter	Value	Unit	Parameter	Value	Unit
D_{eff}	10^{-6}	m^2/s	k_2	10	1/s
k_1	10	1/s	k_m	0.01	m/s
k_{-1}	5	1/s	R_p	10^{-3}	m

The POD basis functions used for order reduction of the constraint (2) were determined from the solutions of the mass balance equations determined with three arrangements of catalyst 1 and catalyst 2. Figure 2a shows the employed distributions of the volume fraction along the particle radius for the catalyst 2, $f_2(\zeta)$.

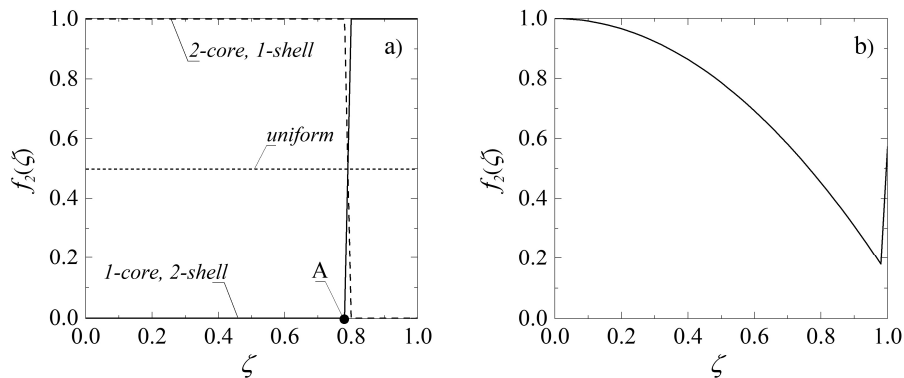


Figure 1. Distributions of the catalyst f_2 used for the determination of the POD basis (a) and optimal distribution of the catalyst f_2 determined via optimization method.

In each case the total volume fraction of each type of active centers was set to $\nu = 0.5$, therefore for both core-shell arrangements the point A (Fig. 2a) corresponds to $\zeta = 0.7937$. Since three leading POD modes resulted to contain more than 99% of the so-called cumulative correlation energy (Bizon, 2017), $2 \cdot N = 102$ algebraic equations obtained from the discretization of the Eq. (2) using finite differences were reduced using the Galärkin projection to $2 \cdot K = 6$ equations.

Figure 2b shows the optimal distribution $f_2(\zeta)$ obtained from the optimization procedure coupled with POD-Galärkin. It needs to be mentioned that the computations were also performed using non-reduced mass balance equations. The results obtained, that is both the optimal profile of the volume fraction and the corresponding value of the cost function Y_{CA} were almost identical to those achieved when applying POD-Galärkin. However, the computational time was about 20 times greater.

The determined optimal distribution $f_2(\zeta)$ provides a substantial yield Y_{CA} enhancement with respect to the values of Y_{CA} that may be obtained with a uniform and core-shell distribution of the catalyst (Table 2).

Table 2. Comparison of the selectivity of A towards C, Y_{CA} , achieved using the uniform, core-shell and optimal distribution of active centers within the catalyst pellet

Catalyst arrangement	Uniform	1-core 2-shell	2-core 1-shell	Optimal
Y_{CA}	0.1808	0.1148	0.1263	0.3093

The analysis of Figure 2 demonstrates that the type of catalyst arrangement within the particle strongly influences the concentration profiles of reactant A (Fig. 2a) and intermediate product B (Fig. 2b) within the particle and, as a consequence, the average process rate and the desired product concentration.

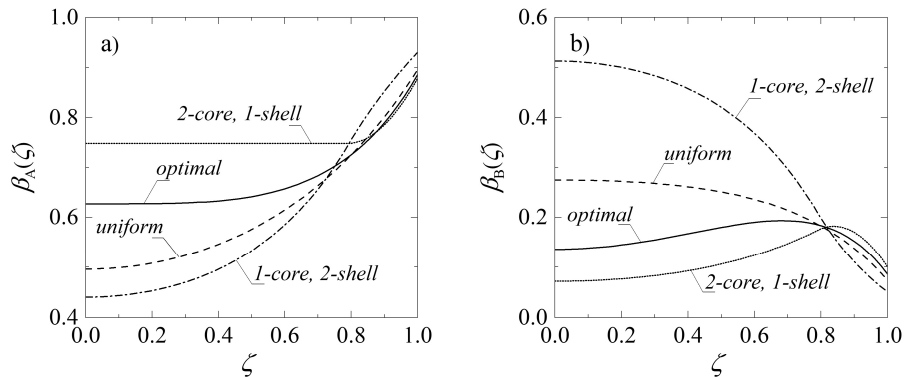


Figure 2. Concentration of reactant A (a) and intermediate product B (b) within particle calculated for different arrangement of the active centers.

Keeping in mind the spherical shape of the particle, it can be observed that in fact the optimal distribution of f_2 (Fig. 2a) provides the highest conversion of the intermediate product B (Fig. 2b) towards the desired product C. Although for the *1-core* and *2-shell* arrangement the average concentration of B is the highest, it should be remembered that in this case the second chemical reaction takes place only in the outer shell of the pellet.

4. Conclusions

Comparison of the catalyst performance indices that may be achieved when using a uniform or a core-shell arrangement of active sites, with the performance achieved for the optimal catalyst distribution within the pellet, confirms that particle microstructuring is a powerful tool for multistep process intensification. The methodology discussed can be easily adapted to more complex chemical kinetics and non-isothermal processes or even to multiscale optimization of the catalyst distribution both at particle and at reactor scale. In such case, computational expenses resulting from additional constraints in the form of a larger number of mass and/or energy equations can still be kept at a reasonable level, thanks to model order reduction based on POD-Galerkin. Moreover, the computed optimal distributions of active centers are non-uniform and can be non-smooth or even discontinuous functions, which is of great importance in view of the catalyst preparation.

Acknowledgements

The research was financed by the Polish National Science Centre, project number 2017/26/D/ST8/00509.

References

- K. Bizon, 2017, Assessment of a POD method for dynamical analysis of a catalyst pellet with simultaneous chemical reaction, adsorption and diffusion: Uniform temperature cases, *Computers & Chemical Engineering*, 97, 259-270.
- M. Grünewald, D.V. Agar, 2004, Enhanced catalyst performance using integrated structured functionalites, *Chemical Engineering Science*, 59, 5519-5526.
- E.L. Lugo, B.A. Wilhite, 2016, A theoretical comparison of multifunctional catalyst for sorption-enhanced reforming processes, *Chemical Engineering Science*, 150, 1-5.
- M. Morbidelli, A. Gavriilidis, A. Varma, 2001, *Catalyst design. Optimal distribution of catalyst, pellets, reactors, and membranes*, Cambridge University Press, UK.
- G.W. Roberts, H.H. Lamb, 1996, The effect of reversibility on the selectivity of parallel reactions in a porous catalyst, 51, 441-448.
- Z. Urgay, L. Lasdon, J. Plummer, F. Glover, J. Kelly, R. Marti, 2007, Scatter search and local NLP solvers: A multistart framework for global optimisation, *INFORMS Journal of Computing*, 19, 328-340.

Sequential and Simultaneous Optimization Strategies for Increased Production of Monoclonal Antibodies

Chrysoula D. Kappatou^a, Oktay Altunok^a, Adel Mhamdi^a, Athanasios Mantalaris^b, Alexander Mitsos^{a*}

^a *RWTH Aachen University, Aachener Verfahrenstechnik – Process Systems Engineering, Forckenbeckstraße 51, 52074 Aachen, Germany*

^b *Dept. of Chemical Engineering, Centre for Process Systems Engineering (CPSE), Imperial College London SW7 2AZ, London, U.K*

amitsos@alum.mit.edu

Abstract

Monoclonal antibodies (mAbs) represent a significant class of biopharmaceuticals with a wide range of diagnostic and therapeutic applications. Typically, mAbs are produced by cultivated mammalian cells, to meet the high quality product specifications. For new products and cell lines, an adaptation of cultivation conditions is required. This is usually performed experimentally. Model-based approaches can be a powerful tool to reduce experimental efforts and accelerate process development. We present optimizations using the process model in Kappatou et al. (2018), which is based on Quiroga et al. (2016). In particular, we perform fed-batch optimizations following a sequential and a simultaneous approach. In the sequential approach, we first find optimal initial conditions for the batch process using different objectives, and then we optimize the feeding for constant initial conditions. In the simultaneous approach, we directly optimize for initial conditions and appropriate feed rates. The optimizations lead to significant improvements compared to the base case presented in Quiroga et al. (2016). The results indicate that the sequential approach is sometimes able to outperform the simultaneous one by overcoming limitations of the local optimization used. This may be due to the flexibility of the sequential approach to use different objectives for the two steps (batch and fed-batch). Therefore, the results further highlight the importance of utilizing good initialization procedures in local optimization.

Keywords: monoclonal antibodies, bioprocess intensification, model-based optimization

1. Introduction

Within the biopharmaceutical industry, monoclonal antibodies (mAbs) are important products. Their increasing demand, together with the advent of biosimilar products and the necessity for incorporation of quality by design (QbD) principles, constitute current challenges (Shukla et al., 2017 & Collins, 2018). Therefore, a shift towards methods that can provide better mechanistic process understanding, and thus facilitate process intensification and control, is needed. To this end, model-based approaches outweigh considerable advantages.

Although recent advances in modelling have paved the way for model-based optimization strategies, there is so far only a limited amount of publications reporting on optimization of mAb production using mathematical models. In batch processes, optimization of the initial nutrient composition is a key feature. In fed-batch, optimal feeding compositions and rates are explored. Nevertheless, the great majority of existing studies considers only feeding of glucose and/or glutamate, which might not be the only growth limiting nutrients (Pörtner and Schäfer, 1996). In an industrial scale, fed-batch optimizations are often performed empirically, based on a long history of data usually obtained from batch experiments. Optimizing the fed-batch culture for both initial concentrations and feeding strategies is advantageous, as it reduces experimental costs (fewer experiments) and product time to market.

We focus on dynamic optimization of mAb producing processes in fed-batch mode of operation. We optimize using a reformulated version of the metabolic model proposed by Quiroga et al. (2016) that we presented in Kappatou et al. (2018). These models enable multiple component feeding. To describe cell's metabolism, metabolic shifts are also incorporated. More information about the modelling part can be found in Quiroga et al. (2016, 2018) and about the undertaken reformulations in Kappatou et al. (2018).

The remainder of the article is organized as follows: In Section 2 we present fed-batch optimizations following the two different methodologies, namely the sequential and the simultaneous approach. Section 3 discusses the formulation of the optimization problems. The optimization results are presented in Section 4. Section 5 summarizes this work and provides conclusions and future directions.

2. Fed-batch process optimization

We consider two different approaches for optimization of initial concentrations and feeding profiles of nutrients, as shown in Fig. 1. The ultimate goal in both cases is to maximize the final antibody concentration (mg/L), which corresponds to the high-value pharmaceutical product.

In the sequential approach, we first find optimal initial concentrations for the batch process (batch optimization), and then we optimize the feeding using the previously derived optimal initial concentrations (fed-batch optimization). Different objectives can be used in these steps. For the batch optimization, we consider to maximize final product concentration (mAb) and/or to maximize viable cell density (X_v), as these turned out to be the most promising objectives for our case study. The subsequent fed-batch optimization maximizes the final product concentration. In the simultaneous approach, we directly optimize for both initial concentrations and appropriate feed rates with the objective to maximize the final antibody concentration. Note that the terminology

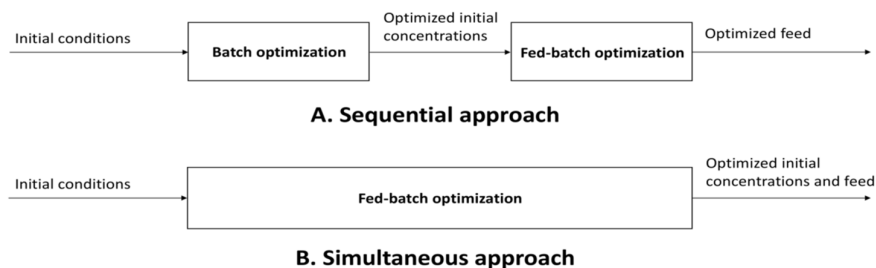


Figure 1- Solution approaches considered in the case studies

sequential and simultaneous should not be confused with that typically used in dynamic optimization theory to describe the indirect numerical solution methods single-shooting and orthogonal collocation, respectively.

3. Problem formulation

We investigate optimization problems with embedded process dynamics, using the reformulated metabolic model in Kappatou et al. (2018). The model consists of 31 differential, 81 algebraic equations and 41 parameters. The key components for the different optimization problems are summarized in Table 1. A brief description of the constraints and the control variables included into the optimization formulations is given.

Table 1- Optimization problem formulations

Optimization approach	Sequential		Simultaneous
Operation mode	Batch	Fed-batch	Fed-batch
Objective	max mAb or Xv	max mAb	max mAb
Constraints			
Viability		Viab \leq 60 %	
Residual nutrients		[NUT](t _r) \leq 0.1 [NUT] ₀	
Glutamate depletion	t _{cr,GLU} \leq 92.5 h	n/a	t _{cr,GLU} \leq 92.5 h
Volume limitation	n/a		V \leq 1.1 V ₀
Control variables			
Final time		t _{batch} \leq t _r \leq 2 t _{batch}	
Feeding rate	n/a	0 \leq F _{in} \leq F _{in,max}	
Initial nutrients	[NUT] _{min} \leq [NUT] ₀	n/a	[NUT] _{min} \leq [NUT] ₀
	\leq [NUT] _{max}		\leq [NUT] _{max}

3.1. Control variables

In this study, six growth limiting nutrients (NUT) are considered, namely glucose (GLC), glutamate (GLU), arginine (ARG), asparagine (ASP), isoleucine (ILE) and leucine (LEU). Optimal initial concentrations for these nutrients are sought. As concentration ranges of the nutrients, we consider the bounds reported by Pörtner et al. (2014). Fed-batch optimization aims at deriving optimal feeding strategies (feeding -composition, -time and -rates). Note that the feeding composition is already optimized in a previous study (Quiroga et al., 2018), and thus is not examined here. The final time of the culture is also an optimization degree of freedom, and is allowed to vary between 144 h (batch time) and 288 h. From our current experience, the upper bound in the culture time is sufficiently large (Kappatou et al., 2018).

3.2. Constraints

Cell viability refers to the percentage of viable cells into the culture. In the considered optimization problems, it represents an indirect quality measure, and thus should be kept above a critical value. This way quality reducing effects are avoided. In this study, we impose a lower value for viability at 60 %. To reduce unnecessary residual nutrients, we impose an additional constraint on the residual concentrations to be lower than 10% of their initial concentrations. This is because, although on the one side nutrient exhaustion induces cell starvation, on the other side, excessive supply can cause inhibition of cell

growth and increased production of inhibitory by-products (Bibila and Robinson, 1995). One of the essential nutrients is glutamate. The cells can only survive for a limited duration, after glutamate depletion (Meister et al., 1980). Therefore, an additional constraint on the culture duration after exhaustion of glutamate (92.5 h) is incorporated to the model. This value corresponds to the value, at which culture was terminated after glutamate depletion at the real batch experiments used for model validation. Finally, in the fed-batch optimizations we impose an additional constraint that the volume is at most increased by 10% to account for dilution effects (Kiparissides et al., 2015).

4. Results and discussion

The optimization studies are performed using gPROMS v.5.0.1 (Process Systems Enterprise, 1997-2018) using a piecewise constant discretization of the controls. The simulation times vary from a few seconds for the batch cases to a few hours for the fed-batch cases with no significant differences with respect to the different approaches.

We show the optimal initial concentrations for all cases in Table 2 and the key indicators for the optimizations of the batch processes in Table 3. The max (mAb) case achieves a higher antibody concentration than maximizing the viable cell concentration, max (Xv). However, the max (Xv) case aiming at (and achieving) a higher viable cell concentration, does not reach the bound on the viability constraint and yields a lower accumulation of toxic lactate. All these are desired characteristics, and indicate the potential of utilizing these optimal concentrations for subsequent fed-batch optimization studies.

We give the optimization results for the fed-batch processes in Table 4. A comparison of the results between the simultaneous and the sequential approach reveals that the simultaneous max (mAb) performs slightly better than the sequential max (mAb, mAb) within identical process duration. This is expected due to the higher degree of freedom in the simultaneous approach. However, the latter is outperformed by the sequential max (Xv, mAb) approach that achieves 7 % higher product concentration with 12 % longer process duration. This approach yields a final mAb improvement of 244 % and an expansion of the culture span around 1.5 days compared to the unoptimized batch case presented in Quiroga et al. (2016).

Table 2- Optimal initial nutrients concentrations in mM

Objectives	Approach	ARG	ASP	GLC	GLU	ILE	LEU
max(mAb)	Sequential batch	3.82	1.38	28.51	2.99	3.13	4.27
max (Xv)	Sequential batch	3.71	1.28	24.80	2.22	2.86	4.27
max (mAb)	Simultaneous fed-batch	4.27	1.43	35.31	3.03	3.33	4.27

Table 3- Batch optimization results

Objectives	mAb (mg/L)	Xv (cells/L)	Culture Duration (h)	LAC (mM)	Viability (%)
max (mAb)	487	3.87E9	166	10.9	60
max (Xv)	393	4.44E9	157	8.8	73

Table 4- Fed-batch optimization results

Optimization Approach	mAb (mg/L)	Culture Duration (h)	LAC (mM)	Viability (%)
Sequential max (mAb, mAb)	582	166	11.5	60
Sequential max (X_v , mAb)	635	186	10.5	60
Simultaneous max (mAb)	592	166	11.7	60

An illustrative representation of the optimization results for the different approaches is shown in Fig. 2. The sequential max (mAb, mAb) and the simultaneous max (mAb) case perform quite similarly. The feeding is introduced early in order to extend the exponential growth phase of the culture. The culture grows faster, but also the release of lactate is faster (results not shown here). In contrast, in the sequential max (X_v , mAb) approach the feeding is added a later time period, which initially slows down the growth, but leads to extended process duration and a higher final product concentration.

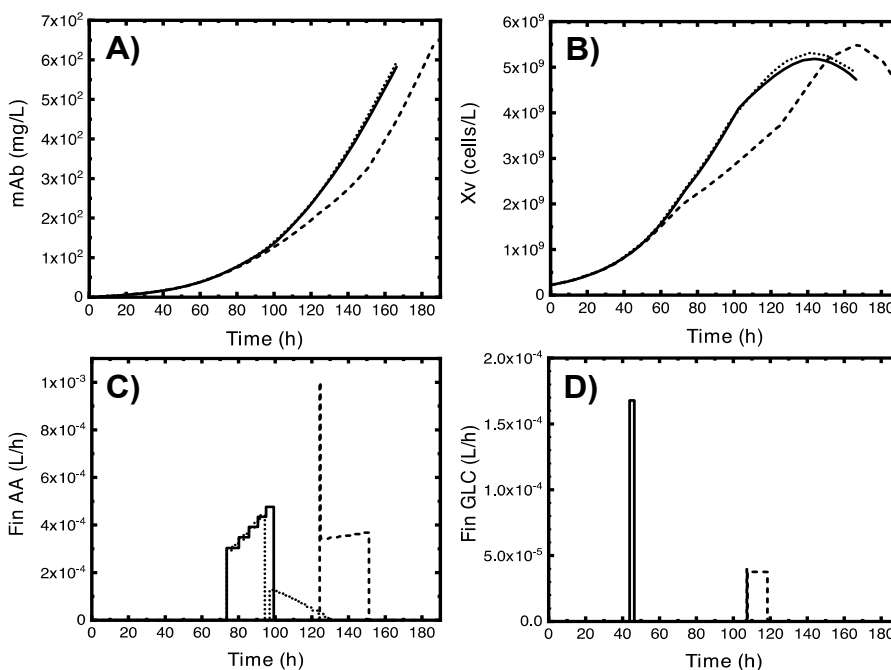


Figure 2- Key trajectories for the different optimization approaches (A) Optimized mAb production [mg/L], (B) Viable cell concentration [cells/L], (C) Optimal feeding profiles of amino acids [L/h], (D) Optimal feeding profiles of glucose [L/h] — Sequential max (mAb, mAb) Sequential max (X_v , mAb) - - - Simultaneous max (mAb)

If the dynamic optimization problem was solved globally, the simultaneous approach would give the best results in terms of maximizing process objective. The better performance of the sequential approach in case that different objectives are used in the two stages can be explained by the limitations of local optimization. More precisely, by solving the optimization problems locally, we end up with suboptimal solutions, the performance of which (as shown) can be strongly affected by good initial guesses.

5. Conclusions

This work applies dynamic optimization studies to a predictive mathematical model developed by Quiroga et al. (2016) and numerically improved by Kappatou et al. (2018). The main scope of the study is to develop computationally efficient and biologically meaningful optimization strategies for mAb process intensification. In practice, being able to optimize a fed-batch culture for both initial concentrations and feeding strategies at the same time provides a real commercial advantage due to its general cost- and time to market- reducing effect. Following a sequential and a simultaneous approach for fed-batch optimization, we exploit different suboptimal solutions to our problem. The higher flexibility of the sequential approach, in terms of being able to utilize different objectives for the two step batch and fed-batch optimization, seems to offer certain advantages. In order to overcome such limitations of local solutions, future research focus should be shifted towards global dynamic optimization techniques.

6. Acknowledgements

This work has received funding from the European Union's Horizon 2020 research and innovation programme under the Marie Skłodowska-Curie grant agreement no.675251.

References

- T. A. Bibila, D. K. Robinson, 1995, In pursuit of the optimal fed-batch process for monoclonal antibody production, *Biotechnology progress*, 11(1), 1-13.
 - P. C. Collins, 2018, Chemical engineering and the culmination of quality by design in pharmaceuticals, *AIChE Journal*, 64(5), 1502-1510.
 - C. D. Kappatou, A. Mhamdi, A. Quiroga-Campano, A. Mantalaris, A. Mitsos, 2018, Model-Based Dynamic Optimization of Monoclonal Antibodies Production in Semibatch Operation—Use of Reformulation Techniques, *Industrial & Engineering Chemistry*, 57(30), 9915-9924.
 - A. Kiparissides, E. N. Pistikopoulos, A. Mantalaris, 2015, On the model-based optimization of secreting mammalian cell (GSNS0) cultures, *Biotechnology & bioengineering*, 112(3), 536-548.
 - A. Meister, 1980, Catalytic mechanism of glutamine synthetase; overview of glutamine metabolism, In *Glutamine: metabolism, enzymology, and regulation*, 1-40.
 - R. Pörtner (ed.), 2014, *Animal Cell Biotechnology*, Humana Press, DOI: 10.1007/978-1-62703-733-4.
 - R. Pörtner, T. Schäfer, 1996, Modelling hybridoma cell growth and metabolism—a comparison of selected models and data, *Journal of biotechnology*, 49(1-3), 119-135.
 - A. L. Quiroga-Campano, N. Panoskaltsis, A. Mantalaris, 2018, Energy-based culture medium design for biomanufacturing optimization: A case study in monoclonal antibody production by GS-NS0 cells, *Metabolic Engineering*, 47, 21-30.
 - A. L. Quiroga-Campano, M. Papathanasiou, E. N. Pistikopolous, A. Mantalaris, 2016, A predictive model for energy metabolism and ATP balance in mammalian cells: towards the energy-based optimization of mAb production, *Computer Aided Chemical Engineering*, Elsevier, 38, 1581-1586.
 - A. A. Shukla, L.S. Wolfe, S. S. Mostafa, C. Norman, 2017, Evolving trends in mAb production processes, *Bioengineering & translational medicine*, 2(1), 58-69.
- Process Systems Enterprise, gPROMS, 1997-2018, www.psenterprise.com/gproms.

An MPCC Reactive Distillation Optimization Model for Multi-Objective Fischer–Tropsch Synthesis

Yizu Zhang ^a, Cornelius M. Masuku ^{a,b} and Lorenz T. Biegler ^{a,*}

^a*Department of Chemical Engineering, Carnegie Mellon University, Pittsburgh, PA 15213, USA.*

^b*Department of Civil and Chemical Engineering, University of South Africa, Private Bag X6, FLORIDA, 1710, South Africa.*

lb01@andrew.cmu.edu

Abstract

In the design of a reactive distillation column, aspects such as column configuration, catalyst loading, tray temperature, and side extraction rates should be well considered. Though preferences in Fischer–Tropsch (FT) synthesis may vary, it is acknowledged that the final product contains a wide range of hydrocarbons including fuel gas, gasoline, diesel, and linear wax. We previously developed an equation-oriented framework for optimal synthesis of integrated reactive distillation systems for FT processes (Zhang et al., 2018).

Here, we extend the mass, equilibrium, summation, and heat equations to a mathematical programming with complementarity constraints model to deal with possible dry trays in the non-reactive sections. The purpose of describing disappearing phases is to avoid infeasibilities due to multiple bilinear terms in the model for complicated model structures. The model is implemented by solving initialization steps and a sequence of nonlinear programming problems to determine an optimal structure and operating conditions.

Design specifications for multiple products could be set as individual objectives to determine design limits. Moreover, a balance of multi-objectives could be reached by formulating the reactive distillation model as a multi-objective optimization problem. In this work, we employ the augmented ϵ -constraint method. The results show that significant design insights can be gained from the Pareto-optimal front regarding acceptable trade-offs amongst various objectives.

Keywords: Equation-Oriented Optimization Framework, Mathematical Programming with Complementarity Constraints, Vapor–Liquid Equilibrium Modeling, Low-Temperature Fischer–Tropsch, Process Intensification.

1. Introduction

The Fischer–Tropsch (FT) reaction is generally assumed to be kinetically determined (Lu et al., 2017) with an Anderson–Schulz–Flory product distribution that describe the product range with a single parameter α (Eze and Masuku, 2018). This presents a challenge in optimizing for a specific product range (Masuku et al., 2015). We recently presented an equation-oriented reactive distillation (RD) model for a typical low-temperature FT processes favoring wax production to overcome the selectivity challenges (Zhang et al.,

2018). In this study, we introduce a method to solve multi-objective optimization (MOO) in FT RD syntheses. The next section discusses relevant model formulation based on a previous study from Zhang et al. (2018). The third section focuses on the implementation procedure by solving a sequence of NLPs and initialization steps to determine optimal structure and operating conditions with multiple objectives. An example is given for a typical low-temperature FT process in the fourth section, along with results, discussions and model validations. The last section summarizes the key points and conclusions of the paper.

2. Model Reformulation

Figure 1 shows the superstructure of the FT RD synthesis problem along with the basic nonreactive stage model as the building block for the purple tray sections. Here, the mass and heat balance equations from Zhang et al. (2018) are extended with stream connection variables γ for each stream and bypass variables ζ for each stage. As bypass variables are used to deal with the optimization of stage numbers, the equilibrium equations for non-reactive stage model with bypass are reformulated as follows (Dowling and Biegler, 2015):

$$\zeta_k \gamma_{V,k+1} V_{k+1} y_{i,k+1} + \zeta_k \gamma_{L,k-1} L_{k-1} x_{i,k-1} - V_k^* y_{i,k}^* - L_k^* x_{i,k}^* = 0 \quad (1.1)$$

$$L_k x_{i,k} = L_k^* x_{i,k}^* + (1 - \zeta_k) L_{k-1} x_{i,k-1} \quad (1.2)$$

$$V_k y_{i,k} = V_k^* y_{i,k}^* + (1 - \zeta_k) V_{k+1} y_{i,k+1} \quad (1.3)$$

$$y_{i,k}^* = \beta_k K_{i,k} x_{i,k}^*, \quad \beta_k = 1 - S_k^L + S_k^V \quad (1.4)$$

$$0 \leq S_k^V \perp V_k^* \geq 0, \quad 0 \leq S_k^L \perp L_k^* \geq 0 \quad (1.5)$$

$$\sum_i y_{i,k} = \sum_i x_{i,k} = \sum_i y_{i,k}^* = \sum_i x_{i,k}^* = 1 \quad (1.6)$$

where S_k^L and S_k^V are non-negative slack variables for the liquid and vapor phases leaving stage k respectively. β_k is the slack variable to relax phase equilibrium. When both phases are present, $V, L \geq 0$ and $S_k^L = S_k^V = 0$, here $\beta = 1$ is not relaxed (Burgard et al., 2018). However, if the liquid phase disappears ($L = 0$), S_k^L moves away from zero and $\beta_k \leq 1$, thus relaxing (1.4). Also note that, γ_k are connecting variables to connect adjacent stages when modifying column structure, ζ_k are bypass variables indicating the existence of stage k . The purpose of describing disappearing phases is to avoid infeasibility issues of bilinear terms in the model when column structure becomes complicated.

For the multi-objective optimization We employ the augmented ε -constraint method proposed by Mavrotas (2009) to formulate the reactive distillation model into the following MOO problem:

$$\mathbf{Problem}(\varepsilon_i) \min f_1(x) - \rho \left(\sum_{i=2}^p s_i / r_i \right), \text{ s.t. } f_i(x) + s_i \leq \varepsilon_i, \quad i = 1, \dots, p, \quad (2)$$

where $\rho > 0$ is a small penalty parameter, and $r_i > 0$ and $s_i \geq 0$ are the range constants and the slack variables for the i^{th} objective function, respectively.

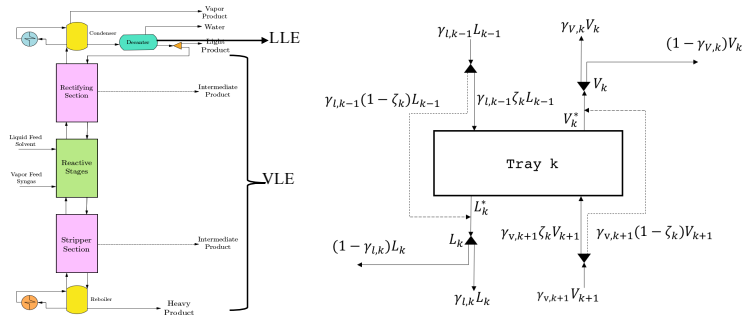


Figure 1: FT reactive distillation superstructure and nonreactive stage model

3. Implementation and Initialization Procedures

The **Algorithm** to find column structure and operating conditions for a multi-objective FT RD production is given below in the form of pseudo-code.

1. Set initial column structure with non-reactive and reactive trays. Set iteration $j = 1$.
2. **If** max. outer loop iteration times reached: **goto** 7; **else**: Implement **base case** run.
3. Implement **adiabatic case** run.
4. Determine $\{f_1^j, f_2^j, \dots, f_p^j\}$, $\{\bar{f}_1^j, \bar{f}_2^j, \dots, \bar{f}_p^j\}$, q_i^j , δ_i^j , r_i^j for multiple objective functions;
Pos ^{j} = \emptyset ; **Pof** ^{j} = \emptyset ; **I** ^{j} = $\{\zeta^j \mid \text{Obj}_{\min} = f_i^j, \forall i = 1 \text{ to } p\}$.
5. Set $\varepsilon_{i,0}^j = \bar{f}_i^j, \forall i = 2 \text{ to } p$;
while $\varepsilon_i^j - \delta_i^j \geq \underline{f}_i^j, \forall i = 2 \text{ to } p$ **do**:
 update ε_i^j by δ_i^j ;
 solve $\{\mathbf{x}, \mathbf{f}(\mathbf{x})\} = \mathbf{Problem}(\varepsilon_i^j)$;
 If ($\{\mathbf{x}\} \not\subset \mathbf{Pos}^j$ or $\{\mathbf{f}(\mathbf{x})\} \not\subset \mathbf{Pof}^j$):
 Pos ^{j} = **Pos** ^{j} $\cup \{\mathbf{x}\}$, **Pof** ^{j} = **Pof** ^{j} $\cup \{\mathbf{f}(\mathbf{x})\}$, **I** ^{j} = **I** ^{j} $\cup \{\zeta\}$;
 If $\{\mathbf{x}\} = \text{null}$: skip; **else**: skip;
end while
6. Visualization of **Pof** ^{j} and analyze to get **Pof** ^{j} .
If (desired subset of **I** ^{j} = **I** ^{$j-1$} **and/or** $\max\{|\frac{f_1^{j-1} - f_1^j}{f_1^{j-1}}|, |\frac{f_2^{j-1} - f_2^j}{f_2^{j-1}}|, \dots, |\frac{f_p^{j-1} - f_p^j}{f_p^{j-1}}|\} \leq \varepsilon$):
goto 7; **else**: update column structure from **I** ^{j} , $j = j + 1$, **goto** 2.
7. Fix column structure from desired subset of **I** ^{j} .

The core of the algorithm lies in two nested loops. In each iteration of the outer loop (steps 2-6), denoted by iteration number j , a new column structure is explored; the inner loop (step 5) transforms the whole objective space as a rectangular axis-parallel domain with respect to objectives f_2 to f_p under a fixed and continuous column structure search space. The output of the outer loop gives information on bypass variables from single-objective and multi-objective optimizations. These results give us information to add or remove additional trays, which updates the outer loop with a new structure.

The **base case** and **adiabatic case** mentioned in steps 2 and 3 refer to the stage model formulations in Zhang et al. (2018) with the updated MPCC reformulation introduced in Section 2. The MPCC reformulation aims to deal with infeasibility issues caused by dry trays or trays with total bypass, which relaxes equilibrium constraints for disappearing phases. The **adiabatic case** reformulates the **base case** into an optimization problem by defining heat duty as an objective to minimize.

In step 4, $\underline{f}_i^j, \overline{f}_i^j$ denote the respective lower and upper bounds of the i^{th} objective function in outer loop j ; the results are obtained by setting f_i^j as a single objective. In step 5, by dividing the range of the i^{th} objective function to q_i^j equal intervals using $\delta_i^j = (\overline{f}_i^j - \underline{f}_i^j)/(q_i^j - 1)$, the original rectangular optimal search space, denoted by vertices $\{f_1^j, \overline{f}_1^j\} \times \dots \times \{f_p^j, \overline{f}_p^j\}$, is gradually reduced, leading to poorer solutions. The detailed implementation of **update** could be found in the flowchart of the AUGMECON method in Mavrotas (2009). The **Pos^j** and **Pof^j** sets collect exclusive Pareto-optimal set and corresponding Pareto-optimal front values. **I^j** is the exclusive set of bypass variables obtained from single-objective (in step 4) and multi-objective optimizations (in step 5). These three sets provide information for visualization of Pareto-optimal front and column structure modification. If the given optimal search space is infeasible, i.e., no **Pos^j** and **Pof^j** are found, or if the same result is found with different optimal search spaces, the results are not recorded, ε_i^j is further updated, and the inner loop continues.

The entire optimal search space is visited through the equally-spaced gridding in step 5. Through visualization of MOO Pareto curve in step 6, we get a better sense of the tradeoffs among multiple objectives. By restricting attention to the subset of choices that are Pareto-efficient (where a gain in one objective leads to a significant loss of another objective), we extract values of corresponding ζ obtained and update the column structure to the next outer loop iteration. The determination of the desired subset is based on preference of the decision maker.

The termination conditions in step 6 could be interpreted as: if no change of bypass variables is observed between the last two outer loop iterations (no indications on column structure change) and/or no great improvements of single objectives from column structure modifications, the outer loop terminates. It should be mentioned, the outer loop also terminates when the "maximum outer loop iteration times" is reached in step 2. The value of "maximum outer loop iteration times" and threshold of improvement ε in step 6 are preferences of the decision maker. $\varepsilon > 0$ is normally set to around 1%, with which all absolute values of normalized improvements on single objectives are compared. With the improvement of column structure after each outer loop, values of $\underline{f}_i^j, \forall i$ are normally smaller under the convention of minimization problems.

4. Case Study Results and Discussions

In this section we consider reactive distillation with low temperature Fischer-Tropsch kinetics, where we minimize $-(\text{wax mass flow rate})$ as the main objective is f_1 and minimize $-(\text{naphtha purity})$ and $-(\text{diesel purity})$ are subsidiary objectives, f_2 and f_3 , respectively. Catalyst loading of reactive stages are fixed during simulation and optimization; heat duty is freed on reactive trays and are minimized to zero for non-reactive trays during **adiabatic case** run; 1000 [kmol/hr] syngas ($H_2 : CO = 2 : 1$) (Kapfunde et al., 2018) is fed to the last reactive tray; pressure of the column is fixed at 21 [bar]; temperature of condenser is fixed at 35 °C; temperature range of reactive stages is from 190 °C to 260 °C; liquid extraction fraction (γ_l) for naphtha and diesel streams are freed from [0,1] after step 3. Also, the following carbon number cut specifications from the previous work (Zhang et al., 2018), naphtha (C_5 - C_7), fuel gas (C_1 - C_4), gasoline (C_8 - C_{12}), diesel (C_{13} to C_{18}), wax (C_{19} - C_{56}) are defined.

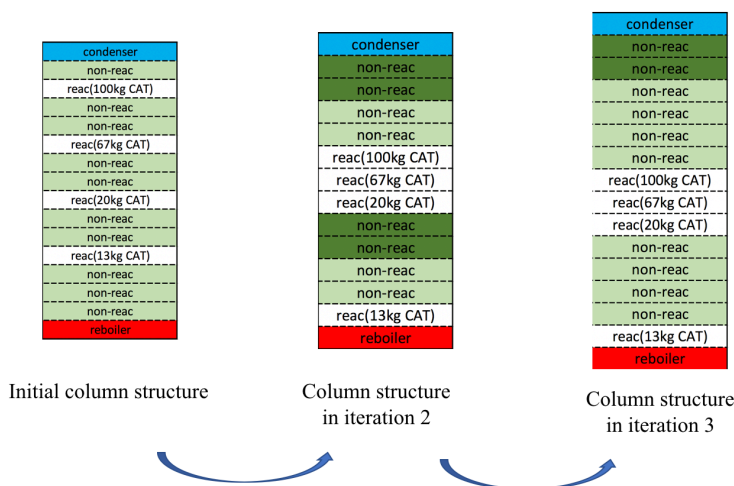


Figure 2: Typical evolution of RD column structure through MOO algorithm. Trays in green are non-reactive trays; those in dark green are from update, those in light green are results from the previous iteration.

The optimal column structure and operating conditions are found through the implementation of **Algorithm** introduced in the previous section over three major iterations. A typical evolution of the column structure (e.g., for $f_1^* \approx -822$) can be observed in Figure 2. From results of **base case** and **adiabatic case** runs, we found that the maximum diesel purity is found on the tray above the last reactive tray; this was set as location for diesel product side-draw all along. The Pareto-front for the three-objective optimization study is shown in Figure 3. The Pareto-front and utopia point (red star) is shown for the final iteration. The three-objective optimization case can then be studied by visiting a uniformed grid of ϵ_i of the defined **Problem**, and selecting the desired subset of the Pareto-front to provide bypass variable information. The iterations terminate because modification of column structure leads to improved single objectives by less than 1%. For instance, by

selecting one Pareto set of interest, we could get 821.73[kg/hr] bottom liquid wax mass flow rate, 0.934 naphtha purity in the top liquid and 0.706 diesel purity on stage 14. This corresponds to the rightmost column in Figure 2.

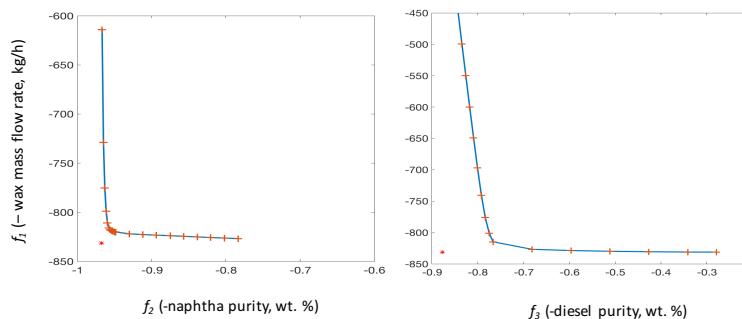


Figure 3: Pareto fronts for three-objective optimization

5. Conclusions

Since the FT reaction produces a range of products, we described a multi-objective optimization model that could be used to optimize the production of one product whilst restricting the negative impact on other valuable products. The model considers disappearing phases in the reactive distillation calculations and uses bypass variable information to avoid large computational efforts on the multi-objective case. The column structure is determined from the Pareto optimal set.

References

- A. Burgard, J. Eason, J. Eslick, J. Ghose, A. Lee, L. Biegler, D. Miller, 2018. A smooth, square flash formulation for equation-oriented flowsheet optimization. *Computer Aided Chemical Engineering* 44, 871–876.
- A. Dowling, L. Biegler, 2015. A framework for efficient large scale equation-oriented flowsheet optimization. *Computers & Chemical Engineering* 72, 3–20.
- P. Eze, C. Masuku, 2018. Vapour–liquid equilibrium prediction for synthesis gas conversion using artificial neural networks. *South African Journal of Chemical Engineering* 26, 80–85.
- N. Kapfunde, C. Masuku, D. Hildebrandt, 2018. Optimization of the thermal efficiency of a fixed-bed gasifier using computational fluid dynamics. *Computer Aided Chemical Engineering* 44, 1747–1752.
- X. Lu, X. Zhu, C. Masuku, D. Hildebrandt, D. Glasser, 2017. A study of the Fischer–Tropsch synthesis in a batch reactor: rate, phase of water, and catalyst oxidation. *Energy & Fuels* 31, 7405–7412.
- C. Masuku, D. Hildebrandt, D. Glasser, 2015. Reactive distillation in conventional Fischer–Tropsch reactors. *Fuel Processing Technology* 130, 54–61.
- G. Mavrotas, 2009. Effective implementation of the ϵ -constraint method in multi-objective mathematical programming problems. *Applied Mathematics and Computation* 213, 455–465.
- Y. Zhang, C. Masuku, L. Biegler, 2018. Equation-oriented framework for optimal synthesis of integrated reactive distillation systems for the Fischer–Tropsch processes. *Energy & Fuels* 32, 7199–7209.

Operating regime model based multi-objective sensor placement for data reconciliation

Gyula Dorgo^a, Mate Haragovics^b and Janos Abonyi^{a*}

^a*MTA-PE Lendület Complex Systems Monitoring Research Group, Egyetem str. 10, Veszprém, H-8200, HUNGARY*

^b*MOL Danube Refinery, Olajmunkás str. 2., Százhalombatta, H-2443, HUNGARY*
janos@abonyilab.com

Abstract

Although the number of sensors in chemical production plants is increasing thanks to the IoT revolution, it is still a crucial problem what to measure and how to place the sensors as such the resulted sensor network be robust and cost-effectively provide the required information. This problem is especially relevant in flexible multi-purpose, multi-product production plants when there are significant differences among the operating regions. The present work aims the development of a sensor placement methodology that utilizes the advantages of local linear models. Realizing the often conflicting nature of the key objectives of sensor placement, the problem is formulated as a multi-objective optimization task taking into consideration the cost, estimation accuracy, observability and fault detection performance of the designed networks and simultaneously seeking for the optimal solutions under multiple operating regimes. The effectiveness of the Non-dominated Sorting Genetic Algorithm-II (NSGA-II)-based solution of the defined problem is demonstrated through benchmark examples.

Keywords: sensor placement, multi-objective optimization, data reconciliation

1. Introduction

Data reconciliation is a widely applied technique to increase the accuracy of the measured variables and calculate the unmeasured variables using the known uncertainty of the applied sensors and the structure and the balance equations as technological constraints. Data reconciliation-based optimal sensor placement can be considered as an optimization problem (Bagajewicz (1997)). As several objectives can be defined to measure the goodness of a sensor placement in a given technology, the visualization of the Pareto optimal solutions can facilitate the work of the decision makers (Bagajewicz and Cabrera (2003)). The problem is much more complex when the process is flexible and its structure changes in time. Xie et al. (2018) incorporated multiple operation modes to data reconciliation. However, in this work the optimal and robust placement of the sensors is not studied although the solution of this crucial problem significantly determines the applicability of data reconciliation in complex multi-mode technologies. To handle this problem we define a multi-objective optimization task that ensures the observability of the system, and generates the Pareto front of the best solutions in terms of estimation accuracy, fault detection performance and cost of the designed sensor networks in all of the operating modes of the technology. Formerly, Brown et al. (2005) incorporated multiple objectives

to process measurement system design.

The core concept of our methodology and the main contributions of the present paper is twofold: first, we describe how a multi-objective optimisation problem can be formulated taking into consideration the general aspects of observability, detectability, estimation accuracy and cost-effectiveness and highlight the conflicting nature of these objectives. Second, as many of the modern production technologies can be operated in multiple modes, the optimal sensor placement solution is sought globally for multiple operating modes. The main steps of the methodology are represented by the blue arrows in Figure 1. The boxes above and below the arrows show the required input and the obtained output information, respectively. Therefore, first the structure of the technology is analysed in order to investigate the observability, estimation accuracy of the variables and the cost of the tested sensor network. Then data reconciliation is applied to reconcile and estimate the variables and determine the reconciliation accuracy. In the following, the detectability of faults is tested based on Type I and II errors using simulated gross errors on the measurement values. Finally, the optimisation algorithm evaluates the given performance measures and creates the next candidate sensor placement.

The roadmap of the present paper is as follows. Section 2 describes the proposed multi-objective and multi-operating mode sensor placement problem. Firstly, the reconciliation and estimation of measured and unmeasured variables are discussed, together with the fault detection basics. This will be followed by the presentation of the performance measures used in the objective function of the multi-objective optimisation problem. The applicability and effectiveness of the proposed solution is described in Section 3.

To stimulate further research, the resultant MATLAB codes of the optimisation algorithms are publicly available on the website of the authors (www.abonyilab.com).

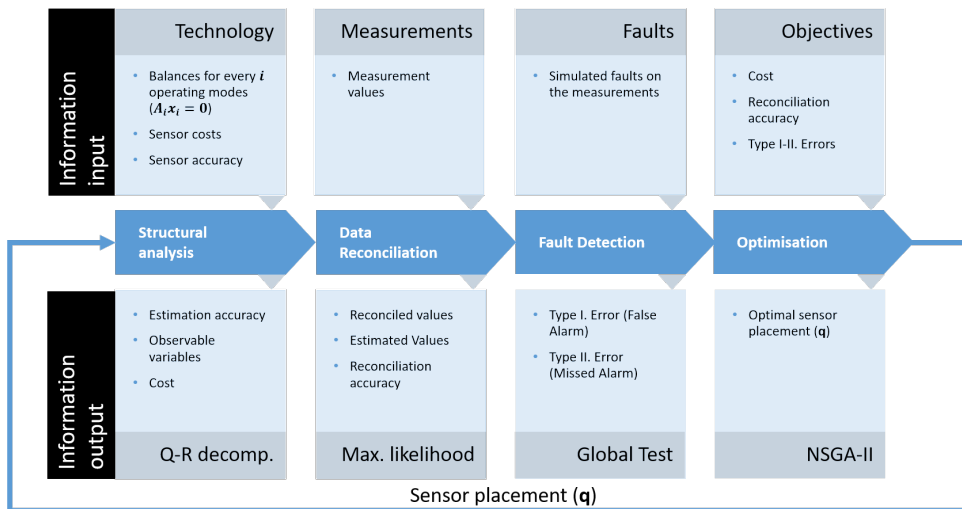


Figure 1: The workflow of the proposed optimisation-based sensor placement methodology. The optimisable variable is the \mathbf{q} binary vector indicating whether the k^{th} variable is measured ($q_k = 1$) or not ($q_k = 0$).

2. The multiobjective multi-mode sensor placement problem

The balance equations of chemical technologies can be compactly represented as the functions of the variables (\mathbf{x}) and the inputs (\mathbf{u}), $\dot{x} = f(\mathbf{x}, \mathbf{u})$, which is represented by a nonlinear algebraic equation system $\mathbf{0} = f(\mathbf{x}, \mathbf{u})$ in the case of steady state operations. Generally, the variables (\mathbf{x}) can be classified into three major groups: variables, whose values are exactly known ($\mathbf{w} = [w_1 \dots w_{N_w}]^T$), measured variables ($\mathbf{y} = [y_1 \dots y_{N_y}]^T$) and unmeasured variables ($\mathbf{z} = [z_1 \dots z_{N_z}]^T$). $[\mathbf{w} \ \mathbf{y} \ \mathbf{z}]^T = \mathbf{P}\mathbf{x}$ where \mathbf{P} is a permutation matrix, which reorders the elements of vector \mathbf{x} according to this classification system. The general $\mathbf{A}\mathbf{x} = \mathbf{0}$ form of the linearised balance equations can be written as $\mathbf{A}\mathbf{x} = \mathbf{A}\mathbf{P}^T\mathbf{P}\mathbf{x} = \mathbf{A}\mathbf{P}^T[\mathbf{w} \ \mathbf{y} \ \mathbf{z}]^T = \mathbf{0}$ where $\mathbf{A}\mathbf{P}^T = [\mathbf{A}_w \ \mathbf{A}_y \ \mathbf{A}_z]$ and the matrices \mathbf{A}_w , \mathbf{A}_y and \mathbf{A}_z are the columns of the original \mathbf{A} matrix assigned to the variables \mathbf{w} , \mathbf{y} and \mathbf{z} , respectively. Hence, the $\mathbf{A}\mathbf{x} = \mathbf{0}$ form of the balance equations can be expressed as $\mathbf{A}_w\mathbf{w} + \mathbf{A}_y\mathbf{y} + \mathbf{A}_z\mathbf{z} = \mathbf{0}$. The aim of data reconciliation is to minimize the difference between the measured and the reconciled values taking into consideration the variance of the measurements and the constraints formed by the balance equations of the system. This can be expressed by the following constrained objective function:

$$\min_{\hat{\mathbf{y}}} (\mathbf{y} - \hat{\mathbf{y}})^T \mathbf{V}^{-1} (\mathbf{y} - \hat{\mathbf{y}}) \quad (1)$$

$$\text{subject to } \mathbf{A}_y\hat{\mathbf{y}} + \mathbf{A}_z\hat{\mathbf{z}} = \mathbf{b} \quad (2)$$

where the vectors $\hat{\mathbf{y}}$ and $\hat{\mathbf{z}}$ are the vectors of estimates (reconciled values) for the measured and the unmeasured variables, respectively. If $\text{rank}(\mathbf{A}_z) = r$ and N_u is the number of unmeasured variables then we know that at least $N_u - r$ variables are unobservable and the vector of unmeasured variables can be divided into observable and unobservable variables $\mathbf{z} = [\mathbf{z}_r \ \mathbf{z}_{N_u-r}]^T$. Since observability is a key aspect of industrial process control, in the following we investigate the observability of \mathbf{z}_r .

Most industrial processes can be operated under multiple operating modes and this can be indicated by the modified incidence matrix of the technology. Therefore, the general $\mathbf{A}\mathbf{x} = \mathbf{0}$ equation can be replaced by the $\mathbf{A}_i\mathbf{x}_i = \mathbf{0}$ equation, where $i = 1 \dots N_m$ indicates the operating mode. However, in order to keep the representation simple, we only indicate the operating modes in situations where it needs to be highlighted. An example for different operating modes can be the optional deletion of Stream 3 in certain operating modes in Figure 2 (marked with red). Since the element $\mathbf{A}_w\mathbf{w}$ is known, it is useful to replace it by $-\mathbf{b}$ and reformulate the equation as $\mathbf{A}_y\mathbf{y} + \mathbf{A}_z\mathbf{z} = \mathbf{b}$.

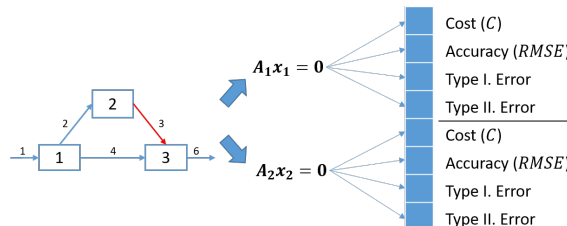


Figure 2: Definition of the operating modes and their objective functions

The core concept of optimal sensor placement design is to determine which process variables to measure in order to maintain an optimal trade-off between the cost (both in terms of capital and operational costs) and accuracy of measurements. However, primarily the cost and accuracy of measurements is mentioned, these goals call for further practical aspects: the control goals of the optimized industrial facility and the robustness of the control network. According to Bagajewicz (1997), the robustness of a network incorporates three properties: availability, error detectability, and resilience. Based on this, the following objectives are defined:

Cost of the network: For all the measured variables there is a measuring instrument with an associated cost c_k . Assuming a binary vector variable \mathbf{q} with the following definition: $q_k = 1$ if x_k is measured, $q_k = 0$ if x_k otherwise. The cost of the sensor network can be expressed as $C(\mathbf{q}) = \sum_k c_k q_k$.

Observability: The observability of the variables of the analysed or planned technology is a crucial industrial factor. Therefore, the placement of sensors aims to maximize the number of observable sensors through both measurements and the estimation of unmeasured variables, $N_{obs} = N_y + N_r$.

Reconciliation error: Assigning the reconciled and estimated observable variables as $\hat{\mathbf{o}} = [\hat{\mathbf{y}} \quad \hat{\mathbf{z}}_r]$ and \mathbf{o} as the nominal value of these variables, the reconciliation error can be calculated. In the following this error term is marked as *RMSE*.

Gross error detection: In most of the cases during data reconciliation, only normally distributed random errors are assumed to be present on the measured data. However, due to different faults in the analysed process, gross errors can be present as well. In order to determine the presence of gross errors, one of the first test proposed by Ripps (1965) and Almsy and Sztano (1975), the global test was applied. However, the test does not indicate the place of the gross error, it provides a good preliminary analysis before the application of more advanced techniques. Therefore, the results of the hypothesis tests are applied as a performance measure to describe the detectability of the network using the *Type I* error (false alarm) and *Type II* error (missed alarm).

Our aim is to design sensor networks that simultaneously meet multiple requirements, so we intend to design sensor networks that optimal from the view of all m properties in every N_m operating modes $\mathbf{Z}(\mathbf{q}) = [Z_{1,1}(\mathbf{q}), \dots, Z_{1,m}(\mathbf{q}) \dots Z_{N_m,1}(\mathbf{q}), \dots, Z_{N_m,m}(\mathbf{q})]$. In practice, we look for four properties to be optimal: $Z_{i,1}(\mathbf{q}) = \min_q C(\mathbf{q})$, $Z_{i,2}(\mathbf{q}) = \min_q RMSE$, $Z_{i,3}(\mathbf{q}) = \min_q Type\ I$, $Z_{i,4}(\mathbf{q}) = \min_q Type\ II$.

The huge search space is further complicated by the often competing objectives of the design process. A genetic algorithm is a promising method for the generation of multi-purpose sensor configurations. Multi-objective optimization algorithms generate a set of optimal solutions. The Pareto fronts of these solutions simultaneously consider several design aspects. Since when solving the problem multiple operating modes and objectives must be taken into consideration at the same time; the problem has been implemented in a well-established genetic algorithm-based multi-objective optimization environment, the Non-dominated Sorting Genetic Algorithm-II (NSGA-II) Deb et al. (2000). The search space is conveniently described by the binary \mathbf{q} vector. The observability is tested by feasibility constraints.

3. Application example

The applicability of the proposed optimisation-based sensor placement methodology is demonstrated on two benchmark data reconciliation tasks, the mass flow network originally published by Rosenberg et al. (1987) and the steady state steam-metering example of the methanol synthesis unit of a large chemical technology Serth and Heenan (1986) as presented in part (a) and (b) of Figure 3. The multiple operating modes are defined by deletion of the streams marked by red in (a) and (b) of Figure 3 (Stream 9 in part (a) and Stream 2 and 14 in part (b)). The networks in part (c) and (d) show an exemplary optimal sensor placement solution for the networks presented in part (a) and (b), respectively.

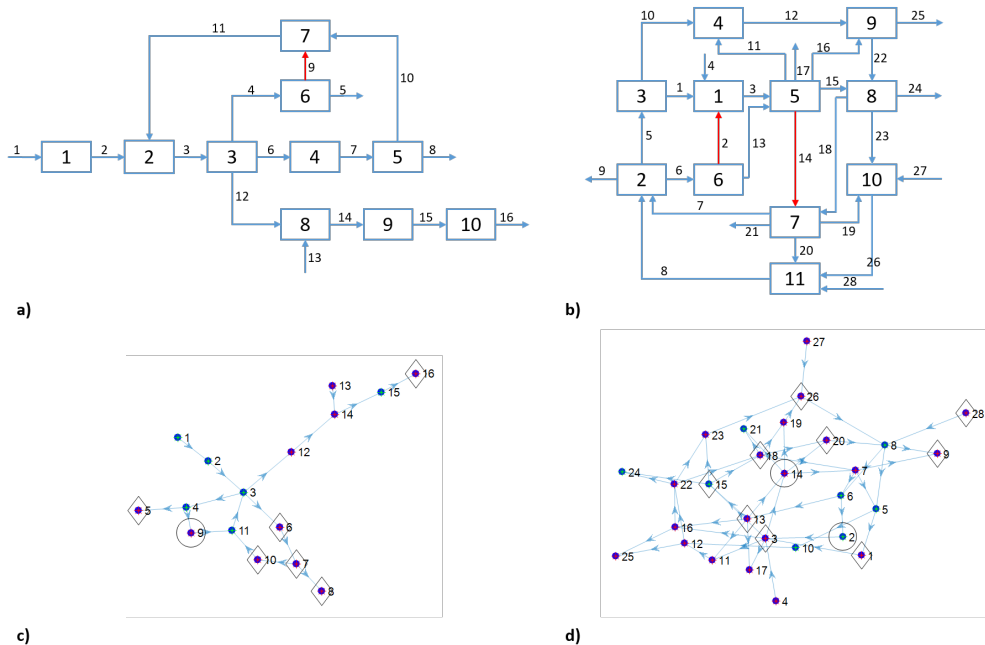


Figure 3: Network representation of the analysed technologies and an exemplary solution of their optimal sensor placement. The mass flow network of Rosenberg et al. (1987) and its solution (a, c) and the steam-metering system for methanol synthesis of Serth and Heenan (1986) and its solution (b, d). In the exemplary solution of networks (c, d) the streams are represented by the nodes, the nodes marked by red and green stars show the measured and estimated variables, respectively, while the nodes framed with a diamond shape are the nonredundant measurements. The circles show the streams that are neglected in certain operating modes (same as the red streams in part (a, b)).

As can be seen in the bottom part of Figure 3, every streams are observable in the network, although some of them are estimated instead of sensory measurements. The redundant measurements increase the accuracy of data reconciliation and increase the detectability of the network. Figure 4 shows the normalized values of the cost function of the obtained Pareto optimal solutions on a parallel coordinates-based visualisation for the problem published by Rosenberg et al. (1987).

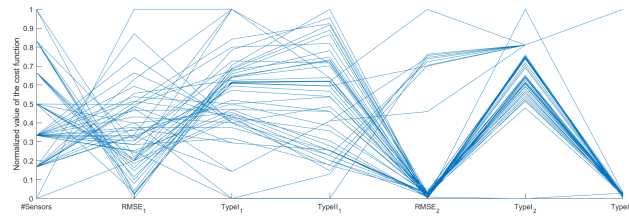


Figure 4: Parallel coordinate representation of the conflicting objectives

4. Conclusions

According to our knowledge, this paper is the first (and yet only introductory) work that defines the problem of multi-mode sensor placement as a multi-objective optimization problem. The cost, accuracy, Type I and II errors of the gross error detection performance were defined as cost functions to evaluate each configurations of the technology, while the constraints were defined to ensure the observability of the system. To handle these conflicting objectives and the complexity of the search space, the NSGA-II evolutionary optimization algorithm has been utilized. The efficiency of the proposed approach is examined through two modified benchmark problems with multiple operating modes. The results prove the applicability of the proposed algorithm and motivate our work for the improvement of the algorithm for dynamic sensor placement with different sensor types.

Acknowledgments This research has been supported by the National Research, Development and Innovation Office (NKFIH) OTKA-116674 project. Gyula Dorgo was supported by the ÚNKP-18-3 New National Excellence Program of the Ministry of Human Capacities.

References

- G. Almasy, T. Sztano, 1975. Checking and correction of measurements on the basis of linear system model. *Problems of Control and Information Theory* 4.
- M. Bagajewicz, E. Cabrera, 2003. Pareto optimal solutions visualization techniques for multiobjective design and upgrade of instrumentation networks. *Industrial & Engineering Chemistry Research* 42 (21), 5195–5203.
- M. J. Bagajewicz, 1997. Design and retrofit of sensor networks in process plants. *AIChE Journal* 43 (9), 2300–2306.
- D. Brown, F. Maréchal, G. Heyen, J. Paris, 2005. Application of multi-objective optimisation to process measurement system design. In: *European Symposium on Computer-Aided Process Engineering-15. Computer-aided chemical engineering*.
- K. Deb, S. Agrawal, A. Pratap, T. Meyarivan, 2000. A fast elitist non-dominated sorting genetic algorithm for multi-objective optimization: Nsga-ii. In: M. Schoenauer, K. Deb, G. Rudolph, X. Yao, E. Lutton, J. J. Merelo, H.-P. Schwefel (Eds.), *Parallel Problem Solving from Nature PPSN VI*. Springer Berlin Heidelberg, Berlin, Heidelberg, pp. 849–858.
- D. L. Ripps, 1965. Adjustment of experimental data. *Chemical Engineering Progress Symposium Series* 61, 8–13.
- J. Rosenberg, R. S. H. Mah, C. Iordache, 1987. Evaluation of schemes for detecting and identifying gross errors in process data. *Industrial & Engineering Chemistry Research* 26 (3), 555–564.
- R. W. Serth, W. A. Heenan, 1986. Gross error detection and data reconciliation in steam-metering systems. *AIChE Journal* 32 (5), 733–742.
- S. Xie, C. Yang, X. Yuan, X. Wang, Y. Xie, 2018. Layered online data reconciliation strategy with multiple modes for industrial processes. *Control Engineering Practice* 77, 63 – 72.

Optimisation of the integrated water – energy systems in small group of islands communities

Christiana M. Papapostolou^a, Georgios T. Tzanes^b, Emilia M. Kondili^{a*}

^a*Optimisation of Production Systems Laboratory,*

^b*Soft Energy Applications and Environmental Protection Laboratory,*

Dept. of Mechanical Engineering, University of West Attica, Campus 2, P. Ralli & Thivon Street, 12244, Egaleo, Greece

*ekondili@uniwa.gr

Abstract

Islands are very special geographical areas with distinct and unique characteristics, often presenting slow infrastructure advancement, rendering the ‘Water-Energy Nexus’ (WEN) subject of increasing attention at all levels of policy making. This work aims to contribute in the optimisation of infrastructure development for the integrated solutions of water-energy systems by devising suitable optimisation models that capture technical and economic aspects. The developed framework is applied to a set of two Aegean Sea islands, assessing alternative scenarios for energy and water planning, with vast RES penetration, either if each island operates in stand-alone mode or the two of them interact as an energy community, via an undersea cable. The results of the work evidence that the solution of interconnection between remote islands could be economic viable, thus leading to downsized plants’ installations and decreased capital investment costs, as greater exploitation of RES is achieved.

Keywords: Water-Energy Nexus, Islands, Frameworks, Desalination, Interconnection.

1. Introduction

Water and energy are two fundamental resources with the supply of one highly depended on the availability of the other. The recognition that their scarcity underpins socio-economic development, has resulted a growing interest of policy makers in the so-called ‘Water-Energy Nexus’, a policy priority which is also reflected in the rising interest of the research community: the water-energy (WE) supply problem affects all types and sizes of contemporary communities around world due to the spatial characteristics of the water availability, also challenged by the availability and the security of energy supply.

With our special focus on small-scale and isolated economies and societies, like the ones of the Aegean Archipelagos that are more likely to be affected by WE problems, the present work seeks to introduce an integrated evaluation framework for the optimal design and operation of water and energy supply chains (WESCs) with special focus on the community-based perspective. To that end, two scenarios are currently elaborated: a) optimisation of the WESCs of two typical Aegean islands operating independently (stand-alone mode), resulting for each one the most economic and environmental viable energy and water supply solution for the upcoming 25 years and b) the two islands operating as a community, being interconnected via undersea cable, revealing possible WE synergies (energy interactions) for the community to exploit. The proposed WESC optimisation framework, apart from achieving the optimal design of the energy and water supply systems (considering RES-based hybrid energy configurations) of the two islands, also

investigates the performance of their interconnection as a feasible and profitable / valuable solution.

2. Background of the work: The island communities' dimension in the WESC optimisation problem

Islands render a special field of study in the WESCs optimisation, focusing on the local specific characteristics of each community namely size, topography, population, energy and water demands. That is why, well-known island communities have been extensively studied by the researchers seeking to identify the optimum WESC, for now and for the future. Focusing on the Aegean Sea, aiming at establishing a sustainable electrification model, the “Green Island” model for (island) communities, Kaldellis et al. (2017) carried out a theoretical analysis estimating the contribution of wind energy curtailments (of both new and existing parks) on the island's energy supply. The results of the work, under the elaborated case study for the island of Kos strongly support the necessity of energy storage introduction, if one may compare the expected and the finally absorbed wind power of the installation: 9.74GWh (final absorbed wind power, according to the official data by the local operator), while the expected wind energy yield was 14.13GWh (on the basis of the available wind potential), thus almost curtailing 4GWh of clean electricity on an annual basis.

Acknowledging the necessity of sustainable energy supply at small-scale islands on the basis of RES, Bertsiou et al. (2018), investigated the implementation possibilities of a Hybrid Renewable Energy System (HRES) in Fournoi island, operating on the basis of hydropower for electricity generation aiming at meeting both drinking and agricultural water demands through desalination of sea water, with wind contribution used for supplying the local power network and for pumping and/or desalination operation depending on the scenario examined. The results of the work support the possibility of achievable high level of water and energy coverage and days of electricity autonomy, according to the water coverage consumption pattern.

Towards the same direction, Papapostolou et al. (2018), emphasising also on small-sized islands, thus energy and water vulnerable islands, studied the case of Irakleia, an island of 151 inhabitants during winter season. With the current energy supply both for the existing desalination plant and the electricity demands of the islanders being met by conventional fuels, which also demanding water imports via shipments to fulfil irrigation needs, the authors propose a RES-based desalination configuration (wind turbine, PV, energy storage battery) limiting the diesel operation to meet just the stability of the network. The results of the work also support high RES energy coverage minimising the CO₂ (diesel-based emissions by ~92%) balancing the calculated capex required for the specific solution (1.87MEUROS).

Tzanes et al. (2017), also dealing with the emerging issue of electrification of remote islandic Greek communities, developed an advanced software tool named Energy System Analysis (ESA), for evaluating different energy and water local scenarios, accounting also the available geographical information and the corresponding RES potential characteristics of the island examined. The study identified optimal solutions comprising HRES and desalination installations for the islands of Anafi and Agios Efstratios, with minimised LCA costs achieved for 85% annual coverage of electricity demand.

Consequently, one may conclude that using hybrid power systems results to better balances in energy supply while facilitates the matching of demand and production, with energy storage contributing also towards this direction. However, of great significance is also proven the consideration of larger spatial distribution of RES generation along with the aggregation of diversified load and water demands (community-based perspective), which, in the majority of the cases, leads to improved cost performances.

3. Case study characteristics

The proposed framework is implemented in two (medium-sized) remote islands of South Aegean Sea, namely Amorgos and Astypalaia. Both islands are characterised by a) high wind and solar potential, capable of achieving high RES capacity factors (Fig. 1a, 1b) and b) by significant water deficits, some of them met by ship transfers (Table 1). The load demand profile in these islands is characterised by high alteration, as tourism is the main economic activity. The most recent official available data (2013 for Amorgos and 2014 for Astypalaia, with no variations till today, as stated by the local authorities) are presented in Fig. 1c. In the case of water (in the absence of official recorded data) a typical (hourly-based) water demand profile is assumed, reflecting the islands’ potable water and irrigation needs (~57,000 m³ for Amorgos and ~37,500 m³ for Astypalaia). The water and electricity needs have a similar pattern in time. However, in the case of water demand, the profiles present a quite low correlation. Therefore, the results of the work include an optimal WE solution for each island separately and in the second case as a community for a time-span of 25 years.

Table 1. Annual water deficits for Amorgos and Astypalaia (YPEKA, 2015)

Island	Irrigation (m ³)	Potable (m ³)	Ship transfers (m ³)	Total (m ³)	Peak demand (m ³ /h)
Amorgos	~7,500	14,000	~35,500	57,000	27,2
Astypalaia	12,500	25,000	-	37,500	24,8

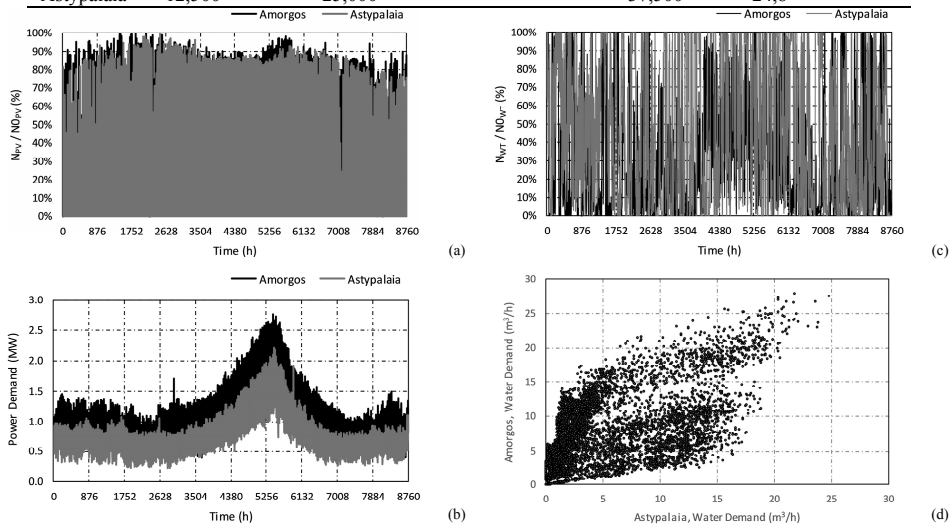


Figure 1. a) PV and b) wind power utilization factors, c) the load demand profiles and d) the islands hourly water demand correlation

4. Optimisation model

For the evaluation of the optimal power and water supply systems size in stand-alone mode, the optimisation model developed by Papapostolou et al. (2018) has been deployed. The key features of the model include two interlinked components, Eq.(1) and Eq.(2), the energy balance of the system (island or islands) and the island's water tank (WT) balance, for a time step of 1h, respectively:

$$\sum_{r=1}^{r=\max} Eg_r(t) + ESSg(t) - ESSs(t) - \sum_{l=1}^{l=\max} Ed_l(t) = 0 \quad (1)$$

$$WTank(t) = WTank(t-1) + \sum_{wr=1}^{wr=\max} F_{wr}(t) - Wd(t) \quad (2)$$

Where, in Eq.(1), ' Eg_r ', represents the energy production of the resource, ' r ' (wind, diesel and solar PV power installations), at time step, ' t ', ' $ESSg$ ' and ' $ESSs$ ', stands for energy storage either generated or stored accordingly, and finally the electricity needs are represented by ' Ed_l ', with the index ' l ' being equal to 1 for the present load demand and 2 for additional demand due to the desalination plant operation. Water balance described in Eq.(2), considers a typical water storage tank operation, whereas the level ' $WTank(t)$ ' at each time step ' t ' is a function of the water initially stored ' $WTank(t-1)$ ', as well as of the sum of the inflows ' $F_{wr}(t)$ ' of water resources ' wr ' minus the water demand ' $Wd(t)$ '.

In the case of integrated operation (two islands operating as a community in terms of exchanging energy), which becomes possible through an undersea cable installation, the main model modifications are applied in the system's electrical balance Eq.(3), the energy storage Eq.(4) and in the objective function Eq.(5):

$$\sum_{r=1}^{r=\max} Eg_r(t) + ESSg(t) - ESSs(t) - \sum_{l=1}^{l=\max} Ed_l(t) - \frac{Et_{load}^{isl}(t)}{\eta t} + Et_{load}^{isl+1}(t) * \eta t = 0 \quad (3)$$

$$ESSs(t) \leq dEres^+(t) - \frac{Et_{storage}^{isl}(t)}{\eta t} + Et_{storage}^{isl+1}(t) * \eta t, \quad (4)$$

$$f_{\rightarrow \min} = \frac{\sum_{r=1}^{r=\max} [N_r * IC_r * (1 + n * FC_r)]}{(1 + i)^n} + \frac{n * \sum_{t=1}^{t=\max} Eg_{r=diesel} * OC_{diesel} + F_{ship}(t) * OC_{ship}}{(1 + i)^n} + IC_{cable}(D, N_{cable}) \quad (5)$$

More precisely, the ' Et ' stands for energy transfers. The index ' $load$ ' refers to the case of energy generated directly addressing (sent) to meet electricity needs, and the index ' $storage$ ' indicates the energy transfers for charging the energy storage systems. The upper index indicates whether the energy is provided, at island ' isl ', or drawn, from every next island ' $isl+1$ '. The term ' $dEres^+$ ' represents the renewable energy surplus, which occurs when the renewable energy production potential is larger than actual utilisation of the installations. The losses of trading energy are represented by the factor ' ηt '. Concerning the objective function to be minimised Eq.(5), it represents the installation ' IC_r ', maintenance ' FC_r ' and operation costs ' OC_r ' for 25-year time-period, of resource

'r'. The last term 'cable' stands for the installation cost of the undersea cable, which is a function of the distance between the two islands and its power capacity (Fig. 2, Kokotsakis 2018). Both optimisation problems, were modelled as Linear Programming Problems (including 30 blocks of equations and 19 of respective variables) in GAMS (www.gams.com) and solved with NEOS Server IBM ILOG CPLEX Optimizer (<https://neos-server.org>) with typical computational times starting from 5s. NEOS Server is hosted by the Wisconsin Institutes for Discovery at the University of Wisconsin in Madison with typical high-level hardware specs.

5. Results

5.1. Stand-alone, island operation

Model implementation resulted viable solutions (in terms of plant-sizes, see Table 2) for both examined scenarios. In stand-alone mode, the islands have a similar behavior, mostly utilising RES for the operation of the corresponding desalination plant (Fig. 2a), which is sized to 0.33 and 0.43 times peak hourly water demand, for Astypalaia and Amorgos island respectively (Fig. 2c). At the same time, the water tanks are mostly utilized until the electricity demand peaks (Fig. 2d).

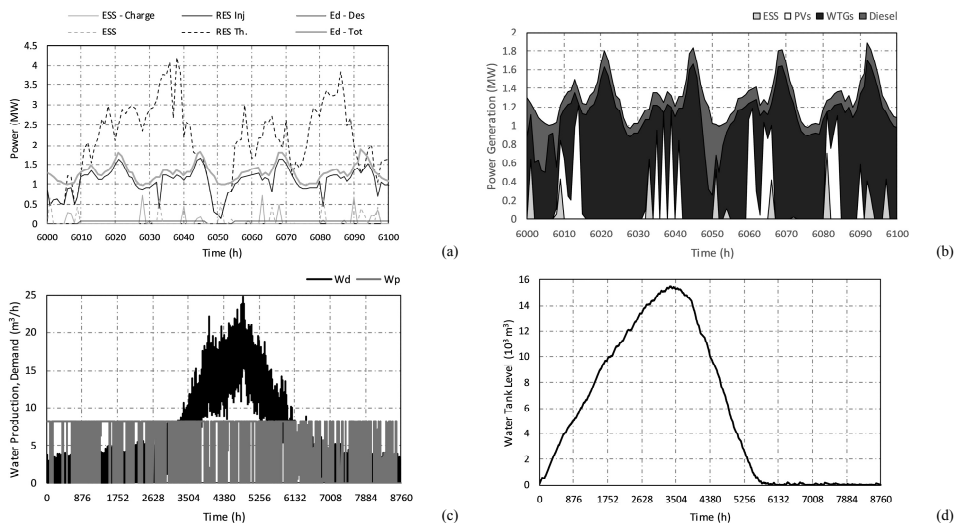


Figure 2. Optimal W-E solutions for Amorgos (a,b) and Astypalaia (c,d)

5.2. Community-based islands' operation

In the scenario of islands operating as a community, via an undersea cable of 1 MW capacity (40km in length), the flexibility in designing (allocation of resources) as well as exploiting individuals' RES surplus for covering the needs of the opposite island accordingly, results mainly to significant downsizing of thermal power and energy storage capacity as well as large increase in installed wind power (Table 2). In terms of cost, accordingly, the total expenditures get reduced from 50.2M€ (stand-alone scenario) to 41.36M€ (community-based scenario). The approx. 8.5M€ difference justifies a further research and application of the framework to islands with similar distance and features (different size, complementarity in energy demand), hence a large number of Aegean islands, heavily relying on diesel.

Table 2. Optimal Capacities- Modeling Results

Stand-alone, island-based operation optimal results					
Island	Diesel Plant (MW)	Wind Park (MW)	PV Park (MW)	ESS Cap. (MWh)	Desalination Plant (m ³ /d)
Amorgos	1.91	3.01	1.39	0.84	287
Astypalaia	2.04	1.74	0.73	0.23	199
Community-based (set of islands) operation optimal results					
Amorgos	1.83	2.88	1.26	0.46	235
Astypalaia	1.72	2.42	0.05	0.17	181

Conclusions

In this work an integrated WESCs optimisation framework has been introduced and tested comparing the single-island to the community-based (island) operation. The results evidenced that RES-based hybrid energy supply solutions including the desalination option are economically attractive for small-sized Aegean Sea islands while also serving at increasing the security of supply, especially under the community-based perspective and for reasonable cable sizes (length and capacity). The present framework will be further tested to other sets of islands (more than 2), with characteristics and complementarities regarding water and energy demand and RES potential (e.g. Santorini-Anafi (distanced ~24km)), for enabling strategic planning with regards to Aegean Sea islands water and energy future infrastructures.

Acknowledgements

"The Post-doctoral Research for Dr C. Papapostolou was undertaken with a scholarship fund by IKY, Act "Supporting Post-Academic Researchers" with resources from the Operational Program "Human Education Development and Lifelong Learning", priority axes 6,8,9, co-funded by the European Social Fund - ESF and the Greek State ".

References

- M. Bertsiou, E. Feloni, D. Karpouzou, E. Baltas, 2018, Water management and electricity output of a Hybrid Renewable Energy System (HRES) in Fourni Island in Aegean Sea, *Renewable Energy*, 118, 790–798
- J.K. Kaldellis, G.T. Tzanes, C. Papapostolou, K. Kavadias, D. Zafirakis, 2017, Analyzing the limitations of vast wind energy contribution in remote island networks of the Aegean Sea Archipelagos, *Energy Procedia*, 142, Volume 142, 787-792
- A. Kokotsakis, D. Zafirakis, 2018, Energy storage in offshore wind farm, in order to avoid over-dimensioning of energy transmission lines from wind farms to the core network, Master dissertation, Heriot-Watt University & Piraeus University of Applied Sciences
- C.M. Papapostolou, E.M. Kondili, G. Tzanes, 2018, Optimisation of water supply systems in the water – energy nexus: Model development and implementation to support decision making in investment planning, *Computer Aided Chemical Engineering*, 43, 1213–1218
- G.T. Tzanes, D. Zafirakis, C. Papapostolou, K. Kavadias, J.K. Kaldellis, 2017, PHAROS: An Integrated Planning Tool for Meeting the Energy and Water Needs of Remote Islands using RES-based Hybrid Solutions, *Energy Procedia*, 142, 2586–2591
- [YPEKA] Ministry of Environment and Energy, 2015, River Basin Management Plan of the Aegean Islands (EL 14), Text only in Greek, URL: wfdver.ypeka.gr/el/management-plans-gr/, Accessed on September, 2018

Techno-economic analysis of alternative reactive purification technologies in the lactic acid production process.

Roberto Gasca-González,^a Oscar A. Prado-Rubio,^b Fernando I. Gómez-Castro,^a
Javier Fontalvo-Alzate,^b Eduardo S. Pérez-Cisneros,^c Ricardo Morales-Rodríguez^{a,*}

^a*Departamento de Ingeniería Química, División de Ciencias Naturales y Exactas, Campus Guanajuato, Universidad de Guanajuato, Noria Alta S/N, Guanajuato, Gto. 36050, México.*

^b*Departamento de Ingeniería Química, Universidad Nacional de Colombia, Km 9 vía al Aeropuerto La Nubia, Campus La Nubia, Bloque L, Manizales, Caldas, Colombia.*

^c*Departamento de Ingeniería de Procesos e Hidráulica, Universidad Autónoma Metropolitana-Iztapalapa, Av. San Rafael Atlixco 186, 09340, México, D.F., México. ricardo.morales@ugto.mx*

Abstract

Lactic acid is one of the most important organic acids on the market due to its wide field of applications. The bio-production of lactic acid has acquired great attention due to the environmental and energy benefits; however, its production bottleneck by fermentation is the cost of the separation and purification stages, representing about 50% of total production cost. Therefore, reducing such costs through the development and design of purification technologies is mandatory. This work presents a techno-economic assessment for lactic acid bio-production process from the residues of the sugar industry, using different alternatives of separation and purification technologies, namely reactive distillation and reactive extraction. The design of the separation systems was performed in Aspen Plus and Matlab. The lactic acid production processes were evaluated to determine the economic feasibility of each separation strategy based on the total annual cost (TAC) and return of investment. It is shown that reactive extraction reduced the total annual cost and energy requirements with respect to reactive distillation by 44% and 37.5%, respectively. Additionally, the return on investment using reactive extraction is 1.2 years faster. Therefore, the reactive extraction process appears as a promising alternative to increase profitability of lactic acid bio-production within a biorefinery. Finally, it is important to highlight that this work discusses the design of a novel reactive extraction system for lactic acid recovery; and, to the best knowledge of the authors, this emerging technology is still under experimental development and has not been extensively investigated from a simulation perspective.

Keywords: Lactic acid production, Aspen plus, Reactive distillation, Reactive extraction

1. Introduction

In a bio-economy, the production of high value-added products from renewable resources, such as biomass, has been established as a strategy to reduce the environmental

impact generated by human activities. Biomass can be used to produce biofuels and other chemicals, thus, decreasing our dependency on fossil fuels as feedstocks. Particularly, one of the chemical products that can be obtained from biomass is lactic acid (LA). Great interest has been placed on this compound due to its diverse applications in the chemical, pharmaceutical, food and plastic industries. More recently, research has focused on LA due to the possibility of transforming it into polylactic acid (PLA), which is considered a biodegradable polymer with applications in the production of packaging, sutures and medical applications in drug delivery systems (Serna et al., 2005). Lactic acid can be produced by chemical synthesis, but it has been estimated that ~90% of the total worldwide production is by bacterial fermentation, since this process uses cheap renewable raw materials, low processing temperatures and low energy consumption (Udachan et al., 2014). However, the bio-production of lactic acid is challenging, especially in the downstream stage, where several separation and purification steps are needed to recover the lactic acid from the fermentation broth. Specifically, it is difficult to obtain high purities of lactic acid mainly due to the high affinity with water and its decomposition at high temperatures. Therefore, separation and purification stages represent up to 50% of total production costs (Komesu et al., 2015).

Several separation techniques have been proposed for lactic acid recovery such as precipitation, distillation, solvent extraction, adsorption and membrane separation processes such as reverse osmosis, electrodialysis, ultrafiltration and ultrafiltration (Prado-Rubio et al., 2009). Despite the efforts, there are still some challenges to overcome, which could be solved at industrial scale, for instance, high equipment cost, solvent recovery and high energy consumption (Komesu et al., 2015). Therefore, the objective of this work is to use a systematic design methodology to perform a techno-economic assessment of the lactic acid bioproduction process, using residues of the sugar industry as main feedstock. Reactive distillation and reactive extraction processes have been investigated to determine their economic feasibility based on total annual cost (TAC) and recovery time. The obtained results showed both technologies potential and could be used as driving force for further technologies development for Lactic acid production.

2. Methodology

For this analysis a calculation base of 28,886.6 kg/h of sugar cane bagasse was considered. The composition of the sugarcane bagasse used was: cellulose (68.22 % w/w), lignin (29.19 % w/w) and xylene (2.59 % w/w). The design of the lactic acid bioproduction process used in this paper has been previously proposed by Mendez-Alva et al. (2018). The bio-production stages including pre-treatment, enzymatic hydrolysis and fermentation stages were taken from Morales-Rodriguez et al. (2016). For the separation and purification stages, they have been based on the studies of Pérez-Cisneros et al. (2015), Su et al. (2013) and Pérez et al. (2016). The process was simulated in the software Aspen Plus V8.8 complemented by integrating a Matlab code where it was necessary. The phase equilibrium has been modeled using the NRTL and Hayden-O'Connell thermodynamic methods, according with a previous work (Méndez-Alva et al., 2018), which employed the NRTL parameters of the National Renewable Energy Laboratory (NREL) database (Wooley and Putsche, 1996).

2.1. Reactive distillation

The scheme shown in Figure 1 was used for the purification of LA by reactive distillation (Su et al., 2013). This separation scheme is composed by four sections: pre-concentrator,

esterification, hydrolysis and the alcohol recovery. The process begins feeding lactic acid aqueous solution (30% w/w) from a filtration and precipitation process to the pre-concentrator column. The pre-concentrator column is used to remove excess water from the feed stream. Lactic acid esterification is performed using methanol in a molar ratio of 2:1 alcohol to acid and using Amberlyst 15 as a catalyst at a concentration of 2.5% w/w. Subsequently, in the hydrolysis section, the lactic ester is hydrolyzed back into lactic acid and alcohol using Amberlyst 15 at the same concentration. Finally, at the recovery section the alcohol is separated from the water and other impurities. The alcohol is recirculated to the esterification section while the water can be recirculated to the hydrolysis section. The kinetic model of Sanz et al. (2004) was used to represent the esterification and hydrolysis reaction. The distillation columns presented in this paper have been modeled with the RADFRAC module in Aspen Plus.

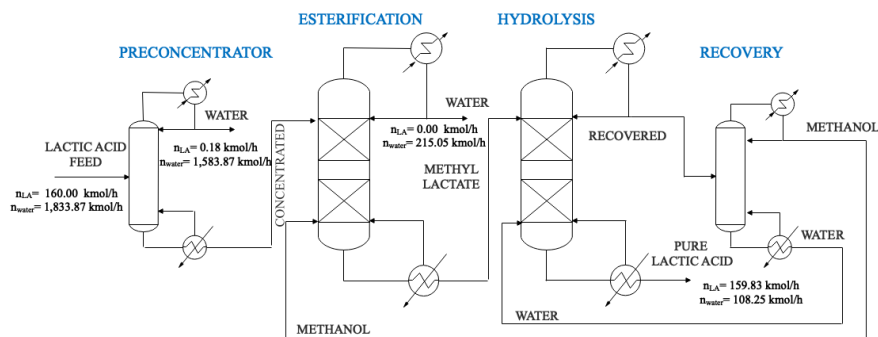


Figure 1. Lactic acid purification process by reactive distillation (Su et al., 2013).

The design of reactive distillation columns was a combinatorial optimization problem with total annual cost (TAC) as objective function. A strategy based on sensitivity analysis was performed to design of the separation scheme considering as degrees of column freedom: number of stages (N), the number of reactive stages (N_{rxn}), feed stage of LA (N_{FLA}) and feed stage of alcohol (N_{FOH}). The design methodology for the reactive and non-reactive distillation columns is presented in Figure 2, where ND is the number of designs obtained in the combinatorial problem. The equilibrium stages, the reactive stages of the column as well as the purities of the required products must be specified, while the position of the feed stages to the column are automatically varied by Aspen Plus. Subsequently, considering the all possible designs obtained through sensitivity analysis, the design that minimizes the total annual cost is selected.

2.2. Reactive extraction

On the other hand, the purification of LA by reactive extraction has been proposed to separate the LA from the fermentation broth using trioctylamine (TOA) and 1-dodecanol as diluent (Pérez et al., 2016). The process has been simulated using the EXTRACT module in Aspen Plus. However, the simulator does not have the binary interaction parameters between amine and system components in its database for the NRTL model; therefore, these parameters could be estimated by the UNIFAC method or employ the NRTL parameters and a chemical equilibrium model with distribution coefficients for this system previously published by Pérez et al. (2016). In this simulation, the parameters

estimated by the UNIFAC method were used since the phase equilibrium could not be reproduced using the parameters reported by Pérez et al. (2016).

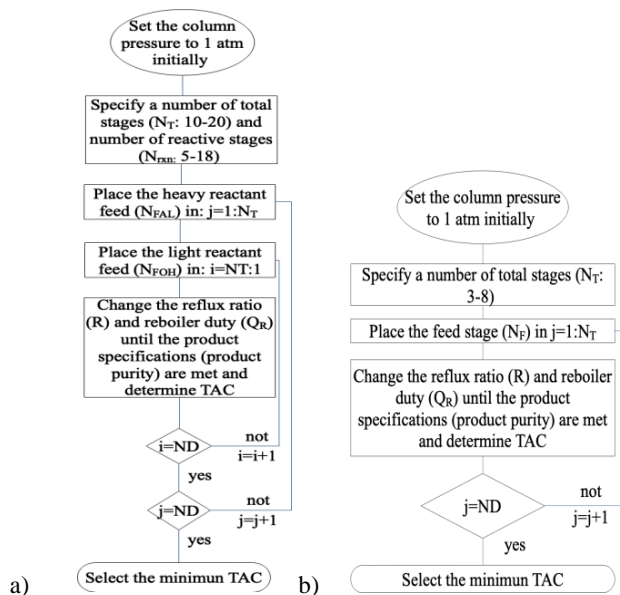


Figure 2. Methodology for the design of the: a) reactive and b) non-reactive distillation columns.

The reactive extraction separation scheme is presented in Figure 3. The extraction was carried out in a counter-current column feeding an aqueous solution of LA (30% w/w) using a molar ratio of 1:1 amine to acid and keeping a concentration of 0.8 mol/L (of TOA in 1-dodecanol). In this system, there is a chemical reaction between LA and TOA producing an amine-lactate complex. This complex promotes separation and provides a greater degree of separation. The extract stream is a mixture of LA-TOA and 1-dodecanol, while the refining stream contains water and a small part of 1-dodecanol. The extract is sent to a distillation column to separate the solvent and TOA from LA and reuse it in the extraction unit.

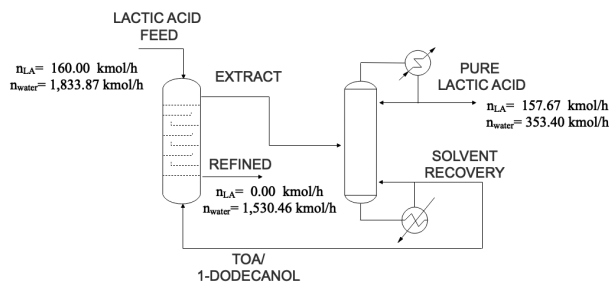


Figure 3. Lactic acid purification process by reactive extraction.

For the design of the extraction column the equilibrium stages have been determined through the equilibrium model reported by Pérez et al. (2016), which considers the

distribution coefficient, the equilibrium constant of the chemical reaction and the mass balances. It is important to mention that the equilibrium model considers that LA is the only compound transferred from the aqueous phase to the organic phase. The analysis of the best design for the extraction column in terms of TAC was limited because the chemical structure of the amine lactate complex changes according to the molar feed ratio. The calculations required the integration of Aspen Plus and Matlab through COM objects since the reactive extraction module was not available in Aspen Plus as a unit operation.

3. Results

Computer-assisted simulation enabled the design of both purification schemes and the economic evaluation of both technologies using Aspen Economic Analyzer.

The best design of the reactive distillation purification scheme consists of four distillation columns: The pre-concentrator column with 8 stages and the feed stream is introduced at the stage number 4. The esterification column has 17 stages and 5 reactive stages (12-16), feeding the stream leaving the concentrator column through stage number 7, while the methanol stream is fed through stage number 13. The hydrolysis column has 30 stages and 25 reactive stages (5-29), feeding the methyl lactate stream through stage number 10, while the water stream is fed through stage number 20. Finally, the column has 14 stages and the stream containing the methanol-water mixture is fed through stage number 6. The separation system operates at 1 atm pressure and the esterification and hydrolysis reactions are carried out at a temperature of 353.15 K.

The reactive extraction process consists of one extraction column and one distillation column. The extraction column has 5 stages, where La is fed at stage number 1, while TOA and diluent are fed at stage number 5, the extraction column operates at 1 atm and 316.1 K. The distillation column has 11 stages and is fed at stage number 7. Both LA purification designs achieved a purity of 88% w/w.

Table 1 presents a comparison of the economic evaluation for both technologies and Table 2 presents a comparison of the energy requirements of both purification schemes.

Table.1 Costs for the proposed purification processes.

Analysis	Reactive distillation	Reactive extraction
Total Capital Cost (USD)	93,107,800.00	93,107,800.00
Total Operating Cost (USD/y)	49,011,200.00	27,654,000.00
Desired Rate of Return (%/y)	20	20
Return of investment (Year)	2.7	1.48
Equipment Cost (USD)	672,500.00	536,500.00
Total Annual Cost (USD/y)	53,666,590.00	27,680,825.00

Table.2 Energy requirements for the proposed purification processes.

Purification process	Heat Duty (kW)
Reactive distillation	31,601.00
Reactive extraction	19,771.00

The economic evaluation of both technologies has shown that reactive extraction substantially reduces the total annual cost of LA purification by 44% compared to reactive distillation. Also, using reactive extraction for LA purification reduces the energy requirements of the purification stage with respect to the use of reactive distillation by 37.5%.

4. Conclusions

A techno-economic analysis of the LA reactive purification technologies has been carried out. Both processes have been designed and analyzed using CAPE tools. The use of reactive extraction in LA purification promises to substantially reduce total LA production costs and energy requirements. However, this technology according to Technology Readiness Level (TRL) is still under development (TRL 3 - TRL 7) because the exact nature of the chemistry involved in acid absorption is unknown and the chemical structure of the complex varies according to several factors, such as: the concentration of the LA in the aqueous phase, the type of diluent and the molar amine to acid feed ratio. Therefore, efforts should be made to provide more reactive extraction system understanding that allows to have more accurate prediction useful for detailed design. However, this work is the starting point for the development of a methodology for the design and simulation of reactive extraction systems for LA recovery in Aspen Plus. Finally, reactive distillation presents a total annual cost and much higher energy requirements, however, the results obtained are much more reliable because it is a mature technology (TRL 8 - TRL 9), which has already been tested industrially.

References

- L. Serna, A. Rodriguez, 2005, Producción biotecnológica de ácido láctico: Estado del arte, *Ciencia y Tecnología Alimentaria*, 5, 1, 54-65 (Spanish).
- I.S. Udachan, A.K. Sahoo, 2014, A study of parameters affecting the solvent extraction of lactic acid from fermentation broth, *Brazilian Journal of Chemical Engineering*, 31, 3, 831-827.
- A. Komesu, P.F. Martins, B.H. Lunelli, J. Oliveira, R.M. Filho, M.R.W. Maciel, 2015, The effect of evaporator temperature on lactic acid purity and recovery by short path evaporation, *Separation Science and Technology*, 50, 10, 1548-1553.
- C.Y. Su, C.C. Yu, I.L. Chien, J. D. Ward, 2013, Plant-wide economic comparison of lactic acid recovery processes by reactive distillation with different alcohols, *Industrial and Engineering Chemistry Research*, 52, 32, 11070-11083.
- J. A. Méndez-Alva, E.S. Pérez-Cisneros, D. Rodriguez-Gomez, O.A. Prado-Rubio, B. Ruiz-Camacho, R. Morales-Rodriguez, 2018, Computer-aided process simulation, design and analysis: lactic acid production from lignocellulosic residues, *Computer Aided Chemical Engineering*, 44, 463-468.
- R. Morales-Rodriguez, E.S. Pérez-Cisneros, J. de los Reyes-Heredia, D. Rodriguez, 2016, Evaluation of biorefinery configuration through a dynamic model-based platform: Integral operation for bioethanol and Xylitol Co-production from lignocellulose, *Renewable Energy*, 89, 135-143.
- E. S. Pérez-Cisneros, L. Avilés-Cabrera, V. Medina-Bañuelos, M. Sales-Cruz, A. Ochoa-Tapia, T. Viveros-García, R. Lobo-Ohemichen, 2015, A computational platform for simulation, Design and analysis of a Poly(Lactic) Acid production process from different lignocellulosic raw materials, *Comput.-Aided Chem. Eng.*, 37, 1187-1192.
- O.A. Prado-Rubio, S.B. Jørgensen, G. Jonsson, 2009, Lactic Acid Recovery in Electro-Enhanced Dialysis: Modelling and Validation. *Comput.-Aided Chem. Eng.*, 26, 1406-1410.
- R. Wooley, V. Putsche, 1996, Development of an ASPEN PLUS physical property database for Biofuels Components, National Renewable Energy Laboratory, NREL/MP-425-20685.
- M.T. Sanz, R. Murga, S. Beltrán, J.L. Cabeza, 2004, Kinetic study for the reactive system of lactic acid esterification with methanol: Methyl lactate hydrolysis reaction, *Ind. Eng. Chem. Res.*, 43, 9, 2049-2053.
- A.D. Pérez, S. Rodríguez-Barona, J. Fontalvo, 2016, Liquid-liquid equilibria for trioctylamine/ 1-dodecanol/ Lactic Acid/ Water system at 306.1m 310.1 and 316.1 K: Experimental data and prediction, *Journal of Chemical and Engineering Data*, 61, 7, 2269-2276.

Life cycle assessment of Jatropha jet biodiesel production in China conditions

Haoyu Liu, Tong Qiu*

Department of Chemical Engineering, Tsinghua University, 100084 Beijing, China
Corresponding author's E-mail: qiutong@tsinghua.edu.cn

Abstract

Jet biodiesel derived from energy crop has been promoted by the Chinese government to decrease oil dependence of the aviation industry. This study carried out a life cycle assessment on jatropha-based jet biodiesel in China condition to evaluate the energy balances and GHG emissions. This life cycle process covered data from Southwest China with the help of CNPC. Detailed information with practical data in the production process and by-products recycling ways were provided. 18 cases were utilized to compare the influence of different planting output, oil extraction model and recycling pathway. Centralized extraction model and by-product re-used as fertilizer and biogas can be developed in the future. The formation of a multi-scene analysis results is useful for policy makers

Keywords: Life-cycle analysis, jet biodiesel, Jatropha, By-product, Scenario analysis

1. Introduction

China had become the world's largest oil consumer and GHGs emitter (EIA, 2014). The aviation industry, which had since long been pointed out as fastest growth contributors to global warming in the transportation sector, emitted 2% of global GHGs emissions (Jong, S. D et al. 2017). A huge increasing demand of jet fuels not only led to an increase crude oil imports and price but also an potential risk for energy safety (Han J. et al. 2013).

Jet biodiesel derived from energy crop had been promoted by the Chinese government to decrease oil dependence of the aviation industry, according to the Medium and Long-term Development Plan for Renewable Energy issued by the National Development and Reform Commission, 2007. However, the controversy surrounding the social impacts such as food safety and environmental impacts promoted the government to impose a ban on expanding grain-based jet biofuel production (Hong, Yuan et al. 2009). In order to find a truly sustainable jet biodiesel, the feedstock should be an effective alternative to mitigate GHGs emissions, should be economically feasible to plant, and should not threat food security.

Jatropha curcas appeared to be an idealized feedstock to produce jet fuel in China conditions (Hou J et al. 2011). These inedible crop grows widely in the Southwest China due to its stable price, drought tolerance, and little agricultural inputs (Blanco-Marigorta et al.2013). While some environmental impact studies were carried out from India (Kumar S, 2012), Mexico (Fuentes A, 2018), US (Han J. et al. 2013; Stratton R W, 2011), Nigeria (Onabanjo T, 2017), a few studies had been carried out in China. Ou X et al. (2009) examined the jatropha curcas as one of six biofuel pathways in China, considering the fossil energy consumption and greenhouse gas emissions. Other impact categories

were taken into account to evaluate the sustainability of *Jatropha curcas* comprehensively by Hou J (2011). Both of them considered LCA on the same scenario. Wei et al. (2018) carried out a LCA of corn-based jet fuel production using Fischer-Tropsch synthesis. Except this, there are few practical data regarding *Jatropha* production process and few case about the use of the by-products from *Jatropha* oil extraction. In addition, studies have little knowledge about whether distributed production or centralized production is better.

Besides, jet biodiesel are considered as a low-carbon alternative to fossil fuels. At a country level, the China National Petroleum Corporation (CNPC) had promoted *Jatropha* jet biodiesel production under the policies and financial supports from the government since 2011. The documents by government and companies both target mitigation of GHG emissions as central sustainability criteria. However, there are a few studies on the GHG balance of jet biodiesel from *Jatropha* to give advice to policymaking.

This study carried out a life cycle assessment on jet biodiesel made from *Jatropha* in China condition to evaluate the energy balances and GHG emissions in order to provide more detailed information and data in the production process and by-products recycling. Different allocation methods were combined to deal with various by-products. Scenario analysis were utilized to predict different plant output and oil extraction model. Three by-products from oil extraction recycling pathways were investigated. The formation of a multi-scene analysis results is useful for policy makers.

2. Methods

2.1. LCA framework

A cradle-to-gate LCA was performed with GaBi ts Education software. The analysis focus on determine the energy consumption and GHGs emissions of jet biodiesel produced by *Jatropha* in Southwest of China, to compare the results with different oil extraction model and to find an eco-friendly by-products recycling pathways.

2.2. System boundary and functional unit

The stages considered and the calculation logic of the energy consumption and the GHGs of the entire process is present in the Figure 1, including the plant cultivation, production and transport process. Effects of fertilizer emissions and land use change will not be considered for the moment due to the data given in the IPCC Guidelines have large deviations. The assessments were compared on the basis of their GHG emissions in g

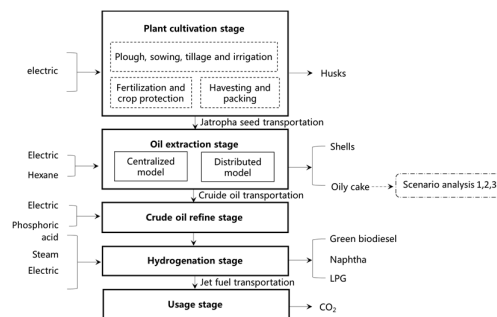


Figure 1. Product system boundary of this study.

Table 1 Allocation method for by-products

By-product	Method	By-product	Method
Husk	Energy method	Jatrophah oily cake recycling as fertilizer	Displacement method
glycerin	Displacement method	Jatrophah oily cake recycling as forage	Economic method
Naphtha	Energy method	Jatrophah oily cake recycling as biogas	Displacement method
LPG	Energy method	Green biodiesel	Energy method

CO2 per MJ and energy consumption in MJ per Kg of jet biodiesel produced from jatrophah.

2.3. Product system description

In the plant stage, three planting output conditions were investigated: low output, basic output and high output which depends on the management level and effect of fertilizer. There were two kinds of oil extraction models: distributed extraction model where famers extracted jatrophah on local plant transported oil to the refine factory, and centralized extraction model where here the jatrophah was transported to the centralized extraction factory. The hydrogenation process was based on technology from the UOP company.

2.4. Method to deal with of by-products

In this case, there were various by-products in the production process. There are four allocation method: displacement method, and the mass, energy, market method. Different allocation methods showed in the Table 1 were combined for different by-product, considering the practical data and usage of the by-product.

2.5. Scenarios for reusing the by-products

For the further applications, the jatrophah oily cake that can be used as forage, fertilizer or biogas will be comprehensive utilized. The data were gained from the factory and the farmers. The possible systems for recycle the jatrophah oily cake are divided into 3 scenarios: Scenario 1: All the jatrophah oily cake is used to fertilizer; Scenario 2: After detoxification, all the jatrophah oily cake is used as forage to replace soybean; Scenario 3: All dried distiller produce biogas, where need extra coal.

2.6. Life cycle inventory

Based on the investigation with the technology developer and farmers, open LCI databases and references, the part of key LCA parameter is showed in the Table 2.

Table 2 Parameter about jet biodiesel production (To produce 1 kg jet biodiesel)

Item Parameter	Value						Item Parameter	Value					
	Jatrophah Output		Low Basic High		Low Basic High			Jatrophah Output		Low Basic High		Low Basic High	
Oil Extraction Model	Distributed			Centralized			Distributed	Distributed			Centralized		
Planting							Oil Refine						
Land (ha)	0.0081	0.0026	0.0015	0.0070	0.0023	0.0013	Electric (Kwh)	0.0498	0.0498	0.0498	0.0498	0.0498	0.0498
N fertilizers (kg)	2.0268	0.6563	0.2369	1.7579	0.5692	0.2055	Phosphoric acid (kg)	0.0418	0.0418	0.0418	0.0418	0.0418	0.0418
P fertilizers (kg)	1.0539	0.3413	0.0939	0.9141	0.2960	0.0814	Refined oil (kg)	2.0180	2.0180	2.0180	2.0180	2.0180	2.0180
K fertilizer (kg)	1.8241	0.5907	0.1848	1.5821	0.5123	0.1602	Hydrogenation						
Electric (Kwh)	0	0.5011	0.2011	0	0.4388	0.1745	Hydrogen (kg)	0.0710	0.0710	0.0710	0.0710	0.0710	0.0710
Gasoline (kg)	0	0.1555	0.0883	0	0.1349	0.0766	Steam (kg)	0.8350	0.8350	0.8350	0.8350	0.8350	0.8350
Husks (kg)	4.7613	4.2407	3.8378	4.1297	3.6781	3.3287	Gas (kg)	0.0795	0.0795	0.0795	0.0795	0.0795	0.0795
Fruit (kg)	12.8685	12.1182	11.2878	11.1615	10.5089	9.7903	Electric (Kwh)	0.3120	0.3120	0.3120	0.3120	0.3120	0.3120
Seed (kg)	8.1072	7.8755	7.4498	7.0317	6.8308	6.4616	Green biodiesel (kg)	0.0170	0.0170	0.0170	0.0170	0.0170	0.0170
Oil Extraction							Naphtha (kg)						
Electric (Kwh)	0.3506	0.3406	0.3222	0.2488	0.2417	0.2286	LPG	0.5330	0.5330	0.5330	0.5330	0.5330	0.5330
Hexane (kg)	0	0	0	0.0144	0.0140	0.0132	Transportation						
Shells (kg)	2.3878	2.3195	2.1942	2.0501	1.9915	1.8839	Electric (Kwh)	0.0056	0.0056	0.0056	0.0056	0.0056	0.0056
Oily cake	3.3188	3.1577	2.8616	2.5214	2.3831	2.1289	Diesel (g)	0.3029	0.3029	0.3029	0.3029	0.3029	0.3029
Crude oil	2.3195	2.3195	2.3195	2.3195	2.3195	2.3195							
Transport gasoline (kg)	0.0040	0.0040	0.0039	0.0105	0.0102	0.0096							
Transport diesel (kg)	0.0096	0.0095	0.0094	0.0253	0.0245	0.0232							

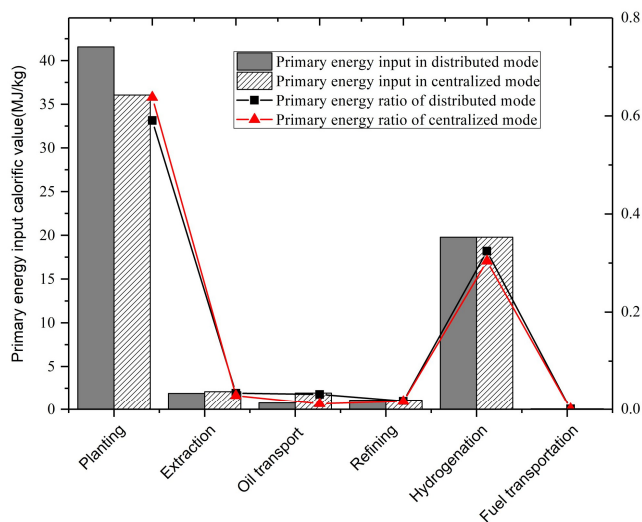


Figure 2. Energy consumption of the basic case in each production process.

3. Result and discussion

3.1. Energy consumption in the basic condition

The contribution of different processes and different oil extraction model to the energy consumption are showed in the Figure 2. The total energy consumption is 61.04 MJ primary energy/kg jet biodiesel in the basic output of centralized extraction model, while the energy product occupy 78.24 MJ including all the by-product. The total energy efficiency is 0.78 MJ primary energy/MJ jet biodiesel. Because of a lot of fertilizer input, the planting unit exhibits high contribution to energy consumption. Besides, the centralized extraction model is benefit for mitigation energy consumptions, it may be because of its advanced technology and high rate of extraction, but it also need time to develop the famers' market. To reduce the GHGs and enhance energy efficiency, enhancing the separation efficiency or using by-product to supply energy can be considered.

3.2. Scenario between output, extraction model and recycling of by-products

To illustrate the impact of output, oily cake extraction model and recycling of by-products, Figure 3 shows that the emissions for the Jatropha range between -36.28 and 466.69 g CO₂/MJ for 18 cases. Scenario 2 increased a lot of GHGs emissions and the detailed reason will be discussed in the next part. For different planting output, it's obvious that the harvest yield is the key factor. The high output cases even cause negative emissions in the scenario 1 and 3, this may be because the by-products replaced a high emission substitution and the professional plantation management increased the efficient of fertilizers. From the Figure 3 it can be concluded that scenario 1 and 3 have positive environment impact, comparing to the fossil fuel, whose baseline is 91.8 g CO₂/MJ in the US renewable fuel standards (WTW).

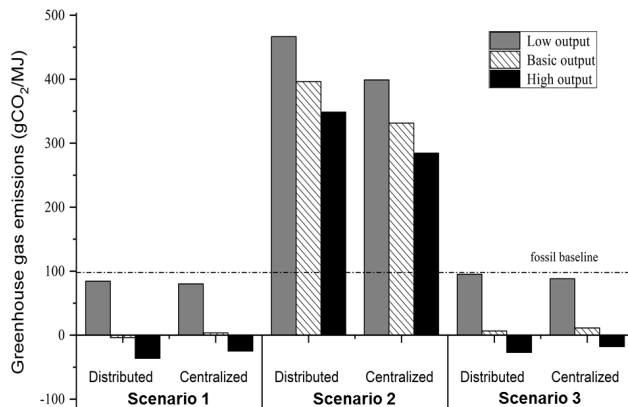


Figure 3. 18 cases with different planting output, recycling scenarios and extraction models.

3.3. Influence of recycling by-product

To examine the high emission in the scenario 2, Figure 4 shows the GHGs emission in each process where the *jatropha* oily cake from the oily extraction process will be used as forage. The detoxification for recycling need huge fuel and chemical substances input such as methyl alcohol. But the high economic value of forage, such as soybean, is an considerable reason to recycle by-product. From the scenario analysis, the conclusion that comprehensive utilization about the by-product especially like *jatropha* oily cake will have huge influence to the environment impact can be drawn.

4. Conclusion

The life cycle analysis about the *jatropha* jet biodiesel in the southwest China was conducted in this study. 18 cases with different oil extraction model, planting output and recycling pathway for by-products was utilized to compare the influence to energy consumption and GHGs emissions in the production process. The result shows that centralized extraction model is better than distributed extraction model especially in the low planting output condition. Scenario 1 and 3 showed the systematic and suitable utilization of by-product will improve the environment impact, with the emission of 80.1-88.28 g CO₂ /MJ even in the low output case of centralized model. The practical data regarding plant process and cases about the use of the by-products is valuable to the researchers. Besides, the formation of a multi-scene analysis results is useful for producer and policy makers.

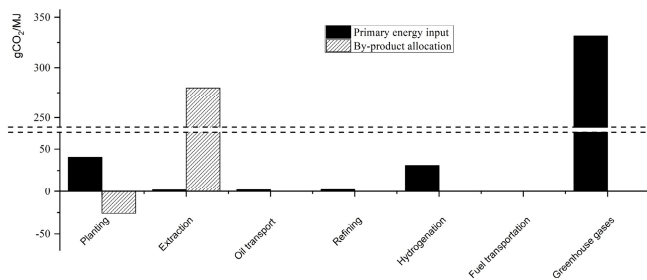


Figure 4. The GHGs emission of Scenario 2 in each process.

Acknowledgements

The authors gratefully acknowledge the National Natural Science Foundation of China for its financial support (Grant No. U1462206).

References

- Blancomarigorta A M , SuárezMedina, J, Veracastellano A . Exergetic analysis of a biodiesel production process from *Jatropha curcas*[J]. *Applied Energy*, 2013, 101(1):218-225.
- EIA, The U.S. Energy Information Administration, 2014. China is Now the World's Largest Net Importer of Petroleum and Other Liquid Fuels. <http://www.eia.gov/todayinenergy/detail.cfm?id%415531>.
- Fuentes A , Carlos García, Hennecke A , et al. Life cycle assessment of *Jatropha curcas* biodiesel production: a case study in Mexico[J]. *Clean Technologies & Environmental Policy*, 2018(1):1-13.
- Han J , Elgowainy A , Cai H , et al. Life-cycle analysis of bio-based aviation fuels[J]. *Bioresour Technol*, 2013, 150(4):447-456.
- Hong, Y., Z. Yuan and J. Liu (2009). "Land and water requirements of biofuel and implications for food supply and the environment in China." *Energy Policy* 37(5): 1876-1885.
- Hou J , Zhang P , Yuan X , et al. Life cycle assessment of biodiesel from soybean, *jatropha* and microalgae in China conditions[J]. *Renewable & Sustainable Energy Reviews*, 2011, 15(9):5081-5091.
- Kumar S . A comprehensive life cycle assessment (LCA) of *Jatropha* biodiesel production in India[J]. *Bioresource Technology*, 2012, 110(32):723-729.
- Onabanjo T, Lorenzo G D, Kolios A. Life-cycle assessment of self-generated electricity in Nigeria and *Jatropha* biodiesel as an alternative power fuel[J]. *Renewable Energy*, 2017, 113.
- Ou X, Zhang X, Chang S, Guo Q (2009) Energy consumption and GHG emissions of six biofuel pathways by LCA in (the) People's Republic of China. *Appl Energy* 86:S197–S208.
- PRC State Development and Reform Commission. Medium and long-term development plan for renewable energy. Beijing: PRC State Development and Reform Commission; 2007.
- S.C. Mao, Z.Y. Li, C. Li Application of biodiesel produced from *Jatropha curcas* L. seed oil *Chin Oils Fats*, 32 (2007), pp. 40-42
- Stratton R W , Wong H M , Hileman J I . Quantifying variability in life cycle greenhouse gas inventories of alternative middle distillate transportation fuels[J]. *Environmental Science & Technology*, 2011, 45(10):4637-44.
- Wei T , Jun X , Kai Y . Life cycle assessment of jet fuel from biomass gasification and Fischer-Tropsch synthesis[J]. *China Environmental Science*, 2018.
- Consulting report of China Engineering Academy, 2014, Development, Demonstration and Application of Key Technology of Biofuels Industry in China.

Optimal design of post combustion CO₂ capture processes based on phase-change solvents

Panagiotis Kazepidis^{a,b}, Athanasios I. Papadopoulos^a, Panos Seferlis^{a,b}, Felipe A. Perdomo^c, Amparo Galindo^c, George Jackson^c, Claire S. Adjiman^c

^a*Chemical Process and Energy Resources Institute (CPERI) – Centre for Research and Technology – Hellas (CERTH), Themi-Thessaloniki 57001 Greece*

^b*Department of Mechanical Engineering, Aristotle University of Thessaloniki, Thessaloniki 54124, Greece*

^c*Department of Chemical Engineering, Centre for Process Systems Engineering, Imperial College London, London SW7 2AZ, UK*

seferlis@auth.gr

Abstract

The current work addresses the investigation of phase-change solvents behaviour during the design of post-combustion CO₂ capture processes. The use of phase-change solvents leads to energetic gains due to their lower regeneration energy demands. The latter are enhanced in this work by the consideration of systematic structural and operating modifications imposed on a reference absorption/desorption flowsheet. Such modifications are realized with the help of a rigorous and flexible model that can represent the phase-change behaviour and includes stream redistribution options that aim to enhance the main process driving forces. An aqueous N-methylcyclohexylamine (MCA) solution is employed in an effort to exploit the solvent's phase separation behaviour towards the reduction of the total process cost and energy requirements.

Keywords: CO₂ capture, optimal design, phase change solvents, MCA, N-methylcyclohexylamine.

1. Introduction

Solvent-based absorption/desorption processes represent a mature technology for post-combustion CO₂ capture. A major drawback is the high regeneration energy requirements which prohibit the wide industrial adoption of such systems. Phase-change solvent processes are emerging as a new and promising technology which enables up to 50% reduction in regeneration energy requirements (Pinto et al., 2014). This is achieved through the use of solvents which exhibit phase-change behavior due to the appearance of a second liquid phase upon reaction with CO₂ and possibly a subsequent increase of temperature. This enables the use of a physical process usually in the form of a decanter to separate the two liquid phases; one of them can be partially or totally recycled directly to the absorber, whereas the other is transferred to the desorber, resulting in significant energy reduction. Despite the obvious advantages, there is very limited research addressing modelling and design of such systems, leaving considerable space for performance improvements. The very few reported studies pertain to techno-economic assessment of specific solvents using commercial software, with no systematic optimisation approaches reported to date (Raynal et al., 2011; Pinto et al., 2014).

In this work, a rigorous and flexible model that can represent the phase-change behaviour of absorption/desorption CO₂ capture processes is proposed. The column models are based on the orthogonal collocation on finite elements (OCFE) technique tailored to three phase systems that support a sufficiently accurate but also computationally tractable process representation. The main advantages include the transformation of discrete process characteristics into continuous decision variables, and the ability to represent and track sharp changes of important variables such as concentration and temperature profiles along the column domain. The model is also employed in the context of a superstructure representation which supports optimisation.

2. Methodology

2.1. Modelling framework

The use of phase-change solvents (PCS) systems in CO₂ capture processes provides the opportunity for enhanced performance as well as the reduction of process energetic demands and economic resources through the exploitation of their liquid-liquid phase separation capabilities. The optimum design of three-phase flowsheets is challenging because it requires (a) a systematic modelling approach able to capture transitions between vapour-liquid (VLE) and vapour-liquid-liquid (VLLE) equilibria regimes, and (b) an underlying framework, which is sufficiently flexible to account for the interactions of the large number of the desired structural and operating features.

The modeling framework employed in this work to meet requirement (a) is based on the OCFE approximating technique (Dalaouti and Seferlis, 2006; Damartzis and Seferlis, 2010) to model three-phase reactive separation systems. The separation column is divided into column sections, defined as the column segment between two successive feed or draw streams. A section is further subdivided into finite elements (FE) of variable size. Within each finite element a given number of collocation points (CP) are defined based on the degree of polynomial approximation. These points are selected as the roots of the discrete Hahn family orthogonal polynomials. A finite element is illustrated in Figure 1 (left) with the two liquid and vapour flows leaving and entering the collocation points.

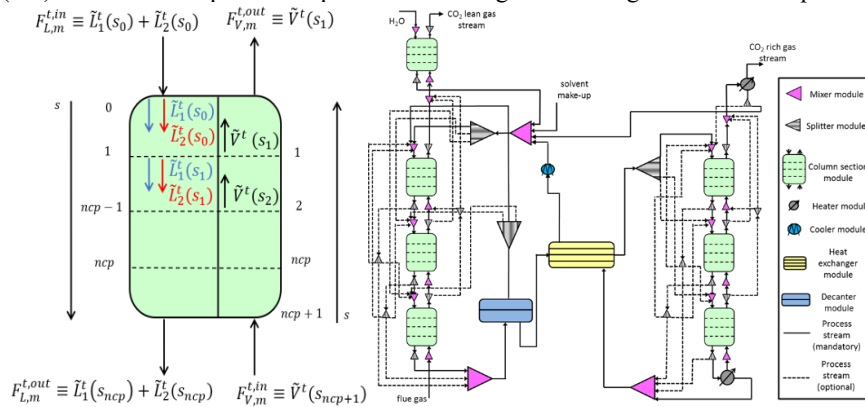


Figure 1: Three-phase OCFE presentation (left), superstructure with indicative placement of liquid-liquid phase separator (right)

Eq. (1) – (5) represent the main equations of a VLLE model with NC components and n collocation points under the assumption of a dispersed second liquid phase. Eq. (1) is the

material balance and Eq. (3) the energy balance at collocation point j that corresponds to a location in the column s_j ; x_i^{L1} and x_i^{L2} are the molar fractions of each component in the two liquid phases and y_i^V is the vapour molar fraction of each component. The reactive absorption is incorporated implicitly in the phase equilibrium model. In Eq. (3) symbol H represents the enthalpies of each phase and ΔH is the heat of reaction. The equilibrium between the vapour and the $L1$ phase is presented in Eq. (4) by K_i^V , whereas Eq. (5) is the equilibrium between the two liquid phases, represented by K_i^L . The dispersed liquid phase (2nd liquid phase) does not interact with the vapour phase and therefore only two interfaces are considered; vapour – liquid $L1$ and liquid $L1$ – liquid $L2$.

$$L1_i(s_j + 1) + L2_i(s_j + 1) - L1_i(s_j) - L2_i(s_j) + V_i(s_j - 1) - V_i(s_j) = 0 \quad (1)$$

$$x_i^{L1}(s_j) = \frac{L1_i(s_j)}{\sum_{i=1}^{NC} L1_i(s_j)}, x_i^{L2}(s_j) = \frac{L2_i(s_j)}{\sum_{i=1}^{NC} L2_i(s_j)}, y_i^V(s_j) = \frac{V_i(s_j)}{\sum_{i=1}^{NC} V_i(s_j)} \quad (2)$$

$$L_1^t(s_j + 1)H^{L1}(s_j + 1) + L_2^t(s_j + 1)H^{L2}(s_j + 1) + V^t(s_j - 1)H^V(s_j - 1) - L_1^t(s_j)H^{L1}(s_j) - L_2^t(s_j)H^{L2}(s_j) - V^t(s_j)H^V(s_j) + \Delta H = 0 \quad (3)$$

$$y_i^V(s_j) = K_i^V(s_j)x_i^{L1}(s_j) \quad (4)$$

$$x_i^{L2}(s_j) = K_i^L(s_j)x_i^{L1}(s_j) \quad i = 1, \dots, NC, \quad j = 1, \dots, n \quad (5)$$

2.2. Design framework

The model shown for the column section is directly adapted on the superstructure proposed by Damartzis et al. (2014) for two-phase post-combustion CO₂ capture processes. The superstructure, shown in Figure 1 (right) consists of modules representing generic process tasks (e.g., reactive, separation, heat transfer) and interconnecting streams emulating material flows. Reactive separation and liquid-liquid phase change processes may be represented by different modules through the column section. Additional information is reported in Damartzis et al. (2014) pertaining to heat transfer tasks. Several different modules may be connected in the same flowsheet using a broad set of stream types (e.g., recycle, bypasses and so forth). The proposed generic tasks account for (a) reaction, mass and heat exchange between different phases within each module, and (b) stream mixing and splitting to enable distribution of materials among different modules. This representation enables the reproduction of any potentially desired representation of solvent-based CO₂ capture processes. For clarity, the liquid-liquid separator is illustrated before the heat exchanger in Figure 1 (right), but it can also be placed after the heat exchanger and connected in any desired way to the columns as in Figure 2.

The combination of the superstructure approach with the OCFE representation introduces important advantages in process optimization. The element length becomes a design variable that indicates the number of stages or equivalent packing height in the column. Accordingly, the size of the separation column can be deduced from the sum of element lengths comprising the column plus the discrete stages, if any, such as the distinct feed stages, reboilers and condensers. Hence, the integer variable denoting the number of stages becomes continuous. Further avoidance of integer variables is achieved by the continuous representation of the location of side feed or draw streams in the columns. Temperature and composition profiles in the column are approximated by continuous Lagrange polynomials of position inside the column. Finally, OCFE supports a significant reduction in terms of the total number of model equations without compromising the resolution of the model, by enabling the solution of the material and energy balances of the equilibrium model on a reduced number of collocation points.

3. Implementation

To investigate the effect of PCS on the optimal design of CO₂ capture processes a N-methylcyclohexylamine (MCA) 35 wt % aqueous solution is considered. MCA is a cyclic secondary aliphatic amine, which has been shown to demonstrate enhanced CO₂ capture capabilities (Jeon et al. 2014; Zhuang et al., 2016) is used. The flowsheet investigated in this work is shown in Figure 2. In addition to the absorption and desorption columns a liquid-liquid phase separator is employed to exploit the phase-split exhibited by MCA.

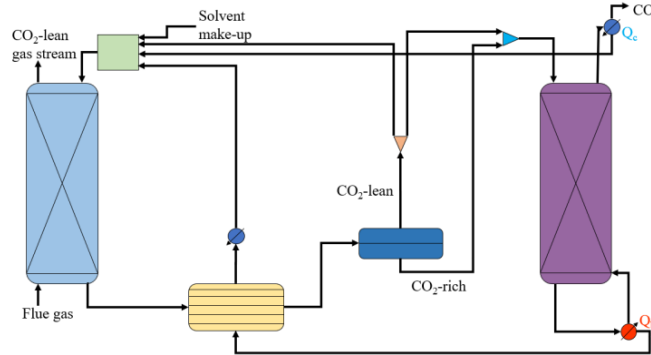


Figure 2: Flowsheet structure used in optimal design.

In the case of MCA, phase separation occurs at 90°C, so the liquid-liquid phase-separator (LLPS) is positioned after the intermediate heat exchanger. In principle, the superstructure may be used to investigate various structural flowsheet options. In this work, for the first time the performance of MCA through systematic process design is investigated and a new structural design option in phase-change flowsheets is explored. After the phase separation, the CO₂-rich phase is directed to the stripper column, whereas the CO₂-lean stream may be recycled entirely or partially to the absorber top through a splitter. The fraction of the CO₂ lean stream leaving the LLPS is a degree of freedom in optimisation. This design option is considered to investigate the trade-off between the regeneration energy requirements and the effects of absorber size on the total process cost. The only flowsheet proposed to date for PCS allows for complete recycle of the CO₂-lean stream to the absorber, leaving the interplay of regeneration energy-absorber size unexplored. A total of seven design decision variables is considered including the split fraction after the LLPS, the pressure in the columns, the reboiler temperature, the amine flowrate as well as the column sizes. The objective function is expressed as the sum of the total process capital and operating expenses as follows:

$$F = \underbrace{\sum_{i=1}^{N_{sep}} C_{sep,i} + \sum_{i=1}^{N_{HEX}} C_{HEX,i} + \sum_{i=1}^{N_{pump}} C_{pump,i}}_{CAPEX} + \underbrace{C_{steam} + C_{cool} + C_{amine}}_{OPEX} \quad (6)$$

CAPEX terms reflect the annualized capital costs of the separation, the heat exchangers and the pumping equipment, whereas the OPEX terms stand for the costs of steam in the reboiler, water (both process and cooling) and the fresh amine used in the system. Employed initial conditions as well as process specifications are listed in Table 1.

The CO₂ vapour pressure (P_{CO_2} in kPa) with respect to loading (a mol CO₂ / mol amine) and temperature (T) is represented by Eq. (7) which is fitted from experimental VLL

data (Tzirakis et al., 2018), with R² = 0.96 for T = 40 °C, 60 °C, and 90 °C. For MCA and H₂O in the vapour phase ideal behavior is assumed. The heat of reaction (ΔH in J/mol) is calculated using Eq. (7) derived by a polynomial approximation (Oexmann, 2011):

Table 1: Initial conditions and process specifications.

Initial Conditions		Specifications	
Vapour flow in absorber (mol/s)	320	CO ₂ Absorption (%)	≥90
CO ₂ composition in flue gas (% v/v)	14.11	Cooler temperature (K)	≥313
Vapour inlet temperature (K)	298	Condenser temperature (K)	313

$$\log_{10}(P_{CO_2}) = 21.65 - 19.81 \cdot a - \frac{7343}{T} - 75720 \cdot \frac{a^2}{T^2} + 721500 \cdot \frac{a}{T^2} + 5435 \cdot \frac{a}{T} \quad (7)$$

$$\Delta H = -R \cdot \left(-7343 - 2 \cdot 75720 \cdot \frac{a^2}{T} + 2 \cdot 721500 \cdot \frac{a}{T} + 5435 \cdot a \right) \quad (8)$$

4. Results and discussion

Table 2 presents the optimal solution for MCA (MCA^{opt}) compared to an optimal solution obtained for monoethanolamine (MEA) 30 wt %. Two more cases are explored, namely MCA¹ and MCA², where the split fraction after the liquid-liquid phase separator is fixed at specific values, one lower and one higher than the optimal solution. This enables the investigation of the effect of the split fraction in the overall performance.

Table 2: Design optimization results

Case	MCA ¹	MCA ^{opt}	MCA ²	MEA
CO ₂ -lean phase split ratio (%) to stripper	20	28.63	50	-
Equivalent Stages:				
Absorber / Stripper	24 / 26	22 / 26	22 / 27	11 / 27
Reboiler Temperature (K)	376.58	376.87	377.35	393.15
Phase Split Ratio (%) (rich/lean)	30.63	30.63	30.63	-
Bottom Pressure (bar):				
Absorber / Stripper	1 / 1	1 / 1	1 / 1	1.9 / 1.8

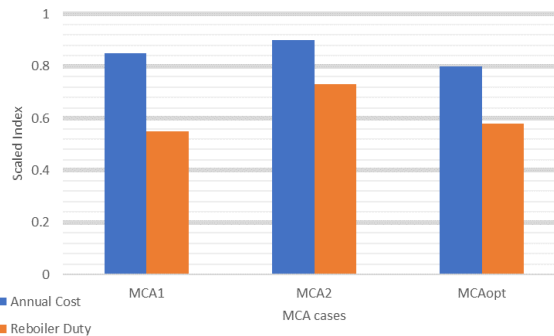


Figure 3: Both reboiler duty and annual cost of MCA aqueous phase split ratio cases, all values scaled with respect to MEA case, values lower than 1 indicate better performance than MEA.

Optimization results reveal that all the cases using MCA exhibit lower operating pressures in both columns as well as reduced operating temperature in the reboiler than MEA. The

second liquid phase is formed above 363.15 K, so this is the target temperature in the decanter for the liquid-liquid phase separation that must be provided by the heat exchanger. Reduced reboiler duty (2.3 GJ/ton CO₂) by 42.5 % at a lower temperature level by 16.2°C is required in the optimised MCA case compared to the conventional MEA case (4.0 GJ/ton CO₂). This is a significant advantage of the phase-change solvent capture system. When the recycle of the CO₂-lean stream to the absorber increases (i.e. in MCA¹), a larger absorber column is needed in order to achieve the overall CO₂ capture specification. A large recycle of the aqueous liquid stream reduces the total amount of CO₂ captured per pass. Eventually, this results in lower regeneration energy, due to lower volume in the desorber, but at a higher investment cost, as shown in Figure 3. MCA performs better even at pressures of 1 bar (thermodynamic data were available only for this pressure). Potential increase of pressure in the desorber would further improve the capture performance.

5. Conclusions

The optimal design of an amine-based post-combustion CO₂ capture process using a phase-change solvent was presented. The process was modelled using a rigorous, equilibrium-based model, able to accurately represent the underlying physical and chemical phenomena, coupled with the OCFE technique for model size reduction. An aqueous MCA solution was used as a representative phase-change solvent, aiming to investigate the impact of phase-splitting behaviour. Stream redistribution possibilities and a flowsheet that takes advantage of the two liquid phases that are formed, were generated using a generalized process design superstructure. Design optimization results indicate a substantial energy reduction in the reboiler and subsequent reduction in the total annual cost compared with a reference plant operating with a MEA solvent, making phase-change solvents a promising alternative for further investigation.

Acknowledgements

This project has received funding from EU Horizon 2020 program under agreement 727503 - ROLINCAP – H2020-LCE-2016-2017/H2020-LCE-2016-RES-CCS-RIA

References

- N. Dalaouti, P. Seferlis, 2006, *Comput. Chem. Eng.*, 30 (8), 1264–1277.
- T. Damartzis, A. I. Papadopoulos, P. Seferlis, 2014, *Clean Technol. Environ. Policy*, 16(7), 1363–1380.
- T. Damartzis, P. Seferlis, 2010, *Ind. Eng. Chem. Res.*, 49 (7), 3275–3285.
- N., Mac Dowell, Pereira, F.E., Llovel, F., Blas, F.J., Adjiman, C.S., Jackson, G., Galindo, A., 2011, *J. Phys. Chem. B*, 115 (25), 8155–8168.
- B. Huepen, E. Y. Kenig, 2010, *Ind. Eng. Chem. Res.*, 49 (2), 772–779.
- S. Bin Jeon, S. W. Cho, S. S. Lee, 2014, S. Y. Jang, K. J. Oh, *J. Taiwan Inst. Chem. Eng.*, 45(5), 2673–2680
- J. Oexmann, 2011, *Post combustion CO₂ capture: Energetic evaluation of chemical absorption processes in coal fired steam power plants*, PhD Thesis, Tech Universität Hamburg-Harburg.
- D. D. D. Pinto, S. A. H. Zaidy, A. Hartono, 2014, H. F. Svendsen, *Int. J. Greenh. Gas Control*, 28, 318–327.
- L. Raynal, P. A. Bouillon, A. Gomez, P. Broutin, 2011, *Chem. Eng. J.*, 171(3), 742–752.
- J. Rodriguez, N. Mac Dowell, F. Llovel, C. S. Adjiman, G. Jackson, A. Galindo, 2012, *Mol. Phys.*, 110 (11–12), 1325–1348.
- F. Tzirakis, I. Tsivintzelis, A. I. Papadopoulos, P. Seferlis, 2019, *Solubility of CO₂ in methylcyclohexylamine*, *Chem. Eng. Sci.*, 199, 20–27.
- Q. Zhuang, B. Clements, J. Dai, L. Carrigan, 2016, *Int. J. Greenh. Gas Contr.*, 52, 449–460.

Optimization of a hydroformulation process in a thermomorphic solvent system using a commercial steady-state process simulator and a memetic algorithm

Tim Janus^{a,b}, Maximilian Cegla^{a,b}, Sabine Barkmann^b and Sebastian Engell^{a,b}

^aZEDO, Dortmund e.V, Joseph-von-Fraunhofer-Str. 20, 44227 Dortmund, Germany

^bTU Dortmund University - Process Dynamics and Operations, Emil-Figge-Str. 70, 44227 Dortmund, Germany

tim.janus@tu-dortmund.de

Abstract

The economic evaluation of alternative process configurations is an important step in process development. It should be based on optimization to correctly investigate the potential of different process routes and process variants. In many companies, such design studies are performed using block-oriented flowsheet simulators such as Aspen Plus to utilize the extensive model libraries and the ease of model building. We developed an optimization framework that integrates a process simulator (specifically Aspen Plus) with a memetic algorithm (MA). This MA combines an evolution strategy (ES) with derivative-free (DFO) local search methods. The ES addresses the global optimization of all design variables, whereas the DFO method locally optimizes the continuous sub-problems that arise by fixing the discrete variables. In this work, the performance of the memetic algorithm is evaluated for different local methods, involving different DFO methods or the internal equation-oriented optimization engine of Aspen Plus. We discuss the results and the efficiency of the different local methods.

Keywords: Chemical process synthesis, Flowsheet simulation, Aspen Plus, Memetic algorithms, Flowsheet optimization

1. Introduction

Chemical process design in industrial practice is usually done by an interdisciplinary team in an iterative process of comparing the performances and costs of alternative process configurations. In many companies, such design studies are performed using block-oriented flowsheet simulators as e. g. Aspen Plus. The optimization of a chemical process is a challenging task as the models that represent the process units, e. g. a reactor, are in general nonlinear. Discrete decisions like the number of stages and the feed stage of a distillation column enlarge the complexity of the optimization problem. In this case, the optimization of a chemical process is a mixed integer nonlinear program (MINLP). In research usually equation-based models are used (see e. g. Urselmann et al. (2011)). From an industrial perspective this approach has the disadvantage that the extensibility and applicability of the models heavily rely on the experts who created them. Often, as in Waltermann and Skiborowski (2017), a tailor-made initialization procedure is needed to converge the model. In contrast, Aspen Plus offers a large model library and the models are initialized automatically. We therefore investigated the coupling of external process simulators, like Aspen Plus, to optimization methods. The biggest drawback from an optimization perspective is the lack of derivative information in commercial process simulators such that optimization of these flowsheets

is not as efficient as the optimization of equations-based models with mathematical programming. In this contribution we extend the approach of Urselmann and Engell (2015), to include features of Aspen Plus that can utilize derivative information. We demonstrate the performance of our approach for a case study that has been studied extensively in other work.

2. Optimization Method - Memetic Algorithm

The optimization of a chemical process can be mathematically formulated by:

$$\min f(\mathbf{x}, \mathbf{y}, \mathbf{z}) \text{ subject to } g_i(\mathbf{x}, \mathbf{y}, \mathbf{z}) \leq 0$$

A cost function f will be minimized in respect to a set of constraints g_i . The variables are divided in three sets, where \mathbf{x} denotes the discrete design variables, \mathbf{y} the continuous design variables and \mathbf{z} the state variables of the process. \mathbf{x} and \mathbf{y} represent degrees of freedom that are determined by an optimization method and \mathbf{z} represents variables that are calculated by the process simulator and are also used by the cost function.

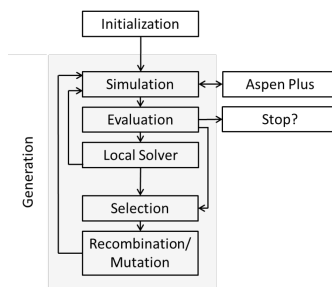


Figure 1: Memetic Algorithm

2.1. Memetic Algorithm

Urselmann et al. (2011) proposed a memetic algorithm to solve MINLPs that formulate an optimization problem for chemical processes. A memetic algorithm is the combination of an evolutionary algorithm, e. g. an evolution strategy (ES), with a local solver (meme). The ES is referred to as the 1st stage and fixes the discrete design variables and provides an initialization of the continuous optimization variables in the NLP problem. The meme solves the NLPs in a more effective manner than the ES and is referred to as the 2nd stage. Figure 1 shows the memetic algorithm. In an initialization step a generation of size μ , i. e. a set of solution candidates, is generated, where the design variables \mathbf{x} and \mathbf{y} are initialized within their bounds by a random uniform distribution. The individuals are simulated by Aspen Plus and then evaluated by the cost function. A meme then computes a local minimum of the continuous sub-problem using Aspen Plus evaluations. After solving the sub-problem for all members of the population the MA is initialized. Then the MA generates a set of λ offspring individuals and evaluates them to select the new μ individuals of the next population. These two steps are repeated until a stop criterion, e. g. the maximum number of function-evaluations, is fulfilled. To generate an offspring, two parents are randomly chosen from the population and act as an input for a recombination operator that generates a new offspring. This offspring is further modified by a mutation operator before it is evaluated.

2.2. Aspen Plus Equation-oriented Mode

Traditionally Aspen Plus uses a sequential modular approach to simulate the flowsheet. Meanwhile, an equation-oriented (EO) mode of Aspen Plus has been implemented which solves the underlying model equations simultaneously. The sequential modular mode is used as an initialization strategy. Aspen Plus supports simulation and optimization in the EO mode. The EO mode distinguishes between calculated and constant types of variables and every variable of the EO mode is initialized by a default type that can be changed. Constant variables are inputs from Aspen Plus, e. g. the reflux ratio. If a constant variable is changed to calculated the underlying equation system becomes over-determined and if a calculated variable is changed to constant it becomes under-determined. Fixing the value for a calculated product purity is permitted if a constant variable, e. g. reflux ratio, is changed to calculated accordingly, such that the equation system is not under-determined. In this way a specification is defined and is realized if the computations

are successful. The EO mode supports an internal local optimizer which has access to derivatives. Variables are marked as degrees of freedom and a cost function is defined in EO mode optimization. The drawback of the internal optimizer is that it does not support arbitrary cost functions, due to technical limitations. In this work we extend the MA by two local solvers, which exploit the EO mode of Aspen Plus. The first meme uses the EO mode simulation to realize specifications and the second meme applies the Aspen Plus internal optimizer to perform a local optimization of an approximated cost function.

3. Flowsheet Optimization of the Hydroformulation of 1-Dodecene

As a case study, the homogeneously catalyzed hydroformulation of 1-dodecene in a thermomorphic solvent system (TMS) is investigated. This case study has been investigated by various groups within the TR SFB Inprompt. Steimel and Engell (2016) optimized this case study based on a simpler model and cost function using an equation-oriented model. The process consists of a reaction step, a decanter and a distillation column, two recycles and includes complex kinetics (Kiedorf et al. (2014)) and uses liquid-liquid separation modelled according to (Merchan and Wozny (2016)) to recover the expensive homogeneous rhodium-based catalyst from the reaction mixture. Due to the coupling of the separation units with the reactor a simple objective function as e. g. the selectivity of the reaction is not sufficient (see Hentschel et al. (2014)). A data-based model describing the catalyst loss is employed, since this loss greatly influences the overall costs.

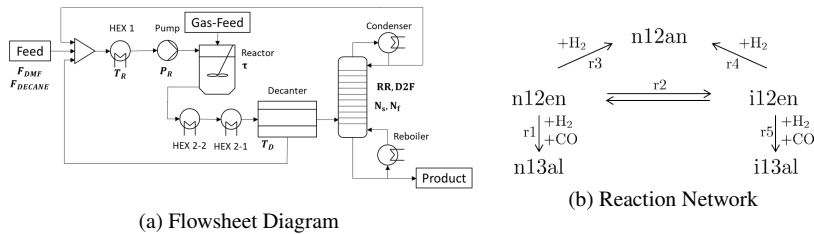


Figure 2: TMS model with DoFs and Specifications

3.1. The Aspen Plus Flowsheet

Figure 2a illustrates the Aspen Plus flowsheet that represents the process. The degrees of freedom are highlighted in bold. The feed flows of the reactant dodecene and the solvents decane and DMF flow are pre-heated and pressurized. The optimizer can change the solvent ratio by adapting F_{DMF} and F_{DECANE} , the residence time τ , the temperature T_R and the pressure P_R to alter the performance of the reaction, in which 1-dodecene reacts to tridecanal. The basic scheme of the reaction network is shown in Figure 2b and is implemented in Aspen Plus. The reacted mixture is cooled down by two heat-exchangers. The first heat exchanger is operated with cooling water and the second heat exchanger is either operated with ammonia or with cooling water depending on the decanter temperature T_E , which is varied by the optimizer. The decanter uses the miscibility gap of the mixture at lower temperature to separate it in a polar phase that contains the catalyst and an unpolar phase that contains the product containing both tridecanal isomers. The polar phase is recycled back to the reactor and the unpolar phase is further purified in a distillation column. The optimizer varies the stage count N_s , the feed position N_f , the distillate to feed ratio $D2F$ and the reflux ratio RR of the column.

Table 2: Variants of Memetic Algorithm

Name	Local Solver	Avg. Costs	Best Costs	Best Purity	Fails
ES-SPECS	EO Sim.	3443 ± 4.76 € / T	3439 € / T	99.00 %	37.6 ± 1.7 %
ES-CATOPT	EO Opt.	3449 ± 3.05 € / T	3445 € / T	99.18 %	26.6 ± 2.5 %
ES	None	3506 ± 5.23 € / T	3500 € / T	99.40 %	27.7 ± 4.0 %
ES-NOMAD	NOMAD	3594 ± 40.6 € / T	3549 € / T	99.49 %	6.1 ± 0.7 %
ES-CMAES	CMAES	3728 ± 217 € / T	3554 € / T	99.43 %	17.5 ± 1.6 %

3.2. Catalyst Loss and Cost Estimation

Our approach supports the definition of arbitrary cost functions. Here the cost function is an indicator of the costs per ton of product depending on the amount of catalyst loss:

$$f(\mathbf{x}, \mathbf{y}, \mathbf{z}) = \frac{C_{OU} + C_{Mat}}{8000 \cdot \dot{m}_{Product}} + Penalty$$

With $C_{Mat} = C_{Raw} + C_{Cat} + C_{Makeup}$ and C_{OU} equals the sum of the capital and utility costs of every operation unit, as proposed by Turton et al. (2008). The capital costs are pressure dependent, e. g. a reactor operated by a pressure of thirty bar instead of twenty raises the capital costs by approximately 45 %. We fitted a 2nd order polynomial model to describe the catalyst loss based on the temperature and solvent data measured by Brunsch and Behr (2013). The catalyst loss is represented by:

$$Loss = (a \cdot DMF_p^2 + b_1 \cdot DMF_p + c_1) \cdot (b_2 \cdot T + c_2)$$

Table 1: Model Parameters

a	0.00112
b_1	-0.1743
c_1	6.9086
b_2	0.2033
c_2	1.7474

where the parameters are defined in Table 1. T represents the temperature in the decanter and DMF_p represents the fraction of DMF of the solvent. With this loss term the costs for catalyst loss regarding the volume flow \dot{V}_F of the decanter is calculated by $C_{Cat}(\dot{V}_F) = \dot{V}_F \cdot Loss \cdot C_{Rhodium}$. The penalty term of the form $Penalty = 4000 + v \cdot 10000$ is used to penalize the constraint violation. Here v represents the constraint violation in molar fraction of the tridencanal purity in the bottom flow of the distillation column.

4. Optimization Results

The optimization problem contains 10 design variables (see Table 3). The purity of the sum of iso- and n-tridencanal is specified as 99 mol % in the bottom stream of the distillation column. We compare the results of several variants of the MA, which are summarized in Table 2. The parameters for the ES are $\mu = 10$ (generation-size), $\lambda = 20$ (number of offsprings) and $\kappa = 5$ (maximum age of an individual) which have been determined in previous studies as a robust setting for a range of problems. We compare the performance of a traditional ES with four MA variants that differ in their meme, i. e.

Table 3: Boundaries of Design Variables

Variable	Unit	Lower	Upper	BFS
T_R	[C°]	80	120	111.34
P_R	[bar]	15	30	23.06
τ	[h]	0.1	5	4.49
T_E	[C°]	-5	25	-5
N_s	unitless	4	40	27
N_f	unitless	2	dynamic	6
$D2F$	unitless	0.6	0.95	0.61
RR	unitless	0.1	15	0.17
F_{dmf}	[kmol/h]	20	100	81.44
F_{dode}	[kmol/h]	20	100	20.76

we test four different local optimization strategies. The Aspen Plus equation-oriented (EO) optimization and the EO simulation represent two memes. The former minimizes the catalyst loss and the latter fixes the tridecanal specification. The derivative free methods (DFO), covariance matrix evolution strategy (CMAES) and the solver NOMAD represent the other two memes. These performed best from a set of DFO methods which have been compared by Urselmann et al. (2016) for water-ethanol-benzene separation case study.

4.1. Cost Distribution

The best found solution (BFS) is shown in Table 3 which has the cost distribution shown in Figure 4. The raw material costs have the biggest impact on the cost. The heat exchangers and the column cause the main equipment costs. The catalyst and solvent makeup costs are only a small fraction of the entire costs of the BFS. The HEX2-1 may use ammonia if the target temperature is below 5 C° and this increases the costs considerably. Nonetheless, the optimizer chooses a decanter temperature of -5 C° because the cost of using ammonia is compensated by the reduction of catalyst loss. The high fraction of DMF in the solvent is also chosen by the optimizer to reduce the loss of catalyst. The design parameters of the reactor are chosen such that there is a good trade-off between selectivity and conversion to reduce the size of the recycle. The high influence of the pressure on the capital costs of the reactor causes the pressure to be below the upper bound.

4.2. Convergence Behavior and Runtime

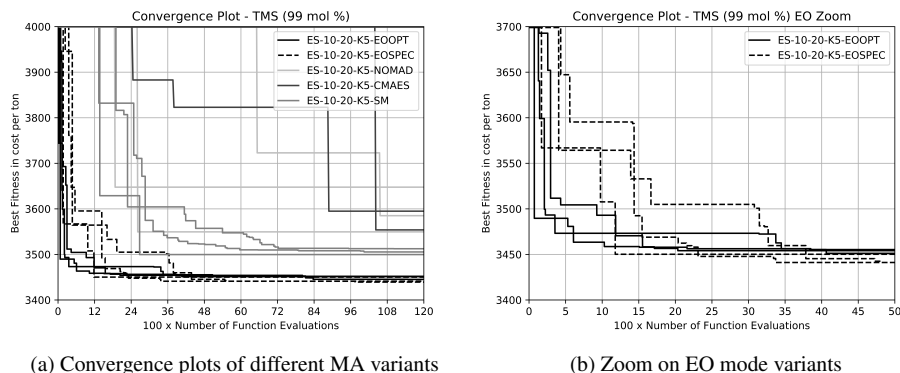


Figure 3: Convergence Plots of three runs of different MA variants

Figure 3 shows the convergence of three runs for each MA variant, i. e. lines of the same type represent different runs of the MA variant that is identified in the legend. Table 2 shows the average and best costs, the best purity and the average percentage of failed simulations and is ordered ascending by costs.

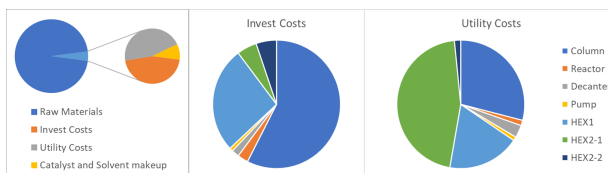


Figure 4: Cost Distribution of Optimal Solution

The memes using Aspen Plus features perform best, as they can access derivatives. All the Aspen Plus meme variants found an optimum that is closer than one percent to the optimal solution after 40 % of the optimization time, i. e. after 4.800 function evaluations which are processed in ten hours on a i7-4790S CPU with 3.20 GHZ. Here 99 % of the time is spent in the Aspen Plus

simulation which is solved in 8.4 seconds on average. The best found solution was detected by the variant that fixes the specification, since a distillation column that operates at a high purity is more expensive. Nonetheless the optimization of the catalyst loss with Aspen Plus leads to a faster convergence in the early stage of the optimization. Although the variants that use DFO methods fail less, the ES variant that does not make use of a local optimization performs better than the DFO variants. This means that the function evaluations used by the DFO methods are not worth the effort. At least at the early stages of the optimization, i. e. using these function evaluations in the ES leads to a faster convergence. Both variants ES and ES-CATOPT fail approximately in 27 % of the simulations. However the ES-SPECS variant fails 10 % more often such that the fraction of failed simulation is traded for a solution that fulfills the specification accurately.

5. Conclusion

Based on the case study of the hydroformylation of 1-dodecene into tridecanal we showed that the new implemented memes that use the equation-oriented (EO) mode of Aspen Plus and therefore utilize derivative information speed up the convergence. As long as the derivative information is not accessible by external tools, the benefit of the ease of modeling larger processes using a process simulator is traded for significantly higher computation times of the optimization. For the example it turned out that in general a MA that uses a derivative-free method (DFO) as a local solver does not outperform a pure evolution strategy with respect to speed of convergence. We therefore propose that a DFO based local optimization should only be performed in the later stages of the optimization.

Acknowledgements

This work is part of the Collaborative Research Centre Integrated Chemical Processes in Liquid Multiphase Systems. Financial support from the Deutsche Forschungsgemeinschaft (DFG) is gratefully acknowledged through TRR 63. The financial support by the German Federal Ministry of Education and Research for the research project SuperOpt (01LY1614) is gratefully acknowledged. The responsibility for the contents rests with the authors.

References

- Y. Brunsch, A. Behr, 2013. Temperature-controlled catalyst recycling in homogeneous transition-metal catalysis : Minimization of catalyst leaching. *Angewandte Chemie - International Edition* 52, 1586–1589.
- B. Hentschel, A. Peschel, H. Freund, K. Sundmacher, 2014. Simultaneous design of the optimal reaction and process concept for multiphase systems. *Chemical Engineering Science* 115, 69–87.
- G. Kiedorf, D. Hoang, A. Miller, A. Jrke, J. Markert, H. Arellano-Garcia, A. Seidel-Morgenstern, C. Hamel, 2014. Kinetics of 1-dodecene hydroformylation in a thermomorphic solvent system using a rhodium-biphephos catalyst. *Chemical Engineering Science* 115, 31 – 48.
- V. A. Merchan, G. Wozny, 2016. Comparative evaluation of rigorous thermodynamic models for the description of the hydroformylation of 1-dodecene in a thermomorphic solvent system. *Industrial & Engineering Chemistry Research* 55 (1), 293–310.
- J. Steimel, S. Engell, 2016. Optimization-based support for process design under uncertainty: A case study. *AIChE Journal* 62 (9), 3404–3419.
- R. Turton, R. C. Bailie, W. B. Whiting, J. A. Shaeiwitz, 2008. *Analysis, synthesis and design of chemical processes*. Pearson Education.
- M. Urselmann, S. Barkmann, G. Sand, S. Engell, 2011. A memetic algorithm for global optimization in chemical process synthesis problems. *IEEE Transactions on Evolutionary Computation* 15 (5), 659–683.
- M. Urselmann, S. Engell, 2015. Design of memetic algorithms for the efficient optimization of chemical process synthesis problems with structural restrictions. *Computers and Chemical Engineering* 72, 87–108.
- M. Urselmann, C. Foussette, T. Janus, S. Tlatlik, A. Gottschalk, M. T. Emmerich, S. Engell, T. Bäck, 2016. Selection of a DFO Method for the Efficient Solution of Continuous Constrained Sub-Problems within a Memetic Algorithm for Chemical Process Synthesis. *Proceedings of the GECCO Conference 2016*, 1029–1036.
- T. Waltermann, M. Skiborowski, 2017. Conceptual Design of Highly Integrated Processes Optimization of Dividing Wall Columns. *Chemie Ingenieur Technik - Special Issue Prozess Optimierung* 89 (5), 562–581.

Exergy analysis for energy integration in a bioethanol production process to determine heat exchanger networks feasibility

J. Cristóbal García-García^a, Jaime D. Ponce-Rocha^b, Danahe Marmolejo-Correa^{c,d}, Ricardo Morales-Rodríguez^{b*}

^a *División de Ciencias e Ingenierías Universidad de Guanajuato, Loma del Bosque 103, León, Guanajuato. 37150, México.*

^b *Departamento de Ingeniería Química, División de Ciencias Naturales y Exactas, Universidad de Guanajuato, Noria Alta S/N, Guanajuato, Gto. 36050, México.*

^c *College of Sciences and Arts, Maryville University, 350 Maryville University Drive, St. Louis, Missouri, 63141, USA*

^d *Department of Engineering, St. Charles Community College, 4601 Mid Rivers Mall Drive, Cottleville, Missouri, 63376, USA*

ricardo.morales@ugto.mx

Abstract

In this study, Exergy Analysis (EA) and Energy Integration (EI) analyses are employed as decision factors to select the best heat exchanger network (HEN) configuration and applied to improve a bioethanol production process plant by evaluating its irreversibilities. The results of EI and EA reveal that the HEN configuration A6 allows to obtain a value of rational efficiency for the process of 87.88 % (an increasing of 12.33 % respect to base case scenario) by a diminution of the process irreversibilities of 28.85 MW. With this HEN configuration, the equipment cost increases by \$158,432.57 with a decrease on services cost of 750,615.06 \$/year, obtaining an energy saving of 21.37 MW.

Keywords: Exergy, Energy Integration, Bioethanol production

1. Introduction

The world is starting to face energy resources depletion and non-renewable resources are the most employed as a fuel in the auto transport sector. The use of non-renewable resources has also showed negative environmental consequences for some decades, which has been catalogued as one of the main global problems that the nations aim to solve, figuring in the list of Sustainable Development Goals that might be reached in 2030 (United Nations General Assembly, 2015). Thus, different alternatives to minimize the negative effects are being evaluated, among them it is the use of alternative fuels such as bioethanol. Bioethanol is an organic biofuel that is obtained from lignocellulosic biomass, a renewable substrate that through a process of numerous unit operations could be converted in an ethanol solution with high purity grade. The second-generation bioethanol production process has begun to be commercially feasible, however, improvements in the process performance are still necessary to reduce production cost.

EA is useful to evaluate thermodynamic efficiency of chemical processes by the calculation of its irreversibilities. EI is a tool that allows development and analysis of several HEN configurations that seeks energy benefits by exchanging the available energy between process streams that may contribute in the reduction of the total cost of the process. Usually, the cost of the process is considered a performance criterion for selection of the best HEN, leaving apart the thermodynamic criteria for the best HEN selection. Therefore, the objective of this work is employing these two tools to design and evaluate HEN configurations in a bioethanol production process, aiming to reduce energy consumption and determine thermodynamic efficiency by using a computer-aided based approach.

2. Exergy Analysis

Exergy is the maximum theoretical work obtainable from a given thermodynamic state when this reaches thermo-mechanical and chemical equilibrium with a reference state on environmental conditions entering in a state called “dead state” (Kotas, 1995). In open systems, exergy content can be classified by its origin: a) exergy accompanying energy flows and b) exergy accompanying material flows. In material flows, excluding kinetic, potential, nuclear and electromagnetics effects, exergy can be then divided into: thermo-mechanical or physical exergy and chemical exergy (Marmolejo-Correa and Gundersen, 2015).

Thermo-mechanical exergy in Eq. (1) is defined by differences in enthalpy ($h-h_0$) and entropy ($s-s_0$) from the current conditions of the system (T, P) to the ambient conditions (T_0, P_0), where T and P stand for temperature and pressure, respectively. Chemical exergy for a non-ideal mixture is shown in Eq. (2), where x_i are the mole fractions, ε_i are the standard chemical exergy and γ_i are the activity coefficient of each component. The irreversibility rate (I) in bioethanol production plant is calculated developing an exergy balance as shown in Eq. (3), where, E_i and E_o are the net exergy rates entering and leaving the system, respectively. ΣE^Q is the net exergy flow accompanying the energy entering in heat exchangers and leaving in coolers, and, ΣE^W is the net exergy flow accompanying the work applied to process. The rational efficiency is a measure of the process performance and is defined by Kotas (1995) as it is illustrated in Eq. (4), this is a relation between useful exergy in the products and exergy driven to the system.

$$e^{ph} = h - h_0 - T_0(s - s_0) \quad (1)$$

$$e^{ch} = \sum_{i=1}^n \varepsilon_i^0 x_i + \sum_{i=1}^n x_i \ln x_i \gamma_i \quad (2)$$

$$I = E_i - E_o + \Sigma E^Q + \Sigma E^W \quad (3)$$

$$\psi = 1 - I / \Delta E_i \quad (4)$$

EA has been previously applied in bioethanol production processes, reporting overall analyses to the complete process configurations (Ojeda et al., 2011; Silva Ortiz and de Oliveira Jr, 2014, Zeineb et al., 2018). However, these studies simulate the process employing other feedstocks and in some cases the papers do not include an EI analysis.

Regarding to exergy calculation, the simulation software employed in this work provides the calculation of physical exergy, but it is necessary to calculate the chemical exergy, in order to obtain the net exergy that material flows contain. Therefore, the usage of computational tools linked to the simulator is a useful strategy. The methodology applied to link the computer-aided tools was already described in a previous work (García-García et al, 2018), thus, it was possible to obtain the exergy balances stage by stage and in overall plant in the bioethanol production process studied.

3. Energy Integration

The EI task relies on proposing several configurations of heat exchanger networks with the aim of minimizing the utility consumption, employing as a performance criterion to determine the best configuration the energy savings, total costs and heat exchangers areas. The EI could be achieved employing the pinch analysis, which provides a systematic methodology for energy saving in process and total sites heat integration (Goodarzvand-Chegini and GhasemiKafrudi, 2017). The exergy analysis has been successfully employed for the EI in previous studies, for example, Janka, A. et al (2018) employed this methodology to evaluate the energy integration in distillation technologies focusing on dividing-wall columns. Goodarzvand-Chegini and GhasemiKafrudi (2017) developed an exergy analysis to improve the heat integration efficiency in a hydrocracking process. On the other hand, Staine and Favrat (1996) proposed a pinch analysis method extended to include exergy factors in the process. The state of the art does not show this type of thermodynamic and process design approach for bio-based production processes, for example for bioethanol production, which is divided in diverse stages and includes several unit operations that need and release energy. Therefore, this work employs the exergy analysis as a performance criterion to select the best HEN obtained by a pinch analysis on a bioethanol production process, the selection also considers the lowest cost on services and equipment.

4. Bioethanol Production Process

The second-generation bioethanol production plant was simulated employing the Aspen Plus v. 8.8 process simulator and divided into six stages: pretreatment, overliming, saccharification, fermentation, separation and waste treatment. The data for the equipment and initial conditions of the streams was taken from (Sánchez et al., 2013). The process simulation was carried out taking wheat straw as raw material with a mass flowrate of 7,752.13 kg/h with composition in mole fraction of 0.47 of water, 0.34 of cellulose, 0.15 of xylan, 0.05 of lignin and traces of ash. In the saccharification section, the cellulose that cannot be dehydrated during the pretreatment section is converted into glucose, with the help of enzymes that favour its reaction. During fermentation the fermentable sugars present in the stream are converted into ethanol by *Zymomonas mobilis*. The separation stage employs a system of sequential distillation columns that allows obtaining high-purity ethanol that can be used as biofuel. Finally, in the waste treatment stage, the residual streams are conducted to biological treatment where three streams are obtained: residual solids, biogas and treated water. The Figure 1 shows a bioethanol process diagram, the streams labelled with points indicate the entering and exit streams using blue and red points, respectively. It is important pointing out these streams are used in the exergy analysis lately.

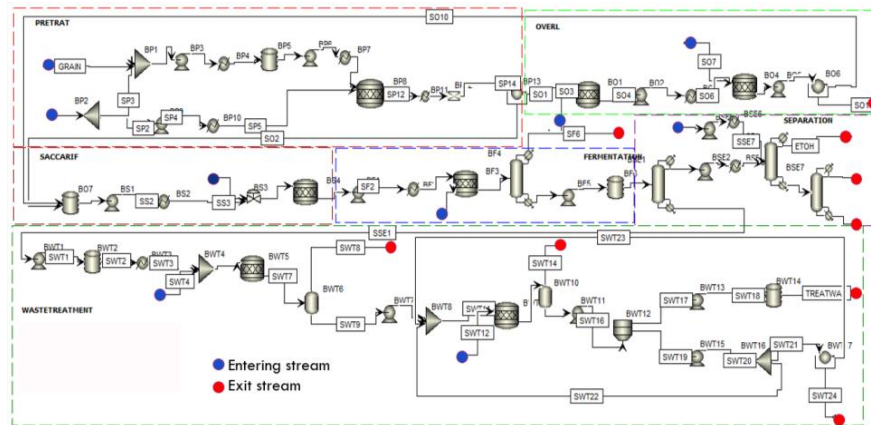


Figure 1. Bioethanol production process diagram

5. Results

The methodology proposed by García-García et al. (2018) was used in this study for calculating the irreversibility rate and rational efficiency, and the previous results were used as the base case scenario. The results of thermal exergy in streams are shown in Table 1. The EI analysis was performed employing the computational tool HINT (Martin and Mato, 2008).

Six HEN configurations were designed and analysed (Table 2). The energy integration and exergy analysis considered the usage of direct flame, high, middle and low pressures steams as heating utilities, and cooling water and Freon as cooling utilities. In Table 2 could be observed that the equipment cost increased in all proposed configurations, due to the number of heat exchangers; in base case scenario the number of heat exchangers were 18 while in all the proposed configurations were 23. It can be also observed that the configurations allow a decrease in the utilities cost in all configurations with energy savings of 21.37 MW, that in fact it was equal in all configurations. Employing only this information obtained from EI analysis was difficult to select the best configurations, because the results are very similar. However, the use of exergy analysis results provided an important and additional information that allowed making a better selection of the best HEN option. Table 2 also shows that the rational efficiency was improved by the selection of any of the proposed HEN, but it was more effectively improved with the configurations A1 or A6 that represents the higher rational efficiency. Comparing the results of energy integration and exergy analyses was possible to select the configuration A6 as the best because improved in 12.10 % the rational efficiency and represents one of the minimum equipment cost in the configurations constructed (US\$ 158,432.56).

The minimum energy requirements for configuration A6 are shown in form of a heat cascade (see Figure 2).

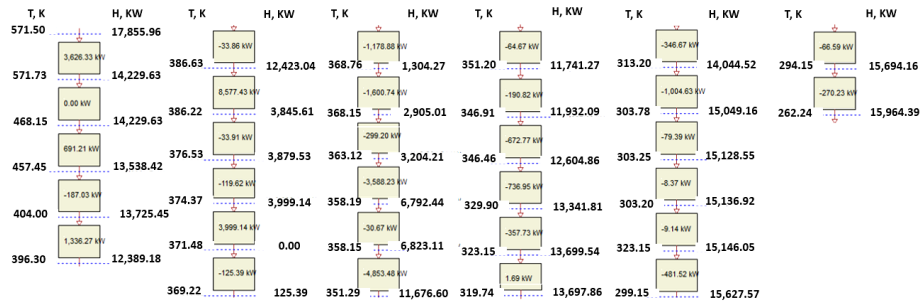


Figure 2. Cascade diagram to determine the energy requirements in scenario A6

Table 1. Exergy of streams that entering and leaving the production process

Category	Stream	e^{ph} , MW	e^{ch} , MW	$e^{ph} + e^{ch}$, MW
Inlets	GRAIN	0.000	23,293.067	23,293.067
	SP1	0.000	2,425.025	2,425.025
	SO3	0.000	136.798	136.798
	SO7	0.216	48.916	49.132
	SS4	0.000	183.514	183.514
	SF4	0.000	138.666	138.666
	SSE5	0.000	50,021.701	50,021.701
	SWT4	0.000	22.033	22.033
	SWT12	0.000	5.873	5.873
Outlets	SO11	0.218	324.830	325.066
	SF6	0.717	343.591	344.308
	SSE10	489.309	50,018.981	50,508.290
	SSE11	29.081	138.182	167.263
	ETOH	7.955	15,170.858	15,178.813
	SWT8	0.010	204.708	204.719
	SWT14	0.678	0.000	0.678
	TREATW	7.734	2,654.332	2,662.066
SWT24	0.731	11,665.444	11,667.171	

Table 2. Results of EI and Exergy analysis

Configuration	Equipment cost, US\$	Utilities cost, US\$/year	Rational efficiency, %	Irreversibility, MW	Energy Saving, MW
Base case	225,151.88	1,715,486.19	75.55	44.76	0
A1	457,430.13	964,871.13	87.88	15.91	21.37
A2	383,584.45	964,871.13	83.96	21.06	21.37
A3	385,959.90	964,870.46	83.76	21.33	21.37
A4	388,128.80	964,870.48	83.55	21.42	21.37
A5	387,922.24	964,871.13	83.88	21.15	21.37
A6	383,584.45	964,870.47	87.65	16.22	21.37

Conclusions

The results reveal that without EI and employing utilities to cover the total energy requirements the rational efficiency and total irreversibility of the process are 19.92% and 68,187.75 KW, respectively. Employing the energy integration and exergy analysis was found that the configuration A6 represent the better option to improve the process performance with a rational efficiency value of 87.65%, total irreversibility of 16.22 MW and savings energy of 21.37 MW. The implementation of both, EI and exergy analysis demonstrates to be a useful methodology to determine the best HEN configuration in accordance with the energy savings and thermodynamic feasibility.

Acknowledgments

The authors acknowledge the partial financial support by the Mexican Bioenergy Innovation Centre, Bioalcohols Cluster (249564) and the Universidad de Guanajuato for the development of this project.

References

- C. García-García, D. Marmolejo-Correa, J. Cárdenas-Guerra, R. Morales-Rodríguez, 2018, Exergy Analysis of an Extractive Distillation Column for Reducing Energy Consumption in a Bioethanol Production Process, *Computer-Aided Chemical Engineering*, 43, p. 513-518.
- F. Goodarzvand-Chegini and E. GhasemiKafrudi, 2017, Application of exergy analysis to improve the heat integration efficiency in a hydrocracking process, *Energy and Environment*, pp. 1-16.
- A. Janka, T. Nagy, A. Toth, E. Haaz, 2018, Thermodynamic and Exergy Analysis of Energy-Integrated Distillation Technologies Focusing on Dividing-Wall Columns with Upper and Lower Partitions, *Industrial and Engineering Chemistry Research*.
- T.J. Kotas, 1995, *The Exergy Method of Thermal Plant Analysis*, Elsevier.
- D. Marmolejo-Correa and T. Gundersen, 2015, A new efficiency parameter for exergy analysis in low temperature processes, *International Journal of Exergy*, 17, pp. 135-170.
- A. Martín and F. A. Mato, Hint: An educational software for heat exchanger network design with the pinch method, *Education for chemical engineers*, Vol. 3, pp 6-14, 2008.
- K. Ojeda, E. Sánchez and V. Kafarov, 2011, Sustainable ethanol production from lignocellulosic biomass - application of exergy analysis. *Energy*, 36, pp. 2119-2128
- A. Sánchez, V. Sevilla-Güitrón, G. Magaña and L. Gutierrez, 2013, Parametric analysis of total cost and energy efficiency of 2G enzymatic ethanol production. *Fuel*, 113, pp. 165-179
- P. Silva Ortiz and S. de Oliveira Jr., 2014, Exergy analysis of pretreatment processes of bioethanol production based on sugarcane bagasse, *Energy*, 76, pp. 130-138.
- F. Staine and D. Favrat, 1996, Energy integration of industrial processes based on the PINCH analysis method extended to include exergy factors, *Applied Thermal Engineering*, Vol.16, No.6, pp 497-507.
- United Nations General Assembly, 2015, Session 70th
- W. Zeineb, K. Zouhour, L. Boulbaba, B. Rachid, H. Noureddine, 2018, Exergetic Analysis of Bioethanol Production from Tunisian Waste Dates, *The Open Waste Management Journal*, pp. 19-32.

ProCAFD: Computer-aided Tool for Sustainable Process Synthesis, Intensification and Hybrid solutions

Anjan K.Tula^a, Mario R. Eden^a, Rafiqul Gani^{b*}

^a *Department of Chemical Engineering, Auburn University, Auburn, AL 36849, USA*

^b *PSE for SPEED, Skyttemosen 6, Allerød, DK-3450, Denmark*

rgani2018@gmail.com

Abstract

Process industry is always in quest for innovative designs which are both efficient, safe and sustainable. The feasible search space of all unit operations that can be combined to generate process flowsheet alternatives for a given synthesis problem can be large and difficult to manually navigate in order to determine the best processing route. Therefore, it is helpful to utilize computer-aided methods and tools to enumerate, analyze and determine within the design space, the more sustainable processes. In this paper, an integrated computer-aided method and corresponding software-tool that's capable of generating and searching the entire design space for more sustainable process options is presented. In this work a comprehensive analysis method consisting of economic, life cycle, sustainability and process safety indicators is used to identify process bottlenecks on the selected alternative which are translated to design targets. Matching of these design targets minimizes/eliminates the process hot-spots and, thereby generating non-trade-off innovative process designs.

Keywords: Process synthesis, ProCAFD, Process Optimization, Process Safety.

1. Introduction

Due to increased emphasis by governments concerning environment, public health and safety through regulatory enforcements and growing competitiveness through globalization, the process industry is moving towards the design of innovative, more sustainable processes. Since synthesis problems are by nature combinatorial and open ended, several approaches have been proposed, these approaches can be broadly classified into three main classes of methods. (1) Rule based heuristic methods, which rely on rules based on a combination of experience, insights and engineering knowledge (data) to solve the synthesis problem; (2) Mathematical programming-based methods, where the best flowsheet alternative is determined from network superstructure optimization. This approach requires one to define and represent the network of alternatives in a mathematical form and solve the resulting mathematical problem using suitable solvers. (3) Hybrid methods that combines different approaches to solve the synthesis problem. Simultaneous based process synthesis approaches require the generation of a superstructure which contains a finite number of processing units with their corresponding interconnections. The resulting superstructure is solved by, using equations that describe the equipment, connectivity together with the process constraints and specifications. Even though it is advantageous to perform simultaneous optimization of the flowsheet structure and operating conditions there are few limitations. The major limitations of this approach are that the solution of the synthesis

problem heavily depends on the superstructure of the alternatives considered. So, in order to find the optimal process topology, the original search space should constitute the optimal pathway. Also, since the process synthesis problem is by default nonlinear in nature, the solution to such optimization problem is difficult. Since applying only knowledge-based methods or optimization-based methods often over simplifies or complicates the process synthesis problem, a more logical way is to use hybrid methods where we can leverage the advantages of the two approaches while still keeping the complexity of the synthesis problem manageable. his work focuses on the development of hybrid method and computer aided software tool (ProCAFD) capable of enumerating all feasible alternatives within the entire search space and efficiently evaluate them. This work also focuses on introducing new analysis methods related to process safety along with economic, sustainability, and life cycle assessments during selection of process alternatives. This paper also shows successful application of ProCAFD on different case studies where different options are highlighted such as generation of integrated/hybrid/intensified configurations based on problem formulation.

2. ProCAFD architecture based on 3-stage Framework for Innovation

An overview of the 12-step method, which is an extension of the synthesis method proposed by Tula et al. (2015), is presented in Figure 1. The method is based on 3 stage approach for innovation proposed by Babi et al. (2015). Brief overview of the steps involved in the method are given below:

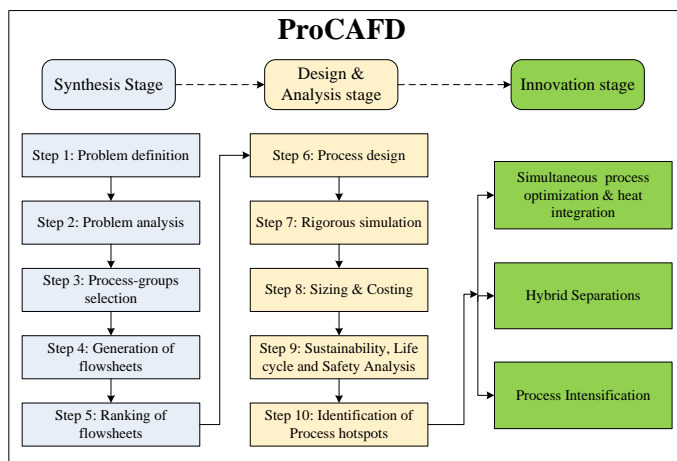


Figure 1: Sustainable process synthesis–design and analysis method (in ProCAFD)

Problem Definition: In this step the synthesis problem is defined along with process specifications, design constraints and performance criteria against which the generated alternatives are screened.

Problem Analysis: In this step, analysis is done to generate information through use of knowledge bases and physical insights methods to solve the synthesis. The outcome of this analysis includes, i) List of all chemical species in the synthesis problem, including

reaction intermediates and/or any mass transfer agents, ii) Reactions, if needed, to convert the given raw materials to desired products, iii) List of all the possible separation tasks along with feasible separation techniques.

Process-groups selection: The selection and initialization of the process groups is based on analysis carried in step 2. This is carried out in three tasks: i) selection and initialization of inlet and outlet process-groups, (based on step 1 information) ii) selection and initialization of reaction process-groups, and iii) selection and initialization of separation process-groups.

Generation of Flowsheets: In this step, the initialized process-groups are combined using connectivity and logical rules to generate structurally feasible process alternatives. These rules also safeguard against any combinatorial explosion that is generally associated with generate and test approaches.

Ranking of Flowsheets: In this step, different flowsheet property models are used to calculate flowsheet properties which are used to screen and rank the generated alternatives. The flowsheet property models are based on a group contribution (GC) approach, where the property of the entire flowsheet is estimated using contributions of individual process-groups present. Flowsheet models are available for carbon footprint, energy consumption, product recovery and, product purity

Process Design: Operational design parameters of the selected process alternative(s) are calculated in this step. This is achieved through the following two tasks: i) the resolution of the mass and energy balance, and ii) calculation of flowsheet design parameters of the process unit operations in the flowsheet structure through reverse simulation. The separation factors and temperature data required for performing mass and energy balance are obtained from the process-group definitions and driving force available. Design parameters for separation process-groups (such as distillation, extractive distillation, and flash), are estimated based on the driving force (DF), while attainable region theory is used to design reactor networks.

Rigorous Simulation: ProCAFD is integrated with commercial simulators like PROII, ASPEN where the design is automatically setup using rigorous models to verify performance of the selected alternatives.

Sizing & Costing: In this step, equipment sizing, and costing calculations are performed for all equipment in the process flowsheet. The sizing and costing values are estimated using ECON (Kalakul et al. 2014).

Analysis: The results of the rigorous simulation, sizing and costing (stream summary, equipment sizing, energy balance etc.) are used to perform economic, safety, sustainability and life cycle analyses.

- *Economic Analysis:* The mass and energy balance results from the rigorous simulation are used to calculate the capital and utility costs for each unit operation which are used to identify hotspots involving high operational and capital costs.
- *Sustainability Analysis:* This analysis is based on an indicator-based methodology (Carvalho et al., 2013), which identifies critical flow paths within the process. Here analysis is done on both open (where a chemical species enters and leaves the process) and closed paths (like recycle loops where mass and energy are recycled without going out of the process). The main indicators, which are estimated, include material value added (MVA), energy and waste cost (EWC), total value added (TVA).
- *Life Cycle Analysis:* This analysis is used for environmental assessment of the selected process alternative. This is carried out through LCSOFT (Kalakul et al. 2014) that helps to quantify potential environmental impacts of chemical process. The main factors which are estimated in this analysis are Carbon Footprint (CF),

Human Toxicity Potential by Ingestion (HTPI), Human Toxicity Potential by Exposure (HTPE) and Global Warming Potential (GWP).

- *Process Safety Analysis*: This analysis is based on Dow's (1987) scoring system to estimate the inherent safety of the process alternative. This method considers different aspects like process conditions, chemicals involved, and equipment types etc. to identify different hazards in the plant. The total inherent safety index is a combined score of chemical inherent safety and process inherent safety. While the chemical inherent safety index considers reactions hazards and chemical hazards; process inherent safety index takes process and equipment conditions

Identification of Hotspots: The indicators from the analysis step are used to identify the process hotspots (Babi et al., 2015), which are in turn used to set design targets for overall process improvement

Innovative Designs: In this step, different strategies/methods are applied individually to the selected alternative to target the hot-spots for overall process improvement.

- *Simultaneous Process Optimization and Heat Integration*: Simultaneous process optimization and heat integration approach is applied to the analyzed base case design, to target process hot-spots involving high operational costs. In this approach, rigorous models from the process simulator are used to calculate the process inputs, which are sent to an integrated heat integration module to estimate the minimum utility requirements. Both module results are used in the optimizer to minimize the total utility of the process. In this method, the heat integration module is based on the condensed LP transshipment model for calculating the minimum utility consumption.
- *Hybrid Separations*: A generalized method based on Tula et al. (2016) for synthesis-design of hybrid distillation-membrane systems is applied to replace the distillation columns in the base case design with a hybrid system to reduce the operational cost substantially. Tula et al. (2016) showed that 30-50 % of energy savings can be achieved for any distillation column by replacing the less efficient region of the distillation operation with membrane based separation technique.
- *Process Intensification*: Phenomena based intensification method proposed by Babi et al. (2015) is applied in this step. This approach breaks tasks into phenomena within the unit operations involved. These phenomena are analyzed and re-combined using combination rules to generate new and/or existing unit operations that constitute the (more sustainable) flowsheet alternatives which satisfy the set design targets.

Case Study

2.1. Synthesis stage:

The synthesis problem definition is to develop an energy efficient process to produce cumene from propylene and benzene. This reaction is exothermic and typical operating conditions are 600 K at atmospheric pressure. In this problem definition, the propylene stream has propane as impurity. As a process specification, the minimum purity of cumene should be 99.5 wt%. A total of 10 binary pairs are formed from 5 compounds present in the synthesis problem. For this synthesis problem, a total 155 process-groups are selected and initialized, which include 148 separation tasks process groups, 6 inlet/outlet process groups and 1 reaction process group. A total of 240 process

alternatives are identified, and the best alternative with respect to energy consumption is shown in Figure 2. The objective from the problem definition step is to find an energy efficient process so, energy consumption property model is used in this case study. Different flowsheet models can be used to screen the alternatives based on the problem definition.

2.2. Design & Analysis stage:

In this stage the selected process alternative (Figure 2) is designed and simulated using rigorous models. Based on the simulation results economic, safety, sustainability and life cycle analyses are performed on the base case. From economic analysis the heat exchangers on the recycles streams (HE3, HE5) along with HE4 share 57% of total equipment cost and 42% of the total utility cost. These results are also complemented by sustainability analysis, which showed a high energy and waste cost (EWC) associated with closed path 3 and loss of material (MVA) for propylene in open path 5. Life cycle analysis showed high carbon footprint associated with heat exchangers HE3 & HE5. LCA analysis also flagged environmental impact from the purge stream AB-P. Safety analysis on the process alternative gave a combined score (total inherent safety index) of 18. The identified hotspots are translated into design targets: Increase plant profit, reduce energy consumption, and improve LCA/sustainability indicators while maintaining the product purity and production rates (kept as the base case values).

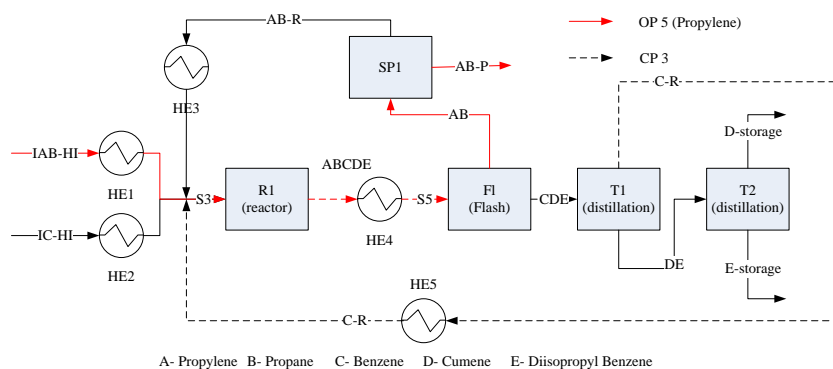


Figure 2 : Selected base case design for further analysis. The open and closed paths (OP, CP).

2.3. Innovation stage:

In this case study, simultaneous optimization and heat integration strategy is used to satisfy the design targets set in stage 2. The process is optimized to maximize the operational profit ($F_{obj} = \text{Revenue} - \text{Cost}$) and the heat integration targeting heat exchangers (HE3, HE4, and HE5). The operational profit has increased by 28% in the optimized case mainly due to reduction of heating and cooling utilities. Since the purge stream ratio is optimized to maximize the profit, waste generation is also reduced which also reduced the environmental impact.

Table 1 shows the application of ProCAFD on various industrially important processes. In all the cases, ProCAFD was able to generate numerous alternatives quickly that are truly innovative and that have not been reported in the literature. This is because the work-flow and data-flow of ProCAFD is organized in such way that all the steps can be performed very fast, consistently and reliably to solve the complete synthesis-design and innovation problem. More details on the solutions can be obtained from the authors.

Table 1 : Solved case examples using ProCAFD. Where improvement is wrt utilities consumption

Case Study	Alternatives Generated	Innovation Strategy	Improvement
Production of Benzene	64	Simultaneous Opt, & Heat Integration	67.0%
Separation of Alkanes	184	Hybrid Separations	60.5%
Production of Cumene	240	Simultaneous Opt, & Heat Integration	27.6%
Production of Biodiesel	502	Process Intensification	24.3%
Production of DMC	53	Process Intensification	86.7%

3. Conclusions

In this work, the main achievement is the development of a computer-aided method and its software to systematically solve complex process synthesis and design problems, which facilitates more efficient and innovative solutions. This work also focuses on extension of previous method to include comprehensive analysis involving sustainability, life cycle, safety and economic in early states of process synthesis. The developed method and software differ significantly from conventional synthesis-design methods/tools as it is not iterative nor is it based solely on mathematical optimization techniques to synthesize an optimal solution. It is a hybrid method based on decomposition-based approach where in the complexity of the synthesis problem is decomposed into a set of sub-problems and solved sequentially.

References

- D. K. Babi, J. Holtbruegge, P. Lutze, A. Gorak, J.M. Woodley, R. Gani, 2015, Sustainable Process Synthesis-Intensification, *Computers & Chemical Engineering*, 81, 218-44.
- A. Carvalho, H.A. Matos, R. Gani, 2013, SustainPro - A tool for systematic process analysis, generation and evaluation of sustainable design alternatives, *Computers & Chemical Engineering*, 50, 8-27.
- Dow Chemical Company. 1987. DOW's Fire & Explosion Index Hazard Classification Guide. 6th ed. New York: American Institute of Chemical Engineers
- S. Kalakul, P. Malakul, K. Siemanond, R. Gani, 2014, Integration of Life Cycle Assessment Software with Tools for Economic and Sustainability Analyses and Process Simulation for Sustainable Process Design, *Journal of Cleaner Production*, 71, 98-109.
- A. K. Tula, B. Befort, N. Garg, K. V. Camarda, R. Gani, 2017. Sustainable Process Design & Analysis of Hybrid Separations, *Computers & Chemical Engineering*, 105, 96-104.
- A. K. Tula, M. R. Eden, R. Gani, 2015, Process synthesis, design and analysis using a process-group contribution method, *Computers & Chemical Engineering*, 81, 245-259.

Component based development of computer-aided tools for different applications

Anjan K.Tula^a, Mario R. Eden^a, Rafiqul Gani^{b*}

^a*Department of Chemical Engineering, Auburn University, Auburn, AL 36849, USA*

^b*PSE for SPEED, Skyttemosen 6, Allerød, DK-3450, Denmark*

rgani2018@gmail.com

Abstract

Computer-aided methods and tools are used at different stages of chemical process development. However new tools are needed to meet the current and future challenges through innovative and more sustainable solutions that the currently available tools may not be able to provide. This work focuses on component-based software architecture for development of tailor-made computer-aided tools for specific application objectives. The architecture is based on “components”, which can be model-objects that are stored in a library; collection of property models; databases; numerical solvers; design-algorithms (work-flows) etc. The main idea of these components is to incorporate a plug & play framework, where for a specific purpose, after the work-flow and associated data-flow are established, a specific computer-aided tool can be configured through a library of software components. Also, through the use of software components that are based on predictive model-based solution techniques, the final software can be reliably used to provide innovative and more sustainable solutions over a wide range of problems.

Keywords: component-based, tailormade tools, software architecture.

1. Introduction

Chemical engineering is in constant evolution and access to computational resources are changing the way chemical engineering problems are addressed. Process simulation, which emerged in the 1960s, has become one of the great success stories in the use of computing in the chemical industry. Process simulators are used today in most of the chemical engineering disciplines ranging from process design, research and development, production planning, optimization to training and education making it one of the most sought-after software. Some well-known process flowsheet simulators are Aspen Plus, ChemCad and PRO/II. This success, however, has led to a negative trend, that is, replacement of the trial and error experiment-based solution approach to a trial and error simulator-based solution approach, which is a faster and less expensive option. However, does it lead to the innovative and significantly better solutions which are required to deal the grand challenges of health, food, water, energy and environment (Negro et al., 2018)? The current unit-operation based process simulators, although having great success and wide applications, are not able to satisfy the demands for the new technologies (multiscale, multipurpose, new concepts leading to new algorithms, visualization, etc.). For example, process simulators can only be used indirectly for synthesis, control, analysis, etc., purposes through iterative approach. In this approach, the simulator is in the inner loop generating the simulation data for each trail while the

outer loop has the techniques for synthesis, design and control. This is not the best way moving forward to solve where innovative and significantly better solutions are need of the hour. Clearly, a new class of methods and associated model-based computer aided tools are needed, and most importantly a structured approach in development of these software. This new software development approaches have to be modular, which can be described as component-based modeling that are flexible and easy to integrate with other components (pieces) of software. In this way one can easily design and develop smaller and flexible tailormade problem specific tools configured from a library of different software components (databases, models, design work-flows, analysis tools, solvers, etc.) according to the needs of the user. Modular based strategies have been proposed in different application areas ranging from modular modeling and simulation of chemical flowsheets to cellular systems however they failed to explain how a common interface can be used to develop software for different applications. This capability is important in industrial research and development where tools are developed for different applications. In this work a standard framework for software development based on components is proposed along with several illustrative examples of new tools that are able to achieve significant improvements through innovative, new and more sustainable solutions. This work also highlights the development of the component library and the common framework (standard interface) for the handling these components.

2. Overview for component-based software development

The main features of this new class of computer-aided tools are that they are based on software components that are taken from a database of components and are assembled through a standard interface (software framework) according to the needs of the user. This modular framework emphasizes separating the functionality of a software into independent, interchangeable components, such that each contains everything necessary to execute only one aspect of the desired functionality. Figure 1 shows the general framework for component-based software development, where it's possible to develop user specific tools by adding the necessary software components from the database. Figure 1 shows how 3 different problem specific software can be developed using components repository.

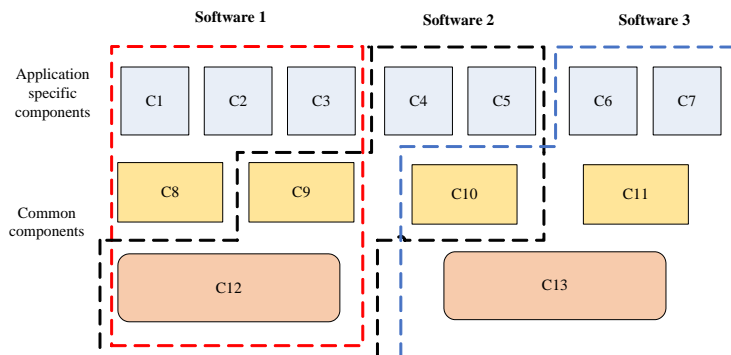


Figure 1: Framework for software component-based software development

Here components C1-C7 represents application specific components while C8-C12 represents common components. Compared to the classic development of large and complex generic software, modular approaches break down the complexity into smaller building blocks, making it easier to modify, maintain and most importantly reuse. This type of modular framework will be beneficial to research centers to reduce the software development times considerably and reuse components effectively. Here the software components can be databases, property models, process models of different types, and method-templates (for example, synthesis, design, analysis, control) with their specific work-flows (for example, step by step algorithms), the associated data-flows and computer-aided tools. Figure 2 shows the example of data and workflow of an integrated system, where in a template for process synthesis-design using superstructure-based optimization is shown. A software component is obtained through a collection of basic-tools and associated methods. A collection of components leads to a computer-aided tool. For example, a simulator for wastewater treatment industry can be constructed through the following software components: databases, membrane library, solver library, chemical dosing models, scaling models, flowsheet representation system. These software components define the application range and predictive capability of the software, so it is very important to select appropriate components keeping in mind the needs of the final software. With regard to system-wide co-ordination, these software components communicate with each other via the main interface.

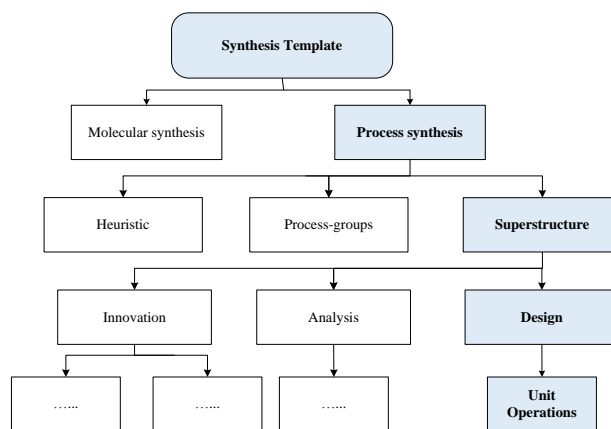


Figure 2 : Template example for Process Synthesis-Design

3. Application examples

3.1. Computer-aided tools for process-product synthesis, design, analysis

ProCAFD (Tula et al., 2017) is an integrated software component-based computer-aided tool that has been tailor-made for synthesis, design, analysis and optimization of chemical and related processes employing 12 hierarchical tasks based sustainable design methodology. It has only one design-template where the work-flow consists of 12 tasks organized into 3 stages. Each task has its associated list of software components, where the user has multiple options to carry out the task. For example, processing route generation may be performed based on well-known heuristics, group contribution based

generate and test or superstructure optimization. Figure 3 illustrates the workflow and software components of ProCAFD, consisting of 12 tasks are performed in 3 stages. First define the problem; then solve the synthesis problem in stage-1; then perform design-analysis after process simulation in stage-2; finally, in the 3rd stage, apply process intensification, hybrid separations etc., to generate alternative more sustainable process designs. In stage 1, once the all the process alternatives are generated, the superstructure can be solved using mathematical optimization method or generate and test approach based on user choice. SUPER-O which is integrated with ProCAFD, can be used to automate the mathematical formulation of the generated superstructure and solve mathematically or the user can choose ProCAFD's built-in ranking algorithm based on generate and test approach to solve. In stage 2, ProCAFD is also integrated external simulation tools like Aspen, PROII, where the generated designs are automatically transferred, and a rigorous simulation model of the alternative is setup. Tula et al. (2015, 2017) illustrates the application of ProCAFD for sustainable chemical process synthesis and design where new innovative solutions have been found. In all the examples ProCAFD was able to quickly generate and evaluate numerous process alternatives that are truly innovative and better than the designs published in literature.

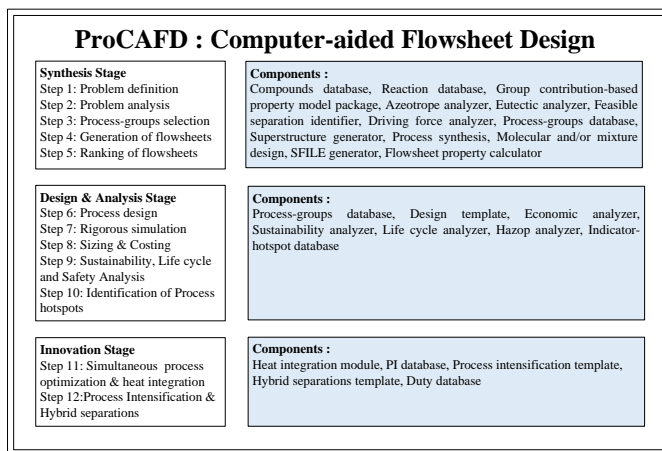


Figure 3 : Architecture of ProCAFD (Computer-aided Flowsheet Design)

ProCAPD (Kalakul et al. 2017) is an integrated tool for computer aided product design. This is analogous to process simulator, that is, it helps make the product design and development easier and faster and provides for a unified and consistent product documentation. However, unlike process simulators, ProCAPD can also be used directly for design of chemicals-based products, such as, single molecule products, formulations, blends, emulsions and devices (using different in-house synthesis design templates). It also has property-process modelling options, a large collection of databases for different classes of chemicals and properties and an interactive design template developer for new products and/or design methods. Figure 4 highlights the architecture and workflow of ProCAPD, where the main interface is at the inner core, then the method-template, then the associated software components and finally, the basic-tools. To design this chemical product simulator (ProCAPD), the components that

must be selected are databases (chemicals, solvents, active ingredients, aroma, color-agents etc.); model objects (properties, product performance, etc.); solvers (product attributes, blend compositions, environmental impact, etc.); design algorithms (single molecules, blends, formulations, emulsions, devices). ProCAPD has been applied to design solvents & refrigerants (Kalakul et al., 2018), surrogate fuel blends (Choudhury et al., 2017) and formulated liquid products (Conte et al., 2011). Note, however, the objective of ProCAPD is not to provide the final design of a chemical product but to quickly screen-out inappropriate alternatives so that focused experiments could be performed on a small set of promising candidates, thereby saving resources by reducing the product development time.

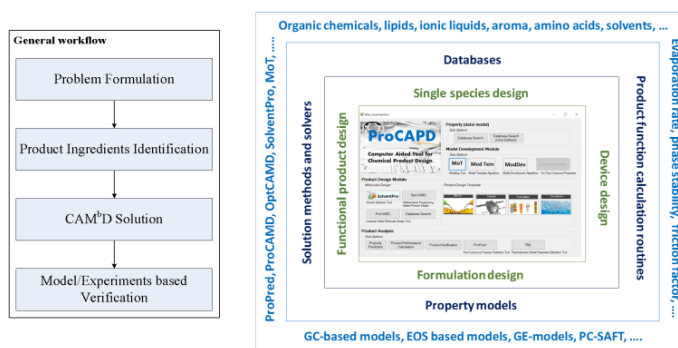


Figure 4 : Architecture of ProCAPD (Computer-aided Product Design)

3.2. ProCAPE: Computer aided property estimation

ProCAPE is a computer-aided property estimation tool consisting of chemicals database, pure component property models, mixture property models & phase equilibrium-based property calculation modules. It has the database for pure component, mixture properties of chemical species. To expand the capability and predictive nature of the software, software components related to property prediction models based on group contribution are also selected.

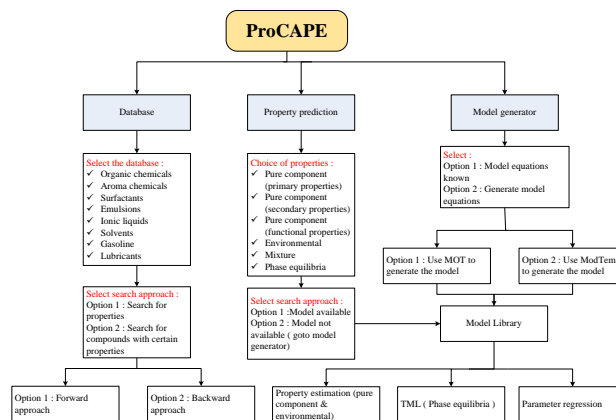


Figure 5 : Overview of ProCAPE (Computer-aided Property Estimation)

ProCAPE has different method templates like thermodynamic model selection guide, equilibrium analysis, parameter fitting for thermodynamic modes and simulation design calculations, etc. ProCAPE also has user model software component, where user can introduce his own models which can be used in performing different calculations. ProCAPE has models to predict 55 pure component properties (such as critical properties, acentric factor and solubility parameter) and 10 functional (temperature dependent) properties (such as vapor pressure, liquid viscosity, and surface tension) and collected measured data in database-tools covering 42,970 compounds. Also, ProCAPE has models (such as SRK, PR, UNIQUAC, UNIFAC, NRTL, PC-SAFT, etc.) for phase equilibrium calculations (vapor–liquid, liquid–liquid or solid–liquid) as well as mixture stability predictions.

4. Conclusions

Process systems engineering can play a leading role to address the current and future challenges of energy, water, food and health. In order to achieve innovative and sustainable solution we need to have access to next generation tools that can handle large datasets, models from different disciplines, establish solution strategies for multidisciplinary nature of problems. The key to these next generation tools would be software component-based computer-aided tools that has the flexibility to handle large and complex problems by breaking them down into smaller solvable problems (as in the case of 12 tasks based sustainable process design) while at the same time, designing different chemicals-based products through similar design templates but having different software components (for example, database and property models). The developed component-based software architecture has been successfully implemented in developing user specific tools ranging from property prediction to sustainable process-product design and analysis.

References

- H.A. Choudhury, S. Intikhab, S. Kalakul, M. Khan, R. Tafreshi, R. Gani, N. Elbashir, 2017, Designing a Surrogate Fuel for Gas-to-Liquid (GTL) Derived Diesel. *Energy & Fuels*, 31, 11266-11279.
- E. Conte E, R. Gani, K.M Ng, 2011, Design of formulated products: a systematic methodology, *AIChE Journal*, 57(9), 2431-2449
- S. Kalakul, M.R. Eden, R. Gani, 2017, The Chemical Product Simulator – ProCAPD, *Computer Aided Chemical Engineering*, 40, 979-984.
- S. Kalakul, L. Zhang, Z. Fang, H.A. Choudhury, S. Intikhab, N. Elbashir, M.R. Eden, R. Gani, 2018, Computer aided chemical product design – ProCAPD & tailor-made blended products, *Computers & Chemical Engineering*, 116, 37-55.
- C. Negro, F. Garcia-Ochoa, P. Tanguy, G. Ferreira, J. Thibault, S. Yamamoto, R. Gani, 2018, Barcelona Declaration – 10th World Congress of Chemical Engineering, 1–5 October 2017, *Chemical Engineering Research & Design*, 129, A1-A2
- A.K. Tula, M.R. Eden, R. Gani, 2015, Process synthesis, design and analysis using a process-group contribution method, *Computers Chem Eng*, 81, 245-259
- A.K. Tula, J. Bottlaender, M.R. Eden, R. Gani, 2017, A computer-aided software-tool for sustainable process synthesis-intensification, *Computers Chem Eng*, 105, 74-95.

Fouling Modelling in Crude Oil Heat Exchanger Networks using Data Reconciliation and Estimation of Unmeasured Process Variables

José Loyola-Fuentes^{a,*}, Megan Jobson^a and Robin Smith^a

^a*Centre for Process Integration, School of Chemical Engineering and Analytical Science, The University of Manchester, M13 9PL, UK*
jose.loyolafuentes@manchester.ac.uk

Abstract

In crude oil refineries, fouling has a significant impact on operating and maintenance costs. The growth of fouling layers on the surface of heat exchangers in a crude oil heat exchanger network (HEN) also increases both energy use and CO₂ emissions. Fouling models facilitate process design and integration while systematically accounting for the impact of fouling. The most common models use a series of parameters that are specific to the type of crude oil, as well as the operating conditions of the pre-heat train. These models are of great importance as they can indicate the set of operating conditions (stream velocities and temperatures) at which the occurrence of fouling might be avoided. A key challenge is to define an accurate method for determining fouling models for each side of a heat exchanger within a network. To achieve this goal, plant-measured data are used to monitor the thermal performance of a pre-heat train, and to obtain specific insights related to the impact of fouling. The main concern related to these data and their interpretation is the effect of measurement error and the limited number of measurements available in the process. This work presents a new methodology for calculating fouling model parameters for both sides of shell-and-tube heat exchangers using simulated plant-data along with data reconciliation and gross error detection. A heat exchanger network model coupled with fouling dynamics is used for simulating a crude oil pre-heat train and for the prediction of fouling behaviour. The effect of full and partial instrumentation in the estimation of reconciled measurements is accounted for in a case study, where the prediction of fouling deposition is assessed.

Keywords: Crude Oil Distillation, Heat Integration, Optimisation, Process Simulation

1. Introduction

The reduction of energy demand is a global concern. A considerable amount of research efforts has been centred in developing new technologies to continuously decrease the energy use, specifically in crude oil refining processes. In general, crude oil is initially pre-heated to approximately 380°C before entering the crude distillation unit (CDU). A heat exchanger network (commonly known as the pre-heat train) is used for this pre-heating, recovering around 60-70% of the heat needed in the CDU (Panchal and Huangfu, 2000). Unfortunately, fouling deposition in the Pre-heat Train decreases the thermal and hydraulic performance of the network. In order to avoid the growth of fouling layers on

the surface of heat exchangers, fouling models can be used for model-based predictions and design of mitigation strategies.

Fouling models can be grouped according to their physical basis. In particular, the concept of the so-called fouling threshold (Ebert and Panchal, 1995) provides a useful theoretical basis for establishing a relationship between the fouling phenomena and the pre-heat train operating conditions. Fouling threshold models are crude oil-dependent; the set of parameters in each model captures the characteristics of a particular crude oil or a crude oil blend. These parameters can be determined using experimental or field data by fitting these data to an appropriate fouling model. Both methods have their own advantages and disadvantages; however, the use of field data contributes to a more realistic representation of the process, when such data is appropriately processed.

Data Reconciliation is a widely used method for processing measured data. This method reduces the impact of measurement error in a data-set. In general, measurement error is defined as the sum of random and gross (or systematic) errors (Narasimhan and Jordache, 2000). To account for these two contributions, gross error detection should be included in the data reconciliation method; this simultaneous strategy is able to estimate the presence and value(s) of miscalibration(s) within the set of data. An equally important challenge is the presence of unmeasured process variables. When a set of process variables is unmeasured, the number of degrees of freedom and available linearly independent equations limit the estimation of this unmeasured variables (Romagnoli and Sánchez, 1999). Therefore, the selection of unmeasured variables should be (in principle) such that the available information is sufficient for the estimation of all unmeasured variables.

This work proposes a methodology to determine fouling threshold models for a crude oil pre-heat train subject to fouling in both the shell and tube sides. Data reconciliation and gross error detection techniques are integrated with an optimisation-based parameter fitting to calculate fouling model parameters associated with different mechanisms within the network. The effects of different gross error and unmeasured process variables is analysed in a case study, in which the set of missing measurements is classified according to whether each missing process variable in the set can be estimated or not.

2. Modelling and Formulation

This work uses a matrix-based HEN simulation strategy along with data reconciliation and gross error detection, together with a hybrid optimisation approach to calculate specific fouling models for a crude oil pre-heat train. The effect of missing process measurements are accounted for by exploiting the matrix formulation of the HEN and by classifying such missing measurements according to the concepts of observability and redundancy defined by Narasimhan and Jordache (2000), as described in Section 2.2.

2.1. HEN and Fouling Modelling and Simulation

The model used in this work calculates the internal flow rates and temperatures of the HEN using inlet information from the crude oil and the CDU side-products streams. The simulation strategy was proposed by de Oliveira Filho et al. (2007) and later modified by Ochoa-Estopier et al. (2015) to include the simulation of unit operations such as desalters and flash units. The proposed approach integrates the dynamic effects of fouling using an

explicit Euler integration, as it was previously shown in Loyola-Fuentes et al. (2017). The HEN is simulated in order to obtain a set of simulation-based data. Random and gross errors are systematically added to these simulated data in order to replicate the variability of an existing process. Following the reconciliation of these measured data, the HEN and fouling models are used for prediction of fouling deposition.

2.2. Data Reconciliation and Gross Error Detection

The data reconciliation algorithm minimises the value of the measurement error, which is defined as the difference between the measurements (y_m) and the reconciled process variables (y_r). These reconciled variables are estimated via nonlinear constrained optimisation, where each measured value is weighted by the corresponding accuracy of the measurement (usually approximated by the variance of such measurement) in matrix ψ . The whole set of constraints considers the presence of unmeasured process variables in the vector y_u . The set of equality constraints $f(y_r, y_u)$ represents mass and energy conservation equations, and the set of inequality constraints $g(y_r, y_u)$ represents specific lower and upper bounds for each measurement. The effect and presence of gross error is accounted for by including the gross error magnitude (measurement bias is assumed in this work) g_ξ in the measurement error vector. The simultaneous optimisation problem is solved by the combinatorial strategy proposed by Romagnoli and Sánchez (1999), which is updated in this work to take into account nonlinear systems. The data reconciliation and gross error detection problem is defined in Eq. (1).

$$\begin{aligned} \min_{y_r, y_u} \quad & (y_m - y_r - g_\xi)^T \psi^{-1} (y_m - y_r - g_\xi) \\ \text{subject to} \quad & f(y_r, y_u) = 0 \\ & g(y_r, y_u) \leq 0 \end{aligned} \tag{1}$$

The minimisation problem in Eq. (1) is solved via Sequential Quadratic Programming (SQP). The values of reconciled and unmeasured process variables are estimated simultaneously. The effect of missing measurements is analysed based on the concepts of observability and redundancy (Narasimhan and Jordache, 2000).

- **Observability:** An unmeasured variable is observable if it can be estimated using measurements and process constraints.
- **Redundancy:** A measured variable is redundant if it is observable even when its measurement is missing.

2.3. Fouling Model Parameter Estimation

A hybrid optimisation approach is implemented for determining fouling parameters. The value of fouling resistance is calculated using the overall heat transfer coefficient in clean and fouled conditions. The parameter estimation is formulated as a nonlinear constrained optimisation problem and solved using Genetic Algorithm. The solution of this problem is then fine-tuned using a deterministic nonlinear programming technique; in this work, the interior point method is implemented.

The objective function shown in Eq. (2) represents the minimisation of the root mean squared error between measured and fitted fouling resistances, defined by R_f^{msr} and R_f^{fit} respectively. The optimisation variables correspond to the specific fouling parameters (vector b) of a fouling model that is previously selected according to operating conditions. Each data-set and the total amount of data-sets are represented by the counter k and number n respectively.

$$\begin{aligned} \min_b \quad & \sqrt{\frac{\sum_{k=1}^n \left(R_{f,k}^{msr} - R_{f,k}^{fit}(b) \right)^2}{n}} \\ \text{subject to} \quad & b^L \leq b \leq b^U \end{aligned} \quad (2)$$

3. Case Study

This new methodology is tested in a HEN case study, comprising of eight process-to-process heat exchangers, one desalter unit, three cold utilities and one hot utility. The pre-heat train is depicted in Figure 1. Fouling is assumed in the shell-side and the tube-side of all process-to-process heat exchangers. Deposition of waxes is considered in both sides of the heat exchangers at the cold end of the pre-heat train (exchangers E1 to E4) as well as in the shell-side of the heat exchangers at the hot end (exchangers E5 to E8). The fouling rate for this mechanism, α_1 , is set to be $5.50 \times 10^{-4} \text{ m}^2\text{K kW}^{-1}\text{h}^{-1}$. Chemical reaction fouling based on the model proposed by Polley et al. (2007) is assumed to occur in the tube-side of exchangers at the hot end of the pre-heat train. The fouling models are shown in Eq. (3) and Eq. (4) respectively, where Re , Pr , R_g and T_W are the relevant Reynolds number, Prandtl number, the ideal gas constant and the tube-wall temperature. The parameters of the chemical reaction model α_2 , E_A and γ are given in Table 1. The simulation time is one year and the operational data are generated using the simulation strategy described in Section 2.1. Random and gross errors are systematically added in order to replicate the variability of a real operating process.

The cold stream outlet flow rate of exchanger E3 and the hot side outlet temperature of exchanger E7 are chosen as unmeasured variables. These variables are to be estimated using the available measurements, in order to check the observability of such missing data. Random errors are added to each measurement across the whole time-span. A constant single gross error of magnitude of 4°C is added to the furnace inlet temperature. After reconciliation and identification of gross errors, the fouling parameters for the shell and tube-sides of all heat exchangers are back-calculated via the parameter estimation method explained in Section 2.3.

$$\frac{dR_f}{dt} = \alpha_1 \quad (3)$$

$$\frac{dR_f}{dt} = \alpha_2 Re^{-0.8} Pr^{-0.33} \exp\left(\frac{-E_A}{R_g T_W}\right) - \gamma Re^{0.8} \quad (4)$$

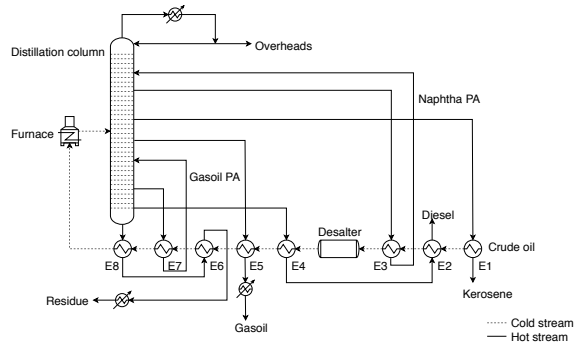


Figure 1: Crude Oil Pre-Heat Train Process Flow Diagram

Table 1: Fouling model parameters for chemical reaction mechanism (Polley et al., 2007)

Parameter	Units	Value
α_2	$\text{m}^2\text{K kW}^{-1}\text{h}^{-1}$	1.00×10^6
E_A	kJ mol^{-1}	48.00
γ	$\text{m}^2\text{K kW}^{-1}\text{h}^{-1}$	1.50×10^{-9}

The results from the estimation of missing measurements are compared with a fully-instrumented scenario. The missing flow rate estimation results give a constant value of 194 kg s^{-1} , as no mass losses are considered. This value is in accordance with the full instrumentation scenario. The comparison for the missing temperature measurement is shown in Figure 2. The agreement between these two scenarios indicates that both of these unmeasured variables are observable, as their magnitudes are accurately estimated.

The average value of the estimated gross error is 3.98°C , which is in good agreement with the initially simulated value of 4°C . The performance of the data reconciliation can be assessed by analysing the values of the fitted fouling parameters for all heat exchangers. These values are shown in Table 2. The agreement of each parameter with respect to their corresponding base-value (see Table 1) shows how well these parameters can be used for the prediction of fouling behaviour in the network.

Table 2: Fitted fouling model parameters for all heat exchangers

	$\alpha_1 (\text{m}^2\text{K kW}^{-1}\text{h}^{-1})$	$E_A (\text{kJ mol}^{-1})$	$\gamma (\text{m}^2\text{K kW}^{-1}\text{h}^{-1})$	$\alpha_2 (\text{m}^2\text{K kW}^{-1}\text{h}^{-1})$
E1	5.42×10^{-4}	–	–	–
E2	5.42×10^{-4}	–	–	–
E3	5.42×10^{-4}	–	–	–
E4	5.42×10^{-4}	–	–	–
E5	9.36×10^{-4}	44.18	1.11×10^{-7}	3.85×10^5
E6	9.70×10^{-4}	51.54	9.89×10^{-8}	2.66×10^6
E7	8.43×10^{-4}	44.10	6.65×10^{-8}	4.16×10^5
E8	8.66×10^{-4}	48.28	5.05×10^{-8}	1.11×10^6

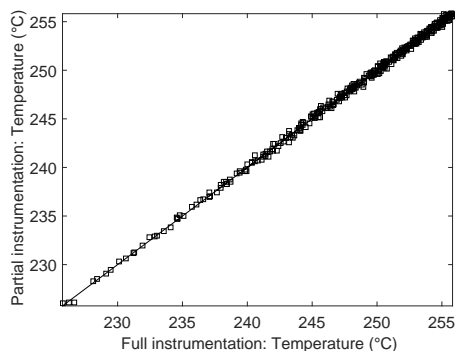


Figure 2: Comparison between full and partial instrumentation scenarios for the missing temperature measurement

4. Conclusions

This work proposes a new method for regressing fouling models for shell and tube-sides of a crude oil pre-heat train using data reconciliation and gross error detection. The Data Reconciliation method accounts for the effect of two different types of measurement errors and the presence of missing measurement(s). These missing measurements are classified according to their observability in order to identify their potential for accurate estimation. The proposed methodology is tested in a case study, where significant agreements were found when full and partial instrumentation scenarios were compared. Further study is needed for multiple combinations of missing measurements presenting different degrees of observability. For achieving this goal, a topological analysis of the network, together with a set of measured values are needed. The degree of observability for this case can be evaluated using matrix-based techniques such as Q-R decomposition.

References

- L. O. de Oliveira Filho, E. M. Queiroz, A. L. Costa, 2007. A matrix approach for steady-state simulation of heat exchanger networks. *Applied Thermal Engineering* 27 (14), 2385–2393.
- W. Ebert, C. B. Panchal, 1995. Analysis of Exxon crude oil-slip-stream coking data. In: *Fouling Mitigation of Industrial Heat-Exchange Equipment*. Begell House, pp. 451–460.
- J. Loyola-Fuentes, R. Smith, M. Jobson, 2017. Fouling modelling in crude oil preheat systems. In: A. Espuña, M. Graells, L. Puigjaner (Eds.), *Computer Aided Chemical Engineering*. Vol. 40. Elsevier, pp. 409–414.
- S. Narasimhan, C. Jordache, 2000. *Data Reconciliation & Gross Error Detection: An Intelligent Use of Process Data*. Gulf Publishing Co., Houston, Texas, USA.
- L. M. Ochoa-Estopier, M. Jobson, L. Chen, C. A. Rodríguez-Forero, R. Smith, 2015. Optimization of heat-integrated crude oil distillation systems. Part II: Heat exchanger network retrofit model. *Industrial & Engineering Chemistry Research* 54 (18), 5001–5017.
- C. Panchal, E.-P. Huangfu, 2000. Effects of mitigating fouling on the energy efficiency of crude-oil distillation. *Heat Transfer Engineering* 21 (3), 3–9.
- G. T. Polley, D. I. Wilson, S. J. Pugh, E. Petitjean, 2007. Extraction of crude oil fouling model parameters from plant exchanger monitoring. *Heat Transfer Engineering* 28 (3), 185–192.
- J. A. Romagnoli, M. C. Sánchez, 1999. *Data Processing and Reconciliation for Chemical Process Operations*. Academic Press, Inc., Orlando, Florida, USA.

Novel Methodology for Cogeneration Targeting with Optimum Steam Level Placement

Julia Jimenez, ^{a,b,*} Adisa Azapagic, ^b Robin Smith^a

^a *Centre for Process Integration, School of Chemical Engineering and Analytical Science, The University of Manchester, Manchester M13 9PL, UK.*

^b *Sustainable Industrial Systems, School of Chemical Engineering and Analytical Science, The University of Manchester, Manchester M13 9PL, UK.*

julia.jimenezromero@manchester.ac.uk

Abstract

This study aims to develop a novel method to synthesise site-wide heat recovery, distribution, cogeneration systems with optimum operating conditions of the steam mains. Previous approaches have simplified the problem to the extent that many important practical issues have been neglected and restricted the scope of the options included. The proposed methodology uses a combination of total site analysis and mathematical programming for a holistic approach to the steam system, which accounts for interactions between site utility system and processes. The optimisation problem involves the selection of more realistic operating conditions of the steam mains (superheating and pressure). The model will also account for water preheating, and superheating and desuperheating for process steam generation and use. Deaerators and let-down stations are also included in the analysis. The application of this methodology to a case study yielded a 7.6 % reduction in total energy requirement, compared to conventional utility system design method. The proposed approach addresses severe shortcomings in previous research on this topic and provides a foundation for future work to explore the next generation of sustainable utility systems.

Keywords: Cogeneration targeting, heat and power integration, total site integration, steam level optimization, mathematical programming.

1. Introduction

Sustainable development, as one of the most significant challenges faced by society, is closely related to the rational generation and use of energy. For this reason, in the process industries it is important to place a focus on the synthesis of energy-efficient sustainable utility systems and how this can shape energy use patterns. The energy transition of existing systems to meet future demands needs to be directed to be on a sustainable basis (Broberg Viklund, 2015). In the future, process utility systems will need to incorporate a much greater contribution from renewable energy sources. This will create a paradigm shift in the way such utility systems are designed and operated.

One of the key performance indicators for the synthesis of utility systems is cogeneration potential, which establishes objectives on heat and power generation as well as steam distribution and boiler fuel requirement (Ghannadzadeh et al., 2012). Steam mains pressures and superheating play an essential role in the performance of both heat and power generation at the site. Research has analyzed the influence of the

steam levels on the energy targets in total site heat integration (Mavromatis and Kokossis, 1998; Shang and Kokossis, 2004; Beangstrom and Majoji, 2016). However, previous methods do not consider the degree of superheat and its effect on the potential shaft power generated by steam expansion.

In addition to these models, Kundra (2005) and Ghannadzadeh et al. (2012) presented targeting approaches, in which both sensible and latent heat of steam has been considered. However, previous methodologies have been based on the assumption of fixed steam mains pressure, usually based on heuristics. This neglects the close interrelation between the processes and the system and its subsequent implications. Moreover, the superheat for both the steam generation and use has been assumed to be the same. This premise might lead to thermodynamically infeasible solutions or further difficulties in practice, because of limitations associated with the materials used for construction, or due to the design complexity.

Sun et al. (2015) proposed a graphical approach to overcome the shortcomings in relation to assessing cogeneration potential and enhancing site-wide heat recovery methodically. Whilst the proposed methodology by Sun et al. (2015) allows for useful thermodynamic and physical insights for understanding some of the interactions within the system It does not provide a systematic decision-making approach to determine the optimum utility system performance since it does not allow the analysis of the trade-off between the cost of the additional steam and the profit from power generation.

Though there is extensive literature for cogeneration targeting in utility systems, the conventional concepts present a number of limitations and drawbacks for the selection of optimum site operating conditions. This study aims to offer the basis for a systematic approach to explore the next generation of sustainable utility systems. For the first time, a study in this area combines an extended transshipment method based on Shang and Kokossis (2004) with total site analysis and more realistic site conditions. In turn, this determines the total site heat and mass flow and ensures that the total operating cost is minimized.

The novelty of this work is derived from the requirement of increased practical and realistic conditions for both steam generation and usage. This is used in combination with an evaluation of the interactions between steam mains conditions (pressure and superheat) and system performance. The effect of process steam generation at a different temperature from the steam mains, as well as the efficiency and the exhaust temperature of the steam turbines based on steam conditions (superheating) and load, is also explored to provide a more realistic and accurate heat recovery. Ultimately, this methodology allows for power targeting of utility systems operating at optimum conditions. In essence, the study provides a framework for the analysis of sustainable steam systems.

2. Methodology

Cogeneration targeting with simultaneous steam mains selection requires making continuous and discrete decisions, where non-linear energy terms are involved. Thus, to produce a linear model and avoid convergence and robustness issues, some properties are fixed during the optimization. Every optimization step is succeeded by a rigorous

simulation, as shown in Figure 1. The following subsections provide a summary of these steps.

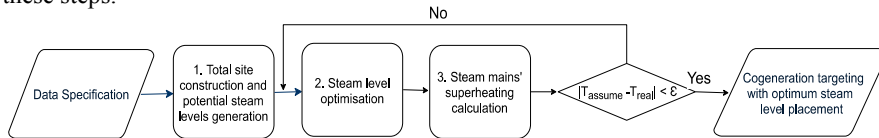


Figure 1. Schematic representation of optimization approach

Step 1 Total site construction and potential steam levels generation

The extended Total Site Profile (TSP) concept of Varbanov et al. (2012) is adopted to obtain the potential steam levels required for the heat recovery and power generation via the utility system. Apart from the stream data specification - i.e. number of processes involved, number of stream of each process, parameters including supply and target temperatures, as well as the heat capacity- the specific minimum approach temperature (ΔT_{min}^{PU}) is used to avoid misleading energy targets that can result from the use of inaccurate global minimum temperature difference (ΔT_{min}) values between process streams.

Saturated temperature (pressure) denotes the potential steam levels. The temperatures are obtained by partitioning the site-wide temperature range into intervals. Since the sink profile defines the quantity and quality of heat required, steam intervals are based on its temperature range. Operational constraints are also taken into account, such as minimum/maximum temperature for process and utility steam generation. Additionally, minimum temperature and pressure difference between each potential level are set by the designer, to guarantee a representative number of options and avoid unnecessary levels. Once generated the potential steam levels, they are classified based on the number of steam main required and the pressure ranges for each header.

Step 2 Steam level optimization

The MILP formulation is based on Total Site Heat and Mass Cascades (TSHMC) employing a transshipment model. An extension of Shang and Kokossis (2004) model enables recording energy and mass balances among process source/sink streams and potential steam levels. The TSHMC are formulated by the temperature intervals (defined by the steam levels) and comprise three cascades: source, steam and sink, as illustrated in Figure 2(a) Process streams act as steam sources or sinks, where the (residual) heat that cannot be used in the interval for either steam generation or use is going to the next lower temperature level, at the respective cascade. Heat flows from the process sources to sinks through steam. Utility steam is raised at boiler house at VHP conditions and distributed to the different headers by either passing through steam turbines or let down stations.

In the source cascade, the heat from process sources is used to raise steam at the steam level pressure, from Boiler Feed Water (BFW) conditions to superheating. The latter is a designer variable and is restricted by the source profile and the heat exchanger equipment. Regarding sink cascade, heat flows from steam level to process sinks via steam desuperheated. Steam is desuperheated prior its use by BFW injection. For the development of the TSHMC, let m^H , m^{ST} , m^{LD} , m^{Cmain} , m^{BFW} be the steam mass flowrates of the process steam generation, steam turbines, let-down stations, process sinks and BFW injected, respectively.

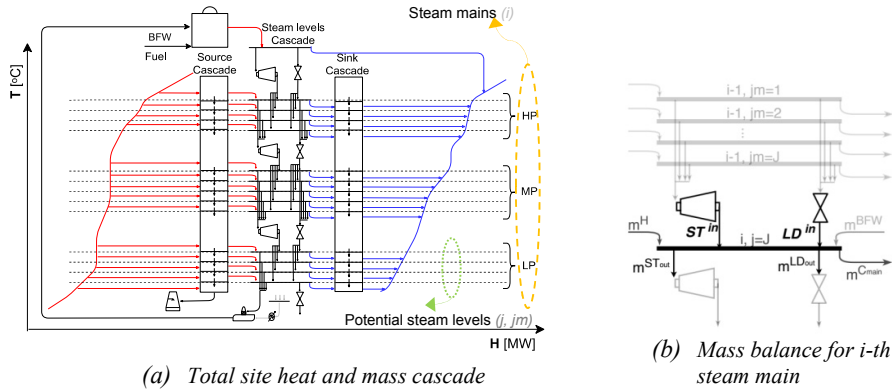


Figure 2. Schematic representation of optimization approach

The MILP formulation is based on the minimum annualised utility cost as the objective function, where the steam flows, heat loads, fuel consumption, electricity generation and cooling water requirement are continuous variables. Binary variables are associated with whether a steam main (defined as i) exists at a given condition, denoted by the set of potential steam levels j or jm . Binary variables are also related to the steam turbines operation between steam mains (i, j) and ($i+1, jm$) and the operating status of boilers at VHP conditions.

Energy and mass balance, as well as the electricity balance are the main equality constraints. While equipment size constraints -- that avoid equipment operating at lower efficiency -- are inequality constraints. Power generation and fuel consumption are estimated employing the linear models of Sun and Smith (2015) and Shang (2000), respectively. Both models accounts for full and part-load operating performance.

Step 3 Calculation of steam mains' superheating

Once the optimum steam level placement (saturated temperature/pressure) has been obtained, the actual superheating temperature of the header is calculated. The superheating is defined through a material and energy balance in each steam main. This is determined by the enthalpy and flow rate of the process steam generation, turbine exhausts, steam passing through let-down valves, and any BFW injected in the steam main. The calculations require top-down iterations that start with the utility steam and work down through the cascade from high to low pressure until superheating constraint is satisfied by all the steam mains. Turbine exhaust properties are obtained using the Willan's linear model presented in the Sun and Smith (2015) research, based on the inlet steam conditions and the steam main pressures. The steam is expanded through letdown valves at isenthalpic conditions. Finally, Step 2 and 3 are repeated until achieving convergence (usually 3-4 iterations).

3. Case Study

Site data was adapted from an example available in the literature (Sun et al., 2015). The number of streams and ΔT_{min}^{PU} for each process are detailed in Table 1. Power site demand is 40 MWh. The site energy requirement is satisfied using a steam system comprising a natural gas boiler, three distribution steam mains, a deaerator, expansion

valves, steam turbines and a single cold utility (cooling water). The utility steam is generated in the boiler house at the very high pressure (VHP) main conditions (100 bar). The inlet temperature of the cooling water is 20 °C. Electricity is generated by single back-pressure steam turbines allocated between each level. The HP, MP and LP steam mains operating conditions are estimated to minimize the total operating cost.

Table 1. Summary of the stream data for case study

	Process A	Process B	Process C	Process D	Process E
No. of streams	4	8	9	6	9
ΔT_{\min} (°C)	15	5	5	10	15

In order to assess the benefit of the methodology, the optimized system configuration is compared against a conventional design based on heuristics, where the HP, MP and LP mains pressure are 40, 20 and 5 bar, respectively. Figure 3 compares the two steam system configurations. Both systems were obtained based on the temperature specifications presented in Table 2. For the optimization, the present case study has considered 65 potential steam levels, based on the specifications and the sink profile temperature. The potential steam levels has been classified in 15 levels for HP (≥ 30 bar), 42 levels for MP (6 – 30 bar) and 8 levels for LP (3 - 6 bar).

Table 2. Temperature specifications for the steam system

Constraints	Temperature [°C]
Maximum boiler steam temperature	570
Minimum process steam generation temperature (saturation)	134
Minimum steam main superheating	20
Degree of superheating for process steam generation	20
Degree of desuperheating for process heating	3

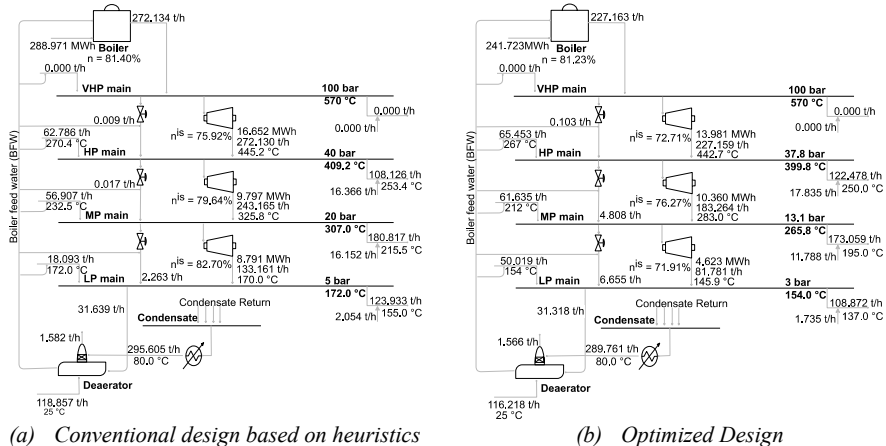


Figure 3. Steam system configuration

The steam main pressures for the optimized system configuration are 37.8, 13.1 and 3 bar, respectively. The manipulation of steam main conditions affects site operational performance. Steam mains selection is affected by several factors i.e. process steam generation, turbine exhausts and let-down flows. Steam passing through let-downs is required to achieve steam balance and more important to maintain the minimum

superheat of 20 °C in each steam main. However, this may result in a reduction in the power generation as it is observed in Table 3. Compared with conventional design cost, the proposed design diminishes the fuel and CW consumption by 16.35 % and 10.61 %, respectively. Even though the power generation is less than the traditional design, the total utility cost decreases 7.61 %.

Table 3. Comparison of steam system designs

<i>Parameter</i>	<i>Conventional</i>	<i>Optimization</i>	<i>Difference in units</i>
Fuel consumption [MWh]	288.97	241.72	- 47.25
Power Generation [MWh]	35.20	28.96	+ 6.24
Cooling Utility [MWh]	237.54	212.33	- 25.21
Fuel Cost [M£ y ⁻¹]	51.19	42.82	- 8.37
Power Cost [M£ y ⁻¹]	3.62	8.38	+ 4.76
Cooling Cost [M£ y ⁻¹]	10.21	9.13	- 1.08
Operating Cost [M£ y⁻¹]	65.02	60.33	- 4.69

4. Conclusions

A new methodology has been developed to provide increased realism and accuracy in utility systems synthesis, operating at optimum conditions for future utility systems. The study shows the close relation between steam level selection and heat recovery and power generation enhancement. In an illustrative example, the new model presents a significant reduction of the total energy requirement at the site compared to a conventional design method (7.61 %). This proves that the energy requirement can be further reduced by holistically optimizing the steam mains operating conditions and the site heat recovery and cogeneration.

5. Acknowledgements

This publication has been funded by HighEFF-Centre for an Energy Efficient and Competitive Industry for the Future. The authors gratefully acknowledge the financial support from the Research Council of Norway and user partners of HighEFF. Also, a special gratitude to the National Secretariat for Higher Education Science, Technology and Innovation of Ecuador (SENESCYT) for its support.

References

- Beangstrom, S. G. & Majoji, T. (2016). Steam system network synthesis with hot liquid reuse: II. Incorporating shaft work and optimum steam levels. *Computers & Chemical Engineering*, 85, 202-209.
- Broberg Viklund, S. (2015). Energy efficiency through industrial excess heat recovery—policy impacts. *Energy Efficiency*, 8(1), 19-35.
- Ghannadzadeh, A., Perry, S. & Smith, R. (2012). Cogeneration targeting for site utility systems. *Applied Thermal Engineering*, 43, 60-66.
- Kundra, V. (2005). *To develop a systematic methodology for the implementation of R-curve analysis and its use in site utility design and retrofit*. Master of Science, The University of Manchester.
- Mavromatis, S. P. & Kokossis, A. C. (1998). Conceptual optimisation of utility networks for operational variations—I. targets and level optimisation. *Chemical Engineering Science*, 53(8), 1585-1608.
- Shang, Z. (2000). *Analysis and Optimisation of Total Site Utility Systems*. Ph.D. Thesis, The University of Manchester.
- Shang, Z. & Kokossis, A. (2004). A transhipment model for the optimisation of steam levels of total site utility system for multiperiod operation. *Computers & Chemical Engineering*, 28(9), 1673-1688.
- Sun, L., Doyle, S. & Smith, R. (2015). Heat recovery and power targeting in utility systems. *Energy*, 84, 196-206.
- Sun, L. & Smith, R. (2015). Performance Modeling of New and Existing Steam Turbines. *Industrial & Engineering Chemistry Research*, 54(6), 1908-1915.
- Varbanov, P. S., Fodor, Z. & Klemeš, J. J. (2012). Total Site targeting with process specific minimum temperature difference (ΔT_{min}). *Energy*, 44(1), 20-28.

A multi-objective multi-period optimization of carbon integration networks in industrial parks

Dhabia M. Al-Mohannadi^{a,*}, Patrick Linke^a, Nialy Shah^b

^a*Department of Chemical Engineering, Texas A&M University at Qatar, Education City, PO Box 23874, Doha, Qatar*

^b*Department of Chemical Engineering, Imperial College of London, London, United Kingdom*

dhabia.al-mohannadi@qatar.tamu.edu

Abstract

The direct link between climate change and anthropogenic industrial activity resulted in a need more prominent than ever to cut emissions. At the Paris climate conference (COP21), 195 countries adopted a legally binding global climate deal to put the world on track to avoid dangerous climate change effects. This sets a challenge for many countries to draft sustainable climate policies by 2030. Climate change has social, environmental and economic consequences. Therefore, it is important to understand the impact of these interconnected factors on climate strategies. Multi-period carbon integration allows carbon reduction over a certain time horizon. The multi-period planning approach identified allocation of carbon dioxide between sources and potential sinks in each period, compared cost elements simultaneously and resulted in a low cost network across all periods. In this work the approach was expanded to evaluate two conflicting objectives. An example was solved to assess climate policies under two objectives. Good carbon reductions were achieved.

Keywords: Optimization, carbon dioxide reduction, renewable energy, sustainability, climate policy

1. Introduction

Policy-making entities have proposed ambitious carbon dioxide emission reduction targets as a means of mitigating global warming effects. Many policies are drafted yearly, in an attempt to successfully reduce carbon dioxide emissions. Most of the policies are outlined for regulatory reasons, by prescribing a required target, over a specified time horizon. Different carbon dioxide emission reduction strategies that are often dictated by over time GHG emission targets, (Huisingsh et al. 2015). While other policies define individual emission reduction targets across different industrial sectors, especially ones associated with carbon dioxide point sources that result in considerable emissions (Pinho and Madaleno, 2011). A number of conventional methods may be applied to reduce carbon dioxide emissions such as energy efficiency, carbon capture utilization and storage (CCUS) and the use of renewable energy. Energy management techniques have been implemented by works like Klemeš and Kravanja (2013) and Varbanov et al. (2004) among others. In CCUS, which minimizes emissions by allocating the CO₂ source to sinks for storage, sequestration and utilization. Works such as Boot-Handford et al. (2014) offer a review of possible CO₂ storage sinks, while work such as Al-Mohannadi and Linke (2016), optimized CO₂ networks converting CO₂ to value added products in sinks among others that can be found at Foo and Tan (2016). Moreover, emissions are reduced further

by the use of renewable energy. Carbon dioxide emission reduction policies may prescribe appropriate target emission goals or specific technologies to achieve their reduction goal such as the European Commission Climate Action Plan of 20-20-20, which specifies carbon reduction by 20% by the year 2020 using 20% renewable technology for energy production and 20% increase in energy efficiency.

Carbon dioxide emission targets are often proposed for a point in time in the future. Multi-period carbon integration methods allow carbon reduction schemes to be identified over certain a time horizon. The same target may be achieved in various ways, depending on how the carbon reduction policy is being implemented over time. Therefore, this work studies the effects that result from incorporating different objectives over a given time horizon onto carbon integration networks, using a multi-period approach (Al-Mohannadi et al, 2016). Economic or environmental objectives often have a trade-off that works such as Jing et al (2018) used in energy planning. This work expands the representation by Al-Mohannadi et al, (2016) to evaluates the impact of different time dependent policies onto CCUS-RE decisions, using a multi-period carbon integration approach and understanding the trade-offs between economic and the reduction targets through assessments of multiobjectives. The next sections include a brief description of the problem statement, and is followed by an illustrative example.

2. Description and problem statement

The overall goal is the identification of climate strategies under two conflicting constraints which are to achieve the maximum economic and maximum environmental performance in terms of carbon reduction. The challenge is to identify the most promising network allocations from the possible reduction alternatives found for each objective.

The problem addressed requires setting a number of periods, knowing for each period the number of plants and their locations. Based on the existing plants, the total CO₂ emission from the cluster is known with defined CO₂ emission sources in terms of flowrates, compositions, condition (temperature and pressure). A given total power requirement of the cluster, a common utility system with known power demand and supply. In addition, to reduce emissions further renewable power generations options are available with known limits and prices. The model was solved for each objective using “What's Best 9.0” Lindo Global solver for MS-Excel 2010 via a desktop PC with Intel Core i7 Duo processor, 8 GB RAM and a 32-bit operating System (Lindo, 2006). Next, a Pareto curve is constructed to evaluate the performance of each objective. The next section illustrates the concept.

3. Case Study

The proposed concept is illustrated in the following case study, which is an industrial cluster that includes a set given plants. The plants are Oil refinery, Steel production, a fertilizer production facility producing both ammonia and urea in addition to a Natural Gas Fired Power Plant which main information is shown in Table 1. In the industrial clusters, plants and processes were included to reduce carbon dioxide footprint such as a Renewable solar power plant, Enhanced Oil Recovery (EOR), Saline Storage, and a Methanol plant, which is also shown in Table 1.

Table 1: Carbon Integration Data obtained from Al-Mohannadi et al, (2016)

Plants		CO ₂ Composition. (wt%)	CO ₂ Flow (t/d)	Sink fixation (t CO ₂ emitted/ t CO ₂ captured)	CO ₂ Cost (USD/ t CO ₂)
Sinks	Enhanced Oil Recovery (EOR)	0.94	6317	0	-30
	Methanol (MEOH)	0.99	1710	0.098	-21
	Fertilizer Complex - Urea	0.99	1126	0.39	-15
	Saline Storage	0.94	8317	0	8.6
Sources	Fertilizer Complex -CO ₂ amine unit	1	977	0	0
	Steel-iron mill	0.44	3451	0	29
	Power Plant-gas turbine	0.07	9385	0	43
	Oil Refinery-boiler	0.27	1092	0	35

Carbon dioxide treatment efficiency parameters, treatment removal, power needed for the compression and transmission were taken from Al-Mohannadi and Linke, (2016). Transmission data including sizes and costs of pipeline and compression were obtained using the method proposed by Kwak, (2016). For a given time frame of five periods over 10 years, the network was first optimized to achieve the maximum economic benefit. The allocation of the network is shown in Table 2.

Table 2: Maximum Economic Benefit Carbon Dioxide Allocation (Period – P, T – Treated Source, U- Untreated Source)

Source	Period	Flow type	EOR	MEOH	UREA	Storage
Fertilizer Complex	P1	T1	-	-	-	-
		U1	977	-	-	-
	P2	T2	-	-	-	-
		U2	977	-	-	-
	P3	T3	-	-	-	-
		U3	977	-	-	-
	P4	T4	-	-	-	-
		U4	977	-	-	-
	P5	T5	-	-	-	-
		U5	977	-	-	-
Iron and Steel Production	P1	T1	2,309	825	-	-
		U1	317	-	-	-
	P2	T2	2,309	825	-	-
		U2	317	-	-	-
	P3	T3	2,309	825	-	-
		U3	317	-	-	-
	P4	T4	2,309	825	-	-
		U4	317	-	-	-
	P5	T5	2,309	825	-	-
		U5	317	-	-	-
Oil Refinery	P1	T1	207	885	-	-
		U1	-	-	-	-

Source	Period	Flow type	EOR	MEOH	UREA	Storage	
	P2	T2	207	885	-	-	
		U2	-	-	-	-	
	P3	T3	207	885	-	-	
		U3	-	-	-	-	
	P4	T4	207	885	-	-	
		U4	-	-	-	-	
	P5	T5	207	885	-	-	
		U5	-	-	-	-	
	Power Plant	P1	T1	2,507	-	-	-
			U1	-	-	-	-
P2		T2	2,507	-	-	-	
		U2	-	-	-	-	
P3		T3	2,507	-	-	-	
		U3	-	-	-	-	
P4		T4	2,507	-	-	-	
		U4	-	-	-	-	
P5		T5	2,507	-	-	-	
		U5	-	-	-	-	

The network resulted in a total profit of 395 million USD. The most profitable sinks, EOR and methanol, were supplied from the sources that has the lowest treatment needed. Next, the network was optimized to achieve the maximum environmental benefit. The network allocation flows are provided in Table 3.

Table 3: Maximum Environmental Benefit Carbon Dioxide Allocation (Period – P, T – Treated Source, U- Untreated Source)

Source	Period	Flow type	EOR	MEOH	UREA	Storage
Fertilizer Complex	P1	T1	-	-	-	-
		U1	-	-	-	977
	P2	T2	-	-	-	-
		U2	-	-	-	977
	P3	T3	-	-	-	-
		U3	-	-	-	977
	P4	T4	-	-	-	-
		U4	-	-	-	977
	P5	T5	-	-	-	-
		U5	-	-	-	977
Iron and Steel Production	P1	T1	2,795	-	-	656
		U1	-	-	-	-
	P2	T2	2,795	-	-	656
		U2	-	-	-	-
	P3	T3	2,795	-	-	656
		U3	-	-	-	-
	P4	T4	2,795	-	-	656
		U4	-	-	-	-
	P5	T5	2,795	-	-	656
		U5	0	-	-	-
Oil Refinery	P1	T1	207	-	-	885

Source	Period	Flow type	EOR	MEOH	UREA	Storage	
	P2	U1	-	-	-	-	
		T2	207	-	-	885	
	P3	U2	-	-	-	-	
		T3	207	-	-	885	
	P4	U3	-	-	-	-	
		T4	207	-	-	885	
	P5	U4	-	-	-	-	
		T5	207	-	-	885	
	Power Plant	P1	T5	-	-	-	-
			T1	3,314	-	-	4,194
P2		U1	-	-	-	-	
		T2	3,314	-	-	4,194	
P3		U2	-	-	-	-	
		T3	3,314	-	-	4,194	
P4		U3	-	-	-	-	
		T4	3,314	-	-	4,194	
P5		U4	-	-	-	-	
		T5	3,314	-	-	4,194	
		U5	-	-	-	-	

When the maximum capture target was imposed without any economic constraint, the network resulted in a cost of -600 million USD and 68 thousand CO₂ captured across all periods. The same structure, sources to sinks, connections were chosen. As EOR and Storage had the largest capacities to reduce CO₂ and the highest efficiency of fixing CO₂. The network also activated the maximum allowed renewable power.

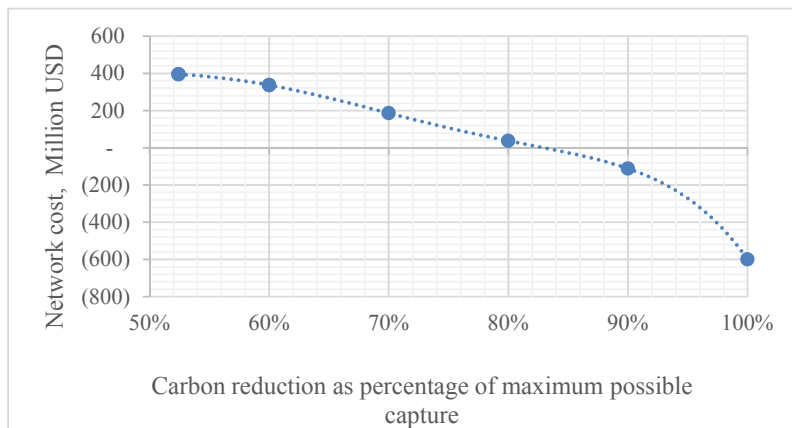


Figure 1: Pareto Optimal Solution of the bi-objective problem

From Figure 1, it can be seen that none of the points within Pareto front were identical, in terms of both of the specified objectives. However, the optimum points for the cost objective, still reduced a good amount of CO₂.

4. Conclusions

The approach takes into account multiple time periods, multiple processes including renewable power generation, CCUS, treatment, compression and transmission options needed to develop carbon dioxide allocation networks. The network optimization problem has been formulated as a MILP and can robustly and quickly be solved for industrial clusters of typical size. Different scenarios for an industrial park were explored using the proposed approach and compared using Pareto curve. The approach gives the regulator or policy makers a tool to develop future mitigation strategies and compare plans.

Acknowledgement

Dhabia M. Al-Mohannadi gratefully acknowledges the support received from the Qatar Research Leadership Program (QRLP), which is part of Qatar Foundation Research Division.

References

- C. Pinho, M. Madaleno, 2001, CO₂ emission allowances and other fuel markets interaction. *Environmental Economics and Policy Studies*. Environmental Economics and Policy Studies. 13, 3, 259–281
- D. Foo, R. Tan, 2016, A review on process integration techniques for carbon emissions and environmental footprint problems, *Process Safety and Environmental Production*, 103B, 291-307
- D. Huisingh, Z. Zhang, J. Moore, Q. Qiao, Qi, Q. Li, 2015, Recent Advances in Carbon Emissions Reduction: Policies, Technologies, Monitoring, Assessment and Modeling. *Journal of Cleaner Production*. 103, 1-12
- D.M. Al-Mohannadi, P. Linke, 2016, On the Systematic Carbon Integration of Industrial Parks for Climate Footprint Reduction *Journal of Cleaner Production*, 112, 4053-4064
- D.M. Al-Mohannadi, S. Y. Alnouri, S.K. Binshu, P Linke, 2016, Multiperiod Carbon Integration. 136, 150-158
- G. Kwak, 2016, A Systematic approach to optimize the cost of carbon integration network. Masters Thesis, Texas A&M University at Qatar, Doha, Qatar
- J.J. Klemeš, Z. Kravanja, 2013, Forty years of Heat Integration: Pinch Analysis (PA) and Mathematical Programming (MP). *Curr. Opin. Chem. Eng.*, 2, 461-474
- Lindo, 2006, What'sBest! 9.0 - Excel Add-In for Linear, Nonlinear, and Integer Modeling and Optimization; Lindo Systems: Chicago, IL
- M.E. Boot-Handford, J.C. Abanades, E.J. Anthony, M.J. Blunt, S. Brandani, N. Dowell, J. R. Fernández, M. Ferrari, R. Gross, J. P. Hallett, R. Haszeldine, P. Heptonstall, A. Lyngfelt, Z. Makuch f, Enzo Mangano, Richard T. J. Porter j, Mohamed Pourkashanian k, Gary T. Rochelle, N. Shah, J. Yao, P. Fennell, 2014, Carbon capture and storage update. *Energy & Environmental Science*, 7, 1, 130-189
- P.S. Varbanov, S. Doyle, R. Smith, 2004. Modelling and Optimization of Utility Systems. *Chemical Engineering Research and Design*, 82, 5, 561-578
- R. Jing, X. Zhu, Z. Zhu, W. Wang, C. Meng, N. Shah, N. Li, Y. Zhao, 2018, A multi-objective optimization and multi-criteria evaluation integrated framework for distributed energy system optimal planning, *Energy Conversion and Management*, 166, 445-462

Life-Cycle Environmental Impact Assessment of the Alternate Subsurface Intake Designs for Seawater Reverse Osmosis Desalination

Abdulrahman H. Al-Kaabi^a, Hamish R. Mackey^{a,*}

^aDivision of Sustainable Development, College of Science and Engineering, Hamad bin Khalifa University, Qatar Foundation, Doha, Qatar

hmackey@hbku.edu.qa

Abstract

The study carried out a life-cycle environmental impact assessment of two reverse osmosis plants located within the Arabian Gulf using three different electric submersible pump (ESP) designs for subsurface intake of seawater and compared these with an existing open intake design. The study used life cycle assessment to quantify impacts for construction and operation of the plant for the various intake options. All values were compared to a functional unit of 1.0 m³ of produced desalinated water based on individual well capacities of 15,000 m³/d and a design life of 50 years. Results showed that the subsurface system performed better across the various impact categories than the open intake. Construction phase impacts of the beach well were insignificant in comparison to operational phase with the exception of abiotic depletion potential, which was still minor. Nevertheless, of the three subsurface beach wells evaluated the slickline ESP design was consistently better than the other two subsurface options, albeit very similar to coil tubing ESP.

Keywords: Desalination, Subsurface Intake, Slickline Electric Submersible Pump, Beach Well, Life-Cycle Assessment, Construction Phase Impacts, Environmental Impact

1. Introduction

Global freshwater scarcity affects at least 2.8 billion people globally. Of this population, at least 43% (1.2 billion people) have no access to clean drinking water (United Nations, 2014; Mekonnen and Hoekstra, 2016). In response, use of desalination as a reliable alternative water source is increasing (Hoekstra and Mekonnen, 2012). Reverse osmosis (RO), which employs semipermeable membrane barriers, is the current desalination method of choice due to its energy efficiency compared to thermal techniques (Raluy et al., 2006).

Subsurface intakes, particularly if abstracting from brackish ground water, are a superior RO feed source to open seawater intakes due to better chemistry, microbiology and physical properties (Stein et al., 2016). In contrast to open seawater intakes which have high fouling potential requiring significant pre-treatment, subsurface intakes allow natural filtration of sediments, salt precipitates, and active biological treatment, which eliminates or reduces the need of pre-treatment (Missimer et al., 2015; Stein et al., 2016).

There are six types of subsurface seawater intakes, which are classified according to onshore location (vertical wells and beach infiltration gallery) and offshore location in

the seabed (slant wells, horizontal wells, radial collector wells, and seabed infiltration galleries). Vertical wells, also commonly called beach wells, are the simplest subsurface intake systems, constructed according to designs and processes that are similar to conventional groundwater production wells. They are typically located along the beach, where they are screened within unconsolidated beach sand and alluvial materials. They are fitted with pumps, installed vertically above the wells, which induce radial inflow of seawater and inland groundwater into the wells. The rate and sustainability of seawater recharge of the beach wells is limited by local hydrogeology, especially the transmissivity of the aquifers (Missimer et al., 2015). Thus, beach wells have a limited production capacity. A recent modeling study, demonstrated that a beach well in Qatar drilled to a depth of 100 m can produce a maximum of only 16,000 m³ per km² in the coastal zone, which can be considered suitable for small-capacity seawater desalination plants (Baalousha, 2016).

The conventional beach well layout includes an electric submersible pump (ESP) design, which was utilized as early as 1928 (Takacs, 2017). Newer ESP designs, such as coil tubing and slickline, were developed to boost production capacity and efficiency in the oil industry and could find useful application for subsurface seawater RO intake (Dieuzeide et al., 2014). The proposed alternative beach well layout designs using coil tubing ESP and slickline ESP designs are shown in Figure 1. Both designs have been proven worldwide in the oil industry (Dieuzeide et al., 2014) and as summarized in Table 1, provide operational and installation advantages, with slickline ESP systems being optimal. Given these benefits this paper aims to evaluate the environmental impact of ESP systems for subsurface seawater RO intakes and assess their performance over conventional vertical wells and open intakes. This is conducted through the use of life cycle assessment (LCA) of environmental loads associated with the construction and operation of the RO plant and intake systems.

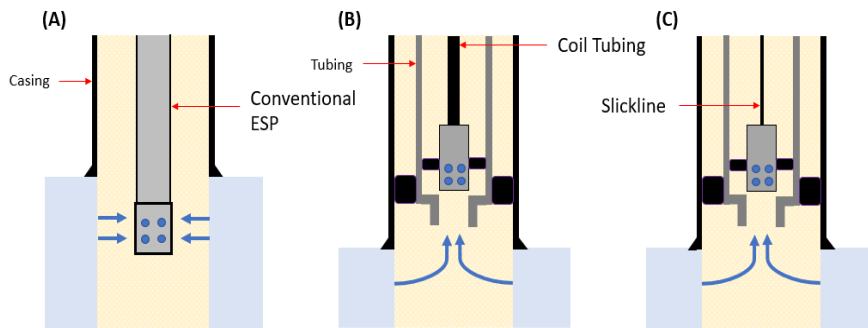


Figure 1: Proposed alternative beach well layouts; A. Current conventional well design; B. Proposed Coil tubing ESP subsurface intake and; C. Proposed Slickline ESP subsurface intake.

Table 1: Comparison between typical beach well design and ESP coil tubing and slickline subsurface intake designs

Design aspects	Typical beach well	Coil tubing beach well	Slickline beach well
Maximum Run Deviation	90°	90°	60°
Installation Mean	Specialized truck or rig	Coil tubing unit	Slickline unit
OPEX	Higher	Lower	Lowest
Production Downtime	3-6 months	1 month	10-15 days

2. Materials and Methods

2.1. Life Cycle Assessment Goal and Scope

LCA is a widely-used process to measure the environmental impacts of different life cycle stages of a system, or compare system alternatives. A cradle to gate boundary LCA was undertaken to investigate the environmental impacts associated with the construction of the various intake systems and the plantwide process operation. The assessment scenarios included an open intake system and three alternative subsurface intake systems (conventional, coil tubing and slickline ESP). The LCA covered materials and diesel associated with machinery for the intake construction, as well as power, material and chemical inputs for the operation phase of the entire plant. The pretreatment and RO unit construction were excluded due to lack of suitable data, but would be identical for all three subsurface systems. All values were compared to a functional unit of 1.0 m³ produced desalinated water based on individual well capacities of 15,000 m³/d and a design life of 50 years. LCA was carried out with GaBi software.

2.2. Life cycle impacts

The LCA considered the following impact categories: global warming potential (GWP), acidification potential (AP), eutrophication potential (EP), ozone layer depletion potential (ODP), abiotic depletion potential of elements (ADP-e), abiotic depletion potential of fossil reserves (ADP-f), freshwater aquatic ecotoxicity potential (FAETP inf.), photochemical ozone creation potential (POCP), human toxicity potential (HTP inf.), marine aquatic ecotoxicity (MAETP inf.), and terrestrial ecotoxicity potential (TETP inf.).

2.3. Life cycle inventory

Data from two existing RO plants located across the Arabian Gulf were utilized for this comparison, both using similar pre-treatment processes of DAF and UF, and operating currently with open intakes. Plant 1 had a capacity close to 175,000 m³/d while Plant 2 had a capacity of close to 275,000 m³/d. Plants with subsurface intakes were modelled with the DAF pre-treatment units removed based on previous literature that indicates even the UF could potentially be dropped (Shahabi et al., 2015). Construction requirements associated with subsurface wells and open intake were taken from an oil and gas company operating within Qatar. Pumping heads were calculated based on 40 m drawdown for

subsurface wells in the local hydrogeology (Baalousha et al., 2015). Distance from the different subsurface wells and RO plant were assumed to be similar.

3. Results and discussion

3.1. Intake construction impacts

Open intakes exhibited the highest overall environmental impacts related to construction in the areas of GWP, AP, EP, ODP, ADP-f, FAETP inf., MAETP inf. and POCP. The conventional ESP intake in contrast showed maximum impacts with respect to ADP-e, HTP inf., MAETP inf. and TETP inf. Coil tubing and slickline ESP intakes generally exhibited lower impacts than conventional ESP, with slickline ESP consistently exhibiting the lowest impact of the ESP systems with the exception of ADP-e, which was 100% for all three ESP systems (Figure 2).

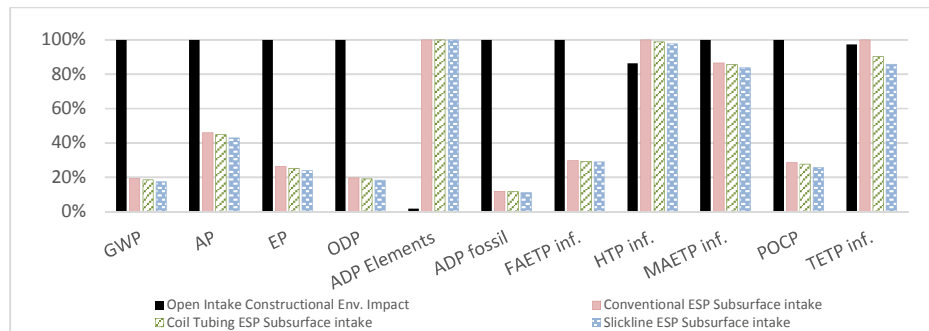


Figure 2: Construction environmental impacts across various RO intake systems.

3.2. Operational impacts of ESP intakes versus conventional vertical wells

The impacts from plant-wide operation at Plant 1 and Plant 2 were significantly higher than construction impacts for all environmental impact categories assessed, as shown in Figure 3. The low construction impacts is due to the minimal excavations and due to the long lifetime of the two plants of 50 years. The most significant contribution was to ADP-e which accounted for around 6.5% of total ADP-e impacts due to the high use of metals in the intake system.

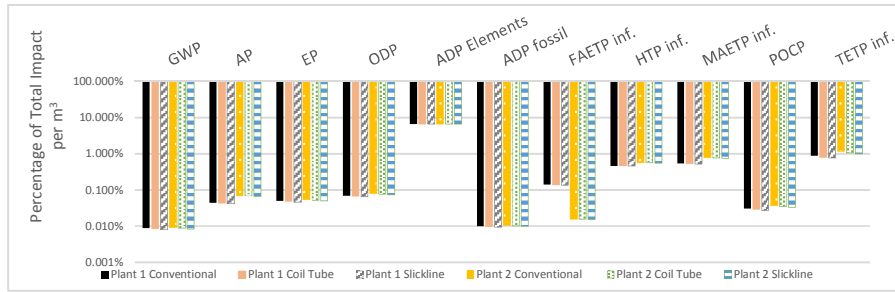


Figure 3: The percentage of total impacts associated with construction of the intake itself at Plant 1 and Plant 2 for the three different types of subsurface intakes.

3.3. Benefits of using subsurface intakes

Figure 4 demonstrates the relative environmental impacts at the two modelled plants using open and subsurface intakes for the operation phase only, given the minor impact from the intake construction phase. It is clear that subsurface intakes provide significant improvements across all selected environmental impact categories, although significant differences exist between the two plants based on chemical usage for the pretreatment.

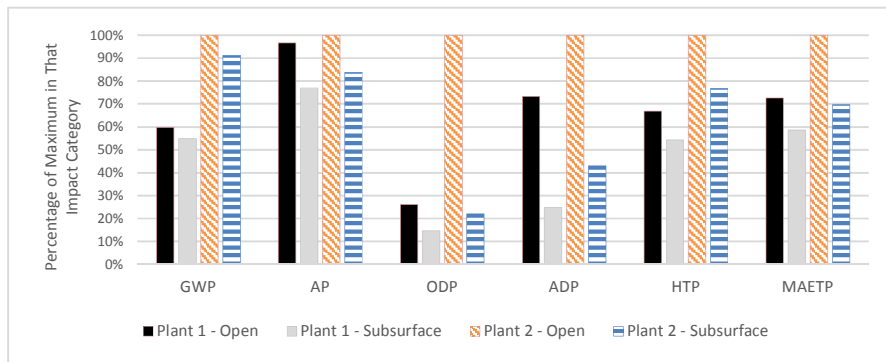


Figure 4: The reduction in various impact categories associated with moving from open intake to subsurface intake (modelled as conventional vertical well) with natural gas as energy source.

4. Conclusions

SWRO has the potential to alleviate water scarcity in coastal regions. While subsurface intakes are suitable due to their low environmental impacts, vertical beach wells have bottle neck effects on their potential production capacity. The current study evaluated the environmental impacts of conventional ESP layout design for beach wells and optimized ESP beach well designs, slickline and coil tubing. The conclusions deduced from the LCA are as follows:

- Construction phase impacts of subsurface beach well intakes are minimal compared to the operational phase requirements.
- Operational phase reductions in impacts are significant for subsurface intakes compare to conventional open-water intakes, particularly for ADP and ODP.

- While only small differences exist between the impacts associated with various beach well designs, slickline ESP consistently had the lowest construction related environmental impacts and is therefore the most suitable candidate given its proven economical value also.

References

- A. Dehwah & T. Missimer, 2016, Subsurface intake systems: Green choice for improving feed water quality at SWRO desalination plants, *Water Res*, 88, 216-224
- A. Hoekstra & M. Mekonnen, 2012, The water footprint of humanity, *Proceedings of the National Academy of Sciences of the United States of America*, 109(9), 3232-3237
- D. Williams, 2015, Slant Well Intake Systems: Design and Construction. Intakes and Outfalls for Seawater Reverse-Osmosis Desalination Facilities. In: Missimer T.M., Jones B., Maliva R.G., *Environmental Science and Engineering*, 275-320
- G. Raluy, L. Serra, & J. Uche, 2006, Life cycle assessment of MSF, MED and RO desalination technologies. *Energy*, 31(13), 2361-2372.
- G. Takács, 2018, *Electrical submersible pumps manual: Design, operations, and maintenance*, Oxford, United Kingdom: Elsevier, Gulf Professional Publishing, an imprint of Elsevier.
- H. Baalousha, 2016, The potential of using beach wells for reverse osmosis desalination in Qatar, *Modeling Earth Systems and Environment*, 2(2), 97
- I. Muralikrishna & V. Manickam, 2017, Principles and Design of Water Treatment. In: *Environmental Management*, 209-248
- M. Mekonnen & A. Hoekstra, 2016, Four billion people facing severe water scarcity, *Science Advances*, 2(2), e1500323-e1500323
- M. Shahabi, A. McHugh & G. Ho, 2015, Environmental and economic assessment of beach well intake versus open intake for seawater reverse osmosis desalination, *Desalination* 357, 259-266
- S. Al-Mashharawi, A. Dehwah, K. Bandar & T. Missimer, 2014, Feasibility of using a subsurface intake for SWRO facility, south of Jeddah, Saudi Arabia, *Desalination and Water Treatment*, 55(13), 3527-3537
- N. Hilal, A. Ismail, T. Matsuura & D. Oatley-Radcliffe, 2017, *Membrane characterization*, Amsterdam, Netherlands, Elsevier
- S. Stein, A. Russak, O. Sivan, Y. Yechieli, E. Rahav, Y. Oren & R. Kasher, 2016, Saline groundwater from coastal aquifers as a source for desalination, *Environmental Science & Technology*, 50(4), 1955-1963
- T. Dieuzeide, A. Bemba, D. Kusuma & G. Anderson, 2014, Wireline Retrievable Electric Submersible Pump: Innovative and Valuable Completion for Offshore Fields. *International Petroleum Technology Conference*
- T. Missimer, B. Jones & R. Maliva, 2015, Intakes and outfalls for seawater reverse-osmosis desalination facilities: Innovations and environmental impacts, Springer
- T. Missimer & R. Maliva, 2018, Environmental issues in seawater reverse osmosis desalination: Intakes and outfalls, *Desalination* 434, 198-215
- United Nations, 2014, International decade for action 'WATER FOR LIFE'

Optimization of biofuel supply chain design via a water-energy-food nexus framework

Dulce Celeste López-Díaz,^{a*} Luis Fernando Lira-Barragán,^a José Maria Ponce-Ortega,^a Mahmoud M. El-Halwagi^{b,c}

^a*Chemical Engineering Department, Universidad Michoacana de San Nicolás de Hidalgo, Morelia 58060, México.*

^b*Chemical Engineering Department, Texas A&T University, College Station TX 77843, USA.*

^c*Adjunct Faculty at the Chemical and Materials Engineering Department, King Abdulaziz University, Jeddah 21589, Saudi Arabia.*

Sanasa_486@hotmail.com

Abstract

Biofuels are attractive energy renewable sources to satisfy the current growing energy demand, but large-scale production requires the installation of complex biorefinery systems that involve strategic decisions for design and operation such as to determine the location, feedstocks, production capacities, as well as the impact on the surrounding environment. This work proposes an optimization model for the design of a biorefinery system through an efficient supply chain considering economic (minimization of the total annual cost) and environmental objectives (minimization of the overall CO₂ emission and the water consumption along the nexus). This approach considers the inherent uncertainty on prices of feedstocks and products, biofuel demands, biomass requirements, weather conditions, agricultural production, etc. Finally, a case study located in Mexico is solved for several scenarios to illustrate the capacity of this approach. The solution shows the trade-off among the considered objectives affected by uncertainty in the biorefinery system.

Keywords: Biorefineries, Supply chain, Nexus, Uncertainty, Material flow analysis.

1. Introduction

Nowadays, the high energy demand has allowed the development of other energy sources such as of biofuels. This energy alternative represents an attractive and renewable option to partially reduce the consumption of fossil fuels. Nevertheless, large-scale production requires the installation of several biorefineries. A biorefinery is an industrial plant that from biomass produces high value-added chemicals and biofuels (bioethanol and biodiesel) [1]. Currently, the design of sustainable processes is essential [2]. Recent advances in processing technologies enable the conversion of non-food biomass resources for the controversy that exists against the food sector through second generation biofuels where the use of residues involves higher environmental benefits. With the variety of feedstocks, processing technologies, portfolio or products, geographic and market conditions, involves complex decisions to determine the optimal location, equipment, and operation of these industrial plants [3]. The objective is to synthesize a supply chain to

satisfy the market demand while the production of feedstock is determined, as well the capacity and location of the processing facilities to convert this biomass to biofuels. Also, to design a robust biorefining system and to have a close estimation of the environmental impact that this energy sector can produce, the uncertain effects should be considered as weather conditions, agriculture parameters, conversion factors, etc. We propose an MFA (Material Flow Analysis) [4] approach for the watershed segmentation in reaches, where in each of them exists the possibility to install a biorefinery. Within each reach, the flow and main characteristics are assumed constant, even considering that several tributaries can feed to each reach. In this regard, this approach accounts for water extractions and discharges associated with domestic, agricultural and industrial uses, in addition to the natural phenomena such as filtration, evaporation and precipitation. Thus, mass balances, property tracking, and physical, chemical, and biochemical phenomena are included for each reach. Also, it estimates the overall CO₂ emissions by the industrial activity related to the biofuels production, and the balance considers the CO₂ fixation by the cultivation lands where the feedstocks are cultivated. The optimization approach is driven by economic (maximization of the total annual costs for the whole supply chain) and environmental (Minimization of the overall greenhouse emission) goals considering simultaneously the effects on the watershed. Because water is the resource of interaction between the sectors that make up the nexus.

2. Model Formulation

The problem is focused on satisfying the biofuel demand in a specific region where several feedstocks are candidate to be processed with existing and new potential cultivation areas, processing technologies, potential location for installing biorefineries, and large portfolio of bioproducts. Given the installation and operation of a biorefinery system (set of biorefineries to supply great demands) the impact on the environment must be considered in a sustainable design, in this case according with numerous studies the water reservoir is the most affected by this industrial activity. Surrounding watershed provides water for different facilities, as well as pollutant effluents are discharged. Implementing a Material Flow Analysis technique, the watershed is analysed to determine the environmental impact through water balances accounting for the availability of resources and environmental constraints along the watershed to avoid affectations for existing tasks as agricultural, residential or industrial activities. The proposed complex industrial system studied as a water-energy-food nexus is design through synthetizing the supply chain obtaining the production and operation specification. Also, the uncertainty that affects several parameters is considered.

The optimization approach is described and proposed as follows:

Watershed at initial conditions before the implementation of the biorefining system

$$Q_{r,s}^{Initial-Out} = Q_r^{In} + P_{r,s} + D_{r,s} + H_{r,s} + \sum_{t=1}^{N(t)} FT_{r,t,s} + \sum_m W_{m,r,s}^{Discharge-feedstocks_Initial} - \sum_m W_{m,r,s}^{Used-feedstocks_Initial} - L_{r,s} - U_{r,s}, \quad \forall r, \forall s \quad (1)$$

Watershed at final condition (once the biorefining system is establish)

$$Q_{r,s}^{Out} = Q_r^{In} + P_{r,s} + D_{r,s} + H_{r,s} + \sum_{t=1}^{N(t)} FT_{r,t,s} + \sum_m W_{m,r,s}^{Discharge-feedstocks} + \sum_k W_{k,r,s}^{Discharge-biorefinery} - \sum_m W_{m,r,s}^{Used-feedstocks} - \sum_k W_{k,r,s}^{Used-biorefinery} - L_{r,s} - U_{r,s}, \quad \forall r, \forall s \quad (2)$$

Wastewater discharges from new biorefineries

$$W_{k,r',s}^{Discharge-biorefinery} = \sum_m \alpha_{k,m,s}^{ww-biorefinery} P_{k,m,r',s}^{Bio}, \quad \forall k, \forall r', \forall s \quad (3)$$

Production at the cultivating fields

$$f_{m,r,s}^{Prod-feedstock} = \alpha_{m,r,s}^{feedstock} \left[a_{m,r}^{exist} + a_{m,r}^{new} \right], \quad \forall m, \forall r, \forall s \quad (4)$$

Activation of binary variables for biorefineries

$$F_{m,r',s} \leq F_{m,r'}^{max} y_{r',s}^{Biorefinery}, \quad \forall r', \forall s \quad (5)$$

Production of biofuels

$$P_{k,m,r',s}^{Bio} = \alpha_{k,m,s}^{Bioref} F_{m,r',s}, \quad \forall k, \forall m, \forall r', \forall s \quad (6)$$

Distribution of products to the markets

$$P_{k,r',s} = \sum_j P_{k,r',j,s}^{Prod-market}, \quad \forall k, \forall r', \forall s \quad (7)$$

Economic equations

Capital cost for biorefineries

The capital cost for biorefineries has associated fixed and variable charges as follows:

$$CapCost_s^{Biorefineries} = k_F \left[\sum_m \sum_{r'} FC_{m,r'}^{Biorefinery} y_{r',s}^{Biorefinery} + \sum_m \sum_{r'} VC_{m,r'}^{Biorefinery} (F_{m,r',s}) \sigma_{m,r'}^{Biorefinery} \right], \quad \forall s \quad (8)$$

Objective function

Total annual profit

The total annual profit accounts for all the sale gains, minus the cost of installation and operation of biorefineries, the agriculture cost to cultivate the biomass, water costs, and product and raw material transportation costs.

$$Profit_s = G_s^{Products} + G_s^{Grains} - CapCost_s^{Biorefineries} - OpCost_s^{Biorefineries} - OpCost_s^{Feedstocks} - \quad (9)$$

$$OpCost_s^{Water-biorefineries} - OpCost_s^{Water-feedstocks} - TCost_s^{Feedstocks} - TCost_s^{Grains} - TCost_s^{Products}$$

For this proposed system, the profit has a different value for each scenario, the involved uncertainty drastically impacts the economic target.

Expected profit

Considering the strong fluctuation that affect the profit, the model formulation defines the expected profit, which corresponds to the distribution profile for all the scenarios:

$$MProfit = \overline{Profit}_s = \frac{1}{scenario(s)} \sum_s Profit_s(s), \quad \forall s \quad (10)$$

Worst Profit

It is particularly important to maximize the worst scenario for the economic performance. Thus, the decision makers can decide among risky configurations for the uncertainty management in the project.

$$MProfit \geq WProfit \quad (11)$$

Total water requirements for the proposed biorefining system

$$Water_s^{required} = Q_s^{Initial} - Q_s^{final}, \quad \forall s \quad (12)$$

Expected fresh water consumption

The available sites to install industrial plants will define the requirements of water for this location, also it is important to include the expected value for the fresh water consumption:

$$MWater = \overline{Water}_s = \frac{1}{scenario(s)} \sum_s Water_s^{required}(s) \quad (13)$$

Worst fresh water consumption

In the same way, it is essential to know the worst scenarios for the performance of the fresh water consumption in the biorefining system:

$$WWater \geq Water_s^{required}, \quad \forall s \quad (14)$$

CO₂ emissions

The overall CO₂ emissions are estimated by the industrial and transportation operation where the capture of emission by cultivating areas is considered:

$$CO_{2s}^{total} = CO_{2s}^{prod} P_s^{biototal} - CO_{2s}^{abs} A_s^{total}, \quad \forall s \quad (15)$$

3. Results

The proposed optimization model corresponds to a mixed integer non-linear programming (MINLP) model. The model was coded in GAMS (General Algebraic Modelling System), and the data of the case study were charged. The uncertainty was considered for several parameters, where N-scenarios are generated through the Latin Hypercube Sampling method under normal distributions. Monte Carlo simulation is implemented to evaluate the risk in quantitative analysis for the parameters analyzed.

A case study was solved to evaluate the capacities of the proposed model. This case study is located in the central part of Mexico that is considered as a high-potential region due to the availability of resources and the predominant agricultural activity. The balsas river is considered as the watershed of analysis to estimate the environmental impact for the water consumption and the effluent discharges using the MFA approach. The watershed was divided in 23 fixed reaches based on hydrologic and geographic studies considering some parameters of the watershed system such as precipitation, filtration, evaporation or discharges due to industrial or residential activities to estimate the biomass and biofuel production. The total demand of biofuels is required by 10 markets, where each one is represented by a city along the studied region. The feedstocks are second generation biomass, where residues of corn, wheat, sorghum, and sugar are used to produce bioethanol, and for biodiesel production are cultivated jatropha and palm oil. The biofuel demands for each market were estimated using projections by the Energy Council of Mexico (SENER), and SENER-BID-GTZ (2016) projected for the next decade that the 10 % of the total energy demand will be satisfied by biofuels. The model was solved using the solver CPLEX. The optimization model consists of 309,650 continuous variables, 84,947 constraints, and 23 binary variables. The CPU time and the average solution for the objectives in expected and the worst scenarios are presented in Table 1. The time horizon is a year with an investment time of ten years. 50 scenarios were generated using Monte Carlo simulations.

The optimization problem was solved for the economic targets. At first, it is obtaining the maximization of profit being the greatest value that represents the optimistic economic condition, and the lowest represents the worst condition. Figure 1 shows the profit and water demands, where 3 interested scenarios were chosen. The solution for each scenario represents a specific configuration for the supply chain, as well the composition and operation of the biorefining system. For example, in scenario 3 with 94 % probability of occurrence, the expected profit is \$US 7.58 x10⁸/y and 3.24 x10⁷ m³/y of demand of fresh water. where 7 biorefineries are required to satisfy the biofuel demands in the considered markets. The total biofuel production is 6.71 x10⁷ L/y of bioethanol and 8.66 x10⁷ L/y of biodiesel, the distribution between the type of biomass used and produced biofuels are presented in the Figure 2. But for the greatest economic risk that we have the worst profit that can be obtained of US\$ 7.32 x10⁸/y and 3.25 x10⁷ m³/y of fresh water consumption.

Also, the satisfied demand of feedstocks and products are estimated. The availability of land to cultivate crops in the region was considered but also the possibility of increment, in the presented solution 19, 377 ha of new area should be cultivated to satisfy the biomass demand. For scenario 2, with 70 % of occurrence, it is possible to obtain approximately at least a profit of US\$ 673 million for the worst profit, when the profit can reach up US\$ 720 million (achieving an increase of 6.98 %). For the optimistic environmental conditions, the system has the lowest consumption of water, where the system with the greatest probability of occurrence yields a profit of US\$ 1.68 x10⁸/y and the demand of water is 2.07x10⁷ m³/y with a biofuel production of 4.4859 x10⁷ L/y for bioethanol and 1.701459x10⁸ L/y for biodiesel, for this scenario the area requires to be increased in 34,224 Ha to cultivate corn, 55 Ha for wheat, and 3,268 ha for oil palm.

Table 1. Case study solutions.

Case	CPU TIME (s)	AVERAGE SOLUTION
<i>Maximizing Mprofit</i>	2426	US\$6.79 x10 ⁸ /y
<i>Maximizing Wprofit</i>	90.4	US\$6.44 x10 ⁸ /y
<i>Minimizing Mwater</i>	244.7	2.01 x10 ⁷ m ³ /y
<i>Minimizing Wwater</i>	27.05	5.04 x10 ⁵ m ³ /y

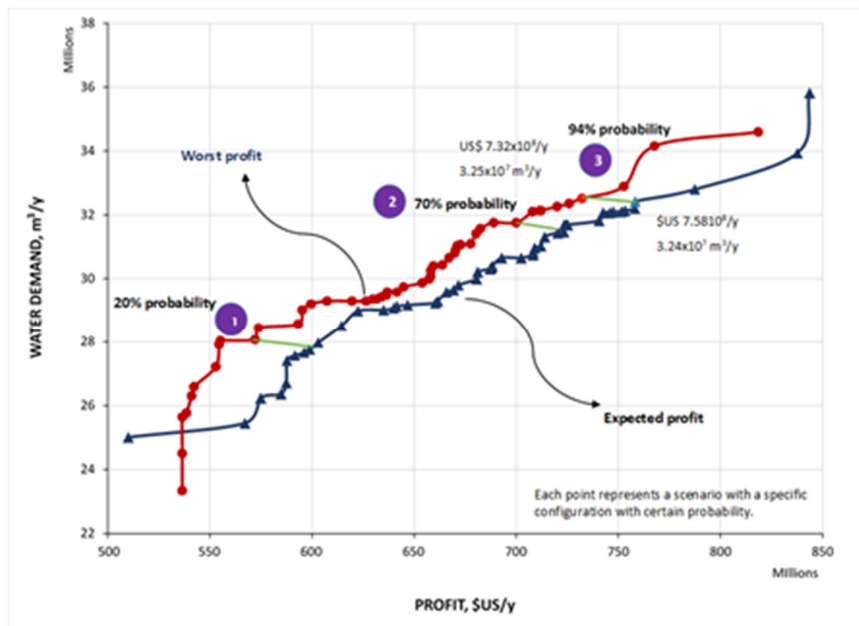


Figure 1. Pareto curve for the profit vs water demand.

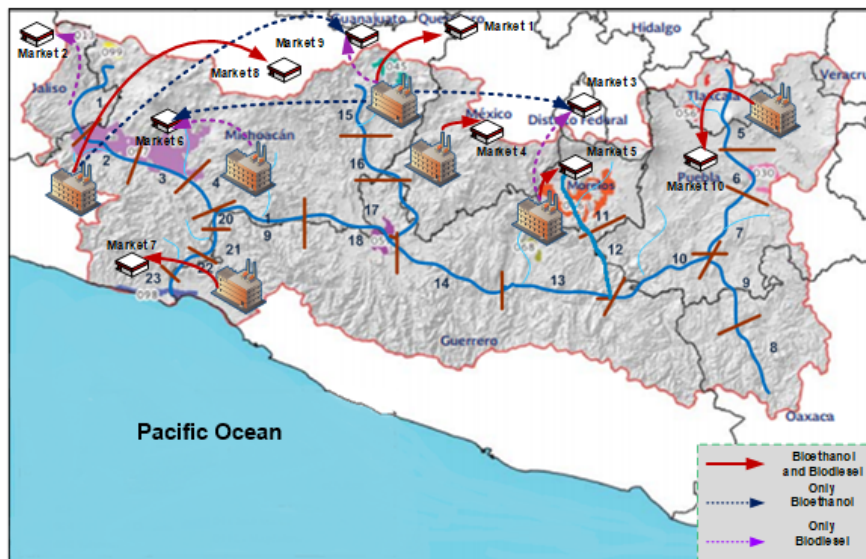


Figure 2. Optimal configuration for the biorefinery system in scenario 3 for expected profit.

4. Conclusions

The proposed mathematical approach incorporates the use of agricultural residues to reduce the environmental impact, as well as an analysis in the watershed to understand the interconnection between sector that works as a nexus, the sale of grains as economic retribution in the system, and the uncertainty to have a robust model.

The optimization approach is an efficient tool that determines the location and operation logistics of biorefineries, new cultivation areas and associated food profits and biomass wastes, fresh water demands, production of feedstock and biofuels, production and capture of greenhouse gas emission, routes of distribution considering environmental and economic objectives. The tradeoffs between these objectives were analyzed and discussed with focus on the strong impact of some environmental constraints on the selection of feedstock growth and location as well as production capacities and impact on the surrounding watershed.

References

- [1] J.E. Satibañez-Aguilar, R. Morales-Rodriguez, J.B. Gonzales-Campos, J.M. Ponce-Ortega, 2016, Stochastic design of biorefinery supply chains considering economic and environmental objectives, *Journal of Cleaner Production*, 136, 224-245.
- [2] P. Staurt, M.M. El-Halwagi, 2013, *Integrated biorefineries: Design, analysis, and optimization*, Taylor and Francis/CRC, Avingdon, Virginia, USA.
- [3] B. Kamm, M. Kamm, 2004, Principles of biorefineries, *Applied Microbiology and Biotechnology*, 64, 2, 137-145.
- [4] F. López-Villareal, L.F. Lira-Barragán, V. Rico-Martinez, J.M. Ponce-Ortega, M.M. El-Halwagi, 2014, An MFA optimization approach for pollution trading considering the sustainability of the surrounded watersheds, *Computers and Chemical Engineering*, 63, 1, 140-151.

Reduced model-based global optimisation of large-scale steady state nonlinear systems

Min Tao^a, Jie Li^a and Constantinos Theodoropoulos^{a*}

^a*School of Chemical Engineering and Analytical Science, The University of Manchester, M13 9PL, UK*

**k.theodoropoulos@manchester.ac.uk*

Abstract

Many engineering systems can be accurately simulated using partial differential equations (PDEs), resulting in large-scale distributed parameter systems. Deterministic global optimisation algorithms (GOP) can compute global optimal solutions offering theoretical guarantees on the global optimality. However, distributed parameter systems pose computational challenges for these optimisation methods. Model reduction techniques can produce low-order systems that are computationally amenable. In this work, a combined principal component analysis (PCA) and artificial neural networks (ANNs)-based model reduction methodology is employed for the global optimisation of large-scale distributed steady state systems. Still, the optimisation problem is hard to solve due to the high nonlinearity of activation functions in the reduced ANN structure. A novel piece-wise linear approximation reformulation is introduced to reduce the complexity of the original problem and to provide a good globally approximate solution. The performance of the proposed PCA-ANN-GOP framework is demonstrated through an illustrative example: a tubular reactor where an exothermic reaction takes place.

Keywords: Model reduction, Distributed parameter systems, Artificial neural networks, Global optimisation

1. Introduction

PDE-constrained black/grey box modelling and optimisation methodologies have wide applicability in industrial engineering areas where many finite approximation-based generic commercial simulators or input-output data from real complex systems are available (Boukouvala et al., 2017). However, many simulators solely provide input-output results of simulation process and can not perform optimisation tasks. Hence, the optimisation of real complex systems is problematic. Even if the high dimensional complex model codes are available, the cost of computing derivatives is often unacceptable. One of the most effective techniques to reduce computational costs for input/output systems is the use of *equation-free* methods (Theodoropoulos, 2011). Recently, equation-free based reduced SQP algorithms have been exploited for large-scale local optimisation with black-box steady-state simulators (Bonis and Theodoropoulos, 2012). With a small set of input-output data from the simulator, matrix-free reduced Jacobian and Hessian matrix techniques can be employed. The aim of this work is to construct deterministic global optimisation methods for large-scale input/output simulators. Such deterministic global optimisation methods are usually computationally intensive due to the repeated utilisation of branch-and-bound algorithms. Hence, in terms of computational cost, detailed models of large-scale problems are very hard or even impossible to deal with.

In this work, a data-driven methodology is employed first to create a good approximate surrogate model for large-scale steady-state systems. Principal component analysis (PCA) in combination with artificial neural networks (ANNs) is used to produce a reduced order model. The reduced model (ANN-constrained model) is then utilized by the global general-purpose optimisation solver BARON (Tawarmalani and Sahinidis, 2005). Furthermore, we present a novel piece-wise linear approximation reformulation for the nonlinear constraints in order to accelerate the computation of the global optimum for the reduced system.

2. Model Reduction

The focus of this work is on optimisation of spatially distributed processes, described by a set of steady-state dissipative PDEs with accompanying boundary and initial conditions:

$$\frac{\partial X}{\partial t} = D\left\{\frac{\partial X}{\partial y}, \frac{\partial^2 X}{\partial y^2}, \dots, \frac{\partial^n X}{\partial y^n}\right\} + R(X, P_m) \quad (1)$$

where D is a dissipative spatial differential operator, $R(X, P_m)$ is a nonlinear function, P_m are the parameter variables and X the set of state variables. If we consider the steady state analysis of these equations, we assume that $X(t, y) \rightarrow X(y)$, and we can set $\frac{\partial X}{\partial t} = 0$, giving the equations:

$$0 = D\left\{\frac{\partial X}{\partial y}, \frac{\partial^2 X}{\partial y^2}, \dots, \frac{\partial^n X}{\partial y^n}\right\} + R(X, P_m) \quad (2)$$

Due to the large number of variables in the corresponding discretised problems, the full model is usually too big for global optimisation (Houska and Chachuat, 2017). This barrier can be overcome by employing model reduction methodologies such as artificial neural networks and principal component analysis. Principal component analysis (PCA) is a powerful methodology for data compression. Common linear PCA is a transformation of the original data space spanned by the principal components (PCs). PCs are the basis vectors for the new space and are ranked by the magnitude of variance of the original data projected onto the corresponding PCs. PCs can be computed by matrix decomposition as in (Jackson, 2005):

$$Y = TP^T + E \quad (3)$$

where $Y \in R^{N \times m}$ is the high dimensional sample data from the large-scale steady state simulator given by Eq.(2), N and m , the number of sample data and data dimension, respectively. $T \in R^{N \times a}$, is the score matrix for the PCs and a ($a \leq m$), the number of PCs. $P \in R^{m \times a}$ is the loading matrix and $E \in R^{N \times m}$ the residual matrix.

In order to compute a representation for the outputs produced by the the black-box simulator, the Latin hyper-cube (LHC) sampling method is applied to collect snapshots. LHC sample method can maximize the sample information content for a limited number of samples. After snapshots collecting and PCA reduction steps applied, the high dimensional input-output data is transformed into lower dimensional PC scores. Subsequently a reduced order model is built through the use of the reduced data obtained. Here, we adopt artificial neural networks (ANNs) because standard

feed-forward artificial neural network (ANN) with one hidden layer can be an universal approximator for any smooth function (Hornik et al., 1989). The structure of the feed-forward ANN is relatively simple and easy to be constructed. In this work, the training process for ANN is performed in MATLAB R2017a with Neural Networks toolbox. The activation function is chosen to be the hyperbolic tangent function. The neural network is trained with the Levenberg-Marquardt back-propagation algorithm, which can reduce the mean square error quickly. The input is the low-dimensional input parameter matrix from the black-box simulators. The output is the reduced principal component scores of the output data from black-box simulators. At this point, data-driven PCA-ANN based surrogate model has been built that can be employed for global optimisation.

3. Model reduced global optimisation

The general nonlinear optimisation problem with embedded neural networks (reduced model) is considered. The general problem can be formulated as follows:

$$\begin{aligned} \min_{x \in R^c, y \in R^d} \quad & f(x, y) \\ \text{s.t.} \quad & h(x, y) = 0, \\ & g(x, y) \leq 0 \end{aligned} \tag{4}$$

where the objective function $f(x, y) : R^c \times R^d \rightarrow R$, $x \in R^c$ is an input vector of the black-box simulator, $y \in R^d$ is an output vector of the black-box simulator, $h(x, y) : R^c \times R^d \rightarrow R$ is ANN constraint derived from the reduced model, and $g(x, y) : R^c \times R^d \rightarrow R$ represents other constraints.

In the current work, $g(x, y)$ are the bound constraints for the state variables. The intrinsic non-linearity of the optimisation problem lies on $h(x, y)$ due to the activation function of the ANN structure. The feed-forward ANN uses the hyperbolic tangent function $\tanh(\cdot)$. The general global optimisation software BARON is employed to solve the above problem. General global solvers in GAMS such ANTIGONE and BARON can not identify $\tanh(\cdot)$, so its explicit algebraic form ($\tanh(x) = \frac{e^x - 1}{e^x + 1}$) is utilized. The basic formulation is transformed into $\tanh(x) = \frac{-2}{e^x + 1} + 1$ in order to produce a tighter under-estimator for the global solver.

However, the computational cost of global solvers increases exponentially when reducing the high non-convexity of the activation function. We propose a novel piece-wise linear approximation (PWA) reformulation for the activation function. With an accurate PWA model, a good approximation to the true global solution can be obtained. It should be, however, noted that a PWA reformulation transforms the high non-convex NLP problem into a set of MILP problems. The global solvers for both NLP and MILP problems are based on the branch and bound framework. The biggest difference is that they turn the continuous variables into auxiliary binary variables on the branch step. The advantage of the PWA reformulation lies on the use proven MILP software such as CPLEX. Here, we present an iterative way to collect piece-wise points for PWA models. $\tanh(x)$ is an odd function of central symmetry, which is concave on $[0, +\infty]$ and convex on $[-\infty, 0)$. So it is easy to compute the grid points for piece-wise approximation of $\tanh(x)$ on $[-\infty, 0)$ when the grid points on $[0, +\infty]$ are available. On the range of $[0, +\infty]$, $\tanh(x)$ experiences a 'short-time' increase and then tends to be 'static' (very slow growth to its limit value). In the current work, we start from only two intervals and three grid points (original point and two static points) in this range. The linear model in a static interval can approximate the activation function accurately. For the 'initial short-time' increasing interval, we reduce the error between the multiple linear models and the nonlinear $\tanh(x)$ by iteratively narrowing the interval sizes.

The iteration procedure is performed by adding more partitioning points where the largest error is calculated. In addition, a sub-interval is acceptable if the biggest error or the number of intervals satisfies a set requirement. This iteration process efficiently produces a set of collecting points, which contribute to a tight piece-wise linear representation of the highly nonlinear activation function. Assume that there are N linear models, $N + 1$ generated grid points $x_1, x_2, \dots, x_{N+1} \in R$ and approximate function $f = \tanh(x_i)$ in the i th interval. By introducing auxiliary variables h_i and λ_i , we can generalize the formulation of a piece-wise linear approximation as follows (Floudas, 1995):

$$\begin{aligned}
 f(x) &= \sum_{i=1}^{N+1} \lambda_i f(x_i) \\
 x &= \sum_{i=1}^{N+1} \lambda_i x_i \\
 \sum_{i=1}^{N+1} \lambda_i &= 1 \\
 \lambda_1 &\leq h_1 \\
 \lambda_i &\leq h_i + h_{i-1}, \forall i \in \{2, 3, \dots, N\} \\
 \lambda_{N+1} &\leq h_N \\
 \lambda_i &\geq 0, \forall i \in \{1, 2, \dots, N+1\} \\
 \sum_{i=1}^N h_i &= 1 \\
 h_i &\in \{0, 1\}^N
 \end{aligned} \tag{5}$$

In the next section, this algorithm is employed to a system of steady-state PDEs after collecting a "good" set of snapshots in order to illustrate its computational capabilities.

4. Application

We first apply our methodology to an example with known global optima for illustration purposes. Then we apply our PCA-ANN-GOP framework to a large-scale steady state nonlinear PDE-based system.

4.1. Illustrative example

In this illustrative example, a two-dimensional multimodal function is chosen, obtained by translating and scaling Gaussian distributions:

$$\begin{aligned}
 g_{peaks} &= 3(1-x)^2 \exp(-x^2 - (y+1)^2) - 10\left(\frac{x}{5} - x^3 - y^5\right) \exp(-x^2 - y^2) \\
 &\quad - \frac{1}{3} \exp(-(x+1)^2 - y^2)
 \end{aligned} \tag{6}$$

where variables $x, y \in [-3, 3]$. Multiple local solutions exist in this defined domain. The known unique global optimum lies on the point $(0.228, -1.626)$ where the function value is -6.551 . We just use it to show the performance of our reduced global optimisation methodology.

Table 1: Comparative results of ANN-constrained model and PWA models

Model	Solver	Optimal value	CPU time (s)	Rel.gap
ANN-constrained model	BARON	-6.555	30294.26	0.002
PWA model1 (31 grid points)	CPLEX	-6.542	1004.71	0.002
PWA model2 (59 grid points)	CPLEX	-6.540	4190.16	0.002

After sampling and ANN learning, we obtain an ANN-constrained reduced model with 52 neurons. We do the global optimisation with reduced model and PWA models. ANN-constrained model is the surrogate model after ANN step. PWA model1 is the piece-wise approximation model for hyperbolic activation function with 31 grid points while PWA model2 is the piece-wise approximation model with 59 grid points. The number of grid points depends on the chosen error during the above iteration process. The NLP with ANN-constrained model is solved by the general global solver BARON 17.4.1/GAMS 24.8.5, and MILP with PWA model is dealt with CPLEX 12.7.1/GAMS 24.8.5 on a Desktop (Intel Core(TM) CPU 3.3 GHz, 8 GB memory, 64-bit operating system) running Windows 7. The results are given in Table 1. From Table 1, we can see that we obtain almost the same optimal solution, very close to the true global optimizer of the original problem. In addition, our proposed PWA formulation can reduce the computation time greatly with high accuracy.

4.2. Case study

The effectiveness of our PCA-ANN-GOP is illustrated using a chemical engineering application; a tubular reactor, where an exothermic reaction takes place. The mathematical formulation of the tubular reactor optimisation is given below:

$$\begin{aligned}
 & \max_{T_{wi}} C_{exit} \\
 s.t. & 0 = \frac{1}{Pe_1} \frac{\partial^2 C}{\partial y^2} - \frac{\partial C}{\partial y} + Da(1-C)\exp(T/(1+T/\gamma)) \\
 & 0 = \frac{1}{LePe_2} \frac{\partial^2 T}{\partial y^2} - \frac{1}{Le} \frac{\partial T}{\partial y} - \frac{\beta}{Le} T + BDa(1-C)\exp(T/(1+T/\gamma)) + \frac{\beta}{Le} T_w \\
 & 0 \leq T_{wi} \leq 5
 \end{aligned} \tag{7}$$

Here C and T are the dimensionless concentration and temperature respectively, while C_{exit} is dimensionless output concentration. The system parameters are $Pe_1 = 5, Pe_2 = 5, Le = 1, Da = 0.1, \beta = 1.5, \gamma = 10, B = 12$; T_w is the adiabatic wall temperature of the cooling problem with three cooling zones, expressed as following:

$$T_w(y) = \sum_{i=1}^N (H(y - y_{i-1}) - H(y - y_i)) T_{wi} \tag{8}$$

The resulting discretised 500 algebraic equations comprise our house-made simulator. After model reduction step (PCA and ANN steps), a small size ANN-constrained optimisation problem (3 input, 12 output, 20 neurons ANN) is generated, which is easy to be solved. In order to compare the computation efficiency of ANN-constrained model and PWA models, we compute the results with different numbers of neurons. All these computation cases converge to almost the same

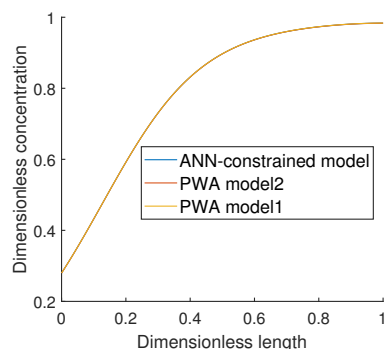


Figure 1: Solution profiles at optimum for concentration

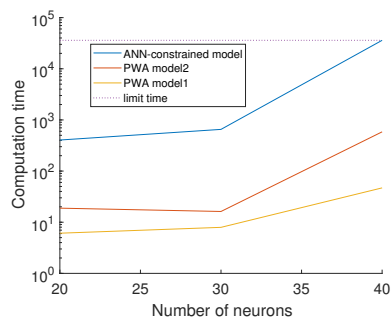


Figure 2: Computation time (sec) under different number of neurons

solution, whose objective values are extremely close to 0.999. Figure 1 gives the optimal solution profiles for concentration distribution under 30-neuron ANN structures. The three concentration distribution curves for different approximate models almost overlap. Hence, our PWA models show high computation accuracy. Figure 2 illustrates the comparison of the computation cost for the different models. The limit time (max time for computations to stop) is set to be 36000 seconds. As it can be seen, computation time increases rapidly as with increasing number of neurons. The computation cost reaches the limit time for the ANN-constrained model with only 40 neurons while the computation times are much smaller for both PWA models. This verifies the high computation efficiency of our PWA models.

5. Conclusion

We propose a reduced model-based global optimisation framework for large-scale steady state nonlinear systems. Data-driven PCA and ANN techniques are employed to produce a small or middle size surrogate model for the original system. To further reduce computation complexity, novel PWA models are utilized to replace the reduced ANN-constrained model. Illustrative examples are presented to verify the efficiency of our framework. Computation results reveal that our PCA-ANN-GOP framework can capture the global optimum with acceptable computational cost, especially when PWA approximations are used.

References

1. Bonis, C. Theodoropoulos, 2012. Model reduction-based optimization using large-scale steady-state simulators. *Chemical engineering science* 69 (1), 69–80.
2. F. Boukouvala, M. F. Hasan, C. A. Floudas, 2017. Global optimization of general constrained grey-box models: new method and its application to constrained pdes for pressure swing adsorption. *Journal of Global Optimization* 67 (1-2), 3–42.
3. C. A. Floudas, 1995. *Nonlinear and mixed-integer optimization: fundamentals and applications*. Oxford University Press.
4. K. Hornik, M. Stinchcombe, H. White, 1989. Multilayer feedforward networks are universal approximators. *Neural networks* 2 (5), 359–366.
5. B. Houska, B. Chachuat, 2017. Global optimization in hilbert space. *Mathematical Programming*, 1–29.
6. J. E. Jackson, 2005. *A user's guide to principal components*. Vol. 587. John Wiley & Sons.
7. M. Tawarmalani, N. V. Sahinidis, 2005. A polyhedral branch-and-cut approach to global optimization. *Mathematical Programming* 103 (2), 225–249.
8. C. Theodoropoulos, 2011. Optimisation and linear control of large scale nonlinear systems: a review and a suite of model reduction-based techniques. In: *Coping with Complexity: Model Reduction and Data Analysis*. Springer, pp. 37–61.

A multiscale model approach for cell growth for lipids and pigments production by *Haematococcus pluvialis* under different environmental conditions.

Alessandro Usai^{a,b}, Jon Pittman^c, and Constantinos Theodoropoulos^{a,b*}

^a*School of Chemical Engineering and Analytical Science, University of Manchester, M13 9PL, UK*

^b*Biochemical and Bioprocess Engineering Group, University of Manchester, M13 9PL, UK*

^c*School of Earth and Environmental Sciences, University of Manchester, M13 9PL, UK*

*k.theodoropoulos@manchester.ac.uk

Abstract

The development of new technologies is essential to contrast the increasing global CO₂ emissions. Microalgae-based biorefineries present a promising tool to reduce the presence of CO₂ in our emissions (Bekirogullari et al 2018, Bekirogullari et al 2017). The development of processes for the simultaneous production of more than one product are essential to increase the possibility of making such biorefineries profitable (García Prieto, Ramos, Estrada, Villar, & Diaz, 2017). Microalgae eukaryotic cells are able to produce pigments and lipids. The production of lipids and pigments could vary depending on the environmental stress conditions such as light intensity, nutrients concentration, medium salinity, and temperature (D'Alessandro & Antoniosi Filho, 2016). *Haematococcus pluvialis* produces lutein, β -carotene, and lipids during growth, which makes it a potential candidate for the simultaneous production of high value products. *H. pluvialis*' division pattern ranges from the formation of two daughters up to 32 cells by multiple-fission (Shah, Liang, Cheng, & Daroch, 2016). New born cells achieve after a dimensional growth step a critical size point, where after that, they are able to keep growing and reproduce without any further input in the system, this point is called commitment point (CP). The achievement of an higher number of CP lead to a higher number of cells in the day/night cycle (Bišová & Zachleder, 2014). The above phenomena reaching one commitment point are described using a population balance model (PBM), in order to evaluate the influence of some environmental conditions on the cell growth. The model was fitted against synchronized experimental data, and then tested on a long duration experiment.

Keywords: microalgae; population balance models, synchronisation.

1. Introduction

The capability to produce high-value products such as neutral lipids, pigments, carbohydrates, proteins, and other products makes the development of the microalgal biorefinery processes interesting. The development of microalgae biotechnology is a

possible candidate to solve significant issues such as the depletion of fossil fuels through the production of biofuels, wastewater removal through the consumption of NH_4^+ , NO_3^- , and PO_4^{3-} and land utilization reduction utilising less land per litre of products produced. Moreover, they have a variety of metabolites produced which can be useful in many fields (Mata, Martins, & Caetano, 2010). Furthermore, CO_2 emissions from fossil-fuel shows an increase during the last decades, especially in developing countries (Olivier, Schure, & Peters, 2017), and microalgae are considered within a biotechnology perspective for CO_2 sequestration (Singh & Ahluwalia, 2013).

Microalgae, during cultivation, cover a series of essential steps leading to multiplication. Starting from the new born cell, the first phase is represented by the cell volume growth up to reach the commitment point (CP) (Bišová & Zachleder, 2014). This first cycle phase could be observed through a synchronisation of the cell population, and then following the cell population volume growth through the light cycle (Hlavová, Vítová, & Bišová, 2016). The given procedure could be improved and applied to other cell constituents, such as lipids and/or pigment. In this work the basis for a volume-structured PBM model was constructed, and the parameters related with the volume growth rate were estimated from synchronous experiments, followed by a prediction of a long-term experiment. Such models can give accurate predictions of individual cell growth and can be subsequently efficiently coupled with kinetic expressions and/or metabolic-level models to predict the production of lipids pigments and of metabolites within.

2. Materials and Methods

Haematococcus pluvialis strain FLOTOW (1844) CCAP 34/6 was purchased from Culture Collection of Algae and Protozoa (CCAP) Scotland, United Kingdom. The medium is carbon-free NIES-C. Two experiments were carried out and the starting point for both experiments is a cell culture inoculated at 5.5×10^3 cell mL^{-1} in 215mL medium in a glass bottles (500mL) with a sponge cap. Both of them were incubated at 27°C , stirred at 130 rpm, and illuminated at $60 \mu\text{mol m}^{-2}\text{s}^{-1}$ by using white fluorescent neon, and considering 16/8 light dark cycle. The first experiment examines microalgae synchronisation, following an adapted procedure suggested by (Hlavová *et al* 2016), and the second experiment is a long-term photoautotrophic growth. The synchronisation experiment reaches around 2.0×10^5 cells mL^{-1} after 16 days. Starting from this point cells were kept at this concentration for 72 hours diluting the culture with NIES-C medium at the beginning of every light cycle. Starting from the 72th hour regular sampling was performed until the end of the light cycle, in order to follow the dimension, and the number of the cell population by using Cellometer Auto T4 purchased from Nexcelom Bioscience LLC. In the second experiment samples were taken starting from time zero every seven days until the 31th day, and the volume and number population properties weremeasured. All of the experimental results presented are the mean of duplicate experiments.

3. Model development

The proposed model is based on the PBM model equations firstly proposed by Fredrickson (1967). The model is represented by an integro-partial differential equation (Eq.1) including a vector of initial conditions (Eq.2), and boundary conditions (Eq.3). The particle state is assumed to depend only on the volume which is an internal coordinate. The choice of the volume is related to the considerations given in many works where the volume seems to be the variable related to the CP achievement in

microalgae (Bišová & Zachleder, 2014; Šetlík & Zachleder, 1984; Zachleder & Vítová, 2016), which aims to give a solid basis for future works in this direction. The term Ψ represents the number concentration density function, r_v and Γ^v are the rate of change for the particle state vector, and the transition rate for the birth term, respectively. They depend on the volume v , and on the attenuated light I_{att} .

$$\frac{\partial \Psi(v,t)}{\partial t} + \frac{\partial [r_v \Psi(v,t)]}{\partial v} = 2 \int_v^\infty \Psi(v',t) \Gamma^v(v', I_{att}) p(v, v') dv' - \Psi(v,t) \Gamma^v(v, I_{att}) \quad (1)$$

$$\Psi(v, t) = \Psi^0(v) \text{ for } t = 0 \text{ and } \forall v \quad (2)$$

$$\Psi(v, t) = 0 \text{ for } t > 0 \text{ and } v = 0 \quad (3)$$

The model was reduced in order to perform an ideal fitting procedure. The birth term is set to zero, and only the part regarding the volume growth considered (Eq.4).

$$\frac{\partial \Psi}{\partial t} + \frac{\partial (r_v \Psi)}{\partial v} = 0 \quad (4)$$

$p(v, v')$ represents the partitioning distribution function, which considers how mother cells internal properties are redistributed in daughter cells. The one used here is able to get unequal partitioning (Hatzis, Srienc, & Fredrickson, 1995), q being a coefficient.

$$p(v, v') = \frac{1}{\beta(q,q)} \frac{1}{v'} \left(\frac{v}{v'}\right)^{q-1} \left(1 - \frac{v}{v'}\right)^{q-1} \quad (5)$$

Light attenuation functionalities related to volume-structured PBM models are not present in literature. In this model a functionality is given (Eq.6), which takes into account the ratio between the total cells volume V_{cell}^T , and the total volume of the culture V^T , α_{att} being a fitting parameter. The total volume of the cells is given by the first order moment of the distribution multiplied by the total cell volume (Eq.7).

$$I_{att} = I_0 \left[1 - \frac{V_{cell}^T}{V^T}\right]^{\alpha_{att}} \quad (6)$$

$$V_{cell}^T = V^T \int_0^\infty v \Psi(v) dv \quad (7)$$

The rate of change for the particle state vector considers the light attenuated by using a Monod functionality (Monod, 1949), where $K_{I_{att}}$ indicates the half saturation light term. Moreover, the volume is considered to influence the volume growth, in particular the raising volume is considered to make the volume growth rate lower, it is represented by an inhibition functionality with K_v inhibition constant. The latter right-hand term represents the decay rate, and μ_C is the decay rate constant (Eq.8).

$$r_v(v, I_{av}) = \mu_v \frac{I_{att}}{I_{att} + K_{I_{att}}} \frac{K_v}{v + K_v} - \mu_C v \quad (8)$$

The transition rate between mother cells and daughters is expressed as a function of the rate of change for the particle state vector multiplied by the gamma function γ^v (Eq.9). The functionality is like the one used in previous a previous work, considering the mass

as internal variable, for microalgae (Concas, Pisu, & Cao, 2016). The probability to undergo division increases when the cells are approaching the critical volume v_c . σ_c^2 is the variance of the Gaussian functionality considered in equation 11.

$$\Gamma^v(v, I_{av}) = r_v(v, I_{att})\gamma^v(v) \quad (9)$$

$$\gamma^v(v) = \frac{f(v)}{1 - \int_0^v f(v') dv'} \quad (10)$$

$$f(v) = \frac{1}{\sqrt{2\pi\sigma_c^2}} \exp\left[-\frac{(v-v_c)^2}{2\sigma_c^2}\right] \quad (11)$$

4. Results and discussion

Parameter estimation has been carried out for the parameters involved in the cell volume growth description by using the data obtained from the synchronisation experiment, following a possible ideal procedure (Fadda, Cincotti, & Cao, 2012). The partial model showed in equation 4 was utilized. The initial volume distribution for the parameter estimation was obtained by fitting the initial number histogram percentage for the synchronisation experiment (Fig.1a) and converting it in terms of the number concentration density function. The parameters are obtained by fitting the mean volume during the synchronisation experiment (Fig.1b). The experimental volume increases in agreement with the model predictions. The normalized density function during the volume growth process (Fig.1c) in the light period agrees qualitatively with the experimental distributions (data not showed). The q parameter was specifically used for binary fission in microalgae (Concas et al., 2016).

The set of parameters obtained was used to predict the long-term experiment. The initial volume distribution showed in figure 1d was obtained by fitting the number histogram percentage of a duplicate experiment at time zero of the long-term experiment, and then it was converted to a number concentration density function. N_0 , σ_0 , and μ_0 were obtained by using this fitting. The critical volume was considered to be the double of the initial volume at time zero of the synchronisation, where the cells should be averagely at the minimum volume related to daughter cells (Bišová & Zachleder, 2014). The σ_c used was the same as the one of the initial distribution. The results of the complete model prediction are shown in figure 1e, where the total cell number shows a good agreement with the experimental data.

Table 1. Definition of model parameters and their respective values.

Parameter	Definition	Value	Units
N_0	Initial total cell number	9.11×10^5	Cells
σ_0	Initial distribution parameter	2.30×10^3	μm^3
μ_0	Mean initial volume	6.94×10^3	μm^3
α_{att}	Light attenuation shape parameter	8.84×10^3	-
q	Coefficient symmetric beta function	4.00×10^0	-
K_v	Volume inhibition constant	5.43×10^3	μm^3
$K_{I_{att}}$	Light half saturation constant	2.24×10^2	$\mu\text{mol m}^{-2}\text{s}^{-1}$

μ_c	Volume decay rate	5.38×10^{-5}	h^{-1}
μ_v	Volume growth rate	1.22×10^3	$\mu\text{m}^3\text{h}^{-1}$
V_T	Total culture volume	2.15×10^2	mL
I_0	Incident light intensity	6.0×10^1	$\mu\text{mol m}^{-2}\text{s}^{-1}$
v_c	Mean critical volume	9.86×10^3	μm^3
σ_c	Critical volume distribution parameter	2.30×10^3	μm^3

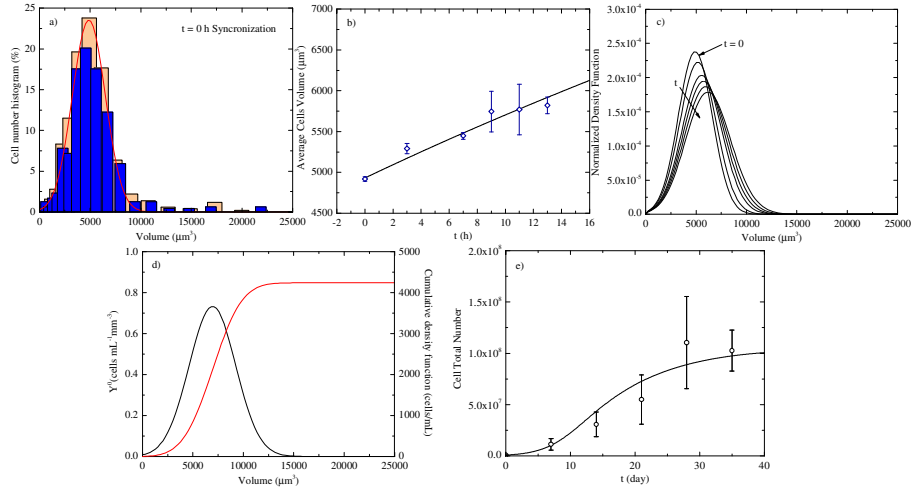


Figure 1. a) Cell number histogram (percentage) at time zero of synchronisation b) Experimental average cell volume (blue diamonds) and model fitting (black line) in synchronisation experiment. c) Normalized density function evolution during cell volume growth in synchronisation model fitting. d) Initial density function (black line), and cumulative density function (red line) at time zero of long-term experiment e) Experimental cell total number (black circles), and model prediction (black line) for the long-term experiment.

5. Conclusions

A population balance model was proposed to describe the growth of microalgae cells. Biomass growth is limited by the light attenuation, and the model takes into account the observed phenomena affecting growth rate decreasing in correspondence of the mean volume growth. The model parameters were estimated observing the volume growth phase during the light cycle in a short duration experiment trying to exclude other phenomena. Model predictions for the long-term experiment show the potential ability of the model to predict cell populations in term of total cell numbers for long-term experiments from a fitting data from short-term experiments. The fitting procedure could be adopted extended to other variables, making the model able to work in a wide range of operative conditions, and including the production of individual metabolites in order to take into account added-value products.

References

- Bekirogullari, M., Pittman J & Theodoropoulos, C (2018). Multi-factor kinetic modelling of microalgal biomass cultivation for optimised lipid production. *Bioresource Technology*.
- Bekirogullari, M., Fragkopoulos I, Pittman J & Theodoropoulos, C (2017). Production of Lipid-Based Fuels and Chemicals from Microalgae: An Integrated Experimental and Model-based Optimization Study. *Algal Research*, 23, 78-87.
- Bišová, K., & Zachleder, V. (2014). Cell-cycle regulation in green algae dividing by multiple fission. *Journal of Experimental Botany*, 65(10), 2585–2602.
- Concas, A., Pisu, M., & Cao, G. (2016). A novel mathematical model to simulate the size-structured growth of microalgae strains dividing by multiple fission. *Chemical Engineering Journal*, 287, 252–268.
- D’Alessandro, E. B., & Antoniosi Filho, N. R. (2016). Concepts and studies on lipid and pigments of microalgae: A review. *Renewable and Sustainable Energy Reviews*, 58, 832–841.
- Fadda, S., Cincotti, A., & Cao, G. (2012). A novel population balance model to investigate the kinetics of in vitro cell proliferation: Part II numerical solution, parameters’ determination, and model outcomes. *Biotechnology and Bioengineering*, 109(3), 782–796.
- Fredrickson, A. G., Ramkrishna, D., & Tsuchiya, H. M. (1967). Statistics and dynamics of procaryotic cell populations. *Mathematical Biosciences*, 1(3), 327–374.
- García Prieto, C. V., Ramos, F. D., Estrada, V., Villar, M. A., & Diaz, M. S. (2017). Optimization of an integrated algae-based biorefinery for the production of biodiesel, astaxanthin and PHB. *Energy*, 139, 1159–1172.
- Hatzis, C., Srien, F., & Fredrickson, A. G. (1995). Multistaged corpuscular models of microbial growth: Monte Carlo simulations. *BioSystems*, 36(1), 19–35.
- Hlavová, M., Vítová, M., & Bišová, K. (2016). Synchronization of green algae by light and dark regimes for cell cycle and cell division studies. In *Methods in Molecular Biology* (Vol. 1370, pp. 3–16). https://doi.org/10.1007/978-1-4939-3142-2_1
- Mata, T. M., Martins, A. A., & Caetano, N. S. (2010). Microalgae for biodiesel production and other applications: A review. *Renewable and Sustainable Energy Reviews*, 14(1), 217–232.
- Monod, J. (1949). a Certain Number. *Annual Reviews in M*, 3(XI), 371–394.
- Olivier, J. G. J., Schure, K. M., & Peters, J. A. H. W. (2017). TRENDS IN GLOBAL CO 2 AND TOTAL GREENHOUSE GAS EMISSIONS 2017 Report Trends in global CO2 and total greenhouse gas emissions: 2017 Report, (December). Retrieved from http://www.pbl.nl/sites/default/files/cms/publicaties/pbl-2017-trends-in-global-co2-and-total-greenhouse-gas-emissions-2017-report_2674.pdf
- Šetlík, I., & Zachleder, V. (1984). The multiple fission cell reproductive patterns in algae. In *The Microbial Cell Cycle* (pp. 253–279).
- Shah, M. M. R., Liang, Y., Cheng, J. J., & Daroch, M. (2016). Astaxanthin-Producing Green Microalga *Haematococcus pluvialis*: From Single Cell to High Value Commercial Products. *Frontiers in Plant Science*, 7(April). <https://doi.org/10.3389/fpls.2016.00531>
- Singh, U. B., & Ahluwalia, A. S. (2013). Microalgae: A promising tool for carbon sequestration. *Mitigation and Adaptation Strategies for Global Change*, 18, 73–95.
- Zachleder, V., & Vítová, M. (2016). The cell cycle of microalgae. <https://doi.org/10.1007/978-3-319-24945-2>

Advanced Model Design Based on Intelligent System Characterization And Problem Definition

Edrisi Munoz ^{a*}, Elisabet Capon-Garcia ^b, Luis Puigjaner^c

^a*Centro de Investigacion en Matemáticas A.C., Jalisco S/N, Mineral y Valenciana 36240, Guanajuato, Mexico*

^b*ABB Switzerland Ltd., Segelhofstrasse 1K, 5405 Baden-Dättwil, Switzerland*

^c*Chemical Engineering Department, EEBE, Universitat Politècnica de Catalunya, Av. Eduard Maristany, 10-14, 08019 Barcelona, Spain*

emunoz@cimat.com

Abstract

Enterprises comprise highly complex systems that need to be coordinated in order to maintain their productivity and competitiveness. During last years, companies have developed information systems to support end users to exploit data and models, with the final objective of improving the decision-making task. Main decisions concern key process characteristics, which are essential for the viability to achieve enterprise wide optimization (EWO) and industry 4.0 approaches. This work focuses on the automated creation of a semantically enriched problem statement of production processes based on system characterization and problem definition. First, features related to the system are defined and the characterized by making use of knowledge models. As a result the system is semantically defined and conceptual enriched. Next, the second step of the approach consists on an automated problem definition process. This process comprises eight main phases to obtain a systematic problem definition. Finally, this work presents a case study base on scheduling problem in order to show the performance of the tool. The case study comprises a system that has been treated with mathematical models for solving a multistage scheduling problem.

Keywords: Artificial Intelligence; Problem Modelling; Intelligent Systems

1. Introduction

Enterprises comprise highly complex systems that need to be correctly managed and coordinated in order to maintain their productivity and competitiveness. During last years, due to accessibility to technological advances, companies have been focused on developing information systems to support end users to exploit data and models, with the final objective of improving the decision-making task in an automated and semi-automated processes environment. Nevertheless, decision-making modeling lies in to human factor (human capacity and expertise). Thus, tools that support fast and reliable problem solve activities related to production process are crucial elements in those information systems.

What is more, nowadays industry is deep into in the fourth industrial revolution, so-called Industry 4.0, where computers and process devices aim for autonomous process by interacting together. In this context, sensors and actuators should be connected remotely to computer systems, equipped with sophisticated algorithms that can

understand, learn and decide with small intervention from human operators. The success on improving decision-making broadly depends on how analytical models and data are integrated. On the one hand, the correct modelling task, when a problem or certain reality is found, increases the success of the decision. On the other hand, the responsiveness and accuracy to get information quality and data complement how good the decision can be. Thus, a key task in the improvement of decision-making depends on having an appropriate and enhanced characterization of the system. This work focuses on the main decisions concerning key process characteristics, which are essential for the viability and competitiveness of the enterprise.

This work presents a methodology for an automated problem definition resulting in a semantically enriched problem statement. This problem statement comprises system characterization and problem definition process, which are based on formal knowledge models namely ontologies. First, features related to the system are defined and then characterizing by making use of knowledge models. System features comprises to general tactical and strategic process issues. Besides, knowledge models enable identifying and matching every process with their functions, objectives and relations regarding different levels of process abstraction within the enterprise structure. As a result of this first step system features are extracted and presented in a taxonomical structure manner conceptually enriched. Next, an automated problem definition comprising nine main phases, namely: a) automated process system definition, b) Problematic situation recognition; c) Solution goal statement; d) General system relations; e) Definition of variables; f) system assumptions; g) parameters and engineering metrics (time & space scales); h) definition of problem statement and solution objectives; and i) search for similar problematic or solutions.

Finally, this work presents a case study base on scheduling problem in order to show the performance of the approach. Scheduling problems are critical in the decision-making of process operations.. The case study comprises a system that has been treated with mathematical models for solving a multistage scheduling problem.

2. Proposal description

Decision Support Systems (DSS) are information technology solutions that can be used to support complex decision-making and problem solving. DSS are defined as aid computer systems at the management company level that combine data and sophisticated analytic models for support decision-making (Simon and Murray, 2007). Classic DSS design is comprised of components for (i) sophisticated database management capabilities with access to internal and external data, information, and knowledge; (ii) modeling functions accessed by a model management system, (iii) simple user interface designs that enable interactive queries, reporting, and graphing functions, and (iv) optimization by mathematic algorithms and or intuition/knowledge.

This work is based on formal knowledge technologies, which allow working in a semantical environment where machines can understand domain and human knowledge. Besides, the development of models and solution strategies to tackle the decision-making from a broad perspective has been the result of integration and collaboration from areas, such as, Process Systems Engineering (PSE), Information Technologies and Communications (ITC), and Operations Research (OR).

Thus, the proposed approach can be generally stated as follows. Given a formal domain knowledge model, the following information must be captured in order to obtain

semantically system features: i) Production system characterization comprising Physical, Procedural and Recipe (Site & General) models; ii) Products to be produced according to the processing order activity in the industry recipes defining the production requirements and production path for the products in the Physical, Process and Recipe (Master & Control) models, and; iii) Resource availability and plant status provided by the process management and production information management activities, as shown in Figure 1, Part I-A and Part I-AA.

The main goal consists on create an enriched problem statement. Thus the following nine steps have been automated comprising: definition of the process system from tactical, strategic and operational views (see Figure 1, Part II - a); an algorithm for monitoring key process features (isolated or integrated) for detecting abnormal or problem situations (see Figure 1, Part II - b); an option for choosing among economical, time or other aim solution perspective (see Figure 1, Part II - c); important relations among problem and direct features in the system are stated (see Figure 1, Part II - d); decision variables, assumptions of the process and the engineering metrics are suggested by the proposal and chosen by the user (see Figure 1, Part II - c, d and e); finally a sematic enriched problem statement is obtained (see Figure 1, Part II - h and i)

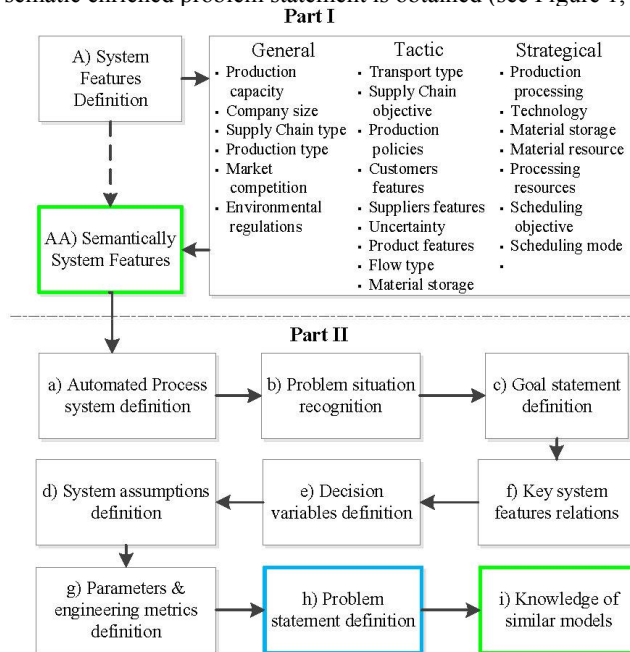


Figure 1. Intelligent system characterization and problem definition procedure diagram.

3. Methodology

This work develops a software platform in Jython, which is integrated to the knowledge models described previously by using OWLAPI as an improved modeling and communication tool in the process domain. Then the proposed framework consists on two main processes, Enterprise Structure Definition and Problem Definition (Figure 1).

On the one hand, enterprise structure definition comprises conception of a real system, considering general, tactic and strategic features (Figure 1, part I). Then, a semantic enriched taxonomical model of the features is obtained. Likewise, this work tackles the conciliation, standardization and management of data and information existing in the process system. On the other hand, the different phases of the proposed framework (Figure 1, part II) define the phases to obtain the systematic problem definition.

4. Case Study

The case study comprises a system that has been treated with mathematical models for solving a multistage scheduling problem. Specifically, the scheduling problem presented in the paper by Capon-Garcia et al. 2011 and detailed in Muñoz et al. 2018, is considered, where acrylic fibers are produced along 14 stages in a batch production plant, structured in 8 recipe unit procedures and 6 recipe operations. As primary information, production process was defined in a master recipe involving 27 different resources, which are basically material and energy resources. Two alternative production processes are assessed in this work, namely acrylic fiber A uses acetone as solvent in the polymerization and acrylic fiber B uses benzene

Thus, system features definition requirements have been defined and fulfill, comprising information as shown in Table 1, based on Enterprise Ontology Project from Munoz et al. 2012.

Table 1. General, tactic and strategic features for system characterization.

General Feature	Value	Tactic features	Value	Strategic features	Value
Production capacity	Medium	Transport type	Land	Production processing	Sequential
Company size	medium	Supply chain objective	Economic	Technology	Multi task
Supply chain type	Good availability	Production policies	Defined	Material storage	Limited
Production Type	Multi Stage	Customer features	-	Material resource	Not perishable
Market competition type	Low	Suppliers features	-	Processing resources	Limited
Environmental regulations	Defined	Process flow type	Forward	Scheduling objective	Timing
Demand feature	High volume	Material storage type	Limited	Scheduling mode	On-line

Next, in order to obtain a problem definition Part II from Figure 1 is explained and detailed.

- a) *Automated Process system definition.* From previous system's instantiation within EOP knowledge model, a semantically enriched machine-readable system structure is obtained. The model comprises 934 instances concerning 295 classes, 257 Object properties, 33 data properties. As example of class instantiation made, the *RawMaterial* class has *Input1_1 (Acrylonitrile)*, *Input1_2 (MethylMetaacrilate)*, *Input1_3 (VinilChloride)*, *Input1_4 (solvent-Acetone)* as instances.
- b) *Problem situation recognition.* In this phase, indicators derived from an automated SWOT are defined. Each indicator is mapped into a semantic concept (class) from the EOP knowledge model. Then, upper and lower boundaries of control are set. One of the main advantages of the system is the fact that problem recognition is coming from the knowledge model. As a result data and information, usually hidden

for a human, can be easily manage by the system. Table 2 shows the different indicators and their corresponding upper and lower boundaries values.

Table 2. Indicators and control boundaries of the problem recognition.

SWOT	Indicator	Related feature	Metric	UBV	LBV
O	Energy consumption	Electric consumption	kWh	30000	50000
		Water consumption	m ³ /ton	6000	10000
		Natural gas consumption	m ³ /ton	39000	45000
W	Time delivered failure	Tardiness finish orders	u/month	15	45
W	Demand unaccomplishment	Orders out of schedule	u/month	5	15
		Outsourcing orders	u/month	10	20
T	Changes in product order	Product demand changes	u/month	30	50
T	Cleaning overtimes	Cleaning task with overtime	u/month	0	5
T	New product order	Order placed out of the schedule	u/month	0	40

- c) *Goal statement.* Once that a problem has been identified an optimization goal can be obtained by specifying the minimization or maximization of the indicator chose in the previous phase. *Time Delivered Failure* indicator has been defined as a problem by the system, due to a violation in the upper boundary. Besides, the goal is stated as a minimization problem.
- d) *Key system features relations.* Based on the EOP knowledge model, the proposed framework is capable of finding the closer relations among the indicator (EOP class) chose in (b) and other process systems' concepts, potentially to be converted into decisions variables. Table 3 shows some examples of properties involved in the query in this phase.

Table 3. Domain and range of "Resource" class and subclasses.

Processing time	
hasID	ResourceID
hasUpperBound/hasLowerBound	float
hasResourceCost	ResourceCost
hasEnvironmentalPerformanceIndex	EnvironmentalPerformanceIndex

- e) *Decision variables definition.* In his phase, a decision about which and which not concepts (EOP classes) are defined as decision variables provided in (d) must be done.

Table 4. Main classes and derived classes potentially become decision variables.

ProcessingTime	TimeInterval	ProcessingActivity
Information	Information	ProcessAction
Parameter	Parameter	ProcessStage
ProcessInformation	ProcessInformation	ProcessOperation
ProcesParameter	ProcessParameter	Thing
Thing	ClainingTime	
TimeInterval	WaitingTime	
	ProcessingTime	
	Thing	

- f) *System assumptions definition.* From the system structure defined in (a), the most important and used assumptions based on the appropriate physical laws governing the process can be chosen to form part of the current problem definition. For this case study the process conditions are fixed according to the recipe definition.

- g) *Parameters & engineering metrics definition.* In the same manner, parameters coming from the EOP's classes' data properties are chosen and defined. Then, engineering metrics are also specified automatically.
- h) *Problem statement definition.* As the main goal of this approach, the proposed framework is capable of creating a problem statement in the form of natural language, which can be used to verify and validate the problem in an easy human readable way. The following paragraph has been obtained as a resulting problem statement from the current case study: "A problem regarding *tardiness finish orders* has been detected, resulting from violating upper bound of control, an optimization problem statement is proposed as follow: Taking into account variables *StartingTime*, *BatchSequencing*; parameters *ChangeOverTime*, *BatchProcessingTime*; Minimize *FinishTime*"
- i) *Knowledge of similar models.* Finally, the framework executed a query that classifies similar optimization problems in order to suggest possible solutions to those similar problems, based on Capon-Garcia et al. (2017).

5. Conclusions

This work develops a semi-automatic process for semantically enriched problem statement based on formal knowledge models. Thus, features related to the system are easily defined and characterized, resulting in a virtualization of the system that comprises strategic, tactical and operational features. Next an automated problem definition process improves how information and data are considered lying in the potential of knowledge models and semantics technologies. In addition, knowledge models provide additional reasoning capabilities to support decision support system for the Wide Optimization and Industry 4.0 approaches. For illustrating purposes, a case study was presented using a scheduling of a multiproduct batch plant, where the systematic approach presented was used resulting in a semantic problem statement and presented in natural language.

Acknowledgements

Financial support received from the Spanish "Ministerio de Economía, Industria y Competitividad" and the European Regional Development Fund, both funding the research Project AIMS (ref. DPI2017-87435-R), and from the "Generalitat de Catalunya" (AGAUR 2017-SGR-1092-CEPEiMA)" is thankfully acknowledged

References

- Grossmann I. E. Advances in mathematical programming models for enterprise-wide optimization. *Computers and Chemical Engineering*, 47, 2012.
- Harjunkoski, I., Maravelias, C.T., Bongers, P., Castro, P.M., Engell, S., Grossmann, I.E., Hooker, J., Méndez, C., Sand, G., Wassick, J., 2014. Scope for industrial applications of production scheduling models and solution methods. *Comput. Chem. Eng.* 62, 161-193.
- Maravelias, C.T., Sung, C., 2009. Integration of production planning and scheduling: Overview, challenges and opportunities. *Comput. Chem. Eng.* 33, 1919-1930.
- Muñoz, E., Capón-García, E., Espuña, A., Puigjaner, L., 2012. Ontological framework for enterprise-wide integrated decision-making at operational level. *Comput. Chem. Eng.* 42, 217-234.
- Edrisi Muñoz, Elisabet Capón-García, and Luis Puigjaner Supervised Life-Cycle Assessment Using Automated Process Inventory Based on Process Recipes. *ACS Sustainable Chemistry & Engineering* 2018 6 (9), 11246-11254.
- Elisabet Capón-García, Edrisi Muñoz, José Miguel Lainez-Aguirre, Konrad Hungerbühler, Knowledge-Driven Multi-Label Classification of Process Scheduling Problems, *Computer Aided Chemical Engineering*, Elsevier 2017, 40, 2353-2358.

Improved problem constraints modeling based using classification

Elisabet Capón-García^{a*}, Edrisi Munoz^b, Luis Puigjaner^c

^a *ABB Switzerland Ltd., Segelhofstrasse 1K, 5405 Baden-Dättwil, Switzerland*

^b *Centro de Investigacion en Matemáticas A.C., Jalisco S/N, Mineral y Valenciana 36240, Guanajuato, Mexico*

^c *Chemical Engineering Department, EEBE, Universitat Politècnica de Catalunya, Av. Eduard Maristany, 10-14, 08019 Barcelona, Spain*

elisabet.capon@ch.abb.com

Abstract

A general classification agent has been developed based on a semantic model for supporting the modelling of problems in the chemical modelling domain. Two case studies are used to illustrate the proposed approach, which stands for a routine that solves the modelling task easily and quicker and less error-prone approach in comparison to the traditional problem.

Keywords: first-principles, mathematical modelling, chemical processes, semantic modelling.

1. Introduction

Currently, chemical and other process industries, such as food, agriculture or pharmaceutical, evolve in a highly dynamic and changing environment. Indeed, the globalization of trade, product customization and stricter environmental and societal requirements, among others, seriously challenge the performance and operation of the process industry. Indeed, time response and solution quality for critical problems are critical issues that motivate the development of new solutions.

In such scenario, enterprises strive to remain competitive by improving their functional, technological and operational advantage. Although chemical processes are intrinsically complex, the underlying chemical and physical phenomena can be explained by a self-contained set of mathematical expressions and models, which derive from physical laws and experimental. In this sense, the quick and flexible development of models that fundamentally support: (i) the understanding of the underlying phenomena and (ii) the implementation of advanced decision support systems, is a crucial issue in the process industry.

Mathematical models use equations and concepts in order to describe a systems and particular situations with the aim of explain, predict and simulate them. The advances in computers systems in recent years have allowed an exponential growth in scientific computation, enhancing the capacity for solving mathematical models with algorithms, easier to treat and solve. In this sense problem modelling has become a key activity where process activities exists as base for make more efficient the mathematical optimization task.

This objective of this work is to support the automatic generation of constraints design by using semantic modelling and mathematical programming, based on problem classification. An intelligent agent proposes a set of model equations which help to understand how those set of constraints can be built up. Besides, the proposed system makes use of semantic technologies enhancing the comprehension among decision variables and parameters. Thus, model constraints using semantic networks link relationship among different components of the system, concepts, physical laws and principles of the phenomenon based on standard conceptualizations.

2. Problem statement

The starting point when posing a model for solving a problem in the chemical process domain mainly consists of defining the problem features, namely the elements which represent the system and describe its behavior, as well as the system parameters and variables.

Hence, a multi-label classification problem can be associated with process modeling. Therefore, given (i) a set of process features (attributes) and (ii) a set of existing mathematical equations related to such problem features (labels); the objective is to match a given instance with a subset of the features in (i) with its corresponding equations in (ii). A goodness function for each label will be used to check the ability of the classification approach to select the appropriate labels (ii).

3. Methodology

On the one hand, an ontology has been created comprising the chemical engineering domain described in Section 3.2. Therefore, Section 3.1 presents the basis for the ontology development. Ultimately, this work develops a software platform in Jython, which is integrated with the semantic model derived as presented in Section 3.1 using OWLAPI, and stands as an improved modeling tool in the chemical process domain.

Different areas in the chemical engineering domain, including basic unit operation principles, transport phenomena, reaction kinetics and thermodynamics, have been revised in order to collect and examine the most relevant formulae (Cameron and Hangos, 2001). In this sense, it is essential to work out the expressions in a very precise and thorough way, since every imaginable system and process configuration has to be considered to account for all possible cases. As a result, a complete table of equations with their attributes has been built up. In summary, 102 distinct equations have been classified to enable a complete and most realistic description of a given system or chemical process. In order to select the appropriate equations, 39 system attributes have been specified. The full description of the knowledge base is provided in Section 3.2.

3.1. Semantic modelling

Ontologies stand for a formal specification of the domain, that is, a body of formally represented knowledge based on conceptualizations, which are abstract, simplified views of the physical or procedural elements. On the one hand, the ontology elements should be part of the model intended to represent a system for some purpose, managing the relationships that hold among the elements of the model, thus allowing the ontology to be usable. On the other hand, reusing ontologies requires not only consideration of

the ontologies, but also of the tasks for which they are intended. The base of this work lies down in the use of an ontology that deals with diversity in scheduling problem representation and allows effective data sharing and information flow. Ontologies are hierarchical domain structures that provide a domain theory, have a syntactically and semantically rich language, and a shared and consensual terminology (Klein et al. 2002). The body of knowledge for this ontology stems from the chemical engineering modelling domain, and a PDCA methodology (Munoz et al., 2012) has been used to create the ontology. The final ontology, called Chemical Engineering Ontology (ChEnOn), contains 154 classes, 33 object properties and 21 data properties.

3.2. Modelling domain and classification approach

The chemical engineering domain can be broadly classified in different knowledge areas. In this work, we have considered mass, energy and momentum balances, as well as mass and heat transfer equations, and thermodynamics and reaction kinetics. Besides, classification approaches are described for each knowledge area, presented next.

3.2.1. Mass balances

First of all, the conservation principle of mass was considered. In general, there are three distinct systems that have to be considered: the isolated system, the closed system and the open system in relation to the surrounding environment. All three systems have to be taken into account to fully study the conservation principles of mass, energy and momentum in every real case example. For mass, there is no difference between the isolated and closed system, since mass can only be exchanged in an open system. The first mass balances for a closed system were stated and the descriptor “State” was introduced to differentiate between a steady state system and a transient state system. These two characteristic, yet clearly opposite attributes of a system were the first guiding principle on how to distinguish and classify equations. In total there are three different situations possible in a closed system. The first two systems time-independent described with the attribute steady state, while the third system’s components change their mass due to the reaction, which results in a transient state system. To differentiate between the first two systems, a new descriptor and its corresponding attributes were introduced, being “Components” and “Single Component” and “Multiple Components”, respectively. Also the descriptor “Reaction” with an attribute “Generation” was proposed. All these parameters and equations are part of the ontological model, where each equation was inserted as a class with a descriptive name and a unique ID code, while the descriptors and its attributes were put into object properties of the ontology. If now a system possesses or an equation fulfils a certain attribute, the corresponding cell between them was marked with a 1 or else with 0. In this way 16 different mass balance equations could be identified and expressed with the help of additional system descriptors like “Mass Flow” (Attributes: Feed, Mass Outflow), “Evolution” (Accumulation/Depletion) and “I/O Structure” (Single Stream, Multiple Streams).

3.2.2. Energy balance

Next, the conservation law of energy and its energy balances for the three aforementioned systems: isolated, closed and open was considered. The approach was similar to the determination of the mass balances and 21 different energy balances could be formulated, covering all imaginable system configurations. To be able to differentiate between these energy balances, additional categories to the old ones of system descriptors and their attributes had to be proposed, namely “Heat”, with the attributes consisting of “Heat Inflow”, “Heat Outflow”, “Conduction”, “Convection”

and “Radiation”, as well as “Work” with “Work Input” and “Work Output” as the corresponding attributes.

For the derivation of the energy balances, it was assumed that the kinetic and potential energy of the system are negligible.

3.2.3. *Momentum balance*

To conclude with the conservation principles, the conservation law of momentum was examined and similar to the energy balances, 21 momentum balances could be postulated. Since most of the momentum balances are simply correlated to the mass balances, only one additional attribute “Force” had to be added in order to account for the sum of gravitational, friction, pressure and shearing forces, which might act on the system. As a result of the conservation principles in chemical systems and processes, 58 different equations could be found to describe a potential real life system.

3.2.4. *Mass transfer*

For this purpose, the descriptor “Diffusion” and five more attributes being “Dilute Solution”, “Concentrated Solution”, “Membrane”, “Diffusion”, and “Convection” have been created. With these, nine more equations concerning diffusion in different systems could be classified and added to the list of classes of the ontology.

3.2.5. *Heat transfer*

Another examined aspect of transport phenomena includes the heat transfer to or from a given system. Heat transfer is a very common issue in chemical engineering. Again the focus was put on the most practical and applicable heat transfer equations and eight common heat transfer equations could be ascertained. For these equations, no further descriptors and attributes had to be assigned, since heat transfer had already been accounted for by the derivation of the energy balances. The transport phenomena encompasses a total of 17 equations.

3.2.6. *Reaction kinetics*

Alongside the classical and convenient reactor kinetics of batch, semibatch, CSTR and PFR, a numerous of typical reactions were investigated and postulated. A total of 19 reaction kinetic equations were amassed with 10 more attributes required to differentiate and classify them all.

3.2.7. *Thermodynamics*

Last but not least, thermodynamics and its equations of state were put into consideration and eight of the vast number of equations has been chosen according to their applicability and frequency of usage. The five specified attributes regarding the thermodynamic equations were “Ideal”, “Non-Ideal”, “Empirical”, “Gas” and “Liquid”. The last two attributes correspond to the phase of the considered fluid.

4. Case study

The applicability of the proposed equations has been tested in two different systems, namely a tank system and an equilibrium stage. The case studies allow to understand the usability of the proposed framework. This validation allows for the direct evaluation of the work and gives insights in the usefulness of having such a tool.

4.1. Tank system

The first example deals with a standard tank system, where both input and output streams are constant and all initial conditions like volume, temperature and concentration of the solution inside the tank are known. The feed stream has constant composition, concentration and temperature and identical properties of both solutions to water as well as perfect mixing are assumed. The goal is to determine the time evolution of the tank level, its concentration and its temperature.

As a first step, the system attributes were determined from the problem description: Open system, transient state, accumulation (since inflow was greater than outflow), single input/output stream, single component, no generation (reaction), no heat or work flows. The time evolution of the tank level is directly correlated to the mass inside the tank, hence a mass balance was required that is described by all the above-mentioned attributes. The overall set of equations proposed by the developed agent consist of M4, M16 and E12 (Figure 1). From the proposed set of equations to the problem solution, a few set of adjustments are required. M4 had to be slightly modified, since volume and not mass was targeted, and integrated to give an exact answer in the form of an analytical expression. M6, which relates mass and concentration, could be used to find an analytical expression for the time evolution of the concentration. In order to determine the temperature evolution of the system, E12 underwent some changes, namely the conversion of the equation from energy to temperature, and the equation could eventually be integrated and the temperature profile of the system with respect to the time was obtained. This methodical way of solving the problem by determining system attributes and supporting agent proved to be very successful and timesaving.

Problem Description	System Attributes	Set of Equations	Problem Solution
Tank (Area: $A = 2 \text{ m}^2$, Height: H) filled with 0.8 m^3 (V) of 0.15 wt\% (c_0) NaCl solution at 35°C (T_0). At constant feed (Q_1) of 0.20 wt\% (c_1) NaCl solution at 25°C (T_1) and outflow (Q_2), determine time evolution of tank level, concentration and temperature.	Open System, Transient State, Accumulation, Single I/O-Stream, Single Component, No Generation (Reaction), No Heat or Work Flows, Perfect Mixing, Ideal Solution (density ρ , heat capacity c_p)	$\frac{dm}{dt} = F - Out \quad [M4]$ $\frac{dm_i}{dt} = \frac{d(Vc_i)}{dt} M_i \quad [M16]$ $\frac{dE}{dt} = F h_F - Out h_{Out} \quad [E12]$	<p>Tank level: $\frac{dm}{dt} = \rho A \frac{dH}{dt} = Q_1 - Q_2$</p> $H(t) = H_0 + \frac{(Q_1 - Q_2)}{\rho A} \cdot t$ <p>Concentration: $\rho \frac{dm}{dt} = c \frac{dV}{dt} + V \frac{dc}{dt} = \rho Q_1 c_1 - \rho Q_2 c$</p> $c(t) = (c_0 - c_1) \cdot e^{-\frac{Q_2}{\rho V} t} + c_1$ <p>Temperature: $\frac{dE}{dt} = m c_p \frac{dT}{dt} = Q_1 c_p T_1 - Q_2 c_p T$</p> $T(t) = (T_0 - T_1) \cdot e^{-\frac{(Q_1 - Q_2)}{m} t} + T_1$

Figure 1. Problem description and solution for a single tank system.

4.2. Equilibrium stage

The following example covers the traditional equilibrium stage of a distillation column. In a distillation column, two streams with different compositions enter an arbitrary stage in counter-current mode, where some components inside the stage change from the liquid phase to the vapour phase or vice versa and the compositions of the two streams leaving the stage are assumed to be in thermodynamic equilibrium. The task is to determine all possible equations to fully describe and solve the system.

The task requires to find the appropriate mass and energy balances, as well as the thermodynamic equilibrium expression. For this purpose, the following system attributes were identified: Open system, steady state, neither accumulation nor depletion, no generation (reaction), multiple input/output streams, multiple components,

no heat or work flows (adiabatic), gas-liquid equilibrium, ideal system (assumption). The developed agent proposed equations M9, E15 and T7 (Figure 2), which had to be adequately adapted. With these three equations, the overall mass balance of the stage, the mass balances of each component, the energy balance of the stage and the equilibrium condition for each component between liquid and gas phase could be obtained. From there, the system was explicitly solvable, which underlined the usefulness of working with system attributes and having the effective classification matrix.

Problem Description	System Attributes	Set of Equations	Problem Solution
Modelling of a Single Stage in a Distillation Column.	Open System, Steady State, No Depletion or Accumulation, No Generation (Reaction), Multiple I/O-Streams, Multiple Components, No Heat or Work Flows, Gas-Liquid Equilibrium, Ideal	$0 = \sum_{s=1}^S F_i - \sum_{s=1}^S Out_i$ [M9] $0 = \sum_{s=1}^S \sum_{i=1}^C h_{F,i}(F_i)_s - \sum_{s=1}^S \sum_{i=1}^C h_{Out,i}(Out_i)_s$ [E15] $py_i = x_i p_i^S$ [T7]	Mass Balance: $0 = V_{i+1} + L_{i-1} - V_i - L_i$ Component Balance: $V_{i+1}y_{i+1} + L_{i-1}x_{i-1} = V_i y_i + L_i x_i$ Energy Balance: $0 = h_{V_{i+1}}V_{i+1} + h_{L_{i-1}}L_{i-1} - h_{V_i}V_i - h_{L_i}L_i$ Equilibrium Condition: $y_i = m_i x_i \quad \text{with} \quad m_i = \frac{p_i^S}{p}$

Figure 2. Problem description and solution for an equilibrium stage.

5. Conclusions

This work presents an intelligent agent which is capable of recognizing the system attributes, and links them to specific equations from the areas of conservation principles, transport phenomena, reaction kinetics and thermodynamics. The agent is based on a semantic model and has been programmed in Java. It has proved to be very helpful in quickly finding the appropriate set of equations to determine or solve for certain properties of the system in a systematic and methodical way. Likewise, a general classification algorithm has been developed to assist in the assignment of the problem to the correct equations. What this all amounts to is that the overall definition of a chemical engineering problem can be monitored on a regular basis and mistakes or inaccuracies in the table are removed at an early stage. As a future work, the developed framework is a cornerstone for a larger enterprise wide framework, which processes the information and data required for the model fitting and problem optimization. The overall framework should be designed such that it is capable of managing, structuring and delivering information as required by the constraints, thus being able to react to production system changes or modeling changes, based on flexible data and information structures.

Acknowledgements

Financial support received from the Spanish "Ministerio de Economía, Industria y Competitividad" and the European Regional Development Fund, both funding the research Project AIMS (ref. DPI2017-87435-R), and from the "Generalitat de Catalunya" (AGAUR 2017-SGR-1092-CEPEiMA) is thankfully acknowledged

References

- I. Cameron and K. Hangos, 2001, Process Modelling and Model Analysis. Elsevier.
- M. Klein et al. 2002, Ontology versioning and change detection on the web. In 13th international conference on knowledge engineering and knowledge management (EKAW02), pp. 197–212.
- E. Muñoz et al. (2012). Towards an ontological infrastructure for chemical batch process management. *Comp. & Chem. Eng.*, 34, 668–682.

Bioethanol Production with Cyanobacteria by a Two-Stage Fermentation Strategy

Romina Lasry Testa^a, Claudio Delpino^a, Vanina Estrada^a, M. Soledad Diaz^{a,*}

^a *Planta Piloto de Ingeniería Química (PLAPIQUI), Universidad Nacional del Sur (UNS)-CONICET, Camino La Carrindanga Km 7, Bahía Blanca 8000, Argentina*
sdiaz@plapiqui.edu.ar

Abstract

In this work, we study *in silico* photoautotrophic bioethanol production with *Synechocystis* sp. PCC6803 by a two-stage approach in two bioreactors in series. In the first stage the conditions are set for the maximization of growth rate, with optimal conditions of light intensity and carbon sources, while in the second a state of nitrogen limited conditions that tends to maximize ethanol production instead of growth rate is considered. Both stages are optimized by Flux Balance Analysis with different objective functions: Maximization of biomass for the first stage and Minimization of ATP production for the second. A previously developed genome scale metabolic network model is used for the optimizations. Results are promising into considering this strategy experimentally.

Keywords: Synechocystis, Bioethanol, FBA, Nitrogen limitation, phosphorus limitation.

1. Introduction

In recent years cyanobacteria have been considered as promising candidates to become cell factories in the context of systems biology research. This is due to the fact that these microorganisms are capable of growing only on ambient carbon dioxide and minimal inorganic nutrients. More specifically, photoautotrophic bioethanol production has been widely studied with mutant strains of *Synechocystis* sp. PCC6803 (*Synechocystis*) harboring the genes *pdh* and *adh* from the ethanol producing bacterium *Zymomonas mobilis*, achieving experimental production rates of 0.261 g L⁻¹ day⁻¹ (Dienst *et al.*, 2014).

Mathematical models of metabolism are useful into quantifying the metabolic capabilities of the microorganism and predicting experimental results through optimization problems. The most useful kind of models are genome scale metabolic networks (GEMs), that include information of all the enzymes, reactions and metabolites, with their corresponding stoichiometry, in the genome of the considered microorganism. GEMs allowed the development of *in silico* strategies to improve the production of high added value products. One of these strategies is coupling the production of the compound of interest to growth by the identification of a set of reactions to eliminate (“knock-outs”), based on a bi-level programming approach, where the knock-outs are represented by binary variables, resulting in MILP programming problems (Chowdhury *et al.*, 2015). In previous work (Lasry Testa *et al.*, 2017) we applied a modification of this strategy to a previously developed GEM of *Synechocystis*

to couple bioethanol production to growth with good results, but requiring a high number of genetic interventions.

In this work we propose a two-stage ethanol production approach in two bioreactors in series to improve ethanol production based on nutrient limiting conditions. In the first stage the conditions are set to maximize growth rate, while in the second stage the conditions are set to limit growth and allow for ethanol production. For the second stage, two different limiting nutrients are considered: Nitrogen and Phosphorus. A similar strategy has been used to produce bioethanol with yeast (Gowtham et al., 2014), but it has not been applied to cyanobacteria to our knowledge so far. We evaluate our model against fluxomic experimental data for a nitrogen limited state (Nakajima et al., 2017). Namakoshi et al. (2016) provide experimental evidence on ethanol production under nitrogen-limited conditions by a mutant strain of *Synechocystis* harbouring deletions for both glycogen and PHB synthesis pathways.

2. Materials and Methods

2.1. Genome Scale Metabolic Network Model and Conditions

We consider a genome scale metabolic network model (GEM) of the cyanobacteria *Synechocystis* that contains 709 reversible and irreversible reactions, 80 exchange reactions and 535 metabolites. The ethanol production pathway is added by incorporating the heterologous gene *pdC* from *Zymomonas mobilis*, which encodes for the enzyme pyruvate decarboxylase (PDC) that catalyzes the non-oxidative decarboxylation of pyruvate (PYR) to produce acetaldehyde (ACAL) and CO₂. Carbon is considered to be taken up as carbon dioxide (CO₂) and bicarbonate (HCO₃³⁻). HCO₃³⁻ uptake is active by a Na⁺ dependent ATP consuming transporter, while CO₂ uptake is passive with the posterior conversion to HCO₃³⁻. The CO₂ from intracellular decarboxylation is considered to be converted into HCO₃³⁻ by a reversible reaction (Nogales et al., 2012). For all the optimizations performed in this work, photoautotrophic growth is considered, and carbon uptake is restricted to 3.7 mmol gDW⁻¹ h⁻¹, divided into CO₂ and HCO₃³⁻, with all other possible carbon sources set to 0. For the light uptake an upper bound of 100 mmol gDW⁻¹ h⁻¹ is considered. Nitrogen is considered to be taken up as nitrate, while phosphorous is taken up as orthophosphate, both through active transport. For the TCA cycle, we take into account two possibilities, proven to be functional by experimental data: (a) The γ -aminobutyric acid shunt (GABA shunt) and (b) the enzymes 2-OGDC and SSDHA.

The model is built in SBML format with the tools provided in COBRA Toolbox and is then turned into the GAMS Data eXchange (GDX) format to be used in the GAMS environment (GAMS Development Corporation, Washington, DC).

2.2. Flux Balance Analysis and evaluation against experimental data

Flux Balance Analysis (FBA) is used to determine the flux distribution of a metabolic network under a specific steady state condition. It consists of a linear programming (LP) problem, which is defined with the steady state mass balances of the network (Eq. (2)), the lower and upper bound on fluxes (Eq. (3)) and an objective function. In this work we consider two different objectives functions (Eq. (1)): (a) Maximization of biomass production and (b) minimization of ATP production.

$$\max v_{biomass} \quad (\min v_{ATP \text{ production}}) \quad (1)$$

$$\sum_j S_{i,j} v_j = 0 \quad (2)$$

$$LB_j \leq v_j \leq UB_j \quad (3)$$

To evaluate the GEM against experimental fluxomic data, Flux Variability Analysis (FVA) is considered. FVA is a strategy derived from FBA, where the fluxes of all the reactions in the model are maximized and minimized subject to FBA constraints (Maranas and Zomorodi, 2016). In the evaluation, the lower and upper confidence bounds of the experimental data are set as bounds for the corresponding reactions in the GEM and the bounds for all other reactions are obtained by FVA. The resulting flux distribution must be feasible and have the same growth rate as reported in the experimental data.

2.3. Two stage production approach

In this *in silico* bioethanol production strategy we consider a first stage where conditions of carbon and light uptake are set for the strain to be in exponential growth phase, where all the carbon flux is directed towards biomass production. This stage is simulated by FBA with biomass objective function (Maximization of Biomass). Then, the biomass produced in the first stage is transferred to a second stage where the conditions are set for the growth to be in stationary phase. For this, we consider two different cases of nutrient limitation that allow for the redirection of carbon flux to the production of biofuels. This stage can also be simulated by FBA with an objective function of ATP production minimization, characteristic of the stationary growth phase where growth rate tends to zero, as the growth and death rates are balanced. The limitations considered are nitrogen and phosphorus. Experimental evidence reveals ethanol production under nitrogen limited conditions in a mutant of *Synechocystis* incapable of glycogen and PHB storage (Namakoshi et al., 2016). With this approach we simulate a nitrogen limited scenario according to experimental values and study the case of phosphorus limitation with different scenarios as there is no experimental evidence to validate it.

3. Results

For both limitation cases we modify our GEM eliminating glycogen and PHB storage as this favours biofuel production (Namakoshi et al., 2016). The first stage of the approach presented in section 2.3 is the same for both cases as it is not limited by any other nutrient than carbon or light. The FBA optimization provides a maximal growth rate of 0.089 h⁻¹ for the first bioreactor, which is consistent with experimental data for these conditions.

3.1. Nitrogen limited conditions

We evaluated our model against experimental fluxomic data from Nakajima et al. (2017) as described in section 2.2. The growth rate reported in this study is 0.015 h⁻¹. We evaluate our model for this growth rate to obtain the nitrogen uptake that corresponds to the experimental flux distribution, which results in a flux of 0.135 mmol gDW⁻¹ h⁻¹. With this uptake value we run FVA and obtain a very accurate correlation between the experimental values and the flux distribution obtained (Table 1), showing that our model is capable to reproduce nitrogen limitation. We only find significant difference for the reaction converting Fumarate to Malate (FUM → MAL) which is

probably due to the different modelling of the TCA cycle. Nakajima et al. (2017) consider the Glyoxylate Shunt and the OGDH complex which are proven to not be present in cyanobacteria. Based on the evaluation against experimental data, we chose to consider a case of nitrogen uptake restricted with an upper bound of 0.135 mmol gDW⁻¹ h⁻¹ to assure that the uptake is feasible and limiting, experimentally. This value and the growth rate of 0.015 h⁻¹ are fixed, and ATP production is minimized by FBA with a result of 6.285 mmol gDW⁻¹ h⁻¹. These conditions provide an ethanol production of 1.547 mmol gDW⁻¹ h⁻¹.

3.2. Phosphorus limited conditions

As there is no experimental data available on cases of phosphorus limitation, we chose to simulate a set of cases for different phosphorus uptakes to study the possibilities for ethanol production in the second stage. The phosphorus uptakes considered are 6: 0.03, 0.025, 0.02, 0.015, 0.01 and 0.005 mmol gDW⁻¹ h⁻¹, respectively. For each of the uptakes maximum growth rate, maximal ethanol production rate and minimal ATP production are obtained with FBA and reported in Figure (1) a, b and c respectively. We can see that as the upper bound on phosphorus uptake decreases the maximal biomass production also decreases, leaving more carbon flux available to be redirected towards ethanol production, which has the opposite tendency. The minimal ATP production required for each state decreases as growth rate, since the ethanol production pathway does not require the production of ATP, contrary to biomass production. We chose the case of 0.01 mmol gDW⁻¹ h⁻¹ of phosphorus uptake as the best one as the growth rate of 0.014 h⁻¹ is very close to the case considered for nitrogen limitation. For this case the ethanol production is 1.57 mmol gDW⁻¹ h⁻¹ and the minimal ATP production is 6.269 mmol gDW⁻¹ h⁻¹.

Table 1: *Experimental and Model flux distributions*

	Our Model	Nakajima et al (2016)		Our Model	Nakajima et al (2016)
G6P -> RU5P	0.389	0.349	GAP -> DHAP	0.938	0.937
RU5P -> RUBP	1.229	1.191	PGA -> GAP	1.166	2.167
RUBP -> 2 PGA	1.229	1.191	PGA -> 2PG	0.192	0.192
DHAP + E4P -> S7P	0.821	0.803	2PG -> PEP	0.193	0.192
PYR -> ACCOA	0.111	0.111	PYR -> PEP	0.444	0.406
ACCOA -> CIT	0.048	0.049	GLU -> AKG	0.042	0.042
CIT -> ACONI	0.048	0.049	SUC -> FUM	0.028	0.027
ACONI -> ICIT	0.048	0.049	FUM -> MAL	1.081	0.039
ICIT -> AKG	0.048	0.048	MAL -> OAA	0.498	0.049
GLU -> ABUT	0.02	0.021	X5P -> RU5P	0.569	0.572
4ABUT -> SUCSAL	0.02	0.021	R5P -> RU5P	0.269	0.269
SUCSAL -> SUCC	0.022	0.021	S7P + GAP -> R5P + X5P	0.282	0.281
MAL -> PYR	0.583	0.537	F6P + GAP -> E4P + X5P	0.288	0.29
F6P -> G6P	0.395	0.366	S7P + GAP -> E4P + F6P	0.539	0.521
FBP -> F6P	0.145	0.136	G6P -> GLYC	0.37	0.372
GAP + DHAP -> FBP	0.145	0.136			

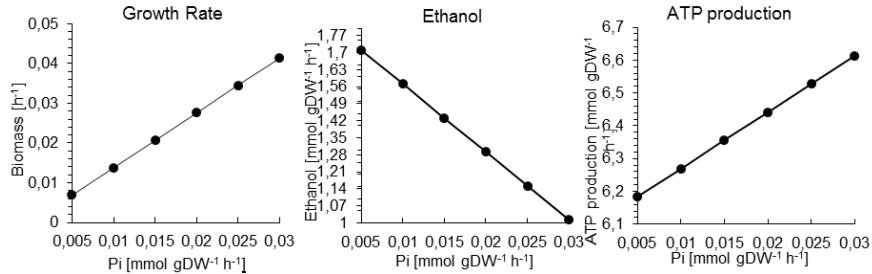


Figure 1: a) Growth rate, b) Maximal ethanol production and c) Minimal ATP production required for 6 different phosphorus scenarios

4. Discussion

To compare the results obtained for the two cases of limitation with data from bibliography, we assume experimental culture conditions to calculate ethanol production rates. The initial biomass concentration (X_0) considered is of 0.078 gDW L^{-1} . For the first stage we consider growth in exponential phase and calculate the final biomass concentration assuming a cultivation time of 2 days (t) and a growth rate (μ) of 0.089 h^{-1} (see section 3). According to Eq. (4), the final biomass concentration for the first stage is 5.589 gDW L^{-1} . This value is the same for both cases of nutrient limitation.

$$\ln X - \ln X_0 = \mu t \tag{4}$$

For the second stage the culture is considered to be in stationary phase, so the net growth rate is 0. With these assumptions the ethanol production is calculated based on the final biomass concentration of the first stage, considering a cultivation time of 1 day. For both stages, a light limitation function is considered to include shade effect of biomass (Laiglecia et al., 2013). The ethanol production for both limitation cases, compared with the case of the coupled mutant presented in Lasry Testa et al. (2017) are shown in Figure 2.

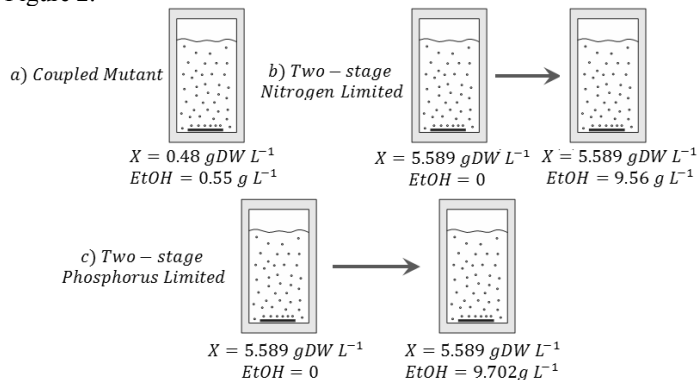


Figure 2: Ethanol and biomass productions for all the cases compared

Numerical results show a very similar ethanol production for the nitrogen and phosphorus cases, with an increase of only $\sim 1.5\%$ for the phosphorus case. In contrast, the results obtained for the two-stage approach are more promising than the ones obtained in previous work for a coupled mutant obtained by a set of genetic

interventions, and higher than the best result of 332 mg L⁻¹ reported by Namakoshi et al. (2016). These results are obtained for constant illumination, so the cultivation needs to be carried out in a closed photobioreactor at industrial scale, where the main obstacle would be the cost of the system compared with open ponds. However, encouraging new photobioreactor designs are beginning to be available to address these difficulties (Johnson et al., 2018)

5. Conclusions

In this work, we have addressed photoautotrophic ethanol production by the genetically modified cyanobacterium *Synechocystis* sp. PCC 6803 with a novel strategy through mathematical modelling. The ethanol productions obtained for both limitation cases are promising as they are higher than the best experimental results from bibliography. The model could be successfully evaluated against experimental data for nitrogen limited conditions, but no experimental data is available for the phosphorus case. Mathematical models of metabolism become more reliable with the inclusion of experimental values. The results obtained are encouraging into testing this kind of approach in experimental studies.

References

- Chowdhury, A., Zomorodi, A.R., Maranas, C.D., 2015. Bilevel optimization techniques in computational strain design. *Comput. Chem. Eng.* 72, 363–372.
- Dienst, D., Georg, J., Abts, T., Jakorew, L., Kuchmina, E., Börner, T., Wilde, A., Dühring, U., Enke, H., Hess, W.R., 2014. Transcriptomic response to prolonged ethanol production in the cyanobacterium *Synechocystis* sp. PCC6803. *Biotechnol. Biof.* 7, 21.
- Gowtham, Y.K., Miller, K.P., Hodge, D.B., Henson, J.M., Harcum, S.W., 2014. Novel two-stage fermentation process for bioethanol production using *Saccharomyces pastorianus*. *Biotechnol. Prog.* 30, 300–310.
- Johnson, T.J., Katuwal, S., Anderson, G.A., Gu, L., Zhou, R., Gibbons, W.R., 2018. Photobioreactor Cultivation Strategies for Microalgae and Cyanobacteria. *Biotechnol. Prog.* 34, 811–827.
- Laiglecia, J., Estrada, V., Vidal, R.V., Florencio, F.J., Guerrero, M.G., Soledad Diaz, M., 2013. Dynamic flux balance analysis of a genetic engineered cyanobacterium for ethanol production. Parameter estimation. *Chem. Eng. Trans.* 32, 955–960.
- Lasry Testa, R., Delpino, C., Estrada, V., Diaz, M.S., 2017. Metabolic network design of *Synechocystis* sp. PCC 6803 to obtain bioethanol under autotrophic conditions. *Comput. Aided Chem. Eng.* 40, 2857–2862.
- Maranas, C.D., Zomorodi, A.R., 2016. Optimization Methods in Metabolic Networks. John Wiley & Sons, Inc.
- Nakajima, T., Yoshikawa, K., Toya, Y., Matsuda, F., Shimizu, H., 2017. Metabolic flux analysis of the *synechocystis* sp. PCC 6803 Δ nrtABCD mutant reveals a mechanism for metabolic adaptation to nitrogen-limited conditions. *Plant Cell Physiol.* 58, 537–545.
- Namakoshi, K., Nakajima, T., Yoshikawa, K., Toya, Y., Shimizu, H., 2016. Combinatorial deletions of *glgC* and *phaCE* enhance ethanol production in *Synechocystis* sp. PCC 6803. *J. Biotechnol.* 239, 13–19.
- Nogales, J., Gudmundsson, S., Knight, E.M., Palsson, B.O., Thiele, I., 2012. Detailing the optimality of photosynthesis in cyanobacteria through systems biology analysis. *Proc. Natl. Acad. Sci.* 109, 2678–2683.

Application of plate heat exchangers into heat exchanger networks retrofit with fixed structure

Kexin Xu^{*}, Robin Smith

*Centre for Process Integration, School of Chemical Engineering and Analytical Science, The University of Manchester, M13 9PL, UK.
kexin.xu@manchester.ac.uk*

Abstract

Heat exchanger enhancement technologies have been widely used into heat exchanger networks (HENs) retrofit. However, the heat recovery is limited through the enhancement, which is restricted by the geometry of existing heat exchanger. Plate heat exchangers are widely used in energy-intensive process industries to increase heat recovery and reduce greenhouse gas emissions with the features of small minimum temperature approach and high effectiveness. Thus, plate heat exchangers are taken into consideration to replace conventional heat exchanger in crude oil preheat trains to enhance heat transfer coefficient and reduce energy consumption. A major limitation of applying plate heat exchanger is lack of reliable optimization method to quantify the energy saving effectively. Due to the high installation cost of plate heat exchangers, the optimization is based on the trade-off between energy reduction and capital cost. This work proposes a new methodology of application of plate heat exchanger in HENs retrofit with a fixed network structure. A change in one component in heat exchanger networks can have an effect on other downstream heat exchangers. Therefore, the proposed methodology also presents a way of eliminating the need for additional heat transfer area after replacement, while ensuring the stream target temperatures are met. Case studies highlight the benefits of the new approach.

Keywords: plate heat exchanger, heat exchanger network retrofit, energy saving

1. Introduction

With the growth of energy consumption and the increase of CO₂ emissions, it is more and more important to improve heat transfer efficiency. Heat exchanger network retrofit is a cost-effective way to increase heat recovery based on the existing heat exchanger network in process industries. Plate heat exchanger, including gasket plate heat exchanger and welded plate heat exchanger, is one of the most high-efficiency heat transfer equipment. Compared with conventional shell-and-tube heat exchangers, plate heat exchangers could significantly increase energy efficiency with minimum approach temperature as low as 2 °C, decrease the possibility of fouling and reduce the fuel consumption and CO₂ emissions. Thus, plate heat exchangers can be considered to improve the energy performance of an existing heat exchanger network.

Established techniques and methodologies for the retrofit of HENs focus on modifying the existing HENs to obtain energy savings and overcome network bottlenecks. Pinch analysis, mathematical programming and hybrid methods are the three main retrofit methods in existing heat exchanger networks. There are several reports in literature dedicated to the retrofit of HENs based on these methods. Sreepathi and Rangaiah

(2014) presented a detailed review of the different methods for HEN retrofit. The book by Smith (2005) has full chapters that introduce the fundamentals of energy targets, capital and total cost targets, and network design of HENs.

In the recent years, there has been an increasing number of research applying heat transfer enhancement techniques in HEN retrofit. Adding inserts and fins in the existing heat exchangers, which could increase the heat transfer coefficient, are the two main techniques in heat transfer enhancement. Heat transfer enhancement increases heat recovery and can also reduce the energy consumption. (Akpomiemie and Smith, 2015) However, for heat transfer enhancement to be effective, one of the film coefficients must be controlling. Besides, although heat transfer enhancement techniques can be performed during the normal shutdown time, the potential risk of damaging the heat exchangers when adding inserts or fins is not negligible. Thus, to overcome these drawbacks, this work presents a new retrofit method that provides insights into the application of plate heat exchangers into heat exchanger network in order to reduce the network energy consumption and increase heat recovery. However, there is no published literature shows the possibility of integrating plate heat exchanger into traditional shell-and-tube heat exchanger networks and quantify the potential effect on energy saving.

The main objective of this work is to develop cost effective retrofit methods for HENs with plate heat exchangers. The benefit of retrofit profit of the existing heat exchanger network is highlighted.

2. Methodology

This section presents a retrofit design methodology of application of plate heat exchanger into an existing fixed structure HEN. The methods, including identify the best candidate heat exchanger to replace, apply plate heat exchanger and set up non-linear model to rebalance network, are detailed in this section.

2.1. Identification of heat exchanger candidate to replace

Utility path is used to identify candidate heat exchanger and sensitivity analysis is used to determine the rank of identified exchangers.

2.1.1. Identification of utility paths

A utility path is a connection between two utilities through process heat exchangers. To develop a cost effective retrofit method of an existing HEN without structure modification and additional heat transfer area, the exchangers to be replaced must be on a utility path so that heat loads can be shifted along the path (Linnhoff and Hindmarsh, 1983). A change in a HEN can affect the performance of other components; thus, the utility path can also be used in the rebalance the HEN after replacement of shell-and-tube heat exchangers. For a simple network, utility paths can be specified by inspection. However, for a complex HEN, Incidence Matrix Approach is used to identify utility paths in the HEN (Akpomiemie and Smith, 2015).

2.1.2. Sensitivity analysis

Sensitivity analysis is used to identify the best heat exchangers, which can bring the most energy saving among others, to be replaced by plate heat exchangers. It also helps users to select the sequence of replacement. Kotjabasakis and Linnhoff (1986a) are the

first researchers that proposed sensitivity analysis. This method is based on the equation:

$$Q = UA\Delta T_{LM}F_T \quad (1)$$

In which Q is the total heat load, W; U is the overall heat transfer coefficient, W/(K·m²); A is surface area of heat exchanger, m²; ΔT_{LM} is the logarithmic mean temperature difference; F_T is the correction factor. The key point of sensitivity analysis is increasing the inlet temperature of key utility, which is identified as the one that have the most energy consumption, by adjusting the heat transfer coefficient, surface area and correction factor of candidate heat exchangers. Wang (2012) developed a mathematical model to identify the high sensitivity heat exchangers. He concluded that the amount of energy saving largely depended on the distance between the heat exchanger and the key utility. Easy implementation and short computation time are the main advantages of sensitivity analysis.

2.1 Application of plate heat exchangers

After the best heat exchangers for replacement are identified, plate heat exchangers need to be applied in the replacement of selected shell-and-tube heat exchangers. The plate heat exchanger model used in this paper is from Xu et al. (2017), where the effects of multi-pass flow arrangement, plate geometries and chevron angle on heat transfer behavior are considered in the model. The input process stream data are derived from candidate heat exchangers. The maximum heat transfer coefficient of the single plate heat exchanger can be derived from the optimization model in GAMS.

2.2 Optimization of HEN

Application of plate heat exchangers to replace the conventional heat exchanger in the existing HEN can affect the other heat exchangers performance. After replacement, the heat transfer coefficient of new plate heat exchanger significant increased, which leads an increase of the inlet temperature of the next heat exchanger in the hot stream and a decrease of the inlet temperature of the next heat exchanger in cold stream correspondingly. These changes could further affect the other components. To rebalance the HEN, the heat loads of heat exchangers need to be relocated. The heat loads can be shifted through the utility paths. Thus, an optimization method to retrofit an existing heat exchanger network without additional heat transfer area and topology modification is proposed. Plate heat exchangers may decrease energy consumption but the high installation cost of plate heat exchanger may be a significant negligible. Thus, there is a trade-off between energy saving and total retrofit cost. The objective of this optimization problem is to maximize retrofit profit. The total cost of retrofit includes the implementation cost of bypass, the capital cost of plate heat exchangers, the cost of adding heat transfer area only if the heat exchangers are not on the utility path. To achieve target temperatures of the process problem and maintain the existing heat exchanger areas (exclude the candidate heat exchangers to be replaced) are the two main constraints of the design.

Objective Function: *Maximize Retrofit Profit* = Profit from energy saving – Total cost of retrofit

Constraints: $A_{ex} = A_E \quad \forall_{\text{exchangers (excluded the candidate heat exchanges)}}$

$TT_s = TT_E \quad \forall_{\text{streams}}$

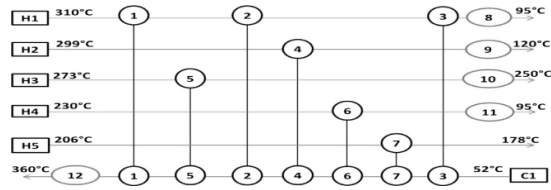


Figure 1. Simplified crude oil preheat train

Variables: heat load for all exchangers on a utility path

heat transfer coefficient for candidate heat exchanger

3. Case study

A simplified preheat train is used to illustrate the benefit of application of plate heat exchanger into retrofit design of HEN in a fixed network structure. The existing structure of the network is shown in Figure 1. There are in total 12 exchangers, and five hot streams and one cold stream. The objective of this study is to maximum the retrofit profit of applying plate heat exchangers into existing network without adding area and structure change. Table 1 summarized the cost parameters used in this study. The streams properties are assumed to be constant. To quantify the retrofit profit, the operating time is fixed as one year.

The first step is to identify the best heat exchanger to replacement. It can be inspected from the Figure 1 that only process heat exchanger 7 is not on the utility path. Thus, heat exchanger 1, 2, 3, 4, 5 and 6 are selected to further sensitivity analysis. According to the result of sensitivity analysis, heat exchanger 5 is the most sensitive exchanger which can bring the most benefit of energy saving. Thus, heat exchanger 5 is identified to be replaced by the plate heat exchanger. To maximum retrofit profit, the heat duties of heat exchanger 5 and corresponding cold utility exchanger 10 are set as variables. After inputting the process stream data of exchanger 5 into the optimization model of a single plate heat exchanger in GAMS, the maximum heat transfer coefficient can be derived with the number of 3.75 m², which is a significant increase compare with shell-and-tube heat exchangers.

The optimization procedure is conducted to rebalance the network by using global solver on LINDO Systems What's Best!. The heat duty of exchanger 5 is increased by 814.96kW and the utility consumption in exchanger 10 decreases to 0. Although the heat load of heat exchanger 5 increases, the area of exchanger 5 decreases from 183.85 m² to 23.83 m² by applying the plate heat exchanger. Three bypasses are implemented

Table 1. Cost data of case study

Utility cost data	Retrofit cost data
Hot Utility Cost: 400 (\$/kW y)	Cost of Installation of plate heat exchangers: 2.5*2070*A0.85(\$)
Cold Utility Cost: 5.5 (\$/kW y)	Implementing By-pass: 5000 (\$)
	Cost of increasing heat exchanger area: 6000 + 200 * A (\$)

Table 2. Results of replacement

	Parameter	Replace E5	Replace E5&E1	Replace E5&E1(allowing extra area on E2 & E3)
Retrofit Cost	Replacement	\$76,630	\$272,893	\$324,287
	Increasing Area	\$0	\$0	\$199,323
	Implementing By-pass	\$15,000	\$15,000	\$15,000
	Total Cost	\$91,631	\$287,893	\$539,110
Retrofit Profit	Utility Savings	\$296,684	\$296,604	\$494,325
	Net Saving (Utility Savings – Total Cost)	\$205,054 (~3.5% of initial utility cost)	\$8,702 (~0.5% of initial utility cost)	-\$44,785
	Payback	0.31 yr	0.97 yr	1.09 yr

to reduce the duty of heat exchangers. The results of retrofit cost and retrofit profit are detailed in Table 2 with the initial utility cost of \$5,801,396.

The procedure is repeated until the net saving starts to decrease since the retrofit objective is to maximize retrofit profit. According to the sensitivity analysis, the next heat exchanger to be replaced is heat exchanger 1. The results after replacement of heat exchanger 5 and heat exchanger 1 are listed in Table 5. The net saving after replacing heat exchanger 1 is smaller than only replacing heat exchanger 5, which violates the objective function, thus the replacement is stopped after replacing heat exchanger 5. The main reason that limits the net saving is the limited utility saving which is restricted to the fixed area of heat exchanger 2 and heat exchanger 3. Thus, another trail allowing extra area on heat exchanger 2 and 3 is carried out.

The comparisons between application of plate heat exchanger and enhancement (Akpomiemie and Smith, 2015) are also highlighted in Table 3. The retrofit profit of replacement is \$11,217.97 smaller than enhancement due to the high installation cost of

Table 3. Comparison of replacement and enhancement

	Parameter	Replacement	Enhancement
Retrofit Cost	Replacement	\$76,630.58	\$3,981.16
	Increasing Area	\$0	\$0
	Implementing By-pass	\$15,000	\$15,000
	Total Cost	\$91,630.58	\$18,981.16
Retrofit Profit	Utility Savings	\$296,684.13	\$237,252.68
	Net Saving	\$205,053.55	\$216,271.52

plate heat exchanger. However, the replacement is more environmental friendly since utility saving in replacement is \$59,431.45 larger than enhancement. Thus, heat transfer enhancement is a cost effective retrofit method. However, when one of the film coefficients is not controlling, applying plate heat exchanger to replace shell-and-tube heat exchanger can be regarded as an alternative option for retrofit, which can bring more energy saving at the same time.

4. Conclusions

A new retrofit method for heat exchanger networks based on the application of plate heat exchangers has been proposed in this work. The case studies highlight the retrofit benefit of the new methods. Compared to the traditional heat transfer enhancement technologies, replacing the shell-and-tube heat exchangers with plate heat exchangers can significantly increase the heat recovery and decrease energy consumption with smaller heat transfer area. However, the installation cost of plate heat exchanger is relatively high. Thus, plate heat exchangers can be used as an alternative retrofit option when one of the heat transfer film is not controlling. The savings are constrained, as all of the existing matches, except the new plate heat exchangers, are being maintained at their original sizes.

References

- Akpomemie, M. O. & Smith, R. (2015). Retrofit of heat exchanger networks without topology modifications and additional heat transfer area. *Applied energy*, 159, 381-390.
- Linnhoff, B. & Hindmarsh, E. (1983). The pinch design method for heat exchanger networks. *Chemical Engineering Science*, 38(5), 745-763.
- Kotjabasakis, E. & Linnhoff, B. (1986a). Sensitivity tables for the design of flexible processes (1)—How much contingency in heat exchanger networks is cost-effective? *Chemical engineering research & design*, 64(3), 197-211
- Smith, R. (2005). *Chemical process: design and integration*: John Wiley & Sons.
- Sreepathi, B. K. & Rangaiah, G. (2014). Review of heat exchanger network retrofiting methodologies and their applications. *Industrial & engineering chemistry research*, 53(28), 11205-11220.
- Wang, Y., Pan, M., Bulatov, I., Smith, R. & Kim, J.-K. (2012). Application of intensified heat transfer for the retrofit of heat exchanger network. *Applied energy*, 89(1), 45-5
- Xu, K., Smith, R., Zhang, N. (2017). Design and optimization of plate heat exchanger networks. *27th European Symposium on Computer Aided Process Engineering*. Barcelona.

Ecosystem Services Valuation and Ecohydrological Management in Salt Lakes with Advanced Dynamic Optimisation Strategies

A.G. Siniscalchi^(a,c), C. Garcia Prieto^(a,c), E.A. Gomez^(b,e), A. Raniolo^(b,d), R.J. Lara^(b),
M.S. Diaz^(a,c)*

^a *Planta Piloto de Ingeniería Química (Universidad Nacional del Sur-CONICET), Camino la Carrindanga Km 7, Bahía Blanca 8000, Argentina*

^b *Instituto Argentino de Oceanografía (IADO-CONICET), Camino La Carrindanga Km7, Bahía Blanca, Argentina*

^c *Departamento de Ingeniería Química, Universidad Nacional del Sur, Bahía Blanca*

^d *Departamento de Ingeniería, Universidad Nacional del Sur, Bahía Blanca*

^e *Universidad Tecnológica Nacional Facultad Regional Bahía Blanca, Bahía Blanca*

Abstract

In this work, we propose a mathematical model within a dynamic optimization framework to address management and economic valuation of ecosystem services in a salt lake basin, located in a semiarid region in Argentina (Chasicó Lake). Ecosystem services are valued by considering water, land and food provision, water flows and disturbance regulation, as well as cultural aspects. Numerical results provide useful insights on optimal management strategies effects and how they can improve services provided by the ecosystem under study.

Keywords: Dynamic Optimisation, Hydrological Mathematical Model, Ecosystem Services, Drought and Flood Mitigation

1. Introduction

The first step to develop useful tools for decision-making in the management of salt lakes is the identification of meteorological, hydrological and ecological components and driving forces of floods, drought and hypersalinisation. Additionally, ecosystem services valuation is essential to assess the relative contribution of the natural capital stock and to effectively manage sustainable human well-being (Costanza et al., 2014). In this work, we extend our previous ecohydrological models formulated as optimal control problems to plan management strategies in salt lakes (Siniscalchi et al., 2018). We formulate optimisation models for dampening extreme hydrological events and related lake salinity oscillations and to irrigate a drought-resistant crop in the grassland basin of a Pampean salt lake, also including equations for the calculation of crop water requirement dynamics. Further, we identify and value the ecosystem services offered by the studied endorheic basin and relate them to the management strategies proposed in this work. Numerical results provide control variables profiles to plan actions and their ecological and hydrologic effects.

2. 2. Mathematical Model

2.1 Hydrological Model

We formulate dynamic water mass balances for a salt lake and an artificial reservoir located nearby. Eqn. (1) and (2) show water and salt mass balances for the salt lake.

$$\frac{dm}{dt} = \left[Q_{pp}(t) \left(\frac{V}{h} \right) + Q_{river}(t) + Q_{gw} - Evap(t) \left(\frac{V}{h} \right) + Q_{res}(t) \right] \delta_w / 1000 \quad (1)$$

where m is total water mass in the lake (kg); δ_w , is water density (kg. m⁻³), which is assumed constant; V corresponds to salt lake volume and h is average depth. Q_{pp} (L.day⁻¹.m²) corresponds to precipitations, Q_{river} (L.day⁻¹) is the tributary flowrate, Q_{gw} (L.day⁻¹) is groundwater flowrate, (Q_{res}) is the flowrate of a water stream that can be diverted from an artificial reservoir to the salt lake for salinity and volume control in drought periods. $Evap$ (L.day⁻¹.m²) corresponds to evaporation per unit area in the lake. As salt concentration in both groundwater and the tributary is negligible, we assume that salt mass is constant within the lake ($d(CsV)/dt=0$) and salt concentration (Cs) is calculated as:

$$\frac{dCs}{dt} = - \frac{Cs}{V} \left[Q_{pp}(t) \left(\frac{V}{h} \right) + Q_{river}(t) + Q_{gw} - Evap(t) \left(\frac{V}{h} \right) + Q_{res}(t) \right] \delta_w / (\delta_w 1000) \quad (2)$$

Equation (3) is the water mass balance for the artificial reservoir of fixed area, located upstream of the tributary, assuming constant water density.

$$\frac{dV_{res}}{dt} = Q_{pp}(t)A \delta H_2O - Evap(t)A \delta H_2O - Q_{res}(t) - Q_r(t) \quad (3)$$

where $Q_r(t)$ is the flowrate of a water stream used for crop irrigation, calculated based on crop evapotranspiration ($ETc(t)$) as:

$$Q_r(t) = ETc(t) - Q_{pp}(t) \quad (4)$$

$ETc(t)$ is calculated for a hypothetical *Chenopodium quinoa* crop after Penman-Monteith, considering the evapotranspiration of a hypothetical crop ($ET0(t)$) and a cultivation coefficient for quinoa (Kc , Garcia et al., 2017) as follows:

$$ET0(t) = \frac{k^* \Delta * Rn + \gamma * \frac{900}{T_{air} + 273} * Fwind * (Prvap - T_{vap})}{\Delta + \gamma * (1 + 0.34 * Fwind)} \quad (5)$$

$$ETc(t) = Kc(t) * ET0(t) \quad (6)$$

Irrigation crop water requirement taken from the artificial lake and diverted flowrate for irrigation are calculated as:

$$CropWR(t) = ETc(t) - Q_{pp}(t) \quad (7)$$

$$Q_r(t) = CropWR(t) * A_{cult} \quad (8)$$

where A_{cult} corresponds to total cultivated area.

Evaporation is calculated taking into account energy and momentum balances (Penman 1948).

$$Evap = \frac{10}{\lambda v} [W Rn(t) + (1 - W)F_{wind} (T_{vap0} - T_{vap})] \quad (9)$$

where W is a weighting factor of the radiation effects on evaporation; $Rn(t)$ is net radiation ($ly \cdot d^{-1}$), F_{wind} expresses wind effects as available energy to evaporate water ($km \cdot d^{-1}$) and $(T_{vap0} - T_{vap})$ is a vapour saturation deficit. Additional algebraic equations include latent heat of vaporization for water and forcing functions, represented by Fourier series, including tributary and groundwater flowrate, air temperature, relative humidity, solar radiation, mean wind rate and related meteorological variables.

The model has three differential and twenty five algebraic equations and has been implemented within a control vector parameterisation environment in gPROMS (2017).

2.3 Dynamic Optimisation Model

We formulate management problems for water bodies as optimal control problems subject to the differential algebraic equation (DAE) systems described in the preceding sections. The goal is to keep salt concentration in the lake (Cs) around a desired value of $23 \text{ kg} \cdot \text{m}^{-3}$ within a drought climate scenario, considering the flowrate of a diverted stream from the artificial reservoir (Q_{diver}) as the control variable. The objective function is:

$$\min Z = \int_0^{tf} (Cs(t) - 23)^2 dt$$

Q_{res}

st

DAE system (1)-(9)

$$Cs(0) = Cs^0, V(0) = V^0, V_{res} = V_{res}^0, Q_{diver}^L \leq Q_{diver} \leq Q_{diver}^U, Cs^L \leq Cs \leq Cs^U, V^L \leq V \leq V^U$$

2.4 Ecosystem Services Valuation

Ecosystem Services for the salt lake basin were identified in previous work (Siniscalchi et al., 2018) and global valuation for each service was carried out following de Groot et al. (2012), in $\text{USD} \cdot \text{ha}^{-1} \cdot \text{yr}^{-1}$. These values were multiplied by the corresponding areas (basin, lake and natural reserve).

3. Case Study

Chasicó Lake is located in a depression, 20 m below sea level in the southwest of the Chaco-Pampean plain ($38^{\circ}38'' \text{ S } 63^{\circ}03'' \text{ W}$), Argentina. The maximum and average depths of this water body are 13.2 and 8 m, respectively. This salt lake (6,500 ha) is part of a natural Reserve (7,800 ha) situated in an endorheic basin (376,400 ha). The hydrologic regime of this basin is closely related to climatic conditions, with dry and wet cycles (D'ambrosio et al., 2013). During the last

century, there were flood events in 1918, 1923, 1924, 1976, 1978, 1983, 1993, 2001 and 2002, alternating with dry periods during 1930–1970 and 2006–2014 (Lara, 2006). Salinity values in the lake during the last fifty years ranged between 100 g.L^{-1} (1963) and 16 g.L^{-1} (1993). A wide variation in lake extension and salinity is the result of natural periods of drought and flooding, and is reflected on changes in water quality and biota (Kopprio et al., 2014). It also affects the economy of the region through losses in cropland area and investment uncertainty in relation to tourism and sport fishing of silverside. The severe impact that droughts and floods cause to inland water resources and to the associated socioeconomic activities requires close monitoring of this lake.

4. Results and Discussion

4.1 Salinity and flood control in Chasicó Lake

In previous work, we proposed a hydrological model for Chasicó Lake calibrated and validated with collected salinity data throughout the last ten years (Siniscalchi et al., 2017, 2018). In this frame, we proposed the construction of an artificial reservoir for water storage during wet periods. In this work, we extend the model to drought scenarios, in which the reservoir is used to damp salinity oscillations in Chasicó Lake and to irrigate a drought-resistant crop. Dynamic optimization problems are formulated within a control vector parameterization framework in gPROMS (PSEnterprise, 2017). Annual rainfall and evaporation during the dry period were 400 and 1100 mm , respectively. Figure 1 shows rainfall and evaporation profiles during a 1.5-year dry period. The basis for hydric calculations for cultivation of *Chenopodium quinoa* in Chasicó basin is 300 ha , which corresponds to 23% of the entire area of the natural reserve that may be used for crop cultivation. Figure 2 shows rainfall and CropWR profiles for quinoa crops, from sowing to harvesting, throughout a drought period in which total CropWR is $1254.2 \text{ m}^3 \cdot \text{ha}^{-1}$. The maximum CropWR, $2.8 \text{ L} \cdot \text{d}^{-1} \cdot \text{m}^{-2}$, corresponds to the onset of grain maturation.

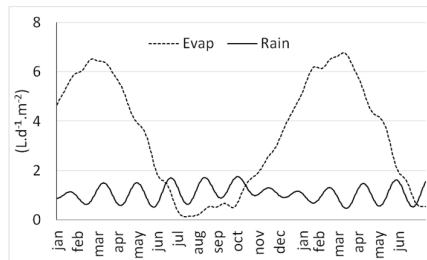


Figure 1. Rainfall and evaporation for 1.5-year drought period in Chasicó Lake

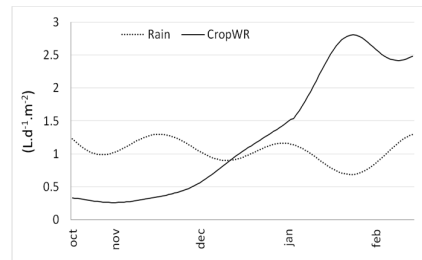


Figure 2. Rainfall and CropWR for *Chenopodium quinoa* crop in Chasicó basin (Oct.15th-Feb.15th)



Figure 3. Inflow profiles into Chasicó Lake from the river (Q_{river}), groundwater (Q_{GW}) and reservoir (Q_{res}), for a 555-day dry period

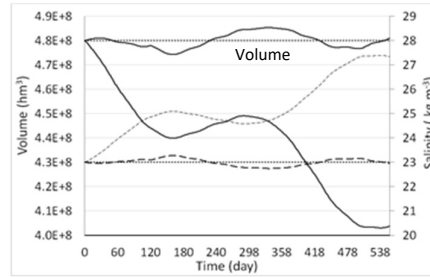


Figure 4. Volume (continuous lines) and salinity profiles (dotted lines) with and without optimal management

Figure 3 shows inflow profiles into Chasicó Lake from the river (Q_{river}), groundwater (Q_{GW}) and reservoir (Q_{res}), being the latter the control variable. Q_{res} peaks correspond to Q_{river} minima and evaporation maxima (see Fig.1). Chasicó Lake volume and salinity profiles with and without optimal management through water input from the artificial reservoir (Q_{res}) are shown in Fig. 4. It is important to remark that the water volume stored during four wet years in an artificial reservoir is enough for keeping salinity at an optimum (23 g.L^{-1}) and simultaneously irrigating a 300 ha-quinoa crop during ca. 1.5 years, thus increasing the socio-ecologic system resilience to extreme drought periods.

3.2. Ecosystem Services Valuation

In this work ecosystem services were valued for the Chasicó region (Gomez, 2015), including regulating (climate, water flows, disturbance dampening), provision (water, land and food) and cultural services (tourism and recreation). Following de Groot et al. (2012), valuation was carried out by multiplying a reference value (MMUS\$/ha.y) for each service by the corresponding area, as follows. For water flows, disturbance dampening, water and land supply, a basin surface of 376,400 ha was taken. A lake surface of 6,500 ha was used in the case of food supply (silverside). To calculate cultural services, the nature reserve surface (7,800 ha) was taken. Ecosystem Services with the highest economic value (in MMUS\$/y) were water flows (2100) and disturbance dampening (1120), further supporting the importance of optimal salinity and lake volume regulation, as well as the construction of a buffering reservoir. Provisioning services valuation include land (450), water (154) and food (4) supply. Additionally to lake food supply services, optimisation results show the possibility of irrigating a 300 ha-quinoa crop. This would produce an improvement of the basin economic value due to quinoa sales of 1.5 MMUS\$/y, considering a 2 t/ha yield. Cultural services were valued in 33 MMUS\$/y.

4. Conclusions

In this work, we propose detailed mechanistic models of salt lakes as constraints for optimal control problems to provide tools for planning water body management and exploring the associated effects. Numerical results show the optimal profile for the water stream flowrate that should be diverted from an artificial reservoir to mitigate drought effects by keeping lake salt concentration at the physiological optimum for a high-commercial value fish and irrigation of 300 ha of drought resistant crops (quinoa). Water flows and disturbance regulation correspond to ecosystem services with highest economic value for the basin where Chasicó Lake is located. Dynamic models provide useful insights for water flow regulation and food provision.

References

- Costanza R., de Groot R., Sutton P., van der Ploeg S., Anderson S.J., Kubiszewski I., Farber S., Turner K. 2014. Changes in the global value of ecosystem services. *Global Environmental Change* 26:152–158
- D'ambrosio, G.T., Bohn, V.Y., Piccolo, M.C., 2013. Evaluación de la sequía 2008–2009 en el oeste de la Región Pampeana (Argentina). *Cuadernos Geográficos* 52 (1), 1–17.
- de Groot R., Brander L., van der Ploeg S., Costanza R., Bernard F., Braat L., Christie M., Crossman N., Ghermandi A., Hein L., Hussain S., Kumar K P., McVittie A., Portela R., Rodriguez L.C., ten Brink P., van Beukering P. 2012. Global estimates of the value of ecosystems and their services in monetary units. *Ecosystem Services* 1: 50–61
- FAO 1998. Evapotranspiración del cultivo Guías para la determinación de los requerimientos de agua de los cultivos. ISSN 0254-5293. p.322
- García Villanueva J, Huahuachampi J; Soto L 2017. Determinación de la demanda hídrica del cultivo de quinoa QML01 (*Chenopodium Quinoa Willd*) en la Molina. *Anales Científicos*, 78 (2): 200-209. ISSN 2519-7398 (Versión electrónica)
- Gómez C. 2015 Revalorización y reutilización turística del Sector Norte del Partido de Villarino. Caso: Laguna Chasicó. <http://sedici.unlp.edu.ar/handle/10915/60544>
- Kopprig G.A, R. Freije, M. Arias-Schreiber, R.J. Lara, 2014. An ecohydrological adaptive approach for a salt lake in semiarid grasslands of Argentina, *Sustain. Sci*, 9: 229-238.
- Lara R.J. 2006. Climate change, sea-level rise and the dynamics of South American coastal wetlands: case studies and the global frame, In *Wissenschaftliche Zusammenarbeit mit Argentinien: Begrenzung und Zuversicht Arbeits und Diskussionspapier* (Frühwald, ed.), Bonn: Von Humboldt Foundation 40-50.
- Millennium Ecosystem Assessment (MEA) 2005. *Ecosystem and human well-being: Current state and trends* Washington. C., USA: Island Press
- Process Systems Enterprise, 2017, gPROMS, www.psententerprise.com/gproms.
- Siniscalchi A.G., Kopprig G., Raniolo L.A., Gomez E.A., Diaz M.S., Lara R.J. 2018. Mathematical modelling for ecohydrological management of an endangered endorheic salt lake in the semiarid Pampean region, Argentina. *Journal of Hydrology* 563: 778–789.
- Siniscalchi A.G., García Prieto, V.C., Raniolo A., Gomez E., Lara R.J., Diaz M.S. 2018. Ecohydrological management and valuation of ecosystem services in salt lakes with advanced dynamic optimisation strategies. *AIChE Annual Meeting 2018*. Oct 28 - Nov 2. Pittsburgh, PA.
- Viglizzo E.F., Franka F.C. 2006. Ecological interactions, feedbacks, thresholds and collapses in the Argentine Pampas in response to climate and farming during the last century. *Quaternary International* 158:122–126.

Life cycle design of indoor hydroponic horticulture considering energy-water-food nexus

Yasunori Kikuchi,^{a,b,c,d,*} Yuichiro Kanematsu,^b Tatsuya Okubo^{b,c}

^a *Integrated Research System for Sustainability Science, The University of Tokyo Institutes for Advanced Study, 7-3-1 Hongo, Bunkyo-ku, Tokyo 113-8654, Japan*

^b *Presidential Endowed Chair for “Platinum Society,” The University of Tokyo, 7-3-1 Hongo, Bunkyo-ku, Tokyo 113-8656, Japan*

^c *Department of Chemical System Engineering, The University of Tokyo, 7-3-1 Hongo, Bunkyo-ku, Tokyo 113-8656, Japan*

^d *Center for Environment, Health and Field Sciences, Chiba University, 6-2-1 Kashiwanoha, Kashiwa, 277-0882 Chiba, Japan*

kikuchi@platinum.u-tokyo.ac.jp

Abstract

Agriculture has become one of the largest concerns in the field of sustainability science, while it is a major consumer of resources such as nitrogen, phosphorus, water, and land. Plant factories, indoor hydroponic farming systems, can be divided into two types according to the light source: plant factories with sunlight (PFSLs) and plant factories with artificial light (PFALs) also called as vertical farming. Through the previous studies, it was revealed that these plant factories reduced the use of irreplaceable resources for food production, i.e., phosphorus, water, and land area, at the expense of additional energy consumption compared with conventional Japanese horticulture systems. In this study, we are tackling with the sustainable agriculture mixing conventional and advanced farming technologies, especially plant factories. Based on the comprehensive assessment, an analysis was conducted on the current energy usage and applicability of technology options in plant factories. The results demonstrated that the regional characteristics should be taken into account in the design of plant factories, especially for the insulation and lighting sources in PFAL. The market fluctuation has also large impacts on the profitability of plant factories.

Keywords: vertical farming, power grid, variable renewable energy

1. Introduction

Agriculture has become one of the largest concerns in the field of sustainability science (Kajikawa et al., 2007), while it is a major consumer of resources such as nitrogen, phosphorus, water, and land (Schnoor, 2014). Although phosphorus is essential for food production (UNEP, 2011), it has not been effectively recycled (Matsubae et al., 2011) and there is a strong need to close the phosphorus loop (Christen, 2007). Many countries face food insecurity and starvation induced by a water deficit (Yang et al., 2003), and water resource management is crucial to food management. Land use is an important index of food environmental impacts (Heller et al., 2013).

Plant factories, indoor hydroponic farming systems, can be divided into two types according to the light source: plant factories with sunlight (PFSLs) and plant factories with artificial light (PFALs) (Kozai et al., 2015). Because PFSLs and PFALs feature semiclosed and closed cultivation rooms, respectively, plants cultivated in these factories can be protected from pathogens and harmful insects, leading to high stability of food production. As a proof of such concept of plant factories, a comprehensive analysis was conducted for the multiple aspects and technology options of plant factories: the use of nitrogen, phosphorus, and potassium (NPK) fertilizers, the consumption of water, the occupation or transformation of land, and greenhouse gas (GHG) emissions for the demonstration PFSL and PFAL located at Chiba University in Kashiwa, Japan (Kikuchi et al., 2018a). It was revealed that these plant factories reduced the use of irreplaceable resources for food production, i.e., phosphorus, water, and land area, at the expense of additional energy consumption compared with conventional Japanese horticulture systems.

Decentralized energy systems have been recognized as a solution to increase the resource utilization including locally available renewable resources (Kikuchi et al., 2018b; 2016). control systems for voltage and frequency should be equipped to accept the massive implementation of variable renewable energy (VRE) such as photovoltaic and wind turbine power generation, e.g., virtual power plant or demand response systems (Kikuchi, 2017) considering the future energy supply and demand structure (Kikuchi et al., 2014; 2016).

In this study, we are tackling with the sustainable agriculture mixing conventional and advanced farming technologies, especially plant factories. An analysis was conducted on the current energy usage and applicability of technology options in plant factories for designing the life cycles of plant factories considering their harmonization with future energy systems.

2. Materials and methods

2.1. Overview of plant factories in this study

Figure 1 shows the plant factories examined in this study (Kikuchi et al., 2018a). The PFSL and PFAL examined in this paper were demonstration factories located at Chiba University in Kashiwa, Japan, where long-stage, high-density cultivation and a 10-stage vertical horticulture system were adopted to produce fresh tomatoes and lettuce in hydroponic culture using rockwool and polyurethane, respectively, as the culture media. The life cycle of plant factories shown in Figure 1(a) includes the market survey and process design before farming of vegetables. As summarized in Figure 1 (b) which was obtained from the comprehensive analysis based on the same methods by Kikuchi et al., (2018), the use of irreplaceable resources for food production can be mitigated at the expense of additional fossil energy consumption indicated as the GHG emission.

2.2. Analysis on current energy utilization and technology options

The suppression of VRE has been conducted in Kyushu area in Japan shown in Figure 2. Especially in remote islands in the area, the capacity of suppression is increasing due to the depopulation within such area and additional installation of photovoltaic power generation.

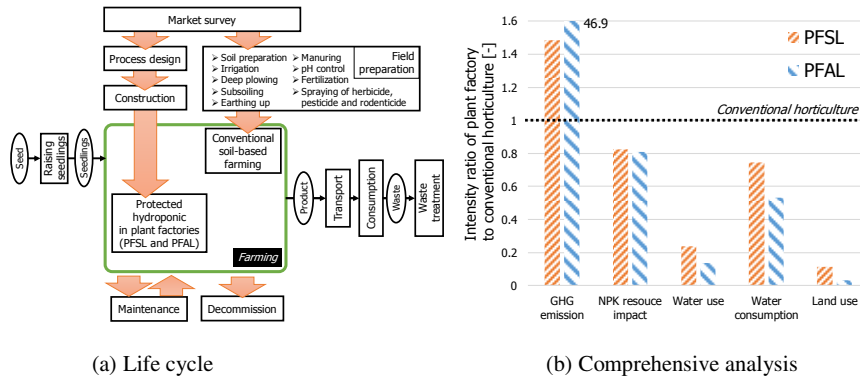


Figure 1 Overview of plant factories examined in this study (Kikuchi et al., 2018a)

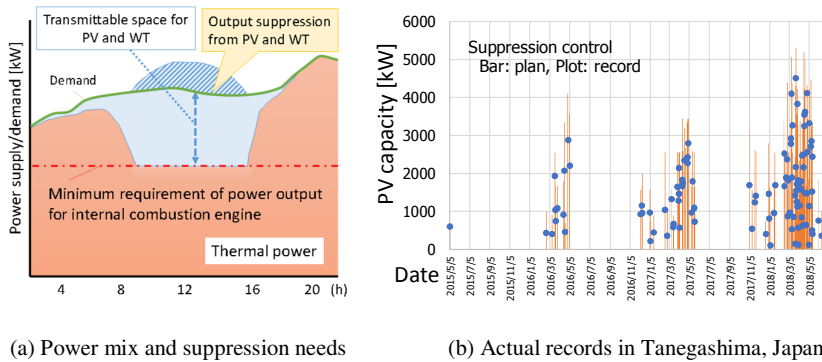


Figure 2 Suppression of VRE in Japan (Kyushu Electric Power Company, 2018)

Considering the harmonization of plant factories with such decentralized energy systems implementing massive amount of VRE, the properties of power demands in plant factories are analysed by utilizing the automatically logged power consumption in the actual PFSL and PFAL in this study for every 1 minute from May 2011 to September 2014. The daily power consumption [Wh/day], maximum power demand [W], and peak demand time are selected as the properties of power demand. These properties can be changed by applying technology options in plant factories. The options to be considered for the plant factories in this study are the utilization of unused heat, a solid-oxide fuel cell, PV power, improved electric devices such as heat pumps and lighting, insulation, and the installation of all options. Their applicability and consequences are analysed and discussed in this paper.

3. Results and discussion

3.1. Current power consumption

Figure 3 shows the power demand properties in PFSL and PFAL in this study. The maximum daily power consumptions were 674 kWh/day and 3.32 MWh/day for PFSL and PFAL, respectively. The maximum power demand were 52.4 kW and 174 kW for PFSL and PFAL, respectively. The largest power demand in PFSL was air conditioning

(Kikuchi et al., 2018a), which gets higher in the morning, evening, and night during winter season. Due to the semiclosed environment of PFSL, the power demand is strongly affected by the seasonal changes, which means not easily controllable. The lighting in the PFAL, the largest power demand, is based on the production amount of vegetable (Kikuchi et al., 2018a). The peak demand time was fluctuated even though the power demand was at the maximum in 2014, which means that the lighting plans are controlled not by the time, but the operation considering the characteristics of plant growth.

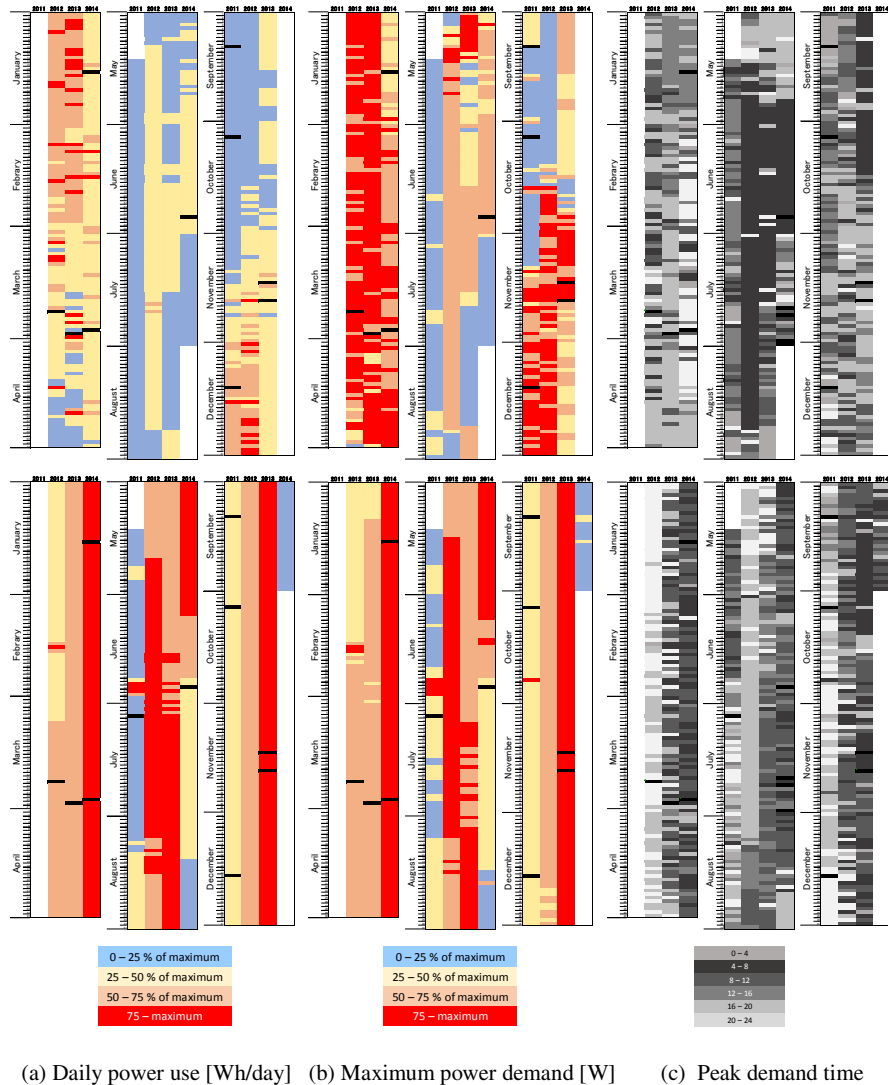


Figure 3 Power demand properties indicated as the ratio to the maximum during all periods (a,b) and ranges of time (c); upper and lower diagrams show the results of PFSL and PFAL, respectively

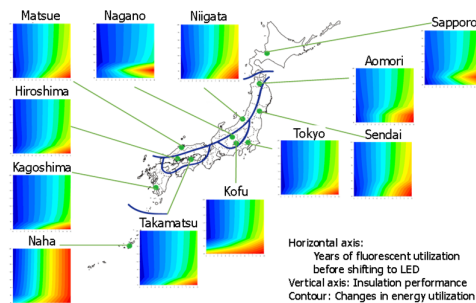


Figure 4 Regional differences of effects of LED implementation in PFALs considering their insulation

3.2. Applicability of technology options

The power demand properties shown in Figure 3 should be taken into account for the harmonization of plant factories with decentralized energy systems in the future. The application of technology options should also be addressed for such harmonization. For example, the implementation of fuel cell into PFSL can achieve the net-zero GHG emission (Kikuchi et al., 2018a), which means that the PFSL can supply power derived from fuel cell. This is partly because the power demand for air conditioning can be supplied by fuel cell as electricity and hot/cold heat with absorption chiller. As for the PFALs, their lighting needs electric power, which cannot be supplied by implementing small scale fuel cell and photovoltaic. At this time, the suppressed power due to the limitation of load following capacity in power grid shown in Figure 2 can be utilized in PFALs as a kind of virtual power plant or demand response, if the power demand can be controlled along with the condition of power grid.

The implementation of LED can also be considered for mitigating power demand in PFALs, where the relationship with insulation of PFALs should be carefully examined. Figure 4 shows the regional differences of effects of LED implementation in PFALs considering their insulation. Because the air conditioning in PFAL is always cooling mode, the lower insulation can reduce power demand in some cold area. However, if the fluorescent is applied at the design of PFALs, the LED implementation can disturb the design rationales and increase the power demand for air conditioning.

4. Conclusions

Food supply security can be also addressed by implementing plant factories (Kikuchi et al., 2018a). They can become a new energy demand to support the regional systems to supply foods. The radical changes in future energy systems should be taken into account for designing the life cycle of plant factories. For this purpose, computer-aided approaches are strongly needed for designing process and operation of plant factories.

Acknowledgement

The authors are grateful to Ms. Hanako Tominaga for her efforts in the modelling and simulation of plant factories. Part of this study is financially supported by JSPS KAKENHI under grant numbers 16H06126 (Grant-in-Aid for Young Scientists A).

Presidential Endowed Chair for “Platinum Society” in the University of Tokyo are supported by the KAITEKI Institute Incorporated, Mitsui Fudosan Corporation, Shin-Etsu Chemical Co., ORIX Corporation, Sekisui House, Ltd., and the East Japan Railway Company.

References

- K. Christen, 2007, Closing the phosphorus loop. *Environ. Sci. Technol.* 41, 2078.
- M.C. Heller, G.A. Keoleian, W.C. Willett, 2013, Toward a life cycle-based, diet-level framework for food environmental impact and nutritional quality assessment: A critical review. *Environ. Sci. Technol.* 47, 12632–12647.
- Y. Kajikawa, J. Ohno, Y. Takeda, K. Matsushima, H. Komiyama, 2007, Creating an academic landscape of sustainability science: An analysis of the citation network. *Sustain. Sci.* 2, 221–231.
- Y. Kikuchi, Y. Kanematsu, M. Ugo, Y. Hamada, T. Okubo, 2016, Industrial symbiosis centered on a regional cogeneration power plant utilizing available local resources: A case study of Tanegashima. *J. Ind. Ecol.* 20, 276–288.
- Y. Kikuchi, S. Kimura, Y. Okamoto, M. Koyama, 2014, A scenario analysis of future energy systems based on an energy flow model represented as functionals of technology options. *Appl. Energy* 132, 586–601.
- Y. Kikuchi, Y. Kanematsu, R. Sato, T. Nakagaki, 2016, Distributed cogeneration of power and heat within an energy management strategy for mitigating fossil fuel consumption. *J. Ind. Ecol.* 20, 289–303.
- Y. Kikuchi, 2017, Simulation-Based Approaches for Design of Smart Energy System: A Review Applying Bibliometric Analysis, *J. Chem. Eng. Jpn.*, 50(6), 385–396.
- Y. Kikuchi, Y. Kanematsu, N. Yoshikawa, T. Okubo, M. Takagaki, 2018a, Environmental and resource use analysis of plant factories with energy technology options: a case study in Japan, *Journal of Cleaner Production*, 186(10) 703–717.
- Y. Kikuchi, Y. Oshita, M. Nakai, A. Heiho, Y. Fukushima, 2018b, A computer-aided analysis on regional power and heat energy systems considering socio-economic aspects: A case study on an isolated island in Japan, *Comput. Aided Chem. Eng.*, 43, 1347–1352.
- T. Kozai, G. Niu, M. Takagaki (ed.), 2015, *Plant factory: An indoor vertical farming system for efficient quality food production*. Elsevier, Tokyo.
- Kyushu Electric Power Company, 2018, Report on the suppression control of renewable energy in Tanegashima, <http://www.kyuden.co.jp/9437tanegashima5628>
- K. Matsubae, J. Kajiyama, T. Hiraki, T. Nagasaka, 2011, Virtual phosphorus ore requirement of Japanese economy. *Chemosphere*. 84, 767–772.
- J.L. Schnoor, 2014, Agriculture: The last unregulated source. *Environ. Sci. Technol.* 48, 4635–4636.
- United Nations Environment Program (UNEP), 2011. Phosphorus and food production. UNEP, Paris, pp. 34–45.
- H. Yang, P. Reichert, K.C. Abbaspour, A.J.B. Zehnder, 2003, A water resources threshold and its implications for food security. *Environ. Sci. Technol.* 37, 3048–3054.

A Data-Driven Robust Optimization Approach to Operational Optimization of Industrial Steam Systems under Uncertainty

Liang Zhao, Chao Ning, Fengqi You

Cornell University, Ithaca, New York 14853, USA

Abstract

This paper proposed a data-driven adaptive robust optimization approach to deal with operational optimization problem of industrial steam systems under uncertainty. Uncertain parameters of the proposed steam turbine model are derived from the semi-empirical model and historical process data. A robust kernel density estimation method is employed to construct the uncertainty sets for modeling these uncertain parameters. The data-driven uncertainty sets are incorporated into a two-stage adaptive robust mixed-integer linear programming (MILP) framework for operational optimization of steam systems. By applying the affine decision rule, the proposed multi-level optimization model is transformed into its robust counterpart, which is a single-level MILP problem. To demonstrate the applicability of the proposed method, the case study of an industrial steam system from a real-world ethylene plant is presented.

Keywords: data-driven, adaptive robust optimization, industrial steam system, operational optimization, uncertainty

1. Background

In recent years, system modelling and optimization methods are employed to improve the efficiency and economic benefits of industrial steam systems. In steam systems, it is an important issue to accurately model the steam turbines to improve the steam system efficiency (Petroulas and Reklaitis, 1984; Li et al. 2014). Turbine models based on thermodynamics were proposed to optimize the performance of steam system (Aguilar et al. 2007). Hybrid models were developed to improve the performances of steam turbine models (Luo et al. 2011). Building upon the developed steam turbine models, several optimization models for synthesis and design of steam systems were proposed (Tveit et al. 2006, Li et al. 2013, Beangstrom et al. 2016). A stochastic programming approach was employed to deal with uncertainties in the site utility system (Sun et al. 2017). However, the optimization results of stochastic programming are highly sensitive to the pre-defined probability distributions, which could deviate significantly from the “true” uncertainty information. The static robust optimization (SRO) approach might make the resulting solutions very conservative (Soyster, 1973; Bertsimas et al. 2011; Ben-Tal and Nemirovski, 1998). More recently, data-driven robust optimization has emerged as an effective tool for optimization under uncertainty (Ning et al. 2017, 2018, Shang et al. 2017). In industrial steam systems, large amounts of historical data are collected and stored in a database that records all operational information of the devices and their connected networks. A semi-empirical model of steam turbine is first developed based on process mechanism and operational data. Then, the uncertain parameters are collected from process historical data. A data-driven two-stage ARO method for operational optimization of steam systems under uncertainty is presented. The robust counterpart of

the proposed data-driven ARO model is derived as a single-level MILP model to facilitate the solution process. A case study of the steam system in a real-world ethylene plant is presented to demonstrate the effectiveness of the proposed method.

2. Deterministic MILP model of industrial steam system

Mixed-integer optimization models were developed for operational optimization of the steam systems, which rely on the linear or nonlinear model of the basic components (Varbanov et al. 2004; Chu and You, 2015). A decomposition method is employed to develop extraction steam turbine model (Aguilar et al. 2007). The semi-empirical model of steam turbine is presented as follows,

$$m_t^{in} = a_t \cdot m_t^{ext} + b_t, \forall t \tag{1}$$

where a_t and b_t , are parameters of the model and can be calculated by process data.

The deterministic MILP model optimization model of steam system (DOSS) is given by,

$$\min c = c^{SS} \sum_{t \in TSS} m_t^{in} + c^e \sum_j y_j^e + c^{water} \sum_{lv} (l_{lv} - 1) m_{lv}^{in} \tag{2}$$

$$\text{s.t.} \sum_t (a_{sh,t}^{in} m_t^{in} + a_{sh,t}^{ext} m_t^{ext}) + \sum_j a_{sh,j}^M (1 - y_j) F_j^S + \sum_{lv} (a_{sh,lv}^{in} m_{lv}^{in} + a_{sh,lv}^{out} m_{lv}^{out}) \geq md^{sh} \tag{3}$$

$$e_t + W_t \geq WD_t \tag{4}$$

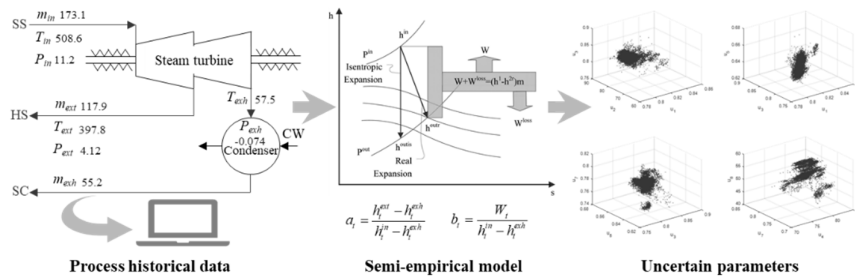
$$m_t^{\min} \leq m \leq m_t^{\max} \tag{5}$$

Equations (2)-(4) are steam demand constraints, mechanical power demand constraints and variables range constraints, respectively.

3. Data-Driven ARO Model for Steam System

3.1 Deriving uncertain parameters of semi-empirical model for steam turbines

The parameters of the steam turbine models are derived from process operation parameters according to equation (1). The schematic diagram of uncertain parameter derivation process is given in Figure 1.



The procedure of deriving uncertainty parameters from historical operation data.

The process historical data of steam system can typically be collected conveniently. A couple of parameters, a_t and b_t , in the proposed semi-empirical model can be calculated by process data, including temperatures, pressures, and flow rates of inlet, extraction and exhausting steam of turbines. Then, the uncertain parameters are derived.

3.2 Data-driven uncertainty sets for ARO

RKDE is employed to construct data-driven uncertainty sets for the ARO framework (Kim et al. 2012). The correlation information is also considered in the construction of uncertainty sets (Ning et al. 2017). The data-driven uncertainty set is reformulated as follows,

$$U^{cor} = \left\{ \zeta \left| \begin{array}{l} \hat{F}_{RKDE}^{i-1}(\alpha) \leq \zeta_i \leq \hat{F}_{RKDE}^{i-1}(1-\alpha), \quad \forall i \\ \sum_i \zeta_i^0 (1-r_i h) \leq \sum_i \zeta_i \leq \sum_i \zeta_i^0 (1+r_i h) \\ \|M(\zeta - \zeta^0)\|_1 \leq \beta \end{array} \right. \right\} \quad (6)$$

where α is a predefined parameter to denote the confidence level $(1-2\alpha)$, h is a predefined uncertainty budget to control the level of conservatism as the parameter α . re $M=\Sigma^{-1/2}$, Σ is the covariance matrix of the uncertain parameters, and β is a parameter used to adjust the size of l_1 norm ball in $\|M(\zeta - \zeta^0)\|_1 \leq \beta$.

3.3 Data-driven robust MILP model of steam system

A novel data-driven adaptive robust MILP model for operational optimization of steam systems is then developed based on the uncertainty sets (6). The multi-level data-driven adaptive robust steam system model based on RKDE incorporating correlation information (DDARSS-RKDECI) is developed as follows. Noted that the model is also subjected to constraint (4) in model DOSS.

$$\min_{m_t^{in}, m_t^{ext}, m_{lv}^{in}, y_j} \max_{\zeta \in U^{cor}} c_e \sum_j y_j^e + c_{water} \sum_{lv} (l_{lv} - 1) m_{lv}^{in} + c_{ss} \sum_{t \in TSS} m_t^{in}(\zeta) \quad (7)$$

$$\begin{aligned} & \sum_t (a_{sh,t}^{in} m_t^{in}(\zeta) + a_{sh,t}^{ext} m_t^{ext}) + \sum_j a_{sh,j}^M (1-y_j) F_j^S \\ \text{s.t.} & \quad + \sum_{lv} (a_{sh,lv}^{in} m_{lv}^{in} + a_{sh,lv}^{out} m_{lv}^{out}) \geq md^{sh}, \quad \forall sh \in SH, \zeta \in U^{cor} \end{aligned} \quad (8)$$

$$m_t^{in, \min} \leq m_t^{in}(\zeta) \leq m_t^{in, \max}, \quad \forall t \in T, \zeta \in U^{cor} \quad (9)$$

$$m_t^{exh, \min} \leq m_t^{in}(\zeta) - m_t^{ext} \leq m_t^{exh, \max}, \quad \forall t \in T, \zeta \in U^{cor} \quad (10)$$

3.4 Robust counterpart reformulation of data-driven ARO model for steam system

Because there are uncertain parameters in the objective function, the epigraph reformulation of objective function (7) is presented by,

$$\min_{m_t^{in}, m_t^{ext}, m_{lv}^{in}, y_j, z} z \quad (11)$$

$$\text{s.t.} \quad c_e \sum_j y_j^e + c_{water} \sum_{lv} (l_{lv} - 1) m_{lv}^{in} + c_{ss} \sum_{t \in SS} m_t^{in}(\zeta) \leq z, \quad \forall \zeta \in U^{cor} \quad (12)$$

By applying the affine decision rule $m_t^{in}(\zeta) = P_t \zeta + q_t$, constraint (12) is reformulated as follows,

$$\max_{\zeta \in U^{cor}} c_{ss} \sum_t P_t \zeta \leq z - c_e \sum_j y_j^e - c_{water} \sum_{lv} (l_{lv} - 1) m_{lv}^{in} - c_{ss} \sum_t q_t \quad (13)$$

Because the left-hand side of constraint (13) is a linear program, dual variables λ_i , γ_i , π , Ω , $C1$, $C2_k$ and $C3_k$ are introduced. Constraint (13) is then reformulated as follows,

$$\sum_i \zeta_i^{\max} \lambda_i - \sum_i \zeta_i^{\min} \gamma_i + \zeta^{\text{sum,max}} \pi - \zeta^{\text{sum,min}} \Omega + \beta C1 + \zeta^{\text{sum,cor}} C2_k - \zeta^{\text{sum,cor}} C3_k \leq z - c_e \sum_j y_j^e + c_w \sum_{lv} (l_{lv} - 1) m_{lv}^{in} - c_{ss} \sum_t q_t \quad (14)$$

$$\lambda_i - \gamma_i + \pi - \Omega + \sum_k M_{k,j} \cdot C2_k - \sum_k M_{k,j} \cdot C3_k = c_{ss} \sum_t P_t, \forall i \quad (15)$$

$$C1 + C2_k - C3_k = 0, \forall k \quad (16)$$

$$\lambda_i, \gamma_i, \pi, \Omega, C1, C2_k, C3_k \geq 0, \forall i, k \quad (17)$$

Similar to constraint (13), constraints (8)-(10) can be transformed to new constraints by dual variables. Then, the data-driven adaptive robust counterpart for steam system operational optimization (DDARCSS-RKDECI) is formulated as a single-level optimization problem, which can be solved by optimization solvers like CPLEX directly.

4. Applications

To demonstrate the applicability of the proposed approach, a case study on the steam system of an ethylene plant is presented. There are four steam grades (SS, HS, MS, and LS), four extractions turbines (T1, T2, T3, and T4), 29 backpressure turbines (T5 to T33), three let-down valves in the given steam system. The prices of SS, water and electricity are set to be 180 m.u./t, 15 m.u./h and 1.5 m.u./kwh, respectively (where m.u. stands for “monetary unit”). In RKDE, the parameter α is set as 0.02, and the parameter h is set as 0.8. The parameter β in uncertainty set U^{cor} is set as 3.2.

The proposed method is compared with the deterministic and RKDE-based method (DDARCSS-RKDE). All optimization problems are coded in GAMS 24.8.3. The CPLEX 12.7.0.0 with an optimality tolerance of 0% is used to solve the single-level MILP problems. The computational results of different methods are given in Table 1.

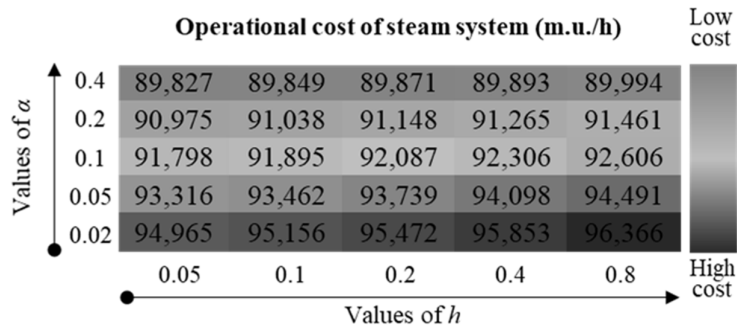
Table 1 Problem sizes and solution comparisons for different methods.

	DOSS	DDARCSS-RKDE	DDARCSS-RKDECI
Binary variables	29	29	29
Continuous variables	11	397	732
Constraints	13	196	369
Min. operating cost(m.u./h)	88,720	96,750	96,366

The optimal operating cost obtained by the deterministic method is 88,720 m.u./h, and it is obviously less than the values determined by the data-driven ARO methods, because the deterministic model uses fixed parameters during the optimization process. Due to the consideration of correlation information among uncertain parameters, the solution of DDARCSS-RKDECI method is less conservative than that of the DDARCSS-RKDE approach.

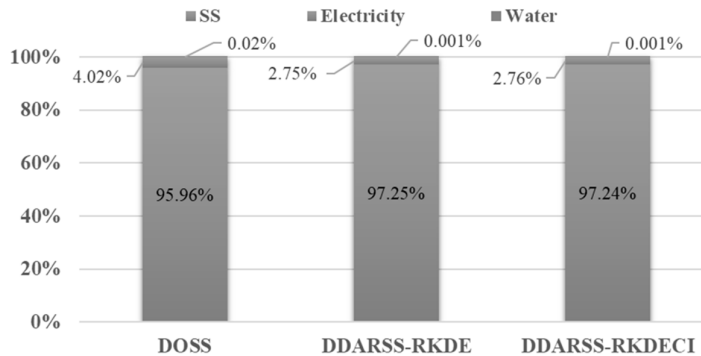
The effects of parameters α and h on the solution of the proposed method are investigated by changing their values. α is set as 0.02, 0.05, 0.1, 0.2 and 0.4, and h is set as 0.05, 0.1, 0.2, 0.4 and 0.8. The heat map of operational cost is shown in Figure 2. When the value of α decreases from 0.4 to 0.02 for any fixed h , the operational cost increases by 6.3% on

average; when h increases from 0.05 to 0.8 for any fixed α , the operational cost increases by 0.9% on average. For a fixed value of parameter h , the operational cost decreases obviously with the increase of α , because the confidence interval becomes smaller with a large value of α . Since h is used to control the effect of uncertainty deviations, the objective value increases slowly as the value of parameter h increases.



Heat map of solutions determined by DDARCSS-RKDECI.

The breakdown of the optimal operational costs determined by different methods in Table 1 are shown in Figure 3. The percentage of electricity obtained by the deterministic method is the largest among the three methods. The parameters of the semi-empirical model are fixed as nominal values, meaning the steam demands from processes can be satisfied easily. As a result, more electrical motors will be turned on, replacing the steam turbines as the method of power generation for the pumps. The data-driven two-stage ARO methods have similar breakdowns of operational costs, because the consumptions of electricity and water are determined at the first stage. The minor differences are caused by the difference of their uncertainty sets.



Comparison of operational cost breakdown for different methods.

5. Conclusion

A novel operational optimization model of steam system under uncertainty using data-driven two-stage ARO was proposed. The uncertain parameters of semi-empirical models for steam turbines were collected from historical process data of an industrial plant. The RKDE method was then employed to construct the uncertainty sets from the derived uncertain parameters. The correlation information was considered in the construction of uncertainty sets through the covariance matrix of uncertain parameters. The data-driven

two-stage ARO model of steam system was formulated based on the constructed uncertainty sets, and the corresponding robust counterpart was developed using affine decision rule. A real-world case study on the steam system of an ethylene plant was presented to demonstrate the effectiveness of the proposed methods.

References

- O. Aguilar, S. Perry, J.-K. Kim and R. Smith, 2007, Design and optimization of flexible utility systems subject to variable conditions: Part 1: Modelling framework, *Chemical Engineering Research and Design* 85(8): 1136-1148.
- S. G. Beangstrom, and T. Majozi, 2016, Steam system network synthesis with hot liquid reuse: II. Incorporating shaft work and optimum steam levels, *Computers & Chemical Engineering* 85: 202-209.
- A. Ben-Tal, A. Nemirovski, 1998, Robust convex optimization. *Mathematics of Operations Research*, 23, 769-805.
- D. Bertsimas, D. B. Brown and C. Caramanis, 2011, Theory and Applications of Robust Optimization, *SIAM Review* 53(3): 464-501.
- Y. Chu, F. You, 2015, Model-based integration of control and operations: Overview, challenges, advances, and opportunities. *Computers & Chemical Engineering*, 83, 2-20.
- J. Kim, and C. D. Scott, 2012, Robust kernel density estimation, *Journal of Machine Learning Research* 13(Sep): 2529-2565.
- Z. Li, W. Du, L. Zhao and F. Qian, 2014, Modeling and Optimization of a Steam System in a Chemical Plant Containing Multiple Direct Drive Steam Turbines, *Industrial & Engineering Chemistry Research* 53(27): 11021-11032.
- Z. Li, L. Zhao, W. Du and F. Qian, 2013, Modeling and Optimization of the Steam Turbine Network of an Ethylene Plant, *Chinese Journal of Chemical Engineering* 21(5): 520-528.
- X. Luo, B. Zhang, Y. Chen and S. Mo, 2011, Modeling and optimization of a utility system containing multiple extractions steam turbines, *Energy* 36(5): 3501-3512.
- C. Ning, F. You, 2017, Data-Driven Adaptive Nested Robust Optimization: General Modeling Framework and Efficient Computational Algorithm for Decision Making Under Uncertainty. *AIChE Journal*, 63, 3790-3817.
- C. Ning, F. You, 2017, A data-driven multistage adaptive robust optimization framework for planning and scheduling under uncertainty. *AIChE Journal*, 63, 4343-4369.
- C. Ning, F. You, 2018, Data-driven stochastic robust optimization: General computational framework and algorithm leveraging machine learning for optimization under uncertainty in the big data era. *Computers & Chemical Engineering*, 111, 115-133.
- C. Ning, F. You, 2018, Data-driven decision making under uncertainty integrating robust optimization with principal component analysis and kernel smoothing methods. *Computers & Chemical Engineering*, 112, 190-210.
- T. Petroulas, G.J.A.j. Reklaitis, 1984, Computer-aided synthesis and design of plant utility systems. 30, 69-78.
- C. Shang, X. Huang, F. You, 2017, Data-driven robust optimization based on kernel learning. *Computers & Chemical Engineering*, 106, 464-479.
- C. Shang, F. You, 2019, A data-driven robust optimization approach to scenario-based stochastic model predictive control. *Journal of Process Control*, 75, 24-39.
- A.L. Soyster, 1973, Convex programming with set-inclusive constraints and applications to inexact linear programming. *Operations Research*, 21, 1154-1157.
- L. Sun, L. Gai and R. Smith, 2017, Site utility system optimization with operation adjustment under uncertainty, *Applied Energy* 186: 450-456.
- T.-M. Tveit, and C.-J. Fogelholm, 2006, Multi-period steam turbine network optimisation. Part II: Development of a multi-period MINLP model of a utility system, *Applied Thermal Engineering* 26(14-15): 1730-1736.
- P. S. P. S., arbanov, S. Doyle and R. Smith, 2004, Modelling and Optimization of Utility Systems, *Chemical Engineering Research and Design* 82(5): 561-578.

Probabilistic Design Space

Linas Mockus,^{a*} Gintaras Reklaitis,^a Ken Morris,^b David LeBlond,^c

^a*Purdue University, 480 W. Stadium Ave., West Lafayette, IN 47907-2100, USA*

^b*Long Island University, 75 Dekalb Ave., Brooklyn, NY 11201-8423, USA*

^c*CMC Statistics, 3091 Midlane Drive, Wadsworth, IL 60083, USA*

lmockus@purdue.edu

Abstract

In this work we develop a Bayesian framework for building surrogate stochastic models of complex multi-step processes for which tractable mechanistic models are difficult to construct. The probabilistic process envelope defined by the design space provides an extra level of assurance of product quality over and above that provided by traditional process control. While the application we report is specific to drug products manufactured using traditional batch processing, the proposed framework is applicable in general to batch and continuous manufacturing of products that must meet a set of critical product quality specifications.

Keywords: stochastic process model; surrogate process model; batch process; continuous process; Bayesian statistics.

1. Introduction

The ICH guideline on pharmaceutical development (ICH, Q8(R2)) introduced the concept of design space, a construct that defines the operating region within which the resulting product can be assured to be at the required quality level. Recognizing the inherently stochastic nature of the design space, (Peterson, 2008) demonstrated the use of Bayesian statistics to facilitate its construction. More recently, (Bano, et al., 2018) proposed an approach based on partial least square regression to establishing a probabilistic design space, under the assumption that product quality is linearly related to process inputs. The key distinctions of the approach proposed in our work is, first, that the stochastic model utilizes historical process performance. Second, it is parametric with regards to product quality attributes as opposed to process performance and therefore aleatoric uncertainties (unknown unknowns) can be implicitly captured. In addition, the proposed framework is independent of linearity assumptions.

To find the design space of a process, quantification of the “assurance of quality” for the product under development or being manufactured is required. In this study, the experimental data for multiple pharmaceutical products manufactured by different manufacturers is used to determine the variation between and within product lots. Uncertainty quantification is obtained by employing multi-level hierarchical models at different levels of fidelity combined with Bayesian inference. This allows prediction of the TRUE between- and within-lot variability. In addition, several ways to predict the TRUE measurement uncertainty are identified.

2. Probabilistic design space

We identify the design space by constructing a process envelope which ensures that the manufactured product is of required quality. The ICH Q8(R2) Guideline (ICH, 2009) defines “Design Space” as: “The multidimensional combination and interaction of input variables (e.g. material attributes) and process parameters that have been demonstrated to provide assurance of quality.” From a Bayesian perspective, one could define the ICH Q8 design space as:

$$DS = \{x \in X \mid \Pr(Y \in A \mid x, data) \geq R\},$$

where X is a vector of process input variables, X is the experimental region, Y is a vector of product attributes defining quality (assay, % dissolved at Q time, tablet hardness, etc.), A is the acceptance region for the product, R is a reliability value which defines the desired level of “assurance” of quality, and DS is the design space. Q is the time point at which the dissolution performance specified in the corresponding pharmacopeial monograph must be satisfied.

The above probability measure is based upon the posterior predictive distribution for Y given the process inputs. The specifications are typically established based on human clinical trials to ensure absence of adverse events and efficacy of the product.

In this work we propose to define the design space in terms of the parameter space associated with the process responses, namely, the product quality attributes. Specifically, these consist of the product grand mean of these attributes as well as the intra and inter lot variability of these attributes. This allows the quality of a product to be determined by measuring the probability of meeting specifications established during pivotal clinical trials. The product quality is deemed sufficient if the probability is equal to, or greater than, an assigned threshold.

For a complex multi-step batch process, it is difficult and often infeasible to derive a rigorous and explicit model, therefore we propose to use a surrogate model expressed in terms of the product quality attributes, specifically, the attribute means and intra/inter lot variabilities. It should be noted that the traditional concept of lot may be extended to continuous processing by defining the lot in terms of an appropriate time interval of production during which product attributes and external intervention (human operator actions, raw material supply, etc.) are constant within some tolerance. Over that time period the process is said to be in the state of control.

In addition, the proposed stochastic model utilizes historical process performance which is incorporated as prior information via a Bayesian framework. It is parametric with regards to product quality attributes as opposed to process performance and therefore aleatoric uncertainty (unknown unknowns) is implicitly considered.

The proposed methodology is easily generalizable to batch and continuous processing industries (i.e., conformance to grade requirements in oil refinery). Significant change in between/within lot variability indicates that measures have to be taken to ensure adequate process control (i.e., quality of incoming materials).

By making the simplifying assumptions of normality, the surrogate process model may be expressed as follows:

$$\begin{aligned} Y_{ij} &= \mu_j + \eta_{ij} \\ \mu_j &\sim N(\mu, \sigma_B^2), \\ \eta_{ij} &\sim N(0, \sigma_W^2) \\ \theta &= (\mu, \sigma_B, \sigma_W) \end{aligned} \tag{1}$$

where Y_{ij} is the true value of product attribute (for assays this is expressed as % of label content, while for dissolution this is expressed as % dissolved), μ_j is the true mean for lot j , and η_{ij} is a deviation of the true value of unit i from lot j from the true lot j mean. σ_B and σ_W are corresponding inter-lot and intra-lot variabilities. μ is the attribute mean. The prior $P(\theta)$ for $\theta=(\mu, \sigma_B, \sigma_W)$ encapsulates expert knowledge and could be derived from historical data.. Without loss of generality and to simplify further development, we assume that $P(\theta) \sim 1$.

It should be noted that the simplifying normality assumptions may be relaxed by treating the intra and inter lot variations to be distributed according to a more robust Student t distribution or even more general distributions such as the four parameter Johnson SU (Johnson, 1949) or the skew-normal or skew- t distributions which can model the presence of skewness and/or kurtosis (Dagne, 2013; Sahu, et al., 2003; Azzalini & Capitanio, 2003). However, in this work we will focus on the simplest normal form since under that assumption the design space may be expressed in terms of an analytical expression. In more complicated cases the design space boundaries have to be estimated using numerical simulation.

The design space boundaries based on the normality assumption may be expressed as:

$$DS_b = pnorm \left(ub, \mu, \sqrt{\sigma_B^2 + \sigma_W^2} \right) - pnorm \left(lb, \mu, \sqrt{\sigma_B^2 + \sigma_W^2} \right), \quad (2)$$

where $pnorm$ is the quantile function for the normal distribution, ub is the upper bound of product attribute, lb is lower bound of product attribute (for assays the typically lower/upper bounds are 90/110%, for dissolution the lower/upper bounds are % dissolved at Q time).

In the multidimensional case (i.e. assay, % dissolved, and tablet hardness are bounded) the design space boundaries may be derived analytically using multivariate normal distribution. For purposes of the present discussion, we assume that inter and intra lot variabilities are independent.

3. Case study

We have experimentally tested 18 different immediate release drug products manufactured by different generic manufacturers and determined their product quality attribute means and inter/intra lot variabilities from the experimental data (Morris, 2018). We also assume that the reliability measure is $R=0.95$. The choice of R is based on acceptable quality level (typically 5%). This choice is very important: higher values may be chosen for narrow therapeutic range products as is the case with some oncology therapies.

The 50% highest probability density region of the estimated joint distribution for mean, intra and inter lot variability of dissolution attribute (% dissolved at Q time) are depicted in Figure 1. To simplify the presentation, we combine the inter and intra lot variabilities by using:

$$\sigma^2 = \sigma_B^2 + \sigma_W^2, \quad (3)$$

where σ is a lumped standard deviation.

The joint probability distribution estimates for mean μ , standard deviations σ_B and σ_W were obtained using Markov Chain Monte Carlo procedure (Morris, 2018) using a hierarchical model by also considering analytical variability.

We observe that for some products those regions are close to the design space boundary (black line). The number beside the product name indicates the probability of the tablet being within design space. Each oval corresponds to a different product and manufacturer combination. The names of the drug products that are below desired quality level are

shown next to their corresponding oval. The probability of a given product being within the design space is shown to the right of the product name. For example, Product P12 manufactured by M11 has probability of 34% being within design space.

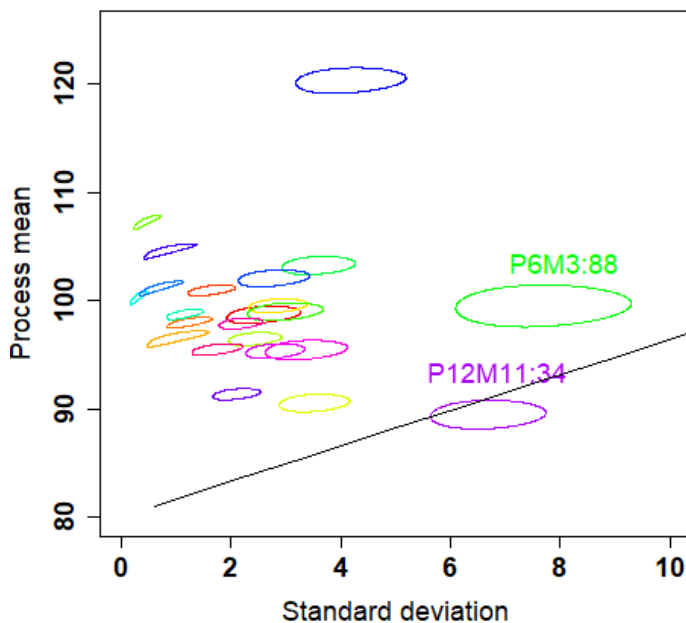


Figure 1. Probabilistic design space for dissolution. Ovals represent various products. The probability of a given product being within the design space is shown to the right of product name. The units of process mean and standard deviation are % dissolved.

The corresponding landscape for the product assay is depicted Figure 2. Since the assay is bounded from both sides of the design space, the boundary has a parabolic shape. Note that there are a number of products that fall outside of the design space boundary. One reason for this being that manufacturers overshoot to ensure that the content of active pharmaceutical ingredient (API) is not too low. Another artefact is that the assay is defined as the average content over several tablets, as specified by US Pharmacopeia. Averaging effectively masks intra-lot variability. While the average active content is below the upper bound the active content in individual tablets fluctuate. The proposed framework allows detecting “unobserved” behaviour.

It is of interest to note that the four large ovals lying outside of the design space on the top right corner of the Figure 2 represent the same product P11 manufactured by different manufacturers M1, M5, M2, and M10. It is very possible that overage is explicitly specified in the corresponding batch record.

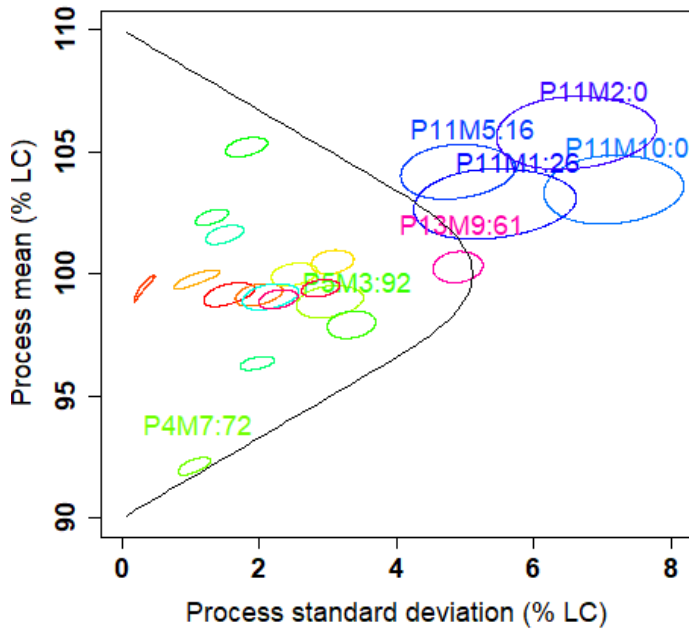


Figure 2. Probabilistic design space for assay. Ovals represent various products. The probability of a given product being within the design space is shown to the right of product name. The units of process mean and standard deviation are % of label claim.

The distributions of the probability that the product is within assay specifications for well performing (within design space) and poorly performing (outside design space) processes are depicted in Figure 3. A well performing process (solid line) is characterized by probability mass concentrated around one which is indicated by a sharp peak close to one. A poorly performing process (dashed line) is characterized by a diffuse probability mass that is indicated by a low and very wide hump in the distribution profile.

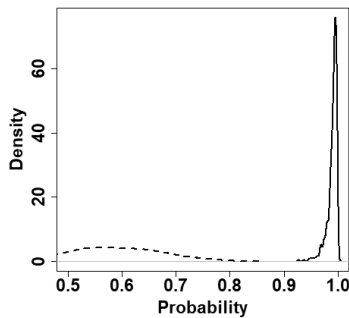


Figure 3. The probability distributions of probability that product is within assay specifications.

4. Conclusion

In this work we develop a Bayesian framework for building surrogate stochastic models of complex multi-step processes for which tractable mechanistic models are not available. The proposed framework may be a valuable tool to detect the “unobserved” process shifts and serve as an additional measure to ensure product quality.

The proposed framework can be easily extended to batch and continuous processing manufacturing of products that must meet a set of critical product quality specifications (i.e., conformance to grade requirements in oil refinery).

In addition, we expect that this work could potentially support FDA’s risk based approach and quality metrics initiative - the proposed framework explicitly identifies the sites that may require attention - as well as continuous process verification as delineated in (FDA, 2011).

References

- Azzalini, A. & Capitanio, A., 2003. Distributions generated by perturbation of symmetry with emphasis on a multivariate skew t distribution. *J. Roy. Statist. Soc., series B*, Volume 65, p. 367–389.
- Bano, G., Facco, P., Bezzo, F. & Barolo, M., 2018. Probabilistic design space determination in pharmaceutical product development: a Bayesian/latent variable approach. *AIChE J*, 64(7), p. 2438–2449.
- Dagne, G. A., 2013. Bayesian Inference for Skew-Normal Mixture Models With Left-Censoring. *J Biopharm Stat.*, 23(5), p. 1023–1041.
- FDA, 2011. *Guidance for Industry – Process Validation: General Principles and Practices*, s.l.: s.n.
- ICH, 2009. *ICH Harmonised Tripartite Guideline Pharmaceutical Development Q8(R2)*, s.l.: s.n.
- Johnson, N. L., 1949. Systems of Frequency Curves Generated by Methods of Translation. *Biometrika*, 36(1/2), p. 149–176.
- Morris, K., 2018. *Annual Report*, New York, NY: Lachman Institute for Pharmaceutical Analysis.
- Morris, K., 2018. *Building towards Statistically-Based Pharmaceutical Quality Standards*, New York, NY: Lachman Institute for Pharmaceutical Analysis.
- Peterson, J., 2008. A Bayesian Approach to the ICH Q8 Definition of Design Space. *Journal of Biopharmaceutical Statistics*, Volume 18, pp. 959–975.
- Sahu, S., Dey, D. & Branco, M., 2003. A new class of multivariate skew distributions with applications to Bayesian regression models. *The Canadian Journal of Statistics*, 31(2), p. 129–150.

Modeling Impacts of Tracking on Greenhouse Gas Emissions from Photovoltaic Power

Ian Miller,^{a,b} Emre Gençer,^{a,*} Francis M. O'Sullivan^a

^a *MIT Energy Initiative, Massachusetts Institute of Technology, 77 Massachusetts Avenue, Cambridge MA 02139, US*

^b *Department of Chemical Engineering, Massachusetts Institute of Technology, 77 Massachusetts Avenue, Cambridge MA 02139, US*

emregencer@mit.edu

Abstract

A life cycle assessment (LCA) of photovoltaic (PV) power is conducted. The PV LCA is used to estimate the emissions impact of a common PV practice that has not been comprehensively analyzed by LCA: solar tracking. Relative to stationary mounting, solar tracking is found to decrease the greenhouse gas emissions of power from multi-crystalline silicon PV in most regions analyzed (by 0 to ~12%, or 0 to ~4 gCO₂e/kWh), and to increase the emissions of power from cadmium telluride PV in most regions analyzed (by 0 to ~12%, or 0 to ~4 gCO₂e/kWh). This dependence on cell type is explained by the interaction of tracker production emissions, module production emissions, and tracking energy gain. For both PV cell types, if the ratio of module production emissions to tracker production emissions increases in future, independent of absolute emission values, tracking will more commonly decrease PV carbon intensity. Conversely, if the ratio decreases, tracking will more commonly increase PV carbon intensity. Equations are presented to explain this relationship between module production emissions and tracker production emissions. These equations apply to emissions of all pollutants, not only greenhouse gases.

Keywords: photovoltaic (PV) power, life cycle assessment (LCA), greenhouse gas (GHG) emission, solar tracking

1. Introduction

Since 2008, solar tracking has grown from rare to common in photovoltaic (PV) power production. In the US from 2008 to 2014, 19 % of new utility-scale projects with cadmium telluride (CdTe) modules employed tracking (16 of 86 projects); in 2015 and 2016, the number was 56 % (44 of 79 projects), including locations outside the exceptionally sunny US southwest, such as Colorado and Tennessee (EIA 2016). For all PV module types, tracking was used on 53 % of cumulative and 70 % of new capacity at utility-scale sites in 2016 in the US (EIA 2016). The impact of solar tracking on emissions from PV generation has not been comprehensively analyzed by life cycle assessment (LCA). This study fills that gap. It provides a general methodology for estimating the emissions impact of adding performance enhancing equipment to PV, and applies this methodology to model the impact of solar tracking on emissions of greenhouse gases (GHGs). This paper refers to life cycle GHG emissions from AC electricity generation as "carbon intensity", and the units of grams-CO₂-equivalent/kilowatthour as "g_c/kWh".

Several LCAs analyzed the impact of solar tracking on carbon intensity, but with limited geographic scope and tracking set-ups that do not (and do not claim to) represent industry practice. Desideri et al. (2013) analyzed 1-axis tracking systems with 30° tilt in southern Europe. In contrast, the industry norm for PV tracking is horizontal 1-axis tracking; in the US in 2016, 97 % of utility-scale tracking PV projects used horizontal 1-axis tracking (Bolinger et al. 2017). Two PV LCAs did analyze industry-representative tracking. Leccisi et al. (2016) found that horizontal 1-axis tracking reduced carbon intensity by 11 % and 1 % for mc-Si and CdTe PV, respectively, given installation in the US southwest. Sinha et al. (2013) estimated that tracking reduced the carbon intensity of CdTe PV by 3 % in the US southwest. This paper aims to build on these studies by calculating and explaining tracking's impact on PV carbon intensity over a range of locations.

2. Methodology

We developed a solar life cycle assessment tool (SoLCAT) following ISO 14040 standards for LCA (ISO 14040 2006) and IEA PV LCA guidelines. To estimate GHG emissions from PV power, SoLCAT integrates four elements: published PV life cycle inventories (LCIs), background emission factors from Ecoinvent, known physical correlations, and capacity factors from PVWatts, a software tool from the US National Renewable Energy Laboratory.

The goal of our LCA is to estimate the impact of solar tracking on the carbon intensity of PV power. The system is electricity production by PV. The functional unit is a kilowatthour of AC electricity supplied to the grid. In addition to electricity, the other system output analyzed is GHG emissions. These two system outputs combine into our central metric: GHGs emitted per AC electricity generated (gC/kWh), or carbon intensity. PV electricity production can be elaborated as shown in Figure 1.

Figure 2 gives an overview of SoLCAT's operation and utilization of data sources. Our primary sources for PV LCIs are the IEA Report "Life Cycle Inventories & Life Cycle Assessments of PV Systems" (Frischknecht et al. 2015) and the ESU Report "Life Cycle Inventories of Photovoltaics" (Jungbluth et al. 2012). Sinha et al. (2013) provides an LCI of a horizontal 1-axis tracking system. For emission factors of background processes, our primary source is the Ecoinvent V3 database. In the absence of data, our model does not account for emissions from PV EOL processes.

SoLCAT converts amounts (a) to GHG emissions (e_{total}) using three general equations:

$$e_{total} = \sum_i e_{stage\ i} \quad (1)$$

$$e_{stage\ i} = \sum_j e_{input\ j\ to\ stage\ i} - \sum_k^{stages\ before\ i} e_{stage\ k} \quad (2)$$

$$e_{input\ j\ to\ stage\ i} = a_{input\ j\ to\ stage\ i} EF_j \quad (3)$$

where e is emissions (gC), a is amount (e.g., kg-iron), and EF is emission factor (e.g., gC/kg-iron). Amounts ($a_{input\ j\ to\ stage\ i}$) are provided by the PV LCIs or determined by parameters input to SoLCAT. Emission factors (EF_j) are provided by Ecoinvent or SoLCAT inputs. Miller et al. (2018) describes how SoLCAT input variables impact amounts and emission factors.

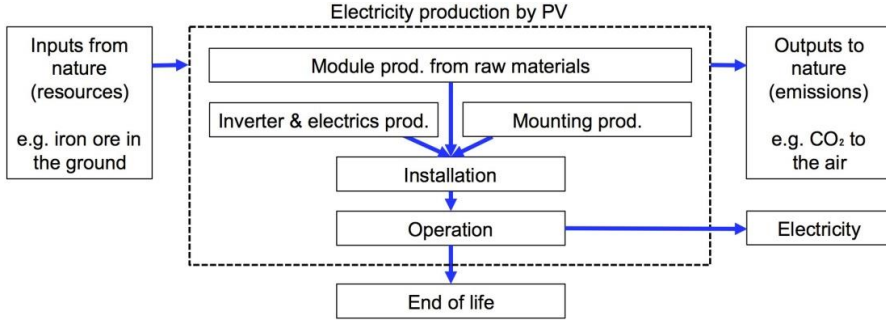


Figure 1. Life cycle stages of PV electricity production.

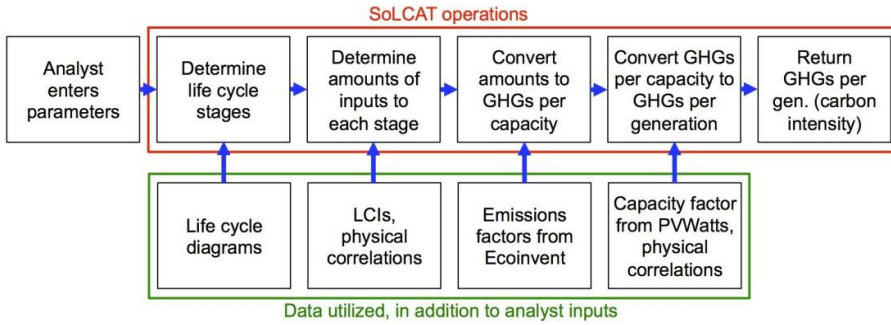


Figure 2. Flowchart of SoLCAT operations and utilization of data sources.

SoLCAT’s last operation utilizes capacity factor estimates from PVWatts (Dobos 2014). As detailed in Miller et. al (2018), our model adjusts capacity factors from PVWatts to account for shading, snow, degradation, and tracker energy consumption, to calculate a lifetime average capacity factor (F). Carbon intensity is then calculated as:

$$I = e_{total} / (F c_g t_{hr}) \tag{4}$$

where I is carbon intensity (gC/kWh), e_{total} is life cycle GHG emissions (gC), c_g is rated power capacity, and t_{hr} is PV system lifetime (h).

Analysis of solar tracking’s impact on carbon intensity requires calculation of tracking energy gain (TEG). TEG is the percent increase in PV power output that results from tracking the sun, relative to a fixed-position system, and can be estimated as

$$TEG = (\bar{P}_{AC,track} - \bar{P}_{AC,fixed}) / \bar{P}_{AC,fixed} \times 100 \% \tag{5}$$

where $P_{AC,track}$ is the AC power output of a PV system with tracking, and $P_{AC,fixed}$ is the output of a PV system with fixed orientation and otherwise identical features (location, modules, etc.). The fixed base case orientation is assumed here to be irradiance-maximizing, with equator-facing azimuth and near-latitude tilt. The tracking system is horizontal 1-axis tracking with $\pm 45^\circ$ rotation limits.

3. Results and discussion

Using SoLCAT, base case results are calculated and shown in Figure 3:

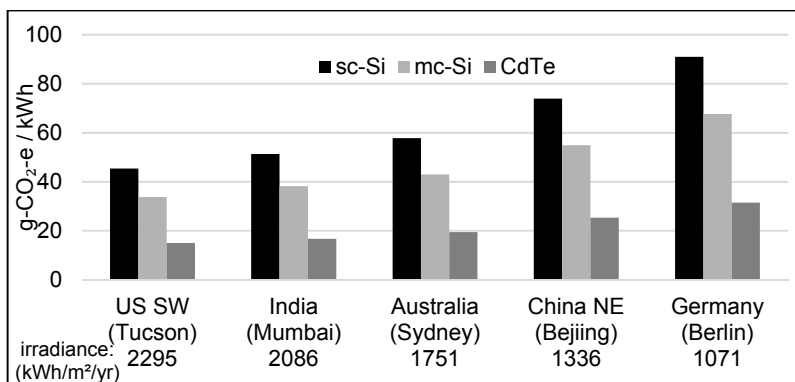


Figure 3. Carbon intensities of PV power installed in different locations circa 2015. Installation type is large-scale, open-ground, fixed-tilt. Lifetime is 30 years. Rated efficiencies are 17, 16, and 15.6 % for sc-Si, mc-Si, and CdTe. Degradation is 0.7 %/yr. GHG emissions of upstream electricity are 660 & 510 g_c/kWh for module and BOS production, assuming 2015 China & world averages.

We find that in the US southwest, for mc-Si PV, horizontal 1-axis tracking reduces carbon intensity by 12 % relative to the fixed-tilt base case (from 34 to 30 g_c/kWh), consistent with previous results (Leccisi, Raugei, and Fthenakis 2016). Tracking produces this reduction despite requiring ~50 % more structural metal and ~30 % more copper cable per module, compared to fixed mounting (Sinha et al. 2013). Emissions from producing tracker materials are offset by increased generation from tracking, such that overall emissions per generation decreases.

Analogous calculations are conducted for PV systems in 4 other locations and presented in Figure 4, which underlines several related findings. (1) location influences the emissions impact of tracking, via TEG; (2) tracking decreases the carbon intensity of mc-Si PV in most locations; (3) consistent with Sinha et al. (2013), tracking reduces the carbon intensity of CdTe PV in the US southwest by ~3 %; and (4) the US southwest is exceptional: for most locations analyzed, tracking increases the carbon intensity of CdTe PV power.

The dependence on location is driven by latitude and cloud cover. The greater the latitude, the greater the module incline that maximizes incident irradiance, and the more irradiance is lost by “reclining” to horizontal for 1-axis tracking. Greater latitude also means more atmosphere for sunlight to travel through. This increases light scattering, as does greater cloud cover. The greater the fraction of ambient light that is scattered (i.e., diffuse), the less energy there is to be gained from tracking the sun's non-diffuse direct beam irradiance. Lower tracking energy gain (TEG) means less extra electricity over which to amortize extra emissions from tracker-production. For both module types, this explains why, as TEG decreases left to right in Figure 4, tracking's emissions impact increases.

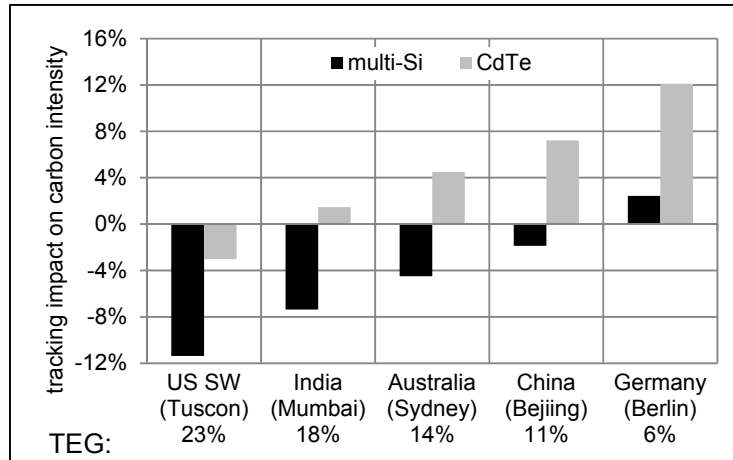


Figure 4. Relative impact of horizontal 1-axis tracking on PV carbon intensity in different locations, for mc-Si PV and CdTe PV.

The varying impact by module type can be explained with the following equations. Let: T \equiv factor by which tracking increases electricity generation.

$e_{f,i}$ \equiv emissions of fixed PV system (gC). i = mc-Si or CdTe

e_t \equiv emissions from adding tracking (gC)

E_f \equiv generation from fixed PV system (kWh)

E_t \equiv generation from tracking PV system (kWh)

I_f \equiv emissions per generation (carbon intensity) of fixed PV system (gC/kWh)

I_t \equiv emissions per generation (carbon intensity) of tracking PV system (gC/kWh)

M \equiv factor by which tracking changes carbon intensity

$$M = I_t / I_f$$

$$= [(e_{f,i} + e_t) / E_t] / [e_{f,i} / E_f] = [(e_{f,i} + e_t) / (TE_f)] / [e_{f,i} / E_f]$$

$$M = (e_{f,i} + e_t) / (Te_{f,i}) \quad (6)$$

Consider Eq. (6) when $e_{f,i} \gg e_t$, i.e., when emissions from module production are much larger than emissions from tracker production:

$$M_{f \text{ large}} = 1 / T \quad (7)$$

$M_{f \text{ large}}$ will always be less than 1, because T always exceeds 1. In other words, for a module type with large production emissions, adding tracking always reduces carbon intensity. This explains why adding tracking reduces the carbon intensity of mc-Si PV in most locations (blue bars in Figure 4). Multi-Si module production is significantly more carbon intensive than CdTe module production, as seen in Figure 3 and previously reported (Frischknecht et al. 2015). $e_{f, \text{multi-Si}}$ is approximately 11 x e_t whereas $e_{f, \text{CdTe}}$ is approximately 5 x e_t . Eq. (6) thus also explains why adding tracking increases CdTe PV's carbon intensity in most locations (red bars in Figure 4):

$$M_{\text{CdTe}} \approx (e_{f, \text{CdTe}} + e_{f, \text{CdTe}} / 5) / (Te_{f, \text{CdTe}}) = 1.2 / T \quad (8)$$

For M_{CdTe} to be less than 1, T must exceed 1.2. In other words, CdTe PV requires TEG above 20 % for tracking to reduce its carbon intensity, a TEG only possible in exceptionally sunny regions like the US southwest.

4. Conclusion

A modeling tool (SoLCAT) is presented. SoLCAT estimates GHG emissions from solar PV generation under a broad range of conditions, partly by combining life cycle inventories and PV performance models. Using this tool, we find that solar tracking decreases the GHG emissions of power from multi-crystalline silicon PV in most regions analyzed (by 0 to ~12 %, or 0 to ~4 gCO₂e/kWh), and increases the emissions of power from cadmium telluride PV in most regions analyzed (by 0 to ~12 %, or 0 to ~4 gCO₂e/kWh). For any PV cell type and any emitted pollutant, if the ratio of module production emissions to tracker production emissions increases in future, independent of absolute emission values, tracking will more commonly decrease PV emissions intensity.

References

- Bolinger, Mark, Joachim Seel, and Kristina Hamachi LaCommare. 2017. "Utility-Scale Solar 2016."
- Desideri, U., F. Zepparelli, V. Morettini, and E. Garroni. 2013. "Comparative Analysis of Concentrating Solar Power and Photovoltaic Technologies: Technical and Environmental Evaluations." *Applied Energy* 102:765–84. <https://doi.org/10.1016/j.apenergy.2012.08.033>.
- Dobos, Aron P. 2014. "PVWatts Version 5 Manual (NREL/TP-6A20-62641)." *National Renewable Energy Laboratory (NREL)*.
- EIA. 2016. "Form EIA-860 : Annual Electric Generator Report."
- Frischknecht, R, R Itten, P Sinha, M de Wild-Scholten, J Zhang, and Vasilis Fthenakis. 2015. "Life Cycle Inventories and Life Cycle Assessment of Photovoltaic Systems; Report IEA-PVPS T12-04:2015." Paris, France.
- ISO 14040. 2006. "The International Standards Organisation. Environmental Management — Life Cycle Assessment — Principles and Framework." *ISO 14040*. <https://doi.org/10.1136/bmj.332.7550.1107>.
- Jungbluth, Niels, Matthias Stucki, Karin Flury, Rolf Frischknecht, and Sybille Büsser. 2012. "Life Cycle Inventories of Photovoltaics." Ulster, CH.
- Leccisi, Enrica, Marco Raugei, and Vasilis Fthenakis. 2016. "The Energy and Environmental Performance of Ground-Mounted Photovoltaic Systems - A Timely Update." *Energies* 9 (8). <https://doi.org/10.3390/en9080622>.
- Miller, Ian, Emre Gençer, Hilary S Vogelbaum, Patrick R Brown, Sarah Torkamani, and O'Su. 2018. "Parametric Modeling of Life Cycle Greenhouse Gas Emissions from Photovol-Taic Power." [Under Review].
- Sinha, P, M Schneider, S Dailey, C Jepson, and M De Wild-Scholten. 2013. "Eco-Efficiency of CdTe Photovoltaics with Tracking Systems." In *39th IEEE Photovoltaic Specialists Conference (PVSC)*. Tampa, FL, US.

Process Intensification and Miniaturization of Chemical and Biochemical Processes

Filip Strniša, Tomaž Urbič, Polona Žnidaršič-Plazl and Igor Plazl

Faculty of Chemistry and Chemical Technology, University of Ljubljana, Večna pot 113, SI-1001 Ljubljana, Slovenia
igor.plazl@fkkt.uni-lj.si

Abstract

In this work, the microscale (bio)process development based on scale-up/numbering-up concept in combination with model-based optimization is presented. The main features of microscale systems are reflected in fluid dynamics, therefore the understanding of fundamental mechanisms involved in fluid flow characteristics at the micro scale is essential since their behaviour affects the transport phenomena and microfluidic applications. Theoretical description of transport phenomena and the kinetics at the micro scale is discussed and illustrated on the cases of a lattice Boltzmann simulations for flow distribution in the packed bed microreactor “between two-plates” and the biocatalytic enzyme surface reaction.

Keywords: process intensification, miniaturization, model-based design

1. Introduction

Process intensification has been considered important for the future of (bio)chemical engineering for a while now. Stankiewicz and Moulijn (2000) defined process intensification as the development of novel and sustainable equipment that compared to the existing state-of-the-art, produces dramatic process improvements related to equipment sizes, waste production, and other factors. The application of microreactor technology in (bio)chemical processes meets these criteria, with the most obvious one being the equipment size reduction. However, besides spatial benefits, microreactors also provide enhanced heat and mass transfer, safety, environmental impact, and others (Pohar and Plazl, 2009). A key advantage that this technology brings is the precise process control that comes with it. This allows for repeatable conditions within the reactor system which leads to improved yields and product quality at a more consistent rate compared to the batch procedures. With the listed advantages there is no doubt that process intensification through the application of microreactor technology holds the potential to revolutionize (bio)chemical synthesis, but specific suggestions for possible replacement of established industrial processes are scarcely encountered. A number of highly innovative and systematic approaches, protocols, tools, and strategies are however currently being developed in both — industry and academia, all to minimize the gap between research and industry, and to enable a smooth transfer of lab-on-a-chip to the industrial scale. To deal with these challenges it is necessary to advance the field from (bio)catalyst discovery to (bio)catalytic microprocess design. Not only will this require a new level of understanding of the underlying reaction mechanisms and transport phenomena at the microscale, but also the

development of relevant computational tools. The quest for high-performance manufacturing technology places the combination of biocatalysis and microscale technology as a key green engineering method for process development and production (Wohlgemuth et al., 2015). The aim of this work is to present the microscale (bio)process development based on scale-up/numbering-up concept in combination with model-based optimization. As microscale systems are flow-based it is essential to understand the fundamental mechanisms involved in fluid flow characteristics at the micro scale, because they affect the transport phenomena and microfluidic applications. Theoretical description of transport phenomena and the kinetics at the micro scale is discussed and illustrated on the cases of lattice Boltzmann simulations for flow distribution in packed bed microreactors “between-two-plates” and the biocatalytic enzyme surface reaction.

2. Model-based design

2.1. Macroscopic models

A theoretical description of transport phenomena and kinetics for different chemical and biochemical processes in the microfluidic devices have to be developed using the bases of continuum theory. The following set of partial differential equations regarding momentum and mass conservation (Eqs. 1, 2), heat conservation (Eq. 3), and species conservation (Eq. 4) have to be solved to describe the convection-diffusion dynamics in all three spatial directions and to depict the governing transport characteristics of processes in microfluidics:

$$\frac{\partial \vec{v}}{\partial t} + \vec{v} \cdot \nabla \vec{v} + \nabla p_k - \nu \nabla^2 \vec{v} = 0 \quad (1)$$

$$\nabla \cdot \vec{v} = 0 \quad (2)$$

$$\frac{\partial}{\partial t} (\rho h) + \nabla \cdot (\rho h \vec{v}) - \nabla \cdot [\lambda \nabla T] - S_h = 0 \quad (3)$$

$$\frac{\partial c_i}{\partial t} + \vec{v} \cdot \nabla c_i - D_i \nabla^2 c_i = 0 \quad (4)$$

where \vec{v} is the velocity vector (m s^{-1}), p_k is the kinematic pressure ($\text{m}^2 \text{s}^{-1}$) and ν is the kinematic viscosity ($\text{m}^2 \text{s}^{-1}$) — Eqs. 1, 2; ρh is the thermal energy (W m^{-3}), λ is the thermal conductivity ($\text{W m}^{-2} \text{K}^{-1}$), T is the temperature (K) and S_h is the volumetric heat source (W m^{-3}) — Eq. 3; c_i is the concentration of the solute i , D_i is the diffusion coefficient of the species i (W m^{-2}) and \vec{v} is the velocity vector obtained from Eqs. 1 and 2 — Eq. 4.

2.2. Mesoscopic models

Lattice Boltzmann methods are computational methods, that were primarily developed to solve fluid-dynamic problems, but can also be used among other to simulate heat and mass transport (Succi, 2015). The core of the method is the lattice Boltzmann equation, which is a special form of the Boltzmann equation, discretized in both — space and time. This gives the methods a base in the statistical mechanics and therefore steers them away

from the “traditional” continuum-based methods, which are usually applied in chemical engineering process simulation. The lattice Boltzmann equation reads as follows:

$$f_a(\vec{x} + \vec{e}_a \Delta t, t + \Delta t) - f_a(\vec{x}, t) = \Omega_a(\vec{u}, \rho, \tau) \quad (5)$$

f is a discrete distribution function, which represents a packet of particles with statistically the same momentum in direction a , which is represented by a set of basic lattice velocities \vec{e} . \vec{x} is the positional vector and t is time. Ω is the collision operator, and it can take on different forms, but they essentially all depend on the local flow velocity and fluid density \vec{u} , and ρ respectively. τ is the relaxation time, which is directly related to species’ physical properties such as kinematic viscosity or molecular diffusivity.

2.3. Model verification and validation

Microfluidic devices have justified the high expectations and successfully demonstrated their advantages for intensification of chemical and biochemical processes in many different research areas and fields. Schematic representation of some typical microfluidic devices, known as enzymatic microreactors is given in Figure 1 (a-g). On these schemes of different microfluidic systems, one can observe the most typical enzyme (or cell) immobilization techniques as well as the most typical flow patterns of two-phase flows: the parallel and droplet flow regime, which allow for efficient performance of various processes from chemical reaction, enzyme catalyzed reaction with immobilized enzyme or cells to separation, extraction, and purification. In order to transfer these systems, successfully developed and tested on the laboratory scale, to the industrial environment and to increase the productivity from microliter scale to bigger scales at the same process efficiency and minimized costs, the optimized scale-up/numbering-up concepts have to be implemented, where the model-based design plays a key role. For this purpose, only pre-verified and validated macroscopic and lower-level mathematical models can be used. Only verified and especially validated models bring about the understanding of basic principles and mechanisms taking place in chemical and biochemical processes at the microscale.

The model equations are usually solved numerically by writing them into computer code. Once the code is complete and error free, the model needs to be verified. In this process the model is tested whether it gives sensible results, which do not necessarily need to be correct (Plazl and Lakner, 2010). The correctness of the model’s predictions is put to the test during model validation. Models can be validated either by comparing them to other already valid models or by testing them against experimental observations. Validating via experimental methods can be done in different ways, such as *e. g.* online validation, and inline validation. Common to all is that theoretical predictions and simulations matched to experimental measurements without any fitting procedures. In our previous work, we showed that macroscopic mathematical models can reliably describe various complex processes in microfluidic devices. In the case of non-homogeneous system with parallel flow pattern the steroid extraction in a microchannel system was studied theoretically and experimentally. In order to analyze experimental data and to forecast microreactor performance, a three-dimensional mathematical model with convection and diffusion terms was developed considering the velocity profile for laminar flow of two parallel phases in

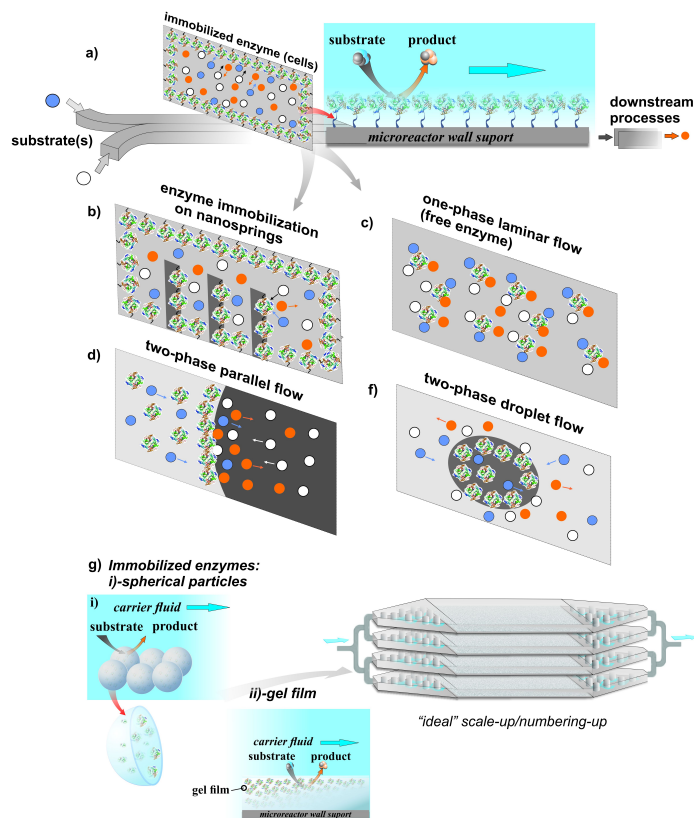


Figure 1: Schematic representation of some typical homogeneous, non-homogeneous and heterogeneous microfluidics systems: a) immobilized biocatalyst on the inner walls of microreactor with integrated down-stream processes; b) immobilized biocatalyst on the inner surface and pillars to increase surface area and biocatalyst loading; c) free enzyme in a one-phase laminar flow; d) free enzyme in a two-phase parallel flow; f) free enzyme in a droplet flow; g) packed-bed microreactor with immobilized enzymes in a spherical particles (i) and gel film (ii) with scale-up in one dimension and numbering-up of microreactor systems “between two-plates”.

a microchannel at steady-state conditions. Very good agreement between model calculations and experimental data was achieved without any fitting procedure (Žnidaršič Plazl and Plazl, 2007).

Online oxygen measurements inside a microreactor with modelling of transport phenomena and enzyme catalyzed oxidation reaction was performed for online model validation of the homogeneous system with biochemical reaction. Continuum based mathematical models, with a full 3D description of transport phenomena, incorporating convection, diffusion and enzymatic reaction terms along with the parabolic velocity profile in a microchannel was developed to simulate the concentration of dissolved oxygen inside

the microchannels, to assess the required model complexity for achieving precise results and to depict the governing transport characteristics at the microscale (Ungerböck et al., 2013). Droplet-based liquid-liquid extraction in a microchannel was studied, both theoretically and experimentally to online validate macroscopic models for complex two-phase droplet flow microfluidics. The finite elements method, as the most common macroscale simulation technique, was used to solve the set of partial differential equations regarding conservation of moment, mass and solute concentration in a two-domain system coupled by interfacial surface of droplet-based flow pattern (Eqs. 1, 2, 4). The model was numerically verified and validated online by following the concentrations of a solute in two phases within the microchannel by means of a thermal lens microscopic (TLM) technique coupled to a microfluidic system, which gave results of high spatial and temporal resolution. Very good agreement between model calculations and online experimental data was achieved without applying any fitting procedure to the model parameters (Lubej et al., 2015).

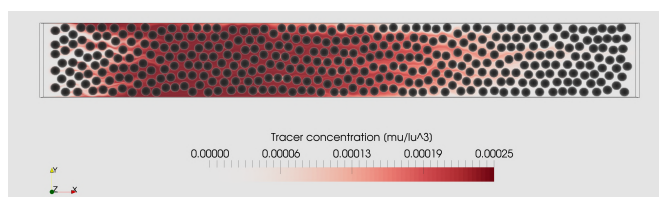


Figure 2: A snapshot of the pulse test simulation. Domain size = $2048 \times 256 \times 32$ lattice units³, Reynolds number = 0.95, Schmidt number = 1000. The flow is from west to east.

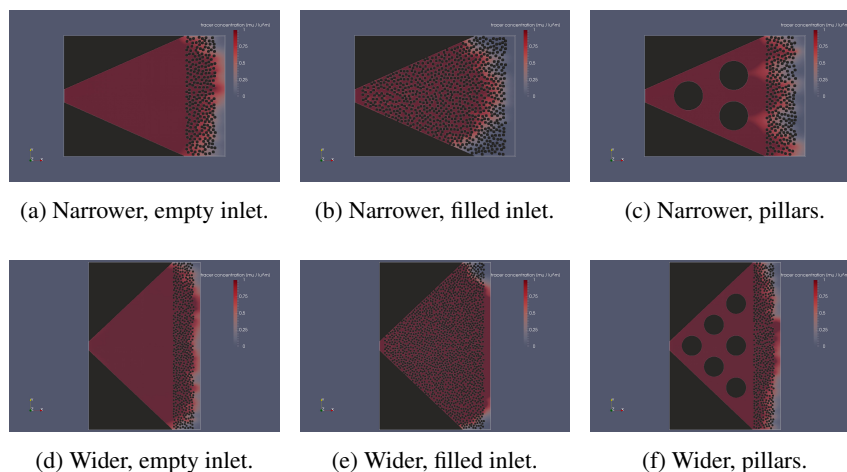


Figure 3: Different scenarios for inlet flow distribution in one-dimensional scale-up. “Empty” channels do not utilize any obstacles to distribute the flow, “filled” channels use the same particles in the flow distribution zone as they do throughout the rest of the channel, and “pillars” channels have pillars in the flow distribution zone. The tracer is colored red, and flows from west to east.

The lattice Boltzmann method was applied to obtain the velocity field in a packed bed

microbioreactor, and to simulate mass transport in a pulse test through it. First a computer program generated a randomly packed bed, then the flow field was calculated, and finally the mass transport of an inert tracer was simulated (Figure 2). The results were recorded and compared to experimentally collected data. In the experiments the channel was packed with enzyme-containing particles, and an inert tracer was injected through it via an HPLC-type 6-port valve. At the outlet an inline biosensor was recording the tracer concentration. The simulations and the experiments show a good agreement (Strniša et al., 2018).

A validated lattice Boltzmann model could then be further used to simulate mass transport in a “near-perfect” scaled-up microchannel, where only one dimension of the channel is increased — its width (Bajić et al., 2017). Similar simulations as above were constructed, where 3 scenarios were tested: empty space at inlet, inlet filled with biocatalytic particles, and pillars in the inlet. Unlike previously the inert tracer was supplied into the system continuously. The results (Figure 3) show that filling the inlet with particles does not create uniform flow conditions downstream, where as leaving the space empty or introducing pillars in it improves the downstream hydrodynamics. Similar simulations should be used further to determine the optimal inlet geometry, which will assure the optimal flow conditions in the microchannel.

3. Conclusions

Several studies have shown the advantages of microfluidic systems. Here it was shown how computer modelling and simulation can (or rather should) work within the research and development of such systems to optimize their performance. We now have the knowledge and technologies for building them, and the (bio)chemical industries need to recognize the potential of process intensification and miniaturization, with the consideration of new modelling approaches, such as multiscale modelling.

References

- M. Bajić, I. Plazl, R. Stloukal, P. Žnidaršič Plazl, 2017. Development of a miniaturized packed bed reactor with ω -transaminase immobilized in lentikats[®]. *Process Biochemistry* 52, 63 – 72.
- M. Lubej, U. Novak, M. Liu, M. Martelanc, M. Franko, I. Plazl, 2015. Microfluidic droplet-based liquid-liquid extraction: online model validation. *Lab on a Chip* 15, 2233—2239.
- I. Plazl, M. Lakner, 2010. Modeling and finite difference numerical analysis of reaction-diffusion dynamics in a microreactor. *Acta Chimica Slovenica* 57 (1), 100—109.
- A. Pohar, I. Plazl, 2009. Process intensification through microreactor application. *Chemical and Biochemical Engineering Quarterly* 23 (4), 537–544.
- A. Stankiewicz, J. Moulijn, 2000. Process Intensification: Transforming Chemical Engineering. *Chemical Engineering Progress* 96, 22–34.
- F. Strniša, M. Bajić, P. Panjan, I. Plazl, A. M. Sesay, P. Žnidaršič Plazl, 2018. Characterization of an enzymatic packed-bed microreactor: Experiments and modeling. *Chemical Engineering Journal* 350, 541 – 550.
- S. Succi, 2015. Lattice boltzmann 2038. *EPL (Europhysics Letters)* 109 (5), 50001.
- B. Ungerböck, A. Pohar, T. Mayr, I. Plazl, 2013. Online oxygen measurements inside a microreactor with modeling of transport phenomena. *Microfluidics and Nanofluidics* 14, 565—574.
- P. Žnidaršič Plazl, I. Plazl, 2007. Steroid extraction in a microchannel system: mathematical modelling and experiments. *Lab on a Chip* 7, 883—889.
- R. Wohlgemuth, I. Plazl, P. Žnidaršič Plazl, K. V. Gernaey, J. M. Woodley, 2015. Microscale technology and biocatalytic processes: opportunities and challenges for synthesis. *Trends in Biotechnology* 33 (5), 302 – 314.

Clustering alternative product formulations using graphs

Fernando P. Bernardo^{a*}, Javier A. Arrieta-Escobar^b

^a*GEPSI-PSE Group, CIEPQPF, Department of Chemical Engineering, University of Coimbra, Portugal*

^b*ERPI (Equipe de Recherche sur les Processus Innovatifs) - University of Lorraine - 8, rue Bastien Lepage, 54010 Nancy Cedex, France*
bernardo@eq.uc.pt

Abstract

This work proposes the use of graph partitioning tools to identify clusters in a possible large space of plausible product formulations, with each cluster representing a significantly different design alternative that deserve to be tested. The partitioning tools are used to find clusters in a large set of previously generated alternatives, and are also incorporated into a mixed-integer programming problem whose solution generates clustered alternatives (within a feasible space defined by available models and heuristics). An example of a cosmetic emulsion is provided.

Keywords: product design, formulated products, graph partitioning, cluster analysis

1. Introduction

Computer-aided design of formulated products, moreover of those having characteristic microstructural attributes, is hindered by the lack of quantitative reliable property models. It is then important to develop tools able to handle qualitative knowledge (Zhang *et al.*, 2017), including lists of often used ingredients, databases of known successful formulations, and a variety of heuristic rules regarding typical combinations of ingredients, amounts used, known effects, synergies and antagonisms. We have recently proposed a method to generate alternative product formulations, based on mixed-integer programming and using propositional logic to model heuristic rules as algebraic restrictions (Arrieta-Escobar *et al.*, 2017, 2018). The list of plausible alternatives thus generated may be long, due to acknowledged uncertainty in the assumed models and heuristics, and therefore it may not be clear what smaller subset of alternatives really deserves to be manufactured and tested.

Here, we propose the use of graph partitioning tools to identify clusters of formulations within a given space of feasible alternatives. Formulations belonging to a given cluster have a certain similarity between them and should be as dissimilar as possible to formulations belonging to other clusters. Therefore, an exploratory design of experiments should include at least one instance from each cluster. As a first contribution to this problem, the only clustering criterion here adopted is the qualitative composition of the formulation, such that similarity between formulations is defined by the number of shared components. Two subproblems are addressed: (i) to find clusters in a given, possibly large, set of alternative formulations (previously generated using e.g. integer programming and/or constructed from databases of product formulations); (ii) to simultaneously generate and cluster alternative formulations obeying to a given set of property models and heuristic constraints.

2. Matrix and graph representations of a set of product formulations

Given a set of available components, $C = \{c_1, \dots, c_{NC}\}$, a product formulation is defined by a vector y^V of binary variables, with dimension NC , indicating which components are present in the formulation, and a corresponding vector x^V of mass fractions.

Solely in terms of qualitative composition (i.e., regardless of x^V values), a set of NF alternative formulations, $F = \{f_1, \dots, f_{NF}\}$, may be represented by a list of vectors y^V organized in a matrix $Y = (y_{fc})_{NF \times NC}$, with $y_{fc} = 1$ if component c is present in formulation f , for all $c \in C, f \in F$. An equivalent representation is that of a bipartite graph $G = (C, F, E)$, with vertex sets C and F , and edge set E . Edge $f - c$ exists if and only if the corresponding matrix entry $y_{fc} = 1$. Figure 1 illustrates both matrix and graph representations.

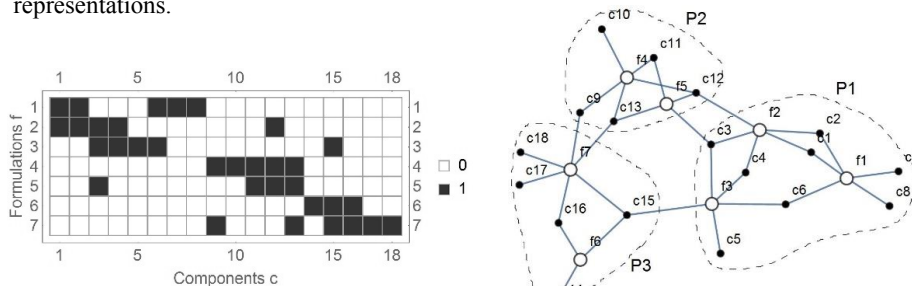


Figure 1. Matrix and graph representations of 7 product formulations (f_1 to f_7), each one having a subset of 18 possible components (c_1 to c_{18}). A partition in three clusters is shown: in the matrix, clusters correspond to diagonal blocks; in the graph, clusters are delimited by dashed lines.

3. Clustering of alternative product formulations

Given a set of product formulations F represented by a 0-1 matrix Y as above defined, the problem of partitioning F in NP clusters may be stated as: “find row and column permutations of Y in order to obtain NP diagonal blocks and minimizing the number of external elements “1” outside the diagonal blocks”. Figure 1 (left) represents a possible solution to this problem with 3 clusters corresponding to 3 diagonal blocks and 5 external elements. Cluster P_1 , for instance, has formulations f_1, f_2 and f_3 , and components c_1 to c_8 . Each external element represents a component from one cluster that is used in a formulation belonging to a different cluster, and therefore the number of external elements is a measure of similarity between clusters that should be minimized.

The same clustering is shown on graph format (Figure 1, right). The external elements of matrix Y here correspond to external edges, which are those connecting vertices located in different clusters. External edges are also designated by cut edges, since their removal decomposes the graph into NP disconnected subgraphs. For this reason, the set of external edges is designated by edge separator.

Using graph language, our problem of partitioning F in NP clusters is thus a problem of graph partitioning by edge separator (known in the graph literature as GPES): “given a set of product formulations F and its graph representation $G = (C, F, E)$, divide the graph into NP subgraphs (also designated by partitions or clusters) minimizing the number of external edges”.

Graph partitioning is a better studied problem than sparse matrix rearrangement. In addition, the latter is often solved first translating the matrix into an equivalent graph and then applying graph partitioning methods (Aykanat *et al.*, 2004). Graph partitioning is thus the basic clustering technique here used, although the representation in the matrix form is preferred for its simplicity.

The graph partitioning problem is an NP-complete combinatorial optimization problem, well studied in multiple contexts (e.g. parallel computing, sparse matrix computations, VLSI design, biological and social networks, data mining). Exact solutions using, for instance, integer programming are in practice limited to relatively small graphs with some hundreds of vertices. For larger graphs, several heuristic algorithms are available with different performances in terms of computational time/quality of solutions (Fjallstrom, 1998). Here, we use integer programming to generate and simultaneously cluster a small set F of alternative formulations (section 4), and a heuristic algorithm to find clusters in large given sets. In particular, we use the multilevel algorithm of the publicly available tool hMeTiS (Karypis and Kumar, 1998). In its simpler form, hMeTiS only requires two inputs: the number of partitions NP and the allowed difference in the cardinality of different partitions (in Karypis Lab, MeTiS is the standard tool for large graphs partitioning, but if the focus is on solution quality rather than on computational efficiency then hMeTiS is advised; hMeTiS is a tool to partition hypergraphs, which are generalization of graphs, and thus may also be applied to our relatively simple graphs G).

4. Simultaneous generation and clustering of alternative formulations

Here, we present a new optimization formulation that extends the one presented in Arrieta-Escobar *et al.* (2017, 2018), in order to solve the following problem: “find the NF most dissimilar formulations of NC components (dissimilarity in qualitative composition defined by yV), obeying to a set of product design constraints (e.g., composition, performance and cost)”. Using a graph representation, what is here being equated is how to connect two given sets of vertices (components C and formulations F) in order to obtain well defined clusters of components c around each formulation f . In other words, this is a graph partitioning problem with edges $f - c$ still to be decided and with each cluster having one and only one formulation ($NP = NF$). Further, the decision about the edges is subject to the condition that the set of edges connected to each f must define a feasible product formulation (according to the available product models).

The standard 0-1 formulation for graph partitioning is adopted (Boulle, 2004), with two sets of binary variables: $y_{fc} = 1$ if component c is chosen to be in formulation f , and $v_{fc} = 1$ if component c is located in cluster f (but not necessarily belongs to formulation f). Then, edge $f - c$ exists if and only if $e_{fc} = y_{fc} \cdot v_{fc} = 1$. The goal is to minimize the number of external edges (NEE) equal to the total number of edges (NE) minus the number of internal edges (NIE):

$$\min_{y_{fc}, x_{fc}, v_{fc}} NEE = \sum_{f,c} y_{fc} - \sum_{f,c} e_{fc} \quad (1.1)$$

$$s. t. \quad e_{fc} \leq a_{fc}, e_{fc} \leq v_{fc}, e_{fc} \geq a_{fc} + v_{fc} - 1, \forall f, c \quad (1.2)$$

$$\sum_f y_{fc} = 1, \forall f, c \quad (1.3)$$

$$v_{fc} = 0, \forall c, ord(f) = ord(c) + 1, \dots, NF \quad (1.4)$$

$$g(yV_f, xV_f, p_f) \leq 0, yV_f = \{y_{fc}, \forall c\}, xV_f = \{x_{fc}, \forall c\}, \forall f \quad (1.5)$$

$$y_{fc}, v_{fc} \in \{0,1\}, 0 \leq e_{fc} \leq 1, 0 \leq x_{fc} \leq 1 \quad (1.6)$$

Restrictions (1.2) are a linear formulation of $e_{fc} = y_{fc} \cdot v_{fc} = 1$; equations (1.3) impose that each component belongs to only one cluster; equations (1.4) are anti-degeneracy constraints (c_1 must belong to cluster f_1 , c_2 must belong either to f_1 or to f_2 , and in general c_k must belong to one of the first k th clusters); restrictions (1.5) represent the available product models, relating the composition of formulation f (vectors yV_f and xV_f) with performance metrics p_f (cost included) and imposing desired limits to these metrics. Although variables $e_{fc} \in \{0,1\}$, they may be treated as continuous due to restrictions (1.2). The decision variables are the composition of all NF formulations (y_{fc}, x_{fc}) plus the assignment of components to clusters (v_{fc}). The total number of binary variables (y_{fc} and v_{fc}) is $2NF \cdot NC$.

For a graph with NE edges, NEE is an absolute measure of the partitioning quality. When comparing solutions for graphs of different dimensions, the fraction of external edges should be used instead: $FEE = NEE/NE$.

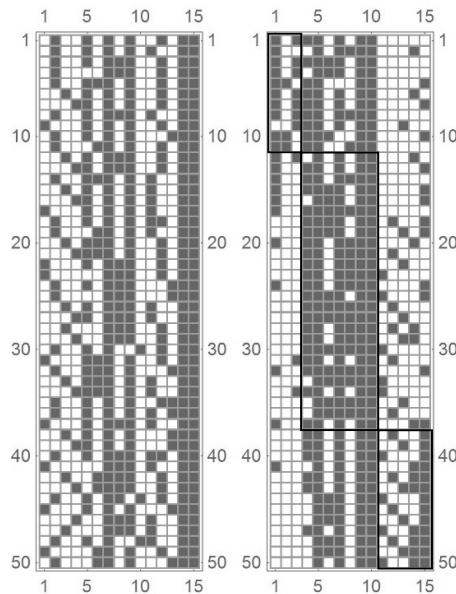


Figure 2. Set of 50 alternative formulations, before (left) and after (right) clustering. Order of components before clustering: $\{i3, i4, i5, i9, j2, j6, j7, j8, k3, k5, m1, m2, m3, r2, r3\}$. Order of components after clustering: $\{i4, k5, m3, j2, j7, j8, k3, m1, r2, r3, i3, i5, i9, j6, m2\}$. Clustering metrics: $NE = 375$, $NEE = 174$, $FEE = NE/NEE = 0.46$.

5. Example of a cosmetic emulsion

Here, the above proposed tools are applied to the example of Arrieta-Escobar *et al.* (2017, 2018). This is the formulation of a hair conditioner (which is an o/w emulsion), from an initial list of 32 possible ingredients organized in 6 subsets: emollients of type i ($i1$ to $i9$),

emollients of type j ($j1$ to $j8$), emollients of type k ($k1$ to $k7$), fatty alcohols ($m1, m2$), thickening polymers ($n1, n2, n3$) and cationic surfactants ($r1, r2, r3$). Known heuristic rules (regarding amounts and combinations of ingredients), together with models for product viscosity and greasiness index, define a space of feasible formulations of the type $g(yV, xV) \leq 0$. All optimization problems here formulated are MILP problems and were solved using GAMS/CPLEX.

Through successive solution of the problem “ $\min Cost, s. t. g(yV, xV) \leq 0$ ”, and using binary cuts to prohibit previous solutions, a rank of 50 formulations with increasing cost (only of raw-materials) is generated. These formulations (Figure 2, left) use 15 different components and have a cost between 0.884 and 0.952 USD/kg. They are then clustered using hMeTiS and with the additional constraint of a minimum of 3 components by cluster. As shown in Figure 2 (right), the result for $NP=3$ is poor, with FEE being quite large (0.46). For larger values of NP , the partitioning quality is even worse. One then concludes that, within this set F of 50 formulations, significantly different subsets of alternatives cannot be identified, which means that F is not diverse enough to there identify a reduced number of exploratory experiments.

Next, the most dissimilar NF formulations obeying to $g(yV, xV) \leq 0$ and also subject to an upper limit on cost ($Cost_f \leq Cmax, \forall f$) are generated by solving the optimization problem (1.1)-(1.6). Figure 3 and Table 1 shows results for different input values of NF and $Cmax$. Set $F1$ contains the three most dissimilar formulations within the considered design space, with only 5 external edges (corresponding to shared components $m2, r2$ and $r3$) of a total of 19, and thus a value of $FEE=5/19=0.26$.

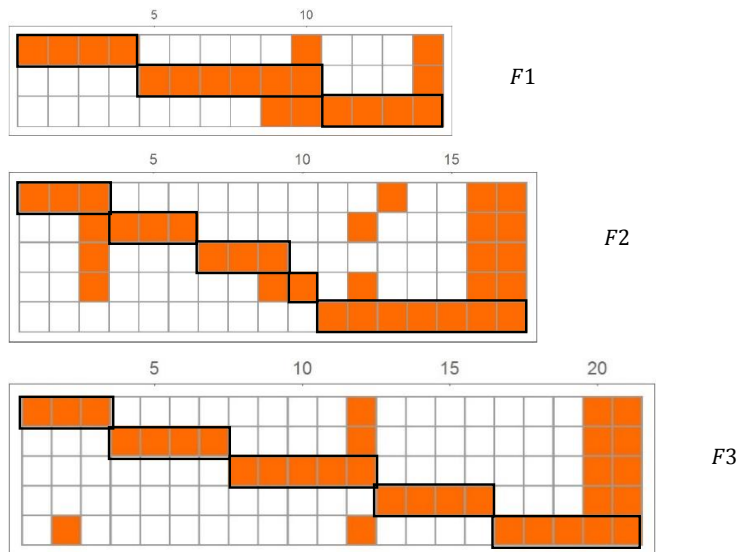


Figure 3. Sets of dissimilar formulations generated solving the optimization problem of section 4. The order of components (columns of the matrices) is shown on Table 1.

Table 1. Data regarding the sets of formulations represented in Figure 3 (C_{max} is in USD/kg).

Set	Em	C_{max}	FEE	Components
$F1$	3	1.1	0.26	{i5, j2, k3, m1, i4, j6, j7, k2, m2, r2, i9, j8, k5, r3}
$F2$	5	1.1	0.47	{i9, k5, m2, i3, j6, k6, i5, j2, k3, i4, i7, j7, j8, k2, m1, r2, r3}
$F3$	5	1.3	0.36	{i2, j2, k5, i3, j1, j7, k6, i4, j5, j8, k4, m2, i9, j6, k2, m1, i5, j4, k3, r2, r3}

Table 2. Data regarding set $F3$. Cost is $C_{max}=1.3$ USD/kg for all formulations.

Formulation	Emollients	Emollients mass percentage
f_1	i2, j2, k5	1.3, 2.8, 1.9; Total = 6.0%
f_2	i3, j1, j7, k6	2.0, 1.5, 1.5, 1.0; Total = 6.0%
f_3	i4, j5, j8, k4	1.1, 1.0, 2.9, 1.0; Total = 6.0%
f_4	i9, j6, k2	1.9, 2.7, 1.5; Total = 6.1%
f_5	i5, j4, k3	2.3, 1.7, 1.0; Total = 6.0%

Keeping C_{max} at the same level and increasing NF to 5, one obtains set $F2$ that uses more components but has less dissimilar formulations ($FEE=0.47$). Relaxing C_{max} to 1.3 USD/kg, the more diverse set $F3$ is obtained, with FEE decreasing to 0.36. Additional data regarding set $F3$ is given in Table 2. For other input values of NF and C_{max} , the same tendency is observed: a more diverse set of alternatives (low value of FEE) come at the price of more expensive formulations.

6. Conclusions

The proposed graph representation and graph partitioning tools are able to identify significantly different alternatives within a space of plausible product formulations (possible large due to uncertain models and heuristics) and thus may be very useful to design an exploratory set of experiments or to build different product lines from a given set of ingredients. Several extensions and refinements of the proposed tools are still to be done, namely the use of additional clustering criteria apart from qualitative composition of the formulation, which was the only one here considered.

References

- J.A. Arrieta-Escobar, F.P. Bernardo, A. Orjuela, M. Camargo, L. Morel, 2017, An Integrated Methodology for Emulsified Cosmetic Product Formulation Using Integer Programming with Logical Constraints, in: A. Espuña, M. Graells, L. Puigjaner (Eds.) ESCAPE-27, Computer-Aided Chemical Engineering, Elsevier, Amsterdam, 985-990.
- J.A. Arrieta-Escobar, F.P. Bernardo, A. Orjuela, M. Camargo, L. Morel, 2018, Incorporation of heuristic knowledge in the optimal design of formulated products: Application to a cosmetic emulsion, *Comput. Chem. Eng.*, In press.
- C. Aykanat, A. Pinar, Ü.V. Çatalyürek, Permuting sparse rectangular matrices into block-diagonal form, 2004, *SIAM J. Sci. Comput.*, 25, 1860-1879.
- M. Boulle, Compact Mathematical Formulation for Graph Partitioning, *Optimization and Engineering*, 5 (2004) 315-333.
- P.-O. Fjällström, Algorithms for graph partitioning: a survey, *Linköping Electronic Articles in Computer and Information Science*, 3 (1998).
- G. Karypis, V. Kumar, hMeTiS. A Hypergraph Partitioning Package. Version 1.5.3, in: Department of Computer & Engineering, University of Minnesota, 1998.
- L. Zhang, K.Y. Fung, X. Zhang, H.K. Fung, K.M. Ng, 2017, An integrated framework for designing formulated products, *Comput. Chem. Eng.*, 107, 61-76.

Recent Advances in Graph-Based Abstractions for Modeling and Simulating Complex Systems

Jordan Jalving^{a,b} and Victor Zavala^{a,*}

^a*Department of Chemical and Biological Engineering, University of Wisconsin-Madison, 1415 Engineering Dr, Madison, WI 53706, USA*

^b*Decision and Infrastructure Sciences Division, Argonne National Laboratory, 9700 South Cass Ave, Lemont, IL 60439, USA*

victor.zavala@wisc.edu

Abstract

Current graph-based approaches for modeling, simulation and optimization of complex cyber-physical systems have motivated the development of new graph-based abstractions. We propose an algebraic graph to represent physical connectivity in complex optimization models and a computing graph to capture computational aspects of cyber/control architectures. The algebraic graph facilitates the analysis and decomposition of optimization problems and the computing graph enables the simulation of optimization and control algorithms in virtual distributed environments. The proposed abstractions are implemented in a Julia software package called `Plasmo.jl`.

Keywords: cyber-physical, structured modeling, complex systems, decomposition

1. Introduction

Modeling and simulating cyber-physical systems is becoming increasingly important, but capturing interdependencies between cyber and physical systems in a coherent manner is technically challenging. Physical systems (such as chemical processes) can be driven by control systems, which in turn are cyber systems comprised of computing devices (e.g. sensors, controllers, actuators) that execute tasks (e.g., data processing, control action computation) and that exchange information (e.g., measurements and control actions) through a communication network. Physical systems are expressed mathematically in the form of *algebraic models* while cyber systems are expressed in the form of *algorithms* which are often executed under heterogeneous computing architectures that exhibit complex communication protocols.

This work discusses newly proposed *graph-based* abstractions that facilitate modeling and simulation of cyber-physical systems. Graph-based modeling approaches have appeared in various engineering applications. Preisig (2007) used graph-theoretic approaches to perform on-line mass and energy balancing in large-scale plants given incomplete sensor data. Couenne et al. (2007) presented bond-graph modeling for chemical engineering applications and highlighted the advantages of model encapsulation and re-use. Elve and Preisig (2018) recently applied graph-based concepts to develop a process simulator with automatic code generation capabilities.

In this work we analyze the concept of an *algebraic model graph* that facilitates the im-

plementation and solution of physical systems and the concept of a *computing graph* that facilitates simulation of cyber systems. The graph abstractions exploit *physical and communication topology* to facilitate model construction, data management, and analysis. Both abstractions are implemented in the Julia package `Plasmo.jl` (<https://github.com/zavalab/Plasmo.jl>).

2. Algebraic Graphs

Here we present a **model graph** abstraction to represent complex optimization models found in physical applications. A model graph $\mathcal{MG}(\mathcal{N}, \mathcal{E})$ is a *hypergraph* wherein each node $n \in \mathcal{N}(\mathcal{MG})$ has an associated component optimization model of the form:

$$\min_{x_n \in \mathcal{X}_n} f_n(x_n). \quad (1)$$

where x_n are decision variables, $\mathcal{X}_n := \{x \mid c_n(x) \geq 0\}$ is the feasible set with associated constraint vector mapping $c_n(\cdot)$, and the mapping $f_n(\cdot)$ is a scalar objective function.

Coupling is captured between component models using *link constraints*. In particular, we consider linear linking constraints of the form:

$$\sum_{n \in \mathcal{N}(e)} \Pi_{e,n} x_n = 0 \quad e \in \mathcal{E}(\mathcal{MG}). \quad (2)$$

where $e \in \mathcal{E}(\mathcal{MG})$ are the hyperedges of the model graph and $n \in \mathcal{N}(e)$ is the set of nodes that support hyperedge e . The matrix $\Pi_{e,n}$ corresponds to the coefficients of the linking constraints between edge e and node n .

We can represent hierarchical optimization structures using subgraphs as shown in Figure 1. A model graph can contain an arbitrary number of subgraphs by defining $\mathcal{SG}(\mathcal{MG}_0)$ (with elements \mathcal{SG}) as the set of subgraphs defined on the parent model graph \mathcal{MG}_0 . This allows us to express the model graph in the form of Equation 3.

$$\min_{x, \mathcal{MG}_0} \sum_{n \in \mathcal{N}(\mathcal{MG}_0)} f_n(x_n) \quad (\text{Graph objective function}) \quad (3a)$$

$$\text{s.t. } x_n \in \mathcal{X}_n, \quad n \in \mathcal{N}(\mathcal{MG}_0) \quad (\text{Local node constraints}) \quad (3b)$$

$$\Pi_{\mathcal{MG}_0} x_{\mathcal{MG}_0} = 0 \quad (\text{Graph link constraints}) \quad (3c)$$

$$\Pi_{\mathcal{SG}} x_{\mathcal{SG}} = 0 \quad \mathcal{SG} \in \mathcal{SG}(\mathcal{MG}_0) \quad (\text{Subgraph link constraints}) \quad (3d)$$

Graph models provide structural information which facilitates decomposition and model management. For example, Formulation (3) has a partially separable structure because eliminating the linking constraints (3c and 3d) results in a fully separable problem. These problems can be solved using Schur decomposition schemes such as done in Chiang et al. (2014). It is also possible to aggregate the nodes in a model graph and into a traditional optimization form which can be solved with an off-the-shelf solver such as Ipopt (Wächter and Biegler (2006)). The graph structure also allows one to produce decompositions using graph analysis techniques such as partitioning and community detection (Tang et al. (2017)).

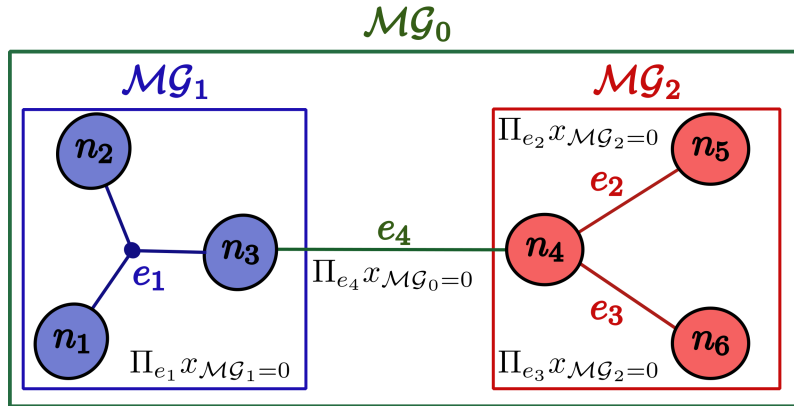


Figure 1: A model graph with two subgraphs. \mathcal{MG}_1 contains three nodes (n_1, n_2, n_3) and one linking constraint (e_1). \mathcal{MG}_2 contains three nodes (n_4, n_5, n_6) and two linking constraints (e_2 and e_3). \mathcal{MG}_0 is the top layer of the graph containing all six nodes and connects the two subgraphs with a single linking constraint between nodes n_3 and n_4 (e_4).

3. Computing Graphs

Simulating a cyber system requires capturing real-time computing aspects such as latency, failures, and asynchronicity. To approach these challenges, we introduce the **computing graph** which is a directed multi-graph that we denote as $\mathcal{CG}(\mathcal{N}, \mathcal{E})$ and that contains a set of nodes $\mathcal{N}(\mathcal{CG})$ which execute tasks and edges $\mathcal{E}(\mathcal{CG})$ which communicate attributes to other nodes.

In a computing graph, A node $n \in \mathcal{N}(\mathcal{CG})$ contains a set of *attributes* \mathcal{A}_n and tasks \mathcal{T}_n and an edge $e \in \mathcal{E}(\mathcal{CG})$ contains a pair of attributes \mathcal{A}_e which it communicates between supporting nodes $\mathcal{N}(e)$. The attributes \mathcal{A}_n represent data and tasks \mathcal{T}_n are computations that operate with and/or change attributes. Tasks require execution time $\Delta\theta_t$ and edges involve communication delay $\Delta\theta_e$. Under the proposed abstraction, computing and communication can be synchronous (a task is not executed until all attributes are received) or asynchronous (a task is executed with current values). This enables capturing a wide range of behaviors seen in cyber-system applications.

A simple computing graph is depicted in Figure 2. Each node contains a single task which operates on its attributes x, y , and z as input and updates one of their values. The nodes communicate attribute values with each other using six edges. For example, attribute y is communicated to both nodes n_2 and n_3 which updates the value of y on these respective nodes. The superscript $+$ means that attributes are updated after a given time which captures computing and communication delays.

The computing graph differs from the model graph abstraction in that it contains a dynamic component (a task) while a node in a model graph contains a static component (a model). Moreover, edges in a computing graph connect attributes while edges connect algebraic variables in a model graph. We highlight that the *solution* of a model graph is a computing task and we can thus use model graphs in individual nodes of the computing graph. This greatly facilitates simulating the behavior of cyber-physical systems.

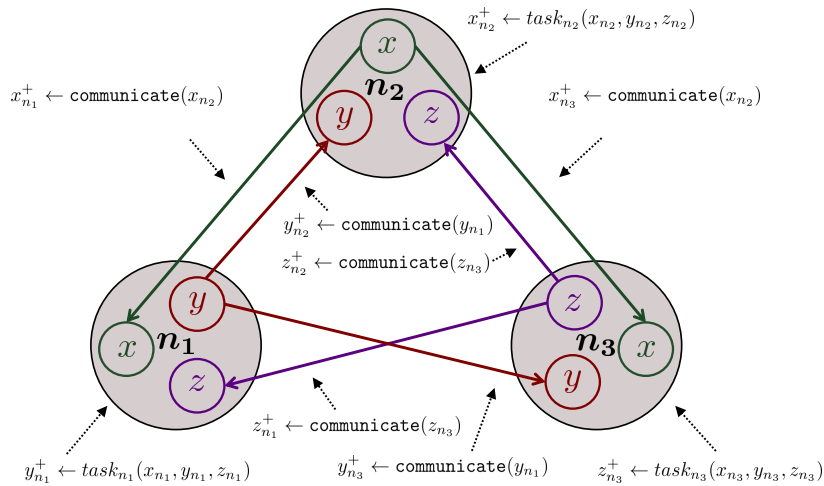


Figure 2: Depiction of a computing graph with three nodes and six edges. Node n_1 computes $task_{n_1}$ using the data attributes (x, y , and z) and updates the value of attribute y . Similarly, node n_2 computes $task_{n_2}$ and updates attribute x , and node n_3 computes $task_{n_3}$ and updates attribute z . Attribute values are communicated between nodes using edges.

4. Case Study: Evaluating Control Architectures

This case study demonstrates how a model graph can be used to formulate and solve an optimal control problem for a dynamic physical system and how solving the model graph can be embedded in a computing graph to evaluate various distributed control architectures subject to real-time latency (i.e., computation and communication times). We consider a reactor-separator system (see Figure 3) from Stewart et al. (2010) which is a standard for evaluating distributed model predictive control.

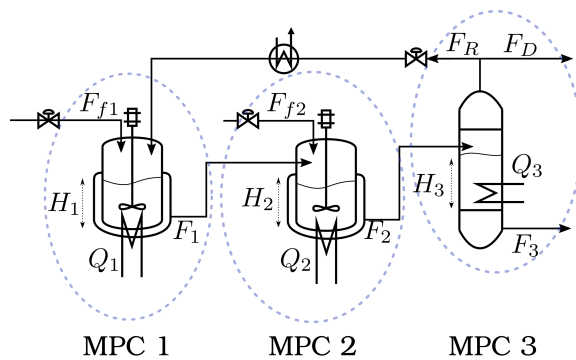


Figure 3: Reactor separator process. The control can be decomposed into 3 MPC controllers.

We first create a model graph using `Plasmo.jl` for the process in Figure 3 using three nodes. Two nodes contain optimization models to track reactor setpoints, and the other node contains a model to track the separator setpoints. The three nodes are linked together using algebraic *link constraints* which represent the flows that couple the systems together.

The process is simulated using the computing graph for three different control architec-

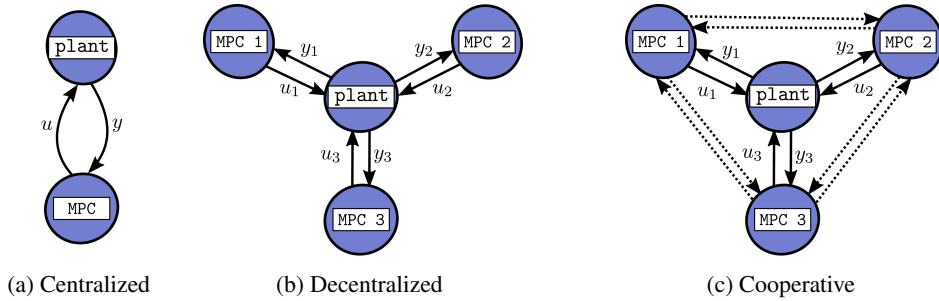


Figure 4: Simulated control architecture topologies. (Left): Centralized control. (Middle): Decentralized Control. (Right): Cooperative Control

tures. We simulate a *centralized* model predictive control (MPC) architecture wherein a central MPC controller calculates all inputs for the process. To do so, we solve the entire model graph as a single MPC node in the computing graph (Figure 4a) and use another computing node to simulate and advance the state of the plant.

We also decompose the process into three MPC controllers and simulate a *decentralized* control architecture wherein controllers do not communicate (Figure 4b) and a *cooperative* architecture (Figure 4c) such that controllers share state and intended control trajectories. For these cases, the nodes in the computing graph (MPC1, MPC2, and MPC3) compute tasks which solve and update the individual model nodes we defined in the model graph. We highlight that the computing graph captures the *asynchronous* behavior of the decentralized and cooperative schemes. Because we account for real computation times, the controllers inject their inputs when they finish their computation as opposed to all at the same time.

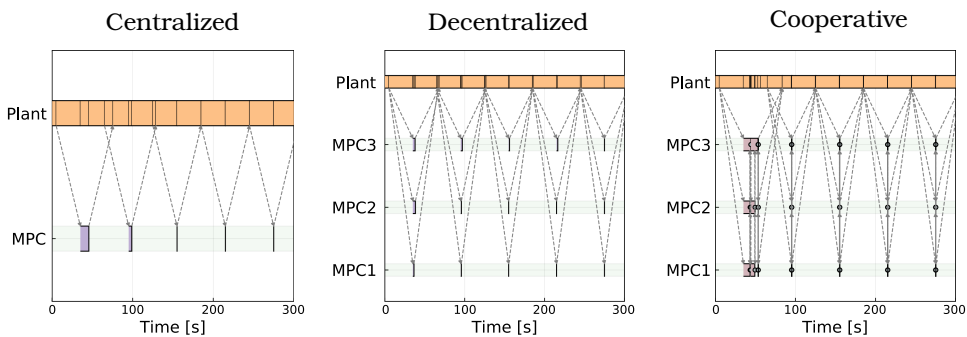


Figure 5: Communication pattern for each simulated MPC architecture

Figure 5 presents communication and computation patterns for each MPC algorithm. The centralized MPC pattern shows the communication delays between the plant and the controller (grey arrows), the time required to compute the control action (the purple bar), and highlights how the plant state advances continuously while computation and communication tasks execute. Despite the delays enforced for the controller, centralized MPC is able to drive the state to the setpoint (as shown in Figure 6). Decentralized MPC does

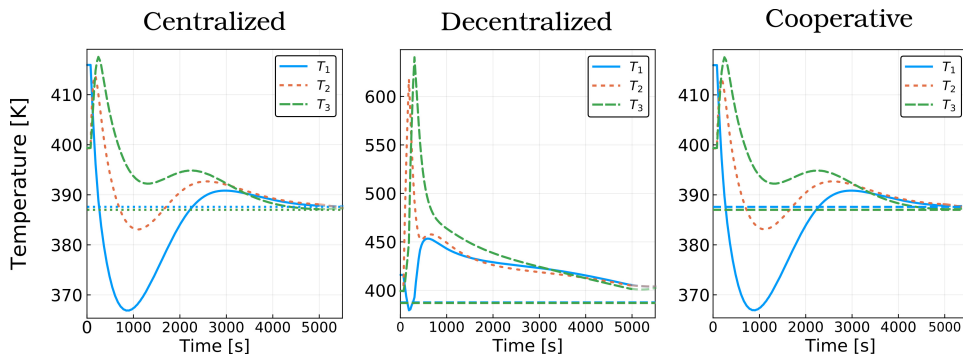


Figure 6: Temperature evolution for each simulated MPC architecture

not require communication between controllers which decreases computing times, but we observe that the setpoint cannot be reached. Finally, cooperative MPC shows a more complex communication pattern but we observe that this mimics the performance of centralized MPC.

5. Conclusions

We have presented graph-based abstractions that facilitate modeling complex cyber-physical systems. We showed how a model graph abstraction facilitates modeling complex physical systems and how a computing graph enables simulating computational behaviors. We provided a case study using the package `Plasmo.jl` that demonstrates how these abstractions can be used to evaluate distributed computing architectures.

6. Acknowledgements

This material is based on work supported by the U.S. Department of Energy (DOE), Office of Science, under Contract No. DE-AC02-06CH11357. This work was also partially supported by the U.S. Department of Energy grant DE-SC0014114.

References

- N. Chiang, C. G. Petra, V. M. Zavala, 2014. Structured Nonconvex Optimization of Large-Scale Energy Systems Using PIPS-NLP. 2014 Power Systems Computation Conference, 1–7.
- F. Couenne, C. Jallut, L. Lefevre, Y. Le Gorrec, B. Maschke, 2007. Basis for bond-graph modeling in chemical engineering. *Computer Aided Chemical Engineering* 24, 69–74.
- A. T. Elve, H. A. Preisig, 2018. From Process Graph to Process Simulation with Proper Model Documentation. *Computer Aided Chemical Engineering* 43, 235–240.
- H. A. Preisig, 2007. A Graph-Theory-Base Approach to the Analysis of Large-Scale Plants. *Computer Aided Chemical Engineering* 24, 81–86.
- B. T. Stewart, A. N. Venkat, J. B. Rawlings, S. J. Wright, G. Pannocchia, 2010. Cooperative distributed model predictive control. *Systems and Control Letters* 59 (8), 460–469.
- W. Tang, A. Allman, D. B. Pourkargar, P. Daoutidis, 2017. Optimal decomposition for distributed optimization in nonlinear model predictive control through community detection. *Computers & Chemical Engineering* 111, 43–54.
- A. Wächter, L. T. Biegler, 2006. On the implementation of an interior-point filter line-search algorithm for large-scale nonlinear programming. *Mathematical Programming* 106 (1), 25–57.

Synthesis technology for failure analysis and corrective actions in process systems engineering

Ákos Orosz^a, Ferenc Friedler^{b,*}

^a*Department of Computer Science and Systems Technology, University of Pannonia, Veszprém H-8200, Hungary*

^b*Institute for Process Systems Engineering & Sustainability, Pázmány Péter Catholic University, Budapest H-1088, Hungary*
friedler.ferenc@ppke.hu

Abstract

The ever increasing complexity of processing systems and the requirements to be satisfied by the processes make process design and process operation more and more complex. Because of that, the reliability/availability is to be taken into account together with other requirements in process design/synthesis. Similarly, failure analysis is also an important part of process operation. In the current work, it has been shown that in addition to the widely used unit level redundancy, process level redundancy must also be considered in synthesizing a process for satisfying high level availability. Therefore, in case of failure, the determination of the best corrective action must be based on more general process networks than considered before. The proposed procedure determines the best or n-best corrective actions for the most general types of highly complex process networks, e.g., including process level redundancy. The P-graph based procedure is effective in generating corrective action suitable for industrial processes.

Keywords: process synthesis, process availability, failure analysis, corrective action.

1. Introduction

Availability, the rate of operability, is an important indicator of a process since it directly influences the profitability. A high level availability can usually be achieved if redundancy is built in the process. If this is the case, the failure of an equipment unit of the process does not necessarily mean that the process becomes non-operational. To keep the process operational in an event of failure of equipment units, a corrective action is to be done. Since a process may have a large number of alternative feasible operating modes with different operating costs, the determination of the corrective action should be systematic and based on optimization if possible.

Corrective actions are, especially, widely used in power distribution networks. Because of the need of an almost immediate action, decisions are usually based on heuristics and genetic algorithms with no guarantee of the optimality. Ela and Spea (2009) applied genetic algorithms to minimize the losses in transmission lines. Korad and Hedman, (2013) developed a hybrid method for taking into account uncertainties in determining the corrective switching action.

Distefano and Puliafito (2007) solved computer system failure problem by two different approaches, one is based on reliability block diagram and the other on fault tree analysis. Though the results were similar for them, the typical issue is that the mathematical model is not generated algorithmically for either method. Goel et al. (2002) simultaneously considered availability and profitability in synthesizing a

chemical process in a mixed integer programming model. The method considers only specific flowsheets, e.g., no redundancy is allowed in the flowsheet of the synthesized process.

Stated formally, if an equipment unit is capable of performing its designated job on a sufficient level, it is called as functional, otherwise, non-functional. Similarly, an operating unit is functional if there are functional equipment units assigned to this operating unit that can perform the transformation identified by the operating unit.

A process is operational if it is capable of generating all products in the required amounts and qualities. An operational process may have several different modes of operations, i.e., the operation can be performed under different process networks. The best of the operating modes is called as on-design operation, all the others are the off-design operations. The mode of operations that is currently working is called as active operating mode. Not necessarily all functional equipment units assigned to the operating units of an active operating mode are in service, consequently, the equipment units of this operating mode can be either active or non-active.

For practical reason, the procedure for determining the corrective action must systematically satisfy the following four criteria:

- (i) Keep the system operational as far as it is possible;
- (ii) Keep the operating cost of the selected operating mode as low as possible, i.e., it is based on optimization;
- (iii) Robust, i.e., it determines the corrective action for any possible flowsheet;
- (iv) Generates the corrective action promptly.

To fulfil criterion (iii), the types of flowsheets (networks) that can appear in a real process must be determined first. For example, Goel et al (2002) considered redundancy free flowsheets. However, if redundancy is allowed, the most common redundancy is realized on operating unit level, i.e., more than one equipment unit is established for an operating unit. The basic question now is if this operating unit level redundancy covers all possible options or more general types of redundancies are to be considered.

The flowsheet or network of a process is determined during its synthesis. Thus, the types of networks to be considered in making a corrective action depend on the possible flowsheets (networks) that can be the result in synthesizing a process. An example, Example 1, will illustrate that unit level redundancy does not necessarily cover all important cases for optimal decision.

In practice, the network of the most preferred processes are usually complex, highly interconnected involving several loops. There are two types of optimization tools for process design in terms of structure representation, implicit, e.g., mathematical programming approaches and explicit, e.g., the P-graph framework. Methods with explicit structure-representation provide additional opportunities on structural properties of process networks including an appropriate interface to failure analysis and to develop systematic method for determining the optimal corrective action. The P-graph framework (see, e.g., Peters et al, 2003) is formulated by combinatorial mathematics, based on the five axioms of feasible process networks and includes combinatorial algorithms, e.g., for synthesizing processes. There is a close relation between the process feasibility in process synthesis and the process operability in failure analysis, since the axioms are valid for both. Therefore, these two types of requirements can be considered simultaneously without compromising any of them. A P-graph is a directed graph and it represents the process network by two types of vertices, i.e., dots for materials and horizontal bars for operating units. Software implementations of the main algorithms are available at www.p-graph.org.

2. Structural redundancy in a process

A processing system is termed as redundancy-free, if the failure of any of its equipment units makes the system non-operational. Because of the high level of requirements on the availability, in most cases, redundancy free systems are not acceptable, redundant systems are to be designed. The redundancies in the process are determined during its synthesis. The availability of a redundancy-free system is simply the product of the availability indicators of the equipment units. The determination of the availability for systems with redundancies is complex both in theory and applications. Since the availability of a processing system can be determined similarly to its reliability, an available method can be applied for that (Kovacs et al., 2018).

Frequently, designing a process with unit-level redundancy satisfies the system's availability requirement, and has been widely used in practice. However, this doesn't necessarily give rise to the optimal process for simple reasons. The off-design operations are performed only a short period of time compared to the on-design operations. It is quite possible that the flowsheet (network) of the off-design operation is different from that of the on-design operation. For example, in total site system, there can be other resources of the intermediate products with possibly higher cost against reduced investment requirements. Another type of process level redundancy is shown in the following example where the synthesis procedure is also given in determining the optimal process.

Example 1

Figure 1 shows the maximal structure (super-structure) of a synthesis problem for producing material A, it is also supposed that the availability of the process must be at least 0.999. Figure 2 shows the optimal process with 9,312 USD/y cost, it is a redundancy free solution. The availability of this process, 0.989, does not satisfy the requirement, and there is no other redundancy free solution with the required availability. Thus, redundancy must be considered during synthesis. On Figure 3, the maximal structure is shown with assigning double equipment units to each operating unit. Figure 4 shows the cost optimal process synthesized by simultaneously taking into account the availability constraint (Kovacs et al, 2018). Bold lines give the on-design operating mode and the thin lines represent the spare part of the system. Note that the optimal solution is based on process level redundancy. Consequently, optimality can only be guaranteed if process level redundancy is taken into account in process synthesis under availability constraint. Furthermore, methods for generating optimal corrective actions must consider flowsheets (networks) with no structural limitations.

3. Systematic procedure for corrective actions in case of failure

The procedure for determining the corrective action in an event of failure is based on P-graph synthesis tools, it is called as procedure CAF. It is supposed that the flowsheet of the process is given in the form of a P-graph. Let the mathematical model of each operating unit with its cost function, the unit cost of each raw material, and the demand of each product be given. If for a running process one or more equipment units become non-functional, their identifiers are assumed to be available immediately for the CAF procedure.

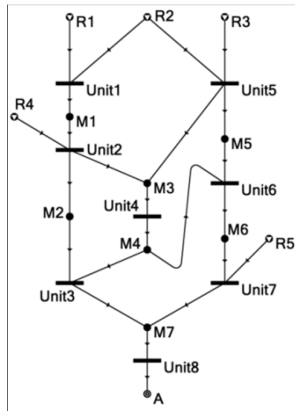


Figure 1. Maximal structure of a process synthesis problem

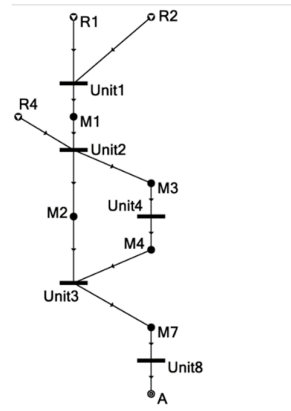


Figure 2. Network of the optimal solution of process synthesis problem given on Figure 1, availability requirement is violated

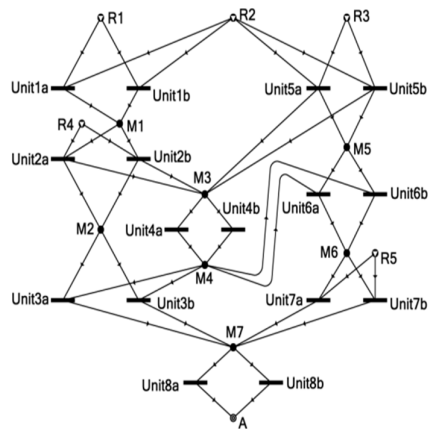


Figure 3. Maximal structure of process synthesis problem given in Figure 1 with redundant equipment units

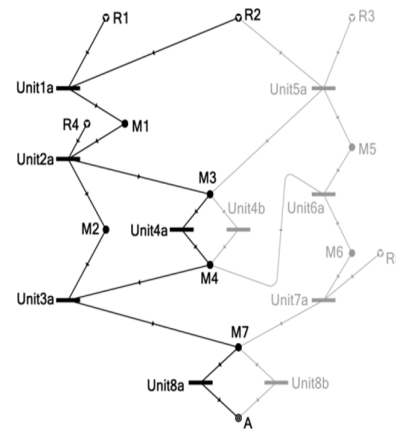


Figure 4. The network of optimal solution of process synthesis problem given on Figure 3 satisfying the availability requirement (bold lines indicate the on-design operating mode)

First, algorithm MSG (Friedler et al., 1993) determines if the remaining functional equipment units may compose a structurally feasible process. In case of negative answer, the procedure halts, there is no feasible operating mode on the basis of the functional equipment units. Otherwise, algorithm ABB (Friedler et al., 1996) is executed to determine the optimal operating mode, if there is one. Note that a structurally feasible process is usually feasible, but not necessarily. Algorithm ABB is a branch&bound type algorithm, the bounding part can be linear or nonlinear depending on the mathematical models of the operating units. The algorithm is also able to give the n-best solutions in addition to the optimal one. Note that algorithms MSG and ABB are available at www.p-graph.org.

Example 2

One product, PMM (Perchloromethyl mercaptan), is produced by a processing system of 16 available operating units from 9 available raw materials. Each operating unit is realized by one equipment unit. The network of a process that includes process level redundancy is shown on Figure 5. The mathematical models of the operating units in this example are linear, they are available at www.p-graph.org/case-study-pmm. There are 24 feasible operating modes producing the product. The best of them in terms of cost is shown on Figure 6, it is considered as the on-design operating mode with the cost of 3,144,010 USD/y.

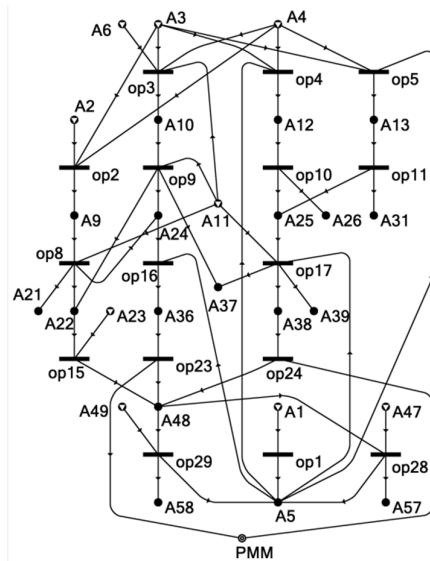


Figure 5. A process with process level redundancy for producing material PMM

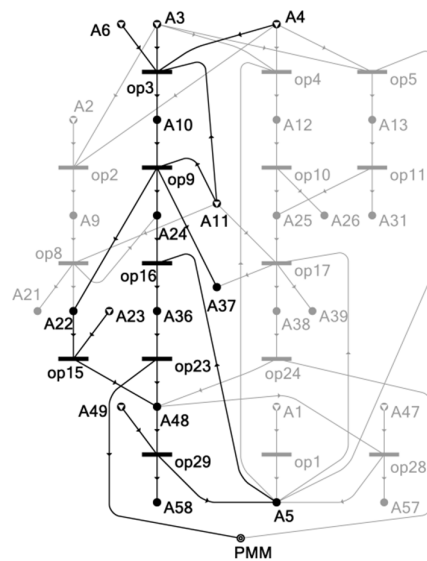


Figure 6. Bold lines indicate the on-design operating mode of production PMM (cost: 3,144,010 USD/y)

Suppose that equipment unit that realizes operating unit op29 fails, then, the number of feasible operating modes is reduced to 12. Figure 7 shows the optimal operating mode under this condition, the cost of operation is increased to 3,228,140 USD/y.

If equipment units op9 and op16 fail simultaneously as a possible consequence of cascading effect, there are 8 remaining feasible operating mode, the optimal of them is shown on Figure 8, its cost is 3,819,490 USD/y. If both equipment units op16 and op17 fail, the process becomes non-operational, as no feasible operating mode exists.

4. Conclusions

It has been shown that process level redundancy must also be considered in process synthesis for optimally satisfying high level availability. Because of that, the corrective action in an event of failure must be prepared for a more general network redundancy. The procedure developed here keeps the process operational as far as it is possible, determines the most cost effective corrective operating mode practically promptly for any possible process network.

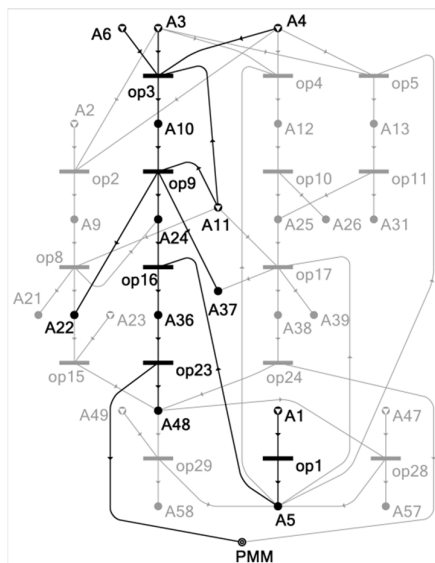


Figure 7. The optimal operating mode in case of failure of equipment unit op29 (cost: 3,228,140 USD/y)

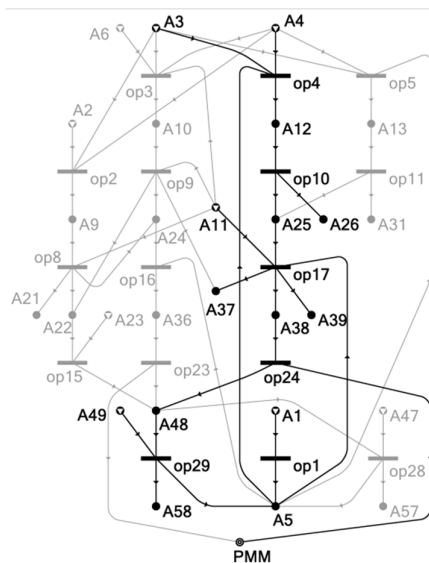


Figure 8. The optimal operating mode in case of failure of equipment units op9 and op16 (cost: 3,819,490 USD/y)

References

- S. Distefano, A. Puliafito, 2007, January. Dynamic reliability block diagrams vs dynamic fault trees, In Reliability and Maintainability Symposium, RAMS'07. Annual, pp. 71-76, IEEE
- A.A.A.E. Ela, S.R. Spea, 2009, Optimal corrective actions for power systems using multi-objective genetic algorithms, *Electric Power Systems Research*, 79(5), pp.722-733
- F. Friedler, K. Tarjan, Y.W. Huang, L.T. Fan, 1993, Graph-theoretic approach to process synthesis: polynomial algorithm for maximal structure generation, *Computers & Chemical Engineering*, 17(9), pp.929-942
- F. Friedler, J.B. Varga, E. Feher, L.T. Fan, 1996, Combinatorially accelerated branch-and-bound method for solving the MIP model of process network synthesis, In State of the art in global optimization, pp. 609-626, Springer, Boston, MA.
- H.D. Goel, J. Grievink, P.M. Herder, M.P. Weijnen, 2002, Integrating reliability optimization into chemical process synthesis, *Reliability Engineering & System Safety*, 78(3), pp.247-258
- A.S. Korad, K.W. Hedman, 2013, Robust corrective topology control for system reliability, *IEEE Transactions on Power Systems*, 28(4), pp.4042-4051
- Z. Kovacs, A. Orosz, F. Friedler, 2018, Synthesis algorithms for the reliability analysis of processing systems, *Central European Journal of Operations Research*, <https://doi.org/10.1007/s10100-018-0577-0>
- M.S. Peters, K.D. Timmerhaus, R.E. West, 2003, *Plant design and economics for chemical engineers*, McGraw-Hill, New York
- <http://www.p-graph.org>

Acknowledgment

Supports of the Pázmány Péter Catholic University under KAP Project and University of Pannonia under EFOP-3.6.1-16-2016-00015 project are acknowledged.

Spatio-Temporal Control of Nutrient Pollution from Organic Waste

Yicheng Hu^a, Gerardo Ruiz-Mercado^b and Victor Zavala^{a*}

^a*Department of Chemical and Biological Engineering, University of Wisconsin-Madison, 1415 Engineering Drive, Madison 53706, USA*

^b*National Risk Management Research Laboratory, U.S. Environmental Protection Agency, 26 W. Martin Luther King Drive, Cincinnati 45268, USA*

victor.zavala@wisc.edu

Abstract

Better management of anthropogenic organic waste and other primary sources of nutrient pollution such as agricultural, municipal, and industrial waste, will reduce the human impact on the environment. Harmful algal blooms (HABs) are a major environmental impact from organic waste and nutrient pollution. HABs can pose severe threats to human health due to the release of dangerous toxins in fresh or marine water that can negatively affect public health, increase treatment costs for drinking water, and cause enormous economic loss in industries that depend on clean water. In this study, the effect of decisions made in the organic waste supply chain (SC) on reducing the potential for HABs is investigated by integrating three types of models: a SC optimization model, a nutrient transport model, and an algae growth model. This contribution presents a comprehensive spatio-temporal management strategy for short-term HAB reduction by adjusting components in the SC, including technologies, logistics, nutrient management plans (NMPs) or environmental costs, and seasonal waste storage planning. In addition, it is presented a case study of the Upper Yahara Watershed in the State of Wisconsin to illustrate the practicability of this modeling framework.

Keywords: supply chain, nutrient pollution, spatial-temporal control, harmful algal blooms

1. Introduction

The role of nutrient pollution (specifically nitrogen and phosphorous) is central to the underlying causes of HABs. Sources of nutrient pollution are classified as either non-point source or point source. Non-point sources include agricultural land, stormwater etc., and the point sources include permitted facilities, e.g. wastewater treatment plants (WWTPs). Complex point and non-point nutrient management strategies will be required to achieve a more comprehensive and permanent solution to controlling the nutrient pollutions. The increasing rate of HAB development is a complicated problem faced by human populations around the world. Algal species involved in a HAB can generate significant levels of toxins threatening public health. According to Heisler et al. (2008), HABs have economic impacts in the form of remediation costs for water treatment and reduction in property value of the impacted areas. Graham et al. (2009) estimated that 30% of lakes from 36 states in the US have reported toxic cyanobacterial bloom issues. The US Environmental Protection Agency (US EPA) reported the tourism losses of one billion dollars annually

and commercial fishing losses on the order of tens of millions of dollars annually ¹.

By designing an appropriate transportation network for organic matter and incorporating technology placement for treatment and processing, the nutrients in organic waste can be more efficiently recycled for agricultural use in the growth of crops, feeding of grazing animals, and ultimately for human benefit. However, from Zandi Atashbar et al. (2018), current sustainable SC design studies typically incorporate metrics such as global warming potential and eutrophication potential which measure the chronic environmental impacts. Yet, the effects of seasonal variations in nutrient loading must be considered. Therefore, an extended modeling framework is needed to better describe the explicit environmental consequences caused by decisions made in the organic waste SC design.

In this work, we apply, adapt, and combine multiple types of modeling tools, including a SC design model, a nutrient transport model, and an algae growth model to create an optimization framework that analyzes the effect of nutrient controlling strategies in SCs on HABs. We present a case study in the Upper Yahara Watershed in the State of Wisconsin.

2. Modeling Framework

In this section, we introduce a modeling framework to connect the decision-making and control strategies in the SC with the environmental consequence of HABs. The modeling structure is shown in Figure 1.

Algae growth shows seasonal dependence, and this is because its growth is affected by water temperature, sunlight, nutrient concentration, and other factors. Steady-state modeling will not adequately capture the impact of seasonality, nor will models with large time steps (e.g. annual based decision making). For example, nutrient leaching in cold months will raise the probability of HABs in the spring. Therefore, management and prevention actions must be taken in advance, but there is still ambiguity about the optimal lead time for actions to be effective. The models for algae growth, nutrient transport, and SC, all have an explicit time dependence.

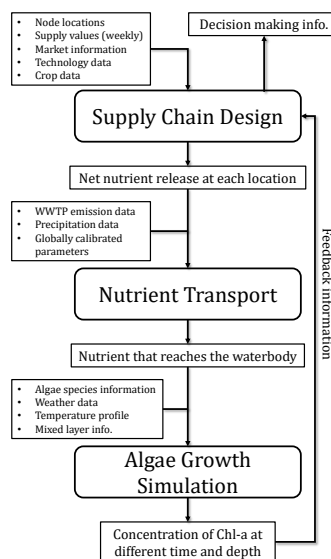


Figure 1: Modeling structure

2.1. Supply Chain Model

We extend the supply chain framework from Sampat et al. (2017) and Hu et al. (2018). The SC model is a constrained dynamic optimization model, which takes the input of node locations (e.g., dairy farms), the weekly supply amount of organic waste, market information including demand amount and price for each product, technology data (yield factors, investment and operational costs), and crop data, such as the crop type, yield, growing season, and nutrient uptake rate.

¹<https://www.epa.gov/nutrientpollution/effects-economy>

The SC structure is shown in Figure 2. The farms can send organic waste to transportation sites to process it, storage systems to store it temporarily, or directly apply it to agriculture lands. The value-added products from technologies can be purchased by external customers. The main decision variables in the model are transportation flows, inventory levels, installation of technologies and storage systems, and amount of commercial fertilizers applied. The SC model can also output the amount of applied organic waste, which can be fed into the nutrient transport model to support runoff calculation.

The constraints in the optimization model include: the flow conservation at each node (product balance), the product conversion at technology sites, capacity constraints for demand, inventory, and processed waste, the nutrient requirement for each crop at each node and time period, and the economic metrics. The objective function is to minimize the overall costs plus the excess nutrients in the system, where the weight can be interpreted as unit environmental costs or the strictness of environmental policies regarding nutrient management plan at each node.

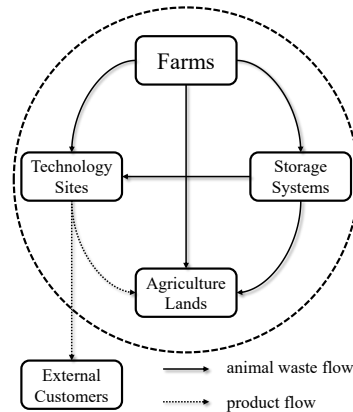


Figure 2: Supply chain structure

2.2. Nutrient Transport Model

A nutrient transport model tracks the nutrient transport process from point and non-point sources to surface water. To reduce the computational burden, increase the compatibility of the framework, and generate results at preliminary development stages, instead of using advanced and data-intensive simulation tools such as SWAT (Neitsch et al. (2011)), we select a watershed-level model called NEWS2 (Nutrient Export from WaterSheds 2) proposed by Mayorga et al. (2010). The NEWS2 model is a more general model that takes input data of WWTP emission data, precipitation data at a watershed level, globally calibrated parameters, and the net nutrient release information from the organic waste SC management model.

The model calculates the phosphorus and nitrogen that reach the water body considering both the contributions from point and non-point sources. The point source part is calculated using the population data and nominal nutrient release per person. The contribution from non-point sources is calculated using some global parameters, precipitation data (which is used for surface runoff calculation), and the net nutrient release accounting for fertilizer, animal waste application, fixation and deposition, and crop need.

We note that in the application of the NEWS2 model, two main assumptions are made. First, the NEWS2 model is originally used for annual nutrient transport. We assume a biweekly nutrient transport amount can be assessed using the same approach with finer input data, and with a transport delay included. Second, we assume the model can be fit into the use of small watershed. The modeling framework is equipped with more powerful functions under these functions, which might lead to lower accuracy. We will continue to extend the scope in the nutrient transport modeling and simulation.

2.3. Algae Growth Model

An algae growth model is used to relate the nutrient concentration in a water body with the HAB level and the corresponding consequences. The algae growth model used in this framework is the PROTECH (Phytoplankton Responses To Environmental CHange) model, which is proposed by Reynolds et al. (2001), and takes the input of nutrient concentration data, algae species information, weather data, lake profile (e.g. temperature). The model uses the concentration of chlorophyll-a (chl-a) as a measurement of the abundance of algae.

The PROTECH model calculates the daily concentration of chl-a by considering the growth rate, the rate of decrease due to animal grazing, settling out (algae movement), and dilution. For each term, the rate is mainly related to temperature, nutrient level, and sunlight intensity. The model can output the concentration of chl-a at different times and at different depths of the lake.

3. Case Study

We apply this modeling framework to a case study considering the region of Upper Yahara Watershed within Dane County in the State of Wisconsin. This region has suffered from nutrient pollution for years. The NBI (nutrient balance index, defined as the ratio of nutrient applied to land over the amount of nutrient that is removed by crops) was 1.95 and 1.35 in the year of 2012 and 2013 respectively (Larson et al. (2016)). For the year 2017, the NBI index was 1.46 based on our estimation. The Lake Mendota has been categorized as eutrophic since the 1980s.

In the case study, we use the crop and weather data of the year 2017. The time period of interest is from April 1st to October 31st, where the HABs are more likely to happen. The data of nutrient recovery technologies are from previous studies (Sharara et al. (2018); Sampat et al. (2018)). The decision-making procedure in this case study is illustrated in Figure 3, and the control techniques in the SC are the strictness of NMPs, the availability of nutrient recovery technologies, and the seasonal storage planning. Although the SC framework has the capability of placing facilities, the facility sites in this case study are predetermined using real data. After solving the SC optimization problem, it can provide a spatio-temporal strategy containing different transportation flows and inventory levels in different times, which is able to control the net nutrient release in the system while balancing the economic objective. Based on this procedure, we start from the worst scenario (no technologies or NMPs, and poor storage planning), and compare the effectiveness of each technique individually. Finally, we study the overall influence of adopting three techniques simultaneously. We obtain economic information from the SC model. From the difference of scenarios, we

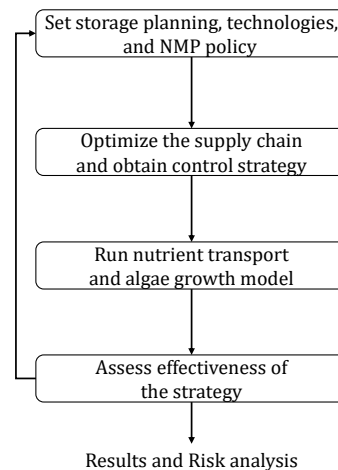


Figure 3: Decision-making scheme

can estimate the preventive cost for reducing HABs risk.

4. Results and Discussion

First, we compare the predicted TSI (trophic state index, proposed by Carlson (1977)) of the scenario closest to reality with observed data. A lake is defined as eutrophic when TSI is between 50-70. The predicted TSI is between 55 and 65; while the observed TSI fluctuates between 50 and 60, which indicates the practicability of the framework.

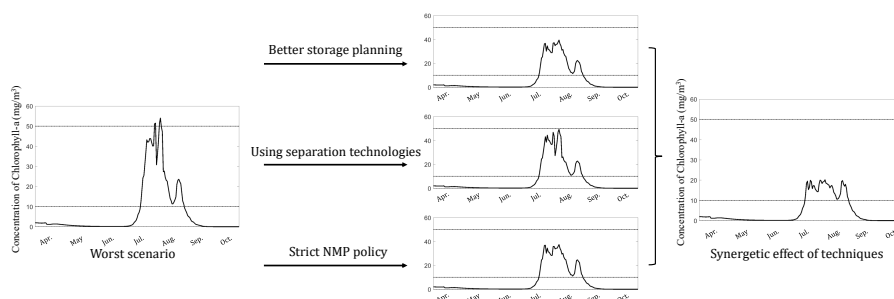


Figure 4: Model prediction

In Figure 4, we show the predicted concentration of chl-a under different control strategies. We observe that, in the worst scenario, the concentration exceeds the warning line of a high risk of acute health effect for humans suggested by the World Health Organization (2003) (50 mg chl-a/m^3), while the control techniques can reduce the HAB level under the warning line. From the comparison between the three control techniques, we find the incorporation of separation technologies is the less effective strategy, which may have attributed to the fact that the derived products are not valuable, and the economic driving force is not large enough. On the other hand, direct environmental policy changes (better storage planning or strict NMP policy) are more effective at controlling the nutrient runoff and thus the HAB level. Additionally, we observe that, by combining the three techniques, the HAB level can be reduced substantially, which means the strategies have an overall synergistic effect. However, even for the best scenario, the concentration of chl-a still exceeds the middle warning line (moderate risk of having acute health problems, 10 mg chl-a/m^3). This indicates that long-term effort (perennial SC optimization and nutrient management) is necessary to further eliminate the HABs risk.

From the economic results of the SC optimization problem, we can obtain the overall cost in the system (operational cost of technology, transportation cost, and fertilizer cost). For the worst scenario, the overall cost is 1.18 million USD while for the best scenario, the overall cost is increased by 32.2 % and reaches 1.56 million USD. This indicates the cost corresponding to the prevention of HABs in the same year can reach 0.38 million USD. We note that this estimation is conservative because the cost of implementing strict policies, the increased holding cost in inventory management, and the investment cost of technologies are not included.

5. Conclusions

In this work, we formulate a dynamic modeling framework by combining a SC optimization model, a nutrient transport model, and an algae growth model. The management elements in the SC network can be regarded as controlling techniques, and the output from the algae growth model can provide feedback information for the SC design. We provide a case study of Upper Yahara Watershed to illustrate the practicability of the model. We find by designing appropriate SCs, the nutrient loading in runoff can be decreased and the risk of HABs will be lower, but a corresponding cost of prevention will be incurred. In future work, we will conduct more scenario analyses and study the influence of logistics and the cost distribution at different times. We will extend our framework so that a perennial influence can be forecast.

6. Acknowledgements

We acknowledge support from the U.S. Department of Agriculture (grant 2017-67003-26055), from the National Science Foundation (grant CBET-1604374), and from the U.S. EPA (contract number EP-18-C-000016).

Disclaimer: The views expressed in this article are those of the authors and do not necessarily reflect the views or policies of the U.S. Environmental Protection Agency. Mention of trade names, products, or services does not convey, and should not be interpreted as conveying, official U.S. EPA approval, endorsement, or recommendation.

References

- R. E. Carlson, 1977. A trophic state index for lakes. *Limnology and oceanography* 22 (2), 361–369.
- J. Graham, K. A. Loftin, N. Kamman, 2009. Monitoring recreational freshwaters. *Lakelines* 29, 18–24.
- J. Heisler, P. M. Glibert, J. M. Burkholder, D. M. Anderson, W. Cochlan, W. C. Dennison, Q. Dortch, C. J. Gobler, C. A. Heil, E. Humphries, et al., 2008. Eutrophication and harmful algal blooms: a scientific consensus. *Harmful algae* 8 (1), 3–13.
- Y. Hu, M. Scarborough, H. Aguirre-Villegas, R. A. Larson, D. R. Noguera, V. M. Zavala, 2018. A supply chain framework for the analysis of the recovery of biogas and fatty acids from organic waste. *ACS Sustainable Chemistry & Engineering* 6 (5), 6211–6222.
- R. Larson, M. Sharara, L. Good, T. Porter, V. Zavala, A. Sampat, A. Smith, 2016. Evaluation of manure storage capital projects in the yahara river watershed. Technical Report for Dane County, WI.
- E. Mayorga, S. P. Seitzinger, J. A. Harrison, E. Dumont, A. H. Beusen, A. Bouwman, B. M. Fekete, C. Kroeze, G. Van Drecht, 2010. Global nutrient export from watersheds 2 (news 2): model development and implementation. *Environmental Modelling & Software* 25 (7), 837–853.
- S. L. Neitsch, J. G. Arnold, J. R. Kiniry, J. R. Williams, 2011. Soil and water assessment tool theoretical documentation version 2009. Tech. rep., Texas Water Resources Institute.
- C. Reynolds, A. Irish, J. Elliott, 2001. The ecological basis for simulating phytoplankton responses to environmental change (protech). *Ecological modelling* 140 (3), 271–291.
- A. M. Sampat, E. Martín, M. Martín, V. M. Zavala, 2017. Optimization formulations for multi-product supply chain networks. *Computers & Chemical Engineering* 104, 296–310.
- A. M. Sampat, E. Martín-Hernández, M. Martín, V. M. Zavala, 2018. Technologies and logistics for phosphorus recovery from livestock waste. *Clean Technologies and Environmental Policy*, 1–17.
- M. A. Sharara, T. Runge, R. Larson, J. G. Primm, 2018. Techno-economic optimization of community-based manure processing. *Agricultural Systems* 161, 117–123.
- World Health Organization, 2003. Guidelines for safe recreational water environments: Coastal and fresh waters. Vol. 1. World Health Organization.
- N. Zandi Atashbar, N. Labadie, C. Prins, 2018. Modelling and optimisation of biomass supply chains: a review. *International Journal of Production Research* 56 (10), 3482–3506.

Optimal design and planning multi resource-based energy integration in process industries

Shabnam Morakabatchiankar^a, Fernando D. Mele^b, Moisés Graells^a, Antonio Espuña^a

^a*Chemical Engineering Department, Universitat Politècnica de Catalunya, EEBE. Av. Eduard Maristany, 10-14, Edifici I, Planta 6, 08019 Barcelona, Spain*

^b*Departamento de Ingeniería de Procesos, FACET, Universidad Nacional de Tucumán (UNT), Avenida Independencia 1800, S. M. de Tucumán T4002BLR, Argentina*
shabnam.morakabatchiankar@upc.edu

Abstract

Recently, process industries have experienced a significant pressure to shift from centralized energy supplying systems to the in-situ exploitation of renewable resources. Special attention has been paid to multi resource-based energy systems, a particular case of distributed generation where processing nodes include energy generation and can operate either grid-connected or isolated. This work proposes a general model to determine the optimal retrofitting of a supply chain integrating renewable energy sources under uncertain conditions and to analyze the effect of different planning horizons in the solution. The proposed mixed integer linear programming (MILP) formulation allows determining the best combination of available technologies that satisfies the internal energy demand of a given set of scenarios while addressing total expected cost and expected environmental impact minimization. The potential of the approach is illustrated through a case study from the sugar cane industry proposed by Mele et al. (2011).

Keywords: Multi resource-based energy, Optimization under uncertainty, renewable energies, closed-loop energy integration

1 Introduction

Growing energy demand about 60% over the last 30 years and increased industrial electricity and gas prices more than double in comparison with 20 years ago ((Zukunft, 2014) force industries to plan their eventual transition to a new energy system that will be largely based on Renewable Energy Sources (RES). This is one of the greatest challenges of our time. Over the latest years, process integration involving different renewable resources for their more efficient use, managing and controlling their uncertain availability, has been considered. Therefore, several alternative approaches are available to satisfy process energy demand and exploit the availability of renewable sources. In this line, a number of studies have been focused on single renewable sources such as first and second generation bioethanol production processes, which were integrated to use the excess of energy when processing lignocellulosic biomass for ethanol dehydration (Čuček et al. 2011; Mele et al. 2011), and cogeneration exploitation (Morakabatchiankar, Hjaila, Mele, Graells, & Espuña, 2018). Different energy sources have also been integrated with biomass types (Martín & Grossmann, 2017; Prasad et al. 2017; Vidal & Martín, 2015). Recently, Martín et al. (2018) proposed an integrated renewable energy resource network to produce biofuels and generate power combining two supply chains that traditionally are developed as independent entities. However, the satisfaction of large scale demands of multiple resources, such the one that should be faced at regional or country level,

requires the integration of resources at a larger scale and needs more flexibility in terms of resources configuration. Hence, this work is focused on the development of a general optimization model for the retrofitting of sustainable process systems integrated with multi-energy generation system. The model is applicable to different ranges and scales while considering energy demand uncertainty to optimize the decisions of country-size SCs in the presence of conflicting objectives at different time spans.

2 Problem statement

According to the objective previously outlined, the proposed model determines a generic multi resource-based integration supply chain network as illustrated in Fig. 1. It is aimed to propose configurations associated with structural decisions that can be considered more sustainable. These decisions include the type, number, location and capacity of the energy generation units and production process plants (including the technologies selected in each of them); their capacity expansion policy and the transportation links between the energy-material SCs entities. The operational decisions are the energy generation level, the production rate at the plants in each time period, the flows of materials and energy between plants, warehouses and product markets, and the sales of final products and excess energy. Then, the SC configurations obtained by means of stochastic mathematical programming at different planning horizons can be compared. Additionally, this generic model determines the power to be installed at each internal or external resource and also the capacity of the required storage systems.

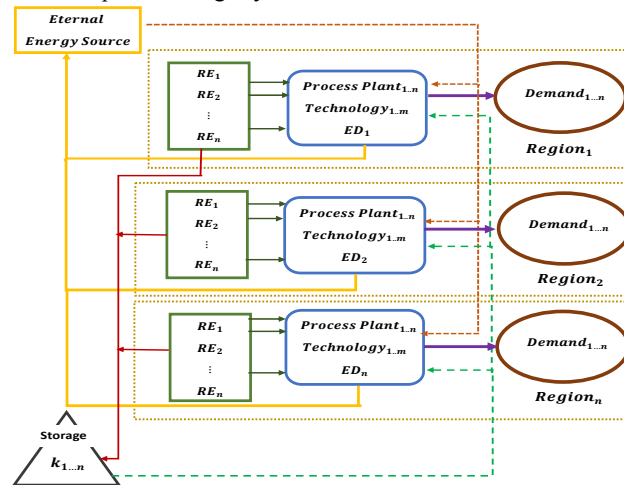


Fig 1. Multi resource-based Energy Integration SC

3 Multi-Objective stochastic Model

In this work, a scenario-based stochastic MILP formulation, considering a given distribution probability along the whole time horizon, based on the models introduced by Mele et al., (2011) (production process part) and Alabert et al., (2016) (multi resource energy integrated part) is proposed. Sizing is constrained to accomplish all scenarios, and operation variables are calculated according to each scenario. The number of necessary scenarios will be set in accordance with the characteristics of the case study to deal with. The model equations are classified as i) production process mass balances and capacity constraints; ii) energy generation mass/energy balances and capacity constraints; iii) energy storage management iv) External resources management; and v) objective

function. The result of the model provides a set of Pareto solutions to be used by the decision maker in order to take the optimum tactical/strategical decision.

3.1 Energy generation

The balance representing the need to meet the (uncertain) energy demand during a certain period is shown in equation 1:

$$\begin{aligned} & \sum_{ei} EnIJ_{ei,g,t,sc} + \sum_{ex} EnXJ_{ex,g,t,sc} \\ & + \sum_k EnKJ_{k,g,t,sc} = ED_{g,t,sc} \end{aligned} \quad \forall g, t, sc \quad (1)$$

where $EnIJ_{ei,g,t,sc}$ is the energy flux between source ei and region g at time period t for scenario sc ; $EnXJ_{ex,g,t,sc}$ is the energy flux between the external source x and region g at time period t for scenario sc ; $EnKJ_{k,g,t,sc}$ is the energy flux between storage k and region g and $ED_{g,t,sc}$ is total energy demand in region g at time period t .

For the management of the own energy sources, the energy balances in equations (2) and (6) consider that all the generated energy has to be consumed or sold. The variable $EnEx_{ei,t,sc}$ represents the eventual excess of energy, and SL represents the slot length.

$$EnIG_{ei,g,t,sc} = PwIG_{ei,g,t,sc} \times SL \quad \forall ei, g, t, sc \quad (2)$$

$$PwI_{ei} \leq PwIMax_{ei} \quad \forall ei, g \quad (3)$$

$$TotalEnIG_{t,sc} \geq TotalED_{g,t,sc} \quad \forall g, t, sc \quad (4)$$

$$\begin{aligned} & \sum_g EnIJ_{ei,g,t,sc} + \sum_{ex} \sum_g EnIX_{ei,g,ex,t,sc} + \\ & \sum_k \sum_g EnIK_{ei,k,g,t,sc} + EnEx_{ei,t,sc} = \sum_g EnIG_{ei,g,t,sc} \end{aligned} \quad \forall ei, t, sc \quad (5)$$

$$PwEx_{ei,t,sc} = EnEx_{ei,t,sc} / SL \quad \forall ei, t, sc \quad (6)$$

Equations (7-9) allow the management of external energy sources; they are similar to (4-5), but adding the possibility to sell energy. In these equations, $EnXP_{ex,t,sc}$ denotes energy purchase, whereas $EnXS_{ex,t,sc}$ represents the energy sales. Energy to be sold can only come from stand-alone generation, and it is considered that extra energy can be accumulated in storage elements.

$$PwX_{ex} \leq PwXMax_{ex} \quad \forall ex \quad (7)$$

$$EnXP_{ex,t,sc} = \sum_g EnXJ_{ex,g,t,sc} + \sum_k EnXK_{ex,k,t,sc} \quad \forall ex, t, sc \quad (8)$$

$$EnXS_{ex,t,sc} = \sum_{ei} \sum_g EnIX_{ei,g,ex,t,sc} \quad \forall ex, t, sc \quad (9)$$

Storage units are modelled through equations (10) to (12), which introduce the charge and discharge limits.

$$EnK_k \leq EnKMax_k \quad \forall k \quad (10)$$

$$EnKCh_{k,t,sc} = \left[\sum_{ei} \sum_g EnIK_{ei,g,k,t,sc} + \sum_{ex} EnXK_{ex,k,t,sc} \right] \times EfcCh_k \quad \forall k, t, sc \quad (11)$$

$$EnKDh_{k,t,sc} = \sum_g EnKJ_{k,g,t,sc} \times 1 / Efdh_k \quad \forall k, t, sc \quad (12)$$

3.2 Costs equations

The objective function considers the installation and operational costs of the facilities along with the planning horizon (eq. (13) and (14)), also considering the environmental impact costs for installation and operation Eq. (15) and (16).

$$CIns = \sum_{ei} \sum_g Pr PwI_{ei} \times PwI_{ei,g} + \sum_k Pr EnK_k \times EnK_k \quad (13)$$

$$COP_{t,sc} = HL / PL \left(\sum_{ei} \sum_g Pr EnI_{ei} \times EnIG_{ei,g,t,sc} \right) + \quad \forall t, sc \quad (14)$$

$$\begin{aligned} & \sum_{ex} (Pr EnP_{ex} \times EnXP_{ex,t,sc} - Pr EnS_{ex} \times EnXS_{ex,t,sc}) + \\ & \sum_{ex} (Pr EnCh_k \times EnKCh_{k,t,sc} + Pr EnDh_k \times EnKDh_{k,t,sc}) \\ GHGIns = & \sum_{ei} \sum_g GHGPwI_{ei} \times PwI_{ei,g} + \sum_k GHGEnK_k \times EnK_k \quad (15) \end{aligned}$$

$$\begin{aligned} & (HL / PL) \sum_{ei} \sum_g GHGEnI_{ei} \times EnIG_{ei,g,t,sc} \\ GHG COP = & \sum_{ex} GHGEnX_{ex} \times EnXP_{ex,t,sc} \quad \forall t, sc \quad (16) \\ & + \sum_k GHGEnCh_k \times EnKCh_{k,t,sc} \\ & + GHGEnDh_k \times EnKDh_{k,t,sc} \end{aligned}$$

3.3 Objective functions

The whole SC system must attain two targets: an economic objective, represented by the NPV, and an environmental objective quantified by the global warming potential (GWP). Different NPV values are obtained for each scenario under study, so an expected value ($E[NPV]$) of the resulting NPV distribution can be computed by considering the estimated probability for each scenario:

$$E[NPV] = \sum_{sc} Prob_{sc} \times NPV_{sc} \quad (17)$$

The resulting objective functions are finally expressed as follows:

$$Min \{-E[NPV]; E[GWP]\} \quad \text{S.t. constraints 1-17 and the constraints} \quad (18)$$

proposed by Alabert et al., 2016; Mele et al.,
2011

The solution of this problem consists of a set of Pareto optimal SC configurations, which can be by applying the \mathcal{E} -constraint method.

4 Case Study

The first example introduced by Mele et al. (2011), which addresses the optimal retrofit of an existing sugar cane industry established in Argentina, is revisited herein: 5 different technologies are available to manufacture 2 main products: ethanol and sugars. Nominal capacity of the sugar mill and the distillery plants are 350 and 300 thousand tons per year. The time horizon is divided into a set of time periods, and the specific geographic area is divided into a set of regions where the facilities of the SC can be located. Each region has

an associated supply capacity (sugar cane crop) at every time interval. Waste (bagasse) is supposed to be sent to cogeneration units to produce electricity as added-value product. Energy demand uncertainty is represented by 3 scenarios. Following Illukpitiya et al. (2013) assumptions, the estimated total electricity requirement for internal use in the processing plants is 0.0441 kWh per kg of cane. It is also assumed that the nominal capacity of the power plant is 8.33 MW and the power generation is available on a continuous basis for at least 7800 h annually. The electricity market price and the operational cost of electricity generation are 0.15USD/kWh and 0.08USD/kWh respectively.

5 Results

Figure 2 shows the Pareto curve obtained using the stochastic approach under several CO₂ emission levels and depicts a compromise between Expected Net Present Value and Expected Global Warming Potential. Each solution represents a specific design configuration of whole energy/material supply chain system. The results show that by increasing planning horizon length NPV value increases so it is also interesting to point out that, for the same cogeneration capacities of renewable resources, NPV increases up to 50% in longer planning horizons but tends to be constant for horizons longer than 10 years (Fig. 3). It is observed that the solutions allow operating at most for satisfying energy demand so that it involves more resources for generating renewable energies. As it is also shown in Fig. 4, a significant part of the expected electricity demand should be supplied by wind turbines.

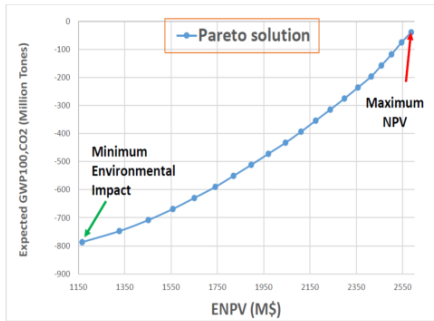


Fig. 2 Pareto set of solutions EGWP100 vs ENPV

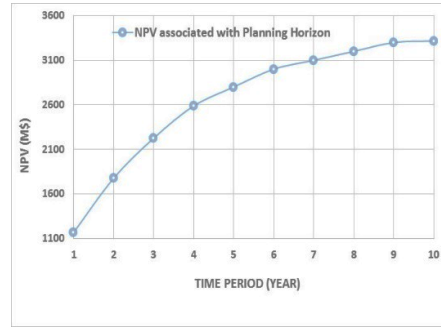


Fig. 3 NPV variation in Planning Horizons

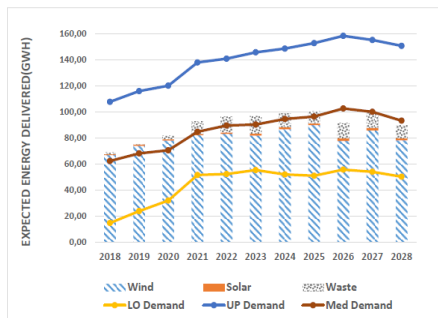


Fig. 4 Energy generation per Resource

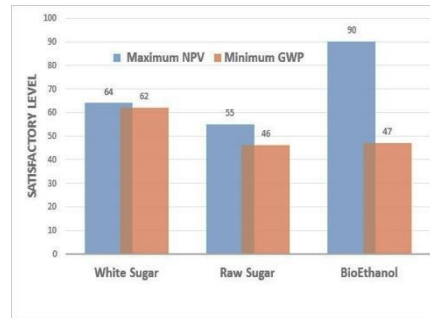


Fig. 5 Satisfaction level of Products Demand

The results show the maximum satisfaction level of products demand with a maximum expected NPV and minimum expected GWP conditions (Fig. 5).

6 Conclusions

A MILP formulation to address the retrofitting problem of a multi-resource based energy integrated SC under uncertainty has been presented. The model produces a set of feasible energy/material networks addressing the optimization of conflictive objectives. The capabilities of the model are highlighted through its application to a case study. The proposed stochastic approach maximizes the expected profit while satisfying a minimum environmental impact for each scenario. The interaction between the objectives has been shown. This way of generating feasible configurations will help the decision-maker to determine the best design according to the selected objectives. In this particular case, the results show that 100% of internal energy demand and 94% of biofuel demand can be met by an entirely renewables-based process network, which majorly generates energy by cogeneration unit and wind power.

References

- Alabert, A., Somoza, A., De La Hoz, J., & Graells, M. (2016). A general MILP model for the sizing of islanded/grid-connected microgrids. *2016 IEEE International Energy Conference, ENERGYCON 2016*. <http://doi.org/10.1109/ENERGYCON.2016.7514112>
- Čuček, L., Martín, M., Grossmann, I. E., & Kravanja, Z. (2011). Energy, water and process technologies integration for the simultaneous production of ethanol and food from the entire corn plant. *Computers and Chemical Engineering*, 35(8), 1547–1557. <http://doi.org/10.1016/j.compchemeng.2011.02.007>
- Illukpitiya, P., Yanagida, J. F., Ogoshi, R., & Uehara, G. (2013). Sugar-ethanol-electricity cogeneration in Hawai'i: An application of linear programming (LP) for optimizing strategies. *Biomass and Bioenergy*, 48, 203–212. <http://doi.org/10.1016/j.biombioe.2012.11.003>
- Martín, M., & Grossmann, I. E. (2017). Optimal integration of a self sustained algae based facility with solar and/or wind energy. *Journal of Cleaner Production*, 145, 336–347. <http://doi.org/10.1016/j.jclepro.2017.01.051>
- Martín, M., & Grossmann, I. E. (2018). Optimal integration of renewable based processes for fuels and power production: Spain case study. *Applied Energy*, 213(November 2017), 595–610. <http://doi.org/10.1016/j.apenergy.2017.10.121>
- Mele, F. D., Kostin, A. M., Guillén-Gosálbez, G., & Jiménez, L. (2011). Multiobjective Model for More Sustainable Fuel Supply Chains. A Case Study of the Sugar Cane Industry in Argentina. *Industrial & Engineering Chemistry Research*, 50(9), 4939–4958. <http://doi.org/10.1021/ie101400g>
- Morakabatchiankar, S., Hjaila, K., Mele, F. D., Graells, M., & Espuña, A. (2018). Economic and environmental benefits of waste-based energy closed-loop integration in process industries under uncertainty. In *Computer Aided Chemical Engineering* (Vol. 43, pp. 501–506). Elsevier.
- Prasad, A. A., Taylor, R. A., & Kay, M. (2017). Assessment of solar and wind resource synergy in Australia. *Applied Energy*, 190, 354–367. <http://doi.org/10.1016/j.apenergy.2016.12.135>
- Vidal, M., & Martín, M. (2015). Optimal coupling of a biomass based polygeneration system with a concentrated solar power facility for the constant production of electricity over a year. *Computers and Chemical Engineering*, 72, 273–283. <http://doi.org/10.1016/j.compchemeng.2013.11.006>
- Zukunft, F. (2014). Process News, (4). Retrieved from https://www.industry.siemens.com/topics/global/en/magazines/process-news/archive/Documents/en/process-news-2014-1_en.pdf

Predictive LCA - a systems approach to integrate LCA decisions ahead of design

Paraskevi Karka^a, Stavros Papadokonstantakis^b, Antonis Kokossis^{a,*}

^a *School of Chemical Engineering, National Technical University of Athens, Iroon Polytechniou 9, 15780 Zografou, Athens, Greece*

^b *Department of Space, Earth and Environment, Division of Energy Technology, Chalmers University of Technology, Hörsalsvägen 7B, 41296 Gothenburg, Sweden*

*Corresponding author: akokossis@mail.ntua.gr

Abstract

Bio-refineries are promising production options of chemicals production, capable to produce a wide range of fuels and chemicals equivalent to the conventional fossil-based products. To establish bio-refineries as mature choices and achieve the commercialization of their technologies, the application of sustainable solutions during the design and development stages are crucial. The innovative character of bio-based production and therefore data availability and access on process modelling details, is a challenging point for decision makers to move towards this direction.

Considering the environmental dimension out of the three aspects of sustainability, Life Cycle Assessment (LCA) is a suitable methodology for the evaluation of environmental impacts of bio-based processes because it highlights the stages with the greatest impact along a production chain. LCA studies require large amount of information, usually extracted from detailed flowsheets or from already completed pilot plants, making this procedure, costly, time consuming and not practical to act as a decision- support tool for the development of a bio-refinery.

The aim of this study is to develop predictive models for the assessment of LCA metrics and use them to highlight sustainable design options for bio-refineries. Models require the least possible information, which can be obtained from chemistry - level data or early (conceptual) design stages.

The modelling techniques used in this study are decision trees and Artificial Neural Networks (ANN), due to their easily interpretable structure and high computational capabilities, respectively. Models are based on the extraction of knowledge from a wide dataset for bio-refineries (it refers to 32 products that is, platform chemicals (e.g., syngas, sugars and lignin) and biofuels (e.g., biodiesel, biogas, and alcohols), starting from diverse biomass sources (e.g., wood chips, wheat straw, vegetable oil)). Input parameters include descriptors of the molecular structure and process related data which describe the production path of a study product.

Models are able to predict LCA metrics which cover the most critical aspects of environmental sustainability such as cumulative energy demand (CED) and Climate Change (CC). The average classification errors for decision- tree models range between 17% ($\pm 10\%$) to 38% ($\pm 11\%$) whereas for ANN models the average R^2_{cv} values (coefficient of determination) range between 0.55 ($\pm 0.42\%$) to 0.87 ($\pm 0.07\%$).

Demonstration of models is provided using case studies found in literature. Models are used to rank options in various design problems and support decisions on the selection of the most profitable option. Examples of such cases are the selection of the appropriate technology or feedstock to produce a desired product or the preliminary design of a biorefinery configuration.

The proposed approach provides a first generation of models that correlate available and easily accessed information to desirable output process parameters and assessment metrics and can be used as pre-screening tools in the development of innovative processes, ahead of detailed design, thus saving time and money.

Keywords: GWP, early stage process design

1. Introduction

Decision making in identifying and developing the most sustainable option among a range of alternatives from biorefinery configurations pre-supposes a great amount of knowledge that is hardly available at early stages of process development. On top of that bio-based processes, in their majority, are characterized by low technology readiness level. Furthermore, there is a strong need to configure sustainability criteria (energy and water consumption, toxicity) as early as possible and identify critical aspects and profitable solutions from the portfolio of possible options.

To give answers for the most profitable option, the commonly used methods such as LCA require data collection and analysis, a kind of information usually obtained from simulations or already existing infrastructures, e.g. pilot plants. In addition, detailed LCA as a standardized method is limited to the final judgment of design decisions, as it is placed at the end of process development steps (that is, conceptual design, mass and energy balances, process integration and optimization) (Fig. 1a). This procedure leads to the formation of economic and environmental data which feed inventory analysis and the assessment of environmental profiles.

This study aims at the development of a streamlined LCA methodology which predicts LCA metrics and it can be applied at early stages of process development of biorefineries using the minimum required information. The proposed method supports decisions towards sustainable design options, providing assessments which can be conducted “ahead of detailed design” and identifies critical parameters which affect LCA metrics, thus providing guidance for design choices (Figure 1b). The concept is based on the FineChem tool (Wernet et al. (2008), Wernet et al (2010)) which predicts LCA metrics for petrochemical industry using as input the molecular structure of the product and no prior knowledge of process flowsheets. The current method expands this concept for bio-based production and, although it adopts molecular descriptors proposed by FineChem, it is enriched with process related information, easily found from laboratory scale and early conceptual design stages.

The proposed method is data-driven and based on a range of biorefinery configurations including all the impacts generated along the production pathways. The predictive LCA models use machine learning techniques and adopt molecular descriptors of the products chemical structure and minimum process information, extracted from a large database of biorefinery case studies. These types of models can be a valuable tool in early design phases for screening alternative biorefinery layouts considering their environmental impact or to guide design considerations without detailed modelling requirements.

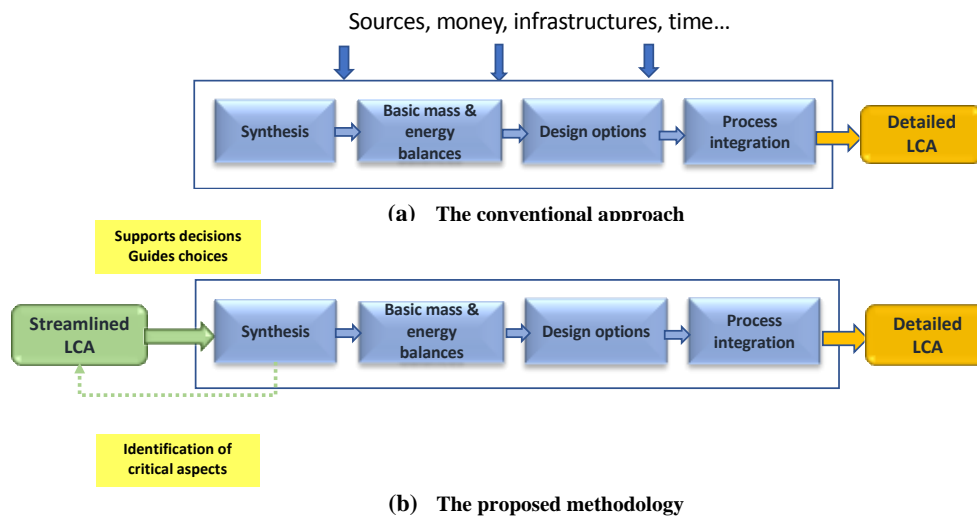


Fig. 1 (a, b) The research question

2. The methodological framework

The predictive models development procedure consists of 4 main steps that is:

- Step 1: Research question
- Step 2. Data collection and pre-processing
- Step 3. Use of data mining techniques to develop prediction models
- Step 4: Modelling performance-validation -demonstration in biorefinery cases

The research question addressed is the development of an amended version of LCA, able to predict LCA metrics for a wide range of environmental issues and guide design options at early design stages (Step 1).

The challenge to guide decisions “ahead of design” comes from the experience of machine learning to exploit data structures and identify patterns. The mathematical formulation aims at the development of functions $Y=f(X)$ which correlate Y , i.e. an LCA metric with a set of input variables $X=[X_1, X_2..X_n]$ easily available at early design stages. Thus, data for predictive model’s training and development (Step 2) are collected from a wide range of biorefinery systems. The training dataset used in this study refers to thirty-two products produced from various synthesis paths which represent the most important groups found in literature (Karka et al. 2017). Training size refers to 91 study systems and data sources for the development of flowsheet models are pilot plant data, combined with literature sources and the knowledge acquired from industrial partners.

Two LCA metrics were selected as target attributes (one for each model), the Climate Change (CC) and the Cumulative Energy Demand (CED) which provide assessments for carbon dioxide emissions and the non-renewable fossil energy demand. Target attributes for the corresponding products were estimated using the LCA method according to the ISO 14040 for each study system as described in Karka et al. 2017. The functional unit is 1kg of product. Values of LCA metrics of each observation of the dataset are also provided for three allocation approaches (mass, market price, substitution).

Input (descriptor) variables refer to the molecular structure of the product of interest (e.g. molecular weight, number of oxygen atoms, number of hydrogen atoms etc.) and process-chain related variables corresponding to chemistry, complexity and generic process conditions (e.g. maximum temperature, efficiency factors, number of processing steps for the synthesis of the final product). Descriptor variables are arranged into two sets of 24 (reduced) and 30 (detailed) input variables depending on the level of access on early design stages, i.e. lab scale and conceptual design level, respectively. Thus, 12 datasets are developed which correspond to an equivalent number of models (2 metrics x 3 allocation approaches x 2 sets of predictor variables).

Data mining techniques used are decision trees which segregate the set of descriptor variables into classes of Low, Medium and High impacts in case of categorical prediction results, and RBF Artificial Neural Networks (ANN) in case of numerical result (Step 3). For the former technique all variables were discretized whereas for the latter they were normalized in the range [-1, 1] before entering the model.

Average modelling capabilities are obtained as a result of an iterative cross validation procedure in Step 4 using average classification error and coefficient of determination (R^2_{cv}). Classification error was defined as $\frac{\sum_{i=1}^l fp_i}{n}$, where fp is the number of wrong predicted class labels to the total number of observations, n , in the dataset and l is the number of class labels.

3. Results

Neural network models present a distinctive performance for both CC and CED metrics for the detailed set of predictor variables and especially for mass and economic allocation approaches. R^2_{cv} values result as an average of 500 cross-validation iterations, varying among 0.55 to 0.87 (Fig. 2).

Compared to the FineChem tool (Wernet et al., 2008) the respective performance ranges are about 0.3 for CC and 0.25-0.4 for CED depending on the number of predictor variables selected each time.

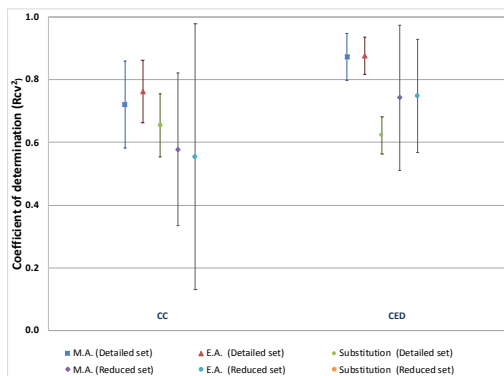


Fig. 2 Average and standard deviation values of R^2_{cv} for NN based models from 500 cross validation iterations (Values for substitution approach for the reduced sets are close to 0 and they are not shown)

The average prediction performance of the decision tree-based models results from a cross-validation procedure for 100 iterations (Table 1). The classification error values for CC and CED metrics (depending of the mass allocation approach and the set of predictor variables) range between 17% to 38%. These values can be acceptable for pre-screening models.

Table 1: Average classification error for CC and CED metrics and for all allocation scenarios and input variables dataset

Predictor variables	Allocation approach	CC		CED	
		Avg.	St. Dev.	Avg.	St. Dev.
Detailed	Mass Allocation	22.2%	8.6%	21.6%	9.0%
	Economic Allocation	28.5%	9.1%	23.4%	9.1%
	Substitution	26.1%	10.2%	33.9%	10.8%
Reduced	Mass Allocation	19.6%	9.0%	17.3%	10.1%
	Economic Allocation	22.5%	8.7%	25.5%	10.7%
	Substitution	32.4%	12.2%	37.8%	11.0%

3.1 Models use in biorefinery processes

For demonstration purposes the graphical representation of the CC model (Fig. 3) for the mass allocation approach and the reduced set of predictor variables is used. Three paths of glucose production are tested, glucose through steam explosion (Option A), concentrated acid hydrolysis (Option B) and through biomass decomposition with organic acids, organosolv (Option C). Table 2, shows the minimum amount of information which is required to obtain an estimation whereas Table 3 summarizes the validation of prediction results using reported data for the options A, B and C.

Table 2: Input data for the assessment of CC metric of glucose following the rules of the tree

	(A)	(B)	(C)
Feedstock	WChips	WChips	WStraw
Reacts	0	0	0
Steps	2	2	2
RME	Medium (0.211)	High (1)	
WAirReacts	100%	100%	
MaxT			Moder (100C)
Oxygen			=1

Table 3: Predictions using the CC metric tree, and respective reported values

Production path	Estimation	Real class	Value	Source
Glucose (steam explosion) (A)	Low	Low	0.7	(Morales et al., 2017)
Glucose (acid hydrolysis) (B)	Low	Low	0.3	(Morales et al., 2017)
Glucose (organosolv) (C)	Medium	Medium	1.46	BIOCORE, 2010-2014, Karka et al. (2017)

✓ Correct ranking
 ✓ Correct class estimations

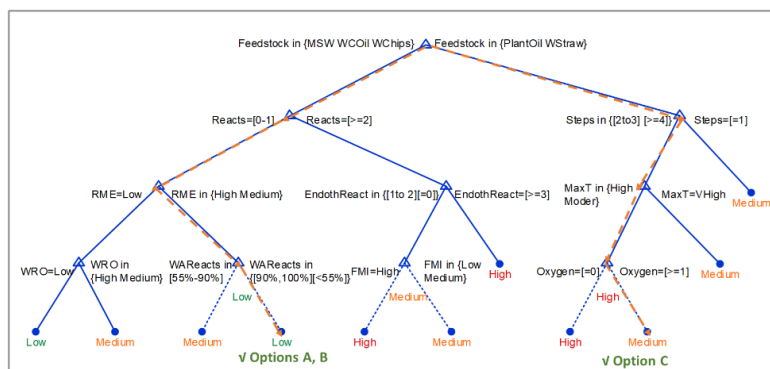


Fig 3. Decision tree for CC metric

Despite the practical use of decision trees, because of their interpretable format, we highlight below an example of using neural networks as a supportive tool to the categorical form of decision trees predictions.

Dihydroxyacetone-DHA (Morales et al., 2015; Lari et al., 2016), produced from biocatalytic processing of glycerine can be derived from plant oil based or waste cooking

oil glycerine. The reported CC values per 1kg of DHA is 9.4 CO₂-eq and 6.4 CO₂-eq, respectively, which have been assessed following the steps of the ISO norm of LCA, both belong to the class of high impacts according to the categorization and classification of decision trees. A prediction like that would not support the designers towards the most profitable selection. Thus, the contribution of a numerical technique would enhance the capability of a classification model to rank the alternative options. In this case, neural networks can give a useful trend on the ranking of solutions even when their predicted values present high deviations from the reported values as shown in Table 4.

Table 4: Neural metrics predictions for CC, and respective reported values

	Production path	30 predictor variables		24 predictor variables
		Reported value	Estimation of NN	Estimation of NN
1	<i>DHA crude (biocatalytic), plant oil</i>	9.4	6.28	4.84
2	<i>DHA crude (biocatalytic), waste cooking oil</i>	6.40	3.44	3.02

4. Conclusions

This study is a contribution towards estimating the environmental impacts of biorefinery products in early stages of process design, based on molecular descriptors of the bio-product and minimum process information. The resulting models for CED and CC show satisfactory accuracy in validation terms (e.g., coefficient of determination values around 0.6-0.85 and average relative errors of 17%-38%), similar to short-cut models previously developed for fossil-based production. The same modeling methodology (both classification trees and NN) was applied in LCA metrics provided by the ReCiPe method giving satisfactory results for other midpoint and endpoint LCA metrics such as Human Health, Ecosystems Quality, Marine Eutrophication etc. It is expected that an enrichment of the database and the appropriate selection of predictor variables will allow the development of a robust tool for predicting/benchmarking the cradle-to-gate environmental performance of the bio-based production.

References

- Karka, P., Papadokonstantakis, S., & Kokossis, A. (2017). Cradle-to-gate assessment of environmental impacts for a broad set of biomass-to-product process chains. *Int J Life Cycle Assess.* doi:10.1007/s11367-017-1262-6
- G. Wernet et al., 2008, Molecular-structure-based models of chemical inventories using neural networks, *Environmental Science & Technology*, 42, 6717-6722
- G. Wernet et al., 2009, Bridging data gaps in environmental assessments: Modeling impacts of fine and basic chemical production, *Green Chemistry*, 11, 1826-1831
- Lari GM, Mondelli C, Papadokonstantakis S, Morales M, Hungerbühler K, Pérez-Ramírez J (2016) Environmental and economic assessment of glycerol oxidation to dihydroxyacetone over technical iron zeolite catalysts. *React Chem Eng* 1:106–118
- Morales M, Dapsens PY, Giovinazzo I, Witte J, Mondelli C, Papadokonstantakis S, Pérez-Ramírez J (2015) Environmental and economic assessment of lactic acid production from glycerol using cascade bio and chemocatalysis. *Energy Environ Sci* 8:558–567

Acknowledgements The authors would like to acknowledge financial support by FP7 KBBE Grant BIOCORE (FP7-241566), Marie-Curie Grant RENESENG (ITN-607415), the BAI4B: Accountable IT Infrastructures for Optimizing Supply Chains in Biomass Symbiotic Networks, General Secretariat for Research and Technology—Hellenic Ministry of Education and Religious Affairs, and Full material and chemical monitoring data and disclosure for the protection of the human health and environment LIFE MATHER (LIFE16 ENV/IT/000211)

From renewable energy to ship fuel: ammonia as an energy vector and mean for energy storage

Francesco Baldi^{a*}, Alain Azzi^a and François Maréchal^a

^a*Laboratory of Industrial processes and energy systems engineering, École Polytechnique Fédérale de Lausanne, EPFL Valais-Wallis, Rue de l'Industrie 17, 1950 Sion, Switzerland
francesco.baldi@epfl.ch*

Abstract

The stochastic and non-controllable nature of most of renewable energy sources makes it necessary to include extensive use of energy storage in national grids to overcome periods with low availability. Hence, effective energy storage technologies will be required for achieving a 100% renewable energy system.

Currently used technologies are only partly suitable for this task. Batteries are efficient but expensive, and mostly suitable for daily storage. Hydrogen has a significant potential, but suffers from a low energy density and difficulties in handling and transportation. Among different potential solutions, ammonia was often pointed out as a high-density and low-cost hydrogen carrier.

In this paper, we analyze the efficiency of an ammonia-based pathway for the storage of excess energy from renewable energy sources, its transportation, and its final use. As a case study, we consider the use on board of a urban car transport vessel as the user of the stored energy. The energy efficiency and cost of the whole chain, from the production at the wind farm until its use on board of the ferry, is evaluated and compared with competitive alternatives, namely batteries and hydrogen storage.

The results show that, while not being a game-changer, the use of ammonia as mean for storing and transporting excess energy from renewable power plants is viable and, in combination with other storage systems, contributes to a relevant part of the share of total installed storage capacity in the most cost-effective solution.

Keywords: energy storage, renewable energy, ammonia, fuel cells

1. Introduction

The challenge of making human activities environmentally sustainable is one of the most important that humanity will have to face in the coming years. While the solution will be provided by a combination of different technological developments, it is widely recognized that renewable energy sources will take a major share of the task.

Given the stochastic and non-controllable nature of most of renewable energy sources, improving the performance of energy storage represents one of the most important challenges to face for achieving a 100% renewable energy system. Batteries, while being the most efficient storage technology, suffer from limitations in energy density and high cost. Hydrogen generated by electrolysis, while still providing a reasonably high round-trip

efficiency, has limitations in energy density and in handling.

As a solution for long-term storage and for transportation, various authors have proposed the conversion of hydrogen to conventional fuels, such as syngas, methane, methanol, and Diesel, but none of these solutions would prove to be carbon neutral, unless the carbon is originated by biomass, or by carbon capture and storage.

The use of ammonia as fuel can provide a valid alternative to carbon-based fuels. Ammonia has a relatively energy density in its liquid phase, that can be achieved at conditions relatively close to ambient conditions. For this reason, we believe that there is an interest in proposing ammonia as an energy vector, and as a mean for energy storage.

In this paper, we aim at investigating the potential role of ammonia as a way to store renewable energy that is produced in excess during low-demand periods. We address this by looking at a specific case study, based on the hypothesis to use the extra energy to propel ferries. The study aims at comparing existing storage technologies (batteries and hydrogen) with the potential case of ammonia.

2. Method

In order to investigate the potential role of ammonia as means for storing renewable energy during periods of excessive availability, in this paper we refer to the case of an off-shore wind farm of a rated power of 200 MW. The excess energy can either be curtailed, and hence lost, or stored and then transferred to a harbor, where it is assumed that a car ferry will be the final user.

The process of storage and transportation of the excess energy is allowed to take different ways, as shown in Figure 1:

Electric way : Excess energy is stored in batteries, and then sent to shore via existing power lines. The power transmission is allowed whenever there is no excess energy generation.

Hydrogen way : Excess energy is used in an electrolyser to generate hydrogen, that is stored in either compressed or liquid form. It is here assumed that the hydrogen is stored in container-sized tanks, that can then be loaded on supply vessels that regularly serve the wind farm. A bi-weekly frequency is assumed for the purpose of this study, as reported by CIT.

Ammonia way : Excess energy is used to generate hydrogen from water in an electrolyser, and nitrogen from air in a cryogenic air separation unit. Hydrogen and nitrogen are then used in an ammonia synthesis plant (here assumed based on the Haber-Bosch technology) that converts them to ammonia, that is then stored in liquid form at low temperature. The transportation is assumed to happen in the same way as assumed for the hydrogen way.

Once delivered to the port, the different fuels can be loaded on board of the ferry that operates on daily round trips. Electrical energy can be stored onboard in batteries, and directly used to power electric motor. Hydrogen is assumed to be used in a proton exchange membrane fuel cell (PEMFC), a well-developed technology extensively tested for

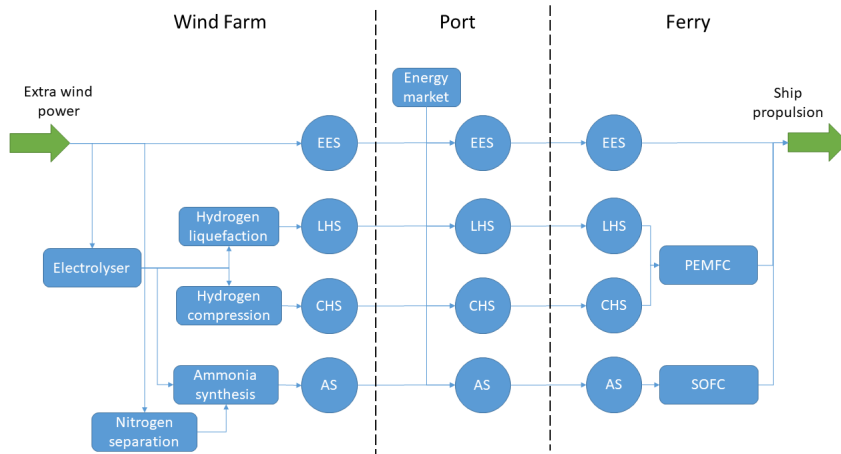


Figure 1: Representation of the superstructure for the optimization model

Name	Location	C_{inv}	Unit	η	Unit
Electrolyser	WF	400 ¹	$\frac{EUR}{kW_{H_2}}$	0.73 ¹	$\frac{kW_{el}}{kW_{H_2}}$
H ₂ Compression plant	WF	180 ²	$\frac{EUR}{kW_{H_2}}$	0.91 ³	$\frac{kW_{el}}{kW_{H_2}}$
H ₂ Liquefaction plant	WF	650 ⁴	$\frac{EUR}{kW_{H_2}}$	0.64 ⁵	$\frac{kW_{el}}{kW_{H_2}}$
N ₂ Separation plant	WF	1450 ¹	$\frac{EUR}{\frac{kg_{H_2}}{h}}$	0.11 ¹	$\frac{kW_{el}}{kg_{N_2}}$
NH ₃ Synthesis plant	WF	3000 ¹	$\frac{EUR}{\frac{kg_{NH_3}}{h}}$	0.64 ¹	$\frac{kW_{el}}{kg_{NH_3}}$

¹Ikäheimo et al. (2018), ²Law et al. (2013), ³Tzimas et al. (2003), ⁴Kelly (2007), ⁵Gardiner (2009)

Table 1: Numerical assumptions employed in the study

use with hydrogen as fuel, also in maritime applications CIT. Ammonia is assumed to be used in a solid oxide fuel cell (SOFC); while the technology of SOFCs is less mature when compared to PEMFCs, particularly when powered by ammonia, recent tests have shown that there is no conceptual, or practical obstacle to a wider adoption of this technology CIT. The assumptions related to unit cost and efficiency are summarized in Table XXX. We assume that the maintenance cost does not significantly vary between different options and technologies and that, hence, can be excluded from the analysis.

The evolution of the excessive power generation over the year is represented using to the processed data provided by Zerrahn et al. (2018), originally retrieved in raw format from ?, and refer to the German electrical grid for the year 2014. This dataset provides hourly values for the curtailed energy from the combination of all renewable power plants. The implicit assumption of using this data in this paper is that the excess power is redistributed among different plants based on the installed power capacity. While this can be considered as a strong assumption, this approach provides a relatively accurate representation of the size and frequency of power curtailment in a European electrical grid. A representation

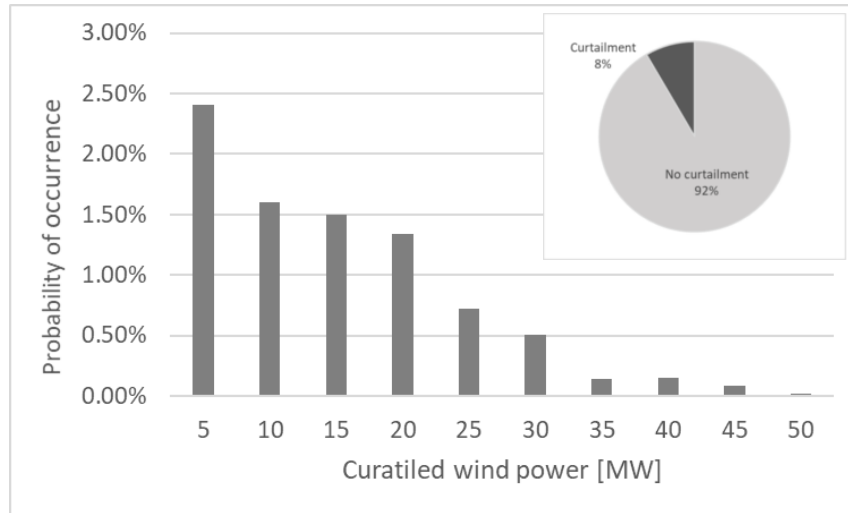


Figure 2: Wind curtailment power, probability of occurrence

of the resulting frequency of different curtailment powers is provided in Figure XXX.

Both the excess power and the power demand of the ferry are represented with a two-hour definition. As this would require a total of 4320 time steps for one year of operation, we assume that yearly operations can be summarized with a total number of four "reference periods" of the duration of two weeks, where the choice of the period length is based on the frequency available for transporting fuel from the wind farm to shore. The four reference periods were defined as follows:

- Maximum cumulated excess energy (for dimensioning the storage), occurring once per year
- Maximum peak excess power (for dimensioning the conversion units), occurring once per year
- Reference period at low cumulated excess energy, occurring 15 times per year
- Reference period at high cumulated excess energy, occurring 9 times per year

3. Results and discussion

The results for the optimal annualized costs in the different cases are provided in Figure 3. The option of using only electric energy storage in the form of batteries is clearly the least convenient case: as a consequence of the high specific investment cost, the optimizer chooses to reduce the total storage installed capacity, hence increasing the operational costs related to energy curtailment. The results also show that, for the selected case study, liquid hydrogen storage is more competitive in comparison to compressed hydrogen storage. Both the increased energy cost for liquefaction and the relatively high investment

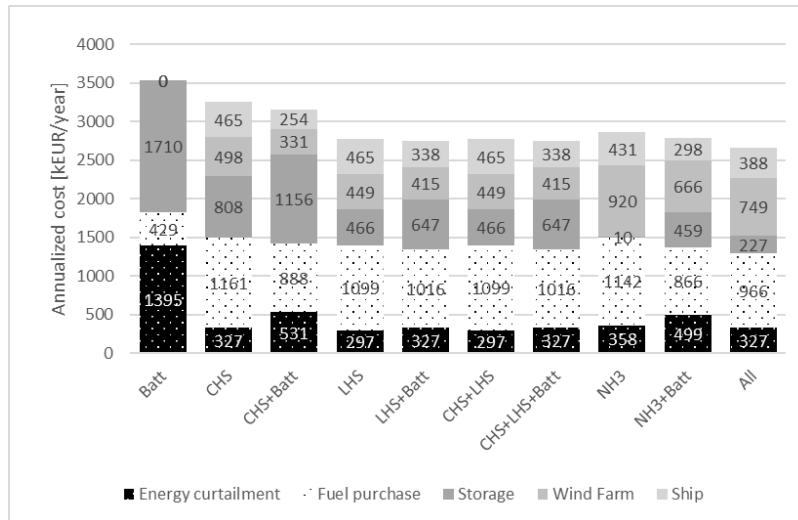


Figure 3: Comparison of operational, investment, and total costs for the different investigated cases

cost of the hydrogen liquefaction plant are offset by the lower investment cost for hydrogen storage.

When ammonia comes into play, a combination of effects can be observed. The use of ammonia alone as storage option is less profitable compared to the case of liquid hydrogen storage. This is mostly due to the high specific investment cost of the ammonia synthesis plant, which in this case is the largest contributor to the investment cost (32%), while the cost of the storage is only marginal (less than 1%). On the other hand, when other storage possibilities are included, the ammonia production plant is downsized (the installed capacity is reduced by 38%), and liquid hydrogen is used for intermediate storage. The detailed cost share in this case is shown in Figure 4: the electrolyser, the SOFC and the ammonia synthesis plant all contribute with 20-25% of the investment costs, while the use of a battery for part of the onboard power generation is favored because of the lower operational costs, particularly when energy is bought from the energy market.

4. Conclusion

References

M. Gardiner, 2009. Energy requirements for hydrogen gas compression and liquefaction as related to storage needs. Technical Report 9013, US Department of Energy, United States.

J. Ikäheimo, J. Kiviluoma, R. Weiss, H. Holttinen, 2018. Power-to-ammonia in future North European 100 % renewable power and heat system. International Journal of Hydrogen Energy 43 (36), 17295–17308.

B. Kelly, 2007. Liquefaction and pipeline costs.

K. Law, J. Rosenfeld, V. Han, M. Chan, H. Chiang, J. Leonard, 3 2013. U.s. department of energy hydrogen storage cost analysis. Tech. rep.

E. Tzimas, C. Filiou, S. Peteves, J.-B. Veyret, 2003. Hydrogen storage: state-of-the-art and future perspective. Tech. Rep. 20995, European Commission, Joint Research Centre (JRC), Directorate General (DG), Institute for Energy, Petten, The Netherlands.

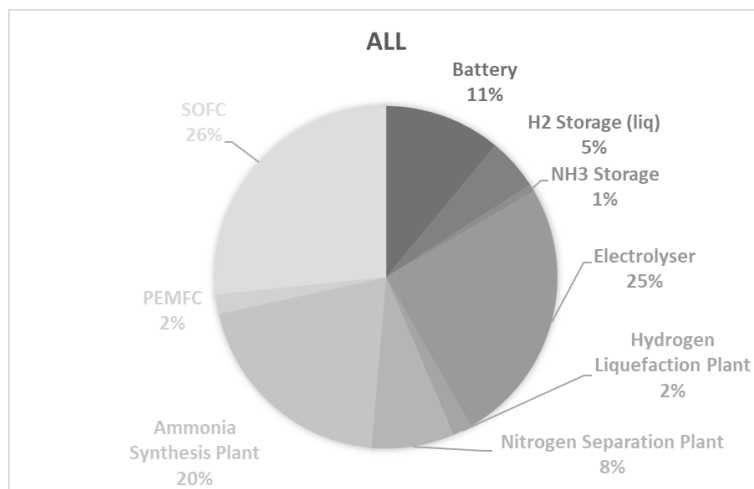


Figure 4: Investment cost breakdown, full case

A. Zerrahn, W.-P. Schill, C. Kemfert, Sep. 2018. On the economics of electrical storage for variable renewable energy sources. *European Economic Review* 108, 259–279.

Heat-integrated water allocation network design: a novel hyperstructure and sequential solution strategy for industrial applications

Maziar Kermani^{a,*}, Ivan Kantor^a, Adriano Ensinas^b and François Maréchal^a

^a*École Polytechnique Fédéral de Lausanne (EPFL) Valais Wallis, , IPESE group, Rue de l'Industrie 17, 1951 Sion, Switzerland*

^b*Universidade Federal de Lavras. Departamento de Engenharia (DEG/UFLA), 3037 Lavras, MG-Brazil*
maziar.kermani@epfl.ch

Abstract

Daily industrial operations consume large quantities of energy and water but are often considered marginal to their processes. Energy is used to heat or cool water; water is frequently used in production or utility systems as steam or cooling water. This emphasizes the interconnectivity of water and energy, stipulating their simultaneous consideration to address resource use in industrial processes which requires systematic methodologies. Two main complications have been observed within methodologies proposed in literature. As discussed in this work, these difficulties affect the overall mathematical formulation in mixed-integer nonlinear programming models; thus, resulting in a complex formulation. These difficulties have been addressed in this work by proposing a novel hyperstructure and a sequential solution strategy for the design of heat-integrated water allocation networks. Emphasis is placed on generating a set of promising solutions by addressing different performance indicators which is achieved via implementation of integer cut constraints to support decision-making for potential configurations. Applying the proposed methodology on several test cases from literature illustrated that the methodology is not only able to reach minimum total cost of the system, but also generates a set of alternative solutions exhibiting various performances with respect to other indicators.

Keywords: mathematical programming, superstructure optimization, heat-integrated mass allocation network, non-linear programming, non-isothermal mixing.

1. Introduction

Savulescu and Smith (1998) published the first work on heat-integrated water allocation network (HIWAN)s. They emphasized the importance of simultaneous consideration of heat and water and provided a graphical approach. Since then, many authors have proposed methodologies to better capture the trade-offs among the two resources which can be categorized into either conceptual or mathematical. The latter is based on developing mathematical models, incorporating all potential alternatives, and optimizing the system with respect to a well-chosen objective function. Several comprehensive reviews have been published on the subject (Ahmetović et al., 2015; Kermani et al., 2018). Two main complications have been observed within the mathematical methodologies proposed in literature, namely, the choice of the thermal state of a water stream (being hot or cold) and

its thermal matches. The formulation of the latter requires the knowledge of the thermal state of the water stream *a priori*. Both complexities have been addressed in the literature via considering binary variables. This results in a mixed-integer nonlinear programming (MINLP) model. Comprehensively addressing the two requires a complex formulation which may fail to provide promising solutions in a reasonable time-horizon. This has prompted researchers to propose several solution strategies to facilitate the solving process (Kermani et al., 2018). This work proposes a novel sequential solution strategy and a novel nonlinear programming (NLP) hyperstructure, addressing the aforementioned difficulties in a systematic manner.

2. Problem definition

Given are two sets of water unit operations (source, sink) with their specific operating temperatures. Maximum allowed inlet (outlet) contamination levels are defined for each sink (source). Mass load removal rates are also defined in case a water unit operation is a mass-transfer unit. Furthermore, non-water process and utility (steam, cooling water) streams are also present. Freshwater sources and wastewater sinks at different temperature and contamination levels are also provided. The objective is to design the total heat-integrated water allocation network exhibiting the lowest total annualized cost. This cost consists of operating costs (consumption of freshwater, wastewater treatment, and thermal utilities) and investment costs (heat exchanger network (HEN) cost, equipment cost, etc.).

3. Methodology

The overall HIWAN problem is generally formulated as an MINLP. In this work the problem is reformulated into three subproblems, namely: targeting, heat load distribution (HLD), and design. The focus of this work is on formulation of the design stage together with the overall solution strategy.

Problem P1 - Targeting: Problem **P1** is formulated as mixed-integer linear programming (MILP) model (Kermani et al., 2017). This problem considers water network constraints, heat network constraints (Maréchal and Kalitventzeff, 1998), and connections between the two. The linearized formulation of non-isothermal mixing (NIM) allows for modeling sets of potential water thermal streams for each water unit operation (assignment of binary variables to each water thermal stream). This formulation solves the first difficulty in design of HIWANs, i.e., the thermal state of water streams. In addition, the solution of problem **P1** provides utility targets and a feasible water allocation network. The problem is solved by minimizing the total annualized cost of the system.

Problem P2 - HLD: Problem **P2** is the well-known HLD model (Papoulias and Grossmann, 1983; Marechal et al., 1989; Cerda and Westerburg, 1983) formulated as MILP with the objective of minimizing the number of thermal matches in each pinch interval, i.e., minimizing the number of heat exchangers. HLD solves the second difficulty in the design of HIWANs, i.e., the potential thermal matches. Furthermore, the solution of problem **P2** provides the heat loads of each thermal match which is used as a good initialization point for the subsequent design stage.

Problem P3 - Design: Knowing the set of thermal streams from problem **P1** and the potential thermal matches from problem **P2**, problem **P3** is formulated as an NLP hyper-

structure. It is adapted from HEN hyperstructure of Floudas and Ciric (1989) for thermal streams. More specifically, in the classical approach by Floudas and Ciric (1989), no interconnection is allowed among different superstructures of thermal streams; however, considering the fact that these thermal streams are water streams, these connections bring potential mixing and splitting opportunities which can further reduce the HEN cost. Several structural changes are implemented in the HEN hyperstructure to consider the new possibilities (Figure 1) including removing the final mixer (initial splitter) from a superstructure if the stream is associated to a source (sink) unit. It should be highlighted that the non-water thermal streams keep the original formulation. Problem **P3** minimizes the HEN cost subject to mass, contamination, and energy balance constraints.

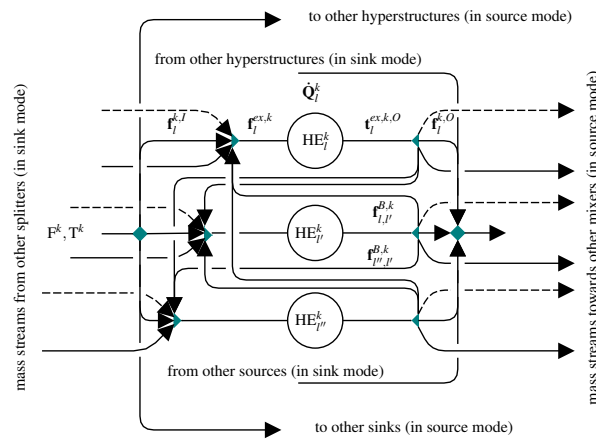


Figure 1: Schematic of the proposed hyperstructure (dashed arrows indicate flows among hyperstructures of the same source (sink) similar to the definition of $f_{I,l'}^{B,k}$ and $f_{p',p'}^{B,k}$)

3.1. solution strategy

Problems **P1**, **P2**, and **P3** are solved in sequence. The original HEN model of Floudas and Ciric (1989) can be solved before problem **P3** to provide an initialization point. The solution of this model is also considered a feasible solution to the overall HIWAN problem. Several drawbacks can be observed in this sequential solution strategy, namely that it fails to: address the trade-off between operating and investment costs, guarantee the global optimality due to non-convexity of the problem, and guarantee a solution with overall minimum HEN cost (Floudas and Ciric, 1989). To address these drawbacks, an iterative sequential solution strategy is proposed, more specifically, by applying integer cut constraints on problems **P1** and **P2** and solving the overall problem for different values of heat recovery approach temperature (HRAT). This approach can be regarded as iteratively optimizing the overall MINLP model within different regions of the global search space (as imposed by the formulations of problems **P1** and **P2** at each iteration).

4. Results and discussion

Two test cases from the literature were selected to validate the proposed approach. The maximum allowed number of integer cuts was limited to 50. The value of HRAT was var-

ied between 1–10°C. These values are passed to problem **P3** as heat exchanger minimum approach temperature (ΔT_{min}). Test case I is a threshold problem and hence the value of HRAT does not affect the utility consumptions. This, however, becomes a decisive factor for test case II where both hot and cold utilities are required. Several key performance indicator (KPI)s are considered:

- Resource indicators: freshwater (\dot{m}_{fw}) and thermal utility consumptions (\dot{Q}_u^H, \dot{Q}_u^C);
- Network indicators: number of thermal streams (N_s^{th}), number of heat exchangers (N_{HE}), total area of heat exchangers (A_{HEN}^{total}), number of mixing points (N_{mixer}), number of non-isothermal mixing points (N_{mixer}^{NIM}), number of mass streams (N_s^m), and total heat load of all heat exchangers (Q_{HEN}^{total});
- Economic indicators: HEN cost (C^{HEN}) and total annualized cost (TAC) (C^{TAC}).

4.1. Test case I: single-contaminant problem

Test case I is a single-contaminant problem proposed by Bagajewicz et al. (2002) that consists of eight water unit operations. The solution with minimum operating cost exhibits 125.94 kg/s of freshwater consumption and 5,289.6 kW of hot utility consumption. Out of 26,010 possible solutions, 5,260 solutions exist to problem **P2**. The objective value of problem **P2** varies between 6–15. From this set of solutions, 565 solutions converged for problem **P3**, among which, HEN cost varies between 272.1–529.3 kUSD/yr for 554 solutions. The minimum HEN cost reported by the literature is 257.2 kUSD/yr (Ibrić et al., 2014), however, the freshwater and utility consumptions were reported to be 126.71 kg/s and 5,322.1 kW, respectively. Several filters were applied to further reduce the number of solutions to aid in visualization based on their corresponding maximum values reported in literature: $N_s^m \leq 32$, $N_{mixer} \leq 21$, $N_{mixer}^{NIM} \leq 17$.

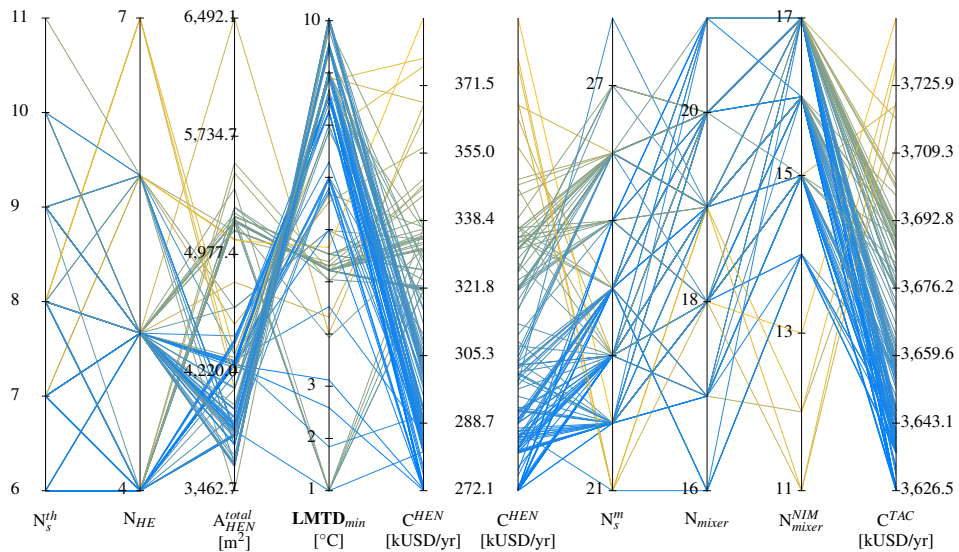


Figure 2: Visualization of selected KPIs for test case I (155 solutions)

Figure 2 presents the remaining 155 solutions. Considering total annualized cost as the

main objective in this case study, the proposed set of solutions encompass the design with the lowest cost of 3,626.5 kUSD/yr. Comparing this with the minimum reported in the literature (3,628 kUSD/yr), one can observe that the proposed sequential solution strategy can reach the minimum while also proposing a set of alternatives which show varying performance for the defined objective and other KPIs. The advantage of such an approach is providing many potential solutions which may yield more desirable solutions in non-objective KPIs which would not be discovered by conventional approaches. For instance, among all solutions with the lowest HEN cost, the solution with the lowest number of mixers and mass streams exhibits a simpler network design while its HEN cost is penalized by less than 0.1%.

4.2. Test case II: multi-contaminant problem

Test case II is a pinch, multi-contaminant problem proposed by Dong et al. (2008) with the minimum freshwater consumption of 70 kg/s. The value of HRAT affects the thermal utility consumptions. Jagannath and Almansoori (2016) proposed a solution in which they constrained the number of heat exchangers and mass exchanges to four and seven, respectively, and reached 74.3 kg/s of freshwater consumption, 8,760 kW of hot utility and 2,520 kW of cold utility ($\Delta T_{min} = 20^\circ\text{C}$). Although they reported the lowest HEN cost (117.2 kSUD/yr), their solution exhibits the highest total cost and the highest thermal utility consumption among the reported values in the literature. Out of 26,010 possible solutions, 982 solutions exist to problem **P2**. The objective value of problem **P2** varies between six and nine thermal matches. Among these solutions, 299 converged for problem **P3** with minimum and maximum HEN costs of 146.3 kUSD/yr and 353.8 kUSD/yr, respectively. Figure 3 illustrates the KPIs of these 299 solutions.

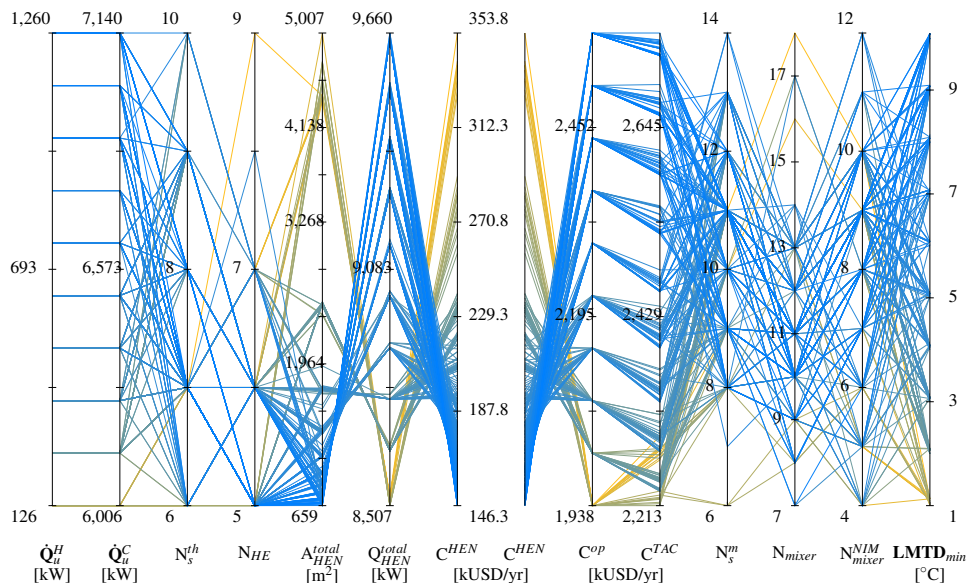


Figure 3: Visualization of selected KPIs for test case II (299 solutions)

5. Conclusions

Two main complexities are observed within literature methodologies for HIWANs. The first difficulty is selecting the thermal state of water streams, leading to the second difficulty of selecting thermal matches with undefined thermal states. Accounting for these complexities results in a complex MINLP formulation which is difficult to solve optimally with current solutions strategies; therefore, this work proposes a novel hyperstructure and solution strategy to treat this complex problem. An initial MILP model provides minimum utility consumptions with a list of potential thermal streams for achieving them. In the second step, thermal matches are identified by solving the HLD model minimizing the number of thermal matches. A novel NLP hyperstructure was developed in the last step for a complete design of the network combining the water allocation the HEN hyperstructures. Results indicate that the approach reaches optimal designs efficiently, and additionally generates a set of near-optimal solutions; thus, providing a practical approach to selecting the final implementation and contrasts the single-solution approach in literature. This approach allows experts to provide additional insights into the performance of all solutions with respect to additional indicators before selecting the solution for implementation. Finally, all possible interconnections are incorporated; therefore, providing a comprehensive approach that allows any type of heating and cooling for any water stream, bringing novel improvements to the state of the art.

Acknowledgements: This research project is financially supported by the Swiss Innovation Agency Innosuisse and is part of the Swiss Competence Center for Energy Research SCCER EIP.

References

- E. Ahmetović, N. Ibrić, Z. Kravanja, I. E. Grossmann, Nov. 2015. Water and energy integration: A comprehensive literature review of non-isothermal water network synthesis. *Computers & Chemical Engineering* 82, 144–171.
- M. Bagajewicz, H. Rodera, M. Savelski, Jan. 2002. Energy efficient water utilization systems in process plants. *Computers & Chemical Engineering* 26 (1), 59–79.
- J. Cerda, A. W. Westerburg, Jan. 1983. Synthesizing heat exchanger networks having restricted stream/stream matches using transportation problem formulations. *Chemical Engineering Science* 38 (10), 1723–1740.
- H.-G. Dong, C.-Y. Lin, C.-T. Chang, 2008. Simultaneous optimization approach for integrated water-allocation and heat-exchange networks. *Chemical Engineering Science - CHEM ENG SCI* 63 (14), 3664–3678.
- C. A. Floudas, A. R. Ciric, Oct. 1989. Strategies for overcoming uncertainties in heat exchanger network synthesis. *Computers & Chemical Engineering* 13 (10), 1133–1152.
- N. Ibrić, E. Ahmetović, Z. Kravanja, Aug. 2014. Two-step mathematical programming synthesis of pinched and threshold heat-integrated water networks. *Journal of Cleaner Production* 77, 116–139.
- A. Jagannath, A. Almansoori, Jul. 2016. Sequential synthesis of heat integrated water networks: A new approach and its application to small and medium sized examples. *Computers & Chemical Engineering* 90, 44–61.
- M. Kermani, I. D. Kantor, F. Maréchal, May 2018. Synthesis of Heat-Integrated Water Allocation Networks: A Meta-Analysis of Solution Strategies and Network Features. *Energies* 11 (5), 1158.
- M. Kermani, Z. Pétrin-Levasseur, M. Benali, L. Savulescu, F. Maréchal, 2017. A novel MILP approach for simultaneous optimization of water and energy: Application to a Canadian softwood Kraft pulping mill. *Computers & Chemical Engineering*.
- F. Maréchal, B. Kalitventzeff, Mar. 1998. Process integration: Selection of the optimal utility system. *Computers & Chemical Engineering* 22, Supplement 1, S149–S156.
- F. Marechal, I. Boursier, B. Kalitventzeff, Apr. 1989. Synep1 : A methodology for energy integration and optimal heat exchanger network synthesis. *Computers & Chemical Engineering* 13 (4–5), 603–610.
- S. A. Papoulias, I. E. Grossmann, 1983. A structural optimization approach in process synthesis—II: Heat recovery networks. *Computers & Chemical Engineering* 7 (6), 707–721.
- L. E. Savulescu, R. Smith, 1998. Simultaneous energy and water minimisation. In: 1998 AIChE Annual Meeting. Miami Beach, Florida, pp. 13–22, unpublished work.

Giving added value to products from biomass: the role of mathematical programming in the product-driven process synthesis framework

Aleksandra Zderic,^a Alexandra Kiskini,^b Elias Tsakas,^c Cristhian Almeida Rivera,^d Edwin Zondervan,^e

^a *Cosun, the Netherlands*

^b *Wageningen University, the Netherlands*

^c *Maastricht university, the Netherlands*

^d *OPCW, the Netherlands*

^e *Bremen University, Germany*

* edwin.zondervan@uni-bremen.de

Abstract

In the first years of the 2000's the late professor Peter Bongers introduced together with his co-workers at Unilever a design methodology that could be applied in the development of new products and processes for structured food products; the product-driven process synthesis method (PDPS). The method was successfully employed in the following years, designing new products from different bio based sources. Although researchers used the method and even made improvements; the structural incorporation of mathematical programming tools has been lacking and this seems to be a crucial component for decision-making processes. In this contribution we will discuss the possibilities to extend the PDPS framework with several of these optimization tools.

Keywords: Product-driven process synthesis, mathematical programming, agro-food products.

1. Introduction

We can agree that the procedures and methods for the development of (petro) chemical processes and products have matured significantly over the last 50 years. However, in new areas such as the bio-based-, food-, pharmaceutical- and water sectors, where feedstock, processing and product are dynamic and complex these developments lag and right now such methods are not at hand. A more structured approach for the synthesis of process and product was developed in the last decade by the late professor Peter Bongers, the so called product-driven process synthesis (PDPS) approach. This method makes use of the synergy of combining product and process work streams. The PDPS delivers a hierarchy of design levels of increasing details, where complex and level-interacting decisions are made from one level to another.

The application of the PDPS approach has resulted in a significant financial benefits in the fast-moving consumer goods industry and lead to novel and differentiating alternatives to current manufacture practices. Although the PDPS is a systematic approach, many of the decisions made at the different levels of the PDPS are based on expertise and knowledge brought in via experienced engineers and scientists (so called heuristics). It is clear that model-based optimization and mathematical programming

could further enhance this decision process. In this work we will outline our vision for the integration of systematic optimization methods into the PDPS.

2. Product driven process synthesis (PDPS)

The product driven process synthesis methodology has been described in detail in (Almeida Rivera et al., 2016) and consists of nine levels of increasing detail, where complex and emerging decisions are made. These levels include the: framing level, consumer wants, product function, input–output level, task network, mechanism and operational window, multiproduct integration, equipment selection and design, and multiproduct equipment integration. Each level follows the general design paradigm cycle (Siirola, 1996): scope and knowledge, generate alternatives, analyse performance of alternatives, evaluate and select, report.

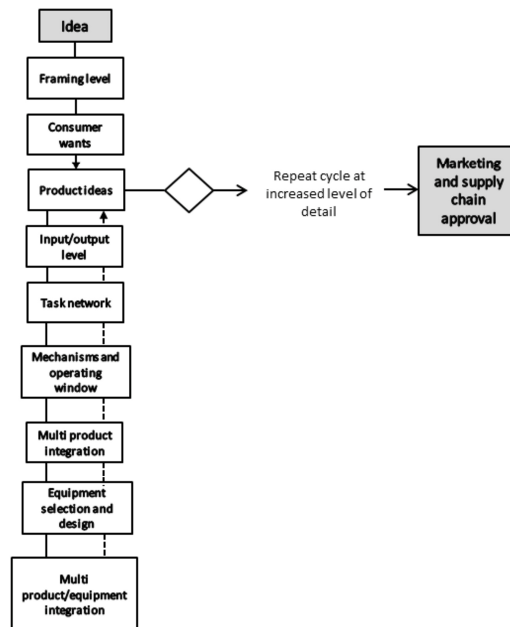


Figure 1: The product-driven process synthesis framework of 9-levels.

At all levels estimates of economic potential, turndown ratio, changeover time, sustainability, process complexity, scalability, hygiene design, among others, and all of them at various degrees of detail are made. The aim is also to include a multi criteria decision-making approach to assist in the “evaluate and select” activity (De Ridder et al. 2008). This approach, termed BROCC (benefits, risks, opportunities, and costs), is used in industrial R&D settings and combines quality function deployment (QFD) and analytic network process (ANP). QFD is a method for structured product planning and development that enables a development team to specify clearly the customer wants and needs, and then to evaluate each proposed product or service capability systematically in terms of its impact on meeting those needs (Cohen, 1995).

The backbone of QFD is the so-called “house of quality”, which displays the customer wants and needs, and the development team technical response to meeting those wants and needs. ANP is a commonly used benchmarking technique to compare alternatives. QFD has been applied to several PDPS cases but only in a qualitative fashion.

3. Examples of successful application of the PDPS to agro-food products

In the last years the PDPS has been successfully employed in several projects in the agro-food industry. These projects focused on the mild disclosure of added value chemicals from biological raw materials. In (Zondervan et al, 2015) a new process is designed for recovering vitality ingredients such as antioxidants from liquid tea-streams via solvent swing adsorption. In (Zderic et al, 2016) the scope was extended and novel methods for disclosing the antioxidants directly from fresh tealeaves using pulsed electric fields and ultrasound techniques were developed. In both studies the PDPS plays an important role for decision-making. (Zderic et al, 2017) also used the PDPS to extract oilbodies from soy.

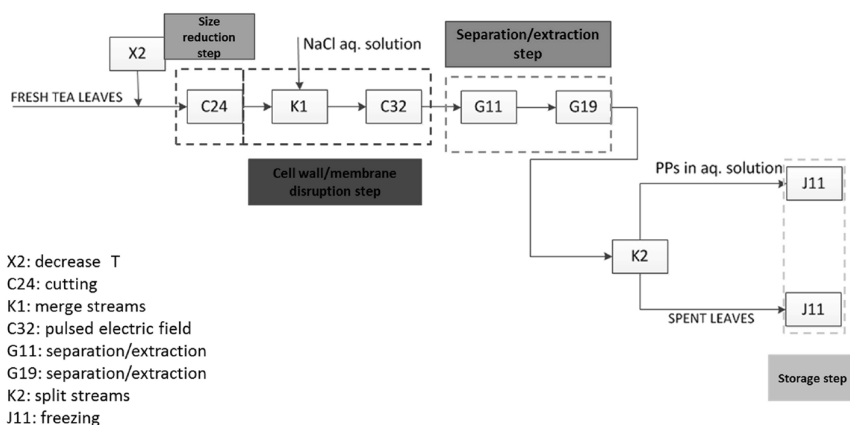


Figure 2: Example of a task-network for the isolation of antioxidants from fresh tealeaves.

In (Jankowiak et al, 2013) the PDPS was used as tool to find new pathways for isolating isoflavones from Okara and in work by (Kiskini et al., 2016) an extensive portfolio of different products that can be obtained from sugar beet leaves was set out, including proteins, carbohydrates, lipids and phenolics.

Although all studies delivered valuable insights and pointed to a strategy for an advanced product portfolio; the main strategy in decision-making was based on brainstorm sessions, experimental work and expert knowledge available in the project teams. The use of mathematical optimization techniques to facilitate decision-making would have certainly been of value, knowing the combinatorial complexity resulting from many different choices that can be made at each of the levels of the PDPS.

4. The use of mathematical optimization in the PDPS framework

4.1. The House of Quality in the PDPS

In the “framing” and the “consumer wants” levels of the PDPS one important question that needs answering is how to link the (qualitative) properties that a consumer wants in

a product to measurable indicators (such as physical properties or product formulations). For example: there might be a clear link between the “mouth feel” and the viscosity of a mayonnaise. The House of Quality (HoQ) is a graphic tool that establishes such links. The HoQ comes in different appearances, but an example is given in figure 3 below, which was taken from (Dawson et al., 1999). The figure shows the interactions between the physical properties of a pencil and how a user experiences the use of the pencil.

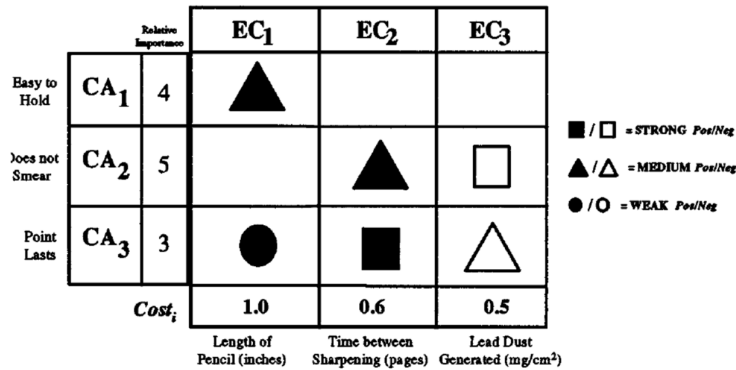


Figure 3: The Pencil design HoQ without roof.

The HoQ has been widely proposed as a method for capturing the voice of the customer when developing requirements for new products. But the methodology lacked a formal mechanism for trading off customer preferences with technical feasibility and economic reality. However, in the work of (Dawson et al., 1999) a non-linear mathematical program for determining the optimal engineering specifications during new product development as a function of elicited customer value functions, engineering development and production costs and development time constraints is proposed. Such models are shown to be computationally feasible for realistic-size problems and to outperform heuristic approaches.

4.2. Superstructure optimization of task networks in de PDPS

In the “Task network” level of the PDPS different definitions of the fundamental tasks that are needed to convert a raw material into product are taken from a cluster of tasks and its subgroup. Then, a network is made from the selected tasks and clusters. This work flow is often done on the basis of knowledge available within the project team. This leads to sound proposals for the task networks, but there are no guarantees that all possible network configurations have been evaluated. This is where superstructure optimization can be brought into the PDPS.

Figure 4 shows the general format of a superstructure, which consists of sources (raw materials), sinks (products), arcs (possible flows of mass/energy) and blocks (contained unit operation- or task models). In superstructure optimization the main question is, which route to take through the network in such way that a criterion is optimized (for example, costs, environmental impact, product yield).

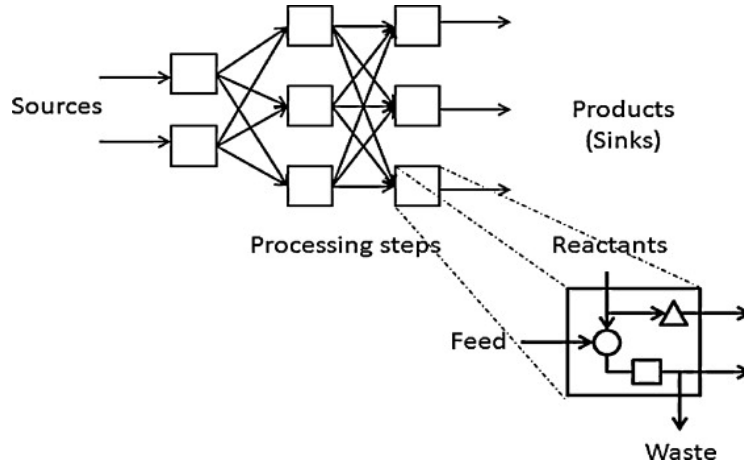


Figure 4: General format of a superstructure (Nawaz et al., 2011)

Of course, there are many possible routes to be evaluated. The number of alternatives increases factorial with the number of components that flow through the network, the number of technology options available and the number of processing stages allowed. The arcs and the blocks in the super structure can be translated into a mathematical program that can be used to evaluate many hundreds or thousands of possible pathways. The general structure of such model is:

$$\begin{aligned}
 & \min f(x, y) \\
 & \text{s.t.} \\
 & g(x, y) = 0 \\
 & h(x, y) > 0 \\
 & x_L \leq x \leq x_U \\
 & x \in X; y \in Y
 \end{aligned}
 \tag{1}$$

With f being the objective function (economic- or environmental criterion), x and y the decision variables, g the equality constraints (often mass- and energy balances), h the inequality constraints (often operating limits). There are also logical constraints (could be equalities as well as inequalities). The decision variables x and y are bounded and defined over the domains X and Y , respectively (this determines the nature of the problem; continuous or discrete). Often these models are captured as mixed integer linear (or nonlinear) programming problems, which can be handled well with appropriate software.

4.3. The use of propositional logic in the PDPS

As a complement to the use of superstructure models to generate and evaluate task networks a more intensive use of propositional logic is foreseen. Propositional logic is a tool that can be used to translate heuristics into mathematical constraints to reduce network complexity. The development of propositional logic in process design finds its roots in the work by (Raman & Grossmann, 1991). Propositional logic can be used to convert logical expressions into inequalities. As an example: “If the dryer or the hydrocyclone is selected, then do not use a crystallization step”. This heuristic can be written as a logic expression:

$$P_D \vee P_H \Rightarrow \neg P_C
 \tag{2}$$

Removing the implication yields:

$$\neg(P_D \vee P_H) \vee \neg P_C \quad (3)$$

After applying de Morgan's theorem:

$$(\neg P_D \wedge \neg P_H) \vee \neg P_C \quad (4)$$

Distributing the OR over the AND:

$$(\neg P_D \vee P_C) \wedge (\neg P_H \vee \neg P_C) \quad (5)$$

After assigning the corresponding binary variables in the above conjunction two inequalities are obtained:

$$y_D + y_C \leq 1 \quad (6)$$

$$y_H + y_C \leq 1 \quad (7)$$

Which can be added to the superstructure model. The house of Quality, superstructure optimization and propositional logic are three examples of applying quantitative methods to the PDPS.

5. Conclusions

Product driven process synthesis has over the years proven to be an effective tool for process- and product design for novel agro-food based products. The method deserves further improvements by the inclusion of mathematical programming tools that can be used to link sensory attributes with product properties (House of quality), the application of superstructure optimization for the evaluation of different task networks and the use of propositional logic in the development of constraints for the superstructure optimization.

References

- C. Almeida Rivera, P. Bongers, E. Zondervan, A structured approach for product driven process synthesis in foods manufacture, *Computer Aided Process Engineering*, 2016, 39, pp. 417-441.
- L. Cohen, *Quality function deployment: How to make QfD work for you*, 1995, Wesley Publishing Company Inc.
- D. Dawson, R. Askin, Optimal new product design using quality function deployment with the empirical value function, *Quality and Reliability Engineering International*, 1999, 15, pp. 17-32.
- D. De Ridder, C. Almeida Rivera, P. Bongers, S. Bruin, S. Flapper, Multi-criteria decision-making in product driven process synthesis, *Computer Aided Process Engineering*, 2008, 25, pp. 1021-1026.
- L. Jankowiak, D. Mendez, R. Boom, M. Ottens, E. Zondervan, A. Van der Goot, A process synthesis approach for isolation of isoflavons from Okara, *I&EC Research*, 2015, 54(2), pp. 691-699
- M. Nawaz, E. Zondervan, J. Woodley, R. Gani, Design of an optimal biorefinery, *Computer Aided Process Engineering*, 2011, 29, pp. 371-376
- A. Kiskini, E. Zondervan, P. Wierenga, E. Poiesz, H. Gruppen, Using product driven process synthesis in the biorefinery, *Computers and Chemical Engineering*, 2016m 91, pp. 257-268
- R. Raman, I. Grossmann, Relation between MILP modeling and logical inference for chemical process synthesis, *Computers and Chemical Engineering*, 1991, 15(2), pp. 73-84.
- J. Sirola, Industrial application of chemical process synthesis, *Advances in chemical engineering, Process synthesis*, 1996, pp. 1-61.
- A. Zderic, C. Almeida Rivera, P. Bongers, E. Zondervan, Product driven process synthesis for the extraction of oilbodies from soy beans, *Journal of food engineering*, 2016, 185, pp. 26-34.
- A. Zderic, E. Zondervan, Product driven process synthesis: the extraction of polyphenols from tea, *Journal of food engineering* (2017), 196, pp. 113-122.
- E. Zondervan, M. Monsanto, J. Meuldijk, Product driven process synthesis for the recovery of vitality ingredients from plant materials, *Chemical Engineering Transactions*, 2015, 43, pp. 61-66.

Energy System Modelling in support of the Energy Transition

Jan van Schijndel,^{a*} Karin Griffioen,^b Levi Ikele,^b Andreas ten Cate^c

^a*VSSC, Frederik Hendriklaan 2, Voorschoten, 2252 KJ, Netherlands*

^b*ORTEC, Houtsingel 5, 2719 EA, Zoetermeer, Netherlands*

^c*ISPT, Groen van Prinstererlaan 37, 3818 JN Amersfoort, Netherlands*

jmg.vanschijndel@gmail.com

Abstract

The Dutch ISPT (Institute for Sustainable Process Technology) executes an innovation program that focusses on system integration and circularity. This program explores amongst others pathways for the re-use of CO contained in waste gases produced by steel making processes so to enable the circular use of carbon. ISPT commissioned an Energy System Modelling (ESM) project to demonstrate how ESM can be used to explore options for the upgrading of these CO-rich waste gas streams and to show which upgrade investments over time could meet CO₂ emission targets in the most cost-effective manner.

Keywords: Multi-Period Mixed Integer Linear Programming, monetisation waste gases from steel manufacturing, CO₂ abatement pathways, impact CO₂ taxation on CCS.

1. Introduction

Deep decarbonization of the energy system is required to mitigate climate change. ISPT executes an innovation program in the Netherlands that focusses on system integration and circularity to enable such a radical transformation. An example is the study on the re-use of CO from waste gases by steel making processes to enable circular use of carbon. Against this backdrop, ISPT commissioned a project to demonstrate how Energy System Modelling (ESM) could be used to explore a set of options for the most effective upgrading of CO-rich waste gas streams produced by a steel manufacturing complex.

2. Energy System Modelling

Energy System Modelling (ESM) is a dedicated application of the more generic network simulation and optimisation algorithm. It is based on a detailed techno-economic description of the conversion of energy flows. ESM systematically explores how to use over a given time horizon optionality in energy resource availability and conversion capacity in order to meet demand for heat, power, mobility and petrochemical products in the most cost-effective manner. An appropriately defined objective function that maximizes the net present value of the energy system whilst obeying CO₂ emission targets supports the evaluation of options how to be best structure the energy system. Scope and granularity for energy system modelling can vary widely: ESM can be applied at country level (Kejun and van der Made, 2014), but also at industrial cluster levels as shown by the example below for a steel manufacturing complex.

3. Mathematics

Energy System Modelling (ESM) is based on a mathematical optimization framework that uses a combination of the mathematical modelling system AIMMS and the mixed-integer solver CPLEX (Lasschuit and Thijssen, 2004). At the heart of ESM lies a Multi-Period Mixed Integer Linear Programming Model designed for strategic value chain studies and supply chain optimization purposes. ESM is a dedicated application of this generic framework with a focus on determining an economically optimal configuration of energy conversion systems such that it meets CO₂ emission targets and energy demand levels given available energy resources.

Mixed-integer Linear Programming (MILP) models have been successful in a vast range of applications. These algorithms evaluate the impact of integer decisions (on-off or 0-1) on the objective simultaneously with continuous variables subject to various constraints. ESM supports the selection and timing of conversion technology investments to meet CO₂ emission targets in the most cost-effective manner. The true value of the implemented mixed-integer linear programming model lies in its multi-period character. In particular, this means that multi-period mixed integer linear programming ensures that from a given set of potential technology investment options, those are selected and timed such that they minimize the total costs over the entire time horizon. This holistic approach avoids “technology lock-in situations” whereby technology options are selected with regrets later on leading to sub-optimal solutions over the time period considered. ESM adopts a complete end-to-end view both on a time-scale as on an infrastructure scale allowing for a fully integrated system optimisation from raw materials, to intermediates, to finished products that serve demand. ESM also allows to model non-linear ‘economy of scale’ features as multiple capacity choices aligned with relevant line-ups.

Figure 1 outlines the Energy System Modelling framework. Inputs define the structure of the energy system model and include data on various constraints and costs. The structure of the energy system may consist of various feedstock sourcing options, yields for conversion technology options and a distribution network to bring product to markets. Additional data are to be provided to define the optimisation space, such as product demand, CAPEX & OPEX for the conversion options and product distribution costs. Furthermore, the scope of the optimization space is defined by strategic input such as the time horizon considered and a set of scenarios to be evaluated. Simulation and Optimisation return a set of attractive energy system options for further analysis.

The model considers an annual planning horizon where t is the time period index, l the location index, p the conversion technology index, m the mode of operation index, s the stream index, i the investment index and r the investment effect time range index. The integer variable $u_{t,r,i}$ specifies the number of investments per investment option i , how many times it is active in period t and r periods after the start period of the investment. With r (relative to start) the aging of a conversion unit is tracked. The continuous variables $\sigma_{t,l,s}$, $\delta_{t,l,s}$, and $\pi_{t,l,p,m}$ denote supply, demand & processing variables for the infrastructure of the system. Processing optimizes the production yields per conversion technology per mode of operation per stream. Input and output yields for the production process are parameters denoted by $IY_{t,l,p,m,s}$ and $OY_{t,l,p,m,s}$. Mass balance constraints ensure that the total inflow equals the total outflow at each node.

$$\sigma_{t,l,s} + \sum_{(p,m)} (\pi_{t,l,p,m} * OY_{t,l,p,m,s}) = \sum_{(p,m)} (\pi_{t,l,p,m} * IY_{t,l,p,m,s}) + \delta_{t,l,s}$$

$$\forall t \in T, l \in L, s \in S$$

$PC_{i,r,l,p,m}$ denotes the processing capacity of a conversion unit with an age of r time periods. Cost minimization steers the investment in processing capacity for conversion technologies and determines the optimal set of conversion technologies.

$$\pi_{t,l,p,m} \leq \sum_{(i,r)} PC_{i,r,l,p,m} * t_{t,r,i} \quad \forall t \in T, l \in L, p \in P, m \in M$$

The yield structure in the ESM denotes the amount of end products and by-products such as CO₂ generated at each production process in the energy system. A CO₂ abatement pathway can be modelled by assigning a cost per ton CO₂ leaving the energy system. Alternatively, direct emission targets can be defined to limit CO₂ emissions and set additional constraints that guide the model towards selection of the optimal energy system layout for the desired CO₂ abatement pathway. Let $MD_{t,l,s}$ be the maximum flow leaving the energy system, then the CO₂ emission limit is defined as follows.

$$\delta_{t,l,s} \leq MD_{t,l,s} \quad \forall t \in T, l \in L, s \in S$$

From Figure 1 it can be inferred that the results of the optimised energy system depend on various input factors such as the layout of the system, conversion technology options, capital intensities & operating expenditures, feedstock availabilities & demand figures, which are deterministically modelled. In practice these input factors are of stochastic nature. This demands for sensitivity analyses to cope with the various types of uncertainties that affect the optimal results. Uncertainties emerge in different ways such as multiple scenarios for the outlook on energy supply and demand, technological developments affecting the capital intensities of conversion technologies or policy changes with regard to imposed CO₂ emission penalties. Therefore, the success of the decision-making process not only relies on the availability of a global optimal solution but also on sensitivity checks on the input data to address and confirm the robustness of the proposed optimal configuration of the energy system.

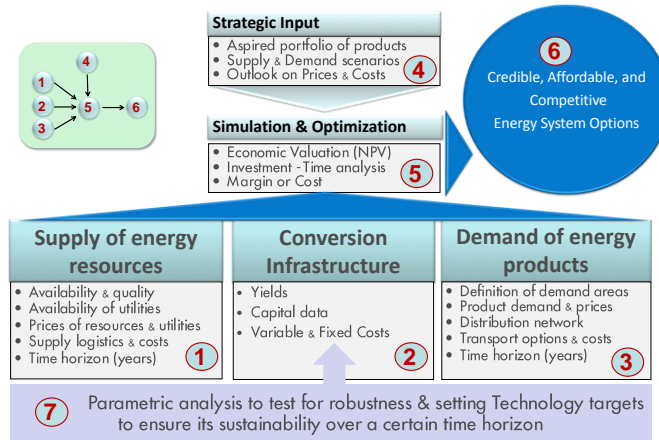


Figure 1: Generic framework for Energy System Modelling

4. Example

Europe produces some 170 million tonnes of steel per year. Significant volumes of waste gas are co-produced, like blast furnace gas (BF) and basic oxygen steel off-gas (BOS). Typically 1,7 tonnes of waste gases are produced per tonne of steel for a world scale plant

producing 7 mln tonnes of steel per year. Apart from a high CO₂ content (40 wt%), waste gases contain high concentrations of valuable components, e.g. 23 wt% of carbon monoxide (CO). The remainder is predominantly N₂. Waste gases are burned to preheat enriched air for the blast furnaces. Waste gases are also used for steam and power generation. The resulting CO₂ footprint is some 1,3 tonnes CO₂ per ton of steel.

The combustion of CO contained in BF and BOS gas (see Figure 2) results in a major loss of potential value from a circular economy perspective. The recovery and conversion of CO into chemicals is therefore an alternative worthwhile pursuing. This has been studied by the CORESYM project (ISPT, 2017). This example builds on this project.

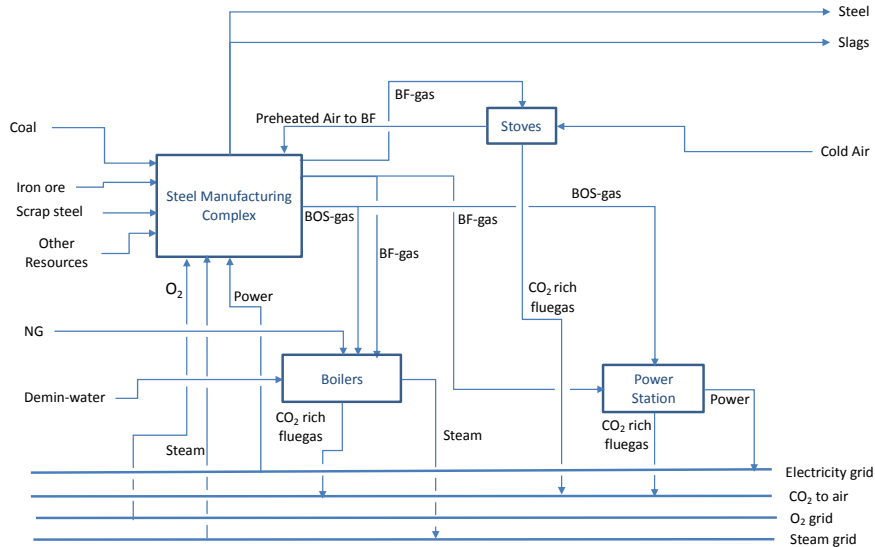


Figure 2: Base case upgrading waste gases from a steel manufacturing complex

Figure 3 below shows a superstructure of options for the upgrading of CO contained in BF and BOS waste gas into valuable products like Fisher-Tropsch (FT)-naphtha and methanol. The deficit in the amount of hydrogen to achieve this is by water electrolysis, steam methane reforming (SMR) and/or by shifting the H₂/CO content of the BOS gas in a dedicated water-gas shift reactor (WGS) or by buying H₂ from the grid. Furthermore, the superstructure shows a number of CO₂ capture units to ensure that remaining CO₂ volumes are captured and can be fed into a CO₂ grid for (deep-sea) storage. The purpose of this EMS pilot project is to analyse the attractiveness of recovery and conversion of CO into chemicals whilst simultaneously addressing the impact of CO₂-to-Air taxation in combination with a feed-in tariff of 50 \$ per ton of CO₂ for a CCS system assumed to be in place. Another task set for the pilot is the development of a CO₂ abatement pathway to meet the 'Paris' goals set for 2030 and 2050 in the most cost-effective manner.

Figure 4 shows the relative attractiveness of the options studied. With CO₂-to-Air priced in accordance with a low ETS (Emission Trading System) price level of 4 \$ per ton of CO₂, ESM identifies the recovery and conversion of CO into methanol (1350 ktpa methanol) with H₂ to be supplied through Steam Methane Reforming as most profitable (bar at the right).

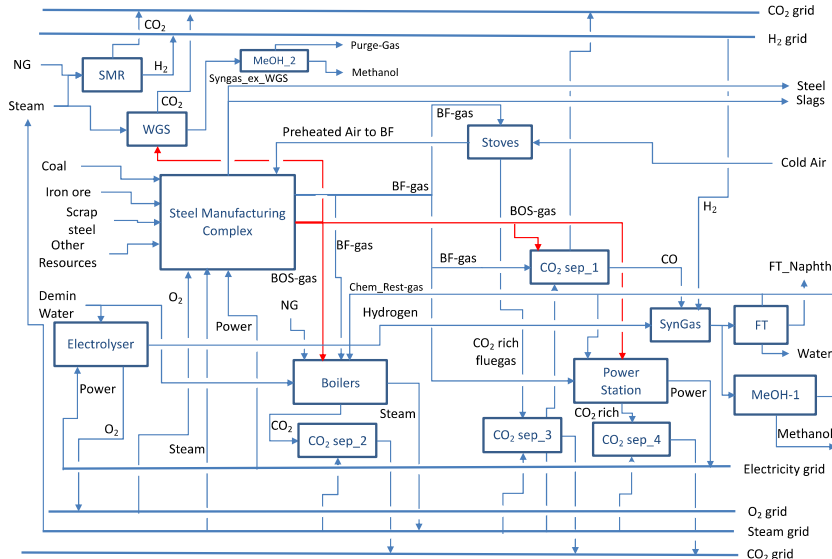


Figure 3: Options for the upgrading of waste gases steel manufacturing complex

Apart from a higher NPV, this option also lowers the CO₂ emission level of the reference case by some 12,5% from 9250 ktpa CO₂ to 8080 ktpa CO₂. This is due to the rerouting of the BOS and BF streams for methanol and hydrogen production and the elimination of NG imports to the boilers. This results in steam and power imports to meet all process requirements. Adjacent steam and power units allow for these imports. The resulting shift of CO₂ emissions to air to outside the complex is not accounted for.

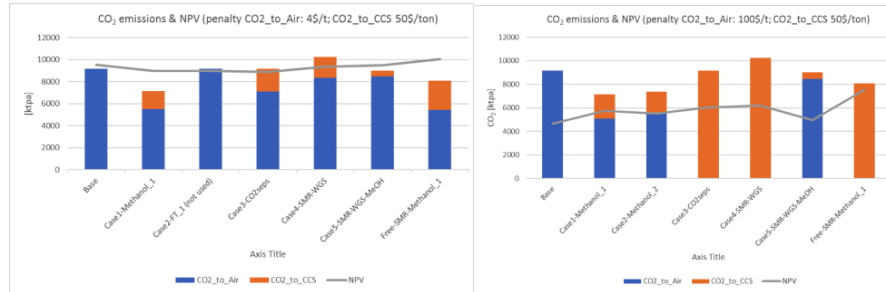


Figure 4: Relative attractiveness of CO monetisation options

Would CO₂ emissions to air be taxed at 100 \$/ton, the most attractive CO-conversion option remains the methanol option. At this 100 \$/ton CO₂ penalty, ESM concludes that it would be more cost-effective to invest in CCS facilities (and capture 50\$ benefit per ton of CO₂) rather than enlarging methanol or FT-naphtha production (the amount of CO contained in the waste gases allows for the production of either 2500 ktpa methanol or 900 ktpa FT-naphtha). FT-naphtha and methanol are feedstocks for Base-Chemicals. Figure 5 shows the CO₂ abatement profile with the CO₂-to-Air penalty set at 0 \$/ton. In order to meet the 50% CO₂ reduction target in 2030 (50% relative to 2017, taken as Reference Year) investments are needed for the separation of CO₂ and CO from the BF and BOS waste gases, the production of Blue H₂ (e.g. through steam-methane-reforming

while capturing and sequestering CO₂), the synthesis of methanol and treatment of flue gas ex boilers for CO₂ capture. Apart from the latter investment (taken in 2030), all other investments are advised to be taken in 2020. To meet the 95% reduction target in 2050 (again relative to 2017, taken as Reference Year), CCS investments are needed in 2050 for Power unit and Stoves. Timing of investments is optimal from an NPV perspective.

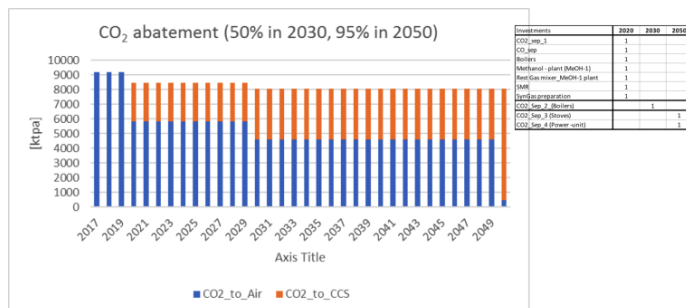


Figure 5: CO₂ abatement curve for steel manufacturing complex

5. Conclusions

ESM is a powerful decision support tool to assess the cost effectiveness of options for the upgrading of CO contained in waste gases from a steel manufacturing complex whilst simultaneously reducing its CO₂ emission footprint. Upgrading of CO into methanol is both economically attractive and it lowers CO₂ production by some 12,5%. This scenario assumes that CO₂-to-Air emissions are not subjected to any tax. In case 100 \$/ton tax would be levied on CO₂-to-Air emissions, methanol remains the preferred upgrading option. Assuming a CO₂ sequestration grid in place with a feed-in tariff of 50 \$/ton of CO₂, ESM shows that capturing and sequestering all CO₂ is economically preferred over increasing methanol production.

ESM supports the development of CO₂ abatement profiles defining which investments over time are needed to meet CO₂-to-Air emissions targets as set by the Paris agreement in the most cost-effective manner.

Acknowledgements

Authors acknowledge Shell Global Solutions International B.V. for making their Network Simulation and Optimisation tool available, TATA Steel for discussing decarbonisation options and Nort Thijssen for the modelling of the example discussed.

References

- ISPT, Report CORESYM study: CarbOn-monoxide RE-use through industrial SYMBiosis between steel and chemical industries; December 2017
- Jiang Kejun and Alexander van der Made: 'The greening and cleaning of China' in: The colours of energy: Essays on the future of our energy system by Kramer G.J. and Vermeer B. (Editors), Shell International B.V., Amsterdam, the Netherlands, ISBN: 978-90-9028343-2, July 2014
- Winston Lasschuit, Nort Thijssen: Supporting supply chain planning and scheduling decisions in the oil and chemical industry; Computers and Chemical Engineering, 28 (2004) 863-870

Are renewables really that expensive? The impact of uncertainty on the cost of the energy transition

Xiang Li^{a,*}, Stefano Moret^a, Francesco Baldi^a and François Maréchal^a

^a*Industrial Process and Energy Systems Engineering, Ecole Polytechnique Fédérale de Lausanne, Sion 1951, Switzerland*

*xiang.li@epfl.ch

Abstract

The dramatic evidence of climate change is making the transition to more renewable energy systems an urgent global priority. As energy planners normally look 20-50 years ahead, it is crucial to consider the key uncertainties stemming from inaccurate forecasts (e.g. of fuel prices, investment costs, etc.) in energy models to ensure making robust investment decisions. Nonetheless, uncertainty is to date seldom accounted for in energy planning models.

In this paper, we challenge the general perception that the transition to a more renewable energy system always comes at a higher price; to do this, we analyze the impact of uncertainty on the cost of this transition for a real-world national energy system. Concretely, we first generate a set of energy planning scenarios with increasing renewable energy penetration (REP); in a second stage, we perform an uncertainty analysis to compare the cost of these scenarios and thus to determine the significance of the difference in their total cost in presence of uncertainty. Our results show that increasing the amount of renewable energy in a national energy system is not necessarily associated to a higher cost, and can even lead to a cost reduction for some specific realizations of the uncertain parameters.

Keywords: Energy planning, Uncertainty, Energy transition, Mixed-integer linear programming

1. Introduction

The Earth is warming up at an alarming pace. Most countries have agreed on ambitious goals for reducing the human impact on the climate (Rogelj et al., 2016) and have started to make plans for a transition towards more sustainable systems (Kern and Rogge, 2016). A major part of this *energy transition* is related to an increased use of renewable energy sources (RESs). Many authors have thus used energy models to evaluate the impact of an increased share of RESs in energy systems planning. Jacobson et al. (2015) investigated the feasibility and cost of a fully renewable-powered system for the United States and concluded that, when externalities are accounted for, such system would be less expensive than a traditional energy system; Schill (2014) performed a similar analysis for the German energy system with the objective of achieving 86% REP by 2050, showing that this can be done with a relatively limited investment in energy storage capacity as long as a higher flexibility in the operation of fossil power plants is allowed.

Despite these results, and despite the fact that today there are several technological options for a cost-competitive generation of renewable energy, the public opinion often still perceives RESs as being far more expensive than fossil fuels. As an example, Ntanos et al. (2018) report the results of a recent survey in Greece, in which the respondents identified in the “high installation costs” the main reason for not using RESs. In this paper, we challenge this general perception. The main

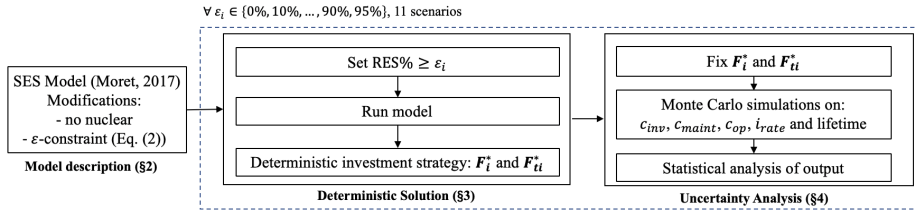


Figure 1: Modeling flowchart

contribution of our work compared to the literature is the consideration of multiple sources of uncertainty in the analysis. In fact, the main shortcoming of most works proposed in the literature lies in the use of “deterministic” models, which do not consider uncertainty and assume that long-term forecasts for the key parameters (e.g. fuel prices) are correct. However, long-term forecasts are inevitably inaccurate (Moret et al., 2017), and thus it is crucial to consider uncertainties in long-term energy modeling (DeCarolis et al., 2017; Mavromatidis et al., 2018).

In this paper, we propose an analysis of the cost and investment decisions for different degrees of REP in an energy system, with a particular focus on the impact of uncertainty in the process, taking the national energy system of Switzerland as a real-world case study. The methodological approach is shown in Figure 1. First, we model the Swiss energy system using the Swiss EnergyScope (SES) framework (Moret et al., 2014; Codina Gironès et al., 2015). SES, which we describe in Section 2, is a mixed-integer linear programming (MILP) model, which identifies the optimal investment and operation strategy to minimize the total annual cost of the energy system. In a second phase, the model is used deterministically (i.e. with all parameters at nominal values) to determine the optimal energy planning scenarios under increasing shares (ε_i) of RESs (Section 3). Third, the impact of uncertainty is evaluated: for each of the previously obtained scenarios, the investment strategy is fixed and the total cost of the system is evaluated with a Monte-Carlo based approach, considering as uncertain parameters all the costs, the discount rates and the lifetime of technologies. This allows to perform an uncertainty analysis of the solution (Section 4).

2. The energy model

The paper is based on the SES model, a framework for the strategic energy planning of the Swiss energy system. In particular, in this paper we use the open-source MILP version of the model by Moret (2017)¹. It is a representative model of an energy system, including electricity, heating and mobility: given the end-use energy demand, the efficiency and cost of energy conversion technologies, the availability and cost of energy resources, the model identifies the optimal investment (\mathbf{F}) and operation (\mathbf{F}_t) strategies to meet the demand and minimize the total annual cost of the energy system. In comparison to other energy models, which often consider hourly timesteps and multi-stage investment plans, it has a lower level of detail, but it offers a reasonable trade-off between CPU time and accuracy; in particular, its multiperiod monthly formulation allows accounting for the main dynamics of concern in energy systems planning, such as seasonal variations, long-term energy storage management, and uncertainties in loads and renewable production.

The objective of the SES model is to minimize the annual total cost \mathbf{C}_{tot} expressed by the sum of the annualized investment cost (\mathbf{C}_{inv}), of the annual operational costs (\mathbf{C}_{op}) and of the annual maintenance cost ($\mathbf{C}_{\text{maint}}$) (1).

$$\min \mathbf{C}_{\text{tot}} = \min \left(\sum_{j \in \mathcal{E}} \mathbf{C}_{\text{inv}}(j) + \sum_{j \in \mathcal{E}} \mathbf{C}_{\text{maint}}(j) + \sum_{r \in \mathcal{R}} \sum_{t \in \mathcal{T}} \mathbf{C}_{\text{op}}(r, t) t_{\text{op}}(t) \right) \quad (1)$$

¹Model available at https://github.com/stefanomoret/SES_MILP and fully documented in (Moret, 2017)

where the sets \mathcal{E} , \mathcal{R} and \mathcal{T} represent the technologies, the resources (renewables and non-renewables as well as electricity import) and the time periods (months) respectively. $t_{op}(t)$ denotes the duration of the period t . The main constraints are the energy and resource balance in each period; the limited availability of resources; the capacity factor of different energy conversion technologies; the limits to the maximum installed capacity of different technologies; and the limits to grid capacity (accounting for the additional investments linked to a higher penetration of stochastic renewables).

In this paper, we modify the model presented by Moret (2017) as follows: *i*) we allow individual technologies to cover the full share of the demand in their sector, e.g. electric vehicles can satisfy all the private mobility demand ($f_{min,\%}(j) = 0, f_{max,\%}(j) = 1 \forall j \in \mathcal{E}$); *ii*) we allow freight transport to be fully satisfied by trains; *iii*) we impose the phase out of nuclear energy, in agreement with the Swiss energy strategy.

3. Deterministic energy planning

In addition, in order to quantify and to constrain the impact of RESs, Eq. (2) is added to the model formulation.

$$\sum_{r \in \mathcal{R}_{RES}} \sum_{t \in \mathcal{T}} \mathbf{F}_t(r,t)t_{op}(t) \geq \varepsilon \sum_{r \in \mathcal{R}} \sum_{t \in \mathcal{T}} \mathbf{F}_t(r,t)t_{op}(t) \quad (2)$$

where the parameter ε represents the minimal renewable penetration ratio in the energy system and the set \mathcal{R}_{RES} is a subset of \mathcal{R} composed of all renewable resources (solar, wind, wood, hydro, geothermal, synthetic natural gas, bioethanol and biodiesel). In Eq. (2), $\mathbf{F}_t(r,t)$ stands for the utilization of resource r at period t . In this paper we analyze 11 scenarios with different values of the ε parameter, ranging from 0 % to 90 % with 10 % steps, plus the “maximum REP” scenario with $\varepsilon = 95$ %.

The energy mixes of the resulting 11 scenarios are shown in Figure 2. It should be noted that scenarios 1, 2 and 3 are equivalent, due to the fact that the REP in the unconstrained (i.e. with 0 % minimum REP) case is approximately 20 %. Among the RESs, wind and (new) hydro-power are the most competitive from a cost perspective and reach their maximum potential at a REP level of

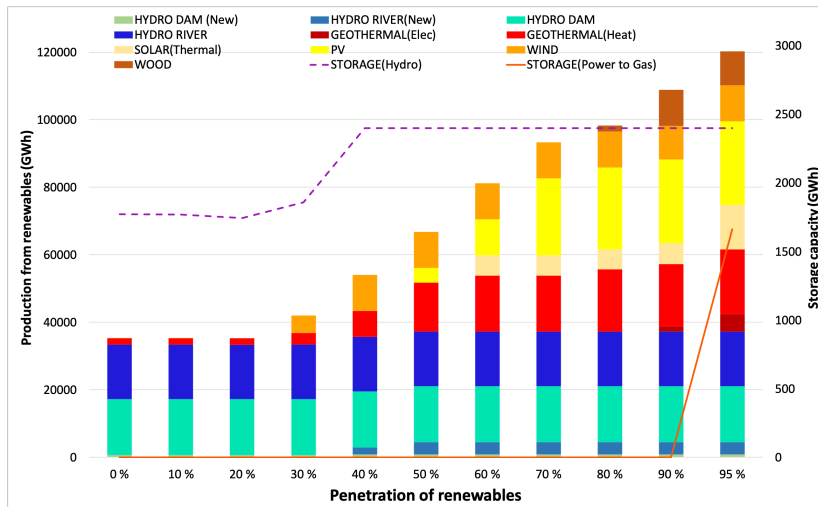


Figure 2: Renewable energy production and storage capacity in different REPs

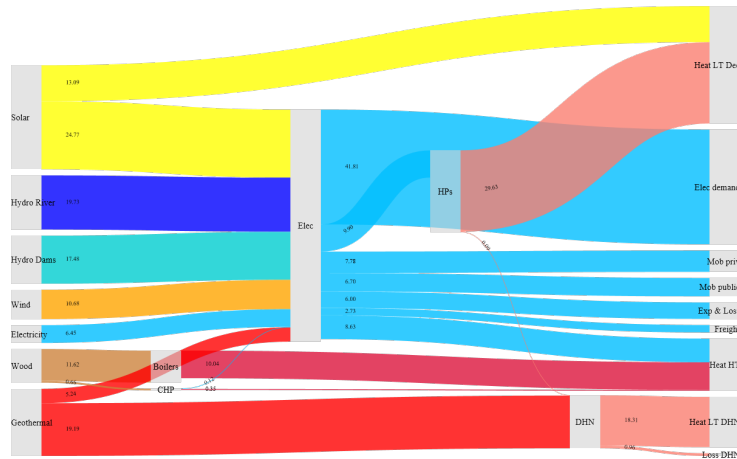


Figure 3: Sankey diagram for energy flows in 95 % REP scenario [TWh]

60 %. The use of solar energy emerges in the optimal solution only starting from a REP of 50 %, and it is only used extensively for $\text{REP} \geq 70\%$. Wood is only used in very high REP scenarios, due to its high assumed cost in the model. The results of the deterministic optimization also show that the required storage capacity is relatively limited: hydro-electric storage reaches its peak in the 40 % REP scenario, at a value approximately 35 % higher than the base case, while power-to-gas is only activated in the 95 % REP scenario, allowing to reach a total seasonal storage capacity of approximately 4,000 GWh. Note that, due to the monthly resolution of the model, here dynamic storage technologies for balancing in-time supply-demand at a daily or more fine time resolution (such as batteries) are not considered. This choice is motivated by computational reasons.

How does an almost completely renewable-based energy system look like? This is shown in Figure 3, where the energy flows in Scenario 11 are represented. As expected, the demand is dominated by the use of electricity, with the exception of part of the high-temperature heat demand (provided by biomass boilers) and of the low-temperature heat demand (provided by thermal solar and by geothermal heat). The use of boilers and gas-driven heat pumps for low-temperature heat is completely discontinued, substituted by electric heat pumps.

4. Uncertainty analysis

As highlighted in the Introduction, the problem of strategic energy planning is subject to a high degree of uncertainty, which should not be neglected. In this article, we consider five main uncertainty categories: interest rate, investment cost, maintenance cost, resource prices, and technology lifetime. In the SES model, this translates to a total of 157 uncertain parameters. We assume that all these uncertain parameters are uniformly distributed between their lower and upper bounds, adopting the methodology and the uncertainty ranges defined by Moret et al. (2017).

In the uncertainty analysis, the decision variables related to the installed capacity of each technology, and the energy utilization for each mobility technology in each period are fixed to the optimal values calculated in the deterministic optimization for each scenario (\mathbf{F}^* and \mathbf{F}_t^* , respectively). Then, for each of the 11 scenarios, the SES model is run for different realizations of the uncertain parameters with a Monte-Carlo approach. This corresponds to a situation where a decision for the strategic energy planning has been taken, and we aim to analyze the cost of the application of that specific strategy with different values for the uncertain parameters, corresponding to different

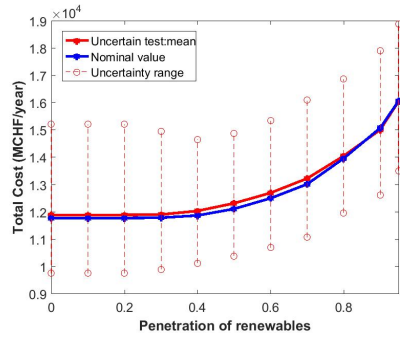


Figure 4: Nominal and uncertain mean total cost

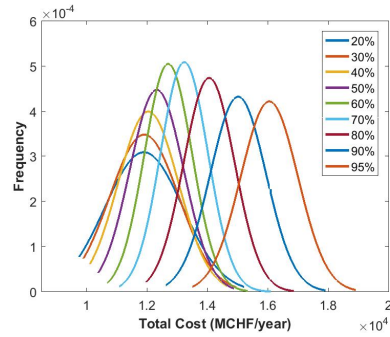


Figure 5: Normalized total cost distribution

possible future scenarios. A total of 3,000 Monte-Carlo simulations (based on an observed convergence after 2,600 simulations) is run for each scenario.

In the Swiss energy system, a large share of the total annual cost (equal to 6,654 MCHF/y) derives from fixed costs, i.e. costs which are equal for all the solutions (such as the investment cost of existing hydroelectric power plants, of the electricity grid and of energy efficiency measures). In the simulation runs, we fix these costs to zero; this means that we do not consider them as uncertain in the simulations, but we add them to the simulation results at their nominal values.

Figure 4 shows the results of the uncertainty analysis. It can be observed that the mean total cost values obtained by Monte-Carlo simulations are consistent with the deterministic results for each scenario, as in both cases the total cost increases with ϵ . However, the results also show that there is a high uncertainty in the total cost of the system for all REP levels, leading to a relatively high overlap between the different distributions (Figure 5). This can lead to the conclusion that, while on average increasing the share of renewable energy beyond 20 % involves a higher cost for the system, this is not necessarily true once uncertainty is accounted for.

A higher REP has also an impact on the variance of the total cost (Figure 6): given the high uncertainty on the price of different fossil fuels, excluding them from the energy mix generates a clear reduction in the uncertainty of operational costs. In contrast, the uncertainty on the investment increases, partially balancing the previous effect, as a consequence of both the larger uncertainty of the investment cost of technologies activated with higher REP, and of the overall higher investment cost of the system, which amplifies the uncertainty related to the interest rate. Overall, it can be concluded that cost uncertainty decreases when the share of RES increases.

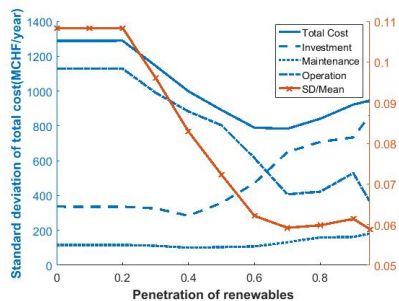


Figure 6: Total cost standard deviation breakdown

	Penetration of renewable energy							
	30%	40%	50%	60%	70%	80%	90%	95%
0%	0.44	0.33	0.23	0.17	0.12	0.05	0.00	0.00
10%	1.00	1.00	0.97	0.62	0.43	0.30	0.12	0.01
20%	1.00	1.00	1.00	0.97	0.76	0.51	0.35	0.18
30%	1.00	1.00	1.00	1.00	0.97	0.75	0.55	0.39
40%	1.00	1.00	1.00	1.00	1.00	0.95	0.77	0.57
50%	1.00	1.00	1.00	1.00	1.00	1.00	0.95	0.78
60%	1.00	1.00	1.00	1.00	1.00	1.00	1.00	0.94
70%	1.00	1.00	1.00	1.00	1.00	1.00	1.00	0.99
80%	1.00	1.00	1.00	1.00	1.00	1.00	1.00	1.00
90%	1.00	1.00	1.00	1.00	1.00	1.00	1.00	1.00
100%	1.00	1.00	1.00	1.00	1.00	1.00	1.00	1.00

Figure 7: Probability of total cost increase for different REP scenarios

Figure 7 shows the percentage of Monte-Carlo simulations where a given REP scenario was more expensive than the base case by a certain amount. An energy system with 70 % REP was less than 20 % more expensive than the base case in 76 % of the simulations, and in 12 % of the simulations it was actually less expensive than the base case. Even the 95 % REP case was, in most (78 %) cases, no more than 50 % more expensive than the baseline case, while the less ambitious 50 % REP scenario is at most 10 % more expensive than the baseline. These results are in accordance with what previously published in the academic literature (e.g. Jacobson et al. (2015)), and the cost difference is expected to be even lower if the external costs were included in the analysis.

5. Conclusions

Are renewable really that expensive? Based on the work that we present in this paper, the answer is that yes, a renewable-based energy system will most likely be more expensive than one where we apply no constraint on the share of renewable energy, but not always, and not by much. Furthermore, a renewable-based energy system will be, overall, inherently more robust against unexpected developments, particularly with respect to fluctuations in fuel prices.

The results of our uncertainty analysis, in fact, reveal that the variance in the total cost of the system is high, and of the same order of magnitude of the average cost difference between different scenarios. This suggests that, when considering uncertainty, increasing the amount of renewable energy in a national energy system is not necessarily associated to a higher cost, and can even lead to a cost reduction in some specific realizations of the uncertain parameters. These results are of particular value to energy planners, as they challenge the common perception of a very high cost related to the energy transition towards a renewable energy-based system. While these conclusions are drawn based on a specific case study (the Swiss energy system), we consider that they are sufficiently general to be applicable to other countries.

References

- V. Codina Gironès, S. Moret, F. Maréchal, D. Favrat, Oct. 2015. Strategic energy planning for large-scale energy systems: A modelling framework to aid decision-making. *Energy* 90, Part 1, 173–186.
- J. DeCarolis, H. Daly, P. Dodds, I. Keppo, F. Li, W. McDowall, S. Pye, N. Strachan, E. Trutnevyte, W. Usher, M. Winning, S. Yeh, M. Zeyringer, May 2017. Formalizing best practice for energy system optimization modelling. *Applied Energy* 194, 184–198.
- M. Z. Jacobson, M. A. Delucchi, G. Bazouin, Z. A. Bauer, C. C. Heavey, E. Fisher, S. B. Morris, D. J. Piekutowski, T. A. Vencill, T. W. Yeskoo, 2015. 100% clean and renewable wind, water, and sunlight (wWS) all-sector energy roadmaps for the 50 united states. *Energy & Environmental Science* 8 (7), 2093–2117.
- F. Kern, K. S. Rogge, Dec. 2016. The pace of governed energy transitions: Agency, international dynamics and the global Paris agreement accelerating decarbonisation processes? *Energy Research & Social Science* 22, 13–17.
- G. Mavromatidis, K. Orehounig, J. Carmeliet, Mar. 2018. Uncertainty and global sensitivity analysis for the optimal design of distributed energy systems. *Applied Energy* 214, 219–238.
- S. Moret, 2017. Strategic energy planning under uncertainty. Ph.D. thesis, École Polytechnique Fédérale de Lausanne, Lausanne, Switzerland.
- S. Moret, V. Codina Gironès, M. Bierlaire, F. Maréchal, Sep. 2017. Characterization of input uncertainties in strategic energy planning models. *Applied Energy* 202, 597–617.
- S. Moret, V. Codina Gironès, F. Maréchal, D. Favrat, 2014. Swiss-EnergyScope.ch: A Platform to Widely Spread Energy Literacy and Aid Decision-Making. *Chemical Engineering Transactions* 39, 877–882.
- S. Ntanos, G. Kyriakopoulos, M. Chalikias, G. Arabatzis, M. Skordoulis, Mar. 2018. Public Perceptions and Willingness to Pay for Renewable Energy: A Case Study from Greece. *Sustainability* 10 (3), 687.
- J. Rogelj, M. den Elzen, N. Höhne, T. Fransen, H. Fekete, H. Winkler, R. Schaeffer, F. Sha, K. Riahi, M. Meinshausen, Jun. 2016. Paris Agreement climate proposals need a boost to keep warming well below 2 °C. *Nature* 534 (7609), 631–639.
- W.-P. Schill, Oct. 2014. Residual load, renewable surplus generation and storage requirements in Germany. *Energy Policy* 73, 65–79.

Bottom-up method for potential estimation of energy saving measures

Anna S. Wallerand^{a*}, Ivan Kantor^a and François Maréchal^a

^a*École Polytechnique Fédérale de Lausanne (EPFL) Valais Wallis, Switzerland*
anna.wallerand@epfl.ch, anna.wallerand@gmail.com

Abstract

Technology and energy saving potentials in the industrial sector are key data that policy makers rely on to drive decision making. A literature review reveals a distinct discrepancy between *general potential estimation* and *detailed design* studies. The former relies principally on top-down conceptual approaches based on temperature levels of the processes' thermal requirements, while the latter aims at mathematically optimized solutions for specific technologies in specific processes under specific economic conditions. This work attempts to close this gap by proposing a bottom-up method for potential estimation of energy saving measures. To this end, a generalized optimization framework was developed which aims at generating a database of optimal solutions which are independent from most economic and environmental input data. By fixing these data, the optimal solution for the same process type in different countries and under various criteria can be identified in the database. The method also increases accessibility of optimization techniques by providing the solution database which then requires limited input parameters and background knowledge to provide expert guidance toward optimal utility integration. The method was applied to the dairy industry, highlighting that energy saving potentials can be achieved through heat recovery and integration of heat pumps, mechanical vapor re-compression, and co-generation units economically favourable especially in Japan and Switzerland.

Keywords: dairy industry, heat pump, co-generation, MINLP, mathematical programming, generalized optimization

1. Introduction

Constant efforts are undertaken to estimate energy saving and technological potentials in the industrial sector. Such analyses are used to formulate policy recommendations, determine target markets, and advance technological development. A state-of-the-art analysis is introduced concerning both *general potential estimation* and *detailed design* studies, before highlighting the contribution of this work and the outline of the study.

General potential estimation: This section concerns studies which aim at estimating energy saving potentials in the industrial sector. Most such studies are based on top-down approaches relying mainly on the temperature levels of the thermal requirements in certain industries and with specific technologies. Concerning heat pump integration, Wolf et al. (2014) presented a study which focused on the German low temperature sectors, estimating the overall energetic potential of heat pumps used as hot utilities. Similarly, Brückner et al. (2015) performed such an analysis for the European industrial sector with compression and absorption heat pumps. For other technologies, analogous studies have

been conducted by Lauterbach et al. (2012) (solar thermal) and Campana et al. (2013) (organic Rankine cycles), as representative examples.

Though top-down approaches offer a clear and simple approach to estimate general potentials, conclusions drawn from such analysis may be misleading. Firstly, they account only for hot utility requirements neglecting the double impact of certain utilities (especially heat pumps) according to the 'more in, more out' principle of pinch analysis. Secondly, they do not consider possible process improvements and efficiency measures such as internal heat recovery.

Bottom-up approaches have also been presented by Wilk et al. (2017) who analyzed different process types and the heat pump integration potential for a set of energy price ratios, and Müller et al. (2014) who suggested an approach for solar thermal integration to the liquid food industry based on the available land surface area and process temperature levels. These approaches are often limited in their scope (in terms of economic and environmental boundary conditions) and lack rigorous methods.

Detailed design: Various detailed design studies are present in academic literature and typically focused on few technologies and processes. Studies by Kamalinejad et al. (2015), Yang et al. (2017), and Becker (2012) presented optimal integration approaches of heat pumps in different industrial processes relying on mathematical programming and superstructure-based design. Most recently Wallerand et al. (2018) presented a comprehensive heat pump integration method based on mathematical programming and expert insight. For organic Rankine cycles, superstructure-based approaches are also common, such as presented by Yu et al. (2017) and Kermani et al. (2018).

Though such approaches offer rigorous solutions to complex problems, the scope of treated problems is usually limited to specific processes, technologies, and economic and environmental boundary conditions.

Synthesis: The state-of-the art analysis can be summarized in two points.

1. Potential studies are either conducted coarsely by top-down approaches, or in a non-rigorous and limited in scope with bottom-up analyses.
2. Detailed design studies provide rigorous methods, however limited to specific conditions.

This work attempts to bridge this gap by suggesting a bottom-up method for potential estimation of energy saving measures through heat recovery and technology integration. The methodology is presented in section 2, followed by the results in section 3 presenting the solutions for various perspectives (from policy-makers to plant managers). The work is summarized and critically reviewed in section 4.

2. Methodology

The methodology presented in this work aims at reducing computational time while producing a large set of feasible and potentially 'good' solutions. The expensive optimization problem is therefore solved once, independent from most input parameters and its solutions are stored in a database from which a large number of scenarios with varying input conditions can be derived. An overview of this approach can be seen in Figure 1. The approach is clarified below in more detail.

Comprehensive solution space generation: The goal of this part is to formulate an op-

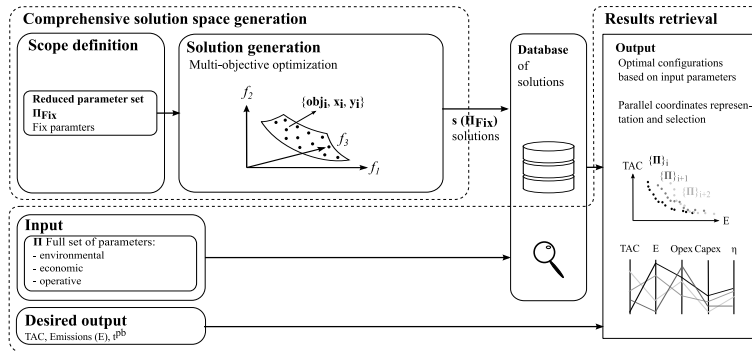


Figure 1: Bottom-up method for potential estimation.

timization problem independent of most typical input parameters. Usually the objectives of main interest for such analyses are the *total annual system cost (TAC)* and/or the *total emissions*. Both of these objectives require a wide range of input parameters ranging from economic (energy prices, investment cost parameters, interest rate, CO₂ tax, maintenance cost), operative (operating time), process specific (product mass flow rates, specific requirements), equipment specific (lifetime, efficiency, fuel consumption) to emissions associated with electricity and natural gas consumption (environmental parameters). Even though the final objectives are *total system cost* and/or the *total emissions*, a different set of objectives is selected at this stage, which requires fewer input parameters with the goal of generating a large set of potentially optimal solutions. The choice of objective depends on the exact goal of the study. In this case, the focus was placed on national differences, which have a drastic effect on energy prices, interest rates, and environmental parameters.

Therefore, the new set of objectives was defined as *consumption* of all resources and *investment cost (capex)*, which requires less input parameters to be fixed. The choice of the new set of objectives requires engineering common sense and needs to be carefully adapted to each problem. The new objectives are fed to a multi-objective optimization framework, similar to the one described by Wallerand et al. (2018) and Weber et al. (2007) to generate a set of solutions. The solution space generation needs to be carried out only once and requires a few days of computational effort.

Database: Depending on the number of objectives, the previous step generates a multi-dimensional surface of solutions. In this study, the resource consumption was distinguished between electricity and natural gas consumption, which led to a total of three objectives. Upon successful completion of the optimization, all solutions and the corresponding values of their decision variables (solution properties) can be stored in a database for later access and evaluation.

Results retrieval: The results retrieval procedure works in two steps: Initially, a solution together with its entire set of properties is retrieved. Subsequently, knowing the optimal values of each decision variable, a user can evaluate the original objective function as well as any other indicators given a new set of parameters (e.g. energy prices, operating time, CO₂ tax). This leads to a new set of objective values among which the user can identify their preferred choice. In this case, the lowest cost and lowest emission solutions were selected. This step is accessible without knowledge of optimization algorithms thus encouraging utilization of such methods by a variety of audiences which is briefly demonstrated in section 3.3. The results retrieval has been implemented in a tool, which can be found [online](#).

3. Results

3.1. Case study

The underlying case study of this section is a dairy plant as presented by Kantor et al. (2018) with a two-stage refrigeration cycle, free cooling water (from a nearby river) and an existing boiler. The heat pump superstructure suggested by Wallerand et al. (2018) with various fluids and a co-generation engine (Becker (2012)) were studied as potential new technology options. Decision variables were the heat pump fluids, temperature levels, and number of stages, as well as the T_{\min} of the heat recovery in the process. The heat exchanger network cost was graphically approximated as proposed by Townsend and Linnhoff (1984).

3.2. Comprehensive solution space generation

The three-dimensional surface of solutions resulting from the multi-objective optimization described in section 2 is shown in Figure 2. It can be seen that points closest to the reference case have lowest capital expenses (capex), while lower electricity and/or natural gas consumption necessitates an increase in capex.

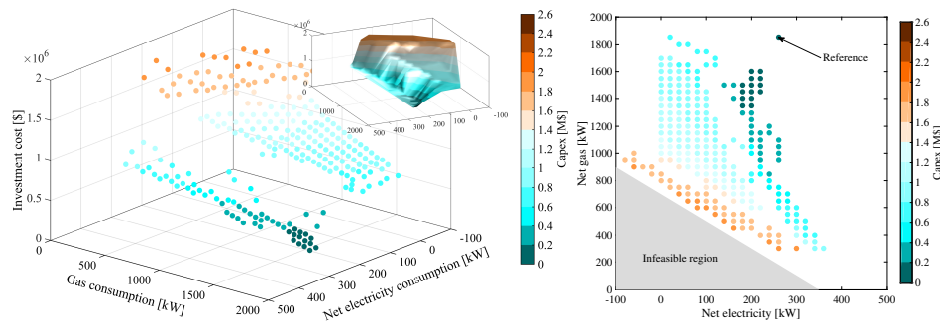


Figure 2: Solutions from multi-objective optimization considering consumption of natural gas and electricity with the corresponding investment required.

3.3. Results retrieval

The retrieval of results is illustrated in Figure 3 for the three exemplary countries, namely Switzerland (CH), Germany (DE), and the United States of America (US). The countries were selected due to their different economic and environmental conditions, as illustrated in the figure, ranging from a high natural gas price and low electricity/natural gas ratio in CH to a low natural gas price and high electricity/natural gas price ratio in the US. The total emissions and TAC are calculated for each solution in the database, but only the minimum cost solutions are selected (indicated with grey circles).

Plant operators: The minimum cost points from Figure 3 are depicted with more cost details in Figure 4, indicating the potential interest of a plant operator in reducing energy-related costs or emissions. CH is visibly the country with highest potential where up to 70% emission reductions could be achieved with heat recovery (firstly), with heat pumping providing options with payback times below 5y. This is in stark contrast to the US context where solutions are not economically attractive compared to the reference case. Here, and in DE, the highest emission reductions can only be achieved with heat pumps and co-generation units, due to the high emissions related to generation of electricity.

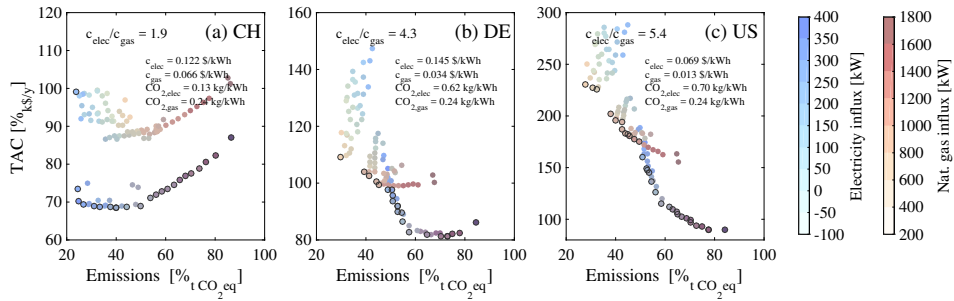


Figure 3: Results retrieval: minimum cost solutions, 8000 h/y operation, 0 \$/t CO₂.

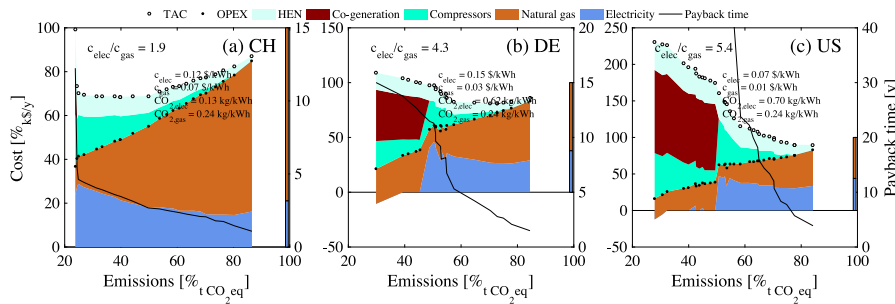


Figure 4: Minimum cost solutions for operating time 8000 h/y, 0 \$/t CO₂.

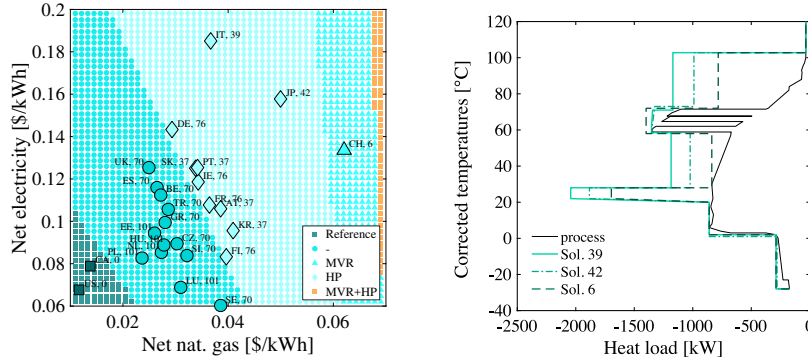


Figure 5: Utility map for operating time 2500 h/y (left), 0 \$/ton CO₂; composite curves of solutions for Italy, Japan and Switzerland (right).

Policy-makers: Another type of analysis can be conducted for policy-makers as shown in Figure 5. With this analysis, the lowest emitting solution for each country (resource price) is selected with a payback time below 3 years. The countries with highest resource prices (Italy (IT), Japan (JP) and Switzerland (CH)), have the highest heat pump potential. The other solutions are principally based on improving process heat recovery to achieve the potential reduction in consumption.

4. Conclusions

This work proposes a bottom-up method for potential estimation of energy saving measures. To this end, a generalized optimization framework was developed based on multi-objective optimization which aims at generating a database of optimal solutions which are

independent from most economic and environmental input data. By fixing this data, the optimal solution for the same process type in different geographical, economic and environmental contexts are retrieved from the database to address various objective criteria.

The method was applied to the dairy industry investigating energy saving and technological potentials through heat recovery and utility integration with heat pumps, mechanical vapor re-compression, and co-generation units. A set of countries was determined in which industrial heat pumping is particularly beneficial from environmental and economic perspectives, namely: Switzerland, Japan, and Sweden. Use cases for plant operators and policy-makers were briefly demonstrated and a variety of additional analyses could be conducted using the solution database; one such example was briefly presented.

References

- H. C. Becker, 2012. Methodology and Thermo-Economic Optimization for Integration of Industrial Heat Pumps. Ph.D. thesis, École Polytechnique Fédérale de Lausanne, Lausanne.
- S. Brückner, S. Liu, L. Miró, M. Radspieler, L. F. Cabeza, E. Lävemann, Aug. 2015. Industrial waste heat recovery technologies: An economic analysis of heat transformation technologies. *Applied Energy* 151, 157–167.
- F. Campana, M. Bianchi, L. Branchini, A. De Pascale, A. Peretto, M. Baresi, A. Fermi, N. Rossetti, R. Vescovo, Dec. 2013. ORC waste heat recovery in European energy intensive industries: Energy and GHG savings. *Energy Conversion and Management* 76, 244–252.
- M. Kamalinejad, M. Amidpour, S. M. M. Naeynian, Jun. 2015. Thermodynamic design of a cascade refrigeration system of liquefied natural gas by applying mixed integer non-linear programming. *Chinese Journal of Chemical Engineering* 23 (6), 998–1008.
- I. Kantor, A. S. Wallerand, M. Kermani, H. Bütün, A. Santecchia, Raphaël Norbert, Sahar Salame, Hélène Cervo, Sebastian Arias, Franz Wolf, Greet van Eetvelde, François Maréchal, Jun. 2018. Thermal profile construction for energy-intensive industrial sectors. In: *Proceedings of ECOS 2018*. Portugal.
- M. Kermani, A. S. Wallerand, I. D. Kantor, F. Maréchal, Feb. 2018. Generic superstructure synthesis of organic Rankine cycles for waste heat recovery in industrial processes. *Applied Energy* 212, 1203–1225.
- C. Lauterbach, B. Schmitt, U. Jordan, K. Vajen, 2012. The potential of solar heat for industrial processes in Germany. *Renewable and Sustainable Energy Reviews* 16 (7), 5121 – 5130.
- H. Müller, S. Brandmayr, W. Zörner, Jan. 2014. Development of an Evaluation Methodology for the Potential of Solar-thermal Energy Use in the Food Industry. *Energy Procedia* 48, 1194–1201.
- D. Townsend, B. Linnhoff, 1984. Surface area targets for heat exchanger networks. In: *ICHEME Annual Research Meeting*, Bath, UK.
- A. S. Wallerand, M. Kermani, I. Kantor, F. Maréchal, Jun. 2018. Optimal heat pump integration in industrial processes. *Applied Energy* 219, 68–92.
- C. Weber, F. Maréchal, D. Favrat, 2007. Design and optimization of district energy systems. In: V. P. a. P. S. Agachi (Ed.), *Computer Aided Chemical Engineering*. Vol. 24 of 17th European Symposium on Computer Aided Process Engineering. Elsevier, pp. 1127–1132.
- V. Wilk, Bernd Windholz, Reinhard Jentsch, Thomas Fleckl, Jürgen Fluch, Anna Grubbauer, Christoph Brunner, Daniel Lange, Dietrich Wertz, Karl Ponweiser, 2017. Valorization of industrial waste heat by heat pumps based on case studies of the project EnPro. In: *Proceedings of the 12th IEA Heat Pump Conference*. IEA Energy Technology Network, Rotterdam.
- S. Wolf, U. Fah, M. Blesl, A. Voß, R. Jakobs, Dec. 2014. Analyse des Potenzials von Industrie - Wärmepumpen in Deutschland. Tech. rep., Universität Stuttgart, Institut für Energiewirtschaft und Rationelle Energieanwendung (IER), Stuttgart.
- T. Yang, Y. Luo, Y. Ma, X. Yuan, Dec. 2017. Optimal synthesis of compression refrigeration system using a novel MINLP approach. *Chinese Journal of Chemical Engineering*.
- H. Yu, J. Eason, L. T. Biegler, X. Feng, Dec. 2017. Process integration and superstructure optimization of Organic Rankine Cycles (ORCs) with heat exchanger network synthesis. *Computers & Chemical Engineering* 107, 257–270.

Analysis of the Tri-Reforming of Methane in a Membrane Reactor

Samuel S. Q. Jardim, José E. A. Graciano and Rita M. B. Alves*

*Universidade de São Paulo, Escola Politécnica, Department of Chemical Engineering,
Avenida Prof. Luciano Gualberto, trav. 3, 380, São Paulo, 05508-010, Brazil
rmbalves@usp.br*

Abstract

This paper analyses the tri-reforming of methane as a reactive way to use natural gas rich in carbon dioxide, without a previous separation. The tri-reforming of methane (TRM) produces syngas suitable for GTL processes and also avoids coke deposition, depending on specific process conditions. For this reason, a thermodynamic analysis was conducted to investigate the possible operating regions to avoid coke formation; then, an operating point was determined by maximizing the CO₂ conversion at a fixed H₂: CO ratio. The given results suggested that the use of large amounts of oxygen are necessary to overcome the coke formation and to increase the syngas yield. In those conditions, the reactor may present hot spots that damage the reactor catalyst. A porous membrane reactor that distributes oxygen along the reactor dropped the sharp thermal profile; the hot spot was mitigated, obtaining 94 % of methane and 30 % of carbon dioxide conversion.

Keywords: membrane reactor, tri-reforming of methane, carbon dioxide, syngas.

1. Introduction

Natural gas is one of the most available sources of energy and a feedstock to the chemical industry. However, in many exploitation sites, the high content of the associated carbon dioxide increases the production cost. For example, in the new Brazilian petroleum offshore fields, the associated CO₂ is usually between 8 and 18 % and, in some cases, up to 79 % (Gaffney et al., 2010). The elevated CO₂ content in NG requires separation previously to its commercialization, increasing the energy requirement and the production cost. An alternative to mitigate this problem is to use the associated CO₂ as a constituent block to produce added-value products, by combining CO₂ and CH₄ to produce syngas.

Tri-reforming of methane (TRM) is a synergetic combination of Steam Methane Reforming (SMR: $CH_4 + H_2O \rightleftharpoons 3 H_2 + 1 CO$), Dry Reforming (DMR : $CH_4 + CO_2 \rightleftharpoons 2 H_2 + 2 CO$) and Partial Oxidation of Methane (POM: $CH_4 + 0.5 O_2 \rightarrow 2 H_2 + 1 CO$), able to convert both methane and carbon dioxide into syngas. The POM is an exothermic reaction which provides energy for endothermic SMR and DMR. As a result, TRM can operate adiabatically, unlike conventional reformers, which demand external heat. Moreover, the coke formation is mitigated due to the introduction of oxygen when compared to DMR and SMR processes. Despite several thermodynamic studies in the literature, less attention has been paid to industrial pressures (> 20 bar) and none to adiabatic conditions. As a result, the benefits reported, such as CO₂ conversion over 90 % (Zhang et al., 2014), might not hold true at industrial conditions. The equilibrium analysis in these conditions

is a good alternative to determine the best operating point for the membrane reactor and to verify if the TRM is: (i) able to efficiently convert the carbon dioxide and (ii) suitable for the downstream process in a GTL plant.

Additionally, the presence of fast and exothermic reactions makes the reactor design challenging, creating hot spots that can damage the reactor materials and threaten the process viability. For example, Arab Aboosadi et al. (2011) optimized a TRM reactor for hydrogen production but obtained a hot spot near to the melting point of nickel (1455 °C), which can easily deteriorate the catalyst activity. The use of a membrane to distribute oxygen along the reactor can be a promising technology to better control the kinetics and the temperature profile of the TRM, as initially proposed by Rahimpour et al. (2012). However, the requirement of large permeation fluxes and severe operating conditions promote the use of porous membranes in detriment of the perm-selective ones. Indeed, α -alumina membranes may be an interesting choice for this application, since they are chemically stable and their permeability can be easily adjusted to a required value (Alibrando et al., 1997; Coronas and Santamaría, 1999; Godini et al., 2014).

In the present work, the TRM is investigated over a large range of feed composition, for an adiabatic operation at 25 bar, aiming to increase the syngas production from a CO₂-rich NG. The initial thermodynamic analysis is conducted using a simplified equilibrium reactor to determine the operating condition that maximizes the CO₂ conversion, syngas yield and prevent coke formation. After that, the obtained optimum operating point is applied to study the behaviour of a phenomenological membrane reactor, in which the ideal oxygen distribution over the membrane is determined by a sensitivity analysis.

2. Modelling

The thermodynamic analysis is performed to convert CO₂-rich natural gas (CO₂: CH₄ = 0.5) into syngas. This process was simulated by an equilibrium reactor model (*RGibbs* in Aspen Plus V8.8[®]), considering seven gaseous species (CH₄, CO₂, H₂O, O₂, CO, H₂, N₂) and solid carbon (C), subjected to the elemental balance at constant pressure (25 bar) and isenthalpic operation (adiabatic). The thermodynamic behaviour of the fluid was predicted by the Peng-Robson equation of state. A parametric analysis is conducted to evaluate the influence of water and oxygen ratio (H₂O: CH₄, O₂: CH₄) in four defined metrics, namely: coke yield (Y_{coke}), syngas yield (Y_{syngas} , eq. 1), CO₂ conversion (X_{CO_2}) and syngas quality (H₂: CO).

$$Y_{syngas} = [(F_{H_2}^{out} + F_{CO}^{out}) - (F_{H_2}^{in} + F_{CO}^{in})] / (4F_{CH_4}^{in}) \quad (1)$$

After that, the operating point for the membrane reactor was determined by maximizing the CO₂ conversion, subjected to: syngas ratio equal to 1.6; syngas yield greater than 70%; absence of solid carbon (coke); and inlet and outlet temperature limited to 900 and 1000 °C, respectively. The set of independent variables was defined as: the inlet composition of oxygen, water and feed stream temperature. The stated optimization problem was solved with the SQP method implemented in Aspen Plus V8.8[®].

The first-principle membrane reactor was modelled as a packed bed tube with an inert porous membrane wall. Oxygen was fed through both feed stream and membrane, from an outer compartment (shell). On the proposed shell side, the oxygen was fed at 900

°C and 29.5 bar. The reactor had 6 m in length, 0.1 m in inner diameter and 0.43 in bed porosity. The nickel catalyst had 0.015 m in diameter and 2100 kg/m³ in density. The TRM kinetics were the same used in Arab Aboosadi et al. (2011). The permeation through the α -alumina porous membrane was modeled by Darcy's equation (eq. 2a) for flow in porous media ($B_0 = 2 \times 10^{-16}$ m² and $\delta_{membrane} = 1.5$ mm) and the pressure drop was determined by Ergun's equation (Salehi et al., 2016).

$$J_{O_2} = \frac{B_0 \rho_{gas}}{\mu \delta_{membrane}} (P_{shell} - P_{tube}) \quad (2a)$$

$$\frac{dF_i}{dz} = A_i \rho_{bed} \sum^q v_i r_q + J_{O_2} \pi D \quad (2b)$$

$$\frac{dH_{total}}{dz} = J_{O_2} \pi D h_{O_2} \quad (2c)$$

A plug-flow regime was assumed with uniform concentrations in the cross-section area. Additionally, no heat conduction is accounted through the wall (membrane). The resulted 1D-pseudo-homogenous model (eq. 2) was implemented in Aspen Custom Modeler[®] (ACM). The system of differential algebraic equations was discretized by backward finite difference method with 300 internal nodes, resulting in a system with (75,156) algebraic equations, solved by a Newton-like method.

3. Results and Discussion

3.1. Thermodynamic analysis

Coke production is one of the major problems encountered in industrial reformers. It is responsible for catalyst deactivation, requiring a high proportion of steam to methane in the feed stream (between 2 to 3). Tri-reforming requires less water due to the presence of a stronger oxidant - O₂. As observed in Figure 1(a), the minimal oxygen amount to mitigate the coke formation is above 40 %. For oxygen feeds below this proportion, more water is required.

The syngas yield is positively affected by both water and oxygen (Figure 1(b)), due to the SMR and the raise of the adiabatic temperature. The yield is more sensitive to oxygen, growing up to a maximum of 0.73 for 55 % of oxygen (O₂:CH₄) and 100 % of water (H₂O:CH₄). The excess of oxygen is also responsible for a decrease in the syngas selectivity, as a result of the higher conversion of methane into carbon dioxide and water (total combustion). In conclusion, both coke and syngas yield profiles stress that a high proportion of oxygen is required for adiabatic operation at 25 bar. However, this imposes a challenge to the reactor design because this high content of oxygen might produce temperatures over the safe operating limits.

The syngas ratio (H₂: CO) grows with water (Figure 1 (c)), as a result of the higher syngas ratio provided by the SMR. On the other hand, it decreases with oxygen, due to the rise of the adiabatic temperature, favoring the DMR. Within the coke free region, the syngas ratio tends to be lower than 2.0. Consequently, more water is needed (> 100 %) to attain syngas ratios stoichiometrically suitable for methanol and Fischer-Tropsch plants (around 2). As observed in Figure 1(d), the carbon dioxide conversion is more influenced by steam

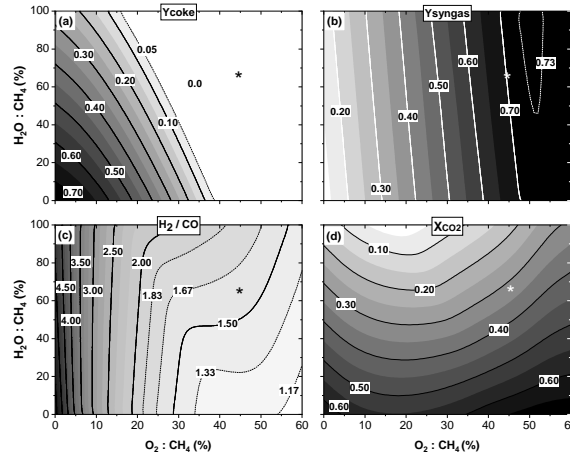


Figure 1: TRM thermodynamic equilibrium analysis at 25 bar, 900°C and 50 % of CO₂: CH₄

than oxygen, due to the presence of the water-gas-shift reaction ($H_2O + CO \rightleftharpoons CO_2 + H_2$). By simultaneously comparing the syngas ratio and CO₂ graphs it is possible to observe a trade-off (Figure 1 (c),(d)). If syngas ratios of 2 or higher are desired, the corresponding CO₂ conversion is low. Conversely, in order to convert the most of the CO₂, the syngas ratio should be the lowest possible. In other words, the maximum conversion of CO₂ is at an active constraint on the syngas quality, which is set at a minimum value of 1.6 (a useful value for some special schemes of Fischer-Tropsch synthesis (Graciano et al., 2018)).

The described optimization found an optimum operating point with the inlet composition of CH₄ : CO₂ : H₂O : O₂ = 1 : 0.5 : 0.679 : 0.4522, at 900 °C and 25 bar. This condition resulted in conversions of 31.2 % of CO₂ and 93 % of CH₄ with 71 % of syngas yield, as indicated by the asterisk shown in Figure 1.

3.2. Membrane Reactor

Since a large amount of oxygen is required for adiabatic operation, it is important to know how the oxygen distribution affects the reactor performance, especially the thermal behavior. Therefore, the effect of the oxygen partition (proportion of oxygen injected at the feed to the one permeated through the porous membrane, $O_{2,feed}|O_{2,membrane}$) is shown in Table 1 and Figure 2. As verified, the kinetic model deviates slightly from the equilibrium results, favoring more conversion of CO₂ and CH₄. The oxygen partition does not significantly shift the overall reactor performance. In contrast, the thermal behavior changes drastically (Figure 2). For example, at 0 % oxygen partition (no oxygen distribution through the membrane) the temperature goes up to 1650 °C, far away from

Table 1: Overall results of oxygen partition in the membrane reactor

$O_{2,feed} O_{2,membrane}$	equilibrium	0% 100%	20% 80%	40% 60%	60% 40%	80% 20%	100% 0%
O_2/CH_4 at feed	45%	45%	36%	27%	18%	9%	0%
J_{O_2} (mol/m ² s)	-	0.00	0.10	0.20	0.30	0.40	0.51
X_{CH_4}	0.93	0.94	0.94	0.94	0.94	0.94	0.93
X_{CO_2}	0.31	0.33	0.33	0.33	0.33	0.33	0.33
Y_{syngas}	0.71	0.71	0.71	0.71	0.71	0.71	0.71
H_2/CO	1.60	1.58	1.58	1.58	1.57	1.57	1.57

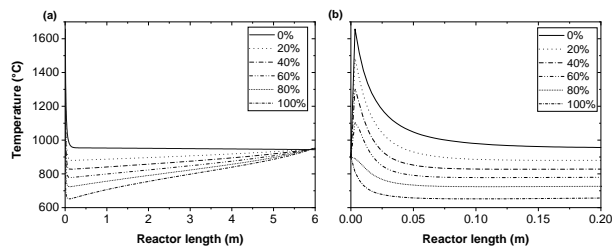


Figure 2: Temperature profile of the membrane reactor for different oxygen partitions, full (a) and zoomed (b) profile.

the melting point of nickel (1455 °C). Cold spots also occur, especially at low oxygen feed because the inlet oxygen is not enough to overcome the endothermic reactions. Despite different profiles for the oxygen distribution, their temperatures coincide at the reactor end (about 950°C). The partition results indicate that a sharp temperature profile is unavoidable. There will always be either a hot or a cold spot due to the extreme enthalpy and reaction velocities at the reactor inlet. Since a hotspot is undesirable for safety reasons, a partition of 80 % is chosen for the porous membrane study.

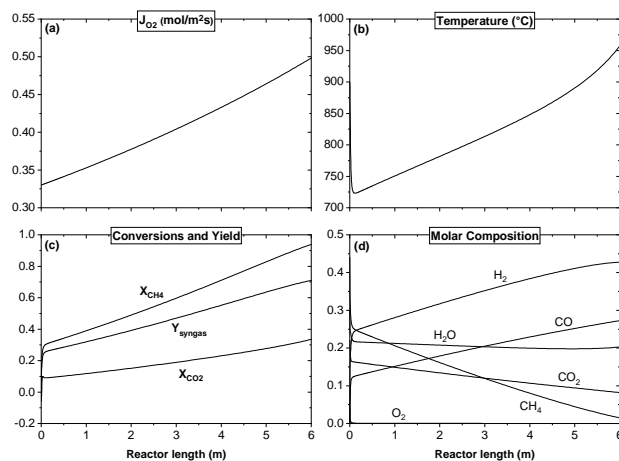


Figure 3: Profile of the membrane reactor using 80 % of oxygen partition. The shell pressure is fixed at 29.5 bar.

Figure 3 shows the reactor behaviour operating at the conditions determined in the thermodynamic analysis and oxygen partition study. As observed in Figure 3 (a), the permeation flux grows from 0.33 up to 0.50 mol/m²s due to the pressure drop in the catalytic bed. Therefore, the transmembrane pressure, pressure drop and the permeability of the membrane should be well designed and controlled to prevent an undesired flux of oxygen. As expected, the temperature profile (Figure 3(b)) reveals no hot spot but rather a cold spot in the inlet region followed by a smooth growth up to the equilibrium temperature, from 725 to 953°C. The conversions and syngas yield profiles (Figure 3(c)) have similar behaviors, a sharp increase at the inlet due to the fast reforming reactions, followed by a smoother growth caused by the temperature increase. The methane and carbon dioxide conversions go up to 94 % and 33.5 % with syngas yield of 71 %. The molar composition shows the same trend with a very steep change at the inlet (Figure 3(d)). Oxygen is extremely low

since it reacts faster as soon as it is introduced in the reactive mixture.

4. Conclusions

The TRM thermodynamic analysis revealed that the adiabatic operation demands substantial oxygen feed to obtain high syngas yields and to avoid coke formation, around half of the methane feed. Moreover, there is a trade-off between the CO₂ conversion and the syngas ratio; CO₂ is converted at the expense of hydrogen production. The membrane reactor showed to be a good alternative to safely provide a high amount of oxygen. The reactor consumed 93 % of the methane and 32 % of the carbon dioxide feed, producing 71 % of the methane into syngas at a 1.6 ratio. As shown, different ratios of oxygen partition do not change the overall reactor performance. No matter how the oxygen is partitioned, drastic temperature behavior is found in the inlet region, either by hot spot or cold spot. However, the chosen oxygen partition of 80 % makes the operation possible by keeping the temperature profile within the limits imposed by the catalyst. The porous membrane imposes a non-uniform distribution of oxygen that grows with the reactor length. As a result, over-oxidation can occur due to the low methane pressure in the outlet region. In short, the proposed porous membrane reactor can perform TRM adiabatically, processing natural gas with high CO₂ content without previous separation.

Acknowledgments: The authors gratefully acknowledge support from FAPESP and SHELL Brasil through the "Research Centre for Gas Innovation – RCGI" (FAPESP Proc. 2014/50279-4), hosted by the University of São Paulo, and the support given by ANP (Brazil's National Oil, Natural Gas and Biofuels Agency) through the R&D levy regulation.

References

- M. Alibrando, H. S. Á. Hahm, E. E. Wolf, 1997. Partial oxidation of methane to synthesis gas on a Rh / TiO₂ catalyst in a fast flow porous membrane reactor. *Catal. Letters* 49, 1–12.
- Z. Arab Aboosadi, A. H. Jahanmiri, M. R. Rahimpour, 2011. Optimization of tri-reformer reactor to produce synthesis gas for methanol production using differential evolution (DE) method. *Appl. Energy* 88 (8), 2691–2701.
- J. Coronas, J. Santamaría, 1999. Catalytic reactors based on porous ceramic membranes. *Catal. Today* 51 (3–4), 377–389.
- C. Gaffney, et al., 2010. Exame e avaliação de dez descobertas e prospectos selecionadas no play do pré-sal em águas profundas na bacia de Santos, Brasil. Documento acessado no endereço eletrônico <http://www.anp.gov.br>.
- H. R. Godini, A. Gili, O. Görke, U. Simon, K. Hou, G. Wozny, Feb 2014. Performance analysis of a porous packed bed membrane reactor for oxidative coupling of methane: Structural and operational characteristics. *Energy and Fuels* 28 (2), 877–890.
URL <http://pubs.acs.org/doi/10.1021/ef402041b>
- J. E. Graciano, B. Chachuat, R. M. Alves, 2018. Conversion of CO₂-Rich Natural Gas to Liquid Transportation Fuels via Tri-reforming and Fischer-Tropsch Synthesis: Model-Based Assessment. *Ind. Eng. Chem. Res.* 57 (30), 9964–9976.
- M. R. Rahimpour, Z. Arab Aboosadi, A. H. Jahanmiri, 2012. Synthesis gas production in a novel hydrogen and oxygen perm-selective membranes tri-reformer for methanol production. *J. Nat. Gas Sci. Eng.* 9, 149–159.
- M. S. Salehi, M. Askarishahi, H. R. Godini, O. Görke, G. Wozny, 2016. Sustainable Process Design for Oxidative Coupling of Methane (OCM): Comprehensive Reactor Engineering via Computational Fluid Dynamics (CFD) Analysis of OCM Packed-Bed Membrane Reactors. *Ind. Eng. Chem. Res.* 55 (12), 3287–3299.
- Y. Zhang, S. Zhang, J. L. Gossage, H. H. Lou, T. J. Benson, 2014. Thermodynamic analyses of tri-reforming reactions to produce syngas. *Energy & Fuels* 28 (4), 2717–2726.

Design of a novel sour water stripping unit

Umer Zahid ^{a*}, Ali Al-Qadri ^a, Baqer Al-Mousa ^a, Ali Al-Nasser ^a, Usama Ahmed ^a

^a *Department of Chemical Engineering, King Fahd University of Petroleum and Minerals, Dhahran, 34464, Saudi Arabia*

uzahid@kfupm.edu.sa

Abstract

This study focusses on the design and simulation of sour water stripping (SWS) unit in the refinery setup for the reuse of sour water. In this study, process simulation has been performed to analyze the energy saving and cost reducing prospects in the sour water stripping unit. First, a base case design has been simulated using a reference sour water stripping unit data. The developed model is validated against the plant data in order to ensure the model validity. A novel design has been proposed in this study that can reduce the energy requirement by 53 % compared to the conventional designs. The results of this study provide a meaningful analysis in terms of energy and economic considerations to improve the performance of the sour water units in the refineries.

Keywords: Sour water stripping, energy efficiency, process simulation, economic analysis.

1. Introduction

Refineries around the world process thousands of barrels of crude oil every day for the production of various petroleum products. The oil refineries generate considerable amounts of sour water from various processes that should be treated before the water can be reused or disposed of. In a typical refinery setup, the stripped sour water can be reused in the crude de-salter section for the removal of chloride salts to inhibit the formation of HCl in the downstream distillation columns (Lieberman, 2013). The stripped water can also be used in the hydrotreater unit for the removal of ammonia sulfide which otherwise could lead to a serious plugging of the condensers in the presence of CO₂ (Gai et al., 2008). Many studies in the past have focused on how to reduce the energy requirement of the sour water stripping process while meeting the environmental regulatory requirements. Sour water strippers can be configured in a variety of ways including column configurations, condensing and reboiler system and stripping methods.

Weiland and Hatcher (Weiland and Hatcher, 2012) studied the sour water stripping process employing a rate based simulation model using ProTreat. Their results showed that depending on the stream rate and H₂S to NH₃ ratio, the overall tray efficiency can vary widely between 15 to 45 %. Bellen (Bellen, 2009) described a step-by-step guide to the design and operation of sour water stripper and showcased the process simulation using Aspen HYSYS and PRO/II simulators. Nabgan et al. (Nabgan et al., 2016) compared the operational performance of single column and double column SWS process using Aspen HYSYS. Their results showed that 100% of NH₃ was stripped in

the two columns model whereas only 24% was stripped using the single column model. Sharma and Nag (Sharma and Nag, 2009) analysed the design modifications in the sour water stripping unit installed at one of the refineries in the India to enhance the H₂S recovery from the sour water before it is fed to the stripper. The simulated the SWS process using Chemcad and showed that approximately 7.5 % more H₂S can be recovered compared to the base design by installing a hot flash drum upstream of the stripper column.

Although, SWS systems have been installed and operational in the industry since decades, however, not enough effort has been done to improve their design and performance. With growing concerns on the environmental issues and energy efficiency improvements in the industry, there is a need to look into SWS system which is an important unit in the refineries. Most of the above mentioned studies simulated the SWS systems and analyzed the process performance. However, very few studies considered the tray efficiencies in their simulation with no details on the model validation. In addition, most of the studies were focused on how to achieve the desired stripped water composition with little attention to the process improvement. Also, to authors knowledge, no previous studies in the open literature have quoted the cost information required for the sour water stripping. The goal of this study is to utilize the process simulation tool for analyzing the sour water stripper process and improve the process performance by design modifications. A novel vapor compression design has been proposed in this study which is compared with other conventional designs reported in the literature. The effect of the design modifications are then evaluated economically in order to check the feasibility of the design.

2. Process Design

The design of the sour water stripping unit considered in this study is based on the refinery data processing a mixture of light and heavy Arabian crude oil. The sour water stripping simulation has been performed using the Aspen HYSYS. The feed specifications along with the major components in the system are shown in table 1. As recommended by previous studies (Nabgan et al., 2016), NRTL has been selected as the thermodynamic property package because the activity coefficient models are suitable in the presence of polar components and non-ideal system.

Table 1: Feed specifications used in the simulation model

Feed flow rate	t/h	185
Temperature	°C	40
Pressure	bar	4.9
Composition		
H ₂ S	mass fr.	0.0030
NH ₃	mass fr.	0.0016
H ₂ O	mass fr.	0.9953
NaCl	mass fr.	0.0001

2.1. Base case design

Most of the new industrial stripper installations are similar to this design scheme. Figure 1 shows the process flow scheme for the base case design. The sour water feed is pre-heated with the stripped water to 60 °C before entering the stripper. The purity requirement of the stripped water is maintained by providing heat through the reboiler. Liquid phase side draw is withdrawn from the stage 6 which is then cooled down to 65 °C using an air-cooler and returned back to the top of the column. The vapor stream leaves at the top of the column mainly comprising of H₂S, NH₃ and water. This design as referred by its name is simple without a condenser that can save the cooling utility along with some capital cost while meeting the purity requirements of the stripped water.

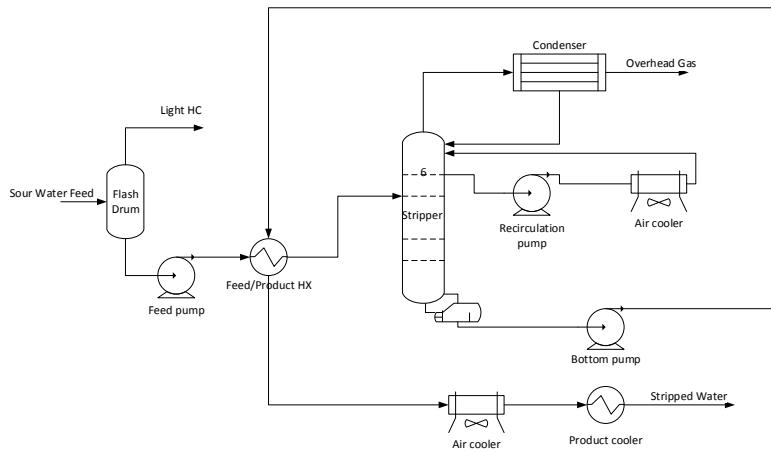


Figure 1: Process flow diagram of base case design

2.2. Bottom cycle vapor compression design

A new design is proposed in this study with the aim to reduce the energy requirements of the conventional sour water stripping process. The proposed design employs mechanical work using a compressor instead of hot and cold utilities. In this design, the stripped water stream leaving at the bottom of the column is flashed to a reduced pressure, whereby, some amount of vapours are generated. The produced vapours leave at the top of the flash drum and are fed to the two-stage compression train. A compression ratio of three is assumed in each compressor stage with an intercooler. The compressed vapor stream at 2.1 bar and 240.7 °C then heats up the incoming feed stream and is fed to the bottom of the column at 121.7 °C. The incoming feed stream is heated from 40 °C to 53.5 °C using the heat available from the compressed vapor. It is then heated to 60 °C using the hot utility before being fed to the 7th stage in the stripper column. The advantage of this design is the elimination of stripper's condenser and reboiler which leads to a reduction in the utilities requirement. Since, the compression also increases the process stream temperature, the heat available from the compression work is supplied to the bottoms of the stripper. However, this design requires an additional compressor work to increase the stream pressure and subsequently the

temperature. Figure 2 shows the process flow diagram for the vapor compression design. The reflux at the top of the column is provided in the same way as that of the simple stripper design by a circulation loop. A recirculation cooling loop withdraws some of the liquid from stage 6, cools it down to 60 °C and pump it back to the top of the column.

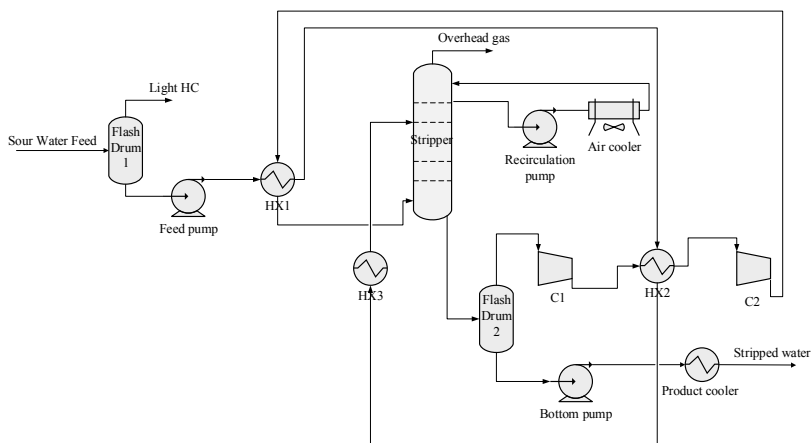


Figure 2: Process flow scheme for the bottom cycle vapor compression design

3. Results

3.1. Tray efficiency

The tray performance and its efficiency depends on the design, active area, weir length and height, down-comer area and so on. Since, no information regarding the tray efficiency was known from the plant data, the efficiency is estimated by fitting the simulation results with the plant data. The results show that the overall efficiency of the stripper trays is approximately 15 % which is a typical value for an industrial sour water strippers (Hatcher and Weiland, 2012; Nagpal, 2014).

3.2. Energy analysis

The stripped water stream is set to contain no more than 10 and 100 ppm of H₂S and NH₃ content respectively. The results show that the base case design consume more energy compared to the bottom cycle vapor compression design. Figure 3 shows the total energy and unit energy requirement per ton of water stripped. The novel design consumes approximately 53 % less energy compared to the base case design. This significant improvement has been made by cutting down the cold and hot utilities for the condenser and reboiler respectively. The largest energy consuming equipment in the base case is the reboiler which requires more than 70 % of the total energy. This hot utility requirement of the reboiler has been saved in the vapor compression design by using the mechanical energy instead of thermal energy. Cooling is the second highest energy consuming process in the base case which in most of the cases is provided by the cooling utility as shown in figure 4. In case of vapor compression design, cooling and

compression are the main energy consuming steps accounting to around 48 % and 36 % respectively.

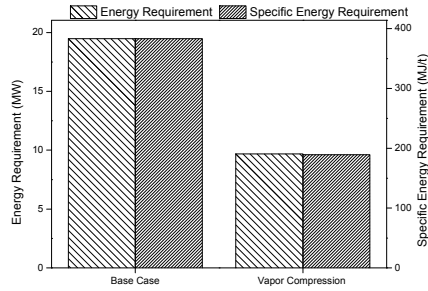
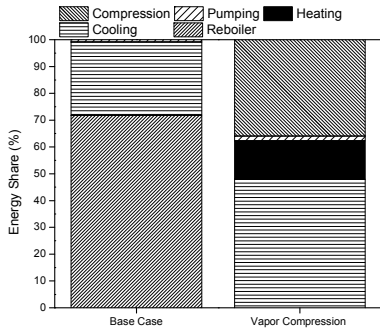


Figure 3: Comparative energy analysis of sour water stripper designs

Figure 4: Percent energy share for the sour water stripper designs

Figure 5 shows the vapor phase composition profile of NH_3 and H_2S in the stripper. The results show that the removal of H_2S is accomplished easily and require less number of stages to achieve the desired stripped water purity specification. However, the removal of NH_3 from the sour water is more difficult and require more number of trays to satisfy the stripped water composition standards.

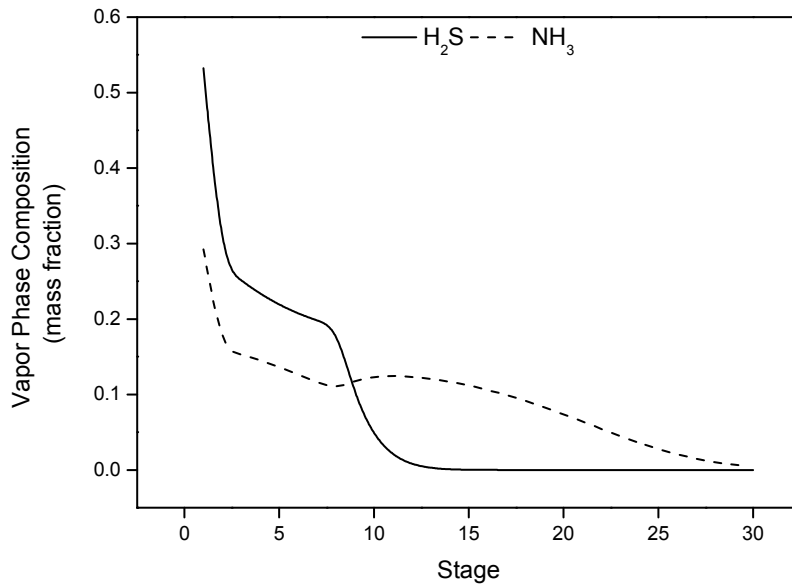


Figure 5: Vapor phase composition of H_2S and NH_3 in the stripper

4. Conclusions

In this study, Aspen HYSYS has been used to simulate the sour water stripping unit of a refinery. The base case design has been compared with a novel vapor compression design. Both the process designs were compared in terms of energy requirement while maintaining the stripped water purity of 10 ppm H₂S and 100 ppm NH₃ content. This study presents a novel design that can reduce the energy requirement of the stripping process significantly compared to the conventional designs. The results show that the proposed vapor recompression design can reduce the hot and cold utilities requirement by 90 % and 22 % respectively compared to the base case design.

Acknowledgment: The authors would like to acknowledge financial support from King Fahd University of Petroleum & Minerals (KFUPM).

References

- Bellen, J., 2009. Design of Sour Water Stripping System, in: Proceedings of the 70th Philippine Institute of Chemical Engineers Annual National Convention.
- Gai, H., Jiang, Y., Qian, Y., Kraslawski, A., 2008. Conceptual design and retrofitting of the coal-gasification wastewater treatment process. *Chem. Eng. J.* 138, 84–94.
- Lieberman, N., 2013. Sour water strippers: Design and operation. *Pet. Technol. Q.* 18, 99–103.
- Nabgan, B., Abdullah, T.A.T., Nabgan, W., Ahmad, A., Saeh, I., Moghadamian, K., 2016. Process simulation for removing impurities from wastewater using sour water 2-strippers
- Nagpal, S., 2014. Fine tune the design of sour-water strippers using rate-based simulation. *Chem. Eng. (United States)* 121, 42–46.
- system via Aspen Hysys. *Chem. Prod. Process Model.* 11, 315–321.
- Sharma, M.K., Nag, A., 2009. Process developed for enhanced H₂S recovery from sour-water strippers. *Oil Gas J.* 107, 44–49.
- Weiland, R.H., Hatcher, N. a, 2012. Sour water strippers exposed 285–298.

Techno-economic Assessment of Future Generation IGCC Processes with Control on Greenhouse Gas Emissions

Usama Ahmed ^{a*}, Umer Zahid^a

^a *Chemical Engineering Department, King Fahd University of Petroleum and Minerals, Dhahran, Saudi Arabia*

usama.ahmed@kfupm.edu.sa

Abstract

Integrated gasification and combined cycle (IGCC) is a pre-combustion carbon capture technology that can be used to generate electricity and hydrogen while reducing the greenhouse gas emissions. In this study, three IGCC based process models are developed in Aspen Plus[®] followed by their techno-economic evaluation. Case 1 is the conventional IGCC process which is considered as a reference model, whereas, case 2 and case 3 are the conceptual process models. In case 2, gasification unit in the conventional IGCC model is integrated with the reforming technology to utilize the steam produced in the gasification unit in the methane reforming process. This concept not only increased the overall yield of syngas but also the H₂ production capacity. On the other hand, the case 3 is modified to convert the conventional IGCC into oxy-fuel IGCC process keeping the reforming unit in place which nullifies the need of using standalone energy intensive water gas shift units and CO₂ capturing unit. The efficiencies calculated for case 1, case 2 and case 3 are 35.86%, 40.7% and 41.3%, respectively. The economic analysis showed that the cost required for each unit of energy generated is 2.93, 2.06 and 2.01 M€/MWe, respectively. The results also showed that the case 3 design not only offers highest process performance and economics but it offers least CO₂ specific emissions compared to the case 1 and case 2 designs.

Keywords: IGCC, SMR, Oxyfuel, CCS, LCOE.

1. Introduction

With the increase in population and industrialization during the last few decades have increased both the energy demand and pollution in the world. The power generation sectors mainly relies on the fossil fuels to compete the world energy demand and are held responsible for 35% of greenhouse gas (GHG) emissions where 75% of total emissions includes CO₂. Among various fossil fuels, coal and natural gas have been receiving a lot of attention for power generation due to their abundance in nature and already developed infrastructures. International Energy Agency (2014) statistics showed that almost 40.58% of electricity in 2010 was generated from only coal where its consumption is expected to increase by 33% in 2035 compared to 2009. Due to an ever increasing energy demand in future also, carbon capture and sequestration (CCS) technologies will play a vital role in controlling and abating GHG emissions. Natural gas combined cycle (NGCC), ultra-supercritical pulverized coal (USPC) and integrated gasification and combined cycle (IGCC) power plants are currently the main sources of electricity generation. However, the efficiency of power plants tremendously drops with the implementation of CCS

technology. For instance, NGCC, USPC and IGCC power plants shows an efficiency drop of 7.1%, 11.4% and 9%, respectively with the CCS technology. Moreover, currently operating post combustion carbon capture processes from coal would nearly double the cost of electricity (COE) while decreasing the net output by 7-10%. On the other hand, pre-combustion processes have higher capital investments but they are more energy efficient if CCS is implemented on large scale. Although, NGCC processes offers higher process performances with CCS, however, the higher and fluctuating cost of natural gas limits its extensive utilization over coal based power plants. Therefore, the state of art technologies for power and H₂ generation can be integrated to enhance the overall process performance while abating the GHG emissions.

Process optimization and intensification techniques along with the better heat integration methods provides an opportunity to increase the reliability and sustainability of processes. Recently, Ahmed et al. (2016) and Cormos et al. (2015) explored the various design routes for enhancing the IGCC performance with CCS techniques. On the other hand, Yi et al. (2014) performed the studies for integrating IGCC and natural gas reforming processes to enhance the H₂/CO content in the syngas followed by their consequent use in various poly generation processes. Recently, Ahmed et al. (2017) presented the model for integrating the gasification and reforming technology that utilizes the in-process generated steam during coal slurry gasification process to assist the reforming process and makes the process more self-sustainable. This study has been performed in continuation of the previous work performed by Ahmed et al. (2016, 2017) with more promising results. In this study, the idea of integrating the available technologies (IGCC, Reforming and Oxyfuel) is presented to enhance the overall process sustainability. The results for the conventional and proposed processes will be compared in terms of both the process performance and economics to assess the design reliability.

2. Simulation Methodology and Process Description:

Three simulation models are developed in Aspen Plus ® using Peng Robinson equation of state as a thermodynamic package. Coal is an un-conventional compound and has been modeled based on proximate and ultimate analysis. The gasification, water gas shift and reformer reactors are modelled on the basis of RGibbs reactor models which are operated on the Gibbs free energy minimization laws to generate syngas reaction products as shown in Table 1.

Table 1: Design Assumptions for Model Development

Unit/Component/System	Modelling Unit	Parameter
Gasification Reactor	RGibbs (Reactor)	Coal flow rate= 38.51kg/s Temp/Press: 1550°C/32 bar
Reformer	RGibbs (Reactor)	NG flow rate: 2.47 kg/sec H ₂ O:CH ₄ = 3:1 Temp/Press: 900-1050°C/ 32 bar
Air Separation Unit (ASU)	HeatX, Compr	Oxygen Purity 99.5% (vol) Energy: 245 kW/t
Shift Conversion (WGS)	RGibbs (Reactor)	(Co-Mo) Sour Catalyst Steam/CO: ~ 2.2
Acid Gas Removal H ₂ S and CO ₂	RadFrac (Slexol Solvent)	H ₂ S/CO ₂ Removal Percentage: 99.9 / 90

2.1. Conventional IGCC process (Case 1):

Case 1 is a conventional IGCC process which is taken as a base case model that sequentially integrates the gasification unit (GU), air separation unit (ASU), water gas shift reactor (WGS), heat recovery steam generation (HRSG), acid gas removal section (AGR), and combined cycle (CC) as shown in Figure 1. Coal water slurry is fed to the entrained flow gasification unit to generate syngas which is a mixture of CO, H₂, CO₂ and H₂O. Syngas leaves the gasification unit at a very high temperature (~1600 °C) and contains high concentration of H₂ and CO. The temperature of the syngas is reduced to 250-500 °C in the radiant and convective heat exchangers to carry out WGS reactions as shown in equation in Eq.(1).

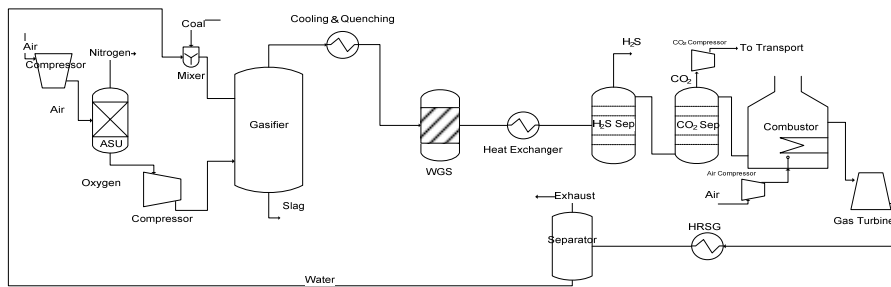
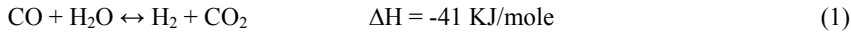
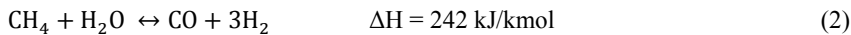


Figure 1: Case 1 – Conventional IGCC design for power generation with CO₂ capture

The syngas from WGS reactors is then passed through AGR section where most of the CO₂ and H₂S is removed and recovered by Selexol solvent. The separated CO₂ is then further processed and compressed to an elevated pressure for its transport and storage, whereas, H₂S is further treated in a Claus plant to recover elemental sulfur. The syngas leaving from AGR section contains high concentration of H₂ which is directed towards CC section to generate electricity and the process heat.

2.2. Integration of IGCC and SMR Process (Case 2):

Steam methane reforming (SMR) technology is extensively used for the commercial production of H₂ gas. SMR is an endothermic process which is carried out by reacting high pressure steam with the methane gas at a temperature range of 627-827°C as shown in equation (2). Reforming process is usually carried out in two sequential steps i.e. pre-reforming and reforming. Firstly, the compressed methane is heated and mixed with a high enthalpy steam in a pre-reforming section. Ahmed et al. (2017) and Lucero et al. (2015) demonstrated the reforming process over the nickel-based catalyst to generate H₂.



Conventional SMR processes requires an additional heat source for preheating the gas stream to assist the reforming process. However, in this case, the syngas generated during gasification process is cooled and mixed with the compressed natural gas where the inlet temperature of the reformer is maintained at 1150 °C. As the mixture passes through the reforming unit, the temperature reduces to 1040 °C due to an endothermic reforming reactions. The conceptual process flow diagram of case 2 can be seen from Figure 2. The

syngas from the reforming section is then directed to the WGS reactors to generate additional H_2 and CO_2 . The CO_2 and H_2S generated in the process is removed in the AGR section using Selexol process, whereas, the H_2 is sent to the CC section to generate electricity. As natural gas used in this case is an important utility, therefore, the corresponding net efficiency of NGCC power plants have been also incorporated for the fair evaluation of the analysis in the next section.

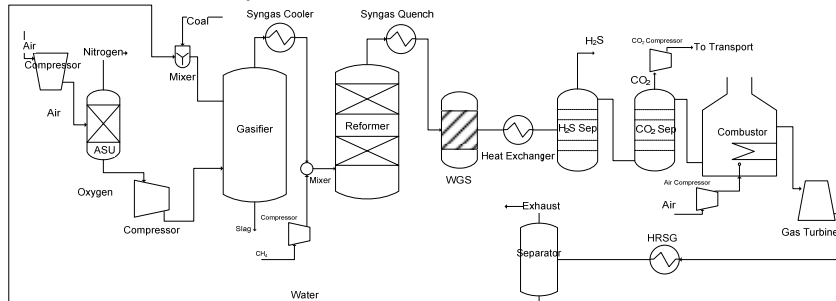


Figure 2: Case 2 – Integration of IGCC and methane reforming process with CO_2 capture

2.3. Integration of IGCC, SMR and Oxyfuel Processes (Case 3):

Oxyfuel combustion technology can be used for burning the fuel in the presence of high purity oxygen to generate more heat compared to air by avoiding its dilution with N_2 . The flue gas generated from the oxyfuel combustion process contain high purity CO_2 and H_2O which do not requires any standalone chemical or physical sorbent process to capture CO_2 . The temperature of the flue gas is reduced in multiple heat exchangers to condense the moisture and pure CO_2 is separated followed by its compressing in the multi-stage compression unit for further utilization. The case 3 design is an advanced version of case 2 in which we can integrate the oxyfuel combustion technology with the gasification and the reforming processes as shown in the Figure 3. The CO_2 generated in the combustion section is partially recycled to the combustion reactor to control both the combustion temperature and maintaining the inlet temperature of flue gas for gas turbine power generation unit. This integration will also nullify the need of installing additional WGS and CO_2 capture units compared to the case 1 and case 2 designs that will also improve both the process performance and economics of the overall process.

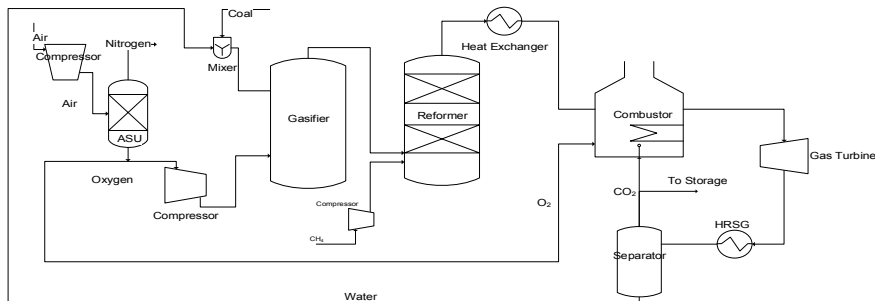


Figure 3: Case 3 - Integration of IGCC with the Reforming and Oxyfuel Technology

3. Results and Discussion

Case 1 is a conventional IGCC process design where the heating value of syngas typically depends on the operational conditions of the gasifier. The addition of reforming unit with the gasification unit in case 2 generates an additional syngas from SMR process. The SMR process utilizes high enthalpy steam from the syngas to convert CH_4 to H_2 while maintaining the reformer's temperature and pressure. Figure 4 provides the comparison of case 1 with the other two cases in terms of syngas composition and heating value at the outlet of the reforming unit. The case 2 and case 3 has the same configuration up to reforming unit so the syngas composition and heating value remained same at the reformer's outlet.

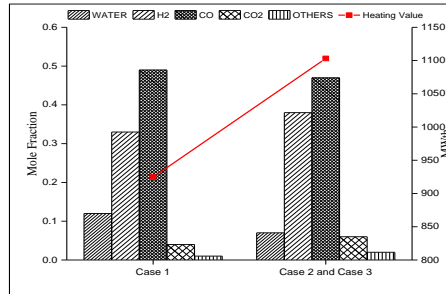


Figure 4: Syngas Composition & Heating Values at the Reformer's Outlet

The results showed that syngas production capacity for case 2 and case 3 has been increased compared to the case 1 design due to installation of the reforming unit. Due to the increase in H_2/CO ratio and heating value of the syngas in the case 2 and case 3 designs, the power generation capacity from both the steam cycle and the gas turbine section are also increased compared to the case 1 design. While comparing case 2 and case 3, it has been analyzed that case 3 generates more power in the steam cycle process due to an oxyfuel nature of the process and also due to an absence of WGS unit which requires steam to convert CO to H_2 . However, the power generation from the gas turbine section for the case 3 is lower than the case 2 design as less flue gas passes through the gas turbine section due to syngas combustion with the high purity oxygen instead of excess air. The net power generated and process efficiency for case 1, case 2 and case 3 is calculated as (375.08, 472.92 and 495.01) MWe and (35.86, 40.7 and 41.3) % respectively. The breakup for power generation from the combined cycle processes is given in Figure 5.

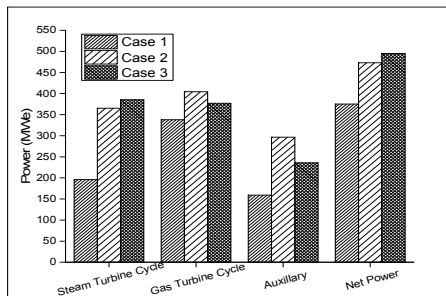


Figure 5: Comparison of process performance of all cases

The key purpose of any power plant is to produce electricity at an economical price. Some of the process performance and economic indicators are used to evaluate the LCOE (cost of electricity) with CCS technology, CO_2 specific emissions and CO_2 capture cost in terms of

CO₂ removal and avoidance cost for all the cases which are summarized in Table 2. It has been seen from results that the case 3 design has a potential to reduce the LCOE by 11.6% and 6.2% compared to the case 1 and case 2 designs, respectively. Moreover, the case 3 design also offers a reduction in both the CO₂ specific emissions and CO₂ capture cost compared to the case 1 and case 2 designs.

Table 2: Comparison of some economic indicators for case 1, case 2 and case 3 designs

	Units	Case 1	Case 2	Case 3
LCOE	€/MW _h	70.57	66.47	62.35
CO ₂ Specific emission	kg/MW _h	87.74	80.26	78.45
CO ₂ avoidance/removal cost	€/t	36.23/26.99	27.97/20.45	25.66/18.35

4. Conclusions

In this study, three IGCC based process models have been developed and techno-economically compared. Case 1 is based on the conventional IGCC process, whereas, case 2 integrates the conventional IGCC with the reforming technology. Case 3 is a further modification of the case 2 design which converts the downstream process into oxyfuel technology which nullifies the utilization of standalone WGS and CO₂ capture units. It has been seen from results that the case 3 design offers higher process efficiency and economics compared to other cases which makes the overall process more reliable and sustainable.

Acknowledgement

The authors would like to acknowledge the support provided by the King Fahd University of Petroleum & Minerals (KFUPM) for funding this work through project No. SR181006.

References

- International Energy Agency (IEA), World Energy Investment Outlook, 2014, France
- Ahmed, U., Zahid, U., Jeong, Y.S., Lee, C. J., Han, C., 2016, IGCC process intensification for simultaneous power generation and CO₂ capture. *Chemical Engineering and Processing: Process Intensification* 101, 72-86.
- Ahmed, U., Kim, C., Zahid, U., Lee, C. J., & Han, C., 2017, Integration of IGCC and methane reforming process for power generation with CO₂ capture. *Chemical Engineering and Processing: Process Intensification*, 111, 14-24.
- Cormos, A.M., Dinca, C., Cormos, C.C., 2015, Multi-fuel multi-product operation of IGCC power plants with carbon capture and storage (CCS). *Applied Thermal Engineering* 74, 20-27.
- Lucero, A. Goyal, J. Carroll, K. McCabe, and S. Gangwal. H₂S resistant steam reforming catalyst for upgrading coal derived syngas for coal to liquid production, <https://www.netl.doe.gov/sites/default/files/2017-11/Lucero-Poster-for-DOE-Gasification-workshop.pdf>
- Yi, Q., Feng, J., Wu, Y., Li, W., 2014, 3E (energy, environmental, and economy) evaluation and assessment to an innovative dual-gas polygeneration system. *Energy* 66, 285-294.

Modelling of Microfluidic Devices for Analysis of Radionuclides

Miguel Pineda^{a,*}, Panagiota Angeli^a, Takehiko Tsukahara^b and Eric S. Fraga^a

^a*CPSE and ThAMeS Multiphase. Department of Chemical Engineering, University College London, London WC1E 6BT, UK*

^b*Laboratory for Advanced Nuclear Energy, Tokyo Tech, Tokyo 2-12-1-N1-6 O-okayama, Meguro-ku, Japan*

m.pineda@ucl.ac.uk

Abstract

Analysis of radionuclides in radioactive waste is performed according to a number of operating protocols which are usually time-consuming and difficult to implement. The use of microdevices for liquid-liquid extraction of radionuclides is promising, since small amounts of materials are needed. In this work, a plug flow modelling approach for the liquid-liquid extraction in microdevices is presented. A multi-component chemical process based on the PUREX-TRUEX waste management treatment is analysed. We evaluate the performance of the coupled micro-units as a function of channel size, superficial mixture velocity, and initial loading. The results show that it is possible to use the model in an optimisation based design procedure for microfluidic devices.

Keywords: Microdevices, Radionuclides, Plug flow, Sensor design

1. Introduction

Liquid liquid extraction (LLE), also known as solvent extraction, is a method used to distribute one or more species (solutes) between two immiscible liquids in contact with each other due to a difference in solubility. It is among the most common separation techniques used in industrial processes. In this regard, computer simulations of LLE processes are very useful tools that can aid the design and testing of process flowsheets. They can form the basis for applications in optimisation, control, and system analysis.

The analysis of radionuclides present in high level radioactive waste (HLRW) is performed using operating protocols including several separation and purification steps which are difficult to implement in glove boxes and hot cells (Hellé, et al., 2015). Among those steps, LLE is essential to obtain a pure fraction containing the radionuclides of interest. However, one of the disadvantage of this separation method is that a large amount of organic solvent is need to dissolve the extractant and the radionuclides of interest. This entails both radiological and chemical risks. Therefore, in order to reduce the amounts of solvents used, as well as the radioactive material needed for the analysis, modifications of operating procedures are important. In the frame of studies aiming to overcome these limitations, microfluidic devices have attracted much attention, and micrototal analysis systems (μ TAS) have been advocated (Ciceri, et al., 2014). Normally, in μ TAS, solvent mixing, reaction, separation, and detection are integrated onto a microfluidic chip. These

microfluidic technologies are suited for the efficient implementation of LLE due to the intrinsic advantages of the small dimension, i.e., high surface-to-volume ratio and laminar flow conditions. Other attractive features of microfluidic devices are the ability to control the contact time of the liquids involved and the use of small manipulating volumes, which decrease both chemical and radiological risk.

Micro-chemical systems that implement two or more liquid streams flowing laminarily in a micro-channel have been developed for some specific radiochemical applications. These studies include the extraction of uranium U(VI) by tributylphosphate (TBP) in *n*-dodecane (*n*-DD) (Hotokezaka, et al., 2005) and the extraction of Am(III) by *n*-octyl(phenyl)-*N,N*-diisobutylcarbamoylmethylphosphine oxide (CMPO) (Ban, et al., 2011). For industrial application of these techniques, however, one of the challenges is to have continuous and multiple separations of individual metal elements occurring in the same microtool (Hellé, et al., 2015).

Despite the interest in the development of μ TAS or lab-on-chip devices, researchers typically do not have large amounts of time and money to build and test several prototypes in order to optimise performance. To reduce the number of iterations of prototyping, it is imperative to develop the best computer-aided design-forecasting methods. With the aim to improve these prediction methods, we present and validate a mathematical modelling framework to simulate continuous separations of radionuclides in a single microdevice. The long term aim is to use the mathematical model with an optimisation based design procedure. This procedure will aim to generate and evaluate alternative channel layouts and identify those that have the best performance for the online determination of radionuclides following microchip extraction by using for example the so-called thermal lens microscopy system (Hotokezaka, et al., 2005).

In the following section, we present the radiochemical system under consideration. Then, we introduce the mathematical model and present the results. We finalize with the conclusions.

2. The chemical system

In this section, we describe the radiochemical process implemented in this work.

2.1. Motivation

Reprocessing of spent nuclear fuels (SNFs) from power reactors by PUREX process is aimed at recovery of uranium and plutonium (Bascone, et al., 2017). It consists of a LLE process using 1.1 M TBP as extractant present in *n*-DD as diluent. Since the trivalent actinides and lanthanides (i.e. Am(III) and Eu(III)), are inextractable by TBP, they are normally rejected to HLRW. However, the trivalents can be then extracted by the TRUEX process, which is a mixture of 0.2 M CMPO - 1.2 M TBP in *n*-DD. In this part of the waste treatment, TBP is added as a diluent modifier in order to minimize third phase formation. It has been also observed that the extraction of trivalent actinides by CMPO decreases with the presence of uranium in the feed as it tends to saturate CMPO in the organic phase (Mathur, et al., 1993). These LLE processes are mostly carried out in pulsed columns and mixer settlers. In the following subsection, we describe a simplified version of the PUREX-TRUEX waste treatment, which will be used in the subsequent sections to

validate our approach.

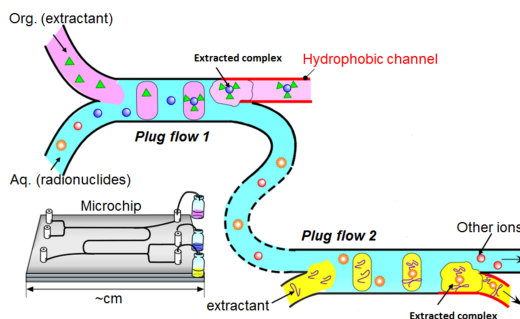


Figure 1: Conceptual diagram of a microchip involving two LLE steps, two different extractants, and three different radionuclides.

2.2. Process description

An HNO_3 aqueous phase, containing U(VI) (in the form of UO_2^{2+}) and Am(III) (in the form of Am^{+3}), is initially brought into contact with the organic phase containing 1.1 M TBP diluted in a hydrocarbon phase. This occurs in a hydrophilic small channel where dispersed plugs (elongated drops) of the organic phase are formed inside the continuous aqueous phase. It is assumed that, after the extraction of uranium, the organic stream will be separated in a side hydrophobic channel. The aqueous stream with the rest of uranium and all the americium will be mixed in a second micro-channel with another organic phase containing 0.2 M CMPO also diluted in a hydrocarbon phase for the extraction of remaining U(VI) and Am(III). We consider the plug flow pattern because it combines improved mixing with large interfacial areas. We will assume a constant HNO_3 concentration along the processes. We refer to Fig. 1 for a general schematic representation of a microchip containing two LLE steps and flow patterns as those described here. In both stages, the extraction proceeds according to the following reaction (Hellé, et al., 2015)



where for the reaction along the first channel, $\text{M}=\text{UO}_2$ and $\text{S}=\text{TBP}$. For the reaction along the second channel $\text{M}=\text{UO}_2$ or Am and $\text{S}=\text{CMPO}$. The symbol S_f represents the free or unbounded extractant along the channel. For uranium $n = 2$ and for americium $n = 3$.

3. Mathematical model

As previously mentioned, the organic phase consists of dispersed plugs moving in a continuous phase containing the aqueous solution which initially contains the two radionuclides. In this work, the $i \in \{1, 2\}$ channel will be modelled as an ideal plug flow reactor with the concentration of the $j \in \{U, \text{Am}\}$ radionuclide in the dispersed (organic) phase described by the so-called operational line given by

$$C_{i,j,d}(x) = C_{i,j,d}(0) - q^{-1} [C_{i,j,c}(x) - C_{i,j,c}(0)], \quad (2)$$

with the concentration of the j radionuclide in the continuous (aqueous) phase, $C_{i,j,c}(x)$, calculated from

$$v_{mix} \frac{dC_{i,j,c}(x)}{dx} = -K_{La_i} (C_{i,j,c}(x) - C_{i,j,c}^e(x)), \quad (3)$$

where the equilibrium concentration of the j radionuclide in the aqueous phase is obtained using the equilibrium line, $C_{i,j,c}^e(x) = C_{i,j,d}(x)/D_{i,j}$. The parameter $q = 1$ is the ratio of the volumetric flow rates of the dispersed phase to the continuous phase. The parameter $D_{i,j}$ is the distribution coefficient defined as the ratio of the concentrations of each radionuclide in the organic and aqueous phases at equilibrium. From the complexation kinetics (see Eq. 1) we have that, $D_{1,U} = K'_{1,U}(C_{TBP_f}(x))^2$, $D_{2,U} = K'_{2,U}(C_{CMPO_f}(x))^2$, and $D_{2,Am} = K'_{2,Am}(C_{CMPO_f})^3$. We also assume that $C_{TBP_f}(x) = 1.1 - 2C_{1,U,d}(x)$ and $C_{CMPO_f}(x) = 0.2 - 2C_{2,U,d}(x) - 3C_{2,Am,d}(x)$ are the concentrations of the free extractants at position x along the channel. The parameters $K'_{1,U}$, $K'_{2,U}$, and $K'_{2,Am}$ are the conditional extraction constants. In Eqs. 2 and 3, $C_{i,j,d}(0)$ and $C_{i,j,c}(0)$ are the inlet concentrations, K_{La_i} is the volumetric overall mass transfer coefficient, and v_{mix} is the superficial mixture velocity. Following previous works using circular channels and plug flow conditions (Bascone, et al., 2017), we assume an average volumetric mass transfer coefficient given by

$$K_{La_i} = 0.88 \frac{v_{mix}}{L_i} Ca_{mix}^{-0.09} Re_{mix}^{-0.09} \left(\frac{ID_i}{L_i} \right)^{-0.1}, \quad (4)$$

where L_i and ID_i are the length and diameter of the channels. The symbols Re_{mix} and Ca_{mix} are the Reynolds and capillary numbers of the mixture, which are functions of the properties of the phases, v_{mix} , ID_i , and q . Crucial for the coupling between the two channels is the assumption that the outlet concentration of radionuclides in the continuous phase of the first channel becomes the inlet concentration of the continuous phase in the second one.

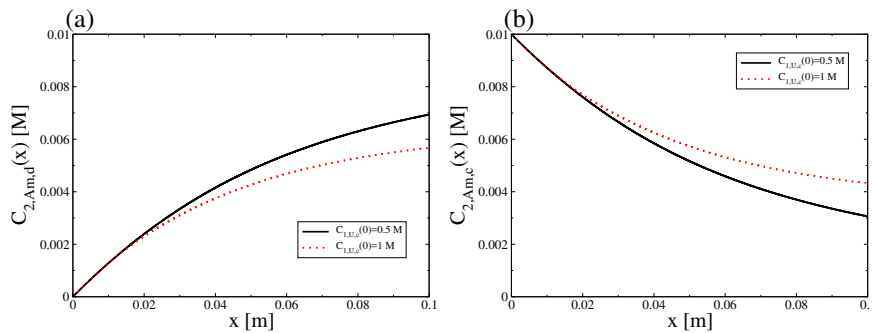


Figure 2: Evolution of the concentration of Am(III) in a) dispersed/organic phase and b) continuous/aqueous phase, for two different values of $C_{1,U,c}(0)$, with $C_{1,Am,c}(0) = 0.01$ M. The fluids along the channels have the same properties. In this case, $K'_{1,U} = K'_{2,Am} = 10^3$ and $K'_{2,U} = 10^2$. For the dimensions, $L_1 = L_2 = 0.1$ m and $ID_1 = ID_2 = 0.002$ m. For the integration of Eq. 3, we use the fourth order Runge-Kutta method with $\Delta x = 5 \times 10^{-6}$ m. Note that $C_{2,U,c}(0) = 0.127$ M and 0.468 M, for $C_{1,U,c}(0) = 0.5$ M and 1 M, respectively.

4. Results and validation of the model

It has been recognised that the extraction of trivalent actinides, like for example Am(III) decreases in the presence of large amounts of uranium in the feed as it tends to saturate CMPO in the organic phase (Mathur, et al., 1993). In the following, we show that our model reproduces, at least in a qualitative manner, this interesting finding. To this end, in Fig. 2 we plot the concentration of americium along the second channel (i.g. $C_{2,Am,d}$ and $C_{2,Am,c}$), for two large enough values of $C_{1,U,c}(0)$ (note that the concentration of Am(III) along the first channel is constant, as TBP does not extract trivalent actinides). The figure clearly shows that the extraction of americium decreases with the initial uranium loading.

Our model also predicts some interesting features that can be tested against future experiments. For example, in Fig. 3 we plot the concentration of americium as a function of the superficial velocity of the mixture v_{mix} . The figure clearly show that the extraction of americium in the microchip device should decrease with v_{mix} . This is due to the fact that an increase of the mixture velocity decreases the residence time available for mass transfer. The model also allows us to analyse the extraction as a function of the geometric

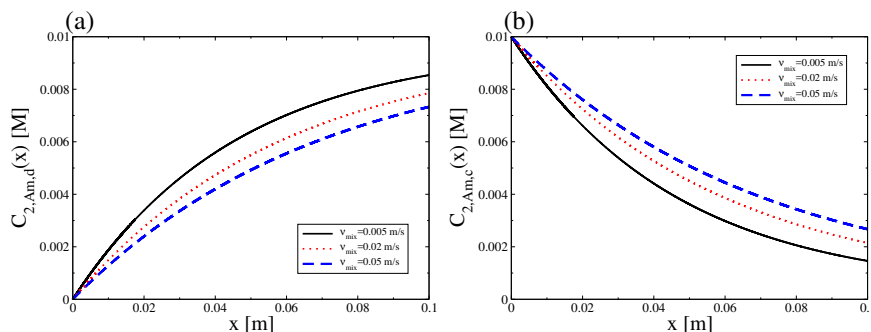


Figure 3: Evolution of the concentration of Am(III) in a) dispersed phase and b) continuous phase, versus v_{mix} . In this case, $K'_{1,U} = K'_{2,U} = K'_{2,Am} = 10^3$. For the dimensions, $L_1 = L_2 = 0.1$ m, and $ID_1 = ID_2 = 0.002$ m. The inlet concentrations are $C_{1,U,c}(0) = 0.05$ M and $C_{1,Am,c}(0) = 0.01$ M. Note that $C_{2,U,c}(0) = 0.006$ M, 0.010 M, and 0.013 M for $v_{mix} = 0.005$ m/s, 0.02 m/s, and 0.05 m/s, respectively.

properties of the microchannel. Figure 4 shows the concentration of americium along the second channel as a function of the channel diameter. The figure shows that the extraction is always higher as the channel size decreases. The interfacial area available for mass transfer decreases with the channel size, because the length of the plugs in the larger channels are longer; thus small number of plugs and reduced interfacial area are available for mass transfer.

5. Summary and conclusions

A mathematical model for the coupling of different LLE micro-unit operations in a single microchip is introduced and validated with a continuous radiochemical process, inspired by the PUREX-TRUEX waste treatment. The model reproduces, in a qualitative manner, the experimental observation that the extraction efficiency of americium decreases with

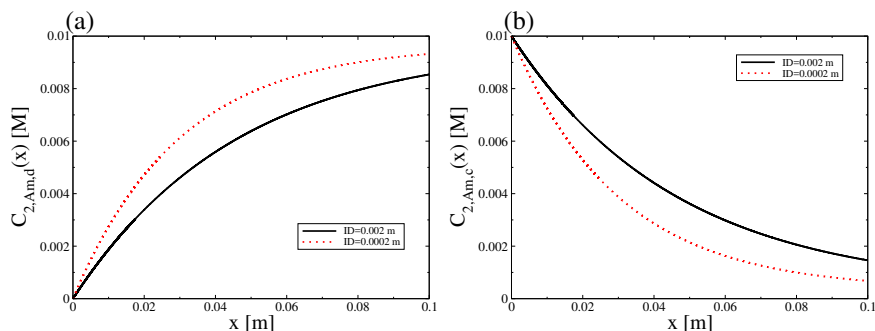


Figure 4: Similar to Fig. 3 but as a function of $ID = ID_1 = ID_2$, with $L_1 = L_2 = 0.1$ m. Note that $C_{2,U,c}(0) = 0.006$ M and 0.002 M, for $ID = 0.002$ M and 0.0002 M, respectively.

the initial loading of uranium. Our results also indicated that for fixed parameter values (i.e. channels size and flow conditions) as the mixture velocity increases the extraction efficiency of Am(III) decreases. It also shows that, for the same mixture velocity, the extraction efficiency is always higher as the diameter of the channel decreases. Our modelling approach constitutes a proof of concept and a first step towards a general modelling of analytical processes with continuous flows in microchips. The next step is to use the mathematical model with an optimisation based design procedure. For example, it could be interesting to determine the optimal channel size and layout in a constrained space for each separation step of the analytical process.

References

- G. Hellé, C. Mariet, G. Cote, 2015, Liquid - liquid extraction of uranium(VI) with Aliquat 336 from HCl media in microfluidic devices:Combination of micro-unit operations and online ICP-MS determination. *Talanta*, 130 123-131.
- D. Ciceri, J. M. Perera, G. W. Stevens, 2014, The use of microfluid devices in solvent extraction. *J. Chem. Technol. Biotechnol.*, 89 771-786.
- H. Hotokezaka, M. Tokeshi, M. Harada, T. Kitamori, Y. Ikeda, 2005, Development of the innovative nuclide separation system for high-level radioactive waste using microchannel chip - extraction behavior of metal ions from aqueous phase to organic phase in microchannel. *Prog. Nucl. Energy*, 47 439-447.
- Y. Ban, Y. Kikutani, M. Tokeshi, Y. Morita, 2011, Extraction of Am(III) at the interface of organic-aqueous two-layer flow in a microchannel. *J. Nucl. Sci. Technol.*, 42 1313-1318.
- J. N. Mathur, M. S. Murali, P. R. Natarajan, L. P. Badheka, A. Banerji, A. Ramanujam, P. S. Dhani, V. Gopalakrishnan, R. K. Dhumwad, and M. K. Rao, 1993, Partitioning of actinides from high-level waste streams of PUREX process using mixtures of CMPO and TBP in dodecane. *Waste management*, 13 317-325.
- D. Bascone, P. Angeli E. S. Fraga, 2017, Mathematical modelling of intensified extraction for spent nuclear reprocessing. In: *Espua, A., Graells, M., Puigjaner, L., (Eds.). Proceedings of the 27th European Symposium on Computer Aided Process Engineering - ESCAPE 27. Barcelona (Spain)*. pp. 355-370.

Comparative analysis of gasification and reforming technologies for the syngas production

Hussain A Alibrahim ^a, Siddig SeedAhmed ^a, Usama Ahmed ^a, Umer Zahid ^{a*}

^a *Department of Chemical Engineering, King Fahd University of Petroleum and Minerals, Dhahran, 34464, Saudi Arabia*

uzahid@kfupm.edu.sa

Abstract

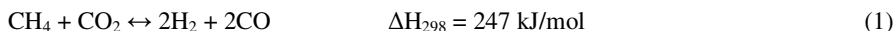
This study is focused on the production of syngas using gasification and dry methane reforming (DMR) technologies. The two processes are compared as a standalone design for a syngas production capacity of 10,000 kmol/h with H₂ to CO ratio of 0.88. The two processes are then integrated to develop a novel design that can reduce the CO₂ emissions to a near-zero level with reasonable amount of energy requirement. In this study, Aspen Plus® has been employed as a process simulation tool. The results reveal that the DMR process consumes 3.4 times less energy compared to a gasification plant of same capacity. The result also shows that the integration of gasification and DMR design off-sets the negative aspects of gasification technology enabling it to utilize conventional solid fossil fuel with low emission levels.

Keywords: Gasification, dry reforming, syngas, energy.

1. Introduction

The production of syngas is one of the important process in the petrochemical industries from which many downstream products like ammonia, methanol and fertilizers are produced. In order to have a sustainable hydrocarbon fuel usage, the amount of carbon dioxide in the atmosphere must be reduced. As in the Paris agreement at COP21 conference in 2015, there are 195 countries who signed a ratification to reduce carbon emissions. The Paris accord can be realized by supplying clean fuels and renewables for the energy production, improving efficiency of the current energy consuming processes, and utilization of fossil fuels by eliminating the pollutants and GHG emissions. Syngas production technologies can play a role in bridging the gap for the use of fossil fuels while keeping the emissions within the limits. Syngas can be produced using gaseous fuels, liquid hydrocarbons and solid feedstocks. The gaseous and liquid feedstocks utilize technologies such as steam reforming, partial oxidation, dry reforming, and auto-thermal reforming. With solid feedstocks such as coal and biomass, gasification is the main technology available for the syngas production.

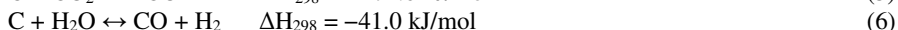
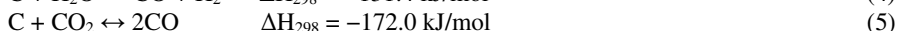
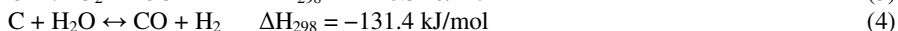
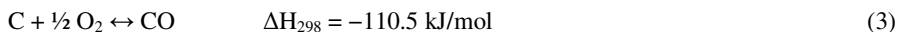
Recently, dry methane reforming is gaining a lot of attention as an environmentally friendly process for syngas production because it consumes two major GHGs, carbon dioxide and methane. It requires 363.6 kg of methane to consume 1 ton of CO₂ for the production of 90.9 kg of H₂ and 1.27 tons of CO. The main reaction taking place in the dry reforming is shown below:



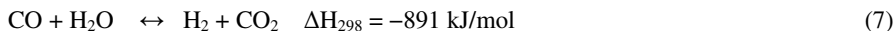
Reverse water gas shift reaction also takes place in the DMR reaction, which combines the CO₂ and H₂ to produce CO and water. The reverse water gas shift reaction is shown below:



The reaction is favoured by low pressure and high temperature which means high energy requirement and high production cost. Gasification is a proven and commercialized technology to convert solid feedstocks into syngas along with other impurities such as H₂S and CO₂. Gasifiers are operated with limited amount of oxygen to conduct the pyrolysis reactions for the formation of syngas. Although there are many simultaneous complex reactions taking place in the gasifier, some of the main reactions are shown below:



Gasification process is usually following by a gas cleaning process where acid gases are removed from the syngas. Depending on the downstream requirement, another reaction known as water gas shift reaction is usually followed to convert CO to CO₂ and increase the syngas ratio as shown below:



Many studies in the past have focussed on the syngas production technologies in order to improve the process performance by developing new catalyst materials, optimizing the process conditions, and integration with other processes. Mallick et al. (Mallick et al., 2018) analysed the effects of co-gasification of coal and biomass experimentally on the process performance. They concluded that the co-gasification of coal and biomass has synergetic effects with merits compared to the individual feedstock gasification. Li et al. (Li et al., 2018) studied the design of dry methane reforming with CO₂ utilization using nickel based catalyst. Their results showed that the catalyst development can be an important factor in the commercialization of DMR technology. Wu et al. (Wu et al., 2005) combined the coal gasification with steam reforming to evaluate the feasibility of process integration. Lim et al. (Lim et al., 2012) studied the combination of steam reforming with dry reforming. Their results showed that the combined process can reduce the net CO₂ emission by 67 % compared to the standalone steam reforming process. Ahmed et al. (Ahmed et al., 2017) studied the integration of gasification with steam reforming for power generation application with CO₂ capture unit.

Although, standalone syngas production technologies have been widely investigated in the literature, however, there is no significant research available that compared the DMR process with that of gasification process and considered their integration. The goal of this study is to compare the process performance of DMR and gasification technologies in terms of energy efficiency and economics. Aspen Plus® V9 is used to simulate the two processes. In order to have a fair comparative analysis, syngas production rate and ratio (H₂/CO) have been fixed for the two processes at 10,000 kmol/h and 0.88 respectively.

2. Process Design

2.1. Dry methane reforming

Dry methane reforming process has been simulated using the design outlined in the literature (Luyben, 2014). Peng-Robinson property method has been used for the simulation of DMR section while Amines package has been employed in the CO₂ removal section. The feed stream containing methane and excess CO₂ is compressed to the required reactor pressure of 4 bar. The temperature of feed stream after compression increases to about 130.6 °C which is further heated using a counter current process heat exchanger. The syngas formation reaction takes place at 4 bar and 1000 °C. The reactor effluent stream is used to cool down the incoming feed stream. The reactor effluent stream contains H₂, CO₂, unreacted CO₂ and CH₄, and small amount of water. The CO₂ is removed from the gas stream using a typical absorber-stripper system by employing MEA as a solvent. The syngas free of CO₂, contains 44 mol % of H₂ and 50.5 mol% of CO is compressed in multi-stage compressor train with intercooling to a product pressure of 30 bar. The capture CO₂ from the absorber is stripped from the solvent in the stripper and is recycled back to the feed compressor.

2.2. Gasification

Feedstock for the syngas production using gasification technology in this study is coal. The composition and heating value for the coal has been adapted from the literature (Ahmed et al., 2016). Multiple property packages have been used to precisely predict the properties of gasification simulation. Solids property method has been used for the feed preparation block, while Peng-Robinson has been used for the gasification, cleaning units and WGS blocks. Figure 1 shows the simplified block diagram of the gasification process for syngas production.

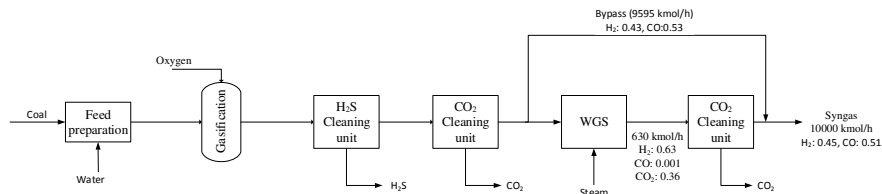


Figure 1: Simplified block diagram of gasification process for syngas production

Coal slurry is first prepared by crushing the coal to a size of 0.2 mm particle diameter along with water addition. The coal slurry is pumped to the gasifier where the reactions take place in the controlled amount of oxygen. The gasifier effluent contains a mixture of gaseous products including CO, H₂, CO₂, H₂O, Ar, H₂S and minor quantities of other gases. The reactions in the gasifier take place at 33 bar and 1200 °C. The hot effluent gas is cooled down in a series of heat exchangers to generate high pressure steam. The cooled gases at 152 °C are then sent to the cleaning unit where H₂S and CO₂ is removed from the syngas in separate absorbers. Methanol is employed as a solvent in the cleaning unit for the removal of acid gases from the syngas. The syngas coming out of the cleaning unit has a H₂/CO ratio of approximately 0.80. In order to meet the required H₂/CO ratio of 0.88, approximately 4.3 % of the total syngas is sent to the water gas shift reactor where CO is converted H₂ by reaction with steam. The additional

CO₂ produced from the water gas shift reaction is removed using methanol absorption to get the syngas product of required purity.

2.3. Integrated design

Integrated design combines the gasification and DMR process in series to enhance the process performance as shown in figure 2. The raw syngas produced from the gasification process is sent to the cleaning unit, where only H₂S is removed and the remaining gas is fed to the DMR section. Methane is also fed to the DMR unit along with the gases entering from the cleaning unit. In this way, the CO₂ generation from the gasification process can be utilized as a feed material for the DMR process. As in the standalone designs, the integrated design is also set to produce 10,000 kmol/h of syngas with the syngas ratio of 0.88. The desired production rate and product purity has been maintained by varying the coal flowrate to the gasifier and methane flowrate to the DMR reactor respectively.

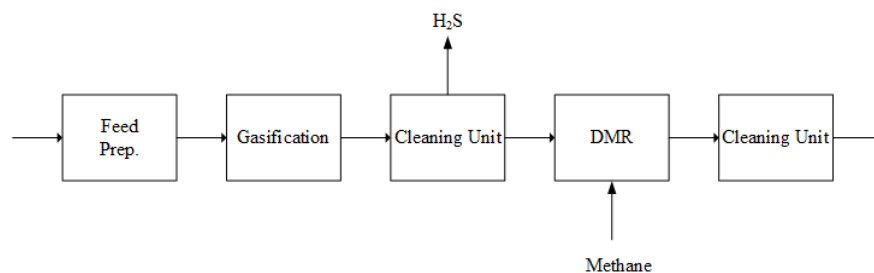


Figure 2: Simplified block diagram of integrated design for syngas production

3. Results

Energy analysis has been performed for the two systems to estimate the power requirement of various units in the process. Table 1 shows the power consumption of various units in the DMR and gasification designs.

Table 1: Energy consumption of various sections in DMR and gasification units

Dry methane reforming (MW)		Gasification (MW)		Integrated design (MW)	
Compression	33	Gasification unit	341	Gasification unit	271
Reactor	183	Cleaning unit	75	Cleaning unit	53
Stripper	7	WGS reactor unit	485	DMR	93
Cooling	42				
Total	265		901		417

The results shows that the DMR process consumes 3.4 times less energy compared to the same size of gasification unit for syngas production. The results also show that since

the DMR process consumes CO₂ as a feed material, the amount of CO₂ consumed in DMR process is approximately 5 times compared to what the gasification process emits. This makes DMR process more environmentally sustainable for the syngas production. The gasification section in the integrated design produces around 500 kmol/h of CO₂ which is used a feed material in the DMR process. In order to maintain the required syngas ratio in the product, CH₄:CO₂ molar ratio in the DMR reactor is maintained at 2.3 in contrast to the standalone DMR design. Figure 3 shows the total energy consumption and CO₂ emissions for the three designs. The results show that the integrated design produce no CO₂ emissions and can reduce the energy requirement by approximately 53.6 % compared to the gasification process. Figure 4 shows the energy requirement per unit of syngas produced from the three processes. The results show that syngas can be produced with a lower energy requirement in case of an integrated design while mitigating the CO₂ emissions.

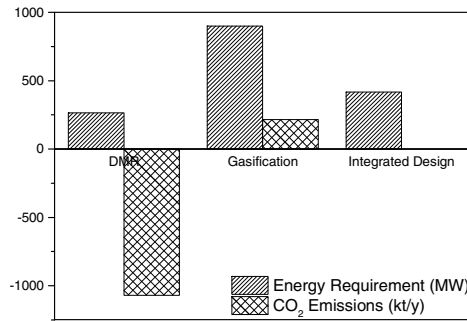


Figure 3: Energy consumption and CO₂ emissions comparison for the standalone and integrated designs

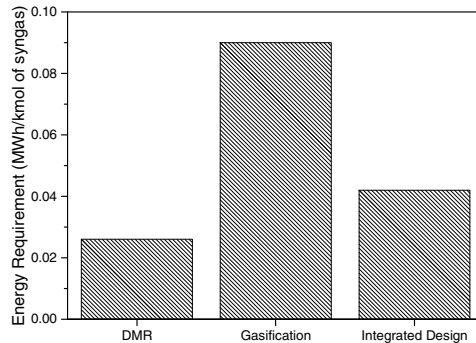


Figure 4: Specific energy requirement for the three designs

4. Conclusion

Dry reforming of methane is considered as an environmentally friendly process to produce syngas as it consumes two GHGs. The energy requirement for the DMR process is significantly lower than what is required in the gasification process. The O/C ratio is an important parameter which controls the syngas composition and its heating value. Adding WGS to gasification process can give a wide range of syngas ratios for downstream consideration. There is a need to further investigate the feasibility of the process by analyzing process economics.

Acknowledgment: The authors would like to acknowledge financial support from King Fahd University of Petroleum & Minerals (KFUPM) under the project no. USRG1803.

References

- Ahmed, U., Zahid, U., Jeong, Y. S., Lee, C. J., & Han, C. (2016). IGCC process intensification for simultaneous power generation and CO₂ capture. *Chemical Engineering and Processing: Process Intensification*, 101, 72-86.
- Ahmed, U., Kim, C., Zahid, U., Lee, C. J., & Han, C. (2017). Integration of IGCC and methane reforming process for power generation with CO₂ capture. *Chemical Engineering and Processing: Process Intensification*, 111, 14-24.
- Li, B., Lin, X., Luo, Y., Yuan, X., & Wang, X. (2018). Design of active and stable bimodal nickel catalysts for methane reforming with CO₂. *Fuel Processing Technology*, 176, 153-166.
- Lim, Y., Lee, C. J., Jeong, Y. S., Song, I. H., Lee, C. J., & Han, C. (2012). Optimal design and decision for combined steam reforming process with dry methane reforming to reuse CO₂ as a raw material. *Industrial & Engineering Chemistry Research*, 51(13), 4982-4989.
- Luyben, W. L. (2014). Design and control of the dry methane reforming process. *Industrial & Engineering Chemistry Research*, 53(37), 14423-14439.
- Mallick, D., Mahanta, P., & Moholkar, V. S. (2018). Synergistic Effects in Gasification of Coal/Biomass Blends: Analysis and Review. In *Coal and Biomass Gasification* (pp. 473-497). Springer, Singapore.
- Wu, J., Fang, Y., Wang, Y., & Zhang, D. K. (2005). Combined coal gasification and methane reforming for production of syngas in a fluidized-bed reactor. *Energy & Fuels*, 19(2), 512-516.

Generating Efficient Wastewater Treatment Networks: an integrated approach comprising of contaminant properties, technology suitability, plant design, and process optimization

Kirti M. Yenkie,^{a*} Sean Burnham,^a James Dailey,^a Heriberto Cabezas,^b Ferenc Friedler^b

^a*Department of Chemical Engineering, Henry M. Rowan College of Engineering, Rowan University, Glassboro NJ – 08028, USA*

^b*Pazmany Peter Catholic University, Institute for Process Systems Engineering and Sustainability, Budapest, Hungary*
yenkie@rowan.edu

Abstract

The rise in world population and industrialization in developing nations has tremendously increased the demand for water and has resulted in wastewater contaminated with several pollutants. Thus, wastewater treatment (WWT), reuse, and safe disposal have become crucial for sustainable existence. We believe that generation of a maximal structure (superstructure) comprising of all possible treatment methods and flow patterns using a systems approach, followed by optimization to decide the best treatment pathway, will enable efficient designing of WWT networks. In this work, the technologies/methods involved in WWT such as sedimentation, filtration, membranes, adsorption, activated sludge, etc. are modelled using material and energy balances, equipment design, costing and environmental impact. Utilizing systematic methods (*e.g.* mixed-integer non-linear programming, MINLP), we frame the WWT network selection as an optimization problem for cost and energy minimization along with sustainable goals. In our analysis, we demonstrate a case study of Municipal WWT and determine the best strategy in compliance with the 1972 US EPA's Clean Water Act to reuse the treated water for cropland irrigation. In the next step, we use the P-graph approach for solving the same problem and this tool provides a ranked list of candidate solutions.

Keywords: water, technology model, optimization, P-graph, sustainable process design

1. Introduction

Water is a necessary commodity, without its services in the industry, agriculture and domestic sectors the human species would cease to exist. The population rise has resulted in increased environmental pollution, majorly influencing urban water resources with issues such as low dissolved oxygen, bacterial contamination, and disruption in aquatic flora and fauna. Thus, strategies for judicious water consumption, pollution prevention, and efficient WWT are required for sustainable existence. Water pollution control boards and federal regulatory agencies (NIH, 2015; US EPA, 2013) have a well-defined list of pollutants and their safety limits, however, with advancements in industrial processing, new and unknown contaminants enter the waste streams ultimately leaching in groundwater sources. Hence, the need for improved

technologies and stage-wise WWT methods (Melo-Guimarães et al., 2013; Ponce-Ortega et al., 2009). Additionally, treatment plants need policies to minimize costs and energy requirements while maintaining the necessary regulations. Some factors that affect technology selection in WWT network are the wastewater characteristics, purity requirements, reliability, sludge handling, and costs.

2. Materials and Methods

2.1. Treatment Stages and Technologies

WWT is usually considered as a four-stage process: pretreatment, primary, secondary, and tertiary. An overview of the treatment stages and technologies involved are described in Figure 1 (Inc et al., 2002; Lipták and Liu, 2000; Liu et al., 2015). Depending on the purity standards and the number of contaminants in the waste stream, WWT plants may utilize one or more technologies from each stage, for example, a treatment path might follow screening, sedimentation, adsorption, and bleaching.

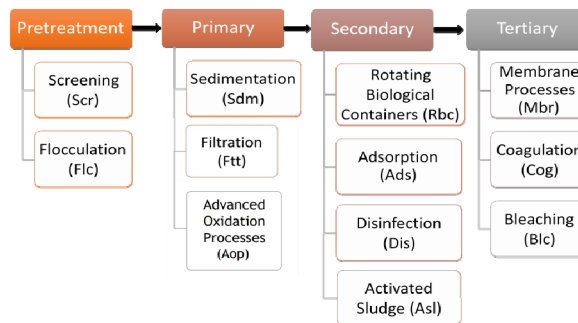


Figure 1 Traditional stage-wise wastewater treatment scheme

Pretreatment methods are used to enhance the operations in the following stages. Primary stage involves the removal of solid wastes. Sdm and Ftt are very successful at removing solid waste from wastewater. Aop can remove other harmful agents such as active pharmaceutical ingredients (API). Secondary stage methods may utilize microorganisms (Rbc, Asl) and disinfectants (Dis) to purify wastewater (Deng and Zhao, 2015; Shukla et al., 2006). Tertiary stage removes leftover contaminants and colour imparting impurities.

2.2. Heuristics, Technology Information and Engineering Judgement

Heuristics can guide in shortlisting the appropriate technology options. For example, characterizing the properties of contaminants present in a stream coming from a specific source of wastewater. Few identifiers for contaminant properties include physical state, size, and shape, density, relative amount, toxicity index, boiling point, biological affinity, chemical reactivity, etc. The second set of information should include the treatment technology options, the principle or driving force behind the purification and the process conditions or specifications that are essential while designing a treatment technology. Table 1 enlists a few technology options with their defining characteristics. However, heuristics can sometimes lead to the elimination of important non-intuitive solutions and thus a more systematic approach, which is more inclusive and unaffected by prior biases, is desired for efficient design.

Table 1. Wastewater treatment technologies and their important characteristics

Technology	Principle/driving force	Specifications/Process conditions
Sedimentation (Sdm)	Density gradient Particle settling velocity	Size, Particle density, Tank depth, Residence time
Filtration (Ftt)	Particle size	Average flux, Pressure gradient, Filtration rate
Advanced Oxidation Process (Aop)	Oxidation reactions for contaminant degradation	Ozone, peroxide, UV reactor
Disinfection (Dis)	Chemical, radiation	Chlorine dosage, Acid/Alkali treatment, UV radiation
Rotating Biological Contactors (Rbc)	Biological mechanism	Biological film on discs, speed of rotation, aeration rate
Membranes (Mbr)	Particle/molecular size Sorption/Diffusion Pressure	Pore size, Mol. wt. cut-off Flux, Pressure gradient, Type - MF, UF, NF and RO
Activated Sludge (Acs)	Microbial activity	Detention time, mixing efficiency, aeration rate

Sources: (Deng and Zhao, 2015; Ho and Sirkar, 1992; Lipták and Liu, 2000; Liu et al., 2015; Melo-Guimarães et al., 2013)

2.3. Wastewater Treatment Superstructure

Superstructure is a systematic representation of all possible treatment technologies available in the four stages of wastewater treatment. It also shows the flow from the initial wastewater stream towards the final purified water stream. Figure 2 shows the current WWT superstructure for treatment of municipal wastewater. The bypass (By) option is included in stages 2, 3 and 4. The current superstructure consists of 4 treatment stages, 10 technologies, 38 streams, 3 splitters, and 3 mixers.

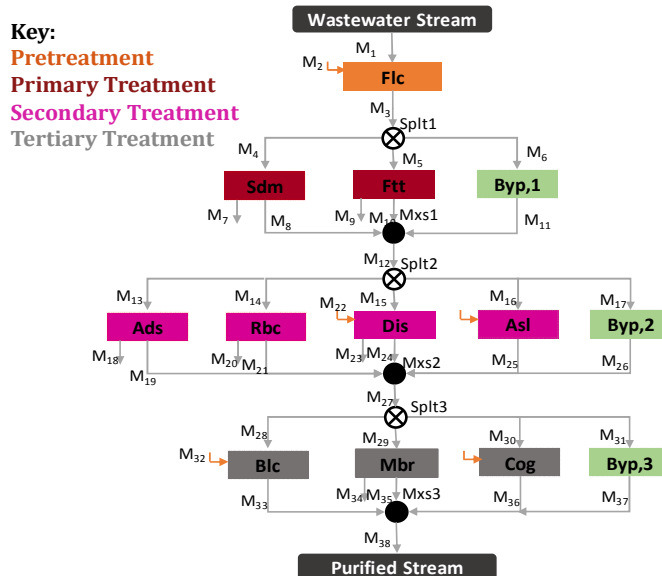


Figure 2 The stage-wise wastewater treatment superstructure for municipal wastewater treatment to reuse it for cropland irrigation

2.4. Framework for Evaluation

- Step#1: Formulate the case study by defining the input stream composition and output stream purity specifications
- Step#2: Construct an optimization model as a Mixed-Integer Non-Linear Programming (MINLP) problem that consists of:
- Mass and energy balances
 - Design equations, cost calculations: capital (equipment) and operating (utility, materials, consumables, labor and overhead requirements) costs
 - Binary integer variables to select technology in use by holding a (0,1) value
- Step#3: Minimize treatment costs while still reaching target values for safe reuse/disposal of wastewater written as a mathematical objective function
- Step#4: Develop the optimization model in GAMS (General Algebraic Modeling System) and solve by global MINLP solvers such as BARON (Branch-and-Reduce Optimization Navigator) (Kılınç and Sahinidis, 2018)
- Step#5: Implement the same case study in P-graph studio (Friedler et al., 1992; Heckl et al., 2010) that utilizes concepts from graph theory to obtain the maximal structure, list alternative paths (solutions) in the superstructure and rank them

3. Results and Discussions

The case study details with the list of inlet contaminant concentrations and the purity requirements for cropland irrigation are presented in Table 2 (Page et al., 1996). Inlet wastewater flowrate is assumed at 100 m³/h and plant operates for 330 days annually.

Table 2. Municipal case study contaminant concentrations and purity levels

Contaminant	Inlet Concentration (g/L)	Outlet Specification (g/L)
Solids (Settleable)	200	≤ 0.5
Metals (Pb, Cu, Zn, Ni)	0.1	≤ 0.05
Chemicals (Acids, chlorides, organics, and inorganics)	1	≤ 0.5

3.1. Solution from the GAMS-MINLP problem

The model in GAMS had a total of 267 equations, 199 variables, and 12 binaries. The solution time was less than a minute with a relative gap of 0.00001. The cost of the wastewater treatment per hour was obtained as 6252.27 USD/h. The technologies selected (Flocculation, Flc, Sedimentation, Sdm and Adsorption, Ads) and active streams are highlighted in Figure 3 and the cost distribution chart shows that the materials cost (flocculent and adsorbent) is the highest contributor. Utility costs are negligible as the selected technologies do not require significant amounts of electricity, cooling or heating.

3.2. Solution from the P-graph framework

The same case study was implemented in P-graph; the maximal structure and the comparable structure to the GAMS-MINLP solution is presented in Figure 4. The cost of wastewater treatment from P-graph is 6219.14 USD/h, which is comparable to the GAMS solution (6252.27 USD/h). This cost discrepancy is due to the linearized cost (capital and operating) equations required in P-graph. However, the cost deviation in

values predicted by GAMS and P-graph is less than 1% and we gain additional insights which were not possible in the GAMS-MINLP framework.

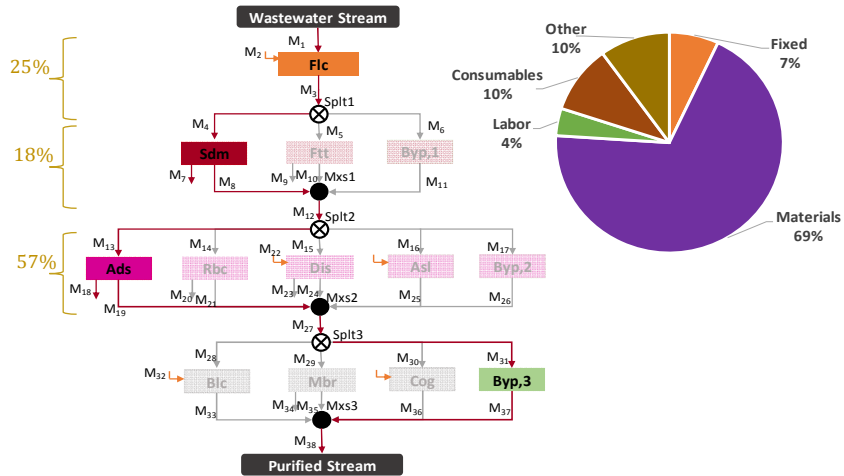


Figure 3. Solution for Municipal WWT case study from GAMS showing the active technologies and streams with cost distribution chart on the right

However, the structure (Flc-Sdm-Ads) is ranked#3 in the optimal feasible structure list. The rank#1 (2673.7 USD/h, consisting of Flc-Sdm-Rbc) and rank#2 (5033.33 USD/h, consisting of Flc-Ftt-Rbc) low-cost feasible structures (networks) are not predicted by the GAMS model. We tested these low-cost structures in GAMS and found that the purity levels of the outlet streams were lower than desired for cropland irrigation. We plan to investigate the differences in costing due to linearizations in the future analysis.

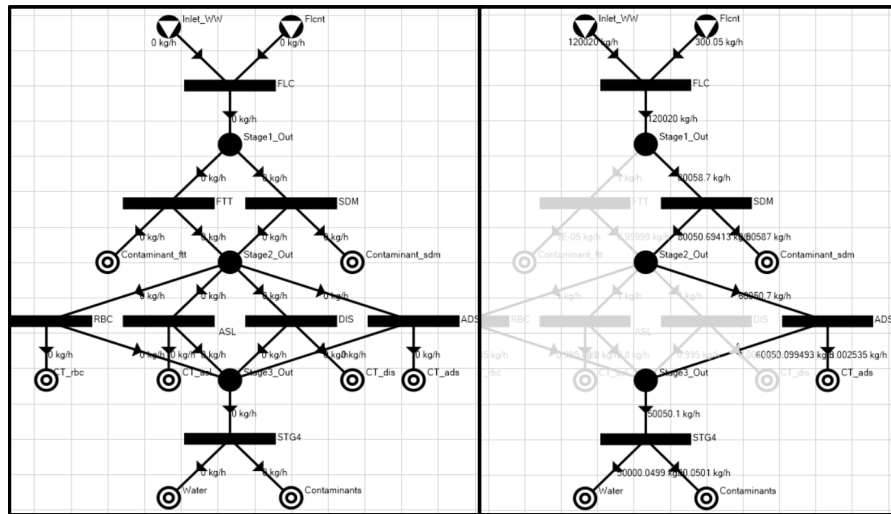


Figure 4. The Municipal WWT case study implemented in P-graph showing the maximal structure on the left and the feasible structure comprising of flocculation, sedimentation, and adsorption with the active streams on the right.

4. Conclusions

In this work, we have proposed a systematic framework for designing wastewater treatment networks. The heuristic-based superstructure is modelled as a MINLP problem in GAMS and the optimal network includes, Flc (stage-1) – Sdm (stage-2) – Ads (stage-3) – Byp (stage-4) with a cost of 6252.27 USD/h. The same case study is modelled in P-graph studio and the results show that the GAMS optimal network is ranked #3 with a comparable cost of 6219.14 USD/h. We believe that the comparative analysis provides a complete perspective into ranked solutions and identifies options, which may prove cost effective by comprising on certain purity constraints. In future, we plan to evaluate the networks with multiple outlet streams with different specifications. Furthermore, we will extend the analysis to include sustainability index for the ranked list of optimal networks predicted by both these approaches.

References

- Deng, Y., Zhao, R., 2015. Advanced Oxidation Processes (AOPs) in Wastewater Treatment. *Curr. Pollut. Rep.* 1, 167–176.
- Friedler, F., Tarján, K., Huang, Y.W., Fan, L.T., 1992. Graph-theoretic approach to process synthesis: axioms and theorems. *Chem. Eng. Sci.* 47, 1973–1988.
- Heckl, I., Friedler, F., Fan, L.T., 2010. Solution of separation-network synthesis problems by the P-graph methodology. *Comput. Chem. Eng., Selected Paper of Symposium ESCAPE 19*, June 14-17, 2009, Krakow, Poland 34, 700–706.
- Ho, W., Sirkar, K., 1992. *Membrane Handbook*. Springer, New York, USA.
- Tchobanoglous, G., Burton, F.L., Stensel, H.D., 2002. *Wastewater Engineering: Treatment and Reuse*, 4th edition. ed. McGraw Hill Higher Education, Boston.
- Kılınç, M.R., Sahinidis, N.V., 2018. Exploiting integrality in the global optimization of mixed-integer nonlinear programming problems with BARON. *Optim. Methods Softw.* 33, 540–562.
- Lipták, B.G., Liu, D.H.F., 2000. *Wastewater treatment*. Boca Raton, FL, London : Lewis.
- Liu, Y., Yu, H.-Q., Ng, W.J., Stuckey, D.C., 2015. Wastewater-Energy Nexus. *Chemosphere, Wastewater-Energy Nexus: Towards Sustainable Wastewater Reclamation* 140, 1.
- Melo-Guimarães, A., Torner-Morales, F.J., Durán-Álvarez, J.C., Jiménez-Cisneros, B.E., 2013. Removal and fate of emerging contaminants combining biological, flocculation and membrane treatments. *Water Sci. Technol.* 67, 877–885.
- Page, 1996. *Use of Reclaimed Water and Sludge in Food Crop Production*.
- Ponce-Ortega, J.M., Hortua, A.C., El-Halwagi, M., Jiménez-Gutiérrez, A., 2009. A property-based optimization of direct recycle networks and wastewater treatment processes. *AIChE J.* 55, 2329–2344.
- Shukla, A.A., Etsel, M.R., Gadam, S., 2006. *Process Scale Bioseparations for the Biopharmaceutical Industry*. CRC Press.
- US EPA, O., 2013. Summary of the Clean Water Act. US EPA. URL <https://www.epa.gov/laws-regulations/summary-clean-water-act>.

Model-based decision-support for waste-to-energy pathways in New South Wales, Australia

Koen H. van Dam^{a*}, Bowen Feng^b, Xiaonan Wang^b, Miao Guo^a, Nilay Shah^a and Stephen Passmore^{c*}

^a*Department of Chemical Engineering, Imperial College London, South Kensington Campus, London SW7 2AZ, UK*

^b*Department of Chemical Engineering, National University of Singapore, 4 Engineering Drive 4, Singapore 117576*

^c*Resilience Brokers Ltd, London, 10 Queen Street Place, London EC4R 1BE, UK*
k.van-dam@imperial.ac.uk and stephen.passmore@resiliencebrokers.org

Abstract

Utility operators involved in energy, waste and water sectors are exploring technology options to generate energy in a sustainable way, while also dealing with waste streams including sewage and municipal solid waste from growing urban environments. The resilience.io platform was developed to study long term changes and development in an urban area of region under a range of policy, behaviour, economic and technological scenarios, to meet local resource demands in a cost-effective and sustainable way. A systems modelling approach studying waste-to-energy in New South Wales suggests initial findings are a suitable starting point for further exploration of the potential in the region using this approach as well as complementary tools and methodologies. Model results show 854 GWh renewable energy could be generated through waste-to-energy pathways in 2036.

Keywords: waste to energy, water, infrastructure modelling

1. Introduction

The Hunter region, in New South Wales, Australia, is undergoing an economic and sustainability transition. Hunter's Smart Specialisation Strategy (Regional Development Australia Hunter, 2016) is Australia's first policy aimed to identify the region's competitive strengths and formulate specific activities to make the most of the key growth areas. "In a post-mining boom economy", it encourages new ideas to "build on [the Hunter's] strong knowledge-base in mining, energy, agriculture and medical research" (ibid: p.14). It also highlights the wider context of climate related challenges, the call for a reduction in greenhouse gas emissions, an energy matrix with an increasing proportion of renewables, demographic shifts and urbanisation (Government of Australia, 2015).

The focus on energy security in a changing environment is reflected at the state level, where the government intends to ensure that NSW is well prepared for the current transformation of the energy markets. Therefore, key actions in the NSW State Infrastructure Policy 2018-2038 (NSW Government, 2018) ensure reliable and affordable energy, focus on supporting private investment in efficient energy generation and horizon-scanning for new approaches. Moreover, the NSW government has set an aspirational goal to achieve

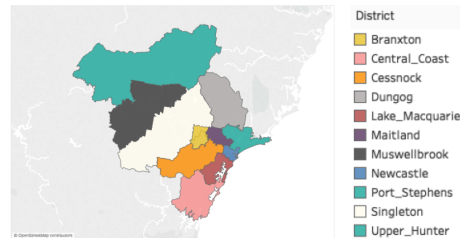


Figure 1: The study area in the Hunter Region, focusing on the area supplied by Hunter Water (highlighted) as well as neighbouring regions in Upper Hunter and Central Coast.

net-zero emissions by 2050 which can be clearly seen as a driver for innovation and development of new climate-compatible growth, jobs and livelihoods in the region.

Utility operators in urban environments, particularly those involved in energy, waste and water sectors, are exploring technology options to generate energy in a sustainable way, while also dealing with waste streams (e.g. sewage and municipal solid waste). Policies at different levels and from different angles appear to provide a window of opportunity to consider waste-to-energy (WtE) as a catalyst for green growth in the region. This paper explores this potential using an optimisation model representing the region and its resources, networks and technologies.

2. Methodology

The resilience.io platform (Triantafyllidis et al., 2018) was developed to study long term changes and development in an urban area of region under a range of policy, behaviour, economic and technological scenarios, to meet local resource demands in a cost-effective and sustainable way. It provides modules to allow forecasting of socio-demographic scenarios, simulating spatio-temporal activities, and planning investment and operational strategies. Agent-based modelling to simulate the population (with their activities and resource demands) is combined with resource-technology-network optimisation to find a suitable combination of technologies, their location and size, to meet these demands. Scenarios can be set up to vary the population, their activities, new technologies and economics properties. To study the nexus between water, energy and waste, this platform can then be used to identify opportunities based on modelled material flows and conversion technologies. Resources available and waste generated can be simulated or included from published data and regional forecasts, with specific technologies (with their economic and environmental performance) selected as input for the optimisation model.

3. Case study

In close cooperation with a local utility operator a model has been set up to simulate the current water and energy demand, supply and networks for a region in New South Wales, Australia, to explore potential future designs and interventions to take advantage of synergies at the water-waste-energy nexus. Figure 1 shows the main case study area. Key resources incorporated in the model include potable water, non-drinking water (industrial use), source water, electricity, gas, domestic waste (municipal solid waste, sewage),

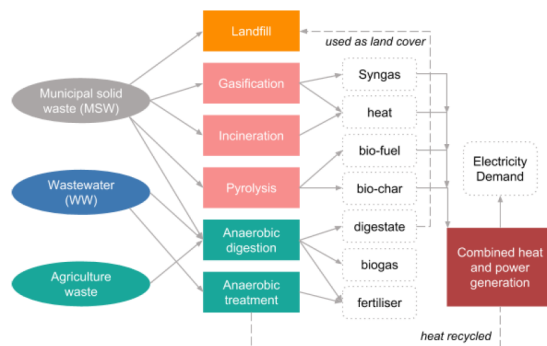


Figure 2: Possible pathways for processing and use of waste from households, waste water and the agriculture sector with technologies that can supply energy. Based on Wang et al. (2018)

Data type	Source
Sociodemographic data per region	Australian Bureau of Statistics (2018)
Water supply and demand	Hunter Water water consumption data
Recycle water supply	Hunter Water effluent reuse data
Wastewater generation and treatment	Hunter Water forward capital program data
Biosolids data	GHD Pty Ltd (2018)
Electricity supply and demand	Ausgrid (2016)
Gas supply and demand	Jemena (2011)
Municipal solid waste generation	WARR Survey provided by Hunter Water
Agricultural waste generation	MRA Consulting Group (2018)
Other organic waste data	MRA Consulting Group (2018)
Waste technology data	Jain et al. (2015); Lofrano (2012); Sun et al. (2015)
Water and wastewater technology data	Hunter Water data
Electricity generation technology data	Aemo (2018)
Existing water / wastewater network	Hunter Water network data
Existing electricity network	Jemena (2011)
Central Coast data	Central Coast Council (2018)

Table 1: Data sources used as input for the optimisation model

agricultural waste, sludge, and carbon dioxide. Potential conversion technologies are compared to alternatives for waste handling such as landfill (see Figure 2). The spatially explicit optimisation model selects which options can be attractive from an economical and environmental perspective, where to locate them to take advantage of local feedstock, and sizing to meet local demands as well as the creation of distribution networks.

The year 2016 is taken as base year, simulating 5 year intervals until 2036 which is the target year for the regional plan (NSW Government, 2018). The population is characterised by Sex, Age, Employment status, Income status, and annual population growth rate for this period is assumed to be the same level as in 2016. Demand data from 2016 was used as baseline, with the growth related to the population growth in the different regions from Figure 1. For modelling the current infrastructure networks, existing technologies for energy, waste and water, and for waste produced (municipal solid waste, agricultural waste, and waste water) a rich selection of local sources was used, see Table 1.

The agricultural and other organic waste data is from MRA’s report to Hunter Water, which identifies a total of 3.3 million tpa of organic feedstock in Lower Hunter and Central

Coast. It is understood that the spatial distribution and amounts of accessible organic waste is unclear at this time. However, since the model investigates the development of Hunter region until 2036, all feedstocks are assumed to be accessible and their spatial distribution is assumed to follow the sociodemographic growth trends in different regions.

4. Scenarios

This section describes the waste to energy scenarios explored in this project using the systems model for the Hunter region described above, leading to insights on the potential contribution of waste to energy pathways in the region. Three scenarios related to waste to energy are explored:

1. Business-as-usual; a baseline scenario using the current infrastructure in the region for water and energy (electricity and gas)
2. Waste to energy scenario (WtE), in which biosolids, municipal solid wastes, agricultural wastes and other organic wastes are considered as the (co-)feedstock of renewable energy generation using anaerobic digestion (with thermal hydrolysis), incineration, gasification and pyrolysis.
3. Economic/policy scenarios, including changes feed-in-tariffs and carbon credit to study the sensitivities of waste to energy. Each scenario is considered at the current situation (based on 2016 data as a baseline) as well as forecasts at 5 year intervals until 2036 following the timeline of the 20-year regional blueprint published by the NSW government.

The Business as usual (BAU) scenario serves as a basis to analyse the changes in other scenarios. In terms of waste management, biosolids is modelled by using BAU options provided by GHD Pty Ltd (2018)'s thermal hydrolysis option comparison. The input waste streams are assumed to leave the system through recycle/recovery and landfill at different prices. The biosolids disposal cost via land application program is included in the system based on cost data provided by Hunter Water. Other than biosolids, MSW will have a landfill levy assumed to be AUD 78.20 dollar per tonne.

5. Results

The model simulation and optimization starts from year 2016 where no WtE facility is installed. With five year intervals, the model progressively suggests optimal WtE strategies up to 2036 based on both economic incentives and spatial-temporal constraints. The results are generated for biosolids, municipal solid waste, agricultural waste and other organic waste. Note that agricultural waste and other organic waste (post-consumer food waste, etc) are shown together as same technology data are used. Figure 3 shows the transportation of biosolids between the different sites in 2036 as a result of optimal allocation of WtE installations, and similar graphs can be generated specifically for e.g. municipal solid waste.

Four biosolids WtE options have been selected by the model at the timestamp of 2036. Plasma gasification with MSW as co-feedstocks (plasma), AD with thermal hydrolysis

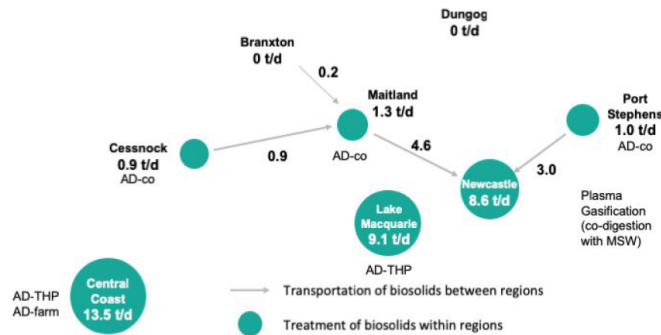


Figure 3: Treatment and transportation of biosolids between and in district (tonnes per day) after the optimisation of WtE technologies and their locations for 2036

(AD-THP) and AD with MSW and wastewater as co-feedstocks (AD-co) are favoured by the model using the objective function and defined economic and environmental performance indicators

Pyrolysis and incineration of biosolids are eliminated by the model, as they are not allocated for waste to energy conversion. The reason is presumed to be their inefficient renewable energy generation under the assumptions of the model. 16.5 GWh of energy can be generated from biosolids mainly in the form of natural gas. If all natural gas is converted to electricity, the value is 5.1 GWh, which can be used to reduce wastewater treatment energy consumption by 16%. Two centralized AD-THP are suggested by the model in Central Coast and Lake Macquarie to treat biosolids only, accounting for 70% of total biosolids in the study area. They are selected for major biosolids WtE pathway due to their relatively low costs. Plasma gasification are proposed to treat 8.6 tonnes per day biosolids together with municipal waste generated in or transported to Newcastle. The plasma plant is mainly used for municipal waste treatment, but the remaining capacity of the facility is identified by the model to be further utilised for biosolids WtE processing. AD co-digestion of MSW with biosolids are also proposed in Port Stephens, Maitland and Cessnock. The plants treat most of the MSW in the corresponding region and also handle a smaller portion of local biosolids. The remaining biosolids will be transported to Newcastle for centralized plasma treatment. The selection of an AD-co plant can be explained by the increased wastewater generation in 2036. With no wastewater reclamation facilities installed over 20 years, AD-co plants can effectively reduce the load of wastewater treatment plant and recover energy from biosolids. A farm AD plant is also allocated in Central Coast to recover energy from the remaining biosolids that will not be treated by the centralized AD-THP. This shows that the model only select decentralized facilities when centralized plants cannot treat all the waste in a region in an efficient way.

A carbon pricing scheme was introduced to Australian industrial sector from 2012 with a cost of 23 AUD\$ per tonne of emitted carbon dioxide, which was abolished later in 2014. The previous WtE scenario thus assumes zero carbon price in the optimization. In a further scenario, the carbon credit prices are set as alternatively 25 AUD\$, 75 AUD\$ or 125 AUD\$ per tonne of CO₂ to study its effects on the three key indicators: CAPEX, OPEX and GHG emission.

6. Conclusions and final remarks

A total of 854 GWh renewable energy can be generated through WtE pathway in 2036. 94% of the generation from waste is in the form of biogas or syngas. By upgrading to natural gas and injecting into gas grid, the gas-to-electricity conversion losses can be avoided, and less energy transmission losses will incur. Biogas generation is thus considered to render more economic benefits than electricity. Decentralised technologies are optimal due to the large amount of waste distributed in each region. Organic feedstocks identified in the study region possess vast potential for WtE pathway, as the WtE energy contributed by agricultural waste in 2036 will cover about 80% of total generation.

The systems approach presented in this report can be seen as a starting point for the exploration of different visions and futures for the region, with local stakeholders at the centre of the decision making process. The data as well as simulated scenarios will enable well-informed decisions and further detailed examination of options deemed attractive at the systems level. Following a systems approach, the interdependencies between infrastructure systems and sectors will continue to be at the core of planning integrated solutions at the national, regional and local level.

Acknowledgements

The authors would like to express their thanks to Hunter Water Corporation, in particular David Derkenne, for their support and contribution to this study.

References

- Aemo, 2018. Australian energy market operator website. <https://www.aemo.com.au/>.
- Ausgrid, 2016. 2015-16 summary community electricity report. <https://www.ausgrid.com.au/-/media/Documents/Data-to-share/Average-electricity-use/Ausgrid-average-electricity-consumption-by-LGA-201516.pdf>.
- Australian Bureau of Statistics, 2018. <http://www.abs.gov.au/>.
- Central Coast Council, 2018. Central coast council website. <https://www.centralcoast.nsw.gov.au/>.
- GHD Pty Ltd, April 2018. Hunter water corporation hunter water-planning technical advice adhoc thermal hydrolysis options comparison. HWC-Planning Technical Advice Adhoc, 2218668.
- Government of Australia, August 2015. Intended nationally determined contribution.
- S. Jain, S. Jain, I. T. Wolf, J. Lee, Y. W. Tong, 2015. A comprehensive review on operating parameters and different pretreatment methodologies for anaerobic digestion of municipal solid waste. *Renewable & Sustainable Energy Reviews* 52, 142–154.
- Jemena, 2011. Average gas consumption. <https://jemena.com.au/about/document-centre/gas/average-gas-consumption>.
- G. Lofrano, 2012. Green technologies for wastewater treatment: energy recovery and emerging compounds removal. Springer Science & Business Media.
- MRA Consulting Group, June 2018. Market analysis of organic waste feedstocks in the lower hunter region.
- NSW Government, March 2018. The NSW state infrastructure strategy 2018-2038. <http://www.infrastructure.nsw.gov.au/expert-advice/state-infrastructure-strategy/>.
- Regional Development Australia Hunter, March 2016. Smart specialisation strategy for the hunter region: A strategy for innovation-driven growth.
- Q. Sun, H. Li, J. Yan, L. Liu, Z. Yu, X. Yu, 2015. Selection of appropriate biogas upgrading technology-a review of biogas cleaning, upgrading and utilisation. *Renewable & Sust. Energy Reviews* 51, 521–532.
- C. P. Triantafyllidis, R. H. Koppelaar, X. Wang, K. H. van Dam, N. Shah, 2018. An integrated optimisation platform for sustainable resource and infrastructure planning. *Env. Mod. & Software* 101, 146–168.
- X. Wang, M. Guo, R. H. Koppelaar, K. H. van Dam, C. P. Triantafyllidis, N. Shah, 2018. A nexus approach for sustainable urban energy-water-waste systems planning and operation. *Env. science & technology* 52 (5), 3257–3266.

Optimal Oversizing and Operation of the Switchable Chlor-Alkali Electrolyzer for Demand Side Management

Kosan Roh^a, Luisa C. Brée^a, Karen Perrey^b, Andreas Bulan^b and Alexander Mitsos^{a,*}

^a*AVT.SVT, RWTH Aachen University, Forckenbeckstraße 51, Aachen 52074, Germany*

^b*Covestro Deutschland AG, Leverkusen 51365, Germany*
alexander.mitsos@avt.rwth-aachen.de

Abstract

Flexible operation of the switchable chlor-alkali process is a novel strategy for minimizing electricity costs in markets with volatile prices (Brée et al. (2018)). This strategy allows for adjusting the process to electricity price profiles, by varying the production rate and by switching the operation between two different modes: the H₂ mode and O₂ mode. The size of the electrolyzer is a crucial factor because oversizing on the one hand leads to higher operational flexibility but on the other hand to increased capital costs. Here, we combine the optimization of the operation and electrolyzer size in the switchable chlor-alkali process for given electricity price profiles. To arrive at the optimum in reasonable computation time, we use a piecewise linear approximation and decomposition method employing the golden-section search. We verify that electrolyzer oversizing in the switchable chlor-alkali process is a suitable strategy for reducing the total production cost when the specific capital costs of the oversizing are low enough and the electricity price strongly fluctuates.

Keywords: demand side management, bifunctional cathode, chlor-alkali electrolysis, decomposition method, MILP

1. Introduction

As intermittent renewable energy penetrates the power grid, electricity prices and availability fluctuate more. A need could arise for power-intensive processes like chlor-alkali (CA) electrolysis to employ smart operation strategies. One possible strategy is demand side management (DSM), which allows for flexible operation of the process to adjust the production rate to electricity price profiles (Daryanian et al. (1989); Ghobeity and Mitsos (2010)). The production rate can be varied when an electrolyzer is oversized; and intermediates are storable or the downstream processes are also operated flexibly. Another DSM strategy for CA electrolysis is to switch its operation mode by implementing a bifunctional cathode. This novel cathode (Bulan et al. (2017)) enables to switch the operation between hydrogen (H₂) and oxygen (O₂) modes. The O₂ mode demands less electricity than the H₂ mode at the expense of not producing H₂.

Brée et al. (2018) examined the optimal operation of an oversized CA electrolyzer with the bifunctional cathode implemented. The operation was optimized by solving a mixed-

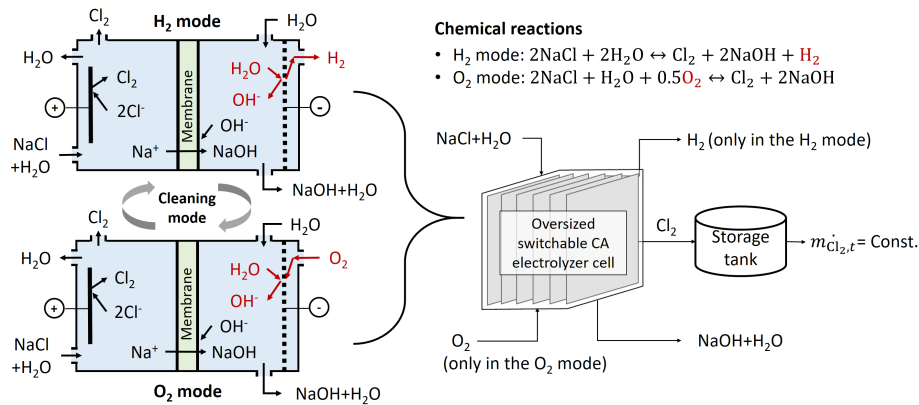


Figure 1: Description of the electrolysis and operation of the switchable CA process.

integer linear program (MILP) that minimized operating costs on the basis of a discrete-time model. The results verified that oversizing the electrolyzer can reduce operating costs when electricity prices fluctuate sharply. Moreover, additional savings are achievable by adopting the switchable operation. When electricity is expensive and H₂ and O₂ are cheap, operation in the O₂ mode is economically preferred.

Oversizing the electrolyzer, however, affects the total production cost of the CA process. It requires extra capital cost, which reduces the profitability. Therefore, the electrolyzer oversizing and reduction of operating costs are at a trade-off (Williams et al. (2012)).

Herein, we examine how electrolyzer oversizing affects the optimal operation of the switchable CA process by modifying the optimization problem formulated by Brée et al. (2018). A sizing factor is introduced as a continuous variable. The modified optimization problem minimizes the total production cost that is the sum of the operating cost and annualized additional capital cost resulting from oversizing the electrolyzer. The modification results in a large-scale mixed-integer nonlinear program (MINLP). Its solution to global optimality is computationally demanding. To reduce the computation cost, we consider the sizing factor as a complicating variable and utilize a decomposition method. At the outer, the golden-section search (GSS) technique is applied to optimize the sizing factor while the subproblems are MILPs. This strategy gives the global optimum in tractable computational time.

2. Description of Operation Strategies

Two operation strategies are applied to the switchable CA process. One is designed to vary the production rate while the other aims to switch the operation between the H₂ and O₂ modes. Figure 1 illustrates the operation scheme.

2.1. Production Rate Variation

Conventional CA electrolyzers in Germany produce chlorine (Cl_2) typically at very high utilization capacity (>95 %), so there is only little potential for flexible operation (Aussfelder et al. (2018)). When a CA electrolyzer is oversized, i.e., its production capacity exceeds the demand in the downstream process, it is possible to adjust the production rate to electricity price fluctuations by changing the voltage applied. When electricity is expensive, the production rate is reduced so that less electricity is consumed. A Cl_2 storage tank is installed as a buffer to guarantee the constant Cl_2 supply to the downstream, that is assumed to operate as is. If necessary, the process can be shut down.

2.2. Switchable Operation

In the H_2 mode, the anode compartment is filled with saturated brine to produce Cl_2 gas and sodium ions (Na^+). Na^+ ions migrate through an ion-exchange membrane, and then sodium hydroxide (NaOH) is produced along with H_2 gas at the cathode compartment. In the O_2 mode, the reactions are the same as in the H_2 mode at the anode side. At the cathode side, gaseous O_2 contacts the cathodic liquid phase and is reduced without H_2 production. The O_2 mode demands less electricity than the H_2 mode by 33 % (Jung et al. (2014)) while still producing the same amount of Cl_2 and NaOH . However, operation in the O_2 mode no longer generates the H_2 by-product while it requires additional O_2 . To avoid the presence of both gases simultaneously, a cleaning process that removes either H_2 or O_2 inside the cell is required when the operation is switched.

3. Problem Formulation and Algorithm for Optimization

3.1. Problem Formulation

In this optimization, the electrolyzer size and the operation of the switchable CA process (the active operation mode and production rate) are simultaneously optimized. A sizing factor (α) is considered as a continuous variable with given bounds as $1 \leq \alpha \leq \alpha^{up}$. For example, α of 1.3 indicates the production capacity is increased by 30 %.

Mass Balance and Mode Transition Constraints to calculate the consumption and production rates ($\dot{m}_{C,t}$) of each component C and control the mode transition and level of the Cl_2 storage tank are the same as Brée et al. (2018) except for the changes described in the following. The CA process can operate only at of three modes $m \in \{\text{H}_2, \text{O}_2, \text{Shutdown}\}$. Once the process is shut down, either the H_2 or O_2 mode can be active after a certain duration for cleaning. The production rate during the operation is limited by the equation

$$\alpha \underline{\dot{m}}_{\text{Cl}_2} y_{m,t} \leq \dot{m}_{\text{Cl}_2,m,t} \leq \alpha \overline{\dot{m}}_{\text{Cl}_2} y_{m,t}, \quad \forall m \in M, t \in T, \quad (1)$$

where $\overline{\dot{m}}_{\text{Cl}_2}$ and $\underline{\dot{m}}_{\text{Cl}_2}$ denote the maximum and minimum active production rates, respectively. When mode m is active at time t , a binary variable $y_{m,t}$ is 1. The production rate is kept above 50 % of the production capacity to ensure the product quality, but it cannot exceed the production capacity. Both the lower and upper bounds are proportional to α .

Power Demand Function The power demand for the reactive modes, calculated as

$$P_t = \frac{a}{\alpha} \dot{m}_{\text{Cl}_2,t}^2 + b \dot{m}_{\text{Cl}_2,t}, \quad t \in T, \quad (2)$$

is a quadratic function of the Cl₂ production rate. The sizing factor influences the power demand function. Here, a and b are parameters. To formulate an MILP, we perform a piecewise linear approximation by dividing the Cl₂ production rate into four ranges:

$$P'_{t,e} = a'_e \dot{m}_{\text{Cl}_2,t} + b'_e \alpha + c'_e, \quad e \in \{1, 2, 3, 4\}, \quad t \in T, \quad (3)$$

where a'_e , b'_e , and c'_e are obtained by parameter estimation from the original power demand P_t calculated.

Ramping Constraints A ramping constraint is imposed on the production rate by

$$\Delta \dot{m}_{\text{Cl}_2} = \alpha (\bar{\dot{m}}_{\text{Cl}_2} - \underline{\dot{m}}_{\text{Cl}_2}) / \theta_{\text{ramp}}, \quad (4)$$

where θ_{ramp} denotes the number of time steps necessary to ramp the production between $\bar{\dot{m}}_{\text{Cl}_2}$ and $\underline{\dot{m}}_{\text{Cl}_2}$. The maximum and minimum allowable production rate of the subsequent time step ($t + 1$) depends via

$$\dot{m}_{\text{Cl}_2,t+1} \leq \dot{m}_{\text{Cl}_2,t} + \sum_m y_{m,t} \Delta \dot{m}_{\text{Cl}_2} + (1 - \sum_m y_{m,t}) \alpha \underline{\dot{m}}_{\text{Cl}_2}, \quad \forall m \in \{\text{H}_2, \text{O}_2\}, \quad t \in T, \quad (5)$$

$$\dot{m}_{\text{Cl}_2,t+1} \geq \dot{m}_{\text{Cl}_2,t} - \sum_m y_{m,t+1} \Delta \dot{m}_{\text{Cl}_2} - (1 - \sum_m y_{m,t+1}) \alpha \underline{\dot{m}}_{\text{Cl}_2}, \quad \forall m \in \{\text{H}_2, \text{O}_2\}, \quad t \in T. \quad (6)$$

Objective Function We minimize the total production cost (C^{TO}) calculated by

$$C^{TO} = C^{OP} + C^{CAP} = \sum_{t=0}^{t_n} (C_{C,t} + C_{El,t}) + (\alpha - 1) a^{CAP} f^{CAP}, \quad \forall C \in \{\text{H}_2\text{O}, \text{O}_2, \text{H}_2\}, \quad (7)$$

which is the sum of the operating cost (C^{OP}) and annualized capital cost (C^{CAP}). Inclusion of the H₂ cost indicates that H₂ should be supplemented when the O₂ mode is active. The annualized capital cost for the oversized portion of the electrolyzer is a function of α and a coefficient a^{CAP} . A 1-year depreciation factor f^{CAP} is calculated by

$$f^{CAP} = (i(1+i)^n) / ((1+i)^n - 1), \quad (8)$$

where i and n denote an interest rate and electrolyzer lifetime, respectively.

3.2. Optimization Algorithm

The inclusion of the sizing factor results in an MINLP problem due to bilinear products (e.g., $\alpha y_{m,t}$) that demands heavy computation costs. Note that since the bilinear products all involve a binary variable, the MINLP can be exactly reformulated as an MILP, e.g., using the big-M method. Our computational experimentation, however, showed that these MILPs are still expensive to solve. To reduce the load, we apply a decomposition method, considering the sizing factor as a complicating variable. This leads to an MILP subproblem. The global solution is then found by the GSS on the complicating variable.

4. Simulation Results

The nominal plant capacity ($\alpha = 1$) is 1 t_{Cl₂}/h. The storage tank can store the nominal Cl₂ supply to the downstream for a maximum of 3 hours. The time horizon T for simulation

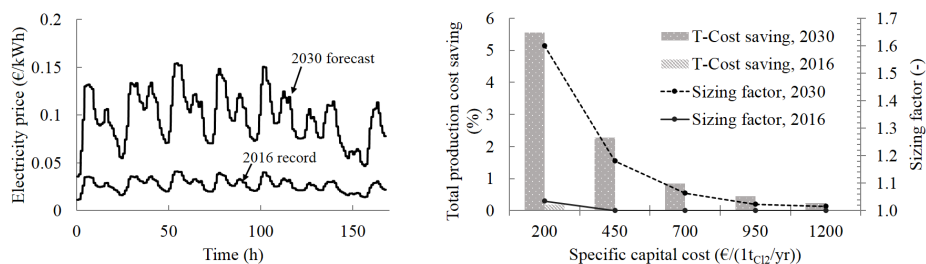


Figure 2: Electricity price profiles in 2016 and 2030 in Germany (left) and simulation results; savings in the total production cost and the optimal sizing factor (right).

is one week and discretized into 672 time steps (15 minutes for one time step). The maximum oversizing is up to 100 % ($\alpha^{up} = 2$). The specific capital cost for oversizing the electrolyzer highly depends on the individual settings of the pre-existing site. To calculate the annualized capital cost, a specific capital cost of €200 up to €1,200 per yearly production of 1 t_{Cl2} (Arnold et al. (2016)), 7 % of the interest rate, and 10 years of the electrolyzer lifetime are assumed. Two electricity price profiles recorded in first week of June in 2016 (Agora Energiewende (2018)) and assumed for 2030 by Brée et al. (2018) are considered (Figure 2, left). The latter one with the higher average price and more pronounced fluctuation reflects the prediction that employment of renewable energy sources in the German power sector will increase in 2030. H₂, O₂, and water (H₂O) prices are 2 €/kg_{H2}, 0.05 €/kg_{O2}, and 0.01 €/kg_{H2O}, respectively. The shutdown mode is active for at least 30 minutes. Once a reactive mode becomes active, such a mode lasts for at least 12 hours to prevent shortening the electrolyzer lifetime. The optimization problem implemented in GAMS 24.9.2 is solved by CPLEX 12.7.1.0 with a relative optimality tolerance of 10⁻⁵ and 12 threads for parallel processing.

Figure 2 (right) shows that, the specific capital cost for oversizing the electrolyzer highly influences the optimal size of the electrolyzer in the switchable CA process as well as the reduction of the total production cost compared to the reference case with no oversizing and operation switch. The lower specific capital cost leads to the larger electrolyzer and higher savings in the total production cost accordingly. The optimal size of the elec-

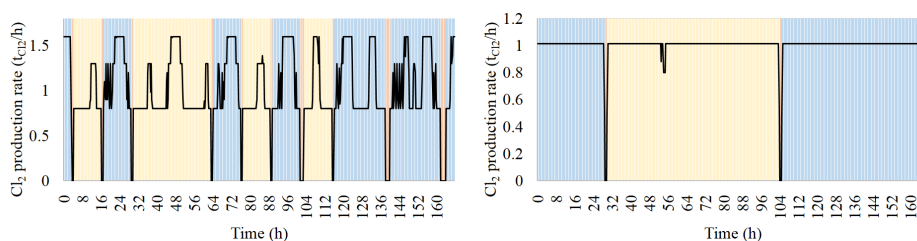


Figure 3: Optimal Cl₂ production rate profile and active mode for the specific capital cost of 200 (left, $\alpha=1.6$) and 1,200 €/1t_{Cl2}/yr (right, $\alpha=1.02$) in the 2030 scenario. Blue indicates the H₂ mode, yellow the O₂ mode, and orange the Shutdown mode.

trolizer in the 2030 scenario is far bigger than in the 2016 scenario. When the electricity price fluctuates sharply, varying the production rate becomes advantageous. Unless the specific capital cost is very low, the oversizing is not recommended in the 2016 scenario.

Figure 3 represents the optimal Cl_2 production rate profile and active mode of the switchable CA process in the case where the specific capital cost for oversizing the electrolyzer is 200 €/($1\text{t}_{\text{Cl}_2}/\text{yr}$) and 1,200 €/($1\text{t}_{\text{Cl}_2}/\text{yr}$) on the basis of the 2030 scenario. More frequent shutdown of the process is observed with the lower specific capital cost: 10 times in the 200 €/($1\text{t}_{\text{Cl}_2}/\text{yr}$) case and only twice in the 1,200 €/($1\text{t}_{\text{Cl}_2}/\text{yr}$) case in a week. The larger electrolyzer provides more flexibility for the operation switch.

5. Conclusions

We investigated the influence of the capital cost for oversizing the electrolyzer in the switchable CA process on its optimal operation for DSM concerning electricity price profiles. We formulated an MINLP problem to minimize the sum of the operating and annualized capital costs while optimizing the electrolyzer size and operations. To find the global solution within reasonable computation time, we applied a decomposition method employing the GSS. As a result, it is noted that the specific capital cost for oversizing the electrolyzer highly affects the optimal operation. The cheaper the specific capital cost, the more frequent the plant is shut down and the higher the savings in the total production cost are. Finally, we verify that oversizing is a suitable strategy for DSM when the electricity price fluctuates strongly and moderate storage of Cl_2 (order of three hours) is allowed.

Acknowledgement

The authors gratefully acknowledge the financial support of the Kopernikus-project Synergie by the Federal Ministry of Education and Research (BMBF) and the project supervision by the project management organization Projektträger Jülich (PtJ). We are also grateful to Pascal Schäfer, Kristina Baitalow, Hatim Djelassi, and Susanne Sass for valuable discussions.

References

- Agora Energiewende, 2018. Agorameter. Accessed on 2018-10-31.
URL <https://www.agora-energiewende.de/>
- K. Arnold, T. Janßen, L. Echternacht, S. Höller, T. Voss, K. Perrey, 2016. Flexind - flexibilisation of industries enables sustainable energy systems.
- F. Ausfelder, A. Seitz, S. v. Roon, 2018. Flexibilitätsoptionen in der grundstoffindustrie : Methodik, potenzielle, hemmnisse. Tech. rep., DECHEMA, Frankfurt am Main.
- L. C. Brée, K. Perrey, A. Bulan, A. Mitsos, 2018. Demand side management and operational mode switching in chlorine production. *AIChE Journal*, in press. DOI: 10.1002/aic.16352.
- A. Bulan, R. Weber, F. Bienen, Oct 2017. Bifunktionelle elektrode und elektrolysevorrichtung für die chloralkali-elektrolyse. WO2017174563A1.
- B. Daryanian, R. E. Bohn, R. D. Tabors, Aug 1989. Optimal demand-side response to electricity spot prices for storage-type customers. *IEEE Transactions on Power Systems* 4 (3), 897–903.
- A. Ghobeity, A. Mitsos, 2010. Optimal time-dependent operation of seawater reverse osmosis. *Desalination* 263 (1), 76 – 88.
- J. Jung, S. Postels, A. Bardow, 2014. Cleaner chlorine production using oxygen depolarized cathodes? a life cycle assessment. *Journal of Cleaner Production* 80, 46 – 56.
- C. M. Williams, A. Ghobeity, A. J. Pak, A. Mitsos, 2012. Simultaneous optimization of size and short-term operation for an RO plant. *Desalination* 301, 42–52.

A process systems engineering approach to designing a solar/biomass hybrid energy system for dairy farms in Argentina

Carolina Alvarez C. Blanchet^a, Antonio M. Pantaleo^{b,c} and Koen H. van Dam^{b,*}

^a*Energy Futures Lab, Imperial College London, South Kensington Campus, London SW7 2AZ, UK*

^b*Department of Chemical Engineering, Imperial College London, South Kensington Campus, London SW7 2AZ, UK*

^c*Department of Agricultural and Environmental Sciences, University of Bari, Italy*
k.van-dam@imperial.ac.uk

Abstract

Argentina targets a 20% share of renewables in the energy mix by 2025 and a 15% emissions reduction by 2030, while at the same time removing subsidies for grid electricity. This paper aims to provide a feasible solution for small farm owners for sustainable and affordable energy: a grid-connected hybrid system able to fulfill the demand in a cheaper, reliable and sustainable way. The case study of an existing dairy farm in Carmen de Areco, Buenos Aires, is taken. A grid-connected hybrid system with solar photovoltaics, unheated anaerobic digestion (AD) coupled to an internal combustion engine and storage system, was selected. The size of the hybrid system was optimized via a mathematical model that compared different technologies. The interrelation between sources was economically optimized in order to match the demand on an hourly basis. The scenario comparison defined the optimal solution for this case study, which was the installation of an unheated AD plant with 2.4 kW capacity, and 16 solar panels with a capacity of 5.2 kW, added to a shift in the demand profile. The initial investment required is 17,042 USD, with a payback of 3.4 years and a GHG reduction of 275.9 tons of CO₂ eq per year.

Keywords: bioenergy, solar energy, dairy farm

1. Introduction

New targets defined by Argentina include an increase in the share of Renewable Energy (RE) to 20% in the energy mix by 2025 and a 15% emissions reduction by 2030 (Porcelli and Martínez, 2018). Together with this shift towards sustainability, the government implemented a subsidy scheme removal in 2016, generating a rise in electricity bills that affected end users in domestic and business segments, including rural sector (Observatorio Economico Social, 2017). The affordability and reliability concerns of the rural grid increased the problems for agricultural farmers. This project aims to provide a feasible solution for small farm owners: a grid-connected hybrid system able to fulfill the demand in a cheaper, reliable and sustainable way. The case study of an existing dairy farm in Carmen de Areco, Buenos Aires, is taken.

The power industry is facing new network challenges worldwide with the rise of the re-

newables. The supply/demand equilibrium can be compared to a RE curtailment in case of an excess of generation, or to a rapid power compensation from fossil fuel power plants in case of unavailability of renewable resources. RE intermittency introduced a new need to the grid operators: today's power plants need to be more flexible, operate within a large load range and minimize emissions in order to react and compensate for possible RE changes. The higher the RE share in the energy mix, the higher the flexibility needed from back up fossil fuel plants to ensure heat and power availability when demanded. Gas-fired power plants will support this balancing given that nuclear energy cannot offer a rapid answer. Available capacity and response times are the key factors for conventional plants, since RE are intermittent (Qadrdan et al., 2017; Welch and Pym, 2017).

In this case study, the combination of an intermittent renewable with a fast responding, flexible biogas plant can deliver secure, reliable, and low-carbon energy. The constant biomass input into an anaerobic digester can produce a secure amount of biogas, being able to balance the supply. The surplus RE generation, rather than being constrained, can be stored (in gas or electricity form) for future use ensuring maximum flexibility. Affordable and reliable electricity can be provided thanks to a fully integrated hybrid system as the one presented before, minimizing environmental impacts and providing dispatchability and flexibility.

2. Approach

The literature mention two approaches: sizing the system and resources needed regarding the demand (Pantaleo et al., 2013), or calculating the energy supply from the resources available (Vis et al., 2010; Elbersen et al., 2012). In this case study, both approaches are proposed, but the heat and power demand will be the decisive approach. First, biomass and solar energy potential are estimated (see Section 3.1) then a demand analysis will define the system sizing; finally, a cost minimization procedure will determine the hybrid system to be implemented, based on the heat and power demand (see Section 3.2). The interrelation between the different sources was economically optimized in order to match the demand on an hourly basis. A baseline scenario was run with available farm data, obtaining a benchmark grid-connected hybrid system configuration. An economic analysis evaluated the investment profitability. Afterwards, multiple scenarios are run, evaluating demand side response, possible regulations outcomes, and technological upgrades (mesophilic AD technologies).

2.1. Case study

The case study is a family business in which the owner takes strategic investment decisions and operates the farm. The company has 7 workers, divided between stable and cattle operation, milk extraction operation, milk refrigeration and raw milk transfer. Having 304 cows, of which 256 in actual milk production, producing approximately 6,000 L of milk per day, it is a small-scale company. Cattle confinement is limited to twice a day for the milking. The mixture of manure, urine and water is held in an open lagoon. This is a normal structure for small and medium farms but lacks in design can potentially generate contamination problems. The decrease in water quality can affect the animal nutrition, minimizing milk production and productivity. In addition, bad water quality can potentially contaminate milk. Moreover, open tanks generate odors, favor insect proliferation

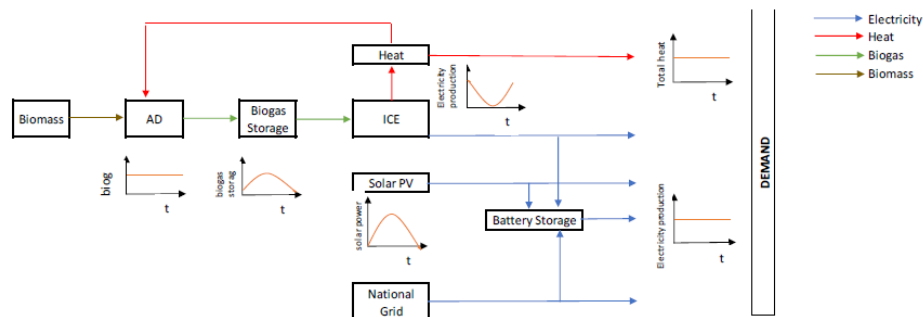


Figure 1: Hybrid System 2 (HS2) model (PV + AD).

(cow health and milk quality could be endangered), and CH₄ emissions (Alessandretti, 2011). The farm's installations are common in small farming operations, including the milking room, the milk process and the waiting stable.

2.2. Hybrid PV + AD system

Eight different hybrid systems were compared, with a hybrid system based on biogas production from an AD digester, an ICE to generate electricity and heat and an array of PV and a storage system (see Figure 1) considered as most attractive option for this case study. The operation modes are the following:

- MODE 1: when the solar power is sufficient to meet the demand and charges the battery with the excess energy produced.
- MODE 2: when the solar power is sufficient to meet the demand, but not to charge the battery, the grid will charge it during off-peak hours if the grid price is lower than the bioenergy price.
- MODE 3: when solar power is insufficient to meet the demand and the ICE starts generating to meet the demand. Excess energy produced will charge the battery.
- MODE 4: when solar power is insufficient to meet the demand and the ICE starts generating to meet the demand, but not to charge the battery. The grid will charge it during off-peak hours.
- MODE 5: when solar power and ICE generation are insufficient to meet the demand and grid electricity is cheap (valley period), the grid starts providing the electricity needed.
- MODE 6: when solar power and ICE generation are insufficient to meet the demand and grid electricity is expensive (peak period), the battery starts providing the electricity needed.
- MODE 7: when solar power, ICE and battery are insufficient to meet the demand, the grid will provide the electricity needed, independent on its price.

The automatic selection of this modes by the energy management system (EMS) will define the instant operation of the system.

3. Methodology

3.1. Energy potential

Bioenergy production and potential depends on the number of cows in the farm, and on breeding and nutritional characteristics (Pantaleo et al., 2013). The total solid manure collected depends on the total number of cows producing milk (N^C), the number of hours in a closed stable (H^C) (manure collection is unfeasible in the fields) and a tabulated potential daily Manure Production per Cow (P^C). Total Manure Production per Day (P^d) becomes:

$$P^d = N^C * \frac{H^C}{24} * P^C \quad (1)$$

From (1) it is possible to obtain the volume of biogas generated per day.

The potential for solar energy varies depending on the power rating of the solar panels installed, the number of panels, the day of the year and the hour of the day. For these calculations, different literature was revised and used: McEvoy et al. (2003); Wenham et al. (2013); Mahachi (2016). Calculations take into account: Installation Relative Azimuth, Installation Tilt, Case Study's Latitude (φ) Sun radiation (P_{sun}), Day number (d), Solar Time max (ω), Temperature max avg, Sun radius (R_{sun}) and Relative distance Sun/Earth (r_o). Potential solar energy produced was calculated for winter and summer solstice, considering the available space for panels.

3.2. Optimisation model for the sizing of hybrid systems

An optimisation model was built in AIMMS with a modular structure. Demand and energy supply were divided into sections in order to organize and aggregate them in different ways. The different sections were demand per day, bioenergy per day, solar energy per day, storage per day, grid per day and finally the optimization and total emissions. The model represents the current Argentinian situation in which it is not possible to sell the energy surplus to the grid.

Demand parameters include hourly electricity demand, maximum electricity demand during peak, and minimum electricity demand during off-peak (in kW). Bio-energy parameters are those ones reported in eqn (1), together with investment and operational bioenergy plant costs. Solar energy parameters include peak power, area of panels, roof area, solar variation, capacity factor, CAPEX and OPEX. Further input parameters include storage investment and potential, grid connection operating costs (energy and power prices during peak and off-peak periods), and emissions.

The objective function for the model then is:

$$\text{minimise } Cost^{Tot} = Cost^{BG} + Cost^{SP} + Cost^{sto} + Cost^{NG} \quad (2)$$

where $Cost^{Tot}$ is the total cost, $Cost^{BG}$ is the cost for bioenergy, $Cost^{SP}$ is the cost for solar power, $Cost^{sto}$ storage costs and $Cost^{NG}$ the cost of supply from the national grid. This

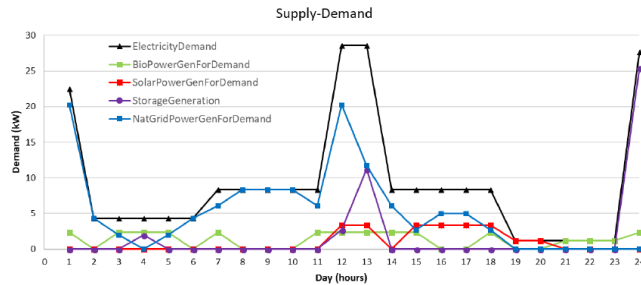


Figure 2: Demand and supply per energy source with the optimised hybrid PV and AD solution.

is subject to constraints on meeting demand, maximum available supply from biogas, available supply from the solar installation, space constraints, battery constraints, and national grid constraints, as well as mass and energy balances.

The objective function in Eqn 2 represents yearly costs considering an annualized CAPEX, as well as fixed and variable OPEX of each technology, so both investment and operational costs of each technology are considered. This economic optimization aims to find the most cost-effective combination of technologies, sizing a hybrid system capable of supplying the electricity demand. However, according to the Argentinian energy market regulation limitations, the model does not take into account selling surplus renewable energy to the grid.

4. Results

For the baseline scenario, the optimal solution was a bioenergy installation of 2.3 kW, a solar energy installation of 5.2 kW (supplied by 16 solar panels) and a storage capacity of 29.9 kW. Figure 2 shows the demand and supply profile with this installation.

The baseline scenario optimization results are very specific of the techno-economic and regulative input conditions assumed for the dairy farm under investigation, and which could be, at some extent, extended to other rural farms in Argentina. However, changes in regulations, demand profile or in the hybrid technology are possible. In order to assess the influences of these key factors, different scenarios have been evaluated: 1) national grid prices before subsidies scheme removal; 2) shifting load demand (mid-night peak) and keeping milk refrigeration on during peak period; 3) regulations evolution, selling electricity to the grid; 4) Mesophilic AD tank with electricity retrofit; 5) mesophilic AD tank with CHP (heat retrofit). Results from these scenarios are shown in Figure 3.

For this small-scale dairy farm the recommended investment is scenario 2: installing a bioenergy plant with 2.4 kW capacity (and no CHP), and 16 solar panels (345 Wp) with a total capacity of 5.2 kW. To avoid the purchase of a battery, a modification in the demand profile is endorsed: a switch of the milking process to after midnight will be sufficient, being able to keep the milk refrigerated after 6 pm. This solution requires an initial investment of 17k USD with 317 USD monthly savings for the first year, and with a payback of 3.4 years. This leads to a GHG reduction of 275.9 tons of CO₂ eq per year.

Description		Scenario (-1)	Baseline-Scenario 1	Scenario 2	Scenario 3.1	Scenario 3.2	Scenario 4.1	Scenario 4.2	Scenario 5.1	Scenario 5.2
		Before subsidies scheme removal	Baseline	Shifting demand	FIT UK	FIT UK with demand shift	Mesophilic AD with ICE	Mesophilic AD with ICE and demand shift	Mesophilic AD with CHP	Mesophilic AD with CHP and demand shift
Bio-Energy installation	kW	0.0	2.3	2.4	2.3	2.3	3.1	3.1	3.1	3.1
Solar Energy installation	kW	0.0	5.2	5.2	5.2	5.2	5.2	3.4	5.2	1.9
Number of solar panels		0	16	16	16	16	16	10	16	6
Storage Capacity	kWh	0.0	29.9	0.0	29.9	0.0	30.1	0.0	29.0	0.0
Final Total Investment	USD	0.0	33684.2	17042.3	33684.2	16579.2	36469.4	16310.8	38071.0	16326.2
Monthly savings (Year 1)	USD	0.0	706.5	317.3	714.9	312.8	687.1	251.9	752.3	297.4
Emission Reduction	tons of CO _{2,eq}	0.0	275.3	275.9	275.3	275.5	274.7	273.3	277.5	274.6
NPV savings	USD	0.0	62646.8	27134.2	63445.7	26729.1	57768.6	19304.5	65057.4	25410.7
Payback period	Years	0.0	3.1	3.4	3.0	3.3	3.4	4.0	3.2	3.4

Figure 3: Comparison of the different scenarios results

5. Discussion and future work

The results show that the proposed model can generate cost-optimal solutions to meet the demand profile of a small dairy farm, and that additional scenarios can be explored to derive optimal solutions in different regulatory framework or technical hybrid solutions implemented. In order to generalize the model, the scheduling of different RE could lead to a complete and more integrated approach. For example, a solar section could have subsections with solar PV (panels, HCPV) and solar thermal (flat plates, PT, HCSP). The model could define which RE and technology or combination of RE and technologies would be the most appropriate from a cost-effective point of view for a particular case study, with results likely to depend on demand profile, location, space constraints etc. Another approach for further work would be a more detailed temporal analysis, considering seasonal variations of resources and energy demand. Various political and economic risks can be faced while developing this project, which is highly uncertain and depends on Argentina's policy stability, but latest trends demonstrate a promising future market.

References

- E. Alessandretti, 2011. Propuesta energética sostenible para establecimientos agropecuarios. Instituto Tecnológico de Buenos Aires (ITBA).
- B. Elbersen, I. Staritsky, G. Hengeveld, L. Jeurissen, J. Lesschen, 2012. Outlook of spatial biomass value chains in eu28. D2. 3 Biomass Policies project.
- T. Mahachi, 2016. Energy yield analysis and evaluation of solar irradiance models for a utility scale solar pv plant in south africa. Ph.D. thesis, Stellenbosch: Stellenbosch University.
- A. McEvoy, T. Markvart, L. Castañer, T. Markvart, L. Castaner, 2003. Practical handbook of photovoltaics: fundamentals and applications. Elsevier.
- Observatorio Economico Social, 2017. Energia electrica en Argentina y Santa Fe. Rosario. Available at: <http://www.observatorio.unr.edu.ar/llego-la-factura-de-la-luz/>.
- A. Pantaleo, B. De Gennaro, N. Shah, 2013. Assessment of optimal size of anaerobic co-digestion plants: an application to cattle farms in the province of Bari (Italy). Renewable and Sustainable Energy Reviews 20, 57–70.
- A. M. Porcelli, A. N. Martínez, 2018. Una inevitable transición energética: el prosumidor y la generación de energías renovables en forma distribuida en la legislación argentina nacional y provincial. Actualidad Jurídica Ambiental (75), 4–49.
- M. Qadrdan, H. Ameli, G. Strbac, N. Jenkins, 2017. Efficacy of options to address balancing challenges: Integrated gas and electricity perspectives. Applied Energy 190, 181–190.
- M. Vis, et al., 2010. Harmonization of biomass resource assessments Volume I: Best practices and methods handbook.
- M. Welch, A. Pym, 2017. Flexible natural gas/intermittent renewable hybrid power plants. In: ASME 2017 11th International Conference on Energy Sustainability. American Society of Mechanical Engineers.
- S. R. Wenham, M. A. Green, M. E. Watt, R. Corkish, A. Sproul, 2013. Applied photovoltaics. Routledge.

Describing CO₂-Absorbent Properties in AspenPlus®

Jasper A. Ros^a, Derk W. F. Brilman^a, Ida M. Bernhardsen^b and Hanna Knuutila^{b,*}

^a*Sustainable Process Technology, University of Twente, Drienerloolaan 5, 7522NB Enschede, The Netherlands*

^b*Department of Chemical Engineering, Norwegian University of Science and Technology, Høgskoleringen 1, Trondheim, N-7491, Norway*

hanna.knuutila@ntnu.no

Abstract

For the modelling of novel solvent systems for CO₂-capture in AspenPlus®, data fitting of physical-chemical properties is needed. In this work the challenges and results are presented for fitting such experimental data for aqueous solutions of 2-(diethylamino)ethanol (DEEA) and 3-(methylamino)propylamine (MAPA). Without CO₂ present, the default regression tool of AspenPlus® gave good data fits for the binary systems H₂O-MAPA and H₂O-DEEA. In the presence of CO₂, regression of parameters was not successful and an additional Particle Swarm Optimization (PSO) algorithm was needed to determine the many molecule-ion parameters for the ELECNRTL model. With this, for DEEA a good fit to experimental data has been obtained, whereas for MAPA, due to the high number of ionic species, the results were still not satisfactory. To resolve this, independent measurement of equilibrium constants for the ionic equilibria is recommended.

Keywords: CO₂ capture, novel solvents, thermodynamic modelling, regression

1. Introduction

Post-combustion CO₂ capture from coal and natural gas fired power plants is widely recognized as one of the most effective techniques to reduce CO₂ emissions. The conventional technology is chemical absorption using aqueous amine solutions, in which amines react with CO₂ and the solvent circulates between the absorption and desorption column. The benchmark solvent is monoethanolamine (MEA), which is a primary amine solvent. However, the energy requirements in the regeneration step of this process are significant, leading to a continuous search for novel solvent systems that require less energy for regeneration (Bernhardsen and Knuutila, 2017). Interesting solvents have higher CO₂ capacities often combined with a lower heat of absorption. Tertiary amines are potentially good candidates, having lower heat of absorption and higher CO₂ capacity compared to primary and secondary amines. Unfortunately, their kinetic absorption rates are much lower compared to primary and secondary amines, which means that larger absorption columns are needed. A promoter (primary/secondary amine) could increase the kinetic absorption rates, while keeping a relatively low heat of absorption and high capacity (Arshad et al., 2013). A blended amine solution consisting of the tertiary amine 2-(diethylamino)ethanol (DEEA) and the primary/secondary amine 3-(methylamino)propylamine (MAPA) is described by Pinto et al. (2014b) as a potential replacement for the conventional MEA solvent. A mixture of these solvents shows high CO₂ capacities, high kinetic absorption rates and relatively low heat of absorption in experiments. This work focused on the thermodynamic modeling of the DEEA+MAPA mixture in the AspenPlus® flowsheet program in order to determine the industrial viability of these novel solvents.

2. Chemistry

The molecular structures of DEEA and MAPA are shown in Figure 1 below. DEEA acts as a free base in the hydration reaction with CO_2 to form bicarbonate and MAPA reacts with the CO_2 to form primary and secondary MAPA carbamate and MAPA di-carbamate, as shown in Equation 1. Additional reactions that are present in both reaction schemes but not shown below are the dissociation reactions of water and bicarbonate (Monteiro et al., 2013).

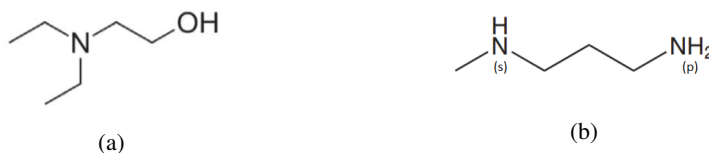
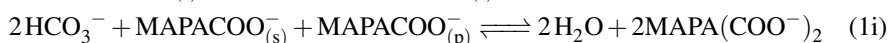
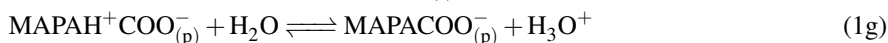
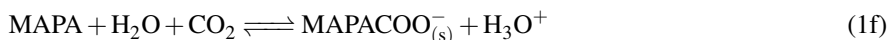
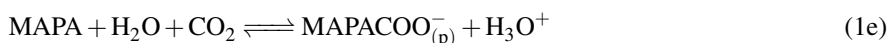
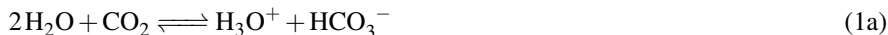


Figure 1: The molecular structures of (a) DEEA and (b) MAPA.

3. Important properties for CO_2 -absorbents

In this work, several properties for DEEA and MAPA were fitted to experimental data. These properties can be divided in three categories, namely: Pure properties, binary properties with water, and loaded properties upon CO_2 loading. The fitting was performed in steps: The pure component properties were fitted to form the boundaries of the binary properties at infinite dilution of either component, which again gave initial values for the loaded properties at a certain concentration of the solvent. Process simulations require detailed sub-models that can describe the absorption kinetics and physical properties like vapor-liquid equilibria and viscosity, describing the absorption capacity and solvent volatility as well as the equilibrium partial pressure of CO_2 at different solvent loadings. Furthermore, heat capacity and heat of absorption have an important role in correctly estimating the energy requirement of a process. Finally, equilibrium constants for the reactions have to be defined to determine the speciation of ions in the liquid phase. The equilibrium constants for the DEEA dissociation reaction were regressed against pKa data from Hamborg and Versteeg (2009) and the constants for the hydration reac-

tion of CO₂ were taken from Edwards et al. (1978). Unfortunately, no equilibrium constants are known for the (bi)carbamate formation reactions in the MAPA reaction scheme. AspenPlus® (Version 8.6) has built in (thermodynamic) models that can be used to represent all the properties described above. The thermodynamic model used in this work was the Electrolyte Non-Random Two Liquid (ELECNRTL) model (Chen et al., 1982). This extended NRTL model takes the activity coefficients of ions in the liquid phase into account. For the vapor phase, the Redlich-Kwong equation of state was used. Additional property models used in this work can be found in Table 1 below.

Table 1: Property models used in this work as defined in AspenPlus®.

	Pure	Binary	Loaded
VLE	PLXANT	NRTL	GMELCC/GMELCD
Density	DNLDIP	VLQKIJ	VLCLK
Viscosity	MULDIP	MUKIJ/MULIJ	IONMOB/IONMUB
Heat capacity	CPLDIP	No model available*	CPAQ0

*Calculated from the liquid enthalpy at constant pressure

4. Available experimental data

DEEA and MAPA have been researched extensively the past years, and data is widely available in literature. The pure vapor pressure data for DEEA and MAPA, the binary VLE data for DEEA-H₂O and the binary VLE data for DEEA-MAPA were taken from Hartono et al. (2013). The binary VLE data for MAPA-H₂O was taken from Kim et al. (2008). The loaded VLE data for the DEEA system was taken from Monteiro (2014) and Xu et al. (2014) and all viscosity and density data were taken from Pinto (2014a). Unfortunately only pure component heat capacities are available in literature and no binary or loaded heat capacities were found. The pure heat capacity for DEEA and MAPA was taken from Maham et al. (1997) and Lin et al. (2014) respectively. AspenPlus® has default values for all H₂O pure component parameters discussed in this work. Furthermore, the default CO₂ Henry coefficients were used.

5. Fitting procedure

The regressed parameters in this work regard the Antoine equation, NRTL, ELECNRTL, density, viscosity and heat capacity parameters. Experimental data is added to the model and the regression tool performs the iterative regression. For the models with typically three parameters to fit the regression tool performs well. However, when the number of parameters to fit increases, the use of the regression tool becomes more challenging. Using this tool is still possible, however it requires substantial amount of trial-and error and understanding of how the different parameters influence the fit. This is the case in fitting the ELECNRTL model which is based on the local composition of molecules and ions. For example in case of the DEEA system, 8 components can be distinguished resulting in 72 parameters whereas, in the MAPA system, 14 components can be distinguished resulting in 360 parameters. Additionally, for the MAPA system, the equilibrium constants of the reactions are regressed together with the molecule-ion parameters. To lower the amount of parameters to fit, the default ELECNRTL parameter values for the sub-system H₂O-CO₂ are typically fixed to the values estimated by the program. This lowered the

amount of parameters in the DEEA and MAPA system to 36 and 300 respectively. Still this is too high for the regression tool, resulting in many regression steps, where only few selected parameters would be regressed at once and manual trial and error is necessary. Therefore in this work, an external MATLAB[®] code is coupled with AspenPlus[®], that provides an alternative solver. This solver is based on the Particle Swarm Optimization (PSO) algorithm (Kennedy and Eberhart, 1995). With this algorithm, more parameters can be regressed simultaneously to experimental data compared to the conventional solver. The MATLAB[®] code generates parameter sets according to the PSO algorithm as input for the AspenPlus[®] model, which uses the ELECNRTL model to calculate the chemical equilibrium and phase equilibrium. This is iteratively done, until a certain threshold is reached for the accuracy of the solution. A drawback of this algorithm is that the computation time for the regression is significantly increased. However, this regression is still much faster than manual fitting by changing a few parameters at a time using the conventional regression tool.

6. Results

The accuracy of the fitted model to the experimental data was assessed using the averaged absolute relative deviation (AARD) error definition, as defined by

$$AARD = \frac{1}{N} \sum_{i=k}^N 100 \frac{|\eta_k - \phi_k|}{|\phi_k|}, \quad (2)$$

where N is the amount of data points, η_k is the value of the fit at a certain point and Φ_k is the experimental value at the same point. The AARD values calculated in this work are listed in Table 2. It can be seen that all pure component properties have accurate fits to the experimental data. Also the considered properties for the binary systems were fitted with an acceptable low AARD. Further, a satisfactory fit of the DEEA model was found to the loaded VLE data, whereas the MAPA model gave no satisfactory fit. It is important to note that without the ELECNRTL parameters, no concentration/activity of ions is known and loaded density, viscosity and heat capacity parameters cannot be fitted, as these parameters are dependent on these concentrations or activities. The reason for the bad fit for the MAPA system is probably due to the high amount of parameters and missing equilibrium constants. The phase envelope diagram for the DEEA-H₂O and MAPA-H₂O mixture is shown in Figure 2. It can be seen that for both mixtures, with the regressed NRTL parameters, the model gives accurate bubble and dew point curves. The DEEA-MAPA mixture data is fitted with an AARD of 3.0 %. The loaded VLE results for the regression of the molecule-ion parameters of the DEEA-H₂O-CO₂ system can be found in Figure 3. As can be seen in this figure, for 2M and 3M DEEA solutions, a satisfactory fit is found and the AARD value is 16.7 %. This is a relatively high error compared to the other component parameters, however it is comparable to other modelled data found in literature for loaded VLE data (Monteiro et al., 2013). The valid range of operation for this model is between 2M and 3M DEEA solutions, and between 40 and 120 °C. The sufficient fit for the DEEA solution proves that the regression algorithm used in this work is an effective algorithm to fit VLE data upon CO₂ loading. The focus of future research should move towards the fitting of the ELECNRTL parameters for the MAPA solution. In order to obtain a satisfactory fit, more molecule-ion pairs should be assumed constant and the equilibrium constants of all reactions should be known. Furthermore, the model results for combining the two solvents should be validated against experimental data.

Table 2: The AARD (%) values obtained in this work.

	DEEA			MAPA		
	Pure	Binary	Loaded	Pure	Binary	Loaded
VLE	0.29	0.71	16.7*	0.85	1.44	No fit
Density	0.01	0.59	0.78	0.20	0.51	No fit
Viscosity	0.64	6.9	9.1	0.21	5.0	No fit
Heat capacity	0.15	No data	No data	0.04	No data	No data

*Regressed with the PSO algorithm

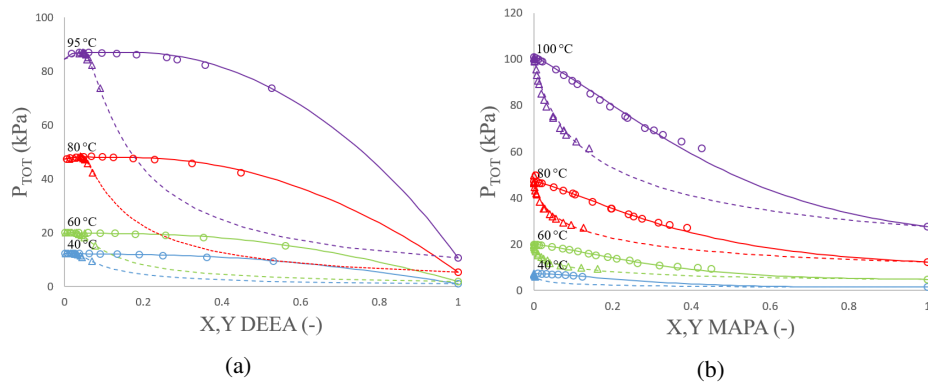


Figure 2: Experimental data from Hartono et al. (2013) and Kim et al. (2008) (O/Δ) and model results (-) for the phase envelope diagram for the (a) DEEA-H₂O binary system and (b) MAPA-H₂O binary system at different temperatures. The continuous lines are the bubble point curves and the dashed lines are the dew point curves.

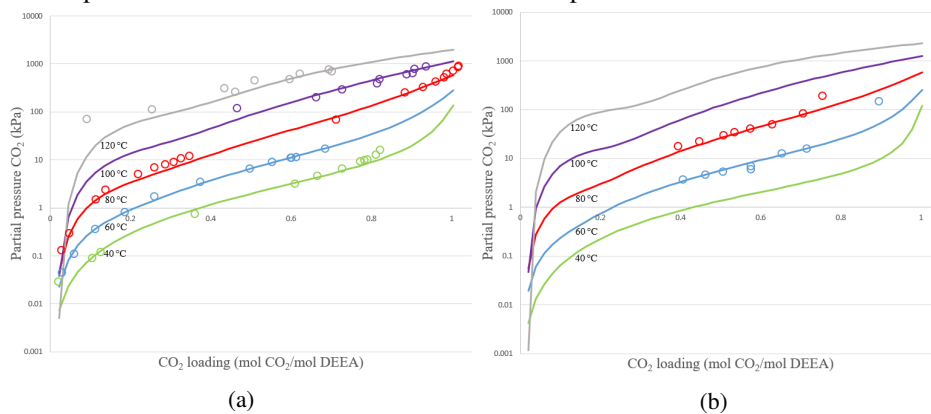


Figure 3: Experimental data from Monteiro et al. (2013) and Xu et al. (2014) (o) and model results (-) for the partial pressure of CO₂ at a certain CO₂ loading for the (a) 2M and (b) 3M DEEA solution at different temperatures.

7. Conclusions

In this work, the basis for the thermodynamic model for the promising DEEA+MAPA solvent for post-combustion CO₂ capture was developed using AspenPlus[®]. Different pure, binary and loaded parameters for the DEEA and MAPA system were regressed with the conventional regression tool, while the PSO algorithm was coupled with AspenPlus[®] to regress the molecule-ion parameters of the ELECNRTL model for the DEEA solution. No good fit was obtained for MAPA, and research should focus on the regression of the ELECNRTL molecule-ion parameters of this MAPA system.

References

- M. W. Arshad, N. von Solms, K. Thomsen, H. F. Svendsen, 2013. Heat of absorption of CO₂ in aqueous solutions of DEEA, MAPA and their mixture. *Energy Procedia* 37, 1532 – 1542.
- I. M. Bernhardsen, H. K. Knuutila, 2017. A review of potential amine solvents for CO₂ absorption process: Absorption capacity, cyclic capacity and pKa. *International Journal of Greenhouse Gas Control* 61, 27 – 48.
- C.-C. Chen, H. I. Britt, J. F. Boston, L. B. Evans, 1982. Local composition model for excess Gibbs energy of electrolyte systems. part I: Single solvent, single completely dissociated electrolyte systems. *AIChE Journal* 28 (4), 588–596.
- T. J. Edwards, G. Maurer, J. Newman, J. M. Prausnitz, 1978. Vapor-liquid equilibria in multicomponent aqueous solutions of volatile weak electrolytes. *AIChE Journal* 24 (6), 966–976.
- E. S. Hamborg, G. F. Versteeg, 2009. Dissociation constants and thermodynamic properties of amines and alkanolamines from (293 to 353) K. *Journal of Chemical & Engineering Data* 54 (4), 1318–1328.
- A. Hartono, F. Saleem, M. W. Arshad, M. Usman, H. F. Svendsen, 2013. Binary and ternary VLE of the 2-(diethylamino)-ethanol (DEEA)/3-(methylamino)-propylamine (MAPA)/water system. *Chemical Engineering Science* 101, 401 – 411.
- J. Kennedy, R. Eberhart, 1995. Particle swarm optimization. *Proceedings of IEEE International Conference on Neural Networks* 4, 1942 – 1948 vol.4.
- I. Kim, H. F. Svendsen, E. Børresen, 2008. Ebulliometric determination of vapor-liquid equilibria for pure water, monoethanolamine, N-methyldiethanolamine, 3-(methylamino)-propylamine, and their binary and ternary solutions. *Journal of Chemical & Engineering Data* 53 (11), 2521–2531.
- S.-Y. Lin, R. B. Leron, M.-H. Li, 2014. Molar heat capacities of diethylenetriamine and 3-(methylamino)propylamine, their aqueous binaries, and aqueous ternaries with piperazine. *Thermochimica Acta* 575, 34 – 39.
- Y. Maham, L. G. Hepler, A. E. Mather, A. W. Hakin, R. A. Marriott, 1997. Molar heat capacities of alkanolamines from 299.1 to 397.8 K group additivity and molecular connectivity analyses. *J. Chem. Soc., Faraday Trans.* 93, 1747–1750.
- J. Monteiro, D. Pinto, S. A.H. Zaidy, A. Hartono, H. Svendsen, 11 2013. VLE data and modelling of aqueous n,n-diethylethanolamine (DEEA) solutions. *International Journal of Greenhouse Gas Control* 19, 432440.
- J.-S. Monteiro, 2014. Contributions to kinetics and equilibrium of CO₂ absorption into n,n-diethylethanolamine (DEEA), N-methyl-1,3-propane-diamine (MAPA) and their blends. Ph.D. thesis, Norwegian university of science and technology, Norway.
- D. Pinto, 2014a. CO₂ capture solvents: modeling and experimental characterization. Ph.D. thesis, Norwegian university of science and technology, Norway.
- D. D. Pinto, S. A. Zaidy, A. Hartono, H. F. Svendsen, 2014b. Evaluation of a phase change solvent for CO₂ capture: Absorption and desorption tests. *International Journal of Greenhouse Gas Control* 28, 318 – 327.
- Z. Xu, S. Wang, G. Qi, A. A. Trollebø, H. F. Svendsen, C. Chen, 2014. Vapor liquid equilibria and heat of absorption of CO₂ in aqueous 2-(diethylamino)-ethanol solutions. *International Journal of Greenhouse Gas Control* 29, 92 – 103.

Challenges in Decision-Making Modelling for New Product Development in the Pharmaceutical Industry

Catarina M. Marques^{a,b,*}, Samuel Moniz^c, Jorge Pinho de Sousa^{a,b},

^a*Faculdade de Engenharia da Universidade do Porto, Portugal*

^b*INESC TEC, Porto, Portugal*

^c*Departamento de Engenharia Mecânica da Universidade de Coimbra, Portugal*
eq98022@fe.up.pt

Abstract

This study presents an assessment of the main research problems addressed in the literature on New Product Development (NPD) and its methodologies, for the pharmaceutical industry. The work is particularly focused on the establishment of an evolutionary perspective of the relevant modelling approaches, and on identifying the main current research challenges, considering the fast-changing business context of the industry. Main findings suggest a generalized misalignment of recent studies with today's technological and market trends, highlighting the need for new modelling strategies.

Keywords: New product development, capacity planning, portfolio management, modelling, decision-making.

1. Introduction

The world is currently experiencing unprecedented fast changes, with major technological breakthroughs that are transforming the way companies operate and manage their systems. Pharmaceutical companies are constantly being challenged to become ever more cost efficient and responsive in the delivery of drugs. Consistently launching new drugs into the market is, therefore, critical to support the industry's economic sustainability. However, the traditional NPD process still imposes considerable challenges for practitioners and researchers. In this sector, the Operations Research (OR) and the Process Systems Engineering (PSE) communities have been developing reliable and effective model-based decision-making tools. Understanding how these developments have been impacting the industry is crucial for establishing new management directions that take into account the paradigm changes currently faced by the industry. The main goal of this work is, therefore, to present a research review with two perspectives: first, identifying the main problems on the pharmaceutical NPD process and the corresponding modelling approaches; and second, analyzing how research has evolved along the years, assessing the methodological main progresses and envision future directions.

2. Literature Review

In order to clearly define the scope of the present study the following research question was formulated: "What have been the main research concerns and modelling approaches in the pharmaceutical NPD process?" Based on this question, the following criteria were

used to perform the review: (i) studies specifically addressing decision-making problems in the pharmaceutical sector; (ii) works within OR, PSE, and related communities; and (iii) full research papers, written in English. The search was performed considering the boolean combination of keywords ((*“planning” OR “scheduling” OR “decision-making” OR “supply chain”*) AND *pharma**), complemented by the analysis of several review papers. After excluding duplicates, review papers, conference papers (with some limited exceptions), and works at a hospital/pharmacy level, a total of 113 research works was obtained covering the complete pharma industry management problems. A second round of analysis was then performed to keep only works related to the development of new products. Finally, a set of 53 papers was considered for a complete analysis.

3. Analysis

The 53 papers selected for full analysis cover the years from 1996 to early 2018 and are distributed in 16 scientific journals and 2 conference proceedings. "Computers and Chemical Engineering" appears as the most represented journal, with 18 published papers. Two broad research areas emerge from the selected papers, namely: (i) the portfolio management area; and (ii) the clinical trial supply chain management area. Portfolio management is the most developed area, being addressed in 31 papers and representing about 58% of the total selected works, while the clinical trial supply chain management area is tackled in the remaining 22 papers. Each one of these areas is described in the following sections.

3.1. Portfolio Management (PM)

The main goal of PM is to determine the portfolio of new products to be developed and the schedule of the associated testing tasks (clinical trials) under uncertainty in the outcomes of the tests. Therefore, two decision problems are usually found in the literature, namely: i) the portfolio selection (PS), and ii) the scheduling of the testing tasks (ST). In the first case, the main decisions include the determination of which targets should be selected for further clinical development. These decisions rely on two issues: i) the assessment of the value of the portfolio, based on its probability of success and on its potential returns; ii) and on the company market strategy.

The ST problem is closely related to the typical Resource-Constrained Project Scheduling (RCPS) problem, but with the possibility of task failing during the development process. The main decisions involved here are related to the determination of the tasks starting and completion times. Uncertainty in trials' outcomes is addressed in 28 of the 31 selected papers, thus highlighting its importance in these problems. In both cases (PS and ST) there are also resource-related decisions, in order to ensure the necessary resources availability. Moreover, most of the studies deal with the two problems simultaneously (17 papers). The modelling details and progresses on portfolio management in the pharmaceutical industry are presented in the next section.

3.1.1. Modelling approaches

Analysing the complete set of the selected papers, the prevailing modelling approaches can be broadly divided in optimization (18 papers), simulation-optimization (11 papers), and simulation (2 papers) approaches. In the optimization case, problems are formulated as deterministic MILP models or as stochastic versions of RCPS problems (two-/multi-stage stochastic programming MILP models). In the simulation-optimization case, there is a combination of combinatorial optimization models with a discrete-event simulation.

Simulation is used to capture uncertainty more realistically and to evaluate the optimization results, thus giving insights to the determination of the optimized solution, in an iterative way. In the simulation case, models are used to perform sensitivity analysis and capture the risk/reward of the portfolio value. Figure 1 depicts the evolutionary path of the most relevant contributions to the PM problem. The first work addressing this problem (Schmidt and Grossmann (1996)) was based on a MILP model and a two-stage stochastic programming (TSSP) approach, to account for uncertainties in task costs, durations, and trials outcomes. The goal was to determine the schedule of testing tasks that maximizes the expected net present value (eNPV), considering task precedence and timing constraints. This model, however, does not account for important features such as product interdependencies or resources limitations.

Later, an evolution has been observed (Figure 1), with works incorporating ever more sophisticated modelling features and broadening the problem scope. It is, therefore possible to outline the basic structure of the MILP formulation that is common to most of the works addressing ST/PS decisions. This formulation can be generalized as follows. We are given: i) a set of time periods $t \in \mathbf{T}$; ii) a set of potential drugs $i \in \mathbf{I}$ to develop; iii) a set of clinical tests $j \in \mathbf{J}$; iv) a set of resource types $r \in \mathbf{R}$; and v) a set of scenarios $s \in \mathbf{S}$. The goal is to determine which tests should be selected and when (X_{ijts} binary variables) to maximize the eNPV, subject to the following general constraints: i) assignment constraints of clinical tests to starting times; ii) test precedence constraints; and iii) resource constraints. The main evolution here was on the resource constraints representation, by considering more industry-specific decisions, such as investment in new resources, outsourcing resources or out-licensing tests.

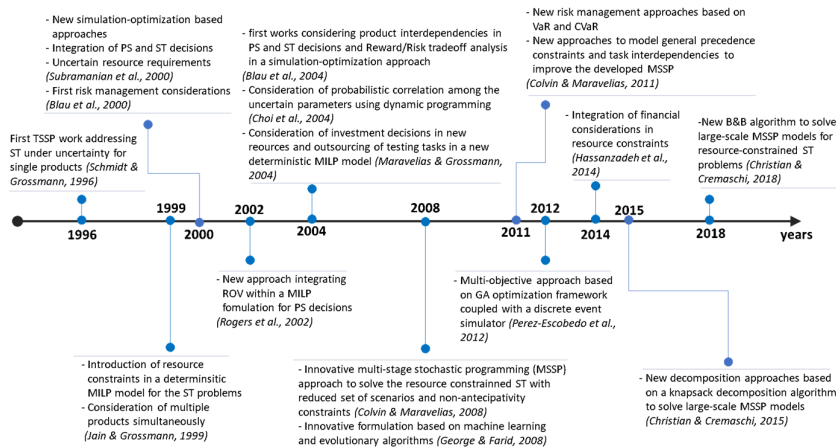


Figure 1. Timeline of the most relevant contributions in Portfolio Management.

3.2. Clinical Trials Supply Chain (CTSC) management

At CTSC management, two broader areas were identified. The first area (*CTSC operations*) is related to management of all the activities required to undertake the clinical trials, including: product manufacturing, packaging, storage, and distribution to clinical sites. In this type of supply chains (SC), special attention needs to be given to aspects such as: the limited time-horizon by trials duration; leftovers at the end of each trial that cannot be reused; delivery failures (seriously compromising time-to-market); and the significant uncertainty affecting the process. The main challenge is, therefore, to

efficiently manage this unique SC, guaranteeing the timely fulfilment of the clinical trials demand. Despite their relevance for the industry, only 8 papers explicitly addressed the CTSC operational problems, showing a very limited attention paid by researchers to this issue. These works span from SC/plant design to production/ inventory planning, with most of the papers integrating these two decision-levels at some extent.

In a second area, the Product Launch planning problem is related to the important link between product development and the capacity planning needed to accommodate both existing and new products. 14 works addressing this link were considered with decisions comprising portfolio selection, capacity and production planning.

3.2.1. Modelling approaches

CTSC operations

CTSC operations are clearly a new area in the OR and the PSE communities, being still at its infancy of development. Selected works can be divided into simulation (2 papers) or simulation-optimization (6 papers) approaches. The early works addressing this problem, particularly regarding inventory management, were based on simulation approaches for assessing different scenarios, and decisions were taken mainly based on sensitivity analysis. The introduction of optimization approaches starts to emerge only recently, and works are still very scarce. The most relevant contributions were by Chen et al. (2012) with an integrated approach to manage the multi-echelon CTSC under uncertainty on patient demand, and the work by Marques et al. (2017), integrating capacity planning and process design decisions under uncertainty with an on time supply of the clinical trials. Both approaches integrate simulation methods to tackle uncertainty with MILP optimization models.

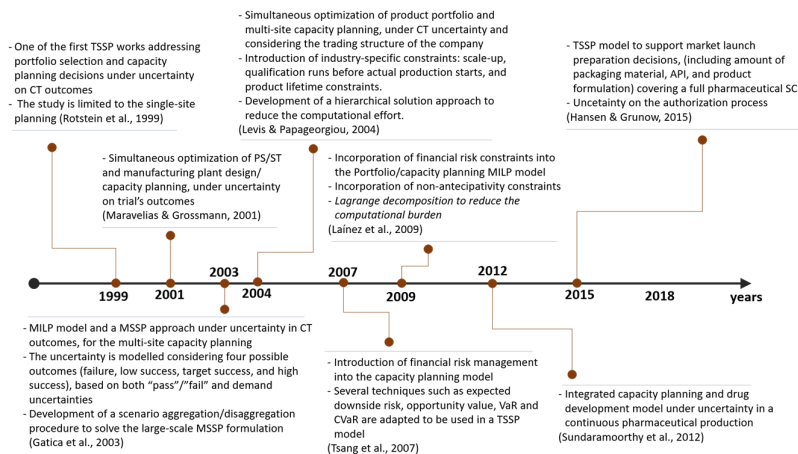


Figure 2. Timeline of the most relevant contributions in Product Launch planning.

Product Launch planning (PL)

Regarding the product launch planning problem, all the selected papers developed optimization approaches based on MILP formulations, and only 3 presented deterministic models. The remaining 11 papers addressed the uncertainty on trials' outcomes through multi-stage stochastic programming (MSSP) approaches. Most of the works deal with the decisions such as portfolio selection and capacity/production planning, and constraints on

material balance, production/manufacturing, resource allocation/investments, or sales/demand.

Figure 2 depicts the evolutionary path of the most relevant contributions to the PL problem. One of the first works addressing this problem was by Rotstein et al. (1999), proposing a MILP model under uncertainty in trial's outcomes for the selection of the most profitable products, capacity planning, and investment strategy to accommodate the new products. Subsequent works tend to deal with ever more complex features by adding problem-specific constraints to the base model, such as: scale-ups; qualification runs; product lifetime, financial, and risk constraints. It is interesting to note that the increase on the models' size/complexity has also motivated a further development of new decomposition techniques, contrasting with the lack of exploitation of alternative modelling approaches.

4. Research directions and final remarks

This work shows that PM problems have been object of significant research activities, contrasting with the CTSC operations with still very modest developments. However, current technological trends (continuous manufacturing and digital capabilities) and market (personalization) trends are still absent or only discreetly considered in research works.

Future modelling approaches should take the following new aspects into account: i) assessment of the portfolio "value", including patient-related considerations (e.g. specific unmet needs); ii) patient-centric delivery models, linking "quantity" variables to new "outcome" variables reflecting benefits for patients; iii) market segmentation constraints; iv) integrated approaches and coordination between actors; v) exploitation of the benefits of continuous manufacturing settings and digital capabilities to leverage efficiency; vi) functional integration between marketing (patient perspective), product development, and manufacturing; vii) exploitation of new performance metrics and multi-objective approaches to capture the multi-dimensionality of the problems; and finally viii) exploitation of innovative modelling approaches to tackle large-scale problems.

In short, future work should extend the analysis throughout the entire drug life-cycle, and define future modelling components (constraints, variables, ...) that are more aligned with the current context of the pharmaceutical industry.

Acknowledgement

The authors gratefully acknowledge the financial support of Fundação para a Ciência e Tecnologia (FCT), under the grant PD/BD/105987/2014.

References

- Blau, G., Mehta, B., Bose, S., Pekny, J., Sinclair, G., Keunker, K., & Bunch, P. (2000). Risk management in the development of new products in highly regulated industries. *Computers & Chemical Engineering*, 24, 659-664.
- Blau, G., Pekny, J. F., Varma, V. A., & Bunch, P. R. (2004). Managing a portfolio of interdependent new product candidates in the pharmaceutical industry. *Journal of Product Innovation Management*, 21, 227-245.
- Choi, J., Realf, M. J., & Lee, J. H. (2004). Dynamic programming in a heuristically confined state space: a stochastic resource-constrained project scheduling application. *Computers & Chemical Engineering*, 28, 1039-1058.

- Christian, B., & Cremaschi, S. (2015). Heuristic solution approaches to the pharmaceutical R&D pipeline management problem. *Computers & Chemical Engineering*, 74, 34-47.
- Christian, B., & Cremaschi, S. (2018). A branch and bound algorithm to solve large-scale multistage stochastic programs with endogenous uncertainty. *AIChE Journal*, 64, 1262-1271.
- Colvin, M., & Maravelias, C. T. (2008). A stochastic programming approach for clinical trial planning in new drug development. *Computers & Chemical Engineering*, 32, 2626-2642.
- Colvin, M., & Maravelias, C. T. (2011). R&D pipeline management: Task interdependencies and risk management. *European Journal of Operational Research*, 215, 616-628.
- Gatica, G., Papageorgiou, L., & Shah, N. (2003). An aggregation approach for capacity planning under uncertainty for the pharmaceutical industry. *Found Comp-Aided Proc Oper*, 4, 245-248.
- George, E. D., & Farid, S. S. (2008). Stochastic combinatorial optimization approach to biopharmaceutical portfolio management. *Industrial & Engineering Chemistry Research*, 47, 8762-8774.
- Hansen, K. R. N., & Grunow, M. (2015). Planning operations before market launch for balancing time-to-market and risks in pharmaceutical supply chains. *International Journal of Production Economics*, 161, 129-139.
- Hassanzadeh, F., Modarres, M., Nemati, H. R., & Amoako-Gyampah, K. (2014). A robust R&D project portfolio optimization model for pharmaceutical contract research organizations. *International Journal of Production Economics*, 158, 18-27.
- Jain, V., & Grossmann, I. E. (1999). Resource-constrained scheduling of tests in new product development. *Industrial & Engineering Chemistry Research*, 38, 3013-3026.
- Laínez, J. M., Reklaitis, G. V., & Puigjaner, L. (2009). Managing financial risk in the coordination of supply chain and product development decisions. *Computer Aided Chemical Engineering*, 26, 1027-1032.
- Levis, A. A., & Papageorgiou, L. G. (2004). A hierarchical solution approach for multi-site capacity planning under uncertainty in the pharmaceutical industry. *Computers & Chemical Engineering*, 28, 707-725.
- Maravelias, C. T., & Grossmann, I. E. (2004). Optimal resource investment and scheduling of tests for new product development. *Computers & Chemical Engineering*, 28, 1021-1038.
- Perez-Escobedo, J. L., Azzaro-Pantel, C., & Pibouleau, L. (2012). Multiobjective strategies for New Product Development in the pharmaceutical industry. *Computers & Chemical Engineering*, 37, 278-296.
- Rogers, M. J., Gupta, A., & Maranas, C. D. (2002). Real options based analysis of optimal pharmaceutical research and development portfolios. *Industrial & Engineering Chemistry Research*, 41, 6607-6620.
- Rotstein, G., Papageorgiou, L., Shah, N., Murphy, D., & Mustafa, R. (1999). A product portfolio approach in the pharmaceutical industry. *Computers & Chemical Engineering*, 23, S883-S886.
- Schmidt, C. W., & Grossmann, I. E. (1996). A mixed integer programming model for stochastic scheduling in new product development. *Computers & Chemical Engineering*, 20, S1239-S1244.
- Subramanian, D., Pekny, J. F., & Reklaitis, G. V. (2000). A simulation—optimization framework for addressing combinatorial and stochastic aspects of an R&D pipeline management problem. *Computers & Chemical Engineering*, 24, 1005-1011.
- Sundaramoorthy, A., Evans, J. M., & Barton, P. I. (2012). Capacity planning under clinical trials uncertainty in continuous pharmaceutical manufacturing. 1: mathematical framework. *Industrial & Engineering Chemistry Research*, 51, 13692-13702.
- Tsang, K., Samsatli, N., & Shah, N. (2007). Capacity investment planning for multiple vaccines under uncertainty: 2: Financial risk analysis. *Food and Bioproducts Processing*, 85, 129-140.

Extension of a Particle Filter for Bioprocess State Estimation using Invasive and Non-Invasive IR Measurements

Julian Kager^{a,b,*}, Vladimir Berezhinskiy^a, Robert Zimmerleiter^c, Markus Brandstetter^c and Christoph Herwig^{a,b}

^aICEBE, TU Wien, Gumpendorfer Straße 1a 166/4, 1060 Wien, Austria

^bCD Laboratory on Mechanistic and Physiological Methods for Improved Bioprocesses, TU Wien, Gumpendorfer Straße 1a 166/4, 1060 Wien, Austria

^cResearch Center for Non Destructive Testing (RECENDT) GmbH, 4040 Linz, Austria
julian.kager@tuwien.ac.at

Abstract

Producers of pharmaceuticals have to guarantee the quality of their products. Therefore, substantial efforts are invested in process monitoring and control. However, crucial parameters, such as the nutrient and product precursor concentrations often require time-consuming analysis of a sample. Infrared (IR) spectroscopy is a promising measurement technique for the online quantification of multianalyte solutions, such as fermentation broths. Besides the high investment cost of devices, chemometric models often are not fully transferable and provide noisy estimates which need to be treated before further usage. To increase robustness and accuracy of these measurements they can be combined with kinetics models under the usage of a state observation algorithms, such as Kalman- or Particle filters.

In this work, we present a unique combination of a transferable mechanistic process description with the real-time information derived from near and mid IR spectroscopy leading to stable, smooth and accurate state estimates. IR spectra were collected in *Penicillium chrysogenum* fed-batch processes. PLS models were trained for the prediction of nitrogen, product and product precursor concentrations, which were used as inputs for the state observer. The resulting probabilistic estimates provide a good basis for automatic control.

Keywords: bioprocess monitoring, spectroscopic measurements, state observation, non-invasive NIR spectroscopy, MIR spectroscopy, PLS-regression

1. Introduction

To control fermentation processes, real-time measurements of critical process parameters are required. Since fermentation broths are a complex mixture of different analytes, their single quantification is difficult. Over the last decades promising technologies emerged to provide real-time information on the reaction kinetics during such processes (Vojinović et al. (2006)).

Near and mid infrared (NIR; MIR) spectroscopy combined with multivariate analysis can be used to quantify multi-analyte solutions. For the penicillin producing organism *P.*

chrysogenum the product, the product precursor and the nitrogen concentration could be successfully determined via NIR and MIR spectroscopy (Luoma et al. (2017); Koch et al. (2014)). Besides advantages like the non-destructive and possible non-invasive measurement, the multivariate models are not fully transferable and provide noisy estimates which need to be treated before further usage (Krämer and King (2017)).

In chemical engineering state observers, which are computational algorithms to estimate unmeasured state variables, are widely applied (Ali et al. (2015)). Hereby, secondary measurements provide real-time information of the ongoing process and Bayesian filters estimate the most probable states. Besides the often used extended Kalman filter, particle filters, which approximate the distribution of the estimated states, gained importance with increasing computational capacities (Goffaux and Wouwer (2005)). In recent works a particle filter configuration was compared to an extended Kalman filter for the examined penicillin production process (Stelzer et al. (2017)), and the better suited particle filter was extended to use delayed offline measurements (Kager et al. (2018)).

Although estimations already show good results the combination of spectroscopy and Bayesian state estimation offers a possibility to further improve bioprocess monitoring. This potential was shown by Golabgir and Herwig (2016) under usage of Raman spectroscopy and by Krämer and King (2017) with NIR spectroscopy for a yeast process. In this work two different IR measurements were carried out. One using an immersion probe in the MIR spectral region and the other through a glass window of the reactor in the NIR spectral region. The acquired IR data was included in a particle filter in order to estimate important process parameters such as product, product precursor, nitrogen and biomass concentration. The possibility to include redundant measurements and to combine them, to get robust and complete state estimates is of high relevance to biochemical production industry.

2. Materials and Methods

2.1. Cultivation & Reference Measurements

Fed-batch experiments were performed in a 2.7 l parallel bioreactor system (Eppendorf AG, Germany) using a spore suspension of an industrial *P. chrysogenum* strain for penicillin production. Dissolved oxygen was controlled above 40% by stirrer speed (350 - 850 rpm) and subsequent oxygen addition to pressurized air, while the reactor was aerated with 1 vvm of gas mixture. The temperature was maintained at 25 °C and the pH value was maintained at 6.5 by addition of KOH and H₂SO₄. Glucose (500 g/l), the penicillin V precursor (POX) (80 g/l phenoxyacetate) and the nitrogen source (100 g/l (NH₄)₂SO₄) were supplied as feeds. As glucose should be the only limiting component, nitrogen and precursor were kept at non-limiting concentrations (1 g/l and 2 g/l), by manipulating the (NH₄)₂SO₄ and POX feeds.

For online analytics, CO₂ and O₂ content in the off-gas were measured by a gas analyzer (DASGIP GA4, Eppendorf AG, Germany). The conversion of O₂ to CO₂ was calculated according to Aehle et al. (2011), giving the carbon evolution rate (CER) and the oxygen uptake rate (OUR) in mol/h. Reference samples were taken every 8 hours. Analysis of penicillin V (PEN) and POX concentration in the culture media was performed by HPLC using a ZORBAX C-18 Agilent column and 28% acetonitrile, 6 mM H₃PO₄ and 5 mM

KH_2PO_4 as elution buffer. Glucose and ammonia concentration were quantified by an enzymatic analyzer (Cedex Bio HT, Roche GmbH, Switzerland). Biomass concentration was determined gravimetrically by separating the cells from 5 ml culture broth via centrifugation at 4800 rpm for 10 min at 4 °C. The cell pellet was dried at 105 °C after a washing step with 5 ml of deionized water in weighted glass tubes.

2.2. Infrared Spectroscopy and Partial Least Square (PLS) Regression

Mid IR absorption ($650\text{-}3000\text{ cm}^{-1}$) was captured by an optical fiber immersion probe (ReactIR 45m, Mettler Toledo, USA) and near IR ($5000\text{-}7500\text{ cm}^{-1}$) was captured, through the glass wall of the reactor (NIRONE, Spectral Engines, Finland).

After data preprocessing (standard normal variate (SNV) transformation and Savitzky-Golay smoothing (SG) and differentiation (1st; 2nd), partial least square regression models (SIMPLS) were build in MATLAB (R2018a, MathWorks, USA). Spectra preprocessing was done according to Koch et al. (2014) for mid and Luoma et al. (2017) for near IR. Suitable wavenumber ranges were selected individually by selecting ranges with high PLS weights in the whole band including 1st and 2nd order derivatives. By a randomly sampling cross-validation procedure the number of latent variables were determined. The selected procedures for different analytes are summarized in Table 1.

Table 1: Near and mid IR PLS regression procedures for penicillin V (PEN), product precursor (POX) and nitrogen (NH_3).

Model	Preprocessing	Wavelength ranges [cm^{-1}]	Latent variables	Datasets
MIR-PEN	1st	1307-1352 ; 1747-1817	4	3
MIR-POX	none	1000-1150 ; 1400-1750 ; 1900-2600	3	3
MIR-NH3	1st	850-1150 ; 1400-1520 ; 1950-2300	4	3
NIR-PEN	SNV, 2nd	6050-7500 ; 5200 -5700	4	4
NIR-POX	SNV, 2nd	5100-5500 ; 6100-6400 ; 6500-7500	4	4
NIR-NH3	1st	6200-7500	4	4

2.3. Non-linear Kinetic Model and Bayesian State Estimation

A kinetic process model taken from Paul et al. (1998) describing the states x (hyphal tips, hyphal bodies, glucose, gluconate, nitrogen, product precursor and product concentration) by ordinary differential equations was adapted to the current process (Stelzer et al. (2017)). In order to use the model during the process a state estimation algorithm, a SIR particle filter derived from Simon (2006) was used. The model states are hereby described by x and linked to the measurements y . As initialization step, a sample of N particles is drawn by the known probability density function $p(x_0)$ of the initial states x_0 . Iteratively, for time steps $k \geq 1$, N particles \tilde{x}_k^i are propagated based on the process model. Importance weights fro every particle, $\tilde{w}_k^i = p(y_k | \tilde{x}_k^i)$, $i = 1, \dots, N$, are calculated at measurement arrival. All measurements are hereby weighted by their error. Applying multinominal resampling, N posteriori particles x_k^i , $i = 1, \dots, N$ are resampled from \tilde{x}_k^i according to their importance weights. The distribution of these particles is an approximation of the probability density function, i.e. $x_k^i \sim p(x_k | y_k)$, from which the actual state estimates can be derived.

3. Results and Discussion

3.1. Model Building and Calibration

In Figure 1 observed vs. predicted plots show the calibrated models, with their confidence intervals and their Root Mean Square Errors (RMSE). PLS models were built according to Table 1 and parameters for the kinetic model were estimated according to the procedures described by Ulonska et al. (2018). For the product, the kinetic model is unable to predict the product degradation properly, which can be seen from the overestimation at high concentrations. Overall the submerged MIR shows the best calibration results, whereas the kinetic model predictions and the non-invasive NIR measurements are within the same error range.

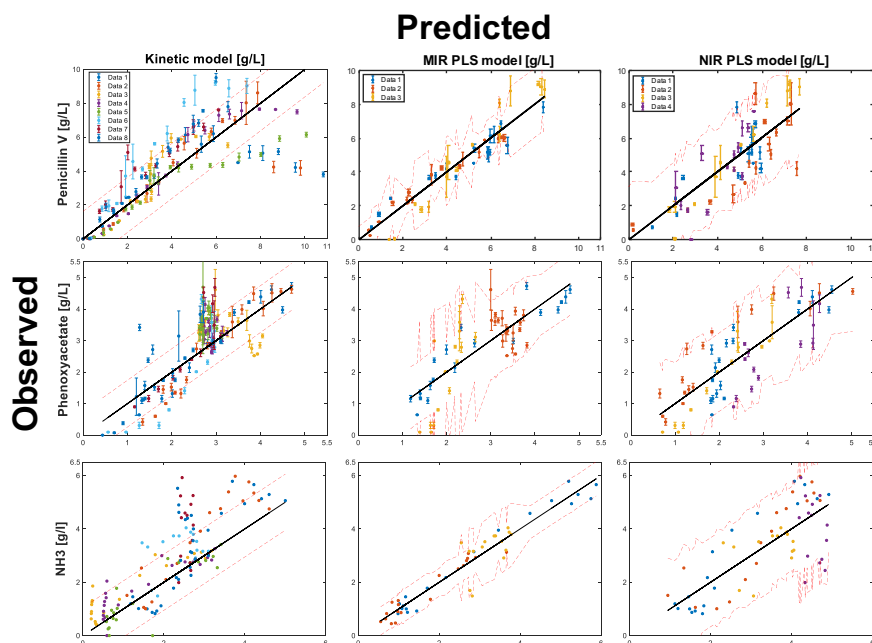


Figure 1: Observed vs. predicted of kinetic model, MIR and NIR PLS model for Penicillin V (RMSE = 1.62; 0.69; 1.33 $R^2 = 0.61$; 0.93; 0.71), Phenoxyacetate (RMSE = 0.74; 0.76; 0.75 $R^2 = 0.59$; 0.62; 0.68) and NH_3 (RMSE = 1.05; 0.41; 1.01 $R^2 = 0.55$; 0.93; 0.58) under usage of historical experiments. Not in all 8 fermentations, IR spectra could be recorded

3.2. Monitoring Results

In Figure 2 prediction results for product and precursor concentrations of an selected process are displayed, whereas the errors are displayed in Table 2. The state observer is able to estimate the biomass concentration, however it fails to estimate the product and precursor concentration correctly as no information of these states are included. By applying the PLS models on the incoming IR spectra good real-time estimates of product,

precursor and nitrogen can be obtained. However, results derived from spectral data are very noisy, outlier need to be removed and the signal needs to be smoothed to obtain meaningful results.

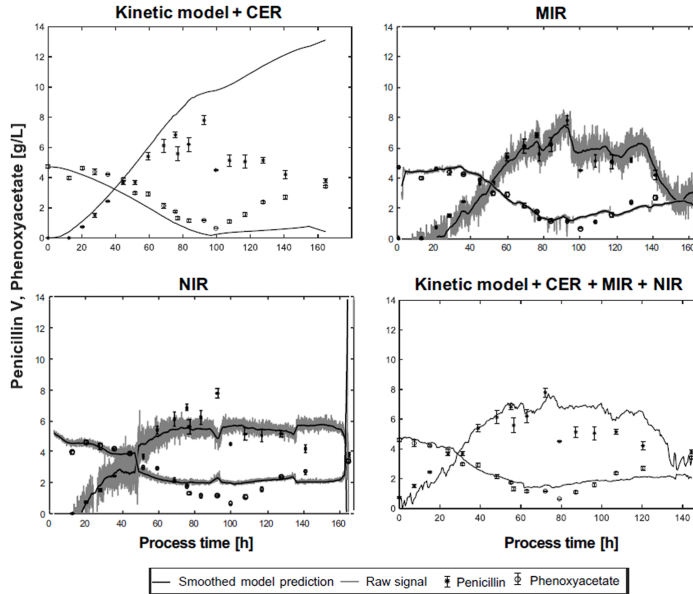


Figure 2: State estimation of validation dataset with kinetic model & CER and MIR & NIR PLS prediction and their combination. Savitzky Golay with a window of 100 datapoints was used to smooth the raw signal.

In order to add needed real-time information to the state observer it can be extended by the IR predictions. This has the advantages that untreated results can be used and by including the measurement errors, redundant measurements derived by the submersed MIR probe and the external NIR sensor can be combined. This combination gives accurate and stable estimates for the entire process.

Table 2: Overall Root Mean Square Errors (RMSE) of different state estimation strategies

	Penicillin V [g/l]	Phenoxyacetate [g/l]	NH_3 [g/l]	Biomass [g/l]
state observer	3.97	1.14	0.90	4.01
MIR (immersion)	0.60	0.50	0.32	-
NIR (non- invasive)	1.11	0.65	0.88	-
state observer + IR	1.15	0.51	0.62	4.26

4. Conclusions

On the example of a *P. chrysogenum* fed batch process penicillin V, product precursor (Phenoxyacetate) and nitrogen (NH_3) concentration could be estimated by invasive MIR

and non-invasive NIR measurements. Through a kinetic model, describing growth, nutrient consumption, product formation and the measurement of the CO₂ production rate, biomass formation during the process can be estimated. The used state estimator, which in our case was a particle filter, is a useful tool for the combination of different and redundant measurements. By including the PLS prediction of the IR spectra, the state observer is able to predict all states accurately. The particle filter hereby filters the measured and partially redundant information and estimates the most probable system states through the kinetic model, giving a solid basis for feedback control.

5. Acknowledgements

This work has been supported by the project “multimodal and in-situ characterization of inhomogeneous materials” (MiCi) by the federal government of Upper Austria and the European Regional Development Fund (EFRE) in the framework of the EU-program IWB2020. Further support was provided by the Christian Doppler Forschungsgesellschaft (Grant No. 171) and the strategic economic- research program "Innovative Upper Austria 2020" of the province of Upper Austria.

References

- M. Aehle, A. Kuprijanov, S. Schaepe, R. Simutis, A. Lübbert, 2011. Simplified off-gas analyses in animal cell cultures for process monitoring and control purposes. *Biotechnology letters* 33 (11), 2103.
- J. M. Ali, N. H. Hoang, M. A. Hussain, D. Dochain, 2015. Review and classification of recent observers applied in chemical process systems. *Computers & Chemical Engineering* 76, 27–41.
- G. Goffaux, A. V. Wouwer, 2005. Bioprocess state estimation: some classical and less classical approaches. In: *Control and Observer Design for Nonlinear Finite and Infinite Dimensional Systems*. Springer, pp. 111–128.
- A. Golabgir, C. Herwig, 2016. Combining mechanistic modeling and raman spectroscopy for real-time monitoring of fed-batch penicillin production. *Chemie Ingenieur Technik* 88 (6), 764–776.
- J. Kager, C. Herwig, I. V. Stelzer, 2018. State estimation for a penicillin fed-batch process combining particle filtering methods with online and time delayed offline measurements. *Chemical Engineering Science* 177, 234–244.
- C. Koch, A. E. Posch, H. C. Goicoechea, C. Herwig, B. Lendl, 2014. Multi-analyte quantification in bioprocesses by fourier-transform-infrared spectroscopy by partial least squares regression and multivariate curve resolution. *Analytica chimica acta* 807, 103–110.
- D. Krämer, R. King, 2017. A hybrid approach for bioprocess state estimation using nir spectroscopy and a sigma-point kalman filter. *Journal of Process Control*.
- P. Luoma, A. Golabgir, M. Brandstetter, J. Kasberger, C. Herwig, 2017. Workflow for multi-analyte bioprocess monitoring demonstrated on inline nir spectroscopy of *p. chrysogenum* fermentation. *Analytical and bioanalytical chemistry* 409 (3), 797–805.
- G. Paul, M. Syddall, C. Kent, C. Thomas, 1998. A structured model for penicillin production on mixed substrates. *Biochemical engineering journal* 2 (1), 11–21.
- D. Simon, 2006. *Optimal state estimation: Kalman, H infinity, and nonlinear approaches*. John Wiley & Sons.
- I. V. Stelzer, J. Kager, C. Herwig, 2017. Comparison of particle filter and extended kalman filter algorithms for monitoring of bioprocesses. In: *Computer Aided Chemical Engineering*. Vol. 40. Elsevier, pp. 1483–1488.
- S. Ulonska, P. Kroll, J. Fricke, C. Clemens, R. Voges, M. M. Müller, C. Herwig, 2018. Workflow for target-oriented parametrization of an enhanced mechanistic cell culture model. *Biotechnology journal* 13 (4), 1700395.
- V. Vojinović, J. Cabral, L. Fonseca, 2006. Real-time bioprocess monitoring: Part i: In situ sensors. *Sensors and Actuators B: Chemical* 114 (2), 1083–1091.

Design of Multi Model Fractional Controllers for Nonlinear Systems: An Experimental Investigation

G Maruthi Prasad^a, A Adithya^a and A Seshagiri Rao^{a,*}

^a*Department of Chemical Engineering, National Institute of Technology, Waranagal - 506 004, Telangana, India*

**Email: seshagiri@nitw.ac.in*

Abstract

Control of nonlinear processes is challenging when compared to those of linear processes. Conventional PID controllers can be used to control nonlinear processes based on a condition that these controllers must be tuned in such a way that they should provide a very stable behaviour over the entire range of operating conditions. In spite of tuning the PID controllers, it still results in a degradation of the control system performance. In order to stabilise nonlinear systems, multi model control approaches are found suitable. Multi-Model Approaches (MMA) rely on the problem decomposition strategy where a nonlinear system is segregated into set of many linear models based on their operating points. These reduced models are used to tune model based PI/PID controllers. In the literature, different methods are proposed to design these controllers in MMA framework and they are all integer order controllers. In this work, fractional controllers based MMA framework is developed for enhanced control of nonlinear systems. Gap metric based weighting methods are used with proper weighting functions to obtain the global controller. The weighting functions are formed by using gap metric to combine local controllers. Three different nonlinear processes (CSTR, conical tank and spherical tank processes) are considered and implemented the proposed methodology. For the purpose of comparison, MMA framework with integer order controllers is considered and it is observed that MMA framework with fractional controllers provide improved closed loop performances. Experimental investigation is also carried out to verify the applicability of the proposed method for level control on conical tank process and it is observed that the proposed method provide enhanced closed loop responses.

Keywords: Multi-model approach, integer order controller, fractional order controller, gap metric, nonlinear system

1. Introduction

In process industries, behavior of most of the systems will be nonlinear and this type of systems mostly have performance degradation by using conventional PID controller. In order to overcome this degradation there are different types of techniques available and one of the most popular techniques which has been consider by several researches is the multi model approach (MMA) Adeniran and El Ferik (2017). This approach divides nonlinear systems into multi linear models sequentially based on the operating points. Controllers are designed by using this linear model and over decades most of the researchers considered integer order controllers only. When integer order controllers are

implemented practically overshoot and resonance are observed and in order to deal such effects fractional order controllers can be used which shows more promising results Podlubny (1999). In this paper an attempt has been made to apply fractional order controllers in order to design a new system called Multi model fractional order controller. This paper presents effectiveness of Multi model fractional order controller and Extensive numerical studies on nonlinear system demonstrate its performance. Section II of the paper describes multi-model approach, gap metric and fractional order controller design. In Section III nonlinear system are studied to demonstrate effectiveness of Multi model fractional order controller. Section IV numerical results and conclusions are presented.

2. Multi Model Fractional controller

2.1. Multi-model approach

The MMA deals with decomposition of nonlinear system into multi linear models based on sequentially steady states and mathematical model is developed for each of the operating range. These models now as a set, can be used as a valid representation of the nonlinear process. These models are further reduced into minimal set using gap metric.

2.2. Gap metric

Recent studies have showed that the most appropriate tool to quantify the difference between different linear systems using metrics based on norms is the gap metric Du et al. (2012); Du and Johansen (2014). The gap metric is calculated based on following formula

$$\delta_g(P_1, P_2) = \max(\vec{\delta}_g^+(P_1, P_2), \vec{\delta}_g^-(P_1, P_2)) \quad (1)$$

Where as P_1 and P_2 are linear models and

$$\delta_g(P_1, P_2) = \inf_{Q \in H_\infty} \left\| \begin{bmatrix} N_1 \\ M_1 \end{bmatrix} - \begin{bmatrix} N_2 \\ M_2 \end{bmatrix} Q \right\|_\infty \quad (2)$$

From eq. (1), the gap metric range is considered as $0 \leq \delta_g(P_1, P_2) \leq 1$. If the value of gap metric is near to 0 a single controller is enough to control two operating regions effectively else it is difficult to use single controller to control the operating regions.

2.3. Fractional Order Controller

Implementation of Fractional calculus which is generalization of Integer order calculus is making a noteworthy advancement. Its significance lies in the fact that practical systems can be better identified as fractional order differential equations instead of integer order differential equations David et al. (2011). Fractional Order PID Controller which is usually described as $PI^\lambda D^\mu$ Controller was introduced by Podlubny (1999).

$$C(s) = K_p + \frac{K_i}{s^\lambda} + k_d s^\mu \quad (3)$$

where K_p is Proportional Gain, K_i is Integral Gain, K_d is Derivative Gain, λ and μ are integral and derivative orders and can be varied between 0 to 2. Non Integer Order Controllers offer more degrees of freedom and by using these controllers for Integer Order

plants, there is more flexibility in adjusting the gain and phase characteristics than using Integer Order controllers. Methods for design of fractional order controllers are discussed in Podlubny (1999); Monje et al. (2008). One such tuning method for Fractional Order PI controllers was proposed by Gude and Kahoraho (2009) in which a performance criteria (J_v) is minimized which is a measure of systems ability to handle low frequency load disturbances. Finally the normalized controller parameters are designed based on normalized dead time τ .

2.4. Multi model integer and fractional order controller

After multi model approach, minimized models are obtained using gap metric. Based on these models, PI values of integer and fractional order controllers are tuned, with the help of IMC technique and Gude method respectively. The global controller is formed by combination of local controllers. The combination is carried out using gap metric weighting function proposed by Du and Johansen (2014).

3. Nonlinear system

Spherical tank, conical tank and isothermal continuous stirred tank reactor(CSTR) are considered to study the behavior of nonlinear process.

3.1. Case study: Spherical Tank System

In a spherical tank process, level (h) is the controlled variable and input flow rate (q_i) is the manipulated variable. Applying mass balance equation, a mathematical model is obtained as

$$q_i - q_o = \pi[2rh - h^2] \frac{dh}{dt} \quad (4)$$

where r is the radius of the spherical tank, q_o is outlet flow rate and α is valve coefficient. Here, R is the resistance of outlet flow and is found experimentally. After linearizing the above Equation by using Taylor series, the transfer function model is obtained as

$$\frac{H(s)}{Q(s)} = \frac{(-K_1/K_2)}{(-K_2)s + 1} \quad (5)$$

where as $K_1 = (\frac{1}{\pi(2rh_s - h_s^2)})$ and $K_2 = (\frac{1}{\pi(2rh_s - h_s^2)})[-2q_{is}(r - h_s) - \frac{\alpha\sqrt{h_s}}{R}(1.5h_s - r)]$

Various steady state values for (h_s, q_{is}), in sequence are considered and the corresponding multi-model transfer functions are derived. Nine different multi linear transfer function models are found. Multi model control schemes states that, the number of linear models for design of controllers should be reduced. This is done by considering the gap metric value ≈ 0.1 and only 3 models are taken as shown in Table 1. Based on these three models, Integer and Fractional PI controllers are designed using the respective methods.

3.2. Case Study: Conical Tank Process

In a conical tank process, the level (h) is controlled by the input flow rate (q_i). It's mathematical model is obtained as

$$q_i - q_o = \frac{\pi D}{12H} \frac{d(h^3)}{dt} \quad (6)$$

Table 1: Reduced models by using gap metric for the nonlinear processes

Spherical Tank		Conical Tank		Isothermal CSTR	
Operating range	Min-imised Model	Operating range	Min-imised Model	Operating range	Min-imised Model
0-15 cm	$M_2 = \frac{0.26261}{330.132s+1}$	0-15 cm	$M_2 = \frac{0.6667}{12.253s+1}$	0-0.5 mole \ L	$M_2 = \frac{0.62834}{21.84s+1}$
15-40 cm	$M_6 = \frac{0.63323}{1194.09s+1}$	15-40 cm	$M_6 = \frac{1.466}{225.68s+1}$	0.5-0.77 mole \ L	$M_6 = \frac{0.32}{11.46s+1}$
40-50 cm	$M_9 = \frac{0.7972}{563.73s+1}$	40-62 cm	$M_9 = \frac{0.9579}{1160.9s+1}$	0.77-1 mole \ L	$M_9 = \frac{0.10417}{3.662s+1}$

Linearizing eq. (6) using Taylors expansion, the transfer function model is obtained as

$$\frac{H(s)}{Q_1(s)} = \frac{\frac{4H}{\pi D h_s^2}}{s + \frac{8q_{is}}{\pi D h_s^2} - \frac{C_D}{2h_s^{5/2}}} \quad (7)$$

where H is height of the tank, D is diameter and C_D outlet valve coefficient. Sequentially different steady state values for (h_s, q_{is}) are considered and derived the corresponding multi-model transfer functions and 12 different multi linear transfer function models as obtained. According to multi-model control schemes, multi models are reduce to the minimum number of local models using gap metric value of 0.1 is considered and only 3 models are retained as shown in Table 1. Based on these three models, the corresponding controller parameter values are tuned.

3.3. Case Study: Isothermal CSTR

An isothermal CSTR, consider a first-order irreversible reaction takes place. The mass balance is

$$\frac{dC_A}{dt} = -KC_A + (C_{Ai} - C_A)u \quad (8)$$

Where reactant concentration(C_A (mol/L)) is controlled variable, input($u = q/V$ (min^{-1})) is the manipulated variable, q ($lmin^{-1}$) is the inlet flow rate and C_{Ai} is the inlet feed concentration(1.0 mol/L) and constant rate k is 0.028 (min^{-1}). Linearizing the above equation using Taylors expansion, the transfer function model is

$$\frac{C_A(s)}{u(s)} = \frac{1 - C_{As}}{s + (0.028 + u_s)} \quad (9)$$

The CSTR model is divided into multi linear model based sequential steady states (u_s, C_{As}) of different operating ranges. Eighteen linear models are found and these are minimized into three model by using gap metric value of ≈ 0.1 are shown in table 1, based on these controller parameters are tuned.

4. Simulation and Experimental Results

Simulation results for spherical and conical tank processes and CSTR are carried out and are given below. Experimental implementation is also carried out for conical tank, the corresponding results are presented here.

4.1. Spherical Tank Process

Comparative results of Multi model integer and fractional order control are implemented in simulation for tracking of different set points of level and the corresponding responses are shown in Figure 1. Quantitative analysis of the spherical tank process has been done and integral absolute error (IAE) values for different set points 10, 30, 45, 35, 15 of integer order control are 32695, 14143, 8940.5, 5475.3, 16853 and fractional order control are 123.55, 2569.9, 2127.4, 579.44, 5512.7. It is observed that multimodel fractional order control approach is efficiently reducing the overshoot and the response is enhanced.

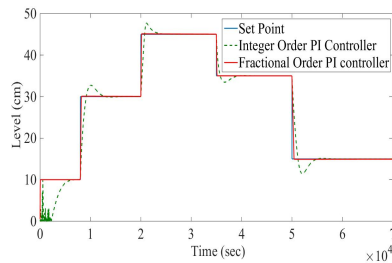


Figure 1: Compared closed loop response of spherical tank process

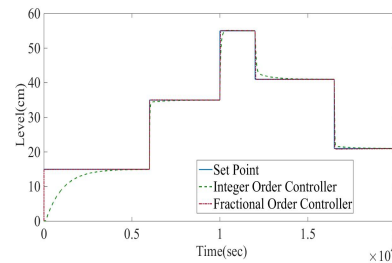


Figure 2: Compared closed loop response of conical tank process

4.2. Conical Tank Process

In the same way, for conical tank also the comparative results of Multi model integer and fractional order control is implemented in the simulation for tracking of different set points of level and the corresponding responses are shown in Figure 2. Quantitative analysis of the conical tank process has been done and IAE values for different set points 15, 35, 55, 41, 21 of integer order control are 1590.4, 91.70, 109.9, 231.64, 123.42 and fractional order control are 4.31, 13.29, 50.14, 37.61, 68.46. Experimental implementation is carried out for this process and response curves are plotted. The Figure 3 shows closed loop response of multi-model integer order controller and Figure 4 shows closed loop response of multi-model fractional order controller. The oscillations observed in Figure 3 (Integer order response) are very low in amplitude and in the case of fractional order controller, these oscillations become miniscule. Quantitative analysis of the conical tank process has been done and IAE values for different set points 15, 35, 55, 41, 21 of integer order control are 70995, 53654, 178050, 60935, 91032 and fractional order control are 862.05, 911.57, 4428.5, 680.81, 897.64.

4.3. Isothermal CSTR

Similarly, for CSTR also the comparative results of Multimodel integer and fractional order control is implemented in the simulation for tracking of different set points of concentration and the corresponding responses are shown in Figure 5. Quantitative analysis

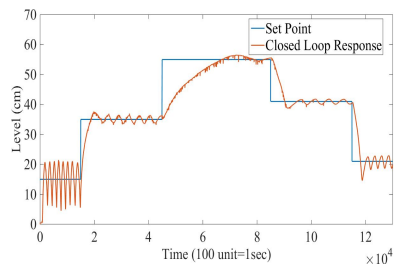


Figure 3: Experimental closed loop response of conical tank process using multi-model integer order controller

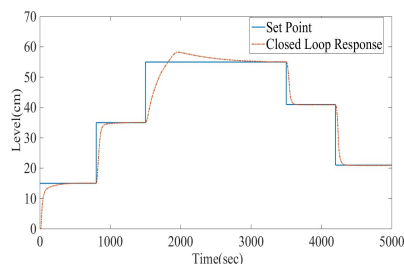


Figure 4: Experimental closed loop response of conical tank process using multi-model fractional order controller

of the CSTR process has been done and IAE values for different set points 0.4, 0.55, 0.85, 0.6, 0.35 of integer order control are 2.71, 0.0872, 0.408, 2.865, 4.3766 and fractional order control are 0.096, 0.0464, 0.2337, 2.865, 4.3766.

5. Conclusion

Multi-model fractional order controller is evaluated for control of nonlinear processes and is compared with multi-model integer order controller. Both the methods are evaluated first by the simulation and then by performing experiments on conical tank process. It is observed that multi model fractional order controller provides better performance when compared to Multi model integer order controller.

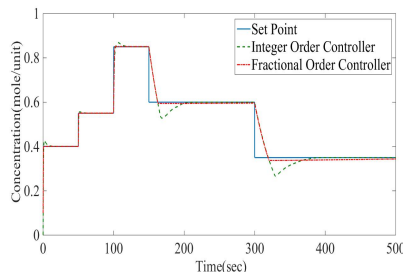


Figure 5: Closed loop response of CSTR

References

- A. A. Adeniran, S. El Ferik, 2017. Modeling and identification of nonlinear systems: A review of the multi-model approach part 1. *IEEE Transactions on Systems, Man, and Cybernetics: Systems* 47 (7), 1149–1159.
- S. David, J. Linares, E. Pallone, 2011. Fractional order calculus: historical apologia, basic concepts and some applications. *Revista Brasileira de Ensino de Física* 33 (4), 4302–4302.
- J. Du, T. A. Johansen, 2014. Integrated multimodel control of nonlinear systems based on gap metric and stability margin. *Industrial & Engineering Chemistry Research* 53 (24), 10206–10215.
- J. Du, C. Song, P. Li, 2012. Multimodel control of nonlinear systems: an integrated design procedure based on gap metric and h_∞ loop shaping. *Industrial & Engineering Chemistry Research* 51 (9), 3722–3731.
- J. J. Gude, E. Kahoraho, 2009. New tuning rules for pi and fractional pi controllers. *IFAC Proceedings Volumes* 42 (11), 768–773.
- C. A. Monje, B. M. Vinagre, V. Feliu, Y. Chen, 2008. Tuning and auto-tuning of fractional order controllers for industry applications. *Control engineering practice* 16 (7), 798–812.
- I. Podlubny, 1999. Fractional-order systems and pi/sup/spl lambda/d/sup/spl mu/-controllers. *IEEE Transactions on automatic control* 44 (1), 208–214.

Modelling and Simulation of Supercritical CO₂ Oil Extraction from Biomass

Rui M. Filipe,^{a,b,*} José A. P. Coelho,^{a,c} David Villanueva-Bermejo,^d Roumiana P. Stateva^e

^a*Instituto Superior de Engenharia de Lisboa, Instituto Politécnico de Lisboa, 1959-007 Lisbon, Portugal*

^b*Centro de Recursos Naturais e Ambiente, Instituto Superior Técnico, Universidade de Lisboa, 1049-001, Lisbon, Portugal*

^c*Centro de Química Estrutural, Instituto Superior Técnico, Universidade de Lisboa, 1049-001 Lisbon, Portugal*

^d*Instituto de Investigación en Ciencias de la Alimentación CIAL (CSIC-UAM), 28049 Madrid, España*

^e*Institute of Chemical Engineering, Bulgarian Academy of Sciences, 1113 Sofia, Bulgaria*

rfilipe@isel.ipl.pt

Abstract

The aim of this work is to model the kinetics of the supercritical CO₂ extraction of oils from biomass, namely from industrial grape seeds and chia seeds. A model introduced by Sovova and Stateva (2015) is used and solved using gPROMS ModelBuilder. The supercritical extraction experiments performed at different temperature, pressure and flow rate conditions, provide the data to the modelling studies and for model parameter estimation, using gPROMS parameter estimation.

The partition coefficient and the maximum oil content corresponding to monolayer adsorption was estimated and the absolute average relative deviation between the experimentally measured and simulated extraction curves for the cases examined is within the range (1-9) %, which may be considered as a good agreement taking into consideration the very complex nature of the systems under study.

Keywords: Grape seeds, chia seeds, supercritical CO₂ extraction, extraction kinetics, mathematical modelling.

1. Introduction

Increasing attention is being drawn to the effective use of waste biomass and vegetal material as renewable resources of high added value compounds with applications in food, cosmetics, pharmaceutical industries, biodiesel production, etc. Grape (*Vitis vinifera* L.) seed biomass contains typically (8-15) % (w/w) of oil rich in long chain polyunsaturated fatty acids (PUFAs) and antioxidants (Bail et al., 2008; Fernandes et al., 2013). Although representing about (20-25) % of the biomass generated by the wine industry, it is still considered a disposable material and rarely valorised. Chia (*Salvia*

hispanica L.) seeds are attracting great attention due to its health beneficial properties and are being studied as a source of protein and dietary fiber. Furthermore, they have a high oil content (20-35 % w/w), rich in PUFAs, mainly the omega-3 α -linolenic acid which represents (60-65) % of total fatty acids (Porrás-Loaiza, 2014).

Supercritical CO₂ extraction (SCE) is known to prevent or minimize the degradation of bioactive compounds due to the comparatively low temperatures applied and oxygen free atmospheres. It also allows obtaining solvent-free products. Unsurprisingly, it is currently establishing itself as the viable and eco-friendly alternative to the use of organic solvents. Yet, kinetic data are not abundant, and, particularly for chia seeds oil extraction they are scarce and superficial.

In view of the above, the aim of our work is to model the kinetics of the SCE of oils from industrial grape seeds, obtained directly from a Portuguese wine industry (Coelho et al., 2018), and from two sets of chia seeds - high oil content (HOCS), and underutilized low oil content (LOCS) seeds, by applying an efficient solution method to a recently introduced kinetics model (Sovova and Stateva, 2015).

2. Methodology

The seeds were prepared prior to extraction. Grape seeds, which were supplied crushed, have been dried for 48 h at 343 K while the chia seeds were cleaned from straws and other extraneous material prior to being grounded and sieved. No other pretreatment was applied. The average particle diameter (d_p) was calculated to be 0.62 mm for the grape seeds and 0.37 mm for the chia seeds.

The SCE of the grape seeds was performed at temperatures of (313 and 333) K, pressures of (20, 30 and 40) MPa and flow rates of (1.8, 2.3 and 2.8) $\times 10^{-3}$ kg \cdot min⁻¹ of CO₂. Regarding the chia seeds, SCEs from LOCS were carried out at (25 and 45) MPa, (313 and 333) K and a CO₂ flow rate of 40 $\times 10^{-3}$ kg \cdot min⁻¹. The extractions of HOCS were performed at 45 MPa, 313 K and several CO₂ flow rates, namely (27, 40 and 54) $\times 10^{-3}$ kg \cdot min⁻¹. The amount of sample used for the experiments was 17 g (grape seeds) and 130 g (chia seeds). A detailed description of the units employed for the extraction of grape and chia seeds can be found, respectively, in the studies reported by Coelho et al. (2018) and Villanueva-Bermejo et al. (2017).

The grape and chia seed oils are very complex mixtures of mainly triacylglycerols (TAGs) with minor amounts of other compounds. Due to this complexity, and in order to reduce the size of the kinetics modelling task, the oils composition is usually being represented by model TAGs. Following the results of the composition analyses, the grape seed oil was represented by triolein (Coelho et al., 2018), while chia seed oil should be represented by trilinolenin. However, considering the lack of any experimental information on the VLE of trilinolenin+scCO₂ and the total lack of data (both experimental and estimated) on the thermophysical properties of trilinolenin, triolein was selected as the model TAG to exemplify the chia seed oil.

To calculate the solubility of the representative TAG in the scCO₂, the VLE of the two-component system (triolein+CO₂) was modelled applying the predictive Soave-Redlich-Kwong (PSRK) cubic EoS (Holderbaum and Gmehling, 1991).

To simulate the extraction curves in terms of yield and composition of the oil extracts for both the grape and chia seeds, the novel model of Sovova and Stateva (2015), which

reflects the complex relationship between kinetics and phase equilibria (solubility), was applied. Although the model was originally developed for multicomponent systems extraction, it remains valid for single component systems too.

This model considers homogeneous concentration in the extractor at both solid and fluid phases and assumes that the extracts are located on the surface of the solid particles. This assumption allows neglecting internal diffusion, which is compatible with finely ground substrates where the diffusion path in the particles is short and the extract is easily accessible, resulting in negligible internal mass transfer resistance. Further details on the model can be found elsewhere (Sovova and Stateva, 2015)

The model was deployed, validated and executed using gPROMS ModelBuilder (Process Systems Enterprise, Ltd.), an equation-oriented modelling and optimisation platform for steady-state and dynamic systems. gPROMS offers an integrated framework where all the tasks can be performed within the same environment, with embedded solvers that can usually complete the simulations without further user input provided that a complete and well formulated model, with the adequate initial conditions, is available.

gPROMS Modelbuilder parameter estimation was used to estimate the partition coefficient (K) for all the cases studied. The maximum oil content corresponding to monolayer adsorption (w_i) was also estimated for the chia seeds cases. gPROMS uses a maximum likelihood parameter estimation problem and attempts to determine values for the uncertain physical and variance model parameters that maximize the probability that the mathematical model will adequately predict the values obtained from the experiments.

In order to compare the fitting accuracy, a standard deviation measure, the absolute average relative deviation, $AARD$, was also calculated after the parameter estimation using Eq. (1), where N is the total number of experimental points, and e_i^{exp} and e_i^{est} - the i -th experimental and estimated point, respectively.

$$AARD = \frac{100}{N} \sum_{j=1}^N \frac{|e_i^{exp} - e_i^{est}|}{e_i^{exp}} \quad (1)$$

3. Results and discussion

Figure 1 shows the experimental and simulated cumulative extraction curves and Figure 2 - the simulated composition profiles for the solid and fluid phases of the SCE of grape seeds oil. The positive effect of the pressure increase on the extraction rate is clearly demonstrated on the yield, while the effect of temperature is not so well-defined. The simulated profiles for solid and fluid phases depicted in Figure 2, where the increase in pressure results in higher extraction rates, are compatible with the behaviour depicted in Figure 1.

For LOCS (Figure 3) analogous effect of the pressure is observed, while the temperature effect on the rate of extraction and on the total amount of extracted oil is more significant. Figure 4 depicts the profiles for HOCS at different scCO₂ flows, with the yield increasing faster for higher flows.

From the analysis of Figure 1, 3 and 4, a steepest ascent in cumulative mass fraction may be observed for chia seeds, indicating that the oil is more readily available than in the in the grape seeds.

The parameter K was estimated for all systems studied, while w_i - only for the chia seeds cases. The values obtained are presented in Table 1. The AARD values obtained ranged approximately from (2 to 9) % for the grape seeds and LOCS, and from (1 to 7) % for HOCS, which should be considered as a good agreement taking into consideration the very complex nature of the systems under study.

The new modelling approach applied incorporates in a rigorous way the interplay between phase equilibria (solubility) and kinetics, and the results obtained demonstrate that albeit the simplifications introduced in representing the grape and chia seed oils, there is a good qualitative and quantitative agreement between the experimental and calculated extraction yields at the SCEs operating conditions examined. It should be emphasized that although the internal diffusion is neglected, the model can still deliver adequate results, providing that the particle size is small, as is the case for the matrix used in this work.

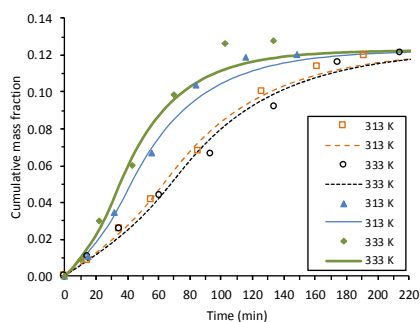


Figure 1. Experimental (symbols) and simulated (lines) extraction curves for grape seeds at different temperatures, $p = 30$ MPa (dashed lines) and $p = 40$ MPa (solid lines) and scCO_2 flow rate of $1.8 \times 10^{-3} \text{ kg} \cdot \text{min}^{-1}$.

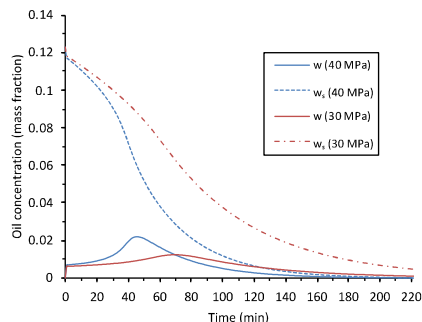


Figure 2. Simulated profile of oil concentration in the grape seeds (w_s) and scCO_2 (w). $T = 333$ K and scCO_2 flow rate of $1.8 \times 10^{-3} \text{ kg} \cdot \text{min}^{-1}$.

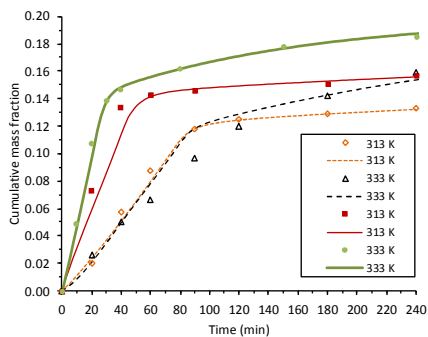


Figure 3. Experimental (symbols) and simulated (lines) extraction curves for LOCS at different temperatures, $p = 25$ MPa (dashed lines) and $p = 45$ MPa (solid lines) and scCO_2 flow rate of $1.8 \times 10^{-3} \text{ kg} \cdot \text{min}^{-1}$.

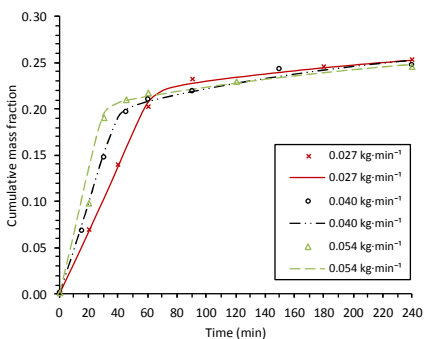


Figure 4. Experimental (symbols) and simulated (lines) extraction curves for HOCS at different at different flow rates. $T = 333$ K and $p = 45$ MPa.

The values of K are directly related with the extraction rate and the values presented in Table 1 follow generically the same trend observed in Figures 1, 3 and 4, namely K increases with the increase of pressure and temperature. Regarding the scCO₂ flow, the trend variation of K is not clear and shows to be system dependent. This behaviour is compatible with the results previously reported by other authors (Honarvar et al., 2013).

Table 1. Estimated values for parameters K and w_i .

System	P (MPa)	T (K)	F (10^{-3} kg·min ⁻¹)	K (kg plant · kg ⁻¹ CO ₂)	w_i	AARD (%)
Grape	30	313	1.8	2.24E-1	-	4.51
Grape	30	333	1.8	2.22E-1	-	8.84
Grape	40	313	1.8	3.65E-1	-	6.73
Grape	40	333	1.8	4.33E-1	-	8.64
Grape	40	333	2.3	5.58E-1	-	6.68
Grape	40	333	2.8	3.46E-1	-	2.16
LOCS	25	313	40	3.22E-3	8.04E-2	4.82
LOCS	25	333	40	1.36E-2	8.04E-2	9.49
LOCS	45	313	40	4.27E-3	5.76E-2	5.64
LOCS	45	333	40	2.47E-2	5.20E-2	2.13
HOCS	45	313	27	2.00E-2	6.01E-2	1.22
HOCS	45	313	40	1.69E-2	8.25E-2	2.47
HOCS	45	313	54	9.28E-3	8.07E-2	6.65

4. Conclusions

This work presents the results of the SCE of biomass from industrial grape seeds, obtained directly from a Portuguese industry without preliminary treatment, and from two sets of chia seeds. The influence of the operating conditions on the extraction yield were analysed in detail and reported.

To simulate the extraction process, a kinetic model assuming that the extracts are located on the surface of the solid particles, thus neglecting internal diffusion, was applied. The solubility in scCO₂ of the oil, represented as triolein, at the temperatures and pressures of interest to both experiments were obtained applying a rigorous thermodynamic framework, which allowed to interweave the respective solubility functions in the mass balance equations.

The model equations were then integrated using gPROMS ModelBuilder. The qualitative and quantitative agreement between the experimental and simulated extraction curves in terms of yields for both the grape and chia seeds oil was good taking into consideration the complex nature of the systems examined. We can also conclude that the model applied can be successfully used in finely ground matrix where the internal diffusion contribution to the extraction phenomena is very small and, thus, negligible.

Acknowledgements

The authors acknowledge the funding received from the European Union's Horizon 2020 research and innovation programme under the Marie Skłodowska-Curie grant agreement No 778168. J. Coelho and R. M. Filipe are thankful for the financial support from Fundação para a Ciência e a Tecnologia, Portugal, under projects UID/QUI/00100/2013 and UID/ECI/04028/2013.

References

- S. Bail, G. Stuebiger, S. Krist, H. Unterweger, G. Buchbauer, 2008, Characterisation of various grape seed oils by volatile compounds, triacylglycerol composition, total phenols and antioxidant capacity *Food Chemistry*, 108, 1122–1132.
- J. Coelho, R. Filipe, M. Robalo, R. Stateva, 2018, Recovering Value from Organic Waste Materials: Supercritical Fluid Extraction of Oil from Industrial Grape Seeds, *Journal of Supercritical Fluids*, 141, 68-77.
- L. Fernandes, S. Casal, R. Cruz, J.A. Pereira, E. Ramalhosa, 2013, Seed oils of ten traditional Portuguese grape varieties with interesting chemical and antioxidant properties, *Food Research International*, 50, 161-166.
- T. Holderbaum, J. Gmehling, 1991, PSRK: A Group Contribution Equation of State Based on UNIFAC, *Fluid Phase Equilibria*. 70,251-265.
- B. Honarvar, S. Sajadian, M. Khorram, A. Samimi, 2013, Mathematical modeling of supercritical fluid extraction of oil from canola and sesame seeds, *Brazilian Journal of Chemical Engineering*, 30, 159–166.
- P. Porras-Loaiza, M. T. Jiménez-Munguía, M. E., Sosa-Morales, E., Palou, A. Lopez-Malo, 2014, Physical properties, chemical characterization and fatty acid composition of Mexican chia (*Salvia hispanica* L.) seeds, *International Journal of Food Science and Technology*, 49, 571-577.
- H. Sovova, R. P. Stateva, 2015, New Approach to Modeling Supercritical CO₂ Extraction of Cuticular Waxes: Interplay between Solubility and Kinetics, *Industrial and Engineering Chemistry Research*, 54, 17, 4861-4870.
- D. Villanueva-Bermejo, F. Zahran, M.R. García-Risco, G. Reglero, T. Fornari, 2017, Supercritical fluid extraction of Bulgarian *Achillea millefolium*, *Journal of Supercritical Fluids*, 119, 283-288.

Immune system modelling in case of a septic shock

Jean Tallon,^a Françoise Couenne,^a Claire Bordes,^a Melaz Tayakout-Fayolle,^{a,*}
Fabienne Venet,^b Guillaume Monneret,^b Patrice Nony,^c François Gueyffier^c

^a*Univ Lyon, Université Claude Bernard Lyon 1, CNRS, LAGEP UMR 5007, 43
boulevard du 11 novembre 1918, F-69100, VILLEURBANNE, France*

^b*Hospices Civils de Lyon, 5 place d'Arsonval 69437 LYON Cedex 03 – France*

^c*Laboratoire de Biologie et Biométrie Evolutive-Equipe Modélisation des Effets
Thérapeutiques, UMR 5558 Université Claude Bernard Lyon1, Lyon, France*

melaz.tayakout-fayolle@univ-lyon1.fr

Abstract

A dynamical pathophysiological model is presented in the case of septic shock. The proposed approach takes into account the environment and the different subsystems. The considered immune system is the blood, the subsystems are leukocyte cells and cytokines. The interactions between blood cells, plasma and the environment are described via mass balances. The transport phenomena between cells and blood and thermodynamic equilibrium are considered. The quantities of pro and anti-cytokines present in the body are combined to propose global information on the inflammatory state of the patient. The proposed model is strongly nonlinear. Simulations showed how the global information evolves after septic shock. In particular, the model has the ability to evolve to alternative homeostatic equilibrium in case of septic shock.

Keywords: septic shock, dynamic modelling, transport phenomena, thermodynamic equilibrium, simulation.

1. Introduction

Homeostasis refers to the ability of living organisms to maintain their internal state constant despite any change in the environment. Sepsis is the body's response to a very strong infectious attack by a pathogen. Septic shock is diagnosed when organ failure is observed with other various clinical symptoms, such as hypotension. The mortality of patients in France with sepsis was 27% in 2016. Worldwide, a person dies from sepsis complications every 4 seconds. Sepsis has been recognized as a major public health problem by World Health Organization in 2017 (WHA resolution, 2017). Alteration of immune homeostasis plays a central role in sepsis pathophysiology. Following the initial pro-inflammatory response leading to organ failure and shock, sepsis and septic shock are associated with the delayed development of immune dysfunctions (Hotchkiss et al., 2013) (Venet and Monneret, 2018). The intensity and duration of sepsis-induced immune alterations have been associated with increased risk of secondary infections and mortality.

However, a more exhaustive understanding of these alterations and of their evolution over time is mandatory and could lead to the elucidation of innovative therapeutic targets and associated companion biomarkers in a personalized medicine approach.

The immune system modelling is not new (Malek et al., 2015), but quickly limited by the number of species.

The system is closed, uniform and thermodynamic or transport phenomena between cells and blood are not considered. The objective of this paper is to improve the knowledge of the homeostasis evolution in the case of septic shock by establishment of dynamical pathophysiological model, to understand mechanisms involved in pro-inflammatory and anti-inflammatory responses and to predict the inflammation level (as shown in Figure 1). Our approach considers the environment and different subsystems. The immune system in this case is the blood, the subsystems are leukocyte cells and cytokine pairs (pro-inflammatory and anti-inflammatory). Cytokines are essential to mechanisms of inflammation and are widely described in the literature. They are released by various cells in the body, such leukocytes, and they induce responses through binding to specific receptors on the surface of target cells. The immune system is open and continuously in interaction with its surroundings. A model considering the previous assumptions has been developed for one cytokine pair, their corresponding receptors and leukocyte cells.

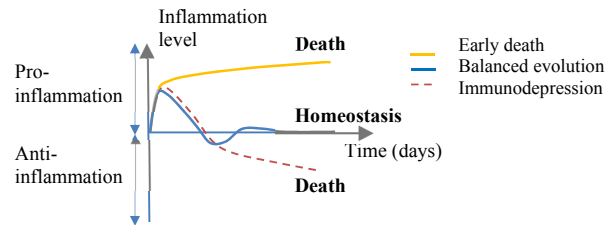


Figure 1: Different scenarios of the supposed evolution of inflammation state of patient

In section 2, assumptions of the model and different material balances are presented. In section 3 simulations of different scenarios of septic shocks are given. Finally, in section 4 we propose conclusion and future work.

2. Model

The objective is to describe the interactions between the cytokines, their receptors, and the leucocyte cells in the blood system. The interaction between the system and surrounding is introduced in the model by constant source terms: cells continually produced by the bone marrow, and cytokines continually produced by tissues and organs.

2.1. Assumptions

The blood system is described with two phases: a fluid phase, and leucocyte cells. The cells are uniformly dispersed in the fluid phase. The blood volume is assumed to be constant. The chosen pair of cytokines is IL10 and IL18 with their associated receptors. All the white blood cells are represented by average leucocyte cells. The receptors are described as being only on the surface of the cells and supposed uniformly distributed. The cytokines and receptors are produced in the cells.

Linear Driving Force model is used to represent the transfer of cytokines from the cell to the blood and the transfer of cytokines from the blood to receptors. The cytokines in the blood are adsorbed on receptors. This adsorption is already described in some existing pharmacokinetic models (Androulakis et al., 2015). Langmuir equilibrium is assumed for the adsorption. The inflammation comes from the variation of the cytokines, which can stimulate or inhibit the leucocytes production as schematically represented in Figure 3.

The adsorbed IL10 and IL18 cytokine on their receptors IL10R and IL18R respectively (see KEGG Pathway Database) can directly trigger the chemical production of the same cytokines and receptors by cells shown in Figure 4.

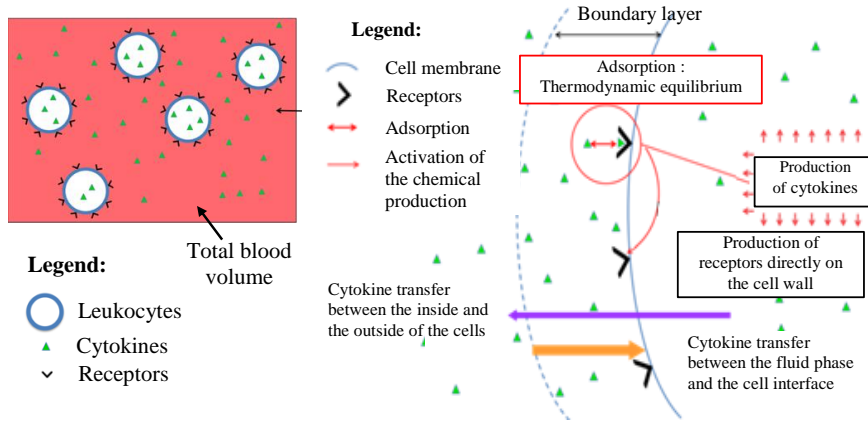


Figure 3: (left) Representation of the blood system and (right) representation of the cytokine adsorption

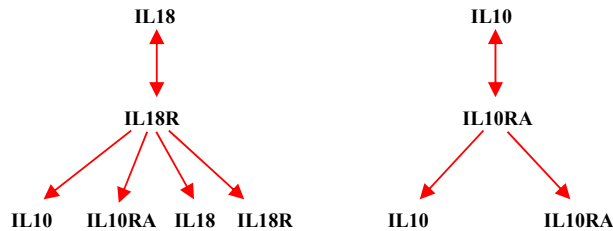


Figure 4 : Schematic representation of the mechanisms of the IL18/IL10 model

2.2. Notations

A and B notations have been chosen for IL18 and IL10 respectively. The adsorbed concentrations of A and B are denoted with index ads. The concentrations of A (mol/m^3) and B (mol/m^3) in the cell are denoted with index c and the ones at the interface with index int. The associated receptors will be denoted R_A (mol/m^3) and R_B (mol/m^3). The expressions of the adsorbed concentrations are given below:

$$A_{ads} = \frac{R_A K_A A_{int}}{1 + K_A A_{int}}, \quad B_{ads} = \frac{R_B K_B B_{int}}{1 + K_B B_{int}}$$

With K_A (m^3/mol) and K_B (m^3/mol) are the Langmuir coefficients.

2.3. Material balances of cytokines

The material balances of A and B in the fluid, at the interface of the cells and in the cells, are as follow:

$$\frac{dV_l A}{dt} = V_c(k_{la}^{intA}(A_{int} - A) + k_{la}^{cA}(A_c - A)) - k_d^A A V_l + S_A(t) \quad (1)$$

$$\frac{dV_c A_{ads}}{dt} = -k_{la}^{intA}(A_{int} - A) V_c \quad (2)$$

$$\frac{dV_c A_c}{dt} = V_c k_A A_{ads} - V_c k_{la}^{cA}(A_c - A) - V_c k_d^A A_c \quad (3)$$

$$\frac{dV_l B}{dt} = V_c(k_{la}^{intB}(B_{int} - B) + k_{la}^{cB}(B_c - B)) - k_d^B B V_l + S_B(t) \quad (4)$$

$$\frac{dV_c B_{ads}}{dt} = -V_c k_{la}^{intB}(B_{int} - B) \quad (5)$$

$$\frac{dV_c B_c}{dt} = V_c k_B B_{ads} + V_c k_{BA} A_{ads} - V_c k_{la}^{cB}(B_c - B) - V_c k_d^B B_c \quad (6)$$

Where V_l (m^3), V_c (m^3) represent the volume of the blood system cells respectively. For cytokine A: k_{la}^{intA} (m/s), k_{la}^{cA} (m/s) represent the mass transfer coefficient between blood and interface and between blood and cell, respectively), k_d^A (s^{-1}) and k_A (s^{-1}) the death and production kinetic constants of cytokine A from A_{ads} , respectively. The same stands for B. k_{BA} (s^{-1}) represents the production kinetic constant of cytokine B from A_{ads} . S_A (mol/s) and S_B (mol/s) are source terms of cytokines from environment.

2.4. Material balances of the receptors at the interface of the cell

$$\frac{dV_c R_A}{dt} = V_c k_{RA} A_{ads} + k_1 \frac{dN_c}{dt} R_A \quad (7)$$

$$\frac{dV_c R_B}{dt} = V_c k_{RB}^A A_{ads} + V_c k_{RB} B_{ads} + k_2 \frac{dN_c}{dt} R_B \quad (8)$$

k_{RA} (s^{-1}), k_{RB} (s^{-1}) and k_{RB}^A (s^{-1}) represent the production kinetic constants of receptor A from A_{ads} , receptor B from B_{ads} and receptor B from A_{ads} , respectively. N_c is the number of cells in the blood. k_1 (m^3) and k_2 (m^3) represent the proportion of receptors A and B, respectively, produced or destroyed induced by the variation of cells numbers.

2.5. Material balances of the cell

Finally, the variation of the number of cells in the fluid is:

$$\frac{dV_l N_c}{dt} = f k_c N_c V_l - k_d^c N_c V_l + S_c(t) \quad (9)$$

With f (mol/m³) the inflammation level function defined as:

$$f(t) = A - \alpha * B \quad (10)$$

The parameter k_c (m³/mol/s) is introduced to adjust the influence of the function f . k_d^c (s⁻¹) is a death kinetic constant for cells. $S_c(t)$ (mol/s) is a source term from the bone marrow.

3. Simulations

We perform three simulations with same parameters: $K_A = 1.5 \cdot 10^{-7}$, $K_B = 9.08 \cdot 10^{-7}$, $k_{la}^{intA} = k_{la}^{intB} = k_{la}^{cA} = k_{la}^{cB} = 10^4$, $k_d^A = k_d^B = 3.3 \cdot 10^{-2}$, $k_d^c = 6.94 \cdot 10^{-4}$, $k_A = 10^7$, $k_B = 0.12 \cdot 10^7$, $k_C = 700$, $k_{BA} = 1.1 \cdot 10^6$, $k_{RA} = k_{RB}^A = k_{RB} = 0.066$, $k_1 = 0.4$, $k_2 = 5 \cdot 10^{-4}$, $V_l = 5 \cdot 10^{-4}$, $V_c = 3 \cdot 10^{-5}$, $A_{healthy} = 3.045$, $B_{healthy} = 3.18$, $\alpha_{healthy} = A_{healthy}/B_{healthy}$, $S_A = 7 \cdot 10^{-3}$, $S_B = \alpha_{healthy} S_A$, $S_c = 7 \cdot 10^{-4}$, $N_{healthy} = 33 \cdot 10^9$ cells, $R_{healthy} = 5.971$. The function f was defined to zero for the healthy patient: $f_{healthy} = 0$. Three different initial (non-stationary) states corresponding to an anti-inflammatory state ($f_0 = -10$) have been used:

IS1: ($A_0 = 3.045$, $A_{0ads} = A_0/10$, $A_{0c} = A_0/10$, $B_0 = 9.18$, $B_{0ads} = B_0/10$, $B_{0c} = B_0/10$, $R_{A0} = 5.971$, $R_{B0} = 7.401$, $N_{c0} = 88.5 \cdot 10^9$),

IS2: ($A_0 = 3.045$, $A_{0ads} = A_0/10$, $A_{0c} = A_0/10$, $B_0 = 9.18$, $B_{0ads} = B_0/10$, $B_{0c} = B_0/10$, $R_{A0} = 5.971$, $R_{B0} = 9.401$, $N_{c0} = 35.5 \cdot 10^9$),

IS3: ($A_0 = 3.045$, $A_{0ads} = A_0/10$, $A_{0c} = A_0/10$, $B_0 = 9.18$, $B_{0ads} = B_0/10$, $B_{0c} = B_0/10$, $R_{A0} = 5.971$, $R_{B0} = 9.401$, $N_{0c} = 82.5 \cdot 10^9$).

A, B, R and N_c were made dimensionless by dividing by $A_{healthy}$, $B_{healthy}$, $R_{healthy}$ and $N_{healthy}$ respectively.

Figure 5 shows dynamic evolution in the case IS1. Figure 6 gives the inflammation function in the case of IS2 and IS3. With IS1 and IS3 the septic shock leads to death of the patient since the inflammation function does not tends to 0. With IS1 conditions the patient reaches a pro-inflammatory state. With IS3 conditions, the patient is initially in an anti-inflammatory state. In case of IS1 and IS2, the cell number is equivalent and high compared to the healthy patient and seems to lead to the early death and immunodepression for IS1 and IS2 respectively. The patient with IS2 initial state begins more initial receptor of anti-inflammatory cytokines that the patient with IS1 initial state. Even though its state (more anti-inflammatory cytokine receptors) seems to be first improved, it finally leads to the patient death. On the other hand, the patient with IS2 state but with a cell number corresponding to healthy state, returns to homeostasis state. It can be noticed that from three different initial conditions we obtain three different steady states. So the model is able to represent the change of homeostasis that appears after septic shock.

4. Conclusion

Very encouraging qualitative results were obtained by the model developed for homeostasis description on the basis of 2 types of cytokines indicating the interest of the proposed approach. However, many cytokines exist and have specific actions. So network modelling will be necessary and essential to better approach the behavior of the inflammation, because there is no species controlling all the others. Each molecule or cell

has its role in the immune system, and none is redundant. This approach will be further investigated. Finally, the simulations have to be confronted with experimental data.

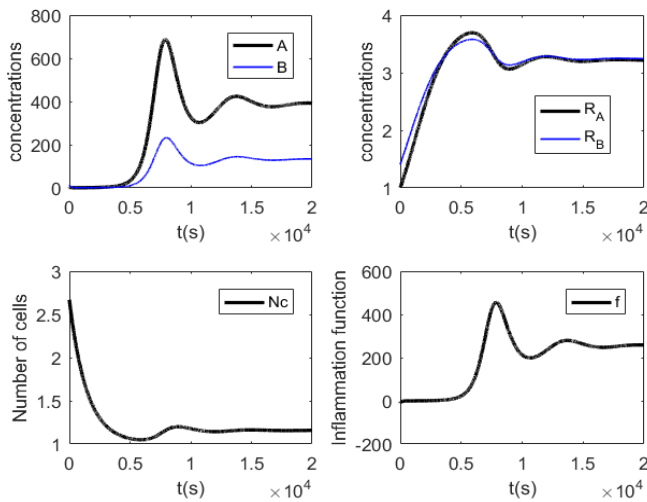


Figure 5: Simulation results with initial state IS1

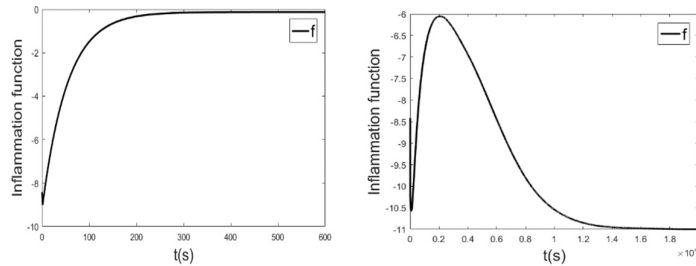


Figure 6: Inflammation function dynamic behaviour with initial state IS2 (right) and IS3 (left)

References

- WHA resolution, 2017, Global Sepsis Alliance. <https://www.global-sepsis-alliance.org/news/2017/5/26/wha-adopts-resolution-on-sepsis>.
- R.S. Hotchkiss, G. Monneret, D. Payen, 2013, Nat Rev Immunol., Vol 13, Is 12, PP 862-74
- F. Venet, G. Monneret, 2018, Nat Rev Nephrol, Vol 14, Is 2, PP 121-137
- H. Malek, M. M. Ebadzadeh, R. Safabakhsh, A. Razavi, J. Zaringhalam, 2015, Comput. Biol. Med. 67, PP 1–12
- I.P. Androulakis, P.D. Mavroudis, S.A. Corbett and S.E. Calvano, 2015, Circadian characteristics of permissive and suppressive effects of cortisol and their role in homeostasis and the acute inflammatory response. Math. Biosci., Vol 260, PP 54–64.
- KEGG Pathway Database : cytokine-cytokine receptor interaction - Homo sapiens

More power to the individual modeller using ontologies

Heinz A Preisig^{a*}, Arne Tobias Elve^a and Sigve Karoliuss^a

^a*Department of Chemical Engineering; NTNU; Trondheim, Norway*

Abstract

Ontology driven process simulation yields a significant improvement not only in terms of accelerating the modelling process itself, but also the quality. Time saving allows for exploring many more alternatives in a shorter time, thus the domain of design for a given process, is readily expanded and quality reduced debugging. To make the use of ontologies successful, one needs to step away from the common data-mining utilisation of ontology, but rather use them to control and guide the modelling process. The construction of the ontology itself is a stage-wise process, where the previously added knowledge is used to control the next stage. From the root definition to the structure of the multi-disciplinary domain, to adding the mathematical description, to designing the controls of the modelling-user graphical interface, the control of constructing the model interactively, to the instantiation and the numerical solution to the visualisation, the ontology is involved at every state improving the overall task equally on every stage.

Keywords: Process Modelling, Automatic Code Generation, Ontology, Graph-based Modelling

1. The Issues

1.1. The Multi-Disciplinary Challenge

Defining modelling as mapping a physical process into a digital twin, being a mathematical model that is realised on a digital device, the modelling activities of the typical chemical engineers would traditionally imply the modelling of unit operations and their combination into plants. Most of the modelling is centred around steady-state processes, with dynamic models mostly being used for control-related activities such as controller design, tuning and testing on a digital plant model. By also allowing for human-in-the-loop then this would also include the operating training with the human acting as a controller, mostly a supervisory controller.

Due to the fast development of computing, both on the hardware and the software side, the use of detailed models in the chemical engineering is rapidly increasing thereby enabling the handling of more and more complex digital twins of our physical plant object. The development affects all disciplines, and with the increasing capabilities, the demand for multi-disciplinary modelling activities is equally rapidly expanding.

Disciplines tend to live their own life generating and solving their problems. The call for interdisciplinary activities requires the integration of the respective software tools and

puts high demands on the users. Many companies have been or are in the process of establishing interdisciplinary modelling groups with the objective to increase the coverage of their modelling activities.

1.2. The Customer Challenge

The software users are primarily facing the need for broader knowledge. Disciplines tend to live their own life, for various reasons, but not at least because of the sheer volume of knowledge required for an individual to become functional in the discipline-specific domains. The users want to have the models to cover a broader range of scales and application domains. A prime example is the utilisation of material models, which has the simple objective to eliminate a large portion of the experimental work required to determine the properties of components but mainly of mixtures. The problem is easy to visualise: a mixture of 2 components covering the range of their concentration range will cover the whole feasible mixing range. Assuming it to cover the full range, thus from pure A to pure B, and performing an experiment in intervals of 10 % one needs 11 experiments to cover the range. With 3 components, this results in 66 experiments, thus naturally multiplying with the number of components and the reduction of the intervals.

The potential substitute is to model the mixture with molecular modelling tools. Programs such as COSMO-RS (Klamt, 2018), LAMMPS (Plimpton, 1995) and suits like MaterialStudio™ are increasingly used to estimate physical properties. Despite having made significant progress on the user-friendliness, these programs typically have a steep learning curve as well as demanding a level of familiarity with the underlying theory to interpret the results. This applies equally to the next upper domain of granularity, the mesoscale, thus all those scales that lie between the molecular level and the macroscopic level whereby macroscopic refers to a scale that captures the dimensions of the product being modelled. The discipline-dependency is probably strongest on both ends of the scale, and weakest in the middle.

Even in the case where one succeeds to assemble a suitable team, the next barrier is the software. The programs, when not in-house developed, need to be evaluated and purchased or licenses must be obtained and maintained. This obviously requires money for the purchase or licence, but it also requires people who administrate and operate the software and the required hardware facilities.

1.3. The Provider Challenge

The customers are asking for integrated simulation environments that make it possible to predict a product based on the complete history being based on the computational integration of all scales. Whilst feasible to link essentially all the scales into a multi-scale modelling environment as was shown in the MoDeNa EC Framework 7 project, the demand on the people is enormous. Having a specialist in the consortium and intense communications are essential. Less of a problem was the construction of a software platform that allows simulating processes including the full range from quantum mechanics for kinetics to mechanical properties of a polymerised polyurethane foam. Having an experienced senior leader of the latter development proved to yield a solution within two years.

The customer is asking for a simple-to-use environment, preferably a graphical interface

that allows the definition of simulations¹ graphically. This implies that the provider is integrated into a platform, which knows about the different "programs" and which knows on how to combine the programs to generate the desired solution to a user-specified problem.

Technically, this implies that this platform knows about the different "programs" that provide solutions to specific problems, which for the time being we term *solvers*. The platform thus requires knowledge of the available solvers as well as the required data inflow and outflow. It also implies that these *solvers* can be connected by a piping mechanism, meaning that the data from one *solver* can be streamed as input to another. The mechanism is thereby not essential for the user. It may be realised as a data stream or may be passed through a file even with intermediate processing integrated. As long as the mechanism is not time limiting the specifics of the integration are of no concern to the customer. This also applies to the *solvers* being linked to the relevant databases. The dream, and thus the task, is to construct the platform such that it can provide this level of convenience and beyond – it should also advise on what to use and how to use all specific to the problem domain relevant to the customer.

2. Controlling the Modelling Processes using Ontologies

Ideally, the platform acts as an adviser and contracted builder of solutions to a domain of problems spanning over a specified set of disciplines. This can range from physics quantum mechanics to mechanical product properties to controlled unit operations, plant models, performance analysis, nearly anything that let itself capture in a mathematical model.

2.1. Simulation – the Core

Simulation is the core operation, whereby *simulation* is the task of computing the response of a mathematical representation of the plant, the mathematical model, to external excitations. For example, what is the effect of changing raw product quality on the product, what is the effect of changing the energy input into a device, the mass flow to be handled by a plant etc. Simulation is also the core of process design, where the design parameters are optimised based on the objective to meet defined production goals, like concentration and mass flow, whilst minimising waste and energy consumption.

A single-block simulation will capture the complete behaviour in a set of equations, which may be very large indeed and solve these equations using suitable methods. In contrast, a multi-scale, multi-block simulation will solve the problem by solving the blocks sequentially or more generically in a logic-controlled sequence. The MoDeNa project is an excellent example, where polyurethane foam was modelled over the full range from quantum to mechanical properties, which also lead to the definition of a standard for modelling processes (CEN workshop committee, 2018) .

Simulations are also the core of controller tuning and performance checking before implementing them on an actual plant. Operating training tests the operator as a human-in-the-loop, a concept which expands to reaction training in accidents. The latter is very much the same as the flight simulator training machinery for pilots.

¹The term *simulation* is here used generically implying all operations that lead to the execution of a simulation.

2.2. Ontology – the Tool

The core of the platform provides the means to specify the problem. In accordance to the MODA (CEN workshop committee, 2018) a graphical interface could provide the means to define the problem interactively as a directed graph, where the nodes represent the computational tasks, some of which are solvers, some of which provide input convert and process output from the various solvers.

2.2.1. Base Ontology

The design philosophy has the main aspects of (i) **small is beautiful** constructing first of all the ontology from a minimal set of classes and a (ii) **context-free approach** constructing mathematical models named by the ontology in the (iii) **state space**.

The first lead to a high-level abstraction of a generic "process" or "system", namely any process/system is represented as a directed graph in which discipline-specific tokens are "living". The nodes/vertices represent the capacities for the tokens, whilst the arcs/edges represent the transfer of tokens, thus model the interaction. The base ontology captures the multi-disciplinary domain into a tree of ontologies where each node in this tree inherits the parent nodes completely. The disciplines are thus split hierarchically into sub-disciplines. A simple example is given in Figure 1. This represents the first step in the construction of the ontology. It allows to control the definition of the *base component models* for each specified knowledge domain whilst providing the hierarchical structure of the different domains. The *base component models* are the mathematical models for the node/vertice and the arc/edge behaviour in the respective domain-specific graphs. For example for process engineering, thus the continuous domain of physical systems, this may be a lumped system for a node giving equations for the conservation of mass, species mass and energy. For the arcs it may be the transfer of mass with the mechanism *convection* or the mechanism *diffusion*, to mention two.

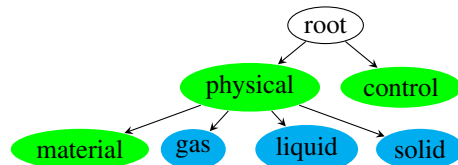


Figure 1: A two-discipline ontology tree

2.2.2. The Multi-Network Framework

A different view is given in Figure 2, which indicates the multi-network for an unspecified example showing the nature of interactions: the intrafaces transfer tokens between subdomains, whilst interfaces transmute tokens from one type into another one. For example, a physical phase interface transfer tokens (energy, mass etc.) whilst the control system observes the state of the physical system and manipulates the physical valve position.

The approach gives an apparent meaning to both types of interaction, at the same time allowing for control of the node connections inside a domain and between domains. For the *interfaces* in the control case, it is the measurement on one side, whilst it is the simplified representation of a set of physical components that convert a control output signal into a valve position. For the *interface* to a material model, it is typically the canonical variables

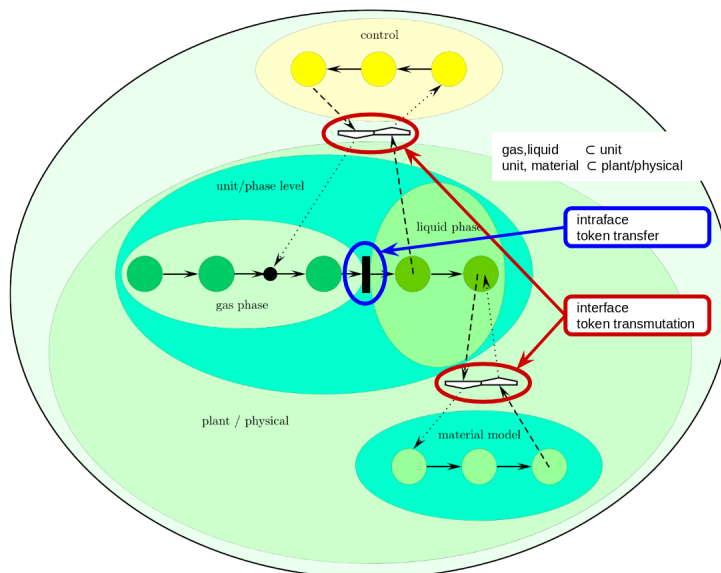


Figure 2: Multi-network view with intra- and interfaces for token transfer & transmutation

of the energy representation whilst it is a physical property that is reported back. If the *interface* connects to a molecular simulation, the one side is typically a lifting whilst on the other side is a homogenisation.

2.2.3. Equations

The equations are appended to the ontology following the rule that they are inherited into all the branches. Thus the node representing the physical systems is populated with the basic conservation principles, whilst the frame variable, time, is in the root node for dynamic systems. The spatial coordinates, being also physical frame variables, are added to the node of the physical system. The population of the ontology with variables and equations is based on the **state-space approach**. The definition starts with the state and the constants as well as the incidence matrix capturing the model's network structure. The tokens in the nodes define the states, thus state variables are defined accordingly in the base ontology. They, together with the constants, define the physical units. Derived quantities can only be defined based on already defined quantities leading to a lower-diagonal definition space, which is also always closed and complete (Preisig, 2010). This provides control not only about the units, but also the indexing for nodes, arcs and tokens. This ensures complete control over the structure of the equation definition. When combined with the ontology it also enforces completeness of the model as an index-one simulation problem with a given sequence in which the equations must be evaluated.

The definition of the equations is done using a parser, the description of which lies outside of the scope of this paper. The parser generates an abstract syntax tree (Elve and Preisig, 2018). Compilation then only requires a set of target-specific templates that implement the syntax of the target language for the basic operations and functions. This can readily be extended to accommodate user-specified functions.

2.2.4. Model Construction

A graphical editor provides the interface for the modeller, the user that builds the process models based on a given ontology. The interface controls the user's input, ensuring that it is consistent with the context provided by the ontology. It makes it impossible to make mistakes that contradict the structures defined in the ontology. The editor allows for a hierarchical definition of the model, to allow for capturing complex models essentially without any limitations than basics of computing, such as the upper limit of an integer for the counter of model elements.

The user only specifies his view on the model topology by specifying the nodes, their dynamic and distribution nature and the arcs as token transfers including their nature, namely the transfer mechanism being modelled. The remaining part is automatically added to the model via a bipartite graph analysis operating on the equation/variable graphs of the respective domain specific equation set.

3. Achievements

- Tools to define a hierarchical multi-disciplinary ontology
- Equation inclusion tool that is controlled by the ontology and constructs lower-triangular equation systems for the discipline-specific base components describing the capacity and transfer properties for all discipline-specific properties.
- Complete control over connecting discipline-specific domains.
- Proper handling of subdomains including the transition over scales and from particulate to continuous domains
- Result is index one differential algebraic or partial differential algebraic systems of equations conserving the model structure, which can be utilised in the solvers.
- Complete separation of model structure from behaviour description.
- Latter allows the implementation of model reduction algorithms that are based on order-of-magnitude assumptions.
- Time/length-scale motivated model reduction is facilitated as an operation on the structure, thus affects only the index sets, not the behaviour equations.
- Complete documentation of the model, structure, equations and all assumptions.
- For simulation, the initialisation is clearly defined.
- Explicit implementation of global boundary conditions.
- Highly efficient modelling tool – a reactor in 5 minutes...

References

- CEN workshop committee, 2018. Materials modelling - terminology, classification and metadata.
URL ftp://ftp.cencenelec.eu/CEN/Sectors/TCandWorkshops/Workshops/WS%20MODA/CWA_17284.pdf
- A. T. Elve, H. A. Preisig, 2018. From ontology to executable program code. *Comp & Chem Eng.*
URL <http://www.sciencedirect.com/science/article/pii/S0098135418309311>
- A. Klamt, 2018. The cosmo and cosmo-rs solvation models. *WIREs Comput Mol Sci* 8, 1–11.
- S. Plimpton, 1995. Fast parallel algorithms for short-range molecular dynamics. *J Comp Phys* 117, 1–10.
- H. A. Preisig, 2010. Constructing and maintaining proper process models. *Comp & Chem Eng* 34(9), 1543–1555.

Optimal Operation and Control of Heat-to-Power Cycles: a New Perspective using a Systematic Plantwide Control Approach

Cristina Zotică^a, Lars O. Nord^b, Jenő Kovács^c and Sigurd Skogestad^{a*}

^a*Norwegian University of Science and Technology (NTNU), Department of Chemical Engineering, 7491, Trondheim, Norway*

^b*Norwegian University of Science and Technology (NTNU), Department of Energy and Process Engineering, 7491, Trondheim, Norway*

^c*University of Oulu, Intelligent Machines and Systems Research Unit, POB4300, Oulu, Finland*

**sigurd.skogestad@ntnu.no*

Abstract

The present control solutions for power plants¹ have been developed to a level where it is difficult to make significant performance improvements using more advanced and systematic control policies, such as model predictive control, unless one has a clear definition of the overall control problem. Hence, the objective of this work is to make a first step in the direction of systematically defining the optimal operation and control problem for power plants. We use a systematic plantwide control framework to analyze a simple heat-to-power steam cycle with a single pressure level and a drum boiler. We evaluate two typical economic modes: I) given plant load, and II) given heat input. We determine that after fulfilling controlling the active constraints there are two unconstrained degrees of freedom left that can be used to achieve optimal operation.

Keywords: Plantwide control, power plant operation, power plant control, steam cycle

1. Introduction

The objective of this work is to provide a new perspective on optimal operation and control of heat-to-power cycles by viewing it from the more general setting of plantwide control. To the best of the authors knowledge, this procedure has so far mainly been applied to chemical plants, and it is yet to be applied to the steam side of heat-to-power cycles. Power plant control systems have been developed by industrial practices over many years, and it is not obvious what are the actual specifications and degrees of freedom. Moreover, power plants contribute to the electric grid stability, which may have priority over optimal operation of the plant itself.

In this paper we analyze this systematically, in the framework of plantwide control, and the goal is to find a control policy, preferably a simple one, which stabilizes the plant on a short time scale (regulatory control), and achieves near-optimal operation on a longer time scale (supervisory control).

The rest of the paper is organized as follows: in Section 2 we present the plantwide procedure; followed by applying it to the water side of a power plant in Section 3; presenting the resulted control structures and operation modes in Section 4 and making the final remarks in Section 5.

¹In this work, the terms heat-to-power cycles and power plants are used interchangeably.

2. Plantwide control procedure

The typical control hierarchy in a process plant is illustrated in Figure 1. It is decomposed based on time scale separation into several simpler layers: scheduling (weeks), site-wide optimisation (days), local optimisation (hours), supervisory control (minutes) and regulatory control (seconds). The layers communicate by sending the process measurements upwards (i.e. from the lower to the upper layers), while the setpoints for each layer are given by solving an optimisation problem in the upper layer (Skogestad, 2004). The procedure consists of a top-down analysis concerning optimal steady-state operation, and a bottom-up analysis targeting the lower regulatory control layer structure. In this work, we focus on the steady-state top-down analysis which involves the following steps (Skogestad, 2004):

Step 1 Define the optimal economic operation (cost function J and constraints).

Step 2 Identify the steady-state control degrees of freedom (DOF) (i.e. manipulated variables that are the setpoints for the lower layers). Use a steady-state model to find the optimal operation for the expected disturbances.

Step 3 Based on the previous step, select the control variables (CVs). Always control the active constraints, and decide to which process variables to allocate the remaining DOF.

Step 4 Select the location of the throughput manipulator (TPM), i.e. choose where to set the production rate. This is a dynamic issue, but with economic implications.

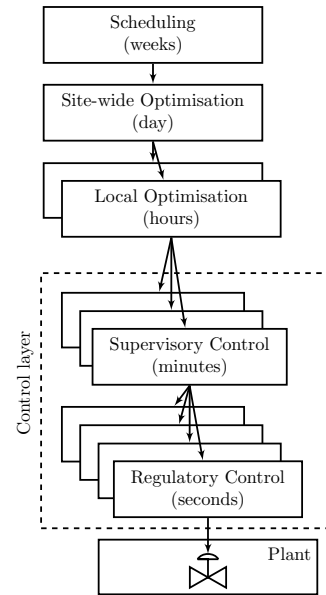


Figure 1: Typical control hierarchy in a process plant.

3. Plantwide control applied to a simple heat to power cycle

3.1. Process Description

We consider the steam side of a heat-to-power cycle with a drum boiler and a single pressure level, as shown in the process flowsheet in Figure 2. In the boiler, there are three physically independent heat exchangers (e.g. economizer (ECO), evaporator (EVAP) and superheater (SH)) dedicated to well defined regimes such as heating of liquid water to or close to boiling point, evaporation and superheating. The superheated steam is expanded in a condensing type turbine, which drives a generator connected to the electric grid. We choose the drum configuration over a once-through boiler (with a single heat exchanger) because it is most common in operating power plants. Further, the drum has the advantage of energy storage which can provide additional operational flexibility.

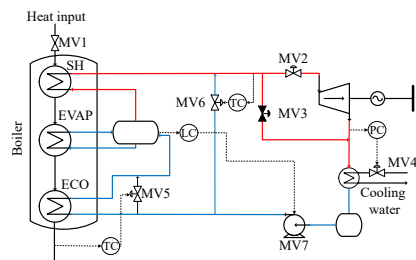


Figure 2: Flowsheet of a power plant with a drum boiler and one pressure level. MV1 and MV2 are the two remaining degrees of freedom considered in this paper. Liquid water is in blue and vapor in red.

3.2. Top-down analysis

We proceed by applying the top-down analysis to the described process.

Step 1. The plant has two operational objectives. On a slow time scale (steady-state) it should achieve the economic optimum, while on a fast time scale it contributes to the grid stability. Due to the time scale separation, these objectives are decoupled. However, the grid stability requirement may impose a back-off from the maximum power production. We define the objective cost function to be minimize the negative profit, given by Eq.1.

$$J = -(p_W W + p_Q Q - p_F F - p_U U) \quad [$/s] \quad (1)$$

Here, W [J/s] is the produced power, Q [kg/s] is the produced steam (if any), F [J/s] is the heat input source, U [kg/s] are the utilities, and p [\$/kg] or [\$/J] is the price of each. As we consider an operating plant, capital costs, personal, and maintenance costs are not included. The cost function should be minimized subject to satisfying a set of constraints, related to products specifications, safe operation and environment. Typical constraints for a heat-to-power cycle include:

- C1 Superheated steam pressure and temperature (e.g. $T \leq 550$ °C, $P \leq 200$ bar to minimize thermal and mechanical stresses and extend the operating life).
- C2 Condenser pressure should be low to maximize the pressure ratio in the turbine, but also above a minimum threshold to minimize condensation on the last turbine blade and reduce erosion (e.g. $P \geq 0.01$ bar).
- C3 Exhaust gas temperature should be low to minimize heat losses, but above the dew point to prevent corrosion (e.g. $T \leq 100$ °C).
- C4 Drum level (stabilizaion and safety).
- C5 Requirement to participate in grid frequency regulation (some plants).
- C6 Fixed turbine speed (equal to the grid frequency, e.g. $n = 50$ Hz in Europe). For this reason, the turbine speed is not a degree of freedom for operation.

In addition, there are operation constraints on the combustion side (e.g. O_2 , CO_2 or NO_x percentage in the flue gas or furnace pressure for combustion power-plants), but these are not relevant for the purpose of this study of the water side.

Step 2. Table 1 shows the degrees of freedom, main disturbances and control variables including the active constraints (a subset of the operational constraints from *Step1*). Here, the active constraints are determined based on engineering insight. The MVs are also shown in Figure 2.

Table 1: Manipulated, disturbances and controlled variables

Manipulated variable	Disturbance	Controlled variable
MV1: Heat (fuel) input	DV1: Quality of heat input	CV1: Power
MV2: Steam turbine valve	DV2: Grid frequency (Load)	CV2: (Live) Steam pressure
MV3: Turbine bypass*	DV3: Cooling water temperature	CV3: Drum level
MV4: Cooling water		CV4: Steam temperature*
MV5: Economizer bypass		CV5: Condenser pressure*
MV6: Feedwater bypass		CV6: Exhaust gas temperature*
MV7: Feedwater pump		

* Active constraint (at steady-state) controlled in Figure 2.

Step 3. We want to select control variables such that desired optimal operation is maintained even when disturbances occur. Firstly, all the active constrains need to be controlled, and one degree of freedom is used to control each of them. One possible pairing for the identified constraints is

shown in Figure 2, and is: control of steam temperature with MV6, gas temperature with MV5, condenser pressure with MV4, and the bypass MV3 should be closed. Further, the drum level can be controlled with MV7. The turbine speed is usually controlled by changing the steam mass flow using MV2. In this case, the setpoint given to the speed controller becomes a new degree of freedom instead of the valve position. In practice, this is often called *droop control*. In practice all turbines have droop control (Kurth and Welfonder, 2006). Note that the pairing of MVs and CVs (here, the active constraints) can be different, and that only the number of the remaining degrees of freedom is important for this step. We now have two degrees of freedom to use for optimal operation: the heat input MV1 and the and the speed controller setpoint MV2.

3.3. Droop Control

Droop control is commonly used to proportionally allocate the load between electrical generators running in parallel, to avoid a scenario where the load is taken by only one of them (Lipták and Bálint, 2003). This is a proportional controller, with a gain of typical 3 %/‰ to 10 %/‰. In droop control, there is a fast MV (i.e. MV2, turbine valve), and a MV with a slow effect (i.e. MV1, heat). For example, when the turbine speed decreases, the droop controller acts by opening MV2, which increasing the steam mass flow. This can be sustained on a long term only if the heat increases as well. Figure 3 shows an example of 4 %/‰ droop, i.e. a change of power of 100 %/‰ gives $50 \cdot 0.04 = 2$ Hz change in turbine frequency setpoint (Anderson and Fouad, 2003).

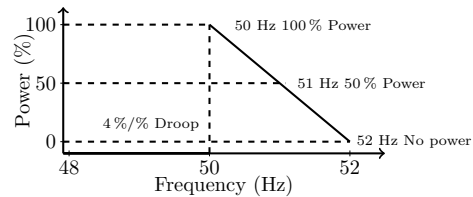


Figure 3: Droop characteristics of 4 %/‰.

Step 4. The location of the throughput manipulator depends on the type of power plant, and we can identify two cases (i.e. economic modes) (Skogestad, 2004):

- Case I** The load is the throughput manipulator and optimal operation means maximizing the fuel usage (efficiency) (i.e. the plant is required to participate in the grid frequency regulation, or to supply utilities to a downstream process).
- Case II** The heat input is the throughput manipulator and optimal operation implies maximizing production (load). This case applies when the heat input is cheap, or “free” (e.g. solar or heat recovery from a gas turbine).

4. Control structures and operation modes

The standard industrial control structures are boiler driven, turbine driven, floating pressure and its variation, sliding pressure (Welfonder, 1999). However, if one disregards the common industrial practices for power plant control, alternative control structures can be proposed. For example, using valve position control (VPC), or both a P and a PI controller with a MID-selector. In the following, we only show the pairing options for the two remaining degrees of freedom (MV1 and MV2), and we assume that the inner turbine speed controller is active. We start with Case I.

4.1. Floating pressure operation

One degree of freedom is used to keep the throughput manipulator to its specification. The simplest options is to use MV1 to control the power output, and have MV2 fully open to minimize throttling losses. This structure is called floating pressure because the live steam pressure is left uncontrolled, as shown in Figure 4a. However, when a constraint on the maximum allowed pressure is reached, and the set of active constraints has changed, we have to give-up another constraint that is less important (Reyes-Lúa et al., 2018). In this case, we have to use the steam turbine bypass (MV3) as a degree of freedom. The disadvantage is a slow time response for load changes.

4.2. Boiler driven operation

To improve the response time of the system, one should control another intermediate variable. The only option is to keep the live steam pressure at a given set-point. The result is the boiler driven control structure, shown in Figure 4b. The output power is controlled with MV1, while the live steam pressure is controlled with MV2. This structure has the advantage that it dynamically responds faster to a change in load by utilizing the energy stored in the system, which comes at an expense of not utilizing the heat input at the maximum. Though it has a faster response compared to the floating pressure, the system still has a large time constant from MV1 to the power output, and the overall response is slow.

4.3. Turbine driven operation

The reverse pairing is turbine driven, as illustrated in Figure 4c. The live steam pressure is controlled with MV1, while the power output is controlled with MV2. It also has the advantage of utilizing the drum and the superheater energy storage, and the response time to load changes is faster. However, it also does not efficiently utilize the heat input due to valve throttling losses.

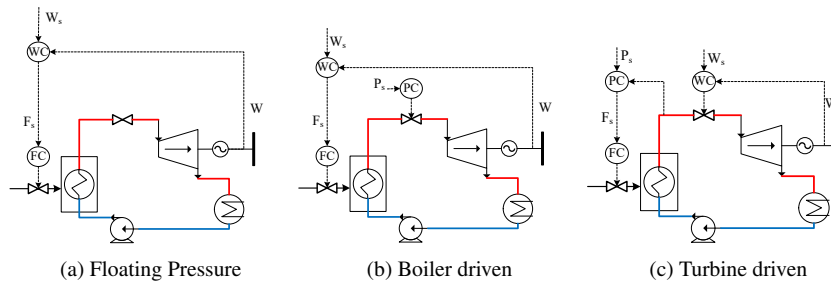


Figure 4: Control structures for three operation modes for a simple heat-to-power cycle.

4.4. Sliding pressure operation

Sliding pressure is when the pressure setpoint is adjusted online, usually for the turbine driven operation mode. In this case, the power plant can participate in the primary frequency control, at the expense of having to back-off from optimal operation and have MV2 partially open (e.g. 90 %) (Weissbach et al., 2006). The cycle efficiency decreases due to throttling losses in the steam valve, but it allows the power plant to have an energy backup that can be dynamically used by fully opening the valve, and participate in the grid frequency control. However, assuming an isenthalpic expansion through the valve, the steady-state effect will be small. In practice, it is common to have a pressure controller with a varying setpoint given by a master controller in a cascade structure that receives the load as input, as shown in Figure 5a (Klefenz, 1986). Here, the pressure setpoint is changed based on a model that has the steam mass flowrate as input and the pressure setpoint as output.

Valve position controller. The conventional sliding pressure control structure can be improved by adding a valve position controller to bring back MV2 to its nominal opening (at steady-state) after it has dynamically contributed to grid frequency regulation, as shown in Figure 5b.

MID selector. We use both MV1 and MV2 to control the power, and the pressure is floating, as illustrated in Figure 5c. Here we use one P-controller, and one PI-controller because we can have only one integral action in a two-inputs one-output system. When pressure becomes an active constraint (i.e. at the minimum or maximum), we use a MID selector to control it using MV1.

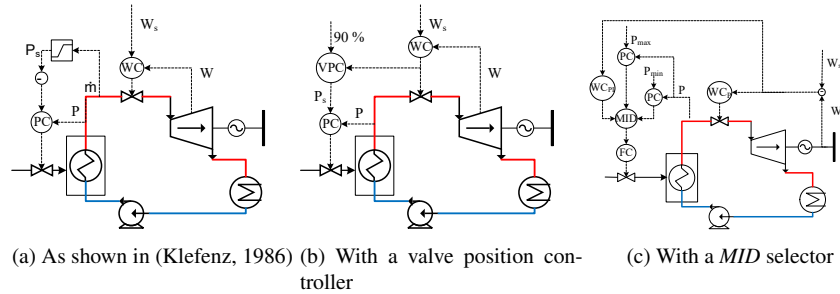


Figure 5: Control structures for sliding pressure operation mode

4.5. Case II - the heat input is the throughput manipulator

From a steady-state point of view, there are no degrees of freedom left to control the power. However, the turbine bypass can be used to reduce the power produced by decreasing the steam mass flow. However, the efficiency of the cycles will also decrease. Ideally, one should make use of energy storage solutions of superheated steam for the situations when more steam can be produced than is needed. This is an attractive idea for power plants using solar energy, especially since the maximum solar power is at midday, when the electricity market demand is lower.

5. Conclusions and final remarks

We have systematically identified the operational objectives, operational and environmental constraints for a heat to power cycle. The degrees of freedom left are MV1, the heat input, and MV2, the steam turbine valve. Now that we have systematically defined the optimal operation and control problem for power plants, it becomes easier to make improvements using more advanced and systematic control policies, such as model predictive control.

6. Acknowledgment

This work is partly funded by HighEFF Centre for an Energy Efficient and Competitive Industry for the Future. The authors gratefully acknowledge the financial support from the Research Council of Norway and user partners of HighEFF, an 8 year Research Centre under the FME-scheme (Centre for Environment-friendly Energy Research, 257632/E20).

References

- Anderson, P., Fouad, A., 2003. *Power System Control and Stability*, 2nd Edition. Wiley.
- Klefenz, G., 1986. *Automatic Control of Steam Power Plants*. Bibliographisches Institut.
- Kurth, M., Welfonder, E., 2006. IMPORTANCE OF THE SELFREGULATING EFFECT WITHIN POWER SYSTEMS. In: *IFAC Proceedings Volumes*. Vol. 39. IFAC, pp. 345–352.
- Lipták, B. G., Bálint, A., 2003. Application and Selection of Control Valves. In: Lipták, B. G. (Ed.), *Instrument Engineers' Handbook*, 4th Edition. ISA - The Instrumentation, Systems and Automation Society, Ch. 8.38, p. 2142.
- Reyes-Lúa, A., Zotică, C., Skogestad, S., 2018. Optimal Operation with Changing Active Constraint Regions using Classical Advanced Control. *IFAC-PapersOnLine* 51 (18), 440–445.
- Skogestad, S., 2004. Control structure design for complete chemical plants. *Computers and Chemical Engineering* 28 (1-2), 219–234.
- Weissbach, T., Kurth, M., Welfonder, E., Haake, D., Gudat, R., 2006. Control Performance of Large Scale Steam Power Plants and Improvements. In: Westwick, D. (Ed.), *IFAC Symposium on Power Plants and Power Systems Control*. Vol. 39. IFAC, Kananaskis, Canada, pp. 183–188.
- Welfonder, E., 1999. Dynamic interactions between power plants and power systems. *Control Engineering Practice* 7 (1), 27–40.

Relative Optimality Index for Evaluation of the Approximate Methods for Synthesis of Flexible Processes under Uncertainty

Klavdija Zirngast, Zdravko Kravanja, Zorka Novak Pintarič*

*University of Maribor, Faculty of Chemistry and Chemical Engineering, Smetanova 17,
2000 Maribor, Slovenia*

zorka.novak@um.si

Abstract

This contribution introduces a new indicator called Relative Optimality Index (ROI) which measures the extent to which the expected objective value of a flexible process flow sheet obtained by an approximate sequential approach is similar to the optimal solution obtained by more rigorous methods. MINLP flexible process syntheses were performed using various approximate robust approaches and the results were compared to the reference value obtained with the Gaussian quadrature method: a) sequential one-scenario method over randomly selected vertices, b) sequential method in which a two-scenario problem was solved in each iteration simultaneously at the nominal point and randomly selected vertex point, c) a method similar to b) but the most violated point from the previous iteration was used in the subsequent iteration instead of a randomly selected vertex, and d) a novel method which identifies a few vertices critical for flexibility, and solves a few-scenario problem simultaneously in the nominal point and these critical vertices. In this way, better trade-offs between first- and second-stage variables are established. These estimated values are then used as target values during the fine tuning of process structure and design variables that should bring both the flexibility index and the ROI as close as possible to the desired value of 1.

Keywords: uncertainty, flexibility, Relative Optimality Index

1. Introduction

Synthesis of flexible process flow sheets with large numbers of uncertain input data suffers from the problem that the exact optimal results usually cannot be obtained, because rigorous methods, such as simultaneous multi-scenario Gaussian quadrature, cannot be carried out due to uncontrolled increase in the size of the mathematical model. Several approximate approaches have been developed that are based on a large reduction of scenarios, for example, a simultaneous few-scenario method at the nominal and critical points (Novak Pintarič et al., 2013), a method based on probability distances (Zeballos et al., 2014), or sequential procedures in which one-scenario problems are solved sequentially in numbers of randomly selected points (Zirngast et al., 2018). Decomposition approaches were also proposed to facilitate the solution of large-scale problems under uncertainty; for example, an improved L-shaped method based on Benders decomposition (Li and Grossmann, 2018).

The problem with approximate approaches is that the results deviate from optimality; moreover, when dealing with large numbers of uncertainty parameters, a compromise is

sought between flexibility, optimality and computational effort. It is therefore important to address challenges in the area of optimization under uncertainty, because industrial engineering problems, such as demand side management, supply chains and process planning, design and synthesis, require that the risk and uncertainties be taken into account (Grossmann et al., 2017).

In this paper, a robust approach is proposed for Mixed Integer NonLinear Programming (MINLP) process synthesis under uncertainty based on a new identification procedure of those points critical for flexibility. In addition, a new Relative Optimality Index (ROI) is proposed for evaluating the precision of the approximate methods. The developed ROI represents, on one hand, a tool to establish how close the expected value obtained by an approximate method is to the exact value. On the other hand, it provides an approach for targeting the expected values and the appropriate trade-offs between the first- and second-stage variables of those flow sheets generated by robust sequential approaches under large numbers of uncertain parameters for which exact results would be impossible to obtain.

2. Methods for synthesis of flexible processes under uncertainty

The presence of uncertain parameters during MINLP synthesis of chemical processes requires discretization of infinite mathematical models at several discrete points i.e. scenarios, and optimization of the expected objective function. The latter involves the solution of a multiple integral which is approximated in discrete scenarios weighted by the corresponding weights or probabilities as shown in Eq. (1).

$$\begin{aligned}
 EZ &= \min \left(c^T y + \sum_s p_s \cdot f(d, x_s, z_s, \theta_s) \right) \\
 \text{s. t. } & h(d, x_s, z_s, \theta_s) = 0 \\
 & g(d, x_s, z_s, \theta_s) + By \leq 0 \quad s \in S \\
 & d \geq g_d(x_s, z_s, \theta_s) \\
 & Ay \leq a \\
 & d, x_s, z_s \geq 0, \quad y \in \{0, 1\}, \quad \theta^{LO} \leq \theta \leq \theta^{UP}
 \end{aligned} \tag{1}$$

Eq. (1) presents a two-stage stochastic model with recourse in which first-stage variables (topology and sizes of process units, y and d) should fit all scenarios, while second-stage variables (operating and control variables, x and z) are specific for each scenario. S is a set of selected scenarios denoted by subscript s , EZ an expected value of scalar objective variable Z , p probability of scenarios, c and f fixed and variable costs, h equality constraints, g inequality constraints, g_d design expressions, θ uncertain parameters, A , B and a are the matrices and vector of constants. The above problem can be solved using various methods which differ in selection of scenarios and in the way they treat the scenarios, either simultaneously or sequentially. The number of scenarios is a crucial factor, as the accuracy of the result and the computational effort increase with it.

2.1. Gaussian quadrature

The scenarios in this method correspond to the zeros of the Legendre polynomials, while their weight coefficients represent probabilities (see Acevedo and Pistikopoulos, 1998). The most accurate results would be obtained if the model would be solved simultaneously in all combinations of quadrature points of uncertain parameters; however, the problem size grows substantially as the number of constraints and second-stage variables are multiplied by $N_Q^{N_p}$, where N_Q is the number of quadrature points and N^U the number of uncertain parameters.

2.2. Sequential one- and two-scenario methods with randomly selected vertex

In order to avoid a tremendous increase in model size when using the Gaussian method, more robust sequential approaches were developed, based on the decomposition of the problem into a) determination of the first-stage variables, and b) adjustment of the second-stage variables (Zirngast et al., 2018). The procedure starts with the optimal process structure obtained by one-scenario MINLP synthesis at the nominal conditions. This structure is then solved at the randomly selected vertex so that the existing process units can enlarge, and new units can be added to achieve feasibility. The procedure continues with new vertices until the first-stage variables change. The flexibility index of the obtained process structure is then determined, and stochastic Monte Carlo optimization is performed in a finite number of randomly selected points for determining second-stage variables and the expected objective value at a specific level of confidence. The two-scenario approach differs from the one-scenario method in that MINLP synthesis problem for first-stage variables is solved simultaneously at the nominal point and random vertex in order to better target the trade-offs between first- and second-stage variables.

2.3. Sequential two-scenario method with most violated vertex

This approach is like the two-scenario method described in section 2.2, except that it does not use a randomly selected vertex next to the nominal point but the most violated vertex from the previous iteration. This vertex is identified by analyzing a flexibility index for the first-stage variables obtained in each iteration, as in (Bansal et al., 2002). The vertex with the lowest flexibility is then identified and added to the nominal point in the subsequent iteration.

2.4. Simultaneous multi-scenario method in critical and nominal points

The approaches described in sections 2.2 and 2.3 start with the initial process structure obtained at the nominal point whose flexibility index is usually close to 0. A new approach is therefore developed that starts with a partly flexible initial topology, and then derives a flexible structure by handling this initial topology through one of the previously described approaches. Identification of critical points starts with a two-scenario MINLP process synthesis at a nominal point and random vertex, followed by determination of the flexibility index of the first-stage variables obtained. After processing a specific set of vertices, those few vertices that produce the lowest flexibility indexes are selected as critical ones. MINLP synthesis is then performed as a few-scenario problem simultaneously at the nominal point and identified critical vertices yielding first-stage variables with flexibility index substantially higher than 0. This topology is then tuned to flexibility index 1 by using one of the approaches described in sections 2.2 and 2.3.

2.5. Relative optimality index

From the above described methods, the simultaneous multi-scenario Gaussian quadrature is regarded as the most precise one, so the results of the other methods are compared with the Gaussian result by defining a Relative Optimality Index (*ROI*) in Eq. (2):

$$ROI = 1 - \frac{|EZ_{\text{Gauss}} - EZ_{\text{appr}}|}{EZ_{\text{Gauss}}} \quad (2)$$

where EZ_{Gauss} and EZ_{appr} represent the expected values obtained by the Gaussian and approximate method, respectively. The closer the ROI value to one, the better the results obtained by an approximate method.

3. Case study

MINLP synthesis of a flexible Heat Exchanger Network (HEN) was selected as a case study. Data for process streams and utilities are given in Table 1, where T_s represents the supply temperatures, T_t target temperatures, CF heat capacity flow rates, and α individual heat transfer coefficients. Four uncertain parameters were supply temperatures of hot streams H1 and H2, supply temperature of cold stream C1, and heat capacity flow rate of hot stream H1. The number of uncertain parameters was intentionally kept low, so that the simultaneous Gaussian method could be performed as a reference. The objective function was minimum Total Annual Cost (TAC) composed of the utility costs plus annualized investment cost of heat transfer units. HEN synthesis was performed using MINLP model (Yee and Grossmann, 1990).

The numerical results obtained by different methods are presented in Table 2, and the optimal HEN structures in Figures 1, 2 and 3. MINLP synthesis at the nominal conditions produced an inflexible network with the lowest TAC. Simultaneous MINLP synthesis by Gaussian method was performed at three quadrature points for each parameter, yielding a flexible HEN with the reference expected TAC of 407,550 \$/y, and flexibility index equal to 1. The model size was 6,230 equations, 8,538 continuous variables and 36 discrete variables, while the required CPU time was 9 h using an SBB optimization solver within GAMS on an average personal computer.

Table 1: Data for case study of HEN synthesis

Stream	T_s (K)	T_t (K)	CF (kW)	α (kW/(m ² ·K))
H1	621 ± 5	350	28 ± 5	1.4
H2	583 ± 13	323	20	1.4
C1	388 ± 15	600	40	1.4
C2	313	393	60	1.4
Hot utility (HU)	620	619		3.5
Cold utility (CU)	298	315		1.4

Cost of heat exchangers and coolers (\$/y) = 1846· $A^{0.65}$ (A in m²)

Cost of heaters (\$/y) = 2350· $A^{0.65}$ (A in m²)

Price of hot utility = 230 \$/kW_y, price of cold utility = 20 \$/kW_y

Table 2: Results of flexible HEN synthesis by different methods

Method for MINLP synthesis	Expected TAC (\$/y)	A (m ²)	Flexibility index	ROI
Nominal point	358,524	663	0.00	0.880
Gaussian quadrature (2.1*)	407,550	742	1.07	1.000
One-scenario method with randomly selected vertex (2.2*)	446,981	956	1.12	0.902
Two-scenario method with randomly selected vertex (2.2*)	426,424	748	1.20	0.954
Two-scenario method with most violated vertex (2.3*)	426,237	748	1.11	0.954
Multi-scenario method in critical and nominal points (2.4*)	424,082	743	1.17	0.959

* Number of section where the method is described

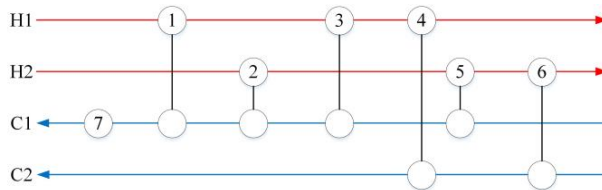


Figure 1: Nominal inflexible HEN (358,524 \$/y)

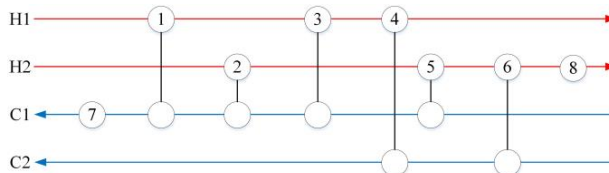


Figure 2: Flexible HEN obtained by Gaussian quadrature (407,550 \$/y) and two-scenario method with most violated vertex (426,237)

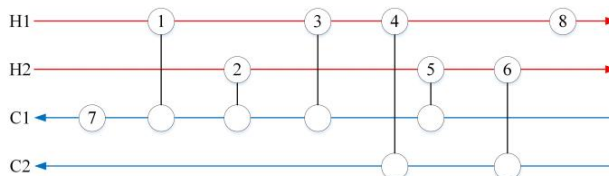


Figure 3: Flexible HEN obtained by two-scenario method with randomly selected vertex (426,424 \$/y), multi-scenario method at nominal and critical points (424,082 \$/y), one-scenario method with randomly selected vertex (446,981 \$/y)

Computation times for the approximate sequential methods were significantly lower than for Gaussian integration, and amounted to around 15 s. Two-scenario approaches produced lower TACs than the one-scenario method, because the presence of the nominal point besides the vertex point during determination of the first-stage variables provides at least rough information about the trade-offs with the second-stage variables.

Those approaches initiating from the nominal inflexible structure (sections 2.2 and 2.3) gave higher costs than the approach that starts from a partially flexible initial structure with flexibility index 0.55 (section 2.4). This structure was then tuned to the required flexibility by using only around 30 vertices in a two-scenario method (section 2.2) while more than 100 vertices were needed when starting the same method from the nominal inflexible structure. All two-scenario approaches achieved a Relative Optimality Index around 95 % with regard to the reference Gaussian method.

4. Conclusions

This paper demonstrates several robust approximate methods for MINLP process synthesis under uncertainty, and compares their results with a more rigorous simultaneous Gaussian quadrature method. A novel indicator, called a Relative Optimality Index, was proposed for measuring how close the results of the approximate methods are to the Gaussian one. It was established that a novel sequential two-scenario approach starting from a partially flexible initial structure produced the closest result with a ROI value of 0.96. In the future work it is intended to upgrade these approaches for determining target ratios between the first- and second-stage variables, and to use them for the approximate synthesis of large processes with many uncertain parameters for which exact optimal results cannot normally be obtained.

Acknowledgment

The authors acknowledge financial support from the Slovenian Research Agency (PhD research fellowships MR-39209, project L2-7633, and program P2-0032) and Perutnina Ptuj.

References

- J. Acevedo, E. N. Pistikopoulos, 1998, Stochastic optimization based algorithms for process synthesis under uncertainty, *Computers & Chemical Engineering*, 22, 4, 647-671
- V. Bansal, J. D. Perkins, E. N. Pistikopoulos, 2002, Flexibility analysis and design using a parametric programming framework, *AIChE Journal*, 48, 12, 2851-2868
- I. E. Grossmann, R. M. Apap, B. A. Calfa, P. Garcia-Herreros, Q. Zhang, 2017, Mathematical Programming Techniques for Optimization under Uncertainty and Their Application in Process Systems Engineering, *Theoretical Foundations of Chemical Engineering*, 51, 6, 893-909
- C. Li, I. E. Grossmann, 2018, An improved L-shaped method for two-stage convex 0–1 mixed integer nonlinear stochastic programs, *Computers & Chemical Engineering*, 112, 165-179
- Z. Novak Pintarič, M. Kasaš, Z. Kravanja, 2013, Sensitivity analyses for scenario reduction in flexible flow sheet design with a large number of uncertain parameters, *AIChE Journal*, 59, 8, 2862-2871
- T. F. Yee, I. E. Grossmann, 1990, Simultaneous optimization models for heat integration—II. Heat exchanger network synthesis, *Computers & Chemical Engineering*, 14, 10, 1165-1184
- L. J. Zeballos, C. A. Méndez, A. P. Barbosa-Povoa, A. Q. Novais, 2014, Multi-period design and planning of closed-loop supply chains with uncertain supply and demand, *Computers & Chemical Engineering*, 66, 151-164
- K. Zirngast, Z. Kravanja, Z. Novak Pintarič, 2018, A Robust Decomposition Methodology for Synthesis of Flexible Processes with many Uncertainty Parameters – Application to HEN Synthesis, submitted to *Chemical and Biochemical Engineering Quarterly*

Process Systems Engineering from an industrial and academic perspective

Anton A. Kiss,^{a,b*} Johan Grievink^c

^a*School of Chemical Engineering & Analytical Science, The University of Manchester, Sackville St, Manchester, M13 9PL, United Kingdom*

^b*Sustainable Process Technology, Faculty of Science and Technology, University of Twente, PO Box 217, 7500 AE Enschede, The Netherlands*

^c*Delft University of Technology, van der Maasweg 9, 2629 HZ Delft, The Netherlands*
tony.kiss@manchester.ac.uk, a.a.kiss@utwente.nl

Abstract

Process Systems Engineering (PSE) deals with decision-making, at all levels and scales, by understanding complex process systems using a holistic view. Computer Aided Process Engineering (CAPE) is a complementary field that focuses on developing methods and providing solution through systematic computer aided techniques for problems related to the design, control and operation of chemical systems. The ‘PSE’ term suffers from a branding issue to the point that PSE does not get the recognition it deserves. This work aims to provide an informative industrial and academic perspective on PSE, arguing that the ‘systems thinking’ and ‘systems problem solving’ have to be prioritized ahead of just applications of computational problem solving methods. A multi-level view of the PSE field is provided within the academic and industrial context, and enhancements for PSE are suggested at their industrial and academic interfaces.

Keywords: PSE, industry, education, research, interface, perspectives

1. Introduction

Process Systems Engineering (PSE) is a discipline concerned with methods and tools to support decision-making for the creation and operation of chemical supply chains, including the discovery, design, manufacturing, processing, and distribution of chemical products (Grossmann and Westerberg, 2000; Stephanopoulos and Reklaitis, 2011). In other words, PSE is all about rational decision-making, at all levels and length / time scales, by understanding complex systems using a holistic view (Kiss et al., 2015). PSE is the wider field embracing Computer Aided Process Engineering (CAPE) as an important sub-domain where computing and information technologies play an essential role in finding solutions for problems of design, control and operation of chemical systems (Cameron and Lewin, 2009; Dimian et al., 2014).

This paper has several contributions: it defines PSE and CAPE areas and their mutual relationship; it questions what makes PSE less effective in chemical engineering (ChE) than it could potentially be; it shows that industrial as well as academic PSE have stronger & weaker points with known causes and amplified by deficient interactions with each other; it offers a model for enhanced PSE interactions between industry and academia covering key topics (e.g. sharing of industrial PSE problems with academia;

knowledge generation by research & know-how transfer by moving PSE professionals between academia and industry; start-ups of companies with deep PSE expertise and tools for industrial services), and it concludes there is ample potential for improvement of effectiveness of PSE by working better across industrial and academic interfaces.

2. Problem statement

The international PSE research community has successfully established a vital science of engineering. Yet, its accomplishments are unevenly absorbed by the process industry and in educational programs. Application potential is lost and locally even branding issues arise. The analysis of this paper is based on authors' experiences in the Dutch process industry and academia, but carries over well to other countries. There is a known divergence between academia and industry due to different focus: research (funding and output) vs economic profit (Klatt and Marquardt, 2009). A key consequence is that industry considers most important the core ChE disciplines, while academia (mainly driven by research funding / input) focuses on biotechnology, nanotechnology, or science-centred topics – as shown in Figure 1 left (Varma and Grossmann, 2014). Some barriers to more daring and effective use of PSE concepts, methods, models and tools (shown in Figure 1, right) include the following:

- The opportunities in making advancements in PSE seem to have moved from its interior (e.g. better models, faster computing) to external interfaces with other chemical engineering disciplines, such as process intensification (PI), product innovation and engineering for multi-phase products (Harmsen et al., 2018).
- The huge application success of CAPE tools has shifted barriers in process engineering projects. In the past doing process data handling and engineering computations fast and consistently was a key barrier. That kind of barrier has largely vanished, resulting in the emergence of other bottlenecks in: the human work processes; the knowledge levels of process engineers being incommensurate with the capabilities of the tools; at the interface of technology and society with societal acceptance of technology applications.

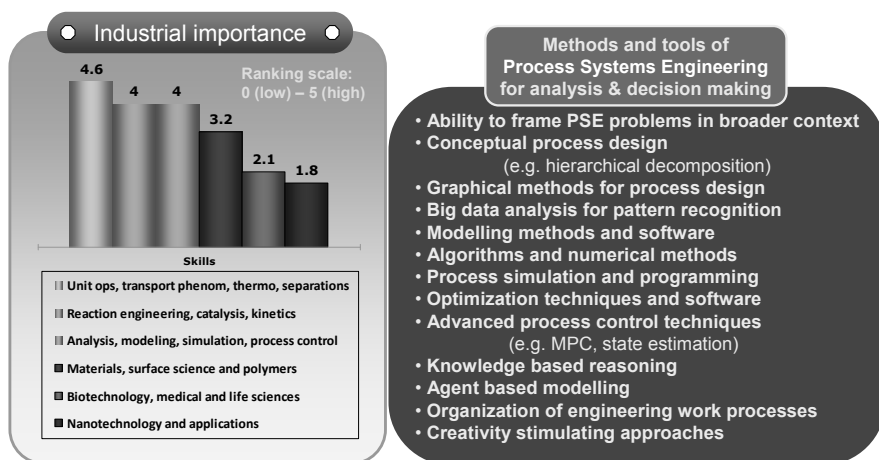


Figure 1. Industrial importance of PSE topics (left). Methods and tools for PSE (right).

3. PSE in industry

Research, development & innovation enable the introduction of new or improved products and processes, and reduce the uncertainty to acceptable levels. PSE supports such reductions: business risks, time, cost & profit, environment, safety, health, social. PSE is perceived as a service provider to “customers” in company applications, making it difficult to put a value (not a cost) on its activities or quantify their contribution.

Many industrial professionals have no idea about PSE, but they do know about process design, modelling, simulation, optimization, control, etc. This is likely due to the having these topics been taught at the university as separate topics without the interactions, but also due to the way in which the process design & engineering activities are compartmentalized in the engineering divisions of companies.

The industrial technology assessment models do take into account the probability of success when applying a new technology with a higher performance (or accounting for risk of failure), but it is rather unclear how does that tie in with PSE methods and tools for products and process innovations. Figure 2 shows a multi-level view of PSE positioning between the upper levels (determining the research directions) and the lower levels (tools and means to achieve the goals), with the “process” being seen as an optimized integrated production system, made up of one or more production plants.

Figure 3 shows that PSE has a key role in delivering more profit in shorter time, along all phases (e.g. research & development, engineering, process optimization, operation) taking into account all sustainability pillars (ten Kate, 2016). Of course, there is a trade-off between multiple criteria in Pareto type of optimization. Moreover, PSE reduces uncertainty along the way from idea to implementation, with the addition that there is also a reverse flow of information from an operational plant to the collection of process models. Plant data periodically collected in operational plants offer a rich base for “big data analysis”: e.g. finding patterns of behaviour that can be exploited to improve process performances and be captured in updated models.

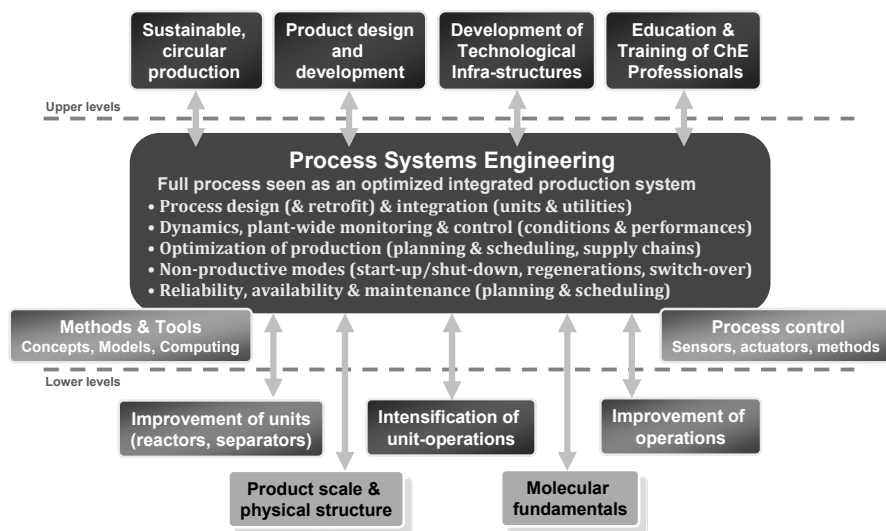


Figure 2. Multi-level view of PSE positioning

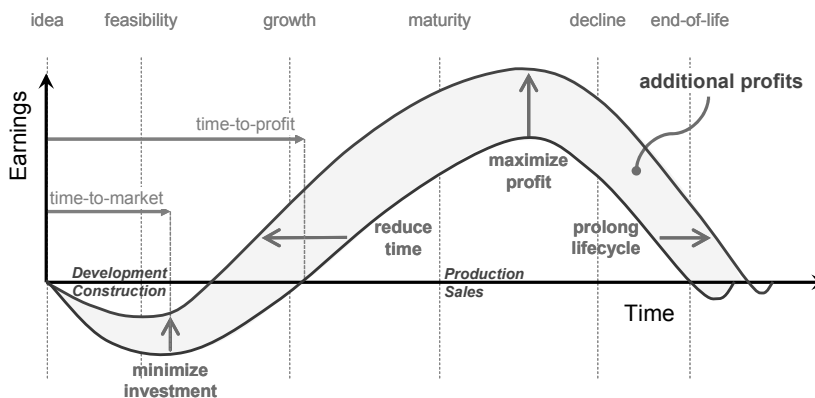


Figure 3. Role of PSE along all phases of plant development and exploitation

In PSE activities, the purpose shapes the models and these models have the role of transferable knowledge carriers (if the physical principles underlying the model are kept transparent in the structure of the equations). Setting up a model provides structured approach to understanding the system. However, a combined approach of experiments supported by modelling is the most effective. PSE offers a structured approach in process and product development: guiding the lab-scale experiments, interpreting the experimental observations, and translating the results into the desired outcome.

4. PSE in academia

Figure 4 illustrates the career span and life-long learning for PSE professionals at the interface of industry and academia, with a required exchange of professionals between academia & industry. But in the academic world, one must make a distinction between the academic research agenda for PSE, and the teaching / education in PSE topics.

PSE research includes: spanning a wider ranges of physical scales in processes & supply chains; broader range of feedstocks; integration of process intensification and PSE; circular systems: integration in design & operation of product manufacturing, product application, recovery and recycling, medical process systems; multi-scale modelling and computing; uncertainty in design & engineering. Major achievements of PSE include the development of methodologies and tools to support process modelling, simulation and optimization (MSO). But MSO technologies have become a commodity; they are not a distinguishing feature of the PSE field any more (Klatt and Marquardt, 2009). Hence PSE has to play a supportive role to the other engineering sub-disciplines that focus on smaller scales with specific objects. The proper integration of such objects in products and/or processes is certainly part of PSE area. Also, a large-scale energy transition with electrified processes and inherent dynamic operations offers challenges.

PSE education proved that one has to gradually build up the complexity, though the systems engineering aspects can be introduced from first year in BSc / BEng onwards. When teaching the PSE core elements in succession (e.g. process analysis, product & process synthesis and design, dynamics and control, optimization of process operations within supply chains, safety and reliability engineering) one could also emphasize the interdependencies between decisions made in these (PSE) activities.

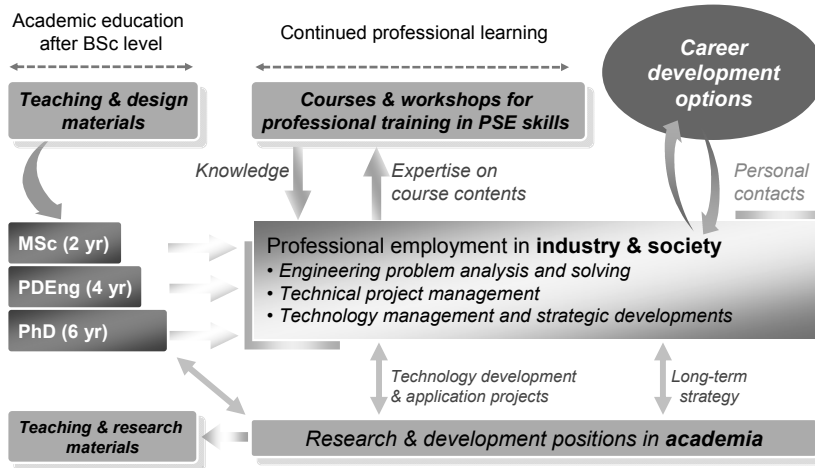


Figure 4. Career span for PSE professionals in academia and industry

5. PSE perspectives

Enhanced PSE interactions between industry and academia needs to cover: sharing of abstracted, generic industrial PSE problems with academia (education and research); knowledge generation by academic research with selective transfer to supportive industrial partners (see framework in Figure 5); as well as knowledge and know-how transfer by moving PSE professionals between academia & industry; and start-ups of small companies (providers) with deep PSE expertise and tools for industrial services.

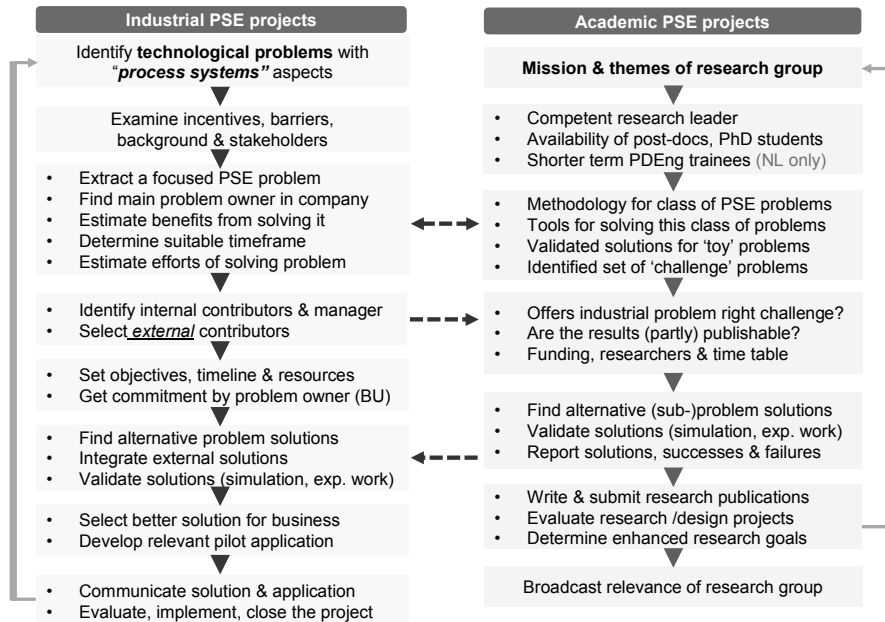


Figure 5. Industrial vs academic PSE projects

What needs to change for more enhanced interactions of both worlds includes:

- *Industry*: awareness from companies that the external development power is actually many times greater than internally in a company (although internally more focus on specific goals can be attained). Open innovation projects can accelerate the technology transfer of novel developments from the academic world into the industry.
- *Academia* needs to accept that the generation and use of engineering knowledge goes wider than writing good publications. The ultimate rationale for generating engineering knowledge is its application (potential) by joint projects & collaborations with industry.

6. Conclusions

PSE contributed significantly to chemical engineering, by providing MSO technology to address demanding and large-scale process problems in academia and industrial practice. Systems thinking and problem solving are indispensable in the academic education of chemical engineers and also in the industrial practice. Industry mainly focuses on profitability and sustainability, while academia aims at scientific progress, causing a potential gap between industrial practice and academic research. Sustainable success of PSE requires consistent co-operations between academia and industry. PSE is a key enabler for process and product innovation, and has a bright future with sustainable impact on the ChE sciences, and on industrial manufacturing processes.

Acknowledgements

AAK gratefully acknowledges the Royal Society Wolfson Research Merit Award.

References

1. T. Cameron, D. R. Lewin, 2009, Curricular and pedagogical challenges for enhanced graduate attributes in CAPE, *Computers and Chemical Engineering*, 33, 1781-1792.
2. A. C. Dimian, C. S. Bildea, A. A. Kiss, 2014, *Integrated design and simulation of chemical processes*, 2nd Edition, Elsevier, Amsterdam.
3. I. E. Grossmann, A. W. Westerberg, 2000, Research challenges in process systems engineering, *AIChE Journal*, 46, 1700-1703.
4. J. Harmsen, A. B. de Haan, P. L. J. Swinkels, 2018, *Product and process design: Driving innovation*, De Gruyter, Germany.
5. A. J. B. ten Kate, 2016, PSE for problem solving excellence in industrial R&D, *Computers and Chemical Engineering*, 89, 127-134.
6. A. A. Kiss, J. Grievink, M. Rito-Palomares, 2015, A systems engineering perspective on process integration in industrial biotechnology, *Journal of Chemical Technology and Biotechnology*, 90, 349-355.
7. K.-U. Klatt, W. Marquardt, 2009, Perspectives for process systems engineering – Personal views from academia and industry, *Computers and Chemical Engineering*, 33, 536-550.
8. G. Stephanopoulos, G. V. Reklaitis, 2011, Process systems engineering - From Solvay to modern bio and nanotechnology. *Chemical Engineering Science*, 66, 4272-4306.
9. A. Varma, I. E. Grossmann, 2014, Evolving trends in chemical engineering education, *AIChE Journal*, 60, 3692-3700.

Optimisation of the integrated water – energy systems: a review with a focus in Process Systems Engineering

Christiana M. Papapostolou^a, Emilia M. Kondili^{a*}, Georgios T. Tzanes^b

^a *Optimisation of Production Systems Laboratory,*

^b *Soft Energy Applications and Environmental Protection Laboratory,*

Dept. of Mechanical Engineering, University of West Attica, Campus 2, P. Ralli & Thivon Street, 12244, Egaleo, Greece,

*ekondili@uniwa.gr

Abstract

The analysis of issues within the ‘water-energy nexus’ has become a topic of increasing attention for the scientific and policy communities. Lately various water, energy and food nexus systems are developed to identify, analyse and better understand the interactions between water and energy systems with the purpose of managing these critical resources in the context of various conflicting requirements on top of the imperative need of their optimal use. The objectives of the present work are at first to identify the wide spectrum of problems being encountered under the term Water – Energy Nexus and to review the existing and recent advancements in the Process Systems Engineering (PSE) field that exploit optimisation models, methods and tools for the analysis and the operation of various integrated water energy systems. In addition, the work aims to provide a perspective to PSE and CAPE experts thus expanding their scope and interests and, at the same time, to provide the WEN with the knowledge, experience, tools and excellent quality researchers able to assist to the solution of these significant global problems.

Keywords: PSE and CAPE fields, Water-Energy Nexus, Optimisation models

1. Introduction – Objectives and Scope of the Work

Water – energy nexus (WEN) deals with the efficient integration of water and energy resources in order to tackle a wide range of design, operation and optimisation issues for systems including both of these two resources. Many problems such as the supply and the continuous availability of the resources, their quality and safety, the environmental and social impacts, along with the cost and/or profit emerged from their exploitation, are problems encountered in a very wide range of real situations. Food is in most cases involved due to its strong interaction with the other two utilities.

However, the present paper focuses mainly to the Water – Energy Nexus, mainly due to the types of problems that are analysed. The water and energy interactions are complex and they affect one another directly and indirectly. The dynamic behavior and the presence of multiple conflicting energy/water demands and the complex interactions between various sources and sinks of water and energy greatly impact decision-making within the water-energy nexus, taking also into account that related decisions depend strongly on the interests of the different stakeholders involved. Therefore, a systematic

and holistic analysis of the nexus is critical and there is a very wide scope for optimisation of the whole system, supporting unbiased decision-making.

2. Background of the Work - WEN representing a wide range of problems

By their definition PSE and CAPE fields investigate solutions for integrated systems and have made a tremendous progress all these years in the understanding, modeling and solving a wide range of problems met initially in process systems and now in a very wide spectrum of fields. Therefore, this integrated approach for problem-solving is very familiar to PSE and CAPE communities and many research works deal with this type of problems. The models, methods and tools of PSE may really be the most added value approaches for the WEN problems due to their integrated approach and their ability to address the complexity of these systems. PSE 2018 conference had a dedicated session in the WEN and in the last 2-3 ESCAPE events there are papers that explicitly deal with this issue. The basic parameters and dimensions of these problems are:

- The type of the problem under consideration.
- The geographic area, i.e. the spatial dimension of the problem
- The scope of the work, i.e. is it for households, for cities, for small isolated communities, for a whole country.
- The temporal dimension, i.e. for which time horizon is the problem being solved.
- The stakeholders and interested parties.
- The objective of the optimisation. For the same problem it will be different for a private investor that might seek for maximum profit, the entire society might seek for minimum environmental impacts, maximum security of water and energy supply, a local authority that might seek for the optimal policy / pricing / management of the resources, for the government that might seek for the best water and energy infrastructure investments.
- The importance for the optimal solution or for a set of feasible solutions.

There are very interesting and very recent review papers that deal with various aspects of the research work relevant to Water Energy (and possibly Food) Nexus. Garcia and You (2016) analyse relevant research works concerning Water – Energy and Food Nexus (WEFN) highlighting challenges and areas where PSE may find interesting research opportunities.

Dai et al. (2018) made an extensive survey of recent scientific literature on the water-energy nexus. The authors identified 70 studies and 35 were selected as comprehensive case studies for review. In their work the reviewed studies have been classified and assessed according to groupings based on both geographic scale and their ‘nexus scope’. The review has also concluded that, while many studies aim to develop new methods and frameworks to comprehensively assess interactions between water, energy and other elements, none can or do provide a singular framework for performing a “nexus study”.

In the context of these excellent review works the current study mainly aims to highlight different types of problems encountered within the WEN scope as well as some modern methods and tools employed to optimise the nexus. It should be stressed that the list of problem types is indicative and various other very significant works have been carried out. The selection has been based on the innovative character of the problem and/or the method being developed for the purposes of the specific work.

3. Types of problems tackled with the Water Energy Nexus

3.1. Water Supply

Although many papers have dealt with the production and the use of energy, much less attention has been paid to the water side of the problems.

Sea Water Desalination

The production of clean water through membrane processes requires large amounts of energy. On the other hand, in remote and isolated from central networks communities, there are a significant technical potential for the simultaneous production of water and energy. A methodology to design desalinated water supply systems including solar energy as an energy source option is proposed by Herrera – Leon et al. (2018). The methodology consists of two stages and uses a MINLP model. The objective of the first stage is to minimize the total cost of the whole system, while the objective of the second stage is to minimize the greenhouse gases (GHG) emissions related to desalinated water transport by considering the opportunity of installing photovoltaic panels. The MINLP model considers the installation and operation costs of the desalination plants, pumping stations, pipes, and photovoltaic panels.

Optimisation of Water Supply systems

A very interesting review has also been carried out by Vakilifard et al. (2018), acknowledging that the utilization of WEN in optimising water supply systems not only ensures the sustainability of the water supply for increasing water demand but also diminishes water-related energy and environmental concerns. The work also presents a review highlighting knowledge gaps in optimisation models related to the water energy nexus in water supply systems or “water supply side of the nexus”. Several major gaps are identified, including the lack of optimisation models capturing spatial aspects as well as environmental impacts of the nexus problems. The main gap is the absence of models for optimising long-term planning of water supply system considering renewable energy within an urban context.

3.2. Water Energy Nexus Optimisation in Remote Communities

Remote communities render a very special issue of investigation within the WEN research umbrella: WE supply problems in these communities are quite intense and require immediate solutions that can only be provided by optimisation approaches. Following that, various research works have been carried out by pioneering in the field teams, indicatively focused in the Greek, Aegean islands and/or in the Mediterranean Region and/or in Maldives islands.

Aiming at providing water and energy sustainable supply solutions for the isolated Aegean islands, Bertsiou et al. (2018), investigated the development of a Hybrid Renewable Energy System (HRES) in Fournoi, a small island in northern Aegean. The proposed methodological framework is designed to produce hydropower for the coverage of electricity needs and for the desalination of the amount of water that is needed for domestic and agricultural use. Data about the island’s population and data of water and electricity consumption are collected, as well as, meteorological data from the nearby station. The authors make a Scenario Analysis with three different scenarios.

In the same field Papapostolou et al. (2017, 2018) implemented an optimisation framework for the optimal design and operation of water and energy supply chains (WESCs) accounting both economic and environment considerations. The framework

consisting of a representation following the Resource-Task-Network approach along with a developed MINLP model and its variations, was implemented and tested in different island topographies (a medium-size and a very small island in Cyclades Complex), so as to prove the most profitable WESC accounting: on the side of energy supply the options of diesel, PV, wind and battery storage, whilst on the side of water supply, the options of the desalination plant vs the traditional water transfer via ships, both acting operating complementary to the island's existing water tank. The results of the work provide a water supply strategy allowing in the case of RES excess the desalination plant to operate "free of charge" so as to allow the water intake to the water tank, a water to be supplied at the island network at a time whereas both peaks loads in energy and water demand occur (thus more expensive). Additionally, results evidence that energy autonomy and water demand fulfilment is possible for small-scale islands as well in a cost-effective way, that being achieved through RES, allowing a reduction of CO₂ emissions more than 90%.

3.3. *Water Energy Nexus Optimisation in Urban – Residential Sector*

Cities are concentrations of demand to water and energy systems that rely on resources under increasing pressure from scarcity and climate change mitigation targets. However, the effect of the end-use water and energy interdependence on urban dynamics had not been studied. In the work of De Stercke et al. (2018), a novel system dynamics model is developed with an explicit representation of the water-energy interactions at the residential end use and their influence on the demand for resources. The model includes an endogenous carbon tax based climate change mitigation policy which aims to meet carbon targets by reducing consumer demand through price. It also encompasses water resources planning with respect to system capacity and supply augmentation. Using London as a case study, the authors show that the inclusion of end-use interactions has a major impact on the projections of water sector requirements.

4. **Modern Methods and Tools in the Optimisation of WEN**

Certainly the well-known optimisation methods and tools (Mathematical Programming as MILP, MINLP, global optimisation, etc.) have extensively been used for the solution of the WEN problems. However, in the latest advancements the authors have used modern approaches concerning optimisation modelling and solution of the corresponding problems. Game Theory and Graph theory are two of the modern methods that have been identified in WEN optimisation works.

4.1. *Game theory*

Land use optimization can have a profound influence on the provisions of interconnected elements that strongly rely on the same land resources, such as food, energy, and water. Avraamidou et al., (2018b) have developed a hierarchical FEW-N approach to tackle the problem of land use optimization and facilitate decision making to decrease the competition for resources. The authors have formulated the problem as a Stackelberg duopoly game, a sequential game with two players – a leader and a follower. The government agents are treated as the leader (with the objective to minimize the competition between the FEW-N), and the agricultural producers and land developers as the followers (with the objective to maximize their profit).

Nie et al (2018) in the context of their work for land use optimisation analyse the FEW-N for crop-livestock systems with the development and implementation of a global

optimisation land allocation framework, providing an adaptive data-driven modeling method based on limited realistic data to predict yields for production components.

For the development of a feasibility model, Namany et al. (2018) developed a bottom-up approach in which the self-interested stakeholders, i.e. the players, are represented based on their own decision variables and objective functions at various levels, i.e. resources and environment systems, engineering systems, and their integration and operations. For this purpose, a combination of optimization models based on linear programming, stochastic programming, and game theoretic approach, represented by a Stackelberg competition, were developed. A case study is set in the State of Qatar with the objective of enhancing food security using hypothetical scenarios. The results obtained demonstrates that interesting interactions between systems can potentially result in the achievement of desired objectives under properly regulated markets.

4.2. Graph theory

Some very interesting modern tools seem to emerge that are exploited in the optimisation of WEN. For example, Tsolas et al. (2018) present a scalable and systematic method for the design and optimization of complex water-energy nexus using graph theory-based network representation and a novel (WEN) diagram. The authors show that for specified external grid demands, the optimal nexus configuration with minimum water and energy generation is the one without any redundant subgraphs. They then propose a systematic method to identify and eliminate redundant cycles, flows and entities within a nexus leading to (i) minimum generation/extraction of water and energy resources from the environment, or (ii) maximum yield of water and energy to meet external demands. Their approach results in optimal nexus configurations that also satisfy operational constraints, restrictions and water quality specifications. The approach is demonstrated using case studies on water-energy nexus systems focusing on power generation, seawater desalination, groundwater and surface water at regional and national scales.

5. Conclusions and Future Prospects

The interest and research challenge in the modelling and optimisation of WEN in various scales, expressions, communities is continuously increasing. There is a very important optimisation scope in these problems since there are a lot of conflicting demands in the resources involved. The present work made an effort to highlight the wide spectrum of real problems that may be encountered under the term Water – Energy Network. For so different problems it is clear that there is no unique modelling framework that could describe all of them. On the other hand it is obvious that there is a serious optimisation scope in these problems due to the different stakeholders, objectives and characteristics. Advanced model development that will describe the details and characteristics of the problems is still required since the interactions between the energy and water resources are complex and not yet clarified. The other important issue in this discussion is the implementation of the above in real problems and how the developed knowledge and knowhow will be useful and exploitable in real operating water – energy systems. Furthermore, it is certain that many investors (on a local or global perspective) will emerge finding business opportunities. Legislation, regulations and infrastructure expansion will definitely be needed in order to make this knowledge exploitable for the social and investor's benefit.

Acknowledgements

"The Post-doctoral Research of Dr C. Papapostolou was undertaken with a scholarship fund by IKY, Act "Supporting Post-Academic Researchers" with resources from the Operational Program "Human Education Development and Lifelong Learning", priority axes 6,8,9, co-funded by the European Social Fund - ESF and the Greek State".

References

- S. Avraamidou, A. Milhorn, O. Sarwar, E.N. Pistikopoulos, 2018, Towards a Quantitative Food-Energy-Water Nexus Metric to facilitate Decision Making in Process Systems: A Case Study on a Dairy Production Plant, Proc. of ESCAPE28, Computer Aided Chemical Engineering, 43
- S. Avraamidou, B. Beykal, I.P.E. Pistikopoulos, E.N. Pistikopoulos, 2018, A hierarchical Food-Energy-Water Nexus (FEW-N) decision-making approach for Land Use Optimization, Computer Aided Chemical Engineering, 44
- M. Bertsiou, E. Feloni, D. Karpouzou, E. Baltas, 2018, Water management and electricity output of a Hybrid (HRES) in Fournoi Island in Aegean Sea, Ren. Energy, 118, 790–798
- J. Dai, S. Wu, G. Han, J. Weinberg, X. Xie, X. Wu, X. Song, B. Jia, W. Xue, Q. Yang, 2018, WEN: A review of methods and tools for macro-assessment, Appl. Energy, 210, 393–408
- S. De Stercke, A. Mijic, W. Buytaert, V. Chaturvedi, 2018, Modelling the dynamic interactions between London's water and energy systems from an end-use perspective, Applied Energy, 230, 615–626
- J. Garcia, F. You, 2016, The water-energy-food nexus and process systems engineering: A new focus, Computers and Chemical Engineering, 91, 49–67
- S. Herrera-León, A. Kraslawski, L.A. Cisternas, 2018, A MINLP model to design desalinated water supply systems including solar energy as an energy source, CACE, 44, 1687–1692
- S. Namany, A-A Tareq, G. Rajesh, 2018, Integrated techno-economic optimization for the design and operations of energy, water and food nexus systems constrained as non-cooperative games, Computer Aided Chemical Engineering, 44, 2018, 1003–1008
- Y. Nie, S. Avraamidou, J. Li, E.N. Pistikopoulos, 2018, Land use modeling and optimisation based on Food-Energy-Water Nexus: A case study on crop-livestock systems, Computer Aided Chemical Engineering, 44
- C. Papapostolou, E. Kondili, J.K. Kaldellis, 2017, Optimising the total benefit of water resources management in combination with the local energy systems in remote communities taking into account sustainability, Computer Aided Chemical Engineering, 40, 2689–2694
- C.M. Papapostolou, E.M. Kondili, G. Tzanes, 2018, Optimisation of water supply systems in the water – energy nexus: Model development and implementation to support decision making in investment planning, Computer Aided Chemical Engineering, 43, 1213–1218.
- R. Segurado, M. Costa, N. Duić, M.G. Carvalho, 2014, Integrated analysis of energy and water supply in islands. Case study of S. Vicente, Cape Verde, Energy, 92, 639–648
- S.D. Tsolas, M.N. Karim, M.M.F. Hasan, 2018, Optimization of water-energy nexus: A network representation-based graphical approach, Applied Energy, 224, 230–250
- G.T. Tzanes, D. Zafirakis, C. Papapostolou, K. Kavadias, J.K. Kaldellis, 2017, PHAROS: An Integrated Planning Tool for Meeting the Energy and Water Needs of Remote Islands using RES-based Hybrid Solutions, Energy Procedia, 142, 2586–2591
- N. Vakili, M.A. Anda, P. Bahri, G. Ho, 2018, The role of water-energy nexus in optimising water supply systems – Review of techniques and approaches, Renewable and Sustainable Energy Reviews, 82, Part 1, 1424–1432

Time Resolved Sensitivity & Identifiability Analysis for Directed Parametrization of Highly Dynamic Models

Sven Daume^{a,+}, Julian Kager^{a,b,+,*} and Christoph Herwig^{a,b}

^aICEBE, TU Wien, Gumpendorfer Straße 1a 166/4, 1060 Wien, Austria

^bCD Laboratory on Mechanistic and Physiological Methods for Improved Bioprocesses,
TU Wien, Gumpendorfer Straße 1a 166/4, 1060 Wien, Austria

⁺Contributed equally to the paper.

julian.kager@tuwien.ac.at

Abstract

Biological systems can be described by ordinary differential equations of the main components with non-linear and interacting reaction kinetics. These models are helpful tools for process development and optimization. The difficulty in building a model is not to find a mathematical expression for the different kinetics but to select the ones with identifiable parameters. Besides that also the right sampling time points are important to capture the needed information for model calibration.

Within this contribution, we show how time resolved sensitivity helps to tackle this question by using the example of an *Escherichia coli* (*E. coli*) growth model. We show how the time resolved parameter sensitivities of the dynamic batch and fed-batch can be used to determine identifiable parameter sets and to schedule samples for off-line and at-line measurements.

For validation of our framework, we compared our approach with equally distributed sampling over time. The results show that our sampling approach is able to determine the best identifiable parameter sets and helps to define sample time points to finally obtain the needed parameter accuracy. Besides that with less effort (number of samples) comparable parameter accuracies could be reached.

Keywords: Sensitivity; Identifiability; Model Parametrization; Sample Timepoint Optimization

1. Introduction

Having accurate process models is of great value for all production industries, offering them to do in-silico process scheduling and optimization and to use them to monitor and control their production processes (Mears et al. (2017)). In order to obtain reliable models that can be successfully used, the model calibration stage requires carefully designed experiments with high informative content (Muñoz-Tamayo et al. (2014)).

Hereby the sampling time points are of central importance to capture the information. Especially in fermentation processes, where sampling bears a contamination risk and off-line analytics are cost and labour intense, a proper sampling strategy is important. Often

equally distributed sampling or only end-points of process phases are sampled, which leads to the loss of important information.

Based on a simple *E. coli* fed-batch model, consisting of three state variables and four parameters (De Pauw and Vanrolleghem (2006)) a workflow is presented, to select identifiable parameter sets and to determine sampling time points and frequencies to obtain the aimed parameter estimation accuracy. The parameter identifiability, which considers the uniqueness of model parameters, is a prerequisite for reliable parameter estimation (Chiş et al. (2011)). Often biological models are over-parameterized, whereas only a subset of parameters are identifiable in practice. By ranking the parameters according to their influence on the model outputs, the so called parameter sensitivity, Brun et al. (2002) showed a procedure how best identifiable parameter sets can be selected for an over-parameterized model. The proposed procedure combines the collinearity, a measure of parameter uniqueness and sensitivity, a measure of parameter importance of all possible combinations.

In this contribution we extended this approach from continuous processes, where steady state conditions are reached to dynamic batch and fed-batch conditions by taking an *E. coli* growth model. The presented subset selection was based on the time resolved collinearity to determine process phases with different identifiable parameter subsets. In contrast to De Pauw and Vanrolleghem (2006) and Kutalik et al. (2004) which determined time points with highest information content, we optimized the sampling time points towards the selected parameter subset, guaranteeing reliable model parameter with preselected accuracies.

2. Materials and Methods

2.1. *E. coli* Fed-batch Model

For illustrating the algorithm an unstructured, unsegregated model describing an *E. coli* fed-batch process was taken from De Pauw and Vanrolleghem (2006). The model was extended by the concentration of dead cells. The model consist of three material balances: the living biomass C_X ,

$$\frac{dC_X}{dt} = (\mu - k_d) \cdot C_X - C_X \frac{F_\alpha}{V}, \quad \mu = \mu_{max} \frac{C_{Glc}}{C_{Glc} + K_{Glc}} \quad (1)$$

the dead biomass C_{Xd} ,

$$\frac{dC_{Xd}}{dt} = k_d \cdot C_X - C_{Xd} \cdot \frac{F_\alpha}{V} \quad (2)$$

and the glucose concentration C_{Glc} ,

$$\frac{dC_{Glc}}{dt} = \frac{Y_{X,Glc}}{\mu} \cdot C_X + (C_{Glc,\alpha} - C_{Glc}) \cdot \frac{F_\alpha}{V} \quad (3)$$

where μ is the specific growth rate, k_d the constant death rate, $Y_{X,S}$ the yield coefficient for biomass on glucose, F_α the flow rate of the glucose feed and $C_{Glc,\alpha}$ the glucose concentration of the feed. A single substrate dependent Monod kinetic was assumed to fully

describe the growth behaviour of *E. coli* in which μ_{max} is the maximum specific growth rate and K_{Glc} the saturation constant.

Normal distributed white noise, ε_{ij} was added to the model states C_j to obtain realistic data $\tilde{C}_j(t_i)$. From this noisy, data samples were taken every 5, 10, 30 and 60 min and model parameters were estimated by minimizing the profile likelihood between simulated and sampled data.

2.2. Sensitivity and Identifiability Analysis

The local sensitivity s_{jk} of the state variable C_j to parameter p_k quantifies the deflection of the state variable C_j due to small changes in p_k (DiStefano III (2015)). To identify the parameters, which influences the outputs of the described *E. coli* model most, the first-order, local sensitivity functions were simultaneously solved with the specified state equations. This local sensitivity information provides a basis for calculation of two parameter selection measures proposed by Brun et al. (2002).

$$s_{jk} = \frac{\partial C_j}{\partial p_k} * p_k \quad \delta_k^{msqr} = \sqrt{\frac{1}{n} \sum_{j=1}^n s_{jk}^2} \quad \gamma_K(t_i) = \frac{1}{\sqrt{\lambda_k(t_i)}} \quad (4)$$

The importance index δ_k^{msqr} , which ranks the parameter according to their influence on the model states and serves as a global importance measurement. Whereas the collinearity index γ_K for a chosen parameter subset k gives the linear dependency between the selected parameters. In contrast to Brun et al. (2002) the collinearity index $\gamma_K(t_i)$ was calculated for every time point t_i . To determine the best set of parameters, the smallest eigenvalue $\lambda_k(t_i)$ of the Fisher Information Matrix $FIM(t_i)$ was used. The FIM is a measure for the information content that is stored in a measurement. It is connected to the covariance matrix of the parameters by its inverse and is defined as follows:

$$FIM = \frac{1}{\sigma^2} \sum_{i=1}^N \sum_{j=1}^n \nabla_p C_j(t_i, p) \nabla_p C_j(t_i, p)^T \quad (5)$$

where σ^2 is the variance of the measurements, p the parameter vector, i the number of measurements and j the number of states (Kutalik et al. (2004)).

2.3. Optimal Sampling Schedule

To determine the best sampling times a D-optimal design was chosen, maximizing the determinant of the FIM (Berger and Wong (2005)). This scalar objective function is optimized by Powell's Method analogous to the publication of Kutalik et al. (2004). This simple algorithm allows to find a suboptimal sampling time vector.

2.4. Description of General Workflow

After stating the model (step 1) the sensitivity analysis (step 2) the importance ranking and collinearity index are calculated (step 3). These two criteria are essential for the parameter subset selection (step 4) including only parameter subsets fulfilling both conditions (high sensitive and uncorrelated). Time optimization (step 5 and 6). Thereafter the optimization algorithm maximizes the determinant of the Fisher information and selects

the most informative measurement points related to the parameter subset. Afterwards the parameter of the subset are estimated (step 7) showing acceptable errors (step 8).

3. Results and Discussion

Figure 2 shows the time series data of the simulated state variables and their corresponding in-silico samples, which were taken with a measurement frequency of 60 min. The fermentation starts in the batch mode with an initial working volume V_0 of 5 L, an initial glucose concentration $C_{Glc,0}$ of 6 g/L and an initial biomass concentration $C_{X,0}$ of 0.5 g/L. After a 6 h lasting batch phase a 4 h fed-batch followed. The fed-batch mode is characterized by a constant inflow of medium $F_\alpha = 5 \cdot 10^{-3}$ L/h with a glucose concentration of 600 g/L.

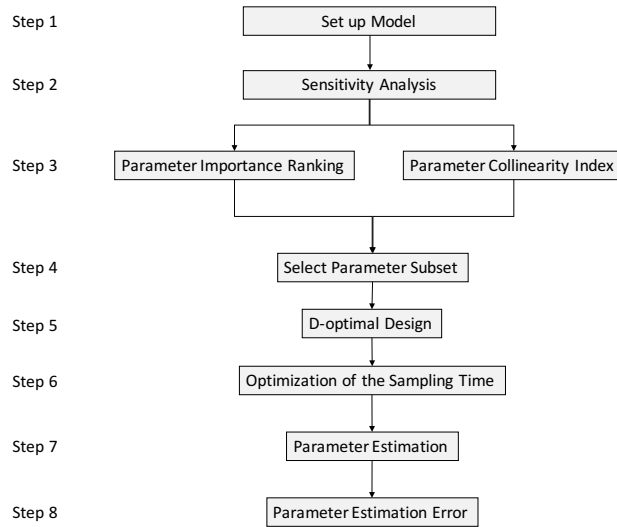


Figure 1: Overview of the workflow for improving the parameter estimation accuracy

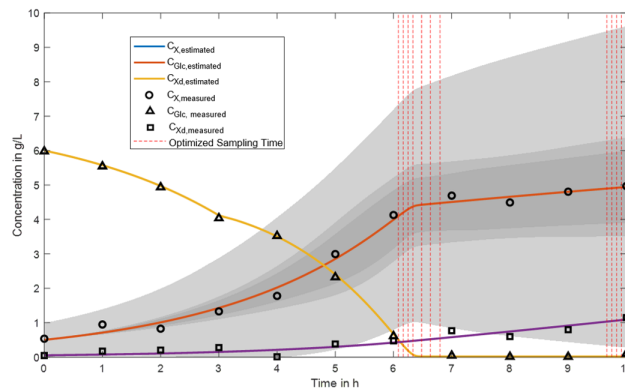


Figure 2: Overview of the optimal sampling times ($n_{sample} = 11$), the measured ($n_{sample} = 11$) and estimated concentration profiles of living biomass, dead biomass and glucose during an *E. coli* fed-batch process with a total process time of 10 h. Shaded areas are the 95 % confidence intervals of the biomass concentration (light grey: before subset selection, grey: after subset selection, dark grey: after sampling time optimization).

In Figure 3 the importance index of the parameters for the *E. coli* model and the time resolved collinearity index of some feasible subsets are illustrated. In total there exist 11 parameter combinations consisting of 2,3 and 4 parameters. All 4 parameters together reached high collinearities. The same goes for combinations with K_{Glc} and μ_{max} , which are not displayed in Figure 3. The parameter ranking revealed that μ_{max} is the most sensitive parameter. A change in μ_{max} leads to the largest change in the state variables. K_{Glc} is characterized by a low importance index, because it is only active in a small time window around 6 h when the glucose is nearly depleted. The subset of μ_{max} , Y_{XS} and k_d is the most linear independent and important triple combination. Within Figure 3 a time window is indicated in gray, where the selected subset shows almost no linear dependency.

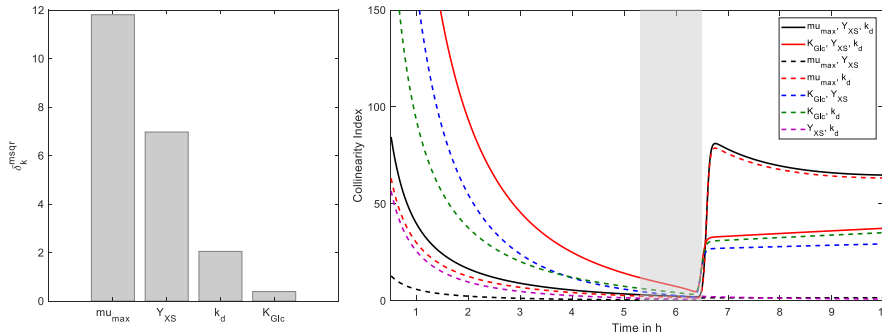


Figure 3: Selection of best identifiable Parameter set. a) Overall parameter importance, b) Time resolved identifiability of feasible parameter sets

In Table 1 the parameter estimation errors of all four parameters and the selected subset are compared for different measurement frequencies. These parameter estimation errors are based on the Cramer Rao lower bound. After parameter subset selection and exclusion

Table 1: Parameter estimation error (%) of the full parameter set with the selected parameter subset, excluding K_{Glc} at different measurement frequencies.

Data Frequency	$\Delta\mu_{max}$	ΔY_{XS}	Δk_d	ΔK_{Glc}	n Samples
(min)	(%)	(%)	(%)	(%)	
5	6.99 2.41	3.82 3.74	18.33 18.33	90.83 -	121
10	9.81 3.41	5.47 5.35	23.13 23.13	148.10 -	61
30	26.61 5.81	9.33 9.03	47.25 43.99	139.50 -	21
60	29.21 7.96	12.58 12.27	56.62 56.59	1145.5 -	11

of K_{Glc} , the parameter estimation error of μ_{max} decreases dramatically from 29 % to 8 % at a low sampling frequency. The other parameters are only slightly affected, which indicates a strong correlation between μ_{max} and K_{Glc} . The sample frequency has also an significant influence on the estimation error, showing a 3-fold increase comparing a 5 min to a hourly sampling rate. The estimation errors of the selected parameter subset with optimized sample time points are summarized in Table 2. It can be seen that by optimizing

the sampling time point the estimation error can be significantly reduced. The errors are in the range of a sampling rate lower than 30 min, with only half of the samples. Compared to the same amount of equally distributed samples (60 min) the estimation error decreased by approx. 35% for μ_{max} and k_d and by 25% for Y_{XS} . The 95 % confidence interval of the biomass is shown in figure 2 before/after the subset selection and at the end of the sampling time optimization .

Table 2: Parameter estimation error (%) of the selected parameter subset consisting of μ_{max} , Y_{XS} and k_d after optimization of the sampling time

Measurement Frequency	$\Delta\mu_{max}$	ΔY_{XS}	Δk_d	n Samples
(min)	(%)	(%)	(%)	
60	7.96	12.27	56.59	11
optim	5.20	9.20	35.70	11

4. Conclusions and Outlook

It is shown that a combination of parameter subset selection and optimization of the sampling time points reduces the parameter estimation error drastically. The presented approach ensures that important samples are taken while at the same time overall sampling effort can be decreased. By evaluating the collinearity and parameter importance, the subsequent parameter estimation leads to more reliable models.

Although the D-optimality criterion proved to be a suitable optimization criterion for the examined fed-batch process, a further improvement might be reached when a combination of different optimality criteria for example D-optimal und E-optimal is implemented.

5. Acknowledgements

This work was supported by the Austrian research funding association (FFG) under the scope of the ‘‘AdaMo’’ project and by the Christian Doppler Forschungsgesellschaft (Grant No. 171).

References

- M. P. Berger, W.-K. Wong, 2005. Applied optimal designs. John Wiley & Sons.
- R. Brun, M. Kühni, H. Siegrist, W. Gujer, P. Reichert, 2002. Practical identifiability of asm2d parameters—systematic selection and tuning of parameter subsets. *Water research* 36 (16), 4113–4127.
- O. Chiş, J. R. Banga, E. Balsa-Canto, 2011. Genssi: a software toolbox for structural identifiability analysis of biological models. *Bioinformatics* 27 (18), 2610–2611.
- D. J. De Pauw, P. A. Vanrolleghem, 2006. Nesting genetic algorithms to solve a robust optimal experimental design problem.
- J. DiStefano III, 2015. Dynamic systems biology modeling and simulation. Academic Press.
- Z. Kutalik, K.-H. Cho, O. Wolkenhauer, 2004. Optimal sampling time selection for parameter estimation in dynamic pathway modeling. *Biosystems* 75 (1-3), 43–55.
- L. Mears, S. M. Stocks, M. O. Albaek, G. Sin, K. V. Gernaey, 2017. Mechanistic fermentation models for process design, monitoring, and control. *Trends in biotechnology* 35 (10), 914–924.
- R. Muñoz-Tamayo, P. Martinon, G. Bougaran, F. Mairet, O. Bernard, 2014. Getting the most out of it: optimal experiments for parameter estimation of microalgae growth models. *Journal of Process Control* 24 (6), 991–1001.

Synthesis of Solar Heat Network for Preheating of Industrial Process Streams

Ben Abikoye,^{a,*} Lidija Čuček,^{b,*} Adeniyi Isafiade,^a Zdravko Kravanja^b

^a*Department of Chemical Engineering, University of Cape Town, Private Bag X3, Rondebosch 7701, Cape Town, South Africa*

^b*Faculty of Chemistry and Chemical Engineering, University of Maribor, Smetanova ulica 17, 2000 Maribor, Slovenia*

abksem001@myuct.ac.za, lidija.cucek@um.si

Abstract

Industrial integration of solar for process heat applications with periodic heat storage and backup utility system ensures reliability and efficiency of renewable heat utilization, thus minimizing the dependence on fossil fuel and energy related emissions. Furthermore, by minimizing heat duty from backup utility, opportunities for matching solar thermal and solar heat storage could be fully explored. This study models the industrial application of solar thermal considering direct and indirect integration, periodic heat storage and backup utility. For the synthesis of the integrated design, a flowsheet superstructure is presented for multi-period heat supply network of industrial processes. The design and optimization of the integrated system is implemented and solved in GAMS with the objective of maximizing total heat output to the heat network. To demonstrate the performance of the model, the proposed solar heat network design for industrial utility retrofit is applied to an illustrative case study of preheating a cold industrial stream.

Keywords: Solar thermal, Solar heat, Thermal storage, Solar heat integration, Industrial solar integration.

1. Introduction

Over the past few decades, the global energy consumption has been on steady increase due to the rising of population and expanding economic activities. According to a recent report, heat consumption accounts for over 50 % of the annual global energy use (WEC, 2016) and analysis has revealed that as at 2014 about 75 % of this share of energy consumption (around 130 EJ) is currently sourced from fossil fuels (OECD/IEA, 2015) which negatively impacts the environment.

Solar thermal is a form of renewable energy with great potentials to substitute/supplement the use of fossil fuels for various heating purposes because it is a low-carbon source of heat and power (electricity). Studies have shown that out of the total global industrial heat consumption of 85 EJ, 30 % is used for low temperature (<150 °C) heat operations (IEA, 2017). Due to the wide range of industrial processes with low temperature heat operations, industrial solar utilization is believed to have great potentials.

Solar industrial utility retrofit in combination with periodic heat storage (Abikoye et al. 2018) is a demonstration of how a renewable source of heat can be effectively planned for and harnessed with industrial heat networks. Due to supply variability and low thermal

splitter is placed at the outlet from the process plant such that the heat transfer fluid can return to the solar collector or to the storage tank depending on whether the temperature level of return could be useful to buffer the heat in the storage tank.

2.2 Model development

The developed model comprises material and energy balances across the solar collector, splitters, mixers, heat storage tank, backup boiler and the plant (two heat exchangers) that is targeted for solar heat integration. It should also be noted that the operational features of a typical solar heating system are transient, therefore to account for the time dependencies, the model is formulated as a mixed-integer non-linear programming (MINLP) problem. Also, the synthesis is implemented simultaneously with the objective of maximizing the average solar heat output to the network ($Q_{mp,dp,hp}^{solar}$) shown in Eq. (1).

$$\max \sum_{mp \in MP} \sum_{dp \in DP} \sum_{hp \in HP} \mid_{(dp,mp) \in DPM} Q_{mp,dp,hp}^{solar} \quad (1)$$

where hp , dp and mp represent the hourly, daily and monthly periods and DPM stands for set of pairs of days and months.

The model takes into account variable flowrates, temperatures and energy flows across each unit within the entire system. Additionally, area of a solar thermal collector and its efficiency and storage tank volume are optimization variables. The data required to achieve this were retrieved as actual measured values of hourly global horizontal irradiation and ambient temperatures. Thermal energy provided by solar collector (in kWh/period) and the data for its calculation are based on the work by Isafiade et al. (2016), however in this work equality constraint is used and is multiplied by the number of hours for specific period.

The MINLP model consists of linear and nonlinear equality and inequality constraints and additionally it includes discrete or binary decisions. The binary variables ($y_{mp,dp,hp}$) are associated with the temperature of heat storage tank and the heat energy provided by heat transfer fluid from the solar collector. Eq. (2) shows such a constraint which states that the temperature in storage tank ($T_{mp,dp,hp}^{storage\ tank}$) should be lower than the difference between outlet temperature of the heat transfer fluid returning to solar collector ($T_{mp,dp,hp}^{out-2, storage\ tank}$) and the minimum temperature difference (ΔT_{min}), in a case the flow is non-zero. On the other hand, when there is no flow, there is no specific constraint on the temperature in storage tank.

$$T_{mp,dp,hp}^{storage\ tank} \leq T_{mp,dp,hp}^{out-2, storage\ tank} - \Delta T_{min} + M \cdot (1 - y_{mp,dp,hp}), \quad \forall (mp \in MP, dp \in DP, hp \in HP) \quad (2)$$

Eq. (2) represents big M constraint, M being big enough scalar, and binary variable $y_{mp,dp,hp}$ is connected to the flow from solar collector to the tank and back to the collector ($F_{mp,dp,hp}^{in-1, storage\ tank}$). If binary variable is 1, the flow should be between a minimum (F^{min}) and a maximum value (F^{max}), and 0 otherwise. Such constraints are shown in Eq. (3).

$$F^{min} \cdot y_{mp,dp,hp} \leq F_{mp,dp,hp}^{in-1, storage\ tank} \leq F^{max} \cdot y_{mp,dp,hp}, \quad \forall (mp \in MP, dp \in DP, hp \in HP) \quad (3)$$

3. Case Study

The developed model is implemented and demonstrated on a specific location near Maribor, Slovenia as a case study, partly because low temperature industrial operations represent approximately 37 % of the total industrial heat demand in Slovenia (RSSO, 2017). This location was a reference point to obtain required meteorological data, such as hourly solar irradiation and ambient temperature. The data, which are based on the year 2016, were extracted from the EC JRC PVGIS (2017) using coordinates 46.552 N: 15.676 E Latitude and Longitude, and an elevation of 267 m above sea level.

In the case study, solar thermal is integrated with an industrial heat network for process stream preheating as shown in Figure 1. As a heat transfer fluid, 50/50 water-ethylene glycol is considered. For simplicity, only 1 cold process stream is considered in this demonstrative example while opportunities for using backup utility are accommodated within the framework of the model (see Figure 1).

To reduce computational time, mathematical model reduction techniques based on an earlier procedure presented by Egieya et al. (2018), which is a modification from presentation of Lam et al. (2011), is adopted. The 24 hours of each day are discretized into 4 periods of different durations: H1: 9 pm – 7 am, H2: 8 am – 10 am, H3: 11 am – 4 pm, H4: 5 pm – 8 pm. The 29 – 31 days of a month are discretized into just one period, while 12 months are considered in total. The input data on an hourly basis were averaged as previously done by Egieya et al. (2018). The model consists of 4,504 single equations, 4,755 single variables, and 48 binary variables. It was solved using SBB solver in GAMS with 1 % optimality gap in up to few hours on a personal computer with an Intel® Core™ i7-8750 H CPU @ 2.20 GHz processor with 8 GB RAM.

The results from the model show that the allowable volume of heat transfer fluid (V^{fluid}) in the storage tank and solar collector area (A_{panel}) have strong influence on the solution. Thus, the model has been solved considering different upper bounds for V^{fluid} and A_{panel} . Additionally, upper bound on flowrates of 100 t/h has been set. In almost all the solutions obtained (except for $A_{\text{panel}} = 100 \text{ m}^2$, where V^{fluid} was 56.6 m^3), both V^{fluid} and A_{panel} were set at their upper bounds. The graphs in Figure 2 show the relationship between the average heat load of solar thermal (Average DH^{solar}) exchanged with the cold process stream and the temperature of the stream achieved with solar (Average T^{solar}) for different values of A_{panel} between 100 and $10,000 \text{ m}^2$.

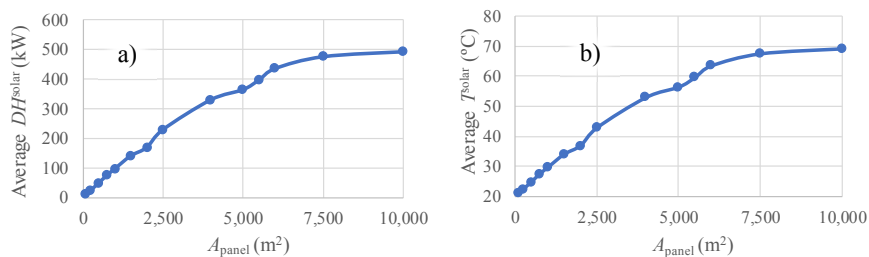


Figure 2: a) Average DH^{solar} and b) average T^{solar} with different sizes of solar collectors

From Figure 2, it could be seen that both DH^{solar} and T^{solar} significantly increase up to a A_{panel} value of $6,500 \text{ m}^2$, DH^{solar} for 80.9 W/m^2 and T^{solar} for 0.008 °C/m^2 in average.

decision support tool for industrial utility planning. For the demonstrative case considered, the solution obtained shows the non-linear relationships between the area of solar collector (and volumes of thermal heat storage fluid) and the quantity of heat captured by the solar panel and thus temperatures achieved in the process. Both variables, A_{panel} and V^{fluid} were mostly set at their upper bounds. Future work will entail investigation of opportunities for inclusion of heat pump to increase thermal efficiency of both the direct and indirect integration. Processes involving a larger number of hot and cold streams, with multiple options of backup utilities, and economics-based objective function, will also be considered.

Acknowledgements

The authors wish to acknowledge the financial supports received from the National Research Foundation (NRF) of South Africa through the grant number 105780, Faculty of Engineering and the Built Environment at the University of Cape Town, South Africa, the Slovenian Research Agency (programs P2-0377 and P2-0032 and project L2-7633) and the Slovenia-Croatia bilateral project INTEGRES.

References

- B. Abikoye, L. Čuček, A. Isafiade, A. Nemet, Z. Kravanja, 2018, Retrofitting of Industrial Utility Systems Considering Solar Thermal and Periodic Heat Storage, Proceedings of 1st International Conference on Technologies & Business Models for Circular Economy (TBMCE 2018), 253-261, doi: 10.18690/978-961-286-211-4.21
- J.M. Egieya, L. Čuček, K. Zirngast, A.J. Isafiade, B. Pahor, Z. Kravanja, 2018, Biogas Supply Chain Optimization Considering Different Multi-Period Scenarios, Chemical Engineering Transactions, 70, 985-990 DOI: 10.3303/CET1870165
- European Commission Joint Research Centre Photovoltaic Geographical Information System (EC JRC PVGIS), 2017, PVGIS tools. <re.jrc.ec.europa.eu/pvg_tools/en/tools.html> (accessed: August 2018)
- International Energy Agency (OECD/IEA), 2015, World Energy Outlook <www.iea.org/publications/freepublications/publication/WEO2014.pdf> (accessed: November 2018)
- International Energy Agency (IEA), 2017, New Report: Renewable Energy for Industry <www.solarpaces.org/new-iea-report> (accessed: February 2019)
- A.J. Isafiade, Z. Kravanja, M. Bogataj, 2016, Design of integrated Solar Thermal Energy System for Multiperiod-Period Process Heat Demand, Chemical Engineering Transactions, 52, 1303-1308 DOI: 10.3303/CET1652218
- C. Kong, L. Sing, J. Shiun, T.G. Walmsley, P. Y. Liew, 2018, Effect of Solar Utility temperature to Costing and Design Parameters of Integrated Solar Thermal System, Chemical Engineering Transactions, 70, 139-144, doi: 10.3303/CET1870024
- H.L. Lam, J.J. Klemeš, Z. Kravanja, 2011, Model Size reduction Techniques for Large Scale Biomass Production and Supply Networks, Energy, 36, 4599-4608.
- Republic of Slovenia Statistical Office (RSSO), 2017, Final Energy Consumption in Slovenia. <www.stat.si/StatWeb/en/News/Index/7722> (accessed: February 2019)
- World Energy Council (WEC), 2016, World Energy Resources <www.worldenergy.org/wp-content/uploads/2016/10/World-Energy-Resources_Report_2016.pdf> (accessed: November 2018)

Novel strategies for predictive particle monitoring and control using advanced image analysis

Rasmus Fjordbak Nielsen^a, Nasrin Arjomand Kermani^b, Louise la Cour Freiesleben^c,
Krist V. Gernaey^a and Seyed Soheil Mansouri^{a,*}

^a*Process and Systems Engineering Centre (PROSYS), Department of Chemical and Biochemical Engineering, Technical University of Denmark, Søtofts Plads, Building 229, DK-2800 Kgs. Lyngby, Denmark*

^b*Section of Thermal Energy, Department of Mechanical Engineering, Technical University of Denmark, Nils Koppels Allé, Building 403, DK-2800 Kgs. Lyngby, Denmark*

^c*ParticleTech ApS, Hirsemarken 1, DK-3520 Farum, Denmark*
seso@kt.dtu.dk

Abstract

Processes including particles, like fermentation, flocculation, precipitation, crystallization etc. are some of the most frequently used operations in the bio-based industries. These processes are today typically monitored using sensors that measure on liquid and gas phase properties. The lack of knowledge of the particles itself has made it difficult to monitor and control these processes. Recent advances in continuous in-situ sensors, that can measure a range of particle properties using advanced image analysis, have now however opened up for implementing novel monitoring and modeling strategies, providing more process insights at a relatively low cost. In this work, an automated platform for particle microscopy imaging is proposed. Furthermore, a model based deep learning framework for predictive monitoring of particles in various bioprocesses using images is suggested, and demonstrated on a case study for crystallization of lactose.

Keywords: Bioprocess Monitoring, Advanced Image Analysis, Modeling Framework

1. Introduction

During the past two decades, bioprocesses have become an increasingly important part of many food, chemical, agrochemical and pharmaceutical industries. This has had an impact on both upstream and downstream processing. Here, fermentation, flocculation, precipitation and crystallization are frequently used processes for formation, separation and purification of products, respectively (Santos et al. (2017)). A common denominator for these processes is that they all contain particles in some form, whether it is cells, aggregates or crystals.

Despite the broad applications of these processes in industry, there is typically a problem of monitoring and controlling them to a satisfactory degree. This is evident in the common use of heuristics based control and the difficulties in obtaining consistent product qualities. Today, most of these bioprocesses are monitored and controlled using traditional sensors that measure gas and liquid phase properties. Only recently, there has been a focus on measuring particle properties continuously (Biechele et al. (2015)).

Historically, particle characterization has been either very time-consuming or associated with relatively high capital costs of the sensors needed. To accommodate this, in the past decade, there

has been a move towards developing soft-sensors, that utilize the measured gas and liquid phase properties, to estimate different process variables that relates to the particles. These have shown great potential (Damour et al. (2009); Mears et al. (2017)). However, these soft-sensors typically require a large amount of infrastructure, in terms of on-line sensors, and significant modeling efforts, as they are only indirect measures of the real process variables.

Meanwhile, there have been significant developments within the application of advanced image analysis in recent years, which has enabled reliable particle analysis in real time, providing an easy way of measuring a range of particle properties. Furthermore, with the current trends towards lab-on-a-chip solutions for industrial sensors, the use of advanced image analysis in bioprocesses can now be implemented at a relatively low cost, and add valuable insights to various bioprocesses.

In this work, a novel platform for automated particle microscopy is presented, where on-line microscopy images are taken from a flow cell. A model-based, predictive monitoring framework is proposed for a generic particle process, utilizing both quantifiable particle properties obtained from advanced image analysis and the captured raw-images themselves. Here, a deep neural network is used for estimating rates of phenomena, that can be used for prediction of process variable trajectories like particle count and size distribution. This model-based framework is subsequently demonstrated on a case study of lactose crystallization, showing the potential of this method, and finally compared to results of conventional white-box modeling.

2. Flow cell microscopy

To measure a whole range of particle properties in a continuous fashion, a robust platform is introduced to automatically transfer samples from the production tank to the flow cell under the microscope for image acquisition and on-line monitoring of the process. The automated platform,

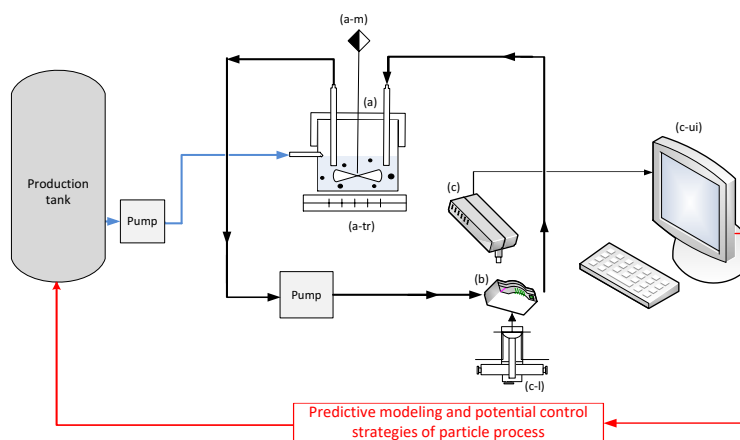


Figure 1: Illustration of proposed platform: (a) Sample unit with automated flowpath (blue and black lines) consists of mixer (a-m), temperature regulator (a-tr) and two pumps; (b) a modular flow cell; (c) Automated microscope with light adjustment (c-l) from bottom side; and a user interface (c-ui)

shown in Figure 1, consists of four core elements:

- Sample unit with automated flowpath consists of a mixer, temperature regulator and two pumps to transfer the sample from the production tank to the flow cell under controlled

conditions. The sample can be diluted inside the sample unit to a convenient volume for on-line microscopy.

- A modular flow cell consist of a monolayer channel, adjustable for a wide range of particle sizes and carrier fluid properties to hold the samples under the microscope for image acquisition
- An automated microscope to capture high quality images
- A user interface to extract meaningful information from an image through several steps such as image processing, segmentation, and characterization of the identified object. The segmented 2D- image will provide valuable information such as particle size, particle shape, and particle size distribution.

The proposed configuration allows rapid and nondestructive visual monitoring of samples with various compositions and enables the extraction of valuable chemical and physical information.

3. Model-Based Framework

To benefit the most from these new real-time measurements, a predictive monitoring framework is proposed, utilizing the large amount of information that is generated from the captured images. The phenomena observed in a generic particle process include particle birth, particle growth (both positive and negative), particle agglomeration and particle breakage. To describe the overall par-

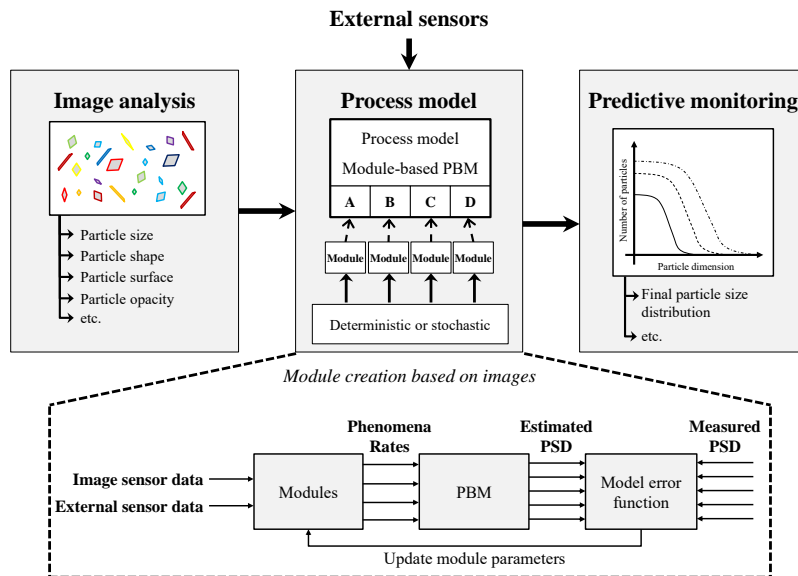


Figure 2: Proposed framework for monitoring of particles in bioprocesses

ticle processes, population balance modeling (PBM) has become a very popular and generic tool (Ramkrishna and Singh (2014)). For each type of process, a range of kinetic expressions are typically derived from experiments, describing the rate of a given phenomenon, as a function of a range of process variables like temperature, pH and composition. To determine these expressions, one has historically tried to study one phenomenon at a time, where a large fraction of these studies have only been looking at the development of a single particle as a function of time.

In this framework, we instead aim towards describing these phenomena, by analyzing sample populations during the process operation, containing several hundreds of particles. For each phenomenon that needs to be explained, a corresponding module will be included in the model. These modules can either be traditional white-box models like power-law expressions, utilizing a limited range of very specific measurements, or black box models like neural networks, random forests etc. that can take into account a much larger range of measured process variables. An overview of the framework can be seen in Figure 2.

By using this framework, with the latter black-box approach, which is combined with the white-box generic PBM, one can potentially save much time in process modeling. One will however still get an accurate description of the system dynamics, and at the same time take into account a lot more possible process disturbances and variables than in the conventional approach. Finally, this framework allows for implementing a robust model predictive control (MPC) in various particle processes.

4. Case study: Lactose crystallization

The presented framework is now demonstrated for a case study of lactose. For this study, a single crystallization experiment was carried out for the model generation and one for process model validation. A scanned 2D plane of $2288.5 \mu\text{m} \times 1408 \mu\text{m}$ was used in both experiments.

A lactose solution was prepared by dissolving 35.0 g lactose per 100.0 g water, by heating the solution to $70 \text{ }^\circ\text{C}$. Afterwards, the solution was cooled down by natural heat loss to the surroundings, which results in crystallization of lactose. Samples were taken regularly (every 3-4 minutes) using the presented flow cell microscopy, obtaining a range of particle properties, including the Feret diameters, projected area and sphericity of each particle detected on each image. Furthermore, the temperature of the crystallization process was measured continuously. Three examples of segmented images, showing the crystallization progress, can be seen in Figure 3. Note how the number of crystals is increasing and the crystals are increasing in size as a function of time.

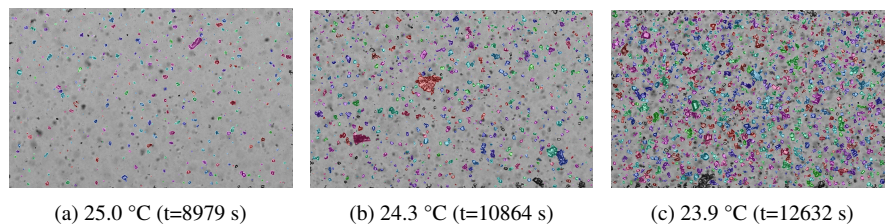


Figure 3: Images after segmentation of crystals.

In this case study, the crystals were binned according to their mean Feret diameter, starting from $20 \mu\text{m}$ moving up to $80 \mu\text{m}$, with a total of 40 bins. Using the presented predictive monitoring modeling framework, a rolling prediction model was generated, using a deep neural network for estimating the nucleation and growth rates, and then compared to a conventional full simulation modeling approach, using white-box power-law expressions. Both approaches utilizes a generic 1D PBM, relying on the method of classes, where the effects coming from agglomeration, breakage and dissolution have been neglected in both.

The deep neural network used here consists of 4 dense layers in total, with a total of 296,000 weights. The inputs provided to the network are: a grey-scale and down-sampled version of the raw image (64×64 pixels) taken at the estimation time, the current temperature, the current temperature gradient and the time-horizon Δt to predict. This results in one growth rate per bin and a single nucleation rate. By transferring these rates to the generic white-box PBM, one can

obtain a grey-box running prediction of the size distribution at time $t + \Delta t$, where the initial size-distribution of the PBM is set to the measured distribution at the current time t .

In the conventional full simulation modeling approach, the solubility of lactose in water as a function of temperature was approximated by a second order polynomial fit of the datapoints measured by Hudson (1908). Furthermore, the density of lactose was set to 1.52 g/cm³ as reported by Lewis (2007). The following three white-box rate expressions, similar to the ones presented by Szilagyí and Nagy (2016), where used in this work:

$$P = k_p \cdot \sigma^p \quad , \quad S = k_s \cdot \sigma^s \cdot V_c \quad , \quad G = k_g \cdot \sigma^g \cdot (1 + \gamma \cdot L) \quad (1)$$

where V_c is the volume of crystals per volume solute and L is the characteristic particle dimension. Thus, in the white-box model, there are seven kinetic parameters that have to be determined by experiments and a single parameter relating to the particle shape, the volumetric shape factor k_v .

The two models were fitted to the experimentally obtained data from a single batch crystallization, by minimizing the absolute error of the relative size distribution. The two fitted models can be seen in Figure 4a + 4b, showing the time-evolution of the relative size distribution. Note that only a selection of size-bins have been included in the figures for improved readability.

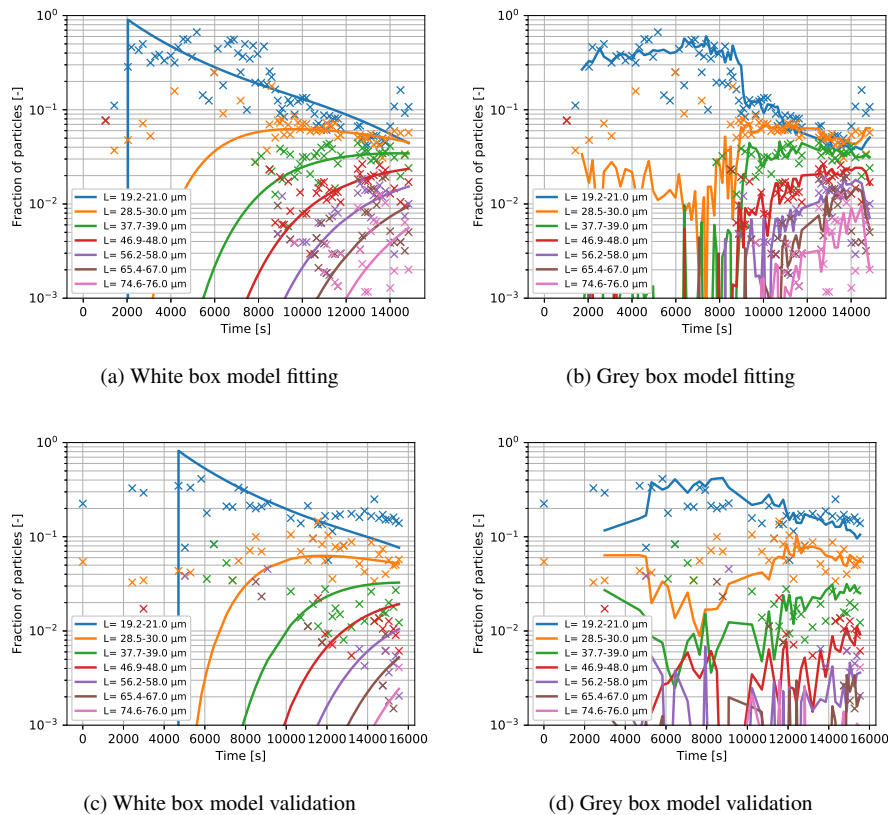


Figure 4: Model fitting and validation for the two modeling approaches.

The two modeling approaches have subsequently been used to predict the evolution of the size distribution as function of time in the validation experiment. These results can be seen in Figure

4c + 4d, where the predicted time-horizon for the rolling prediction is set to 10 minutes. I.e. the deep neural network estimates the appropriate nucleation and growth rates for the next 10 minutes of crystallization operation.

It can be seen that both modeling approaches predicts the trends in the size distribution evolution well. However, the rolling prediction can be seen to produce more accurate predictions. In this, the adaptive nature of the rolling prediction does play a big role, as it is utilizing size distribution data as they become available. However, even for larger predicted time-horizons Δt , the grey-box model approach performs very well, indicating that the deep neural network does estimate the actual phenomena rates to a satisfactory degree.

With the presented grey-box model approach, it is shown possible to capture some effects in the crystallization, that would not be taken into account in a conventional modeling approach. However, the grey-box modeling is also relatively prone to measurement noise in the size-distribution sampling, which can be seen in as fluctuations in Figure 4b + 4d. These sources are especially critical, as they are both used as input and output variables while training the neural network, and would therefore be beneficial to minimize these uncertainties, possibly by using MCMC methods or input noise during training, as previously reported for neural networks (Wright et al. (2000)).

5. Conclusions

In this work, a novel continuous microscopy platform has been presented, showing a simple and cheap way of taking images of particles in suspension. A model-based predictive monitoring framework has been presented, utilizing particle parameters obtained from the images and the raw images themselves. This is used for modeling a generic particle process, and predicting the future particle population, utilizing deep learning neural networks for estimating birth and growth rates. The framework has been tested on a case study of lactose crystallization, where it has been shown that the framework can provide accurate predictions, even for small amounts of training data.

6. Acknowledgments

This work partly received financial support from the Greater Copenhagen Food Innovation project (CPH-Food), Novozymes, from EU's regional fund (BIOPRO-SMV project) and from Innovation Fund Denmark through the BIOPRO2 strategic research center (Grant number 4105-00020B).

References

- P. Biechele, C. Busse, D. Solle, T. Scheper, K. Reardon, 2015. Sensor systems for bioprocess monitoring. *Engineering in Life Sciences* 15, 469–488.
- C. Damour, M. Benne, B. Grondin-perez, J. Chabriat, 2009. Model based soft-sensor for industrial crystallization: on-line mass of crystals and solubility measurement. *World Academy of Science, Engineering and Technology* 54, 196–200.
- C. S. Hudson, 1908. Further studies on the forms of milk-sugar. *Journal of the American Chemical Society* 30, 1767–1783.
- R. J. Lewis, 2007. *Hawley's Condensed Chemical Dictionary*. John Wiley & Sons, Inc.
- L. Mears, S. M. Stocks, M. O. Albaek, G. Sin, K. V. Gernaey, 2017. Application of a mechanistic model as a tool for on-line monitoring of pilot scale filamentous fungal fermentation. *Biotechnology and Bioengineering* 114, 589–599.
- D. Ramkrishna, M. R. Singh, 2014. Population Balance Modeling: Current Status and Future Prospects. *Annual Review of Chemical and Biomolecular Engineering* 5, 123–146.
- R. Santos, A. Carvalho, A. Roque, 2017. Renaissance of protein crystallization and precipitation in biopharmaceuticals purification. *Biotechnology Advances* 35, 41 – 50.
- B. Szilagyi, Z. Nagy, 2016. Graphical processing unit (GPU) acceleration for numerical solution of population balance models using high resolution finite volume algorithm. *Computers and Chemical Engineering* 91, 167–181.
- W. Wright, G. Ramage, D. Cornford, I. Nabney, 2000. Neural Network Modelling with Input Uncertainty: Theory and Application. *Journal of VLSI signal processing systems for signal, image and video technology* 26, 169–188.

Integrating Simulation and Optimization for Process Planning and Scheduling Problems

Miguel Vieira^a, Samuel Moniz^b, Bruno Gonçalves^c, Tânia Pinto-Varela^{a*}, Ana Paula Barbosa-Póvoa^a

^a*CEG-IST, Universidade de Lisboa, Av. Rovisco Pais, 1049-001 Lisboa, Portugal*

^b*Departamento de Engenharia Mecânica, Universidade de Coimbra, Coimbra, Portugal*

^c*Departamento de Produção e Sistemas, Universidade do Minho, Guimarães, Portugal*
tania.pinto.varela@tecnico.ulisboa.pt

Abstract

The development of hybrid simulation-optimization methods has allowed to explore the complexities of planning and scheduling problems. In this work, a simulation-optimization approach is developed to provide decision-support to industrial processes, combining a mathematical formulation with a detailed discrete-event simulation model. To solve industrial planning and scheduling problems, the methodology iteratively estimates the modelling parameters to maximize the output in a multistage production facility, while guaranteeing allocation constraints and main process uncertainties to satisfy the demand. The production plan is evaluated at the MILP model and the capacity-feasible schedule is generated by the dispatching rules in the simulation model. Results highlight the advantages of the hybrid approach to guarantee optimized process performance metrics in a simulated operational planning.

Keywords: simulation-optimization; production planning and scheduling; hybrid methodology

1. Introduction

Current industries are facing competitive environments that demand enhanced performance indicators, such as customer satisfaction, manufacturing/inventory holding costs, and delivery times. These challenging production environments have enabled the development of advanced planning and scheduling support tools, following the increasing digital transformation with process automation. Despite the significant developments in exact/non-exact modelling techniques in recent years, it is acknowledged that generalized mathematical formulations are limited by the inherent computational hindrance of system modelling with combinatorial complexity. As well, the development of novel simulation platforms has empowered the evaluation of scenarios that mimics real operations and explore the complexity of nonlinear and stochastic systems. Therefore, the potential hybridization of simulation with optimization approaches, as noted by Figueira and Almada-Lobo (2014), combines the advantages of the process detail representation with the ability to optimize solutions. With different abstraction levels in each model, the simulation includes features not addressed in the optimization to decrease complexity, while considering iterative parameters adjustment to allow solution convergence. This

methodology is categorized as a Recursive Optimization-Simulation Approach (ROSA), which recursively evaluates performance metrics until a stopping criterion is met.

In this work, we explore this ROSA methodology to address the planning and scheduling optimization problem in multistage production process. Based in Kim and Kim (2001) approach, the proposed hybrid approach combines a mathematical model with a detailed discrete-event simulation model to provide decision-support on the production planning and the required number of allocated shared resources. As follows, we present an overview of methodology of the proposed approach and discuss the results in a case example in order to formulate a planning/scheduling solution for the industrial operational management.

2. Background

The general problem of planning/scheduling operations has become one of the most challenging problems in process industry. Due to arbitrary network configurations of resources that accounts multiple materials recipes, the inherent complexity endures researchers on finding the key modelling solution on how to optimize the sizing, sequencing and allocation while matching the expected performance of an industrial process. Since operational decisions are strongly interconnected, it is difficult to develop competent decomposition approaches to solve real-size applications with good schedules and modest computational hindrance (Castro et al., 2011). And, as note by Harjunkoski et al. (2014), novel optimization methods are required to address the pressure toward further cost-savings, efficient use of resources, regulatory aspects and new technologies.

Among the diverse solution approaches, from mathematical programming to heuristic algorithms, the combination of the best assets of different methods has been gathering significant relevance. Hybrid formulations have been consistently addressing the reduction of the solution search-space to limit the number of operational and strategic decisions to a manageable level (Vieira et al. 2018). Noteworthy, simulation and optimization approaches are widely applied as sole methodologies to address operational problems. But with modern discrete-event simulation platforms, several authors have addressed the drawbacks by exploring the iterative combination of both in the evaluation of parameters, optimization of solution variables, and sampling of scenarios (Martins et al. 2017). For example, Kim and Kim (2001) developed an extended hybrid model for the multiperiod multiproduct production planning problem, based on an iterative process where the release plan determined by a linear programming model is evaluated by the simulation model. One of planning challenges relies in the real estimate of the lead time of production, since the release of the production order to its output dispatch to satisfy the demand, accounting to the uncertainty in resources' workload capacities. When the results are not feasible (e.g. the number of orders released by the optimization exceeds the workload capacity under simulated conditions), the simulation model adjusts a specific set of parameters of the optimization model and repeats the process under more restrict conditions. When the results from the analytical method are feasible and met the stopping criteria (e.g. number of iterations, production demand met or solution convergence), a near-optimal production schedule can be generated. The iteration considers factors that correlate the capacity and workload of the resources, namely loading ratios and unit utilization. The authors verified that the method consistently converges in few iterations, even in real problems of industrial complexity (Kim and Lee, 2016). However, it is acknowledged that the right level of abstraction in each model is

critical to avoid runtime becoming impracticable, since the simulation model is left to include the hard-to-model parameters, with particular significance on solution quality and convergence parameters of the method.

3. Methodology

The hybrid approach proposed in this work consists in the iterative use of optimization and simulation models to address the optimal planning and scheduling of an industrial production process. The problem defines the optimal allocation of shared resources to perform a production mix per demand period in a multistage facility considering the cost-efficient use of resources. This decomposition approach enables to generate a solution at the planning capacity level with a MILP model that is, iteratively, evaluated at the scheduling level with the visualization of the dynamic behavior of the production process. While the optimization model is formulated using GAMS/CPLEX, the detailed simulation model is implemented in SIMIO which systematically reproduces the real production facility. Besides the production mix, the capacities and workload of workstations in the manufacturing system are affected by various factors such as buffer capacity, task sequencing, operational uncertainty, input policy or dispatching rules. The main components and tools available at the SIMIO platform are used to achieve the most accurate representation of the manufacturing system, which requires advanced programming for modelling specific process features.

Based on the approach by Kim and Kim (2001), the proposed algorithm structure considers an iterative procedure to reach solution convergence at stopping criteria, i.e. if the solution objective is identical to the previous iteration. The original mathematical formulation considers four types of continuous variables expressed by product i at time period t : X_{ip} as the orders amount released at time period p , Y_{it} auxiliary variable that defines the effective proportion quantity following the release period ($t \geq p$), I_{it} as the inventory amount, and B_{it} as the backorder amount. That formulation is now extended to consider a binary variable O_{ijr} which defines the set of resources r allocation to perform the sequential operation stage j of a product i , while determining the number of shared resources R_t required to fulfil a demand plan μ_{it} .

$$\text{Min } \sum_i \sum_t (Y_{it} \alpha_{it} + I_{it} \sigma_{it} + B_{it} \pi_{it}) + \sum_t R_t \theta_t \quad (1)$$

$$\sum_i \sum_j \sum_r \sum_{p \leq t} \varepsilon_{ipt} X_{ip} O_{ijr} \tau_{ijkr} \leq \lambda_{kt} \delta_{kt} \quad \forall k, t \quad (2)$$

$$I_{it} - B_{it} = Y_{it} - \mu_{it} + I_{it-1} - B_{it-1} \quad \forall i, t \quad (3)$$

$$Y_{it} = \sum_{p \leq t} \varepsilon_{ipt} X_{ip} \quad \forall i, t \quad (4)$$

$$\sum_i \sum_j \sum_k \sum_{r \in R_A} \sum_{p \leq t} \varepsilon_{ipt} X_{ip} O_{ijr} \tau_{ijkr(A)} \leq \phi_t D_t R_t - S_t \cdot \text{TimeS} \quad \forall t \quad (5)$$

$$\sum_r O_{ijr} = 1 \quad \forall i, j \quad (6)$$

$$X_{ip}, Y_{it}, I_{it}, B_{it}, R_t \geq 0 \quad X_{ip}, R_t \in \mathbb{Z} \quad (7)$$

The objective function Eq. (1) considers the minimization of total costs related to production α_{it} , inventory σ_{it} , backlog π_{it} and number of shared resources θ_t . The capacity constraint of each unit stage k in Eq. (2), with the average operation time given by τ_{ijkr} , is adjusted by the recursive simulated parameters, the average utilization of stage k , λ_{kt} , of the available time per period t , δ_{kt} , and by the effective loading ratio ε_{ipt} per

periods t of the amount released in p . The linearization of $X_{ip}O_{ijr} \equiv \Omega_{ijpr}$ as the released quantity to be performed by resources r was performed, considering the standard auxiliary restrictions to linearize the product of a binary and continuous variables. Eq. (4) considers the inventory balance of material flow and demand per period, and Eq. (3) enables the calculation of auxiliary variable Y_{it} . Eq. (5) considers the capacity constraint related to the operations that make use of shared resources SR_A per time period D_t , accounting the time spent ($TimeS$) with the number of changeovers S_t and the traveling between stages (ϕ_t as average operating rate). Finally, Eq. (6) enforces that all operations of product i are performed by one set of resources and Eq. (7) the non-negativity of variables (details in Kim and Kim (2001)). The first step of the algorithm consists in running the model in GAMS to determine the amount of production released X_{ip} , allocation of resources O_{ijr} , and number of shared resources required per period R_t . In the second step, the feasibility of the sequential release plan (one by one order) is evaluated in the SIMIO model and the statistics on effective loading ratios, unit stages utilization and number of changeovers/utilization of shared resources are collected. In the third step, these iteration statistics in the model updates the capacities constraints by using the recursive parameters from the simulation. The iterations procedure stops when the plan met the stopping criteria and the simulation generates the schedule based on a given dispatching rule.

4. Case study

4.1. Problem description

The example case is based on a multistage industrial process in a production plant composed by seven single-unit stages k (k1-k7) to produce five products i (i1-i5) in a U layout. The different processing stages for each 5 products follow a predefined sequence operation set j given by Table 1, where at each corresponding stage a series of tasks are executed, as displayed in Figure 1. Currently, all tasks are performed by one dedicated operator per stage (Op). Since some of the tasks at each stage can be performed in parallel, the decision-support at the operational level relies on the allocation of a mobile shared resource (Aut) able to perform one of these tasks, therefore existing the option for two sets of resources r per operation i,j . This can enable the decrease of the total processing time per stage, as shown in Table 1 (for this example, only one shared resource is allowed per stage to perform one of the simultaneous tasks.).

Table 1 – Sequence of process stages per product and corresponding processing time

Product i	Unit stage k							Resources r	Average operation time stage j (min/ton)				
	1	2	3	4	5	6	7		1	2	3	4	5
P1	●	●			●	●	●	1 Op	61,2	60,0	116,4	61,2	78,0
								1 Op+1 Aut	61,2	60,0	104,4	60,0	48,0
P2			●	●	●	●		1 Op	93,6	61,2	116,4	61,2	-
								1 Op+1 Aut	74,4	49,2	104,4	60,0	-
P3		●	●	●			●	1 Op	60,0	93,6	61,2	78,0	-
								1 Op+1 Aut	60,0	74,4	49,2	48,0	-
P4	●		●		●		●	1 Op	61,2	93,6	116,4	78,0	-
								1 Op+1 Aut	61,2	74,4	104,4	48,0	-
P5	●	●		●		●		1 Op	61,2	60,0	61,2	61,2	-
								1 Op+1 Aut	61,2	60,0	49,2	60,0	-

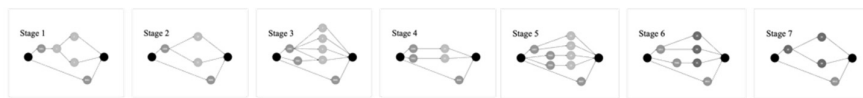


Figure 1 – Sequence of tasks per unit stage

The production follows a pull strategy, which means that the products are manufactured to assess a given demand for a time horizon of seven continuous 24 h production days. While the optimization model considers the Eqs. (1-6), the simulation model is able to accommodate the manufacturing system characteristics as close at the real facility, accounting for the routing distances, queuing, system layout and the detailed tasks sequence at each stage. The simulation inputs the determined release plan, allocation sequence and number of resources, which replicates the process operation during the planning horizon. The uncertainty in the process data is also considered, namely at the processing times of tasks performed by the operator and the changeover time of the shared resource, by assessing the corresponding variability distribution. A FIFO dispatching rule in the simulation is assumed throughout. For the minimization of operational costs, the request cost of one shared resource, θ_t , is assumed of 100 monetary units (mu), while the production α_{it} , inventory σ_{it} , backlog π_{it} costs are, respectively, 100, 25 and 400 mu.

4.2. Computational results

The results of the given example show that the methods quickly converge to a solution where the total output of the production plan is similar between models. The final results were obtained at the third iteration and the results are generated in a few seconds (optimality gap <1%), running on an Intel Core i7-7700HQ with 16GB of RAM. Whenever the optimization results were too optimistic (non-feasible), resources capacity constraints parameters were tightened to generate a more realistic production plan, given the simulation statistics (20 replications for a confidence level of 95%). For example, in the first run of the optimization model, since it considers nonrestrictive capacities of resources, the results match the total demand with only one shared resource allocation (Table 2). But when evaluated in the simulation, the output is a far different solution, due to lower effective loading ratio, percentage utilization of resources and number of setups. Iteratively the solution space is reduced, with a production release on the initial periods to reach a scheduling solution given by the simulation software. In the following iterations, the number of available shared resources per time period is increased to be able to accommodate the production, as well as the increase in inventory backorder and costs since the total demand is not satisfied on this planning horizon. The simulation model also enables to analyze the scenario results on the bottlenecks of the process, where it can be verified that stages 3 and 5 have utilization ratios between 98 to 99%, therefore restraining the fulfillment of demand (assumed to be satisfied in the following plan horizon). The reduction in the number of setups of the shared resources is verified since, with the increase of their availability with almost a full utilization, they were modelled in the simulation to preferably choose same product operations. This number is also influenced by the different allocation of resources to shared tasks performed in each iteration, which increased with the availability of the resources.

Table 2 – Iterations results of order release amount X_{ip}

Time period	Iteration 1						>>> Iteration 3					
	P1	P2	P3	P4	P5	Shared resources	P1	P2	P3	P4	P5	Shared resources
t1	2	6	4	5		1	13	19	6	1	20	1
t2	4	4	2	7	8	1	5	8	8	9		1
t3	5	3		6	3	1	1	6		18	7	2
t4	7	2	8		2	1			10		6	2
t5	6	4	4	5	4	1						1
t6	2	6	4	5		1						2
t7	4	4	2	7	8	1						1
	Opt. model		Total Output ΣY_{it} : 140				Total Output ΣY_{it} : 131					
			Total Costs (mu): 14525				Total Costs (mu): 45117					
	Sim. model		Total Output: 89				Total Output: 122					
			Number Setups: 132				Number Setups: 129					

5. Conclusions

This work presented a hybrid methodology to provide decision-support for the planning and scheduling of multistage industrial systems, combining simulation and optimization approaches. The methodology solution potentiates the advantages of an iterative procedure, combining an upper level optimization plan, which feasibility is tested in a detailed simulation of the real production process, while considering the production mix and allocation of a number of shared resources in order to generate a scheduling solution. The iterative procedure considers recursive parameters obtained from the simulations so that the solution between the two model converges, such as the effective loading ratio, utilization capacities and number of changeovers of the shared resources.

Simulation-optimization methods have been gathering significant relevance to overcome the challenges of dealing with the computational complexity and cost of implementation in industrial planning and scheduling problems. The ability to integrate the stochastic and non-linear constraints, such as allocation of resources and variable processing times or setups, in a solution search with mathematical foundation becomes of key importance. Although further experiments are required to evaluate the quality of convergence solution and the impact of simulation dispatching rules, along with additional decisional variables as the ones proposed in this formulation. The advantages of the simulator should also be explored to provide enhanced information to the decision-maker on the efficiency of resources utilization, while being reactive to changes in the production capacity, operational ergonomic or layout. Future work will aim to explore these issues by evaluating different optimization objectives to assess operational sustainability.

Acknowledgment

The authors would like to acknowledge the financial support from Portugal 2020 project POCI-01-0145-FEDER-016418 by UE/FEDER through the program COMPETE2020.

References

- P. M. Castro, A. M. Aguirre, L. J. Zeballos and C. A. Méndez, 2011, Hybrid mathematical programming discrete-event simulation approach for large-scale scheduling problems. *Industrial & Engineering Chemistry Research*, 50(18), 10665-10680.
- G. Figueira. and B. Almada-Lobo, 2014, Hybrid simulation-optimization methods: A taxonomy and discussion, *Simulation Modelling Practice and Theory*, 46:118-134.
- I. Harjunkoski, C. T. Maravelias, P. Bongers, P.M. Castro, S. Engell, I. E. Grossmann, J. and Wassick, J., 2014, Scope for industrial applications of production scheduling models and solution methods, *Computers & Chemical Engineering*, 62, 161-193
- B. Kim and S. Kim, 2001, Extended model for a hybrid production planning approach, *International Journal of Production Economics*, 73(2): 165-173.
- S. H. Kim and Y. H. Lee, 2016, Synchronized production planning and scheduling in semiconductor fabrication, *Computers & Industrial Engineering*, 96:72-85.
- S. Martins, P. Amorim, G. Figueira and B. Almada-Lobo, 2017, An optimization-simulation approach to the network redesign problem of pharmaceutical wholesalers. *Computers & Industrial Engineering*, 106, 315-328.
- M. Vieira, S. Moniz, T. Pinto-Varela and A.P. Barbosa-Póvoa, 2018, Simulation-optimization approach for the decision-support on the planning and scheduling of automated assembly lines. *IEEE 13th APCA International Conference on Control and Soft Computing*, 265-269.

On Robustness of Mixed-Integer reformulations of Generalized Disjunctive Programs

Miloš Bogataj*, Zdravko Kravanja

Faculty of Chemistry and Chemical Engineering, University of Maribor, Smetanova ulica 17, SI-2000 Maribor, Slovenija

milos.bogataj@um.si

Abstract

In this work, we compare the performance of the Alternative Mixed-Integer (AMI) reformulation of GDPs against those of the Big-M and Hull Reformulation (HR) in a framework of nonconvex mixed-integer nonlinear models. The robustness and efficiency of the reformulations are tested on a synthetic example using commercially available solvers, namely SBB, DICOPT++, SCIP, and Alpha-ECP. The comparison is carried out on the following key criteria: efficiency (CPU usage, number of iterations), robustness (number of successfully solved problems), quality of the obtained solutions (comparison of the objective function values). Results obtained in this study indicate that the AMI reformulation represents a competitive alternative to Big-M and HR.

Keywords: Disjunctive Programming, Mixed-Integer Programming, Nonconvex problems, Robustness, and Efficiency.

1. Introduction

The Generalized disjunctive Programs (GDPs), be it linear or nonlinear, can be formulated as mixed-integer (non)linear problems (MI(N)LPs) in several ways (Nemhauser and Wolsey (1988), Lee and Grossmann (2003), Trespalacios and Grossmann (2015)). This, however, leads to models of different sizes (i.e. in a number of variables and constraints) and tightness – tightness being the relation of the feasible region of a problem to the feasible region of its continuous relaxation. Furthermore, when GDPs are nonlinear and nonconvex, the robustness of nonlinear subproblems becomes an important aspect. We can infer that the ability of the solvers to solve these problems strongly depends on the type of reformulation.

The AMI reformulation was originally proposed by Bogataj and Kravanja (2018). The reformulation of a GDP to a MINLP is analogous to the HR presented by Lee and Grossman (2003), as shown below. The Boolean variables are transformed into 0-1 variables y_{ik} , the continuous variables x into disaggregated variables x_{ik}^D and the logical propositions reformulated into a set of linear constraints. There is, however, an important difference between the reformulations. That is, the disaggregated variables x_{ik}^D are not required to be forced to 0 when $y_{ik} = 0$. Instead, due to mixed-integer translation of variables they are forced to arbitrary fixed values x_{ik}^F , which are usually chosen between nonzero lower and upper bounds of the disaggregated variables.

$$\begin{array}{ll}
\min Z = \sum_{ik} c_{ik} + f(x) & \min Z = \sum_{ik} y_{ik} \gamma_{ik} + f(x) \\
\text{s.t. } h^g(x) \leq 0 & \text{s.t. } h^g(x) \leq 0 \\
\bigvee_{i \in D_k} \begin{bmatrix} Y_{ik} \\ g_{ik}(x) \leq 0 \\ c_{ik} = \gamma_{ik} \end{bmatrix} & k \in K \quad \longrightarrow \quad \begin{array}{ll} x = \sum_{i \in D_k} x_{ik}^D - (1 - y_{ik}) x_{ik}^F & k \in K \\ g_{ik}(x_{ik}^D) - (1 - y_{ik}) g_{ik}(x_{ik}^F) \leq 0 & i \in D_k, k \in K \\ x_{ik}^D \geq x_{ik}^{D,LO} y_{ik} + (1 - y_{ik}) x_{ik}^F & i \in D_k, k \in K \\ x_{ik}^D \leq x_{ik}^{D,UP} y_{ik} + (1 - y_{ik}) x_{ik}^F & i \in D_k, k \in K \\ E y \leq e & \\ \sum_{i \in D_k} y_{ik} = 1 & k \in K \\ x^{LO} \leq x \leq x^{UP}, y_{ik} \in \{0,1\} & \end{array} \\
\bigvee_{i \in D_k} Y_{ik} & k \in K \\
\Omega(Y) = True & \\
x \in \mathbb{R}^n, c_{ik} \in \mathbb{R}, Y_{ik} \in \{True, False\} & \\
\text{(GDP)} & \text{(AMI)}
\end{array}$$

2. Optimization Problem

The problem used in the study represents a nonconvex variation of the Circles Example by Lee and Grossmann (2000). The GDP formulation of the problem is given by (GDP-NC).

$$\begin{array}{ll}
\min Z = (x_1 - 3)^2 - (x_2 - 2)^2 + \sum_{k \in K} c_k & \\
\text{s.t.} & \\
g_j(x_1, x_2) \leq 0 & j \in J \\
\bigvee_{i \in D_k} \begin{bmatrix} Y_{ik} \\ \tilde{h}_{ik}(x_1, x_2) \leq 0 \\ \hat{h}_{ik}(x_1, x_2) \geq 0 \\ c_k = \gamma_{ik} \end{bmatrix} & k \in K \quad \text{(GDP-NC)} \\
\bigvee_{i \in D_k} Y_{ik} & k \in K \\
\Omega(Y) = True & \\
x_1^{LO} \leq x_1 \leq x_1^{UP}, x_2^{LO} \leq x_2 \leq x_2^{UP} & \\
c_k \in R^1, Y_{ik} \in \{True, False\}, i \in D_k, k \in K, j \in J &
\end{array}$$

It represents a minimization of a nonconvex objective function over disjoint nonconvex feasible regions. These are obtained by intersecting the feasible regions described by convex constraints $\tilde{h}_{ik}(x_1, x_2) \equiv (x_1 - \tilde{a}_{ik})^2 + (x_2 - \tilde{b}_{ik})^2 - \tilde{r}_{ik}^2 \leq 0$ and their nonconvex counterparts $\hat{h}_{ik}(x_1, x_2) \equiv (x_1 - \hat{a}_{ik})^2 + (x_2 - \hat{b}_{ik})^2 - \hat{r}_{ik}^2 \geq 0$. Feasible regions of $\tilde{h}_{ik}(x_1, x_2)$ correspond to the interior of circles with centers at $(x_1 = \tilde{a}_{ik}, x_2 = \tilde{b}_{ik})$ and radii \tilde{r}_{ik} , whereas the feasible regions of $\hat{h}_{ik}(x_1, x_2)$ are to the exteriors of the corresponding circles.

The coefficients $\widehat{a}_{ik}, \widehat{b}_{ik}$ and \widehat{r}_{ik} are determined in such a way that the graphical representation of each of the disjoint feasible regions corresponds to either crescent or annulus. The constraints $g_j(x_1, x_2)$ are hyperbolae (i.e. $x_1^2 - x_2^2 + d \leq 0, x_1^2 + x_2^2 - e \geq 0$) globally constraining the disjoint feasible regions.

2.1. Numerical Studies

To provide insights into the studied properties of the reformulations, two numerical examples of different sizes with respect to the number of equations, continuous and discrete variables were considered. The GDP representation of the optimization problem was reformulated into a MINLP problem using Big-M, Hull Reformulation and AMI reformulation. The examples were solved using Branch and Bound, Outer Approximation / Equality Relaxation and Extended Cutting Plane algorithms implemented in SBB, SCIP, DICOPT++ and Alpha-ECP solvers. The models were coded in GAMS 25.1.3 and solved on a PC equipped with Intel® Core™ i7-4770 3.40 GHz processor and 16 GB RAM. The first example is a small instance of (GDP-NC). It is comprised of 6 disjunctions, each having 6 terms. The feasible region is constrained by 2 global constraints. The second example is a larger instance of (GDP-NC), comprised of 2 disjunctions, each having 500 terms. The global constraints were omitted in the latter example. In both, only one term per disjunction can be selected as *True*. The model statistics regarding the MINLPs for the three reformulations is given in Table 1.

Table 1: Model Statistics.

Example 1	Big - M	HR /AMI
Continuous Variables	49	121
Discrete Variables	36	36
Equations	91	247
Example 2	Big - M	HR /AMI
Continuous Variables	1,005	3,005
Discrete Variables	1,000	1,000
Equations	2,003	6,007

3. Results

3.1. Example 1

The example was solved with the four solvers from 100 randomly selected starting points - identical in each run for the different solves. The globally optimal objective value for the given example is -95.98, which was determined by Baron.

By comparing the mean values of the objective functions, as shown in Fig 1, we observe that AMI reformulation produces the most compliant results. The weighted average of objective values obtained by the AMI reformulation is -79.91, the weighted average of objective values obtained by the HR -70.57, and -63.67 by the Big-M reformulation.

In terms of robustness (i.e. number of feasible solutions), Big-M reformulation dominates the three formulations, producing 100% feasible solutions. AMI reformulation averaged at 92% and HR at 51%. A more detailed statistics regarding the robustness of the reformulations are presented in Fig. 2.

In terms of efficiency, the HR is computationally the least demanding (see Fig 3). The weighted average CPU time for HR is 1.7 s, which is, however, comparable to the

weighted average CPU time for AMI reformulation. The Big-M reformulation averages at slightly longer CPU time of 8.6 s.

Finally, there are a few additional results worth mentioning. In the case of the AMI reformulation, the largest standard deviations in objective function values and CPU time are observed when using AlphaECP solver. SCIP failed in each of the HR instances, however, it provided globally optimal solutions in all the instances of the Big-M formulation.

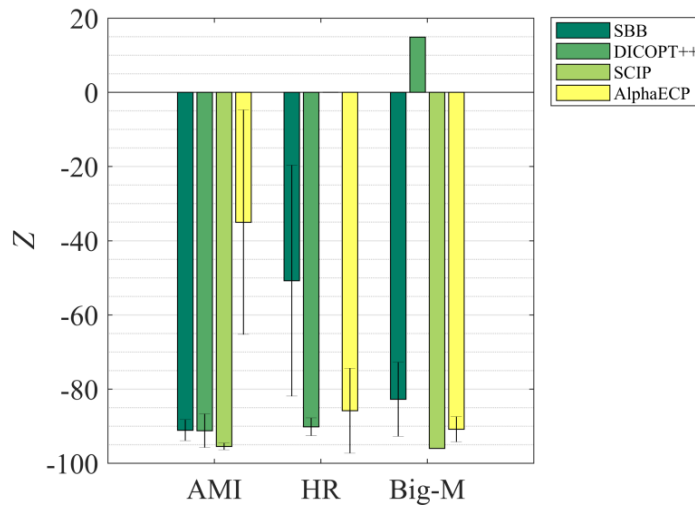


Figure 1: Mean values of objective functions.

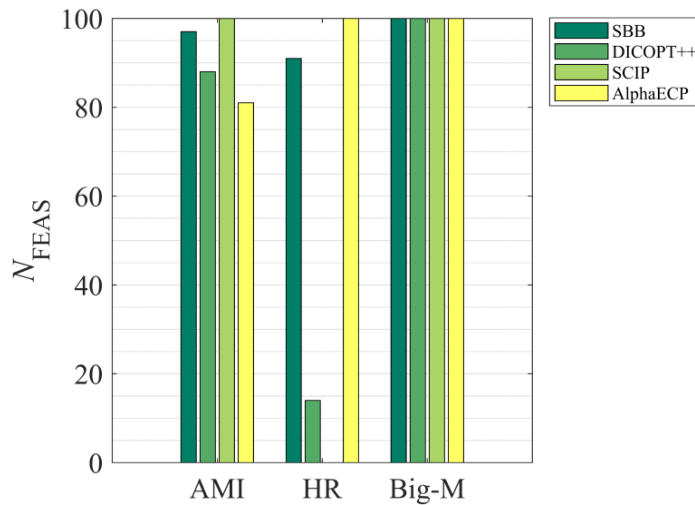


Figure 2: Number of feasible solutions per 100 runs.

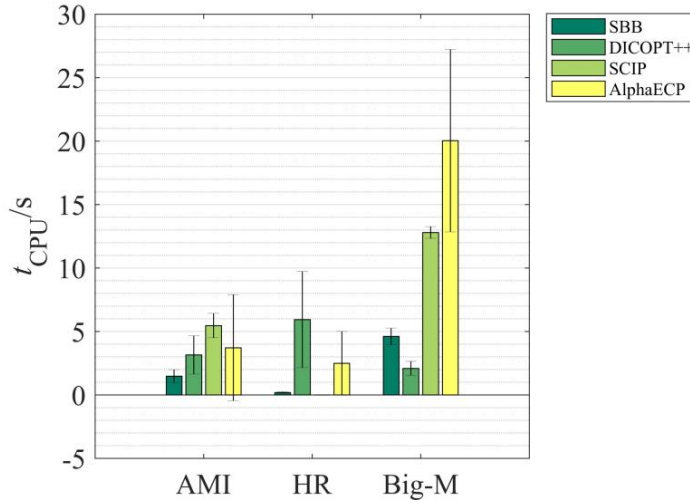


Figure 3: Average computational times.

3.2. Example 2

The example was solved from a starting point that is feasible with respect to the relaxed MINLP of a given reformulation. The CPU time limit was set to 3,000 s. The results are given in Table 2.

Table 2: Statistical results.

Reformulation	Metrics	SBB	DICOPT++	SCIP	AlphaECP
AMI	Z	-128,734	-128,734	-128,734	-95,870
AMI	t_{CPU}/s	96	62	1,632	299
AMI	Nds/Iter	517	14	1,969	274
HR	Z	/	/	-114,809	-41,577
HR	t_{CPU}/s	/	/	3,000	81.5
HR	Nds/Iter	/	/	919,662	114
Big-M	Z	-15,299	141.5	-15,296	-6,872
Big-M	t_{CPU}/s	3,000	35	499	3,000
Big-M	Nds/Iter	40,475	20	9,426	2,700

From the results presented in Table 2 we can conclude that the AMI reformulation outperformed both HR and Big-M reformulation in terms of solution quality and computational efficiency. Note that the CPU time limit was hit in 1 instance of HR (SCIP) and 2 instances of Big-M reformulation (SBB and AlphaECP).

All the solvers utilized in this study provided solutions to the AMI and Big-M reformulation, while two solvers (SBB and DICOPT++) failed to provide solution to the HR because of solver failure.

4. Conclusions

We have presented a study on the performance of the alternative mixed-integer (AMI) reformulation of GDPs against the Big-M and hull reformulation (HR) in a framework nonconvex MINLPs. The result obtained thus far indicate that AMI reformulation exhibits desirable properties that make it favorable for larger nonconvex MINLPs models. Although these results should not be generalized nor considered as conclusive, there are some theoretical indications as to why the AMI reformulation may outperform the other two. First, it tends to reduce the search space of nonlinear subproblems by bounding it to the true lower and upper bounds of continuous variables. Second, the reformulation avoids the usage of the perspective function and thus reduces the number of nonlinearities. Finally, due to the translation of continuous variables, the reformulation does not require the functions being defined at 0.

Future studies will focus on research dedicated to providing theoretical answers regarding the AMI reformulation, and testing it on different optimization/synthesis problems.

Acknowledgements

This research was financially supported by the Slovenian Research Agency (Program P2-0032).

References

- G. L. Nemhauser, L. A. Wolsey, 1988, *Integer and combinatorial optimization*. Wiley-Interscience, Wiley.
- S. Lee, I. E. Grossmann, 2000, New algorithms for nonlinear generalized disjunctive programming. *Computers and Chemical Engineering*, 24, 2125–2141.
- S. Lee, I. E. Grossmann, 2003, Generalized Convex Disjunctive Programming: Nonlinear Convex Hull Relaxation. *Computational Optimization and Applications*, 26 (1), 83–100.
- F. Trespalacios, I. E. Grossmann, 2015, Improved Big-M reformulation for generalized disjunctive programs. *Computers and Chemical Engineering*. 76, 98–103.
- M. Bogataj, Z. Kravanja, 2018, Alternative mixed-integer reformulation of Generalized Disjunctive Programs, *Computer Aided Chemical Engineering*, 43, 549–554.

A Comparison of Data Reconciliation Tools for Modelling Heat Recovery

Petar Sabev Varbanov^{a,*}, Jun Yow Yong^b, Jiří Jaromír Klemeš^a,
Zdravko Kravanja^c

^a*Sustainable Process Integration Laboratory – SPIL, NETME Centre, Faculty of Mechanical Engineering, Brno University of Technology, Technická 2896/2, 616 00 Brno, Czech Republic.*

^b*Department of Computer Science and Systems Technology, Faculty of Information Technology, University of Pannonia, Egyetem u. 10, Veszprém, Hungary.*

^c*University of Maribor, Faculty of Chemistry and Chemical Engineering, Smetanova ulica 17, 2000 Maribor, Slovenia.*

varbanov@fme.vutbr.cz

Abstract

Data Reconciliation is an important step in extracting data from an existing plant. It is especially important for Heat Integration Analysis. In this work, the Iterative PNS Method is introduced as a new method for Heat Exchanger Network Data Reconciliation. This method uses Linear Programming to reduce the computational cost of the complex non-linear data reconciliation problem. The results from the illustrative case study indicate that it performs almost as well as the other state-of-the-art method found in the literature.

Keywords: Heat Exchanger Network, Data Reconciliation, Iterative PNS Method.

1. Introduction

Data extraction is a key activity in performing retrofit of Heat Exchanger Networks (HENs) (Klemeš et al., 2018). It is used to obtain a credible set of data from measurements for the Heat Integration. The topic was briefly mentioned in the HEN synthesis book by Shenoy (1995), providing a non-linear optimisation example. In a previous work (Yong et al., 2016a), an Iterative Method for solving the HEN data reconciliation problem has been proposed. That reduced the model complexity and computational cost required during data reconciliation. VBA tools for energy systems data reconciliation have also been presented (Mayo, 2015). There have been further works – considering rigorous and simplified HEN models (Ijaz et al., 2013), as well as parameter tuning using process-network synthesis (PNS) algorithms (Bartos and Bertok, 2018). Sufficient accuracy of the model with user-friendly data input and acceptable computational time can be key in providing process engineers with a tool for efficient and accurate data extraction.

In this work, a new Iterative PNS Method is derived from the Iterative Method. It uses linear objective functions in the sub-models to reduce the required computational effort. The performance of this method is compared with standard NLP (simultaneous method in this work) and MILP using a linear reformulation.

2. Problem Statement

Consider an existing HEN with total m number of heat exchangers (including heaters and coolers) with $m \in M$. Each hot (H) or cold (C) stream has its own inlet (I) and outlet (O).

These generate a set of streams, $s \in \{HI, HO, CI, CO\}$. For each stream, n measurements are taken ($n \in N$). For the purpose of heat integration analysis, temperature (T) and heat capacity flowrate (CP) are required. It is desired to obtain the reconciled value (R).

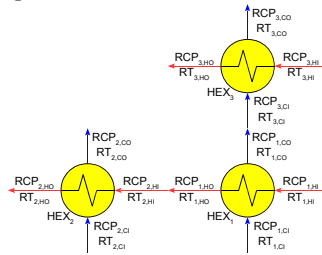


Figure 1: An example of a HEN

3. Models and Equations

3.1. Simultaneous Method

Simultaneous Solving Method	
$\text{Min} \sum_m^M \sum_s^S \sum_n^N \left((RCP_{m,s} - CP_{m,s,n})^2 + (RT_{m,s} - T_{m,s,n})^2 \right)$	(1)
subject to:	
Mass balance constraints around each heat exchanger, for all heat exchanger	
$RCP_{m,HI} = RCP_{m,HO}$	(2)
$RCP_{m,CI} = RCP_{m,CO}$	(3)
Energy balance constraints around each heat exchanger, for all heat exchanger	
$RCP_{m,HI}(RT_{m,HI} - RT_{m,HO}) = RCP_{m,CI}(RT_{m,CO} - RT_{m,CI})$	(4)
Constraints from network arising from the connections between heat exchangers	
$RCP_{m1,HO} = RCP_{m2,HI}$	(5)
$RCP_{m1,CO} = RCP_{m3,CI}$	(6)
$RT_{m1,HO} = RT_{m2,HI}$	(7)
$RT_{m1,CO} = RT_{m3,CI}$	(8)

Figure 2: Data reconciliation model for solving two types of parameters simultaneously

Eq. (1) contains the objective function, combining CP and T values. Since this is only a numerical abstraction without a direct physical meaning, the mixture of the measurement units is not a problem. While in general, the difference in magnitude may cause the model to be biased on either one of the parameters, in the current model such issues have not arisen. In the future work, appropriate weighting and normalization should be introduced for obtaining more robust models. In the simultaneous method, the model shows high non-linearity from the parameters, constraints and objective function. In the case of parameters, CP is a function of T. To reduce this complexity, it is assumed that CP is independent of T. The energy balance constraints, as in Eq. (4), contain bi-linear terms of the reconciliation variables. These non-linear constraints can be reduced to linear by applying the Iterative Method (Yong et al., 2016a)

3.2. Iterative Method

CP Model	T Model
$\text{Min} \sum_m^M \sum_s^S \sum_n^N (RCP_{m,s} - CP_{m,s,n})^2 \quad (9)$	$\text{Min} \sum_m^M \sum_s^S \sum_n^N (RT_{m,s} - T_{m,s,n})^2 \quad (10)$
subject to: Mass balance constraints in Eq. (2) and Eq. (3) Energy balance constraints in Eq. (4) where RT is set to be constant	subject to: Energy balance constraints in Eq. (4) where RCP is set to be constant
Constraints from network in Eq. (5) to Eq. (8)	Constraints from network in Eq. (5) to Eq. (8)

Figure 3: Equations used in the CP model and T model

The Iterative Method divides the model from the simultaneous method into two sub-models. In each sub-model, the instances of one parameter type are reconciled while the instances of the other type are kept constant. By only considering one type of parameter at a time, the energy balance constraints are reduced to linear. This also solves the problems arising from different magnitudes and dimensions in the Iterative Method. The method first chooses one of the sub-models as the starting model. After obtaining the reconciled parameters, they are used as constants in the other sub-model. This process iterates until the convergences or satisfactory level is met. This method is explained in details in the work of Yong et al. (2016b). However, the models used in the Iterative Method are still non-linear, due to the square operation in the objective function.

3.3. Iterative PNS Method

It should be noted that the purpose of the square operation in the objective function is to remove any negative values arising from large measured values, e.g. when $RCP_{m,s} < CP_{m,s,n}$. This is so that the negative values do not reduce any differences for other $RCP_{m,s} > CP_{m,s,n}$. To reduce this non-linearity, the absolute value is proposed i.e.

CP Model	T Model
$\text{Min} \sum_m^M \sum_s^S \sum_n^N RCP_{m,s} - CP_{m,s,n} \quad (11)$	$\text{Min} \sum_m^M \sum_s^S \sum_n^N RT_{m,s} - T_{m,s,n} \quad (12)$

Figure 4: Objective functions that use absolute value in sub-models.

Using these models following Iterative Method changes to mixed integer linear programming (MILP). As the models call for minimisation, $RCP_{m,s}$ are desired to be as close as to $CP_{m,s,n}$. By applying Process Network Synthesis (PNS) algorithm, these models can be further reduced to just linear programming (LP). Consider the following,

$$Y_{m,s,n} = |RCP_{m,s} - CP_{m,s,n}| \quad (13)$$

It can be interpreted as

$$Y_{m,s,n} = RCP_{m,s} - CP_{m,s,n} \quad \text{for } RCP_{m,s} > CP_{m,s,n} \quad (14)$$

$$Y_{m,s,n} = CP_{m,s,n} - RCP_{m,s} \quad \text{for } RCP_{m,s} \leq CP_{m,s,n} \quad (15)$$

To apply the PNS algorithm in the models, let

$$RCP_{m,s} = RCP1_{m,s,n} + RCP2_{m,s,n} \quad (16)$$

RCP_{m,s} is the desired product that has a unit cost of 1. Let there be existing (Y1_{m,s,n}) and new (Y2_{m,s,n}) pre-treatment units. Y1_{m,s,n} is to be fed with streams RCP1_{m,s,n} and vice versa for Y2_{m,s,n}. It is assumed that Y1_{m,s,n} has fixed operating cost at CP_{m,s,n} but its capacity is limited at CP_{m,s,n}. The Y2_{m,s,n} has only the operating cost of 2 × RCP2_{m,s,n}. The net profit is to be

$$\begin{aligned} ZCP_{m,s,n} &= RCP1_{m,s,n} - CP_{m,s,n} + RCP2_{m,s,n} - 2 \times RCP2_{m,s,n} \\ &= RCP1_{m,s,n} - RCP2_{m,s,n} - CP_{m,s,n} \end{aligned} \tag{17}$$

With the following additional constraint

$$e \tag{18}$$

The objective is to maximise the net profit and the objective function for the CP model is

$$Max \sum_m \sum_s \sum_n ZCP_{m,s,n} \tag{18}$$

Eq. (18) has the same purpose as Eq. (9) in the CP model used in the original Iterative Method. It is to have RCP_{m,s} to be as close as to CP_{m,s,n}. The same process is applied for the T model where all CP terms are replaced with T terms. All the equations are linear.

Table 1: Mean values for all the parameters in the illustrative case study.

m	T _{m,HI} (°C)	T _{m,HO} (°C)	CP _{m,HI} (kW/°C)	CP _{m,HO} (kW/°C)	T _{m,C1} (°C)	T _{m,CO} (°C)	CP _{m,C1} (kW/°C)	CP _{m,CO} (kW/°C)
1	184.9	62.0	400.9	399.9	28.6	129.6	498.0	498.3
2	249.6	170.5	501.5	500.9	129.7	210.6	500.1	500.1
3	569.3	369.6	301.1	301.2	210.0	330.1	499.7	500.3
4	410.3	339.3	200.1	200.2	330.9	358.4	501.4	500.5
5	467.9	367.7	299.3	300.1	358.6	418.3	499.5	500.6
6	560.2	524.6	1,000.8	1,000.6	417.8	487.2	500.0	501.1
H1	800.2	700.1	299.5	299.9	488.9	548.3	499.5	499.7
C1	60.3	19.0	299.3	400.1	4.6	9.9	3,197.6	3,199.0
C2	370.9	319.5	302.8	301.2	5.0	9.9	3,000.6	3,000.6

4. An illustrative Case Study

An illustrative case study is used to demonstrate the use of Iterative PNS Method. The HEN is shown in Figure 5. All the measurements are taken at every inlets and outlets of every heat exchangers, heaters and coolers. After sets of measurements are taken repeatedly for a fixed period of time, the outliers are discarded using statistics. Out of these sets of measurements, 10 are chosen to be used as the input data. Table 1 shows the mean value for all the parameters.

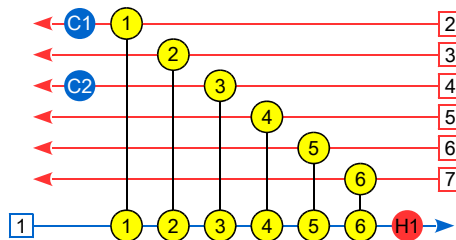


Figure 5: HEN for an illustrative case study

5. Result and Discussion

In this case study, the CP path is chosen and the CP model is to be used first for data reconciliation. Three iterations were done as the work used for comparison in Yong et al. (2016) stopped at third iterations. It should be noted that further iteration can be done to obtain a more accurate result. The percentage difference at this iteration of all the parameters is less than 2 % when compared with the result obtained in the first iteration. Table 2 shows the reconciled values obtained using Iterative PNS Method. The result is compared against mean values, as shown in the percentage difference in Table 3.

Table 2: Reconciled values for all parameters using Iterative PNS Method.

m	T _{m,HI} (°C)	T _{m,HO} (°C)	CP _{m,HI} (kW/°C)	CP _{m,HO} (kW/°C)	T _{m,CI} (°C)	T _{m,CO} (°C)	CP _{m,CI} (kW/°C)	CP _{m,CO} (kW/°C)
1	185.0	62.0	407.3	407.3	28.9	130.0	495.5	495.5
2	250.0	170.8	506.8	506.8	130.0	211.0	495.5	495.5
3	568.1	370.0	297.9	297.9	211.0	330.1	495.5	495.5
4	411.0	339.0	192.0	192.0	330.1	358.0	495.5	495.5
5	469.0	368.3	295.2	295.2	358.0	418.0	495.5	495.5
6	560.9	525.0	967.5	967.5	418.0	488.1	495.5	495.5
H1	801.0	700.0	293.9	293.9	488.1	548.0	495.5	495.5
C1	62.0	18.0	407.3	407.3	4.0	9.6	3,200.0	3,200.0
C2	370.0	319.0	297.9	297.9	5.0	9.9	3,100.6	3,100.6

Table 3: Residual differences (in %) of all reconciled parameters when compared to mean values.

m	$\Delta T_{m,HI}$	$\Delta T_{m,HO}$	$\Delta CP_{m,HI}$	$\Delta CP_{m,HO}$	$\Delta T_{m,CI}$	$\Delta T_{m,CO}$	$\Delta CP_{m,CI}$	$\Delta CP_{m,CO}$
1	0.05	0.00	1.59	1.86	1.09	0.31	-0.50	-0.56
2	0.16	0.18	1.05	1.18	0.23	0.19	-0.92	-0.92
3	-0.22	0.11	-1.06	-1.10	0.48	0.00	-0.84	-0.95
4	0.17	-0.09	-4.05	-4.09	-0.24	-0.11	-1.18	-0.99
5	0.24	0.16	-1.36	-1.61	-0.17	-0.07	-0.80	-1.02
6	0.13	0.08	-3.32	-3.30	0.05	0.18	-0.90	-1.11
H1	0.10	-0.01	-1.88	-2.01	-0.17	-0.05	-0.80	-0.83
C1	2.82	-5.26	2.00	1.79	-13.04	-2.56	0.08	0.03
C2	-0.24	-0.16	-1.62	-1.10	0.00	-0.38	3.33	3.33

From the result, most of the reconciled parameters have values of less than 5 %. Although the reconciled inlet cold stream temperature for C1 only differs by 0.6 °C from 4.6 °C, it has a difference of 13 %. Most of the parameters with high percentage differences are having low value. Another parameter, although has 3 % difference, the reconciled cold stream CP for C2 differs by 100 kW/°C from 3,000 kW/°C. This is a good level of residual errors, comparable with typical values (Romagnoli and Sánchez, 2000) and a recent refinery study (Mayo, 2015). An error level of up to 5 % is very good for the purpose of Heat Integration, where energy savings of 10 % or more would warrant credible investments, while for performing operation optimisation this level may be too high, as the expected cost improvements are of the order 2-5 %.

The results obtained are also compared with results from the simultaneous method and Iterative Method, as shown in Figure 6. From this case study, it can be seen that the Iterative PNS Method performs almost as well as the Iterative Method with less than 10 parameters having higher percentage difference. It is speculated that having a square operation in Iterative Method poses a heavier penalty on outliers. As expected, the simultaneous method performs the best out of these three methods at the cost of high computational cost.

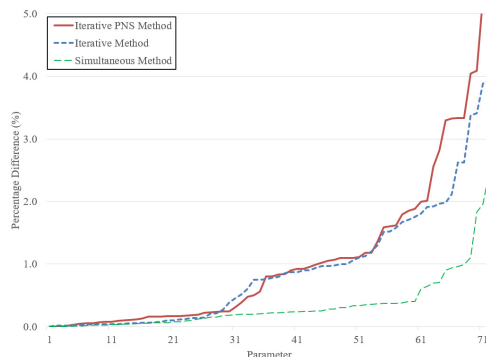


Figure 6: Comparison of three different methods.

6. Conclusions

An Iterative PNS Method is introduced in this work for HEN data reconciliation. It applies the Process Network Synthesis (PNS) Algorithm to augment the previous Iterative Method. In both of the sub-models, the objective functions are reduced from non-linear to linear, thus, it is completely solvable with Linear Programming (LP). Demonstration from an illustrative case study showed that the Iterative PNS Method is performing almost as well as the Iterative Method in terms of precision, at a reduced computational cost.

Acknowledgement

This research has been supported by the EU project “Sustainable Process Integration Laboratory – SPIL”, project No. CZ.02.1.01/0.0/0.0/15_003/0000456 funded by EU “CZ Operational Programme Research, Development and Education”, Priority 1: Strengthening capacity for quality research, in a collaboration with the University of Maribor, Slovenia.

References

- A. Bartos, B. Bertok, 2018. Parameter tuning for a cooperative parallel implementation of process-network synthesis algorithms. *Central European Journal of Operations Research*. DOI: 10.1007/s10100-018-0576-1.
- H. Ijaz, U.M.K. Ati, V. Mahalec, 2013. Heat exchanger network simulation, data reconciliation & optimization. *Applied Thermal Engineering* 52, 328–335
- J.J. Klemeš, P.S. Varbanov, S.R. Wan Alwi, Z.A. Manan, 2018. *Process Integration and Intensification: Saving Energy, Water and Resources*, 2nd ed, de Gruyter Berlin, Germany.
- C.M. Mayo, 2015. *Process Stream Data Analysis: Data Reconciliation and Gross Error Detection for Process Integration Studies* (MSc Dissertation). Chalmers University of Technology, Göteborg, Sweden.
- J.A. Romagnoli, M.C. Sánchez, 2000, *Data processing and reconciliation for chemical process operations*, Process systems engineering. Academic Press, San Diego, CA, USA.
- U.V. Shenoy, 1995. *Heat exchanger network synthesis: Process optimization by energy and resource analysis*. Gulf Pub., Houston, USA.
- J.Y. Yong, A. Nemet, P.S. Varbanov, Z. Kravanja, J.J. Klemeš, 2016. Data reconciliation for Total Site Integration. *Chemical Engineering Transactions* 1045–1050. DOI: 10.3303/CET1652175.
- J.Y. Yong, A. Nemet, M. Bogataj, Ž. Zore, P.S. Varbanov, Z. Kravanja, J.J. Klemeš, 2016b, Data reconciliation for energy system flowsheets, *Computer Aided Chemical Engineering*, 38, 2277–2282.

Process design meets sustainability: overview on the use of modelling tools for process design and sustainability assessment at Corbion

Van Bochove G., Cruz L., Morao A., Rugerio C.*

Process Modelling and Design, R&D, Arkelsedijk 46, 4206MD AC Gorinchem, The Netherlands

carlos.rugerio@corbion.com

Abstract

Bio-based companies must keep up with the needs of the consumers and the developments from their competitors. This needs to be done while managing the inherent risk of launching new products from new technologies to the market. To thrive it is essential to speed up research and development programs, to make the right choices for investment and to evaluate opportunities for reduction of production costs. Today's business ambitions incorporate not only economic growth but also sustainability targets. In this context, mathematical models are crucial to face these challenges. They are key to guarantee economy of scale whilst delivering on the commitments for sustainable development. In this work, the contribution of mathematical models in the process innovation funnel not only for process design but also for sustainability assessment within Corbion is presented. The methodology is illustrated with two case studies, in which it is shown how models help to find the optimal process in terms of economy and sustainability.

Keywords: process design, sustainability assessment, process modelling, bio-based economy

1. Introduction

Bio-based products are totally or partly derived from materials of biological origin, such as crops, plants or other renewable agricultural, marine or forestry materials. These products provide alternative material options to conventional petroleum-based materials by using renewable carbon as feedstock [1]. The use of renewable carbon feedstocks for chemical production has a clear link to reducing the risk of climate change and reduced dependency on fossil resources [2]. However, this is not sufficient to ensure the launching of these products. The newly introduced bio-based chemicals must compete with the well-established petro-based counterparts, in terms of cost and functionality, while outperforming in sustainability performance.

Corbion thrives to turn science into sustainable solutions based on renewable materials for applications in food, bio-chemicals and bio-based innovation products. This needs to be done while managing the inherent risk of launching new products from new technologies to the market. To thrive in this dynamic and challenging market it is essential to speed up research and development programs, to make the right choices for investment and to evaluate opportunities for reduction of production costs, at early stages of innovation.

A key success enabler is the use of mathematical models throughout the different stages of process design, from research to implementation/optimization of commercial processes. It guarantees the speed and the economy of scale whilst delivering on the commitments for sustainable development.

In this paper the applications of mathematical models within the innovation funnel of Corbion for process design and sustainability assessment is shown. Our methodology and achievements are illustrated with two case studies.

2. Process design and sustainability assessment in the innovation funnel of Corbion

To guide, direct and accelerate innovation efforts from idea to launch, Corbion uses the “stage gate pass” model [3]. Projects must pass through a gate to enter a new stage. Figure 1 shows a typical scheme of the development of the process from the feasibility phase to implementation in commercial scale. In each gate, decisions are taken about the continuity of the projects. This decision is based on the marketing perspective of the new product, technical aspects, economy of the process and a sustainability assessment. During all this path, models of different complexity levels are used to evaluate the health of the process.

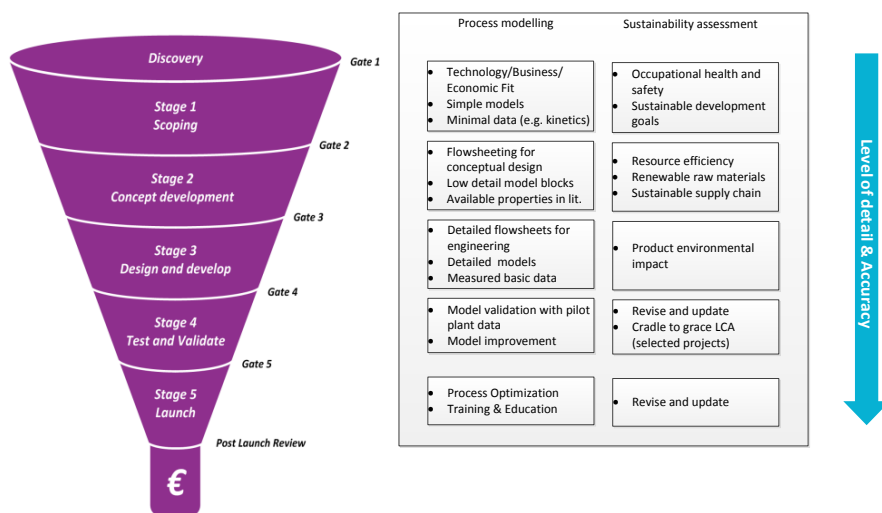


Figure 1. Stage gate pass model used by Corbion to evaluate new process and products.

In the early phase, screening of promising ideas is done. At this stage, typically few basic data are available, e.g. physical properties, and measuring them would be too expensive. Therefore, simple models are used to perform the techno-economical evaluation. Sustainability assessment in this stage consists in checking the safety of the chemicals (solvents, catalyst, etc.) used in the process and the impact of the project on the

Sustainable development goals (SDGs). This is a simple check but assesses safety risks. In case chemicals are found to be unsafe, they are replaced.

During Conceptual Design, different process alternatives are evaluated and the most promising is selected to move forward to the next stage. For this, models with a higher level of detail are developed. In this stage, physical properties available in literature or predicted by group contribution methods are used. Models based on short-cut methods are normally sufficient to achieve the goals of this stage. The aim of the sustainability assessment in this stage is to identify how the new process/product contribute to Corbion KPI's. Typical sustainability activities include comparing water and energy consumptions, waste and emissions to Corbion global average to create awareness of positive/negative impacts. The impact of the project on the SDGs is accessed at this stage.

Once that the project moves to the Design and Develop phase, detailed models of unit operations are used for flowsheeting. In this stage, missing basic data are measured, i.e. phase equilibrium diagrams, reaction kinetics, etc. Mass and energy balance are generated for engineering activities, such as equipment design, piping and pump sizing, etc. Also a more thorough sustainability assessment is made to quantify the environmental impact of the new process/product over its life cycle. This is done by comparing it with commercial benchmark in terms of biobased C-content and life cycle assessment (LCA). To evaluate LCA, an in-house excel based tool has been implemented, which is integrated with our process design software. As one of the inputs to the LCA tool, the mass and energy balance of the process is required [4]. Figure 2, shows a generic workflow followed by Corbion for sustainable process design

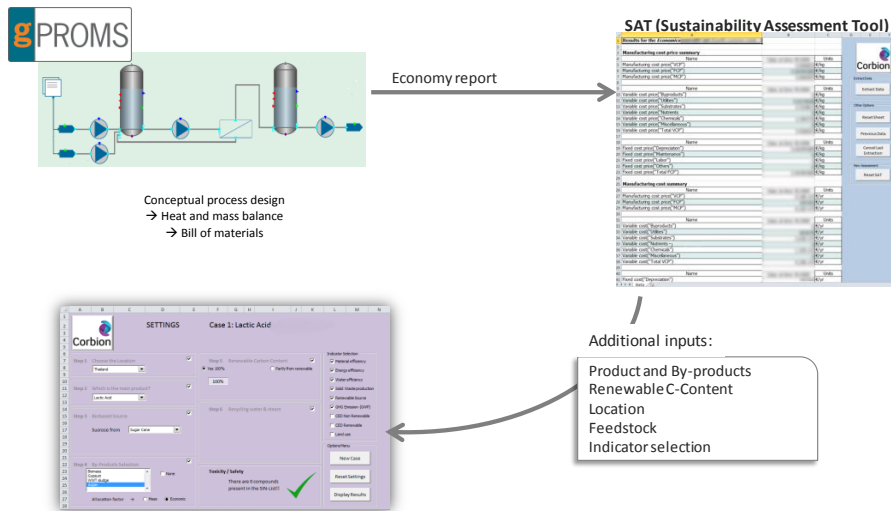


Figure 2. Workflow to reach sustainable process design.

In the next stage of the funnel, the new process/product is tested and validated by e.g. piloting, and experimental data are used to validate the model. Raw experimental data must first be processed before they are used. Methods, such as data reconciliation can be applied to force these data to fulfil the mass and energy balance. In case, important differences between the model and the experimental data are found, the assumptions and basic data are reviewed to improve the quality of the model. LCA is also revised and updated.

Finally, after successful validation of the process/product in pilot scale, the next stage is Launch.

3. Case studies

3.1 Conceptual design

Part of the mission of Corbion is to offer choices to customers to reduce their impact on environment. Bioplastics, such as polylactic acid (PLA) and polyethylene furanoate (PEF), can replace fossil based plastics, such as PET and offer the same or even better properties. Monomer for PEF is 2,5-furan dicarboxylic acid (FDCA). Since 2013, when Corbion acquired BIRD Engineering BV, Corbion has been working on a biotechnological route for production of FDCA, aiming to the lowest possible costs and lowest impact for environment. Like all projects at Corbion, the FDCA project is following the stage gate approach, which involves that economy and LCA are evaluated frequently and used to steer process development and optimization.

The role of process modelling started in 2013 when principles of key unit operations had already been proven on lab scale. A typical start for the *scoping phase* involves brainstorming for process concepts that fit within the boundaries of the project, like no use of toxic chemicals, low energy consumption and low waste production. Subsequently, in the *concept development stage*, process schemes are drafted for the highest ranking options. To generate the mass and energy balance, a flowsheet model of the complete processes from feedstock to FDCA was implemented in the commercial software gPROMS [5]. For this, we have developed an *inhouse model library and inhouse physical property databank*. Where needed new unit operation models were added to the model library, e.g. detailed fermentation models, and the physical property databases were extended with relevant lab data for FDCA and derivatives. Input parameters for the unit operation models were aligned with unit operation experts and are an educated guess representing the expectation of what research can bring to improve the current performance. The gPROMS flowsheet model will automatically produce the mass and energy balance and estimations for Bill of Materials, input for sizing of equipment and estimation of carbon footprint.

The results of the modelling activities were used to select the best feasible process concept. In the *design and develop phase*, sensitivity analysis was carried out to determine the areas that have the largest impact and/or uncertainty on costs and sustainability of the selected process. This is then used to determine further research and the possible need to make changes to the process concept.

In the *test and validate phase*, an iterative process where the model is being extended and validated with new experimental data, proposed changes are evaluated, lacks in our knowledge were identified and results of the model were used to steer further research.

At the stage gates a detailed LCA and economic evaluation is done, which can also lead to process changes, for example when a feedstock was found to have a higher than accepted impact on sustainability or when a solvent choice was not accepted a being sufficiently safe. The LCA and economy of FDCA is benchmarked against the LCA of terephthalic acid to ensure the bio-based alternative represents a large improvement towards to the fossil based alternative.

This process of combining and iterating process modelling, sustainability calculations and lab and pilot research ensured Corbion the process that was being developed for production of FDCA will meet Corbion's targets on sustainability and cost effectiveness, while using resources in the most time-effective way.

3.2 Revamping

To fulfil the higher demand of one of our products, revamping studies were done in one of our facilities. The aim was not only to increase capacity but also to decrease energy consumption and thus, CO₂ emissions. One way to achieve this was to increase the temperature of the feed to the unit using an available hot water stream in the plant. Therefore, the following three concepts were evaluated with help of models.

- Scenario 1: use of a network of heat exchangers to heat up the feed to the unit.
- Scenario 2: application of heat pumps
- Scenario 3: flashing the hot water stream and upgrading the flash vapour with an steam ejector.

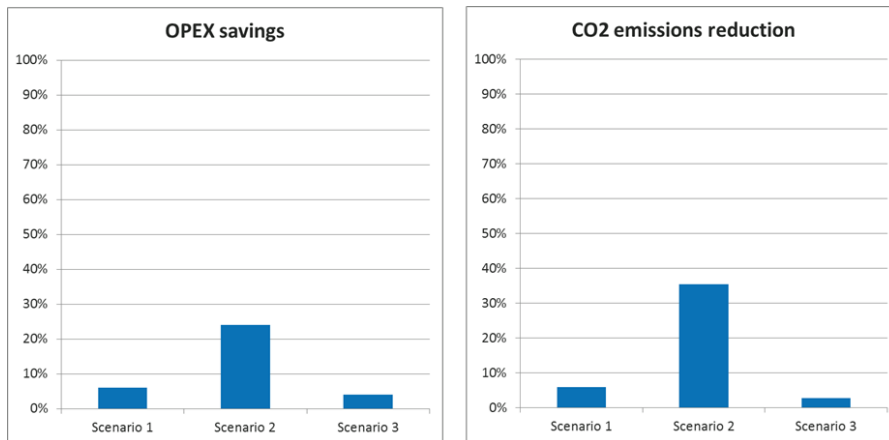


Figure 3. OPEX savings and reduction of CO₂ emissions.

Figure 3 shows the reduction in OPEX for each concept with respect to the base case, and the reduction of CO₂ emissions are also presented. It can be noticed that scenario 2 is the case with both the largest OPEX savings and CO₂ emissions reductions. It is, however, the case with the highest investment, yet, the payback time is less than 3 years. The results of this study were presented during the stage gate assessment and allowed passing the Design and Develop phase.

4. Conclusions

In this paper, the contribution of mathematical models to steer research and development programs within Corbion was presented. By performing a techno-economical evaluation, sustainability assessment and lab/pilot research in each stage of the innovation funnel, Corbion ensures that the new process/product will meet sustainability and economic targets. Moreover, this approach also allows to identify changes needed in the processes and/or chemicals in the early stages of the process development, when this changes involves relatively low cost.

The methodology was illustrated with two different projects running at Corbion. One of them include the production of FDCA. For this case, the stage gate process starting from the scoping to the test and validate phase has been discussed. By process simulations, the most promising process, in terms of economy and sustainability has been determined. A second case study showed how models contributed to find the optimal solution in revamping studies.

References

- [1] European commission. Growth – sectors: Biotechnology – bio-based products (online). Visited: September 26, 2018. http://ec.europa.eu/growth/sectors/biotechnology/bio-based-products_en.
- [2] Carus, Michael. Bio-based economy and climate change - Important links, pitfalls and opportunities. Hürth, Germany: Nova-Institut GmbH, 2017.
- [3] Stage gate International (online), 2018. Visited: November 11, 2018. <https://www.stage-gate.com/stage-gate-model>
- [4] Morao A., Dencic I., Visser D. 2017. Sustainability assessment in the innovation funnel. LCM Conference.
- [5] Process System Enterprise. <https://www.psenterprise.com/products/gproms>

Assessment of the dominant factors during hydroprocessing stabilization

Ngoc Yen Phuong Cao,^a Benoit Celse,^{a,*} Denis Guillaume,^a Isabelle Guibard,^a
Joris W. Thybaut^b

^a*IFP Energies nouvelles, Rond-point de l'échangeur de Solaize, BP 3, 69360 Solaize, France*

^b*Ghent University, Laboratory for Chemical Technology, Technologiepark 914, Ghent, B-9052, Belgium*

benoit.celse@ifp.fr

Abstract

Establishing the steady state in hydrotreating process requires several days, leading to long experimentation times in order to obtain sufficient steady-state data for kinetic modelling. However, during the evolution towards this steady state, effluent analyses are already carried out at regular time intervals to determine whether the steady state has been reached and to ensure that the reaction is under control. In this paper, the stabilization time was assessed by using experimental data during these transient conditions. The stabilization evolution is supposed to follow a first-order response. A characteristic time for stabilization τ was defined. A linear model with interaction for τ prediction was developed. It was found that a higher LHSV leads to a quicker stabilization. The extent of the impact of LHSV on τ depends on the feed resin content, i.e., the polar components with high molecule weight. A direct relationship between reactor pressure and stabilization time was found. Temperature is not a dominant factor. Stabilization of spent catalyst depends on the previous operating conditions.

Moreover, online transient data can be used in order to predict, from the first two experimental points and τ calculated by the model, the future steady-state value. By testing against new data with other feedstocks, the model has been found to provide a good prediction of the stabilization evolution and the steady-state hydrotreating performance. If this value is far from the target, operators can change the operating condition without waiting for stabilization.

Keywords: hydrocarbon, hydrotreating, kinetic modelling, reactor, stabilization, transient data.

1. Introduction

Hydrotreating is a catalytic conversion process in petroleum refining, among others for removing impurities such as nitrogen and sulphur compounds from hydrocarbon streams. A kinetic model is a significant asset in, not to say essential for the adequate design and simulation of such a process (Becker et al., 2015). It is usually developed based on experimental data acquired at steady-state conditions. One of the main challenges of hydrotreating process is that establishing this steady state typically

requires several days, leading to long experimentation times in order to obtain sufficient data for kinetic modelling. However, during the transient phase towards the steady state, effluent analyses are already carried out at regular time intervals to detect the steady state and to ensure that the reaction is under control. These available transient data are currently not used for kinetic modelling because the stabilization behaviour is not well understood.

The aim of this work is, first, to get a better understanding of the stabilization behaviour during these transient conditions and secondly, to use these transient data to predict the steady-state reaction performance. If this value is far from a target, the operators can change the operating condition without waiting for stabilization and without the use of a complex model.

2. Materials & Methods

The experimental data are acquired using the IFPEN Hydrotreatment (HDT) pilot plant operating in a continuous manner. The total catalyst volume in the reactor amounts to 50 cm³. Operating conditions are adjusted after having reached the steady state corresponding with the previous operating conditions. The acquired data cover 11 Vacuum Gas Oil (VGO) feeds over two catalysts. Operating conditions were chosen to cover a wide range for the VGO HDT process: Liquid Hourly Space Velocities (LHSV) from 0.5 to 4 h⁻¹, temperature from 350 to 410 °C and total pressure between 50 and 140 bar. The provided data are the ‘liquid product nitrogen content’ (N) with time on stream (TOS), totalling 920 measurements, see Figure 1. A series of points corresponding to one experimental run is called one ‘episode’. Figure 1 shows 7 episodes corresponding to 42 data points during around 45 days.

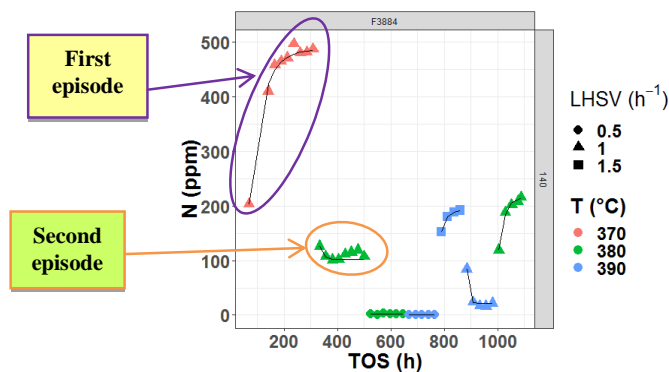


Figure 1. Data representation (P = 140 bar, point: experimental data, solid line: model fitting Equation (1))

A hydrodynamics study on the pilot plant has been carried out using a tracer technique to estimate the stabilization time purely due to hydrodynamic. The objective is to identify whether the stabilization time is determined by hydrodynamic or kinetic phenomena.

Exploratory data analysis (Tukey, 1977) is applied to our available data to assess the stabilization evolution. It resulted in a first-order transfer function as shown in Equation (1).

$$N = N_{init} + (N_{final} - N_{init}) \left(1 - \exp\left(\frac{-(TOS - TOS_{init})}{\tau}\right) \right) \quad (1)$$

Where N is the liquid product nitrogen at a specific time on stream (ppm); N_{init} is the liquid product nitrogen corresponding to the first experimental point of episode (ppm); N_{final} is the last experimental point of episode (ppm); TOS is the time on stream (h); TOS_{init} is the time on stream corresponding to the first experimental point of episode (h) and τ is the characteristic time of the episode (h).

The characteristic time τ of each episode presented in the equation is estimated via nonlinear least-squares (solid line in Figure 1).

A multiple linear regression with interaction technique is then used for τ prediction to evaluate the phenomena underlying the transient data. The general linear model with interaction is illustrated in Equation (2):

$$\tau = a_1x_1 + a_2x_2 + a_{12}x_1x_2 + \dots + b \quad (2)$$

Where x_1 , x_2 are the input variables, which can be LHSV, temperature, pressure or feed properties such as organic nitrogen content, organic sulphur content, resin content in feed, etc.; x_1x_2 is the interaction term between x_1 and x_2 ; a_1 , a_2 , a_{12}, \dots and b are the coefficients.

The most influential input variables of the model are determined via variable selection technique called 'leaps' (Furnival and Wilson, 1974). Fitting linear model and nonlinear model was done by using respectively 'lm' and 'nls' function in 'stats' package in R software. Variable selection was carried out in R by using 'leaps' package obtained from CRAN repository (Lumley, 2017).

The model is then tested against new data with other feedstocks. For each episode, τ is predicted by the model. Knowing τ and the first two points of the episode, it is possible to predict the evolution of the episode as well as the Nitrogen content at steady state calculated via Equation (3) which is developed from Equation (1). The leftover data of the episode are used to validate the model. If the predicted steady-state value is far from the target, the operating condition can be adjusted without waiting for stabilization.

$$N_{final} = \frac{N - N_{init}}{1 - \exp\left(\frac{-(TOS - TOS_{init})}{\tau}\right)} + N_{init} \quad (3)$$

3. Results

The hydrodynamic response to a tracer step reached steady state significantly faster than the stabilization of the HydroDeNitrogenation (HDN) behaviour. Hence, chemical phenomena are involved in the latter.

Stabilization was found to follow a first-order model, which is similar to the observation of Sau et al. (2005) in the study of effect of organic nitrogen compounds on hydroprocessing reaction. The characteristic time τ reflects the time required to reach this steady state. First episodes take more time to stabilize than other episodes. The model was applied on two similar HDT catalysts (Catalyst A and B). Two linear models for τ were built; one for first episodes (model M1) and another for other episodes (model M2).

Model M1 was obtained with a R^2 of 0.83, as shown in the left side of Figure 2. It consists of three variables (LHSV, pressure, resin of feed) and one interaction term LHSV*resin, which are selected by the leaps algorithm. An inverse relationship between LHSV and τ was found. Temperature is not a dominant factor. These two results are coherent with Elizalde et al. (2016) who studied the dynamic behaviour of hydrocracking using the continuous kinetic lumping approach. A direct relationship between pressure and τ was observed. The interaction term shows that the impact of LHSV on τ depends on the value of feed resin, i.e., the polar components with high molecular weight. The resin in VGO can contain nitrogen.

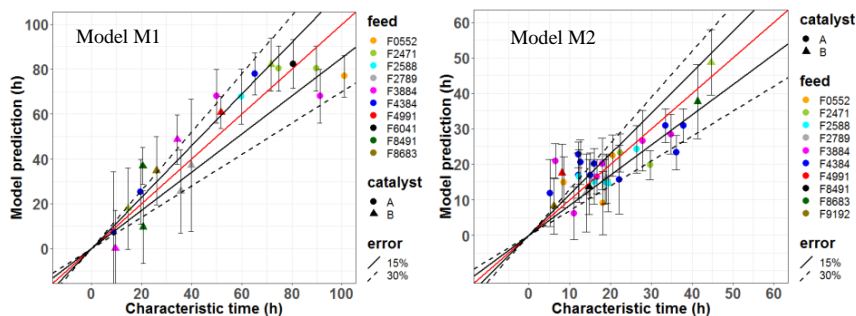


Figure 2. Parity plot with 95% confidence interval for M1 (left, $R^2 = 0.83$) and M2 (right, $R^2 = 0.66$)

However, the stabilization of other episodes seems more complex. The parity plot for model M2 is shown in the right side of Figure 2. The latter includes seven input

variables ($LHSV_{exp}$, $LHSV_{pre}$, T_{pre} , $\frac{LHSV_{exp}}{LHSV_{pre}}$, $\frac{LHSV_{pre}}{LHSV_{exp}}$, $LHSV_{exp} * resin$, S_{feed});

where $LHSV_{exp}$ is the experimental LHSV of the episode; $LHSV_{pre}$ and T_{pre} are respectively LHSV and temperature of the previous episode; resin and S_{feed} are respectively resin content and organic sulphur content in the feed. As can be seen, the model relies by not only on the feed and operating conditions but also on the operating conditions of the previous episode. It shows that the transient behaviour of spent catalyst is more difficult to predict than for the fresh catalyst.

Model was tested by using new data with other feedstocks. τ is predicted by the model and the steady-state value is estimated via Equation (3). Figure 3 shows two examples of such prediction for first episodes (model M1). The two first points of episode which are used to estimate the steady-state value are shown in circle shape. The remaining data in the episode are represented by triangles. The Nitrogen predicted values are very close to the experimental values. The model can predict quite well the transient behaviour and the steady-state value. This algorithm may be linked to an Advanced Process Control method to reach as fast as possible some Nitrogen targets.

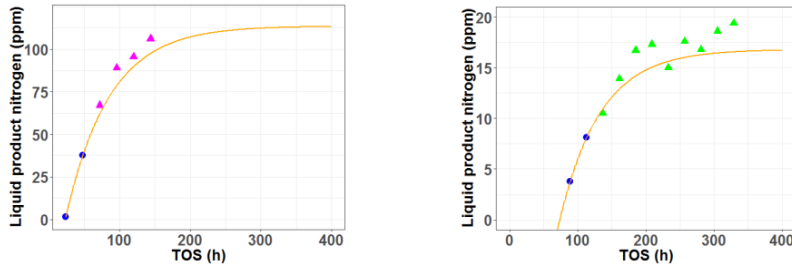


Figure 3. Two examples of the prediction of model M1 (points: experimental data, solid line: model prediction; TOS: time on stream)

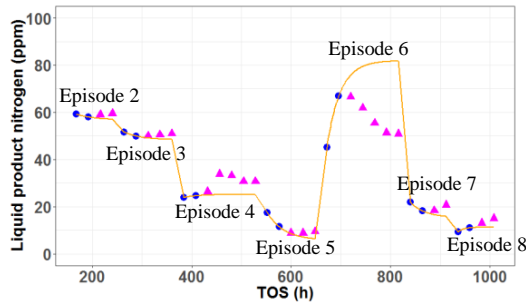


Figure 4. Prediction of model M2 (points: experimental data, solid line: model prediction; TOS: time on stream)

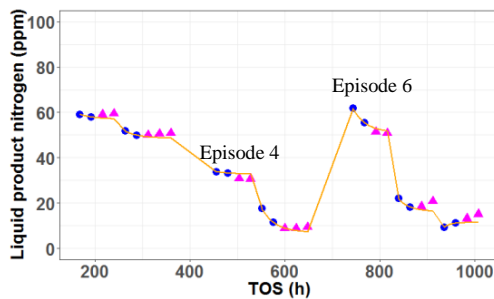


Figure 5. Prediction of model M2 for episode 4 and episode 6 while discarding the first three experimental points of both episodes

Model M2 (for other episodes) is evaluated and is shown in Figure 4. Model predicts well the evolution of episode 2, 3, 5, 7 and 8. Regarding episode 4 and 6, it seems that the transient behaviour did not follow a first-order model, which could be explained by the measurement error/experiment problem or the complex behaviour of spent catalyst. The experimentation duration is longer for these both episodes than for the others. It is possible that there was an experiment problem. If the first three points of episode 4 and 6 are discarded, the prediction is more reliable, see Figure 5. This might be investigated in another study.

4. Conclusions

Stabilization behaviour is a critical point for hydroprocessing experiments. In this work, transient data of hydrotreating process were used to assess this stabilization. It is shown that the stabilization follows the first-order model. A characteristic time for stabilization τ was defined. Two models (one for the first episodes, another for the others) were built to calculate the stabilization time and identify the most influential parameters (LHSV, resin of feed, pressure). Good prediction results were obtained, particularly for the first episodes. The stabilization of other episodes is more complicated to predict.

The model can predict the stabilization time and steady-state value from two initial measures. If the predicted steady-state value would be far from the intended target, operators can change the operating condition without waiting for stabilization. This model will be linked with an Advanced Process Control Algorithm.

This model will be also linked to design of experiment algorithm in order to be used to fit kinetic parameters (Celse et al., 2016).

References

- P.J. Becker, B. Celse, D. Guillaume, H. Dulot, V. Costa, 2015, Hydrotreatment modeling for a variety of VGO feedstocks: A continuous lumping approach, *Fuel*, 139, 133-143.
- B. Celse, J.J. Da Costa, V. Costa, 2016, Experimental Design in Nonlinear Case Applied to Hydrocracking Model: How Many Points Do We Need and Which Ones?, *International Journal of Chemical Kinetics*, 48, 11, 660-670.
- I. Elizalde, F. Trejo, J.A.D. Muñoz, P. Torres, J. Ancheyta, Dynamic modeling and simulation of a bench-scale reactor for the hydrocracking of heavy oil by using the continuous kinetic lumping approach, *Reaction Kinetics, Mechanisms and Catalysis*, 2016, 118, 1, 299-311. DOI: 10.1007/s11144-016-0995-8.
- J. J. Faraway, *Linear Models with R*, Taylor & Francis Group, New York, United States, 2014.
- G. M. Furnival, R.W. Wilson, 1974, Jr, *Regressions by Leaps and Bounds*, *Technometrics*, 499-511.
- T. Lumley, based on Fortran code by A. Miller, 2017, Package 'leaps': Regression subset selection, including exhaustive search, <https://cran.r-project.org/web/packages/leaps/leaps.pdf>.
- R Core Team and contributors worldwide, Package 'stats': R statistical functions.
- M. Sau, K. Basak, U. Manna, M. Santra, R. P. Verma, Effects of organic nitrogen compounds on hydrotreating and hydrocracking reactions, *Catalysis Today*, 2005, 109, 1-4, 112-119. DOI: 10.1016/j.cattod.2005.08.007.
- J. W. Tukey, 1977, *Exploratory Data Analysis*, Addison-Wesley, Reading, MA.

New MINLP Formulations for Flexibility Analysis for Measured and Unmeasured Uncertain Parameters

Maria Paz Ochoa, Ignacio E. Grossmann*

Department of Chemical Engineering, Carnegie Mellon University, Pittsburgh, PA 15213, U.S.A.

grossmann@cmu.edu

Abstract

In this paper, we formulate the flexibility analysis with measured and unmeasured parameters as a rigorous multilevel optimization problem. First, we propose to recursively reformulate the inner optimization problems by the Karush-Kuhn-Tucker conditions and with a mixed-integer representation of the complementarity conditions to solve the resulting multilevel optimization problem. Three types of problems are addressed and solved with the proposed strategy: 1) linear programming problem, 2) nonlinear programming problem with monotonic variation of unmeasured uncertain, and finally 3) nonlinear programming problem. We illustrate the new formulation with a heat exchanger network problem with uncertain heat capacity flowrates.

Keywords: extended flexibility analysis, optimization under uncertainty, MINLP formulation.

1. Introduction

Traditionally, the approach to handle uncertainty in the parameters of a model is to consider nominal conditions in plant operation, and use oversize to compensate for the potential impact of the uncertainty. In contrast, flexibility analysis addresses the guaranteed feasibility of operation of a plant over a range of conditions, with the ultimate goal being on how to design a process for guaranteed flexible operation (Grossmann *et al.*, 2014). The flexibility test problem only determines whether a design does or does not meet the flexibility target. To determine how much flexibility can be achieved in a given design, the flexibility index is defined as the largest value of δ such that the model inequalities hold over the uncertain parameter range (Swaney and Grossmann, 1985).

However, these formulations are based on the assumption that manipulated variables can compensate for any variation in the uncertain parameter set and that during operation stage uncertain parameters can be measured with precision to take the corrective action. Ostrovsky *et al.* (2003) and Rooney and Biegler (2003) extended the analysis by taking into account the level of parametric uncertainty in the mathematical models at the operation stage, by grouping the uncertain parameters, $\theta \in \Theta$, into two types, measured and unmeasured parameters. The flexibility constraint was then extended to account for model parameters, θ_u , that cannot be measured or estimated during the operation stage.

In this paper, we propose a new reformulation of the extended flexibility analysis where the innermost problems are recursively replaced by their optimality conditions and the complementarity conditions are expressed with a discrete representation.

2. Mathematical Model

The basic model for the flexibility analysis involves design variables, d , control variables, z , and uncertain parameters, θ . One of the main problems addressed in the flexibility analysis is the flexibility test problem. It consists in determining whether by proper adjustment of the control variables the process constraints $g_j(d, z, \theta) \leq 0, j \in J$, hold for any realization of uncertain parameters for a given design (Halemane and Grossmann, 1983). This statement can be expressed with the logic expression (1), and is reformulated by the use of min and max operators as shown in Eq. (2).

$$\forall \theta \in \Theta \{ \exists z (\forall j \in J [g_j(d, z, \theta) \leq 0]) \} \quad (1)$$

$$\leftrightarrow \chi(d) = \max_{\theta \in \Theta} \min_z \max_{j \in J} g_j(d, z, \theta) \quad (2)$$

The main difference between the design and control variables is that the design variables are fixed during the operation stage, while the control variables can be adjusted in order to satisfy process constraints. In fact, to solve the flexibility constraint it is required to have accurate estimation of the uncertain parameters. This can only be achieved if there is enough process data for precise determination of all uncertain parameter values. However, this assumption is restrictive, and is often not met in practice.

To address these limitations, two groups of uncertain parameters are identified. The first group of uncertain parameters contains parameters whose values can be determined to within any desired accuracy at the operation stage, namely the measured uncertain parameters, θ_m . Meaning that appropriate sensors are available to determine accurate values of all the uncertain parameters by direct measurement or by solving parameter estimation problems. Therefore, recourse action can be taken in order to compensate for their variation. Examples of this type of parameters include process conditions such as feed flowrates, pressures, temperatures, concentrations, and input variables such as product demands. The second group includes the unmeasured uncertain parameters, θ_u , whose estimation cannot be performed during the operation stage, consequently no control actions can be applied to them.

This distinction has been taken into account and the flexibility constraint was then extended to Eq. (3) and reformulated as the multilevel optimization problem described by Eq. (4) by Ostrovsky *et al.* (2003) and Rooney and Biegler (2003).

$$\forall \theta_m \in \Theta_m \{ \exists z (\forall \theta_u \in \Theta_u, \forall j \in J [g_j(d, z, \theta_m, \theta_u) \leq 0]) \} \quad (3)$$

$$\leftrightarrow \chi(d) = \max_{\theta_m \in \Theta_m} \min_z \max_{\theta_u \in \Theta_u} \max_{j \in J} g_j(d, z, \theta_m, \theta_u) \quad (4)$$

To solve the extended flexibility analysis, Ostrovsky *et al.* (2003) suggested an algorithm for the calculation of the flexibility function based on the branch and bound strategy, while partitioning the uncertain set into subregions. On the other hand, Rooney and Biegler (2003) proposed an extension to the approach presented by Raspanti *et al.*

(2000), which involved the use of the KS smooth function (Krelsselmeler and Steihauser, 1983) that aggregated all of the model inequality constraints, and the KKT derivation together with a smooth approximation of the complementarity conditions for the inner optimization problems. Therefore, the extended flexibility constraint resulted in a nonlinear program.

In this work, we reformulate the extended flexibility constraint by developing the optimality conditions for each nested problems. In addition, in order to make the formulation tighter, the bounds of the nonnegative Lagrange multipliers related to the inequality constraints and the bounds on the slack variables are treated as constraints of the following level optimization problem. Finally, we express the complementarity conditions with a mixed-integer representation and assume that the Haar condition holds, which states that the number of active constraints is equal to the dimension of the control variables plus one. This condition holds true provided the Jacobian is full rank (Grossmann and Floudas, 1987).

In the following subsections, we derive the formulation of three different cases, linear problem, nonlinear problem with monotonic variation of unmeasured parameters with respect to model constraints, and nonlinear problems.

2.1. Special Case 1: Linear Programming problem

The order of the inner max operators in Eq. (4), are interchangeable and can be equivalently expressed as follows.

$$\begin{aligned} \chi(d) &= \max_{\theta_m \in \Theta_m} \psi(d, \theta_m) \\ \text{s.t. } \psi(d, \theta_m) &= \min_z \zeta(d, z, \theta_m) \\ \text{s.t. } \zeta(d, z, \theta_m) &= \max_{j \in J} \max_{\theta_u \in \Theta_u} g_j(d, z, \theta_m, \theta_u) \end{aligned} \quad (5)$$

We consider that the inner problem is described by the linear inequality constraints:

$$g_j(d, z, \theta_m, \theta_u) = a_j \cdot d + b_j \cdot z + c_j \cdot \theta_u + d_j \cdot \theta_m \leq 0, \forall j \in J \quad (6)$$

Constraints g_j in Eq. (6) vary monotonically with respect to θ_u . Hence, the solution of the innermost problem must lie in one of the extreme points of its range of variation, depending on the sign of the derivative, $dg_j/d\theta_{j,u}$.

$$\max_{\theta_u \in \Theta_u} g_j(\theta_{j,u}) \rightarrow \theta_{j,u}^* \quad (7)$$

The bilevel problem M1 described by Eq. (8) is obtained by replacing Eq. (7) in Eq. (5). To obtain a single level optimization problem, the innermost problem of Eq. (8) is replaced by its optimality conditions with a mixed-integer representation of the complementarity condition following the active constraint set strategy (Grossmann and Floudas, 1987). This yields the MILP problem:

$$\begin{aligned} \text{M1: } \chi(d) &= \max_{\theta_m \in \Theta_m} \psi(d, \theta_m) \\ \text{s.t. } \psi(d, \theta_m) &= \min_{z,u} (u \mid g_j(d, z, \theta_m, \theta_u) = a_j \cdot d + b_j \cdot z + c_j \cdot \theta_{j,u}^* + d_j \cdot \theta_m \leq u, \forall j \in J) \end{aligned} \quad (8)$$

Where u is a scalar variable that represents the worst constraint violation.

2.2. Special Case 2: Non-Linear Programming problem with monotonic variation of unmeasured uncertain parameters

If the set of functions $g_j(d, z, \theta_m, \theta_u)$ varies monotonically with respect to the unmeasured uncertain parameters, then the relationship expressed by Eq. (7) holds true. Therefore, the solution of the innermost problem lies at an extreme point of the range of variation of θ_u . Analogously, the following bilevel programming problem M2 is obtained and then reformulated in the same way as the previous case, but leading to the MINLP problem.

$$\begin{aligned} \text{M2: } \chi(d) &= \max_{\theta_m \in \Theta_m} \psi(d, \theta_m) \\ \text{s.t. } \psi(d, \theta_m) &= \min_{z, u} (u | g_j(d, z, \theta_m, \theta_{j,u}^*) \leq u, \forall j \in J) \end{aligned} \quad (9)$$

2.3. General Case: Non-Linear Programming problem

The extended flexibility constraint can be equivalently expressed as the following multilevel optimization problem M3.

$$\begin{aligned} \text{M3: } \chi(d) &= \max_{\theta_m \in \Theta_m} \psi(d, \theta_m) \\ \text{s.t. } \psi(d, \theta_m) &= \min_z \zeta(d, z, \theta_m) \\ \zeta(d, z, \theta_m) &= \max_{\theta_u \in \Theta_u} \varphi(d, z, \theta_m, \theta_u) \\ \text{s.t. } \varphi(d, z, \theta_m, \theta_u) &= \min_u (u | g_j(d, z, \theta_m, \theta_u) \leq u, \forall j \in J) \end{aligned} \quad (10)$$

In order to solve Eq. (10), we propose to replace the inner problems by their optimality conditions in a recursive fashion. Due to space limitations, we cannot report the complete reformulation. To illustrate the solution strategy, we will replace the innermost problem of Eq. (10) by its KKT conditions (Eqns. (11) and (12)) and complementarity conditions (Eq. (13)). Bounds of the Lagrange multipliers, λ_j^0 , and slack variables, s_j^0 , are added as model constraints of the next level optimization problem, described by Eqns. (14) and (15), in order to tighten the formulation.

$$1 - \sum_j \lambda_j^0 = 0 \quad (11)$$

$$g_j(d, z, \theta_m, \theta_{j,u}^*) - u + s_j^0 = 0 \quad \forall j \in J \quad (12)$$

$$\lambda_j^0 \cdot s_j^0 = 0 \quad \forall j \in J \quad (13)$$

$$-\lambda_j^0 \leq 0 \quad \forall j \in J \quad (14)$$

$$-s_j^0 \leq 0 \quad \forall j \in J \quad (15)$$

Following this procedure, we obtain a single level optimization problem. The complementarity conditions are then expressed with a mixed-integer representation, the Haar conditions is assumed, leading to an MINLP problem.

3. Numerical Example

A well-known example in the flexibility analysis literature is the heat exchanger network shown in Figure 1. Grossmann and Floudas (1987) used this NLP example to introduce the active set strategy, which is able to find non-vertex solutions. After the elimination of the state variables, the reduced model consists of four constraints, and

three variables: the cooling load (Q_c) is the control variable and the heat capacity flowrate of streams 1 and 2 (F_{H1} and F_{H2}) are the uncertain parameters. We solve a modified version the problem for three cases. First, considering both uncertain parameters as unmeasured, so no recourse actions can be taken, corresponding to one of the special cases of the traditional flexibility analysis. Second, considering θ_1 as a measured uncertain parameter and θ_2 as an unmeasured uncertain parameter, where control actions can only be adjusted to compensate for variations in θ_1 , solved with the formulation proposed in Section 2.3. Finally, we consider both as measured uncertain parameters like in the traditional flexibility analysis following the active set strategy (Grossmann and Floudas, 1987).

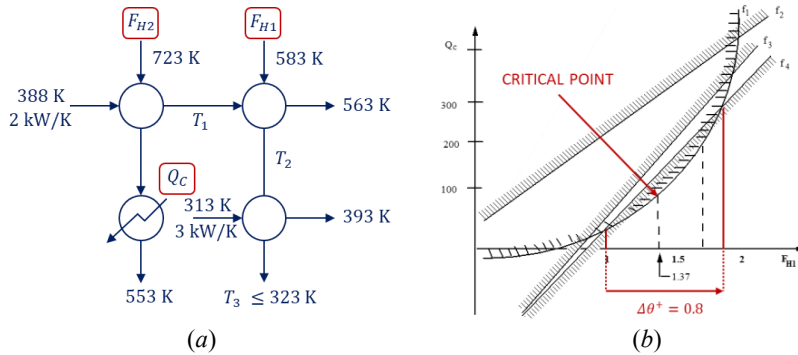


Figure 1. (a) Heat exchanger network scheme. (b) Feasibility diagram for fixed value of $F_{H2}=2$

Numerical results are summarized in Table 1. As we can see, we obtain positive values of u for all the cases, indicating an infeasible design. The worst constraint violation ($u=138.5$) is obtained for the case of no recourse actions. This value can be reduced up to certain degree ($u=20$) when control variables can compensate for the variations in θ_1 . Furthermore, this can be reduced ($u=7.08$) when recourse actions can compensate for variation in both uncertain parameters. It is also important to note, that non-vertex critical points are obtained for the second and third cases. The different problems are implemented in GAMS 25.1.2 (GAMS Development Corporation, 2018) and solved with BARON 18.5.8 (Kilinc and Sahinidis, 2018) in an Intel i7 machine with 16 Gb of RAM. The tolerance of the solver is set to 0.01 and the big M value is 600.

Table 1. Worst constraint violation, critical parameters values for three examples and model size.

	Both unmeasured uncertain parameters* $\theta_u=\theta_1, \theta_2$	Combined type of uncertain Parameters $\theta_m=\theta_1, \theta_u=\theta_2$	Both measured uncertain Parameters $\theta_m=\theta_1, \theta_2$
u	138.5	20	7.08
$\theta_1 = F_{H1}$	1	1.333	1.398
$\theta_2 = F_{H2}$	1.95	2.041	2.034
#bin var	4	36	6
#cont. var	12	161	22
#constraints	13	163	21
CPU time	0.01	1.67	0.09

*For a fixed value of z .

4. Conclusion

In order to obtain more realistic results when dealing with operation under uncertainty, a distinction of the uncertain parameters can be made between the measured and unmeasured uncertain parameters. Thus, the traditional flexibility constraint has been extended. In this work, we have proposed new reformulations of the resulting multilevel optimization problem, which involves the replacement of the innermost problem by its optimality conditions in a recursive fashion and the introduction of a mixed-integer representation of the complementarity conditions, resulting in a MINLP problem.

We have developed the formulation of three different cases, linear problem, nonlinear problem with monotonic variation of unmeasured parameters with respect to model constraints, and nonlinear problems. A particular feature of the first two cases is that the worst constraint violation lies at a vertex of the unmeasured uncertain parameter set; where the formulation can be simplified, leading to a similar formulation as the one obtained by applying the active set constraint strategy, namely the traditional flexibility analysis (Grossmann and Floudas, 1987). An example of a heat exchanger network has been presented to illustrate the proposed reformulation of the general case and compared to cases with different degree of recourse actions.

Acknowledgements

The authors acknowledge the financial support from Eli Lilly and Company and the Center for Advanced Process Decision-making from Carnegie Mellon University.

References

- GAMS Development Corporation, 2018, "General Algebraic Modeling System (GAMS) Release 25.1.2" Washington, DC, USA.
- I.E. Grossmann, B. Calfa and P. Garcia-Herreros, 2014, "Evolution of concepts and models for quantifying resiliency and flexibility of chemical processes," *Computers and Chemical Engineering*, vol. 70, pp. 22-34.
- I.E. Grossmann and C.A. Floudas, 1987, "Active Constraint strategy for flexibility analysis in chemical processes," *Computers and Chemical Engineering*, vol. 6, pp. 675-693.
- K. Halemane and I.E. Grossmann, 1983, "Optimal Process Design under Uncertainty," *AIChE Journal*, vol. 29, no. 3, pp. 425-433.
- M. Kilinc and N.V. Sahinidis, 2018, "Exploiting integrality in the global optimization of mixed-integer nonlinear programming problems in BARON", *Optimization Methods and Software*, vol 33, pp.540-562.
- G. Kreisselmeier and R. Steinhauser, 1983, "Application of vector performance optimization to a robust control loop design for a fighter aircraft," *International Journal of Control*, vol. 37, pp. 251-284.
- G. Ostrovsky, I. Datskov, L. Achenie and Y. Volin, 2003, "Process Uncertainty: Case of Insufficient Process Data at the Operation Stage," *AIChE Journal*, vol. 49, no. 5, pp. 1216-1232.
- C. Raspanti, J. Bandoni and L. Biegler, 2000, "New Strategies for Flexibility Analysis and Design Under Uncertainty," *Computers and Chemical Engineering*, vol. 24, pp. 2193-2209.
- W. Rooney and L. Biegler, 2003, "Optimal Process Design with Model Parameter Uncertainty and Process Variability," *AIChE Journal*, vol. 49, no. 2, pp. 438-449.
- R. Swaney and I.E. Grossmann, 1985, "An index for operational flexibility in chemical process design. Part I. Formulation and Theory," *AIChE Journal*, vol. 31, pp. 621-630.

Mathematical process modelling past, present and future – a personal perspective

J.P. Schmal

Process Systems Enterprise Inc., 4 Century Drive, Ste 130, Parsippany, NJ, 07054, USA¹

p.schmal@psenterprise.com

Abstract

Progress in mathematical process modelling has been tied primarily to hardware developments and secondarily to better software, advanced algorithms and improved data availability. In this paper we review modelling history to extract some trends for the future. Modelling will play an increasingly important role in process industries. Historically separate techniques such as flowsheeting, custom modelling and CFD will likely merge as computational power increases. Initially parallel computing will give the needed additional computation power. Neural nets are expected to play a role in empirical models and analysis. We need to move from storing data to storing useful information.

Keywords: modelling, digitalization, big data, history.

1. Introduction

Mathematical process modelling has been around for many decades, but has evolved significantly with the advent of more powerful computers, better algorithms and the availability of more data. To help understand where mathematical process modelling may go in the future, we need to understand the past and the present. This paper represents a personal view and is based on historic events and personal experiences and beliefs. In a short paper, it is impossible to do justice to all people that contributed to these areas and to cover the history in the detail it deserves. The goal is to abstract general trends in the field and use them to look ahead.

Modelling technology encompasses four main elements: 1) modelling approaches, 2) software & algorithms, 3) hardware and 4) data. We will cover the status of each of these elements. For modelling approaches, we will cover custom modelling, flowsheeting, CFD and neural networks.

2. Past

2.1. Pre-1950

Process modelling has been around for a very long time. Initially the models needed to be solved analytically due to a lack of computers. The art of modelling was therefore to try and find a problem that was as close as possible to reality, yet could be solved analytically. As a consequence many simplifying assumptions were needed to make the

¹ Per May 1st 2019: ExxonMobil, 1545 US-22, Annandale, NJ 08801, USA

problem solvable. Several techniques were employed to get general solutions that could be used for different cases. For example, dimensionless numbers were extensively used to reduce the number of variables and allow for plotting solutions in 2-D. Dynamic behaviour was studied with the help of bifurcation studies, using the steady-state as a demarcation between regions of different dynamic behaviour (Aris, 1994). These general solutions or solutions to certain equations would often be published in books. Process control was all manual and measurements were virtually non-existent. Chemical processes were run based on experience and by trial and error.

2.2. 1950-2018

With the advent of digital computers and the introduction of software, many areas such as modelling, control and neural networks evolved rapidly. Process modelling could relax some of the simplifying assumptions. One of the earliest industrial applications was by Sargent (1958) using a punch card computer to design a distillation column and a multi-stream heat-exchanger. Steady-state models were difficult to solve and dynamic models were used to find the steady-state as they were easier to initialise.

Initial computations could only use limited memory on what were slow computers, but memory, CPU clock speed and hard drive space grew rapidly. This allowed for ever more complex and realistic problems to be solved as demonstrated in Figure 1.

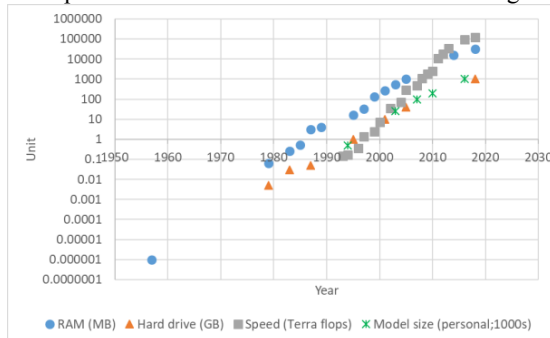


Figure 1: Historic size of RAM and hard drive (created with data from http://organdi.net/article.php?id_article=82, https://en.wikipedia.org/wiki/History_of_supercomputing and personal experience)

Besides hardware improvements, advancements in several other areas were equally important to progress in modelling. New simulation-specific software, advanced algorithms and improved data availability all contributed to the development of more detailed and accurate models.

In 1957, Fortran (FORMula TRANslation) was developed and it allowed for easy implementation of equations. It is worth mentioning Matlab, whose first commercial version became available in 1985, Python, whose first version became available in 1980 and excel (1985; first spreadsheet was developed in 1969). Matlab, Python and excel have found wide spread use in the engineering community.

With regards to algorithms for sets of equations, broadly speaking two types of solutions were considered: sequential modular and simultaneous or equation-oriented. Sequential modular solvers were prominent in flowsheeting tools while simultaneous solvers were

more often used in custom modelling tools. In the sequential modular approach the structure of the problem is exploited and each process unit is solved in turn. This requires the inputs to the units to be known or given. Back to front calculations or including recycles and/or heat-integration is difficult or requires intermediate steps and/or iterations through the loop. Equation-oriented solvers, solve all equations simultaneously, allowing for back to front calculations, easier solution of recycles and heat-integration. Because equation-oriented solvers are Newton-based solvers, good initial guesses are required. Process Systems Enterprise developed automated initialization procedures to get these good initial guesses. As all equations are solved simultaneously, debugging a problem is usually less straightforward than in sequential modular approaches.

Gear was one of the key pioneers in solving sets of Differential-Algebraic equations (DAEs). In 1971 he introduced a multi-step, backward difference formula (BDF) method. Petzold (1982) developed DASSL, which is at the basis of many of today's BDF solvers. In 1989 the semi-implicit Runge-Kutta method, a one-step method, was introduced and the rivalry between BDF and Runge-Kutta caused significant improvements in both solvers. The interest in partial differential equations bloomed in 1996. Although many algorithmic improvements have been made in linear algebra (e.g. MA28 in 1977 & MA48 in 1996), non-linear solvers and integration solvers, the next logical avenue for speed and capability improvements was the exploitation of parallelization.

With regards to software we will briefly consider Computational Fluid Dynamic (CFD), Flowsheeting, custom modelling and neural networks. 2-D CFD solutions were available as early as 1930 and the first CFD calculations using finite differences were done on ENIAC in 1940, one of the world's first computers. In 1957 Los Alamos solved the first 3D CFD calculations with first publications by Douglas aircraft and Boeing in 1967 and 1968 respectively. Unsteady aerodynamic flows were first successfully solved in the 1970's. Two-phase flow and reacting media were developed in the early 1990's until today.

The first flowsheeting tool was developed in 1959 by Monsanto and was called Flowtran. They later participated in the Aspen project with MIT and DOE, which led to first version of Aspen in 1981. Two other notable developments for flowsheeting tools are the development of PRO/II by SimSci which was established in 1967 and later became part of AVEVA and CHESS developed in 1968 at the University of Houston and the US Navy, which became Chemcad in 1985. In 1996 Hyprotech, a company spun out of the University of Calgary, developed HYSYS, which was sold to Aspen and then divested due to the fact it was anticompetitive and bought by Honeywell. Some of the developers of HYSYS also developed Unisim in 2005. Most flowsheeting tools are sequential modular, but Aspen EO, ROMeO, gPROMS ProcessBuilder and gPROMS FormulatedProducts are examples of equation-oriented flowsheeting tools.

Hundreds of tools were developed for custom modelling (able to solve general integral-partial-differential-algebraic equations, IPDAE), but two key developments were SPEEDUP in 1964 developed by Sargent and Westerberg. SPEEDUP was sold to Aspen and later became Aspen Custom Modeller. Pantelides and Barton developed gPROMS in 1993 and Process Systems Enterprise was set-up to commercialize gPROMS in 1997.

Neural networks (NN) were first developed in 1943 where electrical networks were used to represent the neural network. In 1950 IBM had its first successful neural network and in 1957 Cornell university developed perceptron for pattern recognition. In 1959 Stanford used NN to remove echoes in telephone calls, but in 1969 a critical paper proved that

perceptron could not solve the “exclusive or” problem. As a consequence the interest in NN dissipated until 1982 when multi-layer NN were introduced. In 1989 feedforward was introduced, allowing for any function to be implemented in an NN. In 1995 another dead period started since people were unable to teach NN how to play chess. In 2006 the interest in NN rebounded by a rebranding to deep learning. Research led to a couple of key innovations with regards to initialization of the weights used to indicate the influence of each node in the previous layer on a node in the current layer. The weights traditionally were set randomly, requiring huge data sets to “train” the NN. The advent of big data and the use of GPUs (Graphical Processing Units) which sped up calculations drastically, allowed NN to become powerful (e.g. Watson, Google, Amazon etc.).

With the advent of computers and software to simulate complex models, the techniques of optimisation, parameter estimation and design of experiments became readily available. This in turn led to a need for data to estimate unknown or uncertain parameters and optimize the design or operation. In the early days measurements were analogue, often making use of pneumatic measurements, typically a pen moving up and down while a piece of paper was moving underneath it. This meant data had to be transcribed from the scrolls into usable forms. For example, the first electrical signal pressure measurements became available in the 1930’s, but the first digital pressure sensor was developed by Honeywell in 1967 (<http://www.sensorland.com/HowPage059.html>). With the digitalization of operations more sensors were introduced in plants and the sensors were digital, meaning the data was easily accessible. The OPC, OLE (Microsoft Object Linking and Embedding) for Process Control) standard was introduced in 1995 and in 2001 the Historical Data Access (HDA) was introduced. As an example of this change, in 1994 during my internship at Hoechst, the unit I was modelling only had a few measurements (~25), while during my Ph.D. from 1999-2003, I modelled a large petrochemical plant from Shell and 2300 sensors were available, (350 used in the modelling).

3. Present

Present capabilities include among many others: Flowsheets of connected gas processing plants (Aluma et al., 2016), combined product and process design (Martin and Martinez, 2013), coupled DEM (discrete element models), custom multi-scale models of wet granulation (Barrasso et al. 2015), three-phase CFD simulations of units and neural nets that control more and more parts of our daily life.

Tsay et al. (2018) give an overview of optimal process design capabilities and practices. They interviewed 110 industrial people and found that there is limited adoption of optimization and modelling tools.

With regards to hardware there is a clear trend towards parallelization and cloud computing as the improvements of a single core seem to be flattening off. As an example we ran the same large model using the same software version on a high end i7 machine in 2012 taking 156 s CPU time, while on a high end Xeon machine in 2017 it took 105 s CPU time (~32% improvement). During this same time period we have achieved speed improvements of a factor of 3 for large models due to algorithmic improvements. With parallelization we have managed to achieve speed increases of close to a factor of 1000. The latter, is case dependent and not generally applicable however.

Data standards, integration and increased hard disc space have led to much wider availability of data for analysis and training of neural nets. The fact that chemical plants

typically operate in a narrow operating window makes using neural nets both easier and harder: easier because it only needs to cover a limited number of possibilities and harder because it also means the information content in the data is limited and there is a danger of training the neural net how to predict noise.

On-line applications of models both linear and non-linear are common and models are used as soft sensors for unmeasurable quantities and phenomena such as coking and fouling. Advanced model-based control and optimization is applied in many different industries and on hundreds of plants world-wide.

4. Future

All we can do is consider different alternative scenarios and discuss their likelihood. It is clear from history (see Figure 2) that we have always tried to get the most out of the hardware and software. We always have been able to add complexity faster than hardware has been able to grow. The current digitalization trend is expected to increase the use of models both off-line and on-line. As such model-based engineering is expected to be a standard practice (e.g. see INCOSE vision 2025). In on-line models the use of more detailed models is now possible due to robust and fast solvers.

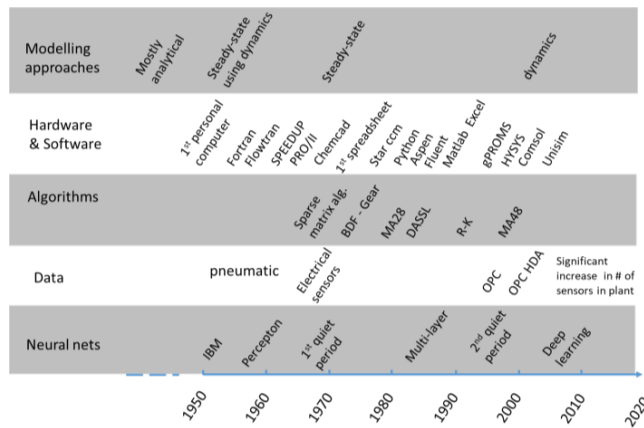


Figure 2: Summary of history

With regards to hardware, the trend we see towards cloud computing and parallelization most likely will continue and it seems it is the most secure way to get more computation power. There are still new developments in miniaturization allowing for more power. The development of the quantum computer is still progressing and has been for a long time (since 1982), chances of a major breakthrough in the next decade seem unlikely. Although progress is steady, the algorithms that can benefit from quantum computing are still limited. A breakthrough in quantum computing would be a disruptive event.

With the availability of more computational power, two trends most likely will continue: bigger envelops/systems and more detailed models. At the moment these bigger problems are solved using relatively simple models. Using more detailed models will require more computational power and bring additional benefits. The level of detail will also increase due to software like CFD, flowsheeting and custom modelling merging into a single tool.

Algorithms will keep on improving and there is still a lot of room for improvement in areas such as global mixed-integer non-linear programming. The application of neural nets will increase, but research interest (measured by hits in Google scholar) shows a decline in papers in this area. Neural nets can play an important role in cases where first-principles are not well-known or in areas such as data analytics.

Compared to nuclear physics, data analytics in chemical engineering can be improved upon. Also, techniques that combine information from signals to get a better overall picture (similar to PAT, Process Analytical Technology) can be improved. Finally, data is simply stored for a certain time and later simply deleted. With the increased availability of data it most likely will be necessary to extract useful information from the data to keep data storage requirements under control and the use of this data manageable.

5. Conclusions

Progress in hardware and software has driven mathematical process modelling and will continue to do so in the future. Single core hardware capabilities are flattening out, but parallelization and cloud-based solutions will allow us to keep expanding. A potentially disruptive technology of quantum computing is not expected to be available to engineers any time soon. Algorithm development has continued steadily and there is still room for improvements. With the availability of more data the application of neural nets will likely grow, but research interest seems to slow down. Neural nets will likely play a role in more traditional roles of pattern recognition for empirical elements of models, raw data analysis and generated data analysis. With the additional availability of data there is room for better analysis techniques such as PAT and a need for smarter storage, e.g. extracting the useful information before storing.

References

- D.Aluma, N. Thijssen, K.M. Nauta, C.C. Pantelides, N.Shah, 2016, Optimize an integrated natural gas production and distribution network, Gas processing & LNG, October
- D. Barrasso, T. Eppinger, F.E. Pereira, R. Algave, K. Debus, S.K. Bermingham and R. Ramachandran, 2015, A multi-scale, mechanistic model of a wet granulation process using a novel bi-directional PBM/DEM coupling algorithm, Chem. Eng. Sc., 123, 500-513
- R. Aris, 1994, Mathematical modelling techniques, General Publishing Company Ltd.
- INCOSE vision 2025, 2014, A world in motion- systemengineering vision 2025, https://www.incose.org/docs/default-source/aboutse/se-vision-2025.pdf?sfvrsn=b69eb4c6_4
- M. Martin and A. Martinez, 2013, A methodology for simultaneous product and process design in the customer products industry: The case study of the laundry business, Comput.Chem. Engng., 32, 715-720
- L. Petzold, 1982, A description of DASSL: A differential/algebraic system solver, IMACS World Congress, August 8-13, Montreal, Canada
- R.W.H. Sargent, 1958, Applications of an electronic digital computer in the design of low temperature plant, Trans. Instit. Chem. Eng. 36, 201-214
- C. Tsay, R.C. Pattison, M.R. Piana and M. Baldea, 2018, A survey of optimal process design capabilities and practices in the chemical and petrochemical industries, Comput. Chem. Engng. 112, 180-189.

The use of optimization tools for the Hydrogen Circular Economy

M. Yáñez,^a A. Ortiz,^a B. Brunaud,^b I.E. Grossmann,^b I. Ortiz^{a,*}

^a *Chemical and Biomolecular Engineering Department, University of Cantabria, Av. los Castros s/n, 39005, Santander, Spain*

^b *Carnegie Mellon University, 15213, Pittsburgh, Pennsylvania, USA*

ortizi@unican.es

Abstract

Hydrogen losses in industrial waste gas streams, estimated as 10 billion Nm³ per year in Europe, constitute potential sources for hydrogen recovery. Further use of this waste hydrogen in fuelled devices promotes a world powered by hydrogen while reinforcing the paradigm of the Circular Economy. This will require the availability of effective technologies for hydrogen recovery and purification as well as the techno-economic assessment of integrating the upcycled gas into a sustainable supply chain using decision-making tools. This work using a mixed-integer programming model (MILP), and scenario analyses, develops the techno-economic modelling over the 2020-2050 period, at a regional scale comprising the north of Spain. Two main industrial waste streams are considered; one produced at integrated steel mills and coke making industries and, the second one, at chlor-alkali plants. The proposed optimization model integrates the following items: i) technology selection and operation, ii) hydrogen demand forecast, iii) geographical information, iv) capital investment models, and v) economic models. The optimal solutions that arise from the combination of all the infrastructure elements into the mathematical formulation, define the gradual infrastructure investments over time that are required for the transition towards a sustainable future energy mix, including surplus hydrogen. The results confirm that the critical factor in the configuration of the proposed energy system is the availability of industrial surplus hydrogen, contrary to conventional hydrogen energy systems that are mainly controlled by hydrogen demand. Additionally, this study confirms that the optimal levelized cost of upcycled hydrogen is in the range of 0.35 to 1.09 €/kg H₂, which is 1.5 to 2 times lower than the price of hydrogen obtained by steam conversion of natural gas.

Keywords: Hydrogen recovery, surplus hydrogen, MILP optimization model, hydrogen infrastructure

1. Introduction

Hydrogen-based energy storage systems could play in the future a key role as a bridge between intermittent electricity provided by alternative sources and the common fossil fuel-based energy system. The versatility and unique properties of hydrogen open the way to accomplish this goal. Although in recent years, the prospects of a shift to a hydrogen economy have created great interest in the scientific community and social stakeholders, the success relies on the availability of the necessary infrastructures. A number of works focused on the use of decision-support tools for the design and operation of hydrogen

supply chains (HSC), have been reported addressing questions such as the design of the hydrogen fuel infrastructure applied at country, region and city levels [1–3].

Likewise, industrial waste streams with a hydrogen content higher than 50% are considered potential and promising sources for hydrogen recovery using cost-effective separation techniques [4]. Meanwhile, among the list of hydrogen-containing waste streams, some studies concentrated on the management, optimization, and utilization of steel-work off gases in integrated iron and steel plants [5,6]. However, little is focused on the optimization of various by-product gases to embed sustainability into HSC. To the best of our knowledge, reported optimization models for HSCs do not consider the competitiveness of upcycling hydrogen-rich waste gas sources for its reuse in both transportation and residential sectors. Hence, the originality of this study is to report the techno-economic feasibility of a HSC with contribution of upcycled hydrogen-rich waste gas sources to fuel both stationary and road transport applications [7].

2. Methodology

The methodology framework of this work is proposed in Figure 1. For that purpose, a mathematical formulation with the objective of maximizing the net present value (NPV) is proposed. The corresponding problem is stated as follows. Given:

- the potential sources for hydrogen recovery composition and their quality;
- a set of suppliers with their corresponding time-dependent maximum supply;
- locations of the key stakeholders in the target region: suppliers, merchants, and customers;
- a set of allowed routes between the three stakeholders, the transportation mode between them, the delivery distance between both routes; supplier-to-merchant and merchant-to-customer;
- hydrogen demand forecast by customer for both transport and residential sectors;
- raw material and product prices;
- a set of production, purification and conditioning technologies, and their yields to upgrade raw materials to hydrogen product, as well as their capacity at different scales;
- investment and operating costs of each intermediate technology, transportation mode, depreciation, and the residual values at the end of the time horizon;
- financial data (such as discount and tax rates).

The goal of the proposed model is to provide the optimum answer to the following questions: how much, where and when stakeholders shall make their investments. The outputs provided by the model are:

- optimal investment plan for all the merchants considered and related logistics;
- location (single- or multiplant), type, scale, and number of installed technologies.
- sourcing and supply routes for the raw materials and product considered;
- connections between the stakeholders, and hydrogen flows through the network.

Within the network presented, the optimization model was developed by integrating the technology selection and operation, the hydrogen demand forecast, geographical information, capital investment models, and economic models.

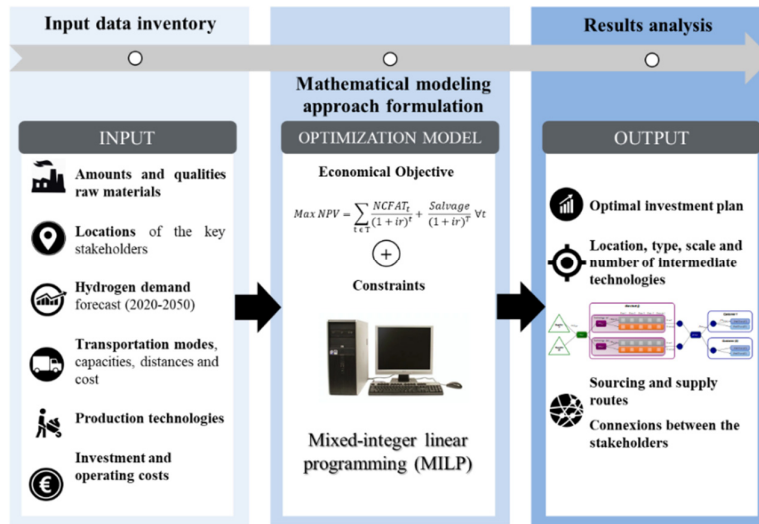


Figure 1. Methodology to optimize a sustainable hydrogen supply chain

3. Optimization model

An optimization modelling approach based on multi-scenario MILP has been developed. The mathematical model was implemented in JuMP (Julia for Mathematical Optimization) and the optimization solver used was Gurobi 7.0.2. The objective of the model is to maximize the NPV over 30 years (2020-2050). Furthermore, the operational planning model regarding plant capacity, production transportation, and mass balance relationships, is considered together with the constraints of these activities.

Because of the complexity of the proposed model, a two-stage hierarchical approach has been used in order to solve the MILP model in reasonable computational time, achieving near-optimal solutions (5% optimality gap) in less than 2 h. The first step consists of the solution of a relaxed single-period problem to determine the location of production plants at the end of the horizon. From this initial assessment, merchant companies that are not selected in the first step are eliminated. Next, in the second step, the 30-year horizon problem is solved with a reduced set of merchants. The optimality gaps have been set to 2% and 5% for the first and second step, respectively.

4. Case study: Upcycled waste gas-based HSC for the North of Spain

This work is focused on the techno-economic feasibility of the upcycling of hydrogen-containing multicomponent gas mixtures to feed stationary and portable fuel cells using optimization tools, geographically located in the north of Spain. The proposed model is focused on two main industrial waste streams.

The first hydrogen source corresponds to high purity hydrogen off gases of the chlor-alkali industry denoted as raw material R99. The second most valuable by-product considered in the optimization model, is coke oven gas (COG) which is produced at integrated steel mills and coke making industries. Hereafter, this raw material has been denoted as R50 because the average hydrogen composition is between 36-62% vol.

Moreover, the geographic distribution of the future hydrogen market comprises a number of stakeholders that correspond to the three nodes of the hydrogen network, as illustrated in Figure 2. Suppliers, which are industrial companies that produce the surplus hydrogen. Merchants, which are the major industrial gases producers and responsible of the raw material transformation into the final product. However, surplus hydrogen transformation onsite was also considered at supplier's plant sites. Finally, the potential customers that are urban areas with more than a hundred thousand inhabitants.

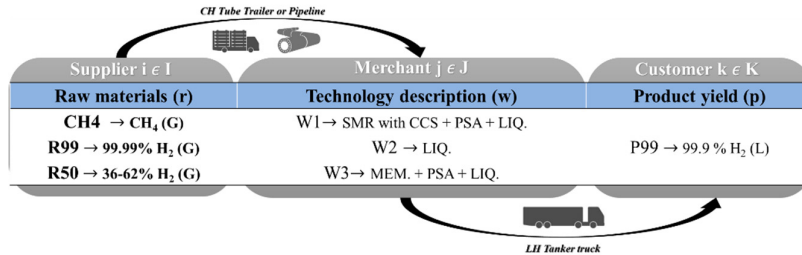


Figure 2. Waste gas streams-based HSC studied for the north of Spain

4.1. Data collection

In this study, two scenarios concerning two levels of demand for road vehicle transportation and residential/commercial sectors have been considered (see Table 1) [8]. Regarding the intermediate technologies, steam methane, CH₄, reforming (SMR) with carbon capture and storage (CCS) has been considered as benchmark technology in order to satisfy the expected demand for hydrogen [9]. With regard to the upcycling of surplus hydrogen, we have selected a combination of two of the most mature technologies for hydrogen purification: membrane technology (MEM) followed by pressure swing adsorption (PSA) [10]. The final product P99, pure liquefied hydrogen, requires a liquefaction stage (LIQ.). Each plant type incurs in fixed capital and unit production costs, as function of its capacity. Furthermore, the transportation costs depend on the selected mode and distance [11]. We considered that raw materials are transported as compressed gas hydrogen (CH₂) by tube trailer or pipeline (already installed), and the final hydrogen products are shipped as liquid hydrogen (LH₂) by truck. We have considered the corresponding unit transportation cost for each type of hydrogen delivery mode.

Table 1. Demand scenarios of hydrogen market penetration by end users and timeframe

	Scenario (S)	End-use (e)	2020	2030	2040	2050
Hydrogen market penetration (%)	S1	e1: Transport sector	0.7	8.4	16.6	25.3
		e2: Residential/Service sector	0.0	0.7	3.0	6.7
	S2	e1: Transport sector	1.4	16.8	33.2	50.6
		e2: Residential/Service sector	1.0	6.0	10.0	13.5
Hydrogen demand	Total S1 (tons H ₂ per year)		8.9E+03	1.2E+05	2.7E+05	4.6E+05
	Total S2 (tons H ₂ per year)		4.0E+04	3.4E+05	6.3E+05	9.2E+05

4.2. Results and Discussion

This section shows the main results obtained by application of the proposed multiperiod mixed-integer programming model to the optimization of the network infrastructure for the fulfilment of low hydrogen demand (S1). The solution of the model determines: i) the amount of hydrogen-rich waste streams (R50 and R99) converted into liquefied hydrogen at the supplier's plants, and ii) the optimum SMR-CCS plant site locations.

Investment Network: Case S1 leads to a solution with a NPV of 941 MM , where the revenue derived from hydrogen sales (3370 MM€) is able to absorb the costs (2030 MM). No single hydrogen production method will be profitable to produce enough hydrogen to fulfil the expected demand on its own. The optimal solution of the integrated surplus HSC leads to the installation of ten units of different technologies until 2050 in northern Spain: W1 (7 units), W2 (2 units) and W3 (1 unit), as shown Table 2.

Table 2. Investment plan obtained for scenario S1

$j \in J$	Location	Period	Technology	Size (ton H ₂ /year)	Investment (MM)
12	Asturias	2020	W3	50000	116.3
14	Huesca	2020	W2	1000	8
16	Cantabria	2020	W2	1000	8
6	Salamanca	2022	W1	200000	605.2
4	BCN (Rubí)	2028	W1	200000	605.2
7	Santander	2033	W1	200000	605.2
6	Salamanca	2037	W1	200000	605.2
5	Huesca	2041	W1	200000	605.2
6	Salamanca	2045	W1	200000	605.2
3	BCN (Parets del Vallés)	2048	W1	200000	605.2

Thus, decentralized on-site hydrogen production by the upcycling of industrial surplus hydrogen is the best choice for market uptake and for avoiding costly distribution infrastructure until the demand increases.

Surplus hydrogen flowrates: As summarized in Figure 3, in Case S1, the full amount of R99 is utilized with an inflow of 293.400 tons over the next 30 years, and R99 can meet 0.5% of the total hydrogen demand in the north of Spain for the whole time period. Whereas the amount of liquefied hydrogen produced from R50, which is 1.497.000 tons of R50, is able to cover a much larger hydrogen demand accounting for 10.1% of the total hydrogen demand. Consequently, the rest of the hydrogen produced to fulfil the total demand is obtained from CH₄ using SMR with CCS as benchmark technology while producing the least CO₂ emissions compared to the rest of the commercially available technologies.

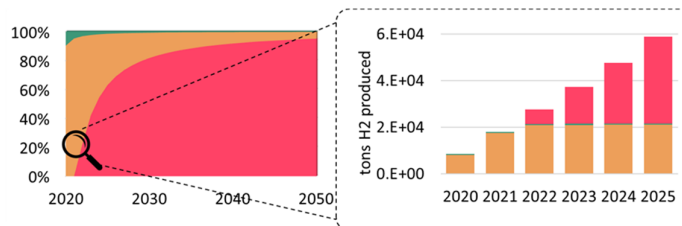


Figure 3. Share of pure H₂ produced per raw material $r \in R$; ■ CH₄; ■ R99; ■ R50

However, the use of inexpensive surplus hydrogen sources may have a central role in the early phase of hydrogen infrastructure build up in the north of Spain. Therefore, industrialized hydrogen will also play an important role in initiating the transition to a hydrogen economy with localized plants of SMR with CCS; this will support the demand before expanding to less populous areas forming a more decentralized green hydrogen production. Analysing the surplus hydrogen flowrates by customer, it can be observed that though R50 is partially marketed to all final end-users, it has a pivotal contribution when the production of the final product is closer to the customers.

5. Conclusions

This research provides the methodology to assess the techno-economic feasibility of upgrading and reusing surplus hydrogen gases promoting the shift to the Circular Economy. The analysis has been performed over two scenarios of hydrogen demand (S1 and S2) and the results show that as long as both scenarios of hydrogen demand (S1 and S2) apply, all generated case studies lead to a solution with positive NPVs. The results confirm that the use of inexpensive surplus hydrogen sources such as R50 and R99 offers an economic solution to cover hydrogen demand in the very early stage of transition to the future global hydrogen-incorporated economy, especially when the industrialized hydrogen generation is closer to the demand markets.

Acknowledgments

This research was supported by the projects CTQ2015-66078-R (MINECO/FEDER, Spain) and SOE1/P1/E0293 (INTERREG SUDOE /FEDER, UE), “Energy Sustainability at the Sudoe Region: Red PEMFC-Sudoe”.

References

- [1] Almansoori, A. and Shah, N. (2009) Design and operation of a future hydrogen supply chain: Multi-period model. *Int. J. Hydrogen Energy*. 34 (19),.
- [2] Ochoa Bique, A. and Zondervan, E. (2018) An outlook towards hydrogen supply chain networks in 2050 — Design of novel fuel infrastructures in Germany. *Chemical Engineering Research and Design*. 134 90–103.
- [3] Sabio, N., Gadalla, M., Jiménez, L., and Guillén-Gosálbez, G. (2010) Multi-objective optimization of a HSC for vehicle use including economic and financial risk metrics. A case study of Spain. *Computer Aided Chemical Engineering*.
- [4] Shalygin, M.G., Abramov, S.M., Netrusov, A.I., and Teplyakov, V. V. (2015) Membrane recovery of hydrogen from gaseous mixtures of biogenic and technogenic origin. *Int. J. Hydrogen Energy*. 40 (8), 3438–3451.
- [5] Lundgren, J., Ekbom, T., Hultheberg, C., Larsson, M., Grip, C.-E., Nilsson, L., et al. (2013) Methanol production from steel-work off-gases and biomass based synthesis gas. *Appl. Energy*. 112 431–439.
- [6] Chen, Q., Gu, Y., Tang, Z., Wei, W., and Sun, Y. (2018) Assessment of low-carbon iron and steel production with CO₂ recycling and utilization technologies: A case study in China. *Appl. Energy*. 220 192–207.
- [7] Yáñez, M., Ortiz, A., Brunaud, B., Grossmann, I.E., and Ortiz, I. (2018) Contribution of upcycling surplus hydrogen to design a sustainable supply chain: The case study of Northern Spain. *Appl. Energy*. 231.
- [8] HyWays (2007) The European Hydrogen Energy Roadmap. *HyWays*.
- [9] Sahdai, M. (2017) Review of modelling approaches used in the HSC context for the UK. *Int. J. Hydrogen Energy*. 42 (39), 24927–24938.
- [10] Alqaheem, Y., Alomair, A., Vinoba, M., and Pérez, A. (2017) Polymeric Gas-Separation Membranes for Petroleum Refining. 2017.
- [11] Reuß, M., Grube, T., Robinius, M., Preuster, P., Wasserscheid, P., and Stolten, D. (2017) Seasonal storage and alternative carriers: A flexible hydrogen supply chain model. *Appl. Energy*. 200 290–302.

Author Index

A

Abikoye, B., 1765
Abildskov, J., 499, 739
Abonyi, J., 1411
Acha, V., 487
Achkar, V.G., 541
Adams II, T.A., 715
Adithya, A., 1711
Adjiman, C.S., 667, 1171, 1435
Ahmed, K., 145
Ahmed, U., 1645, 1651, 1663
Ai, J., 919
Al-Ansari, T., 343, 529, 685, 721, 811, 1051, 1165, 1201
Albahri, T.A., 217
Al-Hmoud, A., 763
Al-hotmani, O.M.A., 181
Al-Hroub, A.M., 247
Alibrahim, H.A., 1663
Alici, M., 1003
Al Jamri, M., 1309
Al-Kaabi, A.H., 1483
Almansoori, A., 505
Almeida-Trasvina, F., 1297
Al-Mohannadi, D.M., 1477
Al-Mousa, B., 1645
Al-Nasser, A., 1645
Alnouri, S.Y., 403
AlNouss, A., 343, 721, 733, 1051, 1201
Al-Obaidi, M.A., 181, 247
Al-Obaidli, H., 1165
Al-Qadri, A., 1645
Al, R., 859
Alsarayreh, A.A., 247
Al-Sobhi, S.A., 523
Altunok, O., 1399
Alves, R.M.B., 1639
Al-Yaeshi, A.A., 685, 1201
Amiri, A., 145, 835
Anantpinijwatna, A., 1189
Anda, M., 301
Andrade Neto, A.S., 709
Andreasen, G., 445
Angeli, P., 1657

Arellano-Garcia, H., 763, 967, 1285, 1291, 1303
Arrieta-Escobar, J.A., 1339, 1567
Asprion, N., 235
Attarakih, M., 433, 511
Ave, G.D., 331
Avraamidou, S., 1195
Azapagic, A., 1471
Azzi, A., 1603

B

Backi, C.J., 127
Bagajewicz, M., 265, 1555
Bahl, B., 463, 475
Bahri, P.A., 301
Baldi, F., 1603, 1627
Bano, G., 325
Barajas, R.C., 655
Barbosa-Póvoa, A.P., 841, 949, 1213, 1273, 1777
Bardow, A., 103, 241, 463, 475, 1267
Barkmann, S., 1441
Barletta, D., 595
Barolo, M., 325
Barrera, R., 607
Barroso-Muñoz, F.O., 1093
Barthe-Delanoë, A.-M., 1009
Bart, H.-J., 433, 511
Barton, P.I., 1141
Basán, N.P., 1153
Baumgärtner, N., 475
Bechtsis, D., 1159
Behera, C.R., 859
Beisheim, B., 1063
Berezhinskiy, V., 1705
Bernardi, A., 1081
Bernardo, F.P., 1339, 1567
Bernhardsen, I.M., 1693
Beykal, B., 1237
Bezzo, F., 319, 325, 421
Bhonsale, S., 1
Biegler, L.T., 1405
Bi, K., 457
Bildea, C.S., 277, 439, 985, 1087
Bisson, J., 1099

Bizakis, A., 1159
 Bizon, K., 1393
 Blanchet, C.A.C., 1687
 Bogataj, M., 1783
 Boix, M., 1351
 Boldrini, A., 7
 Bommireddy, Y., 937
 Bongartz, D., 1129
 Boom, R., 799
 Bordes, C., 1723
 Bortoli, A., 421
 Bortz, M., 259, 295
 Böttcher, R., 235
 Bottegal, G., 337
 Bouaswaig, A.E.F., 331
 Boudouvis, A.G., 373
 Bousbia-Salah, R., 1015
 Bradford, E., 445, 1105
 Brandstetter, M., 1705
 Brée, L.C., 913, 1681
 Brehar, M., 133
 Bremen, A.M., 175
 Brilman, D.W.F., 1693
 Brown, C.J., 1027
 Brown, S., 631, 727
 Brunaud, B., 1819
 Budiarto, T., 79, 91
 Bugrynec, P., 727
 Bulan, A., 1681
 Burnak, B., 1195
 Burnham, S., 1669

C

Caballero, J.A., 37, 61, 1357
 Cabezas, H., 1669
 Cabo, D., 793
 Cabrera-Ruiz, J., 1093
 Cafaro, D.C., 541
 Cafaro, V.G., 541
 Câmara, D., 841
 Camargo, M., 1339
 Cansino-Loeza, B., 1321
 Caoc, Y., 271
 Cao, Y., 1315
 Capón-García, E., 1507, 1513
 Capra, F., 865
 Carpio, R.R., 547
 Carvalho, A., 1213, 1273

Caspari, A., 169, 175
 Cecilio, I., 1057
 Cegla, M., 1441
 Celse, B., 1801
 Chachuat, B., 943, 1069, 1081
 Chandler, E., 631
 Chang, H.-H., 787
 Chang, J.-J.,
 Cheali, P., 571
 Cheng, F., 661
 Chen, W.-H., 1231
 Chen, X., 637
 Chinda, R., 1189
 Chou, C.-H., 757
 Cobden, P.D., 643
 Cóccola, M.E., 1153
 Coelho, J.A.P., 1717
 Colombo, G., 1219
 Continillo, G., 1393
 Contreras-Zarazúa, G., 49, 55, 997
 Cormos, A.-M., 643
 Cormos, C.-C., 643, 817
 Corominas, F., 223
 Costa, A., 265, 1555
 Couenne, F., 1723
 Courtais, A., 985
 Cremaschi, S., 1117
 Cristea, V.M., 133
 Cruz, L., 947, 1795
 Čuček, L., 1765
 Cunha, D.P.S., 1177

D

da Cruz, A.J.G., 13
 Dailey, J., 1669
 Dai, Y., 805
 Dalle Ave, G., 901, 1003
 Damartzis, T., 1381
 d'Amor, F., 319
 Dang, Y., 313
 Daosud, W., 571
 Dashti, H., 835
 da Silva, C., 1273
 Daume, S., 1759
 de Boer, R., 643
 De Buck, V., 163
 de la Fuente, E., 211
 de Las Heras, S.C., 1225

Delpino, C., 1519
 del Rio-Chanona, E.A., 1105
 de Medeiros, E.M., 1075
 de Mello, F.M., 13
 de Prada, C., 1279
 de Sousa, J.P., 1699
 de Sousa, R.Jr., 13
 Diab, S., 373
 Diangelakis, N.A., 1195
 Díaz, I., 31
 Diaz, M.S., 1519, 1531
 Dickson, R., 553, 559
 Dinh, B., 1099
 Di Pretoro, A., 355
 Dirza, R., 703
 Doliente, S.S., 289
 Domenech, S., 1351
 Domingues, L., 1387
 Dorgo, G., 1411
 Dorneanu, B., 1285, 1291, 1303
 Duarte, B.P.M., 1147
 Dua, V., 757, 853
 Dumbava, I., 643
 Duterme, A., 1099
 Dutta, A., 1255

E

Ecker, A.-M., 169
 Eden, M.R., 1453, 1459
 Ehrenstein, M., 895
 Ehsani, A., 619
 Ejeh, J.O., 1135
 Elekidis, A.P., 223
 El-Halwagi, M.M., 1489
 Eljack, F., 523, 733
 Elkamel, A., 217, 505
 Elkhalfá, S., 1051
 Elve, A.T., 1729
 Emebu, S., 127
 Emenike, V.N., 469
 Engell, S., 427, 1003, 1063, 1441
 Ensinas, A., 1609
 Enyedi, F., 1183
 Epelle, E.I., 385
 Eren, A., 769
 Esche, E., 79, 85, 91
 España, A., 1033, 1591
 Estrada, V., 1519

F

Facco, P., 325
 Fairweather, M., 151, 157
 Falconer, R., 631
 Fasahati, P., 559
 Faust, J.M.M., 175
 Feng, B., 1675
 Feng, J., 1249
 Fernández Arranz, I.P., 19
 Fikar, M., 571, 1015
 Filho, P.I.O., 1045
 Filipe, R.M., 1387, 1717
 Filipetto, D., 865
 Filippini, G., 181
 Floquet, P., 1099
 Florence, A.J., 1027
 Fontalvo-Alzate, J., 1423
 Fozer, D., 1525, 1183
 Fracas, P., 397
 Fraga, E.S., 391, 1045, 1657
 Francois, G., 481, 589
 Freiesleben, Louise la Cour, 1771
 Frey, P., 985
 Friedler, F., 1579, 1669
 Frutiger, J., 883
 Furuta, M., 769

G

Gabrielli, P., 7
 Gabrisch, X., 229
 Galán-Martín, Á., 943
 Galanopoulos, C., 595
 Galindo, A., 667, 1171, 1435
 Gallucci, F., 337, 415
 Galvanin, F., 391, 421
 Ganesh, S., 937
 Gani, R., 637, 1453, 1459
 Ganz, K., 463
 Gao, Y., 613, 679
 García del Valle, A., 1153
 García-García, J.C., 1447
 Gasca-González, R., 1423
 Gatti, M., 865
 Gaur, A., 1255
 Gazzani, M., 7
 Gençer, E., 691, 1555
 Georgiadis, G.P., 793
 Georgiadis, M.C., 187, 193, 223, 793

Gerlach, T., 295
 Gernaey, K.V., 829, 859, 1219, 1225, 1771
 Gerogiorgis, D.I., 361, 367, 373, 379, 385
 Gertig, C., 103, 1267
 Giordano, R.C., 547
 Giraldo-Carvajal, V., 1033
 Giuliano, A., 595
 Gkioulekas, I., 853
 Göebel, H., 577
 Gomes, V.V., 1177
 Gómez-Castro, F.I., 73, 187, 655, 1423
 Gomez, E.A., 1531
 Gonçalves, B., 1777
 González-Campos, J.B., 1321, 1327
 Gonzalez, M., 937
 Govindan, R., 529, 685, 811, 1165
 Goz, E., 1039
 Graciano, J.E.A., 1081, 1639
 Graells, M., 1033, 1591
 Graham, E., 667
 Granjo, J.F.O., 1147
 Grievink, J., 1243, 1747
 Griffioen, K., 1621
 Griffiths, L., 361, 367
 Grillo, F., 1243
 Grimes, B.A., 127
 Groenendijk, S., 577
 Grossmann, I.E., 1807, 1819
 Grueters, T., 925
 Gueyffier, F., 1723
 Guibard, I., 1801
 Guillaume, D., 1801
 Guillén-Gosálbez, G., 895, 943
 Guo, M., 1675
 Gutiérrez-Antonio, C., 655
 Gutschmann, B., 1225

H

Haaz, E., 1525, 1183
 Häggblom, K.E., 745
 Halbert, G., 1027
 Hannemann-Tamás, R., 175
 Haragovics, M., 1411
 Harbottle, D., 151, 157
 Harjunkoski, I., 109, 193, 307, 331, 901, 1003

Hasan, S.U., 1255
 Hashem, I., 163
 Hayashi, Y., 991
 Heese, R., 295
 Hennen, M., 463, 475
 Hernández, B., 283
 Hernandez-Castro, S., 1093
 Hernandez-Escoto, H., 1093
 Hernández, S., 655
 Herwig, C., 1705, 1759
 Hirao, M., 991
 Hlawitschka, M.W., 511
 Hoffmann, C., 79, 85, 91
 Ho, G., 301
 Höller, J., 235
 Horiguchi, I., 991
 Houbé, M., 1009
 Hsu, H.-H., 757
 Huang, C.-H., 757
 Huang, Y., 457
 Hui, C.W., 625
 Hu, N., 1249
 Huster, W.R., 1129
 Hu, Y., 1585
 Hwangbo, S., 601

I

Ierapetritou, M., 325
 Ikele, L., 1621
 Ikonen, T.J., 193
 Imre-Lucaci, A., 643
 Imsland, L., 331, 445, 901
 Iqbal, M.U., 1375
 Iruretagoyena, D., 319
 Isafiade, A., 1765
 Iversen, T.B., 847

J

Jackson, G., 667, 1171, 1435
 Jalving, J., 1573
 Jang, S.-S., 787
 Janus, T., 1441
 Jardim, S.S.Q., 1639
 Jasch, C., 1279
 Jasso-Villegas, M.E., 55
 Javaloyes-Antón, J., 1357
 Jiménez-Gutiérrez, A., 979, 1111
 Jimenez, J., 1471

Ji, P., 637
 Ji, X., 313
 Jobson, M., 583, 1465
 Jolliffe, H.G., 1027
 Joulia, X., 355, 1099
 Jung, F., 175

K

Kager, J., 1705, 1759
 Kanematsu, Y., 1537
 Kang, J.-L., 757, 787
 Kantor, I., 1609, 1633
 Kappatou, C.D., 175, 619, 1399
 Karadurmus, E., 1039
 Karimi, I.A., 1363
 Karka, P., 1597
 Karolius, S., 1729
 Katz, J., 1195
 Kazantzis, N., 523
 Kazantzi, V., 523
 Kazepidis, P., 1435
 Kazi, M.-K., 523
 Kedzierski, R., 577
 Kelly, J.D., 115, 121
 Kenig, E.Y., 877
 Kermani, M., 1609
 Kermani, N.A., 1771
 Ketabchi, E., 967
 Khor, C.S., 217
 Kikuchi, Y., 1537
 Kim, J., 775
 Kino-oka, M., 991
 Kiskini, A., 1615
 Kiss, A.A., 439, 583, 985, 1747
 Kittisupakorn, P., 571
 Kleinekorte, J., 241
 Klemeš, J.J., 1789
 Kljajić, N., 907
 Kloye, N., 427
 Knuutila, H., 1693
 Ko, J.-W., 787
 Kokossis, A., 1597
 Kondili, E.M., 1417, 1753
 Konge, U., 955
 Kopanos, G., 793
 Kovács, J., 1735
 Kramer, G.J., 7
 Kravanja, Z., 1741, 1765, 1783, 1789

Krewera, U., 469
 Kröger, L., 241
 Kröhling, D.E., 697
 Kruber, K.F., 925
 Krühne, U., 1225
 Kuhlmann, H., 781

L

Lakerveld, R., 613, 679
 Lampe, M., 427
 Lara-Montaña, O.D., 73
 Lara, R.J., 1531
 Larsen, L.F.S., 451
 Latifi, A., 985, 1015
 LeBlond, D., 1549
 Lee, H., 139
 Leenders, L., 463
 Lee, P.Y., 625
 Lee, S.L., 667
 Leonhard, K., 241, 1267
 Leonzio, G., 67
 Lesage, F., 985, 1015
 Le Vo, D.B., 937
 Li, J., 1309, 1345, 1495
 Linke, P., 1477
 Lin, S.-T., 757
 Lira-Barragán, L.F., 1489
 Liu, H., 1429
 Liu, J., 553, 559
 Liu, S., 1135
 Li, X., 1627
 López-Díaz, D.C., 1489
 Lopez, M., 793
 Lou, X., 835
 Loyola-Fuentes, J., 1465
 Lucia, S., 571

M

Macchietto, S., 487, 493, 1333
 Maciel Filho, R., 1075
 Mackey, H.R., 1051, 1483
 Magli, F., 865
 Mahmoud, B.H., 151, 157
 Manavi, S.A., 877
 Manca, D., 25, 43
 Mancini, M.A., 1237
 Manenti, F., 181, 355
 Mansour, F., 403

- Mansouri, S.S., 739, 829, 1189, 1219,
 1225, 1771
 Mantalaris, A., 1399
 Maravelias, C., 139
 Marcos, M.P., 1279
 Maréchal, F., 1381, 1603, 1609, 1627,
 1633
 Marmolejo-Correa, D., 1447
 Marques, C.M., 1699
 Marquez-Ruiz, A., 415, 703
 Martelli, E., 865
 Martínez, B., 31
 Martínez, E.C., 697
 Martín, M., 211, 283
 Martins, N., 1555
 Masham, E., 1291
 Masuku, C.M., 1405
 Matos, H.A., 1261, 1387
 Max-Hansen, M., 517
 May-Vázquez, M.M., 187
 Mazzali, B., 829
 McKay, G., 343, 721, 1051, 1201
 Mechleri, E., 1285, 1291
 Medina-González, S., 853
 Medina-Herrera, N., 979, 1111
 Medrano-García, J.D., 61, 1357
 Mele, F.D., 1591
 Melo, P.A., 709
 Mendez-Blanco, C.S., 703
 Méndez, C.A., 541, 1153
 Menezes, B.C., 115, 121
 Mesbah, A., 1
 Mhamdi, A., 169, 175, 619, 1399
 Miller, I., 1555
 Milton, R., 727
 Misener, R., 1057
 Mitsos, A., 169, 175, 619, 913, 1129,
 1399, 1681
 Mizsey, P., 1525, 1183
 Mockus, L., 1123, 1549
 Mohammadi, M., 109
 Moniz, S., 1699, 1777
 Monneret, G., 1723
 Montastruc, L., 355, 1351
 Montuir, M., 1099
 Moon, Il., 775
 Morakabatchiankar, S., 1591
 Morales-Rodriguez, R., 1423, 1447
 Morao A., 1795
 Moraru, M.D., 277, 439
 Morel, L., 1339
 Moret, S., 1627
 Morris, K., 1549
 Mortimer, L.F., 151, 157
 Mostafaei, H., 307
 Mousqué, F., 1351
 Mujtaba, I.M., 181, 247
 Mukherjee, R., 1237
 Munoz, E., 1507, 1513
 Muñoz López, C.A., 163
 Murcia Palacios, J.F., 607
 Muthia, R., 583
 Mutran, V.M., 1069
 Mytis, N., 373

N
 Nagy, J., 1525
 Nagy, T., 1525, 1183
 Nagy, Z.K., 673, 769, 937
 Namany, S., 343, 1165
 Nascimentoa, C.O.A., 1069
 Nazemzadeh, N., 739
 Négny, S., 1009, 1351
 Nicoletti, J., 1021
 Niedenfuehr, S., 619
 Nielsen, C.J., 1141
 Nielsen, E.K., 883
 Nielsen, R.F., 1771
 Nijenhuis, J., 823
 Nikaëevi, N., 907
 Nilsson, B., 517
 Nimmegeers, P., 1, 163
 Ning, C., 253, 1021, 1543
 Nony, P., 1723
 Noorman, H., 1075
 Nord, L.O., 1735
 Nukala, A., 937
 Nunes, D.S., 1147
 Nyande, W.B., 613

O
 Ochoa, M.P., 1807
 Offermanns, Chr., 169
 Okeke, I.J., 715
 Okubo, T., 1537
 Oliveira, N.M.C., 1147

- Onel, M., 1237
Öner, M., 499, 601
Orjuela, A., 1339
Orosz, A., 1579
Ortiz, A., 1819
Ortiz, I., 1819
O'Sullivan, F.M., 691, 1555
Özkan, L., 337, 415, 703
- P**
Padding, J.T., 823
Pajalic, O., 517
Pampín, B.M., 793
Pantaleo, A.M., 1687
Papadokostantakis, S., 349, 1597
Papadopoulos, A.I., 1435
Papageorgiou, C., 769
Papageorgiou, L.G., 853, 1135
Papapostolou, C.M., 1417, 1753
Papasavvas, A., 589
Papathanasiou, F., 1027
Pappas, I.S., 1195
Parthasarathy, P., 1051
Passmore, S., 1675
Pastor-Perez, L., 967
Patel, R., 181, 247
Patraşcu, I., 985
Patrut, C., 1087
Paulen, R., 571
Paulson, J.A., 1
Peakall, J., 151, 157
Peccini, A., 265
Perdomo, F.A., 1435
Pereira, M.J., 1261
Pérez-Cisneros, E.S., 1423
Pérez, Y.M., 169
Perrey, K., 1681
Peschel, A., 169
Pesenti, G., 25, 43
Pessoa, F.P., 1189
Petsagkourakis, P., 1105
Petzschmann, J., 103
Phuong Cao, N.Y., 1801
Pilario, K.E.S., 271
Pineda, M., 1657
Pinelo, M., 829
Pinheiro, C.I.C., 1387
Pintarič, Z.N., 1741
Pinto-Varela, T., 841, 1777
Pires-Ribeiro, J., 949
Pistikopoulos, E.N., 1195, 1237
Pitarch, J.L., 1279
Pittman, J., 1501
Plazl, I., 1561
Pokkatt, P.P., 1369
Ponce-Ortega, J.M., 1315, 1321, 1327, 1489
Ponce-Rocha, J.D., 1447
Ponsatorn, R., 1189
Pontes, K.V., 1177
Porru, M., 337
Posada, J.A., 1075
Prado-Rubio, O.A., 49, 1423
Prasad, E., 1027
Prasad, G.M., 1711
Preisig, H.A., 1729
Prieto, C.G., 1531
Privat, Y., 985
Puigjaner, L., 1507, 1513
Punnathanam, V., 889
- Q**
Qiu, T., 457, 1429
Qiu, Y., 805
Quaglio, M., 391
Quattordio, J., 577
Quiroz-Ramírez, J.J., 97
Quon, J., 769
- R**
Rahimi-Adli, K., 1063
Rakovitis, N., 1345
Ramírez-Márquez, C., 49
Ramirez Reina, T., 967
Raniolo, A., 1531
Rao, A.S., 1711
Rato, T.J., 409
Reis, M.S., 409
Reklaitis, G.V., 937, 1123, 1549
Remelhe, M., 427
Repke, J.-U., 79, 85, 91, 229
Reyes-Lúa, A., 445
Ribeiro, C.O., 1069
Ricardez-Sandoval, L., 979
Rice, H.P., 151, 157
Rivera, C.A., 1615

- Rizwan, M., 505
 Robertson, J., 1027
 Rodman, A.D., 361
 Rodríguez-Ángele, M.A., 187
 Rodríguez, M., 19, 31
 Rodríguez-Robles, C.F., 1093
 Rodríguez-Vallejo, D.F., 943
 Roh, J., 775
 Roh, K., 1681
 Romero-García, A.G., 49
 Romero-Izquierdo, A.G., 655
 Ros, J.A., 1693
 Rossi, F., 1123
 Roth, M., 331
 Rugerio C., 1795
 Ruiz-Femenia, R., 37, 61
 Ruiz-Mercado, G., 1585
 Runowski, T., 295
 Rupu, Y., 961
- S**
- Saif, Y., 505
 Samsatli, S., 289, 871
 Sanchez-Ramirez, E., 55, 97
 Sandoval, I.O., 1105
 Sandu, V.C., 643
 Santos, A., 1213
 Sasi, T., 781
 Sass, S., 175
 Savoca, A., 25, 43
 Schäfer, J., 511
 Schäfer, P., 169
 Schenkendorf, R., 469
 Scherrer, A., 295
 Schiekel, T., 913
 Schiermoch, P.D., 1063
 Schilling, J., 103
 Schliebitz, F., 169
 Schmal, J.P., 1813
 Schneider, S.M., 331
 Schulze Spüntrup, F., 901
 Schuppert, A., 619
 Schutyser, M., 799
 Schuurmans, J., 649
 Schwartz, P., 235, 259
 Schweidtmann, A.M., 1129
 Schwientek, J., 235, 259
 Sebastia-Saez, D., 763
- Secchi, A.R., 547, 709
 SeedAhmed, S., 1663
 Seferlis, P., 349, 1435
 Segovia-Hernandez, J.G., 49, 55, 97, 997
 Shafiee, M., 271
 Shah, N., 319, 1477, 1675
 Shahrukh, M., 1363
 Shang, C., 1231
 Sharma, A., 493
 Shastri, Y., 889
 Shen, Q., 367
 Shieh, S.-S., 787
 Shu, D., 475
 Sidnell, T., 1285
 Silk, D., 829
 Sin, G., 499, 601, 847, 859, 883
 Singh, D., 1255
 Siniscalchi, A.G., 1531
 Siwczyk, T., 427
 Skiborowski, M., 781, 925
 Skogestad, S., 127, 451, 1735
 Slavnić, D., 907
 Smith, R., 1297, 1309, 1465, 1471, 1525
 Somoza-Tornos, A., 1033
 Song, Z., 457
 Sousa, A.M., 1261
 Speakman, J., 481
 Srinivasan, B., 1375
 Srinivasan, R., 1363, 1369, 1375
 Stateva, R.P., 1717
 Stocks, S.M., 499
 Stossi, F., 1237
 Stoustrup, J., 451
 Strniša, F., 1561
 Subramanian, S., 955
 Sugiyama, H., 991
 Sun, H.-Y., 787
 Sunny, N., 319
 Sun, W., 919
 Su, Q., 937
 Szafran, A.T., 1237
 Szilagyí, B., 673, 769
 Szima, S., 817
- T**
- Tadé, M.O., 145
 Tallon, J., 1723

Tao, M., 1495
 Tao, Y., 1207
 Tapia, J.F., 871
 Taube, M.A., 739
 Tayakout-Fayolle, M., 1723
 Teixeira, P., 1387
 Telen, D., 1
 Ten Cate, A. 1621
 Terrazas-Rodriguez, J.E., 1093
 Testa, R.L., 1519
 Theodoropoulos, C., 1495, 1501
 Thomas, D., 835
 Thybaut, J.W., 1801
 Tian, Y., 1195
 Tillmanns, D., 97, 103
 Todić, B., 907
 Torres, M.A., 1387
 Toth, A.J., 1525, 1183
 Tovar-Facio, J., 1315
 Tran, C.T., 961
 Tsakas, E., 1615
 Tsimopoulos, E.G., 187, 193
 Tsolakis, N., 1159
 Tsukahara, T., 1657
 Tula, A.K., 637, 1453, 1459
 Tututi-Avila, S., 979, 1111
 Tzanes, G.T., 1417, 1753

U

Udrea, E.C., 1087
 Udugama, I.A., 739, 829, 1219
 Urbi, T., 1561
 Usai, A., 1501

V

Vakilifard, N., 301
 Van Bochove, G., 1795
 van Dam, K.H., 1675, 1687
 Van Impe, J., 1, 163
 van Ommen, J.R., 823, 1243
 van Schijndel, J., 1621
 van Sint Annaland, M., 337, 415
 Varbanov, P.S., 1789
 Várhelyi, M., 133
 Vaupel, Y., 175
 Vazquez-Castillo, J.A., 55, 997
 Vázquez, D., 37, 1357
 Venet, F., 1723

Veys, A., 487
 Vieira, M., 1777
 Vigier, N., 1099
 Villanueva-Bermejo, D., 1717
 Villicaña-García, E., 1321
 Vlachos, D., 1159
 Vuist, J.-E., 799

W

Wallerand, A.S., 1633
 Wang, C.-H., 895
 Wang, J., 637
 Wang, S., 313
 Wang, X., 1675
 Watson, O.L., 1171
 Weaser, M., 361, 367
 Weigert, J., 79, 85, 91
 Weimann, L., 7
 Wendling, L., 1339
 Wenzel, S., 1063
 Wesselmann, J., 781
 Wiebe, J., 1057
 Woldesellasse, H., 529
 Wong, D.S.-H., 757
 Woodley, J.M., 829, 1189
 Wright, F.A., 1237
 Wu, J., 415
 Wu, O., 331

X

Xie, X., 469
 Xu, K., 1525

Y

Yáñez, M., 1819
 Yang, A., 931
 Yenkie, K.M., 1669
 Yentumi, R., 1303
 Yeoh, K.P., 625
 Yfantis, V., 427
 Yong, J.Y., 1789
 You, F., 253, 1021, 1207, 1231, 1543
 Yuceer, M., 1039
 Yu, T., 757

Z

Zahid, U., 1645, 1651, 1663
 Zanella, L., 337

- Zapp, G., 169
Zavala, V.M., 1315, 1573, 1585
Zderic, A., 1615
Zeng, H., 931
Zeng, Z., 1117
Zhai, C., 919
Zhang, D., 457, 1105
Zhang, N., 1345
Zhang, Y., 1405
Zhao, J., 661
Zhao, L., 1543
Zhao, Y., 1249
Zhou, L., 313, 1237
Zimmerleiter, R., 1705
Ziogou, C., 793
Zirngast, K., 1741
Žnidaršič-Plazl, P., 1561
Zondervan, E., 67, 397, 595, 607, 1615
Zotică, C., 1735
Zoughaib, A., 961